

SECOND EDITION

ENERGY
CONVERSION

EDITED BY
D. YOGI GOSWAMI
FRANK KREITH

 CRC Press
Taylor & Francis Group

Energy Conversion

Second Edition

MECHANICAL and AEROSPACE ENGINEERING

Frank Kreith and Efstathios E. Michaelides

Series Editors

RECENTLY PUBLISHED TITLES

- Air Distribution in Buildings, *Essam E. Khalil*
- Alternative Fuels for Transportation, *Edited by Arumugam S. Ramadhas*
- Computer Techniques in Vibration, *Edited by Clarence W. de Silva*
- Design and Control of Automotive Propulsion Systems, *Zongxuan Sun and Guoming (George) Zhu*
- Distributed Generation: The Power Paradigm for the New Millennium, *Edited by Anne-Marie Borbely and Jan F. Kreider*
- Elastic Waves in Composite Media and Structures: With Applications to Ultrasonic Nondestructive Evaluation, *Subhendu K. Datta and Arvind H. Shah*
- Elastoplasticity Theory, *Vlado A. Lubarda*
- Energy Audit of Building Systems: An Engineering Approach, *Moncef Krarti*
- Energy Conversion, Second Edition, *Edited by D. Yogi Goswami and Frank Kreith*
- Energy Efficient Electrical Systems for Buildings, *Moncef Krarti*
- Energy Efficiency and Renewable Energy Handbook, Second Edition, *Edited by D. Yogi Goswami and Frank Kreith*
- Energy Efficiency in the Urban Environment, *Heba Allah Essam E. Khalil and Essam E. Khalil*
- Energy Management and Conservation Handbook, Second Edition, *Edited by Frank Kreith and D. Yogi Goswami*
- Essentials of Mechanical Stress Analysis, *Amir Javidinejad*
- The Finite Element Method Using MATLAB®, Second Edition, *Young W. Kwon and Hyochoong Bang*
- Fluid Power Circuits and Controls: Fundamentals and Applications, *John S. Cundiff*
- Fuel Cells: Principles, Design, and Analysis, *Shripad Revankar and Pradip Majumdar*
- Fundamentals of Environmental Discharge Modeling, *Lorin R. Davis*
- Handbook of Hydrogen Energy, *Edited by S.A. Sherif, D. Yogi Goswami, Elias K. Stefanakos, and Aldo Steinfeld*
- Heat Transfer in Single and Multiphase Systems, *Greg F. Naterer*
- Heating and Cooling of Buildings: Principles and Practice of Energy Efficient Design Third Edition, *T. Agami Reddy, Jan F. Kreider, Peter S. Curtiss, and Ari Rabl*
- Intelligent Transportation Systems: Smart and Green Infrastructure Design, Second Edition, *Sumit Ghosh and Tony S. Lee*
- Introduction to Biofuels, *David M. Mousdale*
- Introduction to Precision Machine Design and Error Assessment, *Edited by Samir Mekid*
- Introductory Finite Element Method, *Chandrakant S. Desai and Tribikram Kundu*
- Large Energy Storage Systems Handbook, *Edited by Frank S. Barnes and Jonah G. Levine*
- Machine Elements: Life and Design, *Boris M. Klebanov, David M. Barlam, and Frederic E. Nystrom*

Mathematical and Physical Modeling of Materials Processing Operations, *Olusegun Johnson Ilegbusi, Manabu Iguchi, and Walter E. Wahnsiedler*

Mechanics of Composite Materials, *Autar K. Kaw*

Mechanics of Fatigue, *Vladimir V. Bolotin*

Mechanism Design: Enumeration of Kinematic Structures According to Function, *Lung-Wen Tsai*

Mechatronic Systems: Devices, Design, Control, Operation and Monitoring, *Edited by Clarence W. de Silva*

The MEMS Handbook, Second Edition (3 volumes), *Edited by Mohamed Gad-el-Hak*

- MEMS: Introduction and Fundamentals
- MEMS: Applications
- MEMS: Design and Fabrication

Multiphase Flow Handbook, Second Edition, *Edited by Efstathios E. Michaelides, Clayton T. Crowe, and John D. Schwarzkopf*

Nanotechnology: Understanding Small Systems, Third Edition, *Ben Rogers, Jesse Adams, and Sumita Pennathur*

Nuclear Engineering Handbook, Second Edition, *Edited by Kenneth D. Kok*

Optomechatronics: Fusion of Optical and Mechatronic Engineering, *Hyungsuck Cho*

Practical Inverse Analysis in Engineering, *David M. Trujillo and Henry R. Busby*

Pressure Vessels: Design and Practice, *Somnath Chattopadhyay*

Principles of Solid Mechanics, *Rowland Richards, Jr.*

Principles of Sustainable Energy Systems, Second Edition, *Edited by Frank Kreith with Susan Krumdieck, Co-Editor*

Thermodynamics for Engineers, *Kau-Fui Vincent Wong*

Vibration and Shock Handbook, *Edited by Clarence W. de Silva*

Vibration Damping, Control, and Design, *Edited by Clarence W. de Silva*

Viscoelastic Solids, *Roderic S. Lakes*

Weatherization and Energy Efficiency Improvement for Existing Homes: An Engineering Approach, *Moncef Krarti*



Taylor & Francis

Taylor & Francis Group

<http://taylorandfrancis.com>

Energy Conversion

Second Edition

Edited by
D. Yogi Goswami and Frank Kreith



CRC Press

Taylor & Francis Group

Boca Raton London New York

CRC Press is an imprint of the
Taylor & Francis Group, an **informa** business

CRC Press
Taylor & Francis Group
6000 Broken Sound Parkway NW, Suite 300
Boca Raton, FL 33487-2742

© 2017 by Taylor & Francis Group, LLC
CRC Press is an imprint of Taylor & Francis Group, an Informa business

No claim to original U.S. Government works

Printed on acid-free paper

International Standard Book Number-13: 978-1-4665-8482-2 (Hardback)

This book contains information obtained from authentic and highly regarded sources. Reasonable efforts have been made to publish reliable data and information, but the author and publisher cannot assume responsibility for the validity of all materials or the consequences of their use. The authors and publishers have attempted to trace the copyright holders of all material reproduced in this publication and apologize to copyright holders if permission to publish in this form has not been obtained. If any copyright material has not been acknowledged please write and let us know so we may rectify in any future reprint.

Except as permitted under U.S. Copyright Law, no part of this book may be reprinted, reproduced, transmitted, or utilized in any form by any electronic, mechanical, or other means, now known or hereafter invented, including photocopying, microfilming, and recording, or in any information storage or retrieval system, without written permission from the publishers.

For permission to photocopy or use material electronically from this work, please access www.copyright.com ([http://www.copyright.com/](http://www.copyright.com)) or contact the Copyright Clearance Center, Inc. (CCC), 222 Rosewood Drive, Danvers, MA 01923, 978-750-8400. CCC is a not-for-profit organization that provides licenses and registration for a variety of users. For organizations that have been granted a photocopy license by the CCC, a separate system of payment has been arranged.

Trademark Notice: Product or corporate names may be trademarks or registered trademarks, and are used only for identification and explanation without intent to infringe.

Library of Congress Cataloging-in-Publication Data

Names: Goswami, D. Yogi. | Kreith, Frank.
Title: Energy conversion / [edited by] D. Yogi Goswami and Frank Kreith.
Description: Second edition. | Boca Raton : CRC Press, 2017. | Series: Mechanical and aerospace engineering series | Includes bibliographical references and index.
Identifiers: LCCN 2016057405 | ISBN 9781466584822 (alk. paper)
Subjects: LCSH: Energy conversion.
Classification: LCC TK2896 .E485 2017 | DDC 621.042—dc23
LC record available at <https://lcn.loc.gov/2016057405>

Visit the Taylor & Francis Web site at
<http://www.taylorandfrancis.com>

and the CRC Press Web site at
<http://www.crcpress.com>

Contents

Prefaceix
Contributors.....xi

1. Global Energy Systems..... 1
D. Yogi Goswami and Frank Kreith

Section I Energy Resources

2. Fossil Fuels.....33
Robert Reuther, Richard Bajura, and Philip C. Crouse

3. Biomass Properties and Resources 61
Mark M. Wright and Robert C. Brown

4. Municipal Solid Waste73
Shelly H. Schneider

5. Nuclear Resources 81
James S. Tulenko

6. Solar Energy Resources..... 85
D. Yogi Goswami

7. Wind Energy Resource 137
Dale E. Berg

8. Geothermal Energy 177
Joel L. Renner and Marshall J. Reed

Section II Energy Conversion

9. Steam Power Plant..... 191
John Kern

10. Gas Turbines.....209
Richard H. Bunce

11. Internal Combustion Engines.....223
David E. Klett, Elsayed M. Afify, Kalyan K. Srinivasan, and Timothy J. Jacobs

12. Hydraulic Turbines257
Roger E.A. Arndt and Leonardo P. Chamorro

13. Advanced Fossil Fuel Power Systems	281
<i>Seyfettin C. (John) Gülen</i>	
14. Stirling Engines	447
<i>Frank Kreith</i>	
15. Nuclear Power Technologies through Year 2035	455
<i>Kenneth D. Kok and Edwin A. Harvego</i>	
16. Nuclear Fusion	491
<i>François Waelbroeck</i>	
17. Energy Storage Technologies	497
<i>Jeffrey P. Chamberlain, Roel Hammerschlag, and Christopher P. Schaber</i>	
18. Solar Thermal Energy Conversion	525
<i>T. Agami Reddy and Jeffrey H. Morehouse</i>	
19. Concentrating Solar Thermal Power	655
<i>Manuel Romero, Jose Gonzalez-Aguilar, and Eduardo Zarza</i>	
20. Photovoltaics Fundamentals, Technology and Application	765
<i>Roger Messenger, D. Yogi Goswami, Hari M. Upadhyaya, Senthilarasu Sundaram, Aruna Ivaturi, Stephan Buecheler, and Ayodhya N. Tiwari</i>	
21. Wind Energy Conversion	851
<i>Dale E. Berg</i>	
22. Biomass Conversion Process for Energy Recovery	897
<i>Mark M. Wright and Robert C. Brown</i>	
23. Geothermal Power Generation	931
<i>Kevin Kitz</i>	
24. Waste-to-Energy Combustion	985
<i>Charles O. Velzy and Leonard M. Grillo</i>	
25. Fuel Cells	1033
<i>Xianguo Li</i>	
26. Direct Energy Conversion	1085
<i>Mysore L. Ramalingam, Jean-Pierre Fleurial, and George Nolas</i>	
Appendix A: The International System of Units, Fundamental Constants, and Conversion Factors	1103
Appendix B: Solar Radiation Data	1109
Appendix C: Properties of Gases, Vapors, Liquids, and Solids	1137
Appendix D: Ultimate Analysis of Biomass Fuels	1151
Index	1153

Preface

Issues related to global climate change are increasing in importance and urgency as people around the world have begun to realize the threats of climate change. These concerns have led the United Nations to adopt the Paris Agreement under the United Nations Framework Convention on Climate Change in December 2015. Major countries including the United States, China, India, and the European Union have agreed to set aggressive targets to reduce emissions from greenhouse gases. With this background, improving the efficiency of energy conversion from fossil fuels and nuclear power as well as increasing the use of renewable energy sources have assumed greater importance. As a result of increased research and development around the world, significant technology developments have taken place in the last 10 years, since the first edition of this book was published. The present edition covers the latest developments in energy conversion from traditional fossil fuels and nuclear power as well as from renewable energy sources.

This book is divided into two parts: Energy Resources and Energy Conversion. Chapter 1 provides a global view of all the energy resources as well as their projected use for the next 20 years. Chapters 2 through 8 deal with available energy resources, including fossil fuels, nuclear power, and renewable energy sources. Chapters 9 through 12 present conventional energy conversion technologies used in steam power plants, gas turbines, internal combustion engines, and hydraulic turbines. Advanced conversion technologies used in coal power plants, combined cycle power plants, Stirling engines, nuclear power plants, etc., are covered in Chapters 13 through 16. Chapter 17 discusses various energy storage technologies. Energy storage is the key to increased use of renewable energy sources because of their intermittent nature, specifically solar and wind.

Renewable energy technologies including solar thermal power, photovoltaics, wind energy, biomass and biofuels, geothermal energy, and waste to energy combustion are covered in Chapters 18 through 24. Chapter 25 presents the fundamentals as well as the technology assessment of fuel cells. Thermionic, thermoelectric, and magneto-hydrodynamic (MHD) methods used for direct energy conversion are discussed in Chapter 26.

The majority of the material presented in this handbook has been extracted from the *Handbook of Energy Efficiency and Renewable Energy* published in 2015, with some new additions to the text. It is hoped that bringing all the information on energy resources and their conversion under one cover will be useful to engineers in designing and building energy generation systems using traditional and renewable energy sources. The editors express their appreciation to the authors for their forbearance and diligence in preparing this work for publication.

In a work of this scope, errors and omissions are unavoidable. The editors would therefore appreciate feedback from readers in order to rectify any errors and improve the coverage in future editions.

D. Yogi Goswami
Frank Kreith



Taylor & Francis

Taylor & Francis Group

<http://taylorandfrancis.com>

Contributors

Elsayed M. Afify

North Carolina State University
Raleigh, North Carolina

Roger E.A. Arndt

St. Anthony Falls Laboratory
University of Minnesota
Minneapolis, Minnesota

Richard Bajura

West Virginia University
Morgantown, West Virginia

Dale E. Berg

Sandia National Laboratories
Albuquerque, New Mexico

Robert C. Brown

Center for Sustainable Environmental
Technologies
Iowa State University
Ames, Iowa

Stephan Buecheler

Laboratory for Thin Films and Photovoltaics
Swiss Federal Laboratories for Materials
Science and Technology
Dübendorf, Switzerland

Richard H. Bunce

Siemens Energy, Inc.
Orlando, Florida

Jeffrey P. Chamberlain

Argonne National Laboratory
Lemont, Illinois

Leonardo P. Chamorro

Department of Mechanical Science and
Engineering
University of Illinois at
Urbana–Champaign
Urbana, Illinois

Philip C. Crouse

Philip C. Crouse and Associates, Inc.
Dallas, Texas

Jean-Pierre Fleurial

Jet Propulsion Laboratory/California
Institute of Technology
Pasadena, California

Nitin Goel

Intel Technology India Pvt. Ltd
Bangalore, India

Jose Gonzalez-Aguilar

IMDEA Energy
Madrid, Spain

D. Yogi Goswami

Clean Energy Research Center
University of South Florida
Tampa, Florida

Leonard M. Grillo

Grillo Engineering Company
Hollis, New Hampshire

Seyfettin C. (John) Gülen

Bechtel Infrastructure and Power, Inc.
Reston, Virginia

Roel Hammerschlag

Institute for Lifecycle Environmental
Assessment
Seattle, Washington

Edwin A. Harvego

Idaho National Laboratory
Idaho Falls, Idaho

Aruna Ivaturi

School of Chemistry
University of Edinburgh
Edinburgh, United Kingdom

Timothy J. Jacobs

Department of Mechanical Engineering
Texas A&M University
College Station, Texas

John Kern

Siemens Power Generation
Milwaukee, Wisconsin

Kevin Kitz

U.S. Geothermal Inc.
Boise, Idaho

David E. Klett

North Carolina A&T State University
Greensboro, North Carolina

Kenneth D. Kok

WSMS Mid-America
Oak Ridge, Tennessee

Frank Kreith

Mechanical Engineering Department
University of Colorado
Boulder, Colorado

Xianguo Li

University of Waterloo
Waterloo, Ontario, Canada

Roger Messenger

Department of Electrical Engineering
Florida Atlantic University
Boca Raton, Florida

Jeffrey H. Morehouse

Department of Mechanical Engineering
University of South Carolina
Columbia, South Carolina

George Nolas

Department of Physics
University of South Florida
Tampa, Florida

Mysore L. Ramalingam

UES, Inc.
Dayton, Ohio

Marshall J. Reed

U.S. Department of Energy
Washington, D.C.

T. Agami Reddy

Julie Ann Wrigley Global Institute of
Sustainability
and
The Design School
Herberger Institute for Design and the
Arts
and
School of Sustainable Engineering and the
Built Environment
Ira A. Fulton Schools of Engineering
Arizona State University
Tempe, Arizona

Joel L. Renner

Idaho National Engineering Laboratory
Idaho Falls, Idaho

Robert Reuther

U.S. Department of Energy
Morgantown, West Virginia

Manuel Romero

Plataforma Solar de Almeria-CIEMAT
Madrid, Spain

Christopher P. Schaber

Institute for Lifecycle Environmental
Assessment
Seattle, Washington

Shelly H. Schneider

Franklin Associates, a Division of ERG
Prairie Village, Kansas

Kalyan K. Srinivasan

Department of Mechanical Engineering
Mississippi State University
Starkville, Mississippi

Senthilarasu Sundaram

Environment and Sustainability Institute
University of Exeter
Penryn, United Kingdom

Ayodhya N. Tiwari

Laboratory for Thin Films and
Photovoltaics
Swiss Federal Laboratories for
Materials
Science and Technology
Zurich, Switzerland

James S. Tulenko

University of Florida
Gainesville, Florida

Hari M. Upadhyaya

Department of Mechanical,
Aerospace, and Civil Engineering
Brunel University
London, United Kingdom

Charles O. Velzy

Private Consultant
White Haven, Pennsylvania

François Waelbroeck

Institute for Fusion Studies
The University of Texas at Austin
Austin, Texas

Mark M. Wright

Department of Mechanical Engineering
Iowa State University
Ames, Iowa

Eduardo Zarza

Plataforma Solar de Almería
Centro de Investigaciones Energéticas,
Medioambientales y Tecnológicas
Madrid, Spain



Taylor & Francis

Taylor & Francis Group

<http://taylorandfrancis.com>

1

Global Energy Systems

D. Yogi Goswami and Frank Kreith

CONTENTS

1.1	Global Energy Needs and Resources.....	2
1.2	Major Sectors of Primary Energy Use.....	5
1.3	Electricity-Generating Capacity Additions to 2040	6
1.4	Transportation.....	6
1.5	World Energy Resources.....	8
1.5.1	Conventional Oil.....	9
1.5.2	Natural Gas.....	10
1.5.3	Coal.....	10
1.5.4	Summary of Fossil Fuel Reserves.....	11
1.5.5	Nuclear Resources	11
1.6	Present Status and Potential of Renewable Energy	13
1.6.1	Wind Power	15
1.6.2	Solar Energy	16
1.6.3	Biomass.....	19
1.6.4	Summary of Renewable Energy Resources	21
1.7	Role of Energy Conservation	22
1.8	Forecast of Future Energy Mix	27
	References.....	29

A thing that will assume enormous importance quite soon is the exhaustion of our fuel resources. Coal and oil have been accumulating in the earth over five hundred million years, and at the present rates of demand for mechanical power, the estimates are that oil will be all gone in about a century, and coal probably in a good deal less than five hundred years. For the present purpose, it does not matter if these are under-estimates; they could be doubled or trebled and still not affect the argument. Mechanical power comes from our reserves of energy, and we are squandering our energy capital quite recklessly. It will very soon be all gone, and in the long run we shall have to live from year to year on our earnings.*

* Quote from *The Next Millennium*, 1953, by Charles Galton Darwin, the grandson of Charles Darwin, author of *On the Origin of Species*.

1.1 Global Energy Needs and Resources

Global energy consumption in the last half century has rapidly increased and is expected to continue to grow over the next 50 years, however, with significant differences. The past increase was stimulated by relatively “cheap” fossil fuels and increased rates of industrialization in North America, Europe, and Japan; yet while energy consumption in these countries continues to increase, additional factors make the picture for the next 50 years more complex. These additional factors include China’s and India’s rapid increase in energy use as they represent about a third of the world’s population; the expected depletion of oil resources in the near future; and, the effect of human activities on global climate change. On the positive side, the renewable energy (RE) technologies of wind, biofuels, solar thermal, and photovoltaics (PV) are finally showing maturity and the ultimate promise of cost competitiveness.

Statistics from the International Energy Agency (IEA) World Energy Outlook 2004 and 2010 show that the total primary energy demand in the world increased from 5,536 MTOE in 1971 to 10,345 MTOE in 2002, representing an average annual increase of 2% (see Figure 1.1 and Table 1.1).*

By 2008, the world energy demand had increased to 12,271 MTOE representing an average annual increase of about 3%. The main reason for a 50% increase in the annual rate is the fast growing energy demand in Asia Pacific, more specifically China. Since the per capita energy used in the most populous countries, China and India is still very small,

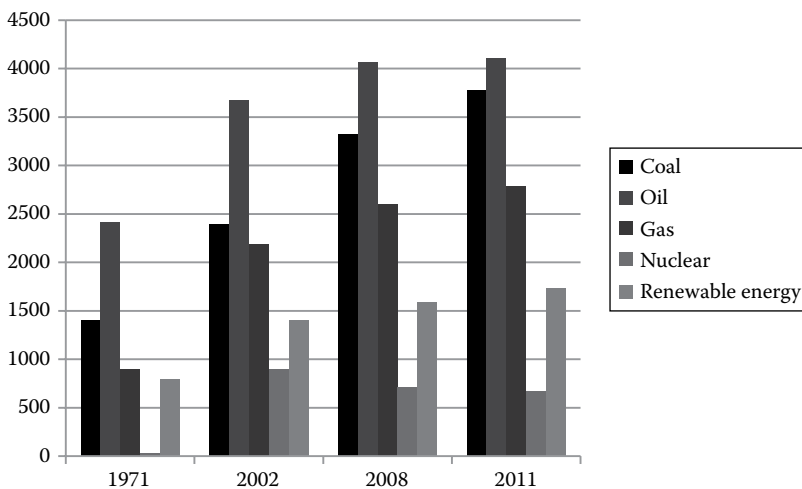


FIGURE 1.1

World primary energy demand (MTOE). (Data from IEA, *World Energy Outlook*, 2004; IEA, *World Energy Outlook 2010*, International Energy Agency, Paris, France, 2010; IEA, *World Energy Outlook 2013*, International Energy Agency, Paris, France, 2013.)

* The energy data for this chapter came from many sources, which use different units of energy, making it difficult to compare the numbers. The conversion factors are given here for a quick reference.

MTOE = Mega tons of oil equivalent; 1 MTOE = 4.1868×10^4 TJ (Terra Joules) = 3.968×10^{13} Btu.

GTOE = Giga tons of oil equivalent; 1 GTOW = 1000 MTOE.

Quadrillion Btu, also known as Quad: 10^{15} British Thermal Units or Btu; 1 Btu = 1055 J.

1 TWh = 10^9 kilowatt hours (kWh), 1 kWh = 3.6×10^6 J.

TABLE 1.1

World Total Energy Demand (MTOE)

Energy Source/Type	1971	2002	2008	2011	Annual Change 1971–2002 (%)	Annual Change 2002–2008 (%)	Annual Change 2008–2011 (%)
Coal	1,407	2,389	3,315	3,773	1.7	5.6	4.4
Oil	2,413	3,676	4,059	4,108	1.4	1.67	0.4
Gas	892	2,190	2,596	2,787	2.9	2.88	2.4
Nuclear	29	892	712	674	11.6	–3.7	–1.8
Hydro	104	224	276	300	2.5	3.6	2.8
Biomass and waste	687	1,119	1,225	1,300	1.6	1.6	2
Other renewables	4	55	89	127	8.8	8.46	12.6
Total	5,536	10,345	12,271	13,069	2.0	2.9	2.1

Sources: Data from IEA, *World Energy Outlook*, 2004; IEA, *World Energy Outlook 2010*, International Energy Agency, Paris, France, 2010; IEA, *World Energy Outlook 2013*, International Energy Agency, Paris, France, 2013.

their energy use may continue to increase at a high rate. From 2008 to 2011, the annual increase in energy use dropped back to 2.1% mainly because of a deep recession in United States and Europe where the energy use actually declined.

The last 10 years data for energy consumption from BP Corp. shows that during the most recent 10-year period even though the total primary energy use in North America and Europe has gone down, the global average increase has gone up to 2.8% (see Table 1.2). The rate of growth has risen mainly due to very rapid growth in Asia Pacific, which recorded an average annual increase of 6.1%. More specifically, China increased its primary energy consumption by approximately 10%/year from 2002 to 2012. Based on the current plans of China this trend will continue for at least another decade (IEA, 2013).

Even at a 2% increase per year, the primary energy demand of 12,271 MTOE in 2008 would double by 2043 and triple by 2063. Of course the global energy use cannot continue to increase at the same rate forever. IEA (2013) estimates that the global energy use will increase at an average annual rate of 1.2 up to 2035. Even at that optimistic slow growth rate of 1.2%, the global energy use will increase by 38% by 2035 reaching a value of 16,934 MTOE/year.

TABLE 1.2Primary Energy Consumption (MTOE)^a

Region	2002	2011	2012	2002–2012 Average Increase/Year (%)	2012 Change Over 2011 (%)
North America including United States	2741.1	2,774.3	2,725.4	–0.1	–2.0
United States	2295.5	2,265.2	2,208.8	–0.5	–2.8
South and Central America	474.9	649.5	665.3	3.5	2.2
Europe and Euro-Asia	2852	2,936.6	2,928.5	0.25	–0.5
Middle East	464.3	727.4	761.9	5.1	4.5
Africa	291.9	384.0	403.3	3.3	4.7
Asia Pacific	2773.7	4,753.2	4,992.2	6.1	4.7
China	1073.8	2,540.8	2,735.2	9.8	7.7
India	310.8	534.8	563.5	6.15	5.1
World	9487.9	12,225.0	12,477.0	2.8	1.8

Source: Data from BP Corp., London, U.K.

^a This data does not include traditional biomass which was approximately 835 MTOE in 2011 according to IEA data.

Of the total world primary energy demand in 2002, fossil fuels accounted for about 80% with oil, coal, and natural gas being 36%, 23%, and 21%, respectively. Biomass accounted for 11% of all the primary energy in the world, with almost all of it being traditional biomass for cooking and heating in the developing countries, which is used very inefficiently. By 2011, fossil fuels contribution increased to approximately 82% of the global primary demand with oil, coal, and natural gas accounting for 31%, 29%, and 21%, respectively. Even though the oil use has continued to increase year after year, its overall share in the primary energy went down from 35% in 2002 to 31% in 2011. On the other hand, the share of coal in the primary energy increased from 23% in 2002 to 29% in 2011. The predominant reason for this shift is the rapid increase in power production in China where coal provides more than 75% of the electrical power (Table 1.3). The power capacity of China has been increasing at an annual rate of 12% since 2000 (Table 1.4) (Zhou, 2012) and has already overtaken the power capacity of United States.

With such high energy demand expected in the future, it is important to look at the available resources to fulfill the future demand 50 years from now, especially for electricity and transportation.

Although not a technical issue in the conventional sense, no matter what types of engineering scenarios are proposed to meet the rising demands of a growing world population, as long as that exponential growth continues, the attendant problems of energy and food consumption, as well as environmental degradation may have no long term solution (Bartlett, 2002). Under current demographic trends, the United Nations forecasts a rise in the global population to around 9 billion in the year 2050. This increase in 2.5 billion people will occur mostly in developing countries with aspirations for a higher standard of living. Thus, population growth should be considered as a part of the overall supply and demand picture to assure the success of future global energy and pollution strategy.

TABLE 1.3

Power Production in China by Energy Source

	1990	%	2008	%	2011	%
Coal	471	72.5	2759	79.0	3598	76.2
Oil	49	7.5	24	0.7	133.2	2.8
Gas	3	0.5	43	1.2	166.2	3.5
Nuclear	0	0.0	68	1.9	87.4	1.9
Hydro	127	19.5	585	16.7	662.6	14.0
Renewables	0	0.0	15	0.4	73.2	1.6
Total	650	100.0	3494	100.0	4720.6	100.0

TABLE 1.4

Power Capacity of China

Year	GW	% Increase/Year
1990	138	
2000	319	8.8
2008	793	12
2011	1056	11

1.2 Major Sectors of Primary Energy Use

The major sectors using primary energy sources include electrical power, transportation, heating and cooling, industrial and others, such as cooking. The IEA data shows that the electricity demand almost tripled from 1971 to 2002 and quadrupled by 2011. This is not unexpected as electricity is a very convenient form of energy to transport and use. Although primary energy use in all sectors has increased, their relative shares except for transportation and electricity have decreased (Figure 1.2). Figure 1.2 shows that the relative share of primary energy for electricity production in the world increased from about 20% in 1971 to about 40% in 2011. This is because electricity is becoming the preferred form of energy for all applications.

Figure 1.3 shows that coal is presently the largest source of electricity in the world. Consequently, the power sector accounted for almost 42% of all CO₂ emissions in 2011. Emissions could be reduced by increased use of RE sources. All RE sources combined accounted for about 20% share of electricity production in the world. Wind and solar power technologies have vastly improved in the last two decades and are becoming more cost effective. Therefore, their share of electricity production has been increasing at a very fast pace. Over the last decade wind power capacity has been increasing at an annual rate of close to 30% and solar photovoltaic power capacity has been increasing at an annual rate of close to 50%, which has resulted in wind and solar providing a combined 2% of all the electricity generation in the world in 2011, almost all of it coming online in less than two decades. Since solar and wind technologies are now mature, substituting fossil fuels with RE for electricity generation must be an important part of any strategy of reducing CO₂ emissions into the atmosphere and combating global climate change.

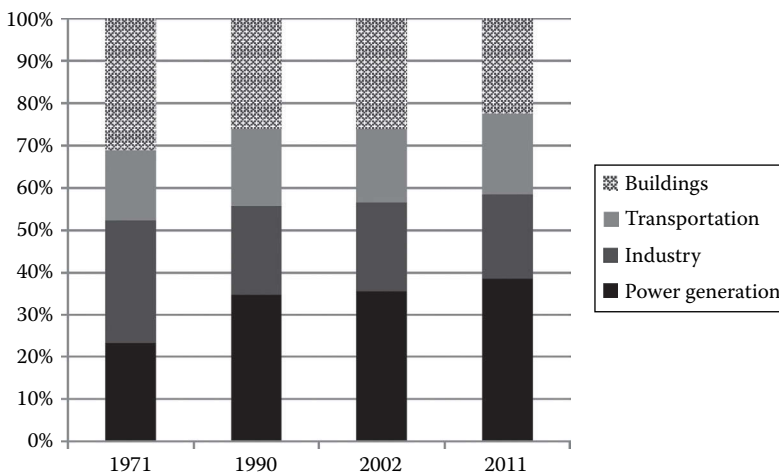


FIGURE 1.2

Sectoral shares in world primary energy demand. (Data from IEA, *World Energy Outlook*, 2004; IEA, *World Energy Outlook 2013*, International Energy Agency, Paris, France, 2013.)

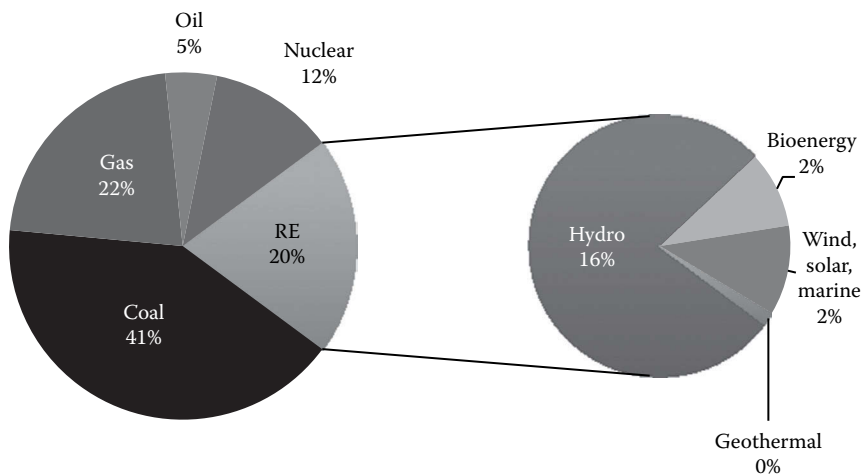


FIGURE 1.3

World electricity production by fuel in 2011. (Data from IEA, *World Energy Outlook 2013*, International Energy Agency, Paris, France, 2013.)

1.3 Electricity-Generating Capacity Additions to 2040

Figure 1.4 shows the global electricity-generating capacity in 2010 and additional electricity-generating capacity forecast by Energy Information Agency (EIA) of the U.S. Department of Energy for different regions in the world. The overall global annual increase of 1.6% in the electricity-generating capacity is in general agreement with the estimates from IEA (2013), which projects an average annual growth of 1.6% up to 2035. It is clear that of all countries, China will add the largest capacity with its projected electrical needs accounting for about 27.5% of the total world electricity-generating capacity. Non-OECD Asian countries (including China, India, Thailand, and Indonesia) combined will add about 60% of all the new capacity of the world. Therefore, what happens in these countries will have important consequences on the worldwide energy and environmental situation. If coal provides as much as 70% of China's electricity in 2030, as forecasted by IEA (2013), it will certainly increase worldwide CO₂ emissions which will further increase global warming.

1.4 Transportation

Transportation is a major sector with a 20% relative share of primary energy. This sector has serious concerns as it is a significant source of CO₂ emissions and other airborne pollutants—and it is almost totally based on oil as its energy source (Figure 1.5). In 2010, the transportation sector accounted for about 20% of all CO₂ emissions worldwide. An important aspect of future changes in transportation depends on what happens to the available

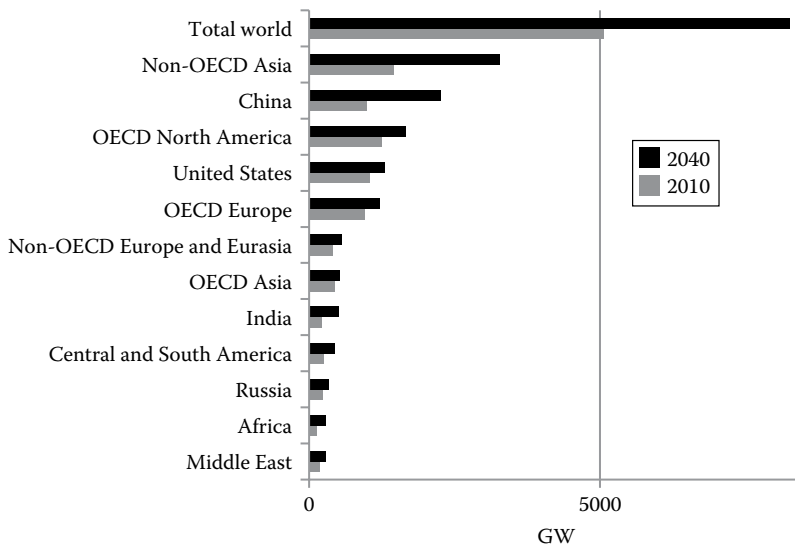


FIGURE 1.4

Electricity-generating capacity and projected additions to 2040 by region. (From EIA, *Annual Energy Outlook 2013*, U.S. Department of Energy, Washington, DC, 2013, www.eia.gov/ies.)

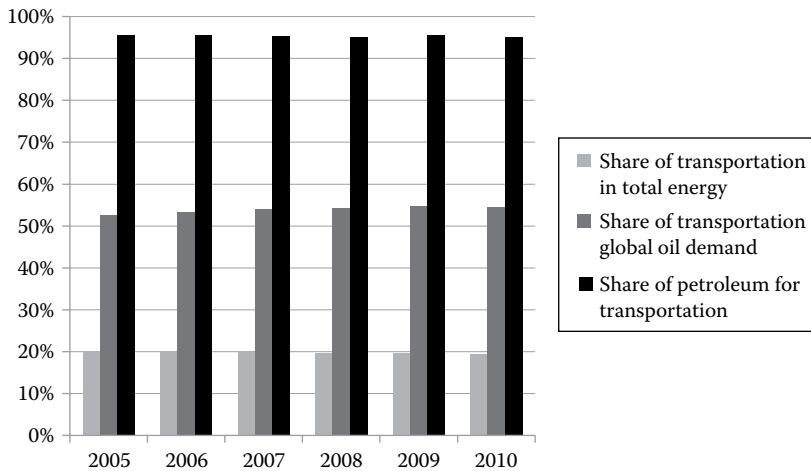


FIGURE 1.5

Share of transport in global oil demand and share of oil in transport energy demand. (Data and Forecast from EIA, *Annual Energy Outlook 2013*, U.S. Department of Energy, Washington, DC, 2013, www.eia.gov/aeo.)

oil resources, production, and prices. At present 95% of all energy for transportation comes from oil, and according to Figure 1.5, the EIA projects that petroleum will still provide 95% of all energy for transportation in 2040. However, with policy changes happening in the world due to serious concerns about global climate change and expected future technology developments, projections simply based on the past use will probably prove to be wrong.

As explained later in this chapter, irrespective of the actual amount of oil remaining in the ground, oil production will peak in the foreseeable future. Therefore, the need for

careful planning for an orderly transition away from oil as the primary transportation fuel is urgent. An obvious replacement for oil would be biofuels such as ethanol, methanol, biodiesel, and biogases. Some believe that hydrogen is another alternative, because if it could be produced economically from renewable energy sources or nuclear energy, it could provide a clean transportation alternative for the future. Some have claimed hydrogen to be a “wonder fuel” and proposed a “hydrogen-based economy” to replace the present carbon-based economy (Veziroglu and Barbir, 1992). However, others (Shinnar, 2003; Kreith and West, 2004; Hammerschlag and Mazza, 2005) dispute this claim based on the lack of infrastructure, problems with storage and safety, and the lower efficiency of hydrogen vehicles as compared to hybrid or fully electric vehicles. Electric transportation presents a promising viable alternative to the oil-based transportation system (West and Kreith, 2006). Already plug-in hybrid-electric automobiles are becoming popular around the world as petroleum becomes more expensive.

The environmental benefits of renewable biofuels could be increased by using plug-in hybrid electric vehicles (PHEVs). These cars and trucks combine internal combustion engines with electric motors to maximize fuel efficiency. But PHEVs have more battery capacity that can be recharged by plugging it into a regular electric outlet. Then these vehicles can run on electricity alone for relatively short trips. The electric-only trip length is denoted by a number, for example, PHEV 20 can run on battery charge for 20 miles. When the battery charge is used up, the engine begins to power the vehicle. The hybrid combination reduces gasoline consumption appreciably. Whereas the conventional vehicle fleet has a fuel economy of about 22 mpg, hybrids can attain about 50 mpg. PHEV 20s have been shown to attain as much as 100 mpg. Gasoline use can be decreased even further if the combustion engine runs on biofuel blends, such as E85, a mixture of 15% gasoline and 85% ethanol (Kreith, 2006; West and Kreith, 2006).

Plug-in hybrid electric technology is already available and could be realized immediately without further R&D. Furthermore, a large portion of the electric generation infrastructure, particularly in developed countries, is needed only at the time of peak demand (60% in the United States), and the rest is available at other times. Hence, if batteries of PHEVs were charged during off-peak hours, no new generation capacity would be required. Moreover, this approach would levelize the electric load and reduce the average cost of electricity, according to a study by the Electric Power Research Institute (EPRI) (Sanna, 2005).

Given the potential of PHEVs, EPRI (2004) conducted a large-scale analysis of the cost, battery requirements, and economic competitiveness of plug-in vehicles today and in the future. As shown by West and Kreith, the net present value of lifecycle costs over 10 years for PHEVs with a 20 mile electric-only range (PHEV 20) is less than that of a similar conventional vehicle (West and Kreith, 2006). Furthermore, currently available nickel metal-hydride (NiMH) batteries are already able to meet required cost and performance specifications. More advanced batteries, such as lithium-ion (Li-ion) batteries, may improve the economics of PHEVs even further in the future.

1.5 World Energy Resources

With a view to meet the future demand of primary energy in 2050 and beyond, it is important to understand the available reserves of conventional energy resources including fossil fuels and uranium, and the limitations posed on them due to environmental considerations.

1.5.1 Conventional Oil

There is a considerable debate and disagreement on the estimates of “ultimate recoverable oil reserves,” however, there seems to be a good agreement on the amount of “proven oil reserves” in the world. According to BP (2013), total identified or proven world oil reserves at the end of 2012 were 1668.9 billion barrels (bbl). This estimate is close to the reserves of 1700 billion bbl from other sources listed by IEA (2013). The differences among them are in the way they account for the unconventional oil sources. Considering the production rate of about 86.5 million bbl/day at the end of 2012, these reserves will last for about 53 years if there is no increase in production. Of course there may be additional reserves that may be discovered in the future. An analysis by the U.S. Energy Information Agency (2006) estimates the ultimately recoverable world oil reserves (including resources not yet discovered) at between 2.2×10^{12} and 3.9×10^{12} bbl. More recently, IEA has estimated that the ultimate remaining recoverable oil resources are as much as 2670 billion bbl of conventional oil (including Natural Gas Liquids), 345 billion bbl of light oil, 1880 billion of extra heavy oil and bitumen, and 1070 billion bbl kerogen oil. It is important to note that for this high estimate the IEA puts in a disclaimer, “However, resource estimates are inevitably subject to a considerable degree of uncertainty; this is particularly true for unconventional resources that are very large, but still relatively poorly known, both in terms of the extent of the resource in place and judgments about how much might be technically recoverable.”

Ever since petroleum geologist M. King Hubbert correctly predicted in 1956 that U.S. oil production would reach a peak in 1973 and then decline (Hubbert, 1974), scientists and engineers have known that worldwide oil production would follow a similar trend. Today, the only question is when the world peak will occur. Bartlett (2002) has developed a predictive model based on a Gaussian curve similar in shape to the data used by Hubbert as shown in Figure 1.6. The predictive peak in world oil production depends on the assumed total amount of recoverable reserves.

If the BP estimated oil reserves are correct, we are close to the peak in the world oil production. If, however, estimates of the ultimate reserves (discovered and undiscovered)

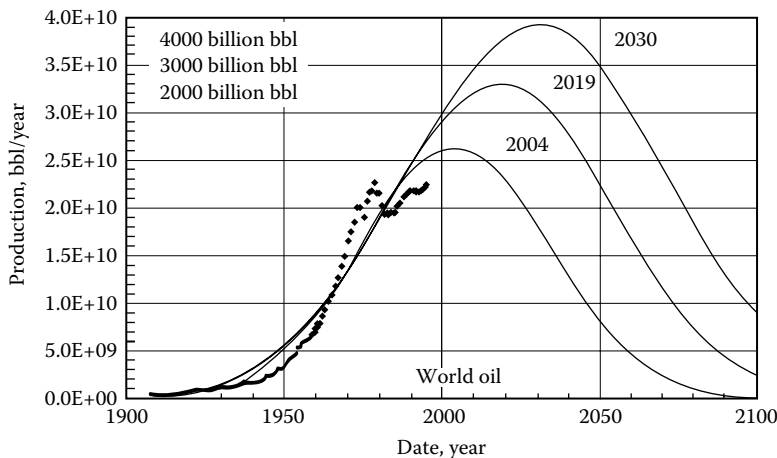


FIGURE 1.6

World oil production vs. time for various amounts of ultimate recoverable resource. (From Bartlett, A.A., *Math. Geol.*, 32, 1, 2002.)

are used, we may expect the oil production to increase a little longer before it peaks. But changing the total available reserves from 3×10^{12} to 4×10^{12} bbl increases the predicted time of peak production by merely 11 years, from 2019 to 2030. IEA World Energy Outlook 2013 estimates that under one policy scenario the oil production will peak at about 91 million bbl/day in 2020 while another policy scenario puts the peak at 101 million bbl/day in 2035. It is clear that no matter which scenario turns out to be true, the global oil production will peak sometime between 2019 and 2035. There is no question that once the world peak is reached and oil production begins to drop, either alternative fuel will have to make up the difference between demand and supply, or the cost of fuel will increase precipitously and create an unprecedented social and economic crisis for our entire transportation system.

The present trend of yearly increases in oil consumption, especially in China and India, shortens the window of opportunity for a managed transition to alternative fuels even further. Hence, irrespective of the actual amount of oil remaining in the ground, peak production will occur soon. Therefore, the need for starting to supplement oil as the primary transportation fuel is urgent because an orderly transition to develop petroleum substitutes will take time and careful planning.

1.5.2 Natural Gas

According to BP (2013) the total proven world natural gas reserves at the end of 2012 were 187.3 trillion m^3 . Considering the production rate of gas in 2012, with no increase in production thereafter, these reserves would last for 55.7 years. However, production of natural gas has been rising at an average rate of 2.7% over the past 5 years. If production continues to rise because of additional use of CNG for transportation and increased power production from natural gas, the reserves would last for fewer years. Of course, there could be additional new discoveries. However, even with additional discoveries, it is reasonable to expect that all the available natural gas resources may last from about 50 to 80 years, with a peak in production occurring much earlier.

1.5.3 Coal

Coal is the largest fossil resource available to us and the most problematic from environmental concerns. From all indications, coal use will continue to grow for power production around the world because of expected increases in China, India, Australia, and other countries. From an environmental point of view this would be unsustainable unless advanced "clean coal technology" (CCT) with carbon sequestration is deployed.

CCT is based on an integrated gasification combined-cycle (IGCC) that converts coal to gas that is used in a turbine to provide electricity with CO_2 and pollutant removal before the fuel is burned (Hawkins et al., 2006). According to an Australian study (Sadler, 2004), no carbon capture and storage system is yet operating on a commercial scale, but may become an attractive technology to achieve atmospheric CO_2 stabilization.

According to BP, the proven recoverable world coal resources were estimated to be 861 billion tons at the end of 2012 with a reserve to production ratio (R/P) of 107 years. The BP data also shows that coal use increased at an average rate of 3.7% from 2007 to 2012, the largest increase of all fossil resources. Since more than 75% of China's electricity-generating capacity is based on coal and both China and India are continuing to build

new coal power plants, it is reasonable to assume that coal use will continue to increase for at least some years in future. Therefore, the R/P ratio will decrease further from the present value of 107 years. The R/P ratio will decrease even more rapidly when clean coal technologies such as coal gasification and liquefaction are utilized instead of direct combustion.

1.5.4 Summary of Fossil Fuel Reserves

Even though there are widely differing views and estimates of the ultimately recoverable resources of fossil fuels, it is fair to say that they may last for around 50–100 years with a peak in production occurring much earlier. However, a big concern is the climatic threat of additional carbon that will be released into the atmosphere. According to the estimates from the IEA, if the present shares of fossil fuels are maintained up to 2040 without any carbon sequestration, a cumulative amount of approximately 1000 gigatons of carbon will be released into the atmosphere (based on Figure 1.7). This is especially troublesome in view of the fact that the present total cumulative emissions of about 500 gigatons of carbon have already raised serious concerns about global climate change.

1.5.5 Nuclear Resources

Increased use of nuclear power presents the possibility of additional carbon-free energy use and its consequent benefit for the environment. However, there are significant concerns about nuclear waste and other environmental impacts, the security of the fuel and the waste, and the possibility of their diversion for weapon production.

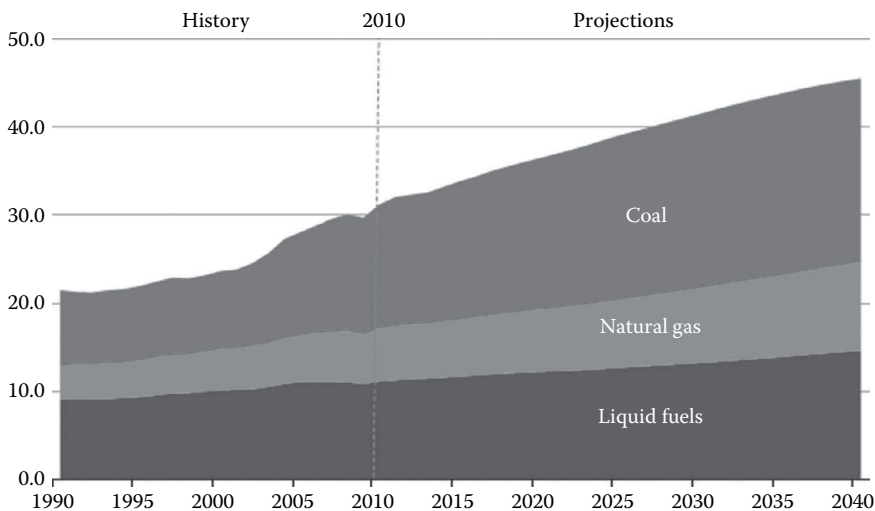


FIGURE 1.7

World energy-related CO₂ emissions by fuel (billion metric tons). (Data and forecast from IEA, *World Energy Outlook 2013*, International Energy Agency, Paris, France, 2013.)

Nuclear fission provided 14% of the electricity in the world in 2011 (IEA, 2013) and the worldwide nuclear capacity in 2011 was 375 GW (IAEA, 2011). Although a number of countries have decided to not build additional nuclear power plants after the Fukushima accident, nuclear power capacity is expected to continue to grow mainly because of the ongoing and planned construction in China and some other countries. IAEA estimates that the worldwide nuclear power capacity will increase at an average rate of 1.5%–2.7% until 2035 (IAEA, 2011). At present, uranium is used as the fissile material for nuclear power production. Thorium could also be used for nuclear fission; however, to date nobody has developed a commercial nuclear power plant based on thorium. Terrestrial deposits of both uranium and thorium are limited and concentrated in a few countries of the world. The International Atomic Energy Agency (IAEA) estimates the total identified recoverable uranium reserves in the world to be about 5 million tons which increase to about 7 million tons if the price of uranium goes up to \$264/kg U (Figure 1.8). Additionally, there are nonconventional uranium resources, such as sea water which contains about 3 parts per billion uranium and some phosphate deposits (more than half of them in Morocco) which contain about 100 parts per million uranium. These resources are potentially huge; however, their cost effective recovery is not certain (Figure 1.9).

For generating 1 TWh of electricity from nuclear fission, approximately 22 tons of uranium are required (UNDP, 2004). Based on the 2011 world capacity of 375 GW, the identified reserves will last about 97 years if there is no change in the generation capacity. At an average annual growth rate of 2%, the uranium reserves of 7 million tons will last for about 60 years. This estimate does not consider regeneration of spent fuel. At present, nuclear fuel regeneration is not allowed in the United States. However, that law could be changed in future. Development of breeder reactors could increase the time period much further. The major impediment may be economic viability. Nuclear fusion could potentially provide a virtually inexhaustible energy supply; however, it is not expected to be commercially available in the foreseeable future.

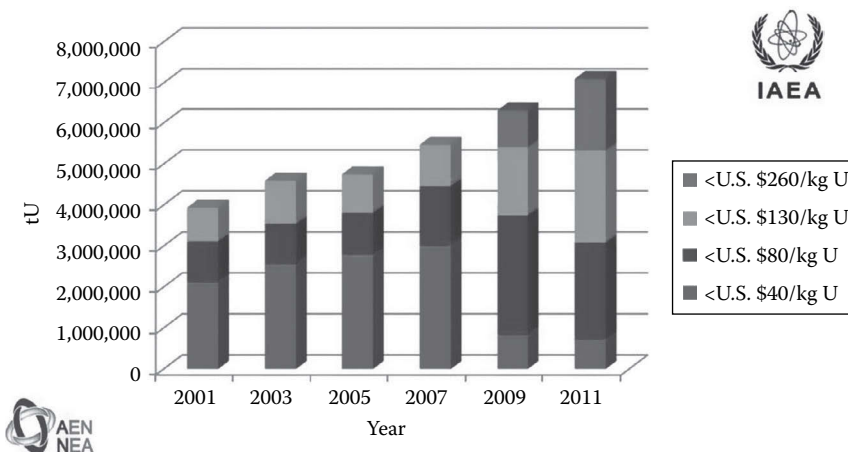


FIGURE 1.8

World identified recoverable uranium resources based on the price of uranium. (From IAEA, *Uranium: Resources, Production and Demand (The Red Book)*, IAEA, Vienna, Austria, 2011.)

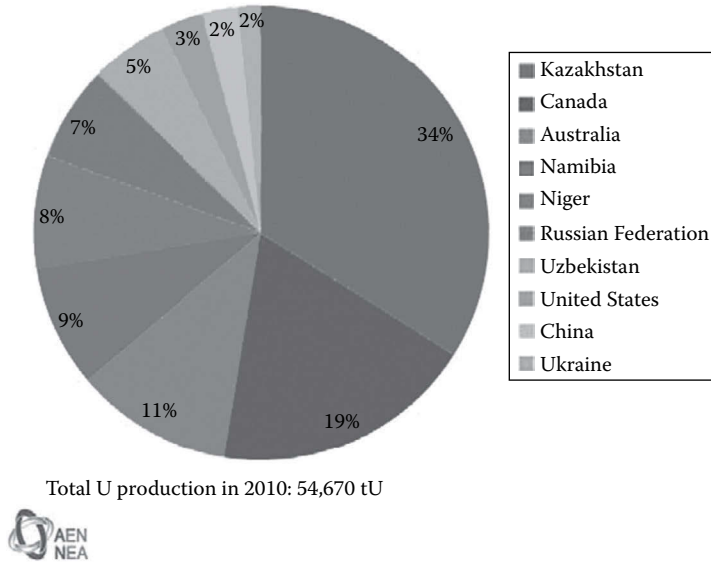


FIGURE 1.9

Top 10 uranium producing countries in 2010. (From IAEA, *Uranium: Resources, Production and Demand (The Red Book)*, IAEA, Vienna, Austria, 2011.)

1.6 Present Status and Potential of Renewable Energy

According to the data in Table 1.5, 13.2% of the world’s total primary energy supply (TPES) came from RE in 2011. However, approximately 75% of the RE supply was from biomass, and in developing countries it is mostly converted by traditional open combustion, which is very inefficient. Because of its inefficient use, biomass resources presently supply only about 20% of what they could if converted by modern, more efficient, available technologies. As it stands, biomass provides only about 10% of the world total primary energy

TABLE 1.5

2011 Fuel Shares in World Total Primary Energy Supply

Source	Share (%)
Oil	31.4
Natural gas	21.3
Coal	28.9
Nuclear	5.2
Renewables	13.2

Source: IEA, *World Energy Outlook 2013*, International Energy Agency, Paris, France, 2013.

which is much less than its real potential. The total technologically sustainable biomass energy potential for the world is 3–4 TW_e (UNDP, 2004), which is about 80% the entire present global electricity-generating capacity of about 5 TW_e.

In 2011, shares of biomass and hydropower in the total primary energy mix of the world were about 10% and 2.3%, respectively. All of the other renewables, including solar thermal, solar PV, wind, geothermal and ocean combined, provided only about 1% of the total primary energy. During the same year, biomass combined with hydroelectric resources provided almost 50% of all the primary energy in Africa. However, biomass is used very inefficiently for cooking in these countries. Such use has also resulted in significant health problems, especially for women. As of 2012, renewable energy contributes more than 40% of their total energy needs in 4 countries (Nigeria, Norway, Brazil, and Sweden) and more than 20% in 10 countries listed in Table 1.6 (Finland, Indonesia, India, Colombia, Chile, and Portugal). Other countries that provide significant shares of their energy from RE but <20% include, New Zealand (19.9%), Canada (18.4), Thailand (18.3%), Romania (15.2%), and Germany (14.2%).

Table 1.7 shows the share of renewable energy in 2011 and projections to 2020 and 2035. Keeping in mind that the future projections are only as good as the assumptions they are based on, and the energy situation is in a flux because of the impact on environment which is a major reason for the global climate change, IEA developed three scenarios for the future projections: (1) Current Energy Policies, (2) New Energy Policies (policies that have already been developed by major countries as of 2012), and (3) 450 Scenario, which assumes that policies around the world will be strengthened to limit the global temperature rise to 2°C or global atmospheric CO₂ concentrations to 450 ppm. Although there is considerable uncertainty about future policies, it is very likely that the future energy developments will lie somewhere in between the last two scenarios. According to these projections, the share of renewable energy will rise to as much as 18%–26% of the global primary energy and 31%–48% of the electricity-generating capacity by 2035. Based on the trends in the development and deployment of wind power and solar power in the last decade, there is reason to believe that values close to 450 scenario are achievable.

TABLE 1.6
Share of Renewable Energy in 2012 TPES for Top 10 Countries

Country	% Share of Renewables in TPES
Nigeria	80.5
Norway	47.2
Brazil	42.8
Sweden	40.0
Finland	30.6
Indonesia	26.2
India	24.3
Colombia	23.5
Chile	22.7
Portugal	22.5
New Zealand	19.9
Canada	18.4
Thailand	18.3
Romania	15.2
Germany	14.2
World	12.9

Source: Enerdata, *Enerdata Energy Statistical Yearbook 2013*, 2013.

TABLE 1.7

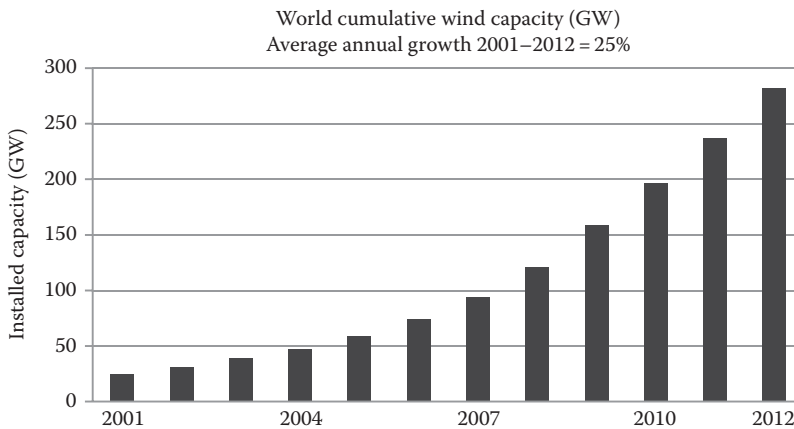
Share of Renewable Energy in 2011 and Projections for 2020 and 2035 Based on New Policies and 450 Scenario

	2011	New Policies		450 Scenario	
		2020	2035	2020	2035
Primary energy demand (MTOE)	1,727	2,193	3,059	2,265	3,918
United States	140	196	331	215	508
Europe	183	259	362	270	452
China	298	392	509	405	690
Brazil	116	148	207	150	225
<i>Share of renewables in total primary energy (%)</i>	13	15	18	16	26
Electricity generation (TWh)	4,482	7,196	11,612	7,528	15,483
Bioenergy	424	762	1,477	797	2,056
Hydro	3,490	4,555	5,827	4,667	6,394
Wind	434	1,326	2,774	1,441	4,337
Geothermal	69	128	299	142	436
Solar PV	61	379	951	422	1,389
CSP	2	43	245	56	806
Marine	1	3	39	3	64
<i>Share of total generation (%)</i>	20	26	31	28	48
Heat demand (MTOE)	343	438	602	446	704
Industry	209	253	316	248	328
Buildings and agriculture	135	184	286	198	376
<i>Share of total final demand (%)</i>	8	10	12	10	16
Biofuels (mboe/day)	1.3	2.1	4.1	2.6	7.7
Road transport	1.3	2.1	4.1	2.6	6.8
Aviation	0	0	0.1	0	0.9
<i>Share of total transport (%)</i>	2	4	6	5	15
Traditional biomass (MTOE)	744	730	680	718	647
<i>Share of total bioenergy (%)</i>	57	49	37	47	29
<i>Share of renewable energy demand (%)</i>	43	33	22	32	17

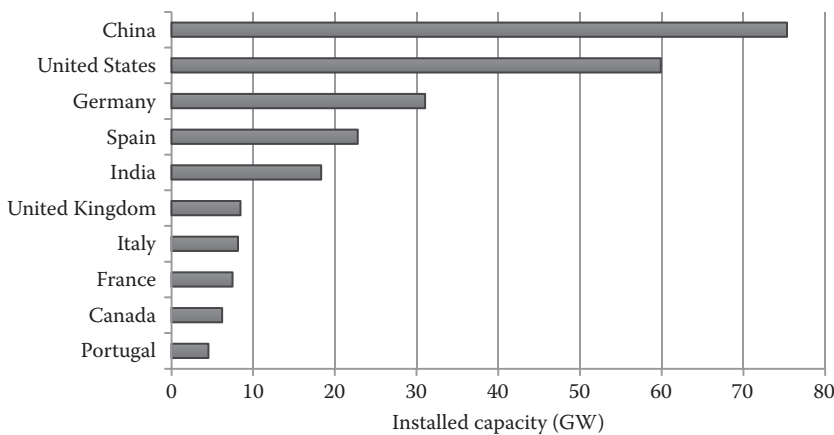
Source: IEA, *World Energy Outlook 2013*, International Energy Agency, Paris, France, 2013.

1.6.1 Wind Power

Wind energy technology has progressed significantly over the last two decades. The technology has been vastly improved and capital costs have come down to as low as \$1000/kW. At this level of capital costs, wind power is already economical at locations with fairly good wind resources. Therefore, the average annual growth in worldwide wind energy capacity from 2001 to 2012 was over 25% (Figure 1.10). The average growth in the United States over the same period was 37.7%. The total worldwide installed wind power capacity which was 24 GW in 2001 (Figure 1.10), reached a level of 282 GW in 2012 (WWEA, 2013). The countries with the largest wind capacity in 2012 include China (75 GW), United States (60 GW), Germany (31 GW), Spain (23 GW), and India (18 GW) (Figure 1.11). The total theoretical potential for onshore wind power for the world is around 55 TW with a practical potential of at least 2 TW (UNDP, 2004), which is about 40% of the entire present worldwide generating capacity. The offshore wind energy potential is even larger.

**FIGURE 1.10**

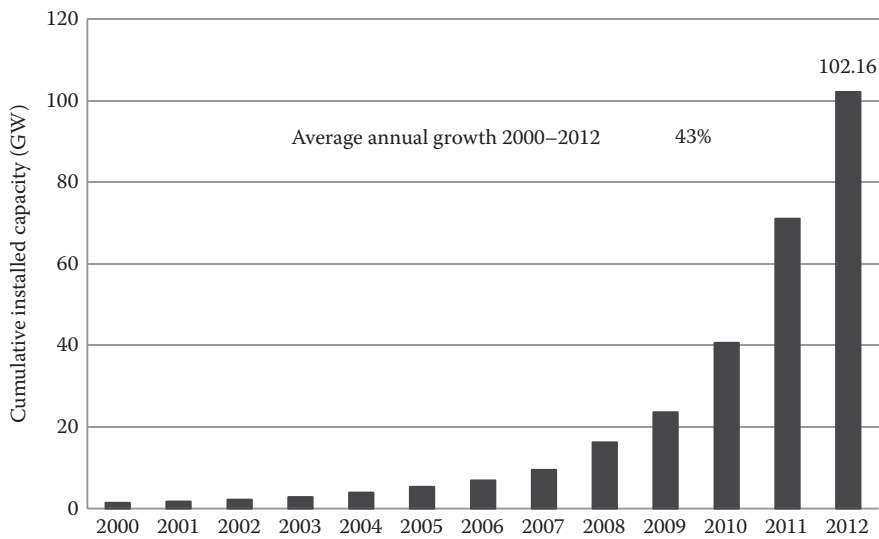
World wind energy installed capacity and growth rates. (Data from WWEA, World Wind Energy Association, 2012, http://www.wwindea.org/webimages/WorldWindEnergyReport2012_final.pdf)

**FIGURE 1.11**

Top 10 countries with installed wind power capacity. (Data from WWEA, World Wind Energy Association, 2012, http://www.wwindea.org/webimages/WorldWindEnergyReport2012_final.pdf)

1.6.2 Solar Energy

The amount of sunlight striking the earth's atmosphere continuously is 1.75×10^5 TW. Considering a 60% transmittance through the atmospheric cloud cover, 1.05×10^5 TW reaches the earth's surface continuously. If the irradiance on only 1% of the earth's surface could be converted into electric energy with a 10% efficiency, it would provide a resource base of 105 TW, while the total global energy needs for 2040 are projected to be about 8–9 TW. The present state of solar energy technologies is such that solar cell efficiencies have reached over 40% and solar thermal systems provide efficiencies of 40%–80%. With the present rate of technological development these solar technologies will continue to improve, thus bringing the costs down, especially with the economies of scale.

**FIGURE 1.12**

World solar PV production, 2000–2012 (GWp). (From EPIA, European Photovoltaic Industries Association, 2012, www.epia.org.)

Solar PV panels have come down in cost from about \$30/W to about \$0.50/W in the last three decades. At \$0.50/W panel cost, the overall system cost is around \$2/W, which is already lower than grid electricity in the Caribbean island communities. Of course, there are many off-grid applications where solar PV is already cost-effective. With net metering and governmental incentives, such as feed-in laws and other policies, grid-connected applications such as building integrated PV (BIPV) have become cost-effective even where grid electricity is cheaper. As a result, the worldwide growth in PV production has averaged over 43%/year from 2000 to 2012 and 61% from 2007 to 2012 (Figure 1.12) with Europe showing the maximum growth.

Solar thermal power using concentrating solar collectors was the first solar technology which demonstrated its grid power potential. A 354 MW_e concentrating solar thermal power (CSP) plant has been operating continuously in California since 1988. Progress in solar thermal power stalled after that time because of poor policy and lack of R&D. However, the last 10 years have seen a resurgence of interest in this area and a number of solar thermal power plants around the world are under construction. The largest CSP plant with a capacity of 400 MW came on line in Nevada in February 2014. The cost of power from these plants (which is so far in the range of 12–16 U.S. cents/kWh_e) has the potential to go down to 5 U.S. cents/kWh_e with scale-up and creation of a mass market. An advantage of solar thermal power is that thermal energy can be stored efficiently and fuels, such as, natural gas or biogas may be used as back up to ensure continuous operation. If this technology is combined with power plants operating on fossil fuels, it has the potential to extend the time frame of the existing fossil fuels.

Low temperature solar thermal systems and applications have been well developed for quite some time. They are being actively installed wherever the policies favor their deployment. Figure 1.13 gives an idea of the rate of growth of solar thermal systems in the world. In 2011, approximately 234 GW_{th} solar collectors were deployed around the world, a vast majority (65%) of those being in China (IEA, 2013) (Figure 1.14).

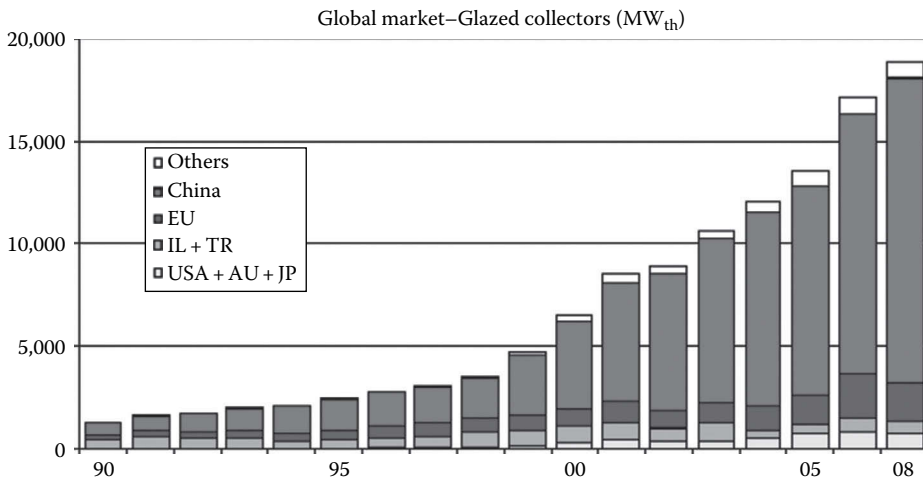


FIGURE 1.13 Deployment of solar heat (glazed) collectors, MW_{th}. (From ESIF, IEA SHC.)

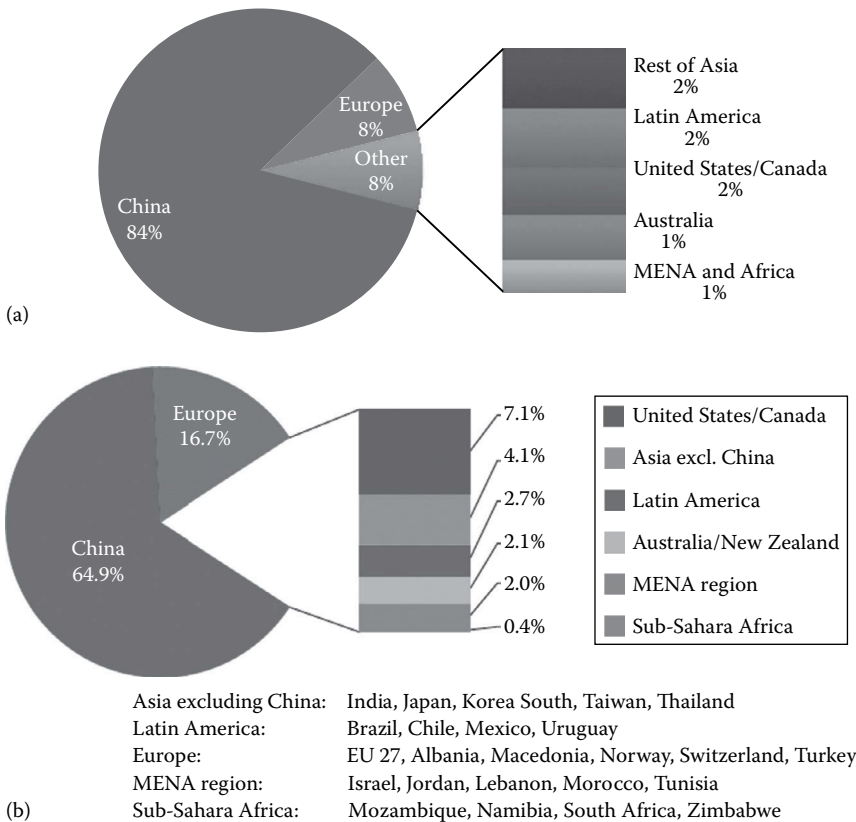


FIGURE 1.14 Worldwide distribution of solar thermal collector markets (a) glazed collectors and (b) total glazed and unglazed in 2012. (From Mauthner, F. and Weiss, W., Solar heat worldwide—Markets and contribution to energy supply 2011, IEA Solar Heating and Cooling Program, Paris, France, May 2013.)

1.6.3 Biomass

Although theoretically harvestable biomass energy potential is of the order of 90 TW, the technical potential on a sustainable basis is of the order of 8–13 TW or 270–450 EJ/year (UNDP, 2005). This potential is 1.6–2.6 times the present electricity-generating capacity of the world. It is estimated that by 2025, even the municipal solid waste (MSW) could generate up to 6 EJ/year.

The biggest advantage of biomass as an energy resource is its relatively straightforward transformation into transportation fuels. Biofuels have the potential to replace as much as 75% of the petroleum fuels in use for transportation in the United States (Worldwatch, 2006). This is especially important in view of the declining oil supplies worldwide. Biofuels will not require additional infrastructure development. Therefore, development of biofuels is being viewed very favorably by governments around the world. Biofuels, along with other transportation options such as electric vehicles and hydrogen, will help diversify the fuel base for future transportation. Table 1.8 and Figure 1.15 show the global production of biofuels from 2001 to 2011. United States, Brazil, and Europe are the top producing countries and region of the world. Biofuel production grew more than five times in 10 years, although it started from a much

TABLE 1.8

Total Biofuels Production (1000 bbl/day)

	2001	2002	2003	2004	2005	2006	2007	2008	2009	2010	2011
United States	115.7	140.3	183.9	223.3	260.6	335.0	457.3	649.7	747.1	889.8	971.7
Brazil	197.6	216.9	249.4	251.7	276.4	307.3	395.7	486.3	477.5	527.1	438.1
Europe	21.2	29.3	39.3	48.9	76.8	123.9	153.8	198.1	233.2	255.2	250.5
Asia	3.1	8.3	17.2	21.1	28.2	44.9	49.2	75.6	93.8	99.8	118.2
Rest of the world	5.3	8.6	9.6	9.8	14.2	29.6	47.3	67.7	83.8	93.3	118.8
World	342.9	403.5	499.4	554.8	656.3	840.6	1,103.3	1,477.3	1,635.4	1,865.4	1,897.2

Sources: Enerdata, *Enerdata Energy Statistical Yearbook 2013*, 2013; IEA, *World Energy Outlook 2013*, International Energy Agency, Paris, France, 2013.

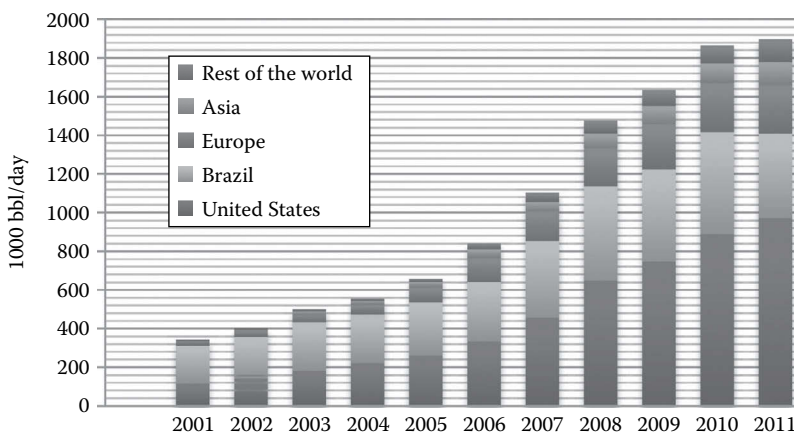


FIGURE 1.15

World biofuel production, 2001–2011. (From IEA, *World Energy Outlook 2013*, International Energy Agency, Paris, France, 2013.)

smaller base. In 2005, the world ethanol production had reached about 36 billion L/year while biodiesel production topped 3.5 billion L during the same year.

The present cost of ethanol production ranges from about €0.25 to about €1/gasoline equivalent L, as compared to the wholesale price of gasoline which is between €0.40 and €0.60/L (Figure 1.16). Biodiesel costs, on the other hand, range between €0.20 and €0.65/L of diesel equivalent (Figure 1.17). Figure 1.18 shows the feedstock used for these biofuels. An important consideration for biofuels is that the fuel not be produced at the expense of food while there are people going hungry in the world. This would not be of concern if biofuels were produced from MSW or nonfood forest resources.

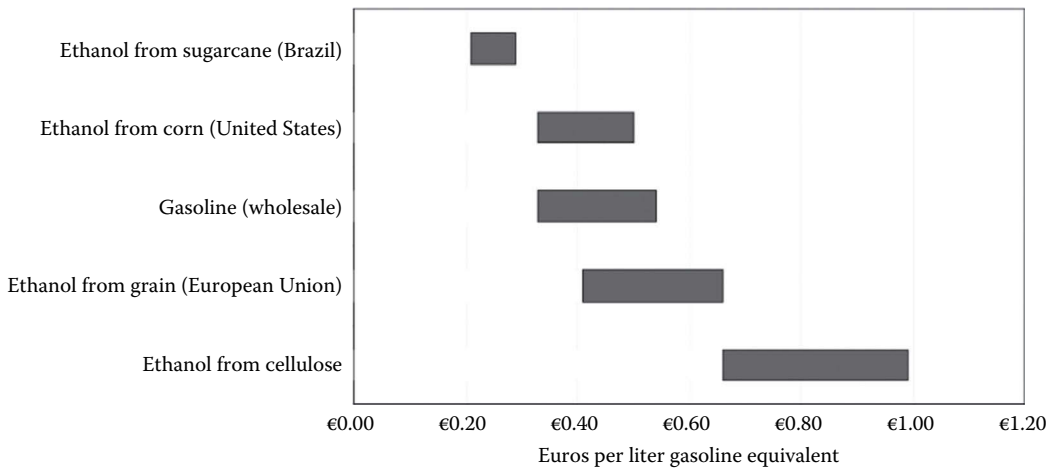


FIGURE 1.16
Cost ranges for ethanol and gasoline production, 2006. (From IEA, Reuters, DOE.)

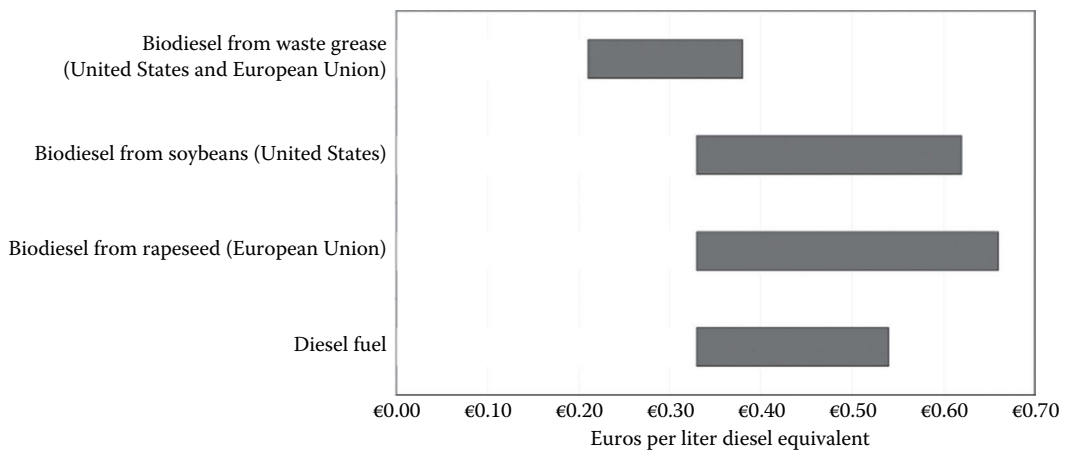


FIGURE 1.17
Cost ranges for biodiesel and diesel production, 2006. (From IEA, Reuters, DOE.)

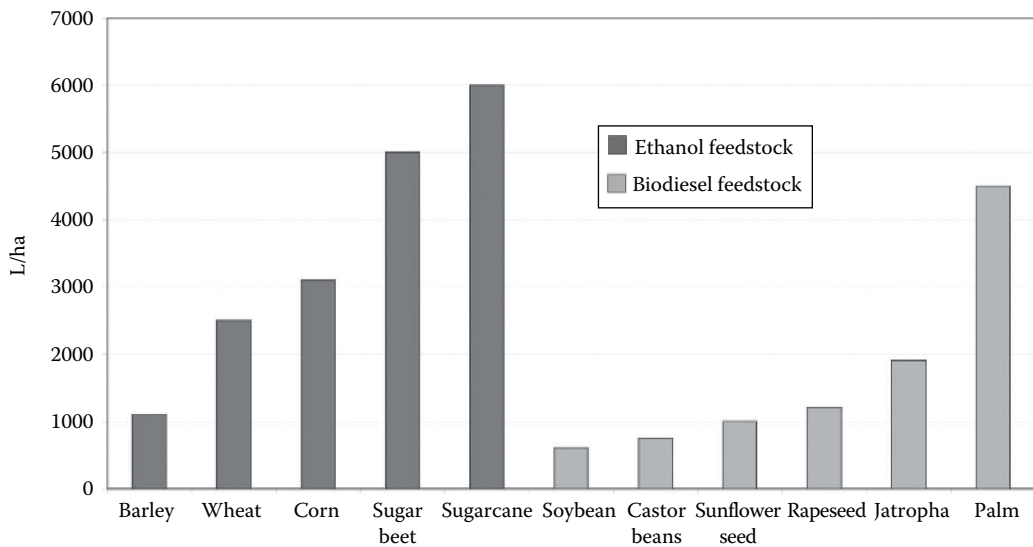


FIGURE 1.18

Biofuel yields of selected ethanol and biodiesel feedstocks. (From Hunt, S. and Forster, E. *Biofuels for Transportation: Global Potential and Implications for Sustainable Agriculture and Energy in the 21st Century*. Worldwatch Institute, Washington, DC, 2006.)

According to the Worldwatch report, a city of one million people produces about 1,800 tons of MSW and 1,300 tons of organic waste every day, which using the present-day technology could produce enough fuel to meet the needs of 58,000 persons in the United States, 360,000 in France, and nearly 2.6 million in China at current rates of per capita fuel use (Worldwatch, 2006).

1.6.4 Summary of Renewable Energy Resources

By definition, the term “reserves” does not apply to renewable resources. So we need to look at the annual potential of each resource. Table 1.9 summarizes the resource potential and the present costs and the potential future costs for each renewable resource.

As in the case of other new technologies, it is expected that cost competitiveness of the renewable energy technologies will be achieved with R&D, scale-up, commercial experience, and mass production. The experience curves in Figure 1.19 show industry-wide cost reductions in the range of 10%–20% for each cumulative doubling of production for wind power, photovoltaics, ethanol, and gas turbines (UNDP, 2004). Similar declines can be expected in solar thermal power and other renewable technologies. As seen from Figure 1.19, wind energy technologies have already achieved market maturity, and PV technologies are well on their way. Even though concentrating solar thermal power (CSP) is not shown in this figure, a GEF report estimates that CSP will achieve the cost target of about \$0.05/kWh by the time it has an installed capacity of about 40 GW (GEF, 2005). As a reference point, wind power achieved that capacity milestone in 2003.

TABLE 1.9

Potential and Status of Renewable Energy Technologies

Technology	Annual Potential	Operating Capacity 2005	Investment Costs U.S. \$/kW	Current Energy Cost	Potential Future Energy Cost
<i>Biomass energy</i>	276–446 EJ Total or 8–13 TW MSW ~ 6 EJ				
Electricity		~44 GW	500–6,000/kW _e	3–12 cents/kWh	3–10 cents/kWh
Heat		~225 GW _{th}	170–1,000/kW _{th}	1–6 cents/kWh	1–5 cents/kWh
Ethanol		~36 billion lit.	170–350/kW _{th}	25–75 cents/lit. (ge) ^a	\$6–\$10/GJ
Biodiesel		~3.5 billion lit.	500–1,000/kW _{th}	25–85 cents/lit. (de) ^b	\$10–\$15/GJ
<i>Wind power</i>	55 TW Theo. 2 TW Practical	59 GW	850–1,700	4–8 cents/kWh	3–8 cents/kWh
<i>Solar energy</i>	>100 TW				
Photovoltaics		5.6 GW	5,000–10,000	25–160 cents/kWh	5–25 cents/kWh
Thermal Power		0.4 GW	2,500–6,000	12–34 cents/kWh	4–20 cents/kWh
Heat			300–1,700	2–25 cents/kWh	2–10 cents/kWh
<i>Geothermal</i>	600,000 EJ useful resource base				
Electricity	5,000 EJ economical in 40–50 years	9 GW	800–3,000	2–10 cents/kWh	1–8 cents/kWh
Heat		11 GW _{th}	200–2,000	0.5–5 cents/kWh	0.5–5 cents/kWh
<i>Ocean energy</i>					
Tidal	2.5 TW	0.3 GW	1,700–2,500	8–15 cents/kWh	8–15 cents/kWh
Wave	2.0 TW		2,000–5,000	10–30 cents/kWh	5–10 cents/kWh
OTEC	228 TW		8,000–20,000	15–40 cents/kWh	7–20 cents/kWh
<i>Hydroelectric</i>	1.63 TW Theo.				
Large	0.92 TW Econ.	690 GW	1,000–3,500	2–10 cents/kWh	2–10 cents/kWh
Small		25 GW	700–8,000	2–12 cents/kWh	2–10 cents/kWh

Sources: Data from UNDP, World Energy Assessment: Energy and the Challenge of Sustainability, 2004. Updated from other sources: Worldwatch, Biofuels for transportation—Global potential and implications for sustainable and energy in the 21st century, Report prepared for the German Federal Ministry for Food, Agriculture and Consumer Protection, Worldwatch Institute, Washington, DC, 2006; World Wind Energy Association Bulletin, 2006, www.wwindea.org; Photovoltaic Barometer; EPIA, European Photovoltaic Industries Association, 2012, www.epia.org; World Geothermal Power Generation 2001–2005; GRC Bulletin; International Energy Annual; U.S. DOE-EIA.

Note: ge, gasoline equivalent liter; de, diesel equivalent liter; kW_e, kilowatt electrical power; kW_{th}, kilowatt thermal power.

1.7 Role of Energy Conservation

Energy conservation can and must play an important role in future energy strategy, because it can ameliorate adverse impacts on the environment rapidly and economically. Figures 1.20 and 1.21 give an idea of the potential of energy efficient improvements. Figure 1.20 shows that per capita energy consumption varies by as much as a factor of 3

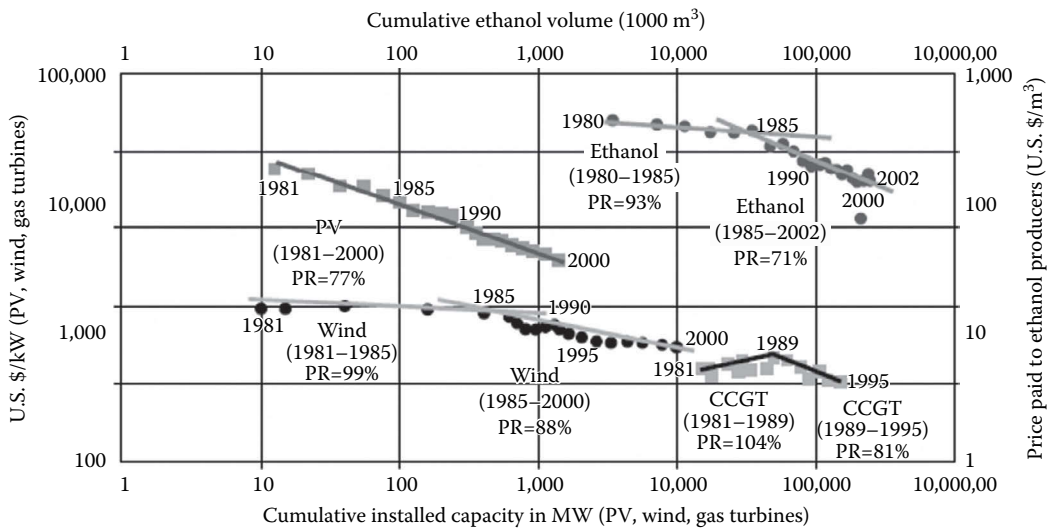


FIGURE 1.19

Experience curves for wind, PV, ethanol and gas turbines. (Adapted from UNDP, *World Energy Assessment: Energy and the Challenge of Sustainability*, 2004. For wind turbines: Neij, L. et al., *Experience curves: A tool for Energy Policy Assessment*, March 2003; For gas turbines: Claeson Colpier, U. and Cornland, D., *Energy Policy*, 30, 209, 2002; For photovoltaics: Parente, V. et al., *Prog. Photovolt. Res. Appl.*, 10(8), 571, 2002; For ethanol: Goldemberg, J. et al., *Biomass Energy*, in press.)

between the United States and some European countries with almost the same level of Human Development Index (HDI). Even taking just the OECD European countries combined, the per capita energy consumption in the United States is twice as much. It is fair to assume that the per capita energy of the United States could be reduced to the level of OECD Europe of 4.2 kW by a combination of energy efficiency improvements and changes in the transportation infrastructure. This is significant because the United States uses about 25% of the energy of the whole world. The present per capita energy consumption in the United States is 284 GJ, which is equivalent to about 9 kW/person, while the average for the whole world is 2 kW. Board of Swiss Federal Institutes of Technology has developed a vision of a 2 kW per capita society by the middle of the century (UNDP, 2004). The vision is technically feasible. However, to achieve this vision will require a combination of increased R&D on energy efficiency and policies that encourage conservation and use of high efficiency systems. It will also require some structural changes in the transportation systems. According to the 2004 World Energy Assessment by UNDP, a 25%–35% reduction in primary energy in the industrialized countries is achievable cost effectively in the next 20 years, without sacrificing the level of energy services. The report also concluded that similar reductions of up to 40% are cost effectively achievable in the transitional economies and more than 45% in developing economies. As a combined result of efficiency improvements and structural changes such as increased recycling, substitution of energy intensive materials, etc., energy intensity could decline at a rate of 2.5%/year over the next 20 years (UNDP, 2004).

McKinsey and Company conducted a comprehensive study of the energy conservation potential in United States in 2020. Figure 1.22 shows the potential in various sectors including the average cost of savings. According to this figure, the total U.S. economical potential of energy conservation to 2020 is 9500 trillion Btu or 25 GTOE.

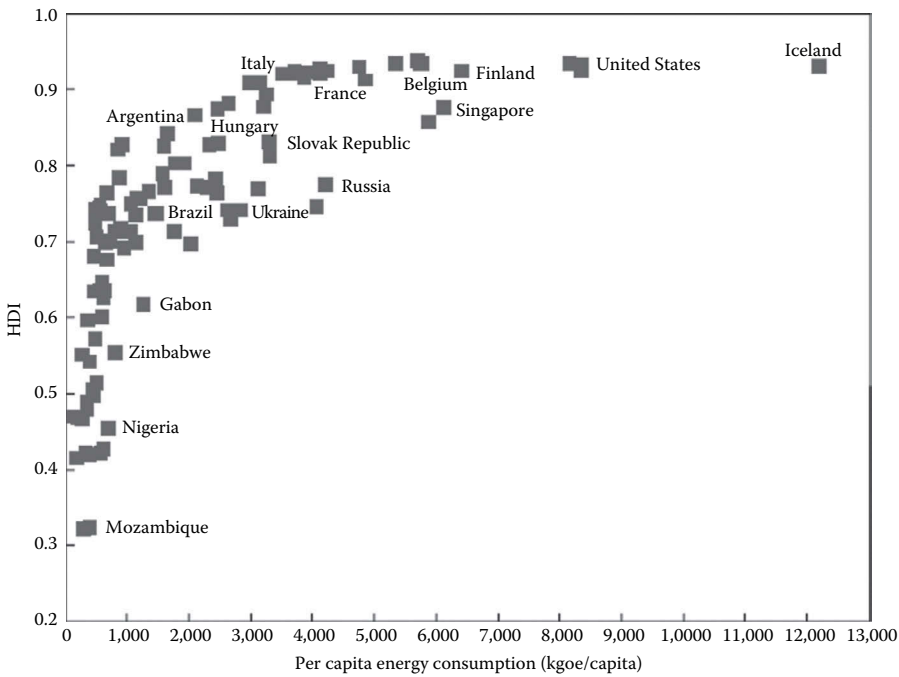


FIGURE 1.20 Relationship between Human Development Index (HDI) and per capita energy use, 1999–2000. (From UNDP, World Energy Assessment: Energy and the Challenge of Sustainability, 2004.)

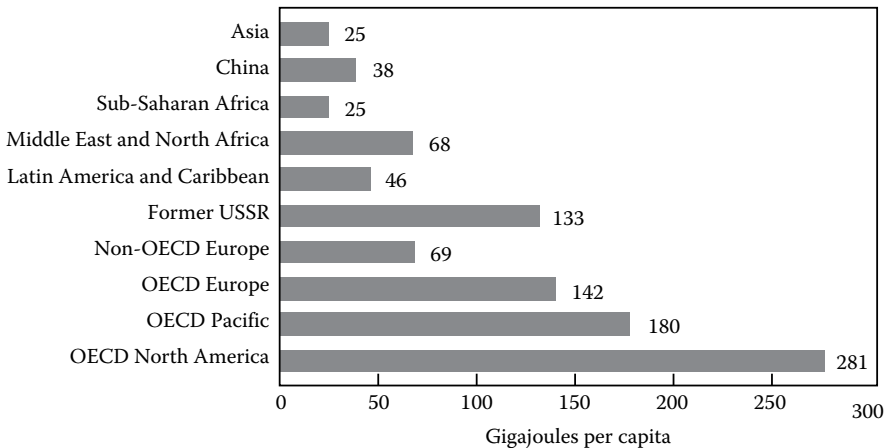


FIGURE 1.21 Per capita energy use by region (commercial and noncommercial) 2000. (From UNDP, World Energy Assessment: Energy and the Challenge of Sustainability, 2004.) *Note:* Asia excludes Middle East, China, and OECD countries; Middle East and North Africa comprises Algeria, Bahrain, Egypt, Iran, Iraq, Israel, Jordan, Kuwait, Lebanon, Libya, Morocco, Oman, Qatar, Saudi Arabia, Syria, Tunisia, United Arab Emirates, and Yemen; Latin America and Caribbean excludes Mexico; OECD Pacific comprises Australia, Japan, Korea, and New Zealand; Former USSR comprises Armenia, Azerbaijan, Belarus, Estonia, Georgia, Kazakhstan, Kyrgyzstan, Latvia, Lithuania, Moldova, Russia, Tajikistan, Turkmenistan, Ukraine, and Uzbekistan; Non-OECD Europe comprises Albania, Bosnia and Herzegovina, Bulgaria, Croatia, Cyprus, Gibraltar, Macedonia, Malta, Romania, and Slovenia; OECD North America includes Mexico.

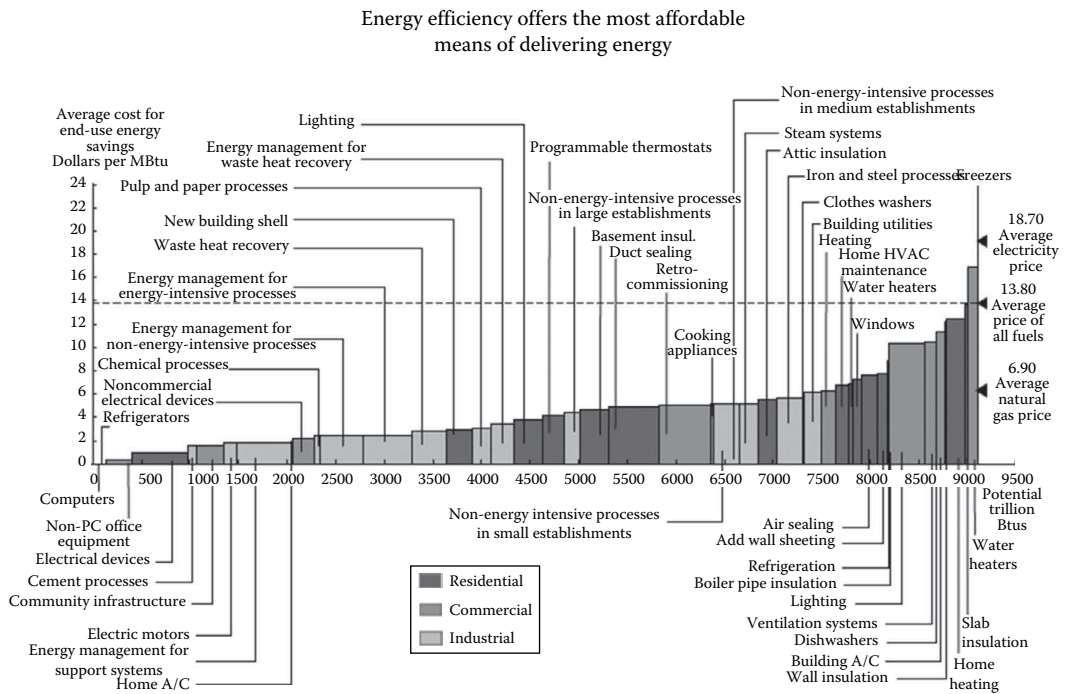


FIGURE 1.22

Energy saving potential of various sectors and cost of savings as compared to the price of electricity. (From Granade, H. et al., *Unlocking energy efficiency in the U.S. economy, 2010 EIA Energy Conference*, Washington, DC, April 2010, www.eia.gov/conference/2010/session9/granade.pdf.)

Rocky Mountain Institute in Colorado, estimates that the total potential of energy savings due to efficiency improvements in the industry sector in United States by 2050 could be as much as 30% of energy use under the business as usual scenario (see Figure 1.23).

Improving energy efficiency across all sectors of the economy should become a worldwide objective (Energy Commission, 2004). It should be noted, however, that free market price signals may not always be sufficient to effect energy efficiency. Hence, legislation on the state and/or national level for energy efficiency standards for equipment in the residential and commercial sector may be necessary. There is considerable debate whether incentives or mandates are the preferred way to improve energy efficiency. Such measures may be necessary because surveys indicate that consumers consistently rank energy use and operating costs quite low on the lists of attributes they consider when purchasing an appliance or construct a building. Incentives may be the preferred option provided they induce decision makers to take appropriate action.

Figure 1.24 shows the projected energy savings from upgraded standards for products installed in the years 2010–2020. Outside the United States, over 30 countries have also adopted minimum energy performance standards. These measures have been shown to be economically attractive and can provide an appreciable reduction in adverse environmental impacts.

This handbook describes energy efficient improvements achievable with available technologies. The challenge is to adopt policies that accelerate the adoption of these technologies all over the world.

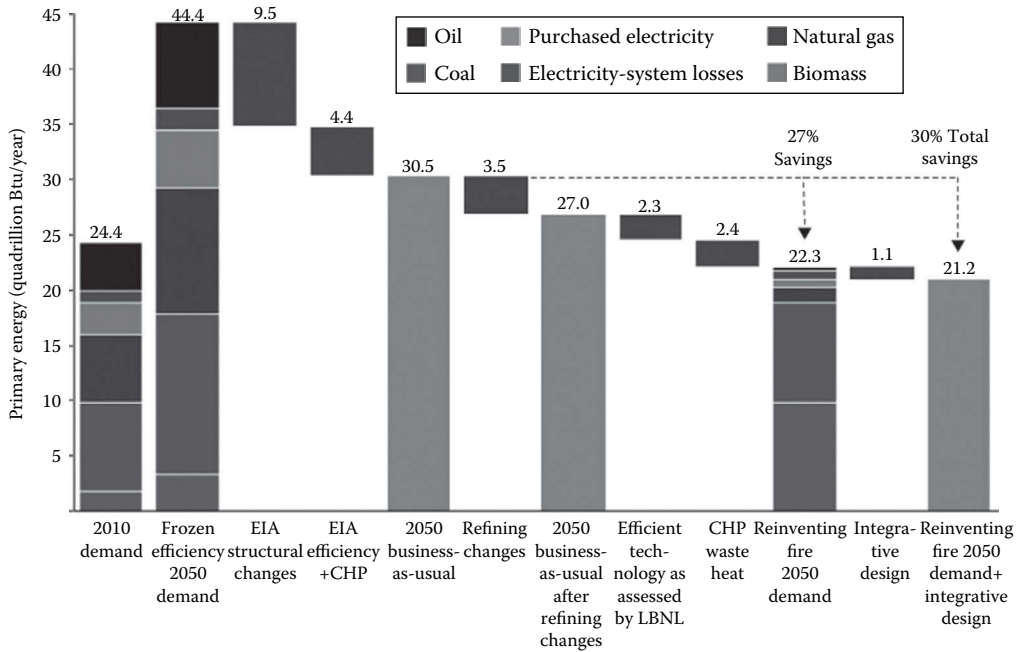


FIGURE 1.23

U.S. industry energy savings potential (2010–2050) as a percentage of the total industrial energy use in business as usual scenario. (From Rocky Mountain Institute, U.S. Industry Energy savings potential, 2010–2050, in: *Reinventing Fire: Bold Business Solutions for the New Energy Era*, RMI, Snowmass, CO, 2012, http://www.rmi.org/RFGGraph-US_industry_energy_saving_potential; www.RMI.org/ReinventingFire.)

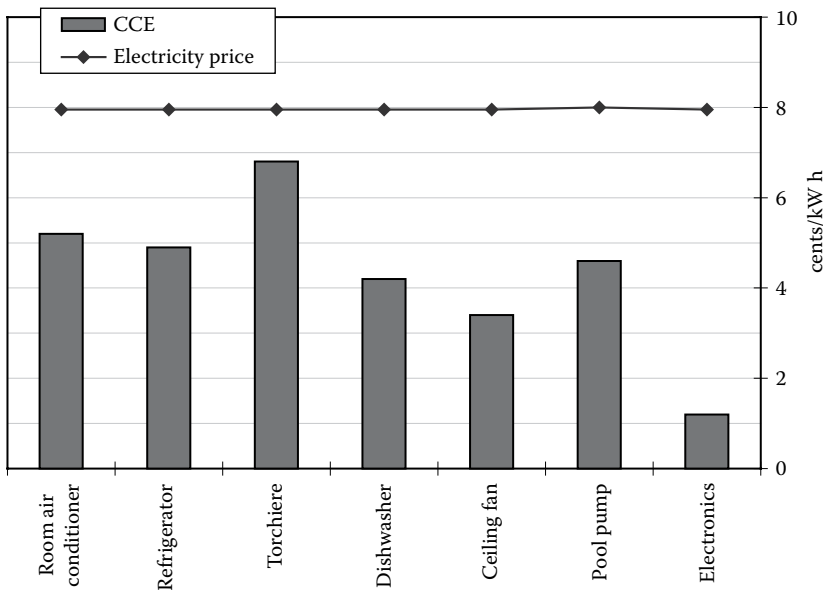


FIGURE 1.24

Comparison of cost of conserved energy for 2010 standards to projected electricity price in the residential sector.

1.8 Forecast of Future Energy Mix

As explained in this chapter, it is clear that oil production will peak in the near future and will start declining thereafter. Since oil comprises the largest share of world energy consumption, a reduction in availability of oil will cause a major disruption unless other resources can fill the gap. Natural gas and coal production may be increased to fill the gap, with the natural gas supply increasing more rapidly than coal. However, that will hasten the time when natural gas production also peaks. Additionally, any increase in coal consumption will worsen the global climate change situation. Although CO₂ sequestration is feasible, it is doubtful that there will be any large-scale application of this technology for existing plants. However, all possible measures should be taken to sequester CO₂ from new coal-fired power plants. Nuclear power does not produce CO₂, however, it is doubtful that nuclear power alone will be able to fill the gap. Forecasts from IAEA show that nuclear power around the world will grow at a rate of 1.2%–2.7% over the next 25 years (IAEA, 2013). This estimate is in the same range as that of IEA.

Based on this information it seems logical that the RE technologies of solar, wind, and biomass will not only be essential but will hopefully be able to fill the gap and provide a clean and sustainable energy future. Although wind and photovoltaic power have grown at rates of over 30%–35%/year over the last few years, this growth rate is based on very small existing capacities for these sources. There are many differing views on the future energy mix. The IEA gives forecasts based on different policy scenarios. Figure 1.25 shows the growth in primary energy demand and the corresponding CO₂ emissions for the

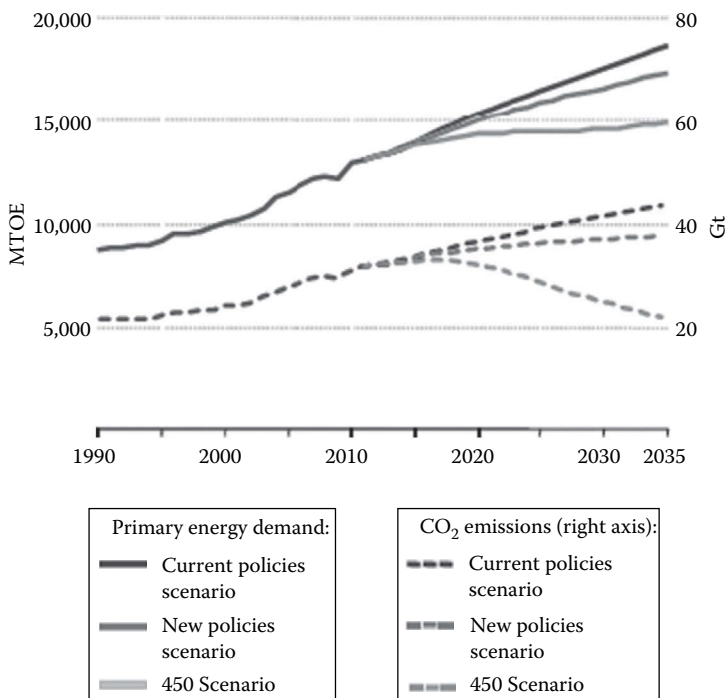


FIGURE 1.25 World primary energy demand by fuel types. (According to IEA, *World Energy Outlook 2013*, International Energy Agency, Paris, France, 2013.)

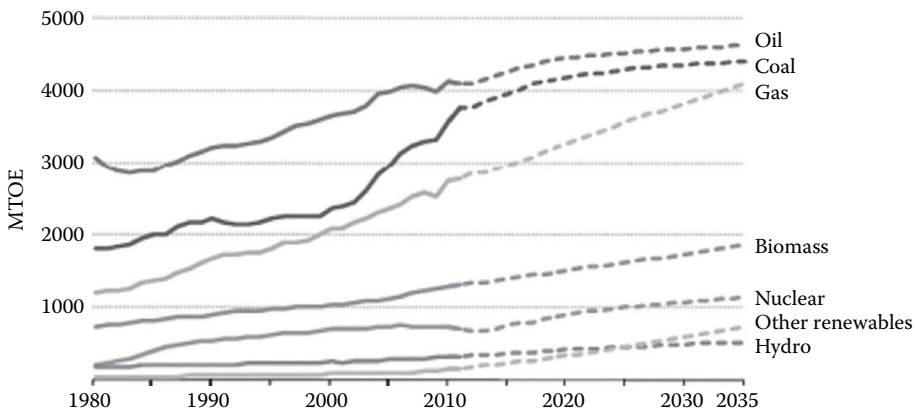


FIGURE 1.26 World primary energy demand by fuel in new policy scenario. (From IEA, *World Energy Outlook 2013*, International Energy Agency, Paris, France, 2013.)

three scenarios. Figure 1.26 shows the demand by fuel type in the “New Policy Scenario,” in which renewable energy will provide 18% of the primary energy demand by 2035. However, in the “450 Scenario,” renewable energy share goes up to 26% by 2035. This estimate is close to the estimate by the German Advisory Council on Global Change (WBGU), which performed a detailed analysis on combating global climate change with an orderly transition to increased energy efficiencies and increased use of renewable energy. WBGU estimates that as much as 50% of the world’s primary energy in 2050 will come from renewable energy, increasing to 80% by 2100 (Figure 1.27). However, to achieve that level of RE use by 2050 and beyond will require a global effort on the scale of Apollo Project.

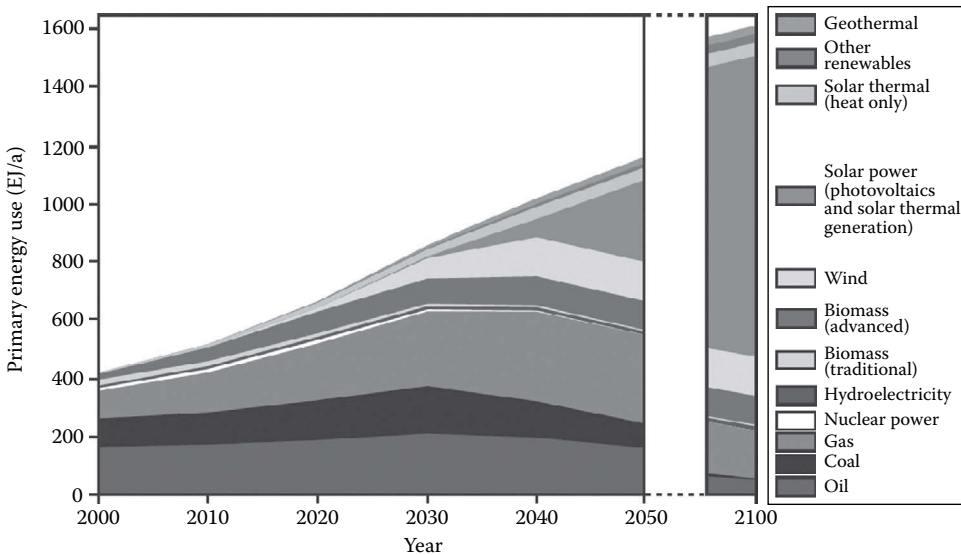


FIGURE 1.27 The global energy mix for year 2050 and 2100. (According to WBGU, *World in transition—Towards sustainable energy systems*, German Advisory Council on Global Change, Berlin, Germany, 2003, Report available at <http://www.wbgu.de>.)

References

- Bartlett, A.A., 2002. An analysis of U.S. and world oil production patterns using Hubbert-style curves. *Mathematical Geology* 32, 1–17.
- BP, 2013. *BP Statistical Review of World Energy 2013*. BP, London, U.K. The report is available on the web at www.bp.com/statisticalreview/.
- EIA, 2013. *International Energy Outlook 2013*. Energy Information Agency, US Department of Energy, Washington, DC, <http://www.eia.gov/forecasts/ieo/index.cfm>.
- Enerdata, 2013. *Enerdata Energy Statistical Yearbook 2013*. <http://yearbook.enerdata.net>.
- Energy Commission, December 2004. *Ending the Energy Stalemate: A Bipartisan Strategy to Meet America's Energy Challenges*. The National Commission on Energy Policy, Washington, DC, www.energycommission.org.
- EPIA, 2012. European Photovoltaic Industries Association, www.epia.org.
- EPRI, 2004. Advanced batteries for electric drive vehicles: A technology and cost-effectiveness assessment for battery electric vehicles, power-assist hybrid electric vehicles, and plug-in hybrid electric vehicles. EPRI Technical Report No. 1009299. EPRI, Palo Alto, CA.
- GEF, 2005. Assessment of the World Bank/GEF strategy for the market development of concentrating solar thermal power. Global Environmental Facility (GEF) Report, GEF/c.25/Inf.11, Washington, DC.
- Granade, H. et al., April 2010. Unlocking energy efficiency in the U.S. economy. *2010 EIA Energy Conference*, Washington, DC, www.eia.gov/conference/2010/session9/granade.pdf.
- Hammererschlag, R. and Mazza, P., 2005. Questioning hydrogen. *Energy Policy* 33, 2039–2043.
- Hawkins, D.G., Lashof, D.A., and Williams, R.H., September 2006. What to do about coal—Carbon capture and storage. *Scientific American*, Special Issue, 68–75.
- Hubbert, M.K., 1974. U.S. Energy Resources: A review as of 1972. A National Fuels and Energy Policy Study, Serial No. 93-40 (92-75). Part 1. U.S. Government Printing Office, Washington, DC.
- Hunt, S. and Forster, E. 2006. *Biofuels for Transportation: Global Potential and Implications for Sustainable Agriculture and Energy in the 21st Century*. Worldwatch Institute, Washington, DC.
- IAEA, 2011. *Uranium: Resources, Production and Demand (The Red Book)*. IAEA, Vienna, Austria.
- IEA, 2004. *World Energy Outlook 2004*. International Energy Agency, Paris, France.
- IEA, 2010. *World Energy Outlook 2010*. International Energy Agency, Paris, France.
- IEA, 2013. *World Energy Outlook 2013*. International Energy Agency, Paris, France.
- Kreith, F., 2006. Plenary Lecture 2006. *ASES Conference*, Denver, CO, available from ASES, Boulder, CO.
- Kreith, F. and West, R.E., 2004. Fallacies of a hydrogen economy. *Journal of Energy Resources Technology* 126, 249–257.
- Mauthner, F. and Weiss, W., May 2013. Solar heat worldwide—Markets and contribution to energy supply 2011. IEA Solar Heating and Cooling Program, Paris, France.
- Rocky Mountain Institute, 2012. U.S. Industry Energy savings potential, 2010–2050. In: *Reinventing Fire: Bold Business Solutions for the New Energy Era*. RMI, Snowmass, CO, http://www.rmi.org/RFGGraph-US_industry_energy_saving_potential.
- Sadler, H., Riedy, C., and Passey, R., September 2004. Geosequestration. Discussion Paper 72. The Australia Institute, Sydney, New South Wales, Australia. ISSN: 1322-5421.
- Sanna, L., Fall 2005. Driving the solution—Plug-in hybrid vehicles. *EPRI Journal*.
- Shinnar, R., 2003. The hydrogen economy, fuel cells, and electric cars. *Technology in Society* 25(4), 453–576.
- UNDP, 2004. *World Energy Assessment: Energy and the Challenge of Sustainability*, UNDP, New York.
- Veziroglu, T.N. and Barbir, F., 1992. Hydrogen: The wonder fuel. *International Journal of Hydrogen Energy* 17(6), 391–404.
- WBGU, 2003. *World in transition—Towards sustainable energy systems*. German Advisory Council on Global Change, Berlin, Germany. Report available at <http://www.wbgu.de>.

- West, R.E. and Kreith, F., 2006. A vision for a secure transportation system without hydrogen. *ASME Journal of Energy Resources Technologies* (to be published), JERT-06-1009-1. ASME, New York.
- Worldwatch, 2006. Biofuels for transportation—Global potential and implications for sustainable and energy in the 21st century. Report prepared for the German Federal Ministry for Food, Agriculture and Consumer Protection, Worldwatch Institute, Washington, DC.
- WWEA, 2012. World Wind Energy Association, http://www.wwindea.org/webimages/WorldWindEnergyReport2012_final.pdf.
- WWEA, 2013. World Wind Energy Association, <http://www.wwindea.org/wwea-publishes-half-year-report-2013-2/>.
- Zhou, X., September 2012. The present and future development of electric power in China. *Keynote Lecture at the International Conference for Energy for the Next Decades*. The Energy Institute, Hong Kong, China.

Section I

Energy Resources



Taylor & Francis

Taylor & Francis Group

<http://taylorandfrancis.com>

2

Fossil Fuels

Robert Reuther, Richard Bajura, and Philip C. Crouse

CONTENTS

2.1	Coal	33
2.1.1	Coal Composition and Classification.....	33
2.1.2	Coal Analysis and Properties.....	36
2.1.3	Coal Reserves	39
2.1.4	Important Terminology: Resources, Reserves, and the Demonstrated Reserve Base	40
2.1.5	Transportation.....	41
2.2	Environmental Aspects.....	47
	Defining Terms	49
	References.....	50
	For Further Information.....	50
2.3	Oil.....	50
2.3.1	Overview.....	50
2.3.2	Crude Oil Classification and World Reserves	51
2.3.3	Standard Fuels.....	54
2.4	Natural Gas.....	55
2.4.1	Overview.....	55
2.4.2	Reserves and Resources.....	56
2.4.3	Natural Gas Production Measurement.....	58
2.4.4	World Production of Dry Natural Gas.....	58
2.4.5	Compressed Natural Gas.....	58
2.4.6	Liquefied Natural Gas (LNG).....	58
2.4.7	Physical Properties of Hydrocarbons	58
	Defining Terms	60
	For Further Information.....	60

2.1 Coal

Robert Reuther

2.1.1 Coal Composition and Classification

Coal is a sedimentary rock formed by the accumulation and decay of organic substances, derived from plant tissues and exudates, which have been buried over periods of geological time, along with various mineral inclusions. Coal is classified by **type** and **rank**. Coal type classifies coal by the plant sources from which it was derived. Coal rank classifies coal

TABLE 2.1

Coal Maceral Groups and Macerals

Maceral Group	Maceral	Derivation
Vitrinite	Collinite	Humic gels
	Telinite	Wood, bark, and cortical tissue
	Pseudovitrinite	? (Some observers place in the inertinite group)
Exinite	Sporinite	Fungal and other spores
	Cutinite	Leaf cuticles
	Alginite	Algal remains
Inertinite	Micrinite	Unspecified detrital matter, <0 μ
	Macrinite	Unspecified detrital matter, 10–100 μ
	Semifusinite	“Burned” woody tissue, low reflectance
	Fusinite	“Burned” woody tissue, high reflectance
	Sclerotinite	Fungal sclerotia and mycelia

Source: Modified from Berkowitz, N., *An Introduction to Coal Technology*, Academic Press, New York, 1979. With permission.

by its degree of metamorphosis from the original plant sources and is therefore a measure of the age of the coal. The process of metamorphosis or aging is termed **coalification**.

The study of coal by type is known as coal petrography. Coal type is determined from the examination of polished sections of a coal sample using a reflected-light microscope. The degree of reflectance and the color of a sample are identified with specific residues of the original plant tissues. These various residues are referred to as **macerals**. Macerals are collected into three main groups: vitrinite, inertinite, and exinite (sometimes referred to as liptinite). The maceral groups and their associated macerals are listed in Table 2.1, along with a description of the plant tissue from which each distinct maceral type is derived.

Coal rank is the most important property of coal because rank initiates the classification of coal for use. Coalification describes the process that the buried organic matter undergoes to become coal. When first buried, the organic matter has a certain elemental composition and organic structure. However, as the material becomes subjected to heat and pressure, the composition and structure slowly change. Certain structures are broken down, and others are formed. Some elements are lost through volatilization, while others are concentrated through a number of processes, including exposure to underground flows, which carry away some elements and deposit others. Coalification changes the values of various properties of coal. Thus, coal can be classified by rank through the measurement of one or more of these changing properties.

In the United States and Canada, the rank classification scheme defined by the American Society of Testing and Materials (ASTM) has become the standard. In this scheme, the properties of **gross calorific value** and **fixed carbon** or **volatile matter** content are used to classify a coal by rank. Gross calorific value is a measure of the energy content of the coal and is usually expressed in units of energy per unit mass. Calorific value increases as the coal proceeds through coalification. Fixed carbon content is a measure of the mass remaining after heating a dry coal sample under conditions specified by the ASTM.

Fixed carbon content also increases with coalification. The conditions specified for the measurement of fixed carbon content result in being able, alternatively, to use the volatile matter content of the coal, measured under dry, ash-free conditions, as a rank parameter. The rank of a coal proceeds from lignite, the “youngest” coal, through subbituminous, bituminous, and semibituminous, to anthracite, the “oldest” coal. The subdivisions within these rank categories are defined in Table 2.2. (Some rank schemes

TABLE 2.2

Classification of Coals by Rank

Class	Group	Fixed Carbon Limits, % (dmmf)		Volatile Matter Limits, % (dmmf)		Gross Calorific Value Limits, Btu/lb (moist, mmf)		Agglomerating Character
		Equal to or Greater Than	Less Than	Greater Than	Equal to or Less Than	Equal to or Greater Than	Less Than	
Anthracitic	Meta-anthracite	98	—	—	2	—	—	Nonagglomerating
	Anthracite	92	98	2	8	—	—	Nonagglomerating
	Semianthracite	86	92	8	14	—	—	Nonagglomerating
Bituminous	Low-volatile bituminous	78	86	14	22	—	—	Commonly agglomerating
	Medium-volatile bituminous	69	78	22	31	—	—	Commonly agglomerating
	High-volatile A bituminous	—	69	31	—	14,000	—	Commonly agglomerating
	High-volatile B bituminous	—	—	—	—	13,000	14,000	Commonly agglomerating
	High-volatile C bituminous	—	—	—	—	11,500	13,000	Commonly agglomerating
	High-volatile C bituminous	—	—	—	—	10,500	11,500	Agglomerating
	Subbituminous	Subbituminous A	—	—	—	—	10,500	11,500
	Subbituminous B	—	—	—	—	9,500	10,500	Nonagglomerating
	Subbituminous C	—	—	—	—	8,300	9,500	Nonagglomerating
Lignitic	Lignite A	—	—	—	—	6,300	8,300	Nonagglomerating
	Lignite B	—	—	—	—	—	6,300	Nonagglomerating

Source: From the American Society for Testing and Materials' Annual Book of ASTM Standards. With permission.

include meta-anthracite as a rank above, or “older” than, anthracite. Others prefer to classify such deposits as graphite—a minimal resource valuable primarily for uses other than as a fuel.)

According to the ASTM scheme, coals are ranked by calorific value up to the high-volatile A bituminous rank, which includes coals with calorific values (measured on a moist, mineral matter-free basis) greater than 14,000 Btu/lb (32,564 kJ/kg). At this point, fixed carbon content (measured on a dry, mineral matter-free basis) takes over as the rank parameter. Thus, a high-volatile A bituminous coal is defined as having a calorific value greater than 14,000 Btu/lb, but a fixed carbon content less than 69 wt%. The requirement for having two different properties with which to define rank arises because calorific value increases significantly through the lower-rank coals, but very little (in a relative sense) in the higher ranks; fixed carbon content has a wider range in higher rank coals, but little (relative) change in the lower ranks. The most widely used classification scheme outside North America is that developed under the jurisdiction of the International Standards Organization, Technical Committee 27, Solid Mineral Fuels.

2.1.2 Coal Analysis and Properties

The composition of a coal is typically reported in terms of its **proximate analysis** and its **ultimate analysis**. The proximate analysis of a coal is made up of four constituents: volatile matter content; fixed carbon content; moisture content; and ash content, all of which are reported on a weight percent basis. The measurement of these four properties of a coal must be carried out according to strict specifications codified by the ASTM. Note that the four constituents of proximate analysis do not exist, per se, in the coal, but are measured as analytical results upon treating the coal sample to various conditions.

ASTM volatile matter released from coal includes carbon dioxide, inorganic sulfur- and nitrogen-containing species, and organic compounds. The percentages of these various compounds or species released from the coal varies with rank. Volatile matter content can typically be reported on a number of bases, such as moist; dry, mineral matter-free (dmmf); moist, mineral matter-free; moist, ash-free; and dry, ash-free (daf), depending on the condition of the coal on which the measurements were made.

Mineral matter and ash are two distinct entities. Coal does not contain ash, even though the ash content of a coal is reported as part of its proximate analysis. Instead, coal contains mineral matter, which can be present as distinct mineral entities or inclusions and as material intimately bound with the organic matrix of the coal. Ash, on the other hand, refers to the solid inorganic material remaining *after combusting* a coal sample. Proximate ash content is the ash remaining after the coal has been exposed to air under specific conditions codified in ASTM Standard Test Method D 3174. It is reported as the mass percent remaining upon combustion of the original sample on a dry or moist basis.

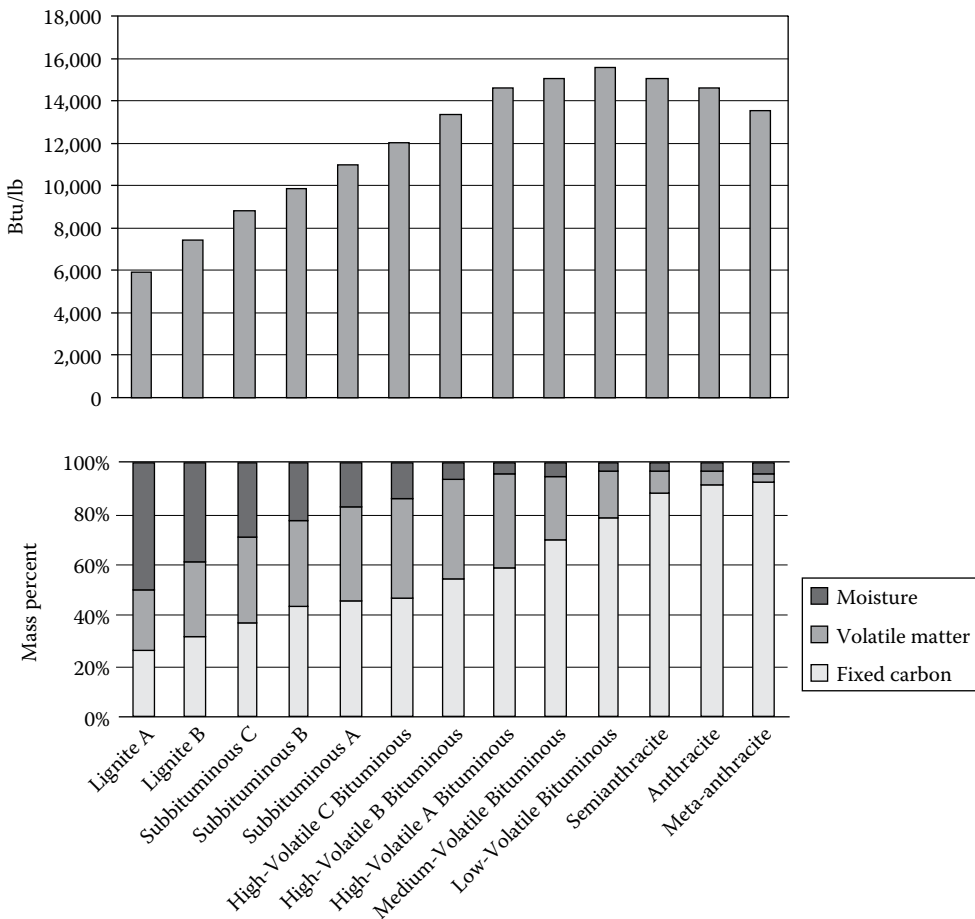
Moisture content refers to the mass of water released from the solid coal sample when it is heated under specific conditions of temperature and residence time as codified in ASTM Standard Test Method D 3173.

The fixed carbon content refers to the mass of organic matter remaining in the sample after the moisture and volatile matter are released. It is primarily made up of carbon. However, hydrogen, sulfur, and nitrogen also are typically present. It is reported by difference from the total of the volatile matter, ash, and moisture contents on a mass percent of the original coal sample basis. Alternatively, it can be reported on a dry basis; a dmmf basis; or a moist, mineral matter-free basis.

The values associated with a proximate analysis vary with rank. In general, volatile matter content decreases with increasing rank, while fixed carbon content correspondingly increases. Moisture and ash also decrease, in general, with rank. Typical values for proximate analyses as a function of the rank of a coal are provided in Table 2.3.

The ultimate analysis provides the composition of the organic fraction of coal on an elemental basis. Like the proximate analysis, the ultimate analysis can be reported on a moist or dry basis and on an ash-containing or ash-free basis. The moisture and ash reported in the ultimate analysis are found from the corresponding proximate analysis. Nearly every element on Earth can be found in coal. However, the important elements that occur in the organic fraction are limited to only a few. The most important of these include carbon; hydrogen; oxygen; sulfur; nitrogen; and, sometimes, chlorine. The scope, definition of the ultimate analysis, designation of applicable standards, and calculations for reporting results on different moisture bases can be found in ASTM Standard Test Method D 3176M.

TABLE 2.3
Calorific Values and Proximate Analyses of Ash-Free Coals of Different Rank



Source: From Averitt, P., Coal Resources of the United States, January 1, 1974. U.S. Geological Survey Bulletin 1412, Government Printing Office, Washington, DC, 1975.

TABLE 2.4

Ultimate Analysis in Mass Percent of Representative Coals of the U.S.

Component	Fort Union Lignite	Powder River Subbituminous	Four Corners Subbituminous	Illinois C Bituminous	Appalachia Bituminous
Moisture	36.2	30.4	12.4	16.1	2.3
Carbon	39.9	45.8	47.5	60.1	73.6
Hydrogen	2.8	3.4	3.6	4.1	4.9
Nitrogen	0.6	0.6	0.9	1.1	1.4
Sulfur	0.9	0.7	0.7	2.9	2.8
Oxygen	11.0	11.3	9.3	8.3	5.3
Ash	8.6	7.8	25.6	7.4	9.7
Gross calorific value, Btu/lb	6,700	7,900	8,400	10,700	13,400

Source: Modified from Probststein, R. and Hicks, R., *Synthetic Fuels*, McGraw-Hill, New York, 1982. With permission.

Typical values for the ultimate analysis for various ranks of coal found in the U.S. are provided in Table 2.4. Other important properties of coal include swelling, caking, and coking behavior; ash fusibility; reactivity; and calorific value.

Calorific value measures the energy available in a unit mass of coal sample. It is measured by ASTM Standard Test Method D 2015M, Gross Calorific Value of Solid Fuel by the Adiabatic Bomb Calorimeter, or by ASTM Standard Test Method D 3286, Gross Calorific Value of Solid Fuel by the Isothermal-Jacket Bomb Calorimeter. In the absence of a directly measured value, the gross calorific value, Q , of a coal (in Btu/lb) can be estimated using the Dulong formula (Elliott and Yohe 1981):

$$Q = 14,544C + 62,028[H - (O/8)] + 4,050S$$

where C , H , O , and S are the mass fractions of carbon, hydrogen, oxygen, and sulfur, respectively, obtained from the ultimate analysis.

Swelling, caking, and coking all refer to the property of certain bituminous coals to change in size, composition, and, notably, strength, when slowly heated in an inert atmosphere to between 450 and 550 or 600°F. Under such conditions, the coal sample initially becomes soft and partially devolatilizes. With further heating, the sample takes on a fluid characteristic. During this fluid phase, further devolatilization causes the sample to swell. Still further heating results in the formation of a stable, porous, solid material with high strength. Several tests have been developed, based on this property, to measure the degree and suitability of a coal for various processes. Some of the more popular tests are the free swelling index (ASTM Test Method D 720); the Gray–King assay test (initially developed and extensively used in Great Britain); and the Gieseler plastometer test (ASTM Test Method D 2639), as well as a host of dilatometric methods (Habermehl et al. 1981).

The results of these tests are often correlated with the ability of a coal to form a coke suitable for iron making. In the iron-making process, the high carbon content and high surface area of the coke are used in reducing iron oxide to elemental iron. The solid coke must also be strong enough to provide the structural matrix upon which the reactions take place. Bituminous coals that have good coking properties are often referred to as metallurgical coals. (Bituminous coals without this property are, alternatively, referred to as steam coals because of their historically important use in raising steam for conversion to mechanical energy or electricity generation.)

Ash fusibility is another important property of coals. This is a measure of the temperature range over which the mineral matter in the coal begins to soften, eventually to melt into a slag, and to fuse together. This phenomenon is important in combustion processes; it determines if and at what point the resultant ash becomes soft enough to stick to heat exchanger tubes and other boiler surfaces or at what temperature it becomes molten so that it flows (as slag), making removal as a liquid from the bottom of a combustor possible.

Reactivity of a coal is a very important property fundamental to all coal conversion processes (such as combustion, gasification, and liquefaction). In general, lower rank coals are more reactive than higher rank coals. This is due to several different characteristics of coals, which vary with rank as well as with type. The most important characteristics are the surface area of the coal, its chemical composition, and the presence of certain minerals that can act as catalysts in the conversion reactions. The larger surface area present in lower rank coals translates into a greater degree of penetration of gaseous reactant molecules into the interior of a coal particle. Lower rank coals have a less aromatic structure than higher ranks. This corresponds to the presence of a higher proportion of lower energy, more reactive chemical bonds. Lower rank coals also tend to have higher proximate ash contents, and the associated mineral matter is more distributed, even down to the atomic level. Any catalytically active mineral matter is thus more highly dispersed.

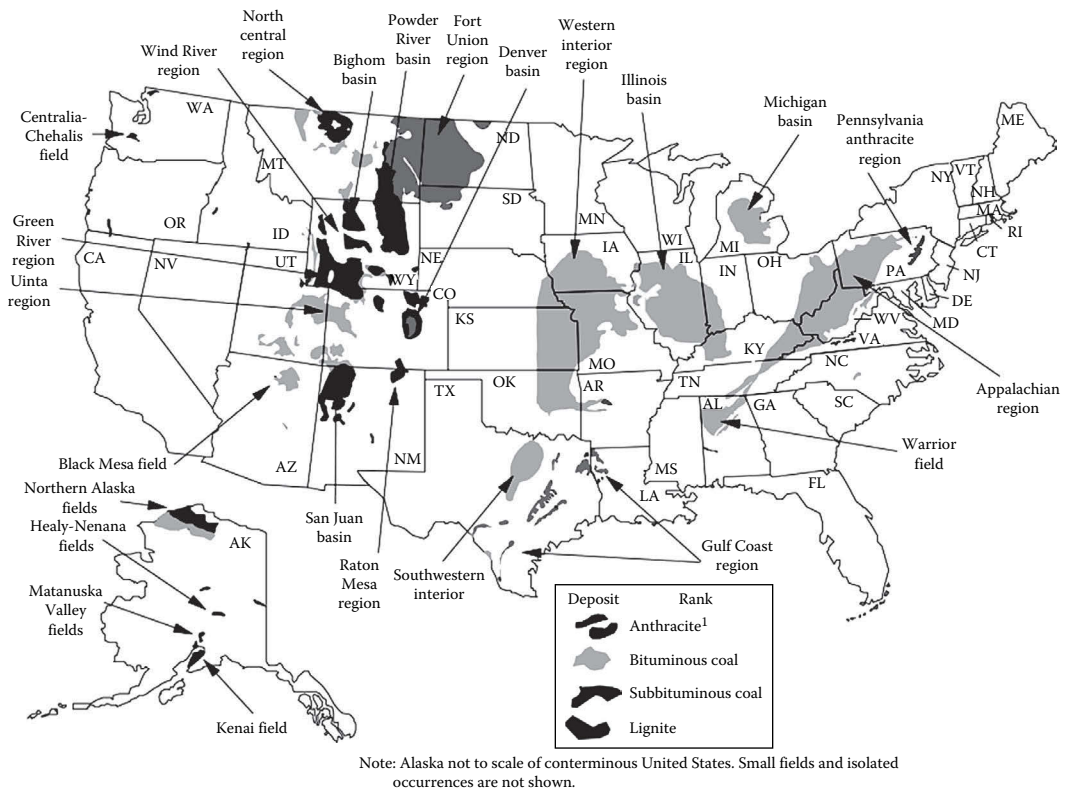
However, the reactivity of a coal also varies depending upon what conversion is attempted. That is, the reactivity of a coal toward combustion (or oxidation) is not the same as its reactivity toward liquefaction, and the order of reactivity established in a series of coals for one conversion process will not necessarily be the same as that for another process.

2.1.3 Coal Reserves

Coal is found throughout the U.S. and the world. It is the most abundant fossil energy resource in the U.S. and the world, comprising 95% of U.S. fossil energy resources and 70% of world fossil energy resources on an energy content basis. All coal ranks can be found in the U.S. The largest resources in the U.S. are made up of lignite and subbituminous coals, which are found primarily in the western part of the country, including Alaska. Bituminous coals are found principally in the Midwest states, northern Alaska, and the Appalachian region. Principal deposits of anthracite coal are found in northeastern Pennsylvania.

The Alaskan coals have not been extensively mined because of their remoteness and the harsh climate. Of the other indigenous coals, the anthracite coals have been heavily mined to the point that little economic resource remains. The bituminous coals continue to be heavily mined in the lower 48 states, especially those with sulfur contents less than 2.5 wt%. The lignite and subbituminous coals in the western U.S. have been historically less heavily mined because of their distance from large population centers and because of their low calorific values and high moisture and ash contents. However, with the enactment of the 1990 Clean Air Act Amendments, these coals are now displacing high sulfur-containing coals for use in the eastern U.S. A map showing the general distribution of coal in the U.S. is included as Figure 2.1.

The amount of coal that exists is not known exactly and is continually changing as old deposits are mined out and new deposits are discovered or reclassified. Estimates are published by many different groups throughout the world. In the U.S., the Energy Information Administration (EIA), an office within the U.S. Department of Energy, gathers and publishes estimates from various sources. The most commonly used definitions for classifying the estimates are provided below.



Note: Alaska not to scale of conterminous United States. Small fields and isolated occurrences are not shown.

¹ Principal anthracite deposits are in Pennsylvania. Small deposits occur in Alaska, Arkansas, Colorado, Massachusetts-Rhode Island, New Mexico, Utah, Virginia, Washington, and West Virginia.

FIGURE 2.1
U.S. coal deposits.

2.1.4 Important Terminology: Resources, Reserves, and the Demonstrated Reserve Base*

Resources are naturally occurring concentrations or deposits of coal in the Earth's crust, in such forms and amounts that economic extraction is currently or potentially feasible.

Measured resources refers to coal for which estimates of the rank and quantity have been computed to a high degree of geologic assurance, from sample analyses and measurements from closely spaced and geologically well-known sample sites. Under the U.S. Geological Survey (USGS) criteria, the points of observation are no greater than ½ mile apart. Measured coal is projected to extend as a ¼-mile-wide belt from the outcrop or points of observation or measurement.

* For a full discussion of coal resources and reserve terminology as used by EIA, USGS, and the Bureau of Mines, see U.S. Coal Reserves, 1996, Appendix A, "Specialized Resource and Reserve Terminology." Sources: U.S. Department of the Interior, Coal Resource Classification System of the U.S. Bureau of Mines and the U.S. Geological Survey, Geological Survey Bulletin 1450-B (1976). U.S. Department of the Interior, Coal Resource Classification System of the U.S. Geological Survey, Geological Survey Circular 891 (1983) U.S. Department of the Interior, A Dictionary of Mining, Mineral, and Related Terms, Bureau of Mines (1968).

Indicated resources refers to coal for which estimates of the rank, quality, and quantity have been computed to a moderate degree of geologic assurance, partly from sample analyses and measurements and partly from reasonable geologic projections. Under the USGS criteria, the points of observation are from ½ to 1½ miles apart. Indicated coal is projected to extend as a ¼-mile-wide belt that lies more than ... mile from the outcrop or points of observation or measurement.

Demonstrated resources are the sum of measured resources and indicated resources.

Demonstrated reserve base (DRB; or simply “reserve base” in USGS usage) is, in its broadest sense, defined as those parts of identified resources that meet specified minimum physical and chemical criteria related to current mining and production practices, including those for quality, depth, thickness, rank, and distance from points of measurement. The “reserve base” is the in-place demonstrated resource from which reserves are estimated. The reserve base may encompass those parts of a resource that have a reasonable potential for becoming economically recoverable within planning horizons that extend beyond those that assume proven technology and current economics.

Inferred resources refers to coal of a low degree of geologic assurance in unexplored extensions of demonstrated resources for which estimates of the quality and size are based on geologic evidence and projection. Quantitative estimates are based on broad knowledge of the geologic character of the bed or region from which few measurements or sampling points are available and on assumed continuation from demonstrated coal for which geologic evidence exists. The points of measurement are from ½ to 6 miles apart. Inferred coal is projected to extend as a 2¼-mile-wide belt that lies more than ¾ mile from the outcrop or points of observation or measurement. Inferred resources are not part of the DRB.

Recoverable refers to coal that is, or can be, extracted from a coalbed during mining.

Reserves relates to that portion of demonstrated resources that can be recovered economically with the application of extraction technology available currently or in the foreseeable future. Reserves include only recoverable coal; thus, terms such as “minable reserves,” “recoverable reserves,” and “economic reserves” are redundant. Even though “recoverable reserves” is redundant, implying recoverability in both words, EIA prefers this term specifically to distinguish recoverable coal from in-ground resources, such as the demonstrated reserve base, that are only partially recoverable.

Minable refers to coal that can be mined using present-day mining technology under current restrictions, rules, and regulations.

The demonstrated reserve base for coals in the U.S. as of January 1, 2001, is approximately 501.1 billion (short) tons. It is broken out by rank, state, and mining method (surface or underground) in Table 2.5. As of December 31, 1999 (December 31, 2000, for the U.S.), the world recoverable reserves are estimated to be 1083 billion (short) tons. A breakdown by region and country is provided in Table 2.6. The recoverability factor for all coals can vary from approximately 40 to over 90%, depending on the individual deposit. The recoverable reserves in the U.S. represent approximately 54% of the demonstrated reserve base as of January 1, 2001. Thus, the U.S. contains approximately 25% of the recoverable reserves of coal in the world.

2.1.5 Transportation

Most of the coal mined and used domestically in the U.S. is transported by rail from the mine mouth to its final destination. In 1998, 1119 million short tons of coal were distributed domestically. Rail constituted 58.3% of the tonnage, followed by water at 21.4%; truck at

TABLE 2.5

U.S. Coal Demonstrated Reserve Base, January 1, 2001

Region and State	Anthracite	Bituminous Coal		Subbituminous Coal		Lignite	Total		Total
		Underground	Surface	Underground	Surface	Surface ^a	Underground	Surface	
Appalachian	7.3	72.9	23.7	0.0	0.0	1.1	76.9	28.1	105.0
Appalachian	7.3	7.40	24.0	0.0	0.0	1.1	78.0	28.5	106.5
Alabama	0.0	1.2	2.1	0.0	0.0	1.1	1.2	3.2	4.4
Kentucky, eastern	0.0	1.7	9.6	0.0	0.0	0.0	1.7	9.6	11.3
Ohio	0.0	17.7	5.8	0.0	0.0	0.0	17.7	5.8	23.5
Pennsylvania	7.2	19.9	1.0	0.0	0.0	0.0	23.8	4.3	28.1
Virginia	0.1	1.2	0.6	0.0	0.0	0.0	1.3	0.6	2.0
West Virginia	0.0	30.1	4.1	0.0	0.0	0.0	30.1	4.1	34.2
Other ^b	0.0	1.1	0.4	0.0	0.0	0.0	1.1	0.4	1.5
Interior	0.1	117.8	27.5	0.0	0.0	13.1	117.9	40.7	158.6
Illinois	0.0	88.2	16.6	0.0	0.0	0.0	88.2	16.6	104.8
Indiana	0.0	8.8	0.9	0.0	0.0	0.0	8.8	0.9	9.7
Iowa	0.0	1.7	0.5	0.0	0.0	0.0	1.7	0.5	2.2
Kentucky, western	0.0	16.1	3.7	0.0	0.0	0.0	16.1	3.7	19.7
Missouri	0.0	1.5	4.5	0.0	0.0	0.0	1.5	4.5	6.0
Oklahoma	0.0	1.2	0.3	0.0	0.0	0.0	1.2	0.3	1.6
Texas	0.0	0.0	0.0	0.0	0.0	12.7	0.0	12.7	12.7
Other ^c	0.1	0.3	1.1	0.0	0.0	0.5	0.4	1.6	2.0
Western	(s)	22.3	2.3	121.3	61.8	29.6	143.7	93.7	237.4
Alaska	0.0	0.6	0.1	4.8	0.6	(s)	5.4	0.7	6.1
Colorado	(s)	8.0	0.6	3.8	0.0	4.2	11.8	4.8	16.6
Montana	0.0	1.4	0.0	69.6	32.8	15.8	71.0	48.5	119.5

(Continued)

TABLE 2.5 (Continued)

U.S. Coal Demonstrated Reserve Base, January 1, 2001

Region and State	Anthracite	Bituminous Coal		Subbituminous Coal		Lignite	Total		Total
		Underground	Surface	Underground	Surface	Surface ^a	Underground	Surface	
New Mexico	(s)	2.7	0.9	3.5	5.2	0.0	6.2	6.1	12.3
North Dakota	0.0	0.0	0.0	0.0	0.0	9.2	0.0	9.2	9.2
Utah	0.0	5.4	0.3	0.0	0.0	0.0	5.4	0.3	5.6
Washington	0.0	0.3	0.0	1.0	(s)	(s)	1.3	0.0	1.4
Wyoming	0.0	3.8	0.5	38.7	23.2	0.0	42.5	23.7	66.2
Other ^d	0.0	0.1	0.0	(s)	(s)	0.4	0.1	0.4	0.5
U.S. total	7.5	213.1	53.5	121.3	61.8	43.8	338.5	162.5	501.1
States east of the Mississippi River	7.3	186.1	44.8	0.0	0.0	1.1	190.1	49.3	239.4
States west of the Mississippi River	0.1	27.0	8.7	121.3	61.8	42.7	148.4	113.3	261.7

Source: Energy Information Administration, Coal Reserves Data Base.

Notes: (s)=Less than 0.05 billion short tons. Data represent known measured and indicated coal resources meeting minimum seam and depth criteria, in the ground as of January 1, 2001. These coal resources are not totally recoverable. Net recoverability ranges from 0% to more than 90%. Fifty-four percent of the demonstrated reserve base of coal in the United States is estimated to be recoverable. Totals may not equal sum of components due to independent rounding.

^a Lignite resources are not mined underground in the U.S.

^b Georgia, Maryland, North Carolina, and Tennessee.

^c Arkansas, Kansas, Louisiana, and Michigan.

^d Arizona, Idaho, Oregon, and South Dakota.

TABLE 2.6

World Recoverable Reserves of Coal

Region/Country	Recoverable Anthracite and Bituminous	Recoverable Lignite and Subbituminous	Total Recoverable Coal
North America			
Canada	3,826	3,425	7,251
Greenland	0	202	202
Mexico	948	387	1,335
U.S.	126,804	146,852	273,656
Total	131,579	150,866	282,444
Central and South America			
Argentina	0	474	474
Bolivia	1	0	1
Brazil	0	13,149	13,149
Chile	34	1,268	1,302
Colombia	6,908	420	7,328
Ecuador	0	26	26
Peru	1,058	110	1,168
Venezuela	528	0	528
Total	8,530	15,448	23,977
Western Europe			
Austria	0	28	28
Croatia	7	36	43
France	24	15	40
Germany	25,353	47,399	72,753
Greece	0	3,168	3,168
Ireland	15	0	15
Italy	0	37	37
Netherlands	548	0	548
Norway	0	1	1
Portugal	3	36	40
Slovenia	0	303	303
Spain	220	507	728
Sweden	0	1	1
Turkey	306	3,760	4,066
United Kingdom	1,102	551	1,653
Yugoslavia	71	17,849	17,919
Total	27,650	73,693	101,343
Eastern Europe and former U.S.S.R.			
Bulgaria	14	2,974	2,988
Czech Republic	2,330	3,929	6,259
Hungary	0	1,209	1,209
Kazakhstan	34,172	3,307	37,479
Kyrgyzstan	0	895	895
Poland	22,377	2,050	24,427
Romania	1	1,605	1,606

(Continued)

TABLE 2.6 (Continued)

World Recoverable Reserves of Coal

Region/Country	Recoverable Anthracite and Bituminous	Recoverable Lignite and Subbituminous	Total Recoverable Coal
Russia	54,110	118,964	173,074
Slovakia	0	190	190
Ukraine	17,939	19,708	37,647
Uzbekistan	1,102	3,307	4,409
Total	132,046	158,138	290,183
Middle East			
Iran	1,885	0	1,885
Total	1,885	0	1,885
Africa			
Algeria	44	0	44
Botswana	4,740	0	4,740
Central African Republic	0	3	3
Congo (Kinshasa)	97	0	97
Egypt	0	24	24
Malawi	0	2	2
Mozambique	234	0	234
Niger	77	0	77
Nigeria	23	186	209
South Africa	54,586	0	54,586
Swaziland	229	0	229
Tanzania	220	0	220
Zambia	11	0	11
Zimbabwe	553	0	553
Total	60,816	216	61,032
Far East and Oceania			
Afghanistan	73	0	73
Australia	46,903	43,585	90,489
Burma	2	0	2
China	68,564	57,651	126,215
India	90,826	2,205	93,031
Indonesia	571	5,049	5,919
Japan	852	0	852
Korea, North	331	331	661
Korea, South	86	0	86
Malaysia	4	0	4
Nepal	2	0	2
New Caledonia	2	0	2
New Zealand	36	594	631
Pakistan	0	2,497	2,497
Philippines	0	366	366

(Continued)

TABLE 2.6 (Continued)

World Recoverable Reserves of Coal

Region/Country	Recoverable Anthracite and Bituminous	Recoverable Lignite and Subbituminous	Total Recoverable Coal
Taiwan	1	0	1
Thailand	0	1,398	1,398
Vietnam	165	0	165
Total	208,719	113,675	322,394
World total	571,224	512,035	1,083,259

Sources: World Energy Council, Survey of Energy Resources 2001, October 2001. U.S. Energy Information Administration. Unpublished file data of the Coal Reserves Data Base (February 2002).

Notes: The estimates in this table are dependent on the judgment of each reporting country to interpret local economic conditions and its own mineral assessment criteria in terms of specified standards of the World Energy Council. Consequently, the data may not all meet the same standards of reliability, and some data may not represent reserves of coal known to be recoverable under current economic conditions and regulations. Some data represent estimated recovery rates for highly reliable estimates of coal quantities in the ground that have physical characteristics like those of coals currently being profitably mined. U.S. coal rank approximations are based partly on Btu content and may not precisely match borderline geologic ranks. Data for the U.S. represent recoverable coal estimates as of December 31, 2000. Data for other countries are as of December 31, 1999.

Millions of tons.

11.0%; and tramway, conveyor, or slurry pipeline at 9.2%. The remaining 0.1% is listed as "unknown method." Water's share includes transportation on the Great Lakes, all navigable rivers, and on tidewaters (EIA 1999).

In general, barge transportation is cheaper than rail transportation. However, this advantage is reduced for distances over 300 miles (Villagran 1989). For distances less than 100 miles, rail is very inefficient, and trucks are used primarily, unless water is available as a mode of transport.

Prior to the signing of the 1990 Clean Air Act Amendments, most coal was transported to the closest power plant or other end-use facility to reduce transportation costs. Because most coal-fired plants are east of the Mississippi River, most of the coal was transported from eastern coal mines. However, once the amendments, which required sulfur emissions to be more strictly controlled, began to be enforced, the potential economic advantage of transporting and using low-sulfur western coals compared to installing expensive cleanup facilities in order to continue to use high-sulfur eastern coals began to be considered. This resulted in increasing the average distance coal was shipped from 640 miles in 1988 to 793 miles in 1997.

In comparing shipments from coal-producing regions, the trend of Figure 2.2 shows that an increasing share of coal was shipped from the low-sulfur coal producing Powder River Basin between 1988 and 1997 and that less coal was shipped from the high-sulfur coal producing Central Appalachian Basin. Overall, coal use continued to increase at about 2.2% per year over this timeframe.

The cost of transporting coal decreased between 1988 and 1997, due to the increased competition from the low-sulfur western coals following passage of the Clean Air Act Amendments in 1990. This decrease held for all sulfur levels, except for a slight increase in medium sulfur B coals over the last couple of years, as shown in Figure 2.3.

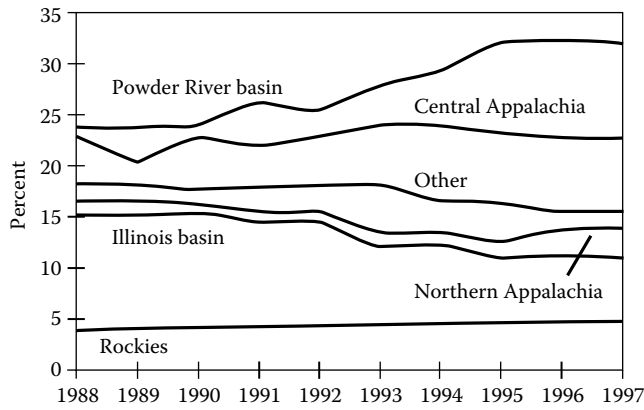


FIGURE 2.2 Supply region shares of domestic coal distribution. (From Energy Information Administration, EIA-6, “Coal Distribution Report.”)

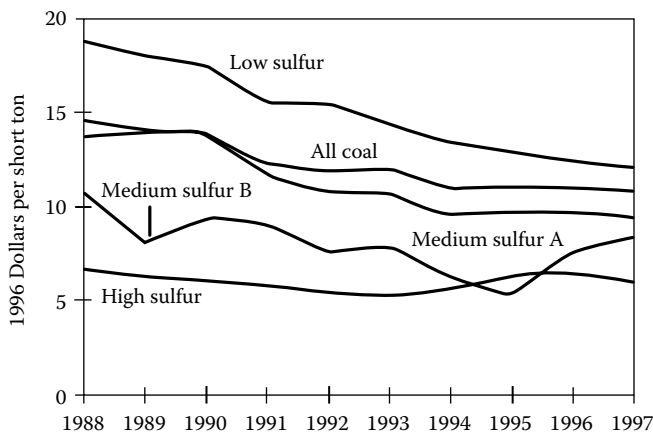


FIGURE 2.3 Average rate per ton for contract coal shipments by rail, by sulfur category, 1988–1997. Notes: low sulfur=less than or equal to 0.6lb of sulfur per million Btu; medium sulfur A=0.61–1.25 lb per million Btu; medium sulfur B=1.26–1.67 lb per million Btu; high sulfur=greater than 1.67 lb per million Btu. 1997. (From Energy Information Administration, Coal Transportation Rate Database.)

2.2 Environmental Aspects

Richard Bajura

Along with coal production and use comes a myriad of potential environmental problems, most of which can be ameliorated or effectively addressed during recovery, processing, conversion, or reclamation. Underground coal reserves are recovered using the two principal methods of room-and-pillar mining (60%) and longwall mining (40%). In room-and-pillar mining, coal is removed from the seam in a checkerboard pattern

(the “room”) as viewed from above, leaving pillars of coal in an alternate pattern to support the roof of the mine. When using this technology, generally half of the reserves are left underground. Depending upon the depth of the seam and characteristics of the overburden, subsidence due to the removal of the coal may affect the surface many years after the mining operation is completed. Because of the danger of collapse and movement of the surface, undermined lands are not used as building sites for large, heavy structures.

Longwall mining techniques employ the near-continuous removal of coal in rectangular blocks with a vertical cross section equal to the height of the seam multiplied by the horizontal extent (width) of the panel being mined. As the longwall cutting heads advance into the coal seam, the equipment is automatically moved forward. The roof of the mine collapses behind the shields, and most of the effects of subsidence are observed on the surface within several days of mining. If the longwall mining operation proceeds in a continuous fashion, subsidence may occur smoothly so that little damage occurs to surface structures. Once subsidence has occurred, the surface remains stable into the future. Longwall mining operations may influence water supplies as a result of fracturing of water-bearing strata far removed from the panel being mined.

When coal occurs in layers containing quartz dispersed in the seam or in the overburden, miners are at risk of exposure to airborne silica dust, which is inhaled into their lungs. Coal workers’ pneumoconiosis, commonly called black lung disease, reduces the ability of a miner to breathe because of the effects of fibrosis in the lungs.

Surface mining of coal seams requires the removal of large amounts of overburden, which must eventually be replaced into the excavated pit after the coal resource is extracted. When the overburden contains large amounts of pyrite, exposure to air and water produces a discharge known as acid mine drainage, which can contaminate streams and waterways. Iron compounds formed as a result of the chemical reactions precipitate in the streams and leave a yellow- or orange-colored coating on rocks and gravel in the streambeds. The acid caused by the sulfur in the pyrite has been responsible for significant destruction of aquatic plants and animals. New technologies have been and continue to be developed to neutralize acid mine drainage through amendments applied to the soil during the reclamation phases of the mining operation. Occasionally, closed underground mines fill with water and sufficient pressure is created to cause “blowouts” where the seams reach the surface. Such discharges have also been responsible for massive fish kills in receiving streams.

The potential for acid rain deposition from sulfur and nitrogen oxides released to the atmosphere during combustion is a significant concern. About 95% of the sulfur oxide compounds can be removed through efficient stack gas cleaning processes such as wet and dry scrubbing. Also, techniques are available for removing much of the sulfur from the coal prior to combustion. Combustion strategies are also being developed that reduce the formation and subsequent release of nitrogen oxides.

The potential for greenhouse warming due to emissions of carbon dioxide during combustion (as well as methane during mining and mine reclamation) has also been raised as a significant concern. Because coal is largely composed of carbon with relatively little hydrogen, its combustion leads to a higher level of carbon dioxide emissions per unit of energy released than for petroleum-based fuels or natural gas.

Defining Terms

Coalification: The physicochemical transformation that coal undergoes after being buried and subjected to elevated temperature and pressure. The classification of a particular coal by rank is a measure of the extent of its coalification. Thus, coalification is a measure of the “age” of a particular coal.

Fixed carbon content: One of the constituents that make up the proximate analysis of a coal. It is normally measured by difference. That is, one measures the volatile matter content and the moisture and ash contents, if the fixed carbon content is reported on a basis containing one or both of those constituents, and subtracts the result(s) from 100% to find the fixed carbon content. One should not confuse the fixed carbon content of a coal with its (elemental) carbon content found in the ultimate analysis. Although carbon is certainly in the material making up the fixed carbon content, it is not all of the carbon present in the original coal, and other elements are also present.

Gross calorific value: Calorific value is a measure of the energy content of a material—in this case, a coal sample. Calorific value is measured by ASTM Standard Test Method D 2015M, Gross Calorific Value of Solid Fuel by the Adiabatic Bomb Calorimeter, or by ASTM Standard Test Method D 3286, Gross Calorific Value of Solid Fuel by the Isothermal-Jacket Bomb Calorimeter. The *gross* calorific value takes into account the additional heat gained by condensing any water present in the products of combustion, in contrast to the *net* calorific value, which assumes that all water remains in the vapor state.

Maceral: An organic substance or optically homogeneous aggregate of organic substance in a coal sample that possesses distinctive physical and chemical properties.

Proximate analysis: A method to measure the content of four separately identifiable constituents in a coal: volatile matter content; fixed carbon content; moisture content; and ash content, all of which are reported on a weight percent basis. The standard method for obtaining the proximate analysis of coal or coke is defined by the ASTM in Standard Test Method D 3172.

Rank: A classification scheme for coals that describes the extent of coalification that a particular coal has undergone. The structure, chemical composition, and many other properties of coals vary systematically with rank. The standard method for determining the rank of a coal sample is defined by the ASTM in Standard Test Method D 388.

Type: A classification scheme for coals that references the original plant material from which the coal was derived.

Ultimate analysis: A method to measure the elemental composition of a coal sample. Typical ultimate analyses include carbon, hydrogen, oxygen, sulfur, and nitrogen contents, but other elements can also be reported. These other elements are usually not present to any appreciable extent. However, if they are reported, the sum of all the elements reported (including moisture and ash content) should equal 100%. The standard method for the ultimate analysis of coal or coke is defined by the ASTM in Standard Test Method D 3176.

Volatile matter content: The mass of material released upon heating the coal sample under specific conditions, defined by the ASTM Standard Test Method D 3175.

References

- Elliott, M. A. and Yohe, G. R. 1981. The coal industry and coal research and development in perspective. In *Chemistry of Coal Utilization. Second Supplementary Volume*, M. A. Elliott, ed., pp. 26–328. Wiley, New York.
- Habermehl, D., Orywal, F., and Beyer, H.-D. 1981. Plastic properties of coal. In *Chemistry of Coal Utilization. Second Supplementary Volume*, M. A. Elliott, ed., pp. 319–328. Wiley, New York.
- Villagran, R. A. 1989. *Acid Rain Legislation: Implications for the Coal Industry*, pp. 37–39. Shearson, Lehman, Button, New York.
-

For Further Information

An excellent resource for understanding coal, its sources, uses, limitations, and potential problems is the book by Elliott referenced under Elliott and Yohe (1981) and Habermehl et al. (1981). A reader wishing an understanding of coal topics could find no better resource. Another comprehensive book, which includes more-recent information but is not quite as weighty as Elliott's (664 pages vs. 2374 pages), is *The Chemistry and Technology of Coal*, edited (second edition, revised and expanded) by James G. Speight. For information specific to the environmental problems associated with the use of coal, the reader is referred to Norbert Berkowitz's chapter entitled "Environmental Aspects of Coal Utilization" in *An Introduction to Coal Technology*. For information on the standards for coal analyses and descriptions of the associated procedures, the reader is referred to any recent edition of the ASTM's *Annual Book of ASTM Standards*. Section 5 covers petroleum products, lubricants, and fossil fuels, including coal and coke.

2.3 Oil

Philip C. Crouse

2.3.1 Overview

The U.S. Department of Energy's Energy Information Administration (EIA) annually provides a wealth of information concerning most energy forms including fossil fuels. The oil and natural gas sections are extracted summaries for the most germane information concerning oil and natural gas. Fossil fuel energy continues to account for over 85% of all world energy in 2000. The EIA estimates that in 2025, fossil fuels will still dominate energy resources with natural gas having the most growth. The base case of the EIA predicts that world energy consumption will grow by 60% over the next two decades. Figure 2.4 shows steady growth in global energy consumption. The projections show that in 2025 the world will consume three times the energy it consumed in 1970.

In the United States, wood served as the preeminent form of energy for about half of the nation's history. Around the 1880s, coal became the primary source of energy. Despite its tremendous and rapid expansion, coal was overtaken by petroleum in the middle of the 1900s. Natural gas, too, experienced rapid development into the second half of the

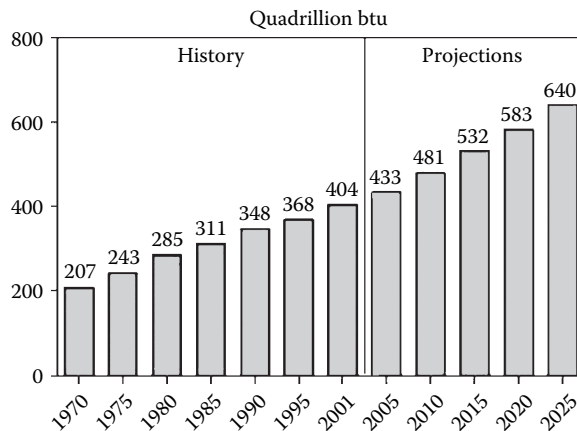


FIGURE 2.4

World energy consumption, 1970–2025. (History from EIA, *International Energy Annual 2001*, DOE/EIA-0219(2001), Washington, DC, Feb. 2003, www.eia.doe.gov/iea/. Projections from EIA, *System for the analysis of Global Energy Markets* (2003).)

20th century, and coal began to expand again. Late in the 1900s, nuclear electric power was developed and made significant contributions.

Although the world's energy history is one of large-scale change as new forms of energy have been developed, the outlook for the next couple of decades is for continued growth and reliance on the three major fossil fuels of petroleum, natural gas, and coal. Only modest expansion will take place in renewable resources and relatively flat generation from nuclear electric power, unless major breakthroughs occur in energy technologies. Table 2.7 shows EIA's estimate of growth of selected energy types with oil needs dominating the picture over the next 20 years.

2.3.2 Crude Oil Classification and World Reserves

Obtaining accurate estimates of world petroleum and natural gas resources and reserves is difficult and uncertain, despite excellent scientific analysis made over the years. Terminology standards used by industry to classify resources and reserves has progressed over the last 10 years with the Society of Petroleum Evaluation Engineers leading an effort to establish a set of standard definitions that would be used by all countries in reporting reserves. Classifications of reserves, however, continue to be a source of controversy in the international oil and gas community. This subsection uses information provided by the Department of Energy classification system. The next chart shows the relationship of resources to reserves. **Recoverable reserves** include discovered and undiscovered resources. **Discovered resources** are those resources that can be economically recovered. Figure 2.5 shows the relationship of petroleum resource and reserves terms.

Discovered resources include all production already out of the ground and reserves. Reserves are further broken down into proved reserves and other reserves. Again, many different groups classify reserves in different ways, such as measured, indicated, internal, probable, and possible. Most groups break reserves into producing and nonproducing categories. Each of the definitions is quite voluminous and the techniques for qualifying reserves vary globally. Table 2.8 shows estimates made by the EIA for total world oil resources.

TABLE 2.7

World Total Energy Consumption by Region and Fuel, Reference Case, 1990–2025

Region/Country	History			Projections					Average Annual Percent Change, 2001–2025
	1990	2000	2001	2005	2010	2015	2020	2025	
Industrialized Countries									
North America									
Oil	40.4	46.3	45.9	48.3	54.2	59.7	64.3	69.3	1.7
Natural Gas	23.1	28.8	27.6	30.6	34.0	37.9	42.0	46.9	2.2
Coal	20.7	24.5	23.9	24.9	27.3	28.7	30.0	31.8	1.2
Nuclear	6.9	8.7	8.9	9.4	9.6	9.7	9.7	9.5	0.3
Other	9.5	10.6	9.4	11.3	12.0	12.7	13.4	13.9	1.7
Total	100.6	118.7	115.6	124.6	137.2	148.7	159.4	171.4	1.7
Western Europe									
Oil	25.8	28.5	28.9	29.2	29.7	30.3	30.6	31.6	0.4
Natural gas	9.7	14.9	15.1	15.9	17.5	20.1	23.4	26.4	2.4
Coal	12.4	8.4	8.6	8.3	8.2	7.5	6.8	6.7	-1.0
Nuclear	7.4	8.8	9.1	8.9	9.1	8.8	8.1	6.9	-1.1
Other	4.5	6.0	6.1	6.8	7.5	8.0	8.4	8.8	1.5
Total	59.9	66.8	68.2	69.1	72.1	74.7	77.3	80.5	0.7
Industrialized Asia									
Oil	12.1	13.2	13.0	13.5	14.3	15.1	15.8	16.7	1.1
Natural gas	2.5	4.0	4.1	4.4	4.6	5.0	5.3	5.9	1.5
Coal	4.2	5.7	5.9	5.8	6.3	6.7	7.0	7.4	0.9
Nuclear	2.0	3.0	3.2	3.2	3.6	3.9	4.0	3.9	0.9
Other	1.6	1.6	1.6	1.9	2.0	2.1	2.3	2.4	1.7
Total	22.3	27.5	27.7	28.8	30.8	32.8	34.4	36.4	1.1
Total industrialized									
Oil	78.2	88.1	87.8	90.9	98.2	105.1	110.7	117.6	1.2
Natural Gas	35.4	47.7	46.8	50.9	56.1	63.0	70.7	79.2	2.2
Coal	37.3	38.6	38.5	39.1	41.9	42.9	43.7	45.9	0.7
Nuclear	16.3	20.5	21.2	21.5	22.3	22.3	21.8	20.4	-0.2
Other	15.6	18.2	17.1	20.0	21.6	22.8	24.0	25.2	1.6
Total	182.8	213.0	211.5	222.5	240.1	256.2	271.1	288.3	1.3
EE/FSU									
Oil	21.0	10.9	11.0	12.6	14.2	15.0	16.5	18.3	2.1
Natural gas	28.8	23.3	23.8	27.9	31.9	36.9	42.0	47.0	2.9
Coal	20.8	12.2	12.4	13.7	12.7	12.5	11.2	10.2	-0.8
Nuclear	2.9	3.0	3.1	3.3	3.3	3.3	3.0	2.6	-0.7
Other	2.8	3.0	3.2	3.6	3.7	3.9	4.0	4.1	1.1
Total	76.3	52.2	53.3	61.1	65.9	71.6	76.7	82.3	1.8

(Continued)

TABLE 2.7 (Continued)

World Total Energy Consumption by Region and Fuel, Reference Case, 1990–2025

Region/Country	History			Projections					Average Annual Percent Change, 2001–2025
	1990	2000	2001	2005	2010	2015	2020	2025	
Developing Countries									
Developing Asia									
Oil	16.1	30.2	30.7	33.5	38.9	45.8	53.8	61.9	3.0
Natural gas	3.2	6.9	7.9	9.0	10.9	15.1	18.6	22.7	4.5
Coal	29.1	37.1	39.4	41.3	49.4	56.6	65.0	74.0	2.7
Nuclear	0.9	1.7	1.8	2.6	3.1	4.1	4.5	5.0	4.3
Total	52.5	80.5	85.0	92.5	110.1	130.5	151.9	174.6	3.0

Quadrillion Btu.

Source: International Energy Outlook-2003, U.S. Dept. of Energy, Energy Information Administration.

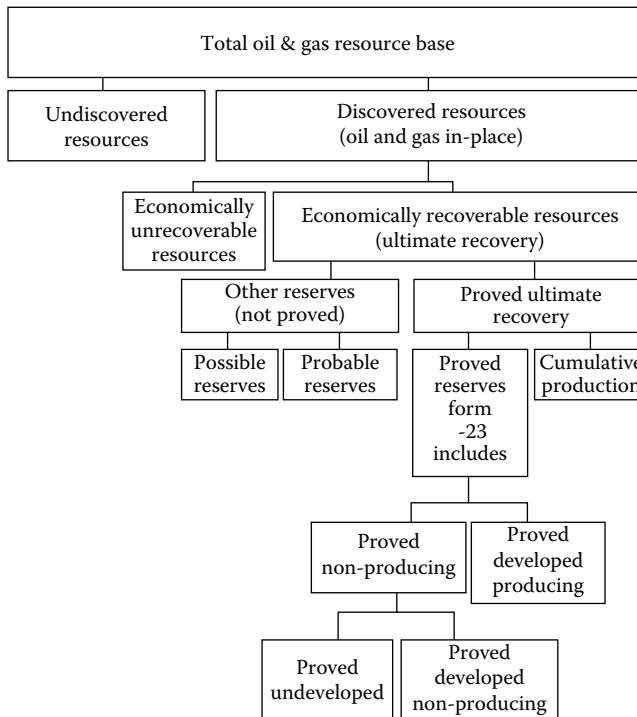


FIGURE 2.5

Components of the oil and gas resource base. (From EIA, Office of Gas and Oil.)

TABLE 2.8

Estimated World Oil Resources, 2000–2025

Region and Country	Proved Reserves	Reserve Growth	Undiscovered
Industrialized			
U.S.	22.45	76.03	83.03
Canada	180.02	12.48	32.59
Mexico	12.62	25.63	45.77
Japan	0.06	0.09	0.31
Australia/New Zealand	3.52	2.65	5.93
Western Europe	18.10	19.32	34.58
Eurasia			
Former Soviet Union	77.83	137.70	170.79
Eastern Europe	1.53	1.46	1.38
China	18.25	19.59	14.62
Developing countries			
Central and South America	98.55	90.75	125.31
India	5.37	3.81	6.78
Other developing Asia	11.35	14.57	23.90
Africa	77.43	73.46	124.72
Middle East	685.64	252.51	269.19
Total	1,212.88	730.05	938.90
OPEC	819.01	395.57	400.51
Non-OPEC	393.87	334.48	538.39

Source: U.S. Geological Survey, *World Petroleum Assessment 2000*, web site <http://greenwood.cr.usgs.gov/energy/WorldEnergy/DDS-60>.

Note: Resources include crude oil (including lease condensates) and natural gas plant liquids. Billion barrels.

2.3.3 Standard Fuels

Petroleum is refined into petroleum products that are used to meet individual product demands. The general classifications of products are:

1. *Natural gas liquids and liquefied refinery gases*. This category includes ethane (C_2H_6); ethylene (C_2H_4); propane (C_3H_8); propylene (C_3H_6); butane and isobutane (C_4H_{10}); and butylene and isobutylene (C_4H_8).
2. *Finished petroleum products*. This category includes motor gasoline; aviation gasoline; jet fuel; kerosene; distillate; fuel oil; residual fuel oil; petrochemical feed stock; naphthas; lubricants; waxes; petroleum coke; asphalt and road oil; and still gas.
 - *Motor gasoline* includes reformulated gasoline for vehicles and oxygenated gasoline such as gasohol (a mixture of gasoline and alcohol).
 - *Jet fuel* is classified by use such as industrial or military and naphtha and kerosene type. Naphtha fuels are used in turbo jet and turbo prop aircraft engines and exclude ram-jet and petroleum rocket fuel.
 - *Kerosene* is used for space heaters, cook stoves, wick lamps, and water heaters.
 - *Distillate fuel oil* is broken into subcategories: No. 1 distillate, No. 2 distillate, and No. 4 fuel oil, which is used for commercial burners.

TABLE 2.9

World Crude Oil Refining Capacity, January 1, 2002

Region/Country	Number of Refineries	Thousand Barrels per Day			
		Crude Oil Distillation	Catalytic Cracking	Thermal Cracking	Reforming
North America	180	20,254	6,619	2,450	4,140
Central and South America	70	6,547	1,252	435	447
Western Europe	112	15,019	2,212	1,603	2,214
Eastern Europe and Former U.S.S.R.	87	10,165	778	516	1,353
Middle East	46	6,073	312	406	570
Africa	46	3,202	195	88	387
Asia and Oceania	203	20,184	2,673	421	2,008
World Total	744	81,444	14,040	5,918	11,119

Source: Last updated on 3/14/2003 by DOE/EIA.

- *Petrochemical feedstock* is used in the manufacture of chemicals, synthetic rubber, and plastics.
- *Naphthas* are petroleums with an approximate boiling range of 122°F–400°F.
- *Lubricants* are substances used to reduce friction between bearing surfaces, as process materials, and as carriers of other materials. They are produced from distillates or residues.
Lubricants are paraffinic or naphthenic and separated by viscosity measurement.
- *Waxes* are solid or semisolid material derived from petroleum distillates or residues. They are typically a slightly greasy, light colored or translucent, crystallizing mass.
- *Asphalt* is a cement-like material containing bitumens. *Road oil* is any heavy petroleum oil used as a dust pallatine and road surface treatment.
- *Still gas* is any refinery by-product gas. It consists of light gases of methane; ethane; ethylene; butane; propane; and the other associated gases. Still gas is typically used as a refinery fuel.

Table 2.9 shows *world refining capacity* as of January 1, 2002. The number of oil refineries continues to grow as demands for petroleum products have continued to grow.

2.4 Natural Gas

Philip C. Crouse

2.4.1 Overview

Natural gas has been called the environmentally friendly fossil fuel because it releases fewer harmful contaminants. World production of dry natural gas was 73.7 trillion ft³ and accounted for over 20% of world energy production. In 1990 Russia accounted for about

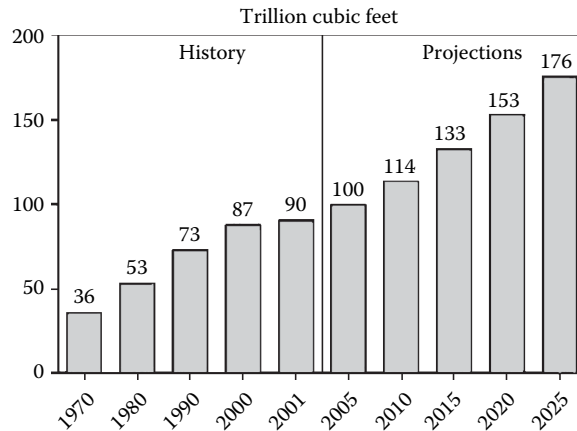


FIGURE 2.6

World natural gas consumption, 1970–2025. (History from EIA, International Energy Annual 2001, DOE/EIA-0219(2001), Washington, DC, Feb. 2003, www.eia.doe.gov/iea/. Projections from EIA, System for the analysis of Global Energy Markets (2003).)

one third of world natural gas. With about one quarter of the world's 1990 natural gas production, the second largest producer was the U.S.

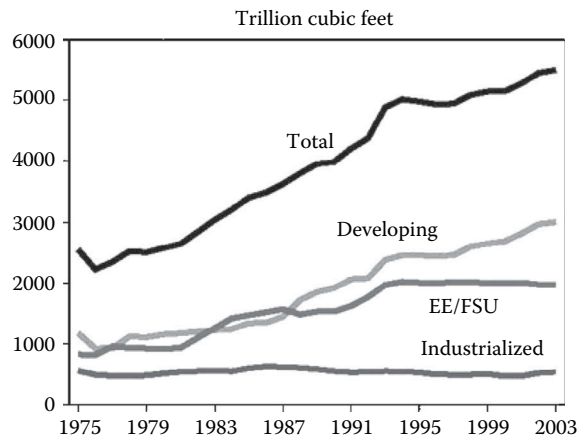
According to the U.S. Department of Energy, natural gas is forecast to be the fastest growing primary energy. Consumption of natural gas is projected to nearly double between 2001 and 2025, with the most robust growth in demand expected among the developing nations. The natural gas share of total energy consumption is projected to increase from 23% in 2001 to 28% in 2025.

Natural gas traded across international borders has increased from 19% of the world's consumption in 1995 to 23% in 2001. The EIA notes that pipeline exports grew by 39% and liquefied natural gas (LNG) trade grew by 55% between 1995 and 2001. LNG has become increasingly competitive, suggesting the possibility for strong worldwide LNG growth over the next two decades. Figure 2.6 shows projections of natural gas consumption in 2025 to be five times the consumption level in 1970.

2.4.2 Reserves and Resources

Since the mid-1970s, world natural gas reserves have generally trended upward each year. As of January 1, 2003, proved world natural gas reserves, as reported by *Oil & Gas Journal*, were estimated at 5501 trillion ft³. Over 70% of the world's natural gas reserves are located in the Middle East and the EE/FSU, with Russia and Iran together accounting for about 45% of the reserves. Reserves in the rest of the world are fairly evenly distributed on a regional basis.

The U.S. Geological Survey (USGS) regularly assesses the long-term production potential of worldwide petroleum resources (oil, natural gas, and natural gas liquids). According to the most recent USGS estimates, released in the *World Petroleum Assessment 2000*, the mean estimate for worldwide undiscovered gas is 4839 trillion ft³. Outside the U.S. and Canada, the rest of the world reserves have been largely unexploited. Outside the U.S., the world has produced less than 10% of its total estimated natural gas endowment and carries more than 30% as remaining reserves. Figure 2.7 shows world natural gas reserves by region from 1975 to 2003. Table 2.10 shows natural gas reserves of the top 20 countries compared to world reserves. Russia, Iran, and Qatar account for over half of estimated world gas reserves.

**FIGURE 2.7**

World natural gas reserves by region, 1975–2003. (Data for 1975–1993 from *Worldwide oil and gas at a glance, International Petroleum Encyclopedia*, Tulsa, OK: PennWell Publishing, various issues. Data for 1994–2003 from *Oil & Gas Journal*, various issues.)

TABLE 2.10

World Natural Gas Reserves by Country as of January 1, 2003

Country	Reserves (trillion ft ³)	Percent of World Total
World	5501	100.0
Top 20 countries	4879	88.7
Russia	1680	30.5
Iran	812	14.8
Qatar	509	9.2
Saudi Arabia	224	4.1
United Arab Emirates	212	3.9
U.S.	183	3.3
Algeria	160	2.9
Venezuela	148	2.7
Nigeria	124	2.3
Iraq	110	2.0
Indonesia	93	1.7
Australia	90	1.6
Norway	77	1.4
Malaysia	75	1.4
Turkmenistan	71	1.3
Uzbekistan	66	1.2
Kazakhstan	65	1.2
Netherlands	62	1.1
Canada	60	1.1
Egypt	59	1.1
Rest of World	622	11.3

Source: *Oil Gas J.*, 100 (December 23, 2002), 114–115.

2.4.3 Natural Gas Production Measurement

Natural gas production is generally measured as “dry” natural gas production. It is determined as the volume of natural gas withdrawn from a reservoir less (1) the volume returned for cycling and repressuring reservoirs; (2) the shrinkage resulting from the removal of lease condensate and plant liquids; and (3) the nonhydrocarbon gases. The parameters for measurement are 60°F and 14.73lb standard per square inch absolute.

2.4.4 World Production of Dry Natural Gas

From 1983 to 1992, dry natural gas production grew from 54.4 to 75 trillion ft³. The breakdown by region of world is shown in Table 2.11.

2.4.5 Compressed Natural Gas

Environmental issues have countries examining and supporting legislation to subsidize the development of cleaner vehicles that use compressed natural gas (CNG). Even with a push toward the use of CNG- burning vehicles, the numbers are quite small when compared with gasoline vehicles. Recent efforts toward car power have been focused on hybrid electric-gasoline cars and fuel cell vehicles.

2.4.6 Liquefied Natural Gas (LNG)

Natural gas can be liquefied by lowering temperature until a liquid state is achieved. It can be transported by refrigerated ships. The process of using ships and providing special-handling facilities adds significantly to the final LNG cost. LNG projects planned by a number of countries may become significant over the next 20 years, with shipments of LNG exports ultimately accounting for up to 25% of all gas exports.

2.4.7 Physical Properties of Hydrocarbons

The most important physical properties from a crude oil classification standpoint are density or specific gravity and the viscosity of liquid petroleum. Crude oil is generally lighter

TABLE 2.11

World Dry Natural Gas Production

Country/Region	1983	1992	2000
North, Central, and South America	21.20	25.30	30.20
Western Europe	6.20	7.85	10.19
Eastern Europe and former U.S.S.R.	21.09	28.60	26.22
Middle East and Africa	2.95	6.87	12.01
Far East and Oceania	<u>2.96</u>	<u>6.38</u>	<u>9.48</u>
World total	54.40	75.00	88.10

Trillion ft³.

Source: From EIA, Annual Energy Review 1993, EIA, Washington, DC, July 1994, 305, and International Energy Outlook-2003.

than water. A Baume-type scale is predominantly used by the petroleum industry and is called the API (American Petroleum Institute) gravity scale (see Table 2.12). It is related directly to specific gravity by the formula:

$$\phi = (141.5)/(131.5 + \text{°API})$$

where ϕ = specific gravity. Temperature and pressure are standardized at 60°F and 1atm pressure.

Other key physical properties involve the molecular weight of the hydrocarbon compound and the boiling point and liquid density. Table 2.13 shows a summation of these properties.

TABLE 2.12

Relation of API Gravity, Specific Gravity, and Weight per Gallon of Gasoline

Degree API	Specific Gravity	Weight of Gallon (lb)
8	1.014	8.448
9	1.007	8.388
10	1.000	8.328
15	0.966	8.044
20	0.934	7.778
25	0.904	7.529
30	0.876	7.296
35	0.850	7.076
40	0.825	6.870
45	0.802	6.675
50	0.780	6.490
55	0.759	6.316
58	0.747	6.216

Note: The specific gravity of crude oils ranges from about 0.75 to 1.01.

TABLE 2.13

Other Key Physical Properties of Hydrocarbons

Compound	Molecular Weight	Boiling Point at 14.7 psia in °F	Liquid Density at 14.7 psia and 60°F-lb/gal
Methane	16.04	-258.7	2.90
Ethane	30.07	-125.7	4.04
Propane	44.09	-43.7	4.233
Isobutane	58.12	10.9	4.695
<i>n</i> -Butane	58.12	31.1	4.872
Isopentane	72.15	82.1	5.209
<i>n</i> -Pentane	72.15	96.9	5.262
<i>n</i> -Hexane	86.17	155.7	5.536
<i>n</i> -Heptane	100.2	209.2	5.738
<i>n</i> -Octane	114.2	258.2	5.892
<i>n</i> -Nonane	128.3	303.4	6.017
<i>n</i> -Decane	142.3	345.4	6.121

Defining Terms

API gravity: A scale used by the petroleum industry for specific gravity.

Discovered resources: Include all production already out of the ground and reserves.

Proved resources: Resources that geological and engineering data demonstrate with reasonable certainty to be recoverable in future years from known reservoirs under existing economic and operating conditions.

Recoverable resources: Include discovered resources.

For Further Information

The Energy Information Agency of the U.S. Department of Energy, Washington, DC, publishes *International Energy Outlook* and other significant publications periodically.

3

Biomass Properties and Resources

Mark M. Wright and Robert C. Brown

CONTENTS

3.1	Introduction.....	61
3.2	Solar Energy Conversion to Biomass.....	61
3.3	Biomass Properties.....	63
3.3.1	Plant Composition.....	63
3.3.2	Biomass Analysis.....	64
3.4	Biomass Resources.....	66
3.4.1	Waste Materials.....	66
3.4.2	Energy Crops.....	67
3.4.3	Algae.....	69
3.5	Land Use for Biomass Production.....	69
	References.....	71

3.1 Introduction

The term “biomass” encompasses a wide range of materials of recent origin classified as either waste or dedicated energy crops. Waste biomass includes any organic material that has negligible apparent value, represents a nuisance, or is a pollutant to the local environment. Dedicated energy crops are biomass grown specifically for the production of biobased products and fuels. This term excludes crops grown for food or feed even though they can also be used to produce energy. It also includes organic material with maturation times of hundreds to millions of years such as fossil fuels and some forest trees with long maturity terms. Biomass is primarily a form of solar energy stored as chemical energy within organic compounds. The solar-to-biomass conversion process involves interactions among numerous factors, leading to different types of biomass.

In the following sections, we describe the principles of solar energy conversion, biomass types and their properties, and the role of land use for crop production. These concepts help to understand the quantity and quality of global biomass resources.

3.2 Solar Energy Conversion to Biomass

Solar energy is the most abundant source of renewable energy on planet earth. Every year, the planet receives 5.6 million exajoules (EJ— 10^{18} J) upon its atmosphere. Given that the world consumes about 570 EJ per year, this is enough energy to supply for several thousand

TABLE 3.1
Photosynthesis Steps and Efficiencies

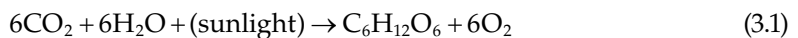
Photosynthesis Step	Total Energy (%)	
Incident solar energy (on leaf surface)	100	
Energy in photosynthetically active spectrum	48.7	
Absorbed energy	43.8	
Photochemically converted energy	37.2	
Carbon fixation pathway	C3	C4
Energy in synthesized carbohydrates	12.6	8.5
Energy available after photorespiration	6.5	8.5
Energy available after respiration	4.6	6.0

Source: Zhu, X.G. et al., *Curr. Opin. Biotechnol.*, 19(2), 153, 2008.

years. Unfortunately, solar energy is very diffuse and difficult to convert efficiently. Most of the atmosphere's solar energy never reaches land surfaces, and only a minuscule amount is converted to biomass.

The planet's atmosphere absorbs, reradiates, and reflects 30% of the incident solar radiation and allows 70% to reach the planet's surface. Earth's surface area consists of 29.2% land, of which about 21% is covered by biomass. Overall, only 6.1% of the atmosphere's solar radiation remains available for biomass production. Plants have developed photosynthetic means of storing solar energy that are suitable for their needs but inefficient in their ability to convert solar to chemical energy.

Table 3.1 compares the percent of total energy captured by C3 and C4 plants after several photosynthesis steps. Starting from 100% of the solar energy available at the plant's surface, only 48.7% is in the photosynthetically active spectrum. The absorbed energy represents 43.8%, and 37.2% of the incident solar energy on the leaf's surface is photochemically converted to biomass energy via carbon fixation. C3 and C4 are carbon fixation pathways labeled after the carbon chain length of the first carbohydrate formed during photosynthesis. The vast majority of plants employ three carbon-chain length molecules to fixate carbon, whereas about 3% of known species employ four carbon-chain carbohydrates. Corn, sugarcane, and sorghum are common C4 plants. The process of photosynthetically converting solar energy into chemical compounds can be generalized by the formula 3.1. This formula describes the conversion of CO₂, H₂O, and sunlight into sugar (glucose) and oxygen.



C3 and C4 plants can theoretically store up to 4.6% and 6.0% of the solar energy on their leaf surfaces into biomass. This is the amount leftover after the energy spent during carbohydrate synthesis, photorespiration, and respiration. C3 plants are more efficient at carbohydrate synthesis and respiration, but C4 plants have an overall higher efficiency, because they avoid photorespiration penalties. In practice, the most efficient conversion measured in C3 and C4 plants is 2.4% and 3.7%, respectively. There are many environmental factors that lower the efficiency of crops in the field including nutrient availability, weather patterns, and pest activity.

The efficiency of solar energy conversion to biomass can be estimated based on the incident energy and biomass available in a given area. Data for solar incident energy measurements are publicly available from sources such as the National Renewable Energy Laboratory [9]. The U.S. Department of Agriculture (USDA) publishes biomass

productivity data (<http://quickstats.nass.usda.gov/>). USDA data are based on above-ground biomass. However, the biomass efficiency calculations should include the amount of belowground biomass that can exceed a quarter of the total biomass material. The ratio of below- to aboveground biomass is commonly known as the root-to-shoot ratio, and values for different crops are available in the literature [3].

3.3 Biomass Properties

3.3.1 Plant Composition

Plant composition and physical properties have a significant impact on biomass energy content. Biomass is commonly characterized by its organic composition, elemental analysis, proximate analysis, and bulk properties such as heating value and bulk density. Table 3.2 shows physical and thermochemical data of representative grain, herbaceous, and woody biomass. Organic composition includes cellulose, hemicellulose, and lignin mass content. Elemental analysis typically reports carbon, hydrogen, oxygen, nitrogen, and ash. Other elements are often reported if they are found in high quantities or important for the target application (such as sulfur for combustion). Proximate analysis is a measure of the moisture content, volatile matter, fixed carbon, and ash content. Heating value is the amount of energy released during complete biomass combustion.

Biomass is mostly composed of lignocellulosic material. Lignocellulose is a term that describes the three-dimensional polymeric composites formed by plants as structural material [1]. Plants contain varying quantities of lignin, cellulose, and hemicellulose.

Lignin is a polymer whose primary function is to provide structural support and protect the plant from microbial activity. Therefore, lignin is a common by-product of biochemical processes, since microbes are unable to easily utilize it as a substrate. On the other hand,

TABLE 3.2

Physical and Thermochemical Properties of Selected Biomass

	Feedstock	Corn Stover	Herbaceous Crop	Woody Crop
Organic composition (wt.%)	Cellulose	53	45	50
	Hemicellulose	15	30	23
	Lignin	16	15	22
	Others	16	10	5
Elemental analysis (dry wt.%)	C	44	47	48
	H	5.6	5.8	5.9
	O	43	42	44
	N	0.6	0.7	0.5
	Ash	6.8	4.5	1.6
Proximate analysis (dry wt.%)	Volatile matter	75	81	82
	Fixed C	19	15	16
	Ash	6	4	1.3
HHV (MJ/kg)		17.7	18.7	19.4
Bulk density (kg/m ³)		160–300	160–300	280–480
Yield (Mg/ha)		8400	14,000	14,000

Source: Brown, R.C., *Biorenewable Resources: Engineering New Products from Agriculture*, Iowa State Press, A Blackwell Publishing Company, Ames, IA, 2003, pp. 59–75.

thermochemical processes can decompose lignin although the products are still hard to predict. Instead of breaking apart into its monomers, lignin decomposition tends to form oligomers from the repolymerization of smaller hydrocarbons. These oligomers can be gasified or catalytically upgraded to desired fuels and chemicals.

Cellulose is a polysaccharide made of glucose chains. Its basic building block is the cellobiose, which consists of two linked glucose units. The typical cellulose chain has a degree of polymerization of 10,000 units. Cellulose tends to agglomerate and with high packing densities can form crystalline cellulose. Crystalline cellulose is inert to chemical treatment and insoluble in most solvents. Cellulose with low packing densities is known as amorphous cellulose. Microbes consume cellulose efficiently, and they can convert it into a variety of chemicals most notably ethanol.

Hemicellulose consists of a large number of heteropolysaccharides built from hexoses, pentoses, and deoxyhexoses. Its degree of polymerization is much lower than cellulose and in the order of 100–200. Hemicellulose requires acid or enzymatic treatment before its sugars become available to microbial activity.

The organic composition of biomass feedstock has a significant impact on the types of processes that can convert it to fuels and chemicals. The proportions of all three organic compounds impact the types and quantities of degradation compounds formed during thermochemical biomass conversion. Furthermore, there are interaction effects among these compounds that are not well understood. Therefore, increasingly powerful analysis techniques are under development to measure not just the quantity but also the physical properties of organic compounds.

3.3.2 Biomass Analysis

Proximate analysis is primarily important in thermochemical applications, because it describes the general evolution of biomass combustion products. Proximate analysis is measured by heating biomass under controlled temperature and heating rate conditions. The total weight loss from holding the biomass temperature at 100°C represents its moisture content. Volatile matter is the fraction of biomass that decomposes into gases at moderate temperatures of about 400°C in an inert environment. The remaining fraction is a mixture of solid carbon (fixed carbon) and mineral matter (ash). The ash content can be determined by introducing oxygen and burning the remaining carbon material.

Ultimate analysis is often reported on a dry, ash-free (daf) basis and often used to estimate thermal biomass properties. One correlation of the higher heating value (HHV) of biomass is the formula 3.2 that is based solely on the feedstock carbon content. Although carbon is the primary factor in determining heating value, oxygen is important because of its detrimental effect to heating value and recalcitrance to removal. Researchers have published alternative HHV correlations that incorporate a greater number of factors.

$$\text{HHV(dry)} \left[\frac{\text{MJ}}{\text{kg}} \right] = 0.4571(\% \text{ C on dry basis}) - 2.70 \quad (3.2)$$

The thermal performance of biomass fuel depends heavily on its heating value. Heating value is the net enthalpy released upon reacting fuel with oxygen at stoichiometric conditions. It is reported on either a lower heating value (LHV) or higher heating value (HHV) basis. The difference between LHV and HHV depends on whether the combustion gases are released above or below the water condensation temperature. Below the

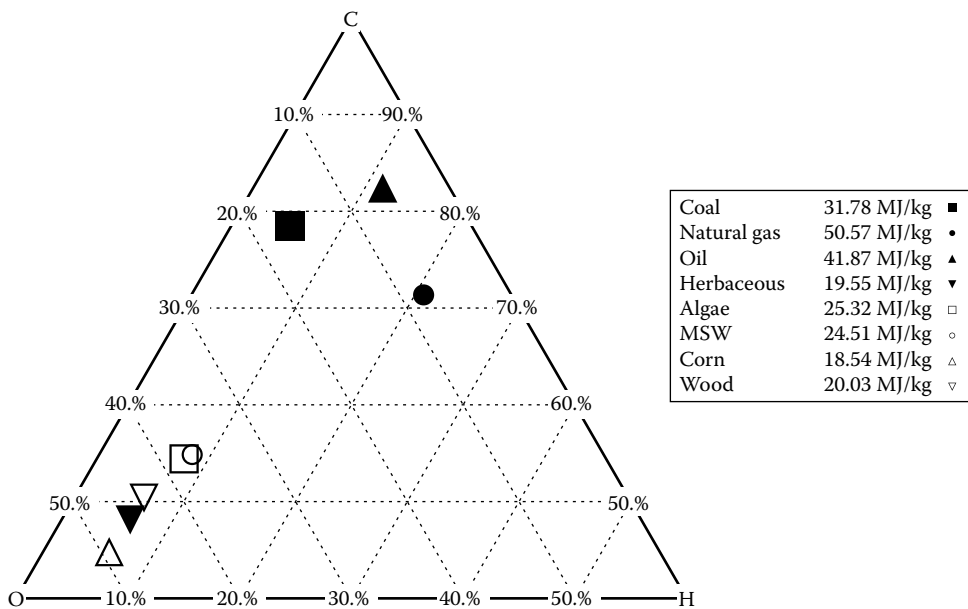


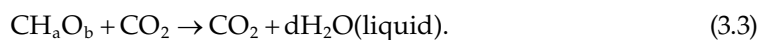
FIGURE 3.1

Ternary plot of average elemental carbon, hydrogen, oxygen in fossil and biomass materials and their higher heating values. (Adapted from Anon. Phyllis2 database by ECN (July 2013) available at <http://www.ecn.nl/phyllis2/Browse/Standard/ECN-Phyllis>, accessed March 2015.)

water condensation temperature, the moisture in the fuel contributes a latent enthalpy heat release, resulting in a higher heat output. Biomass heating value is typically about 18 MJ/kg, but it varies by biomass type as shown in Table 3.2.

There are several comprehensive sources of biomass composition available in textbooks and online databases. The U.S. Department of Energy (DOE) *Biomass Feedstock Composition and Property Database*, and the ECN Phyllis database for example are freely available online. These databases contain composition and material property data for a wide range of organic and nonorganic materials. Figure 3.1 compares the HHV of fossil and biomass materials based on their carbon, hydrogen, and oxygen content [10]. As shown, higher carbon content and lower oxygen generally correspond with increasing HHV. However, the greater hydrogen content in natural gas compensates for a slightly higher oxygen content than crude oil.

Combustion calculations require knowledge of the fuel's enthalpy (heat) of formation. This information is difficult to determine from biomass composition information. It can however be estimated after measuring the combustion reaction heating value. Consider the reaction in the following equation:



The heating value (ΔH_R) can be calculated using Equation 3.4, thermodynamic property data, and feedstock composition (such as Table 3.2):

$$\Delta H_R = h_{f,\text{CO}_2}^\circ + dh_{f,\text{H}_2\text{O}}^\circ - (h_{f,\text{CH}_a\text{O}_b}^\circ + ch_{f,\text{O}_2}^\circ). \quad (3.4)$$

3.4 Biomass Resources

Biomass is a term that encompasses a wide range of materials. Scientists generally classify biorenewable resources as either wastes or dedicated energy crops. A waste is a material that has been traditionally discarded, because it has no apparent value or represents a nuisance or even a pollutant to the local environment. Dedicated energy crops are plants grown specifically for production of biobased products, that is, for purposes other than food or feed. This section describes estimates for U.S. biorenewable resources.

3.4.1 Waste Materials

Categories of waste materials that qualify as biorenewable resources include municipal solid wastes (MSWs), agricultural and forest residues and their by-products, and manure. MSWs refer to anything thrown out in the garbage, and clearly include materials that do not qualify as biorenewable resources, such as glass, metal, and plastics. MSW includes food processing waste that is the effluent from a wide variety of industries ranging from breakfast cereal manufacturers to alcohol breweries. Another category of waste product is agricultural residues. Agricultural residues are simply the part of a crop discarded by farmers after harvest such as corn stover (husks and stalks), rice hulls, wheat straw, and bagasse (fibrous material remaining after the milling of sugarcane). Modern agriculture continues to heavily employ animals. The recent concentration of animals into giant livestock facilities has led to calls to treat animal wastes in a manner similar to that for human wastes. Table 3.3 shows the potential quantities of agricultural and forest residue available in the United States.

Waste materials share few common traits other than the difficulty of characterizing them because of their variable and complex composition. Thus, waste biomass presents special problems to engineers who are tasked with converting this sometimes unpredictable feedstock into reliable power or high-quality fuels and chemicals. The major virtue of waste materials is their low cost. By definition, waste materials have little apparent economic value and can often be acquired for little more than the cost of transporting the material from its point of origin to a processing plant. In fact, it is possible to acquire wastes at a negative cost because of the rising costs for solid waste disposal and sewer

TABLE 3.3

Potential Agricultural, Forest, and Process Waste Supply in the United States

	Annual Biomass Supply (Million Dry Mg/Year)
Logging and other residue	58
Fuel treatments	54
Urban wood residues	43
Wood processing residues	64
Pulping liquor	67
Fuelwood	47
Crop residues	405
Process residues	79

Source: Perlack, R. et al., Biomass as feedstock for a bioenergy and bioproducts industry: The technical feasibility of a billion-ton annual supply, Technical Report A357634, Oak Ridge National Laboratory, Oak Ridge, TN, 2005.

discharges and restrictions on landfilling certain kinds of wastes; that is, a biorenewable resource processing plant is paid by a company seeking to dispose of a waste stream. For this reason, many of the most economically attractive opportunities in biorenewable resources involve waste feedstocks.

Clearly, a waste material that can be used as feedstock for an energy conversion process is no longer a waste material. As demand for these new-found feedstocks increases, those that generate it come to view themselves as suppliers and may demand payment for the one-time waste: a negative feedstock cost becomes a positive cost. Such a situation developed in the California biomass power industry during the 1980s [4]. Concerns about air pollution in California led to restrictions on open-field burning of agricultural residues, a practice designed to control infestations of pests. With no means for getting rid of these residues, an enormous reserve of biomass feedstocks materialized. These feedstocks were so inexpensive that independent power producers recognized that even small, inefficient power plants using these materials as fuel would be profitable. A number of plants were constructed and operated on agricultural residues. Eventually, the feedstock producers had plant operators bidding up the cost of their once nuisance waste material. In the end, many of these plants were closed because of the escalating cost of fuel.

3.4.2 Energy Crops

Energy crops are defined as plants grown specifically as an energy resource. We should note that firewood obtained from cutting down an old-growth forest does not constitute an energy crop. An energy crop is planted and harvested periodically. Harvesting may occur on an annual basis, as with sugar beets or switchgrass, or on a 5–7 year cycle, as with certain strains of fast-growing trees such as hybrid poplar or willow. The cycle of planting and harvesting over a relatively short time period assures that the resource is used in a sustainable fashion; that is, the resource will be available for future generations.

Energy crops contain significant quantities of one or more of four important energy-rich components: oils, sugars, starches, and lignocellulose (fiber). Farmers historically cultivated crops rich in the first three components for food and feed: oils from soybeans and nuts; sugars from sugar beets, sorghum, and sugarcane; and starches from corn and cereal crops. Oil, sugars, and starches are easily metabolized. On the other hand, humans find it hard to digest lignocellulose. Certain domesticated animals with specialized digestive tracts are able to break down the polymeric structure of lignocellulose, and use it as an energy source. From this discussion, it might appear that the best strategy for developing biomass resources is to grow crops rich in oils, sugars, and starches. However, even for *oil crops* or *starch crops*, the largest single constituent is invariably lignocellulose (Table 3.4), which is the structural (fibrous) material of the plant: stems, leaves, and roots. If we harvest oils, sugars, and starches and leave the lignocellulose behind as an agricultural residue rather than use as fuel, we will waste the greatest portion of the biomass crop.

TABLE 3.4
Typical Woody Biomass Compositions

Component	Weight (%)
Cellulose	44 ± 6
Hemicellulose	28 ± 4
Lignin	20 ± 5

Research has shown that energy yields (Joules per km² per year) are usually greatest for plants that are mostly *roots and stems*; in other words, plant resources are directed toward the manufacture of lignocellulose rather than oils, sugars, and starches. As a result, there has been a bias toward development of energy crops that focus on lignocellulosic biomass, which is reflected in the discussion that follows.

Dedicated energy crops are typically high fiber crops grown specifically for their high productivity of holocellulose (cellulose and hemicellulose). Harvesting may occur on an annual basis, as with switchgrass, or on a 5–7 year cycle, as with certain strains of fast-growing trees such as hybrid poplar. Lignocellulosic crops are conveniently divided into herbaceous energy crops (HECs) and short rotation woody crops (SRWCs) [7].

Herbaceous crops are plants that have little or no woody tissue. The aboveground growth of these plants usually lives for only a single growing season. However, herbaceous crops include both annuals and perennials. Annuals die at the end of a growing season and must be replanted in the spring. Perennials die back each year in temperate climates but reestablish themselves each spring from rootstock. Both annual and perennial HECs are harvested on at least an annual basis, if not more frequently, with yields averaging 550–1100 Mg/km²/year, with maximum yields between 2000 and 2500 Mg/km²/year in temperate regions [7]. As with trees, yields can be much higher in tropical and subtropical regions.

Herbaceous crops more closely resemble hardwoods in their chemical properties than they do softwoods. Their low lignin content makes them relatively easy to delignify, which improves accessibility of the carbohydrate in the lignocellulose. The hemicellulose contains mostly xylan, which is highly susceptible to acid hydrolysis, compared to the cellulose. As a result, microbes can easily degrade agricultural residues, destroying their processing potential in a matter of days if exposed to the elements. Herbaceous crops have relatively high silica content compared to woody crops, which can present problems during processing.

SRWC is used to describe woody biomass that is fast growing and suitable for use in dedicated feedstock supply systems. Desirable SRWC candidates display rapid juvenile growth, wide site adaptability, and pest and disease resistance. Woody crops grown on a sustainable basis are harvested on a rotation of 3–10 years. Annual SRWC yields range between 500 and 2400 Mg/km²/year.

Woody crops include hardwoods and softwoods. Hardwoods are trees classified as angiosperms, which are also known as flowering plants. Examples include willow, oak, and poplar. Hardwoods can be regrown from stumps, a process known as coppicing, which reduces their production costs compared to softwoods. Advantages of hardwoods in processing include: high density for many species; relative ease of delignification and accessibility of wood carbohydrates; the presence of hemicellulose high in xylan, which can be removed relatively easily; low content of ash, particularly silica, compared to softwoods and herbaceous crops; and high acetyl content compared to most softwoods and herbaceous crops, which is an advantage in the recovery of acetic acid.

Softwoods are trees classified as gymnosperms, which encompass most trees known as evergreens. Examples include pine, spruce, and cedar. Softwoods are generally fast growing, but their carbohydrate is not as accessible for chemical processing as the carbohydrates in hardwood. Since softwoods have considerable value as construction lumber and pulpwood, they are more readily available as waste material in the form of logging and manufacturing residues compared to hardwoods. Logging residues, consisting of a high proportion of branches and tops, contain considerable high-density compression wood, which is not easily delignified. Therefore, logging residues are more suitable as boiler fuel or other thermochemical treatments than as feedstock for chemical or enzymatic processing.

3.4.3 Algae

Algae is a broad term that encompasses several eukaryotic organisms. Eukaryotic organisms are characterized by complex structures enclosed within their cell membranes. Although algae do not share many of the structures that define terrestrial biomass, they are capable of photosynthesis and capturing carbon. Algae's affinity to convert CO₂ into lipids has drawn academic and industrial attention as a means to simultaneously lower carbon emissions and produce biofuels.

Algal biomass uses CO₂ as its carbon source and sunlight as its energy source. About 1.8 kg of CO₂ is fixed for every kg of algal biomass, which contains up to 50% carbon by dry weight. Controlled production of renewable fuels from algae has been proposed in either raceway ponds or photobioreactors. Raceway ponds consist of open, shallow recirculation channels with mechanical flow control and surfaces that enhance light retention. Raceway ponds are inexpensive, but relatively inefficient when compared to photobioreactors. There are various photobioreactor designs with the common goal of maintaining a monoculture of algae that is efficiently exposed to sunlight and carbon dioxide. A common design employs arrays of tubes arranged vertically to minimize land use and oriented north–south to maximize light exposure.

Given that algae do not require fresh water or fertile soils, waste lands have been suggested as potential locations to grow algae. One suggestion is to build algae ponds in the desert Southwest United States where inexpensive flat land, abundant sunlight, water from alkaline aquifers, and CO₂ from power plants could be combined to generate renewable fuels. Algae's potential for yields of 1.12–9.40 million liters of oil/km²/year promises significant reductions in the land footprint required to produce biofuels.

3.5 Land Use for Biomass Production

Global land use is broadly defined by five categories: pasture, crop, forest, urban, and abandoned. Pasture is land devoted primarily to animal grazing; crop lands are areas actively cultivated for food production; forest land contains primarily large trees; urban areas are heavily populated regions; and abandoned lands are territories that formerly fit one of the previous categories but are no longer employed for human activities. Humans, because of population migrations or land use change, alter the portions of land devoted to each of these categories over time.

Researchers estimate that 14.5 and 33.2 million km² of global land area were devoted to crops and pasture respectively in 2000 [2]. These land use groups can coexist within the same region. For example, the U.S. Midwest and parts of the Southeast include regions with more than 70% of the land devoted to crops, and the western sides of the Midwest and Southern U.S. states have a high concentration of land for pasture.

Modern day farmers devote their production to a small selection of crops depending on socioeconomic factors. Table 3.5 shows a sample of biomass crops grown in various geographical regions and their annual yields. Crops such as corn and sugarcane can serve both food and energy needs due to their high yields of sugar-rich biomass and biomass residue (stover and bagasse respectively).

TABLE 3.5

Nominal Annual Yields of Biomass Crops

Biomass Crop	Geographical Location	Annual Yield (Mg/km ²)
Corn: grain	North America	700
Corn: cobs	North America	130
Corn: stover	North America	840
Jerusalem artichoke: tuber	North America	4500
Jerusalem artichoke: sugar	North America	640
Sugarcane: crop	Hawaii	5500
Sugarcane: sugar	Hawaii	720
Sugarcane: bagasse (dry)	Hawaii	720
Sweet sorghum: crop	Midwest United States	3800
Sweet sorghum: sugar	Midwest United States	530
Sweet sorghum: fiber (dry)	Midwest United States	490
Switchgrass	North America	1400
Hybrid poplar	North America	1400
Wheat: grain	Canada	220
Wheat: straw	Canada	600

Source: Wayman, M. and Parekh, S., *Biotechnology of Biomass Conversion: Fuels and Chemicals from Renewable Resources*, Open University Press, Philadelphia, PA, 1990.

We can estimate the amount of biomass available in a given region by assuming nominal values for crop productivity and available land use data using the equation:

$$\text{Total biomass} \left[\frac{\text{kg}}{\text{year}} \right] = f \times \text{crop}_{\text{yield}} \left[\frac{\text{kg}}{\text{km}^2 \times \text{year}} \right] \times \text{land}_{\text{area}} [\text{km}^2] \quad (3.5)$$

In Equation 3.5, f is a factor that accounts for crop rotations, farmer participation, and land conservation among other considerations that restrict the land use. As an example, Iowa has a total land area of 144,700 km² that is predominantly covered by corn and soybeans. In 2010, farmers planted 37.5% of Iowa land with corn, netting an average yield of 165 bushels per acre (1035 Mg/km²). Thus, the total amount of corn grown in Iowa that year was 56.2 million Mg.

Farmers and seed companies have managed to increase crop yields every year for the past couple of decades. Crop yield increases follow the exponential growth formula:

$$\text{Crop}_{\text{yield}}(t) \left[\frac{\text{kg}}{\text{km}^2} \right] = \text{crop}_{\text{yield},0} e^{kt}, \quad (3.6)$$

where

k is the growth rate

t is the period of time since the initial value $\text{Crop}_{\text{yield},0}$

The USDA maintains a comprehensive database of agricultural statistics (available online at <http://quickstats.nass.usda.gov/>). The data span several years, and include county-level data for crops, demographics, economics, animals and products, and environmental impacts.

The United States benefits from large biomass resources. Based on crop historical data and growth projections, we can expect traditional biomass resources to continue as a significant potential energy resource. The development of fast-growing dedicated energy crops and algae could help address concerns over land use. Much work remains to continue the production and conversion of biomass in economic and environmentally friendly ways.

References

1. Brown, R. C. (2003). *Biorenewable Resources: Engineering New Products from Agriculture*, pp. 59–75. Iowa State Press, A Blackwell Publishing Company, Ames, IA.
2. Field, C., J. Campbell, and D. Lobell (2008). Biomass energy: The scale of the potential resource. *Trends in Ecology and Evolution* 23(2), 65–72.
3. Mokany, K., R. Raison, and A. S. Prokushkin (2006). Critical analysis of root: Shoot ratios in terrestrial biomes. *Global Change Biology* 12(1), 84–96.
4. Morris, G. (December 2003). The status of biomass power generation in California, July 31, 2003. Technical Report NREL//SR-510–35114, National Renewable Energy Laboratory, Golden, CO.
5. Perlack, R., L. Wright, A. Turhollow, R. Graham, B. Stokes, and D. Erbach (2005). Biomass as feedstock for a bioenergy and bioproducts industry: The technical feasibility of a billion-ton annual supply. Technical Report A357634, Oak Ridge National Laboratory, Oak Ridge, TN.
6. Wayman, M. and S. Parekh (1990). *Biotechnology of Biomass Conversion: Fuels and Chemicals from Renewable Resources*. Open University Press, Philadelphia, PA.
7. Wright, L. and W. Hohenstein (1994). Dedicated feedstock supply systems: Their current status in the USA. *Biomass and Bioenergy* 6(3), 159–241.
8. Zhu, X. G., S. P. Long et al. (2008). What is the maximum efficiency with which photosynthesis can convert solar energy into biomass? *Current Opinion in Biotechnology* 19(2), 153–159.
9. Anon. Dynamic Maps, GIS Data, & Analysis Tools—Solar Data, National Renewable Energy Laboratory, Golden, CO, 2015. <http://www.nrel.gov/gis/datasolar.html> (accessed March 2015).
10. Anon. ECN Phyllis2 Database for biomass and waste. Energy Centre of the Netherlands, Petten, the Netherlands. <http://www.ecn.nl/phyllis2/Browse/Standard/ECN-Phyllis> (accessed March 2015).



Taylor & Francis

Taylor & Francis Group

<http://taylorandfrancis.com>

4

Municipal Solid Waste

Shelly H. Schneider

CONTENTS

4.1 Materials and Products in MSW.....	73
4.2 Management of MSW.....	76
4.3 Summary.....	78
References.....	79

This chapter has been extracted from the most recent in a series of reports released by the U.S. Environmental Protection Agency (EPA) to characterize municipal solid waste (MSW) in the United States. This report characterizes the national municipal waste stream based on data through 2011. As characterized in the EPA report, MSW includes wastes from residences and commercial establishments. No construction and demolition debris or industrial wastes are included. (Some wastes from industrial establishments, such as packaging and office wastes, are, however, included.)

Identifying the components of the MSW stream is an important step toward addressing the issues associated with using it for energy generation. MSW characterizations, which analyze the quantity and composition of the waste stream, involve estimating how much MSW is generated, recycled, combusted, and disposed of in landfills. This chapter characterizes the MSW stream *of the nation as a whole*. Local and regional variations are not addressed.

The methodology used for the characterization of MSW for this chapter estimates the waste stream on a nationwide basis by a “material flows methodology.” EPA’s Office of Solid Waste and its predecessors in the Public Health Service sponsored work in the 1960s and early 1970s to develop this methodology, which is based on production data (by weight) for the materials and products in the waste stream, with adjustments for imports, exports, and product lifetimes.

4.1 Materials and Products in MSW

In 2011, generation of MSW totaled 250.4 million tons. A breakdown by percentage of the materials generated in MSW in 2011 is shown in Figure 4.1. Paper and paperboard products are the largest component of MSW by weight (28% of generation), and food waste and yard trimmings are the second and third largest components (14.5% and 13.5% of generation). Plastics come next, at 23.7% of MSW generation. Inorganic portions of the waste stream—metals and glass—total 13.4% of generation. (The “other” category also

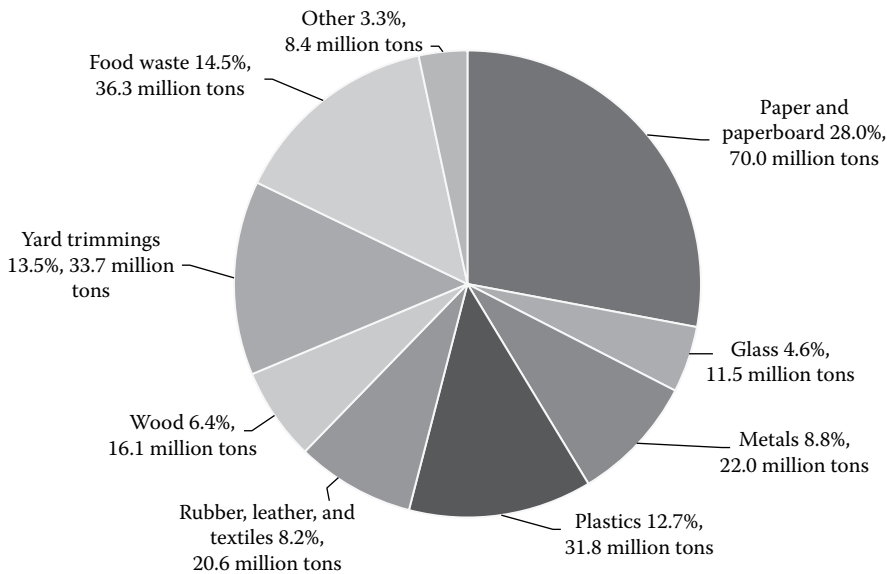


FIGURE 4.1
Materials generated in MSW by weight and percentage, 2011.

contains some inorganic materials such as broken pottery and kitty litter.) Rubber, leather, textiles, and wood make up about 14.6% of MSW generation.

Most of the materials in MSW have some level of recovery for recycling or composting. This is illustrated in Table 4.1. Since each materials category (except for yard trimmings and food waste) is made up of many different products, some of which may not be recovered at all, the overall recovery rate for any particular material will be lower than recovery rates for some products within the materials category.

The highest recovery rate shown in Table 4.1 is that for nonferrous metals other than aluminum (68.4% of generation). This is because the lead in lead-acid batteries is recovered at very high rates. Paper and paperboard were recovered at 65.6% of generation in 2011, and they had by far the highest recovered tonnage. Within that category, newspapers were recovered at 72.5% and corrugated boxes at 91% of generation. Yard trimmings were recovered for composting at a rate of 57.3% in 2011. Recovery rates for other materials are shown in the table.

The many products in MSW are grouped into three main categories: durable goods (e.g., appliances), nondurable goods (e.g., newspapers), and containers and packaging (e.g., beverage cans and corrugated boxes) (see Figure 4.2). The materials in MSW are generally made up of products from each category. There are, however, exceptions. The durable goods category contains no paper and paperboard. The nondurable goods category includes only small amounts of metals and essentially no glass or wood. The containers and packaging category includes only very small amounts of rubber, leather, and textiles.

Generation and recovery of MSW by product category are shown in Table 4.2. Overall, the materials in durable goods were recovered at a rate of 18.4% in 2011. Recovery of materials (lead and plastic) from lead-acid batteries was at 96.2% in 2011. Major appliances were recovered at an overall rate of 64.2% because of the high rate of recovery of steel in appliances. Recovery of tires at 44.6% is due to recovery of rubber and some steel.

The overall recovery rate for nondurable goods was estimated at 36.5% in 2011. Recovery of paper products such as newspapers and other paper products accounts for most of this. Recovery of containers and packaging is at the highest rate—50.7% in 2011. Large tonnages

TABLE 4.1
 Generation and Recovery of Materials in MSW, 2011

Material	Weight Generated	Weight Recovered	Percentage of Generation (%)
Paper and paperboard	70.02	45.90	65.6
Glass	11.47	3.17	27.6
<i>Metals</i>			
Steel	16.52	5.45	33.0
Aluminum	3.47	0.72	20.7
Other nonferrous metals	1.96	1.34	68.4
Total metals	21.95	7.51	34.2
Plastics	31.84	2.65	8.3
Rubber and leather	7.49	1.31	17.5
Textiles	13.09	2.00	15.3
Wood	16.08	2.38	14.8
Other materials	4.59	1.28	27.9
Total materials in products	176.53	66.20	37.5
<i>Other wastes</i>			
Food, other	36.31	1.40	3.9
Yard trimmings	33.71	19.30	57.3
Miscellaneous inorganic wastes	3.87	Negligible	Negligible
Total other wastes	73.89	20.70	28.0
Total municipal solid waste	250.42	86.90	34.7

Source: U.S. Environmental Protection Agency, *Municipal Solid Waste in the United States: 2011 Facts and Figures*, U.S. Environmental Protection Agency.

Note: In millions of tons and percentage of generation of each material. Negligible = less than 5000 tons or 0.05%.

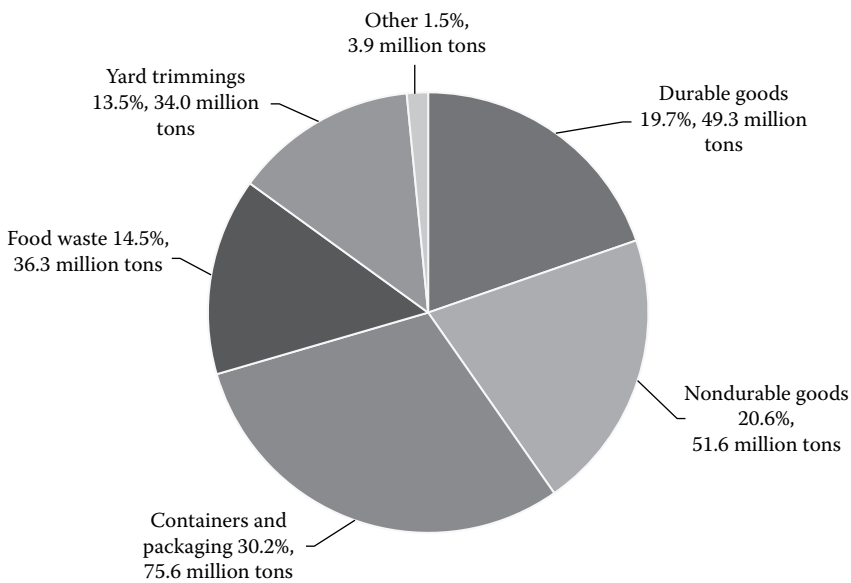


FIGURE 4.2
 Products generated in MSW by weight and percentage, 2011.

TABLE 4.2

Generation and Recovery of Products in MSW, 2011

	Weight Generated	Weight Recovered	Percentage of Generation (%)
Durable goods	49.3	9.07	18.4
Nondurable goods	51.61	18.83	36.5
Containers and packaging	75.58	38.3	50.7
<i>Other wastes</i>			
Food, other	36.31	1.40	3.9
Yard trimmings	33.71	19.30	57.3
Miscellaneous inorganic wastes	3.87	Negligible	Negligible
Total other wastes	73.89	20.70	28.0
Total municipal solid waste	250.42	86.90	34.7

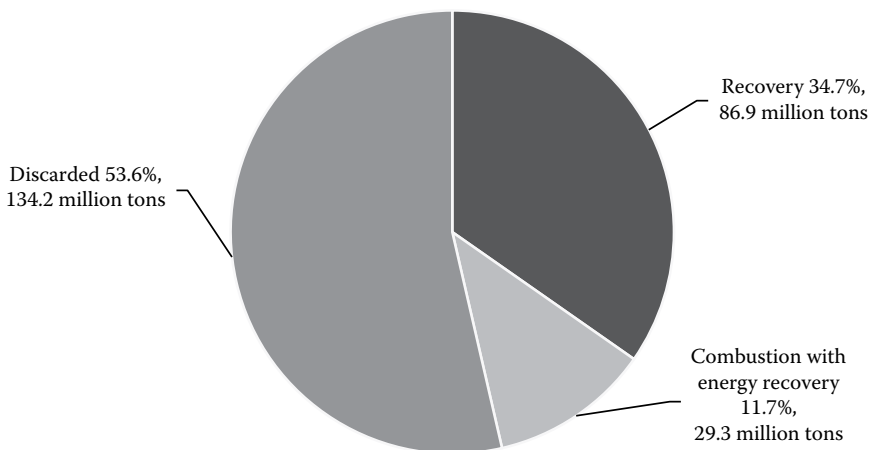
Source: U.S. Environmental Protection Agency, *Municipal Solid Waste in the United States: 2011 Facts and Figures*, U.S. Environmental Protection Agency.

Note: In millions of tons and percentage of generation of each product category. Negligible = less than 5000 tons or 0.05%.

of corrugated boxes were recovered, at a rate of 91.0%. Steel cans were recovered at a rate of 70.6%, and aluminum cans at 54.5%. Other packaging made of glass, plastics, and wood was also recovered.

4.2 Management of MSW

The breakdown of how much MSW went to recycling and composting, combustion, and land disposal* in 2011 is shown in Figure 4.3. Recovery of materials for recycling and composting was estimated to have been 86.9 million tons, or 34.7% of generation, in 2011.

**FIGURE 4.3**

Management of MSW in the United States, 2011.

* Land disposal is calculated as the remainder after recycling, composting, and combustion are deducted from generation. This disposal is overwhelmingly landfilled; however, small amounts are littered, self-disposed (e.g., by on-site burning), or otherwise not taken to landfills.

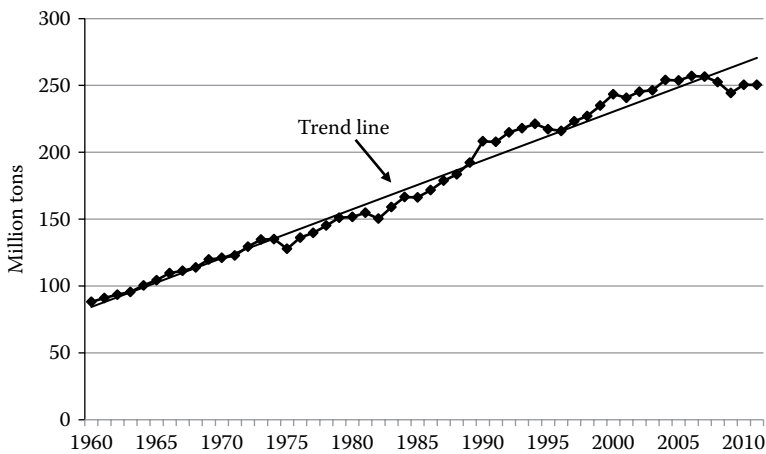


FIGURE 4.4
The trend of municipal solid waste generation, 1960–2011.

Combustion of MSW (with energy recovery) was estimated to have been 29.3 million tons, or 11.7% of generation. The remainder—134.2 million tons, or 53.6% of generation—was land disposed.

Generation of MSW grew steadily from 1960 to 2011, from 88.1 million tons to 250.4 million tons per year (Figure 4.4). As illustrated by the graph, the growth of generation is not continuous, but fluctuates with the economy and, of course, with population growth. It has been demonstrated that there is a high degree of correlation between MSW generation and gross domestic product, and recession years can be identified on the graph. Another way to look at generation is in pounds per capita (pcd) (Figure 4.5). After years of steady growth, pcd peaked at 4.74 pounds per capita per day in 2000, decreasing slightly between 2001 and 2003, rising again to 4.74 pcd in 2004 followed by a steady decline to 4.36 pcd in 2009. The per capita rate rose to 4.44 in 2010 followed by a decline to 4.40 in 2011. Decreasing per capita rates follow periods of economic turndowns.

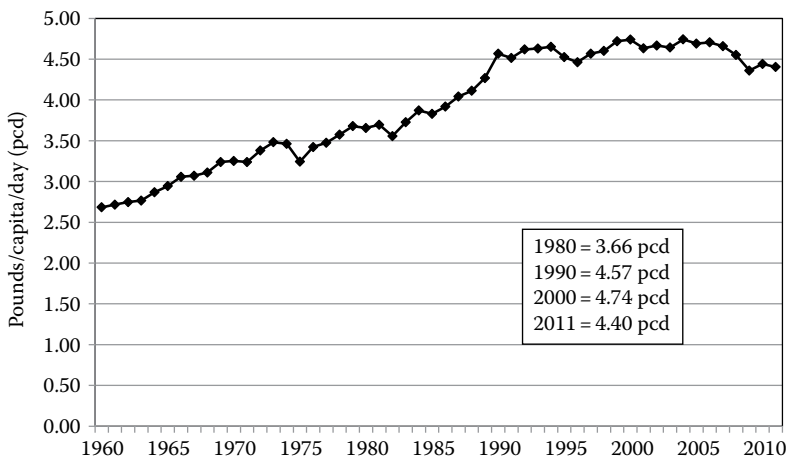


FIGURE 4.5
Generation of municipal solid waste in pounds per capita per day, 1960–2011.

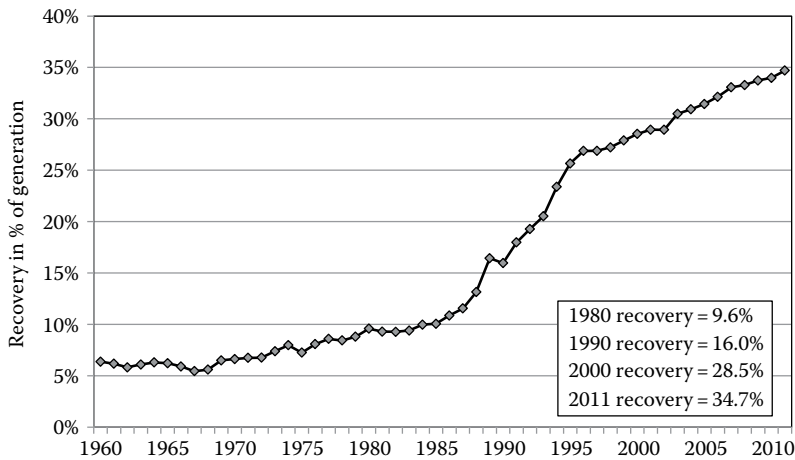


FIGURE 4.6

Recovery of MSW for recycling and composting, in percentage of generation, 1960–2011.

Recovery for recycling and composting has increased dramatically since the late 1980s (Figure 4.6). Recovery of MSW was minimal in the 1960s and early 1970s. The percentage recovered crept up to 9.6% by 1980. Interest in recovery grew rapidly in the late 1980s as concerns were raised about diminishing landfill space in parts of the United States, especially the northeast. Recovery reached 16% in 1990, 28.5% in 2000, and 34.7% in 2011. While most recovered material is made up of products in MSW, there also has been an increase in composting of yard trimmings and, to a much lesser extent, food waste.

Combustion handled an estimated 30% of MSW generated in 1960, mostly through incinerators with no energy recovery and no air pollution controls. In the 1960s and 1970s, combustion dropped steadily as the old incinerators were closed, reaching a low of less than 10% of MSW generated by 1980. The percentage of MSW managed by combustion reached about 14.2% in 1990 and 13.9% in 2000; it has been declining slowly since 2000 to 11.7% in 2011.

Land disposal has been declining since the 1980s. Land disposal was 81.4% (U.S. Environmental Protection Agency 2005) of generation in 1980, 69.8% in 1990, and 53.6% in 2011 (U.S. Environmental Protection Agency 2013).

4.3 Summary

The history of MSW generation and management is shown in Figure 4.7. The top line of the area graph is MSW generation, while management methods are shown as area plots. Major findings from the referenced EPA report are as follows:

- MSW generation in the United States has grown from 88 million tons in 1960 to 250.4 million tons in 2011. On a per capita basis, generation of MSW during the 1990s was around 4.5 pounds per capita per day, increasing to 4.74 pounds per capita per day in 2000. In 2011, the per capita generation rate had declined to 4.40 pounds per person per day.

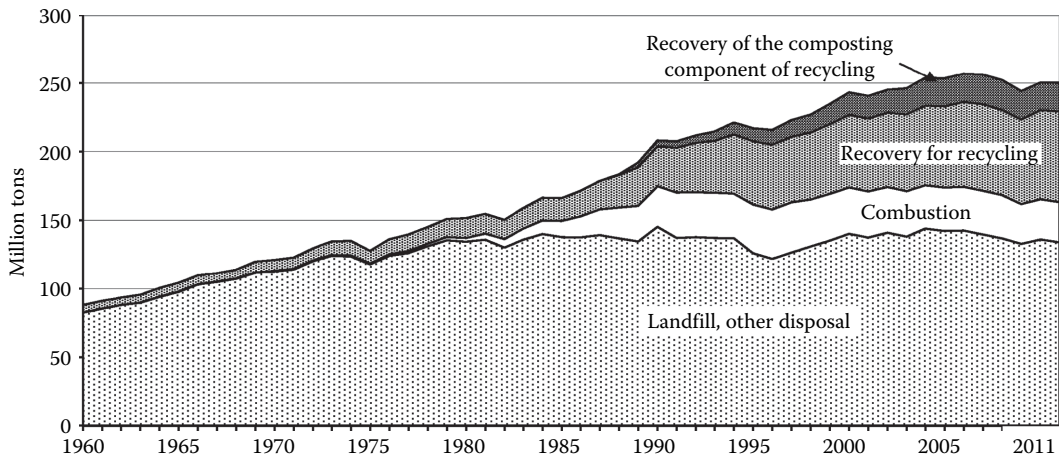


FIGURE 4.7
Generation and management of municipal solid waste, 1960–2011.

- In the 1960s and early 1970s, a large percentage of MSW was burned, with little recovery for recycling. Landfill disposal typically consisted of open dumping, often accompanied with open burning of the waste for volume reduction.
- Through the mid-1980s, incineration declined considerably, and landfills became difficult to site, and waste generation continued to increase. Materials recovery rates increased very slowly in this time period, and the burden on the nation's landfills grew dramatically. As Figure 4.7 shows, discards of MSW to landfill or other disposal apparently peaked in 1990 and then began to decline as materials recovery and combustion with energy recovery increased.
- Over time, recycling rates have increased from just over 6% of MSW generated in 1960 to about 10% in 1980, to 16% in 1990, to about 29% in 2000, and to over 34% in 2011.
- Combustion of MSW reached a low point of about 10% of generation around 1980. Since 2004, combustion with energy recovery has held steady at about 12% of generation.
- MSW discards to landfills rose to about 142.3 million tons in 2005 and then declined to 134.3 million tons in 2011. As a percentage of total MSW generation, discards to landfills has consistently decreased—from 69.8% of generation in 1990 to 53.6% in 2011.

References

- U.S. Environmental Protection Agency. *Municipal Solid Waste in the United States: 2011 Facts and Figures*, May 2013. www.epa.gov/epaoswer/non-hw/muncpl/msw99.htm (accessed July 2013).
- U.S. Environmental Protection Agency. *Municipal Solid Waste in the United States: 2003 Data Tables*, 2005. www.epa.gov/epaoswer/non-hw/muncpl/msw99.htm (accessed July 2013).



Taylor & Francis

Taylor & Francis Group

<http://taylorandfrancis.com>

5

Nuclear Resources

James S. Tulenko

CONTENTS

5.1	The Nuclear Fuel Cycle	81
5.1.1	Sources of Nuclear Fuels and World Reserves	81
5.2	Processing of Nuclear Fuel	82

5.1 The Nuclear Fuel Cycle

5.1.1 Sources of Nuclear Fuels and World Reserves

Nuclear power can use two naturally occurring elements, uranium, and thorium, as the sources of its fissioning energy. Uranium can be a fissionable source (fuel) as mined (Candu Reactors in Canada), while thorium must be converted in a nuclear reactor into a fissionable fuel. Uranium and thorium are relatively plentiful elements ranking about 60th out of 80 naturally occurring elements. All isotopes of uranium and thorium are radioactive. Today, natural uranium contains, in atomic abundance, 99.2175% uranium-238 (U^{238}); 0.72% uranium-235 (U^{235}); and 0.0055% uranium-234 (U^{234}). Uranium has atomic number 92, meaning all uranium atoms contain 92 protons, with the rest of the mass number being composed of neutrons. Uranium-238 has a half-life of 4.5×10^9 years (4.5 billion years), U-235 has a half-life of 7.1×10^8 years (710 million years), and U-234 has a half-life of 2.5×10^5 years (250 thousand years). Since the age of the earth is estimated at 3 billion years, roughly half of the U-238 present at creation has decayed away, while the U-235 has changed by a factor of sixteen. Thus, when the earth was created, the uranium-235 enrichment was on the order of 8%, enough to sustain a natural reactor of (there is evidence of such an occurrence in Africa). The U-234 originally created has long disappeared, and the U-234 currently present occurs as a product of the decay of U-238.

Uranium was isolated and identified in 1789 by a German scientist, Martin Heinrich Klaproth, who was working with pitchblend ores. No one could identify this new material he isolated, so in honor of the planet Uranus which had just been discovered, he called his new material uranium. It wasn't until 1896, when the French scientist Henri Becquerel accidentally placed some uranium salts near some paper-wrapped photographic plates, that radioactivity was discovered.

Until 1938, when the German scientists Otto Hahn and Fritz Shassroen succeeded in uranium fission by exposure to neutrons, uranium had no economic significance except in coloring ceramics, where it proved valuable in creating various shades of orange, yellow, brown, and dark green. When a uranium atom is fissioned it releases 200 million electron volts of energy; the burning of a carbon (core) atom releases 4 eV. This difference of

50 million times in energy release shows the tremendous difference in magnitude between chemical and nuclear energy.

Uranium is present in the earth's crust to the extent of four parts per million. This concentration makes uranium about as plentiful as beryllium, hafnium, and arsenic; and greater in abundance than tungsten, molybdenum, and tantalum. Uranium is an order of magnitude more plentiful than silver and a hundred times more plentiful than gold. It has been estimated that the amount of uranium in the earth's crust to a depth of 12 miles is of the order of 100 trillion tons.

Thorium, which is composed of only one isotope, thorium-232, has a half-life of 14 billion years (1.4×10^{10} years), is more than three times more abundant than uranium, and is in the range of lead and gallium in abundance. Thorium was discovered by Berzelius in 1828 and named after Thor, the Scandinavian god of war. For reference, copper is approximately five times more abundant than thorium and twenty times more abundant than uranium.

Uranium is chemically a reactive element; therefore, while it is relatively abundant, it is found chemically combined as an oxide (U_3O_8 or UO_2) and never as a pure metal. Uranium is obtained in three ways, either by underground mining, open pit mining, or in situ leaching. An economic average ore grade is normally viewed as 0.2% (4 pounds per short ton), though recently ore grades as low as 0.1% have been exploited. A large quantity of uranium exists in sea-water which has an average concentration of 3×10^{-3} ppm, yielding an estimated uranium quantity available in sea-water of 4000 million tons. A pilot operation was successfully developed by Japan to recover uranium from sea-water, but the cost was about \$900/lb, and the effort was shut down as uneconomical.

The major countries with reserves of uranium in order of importance are Australia, United States, Russia, Canada, South Africa, and Nigeria. The countries with major thorium deposits are India, Brazil, and the United States. It is estimated that for a recovery value of \$130/kg (\$60/lb), the total uranium reserves in these countries are approximately 1.5 million tonnes of uranium in the U.S., 1 million tonnes of uranium in Australia, 0.7 million tonnes of uranium in Canada, and 1.3 million tonnes of uranium in the former Soviet Union. As mentioned earlier, thorium reserves are approximately four times greater. With the utilization of breeder reactors, there is enough uranium and thorium to provide electrical power for the next thousand years at current rates of usage.

5.2 Processing of Nuclear Fuel

Once the uranium ore is mined it is sent to a concentrator (mill) where it is ground, treated, and purified. Since the ore is of a grade of 0.1%–0.2% uranium, a ton of ore contains only between 1 and 2 kg of uranium per 1000 kg of ore. Thus, thousands to tonnes of ore have to be extracted and sent to a mill to produce a relatively small quantity of uranium. In the concentration process approximately 95% of the ore is recovered as U_3O_8 (yellowcake) to a purity grade of about 80%. Thus, assuming 0.15% uranium ore, the milling and processing of a metric ton (1000 kg) of ore yields a concentrate of 1.781 kg (1.425 kg of uranium and 0.356 kg of impurities). For this reason the mills must be located relatively close to the mine site. The ore tailings (waste) amounts to 998.219 kg and contains quantities of radon and other uranium decay products and must be disposed of as a radioactive waste.

The U_3O_8 concentrate is then taken to a conversion plant where the concentrate is further purified (the 20% impurities are removed) and the uranium yellowcake is converted to uranium hexafluoride (UF_6). The uranium hexafluoride is a gas at fairly low temperature and is an ideal material for the U-235 isotope enriching processes of either gaseous diffusion or gaseous centrifuge. The UF_6 is shipped in steel cylinders in a solid state, and UF_6 is vaporized by putting the cylinder in a steam bath.

If the uranium is to be enriched to 4% U^{235} , then 1 kg of 4% U^{235} product will require 7.4 kg of natural uranium feed and will produce 6.4 kg of waste uranium (tails or depleted uranium) with a U^{235} isotope content of 0.2%. This material is treated as a radioactive waste. Large quantities of tails (depleted uranium) exist as UF_6 in their original shipping containers at the enriching plants. Depleted uranium (a dense material) has been used as shields for radioactive sources, armor piercing shells, balancing of helicopter rotor tips, yacht hold ballast, and balancing of passenger aircraft.

The enriched UF_6 is then sent to a fabrication plant where it is converted to a uranium dioxide (UO_2) powder. The powder is pressed and sintered into cylindrical pellets which are placed in zircaloy tubes (an alloy of zirconium), pressurized with helium, and sealed. The rods are collected in an array ($\sim 17 \times 17$) bound together by spacer grids, with top and bottom end fittings connected by tie rods or guide tubes. Pressurized water reactor fuel assemblies, each containing approximately 500 kg of uranium, are placed in a reactor for 3–4 years. A single fuel assembly produces 160,000,000 kilowatt hours of electricity and gives 8000 people their yearly electric needs for its three years of operation. When the fuel assembly is removed from the reactor it must be placed in a storage pond to allow for removal of the decay heat. After approximately five years of wet storage, the fuel assembly can be removed to dry storage in concrete or steel containers. In the United States the current plan is to permanently store the nuclear fuel, with the Department of Energy assuming responsibility for the “spent”

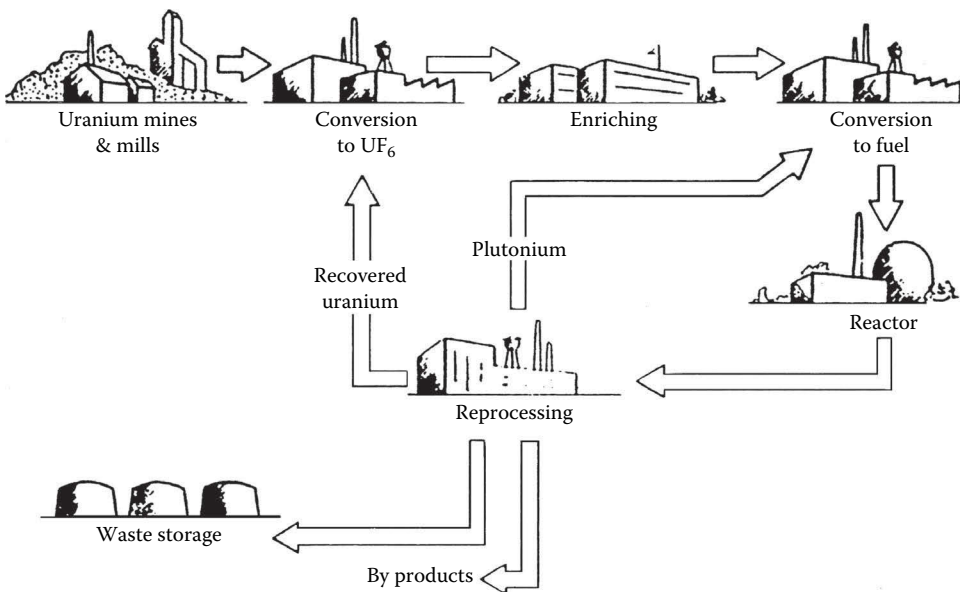


FIGURE 5.1
The nuclear fuel cycle.

fuel. The money for the government to handle the storage comes from a fee of 1 mill per kilowatt hour paid by consumers of nuclear-generated electricity. A mill is a thousandth of a dollar or a tenth of a penny. Thus, the fuel assembly described above would have collected \$160,000 in the waste fund for the Department of Energy to permanently store the fuel. In Europe, when the fuel is taken out of wet storage it is sent to a reprocessing plant where the metal components are collected for waste disposal; and the fuel is chemically recovered as 96% uranium, which is converted to uranium dioxide for recycling to the enrichment plant, 1% plutonium, which is converted to fuel or placed in storage, and 3% fission products which are encased in glass and permanently stored.

The important thing to remember about the fuel cycle is the small quantity of radioactive fission products (1.5 kg) which are created as radioactive waste in producing power which can serve the yearly electricity needs of 8000 people for the three years that it operates. The schematic of the entire fuel cycle showing both the United States system (once-through) and the European (recycle) system is given in Figure 5.1.

6

Solar Energy Resources

D. Yogi Goswami

CONTENTS

6.1	Introduction.....	85
6.2	Sun–Earth Geometric Relationship.....	86
6.2.1	Solar Time and Angles.....	92
6.2.2	Sun-Path Diagram.....	93
6.2.3	Shadow-Angle Protractor.....	95
6.3	Solar Radiation.....	98
6.3.1	Extraterrestrial Solar Radiation.....	99
6.4	Estimation of Terrestrial Solar Radiation.....	100
6.4.1	Atmospheric Extinction of Solar Radiation.....	101
6.4.2	Clear Sky Radiation Model.....	103
6.4.3	Solar Radiation on a Tilted Surface.....	105
6.4.4	Monthly Solar Radiation Estimation Models.....	112
6.5	Models Based on Long-Term Measured Horizontal Solar Radiation.....	113
6.5.1	Monthly Solar Radiation on Tilted Surfaces.....	115
6.5.2	Circumsolar or Anisotropic of Diffuse Solar Radiation.....	118
6.5.3	Hourly and Daily Solar Radiation on Tilted Surfaces.....	119
6.5.4	Spectral Models.....	122
6.6	Measurement of Solar Radiation.....	123
6.6.1	Instruments for Measuring Solar Radiation and Sunshine.....	124
6.6.2	Detectors for Solar Radiation Instrumentation.....	127
6.6.3	Measurement of Sunshine Duration.....	128
6.6.4	Measurement of Spectral Solar Radiation.....	128
6.6.5	Wideband Spectral Measurements.....	129
6.6.6	Solar Radiation Data.....	129
6.7	Solar Radiation Mapping Using Satellite Data.....	131
6.7.1	Estimation of Solar Resource from Satellite Data.....	132
	References and Suggested Readings.....	134

6.1 Introduction

Solar energy is the world’s most abundant permanent source of energy. The amount of solar energy intercepted by the planet Earth is a tiny fraction of the solar radiation emitted by the sun. However, even that tiny amount is 5000 times greater than the sum of all other inputs (terrestrial nuclear, geothermal, and gravitational energies and lunar gravitational energy).

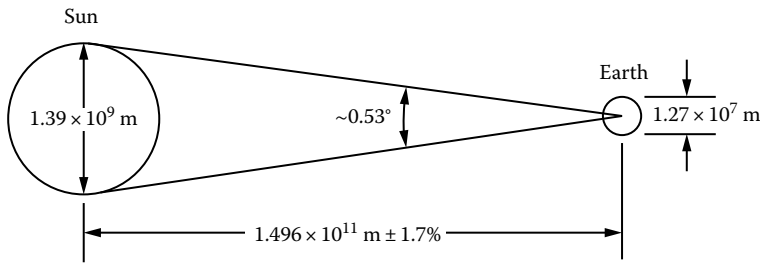


FIGURE 6.1
Relationship between the sun and the earth.

The sun is a $13.9 \times 10^5 \text{ km}$ diameter sphere comprising many layers of gases, which are progressively hotter toward its center. The outermost layer, from which energy is radiated into the solar system, is approximately at an equivalent blackbody temperature of $5,760 \text{ K}$ ($10,400^\circ \text{ R}$). The rate of energy emission from the sun is $3.8 \times 10^{23} \text{ kW}$. Of this total, only a tiny fraction, approximately $1.7 \times 10^{14} \text{ kW}$, is intercepted by the earth, which is located about 150 million km from the sun (Figure 6.1). Of this amount, 30% is reflected to space, 47% is converted to low-temperature heat and reradiated to space, and 23% powers the evaporation/precipitation cycle of the biosphere. Less than 0.5% is represented in the kinetic energy of the wind and waves and in photosynthetic storage in plants.

Total terrestrial radiation is only about one-third of the extraterrestrial total during a year, and 70% of that falls on the oceans. However, the remaining $1.5 \times 10^{17} \text{ kWh}$ that falls on land is a prodigious amount of energy—about 6000 times the total energy usage of the United States in 2009. Only a small fraction of this total can be used because of physical and socioeconomic constraints.

6.2 Sun–Earth Geometric Relationship

Figure 6.2 shows the annual orbit of the earth around the sun. The distance between the earth and the sun changes throughout the year, the minimum being $1.471 \times 10^{11} \text{ m}$ at winter solstice (December 21) and the maximum being $1.521 \times 10^{11} \text{ m}$ at summer solstice (June 21). The year-round average earth–sun distance is $1.496 \times 10^{11} \text{ m}$. The amount of solar radiation intercepted by the earth, therefore, varies throughout the year, the maximum being on December 21 and the minimum on June 21.

The axis of the earth's daily rotation around itself is at an angle of 23.45° to the axis of its ecliptic orbital plane around the sun. This tilt is the major cause of the seasonal variation of the solar radiation available at any location on the earth. The angle between the earth–sun line (through their centers) and the plane through the equator is called the *solar declination*, δ_s . The declination varies between -23.45° on December 21 and $+23.45^\circ$ on June 21. Stated another way, the declination has the same numerical value as the latitude at which the sun is directly overhead at solar noon on a given day. The tropics of Cancer (23.45° N) and Capricorn (23.45° S) are at the extreme latitudes where the sun is overhead at least once a year as shown in Figure 6.2. The Arctic and Antarctic circles are defined as those latitudes above which the sun does not rise above the horizon plane at least once per year. They are located, respectively, at $66\frac{1}{2}^\circ \text{ N}$ and

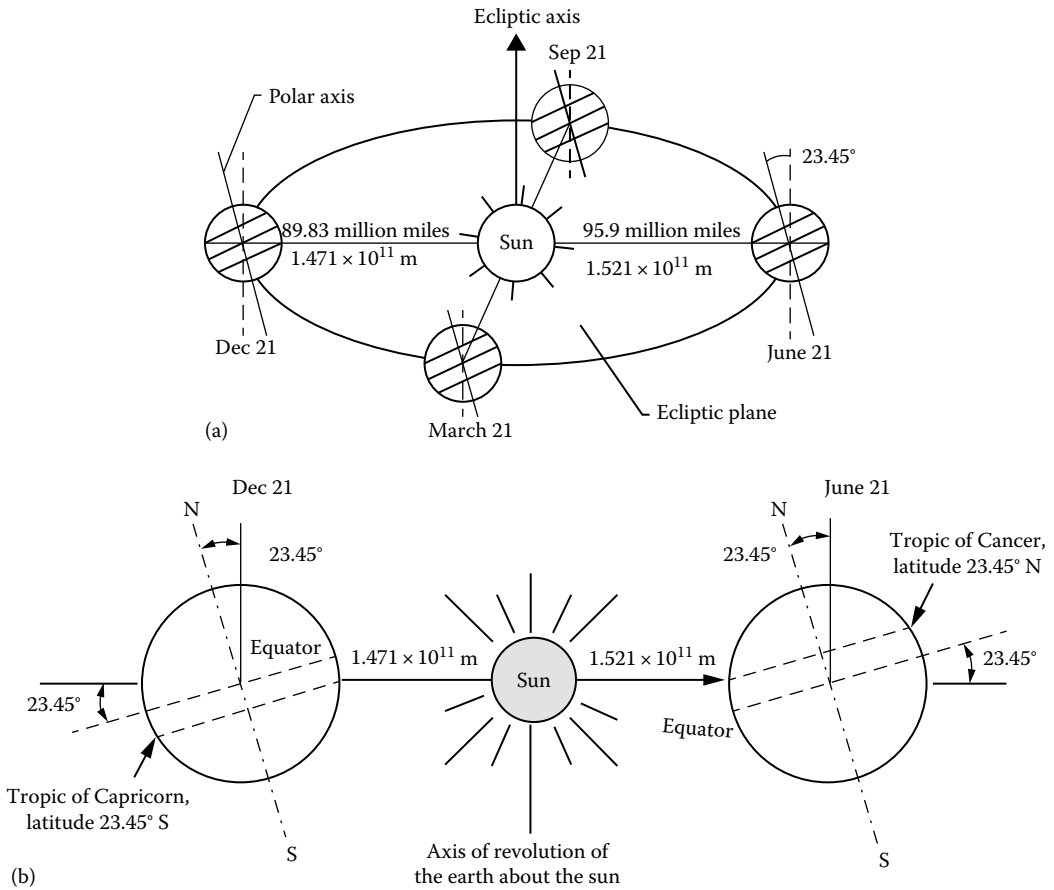


FIGURE 6.2

(a) Motion of the earth about the sun and (b) location of tropics. Note that the sun is so far from the earth that all the rays of the sun may be considered as parallel to one another when they reach the earth.

$66\frac{1}{2}^\circ$ S. Declinations north of the equator (summer in the northern hemisphere) are positive; those south, negative. The solar declination may be estimated by the relation*

$$\delta_s = 23.45^\circ \sin\left[\frac{360(284 + n)}{365}\right]^\circ, \tag{6.1}$$

where n is the day number during a year with January 1 being $n = 1$. Approximate values of declination* may also be obtained from Table 6.1 or Figure 6.3. For most calculations, the declination may be considered constant during any given day.

For the purposes of this book, the Ptolemaic view of the sun's motion provides a simplification to the analysis that follows. It is convenient to assume the earth to be fixed and to describe the sun's apparent motion in a coordinate system fixed to the earth with its origin at the site of interest. Figure 6.4 shows an apparent path of the sun to an observer. The position of the sun can be described at any time by two angles, the altitude and azimuth angles,

* A more accurate relation is $\sin \delta_s = \sin(23.45^\circ) \sin[360(284 + n)/365]^\circ$. Because the error is small, Equation (2.23) is generally used.

TABLE 6.1Summary Solar Ephemeris^a

Date	Declination		Equation of Time		Date	Declination		Equation of Time			
	Deg	Min	Min	Sec		Deg	Min	Min	Sec		
Jan.	1	-23	4	-3	14	Feb.	1	-17	19	-13	34
	5	-22	42	-5	6		5	-16	10	-14	2
	9	-22	13	-6	50		9	-14	55	-14	17
	13	-21	37	-8	27		13	-13	37	-14	20
	17	-20	54	-9	54		17	-12	15	-14	10
	21	-20	5	-11	10		21	-10	50	-13	50
	25	-19	9	-12	14		25	-9	23	-13	19
	29	-18	9	-13	5						
Mar.	1	-7	53	-12	38	Apr.	1	+4	14	-4	12
	5	-6	21	-11	48		5	5	46	-3	1
	9	-5	48	-10	51		9	7	17	-1	52
	13	-3	14	-9	49		13	8	46	-0	47
	17	-1	39	-8	42		17	10	12	+0	13
	21	-0	5	-7	32		21	11	35	1	6
	25	+1	30	-6	20		25	12	56	1	53
	29	3	4	-5	7		29	14	13	2	33
May	1	+14	50	+2	50	June	1	+21	57	2	27
	5	16	2	34	17		5	22	28	1	49
	9	17	9	3	35		9	22	52	1	6
	13	18	11	3	44		13	23	10	+0	18
	17	19	9	3	44		17	23	22	-0	33
	21	20	2	3	24		21	23	27	-1	25
	25	20	49	3	16		25	23	25	-2	17
	29	21	30	2	51		29	23	17	-3	7

(Continued)

TABLE 6.1 (Continued)Summary Solar Ephemeris^a

Date	Declination		Equation of Time		Date	Declination		Equation of Time			
	Deg	Min	Min	Sec		Deg	Min	Min	Sec		
July	1	+23	10	-3	31	Aug.	1	+18	14	-6	17
	5	22	52	-4	16		5	17	12	-5	59
	9	22	28	-4	56		9	16	6	-5	33
	13	21	57	-5	30		13	14	55	-4	57
	17	21	21	-5	57		17	13	41	-4	12
	21	20	38	-6	15		21	12	23	-3	19
	25	19	50	-6	24		25	11	2	-2	18
	29	18	57	-6	23		29	9	39	-1	10
Sep.	1	+8	35	-0	15	Oct.	1	-2	53	+10	1
	5	7	7	+1	2		5	-4	26	11	17
	9	5	37	2	22		9	-5	58	12	27
	13	4	6	3	45		13	-7	29	13	30
	17	2	34	5	10		17	-8	58	14	25
	21	1	1	6	35		21	-10	25	15	10
	25	0	32	8	0		25	-11	50	15	46
	29	-2	6	9	22		29	-13	12	16	10
Nov.	1	-14	11	+16	21	Dec.	1	-21	41	11	16
	5	-15	27	16	23		5	-22	16	9	43
	9	-16	38	16	12		9	-22	45	8	1
	13	-17	45	15	47		13	-23	6	6	12
	17	-18	48	15	10		17	-23	20	4	47
	21	-19	45	14	18		21	-23	26	2	19
	25	-20	36	13	15		25	-23	25	+0	20
	29	-21	21	11	59		29	-23	17	-1	39

^a Since each year is 365.25 days long, the precise value of declination varies from year to year. *The American Ephemeris and Nautical Almanac*, published each year by the U.S. Government Printing Office, contains precise values for each day of each year.

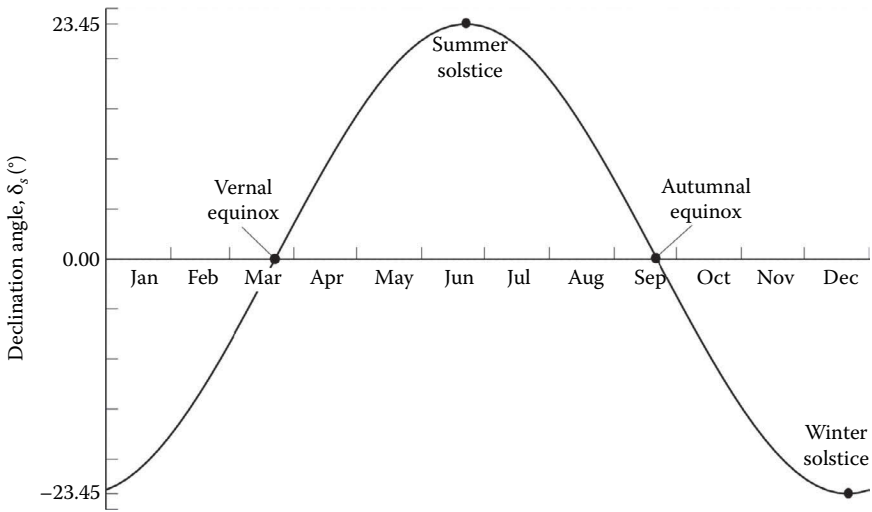


FIGURE 6.3
Graph to determine the solar declination.

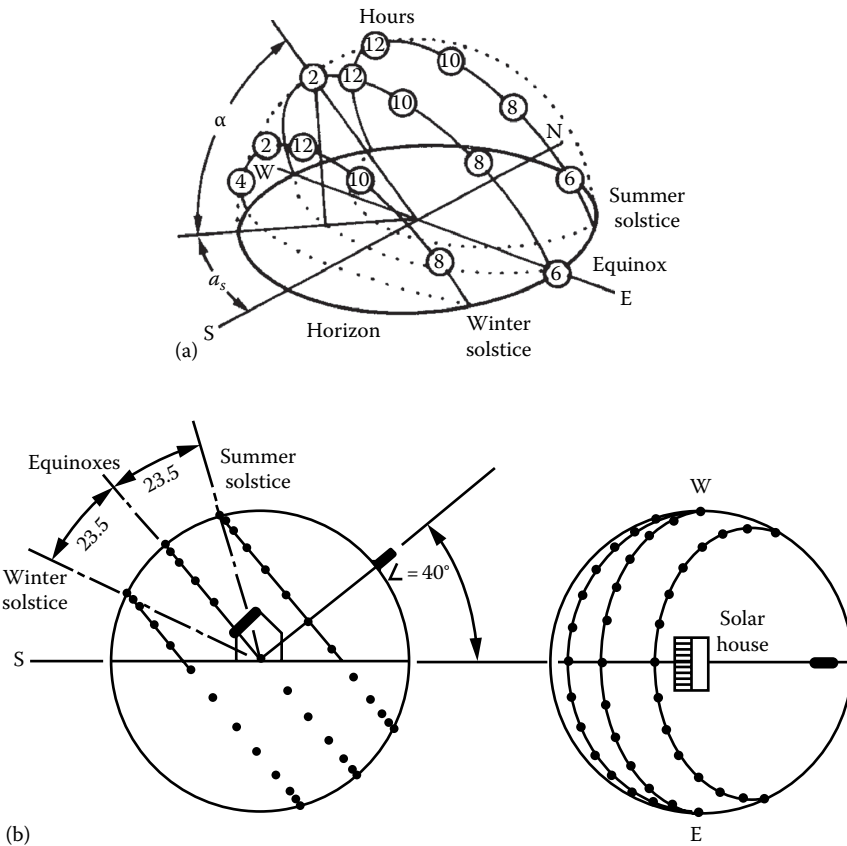
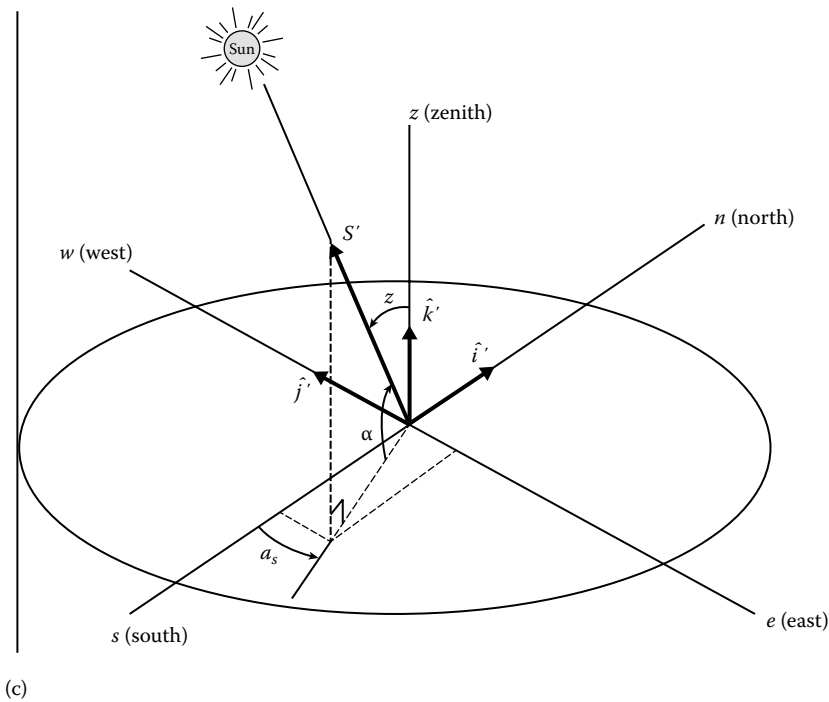


FIGURE 6.4
Sun paths for the summer solstice (6/21), the equinoxes (3/21 and 9/21), and the winter solstice (12/21) for a site at 40° N: (a) isometric view, (b) elevation and plan views. (Continued)

**FIGURE 6.4 (Continued)**

Sun paths for the summer solstice (6/21), the equinoxes (3/21 and 9/21), and the winter solstice (12/21) for a site at 40° N: (c) solar altitude and azimuth angles.

as shown in Figure 6.4c. The *solar altitude angle*, α , is the angle between a line collinear with the sun's rays and the horizontal plane. The *solar azimuth angle*, a_s , is the angle between a due south line and the projection of the site to sun line on the horizontal plane. The sign convention used for the azimuth angle is positive west of south and negative east of south. The *solar zenith angle*, z , is the angle between the site to sun line and the vertical at the site:

$$z = 90^\circ - \alpha. \quad (6.2)$$

The solar altitude and azimuth angles are not fundamental angles. Hence, they must be related to the fundamental angular quantities *hour angle*, *latitude*, and *declination*. The three angles are shown in Figure 6.5. The solar hour angle h_s is based on the nominal time of 24 h required for the sun to move 360° around the earth or 15° per hour. Therefore, h_s is defined as

$$h_s = (15^\circ/\text{h}) \cdot (\text{Hours from local solar noon}) = \frac{\text{Minutes from local solar noon}}{4 \text{ min/degree}}. \quad (6.3)$$

Again, values east of due south, that is, morning values, are negative; and values west of due south are positive.

The latitude angle L is the angle between the line from the center of the earth to the site and the equatorial plane. The latitude may be read from an atlas and is considered positive north of the equator and negative south of the equator.

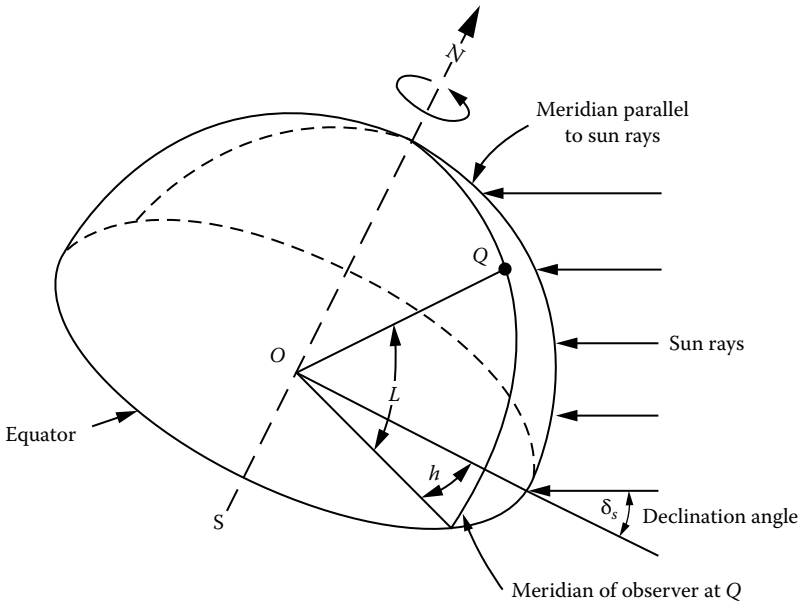


FIGURE 6.5
 Definition of solar hour angle h_s , solar declination δ_s , and latitude L ; Q site of interest.

6.2.1 Solar Time and Angles

The sun angles are obtained from the local solar time, which differs from the local standard time (LST). The relationship between the local solar time and the LST is

$$\text{Solar time} = \text{LST} + \text{ET} + (l_{st} - l_{local}) \cdot 4 \text{ min/degree}, \tag{6.4}$$

where

ET is the equation of time, which is a correction factor that accounts for the irregularity of the speed of earth’s motion around the sun

l_{st} is the standard time meridian

l_{local} is the local longitude

ET may be estimated from Table 6.1 or Figure 6.6 or calculated from the following empirical equation:

$$\text{ET}(\text{in min}) = 9.87 \sin 2B - 7.53 \cos B - 1.5 \sin B, \tag{6.5}$$

where $B = 360(n - 81)/360^\circ$.

The solar altitude angle, α , can be found from the application of the law of cosines to the geometry of Figures 6.4c and 6.5 and simplification as

$$\sin \alpha = \sin L \sin \delta_s + \cos L \cos \delta_s \cos h_s. \tag{6.6}$$

Using a similar technique, the solar azimuth angle, a_s , can be found as

$$\sin a_s = \cos \delta_s \sin h_s / \cos \alpha. \tag{6.7}$$

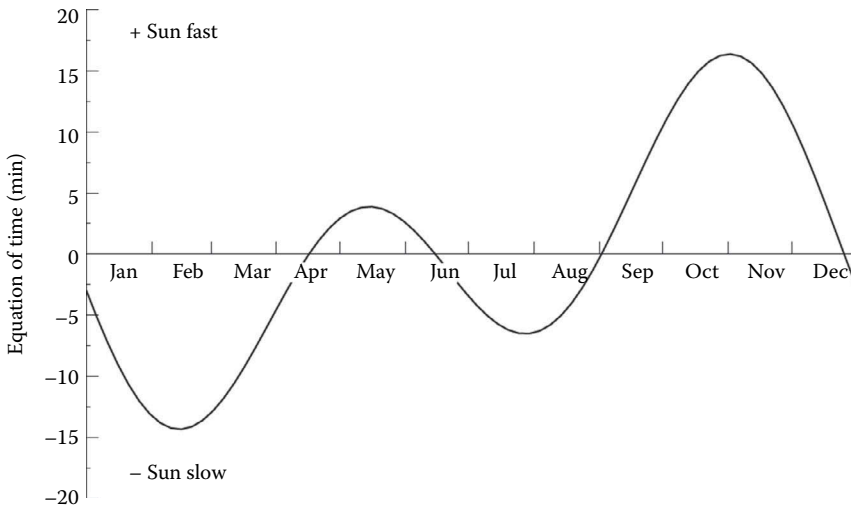


FIGURE 6.6
Equation of time.

At local solar noon, $h_s = 0$; therefore, $\alpha = 90 - |L - \delta_s|$, and $a_s = 0$.

In calculating the solar azimuth angle from Equation 6.7, a problem occurs whenever the absolute value of a_s is greater than 90° . A computational device usually calculates the angle as less than 90° since $\sin a_s = \sin(180 - a_s)$. The problem can be solved in the following way:

For $L > \delta_s$, the solar times when the sun is due east (t_E) or due west (t_W) can be calculated by t_E or $t_W = 12:00 \text{ noon} \mp (\cos^{-1}[\tan \delta_s / \tan L])^0 / (15^\circ/\text{h})$ ($-$ for t_E , $+$ for t_W).

For solar times earlier than t_E or later than t_W , the sun would be north (south in the southern hemisphere) of the east-west line and the absolute value of a_s would be greater than 90° , which may be calculated as $a_s = +$ or $- (180^\circ - |a_s|)$.

For $L \leq \delta_s$, the sun remains north (south in the southern hemisphere) of the east-west line and the true value of a_s is greater than 90° .

Sunrise and sunset times can be estimated by finding the hour angle for $\alpha = 0$. Substituting $\alpha = 0$ in Equation 19.6 gives the hour angles for sunrise (h_{sr}) and sunset (h_{ss}) as

$$h_{ss} \text{ or } h_{sr} = \pm \cos^{-1}[-\tan L \cdot \tan \delta_s]. \tag{6.8}$$

It should be emphasized that Equation 6.8 is based on the center of the sun being at the horizon. In practice, sunrise and sunset are defined as the times when the upper limb of the sun is on the horizon. Because the radius of the sun is $16'$, the sunrise would occur when $\alpha = -16'$. Also, at lower solar elevations, the sun will appear on the horizon when it is actually $34'$ below the horizon. Therefore, for apparent sunrise or sunset, $\alpha = -50'$.

Knowledge of the solar angles is helpful in the design of passive solar buildings, especially the placement of windows for solar access and the roof overhang for shading the walls and windows at certain times of the year.

6.2.2 Sun-Path Diagram

The projection of the sun's path on the horizontal plane is called a *sun-path diagram*. Such diagrams are very useful in determining shading phenomena associated with solar

collectors, windows, and shading devices. As shown earlier, the solar angles (α, a_s) depend upon the hour angle, declination, and latitude. Since only two of these variables can be plotted on a 2D graph, the usual method is to prepare a different sun-path diagram for each latitude with variations of hour angle and declination shown for a full year. A typical sun-path diagram is shown in Figure 6.7 for 30° N latitude.

Sun-path diagrams for a given latitude are used by entering them with appropriate values of declination δ_s and hour angle h_s . The point at the intersection of the corresponding δ_s and h_s lines represents the instantaneous location of the sun. The solar altitude can then be read from the concentric circles in the diagram, the azimuth, from the scale around the circumference of the diagram.

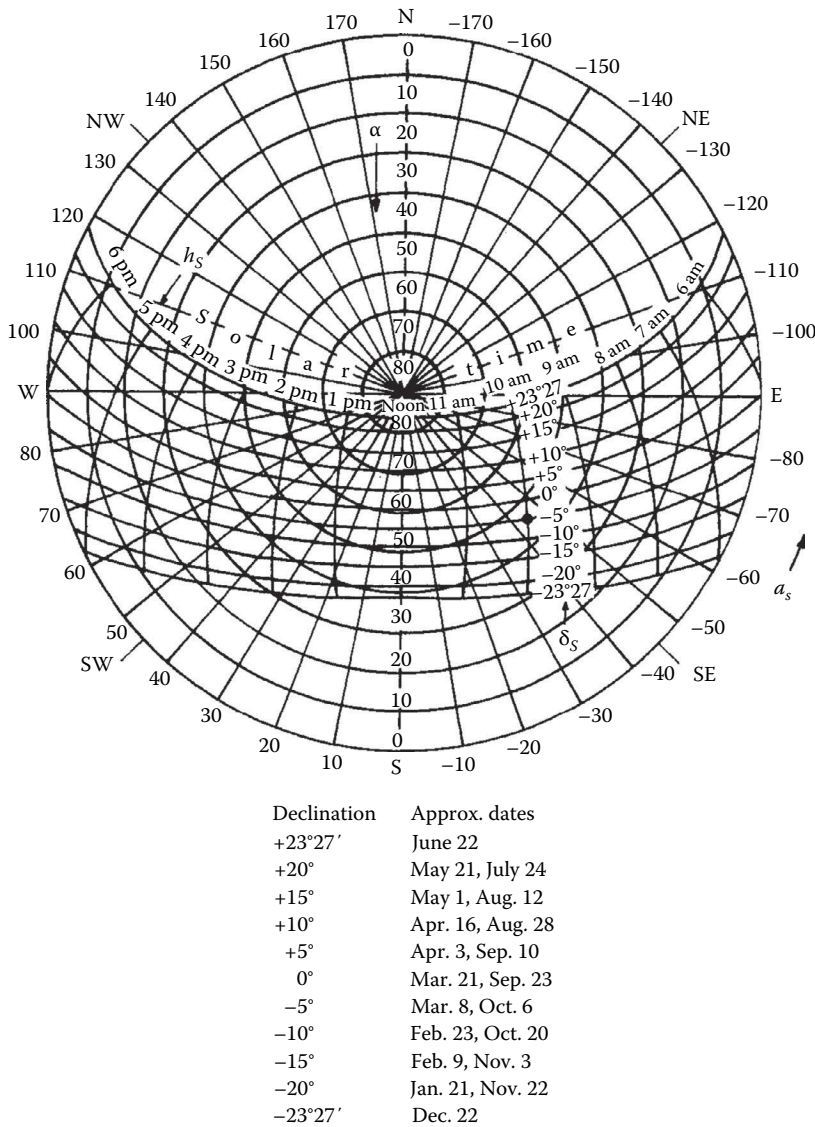


FIGURE 6.7 Sun-path diagram for 30° N latitude showing altitude and azimuth angles.

altitude angle. The profile angle, which is always used in sizing shading devices, is given by

$$\tan \gamma = \sec a \tan \alpha, \tag{6.9}$$

where a is the solar azimuth angle with respect to the wall normal.

Figure 6.8b shows the shadow-angle protractor to the same scale as the sun-path diagram in Figure 6.7. It is used by plotting the limiting values of profile angle γ and azimuth angle a , which will start to cause shading of a particular point. The shadow-angle protractor is usually traced onto a transparent sheet so that the shadow map constructed on it can be placed over the pertinent sun-path diagram to indicate the times of day and months of the year during which shading will take place. The use of the shadow-angle protractor is best illustrated by an example.

Example 6.1

A solar building with a south-facing collector is sited to the north-northwest of an existing building. Prepare a shadow map showing what months of the year and what part of the day point C at the base of the solar collector will be shaded. Plan and elevation views are shown in Figure 6.9. Latitude = 40° N.

Solution

The limiting profile angle for shading is 40° and the limiting azimuth angles are -45° and +10° as shown in Figure 6.9. These values are plotted on the shadow-angle protractor (Figure 6.10a). The shadow map, when superimposed on the sun-path

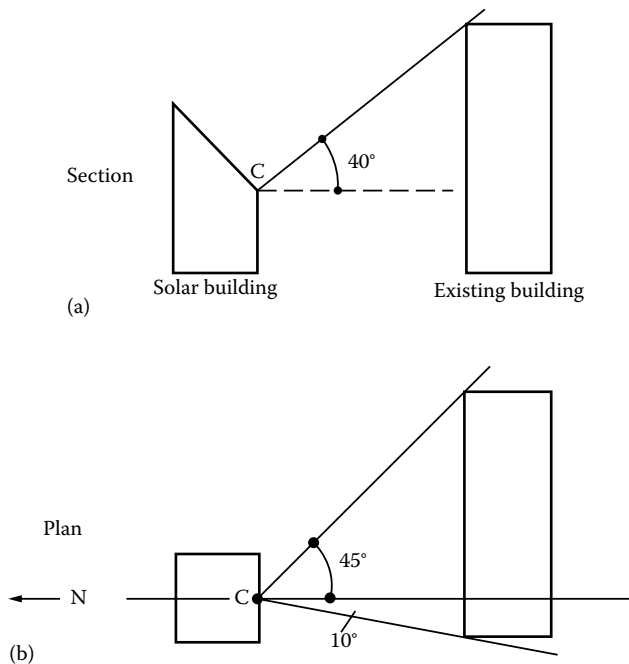
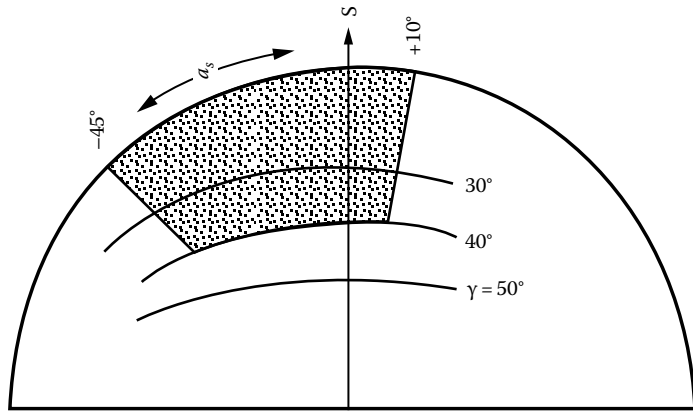
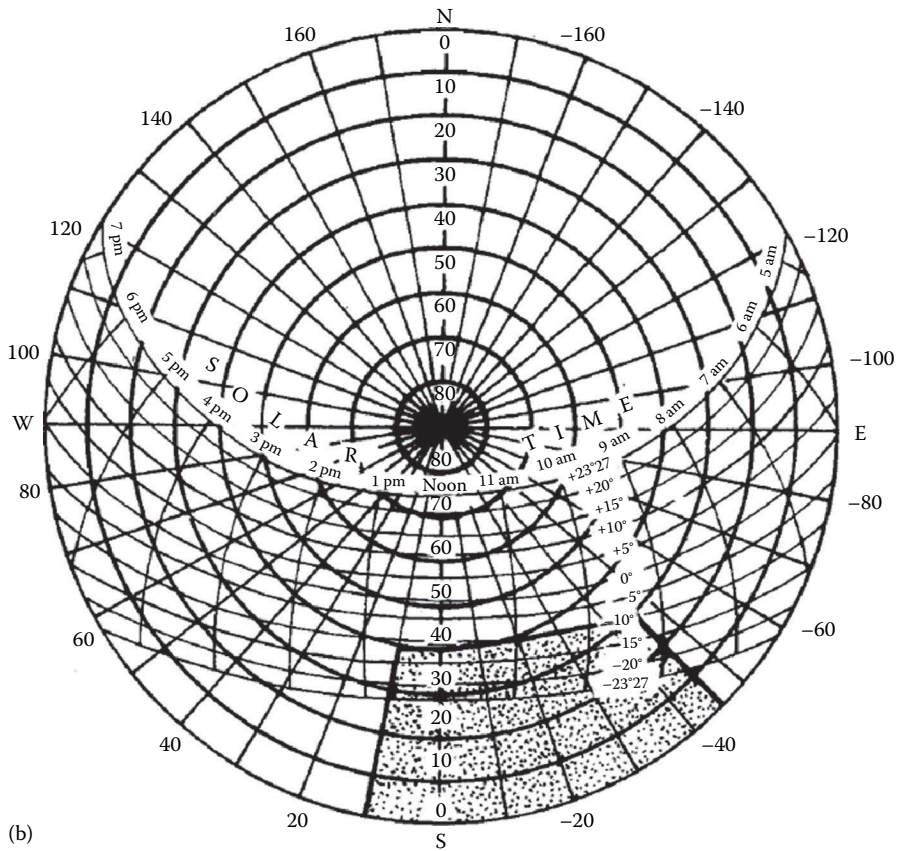


FIGURE 6.9 Elevation (a) and plan (b) view of proposed solar building and existing building, which may shade solar collector at point C.



(a)



(b)

FIGURE 6.10

(a) Shadow map constructed for the example shown in Figure 2.13 and (b) shadow map superimposed on the sun-path diagram.

diagram (Figure 6.10b), shows that point C will be shaded during the following times of day for the periods shown:

Declination	Date	Time of Day
-23°27'	Dec 22	8:45 AM-12:40 PM
-20°	Jan 21, Nov 22	8:55 AM-12:35 PM
-15°	Feb 9, Nov 3	9:10 AM-12:30 PM

In summary, during the period from November 3 to February 9, point C will be shaded between 3 and 4 h. It will be shown later that this represents about a 50% loss in collector performance for point C, which would be unacceptable for a collector to be used for heating a building in winter.

6.3 Solar Radiation

Detailed information about solar radiation availability at any location is essential for the design and economic evaluation of a solar energy system. Long-term measured data of solar radiation are available for a large number of locations in the United States and other parts of the world. Where long-term measured data are not available, various models based on available climatic data can be used to estimate the solar energy availability. Solar energy is in the form of electromagnetic radiation with the wavelengths ranging from about 0.3 μm (10^{-6} m) to over 3 μm , which correspond to ultraviolet (less than 0.4 μm), visible (0.4 and 0.7 μm), and infrared (over 0.7 μm). Most of this energy is concentrated in the visible and the near-infrared wavelength range (see Figure 6.11). The incident solar radiation,

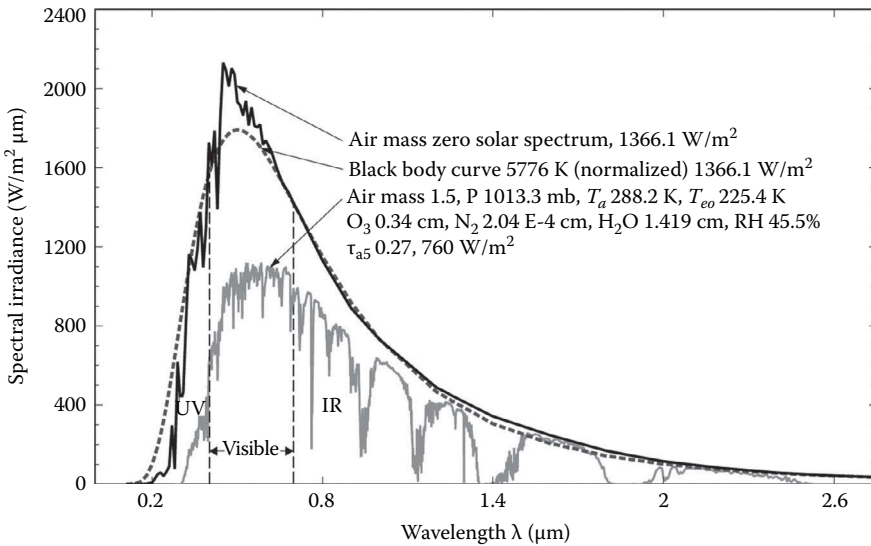


FIGURE 6.11 Extraterrestrial solar radiation spectral distribution. Also shown are equivalent blackbody and atmosphere-attenuated spectra.

sometimes called *insolation*, is measured as irradiance, or the energy per unit time per unit area (or power per unit area). The units most often used are watts per square meter (W/m^2), British thermal units per hour per square foot ($Btu/h-ft^2$), and langley's per minute (calories per square centimeter per minute, $cal/cm^2/min$).

6.3.1 Extraterrestrial Solar Radiation

The average amount of solar radiation falling on a surface normal to the rays of the sun outside the atmosphere of the earth (extraterrestrial) at mean earth–sun distance (D_0) is called the *solar constant*, I_0 . Measurements by NASA indicated the value of the solar constant to be $1353 W/m^2$ ($\pm 1.6\%$), $429 Btu/h-ft^2$, or $1.94 Cal/cm^2/min$ (langley's/min). This value was revised upward by Fröhlich et al. [7] to $1377 W/m^2$ or $437.1 Btu/h-ft^2$ or 1.974 langley's/min, which was the value used in compiling SOLMET data in the United States [37,38]. At present, there is no consensus on the value of the solar constant. Recently, new measurements have found the value of the *solar constant* to be $1366.1 W/m^2$. A value of $1367 W/m^2$ is also used by many references.

The variation in seasonal solar radiation availability at the surface of the earth can be understood from the geometry of the relative movement of the earth around the sun. Since the earth's orbit is elliptical, the earth–sun distance varies during a year, the variation being $\pm 1.7\%$ from the average. Therefore, the extraterrestrial radiation, I , also varies by the inverse square law as follows:

$$I = I_0 \left(\frac{D_0}{D} \right)^2, \quad (6.10)$$

where

D is the distance between the sun and the earth

D_0 is the yearly mean earth–sun distance (1.496×10^{11} m)

The $(D_0/D)^2$ factor may be approximated as [42]

$$\begin{aligned} (D_0/D)^2 = & 1.00011 + 0.034221 \cos(x) + 0.00128 \sin(x) \\ & + 0.000719 \cos(2x) + 0.000077 \sin(2x), \end{aligned} \quad (6.11)$$

where

$$x = \frac{360(n-1)}{365^\circ}, \quad (6.12)$$

and n = day number (starting from January 1 as 1). The following approximate relationship may also be used without much loss of accuracy:

$$I = I_0 [1 + 0.034 \cos(360n/365.25)^\circ]. \quad (6.13)$$

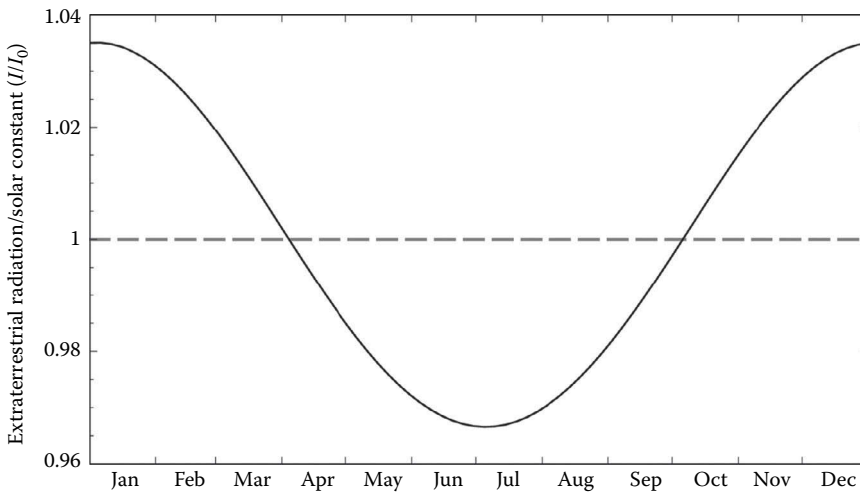


FIGURE 6.12
Effect of the time of year on the ratio of extraterrestrial radiation to the nominal solar constant.

Figure 6.12 also shows the relationship of the extraterrestrial solar radiation to the solar constant. For many solar energy applications, such as photovoltaics and photocatalysis, it is necessary to examine the distribution of energy within the solar spectrum. Figure 6.11 shows the spectral irradiance at the mean earth–sun distance for a solar constant of 1366.1 W/m^2 as a function of wavelength. The data are also presented in Table 6.2 and their use is illustrated in the following example.

Example 6.2

Calculate the fraction of extraterrestrial solar radiation within the visible part of the spectrum, that is, between 0.40 and $0.70 \mu\text{m}$.

Solution

The first column in Table 6.2 gives the wavelength. The second column gives the averaged solar spectral irradiance in a band centered at the wavelength in the first column. The fourth column, D_λ , gives the percentage of solar total radiation at wavelengths shorter than the value of λ in the first column. At a value of $0.40 \mu\text{m}$, 8.12% of the total radiation occurs at shorter wavelengths. At a wavelength of $0.70 \mu\text{m}$, 47.25% of the radiation occurs at shorter wavelengths. Consequently, 39.13% of the total radiation lies within the band between 0.40 and $0.70 \mu\text{m}$, and the total energy received outside the earth's atmosphere within that spectral range is 535 W/m^2 during equinoxes.

6.4 Estimation of Terrestrial Solar Radiation

As extraterrestrial solar radiation, I , passes through the atmosphere, a part of it is reflected back into space, a part is absorbed by air and water vapor, and some gets scattered by molecules of air, water vapor, aerosols, and dust particles (Figure 6.13). The part of solar radiation that reaches the surface of the earth with essentially no change in direction is

TABLE 6.2

Extraterrestrial Solar Irradiance

λ (μm)	E_{λ} ^a ($\text{W}/\text{m}^2 \mu\text{m}$)	D_{λ} ^b (%)	λ (μm)	E_{λ} ($\text{W}/\text{m}^2 \mu\text{m}$)	D_{λ} (%)	λ (μm)	E_{λ} ($\text{W}/\text{m}^2 \mu\text{m}$)	D_{λ} (%)
0.115	0.00799	3.76E-04	0.43	1389	11.98	0.90	889.60	63.91
0.14	0.07694	1.07E-03	0.44	1848	13.25	1.00	730.70	69.84
0.16	0.20640	1.25E-03	0.45	2131	14.72	1.2	488.60	78.55
0.18	2.06	2.45E-03	0.46	2092	16.26	1.4	342.90	84.58
0.20	7.93	8.68E-03	0.47	2010	17.79	1.6	247.70	88.89
0.22	51.91	0.05	0.48	2102	19.32	1.8	168.20	91.88
0.23	59.09	0.08	0.49	2072	20.78	2.0	115.90	93.91
0.24	42.19	0.12	0.50	1932	22.24	2.2	82.58	95.35
0.25	62.28	0.16	0.51	1915	23.66	2.4	58.47	96.36
0.26	90.16	0.22	0.52	1864	25.00	2.6	43.54	97.10
0.27	297.50	0.38	0.53	1938	26.38	2.8	33.25	97.65
0.28	78.46	0.52	0.54	1813	27.78	3.0	25.60	98.08
0.29	617.70	0.74	0.55	1905	29.16	3.2	20.08	98.42
0.30	416.60	1.14	0.56	1812	30.52	3.4	15.75	98.68
0.31	464.80	1.56	0.57	1803	31.86	3.6	12.83	98.89
0.32	836.30	2.08	0.58	1818	33.19	3.8	10.39	99.06
0.33	1162	2.72	0.59	1716	34.51	4.0	8.30	99.19
0.34	1133	3.42	0.60	1737	35.80	4.5	5.03	99.43
0.35	1081	4.12	0.62	1681	38.29	5.0	3.27	99.58
0.36	1188	4.84	0.64	1591	40.68	6.0	1.64	99.75
0.37	1376	5.67	0.66	1517	42.94	7.0	0.90360	99.84
0.38	1096	6.50	0.68	1474	45.14	8.0	0.53890	99.89
0.39	1301	7.26	0.70	1413	47.25	10.0	0.22720	99.94
0.40	1727	8.12	0.72	1361	49.29	15.0	0.04418	99.98
0.41	1610	9.39	0.75	1273	52.16	20.0	0.01385	99.99
0.42	1787	10.71	0.80	1129	56.54	50.0	0.00036	100.0

Source: Adapted from Gueymard, C., *Sol. Energ.* 76, 423, 2003.

Note: Solar constant = 1366.1 W/m^2 .

^a E_{λ} is the solar spectral irradiance.

^b D_{λ} is the percentage of the solar constant associated with wavelengths shorter than λ .

called *direct* or *beam radiation*. The scattered diffuse radiation reaching the surface from the sky is called the *sky diffuse radiation*.

Although extraterrestrial radiation can be predicted with certainty,* radiation levels on the earth are subject to considerable uncertainty resulting from local climatic interactions. The most useful solar radiation data are based on long-term (30 years or more) measured average values at a location, which unfortunately are not available for most locations in the world. For such locations, an estimating method (theoretical model) based on some measured climatic parameter may be used. This chapter describes several ways of estimating terrestrial solar radiation; all have large uncertainties (as much as $\pm 30\%$) associated with them.

6.4.1 Atmospheric Extinction of Solar Radiation

As solar radiation I travels through the atmosphere, it is attenuated due to absorption and scattering. If K is the local extinction coefficient of the atmosphere, the

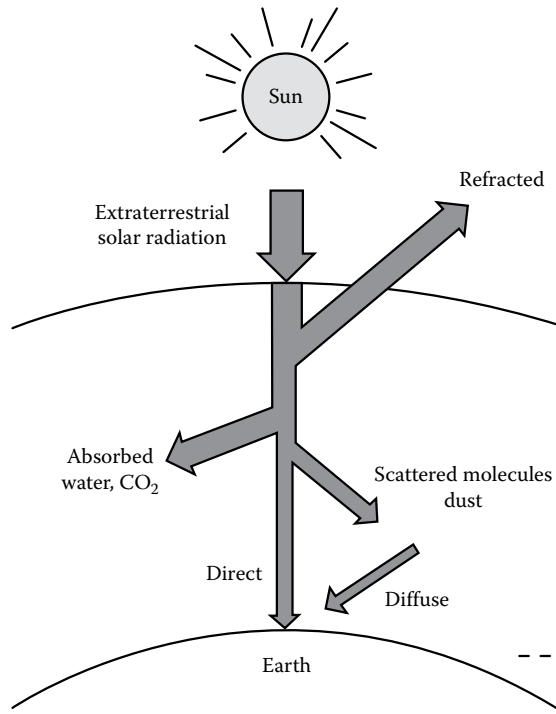


FIGURE 6.13
Attenuation of solar radiation as it passes through the atmosphere.

beam solar radiation at the surface of the earth can be written according to Bouger’s law as

$$I_{b,N} = Ie^{-\int kdx}, \tag{6.14}$$

where $I_{b,N}$ is the instantaneous beam solar radiation per unit area normal to the sun’s rays and x is the length of travel through the atmosphere. If L_o is the vertical thickness of the atmosphere and

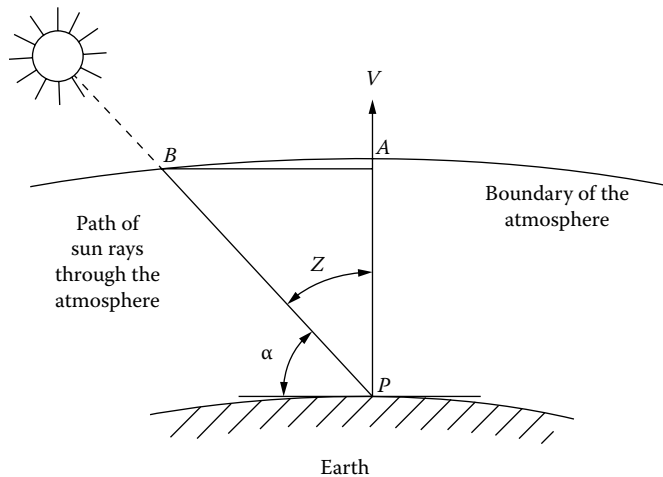
$$\int_0^{L_o} Kdx = k, \tag{6.15}$$

the beam normal solar radiation for a solar zenith angle of z will be

$$I_{b,N} = Ie^{-k\sec z} = Ie^{-k/\sin \alpha} = Ie^{-km}, \tag{6.16}$$

where m is a dimensionless path length of sunlight through the atmosphere, sometimes called the *air mass ratio* (Figure 6.14):

$$m = \frac{\overline{BP}}{AP} \approx \frac{1}{\cos z} \approx \frac{1}{\sin \alpha}. \tag{6.17}$$

**FIGURE 6.14**

Air mass definition; air mass $m = BP/AP = \text{cosec } \alpha$, where α is the altitude angle. The atmosphere is idealized as a constant thickness layer.

The following equation gives a more accurate value of air mass according to Kasten and Young (1989):

$$m \approx \frac{1}{\sin \alpha + 0.50572 (6.07995 + \alpha)^{-1.6364}} \quad (6.18)$$

where α is expressed in degrees. When solar altitude angle is 90° (sun is overhead), $m = 1$.

6.4.2 Clear Sky Radiation Model

Gueymard and Thevenard (2009) have described a model that can be used to model solar radiation for clear days for a large number of locations in the world. This model was developed for ASHRAE to calculate the solar heat gain for fenestration; therefore, they named it the ASHRAE clear sky model. This is a simple model that was developed based on a large number of simulations using sophisticated spectral simulations using the spectral model of the atmospheric radiative transfer of sunshine (SMARTS) spectral code developed by Gueymard (2000, 2005b, 2008a) and validating with ground-based measurements. Based on the detailed simulations, Gueymard developed a simple two-band solar irradiance model, the reference evaluation of solar transmittance, 2 (REST2), that can model clear sky solar irradiance very accurately. The proposed model was developed in two steps:

1. Solar transmittance of clear sky was modeled based on two spectral bands, the first band from 290 to 700 nm, characterized by absorption by molecules and aerosols, and the second band from 700 to 4000 nm, characterized by absorption by water vapor and CO_2 . The two-band clear sky radiation model was used to calculate clear sky solar irradiance for a large number of *typical* cases and compared with the data covering a large part of the world. Figure 6.15 shows the global sites used in the validation.
2. The second step consisted in developing a condensed model depending on only two monthly parameters described later in this section.

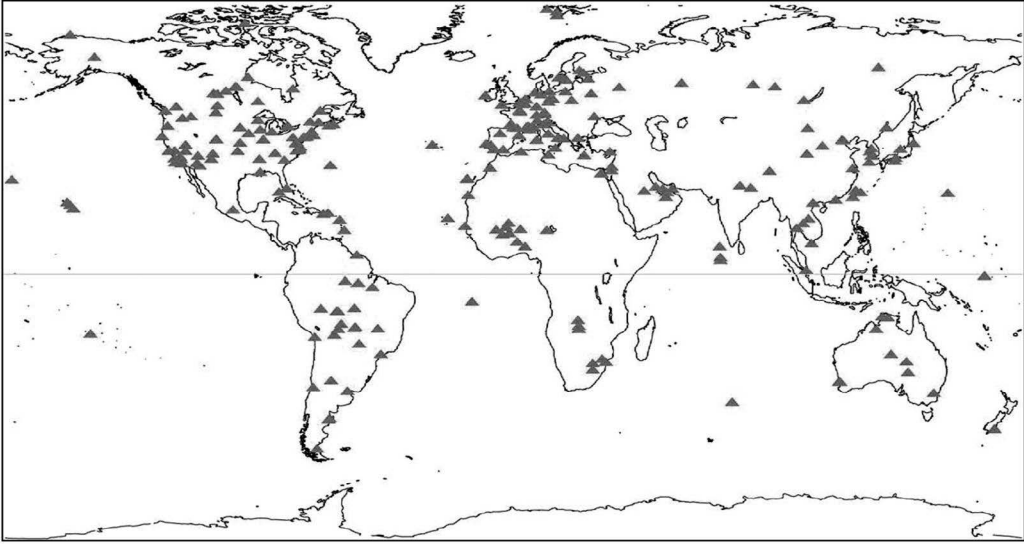


FIGURE 6.15

World sites of interest used in the model. (From Gueymard, C.A. and Thevenard, D., *Solar Energy*, 82, 272, 2009.)

According to the ASHRAE model, the beam and diffuse components are calculated as

$$I_{b,N} = I(e^{-\tau_b m^b}), \quad (6.19)$$

$$I_{d,h} = I(e^{-\tau_d m^d}), \quad (6.20)$$

where

$I_{b,N}$ is the beam normal irradiance per unit area normal to the sun rays

$I_{d,h}$ is the diffuse horizontal irradiance per unit area on a horizontal surface

I is the extraterrestrial normal irradiance

m is the air mass

τ_b , τ_d are the beam and diffuse optical depths (τ_b and τ_d are more correctly termed pseudo-optical depths, because optical depth is usually employed when the air mass coefficient is unity)

b , d are the beam and diffuse air mass exponents

Values of τ_b and τ_d are location-specific and vary during the year. They embody the dependence of clear sky solar radiation upon local conditions, such as elevation, precipitable water content, and aerosols. Their average values are tabulated for the 21st day of each month for all the locations in the tables of climatic design conditions (*ASHRAE Handbook*, 2009 Fundamentals).

Air mass exponents b and d are correlated to τ_b and τ_d through the following empirical relationships:

$$b = 1.219 - 0.043 \tau_b - 0.151 \tau_d - 0.204 \tau_b \cdot \tau_d \quad (6.21)$$

$$d = 0.202 + 0.852 \tau_b - 0.007 \tau_d - 0.357 \tau_b \cdot \tau_d. \quad (6.22)$$

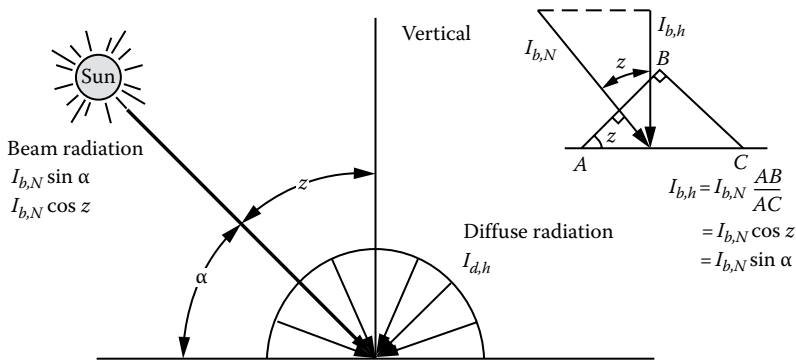


FIGURE 6.16
Solar radiation on a horizontal surface.

This radiation model describes a simple parameterization of a sophisticated broadband radiation model and provides accurate predictions of $I_{b,N}$ and $I_{d,h}$ even at sites where the atmosphere is very hazy or humid most of the time.

Solar radiation on a horizontal surface is given by (Figure 6.16)

$$I_h = (I_{b,N} \sin \alpha + I_{d,h}). \tag{6.23}$$

6.4.3 Solar Radiation on a Tilted Surface

Solar radiation on an arbitrary tilted surface having a tilt angle of β from the horizontal and an azimuth angle of a_w (assumed + west of south), as shown in Figure 6.17, is the sum of components consisting of beam ($I_{b,c}$), sky diffuse ($I_{d,c}$), and ground-reflected solar radiation ($I_{r,c}$):

$$I_c = I_{b,c} + I_{d,c} + I_{r,c}. \tag{6.24}$$

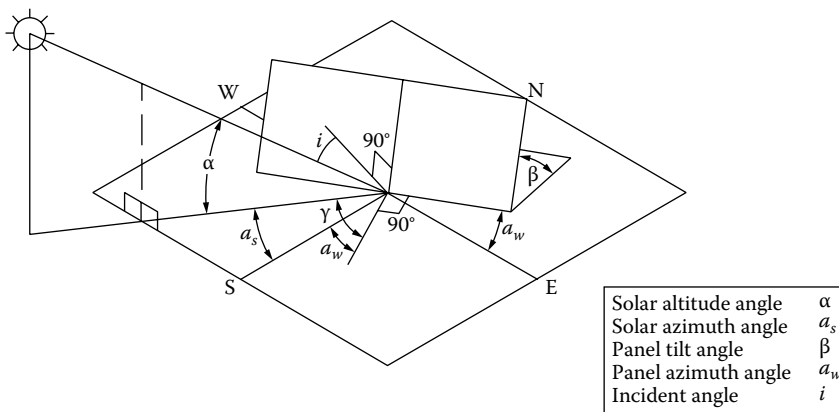


FIGURE 6.17
Definitions of solar angles for a tilted surface.

If i is the *angle of incidence* of the beam radiation on the tilted surface, it is simple to show that the instantaneous beam radiation on the surface per unit area is

$$I_{b,c} = I_{b,N} \cos i. \quad (6.25)$$

From the geometry in Figure 6.17, it can be shown that the angle of incidence i for the surface (angle between the normal to the surface and a line collinear with the sun's rays) is related to the solar angles as

$$\cos i = \cos \alpha \cos (a_s - a_w) \sin \beta + \sin \alpha \cos \beta. \quad (6.26)$$

The diffuse radiation on the surface ($I_{d,c}$) can be obtained by multiplying the sky diffuse radiation on a horizontal surface by the view factor between the sky and the surface:*

$$\begin{aligned} I_{d,c} &= I_{d,h} (I + \cos \beta) / 2 \\ &= I_{d,h} \cos^2(\beta/2). \end{aligned} \quad (6.27)$$

The ground-reflected solar radiation can be found from the total solar radiation incident on a horizontal surface and the ground reflectance ρ as

$$I_{r,c} = I_h \rho. \quad (6.28)$$

The part of I_r intercepted by the tilted surface can be found by multiplying the ground-reflected radiation by the view factor between the surface* and the ground:

$$\begin{aligned} I_{r,c} &= \rho I_h (1 - \cos \beta) / 2 = \rho I_h \sin^2(\beta/2) \\ &= \rho (I_{b,h} \sin \alpha + I_{d,h}) \sin^2(\beta/2). \end{aligned} \quad (6.29)$$

For ordinary ground or grass, ρ is approximately 0.2, and for snow-covered ground, it can be taken as approximately 0.8.

Example 6.3a

Find the instantaneous solar radiation at 12:00 noon Eastern Standard Time on a solar collector surface ($\beta = 30^\circ$, $a_w = +10^\circ$) on February 1st in Tampa, FL.

Solution

For Tampa International Ap, $L = 2796$ N (+), $L_{local} = 82.54$ W (+), and $L_{ST} = 75$ W (+) for February 1st; $n = 32$.

The declination angles for this day are

$$\begin{aligned} \delta_s &= 23.45^\circ \sin \left[\frac{360}{365} (284 + 32) \right] \\ \delta_s &= -17.51^\circ \end{aligned}$$

The local time is 12:00 PM. The solar time is given by

$$ST = LST + ET + (L_{st} - L_{local}) \cdot 4 \frac{\text{min}}{1^\circ}.$$

The equation of time is

$$B = \frac{360}{364}(32 - 81) = -48.46^\circ$$

$$\begin{aligned} ET(\text{min}) &= 9.87(2 \times (-48.46^\circ)) - 7.53 \cos(-48.46^\circ) - 1.5 \sin(-48.46^\circ) \\ &= -13.66 \text{ min.} \end{aligned}$$

Then the solar time is

$$ST = 12:00 - 13.66 \text{ min} + (75^\circ - 82.54^\circ) \times 4 = 11:16 \text{ AM.}$$

The hour angle is

$$h_s = (ST - 12) \frac{15^\circ}{\text{h}} = (11.26 - 12) \frac{15^\circ}{\text{h}} = -11.1^\circ.$$

The solar altitude angle is

$$\begin{aligned} \sin \alpha &= \cos \delta_s \cos L \cosh_s + \sin \delta_s \sin L \\ &= \cos(-17.51^\circ) \cos(27.96^\circ) \cos(-11.1^\circ) + \sin(-17.51^\circ) \sin(27.96^\circ) \end{aligned}$$

and

$$\alpha = 43.30^\circ.$$

The solar azimuth angles are defined by

$$\sin a_s = \cos \delta_s \frac{\sin h_s}{\cos \alpha} = \cos(-17.51^\circ) \frac{\sin(-11.1^\circ)}{\cos(43.30^\circ)}$$

and

$$a_s = -14.61^\circ.$$

We need to find out if $|a_s|$ is greater than 90° .

For

$$L > \delta_s,$$

$$\begin{aligned} t_E &= 12:00 - \left[\cos^{-1} \left(\frac{\tan \delta_s}{\tan L} \right) \right] \frac{\text{h}}{15^\circ} \\ &= 12:00 - \left[\cos^{-1} \left(\frac{\tan(-17.51^\circ)}{\tan(27.96^\circ)} \right) \right] \frac{\text{h}}{15^\circ} \\ &= 3.5689 \text{ h} \end{aligned}$$

Given that $ST > t_E$, the sun is south, and $a_s = -14.61^\circ$. The air mass is as follows

$$\begin{aligned} m &= \frac{1}{\sin(43.30^\circ) + 0.50572(6.07995 + 43.30^\circ)^{-1.6364}} \\ &= 1.4565. \end{aligned}$$

TABLE 6.3

Data for Tampa International AP, FL

Lat, 27.96N; long, 82.54W; elev, 3 m												
Month	Jan	Feb	Mar	Apr	May	Jun	Jul	Aug	Sep	Oct	Nov	Dec
τ_b	0.344	0.364	0.391	0.403	0.47	0.473	0.509	0.493	0.445	0.398	0.36	0.346
τ_d	2.531	2.403	2.271	2.272	2.029	2.07	1.95	2.01	2.19	2.356	2.488	2.512
$I_{b,N}$, noon (W/m ²)	902	908	899	895	831	823	793	805	836	861	876	882
$I_{d,h}$, noon (W/m ²)	94	113	134	137	174	167	188	175	143	116	97	93

Source: Data taken from *ASHRAE Handbook: Fundamentals: SI Edition*, American Society of Heating, Refrigeration and Air-Conditioning Engineers, Inc., 2009.

The data for the Tampa International AP, FL, are shown in Table 6.3.

The *pseudo*-optical depths are tabulated for the 21st day of each month for all the locations in the tables of climatic design. Values for other days of the year should be found by interpolation. For this example, by using linear interpolation between January and February, the *pseudo*-optical depths are

$$\tau_b = 0.35109$$

$$\tau_d = 2.48558.$$

The parameters for air mass are as follows:

$$b = 1.219 - 0.043\tau_b - 0.151\tau_d - 0.204\tau_b\tau_d = 0.6506$$

$$d = 0.202 - 0.852\tau_b - 0.007\tau_d - 0.357\tau_b\tau_d = -0.4261.$$

The extraterrestrial solar radiation is given by

$$\begin{aligned} I &= I_0 \left[1 + 0.034 \cos \left(\frac{360n}{365.25} \right)^\circ \right] \\ &= 1366.1 \left[1 + 0.034 \cos \left(360 \times \frac{32}{365.26} \right)^\circ \right] = 1406 \text{ W/m}^2. \end{aligned}$$

The direct solar radiation component is

$$\begin{aligned} I_{b,N} &= Ie^{-\tau_b m^b} \\ &= 1406 \exp(-0.35109 \cdot 1.4565^{0.6506}) \\ &= 898 \text{ W/m}^2. \end{aligned}$$

The diffuse solar radiation on a horizontal surface is

$$\begin{aligned} I_{d,h} &= Ie^{-\tau_d m^d} \\ &= 1406 \exp(-2.48558 \cdot 1.4565^{-0.4261}) \\ &= 169 \text{ W/m}^2. \end{aligned}$$

The instantaneous beam radiation on the surface per unit area is given by

$$I_{b,c} = I_{b,N} \cos i.$$

For this geometry, the cosine of the angle of incidence is

$$\begin{aligned} \cos i &= \cos \alpha \cos(a_s - a_w) \sin \beta + \sin \alpha \cos \beta \\ &= \cos(43.30^\circ) \cos(-14.61^\circ - (+10^\circ)) \sin(30^\circ) + \sin(43.30^\circ) \cos(30^\circ) \\ &= 0.9248. \end{aligned}$$

Then the beam radiation is

$$I_{b,c} = 898 \times 0.9248 = 830 \text{ W/m}^2.$$

The diffuse radiation on the collector surface will be

$$\begin{aligned} I_{d,c} &= I_{d,h} \cos^2\left(\frac{\beta}{2}\right) \\ &= 169 \cos^2\left(\frac{30^\circ}{2}\right) \\ &= 158 \text{ W/m}^2. \end{aligned}$$

The ground-reflected solar radiation is

$$I_{r,c} = \rho(I_{b,N} \sin \alpha + I_{d,h}) \sin^2\left(\frac{\beta}{2}\right).$$

Assuming that the solar collector is surrounded by ordinary ground or grass, then $\rho \approx 0.2$:

$$\begin{aligned} I_{r,c} &= 0.2(898 \sin(43.30^\circ) + 169.10) \sin^2\left(\frac{30^\circ}{2}\right) \\ &= 11 \text{ W/m}^2. \end{aligned}$$

Finally, the total radiation on a tilted collector surface is

$$I_c = I_{b,c} + I_{d,c} + I_{r,c} = 830 + 158 + 11 = 999 \text{ W/m}^2.$$

Example 6.3b

Repeat the calculations in Example 6.3a for a north-facing solar collector ($\beta = 30^\circ$, $a_w = 10^\circ$) in Canberra, Australia (latitude = $35^\circ - 18' \Sigma$, longitude = $149^\circ - 11' \text{ E}$, Standard Meridian = 150° E).

Solution

As the day number has not been changed, the values of the δ_s and ET remain the same:

$$\delta_s = -17.51^\circ$$

$$ET = -13.66 \text{ min.}$$

The local time is 12:00 PM. The solar time is given by

$$ST = 12:00 - 13.66 \text{ min} + (-150^\circ + 149.18^\circ) \times 4 \frac{\text{min}}{1^\circ} = 11:43 \text{ AM.}$$

The hour angle is

$$h_s = (ST - 12) \frac{15^\circ}{\text{h}} = (11.72 - 12) \frac{15^\circ}{\text{h}} = -4.2^\circ.$$

The solar altitude angle is

$$\begin{aligned} \sin \alpha &= \cos \delta_s \cos L \cosh_s + \sin \delta_s \sin L \\ &= \cos(-17.51^\circ) \cos(-35.3^\circ) \cos(-4.2^\circ) + \sin(-17.51^\circ) \sin(-35.3^\circ) \end{aligned}$$

and

$$\alpha = 71.82^\circ.$$

The solar azimuth angles are defined by

$$\sin a_s = \cos \delta_s \sin h_s / \cos \alpha = \cos(-17.51^\circ) \sin(-4.2^\circ) / \cos(71.82^\circ)$$

and

$$a_s = -12.93^\circ.$$

The air mass is as follows:

$$m = \frac{1}{\sin(71.82^\circ) + 0.50572(6.07995 + 71.82^\circ)^{-1.6364}} = 1.052.$$

The data for the Canberra airport are shown in Table 6.4.

By using linear interpolation between January and February, the *pseudo*-optical depths are

$$\tau_b = 0.3548$$

$$\tau_d = 2.4584.$$

TABLE 6.4

Data for Canberra Airport

Lat, 35.30S; long, 149.20E; elev, 580 m												
Month	Jan	Feb	Mar	Apr	May	Jun	Jul	Aug	Sep	Oct	Nov	Dec
τ_b	0.363	0.340	0.326	0.313	0.299	0.291	0.292	0.297	0.315	0.318	0.334	0.342
τ_d	2.403	2.559	2.606	2.638	2.730	2.747	2.702	2.678	2.582	2.609	2.520	2.519
$I_{b,N}$, noon (W/m ²)	972	974	952	908	871	853	869	915	948	986	995	998
$I_{d,h}$, noon (W/m ²)	126	104	94	82	69	64	70	78	94	98	111	113

Source: Data taken from: 2009 ASHRAE Handbook: Fundamentals: SI Edition, American Society of Heating, Refrigeration and Air-Conditioning Engineers, Inc.

The parameters for air mass are as follows:

$$b = 1.219 - 0.043\tau_b - 0.151\tau_d - 0.204\tau_b\tau_d = 0.6546$$

$$d = 0.202 - 0.852\tau_b - 0.007\tau_d - 0.357\tau_b\tau_d = -0.4289.$$

The extraterrestrial solar radiation is given by

$$I = I_0 \left[1 + 0.034 \cos \left(\frac{360n}{365.25} \right)^\circ \right] = 1406 \text{ W/m}^2.$$

The direct solar radiation component is

$$I = I_0 \left[1 + 0.034 \cos \left(\frac{360n}{365.25} \right)^\circ \right] = 1406 \text{ W/m}^2.$$

The diffuse solar radiation on a horizontal surface is

$$I_{d,h} = Ie^{-\tau_a m^d}$$

$$= 1406 \exp(-2.4584 \times 1.0521^{-0.4289})$$

$$= 127 \text{ W/m}^2.$$

The cosine of the angle of incidence is

$$\cos i = \cos \alpha \cos(a_s - a_w) \sin \beta + \sin \alpha \cos \beta$$

$$= \cos(71.82^\circ) \cos(-12.93^\circ - (+10^\circ)) \sin(30^\circ) + \sin(71.82^\circ) \cos(30^\circ)$$

$$= 0.9665.$$

Then the beam radiation is

$$I_{b,c} = I_{b,N} \cos i$$

$$I_{b,c} = 974 \times 0.9665 = 941 \text{ W/m}^2.$$

The diffuse radiation on the collector surface will be

$$I_{d,c} = I_{d,h} \cos^2 \left(\frac{\beta}{2} \right)$$

$$= 127 \cos^2 \left(\frac{30^\circ}{2} \right)$$

$$= 118 \text{ W/m}^2.$$

The ground-reflected solar radiation is

$$I_{r,c} = \rho(I_{b,N} \sin \alpha + I_{d,h}) \sin^2 \left(\frac{\beta}{2} \right).$$

Assuming that the solar collector is surrounded by ordinary ground or grass, then $\rho \approx 0.2$:

$$\begin{aligned} I_{r,c} &= 0.2(974 \sin(71.82^\circ) + 127) \sin^2\left(\frac{30^\circ}{2}\right) \\ &= 14 \text{ W/m}^2. \end{aligned}$$

Finally, the total radiation on a tilted collector surface is

$$I_c = I_{b,c} + I_{d,c} + I_{r,c} = 941 + 118 + 14 = 1073 \text{ W/m}^2.$$

6.4.4 Monthly Solar Radiation Estimation Models

One of the earliest methods of estimating solar radiation on a horizontal surface was proposed by the pioneer spectroscopist Angström. It was a simple linear model relating average horizontal radiation to clear-day radiation and to the sunshine level, that is, percent of possible hours of sunshine. Since the definition of a clear day is somewhat nebulous, Page [34] refined the method and based it on extraterrestrial radiation instead of the ill-defined clear day:

$$\begin{aligned} \bar{H}_h &= \bar{H}_{o,h} \left(a + b \frac{\bar{n}}{\bar{N}} \right) \\ &= \bar{H}_{o,h} \left(a + b \frac{\overline{PS}}{100} \right) \end{aligned} \quad (6.30)$$

where

\bar{H}_h and $\bar{H}_{o,h}$ are the horizontal terrestrial and horizontal extraterrestrial radiation levels averaged for a month

\overline{PS} is the monthly averaged percent of possible sunshine (i.e., hours of sunshine/maximum possible duration of sunshine $\times 100$)

a and b are constants for a given site

\bar{n} and \bar{N} are the monthly average numbers of hours of bright sunshine and day length, respectively

The ratio \bar{n}/\bar{N} is also equivalent to the monthly average percent sunshine (\overline{PS}). $\bar{H}_{o,h}$ can be calculated by finding $H_{o,h}$ from Equation 6.31, using Equations 6.13 and 6.30, and averaging $I_{o,h}$ for the number of days in each month:

$$H_{o,h} = \int_{t_{sr}}^{t_{ss}} I \sin \alpha dt. \quad (6.31)$$

Some typical values of a and b are given in Table 6.5 [26].

A number of researchers found Angström–Page-type correlations for specific locations that are listed in Table 6.6. Some of these include additional parameters such as relative humidity and ambient temperature. Correlations listed in the table may be used for the specific locations for which they were developed.

Another meteorological variable that could be used for solar radiation prediction is the opaque cloud cover recorded at many weather stations around the world. This quantity is

TABLE 6.5Coefficients *a* and *b* in the Angström–Page Regression Equation

Location	Climate ^a	Sunshine Hours in Percentage of Possible		<i>a</i>	<i>b</i>
		Range	Avg.		
Albuquerque, NM	BS-BW	68–85	78	0.41	0.37
Atlanta, GA	Cf	45–71	59	0.38	0.26
Blue Hill, MA	Df	42–60	52	0.22	0.50
Brownsville, TX	BS	47–80	62	0.35	0.31
Buenos Aires, Argentina	Cf	47–68	59	0.26	0.50
Charleston, SC	Cf	60–75	67	0.48	0.09
Dairen, Manchuria	Dw	55–81	67	0.36	0.23
El Paso, TX	BW	78–88	84	0.54	0.20
Ely, NV	BW	61–89	77	0.54	0.18
Hamburg, Germany	Cf	11–49	36	0.22	0.57
Honolulu, HI	Af	57–77	65	0.14	0.73
Madison, WI	Df	40–72	58	0.30	0.34
Malange, Angola	Aw-BS	41–84	58	0.34	0.34
Miami, FL	Aw	56–71	65	0.42	0.22
Nice, France	Cs	49–76	61	0.17	0.63
Poona, India (monsoon)	Am	25–49	37	0.30	0.51
Poona, India (dry)		65–89	81	0.41	0.34
Stanleyville, Congo	Af	34–56	48	0.28	0.39
Tamanrasset, Algeria	BW	76–88	83	0.30	0.43

Source: From Lóf, G.O.G. et al., World distribution of solar energy, Engineering Experiment Station Report, University of Wisconsin, Madison, WI, 1966. With permission.

Note: Am, tropical forest climate, monsoon rain, short dry season, but total rainfall sufficient to support rain forest; Aw, tropical forest climate, dry season in winter; BS, steppe or semiarid climate; BW, desert or arid climate; Cf, mesothermal forest climate, constantly moist, rainfall all through the year; Cs, mesothermal forest climate, dry season in winter; Df, microthermal snow forest climate, constantly moist, rainfall all through the year; Dw, microthermal snow forest climate, dry season in winter.

^a Af, tropical forest climate, constantly moist, rainfall all through the year.

a measure of the percent of the sky dome obscured by opaque clouds. Because this parameter contains even less solar information than sunshine values, it has not been useful in predicting long-term solar radiation values. A subsequent section, however, will show that cloud cover, when used with solar altitude angle or air mass, is a useful estimator of hourly direct radiation.

6.5 Models Based on Long-Term Measured Horizontal Solar Radiation

Long-term measured solar radiation data are usually available as monthly averaged total solar radiation per day on horizontal surfaces. In order to use these data for tilted surfaces, the total solar radiation on a horizontal surface must first be broken down into beam and diffuse components. A number of researchers have proposed models to do that, prominent among them being Liu and Jordan, Collares-Pereira and Rabl, and Erbs, Duffie, and Klein.

TABLE 6.6
Angström–Page-Type Correlations for Specific Locations

Authors	Measured Data Correlated	Correlation Equations ^a
Iqbal [16]	Canada, 3 locations	$\frac{\bar{D}_h}{\bar{H}_h} = 0.791 - 0.635 \left(\frac{\bar{n}}{\bar{N}} \right)$ $\frac{\bar{H}_d}{\bar{H}_h} = 0.163 + 0.478 \left(\frac{\bar{n}}{\bar{N}} \right) - 0.655 \left(\frac{\bar{n}}{\bar{N}} \right)^2$ $\frac{\bar{H}_b}{\bar{H}_{o,h}} = -0.176 + 1.45 \left(\frac{\bar{n}}{\bar{N}} \right) - 1.12 \left(\frac{\bar{n}}{\bar{N}} \right)^2$
Garg [8]	India, 11 locations, 20 years' data	$\frac{\bar{H}_h}{\bar{H}_{o,h}} = 0.3156 - 0.4520 \left(\frac{\bar{n}}{\bar{N}} \right)^2$ $\frac{\bar{D}_h}{\bar{H}_{o,h}} = 0.3616 - 0.2123 \left(\frac{\bar{n}}{\bar{N}} \right)$ $\frac{\bar{D}_h}{\bar{H}_h} = 0.8677 - 0.7365 \left(\frac{\bar{n}}{\bar{N}} \right)$
Hussain [14]	India	$\frac{\bar{H}_h}{\bar{H}_{o,h}} = 0.394 + 0.364 \left[\frac{\bar{n}}{\bar{N}'} \right] - 0.0035 W_{at}$ $\frac{\bar{D}_h}{\bar{H}_{o,h}} = 0.306 - 0.165 \left[\frac{\bar{n}}{\bar{N}'} \right] - 0.0025 W_{at}$
Coppolino [5]	Italy	$\frac{\bar{H}_h}{\bar{H}_{o,h}} = 0.67 \left(\frac{\bar{n}}{\bar{N}} \right)^{0.45} \sin(\alpha_{sn})^{0.05}$ <p style="text-align: center;">α_{sn} = Solar elevation at noon on the 15th of each month, degrees</p> $0.15 \leq \frac{\bar{n}}{\bar{N}} \leq 0.90$
Akinoglu and Ecevit [1]	Italy	$\frac{\bar{H}_h}{\bar{H}_{o,h}} = 0.145 + 0.845 \left(\frac{\bar{n}}{\bar{N}} \right) - 0.280 \left(\frac{\bar{n}}{\bar{N}} \right)^2$
Ögelman et al. [33]	Turkey, 2 locations, 3 years' data	$\left(\frac{\bar{H}_h}{\bar{H}_{o,h}} \right) = 0.204 + 0.758 \left(\frac{\bar{n}}{\bar{N}} \right) - 0.250 \left\{ \left[\left(\frac{\bar{n}}{\bar{N}} \right)^2 \right]^2 + \sigma \frac{2/n}{\bar{N}} \right\}$ $\sigma \frac{2/n}{\bar{N}} = 0.035 + 0.326 \left(\frac{\bar{n}}{\bar{N}} \right) - 0.433 \left(\frac{\bar{n}}{\bar{N}} \right)^2$
Gopinathan [10]	40 locations around the world	$\frac{\bar{H}_h}{\bar{H}_{o,h}} = a + b \left(\frac{\bar{n}}{\bar{N}} \right)$ $a = -0.309 + 0.539 \cos L - 0.0639h + 0.290 \left(\frac{\bar{n}}{\bar{N}} \right)$ $b = 1.527 - 1.027 \cos L + 0.0926h - .359 \left(\frac{\bar{n}}{\bar{N}} \right)$

Note: \bar{N}' , maximum duration for which Campbell–Stokes recorder can be active, that is, solar elevation $>5^\circ$; W_{at} , relative humidity $\times (4.7923 + 0.3647T + 0.055T^2 + 0.0003 T^3)$; T , ambient temperature, $^\circ\text{C}$; W_{at} , gm moisture/ m^3 ; h , elevation in km above sea level; L , latitude.

^a \bar{H}_a , \bar{H}_b , $\bar{H}_{o,h}$, \bar{D}_h are monthly averaged daily values.

6.5.1 Monthly Solar Radiation on Tilted Surfaces

In a series of papers, Liu and Jordan [21–25] have developed an essential simplification in the basically complex computational method required to calculate long-term radiation on tilted surfaces. This is called the Liu and Jordan (LJ) method. The fundamental problem in such calculations is the decomposition of long-term measured total horizontal radiation into its beam and diffuse components.

If the decomposition can be computed, the trigonometric analysis presented earlier can be used to calculate incident radiation on any surface in a straightforward manner. Liu and Jordan (LJ) correlated the diffuse-to-total radiation ratio (\bar{D}_h/\bar{H}_h) with the *monthly clearness index* \bar{K}_T , which is defined as

$$\bar{K}_T = \frac{\bar{H}_h}{\bar{H}_{o,h}}, \quad (6.32)$$

where

\bar{H}_h is the monthly averaged terrestrial radiation per day on a horizontal surface

$\bar{H}_{o,h}$ is the corresponding extraterrestrial radiation, which can be calculated from Equation 6.31 by averaging each daily total for a month

The original LJ method was based upon the extraterrestrial radiation at midmonth, which is not truly an average.

The LJ correlation predicts the monthly diffuse (\bar{D}_h) to monthly total \bar{H}_h ratio. It can be expressed by the following empirical equation:

$$\frac{\bar{D}_h}{\bar{H}_h} = 1.390 - 4.027\bar{K}_T + 5.531\bar{K}_T^2 - 3.108\bar{K}_T^3. \quad (6.33)$$

Note that the LJ correlation is based upon a solar constant value of 1394 W/m² (442 Btu/h-ft²), which was obtained from terrestrial observations, whereas the newer value, based on satellite data, is 1377 W/m² (437 Btu/h-ft²). The values of \bar{K}_T must be based on this earlier value of the solar constant to use the LJ method. Collares-Pereira and Rabl [4] conducted a study and concluded that although LJ's approach is valid, their correlations would predict significantly smaller diffuse radiation components. They also concluded that LJ were able to correlate their model with the measured data because they used the measured data that were not corrected for the shade ring (see solar radiation measurements). Collares-Pereira and Rabl also introduced the sunset hour angle h_{ss} in their correlation to account for the seasonal variation in the diffuse component. The Collares-Pereira and Rabl (C-P&R) correlation is

$$\frac{\bar{D}_h}{\bar{H}_h} = 0.775 + 0.347 \left(h_{ss} - \frac{\pi}{2} \right) - \left[0.505 + 0.0261 \left(h_{ss} - \frac{\pi}{2} \right) \right] \cos(2K_T - 1.8), \quad (6.34)$$

where h_{ss} is the sunset hour angle in radians. The C-P&R correlation agrees well with the correlations for India [3], Israel [43], and Canada [39] and is, therefore, preferred to Equation 6.33.

The monthly average beam component \bar{B}_h on a horizontal surface can be readily calculated by simple subtraction since \bar{D}_h is known:

$$\bar{B}_h = \bar{H}_h - \bar{D}_h. \quad (6.35)$$

It will be recalled on an instantaneous basis from Equations 6.23 and 6.25 and Figure 6.17 that

$$I_{b,N} = \frac{I_{b,h}}{\sin \alpha}, \quad (6.36)$$

$$I_{b,c} = I_{b,N} \cos i, \quad (6.37)$$

where $I_{b,h}$ is the instantaneous horizontal beam radiation. Solving for $I_{b,c}$, the beam radiation on a surface,

$$I_{b,c} = I_{b,h} \left(\frac{\cos i}{\sin \alpha} \right). \quad (6.38)$$

The ratio in parentheses is usually called the beam radiation *tilt factor* R_b . It is a purely geometric quantity that converts instantaneous horizontal beam radiation to beam radiation intercepted by a tilted surface.

Equation 6.38 cannot be used directly for the long-term beam radiation \bar{B}_h . To be strictly correct, the instantaneous tilt factor R_b should be integrated over a month with the beam component $I_{b,h}$ used as a weighting factor to calculate the beam tilt factor. However, the LJ method is used precisely when such short-term data as $I_{b,h}$ are not available. The LJ recommendation for the monthly mean tilt factor \bar{R}_b is simply to calculate the monthly average of $\cos i$ and divide it by the same average of $\sin \alpha$. In equation form for south-facing surfaces, this operation yields

$$\bar{R}_b = \frac{\cos(L - \beta) \cos \delta_s \sin h_{sr} + h_{sr} \sin(L - \beta) \sin \delta_s}{\cos L \cos \delta_s \sin h_{sr}(\alpha = 0) + h_{sr}(\alpha = 0) \sin L \sin \delta_s}, \quad (6.39)$$

where the sunrise hour angle $h_{sr}(\alpha = 0)$ in radians is given by Equation 6.8 and h_{sr} is the min $\left[|h_s(\alpha = 0)|, |h_s(i = 90^\circ)| \right]$, respectively, which are evaluated at midmonth. Non-south-facing surfaces require numerical integration or iterative methods to determine \bar{R}_b . The long-term beam radiation on a tilted surface \bar{B}_c is then

$$\bar{B}_c = \bar{R}_b \bar{B}_h, \quad (6.40)$$

which is the long-term analog of Equation 6.27.

Diffuse radiation intercepted by a tilted surface differs from that on a horizontal surface, because a tilted surface does not view the entire sky dome, which is the source of diffuse radiation. If the sky is assumed to be an isotropic source of diffuse radiation, the instantaneous and long-term tilt factors for diffuse radiation, R_d and \bar{R}_d , respectively, are equal and are simply the radiation view factor from the plane to the visible portion of a hemisphere. In equation form,

$$R_d = \bar{R}_d = \cos^2 \frac{\beta}{2} = \frac{(1 + \cos \beta)}{2}. \quad (6.41)$$

In some cases where solar collectors are mounted near the ground, some beam and diffuse radiation reflected from the ground can be intercepted by the collector surface. The tilt factor \bar{R}_r for reflected total radiation ($\bar{D}_h + \bar{B}_h$) is then calculated to be

$$\bar{R}_r = \frac{\bar{R}}{\bar{D}_h + \bar{B}_h} = \rho \sin^2 \frac{\beta}{2} = \frac{\rho(1 - \cos \beta)}{2}, \quad (6.42)$$

in which ρ is the diffuse reflectance of the surface south of the collector assumed uniform and of infinite extent.

For snow, $\rho \cong 0.75$; for grass and concrete, $\rho \cong 0.2$. The total long-term radiation intercepted by a surface \bar{H}_c is then the total of beam, diffuse, and diffusely reflected components:

$$\bar{H}_c = \bar{R}_b \bar{B}_h + \bar{R}_d \bar{D}_h + \bar{R}_r (\bar{D}_h + \bar{B}_h). \quad (6.43)$$

Using Equations 6.41 and 6.42, we have

$$\bar{H}_c = \bar{R}_b \bar{B}_h + \bar{D}_h \cos^2 \frac{\beta}{2} + (\bar{D}_h + \bar{B}_h) \rho \sin^2 \frac{\beta}{2}, \quad (6.44)$$

in which \bar{R}_b is calculated from Equation 6.39.

Example 6.4

Using a value of \bar{H}_h as 16,215 kJ/m²/day for January in place of the long-term measured data for the North Central Sahara Desert at latitude 25° N, find the monthly averaged insolation per day on a south-facing solar collector tilted at an angle of 25° from the horizontal.

Solution

The following solution is for the month of January. Values for the other months can be found by following the same method:

$$\bar{H}_h = 16,215 \text{ kJ/m}^2/\text{day}.$$

From Table A2.2a,

$$\bar{H}_{o,h} = 23,902.$$

Therefore,

$$\bar{K}_T = \frac{\bar{H}_h}{\bar{H}_{o,h}} = 0.678.$$

δ_s and h_{sr} can be found for the middle of the month (January 16):

$$\begin{aligned} \delta_s &= 23.45^\circ \sin[360(284 + 16)365]^\circ \\ &= -21.1^\circ, \end{aligned}$$

$$\begin{aligned} h_{sr}(\alpha = 0) &= -\cos^{-1}(-\tan L \tan \delta) \\ &= -79.6^\circ \quad \text{or} \quad -1.389 \text{ rad} \end{aligned}$$

and

$$h_{ss} = 1.389.$$

Using the C-P&R correlation,

$$\begin{aligned}\frac{\bar{D}_h}{\bar{H}_h} &= 0.775 + 0.347(1.389 - 1.5708) - [0.505 + 0.0261(1.389 - 1.5708)]\cos(2 \times 0.678 - 1.8) \\ &= 0.212.\end{aligned}$$

Therefore,

$$\bar{D}_h = 0.212 \times 16,215 = 3,438 \text{ kJ/m}^2/\text{day}$$

and

$$\bar{B}_h = \bar{H}_h - \bar{D}_h = 12,777 \text{ kJ/m}^2/\text{day}$$

Insolation on a tilted surface can be found from Equation 6.43. We need to find \bar{R}_b from Equation 6.39.

Therefore,

$$\begin{aligned}\bar{R}_b &= \frac{\cos(0)\cos(-21.1^\circ)\sin(-79.6^\circ) - 1.389\sin(0)\sin(-21.1^\circ)}{\cos(25^\circ)\cos(-21.1^\circ)\sin(-79.6^\circ) - 1.389\sin(25^\circ)\sin(-21.1^\circ)} \\ &= 147.\end{aligned}$$

$$\bar{R}_d = \cos^2(25/2) = 0.953.$$

$$\begin{aligned}\bar{R}_r &= \rho \sin^2(\beta/2) \text{ (Assume } \rho = 0.2) \\ &= 0.2\sin^2(12.5^\circ) \\ &= 0.009.\end{aligned}$$

Therefore,

$$\begin{aligned}\bar{H}_c &= (1.47)(12,777) + 0.953(3,438) + 0.009(16,215) \\ &= 22,205 \text{ kJ/m}^2.\end{aligned}$$

6.5.2 Circumsolar or Anisotropic of Diffuse Solar Radiation

The models described in the earlier sections assume that the sky diffuse radiation is isotropic. However, this assumption is not true because of circumsolar radiation (brightening around the solar disk). Although the assumption of isotropic diffuse solar radiation does not introduce errors in the diffuse values on horizontal surfaces, it can result in errors of 10%–40% in the diffuse values on tilted surfaces. A number of researchers have studied the anisotropy of the diffuse solar radiation because of circumsolar radiation. Temps and Coulson [45] introduced an anisotropic diffuse radiation algorithm for tilted surfaces for

clear sky conditions. Klucher [20] refined the Temps and Coulson algorithm by adding a cloudiness function to it:

$$R_d = \frac{1}{2}(1 + \cos\beta)M_1M_2, \quad (6.45)$$

where

$$M_1 = 1 + F \sin^3(\beta/2), \quad (6.46)$$

$$M_2 = 1 + F \cos^2 i \sin^3(z), \quad (6.47)$$

$$F = 1 - \left(\frac{D_h}{H_h} \right)^2. \quad (6.48)$$

Examining F , we find that under overcast skies ($D_h = H_h$), R_d in Equation 6.45 reduces to the isotropic term of LJ. The Klutcher algorithm reduces the error in diffuse radiation to about 5%.

In summary, monthly averaged, daily solar radiation on a surface is calculated by first decomposing total horizontal radiation into its beam and diffuse components using Equation 6.34 or 6.35. Various tilt factors are then used to convert these horizontal components to components on the surface of interest.

6.5.3 Hourly and Daily Solar Radiation on Tilted Surfaces

Accurate determinations of the hourly solar radiation received during the average day of each month are a prerequisite in different solar energy applications. In the early 1950s, Whillier introduced the *utilizability* method to analytically predict the performance of active solar collectors. This method used a simple formulation to estimate the mean hourly radiation during each hour of an average day of the month, based on the ratio of the hourly to daily irradiation received by a horizontal surface outside of the atmosphere. The long-term models provide the mean hourly distribution of global radiation over the average day of each average month.

Three methods are described as follows:

1. C-P&R model, CPR (Figure 6.18)

Given the long-term average daily total and diffuse irradiation on a horizontal surface \bar{H}_h and \bar{H}_d , it is possible to find the long-term average hourly irradiances \bar{I}_d , \bar{I}_h , and \bar{I}_b .

The ratio of the hourly diffuse to the long-term average daily diffuse irradiation on a horizontal surface, r_d , is given by

$$r_d = \frac{I_d}{\bar{H}_d} = \frac{\pi}{24} \frac{\cos h_s - \cos h_{ss}}{\sin h_{ss} - \left(\frac{\pi}{180} \right) h_{ss} \cos h_{ss}}. \quad (6.49)$$

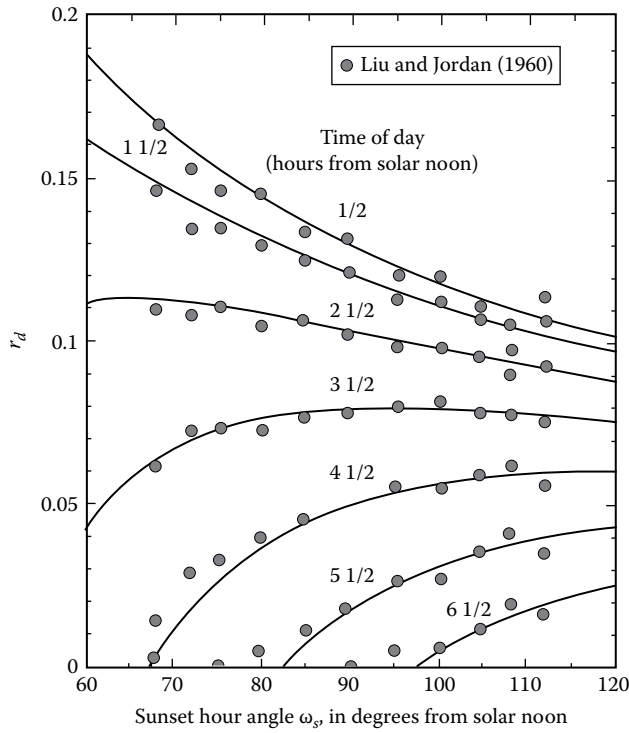


FIGURE 6.18 C-P&R model, CPR. (Adapted from Collares-Pereira, M. and Rabl, A., *Sol. Energ.*, 22, 155, 1979; Liu, B.H.Y. and Jordan, R.C., *Sol. Energ.*, 4, 1, 1960.)

The ratio of hourly total to the long-term average daily total irradiation on a horizontal surface, r_t , is given by

$$r_t = \frac{I_h}{H_h} = (a + b \cos h_s) r_d \tag{6.50}$$

with

$$a = 0.409 + 0.5016 \sin (h_{ss} - 60^\circ)$$

$$b = 0.6609 - 0.4767 \sin (h_{ss} - 60^\circ)$$

This fit satisfies, within 1% for all h_{ss} , the normalization condition:

$$\int_{-t_s}^{t_s} I_d dt = \overline{H}_h \tag{6.51}$$

2. C-P&R model modified by Gueymard, CPRG (Figure 6.19)

For the CPRG method, the ratio of hourly total to the long-term average daily total irradiation on a horizontal surface, r_t , is given by [52]

$$r_t = \frac{I_h}{H_h} = \frac{(a + b \cos h_s) r_d}{f_c} \tag{6.52}$$

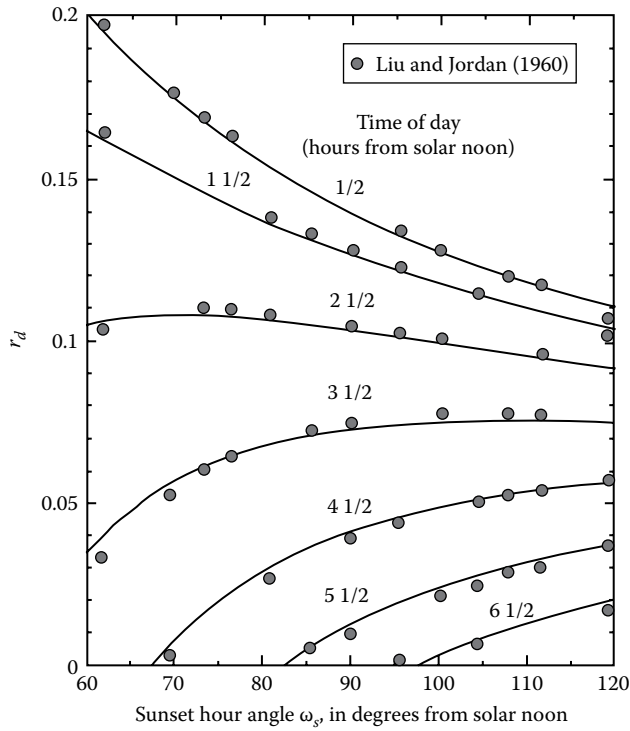


FIGURE 6.19 C-P&R model modified by Gueymard [51]. (Adapted from Collares-Pereira, M. and Rabl, A., *Sol. Energ.*, 22, 155, 1979; Liu, B.H.Y. and Jordan, R.C., *Sol. Energ.*, 4, 1, 1960.)

with

$$f_c = a + kb \left[\left(\frac{\pi}{180} \right) h_{ss} - \frac{1}{2} \sin 2h_{ss} \right]. \tag{6.53}$$

$$k = \left(2 \left[\sin h_{ss} - \left(\frac{\pi}{180} \right) h_{ss} \cos h_{ss} \right] \right)^{-1}. \tag{6.54}$$

The normalization condition is expressed by

$$\int_{-t_s}^{t_s} r_t dt = 1. \tag{6.55}$$

3. For both CPR and CPRG models

The instantaneous solar beam radiation on a horizontal surface, $I_{b,hr}$ is given by

$$I_{b,hr} = r_t \bar{H}_h - r_d \bar{H}_d. \tag{6.56}$$

The instantaneous solar beam radiation on a tilted surface, $I_{b,c}$ is

$$I_{b,c} = I_{b,h} \frac{\cos i}{\sin \alpha}. \quad (6.38)$$

Then the total radiation on a tilted surface, I_c is

$$I_c = (r_i \bar{H}_h - r_d \bar{H}_d) \frac{\cos i}{\sin \alpha} + r_d \bar{H}_d \cos^2 \left(\frac{\beta}{2} \right) + \rho r_i \bar{H}_h \sin^2 \left(\frac{\beta}{2} \right). \quad (6.57)$$

The following websites give information about long-term measured or satellite solar radiation data.

- Surface meteorology and solar energy (version 6.0)—<https://eosweb.larc.nasa.gov/sse/>
- EnergyPlus weather data—http://apps1.eere.energy.gov/buildings/energyplus/weatherdata_about.cfm?CFID=777061&CFTOKEN=999ebda95de32b46-A8949F8C-E3B6-3771-7E42A53F29DDF35C
- National Solar Radiation Data Base (NSRDB), 1961–1990: Typical Meteorological Year (TMY) 2—[http://webcache.googleusercontent.com/search?q=cache; http://rredc.nrel.gov/solar/old_data/nsrdb/tmy2/](http://webcache.googleusercontent.com/search?q=cache;http://rredc.nrel.gov/solar/old_data/nsrdb/tmy2/)
- NSRDB, 1991–2005 update: TMY 3—http://rredc.nrel.gov/solar/old_data/nsrdb/1991-2005/tmy3/; http://rredc.nrel.gov/solar/old_data/nsrdb/1991-2005/tmy3/
- The Solar and Wind Energy Resource Assessment (SWERA)—<http://en.openei.org/apps/SWERA/>
- National Renewable Energy Laboratory (NREL)—http://www.nrel.gov/international/geospatial_toolkits.html; http://www.nrel.gov/international/geospatial_toolkits.html#HOMER

6.5.4 Spectral Models

Many biological, chemical, and physical processes are activated more powerfully at some wavelengths than at others. Therefore, it is important to know the spectral characteristics of the incident radiation. In order to model spectral solar radiation at a location, radiation needs to be modeled as it travels through the atmosphere. These models are complex to begin with and are made more complex since different wavelengths are absorbed, reflected, and scattered differently in the atmosphere. Examples of radiative transfer numerical models include the Santa Barbara DISORT, the atmospheric radiative transfer code SBDART, and the moderate resolution transmission code MODTRAN. SBDART, developed at the University of California at Santa Barbara, is relatively simpler to use than MODTRAN, is freely accessible, and even has a convenient user interface online: <http://arm.mrcsb.com/sbdart/>

MODTRAN, developed by the Air Force Geophysical Laboratory (AFGL), has a much higher resolution and is considered as the standard in atmospheric applications.

These models, however, are not convenient for solar energy or other engineering-type applications.

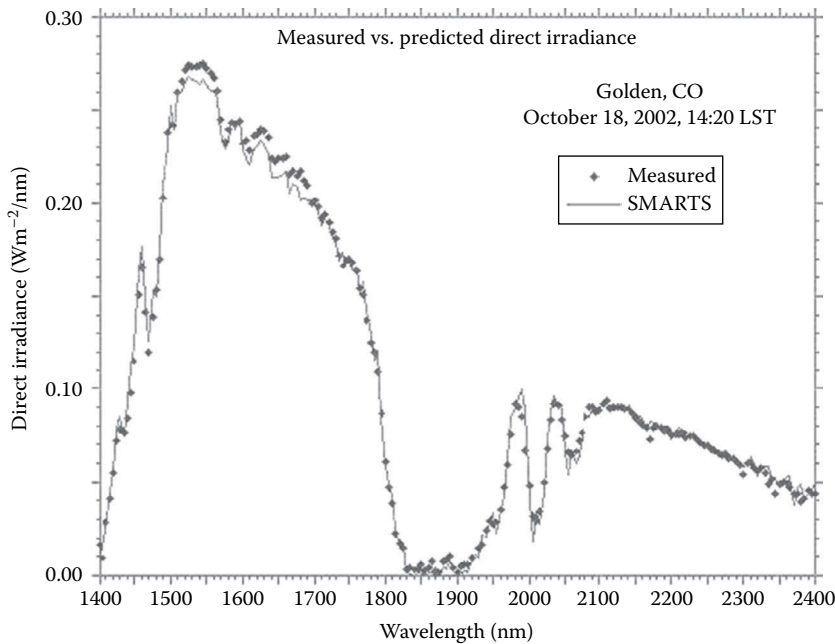


FIGURE 6.20

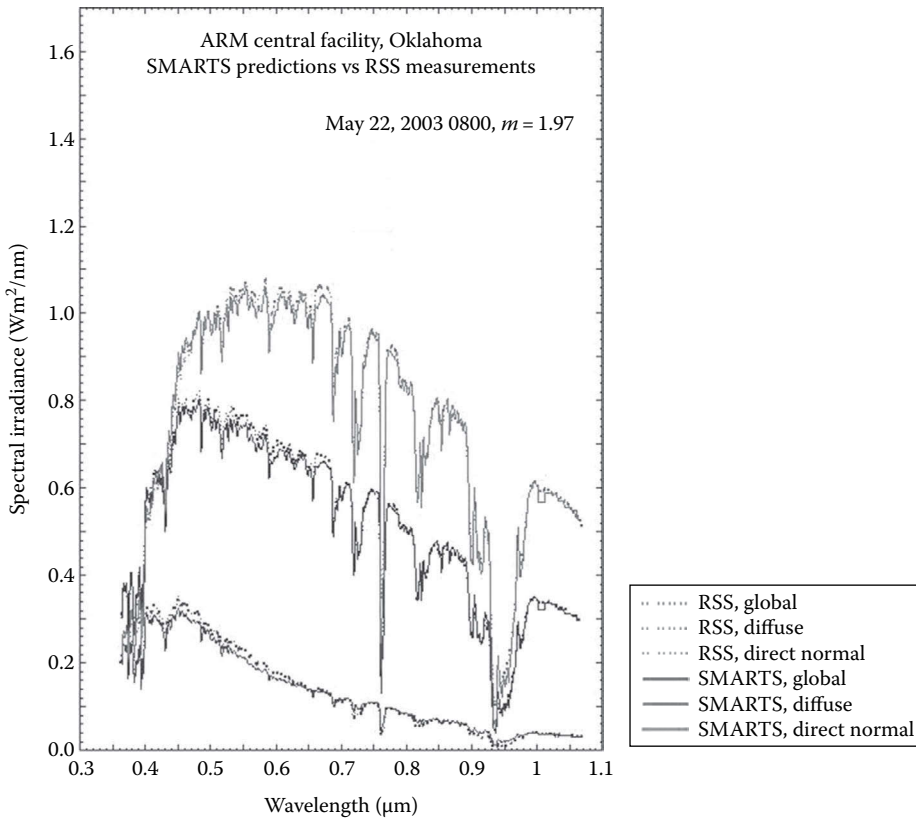
A sample spectral irradiance prediction compared with measured data for Golden, Colorado.

Bird's simple spectral model (SPCTRAL2), the SMARTS, and REST2 can be used for solar engineering applications. Even though these models are limited to clear sky conditions, they can also be empirically modified to predict spectra under cloudy conditions. SMARTS model offers fast and accurate predictions of spectral irradiance on any tilted surface without the difficulties and limitations associated with the atmospheric models mentioned earlier. Sample outputs produced by SMARTS, compared with actual spectroradiometric measurements from high-performance instruments, are shown in the Figures 6.20 and 6.21.*

6.6 Measurement of Solar Radiation

Solar radiation measurements of importance to most engineering applications, especially thermal applications, include total (integrated over all wavelengths) direct or beam and sky diffuse values of solar radiation on instantaneous, hourly, daily, and monthly bases. Some applications such as photovoltaics, photochemical, and daylighting require knowledge of spectral (wavelength specific) or band (over a wavelength range—e.g., ultraviolet, visible, infrared) values of solar radiation. This section describes some of the instrumentation used to measure solar radiation and sunshine and some sources of long-term measured data for different parts of the world. Also described briefly in this section is the method of satellite-based measurements.

* Taken from <http://www.solarconsultingservices.com/smarts.php>; <http://www.solarconsultingservices.com/smarts.php>.

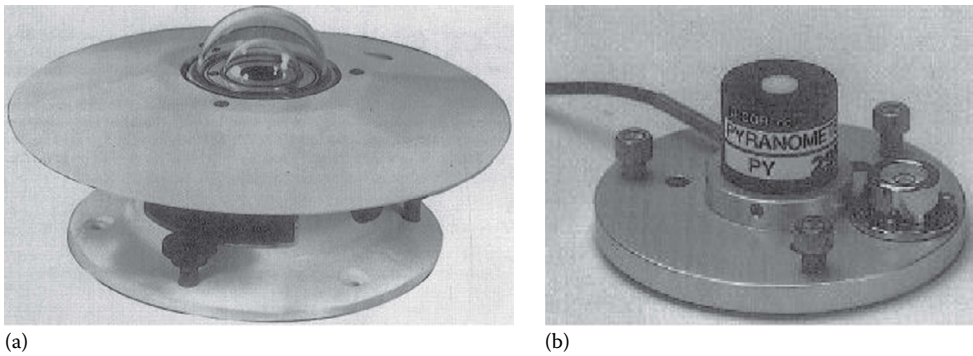
**FIGURE 6.21**

A sample prediction for direct normal, diffuse, and global horizontal spectral irradiance.

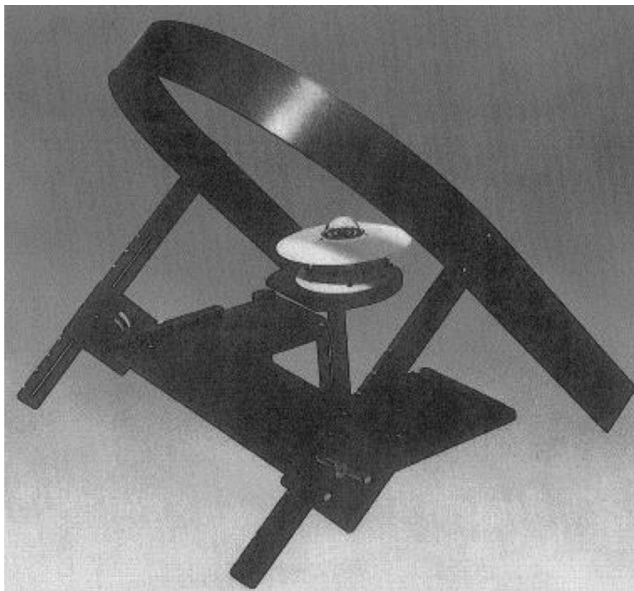
6.6.1 Instruments for Measuring Solar Radiation and Sunshine

There are two basic types of instruments used to measure solar radiation, *pyranometer* and *pyrheliometer*. A pyranometer has a hemispherical view of the surroundings and therefore is used to measure total, direct and diffuse, solar radiation on a surface. A pyrheliometer, on the other hand, has a restricted view (about 5°) and is, therefore, often used to measure the direct or beam solar radiation by pointing it toward the sun. Pyranometers are also used to measure the sky diffuse radiation by using a shadow band to block the direct sun view. A detailed discussion of the instrumentation and calibration standards is given by Iqbal [15] and Zerlaut [48].

A pyranometer consists of a flat sensor/detector (described later) with an unobstructed hemispherical view, which allows it to convert and correlate the total radiation incident on the sensor to a measurable signal. The pyranometers using thermal detectors for measurements can exhibit serious errors at tilt angles from the horizontal due to free convection. These errors are minimized by enclosing the detector in double hemispherical high-transmission glass domes. The second dome minimizes the error due to infrared radiative exchange between the sensor and the sky. A desiccator is usually provided to eliminate the effect due to condensation on the sensor or the dome. Figure 6.22 shows pictures of typical commercially available precision pyranometer.

**FIGURE 6.22**

Typical commercially available pyranometers with (a) thermal detector and (b) photovoltaic detector.

**FIGURE 6.23**

A pyranometer with a shade ring to measure sky diffuse radiation.

A pyranometer can be used to measure the sky diffuse radiation by fitting a shade ring to it, as shown in Figure 6.23, in order to block the beam radiation throughout the day. The position of the shade ring is adjusted periodically as the declination changes. Since the shade ring obstructs some diffuse radiation from the pyranometer, correction factors must be applied.

Geometric correction factors (GCFs) that account for the part of the sky obstructed by the shade ring can be easily calculated. However, a GCF assumes isotropic sky, which results in errors because of the circumsolar anisotropy. Eppley Corp. recommends additional correction factors to account for anisotropy as +7% for clear sky, +4% for partly cloudy condition, and +3% for cloudy sky. Mujahid and Turner [30] determined that these correction factors gave less than 3% errors on partly cloudy days but gave errors of -11% for clear sky conditions and +6% on overcast days. They suggested correction factors due

TABLE 6.7
Shading Band Correction Factors due to Anisotropy

Solar Altitude Angle	k_T									
	0.0	0.1	0.2	0.3	0.4	0.5	0.6	0.7	0.8	0.9
<20°	0.0	0.0	0.0	0.0	0.015	0.06	0.14	0.23	0.24	0.24
20°–40°	0.0	0.0	0.0	0.0	0.006	0.05	0.125	0.205	0.225	0.225
40°–60°	0.0	0.0	0.0	0.0	0.003	0.045	0.115	0.175	0.205	0.205
60°+	0.0	0.0	0.0	0.0	0.0	0.035	0.09	0.135	0.17	0.17

Source: Mujahid, A. and Turner, W.D., Diffuse sky measurement and model, ASME Paper No. 79-WA/Sol-5, 1979.

to anisotropy as tabulated in Table 6.7, which reduce the errors to less than $\pm 3\%$. It must be remembered that these correction factors are in addition to the GCFs. Recently, a sun occulting disk has been employed for shading the direct sun.

Beam or direct solar radiation is usually measured with an instrument called a pyrheliometer. Basically a pyrheliometer places the detector at the base of a long tube. This geometry restricts the sky view of the detector to a small angle of about 5° . When the tube points toward the sun, the detector measures the beam solar radiation and a small part of the diffuse sky radiation within the view angle. Figure 6.24 shows the geometry of a pyrheliometer sky occulting tube.

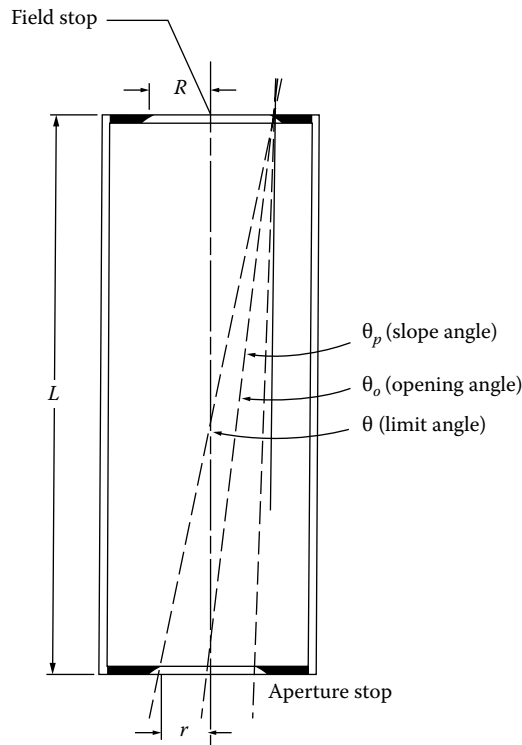


FIGURE 6.24
Geometry of a pyrheliometer sky occulting tube.

In this figure, the opening half angle

$$\theta_o = \tan^{-1} \frac{R}{L}. \quad (6.58)$$

The slope angle

$$\theta_p = \tan^{-1} \left[\frac{(R-r)}{L} \right]. \quad (6.59)$$

The limit half angle

$$\theta = \tan^{-1} \left[\frac{(R+r)}{L} \right]. \quad (6.60)$$

The field of view is $2\theta_o$. The World Meteorological Organization (WMO) recommends the opening half angle θ_o to be 2.5° [48] and the slope angle θ_p to be 1° .

Continuous tracking of the sun is required for the accuracy of the measurements. This is obtained by employing a tracking mechanism with two motors, one for altitude and the other for azimuthal tracking. Another problem is that the view angle of a pyrheliometer is significantly greater than the angle subtended by the solar disk (about 0.5°). Therefore, the measurements using a pyrheliometer include the beam and the circumsolar radiation. These measurements may present a problem in using the data for central receiver systems that use only direct beam radiation. However, this is not a significant problem for parabolic trough concentrators that in most cases have a field of view of the order of 5° .

6.6.2 Detectors for Solar Radiation Instrumentation

Solar radiation detectors are of four basic types [15,48]: thermomechanical, calorimetric, thermoelectric, and photoelectric. Of these, thermoelectric and photoelectric are the most common detectors in use today.

A *thermoelectric detector* uses a thermopile that consists of a series of thermocouple junctions. The thermopile generates a voltage proportional to the temperature difference between the hot and cold junctions that, in turn, is proportional to the incident solar radiation. Figure 6.25 shows different types of thermopile configurations. The Eppley black and white pyranometer uses a radial differential thermopile with the hot junction coated with 3M Velvet Black™ and the cold junction coated with a white barium sulfate paint.

Photovoltaic detectors normally use silicon solar cells measuring the short circuit current. Such detectors have the advantage of being simple in construction. Because heat transfer is not a consideration, they do not require clear domes or other convection suppressing devices. They are also insensitive to tilt as the output is not affected by natural convection. One of the principal problems with photovoltaic detectors is their spectral selectivity. Radiation with wavelengths greater than the bandgap of the photovoltaic detector cannot be measured. Silicon has a bandgap of 1.07 eV corresponding to a wavelength of $1.1 \mu\text{m}$. A significant portion of the infrared part of solar radiation has wavelengths greater than $1.1 \mu\text{m}$. Therefore, photovoltaic detectors are insensitive to changes in the infrared part of solar radiation.

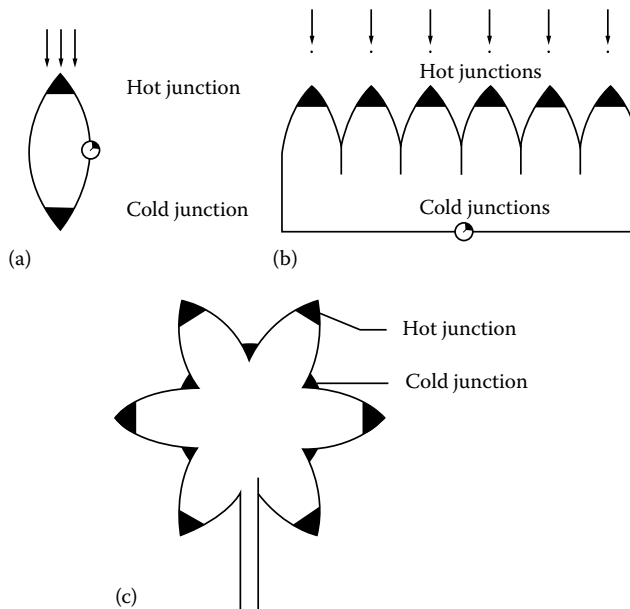


FIGURE 6.25

Various thermopile configurations. (From Zerlaut, G., *Solar radiation instrumentation*, in *Solar Resources*, Roland L. Hulstrom, ed., MIT Press, Cambridge, MA, 1989.)

6.6.3 Measurement of Sunshine Duration

The time duration of bright sunshine data is available at many more locations in the world than the solar radiation. That is why a number of researchers have used these data to estimate the available solar radiation. Two instruments are widely used to measure the sunshine duration. The device used by the U.S. National Weather Service is called a *sunshine switch*. It is composed of two photovoltaic cells—one shaded, the other not. During daylight a potential difference is created between the two cells, which in turn operates the recorder. The intensity level required to activate the device is that just sufficient to cast a shadow. The other device commonly used to measure the sunshine duration is called the *Campbell–Stokes sunshine recorder*. It uses a solid, clear glass sphere as a lens to concentrate the solar beam on the opposite side of the sphere. A strip of standard treated paper marked with time graduations is mounted on the opposite side of the sphere where the solar beam is concentrated. Whenever the solar radiation is above a threshold, the concentrated beam burns the paper. The length of the burned part of the strip gives the duration of bright sunshine. The problems associated with the Campbell–Stokes sunshine recorder include the uncertainties of the interpretation of burned portions of the paper, especially on partly cloudy days, and the dependence on the ambient humidity. Figure 6.26 shows a Campbell–Stokes sunshine recorder.

6.6.4 Measurement of Spectral Solar Radiation

Spectral solar radiation measurements are made with spectroradiometers. Full-spectrum scanning is difficult, requires constant attention during operation, and is therefore expensive. Zerlaut [48] has described a number of solar spectroradiometers. These instruments consist basically of a monochromator, a detector–chopper assembly, an integrating sphere, and a signal conditioning/computer package. They have the capability of measuring solar radiation in the wavelength spectrum of 280–2500 nm.



FIGURE 6.26
Campbell–Stokes sunshine recorder.

6.6.5 Wideband Spectral Measurements

Some applications of solar energy require solar radiation data in wideband wavelength ranges such as visible, ultraviolet, and infrared rather than complete spectral data. For example, solar photocatalytic detoxification using TiO_2 as the catalyst needs data in the UV wavelength range, while passive solar applications need data in the infrared wavelength range. Instruments such as pyranometers and pyrhemometers can be adapted for wideband spectral measurements by using cut-on and cutoff filters. Eppley instruments provide standard cut-off filters at wavelengths 530 nm (orange), 630 nm (red), and 695 nm (dark red). They are provided as plain filters at the aperture of a pyrhemometer tube and as outer glass domes for pyranometers. Instrument manufacturers provide various interference filters peaking at different wavelengths in the solar spectrum.

Solar UV measurements are important in general since prolonged exposure to solar UV can cause skin cancer, fading of colors, and degradation of plastic materials. Such measurements have become even more important because the photocatalytic effect based on TiO_2 as a catalyst depends only on the solar UV wavelength range. Figure 6.27 shows an Eppley model total ultraviolet radiometer (TUVR) that measures the total hemispherical UV radiation from 295 to 385 nm. This radiometer uses a selenium photoelectric cell detector, a pair of band pass filters to allow wavelengths from 295 to 385 nm to pass through, and a beveled Teflon diffuser.

6.6.6 Solar Radiation Data

Measured solar radiation data are available at a number of locations throughout the world. Data for many other locations have been estimated based on measurements at similar climatic locations.

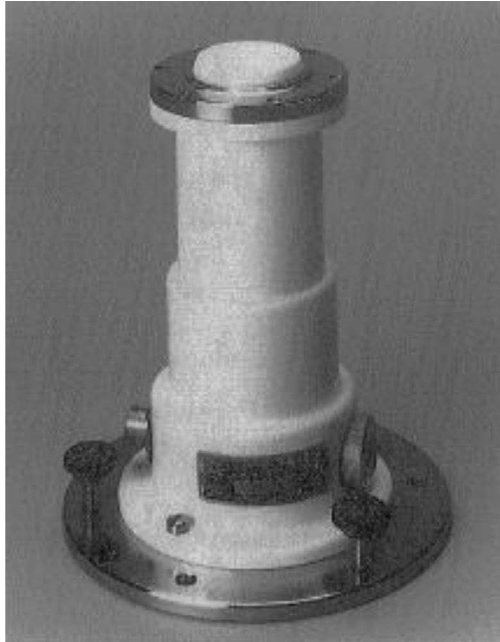


FIGURE 6.27
Eppley TUVR®. (Courtesy of Eppley Lab, Newport, RI)

Solar radiation data for the United States are available from the National Climatic Data Center (NCDC) of the National Oceanic and Atmospheric Administration (NOAA) and the NREL. In the mid-1970s, NOAA compiled a database of measured hourly global horizontal solar radiation for 28 locations for the period 1952–1975 (called SOLMET) and of data for 222 additional sites (called ERSATZ) estimated from SOLMET data and some climatic parameters such as sunshine duration and cloudiness. NOAA also has two data sets of particular interest to engineers and designers: the TMY and the Weather Year for Energy Calculations (WYEC) data sets. TMY data set represents typical values from 1952 to 1975 for hourly distribution of direct beam and global horizontal solar radiation. The WYEC data set contains monthly values of temperature, direct beam and diffuse solar radiation, and estimates of *illuminance* (for daylighting applications). Illuminance is solar radiation in the visible range to which the human eye responds. Recently, NREL compiled an NSRDB for 239 stations in the United States [28,32]. NSRDB is a collection of hourly values of global horizontal, direct normal, and diffuse solar radiation based on measured and estimated values for a period of 1961–1990. Since long-term measurements were available for only about 50 stations, measured data make up only about 7% of the total data in the NSRDB. A TMY data set from NSRDB is available as TMY2.

The data for other locations in the world are available from national government agencies of most countries of the world. Worldwide solar radiation data are also available from the World Radiation Data Center (WRDC) in St. Petersburg, Russia, based on worldwide measurements made through local weather service operations [47]. WRDC, operating under the auspices of the World Meteorological Organization (WMO), has been archiving data from over 500 stations and operates a website in collaboration with NREL with an

address of <http://wrdc.mgo.nrel.gov>. An International Solar Radiation Data Base was also developed by the University of Lowell [46].

- Surface meteorology and solar energy (version 6.0) (<http://eosweb.larc.nasa.gov/sse/>)
- EnergyPlus weather data (http://apps1.eere.energy.gov/buildings/energy-plus/weatherdata_about.cfm?CFID=5019287&CFTOKEN=b54041e7be537f1f-B598302C-5056-BC19-15C492F462EE1BAC)
- NSRDB, 1961–1990: TMY (http://rredc.nrel.gov/solar/old_data/nsrdb/)
- (<http://rredc.nrel.gov/solar/pubs/NSRDB/>)
- NSRDB, 1991–2005 update: TMY3 (http://rredc.nrel.gov/solar/old_data/nsrdb/)
- (<http://www.nrel.gov/docs/fy12osti/54824.pdf>)
- The SWERA ([http://en.openei.org/wiki/Solar_and_Wind_Energy_Resource_Assessment_\(SWERA\)](http://en.openei.org/wiki/Solar_and_Wind_Energy_Resource_Assessment_(SWERA)))
- NREL (<http://www.nrel.gov/>)

6.7 Solar Radiation Mapping Using Satellite Data

Remote sensing satellite data have been used since the early 1960s to extract quantitative and qualitative cloud data. The most important application of cloud cover mapping has been the observation of storms and hurricanes, etc. Recently, however, considerable interest has been developed in using the cloud mapping data to estimate terrestrial solar radiation. Since meteorological satellites from a number of countries can now cover most of the earth, the data can be used to estimate solar radiation where no measured data exist or none is being measured.

Weather satellites are available in three main orbiting configurations—equatorial, polar, and geostationary. The equatorial satellites are low-level orbiting satellites (~600 km altitude) that generally orbit the earth in a west to east direction in a sinusoidal path that crosses the equator at least twice per orbit. Polar satellites are also low-orbit satellites that orbit the earth from the north to the south pole while the earth rotates underneath. Sun synchronous polar orbits have their orbits synchronized with the sun such that the same point on the earth is viewed at the same time each day. Low-orbit satellites are capable of gathering high-resolution spatial data. A geostationary satellite orbits in such a way that it is always over the same point on the earth's surface. Geostationary satellites have very high altitudes (approximately 36,000 km) and can provide high-temporal-resolution images over a large portion of the earth's surface. A number of countries maintain geostationary satellites including the United States (GOES, longitudes 70° W and 140° W), Europe (METEOSAT, longitude 0°), India (INSAT, longitude 70° E), and Japan (GMS, longitude 140° E).

Various types of high-resolution radiometers collect radiative data images of the earth's atmosphere below. These radiometers scan spectral measurements in the wavelength ranges of shortwave (0.2–3.0 μm), longwave (6.5–25 μm), and total irradiance (0.2–100 μm). The spatial resolution of images from the satellite is given by a *pixel* that represents the smallest area of data, generally of the order of 2 km \times 2 km. However, several pixels of data

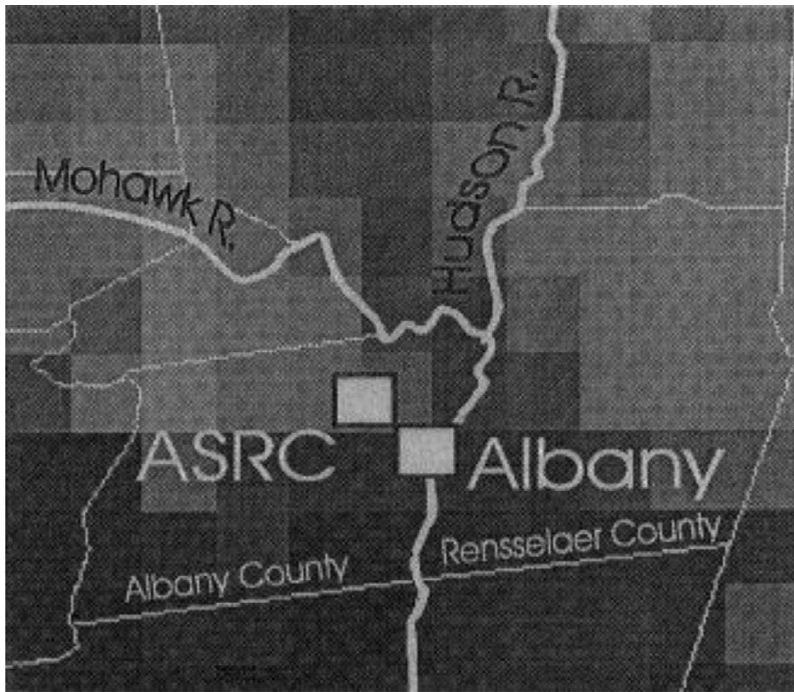


FIGURE 6.28

GOES-8 intermediate-resolution image close-up around Albany. (From Perez, R., The strengths of satellite based resource assessment, *Proceedings of the 1997 ASES Annual Conference*, Washington, DC, pp. 303–308, 1997.)

are required to derive a surface value giving a surface resolution of the order of $10 \text{ km} \times 10 \text{ km}$. Figure 6.28 shows an example of an intermediate-resolution GOES-8 image around Albany, New York, overlaid on a local map.

6.7.1 Estimation of Solar Resource from Satellite Data

The signal recorded by a radiometer on a satellite measures the solar radiation flux reflected back from the earth's atmosphere. The basic method behind estimation of ground solar radiation from these data is to apply the principle of energy conservation in the earth-atmosphere system [31], as shown in Figure 6.29. From this figure we can write

$$I_{in} = I_{out} + I_a + I_g, \quad (6.61)$$

where

I_{in} represents the solar radiation incident on the atmosphere

I_{out} represents the outward radiation from the atmosphere

I_a is the radiation absorbed by the atmosphere

I_g is the radiation absorbed by the ground

I_g can be expressed in terms of the surface albedo* ρ (reflectivity) and the solar radiation I_s , incident on the earth's surface:

$$I_g = I_s(1 - \rho). \quad (6.62)$$

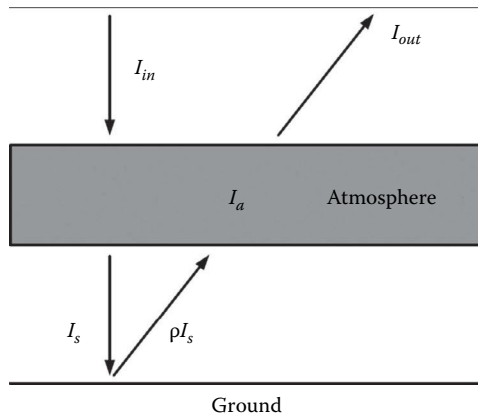


FIGURE 6.29
Solar radiation in the earth-atmosphere model.

From Equations 6.61 and 6.62 we can obtain

$$I_s = \frac{(I_{in} - I_{out} - I_a)}{(1 - \rho)} \tag{6.63}$$

I_{out} is measured by the satellite radiometers. I_{in} depends on the sun–earth distance and the solar zenith angle and can be calculated using Equation 6.11 as

$$I_{in} = I_o \left(\frac{D_o}{D} \right)^2 \cdot \cos(z) \tag{6.64}$$

If we could estimate I_a , and A were known a priori, I_s could be estimated using Equation 6.63 from the value of I_{out} measured by a satellite. However, I_a cannot be estimated easily since it depends on the atmospheric conditions such as cloud cover, dust particles, and air mass, and surface albedo (reflectance) ρ varies for every point of the region under consideration. In order to deal with these factors, two types of empirical methods are under development. These are known as statistical and physical methods. These methods have been reviewed in detail by Schmetz [40], Hay [12], Noia et al. [31], Islam [17], and Pinker et al. [36].

Statistical Methods: Statistical methods are based on finding a relationship between the radiative flux measured by a satellite radiometer and the simultaneous solar radiation value measured at the earth’s surface in the area under consideration. Some of the models developed on statistical approach include Hay and Hanson [13], Tarpley [44], Justus et al. [18], Cano and Sorapipatana et al. [41].

Physical Methods: Physical methods are based on the analysis of radiative processes in the atmosphere as the solar radiation passes through it. Some of the models developed with this approach include Gautier [9], Moser and Raschke [29], Dedieu et al. [6], and Marullo et al. [27].

The simplest of the previously mentioned models is by Hay and Hanson [13], which gives the atmospheric transmittance T as

$$T = \frac{I_s}{I_{in}} = a - b \frac{I_{out}}{I_{in}},$$

or $I_s = aI_{in} - bI_{out}$. (6.65)

The values of regression coefficients given by Hay and Hanson [13] are $a = 0.79$, $b = 0.71$. This method is simple; however, the coefficients, particularly b , vary considerably with parameters such as cloud reflectivity. More recent investigations suggest that it is necessary to determine the coefficients a and b for different locations.

It is beyond the scope of this book to discuss all the models. It suffices, however, to point out that all the models, including the Hay and Hanson model, more or less give values within 10% of the ground measured values [31]. The methods usually break down under partly cloudy conditions and under snow-covered ground conditions.

References and Suggested Readings

1. Akinoglu, B.G. and A. Ecevit. 1990. Construction of a quadratic model using modified angstrom coefficients to estimate global solar radiation. *Solar Energy* 45: 85.
2. Choudhury, N.K.O. 1963. Solar radiation at New Delhi. *Solar Energy* 7(44).
3. Collares-Pereira, M. and A. Rabl. 1979. The average distribution of solar radiation-correlation between diffuse and hemispherical. *Solar Energy* 22: 155–166.
4. Coppolino, S. 1994. New correlation between clearness index and relative sunshine. *Renewable Energy* 4(4): 417–423.
5. Dedieu, G., P.Y. Deschamps, and Y.H. Kerr. 1987. Satellite estimation of solar irradiance at the surface of the earth and of surface albedo using a physical model applied to METEOSAT data. *Journal of Climate and Applied Meteorology* 26: 79–87.
6. Frohlich, C. et al. 1973. The third international comparison of pyrhemometers and a comparison of radiometric scales. *Solar Energy* 14: 157–166.
7. Garg, H.P. and S.N. Garg. 1985. Correlation of the monthly average daily global, diffuse and beam radiation with bright sunshine hours. *Energy Conversion and Management* 25(4): 409–417.
8. Gautier, C. 1980. Simple physical model to estimate solar radiation at the surface from GOES satellite data. *Journal of Applied Meteorology* 19(8): 1005–1012.
9. Gopinathan, K. 1988. A general formula for computing the coefficients of the correlation connecting global solar radiation to sunshine duration. *Solar Energy* 41: 499.
10. Gueymard, C.A. and Thevenard, D. 2009. Monthly average clear-sky broadband irradiance database for solar heat gain and building cooling load calculations. *Solar Energy* 82: 272–285.
11. Hay, J.E. 1993. Satellite based estimates of solar irradiance at the earth's surface: I. Modelling approaches. *Renewable Energy* 3: 381–393.
12. Hay, J.E. and K.J. Hanson. 1978. A satellite-based methodology for determining solar irradiance at the ocean surface during GATE. *Bulletin of the American Meteorological Society*. 59: 1549.
13. Hussain, M. 1994. Estimation of the global and diffuse irradiation from sunshine duration and atmospheric water vapor content. *Solar Energy* 33(2): 217–220.
14. Iqbal, M. 1983. *An Introduction to Solar Radiation*. New York: Academic Press.
15. Iqbal, M. 1979. Correlation of average diffuse and beam radiation with hours of bright sunshine, *Solar Energy* 23: 169–173.
16. Islam, M.R. 1994. Evolution of methods for solar radiation mapping using satellite data. *RERIC International Energy Journal* 16(2).
17. Justus, C., M.V. Paris, and J.D. Tarpley. 1986. Satellite-measured insolation in the United States, Mexico and South America. *Remote Sensing of Environment* 20: 57–83.
18. Klucher, T.M. 1979. Evaluation of models to predict insolation on tilted surfaces. *Solar Energy* 23(2): 111–114.
19. Liu, B.Y.H. and R.C. Jordan. 1961. Daily insolation on surfaces titled toward the equator. *ASHRAE Transactions* 67: 526–541.

20. Liu, B.Y.H. and R.C. Jordan. 1961. Daily insolation on surface tilted toward the equator. *ASHRAE Transactions* 3(10): 53–59.
21. Liu, B.Y.H. and R.C. Jordan. 1967. Availability of solar energy for flat-plate solar heat collectors. In *Low Temperature Engineering of Solar Energy*, Chapter 1. New York: ASHRAE; see also 1977 revision.
22. Liu, B.Y.H. and R.C. Jordan. 1963. A rational procedure for predicting the long-term average performance of flat-plate solar energy collectors. *Solar Energy* 7: 53–74.
23. Liu, B.Y.H. and R.C. Jordan. 1960. The interrelationship and characteristic distribution of direct, diffuse and total solar radiation. *Solar Energy* 4: 1–19. See also Liu, B.Y.H. Characteristics of solar radiation and the performance of flat plate solar energy collectors, Ph.D. dissertation, Minneapolis, MN: University of Minnesota, 1960.
24. Löf, G.O.G. et al. 1966. World distribution of solar energy. Engineering Experiment Station Report 21, Madison, WI: University of Wisconsin.
25. Marullo, S., G. Dalu, and A. Viola. 1987. Incident short-wave radiation at the surface from METEOSAT data. *Il Nuovo Cimento* 10C: 77–90.
26. Maxwell, E.L. 1998. METSTAT—The solar radiation model used in the production of the national solar radiation data base (NSRDB). *Solar Energy* 62: 263–279.
27. Moeser, W. and E. Raschke. 1984. Incident solar radiation over Europe estimated from METEOSAT data. *Journal of Climate and Applied Meteorology* 23(1): 166–170.
28. Mujahid, A. and W.D. Turner. 1979. Diffuse sky measurement and model. ASME Paper No. 79-WA/Sol-5.
29. Noia, M., C. Ratto, and R. Festa. 1993. Solar irradiance estimation from geostationary satellite data: I. statistical models; II. physical models. *Solar Energy* 51: 449–465.
30. NSRDB. 1992. Volume 1: Users Manual: National Solar Radiation Data Base (1961–1990), Version 1.0. Golden, CO: National Renewable Energy Laboratory.
31. Ögelman, H., A. Ecevit, and E. Tasdemiroglu. 1984. A new method for estimating solar radiation from bright sunshine data. *Solar Energy* 33(6): 619–625.
32. Page, J.K. 1966. The estimation of monthly mean values of daily total short-wave radiation on vertical and inclined surfaces from sunshine records or latitudes 40°N–40°S. *Proceedings of U.N. Conference on New Sources of Energy* 4: 378.
33. Perez, R., R. Seals, A. Zelenka, and D. Renne. 1997. The satellite based resource assessment. *Proceedings of the 1997 ASES Annual Conference*, pp. 303–308, Washington, DC.
34. Pinker, R.T., R. Frouin, and Z. Li. 1995. A review of satellite methods to derive surface shortwave irradiance. *Remote Sensing of Environment* 51: 108–124.
35. Quinlan, E.T.(ed.) 1977. *Hourly Solar Radiation Surface Meteorological Observations*. Asheville, NC: NOAA, SOLMET Vol. 1.
36. Quinlan, F.T.(ed.) 1979. *Hourly Solar Radiation Surface Meteorological Observations*. Asheville, NC: NOAA, SOLMET Vol. 2.
37. Ruth, D.W. and R.E. Chant. 1976. The relationship of diffuse radiation to total radiation in Canada. *Solar Energy* 18: 153.
38. Schmetz, J. 1989. Towards a surface radiation climatology: Retrieval of downward irradiances from satellites. *Atmospheric Research* 23: 287–321.
39. Sorapipatana, C., R.H.B. Exell, and D. Borel. 1988. A bispectral method for determining global solar radiation from meteorological satellite data. *Solar and Wind Technology* 5(3): 321–327.
40. Spencer, J.W. 1971. Fourier series representation of the position of the sun. *Search* 2: 172.
41. Stanhill, G. 1966. Diffuse sky and cloud radiation in Israel. *Solar Energy* 10: 66.
42. Tarpley, J.D. 1979. Estimating incident solar radiation at the surface from geostationary satellite data. *Journal of Applied Meteorology* 18(9): 1172–1181.
43. Temps, R.C. and K.L. Coulson. 1977. Solar radiation incident upon slopes of different orientations. *Solar Energy* 19(2): 179–184.
44. University of Lowell Photovoltaic Program. 1990. International Solar Irradiation Database. Version 1.0. Lowell, MA: University of Lowell Research Foundation.

45. Voikov Main Geophysical Observatory. 1999. Worldwide daily solar radiation. Available from: <http://www.mgo.rssi.ru>.
46. Zerlaut, G. 1989. Solar radiation instrumentation. In *Solar Resources*, Roland L. Hulstrom (ed.), Cambridge, MA: MIT Press.
47. M. Collares-Pereira and A. Rabl. 1979. The average distribution of solar radiation correlations between diffuse and hemispherical and between daily and hourly insolation values. *Solar Energy* 22: 155.
48. B.H.Y. Liu and R.C. Jordan. 1960. The interrelationship and characteristic distribution of direct, diffuse and total solar radiation. *Solar Energy* 4: 1.
49. Gueymard, C. 2000. Prediction and performance assessment of mean hourly global radiation. *Solar Energy* 68: 285–303.
50. Gueymard, C. 1986. Mean daily averages of beam radiation received by tilted surfaces as affected by the atmosphere. *Solar Energy* 37: 262–267.
51. Vasquez-Padilla, R. 2011. Simplified methodology for designing parabolic trough solar power plants, Ph.D dissertation, Tampa, FL: University of South Florida.
52. Gueymard, C. 2003. The sun's total and spectral irradiance for solar energy applications and solar radiation models. *Solar Energy* 76: 423–453.
53. ASHRAE. 2009. *ASHRAE Handbook. Fundamentals: SI Edition*, Atlanta, GA: American Society of Heating, Refrigeration and Air-Conditioning Engineers, Inc.

7

Wind Energy Resource

Dale E. Berg

CONTENTS

7.1	Wind Origins.....	137
7.2	Energy Available from the Wind.....	141
7.2.1	Wind Power	141
7.2.2	Wind Shear	142
7.2.3	Available Resource.....	143
7.2.4	Environmental/Societal Restrictions.....	149
7.2.4.1	Impacts of Wind Facilities on Birds and Bats	149
7.2.5	Impact of Wind Facilities on Radar.....	151
7.3	Wind Resource Assessment	152
7.3.1	Prospecting	152
7.3.1.1	Biological Indicators	153
7.3.1.2	Effects of Topography.....	153
7.3.2	Wind Resource Evaluation	157
7.3.2.1	Data Measurement.....	159
7.3.2.2	Sampling Rates and Statistical Quantities	164
7.3.2.3	Lightning Protection Devices.....	165
7.3.2.4	Towers and Sensor Mounting	165
7.3.2.5	Data Collection and Handling.....	166
7.4	Example: Initial Wind Farm Development in New Mexico	171
	References.....	173
	Further Information.....	175

7.1 Wind Origins

The primary causes of horizontal atmospheric air motion, or wind, are the uneven heating of the earth and its atmosphere by solar radiation and the earth's rotation. The earth's atmosphere reflects about 43% of the incident solar radiation back into space, absorbs about 17% of it in the lower portions of atmosphere, and transmits the remaining 40% to the surface of the earth, where much of it is then reradiated into the atmosphere. The radiation from the hot sun is at short wavelengths (0.15–4 μm) and passes readily through the atmosphere, while the radiation from the cooler earth is at longer wavelengths (5–20 μm) and is readily absorbed by the water vapor in the atmosphere. Thus, the radiation from the earth is primarily responsible for the warmth of the atmosphere near the earth's surface. Heat is also transferred from the earth's surface to the atmosphere by conduction and convection.

On average, the total amount of energy radiated to space from the earth and its atmosphere must be equivalent to the total amount of solar radiation absorbed, or the temperature of the earth and its atmosphere would steadily increase or decrease. The more nearly perpendicular the sun's rays strike the earth, the more solar radiation is transferred through the atmosphere. Thus, during the year, tropical regions receive much more solar energy than do polar regions. Winds and ocean currents level out this imbalance in thermal energy, preventing the tropical regions from getting progressively hotter and the polar regions from getting progressively colder. In addition, the lack of homogeneity of the earth's surface—the land, water, desert, forest, rock, sand, black loam soil, etc.—leads to differences in solar radiation absorption and reflection back to the atmosphere, creating differences in atmospheric temperature, density, and pressure. These differences, in turn, create forces that contribute to wind. For example, the difference in radiation absorption and emission by land and water along a coastline is the dominant cause of the light shore winds or breezes; the difference in radiation absorption and emission by mountains and valleys is a significant contribution to the light upslope and downslope breezes often found in mountainous terrain. The earth's rotation results in Coriolis forces, which accelerate each moving particle of air. This acceleration moves an air particle to the right of its direction of motion in the Northern Hemisphere and to the left in the Southern Hemisphere. The geostrophic winds in the upper atmosphere (above 600 m or so) are due to the balance of these Coriolis forces and the pressure gradient forces due to the uneven heating of the atmosphere.

The earth's rotation also imparts an angular momentum to each particle of air in a west-to-east direction. Conservation of angular momentum results in an increase in its west-to-east velocity as the particle moves from the equator toward the poles. In the temperate zones, this causes the westerlies, winds opposite to the general flow, in both hemispheres.

The other long-term, large-scale global wind patterns such as equatorial doldrums, trade winds, easterlies, and subtropical and polar jets, illustrated in Figure 7.1, are also caused by the combination of differential solar heating and the rotation of the earth. These wind patterns are often referred to as the general circulation patterns. In actuality, these patterns are complicated by seasonal effects due to changes in the earth's position relative to the sun during the course of a year and geographical effects due to the uneven distribution of, and physical properties of, water and land surfaces. Centers of high or low pressure, caused by heating or cooling of the lower atmosphere, include hurricanes, monsoons, and extratropical cyclones. Small-scale phenomena characterized by local wind include land and sea breezes, valley and mountain winds, monsoon-like flow, Foehn winds (dry, high-temperature winds on the downwind side of mountain ranges, commonly referred to in the western United States as "chinooks"), thunderstorms, and tornadoes.

Variations of wind speed in time can be divided into the categories of interannual, annual, diurnal, and short-term. Interannual variations in wind speed occur over timescales greater than 1 year. They can have a large effect on long-term wind turbine production. Meteorologists generally conclude that it takes 30 years of data to accurately determine long-term values of weather or climate and that it takes at least 5 years of data to arrive at a reliable average annual wind speed at a given location. However, that doesn't mean that data spanning shorter periods of time are useless.

Annual variations refer to significant variations in seasonal or monthly averaged wind speeds that are common over most of the world. For example, for the eastern one-third of the United States, maximum average wind speeds occur during the winter and early spring. Spring maximums occur over the Great Plains, the North Central States, the Texas Coast, in the basins and valleys of the West, and the coastal areas of Central and Southern California.

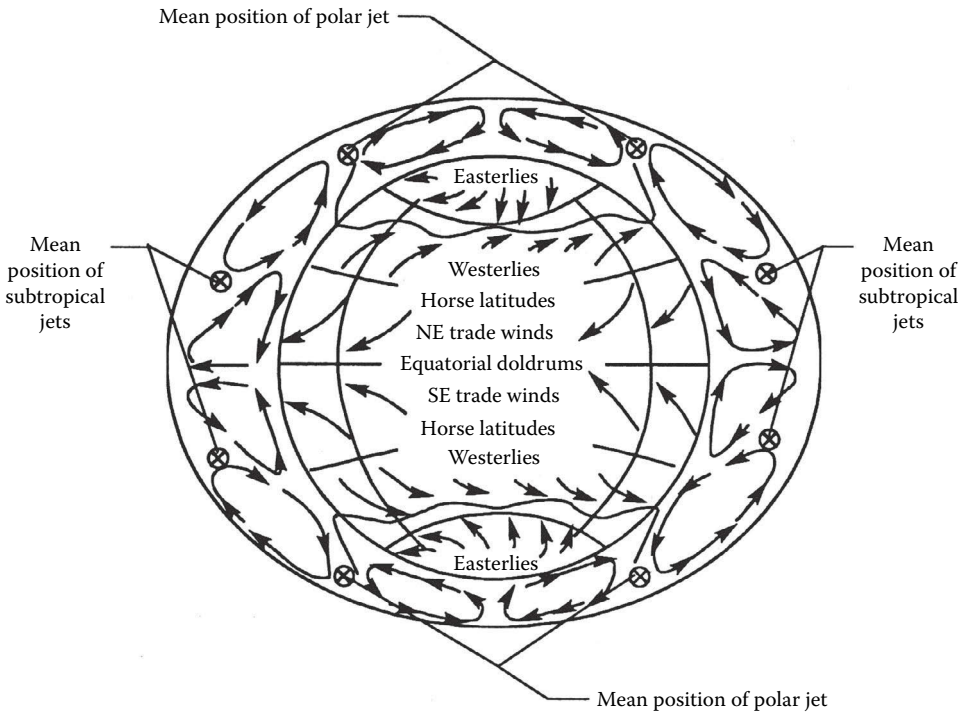


FIGURE 7.1

Semipermanent global wind patterns. (From Spera, D. (ed.), *Wind Turbine Technology: Fundamental Concepts of Wind Turbine Engineering*, ASME Press, New York, 1994. Reproduced by permission of ASME.)

Winter maximums occur over all U.S. mountainous regions, except for some areas in the lower southwest, where spring maximums occur. Spring and summer maximums occur in the wind corridors of Oregon, Washington, and California. Figure 7.2 illustrates how the monthly average wind speed at a location can vary significantly from year to year.

Large diurnal or time-of-day variations in wind occur in both tropical and temperate latitudes. This type of wind speed variation is mainly due to differential heating of the earth's surface during the daily radiation cycle; this is especially true in temperate latitudes over relatively flat areas. A typical diurnal variation is an increase in wind speed during the day, with the wind speeds lowest during the hours from midnight to sunrise. The largest diurnal changes generally occur in spring and summer, and the smallest in winter. However, the diurnal variation may vary with location and altitude above sea level. For example, at altitudes high above surrounding terrain, for example, mountains or ridges above a plain, the diurnal pattern may be very different from the pattern for the surrounding terrain. This variation is due to mixing or transfer of momentum from the upper air to the lower air. There may be significant year-to-year differences in diurnal behavior, even at fairly windy locations. Although gross features of the diurnal cycle can be established with a single year of data, a good characterization of more detailed features, such as the amplitude of the diurnal oscillation and the time of day that the maximum winds occur, requires multiple years of data.

Variations in wind speed with periods of less than 10 min and that have a stochastic or random character are generally considered to represent turbulence or fluctuations

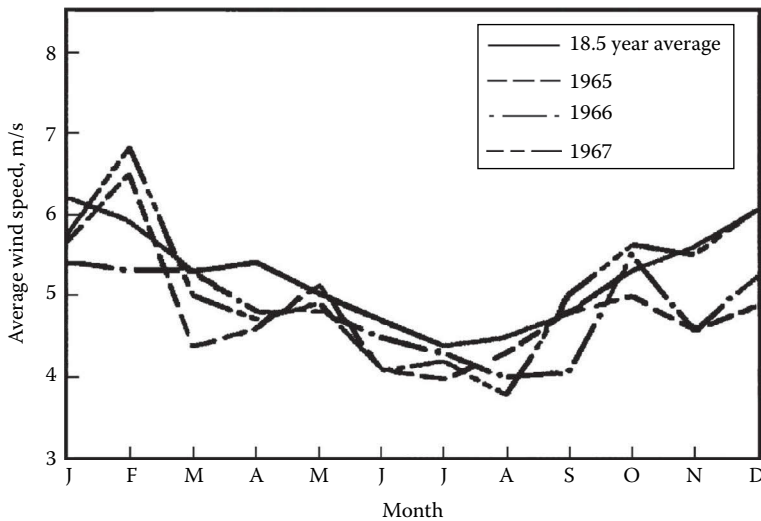


FIGURE 7.2

Seasonal changes of monthly average wind speeds for Billings, MT. (From Hiester, T.R. and Pennell, W.T., *The meteorological aspects of siting large wind turbines*, PNL-2522, Pacific Northwest Laboratory, Richland, WA, 1981.)

imposed on the mean wind speed. A gust is a short-term discrete event within a turbulent wind field. The common method of characterizing a gust is to measure or specify the amplitude, the rise time, the maximum gust variation, and the lapse time associated with it. Wind speed is very dependent on local topographical and ground cover variations. Figure 7.3 illustrates differences between two sites that are located in nominally flat terrain only 21 km apart. In spite of the close proximity and the flat terrain, the 5-year average mean wind speeds differ by about 12%.

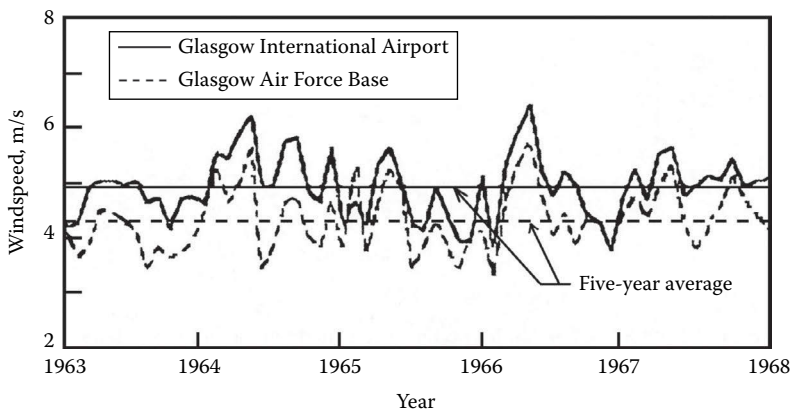


FIGURE 7.3

Time series of monthly wind speed for Glasgow, MT, International Airport and Air Force Base. (From Hiester, T.R. and Pennell, W.T., *The meteorological aspects of siting large wind turbines*, PNL-2522, Pacific Northwest Laboratory, Richland, WA, 1981.)

7.2 Energy Available from the Wind

Given the fact that the wind blows everywhere, the idea of harnessing it to provide power is very appealing. Mankind has harnessed the power of the wind to produce mechanical power for well over 1000 years; the use of the wind to mill grain in Persia in the tenth century is well documented, and many experts speculate that the Chinese may have invented the windmill as much as 2000 years ago. How much power is available in the wind? Is it enough to be a viable source of energy in the modern world? Answers to these questions require knowledge of several wind energy basics.

7.2.1 Wind Power

Consider the air with an average velocity U and density ρ in a cylinder of cross section A and length L as shown in Figure 7.4. The mass of the air in that cylinder is ρAL , and the kinetic energy (KE) of that air is $\frac{1}{2}\rho ALU^2$ (Watt-hours or Wh). Now assume that there is a wind turbine rotor at the downwind end of that cylinder of air. The cylinder of air will pass through that rotor in a period of time, T , where $T = L/U$. The power, or time rate of change of the KE, available at the rotor then is $\frac{1}{2}\rho ALU^2/T$, which becomes

$$\text{Power} = \frac{1}{2}\rho AU^3 \text{ (W)} \quad (7.1)$$

This is often rearranged and expressed as power per unit area:

$$\text{WPD (wind power density)} = \frac{\text{Power}}{A} = \frac{1}{2}\rho U^3 \text{ (W/m}^2\text{)} \quad (7.2)$$

From Equation 7.1, it is obvious that the most important factor in the available wind power is the velocity of the wind. Increasing the wind velocity by only 20%, say from 5 to 6 m/s, increases the available wind power by 73%. Figure 7.5 illustrates the impact of normal annual wind speed variations at a location on the available wind power at that location.

The standard value for air density at sea-level reference conditions of 101,325 Pa pressure and 15°C is 1.225 kg/m³. The actual density depends on the moisture content or humidity of the air, the temperature, and the atmospheric pressure; however, the influence of

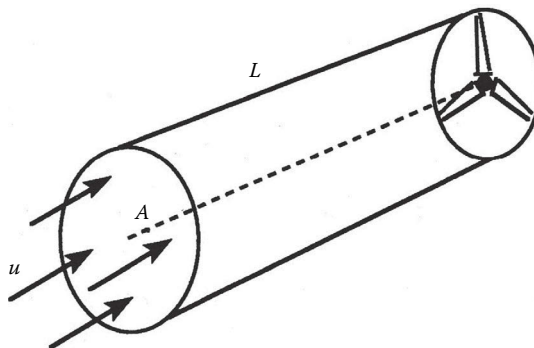


FIGURE 7.4
Steady wind passing through turbine rotor disk.

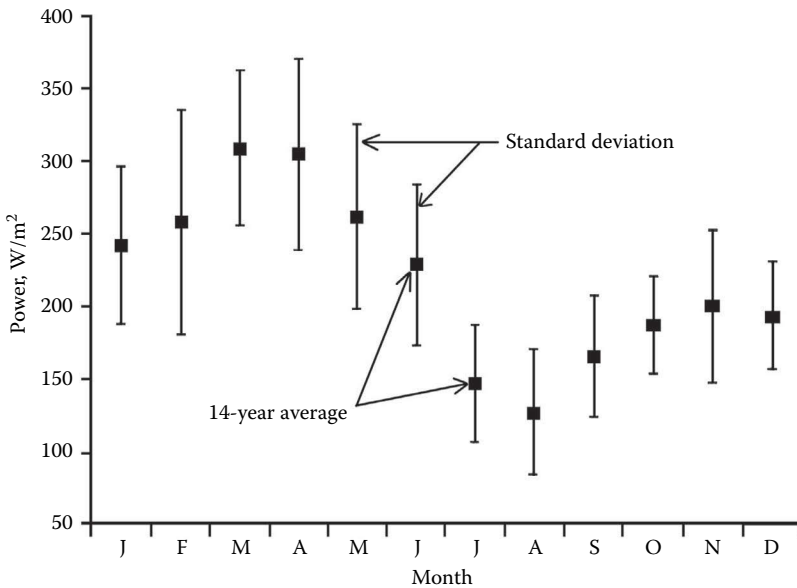


FIGURE 7.5

Seasonal variation of available wind power density for Amarillo, TX. (From Rohatgi, J.S. and Nelson, V., *Wind Characteristics: An Analysis for the Generation of Wind Power*, Alternative Energy Institute, West Texas A&M University, Canyon, TX, 1994. Reproduced by permission of Alternative Energy Institute.)

humidity is very small and is normally neglected. Under this condition, the air density can be calculated from the perfect gas law

$$\rho = \frac{P}{RT} \text{ (kg/m}^3\text{)} \quad (7.3)$$

where

P is the atmospheric pressure in Pa or N/m²

R is the specific gas constant for air (287 J/kg K)

T is the absolute air temperature in Kelvin

If site air pressure is not available, air density can be estimated as a function of site elevation, z , and absolute temperature as [1]

$$\rho = \left(\frac{353.05}{T} \right) e^{-0.034(z/T)} \text{ (kg/m}^3\text{)} \quad (7.4)$$

For example, the air density at Denver, Colorado (elevation 1600 m or 5300 ft above sea level), is approximately 15% lower than that at sea level, so wind of a given velocity at Denver contains 15% less power than wind of the same velocity at sea level (assuming the temperature is the same).

7.2.2 Wind Shear

Wind moving across the earth's surface is slowed by trees, buildings, grass, rocks, and other obstructions in its path, resulting in a wind velocity that varies with height above the earth's surface—a phenomena known as the *vertical wind profile* or *vertical wind shear*.

In most locations, wind shear is positive (wind speed increases with height), but situations in which the wind shear is negative or inverse are not unusual. In the absence of actual data for a specific site, a commonly used approximation for wind shear in an open area is

$$\frac{U}{U_o} = \left(\frac{h}{h_o} \right)^\alpha \quad (7.5)$$

where

U is the velocity at a height h

U_o is the measured velocity at height h_o

α is the wind shear exponent

The instantaneous wind shear exponent varies widely with elevation, time of day, season of the year, wind speed, temperature, and nature of the terrain. It could be, say, 0.1 during the day and then reach 0.5 at night [2]. The time-averaged shear exponent is the value that is normally used (averaged over several weeks); this varies with terrain characteristics, but usually falls between 0.10 and 0.25. Wind over a body of open water is normally well modeled by a value of α of about 0.10; wind over a smooth, level, grass-covered terrain such as the U.S. Great Plains by a value of α of about 0.14; wind over row crops or low bushes with a few scattered trees by a value of α of 0.20; and wind over a heavy stand of trees, several buildings, or hilly or mountainous terrain by a value of α of about 0.25. Short-term time-averaged shear factors as large as 1.25 have been documented in rare, isolated cases.

As a result of wind shear, the available wind power at a site may vary dramatically with height. For example, for $\alpha = 0.20$, Equations 7.1 and 7.5 reveal that the available wind power density (WPD) at a height of 50 m is approximately $\{(50/10)^{0.2}\}^3 = 2.63$ times the available WPD at a height of 10 m. Keep in mind that Equation 7.5 is only an estimate; a specific site may display much different wind shear behavior, and that will dramatically affect site WPD, so it is very important to measure the wind resource at the specific site and height where the wind turbine will be located.

National Renewable Energy Laboratory (NREL) scientists recently analyzed wind data obtained from several tall towers at heights of up to 110 m and found that the annual average wind shear exponent at Great Plains sites for heights between 50 and 100 m ranges from 0.15 to 0.25, with a daytime shear between 0.05 and 0.1 and a nighttime shear between 0.25 and 0.40 [3]. They also found that surface roughness effects on wind shear can be significant at heights up to 100 m, wind shear exponents at heights of 100–150 m can exceed those at heights of 50–100 m, and large differences in shear exponents at elevated heights can exist among sites, even in local areas of similar wind climate [4]. Their recommendation from these studies is that direct measurement data at elevated heights are needed to validate model-derived wind resource estimates.

7.2.3 Available Resource

The amount of energy available in the wind (the wind energy resource [WER]) at a site is the average amount of power available in the wind over a specified period of time, commonly 1 year. If the wind speed is 20 m/s, the available power is very large at that instant, but if it blows at that speed for only 10 h/year and the rest of the time the wind speed is near zero, the resource for the year is small. Therefore, the relative frequency of occurrence for each wind speed (the wind speed distribution) is very important in determining the resource at the site. This distribution is determined experimentally as the relative

frequency of occurrence of uniform width wind speed ranges extending over the entire range of possible wind speeds (i.e., 0.5 m/s increments from 0 to 30 m/s). The wind speed associated with each range is that at the center of the range. This distribution may be approximated by a continuous curve, the probability density function or pdf, which corresponds to wind speed ranges of infinitesimal width.

If the actual wind speed probability density distribution is not available, it is commonly approximated with the generalized two-parameter Weibull distribution given by

$$f(U) = \frac{k}{C} \left(\frac{U}{C}\right)^{k-1} \exp\left[-\left(\frac{U}{C}\right)^k\right] \quad (7.6)$$

where

$f(U)$ is the frequency of occurrence of wind speed U

k is the Weibull shape factor

C is the Weibull scale factor

For the special case with parameter k equal to 2, this reduces to the commonly used Rayleigh distribution:

$$f(U) = \frac{\pi}{2} \frac{U}{\bar{U}^2} \exp\left[-\frac{\pi U^2}{4 \bar{U}^2}\right] \quad (7.7)$$

where \bar{U} is the yearly average wind speed.

It is readily apparent that the average wind speed at a site yields a unique Rayleigh distribution for that site. Experimental data from a site also determine the best Weibull distribution for that site, but the process of determining k and C from the experimental data is not straightforward.

The measured wind speed distribution at the Amarillo, Texas, airport (yearly average wind speed of 6.6 m/s) is plotted in Figure 7.6, together with the Weibull and Rayleigh distributions for that wind speed. It is obvious that the Rayleigh distribution is not a good representation for these data; the data have a higher peak, have a lower probability of lower wind speeds, and have a significantly higher probability of winds in the 4–12 m/s range. The Weibull distribution (the shape factor k was picked as 2.6, yielding an estimate for the scale factor C of 7.4) is a much better approximation of the data. It shows a good match to the peak probability, but it still is not a good match; the data consistently have a somewhat lower probability for wind speeds below about 10 m/s and a somewhat higher probability for wind speeds above 10 m/s.

With a discrete wind speed distribution and the local air density, the WER, or average wind power availability, for a specific site can be estimated as

$$\text{WER} = \frac{1}{2} A \sum_{i=1}^n \rho f(U_i) \Delta U_i U_i^3 (W) \quad (7.8)$$

where

n is the number of wind speeds included in the distribution

$f(U_i) \Delta U_i$ is the probability of the wind speed occurring in the wind speed range ΔU_i centered on wind speed U_i

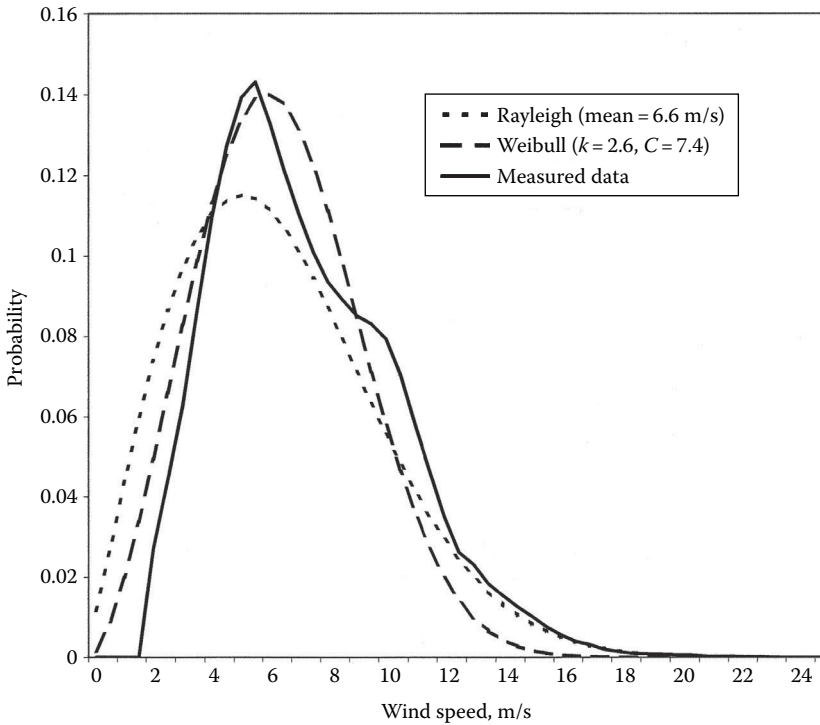


FIGURE 7.6
Measured and analytical wind speed distributions for Amarillo, TX, airport.

If an analytical pdf (such as the Rayleigh or Weibull) is used, this becomes

$$WER = \frac{1}{2}A \int \rho f(U)U^3 dU(W) \tag{7.9}$$

The wind energy potential (WEP) or potential gross annual wind energy production for a specific site and a specific wind turbine can be calculated with a wind speed distribution and the turbine power curve (the electrical power generated by the turbine at each wind speed), properly adjusted for the local air density. For a discrete wind speed distribution,

$$WEP = 8760 \sum_{i=1}^n f(U_i)\Delta U_i P(U_i)(Wh) \tag{7.10}$$

where

8760 is the number of hours in a year

$P(U_i)$ is the electrical power produced by the turbine at wind speed U_i , the center of the range ΔU_i

With an analytical pdf (the Rayleigh or Weibull), this becomes

$$WEP = 8760 \int f(U)P(U)dU(Wh) \tag{7.11}$$

It is quite obvious that using an analytical pdf that is not a good match to the actual distribution at a site (such as the Weibull and Rayleigh distributions shown in Figure 7.6) will yield values for WER and WEP that are not good estimates of the actual values for that site. In order to get good estimates for these quantities, the actual wind speed distribution must be used.

In 1987, Elliott, Holladay, Barchet, Foote, and Sandusky at Battelle Pacific Northwest Laboratory in the United States carefully analyzed and interpreted the available long-term wind data for the United States and summarized their estimate of the WERs in the *Wind Energy Resource Atlas of the United States* [5]. Their summary for the entire United States is reproduced in Figure 7.7. The results are presented in terms of wind power classes based on the annual average power available per square meter of intercepted area (see the legend on Figure 7.7). Sites of wind power class 3 or higher (at least 150 W/m^2 at 10 m height or 300 W/m^2 at 50 m height) are usually considered economic for utility-scale wind power development with available wind technology. Sites of wind power class 2 or lower (less than 150 W/m^2 at 10 m height or 300 W/m^2 at 50 m height) are usually considered economic only for remote or hybrid wind power systems. Troen and Petersen at Denmark's Risø National Laboratory produced a European Wind Atlas [6] in 1989 that used somewhat different techniques to estimate the wind resources of the European Community countries. Their work summarizes the resource available at a 50 m height for five different topographic conditions.

The estimates shown in Figure 7.7 and those presented in [6] are quite crude and have been superseded in recent years by much higher-resolution maps at higher elevations, made possible by improvements in wind resource computer modeling programs, increases in computer speed, and development of high-altitude wind speed-measuring capabilities. In particular, NREL, in collaboration with AWS Truepower, has recently released new maps of the U.S. wind resource at 50, 80, and 100 m elevations [7]. The new 100 m resource map, displayed in Figure 7.8, reveals that many areas in the U.S. Midwest and Southeast thought to lack an adequate wind resource (see Figure 7.7) actually have commercially viable wind resources at turbine tower heights of 100 m or greater. Many countries around the world have embarked on similar high-resolution mapping efforts to accurately quantify their wind resources and identify those areas of highest resource. The resultant resource maps are frequently available to the public, but in some cases, a payment is required to obtain them. High-resolution wind resource maps of the individual states in the United States may be found on the web at www.windpoweringamerica.gov/wind_maps.asp. Some states have developed even more detailed maps in recent years, and these may be found on websites for the individual states. Similar maps for some other countries may be found at www.nrel.gov/wind/international_wind_resources.html, and information on where to find maps and/or data for other countries may be found at www.windatlas.dk/index.htm. These newer wind resource evaluations frequently reveal far greater wind resource than earlier evaluations. In some cases, this is due to the higher resolution now available, but in some cases, this is because the early evaluations sometimes used unverified long-term data from existing weather stations where the anemometers had not been properly maintained—the bearings had deteriorated over time, and the anemometers registered lower winds than what actually existed. The verification procedures used in the newer evaluations are designed to help identify and eliminate this type of biased data. But even the highest resolution resource estimates are just that—estimates. The actual wind resources in any specific area can vary dramatically from those estimates and must be determined with long-term, site-specific, and elevation-specific measurements.

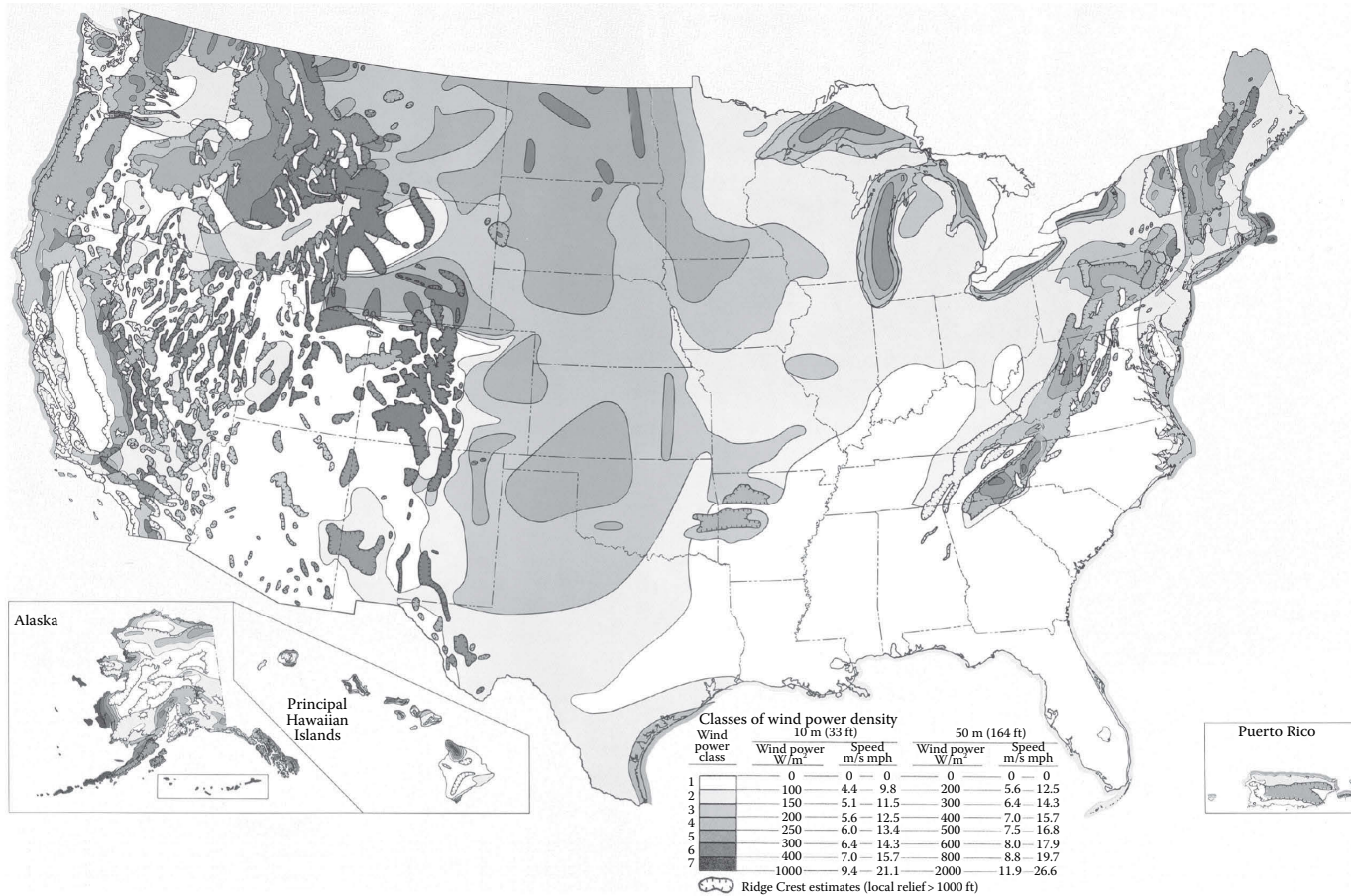


FIGURE 7.7

The U.S. wind energy resources. (From Elliott, D.L. et al., Wind energy resource atlas of the United States, DOE/CH10094-4, Solar Energy Research Institute, Golden, CO, 1987. Reproduced by permission of National Renewable Energy Laboratory, Golden, CO)

United States—land-based and offshore annual average wind speed at 100 m

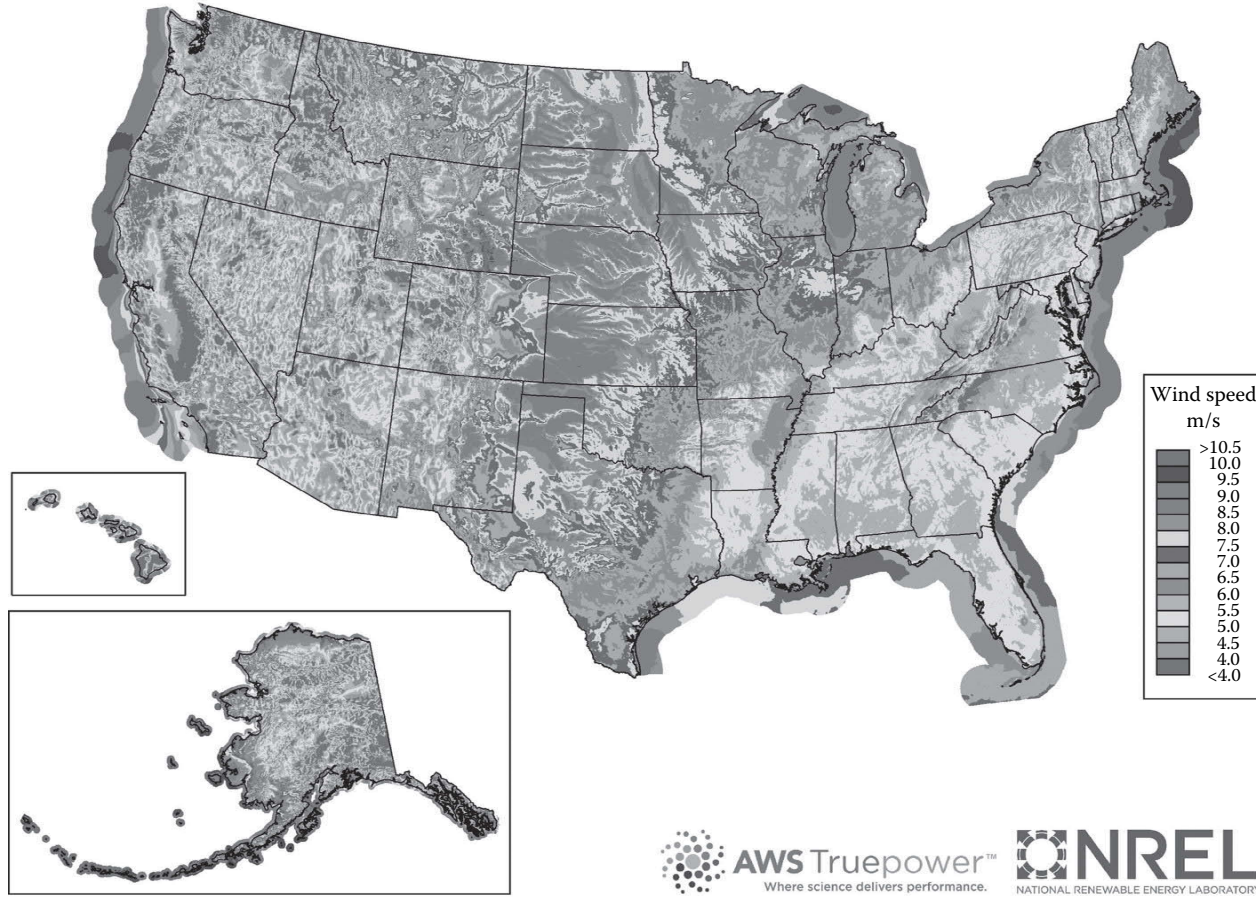


FIGURE 7.8

The U.S. high-altitude wind energy resources. (From Office of Energy Efficiency and Renewable Energy, U.S. Department of Energy, http://energy.gov/sites/prod/files/styles/media_energy_gov_wysiwyg_fullwidth/public/wind_speed_map_lg.jpg?itok=ITLo1T1G, accessed March 2015.)

Archer and Jacobson from Stanford University [8] have estimated the average global wind power potential for all land-based locations with wind class 3 or better (mean annual wind speeds in excess of 6.9 m/s at 80 m height) to be on the order of 72 TW (1 TW = 10^{12} W) for the year 2000, yielding an average WEP of 627,000 TW h/year. In reality, the use of approximately 90% of the land mass is restricted, leaving only about 10% available for wind power generation. Thus, a realistic WEP from the Stanford study is on the order of 62,700 TW h/year. This figure is consistent with the published European Wind Energy Association [9] figure of 53,000 TW h/year of WEP and corresponds to over three times the world's total electricity needs in 2001 of 14,000–16,000 TW h/year. Many of the countries around the world have adequate wind resources to supply their entire energy consumption. Of course, this resource is not necessarily available at the right time or the right place, and actually capturing wind energy on this vast a scale is not apt to happen.

The wind resource over the water-covered portion of the earth's surface is many, many times greater than that over the land, but current wind energy technology is restricted to shallow water (water depths on the order of 30 m or less). The available wind resource over water restricted to these depths is still significant—recent NREL work has shown that the U.S. offshore gross wind resource at these depths is estimated at over 1000 GW, or roughly the generating capacity currently carried on the U.S. electric grid [10]. Keep in mind that this resource value will likely shrink by 60% or more after all environmental and socioeconomic constraints have been taken into account. Development of the technology required to enable utilization of the much larger WERs at greater water depths is the focus of much current research.

7.2.4 Environmental/Societal Restrictions

The fact that a site has great wind resources and access to transmission lines with excess capacity does not mean that it is suitable for wind power development. Potential environmental and social issues must be considered and resolved before a wind facility can be built. In the best possible scenario, such issues will add expense and development time to a project. In the worst scenario, such issues could cause cancellation of a project. Some of the issues that could affect the suitability of a proposed site include the presence of endangered or protected species, nearby residences or airports (which might require significant setbacks of the nearest wind turbines), nearby scenic areas, recreational use or other specific use restrictions of the candidate site, or religious significance of the site. The following sections discuss two issues that are topics of research today.

7.2.4.1 Impacts of Wind Facilities on Birds and Bats

The greatest environmental issues that the wind industry has had to face are the possible impacts of wind facilities on birds and bats and their habitats. Concerns about the bird fatality issue were, in large part, the result of relatively high numbers of raptor deaths in the Altamont Pass wind farms east of San Francisco, CA, in the 1980–1985 time frame. Dozens of studies of this issue have been conducted during the past 30 years. Sinclair and Morrison [11] and Sinclair [12] give overviews of some of the early U.S. studies, and the National Wind Coordinating Committee has recently published a fact sheet summarizing the research performed prior to 2010 [13]. One conclusion of these studies is that the Altamont Pass situation appears to be a worst-case scenario, due in large part to bad turbine siting and to the presence of overhead power lines that led to a large number of bird electrocutions. Colson [14] and Wolfe [15] report that the numerous

recommendations for minimizing the impact of new wind farms on birds resulting from these studies include the following:

- Conduct site-specific mitigation studies.
- Avoid bird migration corridors and areas of high bird population such as micro-habitats or fly zones.
- Use fewer, larger turbines.
- Minimize the number of perching sites on turbine towers by using tubular, rather than lattice, towers.
- Bury electrical lines.

The subsequent development of industry siting guidelines for wind farms has proven to be quite effective; recent studies have shown that relatively low raptor fatality rates exist at most wind energy developments, with the possible exception of those wind farms in California that were developed prior to the establishment of these siting guidelines.

If large numbers of raptors are present, additional restrictions on turbine placement, style, height, etc., may be required by local authorities to minimize the potential for collisions with turbines. In reality, far more songbirds than raptors are killed by turbines; in spite of this, the estimated cumulative impact of songbird collisions with wind turbines is several orders of magnitude lower than the estimated impacts from the leading human-related causes of songbird mortality (vehicles, buildings and windows, power transmission lines, communication towers, toxic chemicals, and feral and domestic cats), according to the NWCC [13,16]. Bird collisions with wind turbines caused the deaths of only 0.01%–0.02% of all the birds killed by collisions with man-made structures across the United States in 2001. In contrast, bird collisions with buildings and windows accounted for about 55% of structure-related bird deaths, while collisions with vehicles, high-tension power lines, and communication towers accounted for about 17%.

Relatively small numbers of bat fatalities were reported at wind energy facilities in the United States before 2001, largely because most monitoring studies were designed to assess bird fatalities, according to Kunz et al. [17]. Bat carcasses are much more difficult to find than are bird carcasses, and they are quickly removed by predators, so it is quite likely that these studies underestimated bat fatalities. However, once more careful studies revealed that some wind farms were causing a large number of bat fatalities, the wind industry joined with Bat Conservation International, the U.S. Fish & Wildlife Service, and NREL to identify and quantify the problem and to explore ways to mitigate these deaths. Several wind energy companies are providing a portion of the funding for cooperative efforts to resolve this issue.

Although bat fatalities at wind energy facilities appear to be highest along forested ridgetops in the eastern United States, studies have revealed that bat fatalities are a widespread problem—turbine-related bat deaths have been reported at every wind facility studied to date, both in the United States and in Europe [13].

This problem has been actively studied for over a decade at this point, but it is still poorly understood. A few of the findings to date are as follows:

- Some migratory tree-roosting bat species appear particularly vulnerable to wind power fatalities.
- Bat fatalities peak at wind facilities during the late summer and early fall bat migration seasons.
- Most bat fatalities occur during periods of low wind, when flying insects, which are their primary source of food, are most common, and bats are most active.

Why are bats being killed by turbines? As documented by Baerwald et al. [18], given that echolocating bats detect moving objects better than stationary ones, their relatively high fatality rate at wind farms is perplexing. According to the NWCC [13], bats may be attracted to the turbines; possibly because the towers appear to be potential roosting trees, there is a high concentration of insects around the turbines (due to the favorable conditions created during turbine installation); or the sounds produced by turbines are attractive. On the other hand, the bats may become disoriented by the turbine sounds or by the electromagnetic fields in the vicinity of the turbine nacelles. This remains a research topic at this time.

In contrast to turbine-related bird deaths, which appear to be caused entirely by collisions with the turbines, the manner in which bats are killed by turbines is not well understood. While direct collisions with the turbines certainly account for many of the deaths, some researchers hypothesize that a large portion of the bat fatalities are caused by barotrauma; Baerwald et al. [18] have found that the internal organs of a sizable portion of the dead bats they found in the vicinity of wind turbines have been damaged by the low-pressure areas present near the blade tips and in the blade wake.

Preliminary studies reported by Baerwald et al. [19] and Arnett et al. [20] have demonstrated that bat fatalities have been reduced by 50%–87% by increasing the cut-in wind speed of the turbine, but much work remains to be done before this issue is resolved. Until this problem is better understood, the prudent course of action would be to postpone the development of promising sites that have significant numbers of bats nearby. At the very least, the latest information from the appropriate national wind energy association regarding bat collisions with wind turbines should be obtained and carefully studied.

7.2.5 Impact of Wind Facilities on Radar

While fixed objects in the vicinity do not generally create a problem for radar installations, the rotating blades of wind turbines do; wind turbine blades have a very large radar signature, especially when turbines are grouped together in a wind farm. As a result, wind farms located in the near vicinity of government radar installations used for national defense, national security, aviation safety, and weather forecasting interfere with those radars by creating clutter, reducing detection sensitivity, obscuring potential targets, and scattering target returns. These effects tend to decrease radar sensitivity, generate false targets, interfere with target tracking, and impede critical weather forecasts. Many hundreds of MW of proposed U.S. wind developments in the vicinity of radar installations are on hold because of this issue—developers cannot get approval from one or more government agencies due to concerns that these developments will interfere with the existing radar installations.

In an effort to resolve this problem in order to accommodate future wind energy growth, the U.S. Departments of Energy, Defense, and Homeland Security and the Federal Aviation Administration are currently funding a field test and evaluation of commercial off-the-shelf wind–radar interference mitigation technologies. Results of this effort should be available in the 2014 time frame, but widespread implementation of any successful mitigation technology is apt to take several years. In the meantime, the prudent course of action would be to postpone the development of promising sites that might create a radar interference issue.

7.3 Wind Resource Assessment

Three things must be present before a commercial wind energy generation plant can be successfully developed: a site with a good wind resource, access to a transmission line with the capacity to accept the plant output, and a buyer to purchase the energy generated. Only the identification of sites with adequate wind resource will be considered here. In addition, this discussion will be limited to the evaluation of onshore wind resources. Evaluation of offshore resources requires significantly more effort and a much larger financial investment.

Many different approaches are available when investigating the wind resource in a given land area. The preferred approach will depend on your wind energy program objectives and on previous experience with wind resource assessment. In any case, the process normally consists of three basic scales or stages of assessment:

1. Prospecting or identifying general areas of high wind resource. In this stage, wind developers typically rely on existing wind resource information to narrow the search region to the most promising areas.
2. Area wind resource evaluation to determine the actual wind resource. Wind measurement programs are normally undertaken in areas under serious consideration for wind power development. Wind developers use these measurements to determine the actual quality of the resource, compare different candidate sites, estimate the performance of specific turbines, analyze the economic potential of wind development, and make preliminary determinations of turbine placements.
3. Micrositing, in which the siting of the individual wind turbines is optimized. By carefully studying the small-scale variability of the wind resource at a particular location, the developer can position the wind turbines to get maximum wind exposure with minimal interference from other turbines or obstructions, and thus maximize the overall energy output. There are many computer codes available to perform this function. The level of sophistication of these codes varies widely. The better ones use computational fluid dynamics to model the wind farm, utilizing digital elevation data to define the terrain of the wind farm and site measurement data to provide calibration and wind input information. In some cases, professional wind energy development companies may be willing to perform this service gratis, in hopes of getting the rights to develop the site. Advertisements for these programs can be found in most wind energy trade magazines. Further discussion of micrositing is beyond the scope of this contribution.

7.3.1 Prospecting

The goal of prospecting for wind energy development sites is to identify areas within a fairly large region such as a utility service area, a county, or even a multistate region that are likely to have good wind resources and that are located near existing power transmission lines with the capacity to handle the power generated by the new development. A good initial step in this process is to obtain the highest resolution available wind resource maps of the entire area of interest (see Section 7.2.3 for links to some map sources) and use those to identify areas of high winds. Keep in mind that values on the wind resource maps are just estimates—some areas of good resource may not be identified, and some areas identified as

having good resource may actually have very poor resources. Use these maps in conjunction with topographic maps that show the location of major transmission lines, roads, etc., to narrow the general search area. Use of geographic information system (GIS) will permit the overlaying of the resource information with topographic information and road and transmission line information, greatly facilitating the identification of promising sites. Even with all the information that can be gleaned from GIS systems and hard copy and online maps, field visits to prospective sites are very worthwhile, as observation of biological indicators and topographic features often help identify the best wind resource areas.

7.3.1.1 Biological Indicators

Persistent winds can cause plant deformation; careful observation of these plant deformations can be used to compare candidate sites and, in at least some cases, to estimate the average wind speed. Figure 7.9 illustrates various levels of tree deformity, corresponding to increasing levels of wind from one prevailing direction. The Griggs–Putnam index, explained in Hewson et al. [21], correlates these degrees of deformation to specific wind speeds for one particular type of tree. While the vegetation in an area of interest may not permit the estimation of actual wind speeds based upon the sketches in this figure, the relative wind speeds in the area might well be established by observing the amount of flagging or throwing that is present. It should be noted that, although wind-flagged trees (i.e., trees with branches bent away from a prevailing wind) may indicate that the annual average wind speed is quite strong, trees that are not flagged do not necessarily indicate that the winds are light; those trees may be exposed to strong winds from several directions, with insufficient persistence in any one direction to cause flagging.

7.3.1.2 Effects of Topography

The effects of surrounding terrain on the wind speed at a specific site are discussed in various wind turbine siting handbooks including Troen and Petersen [6], Hiester and Pennell [22], Wegley et al. [23], and Rohatgi and Nelson [24]; the following discussion borrows heavily from these sources. Numerous researchers emphasize that the influence of terrain features on the energy output from a turbine may be so great that the economics of the whole project may depend on the proper selection of the site. The ready availability of detailed GIS maps and mapping technology today has greatly simplified this aspect of prospecting.

7.3.1.2.1 Terrain Classification

The most basic classification divides terrain into flat and non-flat categories. In a strict sense, the earth's surface is never truly flat; there are always some irregularities such as forest and shelterbelts (or wind breaks), and/or gentle slopes. However, according to Frost and Nowak [25], the terrain can be considered flat (for the purpose of wind turbine siting) if it meets the following conditions:

- Elevation differences between the wind turbine site and the surrounding terrain are not greater than about 60 m anywhere in an 11.5 km diameter circle around the turbine site.
- No hill has an aspect ratio (height to width) greater than 1/50 within 4 km upwind and downwind of the site.
- The elevation difference within 4 km upwind is small compared to the rotor ground clearance.

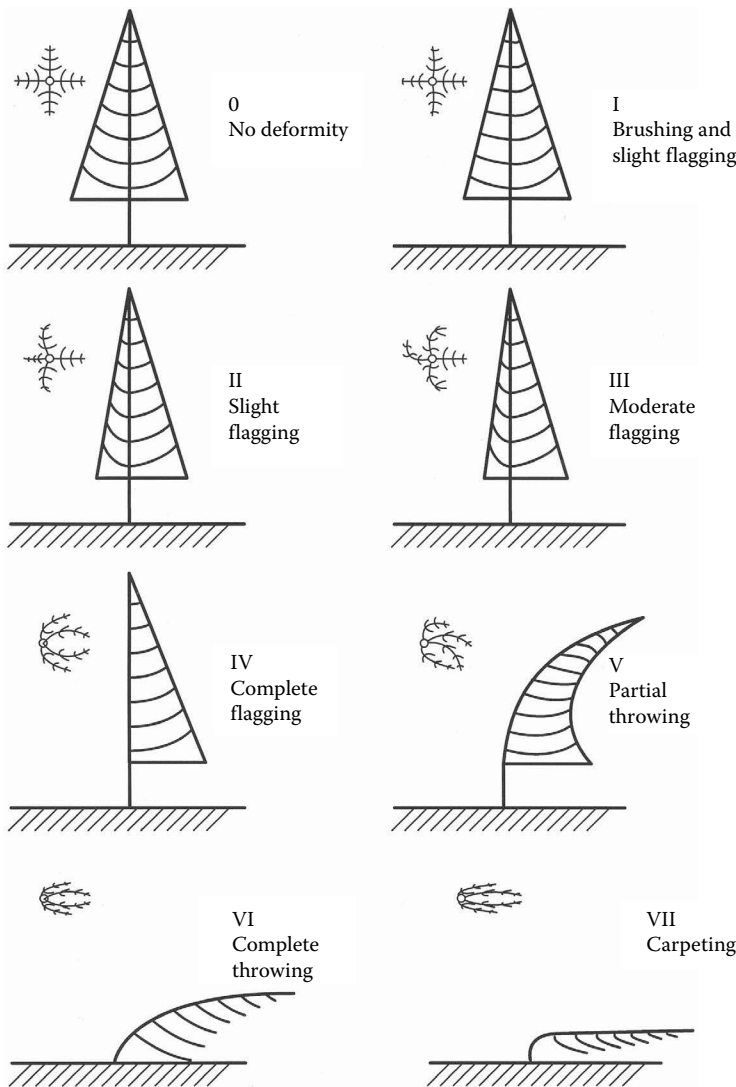


FIGURE 7.9

Griggs-Putnam index of tree deformation. (From Hewson, E.W. et al., *Vegetation as an indicator of high wind velocity*, RLO/2227-T24-78-2, Oregon State University, Corvallis, OR, 1978.)

Flat terrain is obviously the simplest type of terrain for siting a turbine—the wind speed at a given height is nearly the same over the entire area. In the absence of any obstructions to speed up wind flow, typically the best way to increase the available wind power is to raise the rotor higher above the ground to take advantage of positive wind shear. In most natural terrain, however, the surface of the earth is not uniform but changes significantly from location to location, affecting the local wind profile. Figure 7.10 illustrates the significant change in a vertical wind profile that results from wind flow going from a smooth to a rough surface—the shape of the profile shifts quite dramatically over a relatively short horizontal distance. In addition, most flat terrain has a variety of man-made (buildings, silos, etc.) and natural obstacles that affect the flow of wind. The effects of these obstacles

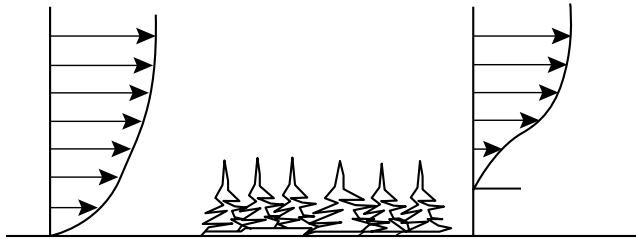


FIGURE 7.10 Effect of change in surface roughness from smooth to rough. (From Wegley, H.L. et al., *A Siting Handbook for Small Wind Energy Conversion Systems*, PNL-2521, Pacific Northwest Laboratory, Richland, WA, 1980.)

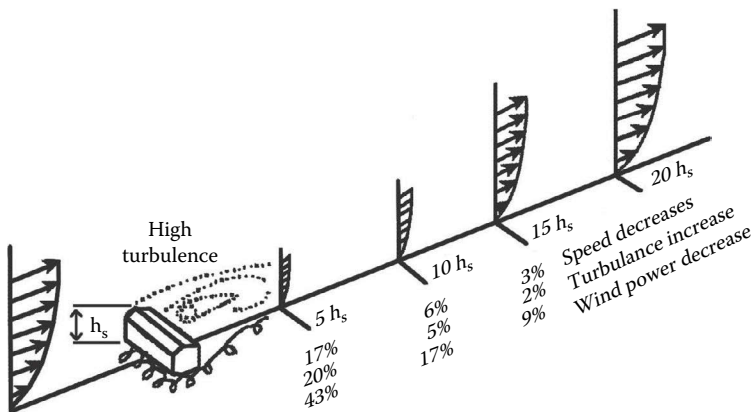
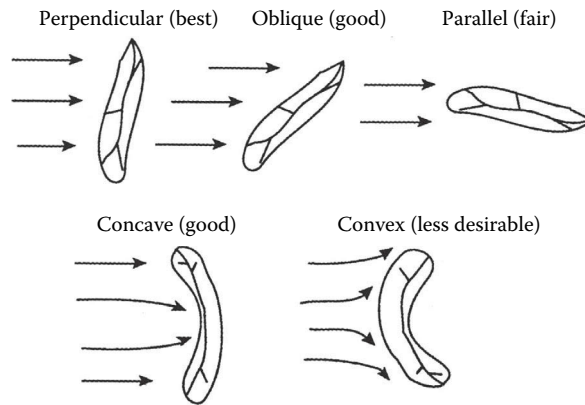


FIGURE 7.11 Wind speed, power, and turbulence effects downstream of a building. (From Wegley, H.L. et al., *A Siting Handbook for Small Wind Energy Conversion Systems*, PNL-2521, Pacific Northwest Laboratory, Richland, WA, 1980.)

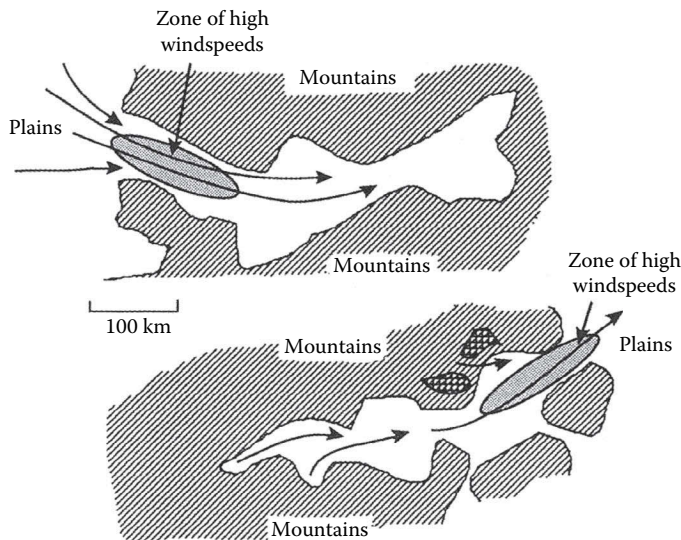
have been studied extensively; an example of the effect of a building on wind speed, available power, and turbulence is shown in Figure 7.11. Note that the estimates in the figure apply at a height equal to 1 building height above the ground, and that power losses become small (<10%) after a downwind distance equal to 15 building heights.

Ridges are elongated hills with a length-to-height ratio of at least 10 that have little or no flat area on the summit. As illustrated in Figure 7.12, the ideal prevailing wind direction for wind turbine siting should be perpendicular to the ridge axis. When the prevailing wind is not perpendicular to the axis, the ridge will not be as attractive a site. Concavity in the windward direction enhances speedup, and convexity reduces speedup by deflecting the wind flow around the ridge. The slope of a ridge is also an important parameter; steeper slopes give rise to stronger wind flow, but they also give rise to high turbulence in the lee of the ridge.

Depressions are characterized by terrain features lower than the surroundings and include valleys, canyons, basins, and passes. These can cause significant speedup of the wind if they effectively channel the wind. The factors that influence the flow in depressions, in addition to diurnal flow variations, include orientation of the wind in relation to the depression, atmospheric stability, the width, length, slope and roughness of the depression, and the regularity of the section of valley or canyon. Canyons in mountainous terrain, such as those illustrated in Figure 7.13, can be very effective in creating high wind speeds.

**FIGURE 7.12**

Effect of ridge orientation and shape on site suitability. (From Wegley, H.L. et al., *A Siting Handbook for Small Wind Energy Conversion Systems*, PNL-2521, Pacific Northwest Laboratory, Richland, WA, 1980.)

**FIGURE 7.13**

Increased wind speeds due to channeling of prevailing winds by mountains. (From Rohatgi, J.S. and Nelson, V., *Wind Characteristics: An Analysis for the Generation of Wind Power*, Alternative Energy Institute, West Texas A&M University, Canyon, TX, 1994. Reproduced by permission of Alternative Energy Institute.)

Non-flat or complex terrain has large-scale elevations or depressions such as hills, ridges, valleys, and canyons. Keep in mind that information on wind direction should be considered when defining the terrain classification. For example, if an isolated hill (200 m high and 1000 m wide) were situated 1 km south of a proposed site, the site would normally be classified as complex. If, however, the wind blows only 5% of the time from this direction and the average speed from this direction is low, say 2 m/s, then this terrain would be classified as flat. Additional summaries of the effects on wind flow of many types of large-scale features, including mountains, large cliffs and escarpments, valleys and canyons (including

slope winds, prevailing winds in alignment, and prevailing winds in nonalignment), gaps and gorges, passes and saddles, and large basins, are given in Rohatgi and Nelson [24].

7.3.2 Wind Resource Evaluation

Once general areas of high wind resources have been identified, the actual resource available at one or more of those sites can be determined by performing a full wind resource evaluation or site assessment. This is a costly, complex, and time-consuming activity. Numerous companies perform this service; a good method for locating some is to access the appropriate national wind energy association membership list and search for “meteorology consultants.” Even if the service is contracted out, a cursory knowledge of the process is important to ensure that the contractor does a good job. Numerous handbooks detailing the steps for conducting successful measurement programs are available. While the following discussion, which borrows heavily from AWS Scientific, Inc. [1], is for land-based resource assessment, many of the important aspects are also applicable to off-shore resource assessment [26].

Long-term wind speed variability at a site is nearly as important as mean wind speed, as far as long-term energy production is concerned. Meteorologists generally agree that a well-done evaluation/assessment project will take a minimum of 1 year to complete [23], but a project duration of 2 or more years will produce more reliable results and is recommended by Schwartz and Elliott [27] and many other experts. One year is usually sufficient to determine the diurnal and seasonal variability of the wind with an accuracy of 10% at a confidence level of 90%, according to Aspliden et al. [28] and Corotis [29]. In some cases, high-quality data may be available from a nearby representative site, and this might be used to shorten the duration of the assessment project and to estimate the interannual variability of the wind. In particular, long-term data from the nearest airport or weather recording station can help determine whether the data obtained at a site is representative of normal winds for the site or whether it is representative of higher- or lower-than-average winds. Wegley et al. [23] and Gipe [30] give suggestions on methods of using available data from nearby sites to estimate site wind speed with minimal on-site data.

A single site assessment with a very basic single monitoring station (cup anemometer and wind vane instrumentation) on a 50 m tilt-up tower operated for 2 years can be expected to run in excess of \$20,000 (2005\$); a 60 m monitoring station will run about \$2500 more. Multiple sites will see some economies of scale, depending on how close the sites are to each other. The total cost to operate a second site can be expected to be 10%–15% less than the cost for the first site. Five sites in fairly close proximity can probably be operated for an average site cost about 25% less than for a single site. Most savings will be realized in the labor and travel categories, although equipment cost savings may be realized as a result of quantity discounts, by sharing installation equipment, and by sharing parts inventories. Conducting an abbreviated resource assessment program to minimize expenses may well turn out to be a case of “penny wise, pound foolish” in that the return on investment of the entire wind farm project will be directly affected by the quality of the actual wind resource at each turbine site. Without a proper site assessment, the resource estimates may not be a good reflection of the actual resource, and the production of the wind project may be much different than projected.

For small wind turbines, the expense of anemometers, data logger, and data analysis may be more than the price of the wind turbine. In this case, historical regional data may be judged to be adequate for estimating the wind resource. Inexpensive digital weather stations, including rudimentary data loggers that work with a personal computer, are

available for under \$1000, and one of these could be used in conjunction with the historical data to improve the accuracy of the resource assessment. While these inexpensive weather stations may be adequate for this particular application, they are not highly accurate and are not designed for long-term durability, so they are not suitable for collecting long-term data for accurate wind resource assessment as is needed for commercial enterprises. Wind speed, direction, distribution, and shear can vary significantly over fairly short distances in either the horizontal or the vertical direction, so in order to get the best possible estimate of the WER at a particular location, it is important to measure the wind resource at the specific site and height of interest. In complex terrain, this probably means the use of several monitoring stations to adequately assess a single site.

The keys to a successful assessment program are the early identification of the objectives of the program and the timely development of a detailed plan of action to ensure that the data needed to meet the objectives are acquired. Such a plan should include, at a minimum, the following:

- Quality control measures, including a quality assurance (QA) program
- Site data to be measured
- The program duration, minimum measurement accuracy, and target data recovery rate (these heavily impact the equipment type and quality)
- Number and tentative location of monitoring towers, together with sensor measurement heights
- Data sampling and recording intervals
- Data storage, handling, and processing procedures

The data recovery rate is defined as the percentage of possible data records that have actually been collected over a reporting period:

$$\text{Data recovery rate} = \frac{\text{Data records collected}}{\text{Data records possible}} \times 100(\%)$$

where

$$\text{Data records collected} = \text{Data records possible} - \text{Number of invalid records}$$

For example, assume that the total possible number of 10 min records in December is 4464. If 264 records were deemed invalid, the number of valid data records collected would be 4200 (4464–264). The data recovery rate for this example would be

$$\text{Data recovery rate} = \frac{4200}{4464} \times (100) = 94.1\%$$

A data recovery rate of at least 90% (95% or better should be possible) for all measured parameters over the duration of the program, with any data gaps kept to a minimum (less than 1 week), should be a major goal of any measurement program.

A QA program for flagging and handling suspect data is imperative to ensure the acquisition of high-quality data and the successful completion of the assessment

program. The specifics of the components of this QA program should be determined and documented early in the assessment program and should include, at a minimum, the following:

- Acquisition of equipment that meets accuracy and reliability specifications
- Equipment calibration methods and frequency of calibration
- Installation and maintenance instructions for equipment
- Data validation methods, including specifics on evaluating, removing and/or replacing suspect data, and reporting all of these actions
- Data analysis instructions, including specific calculations to be performed

QA will also help to minimize the uncertainties that are always inherent in the data. If the assessment process is carefully followed, these uncertainties can be characterized and controlled to maximize the usefulness of the assessment program conclusions.

7.3.2.1 Data Measurement

The core of the monitoring program is the collection of wind speed, wind direction, and air temperature data. Keep in mind that it is generally less expensive to provide and monitor extra sensors than to conduct an unscheduled site visit to replace or repair a failed sensor that is the sole source of an essential measurement. Care must be used in mounting the various sensors to minimize any interference of one sensor on another. It is especially important to avoid any interference with the wind measurements.

If the rotor is relatively small, wind speed measurements at the turbine hub height will suffice, but for larger rotors, acquiring wind speed data at multiple measurement heights is necessary for determining the site vertical wind shear characteristics, for conducting turbine performance simulations at several turbine hub heights, and to assist in data validation (multiple anemometers make spotting a bad one fairly easy). Redundant anemometers are sometimes used to minimize the risk of wind speed data loss due to a failed primary anemometer and to provide substitution data when the primary anemometer is shadowed by the tower (when it is directly downwind of the tower). Typical anemometer heights are every 10 m, starting at 20 or 30 m and going up to maximum tower height (50–60 m for a tilt-up tower). The vertical distances between anemometers mounted at different heights are referred to as *height layers*. For example, for anemometers installed at heights of 30, 40, and 50 m, height layers would be 30–50, 30–40, and 40–50 m.

The following sensor types have traditionally been those commonly used for the measurement of near-horizontal wind speed:

- *Cup anemometer*: This instrument consists of a cup assembly (three or four cups) centrally connected to a vertical shaft for rotation. At least one cup always faces the oncoming wind. The cups convert wind pressure force to rotational torque, and the transducer in the anemometer produces an electrical signal that is proportional to wind speed.
- *Propeller anemometer*: This instrument consists of a propeller mounted on a horizontal shaft that is oriented into the wind through the use of a tail vane. The propeller anemometer also generates an electrical signal proportional to wind speed.

The current trend toward taller turbine towers and the large expense of erecting met towers of comparable height has encouraged the development of ground-based remote sensing technology, capable of monitoring wind conditions at heights well above 100 m. The two major types of remote sensing are light detection and ranging (LIDAR) and sonic detection and ranging (SODAR). Detailed information on these technologies and their use is available in [26,31–32]. These are also commonly used to characterize off-shore wind resources. Further discussion of these technologies is beyond the scope of this contribution; the remainder of this discussion will focus on data systems that utilize traditional anemometers.

Although the two anemometer types differ somewhat in their responsiveness to wind speed fluctuations, there is no clear advantage of one type over the other. In practice, the cup type is most commonly used for resource assessment. When selecting an anemometer model, the following should be considered:

- *Intended application:* Anemometers intended for low-wind-speed applications, such as air pollution studies, are usually made from lightweight materials. These are probably not suitable for very windy or icy environments.
- *Survival wind speed:* Be sure the anemometer is capable of withstanding the maximum wind speed that it is likely to see. An anemometer with a survival wind speed of 25 m/s is not apt to survive in most windy sites. A survival speed of 50 m/s should be adequate for most sites.
- *Starting threshold:* This is the minimum wind speed at which the anemometer starts and maintains rotation. For wind resource assessment purposes, it is more important for the anemometer to survive a 25 m/s wind gust than to be responsive to winds under 1 m/s.
- *Distance constant:* This is the distance the air travels past the anemometer during the time it takes the cups or propeller to reach 63% of the equilibrium speed after a step change in wind speed (the *response time* of the anemometer to a change in wind speed). Longer-distance constants are usually associated with heavier anemometers; inertia causes them to take longer to slow down when the wind decreases. These instruments may overestimate the wind speed.
- *Reliability and maintenance:* Wind sensors are mechanical and eventually wear out, although most have special, long-life bearings that will normally last for at least 2 years. Be sure to get units with bearings that will last for the entire duration of the measurement project.

Anemometers are subject to a variety of errors in the determination of true wind speed, and equations that may be used to estimate the size of these errors are given in Justus [33]. When anemometers are calibrated in steady air flows in a wind tunnel, they may measure the true wind within $\pm 1\%$. In gusty winds, however, anemometers generally speed up faster than they slow down, so that accuracies of $\pm 5\%$ may be more realistic in application. Additional information on anemometers may be found in publications by American Wind Energy Association (AWEA) [34] and ASME [35].

Wind direction vanes should be installed at all significant monitoring levels. Wind direction information is important for identifying preferred terrain shapes and orientations and for optimizing the layout of wind turbines within a wind farm. The most familiar type of vane uses a fin connected to a vertical shaft. The vane constantly seeks a position of force equilibrium by aligning itself into the wind and produces an electrical

signal proportional to the position of the vane relative to some reference direction (usually selected as true—not magnetic—north). Some wind vanes have a *dead band*, a narrow section of the rotation where the sensor transitions from the full rotation reading of nearly 360° to the initial reading of 0°. The output of the sensor in this section is usually unpredictable. The position of this dead band should be carefully noted for reference when the vane is mounted to the tower. Newer direction vanes have eliminated this dead band.

Air temperature is used to calculate air density, a quantity required to estimate the WPD and the power that a wind turbine will generate. It is normally measured either near ground level (2–3 m) or near hub height. In most locations, the average near-ground-level air temperature will be within 1°C of the average temperature at hub height. Ambient air temperature sensors are readily available. The temperature sensor must be protected from direct solar radiation by mounting it within a radiation shield.

Once the basic measurement system is installed, additional resource-related parameters can be acquired at minimal cost. The most common additional parameters are vertical wind speed, change in temperature with height (commonly referred to as ΔT), barometric pressure, and solar radiation.

The vertical wind speed provides more detail about site turbulence and can be a good predictor of wind turbine loads. Historically, this parameter has only been a research measurement, but as wind energy development spreads into new regions of the country, regional information on vertical wind velocity may become important. The propeller anemometer is especially well suited for measuring the vertical wind component. For this application, the rotation axis would be mounted vertically. The polarity of the DC output signal indicates rotational direction, and the signal magnitude indicates actual vertical speed. The vertical wind speed anemometer should be located near the upper basic wind speed monitoring level.

ΔT provides information about turbulence and atmospheric stability. This is measured with a matched set of temperature sensors located near the lower and upper measurement levels; the existing air temperature sensor may be matched with an identical sensor and used to measure ΔT , or a separate pair of matched sensors may be used. Sensors for this application are usually tested over a specified range and matched by the manufacturer. Be sure to use identical equipment (e.g., radiation shield and mounting hardware) with both sensors so the inherent errors in the signals will cancel out when the difference between the two values is taken. Radiation shields that use either forced (mechanical) or natural (passive) aspiration are normally used on both sensors to reduce the radiation-induced errors.

Barometric pressure is used with air temperature to determine air density. Since it does not vary much over relatively short distances, many resource assessment programs do not measure barometric pressure; they use elevation-adjusted data taken at a nearby regional National Weather Service station. Several atmospheric (barometric) pressure sensors that are suitable for this application are commercially available. Be sure to select one that will give accurate readings in a windy environment.

Solar radiation, when used in conjunction with wind speed and time of day, can be an indicator of atmospheric stability and is often used in numerical wind-flow modeling. These measurements may also be useful for later solar energy evaluation studies. A *pyranometer* is used to measure global (or total) solar radiation, the combination of direct sunlight and diffuse sky radiation. Remember that the pyranometer must be in a position where it will never be shaded in order to measure accurately. The recommended measurement height is 3–4 m above ground.

Table 7.1 lists nominal specifications for the most common types of sensors. Some sensors require the use of separate signal conditioners, electronic packages that supply power

TABLE 7.1

Typical Specifications for Sensors

Specification	Wind Speed	Wind Direction	Air Temperature	Vertical Wind Speed	ΔT	Atmospheric Pressure	Solar Radiation
Measurement range	0–50 m/s	0°–360°	–40° to 60°C	0–50 m/s	–40° to 60°C	94–106 kPa (sea level equivalent)	0–1500 W/m ²
Starting threshold	≤1.0 m/s	≤1.0 m/s	N/A	≤1.0 m/s	N/A	N/A	N/A
Distance constant	≤4.0 m/s	N/A	N/A	≤4.0 m/s	N/A	N/A	N/A
Allowable sensor error	≤3%	≤5°	≤1°C	≤3%	≤1°C	≤1 kPa	≤5%
Sensor resolution	≤0.1 m/s	≤1°	≤0.1°C	≤0.1 m/s	≤0.1°C	≤0.2 kPa	≤1 W/m ²

Source: AWS Scientific, Inc., *Wind Resource Assessment Handbook: Fundamentals for Conducting a Successful Monitoring Program*, SR-440-22223, National Renewable Energy Laboratory, Golden, CO, 1997.

Note: All sensors should have an operating temperature range of –40°C to 60°C and an operating humidity range of 0%–100%.

to the sensor, and process the signal received from the sensor to convert it into a form that can be used by the data logger, the device that actually acquires the raw data and calculates and saves the average statistics. Data loggers (or data recorders) come in a variety of types, sizes, and capabilities; most include peripheral storage and data transfer devices. Be sure the data logger is compatible with the sensor types, number of sensors, and desired sampling and recording intervals. The data logger should also

- Be capable of recording the time and date corresponding to each data record with that data record
- Contribute negligible errors to the signals received from the sensors
- Operate over the temperature range of –40°C to 60°C and over a relative humidity range of 0%–100%
- Offer retrievable data storage media
- Operate on battery power (with an AC adaptor to permit the use of AC power when it is available)

The amount of data logger storage capacity that is needed depends on the averaging interval, the number of active data channels, the need for calculating derived quantities such as wind shear exponent and turbulence intensity, and the maximum time span between data retrievals, including potential delays. Manufacturers usually provide tables or methods to calculate the approximate available storage capacity in days for various memory configurations. To be safe, get enough storage capacity to store an additional week of data, in case a data retrieval or site access problem develops.

While all data loggers allow manual retrieval of stored data, many either come equipped with or can easily be equipped with communications equipment to enable remote retrieval of data, typically via cell phone or satellite phone link. The manual method promotes frequent visual on-site inspection of the equipment during the site visits required to retrieve the data, which may be beneficial. However, this method also requires frequent expensive site visits and additional data-handling steps (thus increasing potential data loss).

Remote data retrieval permits more frequent data retrieval and inspection than that is feasible with manual data retrieval. This allows for prompt identification and resolution of site problems and enhances the data recovery rate. The disadvantages include the up-front cost of the required additional equipment, the cost of monthly service, and the risk of communication system problems. The additional costs are usually quickly offset by the savings from not having to make site visits, and choosing good quality equipment helps minimize the communication problem risk.

Data loggers with cell phone capability are extremely popular due to their ease of use and reasonable cost. A major concern with these units is whether the signal strength at the measurement site will be sufficient to establish a solid communication link. Keep in mind that the data logger cell phone is much more powerful than a typical cell phone—it will normally be equipped with a high gain antenna to permit communication at a much greater range. A general rule of thumb is that a good connection is usually possible as long as there is a cell phone tower in line of sight within about 120 km. Replacement of the standard antenna with one with higher gain may be an option if the nearest cell tower is further away. Additional information regarding cell phone links and accounts should be available from the data logger supplier or manufacturer.

Satellite telephone service may be all that is available in really remote locations, but that service is usually quite expensive—the transceiver is much more costly, and the monthly fees are usually much higher than is the case for cell phone service. In addition, utilizing a satellite communication link may require the development of specialized data transfer software for the specific application. Again, additional information should be available from the data logger supplier or manufacturer.

If phone service (either cellular or satellite) is either unavailable at the site or is prohibitively expensive, try to arrange for manual data retrieval by someone who lives near the monitoring site. That individual may then be able to send the data media by mail or transmit the data via e-mail or landline phone transmission. If this means of data retrieval is utilized, be sure to incorporate additional procedures to protect against data loss in the event that the data media gets damaged or lost in the mail or the transmitted data become corrupted.

The overall accuracy of any system is determined by its weakest link or least accurate component. It is also influenced by its complexity, the total number of components or links. The measurement of any parameter (wind speed, wind direction, etc.) requires that several components (sensor, signal conditioner, cabling, and data logger), each potentially contributing an error to the measured parameter, be interconnected. The combination of these errors will determine the system error (the difference between the measurement result and the actual value sensed) for that parameter. Errors contributed by the sensors represent the main concern, because those associated with the electronic subsystem (data logger, signal conditioner, and associated wiring and connectors) are typically negligible (less than 0.1%). Using wind speed as an example, the allowable system error in the measured wind speed might be specified as less than or equal to 3% of the true wind speed value, allowing for a 6% error window ($\pm 3\%$) centered about the true wind speed. This means that the wind speed sensor must have a system error of 3% or less.

The resolution of a data measurement is the smallest change in a measured quantity that can be detected by the measuring system. Again, this is primarily a function of the sensor, as most data loggers have far more resolution than is normally required. For example, an anemometer system with an 8-bit data logger analog-to-digital converter or digitizer (a very low resolution for a data logger) that is set up to measure a maximum wind speed of 50 m/s has a data logger resolution of $50/(2^8) = 0.2$ m/s. Most data loggers will have higher-precision digitizers

(10-bit or 12-bit are common) with a resolution of much less than this (0.05 or 0.01 m/s, respectively). Thus, to achieve the resolution of 0.1 m/s specified for anemometers in Table 7.1, the anemometers themselves must have a resolution of 0.1 m/s or better.

System reliability is the measure of how well an instrumentation system will consistently provide valid data for a measured parameter over its measurement range—how well it performs in the long run. In selecting instrumentation, it is important to identify and select components that are designed to reliably measure the selected parameters at the prescribed heights for the full monitoring duration and at the required levels of data recovery and accuracy. The instrumentation must also be capable of withstanding the environment of the specific location (e.g., weather extremes, dust, and salt) and be tailored to the selected mode of data retrieval (manually or via cell phone or satellite phone communication link). Although vendors often provide reliability information in terms of a mean time between failures under certain conditions, the best indication of a product's reliability is its performance history. Ask the vendor for a few references and check with those references to determine their satisfaction or lack of satisfaction with the product of interest. Comprehensive QA procedures and the use of redundant sensors are two of the best ways that the user can maximize system reliability. However, there is little that can be done to improve the reliability of sensors or data loggers that are prone to failure.

The equipment should also be proven, affordable, and user-friendly. Complete monitoring systems can be purchased from a single vendor, or components from different vendors can be combined. If components from different vendors are used, be sure the individual components are compatible with each other.

Lists of wind resource assessment equipment vendors may be found in the member lists of the various national wind associations. At the AWEA site (www.awea.org), for instance, they may be found by accessing the member directory, selecting "search," "consultants," and then "meteorology."

7.3.2.2 Sampling Rates and Statistical Quantities

All data sensors should be sampled once every 1 or 2 s. The resultant data are not typically recorded, but stored into data logger accumulators for the specified averaging period (10 min is the default international averaging period for wind measurements). At the end of the averaging period, the statistics are calculated and stored, the accumulators are cleared, and the storage of data into the accumulators begins anew. The data logger should contain built-in programming to calculate and store, as a minimum, the following statistics:

- The average, standard deviation, and maximum and minimum values for the wind speed at each anemometer level, together with the wind directions associated with each maximum and minimum value
- The average and standard deviation for the wind direction at each level
- The average, standard deviation and maximum and minimum wind speed difference for each height layer, together with the wind direction associated with each maximum and minimum difference
- The air temperature
- The vertical wind speed (if measured)

- The ΔT (if measured)
- The barometric pressure (if measured)
- The solar radiation (if measured)

These statistics, together with a corresponding time and date stamp, constitute the data to be recorded; as mentioned earlier, the individual data samples are not normally saved.

Except for wind direction, the average is defined as the numeric mean of all samples. For wind direction, the average is defined as the mean direction on a 0° – 360° scale. The standard deviation is defined as the true population standard deviation for all samples within the averaging interval.

7.3.2.3 Lightning Protection Devices

Keep in mind that a single lightning strike can destroy the entire site monitoring system and all associated electronics, and repairing lightning damage will require a large investment in both time and replacement parts. While no amount of protection can ensure that lightning will not strike the system, appropriate protection can minimize that risk. Consult with the data logger and instrumentation suppliers to ensure that adequate lightning protection is incorporated in the data logger and in all sensors, signal conditioners, and power supplies that will be used. If the supplied lightning protection is not adequate for application, determine what additional protection is needed and add it before installing the monitoring system.

7.3.2.4 Towers and Sensor Mounting

Towers for mounting sensors are available in either tubular or lattice types. Both types are available in tilt-up, telescoping, and fixed versions. For new sites, the tubular, tilt-up, guyed tower, which makes possible the assembly of the tower and the mounting of the sensors on the ground, is an excellent and convenient choice. It also requires very little ground preparation and is relatively low cost. The current maximum height of available tilt-up towers is about 60 m; if the tower is to be used in icing conditions, the maximum height is reduced to about 50 m. Keep in mind that raising a tower of this size is not a simple task, and neither is replacing tower-mounted sensors; they both require experienced personnel and proper equipment. Taller towers can certainly be constructed, but they are far less portable and much more expensive. If you need measurements above 60 m and you intend to evaluate multiple sites, you may want to consider the remote sensing systems mentioned earlier [26].

The sensor support hardware includes the masts (vertical extensions) and mounting booms (horizontal extensions). Tubing, not solid stock, masts, and booms should be used. These are used to position the sensors away from the support tower so as to minimize any influence of the tower, mounting hardware, and other equipment and sensors on each of the measured parameters. This can be achieved by consulting specific manufacturers' instructions and referring to the sample installation configuration shown in Figure 7.14. Detailed information may be found in [34] and virtually any other wind measurement handbook.

Refer to the manufacturer's instructions for the proper sensor and data logger wiring configurations. Wiring to connect the sensors, signal conditioners, and data logger should be shielded and/or twisted pair cable, whenever possible, to prevent ambient electrical noise from affecting the accuracy of the measurements. Be sure to use insulation and conductor types that are flexible over the full temperature range expected at the site and use

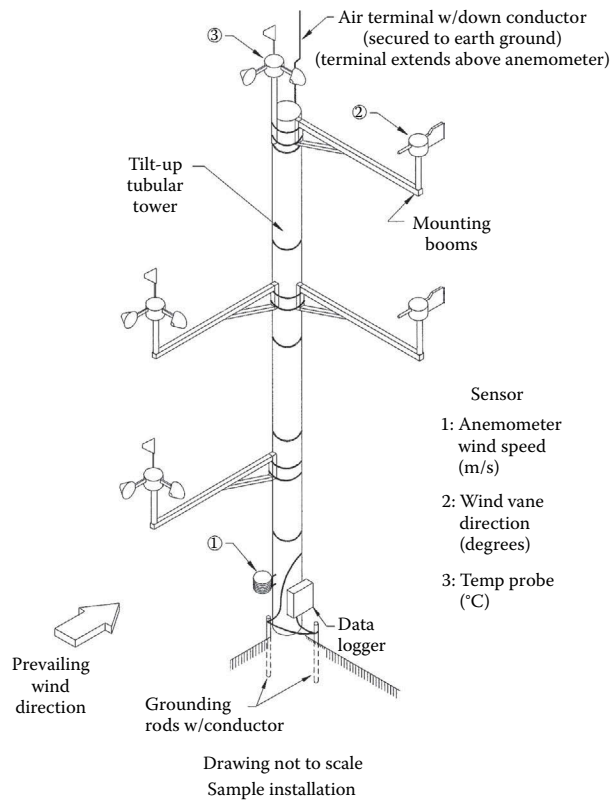


FIGURE 7.14
Typical instrumentation placement on meteorological tower.

wire with UV-resistant insulation. Rodents and raptors, in particular, seem to have an affinity for wire insulation, so consider using armored cable or protective conduit in areas that are accessible by them. Try to mount the data logger and communications equipment in a substantial locked container. Mount the communications antenna high enough to discourage vandalism but where it can still be easily accessed by service personnel. Vandals are a concern, even in very remote locations.

Seal all sensor terminal connections with silicone caulking and protect them from direct exposure to sunlight and water with rubber boots or electrical tape. Wrap the sensor cabling along the length of the support arm and tower and secure it with UV-resistant wire ties or electrical tape. Wrap tape around the sensor wire and leave sufficient slack in the wire wherever chafing can occur between the sensor wire(s) and the support structure (e.g., tilt-up tower anchor collars).

7.3.2.5 Data Collection and Handling

All of these efforts devoted to selecting and mounting sensors and ensuring that acquired data are free of interference are for naught if the resultant data are subsequently lost or contaminated. The data collection and handling elements of the monitoring system must incorporate procedures that offer a high level of data protection. In general, the procedures should comply with those specified by the data logger manufacturer and reflect good common sense. A few pertinent comments are listed here.

7.3.2.5.1 Data Retrieval Frequency

A key factor in achieving a high level of data recovery is the ability to identify potential data acquisition problems and to quickly determine if a problem exists (a failed sensor, icing, possible loss of ground, etc.) and, if necessary, initiate the steps required to fix the problem. Data transfer and review are the first-order means of achieving this end. A schedule of regular site data transfers or downloads should be developed and maintained. The maximum recommended manual download interval is every 2 weeks. For remote data transfer systems, a weekly retrieval rate may suffice, but a shorter interval, such as every other day, may be preferable to minimize potential loss of data if a problem arises and to efficiently transfer the large amount of data resulting from 10-min data averaging. Situations may arise that warrant additional data transfers. For example, sensor data irregularities may become apparent during the review of site data, or the site may experience severe weather, such as icing or thunderstorms. Either of these situations merits a prompt follow-up data transfer (either manual or remote) and review.

Any time a site visit is made, the first order of business should be retrieval of the raw data from the data logger, either by manually downloading it to an in-field laptop computer or by transferring it over a telephone link to a central site computer. This will minimize the risk of potential data loss from operator error, static discharges, or electrical surges during handling and/or checking of system components. The last order of business before leaving the site should be a verification that the monitoring system is functioning properly.

7.3.2.5.2 Data Protection and Storage

Sensor data that have not been subjected to a validation or verification process are commonly referred to as raw data. There is a constant risk of raw data loss or alteration during any measurement program. Aside from the data logger programming requirements, the actual data collection process requires minimal human intervention, and data are adequately protected by following recommended installation and operation procedures, including grounding all equipment. These field data will eventually be transferred to a personal computer for analysis; while this may be the primary location of the working database, it should not be the storage area for the archived or raw database, as frequent usage of a computer increases the likelihood of electrical surges, static discharges, and other events that may damage hard drives and destroy any databases. Preserve the original raw data; make at least two copies of that data set on removable media and store the original and all but one of the copies in separate locations (not in the same building). Then, apply the validation and processing steps to the remaining copy. Back up this active database on a regular schedule during the validation process. Once the database is fully validated, create multiple copies of it and again store each copy in a separate location (not in the same building).

Improper data-handling procedures represent a high risk for data loss. The data reduction and analysis staff will be handling the data medium and be in constant contact with significant numbers of raw and processed databases. Ensure that all personnel are fully trained and understand the data retrieval software and computer operating system, that they are well aware of all instances in which data can be accidentally overwritten or erased, and that they employ good handling practices for all data storage media.

7.3.2.5.3 Data Validation

After the field data are collected, transferred to an office computing environment, and appropriate copies are made, the next steps are to validate and process that data. Again, these steps should be performed on a copy of the database, not on the original data. Data validation consists of the inspection of all the collected data for completeness and reasonableness, and the elimination of erroneous values. This step transforms raw data into validated data and is

crucial to maintaining high rates of data recovery during the course of the monitoring program. There are many possible causes of erroneous data: faulty or damaged sensors, loose wire connections, broken wires, damaged mounting hardware, data logger malfunctions, static discharges, sensor calibration drift, and icing conditions are some of the contributors. The goal of data validation is to detect as many significant errors from as many causes as possible; catching all the subtle ones is impossible. For example, a disconnected wire can be easily detected by a long string of zero (or random) values, but a loose wire that becomes disconnected intermittently may only partly reduce the recorded value, yet produce data that appear reasonable. Therefore, slight deviations in the data can escape detection (although the use of redundant sensors can reduce this possibility). Properly exercising the other QA components of the monitoring program will also reduce the chances of data problems.

Data should be validated as soon as possible after they are transferred from the site to the office; the sooner a potential measurement problem is spotted, the quicker it can be addressed, and the lower the risk of losing large amounts of data. Data can be validated either manually or automatically, with computer processing. Obviously, manual verification can be extremely tedious and time consuming, but it is a good practice to validate the initial data from a site in this manner, in order to learn the characteristics of the data and become familiar with the types of suspect data that can be expected. This knowledge then makes possible the tailoring of the computer routines to optimize the automated validation process. Validation software is available from several sources, including from data logger vendors, but it is still commonly homegrown and tailored for particular applications.

Data validation can be split into two distinct operations: data screening and data verification.

7.3.2.5.3.1 Data Screening This operation uses a series of validation routines or algorithms to screen all the data to identify suspect or questionable values—values that deserve scrutiny but are not necessarily erroneous. For example, an unusually high hourly wind speed caused by a locally severe thunderstorm may appear on an otherwise average windy day. The result of this data screening is a report that lists the suspect values and which validation routine each of those suspect values failed.

General system checks ensure that each data record contains the appropriate number of data fields and that records are contiguous in time (i.e., time and date stamps are in order, and none are missing). Measured data checks, on the other hand, ensure that the actual data are reasonable. These normally include range tests, relational tests, and trend tests.

- Range tests are the simplest and most commonly used validation tests. The measured data are compared to upper and lower limiting values that include nearly (but not absolutely) all of the expected values for the site for each data parameter. For example, a reasonable range for average wind speeds for most sites is 0–25 m/s. Negative values clearly indicate a problem; speeds above 25 m/s are possible, but should be verified with other information. Data reduction and analysis personnel can fine-tune these limiting values as they gain experience. In addition, the limits for appropriate data parameters should be adjusted seasonally. For instance, the limits for air temperature and solar radiation should be lower in winter than in summer. In general, a single item of data should be subjected to more than one range check before it is judged to be valid, because a single check is unlikely to detect all problems. For example, if a frozen wind vane reports an average direction of exactly 180° for six consecutive 10 min intervals, the values would pass the 0°–360° range test, but a check on the standard deviation would reveal a value of zero and should be flagged as suspect.

- Relational tests are based on expected physical relationships between various parameters. These ensure that physically improbable situations are flagged as suspect. For example, a significantly higher wind speed at the 25 m level than at the 40 m level should be flagged as suspect.
- Trend tests are based on the rate of change in a parameter over time. An example of a trend that indicates an unusual circumstance and a potential problem is a change in air temperature greater than 5°C in 1 h.

Some data loggers include the capability to record the system battery voltage for each averaging interval. Range and relational tests for a reduction in battery voltage may be used to give early warning of site hardware problems and ensure that data are not lost due to a bad battery or a blown fuse.

With experience, the data analysis personnel directly involved in the validation process will become very familiar with the local wind climatology and will learn which criteria are most often triggered and under which conditions. The behavior of the wind under various weather conditions will become apparent, as will the relationship between various parameters. This is an invaluable experience that cannot be gained solely by scanning monthly summary tables, and it may prove to be important for evaluating the impact of the local meteorology on wind turbine operation and maintenance. For example, some validation tests may almost always be failed under light wind conditions, yet the data are valid. This occurrence may argue for one set of test criteria under light wind conditions (below 4 m/s perhaps) and another set for stronger winds. The data analysis personnel should be authorized and encouraged to modify validation test criteria and create new ones as needed, based on their experience with the site data. However, be sure to establish operating procedures to ensure appropriate documentation and reporting of any such changes that are made.

7.3.2.5.3.2 Data Verification Once suspect data are identified, case-by-case decisions must be made on what to do with the suspect values—retain them as valid, reject them as invalid, or replace them with redundant valid values (if available). This operation requires the application of judgment of a qualified person familiar with the monitoring equipment and local meteorology. The disposition of each suspect value should be noted in a data verification report. This report should include, for each suspect value, the sensor from which the value was obtained, the date and time that the value was obtained, and the disposition of the suspect value, including the source for the replacement value or the validation code for the rejected value.

If a suspect data value is judged to be valid, leave the value as is. If a suspect value is judged to be invalid, but valid data from a redundant sensor is available, replace the invalid value with that from the redundant sensor. If a suspect value is judged to be invalid, and no data from a redundant sensor are available, replace the value with a unique error code that will serve as both a flag for later data processing programs and an indication of the specific problem with the original value. Selection of the specific error code may require review of the site log or other site data. The data processing and reporting software must incorporate means for handling these error codes. The results of this process are a validated database and a data verification report itemizing the disposition of each suspect data value.

7.3.2.5.4 Data Processing and Reporting

Once the data validation step is complete, the validated data set is ready to be processed to quantify the wind resource. This typically involves performing calculations on the data set, as well as binning or sorting the recorded 10-min average data values into

useful subsets based on other chosen averaging intervals, such as hourly or weekly. Hourly averages are normally used for reporting purposes. The processed data are then summarized into weekly or monthly informative reports of summary tables and performance graphs. Items included in these reports typically include mean wind speed, wind direction frequency distribution, maximum gust, mean turbulence intensity, mean power density, and diurnal wind speed and power density (by time of day) for each anemometer and wind direction level, mean shear for each height layer, daily and monthly wind speed distribution for the primary height anemometer, and hourly temperature. Data processing and reporting software is available from several sources, including many data logger manufacturers and vendors of spreadsheet, database, and statistical software. Whatever method is used, procedures must be developed to ensure that flagged data points or invalid data codes are excluded from the computations of hourly averages and other quantities. These procedures should be developed and implemented before the first data are recorded.

The wind shear exponent, turbulence intensity, and WPD are items that are usually included in wind resource reports, but may not be routinely produced by some data loggers. These parameters can be easily calculated using a spreadsheet software application to obtain hourly and monthly averages. A description of each parameter and calculation method is presented in detail as follows:

- Vertical wind shear exponent

Wind shear is defined as the change in horizontal wind speed with a change in height. The wind shear exponent (α) must be determined for a set of anemometry levels at each site, because the magnitude of α is influenced by site-specific characteristics. Solving the power law equation (Equation 7.5) for α gives

$$\alpha = \frac{\ln(U/U_0)}{\ln(h/h_0)} \quad (7.12)$$

where

U is the wind speed at height h

U_0 is the wind speed at height h_0

- Turbulence intensity

Wind turbulence is the rapid disturbances or irregularities in the wind speed, direction, and vertical component. It is an important site characteristic, because high turbulence levels may decrease power output and cause extreme loading on wind turbine components. The most common indicator of turbulence for siting purposes is the standard deviation (σ) of wind speed. Normalizing this value with the mean wind speed gives the turbulence intensity (TI), defined as

$$TI = \frac{\sigma}{\bar{U}} \quad (7.13)$$

where

σ is the standard deviation of wind speed

\bar{U} is the mean wind speed (m/s)

- WPD

WPD is defined in Equation 7.14 as the wind power available per unit area swept by the turbine blades. It combines the effects of the wind speed distribution and its dependence on air density and wind speed. For experimental data, WPD may be calculated as

$$\text{WPD} = \frac{1}{2n} \sum_{i=1}^n \rho U_i^3 \quad (\text{W/m}^2) \quad (7.14)$$

where

n is the number of records in the averaging interval

ρ is the air density (kg/m^3)

U_i^3 is the cube of the i th wind speed value (m/s)

7.4 Example: Initial Wind Farm Development in New Mexico

By 2001, the New Mexico Public Utility Commission (PUC) had, for some time, been looking at the idea of implementing a Renewable Portfolio Standard (RPS) requiring the Public Service Company of New Mexico (PNM), the state electrical utility, to obtain some of its electricity from renewable sources. The state legislature was also seriously considering enacting an RPS, but it had not yet done that in 2002. PNM had been investigating wind energy and monitoring the wind resource at some promising wind sites for several years, but had not yet been seriously considering adding wind to its generation mix. With the RPS under consideration in both the PUC and the legislature, PNM saw the handwriting on the wall and started seriously considering renewable energy, in general, and wind energy, in particular.

PNM decided to encourage the development of the first large wind farm in the state of New Mexico—they would purchase all of the electricity produced by the facility. New Mexico has fairly good wind resources to the east of the north/south central mountain range and in the eastern part of the state, so those are logical areas in which to start prospecting. The state has worked with NREL and True Solutions (now AWS Truepower) to develop a high-resolution wind map (available at www.emnrd.state.nm.us/ECMD/RenewableEnergy/images/WindMapForWeb.jpg). This map also shows the route of high-power transmission lines across the state. A map with transmission line details reveals a 345 kV PNM transmission line running from Clovis, in eastern New Mexico, to Albuquerque in the north-central part of the state. That line directly feeds the 1 GW Albuquerque load, and 2002, it had significant excess capacity.

This line passes through or near several areas with reasonable winds (annual average of 7 m/s or greater), mostly just east of Albuquerque. In the eastern part of the state, one of the areas near the line with reasonable winds appears to be near the intersection of Guadalupe, De Baca, and Quay counties. The statewide map in Figure 7.15 locates this area of interest, and the expanded scale map shows the estimated resource from the wind map. The wind map indicates average wind speeds of 7 m/s right in the area of the transmission line, with somewhat higher winds just a little to the north.

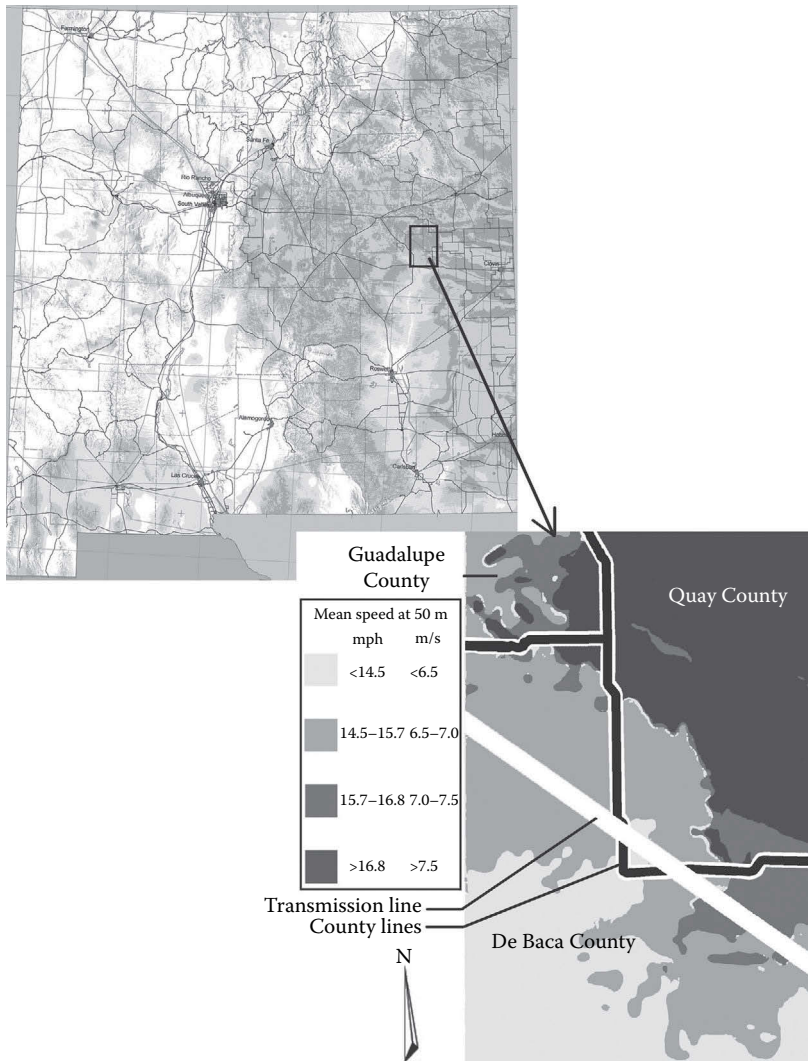


FIGURE 7.15

Wind resource map of the western edge of Tiaban Mesa in eastern New Mexico. (Reproduced by permission of AWS Truewind and the New Mexico Energy, Minerals, and Natural Resources Department. www.emnrd.state.nm.us/ECMD/RenewableEnergy/images/WindMapForWeb.jpg, accessed August 2005.)

Closer inspection of the topography in the area shows that the western edge of this high resource corresponds to the western edge of Tiaban Mesa. The mesa edge runs generally north/south in this area, and the top of the mesa is 60–90 m above the plains just to the west. This topography can certainly be expected to enhance the wind speed near the mesa edge. A site visit reveals heavy flagging of the vegetation from the southwest, indicative of a predominant wind direction. The land is privately owned, with no use restrictions, no large bird populations, and no environmental concerns. A measurement program quickly confirmed that the winds are predominantly southwest and that the annual average wind speeds along the mesa edge, from just south of the transmission line crossing to several miles north, are 7 m/s or better. Prospective developers thus had the

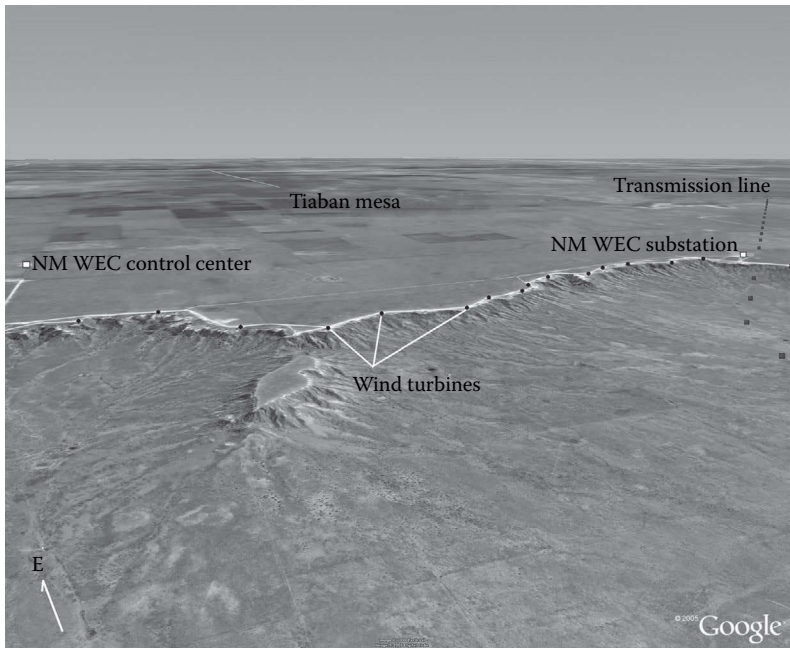


FIGURE 7.16

Perspective view of western edge of Tiaban Mesa. Every second wind turbine and transmission line tower indicated.

three essential components for a wind farm development—access to a transmission line with excess capacity, a customer for the power (PNM), and a good wind resource.

In August 2002, FPL Energy and PNM announced their agreement to develop the first large wind energy project in the state of New Mexico. FPL Energy built the 204 MW New Mexico Wind Energy Center on the western edge of Tiaban mesa in 2003. A perspective view of the mesa edge, with the turbine locations and transmission line indicated, is given in Figure 7.16. The PNM-built substation lies right under the existing transmission line and immediately adjacent to the line of turbines on the mesa edge; this ready access to the transmission line was a key driver in the decision to locate the wind farm in this spot. PNM purchases the entire output of the wind farm and sells it at a premium to residential and small business customers through their “Sky Blue” renewable energy program. Two years of operation have confirmed that the site resource is a good one: the yearly average wind speed at the 65 m turbine hub height has been 8 m/s. At the wind farm elevation of 1460 m, this wind speed yields a power density of 460 W/m², which corresponds to an NREL wind class 4 site.

References

1. AWS Scientific, Inc. 1997. *Wind Resource Assessment Handbook: Fundamentals for Conducting a Successful Monitoring Program*, SR-440-22223. National Renewable Energy Laboratory, Golden, CO.
2. Golding, E. 1977. *The Generation of Electricity by Wind Power*. E. & F.N. Spon Ltd., London, U.K.
3. Schwartz, M. and Elliott, D. 2006. Wind shear characteristics at central plains tall towers. *Windpower '06*. American Wind Energy Association, Washington, DC.

4. Elliott, D., Schwartz, M., and Scott, G. 2009. Wind shear and turbulence profiles at elevated heights: Great lakes and midwest sites. *Windpower 2009*. American Wind Energy Association, Washington, DC.
5. Elliott, D.L., Holladay, C.G., Barchet, W.R., Foote, H.P., and Sandusky, W.F. 1987. Wind energy resource atlas of the United States, DOE/CH10094-4. Solar Energy Research Institute, Golden, CO.
6. Troen, I. and Petersen, E.L. 1989. *European Wind Atlas*. Risø National Laboratory, Roskilde, Denmark.
7. Elliott, D., Schwartz, M., Haymes, S., Heimiller, D., Scott, G., Brower, M., Hale, E., and Phelps, B. 2011. New wind energy resource potential estimates for the United States. *Second Conference on Weather, Climate and the New Energy Economy*, Seattle, WA.
8. Archer, C.L. and Jacobson, M.Z. 2005. Evaluation of global wind power. *Journal of Geophysical Research*, 110, D12110.
9. European Wind Energy Association (EWEC)/Greenpeace. 2003. *Wind Force 12: A Blueprint to Achieve 12% of the World's Electricity from Wind Power by 2020*. EWEC and Greenpeace, Brussels, Belgium.
10. Musial, W. and Ram, B. 2010. *Large-Scale Offshore Wind Power in the United States: Assessment of Opportunities and Barriers*, NREL TP-500-40745. National Renewable Energy Laboratory, Golden, CO.
11. Sinclair, K.C. and Morrison, M.L. 1997. Overview of the U.S. Department of Energy/National Renewable Energy Laboratory avian research program. *Proceedings of Windpower '97*. American Wind Energy Association, Washington, DC, pp. 273–279.
12. Sinclair, K.C. 1999. Status of the U.S. Department of Energy/National Renewable Energy Laboratory Avian Research Program. *Proceedings of Windpower '99*. American Wind Energy Association, Washington, DC, pp. 273–279.
13. National Wind Coordinating Committee. 2010. Wind turbine interactions with birds, bats, and their habitats: A summary of research results and priority questions. <http://www.national-wind.org/publications/bbfactsheet.aspx> (accessed November 2014).
14. Colson, E.W. 1995. Avian interactions with wind energy facilities: A summary. *Proceedings of Windpower '95*. American Wind Energy Association, Washington, DC, pp. 77–86.
15. Wolf, B. 1995. Mitigating avian impacts: Applying the wetlands experience to wind farms. *Proceedings of Windpower '95*. American Wind Energy Association, Washington, DC, pp. 109–116.
16. Erickson, W.P., Johnson, G.D., Strickland, M.D., Young, D.P., Sernka, K.J., and Good, R.E. 2001. Avian collisions with wind turbines: A summary of existing studies and comparisons to other sources of avian collision mortality in the United States. National Wind Coordinating Committee, Washington, DC. http://www.nationalwind.org/publications/wildlife/avian_collisions.pdf (accessed November 2014).
17. Kunz, T.H., Arnett, E.B., Erickson, W.P., Hoar, A.R., Johnson, G.D., Larkin, R.P., Strickland, M.D., Thresher, R.W., and Tuttle, M.D. 2007. Ecological impacts of wind energy development on bats: Questions, research needs, and hypotheses. *Frontiers in Ecology and the Environment*, 5(6), 315–324.
18. Baerwald, E.F., D'Amours, G.H., Klug, B.J., and Barclay, R.M.R. 2008. Barotrauma is a significant cause of bat fatalities at wind turbines. *Current Biology*, 18(16), R695–R696.
19. Baerwald, E.F., Edworthy, J., Holder, M., and Barclay, R.M.R. 2009. A large-scale mitigation experiment to reduce bat fatalities at wind energy facilities. *Journal of Wildlife Management*, 73(7), 1077–1081.
20. Arnett, E.B., Schirmacher, M., Huso, M.M.P., and Hayes, J.P. 2009. Effectiveness of changing wind turbine cut-in speed to reduce bat fatalities at wind facilities. An annual report submitted to the Bats and Wind Energy Cooperative. Bat Conservation International. Austin, TX.
21. Hewson, E.W., Wade, J.E., and Baker, R.W. 1978. Vegetation as an indicator of high wind velocity. RLO/2227-T24-78-2. Oregon State University, Corvallis, OR.

22. Hiester, T.R. and Pennell, W.T. 1981. The meteorological aspects of siting large wind turbines. PNL-2522. Pacific Northwest Laboratory, Richland, WA.
23. Wegley, H.L., Ramsdell, J.V., Orgill, M.M., and Drake, R. L. 1980. *A Siting Handbook for Small Wind Energy Conversion Systems*, PNL-2521. Pacific Northwest Laboratory, Richland, WA.
24. Rohatgi, J.S. and Nelson, V. 1994. *Wind Characteristics: An Analysis for the Generation of Wind Power*. Alternative Energy Institute, West Texas A&M University, Canyon, TX.
25. Frost, W. and Nowak, D.K. 1979. Summary and guidelines for siting wind turbine generators relative to small-scale two-dimensional terrain features. Report RLO-2443-77/1. Battelle Pacific Northwest Laboratory, Richland, WA.
26. International Energy Agency. 2013. *Ground-Based Vertically-Profiling Remote Sensing for Wind Resource Assessment*, 1st edn. IEA Wind RP 15.
27. Schwartz, M. and Elliott, D. 2005. Towards a wind energy climatology at advanced turbine hub heights, NREL/CP-500-38109. National Renewable Energy Laboratory, Golden, CO.
28. Aspliden, C.I., Elliot, D.L., and Wendell, L.L. 1986. Resource assessment methods, siting and performance evaluation, in *Physical Climatology for Solar and Wind Energy*, Guzzi, R. and Justus, C.G., eds., pp. 321–326. World Scientific, Hackensack, NJ.
29. Corotis, R.B. 1977. Stochastic modeling of site wind characteristics, RLO/2342-77/2. Northwestern University, Evanston, IL.
30. Gipe, P. 1993. *Wind Power for Home & Business—Renewable Energy for the 1990s and Beyond*. Chelsea Green Publishing Company, Post Mills, VT.
31. Aranda, F., ed. 2009. Remote wind speed sensing techniques using SODAR and LIDAR. *59th IEA Wind Topical Experts Meeting*. International Energy Agency, Boulder, CO.
32. Thor, S., ed. 2007. State of the art of remote wind speed sensing techniques using sodar, lidar and satellites. *51st IEA Wind Topical Expert Meeting*. International Energy Agency, Roskilde, Denmark.
33. Justus, C.G. 1978. *Winds and Wind System Performance*. Franklin Institute Press, Philadelphia, PA.
34. American Wind Energy Association (AWEA). 1986. Standard procedures for meteorological measurements at a potential wind turbine site, D-FC02-86CH10302. American Wind Energy Association, Washington, DC.
35. American Society of Mechanical Engineers (ASME). 1989. Performance test code for wind turbines, ASME/ANSI PTC 42-1988. American Society of Mechanical Engineers, New York.

Further Information

Wind Characteristics—An Analysis for the Generation of Wind Power, by J. S. Rohatgi and V. Nelson, Alternative Energy Institute, West Texas A&M University, is an excellent source for additional information on the wind resource. *Wind Resource Assessment Handbook: Fundamentals for Conducting a Successful Monitoring Program*, by AWS Scientific, Inc., report SR-440-22223, National Renewable Energy Laboratory, Golden, CO, 1997, gives step-by-step instructions for a successful land-based resource monitoring effort. *Ground-Based Vertically-Profiling Remote Sensing for Wind Resource Assessment*, by the International Energy Agency, is an excellent resource on the use of Lidar and Sodar for wind resource measurement. *Wind Turbine Technology, Fundamental Concepts of Wind Turbine Engineering*, D. Spera (editor), ASME Press, New York, 1994; *Wind Energy Handbook* (2nd edn.) by T. Burton, D. Sharpe, N. Jenkins, and E. Bossanyi, John Wiley & Sons, Chichester, U.K., 2011, and *Wind Energy Explained: Theory, Design and Application* (2nd edn.) by J. Manwell, J. McGowan,

and A. Rogers, John Wiley & Sons, Chichester, U.K., 2010, contain a wealth of fairly current information on wind energy resources, history, and technology, together with extensive reference lists. The reference site for the National Wind Coordinating Collaborative bird/bat fact sheet [13] at www.nationalwind.org/publications/bbfactsheet.aspx has links to a very extensive list of publications dealing with studies of the interactions of birds and bats with wind turbines. Extensive information on wind energy resources and technology may also be found on the world wide web. Excellent sites to start with include those of the U.S. National Renewable Energy Laboratory Wind Energy Technology Center at www.nrel.gov/nwtc/, the Danish Technical University Department of Wind Energy at www.vindenergi.dtu.dk, the American Wind Energy Association at www.awea.org, the European Wind Energy Association at www.ewea.org, and the Danish Wind Energy Association at www.windpower.org/en.

8

Geothermal Energy

Joel L. Renner and Marshall J. Reed

CONTENTS

8.1 Heat Flow	177
8.2 Types of Geothermal Systems.....	178
8.3 Geothermal Energy Potential.....	178
8.4 Geothermal Applications.....	179
8.5 Environmental Constraints.....	181
8.6 Operating Conditions.....	183
Defining Terms	185
Acknowledgments.....	186
References.....	186
For Further Information.....	187

The word Geothermal comes from the combination of the Greek words *gê*, meaning Earth, and *thêrm*, meaning heat. Quite literally, geothermal energy is the heat of the Earth. Geothermal resources are concentrations of the Earth's heat, or geothermal energy, that can be extracted and used economically now or in the reasonable future. Currently, only concentrations of heat associated with water in permeable rocks can be exploited. Heat, fluid, and permeability are the three necessary components of all exploited geothermal fields. This section of Energy Resources will discuss the mechanisms for concentrating heat near the surface, the types of geothermal systems, and the environmental aspects of geothermal production.

8.1 Heat Flow

Temperature within the Earth increases with depth at an average of about 25°C/km. Spatial variations of the thermal energy within the deep crust and mantle of the Earth give rise to concentrations of thermal energy near the surface of the Earth that can be used as an energy resource. Heat is transferred from the deeper portions of the Earth by conduction of heat through rocks, by the movement of hot, deep rock toward the surface, and by deep circulation of water. Most high-temperature geothermal resources are associated with concentrations of heat caused by the movement of magma (melted rock) to near-surface positions where the heat is stored.

In older areas of continents, such as much of North America east of the Rocky Mountains, heat flow is generally 40–60 mW/m² (milliwatts per square meter). This heat flow coupled

with the thermal conductivity of rock in the upper 4 km of the crust yields subsurface temperatures of 90°C–110°C at 4 km depth in the Eastern United States. Heat flow within the Basin and Range (west of the Rocky Mountains) is generally 70–90 mW/m², and temperatures are generally greater than 110°C at 4 km. There are large variations in the Western United States, with areas of heat flow greater than 100 mW/m² and areas which have generally lower heat flow such as the Cascade and Sierra Nevada Mountains and the West Coast. A more detailed discussion of heat flow in the United States is available in Blackwell et al. (1991).

8.2 Types of Geothermal Systems

Geothermal resources are hydrothermal systems containing water in pores and fractures. Most hydrothermal resources contain liquid water, but higher temperatures or lower pressures can create conditions where steam and water or only steam are the continuous phases (White et al. 1971; Truesdell and White 1973). All commercial geothermal production is expected to be restricted to hydrothermal systems for many years because of the cost of artificial addition of water. Successful, sustainable geothermal energy usage depends on reinjection of the maximum quantity of produced fluid to augment natural recharge of hydrothermal systems.

Other geothermal systems that have been investigated for energy production are (1) geopressured- geothermal systems containing water with somewhat elevated temperatures (above normal gradient) and with pressures well above hydrostatic for their depth; (2) magmatic systems, with temperature from 600°C–1400°C; and (3) hot dry rock geothermal systems, with temperatures from 200°C–350°C, that are subsurface zones with low initial permeability and little water. These types of geothermal systems cannot be used for economic production of energy at this time.

8.3 Geothermal Energy Potential

The most recent report (Huttrer 1995) shows that 6800 MW_e (megawatts electric) of geothermal electric generating capacity is on-line in 21 countries (Table 8.1). The expected capacity in the year 2000 is 9960 MW_e. Table 8.2 lists the electrical capacity of U.S. geothermal fields. Additional details of the U.S. generating capacity are available in McClarty and Reed (1992) and DiPippo (1995). Geothermal resources also provide energy for agricultural uses, heating, industrial uses, and bathing. Freeston (1995) reports that 27 countries had a total of 8228 MW_t (megawatts thermal) of direct use capacity. The total energy used is estimated to be 105,710 TJ/year (terajoules per year). The thermal energy used by the ten countries using the most geothermal resource for direct use is listed in Table 8.3.

The U.S. Geological Survey has prepared assessments of the geothermal resources of the U.S. Muffler (1979) estimated that the identified hydrothermal resource, that part of the **identified accessible base** that could be extracted and utilized at some reasonable future time, is 23,000 MW_e for 30 years. This resource would operate power plants with an aggregate capacity of 23,000 MW_e for 30 years. The undiscovered U. S. resource (inferred from knowledge of Earth science) is estimated to be 95,000–150,000 MW_e for 30 years.

TABLE 8.1
Installed and Projected Geothermal Power Generation Capacity

Country	1995	2000
Argentina	0.67	n/a ^a
Australia	0.17	n/a
China	28.78	81
Costa Rica	55	170
El Salvador	105	165
France	4.2	n/a
Greece ^b	0	n/a
Iceland	49.4	n/a
Indonesia	309.75	1080
Italy	631.7	856
Japan	413.705	600
Kenya	45	n/a
Mexico	753	960
New Zealand	286	440
Nicaragua	35	n/a
Philippines	1227	1978
Portugal (Azores)	5	n/a
Russia	11	110
Thailand	0.3	n/a
Turkey	20.6	125
U.S.	2816.775	3395
Total	6797.975	9960

Source: From Hutterer, G. W., in Proceedings of the World Geothermal Congress, 1995, International Geothermal Association, Auckland, New Zealand, 1995, 3–14. With permission.

^a n/a, information not available.

^b Greece has closed its 2.0 MWe Milos pilot plant.

8.4 Geothermal Applications

In 1991, geothermal electrical production in the United States was 15,738 GWh (gigawatt hours), and the largest in the world (McLarty and Reed 1992).

Most geothermal fields are water dominated, where liquid water at high temperature, but also under high (hydrostatic) pressure, is the pressure-controlling medium filling the fractured and porous rocks of the reservoir. In water-dominated geothermal systems used for electricity, water comes into the wells from the reservoir, and the pressure decreases as the water moves toward the surface, allowing part of the water to boil. Since the wells produce a mixture of flashed steam and water, a separator is installed between the wells and the power plant to separate the two phases. The flashed steam goes into the turbine to drive the generator, and the water is injected back into the reservoir.

TABLE 8.2

U.S. Installed Geothermal Electrical Generating Capacity in MWe

Rated State/Field	Plant Capacity	Type
California		
Casa Diablo	27	B
Coso	240	2F
East Mesa	37	2F
East Mesa	68.4	B
Honey Lake Valley	2.3	B
Salton Sea	440	2F
The Geysers	1797	S
Hawaii		
Puna	25	H
Nevada		
Beowawe	16	2F
Brady Hot Springs	21	2F
Desert Peak	8.7	2F
Dixie Valley	66	2F
Empire	3.6	B
Soda Lake	16.6	B
Steamboat	35.1	B
Steamboat	14.4	1F
Stillwater	13	B
Wabuska	1.2	B
Utah		
Roosevelt	20	1F
Cove Fort	2	B
Cove Fort	9	S

Note: S, natural dry steam; 1F, single flash; 2F, double flash; B, binary; H, hybrid flash and binary.

TABLE 8.3

Geothermal Energy for Direct Use by the Ten Largest Users Worldwide

Country	Flow Rate (kg/s)	Installed Power (MW _e)	Energy Used (TJ/year)
China	8,628	1,915	16,981
France	2,889	599	7,350
Georgia	1,363	245	7,685
Hungary	1,714	340	5,861
Iceland	5,794	1,443	21,158
Italy	1,612	307	3,629
Japan	1,670	319	6,942
New Zealand	353	264	6,614
Russia	1,240	210	2,422
U.S.	3,905	1,874	13,890
Total	37,050	8,664	112,441

Source: From Freeston, D. H., in *Proceedings of the World Geothermal Congress, 1995*, International Geothermal Association, Auckland, New Zealand, 1995, 15–26. With permission.

Many water-dominated reservoirs below 175°C used for electricity are pumped to prevent the water from boiling as it is circulated through heat exchangers to heat a secondary liquid that then drives a turbine to produce electricity. **Binary geothermal** plants have no emissions because the entire amount of produced geothermal water is injected back into the underground reservoir. The identified reserves of lower-temperature geothermal fluids are many times greater than the reserves of high-temperature fluids, providing an economic incentive to develop more-efficient power plants.

Warm water, at temperatures above 20°C, can be used directly for a host of processes requiring thermal energy. Thermal energy for swimming pools, space heating, and domestic hot water are the most widespread uses, but industrial processes and agricultural drying are growing applications of geothermal use. In 1995, the United States was using over 500 TJ/year of energy from geothermal sources for direct use (Lienau et al. 1995). The cities of Boise, ID; Elko, NV; Klamath Falls, OR; and San Bernardino and Susanville, CA have geothermal district-heating systems where a number of commercial and residential buildings are connected to distribution pipelines circulating water at 54°C–93°C from the production wells (Rafferty 1992).

The use of geothermal energy through ground-coupled heat pump technology has almost no impact on the environment and has a beneficial effect in reducing the demand for electricity. Geothermal heat pumps use the reservoir of constant temperature, shallow groundwater and moist soil as the heat source during winter heating and as the heat sink during summer cooling. The energy efficiency of geothermal heat pumps is about 30% better than that of air-coupled heat pumps and 50% better than electric-resistance heating. Depending on climate, advanced geothermal heat pump use in the United States reduces energy consumption and, correspondingly, power-plant emissions by 23%–44% compared to advanced air-coupled heat pumps, and by 63%–72% compared with electric-resistance heating and standard air conditioners (L'Ecuyer et al. 1993).

8.5 Environmental Constraints

Geothermal energy is one of the cleaner forms of energy now available in commercial quantities. Geothermal energy use avoids the problems of acid rain, and it greatly reduces greenhouse gas emissions and other forms of air pollution. Potentially hazardous elements produced in geothermal brines are removed from the fluid and injected back into the producing reservoir. Land use for geothermal wells, pipelines, and power plants is small compared with land use for other extractive energy sources such as oil, gas, coal, and nuclear. Geothermal development projects often coexist with agricultural land uses, including crop production or grazing. The average geothermal plant occupies only 400 m² for the production of each gigawatt hour over 30 years (Flavin and Lenssen 1991). The low life-cycle land use of geothermal energy is many times less than the energy sources based on mining, such as coal and nuclear, which require enormous areas for the ore and processing before fuel reaches the power plant. Low-temperature applications usually are no more intrusive than a normal water well. Geothermal development will serve the growing need for energy sources with low atmospheric emissions and proven environmental safety.

All known geothermal systems contain aqueous carbon dioxide species in solution, and when a steam phase separates from boiling water, CO₂ is the dominant (over 90% by weight) **noncondensable gas**. In most geothermal systems, noncondensable gases make

up less than 5% by weight of the steam phase. Thus, for each megawatt-hour of electricity produced in 1991, the average emission of carbon dioxide by plant type in the United States was 990 kg from coal, 839 kg from petroleum, 540 kg from natural gas, and 0.48 kg from geothermal flashed-steam (Colligan 1993). Hydrogen sulfide can reach moderate concentrations of up to 2% by weight in the separated steam phase from some geothermal fields.

At The Geysers geothermal field in California, either the Stretford process or the incineration and injection process is used in geothermal power plants to keep H_2S emissions below 1ppb (part per billion). Use of the Stretford process in many of the power plants at The Geysers results in the production and disposal of about 13,600 kg of sulfur per megawatt of electrical generation per year. Figure 8.1, shows a typical system used in the Stretford process at The Geysers (Henderson and Dorigi 1989).

The incineration process burns the gas removed from the steam to convert H_2S to SO_2 , the gases are absorbed in water to form SO_3^{2-} and SO_4^{2-} in solution, and iron chelate is used to form $\text{S}_2\text{O}_3^{2-}$ (Bedell and Hammond 1987). Figure 8.2 shows an incineration abatement system (Bedell and Hammond 1987). The major product from the incineration process is a soluble thiosulfate which is injected into the reservoir with the condensed water used for the reservoir pressure-maintenance program. Sulfur emissions for each megawatt-hour of electricity produced in 1991, as SO_2 by plant type in the United States was 9.23 kg from coal, 4.95 kg from petroleum, and 0.03 kg from geothermal flashed-steam (Colligan 1993). Geothermal power plants have none of the nitrogen oxide emissions that are common from fossil fuel plants.

The waters in geothermal reservoirs range in composition from 0.1 to over 25 wt% dissolved solutes. The geochemistry of several representative geothermal fields is listed in Table 8.4. Temperatures up to 380°C have been recorded in geothermal reservoirs in the United States, and many chemical species have a significant solubility at high temperature. For example, all of the geothermal waters are saturated in silica with respect to quartz. As the water is produced, silica becomes supersaturated, and, if steam is flashed, the silica becomes

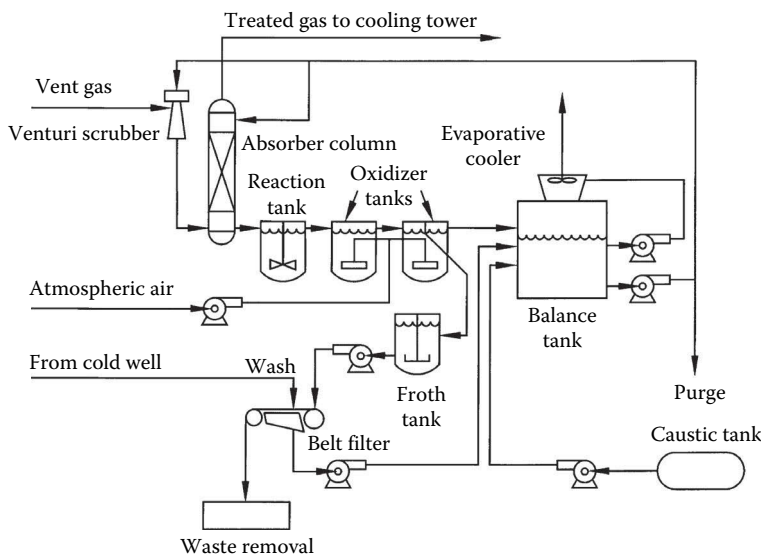


FIGURE 8.1

Typical equipment used in the Stretford process for hydrogen sulfide abatement at The Geysers geothermal field. (Based on the diagram of Henderson, J.M. and Dorigi, G.P., *Geotherm. Resour. Counc. Trans.*, 13, 593–595, 1989.)

TABLE 8.4

Major Element Chemistry of Representative Geothermal Wells

Field	T (°C)	Na	K	Li	Ca	Mg	Cl	F	Br	SO ₄	Total ^a CO ₂	Total ^a SiO ₂	Total ^a B	Total ^a H ₂ S
Reykjavik, Iceland	100	95	1.5	<1	0.5	—	31	—	—	16	58	155	0.03	—
Hveragerdi, Iceland	216	212	27	0.3	1.5	0.0	197	1.9	0.45	61	55	480	0.6	7.3
Broadlands, New Zealand	260	1,050	210	1.7	2.2	0.1	1,743	7.3	5.7	8	128	805	48.2	<1
Wairekai, New Zealand	250	1,250	210	13.2	12	0.04	2,210	8.4	5.5	28	17	670	28.8	1
Cerro Prieto, Mexico	340	5,820	1,570	19	280	8	10,420		14.1	0	1,653	740	12.4	700
Salton Sea, California	340	50,400	17,500	215	28,000	54	155,000	15	120	5	7,100	400	390	16
Roosevelt, Utah ^b	<250	2,320	461	25.3	8	<2	3,860	6.8	—	72	232	563	—	—

^a Total CO₂, SiO₂, etc., is the total CO₂+HCO⁻²+CO₃²⁻ expressed as CO₂, silica+silicate as SiO₂, etc.

^b From Wright (1991); remainder of data from Ellis and Mahon (1977).

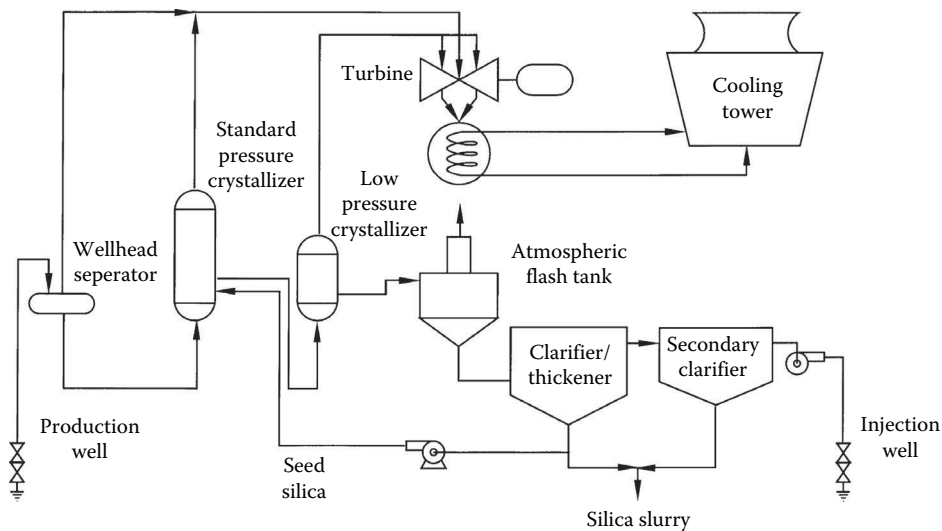


FIGURE 8.3

The flow stream for removal of solids from the vapor and brine in typical power plants in the Salton Sea geothermal field. (Modified from the diagram of Signorotti, V. and Hunter, C.C., *Geotherm. Resour. Coun. Bull.*, 21(9), 277–288, 1992.)

ranges from 100% liquid to almost 100% steam. Production wells have a wide range of flow rates, but the average production flow rate is 135,000 kg/h (Mefferd 1991). Much of the produced fluid is evaporated to the atmosphere in the cooling towers of the power plant, and only about 65% of the produced mass is available for injection into the reservoir at an average rate of 321,000 kg/h (Mefferd 1991).

The Salton Sea geothermal system in the Imperial Valley of southern California has presented some of the most difficult problems in brine handling. Water is produced from the reservoir at temperatures between 300 and 350°C and total dissolved solid concentrations between 20 and 25% by weight at an average rate of 270,000 kg/h (Mefferd 1991). When up to 20% of the mass of brine boils during production, the salts are concentrated in the brine causing supersaturation with respect to several solid phases. Crystallizers and clarifier and thickener tanks are needed to remove solids from the injection water. Figure 8.3 shows the flow stream for removal of solids from the vapor and brine (Signorotti and Hunter 1992). Other power plants use the addition of acid to lower the pH and keep the solutes in solution (Signorotti and Hunter 1992). The output from the crystallizers and clarifiers is a slurry of brine and amorphous silica. The methods used to dewater the salt and silica slurry from operations in the Salton Sea geothermal system are described by Benesi (1992). Approximately 80% of the produced water is injected into the reservoir at an average rate of 310,000 kg/h.

Defining Terms

Binary geothermal plant: A geothermal electric generating plant that uses the geothermal fluid to heat a secondary fluid that is then expanded through a turbine.

Identified accessible base: That part of the thermal energy of the Earth that is shallow enough to be reached by production drilling in the foreseeable future. *Identified* refers to concentrations of heat that have been characterized by drilling or Earth science evidence. Additional discussion of this and other resource terms can be found in Muffler (1979).

Noncondensable gases: Gases exhausted from the turbine into the condenser that do not condense into the liquid phase.

Acknowledgments

This study was supported in part by the U.S. Department of Energy, Assistant Secretary for Energy Efficiency and Renewable Energy, Geothermal Division, under DOE Idaho Operations Office Contract DE-AC07-94ID13223.

References

- Bedell, S. A. and Hammond, C. A. 1987. Chelation chemistry in geothermal H₂S abatement. *Geotherm. Resour. Counc. Bull.*, 16 (8), 3–6.
- Benesi, S. C. 1992. Dewatering of slurry from geothermal process streams. *Geotherm. Resour. Counc. Trans.*, 16, 577–581.
- Blackwell, D. B., Steele, J. L., and Carter, L. S. 1991. Heat-flow patterns of the North American continent; a discussion of the geothermal map of North America. In *Neotectonics of North America*, D. B. Slemmons, E. R. Engdahl, M. D. Zoback, and D. B. Blackwell, eds., Vol. 1, pp. 423–436. Geological Society of America, Boulder, CO.
- Colligan, J. G. 1993. U.S. electric utility environmental statistics. In *Electric Power Annual 1991*, U. S. Department of Energy, Energy Information Administration, DOE/EIA-0348(91), Washington, DC.
- DiPippo, R. 1995. Geothermal electric power production in the United States: a survey and update for 1990–1994. In *Proceedings of the World Geothermal Congress, 1995*, pp. 353–362. International Geothermal Association, Auckland, New Zealand.
- Ellis, A. J. and Mahon, W. A. J. 1977. *Chemistry and Geothermal Systems*. Academic Press, New York.
- Flavin, C. and Lenssen, N. 1991. Designing a sustainable energy system. In *State of the World, 1991, A Worldwatch Institute Report on Progress Toward a Sustainable Society*, pp. 1–595. W. W. Norton and Company, New York.
- Freeston, D. H. 1995. Direct uses of geothermal energy 1995—preliminary review. In *Proceedings of the World Geothermal Congress, 1995*, pp. 15–26. International Geothermal Association, Auckland, New Zealand.
- Henderson, J. M. and Dorigi, G. P. 1989. Operating experience of converting a Stretford to a Lo-Cat(R) H₂S abatement system at Pacific Gas and Electric Company's Geysers unit 15. *Geotherm. Resour. Counc. Trans.*, 13, 593–595.
- Hirtz, P., Lovekin, J., Copp, J., Buck, C., and Adams, M. 1993. Enthalpy and mass flowrate measurements for two-phase geothermal production by tracer dilution techniques. In *Proceedings of 18th Workshop on Geothermal Reservoir Engineering*, pp. 17–27. Stanford University, Palo Alto, CA, SGPTR-145.

- Huttrer, G. W. 1995. The status of world geothermal power production 1990–1994. In *Proceedings of the World Geothermal Congress, 1995*, pp. 3–14. International Geothermal Association, Auckland, New Zealand.
- L'Ecuyer, M., Zoi, C., and Hoffman, J. S. 1993. *Space Conditioning—The Next Frontier*. U.S. Environmental Protection Agency, Washington, DC, EPA430-R-93-004.
- Lienau, P. J., Lund, J. W., and Culver, G. G. 1995. Geothermal direct use in the United States, update 1990–1995. In *Proceedings of the World Geothermal Congress, 1995*, pp. 363–372. International Geothermal Association, Auckland, New Zealand.
- McLarty, L. and Reed, M. J. 1992. The U.S. geothermal industry: three decades of growth. *Energ. Sources*, 14, 443–455.
- Mefferd, M. G. 1991. *76th Annual Report of the State Oil & Gas Supervisor: 1990*, California Division of Oil & Gas, Pub. 06, Sacramento, CA.
- Muffler, L. J. P., ed. 1979. Assessment of geothermal resources of the United States—1978, U.S. Geological Survey Circular 790, Washington, DC.
- Rafferty, K. 1992. A century of service: the Boise Warm Springs water district system. *Geotherm. Resour. Counc. Bull.*, 21 (10), 339–344.
- Signorotti, V. and Hunter, C. C. 1992. Imperial Valley's geothermal resource comes of age. *Geotherm. Resour. Counc. Bull.*, 21 (9), 277–288.
- Truesdell, A. H. and White, D. E. 1973. Production of superheated steam from vapor-dominated reservoirs. *Geothermics*, 2, 145–164.
- White, D. E., Muffler, L. T. P., and Truesdell, A. H. 1971. Vapor-dominated hydrothermal systems compared with hot-water systems. *Econ. Geol.*, 66 (1), 75–97.
- Wright, P. M. 1991. Geochemistry. *Geo-Heat Cent. Bull.*, 13 (1), 8–12.

For Further Information

- Geothermal education materials are available from the Geothermal Education Office, 664 Hilary Drive, Tiburon, CA 94920.
- General coverage of geothermal resources can be found in the proceedings of the Geothermal Resources Council's annual technical conference, *Geothermal Resources Council Transactions*, and in the Council's *Geothermal Resources Council Bulletin*, both of which are available from the Geothermal Resources Council, P.O. Box 1350, Davis, CA 95617-1350.
- Current information concerning direct use of geothermal resources is available from the Geo-Heat Center, Oregon Institute of Technology, Klamath Falls, OR 97601.
- A significant amount of geothermal information is also available on a number of geothermal home pages that can be found by searching on "geothermal" through the Internet.



Taylor & Francis

Taylor & Francis Group

<http://taylorandfrancis.com>

Section II

Energy Conversion



Taylor & Francis

Taylor & Francis Group

<http://taylorandfrancis.com>

9

Steam Power Plant

John Kern

CONTENTS

9.1	Introduction.....	191
9.2	Rankine Cycle Analysis.....	193
	References.....	195
9.3	Topping and Bottoming Cycles.....	196
	For Further Information.....	196
9.4	Steam Boilers.....	196
9.4.1	Drum-Type Boilers.....	197
9.4.2	Once-Through Boilers.....	197
9.4.3	Major Boiler Components.....	197
9.5	Steam Turbines.....	198
9.5.1	General.....	198
9.5.2	Blading.....	199
9.5.3	Rotors.....	200
9.5.4	Choosing the Turbine Arrangement.....	201
9.5.5	Materials.....	202
9.5.6	Cylinders and Bolting.....	202
9.5.7	Valves.....	203
	For Further Information.....	203
9.6	Heat Exchangers, Pumps, and Other Cycle Components.....	203
9.6.1	Heat Exchangers.....	203
9.6.2	Pumps.....	205
	For Further Information.....	206
9.7	Generators.....	206
9.7.1	Generator Ventilation.....	207
9.7.2	Generator Auxiliaries.....	207
9.7.3	Excitation.....	208
	For Further Information.....	208

9.1 Introduction

This section provides an overview of the steam power cycle. There are noteworthy omissions in the section: site selection; fuel handling; activities related to civil engineering (such as foundations); controls; and nuclear power. Thermal power cycles take many forms, but the majority are fossil steam, nuclear, simple-cycle gas turbine, and combined cycle. Of those listed, conventional coal-fired steam is the predominant power producer—especially in

developing countries that have indigenous coal or can import coal inexpensively. A typical steam power plant is shown in Figure 9.1.

Because the Rankine cycle is the overwhelmingly preferred process for steam power generation, it is discussed first. Topping and bottoming cycles, with one exception, are rare and mentioned only for completeness. The exception is the combined cycle, in which the steam turbine cycle is a bottoming cycle. Developed countries have been moving to the combined cycle because of relatively low capital costs when compared with coal-fired plants; its high thermal efficiency, which approaches 60%, and low emissions.

The core components of a steam power plant are boiler; turbine; condenser and feedwater pump; and generator. These are covered in successive subsections. The final subsection is an example of the layout and contents of a modern steam power plant.

As a frame of reference, the following efficiencies are typical for modern, subcritical, fossil fuel steam power plants. The specific example chosen has steam conditions of 2400 psia; 1000°F main steam temperature; and 1000°F reheat steam temperature: boiler thermal 92; turbine/generator thermal 44; turbine isentropic 89; generator 98.5; boiler feedwater pump and turbine combined isentropic 82; condenser 85; plant overall 34 (Carnot 64). Supercritical steam plants operate with main steam above the “critical” pressure for water where water and steam have the same density and no longer exist as separate phase states. They are generally used when higher efficiency is desired. Modern supercritical coal plants with main steam conditions of 3600 psia at 1050 and 1050°F for reheat steam can exceed 40% in overall net plant efficiency.

Nuclear power stations are so unique that they are worthy of a few closing comments. Modern stations are all large, varying from 600 to 1500 MW. The steam is low temperature and low pressure ($\sim 600^\circ\text{F}$ and ~ 1000 psia), compared with fossil applications, and hovers around saturation conditions. Therefore, the boilers, superheater equivalent (actually a combined moisture separator and reheater), and turbines are unique to this cycle. The turbine generator thermal efficiency is around 36%.

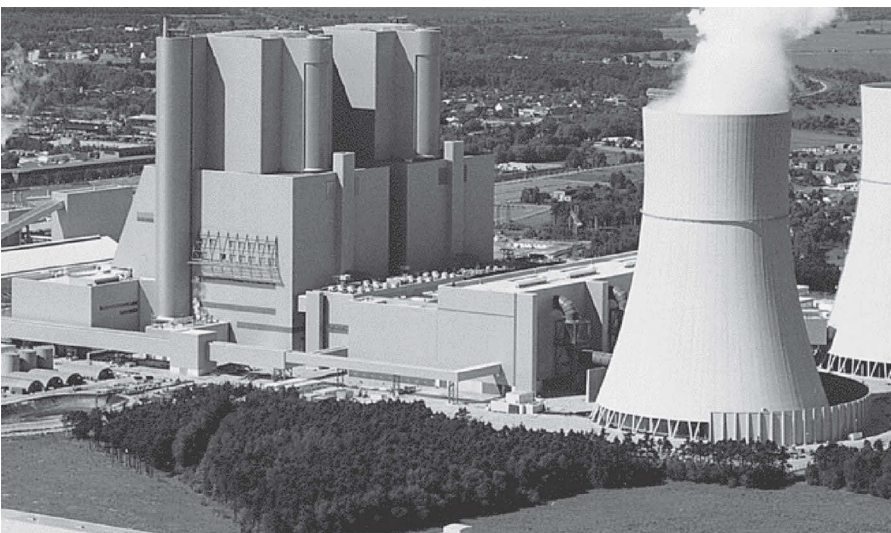


FIGURE 9.1
Modern steam power plant.

9.2 Rankine Cycle Analysis

Modern steam power generation is based on the Rankine cycle and thermodynamics govern the ultimate performance of the cycle whether used in a coal-fired steam plant or the bottoming cycle of a combined-cycle plant. The basic, ideal Rankine cycle is shown in Figure 9.2. The ideal cycle comprises the processes from state 1:

- 1–2: Saturated liquid from the condenser at state 1 is pumped isentropically (i.e., $S_1 = S_2$) to state 2 and into the boiler.
- 2–3: Liquid is heated at constant pressure in the boiler to state 3 (saturated steam).
- 3–4: Steam expands isentropically (i.e., $S_3 = S_4$) through the turbine to state 4, where it enters the condenser as a wet vapor.
- 4–1: Constant-pressure transfer of heat in the condenser takes place to return the steam to state 1 (saturated liquid).

If changes in kinetic and potential energy are neglected, the total heat added to the Rankine cycle can be represented by the shaded area on the T – S diagram in Figure 9.2; the work done by this cycle can be represented by the crosshatching within the shaded area. The thermal efficiency of the cycle (η) is defined as the work (W_{NET}) divided by the heat input to the cycle (Q_H).

The Rankine cycle is preferred over the Carnot cycle for the following reasons:

- The heat transfer process in the boiler must be at constant temperature for the Carnot cycle, whereas in the Rankine cycle it is superheated at constant pressure. Superheating the steam can be achieved in the Carnot cycle during heat addition, but the pressure must drop to maintain constant temperature. This means the steam is expanding in the boiler while heat is being added, which is not a practical method.

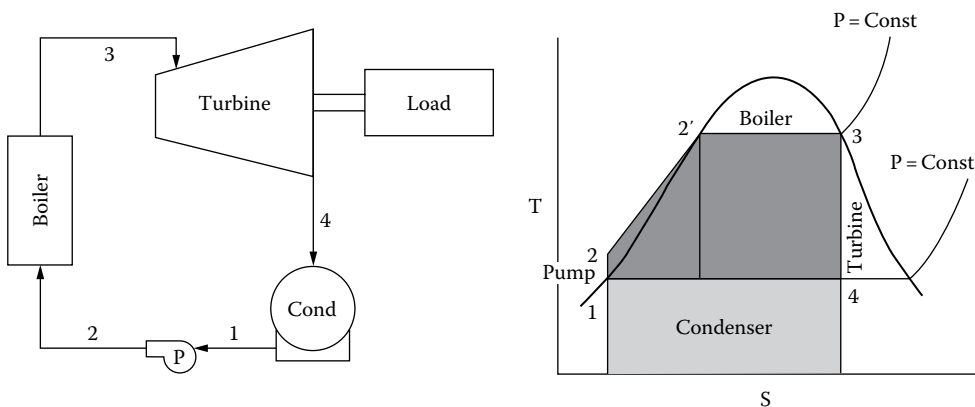


FIGURE 9.2
Basic Rankine cycle.

- The Carnot cycle requires that the working fluid be compressed at constant entropy to boiler pressure. This would require taking wet steam from point 1' in Figure 9.2 and compressing it to saturated liquid condition at 2'. A pump required to compress a mixture of liquid and vapor isentropically is difficult to design and operate. In comparison, the Rankine cycle takes the saturated liquid and compresses it to boiler pressure. This is more practical and requires much less work.

The efficiency of the Rankine cycle can be increased by utilizing a number of variations to the basic cycle. One such variation is superheating the steam in the boiler. The additional work done by the cycle is shown in the crosshatched area in Figure 9.3.

The efficiency of the Rankine cycle can also be increased by increasing the pressure in the boiler. However, increasing the steam generator pressure at a constant temperature will result in the excess moisture content of the steam exiting the turbine. To take advantage of higher steam generator pressures and keep turbine exhaust moistures at acceptably low values, the steam is expanded to some intermediate pressure in the turbine and then reheated in the boiler. Following reheat, the steam is expanded to the cycle exhaust pressure. The reheat cycle is shown in Figure 9.4.

Another variation of the Rankine cycle is the regenerative cycle, which involves the use of feedwater heaters. The regenerative cycle regains some of the irreversible heat lost when condensed liquid is pumped directly into the boiler by extracting steam from various points in the turbine and heating the condensed liquid with this steam in feedwater heaters. Figure 9.5 shows the Rankine cycle with regeneration.

The actual Rankine cycle is far from ideal because losses are associated with the cycle. They include piping losses due to friction and heat transfer; turbine losses associated with steam flow; pump losses due to friction; and condenser losses when condensate is sub-cooled. The losses in the compression (pump) and expansion process (turbine) result in an increase in entropy. Also, energy is lost in heat addition (boiler) and rejection (condenser) processes as they occur over a finite temperature difference.

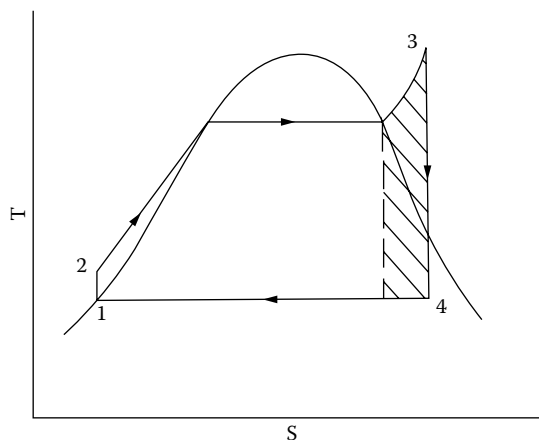


FIGURE 9.3
Rankine cycle with superheat.

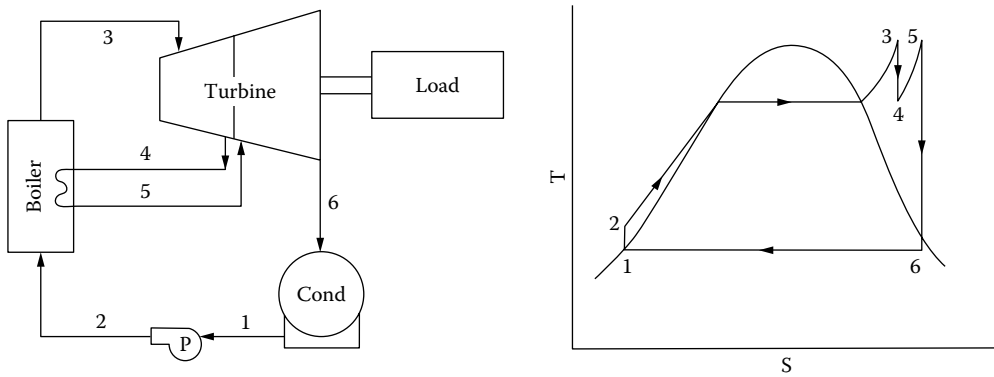


FIGURE 9.4
Rankine cycle with reheat.

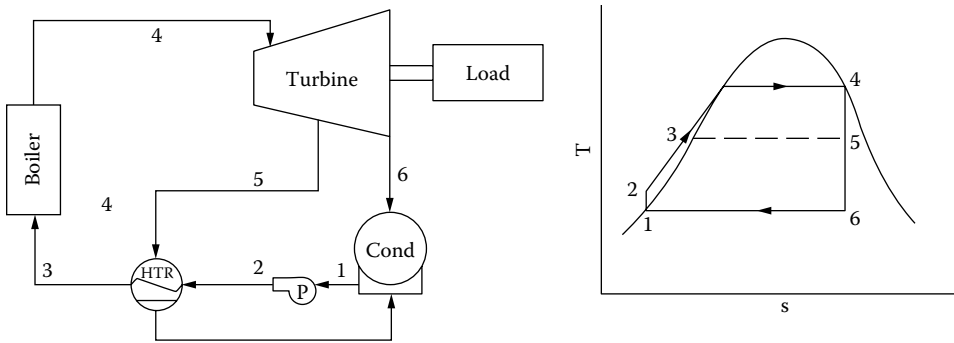


FIGURE 9.5
Rankine cycle with regeneration.

Most modern power plants employ some variation of the basic Rankine cycle in order to improve thermal efficiency. For larger power plants, economies of scale will dictate the use of one or all of these variations to improve thermal efficiency. In most cases, power plants in excess of 200,000 kW will have 300°F superheated steam leaving the boiler reheat and seven to eight stages of feedwater heating.

References

- Salisbury, J. K. 1950. *Steam Turbines and Their Cycles*, reprint 1974. Robert K. Krieger Publishing, Malabar, FL.
- Van Wylen, G. J. and Sonntag, R. E. 1986. *Fundamentals of Classical Thermodynamics*, 3rd Ed. Wiley, New York.

9.3 Topping and Bottoming Cycles

Steam Rankine cycles can be combined with topping and/or bottoming cycles to form binary thermodynamic cycles. These topping and bottoming cycles use working fluids other than water. Topping cycles change the basic steam Rankine cycle into a binary cycle that better resembles the Carnot cycle and improves efficiency. For conventional steam cycles, state-of-the-art materials allow peak working fluid temperatures higher than the supercritical temperature for water. Much of the energy delivered into the cycle goes into superheating the steam, which is not a constant-temperature process. Therefore, a significant portion of the heat supply to the steam cycle occurs substantially below the peak cycle temperature.

Adding a cycle that uses a working fluid with a boiling point higher than water allows more of the heat supply to the thermodynamic cycle to be near the peak cycle temperature, thus improving efficiency. Heat rejected from the topping cycle is channeled into the lower-temperature steam cycle. Thermal energy not converted to work by the binary cycle is rejected to the ambient-temperature reservoir. Metallic substances are the working fluids for topping cycles. For example, mercury has been used as the topping cycle fluid in a plant that operated for a period of time but has since been dismantled. Significant research and testing has also been performed over the years toward the eventual goal of using other substances, such as potassium, sodium, or cesium, as a topping-cycle fluid, but none has proven to be commercially successful.

Steam power plants in a cold, dry environment cannot take full advantage of the low heat rejection temperature available. The very low pressure to which the steam would be expanded to take advantage of the low heat sink temperature would increase the size of the low-pressure (LP) turbine to such an extent that it is impractical or at least inefficient. A bottoming cycle that uses a working fluid with a vapor pressure higher than water at ambient temperatures (such as ammonia or an organic fluid) would enable smaller LP turbines to function efficiently. Thus, a steam cycle combined with a bottoming cycle may yield better performance and be more cost effective than a stand-alone Rankine steam cycle. However, again, these techniques are not at present commercially viable and are not being broadly pursued.

For Further Information

Fraas, A. P. 1982. *Engineering Evaluation of Energy Systems*. McGraw-Hill, New York.

Horlock, J. H. 1992. *Combined Power Plants, Including Combined Cycle Gas Turbine (CCGT) Plants*. Pergamon Press, Oxford.

Lezuo, A. and Taud, R. 2001. Comparative evaluation of power plants with regard to technical, ecological and economical aspects. In *Proceedings of ASME Turbo Expo 2001*, New Orleans.

9.4 Steam Boilers

A boiler, also referred to as a steam generator, is a major component in the plant cycle. It is a closed vessel that efficiently uses heat produced from the combustion of fuel to convert water to steam. Efficiency is the most important characteristic of a boiler because it has

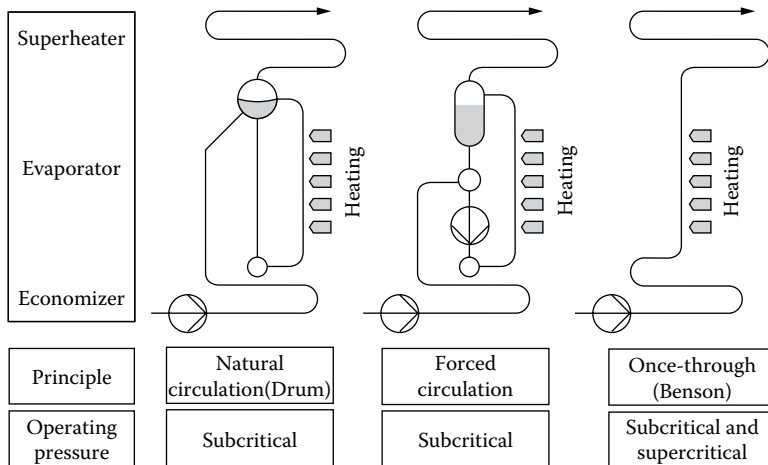


FIGURE 9.6
Boiler principles.

a direct bearing on electricity production. Boilers are classified as drum-type or once-through (Figure 9.6). Major components of boilers include an economizer, superheaters, reheaters, and spray attemperators.

9.4.1 Drum-Type Boilers

Drum-type boilers depend on constant recirculation of water through some of the components of the steam–water circuit to generate steam and keep the components from overheating. These boilers circulate water by natural or controlled circulation.

Natural Circulation Boilers. Natural circulation boilers use the density differential between water in the downcomers and steam in the waterwall tubes for circulation.

Controlled Circulation Boilers. Controlled circulation boilers use boiler-water-circulating pumps to circulate water through the steam–water circuit.

9.4.2 Once-Through Boilers

Once-through boilers convert water to steam in one pass through the system rather than re-circulating through the drum. Current designs for once-through boilers use a spiral-wound furnace to assure even heat distribution across the tubes.

9.4.3 Major Boiler Components

- *Economizer.* The economizer is the section of the boiler tubes in which feedwater is first introduced into the boiler and flue gas is used to raise the temperature of the water.
- *Steam drum (drum units only).* The steam drum separates steam from the steam–water mixture and keeps the separated steam dry.
- *Superheaters.* Superheaters are bundles of boiler tubing located in the flow path of the hot gases created by the combustion of fuel in the boiler furnace. Heat is transferred from the combustion gases to the steam in the superheater tubes.

Superheaters are classified as primary and secondary. Steam passes first through the primary superheater (located in a relatively cool section of the boiler) after leaving the steam drum. There the steam receives a fraction of its final superheat and then passes through the secondary superheater for the remainder.

- *Reheaters.* Reheaters are bundles of boiler tubes that are exposed to the combustion gases in the same manner as superheaters.
- *Spray attemperators.* Attemperators, also known as desuperheaters, are spray nozzles in the boiler tubes between the two superheaters. These spray nozzles supply a fine mist of pure water into the flow path of the steam to prevent tube damage from overheating. Attemperators are provided for the superheater and the reheater.

Worldwide, the current trend is to use higher temperatures and pressures to improve plant efficiency, which in turn reduces emissions. Improvements in high-temperature materials such as T-91 tubing provide high-temperature strength and improved corrosion resistance permitting reliable operation in advanced steam cycles. In addition, the development of reliable once-through Benson type boilers has resolved most of the operational problems experienced with first- and second-generation supercritical plants.

Steam plant boilers burning coal require advanced exhaust gas clean-up systems to meet today's strict environmental emissions limits. A typical plant burning high-sulfur eastern coal will have an SCR (selective catalytic reduction) for NO_x control, a precipitator for particulate control, and a wet limestone scrubber to reduce SO_x . A typical plant burning low-sulfur western coal might include an SCR, a baghouse filter for particulate control, and a dry scrubber for SO_x reduction.

9.5 Steam Turbines

9.5.1 General

Each turbine manufacturer has unique features in its designs that affect efficiency, reliability, and cost. However, the designs appear similar to a non-steam-turbine engineer. Figure 9.7 shows a modern steam turbine generator as used in a coal-fired steam power plant. Steam turbines for power plants differ from most prime movers in at least three ways:

- All are extremely high powered, varying from about 70,000 to 2 million hp, and require a correspondingly large capital investment, which puts a premium on reliability.
- Turbine life is normally between 30 and 40 years with minimal maintenance.
- Turbines spend the bulk of their lives at constant speed, normally 3600 or 1800 rpm for 60-Hz operation.

These three points dominate the design of the entire power station, particularly of the steam turbine arrangement and materials. Figure 9.8 shows the dramatic increase of steam turbine power output for one manufacturer over the past 50 years. This is reasonably typical of the industry.

In an earlier subsection it was shown that high steam-supply temperatures make for more efficient turbines. In Europe and Japan, the trend is to use increasingly higher steam-supply temperatures to reduce fuel cost and emissions.

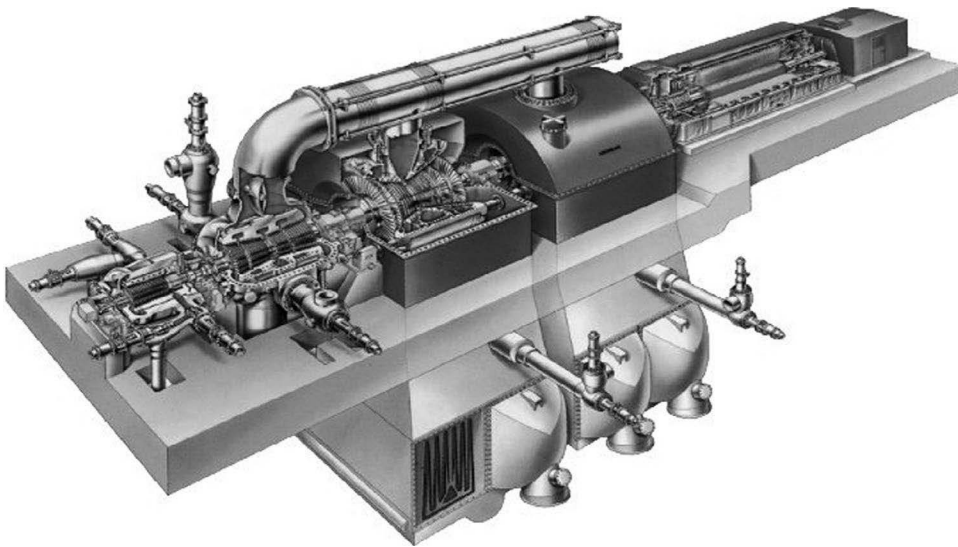


FIGURE 9.7
Modern steam turbine generator for a coal-fired steam plant.

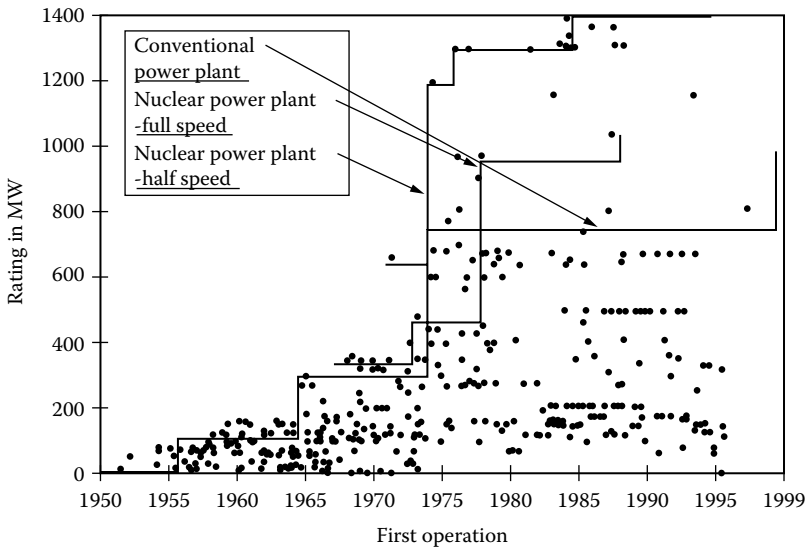


FIGURE 9.8
Increase of steam turbine power.

9.5.2 Blading

The most highly stressed component in steam turbines is the blades. Blades are loaded by centrifugal and steam-bending forces and also harmonic excitation (from nonuniform circumferential disturbances in the blade path). All blades are loaded by centrifugal and steam-bending loads, and smaller blades are designed to run when the harmonic excitation is resonant with the natural modes of the blade. If harmonic excitation is permitted

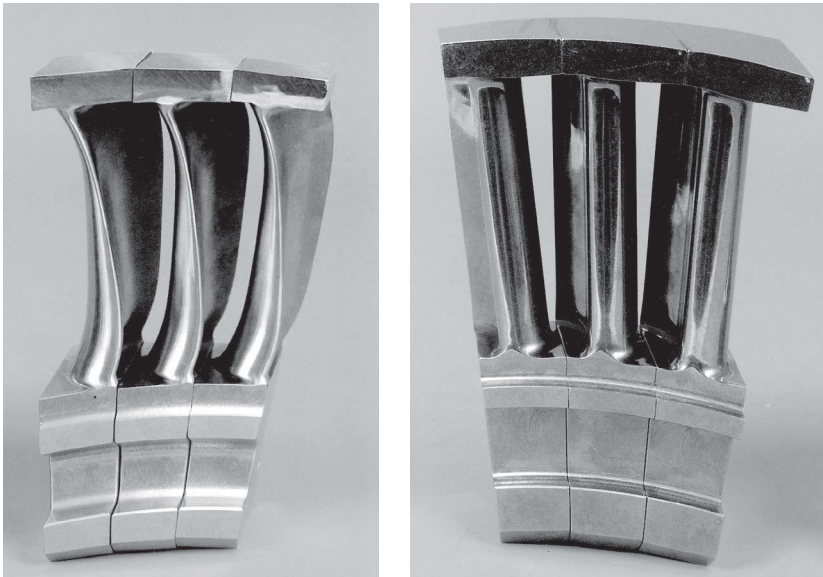


FIGURE 9.9
Typical steam turbine blades.

on very long blades, however, the blades become impractically large. Fortunately, because the turbine runs at constant speed, the blade modes can be tuned away from resonant conditions so that the harmonic loads are significantly reduced. This forms a split in blade design, commonly referred to as tuned and untuned blading.

Blades guide steam throughout the turbine in as smooth and collision-free a path as possible. Collisions with blades (incidence) and sudden expansions reduce the energy available for doing work. Until recently, designers would match flow conditions with radially straight blades (called parallel-sided blades). Turbine physics does not recognize this convenience for several reasons. The most visually obvious is the difference in tangential velocity between blade hub and tip. The latest blades address the full three-dimensional nature of the flow by curving in three dimensions (bowed blades). Three dimensional design techniques allow for better matching of the flow (and area) conditions and now, with the use of numerical control machine tools to make it more cost competitive, three-dimensional blading is used extensively in many modern turbines. Examples of three-dimensional and parallel-sided blades are shown in Figure 9.9.

9.5.3 Rotors

After blades, steam turbine rotors are the second most critical component in the machine. Rotor design must take into account

- The large high-strength alloy steel rotor forging that must have uniform chemistry and material properties
- Centrifugal force from the rotor body and the increased centrifugal pull from the attached blades

- The need to have high resistance to brittle fracture, which could occur when the machine is at high speed and the material is still not up to operating temperature
- Creep deformation of the high-pressure (HP) and intermediate-pressure (IP) rotors under steady load while at high temperature.

The life cycle is further complicated by transient fatigue loads that occur during power changes and start-up. Two further events are considered in rotor design: torsional and lateral vibrations caused by harmonic steam and electrical loads. As with tuned blades, this is normally addressed by tuning the primary modes away from resonance at full running speed.

9.5.4 Choosing the Turbine Arrangement

Because the turbine shaft would be too long and flexible if it were built in one piece with all the blades in sequence, the rotor is separated into supportable sections. The “cuts” in the shaft result in HP (high pressure), IP (intermediate pressure), and LP (low pressure) cylinders. Manufacturers address the grouping of cylinders in many different ways, depending upon steam conditions. It is common practice to combine HPs and IPs into one cylinder for subcritical units in the power range of about 250 to 600 MW. One manufacturer’s grouping, shown in Figure 9.10, is fairly representative of the industry.

So far, the text has discussed the steam flow as though it expanded monotonically through the turbine. This is usually not the case for two reasons. First, the most common steam conditions would cause steam exiting the last row of blades to be very wet, creating excessive erosion. Second, thermal efficiency can be raised by removing the steam from the turbine, reheating, and then returning it to the blade path; this increases the “average” heat supply temperature and reduces moisture levels in the turbine exhaust. The turbine position for reheat is normally between the HP and IP turbines.

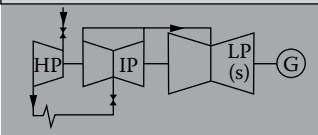
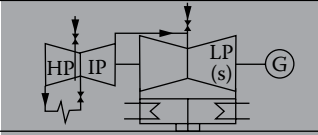
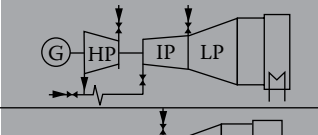
Type	Basic configuration	Power
HP-IP-LP (with reheat)		200Ð1200 MW
HP/IP-LP (with reheat)		160Ð700 MW
HP-IP/LP (with reheat)		120Ð260 MW
Single case (without reheat)		50Ð300 MW

FIGURE 9.10
Steam turbine product combinations.

There is one further geometric arrangement. Cylinders need not be all on one shaft with a single generator at the end. A cross-compound arrangement exists in which the steam path is split into two separate parallel paths with a generator on each path. Commonly, the split will be with paths of HP-LP generator and IP-LP generator. Torsional and lateral vibrations are more easily analyzed with shorter trains, which make the foundation systems more compact. The primary shortcoming is the need for two generators, two control systems, and a larger power house—all of which increase overall plant cost.

Historically, steam turbines have been split into two classes, reaction and impulse, as explained in Basic Power Cycles. This difference in design makes an observable difference between machines. Impulse turbines have fewer, wider stages than reaction machines. As designs have been refined, the efficiencies and lengths of the machines are now about the same. For a variety of reasons, the longer blades in the LP ends are normally reaction designs. Because each stage may now be designed and fabricated separately, the line between impulse and reaction turbines is diminishing with most manufacturers supplying blading that has characteristics of both technologies. Turbine blading is broadly split between machines as shown in the following table.

9.5.5 Materials

Materials are among the most variable of all turbine parts, with each manufacturer striving to improve performance by using alloying and heat-treatment techniques. It follows that accurate generalizations are difficult. Even so, the following table is reasonably representative for steam turbines with 1000°F–1050°F inlet temperatures:

	Cylinder			
	HP	IP	LP	
			Short Blades	End Blade(s)
Reaction turbines	Reaction	Reaction	Reaction	Reaction
Impulse turbines	Impulse	Impulse	Impulse	Reaction

Item	Common Material Description								
High-temperature HP and IP blades	Moderate- and cold-temperature stator blades	Moderate-temperature rotating blades	Cold LP rotating blades	High-temperature rotors	Low-temperature rotors	Hot	LP	High-temperature bolting	Cold bolting
Mod'd SS403	SS304	SS403	SS403 or 17/4 PH	1CrMoV, occasionally 10Cr	3.5 NiCrMoV	1.25Cr or 2.25Cr	Carbon, steel	SS422	B16

9.5.6 Cylinders and Bolting

These items are relatively straightforward, except for the very large sizes and precision required for the castings and fabrications. In a large HP-IP cylinder, the temperature and pressure loads split between an inner and outer cylinder. In this case, finding space and requisite strength for the bolting presents a challenge for the designer.

9.5.7 Valves

The turbine requires many valves for speed control, emergency control, drains, hydraulics, bypasses, and other functions. Of these, four valves are distinguished by their size and duty: throttle or stop; governor or control; reheat stop; and reheat interceptor. The throttle, reheat stop, and reheat interceptor valves normally operate fully open, except in some control and emergency conditions. Their numbers and design are selected for the appropriate combination of redundancy and rapidity of action. The continuous control of the turbine is accomplished by throttling the steam through the governor valve. This irreversible process detracts from cycle efficiency. In more modern units, the efficiency loss is reduced by reducing the boiler pressure (normally called sliding pressure) rather than throttling across the valves when reducing output.

For Further Information

- Japikse, D. and Nicholas, C. B. 1994. *Introduction to Turbomachinery*. Concepts ETI, Norwich, VT.
- Kutz, M. 1986. *Mechanical Engineers' Handbook*. Wiley, New York.
- Stodola, A. and Loewenstein, L. C. 1927. *Steam and Gas Turbines*, reprint of 6th Ed., 1945. Peter Smith, New York.

9.6 Heat Exchangers, Pumps, and Other Cycle Components

9.6.1 Heat Exchangers

Heaters. The two classifications of condensate and feedwater heaters are the open or direct contact heater and the closed or shell-and-tube heater.

Open Heaters. In an open heater, the extraction or heating steam comes in direct contact with the water to be heated. Although open heaters are more efficient than closed heaters, each requires a pump to feed the outlet water ahead in the cycle. This adds cost and maintenance and increases the risk of water induction to the turbine, making the closed heater the preferred heater for power plant applications.

Closed Heaters. These heaters employ tubes within a shell to separate the water from the heating steam (see Figure 9.11). They can have three separate sections in which the heating of the feedwater occurs.

First is the drain cooler section where the feedwater is heated by the condensed heating steam before cascading back to the next-lower-pressure heater. The effectiveness of the drain cooler is expressed as the drain cooler approach (DCA), which is the difference between the temperature of the water entering the heater and the temperature of the condensed heating steam draining from the heater shell. In the second section (condensing section), the temperature of the water is increased by the heating steam condensing around the tubes. In the third section (desuperheating section), the feedwater reaches its final exit temperature by desuperheating the extraction steam. Performance of the condensing and superheating sections of a heater is expressed as the terminal temperature difference (TTD). This is the difference between the saturation temperature of the

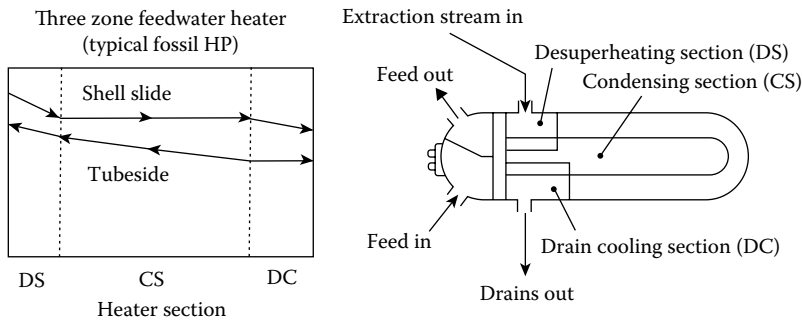


FIGURE 9.11
Shell-and-tube feedwater heater.

extraction steam and the temperature of the feedwater exiting the heater. Desuperheating and drain cooler sections are optional depending on the location of the heater in the cycle (for example, desuperheating is not necessary in wet extraction zones) and economic considerations.

The one exception is the deaerator (DA), which is an open heater used to remove oxygen and other gases that are insoluble in boiling water. The DA is physically located in the turbine building above all other heaters, and the gravity drain from the DA provides the prime for the boiler feed pump (BFP).

Two other critical factors considered in heater design and selection are (1) venting the heater shell to remove any noncondensable gases; and (2) the protection of the turbine caused by malfunction of the heater system. Venting the shell is required to avoid air-binding a heater, which reduces its performance. Emergency drains to the condenser open when high water levels are present within the shell to prevent back-flow of water to the turbine, which can cause serious damage. Check valves on the heating steam line are also used with a water-detection monitor to alert operators to take prompt action when water is present.

Condenser. Steam turbines generally employ surface-type condensers comprising large shell-and-tube heat exchangers operating under vacuum. The condenser (1) reduces the exhaust pressure at the last-stage blade exit to extract more work from the turbine; and (2) collects the condensed steam and returns it to the feedwater-heating system. Cooling water circulates from the cooling source to the condenser tubes by large motor-driven pumps. Multiple pumps, each rated less than 100% of required pumping power, operate more efficiently at part load and are often used to allow for operation if one or more pumps are out of service. Cooling water is supplied from a large heat sink water source, such as a river, or from cooling towers. The cooling in the cooling tower is assisted by evaporation of 3%–6% of the cooling water. Airflow is natural draft (hyperbolic towers) or forced draft. Noncondensable gases are removed from the condenser with a motor-driven vacuum pump or, more frequently, steam jet air ejectors, which have no moving parts.

When adequate cooling water is not available, a dry condenser can be used. This device uses large motor-driven fans to move air across a large radiator-like heat exchanger to condense the steam at ambient temperature. Air condensers are significantly more

expensive than wet condensers and generally decrease overall plant efficiency, so they are used only when necessary.

9.6.2 Pumps

Condensate pump. Condensate is removed from the hot well of the condenser and passed through the LP heater string via the condensate pump. Typically, two or more vertical (larger units) or horizontal (medium and small units) motor-driven centrifugal pumps are located near the condenser hot well outlet. Depending on the size of the cycle, condensate booster pumps may be used to increase the pressure of the condensate on its way to the DA.

Feedwater booster pump. The DA outlet supplies the feedwater booster pump, which is typically a motor-driven centrifugal pump. This pump supplies the required suction head for the BFP (boiler feed pump).

Boiler feed pump. These pumps are multiple-stage centrifugal pumps that, depending on the cycle, can be turbine or motor driven. BFP turbines (BFPT; Figure 9.12), are single-case units that draw extraction steam from the main turbine cycle and exhaust to the main condenser. Typical feed pump turbines require 0.5% of the main unit power at full-load operation. Multiple pumps rated at 50%–100% each are typically used to allow the plant to operate with one pump out of service.

With the increasing reliability of large electric motors, many plant designers are now using motors to drive the feed pumps for plants up to about 800 MW. Although the cycle is not quite as efficient as using a turbine drive, the overall plant capital cost is significantly less when motor BFP drives are used.

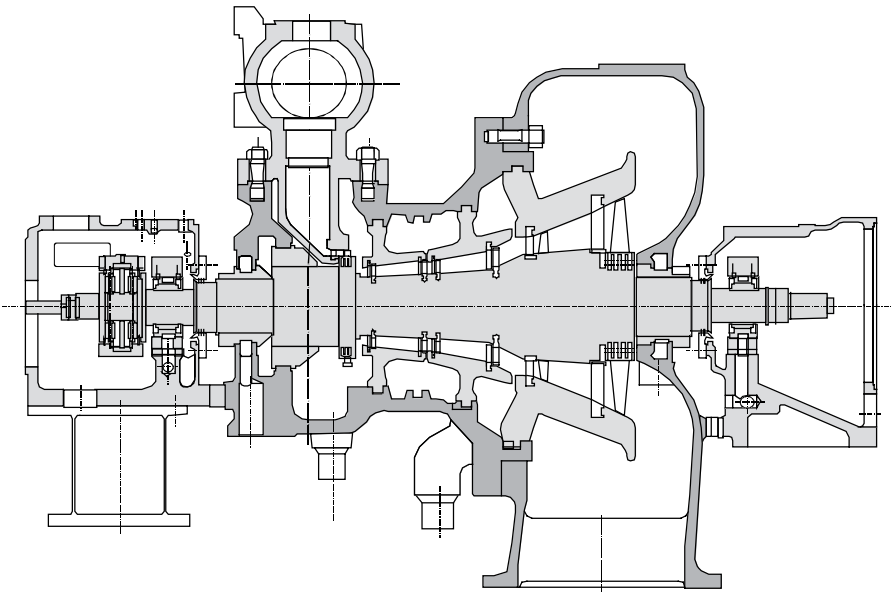


FIGURE 9.12
Boiler feed pump turbine.

For Further Information

British Electricity International 1992. *Modern Power Station Practice 3rd Ed.* Pergamon Press, Oxford.
Lammer, H. B. and Woodruff 1967. *Steam Plant Operation*, 3rd Ed. McGraw-Hill, New York.
Powell, C. 1955. *Principles of Electric Utility Operation*. Wiley, New York.

9.7 Generators

The electric generator converts rotating shaft mechanical power of the steam turbine to three-phase electrical power at voltages between 11.5 and 27 kV, depending upon the power rating. The generator comprises a system of ventilation, auxiliaries, and an exciter. Figure 9.13 shows an installed hydrogen-cooled generator and brushless exciter of about 400 MW. Large generators greater than 25 MW usually have a solid, high-strength steel rotor with a DC field winding embedded in radial slots machined into the rotor. The rotor assembly then becomes a rotating electromagnet that induces voltage in stationary conductors embedded in slots in a laminated steel stator core surrounding the rotor (see Figure 9.14).

The stator conductors are connected to form a three-phase AC armature winding. The winding is connected to the power system, usually through a step-up transformer.

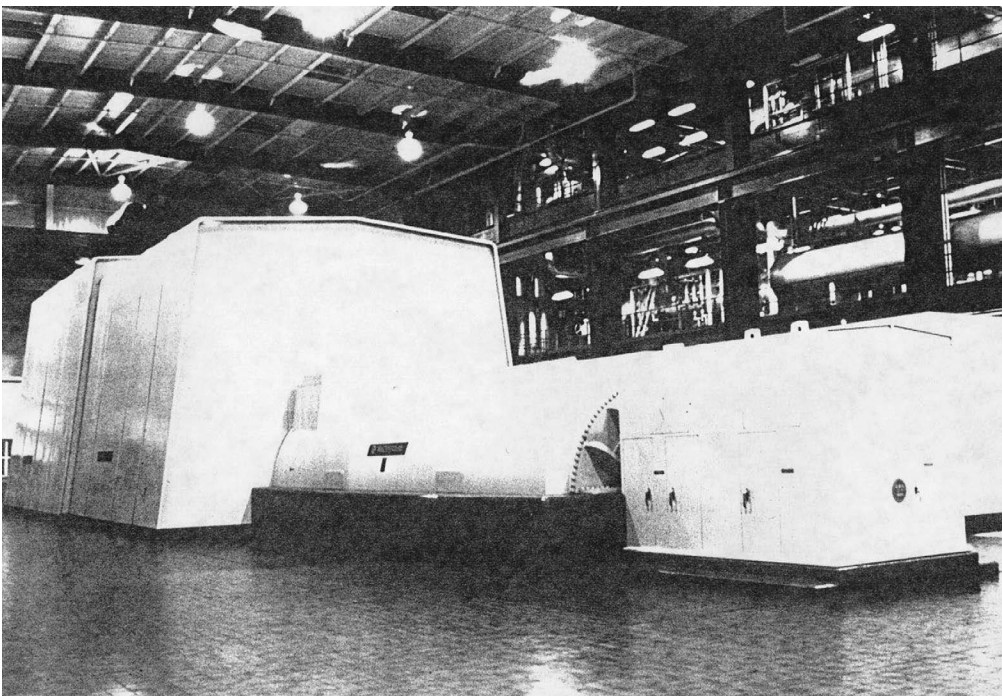


FIGURE 9.13
Generator and exciter.

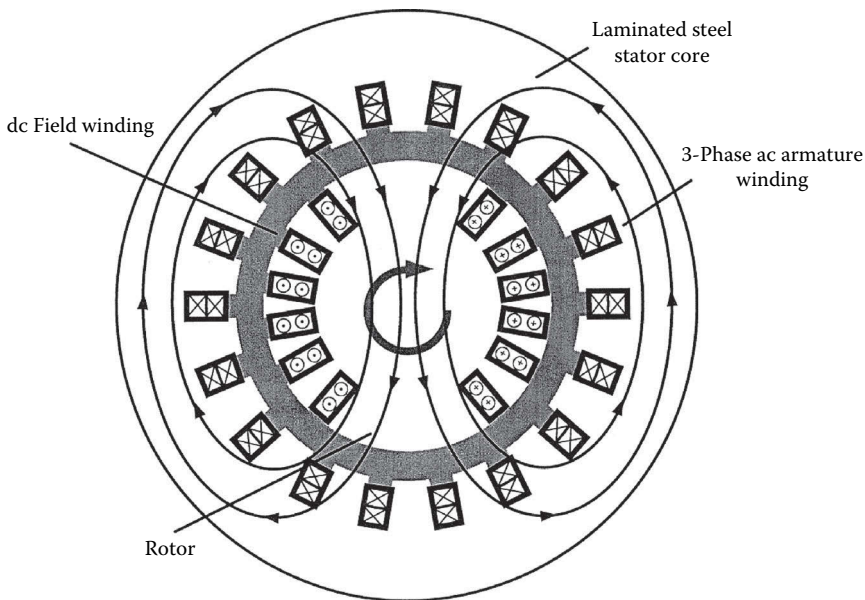


FIGURE 9.14
Generator magnetic paths.

Most steam turbines driven by fossil-fired steam use a two-pole generator and rotate at 3600 rpm in 60-Hz countries and 3000 rpm in 50-Hz countries. Most large steam turbines driven by nuclear steam supplies use a four-pole generator and rotate at 1800 or 1500 rpm for 60 and 50 Hz, respectively.

9.7.1 Generator Ventilation

Cooling the active parts of the generator is of such importance that generators are usually classified by the type of ventilation they use. Air-cooled generators are used commonly up to 300 MW. Some use ambient air, drawing air through filters, and others recirculate air through air-to-water heat exchangers. Above 250 MW, most manufacturers offer hydrogen for overall cooling. Hydrogen has 14 times the specific heat of air and is 14 times less dense. This contributes to much better cooling and much lower windage and blower loss. The frame must be designed to withstand the remote circumstance of a hydrogen explosion and requires shaft seals. Hydrogen is noncombustible with purities greater than 70%. Generator purities are usually maintained well above 90%. Depending upon the manufacturer, generators with ratings above 500 MW generally have water-cooled stator winding; the remaining components are cooled with hydrogen.

9.7.2 Generator Auxiliaries

Large generators must have a lubrication oil system for the shaft journal bearings. Major components of this system are pumps, coolers, and a reservoir. In most cases, the turbine and generator use a combined system. For hydrogen-cooled generators, a shaft seal system and hydrogen supply system are needed. The shaft seal system usually uses oil pumped to a journal seal ring at a pressure somewhat higher than the hydrogen pressure. Its major

components are pumps, coolers, and reservoir, similar to the lubrication system. The hydrogen supply system consists of a gas supply and regulators. A CO₂ supply is used to purge the generator when going from air to hydrogen or vice versa to avoid a combustible hydrogen–air mixture. The stator winding water supply again uses pumps, coolers, and a reservoir. It requires demineralizers to keep the water nonconducting because the water flow provides a path between the high-voltage conductors and ground. Depending upon the design approach, it may also include chemistry or oxygen content control to avoid corrosion in the winding cooling passages.

9.7.3 Excitation

The rotor field winding must have a DC source. Many generators use rotating “collector” rings with stationary carbon brushes to transfer DC current from a stationary source, such as a thyristor-controlled “static” excitation system, to the rotor winding. A rotating exciter, known as a brushless exciter, is used for many applications. It is essentially a small generator with a rotating rectifier and transfers DC current through the coupling into the rotor winding without the need for collectors and brushes.

For Further Information

- Fitzgerald, A. E., Kingsley, C. F., and Umans, S. D. 2002. *Electric Machinery, 6th Ed.* McGraw-Hill, New York.
- IEEE C50.13-2003 Standard for Cylindrical-Rotor 50 and 60 Hz Synchronous Generators Rated 10 MVA and Above.
- IEEE 67-1990 (R1995) Guide for Operation and Maintenance of Turbine Generators.
- IEEE 37.102-1995 Guide for AC Generator Protection.
- Nelson, R. J., et al. 2000. Matching the capabilities of modern large combustion turbines with air- and hydrogen-cooled generators. In *Proceedings of the American Power Conference*, Chicago, April 2000.

10

Gas Turbines

Richard H. Bunce

CONTENTS

10.1	Overview.....	209
10.2	History.....	210
10.3	Fuels and Firing.....	210
10.4	Efficiency.....	211
10.5	Gas Turbine Cycles.....	212
10.6	Cycle Configurations.....	213
10.7	Components Used in Complex Cycles.....	215
10.8	Upper Temperature Limit.....	219
10.9	Materials.....	220
10.10	Combustion.....	221
10.11	Mechanical Product Features.....	221
	Defining Terms.....	221

10.1 Overview

Gas turbines are steady-flow power machines in which a gas (usually air) is compressed, heated, and expanded for the purpose of generating power. The term *turbine* is the component that delivers power from the gas as it expands; it is also called an *expander*. The term gas turbine refers to a complete power machine. The term gas turbine is often shortened to simply turbine, which can lead to confusion with the term for an expander.

The basic thermodynamic cycle on which the gas turbine is based is known as the Brayton cycle. Gas turbines may deliver their power in the form of torque or one of several manifestations of pneumatic power, such as the thrust produced by the high-velocity jet of an aircraft propulsion gas turbine engine. Gas turbines vary in size from large, 775,000 hp utility machines, to small, 5 hp automobile and motorcycle turbochargers and microturbines. Now, 25–250 kW, recuperated gas turbines are being sold.

Gas turbines are used in electric power generation, propulsion, and compressor and pump drives. The most efficient power generation systems in commercial service are gas turbine combined-cycle plants with net power-to-fuel energy efficiencies of more than 60% (lower heating value [LHV] basis). Simple-cycle plants used in electric power generation have achieved efficiencies of over 40% (LHV basis).

10.2 History

The fourth quarter of the nineteenth century was one of great innovation in power machinery. Along with the spark-ignited gasoline engine, the compression-ignited diesel engine, and the steam turbine, engineers applied their skills to several hot-air engines. Charles Curtis received the first U.S. patent for a complete gas turbine on June 24, 1895. Jens William Aegidius Elling designed and built the first gas turbine in Norway in 1903, which produced 11 hp.

The first commercial stationary gas turbine engineered for power generation was a 4000 kW machine built by the Brown Boveri Company in Switzerland in 1939.

Aviation provided the impetus for gas turbine development in the 1930s. In Germany, Hans von Ohain's first engine ran in March 1937. Frank Whittle's first engine ran in England in April 1937. The first airplane flight powered by a gas turbine jet engine was undertaken in Germany on August 27, 1939. The first British airplane powered by a gas turbine flew on May 15, 1941.

A Swiss railway locomotive using a gas turbine was first run in 1941. The first automobile powered by a gas turbine was a British Rover, which ran in 1950. And, in 1956, a gas turbine-powered Plymouth car drove over 3000 miles on a coast-to-coast exhibition trip in the United States.

10.3 Fuels and Firing

The first heat engines were external combustion steam engines. The combustion products never came in contact with the working fluid, so ash, corrosive impurities, and contaminants in the fuel or exhaust did not affect the internal operation of the engine. Later, internal combustion (piston) engines were developed. In these engines, a mixture of air and fuel burned in the space enclosed by the piston and cylinder walls, thereby heating the air. The air and combustion products formed the working fluid, and contacted internal engine parts.

Most gas turbines in use today are internal combustion engines and, consequently, require clean fuels to avoid corrosion and erosion of critical turbine components. Efforts were made to develop gas turbines rugged enough to burn residual or crude oil. However, due to the higher efficiencies obtainable by burning extremely clean fuel at higher temperatures, there is little current interest in using fuels other than clean gas and distillate oil in gas turbines. Interest in the use of coal and residual oil is now centered on gasifying and cleaning these fuels prior to use.

A few external combustion gas turbines have been built for use with heavy oil, coal, nuclear reactor, radioisotope, and solar heat sources. However, none of these has become commercial. The added cost and pressure drop in the fired heater make externally fired gas turbines expensive. Because the working fluid temperature cannot be greater than that of the walls of the fired heater, externally fired gas turbines are substantially less efficient than modern internal combustion gas turbines with internally cooled blades.

The only internal combustion, coal-fired gas turbine of current interest is the pressurized fluidized bed (PFB) combustion system. In the PFB, air discharged from the compressor of the turbine is used to fluidize a bed of limestone or dolomite in which coal is burned. The

bed is maintained at a modest temperature so that the ash in the coal does not form sticky agglomerates. Fortunately, this temperature range also minimizes oxides of nitrogen (NO_x) formation and allows capture of sulfur dioxide (SO_2) in the bed. Bed temperature is maintained in the desired range by immersed boiler tubes. Carryover fly ash is separated from gaseous combustion products by several stages of cyclone inertial separators and, in some cases, ceramic filters. The power turbine is modified to accommodate the combustion products, which after mechanical cleanup may still contain particles as large as 3–5 μm . The most common gas turbine fuels today are natural gas and distillate oil. To avoid hot corrosion by alkali metal sulfates, the total sodium and potassium content of the fuel is typically limited to less than 5 ppm. Liquid fuels may also contain vanadium, which also causes corrosion. Fuels must be ash-free because particles larger than 3–5 μm rapidly erode blades and vanes.

10.4 Efficiency

The term *efficiency* is applied not only to complete power generation machines but also to the individual compression, expansion, and combustion processes that make up the gas turbine operating cycle. Different definitions of efficiency apply in each case. In an expansion process, the turbine efficiency is the ratio of the actual power obtained to the maximum power that could have been obtained by expanding the gas reversibly and adiabatically between the same initial and final pressures.

Gas turbines typically involve high-speed gas flows, so appreciable differences exist between the static pressure and temperature and the total (or stagnation) pressure and temperature. Care must be taken in interpreting data to be sure that the pressure condition—static or stagnation—at each component interface is properly used.

Irreversible losses in one stage of an expansion process show up as heat (increased temperature) in later stages and add to the power delivered by such stages. Hence, a distinction exists between the polytropic efficiency (used to describe the efficiency of a process of differential pressure change) and the adiabatic (complete pressure change) efficiency. The efficiency of compressors and turbines based on their inlet and outlet pressures is called the isentropic or adiabatic efficiency. Unfortunately, both terms are reported in the literature, and confusion can exist regarding the meaning of the term *efficiency*.

The combustion efficiency in well-engineered and well-built internal combustion gas turbines is almost always close to 100%. The combustion losses appear as carbon monoxide, unburned hydrocarbons, and soot, which, combined, are typically well below 50 ppm, with clean fuels. Oxides of carbon emissions of less than 1 ppm have been commercially demonstrated.

The gas turbine or engine efficiency is the ratio of the net power produced to the energy in the fuel consumed. The principal gas turbine fuels are liquid and gaseous hydrocarbons (distillate oil and natural gas) that have high hydrogen content. Consequently, the term *engine efficiency* needs to be qualified as to whether it is based on the higher or the lower heat content of the fuel (the difference between the two being the latent heat of condensation of the water vapor in the products of combustion). Utility fuel transactions are traditionally based on higher heating values (HHVs), and most engine publications presume the LHV of the fuel as the efficiency basis. In the case of natural gas fuel, the HHV efficiency is greater than the LHV efficiency by 10% of the value of the HHV efficiency.

Engineers analyze gas turbine machines to evaluate improvements in component performance, in higher temperature and pressure ratio designs, and in innovative cycles. Ideal-case cycle calculations generally assume the following:

- Air (with either constant or temperature-dependent specific heats) is the working fluid in both turbine and compressor (with equal mass flows).
- Air is the working fluid in both turbine and compressor, but with the turbine mass flow greater than the amount of fuel used.

Components are modeled with or without frictional pressure drops, and heat transfer effectiveness may be ideal (unity) or actual, depending on the purpose of the analysis. The use of compressor air for cooling of high-temperature structure, nozzles, and blades is modeled in varying degrees of complexity. Three-dimensional temperature profiles or pattern factors exist. Component inlet and exit total pressure losses should be included in cycle analyses.

10.5 Gas Turbine Cycles

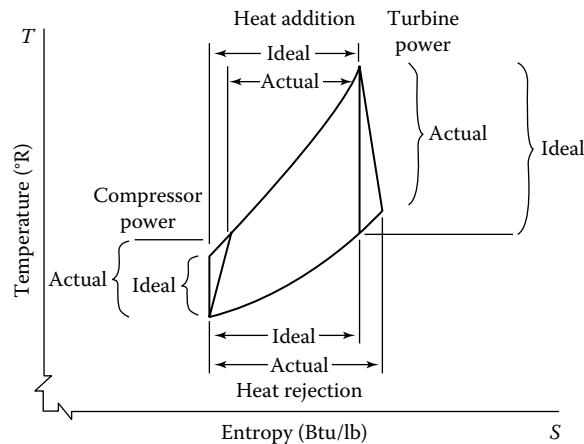
Gas turbine cycles are usually plotted on temperature–entropy (T - s) coordinates, entropy being a measurement of energy density. The T - s plot is useful in depicting cycles because, in an adiabatic process—as is the case for turbines and compressors—the power produced or consumed is the product of the mass flow and the enthalpy change through the process. Thus, the temperature difference, which is found on a T - s plot, is proportional to the power involved. Additionally, the heat exchange in a process involving zero power—such as a combustor or heat exchanger—is the product of the absolute temperature and the entropy change. On a T - s chart, the area under a process line for a combustor or heat exchanger is the heat exchanged.

The slope of a constant-pressure line on a T - s diagram is proportional to the absolute temperature; consequently, lines of constant pressure become steeper and diverge as the temperature increases. This illustrates that more work is obtained by expanding a gas between fixed pressures at higher temperatures than at lower temperatures. Figure 10.1 shows a comparison of the process of an ideal and an actual simple-cycle gas turbine on a T - s diagram. The increased compressor power consumption and the decreased turbine power generation in the actual cycle are shown to provide an understanding of the differences that component efficiencies make on machine performance.

The incremental amount of power produced per differential pressure change in the gas is given by

$$d\left(\frac{\text{Power}}{\text{Mass flow}}\right) = -RT \frac{dp}{p}$$

Two phenomena are illustrated by this equation. First, power is proportional to the absolute temperature of the gas. Second, power is proportional to the percent change in pressure. This latter point is important in understanding the effect of pressure losses in cycle components. In heat exchangers, the proper measure of power lost is the percent pressure drop.

**FIGURE 10.1**

$T-s$ diagram for a simple cycle illustrating the differences in compressor and turbine power for ideal (100% efficient) and actual components.

10.6 Cycle Configurations

The basic Brayton cycle consists of a compressor, a combustor or burner, and an expander. This configuration is known as the simple cycle. In idealizing the actual cycle, combustion is replaced by constant-pressure heat addition, and the cycle is completed by the assumption that the exhaust to ambient pressure is followed by a zero-pressure-loss cooling to inlet conditions.

A $T-s$ diagram of the simple-cycle gas turbine with an upper temperature limit set by metallurgical conditions is illustrated in Figure 10.2 for cycles of low, medium, and high pressure ratios. The heat addition is only by fuel combustion, simplified here to be without mass addition or change in specific heat of the working fluid.

It is seen that the low-pressure-ratio cycle requires a large heat addition, which leads to a low efficiency, and the high-pressure-ratio cycle has a turbine power output barely greater than the compressor power requirement, thereby leading to a low net output and low efficiency. At intermediate-pressure ratios, the turbine power output is substantially higher than the compressor power requirement, and the heat addition is modest in comparison with the difference between the turbine and compressor powers.

There is an optimum pressure ratio for maximum efficiency, which is mainly a function of the maximum gas temperature in the machine and, to a lesser extent, of the component efficiencies, internal pressure losses, and the isentropic exponent. There is another optimum pressure ratio for maximum specific power (power per unit mass flow).

As the achievable turbine inlet temperature increases, the optimum pressure ratios (for both maximum efficiency and maximum specific power) also increase. The optimum pressure ratio for maximum specific power is at a lower pressure level than that for maximum efficiency for all cycles not employing a recuperator. For cycles with a recuperator, the reverse is true: Maximum efficiency occurs at a lower pressure ratio than maximum specific power. Heavy-duty utility and industrial gas turbines are typically designed to operate near the point of maximum specific power, which approximates lowest equipment cost,

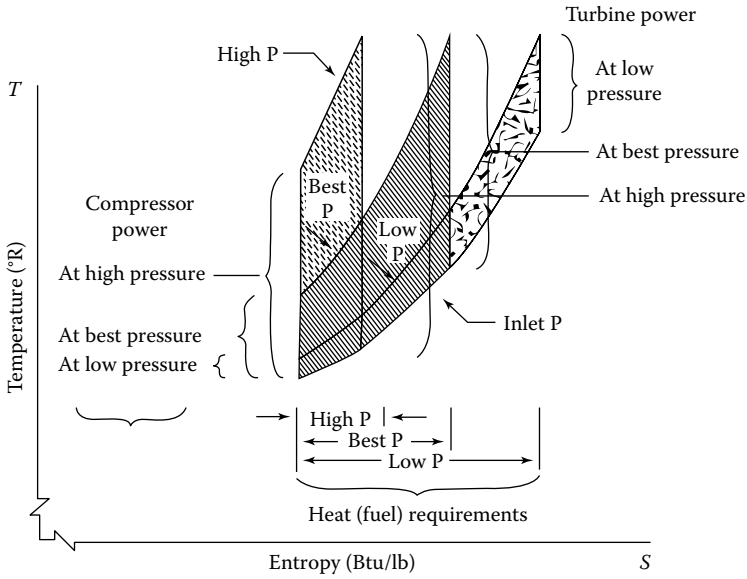


FIGURE 10.2
 $T-s$ diagram illustrating the power and heat (fuel) requirements at low, best, and high cycle pressures.

while aeroderivative gas turbines are designed to operate near the point of maximum efficiency, approximating highest thrust. Figure 10.3 shows a performance map (efficiency as a function of power per unit of air flow) for a simple-cycle gas turbine for two turbine inlet temperatures. It is seen that at higher temperatures, both the efficiency and the specific power increase, as well as the optimum pressure ratios for both the maximum efficiency and maximum specific power conditions.

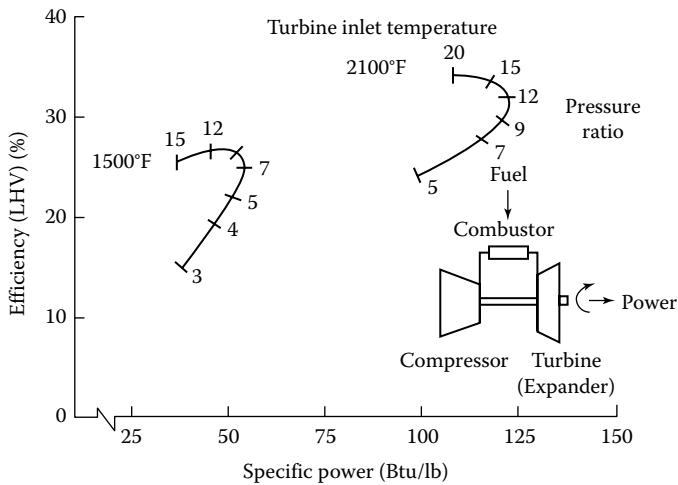


FIGURE 10.3
 Performance map of a simple cycle gas turbine.

Both aircraft and heavy industrial gas turbines used in the stationary power markets operate at temperatures above the limit of the turbine materials. Manufacturers use complex internal cooling passages in the blades and vanes as well as thermal barrier coatings on the aerodynamic surfaces of the airfoils to accommodate the high process gas temperature.

10.7 Components Used in Complex Cycles

Recuperators and regenerators recover heat from the turbine exhaust and use it to preheat the air from the compressor before it enters the combustor, thereby saving fuel. This heat transfer is shown in Figure 10.4. While recuperators and regenerators are quite similar thermodynamically, they are totally different in design. Recuperators are conventional heat exchangers in which hot and cold gases flow steadily on opposite sides of a solid (usually metal) wall.

Regenerators are periodic-flow devices. Fluid streams flow in opposite directions through passages in a wheel with heat storage walls. The wheel rotates, transferring heat from one stream to the other. Regenerators usually use a nest of very small parallel passages oriented axially on a wheel that rotates between hot and cold gas manifolds. Such regenerators are sometimes used in industrial processes for furnace heat recovery, where they are referred to as heat wheels. Because regenerators are usually more compact than recuperators, they are used in experimental automotive gas turbines. The difficulty in using regenerators on gas turbines intended for long life is that the two gas streams are at very different pressures. Consequently, the seals between the manifolds and the wheel must not leak excessively over the maintenance overhaul interval of the engine. If they

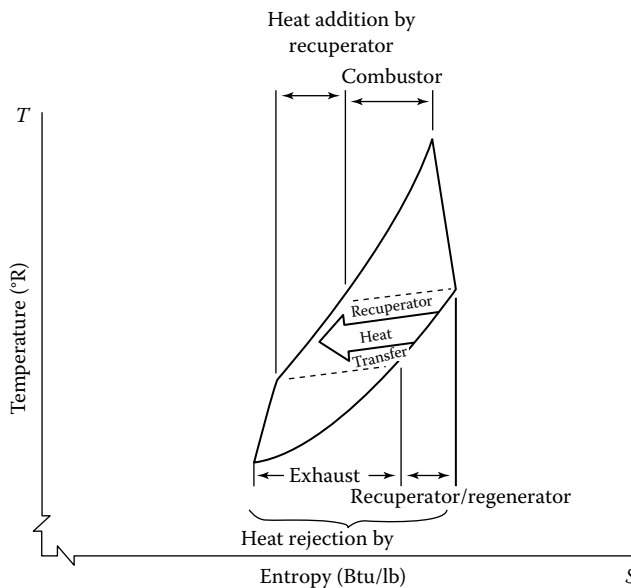


FIGURE 10.4 T-s diagram illustrating the heat transfer from the turbine exhaust to the compressor discharge accomplished by a recuperator/regenerator.

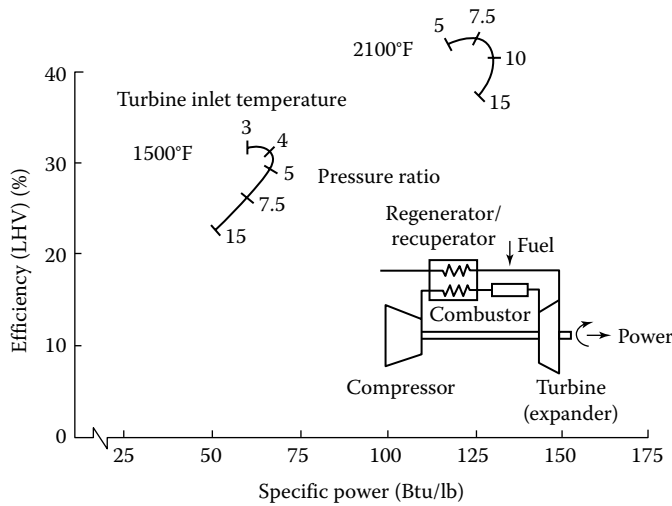


FIGURE 10.5
Performance map of a regenerative cycle gas turbine.

do, the power loss due to seal leakage will compromise the engine power and efficiency. Figure 10.5 shows a performance map for the regenerative gas turbine cycle for two temperatures. It is seen that as the temperature increases, the efficiency, specific power, and optimum pressure ratio all increase.

Current research on the recovery of gas turbine exhaust heat includes examination of thermochemical recuperation, where exhaust heat is used to effect a chemical reaction (reforming) of the fuel with steam, thereby increasing the heating value of the fuel. Although this process is feasible, research is underway to determine if it is practical and economic.

Industrial process compressors frequently use intercoolers to reduce compressor power when the compressor has a high pressure ratio and operates for a large number of hours per year. When analyzing cycles with intercoolers, the added pressure drops in the compressor interstage entrance, exit diffuser, compressor and the pressure drop in the intercooler itself should be included.

In a similar manner, turbine reheat can be used to increase the power output of a large-pressure-ratio turbine. This is the thermodynamic principle in turbojet afterburner firing. Turbine reheat increases power but decreases efficiency, unless the turbine exhaust heat is used for additional power generation, as is the case with a combined cycle, or is used with a recuperator to preheat combustor inlet air.

Intercoolers and reheat burners increase the temperature difference between the compressor and turbine discharges, thereby increasing the opportunity to use a recuperator to preheat the burner air with exhaust heat. An intercooled recuperated (ICR) machine is at present in development. The efficiency decrease at part load of an ICR gas turbine is much less than of conventional simple-cycle machines.

Small gas turbines have uncooled turbine blades as a result of the difficulty in manufacturing extremely small cooling passages in small blades. This results in low efficiencies, making it difficult for such turbines to compete with high-volume production (low-cost) reciprocating (piston) engines. The low-pressure-ratio recuperated cycle has greater

efficiency, although at higher cost. The recuperated cycle is finding favor in programs for small (under 300 kW) gas turbines used for stationary power generation.

Because of their compact size, low emissions, and light weight, gas turbines are also being considered for hybrid engine–battery vehicles. Proponents are pursuing the low-pressure-ratio recuperated gas turbine as the way to obtain high efficiency and low emissions in a compact power plant.

An ingenious gas turbine cycle is the closed cycle in which the working fluid is sealed in the system. Heat is added to the fluid using an externally fired heater and extracted from the fluid through heat exchangers. The working fluid may be any gas, and the density of the gas may be varied—to vary the power delivered by the machine—by using a gas storage cylinder connected to the compressor discharge and inlet. The gas storage system is at an intermediate pressure so that it can discharge gas into the lowest pressure point in the cycle and receive gas from the highest pressure point in the cycle. About ten such units were built between 1938 and 1968. However, in spite of its sophistication, the added cost and low efficiency inherent in external combustion systems prevented the gas storage system from becoming economic.

A closed cycle under current development is the recuperated recompression Brayton cycle using supercritical carbon dioxide (SCO_2) as the working fluid. The SCO_2 operates at very high pressure and at target temperatures of over 1000°F. The system would include compressors, coolers, heaters, recuperators, and a turbo-expander.

The exhaust from a gas turbine is quite hot and can be used to raise steam, which can then be used to generate additional power using a steam turbine. Such a compound gas turbine–steam turbine system is referred to as a combined cycle. Figure 10.6 shows a schematic diagram of the equipment in a combined cycle. Because the exhaust of heavy-duty machines is hotter than that of aeroderivative machines, the gain in the combined-cycle system efficiency through the use of the lower temperature steam bottoming cycle operating from the exhaust heat exchanger to the steam condenser is greater for heavy-duty machines than for aeroderivatives. Indeed, heavy-duty machines are designed with two criteria in mind: achieving the lowest cost for peaking (based on the simple-cycle configuration) and achieving the highest efficiency in a combined-cycle configuration for base load use. The optimum pressure ratios for these two system configurations are very close. Steam bottoming cycles used in combined cycles usually use steam at multiple pressure levels to increase the efficiency.

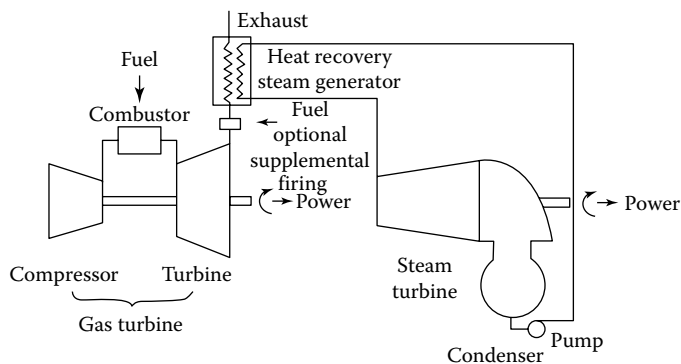


FIGURE 10.6
Combined (Brayton–Rankine) cycle.

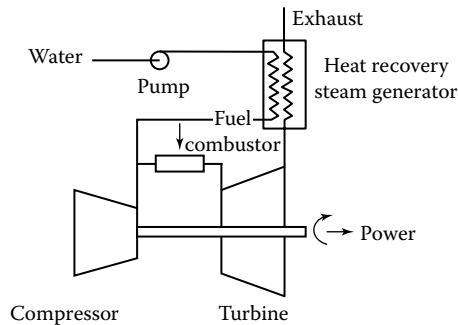


FIGURE 10.7
Steam-injected gas turbine.

Another system in which the power and efficiency of a gas turbine is increased through the use of steam is the steam-injected gas turbine. Figure 10.7 shows a schematic diagram of a steam-injected gas turbine cycle. Here, the turbine exhaust flows into a heat recovery steam generator (HRSG) operating at a pressure somewhat higher than the compressor discharge pressure. The steam is introduced into the gas turbine at the combustor. The steam–air mixture then passes into the turbine, where the augmented mass flow increases the power produced by the turbine. Additional fuel is required by the combustor because the steam must be heated from the HRSG delivery temperature to the combustor discharge temperature.

Typical turbines can accommodate only a limited additional mass flow—from 5% to 15%, depending on the design of the original gas turbine. Steam-injected gas turbines enable the use of the steam for industrial purposes, space heating, or for the generation of additional power.

Alternatively, manufacturers of industrial gas turbines will use the technique of inlet air fogging to generate higher power. Fogging consists of spraying tiny water droplets into the compressor inlet air flow, thus increasing the mass flow of the working fluid and lowering the effective inlet temperature. Power increase in large industrial gas turbines is over 0.5%, and it is over 2.0% for large aeroderivative turbines for each 2°F of inlet air cooling. Wet compression, or overspray fogging, can produce a 5% power boost for every 1% increase in air mass flow due to the water injected.

A group of cycles under consideration for development involve the use of adiabatic saturators to provide steam at compressor discharge pressure to augment greatly the mass flow through the turbine and, consequently, increase the cycle power and efficiency. In the adiabatic saturator, water flows in a countercurrent path to the compressor discharge air in a mass transfer tower. Such equipment is often used in the chemical processing industries. The saturated air is preheated in a turbine exhaust heat recuperator. This cycle is called the humid air turbine, or HAT, cycle. The HAT cycle is particularly useful in using the low-temperature heat generated in coal-gasification-fueled gas turbine power plants. As the mass flow through the turbine is significantly augmented, engineers can no longer use the expansion turbine that was matched to the compressor in a conventional simple-cycle gas turbine.

Figure 10.8 shows performance maps for the gas turbine cycles of major interest for a turbine inlet temperature typical of new products. Intercooling increases the specific power appreciably when compared with a simple cycle; however, such improvement requires an

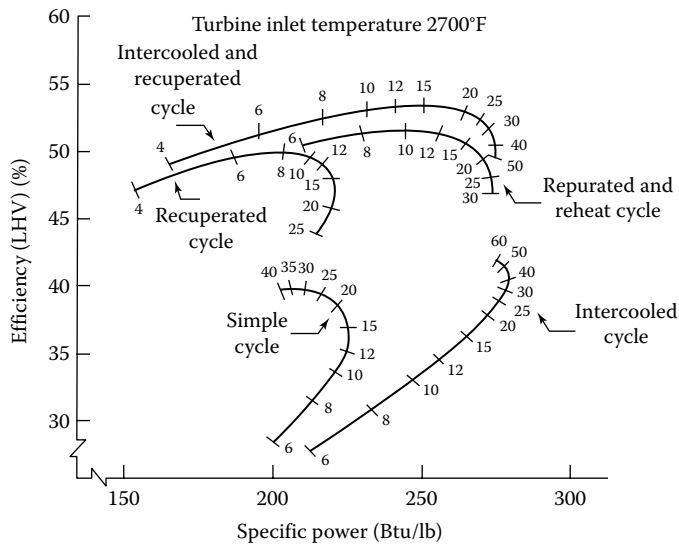


FIGURE 10.8
Specific power (Btu/lb).

increase in the pressure ratio. Recuperated cycles have a considerably higher efficiency than similar cycles without recuperation. The effect of the pressure ratio on the performance of recuperated cycles is opposite to that of similar cycles without recuperation. For recuperated cycles, the pressure ratio for maximum efficiency is considerably lower than for maximum specific power. Performance maps such as these are used in screening cycle alternatives for improved performance. Individual curves are generated for specific component performance values for use as a guide in developing new or improved machines.

10.8 Upper Temperature Limit

Classically, gas turbine engineers often spoke of a metallurgical limit in reference to maximum turbine inlet temperature. Later, turbine vane and blade cooling became standard on large machines. This situation creates a temperature difference between the combustion products flowing through the turbine and the turbine blade wall. Thus, because heat can be removed from the blades, the turbine can be operated with a combustion gas temperature higher than the metallurgical limit of the blade material.

Typically, the blades and vanes in new large gas turbines contain complex internal passages. Up to 20% of compressor discharge air may be directed through these internal passages. The cooling air first flows through internal convective cooling passages, then through impingement passages, where the air is directed at the blade and vane walls, and finally through small holes in the blade, where it is used to provide a low-temperature film over the blade surface. This film cooling of the surface reduces heat transfer to the blade.

The design of blade and vane cooling passages is an extremely competitive endeavor because greater cooling enables the use of higher combustion temperatures without

exceeding the metallurgical limit of the blade material. However, a balance between air flow for cooling and air flow for power must be achieved; the cooling air flowing within a blade drops in pressure without producing any power within that stage (although it is available for power in later stages). In the newest gas turbines, with regard to blade cooling, the difference between turbine inlet gas temperature and blade metal temperature is around 1000°F.

Water-cooled large gas turbines have been developed and introduced into the market using closed-circuit steam cooling in selected hot-section parts. Steam cooling reduces the need for air cooling, so more of the compressor discharge air can be used for NO_x reduction in the combustor and for power generation. The heat transferred to the steam increases the efficiency of the bottoming cycle in a combined-cycle gas turbine plant at the same firing temperature. The additional combustion products that flow through the high-pressure portions of the turbine generate substantially more power, thereby increasing both the power output and the efficiency of the machine. Water cooling adds significant complexity to the engine design. Early water-cooled concepts proved difficult because cooling rotating airfoils was an insurmountable problem at the time. Advanced air cooling technologies that allow higher firing temperatures have been developed such that the water cooling approach is not currently being actively pursued in heavy industrial gas turbine engines typically used for power generation.

10.9 Materials

The high-technology parts of a gas turbine are its hot-section parts: blades, vanes, combustors, and transition pieces. Gas turbine power, efficiency, and economics increase with the temperature of the gas flowing through the turbine blade passages. Materials are selected to survive in serviceable condition for over 50,000 h and associated numbers of thermal cycles. Ceramic coatings protect materials from oxidation and corrosion and provide thermal insulation, permitting higher gas temperatures.

Gas turbine alloys are frequently referred to as superalloys because of their extremely high strength at high temperatures. These superalloys are nickel based (such as IN 738), cobalt based (such as FSX-414), or with a nickel–iron base (such as Inconel 718). Nickel is oxidation and creep resistant, but is subject to corrosive sulfidation.

The key property of ceramic thermal barrier coatings is thermal conductivity. Reduced thermal conductivity on the surface of the components facing the process gas permits higher gas temperatures. The industry relies largely on ceramic materials applied to the metallic substrate surface using a spray process that melts and then solidifies the thermal barrier coating on the component.

Alloy and manufacturing advancements have been led by the needs of military aircraft engines. Coating developments for corrosion resistance have been led by the needs of stationary power for overhaul intervals as large as 50,000 h. The developmental needs of automotive gas turbines have led to significant advances in the strength and reliability of high-temperature ceramic components, including radial inflow turbines. Ceramic materials, principally silicon nitride, are of interest to developers of ceramic components for small gas turbines.

10.10 Combustion

Gas turbine combustors appear to be simple in design, yet they solve several difficult engineering challenges. Until relatively recently, gas turbine combustors employed a (turbulent) diffusion flame design approach, which created the most compact flame. European heavy-duty gas turbine manufacturers—with substantial interest in burning heavy fuel oils—preferred large, off-engine combustors, often called silo combustors because of their appearance, in order to obtain lower flame velocities and longer residence times. American heavy-duty gas turbine manufacturers use compact on-engine combustors and design for gaseous and clean (distillate) liquid fuels. Aeropropulsion gas turbines require the smallest-possible frontal area and use only clean liquid fuels; hence, they use on-engine combustors.

Until recently, stationary engines have been required to reduce NO_x emissions to the greatest extent possible, and combustors on stationary gas turbines first modified their diffusion flame combustors and employed water and steam injection to quench flame hot spots. Most current designs have changed to the lean-premixed process. With the improved blade cooling, materials, and coatings now in use, the material limits on turbine inlet temperature and the NO_x emission limits on combustor temperature appear to be converging on a combustion–temperature asymptote around 2900°F (1600°C class).

10.11 Mechanical Product Features

In view of the need to achieve all the performance features described in the chapter, one must keep in mind that a gas turbine is a high-speed dynamic machine with numerous machine design, materials, and fabrication features to consider. Major issues include the following: critical shaft speed considerations, bearing rotational stability, rotor balancing, thrust bearing design, bearing power loss, oil lubrication system, oil selection, air filter design and minimization of inlet and exhaust diffuser pressure drops, instrumentation, controls, diagnostic systems, scheduled service and inspection, overhaul, and repair. All of these topics must be addressed to produce a cost-effective, reliable, long-lived, practical gas turbine product that will satisfy users while also returning to investors sufficient profit for them to continue to offer better power generation products of still higher performance.

Defining Terms

Adiabatic saturator: A combined heat-and-mass exchanger whereby a hot gas and a volatile liquid pass through a series of passages such that the liquid is heated and evaporates into the gas stream.

Combined cycle: An arrangement of a gas turbine and a steam turbine whereby the heat in the exhaust from the gas turbine is used to generate steam in a heat recovery boiler, which then flows through a steam turbine, thereby generating additional power from the gas turbine fuel.

Combustion efficiency: The ratio of the rate of heat delivered in a device that burns fuel to the rate of energy supplied by the fuel.

Expansion process: A process of power generation whereby a gas passes through a machine while going from a condition of high pressure to one of low pressure.

Gas turbine or engine efficiency: The ratio of the net power delivered (turbo-expander power minus compressor and auxiliary power) to the rate of energy supplied to the gas turbine or engine in the form of fuel, or directly in the form of heat.

Humid air turbine: A gas turbine in which the flow through the expander is augmented by large amounts of steam generated by the use of an adiabatic saturator.

Intercooler: A heat exchanger used to cool the flow between sections of a compressor such that the high-pressure section of the compressor acts on a stream of reduced volumetric flow rate, thereby requiring less overall power to compress the stream to the final pressure.

Recuperator: A heat exchanger in which the hot and cold streams pass on opposite sides of a wall where temperature rises and falls, thereby transferring heat between the streams.

Steam cooling: A process in which steam is used as the heat transfer fluid to cool a hot component.

Steam-injected gas turbine: A system in which the gas turbine flow is augmented by steam, usually directly into the combustion section of the gas turbine, thereby generating additional power.

Turbine efficiency: The ratio of the actual power delivered in an expansion process employing a turbine as the expander to the maximum power that could be produced by expanding the gas in a reversible adiabatic (isentropic) process from its initial pressure and temperature to its final pressure and temperature.

11

Internal Combustion Engines

David E. Klett, Elsayed M. Afify, Kalyan K. Srinivasan, and Timothy J. Jacobs*

CONTENTS

11.1	Introduction	224
11.2	Engine Types and Basic Operation	224
11.2.1	Four-Stroke SI Engine	224
11.2.2	Two-Stroke SI Engine	225
11.2.3	Compression Ignition Engine	228
11.3	Air Standard Power Cycles.....	230
11.3.1	Constant-Volume Heat Addition—Ideal Otto Cycle.....	230
11.3.2	Constant-Pressure Heat Addition—Ideal Diesel Cycle.....	232
11.4	Actual Cycles	233
11.5	Combustion in IC Engines.....	236
11.5.1	Combustion in Spark Ignition Engines	236
11.5.1.1	Normal Combustion Process	237
11.5.1.2	Abnormal Combustion.....	238
11.5.2	Compression Ignition Engine Combustion	239
11.5.2.1	Knock in CI Engines	240
11.6	Exhaust Emissions	240
11.6.1	Harmful Constituents	240
11.6.1.1	Carbon Monoxide.....	240
11.6.1.2	Unburned Hydrocarbons.....	241
11.6.1.3	Oxides of Nitrogen.....	241
11.6.1.4	Particulates.....	241
11.6.2	Control of Emissions from IC Engines	242
11.7	Fuels for SI and CI Engines	244
11.7.1	Background.....	244
11.7.2	Gasoline.....	244
11.7.3	Diesel Fuels	245
11.8	Intake Pressurization—Supercharging and Turbocharging.....	247
11.8.1	Background.....	247
11.8.2	Supercharging	247
11.8.3	Turbocharging.....	248
11.8.4	Exhaust Waste Energy Recovery	250
	Defining Terms	252
	References.....	254
	For Further Information	255

* The original authors of this chapter were David E. Klett and Elsayed M. Afify, and it was revised for this edition by Kalyan K. Srinivasan and Timothy J. Jacobs.

11.1 Introduction

This section discusses the two most common reciprocating internal combustion (IC) engine types in current use: the **spark ignition** (SI) and the **compression ignition** (CI or Diesel) **engines**. Space limitations do not permit detailed coverage of the very broad field of IC engines. For a more detailed treatment of SI and CI engines and for information on variations, such as the Wankel rotary engine (Norbye, 1971) and the Miller cycle engine (a variation on the reciprocating four-stroke engine), several textbooks, technical papers, and other sources on the subject are included in the list of references.

Of course, the fundamental operation of the IC engine remains true to its original concept. Major advances in the areas of materials, manufacturing processes, electronic controls, computer-aided design, and advanced combustion and thermodynamic understanding have led to significant improvements in dependability, longevity, thermal efficiency, and emissions. Electronic controls, in particular, have played a major role through improved control of the fuel and air systems, ignition, and exhaust gas recirculation (EGR).

This section presents the fundamental theoretical background of IC engine function and performance, including **four-stroke** and **two-stroke** SI and CI **engines**. Sections on combustion, emissions, fuels, and intake pressurization (**turbocharging** and **supercharging**) are also included.

11.2 Engine Types and Basic Operation

IC engines may be classified by a wide variety of characteristics; the primary category includes the type of ignition (e.g., SI and CI) and the type of stroke (e.g., four stroke and two stroke). Other possible categories of classification include intake type (e.g., naturally aspirated, turbocharged, and supercharged), number of cylinders, cylinder arrangement (e.g., in-line, vee, opposed), cooling method (e.g., air and water), fueling system (e.g., injected and carbureted), valve gear arrangement (e.g., overhead cam and pushrod), and type of **scavenging** for two-stroke engines (e.g., cross, loop, and uniflow).

11.2.1 Four-Stroke SI Engine

Figure 11.1 is a cross-section schematic of a four-stroke SI engine. The SI engine relies on an external (usually via a plug) spark to ignite a volatile air–fuel mixture as the piston approaches **top dead center (TDC)** on the compression stroke. This mixture may be supplied from a carburetor, a single throttle-body fuel injector, individual fuel injectors mounted above the intake port of each cylinder, or individual fuel injectors mounted in each cylinder (direct injection). One combustion cycle involves two revolutions of the crankshaft and thus four strokes of the piston, referred to as the intake, compression, combustion/power, and exhaust strokes. Intake and exhaust valves control the flow of intake and exhaust gases into and out of the cylinder, and an ignition system supplies a spark-inducing high voltage to the spark plug at the proper time in the cycle to initiate combustion. Sometimes, the intake mixture may include high concentrations of exhaust gas/residual fraction, usually purposeful to improve efficiency and/or emissions.

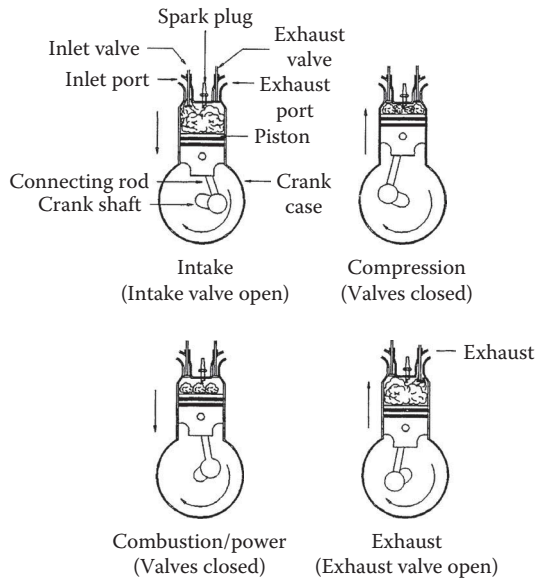


FIGURE 11.1
Schematic diagram of four-stroke SI engine.

On the intake stroke, the intake valve opens and the descending piston draws a fresh charge into the cylinder. For some SI engines, the intake charge might be a mixture of fuel and air. As described above, exhaust gas may be recirculated and inducted during intake. Direct injection engines usually only induct air (plus EGR if being used) and introduce fuel directly into the cylinder either during intake or after intake valve closes during compression. During the compression stroke, the intake valve closes and the mixture is compressed by the upward piston movement. The mixture is ignited by the external spark, typically before TDC. The rapid, **premixed, homogeneous combustion** process causes a sharp increase in cylinder temperature and pressure that forces the piston down for the combustion/power stroke. Near **bottom dead center (BDC)**, the exhaust valve opens and the cylinder pressure drops rapidly to near atmospheric. The piston then returns to TDC, expelling the exhaust products. At TDC, the exhaust valve closes and the intake valve opens to repeat the mechanical cycle again. Figure 11.2 is a cutaway drawing of a modern high-performance automotive SI engine. This is a fuel-injected normally aspirated aluminum alloy V-8 engine of 3.9 L displacement with dual overhead cams for each cylinder bank and four valves per cylinder. Peak power output is 188 kW at 6100 rpm and peak torque is 354 N·m at 4300 rpm.

11.2.2 Two-Stroke SI Engine

The two-stroke SI engine completes a combustion cycle for every revolution of the crankshaft by essentially overlapping the power and exhaust functions in one downward stroke and the intake and compression processes in one upward stroke. A single-cylinder, crankcase-scavenged, two-stroke SI engine is illustrated schematically in Figure 11.3. The operation is as follows.

On the upward stroke, the piston first covers the transfer port and then the exhaust port. Beyond this point, the mixture is compressed and ignited near TDC. During the upward stroke, the negative pressure created in the crankcase below the piston draws in a fresh

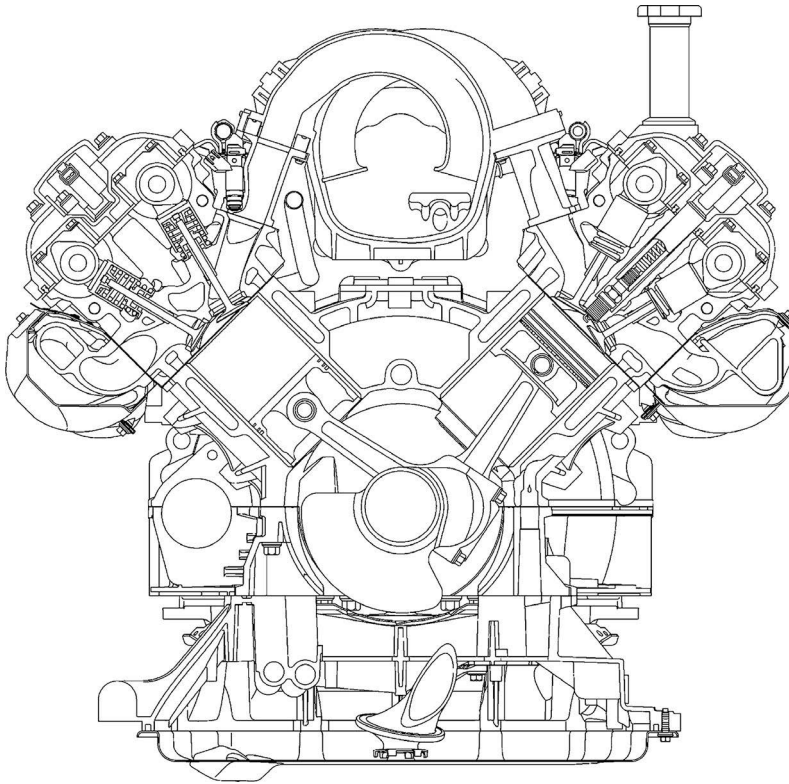


FIGURE 11.2
Ford 4.6-L aluminum V-8 SI engine. (Courtesy of Ford Motor Company, Dearborn, MI.)

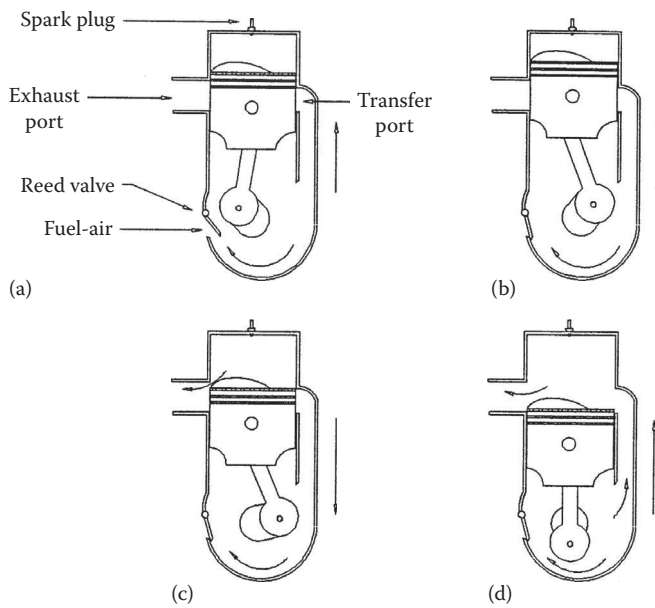


FIGURE 11.3
Schematic drawing of two-stroke SI engine. (a) Compression intake, (b) power, (c) exhaust, and (d) transfer.

charge through a one-way valve, known as a reed valve. Depending on the design of the engine, the charge might consist of different combinations of air, fuel, and EGR. If only air, or air and EGR, fuel is then typically injected directly into the cylinder after port closure. On the downward power stroke, the mixture in the crankcase is pressurized. The piston uncovers the exhaust port and the high-pressure exhaust gases exit. Near BDC, the transfer port is uncovered and the pressurized mixture flows from the crankcase into the cylinder and the cycle repeats. Because the crankcase is part of the induction system, it commonly does not contain oil; in such a case, lubrication is usually accomplished by mixing oil with the fuel. With the cross-flow scavenging configuration illustrated in Figure 11.3, there will be a certain degree of mixing of the fresh charge with the combustion products remaining in the cylinder and some loss of fresh charge out the exhaust port. Note that the piston in Figure 11.3 is designed to assist with removing exhaust products while preventing “short-circuiting” of the fresh charge.

Because two-stroke engines produce twice the power impulses of four-stroke engines for the same rpm, a two-stroke engine generally has a higher **power density** and is thus smaller and lighter than a four-stroke engine of equal output. The disadvantages of some two-stroke engines have historically been lower fuel conversion efficiency and higher exhaust emissions because of overlapping intake and exhaust processes and the loss of some fresh intake mixture with the exhaust products. For this reason, two-stroke SI engines have largely been confined to either small-displacement applications, such as small motorcycles, outboard marine engines, and small equipment, or large-displacement, stationary applications such as those used in oil and gas industry. Several manufacturers have addressed these shortcomings in recent years and have achieved significant improvements in two-stroke engine fuel economy and emissions (Blair 1988).

The orbital combustion process (OCP), as illustrated in Figure 11.4, applies air-assisted direct injection of the fuel into the cylinder of a two-stroke engine and, in conjunction with

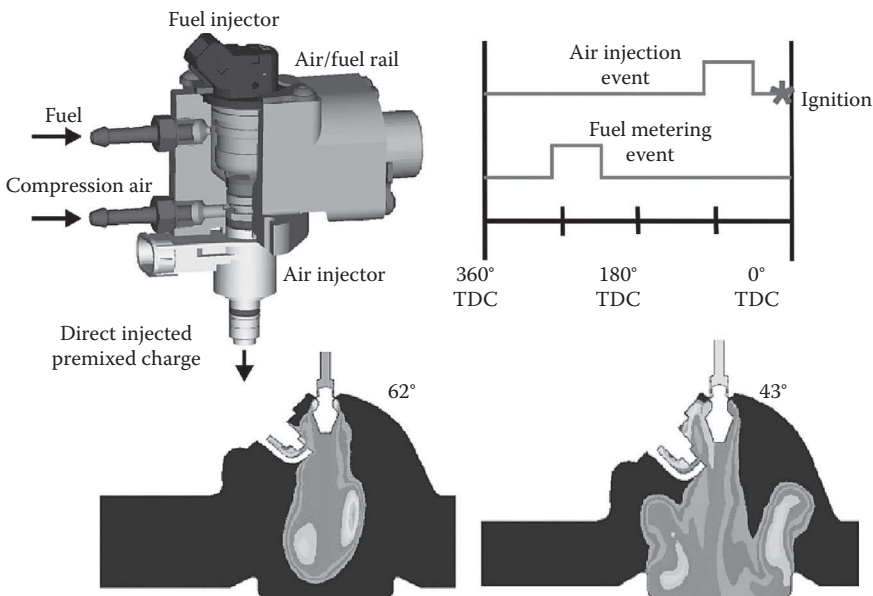


FIGURE 11.4 Orbital OCP combustion system. (Courtesy of Orbital Engine Company, Lapeer, MI)

a high turbulence combustion chamber design, achieves very favorable fuel economy and significantly reduced levels of hydrocarbon emissions. This system, in use today on single-cylinder scooters and on 2-, 3-, and 6-cylinder marine two-stroke engine applications, is also applicable to four-stroke engines.

Some large-bore natural gas engines relying on two-stroke principle also make use of indirect injection, using a separate but connected volume called a prechamber. These small prechambers, incorporated in the cylinder head, help promote rapid mixing of fuel and air. Swirl chambers are designed to produce a strong vortex in the prechamber during compression. The fuel is sprayed into the chamber through a single-hole nozzle, and the high vorticity promotes rapid mixing. Precombustion chambers do not attempt to generate an orderly vortex motion within the chamber; instead, to promote mixing, they rely on a high level of turbulence created by the rush of air into the chamber during compression.

11.2.3 Compression Ignition Engine

The basic valve and piston motions are the same for the CI, or Diesel, engine as discussed above for the SI engine. The CI engine relies on the high temperature and pressure of the cylinder air resulting from the compression process to cause **autoignition** of the fuel, which is injected directly into the combustion chamber of **direct injection (DI)** engines or into the prechamber of **indirect injection (IDI)** engines, when the piston approaches TDC on the compression stroke. Compression ratios are typically much higher for CI than for SI engines, which helps to achieve the high air temperatures required for autoignition. The fuels used must have favorable autoignition qualities as well. The higher compression ratios of CI engines is one reason they generally have higher fuel conversion efficiencies than SI engines.

The time period between the start of fuel injection and the occurrence of autoignition is called the **ignition delay period**. Long ignition delay periods allow more time for fuel vaporization and fuel–air mixing and result in objectionable Diesel knock when this larger premixed charge autoignites. Combustion chambers and fuel injection systems must be designed to avoid extended ignition delay periods under conventional combustion conditions. Diesel engines may be classified as DI or IDI. In DI engines, the combustion chamber consists of a bowl formed in the top of the piston; the fuel is injected into this volume. The injector tip generally has from four to eight holes to form multiple spray cones.

Two variations are illustrated in Figure 11.5. The quiescent chamber engine utilizes a large-diameter shallow bowl shape that produces low swirl and low turbulence of the air during compression. Fuel is injected at high pressure through a multihole nozzle; mixing of the fuel and air relies primarily on the energy of the injected fuel to cause air entrainment in the spray cone and diffusion of vaporized fuel into the air. This system is suited to large slow-speed engines that are operated with significant excess air.

The toroidal bowl combustion chamber is used in conjunction with intake ports and/or valve shrouds designed to produce air swirl to enhance fuel–air mixing. The **swirl ratio** is defined by $\text{swirl ratio} = \text{swirl speed (rpm)} / \text{engine speed (rpm)}$. The swirl velocity component is normal to the fuel spray direction and tends to promote mixing in the regions between the individual spray cones. This system makes better use of the available air and is utilized extensively in moderate-speed engines such as over-the-road truck engines. In the past, DI did not lend well to high-speed operation because less time is available for proper mixing and combustion. Diesel engines for passenger car applications are generally designed for higher speed operation to produce higher specific output. Because of this, they typically utilized IDI combustion systems, two of

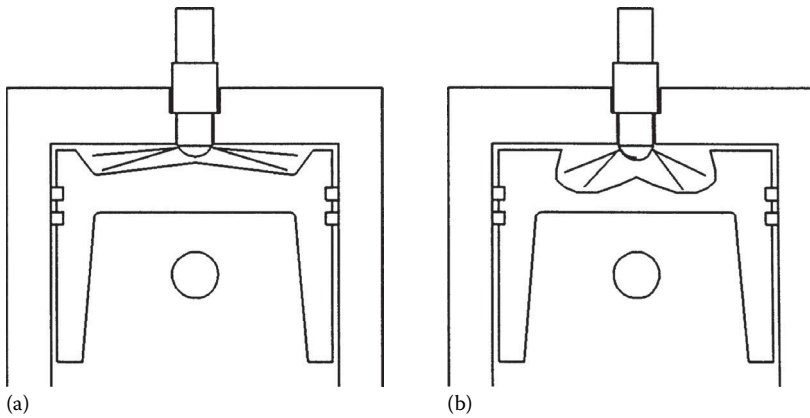


FIGURE 11.5
Examples of DI Diesel combustion chamber design. (a) quiescent bowl and (b) toroidal bowl.

which are illustrated in Figure 11.6. Nowadays, however, improved combustion chamber design along with advanced turbocharging systems allows even high-speed Diesel engines to use DI.

CI engines have suffered from poor cold-start characteristics due to vaporability of most Diesel fuels. **Glow plugs** are often installed in each cylinder to heat the air to improve cold starting. Higher compression ratios also improve cold starting. The compression ratios, typically 18–24, might be higher than the optimum for fuel efficiency (due to decreased mechanical efficiency resulting from higher friction forces).

CI engines are produced in two-stroke and four-stroke versions. Because the fuel is injected directly into the combustion chamber of CI engines just prior to TDC, two-stroke CI engines do not suffer the same emission and efficiency shortcomings as do older crank-case-scavenged two-stroke SI engines. Thus, they are available in much larger displacements for high-power-requirement applications such as locomotive and ship propulsion and electric power generation systems. Two-stroke CI engines are generally of the DI type because the use of IDI in a two-stroke engine would lead to aggravated cold-start problems due to lower effective compression ratios.

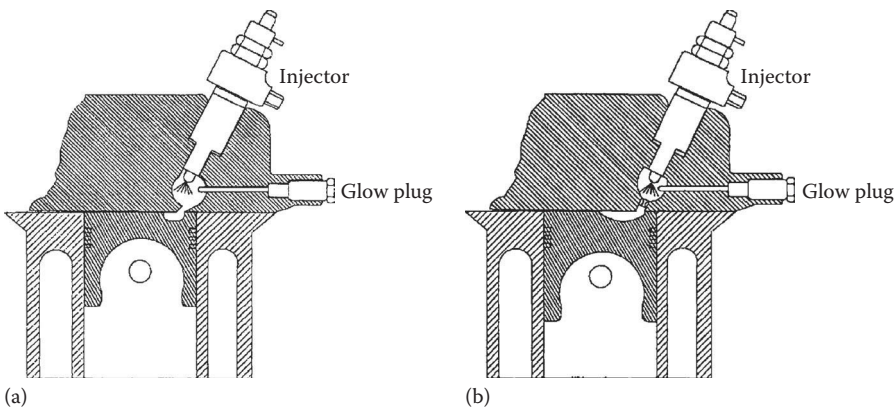


FIGURE 11.6
Two examples of IDI combustion chambers. (a) Swirl chamber and (b) pre-combustion chamber.

11.3 Air Standard Power Cycles

The actual operation of IC engines is idealized at a very basic level by the air standard power cycles (ideal thermodynamic cycles for converting heat into work on a continuous basis). The following simplifying assumptions are common to the air standard cycles: (1) the working substance is air, (2) the air is assumed to behave as an ideal gas with constant specific heats, (3) heat is added to the cycle from an external source, and (4) expansion and compression processes not involving heat transfer occur isentropically. The air standard cycles, while grossly oversimplified in terms of the complex processes occurring within actual engines, are nevertheless useful in understanding some fundamental principles of SI and CI engines. The simplified models also lend insight into important design parameters, e.g., **compression ratio**, that govern theoretical maximum thermal efficiencies.

11.3.1 Constant-Volume Heat Addition—Ideal Otto Cycle

One such idealization is the Otto cycle, which assumes that heat is added to the system at constant volume. Constant-volume heat addition would idealize the combustion process taking place instantly when the piston is at TDC. A P - V diagram for the Otto cycle is illustrated in Figure 11.7. The cycle consists of the following processes: 1 \rightarrow 2 isentropic compression; 2 \rightarrow 3 constant-volume heat addition; 3 \rightarrow 4 isentropic expansion; and 4 \rightarrow 1 constant-volume heat rejection.

Thermal efficiency for a power cycle is defined as the ratio of work output to heat input per cycle:

$$\eta = \frac{W_{net}}{Q_{in}} \quad (11.1)$$

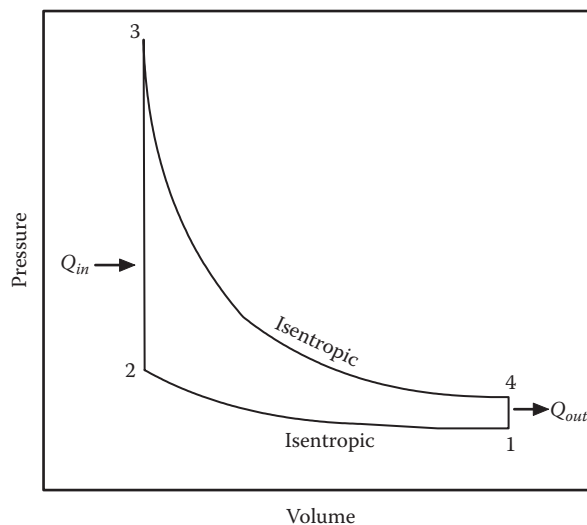


FIGURE 11.7
Schematic pressure–volume diagram for the ideal Otto cycle.

For the Otto cycle, the basic efficiency expression can be manipulated into the form

$$\eta = 1 - \frac{1}{r^{\gamma-1}} \quad (11.2)$$

where

γ is the ratio of specific heats ($\gamma = C_p/C_v$)

r is the compression ratio, or ratio of the maximum to minimum cycle volumes ($r = V_1/V_2$).

In actual IC engines, the minimum cycle volume is referred to as the **clearance volume** and the maximum cycle volume is the **cylinder volume**. The ideal Otto cycle efficiency for air, with $\gamma = 1.4$, is shown plotted in Figure 11.8. The theoretical efficiency of the constant volume heat addition cycle increases rapidly with compression ratio, up to about $r = 8$. Further increases in compression ratio bring moderate gains in efficiency.

Compression ratios in practical SI engines are limited because of autoignition (knock) and high NO_x emission problems that accompany high compression ratios. Production SI automotive engines typically have compression ratios in the range of 8–10, whereas high-performance normally aspirated racing engines may have compression ratios as high as 14, but require the use of special fuels to avoid autoignition. Compression ratios in practical CI engines are limited because of increasing friction that results from the high in-cylinder pressures that cause increased bearing, wrist pin, and piston ring forces at high compression ratios. Regardless, CI engines generally operate at much higher compression ratios, usually in the range of 14–21.

Historically, initially because of the need to spark-ignite the fuel–air mixture but more recently to support effective after-treatment catalysis for exhaust emissions, SI engines had been limited to stoichiometric, or chemically correct, fuel–air mixtures. Thus, there had been little opportunity to increase SI efficiency through mixture leaning. CI engines, however, are able to ignite very lean mixtures due to the independence from an external ignition source. In fact, in many cases CI engines are limited as the fuel–air mixture approaches stoichiometric

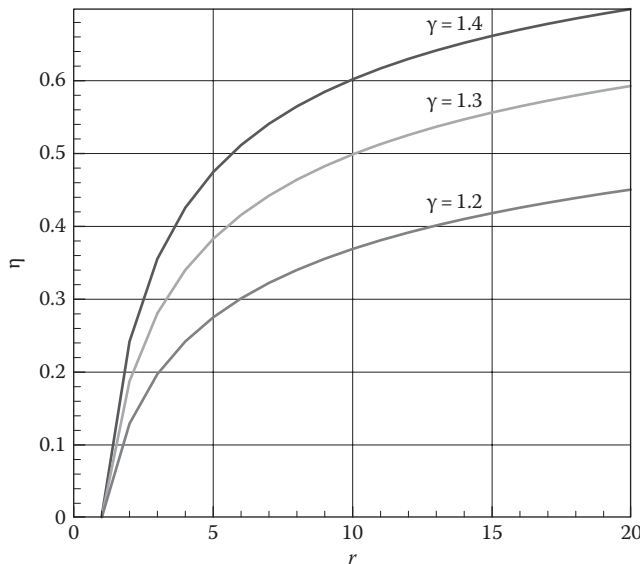


FIGURE 11.8
Efficiency of the ideal Otto cycle.

ratios, where smoke and particulate matter formation become excessive; such a limit is called the engine's "smoke limit." Consequently, CI engines generally operate lean. The combination of high compression ratios and lean fuel–air mixtures are the leading reasons for CI engines typically having higher efficiencies than SI engines. Recent advances, however, in both engine designs are allowing SI engines to operate lean with higher compression ratios (through the use of, for example, gasoline direct injection) and CI engines to operate with higher power densities (through the use of, for example, advanced turbocharging).

The diminishing increase in efficiency with compression ratio results from the decreasing increase in the ratio between maximum and minimum temperatures in the cycle; the same behavior is observed in the ideal heat engine cycle (i.e., the Carnot cycle). Also shown in Figure 11.8 is the behavior with ratios of specific heats. Note that efficiency decreases as the ratio of specific heats decreases. Mixtures with lower ratios of specific heats have less stored energy for any given temperature; thus, a mixture with a lower ratio of specific heats transfers less energy per temperature change than a mixture with a higher ratio of specific heats. In a practical IC engine, adding fuel to air decreases the mixture's ratio of specific heats. Thus, lean mixtures (mixtures with more air than is chemically necessary to react all the fuel) tend to have higher ratios of specific heats than chemically correct (i.e., stoichiometric) mixtures. Therefore, based on fundamental thermodynamics, raising compression ratio and/or leaning the fuel–air mixture tends to raise engine efficiency.

11.3.2 Constant-Pressure Heat Addition—Ideal Diesel Cycle

Another idealization is the air standard Diesel cycle. The Diesel cycle, illustrated by the P – V diagram in Figure 11.9, consists of the following processes: $1 \rightarrow 2$ isentropic compression from the maximum to the minimum cycle volume; $2 \rightarrow 3$ constant-pressure heat addition during an accompanying increase in volume to V_3 ; $3 \rightarrow 4$ isentropic expansion to the maximum cycle volume; and $4 \rightarrow 1$ constant-volume heat rejection. Although this ideal cycle is called the Diesel cycle, it should not be misinterpreted to be the ideal cycle of the Diesel, or CI, engine (just like the Otto cycle should not be misinterpreted to be the ideal cycle of the SI engine). It's best to think of both the Otto and Diesel cycles as

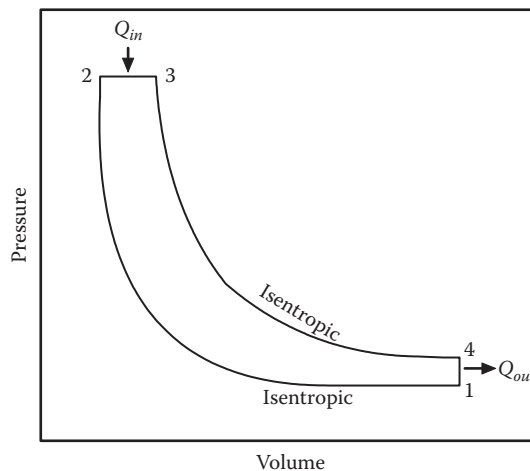


FIGURE 11.9
Schematic pressure–volume diagram of ideal Diesel cycle.

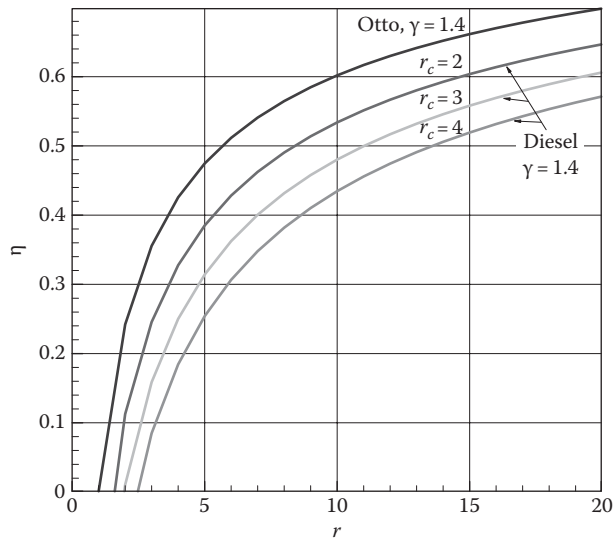


FIGURE 11.10
Efficiency of the ideal Diesel cycle.

two different opportunities to combine different ideal processes (i.e., constant volume heat addition vs. constant pressure heat addition, in considering Otto and Diesel cycles) to provide some guidance on how certain fundamental parameters (e.g., compression ratio, ratios of specific heats, and cut-off ratio) affect an engine's efficiency.

The efficiency of the ideal Diesel cycle is given by

$$\eta = 1 - \frac{1}{r^{\gamma-1}} \left[\frac{r_c^\gamma - 1}{\gamma(r_c - 1)} \right] \quad (11.3)$$

The efficiency of the ideal Diesel cycle depends not only on the compression ratio, r , but also on the **cut-off ratio**, $r_c = V_3/V_2$, the ratio of the volume when heat addition ends to the volume when it begins. Equation 11.3 is shown plotted in Figure 11.10 for several values of r_c and for $\gamma = 1.4$. An r_c value of 1 is equivalent to constant-volume heat addition—i.e., the Otto cycle. This is also shown in Figure 11.10 for $\gamma = 1.4$. The efficiency of the ideal Diesel cycle is less than the efficiency of the ideal Otto cycle for any given compression ratio and any value of the cut-off ratio greater than 1. Both these features (i.e., Diesel cycle efficiency being less than Otto cycle efficiency and the decrease in Diesel cycle efficiency as cut-off ratio increases) result from the decreasing opportunity to expand the added heat energy to work energy. The Otto cycle, because of constant-volume heat addition, utilizes the full expandability of the volume ratios; the Diesel cycle uses decreasing levels of expandability as cut-off ratio increases.

11.4 Actual Cycles

IC engines do not operate on closed thermodynamic cycles, such as the air standard power cycles, but rather on open mechanical cycles; energy supplied to the engine is not done in the form of a heat addition (rather, chemical energy addition via fuel) and this chemical

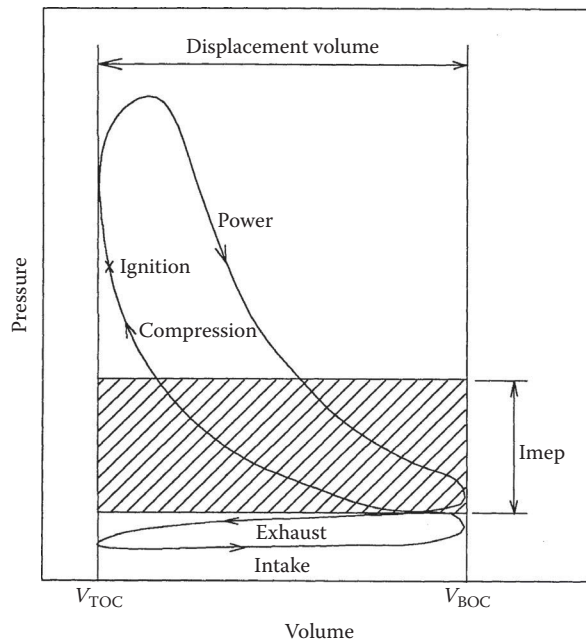


FIGURE 11.11
Schematic indicator diagram.

energy is released neither at constant volume nor at constant pressure. Figure 11.11 is a schematic representation of an **indicator diagram** (pressure–volume history) of a four-stroke IC engine; it could be SI or CI. The pressure changes during the intake and exhaust strokes are exaggerated in the diagram. The **indicated work** performed per cycle can be calculated by taking the integral of PdV for the complete cycle. The **indicated mean effective pressure, imep**, is defined as the ratio of the net indicated work output to the **displacement volume**:

$$\text{imep} = \frac{\text{Indicated work output per cycle}}{\text{Displacement volume}} \quad (11.4)$$

The shaded area in Figure 11.11 thus represents the net indicated work output per cycle. During the intake and exhaust processes of a normally aspirated engine, the negative work performed represents pumping losses and acts to decrease the network output of the engine. The magnitude of the pumping losses depends on the flow characteristics of the intake and exhaust systems, including the valves, ports, manifolds, piping, mufflers, etc. The more restrictive these passages are, the higher the pumping losses will be.

SI engines control power output by throttling the intake air. Thus, under partial-load conditions, the pressure drop resulting from the air throttling represents a significant increase in pumping loss with a corresponding decrease in operating efficiency. SI engines are therefore less efficient at partial-load operation than at full load. The power level of CI engines, on the other hand, is controlled by varying the amount of fuel injected, as opposed to throttling the intake air; this is a third primary reason CI engines are generally more efficient than SI engines.

Brake work (or power) is the actual work (or power) produced at the output shaft of an engine, as measured by a dynamometer. The brake work will be less than the indicated

work due to friction losses and any parasitic power requirements for oil pumps, water pumps, etc. The **brake mean effective pressure, bmep**, is defined as

$$\text{bmep} = \frac{\text{Brake work output per cycle}}{\text{Displacement volume}} \quad (11.5)$$

The mechanical efficiency can then be defined as

$$\eta_m = \frac{\text{Brake work (power)}}{\text{Indicated work (power)}} = \frac{\text{bmep}}{\text{imep}} \quad (11.6)$$

Engine fuel conversion efficiency can be determined from the ratio of power output to rate of fuel energy input, or

$$\eta_{fc} = \frac{\text{Power}}{m_f Q_c} \quad (11.7)$$

where

m_f is the rate of fuel consumption per unit time

Q_c is the heat of combustion per unit mass of fuel

Q_c is commonly estimated with the lower heating value of the fuel, Q_{LHV} . The fuel conversion efficiency in Equation 11.7 could be indicated or brake-specific fuel consumption depending on the nature of the power used in the calculation. Uncertainty associated with variations of energy content of fuels may present a practical difficulty with determining engine efficiency. In lieu of efficiency, **brake-specific fuel consumption (bsfc)** is often used as an efficiency index.

$$\text{bsfc} = \frac{\text{Fuel consumption rate (kg/h)}}{\text{Brake power (kW)}} \quad (11.8)$$

The efficiency of engines operating on the same fuel may be directly compared by their bsfc. Caution is advised, however, when comparing bsfc of engines using different fuels, such as natural gas or biodiesel.

Volumetric efficiency, η_v is an important performance parameter for four-stroke engines defined as

$$\eta_v = \frac{m_{\text{actual}}}{m_d} \quad (11.9)$$

where

m_{actual} is the mass of intake air per cycle

m_d is the ideal mass of air contained in the displacement volume at inlet conditions (pressure and temperature near the inlet port)

For most SI engines, the intake mass includes air and fuel; for CI engines only air is present during intake. Thus, the fuel present in most SI engines' intake mixture causes a decrease in volumetric efficiency. With the intake mixture density determined at inlet conditions, η_v accounts for pressure losses and charge heating associated with the intake

ports, valves, and cylinder. Sometimes, for convenience, the mixture density is taken at ambient conditions. In this case, η_v is called the overall volumetric efficiency and includes the flow performance of the entire intake system.

Because a certain minimum amount of air is required for complete combustion of a given amount of fuel, it follows that the maximum power output of an engine is directly proportional to its air-flow capacity. Therefore, although not affecting the fuel conversion efficiency of the engine in any way, the volumetric efficiency directly affects the maximum power output for a given displacement and thus can affect the efficiency of the overall system in which the engine is installed because of the effect on system size and weight. Volumetric efficiency is affected primarily by intake and exhaust valve geometry; valve lift and timing; intake port and manifold design; mixing of intake charge with residual exhaust gases; engine speed; ratio of inlet pressure to exhaust back pressure; and heat transfer to the intake mixture from warmer flow passages and combustion chamber surfaces. For further information on the fundamentals of IC engine design and operation, see Taylor (1985), Heywood (1988), Stone (1993), and Ferguson and Kirkpatrick (2001).

11.5 Combustion in IC Engines

11.5.1 Combustion in Spark Ignition Engines

Background. In modern fuel-injected SI engines, gasoline is either injected near the intake valve into the cylinder during the intake process in multipoint port injected configurations or later during the compression process directly into the cylinder in gasoline direct injection configurations. In both SI engine configurations in-cylinder fluid motion strongly influences air–fuel mixture preparation, which ultimately governs combustion, performance, and emissions. In SI engines, a near stoichiometric air–fuel mixture is ignited using a spark generated between the electrodes of a spark plug. Large-scale flow structures such as tumble and swirl are generated by intake valve motion and/or geometric orientation of the intake valves with respect to the cylinder. Tumble or barrel swirl is characterized by the bulk air motion along an axis that is perpendicular to the cylinder axis and is more common in SI engines, whereas swirl is ordered air motion about the cylinder axis and is more common in Diesel engines. Due to their longer time and length scales, tumble and swirl are effective storehouses of turbulent kinetic energy. Toward the end of compression stroke, the stored turbulent kinetic energy is released by a phenomenon called the tumble vortex breakdown. As a result, in-cylinder turbulence is increased just prior to ignition and near the spark plug. Turbulence can be imagined to be random fluid motion in three dimensions characterized by the superimposition of vortices or eddies of varying sizes. Viscous shear stresses within these vortices lead to rapid dissipation of energy and decay in turbulence. Although the spark provides the required activation energy to generate the initial flame kernel in the near stoichiometric air–fuel mixture within the spark gap, it is this increased preignition turbulence from the tumble vortex breakdown that ensures the necessary flame propagation of the remainder air–fuel mixture within the cylinder.

Carburetors and fuel injection systems are used for fuel-metering control. Because of the superior control capabilities of fuel injection systems, they are nearly universally used today in production automotive applications. Carburetors are used for applications with less-stringent emission requirements, e.g., small engines for lawn and garden equipment.

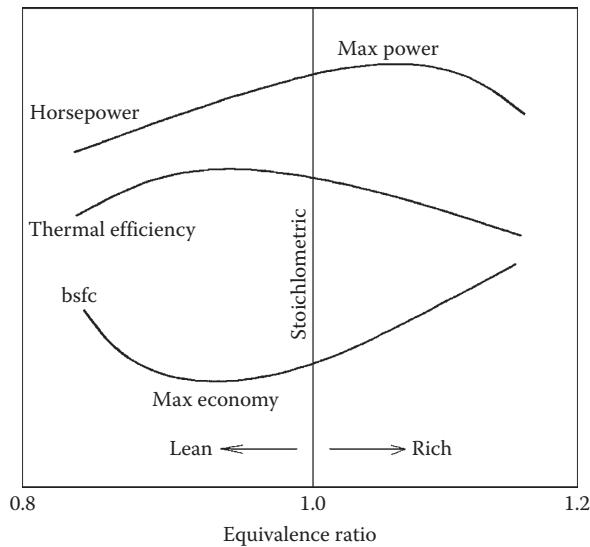


FIGURE 11.12
Effect of fuel–air mixture on indicated performance of an SI engine.

Figure 11.12 illustrates the effect of **fuel–air** ratio on the indicated performance of an SI engine. The **equivalence ratio** (ϕ) is defined by the ratio $\text{fuel–air}_{\text{actual}}/\text{fuel–air}_{\text{stoichiometric}}$. Rich mixtures have fuel–air ratios greater than stoichiometric ($\phi > 1$) and lean mixtures have fuel–air ratios less than stoichiometric ($\phi < 1$). Optimum fuel economy, coinciding with maximum thermal efficiency, is obtained at part throttle with a lean mixture as a result of the fact that the heat release from lean mixtures suffers minimal losses from dissociation and variation of specific heat effects when compared with stoichiometric and rich fuel–air ratios.

Maximum power is obtained at full throttle with a slightly rich mixture—an indication of the full utilization of the air within the cylinders. Idling with a nearly closed throttle requires a rich mixture due to the high percentage of residual exhaust gas that remains in the cylinders. The fuel–air mixture requirement under transient operation, such as acceleration, requires a rich mixture to compensate for the reduced evaporation caused by the sudden opening of the throttle. Cold starting also requires a rich mixture to ensure the vaporization of sufficient amounts of the highly volatile components in the fuel to achieve proper ignition.

11.5.1.1 Normal Combustion Process

The combustion processes in SI engines can be divided into two categories: normal and abnormal. The normal combustion process occurs in three stages: initiation of combustion; flame propagation; and termination of combustion. Combustion normally starts within the spark plug gap when the spark is discharged. The fuel molecules in and around the spark discharge zone are ignited and a small amount of energy is released. The important criterion for the initial reaction to be self-sustaining is that the rate of heat release from the initial combustion be larger than the rate of heat transfer to the surroundings. The factors that play an important role in making the initial reaction self-sustaining, and thereby establishing a flame kernel, are the ignition energy level; the spark plug gap; the fuel–air ratio; the initial turbulence; and the condition of the spark plug electrodes.

After a flame kernel is established, a thin spherical flame front advances from the spark plug region progressively into the unburned mixture zone. Flame propagation is supported and accelerated by two processes. First, the combined effect of the heat transfer from the high-temperature flame region and the migration of active radicals from the flame front into the adjacent unburned zone raise the temperature and accelerate the reactivity of the unburned mixture region directly ahead of the flame front. This helps to condition and prepare this zone for combustion.

Second, the increase in the temperature and pressure of the burned gases behind the flame front will cause it to expand and progressively create thermal compression of the remaining unburned mixture ahead of the flame front. The flame speed will be slow at the start of combustion, then reach a maximum at about half the flame travel, and finally decrease near the end of combustion. Overall, the flame speed is strongly influenced by the level of turbulence in the combustion chamber; the shape of the combustion chamber; the mixture strength; the type of fuel; and the engine speed.

When the flame front approaches the walls of the combustion chamber, the high rate of heat transfer to the walls slows down the flame propagation and, finally, the combustion process terminates close to the walls because of surface quenching. This leaves a thin layer of unburned fuel close to the combustion chamber walls that shows up in the exhaust as unburned hydrocarbons.

11.5.1.2 Abnormal Combustion

Abnormal combustion may occur in SI engines associated with two combustion phenomena: **knock** and **surface ignition**. Knock occurs near the end of the combustion process if the end portion of the unburned mixture, which is progressively subjected to thermal compression and seeding by active radicals, autoignites prematurely before the flame front reaches it. As a result of the sudden energy release, a violent pressure wave propagates back and forth across the combustion chamber, causing the walls or other parts of the engine to vibrate, producing a sharp metallic noise called knock. If knock persists for a period of time, the high rate of heat transfer caused by the traveling high pressure and temperature wave may overheat the spark plug electrode or ignite carbon deposits that may be present in the combustion chamber, causing uncontrolled combustion and surface ignition. As a result, loss of power and serious engine damage may occur.

Knock is sensitive to factors that increase the temperature and pressure of the end portion of the unburned mixture, as well as to fuel composition and other time factors. Factors that increase the probability of knock include: (1) increasing the temperature of the mixture by increasing the charge intake temperature, increasing the compression ratio, or turbo/supercharging; (2) increasing the density of the mixture by turbo/supercharging or increasing the load; (3) advancing the spark timing; (4) increasing the time of exposure of the end portion of the unburned mixture to autoignition conditions by increasing the length of flame travel or decreasing the engine speed and turbulence; and (5) using low-octane fuel and/or maximum power fuel–air ratios.

Other engine design factors that affect knock in SI engines include the shape of the combustion chamber and the location of the spark plug and inlet and exhaust valves relative to the location of the end portion of the unburned mixture. Modern computerized engine management systems that incorporate a knock sensor can automatically retard the ignition timing at the onset of knock, greatly reducing the possibility of engine damage due to knock.

Surface ignition is the ignition of the unburned mixture by any source in the combustion chamber other than the normal spark. Such sources could include overheated exhaust

valves or spark plug electrodes, glowing carbon deposits, or other hot spots. Surface ignition will create secondary flame fronts, which cause high rates of pressure rise resulting in a low-pitched, thudding noise accompanied by engine roughness. Severe surface ignition, especially when it occurs before spark ignition, may cause serious structural and/or component damage to the engine.

11.5.2 Compression Ignition Engine Combustion

Combustion in Diesel engines commences by the autoignition of high-pressure Diesel jets (in excess of 2000 bar) injected from a common rail injection system into high-temperature air toward the end of the compression process. Modern Diesel engines utilize more than one fuel injection event per combustion cycle due to high precision control of fuel injection using solenoid-controlled injectors. Upon injection, the Diesel fuel enters the combustion chamber at very high exit velocities and has an intact liquid length near the exit of the nozzle. At the periphery of this liquid length, the surrounding hot air (from the compression process) is entrained into the jet and a vapor region is formed. This vapor region expands radially and continues to entrain air, and when the temperature and pressure in the cylinder are conducive, the vaporized Diesel fuel autoignites after an ignition delay period, which is defined as the time duration between fuel injection start and start of combustion. Upon autoignition, the jet penetrates further downstream to a spatial location where a stable diffusion flame is anchored. This location is known as the diffusion flame lift-off length (FLOL) and is characterized by the simultaneous sudden radial expansion of the fuel jet and intense OH* chemiluminescence (Dec 1997). Combustion progresses via rich premixed burn near the center of the fuel jet and simultaneous turbulent mixing-controlled burn near the jet periphery (see Figure 11.13). While NO_x emissions form in regions of high temperature near the stoichiometric diffusion flame surrounding the periphery of the jet, soot predominantly forms near the

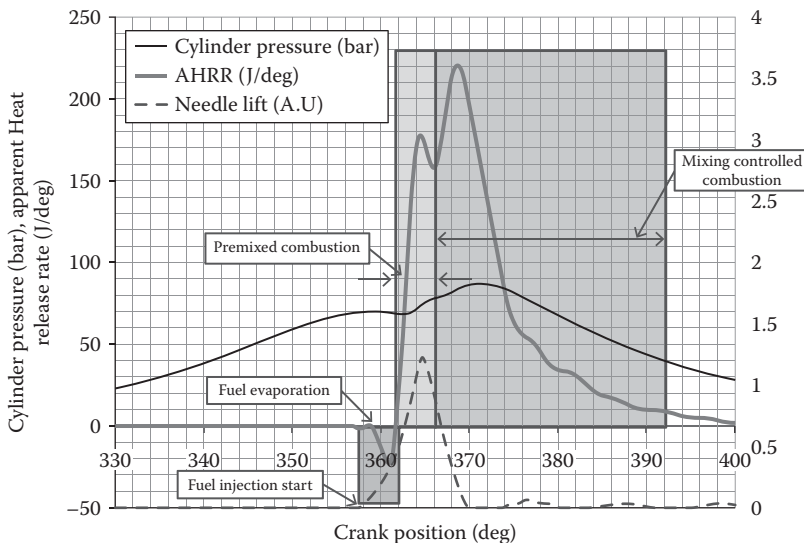


FIGURE 11.13

Cylinder pressure and apparent heat release rate schedules from Diesel combustion in a 1.875 liter single cylinder Diesel engine with geometric compression ratio 17:1 operated at a speed of 1500 rev/min and a load of 5 bar b.m.e.p.

center of the jet where the air entrainment rates upstream of the FLoL govern local equivalence ratios. Typical strategies to control oxides of nitrogen (NO_x) emissions include the use of exhaust gas recirculation (EGR) and retarding the Diesel fuel injection timing closer to the top dead center (TDC). The use of EGR to reduce NO_x results in reduced air availability near the center of the Diesel jet upstream of the FLoL, which simultaneously results in increased soot emissions, thereby leading to the familiar smoke– NO_x trade-off in Diesel engines.

The ignition delay period plays a key role in controlling the time duration of the two modes of combustion. Prolonging the ignition delay, through engine design factors or variations in operating conditions, will generate a larger portion of premixed fuel–air mixture and thus tend to increase the premixed combustion mode duration and decrease the diffusion mode duration. This may lead to higher peak cylinder pressure and temperature; this may improve thermal efficiency and reduce CO and **unburned hydrocarbon (UHC)** emissions at the expense of increased emissions of oxides of nitrogen (NO_x).

Large increases in the ignition delay period will cause high rates of pressure rise during premixed combustion and may lead to objectionable Diesel knock. Reducing the ignition delay period causes the premixed combustion duration to decrease while increasing the diffusion combustion duration. A large reduction in ignition delay may lead to loss of power, decrease in thermal efficiency, and possible deterioration of exhaust emissions. Several factors related to the fuel–air mixture temperature and density, engine speed, combustion chamber turbulence, injection pressure, rate of injection, and fuel composition influence the duration of the ignition delay period.

11.5.2.1 Knock in CI Engines

Because the combustion process in CI engines is triggered by autoignition of the fuel injected during the ignition delay period, factors that prolong the ignition delay period will increase the premixed combustion duration, causing very high rates of energy release and thus high rates of pressure rise. As a result, Diesel knock may occur. The phenomenon is similar to knock in SI engines except that it occurs at the beginning of the combustion process rather than near the end, as observed in SI combustion. Factors that reduce the ignition delay period will reduce the possibility of knock in Diesel engines. Among them are increasing the compression ratio; supercharging; increasing combustion chamber turbulence; increasing injection pressure; and using high-**cetane-number (CN)** fuel. For a more detailed discussion of the combustion process in IC engines, see Henein (1972), Lenz (1992), and Keating (1993).

11.6 Exhaust Emissions

11.6.1 Harmful Constituents

The products of combustion from IC engines contain several constituents that are considered hazardous to human health, including CO, UHCs NO_x , and **particulates** (from Diesel engines). These emission products are discussed briefly next, followed by a description of the principal schemes for their reduction.

11.6.1.1 Carbon Monoxide

CO is a colorless, odorless, and tasteless gas that is highly toxic to humans. Breathing air with a small volumetric concentration (0.3%) of CO in an enclosed space can cause death in a

short period of time. CO results from the incomplete combustion of hydrocarbon fuels. One of the main sources of CO production in SI engines is the incomplete combustion of the rich fuel mixture that is present during idling and maximum power steady-state conditions and during such transient conditions as cold starting, warm-up, and acceleration. Fuel maldistribution, poor condition of the ignition system, and slow CO reaction kinetics also contribute to increased CO production in SI engines. CO production is not as significant in CI engines because these engines are always operated with significant excess air.

11.6.1.2 Unburned Hydrocarbons

When UHCs combine with NO_x (see following) in the presence of sunlight, ozone and photochemical oxidants form that can adversely affect human health. Certain UHCs are also considered to be carcinogenic. The principal cause of UHC in SI engines is incomplete combustion of the fuel–air charge, resulting in part from flame quenching of the combustion process at the combustion chamber walls and engine misfiring. Additional sources in four-stroke engines may include fuel mixture trapped in crevices of the top ring land of the piston and outgassed fuel during the expansion (power) stroke that was absorbed into the lubricating oil film during intake. In two-stroke SI engines, the scavenging process often results in a portion of the fresh mixture exiting the exhaust port before it closes, resulting in high UHC emissions.

The presence of UHC in CI engines is related to the heterogeneous nature of the fuel–air mixture. Under certain conditions, fuel–air mixtures that lie outside the flammability limits at the lean and rich extremes can exist in portions of the combustion chamber and escape combustion, thus contributing significantly to UHC in the exhaust. Fuel injected near the end of the combustion process and fuel remaining in the nozzle **sac volume** at the end of injection contribute to UHC emission in CI engines. Engine variables that affect UHC emissions include the fuel–air ratio; intake air temperature; and cooling water temperature.

11.6.1.3 Oxides of Nitrogen

Nitric oxide (NO) is formed from the combination of nitrogen and oxygen present in the intake air under the high-temperature conditions that result from the combustion process. As the gas temperature drops during the expansion stroke, the reaction is frozen, and levels of NO persist in the exhaust products far in excess of the equilibrium level at the exhaust temperature. In the presence of additional oxygen in the air, some NO transforms to nitrogen dioxide (NO_2), a toxic gas.

The combined NO and NO_2 are referred to as oxides of nitrogen or NO_x . The production of NO_x is in general aggravated by conditions that increase the peak combustion temperature. In SI engines, the most important variables that affect NO_x production are the air/fuel ratio; spark timing; intake air temperature; and amount of residual combustion products remaining in the cylinder after exhaust. In modern CI engines, NO_x is formed in the high-temperature anchored diffusion flame surrounding the Diesel jet periphery late during the mixing-controlled combustion phase and also in the surrounding postcombustion gases, where despite lower (than diffusion flame) temperatures, there is sufficient residence time for the thermal NO generation reactions to form NO_x emissions (Dec 1997).

11.6.1.4 Particulates

Particulates are a troublesome constituent in the exhaust from CI engines. They are defined by the U.S. Environmental Protection Agency (EPA) as any exhaust substance

(other than water) that can be trapped on a filter at temperatures of 325 K or below. Particulates trapped on a filter may be classified as soot plus an organic fraction of hydrocarbons and their partial oxidation products. Soot consists of agglomerates of solid uncombusted carbon particles. Particulates are of concern because their small size permits inhalation and entrapment in the lung walls, making them potential lung carcinogens.

Soot is formed in CI engines under conditions of heavy load when the gas temperature is high and the concentration of oxygen is low. Smoke production is affected by such parameters as fuel CN; rate of fuel injection; inlet air temperature; and the presence of secondary injection.

11.6.2 Control of Emissions from IC Engines

Figure 11.14 depicts the relative concentrations of CO, NO_x, and UHC in the exhaust products of an SI engine as a function of the fuel–air mixture. Lean mixture combustion, which promotes good thermal efficiency, also results in low UHC and CO production but causes high levels of NO_x emission. Increasing the fuel/air ratio to reduce NO_x results in increased CO and UHC emission. Approaches to reduce total emissions fall under two categories: (1) engine design and fuel modifications; and (2) treatment of exhaust gases after they leave the engine.

In SI engines, the first approach focuses on addressing engine variables and design modifications, which improve in-cylinder mixing and combustion in an effort to reduce CO and UHC emissions. To reduce NO_x, attention is focused on factors that reduce peak combustion temperature and reduce the oxygen available in the flame front. Design and operating parameters implemented or modified for decreased emissions include compression ratio reduction, increased coolant temperature, modification of the combustion chamber shape to minimize surface-to-volume ratio and increase turbulence, improvement of intake manifold design for better charge distribution, use of fuel injection instead of carburetors for better mixture control, use of exhaust gas recirculation to reduce NO_x

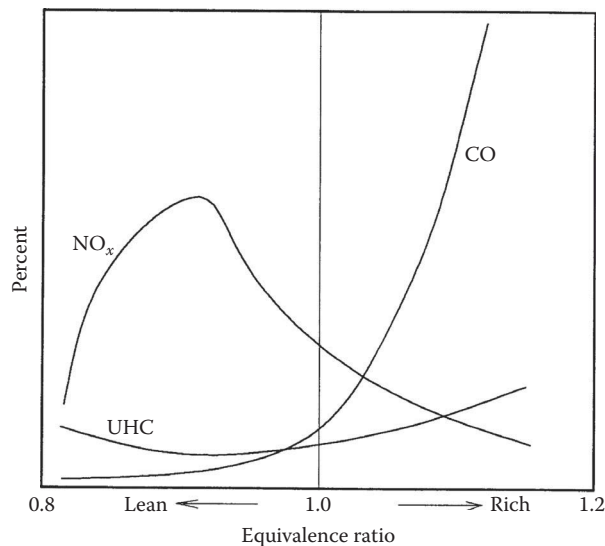


FIGURE 11.14
Emission levels from an SI engine vs. fuel–air mixture.

by lowering combustion temperatures, positive crankcase ventilation to reduce UHC, and increased aromatic content in gasoline.

Engine modifications that have been implemented to reduce emissions from CI engines include modifications to the combustion chamber shape to match the air swirl pattern and fuel spray pattern for better mixing and complete combustion; use of exhaust gas recirculation to limit NO_x production; use of higher injection pressure for better atomization to reduce soot and UHC; and the use of precise injection timing with electronic control.

In the second approach, several devices have been developed for after treatment of exhaust products. A thermal reactor may be used to oxidize UHC and CO. These typically consist of a well-insulated volume placed close to the exhaust manifold, with internal baffles to increase the gas residence time and an air pump to supply fresh oxygen for the oxidation reactions. Thermal reactors are ineffective for NO_x reduction and thus have limited application.

Catalytic converters utilize a catalyst, typically a noble metal such as platinum, rhodium, or palladium, deposited on a ceramic substrate to promote reactions at lower temperatures. Two types are in use: oxidation converters and reduction converters. Oxidation catalytic converters use the excess air available in lean mixtures (or supplied from an external air pump) to oxidize CO and UHC emissions. Reduction catalytic converters operate with low levels of oxygen to cause reduction of NO_x . Sometimes, dual catalytic converters are employed to treat all three pollutants with a reducing converter, to reduce NO_x , placed upstream of an oxidation converter for treating CO and UHC. This arrangement requires that the engine be operated with a rich mixture, which decreases fuel economy.

Three-way catalytic converters are a recent development that permits treatment of NO_x , CO, and UHC in a single device, thus reducing size and weight of the exhaust system. Proper operation of a three-way catalyst requires very nearly stoichiometric combustion. If the combustion is too lean, NO_x is not adequately reduced, and if it is too rich, UHC and CO are not adequately oxidized. Within a narrow band for equivalence ratio (from about 0.999 to 1.007), conversion efficiency is 80% or better for all three pollutants (Kummer 1980). Maintaining engine operation within this narrow mixture band requires a closed-loop fuel-metering system that utilizes an oxygen sensor placed in the exhaust system to monitor excess oxygen and control the fuel injection to maintain near stoichiometric combustion.

Diesel engines suffer from the familiar soot- NO_x trade-off; therefore, most modern engines operate with both particulate traps and urea-selective catalytic reduction (SCR) systems to reduce engine-out soot and NO_x emissions. Particulates emitted by Diesel engines are typically in the micron (10 μm) size range and are composed of carbon, ash, and volatile hydrocarbons. Particulate traps are essentially porous ceramic filters made of silicon carbide (typically). Exhaust flows through these walls and the soot particles diffuse through to the wall surface and adhere. As a consequence, the particulate filters have to be periodically regenerated. Selective catalytic reduction (NH_3 SCR) uses ammonia to reduce nitrogen oxides to nitrogen and water. Typically, a urea solution is injected into the exhaust stream where ammonia is generated from catalytic hydrolysis of urea solution. This ammonia reacts with NO/NO_2 in the SCR catalytic converter and reduces NO_x emissions to nitrogen and water. It is interesting to note that the reason urea is chosen is primarily due to the fact that it is environmentally stable and is already mass produced as fertilizer and has an excellent freezing point (about -11°C) (*Bosch Automotive Handbook*, 6th edn., 2007, SAE Publication). While SCR is the best available solution to deal with NO_x emissions in Diesel engines, it also poses the danger of "ammonia slip," that is, the leakage of ammonia. This potential leakage of ammonia is prevented by using another oxidizing catalyst downstream of the SCR to oxidize any leaked ammonia to nitrogen and water, thereby ensuring environmental safety.

11.7 Fuels for SI and CI Engines

11.7.1 Background

The primary distinguishing factor between SI and CI engines is the fundamental difference in the combustion process. SI engines rely on homogeneous, spark-ignited, premixed combustion, while CI engines are designed for heterogeneous combustion with an autoignited premixed combustion period followed by a diffusion combustion period. The differences in the combustion process call for quite different qualities in the fuels to achieve optimum performance.

By far the most common fuel for SI engines is gasoline, although other fuels can be used in special circumstances, including alcohol, natural gas, and propane. Even such low-grade fuels as wood gas and coal gas have been used to fuel SI engines during wartime when conventional fuels were in short supply. Diesel fuel is the predominant fuel for CI engines, but they too can be designed to operate on a variety of other fuels, such as natural gas, bio-gas, and even coal slurries. This discussion is confined to gasoline and Diesel fuel, both of which are distilled from crude oil.

Crude oil is composed of several thousand different hydrocarbon compounds that, upon heating, are vaporized at different temperatures. In the distillation process, different “fractions” of the original crude are separated according to the temperatures at which they vaporize. The more volatile fraction, naphtha, is followed in order of increasing temperature of vaporization by fractions called distillate, gas oil, reduced crude, and residual oil. These fractions may be further subdivided into light, middle, and heavy classifications. Light virgin naphtha can be used directly as gasoline, although it has relatively poor anti-knock quality. The heavier fractions can be chemically processed through coking and catalytic cracking to produce additional gasoline. Diesel fuel is derived from the light to heavy virgin gas oil fraction and from further chemical processing of reduced crude.

11.7.2 Gasoline

Gasoline fuels are mixtures of hydrocarbon compounds with boiling points in the range of 32°C–215°C. The two most important properties of gasoline for SI engine performance are volatility and octane rating. Adequate volatility is required to ensure complete vaporization, as required for homogeneous combustion, and to avoid cold-start problems. If the volatility is too high, however, vapor locking in the fuel delivery system may become a problem. Volatility may be specified by the distillation curve (the distillation temperatures at which various percentages of the original sample have evaporated). Higher volatility fuels will be characterized by lower temperatures for given fixed percentages of evaporated sample or, conversely, by higher percentages evaporated at or below a given temperature. Producers generally vary the volatility of gasoline to suit the season, increasing the volatility in winter to improve cold-start characteristics and decreasing it in summer to reduce vapor locking.

The octane rating of a fuel is a measure of its resistance to autoignition or knocking; higher octane fuels are less prone to autoignition. The octane rating system assigns the value of 100 to iso-octane (C_8H_{18} , a fuel that is highly resistant to knock) and the value 0 to *n*-heptane (C_7H_{16} , a fuel that is prone to knock). Two standardized methods are employed to determine the octane rating of fuel test samples: the research method and the motor method; see ASTM Standards Part 47—Test Methods for Rating Motor, Diesel and Aviation Fuels (ASTM 1995).

Both methods involve testing the fuel in a special variable compression-ratio engine (cooperative fuels research or CFR engine). The test engine is operated on the fuel sample and the compression ratio is gradually increased to obtain a standard knock intensity reading from a knock meter. The octane rating is obtained from the volumetric percentage of iso-octane in a blend of iso-octane and *n*-heptane that produces the same knock intensity at the same compression ratio.

The principal differences between the research method and the motor method are the higher operating speed, higher mixture temperature, and greater spark advance employed in the motor method. Ratings obtained by the research method are referred to as the **research octane number (RON)**; those obtained with the motor method are called the motor octane number (MON). MON ratings are lower than RON ratings because of the more stringent conditions, that is, higher thermal loading of the fuel. The octane rating commonly advertised on gasoline pumps is the **antiknock index**, $(R + M)/2$, which is the average of the values obtained by the two methods. The typical range of antiknock index for automotive gasolines currently available at the pump is 87–93. In general, higher compression SI engines require higher octane fuels to avoid autoignition and to realize full engine performance potential from engines equipped with electronic control systems incorporating a knock sensor.

Straight-run gasoline (naphtha) has a poor octane rating on the order of 40–50 RON. Higher octane fuels are created at the refinery by blending with higher octane components produced through alkylation wherein light olefin gases are reacted with isobutane in the presence of a catalyst. Iso-octane, for example, is formed by reacting isobutane with butene. Aromatics with double carbon bonds shared between more than one ring, such as naphthalene and anthracene, serve to increase octane rating because the molecules are particularly difficult to break.

Additives are also used to increase octane ratings. In the past, a common octane booster added to automotive fuels was lead alkyls—tetraethyl or tetramethyl lead. For environmental reasons, lead has been removed from automotive fuels in most countries. It is, however, still used in aviation fuel. Low-lead fuel has a concentration of about 0.5 g/L, which boosts octane rating by about five points. The use of leaded fuel in an engine equipped with a catalytic converter to reduce exhaust emissions will rapidly deactivate the catalyst (typically a noble metal such as platinum or rhodium), quickly destroying the utility of the catalytic converter. Octane-boosting additives in current use include the oxygenators methanol, ethanol, and methyl tertiary butyl ether (MTBE).

RON values of special-purpose, high-octane fuels for racing and aviation purposes can exceed 100 and are arrived at through an extrapolation procedure based on the knock-limited indicated mean effective pressure (klimep). The klimep is determined by increasing the engine intake pressure until knock occurs. The ratio of the klimep of the test fuel to that for iso-octane is used to extrapolate the octane rating above 100.

11.7.3 Diesel Fuels

Diesel fuels are blends of hydrocarbon compounds with boiling points in the range of 180°C–360°C. Properties of primary importance for CI fuels include the density, viscosity, cloud point, and ignition quality (CN). Diesel fuel exhibits a much wider range of variation in properties than does gasoline. The density of Diesel fuels tends to vary according to the percentages of various fractions used in the blend. Fractions with higher distillation temperatures tend to increase the density. Variations in density result in variations in volumetric energy content and thus fuel economy, because fuel is sold by volume measure. Higher density fuel will also result in increased soot emission.

Viscosity is important to proper fuel pump lubrication. Low-viscosity fuel will tend to cause premature wear in injection pumps. Too high viscosity, on the other hand, may create flow problems in the fuel delivery system. Cloud point is the temperature at which a cloud of wax crystals begins to form in the fuel. This property is critical for cold-temperature operation because wax crystals will clog the filtration system. ASTM does not specify maximum cloud point temperatures, but rather recommends that cloud points be no more than 6°C above the 10th percentile minimum ambient temperature for the region for which the fuel is intended; see ASTM D 975 (ASTM 1995).

CN provides a measure of the autoignition quality of the fuel and is the most important property for CI engine fuels. The CN of a fuel sample is obtained through the use of a CI CFR engine in a manner analogous to the determination of octane rating. The test method for CN determination is specified in standard ASTM D 613. *n*-Cetane (same as hexadecane, C₁₆H₃₄) has good autoignition characteristics and is assigned the cetane value of 100. The bottom of the cetane scale was originally defined in terms of α -methyl naphthalene (C₁₁H₁₀), which has poor autoignition characteristics and was assigned the value 0. In 1962, for reasons of availability and storability, the poor ignition quality standard fuel used to establish the low end of the cetane scale was changed to heptamethylnonane (HMN), with an assigned CN of 15. The CN of a fuel sample is determined from the relative volumetric percentages of cetane and HMN in a mixture that exhibits the same ignition delay characteristics as the test sample using the relation

$$\text{CN} = \%n\text{-cetane} + 0.15(\%\text{HMN}) \quad (11.10)$$

ASTM standard D 976 (ASTM 1995) provides the following empirical correlation for calculating the **cetane index** of straight petroleum distillate fuels (no additives) as an approximation to the measured CN:

$$\text{Cetane index} = 454.74 - 1641.416D + 774.74D^2 - 0.554B + 97.803(\log B)^2 \quad (11.11)$$

where

D is the density at 15°C (g/mL)

B is the mid-boiling temperature (°C)

ASTM standard D 975 (ASTM 1995) establishes three classification grades for Diesel fuels (No. 1-D, No. 2-D, and No. 4-D) and specifies minimum property standards for these grades. No. 1-D is a volatile distillate fuel for engines that must operate with frequent changes in speed and load. No. 2-D is a lower volatility distillate fuel for industrial and heavy mobile service engines. No. 4-D is a heavy fuel oil for low- and medium-speed engines. Nos. 1-D and 2-D are principally transportation fuels, while No. 4-D is for stationary applications. The ASTM minimum CN for No. 1-D and No. 2-D is 40, and for No. 4-D the minimum is 30. Typical CNs for transportation fuels lie in the range of 40–55. Use of a low-cetane fuel aggravates Diesel knock because of the longer ignition delay period, which creates a higher fraction of premixed combustion.

Antiknock quality (octane number) and ignition quality (CN) are opposing properties of distillate fuels. The CN increases with decreasing octane rating of various fuels. Gasoline, with good antiknock quality, has a CN of approximately 10, while a Diesel fuel with a CN of 50 will have an octane number of about 20. Thus, gasoline is not a suitable fuel for CI engines because of its poor autoignition quality, and Diesel fuel is inappropriate for use in SI engines as a result of its poor antiknock quality. For additional information on fuels for IC engines see the SAE (1993a,b) and Owen and Coley (1995).

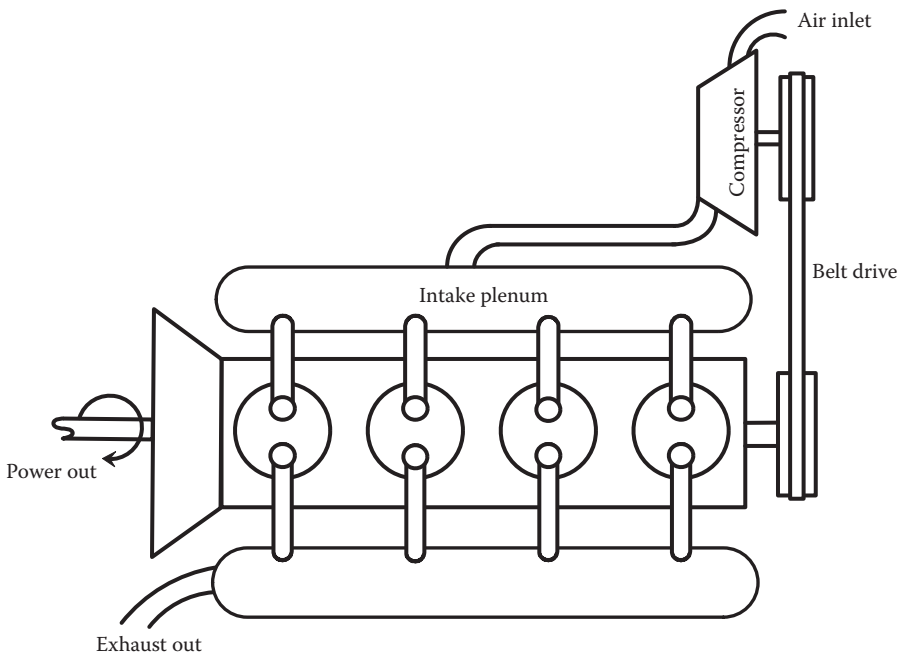


FIGURE 11.16
Schematic diagram of supercharged engine.

to improve the scavenging process in two-stroke direct-injection engines. Figure 11.16 is a schematic of an engine with a mechanically driven supercharger. Superchargers may be belt, chain, or gear driven from the engine crankshaft.

Two types of superchargers are in use: the positive displacement type (Roots blower) and the centrifugal type. Roots blowers may be classified as: (1) straight double lobe; (2) straight triple lobe; and (3) helix triple lobe (twisted 60%). The helix triple-lobe type runs more quietly than the others and is generally recommended, especially for Diesel engines operating under high torque at various speed conditions. Because of its high capacity and small weight and size, the centrifugal type is best suited for applications in which power and volumetric efficiency improvement are required at high engine speed, e.g., with aircraft engines. A centrifugal blower will also survive a backfire more readily than a Roots blower in SI applications. Because superchargers are directly driven from the engine output shaft, no inherent lag in the rate of pressure increase with engine speed is present, as is typically the case with turbochargers.

11.8.3 Turbocharging

Turbochargers utilize a centrifugal compressor directly connected to a turbine that extracts energy from the exhaust gases of the engine and converts it to the shaft work necessary to drive the compressor. Turbocharging is widely used to increase power output in automotive and truck applications of four-stroke SI and CI engines and to improve scavenging of two-stroke CI engines.

There are three methods of turbocharging: the constant pressure; the pulse; and the pulse converter. In the constant-pressure method, as illustrated in Figure 11.17, the exhaust pressure is maintained at a nearly constant level above atmospheric. To accomplish this,

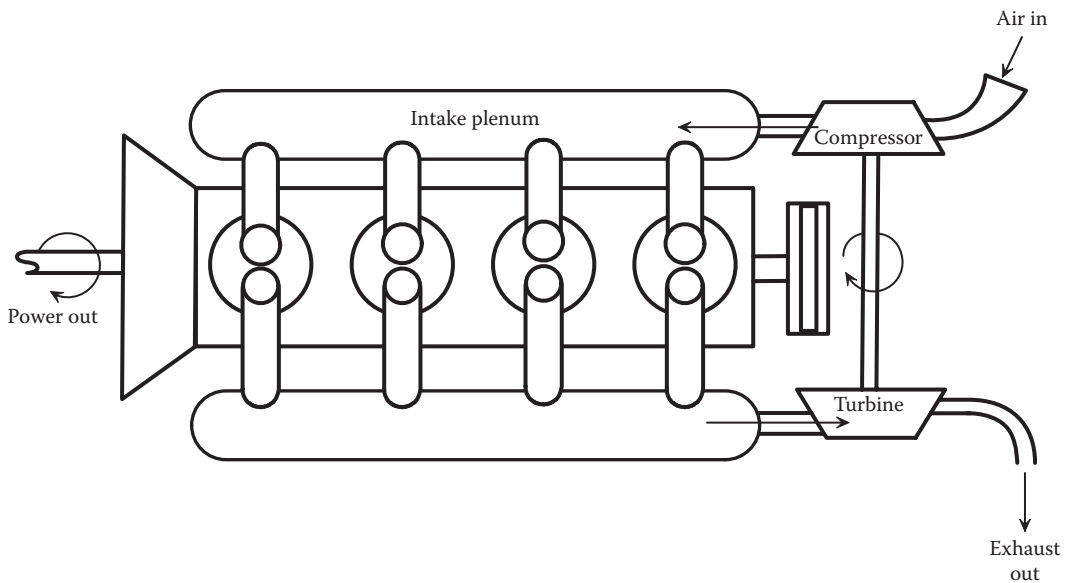


FIGURE 11.17
Schematic diagram of a constant-pressure turbocharger.

the exhaust manifold must be large enough to damp out the pressure fluctuations caused by the unsteady flow characteristic of the engine exhaust process. In this method, the turbine operates efficiently under steady-flow conditions; however, some engine power is lost because of the increased backpressure in the exhaust manifold.

The pulse turbocharger, as illustrated in Figure 11.18, utilizes the kinetic energy generated by the exhaust blow-down process in each cylinder. This is accomplished by using small exhaust lines grouped together in a common manifold to receive the exhaust from the cylinders, which are blowing down sequentially. In this method, the pressure at the turbine inlet tends to fluctuate; this is not conducive to good turbine efficiency. This is offset to a large degree, however, by improved engine performance as a result of the lower exhaust backpressure relative to the constant-pressure method. The pulse converter method represents a compromise between the previous two techniques. In principle, this is accomplished by converting the kinetic energy in the blow-down process into a pressure rise at the turbine by utilizing one or more diffusers. Details of the different methods of turbocharging may be found in Watson and Janota (1982).

Recent advances in turbocharging technology have focused mainly on (1) improving turbine transient response (turbo-lag); (2) improving torque-speed characteristics of the engine; and (3) increasing the power output by increasing the boost pressure and using charge cooling (intercooling). The use of ceramic materials in fabricating turbine rotors improves the turbine transient response because they are lighter in weight and have less rotational inertia. Ceramic rotors also have greater thermal operating range because of their lower thermal expansion. The use of variable-geometry turbochargers can improve the low-speed torque characteristics of the engine and help reduce the transient response time. This is due to the ability of the variable-geometry turbocharger to change its internal geometry to accommodate low flow rates at low engine speeds and higher volume flow rates at high engine speeds.

However, because the geometry of the turbine rotor remains unchanged while the internal geometry varies, the turbine efficiency will be reduced for all internal geometries other than

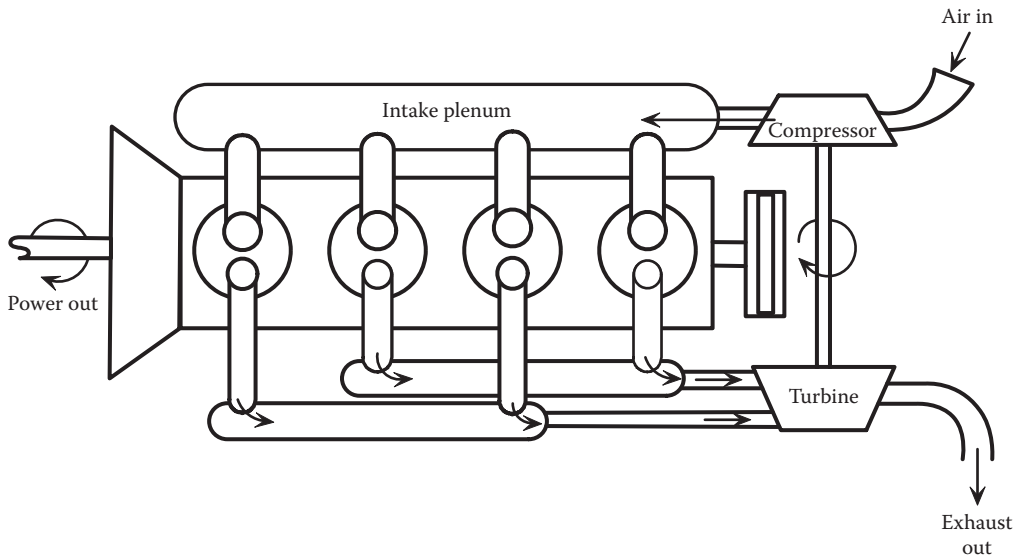


FIGURE 11.18
Schematic diagram of a pulse turbocharger.

the optimum design geometry. In response to increased demand for Diesel engines with high boost pressure and with size constraints, advances in the aerothermodynamics of axial/radial flow and of two-stage turbochargers, as well as in the design of compressor and turbine blades, have allowed high boost pressure at improved overall turbocharger efficiency.

Charge cooling by means of a heat exchanger (intercooler) between the compressor and the intake ports is effective in reducing NO_x emissions and improving the power output of turbocharged Diesel engines and in reducing the probability of knock in SI engines. Two types of charge cooling are in use: air–air and air–water. Air-to-water cooling is used in marine applications, in which a source of cool water is available; air-to-air intercoolers are used for automotive and truck applications.

11.8.4 Exhaust Waste Energy Recovery

Considerable effort has been expended to improve internal combustion engines (ICEs) since they have become a leading powertrain choice, and as a consequence, peak brake thermal efficiencies of on-road spark ignition and compression ignition powertrains have approached 30% and 40%, respectively. However, anywhere between 60% and 70% of the energy contained in the fuel used in conventional ICEs is wasted, mainly through exhaust and engine cooling. Therefore, it is imperative to harness the energy in the exhaust stream of IC engines to further increase the fuel economy of ICEs.

Waste energy recovery (WER) typically describes the use of a bottoming cycle, such as a Rankine cycle, to increase overall fuel conversion efficiency (FCE) and engine power where a secondary working fluid is heated by a portion of otherwise discarded exhaust enthalpy. Due to its simplicity over other additional cycles, the organic Rankine cycle (ORC) is the most common indirect WER system to be coupled with ICEs. Waste energy recovery using Rankine bottoming cycles involves the utilization of the sensible enthalpy of the hot exhaust from the IC engine to heat a suitable fluid, preferably to saturated/superheated vapor, and then the sensible enthalpy of the vapor is used to obtain useful

work from a turbine. Examples of practical Rankine bottoming cycles in the automotive and power industry can be found in these references (Leising et al., 1978; Brands et al. 1981; DiBella et al. 1983; Teng 2006; Ringler et al. 2009).

The efficiency of the Rankine cycle depends on the choice of the working fluid. As shown in Figures 11.19 through 11.21, Rankine cycle working fluids can be classified as

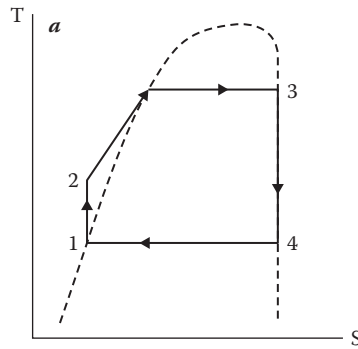


FIGURE 11.19

Isentropic fluid is characterized by a near “infinite” slope of the saturation vapor curve on a T - s diagram.

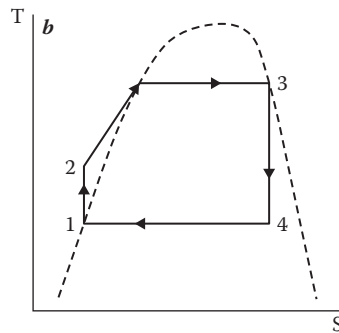


FIGURE 11.20

A wet fluid is characterized by a “negative” slope of the saturation vapor curve on a T - s diagram.

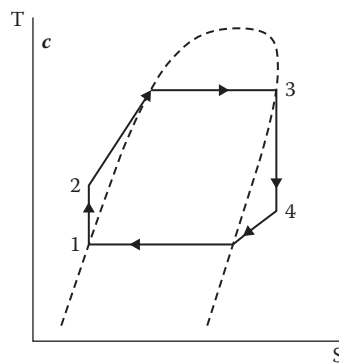


FIGURE 11.21

A dry fluid is characterized by a “positive” slope of the saturation vapor curve on a T - s diagram.

isentropic, wet, and dry, depending on the slope of the saturated vapor line on a T - s diagram. A classical example of a wet fluid is water; however, some problems associated with wet fluids include the need for superheating and, more practically, potential pitting and corrosion in the expansion turbine blades in the energy recovery turbine. Therefore, there is widespread preference for dry (e.g., isopentane) or isentropic (R11) fluids. The choice of the optimum ORC fluid depends on the thermodynamic cycle and the type of expander being used for energy recovery, and this means there is no silver bullet, but an appropriate choice of working fluid can be made by simultaneous optimization of both the expander and the working fluid for a given WER cycle.

Defining Terms

Antiknock index: The average of the two octane numbers obtained by the research method and the motor method.

Autoignition: The ability of a fuel–air mixture to ignite spontaneously under conditions of high temperature and pressure.

Bottom dead center (BDC): Piston located at its lowest position in the cylinder. Cylinder volume is maximum at BDC.

Brake mean effective pressure (bmep): Ratio of brake work output per cycle to the displacement volume.

Brake specific fuel consumption (bsfc): The ratio of fuel consumption rate in kilograms per hour to the engine output in kilowatts.

Brake work: Work produced at the output shaft of an IC engine as measured by a dynamometer.

Cetane index: An approximation to the measured cetane number determined from an empirical relationship specified in ASTM D 976.

Cetane number: A measure of the autoignition quality of a fuel important for proper performance of CI engines determined experimentally through use of a CI CFR test engine.

Clearance volume: Combustion chamber volume remaining above the piston at TDC.

Compression ignition (CI) engine: Air alone is compressed in the cylinder and fuel is injected near TDC. Combustion results from autoignition of the fuel–air mixture due to the high temperature of the air.

Compression ratio: The ratio of the cylinder volume at BDC to the volume at TDC.

Cut-off ratio: Ratio of cylinder volume at the end of heat addition to the volume at the start of heat addition in the ideal Diesel cycle.

Cylinder volume: Volume above piston at BDC; equals displacement volume plus clearance volume.

Direct injection (DI): Method of fuel injection in low- and medium-speed CI engines wherein fuel is injected into the main combustion chamber formed by a bowl in the top of the piston.

Displacement volume: Difference in cylinder volume between TDC and BDC.

Equivalence ratio: Actual fuel–air ratio divided by stoichiometric fuel–air ratio.

Four-stroke engine: Entire cycle completed in two revolutions of the crankshaft and four strokes of the piston.

Fuel–air ratio: Ratio of mass of fuel to mass of air in the cylinder prior to combustion.

Glow plug: Electric heater installed in prechamber of an IDI Diesel engine to aid cold starting.

Heterogeneous combustion: Refers to the mixture of liquid fuel droplets and evaporated fuel vapor and air mixture present in CI engine combustion chambers prior to ignition.

Ignition delay period: Period between start of injection and onset of autoignition in a CI engine.

Indicated mean effective pressure (imep): Ratio of net indicated work output of an IC engine to the displacement volume.

Indicated work: Work output of an IC engine cycle determined by an area calculation from an indicator diagram.

Indicator diagram: Pressure–volume trace for an IC engine cycle; area enclosed by diagram represents work.

Indirect injection (IDI): Method of fuel injection used in high-speed CI engines wherein the fuel is injected into a precombustion chamber to promote fuel–air mixing and reduce ignition delay.

Knock: In SI engines: the noise that accompanies autoignition of the end portion of the uncombusted mixture prior to the arrival of the flame front. In CI engines: The noise that accompanies autoignition of large premixed fractions generated during prolonged ignition delay periods. Knock is detrimental to either type of engine.

NO_x: Harmful oxides of nitrogen (NO and NO₂) appearing in the exhaust products of IC engines.

Octane number: Antiknock rating for fuels important for prevention of autoignition in SI engines.

Particulates: Any exhaust substance, other than water, that can be collected on a filter. Harmful exhaust product from CI engines.

Power density: Power produced per unit of engine mass.

Premixed homogeneous combustion: Fuel and air are mixed in an appropriate combustible ratio prior to ignition process. This is the combustion mode for SI engines and for the initial combustion phase in CI engines.

Sac volume: Volume of nozzles below the needle of a Diesel fuel injector that provides a source of UHC emissions in CI engines.

Scavenging: The process of expelling exhaust gases and filling the cylinder with fresh charge in two-stroke engines. This is often accomplished in SI engines by pressurizing the fresh mixture in the crankcase volume beneath the piston and in CI engines by using a supercharger or turbocharger.

Spark ignition (SI) engine: Homogeneous charge of air–fuel mixture is compressed and ignited by a spark.

Stroke: Length of piston movement from TDC to BDC; equal to twice the crankshaft throw.

Supercharging: Pressurizing the intake of an IC engine using a compressor that is mechanically driven from the crankshaft.

Surface ignition: A source of autoignition in SI engines caused by surface hot spots.

Swirl: Circular in-cylinder air motion designed into CI engines to promote fuel-air mixing.

Swirl ratio: Ratio of rotational speed of in-cylinder air (rpm) to engine speed (rpm).

Top dead center (TDC): Piston located at its uppermost position in the cylinder. Cylinder volume (above the piston) is minimum at TDC.

Turbocharging: Pressurizing the intake of an IC engine with a compressor driven by a turbine that extracts energy from the exhaust gas stream.

Two-stroke engine: Entire cycle completed in one revolution of the crankshaft and two strokes of the piston.

Unburned hydrocarbons (UHC): Harmful emission product from IC engines consisting of hydrocarbon compounds that remain uncombusted.

Volumetric efficiency: Ratio of the actual mass of air intake per cycle to the displacement volume mass determined at inlet temperature and pressure.

References

- ASTM. 1995. *Annual Book of ASTM Standards*. American Society for Testing and Materials, Philadelphia, PA.
- Blair, G. P. (Ed.) 1988. *Advances in Two-Stroke Cycle Engine Technology*, Society of Automotive Engineers, Inc., Warrendale, PA.
- Brands, M. C., Werner, J. R., Hoehne, J. L., and Kramers, S. 1981. Vehicle testing of Cummins turbo-compound Diesel engine. SAE Paper No. 810073, Warrendale, PA.
- Dec, J. A. 1997. A conceptual model of DI Diesel combustion based on laser-sheet imaging. SAE Paper 970873, Warrendale, PA.
- DiBella, F. A., DiNanno, L. R., Koplrow, M. D. 1983. Laboratory and on-highway testing of Diesel organic Rankine compound long-haul vehicle engine. SAE Paper No. 830122, Warrendale, PA.
- Ferguson, C. R. and Kirkpatrick, A. T. 2001. *Internal Combustion Engines, Applied Thermosciences*. Wiley, New York.
- Henein, N. A. 1972. *Emissions from Combustion Engines and Their Control*. Ann Arbor Science Publishers, Ann Arbor, MI.
- Heywood, J. B. 1988. *Internal Combustion Engine Fundamentals*. McGraw-Hill, New York.
- Keating, E. L. 1993. *Applied Combustion*. Marcel Dekker, New York.
- Kummer, J. T. 1980. Catalysts for automobile emission control. *Prog. Energy Combust. Sci.*, 6, 177–199.
- Leising, C. J., Purohit, G. P., DeGrey, S. P., and Finegold, J. G. 1978. Waste heat recovery in truck engines, SAE Paper No. 780686, Warrendale, PA.
- Lenz, H. P. 1992. *Mixture Formation in Spark-Ignition Engines*. Springer, New York.
- Norbye, J. P. 1971. *The Wankel Engine*. Chilton Press, Philadelphia, PA.
- Obert, E. F. 1973. *Internal Combustion Engines and Air Pollution*, 3rd edn. Harper & Row, New York.
- Owen, K. and Coley, T. 1995. *Automotive Fuels Reference Book*, 2nd edn. Society of Automotive Engineers, Inc., Warrendale, PA.

- Ringler, J., Seifert, M., Guyotot, V., and Huebner, W. 2009. Rankine cycle for waste heat recovery of IC engines, SAE Paper No. 2009-01-0174, Presented at *SAE World Congress & Exhibition*, Detroit, MI, , April 2009. Session: Thermal Management Systems (Part 2 of 2).
- SAE. 1993a. *SAE Fuels and Lubricants Standards Manual*. Society of Automotive Engineers, Inc., Warrendale, PA.
- SAE. 1993b. *SAE Surface Vehicle Emissions Standards Manual*. Society of Automotive Engineers, Inc., Warrendale, PA.
- Stone, R. 1993. *Introduction to Internal Combustion Engines*, 2nd edn. Society of Automotive Engineers, Inc., Warrendale, PA.
- Taylor, C. F. 1985. *The Internal Combustion Engine in Theory and Practice*, 2nd edn., Vols. I and II. MIT Press, Cambridge, MA.
- Teng, H. 2006. Achieving high engine efficiency for heavy-duty Diesel engines by waste heat recovery using supercritical organic-fluid Rankine Cycle, SAE Paper No. 2006-01-3522, Presented at *SAE 2006 Commercial Vehicle Engineering Congress & Exhibition*, Rosemont, IL, , October 2006. Session: New Developments in Engines and Transmission Systems.
- Watson, N. and Janota, M. S. 1982. *Turbocharging the Internal Combustion Engine*. Wiley, New York.

For Further Information

The textbooks on IC engines by Obert (1973), Taylor (1985), Heywood (1988), Stone (1993), and Ferguson and Kirkpatrick (2001) listed under the references provide excellent treatments of this subject. In particular, Stone's book is up to date and informative. The *Handbook of Engineering* (1966) published by CRC Press, Boca Raton, Florida, contains a chapter on IC engines by A. Kornhauser. The Society of Automotive Engineers (SAE) publishes transactions, proceedings, and books related to all aspects of automotive engineering, including IC engines. Two very comprehensive handbooks distributed by SAE are the *Bosch Automotive Handbook* and the *SAE Automotive Handbook*. For more information contact: SAE Publications, 400 Commonwealth Drive, Warrendale, PA, 15096-0001; (412)776-4970.



Taylor & Francis

Taylor & Francis Group

<http://taylorandfrancis.com>

12

Hydraulic Turbines

Roger E.A. Arndt and Leonardo P. Chamorro

CONTENTS

12.1	General Description.....	258
12.1.1	Typical Hydropower Installation	258
12.1.2	Turbine Classification.....	258
12.1.2.1	Impulse Turbines	259
12.1.2.2	Reaction Turbines.....	260
12.2	Principles of Operation	261
12.2.1	Power Available and Efficiency	261
12.2.2	Similitude and Scaling Formulae	262
12.3	Factors Involved in Selecting a Turbine.....	265
12.3.1	Performance Characteristics	265
12.3.1.1	Impulse Turbines	265
12.3.1.2	Reaction Turbines.....	266
12.3.1.3	Performance Comparison.....	267
12.3.2	Speed Regulation	268
12.3.3	Cavitation and Turbine Setting.....	270
12.4	Performance Evaluation.....	271
12.4.1	Model Tests	271
12.5	Numerical Simulations	271
12.6	Field Tests.....	276
12.7	Other Concepts: Hydrokinetic Turbines.....	277
	Defining Terms	278
	References.....	278
	Further Information.....	279

A hydraulic turbine is a mechanical device that converts the potential energy associated with a difference in water elevation (*head*) into mechanical work. Modern hydraulic turbines are the result of many years of gradual development. Economic incentives have resulted in the development of very large units (exceeding 800 MW in capacity, i.e., two orders of magnitude larger than their wind counterparts) with efficiencies that are sometimes in excess of 95%.

However, the emphasis on the design and manufacture of very large turbines has shifted to the production of smaller units, especially in developed nations, where much of the potential for developing large base-load plants has been realized. At the same time, the sustained increase in the cost of energy has made many smaller sites economically feasible and has greatly expanded the market for smaller turbines. The increased value of energy

also justifies the cost of refurbishment and increasing the capacity of older facilities with modern runners having higher efficiency and greater capacity. The introduction of high-performance computational tools in the last decade has had considerable influence on the design of hydraulic systems, their operation, and control.

12.1 General Description

12.1.1 Typical Hydropower Installation

As shown schematically in Figure 12.1, the basic hydraulic components of a hydropower installation consist of an intake, a penstock, guide vanes or distributor, a turbine, and a draft tube. Trash racks are also commonly provided to prevent ingestion of debris into the turbine. Intakes usually require some type of shape transition to match the passageway to the turbine and also incorporate a gate or some other means of stopping the flow in case of an emergency or turbine maintenance. Some types of turbines are set in an open flume, the so-called hydrokinetic turbines; others are attached to a closed-conduit penstock.

12.1.2 Turbine Classification

There are two types of turbines, denoted as impulse and reaction. In an *impulse turbine*, the available head is converted to kinetic energy before entering the runner, the power available being extracted from the flow at approximately atmospheric pressure. In a *reaction turbine*, the runner is completely submerged and both the pressure and the velocity decrease from inlet to outlet. The velocity head in the inlet to the turbine runner is typically less than 50% of the total head available.

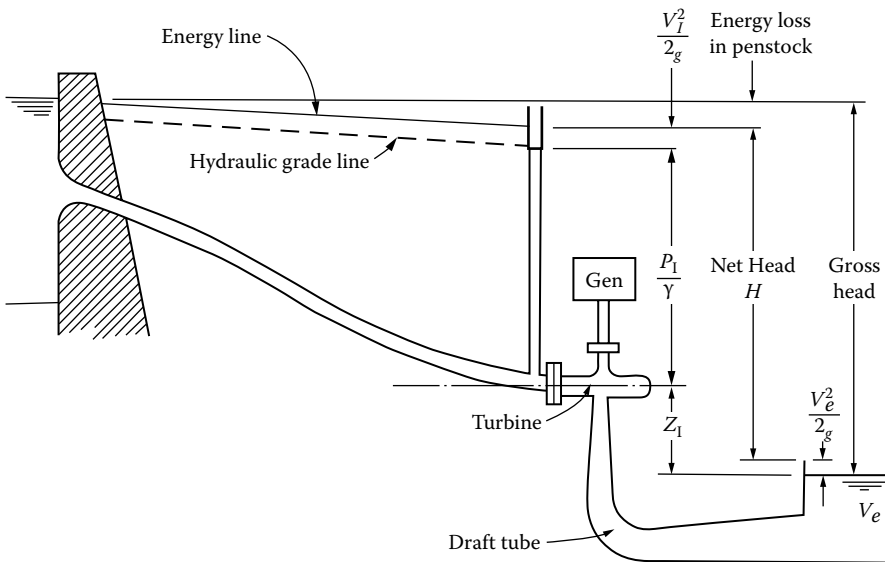


FIGURE 12.1
Schematic of a hydropower installation.

12.1.2.1 Impulse Turbines

Modern impulse units are generally of the Pelton type and are restricted to relatively high head applications (Figure 12.2). One or more jets of water impinge on a wheel containing many curved buckets. The jet stream is directed inwardly, sideways, and outwardly, thereby producing a force on the bucket, which in turn results in a torque on the shaft. All kinetic energy leaving the runner is “lost.” A draft tube is generally not used since the runner operates under approximately atmospheric pressure, and the head, represented by the elevation of the unit above tailwater, cannot be utilized. (In principle, a draft tube could be used, which requires the runner to operate in air under reduced pressure. Attempts at operating an impulse turbine with a draft tube have not met with much success.) Since this is a high-head device, this loss in available head is relatively unimportant. As will be shown later, the Pelton wheel is a *low specific speed* device. The specific speed can be increased by the addition of extra nozzles, with the specific speed increasing by the square root of the number of nozzles. The specific speed can also be increased by a change in the manner of inflow and outflow. Special designs such as the Turgo or cross-flow turbines are examples of relatively high specific speed impulse units (Arndt, 1991).

Most Pelton wheels are mounted on a horizontal axis, although newer vertical-axis units have been developed with hydrodynamically improved bucket designs. Because of physical constraints on orderly outflow from the unit, the number of nozzles is generally limited to six or less. Whereas *wicket gates* control the power of a reaction turbine, the power of the Pelton wheel is controlled by varying the nozzle discharge by means of an automatically adjusted needle, as illustrated in Figure 12.2. Jet deflectors or auxiliary nozzles are provided for emergency unloading of the wheel. Additional power can be obtained by connecting two wheels to a single generator or by using multiple nozzles. Since the needle valve can throttle the flow while maintaining essentially constant jet velocity, the relative velocities at entrance and exit remain unchanged, producing nearly constant efficiency over a wide range of power output.

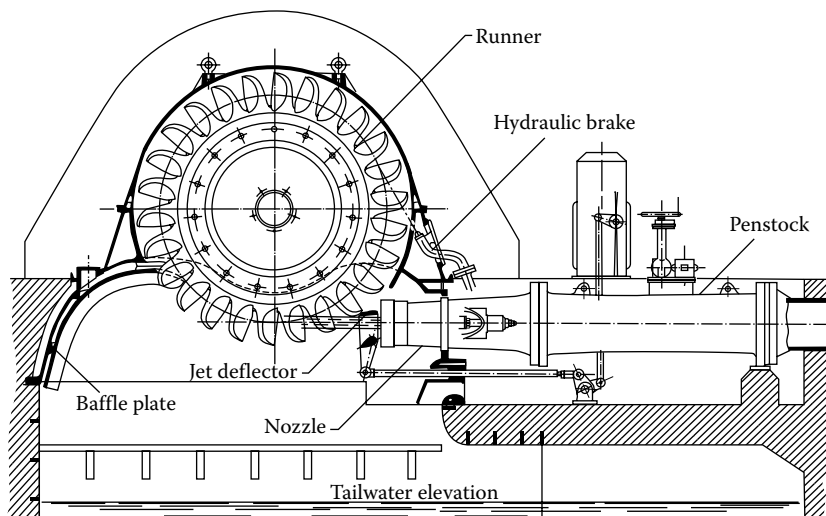


FIGURE 12.2

Cross section of a single-wheel, single-jet Pelton turbine. This is the third highest head Pelton turbine in the world, $H = 1447$ m, $n = 500$ rpm, $P = 35.2$ MW, and $N_s \sim 0.038$. (Courtesy of Vevey Charmilles Engineering Works; adapted from Raabe, J. 1985. *Hydro Power: The Design, Use, and Function of Hydromechanical, Hydraulic, and Electrical Equipment*, VDI Verlag, Dusseldorf, Germany.)

12.1.2.2 Reaction Turbines

Reaction turbines are classified according to the variation in flow direction through the runner. In radial- and mixed-flow runners, the flow exits at a radius different from the radius at the inlet. If the flow enters the runner with only radial and tangential components, it is a radial-flow machine. The flow enters a mixed-flow runner with both radial and axial components. Francis turbines are of the radial- or mixed-flow type, depending on the design specific speed. A Francis turbine is illustrated in Figure 12.3.

Axial-flow propeller turbines are generally either of the fixed-blade or the Kaplan (adjustable-blade) variety. The “classical” propeller turbine, illustrated in Figure 12.4, is a vertical-axis machine with a scroll case and a radial wicket gate configuration that is very similar to the flow inlet for a Francis turbine. The flow enters radially inward and makes a right-angle turn before entering the runner in an axial direction. The Kaplan turbine has both adjustable runner blades and adjustable wicket gates. The control system is designed in a way that the variation in blade angle is coupled with the wicket gate setting in a manner that achieves best overall efficiency over a wide range of flow rates.

Some modern designs take full advantage of the axial-flow runner; these include the tube, bulb, and Straflo types illustrated in Figure 12.5. The flow enters and exits the turbine with minor changes in direction. A wide variation in civil works design is also permissible. The tubular type can be fixed-propeller, semi-Kaplan, or fully adjustable. An externally mounted generator is driven by a shaft that extends through the flow passage either upstream or downstream of the runner. The bulb turbine was originally designed as a high-output, low-head unit. In large units, the generator is housed within the bulb and is driven by a variable-pitch propeller at the trailing end of the bulb. Pit turbines are similar in principle to bulb turbines, except that the generator is not enclosed in a fully submerged compartment (the bulb). Instead, the generator is in a compartment that extends above water level. This improves access to the generator for maintenance.

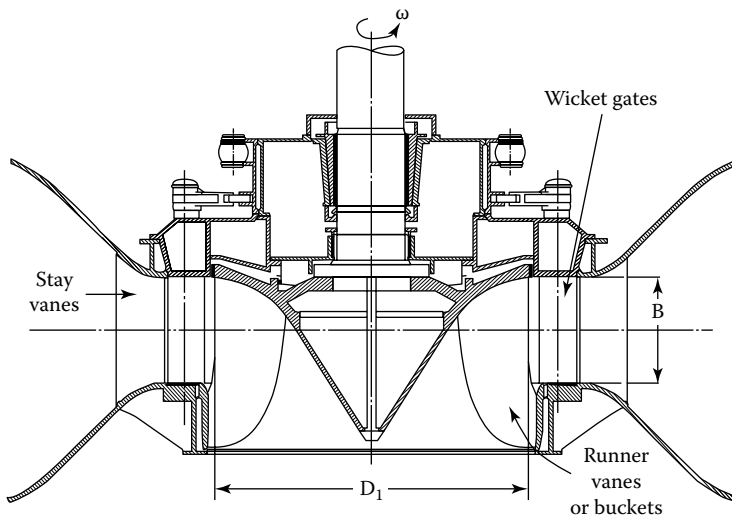
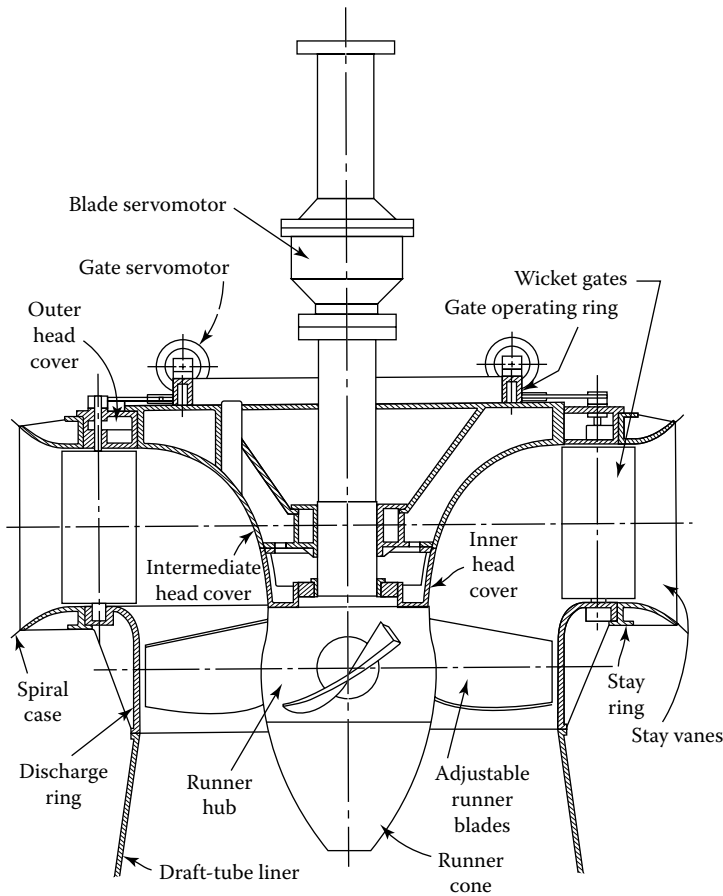


FIGURE 12.3

Francis turbine, $N_s \sim 0.66$. (Adapted from Daily, J.W., Hydraulic machinery, in *Engineering Hydraulics*, ed. H. Rouse, Wiley, New York, 1950. Reprinted with permission.)

**FIGURE 12.4**

Smith–Kaplan axial-flow turbine with adjustable-pitch runner blades, $N_s \sim 2.0$. (From Daily, J.W., *Hydraulic machinery*, in *Engineering Hydraulics*, ed. H. Rouse, Wiley, New York, 1950. Reprinted with permission.)

12.2 Principles of Operation

12.2.1 Power Available and Efficiency

The power P that can be developed by a turbine is a function of both the head and the flow available:

$$P = \eta \rho g Q H \quad (12.1)$$

where

η is the turbine efficiency

ρ is the density of water (kg/m^3)

g is the acceleration due to gravity (m/s^2)

Q is the flow rate (m^3/s)

H is the net head (m)

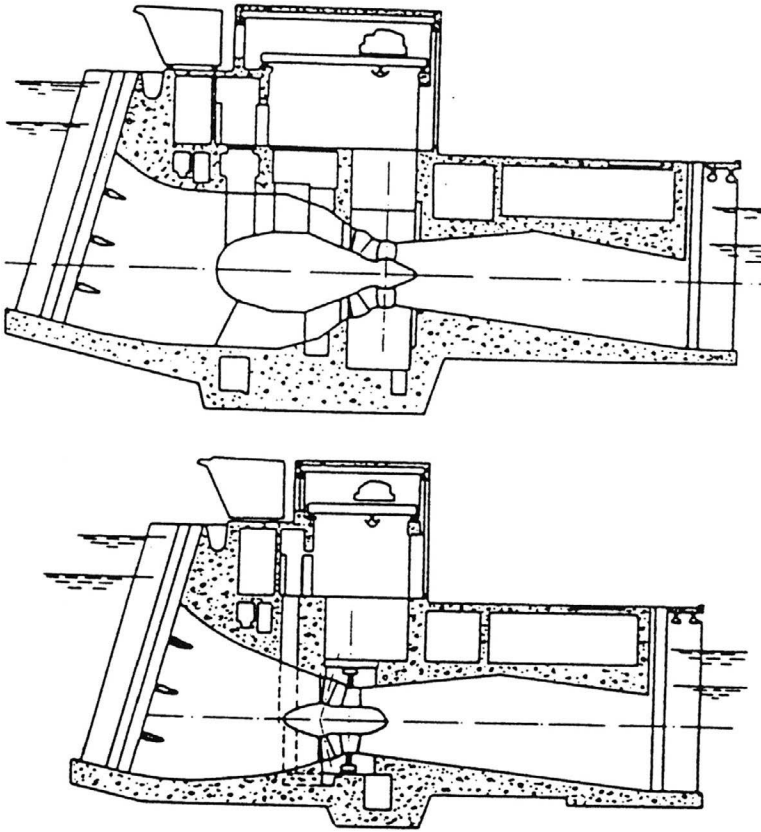


FIGURE 12.5
Comparison between bulb (upper) and Straflo (lower) turbines. (Courtesy of U.S. Department of Energy.)

Net head is defined as the difference between the *total head* at the tailrace, as illustrated in Figure 12.1. Various definitions of net head are used in practice, which depend on the value of the exit velocity head, $V_e^2/2g$, that is used in the calculation. The International Electrotechnical Test Code uses the velocity head at the draft tube exit.

The efficiency depends on the actual head and flow utilized by the turbine runner, flow losses in the draft tube, and the frictional resistance of mechanical components.

12.2.2 Similitude and Scaling Formulae

Under a given head, a turbine can operate at various combinations of speed and flow depending on the inlet settings. For reaction turbines, the flow into the turbine is controlled by the wicket gate angle, α . The nozzle opening in impulse units typically controls the flow. Turbine performance can be described in terms of nondimensional variables:

$$\psi = \frac{2gH}{\omega^2 D^2} \quad (12.2)$$

$$\phi = \frac{Q}{\sqrt{2gHD^2}} \quad (12.3)$$

where

ω is the rotational speed of the turbine (rad/s)

D is the diameter of the turbine

The hydraulic efficiency of the runner alone is given by

$$\eta_h = \frac{\phi}{\sqrt{\psi}} (C_1 \cos \alpha_1 - C_2 \cos \alpha_2) \quad (12.4)$$

where

C_1 and C_2 are constants that depend on the specific turbine configuration

α_1 and α_2 are the inlet and outlet angles that the absolute velocity vectors make with the tangential direction, respectively

The value of $\cos \alpha_2$ is approximately zero at peak efficiency. The terms ϕ , ψ , α_1 , and α_2 are interrelated. Using model test data, isocontours of efficiency can be mapped in the $\phi\psi$ plane. This is typically referred to as a *hill diagram*, as shown in Figure 12.6.

The *specific speed* is defined as

$$N_s = \frac{\omega\sqrt{Q}}{(2gH)^{3/4}} = \sqrt{\frac{\phi}{\psi}} \quad (12.5)$$

A given specific speed describes a specific combination of operating conditions that ensures similar flow patterns and the same efficiency in geometrically similar machines regardless of the size and rotational speed of the machine. It is customary to define the design specific speed in terms of the value at the design head and flow where peak efficiency occurs. The value of specific speed so defined permits a classification of different turbine types.

The specific speed defined herein is dimensionless. Many other forms of specific speed exist that are dimensional and have distinct numerical values depending on the system of units used (Arndt, 1991). (The literature also contains two other minor variations of the dimensionless form. One differs by a factor of $1/\pi^{1/2}$ and the other by $2^{3/4}$.) The similarity arguments used to arrive at the concept of specific speed indicate that a given machine of diameter D operating under a head H will discharge a flow Q and produce a torque T and power P at a rotational speed ω given by

$$Q = \phi D^2 \sqrt{2gH} \quad (12.6)$$

$$T = T_{11} \rho D^3 2gH \quad (12.7)$$

$$P = P_{11} \rho D^2 (2gH)^{3/2} \quad (12.8)$$

$$\omega = \frac{2u_1}{D} = \omega_{11} \frac{\sqrt{2gH}}{D}, \quad \left[\omega_{11} = \frac{1}{\sqrt{\psi}} \right] \quad (12.9)$$

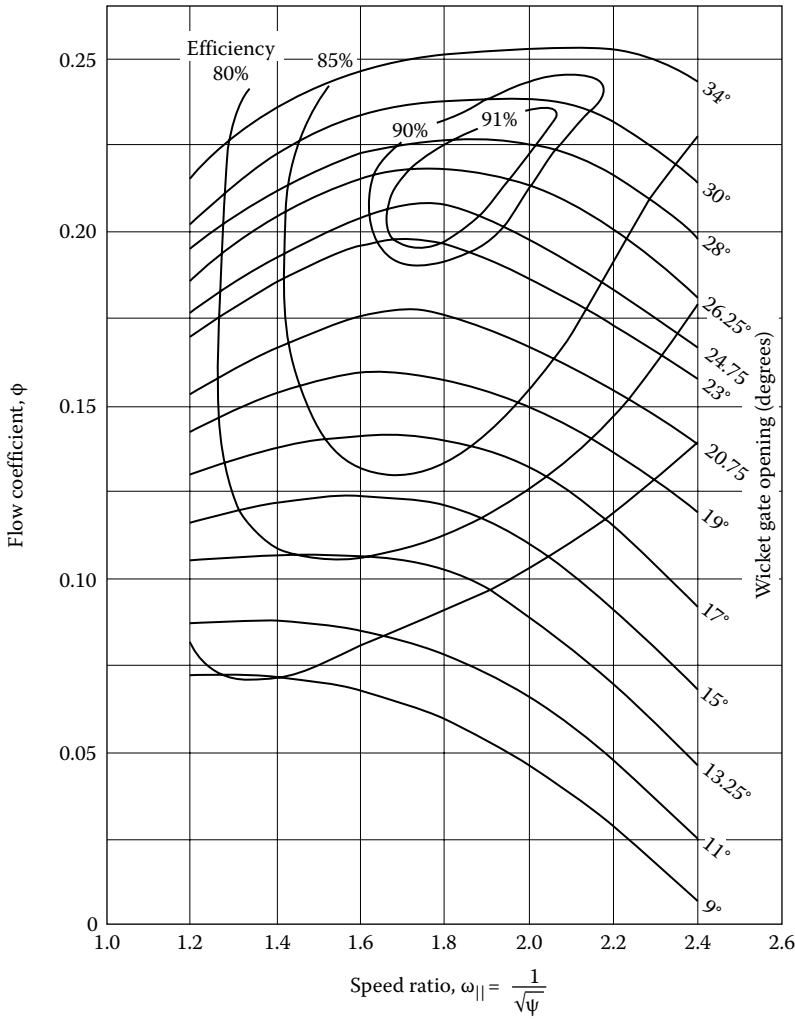


FIGURE 12.6 Typical hill diagram. Information of this type is obtained in turbine test stand (see Figure 12.9). (Adapted from Wahl, T.L., *Hydro Rev.*, 13(1), 60, 1994. With permission.)

with

$$P_{11} = T_{11}\omega_{11} \tag{12.10}$$

where T_{11} , P_{11} , and ω_{11} are also nondimensional. (The reader is cautioned that many texts, especially in the American literature, contain dimensional forms of T_{11} , P_{11} , and ω_{11} .) In theory, these coefficients are fixed for a machine operating at a fixed value of specific speed, independent of the size of the machine. Equations 12.6 through 12.10 can be used to predict the performance of a large machine using the measured characteristics of a smaller machine or model.

12.3 Factors Involved in Selecting a Turbine

12.3.1 Performance Characteristics

Impulse and reaction turbines are the two basic types of turbines. They tend to operate at peak efficiency over different ranges of the specific speed due to geometric and operational differences.

12.3.1.1 Impulse Turbines

Of the head available at the nozzle inlet, a small portion is lost to friction in the nozzle and to friction on the buckets. The rest is available to drive the wheel. The actual utilization of this head depends on the velocity head of the flow leaving the turbine and the setting above tailwater. Optimum conditions, corresponding to maximum utilization of the head available, dictate that the flow leaves at essentially zero velocity. Under ideal conditions, this occurs when the peripheral speed of the wheel is one half the jet velocity. In practice, optimum power occurs at a speed coefficient, ω_{11} , somewhat less than 1.0. This is illustrated in Figure 12.7. Since maximum efficiency occurs at a fixed speed for a fixed H , V_j must remain constant under varying flow conditions. Thus, the flow rate Q is regulated with an adjustable nozzle. However, maximum efficiency occurs at slightly lower values of ω_{11} under partial power settings. Present nozzle technology is such that the discharge can be regulated over a wide range at high efficiency.

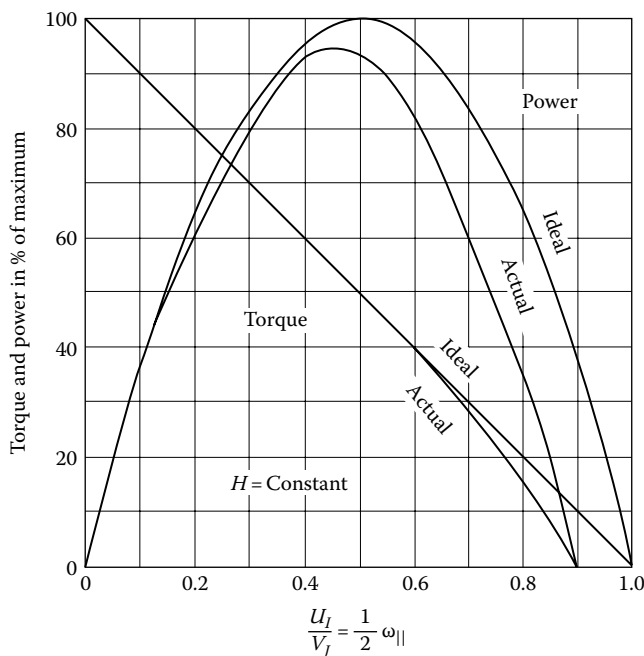


FIGURE 12.7

Ideal and actual variable-speed performance for an impulse turbine. (Adapted from Daily, J.W., *Hydraulic machinery*, in *Engineering Hydraulics*, ed. H. Rouse, Wiley, New York, 1950. With permission.)

A given head and penstock configuration establishes the optimum jet velocity and diameter. The size of the wheel determines the speed of the machine. The design specific speed is approximately

$$N_s = 0.77 \frac{d_j}{D} \text{ (Pelton turbines)} \quad (12.11)$$

Practical values of d_j/D for Pelton wheels to ensure good efficiency are in the range 0.04–0.1, corresponding to N_s values in the range 0.03–0.08. Higher specific speeds are possible with multiple nozzle designs. The increase is proportional to the square root of the number of nozzles. In considering an impulse unit, one must remember that efficiency is based on net head; the net head for an impulse unit is generally less than the net head for a reaction turbine at the same gross head because of the lack of a draft tube.

12.3.1.2 Reaction Turbines

The main difference between impulse units and reaction turbines is that a pressure drop takes place in the rotating passages of the latter. This implies that the entire flow passage from the turbine inlet to the discharge at the tailwater must be completely filled. A major factor in the overall design of modern reaction turbines is the draft tube, where the presence of energetic coherent motions and highly three-dimensional flow can affect the efficiency of the system. It is usually desirable to keep the overall equipment and civil construction costs relatively low by using high-specific-speed runners. Under these circumstances, the draft tube is also extremely critical for flow stability. This should be kept in mind when retrofitting on older, low-specific-speed turbine with a new runner of higher capacity. At higher specific speed, a substantial percentage of the available total energy is in the form of kinetic energy leaving the runner. To recover this energy, considerable emphasis should be placed on the draft tube design.

The practical specific speed range for reaction turbines is much broader than for impulse wheels. This is due to the wider range of variables that control the basic operation of the turbine. The pivoted guide vanes allow for control of the magnitude and direction of the inlet flow. Because there is a fixed relationship between blade angle, inlet velocity, and peripheral speed for shock-free entry, this requirement cannot be completely satisfied at partial flow without the ability to vary blade angle. This is the distinction between the efficiency of fixed-propeller and Francis types at partial loads and that of the fully adjustable Kaplan design.

In Equation 12.4, optimum hydraulic efficiency of the runner would occur when α_2 is equal to 90° . However, the overall efficiency of the turbine is dependent on the optimum performance of the draft tube as well, which occurs with a little swirl in the flow. Thus, the best overall efficiency occurs with $\alpha_2 \approx 75^\circ$ for high-specific-speed turbines.

The determination of optimum specific speed for a reaction turbine is more complicated than for an impulse unit since there are more variables. For a radial-flow machine, an approximate expression is

$$N_s = 1.64 \left[C_v \sin \alpha_1 \frac{B}{D_1} \right]^{1/2} \omega_{11} \text{ (Francis turbines)} \quad (12.12)$$

where

C_v is the fraction of net head that is in the form of inlet velocity head

B is the height of the inlet flow passage (see Figure 12.3)

N_s for Francis units is normally found to be in the range 0.3–2.5

Standardized axial-flow machines are available in the smaller-size range. These units are made up of standard components, such as shafts and blades. For such cases,

$$N_s \sim \frac{\sqrt{\tan \beta}}{n_B^{3/4}} \text{ (Propeller turbines)} \quad (12.13)$$

where

β is the blade pitch angle

n_B is the number of blades

The advantage of controllable pitch is also obvious from this formula, the best specific speed simply being a function of pitch angle.

It should be further noted that ω_{11} is approximately constant for Francis units and N_s is proportional to $(B/D_1)^{1/2}$. It can also be shown that the velocity component based on the peripheral speed at the throat, ω_{11e} , is proportional to N_s . In the case of axial-flow machinery, ω_{11} is also proportional to N_s . For minimum cost, the peripheral speed should be as high as possible—consistent with cavitation-free performance. Under these circumstances, N_s would vary inversely with the square root of head (H is given in meters):

$$N_s = \frac{C}{\sqrt{H}} \quad (12.14)$$

where the range of C is 8–11 for fixed-propeller units and Kaplan units and 6–9 for Francis units.

12.3.1.3 Performance Comparison

The physical characteristics of various runner configurations are summarized in Figure 12.8. It is obvious that the configuration changes with speed and head. Impulse turbines are efficient over a relatively narrow range of specific speed, whereas Francis and propeller turbines have a wider useful range. An important consideration is whether or not a turbine is required to operate over a wide range of load. Pelton wheels tend to operate efficiently over a wide range of power loading because of their nozzle design. In the case of reaction machines that have fixed geometry, such as Francis and propeller turbines, efficiency can vary widely with load. However, Kaplan and Deriaz [an adjustable-blade mixed-flow turbine [see Arndt, 1991]] turbines can maintain high efficiency over a wide range of operating conditions. The decision of whether to select a simple configuration with a relatively “peaky” efficiency curve or incur the added expense of installing a more complex machine with a broad efficiency curve depends on the expected operation of the plant and other economic factors.

Note in Figure 12.8 that there is an overlap in the range of application of various types of equipment. This means that either type of unit can be designed for good efficiency in this range, but other factors, such as generator speed and cavitation, may dictate the final selection.

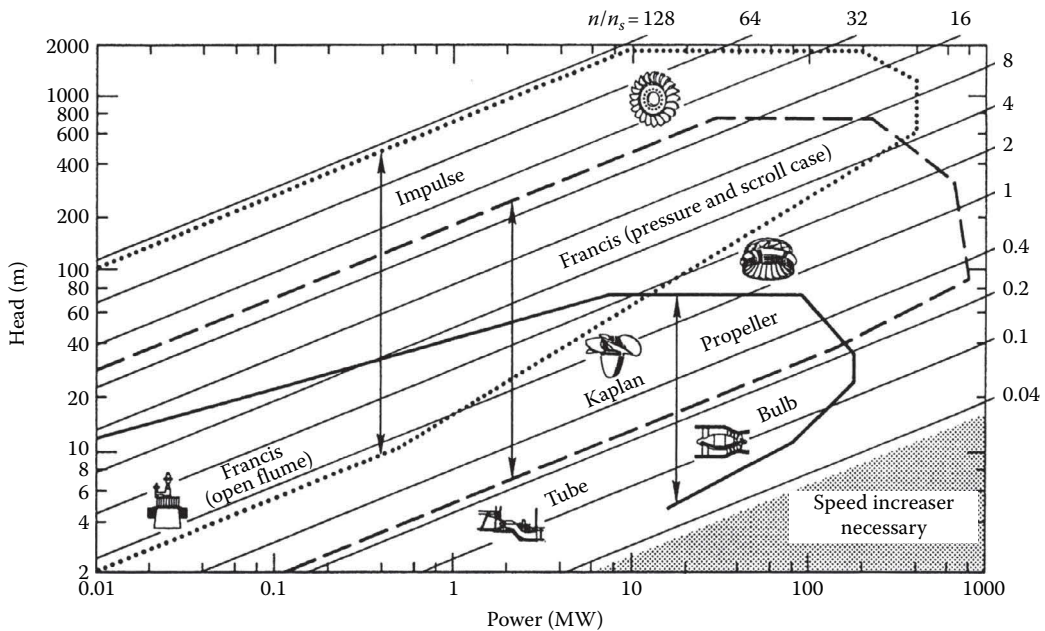


FIGURE 12.8

Application chart for various turbine types (n/n_s is the ratio of turbine speed in rpm, n , to specific speed defined in the metric system, $n_s = nP^{1/2}/H^{5/4}$, with P in kilowatts). (From Arndt, R.E.A., *Hydraulic turbines*, in *Hydropower Engineering Handbook*, eds. Gulliver, J.S. and Arndt, R.E.A., McGraw-Hill, New York, 1991, pp. 4.1–4.67. With permission.)

12.3.2 Speed Regulation

Speed regulation of a turbine is an important and complicated problem. The magnitude of the problem varies with size, type of machine and installation, type of electrical load, and whether the plant is tied to an electrical grid. It should also be kept in mind that runaway or no-load speed can be higher than the design speed by a factor as high as 2.6. This is an important design consideration for all rotating parts, including the generator.

The speed of a turbine has to be controlled to a value that matches the generator characteristics and the grid frequency:

$$n = \frac{120f}{N_p} \quad (12.15)$$

where n is the turbine speed in rpm, f is the required grid frequency in Hz, and N_p is the number of poles in the generator. Typically, N_p is in multiples of 4. There is a tendency to select higher-speed generators to minimize weight and cost. However, consideration has to be given to speed regulation.

It is beyond the scope of this chapter to discuss the question of speed regulation in detail. The regulation of speed is normally accomplished through flow control. Adequate control requires sufficient rotational inertia of the rotating parts. When load is rejected, power is absorbed, accelerating the flywheel; when load is applied, some additional power is available from the deceleration of the flywheel. Response time of the governor must be carefully selected, since rapid closing time can lead to excessive pressures in the penstock.

Opening and closing the wicket gates, which vary the flow of water according to the load, control a Francis turbine. The actuator components of a governor are required to overcome the hydraulic and frictional forces and to maintain the wicket gates in fixed position under steady load. For this reason, most governors have hydraulic actuators. On the other hand, impulse turbines are more easily controlled. This is due to the fact that the jet can be deflected or an auxiliary jet can bypass flow from the power-producing jet without changing the flow rate in the penstock. This permits long delay times for adjusting the flow rate to the new power conditions. The spear on the needle valve controlling the flow rate can close quite slowly, say, in 30–60 s, thereby minimizing any pressure rise in the penstock.

Several types of governors are available that vary with the work capacity desired and the degree of sophistication of control. These vary from pure mechanical to mechanical-hydraulic and electro-hydraulic. Electro-hydraulic units are sophisticated pieces of equipment and would not be suitable for remote regions. The precision of governing necessary depends on whether the electrical generator is synchronous or asynchronous (induction type). There are advantages to the induction type of generator. It is less complex and therefore less expensive, but typically has slightly lower efficiency. Its frequency is controlled by the frequency of the grid it feeds into, thereby eliminating the need for an expensive conventional governor. It cannot operate independently but can only feed into a network and does so with a lagging power factor, which may or may not be a disadvantage, depending on the nature of the load. Long transmission lines, for example, have a high capacitance and, in this case, the lagging power factor may be an advantage.

Speed regulation is a function of the flywheel effect of the rotating components and the inertia of the water column of the system. The start-up time of the rotating system is given by

$$t_s = \frac{I\omega^2}{P} \quad (12.16)$$

where I is the moment of inertia of the generator and turbine (kg m^2) (Bureau of Reclamation, 1966).

The start-up time of the water column is given by

$$t_p = \frac{\sum LV}{gH} \quad (12.17)$$

where

L is the length of the water column

V is the mean velocity in each component of the water column

For good speed regulation, it is desirable to keep $t_s/t_p > 4$. Lower values can also be used, although special precautions are necessary in the control equipment. It can readily be seen that higher ratios of t_s/t_p can be obtained by increasing I or decreasing t_p . Increasing I implies a larger generator, which also results in higher costs. The start-up time of the water column can be reduced by reducing the length of the flow system, by using lower velocities, or by adding surge tanks, which essentially reduce the effective length of the conduit. A detailed analysis should be made for each installation, since, for a given length, head,

and discharge, the flow area must be increased to reduce t_p , which leads to associated higher construction costs.

12.3.3 Cavitation and Turbine Setting

Another factor that must be considered prior to equipment selection is the evaluation of the turbine with respect to tailwater elevations. Hydraulic turbines are subject to pitting, loss in efficiency, and unstable operation due to cavitation (Arndt, 1981, 1991, Arndt, et al., 2000). For a given head, a smaller, lower-cost, high-speed runner must be set lower (i.e., closer to tailwater or even below tailwater) than a larger, higher-cost, low-speed turbine runner. Also, atmospheric pressure or plant elevation above sea level is a factor, as are tailwater elevation variations and operating requirements. This is a complex subject that can only be accurately resolved by model tests. Every runner design will have different cavitation characteristics. Therefore, the anticipated turbine location or setting with respect to tailwater elevations is an important consideration in turbine selection.

Cavitation is not normally a problem with impulse wheels. However, by the very nature of their operation, cavitation is an important factor in reaction turbine installations. The susceptibility for cavitation to occur is a function of the installation and the turbine design. This can be expressed conveniently in terms of Thoma's sigma, defined as

$$\sigma_T = \frac{H_a - H_v - z}{H} \quad (12.18)$$

where

H_a is the atmospheric pressure head

H is the vapor pressure head (generally negligible)

z is the elevation of a turbine reference plane above the tailwater (see Figure 12.1)

Draft tube losses and the exit velocity head have been neglected.

The term σ_T must be above a certain value to avoid cavitation problems. The critical value of σ_T is a function of specific speed (Arndt, 1991). The Bureau of Reclamation (1966) suggests that cavitation problems can be avoided when

$$\sigma_T > 0.26N_s^{1.64} \quad (12.19)$$

Equation 12.19 does not guarantee total elimination of cavitation, only that cavitation is within acceptable limits. Cavitation can be totally avoided only if the value of σ_T at an installation is much greater than the limiting value given in Equation 12.19. The value of σ_T for a given installation is known as the plant sigma, σ_p . Equation 12.19 should only be considered a guide in selecting σ_p , which is normally determined by a model test in the manufacturer's laboratory. For a turbine operating under a given head, the only variable controlling σ_p is the turbine setting z . The required value of σ_p then controls the allowable setting above tailwater:

$$z_{allow} = H_a - H_v - \sigma_p H \quad (12.20)$$

It must be borne in mind that H_a varies with elevation. As a rule of thumb, H_a decreases from the sea-level value of 10.3 m by 1.1 m for every 1000 m above sea level.

12.4 Performance Evaluation

12.4.1 Model Tests

Model testing is an important element in the design and development phases of turbine manufacture. Manufacturers own most laboratories equipped with model turbine test stands. Major hydro projects have traditionally had proof-of-performance tests in model scale at either an independent laboratory or the manufacturer's laboratory as part of the general design. Model testing at an independent laboratory can lead to large savings at a major project because of improved efficiency. Recently, turbine design procedures have been dramatically improved through the use of advanced numerical analysis of the three-dimensional flow characteristics. Such analysis techniques, linked with design programs, provide the turbine designer with powerful tools for achieving highly efficient turbine designs. In spite of this progress, computational methods require fine-tuning with model tests. In addition, model testing is necessary for determining performance over a range of operating conditions and for determining quasi-transient characteristics. Model testing can also be used to eliminate or mitigate problems associated with vibration, cavitation, hydraulic thrust, and pressure pulsation (Fisher and Beyer, 1985).

A typical turbine test loop is shown in Figure 12.9. All test loops perform basically the same function. A model turbine is driven by high-pressure water from a head tank, which then discharges into a tail tank. The flow is recirculated by a pump, usually positioned well below the elevation of the model to ensure cavitation-free performance of the pump while performing cavitation testing of the turbine model. One important advantage of a recirculating turbine test loop is that cavitation testing can be done over a wide range of cavitation indices at constant head and flow.

The extrapolation of model test data to prototype values has been a subject of considerable debate for many years. Equations 12.6 through 12.10 can be used to predict prototype values of flow, speed, power, etc., from model tests. Unfortunately, there are many factors that lead to scale effects, that is, the prototype efficiency and the model efficiency are not identical at a fixed value of specific speed. The cited scale-up formulae are based on inviscid flow. There are several sources of energy loss, which lead to an efficiency that is less than ideal. All of these losses follow different scaling laws, and in principle, perfect similitude can only be achieved by testing the prototype. There have been several attempts at rationalizing the process of scaling up model test data. The International Electrotechnical Test Code and various American Society of Mechanical Engineers (ASME) publications (IEC, 1991) outline in detail the differences in efficiency between model and prototype. It should also be pointed out that other losses such as in the draft tube and "shock losses" at the runner inlet might not be independent of the Reynolds number.

12.5 Numerical Simulations*

The analysis of turbines and other components of hydropower facilities has been largely dependent on approximate models using the Euler and Reynolds-averaged Navier–Stokes (RANS) equations because the solutions of the Navier–Stokes equations are computationally

* This section has been prepared by Professor Charles Song of the Saint Anthony Falls Laboratory, Minneapolis, MN, University of Minnesota, Saint Paul, MN.

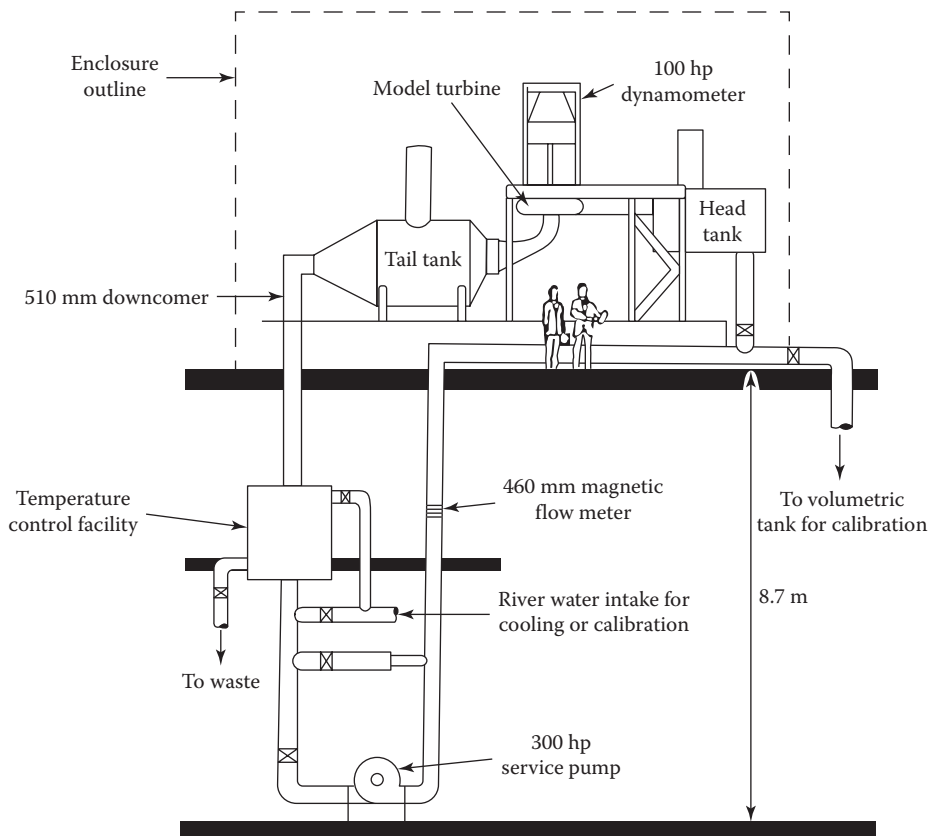


FIGURE 12.9

Schematic of the SAFL independent turbine test facility. (Courtesy of the Saint Anthony Falls Laboratory [SAFL], Minneapolis, MN, University of Minnesota, Saint Paul, MN.)

too demanding to be solved for hydropower components. The Euler equation model has been applied with reasonable success for the simulation of turbine runners, but energy losses and efficiency cannot be calculated. RANS models have been applied for the spiral case and for the draft tube simulations also with reasonable success. Commercial codes have become available and are being used with increasing frequency. They mostly rely on variants of RANS models, although rapid progress is being made in adapting large-eddy simulation (LES).

LES is a step forward in the application of computational fluid dynamics (Song et al., 1995). This technique is able to more accurately capture the large-scale effects of turbulent flows in a turbine than other techniques. The use of parallel computing has allowed the use of LES in turbine applications and, consequently, has helped to achieve sufficient resolution and good accuracy for final design purposes. Even parallel processing with desktop computers shows promise and can presently be used for relatively simple geometry or for preliminary evaluation purposes. However, progress in its application is very rapid, and it is anticipated that an entire computation may be carried out on a high-end desktop computer in the near future.

The components that require simulation include the spiral case, wicket gates, the runner, and the draft tube. Often, the spiral case, including stay vanes, and wicket gates are

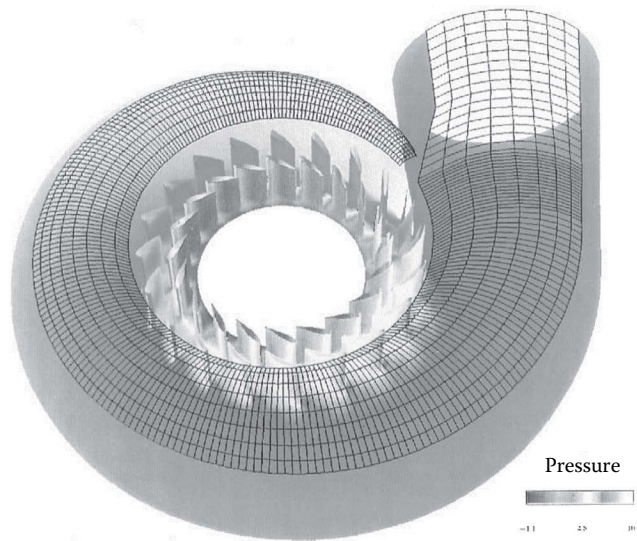


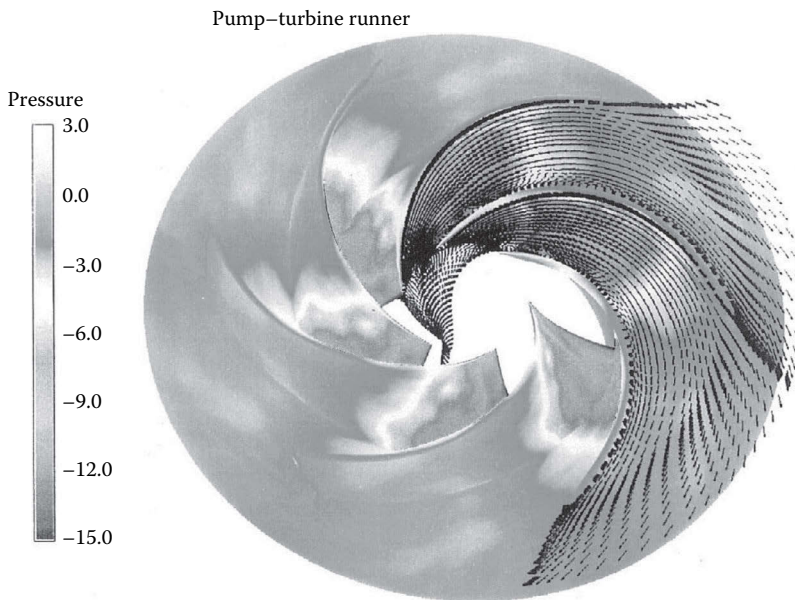
FIGURE 12.10

Simulated velocity field in a spiral case showing the pressure distribution on the boundaries of the spiral case, the stay vanes, and the wicket gates. (Adapted from Song, C.C.S. et al., *Hydro Rev.*, XIV(4), 104. With permission.)

modeled as a unit. This is necessary because the stay vanes and wicket gates are so close to each other that their mutual interactions cannot be ignored and each stay vane may be of slightly different shape and orientation and cannot be modeled separately. A typical spiral case contains more than 20 stay vanes, and an equal number of wicket gates, requiring extensive computational resources for a complete simulation. A sample calculation is shown in Figure 12.10. In this example, the calculated energy loss through this device is 2.62% of the net available energy for this particular case. This is significant and justifies additional computational effort to minimize the losses.

The runner is the most extensively studied component of a turbine. Since all the blades in a runner are of the same geometrical shape, only one or two flow passage models are commonly used for runner simulation. A complete model is required if vibration or cavitation due to nonsymmetrical modes of interactions between blades and vortices are to be studied. An important application of computer simulation is in the design of runners for units used for pumped storage. *Pumped-storage* schemes are becoming very popular for smoothing out the difference between energy demand and supply. Special care is required in the design because a runner must be designed to act efficiently both as a turbine and as a pump. Because of viscous effects, a runner optimized in the turbine mode may have poor efficiency in the pump mode. Flow in the pump mode can be unstable and more difficult to calculate. An LES-based analysis greatly facilitates the optimum design of this type of runner. Figure 12.11 is an example of the calculated flow in the pump mode. A small flow separation near the entrance can be observed. This kind of information is very useful to determine how the blade geometry can be modified to improve the performance.

As pointed out, draft tube design is an important factor affecting the efficiency and stability of a turbine. Although typical draft tube geometry is somewhat simpler than that of a runner, it takes much more advanced computational techniques to accurately simulate

**FIGURE 12.11**

Simulation of the velocity and pressure distribution in a pump turbine runner operating in the pumping mode. (Adapted from Song, C.C.S. et al., *Hydro Rev.*, XIV(4), 104. With permission.)

its performance. This is because the diffuser-like flow produces secondary currents, three-dimensional vortex shedding, and large-scale vortices, which are all very important contributors to energy loss. Current RANS models are ineffective in accounting for this flow phenomenon. At the present time, only the LES model can fulfill the requirements for draft tube simulation. Figure 12.12 illustrates the three-dimensionality and complexity of the flow field. The instantaneous pressure distribution on the walls of an elbow-type draft tube with a divider wall is compared with the same draft tube with the divider wall removed. A dramatic change in the flow pattern and pressure distribution occurs when the divider wall is removed. By removing the wall, the draft tube becomes a diffuser of large angle with very unstable flow. Clearly, the divider wall stabilizes the flow and reduces the energy loss due to vortex shedding. These types of simulations are invaluable in predicting draft tube performance. This is underscored by the fact that many projects involve refurbishing existing units. Typically, only the runner is replaced, usually with increased design flow. On many occasions, the existing draft tube is unable to operate efficiently at higher flow rates, canceling out any improvements that a new runner can provide.

Current challenges and target problems in numerical simulations of hydraulic systems include the following: (1) the effects of erosion in reaction runners; (2) the development of advanced predictive control strategies, considering the turbine system (penstock, servomechanism, turbine, and generator) as a time-dependent nonlinear system; (3) the coupled simulations of turbine runners and draft tube system, which can provide details on the pressure, stresses, and turbulence fields necessary to design highly efficient and long-lasting systems; (4) spatial and temporal characterization of runaway transients in Francis turbines; and (5) stability of hydropower systems, including active flow control, to extend the operating range, among others.

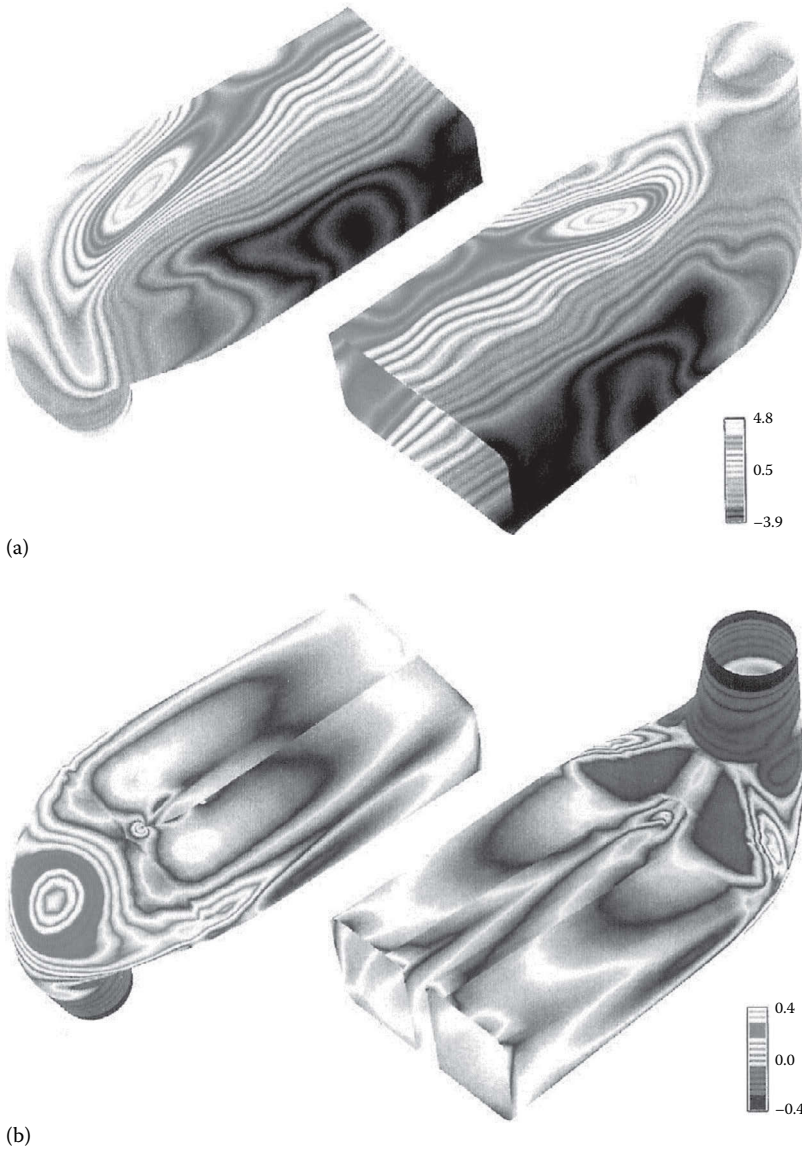


FIGURE 12.12

Simulation showing a comparison of the flow in a draft tube with and without a dividing wall. The pressure patterns on the walls indicate a very asymmetrical flow pattern without a divider wall (a). With a wall in place, a very uniform flow pattern is evident (b). (Adapted from Song, C.C.S. et al., *Hydro Rev.*, XIV(4), 104. With permission.)

12.6 Field Tests

Model tests and numerical simulations are only valid when geometric similitude is adhered to, that is, there is no guarantee that the prototype machine is an accurate reproduction of the design. In addition, approach flow conditions, intake head losses, the effect of operating other adjacent units, etc., are not simulated in model tests. For these reasons, field performance tests are often performed. There are several types of field tests, which serve different purposes. *Absolute* efficiency is measured for acceptance or performance tests. *Relative* efficiency is often measured when operating information or fine-tuning of turbine performance is desired. Field tests are also carried out for commissioning a site and for various problem-solving activities. Basic procedures are covered by codes of the ASME and the International Electrotechnical Commission. The major difference between an “absolute” and a “relative” or index test is in the measurement of the flow rate. Net head is evaluated in the same manner for each procedure. There are a variety of methods for measuring flow rate that are code accepted. These include the pressure–time technique, tracer methods (salt velocity, dye dilution), area–velocity measurements (Pitot tubes or current meters), volumetric measurements (usually on captive pumped-storage sites), Venturi meters, and weirs. The thermodynamic method is actually a direct measure of efficiency. Flow is not measured. In addition to the code-accepted methods, it has been demonstrated that acoustic meters can measure flow rate in the field with comparable accuracy.

The *pressure–time technique* relies on measuring the change in pressure necessary to decelerate a given mass of fluid in a closed conduit. The method requires the measurement of the piezometric head at two cross sections spaced a distance L apart. A downstream valve or gate is necessary for this procedure. This technique requires load rejection for each test point, and the need to estimate or measure any leakage. An adequate length of conduit is required, and the conduit geometry must be accurately measured (Hecker and Nystrom, 1991).

The *salt velocity method* is based on measuring the transit time, between two sensors, of an injected cloud of concentrated salt solution. Given the volume of the conduit between sensors, the flow rate may be calculated from the average transit time. Electrodes that measure the change in the conductivity of the liquid detect the passage of the salt cloud at a given location.

The *dye dilution method* is based on the conservation of a tracer continuously injected into the flow. A sufficient length for complete mixing is necessary for accurate results. The data required are the initial concentration and injection flow rate of the tracer and the measured concentration of the fully mixed tracer at a downstream location. The method is quite simple, but care is necessary to achieve precise results.

In principle, *area–velocity measurements* are also quite simple. Either Pitot tubes or propeller-type current meters are used to measure point velocities that are integrated over the flow cross section. The method is applicable to either closed conduits or open channels. A relatively uniform velocity distribution is necessary for accurate results. A single unit can be traversed across the conduit or a fixed or movable array of instruments can be used to reduce the time for data collection.

The *thermodynamic method* is a direct indication of turbine efficiency. The flow rate is not measured. In its simplest form, the method assumes adiabatic conditions, that is, no heat transfer from the flow to its surroundings. Under these conditions, that portion of the

available energy not utilized in the machine to produce useful work results in increased internal energy of the fluid, which is sensed as an increase in temperature.

Acoustic flow meters have been developed that produce results with a precision equal to or greater than the code-accepted methods. The flow velocity is determined by comparing acoustic travel times for paths diagonally upstream and downstream between pairs of transducers. The speed of sound is assumed constant. The difference in travel time is related to the component of flow velocity along the acoustic path (increased travel time upstream, decreased travel time downstream). An extensive evaluation and comparison of this method has been reported (Sullivan, 1983).

Index tests circumvent the problem of accurate flow measurement by measuring relative flow detected by the differential pressure between two points in the water passages leading to the runner. Often, the differential pressure is measured with Winter–Kennedy taps, which are positioned at the inner and outer radii of the spiral case of a turbine. Calibration of properly placed Winter–Kennedy taps shows that the flow rate is very closely proportional to the square root of the pressure difference. Index testing is useful for calibrating relative power output versus gate opening and for optimizing the various combinations of gate opening and blade setting in Kaplan units. The use of index testing to optimize cam settings in Kaplan turbines has resulted in substantial increases in weighted efficiency (i.e., a flatter efficiency curve over the full range of operation).

12.7 Other Concepts: Hydrokinetic Turbines

Alternative ways of energy conversion include the direct use of the kinetic energy of currents in natural environments. Hydrokinetic turbines can provide clean and renewable energy harnessed from streams, rivers, and tidal currents, where the flow velocity is sufficiently high (Fraenkel, 2002). Other concepts, including wave-energy converters and wave attenuators, require major research and development efforts before becoming competitive options. Installation and operations and maintenance costs and bathymetric constraints have, to date, prevented extensive deployment of hydrokinetic turbines. In addition, optimum operating conditions (peak efficiency with the lowest dynamic loadings) of the current technology are not easily achieved due to the distinctive turbulence features of natural flows, which induce dynamic loading and power fluctuations on hydrokinetic units. Coherent turbulent motions on the order of the rotor diameter and larger have a direct effect on turbines (Chamorro et al., 2013). The performance of hydrokinetic turbines is characterized through the so-called power coefficient, C_p , defined in terms of the power equation:

$$P = C_p \frac{1}{2} \rho A U^3 \quad (12.21)$$

where A is the area swept by the blades in the case of axial-flow rotors. The maximum efficiency or maximum power coefficient of an ideal turbine was developed independently by Betz and Joukowski (see Okulov and van Kuik, 2012). It is $C_{p_{\max}} = 16/27 \approx 0.593$ for uniform flow. This limit can be exceeded in constrained flows (Garrett and Cummins, 2007;

Vennell, 2010) and can also be slightly affected by the mean shear approaching the rotor (Chamorro and Arndt, 2011). Several factors affect the efficiency of a hydrokinetic turbine. Most important include the number of blades, tip losses, and foil profile losses, which usually result in an overall $C_p \sim 0.45$. Current efforts on the subject are focused on defining the most appropriate configurations across a wide range of operational conditions and on the impact on the surrounding ecosystem.

Defining Terms

Draft tube: The outlet conduit from a turbine that normally acts as a diffuser. This is normally considered an integral part of the unit.

Forebay: The hydraulic structure used to withdraw water from a reservoir or river. This can be positioned a considerable distance upstream from the turbine inlet.

Head: The specific energy per unit weight of water. *Gross head* is the difference in water surface elevation between the forebay and the tailrace. *Net head* is the difference between the *total head* (the sum of velocity head, $V^2/2g$, pressure head, p/ρ_g , and elevation head, z) at the inlet and the outlet of a turbine. Some European texts use specific energy per unit mass, for example, specific kinetic energy is $V^2/2$.

Power coefficient: It is the ratio of the power produced by a turbine to the total available in the flow stream.

Pumped storage: A scheme in which water is pumped to an upper reservoir during off-peak hours and used to generate electricity during peak hours.

Runner: The rotating component of a turbine in which energy conversion takes place.

Specific speed: A universal number for a given machine design.

Spiral case: The inlet to a reaction turbine.

Surge tank: A hydraulic structure used to diminish overpressures in high-head facilities due to water hammer resulting from the sudden stoppage of a turbine.

Wicket gates: Pivoted, streamlined guide vanes that control the flow of water to the turbine.

References

- Arndt, R. E. A. 1981. Cavitation in fluid machinery and hydraulic structures. *Ann. Rev. Fluid Mech.* 13, 273–328.
- Arndt, R. E. A. 1991. Hydraulic turbines. In *Hydropower Engineering Handbook*, eds. J. S. Gulliver and R. E. A. Arndt, pp. 4.1–4.67. McGraw-Hill, New York.
- Arndt, R. E. A., Keller, A., and Kjeldsen, M. 2000. Unsteady operation due to cavitation. *Proceedings 20th IAHR Symposium on Hydraulic Machinery and Systems*, Charlotte, NC, August 2000.
- American Society of Mechanical Engineers. 2011. *ASME Performance Test Code 18 on Hydraulic Turbines and Pump-Turbines*.

- Bureau of Reclamation. 1966. *Selecting Hydraulic Reaction Turbines*. Engineering Monograph No. 20.
- Chamorro, L. P., Hill, C., Morton, S., Ellis, C., Arndt, R. E. A., and Sotiropoulos, F. 2013. On the interaction between a turbulent open channel flow and an axial-flow turbine. *J. Fluid Mech.* 716, 658–670.
- Chamorro, L. P. and Arndt, R. E. A. 2011. Non-uniform velocity distribution effect on the Betz–Joukowski limit. *Wind Energy* 16(2), 279–282.
- Daily, J. W. 1950. Hydraulic machinery. In *Engineering Hydraulics*, ed. H. Rouse. Wiley, New York.
- Fraenkel, P. L. 2002. Power from marine currents. *Proc. Inst. Mech. Eng., A: J. Power Energy* 216, 1–14.
- Fisher, R. K. and Beyer, J. R. 1985. The value of model testing for hydraulic turbines. *Proc. Amer. Power Conf., ASME* 47, 1122–1128.
- Garrett, C. and Cummins, P. 2007. The efficiency of a turbine in a tidal channel. *J. Fluid Mech.* 588, 243–251.
- Hecker, G. E. and Nystrom, J. B. 1991. Which flow measurement technique is best? *Hydro Rev.* 6(3), June.
- IEC. 1991. *International Code for the Field Acceptance Tests of Hydraulic Turbines*. Publication 41. International Electrotechnical Commission. <http://www.iec.ch/standardsdev/>.
- Okulov, V. and Van Kuik, G. A. M. 2012. The Betz–Joukowski limit: on the contribution to rotor aerodynamics by the British, German and Russian scientific schools. *Wind Energy* 15, 335–344.
- Raabe, J. 1985. *Hydro Power: The Design, Use, and Function of Hydromechanical, Hydraulic, and Electrical Equipment*. VDI Verlag, Dusseldorf, Germany.
- Song, C. C. S., Chen, X., He, J., Chen, C., and Zhou, F., July 1995. Using computational tools for hydraulic design of hydropower plants. *Hydro Rev.* XIV(4), 104–111.
- Sullivan, C. W. 1983 Acoustic flow measurement systems: economical, accurate, but not code accepted. *Hydro Rev.* 6(4), August.
- Vennell, R. 2010 Tuning turbines in a tidal channel. *J. Fluid Mech.* 663, 253–267.
- Wahl, T. L. 1994. Draft tube surging times two: The twin vortex problem. *Hydro Rev.* 13(1), 60–69.

Further Information

J. Fluids Eng. Published quarterly by the ASME.

ASME Symposia Proceedings on Fluid Machinery and Cavitation. Published by the Fluids Eng. Div.

Hydro Rev. Published eight times per year by HCI Publications, Kansas City, MO.

Moody, L. F. and Zowski, T. 1992. Hydraulic machinery. In *Handbook of Applied Hydraulics*, eds. C. V. Davis and K. E. Sorenson. McGraw-Hill, New York.

Waterpower and Dam Construction. Published monthly by Reed Business Publishing, Surrey, U.K.



Taylor & Francis

Taylor & Francis Group

<http://taylorandfrancis.com>

13

Advanced Fossil Fuel Power Systems

Seyfettin C. (John) Gülen

CONTENTS

13.1	Introduction	282
13.2	Organization of the Chapter	284
13.2.1	Performance Terminology	286
13.2.2	Fuels Covered	288
13.3	Fossil Fuel Power System	290
13.3.1	System Components	291
13.3.2	Main Equipment	292
13.3.3	Auxiliary Equipment.....	294
13.3.3.1	Fuel System	294
13.3.3.2	Air Quality Control System.....	295
13.3.3.3	Post-Combustion Carbon Capture System	295
13.3.3.4	Water Treatment System	296
13.4	Advanced Fossil Fuel Power System.....	296
13.5	Past, Present, and Future	302
13.5.1	Past	302
13.5.2	Present	304
13.5.3	Future	305
13.6	Thermodynamics	308
13.7	Economics	319
13.8	Combustion.....	330
13.8.1	Combustion Reaction	330
13.8.2	NO _x Emissions.....	334
13.8.3	Dry Low NO _x Combustors	336
13.8.4	Catalytic Combustor.....	339
13.8.5	Coal Combustion	340
13.8.6	Pressure-Gain Combustion	341
13.9	USC Power Plants	345
13.10	Gas Turbines	351
13.10.1	Cycle Variants.....	355
13.10.1.1	Closed-Loop Steam Cooling.....	355
13.10.1.2	Intercooling and Recuperation	357
13.10.1.3	Reheat Combustion	357
13.10.1.4	Kalina Cycle.....	358
13.10.1.5	Humid Air Turbine.....	359
13.10.2	Indirectly Fired Gas Turbines	361
13.10.3	Repowering.....	362

13.10.4	Cogeneration.....	364
13.10.5	Operational Flexibility	367
13.10.6	Fuel Flexibility.....	369
13.11	Gas Engines	372
13.11.1	Low-Quality Waste Heat Recovery	375
13.11.2	Supercritical CO ₂ Cycle	377
13.12	Materials.....	380
13.12.1	General	380
13.12.2	Superalloys.....	387
13.12.3	Thermal Barrier Coatings	390
13.13	Synthetic Fuel Production	391
13.13.1	Gasification	391
13.13.2	Underground Coal Gasification.....	397
13.13.3	Substitute Natural Gas	398
13.13.4	Hydrogen	399
13.14	Post-Combustion Carbon Capture	401
13.15	Oxy-Fuel Combustion	408
13.15.1	Oxy-Fuel Combustion of Coal.....	408
13.15.2	Oxy-Fuel Combustion of Natural Gas	410
13.15.3	Oxy-Fuel Combustion with Supercritical CO ₂ Cycle.....	413
13.15.4	Chemical Looping Combustion.....	416
13.16	Air Quality Control	417
13.17	Water Treatment.....	424
13.17.1	Why Treatment?	424
13.17.2	Usage Minimization.....	427
13.17.3	Wastewater Treatment.....	429
13.17.4	Zero Liquid Discharge	430
13.18	Recap.....	433
	References.....	437
	General References.....	437
	References Cited in the Text	438
	Periodicals	444
	Codes and Standards.....	445

13.1 Introduction

At the time of writing (fall of 2015), fossil-fuel-fired electric generation constitutes a significant portion of the worldwide generation portfolio—70% or more in most regions. Whether this is going to be the case, say, by the mid-century is debatable. Climate change concerns and related initiatives to reduce greenhouse gas emissions, and rules and regulations aiming to address water scarcity and air pollution, all point to an increasing share of renewables and nuclear in a not-too-distant future. Projections from various organizations such as the U.S. Energy Information Administration (EIA) and the World Energy Council can be readily found on the Internet. They are not quoted here simply because they will be out of date within a few years. Interested readers are encouraged to “google” to find and consult those sources and many others, which are typically revised annually. While it

is very difficult to predict the future in energy resources and power generation (shale gas revolution* in the United States is a good example of how things can change dramatically within a mere decade or less), it is a good bet that fossil fuel power systems will continue to play a major role in the global economy far into the current century.

Major fossil fuels (coal, natural gas, and petroleum) and their properties have been discussed in detail in other chapters of this handbook. Similarly, key technologies utilized in the combustion of fossil fuels, and conversion of the resulting heat into electric power, have also been covered in the respective chapters. As such, the present chapter is primarily dedicated to a discussion of the most advanced variants of those technologies. To the extent possible, the focus will be on technologies falling under the first definition of the term “advanced,” namely, those which are “far on or ahead in development or progress.” Simple formulas, charts, rules of thumb, and similar estimating tools will be provided so that the readers can make an informed decision on the applicability of the said technologies to their own ends. Technologies that can be best described by the second definition of the term, that is, “new technologies under development,” will be touched upon briefly, including primary references to be consulted for more information.

In keeping with this general philosophy, advanced power systems falling into the first category can be divided into two distinct groups:

1. Technologies that made it to commercial products and can be considered field-proven but have failed to become *mainstream* (e.g., integrated gasification combined cycle [IGCC][†] [82])
2. State-of-the-art (SOA), that is, the *crème de la crème* that is already deployed in the field and is all but guaranteed to become mainstream in the near future (e.g., H and J class gas turbines[‡] in combined cycle, ultra-supercritical (USC) coal plants [157])

Advanced power systems falling into the second category can be divided into three groups:

1. Technologies that had been the subject of quite extensive research and development but did not achieve commercial viability (e.g., *Kalina* cycle [114], *Humid Air Turbine* [HAT] [144], etc.)
2. Perennially *new* technologies that have been around for decades but have not made it beyond prototype—if that (i.e., *pressure-gain combustion* [111])—but refuse to disappear completely
3. New technologies under development, for example, *supercritical CO₂* cycles with *oxy-fuel combustion* [26]

* This is a reference to the large increase in natural gas production in the United States spurred by horizontal drilling and hydraulic fracturing technologies, which enabled production of oil and gas from previously inaccessible shale deposits (e.g., the Marcellus basin).

[†] Extensive usage of acronyms is hard to avoid in a specialized technical treatise. In this chapter, acronyms are defined where they first appear in the text. Most of them have found industrywide acceptance and are expected to be familiar to the reader (e.g., IGCC, USC, CCS, etc.). Some are easy to guess within the context of the narrative (e.g., GT, ST, etc.). Those that are specific to the coverage herein (e.g., FFPS, SOA) are used intermittently so that the reader focusing on select sections does not have to go back and forth to look for their definition.

[‡] For the class “hierarchy” of gas turbines, please consult the relevant chapter of this handbook or refer to Figure 13.39 in Section 13.10.

In addition to these categories, one must also be cognizant of the key *auxiliary* technologies, which are destined to become an integral part of the future generation of fossil-fuel-fired power plants—if they are not already so. Primarily, these are the technologies designed to reduce or, preferably, eliminate emissions of combustion-generated pollutants (i.e., NO_x , SO_x , particulate matter [PM], mercury, etc.), carbon dioxide (CO_2), and wastewater (for discharge or reuse in the power plant). The best-known example of these technologies is *carbon capture and sequestration* (CCS) [53].

In keeping with the main theme of the chapter, most basic items will not be described in excessive detail. It is expected that the reader is familiar with the fundamental concepts and building blocks of typical fossil-fuel-fired power plants—either from the relevant chapters of this handbook or from individual experience. For example, a steam turbine condenser or boiler feed pump or the basic structure of a typical gas turbine is not going to be elaborated upon herein; they will just be mentioned in passing. Only variations that make them *advanced* will be discussed in detail. In order to keep the narrative concise and to the point, no references or descriptions are provided for terms and/or concepts that can be easily “googled” for information on their definition, details, etc. (e.g., from *Wikipedia*)—these include technical terms such as “pH,” a particular product such as “LMS 100” gas turbine, definitions such as NASA’s TRL, etc.

13.2 Organization of the Chapter

To paraphrase Frederick the Great of Prussia, he who tries to cover everything covers nothing. An attempt to write a comprehensive discourse on fossil fuel power systems would lead to a hefty tome and, even then, it would have severe deficiencies. In a chapter within a larger book, the prudent approach is to be selective in the material that is covered in some detail and provide a glimpse of what is out there in a logically coherent manner.

Consequently, to the extent possible, information that is bound to be out of date within a few years is omitted (a good example is detailed cost data). In keeping with the true definition of a handbook, as much as possible, crucial, timeless, and quantitative information (rules of thumb, typical factors, simple formulas, etc.) is favored at the expense of lengthy descriptions. It is hoped that this will enable the following treatise to be relevant for quite a long time down the road. In addition, the “References” section contains time-tested books and long-standing periodicals that should provide in-depth coverage requisite for a full understanding of the subject matter.

1. Establish the framework

The coverage starts with a concise description of fossil fuel power system and its advanced variant. In particular, Figure 13.4 can be used as a map for locating individual discussion items within the power plant framework. The bewildering array of carbon capture technologies can be deciphered with the help of the chart in Figure 13.5.

2. Those who don’t remember the past

In order to know and appreciate where one is headed, one must be cognizant not only of today but also of the past. All major fossil fuel-based power generation

technologies can be deemed fully mature. In other words, in terms of internal and external combustion engine development, we are at the end of the technology *S-curve*. As such, a brief discussion of what was in the past and what lies in future—within reason—is imperative for a well-rounded discussion of advanced technologies.

3. Performance vs. cost

Performance is the ultimate target of power plant design. Cost is the ultimate hurdle facing the designer. Performance disregarding cost is not realistic. Thermodynamics dictate the performance. Economics dictate the cost. Balancing the two is more an *art* than *science* but the latter must be firmly understood to master the former.

Thus, the more in-depth discussion commences with a crash course in thermodynamics. The aim is to arm the reader with crucial quantitative and qualitative tools to understand the concepts in the rest of the chapter and compare alternatives.

This is followed by another crash course, this one on the basic economics of electric power generation via combustion of fossil fuels. Once again, the aim is to provide a few basic tools to make the arguments in the rest of the chapter transparent to the reader.

4. The heart of the system

Combustion is the fundamental process in all power generation technologies based on fossil fuels. Thus, it is covered in Section 13.8. This is requisite for a proper understanding of fossil-fuel-fired power plant performance and emissions.

5. Three major technologies

The future of coal-burning power plants is *advanced ultra-supercritical* (A-USC) technology, which is covered in its own section.

The undisputed king of the fossil fuel power systems realm, today and tomorrow, is advanced *gas turbine combined cycle* (GTCC)—both in terms of performance (i.e., thermal efficiency) and emissions. The next section is devoted to it.

Liquid-fuel-fired reciprocating (piston-cylinder) internal combustion engine (ICE) is the anchor of land and—to a large extent—marine propulsion. In the recent past, however, it has made a significant inroad to land-based electric power generation. This is mainly driven by highly efficient (approaching 50% in *lower heating value*), *gas-fired spark-ignition engines* of large sizes (i.e., 10 or 20 MWe engines). They are covered briefly in their own section.

6. The “real” ultimate hurdle

Cost (i.e., euros, dollars, etc.) is the ultimate hurdle; this was the statement made earlier. This is a true but incomplete statement; cost is the expression in monetary terms of the *real* ultimate hurdle: materials.

Most of the advancements in combustion engines are dependent on available materials. Nickel-based *superalloy* and casting technology developments have been by far the largest factor in the rapid ascent of gas turbines to the top of the technology portfolio within less than two decades. A brief survey of the SOA in major equipment and balance of plant (BOP) materials and future development requirements is presented in a separate section.

7. Synthetic fuels

In addition to naturally available fossil fuels, one should also be aware of man-made synthetic fuels produced by chemical processing of fossil fuels (primarily coal). The key driver for synthetic fuels is carbon-free energy conversion and clean coal technology. The best-known example with considerable field experience is the IGCC. Synthetic fuel-based power generation is covered in a separate section.

8. Cleaning up the mess

Scrubbing pollutants from power plant stack gas and other plant effluents is as important as efficient generation of electric power. Carbon dioxide (CO₂) is a potent greenhouse gas and, as such, the center of attention from an environment-friendly fossil-fuel-fired power generation perspective.

In terms of technology readiness and feasibility, post-combustion CO₂ capture approach is at the top of the list; not only for the new power plants but also for retrofitting existing ones (depending on site availability, existing plant vintage, and project economics). The primary post-combustion technology is the amine-based absorption process, which will be the focus of Section 13.3.3.3.

The next section is devoted to *oxy-fuel combustion*, which is a promising technology amenable to carbon capture with less complexity and cost (on the capture side, that is; from an overall plant perspective, not necessarily so) than pre- and post-combustion technologies. While still mostly on paper, it is actively developed by private, government, and academic organizations and research institutes.

Air quality control is the generally accepted industry term for fossil-fuel-fired power plant flue gas cleaning by scrubbing off criteria pollutants between the furnace/combustor exit and the stack. Such cleanup systems are especially complex and costly for coal-fired power plants. Their impact on plant performance via parasitic power consumption of air quality control system (AQCS) components is significant for the competitiveness of advanced fossil fuel power system technologies and merits a closer look.

Finally, water treatment, on both ends of the power generation process, that is, input and output, is becoming increasingly important in the face of diminishing water resources. Just to give an example, in the United States, nearly 40% of all freshwater withdrawals in 2010 were attributed to the fossil-fuel-fired power generation industry [166]. Consequently, reducing freshwater usage is a key environmental protection initiative. As a result, *zero liquid discharge* (ZLD) facilities are on their way to become a standard feature of advanced fossil fuel power systems and thus deserve a closer look.

The chapter closes with a recapitulation of major technologies and their impact on global energy sustainability.

13.2.1 Performance Terminology

The most important fossil fuel power system performance parameter is thermal efficiency, η , which is the ratio of power output to the amount of fuel burned and expressed either as a percentage in text or as a fraction in calculations (i.e., 50% or 0.50, respectively). Its inverse is the *heat rate* (HR), which is found by the following formula (in U.S. customary and SI units):

$$\text{HR [Btu/kWh]} = 3.412/\eta$$

$$\text{HR [kJ/kWh]} = 3600/\eta$$

The amount of fuel burned can be expressed in terms of *lower heating value* (LHV) or *higher heating value* (HHV). The difference between the two is the latent energy of gaseous H_2O in the combustion products. Fuel is always purchased by HHV; therefore, the price is always quoted in dollars per million Btu (HHV). Utility practice in the United States is to use HHV in performance calculations for steam power plants (coal, oil, or gas fired) and LHV for gas turbine power plants. In Europe, the practice is to use LHV for all. In Japan, one can see plant efficiencies for gas turbine power plants quoted in HHV as well.

This can be a major source of confusion in making apples-to-apples comparisons. The convention in this chapter is, as much as possible, to use LHV in all performance discussions and calculations. The reason for that is simple: it is prohibitively expensive to add a heat exchanger to the stack of a fossil fuel power system to condense the water vapor in the flue gas and utilize the released latent heat in additional power production (e.g., by using an *organic Rankine cycle* [ORC] device—see Section 13.11.1). Thus, LHV is the more logical yardstick. For natural gas, the ratio of HHV to LHV is 1.109. For coal the ratios differ between different ranks. For Illinois #6 (bituminous) it is 1.052, for Texas lignite it is 1.107.

The second major source of confusion is gross vs. net. The total output measured at the terminals of the prime mover electric generators of the power plant is the *gross* output. To arrive at the *net* output, one should subtract the *parasitic* power consumption of myriad plant equipment and users (i.e., electric motors of the BOP pumps and fans, lighting, HVAC, etc.). The difference is commonly referred to as the *auxiliary* power. Auxiliary power for GTCC power plants ranges between 1.6% and 2.5% (mainly determined by the type of heat sink), whereas for steam power plants with typical AQCS, it is around 6% with steam turbine-driven boiler feed pumps (it can be as high as 9%–10% with electric motor-driven pumps). The convention in this chapter is to use net output, efficiency, and heat rate.

Kilowatts (kW) and megawatts (MW), and sometimes gigawatts (GW), are the generally accepted units for power—in British as well as SI systems. However, the same units can also be applied to the rate of heat transfer (i.e., $1 \text{ Btu/s} = 1.05506 \text{ kW}$ —one of the rare instances when the often-confusing British units come in quite handy). This is not surprising since the science of thermodynamics is founded on the idea that the two rates of transfer, namely, heat and work, are interchangeable. Herein, the distinction is made by using *kWe* or *MWe* for power and *kWth* or *MWth* for rate of heat transfer.

Finally, there is the issue of how to quantify the improvements in efficiency and/or heat rate. First of all, the preference herein is to use the efficiency in lieu of heat rate for the simple reason that it has a well-defined upper boundary (the Carnot efficiency, *not* 100%—see Section 13.6) and makes comparisons easier, more intuitive. (In that context, note that an improvement in heat rate is a *negative* incremental change.) Second, efficiency changes are reported in *absolute* terms as *percentage points*. In other words, improvement in net efficiency from 40% to 41% is plus 1% point. In *relative* terms, however, it is $1/40 = 0.025$ or 2.5%. Within a sentence, stating that “the efficiency increased by 2.5% from 40% to 41%” is both awkward and very confusing. The user, who is more comfortable in heat rate terminology, should note that, *x%* *relative* improvement in efficiency is *x%* improvement (i.e., *x%* *reduction*) in heat rate.

The chapter primarily uses the U.S. customary system (essentially, the “imperial” or British units with a few exceptions). Conversion to the SI (or metric) units is provided in some instances (e.g., steam pressures and temperatures in Section 13.4), where the reader might be more familiar with the latter. For large masses, one metric *tonne* (mt) is 2204.6 lb or 1.1023 U.S. *tons* (1 U.S. ton is 2000 lb).

13.2.2 Fuels Covered

The focus will be on coal (for steam turbine–based power plants) and gaseous fuels (for gas turbine–based and gas engine–based power plants). Gaseous fuels include natural gas and *synthetic gas* (syngas), which are produced via coal gasification. Hydrogen will also be covered as a special case of syngas.

The last oil-fired boiler-based power plant in the United States was built nearly 35 years ago. No new liquid fuel (distillate or residual oil)–fired boiler-based power plant is expected to be built in the future. In fact, if one goes by the projection published in the *Annual Energy Outlook 2015* by the U.S. EIA, one would not be amiss in omitting coal as well (see Figure 13.1). Nevertheless, the memory of \$13 per MMBtu natural gas is still fresh. One should also keep in mind that industry experts had declared gas-fired generation “dead” just before horizontal drilling and hydraulic fracturing (“fracking”) technology sparked the shale gas revolution in the United States.

At one time, gas turbines were exclusively designed to burn liquid fuels (1960s and 1970s). Presently, liquid fuels (e.g., light distillates such as No. 2 fuel oil) are used as backup fuel in gas turbines.* In advanced heavy-duty industrial GTs (such as H or J class), the capability to burn liquid fuel or natural gas requires “dual fuel” combustors and liquid fuel treatment skids. Old frame engines (E class or even older) are well suited to burning more difficult liquid fuels such as residual or crude oil. Nevertheless, it is unlikely that a GT power plant will ever be designed to burn more expensive and more polluting liquid fuels, which are notoriously detrimental to turbine parts’ life. (The only GTCC power plant designed to burn residual oil in the United States is a cogeneration plant in Hawaii, which burns a low sulfur fuel oil [42].) More details on burning liquid fuels in gas turbines can be found in [42].

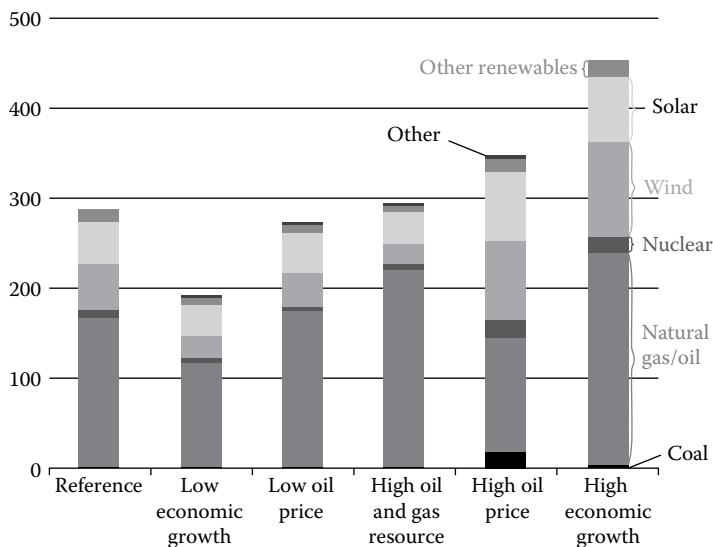


FIGURE 13.1

Cumulative additions to U.S. electricity generation capacity under different scenarios, 2013–2040 (GW). (From the U.S. Energy Information Administration, *Annual Energy Outlook 2015*.)

* Typically, sufficient liquid fuel is stored on site to enable 8–24 h of operation of the GT—for example, enough time to rectify, say, a gas pipeline pressure-loss malfunction.

It is a safe bet that expensive liquid fuels will be largely reserved for transportation applications (except in a few select cases, such as in Saudi Arabia). One could also be certain of the ever-increasing share of renewables in the global power generation portfolio. Other than that, all future predictions concerning the demise of coal in the United States and the exact share of natural gas and coal in the global power generation portfolio are subject to unexpected changes due to “black swan” type events (in any event, coal should be still significant at least in China and India*).

Synthetic liquid and gaseous fuels can and are produced from coal and other solid fuels. A well-known example is the *Fischer–Tropsch* (F-T) process for production of liquid fuels from coal, which has been in extensive use in South Africa since the 1980s. For land-based utility-scale electric power generation, however, the better candidate is the gasification process, which results in a lower heating value gaseous fuel comprising CO and H₂. Further refinement of the gasification product, *syngas*, can result in nearly pure methane, which is referred to as *substitute natural gas* (SNG), or in hydrogen fuel. Such gaseous fuels are readily amenable to utilization in GTCC power plants. For a comprehensive treatment of the synthetic fuels subject, the reader can consult the book by Probststein and Hicks [16].

Finally, one should mention *blast furnace gas* (BFG) and *coke oven gas* (COG), which are by-products of the steel-making process. Mixing these two off-gases (BFG with ~800 kcal/Nm³ or ~90 Btu/scf heating value and COG with 4500 kcal/Nm³ or ~500 Btu/scf heating value) results in a low-Btu fuel gas that can be burned in a GT combustor with 1300–1600 kcal/Nm³ LHV (~150–200 Btu/scf).[†] This off-gas blend is at atmospheric pressure and requires treatment to remove the impurities detrimental to the gas turbine hot gas path components. Older-generation E or even F class gas turbines with diffusion flame combustors are highly suitable for burning this gas with some modifications. In a combined cycle configuration, several hundred MWe worth of electric power can be generated by making use of waste gas, which otherwise would simply be vented to the atmosphere.

A typical single-shaft configuration, originally developed by a major OEM in 1990s for steel mill BFG applications is shown in Figure 13.2 [93]. An E class gas turbine is connected to the fuel gas compressor, which is a two-stage intercooled centrifugal unit, with a synchronous AC generator between the two. This configuration has been successfully operational in many steel mills in Europe and China.

Alternative single-shaft configurations are possible; for example, the power train equipment consisting of the gas turbine, generator, steam turbine, and a single-casing axial fuel gas compressor (connected to the ST via a stepup gearbox) supplied by a Japanese OEM

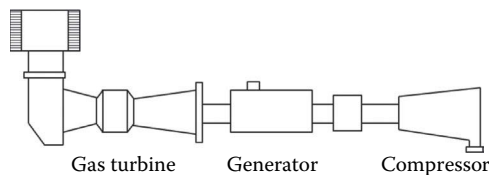


FIGURE 13.2

Single-shaft BFG firing gas turbine power train configuration (e.g., Wuhan and Handan steel mills in China [93]).

* China is the world’s biggest coal user, producer and importer. It burns 4 billion tons of coal a year, four times as much as the United States. Coal-fired plants account for about 60% of India’s installed power capacity.

[†] For comparison, consider that natural gas has a heating value of about 1000 Btu/scf LHV.

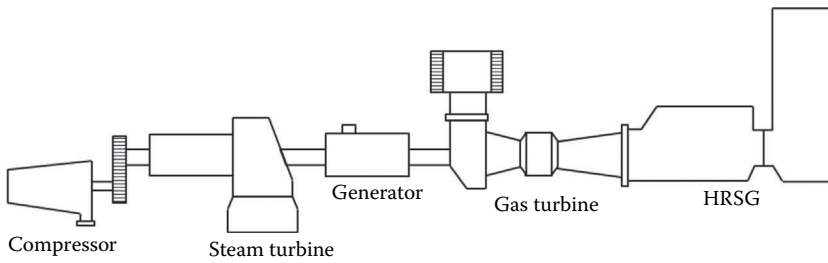


FIGURE 13.3
Single-shaft BFG firing gas and steam turbine power train configuration (e.g., in Anshan steel mill in China [136]).

for the Anshan BFG firing combined cycle power plant [136]. For design considerations pertaining to BFG firing gas turbine power generation systems, please refer to [116]. They are quite similar to those that will be discussed in Section 13.13 (Figure 13.3).

13.3 Fossil Fuel Power System

In order to treat the subject at hand, a suitable framework is needed. In cognitive sciences, such a framework is called a *schema*, which describes a well-defined pattern of thought or behavior that organizes categories of information and the relationships among them. A basic schema for the study of a generic fossil fuel power system (FFPS hereafter) is provided in Figure 13.4. Admittedly, as will be apparent in later paragraphs, this is not a fully complete rendering. Nevertheless, it establishes a starting point for the ensuing discussion.

Everything inside the big central box in Figure 13.4 is the FFPS proper; they constitute the *main* components thereof. Without them, the FFPS will not function. Everything outside are the *auxiliary* components; even without them, the FFPS will function to generate electric power (its *raison d'être*). Yet without most of those auxiliary components, almost anywhere in the world today, the governing bodies will *not* permit the FFPS to run.

Of course, one can argue that, without the *air separation unit* (ASU) to provide oxygen, the *oxy-fuel combustor* of the FFPS will not function and, therefore, the ASU should be considered a main component. This is a valid argument (which, by the way, can be made equally strongly for the *methanation unit* [METH], the *gasifier* [GASF], and the *steam methane reformer* [SMR], which generate the *syngas* or *substitute natural gas* (SNG) or pure *hydrogen* for the FFPS combustor, respectively) and points to a *fuzziness* in the distinction between main and auxiliary components.

This difficulty is avoided by limiting the definition of the FFPS, for the purposes of the present discussion, to a system with

1. Inputs of fuel, oxidizing agent, and working fluid makeup (if necessary) and
2. *Desired* outputs of electric power and useful heat (in the form of steam or hot water) while generating
3. *Undesired* or waste outputs (i.e., streams of flue gas, wastewater, etc.)

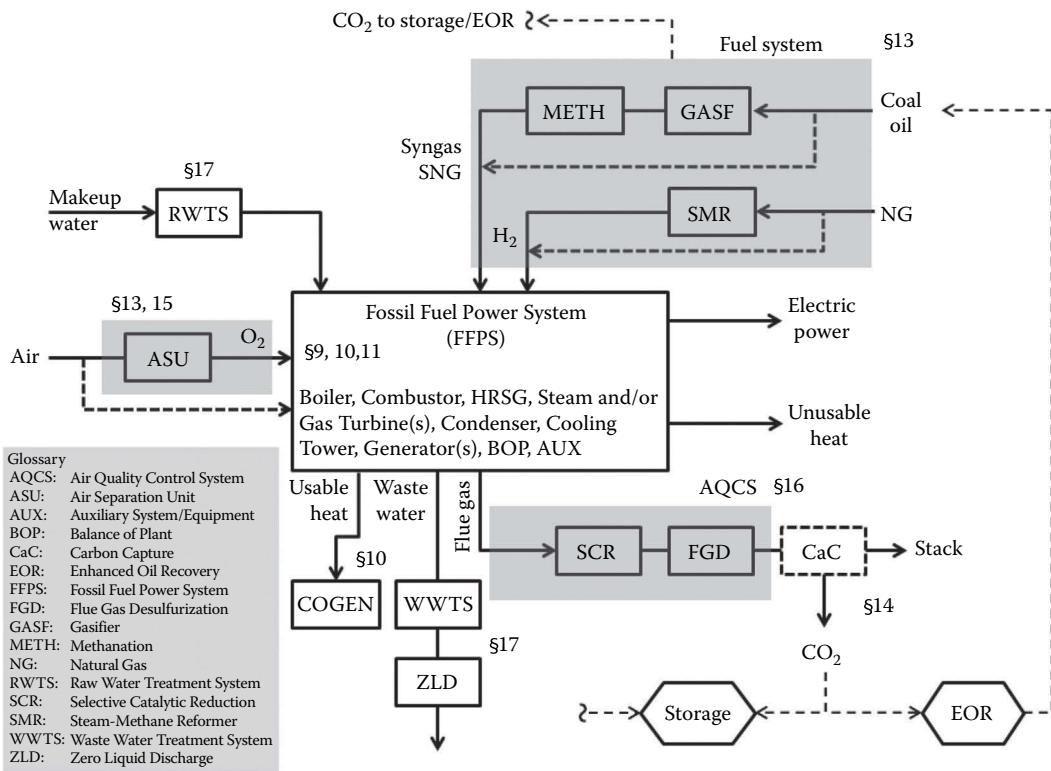


FIGURE 13.4 Fossil fuel power system—see the inset for the glossary of acronyms (annotations indicate sections where specific items are covered).

When a particular FFPS is designed to generate more than one desired output, it is referred to as a *cogeneration* (U.S. terminology) or *combined heat and power* (CHP, the term preferred in Europe) system. Most common cogeneration applications are industrial systems with process steam supplied to a, say, chemical plant and district heating systems drawing hot water or low-pressure steam from the power plant.

13.3.1 System Components

Plants utilizing fossil fuels to generate electric power can be divided into two groups based on the type of *prime mover* (i.e., engines originally conceived to convert power into motion) forming the core of the power system:

1. Internal combustion engines (ICE)
 - a. Reciprocating (piston–cylinder) engines (characterized by unsteady or intermittent flow of the working fluid)
 - i. Spark ignition
 - ii. Compression ignition
 - b. Open-cycle gas turbines (characterized by the *steady* flow of the working fluid)

2. External combustion engines (XCE)
 - a. Steam turbines
 - b. Closed-cycle gas turbines

Internal and external combustion engines are heat engines whose operations are described by well-known thermodynamic cycles (details of which can be found in any engineering textbook [14]):

1. ICE cycles
 - a. Otto, Diesel, Stirling (reciprocating engines)
 - b. *Brayton* (gas turbine)
2. XCE cycles
 - a. Steam RBC
 - b. *Brayton* (gas turbine)
3. *Combined cycles* (please refer to the respective chapter of the handbook for the pertinent details)
 - a. *Brayton* or *Otto/Diesel* (the topping cycle)
 - b. *Rankine* (the bottoming cycle)

13.3.2 Main Equipment

The thermodynamic cycles listed earlier are translated from paper (thermodynamic theory) to practice (a plant operating in the field) via the following *main* equipment:

1. Heat source
 - a. XCE *boiler* (coal, oil, or gas fired)—fuel, oxidizer (usually air), and cycle working fluid (H_2O as water and steam) do *not* mix
 - b. ICE *combustor* (oil or gas fired)—fuel and oxidizer (usually air) mix and constitute the working fluid (at least for the “hot” section of the cycle)
 - c. ICE cylinder (reciprocating engines)
2. Shaft power producer
 - a. XCE *steam turbine* (also for the bottoming cycle of the combined cycle)
 - b. ICE *gas turbine*
 - c. ICE piston (reciprocating engines)
3. Electric *generator* (transforms shaft power to electric power)
4. Heat sink—ultimately the atmosphere via
 - a. XCE *condenser* (water or air-cooled) and *cooling tower*—also for the bottoming cycle of the combined cycle or
 - b. ICE exhaust/flue gas (reciprocating engines and gas turbines)
5. Waste heat recovery (WHR) heat exchanger—also known as *heat recovery steam generator* (HRSG)—is the piece of equipment serving as the interface between the topping (*Brayton*) and bottoming (*Rankine*) cycles of the combined cycle

6. Myriad pumps and heat exchangers
7. Ducts, pipes, and valves
8. Plant distributed control system (DCS)
9. Myriad motors, transformers, and other electrical equipment

Equipment except those italicized in this list are typically covered under the heading *balance of plant* (BOP). One should also consider the *main step-up transformers* and the *switchyard*, requisite for connecting the plant to the electric grid, among the major equipment. It is the new and improved variants of non-BOP equipment that decide whether an FFPS can be deemed to be advanced or not (more on that in the next section).

Major equipment has different variants, which can be summarized as follows:

1. Steam power plant boilers (coal, oil, or gas fired)
 - a. Pulverized coal (PC)
 - b. Circulating fluidized bed (CFB)
2. Gas turbine combustors
 - a. Diffusion
 - b. Dry low NO_x (DLN)—also referred to as dry low emissions (DLE)
 - c. Single (usually natural gas) or dual fuel (#2 distillate as backup fuel)
 - d. Configuration—can-annular, annular, or silo (mostly obsolete)
 - e. Single or sequential (i.e., reheat combustion)
3. Steam turbines
 - a. Aerothermal design—impulse or reaction stages
 - b. Configuration
 - i. Reheat or non-reheat (RH or NRH)
 - ii. Condensing (pure power) or back pressure (cogeneration)
 - iii. Tandem or cross-compound
4. Gas turbines
 - a. Hot gas path (turbine) cooling
 - i. Air cooled (open loop)
 - ii. Steam cooled (closed loop)
 - b. Intercooled compressor
 - c. Recuperative
5. Synchronous AC generators
 - a. Air or water cooled
 - b. Hydrogen cooled
6. Steam condensers
 - a. Once-through open loop (water cooled, no cooling tower)
 - b. Closed loop (water cooled with mechanical or natural draft cooling tower)
 - c. Air cooled (A-frame)

7. HRSG

- a. Reheat or non-reheat (RH or NRH)
- b. One, two, or three pressure levels (1P, 2P, and 3P, respectively)
- c. Vertical (common in Europe and Asia) or horizontal (common in the United States)
- d. With or without bypass stack

13.3.3 Auxiliary Equipment

The *auxiliary* equipment can be grouped into four categories:

1. Fuel system—comprises fuel generation, delivery, preparation, and conditioning
2. Air quality control system
3. *Post-combustion* carbon capture system
4. Water treatment system
 - a. Raw water treatment system
 - b. Wastewater treatment system

13.3.3.1 Fuel System

For the fuels, which are readily available at the FFPS boundary, the fuel system comprises preparation, conditioning, and delivery components. For a typical *pulverized coal* (PC) boiler, this can be a bin or direct firing system with raw coal bunker, crusher, pulverizer, cyclone, bag filter, etc. For the natural gas-fired gas turbines, there is a “fuel skid” comprising a multiplicity of valves and controls to supply the gaseous fuel to the combustor at the requisite pressure and quantity. Depending on the pipeline pressure and gas turbine cycle pressure ratio (PR), a booster compressor may be required (especially for the reheat combustion units with cycle pressures well above 30 bars and aeroderivative gas turbines). In addition to fuel gas heaters to provide sufficient superheat to prevent hydrocarbon condensation, “performance” fuel gas heaters are present in all advanced combined cycle power plants to heat the gaseous fuel to temperatures as high as 200+°C (400+°F) in order to improve the plant’s thermal efficiency. Such heaters typically use the intermediate pressure (IP) feedwater from the HRSG as the hot fluid.

The most efficient FFPS today (and in future) is a gas turbine combined cycle (GTCC) power plant. In theory, a gas turbine combustor can burn any fuel.* Indeed, there are industrial gas turbines in Saudi Arabia burning crude or residual oil for power generation (mainly old Frame 5 units). All modern gas turbines with DLN combustors are designed to burn distillate fuel (No. 2 fuel oil) as a backup [42]. Nevertheless, burning solid fuels (e.g., coal or biomass) in a gas turbine combustor cleanly and efficiently is not a realistic possibility. Therefore, gasification of solid fuels has been a primary area of research and development for “clean” power generation utilizing abundant but environmentally problematic fossil fuel resources such as coal.

The key enabling technology is *gasification*, which produces a gaseous fuel of low or medium heating value with carbon monoxide (CO) and hydrogen (H₂) as primary

* A striking, and likely to be apocryphal, example used to emphasize this capability is Chrysler’s Ghia turbine car in the early 1960s, whose combustor was claimed to burn even Chanel No. 5 perfume as fuel.

constituents. The combination of the gasification and GTCC plants (the latter burning syngas for electric power generation) is referred to as *integrated gasification combined cycle* (IGCC). A variation on gasification comprises the additional step of *methanation*, which generates a final gaseous product with methane (CH_4) as the primary constituent, also known as *substitute natural gas*.

Hydrogen is touted as the perfect fuel for clean combustion. With +95% pure oxygen (O_2) as the oxidizing agent, the main combustion product is H_2O (steam). It seems to solve all major pollutant emission problems in one stroke, that is, no NO_x , no SO_x , no carbon dioxide (of course, the reality is not so simple). Catalytic and noncatalytic *steam methane reforming* (SMR) is one way to produce H_2 as gas turbine fuel.

All gaseous fuel production technologies for electric power generation in gas turbine-based power plant systems can be classified as advanced and will be covered later in the chapter.

13.3.3.2 Air Quality Control System

Emission of pollutants in the flue gas of an FFPS into the atmosphere is stringently regulated by governmental agencies (e.g., Environmental Protection Agency [EPA] in the United States). Most notorious pollutants are nitrous oxides (NO_x), sulfur oxides (SO_x), particulate matter (PM), lead, carbon monoxide (five of the six *criteria pollutants* defined by the EPA), and mercury. While carbon dioxide (CO_2) is not a pollutant per se, it is a major greenhouse gas, and reduction of its release into the atmosphere from the FFPS stack is a major endeavor.

A *bona fide* AQCS comprises several major pieces of equipment and can be considered a “mini plant” in its own right. It is an integral part of coal-fired boiler steam turbine FFPS and will be covered in a separate section in the following text.

Natural gas is a relatively clean burning fuel. From an air quality control perspective, the major pollutants in a gas-fired FFPS are NO_x and carbon monoxide (CO)—and volatile organic compounds (VOC) to a lesser extent. (Particulate matter and sulfur oxides are a concern when liquid fuels are burned—as a backup fuel mostly—in gas turbines.) Reduction of NO_x emissions in gas turbine power plants is done in two steps: (1) *dry low NO_x* (DLN) combustion and (2) selective catalytic reduction (SCR) of the flue gas. DLN combustors will be covered in Section 13.8; SCR technology for the gas-fired FFPS will be touched upon in Section 13.3.3.2.

13.3.3.3 Post-Combustion Carbon Capture System

There are three types of carbon capture: *pre-* or *post-*combustion and *oxy-fuel* combustion. The first one is a part of the advanced fuel system and results in a carbon-free fuel, for example, hydrogen; the main combustion product is water vapor (steam). Oxy-fuel combustion, as the name implies, utilizes nearly pure oxygen as the oxidizing agent in lieu of air (more than two-thirds of which, on a volumetric basis, is nitrogen). Oxy-fuel combustion can be combined with pre-combustion capture, resulting in steam as the combustion product (using steam or water as combustion diluent). Otherwise, the combustion products are mainly water vapor and CO_2 , which is easy to separate for sequestration by knocking out the water vapor in a condenser.

There are three types of post-combustion CO_2 capture technologies: via *absorption*, *adsorption*, or *membrane* [25]. A fourth one, regenerable solid solvent, can be added to the list. At the time of writing, from technology maturity and economic viability perspectives,

scrubbing of flue gas in an *amine-based absorption/stripper* process is the most feasible. From a conceptual standpoint, this process can be thought of as an add-on (a mini chemical process plant if you will) to the AQCS of a coal-fired FFPS (itself a mini plant, as stated earlier) or to the GTCC proper. It will be covered in more detail in a separate section in the following text.

13.3.3.4 Water Treatment System

Steam generated when boiling water in a pan on the kitchen range at home is not suitable for a steam turbine. Even though invisible to the naked eye, untreated boiler feedwater is full of stuff harmful to the FFPS equipment: suspended solids (e.g., metallic particles), dissolved solids (e.g., Na, Cl, SO₄, etc.), and gases such as CO₂, O₂, vaporized silica, and “organics.” Ideal steam turbine steam is dry (quality of 1.0) and pure H₂O with a pH of ~9.0. Poor steam purity leads to severe problems, for example, deposition on turbine blades, corrosion fatigue of blades and disks, particle erosion, etc.

Water and steam lost via blowdown and leakages must be made up. The added makeup water must be treated to preserve cycle water and steam purity to prevent boiler and turbine damage. Raw makeup water treatment comprises several steps: filtration, clarification, softening, demineralization, and condensate polishing.

Water discarded from the power plant must also be treated in compliance with applicable rules and regulations. Gas-fired power plants do not produce a significant amount of wastewater, mainly HRSG evaporator drum and cooling tower blowdowns. Coal-fired steam power plants with AQCS have more wastewater producers and more contaminants. For both gas- and coal-fired FFPS, if/when post-combustion carbon capture add-on becomes a standard plant future, wastewater treatment systems will be more complex and costlier. Furthermore, growing water scarcity across the globe makes *zero liquid discharge* (ZLD) increasingly common. In ZLD plants, wastewater from the FFPS is treated for water recovery and reuse (e.g., as cooling tower makeup).

These technologies will be covered in Section 13.17.

13.4 Advanced Fossil Fuel Power System

What makes a fossil-fuel-fired power system deserve the moniker “advanced,” that is, AFFPS? Those determining factors can be summed up in three categories:

1. Technologies that make the *cycle* advanced—for example, double-reheat steam RBC for advanced USC power plants or 1600°C (+2900°F) turbine inlet temperature (TIT) J class turbine (Brayton cycle)
2. Technologies that make the *equipment* advanced—for example, sequential combustion or closed-loop steam cooling in a gas turbine
3. Technologies that make the *overall* power plant advanced—for example, amine-based post-combustion carbon capture in a gas turbine combined cycle power plant

As described earlier, the key foundation blocks of FFPS are internal and external combustion engines. These are heat engines, whose basic operation is described by fundamental thermodynamic cycles. There are four such cycles that describe by far the largest majority

of heat engines: Brayton (gas turbine), steam RBC, and Otto/Diesel (piston–cylinder or reciprocating engines).

All fundamental engine cycles have been around for many decades. In particular, the emergence of the two engine types, namely steam turbine and reciprocating engines, goes as far back as the nineteenth century. The gas turbine, in its aircraft propulsion and land-based power generation guises, is not exactly new either. Depending on where one marks the beginning, its origins (in its readily recognizable form) can be traced to the 1930s. As such, all these engines, from a thermodynamic cycle perspective, represent mature technologies. At the time of writing, developments that one can call advanced in terms of heat engine cycles are quite limited.

Today's SOA in gas turbine (GT) Brayton cycles are cycle pressure ratios (PR) of ~23 and TIT of 1600°C (+2900°F) with the next step being identified as 1700°C (~3100°F) and PR of about 25.

By far the most widely used Brayton GT variant is the standard, four-process cycle with compression, combustion, expansion, and exhaust. Textbook variations such as intercooling (to reduce compression power) and exhaust gas recuperation (heating of combustion air with gas turbine exhaust) are available in limited units (exclusively in aeroderivative units). Recuperation is advantageous for the simple cycle, especially in combination with intercooling, but not so for the combined cycle (limiting the waste heat recovery in the HRSG).

Today's SOA in steam RBCs can be covered in two groups:

1. For GTCC bottoming cycles with high-pressure (HP) or throttle steam conditions of ~2400 psi (165 bar) and 1112°F (600°C); hot reheat (HRH) steam temperature of also 1112°F (600°C)
2. For steam power plants USC cycles of 280 bar HP steam and 1112°F (600°C) HP and HRH steam temperatures

GTCC bottoming cycle steam conditions are directly tied to the GT exhaust flow and temperature. Supercritical steam bottoming cycles have been considered but are unlikely to be economically feasible any time soon—if ever [82]. The goal in advanced USC is 300 bar HP steam with 700°C HP (760°C in the U.S. DOE–sponsored programs) and HRH steam temperatures with *double-reheat* cycle. Advanced USC systems will be covered separately in the following text.

Whether reheat gas turbine is an advanced cycle or advanced equipment technology is debatable. It is probably both. Reheat is a textbook cycle improvement applicable to both Brayton and Rankine cycles [14]. It is indeed a main feature of all modern fossil-fuel–fired boiler steam turbine power plant cycles. Its application to a gas turbine is more complicated due to excessive combustion pressure loss, sealing difficulties, and *hot gas path* (HGP) parts' cooling load increase. Nevertheless, sequential combustion GTs offered by one *original equipment manufacturer* (OEM) with two combustion–expansion steps in series are the second most widely deployed heavy-duty industrial gas turbine configuration out there.

One can also add the steam-cooled GTs to the advanced equipment technology; G and J class GTs with steam cooling limited to the stationary HGP parts and the H-System™ with fully steam-cooled first and second turbine (expansion) stages. Those technologies will be discussed in Section 13.6.

It is a safe bet that the steam and gas turbines as well as the reciprocating ICEs and their respective cycles in the foreseeable future, say, 20 years down the road, will not be different from the advanced technology units that we have today (and, one might add, those

we had half a century ago). The improvements will be incremental and mostly driven by advancements in materials and manufacturing technologies.

By far the largest advances in FFPS should be expected from the add-ons to the basic plant, primarily in advanced fuel systems and emission control technologies. An overriding majority of such advances will be driven by initiatives (1) to burn fossil fuels and especially coal cleanly and (2) to reduce or eliminate CO₂ emissions. Such technologies constitute a major part of this chapter.

There are a large variety of proposed technologies for *carbon capture and sequestration or storage* (CCS). This is a distinctly two-pronged process:

1. Capture: Separate or scrub CO₂ from a stream of gas mixture, which can be one of the following three types:
 - a. FFPS flue/stack gas (*after* combustion)
 - b. Synthetic fuel gas or syngas (*before* combustion)
 - c. Carbon dioxide plus water vapor (*after* combustion with O₂ or via *chemical looping*)
2. Sequester*: Compress the “captured” CO₂ to a pressure commensurate for (1) transporting away (if necessary) from the FFPS via pipeline and (2) injecting into a suitable underground storage well (e.g., depleted oil or gas reservoirs, unminable coal beds, deep saline aquifer, deep ocean, etc.).

The second part is pretty straightforward: one just needs a large enough process compressor train to increase the pressure of CO₂ to the requisite level (typically, around 2000 psia or higher). In order to reduce the compression power, which is a parasitic consumption debited to the net electric output of the FFPS, a multicasing compressor train with intercoolers is utilized. State-of-the-art designs incorporate a pump-like final stage where CO₂ is in a supercritical state (critical pressure of carbon dioxide is about 1150 psig) with or without an upstream refrigeration cycle to liquefy it [41]. It is a case of cost vs. performance trade-off, which must be done on a case-by-case basis. Dehydration may be required to reduce water moisture to less than 50 ppmv for *enhanced oil recovery* (EOR) application. As a rule of thumb, one should allow for 170 ± 20 Btu/lb (400 ± 50 kJ/kg) for CO₂ compression via an intercooled, multistage centrifugal compressor. Advanced technologies such as a single-stage shock compressor have been proposed [34]. It is unclear when or if they would be viable competitors to centrifugal compressors.

In order to visualize the capture technology landscape in a digestible manner, the schema shown in Figure 13.5 is proposed. The main distinction is between two approaches, which involves separation or stripping (or *scrubbing*) of CO₂

1. From flue gas or syngas (difficult/costly)
2. From CO₂ plus water vapor (easy/cheaper)

The difficulty and costliness are not limited to the separation process. Those challenges are also involved in the *production of*

1. Syngas
2. CO₂ + H₂O post-combustion product stream

and make the carbon capture technology selection process even more complicated.

* Isolate or hide away.

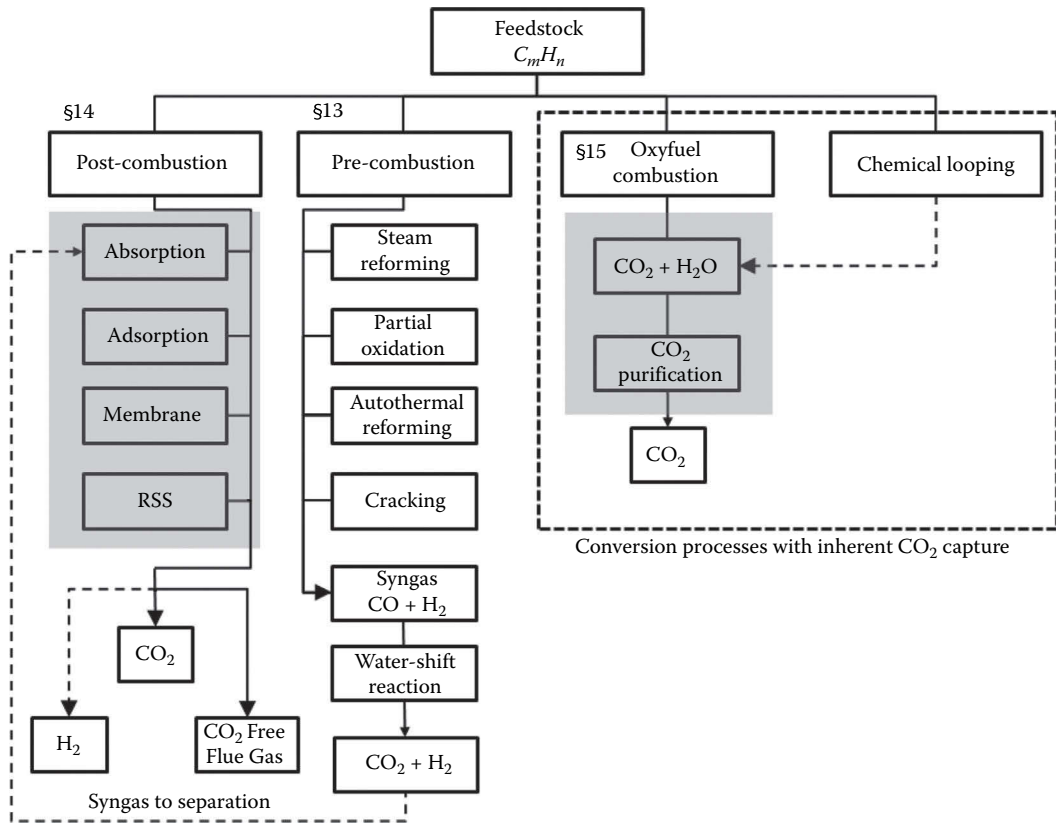


FIGURE 13.5

Carbon capture technology landscape (annotations indicate sections where specific items are covered). RSS, regenerable solid solvent.

Oxy-fuel combustion is covered in Section 13.15. This is also where the *supercritical* CO_2 cycle is covered within the context of the *Allam* cycle. Furthermore, *chemical looping combustion* (CLC) is also covered under oxy-fuel combustion. Pre-combustion technologies are covered in the context of syngas production, which includes the IGCC. Post-combustion technologies are covered in a separate section, with an emphasis on amine-based absorption system, which is currently the most readily available carbon capture technology.

A useful concept in assessing new technologies is the *technology readiness level* (TRL), which was originally adopted by the NASA to help and guide their research and development (R&D) process. It is intended to provide a systematic approach to assessing the maturity of a particular technology and to compare it consistently with other technologies in terms of maturity. The TRL score (from 1 to 9) is established based on three key attributes: (1) scale or size, (2) degree of system integration, and (3) the test environment in which the technology has been successfully demonstrated (see Figure 13.6).

Each of the stages in Figure 13.6 can take at least 5–10 years, maybe longer. Artificial acceleration of the process is actually harmful to the technology in question. The introduction of the FGR technology in the 1970s is a good cautionary example. Although it is a widely accepted technology today, it took nearly three decades to make the transition from “novel” to “mature.” The end goal of “commercial deployment” has also different stages.

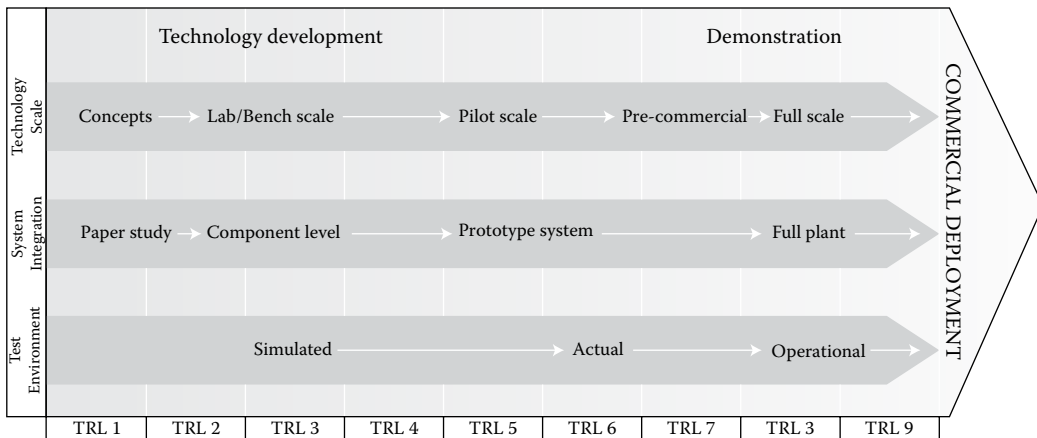


FIGURE 13.6

Technology readiness level—relationship to scale, degree of integration, and test environment. (From Carbon Capture Technology Program Plan, Clean Coal Research Program, U.S. DOE, Office of Fossil Energy, NETL, January 2013).

According to a report by the National Coal Council [68], a technology that has achieved at least TRL 7 or 8 is commercially viable. Such a technology has the potential to be commercially available. In order to be commercially available, the technology in question should meet the following criteria [68]:

1. One year of operation, with 70% availability at scale within 5 years after startup.
2. Reasonable cost and performance.
 - a. Meets the *pro forma* requirements of the facility's balance sheet.
 - b. Project wrap performance guarantees are available.
 - c. Reasonable insurance policies are available.
 - d. Risks to ratepayers are minimized (e.g., cost overruns, underperformance, etc.).
 - e. Risks of prudency-type reviews downstream are minimal.
 - f. Performance objectives are met (i.e., heat rate, availability, reliability, market and grid dispatch, flexibility, emissions criteria).
 - g. Project finance can be obtained without the need for a consortium.

According to the aforementioned NCC report [68], *(full) commercialization* is defined as being that point where either the new technology claims 10% of the installed base or at least 50% market share of new installations for several years.

Many new technologies do not make it beyond TRL 4 or 5. Even if a technology eventually reaches TRL 7 or 8, it is not a guarantee that it will be widely accepted by the industry and become a mainstay of generation technology portfolio. A good example is the IGCC, which has been commercially deployed since 1980s but failed to make an inroad—primarily due to economic reasons (made worse by cheap natural gas in the United States). A table of TRL levels as defined by the DOE Office of Fossil Energy is provided in Table 13.1. It will be helpful in gauging the maturity of advanced technologies covered in the following paragraphs.

TABLE 13.1

U.S. DOE Office of Fossil Energy Definitions of Technology Readiness Levels

TRL	DOE-FE Definition	DOE-FE Description
1	Basic principles observed and reported	Lowest level of technology readiness. Scientific research begins to be translated into applied R&D. Examples might include paper studies of a technology's basic properties.
2	Technology concept and/or application formulated	Invention begins. Once basic principles are observed, practical applications can be invented. Applications are speculative, and there may be no proof or detailed analysis to support the assumptions. Examples are still limited to analytic studies.
3	Analytical and experimental critical function and/or characteristic proof of concept	Active R&D is initiated. This includes analytical studies and laboratory-scale studies to physically validate the analytical predictions of separate elements of the technology. Examples include components that are not yet integrated or representative. Components may be tested with simulants.
4	Component and/or system validation in laboratory environment	The basic technological components are integrated to establish that the pieces will work together. This is relatively "low fidelity" compared with the eventual system. Examples include integration of "ad hoc" hardware in a laboratory and testing with a range of simulants.
5	Laboratory scale, similar system validation in relevant environment	The basic technological components are integrated so that the system configuration is similar to (matches) the final application in almost all respects. Examples include testing a high-fidelity, laboratory-scale system in a simulated environment with a range of simulants.
6	Engineering/pilot scale, similar (prototypical) system demonstrated in a relevant environment	Engineering-scale models or prototypes are tested in a relevant environment. This represents a major step up from a TRL5. Examples include testing an engineering scale prototype system with a range of simulants. TRL 6 begins true engineering development of the technology as an operational system.
7	System prototype demonstrated in a plant environment	This represents a major step up from TRL 6, requiring demonstration of an actual system prototype in a relevant environment. Examples include testing full-scale prototype in the field with a range of simulants. Final design is virtually complete.
8	Actual system completed and qualified through test and demonstration in a plant environment	The technology has been proven to work in its final form and under expected conditions. In almost all cases, this TRL represents the end of true system development. Examples include developmental testing and evaluation of the system within a plant/CCS operation.
9	Actual system operated over the full range of expected conditions	The technology is in its final form and operated under the full range of operating conditions. Examples include using the actual system with the full range of plant/CCS operations.

Source: Carbon Capture Technology Program Plan, Clean Coal Research Program, U.S. DOE, Office of Fossil Energy, NETL, January 2013.

13.5 Past, Present, and Future

The moniker “advanced” designates a given technology’s most favorable embodiment currently available or soon to be available (“far on or ahead in development or progress”). The two obvious follow-up questions are (1) where the technology was before it became advanced and (2) where it can go by being even more advanced. These questions are especially relevant for a mature technology such as fossil-fuel-fired electric power generation. The conceptual tool that addresses the evolution of a technology is widely known as the “S curve” (Figure 13.7).

According to the S curve, the evolution of a technology over time (as represented by a suitable figure of merit that characterizes the advancement of the technology in question) can be divided into three conceptual phases: (1) invention and early development, (2) rapid innovation and advancement, and (3) maturity.

During the maturity phase, any further innovation adds only incremental improvements with diminishing returns. In this phase, research and development efforts increasingly focus on new “replacement” technologies, which are expected to go through their own S curve evolution.

13.5.1 Past

At this point, it is instructive to look at the evolution of fossil-fuel-fired (mostly coal), steam-driven power generation technology (see Figure 13.8). The early steam engine and Parsons’ *fin de siècle* steam turbine data are from W.S. Jevons’ incredibly prescient treatise on coal [106] and Aurel Stodola’s seminal book [20]. The modern-age data (containing historical and forecasted numbers) are compiled from various sources such as International Energy Agency (IEA) databases published in several reports and articles. They show the classical stages of the technology life cycle or the “S curve,” ending up in the mature phase capped by about 45% net HHV efficiency. That barrier seems highly unlikely to

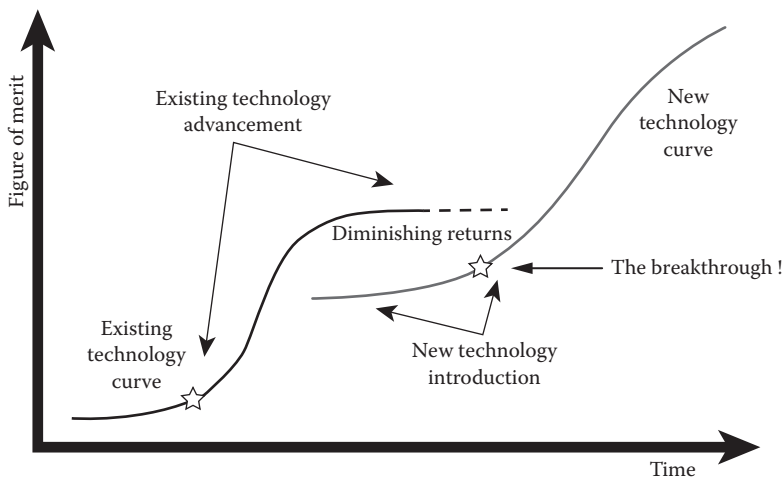


FIGURE 13.7
Conceptual technology evolution S curve.

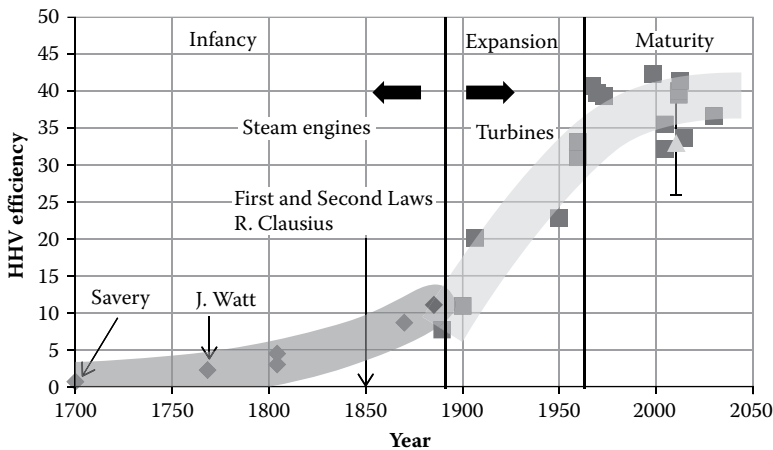


FIGURE 13.8

Historical development of fossil-fuel-fired, steam-driven power generation technology. Today's average is around 33% (the triangle with error bars), with the range of technology from around 25% to 40%. The current world record holder is a USC unit with double reheat in Denmark (>42%). The first USC plant in the United States is J.W. Turk, with 40%.

be broken for quite a while (maybe never, considering the increasingly stringent limits imposed on the generators by the regulatory agencies).

At this point, a *caveat* is in order. At any given time during a technology's development history, pouring in resources into R&D can lead to "blips"—that is, performances well ahead of their time. The best example for this situation is Lockheed's SR-71 "Blackbird" strategic reconnaissance aircraft with two Pratt & Whitney J58 "turbo-ramjet" engines [57]. Designed in the early 1960s by engineers using slide rules, the aircraft was capable of reaching a cruise speed of Mach 3.0+ at 80,000 ft—a feat still unsurpassed even today.* In a similar vein, two noteworthy examples are AEP's *Philo 6* and *Eddystone 1* ultra-supercritical, double-reheat power plants (both ASME historic mechanical engineering landmarks today) built and commissioned in the late 1950s (40% net HHV) [64].† In fact, *Eddystone 1* was designed to operate at the highest steam pressure and temperature ever utilized in a power plant, 5000 psi (345 bars) and 1200°F (650°C), respectively. However, repeated failures after a few years of operation forced the plant operators to reduce the steam temperatures back to 1130°F (610°C). While the trend started by these units continued by the high-performance levels of supercritical TVA power plants built in the late 1960s (i.e., Bull Run, Paradise Unit 3, etc.), a plateau in steam conditions has existed since then. Furthermore, added cost and complexity (notwithstanding the impact on efficiency) of the AQCS, in addition to environmental regulations‡ severely precluding the use of once-through, open-loop heat rejection to rivers and lakes, actually led to a much reduced level of average plant performance.

* One could also mention the development, introduction, long and successful (albeit on a limited scale) service but ultimate failure of supersonic Concorde for commercial air travel in that context.

† Cost of building *Philo 1* is reported as \$20.3 million, which translates to about \$175 million or \$1450 per kilowatt in today's dollars [64].

‡ For example, U.S. EPA's final rule issued under Section 316(b) of the Clean Water Act, which applies to facilities that each withdraw at least 2 million gal per day of cooling water from waters of the United States.

13.5.2 Present

Is there a breakthrough in fossil-fuel-fired power generation technology depicted in Figure 13.8? As a matter of fact, yes; there is the gas turbine combined cycle technology. The history of GTCC can be taken as far back as late 1940s when a GE Frame 3 gas turbine was used as “forced draft fan” in a steam power plant in the United States [154]. Nevertheless, gas turbines did not play a significant role in electric power generation until 1960s. Up to that point, their role was limited to industrial process and natural gas transmission applications. Their subsequent role was as emergency generators in simple cycle configuration to alleviate demand peaks. However, this started to change soon when coal-fired generation technology hit an efficiency “wall,” while technology transfer from aircraft engines pushed gas turbine efficiencies higher. Higher firing and exhaust temperatures made the combined cycle a feasible option, which from the get-go matched and surpassed the best-available coal-fired power plant efficiency. The pace of evolution picked up with the introduction of the F class in the 1980s, when 50% net efficiency barrier was broken by the end of the decade. The “bubble” at the end of the 1990s speeded up the introduction of new technologies, with 60% net efficiency as the next goalpost. The gas turbine CC technology evolution trend from the 1980s to the present is captured in Figure 13.9 [85].

It seems that the GTCC technology is about to enter its own maturity phase. Based on the trend in Figure 13.9, one can reasonably expect ~62% by 2025 and ~62.5% by 2035 (ISO base load rating performance). Going by the error of the fit, these numbers can be bumped up by 1% point. Details of specific technology enablers requisite for achieving those performances (or better) will be covered in the “GTCC” section.

The existence of an efficiency “wall” for the GTCC technology can also be discerned by the technology curves of its major building blocks, that is, gas turbine Brayton and steam RBCs. The Brayton cycle gas turbine efficiency evolution is shown in Figure 13.10. The Rankine cycle efficiency will be discussed in Section 13.6.

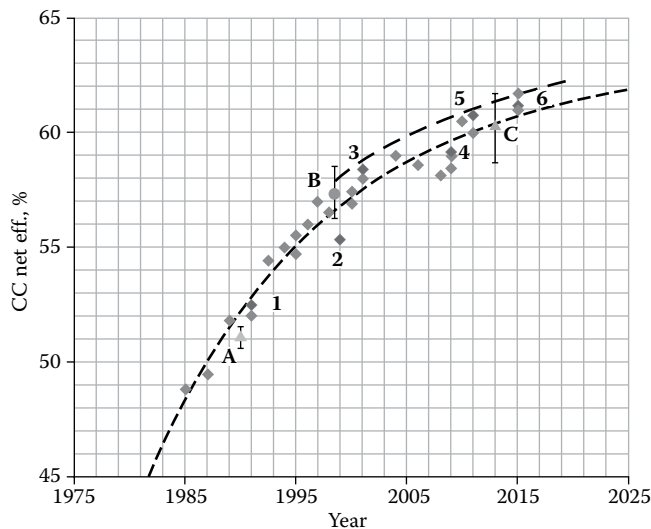


FIGURE 13.9

GTCC evolution, 1985–2015 (A: *TMI 1990 Handbook*, B: *GTW 1998–1999 Handbook*, C: *GTW 2013 Handbook*, 1: Ambarli, Turkey, 2: Tapada do Outerio, Portugal, 3: Mainz Wiesbaden, Germany, 4: Kawasaki, Japan, 5: Irsching, Germany, 6: Cengiz Enerji, Turkey).

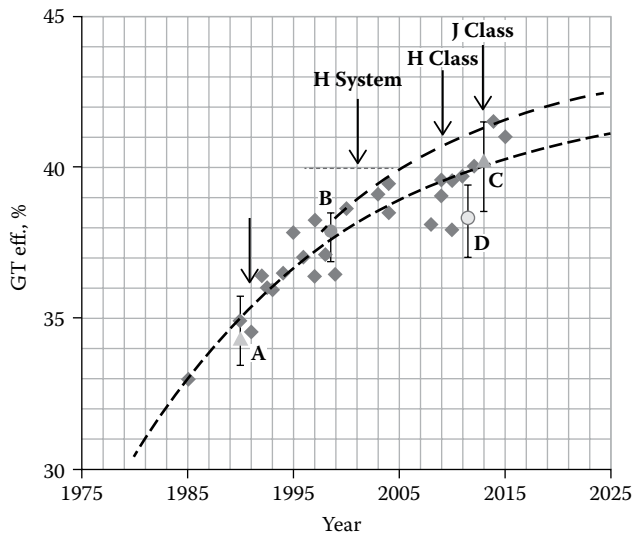


FIGURE 13.10

Gas turbine evolution, 1985–2015. See the caption of Figure 13.9 for data sources (D: *GTW 2003 Handbook*).

13.5.3 Future

All fossil fuel power systems, whether they are advanced or not, are based on prime movers, which are heat engines. As such, their performance is capped by the second law of thermodynamics, that is, the *Carnot limit*. The inescapability of its iron grip is dramatically illustrated by the second law treatment in Section 13.6. Unless a “non-heat engine” technology emerges to replace the entire system or parts of it, this hurdle will be impossible to overcome.

By far the most promising non-heat engine candidate, at least on paper, is the *fuel cell* technology [45]. A fuel cell converts chemical energy of a fuel directly into electrical energy. It is different from a battery in the sense that, rather than being a *storage* device, it is a *conversion* device to which fuel and oxidant are supplied continuously. The intermediate processes of heat generation, transfer, and conversion to shaft power are avoided so that fuel cells are *not* subject to the Carnot limit. Since there is no combustion, fuel cells generate power with minimal pollutants (e.g., no NO_x because operating temperatures are about 1650°F or lower). For details of the fuel cell technology, the reader is referred to Chapter 25 of this handbook.

Fuel cells, as standalone individual power generation systems, are ideally suited to distributed generation. From an AFFPS perspective, especially for utility-scale electric power generation, the application of most interest is a *fuel cell hybrid system*, wherein the fuel cell acts as the “combustor” of a gas turbine [45]. From a different perspective, the hybrid system is a *combined* cycle with the fuel cell as the *topping* cycle. (Another variant has the fuel cell as the *bottoming* cycle.) A hybrid gas turbine fuel cell (as the topping cycle) system is shown in Figure 13.11. Fuel cell hybrid systems are based on *molten carbonate* and *solid oxide* fuel cells (MCFCs and SOFCs, respectively) due to their high operating temperatures (650°C–900°C). Typical fuel cell fuel is hydrogen (H_2), carbon monoxide (CO), and methane.

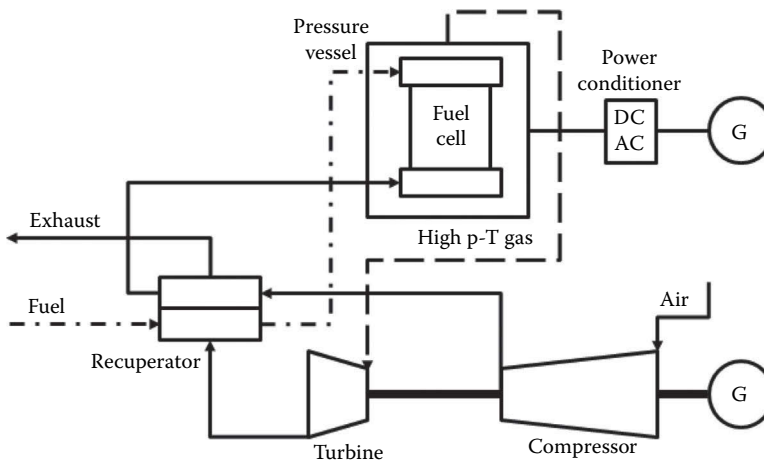


FIGURE 13.11
Basic fuel cell—gas turbine hybrid power generation system.

A detailed study of fuel cell GT hybrid systems was done by Bhargava et al. [37]. Their findings are summarized in Table 13.2. For a detailed analysis, please refer to the cited work. The fuel cell technology is characterized by cell voltage (0.70 V), fuel cell *utilization factor* (UF, with a typical value of 0.80), and air utilization factor (0.25). Fuel cell UF (for MCFCs and SOFCs) is defined as the ratio of the oxidized hydrogen mass flow to the equivalent hydrogen mass flow available at the cell inlet, taking into account the internal reforming reactions. Air UF (for MCFCs) is defined as a ratio of oxygen mass flow consumed by the FC electrochemical reactions to the oxygen total mass flow available. The gas turbine technology was defined by two cooled stages and compressor/turbine polytropic efficiencies (0.90/0.89).

The U.S. Department of Energy (DOE)'s National Energy Technology Laboratory (NETL) conducts an SOFC program under the Clean Coal Research Program (CCRP), specifically within the *CCS and Power Systems* program. Solid oxide fuel cells constitute one of the four areas within the *Advanced Energy Systems* subprogram.*

TABLE 13.2
Comparison of Optimum Performance Data for Fuel Cell GT Hybrid Cycles

Technology	Cycle PR	TIT, °C	Eff., %	Sp. Output, kJ/kg
SOFC + GT	30	1300	65.0	588
SOFC + REC	3.5	1300	68.7	620
SOFC + ICR	4	1300	67.8	614
MCFC + GT	3.5	1300	63.5	464
Modern CC [71]	23	1600	62.0	650–700

Source: Bhargava, R.K. et al., *J. Eng. Gas Turbines Power*, 132, #022001, 2010.

Note: REC, recuperated; ICR, intercooled and recuperated.

* The other three are (1) gasification systems, (2) advanced combustion system, and (3) advanced turbines.

Research and development of key technologies within the SOFC program leading to electric power generation systems is coordinated through the *Solid State Energy Conversion Alliance* (SECA). The primary objective of the SECA program is utility-scale power generation with a coal feedstock that generates cost-effective electricity, with near-zero levels of air pollutants, facilitates >97% CO₂ capture, and has an efficiency of +60% in HHV (which corresponds to +63% net LHV efficiency for subbituminous coal feedstock), with minimal raw water consumption [155]. This is more than *twice* that for a typical pulverized coal (PC) power plant with CCS.

Solid oxide fuel cell can also use syngas generated in a gasification plant from a solid feedstock, for example, coal, in which case, the overall system is referred to as an *integrated gasification fuel cell* (IGFC). Another option is to use syngas generated by *steam methane reforming* (SMR), which is known as the *natural gas fuel cell* (NGFC). Basic IGFC and NGFC configuration is shown in Figure 13.12. The gasification island of an IGFC is similar to that of an IGCC power plant (see Section 13.13). There are two system configurations: *atmospheric* (as shown in Figure 13.12) and *pressurized*.

In the *atmospheric IGFC*, SOFC modules are operated at near-atmospheric pressure. Coal is fed to the gasifier, where it is converted to syngas (comprising CO and H₂). Contaminants are removed from the syngas via conventional gas cleanup technology (e.g., Selexol™ or Rectisol®). Pressurized, clean syngas is expanded to near-atmospheric pressure in a syngas expander. The syngas exiting the expander is processed to reduce sulfur to acceptable levels, and subsequently delivered to the SOFC power island. The SOFC electrochemically utilizes 85%–90% of the incoming fuel to produce electric power.

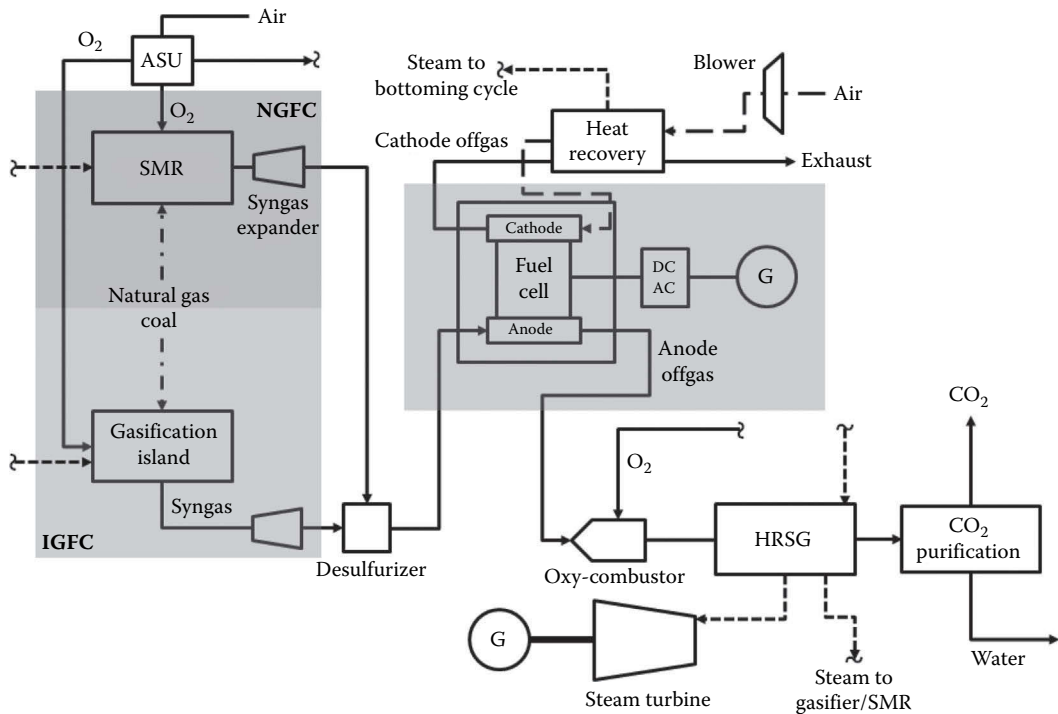


FIGURE 13.12 IGFC and NGFC power systems [155] (condenser and feedwater BOP not shown for simplicity).

The anode off-gas (mainly depleted fuel in addition to CO_2 and H_2O) is combusted in an oxy-fuel combustor. Heat is recovered from this process and used to generate steam for use in a bottoming cycle and for the gasification process. Process air for the electrochemical reaction and for module cooling is delivered by an air blower. Heat is recovered from the cathode off-gas (mainly vitiated air) and the process air to generate steam for use in the bottoming cycle.

In the *pressurized IGFC*, syngas from the gasification block or the SMR is supplied to the anode of the fuel cell. The cathode off-gas can be utilized to generate power in a turbine. The anode off-gas is sent to an oxy-fuel combustor for combustion with oxygen supplied by the ASU. The combustion products (mainly CO_2 and H_2O) are used to generate power in a turbine, with the exhaust treated in a heat recovery unit to generate CO_2 for storage or EOR (about 97% is captured). Condensed water is recycled to the gasifier or the SMR.

The pressurized IGFC is more efficient vis-à-vis the atmospheric variant due to the increase in cell voltage (e.g., at 40 bars pressure, cell voltage is about 90 mV higher than that at 1 bar), but it also has a more complex system configuration. The air blower is replaced by a compressor, and both the anode and cathode off-gas streams utilize a turbo-expander generator. Along with increased system complexity, pressurization also presents operational challenges, particularly during startup and shutdown and during transients. High-integrity seals are required to keep the anode and cathode streams separated. The steam bottoming cycle is eliminated since there is insufficient heat remaining in the off-gas streams to raise steam. In addition to reducing system complexity and cost, eliminating the steam bottoming cycle also reduces the pressurized IGFC power system's water requirements.

IGFC systems with existing gasifiers are projected to have efficiencies in the 45%–50% range (in HHV). With a *catalytic gasifier* (lower process temperature, less oxygen input, product syngas with a significantly higher methane concentration, 15%–30% (v), in addition to H_2 and CO), 5%–10% points of efficiency increase is projected [155]. Similar efficiencies can be achieved by enriching the syngas produced by a conventional gasifier (typically 4%–5% (v) methane) with natural gas.

The ultimate SOFC-based power plant envisioned by the SECA is an NGFC system that features complete *internal reformation* (IR) of the natural gas within the SOFC to utilize its ability to internally reform methane, that is, IR-NGFC [102]. Since its inception in 2001, the SECA program has been reported to manage to drop the SOFC cost by a factor of ten in 2010 while maintaining the power density [155]. The goal, as recently stated in 2013, is to begin IGFC commercial operation by 2035.

13.6 Thermodynamics

The fundamental tool that is needed for high-level engineering analysis of a heat engine is the *Kelvin–Planck* statement of the second law of thermodynamics: *It is impossible to conceive a device operating in a cycle, the sole effect of which is to absorb energy in the form of heat from a single thermal reservoir and to deliver an equivalent amount of work.* In layman's terms, one cannot conceive a heat engine whose efficiency is greater than the efficiency of the "equivalent" *Carnot* cycle [154]. The operative term here is "equivalent," which is explained in the following text.

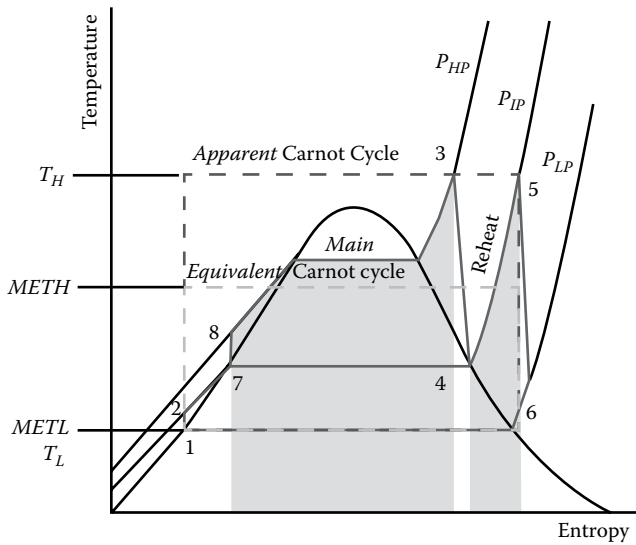


FIGURE 13.13
Temperature–entropy diagram of the steam RBC.

The most basic heat engine cycle is the *Rankine cycle* (see Figure 13.13) with reheat [14]. Like all practical heat engine cycles, it is an attempt to approximate the ideal Carnot cycle with (1) isothermal heat addition and rejection and (2) isentropic compression and expansion. Indeed, the cycle that is being aspired to is the Carnot cycle operating between T_H and T_L , which is the “Carnot target” of the Rankine cycle shown in the figure and whose efficiency is given by*

$$\eta_C = 1 - \frac{T_L}{T_H} \tag{13.1}$$

Even if one can design a perfect cycle with zero losses and isentropic pumping and turbine expansion, the resulting efficiency is much less than the “Carnot target” given by Equation 13.1. This can be easily proven by using a commercially available heat balance tool to perform the relatively straightforward calculation. In fact, the efficiency of such a perfect cycle is equal to the efficiency of the “Carnot equivalent” cycle defined as [81,154]:

$$\eta_{C,e} = 1 - \frac{METL}{METH} \tag{13.2}$$

where

- METH is the cycle’s mean effective heat addition temperature
- METL is the cycle’s mean effective heat rejection temperature

* In this and other equations, temperatures are in degrees Rankine or degrees Kelvin.

Using basic thermodynamic relationships, one can show that METH and METL are logarithmic means of the initial and final temperatures of their respective heat transfer processes [77,91,154]. Furthermore,

- The difference between T_H and METH is a measure of *exergy* destruction (also known as *irreversibility*) during cycle heat addition.
- The difference between T_L and METL is a measure of *exergy* destruction during cycle heat rejection.

Exergy (also known as *availability*) is defined as the maximum theoretical work obtainable as the system in question interacts with the environment to reach equilibrium [14]. For a given cycle working fluid, exergy per unit mass is a thermodynamic property and can be calculated from two other (known) properties, say, pressure and temperature, using a suitable equation of state. Exergy is a very powerful concept to simplify thermodynamic analysis of heat engines. For example, the exergy of the exhaust gas of a gas turbine or gas engine with known composition, pressure, and temperature is the maximum theoretical work obtainable from any bottoming cycle that one can conceive of. At that maximum, the bottoming cycle is in effect a Carnot cycle. Thus, any real bottoming cycle can be characterized by reference to that maximum via a *Carnot factor*.

By virtue of the constant-pressure–temperature heat rejection process via condensation, Rankine cycle METL is indeed equal to the real temperature T_L . However, METH is a hypothetical temperature, which, for a hypothetical isothermal heat addition process between state 8 and state 5 in Figure 13.13, results in the same amount of heat addition, which is the sum total of non-isothermal main and reheat heat addition processes (the shaded area in Figure 13.13). Thus, starting from the general expression for an arbitrary number of constant-pressure heat addition processes ($i = 1, 2, \dots, N$)

$$\text{METH} = \frac{\sum_{i=1}^N \Delta h_i}{\Delta s_{\text{overall}}} \quad (13.3)$$

where

h is enthalpy

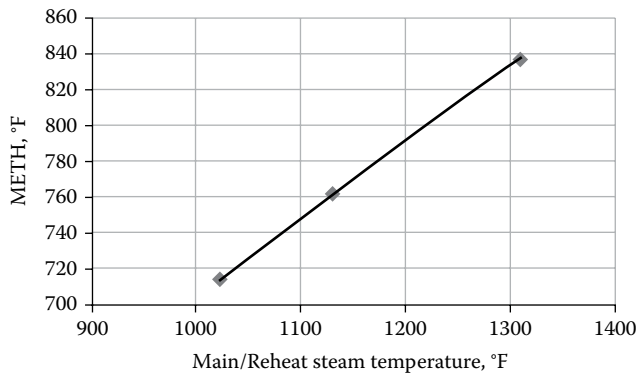
s is entropy (from a suitable equation of state using pressure, p , and temperature, T); for the specific reheat boiler in Figure 13.13, one arrives at

$$\text{METH} = \frac{(h_3 - h_8) + (h_5 - h_4)}{(s_5 - s_8)} \quad (13.4)$$

The calculation is simple and straightforward using steam tables—all one needs is cycle main and reheat steam pressures and temperatures (readily available). For typical subcritical, SC, and USC cycles, the relationship between METH and cycle’s main and reheat steam temperatures (use the average if they are not the same) is shown in Figure 13.14.

Let us consider an advanced steam turbine cycle with 1100°F main and reheat steam temperatures and condenser pressure of 0.7 psia (saturation temperature is 90°F). The “target” Carnot cycle efficiency is

$$\eta_c = 1 - (90 + 460)/(1100 + 460) = 0.647 \text{ or } 64.7\%$$

**FIGURE 13.14**

Rankine steam cycle mean effective heat addition temperature (for 3625 psia [250 bara] steam). For each 725 psia (50 bara) increase in steam pressure, add 10°F to METH.

The “equivalent” Carnot cycle efficiency is

$$\eta_{C,e} = 1 - (90 + 460)/(740 + 460) = 0.542 \text{ or } 54.2\%$$

Therefore, the benchmark to use to evaluate the “goodness” of a real steam cycle design is the latter, which one would obtain with ideal processes and zero losses. The ratio of the actual steam cycle thermal efficiency to that of its Carnot equivalent is the *Carnot factor* (CF). Today’s state of the art in SC and USC design achieves a CF of about 0.90 (caution: steam turbine cycle only, *not* the entire plant) at a METH of about 740°F. For quick estimates, one can assume that each 60°F in METH is worth 0.01 (equivalent to 1% point) in CF. Thus, using a boiler LHV efficiency of 90% and a plant auxiliary load of 5%, one can expect a coal-fired steam generating plant efficiency (net LHV) of

$$\eta_{net} = 0.90 \times (0.90 \times 0.542) \times (1 - 0.05) = 0.417 \text{ or } 41.7\%.$$

For the entire plant, the CF is $41.7/54.2 = 0.77$ —this is a very important number, as will be clearer further on.

The same analysis can be done for the GT Brayton cycle and the Brayton–Rankine combined cycle (see Figure 13.15). Following the standard cycle notation in the figure, for the Brayton cycle, one finds that [81]

$$\text{METH} = \frac{T_3 - T_2}{\ln(T_3/T_2)} \quad (13.5)$$

$$T_2 = T_1 \cdot PR^{k_{air}} \quad (13.6)$$

$$\text{METL} = \frac{T_4 - T_1}{\ln(T_4/T_1)} \quad (13.7)$$

$$T_4 = T_3 \cdot PR^{-k_{gas}} \quad (13.8)$$

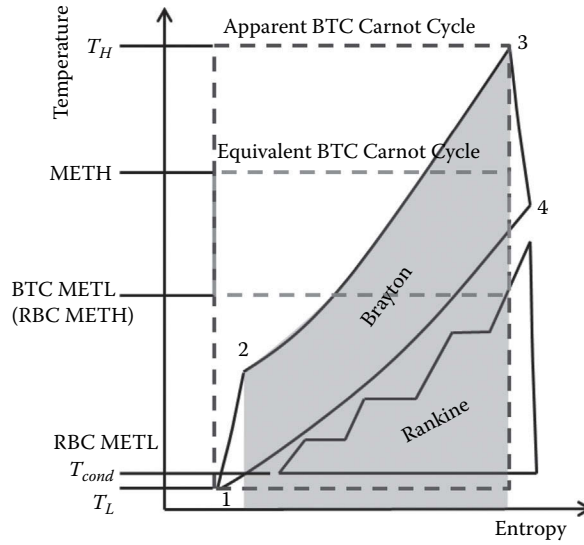


FIGURE 13.15
Temperature–entropy diagram of Brayton–Rankine combined cycle.

In Equations 13.5 through 13.8, the exponent k is given by

$$k = \frac{\gamma - 1}{\gamma}$$

where γ is the ratio of the specific heats (c_p/c_v) of the cycle working fluid [14]. The ideal gas value of γ is 1.40, which is appropriate for air and GT compressor calculations. A good value of γ for combustion products is 1.33 [18], which is appropriate for turbine (expansion) calculations. The values of k in Equations 13.5 through 13.8, $k_{air} = 0.2831$ and $k_{gas} = 0.2270$, are indeed very close to what one would obtain with the stated values of γ , respectively. They are slightly tweaked (more like curve-fitting constants) to match the ideal cycle performance that one would obtain from a heat balance simulation tool (e.g., see [160]) with zero losses, isentropic compression, and isentropic expansion.

In Equations 13.5 through 13.8, T_3 is the *turbine inlet temperature* (TIT) for the ideal engine; PR is the cycle pressure ratio, p_2/p_1 . Thus, from Equation 13.2, with Equations 13.5 through 13.8, the equivalent *Brayton topping cycle* (BTC) Carnot efficiency is

$$\eta_{C,BTC} = 1 - \frac{\tau - PR^{-0.227}}{\tau - PR^{0.2831}} \cdot \frac{\ln(\tau PR^{-0.2831})}{\ln(\tau_x)} \tag{13.9}$$

In Equation 13.9, τ and τ_x are gas turbine inlet and exhaust temperatures, respectively, normalized by dividing by T_1 (59°F for ISO ambient conditions). Note that the “Carnot equivalent” efficiency of Equation 13.9, similar to that for the Rankine cycle discussed earlier, is much lower than the “Carnot target” efficiency given by

$$\eta_C = 1 - \frac{T_1}{T_4} \tag{13.10}$$

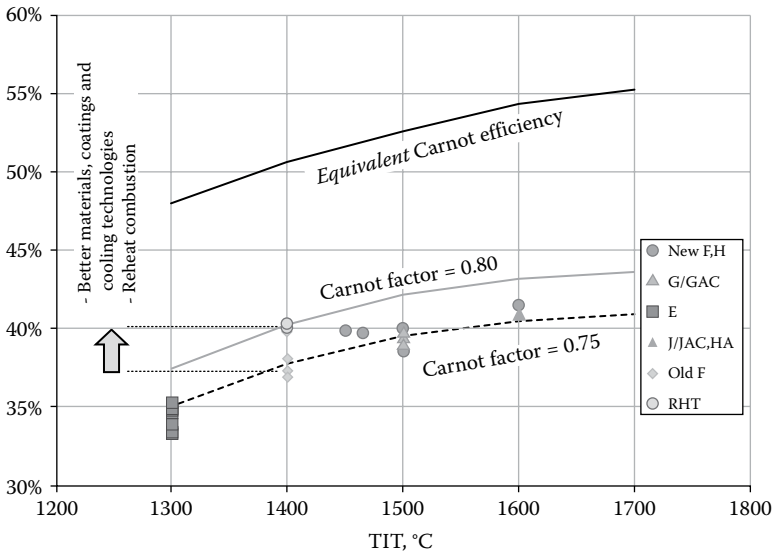


FIGURE 13.16

Industrial heavy-duty gas turbine efficiencies. Please refer to Section 13.10 for GT classification system description.

When the efficiencies of actual gas turbines reported in the trade literature are plotted as a function of TIT in Figure 13.16, the regression line going through the data points is almost a perfect match with Equation 13.9—corresponding to a CF of 0.75.

Several interesting observations can be made from Figure 13.16:

1. Modern gas turbine technology is doing a laudable job of achieving 75% of the theoretical maximum.
2. While “brute force” approach, that is, ever higher TITs, is still the main driver of efficiency, advances in materials, coatings, and cooling technologies make inroads without pushing the TIT further.
3. One should also mention the reheat combustion, which is effective in reducing the combustion irreversibility without increasing the TIT. (The reader can consult any undergraduate thermodynamics book for the physical mechanism behind this beneficial effect [14].)

Note that the METL for the Brayton topping cycle of a GTCC given by Equations 13.7 and 13.8 is the METH for the RBC of the GTCC. Thus, the equivalent Carnot efficiency for the RBC is

$$\eta_{C,RBC} = 1 - \frac{T_{cond}}{METL} \tag{13.11}$$

$$\eta_{C,RBC} = 1 - \frac{T_1}{METL} \tag{13.12}$$

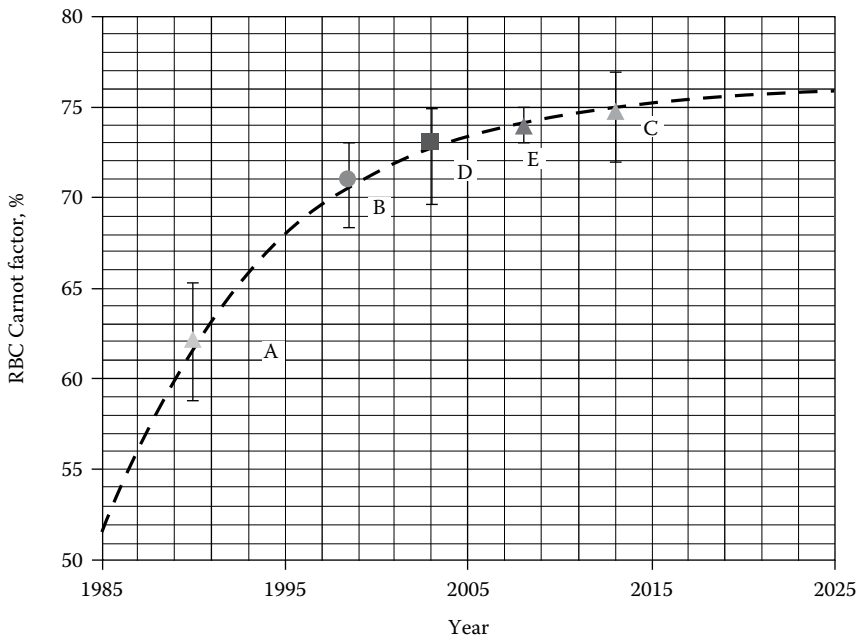


FIGURE 13.17

Gas turbine combined cycle, steam RBC evolution, 1985–2015. See the caption of Figures 13.9 and 13.10 for data sources (E: *GTW 2008 Handbook*).

In Equation 13.11, METL for the RBC is T_{condr} that is, the steam temperature in the condenser. One can also use T_1 in lieu of condenser steam temperature with little impact on the final numerical result, that is, Equation 13.12. In that case, the implicit assumption is that the exergy loss in the condenser will be a part of the cycle Carnot factor. Steam RBC Carnot factor evolution is shown in Figure 13.17. The trend clearly points to the increasingly incremental nature of recent and possible future advances, which, by the way, come at significantly increasing cost [92].

For the overall Brayton–Rankine combined cycle, the equivalent Carnot efficiency is

$$\eta_{C,CC} = 1 - \frac{T_1}{METH} \quad (13.13)$$

Using Equations 13.5 through 13.8, Equation 13.13 translates into

$$\eta_{C,CC} = 1 - PR^{-0.227} \frac{\ln(\tau_x / PR^{0.0561})}{\tau_x - PR^{0.0561}} \quad (13.14)$$

In Equation 13.14, the gas turbine exhaust temperature is used as a proxy for TIT because it is the most readily available piece of information. The exponents are consistent with those in Equations 13.5 through 13.9.

For the GTCC, using the second law concepts, one can now write the net thermal efficiency as

$$\eta_{CC,net} = \left[CF_{BTC} \cdot \eta_{C,BC} + (1 - CF_{BTC} \cdot \eta_{C,BC}) \cdot CF_{RBC} \cdot \eta_{C,RBC} \right] \cdot (1 - \alpha) \quad (13.15)$$

where

$\eta_{C,BC}$ and $\eta_{C,RBC}$ are ideal efficiencies from Equations 13.9 and 13.12, respectively

CF_{BTC} is the Carnot factor for the GT Brayton topping cycle (0.75 for SOA and 0.80 for advanced—see Figure 13.16)

CF_{RBC} is the Carnot factor for three-pressure, reheat (3PRH) steam RBC (0.75 for SOA, ± 0.05 for advanced and *cheap* versions—see Figure 13.17)

α is the plant auxiliary load as fraction of the gross output

The standard reference plant value for α is 1.6%, which is appropriate for nominal rating purposes (roughly, a plant with once-through, open-loop steam condenser with access to a natural coolant source such as a river, lake, etc.) [78]. Real installations, say, with air-cooled condenser systems can be much higher than this, for example, as much as 2.5% of the gross output [78]. In first-law terms, which may be more familiar to the reader, Equations 13.15 is

$$\eta_{CC,net} = \left[\eta_{GT} + (1 - \eta_{GT}) \cdot \eta_{HRSG} \cdot \eta_{ST} \right] \cdot (1 - \alpha) \quad (13.16)$$

In Equation 13.16, η_{HRSG} is the *HRSG effectiveness*, that is, percentage of the GT exhaust gas energy utilized in steam production [92]. For a given GT exhaust temperature, it dictates the HRSG stack gas exit temperature.* For modern GTs with three-pressure, reheat (3PRH) bottoming cycles, HRSG effectiveness is about 90% (corresponding to stack temperature of 180°F). One key takeaway from Equation 13.16 is the “tug of war” between HRSG effectiveness and the ST efficiency; the product of the two giving the overall RBC efficiency, that is,

$$\eta_{RBC} = \eta_{HRSG} \cdot \eta_{ST} \quad (13.17)$$

Comparing with Equation 13.15, one finds that

$$\eta_{RBC} = CF_{RBC} \cdot \eta_{C,RBC} \quad (13.18)$$

$$CF_{RBC} = \frac{\eta_{HRSG} \cdot \eta_{ST}}{\eta_{C,RBC}} \quad (13.19)$$

For the optimal RBC design, both terms in the numerator of the term on the right-hand side of Equation 13.19 should be balanced carefully. This is best illustrated by a single-pressure bottoming cycle. Best HRSG effectiveness requires lowest-possible steam pressure (or, equivalently, lowest stack gas temperature), which, of course, severely hurts the ST efficiency. Similarly, best ST efficiency requires highest-possible steam pressure, which is

* Note that Equation 13.16 is a rough approximation. GT exhaust energy, as a fraction of GT heat consumption, is slightly lower than $(1 - \eta_{GT})$ by about 2% (miscellaneous losses, fuel heating, etc.).

detrimental to the HRSG effectiveness (i.e., high stack temperature). Optimal design point balances the two at a particular steam pressure. This vital RBC design principle will again come up in the following text during the discussion of the suitability of *supercritical CO₂* cycle as the bottoming cycle of an advanced GTCC plant.

Note that, for the GTCC net thermal efficiency, one can also write

$$\eta_{CC,net} = CF_{GTCC} \cdot \eta_{C,CC} \quad (13.20)$$

Equation 13.20 provides a more illustrative perspective for predicting the future room for GTCC improvement by treating the *entire system* as a heat engine. Thus, the theoretical upper limit is set by the equivalent Carnot efficiency of the Brayton–Rankine combined cycle. Carnot factors implied by published rating data over the last three decades have been plotted in Figure 13.18. The trend in Figure 13.18 speaks for itself and does not require additional commentary. Suffice to note that, with 1700°C TIT and PR of 25, a Carnot factor of 0.85 is required for 65% efficiency (on an ISO base load rating basis—not consistently and comfortably achievable field performance).

In summary, from a fundamental perspective, the two objectives of fossil-fuel-fired power plant design engineering are as follows:

1. Increase cycle METH
2. Reduce cycle METL

(If both can be achieved simultaneously, it is even better!) If one can set the origin of energy conversion engineering to James Watt’s steam engine, one must admit that the achievement in the ensuing two centuries and several score years is truly impressive. Today’s SOA in heat engines, represented by the most advanced steam and gas turbine power plants burning fossil fuels, is equivalent to a Carnot factor of 0.75–0.80. In other words, as

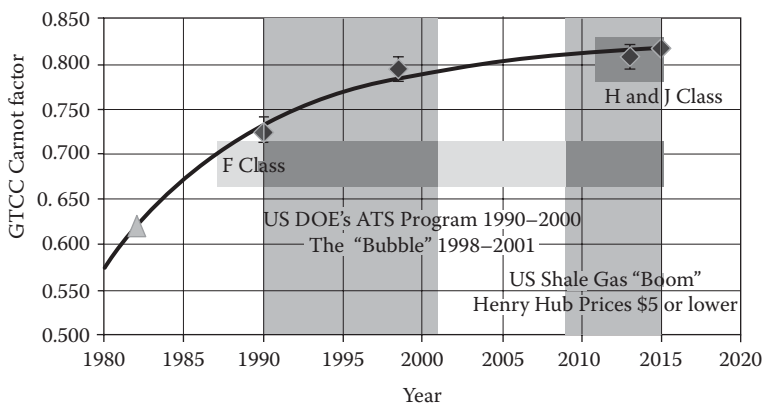


FIGURE 13.18

Evolution of GTCC technology as represented by the Carnot factor. Data points are from trade publications such as annual *TMI Handbook* (red diamonds). The green triangle represents OEM data culled from several published sources.

quantified by the net thermal efficiency, under the most favorable site and operating conditions, a modern FFPS is performing at a level only 20%–25% below that of the theoretical maximum set by a fundamental law of physics.

Returning to the mean effective cycle temperatures and the equivalent Carnot cycle defined by them, they constitute a readily calculable yardstick for evaluating the “goodness” of any heat engine cycle. No matter how complicated a given cycle may look at a first glance, it can be reduced to its bare essentials. Once this is done, it is impossible to be distracted by obfuscating claims and obscure or minor details. Today’s gold standard is set by the natural gas–fired Brayton–Rankine combined cycle with the latest H and J class gas turbines—a Carnot factor of +0.80 (see Figure 13.18). Not far behind is the fossil-fuel–fired boiler plant with ultra-supercritical steam cycle. Any technology that has a realistic chance of competing with these two “olden but golden” technologies must (1) either surpass them in performance (extremely difficult) or (2) match them at a lower cost and/or emissions.

In order to clarify the points made in this section with actual product ratings, consider the data in Table 13.3. Ideal, air standard cycle calculations ($\gamma = 1.40$) are carried out for three types of heavy-duty industrial GTs (E, J, and future “K” class), a heavy-duty *reheat combustion* GT, and an *aeroderivative* GT with high cycle PR—all in a combined cycle configuration. Underlying formulas can be found in any undergraduate textbook [14]. Equivalent Carnot efficiency is from Equation 13.2, with METL = 59°F, and METH from Equations 13.5 and 13.6, with $k = 1 - 1/\gamma = 0.2857$. Rating numbers for E, J, and reheat machines are from [71].

J class and reheat GT cycle T – s diagrams are shown in Figure 13.19. Table 13.3 and Figure 13.19 provide very interesting and important insights into the thermal performance of gas turbines. As mentioned earlier, the steam RBC does a very good job of recovering the cycle

TABLE 13.3

Air-Standard (Ideal) Brayton Cycle Data

	E Class			J Class			K Class			Reheat			Aero			
	P	T	s	P	T	s	P	T	s	P	T	s	P	T	s	
Cycle PR	13.7			23.0			25.0			35.0			45.0			
Precomp.	NA			NA			NA			NA			NA			
1	15	59	0.00	15	59	0.00	15	59	0.00	15	59	0.00	15	59	0.00	
2	201	636	0.00	338	811	0.00	368	842	0.00	515	973	0.00	662	1080	0.00	
3	201	2,372	0.23	338	2912	0.23	368	3092	0.24	515	2372	0.16	662	2372	0.15	
4r	NA	NA		NA	NA		NA	NA		257	1863	0.16	NA	NA		
3r	NA	NA		NA	NA		NA	NA		257	2372	0.21	NA	NA		
4	15	881	0.23	15	917	0.23	15	956	0.24	15	790	0.21	15	494	0.15	
1	15	59	0.00	15	59	0.00	15	59	0.00	15	59	0.00	15	59	0.00	
METL	59			59			59			59			59			
METH	1,369			1694			1782			1710			1661			
IHA	228			285			25%	315	38%	108			-53%	104		-54%
Carnot η	71.6%			75.9%			76.8%			76.1%			75.5%			
Rating η	56.0%			61.7%			63.0%			59.5%			56.0%			
CF	0.782			0.813			0.820			0.782			0.741			

Note: I_{HA} cycle heat addition irreversibility.

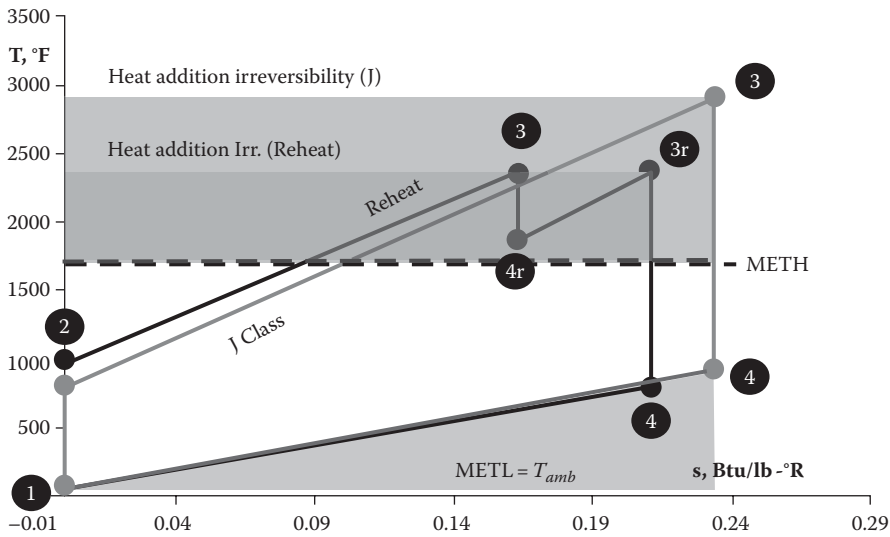


FIGURE 13.19
Air-standard (ideal) Brayton cycle T - s diagrams.

heat rejection irreversibility. Thus, the focus is on the combined cycle performance and, specifically, cycle heat addition irreversibility:

1. There is no doubt that increasing TIT (accompanied by increasing cycle PR) improves the cycle performance. However, as indicated by the increase in cycle heat rejection irreversibility from E to J and K class, this is a “brute force” approach.
2. The more elegant solution, at least from a purely theoretical perspective, is the reheat combustion, which improves cycle performance while reducing the cycle heat addition irreversibility.
3. The aeroderivative cycle demonstrates the superiority of the cycle pressure ratio as the major driver of gas turbine efficiency.

However, as evidenced by the cycle Carnot factors in Table 13.3, transition from theory to practice is not straightforward:

1. While reheat combustion, in theory, can match J class performance at much lower E class TIT, hardware design compromises (material limits, HGP cooling load, seals at high pressures and temperatures) limit the field performance (i.e., low CF).
2. Aeroderivative GTs can also match their J class cousins with E class TIT, but their low exhaust temperatures preclude strong bottoming cycle contribution and result in poorer field performance (i.e., even lower CF than reheat combustion turbine).

In summary, whenever a new FFPS technology is evaluated, these questions must be asked:

- What is the METH?
- What is the METL?
- What is the Carnot factor implied by the claimed performance?

- Is it better than SOA Brayton–Rankine GTCC?
- If so, is it cheaper and/or “cleaner” (in terms of emissions and effluents)?
- Are the cycle pressures and temperatures commensurate with existing materials and hardware design practices?

Answering these questions with a few basic calculations should provide a good idea about the potential of new heat engine technologies without resorting to complex simulation models, which, more often than not, mask the underlying principles.

The benchmark to use for deciding whether a proposed technology has a reasonable chance to commercial viability is the GTCC with advanced F, G, H, and J class gas turbines and 3PRH bottoming cycles incorporating advanced steam turbines. This particular FFPS represents the current SOA (in the second decade of the twenty-first century) with more than 60% net thermal efficiency (ISO base load) at roughly \$1000 per kW. Its Carnot factor is above 0.8 (see Figure 13.18); in other words, its rated thermal efficiency is *more than 80%* of what one would achieve with zero losses and isentropic components. Even without a post-combustion CCS add-on, its CO₂ emissions are less than half of that for coal-fired plants (see Section 13.8). At a conservative 50% cost adder and 12% parasitic power load via CCS (see Section 13.3.3.3), this represents essentially carbon-free +53% net thermal efficiency at \$1500 per kW, which is less than half of what it would cost for an advanced USC power plant without carbon capture.

13.7 Economics

In evaluating electric power generation technologies using dollars and cents, the most widely used metric is the *levelized cost of electricity* (LCOE), which combines plant output, efficiency, and operations and maintenance (O&M) with capital investment and fuel expenditure in a simple formula. This metric is useful when comparing power generation alternatives that use *similar technologies*. The standard formulation of COE is the sum of capital, fuel, and operations and maintenance (O&M) costs of plant ownership, that is [91],

$$COE = \frac{\beta \cdot C}{P \cdot H} + \frac{f}{\eta} + \left\{ \frac{OM_f}{P \cdot H} + \mu \cdot OM_{v,b} \right\} \quad (13.21)$$

where

β is the levelized carrying charge factor or cost of money

C is the total plant cost (\$)

H is the annual operating hours

P is the net rated output (kW)

f is the levelized fuel cost (\$/kWh [LHV])

η is the net rated efficiency of the combined cycle plant (LHV)

OM_f is the fixed O&M costs (\$ or \$/kW year)

$OM_{w,b}$ is the variable O&M costs for base load operation (\$/kWh)

μ is the maintenance cost escalation factor (1.0 for base load operation)

The cost of generation as provided by this COE formula can be interpreted as the price at which electricity must be sold in order to cover all fixed and variable generating expenses and to match the return on company's equity implicit in the assumed *capital charge factor* (β). The COE is limited to a single operating condition, typically new and clean-rated performance, and is usually calculated at full load at *International Organization for Standardization* (ISO) ambient conditions* (commonly referred to as the "base load").

The fuel cost used in the COE formula should be in \$/kWh (LHV) and is given by

$$f = \frac{f_0 \cdot h}{293.071} \quad (13.22)$$

where

h is the ratio of fuel HHV to LHV (1.109 for natural gas as 100% CH₄)

f_0 is the base fuel cost in \$/MMBtu (HHV)

The levelized COE can be calculated as

$$\text{LCOE} = \text{LF} \times \text{COE} \quad (13.23)$$

where LF is the levelization factor.

Typical values for the financial parameters that can be used in the LCOE equation are as follows [59]:

- For *investor-owned utilities* (IOUs), β is 10%–13%.
- For *independent power producers* (IPPs), β is 15% to +20%.
- For IOUs, LF is 1.268, and for IPPs, 1.169.

The total plant cost, C in Equation 13.21, is by far the most difficult number to come up with. The problems start with the definition of the "cost scope," that is, what to include in that number? Since there is not an industry standard on that subject, the literature is full of widely varying numbers based on myriad assumptions, estimation models, escalation factors, etc. To make matters worse, there is the price–cost dichotomy. Depending on market demand–supply dynamics (a good example to remember is the natural gas–fired power "bubble" in late 1990s), commodity prices, craft labor availability, and many other factors, what is estimated to "cost" \$100 today can easily be \$300 or \$500 tomorrow—well beyond what is suggested by simple inflation. Even projects with mature technologies (e.g., GTCC) are subject to changes in total installed cost estimates depending on site- and/or project-specific complexities (see Figure 13.20). For example, adding a ZLD system to a GTCC project, which in other aspects is pretty much identical to earlier ones, can result in substantial cost increases. The only remedy is learning gained during early implementation so that potential risks and pitfalls are better understood and quantified at different stages of the subsequent projects.

The other component that makes capital cost estimation difficult is the "lead time," that is, the total time spent on project definition, environmental permitting, licensing, conceptual and final engineering design, and finally construction, followed by startup and commissioning. Some activities can overlap at certain times. The lead time can have a

* 59°F, 14.7 psia, and 60% relative humidity.

- Conceptual (EPRI Class I – 30%–50% Contingency)
 - Project development complete
 - No quantities
 - Budgetary estimates from OEMs
- Preliminary (EPRI Class II – 15%–30% Contingency)
 - Preliminary engineering complete
 - Some quantities
 - Firm estimates from OEMs
- Detailed (EPRI Class III – 10%–20% Contingency)
 - Ready to start construction
 - Most quantities
 - Major equipment purchased

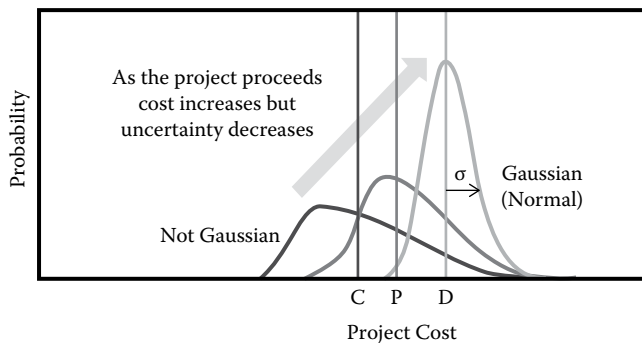


FIGURE 13.20

Project cost estimate evolution. (From Kuhr, R. et al., How power project complexity affects financing, *Powergen International* 2012, Orlando, FL, December 11–13, 2012.)

substantial impact on the total cost through financing requirements during that time (interest during construction—also known as *allowance for funds during construction* or AFUDC). Typical values are 4 years for GTCC, 5–6 years for supercritical pulverized coal (SCPC), and 6–8 years for the IGCC power plants. (Nuclear power plants can easily take more than 10 years—the average lead time for them in 1970s was 14 years.) Even slight variations and/or unforeseen problems (mainly due to a lack of prior experience) can substantially add especially to the construction phase so that the final bill becomes even more inflated than what is suggested by the conceptual cartoon in Figure 13.20. The project cost in the figure should be interpreted as the “total plant investment” (TPI) per the Electric Power Research Institute (EPRI) TAG® definition (see p.323 for more on this), which is the *total plant cost* (TPC)* plus AFUDC. It does *not* include myriad owner/developer costs such as royalties, permits, preproduction (startup) costs, working capital, land, etc., which are added to the TPI to find the *total capital requirement* (TCR).

Contingencies in Figure 13.20 are *project* contingencies. *Process* contingency is a cost added to inflate the estimated capital cost to quantify the uncertainty in the technical performance and cost of the commercial scale equipment requisite for a new technology. Per EPRI guidelines, process contingency for a new concept with limited data is 40% or more. In other words, if one estimates \$1000/kW for a new technology, it is likely to end up at \$1400/kW or even more.

* Also known as “overnight” construction cost.

The reality is in fact quite bleak for emerging and/or “first-of-a-kind” (FOAK) technologies. A case in point is the 630 MWe Duke Edwardsport IGCC power plant in Indiana, United States. The plant was started as a 1600–2000 kW target cost project (about \$1–\$1.5 billion give or take), which ended up with more than three times as high a price tag at the time of writing.* Another example is the 582 MWe Kemper County IGCC project with 65% carbon capture, which, originally estimated at \$2.4 billion (\$4,125 per kW), ended up at \$6.49 billion (a stunning \$11,150 per kW!)† due to cost increases and schedule delays due to myriad causes such as erroneous calculations of pipe thickness, length, quantity, and metallurgy, leading to structural support changes.

The problems besetting new and advanced technologies such as IGCC can be best explained by the *capital cost learning curve* in Figure 13.21, which is used by the EPRI. As the real cost overrun examples cited earlier indicate, in the early development phase of a new technology, cost estimates can be low by a factor of 2 or more. After the first unit is commercialized, new learning by the OEMs and the EPC contractors, if spurred by customer demand and lining up of new projects as well, can rapidly accumulate to bring the cost down to a level commensurate with a mature technology. Unfortunately, as dramatically illustrated by the IGCC example, if the new plants are built sporadically, over a long period of time with a multiplicity of technology variants by different OEMs and EPC contractors, the learning curve effect never happens. For all practical purposes, each new project is a FOAK. Invariably, this scattershot approach to technology introduction decreases the receptiveness of the industry to not only the particular technology in question but also to any new technology in general.

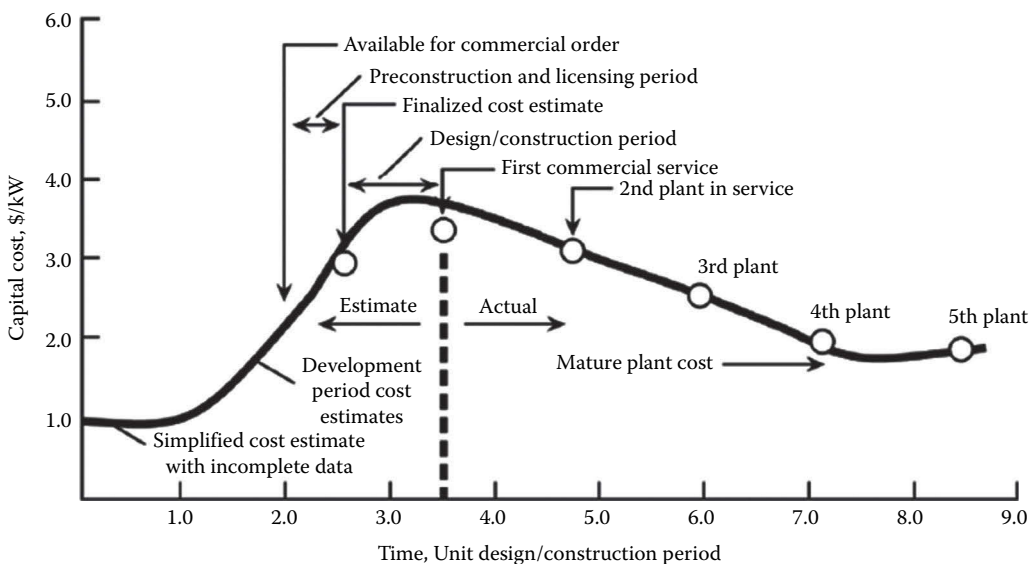


FIGURE 13.21
EPRI capital cost learning curve.

* \$3.55 billion based on news articles obtained from the Internet. This corresponds to a specific cost about \$5650 per kW.

† Data are obtained from the Massachusetts Institute of Technology (MIT) CCS Project Database.

Due to that reason, no attempt is made herein to provide detailed capital cost data about any technology, especially about technologies involving gasification, carbon capture, etc. Suffice to say that (1) addition of carbon capture (and sequestration) will add significantly to the FFPS cost, coal or gas fired; (2) coal-fired FFPS will cost much more than natural gas-fired GTCC on a \$/kW basis; and (3) GTCC, due to its amenability to standardized "reference plant" design and relatively short construction period (roughly 2 years) has the lowest cost estimation uncertainty. This is the reason why gas turbine simple and combined cycle budgetary price estimates can be found in trade publications in tabular form (e.g., *Gas Turbine World Handbook* [71]). A few things to keep in mind when using those estimates are as follows:

1. Plant total cost should include the cost of equipment, materials, labor, engineering and construction management, contingencies related to the construction of a facility, and owner's costs (land acquisition, licenses, and administrative costs). If the interest used during construction (typically 2 years for GTCC) for funds borrowed to pay for items listed above is excluded, this gives the *total overnight construction* (TOC) cost (TPC per EPRI definition mentioned earlier).
2. 2015 budget price cost for a typical GTCC is \$675 (*GTW Handbook* scope) with $\pm 15\%$ uncertainty.
3. To this at least 30% should be added for TOC (interest during construction excluded). This gives a range of \$750–\$1000 per kW. (Note that a 2010 survey of construction costs for GTCC power plants indicated a range of costs from about \$670 to slightly more than \$1400 per kW of installed capacity.)
4. Capacity factoring exponent for GTCC plants is about 0.75 (recall the famous *six-tenths rule* [15] with 0.60 as the exponent) for plants rated 400 MWe or less. For larger plants, the exponent is 0.93.* In other words, there is little economy of scale for large GTCC plants. Doubling the capacity from, say, 500–1000 MWe will reduce the specific capital cost (\$/kW) by only 5%.

For more detailed information and methodologies in FFPS capital cost estimation and LCOE calculations, the reader is encouraged to consult the reference books [2,15] and the works cited therein. A good source for large power plants of all types is the recent report by the U.S. EIA [161] (or its more recent editions when/if available). A pricey but highly useful source for technical and cost information is the *Technical Assessment Guide*TM (TAG) published by the EPRI (the latest 2013 edition has a price tag of \$75,000). Readers with access to it (through their organizations or a library) are encouraged to consult it as the first source. It must be emphasized that any *generic* cost information from the cited and similar sources must be verified and/or adjusted by real project information (if/when available, of course).

A good rule-of-thumb fixed O&M cost for GTCC is \$10–\$15 per kW year (higher values for advanced H and J class machines). For the variable O&M, one can use \$0.50–\$1.50 per MWh. The lower value is appropriate for base-loaded plants; the higher value for cyclic operation. Somewhat higher values may be adopted for H and J class machines comprising advanced single-crystal alloys and coatings. The reader is encouraged to refer to [161] for more information on generic O&M costs for gas turbine and other fossil fuel technologies. In a GTCC power plant, gas turbine is the largest O&M cost

* Refer to the chart on page 44 of [67].

contributor. Gas turbine maintenance comprises three major activities: combustor inspection, HGP inspection, and major inspection [35]. Periodicity of these maintenance activities is a function of fired operating hours and start–stop cycles. For the SOA advanced machines comprising high-technology parts and operating at high firing temperatures, the prudent but costly approach is to enter into *long-term service agreements* (LTSA) with the OEM.* For the more mature technologies such as the older F class or E class machines, independent (third-party) service providers can be the less costly choice with minimal risk [132].

An example of U.S. natural gas spot prices is shown in Figure 13.22. In the past, before the shale gas glut hit the market, it was as high as \$13 per MMBtu (HHV). Depending on unexpected weather conditions (pushing up the demand for home heating), it can still show significant spikes (e.g., see winter of 2014 in Figure 13.22). For the time being \$3 natural gas seems to be a reality in the United States, which makes widespread acceptance of advanced but proven technologies such as IGCC (especially with their cost and schedule creep problems) extremely difficult. Overseas, especially in countries dependent on imported natural gas or LNG, it is around \$7–\$8 at the time of writing (late 2015), but it went up as high as \$15 in the recent past (*landed* price, that is, as received at the terminal). This is one reason why coal-burning technologies such as advanced USC and carbon capture are expected to make significant inroads in Europe and Japan well before the United States.

Strictly speaking, the basic LCOE formula has a very limited applicability; it is only appropriate for comparing *similar technologies of the same vintage*, that is, a coal-fired SCPC power plant with another coal-fired SCPC power plant or the same SCPC power plant with an advanced feature. The technologies must have similar rated performance, part load and ambient condition efficiency lapse, degradation, RAM (reliability, availability, and maintenance), emissions, etc. In other words, for a given operating scenario, they must

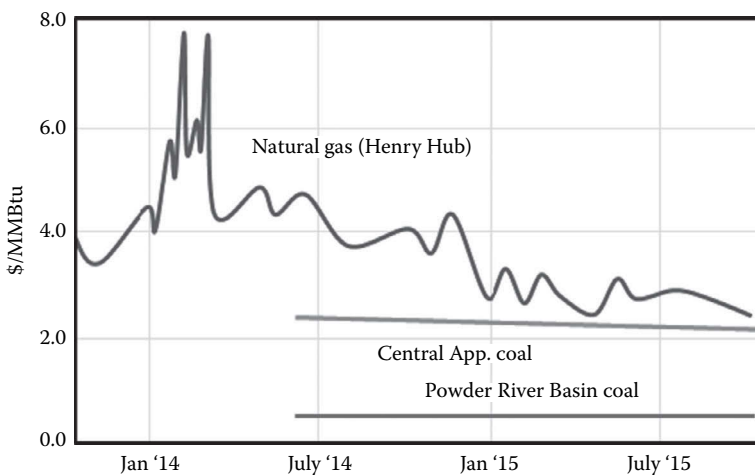


FIGURE 13.22

An example of U.S. natural gas and coal spot prices (Henry Hub prices from the U.S. EIA *Natural Gas Intelligence*). In Central Appalachia, mines are very deep and expensive to excavate. Powder River Basin coal is much cheaper due to less cost-intensive formation spreading across Montana and Wyoming.

* Also known as contractual service agreements (CSA).

deliver approximately the same annual megawatt-hour generation. Unfortunately, it has been used for comparing different technologies (e.g., IGCC with GTCC) with total disregard of the aforementioned technology characteristics. The most glaring omission is RAM, whose importance can be demonstrated by a simple example.

Suppose that two technologies, A and B, are considered for base load generation at 800 MW nominal rating for 7000 h a year. Technology A is proven and has a reliability of 99%; that is, one has to account for an unexpected failure probability of only 1%. Technology B is relatively new (and more efficient), with only a few operating units in the field; its reliability is estimated at 80%—that is, there is a 20% probability that it will be down, when it is expected to run and generate power, due to an unforeseen component failure. Thus, while both technologies have nominally the same annual generation capability, that is, $800 \times 7,000 = 5,600,000$ MWh, in reality, technology A has an expected annual generation capability of $0.99 \times 800 \times 7,000 = 5,544,000$ MWh, whereas technology B has an expected annual generation capability of $0.80 \times 800 \times 7,000 = 4,480,000$ MWh. If one goes ahead with technology B, allowance must be made for the purchase of nearly 1,000,000 MWh from other generators on the grid. The simple LCOE formula in Equation 13.21 does not and cannot account for that huge handicap.

Average F Class GTCC outage factors in Table 13.4 provide a good measure of technology reliability.* As shown in the table, GT-only unexpected outage rate is 2.4%, whereas for the entire plant, that is, GT, ST, and HRSG combined, the unexpected outage rate increases to 3.9% (2005–2009 time frame). What this means is that, on average, one should expect annually ~300 h of lost power generation opportunity due to unforeseen events.

Gas turbine forced outage data in Table 13.4 illustrate the “learning” effect. As a technology matures, OEMs and operators become more adept in its design, operation, and maintenance. Nevertheless, as shown in Figure 13.23, effects of equipment and changes in the duty cycle of a plant can be detrimental to reliability (and availability).

TABLE 13.4

Average Outage Factors for F Class GTs in Combined Cycle Configuration and Other Major Equipment (Based on Units with Minimum 6500 Annual Operating Hours)

	1995–1999	2000–2004	2005–2009
Combustion turbine subsystem			
Forced outage, %	2.67	2.09	1.59
Unscheduled maintenance, %	1.78	0.55	0.79
Service factor, %	78.7	62.4	60.9
HRSG subsystem			
Forced outage, %	0.11	0.28	0.21
Unscheduled maintenance, %	0.93	0.26	0.26
Steam turbine subsystem			
Forced outage, %	0.36	0.39	0.81
Unscheduled maintenance, %	0.59	0.24	0.26

Source: Grace, D. and Christiansen, T., Risk-based assessment of unplanned outage events and costs for combined cycle plants, GT2012-68435, ASME Turbo Expo 2012, Copenhagen, Denmark, June 11–15, 2012.

* RAM data is from the *Operational Reliability Analysis Program* (ORAP®) data system maintained by SPS, Inc. in Charlotte, NC.

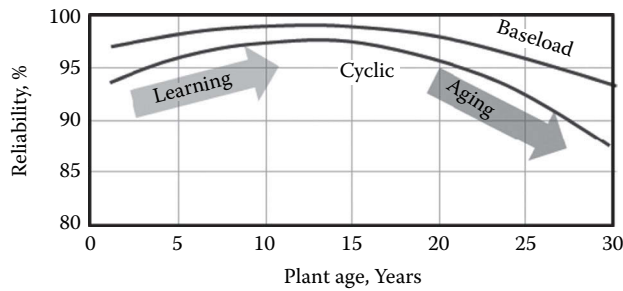


FIGURE 13.23

Impact of cyclic operation on GTCC reliability. (From Walsh, D, Impact of cyclic/two shift operation on the reliability, economics, and emissions of fossil generation (coal and combined cycle gas turbine), *Powergen International 2015*, Las Vegas, NV, December 8–10, 2015.)

The basic LCOE formula can be expanded to account for the technology reliability and other factors [91], that is,

$$COE = \frac{\beta \cdot C}{P_{eff} \cdot H_{eff}} + \frac{f}{\eta_{eff}} + \left\{ \frac{OM_f}{P \cdot H} + \mu \cdot OM_{v,b} \right\} + \sum_i c_i \cdot m_{p,i} + \frac{S_c \cdot \Delta P + S_e \cdot \Delta E}{P_{eff} \cdot H_{eff}} \quad (13.24)$$

First of all, output, efficiency, and annual operating hours are replaced by their “mean effective” values (denoted by the subscript $_{eff}$). Mean effective values include annual average load factor, site ambient conditions, and reliability (see [91] for details). Emission costs (or penalties) can be added to the LCOE via a term comprising two new parameters:

1. c_i (price/cost of pollutant i in terms of \$/ton)
2. $m_{p,i}$ (plant generation of pollutant i in tons/kWh)

These terms can also be used to represent a cost of emissions during startup. The last new term, system impact, accounts for the variation in effective total MWh generation and output that must be provided when a deficiency in energy (kWh or MWh) must be made up by bringing another unit in the system online and/or when a deficiency in capacity (kW or MW) must be made up by purchasing firm capacity from neighboring systems. The COE analysis is adjusted to a common annual total energy generation basis using the following terms:

- S_c —system replacement capacity cost (\$/kW year)
- S_e —system replacement energy cost (\$/kWh)
- ΔP —capacity to be replaced (kW)
- ΔE —energy to be replaced (kWh)

For multiple-unit comparisons, the alternative with highest total energy production can be selected as the basis to determine ΔP and ΔE (unless there is a known target value). Energy replacement cost (S_e) is dependent on the makeup of the particular generating system, for which the alternatives are evaluated using the COE. Note, however, that the

economic dispatch principle requires using a variable generation cost at least equal to or higher than that of the units under consideration. Otherwise, the replacing unit would already be online and generating electricity.

For a quick evaluation of technology improvements for a given system, a useful tool is *maximum acceptable increase in capital cost* (MACC), which is the capital cost equivalent of a given plant performance improvement (output and/or heat rate) with no change in the COE. Using the basic COE formula and ignoring the change in O&M costs, MACC is calculated by equating before and after values of the COE for a given plant improvement, that is,

$$\text{MACC} = \frac{H \cdot f}{\beta} \cdot \left(\frac{\Delta P}{\eta_0} - \Delta HC \right) + k_0 \cdot \Delta P \quad (13.25)$$

where

- f is the levelized fuel cost (in \$/kWh in LHV)
- ΔP is the change in plant net output (kW)
- ΔHC is the change in plant heat consumption (in kW)
- η_0 is the base plant net efficiency
- k_0 is the base plant-specific capital cost (\$/kW)

The two terms on the right-hand side of the MACC formula in Equation 13.25 give the value of plant heat rate, HR (or its equivalent, efficiency, η), and output, P . In general, an improvement in GTCC heat rate (efficiency) comes with a change in output and heat (i.e., fuel) consumption, HC. If the improvement is limited to the bottoming cycle or gas turbine hot gas path section, however, there is no change in GT heat consumption, that is, $\Delta HC = 0$. Using the well-known definition of efficiency and heat rate, that is, $\eta = P/HC$ and $HR = 3412/\eta$ Btu/kWh in the U.S. customary system, it can be shown that the value of 1 Btu/kWh reduction in heat rate is given by

$$\text{VHR} = 10^{-6} \cdot \frac{H \cdot f}{\beta} \cdot P_0 \cdot \left(1 + \frac{\Delta P}{P_0} \right) \approx 10^{-6} \cdot \frac{H \cdot f}{\beta} \cdot P_0 \quad (13.26)$$

where

- P is in kW, with f in \$/MMBtu (LHV)
- P_0 is the base value of plant output

Alternatively, one can also use the value of 1 *basis point* improvement in net efficiency* as a yardstick, that is,

$$\text{VEFF} = 10^{-4} \cdot \frac{H \cdot f}{\beta} \cdot \frac{HC_0}{\eta_0} \cdot \left(1 + \frac{\Delta HC}{HC_0} \right) \approx 10^{-4} \cdot \frac{H \cdot f}{\beta} \cdot \frac{HC_0}{\eta_0} \quad (13.27)$$

Note that HC in Equation 13.27 is in MMBtu/h, with f in \$/MMBtu, both in LHV. HC_0 is the base value of gas turbine (i.e., plant) heat consumption. Values of VHR and VEFF

* A basis point is one-hundredth of 1 percentage point or 1/10,000.

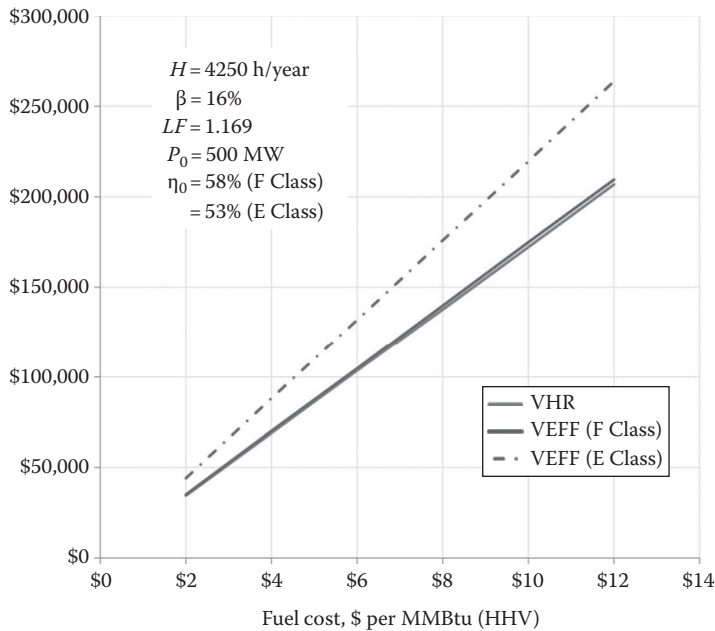


FIGURE 13.24

Value of 1 Btu/kWh improvement in net CC heat rate (VHR) and 1 basis point improvement in net CC efficiency (VEFF).

are plotted as a function of fuel cost in Figure 13.24. Two things to note in the figure are as follows:

1. For F class technology, VHR and VEFF are nearly equivalent and can be used interchangeably.
2. For E class technology with lower efficiencies, VEFF is higher than VHR (which does *not* change with η_0).

Furthermore, the difference between E class VEFF and VHR is more pronounced at higher fuel costs. This is not surprising because the same incremental change (i.e., 1 basis point) in efficiency is more valuable for older technologies burning a lot more fuel. The values read from the curves in Figure 13.24 can be scaled up or down for different values of H , β , LF , and P_0 as needed.

Equations 13.26 and 13.27 are frequently used to evaluate the value of 1 Btu of heat rate or 1 basis point of efficiency. Unfortunately, for the special cases where ΔHC is zero, they are incorrect and overstate the value of heat rate by a very large margin. This was shown via detailed mathematical analysis in [88]. The inherent fallacy can be easily grasped by considering the two special cases of GTCC efficiency improvement:

1. Via an improvement in the bottoming cycle (e.g., a better steam turbine), that is, ΔHC is zero
2. Via an improvement in the topping cycle (e.g., a better compressor efficiency), that is, ΔHC is non-zero—in fact, negative (i.e., less fuel consumed for the same power output)

In one case, that is, when ΔHC is zero, the plant owner's fuel bill does not change at all. In either case, however, Equation 13.26 returns a positive value.

The "intrinsic" value of heat rate (or efficiency) is fully independent of any change in power output and can be evaluated by applying a *realization factor*, RF, which is rigorously evaluated in [88] and represented by the curve in Figure 13.25. The independent variable, E , is the *efficiency improvement factor*, which is defined as percent change in η per percent change in P . As an example, consider a GTCC with 500 MWe and 58%. The GT compressor is upgraded with new technology to give 0.7% higher CC output and 0.3% higher CC efficiency (i.e., new CC performance is 503.5 MW—58.17%). The efficiency improvement factor E is $0.3/0.7/100 \sim 0.0043$ (or 0.43% for each 1% in P). Using this value, from Figure 13.25, RF is read as 0.38. At \$3 fuel, using Figure 13.24, VHR predicted via Equation 13.26 is read as \$50,000. Thus, using the RF of 0.38, the intrinsic value of 1 Btu in heat rate at \$3 fuel is $0.38 \times \$50,000 = \$19,000$.

In addition to the significant difficulty and uncertainty involved in capital investment estimation, the uncertainty in predicting future price of fuel, load, demand growth, inflation, and other economic and/or financial fluctuations (e.g., interest rates) resulting from social and political turmoil makes LCOE a very tricky tool. As such, to the extent possible, probabilistic methods such as *Monte Carlo simulation* should be preferred over deterministic comparisons. By assigning probabilities to the key parameters in the LCOE formula (by no means an easy task), the end result from any LCOE comparison should be the *probability* of "option A being lower/higher than option B" and *not whether* "option A is lower/higher than option B."

The application of *real options theory* to the valuation of power generation assets is a powerful technique that should be superior to *deterministic* methods such as LCOE evaluation.

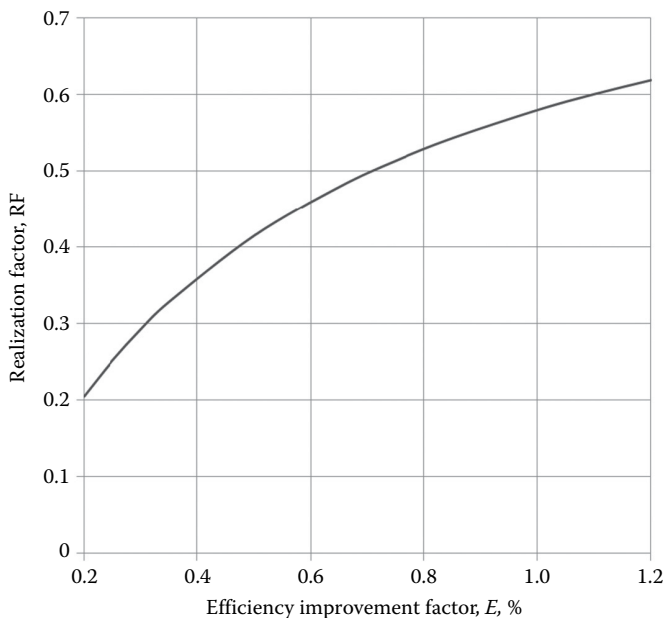


FIGURE 13.25

Realization factors (RF) to be applied to VHR in Equation 13.26 as a function of E , which is the efficiency improvement factor, which is defined as percent change in η per percent change in P .

This is especially true for the currently (and most likely in future as well) prevalent deployment mode of fossil generation assets—especially the simple and combined cycle gas turbines. While the real options theory provides a powerful *stochastic* tool for economic analysis, its application requires sophisticated mathematical modeling and computer programming expertise. Nevertheless, the reader is strongly encouraged to consult the introductory book by Mun [130] to obtain an idea on the key principles underlying the real options theory, which should also help with applying probabilistic techniques such as Monte Carlo simulation to the LCOE modeling.

The takeaways from this section can be summarized as follows:

1. Simple LCOE formula (Equation 13.21) is only appropriate for comparison of similar technologies (e.g., heavy-duty GTCC with heavy-duty GTCC) and similar operational profiles (e.g., cyclic with cyclic).
2. For comparing different technologies (e.g., GTCC with IGCC), the expanded formula (Equation 13.24) should be used by accounting for all the pertinent factors (e.g., RAM).
3. Deterministic comparisons (to the extent possible) should be avoided—whenever possible probabilistic approaches should be preferred (e.g., Monte Carlo simulation).
4. Cost estimates should be made carefully, accounting for all applicable determinants (e.g., lead time and interest during construction); real project information must be taken into account (whenever possible).
5. For simple technology improvement evaluation, the MACC approach with the appropriate RF is sufficient. For “back of the envelope” type evaluations, RF = 0.5 is a good rule of thumb.

13.8 Combustion

Combustion of natural gas with air as the oxidizer is the most basic FFPS heat addition process. For a given fuel and fuel-to-air ratio, calculation of flame temperature from equilibrium chemistry is relatively straightforward and essential. Unfortunately, due to the strongly non-equilibrium nature of actual chemical reactions taking place in the flame zone, combustor design and emissions calculations are based on mostly empirical correlations and experimental data. For a comprehensive coverage, the reader should consult specialized treatises on the subject such as [11] and [13]. A relatively brief but practically helpful coverage of the basic relationships can be found in the first chapter of [8].

13.8.1 Combustion Reaction

For simple estimates, natural gas can be assumed to be 100% methane (CH_4), and air can be approximated by $\text{O}_2 + 3.76\text{N}_2$ (based on the assumption of 21% O_2 and 79% N_2 by volume). Thus, stoichiometric combustion (i.e., all oxygen in the air is used up) of 1 mol of methane (16 lbs/lbmol, LHV of 21,515 Btu/lb) is given by



Based on this simple chemical reaction equation,

1. Stoichiometric combustion of 1 mol of methane requires about 9.5 mol of air (about 275 lb).
2. Stoichiometric air-to-fuel ratio is about 17 (i.e., 275/16); consequently, the stoichiometric fuel-to-air ratio is about 0.06.
3. Combustion products include 1 mol (44 lb/lb mol) of CO_2 per mole of CH_4 or $44/16 = 2.75$ lb of CO_2 per lb of CH_4 .

The *equivalence ratio* is the actual fuel-to-air ratio to the stoichiometric fuel-to-air ratio:

$$\phi = (f/a)/(f/a)_{\text{stoich}} \quad (13.29)$$

The inverse of the equivalence ratio is the *excess air ratio*, that is,

$$\lambda = 1/\phi \quad (13.30)$$

Thus,

$$\phi < 1 \ (\lambda > 1) \rightarrow \text{fuel-lean combustion}$$

$$\phi > 1 \ (\lambda < 1) \rightarrow \text{fuel-rich combustion}$$

The *flame temperature* is calculated by solving the mass and energy balance problem for the adiabatic combustion reaction shown in Figure 13.26. This is commonly known as a *stirred reactor* model (see Figure 13.26). In other words, the control volume representing the combustor is an idealization where combustion products are back-mixed with reactants so quickly that the reaction zone is distributed uniformly in space. The stirred reactor model is essentially the only practical approach to combustion calculations.

Calculation of the temperature of combustion products via enthalpy balance of reactants (i.e., fuel and air) and products is a straightforward but tedious process. How it can be done in a simple spreadsheet can be found in many references (e.g., see [19]). In any event, today, there are many commercially available software tools to perform such mundane calculations on a desktop or laptop computer (maybe even on an iPad) in a fraction of second [160]. Herein, a lookup chart is provided and might come in handy for quick exploratory calculations (see Figure 13.27).

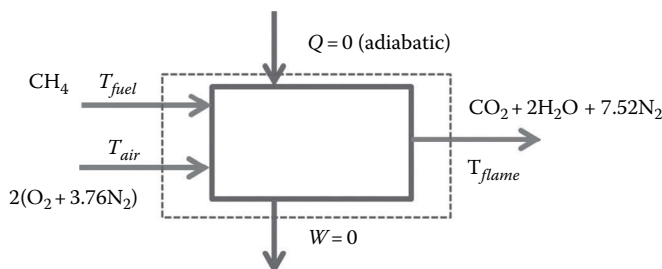


FIGURE 13.26

Stirred reactor control volume for combustion of methane.

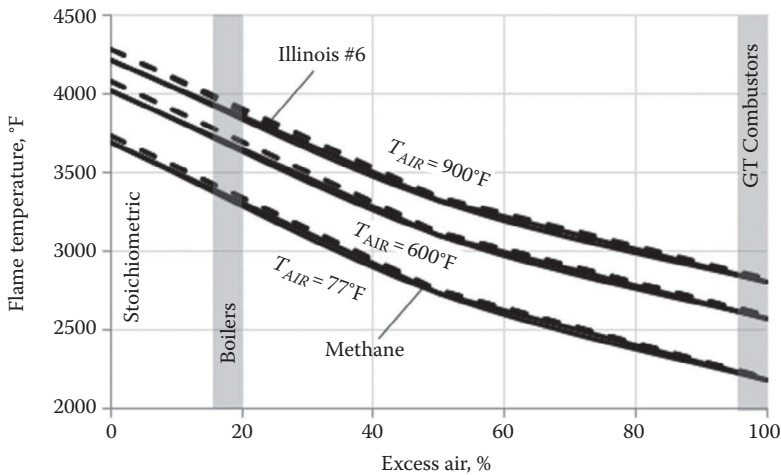


FIGURE 13.27
Flame temperature for typical gas and solid fuels.

By definition, stoichiometric combustion is with 0% excess air. Typical excess air for coal-fired steam boilers is 15%–20%; modern GT combustors operate with about 100% excess air. The stoichiometric combustion of methane with 77°F air results in ~3700°F products. This is also known as the *flame temperature*. As seen in Figure 13.27, (1) combustion with hotter air results in higher flame temperatures; (2) for fuel-lean combustion, the flame temperature is lower; and (3) for fuel-rich combustion, it is higher.

Coals are typically specified by *ultimate* or *proximate* analysis (both by weight percentage)—see Table 13.5 for two typical coals (subbituminous and lignite)—instead of simple clean C_mH_n -type formulas for gaseous fuels. Some generic (average) property data for coal used in the United States for electric power production are shown in Table 13.6. The combustion equation becomes somewhat more involved for the actual coal composition. Basically, on the left-hand side of the chemical reaction formula, each

TABLE 13.5
Ultimate Analysis for Typical Bituminous and Lignite Coals

		Illinois #6	TX Lignite
LHV (moisture and ash included)	BTU/lb	9,599	6398
HHV (moisture and ash included)	BTU/lb	10,100	7080
Ultimate analysis (weight %)			
Moisture	%	12	37.7
Ash	%	16	6.479
Carbon	%	55.35	41.3
Hydrogen	%	4	3.053
Nitrogen	%	1.08	0.623
Chlorine	%	0.1	0
Sulfur	%	4	0.7476
Oxygen	%	7.47	10.09

TABLE 13.6

Average Properties of Coals Delivered for U.S. Electric Power Production in 2008

Coal Rank	HHV, Btu/lb	Typical Moisture Content, %	Average Ash Content, %	Average Sulfur Content, %
Bituminous	>10,500	2–16	~11	1.70
Subbituminous	<10,500	15–30	~6	<0.5
	>8,300			
Lignite	<8,300	25–40	~14	<1

Source: U.S. Environmental Protection Agency, Available and emerging technologies for reducing greenhouse gas emissions from coal-fired electric generating units, Sector Policies and Programs Division Office of Air Quality Planning and Standards, U.S. Environmental Protection Agency, Research Triangle Park, NC, October 2010.

constituent's molar amount is found by dividing the ultimate analysis weight percentage by the respective molecular weight. For example, for the Illinois #6 coal, 100 lb of solid fuel contains $55.35/12 = 4.6$ moles of carbon. Just like for methane, each mole of C in the fuel results in 1 mole of CO_2 in the products. Stoichiometric air-to-fuel ratio for Illinois #6 coal is about 7.5. As shown in Figure 13.27, flame temperatures for combustion of Illinois #6 (subbituminous) coal are quite similar to those for the combustion of methane.

Simple combustion calculations help to illustrate the dramatic advantage of natural gas-fired CC power plants vis-à-vis coal-fired steam power plant in terms of CO_2 emissions. For example, given FFPS net output and efficiency (heat rate), CO_2 in the flue gas can be found as follows*:

$$e_{\text{CO}_2} = 1000 \cdot \frac{HR}{LHV} \cdot \frac{MW_{\text{CO}_2}}{MW_f} \text{ lb/MWh (gas fuel)} \quad (13.31)$$

$$e_{\text{CO}_2} = 1000 \cdot \frac{HR}{LHV} \cdot c \cdot \frac{MW_{\text{CO}_2}}{MW_C} \text{ lb/MWh (coal)} \quad (13.32)$$

where

HR is the plant heat rate in Btu/kWh

LHV is the lower heating value of the fuel in Btu/lb

c is the fraction of carbon in coal per ultimate analysis

MW refers to the molecular weights of fuel gas (~16 lb/lb mol), CO_2 (44 lb/lb mol), and carbon (12 lb/lb mol)

Calculations for three different fuels are plotted in Figure 13.28. The lignite and bituminous coal carbon emissions per unit of heat input (CO_2 emission factor) from this simple calculation correspond to 211.4 and 236.7 lbs/MMBtu, respectively (127.9 lbs/MMBtu for natural gas). Corresponding U.S. EIA emissions factors are 201.3–211.6 (bituminous) and 211.7–220.6 (lignite), provided as a range across the states with coal deposits [32].

* This formula is similar to that in Federal Emissions Regulation Code for Continuous Emissions Monitoring (CEM), CFR 75.10(3)(ii): W_{CO_2} [tons/h] = $(F_c \times H \times U_f \times MW_{\text{CO}_2})/2000$, where the F_c factor is 1040 scf/MMBtu for natural gas, H is the heat input in MMBtu/h, and U_f is 1/385 scf CO_2 /lbmol at 14.7 psia and 68°F. For typical natural gas (19,900 Btu/lb, 17.75 lb/lbmol), Equation 13.31 gives 5% higher values.

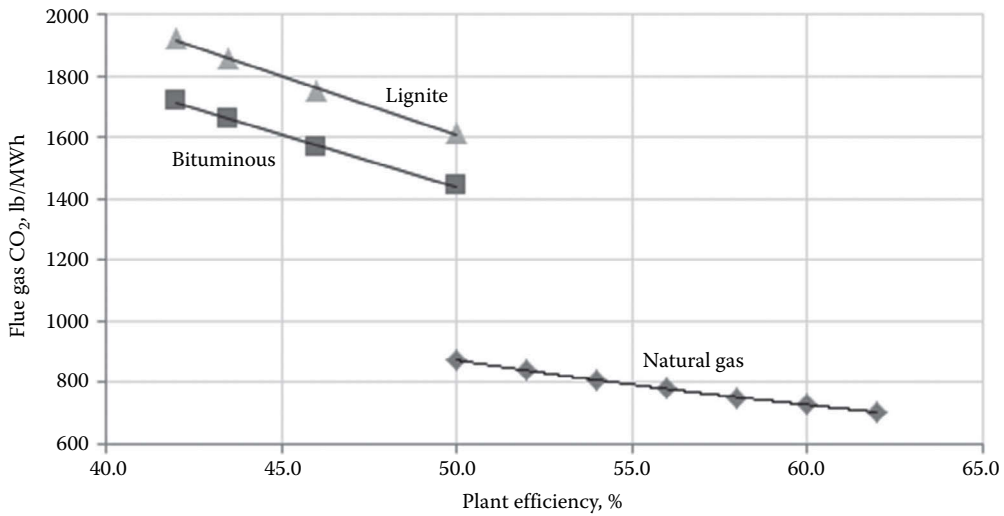


FIGURE 13.28

Flue gas carbon dioxide content for coal- and gas-fired power plants (from Equations 13.31 and 13.32).

The difference between coal and natural gas is striking. Even at the same plant efficiency, CO_2 in the flue gas of the most advanced coal-fired power plant is almost twice that of the least advanced gas-fired GTCC power plant.

13.8.2 NO_x Emissions

Theoretical combustion of a hydrocarbon fuel converts C, H, and S in the fuel completely to CO_2 , H_2O , and SO_2 . (Excess O_2 and N_2 in the combustion air do not enter the reaction.) Combustion process in FFPS combustors and boiler furnaces is incomplete and the products, that is, the flue gas, contain *carbon monoxide* (CO). At sufficiently high temperatures (about 2600°F and higher), nitrogen in the air combines with oxygen to form nitric oxide, NO. This NO is oxidized into NO_2 , especially in zones of excess air in the combustor and in the exhaust.

There are three mechanisms for NO_x production in the combustor of a gas turbine: thermal, nitrous oxide, and prompt. Each mechanism is described by a different chemical reaction path. Of these three, when flame temperatures are above 2780°F , the dominant mechanism is the *thermal* NO_x or the *extended Zel'dovich* mechanism [11]. Below this temperature, the thermal reactions are relatively slow. Beyond about 3100°F (1700°C), thermal NO_x production grows exponentially. This can be considered as an upper limit for DLN combustion.

Simple estimation of NO_x and CO in the flue gas is not possible. Even highly detailed chemical kinetics models require significant adjustment using empirical constants. In general, NO_x formation is a function of three parameters: residence time in the combustion zone, chemical reaction rate, and mixing rate [11]. The following discussion uses the gas turbine combustors (especially the *dry low NO_x* (DLN) combustors) for exploring the fundamental processes. However, the same principles apply to the *low NO_x burners* (LNB) in coal-fired boiler furnaces as well.

For the gas turbine combustors, the three reaction parameters can be related to the turbine operating conditions and combustor size. From that, it is found that NO_x production rate for a given system can be expressed in an empirical formula that can be written as [11]

$$\text{NO}_x \propto p^n \cdot e^{\alpha T_f} \quad (13.33)$$

where

p is combustion pressure

T_f is the stoichiometric flame temperatures

n and α are empirical constants

The normalized NO_x behavior in Figure 13.29 is typical of modern gas turbine DLN combustors. This curve can be used to gauge NO_x emissions of a given GT combustor with known (or guessed or estimated) performance (denoted by the subscript 0 in the following equation). Gas turbine inlet or firing temperature (e.g., TIT) can be used as a *proxy* for the flame temperature:

$$\text{NO}_x = \left(\frac{\text{TIT}}{\text{TIT}_0} \right)^{20.724} \left(\frac{\text{PCOMB}}{\text{PCOMB}_0} \right)^{1/3} \text{NO}_{x0} \quad (13.34)$$

Thus, reducing the combustion (flame) temperature is the key to NO_x control. There are two types of flames: *diffusion* and *premixed*. These two types of flames characterize the two types of combustors as well. In diffusion combustors, the flame temperature in the reaction zone can approach the maximum (stoichiometric) value, independent of excess air mixed downstream of the reaction zone. The only way to control NO_x via diffusion flame temperature reduction is by injecting a *diluent*, that is, water or steam, into the reaction zone. There are several problems associated with this method, including reduced performance, water consumption, operability issues, etc. The only alternative is post-combustion exhaust gas cleanup using *selective catalytic reduction* (SCR).

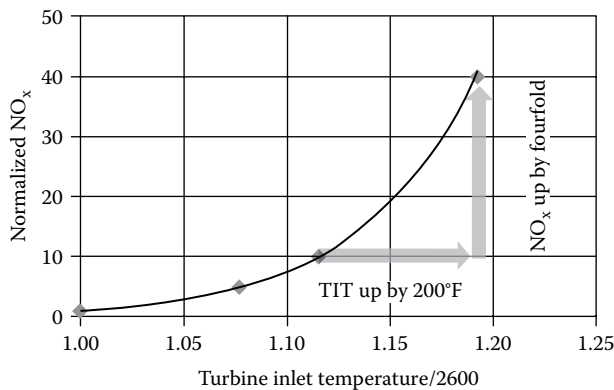


FIGURE 13.29

Normalized NO_x emissions as a function of TIT (as a proxy for the flame temperature, from Equation 13.34).

13.8.3 Dry Low NO_x Combustors

Premixed flame is the enabler of *dry low NO_x* (DLN) technology, which is also known as *lean premix* (LPM) combustion. The moniker “dry” obviously refers to the absence of water/steam as a diluent, because in DLN/LPM combustors, this role is played by atmospheric nitrogen in the combustion air. In DLN combustors, fuel is mixed with air upstream of the reaction zone at fuel-lean conditions (about $\phi \sim 0.5$) to prevent high flame temperatures that create thermal NO_x.

The main problem in designing a DLN combustor is to keep the combustion fuel-lean at *all* operating conditions. In order to fully appreciate this difficulty, assume that there is only *one* nozzle designed for $\phi = 0.5$ at the design point (full load) operation. To reduce the GT load by reducing the fuel flow and keeping the same fuel-lean condition with this single degree of freedom is not possible. The obvious solution is to increase the degrees of freedom, that is, the number of nozzles and stages of the fuel flow. This is the premise behind the modern DLN combustor design. This is sometimes referred to as radial or parallel fuel staging. Radial staging involves the use of pilot flames and reducing/eliminating fuel from some injectors completely [62].

Even with multiple nozzles and fuel staging, there are only a limited number of degrees of freedom. This limitation presents itself in MECL (*minimum emissions compliance load*), which is illustrated in Figure 13.30 [152]. Gas turbine and GTCC load is controlled via GT firing temperature (i.e., fuel flow) and airflow (via *inlet guide vanes* or IGVs). For maximum GTCC efficiency at part load, load is first reduced by closing the IGVs and reducing GT airflow until the exhaust temperature reaches its maximum value (typically 1200°F–1250°F). Thereafter, load is controlled via combined control of fuel flow and IGVs while keeping the exhaust temperature at its maximum. Once the IGVs reach their minimum position, further reduction in load is only possible by reducing the fuel flow. Major pollutant emissions

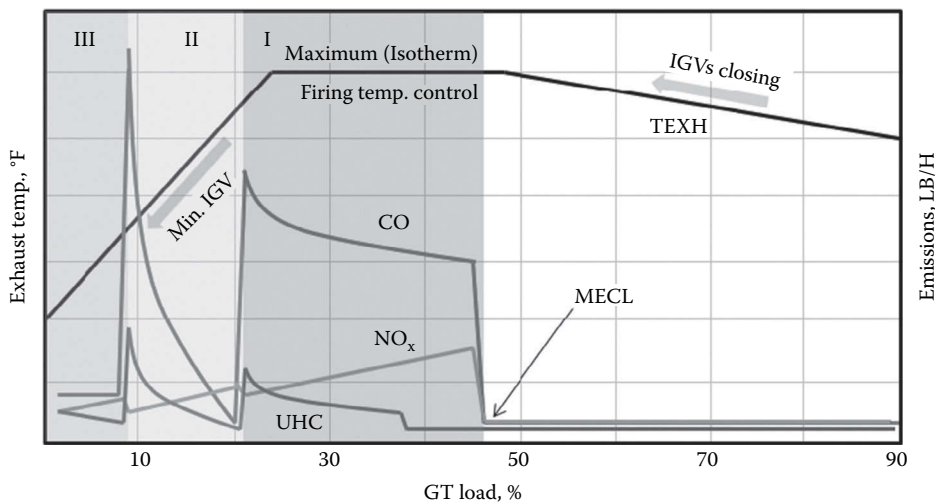


FIGURE 13.30

Typical gas turbine DLN combustor emissions (CO, NO_x, and unburned hydrocarbons [UHC]) and exhaust temperature (TEXH) as a function of GT load. (Adapted from Smith, G.R. et al., Transient operation of combined cycle power plants and the associated air emissions, *Powergen International 2012*, Orlando, FL, 2012.)

display large discontinuities as the combustion mode changes (e.g., one premix passage is closed) at a sufficiently low airflow and fuel flow combination, as dictated by requested GT load and exhaust temperature (or IGV opening) limit. The first such “jump” takes place at MECL (typically around 40%–50% GT load), below which the combustor emissions cannot be maintained at their environmentally regulated levels. This is a significant concern due to increasingly stringent government regulations and cyclic operation duties imposed on GT power plants as a result of the grid fluctuations caused by renewable generation (i.e., wind and/or solar) interruptions.

From a *full-load* (i.e., 100% load at given site ambient conditions with IGVs at their fully open position) operation performance perspective, the limitations of LPM/DLN combustors with fuel staging and single reaction zone can be seen in Figure 13.31. For high combustor exit (i.e., turbine inlet) temperatures, reaction zone temperature increases to the point that the increase in thermal NO_x becomes exponentially high. This is a significant impediment to further increase in gas turbine TIT for even higher thermal performance. Today’s SOA is 1600°C with 1700°C TIT under active development by one OEM [101]. According to the OEM, the development focuses on a 1700°C-class DLN combustor with steam-cooled casing and an *exhaust gas recirculation* (EGR) system [158]. With nearly 30% EGR (i.e., about 30% of the HRSG stack gas is recirculated to the GT inlet) and 17% (by volume) combustor inlet air O_2 (cf. about 21% O_2 in ambient air), NO_x emissions are reduced by 40%. The significance of this can be appreciated by considering the conceptual

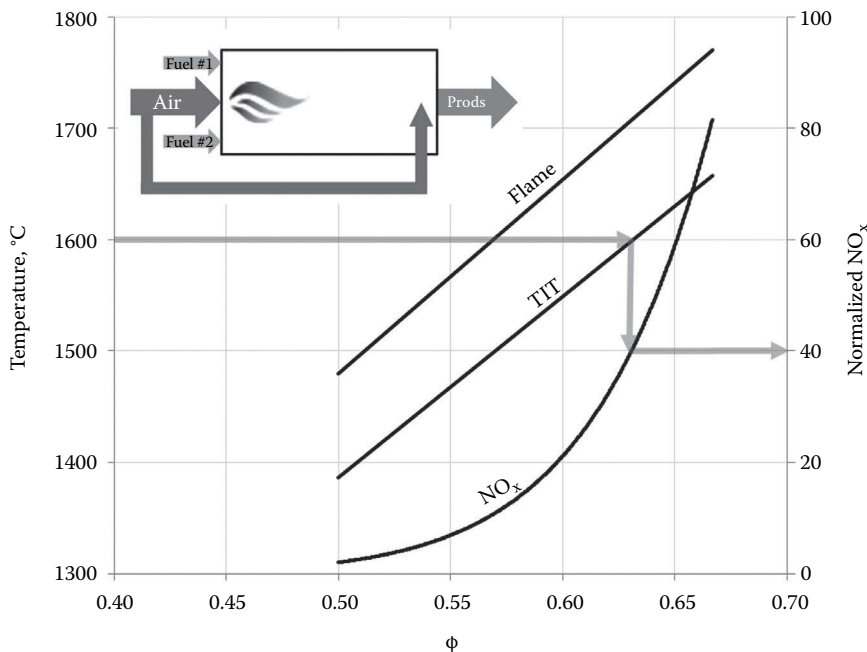


FIGURE 13.31

Flame temperature and normalized NO_x as a function of equivalence ratio (DLN combustor with radial/parallel fuel staging and single reaction zone). Note that ϕ is based on the airflow through the flame zone (*not* the total combustor airflow). Calculations are done with a heat balance simulation tool. (From Thermoflow Suite, Version 25, Thermoflow, Inc., www.thermoflow.com, Southborough, MA, 2015.)

curve in Figure 13.29. Assuming 25 ppmvd* NO_x (15% O_2) at 1600°C TIT, going to 1700°C (ignoring the change in compressor PR) would result in nearly 100 ppmvd NO_x , which corresponds to 60 ppmvd with 40% reduction via EGR. Indeed, the OEM-targeted NO_x concentration is 50 ppm (15% O_2) [158].

Axial staging injects fuel at two places along the combustor flow path (see Figure 13.32). Products from the first combustion zone are mixed with fuel and air in a second, subsequent combustion zone, providing an advantage for fuel-lean operation of the second zone. Combustion with axial fuel staging can be approximated by two stirred reactors in series. Assuming that 25% of total fuel flow is sent to the second reactor, the results in Figure 13.32 clearly illustrate the advantage of axial fuel staging (e.g., compare the curves in Figure 13.32 with those in Figure 13.31).

One promising method for achieving high TIT in DLN combustors without excessive NO_x generation is *fuel moisturization*. The method was introduced to utilize the lowest-grade energy in the HRSG (i.e., flue gas downstream of the low pressure (LP) section) to heat the fuel in a direct-contact heat exchanger (called moisturizer or saturator), which is a randomly packed column [153]. Similar to steam or water injection in diffusion combustors, water vapor in the fuel gas acts as a heat sink and reduces the flame temperature and lowers the thermal NO_x production. Performance improvement, subject to cycle

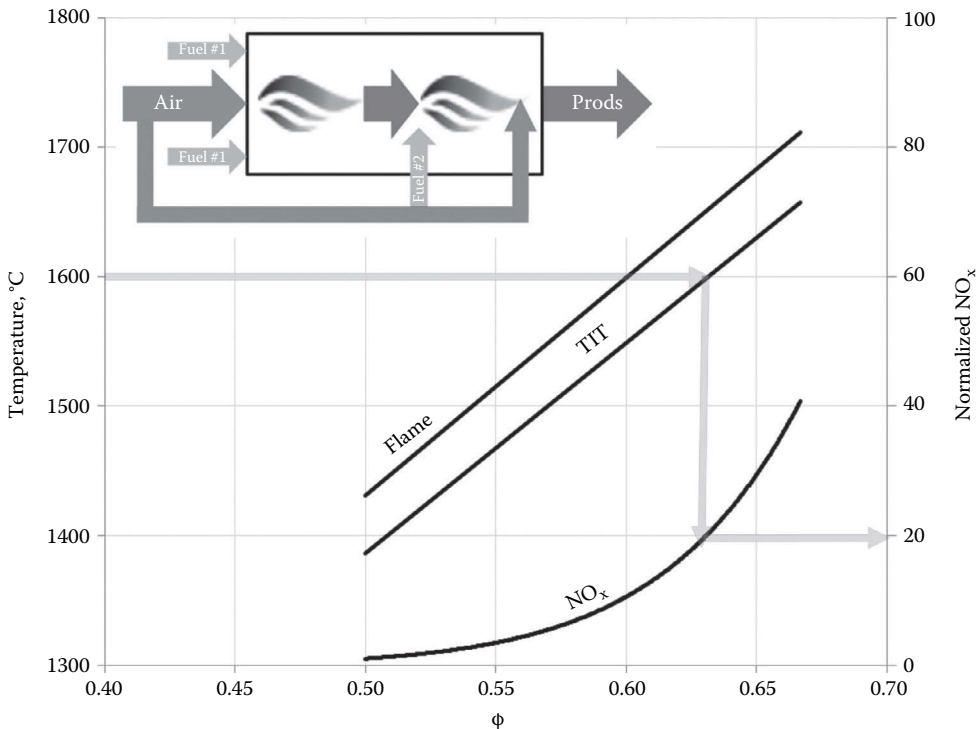


FIGURE 13.32

Flame temperature and normalized NO_x as a function of equivalence ratio (DLN combustor with axial fuel staging and two reaction zones). Note that normalized NO_x at 1600°C TIT is ~20 vis-à-vis ~40 in Figure 13.31 for a reduction of about 50%.

* Parts per million by volume on a dry basis.

optimization, is about 0.20% point increase in net efficiency and about 1.25% increase in net output. The system was deployed successfully in a GTCC power plant in California,* but complexity and cost prevented widespread commercial acceptance.

13.8.4 Catalytic Combustor

One alternative to the lean premix combustion for low emissions in advanced gas turbines is catalytic combustion, which was investigated heavily in the 1990s [13], especially in conjunction with the U.S. DOE's *Advanced Turbine Systems (ATS)* program. It has two variants: catalytically stabilized thermal combustion (also known as *lean catalytic lean burn* or LCL—shown in Figure 13.33) and fuel-rich catalytic combustion (also known as *rich catalytic lean burn* or RCL).

As shown in Figure 13.33, fuel is premixed with compressed air ($\phi < 0.5$, that is, fuel-lean) upstream of the palladium (Pd)-based catalyst. A pre-burner raises the gas inlet temperature to a level requisite for catalytic ignition. If the compressor discharge air is sufficiently high (i.e., in a gas turbine with high cycle pressure ratio), a pre-burner may not be necessary. The catalyst preheats the gas to a temperature at which homogeneous reaction burns out remaining, unreacted fuel. Due to material stability limitations, it is not possible to design a pure catalytic burner where all of the fuel is reacted in the catalyst section and delivers combustion products to the turbine at temperatures requisite for the SOA machines. In the RCL variant, only a portion of the compressed air is mixed with the fuel, which then reacts in the catalyst section under fuel-rich conditions ($2 < \phi < 4$). The remaining lean air-fuel mixture cools the catalyst section while flowing around it. The two streams mix at the catalyst section exit and then react and burn out in the homogeneous reaction zone.

Catalytic combustion can be applied to natural gas and syngas (including hydrogen) combustion. It has been shown to be capable of single-digit NO_x emissions in rig tests. The technology never came close to commercial acceptance due to issues related to operational reliability over a wide range of fuel-to-air ratios and at high temperatures. It is not likely to offer a solution at SOA turbine inlet temperatures, which are much higher than those considered during the ATS program in the 1990s.

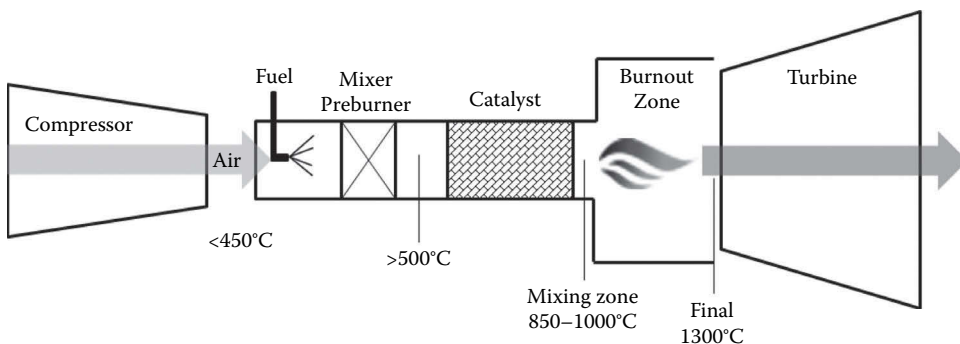


FIGURE 13.33
Gas turbine with LCL combustor.

* The plant, Inland Empire Energy Center in southern California, comprises two 107H single-shaft CC blocks. For the last several years, it was in the top 20 list of GTCC power plants with least NO_x emissions published in the *EP&L* magazine every year in November/December issue (available online).

13.8.5 Coal Combustion

The counterpart of the GT combustor in conventional coal-fired boiler furnaces is the *burner*. The reader is referred to [19] for a comprehensive coverage of pulverized coal burners. From an NO_x emissions standpoint, similar fundamental considerations apply to the PC burners. Fuel and air staging (also referred to as *reburning* [36] and *over-fire air* (OFA), respectively) are employed by the low NO_x burners to reduce NO_x emissions. It is not possible to achieve stringent emission requirements (down to single-digit NO_x by ppmvd in many places) via low NO_x burners only; to that end, SNCR systems in the boiler or SCR systems in the AQCS are requisite. Products of incomplete combustion, for example, unburned carbon (UBC) and CO, are controlled and minimized via advanced control systems monitoring and controlling air–fuel mixing rates.

Cyclone furnaces were developed to burn coals that are difficult to burn in conventional furnaces. It is a form of *slagging combustion* technology. Crushed (not pulverized) coal along with primary air enters the cyclone and the flow transitions into a vortex via tangential injection of secondary air. This results in higher heat release and higher combustion zone temperatures. About 85% of the coal ash is removed in molten form in a single pass (no ash recirculation) [36]. High combustion temperature is the reason for one major drawback of the cyclone furnace: high NO_x emissions. Air-staging, reburning, and post-combustion treatment (e.g., SCR) provides varying degrees of NO_x control capability.

Fluidized bed combustion, especially the circulating type known as the *circulating fluidized bed* (CFB) combustion, leads essentially to a *vertical cyclone furnace* with concurrent removal of sulfur dioxide (SO_2) in addition to fly ash. Primary air (40%–70% of the total) enters from the bottom of the furnace and carries the crushed coal particles (5–10 mm size, fed by gravity through the openings in the furnace walls) entrained in its flow upward. The “fluidized bed” comprises 0.5–3.0 mm size inert solids [36]. The term “circulating” refers to the solids separated from the flue gas after exiting the furnace and returned (recycled) to it (see Figure 13.34). Sulfur dioxide removal is accomplished by addition of *limestone* sorbent (i.e., calcium carbonate, CaCO_3) directly to the fluidized bed, together with the crushed coal. Comparison of CFB and PC capabilities in terms of coal feedstock, boiler size, and steam cycle are shown in Table 13.7.

Advantages of CFB boilers include low furnace temperatures (low NO_x , no slagging), coarse circulating solids (simple feed systems, handles poor fuels), and long residence time (complete combustion for reduced UBC and CO, good sorbent utilization). In addition to a wide variety of coals, CFB boilers can burn hard-to-burn fuels such as petroleum coke and anthracite as well as opportunity fuels such as waste coals and biomass (or even discarded tires). They also have very good emissions performance with smaller scrubber systems (with selective noncatalytic reduction for NO_x in the boiler). Proper fuel analysis is requisite for proper CFB selection and design (for a range of expected feedstock parameters—especially for the ultimate analysis—see Table 13.8).

Fluidized bed combustion technology is proven and industry accepted for subcritical steam cycle power plants at sizes less than 500 MWe. Scale-up to much larger sizes (e.g., up to 1000 MWe) has been problematic because uniform distribution of coal in the fluidized bed for complete combustion requires a large number of feeders (less of a problem in CFB) [36]. Due to its superior emissions performance vis-à-vis the PC technology, supercritical and ultra-supercritical CFB boiler plants are attractive for continued coal-fired power generation in an atmosphere of increasingly stringent environmental regulations. The first supercritical CFB boiler power plant (460 MWe, 43.3% LHV, 282 bar, 563°C/582°C steam cycle)

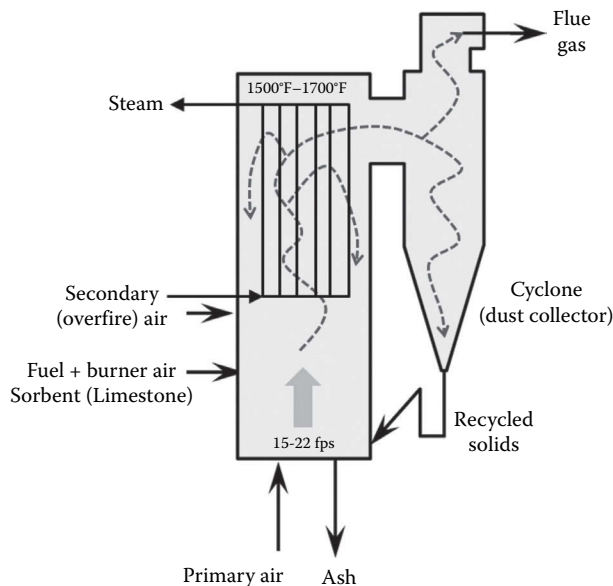


FIGURE 13.34
Circulating fluidized bed (CFB) boiler.

TABLE 13.7

Comparison of CFB and PC

	PC	CFB
Ash content	<20%	15%–60%
Moisture	<30% (PRB)	up to 50%
Heating value	>8000 Btu/lb	4500 to 9500 Btu/lb
Turndown	Down to 20%	Down to 70%
Boiler size	up to 1000 MW	Typically up to 300 MW Larger sizes avail. now
Cycle	Supercritical	Typically Subcritical Supercrit. avail. now
Sulfur capture	94% (Dry) 98% (Wet)	97%

went commercial in 2009 [104]. A 600 MWe SC-CFB power plant (254 bar, 570°C/570°C steam cycle) entered commercial operation in 2013 in China [75].

The natural extension of the CFB technology, which is essentially a *steam-cooled gas generator* at atmospheric pressure, is the *pressurized fluidized bed combustion* (PFBC) technology. In other words, if one could treat the CFB boiler conceptually as a “combustor,” the resulting system would end up being a coal-fired gas turbine combined cycle. The PFBC power plant will be covered in Section 13.10 in conjunction with closed-cycle gas turbines.

13.8.6 Pressure-Gain Combustion

The combustor of a gas turbine is a steady-state steady-flow (SSSF) device with a small pressure loss (about 5%–6%) and significant temperature rise (nearly 2000°F for J class gas turbines). The air-standard Brayton cycle comprises a *constant-pressure heat addition*

TABLE 13.8

Fuel Analysis Requirements for CFB

Ultimate analysis	Required for combustion calculations
Proximate analysis	Volatiles—ease of combustion
Size distribution	Fluidization and combustion zone
Hardness	Crushing and friability
Ash constituents	Agglomeration
Chlorine	Emissions, Hg capture, corrosion, agglomeration
Alkalies	Refractory attack and ash agglomeration
Trace/Toxic elements	Emissions, Hg capture, corrosion, agglomeration
Limestone analysis	CaCO ₃ , MgCO ₃ , Inerts, and moisture content, reactivity with SO ₂

(CPHA) process between the compression and expansion parts of the cycle. Another cycle heat addition possibility is the *constant-volume heat addition* (CVHA) process, which leads to the *Otto cycle*, that is, the air-standard (ideal) proxy for the gasoline ICE. From the ideal gas equation of state, it is straightforward to deduce that this process increases the pressure and the temperature of the cycle working fluid simultaneously. The advantage of CVHA over CPHA from a cycle performance perspective is obvious: A portion of the working fluid compression is shifted from the compressor (consumer of expander power) to the “heat adder,” resulting in an increase in cycle net power. This, in fact, is the physical mechanism underlying the significant efficiency advantage of reciprocating (piston–cylinder) gas engines over their turbomachine cousins (about 50% vis-à-vis 40% for the SOA representatives of either, respectively).

Numerically, for the ideal constant-volume heat addition process, Equations 13.5 and 13.6 becomes

$$\text{METH} = \frac{T_3 - T_2}{\ln\left(\frac{T_3}{T_2}\right) - \left(1 - \frac{1}{\gamma}\right) \cdot \ln\left(\frac{p_3}{p_2}\right)} \quad (13.35)$$

$$\text{METH} = \gamma \frac{T_3 - T_2}{\ln\left(\frac{T_3}{T_2}\right)} \quad (13.36)$$

In other words, since ideal gas γ is 1.40, for the same temperature delta across the cycle heat addition process, ideal CVHA results in 40% higher METH vis-à-vis CPHA. On a combined cycle basis, this can translate into a significant advantage. Using Equation 13.13 for the equivalent Carnot efficiency for the GTCC power plant, for METL of 59°F and METH of ~1370°F (e.g., the E class technology in Table 13.3), going from CPHA to CVHA would result in about a 10% (relative, *not* percentage points) increase in CC efficiency. In other words, one could achieve about a 62% net GTCC efficiency at E class TIT, which is equivalent to the J class performance at more than 300°F higher METH. The cycle state point data are shown in Table 13.9 (compare it with the E class cycle in Table 13.3). Comparison of the cycle T - s diagrams and METHs in Figure 13.35 illustrates the dramatic impact of CVHA on Brayton cycle heat addition irreversibility reduction (nearly by 80%).

TABLE 13.9

Cycle State Points (Brayton Cycle with CVHA and E class TIT)

	E Class with CVHA			
	P	T	v	s
Cycle PR	35.4			
CVHA PR	2.6			
1	14.7	59	13.07	0.00
2	201	636	2.015	0.00
3	520	2372	2.015	0.16
4r	NA	NA		
3r	NA	NA		
4	14.7	562	25.74	0.16
1	14.7	59	13.07	0.00
METL		59		
METH		2,100		
IHA		44		
Carnot η		79.7%		
Rating η		62.3%		
CF		0.782		

Note: Total cycle PR is 35.4 with precompression PR of 13.7 and PR during CVHA of 2.6 (which is the same as the temperature ratio [TR] during CVHA).

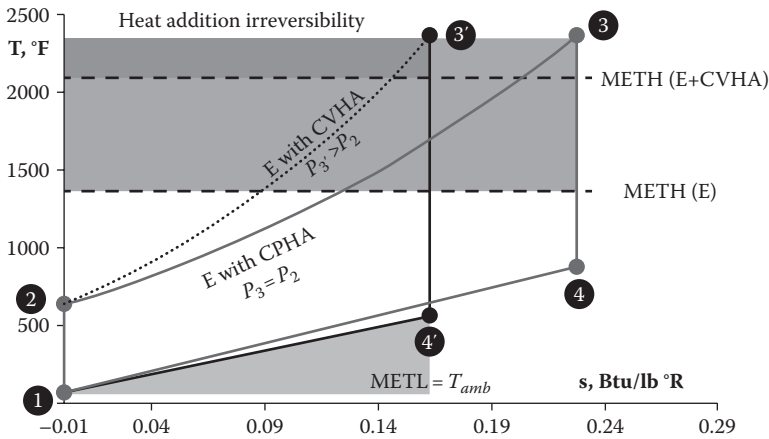


FIGURE 13.35

Brayton cycle T-s diagrams (E class with CPHA {1-2-3-4-1} and with CVHA {1-2-3'-4'-1}).

Fundamental thermodynamics via air-standard cycle analysis establishes the superiority of the Brayton cycle with CVHA over that with CPHA. The difficulty is in designing (conceptually as well as physically) a steady-flow device to accomplish combustion with temperature *and* pressure rise. Unsteady-flow examples approximating the ideal constant-volume combustion are the Holzwarth turbine, the Pescara turbine (which is a combined GT-Diesel machine as described by Reynst), and pulsating combustor engines [146]. The only possibility for an adiabatic and steady-flow process with pressure rise is a supersonic

flow with a standing *shock wave* (idealized as a discontinuity in the flow field.) Similarly, the only possibility for a steady-flow process with pressure rise *and* heat addition is a supersonic flow with a standing *detonation wave*. Therefore, from a conceptual perspective, one option to realize the Brayton cycle with the ideal CVHA is a modified Brayton cycle in which the heat addition process between state 2 and state 3' (see Figure 13.35) is via *detonation combustion*.

Detonation is a “rapid and violent form of combustion” that differs from other modes (e.g., flames) in that the main energy transfer mechanism is mass flow in a strong compression wave, that is, a shock wave, with negligible contribution from other mechanisms (e.g., heat conduction in flames) [10,21,22,65,119]. In other words, detonation is a “composite” wave that has two parts: An ordinary shock wave, which raises the temperature and pressure of a mixture of reactants, followed by a thicker reaction zone, in which the chemical reaction (ideally but not necessarily) goes to completion [22].* Strictly speaking, the Brayton cycle with heat addition via detonation combustion is *not* an ideal air-standard cycle in that the irreversible shock-driven heat addition process cannot be depicted on an equilibrium T - s diagram.[†] Furthermore, detonation combustion is *not* a true constant-volume combustion process. For sufficiently high PR across the C-J detonation wave, the specific volume ratio is approximately $\gamma/(1 + \gamma)$, where γ is the specific heat ratio of the combustion products downstream of the wave. For a typical γ of 1.3, this gives about 0.6, which is close to an ideal CVHA process. Nevertheless, detonation combustion is a practically feasible method to approximate CVHA in an actual engine configuration.

Alas, it is not possible to design a combustor with steady supersonic flow (Mach number of about 3–4) and a standing detonation wave in a land-based power generation turbine. The only possibility is to create detonation waves at a high frequency (say, tens of times per second) inside a semi-closed channel (tube) utilizing a suitable ignition system. The inherent unsteadiness of the practical detonation combustion led to the concept of intermittent or *pulse(d) detonation combustion* (PDC), which has been seriously investigated for aircraft propulsion systems for more than half a century [111]. In its most basic configuration, the resulting aircraft gas turbine engine, widely known as a *pulse detonation engine* (PDE), comprises a semi-closed multitubular combustion chamber in which detonations are created at a high frequency, for example, 80–100 times in a second, for practical flight units. For the application of PDC to land-based gas turbines for electric power generation, see references [76,79]. Realistic gas-dynamic calculations for the C-J detonation [76] suggest that the PR accompanying the TR in a PDC is much smaller than that suggested by the ideal CVHA (i.e., PR = TR). As shown in Figure 13.36, for the temperature ratio 2.58 in Table 13.9, a more realistic CVHA PR is 1.74. Substituting that value in the calculations, the equivalent Carnot efficiency becomes 76.4% (instead of nearly 80% in Table 13.9) and the implied GTCC efficiency with a CF of 0.782 is 59.7%–2.5% points lower than the “true” CVHA Brayton cycle efficiency in Table 13.9. Even so, the performance is still impressive: nearly 60% GTCC efficiency with E class TIT (cheaper materials, lower emissions).

* The most common mode of detonation that is of interest for practical applications is the *Chapman–Jouget* (C-J) detonation. Please refer to the works cited in the text for details.

[†] In the literature, detonation combustion Brayton cycle is commonly shown on a T - s diagram, along with the other cycles, via an artifice: The leading shock wave part of the detonation process is depicted as a dashed line combining the states upstream and downstream of the shock wave.

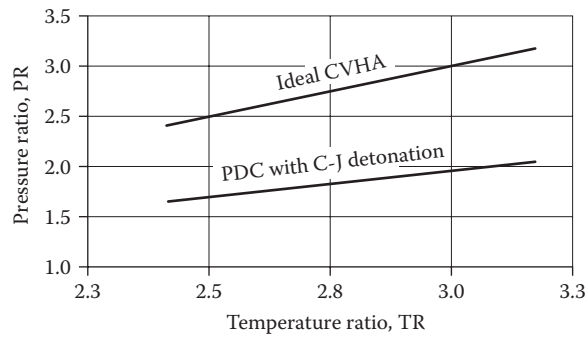


FIGURE 13.36
Pressure rise across pressure-gain combustion.

13.9 USC Power Plants

For a long time, coal-fired steam plants accounted for nearly 50% of U.S. electric power generation. At the time of writing (late 2015), the share of coal had dropped below 40%.* There are myriad factors for the declining share of coal in U.S. power generation portfolio, for example, low natural gas prices (prompted by the shale gas glut), environmental benignness of natural gas relative to other fossil fuels, and increasingly stringent rules and regulations. For example, at the time of writing, many coal-fired plants are being shut down to avoid costly compliance with Mercury and Air Toxics Standards (MATS) enforced by the U.S. EPA.

The future of coal-fired generation in the United States and, maybe to a lesser extent, in the rest of the world is closely tied to highly efficient power plants with some means of carbon capture. A coal-fired steam plant comprises three key components:

1. Steam generator (boiler)
2. Steam turbine generator (including feedwater heaters)
3. Air quality control system (AQCS)

From a thermal conversion efficiency perspective, the opportunities in improvement are in steam cycle parameters (pressure and temperature) and cycle optimization. This can be seen from the basic thermal efficiency formulas for the Rankine steam cycle power plant:

$$\eta_{th} = \eta_B \cdot \{CF \cdot \eta_{C,e}\} \cdot (1 - \alpha) \tag{13.37}$$

$$\eta_{C,e} = 1 - \frac{T_{cond}}{METH} \quad (\text{equivalent Carnot efficiency}) \tag{13.38}$$

$$CF \cdot \eta_{C,e} = \eta_{Gen} \cdot \eta_{Rank} \tag{13.39}$$

* In fact, twice in 2015, in April and July, gas-fired generation surpassed coal-fired generation (e.g., 35% vs. 34.9%, respectively).

$$\eta_{Rank} = \frac{\dot{W}_{ST,shaft}}{\dot{Q}_{in}} = \frac{\dot{W}_{ST,shaft}}{\eta_B \cdot (\dot{m} \cdot LHV)_{Fuel}} \quad (13.40)$$

In these formulas, METH is the steam cycle's mean effective heat addition temperature, which is a function of steam cycle parameters (see Figure 13.14), and CF is the cycle's Carnot factor, which is estimated as

$$CF = 0.79 + 0.0152 \frac{METH}{100} \quad (13.41)$$

Combined with the condenser temperature (T_{cond}), METH establishes the ideal cycle efficiency. Multiplication with the CF gives the steam turbine net efficiency (measured at the generator low-voltage terminals). In more familiar terms, the latter is the product of the Rankine cycle efficiency (η_{Rank}) and the ST generator efficiency (η_{Gen}). Utilizing advanced materials in boiler, steam turbine, and plant BOP leads to higher steam pressures and temperatures and, consequently, to higher steam cycle efficiency. Cycle optimization and better steam path efficiencies improve the cycle's Carnot factor. Optimization of the AQCS and other BOP parasitic power consumers leads to a lower auxiliary load fraction, α , and better overall conversion efficiency.

Assuming 165 bars (2400 psia) and 538°C (1000°F) for a typical subcritical PC power plant, 90% boiler efficiency and 6% auxiliary load fraction, it is found that METH is about 700°F (from Figure 13.14) and net plant efficiency is 42.1%. Using the simple calculations presented in Section 13.6, estimated improvement in coal-fired FFPS efficiency is plotted in Figure 13.37. Thus, an advanced USC plant with 300 bars (4350 psia) main steam pressure and 700°C (1300°F) steam temperature adds nearly 6% points to the plant efficiency. One should not expect significant improvement in boiler efficiency or Carnot factor (both are at around 90% at present). In other words, to expect more than 7%–8% points overall plant net thermal efficiency improvement is not realistic.

This quick estimate is confirmed by information from different sources of published information (presumably derived from detailed cycle calculations). An overall perspective is provided in Figure 13.38 [149]. Cycle enhancements such as dual reheat and increasing

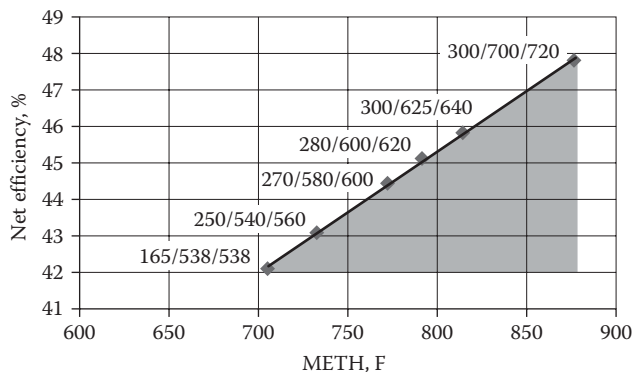


FIGURE 13.37

Improvement in coal-fired steam generation power plant thermal efficiency (Equations 13.38 through 13.40). Cycle conditions shown are in SI units (main pressure, main steam temperature, and reheat steam temperature).

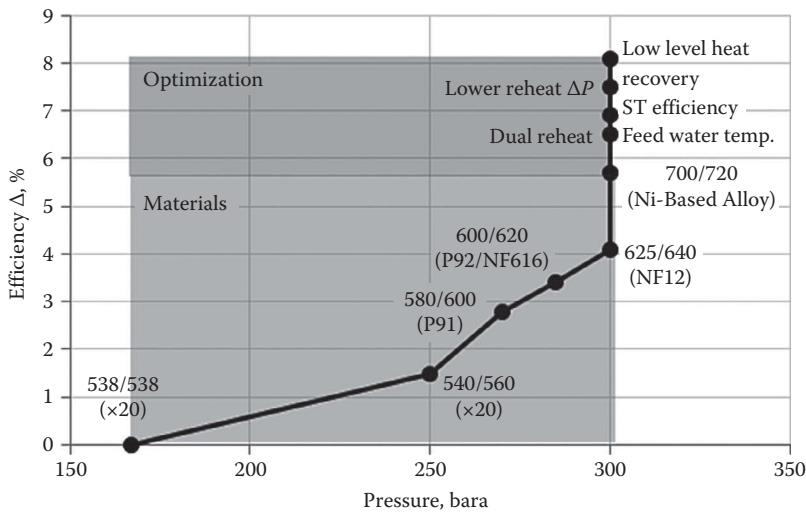


FIGURE 13.38

Impact of materials and system optimization on coal-fired power plant efficiency. (From Rukes, B. and Taud, R., *Energy*, 29, 1853, 2004).

final feedwater temperature increase directly impact METH (each 10°F increase in METH is worth 0.4 net efficiency points). Both improvements come at significant additional cost (e.g., additional piping, valves, heat exchangers, construction materials and labor, etc.) and are subject to careful optimization on a case-by-case basis. Steam turbine steam path efficiency improvement and lower reheat pressure loss are reflected in higher CF (each 0.01 in CF is worth 0.6 net efficiency points).

Steam cycle pressures as high as 5000 psia (344 bars) and steam temperatures as high as 760°C have been considered. These parameters lead to another 1.2% points improvement in net plant thermal efficiency. Thus, starting from about 42% net LHV for today's SOA, about 50% should be considered the entitlement performance for an A-USC power plant. Note that the auxiliary power assumption of 6% is based on the assumption of ST-driven boiler feed pump, which is pretty much the case for all large coal-fired power plants. For smaller plants with electric motor-driven pumps, it can be as high as 10% of the gross output. Depending on the particular site characteristics and heat sink availability, performances in Figure 13.37 can be difficult to achieve in an actual power plant.

The key to achieving this projected improvement is the availability of advanced materials for major plant equipment, that is, boiler and furnace, steam turbine, and plant BOP (primarily pipes and valves). This will be covered in detail in Section 13.12.

Another important consideration is what one can do with regard to existing coal-fired plants to improve their efficiency. This would also make a significant impact on carbon emissions per megawatt-hour of electricity generation. Table 13.10 summarizes the findings from a study based on a literature review of published articles and technical papers identifying potential efficiency improvement techniques applicable to existing coal-fired power plants [32]. The reference plant representing a common basis for the data in the table is as follows: 87% boiler efficiency (HHV basis), 40% steam turbine efficiency, 98% generator efficiency, and 6% auxiliary load. Based on these assumptions, from Equation 13.37, the reference plant HHV efficiency is 32% and the net heat rate is 10,600 Btu/kWh in HHV. Thus, if all the improvements are implemented (and not all coal-fired power plants

TABLE 13.10

Existing Coal-Fired Power Plant Efficiency Improvements Reported for Actual Heat Rate Improvement Projects (Improvement Is a Reduction in Heat Rate by the Indicated Percentage)

Efficiency Improvement Technology	Description	Minimum Improvement	Maximum Improvement
Combustion control optimization	Combustion controls adjust coal and air flow to optimize steam production for the steam turbine/generator set. However, combustion control for a coal-fired power plant is complex and impacts a number of important operating parameters including combustion efficiency, steam temperature, furnace slagging and fouling, and NO _x formation. The technologies include instruments that measure carbon levels in ash, coal flow rates, air flow rates, CO levels, oxygen levels, slag deposits, and burner metrics as well as advanced coal nozzles and plasma assisted coal combustion.	0.15%	0.84%
Cooling system heat loss recovery	Recover a portion of the heat loss from the warm cooling water exiting the steam condenser prior to its circulation thorough a cooling tower or discharge to a water body. The identified technologies include replacing the cooling tower fill (heat transfer surface) and tuning the cooling tower and condenser.	0.20%	1.00%
Flue gas heat recovery	Flue gas exit temperature from the air preheater can range from 250°F to 350°F depending on the acid dew point temperature of the flue gas, which is dependent on the concentration of vapor phase sulfuric acid and moisture. For power plants equipped with wet FGD systems, the flue gas is further cooled to approximately 125°F as it is sprayed with the FGD reagent slurry. However, it may be possible to recover some of this lost energy in the flue gas to preheat boiler feedwater via use of a condensing heat exchanger.	0.30%	1.50%
Low rank coal drying	Subbituminous and lignite coals contain relatively large amounts of moisture (15%–40%) compared to bituminous coal (less than 10%). A significant amount of the heat released during combustion of low-rank coals is used to evaporate this moisture, rather than generate steam for the turbine. As a result, boiler efficiency is typically lower for plants burning low-rank coal. The technologies include using waste heat from the flue gas and/or cooling water systems to dry low-rank coal prior to combustion.	0.10%	1.70%
Sootblower optimization	Sootblowers intermittently inject high velocity jets of steam or air to clean coal ash deposits from boiler tube surfaces in order to maintain adequate heat transfer. Proper control of the timing and intensity of individual sootblowers is important to maintain steam sootblowing (i.e., sootblowing in response to real-time conditions in the boiler) and detonation sootblowing.	0.10%	0.65%
Steam turbine design	There are recoverable energy losses that result from the mechanical design or physical condition of the steam turbine. For example, steam turbine manufacturers have improved the design of turbine blades and steam seals which can increase both efficiency and output (i.e., steam turbine dense pack technology).	0.84%	2.60%
Total		1.70%	8.57%

Source: U.S. Environmental Protection Agency, Available and emerging technologies for reducing greenhouse gas emissions from coal-fired electric generating units, Sector Policies and Programs Division Office of Air Quality Planning and Standards, U.S. Environmental Protection Agency, Research Triangle Park, NC, October 2010.

can accommodate all of them), one could expect an improved net HHV efficiency between 32.7% and 35%. For a 500 MWe coal-fired plant, 3% point improvement in efficiency reduces the CO₂ emissions from 1.13 to 1.03 tons/MWh. For annual 6000 h of operation, this corresponds to nearly 300,000 tons of reduction in CO₂ emissions in a year.

There is a significant variability in the quality and heating value of coals available for power generation. In particular, sulfur, moisture, and ash content of the coal significantly affect the boiler and flue gas cleanup performances (i.e., coal needs to be dried to reduce the coal moisture, the *flue gas desulfurization* [FGD] system is loaded higher to remove sulfur from the stack gas, etc.). Typically, performance ratings are quoted based on a higher quality coal with a heating value of about 11,000 Btu/lb (6,100 kcal/kg) HHV. When lignite with a reduced HHV is the feedstock to the boiler, the boiler efficiency is lower. It is difficult to burn a coal with, say, 50% moisture and 2160 Btu/lb (1200 kcal/kg) heating value in a conventional PC steam boiler. A good portion of the fuel energy would be wasted in evaporating the moisture in the coal instead of generating steam in the boiler tubes. There are about 10 different proprietary methods to deal with this problem; one of them is to dry the coal in a two-step process utilizing the flue gas. Table 13.11 shows how the PC plant cost and efficiency change with coal quality. Note that the coal-fired plant capital cost increases significantly with decreasing rank (and the heating value) of the coal feedstock.

Equally important but typically neglected factors are design for reliability, operational flexibility (e.g., startup, shutdown, and load ramps), constructability, maintenance, and repair considerations. All these factors will enter the life-cycle COE calculation via total installed cost and fixed/variable O&M costs. Considering the already astronomic cost of utility-scale coal-fired power plants, one can certainly appreciate the magnitude of the hurdle to be overcome. Note that this is *before* the addition of the carbon capture and sequestration system, without which it will be increasingly difficult to contemplate the construction of coal-fired power plants—at least in the developed countries (with the possible exception of Germany with its large lignite reserves).

From a performance perspective, steam turbine back pressure is a very strong factor. It is primarily dependent on the availability of a suitable heat sink to achieve a low condenser pressure. The best choice is a once-through, open-loop system utilizing cold water from a natural source (e.g., a lake, river, etc.). Apart from the geographic constraints, this is an increasingly rare option due to increasingly stringent environmental regulations precluding the use of water resources for thermal power plant cooling (preservation of scarce resources, ecological concerns, etc.). In order to exploit low

TABLE 13.11

Impact of Coal Rank on PC Plant Heat Rate and Capital Cost

	Pittsburg #8	Illinois #6	PRB	TX Lignite
HHV, Btu/lb	12,450	10,100	8149	7080
Moisture, %	6	12	32	38
Ash, %	10	16	5	6.5
Heat rate	1.00	1.03	1.06	1.11
Furnace size	1.00	1.21	2.03	2.36
Cost	1.00	1.04	1.15	1.24

Source: Cost Comparison IGCC and Advanced Coal, An EPRI Presentation (by S. Dalton), Roundtable on Deploying Advanced Clean Coal Plants, July 29, 2004.

Note: PRB, Powder River Basin.

condenser pressure, the steam turbine must have a suitably large exhaust annulus to prevent excess leaving losses. This translates into expensive hardware with large last-stage buckets (made from titanium in extreme cases) and/or multicasing LP sections (e.g., two double-flow LP configuration). Optimized designs with multi-pressure condensers help in that regard (e.g., each double-flow LP turbine section exhausting to a dedicated condenser, one with a higher pressure than the other, instead of a single condenser for both sections at a single low pressure).

No big difference is expected in A-USC boiler configuration and furnace design vis-à-vis existing SC/USC boilers. Additional heat transfer surface area is requisite in the convective sections due to lower log-mean temperature difference (LMTD) caused by higher steam temperatures. From protection against corrosion perspective, even with the best-possible materials and claddings used to construct superheater and reheater sections of the A-USC boiler, the design might have to allow for more frequent tube replacement (i.e., additional O&M expenditure). Weld overlay in the furnace section, cladding, or duplex furnace tubes with Ni-Cr alloys are expected to mitigate excessive fireside corrosion problems.

Oxygenated water treatment is recommended for the SC through A-USC systems for higher reliability compared with the all-volatile treatment (except during commissioning). This will be covered in more detail in Section 13.17. No change is expected in the boiler efficiency (per ASME PTC 4), which will be fuel dependent and in the same range as the current boilers (about 90%).

Constructability, ease of installation, and maintenance considerations stem from the requisite alloy materials (difficult to weld) and additional heat transfer equipment, larger and heavier due to higher pressures and temperatures (longer erection time, requirement of new standards, etc.). Availability of qualified craft labor for welding is already a big concern and a source of cost overrun due to schedule slip for EPC contractors. This could be magnified significantly for the erection and repair of the A-USC power plants with extensive use of alloy materials.

In order to emphasize the cost hurdle faced by the A-USC technology, a performance-cost comparison of two 1000 MW power plants is undertaken. Plant A is an advanced GTCC with F or H class gas turbine with 59% rated efficiency. For the purpose of illustration, plant B is a readily available A-USC coal-fired power plant with 50% (net LHV) efficiency. For simplicity, difference in O&M costs, emission penalties, etc. are ignored. Using the formula presented in Section 13.7 with 6000 h per year operation at a load factor of 75% and assuming \$1000 per kW for the GTCC,

- For \$5 natural gas and \$2 coal, to achieve the same LCOE as the GTCC power plant, the A-USC plant's total installed cost should be around \$1600 per kW.
- For \$13 natural gas, the break-even total installed cost for the A-USC plant is around \$3500.

In order to have a reference point for the cited numbers, consider that the construction cost of 600 MW John W. Turk Jr. USC power plant in Arkansas, United States, which came online in 2012, was \$1.8 billion or \$3000 per kW (construction started in 2008 and took four years—cf. about 2 years for the comparable GTCC).

Referring to Figure 13.28, CO₂ emissions from the hypothetical 50% efficient USC power plant would be twice as high as that of a typical advanced GTCC, that is, 1400 lb/MWh vis-à-vis 700 lb/MWh. According to the 2013 EPA proposal for carbon dioxide reductions from new coal- and natural gas-fired power plants, "Standards of Performance for Greenhouse Gas emissions From New Stationary Sources: Electric Utility Generating Units," emission limits

are set at 1100 lb/MWh for coal-fired plants and 1000 lb/MWh for large natural gas-fired turbines. An advanced GTCC with F, H, or J class turbines is already below the EPA limit for CO₂ emissions; in order to bring the hypothetical A-USC plant below the limit, about 25% carbon capture is requisite; in order to bring it to the same footing as the GTCC (without capture), the requirement becomes 50% carbon capture. Accompanied by the hits to its performance and cost, it is practically impossible for the A-USC technology, even if it *were* available today, to compete with gas-fired generation economically when the latter is readily available and reasonably cheap (e.g., the United States in the second decade of the twenty-first century).

13.10 Gas Turbines

Gas turbine combined cycle is the most efficient FFPS technology as of today and tomorrow. (As discussed earlier, the only exception is the fuel cell hybrid arrangement, which is not bound by the Carnot limit.) The workhorses of utility-scale gas-fired electric power generation are the *heavy-duty industrial gas turbines* (also referred to as “frame” machines). The technology hierarchy of frame machines is defined by the *turbine inlet temperature* (TIT). Each technology class is designated by a letter, as shown in Figure 13.39 [81]. At the time of writing (late 2015), the state of the art is 1600°C class designated by the letter “J” (offered by one OEM with the designation “HA” for “air-cooled H”).

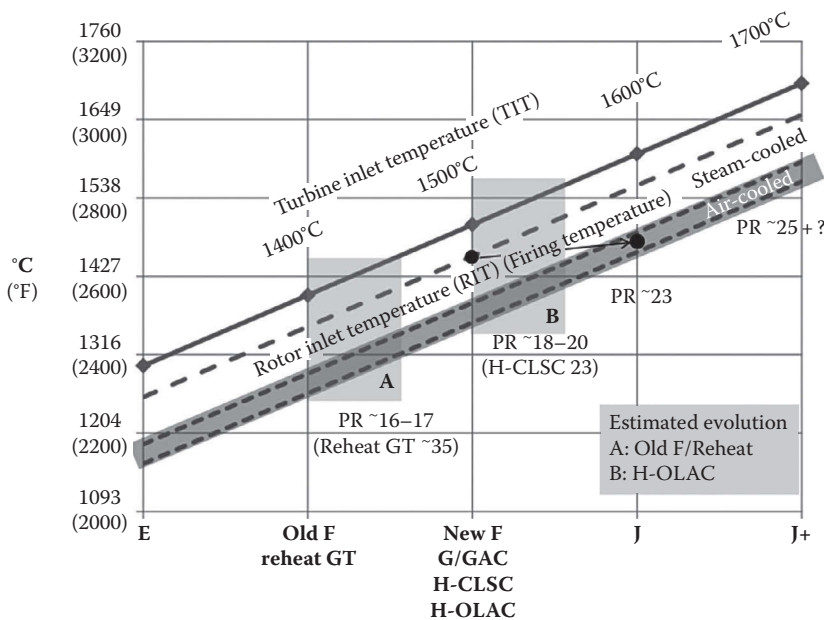


FIGURE 13.39

Heavy-duty industrial gas turbine classification by turbine inlet temperature (solid line). Dashed lines represent the corresponding “firing” temperatures (see the text) (CLSC, closed loop steam cooling; OLAC, open loop air cooling).

Gas turbine operation is thermodynamically described by the Brayton cycle (see Chapter 10 in this handbook). As such, the performance is controlled by the highest temperature of the cycle and the compressor pressure ratio. The former, strictly speaking, is the flame temperature inside the combustor, which is well above 3000°F. From a practical point of view, however, two temperatures define the GT performance: TIT and RIT (rotor inlet temperature). The former is the gas temperature at the combustor exit prior to entering the stage 1 nozzle (S1N) or vane. The latter, also known as the *firing temperature*, is the gas temperature at the inlet of the stage 1 bucket (S1B), which is lower than the TIT due to dilution with S1N and wheel space cooling air flow. A third definition, which is preferred by European manufacturers, is based on airflow and fuel flow: TIT per *ISO-2314* [72]. It is not a “real” temperature in the sense that it cannot be measured by a thermocouple or other device in the hot gas path (HGP).* All three definitions are explained graphically in Figure 13.40.

The difference between TIT and RIT is about 200°F; in other words, higher gas temperatures achieved in the combustor at the expense of higher NO_x formation are diluted before the gas starts generating useful shaft work. Using advanced alloys and *thermal barrier coatings* (TBC), in conjunction with intricate film cooling techniques, aims to reduce the gap. Possible remedies include *ceramic matrix composites* (CMCs) as S1N material, which practically eliminates the need for cooling and *additive manufacturing* (commonly known as *3D printing*) to produce airfoils with many small-sized holes to facilitate *effusion cooling* (the ultimate form of film cooling).

The current GT technology landscape is summarized in Figure 13.41 and Table 13.12. Performances shown are at ISO base load. On hot and humid days, GT output drops significantly due to lower airflow (same volume flow but much lower density). Since those are the times when electric power demand rises sharply due to excessive air conditioning, power augmentation methods are deployed to close the gap, with some sacrifice in heat rate. The most common power augmentation options are shown in Table 13.13. *Duct firing* increases the net capacity of the plant but reduces efficiency due to the higher incremental heat rate of the additional combustion in the HRSG duct burners

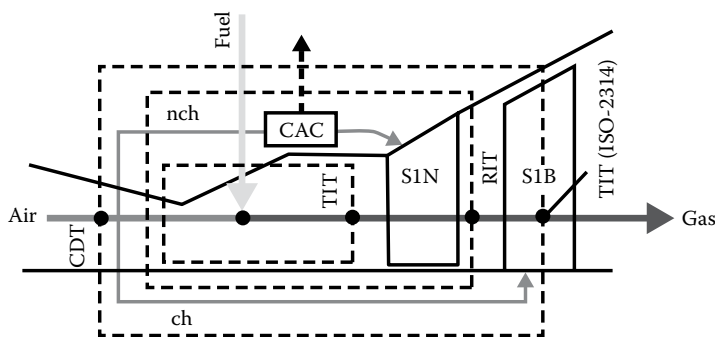


FIGURE 13.40

Gas turbine hot gas path temperature definitions. CDT, compressor discharge temperature; CAC, cooling air cooler; “ch” and “nch” refer to “chargeable” and “non-chargeable” turbine hot gas path cooling air flows, respectively. RIT is also known as the *firing temperature*. The fictitious ISO-2314 TIT is about 100°C (180°F) lower than the corresponding RIT.

* While the other two temperatures can be measured, this would be a very a difficult feat to accomplish reliably and continuously, which makes it possible only in a controlled lab environment.

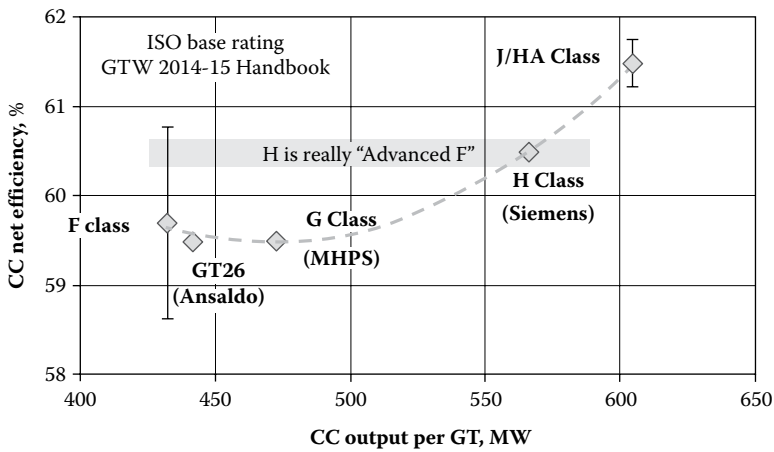


FIGURE 13.41 State-of-the-art GT technology. (Data from *Gas Turbine World 2014–2015 Handbook*, Vol. 31, Pequot Publishing Inc., Fairfield, CT, p. 66.) The wide variation in F class efficiency is a reflection of technology flow-down from advanced classes. There are several generations of F, with the newer ones incorporating materials, coatings, and film cooling techniques from H and J classes. Those are more efficient than the older generations of F and legacy machines manufactured by licensees of OEMs.

TABLE 13.12

A Composite Picture of State-of-the-Art F, Advanced F, Air-Cooled G, Air-Cooled H, and Air-Cooled J Class Gas Turbines (Simple Cycle GT Data from *Gas Turbine World 2013 Handbook* and Selected Issues)

	Average	"Best"
GT output, MW	337 ± 64	300 to ~500
GT efficiency, %	39.9 ± 1.3	41+
Compressor pressure ratio	19.9 ± 1.9	22–23
Turbine inlet temperature, °C	1450–1600	1600
Turbine inlet temperature, °F	2642–2912	2912
Exhaust temperature, °F	1137 ± 29	~1145
CC net efficiency, %	60.2 ± 0.9	61+

TABLE 13.13

GTCC Power Augmentation Options

Evaporative Cooling or Inlet Fogging	HRSG Duct (Supplementary) Firing	Impact on Output, %	Impact on Efficiency, %
×		+4	-0.2
	×	+14	-4.0
×	×	+18	-4.0

(when operating in duct firing mode) and the reduced efficiency of steam turbine (when not operating at full output). Since 2002, nearly 36 GWe capacity (56 plants at an average size of 640 MWe) was built in the United States. The average duct firing capacity was 77 MWe (roughly 14% increase over unfired capacity).^{*} The most commonly deployed GT inlet conditioning technology is *evaporative cooling*. *Inlet foggers* with overspray saturate the inlet air and cool it down to nearly wet-bulb temperature. Unevaporated water in the form of microscopic droplets evaporates during the compression, which results in a mild intercooling effect. Another form of inlet fogging is *wet compression* (also referred to as *high fogging*), which is promoted by some OEMs [109,134].

The state-of-the-art and future GTCC technology landscape is summarized in Figure 13.42 (based on the simple formula in Equations 13.18 and 13.19). For 60% efficiency, minimum 39% GT efficiency, high exhaust temperature (implying system-level optimization to determine gas turbine firing temperature and cycle pressure ratio), and a state-of-the-art bottoming cycle are requisite. In near future, 63% net GTCC efficiency seems to be the upper limit, which requires 43% gas turbine efficiency and a Carnot factor of 0.76 for the steam RBC. To reach 65%, one needs 45% Brayton cycle efficiency and 0.78 bottoming cycle CF (with 700°C GT exhaust temperature).

It is fairly certain that future GTCC performance improvement is a function of GT technology advances. A qualitative synopsis of such advances in terms of their impact on key

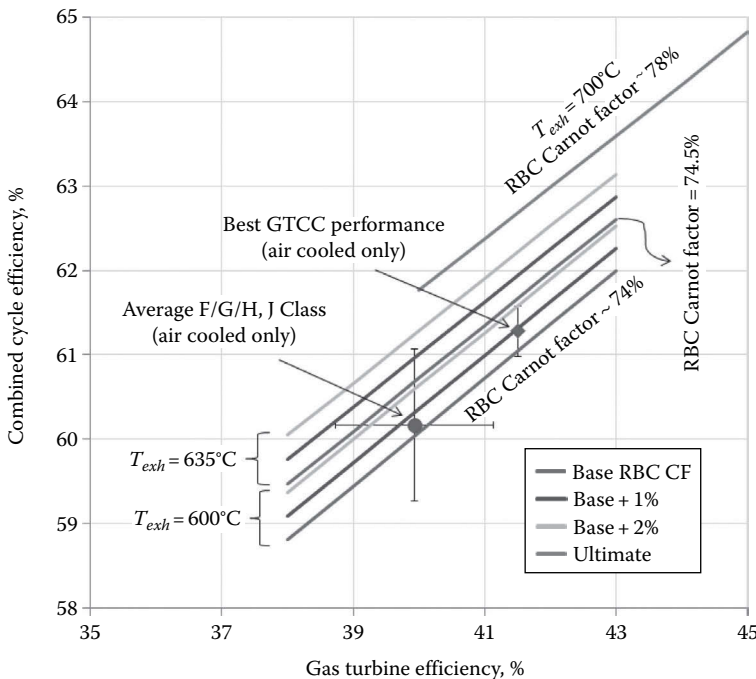


FIGURE 13.42

GTCC net cycle efficiency map (steam RBC); GT exhaust temperature is used as a proxy for GT cycle pressure ratio).

^{*} From a 2014 report by Sargent & Lundy, prepared for PJM.

TABLE 13.14

Gas Turbine Parameter Improvement Impact on GTCC Efficiency

Parameter	Improvement	GTCC Efficiency Impact (Percentage Points)
Compressor efficiency	+1 percentage point	+0.25
Firing temperature	+50°F	+0.35
Fuel temperature	+50°F	+0.07
Turbine efficiency	+1 percentage point	+0.35
Chargeable flow	-1% of airflow	+0.20
HGP bucket tip clearance	-10 mils	+0.04

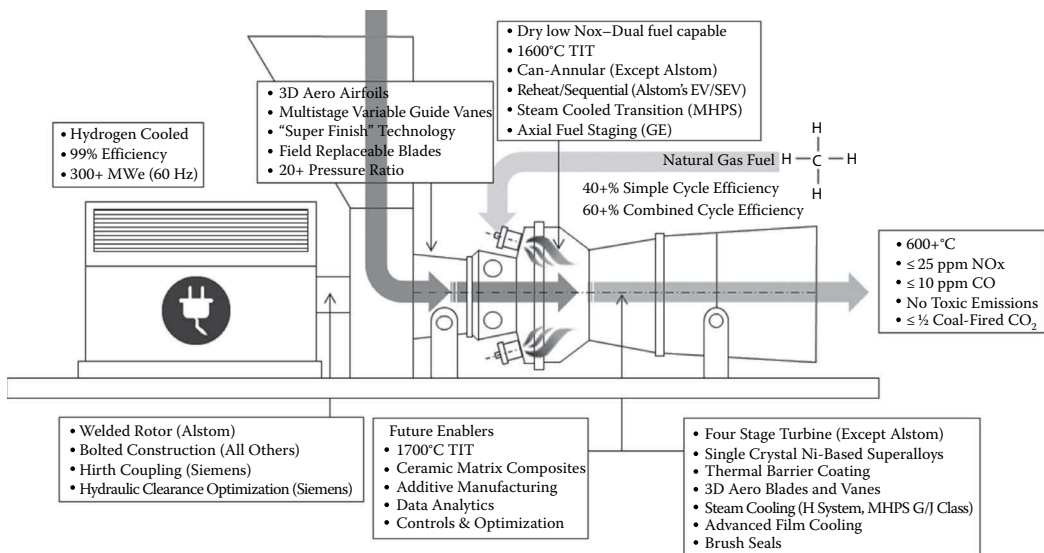


FIGURE 13.43

Current and future gas turbine technology drivers. (From Gülen, S.C., Powering sustainability with gas turbines, *Turbomachinery International*, September–October 2015, pp. 24–26).

gas turbine design parameters and GTCC efficiency are provided in Table 13.14. Current and future technology highlights to accomplish that are summarized in Figure 13.43.

13.10.1 Cycle Variants

13.10.1.1 Closed-Loop Steam Cooling

Another technique to reduce the TIT–RIT temperature loss across the S1N is closed-loop steam cooling (see Figure 13.44). At present, there is only one *closed-loop steam cooled* gas turbine, the H-System, which is not offered commercially anymore.* It is true that G

* Steam-cooled gas turbines, by necessity, come only in combined cycle configuration. That is why the term “system” was adopted by their OEM.

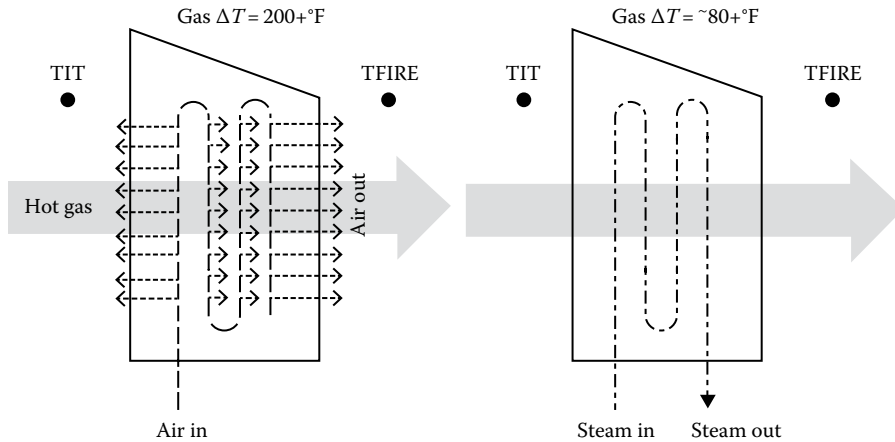


FIGURE 13.44

Stage 1 nozzle (stator) cooling technology impact. For simplicity, small secondary cooling flows are not shown. The firing temperature (TFIRE) is at the inlet plane of stage 1 bucket (rotor). (From Gülen, S.C., General electric—Alstom merger brings visions of the Überturbine, *Gas Turbine World*, pp. 28–35, July/August 2014).

and J class gas turbines by a different OEM* also employ steam cooling for combustor liner, transition piece, and stages 1 and 2 turbine rotor rings (J class). In terms of HGP “chargeable” (entering HGP *downstream* of RIT) and “non-chargeable” (entering HGP *upstream* of RIT) cooling air reduction, however, G and J class gas turbines are essentially air-cooled machines.

In H-System gas turbines, on the other hand, closed-loop steam cooling reduces hot gas temperature drop across stage 1 nozzle to less than 80°F. For the same combustor temperature and TIT, this results in an increase of 100°F–150°F in firing temperature vis-à-vis advanced F class machines with air cooling (one OEM’s H class gas turbines also belong in this category). An additional benefit of steam cooling is the less parasitic extraction of compressor discharge air and higher flow to the head-end of the DLN combustor for fuel premixing. If the firing temperature is kept at the F class level, the benefit of steam cooling presents itself as reduced TIT and combustor temperature, that is, reduced NO_x production.

In the H-System, the first two turbine stages, including nozzles and buckets, are fully steam cooled. This reduces the amount of “chargeable” cooling air and increases gas turbine output via higher gas flow through the HGP.† Heat rejected to the coolant steam is converted into additional steam turbine power output. The net benefit of full steam cooling is an increase of 2% points in combined cycle efficiency [50].

There are only six H-System power plants in existence. It is highly unlikely that another fully steam-cooled gas turbine combined cycle system will be offered by an OEM in near

* Note that the same OEM designed and tested a fully steam-cooled “H” machine around 2000. This machine, with a cycle pressure ratio of 25, was never offered commercially, but its compressor lives on in current G and J class gas turbines.

† It should be noted that closed-loop steam cooling does not eliminate air cooling altogether. Purge flow is still needed to prevent the ingestion of hot gas into wheel spaces. Furthermore, cooling of the trailing edges of stage 1 and 2 nozzle vanes via internal coolant flow presents a challenge. Supplementary cooling of inner and outer side walls (platforms) and trailing edge of the nozzle vanes with wheel space purge air is requisite to ensure adequate parts life.

future—if ever. As such, today (late 2015) and in the near future (next 10 years at least), the dominant gas turbine technology will comprise air-cooled advanced, F, G, H, and J class “frame” machines.

13.10.1.2 Intercooling and Recuperation

Intercooling and recuperation are textbook Brayton cycle variations, which are available in several commercially available gas turbines, specifically aeroderivative machines [14]. From an ideal cycle perspective, intercooling is not desirable because it lowers cycle METH. However, in high cycle PR machines (i.e., aeroderivatives), intercooling reduces compressor power consumption (thus increasing the specific power output of the machine) and discharge temperature, which translates into reduced HGP cooling air flow. In fact, the largest (and most efficient) commercially available aeroderivative GT is an intercooled machine rated at 100 MWe. The only commercially available machine with recuperation is a small aeroderivative GT rated at 5 MWe (which was developed with support from the U.S. DOE’s ATS program). At 38.5%, it is quite efficient within its size class. However, recuperation is detrimental to CC efficiency due to low exhaust gas temperature (only 690°F for the cited example). The only gas turbine combining intercooling and recuperation (ICR) in one cycle is a marine propulsion unit rated at 21 MW [60]. It is not expected that recuperation is going to be a feature to find its way into future advanced GT technologies (an exception can be made for the supercritical CO₂ cycle, which will be discussed later in the chapter). Intercooling, on the other hand, may be necessary at high cycle pressure ratios driven by high TITs to reduce the compressor power consumption and to keep the HGP cooling air flow at a manageable level. It is interesting to note that, in the 1950s and 1960s, venerable Swiss engineering company Brown Boveri Corporation (BBC) developed and built many gas turbine power stations with intercooling (and reheat). These gas turbines were very efficient power stations, with key components (i.e., compressors, combustors, expanders, and heat exchangers) installed in a complex plant arrangement rather than in a compact “jet engine” frame [163]. They were superseded with the advancement of efficient and compact frame machines, starting in the late 1960s.

13.10.1.3 Reheat Combustion

The most significant Brayton cycle variation, which is available in a commercially offered heavy-duty industrial GT, is reheat or *sequential combustion*, which is a very crude approximation of isothermal heat addition and can be found in any undergraduate textbook [14]. The goal of reheat combustion is to realize an increase in the cycle’s effective heat addition temperature, METH, without increasing TIT, which is the maximum cycle temperature [84]. On an ideal cycle basis, the advantage of reheat cycle over the non-reheat cycle is illustrated in Figure 13.45.

Also shown in Figure 13.45 is an estimate of the realistically achievable performance advantage of reheat combustion, which is much more modest than predicted by the ideal cycle comparison. The primary drivers for this are increased HGP component cooling load and combustor design requirements. In fact, for TIT values of ~1450°C (~2642°F) or above, the reheat cycle efficiency advantage disappears due to a significant increase in cooling losses [83]. This is where the closed-loop steam cooling concept might be of help by reducing the cooling air consumption. In lieu of a full “H” configuration, closed-loop steam cooling of the HP and LP turbine stage one nozzle vanes should be sufficient. Obviously, ceramic matrix composite (CMC) parts would be equally advantageous (if/when they become available, which may not be too far ahead—see Section 13.12).

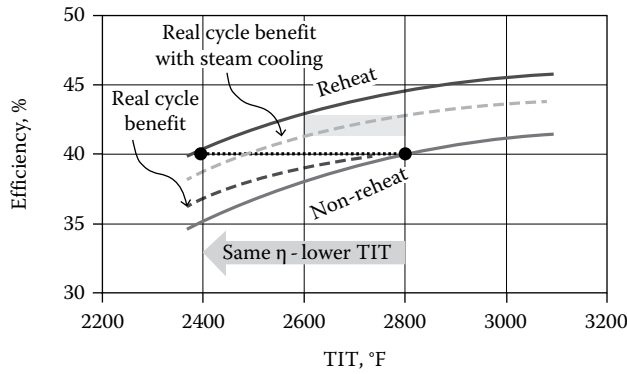


FIGURE 13.45

Advantage of ideal reheat Brayton cycle over non-reheat variant. Also shown are “real” cycle entitlement values (approximate). The shaded rectangle designates the most likely near- to mid-term impact of closed-loop steam-cooled reheat gas turbine. (From Gülen, S.C., General electric—Alstom merger brings visions of the Überturbine, *Gas Turbine World*, July/August 2014, pp. 28–35.)

13.10.1.4 Kalina Cycle

The largest exergy destruction in the steam RBC of a modern GTCC power plant is in the HRSG [92]. A major contributor to that is the temperature mismatch between the GT exhaust gas and the boiling water/steam (constant pressure and temperature) in the HRSG evaporators—especially the HP evaporator. Conceptually, this is illustrated in Figure 13.46. For minimum heat exchange irreversibility, the temperature of the “ideal” working fluid would rise in lockstep with the cooling exhaust gas. One way to approximate that ideal is to use water at supercritical pressures as the working fluid [82]. Another way was proposed by Kalina via using a binary working fluid, ammonia and water mixture, specifically, with variable boiling and condensing temperatures. The reduction in HRSG evaporator

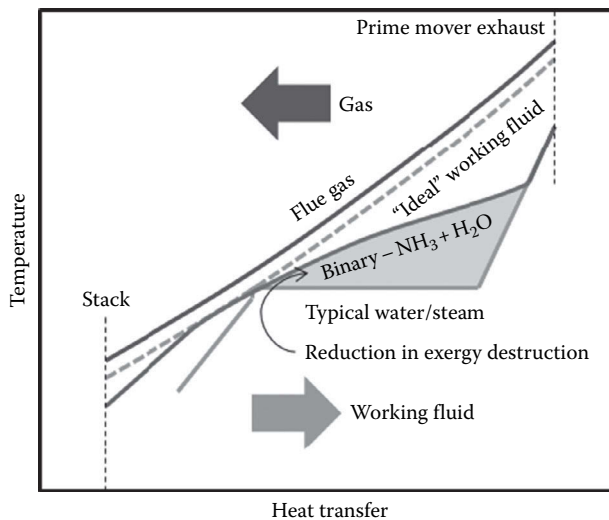


FIGURE 13.46

HRSG evaporator T - Q diagram.

irreversibility is conceptually illustrated in Figure 13.46. Significant efficiency improvement was claimed over a comparable GTCC with steam RBC [169]. However, as was shown in [82], the improvement opportunity just by reducing HP evaporator irreversibility is rather limited. It is not clear how the Kalina cycle can be significantly more efficient than a modern 3PRH bottoming cycle with advanced steam conditions.* Several pilot plants have been built and operated [169]. All of them were small units to generate power from different types of low-grade heat source, including industrial waste heat, waste incineration, and geothermal springs. Severe corrosion problems were reported in one plant in Finland. In addition to corrosion, chemical stability of the ammonia–water solution, nitridation of high-temperature components, and maintaining water quality are main concerns. Overall, the cycle is considered a good alternative to organic Rankine cycle for low-grade heat applications such as geothermal. It is doubtful that it will ever be a feasible candidate for utility-scale electric power generation.

13.10.1.5 Humid Air Turbine

Humid air turbine (HAT) is an inter- and after-cooled recuperated system in which the exhaust gas energy is used to heat and saturate combustion air with moisture [144]. There is no steam turbine since the gas turbine is acting as a quasi-steam turbine due to the high water vapor content of the hot gas. The exhaust gas first heats the combustion air in a recuperator, and then it heats water in an economizer. Hot water is used in a randomly packed column (saturator), a direct-contact heat and mass transfer device widely used in the chemical process industry (CPI), to heat compressed air and moisturize it. Humid air (up to 15% water vapor by mass) for combustion is advantageous for NO_x control. The optimal HAT cycle design (from the proverbial “blank sheet”) requires new combustor and turbine development. A variant utilizing off-the-shelf components (with the exception of an HP turbine), *cascaded HAT* (CHAT), was proposed in the 1990s. Several HAT pilot plants as well as a 40 MWe advanced HAT with an inlet fogger were built and operated. The test facility humidification achieved 5% moisture by weight in combustion air. The development target is a HAT plant rated up to 200 MWe output at around 55% net LHV efficiency with 13% moist air [122]. A typical 40 MWe HAT cycle with 2550°F (1400°C) TIT and 17% (by weight) H₂O in combustion air is depicted in Figure 13.47. Cycle efficiency is ~50% net, with nearly 20 lb/s (about 140 gpm) water consumption. Based on the METH and METL from Equations 13.5 through 13.8, the equivalent Carnot efficiency from Equation 13.2 is 65.9%, which translates into a HAT cycle Carnot factor of 0.76, which is perfectly in line with F class GTCC. As in many other cases, from a base load performance perspective, the HAT plant is not better than a comparable GTCC with 3PRH steam RBC. However, HAT cycle’s part load (turn-down) performance and hot ambient efficiency lapse characteristic are much better than those of a typical GTCC [144]. This is a direct result of the *third* degree of freedom in cycle output control afforded by the mass addition in the saturator (in addition to airflow control via compressor inlet guide vanes (IGVs) and firing temperature control via fuel flow).

For specific design issues pertaining to the combustor and the turbine, please refer to [122]. Since the water added to the motive air ends up in the gas turbine, makeup water treatment requirements are as stringent as they would be for steam or water injection. Water consumption of the HAT cycle is a concern in many areas. In fact, in the United States, for example, obtaining site permit for new plant construction for HAT may turn

* This point was dramatically illustrated by an exchange of letters, between A. Kalina and a recognized expert in the field, published in two issues of the *Gas Turbine World* in 1995 (#6) and 1996 (#2).

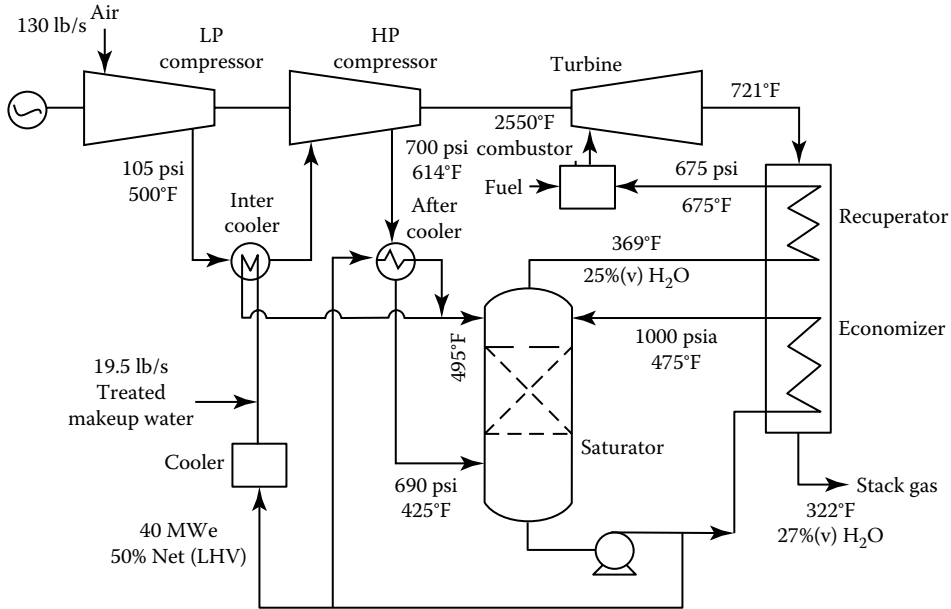


FIGURE 13.47

Humid air turbine (HAT)—calculation using heat balance simulation tool by ThermoFlow, Inc. [160].

out to be very difficult, if not impossible. One way to alleviate this problem is to deploy a *dehumidification* technology to efficiently extract water from the stack gas. This would add to plant cost and complexity, along with performance loss (e.g., additional GT exhaust loss, auxiliary load, etc.) and operability issues (corrosion, fouling, or discharge of non-buoyant stack gas). For a review of available technologies and their comparison in terms of water capture performance and energy consumption, please refer to [61].

A comprehensive study of gas turbine Brayton cycle variants had been conducted by Bhargava et al. [37]. Their findings are summarized in Table 13.15. At the same TIT, none of the cycles can match the efficiency of a GTCC—even with a two-pressure (2P) bottoming cycle.

TABLE 13.15

Comparison of Optimum Performance Data for Examined High Performance Cycles

Technology	Cycle PR	TIT, °C	Eff., %	Specific Output, kJ/kg	Water Consumption, L/kWh
CC (2PRH)	15	1300	55.1	587	
CHAT	84	1300	53.8	832	0.227
HAT	24	1300	53.6	637	0.611
RWI	14	1300	52.6	554	0.650
ISTIG	36	1300	51.7	635	0.644
STIG	30	1300	51.2	572	0.833
ICR	10	1300	48.3	407	
Brayton	42	1300	42.3	320	

Source: Bhargava, R.K. et al., *J. Eng. Gas Turbines Power*, 132, #022001, 2010.

Note: RWI, recuperated water injection; STIG, steam-injected GT; ISTIG, intercooled STIG.

project was scheduled to be completed in 2006. At the time of writing, externally fired GT power plants still have not materialized as commercially viable options. The system is fairly straightforward, with mostly mature equipment. However, significant design and operability challenges exist (e.g., material selection for convective and radiant air heaters—superalloys or ceramics).

The highly simplified schematic in Figure 13.48 illustrates that the HIPPS is essentially a coal-fired GTCC with the combustor replaced by a furnace. The gas turbine cycle PR (about 18) and the TIT indicate that it is equivalent to an old E class unit. From Table 13.3, the rated efficiency of an E class GTCC with cycle PR of ~14 is 56% (CF of 0.782). Correcting for the cycle PR suggests a GTCC efficiency of ~57% (LHV) with the same technology or ~51% (HHV). This is about 4% points higher than the projected HIPPS efficiency (which can be ascribed to the higher plant auxiliary loads and excessive “combustor” pressure loss).

A technology similar to HIPPS in spirit as well as in main features of the coal combustion process is the *pressurized fluidized bed combustion* (PFBC). Due to its attractive environmental performance and high fuel flexibility, the technology has been intensively studied for implementation in power generation in the 1990s. Several first-generation PFBC power plants have entered commercial operation (see the list in Table 13.16).

The second-generation or advanced PFBC systems combine gasification and FBC technologies for higher efficiencies (46% net HHV) and reduced emissions [112]. A highly simplified system diagram is shown in Figure 13.49. Similar to the HIPPS, the advanced PFBC system is also a coal-fired GTCC with the combustor replaced by a gasifier–FBC combo. The difficulty in either case is in the development of (1) a “topping” combustor that can handle the hot vitiated gas entering it (at a temperature well above that in conventional gas turbine DLN combustors) and (2) a hot gas cleanup system. Despite projections in late 1990s and significant R&D effort, the advanced PFBC failed to materialize as a viable commercial technology. For a concise but informative review of the indirectly fired gas turbine combined cycles, the reader is referred to the paper by Beér [36].

13.10.3 Repowering

Repowering is the term used to describe the addition to or replacement of aging power generation equipment with obsolete technology (i.e., a fossil-fuel–fired boiler plant with a steam turbine generator) with newer equipment comprising up-to-date technology

TABLE 13.16

Commercial PFBC Power Plants

Plant	Country	Rating	Steam Cycle	Startup	HHV Efficiency
Värtan	Sweden	135	137 bar/530°C	1989	33.5
Escatrón	Spain	80	94 bar/513°C	1991	36.4
Tidd	United States	70	90 bar/496°C	1991	35.0
Wakamatsu	Japan	70	103 bar/593°C/593°C	1994	37.5
Cottbus	Germany	75	142 bar/573°C/537°C	1998	42.0
Karita	Japan	350	241 bar/565°C/593°C	1999	42.0

Source: Kakaras, E. et al., Pressurized fluidized bed combustion (PFBC) combined cycle systems, in: *Combined Cycle Systems for Near-Zero Emission Power Generation*, Rao, A. (ed.), Woodhead Publishing Ltd., Cambridge, U.K., Chapter 8.

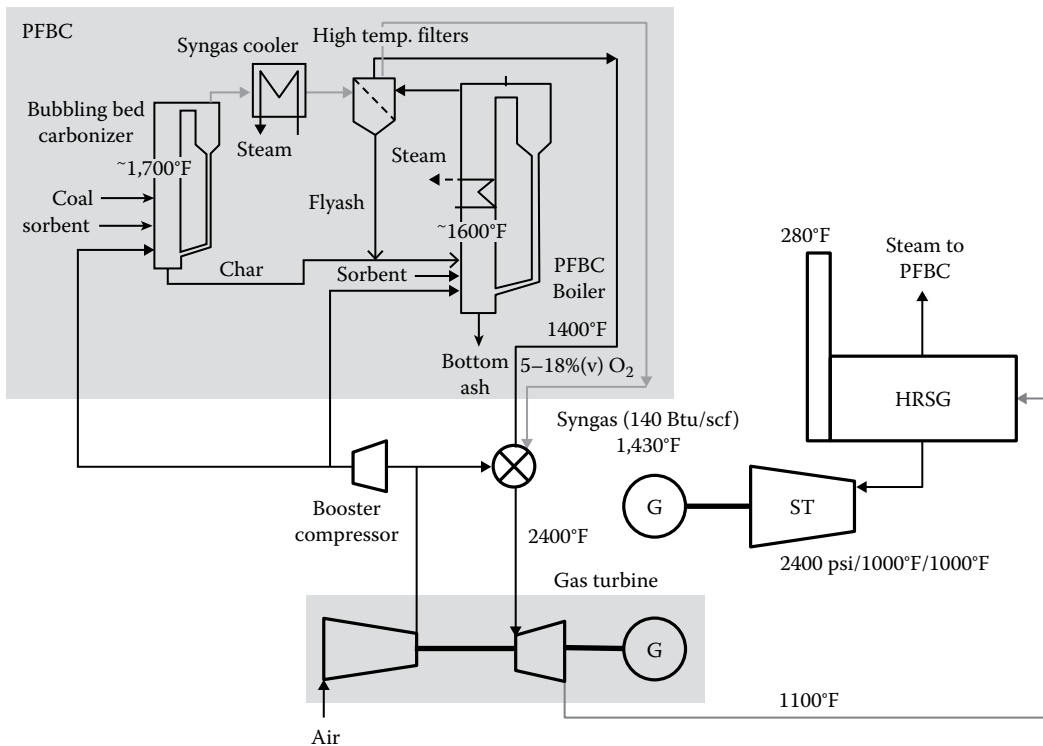


FIGURE 13.49

Schematic of second generation (advanced) PFBC combined cycle power plant with “topping” combustor.

(i.e., natural gas-fired gas turbine in simple or combined cycle) while retaining still-usable components toward more effective utilization of an existing site, which involves one or more of the following [156]:

- Improve generation economics (higher output and efficiency)
- Extend plant life
- Improve environmental performance
- Enhance operability and maintainability

The hurdle for repowering is the *life cycle cost* of generation: that is, the new power plant must have better LCOE than the old one. The aging steam power plants (the average age of “ripe-for-retirement” coal power plants is nearly 50 years [52]) are fully paid-off generating assets, whose generating costs are limited to the variable expenses for fuel (typically coal) and O&M. Unless the equipment is in such a terrible shape that O&M costs to maintain a reasonable efficiency (in order to keep the fuel costs in check) become intolerable, these plants could be operational for quite a long time (albeit at a reduced capacity factor).

Repowering projects have been dormant since the 1990s. Economic factors and the difficulties associated with brownfield construction have been the primary reasons for that. Nevertheless, there may be a revival in repowering projects due to much more stringent emissions control requirements enforced by government agencies that make the aging fossil-fuel-fired power plants impossible to keep running. The investment into new equipment to

reduce harmful stack emissions and improve the efficiency is simply too high. The situation is made even worse by low natural gas prices, driven by increased production of shale gas using new technology such as fracking. Thus, natural gas-fired gas turbine technology with efficiencies pushing 60% becomes economically a much more attractive alternative.

There are *four* major gas turbine-based repowering options:

1. Site repowering (a completely new GTCC power plant)
2. Heat recovery repowering, that is, boiler replacement with a gas turbine plus HRSG train
3. Hot wind-box repowering (utilizing a GT as a “forced draft fan”)
4. Feedwater heater repowering (utilizing GT exhaust gas for feedwater heating)

Only two of the four possible types of GT-based repowering options are applicable to repowering of retired coal-fired power plants:

1. Site replacement (a new *brownfield* GTCC project)
2. Replacement of original boiler with a GT + HRSG train (heat recovery repowering)

Heat recovery repowering is where the existing boiler is replaced by a GT and an HRSG. This approach increases the unit’s net generating capacity by about 150%–200%, reduces the heat rate by up to 30%–40%, and reduces NO_x emissions. The performance change is application specific and depends on the match of the new gas turbine with the existing power plant [156]. Since heat recovery repowering delivers the biggest “bang for the buck,” most of the existing repowering experience in the United States involves this system type. Due to the relatively large capacity increase, this approach is normally considered for older units less than 250 MW with steam pressures up to 1800 psia.

A cheaper and simpler variant of heat recovery repowering with an advanced GT and single-pressure, duct-fired bottoming cycle has been proposed as a possible alternative to costlier and complex GTCC-based repowering option (see Figure 13.50). This option can repower an old, subcritical PC power plant with obsolete technology, which is no longer economic to operate. Calculations show that it can match the output of a modern GTCC with an advanced F class GT at roughly half the capital cost [87]. While the resulting efficiency is of course significantly lower (but still much higher than that of the replaced PC plant), at low natural gas prices, the LCOE will be cheaper. The feasibility of any power generation concept hinges around the reduced capital investment and project technology risk. The latter is a known Achilles’ heel for repowering projects, which is exacerbated by the brownfield nature of the construction phase. Thus, the first and foremost requirement is a diligent evaluation of the equipment (age, degradation, requisite repairs, modifications, and/or upgrades to ensure continued service with no excessive O&M expenditures) in the fossil-fuel-fired plant slated for retirement (and thus a candidate for repowering). It should be done on a case-by-case basis to ensure that the plant in question is suitable to the implementation of the proposed simple heat recovery repowering concept.

13.10.4 Cogeneration

Cogeneration is the term used for simultaneous production of electric power and useful heat (usually in the form of steam exported to an industrial user) in the same power plant. Another term for cogeneration is *combined heat and power* (CHP), which is more

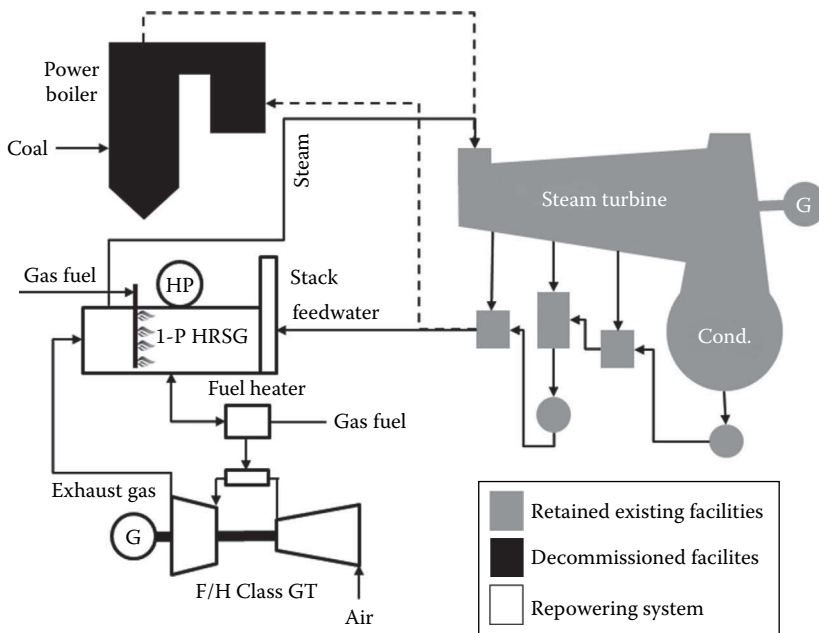


FIGURE 13.50

Heat recovery repowering with an advanced F-Class GT and single-pressure, supplementary-fired HRSG. (From Gülen, S.C., Repowering revisited, *Power Engineering*, November 2015, pp. 34–44.)

common in Europe, where cogeneration is more popular. The goal in cogeneration is to make the maximum use of fuel burned in the prime movers. The holy grail in cogeneration is to make use of the *lowest grade of heat* in the power cycle, which otherwise would be rejected to an external heat sink (e.g., atmosphere, lake, river, etc.). Obvious examples are boiler or HRSG stack gas and steam turbine condenser heat rejection. Otherwise, any stream of hot water, steam, and/or flue gas extracted for use in an industrial facility and/or district heating (or any other purpose) comes *at the expense of shaft and electric power generation*. Nevertheless, from a fuel economy perspective, using a separate boiler plant for heat generation, as opposed to sacrificing some electricity generation from a power plant, might not be attractive (see Figure 13.51). In the example case shown in Figure 13.51, fuel utilization factor increased from 0.58 to 0.85. This is the economic driver behind most cogeneration projects. Examples of cogeneration and basic considerations in its myriad applications are described in detail in [8,66,154]. Correct accounting for cogeneration heat product in efficiency calculations is discussed in [76]. As an example, the electrical efficiency of the cogeneration plant in Figure 13.51 is *not 85%**, which is rather obvious, but it is not 30% either. The overall electrical efficiency would be a function of the “exergy” of the 55 units of heat provided to the process user. If the latter is equivalent to, say, 27.5 units of electric power, the equivalent electrical efficiency of the cogeneration plant is 57.5%.

From a fuel-saving perspective, however, a numerically more attractive case can be made. Fuel saved by using steam export from a CHP plant, in lieu of, say, using a separate

* A more correct description of 85% is “fuel utilization factor.”

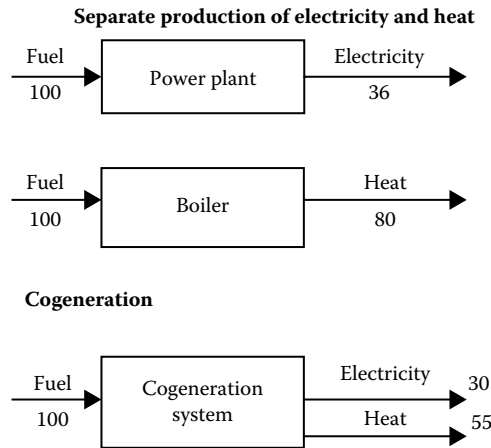


FIGURE 13.51
Cogeneration principle.

boiler plant, can be credited to the CHP plant's fuel consumption. Therefore, the CHP plant efficiency becomes

$$\eta_{CHP} = \frac{\dot{W}_0 - \dot{W}_{lost}}{HC_0 - \frac{\dot{Q}_{stm}}{\eta_B}} = \frac{\dot{W}_{CHP}}{HC_0} \frac{1}{1 - \frac{\dot{Q}_{stm}}{\eta_B HC_0}} = \eta'_{CHP} \frac{1}{1 - \frac{\dot{Q}_{stm}}{\eta_B HC_0}} \quad (13.42)$$

In this equation, the subscript 0 denotes the plant performance parameters with no steam export. Exporting steam causes a "loss" in the net power output (denoted by the subscript *lost*). The new electrical efficiency is denoted by the *prime* and η_B is the (eliminated) boiler efficiency. To a very good approximation, the earlier formula can be written as

$$\eta_{CHP} \approx \eta'_{CHP} \left(1 + \frac{\dot{Q}_{stm}}{\eta_B HC_0} \right) \quad (13.43)$$

$$\eta_{CHP} = \frac{\dot{W}_{CHP}}{HC_0} + \frac{\eta'_{CHP} \dot{Q}_{stm}}{\eta_B HC_0} \quad (13.44)$$

$$\dot{W}'_{CHP} = \dot{W}_{CHP} + \frac{\eta'_{CHP}}{\eta_B} \dot{Q}_{stm} \quad (13.45)$$

In essence, ignoring all exports of heat and/or power except process steam, Equation 13.45 illustrates how the gross power output of a cogeneration power plant is defined in the EPA standards. Depending on the exact point of process steam extraction, if

$$\frac{\eta'_{CHP}}{\eta_B} \dot{Q}_{stm} > \dot{W}_{lost}, \text{ then}$$

$$\eta_{CHP} > \eta_0$$

This is indeed the case unless steam export is taken upstream of the steam turbine's HP throttle. Furthermore, this may be one possibility to enable coal-fired power plants to achieve the U.S. EPA's new source performance standard of 1400 lb (636 kg) of CO₂ emission per MWh of gross power output [138].

Another technically "correct" measure for CHP effectiveness is *fuel chargeable to power* (FCP), which is an incremental heat rate defined as the ratio of the incremental fuel consumption between the cogeneration plant and the boiler plant dedicated to heat production only to the net incremental power production by the cogeneration plant. Thus, mathematically

$$FCP = \frac{HC_{CHP} - HC_{boiler}}{\dot{W}_{net,CHP} + \dot{W}_{aux,boiler}} \quad (13.46)$$

For a pure power generation facility, FCP is identical to the plant heat rate. Obviously, the inverse of the FCP is the incremental efficiency of the cogeneration plant.

Some combinations of steam demand and electric power can only be met by supplementary firing in the HRSG. A typical steam-power cogeneration map is shown in Figure 13.52. A comprehensive coverage of cogeneration system design considerations can be found in [103]. Widespread deployment of CHP is precluded by the impossibility of transporting thermal energy over long distances efficiently. This limits the application opportunities to relatively small-sized plants near the end user (i.e., cities for district heating and industrial facilities). This is probably one reason why CHP is more popular in Europe vis-à-vis the United States (i.e., densely populated small countries with relatively small distances in between).

13.10.5 Operational Flexibility

The increasing share of renewable technologies (solar and wind) in the power generation portfolio impacts the duty cycle of fossil-fuel-fired power plants—especially the gas turbine power plants in simple and combined cycle. Fluctuations in power generation due to unforeseen atmospheric conditions such as cloud coverage, change in wind direction, or speed at times of high demand require compensation from other generators on the grid.

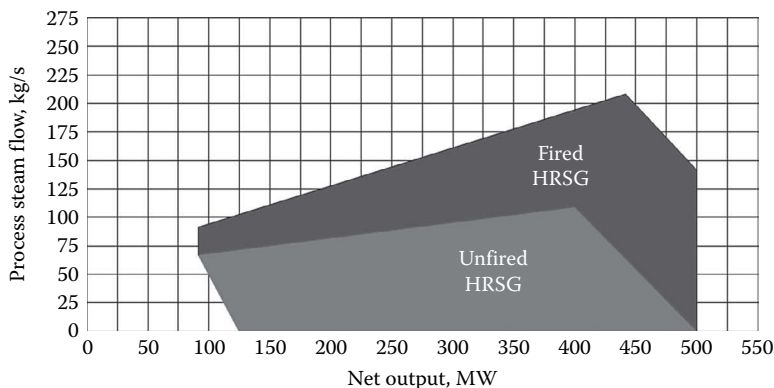


FIGURE 13.52

Typical cogeneration power plant steam-power map (1 kg/s ~ 8 kpph).

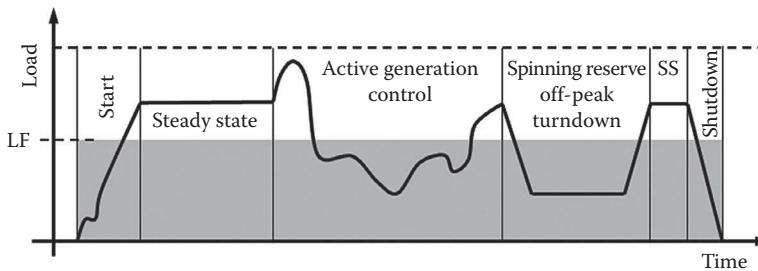


FIGURE 13.53
Typical operating regime of a modern GTCC.

This is usually in the form of *spinning* and *non-spinning* reserve. In the former, a fossil-fuel-fired power plant, say, a GTCC, is running at a low load level, say, at 40% load. Upon demand, when a renewable generator suddenly comes down, the GTCC is asked by the grid operator to rapidly come up to full load to make up for the lost power generation. Even more desirable is the ability to accomplish this feat from standstill (i.e., non-spinning reserve) so that the GTCC in question does not burn a lot of fuel at a significantly lower efficiency at a low load while waiting to be called on.

A typical GTCC daily load profile is shown in Figure 13.53. As shown, during midday, the plant runs in an *automatic* (or *active*) *generation control* (AGC) mode. In the AGC mode, the grid operator adjusts the power output of the generators on the power grid actively so that, at any given moment, power demand and power supply, that is, load and generation, respectively, are exactly matched. At off-peak times, the plant runs at a spinning reserve mode, that is, at part load, where it can still meet the emissions requirements. This load level is referred to as the *minimum emissions compliance load* (MECL). The average load factor (LF) in Figure 13.53 is the plant load, at which the plant should run at a steady state over the same time period to generate the same megawatt-hours (represented by the blue rectangle in the figure). In mathematical terms, it is a *mean effective average* value. When taking into account all factors that impact the performance of a GTCC power plant, typical LF for a cycling plant is around 75%–77% [91].

In order to operate in a daily start–stop cycle (sometimes twice a day) with rapid load ramps (up or down), an FFPS should be designed for durability under the thermal stresses imposed on the equipment, especially the HRSG and the ST with large metal masses. “Lighter” and agile units such as aeroderivative GTs, gas engines, and even some heavy-duty industrial GTs in simple cycle can start from a cold standstill to full load within 10 min with no detrimental effects. However, these units are more appropriate for short-duration peak saving duties where fuel consumption at relatively low efficiency is not a big consideration.

Gas turbine combined cycle plants require much longer time for controlled warming of the HRSG, steam pipes and valves, and the ST to minimize thermal stresses* and prevent premature failure due to *low cycle fatigue* (LCF) [80]. This is especially important for “cold” starts when the plant has been down for more than 72 h. Conventional methods accomplish this by GT loading and exhaust gas temperature control with cascaded steam bypass from the HRSG to the condenser (as shown in Figure 13.54) [90]. This takes a long time,

* Thermal stresses are caused by the temperature gradients across the thick metal walls of evaporator drums, certain steam pipes, steam valve bodies, ST casings, and ST rotor. If the warming of such components is rapid enough to cause large temperature gradients between hot and cold sides, resulting thermal stresses will also be high and detrimental to parts’ life.

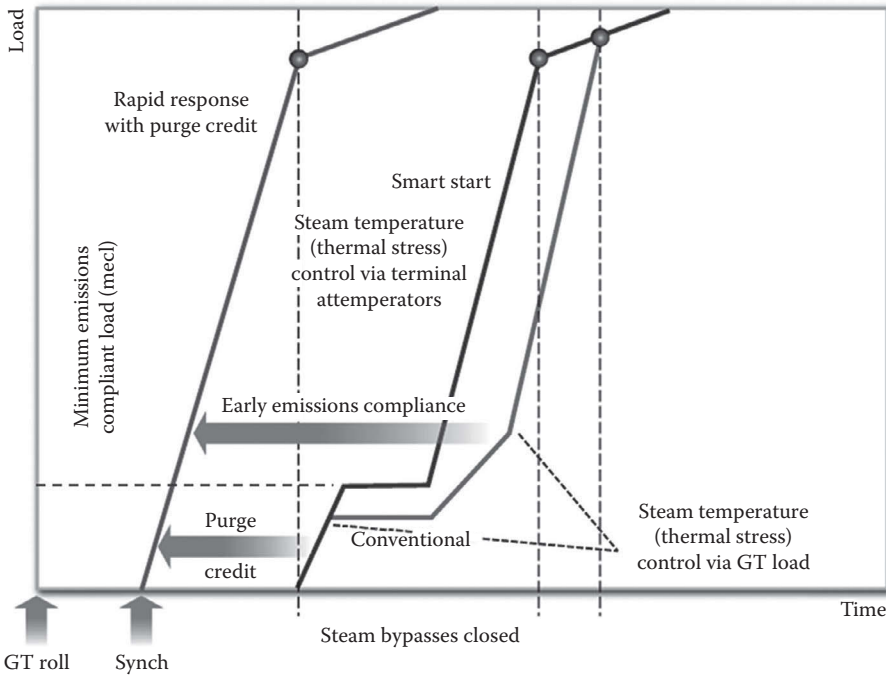


FIGURE 13.54

GTCC startup curves. (From Gülen, S.C. and Jones, C.M., *Modern Power Syst.*, June, 16, 2011.)

typically about 1 h for “hot” starts after an overnight shutdown. While this was acceptable in the past, as mentioned earlier, with the increasing share of renewables in the power generation mix, more agile response is expected from the most efficient units on the grid (i.e., the GTCC).

New GTCC plants are designed for “fast start” or “rapid response” by decoupling the startup sequence of the GT and the ST and pushing the HRSG purge sequence* from the startup to the shutdown. This is accomplished by starting the GT in a simple cycle mode and bringing it to full load as soon as possible [80]. Steam generated in the HRSG and not sent to the ST is bypassed to the condenser. Steam temperature is actively controlled by terminal attemperators (also known as desuperheaters) to exactly the level required by the ST stress controller. In this mode, the GTCC can start in about 30 min or slightly less after an overnight shutdown (leftmost curve in Figure 13.54). Another mode of fast start brings the GT to its MECL and keeps it there until the steam temperature is deemed to be ready for admission by the ST stress controller (middle curve in Figure 13.54) [90].

13.10.6 Fuel Flexibility

The development of heavy-duty industrial GT combustion systems was focused on natural gas (essentially methane) as the primary fuel, with distillate oil as secondary fuel. However, the ability to burn a wide variety of fuels, known as fuel flexibility, is a critical GT feature that provides a hedge against increasing fuel costs and reducing fossil fuel

* This is the 10–15 min period when the GT cranks in an unfired mode to push air through the HRSG and purge it from any unburned fuel to prevent explosions when the GT is started and hot exhaust gas enters the system.

resources. For comprehensive coverage of gas turbine fuel flexibility, please consult Meher-Homji et al. [127]. The critical GT system component from a fuel flexibility perspective is the combustion system. Apart from emissions, the key areas of combustor operability that are affected by fuel composition and LHV are lean blowout (LBO), flashback, combustion dynamics (noise), and autoignition. The key fuel characteristics that have an impact on the aforementioned operability problems are composition (specifically H₂ content), heating value (Btu/scf), stoichiometric flame temperature, and *flammability*. Flammability of a fuel is expressed by upper and lower fuel limits, UFL and LFL, respectively, which refer to the range of compositions, for fixed pressure and temperature, within which an explosive reaction is possible when an external source of ignition is introduced. A representative selection of fuel gases in the order of decreasing volumetric heating value is given in Table 13.17 [1]. Note that syngas in the table is carbureted water gas, which is produced by passing steam over red-hot coke. The calorific value is boosted by passing the gas through a heated retort into which oil is sprayed.

For stable diffusion flame operation, a *flammability ratio* in excess of 2.0 (ratio of UFL to LFL) is required. From Table 13.17, this value for natural gas or methane at 1 atm is around 3.0 (cf. close to 20 for hydrogen). Fuels with very low flammability ratios such as BFG are usually blended with other fuels (e.g., COG in steel mill applications). In low-Btu fuel combustion systems, a conventional fuel such as natural gas or fuel oil is always utilized for startup and shutdown.

Flammability limits depend on the type and strength of the ignition source, type of atmosphere (e.g., in oxygen, limits are much wider than in air), and pressure and temperature of atmosphere. Natural gas UFL at 20 atm is nearly 60% for a flammability ratio of ~12.0 (LFL dependence on pressure is much weaker). Increasing temperature reduces both UFL and LFL.

Autoignition temperature (AIT) is the temperature, at a given pressure, for which an explosive reaction at a fixed composition mixture within its flammable range is possible. The reaction is initiated by autocatalytic reaction without any external ignition source. The minimum AIT is a strong function of fuel type, pressure, and concentration. At 1 atm, minimum AIT for methane and hydrogen are 1350°F and 1140°F, respectively. Increased pressures typically reduce the AIT.

TABLE 13.17

Selected Fuel Properties

	Flame Temp.		NOx	H ₂	CO	LHV	LFL	UFL
	°F	°C						
Natural gas	3720	2049	1.42	—	—	929.3	4.8	13.5
Methane	3550	1954	1.00	—	—	896.0	5.0	15.0
Coke oven gas	3590	1977	1.10	53.2	5.9	579.7	4.8	33.5
Syngas	3690	2032	1.34	32.5	24.1	431.8	5.3	40.7
CO	3860	2127	1.74	—	100.0	316.0	12.5	74.2
Hydrogen	3930	2166	1.91	100.0	—	270.0	4.0	75.0
Blast furnace gas	2600	1427	0.10	3.5	26.5	95.0	35.0	73.5

Source: Baumeister, T. (Editor-in-Chief), *Marks' Standard Handbook for Mechanical Engineers*, 8th edn., McGraw-Hill, Book Company Inc., New York.

Note: UFL and LFL are upper and lower flammability levels, respectively, at 1 atm and 77°F, and given in terms of fuel concentration by volume.

Another important fuel characteristic is *flame speed* or burning velocity, which quantifies the rate of flame propagation. Flame speed is a function of fuel concentration and is less than 2 ft/s for most hydrocarbon fuels, whereas it can be more than 8 ft/s for hydrogen at 40% concentration. This is the primary reason for the difficulty in designing DLN combustors for fuels with large hydrogen content (due to flashback concerns). Therefore, conventional diffusion combustors are used for most hydrogen-containing fuels with diluent nitrogen or steam/water injection for NO_x control. Another concern for combustor design is the tendency of the combustion flame to be “blown out” from its anchor point. For many low-Btu fuels, H_2 and CO are the two key components. Fuels or fuel mixtures with high H_2 content (very high flame speed) have much smaller reaction times than fuel mixtures with high CO content (low flame speeds). Thus, “fast” mixtures with higher H_2 content will blow out at leaner equivalence ratios than “slow” mixtures with high CO content.

Combustion dynamic instability, also referred to as combustion noise or “humming,” is characterized by large-amplitude pressure oscillations driven by unsteady heat release. The problem is especially severe when pressure and heat release oscillations are nearly “in phase,” that is, the phase difference is less than 90° . Fuel composition and LHV variations (especially in fuels such as BFG) affect the combustion dynamics by altering the phase angle. Dry low NO_x combustors are especially susceptible to this problem due to the fact that they operate near the lean blowout limit, where small perturbations are amplified to large effects. Combustion dynamic instabilities are potentially harmful to the combustor parts and downstream HGP components.

The key engineering parameter that is used to characterize gas composition is the *Wobbe index*. The basic WI is usually modified to incorporate the gas compressibility effects and is known as the *modified Wobbe index* (MWI):

$$\text{MWI} = \frac{\text{LHV}}{\sqrt{T_{\text{fuel}} \frac{\text{MW}_{\text{fuel}}}{28.96}}}$$

where MW is the molecular weight and T is its temperature in $^\circ\text{R}$, with the LHV in Btu/scf. In essence, MWI is a relative measure of the energy input to the combustor at a fixed pressure ratio and determines the ability of the fuel cleanup and injection system to accommodate the variations in composition and heating value.

There is an allowable range of MWI to ensure proper operation of the fuel injection system with the requisite fuel nozzle pressure ratios at all modes of operation. That range is typically $\pm 5\%$; however, OEMs for most modern H class machines claim allowable MWI ranges up to $\pm 10\%$. For example, for the natural gas fuel with 1000 Btu/scf at 365°F , the value of the MWI is about 47. Thus, the allowable variation can be up to about ± 5 . As the MWI formula indicates, in systems with performance fuel heating, some of the effects of composition variation can be moderated by changing the fuel gas temperature. Within certain MWI limits, the gas turbine can operate successfully without requiring combustion system hardware modification. Dual-fuel systems require separate independent fuel handling trains, which include control valves, manifolds, and fuel nozzles.

Composition and MWI variability in low-Btu fuels is a significant concern, which is amplified by fuel blending and “co-firing.” For example, in steel mill applications, a fuel compressor is required to ensure delivery of the fuel to the GT at a sufficiently high pressure to ensure stable and reliable fuel flow control. In most cases, BFG is blended with

COG to provide a higher-LHV mixed-gas fuel to the GT combustor. Fuel blending and compression are accommodated by improved controls and system design changes with allowable MWI limit of $\pm 10\%$.

13.11 Gas Engines

Stationary, reciprocating gas engines (in industry parlance, simply “recips”) are ideally suitable for distributed electric power generation and cogeneration applications. (Please refer to Chapter 11 in this handbook.) Due to their low power density (roughly 200 kW/m² of engine footprint vis-à-vis a frame gas turbine with nearly 3000 kW/m²), they are not preferred for large power stations. In certain areas of the world, however, depending on site-specific requirements, they are even used for utility-scale power generation in lieu of GTCC or steam power plants. In such instances, a large number of engines, for example, 10 or 20 or even more, are combined with several HRSGs and an steam turbine into an $N \times 1$ combined cycle configuration (e.g., the 573 MWe IPP3 power plant in Jordan with 38 dual-fuel 18 MWe gas engines). Even though the recips are highly efficient prime movers, with net thermal efficiencies approaching almost 50% for the SOA turbocharged units, their low exhaust temperatures (well below 1000°F) preclude an efficient steam RBC.

The advantage of recips vis-à-vis gas turbines in a large simple or combined cycle application stems from a few factors:

- Low output loss with ambient temperature (see Figure 13.55) and site elevation
- High efficiency at low loads (via turning off multiple engines—see Figure 13.56)

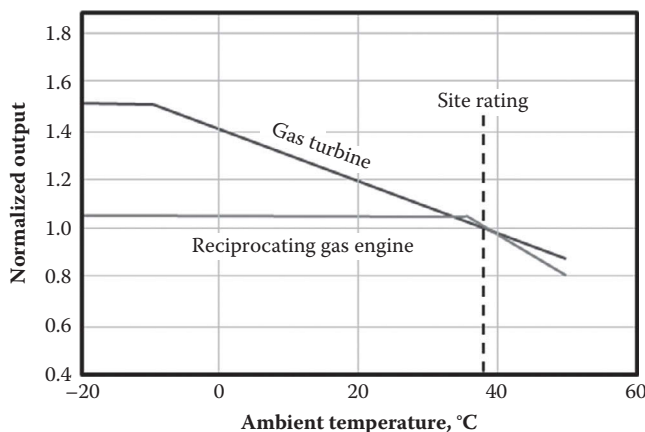


FIGURE 13.55

Reciprocating engine and gas turbine performance as a function of ambient temperature.

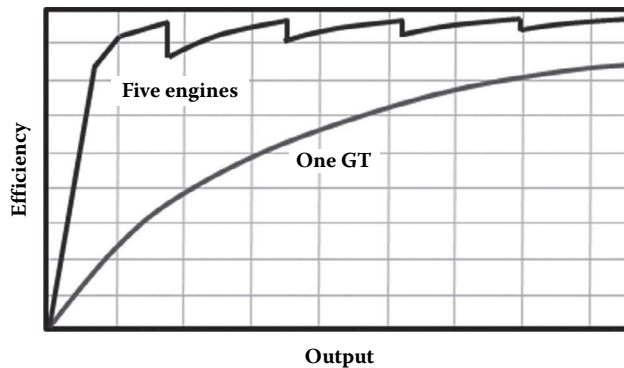


FIGURE 13.56
Part load performance of multiengine plant vs. single gas turbine.

Thus, on a high-altitude site (say, several hundred meters or higher) where power demand on hot days is a significant determining factor, a power plant comprising multiple gas engines can be the optimal solution. Another factor that may be in favor of gas engines is their flexibility (i.e., fast startup and shutdown, maintaining efficiency at low loads, etc.)

Obviously, no matter what the specific site and project conditions and requirements (e.g., availability, startup time, fuel flexibility, capital and operating costs, cycling capability, footprint, heat requirement, etc.) are, reciprocating engines in a simple or combined cycle configuration cannot compete with H or J class GTCC power plants with rated efficiencies around 60%. This is the case for most large-scale projects with 500 MWe or more capacity requirement. In applications where capacity requirement is around 200 MWe with cogeneration (e.g., steam for industrial process, hot water for district heating, etc.), where E or old F class GTCC present a good fit, plant efficiencies, especially at low load factors, are comparable to those achievable with gas engines (i.e., low fifties in percentage points).

In terms of availability (the amount of time during a year when a plant is available to generate power), typical values for reciprocating engines and gas turbines are 92% and 97%, respectively. The difference is equivalent to $5\% \times 8760/24 \sim 18$ days per year of not being available for generation. Dual-fuel gas turbines can operate on 100% backup fuel (typically, No. 2 distillate) and can switch from one to the other while running. In the United States, power plants rarely require to be run with the backup fuel. In other places in the world, for instance, in Africa, this is a key requirement. Most modern gas turbines have dual-fuel DLN combustors. Some spark-ignition reciprocating engines do not have that capability. Some dual-fuel reciprocating engines, on the other hand, always require a small amount of pilot liquid fuel, which is around 1% of total fuel flow. Furthermore, some dual-fuel reciprocating engines might require load to be reduced to around 80% of full load when transferring from liquid fuel to gas fuel (which can take about 1 min). However, the gas turbine converts from gas to fuel oil operation at any load instantaneously. These differences can be important to plant economics.

From a plant startup time perspective, reciprocating engines and gas turbines, especially aeroderivatives, are similar. They can reach full load in 10 min from ignition. In order to achieve the “ready-to-start” status, however, there can be differences. In addition to

the standard checks, to bring the unit to a ready state, purging the exhaust duct and the HRSG (if present) and heating the lube oil to the required temperature need to be accomplished. This can be more onerous for recips because they typically require the cooling water circulating through the cylinders to be preheated to at least 60°C, preferably 70°C (especially for units that are designed to operate on heavy fuel). The energy required for preheating of the cooling water can be supplied by a separate source or by a running engine, or a combination of both. A typical heating power is 12 kW per cylinder (216 kW for an 18-cylinder engine), which makes it possible to warm up the engine from 20°C to 60°C–70°C in 10–15 h. In contrast, gas turbines only require the lube oil to be at or above 20°C.

Emissions of NO_x, CO, and UHC from gas engines are significantly higher than those from gas turbines. Typical guarantee numbers for NO_x and CO are well above 300 ppmvd (5% O₂) for the recips (about 110 ppmvd on 15% O₂ basis). For most modern GTs with DLN numbers, typical NO_x/CO guarantee numbers are 25/10 ppmvd (15% O₂). Furthermore, UHC emissions for gas turbines are almost negligible, whereas they are in excess of 1000 ppm for gas engines (most of it is methane, which is a more potent greenhouse gas than CO₂). Considering that “single digit” NO_x/CO emissions are required in many places by environmental regulations, recips require a secondary reduction system, which is typically an SCR, adding cost and complexity to the project.

On a pounds per MWh basis, CO₂ emissions from natural gas-fired recips can be read from the chart in Figure 13.29. However, as a greenhouse gas, methane, which makes up most of the engine UHC emissions, is 20 times more potent than CO₂. Therefore, an emission of, say, 1000 ppmv UHC is equivalent to another 2% of CO₂ and would bring the equivalent CO₂ emissions of a recip closer to those of a coal-fired power plant.

At present, the range of gas engines available for power generation is 4–20 MWe. Efficiencies of the most advanced engines are well above 45%—some approaching 50% (see Table 13.18). They are readily amenable to distributed power generation and cogeneration. In certain geographical locations, for example, high altitudes, high annual average ambient temperatures, and scarce water resources (the engines’ water consumption is minimal due to their closed-loop air-cooled coolant circuit), they are ideally suited as a comparatively low cost and flexible alternative. In that sense, one area where recips can prove valuable is as a backup to renewable power generation (solar and/or wind) during emergencies (e.g., cloud cover, etc.).

Gas engines can also be deployed in a combined cycle configuration, with multiple engines supplying a single HRSG or multiple HRSGs with a single ST generator. Due to the low exhaust temperature (especially with the turbocharger turbine), the bottoming cycle boost is limited. Whereas an advanced heavy-duty GT with +1100°F exhaust gas can have a 50% boost in overall thermal efficiency (e.g., from 40% in simple cycle to 60% in combined cycle), the economically feasible thermal efficiency boost for a gas engine is more like 10% (e.g., from 45% to about 50%). This, however, is not as big a disadvantage as it looks at

TABLE 13.18

Selected Reciprocating (Piston–Cylinder) Gas Engines for Stationary Power Generation

	RPM	Exhaust Temp., °F	Exhaust Flow, lb/s	Output, kW	Efficiency, %
GE Jenbacher J920	900	617	28.8	8,569	48.7
Wärtsilä 20V34SG	720	687	34.9	9,341	45.0
Wärtsilä 18V50SG	514	714	68.8	18,759	45.9

TABLE 13.19

Comparison of Gas Engine CC Performances with Gas Turbine Power Plants

	Output, kW	Efficiency, %
10 × Wärtsila 18V50SG	187,590	45.9
10 × Wärtsila 18V50SG CC	206,555	50.5
Ansaldo AE94.2	185,300	36.2
MHPS M501F3	185,400	37.0
1 × SGT6–2000F	171,000	51.3
1 × M701DA	212,500	51.4

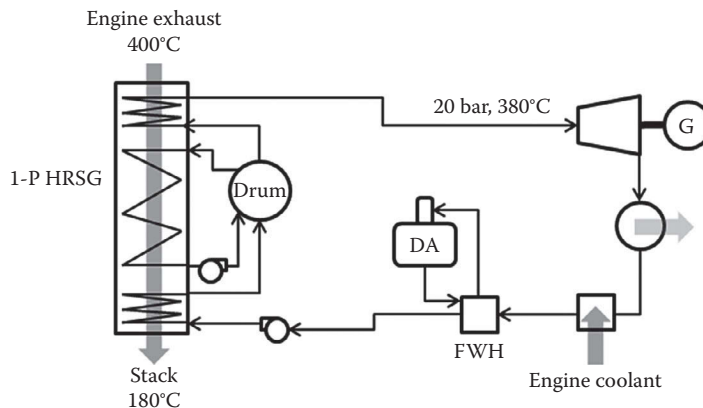
Note: ISO base load.

the first glance. A comparison of gas engine performances in simple and combined cycle to similar gas turbine performances (in the same net power output range) is shown in Table 13.19. At that rating range (200 MWe or lower), the available gas turbines are mostly old D/E or early F class units with simple cycle efficiencies in mid-thirties and low exhaust gas temperatures (around 1000°F). Thus, they do not allow for the same proverbial “bang for the buck” in a combined cycle configuration as their state-of-the-art G, H, or J class descendants. Consequently, especially at high-altitude and/or high-ambient-temperature sites, multiengine CC power plants may present an attractive alternative to comparable GTCC units. The ultimate arbiter is an LCOE evaluation using site-specific criteria.

13.11.1 Low-Quality Waste Heat Recovery

As mentioned earlier, low exhaust temperature of gas engines (as well as small industrial and aeroderivative GTs) are commensurate with simple steam bottoming cycles. Typical configuration is a single-pressure HRSG with a non-reheat industrial steam turbine (see Figure 13.57). Such a modest bottoming cycle can add only about 10% to the plant output (cf. +50% for the advanced bottoming cycles with heavy-duty industrial GTs).

There is no sharp delineation between high- and low-quality waste heat. For most practical purposes, exhaust gas temperatures lower than 500°C (~930°F) could be considered

**FIGURE 13.57**

Typical steam bottoming cycle for recip engines. (From Ahngers, A., *Wärtsila Techn. J.*, 2, 4, 2007.)

low quality. In terms of *quantity*, one can put the boundary at around 150 kg/s (~330 lb/s), which is typical for the exhaust flow of old frame machines and aeroderivative GTs. This is still big enough to fit a HRSG–ST bottoming cycle behind a single unit. However, the exhaust gas flow of gas engines is too small (30 kg/s or less) to merit a bottoming cycle on single-unit basis (i.e., 1 × 1 with one ICE and one steam turbine) and they come usually in multiple-ICE configurations [26]. These engines have very small exhaust flows and very low exhaust temperatures (<400°C). The Carnot factor for the bottoming cycle of recip engines, similar to the one shown in Figure 13.57, is about 0.35–0.40 (cf. 0.75–0.80 for advanced GTCC). This should be considered a reasonable technology level for steam Rankine BCs at this size. Similarly, heat recovery effectiveness is about 60% (cf. ~90% for advanced three-pressure, reheat HRSG) and the associated ST efficiency is 22%–25% (around 40% for modern GTCC steam turbines).

For such low-quality and/or low-quantity waste heat recovery applications, the *organic Rankine cycle* (ORC) emerges as a feasible option. It is essentially a Rankine cycle where the working fluid, instead of H₂O, is an organic hydrocarbon such as isopentane. Such working fluids are characterized by their high *standard heat capacity*, $c_v(T_{crit})/R$ (typically, 20 or higher—cf. 3.5 for H₂O) and T - s diagrams skewed to the right (cf. H₂O T - s diagram is similar to the Gaussian bell curve), as shown in Figure 13.58. The advantage is dry expansion in the turbine at very low temperatures (however, a recuperator is required since the end point of expansion is far into the superheated vapor region). The Carnot factor for the state-of-the-art ORCs with small gas turbines is around 0.4–0.5 [135]. Heat recovery effectiveness is about 75%, with about 25% steam turbine efficiency.

In summary, designing efficient bottoming cycles with low-quality and small prime mover exhaust streams is difficult. Since the waste heat quality is low (quantified by *exergy*), heat recovery effectiveness is low. (Note that what makes the stack temperature of a three-pressure HRSG low [and, therefore, the HRSG effectiveness high] is the LP pressure, which is the pressure of the third HRSG section. It is difficult to squeeze multiple pressure levels in such small systems. And if the HRSG steam pressure is kept low to drive the stack temperature low and increase the HRSG effectiveness, the ST efficiency suffers due to the low available steam exergy.)

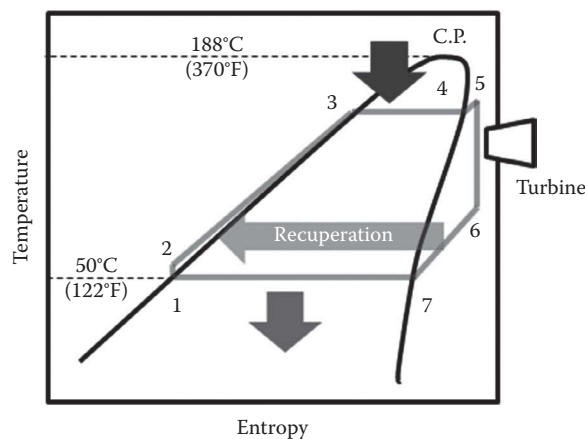


FIGURE 13.58
The T - s diagram for a typical organic Rankine cycle.

Small mass flows mean small volumetric flows, which makes it difficult to design efficient steam turbines and turbo-expanders. Thus, steam turbine efficiencies for such systems are 25% or lower, with bottoming cycle efficiencies less than 20%. This is why the supercritical CO₂ emerges as an attractive, alternative cycle working fluid.

13.11.2 Supercritical CO₂ Cycle

Supercritical CO₂ (from here on SCO₂) is an extremely dense fluid at pressures above 1000 psi and temperatures above 100°F, which is an intriguing alternative to H₂O (steam) and air as working fluid in traditional thermodynamic cycles such as Rankine and Brayton. In particular, a power plant based on a cycle with SCO₂ as the working fluid is bound to be smaller (and cheaper) than its steam and/or air counterparts at the same power rating and, possibly, with better efficiency.

Supercritical CO₂ Brayton cycle is a closed cycle (it needs to be hermetically sealed) with very low cycle pressure ratio (i.e., about 3—cf. +20 for modern heavy-duty industrial GTs). Even at a PR of 3, the cycle’s high pressure leg becomes >3000 psi—thus, higher PRs are unlikely to be feasible. Due to this reason, the SCO₂ cycle is difficult to seal, highly sensitive to pressure losses, and very inefficient if not recuperated (e.g., see the cycle shown in Figure 13.59). In the recuperated SCO₂ cycle, compressed working fluid

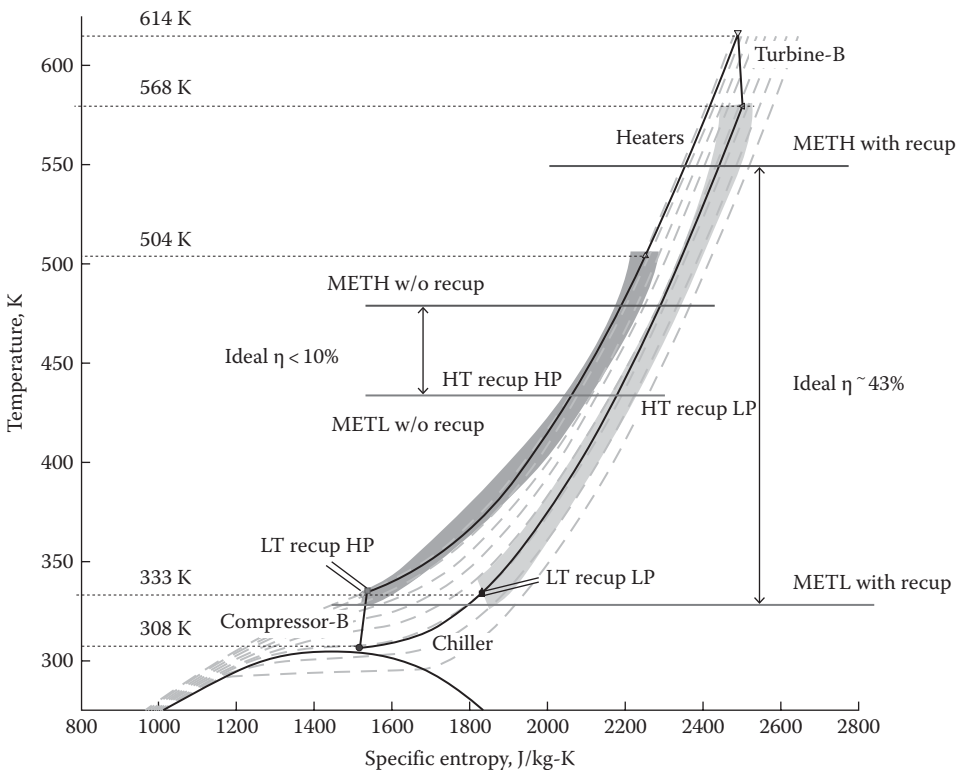


FIGURE 13.59

Supercritical CO₂ Brayton cycle. METH (with recuperation) is around 560 K (see Equation 13.5). METL (with recuperation) is around 320 K (see Equation 13.7). Thus, the ideal cycle efficiency from Equation 13.2 is about 43% (no losses, isentropic compression/expansion). (From Conboy, T. et al., *J. Eng. Gas Turbines Power*, 134, 111703, 2012.)

(dark gray highlight in Figure 13.59) is heated by using the expander exhaust (light gray highlight in Figure 13.59). Thus, recuperation raises the cycle's mean effective heat addition temperature (METH, top two lines in Figure 13.59) and lowers the cycle's mean effective heat rejection temperature (METL, bottom two lines in Figure 13.59).

This is the main quandary for the SCO_2 system designer. If there is no recuperation, due to very low cycle PR, METH and METL become very close to each other: the end result is low cycle efficiency (see Figure 13.59). With recuperation, quite good efficiency can be achieved, but

- Little room is left for waste heat recovery (upper parallelogram in Figure 13.60).
- Little room is left for a bottoming cycle (lower triangle in Figure 13.60).

The simple SCO_2 Brayton cycle in Figure 13.59 is potentially about 32%–34% efficient (corresponding to a CF of 0.75–0.80). A well-known variation is the *part-flow* or *split-compression* cycle, with recuperation divided into two parts to achieve the lowest-possible recuperator pinch (especially with microchannel heat exchangers to minimize pressure losses) [162]. Depending on the cycle maximum temperature and expander

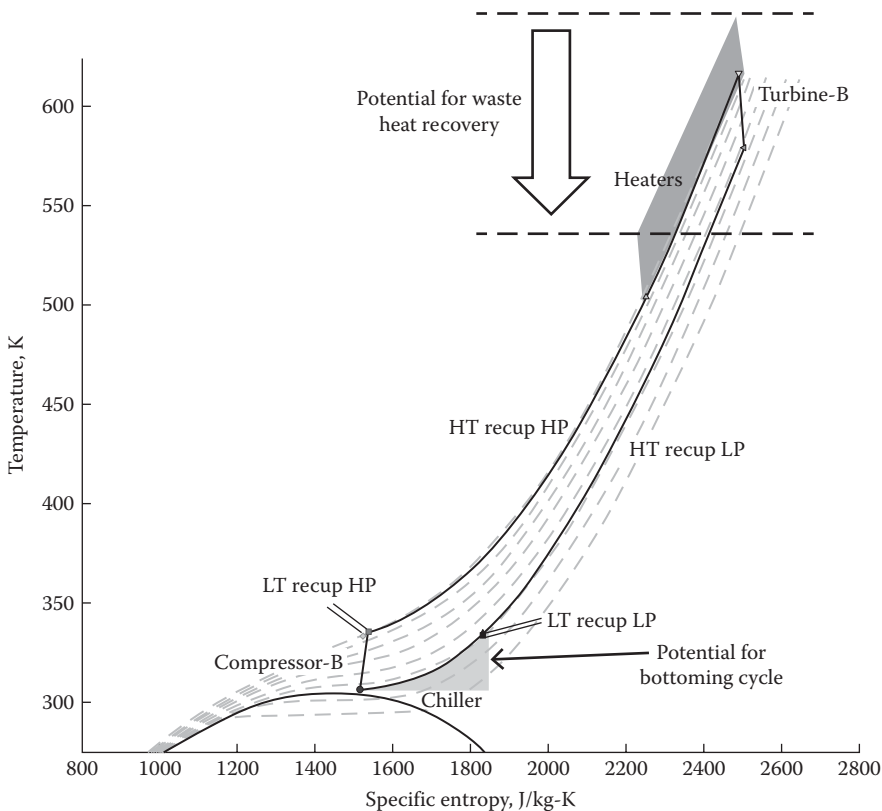


FIGURE 13.60

Supercritical CO₂ Brayton cycle. Recuperation results in high cycle efficiency but leaves little room for waste heat recovery (from a topping cycle) or for a bottoming cycle. (From Conboy, T. et al., *J. Eng. Gas Turbines Power*, 134, 111703, 2012.)

PR (unlikely to be much above 3, as mentioned earlier), a cycle efficiency of about 45% is possible (based on the information in [162]—the implied CF is 0.85 with the cycle maximum temperature of 800°K and expander PR of about 2.5). Cycle efficiencies as high as 50% have been reported with the cycle maximum temperature of about 1000°K; this should be considered as an entitlement value for the SCO₂ Brayton cycle.

The SCO₂ cycle can also be a Rankine cycle. Both, Brayton and Rankine SCO₂ are the same on the high pressure leg (heat addition). Rankine is better for heat rejection (low pressure leg) because it helps the cycle's METL to be lower (e.g., see Equation 13.2). In any event, the room for improvement is very limited because the critical point is too cold already (~31°C). Thus, there is not much room to go down in pressure to take advantage of constant p - T "condensation" and lower the METL. This is especially for applications where heat rejection will be via air-cooled condensers (very hot ambient and/or scarce cooling water).

The recuperation vs. waste heat recovery dichotomy (one always improves at the expense of the other) limits the viability of the SCO₂ cycle as a bottoming cycle for utility-scale power generation. Recall the "tug of war" between the HRSG effectiveness and the ST efficiency in the "GTCC" section, summarized by Equation 13.17. Herein, the optimization parameter is the *degree of recuperation*, which determines the overall SCO₂ bottoming cycle efficiency. In a modern GTCC with advanced frame machines, η_{HRSG} and η_{ST} are roughly 90% (stack temperature of ~180°F) and 40%, respectively, resulting in the RBC efficiency of 36%. Even with the entitlement efficiency of 50% for the SCO₂, to match the steam RBC performance, the requisite HRSG effectiveness is 72%. With a modern GT exhaust temperature of 1150°F (~900°K), this requires stack gas exit temperature of ~400°F (~475°K). From Figure 13.60, one can see that this is well below the stack gas temperature requisite for good SCO₂ cycle efficiency (+500 K for an implied exhaust gas temperature of 650–700 K at most). Achieving the requisite stack gas exit temperature, however, will hamper the degree of recuperation and drive the SCO₂ efficiency down. The magnitude of the difficulty facing the system designer is, thus, obvious.

Scalability to several hundred megawatt sizes is another issue [67]. Scaling SCO₂ turbo-machinery components (compressors and expanders) from 5–10 MW to 500–1000 MW is not a significant hurdle and can be done in a relatively short development phase. To achieve the same level of GT exhaust heat recovery with the same efficiency is a huge hurdle for the SCO₂ cycle with advanced heavy-duty GTs pushing 1200°F in exhaust temperature. Thus, SCO₂ cannot be considered an alternative to steam Rankine technology in utility-scale power generation with advanced GTCC power plants. Its advantage vis-à-vis coal-fired USC steam Rankine technology is too close to call (and might be a moot point anyway—in light of environmentalist hostility toward coal in many countries).*

At a smaller scale, however, SCO₂ is a viable and attractive waste heat recovery (i.e., bottoming cycle) alternative to the ORC and steam RBC. Potential applications are CC power plants with small and vintage GTs (e.g., aeroderivative or smaller frame engines) and reciprocating engines with exhaust gas temperatures of ~800°F or even lower. SCO₂ delivers same or better performance at a smaller footprint (i.e., smaller and cheaper) with less problems vis-à-vis ORC working fluids (toxicity, flammability). A commercially available 8 MWe engine is based on SCO₂ Rankine cycle and can be applied as a bottoming cycle to small aeroderivative gas turbines [95].

* Semi-closed supercritical CO₂ cycles in oxy-fuel combustion applications are discussed later in the chapter.

13.12 Materials

13.12.1 General

Thermodynamics dictate highest-possible cycle heat addition temperature (METH) for maximum thermal efficiency.* In order to achieve the highest-possible METH, the highest-possible cycle working fluid pressure and temperature are requisite. If design engineers had access to a fictional material “unobtainium” that would preserve its strength and integrity under arbitrarily high pressures and temperatures as well as in any corrosive environment, performances envisioned for advanced FFPS in not-so-near future would have been obtained decades ago.

Unobtainium, of course, does not exist. What engineers have to work with are metals, that is, mainly steels and alloys. Metals used in the construction of FFPS equipment and structures lose their strength and resistance to corrosion as the temperature of the environment they are in increases and they tend to undergo structural changes. In terms of their resistance to degradation by high temperatures, metals are ordered as shown in Figure 13.61.

Degradation of metal leads to a shortening of components’ design life and premature failure. Failure mechanisms in FFPS components can be physical (i.e., stress rupture) or chemical (i.e., corrosion). The end result of failure is deformation and fracture. The resistance of metals to deformation and fracture decreases with increasing temperature (*creep*) and pressure (*stress*) of the environment they exist in. Creep is defined as time-dependent,

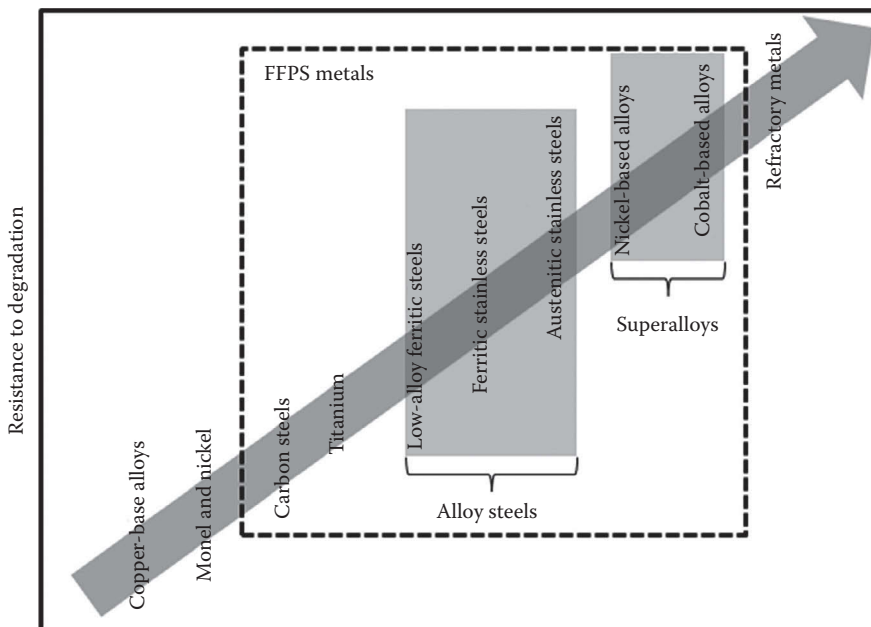


FIGURE 13.61

Qualitative ordering of metals based on resistance to degradation (mechanical and chemical). (From Horger, O.J. (Ed.), *Metals Engineering Design*, ASME Handbook, McGraw-Hill Book Co., New York, 1965.)

* Equally important is the lowest-possible cycle heat rejection temperature (METL); however, from a materials availability perspective, the higher temperature is the determining factor.

thermally assisted deformation of components under load (stress). The critical parameter is the *time to rupture*, which is a function of the *yield strength* of the metal in question (in other words, its inherent strength), and its environment (temperature and stress). An increase in either or both of the latter two will shorten the time to rupture. Obviously, short-term phenomena, such as extreme overheating due to an accidental loss of coolant flow, can accelerate the failure process. From an advanced cycle design perspective, the main concern is the long-term, high-temperature creep. Thus, the material selected should comply with the design life, with sufficient margin of safety under the requisite pressure and temperature. This is the basic premise of advanced materials for advanced power plants.

The other key feature from an advanced materials perspective is resistance to water-side and fire-side (in steam boilers) corrosion. *Corrosion* and oxidation are chemical reactions, and as such, their rates increase with temperature. They either occur uniformly over the metal surface or are limited to small areas (pitting). The rate of corrosion manifests itself in the loss of material, expressed as loss in weight per unit area and time (e.g., milligrams per square centimeter per day) or penetration in length per unit time (e.g., inches per years). Pitting corrosion is, in general, a much more serious problem than general corrosion—its rate can be as high as 1000 times the uniform corrosion rate.

Maintaining proper water chemistry (e.g., pH range and dissolved oxygen content) is the key to controlling water-side corrosion. It is also important to prevent *stress corrosion cracking* (SCC), which is caused by chlorides and alkalis in boiler water.

Avoiding problem fuels such as coal containing chlorides and temperatures for maximum corrosion rates (around 1200°F) is one obvious way to combat fire-side corrosion in boiler superheater/reheater tubes. The latter would be difficult in advanced USC power plants targeting 700°C (~1300°F) steam. Fire-side chloride corrosion of furnace-wall tubes can be influenced by interaction with other fuel constituents and is worse in reducing zones on the furnace wall. Introduction of boundary air at the furnace wall or even fuel additives have been known to help mitigate chloride corrosion. In all likelihood, especially in the furnace section, *weld overlay*, cladding, or duplex water-wall tubes will be requisite. In other words, a relatively thick layer of weld metal (about 1/8 in.) is applied to the alloy tube surface to provide a corrosion-resistant protective layer as the most direct and sure method of protection.

There is a wide range of pressures and temperatures across the steam cycle of an advanced FFSB (see Figure 13.62). Therefore, a variety of carbon and alloy steels will be used in the construction of different steam power plant equipment and their components. In order to make sense of the extremely confusing maze of terminology (differing widely from one standard to another) and definitions, a very brief review is provided first.

According to the European Standard DIN EN 10020 (July 2000), *steel* is a material (1) with a mass fraction of iron (Fe) higher than that of every other element, (2) with carbon content lower than 2%, and (3) with other elements in its chemical composition. A limited number of chromium steels might contain a carbon content that is higher than 2%, but 2% is the common boundary between steel and cast iron. Per DIN EN 10020, *stainless steels* are grades of steel with a mass fraction of chromium (Cr) of at least 10.5% and a maximum of 1.2% of carbon.

DIN EN 10020 defines *alloy steels* (of most interest herein) as steel grades (1) that do not comply with the definition of stainless steels and (2) where one alloying element exceeds the limit value prescribed in the standard. The alloyed steels are labeled with the code letter X, a number that complies with the 100-fold of the mean value of the range stipulated for the carbon content, the chemical symbols of the alloying elements (ordered according to decreasing contents of the elements), and numbers, which, in sequence of the designating alloying

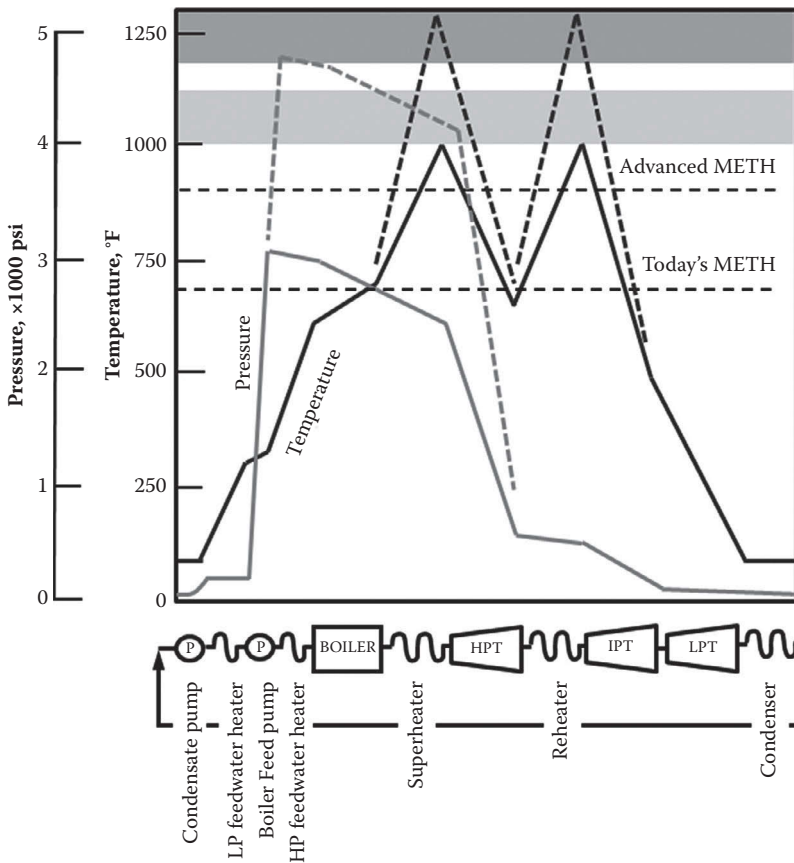


FIGURE 13.62

Typical pressures and temperatures in the steam cycle of typical subcritical PC (solid lines) and advanced USC (dashed lines) power plants. (From Davis, J.R. (Ed.), *Heat-Resistant Materials*, ASM Specialty Handbook, ASM International, Materials Park, OH, 1999.)

elements, refer to their content. For example, $X_{10}CrNi_{18-10}$ has $10/100 = 0.1\%$ C, 18% Cr, and 10% Ni in its chemical composition. As such, it is equivalent to SA-213 per ASME or ASTM specification (grade TP321H or TP347H depending on other elements in its composition).

ASTM specifications do not have the Teutonic discipline of the DIN specifications. The letter "A" describes a ferrous metal, but does not subclassify it as cast iron, carbon steel, alloy steel, tool steel, or stainless steel. It is followed by a three-digit sequential number without any relationship to the metal's properties. There might be a letter "M" appended to the sequential number to indicate that the standard is written in rationalized SI units. A two-digit number following a dash indicates the year of adoption or last revision. Grade is used to describe chemical composition. Type is used to define the deoxidation practice. Class is used to indicate other characteristics such as strength level or surface finish. (However, within the ASTM standards, these terms were adopted and used to identify a particular metal within a metal standard and used without any strict definition.) Another use of ASTM grade designators is found in pipes, tubes, and forging products, where the first letter P refers to pipe, T refers to tube, TP may refer to tube or pipe, and F refers to forging. For example, ASTM A335/A335-03, *Grade P22* refers to seamless ferritic alloy steel pipes for high-temperature service.

The most common alloying elements are as follows:

- *Manganese (Mn)*—Manganese is present in most commercially made steels (it acts as a deoxidizer in the manufacturing of steel). It increases the strength and hardness of steel.
- *Chromium (Cr)*—Chromium increases the toughness and wear resistance of steel as well as its corrosion resistance.
- *Silicon (Si)*—Silicon is also used as a deoxidizer in the manufacturing of steel. It slightly increases the strength of steel, and when used in conjunction with other alloys, it can help increase the toughness and hardness of steel.
- *Nickel (Ni)*—Nickel increases the strength of steel. It is used in low alloy steels to increase toughness and hardenability. Nickel forms the base of high-temperature superalloys because of its ability to develop an adherent oxide and precipitation hardening phases based on Ni₃Al.
- *Molybdenum (Mo)*—Molybdenum increases the hardness and high-temperature tensile strength of steel (due to its high melting point). It improves resistance to pitting corrosion in chloride environments and to crevices in both Fe–Cr alloys and Fe–Cr–Ni alloys.
- *Vanadium (V)*—Vanadium increases the toughness and strength of steel.

Obviously, the element with the largest share in steel chemical composition is *iron (Fe)*. At room temperature, iron is composed of atoms arranged in a *body-centered cubic (BCC)* lattice; irons of this type of crystal structure are referred to as *ferrite* or *alpha (α) iron*. The crystal structure changes to *face-centered cubic (FCC)* at around 1670°F; at that temperature, alpha iron is transformed to *austenite* or *gamma (γ) iron* and is nonmagnetic. Alloys of BCC and FCC crystal structures are thus referred to as *ferritic* and *austenitic*, respectively. Typical alloys used in SCPC FFPS boiler construction are listed in Table 13.20. Selected advanced alloys suitable for the construction of advanced USC boilers are described in Table 13.21.

Figure 13.63 shows the allowable metal temperatures at a constant stress of 50 MPa (about 7.25 ksi or 7250 psi) as a function of chromium content for various alloys. Figure 13.64 conveys the same information from a different perspective, which is somewhat more convenient for predicting what is needed in future to achieve the ultimate USC performance. For a given strength requirement (15 ksi or 100 MPa) and life expectancy of 100,000 h, materials requisite for different technology levels (expressed in maximum steam temperature) can be found in Figure 13.64. (Note that the U.S. DOE program—Ohio Coal Development Office [OCDO] A-USC Steam Boiler and Turbine Consortium—has a more aggressive goal than the European programs, namely 760°C [1400°F] steam temperature.)

The life expectancy of 100,000 h is equivalent to about 11 years (continuous) operation or, more realistically, 15–20 years in a more typical duty cycle. To prove that a selected material for the new advanced steam cycle conditions will indeed survive that long is a difficult proposition. This is one of the big hurdles in the ASME code approval (see p.388 for more on this) for the materials in question for use in plant equipment construction and, ultimately, widespread commercial acceptance. Usually, tests are conducted in the laboratory for shorter durations and expected creep is extrapolated using accepted theoretical approaches (e.g., *Larson–Miller* curves for creep rupture, *Manson–Coffin S-N* curves for low cycle fatigue, and *Goodman* diagram for high cycle fatigue [24]).

Corrosion resistance of alloy steels as a function of chromium content is shown in Figure 13.65. Based on the steam temperature–pressure profile in Figure 13.62 and the

TABLE 13.20

Typical Materials Used in PC Boiler Construction

Alloy	Product	ASTM	Grade	Min. Tensile Strength, ksi	Min. Yield Strength, ksi	Composition
Ferritic alloys						
1Cr-1/2Mo	Tubes	A 213	T12	60	30	0.15% C, 0.30%–0.60% Mn, 0.50% Si
	Pipes	A 335	P12	60	30	0.15% C, 0.30%–0.60% Mn, 0.50% Si
1.25Cr-0.5Mo	Tubes	A 213	T11	60	30	0.15% C, 0.30%–0.60% Mn, 0.50%–1.00% Si
	Pipes	A 335	P11	60	30	0.15% C, 0.30%–0.60% Mn, 0.50%–1.00% Si
2.25Cr-1Mo	Tubes	A 213	T22	60	30	0.15% C, 0.30%–0.60% Mn, 0.50% Si
	Pipes	A 335	P22	60	30	0.15% C, 0.30%–0.60% Mn, 0.50% Si
9Cr-1Mo	Tubes	A 213	T9	60	30	0.15% C, 0.30%–0.60% Mn, 0.25%–1.00% Si
Austenitic stainless steel alloys						
18Cr-8Ni	Tubes	A 213	TP304H	75	30	0.04%–0.1% C, 2.00% Mn, 0.75% Si
	Pipes	A 376	TP304H	75	30	0.04%–0.1% C, 2.00% Mn, 0.75% Si
18Cr-10Ni-Ti	Tubes	A 213	TP321H	75	30	0.04%–0.1% C, 2.00% Mn, 0.75% Si
18Cr-10Ni-Cb	Tubes	A 213	TP347H	75	30	0.04%–0.1% C, 2.00% Mn, 0.75% Si
16Cr-12Ni-2Mo	Tubes	A 213	TP316H	75	30	0.04%–0.1% C, 2.00% Mn, 0.75% Si
	Pipes	A 376	TP316H	75	30	0.04%–0.1% C, 2.00% Mn, 0.75% Si

Source: Viswanathan, R., *Damage Mechanisms and Life Assessment of High-Temperature Components*, ASM International, Metals Park, OH, 1989.

properties of alloys depicted in Figures 13.63 through 13.65, it is possible to deduce that the boiler of an advanced USC power plant of future will comprise a multiplicity of alloys ranging from ferritic to austenitic, with high Cr content in sections with high probability of hot corrosion. In the superheater/reheater sections subject to the highest temperatures and pressures, superalloys might be requisite (i.e., HR6W, Inconel 617, Inconel 671, etc.). For the most aggressive goal of 760°C steam temperatures, superalloys are the only option.

The boiler materials list for an advanced USC with double-reheat steam cycle (5000 psi; 1200°F/1100°F/1100°F) is as follows [24]:

- *Furnace wall*: T11, T12
- *Final superheater*
 - *Non-corrosive*: 15Cr-15Ni steel
 - *Corrosive*: NF709, Inconel 617, chromized 15Cr-15Ni or coextruded with Inconel 671 or 310 SS

TABLE 13.21

Selected Advanced Alloy Steel and Superalloy Materials

Alloy	Name	Min. Tensile Strength, ksi	Min. Yield Strength, ksi	Description
20Cr–11Ni	NF709	90	40	<ul style="list-style-type: none"> • Highest creep rupture strength among austenitic stainless steel • Good steam oxidation resistance due to higher Cr, Ni content • Better hot corrosion resistance for chloride and alkaline than TP310. • Matching welding consumable available (strength and corrosion resistance). • Applicable as superheater and reheater tube material for coal fired boiler and HRSG.
27Cr–23Ni	HR3C	95–130	+40	<ul style="list-style-type: none"> • Much higher strength than conventional 310 stainless steels. • Much better steam oxidation resistance than 18Cr–8Ni austenitic stainless steels due to 25Cr–20Ni chemical composition. • Weldability is equivalent to TP347H, and matching welding consumable is available.
24.5Cr–40+ Ni (Superalloy)	HR6W	85–115	40	<ul style="list-style-type: none"> • Stability of long term creep rupture strength and superior creep rupture ductility • Much better corrosion resistance than 18Cr–8Ni austenitic stainless steels • Microstructural phase stability at elevated temperature, which contributes to superior stress relaxation properties and enough fatigue properties for various applications • Better formability, wider available size range and better weldability than γ-phase present Ni based alloys

Note: For advanced USC.

- *Final reheater*: 347HFG (18Cr–12Ni stainless steel that has been subject to a thermo-mechanical treatment to obtain a *fine grain* size)
- *Headers and steam pipes*: 316H, P91

For steam cycles with 700°C (~1300°F) steam temperatures, superalloys have to be substituted where needed. The steam turbine materials list for the same is as follows:

- *HP and IP rotor*: austenitic superalloy or equivalent (forging)
- *HP and IP inner cylinder*: 316 austenitic steel (casting or forging)
- *HP and IP outer cylinder*: Cr–Mo steel (casting)
- *Blades*: superalloy (if necessary)—rolled or forged
- *Steam valves*: 316 austenitic steel (forging)
- *Inlet steam pipe at high temperature*: 316 austenitic steel (forging) with dissimilar metal weld (DMW)
- *LP rotor*: If steam temperature at the LP inlet is 750°F–850°F, Ni–Cr–Mo–V steel (forging); if higher, to eliminate susceptibility to temper embrittlement, super-clean Ni–Cr–Mo–V steel manufacturing techniques must be adopted

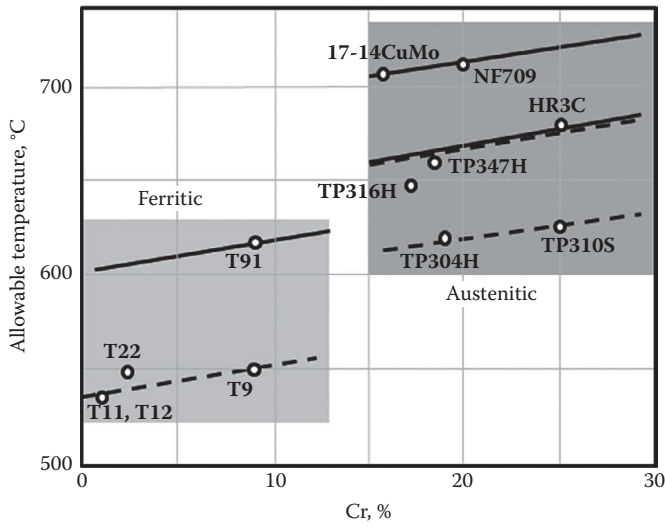


FIGURE 13.63

Allowable metal temperatures at a constant stress of 50 MPa (about 7.25 ksi) as a function of chromium content for various alloys. (From Viswanathan, R., *Damage Mechanisms and Life Assessment of High-Temperature Components*, ASM International, Metals Park, OH, 1989.)

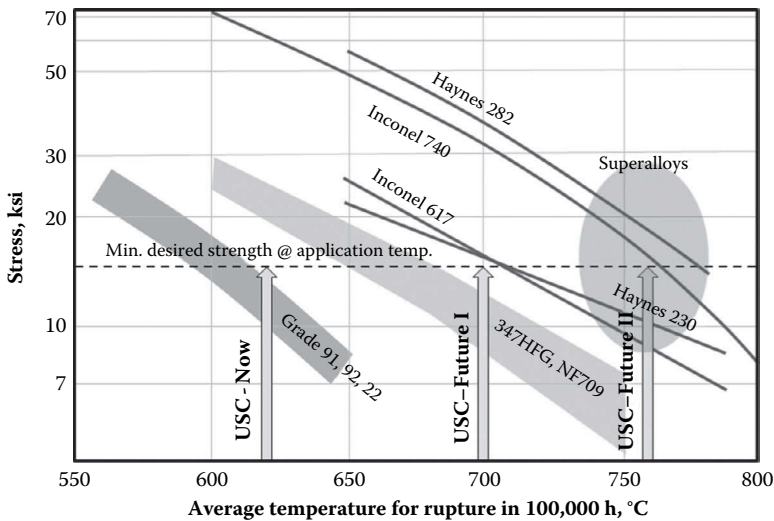
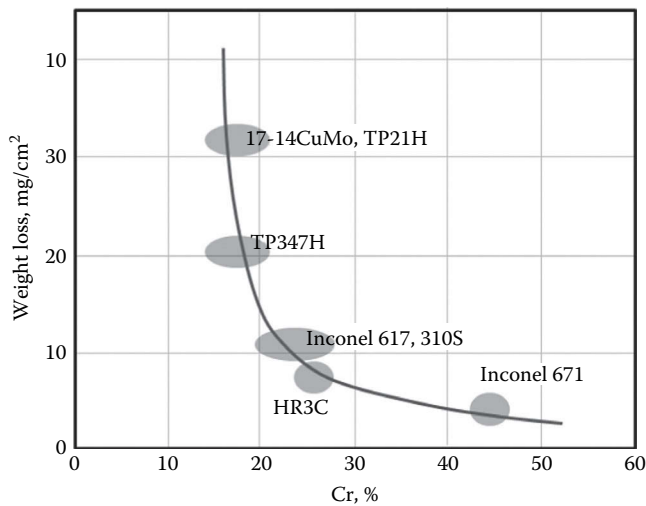


FIGURE 13.64

Steam turbine materials for A-USC coal power plants. (Based on a presentation in May 2014, *NETL Crosscutting Research Review Meeting*, Pittsburgh, PA.)

**FIGURE 13.65**

Hot corrosion resistance of alloy steels as a function of chromium content. Test conditions are 5 h at 650°C. Test gas contains 5% O₂ and 1% SO₂ and ash (contains potassium and sodium sulfates and ferric oxide).

13.12.2 Superalloys

Superalloys have good creep and oxidation resistance. They are ideally suited to functioning under high temperatures and mechanical stress. There are three groups of alloys: cobalt-based, nickel-based, and iron-based alloys. They can be used at temperatures as high as 85% of their melting point [3]. The melting temperature range of most superalloys is 1260°C–1370°C (2300°F–2500°F) [3]. Thus, all three types of superalloys can be used at temperatures well above 540°C (1000°F).

As an example, *Inconel 617* is a solid-solution strengthened alloy and has good oxidation resistance and a wide variety of corrosive media (see Table 13.22 for chemical composition). Its tensile strength is +70 ksi; its yield strength is +40 ksi. Its melting point is 1363°C (2485°F). Another superalloy is *Haynes 263*, which is a nickel–cobalt–chromium alloy that also contains molybdenum to provide it hot strength (see Table 13.22 for chemical composition). It is amenable to precipitation hardening (a heat treatment technique to increase the yield strength of the material) and comparatively easy to form, with a good

TABLE 13.22

Chemical Composition of Select Superalloys

Elements	Inconel 617	Haynes 263
Nickel, Ni	48.85–62	52
Chromium, Cr	20–24.0	20
Cobalt, Co	10–15	20
Molybdenum, Mo	8–10	6
Manganese, Mn	≤1	0.6
Silicon, Si	≤1	0.4
Carbon, C	≤0.15	0.06

high-temperature performance. This alloy is primarily used for high-temperature applications up to 900°C (1650°F). Its tensile strength is +150 ksi; its yield strength is +90 ksi. Its melting point is around 1350°C (2450°F).

Many alloys and superalloys have been investigated for utilization in advanced USC power plants. Some of those tested have obtained ASME code approval. For an alloy or superalloy, rigorous testing is necessary to demonstrate that the material has a stable microstructure at elevated temperatures and that it has adequate stress-rupture properties after long-term, elevated temperature exposure to accommodate the design stresses. Creep testing usually requires at least 30,000 h and data are then extrapolated to 100,000 h. (For example, a base load plant operating 8,000 h/yr for 20 years is expected to have a design life of 160,000 h. Obviously, not all parts are expected to survive such a long time without replacement and, thus, allowance must be made for periodic replacement. However, some parts, for example, steam turbine casings and rotor, must be able to reach the end line in one piece.)

Cast, nickel-based superalloys are primarily used to manufacture gas turbine hot gas path components, for example, nozzle vanes and rotor blades (stationary and rotating airfoils, respectively). The relationship between the temperature capabilities of turbine HGP materials and GT firing temperature is clearly and concisely illustrated in Figure 13.66. There are three types of casting techniques used in HGP component manufacturing: conventional (equiaxed grain) investment casting, vacuum casting with *directional solidification* (DS), and *single-crystal* (SC or SX) [3]. The latter two provide higher resistance to thermal fatigue at elevated temperatures. As such, they are used for manufacturing vanes and blades in the first two stages of the turbine, which experience the highest gas temperatures. (Wrought superalloys are used for turbine disks, on which the airfoils are mounted.)

With the advance of film cooling techniques, first stage nozzle vanes and rotor blades made from DS or SX alloys are the key enablers for 1600°C TIT J class gas turbines. Nevertheless, going to even higher temperatures (e.g., 1700°C TIT) is pushing the limits of

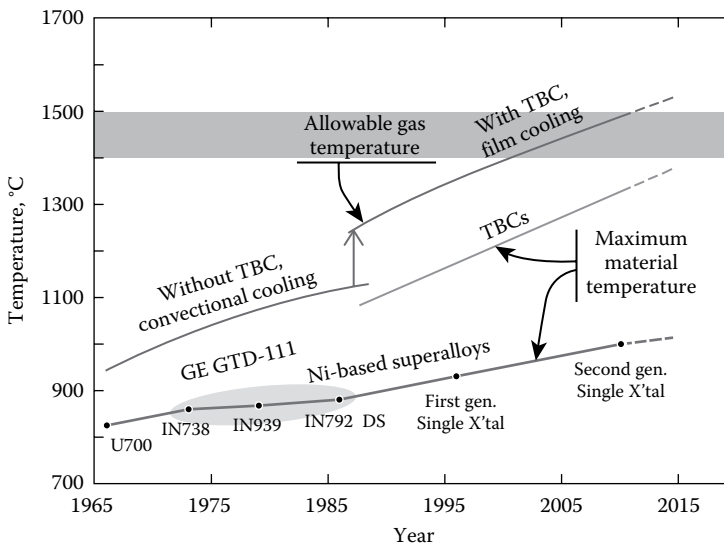


FIGURE 13.66

Historical evolution of nickel-based superalloys and thermal barrier coatings. (From Clark, D.R. et al., *MRS Bull.*, 37, 891, 2012.)

the current metallurgy. Refractory metal alloys have been looked at as possible substitutes for nickel-based and cobalt-based superalloys. However, they have several deficiencies, such as severe lack of oxidation resistance, which preclude them from being viable alternatives at this point (Figure 13.67).*

Although there is no “unobtanium,” of course, there is a reasonably close substitute: *ceramic matrix composites* (CMC). Ceramic matrix composites are produced from ceramic fibers embedded in a ceramic matrix. For GT applications, the most promising candidate is SiC/SiC, a CMC made of silicon carbide fibers and a silicon carbide matrix. Just like their monolithic forebears, CMCs have excellent creep resistance and show high stiffness at one-third the weight of nickel-based alloys. Furthermore, their high fracture toughness solves the main shortcoming of the former, namely, susceptibility to brittle

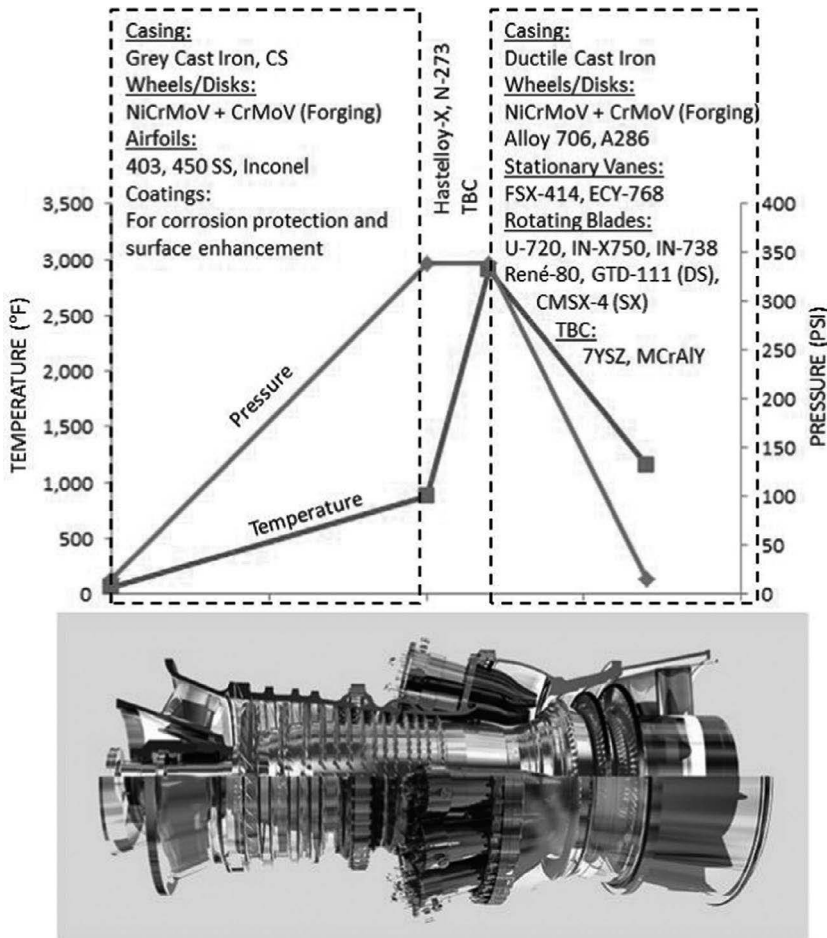


FIGURE 13.67

Gas turbine materials and coatings. (From Schilke, P.W., *Advanced gas turbine materials and coatings*, GER-3569G, GE Energy, 2004; Photo Courtesy of GE.)

* Another important consideration is the dwindling supplies and increasing prices for refractory metals such as rhenium, which are predominantly imported materials.

fracture and low thermal shock resistance. Single-crystal nickel-based alloys with TBC have a temperature capability of around 1150°C, whereas CMCs can go up to 1300°C with *environmental barrier coatings* (EBCs) for protection from oxidation without air cooling (or very little of it).*

CMC materials have been in development since 1990s. Static (non-rotating) parts such as combustor liners and stage 1 shrouds made from SiC/SiC with EBCs by different OEMs have survived several thousands of hours in field installations [164]. One OEM tested low-pressure turbine blades made from CMCs in an aircraft test engine in early 2015. Thus, it appears that a breakthrough has been made. How long it will take for full aircraft engine implementation and technology transfer into heavy-duty industrial GTs remains to be seen. Cost and durability under fire, specifically component life demonstration (25–30,000 h) under the combined centrifugal and thermal stresses plus high aerodynamic loading (rotating parts), are the key hurdles to commercialization.

Advanced GTCC power plants require efficient bottoming cycles. Along with the increase in GT firing and exhaust temperatures, optimal thermodynamic design dictates commensurately high steam temperatures. For the most advanced J class machines with exhaust temperatures pushing 1200°F (650°C), steam temperatures of 600°C are requisite for good performance. Combined with high steam pressures of around 2400–2500 psi (160–170 bars), T91 and P91 are requisite as HRSG tube, header, and steam pipe materials. Higher steam pressures (even supercritical) are possible with once-through evaporator designs. With supplementary firing, steam conditions similar to those in A-USC power plants can be achieved. Whether such a design with requisite materials, including superalloys, would be cost effective is difficult to predict.

13.12.3 Thermal Barrier Coatings

Corrosion resistance of superalloys due to limited amount of Cr (to make room for refractory metals in the composition) has been supplemented by special coatings. Protective coatings are primarily of two types: *diffusion* (e.g., platinum–aluminide) and *overlay* (e.g., MCrAlY, where M is Co, Ni, or Co/Ni). There are several different processes to apply these coatings on the component. For the overlay coatings, they are electron beam physical vapor deposition (EB-PVD), low pressure plasma spraying (LPPS), vacuum plasma spraying (VPS) or air plasma spraying (APS), and high-velocity oxy-fuel (HVOF) spraying. The choices for diffusion coating are pack cementation and chemical vapor deposition (CVD). *Thermal barrier coatings* (TBCs) add another 200°C or so to the maximum allowable metal temperature (see Figure 13.66). They were first deployed in aircraft engines in the 1960s and eventually found their way into land-based industrial gas turbines in the 1980s. TBC is a multilayer coating comprising an insulating ceramic *top coat* and a metallic *bond coat*. The most common top coat material is 7% (wt.) yttria partially stabilized zirconia (7YSZ) with MCrAlY as the bond coat. Gas turbine OEMs and third-party (aftermarket) suppliers actively develop their own TBCs and application technologies. One example for the latter is DVC (dense vertical cracking), wherein the thermal spray process produces vertical cracks in the microstructure of the ceramic coating layer to provide strain compliance as well as resistance to material loss via chipping, erosion, etc.

* About 20% of compressor airflow is utilized for component cooling. The resulting dilution of combustion exit gas temperature (by about 100+°C) across the stage one nozzle and loss of shaft output via airflow bypassing turbine stages severely hamper the gas turbine efficiency.

Research and development in the TBC area includes sensor coatings (enables remote detection of coating temperature), thermal memory coatings, gadolinium zirconate (GdZ) coatings, addition of rare earth elements to the coating composition to lower thermal conductivity, and application technologies such as suspension plasma spray (SPS).

13.13 Synthetic Fuel Production

Burning coal and other solid or liquid fuels is problematic from an emissions and performance perspective. One way to mitigate the emissions problem is to convert such fuels into a gaseous fuel suitable to combustion in the most efficient, gas turbine-based power plants. The generic term for such fuels is synthesis gas or, simply, *syngas*. Typical syngas comprises primarily CO and H₂. Further processing can produce nearly pure hydrogen or methane.

13.13.1 Gasification

The commercially available technology for syngas production from all forms of hydrocarbon feedstock is *gasification*. Coal gasification goes back to the 1800s, when it was used to make “town gas” for local cooking, heating, and lighting. Gasification is a sub-stoichiometric reaction of coal with oxygen and steam under high pressure and temperature to form a gaseous product consisting primarily of carbon monoxide and hydrogen. The gasification process typically takes place at temperatures of 1200°C–1400°C (2200°F–2600°F) and pressures of 30–60 bar (435–870 psi). The resulting gas contains CO, H₂, CH₄, and other fuel constituents, which can be referred to as desirable products (i.e., suitable to be used as GT fuels), in addition to undesirable products such as CO₂, H₂S, NH₃, and particulate matter (PM), and neutral products such as N₂ and water vapor.

When the destination of the gaseous product of gasification is a gas turbine combustor, the entire system is referred to as *integrated gasification combined cycle* or IGCC (because the power block is generally a gas turbine combined cycle). For a concise but well-rounded review of IGCC technology with different gasifiers, please refer to [8]. For detailed coverage of the fundamental physical and chemical principles and gasification technologies, see [16]. A simplified method for IGCC performance estimation can be found in [89].

Environmental regulations and GT hardware design and life requirements preclude the direct utilization of the raw syngas as turbine fuel. It must be cleaned of particulate and sulfur compounds. Thus, it is first cleaned by steam at a high pressure or via quenching and then “scrubbed” with water to remove particulates. Scrubbing also removes some NH₃ and further cools the syngas to about 200°C. (This is the so-called cold gas cleanup process. Alternative *hot gas cleanup* processes have been investigated in the past for their potential benefits [lower capital cost and higher efficiency] but they did not overcome their technical difficulties. For the most common variant of gasification technology for IGCC applications, slagging entrained-bed systems, the efficiency benefit was about 1 percentage point.)

If the IGCC power plant is designed for CCS, the next step is the so-called sour shift process, where catalyst-filled reactors reacts most of the CO in the raw syngas with water vapor to produce H₂ and CO₂ (which is then removed from the predominantly H₂ stream prior to combustion in the gas turbine). This reaction is exothermic and typically

generates intermediate pressure (IP) steam, which is exported to the steam turbine for power generation. This steam can also be used to increase the syngas H_2/CO ratio from less than 1.0 (for most gasifiers) to 2.0 (for subsequent conversion to liquid fuels such as diesel or gasoline) or 3.0 (suitable for methane production, which is also referred to as substitute natural gas or SNG).

In plants without CCS, a hydrolysis reactor is required to react the carbonyl sulfide (COS) in the syngas to H_2S for easier sulfur removal. In plants with CCS, this conversion takes place simultaneously with the shift reaction and no separate hydrolysis reactor is needed.

Either way, the syngas is still too hot, so it is cooled down to near-ambient temperature suitable for the cleanup process, which is referred to as *acid gas removal* (AGR). A significant part of the heat can be recovered during the cooling process to generate low pressure (LP) or IP steam and sent to the power block (parts might be utilized in the process block).

There is a variety of processes for AGR, either commercially available or under development. The most common technique involves absorption into a liquid with chemical (e.g., methyl diethanolamine [MDEA], etc.) or physical (e.g., Selexol, Rectisol, etc.) solvents. The selection of the optimal AGR technology in the IGCC is controlled by factors such as required degree of H_2S control and the need for removal of CO_2 (i.e., a plant to be built with or retrofitted to CCS). Detailed cost–performance trade-off is required for a final choice. However, the most likely choice for high-pressure systems, especially with CCS, is a physical solvent process. Whatever the chosen technology, the process involves absorption (removal of acid gases from the syngas into the liquid absorbent) and solvent regeneration (removal of the acid gases from the liquid absorbent). The latter process requires significant energy, which is typically supplied by LP steam extraction from the CC bottoming. In plants with CCS, staged flashing is the technique used for the regeneration of the CO_2 -rich, physical solvent from the CO_2 absorber, which is the second stage of the AGR. A promising, but not yet commercially proven, alternative technology is the use of gas separation membranes [113].

Syngas is a medium calorific or heating value fuel. While it is eminently suitable for gas turbine combustion, it requires modification to the existing gas turbine hardware designed for natural gas, especially in the combustor and either turbine or compressor design. Alternatively, the IGCC plant can then convert the syngas into *substitute natural gas* (SNG or methane), through a process called *methanation* [16]. SNG is higher in energy content than syngas, and in fact, it is the fuel for which modern gas turbines are designed. Thus, SNG can be burned in a heavy-duty industrial GT without any modification. The negative impact on efficiency, however, would make conversion to SNG a consideration only if the gasifier and gas turbines were long distances from one another.

In essence, IGCC is a CC power plant with a complex fuel skid, which converts a solid fuel, namely coal, into a gaseous fuel, that is, syngas or SNG. A typical IGCC comprises three separate plants or “blocks”:

1. Power block (gas and steam turbine combined cycle power plant)
2. Oxygen plant (air separation unit or ASU)—generates O_2 used in the gasifier*
3. Process block (gasification and cleanup)

There are many variations to the basic IGCC design (especially when it comes to “integration” between the process block, ASU, and power block). Nonetheless, the general consensus among IGCC plant designers is that the preferred design today is one in which the

* Some gasifier technologies uses air instead of O_2 , but these are generally not considered for IGCC.

ASU derives 25%–50% of its oxygen supply from the gas turbine compressor and the rest from the ASU [89]. Pressurized gasification is generally preferred to avoid large auxiliary power losses for compression of syngas. (High-pressure oxygen-blown gasification also provides advantages when CO₂ capture is mandated.) Entrained-flow gasifiers that operate in the higher-temperature slagging regions have been selected for the majority of IGCC project applications. A major advantage of using high-temperature entrained-flow gasifiers in an IGCC project is that they avoid tar formation and its related problems. The high pressure also allows individual gasifiers to be built with sufficient capacity to fuel the large commercial gas turbines now entering the marketplace.

Although coal gasification is a mature technology, it is only in the last 30 years that gasification has been used for the production of electricity using the IGCC process. (Historically, and even today, syngas from most gasifiers around the world is converted to hydrogen and to liquids such as ammonia, methanol, transportation fuels, and chemicals for plastics production.) There are currently three operating commercial-sized, coal-based IGCC plants in the United States, one in Japan (a 250 MWe unit air-blown gasifier demo plant), and three in Europe (Buggenum in the Netherlands [NUON], Puertollano in Spain [Elcogas], and Vresova in the Czech Republic). There is also one residual oil gasifying IGCC plant in Japan (Negishi in Japan—in fact, it is the world's largest IGCC, with 343 MWe net output). The U.S. projects received support from the U.S. Department of Energy (DOE). The most recent U.S. plant is Duke Energy's 618 MW Edwardsport (Knox County, Indiana) IGCC power plant. Southern Company's Kemper County IGCC project is currently under construction. Several IGCC projects are also in various stages of development, construction, and operations in China, Japan, Korea, and India. Performances of five of those eight IGCC plants are summarized in Table 13.23. For a discussion of the operating experience of these plants and improvement opportunities, please refer to Reference 98.

Only two IGCC plants are under active development in the United States, both sized at 400 MWe and both with 90% carbon capture for EOR. Furthermore, both U.S. projects are *polygeneration* plants, with fertilizers as a major product for sale. At the time of writing,

TABLE 13.23

Commercial Scale IGCC Power Plants

	NUON	Elcogas	TECO	Wabash River	Nagoso
Year	1994	1997	1996	1996	2007
Fuel	Bituminous coal	Bituminous coal, petcoke	Bituminous coal, petcoke	Bituminous coal, petcoke	Bituminous/subbituminous coal
Coal use, mt/day	2,000	2175	2270	2300	1700
Coal feed	Dry	Dry	Slurry	Slurry	Dry
Oxidant	Oxygen	Oxygen	Oxygen	Oxygen	Air
Availability, %	≥80	NA	≥85	≥70	4679 h (2011)
GT power, MW	156	182	192	192	124.4
ST power, MW	128	135	120	105	125.8
Auxiliary load, MW	31	35	60	36	36.2
Net output, MW	253	282	252	261	214
Net efficiency, % LHV	43.2	45	39.1	41.9	42.9
SO ₂ , g/kWh	0.2	0.07	<0.61	0.49	1 ppm
DeSO _x , %	>99	99.9	>98	>98	NA
NO _x , ppmv	<10	<10	15	25	3.4
PM, g/kWh	0.005	0.02	<0.02	<0.05	<0.1 mg/Nm ³

both projects were delayed due to financing difficulties. One plant in China (“GreenGen” project) is under way, with construction having started in 2009. The first 250 MWe unit has been fired with syngas in 2014. A second 400 MWe unit is under development on the same site. This project also incorporates carbon capture for EOR. Full commercialization is expected by 2020. Interestingly, one of the investors in the China project is a U.S. coal company. Worldwide, there are about a dozen IGCC projects under various stages of development.*

A highly simplified block diagram of an IGCC plant is shown in Figure 13.68. It illustrates the basic premise of the concept stated earlier, namely a gas-fired combined cycle power plant with a complex fuel skid. The performance of the IGCC power plant can be described by the following simple formula:

$$\eta_{IGCC} = \frac{\dot{W}_{PWR} - \dot{W}_{PROC} - \dot{W}_{ASU}}{HC_{Feed}} \quad (13.47)$$

where the terms in the numerator, from left to right, designate net electric power output of the power block, net electric power consumed by the process block, and the oxygen plant (ASU), respectively. The term in the denominator is the IGCC heat consumption (HC) in terms of the HHV of the feedstock (e.g., coal). Note that the net electric power consumption by the process block includes the power generated by the syngas expander

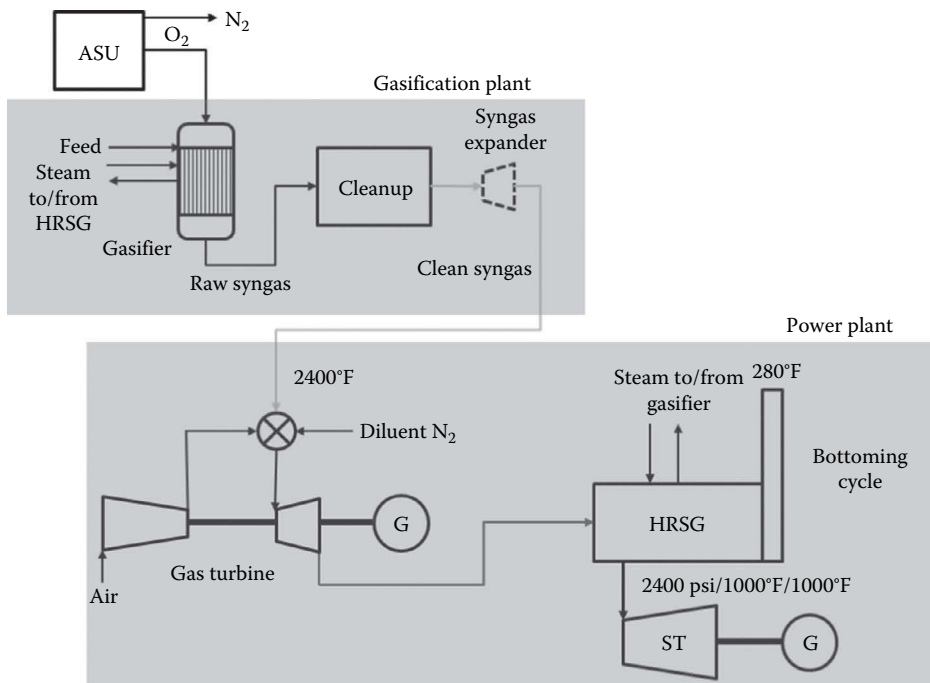


FIGURE 13.68

Simplified IGCC block diagram (for simplicity, steam RBC condenser and other BOP equipment such as feed pumps are not shown).

* Detailed and up-to-date information on the active projects can be found on the Internet.

(if one is available) and the power block steam turbine power generation (or loss of that) due to the net steam exchange between the HRSG and the gasifier syngas coolers and other heat process heat exchangers.

Significant heat is released when cooling the syngas from a high-pressure, high-temperature gasifier (e.g., 70 bar and 1250°C). This heat is typically utilized to generate high- or medium-pressure steam to be utilized in the CC steam turbine (after being superheated in the HRSG). The amount of steam generated and the additional ST output depends on the type of gasifier and heat recovery in the gasifier (i.e., radiant heat transfer or quench cooling). In terms of additional steam generation, it is typically equivalent to 8%–13% of gasifier feedstock input (i.e., coal mass flow rate multiplied by its LHV) [89].

Major IGCC electric power consumers are the oxygen plant's (ASU) main air and nitrogen compressors. Compression need is due to two reasons: high operating pressure of the gasifier (about 70 bar) and the use of separated nitrogen (N₂) as a diluent in the GT for NO_x reduction. On a mass flow basis, the oxygen consumption of a gasifier is nearly the same as the coal feed rate. A rule of thumb is about 250 kW ASU power consumption per thousand pounds per hour of O₂. Thus, taking the TECO plant in Table 13.24 as an example, 2270 tons/day is about 190,000 lb/h, so the ASU consumption is 250 × 190 = 47 MW.*

The fuel input to the power block, that is, the gas turbine CC power plant, of the IGCC is not the fuel input to the IGCC. The fuel consumed by the IGCC plant is the coal feedstock supplied to the gasifier. The ratio of the syngas fuel energy to the coal feedstock energy on an LHV basis is the *cold gas efficiency* (CGE). It is usually defined in terms of HHV. In terms of LHV, then, the relationship is

$$\eta_{CG} = h_{Feed} \frac{HC_{SG,LHV}}{HC_{Feed}} \quad (13.48)$$

where h is the HHV/LHV ratio for the gasifier feedstock. Combining Equations 13.47 and 13.48

$$\eta_{IGCC} = \frac{\eta_{CG}}{h_{Feed}} \cdot \eta_{CC} - \frac{\dot{W}_{PROC} + \dot{W}_{ASU}}{HC_{Feed}} \quad (13.49)$$

The value of the CGE depends on the gasifier technology and the feedstock quality. The higher the coal quality, the higher is the CGE. A typical value for the type of gasifier in

TABLE 13.24

Effect of Coal Rank on IGCC Heat Rate and Capital Cost

	Pittsburg #8	Illinois #6	PRB	TX Lignite
HHV, Btu/lb	12,450	10,100	8,149	7,080
Moisture, %	6	12	32	38
Ash, %	10	16	5	6.5
Heat Rate	1.00	1.06	1.14	1.22
Cost	1.00	1.08	1.22	1.36

* *Air-blown gasification* can alleviate the ASU parasitic power consumption but results in larger and costlier gas cleanup equipment. See [120] for comparison of air-blown and oxygen-blown IGCC performances.

TECO with high-sulfur bituminous coal is about 80% on HHV basis or 75% on LHV basis. For an O₂-blown gasifier ASU, power consumption is about 8%–9% of the feedstock heat input in HHV. Gasifier power usage is about 2%, while power consumed by the cleanup block is about 2.5%. Positive contribution from steam export to the HRSG and/or the syngas expander can be about 3%–6% [89]. Assuming a typical bituminous coal (with h of 1.05), gasifier CGE of 75% (for an O₂-blown, entrained-flow gasifier with a radiant syngas cooler), and F class GTCC efficiency of 57% (commensurate with the firing temperatures typical of a syngas-fired GT), we find that

$$\eta_{IGCC} = 0.75 \times 0.57/1.05 - (0.02 + 0.025 - 0.06 + 0.085) = 0.427 \text{ or } 42.7\% \text{ LHV}$$

(In the roll-up mentioned earlier, net steam export from the process block to the power block and syngas expander output are assumed to be equivalent to 6% of the feedstock heat input [HHV] in electric power generation.)

IGCC competes most directly against other clean coal technologies—especially the *supercritical pulverized coal* (SCPC) design. The comparison can be made on three aspects of an electric power plant:

1. Capital costs and cost of energy produced
2. Environmental impacts
3. Potential for cost-effective carbon dioxide capture

IGCC is expensive; in fact, it is very expensive. This is not surprising when one considers, as discussed earlier, that IGCC is a combination of three separate plants. How much more expensive, however, is not easy to answer. Presently, the rule-of-thumb expectation is that IGCC plants cost 20%–25% more than a comparable SCPC power plant at any given site. Duke Energy's current estimate for the 630 MW IGCC plant in Edwardsport is approximately \$3.55 billion. At \$5635/kW, it is about 40% more expensive than a comparable SCPC power plant at \$4000/kW. The project has been awarded local, state, and federal tax incentives totaling more than \$460 million. This brings the effective cost to the plant owners to \$4900/kW.

Similar to the PC boiler systems, lower-quality coals (e.g., lignite) result in lower CGE and higher parasitic power consumption. In slurry fed gasifiers, the energy density of high moisture and/or high ash coal slurries is markedly lower, which increases the oxygen consumption and reduces the gasification efficiency. For dry coal-fed gasifiers, there is an energy penalty (and therefore reduced steam turbine output) for drying the high-moisture coals to the low moisture content necessary for reliable feeding via lock hoppers and pneumatic conveying. For a discussion of coal quality on gasifier and IGCC performance, please consult [124].

It is somewhat difficult to make a case for IGCC over PC plants in terms of cost and/or performance. This is especially so for countries where the most abundant coal resource is high-moisture/ash (and low heating value) lignite, which is eminently unsuitable as a gasifier feedstock. However, IGCC really shines when it comes to stack emissions of pollutants. IGCC facilities:

1. Meet or exceed the U.S. EPA standards
2. Emit fewer criteria air pollutants than SCPC plants
3. Compare favorably with natural gas-fired gas turbine CC facilities

Detailed comparison of IGCC emissions with other fossil fuel technologies can be found in [121]. In terms of mercury emissions, emissions of criteria pollutants, and solid wastes, the IGCC is superior to other coal-fired technologies. IGCC-produced syngas is virtually free of fuel-bound nitrogen, and NO_x formation is primarily the result of thermal NO formation in the gas turbine combustor. NO_x control in the combustor is possible via diluent nitrogen (from the ASU) injection. Further reduction can be achieved via SCR in the HRSG.

In conventional coal-fired plants, post-combustion CO_2 capture via amine-based absorption technology is possible but expensive (see the next section). Carbon capture and sequestration is projected to increase the LCOE from such plants by 50% or more. Of course, the cost of capturing and sequestering CO_2 in an IGCC plant is also expensive, but to a lesser degree, that is, adding 25%–35% to the LCOE [121]. The principal reason for this cost differential is that CO_2 in an IGCC plant is separated from syngas *before* combustion, but CO_2 in a conventional coal plant is removed from post-combustion exhaust gases.

13.13.2 Underground Coal Gasification

In underground coal gasification (UCG), air or oxygen (plus steam in some cases) is introduced into the coal while it is still in the ground by pumping air or oxygen down “injection wells.” These wells are essentially boreholes, which are drilled into the coal seam from the surface. There are two UCG technologies: *linked vertical well* (LVW) and *controlled retractable injection point* (CRIP). The former is well suited to shallow coal seams, the latter is more suitable for deeper seams. The UCG was first developed more than a century ago and was commercially deployed in the former Soviet Union in the 1950s. There are several pilot UCG projects in the world, with some of the more notable ones in Australia (two), Canada, China (largest UCG program in the world), and South Africa [133]. While both UCG technologies are considered in those projects, LVW is the more common method.

In LVW, coal is ignited from the “production well” and the combustion front moves toward the oxidant injection well (so-called reverse combustion). Once the linkage between the wells is established, the combustion front moves in the same direction as the oxidant, that is, toward the production well. The UCG rate is controlled by controlling the amount of oxidant injection and its pressure. The process stops when oxidant injection stops. After the coal is converted to syngas in a particular location, there are two options for the remaining cavity (which will contain the leftover ash or slag from the coal):

- Flooding with saline water and capping the wells
- Using the wells to store CO_2 captured from the aboveground syngas processing

Once a particular section of a coal seam is exhausted, new wells are drilled to initiate the gasification reaction in a different section of the coal seam. The syngas that is produced from UCG is the same as that produced by aboveground gasification processes.

It is estimated that UCG can increase the U.S. recoverable coal reserves by as much as two to three times.* Cold gas efficiency of UCG is estimated at around 80% (similar to other gasification technologies). Economic benefits of UCG include elimination of coal mining,

* Accelerating Development of Underground Coal Gasification, S.J. Friedmann, Lawrence Livermore National Laboratory, 2007.

handling, transportation, and preparation prior to being fed into the gasifier; elimination of ash or slag disposal; and elimination of the gasification plant (but not the cleanup section), leading to significantly lower capital cost than that for IGCC plants.

Environmental benefits of UCG are listed as minimal land use, reduced use of groundwater or freshwater (because underground saline water is used), elimination of environmental impacts traditionally associated with coal mining and handling, and reduced criteria pollutants. Furthermore, all or a substantial portion of the sulfur, mercury, arsenic, tar, ash, and particulates found in coal remain underground. It is projected that, since any sulfur or metals that reach the surface do so in a chemically reduced state, they are easier to remove. Finally, there is no landfill disposal required for ash or slag.

A signification issue facing UCG, at least in the United States, is low natural gas prices. In some areas of the world, uncertainty in the regulatory environment can be a significant hurdle (as in the case of CCS). In addition, certain coal seams may not be suitable for UCG because of geologic/hydrologic conditions and/or insufficient seam thickness. As it was the case for the IGCC with several commercial plants in operation, project economics are highly uncertain and will remain so until several commercial-scale plants are built and operated. Nevertheless, if the technology reaches a comfortable level of maturity, its LCOE is estimated at about 60% of that for the A-USC and IGCC (all with CCS) [133]. Site selection needs to be done properly to avoid potential groundwater contamination (coal seams selected are below the fresh drinking water supplies) and surface subsidence (propagation of the UCG cavity toward the surface following collapse of the cavity roof rocks).

13.13.3 Substitute Natural Gas

As mentioned earlier, synthetic gas (syngas) from the gasifier is burned in a gas turbine for electric power production. The problem with typical coal gasification syngas is its low calorific value. Thus, more syngas flow is required to satisfy the fuel energy consumption requirement of an advanced, heavy-duty industrial gas turbine. This higher fuel flow rate dictates design modifications and/or derating (e.g., reduced firing temperature) so that the turbine design originally intended for natural gas (mostly methane) can handle it [49,108].

One can, however, take the coal gasification one step further and add one more process to convert syngas to nearly pure methane. This process is called *methanation*, which converts H_2 , CO, and CO_2 into methane and water/steam. The resulting *substitute natural gas* (SNG) can then be burned in a local gas turbine-based power plant or can be transported to a power plant in a distant location via an existing natural gas pipeline. The basic process thermodynamics can be found in [48].

This process is demonstrated in the North Dakota Gasification Plant in Beulah, ND, where approximately 18,000 tons/day of lignite is converted to 160 million standard cubic feet of methane. The calculated thermal efficiency is 61.9% for the conversion of the heating value of lignite to the heating value of the methane produced.

The \$2.1 billion plant began operating in 1984. Lignite is gasified in 14 Lurgi Mark IV gasifiers. The raw gas is cooled after it exits the gasifier, removing tar, oils, phenols, ammonia, and water via condensation from the gas stream. These products are then purified, transported, or stored for later use as a fuel for steam generation. After cooling, the gas is further treated to remove impurities.

Following cleanup, syngas is sent to a methanation unit where CO and most of the remaining CO_2 are reacted over a nickel catalyst with free hydrogen to form methane (CH_4). The product gas, now referred to as SNG, is then further cooled, dried, and compressed.

The compressed gas with a heating value of 975 Btu/ft³ leaves the facility for sale. The product joins the Northern Border Pipeline, which supplies natural gas to the Eastern United States. Incidentally, this project also captures some of the CO₂ from the process and sells it into Canada for EOR.

Another gasification project producing SNG is now in startup. POSCO of South Korea, one of the largest steel producers in the world, will gasify coal and petroleum coke to produce 500,000 mtons/year of pipeline-ready SNG.

Catalytic hydromethanation (HM) combines gasification and methanation into a single process for direct conversion of carbon into methane [48]. Pulverized coal is mixed with the catalyst and, after drying to remove moisture, fed into the HM reactor. Steam is injected into the HM reactor to “fluidize” the mixture and ensure continuous contact between the catalyst and the carbon particles. The catalyst facilitates simultaneous gasification (to produce CO and H₂), water gas shift, and methanation reactions at low temperature to generate a mixture comprising primarily methane and CO₂. The catalyst (a proprietary formula by the technology owner) is continuously recycled and reused within the HM process. The technology was demonstrated in the lab and in two pilot plants (in Illinois and Massachusetts). Commercialization prospects are not too good at this point.

In countries with abundant, cheap coal resources and very expensive imported natural gas or LNG, SNG technology can be an attractive alternative (such as China, Japan, and Korea). Produced SNG can be fed to an existing pipeline and sent to existing gas turbine CC power plants. In that case, the analysis should consider the cost of the coal-based substitute natural gas vis-à-vis natural gas from natural sources on a dollar per unit heating value basis. In fact, China seems to be betting big on SNG, with more than 30 proposed SNG projects going back to 2012 and is on its way to become the world leader in this technology [168]. Recently decreasing LNG prices, however, will likely reduce this bet. Similarly, with the current natural gas prices (less than \$3/million Btu in 2016), SNG is not economically feasible in the United States.

13.13.4 Hydrogen

The advantage of H₂ as gas turbine fuel is obvious: the combustion products do not contain carbon dioxide. One is then compelled to ask why it is not already in widespread use. To begin with, hydrogen combustion in gas turbine in DLN combustors presents problems, which are not insurmountable but require significant development effort (see Section 13.10.6 for more on this). Second, the main problem of carbon emissions does not disappear magically; it simply shifts from post-combustion to pre-combustion, along with all concomitant cost and complexity. For example, when hydrogen is produced in a steam methane reformer, each 1 ton of hydrogen produced will also produce about 9 tons of carbon dioxide [54].

Steam methane reforming (SMR) is widely used for hydrogen production in CPI. Natural gas (free from sulfur and other contaminants) is fed to the reformer, which converts the feed and steam to syngas (mainly hydrogen and carbon monoxide) in an endothermic reaction at high temperature (~1500°F–1600°F) and moderate pressure (~300–400 psia). The requisite energy is provided by additional fuel gas combustion (see Figure 13.69). Hot syngas from the reformer is cooled in a heat recovery heat exchanger and fed to the CO shift reactor. In earlier versions, the shift reaction took place in a two-stage process (high- and low-temperature shift reactors at 650°F–700°F and 450°F, respectively). The exothermic water gas shift reaction converts CO and steam to CO₂ and H₂. In modern systems, hydrogen from the shift reactor(s) is purified in a *pressure swing adsorption* (PSA) unit to achieve

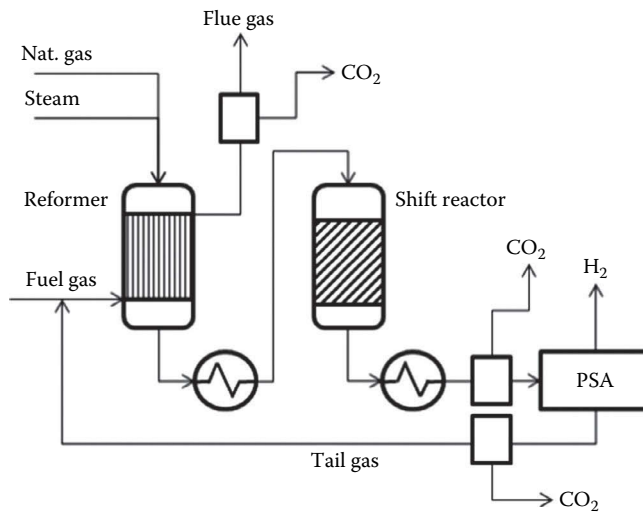


FIGURE 13.69
Steam methane reforming process.

the final product purity (+99% in newer designs).^{*} Tail gas from the PSA is recycled back to the SMR. Older systems used amine-based CO₂ stripping. Residual CO and CO₂ are converted to methane in a fixed-bed, catalytic methanation reactor (700°F–800°F).

As shown in Figure 13.69, CO₂ could be captured at three locations [54]: from the PSA tail gas or from the reformer flue gas with about 90% efficiency (~45% (v) and ~20% (v) concentration, respectively, and less than 1 bar partial pressure) or from the raw H₂ at the shift reactor exit with +99% efficiency (~15% (v) concentration and ~3.5 bar partial pressure). The removal technologies include amine-based scrubbing, physical solvents, and membranes, and there is widespread experience in CPI in CO₂ removal from raw hydrogen at high pressure. CO₂ scrubbing from the flue gas at low partial pressures and high-volume flows requires larger and more expensive equipment and consumes more parasitic power (e.g., see Section 13.14).

A cryogenic process to capture CO₂ from the PSA tail gas has been inaugurated at a hydrogen plant in France in late 2015.[†] The unit has a capture capacity of 100,000 mtons/year and is based on a combined partial condensation and distillation process, which separates CO₂ from other components.

Gas turbines burning syngas in general and hydrogen in particular are not designed from the proverbial “blank sheet” specifically for these particular gaseous fuels. There is simply not a big enough market to justify the huge cost and lengthy development time requisite for such an endeavor. Thus, major OEMs either modify their existing machines for specific applications or, as is the case recently, make their new models “fuel flexible” to the extent possible.

^{*} PSA is based on physical binding of gas molecules to a solid absorbent such as activated carbon, silica gel, zeolites, or a combination thereof. Separation is based on the fact that highly volatile compounds with low polarity such as H₂ are not adsorbed at all. The process takes place at constant temperature (no heating or cooling) because adsorption and desorption are driven by the effect of alternating pressure and partial pressure.

[†] Cryocap™ by Air Liquide—see www.airliquide.com for more information.

Due to its high flammability and lower ignition temperature, burning H_2 or any other syngas with high H_2 content in standard DLN combustors with fuel–air premixing is not possible. Such gaseous fuels are burned in diffusion flame combustors with steam (from the bottoming cycle) or nitrogen (from the ASU if H_2 is generated in a gasification plant) diluent injection for NO_x control. For those and other issues pertaining to H_2 combustion in heavy-duty industrial gas turbines (i.e., enthalpy drop difference in turbine expansion, turbine–compressor mismatch due to changing turbine mass flow rate and increased heat transfer rate with impact on HGP cooling), please refer to [48]. For detailed information on basics and specific problems related to the combustion of syngas, including blowout and stability (so-called humming), please consult [11] for a general understanding and [13] for syngas-specific issues.

The aforementioned “mismatch” stems from the disturbance of the pressure–flow balance between the compressor and the turbine. For low or medium heating value syngas, the main driver for modification is the increased turbine mass flow rate due to higher fuel flow in the combustor. Some of the increase can be absorbed by opening up the turbine inlet flow area (e.g., via staggering the nozzle vanes). This can account for maybe 6%–8% of the increased mass flow. The rest is achieved by modifications to the compressor to accommodate the increased cycle pressure ratio and/or by closing the inlet guide vanes to reduce the airflow. A detailed description can be found in [108].

13.14 Post-Combustion Carbon Capture

Post-combustion carbon capture refers to the scrubbing of CO_2 from the flue gas of a fossil-fuel–fired power plant before the stack. It can be applied to existing gas- or solid-fuel–fired power plants as a retrofit or during the design phase as an integral part of the overall plant. The primary commercially available technology at the present time is chemical absorption using an amine-based solvent, such as monoethanolamine (MEA), diethylamine (DEA), *methyl diethanolamine* (MDEA), piperazine (PIPA), and 2-amino-2-methylpropanol (AMP). The system, as shown in Figure 13.70, comprises two main components—an *absorber* column in which the CO_2 is removed and a *stripper* column in which the CO_2 is released in a concentrated form and the solvent is recovered. Prior to the absorber, the flue gas has to be cooled to about $50^\circ C$ and scrubbed to remove impurities such as SO_x , NO_x , HCl, Hg, NH_3 , etc., to prevent solvent degradation.

Minimum work required to remove CO_2 from the flue gas can be calculated from basic thermodynamic principles [25]. It is inversely proportional to the flue gas CO_2 content and increases exponentially at low concentrations. (Flue gas CO_2 concentration varies from typically around 5% [by volume on a dry basis] for a natural gas–fired combined cycle power plant to about 15% for a coal-fired power plant.) A typical range is from about 6 kJ/mol of CO_2 (coal-fired power plant) to about 10 kJ/mol of CO_2 (gas-fired combined cycle) [25]. More work is required as capture rate and purity increase (see Figure 13.71).

The actual system consumes more power than suggested by the thermodynamic minimum. Significant contributors are gas blowers (to provide the pressure head driving the flue gas from the power plant exhaust to the stack discharge and through all the capture equipment), solvent pumps, and the addition of heat for solvent regeneration, which comes in the form of steam at the expense of power plant steam turbine output. The second-law efficiency, defined as the ratio of the minimum work to the real work, is around 20%–25%

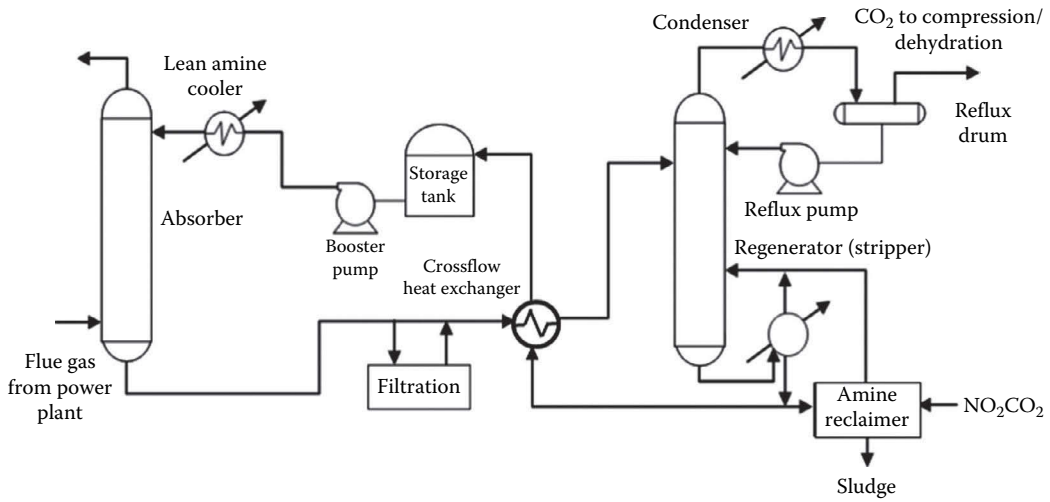


FIGURE 13.70 Absorber/stripper system for CO₂ removal from the flue gas. (Flue gas blower/fan and direct-contact cooler/scrubber are not shown—they are upstream of the absorber column.)

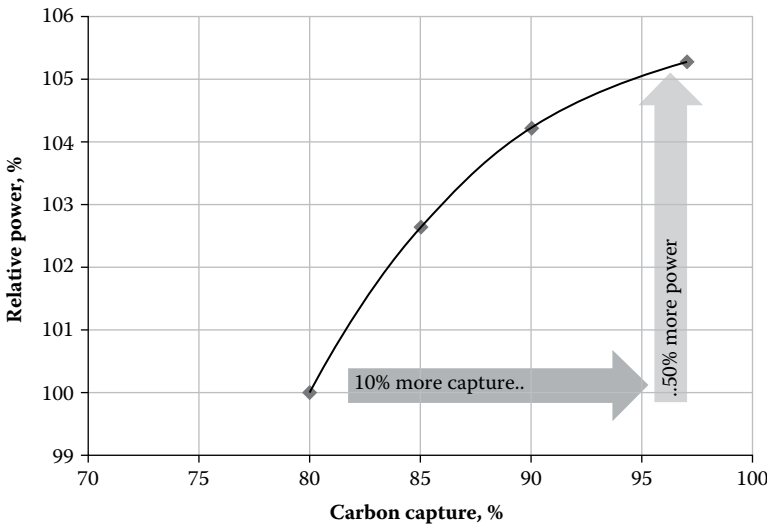


FIGURE 13.71 Power saving (%) at various CO₂ capture rates.

[25]. Armed with these rough numbers, making some quick estimates of CCS impact on FFPS performance is possible.

To start with, using the relationships in Section 13.8, molar flow of CO₂ in the flue gas for a 500 MW power can be calculated (see Figure 13.72).

From Figure 13.72, for a typical GTCC, CO₂ molar flow is about 1100 mol/s. At 8.5 kJ/mol and 90% capture rate, this corresponds to minimum capture work of about 8.5 MW. With 20% second-law efficiency, the real power consumed by the post-combustion capture

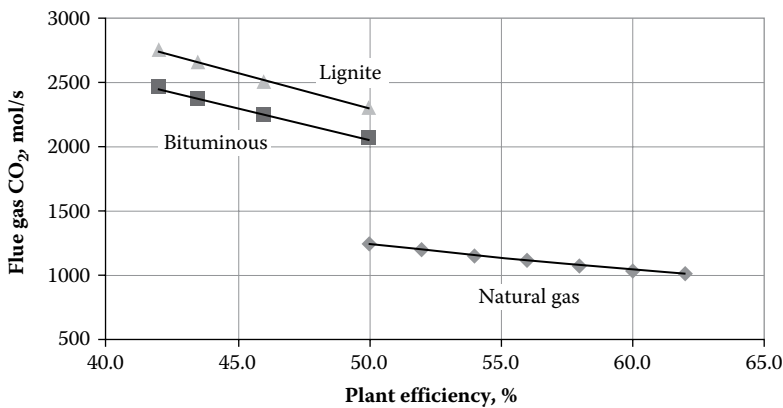


FIGURE 13.72
Flue gas CO₂ molar flow rate.

plant would be ~40 MW, which is ~8% of the GTCC output. On top of this, one should also include the CO₂ compressor for pipeline transportation and underground sequestration. Typical power consumption is anywhere between 15% and 25% of gross output as a function of final CO₂ pressure and compressor configuration (efficiency). For the example herein, this adds another 22 MW to the power expenditure for a total of 62 MW or 12% of the GTCC output. This “parasitic” power consumption can be as high as 15% on a case-by-case basis.

Using the same approach, for an advanced coal-fired plant (say, 42% LHV efficiency), the power penalty for CCS is 20%–25% of gross output. For the older power plants, with efficiencies in low thirties, it can be as high as +30%. In other words, retrofitting an old coal-fired power plant with post-combustion CCS can cause nearly one-third of the plant’s electric power output to vanish.

Due to the low-pressure and high-volume flow of the flue gas, the capture plant comprises large and costly equipment and piping. Furthermore, the CO₂ capture hardware has a large footprint; absorber and stripper columns, compression stations, and various cooling and storage tanks occupy a significant area. One should also make an allowance for accommodation of large ducts for the flue gas routed from the exit of the AQCS block (for coal-fired power plants) or the HRSG stack (for GTCC power plants) to the amine scrubber. Large-diameter pipes are needed to transfer the LP steam from the steam turbine generator to the amine scrubber; this requires pipe racks with adequate support.

Other items to consider constitute a fairly long list. For example, the existing BOP equipment has to be able to cater to the CCS requirements. Similarly, electrical system design for transformers, transmission cables, and motor control centers should be examined for requisite expansion. Plant heat sink should be sized to allow the condenser and cooling tower to deal with additional steam when the CCS is not in operation and with compression cooling loads.

The last item is an operability issue, which requires some attention. One should plan with frequent (and extended) downtime of the CCS plant. Thus, the significant amount of steam (roughly about 165 kJ/mol of captured CO₂) consumed by the stripper should be diverted back to the steam turbine. This steam is equivalent to nearly 20% of the ST output. In retrofitting an existing power plant, coal-fired or GTCC, this will require careful examination of the existing equipment and control system. For “clean sheet” designs where the

power plant is designed as a total system comprising the power and post-combustion CCS blocks, innovative design options should be explored. One option is a multisection LP turbine with a *synchro-self-shifting* (SSS) clutch separating one section from the rest of the power train. When the CCS block is operational, the clutch is disengaged and the LP section is idle. When the CCS block is down, the clutch engages and the LP section uses the stripper steam for power generation.

As far as the cost is concerned, it is very difficult to provide a simple answer. It is a highly site-specific problem. According to the Sherwood plot [25], one should figure around \$50–\$75/mtons of captured CO₂. For the earlier example case, at \$50, one gets around \$8000 per hour of operation. For a typical 6000 h/year, this is about \$50 million or about 1/10th of the total installed cost of a 500 MW combined cycle power plant. State-of-the-art capture systems can add anywhere from 30% to 40% to the GTCC-specific plant cost (\$/kW) [40].

Post-combustion carbon capture evaluation is quite controversial due to the costs, penalties (e.g., carbon tax), and incentives (e.g., carbon credits) involved. There are basically four scenarios:

1. Retrofit an old coal-fired power station with CCS.
2. Close the old station and build a new coal-fired power station (more efficient) with CCS.
3. Close the old station and build a new gas-fired GTCC without CCS.
4. Close the old station and build a new gas-fired GTCC with CCS.

Using a 500 MW old coal-fired power station with 35% net LHV efficiency as a basis, the four scenarios are summarized in Table 13.25 from a purely electric output and CO₂ emission reduction perspective. Interested readers can use their case-specific economic criteria and financial parameters to evaluate each option in terms of dollars and cents. A reasonably good starting point for detailed technical and cost information can be found in a fairly recent IEA technical study [53]. For a high-level coverage of the current landscape and future R&D needs, please refer to the findings of a symposium at MIT [145]. It is clear, however, that, especially at low natural gas prices at the present time (i.e., the second decade of the twenty-first century), the hurdle for post-combustion CCS to gain a solid foothold is rather high (at least in the United States).

TABLE 13.25

Comparison of Four Post-Combustion Carbon Capture Scenarios

	Coal	Coal	GTCC	GTCC
	Retrofit	New	New	New
Base LHV efficiency, %	35	42	56	56
Without CCS, MW	500	628	500	567
CO ₂ emitted, pph	1,030,562	1,078,393	389,659	441,676
CCS penalty, MW	122	128	NA	67
With CCS, MW	378	500	NA	500
CO ₂ emitted, pph	103,056	107,839	NA	44,168
CO ₂ reduction, pph	927,506	922,723	640,902	986,394
Lost output, MW	122	0	0	0
Sequestration?	Yes	Yes	No	Yes
New CO ₂ , lb/MWh	273	216	779	88

From the preceding discussion and typical numerical examples, one can infer that post-combustion CCS is a significantly expensive option with high parasitic power consumption. Current research is based on carbon capture systems with reduced impact on plant heat rate (mostly steam *stolen* from the GTCC bottoming cycle or steam RBC), including [145]

- Advanced amines [33]
- Other solvents such as NH_3 (the lowest form of amine)
- Adsorption
- Membrane separation
- Mechanical separation (“supersonic CCS”)
- Cryogenic separation
- Biomimetic* and microalgae systems

Membrane technologies require sufficient driving force for effective separation of the more permeable species in the gas mixture. This can be achieved by increasing the concentration of CO_2 in flue gas (e.g., exhaust gas recirculation or EGR). Optimization and demonstration of this technology at large scale is difficult and still in the future. *Adsorption* is a surface-based process in which molecules of the gaseous or liquid adsorbate (in this case CO_2) accumulate on the surface of the solid adsorbent material. In that sense, it differs from absorption, which involves one substance entering the bulk or volume of another. Classes of adsorbents include aluminas (used as desiccants), silicates and aluminosilicates (includes zeolites), carbons, and organic polymers. Advanced solid adsorbents such as *metal organic frameworks* (MOF), basically sponge-like solid materials, have the potential for significant reduction in parasitic power consumption because their regeneration energy requirement is much smaller than that for amine-based solvents. If or when they can reach commercial readiness remains to be seen.

An intriguing mechanical method for carbon capture is ICES (*inertial CO_2 extraction system*), wherein flue gas is first compressed and then expanded supersonically in a converging–diverging nozzle to cool it to very low temperatures so that CO_2 is turned into solid particles (dry ice), which are then removed from the system by a cyclone separator. The system is very simple with no moving parts, moderate operating conditions, and no chemical additives and absorbents. Its parasitic power consumption is estimated to be much lower than that of a typical amine-based scrubber.[†] The system occupies a footprint about 25% of that of an equivalent amine-based system. Technical challenges include pressure losses due to condensation in supersonic flow, agglomeration or sublimation of CO_2 particles in the capture duct and cyclone particle separator, erosion of the duct via solid particle impact, and design of an efficient CO_2 self-pressurization system. More information on the technology, which is still in the early development stage, can be found on the U.S. DOE’s ARPA-E[‡] website.

* Biomimetic refers to synthetic methods that mimic biochemical processes. One biomimetic approach to CCS is based on accelerating the rate of carbon capture by the engineering of an enzyme called carbonic anhydrase, which is combined with a conventional MEA.

† It is very difficult to verify such claims via independent calculations; primary difficulty lies in modeling two-phase flows with solid particles.

‡ Advanced Research Projects Agency—Energy

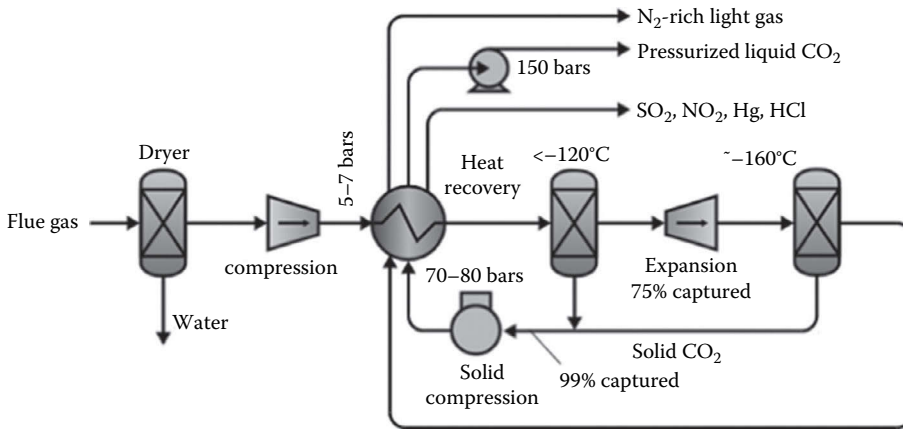


FIGURE 13.73

Cryogenic Carbon Capture™ process flow diagram. (From the U.S. DOE's ARPA-E website—represents Sustainable Energy Solutions [SES] technology).

Cryogenic separation is another novel technology that aims to convert CO_2 in flue gas first to solid (via expansion to very low temperatures, that is, $-140^{\circ}\text{C}/280^{\circ}\text{F}$) for cryogenic heat exchange and then to liquid for pumping to pressures requisite for transportation and sequestration. The system is shown in Figure 13.73. The dewatered flue gas is compressed to 5–7 bars and cooled in a *desublimating* heat exchanger. During the cooling, up to 75% of the CO_2 forms a solid and is separated along with pollutants such as mercury, SO_2 , NO_2 , Hg, and HCl. The gas is expanded and cooled in a turbine, causing more CO_2 to solidify. At this point, 99% of the original CO_2 has been captured. The captured CO_2 is pressurized to 70–80 bars. The cold products are used to cool the incoming flue gas in the desublimating heat exchanger. The warm, liquid CO_2 is pumped to the final delivery pressure. The technology is claimed to reduce the CCS parasitic load to 50% of that for a comparable amine-based process. It is still in the early development stage. More information can be found on the U.S. DOE's ARPA-E website.

Another research area is reduction in CO_2 compression power requisite for pipeline transportation and injection into the underground sequestration depository:

- Shock wave compressor [34]
- Optimization of CO_2 compression “path” [41]

Current (i.e., amine-based absorption) and emerging post-combustion CCS technologies are in various stages of development. Some of those, which have been demonstrated in the field at reasonably sized pilot plants or proof-of-concept test-bed settings, are listed as follows:

- CO_2 separation plant in Niederaussem, Germany [110]
- CO_2 separation plant in Dürnrrohr, Germany [141]
- Chilled Ammonia Process (CAP) Technology [120]
- KM-CDR® Process Technology—Petra Nova Parish Holdings, W.A. Parish Generating Station in Thompsons, TX [99]

The *Petra Nova* project is designed to capture and store 1.4 million mtons of CO₂/year. At a flue gas stream equivalent to 240 MWe, this is the largest post-combustion CO₂ capture project installed on an existing coal-fueled power plant. (Note that only a portion of the 610 MWe power plant flue gas, a “slip stream,” is sent to the CCS plant.) It is built around an advanced amine-based carbon capture process and reuse of the captured CO₂ in an EOR application. The technology was deployed earlier in a 25 MWe-equivalent pilot plant in a coal-fired power station in Alabama. The project is expected to boost production at West Ranch oil field in Vanderbilt, TX, (82 miles away) from 500 barrels/day to approximately 15,000 barrels/day. It is estimated that the field holds 60 million barrels of oil recoverable from EOR operations. If ultimately successful, this project is expected to demonstrate that post-combustion CO₂ capture and reuse can be done economically for existing plants when the plant has the opportunity to recover oil from nearby oilfields. At the time of writing, the construction of the project was under way, and it was expected to be operational in late 2016.

A full-scale post-combustion capture initiative resulted in the first and largest commercial-scale CCS project, a 115 MW coal-fired power plant in Saskatchewan, Canada. An old unit of the *Boundary Dam Power Station* was retrofitted with a proprietary amine-based carbon capture process technology for 90% capture. The reported capital cost was \$600 million (Canadian). The captured CO₂ is transported by pipelines to nearby oil fields in southern Saskatchewan to be used for EOR. Other by-products captured from the project are also planned to be sold. For example, captured SO₂ is converted to sulfuric acid and sold for industrial use. Fly ash will be sold for use in ready-mix concrete, pre-cast structures and concrete products. This project was one of the 10 large-scale* post-combustion capture projects (all of them being power plants) identified by the Global CCS Institute in 2014 (and the only one in the execution stage).

The plant went into operation in 2014. At the time of writing (late 2015), reports in the media suggested that the project had run into design, operational, and cost problems [63]. In particular, the process was reported to have captured more than 400,000 mtons of CO₂, well short of the planned 1 million mtons annually. This was explained by “mechanical problems,” which resulted in 40% availability—even though the capture plant, when operational, performed as planned to achieve 90% capture. Such teething problems are to be expected in the initial field deployment of a FOAK technology. Nevertheless, it is instructive in the sense that, even when all the major components are mature and field proven (after all, absorber/stripper systems are mainstays of CPI plants all over the world), deployment of them in a different application is subject to many unforeseen pitfalls.

On the other hand, one should recognize that the FGD technology went through its own trials and tribulations in the 1980s. Spurred on by the Clean Air Act of 1970 and governmental regulations requiring large reduction in SO₂, scrubbing technologies achieved a comfortable level of maturity and cost-effectiveness over the next two decades. There is no reason that CCS cannot go through that phase even quicker. In fact, the biggest problem facing widespread deployment of CCS may very well be the sequestration part of the system, in particular, the choice of location, which is mainly a legislative—and a quite intractable one at that—issue (“Not in my backyard!” or NIMBY). One technology that currently provides a ready-made solution is EOR. Carbon dioxide injection is already the

* Large-scale projects are defined as those that involve the capture, transport, and storage of CO₂ at a scale of at least 800,000 mt/year of CO₂ for a coal-fired power plant, or at least 400,000 mt/year of CO₂ for other emissions-intensive industrial facilities (including GTCC). For details, refer to the article on pp. 21–23 in *Chemical Engineering* April 2014 issue.

most common EOR method, where injected gas displaces the crude oil in the reservoir and allows more of the reservoir's oil reserve to be extracted. Thus, combined with CCS, EOR is a *two-in-one* solution to oil scarcity and GHG emissions with readily available CO₂ storage space. (A similar technology is *enhanced coal bed methane* [ECBM] technology [74]. In the United States, for example, the mines most suitable to ECBM applications are the very deep bituminous coal mines such as in Alabama's Warrior Basin and in the western part of Virginia.) There is also the possibility, on a very limited scale, of course, of turning captured CO₂ into a saleable product such as calcium carbonate (limestone). The technology has been demonstrated on a pilot plant scale (up to 2 mtons/day*), but its feasibility on a meaningful scale has not been established.

13.15 Oxy-Fuel Combustion

Oxy-fuel combustion is conceptually very simple (and *obvious* one might add): use +95% pure O₂ as oxidizer in the combustor instead of air, which contains nearly 79% (v) N₂ and results in significant dilution of the flue gas. The result is a combustion product gas comprising mostly steam and CO₂, from which CO₂ is separated via cooling in a condenser (water is simply knocked out of the gas). This completely eliminates the parasitic load associated with CO₂ absorption in traditional scrubber systems. What is the problem, then, one could justifiably wonder. The problem is that almost the same amount of power is now spent in a cryogenic air separation unit (ASU), where O₂ is separated from ambient air and compressed to the combustor pressure.

13.15.1 Oxy-Fuel Combustion of Coal

There are two potential applications using oxy-fuel combustion technologies:

1. Coal-fired boiler system: new boiler or retrofit (some claim it would rather be a *rebuild*)
2. New turbine system with oxy-fuel combustor(s)

The former is the path followed by one OEM with its oxy-fired PC and CFB technologies (see Figure 13.74) [118]. Several large pilot test programs have been undertaken (such as Vattenfall's 30 MWth oxy-fired boiler plant at Schwarze Pumpe,[†] Germany). Based on its experience with pilot plants, the said OEM was shooting for large (100–350 MWe) oxy-fired CCS demonstration plants. No further information was available at the time of writing.

Oxygen firing reduces combustion gas flow (because nitrogen is eliminated) by 25%–30% and changes the thermal and radiative properties of the gas containing mostly CO₂ (about 85% by dry volume). Recycling a portion of flue gas (75%–80% depending on configuration) compensates for these effects and maintains the furnace temperature at a level to avoid ash slagging, fouling and corrosion, and the heat flux to furnace walls to prevent

* Interested readers can google the Calera® technology.

[†] The town's name translates as "black pump," based on a tale that, in the Thirty Years' War of the 1600s, townspeople painted their water pump black to trick invaders into thinking that the water was infected with plague (the "black death").

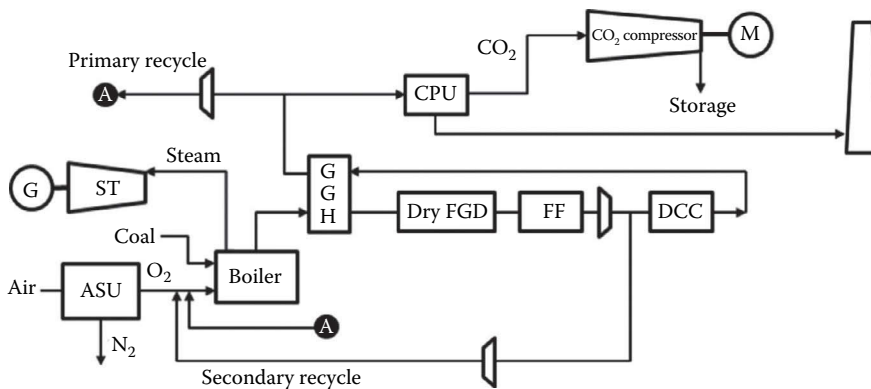


FIGURE 13.74

O₂/CO₂ recycle oxy-fuel combustion and CO₂ capture (GGH, gas-gas heat exchanger; FF, fabric filter; DCC, direct-contact cooler; CPU, CO₂ purification unit). Recycle gas heating is not shown.

overheating. Depending on the location of recycle gas extraction, three gas cleanup processes or systems can be identified: warm, cool, and cold recycle processes [19]. The warm recycle process with dry FGD is the most efficient option but is limited to low sulfur coals. The cool recycle process (as shown in Figure 13.74) with dry or wet FGD is suitable for medium- and high-sulfur coals. For a new design (no retrofit), heat integration can improve the plant performance by incorporating the heat rejected from the ASU and CPU compressor intercoolers into the cycle. Minimizing air infiltration (to maximize CO₂ concentration in flue gas) is an important design concern and achieved via minimizing the locations where the internal gas pressure is below atmospheric pressure.

Significant reduction in the recycle rate is not possible in conventional boilers [19]. However, CFB technology can be combined with oxy-fuel combustion so that the external fluidized-bed heat exchanger can replace some or, in theory, all of the flue gas recycling needed to compensate for the removal of nitrogen from the combustion gas.

At present, cryogenic air separation (distillation) is the only available technology for O₂ production. In the ASU, air is compressed to about 6 bar (depending on the purity required) and cooled down to about -180°C. Cooling is achieved through highly efficient heat exchange with outgoing products. The distillation takes part in a double column with an integrated boiler/condenser. The energy requirement of cryogenic air separation is about 250–270 kWh/mtons of O₂, with the lower energy consumption for an O₂ concentration of about 93% and higher for a concentration of 99.7%. Decreasing the purity to 95% results in a lower energy consumption because only nitrogen and oxygen have to be separated (the remaining 5% is mostly argon). The unit is highly integrated, which makes potential savings difficult, although it should still be possible to improve the equipment by decreasing pressure losses and improving the efficiency of the boiler/condenser heat exchanger. The largest cryogenic air separation unit built today produces about 5000 mtons/day of O₂, which is suitable for a 300 MWe coal-fired boiler with O₂/CO₂ recycle combustion. Multiple units are needed to supply a large coal-fired power plant boiler with oxygen.

Calculations show that the total parasitic power consumption for an oxy-fuel boiler system is about the same as that of a coal-fired power plant with amine-based post-combustion CCS [140]. Typical numbers are provided in Table 13.26 for a power plant burning subbituminous coal [19]. In addition to increased parasitic power consumption, the ASU

TABLE 13.26

Comparison of Coal-Fired Power Plant Performance with Air and Oxy-Fuel Combustion

		BASE	Oxy-Fuel
STG output	MWe	698	702
Power block aux.	MWe	19	17
BOP and transformer	MWe	22	26
Plant output—w/o ASU/CPU	MWe	657	659
Plant heat input (HHV)	MWth	1683	1616
Plant eff.—w/o ASU/CPU	—	39.0%	40.8%
ASU power	MWe	—	89
CPU power	MWe	—	61
Plant net output	MWe	657	509
Plant net efficiency, %	—	39.0	31.5
CO ₂ capture	—	None	90% Cap.
NO _x	lb/106 Btu	0.05	<0.03
SO ₂	lb/106 Btu	0.04	~0
Total PM	lb/106 Btu	0.018	~0
Mercury	—	90% Red.	~0
Capex	—	BASE	+50%–70%

Source: Babcock & Wilcox Company, *Steam, Its Generation and Use*, 42nd edn., Babcock & Wilcox Company, New York, 2015.

and CPU add 60%–80% to the plant footprint. Furthermore, to satisfy the additional cooling burden imposed by the ASU and CPU, freshwater usage is 25%–30% higher. On a per MWh basis, since the net output is lower than the comparable air-fired unit, water consumption is higher by 60%–70%. Similarly, wastewater production is 1.5–2 times higher than the comparable baseline unit. Lower net output and higher capital investment, along with increased O&M expenses, result in higher LCOE. Even though its environmental benefits are significant, in the absence of carbon tax credits or similar financial benefits, the hurdle to commercial deployment of oxy-fuel is significant as well (especially with low natural gas prices).

13.15.2 Oxy-Fuel Combustion of Natural Gas

A recent joint venture between an oxy-fuel combustion technology developer and a major gas turbine OEM is aiming to develop an oxy-fired turbine. This is a hybrid machine using the developer's high-pressure oxy-fuel combustor technology (a 170 MWth version tested with a GE J79 aircraft jet engine turbine) and heavy-duty industrial GT technology [30]. What is currently in development with a \$30 million grant from the DOE is referred to as the second generation oxy-fuel turbine by the joint venture and combines an oxy-fuel combustor with the turbine section of the industrial machine [31]. The cycle itself is also referred to as "water cycle" in some other papers. (Variants or close competitors are *Graz* [105] and *Matiant* cycles [123] and, recently, the *Allam* cycle [26–28].) Detailed thermodynamic calculations show that the entitlement performance of an oxy-fuel turbine with CCS is similar to that of an advanced GTCC with post-combustion carbon capture in the most optimal configuration, that is, ~50% net (LHV).

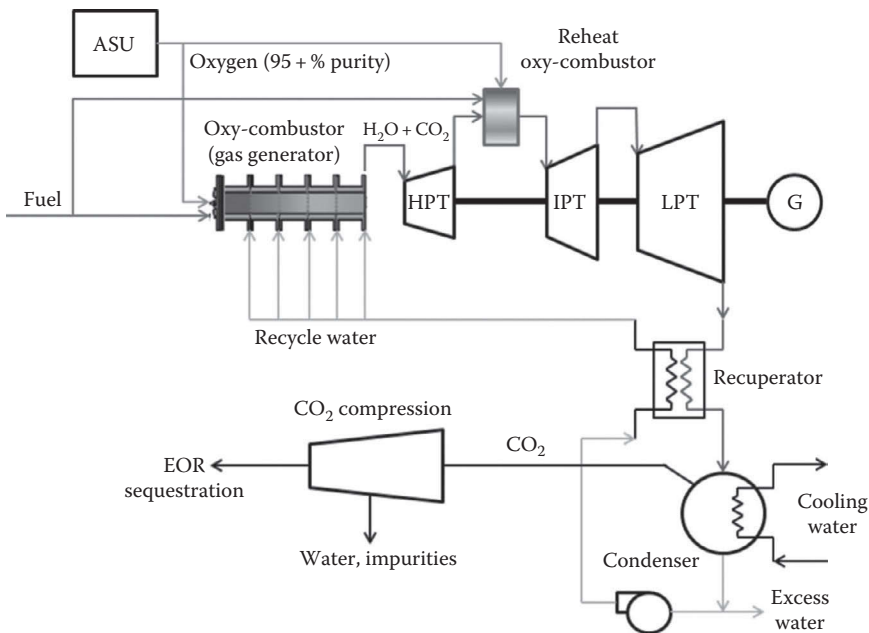


FIGURE 13.75

Oxy-fuel combustion cycle (“water cycle”)—based on the description. (From Anderson, R.E. et al., Adapting gas turbines to zero-emission oxy-fuel power plants, ASME Paper GT2008-51377, 2008.)

The projected commercial deployment for the second-generation oxy-fuel turbine* is a 150–200 MWe net power plant with 30%–40% net efficiency and 2500 mtons/day of CO₂ for EOR. This should be taken as a more realistic near-term performance standard. The cycle is shown in Figure 13.75. Natural gas fuel and oxygen are supplied to the oxy-fuel combustor operating at about 80 bar (about 1200 psi). Water is injected to maintain a flame temperature of about 1700°C (around 3000°F) and deliver diluted combustion gas (roughly 85%–90% H₂O and 10%–15% CO₂—this is why it is called “water cycle”) to the high-pressure turbine (HPT) at 500°C–600°C (930°F–1110°F). Thus, the HPT is essentially a steam turbine with a pressure ratio subject to optimization. Cycle performance is enhanced by reheat combustion before the process moves to the intermediate-pressure turbine (IPT). Typically, the IPT can be selected from the existing gas turbine technology and the inlet temperature can be as high as 1200°C (about 2200°F) or even higher.

Calculations carried out by third-party researchers over a range of HPT inlet pressures (80–200 bar), HPT inlet temperatures (600°C–1450°C), and condenser pressures (0.15–1 bar) returned net plant efficiencies of 38%–48% (after subtracting ASU and CO₂ compression loads) [39]. This is at best comparable to what one can achieve with a modern gas turbine combined cycle with amine-based post-capture technology [40]. On paper, one can come up with net efficiencies higher than 50%, but this requires currently unavailable technologies with a long development time (e.g., 1200°C and 150 bar at HPT inlet for about ~51% or 1400°C and 200 bar at HPT inlet for 53%) [39]. Myriad design challenges (in addition

* This was predicted in 2008 to happen in the time frame 2014–2015; no new development was announced at the time of writing in late 2015.

to those involved in developing oxy-fuel combustors with near-stoichiometric combustion) have been discussed by the technology advocates [30,31]. Most publications focus on applications to natural gas combustion, but variations of the basic water cycle for syngas applications have also been proposed [139]. This requires facing and overcoming the tremendous challenge involved in commercializing an already extremely costly and complex power-*cum*-process plant comprising yet-to-be developed components.

The other oxy-fuel combustion variant is the *Graz cycle*, in which the recuperator of the water cycle in Figure 13.75 is an HRSG. The cycle is shown in Figure 13.76. The composition of working fluid downstream of the oxy-fuel combustor is about 75% H₂O and 25% CO₂. The steam generated in the HRSG is utilized for power generation in a high pressure turbine (HPT) and sent to the oxy-fuel combustor as diluent. Some of the spent steam is used as coolant in the high-temperature turbine (HTT). Reported gross efficiencies, excluding ASU and CO₂ compression, are indeed impressive, well above 60%. However, the net efficiency drops to about 50% after accounting for all parasitic losses [39], which add up to about 10–11 percentage points in cycle efficiency. (Interestingly, the latter number is very similar to the efficiency penalty of MEA-based post-combustion carbon capture.) The *Graz cycle* has, thus, slightly higher efficiency than the water cycle. Similar design and development challenges must be overcome, that is, oxy-fuel combustor and high-temperature steam (or, more appropriately, “steam-like”) turbines, HTT, and HPT. A truly “apples-to-apples” comparison with today’s SOA in GT combined cycle and steam turbine technologies (applied to *all* cycle options) at the same condenser pressure shows that the oxy-fuel combustion cycles do not represent performances much too different from GTCC with MEA-based post-combustion carbon capture (especially with H and J class gas turbines, which would result in an ~53% net efficiency with capture).

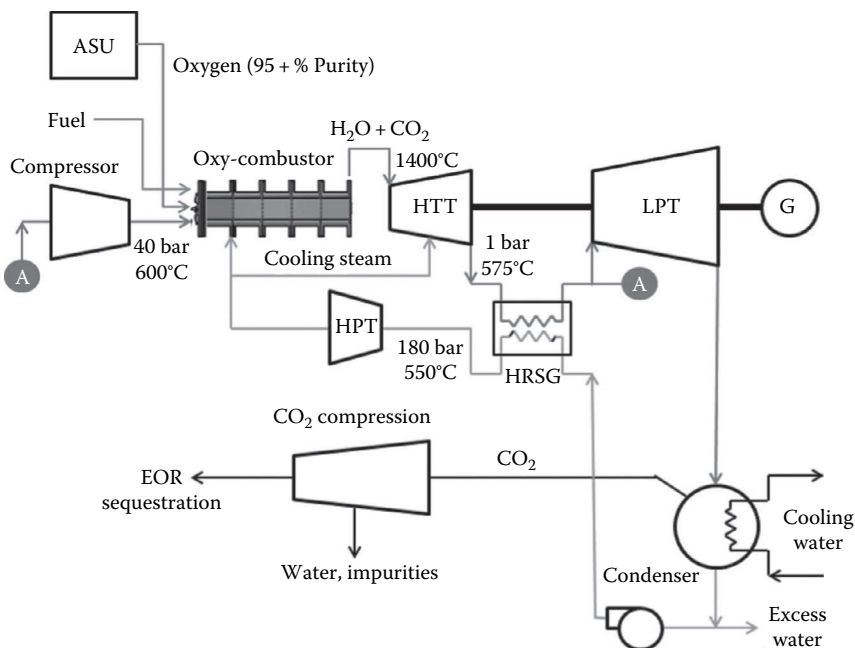


FIGURE 13.76

Graz cycle—based on the description. (From Bolland, O. et al., A thermodynamic comparison of the oxy-fuel power cycles, *Proceedings of the International Conference on Power Generation and Sustainable Development*, Liège, Belgium, October 8–9, 2001, p. 6.)

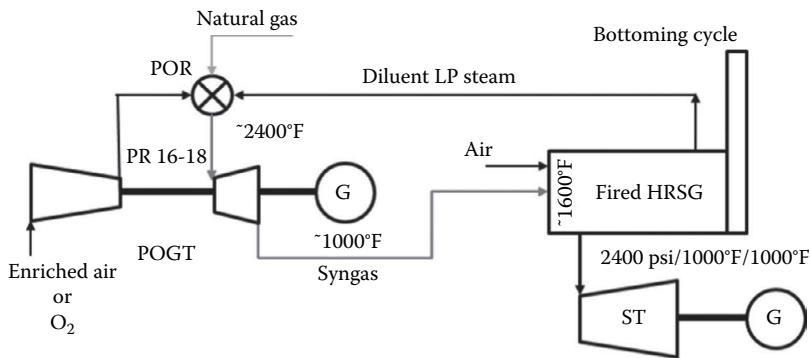


FIGURE 13.77

Partial oxidation gas turbine (POGT). (ASU is not shown. For simplicity, steam RBC condenser and other BOP equipment such as feed pumps are not shown either.)

Another oxy-fuel combustion cycle utilizing natural gas as a fuel is the *partial oxidation gas turbine* (POGT). This is a gas turbine with its combustor replaced by a *partial oxidation reactor* (POR). The noncatalytic POR (which can be thought of as a noncatalytic *auto-thermal reformer*) produces syngas via partial oxidation of methane at fuel-rich conditions (ϕ is about 2.5) [143]. A POGT combined cycle is shown in Figure 13.77. Syngas generated in the POR is used as HRSG duct burner fuel. Some of the LP steam generated in the HRSG is injected into the POR. Note that steam can also be used as a coolant for the POGT hot gas path. Alternatively, nitrogen generated in the ASU can also be used as diluent and HGP coolant. Either option results in improved efficiency.

Alternative POGT configurations have been proposed [143]. Examples are steam-injected POGT (HRSG generates only steam for injection and as HGP coolant), reheat POGT (syngas exhaust from the POGT is used as fuel in a second combustor–turbine combo), hybrid fuel cell POGT, and POGT for coproduction of hydrogen and power. In another variant, syngas from the POGT exhaust is the feedstock to *gas-to-liquid* (GTL) process for gasoline production. Significantly high efficiencies have been claimed for the POGT. One POGT combined cycle variant with a natural gas–fired heavy-duty industrial GT in parallel was calculated to have a gross efficiency of nearly 65% [142]. However, accounting for the power consumption of the ASU requisite for O_2 production and other plant auxiliaries, the net efficiency is well below 60%.

13.15.3 Oxy-Fuel Combustion with Supercritical CO_2 Cycle

Unlike the water cycles, where the post-combustion cycle working fluid is mostly H_2O (steam), Matiant and Allam cycles are *supercritical CO_2* cycles. The former is essentially an intercooled–recuperated reheat cycle with supercritical CO_2 as the working fluid and O_2 as the oxidizer. When the ASU power consumption is accounted for, the cycle does not look attractive from an efficiency perspective. A combined cycle version, *CC–Matiant cycle*, eliminates intercooling and uses a steam bottoming cycle, with the recuperator limited to the hottest (exhaust) and coolest (compressor discharge) working fluid streams. The net plant efficiency is limited to 47%–49% and does not seem to justify the requisite high-temperature component development effort ($1300^\circ C$ turbine inlet at 300 bars). More details on these cycles, including their history and relevant references, can be found in [69].

The *Allam cycle* [26] differs from the other oxy-fuel combustion cycles in that CO_2 constitutes 95% of the fluid flow in the combustor (by mass), with the rest, 5%, made up by O_2 and fuel (see Figure 13.78). The resulting combustion product is 90% CO_2 and the ASU parasitic power consumption is minimized by the lower O_2 requirement. For comparison, consider that, for the “third generation” water cycle design in [31], combined inlet stream composition to the “gas generator” oxy-fuel combustor is roughly 30% O_2 , 65% water (diluent), and 5% fuel. The claimed net LHV efficiency of the Allam cycle is nearly 59% [26]. A 50 MWh demonstration plant in Texas was announced in late 2014 (at a projected cost of \$140 million, undertaken partly by major players in the power industry). The projected commissioning date is sometime in 2016 or 2017. The heart of the cycle is, just like all the other oxy-fuel combustion cycles, the combustor and the turbine (a hybrid of steam and gas turbine technologies), which are said to be under development by a major OEM. Design details and other information can be found in [33]. At the time of writing (late 2015), no further information was publicly available on the project status.

In order to assess the realism in the claimed performance, consider that the METH of the cycle in Figure 13.78, as calculated from Equation 13.5 with stated T_2 and T_3 , is about 1050°C (1920°F). Using Equation 13.11 with 20°C condenser temperature, the equivalent Carnot cycle has an efficiency of nearly 78%. Thus, the Allam cycle with 59% has a Carnot factor of 0.758, which is well within the realm of the current SOA in GTCC technology. Although modest at first glance, this CF might, however, be somewhat

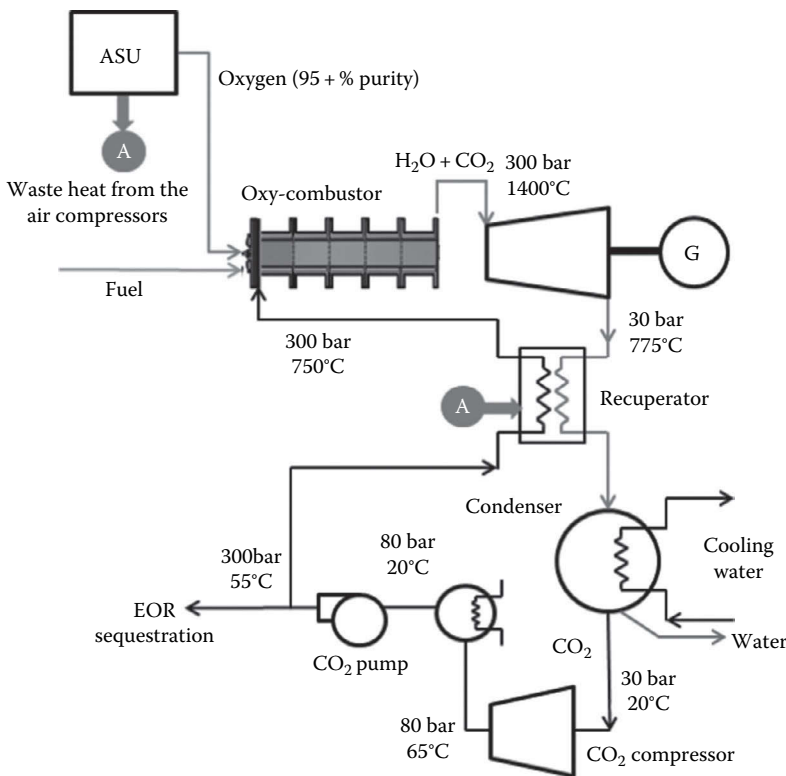


FIGURE 13.78

Allam cycle. (Based on the description in Ahngers, A., *Wärtsila Techn. J.*, 2, 4, 2007.)

high for a system with first-of-a-kind equipment. Even so, considering that the cited performance is inclusive of O_2 generation as well as CO_2 capture and compression (presumably), even coming up a few percentage points short would result in an impressive performance.

Note that, at present, reliable prediction of supercritical CO_2 cycle performance via detailed heat balance simulation is subject to some uncertainty. The reason for that is the lack of highly accurate equation of state data widely accepted by the industry (similar to the ASME steam tables). The performance of the cycle is highly sensitive to the fluid state at the pump inlet near the vapor–liquid critical point, which is the key driver of the remarkable cycle efficiency (it also presents problems from a system control perspective). Compressing air, for example, to 300 bar without intercooling would result in more than $1200^\circ C$ at the compressor discharge (cf. $55^\circ C$ in Figure 13.78), which implies a very large amount of power consumption. Thus, it is very difficult to verify myriad performance claims via rigorous simulation models.

A recently proposed FFPS concept, which is based on the PFBC for burning coal, combines oxy-fuel combustion with a supercritical CO_2 cycle [107]. In the *Zero Emission Power and Steam* (ZEPSTTM) power plant, coal is burned in a PFBC with oxygen to produce a flue gas containing primarily CO_2 and H_2O at 120 psi. Heat produced in the PFBC is transferred to the supercritical CO_2 passing through the in-bed and convective heat exchangers in the fluidized bed and the free-board volume above the fluidized bed. The PFBC bed is operated at 120 psia and $1600^\circ F$ ($870^\circ C$). The supercritical CO_2 cycle is a *split-flow recompression* cycle [162] with separate compressor drive and power turbines, with $1300^\circ F$ ($700^\circ C$) and 3000 psi (~ 210 bars) at the turbine inlet. The system is shown in Figure 13.79.

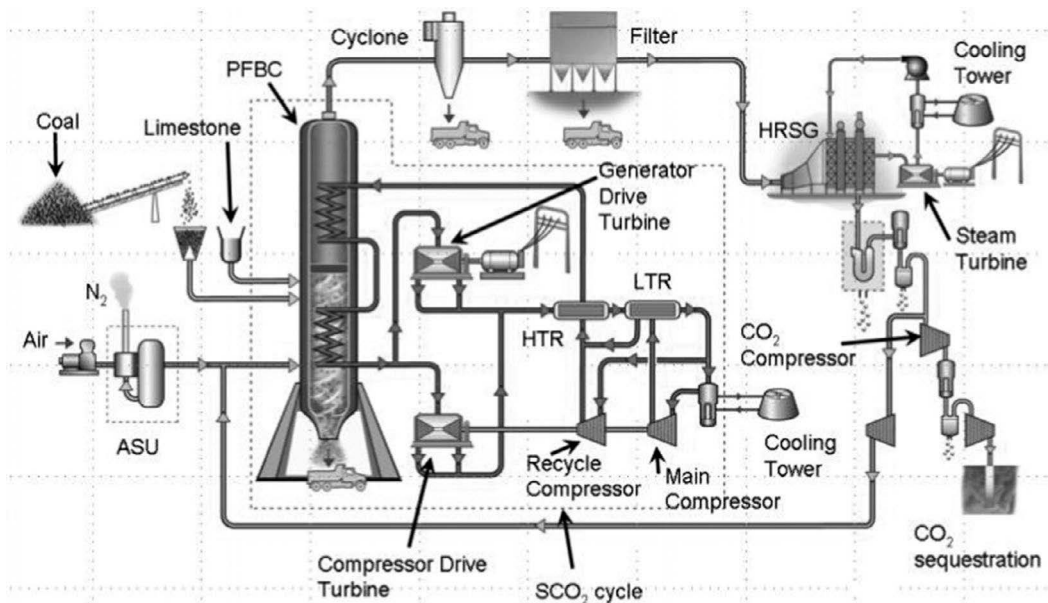


FIGURE 13.79

Zero emission oxy-coal power plant with supercritical CO_2 cycle. (From Johnson, G.A. et al., Supercritical CO_2 cycle development at Pratt & Whitney Rocketdyne, GT2012-70105, ASME Turbo Expo 2012, Copenhagen, Denmark, June 11–15, 2012.)

The ZEPS system in Figure 13.79 includes carbon capture and compression for sequestration. It also has a small steam RBC (HRSG and ST), which utilizes remaining heat in the scrubbed PFBC flue gas (primarily steam and CO_2) to make additional power (about 2% of the supercritical CO_2 power turbine). The exhaust of the HRSG is sent to the CCS system. Significant efficiency gain is claimed with the high-pressure and high-temperature supercritical CO_2 cycle over the steam cycles with CCS and oxy-fired PFBC. At the same TIT, that is, 1100°F (i.e., today's SC fossil-fuel-fired power plant ST technology) and 1300°F (for future USC plants with advanced materials), same PFBC pressures, and same flue gas exit temperatures, ZEPS™ is claimed to have 2.4 and 3.7 percentage points (HHV), respectively, advantage over the SC/USC steam systems [107].

13.15.4 Chemical Looping Combustion

Chemical looping combustion (CLC) is a variant of oxy-fuel combustion. Instead of an ASU, oxygen is provided by a separate reactor (*oxidation reactor* or OR) in the form of a metal oxide (MeO). In the OR, metal reacts with air to create MeO, which is sent to the *fuel reactor* (FR), where it is reduced back to metal while O_2 reacts with the fuel to create CO_2 and H_2O [13]. A neat analogy can be made between CLC and the human bloodstream cycle. Blood stream (oxygen carrier in CLC) cycles through the human body. During this cycle, red blood cells absorb oxygen from the lungs (OR in CLC) and deliver it to muscles (FR in CLC) for burning sugar (fuel in CLC) to provide energy requisite for the body to function. Variants have been proposed to use coal or natural gas as fuel. If the oxygen is not enough for complete reaction, the product is a syngas. In that case, the process is referred to as *chemical looping reforming*. One way to utilize CLC in power generation is to use it as a replacement for a gas turbine combustor in a combined cycle configuration [131]. A simplified block diagram of the resulting CLC-CC system is shown in Figure 13.80.

Compressed air enters the OR, where it reacts with the reduced metal. Natural gas fuel reacts with the metal oxide in the FR in a continuous process. The key to a reliable CLC design is the prevention of gas leakage between the reactors as solids (Me and MeO) are transported back and forth between them. This is achieved by a system of valves and relative positioning of the two reactors (which are essentially two fluidized beds), that is, OR above the FR. Oxygen-depleted air from the OR is sent to the *air turbine*, which is cooled by air extracted from the compressor. A typical steam bottoming cycle utilizes the air turbine exhaust for additional power generation.

Exhaust gas from the FR, comprising mainly CO_2 (and some H_2O as steam), is expanded in the *CO_2 turbine*. CO_2 turbine exhaust is utilized to heat natural gas in a fuel gas heater. Cooled exhaust gas is sent to the CCS block, which comprises CO_2 dehydration and recompression for sequestration. Plant performance is a function of air turbine inlet temperature and cycle pressure ratio. At 1100°C–1200°C and a PR of 10, net efficiencies (including CO_2 compression) around 50% have been calculated [131]. At the given parameters, excluding CO_2 compression, this corresponds to a CF of 0.75. This CF is about the same as that of an F class GTCC (1400°C TIT with a PR of 16–18)—see Figure 13.19. As such, it should be considered somewhat optimistic.

Cycle maximum temperature is limited by the properties of the O_2 -carrying metal. Some promising candidate materials for use in CLC are NiO, CuO, CoO, and Fe_2O_3 converted to Fe_3O_4 [131]. Performance and durability of the selected metal oxide and CLC reactor design (i.e., high fuel conversion, high solid–gas heat transfer, and solids' circulation with minimal gas leakage) are the main R&D subjects on the path to viability for CLC-based FFPS.

everywhere, most certainly in developing regions of the world, where fossil fuels in general and coal in particular will continue to be the driving power of human development. However, the developed world exerts its preference to limit coal-firing power production through institutions such as the World Bank, which in 2013 instituted a policy of only financing coal projects in rare circumstance.*† While the onus will be for the air quality control systems (AQCS) to scrub the flue gas from pollutants to minimize the environmental impact of FFPS in an efficient and cost-effective manner, the opportunities to do so are not widespread.

In the United States, the driving force behind the air quality control is the EPA via the Clean Air Act and its five amendments (latest in 1990). Specifically, *six criteria pollutants* defined by the National Ambient Air Quality Standards (NAAQS) must be kept at or below prescribed levels in by-product streams emitted from industrial processes: sulfur dioxide (SO₂), nitrogen dioxide (NO₂), carbon monoxide (CO), ozone (O₃), particulate matter (PM), and lead. Furthermore, under the National Emission Standards for Hazardous Air Pollutants (NESHAP) and one particular rule thereof, commonly known as Mercury and Air Toxic Standards (MATS) for utility steam generators, numerical limits are set for mercury (Hg) and other HAP metals as well as for hydrogen chloride (HCl) as a surrogate for acid gas. This rule, which became effective April 16, 2012, prompted a wave of smaller coal-fired power plant retirement announcements between 2013 and 2015. Although the Supreme Court in June 2015 ruled that the regulation was improperly developed, the plant retirement of 4% of installed U.S. coal capacity in 2015 alone was a timely retrenchment for the power industry economizing on low natural gas fuel prices.‡ Along with MATS' stringent mercury limits for new sources, new coal-fired projects were curtailed in the United States for the most part and now regarded as economically irrelevant.§ For detailed information on these pollutants, including their regulation and control, the reader is referred to [19]. A representative selection is provided in Table 13.27.

There are three ways to control SO₂ emissions: switching to a low-sulfur fuel (indeed, nearly 50% of U.S. power plants burn low-sulfur Powder River Basin [PRB] coal despite the added transportation costs), coal cleaning (to remove sulfur-bearing constituents such as pyrite), and post-combustion cleanup. The key post-combustion cleanup technology for SO₂ control in coal-fired plants is *flue gas desulfurization* (FGD). In 2011, more than 60% of coal-fired generating capacity in the United States had FGD; the same number for the world was about 50% [38]. (The highest is Germany, with nearly 90% of coal-generating capacity with FGD.) In 2015, according to the EPA's National Electric Energy Data System (NEEDS), the U.S. number had risen to more than 75% (280 MWe total generating capacity).¶ Many of the U.S. FGD systems in service today are more than 40 years old. While many of those were upgraded over the years, some might (and did) require complete replacement to comply with the new rules. Many plants, however, are slated for retirement due to the infeasibility of expected upgrades, replacements, and other modifications.

There are several FGD processes: wet scrubbing and dry scrubbing, including *spray dryer absorber* (SDA), *circulating dry scrubbing* (CDS), and *dry sorbent injection* (DSI). Wet FGD has by far the largest share of the existing scrubbing systems (the United States and

* Board Report, "Toward a Sustainable Energy Future for All: Direction of the World Bank Group Energy Sector," World Bank Groups, Report 79597, July 9, 2013, p. 5.

† Plumer, B., 2013, The World Bank cuts on funding for coal. *Washington Post*, July 17, 2013.

‡ Market Watch, With MATS in Effect, Coal Unit Retirements Will Hit Peak in 2015, *Coal Age*, July 2015.

§ In fact, twice in 2015, in April and July, gas fired generation surpassed coal fired generation (e.g., 35% versus 34.9%, respectively).

¶ Patel, S., 2015, The big picture: Emission controls, *Power*, July 2015, p. 12.

TABLE 13.27

Typical Coal-Fired Power Plant Emissions and Saleable By-Products

Cycle	Subcritical (500 MWe Net)		Supercritical (615 MWe Net)	
Coal	2.5% sulfur, 16% ash, 12,360 Btu/lb HHV		2.3% sulfur, 7.7% ash, 13,100 Btu/lb HHV	
SO _x control system	Wet limestone scrubber		Wet FGD (WFGD)	
NO _x control system	LNB and SCR		LND and SCR	
Particulate control system	Electrostatic precipitator (ESP) or fabric filter (FF)		ESP or FF plus WFGD	
	Uncontrolled	Controlled	Uncontrolled	Controlled
SO _x as SO ₂ , tons/h	9.3	0.3	9.1	0.27
NO _x as NO ₂ , tons/h	2.9	0.1	0.8	0.08
CO ₂ , tons/h	485		536	
Fly ash to air, tons/h	22.9	0.05	13	0.03
Thermal discharge	821 MWth	~0 ^a	750 MWth	~0 ^a
Ash to landfill, tons/h	9.1	32	2.6	16
Scrubber sludge (subcrit.) Wet FGD gypsum (supercrit.)	0	27.7	0	24

Source: Babcock & Wilcox Company, *Steam, Its Generation and Use*, 42nd edn., Babcock & Wilcox Company, New York, 2015

Note: For example, ash and gypsum.

^a With natural draft cooling tower.

worldwide). Less than 20% of coal-fired plants have dry scrubbers (mostly SDA) and only a few DSI. A very small fraction have CFB boilers with no SO₂ control other than the limestone in the bed material.

Nitrogen oxide control technologies include low-NO_x burners, fuel staging (e.g., see Section 13.8 in the context of GT combustors with AFS), flue gas recirculation and post-combustion scrubbing techniques, and selective catalytic and noncatalytic reduction (SCR and SNCR, respectively). For PM removal, the AQCS system includes *fabric filters* (also known as baghouses) and *electrostatic precipitators* (ESP), which have similar removal efficiencies (99% or more). For details of these technologies, including hardware description, process chemistry, cost, and performance, the reader is referred to [19] and [129]. A typical AQCS comprising all requisite cleanup equipment is shown in Figure 13.81.

Activated carbon injection (ACI) is the primary commercially available mercury control technology. Mercury is adsorbed onto the surface of the *powdered activated carbon* (PAC) injected into the flue gas stream and is removed as solid particulates in the ESP. There are two types of PAC, bromide (more effective) and non-bromide, and several generations of each by different manufacturers, who strive to come up with products with better capture efficiency (e.g., SO₃-tolerant PACs to overcome the poisoning effect of SO₃ on PAC performance*). Mercury control can also be achieved by optimizing the other equipment in the AQCS to promote mercury oxidation. In that case, if still necessary, ACI is used for the final “polishing.” Oxidizing elemental mercury to Hg²⁺ (enhanced by the SCR system) significantly improves its capture efficiency in a wet or dry FGD system. This is so because Hg²⁺ is water soluble whereas elemental mercury is not. Thus, the SCR emerges as a key AQCS component with multipollutant removal capability. If the level of mercury oxidation is high enough

* For example, SO₃ concentration increase from 1 to 6 ppm requires doubling of PAC injection amount [18].

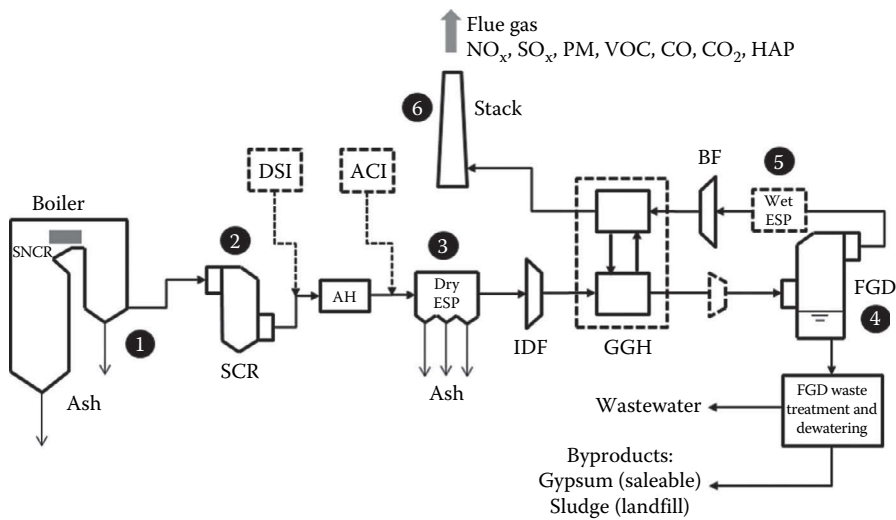


FIGURE 13.81

Typical coal-fired boiler AQCS with wet FGD (for generic eastern bituminous coal)—see the text for acronyms (AH, air heater; IDF, induced draft fan; BF, booster fan). Wet ESP (to collect mists, aerosols, and particulates) can be integrated into the FGD scrubber tower. A gas-gas heater (GGH) may be required to heat the flue gas before the stack for improved plume dispersion (e.g., in Japan).

(80%–85%), cheaper but less effective non-bromide PAC can be used. Another enhancer in mercury oxidation is chlorine in the fuel. In a similar manner, bromine injection can also be used to promote mercury oxidation with either a wet or a dry FGD system. Note that, however, the increased concentration of bromides in FGD wastewater and of Hg in saleable FGD by-products can be a problem. Another method involves injecting sulfides into a wet FGD system to turn the captured oxidized and elemental mercury into highly insoluble and stable mercuric sulfides, which are then removed with the solids.

A non-carbon adsorbent for mercury capture is bentonite amended by metal sulfides [44]. This mineral-based reagent captures mercury via a chemical reaction that forms mercuric sulfide on the flue gas particle surfaces. The reaction captures both elemental and oxidized mercury and does not contaminate saleable FGD by-products. The non-carbon adsorbent is claimed to be a cheaper alternative to the bromide PAC, with a lower rate of injection for the same capture efficiency [44]. It is able to maintain its advantage at high concentrations of SO_3 as well. The product, which has been tested at several facilities, is commercially available, but it is too recent to predict its acceptance by the industry over PACs.

Dry sorbent injection (DSI) can be utilized in wet FGD systems to prevent “blue plume” formation due to sulfuric acid in the flue gas (5–7 ppm is enough). Sulfuric acid (H_2SO_4) is formed in the wet scrubber from sulfur trioxide (SO_3), which increases in the SCR via oxidation of SO_2 . As discussed earlier, its presence is detrimental to mercury capture efficiency, too. A sodium-based chemical solution (sodium bisulfite and/or sodium sulfite) can be injected into the flue gas stream upstream of the air preheater to remove SO_3 (via formation of sodium sulfate and SO_2). In certain cases, especially with low-sulfur coals such as PRB, DSI with sodium bicarbonate sorbent, in combination with SCR and ESP, can be a cheaper alternative to a wet FGD system. The system can achieve removal efficiencies up to 85%–90%. If this is sufficient to meet emissions standards, a careful cost–performance

trade-off study is required to determine whether DSI (low capex but high sorbent consumption and operating costs) is a viable alternative to a wet FGD system (high capex but low operating costs).

Wet FGD systems are typically designed to achieve 98% or more SO_2 removal for high-sulfur coal. However, they come at a high cost, including initial capital investment, increased footprint, higher O&M costs, and, most importantly, increased parasitic power consumption. For a limestone forced oxidation (LSFO) scrubber, the parasitic power consumed by myriad pumps, blowers, mills, and fans is nearly 2% of the gross power output (i.e., nearly 10 MWe for a nominal 500 MWe power plant burning 4% sulfur coal). Originally used for lower removal requirements on lower-sulfur coals (typically 70%–85% removal), state-of-the-art SDA systems can reliably achieve greater than 96% SO_2 removal on lower-sulfur fuels (see Figure 13.82). For a power plant with a dry system comprising SDA and fabric filters, the power hit is slightly lower, for example, around 1.65% of gross output (500 MWe power plant burning 0.44% sulfur coal). The reader is referred to [129] for typical capital and operating costs, which are very difficult to compare on a consistent basis due to high variability from site to site (depending on coal type, sorbent type and consumption, and respective equipment and sorbent prices, among other things). In general, on a per MWh basis, SDA is more expensive than wet FGD (capex plus O&M) and cheaper than CDS when used with low-sulfur PRB coal (although CDS has higher removal efficiency).

The holy grail in coal-fired power plant AQCS design is a single system to control and remove more than one pollutant (i.e., SO_x , NO_x , and particulates) to minimize equipment footprint, size/cost, and parasitic power consumption. Several technologies were developed and tested in the DOE's Clean Coal Technology program in early 1990s, for example, *SNOX*TM (by Halder-Topsoe), *SNRB*TM (by Babcock & Wilcox), and *integrated dry NO_x/SO_2 emissions control systems* [129]. None of these technologies have made their way to widespread commercial acceptance. Currently investigated integrated AQCS technologies include Powerspan Corporation's *Electro-Catalytic Oxidation* (ECO[®]) [129], *Airborne Process*TM (by Airborne Clean Energy) [126], and *ROFA*[®] (Rotating Opposed Fire Air) and *Rotamix*[®] *Advanced SNCR* by Nalco Mobotec [58]. ECO and Airborne are post-combustion cleanup systems. ROFA is a combustion optimization technology resulting in reduced NO_x , SO_3 , and CO. Combined with Rotamix SNCR, ROFA aims to reduce pollutant formation.

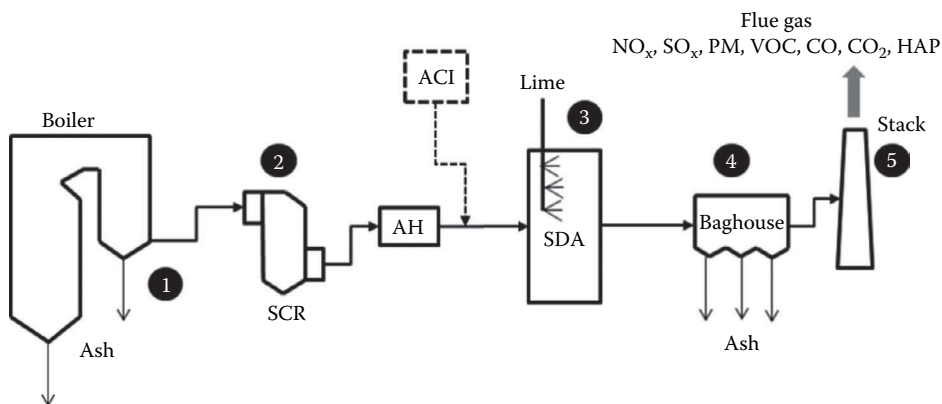


FIGURE 13.82

Typical coal-fired boiler AQCS with dry FGD (for low-sulfur PRB coal)—see the text for acronyms.

The overall control system includes *furnace sorbent injection* (FSI) using limestone (calcium carbonate) or trona (sodium carbonate) or DSI. These technologies are marketed but, at the time of writing, have not made it beyond pilot or demo plant stage.

Since pipeline quality natural gas is essentially sulfur-free and does not contain all the other harmful pollutants present in coal, AQCS in gas-fired systems comprises only the SCR (GT exhaust gas temperatures are not suitable for SNCR). In combined cycle applications, the SCR is placed between the HRSG tube bundles (typically downstream of the HP evaporator section), where the gas temperature is suitable for the SCR operation. The optimum operating temperature is a function of the SCR catalysts; typically, it is above 350°C (570°F). In simple cycle (gas turbine only) applications, either a high-temperature catalyst is employed or the GT exhaust gas is cooled via air injection. The exact configuration is subject to a cost-performance trade-off involving catalyst efficiency (NO_x reduction), cost, and catalyst life. Ammonia (NH₃) is injected upstream of the SCR catalyst, where it combines with oxides of nitrogen in the exhaust gas to form nitrogen and water vapor. Often, there is a separate catalyst layer designed to oxidize CO to CO₂ upstream of the *ammonia injection grid* (AIG). The reason is the strong dependence of CO conversion rate on gas temperature. Carbon monoxide emissions are particularly high at low GT loads (e.g., see Figure 13.31 in Section 13.8).

A “multifunction” SCR catalyst can achieve NO_x and CO/VOC reduction in one layer. Elimination of the separate catalyst section reduces the exhaust gas pressure drop, with a beneficial impact on GT performance. Note that an SCR system can add 2–3 in. of water column to the exhaust gas pressure loss in the HRSG. (Each extra 1 in. of water column in GT exhaust pressure is worth about 0.4% in lost output and 0.1% in higher heat rate.) An extra 1 in. of water column pressure loss can be attributed to the CO catalyst (Figure 13.83).

Emissions of NO_x are typically quoted at a reference condition on a volumetric basis, for example, 25 ppmvd (parts per million by volume dry) at 15% O₂ (for gas turbines) or 5% O₂ (for some gas engines). For the fraction of NO_x in the GT exhaust gas, conversion from a mass basis to a volume basis (dry) can be done as follows:

$$v = \frac{\dot{m}_{\text{NO}_x} \cdot MW_{\text{exh}}}{\dot{m}_{\text{exh}} \cdot 46} \cdot \frac{1}{1 - y_{\text{H}_2\text{O}}} \quad (13.50)$$

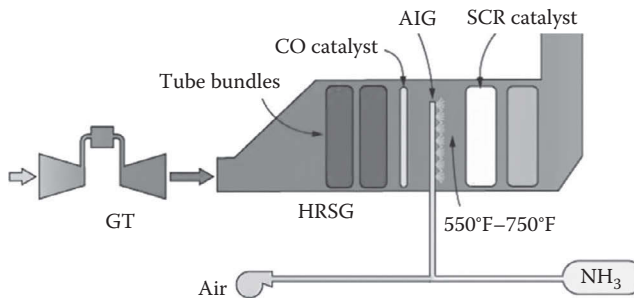


FIGURE 13.83

Typical selective catalytic reduction (SCR) system in GTCC.

where the terms in the numerator refer to the mass flow rates of NO_2 (proxy for NO_x in the exhaust gas), GT exhaust gas, and the molecular weight thereof. The term in the denominator is the fraction of water vapor in the exhaust gas on a volume basis. Correction to $x\%$ O_2 results in (assuming air is 21% oxygen)

$$v_c = 10^6 \frac{\left(0.21 - \frac{x}{100}\right) \cdot v}{0.21 - (1 - y_{\text{H}_2\text{O}}) \cdot y_{\text{O}_2}} \quad (13.51)$$

For a typical heavy-duty industrial GT, exhaust gas molecular weight is about 29 lb/lbmol; exhaust gas oxygen and water vapor volume fractions are 12% and 9%, respectively (for 100% methane fuel). Thus, for a machine rated at 25 ppmvd NO_x (15% O_2), from Equation 13.51, v is found as 0.0000415. If the exhaust gas mass flow rate is 1175 lb/s, from Equation 13.50, NO_x mass flow rate is about 260 lb/h. For a 230 MW unit, this corresponds to about 1.1 lb/MWh NO_x emissions. Thus, as a rule of thumb, about 1 lb/MWh is a good NO_x estimator for modern units with DLN combustors. Same calculations can be done for CO emissions by using 28 instead of 46 in Equation 13.50.

Another method, provided by the EPA, is based on an *emissions index* ($E\text{INO}_x$) in units of lb NO_x per 1000 lb fuel, which is proportional to the exhaust NO_x emission levels in ppmv by a constant, K [29]:

$$\frac{v_c}{E\text{INO}_x} = K \quad (13.52)$$

The equation and K values (for v_c at 15% O_2) were provided by OEMs for different gas turbines and fuels (e.g., $K = 11.6$ for methane, $K = 12.1$ for pipeline quality natural gas and $K = 13.2$ for #2 distillate). The earlier calculation with NO_2 as a proxy for NO_x suggests a K value of 8.9.

EPA's Method 19 allows the use of following estimating factors [71]:

- 1 ppmv NO_x (at 15% O_2) = 0.0036 lb/MMBtu (natural gas fuel)
- 1 ppmv NO_x (at 15% O_2) = 0.0040 lb/MMBtu (distillate)

Note that Equation 13.52 with the given K values returns a value of 0.0040 in lb/MMBtu of NO_x emissions for each ppmv of NO_x . The corresponding value from the earlier sample calculation with NO_2 as a proxy for NO_x is 0.0052 lb/MMBtu. The difference can be explained by the composition of NO_x emissions, which are typically 90%–95% NO, with the balance being NO_2 . Once the flue gas is out of the stack, most of the NO is eventually oxidized to NO_2 in the atmosphere, which contributes to the so-called yellow plume. Thus, using a weighted average molecular weight of 31.6 lb/lbmol for NO_x in Equation 13.50 (instead of 46 lb/lbmol for NO_2), one obtains a K value of 12.9 and 0.0036 lb/MMBtu for each 1 ppmv of NO_x from the earlier sample calculation.

13.17 Water Treatment

13.17.1 Why Treatment?

Steam RBC equipment requires essentially pure water as working fluid. Unfortunately, pure water does not occur in nature. To make matters worse, water quality shows a large variability from site to site. Thus, water treatment equipment make up a vital auxiliary system of an FFPS. Major types of water impurities are summarized in Table 13.28. There are many treatment technologies available to handle one or more of those contaminants (see Table 13.29). Detailed information on these technologies can be found in [17]. Specific information on power plant water treatment can be found in [4]. The reader can also consult [19] for water chemistry information specific to steam power plants.

TABLE 13.28

Water Impurities and Contaminants

Contaminant Type	Examples
Suspended solids	Clay, dirt, silt, dust, insoluble metal oxides and hydroxides, colloidal materials
Dissolved organic compounds	Synthetic organic compounds, trihalomethanes, humic and fulvic acids
Dissolved ionic compounds	Heavy metals, silica, arsenic, nitrates, chlorides, carbonates
Microorganisms	Bacteria, viruses, protozoan cysts, fungi, algae, molds, yeast
Gases	Hydrogen sulfide, carbon dioxide, methane, radon

Source: Cartwright, P., *Chem. Eng.*, March, 50, 2006.

TABLE 13.29

Water Treatment Technologies

Technology	Suspended Solids	Dissolved Organics	Dissolved Ionic Compounds	Microorganisms	Gases ^a
Filters (bed, cartridge, or bag)	Very effective	NA	NA	NA	NA
Precoat filtration	Very effective	Partially effective	NA	NA	NA
Activated carbon	NR	Very effective	NA	NA	Partially effective
Reverse osmosis	NR	Very effective	Very effective	Very effective	NA
Distillation	NR	Partially effective	Very effective	Very effective	NA
Electrodialysis	NA	NA	Effective	NA	NA
Electrodeionization	NA	NR	Effective	NR	NA
Ion exchange	NR	NA	Very effective	NA	NA
Ozonation	NA	Partially effective	Partially effective	Very effective	NA
Chlorine	NA	NA	NA	Effective	NA
Ultraviolet Radiation	NA	Partially Effective	NA	Effective	NA

Source: Cartwright, P., *Chem. Eng.*, March, 50, 2006.

Note: NA, not applicable; NR, not recommended.

^a Gases are removed by deaeration.

The ultimate goal of water treatment is steam purity, which can have a detrimental impact on performance and availability if not maintained adequately. For example, the presence of contaminants can lead to corrosion damage of steam turbine components, including pitting, *stress corrosion cracking* (SCC), and corrosion fatigue. The damage is proportional to exposure time and concentration of contaminants. The objective in establishing proper water and steam cycle chemistry is to minimize deposits and prevent corrosion damage to major equipment (steam turbine, boiler, HRSG, and condenser) and components (e.g., valves, seals, and bearings).

Potential sources and/or causes of contamination are boiler carryover (silica at 900 psig, salts at 1800 psig), steam attemperation (desuperheating) with contaminated water, silica vaporization, and vaporization of organic compounds. Detailed chemical background and quantitative data can be found in [124].

In drum-type boiler systems, carryover of impurities from the feedwater in vapor or solid phase is the key mechanism of contamination. In once-through systems (e.g., Benson-type boiler), steam contamination is directly tied to the purity of the condensate prior to entering the boiler inlet. Therefore, treatment requirements for once-through boiling systems are more stringent, thus requiring expensive equipment. The differences are summarized in Tables 13.30 and 13.31. For the steam RBC of a GTCC, feedwater and steam quality requirements are similar to those in Table 13.31. Slightly more stringent requirements may apply to steam-cooled G and H class systems, where cooling steam may leak into the turbine HGP.

TABLE 13.30

Differences in Water Treatment for Subcritical (Drum Type) and Supercritical Boilers

Drum Type Subcritical	Once-Through Supercritical
All Volatile Treatment (AVT)	Oxygenated Treatment (OT)
Polisher may not be needed (Needed for faster startups)	Combined Water Treatment (CWT) 100% polisher for startup with AVT, OT (CWT) Reduced use during normal operation possible
50% precoat type demineralizer	Precoat and deep-bed demineralizer

TABLE 13.31

Recommended Boiler Feedwater Limits for Once-Through and High-Pressure Drum Type Boilers^a

	Units	Drum	Once-Through	
		AVT	AVT	OT
pH		9.3–9.6	9.3–9.6	8.0–8.5
Total hardness	ppm CaCO ₃	0.003	0.003	0.001
Oxygen	ppm	0.007	0.007	0.03–0.15
Iron	ppm	0.01	0.01	0.005
Copper	ppm	0.005	0.002	0.001
Organic	ppm TOC	0.2	0.2	0.2
Cation conductivity	µS/cm	0.2	0.2	0.15

Source: Babcock & Wilcox Company, *Steam, Its Generation and Use*, 42nd edn., Babcock & Wilcox Company, New York, 2015.

^a Conductivity is a measure of the concentration of (ionized) dissolved solids in water. Its units are “micro-Siemens per centimeter,” or µS/cm. For most public waters, 1.55 µS/cm is about 1 mg/L or 1 ppm (part per million as CaCO₃) in total dissolved solids (TDS). TOC stands for total organic carbon.

In *all-volatile treatment* (AVT), boiler feedwater quality is controlled by adding non-solid chemicals such as ammonia (to control pH to prevent corrosion) and hydrazine (to scavenge oxygen). When the latter is used, the process is referred to as AVT-R. *Oxygenated treatment* (OT) or AVT-O with no hydrazine addition is based on the theory that slightly soluble oxides, such as Fe^{3+} oxide, forming on the boiler tube surface act as a protector against *flow accelerated corrosion* (FAC). There are two types of OT, *neutral water treatment* (NWT), in which dissolved oxygen is allowed to coexist in neutral water, and *combined water treatment* (CWT), in which dissolved oxygen is allowed to coexist in weak alkaline water adjusted to a pH range of 8.0–9.3 by ammonia.

A typical advanced boiler water treatment system is shown in Figure 13.84. More or less the same type of systems and principles apply to an advanced GTCC with a drum-type or once-through HRSG as well. Typically, modern GTCC plants do not have a separate deaerator or combined LP drum and deaerator. They utilize a *deaerating condenser*. As shown in Figure 13.84, boiler feedwater is a combination of condensate return and makeup water. The latter is about 1%–2% of the total feedwater flow (unless it is a cogeneration system). Treatment starts with *clarification* of the makeup (raw) water to coagulate and settle suspended matter with the help of chemical additives (alum and iron sulfate). It is followed by *filtering* to remove trace impurities and excess chlorine (which is used to kill microorganisms). Next comes *softening*, which removes calcium and magnesium ions (major hardness ions) by replacing them with sodium salts (i.e., ion exchange). Some other dissolved impurities are also removed during this process. The removal of dissolved solids still present after softening (now including sodium cations as well) is known as *demineralization*. There are several methods of demineralization, including *ion exchange* (IX), *reverse osmosis* (RO), and *electrodeionization*. One or more of those (in series) can be used to satisfy the boiler feedwater

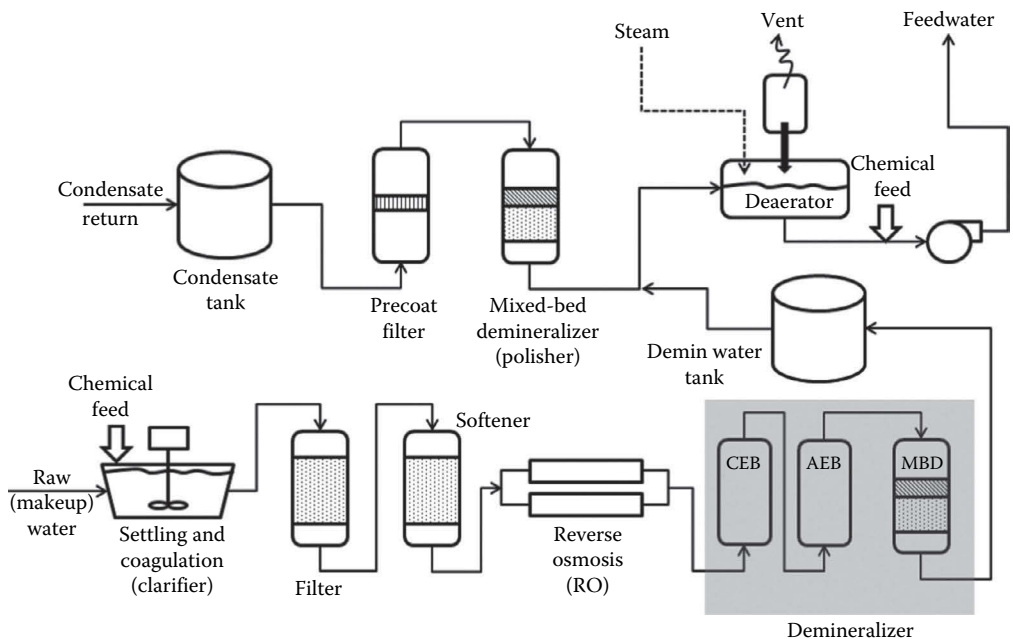


FIGURE 13.84

Conceptual boiler feedwater treatment system for an advanced FFPS (CEB, cation exchange bed; AEB, anion exchange bed).

purity requirements (see Table 13.31). The exact system configuration is a function of the particular site raw water analysis. Complete removal of solids is ideal for once-through SC and USC systems. In that case, the process is finished by a *mixed-bed demineralizer* (MBD).

In theory, condensate return from the steam turbine condenser should be pure. Nevertheless, it may contain contaminants resulting from corrosion of tubes and pipes, air in-leakage, and in-leakage of condenser cooling water (especially if the circulating coolant is seawater). Thus, *condensate polishing* using MBD is desirable for all modern high-pressure systems with AVT and seawater-cooled condensers. Finally, dissolved O₂ and CO₂ in the feedwater are vented out in the *deaerator*.

Long-term exposure is not necessary for serious damage to equipment. In fact, short-duration contamination events associated with accidents and upset conditions (especially during plant commissioning and startup) are sufficient to plant the seeds for future failure. Avoiding such events requires constant vigilance on the part of operators, with proper maintenance of the water treatment equipment to prevent leakages and deviations from OEM-specified contaminant levels. Some critical parameters such as *cation conductivity** must be monitored continuously for their target levels (e.g., less than several parts per billion by weight for the former). Others are checked less frequently (e.g., once or twice per week for silica and total organic carbon) or only during commissioning, regular maintenance, and troubleshooting periods.

Recommended on-line analysis/monitoring locations are condensate pump discharge, feedwater pump discharge, deaerator outlet, economizer inlet (HRSG), and boiler (evaporator) drum (blowdown line or down-comer). Some measurements can even lead to a plant shutdown (e.g., if the boiler water pH goes down below 8.0 for an HRSG per EPRI guidelines). For the modern, advanced GTCC plants with fast-start features, steam purity achievement is critical. Since the presence of CO₂ in the sample (via air in-leak in the condenser, for example) increases its conductivity (by about 5 μS/ppm of CO₂), *degassed* cation conductivity is recommended in order not to hold up the startup sequence due to artificially high conductivity readings.

13.17.2 Usage Minimization

The quantity and quality of global water resources has been a major concern for some time. Severe drought and resulting problems have even been associated with recent major sociopolitical problems in certain areas of the world. Combined with the uncertainty tied to climate change, water scarcity looms as an urgent problem facing humanity. Thus, conservation of precious freshwater resources is a major initiative of many governmental agencies, with a significant impact on electric power generation technology.

Consider that fossil fuel power systems, combined with nuclear power plants, accounted for nearly 40% of freshwater withdrawals in the United States (mainly as circulating cooling water for steam turbine condensers), while they accounted for 3% of freshwater consumption (via evaporation into the atmosphere or as moisture in disposed solid wastes) [166]. In terms of withdrawal, coal-fired steam power plants (along with nuclear power plants) utilize nearly three times more cooling water than gas-fired GTCC (i.e., 25,000–45,000 gal/MWh of generation with once-through open-loop systems or 550–800 gal/MWh for closed-loop systems with wet cooling tower) [167]. Furthermore, dry or wet FGD systems of coal-fired power plants consume an additional 40–80 gal/MWh of freshwater (none for GTCC with modern DLN combustion systems).

* A cation is a positively charged ion, for example, Na⁺; cations attract oxides and lead to corrosion. Elevated levels of cation conductivity indicate an increase in salts such as chlorides and sulfates.

While the consumption of freshwater by FFPS seems small, consider that a 500 MWe base-loaded coal-fired power plant, using the lower estimate, consumes annually $7000 \text{ h/year} \times 500 \text{ MWe} \times 550 \text{ gal/MWh} \sim 2 \text{ billion gal}$ of freshwater. The comparable number for a 500 MWe GTCC is about 500 million gal. Thus, the incentive for FFPS freshwater consumption minimization is quite strong. There are several options:

1. Use of water of a quality only as good as required by the power plant processes
2. Use of advanced (dry, hybrid, other) cooling systems
3. Reuse and recycling of power plant wastewater with requisite treatment
4. Proper selection of water treatment chemicals to reduce hazardous wastes
5. A combination of the above

One example for the first item is using *membrane distillation* (MD) technology to remove salts and other dissolved solids from brackish groundwater or seawater. Using the waste heat in the flue gas (say, downstream of the economizer prior to discharge to atmosphere through the stack), MD could be used to desalinate water without a penalty in terms of extra parasitic power consumption. There is ongoing research to establish the economic viability of applying MD to coal-fired power plants [43]. Another related concept is carbon nanotube-enabled MD, which can also be applied to cooling tower blowdown treatment [43].

By far the majority of fossil-fuel-fired power plants have wet cooling systems, which use water to condense the steam turbine exhaust. There are two types of wet cooling systems. Once-through, open-loop (OT-OL) systems utilize cold water from a natural reservoir (e.g., a lake, river, etc.) and return the warm condenser discharge (roughly by 20°F) water to the same reservoir. Closed-loop or recirculating systems with mechanical or natural draft cooling towers (CL-CT) circulate the cooling water, which gives up its heat to air, in counter- or cross-flow inside the tower. They began to replace the once-through cooling systems in the 1970s following the restrictions imposed by the Clean Water Act. A high-level comparison of currently available power plant heat rejection technologies, including the dry or air-cooled option, is provided in Table 13.32. (There are also hybrid systems [e.g., *Heller*], which use a combination of wet and dry cooling methods [159].)

TABLE 13.32

Fossil-Fuel-Fired Power Plant Heat Sink Options

	OT-OL	CL-CT	DRY (A/C)
Water withdrawal	10–100×	BASE (per unit kWh)	Negligible
Water consumption	~50%	BASE (per unit kWh)	0%–5%
Installed cost	BASE	~1.5×	4–6×
Parasitic power cons.	~1% of STG	~1.7% of STG	>2.0% of STG
Environmental Impact			
OT-OL	Mortality of marine organisms due to impingement and entrainment; thermal impact of heated water discharge		
CL-CT	Visible plume from CT forming localized fog or icing in freezing weather; higher pollutants per kWh than OT-OL (lower efficiency)		
Dry (A/C)	Largest footprint; highest pollutants per kWh than wet technologies (lowest efficiency)		

In 2008, about one-third of the electricity generated in the United States was by plants with once-through wet cooling systems and about half by plants with closed-loop wet cooling systems [166]. Only about 2% was by plants with dry or other cooling systems. However, concerns about water resource scarcity and other environmental regulations have been increasing, and expected to grow in future, leading to greater deployment of dry cooling systems (mostly, air-cooled condensers or A-Frame condensers [159]). Air-cooled condensers essentially reduce cooling water consumption to zero. Unfortunately, this benefit comes at the cost of increased parasitic power consumption by the forced-draft fans pushing the air through the condenser and reduced steam turbine output (higher backpressure). For a typical GTCC, the difference can be as much as 0.3% of gross plant output [78] or even more.

There are several new dry cooling technologies at various stages of development: thermosyphon cooling (TRL of 6), advanced M-cycle dew point cooling (TRL of 4), and adsorption chiller (TRL of 3) [43,166]. A high-level assessment of these technologies can be found in References 43 and 166.

13.17.3 Wastewater Treatment

Boiler or steam generator feedwater and makeup (raw) water treatment is critical to trouble-free operation of the power plant. Equally important is wastewater treatment prior to discharge to a receiving water body in order to comply with environmental regulations. A good example is wet FGD system purge or blowdown water in a coal-fired power plant, which contains many pollutants. The exact composition of FGD blowdown water shows a large variability depending on coal properties and system characteristics. Detailed information on FGD wastewater characteristics, treatment system options, equipment cost, and O&M considerations can be found in Reference 147. Gas turbine combined cycle power plants do not present as significant a challenge as coal-fired power plants since their wastewater mainly constitutes HRSG and cooling tower blowdown.

There are many different types of wastewater from FFPS processes, including boiler blowdown, drains, leakages, etc. There are several disposal options for treated wastewater: discharge to surface water (e.g., oceans, rivers, etc.), discharge to sewers, deep-well injection, or evaporation ponds. The first two are not permitted by regulatory agencies in many places. There are concerns associated with the latter two, for example, well-plugging, insufficient evaporation, lack of space, etc.

Wastewater can be in the form of liquid and *sludge* (e.g., from the FGD, boiler bottom ash removal system, etc.). Sludge is ultimately sent to a solid waste disposal system. Heavily polluted streams, for example, wastewater from the FGD (high chlorides, heavy metals, particulates—typically, 60–300 gpd/MWe) or flue gas condensate, are sent to an evaporation pond. If one is not available, they have to be treated for discharge or (if possible) reuse. FGD wastewater treatment requires special care. It contains PM such as gypsum, unreacted limestone, inert materials from raw limestone, fly ash, and unburnt coal. Dissolved impurities are metal cations from coal (fly ash and volatiles) and limestone (e.g., Cd, Hg, Ag, Cu, Fe, Mn, Mo, Ni, Pb, Sn, V, Zn), metal oxy-anions (e.g., As, Sb, Se, B), anions mainly from Cl and F in the fuel, sulfates, and trace amounts of nitrate. Treatment steps include the following [147]:

- pH is increased with an alkali (NaOH or Ca(OH)₂) to precipitate metal hydroxides.
- A sodium sulfide solution is added to precipitate metal sulfides.
- A coagulant (e.g., ferric chloride) is added to capture precipitated hydroxides and sulfides as well as fine PM.

- A flocculation aid (polymer) is added to promote settlement of sludge.
- Water and sludge are separated in a clarifier and sludge thickener.
- Sludge is dried and disposed to a landfill or re-fired with coal.
- Clarified water is pH adjusted with HCl and polished by gravity filtration to enhance total suspended solids and metals reduction prior to discharge.

Wastewater from the boiler blowdown and certain drains (e.g., feedwater storage tank, boiler, sampling system, etc.) is collected in an oil-free basin and either discharged (if permitted) or sent to a WWT. Wastewater from miscellaneous cooler drains, operation leakages, and other “less clean” sources is collected in a drain pit and sent to a central *wastewater treatment plant* (WWT).

Wastewater from maintenance activities (e.g., boiler lay-up drains, boiler cleaning water, etc.) is neutralized and collected in a separate pit before being sent to a WWT.

Reverse osmosis (RO) is the most widely used technology to purify water. It is a membrane technology using an applied pressure to overcome osmotic pressure. Thus, water is forced from a region of high concentration through a semipermeable membrane to a region of low concentration. Newer technologies include *forward osmosis* (FO) and *membrane bioreactor* (MBR), which combines biological treatment with conventional filtration. The former is also a membrane technology, which, unlike the RO using hydraulic pressure as the driving force, uses a “draw” solution of high concentration of ammonium bicarbonate to induce a net flow of water through the semipermeable membrane into the draw solution. Separation of clean water from the diluted draw solution takes place in a heated recovery vessel via evaporation. Forward osmosis can treat water up to four times as concentrated water as that treated by conventional RO systems.

13.17.4 Zero Liquid Discharge

Power plant wastewater recovery for reuse and recycling is the driving force underlying the high recovery (92% to +99%) and *zero liquid discharge* (ZLD) systems. Available technologies can be classified broadly in two groups:

1. Thermal evaporation (brine concentrator and crystallizer)
2. Membrane technology (reverse osmosis, RO)
 - a. Conventional RO (65%–85% recovery)
 - b. High-recovery RO (i.e., two-stage RO used in seawater desalination)
 - c. High-efficiency reverse osmosis or HERO™

These two technologies can be deployed alone or combined, resulting in *five* basic configurations:

1. Thermal evaporation
 - a. Brine concentrator (BC) only (with evaporation pond or deep-well injection)
 - b. Brine concentrator and crystallizer (solidification for landfill)
2. Combined
 - a. Softener and reverse osmosis with brine concentrator
 - b. Softener and reverse osmosis with brine concentrator and crystallizer
3. Softener and reverse osmosis only (with evaporation pond or deep-well injection)

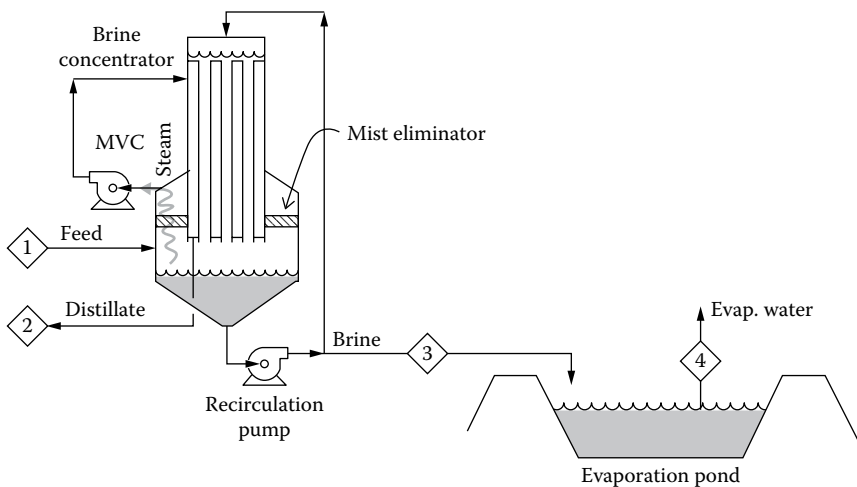


FIGURE 13.85

Thermal evaporation system with evaporation pond. (From Mickley, M., Survey of high-recovery and zero liquid discharge technologies for water utilities, WRF-02-006a, WaterReuse Foundation, Alexandria, VA, 2008.)

These five configurations are described in detail and compared with each other in terms of cost and performance in [128]. The most widely deployed system is thermal evaporation, which is shown in Figure 13.85. Feed 1 is wastewater (e.g., GTCC cooling tower blowdown) heated close to its atmospheric boiling temperature by recovering heat from distillate 2 (the heat exchanger is not shown). Deaerated feed (to remove corrosive and scale-forming constituents) is introduced into the BC sump, where it is mixed with concentrated slurry (brine), which is continuously recirculated to the top of the BC evaporator column. The evaporator is a vertical tube heat exchanger. The brine falls down the evaporator while forming a thin film on the inside of the tubes, from which water evaporates into steam flowing down along with the brine. Upon exiting the tubes at the top of the sump, steam flows through mist eliminators and enters the *mechanical vapor compressor* (MVC). The MVC (usually a centrifugal fan) increases the pressure and temperature of steam. It consumes about 70–90 kW/1000 gal/h of feed. This provides the heat for evaporation of water from the brine, which is supplied by the latent heat of evaporation of compressed steam on the shell side of the evaporator. The condensed water flows down the tubes (outside) and is collected as distillate in the evaporator bottom. Concentrated brine 3 from the BC is sent to an evaporation pond or to a steam-driven *crystallizer* (steam consumption is equivalent to 150–200 kWh/1000 gal/h of BC feed). Distillate 2 from the BC is ready for reuse in the power plant. The water recovery rate in the BC is in the range of 90%–99%.

Selection of a particular ZLD system configuration requires a careful performance–cost trade-off study on a case-by-case basis. Performance herein is the rate of recovery, that is, water recovered for reuse in the power plant as a percentage of the ZLD plant feedwater. The main drivers are quantity of feedwater and water quality (i.e., total dissolved solids [TDS], composition of cations and anions, total hardness [TH], silica content, etc.). There are little economies of scale, that is, multiple trains are required for the larger sizes.

In general, for low TDS feedwater, the best option is a membrane-only system with an evaporation pond. For all others, a combined system comprising pretreatment with a membrane system followed by thermal evaporation is the best option. In such an arrangement with

several components or subsystems in series, the overall system reliability is low (product of reliabilities of individual components). When one component breaks down, the entire ZLD system breaks down (i.e., forced outage or decreased processing capacity). Since the power plant cannot run when the ZLD system is down, this has a big impact on plant availability.

The simplest way to address the reliability problem is storage. Storage options are brine- and concentrate-holding tanks and/or storage ponds. The latter essentially disconnects the ZLD system from the power plant to enable continued power generation while the ZLD system is in forced or planned outage. Factoring in the capital cost of sufficient storage and including design margins to account for system degradation can change the cost picture significantly [150].

Consequently, taking into consideration the probability of a forced outage and capacity degradation when calculating annualized unit cost, one may very well end up with a simple brine concentrator (with evaporation pond) or softener plus RO system and evaporation pond (where feasible) as the most optimal solution. It should be pointed out that the latter may not be an option for sites with very high TDS feedwater. Another, guaranteed to be more expensive in terms of upfront capital expenditure, solution is a multitrain design with parallel components, that is, $2 \times 50\%$ or $3 \times 50\%$. Depending on the resulting overall system reliability without resorting to a large storage capacity, this may also be a feasible path. The ultimate solution can only be determined by a detailed analysis on a case-by-case basis.

General industry experience suggests that ZLD systems are notoriously difficult, costly, and time-consuming processes to operate and maintain [55,150]. Investigation of the possibility of other options such as subsurface (deep well) injection and evaporation ponds is critical.

ZLD system selection should be made after a diligent analysis of raw water chemistry (average, best, and worst cases), site ambient conditions, and environmental regulations and/or permits pertaining to the final disposal of the concentrate (liquid and/or solid). Important lessons learned are summarized as follows:

- System capacity/sizing with ample margin (i.e., the worst-case scenario under *fouled* conditions should be considered—especially brine concentrator and crystallizer heat exchangers).
- Redundancy of certain critical components should be carefully evaluated.
- Materials selection (opting for cheaper materials to save capex may not be a good idea—for example, use alloy steel for crystallizer feed-tank fabrication).
- Availability of ample spares (e.g., smaller pumps, pump motors, MVC impeller, bearings, etc.).
- Availability of storage tanks (to ensure continued operation when the system or a subsystem is down).
- Availability of substitute steam source (in case of brine concentrator MVC outage).

ZLD systems can add significantly to the parasitic power burden of a power plant. For example, at 40–80 gal/MWh, MVC power consumption for a ZLD system treating the FGD blowdown of a coal-fired power plant is anywhere between 2 and 4 MWe. Clearly, dry FGD systems such as SDA are more advantageous from a ZLD perspective (i.e., less blowdown). Minimization of blowdown rate is critical for reliable and economic system operation (e.g., by increasing the allowable chloride concentration). The impact on construction materials, overall system cost, and O&M expenditure must be carefully balanced for an optimal system design (e.g., see [94]).

The impact of ZLD requirement on GTCC parasitic power consumption can be onerous as well. Cooling tower makeup water requirement of a typical GTCC is 220 gal/MWh. For a 500 MWe power plant, this comes to about 1850 gpm, which covers the cooling tower water loss via evaporation (ignoring the drift), E , and blowdown, B . For a cycle of concentration (CoC) of 5, E and B can be determined from

$$E + B = 1850$$

$$\text{CoC} = 5 = (E/B) + 1$$

as $E = 1480$ gpm and $B = 370$ gpm. At 90 kWh/1000 gal of feed, brine concentrator MVC would consume nearly 2 MWe of power. One should also add the lost ST output via steam provided to the crystallizer to that amount (if one is present). The impact on plant performance is significant. Assuming that the GTCC in question is an advanced H or J class unit rated at 60% net efficiency with auxiliary power consumption at 2% of gross, addition of the ZLD reduces the net efficiency to $498/500 \times 60 = 59.76\%$.

There are several new technologies for “volume reduction” (i.e., reducing the feed flow to the brine concentrator to reduce its size or completely eliminate it) for high recovery at various stages of development. Respective approaches taken by these technologies and their development status can be found in [128]. The most common and commercially available approach is *high efficiency reverse osmosis* (HERO), which involves chemical pretreatment of the feedwater to remove its hardness and raise its pH before it is subjected to RO. Depending on the particular wastewater characteristics, the HERO process has a 95%–99% recovery effectiveness.

13.18 Recap

A wide variety of advanced power systems for electric power generation via combustion of fossil fuels have been reviewed. The coverage included synthetic fuels, in addition to coal and natural gas, as well as treatment systems requisite for environment-friendly power generation. Many of the covered advanced technologies have not progressed beyond TRL 4 or 5. As one can deduce from the narrative and references, some have not been a focus of ongoing R&D for the last decade or more. Pilot or demo plants projected to have been in place and running by the time of this writing (late 2015) have either not materialized or have failed to make it to the next step. Some promising technologies are still in the early development stage (TRL 4–5).

The two workhorses of the industry, coal-fired boiler and natural gas-fired gas turbine combined cycle power plants, are very likely to carry the burden in the foreseeable future as well. They will continue to do so in their own advanced variations: ultra-supercritical steam cycles with very high pressures and temperatures (definitely), CFB systems with supercritical steam cycles (most likely), and J class and next-generation gas turbines with 1700°C turbine inlet temperatures (definitely).

Advanced USC and GTCC power plants with post-combustion combined cycle addition have so far failed to become a commercially accepted reality. Whether they will become so in the future remains to be seen. Three uncertainties will play a key role in the outcome: legislation, technology selection, and sequestration options.* Based on everything that is

* The uncertainty in the future of CCS technology was highlighted by the withdrawal of 1 billion GBP promised by the UK government to the winner of the two CCS projects in competition in November 2015.

known today, the amine-based post-combustion scrubbing method is the apparent solution. Nevertheless, requisite capital investment is substantially high and the risk of the technology becoming obsolete and turning a facility built on it into a stranded asset is not small either. (One factor in favor of *add-on* post-combustion combined cycle option without excessive integration with the power block [or as a retrofit to an existing power plant] is that, in the event of a system failure, it can simply be switched off while electricity generation goes on unimpededly. In that sense, unlike the other two CCS options, at least the most important part of the facility will survive.)

Even after several plants with years of commercial operation under their belt, IGCC technology is still an unattractive option for the power market. The biggest obstacle that IGCC has not been able to fully overcome is its high cost and (comparatively) low efficiency not commensurate with its price tag. The latter is exacerbated by the fact that field experience suggests that, from an operability and maintenance perspective, high-level integration between the ASU and the GT (a must for optimal performance) is a liability. Unavoidably, any existing cost, performance, operability, and O&M issue is exacerbated when IGCC is combined with CCS and multiplied by the addition of new ones. Cost and schedule overrun difficulties encountered by ongoing projects in the United States have been mentioned earlier in the chapter. Another cautionary tale worth mentioning is the 450 MWe “carbon free” IGCC–CCS project, which had been announced by a large German utility in 2006 to go into service in 2014. In 2010, the project was suspended indefinitely primarily due to a lack of political support and public acceptance pertaining to the pipeline and final storage space.*

As of 2015, none of the DOE CCS programs have evolved above TRL 6 [68]. The Kemper County IGCC plant (which experienced significant cost and schedule overruns) will be the first IGCC plant with CCS and, if successful, would be at TRL 8. The Petra Nova post-combustion CCS–EOR plant would be at TRL 7. The Boundary Dam demonstration project would be at TRL 7, after some longer period of successful operation. (Commercialization occurs after the successful completion of TRL 9—see Section 13.4 for more on this.)

With all those caveats in mind, the most likely mixture of proven and projected advanced FFPS technologies that will be the focus of the industry and research communities in the near future is summarized in Table 13.33. While the last two in Table 13.33 (both based on fuel cell technology) are very long shots at this point, their projected performance is so attractive that they will be on the table until the technological and/or cost challenges prove insurmountable.†

The other technologies (except the oxy-fuel SCO_2 technology) do not present a technology risk as long as (1) design parameters do not exceed those with established experience base and (2) no carbon capture feature is present. Technology risk (performance and RAM) and cost will determine whether owners, lenders, and insurers will deem the returns attractive enough to finance the first few proposed advanced plants. After that, it is a question whether the technology will operate long enough in the field while accumulating valuable experience that will translate into robust future designs at acceptable capital cost so that the installed base will increase to a point where the industry can declare the technology mature. While this is an onerous requirement, one should consider the large capital expenditure involved in building a utility-scale power plant (billions of dollars) and the risks involved in securing a financial return on that expenditure.

* Interested readers can google “RWE’s 450 MW IGCC–CCS project in Hürth near Köln.”

† A very recent article, published right after the completion of the current chapter’s final draft, goes over a very similar technology landscape and provides detailed performance and CO_2 emission data for most of the technologies in Table 13.32 and their variants (based on several related EPRI studies) [137] with similar conclusions and predictions.

TABLE 13.33

Advanced Fossil Fuel Power Systems in the First Quarter of the Twenty-First Century

Technology	Acronym	TRL	Capex	Capex w/CCS	LHV Efficiency (%) Current (2015)	Long-Term Potential (% LHV)	CCS Derate to Net Output
Gas turbine combined cycle	GTCC	Commercial	Base	+30%–40%	58–59 (F Class) 60+ (J Class)	Target: 65	–10%to –12%
Supercritical pulverized coal	(U)SCPC	Commercial	3–4 X	+50%–60%	39–41 (supercritical) 42–47 (ultra-Supercritical)	Target: 50 with Advanced USC	–20% to –25%
Integrated gasification combined cycle	IGCC	8–9 commercially viable	5 X	+40%	37–42	46-50 with H/J GT and Membrane ASU	–10% to –15%
Pressurized fluidized bed combustion	PFBC	8–9 commercially viable	>SCPC	>SCPC	40–42	50 with advanced PFBC	~SCPC
Atmospheric fluidized bed combustion	AFBC	Commercial	>SCPC	>SCPC	35-37	40 with supercritical cycle	~SCPC
Oxyfuel supercritical CO ₂	OF- SC02	5–6	TBD	Incl.	Not available	~50	Incl.
Fuel cell—GTCC	FC-GTCC	3–4	TBD	TBD	Not available	70+	~GTCC
Pressurized integrated gasification fuel cell	IGFC	3–4	TBD	Incl.	Not available	Target: 60+	Incl.

Note: TBD, to be determined.

Two items in Table 13.33 should be emphasized. First of all, the “Capex” in the table refers to the TPI discussed in Section 13.7. Its closest real-life approximation is the *lump-sum turnkey* (LSTK) amount agreed upon by the owner/developer and the EPC contractor at the beginning of a project. It can be estimated with reasonable certainty only for those projects that are amenable to a certain level of modularization, automation, and repetition (e.g., the *reference plant* concept) based on extensive experience with similar projects in the past. (See more on this in Section 13.7)

Second, the efficiencies in the table are “sticker” values (e.g., ISO base load rating for the GTCC), that is, they do *not* represent the day-to-day operating performance of a commercial unit in the field. Based on the Form EIA 923 “Power Plant Report” published annually by the U.S. EIA, the average efficiency of the top 20 GTCC in the United States in 2014 was 54.7% (LHV) with an average capacity factor of 54%.^{*} The corresponding numbers for the top 20 coal-fired power plants in the United States was 36.1% (HHV)[†] and 66%, respectively.

Finally, many of the technologies discussed in this section can be combined into a *poly-generation* plant (see Figure 13.86). While similar in spirit to PC and IGCC plants with saleable by-products (e.g., slag, ash, gypsum, sulfuric acid, etc.), this is a much more ambitious

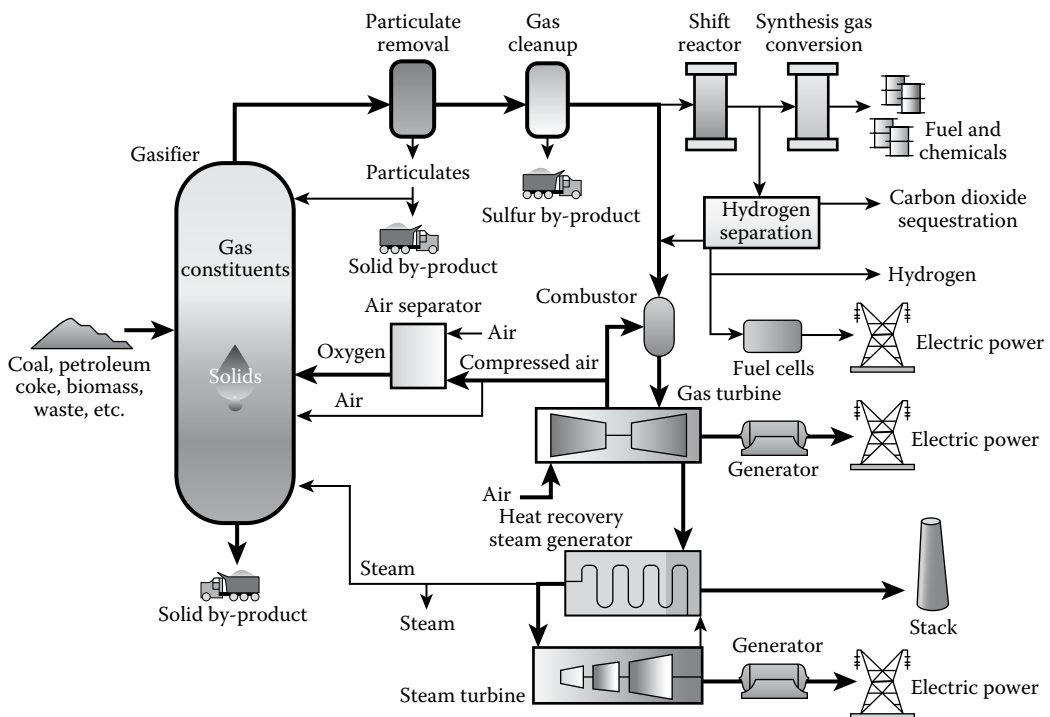


FIGURE 13.86
Polygeneration power plant concept. (Courtesy of DOE/NETL.)

^{*} The data does not allow the calculation of load factor and site ambient characteristics. Thus, converting to an approximate ISO base load rating is not possible.

[†] Numbers are reported in HHV. Due to the variety in HHV/LHV ratios for different coals, converting the average heat rate to LHV basis is not possible.

concept, which is designed from the get-go to be a *bona fide* producer of multiple products (including electric power) in significant quantities. In fact, the two active U.S. projects with CCS are envisioned as polygeneration plants (fertilizer is the other plant product). The idea of an industrial facility with multiple, high-value revenue streams to relieve the cost pressure imposed by CCS to enable burning widely available but environmentally undesirable fossil fuels is undoubtedly intriguing. Nevertheless, the challenges imposed by the immense complexity of a project of this scope severely impacting every conceivable phase of it (development, financing, permitting, front-end engineering design, construction, and, finally, operating and maintaining the facility) are enormous as well. The only conceivable path to fruition is probably limited to those cases where infrastructure already exists and the owner/operator (e.g., a refinery) is willing to share in the development and operations.

References

The following references are listed in alphabetical order by the lead author's name (or the lead editor's name for handbooks). If there are more than three authors, those other than the lead author are grouped by et al. For anonymous works (e.g., reports by agencies, technical standards, etc.), the document title is used for their placement in the list.

General References

These are books that are indispensable for a thorough understanding of fossil-fuel-fired electric power generation technologies.* They include textbooks covering the three fundamental mechanical engineering disciplines (thermodynamics, heat transfer, and fluid mechanics), specialty books on turbomachinery and other major plant equipment and treatises on costing and optimization. Most are excellent sources that a practitioner can frequently turn to for help in day-to-day tasks as well as for learning new subjects. Some are classics providing a valuable historical perspective but contain long-forgotten gems that can still spark new ideas. Note that some books do have updated editions (newer than those in the author's library, which are cited as follows). The reader is encouraged to search for and obtain those newer editions.

1. Baumeister, T. (Editor-in-Chief), 1978, *Marks' Standard Handbook for Mechanical Engineers*, 8th edn., McGraw-Hill, Book Company Inc., New York.
2. Bejan, A., Tsatsaronis, G., Moran, M., 1996, *Thermal Design and Optimization*, John Wiley & Sons, New York.
3. Davis, J.R. (Ed.), 1999, *Heat-Resistant Materials*, ASM Specialty Handbook, ASM International, Materials Park, OH.
4. Elliott, T.C. (Ed.), 1989, *Standard Handbook of Powerplant Engineering*, McGraw-Hill, Book Company Inc., New York.
5. El-Wakil, M.M., 1984, *Powerplant Technology*, McGraw-Hill, Inc., New York.

* Unavoidably, this is a subjective list. While it is hard to think that there would be a disagreement on the place of works by Stodola or Traupel or industry standards such as *Steam* by Babcock & Wilcox in the *pantheon* of technical literature, some quibble on the worthiness of each and every item in the list is to be expected. Nevertheless, it is a starting point for the novice reader. For the rest, undoubtedly, the best resource is their personal library.

6. Fitzgerald, A.E., Kingsley, Jr., C., Kusko, A., 1971, *Electric Machinery*, 3rd edn., McGraw-Hill, Inc., New York.
7. Incropera, F.P., DeWitt, D.P., 2002, *Introduction to Heat Transfer*, 4th edn, John Wiley & Sons, New York.
8. Khartchenko, N.V., 1998, *Advanced Energy Systems*, Taylor & Francis, Washington, DC.
9. Lakshminarayana, B., 1996, *Fluid Dynamics and Heat Transfer of Turbomachinery*, John Wiley & Sons, New York.
10. Landau, L.D., Lifshitz, L.M., 1987, *Fluid Mechanics*, 2nd edn., Pergamon Press, London, U.K.
11. Lefebvre, A.H., 1983, *Gas Turbine Combustion*, Hemisphere Publishing Corporation, Washington, DC.
12. Leyzerovich, A.S., 2007, *Steam Turbines for Modern Fossil-Fuel Power Plants*, CRC Press, The Fairmont Press Inc., Lilburn, GA.
13. Lieuwen, T., Yang, V., Yetter, R. (Eds.), 2010, *Synthesis Gas Combustion—Fundamentals and Applications*, CRC Press, Boca Raton, FL.
14. Moran, M.J., Shapiro, H.N., 1988, *Fundamentals of Engineering Thermodynamics*, John Wiley & Sons, New York.
15. Peters, M.S., Timmerhaus, K.D., West, R.E., 2004, *Plant Design and Economics for Chemical Engineers*, 5th edn., Mc-Graw Hill, Inc., New York.
16. Probst, R.F., Hicks, R.E., 2006, *Synthetic Fuels*, Dover Publications, Inc., Mineola, NY.
17. Randtke, S. J., Horsley, M.B. (Eds.), 2012, *Water Treatment Plant Design*, 5th edn., McGraw-Hill, Book Company Inc., New York.
18. Saravanamuttoo, H.I.H. et al., 2009, *Gas Turbine Theory*, 6th edn., Pearson Education Limited, Harlow, U.K.
19. Babcock & Wilcox Company, 2015, *Steam, Its Generation and Use*, 42nd edn., Babcock & Wilcox Company, New York.
20. Stodola, A., 1927, *Steam and Gas Turbines*, 6th German edn., Löwenstein, L.C. (Ed.), Vol. 2, pp. 1237, McGraw-Hill Book Company Inc., New York.
21. Strehlow, R., 1984, *Combustion Fundamentals*, McGraw-Hill, New York.
22. Thompson, P.A., 1988, *Compressible Fluid Dynamics*, Advanced Engineering Series, McGraw-Hill, Inc., New York.
23. Traupel, W., 2001, *Thermische Turbomaschinen*, Band I-II, 4. Auflage, Springer Verlag, Berlin, Germany. (Unfortunately, it is not yet translated to English.)
24. Viswanathan, R., 1989, *Damage Mechanisms and Life Assessment of High-Temperature Components*, ASM International, Metals Park, OH.
25. Wilcox, J., 2014, *Carbon Capture*, Springer, New York.

References Cited in the Text

26. Ahngers, A., 2007, Engine combined cycle (ECC) with internal combustion engines, *Wärtsila Technical Journal*, 2, 4–6.
27. Allam, R.J. et al., 2014, The oxy-fuel, supercritical CO₂ Allam cycle, ASME Paper GT2014-26952.
28. Allam, R.J., 2013, Net power's CO₂ cycle: The breakthrough that CCS needs, *Modern Power Systems*, July 2013.
29. Alternative control techniques document—NO_x emissions from stationary gas turbines, U.S. Environmental Protection Agency, EPA-453/R-93-007, January 1993, Office of Air and Radiation, Office of Air Quality Planning and Standards, Research Triangle Park, NC.
30. Anderson, R. et al., 2010, Oxy-fuel gas turbine, gas generator and reheat combustor technology development and demonstration, ASME paper GT2010-23001.
31. Anderson, R.E. et al., 2008, Adapting gas turbines to zero-emission oxy-fuel power plants, ASME Paper GT2008-51377.
32. Available and emerging technologies for reducing greenhouse gas emissions from coal-fired electric generating units, October 2010, Sector Policies and Programs Division Office of Air Quality Planning and Standards, U.S. Environmental Protection Agency, Research Triangle Park, NC.

33. Baburao, B. et al., 2014, Advanced amine process technology operations and results from demonstration facility at EDF Le Havre, *Energy Procedia*, 63, 6173–6187.
34. Baldwin, P., Williams, J., 2009, Capturing CO₂: Gas compression vs. liquefaction, *Power*, June, 68–71.
35. Balevic, D., Burger, R., Forry, D., 2004, Heavy-duty gas turbine operating and maintenance considerations, GER-3620K, GE Energy.
36. Beér, J.M., 2000, Combustion technology developments in power generation in response to environmental challenges, *Progress in Energy and Combustion Science*, 26, 301–327.
37. Bhargava, R.K. et al., 2010, Parametric thermodynamic evaluation of high performance gas turbine based power cycles, *Journal of Engineering for Gas Turbines and Power*, 132, 022001.
38. Bielawski, G.T., 2013, Air quality control system choices for U.S. utility power plants, *Power-Gen International 2013*, Orlando, FL, November 12–14, 2013.
39. Bolland, O., Kvamsdal, H.M., Boden, J.C., 2001, A thermodynamic comparison of the oxy-fuel power cycles, *Proceedings of the International Conference on Power Generation and Sustainable Development*, Liège, Belgium, October 8–9, 2001, p. 6.
40. Botero, C. et al., 2008, Redesign, optimization and economic evaluation of a NGCC with the best integrated technology CO₂ capture, *Energy Procedia*, 1, 3835–3842.
41. Botero, C. et al., 2009, Thermoeconomic evaluation of CO₂ compression strategies for CO₂ capture applications, GT2009-60217, *ASME Turbo Expo 2009*, Orlando, FL, June 8–12, 2009.
42. Bromley, A.F., 2006, Attention to detail critical for maintaining high availability when firing liquid fuels, *Combined Cycle Journal*, 3rd Quarter, 33–39.
43. Bushart, S., Shi, J., 2014, Advanced cooling and water treatment technology concepts for power plants, *Power*, April, 62–67.
44. Butz, J., 2014, Non-carbon reagent injection for MATS compliance, *Power*, October, 62–65.
45. Campanari, S., Macchi, E., 1998, Thermodynamic analysis of advanced power cycles based upon solid oxide fuel cells, gas turbines, and Rankine bottoming cycles, ASME Paper 98-GT-585.
46. Carbon Capture Technology Program Plan, Clean Coal Research Program, U.S. DOE, Office of Fossil Energy, NETL, January 2013.
47. Cartwright, P., 2006, Process water treatment—Challenges and solutions, *Chemical Engineering*, March, 50–56.
48. Chen, L., Nolan, R., Avadhany, S., 2009, *Thermodynamic Analysis of Coal to Synthetic Natural Gas Process*, Mechanical Engineering Department, Massachusetts Institute of Technology, Cambridge, MA.
49. Chiesa, P., Lozza, G., Mazzocchi, L., 2005, Using hydrogen as gas turbine fuel, *Journal of Engineering for Gas Turbines and Power*, 127(1), 73–80.
50. Chiesa, P., Macchi, E., 2004, A thermodynamic analysis of different options to break 60% electric efficiency in CC power plants, *Journal of Engineering for Gas Turbines and Power*, 126, 770–785.
51. Clark, D.R., Oechsner, M., Padture, N.P., 2012, Thermal barrier coatings for more efficient gas turbine engines, *MRS Bulletin*, 37, 891–897.
52. Cleetus, R. et al., Ripe for retirement: The case for closing America's costliest coal plants, Union of Concerned Scientists, November 2012.
53. CO₂ capture ready plants, International Energy Agency (IEA) Greenhouse Gas R&D Programme, Technical Study Report Number: 2007/4, May 2007.
54. Collodi, G., 2010, Hydrogen production via steam reforming with CO₂ capture, *Proceedings of the Fourth International Conference on Safety and Environment in the Process Industry (CISAP4)*, Florence, Italy, March 14–17, 2010.
55. Como, V.A., Cannon, T., Mueller, M., 2013, Operating a ZLD, what does it take? *Proceedings of the 74th Annual International Water Conference*, Orlando, FL, November 17–21, 2013.
56. Conboy, T. et al., 2012, Performance characteristics of an operating supercritical CO₂ Brayton cycle, *Journal of Engineering for Gas Turbines and Power*, 134, 111703.
57. Connors, J., 2009, *The Engines of Pratt & Whitney: A Technical History*, AIAA Library of Flight, Reston, VA.

58. Coombs, K.A. et al., 2004, SCR levels of NO_x reduction with ROFA and Rotamix (SNCR) at dynegey's vermilion power station, *2004 Stack Emissions Symposium*, Clearwater Beach, FL, July 28–30, 2004.
59. Cost estimation methodology for NETL assessments of power plant performance, U.S. DOE report DOE/NETL-2011/1455, April 2011.
60. Cox, J.C., Hutchinson, D., Oswald, J.I., 1995, The Westinghouse Rolls-Royce WR-21 gas turbine variable area power turbine design, 95-GT-54, *Proceedings of the International Gas Turbine and Aeroengine Congress and Exposition*, Houston, TX, June 5–8, 1995.
61. Daal, L. et al., 2012, Evaluation of different water vapor capture technologies and energy modeling results for membrane technology, Project CapWa, www.watercapture.eu.
62. Davis, L.B., Black, S.H., 2000, Dry low NO_x combustion systems for GE heavy-duty gas turbines, GER-3568G.
63. Downloaded on 11/10/2015 from <http://www.powermag.com/saskpower-admits-to-problems-at-first-full-scale-carbon-capture-project-at-boundary-dam-plant/>.
64. Fiala, S.N., 1957, First commercial supercritical-pressure steam-electric generating unit for philo plant, *Transactions American Society of Mechanical Engineering*, 79, 389–407.
65. Fickett, W., Davis, W.C., 1979, *Detonation*, University of California Press.
66. Fisk, R.W., VanHousen, R.L., 1996, Cogeneration application considerations, GER-3430F, GE Energy.
67. Fleming, D. et al., 2012, Scaling considerations for a multi-megawatt class supercritical CO₂ Brayton Cycle and Path Forward for Commercialization, GT2012-68484, *ASME Turbo Expo*, Copenhagen, Denmark, June 11–15, 2012.
68. Fossil forward: Revitalizing CCS bringing scale and speed to CCS deployment, Study Report by National Coal Council, info@NCC1.org, Washington, DC.
69. Foy, K., Yantovsky, E., 2006, History and state-of-the-art of fuel fired zero emission cycles, *International Journal of Thermodynamics*, 9(2), 37–63.
70. Frutschi, H.U., 2005, *Closed Cycle Gas Turbines*, ASME Press, New York.
71. *Gas Turbine World 2014–2015 Handbook*, Vol. 31, p. 66, Pequot Publishing Inc., Fairfield, CT.
72. *Gas Turbines—Acceptance Tests, International Standard ISO 2314*, 2nd edn., 1989-05-01, International Organization for Standardization, Genève, Switzerland.
73. Grace, D., Christiansen, T., 2012, Risk based assessment of unplanned outage events and costs for combined cycle plants, GT2012-68435, *ASME Turbo Expo 2012*, Copenhagen, Denmark, June 11–15, 2012.
74. Greb, S.F. et al., 2010, Storing and using CO₂ for enhanced coalbed methane recovery in unmineable coal beds of the Northern Appalachian Basin and parts of the Central Appalachian Basin, MRCSP Phase II Topical Report, DOE Cooperative Agreement No. DE-FC26-05NT42589, OCDO Grant Agreement No. DC-05-13.
75. Guangxi, Y., Wen, L., Li, N., 2015, China brings online the world's first 600-MW, supercritical CFB boiler, *Cornerstone*, Spring, 43–47.
76. Gülen, S.C., 2010, A proposed definition of CHP efficiency, *Power*, June, 58–63, www.powermag.com.
77. Gülen, S.C., 2010, Gas turbine with constant volume heat addition, ESDA2010–24817, *ASME 2010 10th Biennial Conference on Engineering Systems Design and Analysis*, Istanbul, Turkey, July 12–14, 2010.
78. Gülen, S.C., 2011, Importance of auxiliary power consumption on combined cycle performance, *Journal of Engineering for Gas Turbines and Power*, 133, 041801.
79. Gülen, S.C., 2013, Constant volume combustion: The ultimate gas turbine cycle, *Gas Turbine World*, November/December, 20–27.
80. Gülen, S.C., 2013, Gas turbine combined cycle fast start: The physics behind the concept, *Power Engineering*, June, 40–49.
81. Gülen, S.C., 2013, Modern gas turbine combined cycle, *Turbomachinery International*, November/December, 31–35.
82. Gülen, S.C., 2013, Performance entitlement of supercritical steam bottoming cycle, *Journal of Engineering for Gas Turbines and Power*, 135, 124501.

83. Gülen, S.C., 2014, General electric—Alstom merger brings visions of the Überturbine, *Gas Turbine World*, July/August, 28–35.
84. Gülen, S.C., 2015, Combined cycle trends: Past, present and future, *Turbomachinery International Handbook 2016*, pp. 24–26.
85. Gülen, S.C., 2015, Étude on gas turbine combined cycle power plant—Next 20 years, *Journal of Engineering for Gas Turbines and Power*, 138, 051701.
86. Gülen, S.C., 2015, Powering sustainability with gas turbines, *Turbomachinery International*, September–October, 24–26.
87. Gülen, S.C., 2015, Repowering revisited, *Power Engineering*, November, 34–44.
88. Gülen, S.C., 2015, What is the worth of 1 Btu/kWh of heat rate, *Power*, June, 60–63, www.powermag.com.
89. Gülen, S.C., Driscoll, A.V., 2013, Simple parametric model for quick assessment of IGCC Performance, *Journal of Engineering for Gas Turbines and Power*, 135, 010802.
90. Gülen, S.C., Jones, C.M., 2011, GE's next generation CCGT plants: Operational flexibility is the key, *Modern Power Systems*, June, 16–18.
91. Gülen, S.C., Mazumder, I., 2013, An expanded cost of electricity model for highly flexible power plants, *Journal of Engineering for Gas Turbines and Power*, 135, 011801.
92. Gülen, S.C., Smith, R.W., 2010, Second law efficiency of the Rankine bottoming cycle of a combined cycle power plant, *Journal of Engineering for Gas Turbines and Power*, 132, 011801.
93. Hall, J.M. et al., 2011, Development and field validation of a large-frame gas turbine power train for steel mill gases, GT2011-45923, *ASME Turbo Expo 2011*, Vancouver, British Columbia, Canada, June 6–10, 2011.
94. Hansen, B.D., 2006, Minimizing FGD costs, burns & McDonnell Technical Paper, www.burn-smcd.com.
95. Held, T.J., 2014, Initial test results of a megawatt class supercritical CO₂ heat engine, *The Proceedings of the Fourth International Symposium on Supercritical CO₂ Power Cycles*, Pittsburgh, PA, September 9–10, 2014.
96. Hejzlar, P. et al., 2006, Assessment of gas cooled fast reactor with indirect supercritical CO₂ cycle, *Nuclear Engineering and Technology*, 38(2), 109–118.
97. Higgins, T.E., Sandy, A.T., Givens, S.W., 2009, Flue gas desulfurization wastewater treatment primer, *Power*, March.
98. Holt, N.A.H., 2003, Operating experience and improvement opportunities for coal based IGCC plants, *Materials at High Temperatures*, 20(1), 1–6.
99. Horgler, O.J. (Ed.), 1965, *Metals Engineering Design*, *ASME Handbook*, McGraw-Hill Book Co., New York.
100. Iijima, M. et al., 2011, MHI's energy efficient flue gas CO₂ capture technology and large scale CCS demonstration test at coal-fired power plants in USA, *Mitsubishi Heavy Industries Technical Review*, 48(1), 26–32.
101. Ito, E. et al., 2011, Development of key technologies for an ultra-high-temperature gas turbine, *Mitsubishi Heavy Industries Technical Review*, 48(3).
102. Iyengar, A.K.S. et al., 2013, Performance and cost of a natural gas fuel cell plant with complete internal reformation, DOE/NETL-2014/1635.
103. Jacobs III, J.A., Schneider, M., 2009, Cogeneration application considerations, GER-3430G, GE Energy.
104. Jäntti, T., Räsänen, K., 2011, Circulating fluidized bed technology, towards 800 MWe scale—Lagisza 460 MWe supercritical CFB operation experience, *Powergen Europe*, Milan, Italy, June 7–9, 2011.
105. Jericha, H., Fesharaki, M., 1995, The graz cycle—1500°C max. temperature potential H₂–O₂ fired CO₂ capture with CH₄–O₂ firing, ASME Paper 95-CTP-79.
106. Jevons, W.S., 1906, *The Coal Question*, 3rd edn., Revised, Macmillan and Company, Ltd., London, U.K.
107. Johnson, G.A. et al., 2012, Supercritical CO₂ cycle development at Pratt & Whitney Rocketdyne, GT2012-70105, *ASME Turbo Expo 2012*, Copenhagen, Denmark, June 11–15, 2012.

108. Johnson, M.S., 1992, Prediction of gas turbine on- and off-design performance when firing coal-derived syngas, *Journal of Engineering for Gas Turbines and Power*, 114(2), 380–385.
109. Jolly, S., Cloyd, S., 2003, Performance enhancement of GT 24 with wet compression, *Power-Gen International*, Las Vegas, NV, December 9–11, 2003.
110. Jovanovich, S. et al., 2012, Slipstream pilot-scale demonstration of a novel amine-based post-combustion technology for carbon-dioxide capture from coal-fired power plant flue gas, Report submitted to U.S. DOE NETL, DE-FE0007453.
111. Kailasanath, K., 2000, Review of propulsion applications of detonation waves, *AIAA Journal*, 38(9), 1698–1708.
112. Kakaras, E., Koumanakos, A.K., Doukelis, A., Pressurized fluidized bed combustion (PFBC) combined cycle systems, Chapter 8, *Combined Cycle Systems for Near-Zero Emission Power Generation*, Rao, A. (Ed.), Woodhead Publishing Ltd., Cambridge, U.K.
113. Kaldis, S.P., Skodras, G., Sakellaropoulos, G.P., 2004, Energy and capital cost analysis of CO₂ capture in coal IGCC processes via gas separation membranes, *Fuel Processing Technology*, 85, 337–346.
114. Kalina, A.I., 1984, Combined-cycle system with novel bottoming cycle, *Journal of Engineering for Gas Turbines and Power*, 106(4), 737–742.
115. Kang, S.G., Marion, J.L., 2013, Revolutionary chemical looping technology advances clean coal, *Power Engineering*, November, 22–28.
116. Komori, T. et al., 2003, Design for F class BFG Firing 300 MW gas turbine combined cycle plant, TS-103, *Proceedings of the International Gas Turbine Congress 2003*, Tokyo, Japan, November 2–7, 2003.
117. Kuhr, R., Richert, D., Hannink, R., 2012, How power project complexity affects financing, *Powergen International 2012*, Orlando, FL, December 11–13, 2012.
118. Levasseur, A.A. et al., 2009, Alstom's oxy-firing technology development and demonstration—Near term CO₂ solutions, *34th International Technical Conference on Clean Coal & Fuel Systems*, Clearwater, FL, May 31 to June 4, 2009.
119. Liepmann, H.W., Roshko, A., 1957, *Elements of Gasdynamics*, John Wiley & Sons.
120. Lombardo, G., Agarwal, R., Askander, J., 2014, Chilled ammonia process at technology center mongstad first results, *Energy Procedia*, 51, 31–39.
121. Ratafia-Brown, J., Manfredo, L., Hoffmann, J., and Ramezan, M., 2002, Major environmental aspects of gasification-based power generation technologies, Report prepared for the U.S. DOE, Office of Fossil Energy, NETL, December 2002, Contract no. DE-AT26-99FT20101.
122. Manabu, Y. et al., 2013, Progress of the 40 MW-class advanced humid air turbine tests, *Journal of Engineering for Gas Turbines and Power*, 135(11), 112002.
123. Mathieu, P., Nihart, R., 1998, Zero emission matiant cycle, ASME Paper 98-GT-383.
124. Maurstad, O. et al., 2009, *Impact of Coal Quality and Gasifier Technology on IGCC Performance*, Norwegian University of Science and Technology (NTNU), Trondheim, Norway and Massachusetts Institute of Technology, Cambridge, MA.
125. McCoy, J.W., 1981, *The Chemical treatment of Boiler Water*, Chemical Publishing Co., New York.
126. McMahon, T. (ed.), 2005, Benefits of the Airborne Process™ commercial scale demonstration project, Clean coal power initiative-round 2, U.S. DOE NETL, www.airbornecleanenergy.com.
127. Meher-Homji, C.B., Zachary, J., Bromley, A.F., 2010, Gas turbine fuels—System design, combustion and operability, *Proceedings of the 39th Turbomachinery Symposium*, Houston, TX, October 4–7, 2010.
128. Mickley, M., 2008, Survey of high-recovery and zero liquid discharge technologies for water utilities, WRF-02-006a, WaterReuse Foundation, Alexandria, VA.
129. Miller, B.G., 2011, *Clean Coal Engineering Technology*, Butterworth-Heinemann (an imprint of Elsevier), Burlington, MA.
130. Mun, J., 2005, *Real Options Analysis: Tools and Techniques for Valuing Strategic Investment and Decisions*, 2nd edn., John Wiley & Sons, Inc., Hoboken, NJ.
131. Naqvi, R., 2006, Analysis of natural gas-fired power cycles with chemical looping combustion for CO₂ capture, Doctoral thesis, Norwegian University of Science and Technology, Faculty of Engineering Science and Technology, Department of Energy and Process Engineering, Trondheim, Norway.

132. Nagy, D., Savic, S., 2015, Alternative gas turbine maintenance concepts by independent service providers, *Powergen International 2015*, Las Vegas, NV, December 8–10, 2015.
133. Neville, A., 2011, Underground coal gasification: Another clean coal option, *Power*, July, 36–42.
134. Nuding, J.-R., Johnke, T., 2002, Increasing GT power and efficiency through wet compression, *Powergen Europe 2002*, Milan, Italy, June 11–13, 2002.
135. O'Regen*, Waste heat recovery system for GE and other OEM gas turbines, GE Oil & Gas, www.ge.com/oilandgas, 2010, COMK/MARK 839/IL.
136. Otsuka, H. et al., 2007, Anshan Iron & Steel Group Corporation, China, construction and operation experience of 300 MW blast furnace gas firing combined cycle power plant, *MHI Technical Review*, 44(4).
137. Parulekar, P., 2011, Comparison between oxygen-blown and air-blown IGCC power plants: A gas turbine perspective, GT2011-45154, *ASME Turbo Expo 2011*, Vancouver, British Columbia, Canada, June 6–10, 2011.
138. Phillips, J., 2016, CHP and other technologies could breathe new life into U.S. coal-fired power plants, *Power*, February, 22–16.
139. Pronske, K. et al., 2006, An overview of turbine and combustor development for coal-based oxy-syngas systems, ASME Paper GT2006-90816.
140. Pulverized coal oxy-combustion power plants, Vol. 1: Bituminous coal to electricity, U.S. DOE NETL, Report DOE/NETL-2007/1291, October 2007.
141. Rabensteiner, M. et al., 2014, Pilot plant studies of the CO₂ post-combustion process at the Dürnröhr power plant, *VGB Power Technology*, 10, 61–65.
142. Rabovitser, J., 2010, Partial oxidation gas turbine for power and hydrogen co-production from coal-derived fuel in industrial applications, Gas Technology Institute (GTI) Final Report, DOE Contract DE-FC26-05NT42649, Des Plaines, IL.
143. Rabovitser, J. et al., 2007, Development of a partial oxidation gas turbine (POGT) for innovative gas turbine systems, *ASME Turbo Expo 2007*, Montreal, Quebec, Canada, May 14–17, 2007.
144. Rao, A., 2015, Evaporative gas turbine (EvGT)/humid air turbine (HAT) cycles, *Handbook of Clean Energy Systems*, Yen, J. (Ed.), John Wiley & Sons, Ltd., New York.
145. Retrofitting of coal-fired power plants for CO₂ emissions reductions, Report on MIT Energy Initiative Symposium, Massachusetts Institute of Technology, March 23, 2009.
146. Reynst, F.H., 1961, *Pulsating Combustion—The Collected Works*, Thring, M.W. (Ed.), Pergamon Press.
147. Riffe, M.R. et al., 2008, Wastewater treatment for FGD purge streams, Paper presented at *MEGA Symposium 2008*, Baltimore, MD, August 25–28, 2008.
148. Robson, F., Rao, A., 2012, Externally fired combined cycle (EFCC) systems, Chapter 8, *Combined Cycle Systems for Near-Zero Emission Power Generation*, Rao, A. (Ed.), Woodhead Publishing Ltd., Cambridge, U.K.
149. Rukes, B., Taud, R., 2004, Status and perspectives of fossil power generation, *Energy*, 29, 1853–1874.
150. Sampson, D., 2012, No easy answers: ZLD improvement options for a 720-MW power generation facility, IWC-12–13, *Proceedings of the 73rd Annual International Water Conference*, San Antonio, TX, November 4–8, 2012.
151. Schilke, P.W., 2004, Advanced gas turbine materials and coatings, GER-3569G, GE Energy.
152. Smith, G.R., Kulkarni, P., Hoskin, R.F., 2012, Transient operation of combined cycle power plants and the associated air emissions, *Proceedings of the Powergen International 2012*, Orlando, FL.
153. Smith, R.W. et al., 2005, Fuel moisturization for natural gas fired combined cycles, GT2005-69012, ASME Turbo Expo 2005, Reno, NV, June 6–9, 2005.
154. Smith, R.W., Gülen, S.C., 2012, Natural gas power, *Encyclopedia of Sustainability Science and Technology*, Meyers, R.A. (Ed.), Springer Reference, January 2012.
155. Solid oxide fuel cells, Technology Program, January 2013, U.S. DOE, National Energy Technology Laboratory (NETL), Morgantown, WV.
156. Stoll, H.G. et al., 1994, Performance and economic considerations of repowering steam power plants, GER-3644D, GE Energy.

157. Tanaka, Y. et al., 2012, Development of advanced ultra-supercritical technologies for high temperature steam turbines, *Proceedings of the Powergen International 2012*, Orlando, FL, December 11–13, 2012.
158. Tanaka, Y. et al., 2013, Development of low NO_x combustion system with EGR for 1700°C-class gas turbine, *Mitsubishi Heavy Industries Technical Review*, 50(1).
159. Tawney, R., Khan, Z., Zachary, J., 2005, Economic and performance evaluation of heat sink options in combined cycle applications, *Journal of Engineering for Gas Turbines and Power*, 127(2), 397–403.
160. Thermoflow, Inc., 2015, Thermoflow suite, Version 25, Thermoflow, Inc., Southborough, MA., www.thermoflow.com.
161. U.S. Energy Information Administration, April 2013, Updated capital cost estimates for utility scale electricity generating plants, U.S. Energy Information Administration, Washington, DC.
162. Utamura, M., 2010, Thermodynamic analysis of part-flow cycle supercritical CO₂ gas turbines, *Journal of Engineering for Gas Turbines and Power*, 132, 111701-1.
163. Van der Linden, S., 2012, Intercooling key to the success of gas turbines, *Combined Cycle Journal*, 1Q/2012, 120–121.
164. Van Roode, M., 2010, Ceramic gas turbine development: Need for a 10 year plan, *Journal of Engineering for Gas Turbines and Power*, 132, 011301.
165. Walsh, D., 2015, Impact of cyclic/two shift operation on the reliability, economics, and emissions of fossil generation (coal and combined cycle gas turbine), *Proceedings of the Powergen International 2015*, Las Vegas, NV, December 8–10, 2015.
166. Water in the energy sector, August 2015, U.S. Government Accountability Office (GAO), Center for Science, Technology, and Engineering, Technology Assessment Report, GAO-15-545.
167. Water use for electric power generation, 2008, EPRI Report 1014026, EPRI, Palo Alto, CA.
168. Yang, C.-J., Jackson, R.B., 2013, China's synthetic natural gas revolution, *Nature Climate Change*, 3, 852–854.
169. Zhang, X., He, M., Zhang, Y., 2012, A review of research on the Kalina cycle, *Renewable and Sustainable Energy Reviews*, 16, 5309–5318.

Periodicals

The best sources for new and emerging technologies are academic journals (requires subscription and/or membership to professional organizations), conference proceedings, and trade publications (almost all of them available online at no charge). The reader is encouraged to consult them for up-to-date information on new research and development. The following list, by no means comprehensive, is provided as a starting point:

1. *ASME Journal of Energy Resources Technology*
2. *ASME Journal of Engineering for Gas Turbines and Power*
3. *ASME Journal of Turbomachinery*
4. *Chemical Engineering* (www.che.com)
5. *Combined Cycle Journal* (www.ccj-online.com)
6. *Electric Power & Light* (www.elp.com)
7. *Energy, The International Journal*, Elsevier
8. *Gas Turbine World* (www.gasturbineworld.com)
9. *Hydrocarbon Processing* (www.HydrocarbonProcessing.com)
10. *Modern Power Systems* (www.modernpowersystems.com)

11. *POWER* (www.powermag.com)
12. *Power Engineering* (www.power-eng.com)
13. *Turbomachinery International* (www.turbomachinerymag.com)

Codes and Standards

Plant performance tests are performed to demonstrate that the plant meets the guaranteed performance (primarily output and efficiency or heat rate) offered by the EPC contractor to the plant owner. The American Society of Mechanical Engineers (ASME) Power Test Codes (PTC) have been developed to provide guidance on how to conduct power plant performance testing. The codes provide comprehensive, practical information on calculations pertaining to major FFPS equipment and, as such, constitute very useful resources for information on the core subject matter of the chapter.

First published in 1914, the ASME Boiler and Pressure Vessel Code, especially its sections on the boiler and pressure vessel sections, is an indispensable resource in the United States as well as global electric power generation industry (in addition to other industries):

1. PTC 22—Gas Turbines
2. PTC 4 (or 4.1)—Fired Steam Generators
3. PTC 4.4—HRSGs
4. PTC 46—Overall Plant Performance
5. PTC 47–2006—Integrated Gasification Combined Cycle Power Generation Plants
6. PTC 6—Steam Turbines (Rankine Cycle)
7. PTC 6.2—Steam Turbines (Combined Cycle)
8. ASME Boiler and Pressure Vessel Code (BPVC)
9. ASME B31.1 Power Piping Code



Taylor & Francis

Taylor & Francis Group

<http://taylorandfrancis.com>

14

Stirling Engines

Frank Kreith

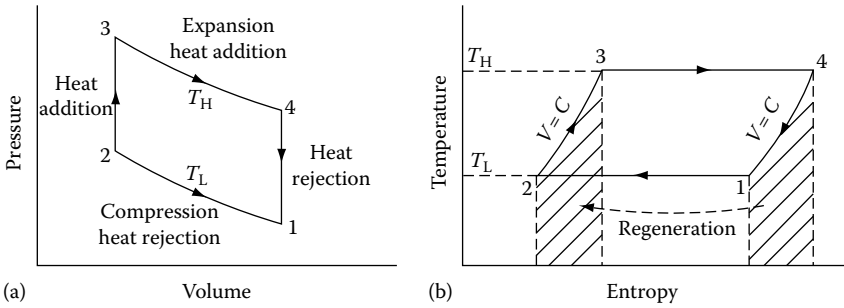
CONTENTS

14.1 Thermodynamics of a Sterling Cycle	447
14.2 Examples of Solar Stirling Power Systems	450
References	454

The efficiency of the ideal Sterling cycle is the same as that of a Carnot cycle operating between the same temperatures. The Sterling cycle was originally proposed by a Scottish minister, Reverend Robert Sterling, as an alternative to a steam engine. Sterling engines have recently received increased attention because they can utilize concentrated solar energy, which can be produced by parabolic concentrators. Since a Sterling engine is an external combustion engine, it can use any fuel or concentrated energy. Sterling engines can operate at high temperatures, typically between 600°C and 800°C, resulting in conversion efficiency of 30%–40%. Sterling engines have also recently been developed for cryogenic applications [1], and the advances in that field can be applied to solar-driven Sterling systems.

14.1 Thermodynamics of a Sterling Cycle

Figure 14.1 shows the thermodynamic diagram of an ideal Sterling cycle with a perfect gas as the working fluid. The gas is compressed isothermally (at constant temperature) from state 1 to 2 by means of heat rejection at the low temperature of the cycle, T_L . The gas is then heated at constant volume from state 2 to 3, followed by an isothermal expansion from state 3 to 4. During this expansion process, heat is added at the high temperature in the cycle, T_H . Finally, the gas is cooled at constant volume from T_H to T_L during the process from state 4 to 1. Figure 14.1 shows the thermodynamic diagrams of an ideal Sterling engine on pressure–volume and temperature–entropy diagrams. The cross-hatched areas in the temperature–entropy diagram during the constant-volume process between states 2 and 3 represent the heat addition to the working gas while raising its temperature from T_L to T_H . Similarly, the cross-hatched area between states 4 and 1 represents the heat rejection as the gas is cooled from T_H to T_L . Note that the heat addition from state 2 to 3 is equal

**FIGURE 14.1**

Thermodynamic diagrams of an ideal Stirling engine cycle. (a) Pressure–volume and (b) temperature–entropy. (From Goswami, Y. et al., *Principles of Solar Engineering*, 2nd edn., Taylor & Francis, Philadelphia, PA, 2000. With permission.)

to the heat rejection from state 4 to 1 and that the processes occur between the same temperature limits. In the ideal cycle, the heat rejected between 4 and 1 is stored and transferred by perfect regeneration to the gas in processes 2–3. Hence, the only external heat addition in the cycle occurs in the process between states 3 and 4, and is given by

$$Q_{3-4} = -W_{3-4} = \int_3^4 p dV = mRT_H \ln \frac{V_4}{V_3}. \quad (14.1)$$

The work input during compression from state 1 to 2 is

$$\begin{aligned} W_{1-2} &= -\int_1^2 p dV = mRT_L \ln \frac{V_1}{V_2} \\ &= -mRT_L \ln \frac{V_2}{V_1}. \end{aligned} \quad (14.2)$$

Noting that the ratio $V_2/V_1 = V_3/V_4$, and combining the earlier two equations, the net work output is

$$mR \ln \frac{V_3}{V_4} (T_H - T_L). \quad (14.3)$$

Therefore, the cycle efficiency

$$\eta = \frac{\text{Net work out}}{\text{Heat input}} = \frac{T_H - T_L}{T_L}. \quad (14.4)$$

This efficiency, which is equal to the Carnot cycle efficiency, is based on the assumption that regeneration is perfect, which is not possible in practice. Therefore, the cycle efficiency

would be lower than that indicated by the earlier equation. For a regeneration effectiveness e as defined later, the efficiency is given by

$$\eta = \frac{T_H - T_L}{T_H + [(1-e)/(k-1)][T_H - T_L/\ln(V_1/V_2)]}, \quad (14.5)$$

where

$$e = (T_R - T_L)/(T_H - T_L) \text{ and } T_R = \text{regenerator temperature}$$

$$k = C_p/C_v \text{ for the gas}$$

For perfect regeneration ($e = 1$), this expression reduces to the Carnot efficiency. It is also seen from the earlier equation that regeneration is not necessary for the cycle to work because even for $e = 0$, the cycle efficiency is not zero.

Example 14.1

A Stirling engine with air as the working fluid operates at a source temperature of 400°C and a sink temperature of 80°C. The compression ratio is 5.

Assuming perfect regeneration, determine the following:

1. Expansion work
2. Heat input
3. Compression work
4. Efficiency of the machine

If the regenerator temperature is 230°C, determine

5. The regenerator effectiveness
6. Efficiency of the machine
7. If the regeneration effectiveness is zero, what is the efficiency of the machine?

Solution

1. Expansion work per unit mass of the working fluid
Assuming air as an ideal gas,

$$w_{34} = -\int_3^4 p dv = RT_H \ln \frac{v_4}{v_3} = (0.287)(400 - 273) \ln 5 = -310.9 \text{ kJ/kg.}$$

Minus sign shows work output.

2. Heat input per unit mass of the working fluid

$$q_{34} = w_{34} = 310.9 \text{ kJ/kg.}$$

3. Compression work per unit mass of the working fluid

$$w_{12} = -\int_1^2 p dv = RT_L \ln \frac{v_2}{v_1} = -(0.287)(80 + 273) \ln \left(\frac{1}{5}\right) = 163.1 \text{ kJ/kg.}$$

4. Efficiency of the machine

$$\eta = \frac{T_H - T_L}{T_H} = \frac{400 - 80}{(400 - 273)} = 0.475 = 47.5\%.$$

5. The regenerator effectiveness

$$e = \frac{T_R - T_L}{T_H - T_L} = \frac{230 - 80}{400 - 80} = 0.469.$$

6. Efficiency of the machine

$$\eta = \frac{T_H - T_L}{T_H + \frac{(1-e)(T_H - T_L)}{(k-1)\ln(v_1/v_2)}} = \frac{400 - 80}{(400 + 273) + \frac{(1-0)(400 - 80)}{(1.4 - 1) \ln(5)}} = 0.341,$$

$$\eta = 34.1\%.$$

7. If the regeneration effectiveness is zero, the efficiency of the machine is

$$\eta = \frac{T_H - T_L}{T_H + \frac{(1-e)(T_H - T_L)}{(k-1)\ln(v_1/v_2)}} = \frac{400 - 80}{(400 + 273) + \frac{(1-0)(400 - 80)}{(1.4 - 1) \ln(5)}} = 0.273,$$

$$\eta = 27.3\%.$$

14.2 Examples of Solar Stirling Power Systems

In order to understand how the Stirling cycle shown in Figure 14.1 may operate, in practice, the simple arrangement and sequence of processes shown in Figure 14.2 are helpful. In the proposed arrangement, two cylinders with pistons are connected via a porous media, which allows gas to pass through from one cylinder to the other. As the gas passes through the porous media, it exchanges heat with the media. The porous media, therefore, serves as the regenerator. In practice, this arrangement can be realized in three ways, as shown in Figure 14.3, by alpha, beta, and gamma types.

The choice of a working fluid for Stirling engine depends mainly on the thermal conductivity of the gas in order to achieve high heat transfer rates. Air has traditionally been used as the working fluid. Helium has a higher ratio of specific heats (k), which lessens the impact of imperfect regeneration.

In the alpha configuration, there are two cylinders and pistons on either side of a regenerator. Heat is supplied to one cylinder, and cooling is provided to the other. The pistons move at the same speed to provide constant-volume processes. When all the gas has moved to one cylinder, the piston of that cylinder moves with the other remaining fixed to provide expansion or compression. Compression is done in the cold cylinder and

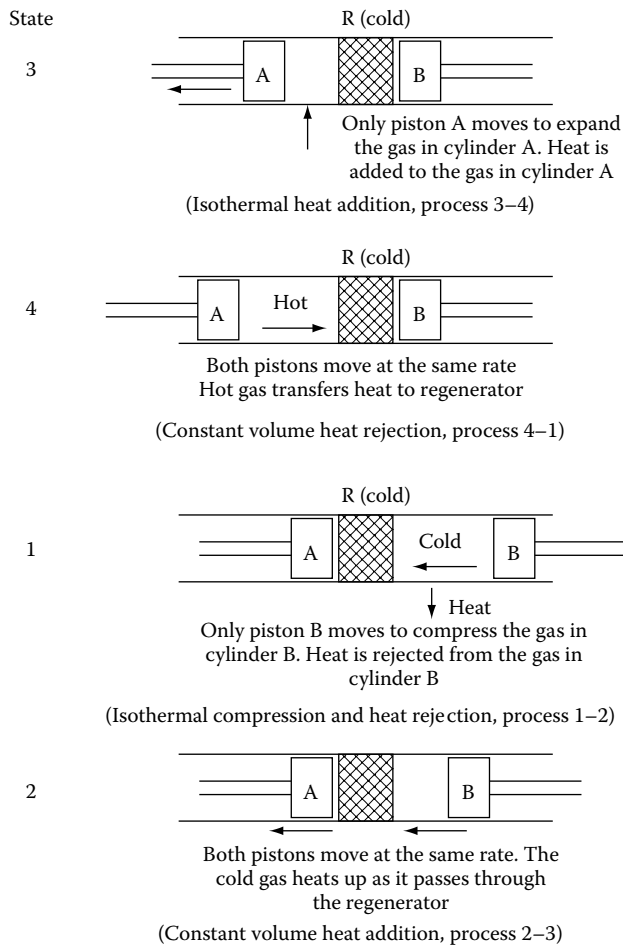


FIGURE 14.2
Stirling cycle states and processes with reference to Figure 14.1.

expansion in the hot cylinder. The Stirling Power Systems V-160 engine (Figure 14.4) is based on an alpha configuration.

The beta configuration has a power piston and a displacer piston, which divides the cylinder into hot and cold sections. The power piston is located on the cold side and compresses the gas when the gas is in the cold side and expands it when it is in the hot side. The original patent of Robert Stirling was based on beta configuration, as are free-piston engines.

The gamma configuration also uses a displacer and a power piston. In this case, the displacer is also the regenerator, which moves gas between the hot and cold ends. In this configuration, the power piston is in a separate cylinder.

In a piston/displacer drive, the power and displacer pistons are designed to move according to a simple harmonic motion to approximate the Stirling cycle. This is done by a crankshaft or a bouncing spring/mass second-order mechanical system [2].

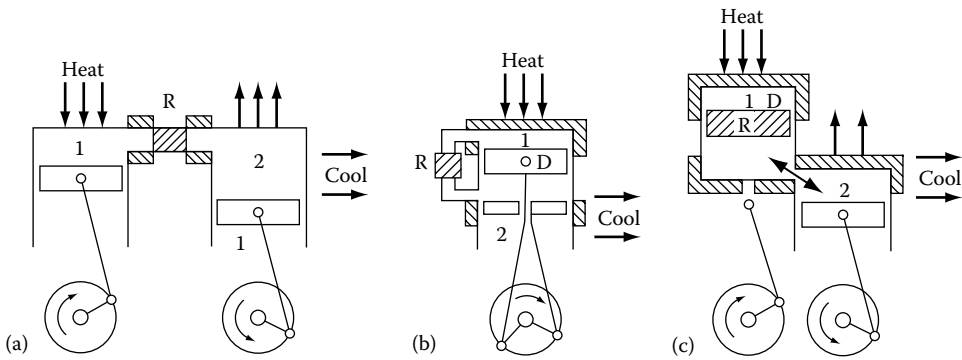


FIGURE 14.3

Three basic types of Stirling engine arrangements. (a) Alpha type, (b) beta type, and (c) gamma type. R, regenerator; D, displacer; 1, expansion space; 2, compression space.

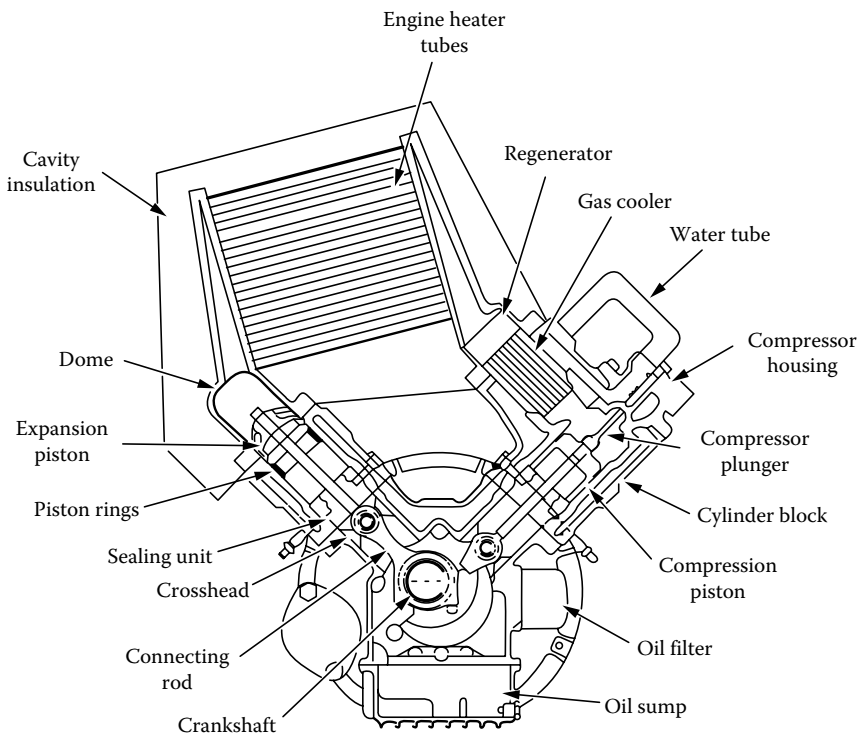
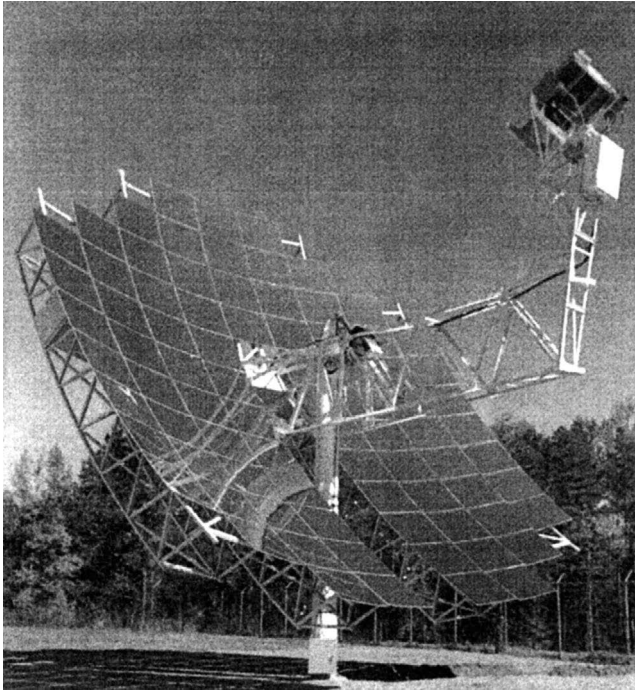


FIGURE 14.4

Stirling power systems/Solo Kleinmotoren V-160 alpha-configuration Stirling engine. (Adapted from Kistler, B.L., A user's manual for DELSOL3: A computer code for calculating the optical performance and optimal system design for solar thermal central receiver plants, Sandia National Labs, Albuquerque, NM, 1986, SAND86-80112.1.)

**FIGURE 14.5**

The McDonnell Douglas/United Stirling dish–Stirling 25 kW_e module. (From Goswami, Y. et al., *Principles of Solar Engineering*, 2nd edn., Taylor & Francis, Philadelphia, PA, 2000. With permission.)

In a kinematic engine, the power piston is connected to the output shaft by a connecting rod crankshaft arrangement. Free-piston arrangement is an innovative way to realize the Stirling cycle. In this arrangement, the power piston is not connected physically to an output shaft. The piston bounces between the working gas space and a spring (usually a gas spring). The displacer is also usually free to bounce. This configuration is called the Beale free-piston Stirling engine after its inventor, William Beale [2]. Since a free-piston Stirling engine has only two moving parts, it offers the potential of simplicity, low cost, and reliability. Moreover, if the power piston is made magnetic, it can generate current in the stationary conducting coil around the engine as it moves. This is the principle of the free piston/linear alternator in which the output from the engine is electricity.

Stirling engines can provide very high efficiencies with high-concentration solar collectors. Since practical considerations limit the Stirling engines to relatively small sizes, a Stirling engine fixed at the focal point of a dual tracking parabolic dish provides an optimum match, as shown in Figure 14.5. Therefore, all of the commercial solar developments to date have been in parabolic dish–Stirling engine combination. The differences in the commercial systems have been in the construction of the dish and the type of Stirling engine. A thorough description of past and current dish–Stirling technologies is presented in Ref. [3].

References

1. www.stirlingcryogenics.com (accessed March 31, 2015).
2. Stine, W.B. (1998) Stirling engines, in: *The CRC Handbook of Mechanical Engineering*, F. Kreith. (Ed.), CRC Press, Boca Raton, FL.
3. Mancini, T. et al. (May 2003) Dish-stirling systems: An overview of development and status, *JSEE* 125, 135–151.
4. Kistler, B.L. (1986) A user's manual for DELSOL3: A computer code for calculating the optical performance and optimal system design for solar thermal central receiver plants, SAND86-80112.1. Sandia National Labs, Albuquerque, NM.
5. Goswami, Y. et al. (2000) *Principles of Solar Engineering*, 2nd edn., Taylor & Francis, Philadelphia, PA.

15

Nuclear Power Technologies through Year 2035

Kenneth D. Kok and Edwin A. Harvego

CONTENTS

15.1	Introduction	456
15.2	Development of Current Power Reactor Technologies	457
15.2.1	Current Nuclear Power Plants Worldwide	457
15.2.1.1	Pressurized Water Reactors	457
15.2.1.2	Boiling Water Reactors	459
15.2.1.3	Pressurized Heavy-Water Reactor	459
15.2.1.4	Gas-Cooled Reactors	460
15.2.1.5	Other Power Reactors	461
15.2.2	Growth of Nuclear Power	461
15.2.2.1	Increased Capacity	461
15.2.2.2	Plant Life Extension	461
15.2.2.3	New Nuclear Plant Construction	462
15.3	Next-Generation Technologies	462
15.3.1	Light-Water Reactors	465
15.3.2	Heavy-Water Reactors	468
15.3.3	High-Temperature Gas-Cooled Reactors	468
15.3.4	Fast Neutron Reactors	469
15.3.5	Summary of Generation III Reactors	470
15.4	Small Modular Reactors	470
15.5	Generation IV Technologies	471
15.5.1	Gas-Cooled Fast Reactor (GFR) System	472
15.5.2	Very-High-Temperature Reactor	472
15.5.3	Supercritical-Water-Cooled Reactor (SWR)	473
15.5.4	Sodium-Cooled Fast Reactor	474
15.5.5	Lead-Cooled Fast Reactor	475
15.5.6	Molten Salt Reactor	477
15.6	Fuel Cycle	478
15.6.1	Uranium and Thorium Resources	478
15.6.2	Mining and Milling	480
15.6.3	Conversion and Enrichment	480
15.6.4	Fuel Fabrication and Use	481
15.6.5	Reprocessing	481
15.6.5.1	PUREX	483
15.6.5.2	UREX+	484
15.6.5.3	Pyroprocessing	484

15.6.6 Spent Fuel Storage.....	484
15.6.7 Spent Fuel Transportation	484
15.7 Nuclear Waste.....	485
15.7.1 Types of Radioactive Wastes	485
15.7.1.1 Mine Tailings	485
15.7.1.2 Low-Level Wastes	485
15.7.1.3 Intermediate-Level Wastes	485
15.7.1.4 High-Level Wastes	486
15.7.2 Managing HLW from Spent Fuel	486
15.7.3 Managing Other Radioactive Wastes	486
15.8 Nuclear Power Economics	486
15.8.1 Comparison of Generation Technologies	488
15.9 Conclusions.....	489
References.....	490

15.1 Introduction

Nuclear power is derived from the fission of heavy element nuclei or the fusion of light element nuclei. This chapter will discuss nuclear power derived from the fission process, since fusion as a practical power source will not reach the stage of commercial development in the next 20–25 years. In a nuclear reactor, the energy available from the fission process is captured as heat which is transferred to working fluids that are used to generate electricity. Uranium-235 is the primary fissile fuel currently used in nuclear power plants. It is an isotope of uranium that occurs naturally at about 0.72% of all natural uranium deposits. When uranium-235 is “burned” (fissioned) in a reactor, it provides about one megawatt day of energy for each gram of uranium-235 fissioned ($3.71\text{E}+10$ Btu/lb).

Nuclear power technology includes not only the nuclear power plants which produce electric power but also the entire nuclear fuel cycle. Nuclear power begins with the mining of uranium. The ore is processed and converted to a form that can be enriched in the U235 isotope so that it can be used efficiently in today’s light-water moderated reactors. The reactor fuel is then fabricated into appropriate fuel forms for use in nuclear power plants. Spent fuel can then be either reprocessed or stored for future disposition. Radioactive waste materials are generated in all of these operations and must be disposed of. The transportation of these materials is also a critical part of the nuclear fuel cycle.

In this chapter, the development, current use, and future of nuclear power will be discussed. The first section is a brief review of the development of nuclear energy as a source for the production of electric power. The second section looks at nuclear power as it is deployed today both in the United States and worldwide. The third section examines the next generation of nuclear power plants that will be built. The fourth section reviews concepts being proposed for a new generation of nuclear power plants. The fifth section provides a brief introduction to small modular reactors. The sixth section describes the nuclear fuel cycle beginning with the availability of fuel materials and ending with a discussion of fuel reprocessing technologies. The seventh section discusses nuclear waste and the options for managing this waste. The eighth section addresses nuclear power economics. Conclusions are presented in Section 15.9.

15.2 Development of Current Power Reactor Technologies

The development of nuclear reactors for power production began following World War II, when engineers and scientists involved in the development of the atomic bomb recognized that controlled nuclear chain reactions could provide an excellent source of heat for the production of electricity. Early research on a variety of reactor concepts culminated in President Eisenhower's 1953 address to the United Nations in which he gave his famous "Atoms for Peace" speech, where he pledges the United States "to find the way by which the miraculous inventiveness of man shall not be dedicated to his death, but consecrated to his life." In 1954, President Eisenhower signed the 1954 Atomic Energy Act, which fostered the cooperative development of nuclear energy by the Atomic Energy Commission (AEC) and private industry. This marked the beginning of the commercial nuclear power program in the United States.

The world's first large-scale nuclear power plant was the Shipping port Atomic Power Station in Pennsylvania, which began its operation in 1957. This reactor was a pressurized water reactor (PWR) nuclear power plant designed and built by the Westinghouse Electric Company and operated by the Duquesne Light Company. The plant produced 68 MWe and 231 MWt.

The first commercial size boiling water reactor (BWR) was the Dresden Nuclear Power Plant which began its operation in 1960. This 200-MWe plant was owned by the Commonwealth Edison Company and was built by the General Electric Company at Dresden, Illinois, about 50 miles southwest of Chicago.

While other reactor concepts, including heavy-water moderated, gas-cooled, and liquid-metal-cooled reactors, have been successfully operated, the PWR and BWR designs have dominated the commercial nuclear power market, particularly in the United States.

These commercial power plants rapidly increased in size from tens of MWe generating capacity to over 1000 MWe. Today nuclear power plants are operating in 33 countries. The following section presents the current status of nuclear power plants operating or under construction around the world.

15.2.1 Current Nuclear Power Plants Worldwide

At the end of 2012, there were 433 individual nuclear power reactors operating throughout the world. More than half of these nuclear reactors are PWRs. The distribution of current reactors by type is listed in Table 15.1. As shown in Table 15.1, there are six types of reactors currently used for electricity generation throughout the world. The following sections provide a more detailed description of these different reactor types.

15.2.1.1 Pressurized Water Reactors

PWRs represent the largest number of reactors used to generate electricity throughout the world. They range in size from about 400 to 1500 MWe. The PWR, shown in Figure 15.1, consists of a reactor core contained within a pressure vessel and is cooled by water under high pressure. The nuclear fuel in the core consists of uranium dioxide fuel pellets enclosed in zircaloy rods that are held together in fuel assemblies. There are 200–300 rods in an assembly and 100–200 fuel assemblies in the reactor core. The rods are arranged vertically and contain 80–100 tons of enriched uranium.

TABLE 15.1

Nuclear Power Units by Reactor Type, Worldwide

Reactor Type	Main Countries	# Units Operational	GWe	Fuel
Pressurized light-water reactors (PWR)	United States, France, Japan, Russia	271	251	Enriched UO_2
Boiling light-water reactors (BWR) and Advanced boiling light-water reactors (AWBR)	United States, Japan, Sweden	83	78	Enriched UO_2
Pressurized heavy-water reactors—CANDU (PHWR)	Canada	48	24	Natural UO_2
Gas-cooled reactors (Magnox and AGR)	United Kingdom	15	8	Natural U (metal), enriched UO_2
Graphite-moderated light-water reactors (RMBK)	Russia	15	10	Enriched UO_2
Liquid-metal-cooled fast-breeder reactors (LMFBR)	Japan, France, Russia	1	1	PuO_2 and UO_2
		433	371	

Source: Information taken from *Nuclear News*, American Nuclear Society, 15th Annual Reference Issue, March 2013.

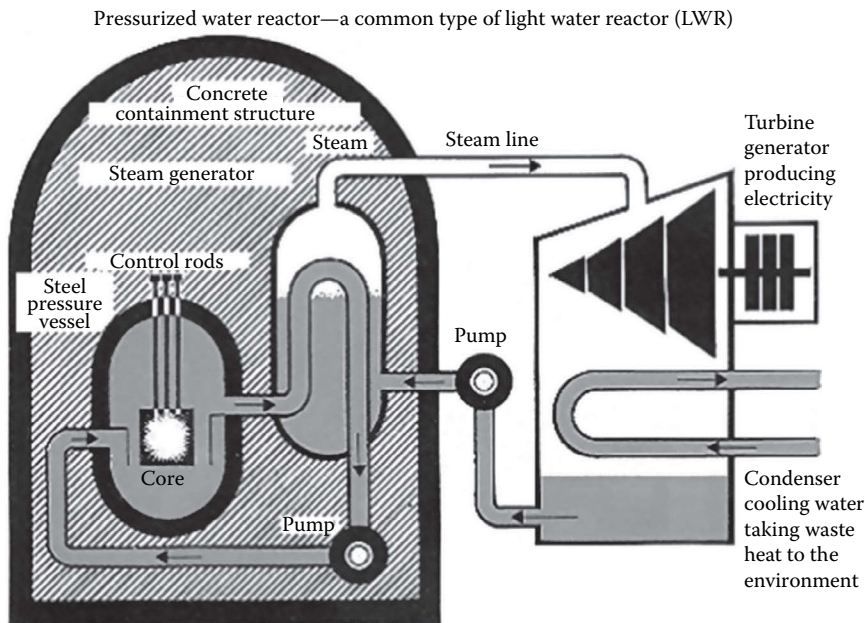


FIGURE 15.1

Sketch of a typical PWR power plant. (Courtesy of World Nuclear Association.)

The pressurized water at 315°C is circulated to the steam generators. The steam generator is a tube and shell type of heat exchanger with the heated high pressure water circulating through the tubes. The steam generator isolates the radioactive reactor cooling water from the steam which turns the turbine generator. Water enters the steam generator shell side and is boiled to produce steam which is used to turn the turbine generator producing electricity. The pressure vessel containing the reactor core and the steam generators are

located in the reactor containment structure. The steam leaving the turbine is condensed in a condenser and returned to the steam generator. The condenser cooling water is circulated to cooling towers where it is cooled by evaporation. The cooling towers are often pictured as an identifying feature of a nuclear power plant.

15.2.1.2 Boiling Water Reactors

The BWR power plants represent the second largest number of reactors used for generating electricity. BWRs range in size from 400 MWe to the largest being about 1200 MWe. The BWR, shown in Figure 15.2, consists of a reactor core located in a reactor vessel that is cooled by circulating water. The cooling water is heated to 285°C in the reactor vessel and the resulting steam is sent directly to the turbine generators. There is no intermediate loop as in PWR. The reactor vessel is contained in the reactor building. The steam leaving the turbine is condensed in a condenser and returned to the reactor vessel. The condenser cooling water is circulated to the cooling towers, where it is cooled by evaporation.

15.2.1.3 Pressurized Heavy-Water Reactor

The so-called “CANDU reactor” was developed in Canada, beginning in the 1950s. It consists of a large tank called calandria containing the heavy-water moderator. The tank is penetrated horizontally by pressure tubes which contain the reactor fuel assemblies. Pressurized heavy water is passed over the fuel and heated to 290°C. As in the PWR, this pressurized water is circulated to a steam generator where light water is boiled to form the steam, used to drive the turbine generators.

The pressure tube design allows the CANDU reactor to be refueled while it is in operation. A single pressure tube can be isolated and the fuel can be removed and replaced while the reactor continues to operate. The heavy water in the calandria is also circulated and the heat is recovered from it. The CANDU reactor is shown in Figure 15.3.

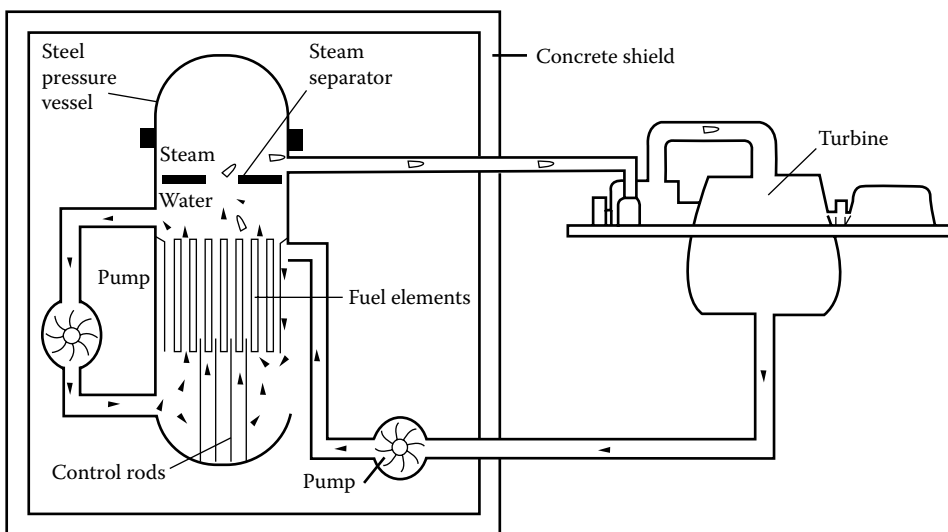


FIGURE 15.2
Sketch of a typical BWR power plant. (Courtesy of World Nuclear Association.)

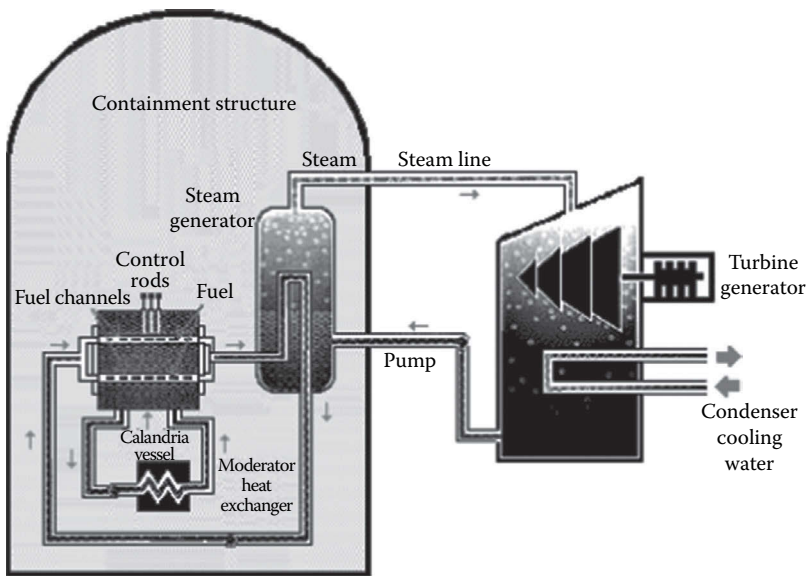


FIGURE 15.3
Sketch of a typical CANDU reactor power station. (Courtesy of World Nuclear Association.)

15.2.1.4 Gas-Cooled Reactors

Gas-cooled reactors were developed and implemented in the United Kingdom. The first generation of these reactors was called “Magnox” and they were followed by the advanced gas-cooled reactor (AGR). These reactors are graphite moderated and cooled by CO_2 . Magnox reactors are fueled with uranium metal fuel, while the AGRs use enriched UO_2 as the fuel material. The CO_2 coolant is first circulated through the reactor core and then to a steam generator. The reactor and the steam generators are located in a concrete pressure vessel. As with the other reactor designs, the steam is used to turn the turbine generator to produce electricity. Figure 15.4 shows the configuration for a typical gas-cooled reactor design.

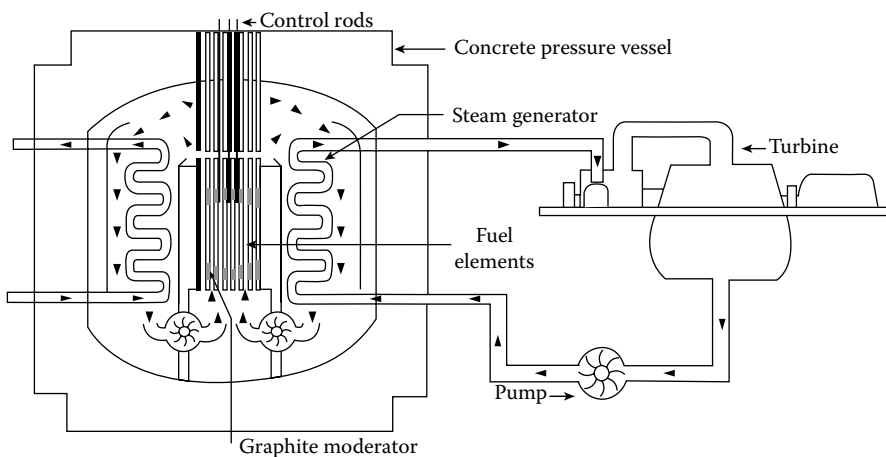


FIGURE 15.4
Sketch of a typical gas-cooled reactor power station. (Courtesy of World Nuclear Association.)

15.2.1.5 Other Power Reactors

The remaining reactors listed in Table 15.1 are the light-water graphite-moderated reactors used in Russia, and the liquid-metal-cooled fast-breeder reactors (LMFBRs) in Japan, France, and Russia. In the light-water graphite-moderated reactors, the fuel is contained in vertical pressure tubes where the cooling water is allowed to boil at 290°C, and the resulting steam is circulated to the turbine generator system as in BWR. In the case of the LMFBR, sodium is used as the coolant and a secondary sodium cooling loop is used to provide heat to the steam generator.

15.2.2 Growth of Nuclear Power

The growth of nuclear power generation is being influenced by three primary factors. These factors are (1) current plants are being modified to increase their generating capacity, (2) the life of old plants is being lengthened by life extension practices that include relicensing, and (3) new construction is adding to the number of plants operating worldwide. According to the IAEA, following the Fukushima accident, the World Energy Outlook 2011 New Policies scenario has a 60% increase in nuclear capacity to 2035, compared with about 90% the year before. At the end of 2012, there were 433 nuclear power plants in operation with a total net installed capacity of 371 GWe. They now anticipate the installed capacity to reach 630 GWe by 2035. This implies that over 250 new nuclear plants will be built over the next 20 years and this does not account for replacement of current plants that reach the end of life and it assumes that the overall average capacity will remain the same.

15.2.2.1 Increased Capacity

Operating nuclear plants are being modified to increase their generating capacity. Reactors in the United States, Belgium, Sweden, Switzerland, Spain, and Finland are being uprated. In the United States, the Nuclear Regulatory Commission has approved 140 uprates totaling over 6500 MWe since 1977 with some of them having capacity increased up to 20%. The number of operating reactors in the United States as of June 2013 is 102, which have a generating capacity exceeding 100 GWe. The generating capacity increase was due to both power uprating and improvements in operation and maintenance practices to produce higher plant availability. Switzerland increased the capacity of its plants by over 13%, while in Spain uprating has added 11% to that country's nuclear capacity. The uprating process has proven to be a very cost-effective way to increase overall power production capacity, while avoiding the high capital cost of new construction.

15.2.2.2 Plant Life Extension

Life extension is the process by which the life of operating reactors is increased beyond the original planned and licensed life. Most reactors were originally designed and licensed for an operational life of 40 years. Without life extension, many of the reactors that were built in the 1970s and 1980s would reach the end of their operational lives during the years 2010–2030. If they are not replaced with new plant construction, there would be a significant decrease in nuclear-based electricity generation as these plants reached the end of their useful life.

Engineering assessments of current nuclear plants have shown that they are able to operate for longer than their original planned and licensed lifetime. Over 70 plants in the

United States have been granted 20-year extensions to their operating licenses by the U.S. Nuclear Regulatory Commission (NRC). The operators of most of the remaining plants are also expected to apply for license extensions. This will give the plants an operating life of 60 years. In Japan, operating lifetimes of 70 years are envisaged.

The oldest nuclear power stations in the world were operated in Great Britain. Chalde Hall and Chaplecross were built in the 1950s and were expected to operate for 20–25 years. They were authorized to operate for 50 years but were shut down in 2003 and 2004 for economic reasons. In 2000, the Russian government extended the lives of their 12 oldest reactors by 15 years for a total of 45 years.

While life extension has become the norm throughout the world, many reactors have been shut down due to economic, regulatory, and political reasons. Many of these reactors were built early in the development of nuclear power. They tended to be smaller in size and were originally built for demonstration purposes. However the political and regulatory process in some countries has led to the termination of nuclear power programs and the shutdown of viable reactor plants. Germany is probably the best example having made a political decision to phase out nuclear power. Plants such as San Onofre Units 2 and 3, in southern California, and Kewaunee, in Wisconsin, are being shut down for economic reasons.

15.2.2.3 New Nuclear Plant Construction

New nuclear power plants are currently being constructed in several countries. The majority of these constructions are in Asia. Plants currently under construction are listed in Table 15.2.

15.3 Next-Generation Technologies

The next generation, Generation III, nuclear power reactors are being developed to meet the power production needs throughout the world. These reactors incorporate the lessons that have been learned by operation of nuclear power systems since the 1950s. The reactors are designed to be safer, more economic, and more fuel-efficient. The first of these reactors were built in Japan and began operation in 1996.

The biggest change in the Generation III reactors is the addition of passive safety systems. Earlier reactors relied heavily on operator actions to deal with a variety of operational upset conditions or abnormal events. The advanced reactors incorporate passive or inherent safety systems that do not require operator intervention in the case of a malfunction. These systems rely on such things as gravity, natural convection, and resistance to high temperatures.

Generation III reactors also have the following advantages:

- Standardized designs with many modules of the reactor being factory constructed and delivered to the construction site leading to expedited licensing, reduction of capital cost, and reduced construction time.
- Simpler designs with fewer components that are more rugged, easier to operate, and less vulnerable to operational upsets.

TABLE 15.2

Power Reactors under Construction

Start Operation	Country, Organization	Reactor	Type	MWe (Net)
2013	Iran, AEOI	Bushehr 1 ^a	PWR	950
2013	India, NPCIL	Kudankulam 1	PWR	950
2013	India, NPCIL	Kudankulam 2	PWR	950
2013	China, CGNPC	Hongyanhe 1 ^a	PWR	1080
2013	China, CGNPC	Ningde 1 ^a	PWR	1080
2013	Korea, KHNP	Shin Wolsong 2	PWR	1000
2013	Korea, KHNP	Shin-Kori 3	PWR	1350
2013	Russia, Rosenergoatom	Leningrad II-1	PWR	1070
2013	Argentina, CNEA	Atucha 2	PHWR	692
2013	China, CGNPC	Ningde 2	PWR	1080
2013	China, CGNPC	Yangjiang 1	PWR	1080
2013	China, CGNPC	Taishan 1	PWR	1700
2013	China, CNNC	Fangjiashan 1	PWR	1080
2013	China, CNNC	Fuqing 1	PWR	1080
2013	China, CGNPC	Hongyanhe 2	PWR	1080
2014	Russia, Rosenergoatom	Novovoronezh II-1	PWR	1070
2015	Russia, Rosenergoatom	Rostov 3	PWR	1070
2014	Slovakia, SE	Mochovce 3	PWR	440
2014	Slovakia, SE	Mochovce 4	PWR	440
2014	Taiwan Power	Lungmen 1	ABWR	1300
2014	China, CNNC	Sanmen 1	PWR	1250
2014	China, CPI	Haiyang 1	PWR	1250
2014	China, CGNPC	Ningde 3	PWR	1080
2014	China, CGNPC	Hongyanhe 3	PWR	1080
2014	China, CGNPC	Yangjiang 2	PWR	1080
2014	China, CGNPC	Taishan 2	PWR	1700
2014	China, CNNC	Fangjiashan 2	PWR	1080
2014	China, CNNC	Fuqing 2	PWR	1080
2014	Korea, KHNP	Shin-Kori 4	PWR	1350
2014?	Japan, Chugoku	Shimane 3	ABWR	1375
2014	India, Bhavini	Kalpakkam	FBR	470
2014	Russia, Rosenergoatom	Beloyarsk 4	FNR	750
2015	United States, TVA	Watts Bar 2	PWR	1180
2015	Taiwan, Power	Lungmen 2	ABWR	1300
2015	China, CNNC	Sanmen 2	PWR	1250
2015	China, CGNPC	Hongyanhe 4	PWR	1080
2015	China, CGNPC	Yangjiang 3	PWR	1080
2015	China, CGNPC	Ningde 4	PWR	1080
2015	China, CGNPC	Fangchenggang 1	PWR	1080
2015	China, CNNC	Changjiang 1	PWR	650
2015	China, CNNC	Changjiang 2	PWR	650
2015	China, CNNC	Fuqing 3	PWR	1080
2015	India, NPCIL	Kakrapar 3	PHWR	640
2015?	Japan, EPDC/J Power	Ohma 1	ABWR	1350

(Continued)

TABLE 15.2 (Continued)

Power Reactors under Construction

Start Operation	Country, Organization	Reactor	Type	MWe (Net)
2016	Finland, TVO	Olkilouto 3	PWR	1600
2016	France, EdF	Flamanville 3	PWR	1600
2016	Russia, Rosenergoatom	Novovoronezh II-2	PWR	1070
2016	Russia, Rosenergoatom	Leningrad II-2	PWR	1200
2016	Russia, Rosenergoatom	Vilyuchinsk	PWR x 2	70
2016	India, NPCIL	Kakrapar 4	PHWR	640
2016	India, NPCIL	Rajasthan 7	PHWR	640
2016	Pakistan, PAEC	Chashma 3	PWR	300
2016	China, China Huaneng	Shidaowan	HTR	200
2016	China, CPI	Haiyang 2	PWR	1250
2016	China, CGNPC	Yangjiang 4	PWR	1080
2016	China, CGNPC	Hongyanhe 5	PWR	1080
2015	China, CNNC	Hongshiding 1	PWR	1080
2015	China, CGNPC	Fangchenggang 2	PWR	1080
2016	China	Several others	PWR	
2017	United States, Southern	Vogtle 3	PWR	1200
2017	Russia, Rosenergoatom	Baltic 1	PWR	1200
2017	Russia, Rosenergoatom	Rostov 4	PWR	1200
2017	Russia, Rosenergoatom	Leningrad II-3	PWR	1200
2017	Ukraine, Energoatom	Khmelnitsky 3	PWR	1000
2017	Korea, KHNP	Shin-Ulchin 1	PWR	1350
2017	India, NPCIL	Rajasthan 8	PHWR	640
2017	Romania, SNN	Cernavoda 3	PHWR	655
2017?	Japan, JAPC	Tsuruga 3	APWR	1538
2017	Pakistan, PAEC	Chashma 4	PWR	300
2017	United States, SCEG	Summer 2	PWR	1200
2017	China	Several		
2018	Korea, KHNP	Shin-Ulchin 2	PWR	1350

Source: Information taken from Plans for new reactors worldwide, World Nuclear Association Information Paper, www.world-nuclear.org, March, 2013.

^a Is the latest announced date as of March 2013; ? for the reactors in Japan is because of the uncertainty following the Fukushima event.

- Longer operating lives of 60 years and designed for higher availability.
- Reduced probability of accidents leading to core damage.
- Safety systems that allow 72 h after an accident before active intervention is required.
- Resistance to serious damage that would allow release of radioactivity following an aircraft impact.
- Higher fuel burnup reducing refueling outages and increasing fuel utilization with less waste produced.

The following sections describe the different types of Generation III reactors being developed worldwide. Many of them are larger than their predecessors and involve consortiums of international companies. Certification of the design concepts continues on a country-by-country basis.

In Europe, there is an effort to harmonize requirements for nuclear plant licensing. Plants certified to comply with the European Utilities Requirements (EUR) include the Westinghouse AP1000, Gidropress' AES-92, Areva's EPR, GE-s ABWR, Areva's Kerena, and Westinghouse BWR 90. In the United Kingdom, the Office of Nuclear Regulation is processing the Areva EPR and the Westinghouse AP1000.

In the United States, the commercial nuclear industry in conjunction with the U.S. Department of Energy (DOE) has developed four advanced light-water reactor designs. Two of these are based on experience obtained from operating reactors in the United States, Japan, and Western Europe. These reactors will operate in the 1300 MW range. One of the designs is the advanced boiling water reactor (ABWR). It was designed in the United States and is already being constructed and operated in Asia. The NRC gave final design certification to the ABWR in 1997. It was noted that the design exceeded NRC "safety goals by several orders of magnitude." The other type, designated System 80+, is an advanced PWR. This reactor system was ready for commercialization but the sale of this design is not being pursued.

Advanced thermal reactors currently being marketed are summarized in Table 15.3, and the various types of reactors and specific identified designs will be discussed in the following sections.

15.3.1 Light-Water Reactors

Generation III advanced light-water reactors are being developed in several countries.

EPR: Areva in France has developed a large 1630-MWe PWR, which is designated as the European pressurized water reactor (EPR). It is designed with double containment with four separate redundant active safety systems. The first EPR is being built in Olkiluoto, Finland, the second two will be built in France. Areva has also designed a US-EPR and has been submitted to the USNRC for design certification. It is known as the Evolutionary PWR (EPR).

AP1000, CAP1400: The Westinghouse AP1000 (scaled up from the AP-600) received final design approval from the NRC and has received full design certification 2011. The passive safety systems in this reactor design lead to a large reduction in components including 50% fewer valves, 35% fewer pumps, 80% less pipe, 45% less seismic building volume, and 70% less cable. The AP1000 is designated the CAP1000 in China. Another aspect of the AP1000 is the construction process. Once the plant is ordered, the plant will be constructed in a modular fashion with modules being fabricated in a factory setting and then transported to the reactor site. The anticipated design construction time for the plant is 36 months. The construction cost of an AP1000 is expected to be greater than \$5000 per kW in the United States and less than \$2000 per kW in China. The plant is designed to have a 60 year operating life. AP1000 plants are under construction in China and the United States.

ABWR: Advanced boiling water reactor is offered in slightly different versions by GE Hitachi, Hitachi-GE, and Toshiba. This design produces 1350–1600 MWe. Two of the Hitachi versions and two of the Toshiba versions have been built in Japan and are in commercial operation, Hitachi is promoting the UK-ABWR while Toshiba has the EU-ABWR. The design can operate with MOX fuel and has a design life of 60 years. The emergency cooling system uses pump mounted at the bottom of the reactor vessel and are part of an active safety system.

TABLE 15.3

Advanced Thermal Reactors Being Marketed

Country and Developer	Reactor	Size (MWe)	Design Progress	Main Features
United States–Japan (GE–Hitachi–Toshiba)	ABWR	1380	Commercial operation in Japan since 1996–1997. In the United States: NRC certified 1997, first-of-a-kind engineering (FOAKE).	Evolutionary design More efficient, less waste Simplified construction (48 months) and operation
South Korea (derived from Westinghouse)	APR-1400 (PWR)	1450	Under construction—Shin Kori 3 and 4. Sold to UAE.	Evolutionary design Increased reliability Simplified construction and operation
United States (Westinghouse)	AP-600	600	AP-600: NRC certified 1999, FOAKE	Passive safety features Simplified construction and operation 3 years to build 60-year plant life
	AP1000 (PWR)	1200	AP1000 NRC design approval 2011.	
Japan (Utilities, Westinghouse, Mitsubishi)	APWR	1530	Basic design in progress, planned for Tsuruga U.S.-design certification application.	Hybrid safety features Simplified construction and operation
	US-APWR	1700		
	EU-APWR	1700		
Europe (Areva NP)	EPR	1750	Future French standard. French design approval. Being built in Finland, France, and China. Undergoing certification in the United States.	Evolutionary design Improved safety features High fuel efficiency Low cost electricity
	US-EPR (PWR)			
United States (GE)	ESBWR	1600	Developed from the ABWR, pre-certification in the United States.	Evolutionary design Short construction time Enhanced safety features Innovative design High fuel efficiency
	Atmea1 (PWR)	1150	French design approval February 2012, ready for deployment.	
Russia (Gidropress)	VVER-1200 (PWR)	1200	Under construction at Leningrad, Novovoronezh and Baltic plants.	Evolutionary design 50-year plant life High fuel efficiency
Canada (CANDU Energy)	Enhanced CANDU-6—EC6	750	Improved model Design review in progress.	Evolutionary design Flexible fuel requirements Modular plant, low cost High temperature High fuel efficiency
	HTR-PM	2 × 105 (module)	Demonstration plant being built at Shidaowan.	

Source: World Nuclear Association, Advanced nuclear power reactors. Information paper, www.world-nuclear.org, September 2013.

ESBWR: GE Hitachi is working on this design which is known as the Economic and Simplified BWR. It is in the final stages of certification by the USNRC. This design eliminates the need for pumps for emergency cooling and uses passive systems and stored energy instead. It has a design life of 60 years and produces 1535 MWe.

APWR: APWR is an advanced PWR marketed by Mitsubishi. The first of these reactors was planned for construction at Tsuruga in Japan. The U.S. version of this

- reactor will have a 1620 MWe output. Another version of this reactor was planned for construction in Texas but the request for certification has been delayed because the utility is looking at other electrical generating systems. It combines active and passive emergency cooling systems in a double containment and features high burnup fuel.
- APR1400*: The APR1400 is an advanced design, earlier known as Korean Next-Generation Reactor. The design was certified by Korean Institute of Nuclear Safety in 2003 and the first two units have been constructed in Korea. The reactor is being marketed in the Middle East as a heat source for large desalinization systems. It has a generating capacity of 1350–1400 MWe.
- Atmea1*: The Atmea1 was developed by the Atmea joint venture by Areva and Mitsubishi to produce an evolutionary PWR which would use the same steam generators as the EPR. The reactor was designed to have load-following capability and frequency control capacity. The design has been approved by the French regulator ASN and is designed for sale to countries that do not have previous nuclear experience. It has three redundant active and passive safety systems and a backup cooling system similar to the EPR.
- Areva-EdF-CGNPC*: This is a proposed effort between the French companies and China Guangdong Nuclear Power Group to develop a mid-sized PWR with third-generation safety features. No reactor design has yet come from this effort.
- Kerena*: This reactor design was developed by Areva in conjunction with two German utilities. Kerena is based on the design of a German plant designed and built by Siemens and completed in 1999. This reactor can operate with MOX fuel and also has load-following capability.
- AES-92, V392*: These are late model VVER-1000 with enhanced safety systems and are designed by Gidropress. This reactor model is being built in China and India. AES-92 is certified as meeting EUR.
- AES-2006, MIR-1299, VVER-TOI*: These are third-generation standardized VVER-1200 reactors that will operate at 1070 MWe. Models of this system are being built in Russia and are expected to begin operation in 2014. The systems are designed for 60 years of operation at a 90% capacity factor. They have enhanced safety systems including those related to earthquakes and aircraft impact with some passive safety features. The MIR-1200 (Modernized International Reactor) is intended for sale and operation outside of Russia.
- ACPR1000 and ACP1000*: These are essentially Chinese designed versions of French designs with modern features. The ACP1000 is an 1100-MWe plant with load-following capability. The ACPR1000 is also an 1100-MWe plant with a double containment and a core catcher.
- IRIS*: An international project being led by Westinghouse is designing a modular 335 MWe reactor known as the “International Reactor Innovative & Secure” (IRIS). This PWR is designed with integral steam generators and a primary cooling system that are all contained in the reactor pressure vessel. The goal of this system is to reach an 8-year refueling cycle using 10% enriched fuel with an 80,000 MWd/t burnup.
- VBER-300*: The VBER is a small PWR based on naval reactors and was designed to be a barge-mounted floating nuclear power plant (295–325 MWE unit) with an

expected life of 90 years with a 90% capacity factor. The first land-based reactor of this design will be built in Kazakhstan.

RMWR, RBWR: The reduced moderation water reactor (RMWR) is a light-water reactor with the fuel array packed more tightly than the typical PWR and BWR of today. These Hitachi-designed reactors are expected to produce more plutonium, and thus make better use of the uranium resource. The breeding ratio is near 1 instead of 0.6 of today's reactors. Reprocessing through an advanced fluoride volatility process leaves a uranium-plutonium mixture that can be made directly into MOX fuels of standard light-water reactors. Thor Energy in Norway is exploring the use of an RBWR with a thorium oxide (Th-MOX) fuel because high conversion factors for production of U233 can be achieved with this design. The core of the reactor is flatter with tightly packed fuel rods to ensure sufficient fast neutron leakage and a negative void reactivity coefficient.

15.3.2 Heavy-Water Reactors

Heavy-water reactors are primarily designed and used in Canada and India. Both countries are actively taking steps in developing and making advances in this technology. In 2011 AECL sold the reactor division which now operates as Candu Energy, Inc.

EC6: The EC6 is an advancement of the CANDU-9, which was designed in the late 1990s and never built. This design is proposed for building in China after the successful construction of CANDU-6 units and is known as the "Enhanced CANDU-6." It is a versatile reactor which will be able to use natural uranium fuel as well as reprocessed PWR uranium and various mixtures of plutonium, uranium, and thorium. The reactor operates at 690 MWe.

ACR: The advanced CANDU reactor was designed as a more innovative concept, but the design and regulatory approval efforts have now been terminated.

AHWR: Advance heavy-water reactor is being developed in India. The purpose of this reactor is to use a thorium-based fuel cycle. The thorium-based fuel will be seeded with both U233 and Pu239. It is a 284-MWe reactor moderated with heavy water and cooled with boiling light water. It is designed for a 100-year plant life. The AHWR-LEU is an export version of this design. It will use low-enriched uranium and thorium as fuel.

15.3.3 High-Temperature Gas-Cooled Reactors

These reactors use high-temperature helium as a coolant at up to 950°C which is used to make steam via a steam generator or is used directly to drive a gas turbine. The fuel is in the form of small particles coated with carbon and silicon carbide which will provide containment of the fission products to temperatures up to 1600°C or more.

HTR-PM: The first commercial version of the HTGR will be China's HTR-PM. This reactor is being built in China and will consist of two 105-MWe modules. The reactor will have an outlet temperature of 750°C. This will be a demonstration system for a complete 18-module power station.

PMRB: The pebble bed modular reactor is being developed by a consortium in South Africa led by Eskom along with Mitsubishi Heavy Industries. Production

units were planned to be 165 MWe with a direct cycle gas turbine generator. Development of this system has ceased due to lack of funds and customers.

GT-MHR: The gas turbine—modular helium reactor is a U.S. design with modules of 285 MWe each, generated by a directly driven gas turbine at a 48% efficiency. The reactor was being developed by General Atomics in partnership with Russia's OKBM Afrikantov and supported by Fuji in Japan. The preliminary design stage was completed in 2001, but the program has stalled then.

15.3.4 Fast Neutron Reactors

Several countries are working on the development of fast breeder reactors (FBR), which are fast neutron reactor (FNR) configured with a breeding ratio greater than 1.0. About 20 of these reactors have been built and operated since the 1950s. The FBR can use uranium much more efficiently than the light-water reactor but they are more expensive to construct; so long as the price of uranium remains low, they are not economic.

India has operated a 40 mMWt fast breeder test reactor since 1985. Construction of 500-MWe prototype fast reactor was started in 2004 with expected operation in 2012. The reactor is fueled with U–Pu fuel with a thorium blanket to breed U233. This will provide support for India's efforts to make use of the abundant supply of thorium available there.

The Russian BN-600 reactor has been supplying electricity to the grid since 1981 and has the best operating and production record of any reactor in the country. The BN-350 reactor is operated in Kazakhstan for 27 years and about half of the output was used for water desalinization.

BN-800: The BN-800 is a new and more powerful FBR designed by OKBM. It has a wide fuel flexibility, enhanced safety, and improved economy. It will be used to burn plutonium from dismantled weapons and to test the recycle of minor actinides. Two units of this reactor design have been sold to China and are under construction.

BN-1200: The BN1200 is designed to operate with MOX fuel and also U–Pu nitride in a closed cycle. It can be sodium or lead cooled and will produce 1220 MWe. The BN-1200 is being considered to be a Gen-IV design.

BREST: Russia has used lead–bismuth cooling for 40 years in submarine reactors. BREST is a new fast neutron reactor designed to produce 300 MWe with lead coolant. Construction of the first reactor of this type is expected to begin in 2015 with operation in 2020. It is designed to have an equilibrium core that will allow it to use its own recycled fuel but will not produce excess material for additional reactors.

ELSY: The European Lead-Cooled System is a 600-MWe fast reactor being designed in Italy. ELSY is designed to be fueled by either depleted uranium or thorium and also burn the actinides from light-water reactor fuel. It is cooled by either lead or lead–bismuth eutectic.

PRISM: PRISM is a GE-Hitachi design fast reactor of the pool type with passive cooling for decay heat removal. PRISM is designed to produce 311 MWe and will operate in blocks of two reactors using a metal fuel of depleted uranium and plutonium. It is designed to be used with the electrometallurgical reprocessing so that all the transuranics are recycled with the fuel.

KALIMER: The Korea Advanced Liquid Metal Reactor is the Korean-designed fast reactor system. This is a 600-MWe pool type system that is expected to be developed as a Gen-IV reactor.

15.3.5 Summary of Generation III Reactors

As can be seen from the discussion earlier, there are many reactor systems of many types under development. The key feature of all of these reactors is the enhancement of safety systems. Some of these reactors have already been built and are in operation while others are under construction. This activity indicates that there will be a growth of nuclear reactor generated electricity during the next 20 years. Table 15.3, taken from World Nuclear Association information on advanced nuclear power reactors shows the advanced thermal reactors that are being marketed around the world.

15.4 Small Modular Reactors

In the early days of nuclear power reactors, most of the reactors had small power outputs and many had unique first of a kind designs. Most of the nuclear power plants had electric power outputs below 100 MW and were considered demonstration plants which used a variety of technologies. They include sodium-cooled fast reactors, heavy-water moderated reactors, BWRs, PWRs, and gas-cooled reactors.

Today the concept of the small modular reactor (SMR) is being developed using modern technologies with advanced safety systems. The International Atomic Energy Agency (IAEA) defines “small” as under 300 MWe; it also defines a medium-sized reactor as the one up to 700 MWe. The driving force behind the ideas for reactors of this size is based on several factors including

- Smaller reactors can be produced in a factory and moved as a single unit to the reactor site to be installed. This will shorten the time for construction of the power station and should be less costly.
- If a large power station is needed in the future, it could be made up of multiple small units each being added as the need arises. This is not unlike the manner in which fossil-fired plants were originally built with multiple smaller units.
- Smaller reactors can be used to serve remote area, where large amounts of power are not required and where service via transmission from larger plants is difficult.
- Smaller reactors can more easily be designed to operate with passive safety systems since the residual heat loads are smaller.
- They can also be built underground which would protect them from attack and also make siting possible in more urban areas.

The development of SMRs is in process across the world by nuclear system supplier. The whole industry in this area is in a state of flux and details on specific reactor are changing rapidly. Specific current information of designs being considered is best found in the World Nuclear Association Information Library.⁸

15.5 Generation IV Technologies

As discussed earlier, the development of nuclear power occurred in three general phases. The initial development of prototype reactor designs occurred in the 1950s and 1960s, development and deployment of large commercial plants occurred in the 1970s and 1980s, and development of advanced light-water reactors occurred in the 1990s.

While the earlier generations of reactors have effectively demonstrated the viability of nuclear power, the nuclear industry still faces a number of challenges that need to be overcome in order for nuclear power to achieve its full potential. Among these challenges are (1) public concern about the safety of nuclear power in the wake of the Three Mile Island accident in 1979 and the Chernobyl accident in 1986, (2) high capital costs and licensing uncertainties associated with the construction of new nuclear power plants, (3) public concern over potential vulnerabilities of nuclear power plants to terrorist attacks, and (4) issues associated with the accumulation of nuclear waste and the potential for nuclear material proliferation in an environment of expanding nuclear power production.

To address these concerns and to fully realize the potential contributions of nuclear power to future energy needs in the United States and worldwide, the development of a new generation of reactors, termed Generation IV, was initiated in 2001. The intent or objective of this effort is to develop multiple Generation IV nuclear power systems that would be available for international deployment before 2030. The development of the Generation IV reactor systems is an international effort, initiated by the U.S. Department of Energy (DOE) with participation from 10 countries. These countries established a formal organization referred to as the Generation IV International Forum (GIF). The GIF countries included Argentina, Brazil, Canada, France, Japan, the Republic of Korea, the Republic of South Africa, Switzerland, the United Kingdom, and the United States. The intent of the GIF is "... to develop future-generation nuclear energy systems that can be licensed, constructed, and operated in a manner that will provide competitively priced and reliable energy products while satisfactorily addressing nuclear safety, waste, proliferation, and public perception concerns."

The process used by the GIF to identify the most promising reactor concepts for development (referred to as the Generation IV Technology Roadmap) consisted of three steps. These steps were (1) to develop a set of goals for new reactor systems, (2) solicit proposals from the worldwide nuclear community for new reactor systems to meet these goals, and (3) using experts from around the world, evaluate the different concepts to select the most promising candidates for further development.

The eight goals developed by the GIF for Generation IV nuclear systems [Ref. 7] were

- *Sustainability-1.* Generation IV nuclear energy systems will provide sustainable energy generation that meets clean air objective and promotes long-term availability of systems and effective fuel utilization for worldwide energy production.
- *Sustainability-2.* Generation IV nuclear energy systems will minimize and manage their nuclear waste and notably reduce the long-term stewardship burden in the future, thereby improving protection for the public health and the environment.
- *Economics-1.* Generation IV nuclear energy systems will have a clear life-cycle cost advantage over other energy sources.
- *Economics-2.* Generation IV nuclear energy systems will have a level of financial risk comparable to other energy projects.

- *Safety and Reliability-1.* Generation IV nuclear energy systems operations will excel in safety and reliability.
- *Safety and Reliability-2.* Generation IV nuclear energy systems will have a very low likelihood and degree of reactor core damage.
- *Safety and Reliability-3.* Generation IV nuclear energy systems will eliminate the need for offsite emergency response.
- *Proliferation Resistance and Physical Protection-1.* Generation IV nuclear energy systems will increase the assurance that they are very unattractive and the least desirable route for diversion or theft for weapons-usable materials, and provide increased physical protection against acts of terrorism.

Over 100 Generation IV candidates were evaluated by experts from the GIF countries and six reactor systems were selected for further evaluation and potential development. These six reactor systems selected are described as follows.

15.5.1 Gas-Cooled Fast Reactor (GFR) System

Gas-cooled fast reactor (GFR) System is a fast neutron spectrum reactor that uses helium as the primary coolant. It is designed to operate at relatively high helium outlet temperatures, making it a good candidate for the high-efficiency production of electricity or hydrogen. As shown in Figure 15.5, a direct Brayton cycle is used for the production of electricity with the helium gas delivered from the reactor outlet to a high-temperature gas turbine connected to a generator that produces electricity. In alternative designs, the high-temperature helium can also be used to produce hydrogen using either a thermochemical process or high-temperature electrolysis, or for other high-temperature process heat applications.

The reference plant is designed to produce 288 MWe using the direct Brayton cycle with a reactor outlet temperature of 850°C. The fuel forms being considered for high-temperature operation include composite ceramic fuel, advanced fuel particles, or ceramic clad elements of actinide compounds. Alternative core configurations include prismatic blocks, pin- or plate-based assemblies. GFR's fast neutron spectrum also makes it possible to efficiently use available fissile and fertile materials in a once-through fuel cycle.

15.5.2 Very-High-Temperature Reactor

Very-high-temperature reactor (VHTR) is a helium-cooled reactor designed to provide heat at very high temperatures, in the range of 1000°C for high-temperature process heat applications. In particular, the 1000°C reactor outlet temperature makes it a good candidate for the production of hydrogen using either thermochemical or high-temperature electrolysis processes. As shown in Figure 15.6, heat for the production of hydrogen is delivered through an intermediate heat exchanger that serves to isolate the reactor system from the hydrogen production process.

The reference design for VHTR is a 600 MW(t) reactor with an outlet temperature of 1000°C. The reactor core uses graphite as a moderator to produce thermal neutrons for the fission process. The core configuration can be either graphite blocks or pebbles about the size of billiard balls in which fuel particles are dispersed. For electricity production, either a direct Brayton cycle gas turbine using the primary helium coolant as the working

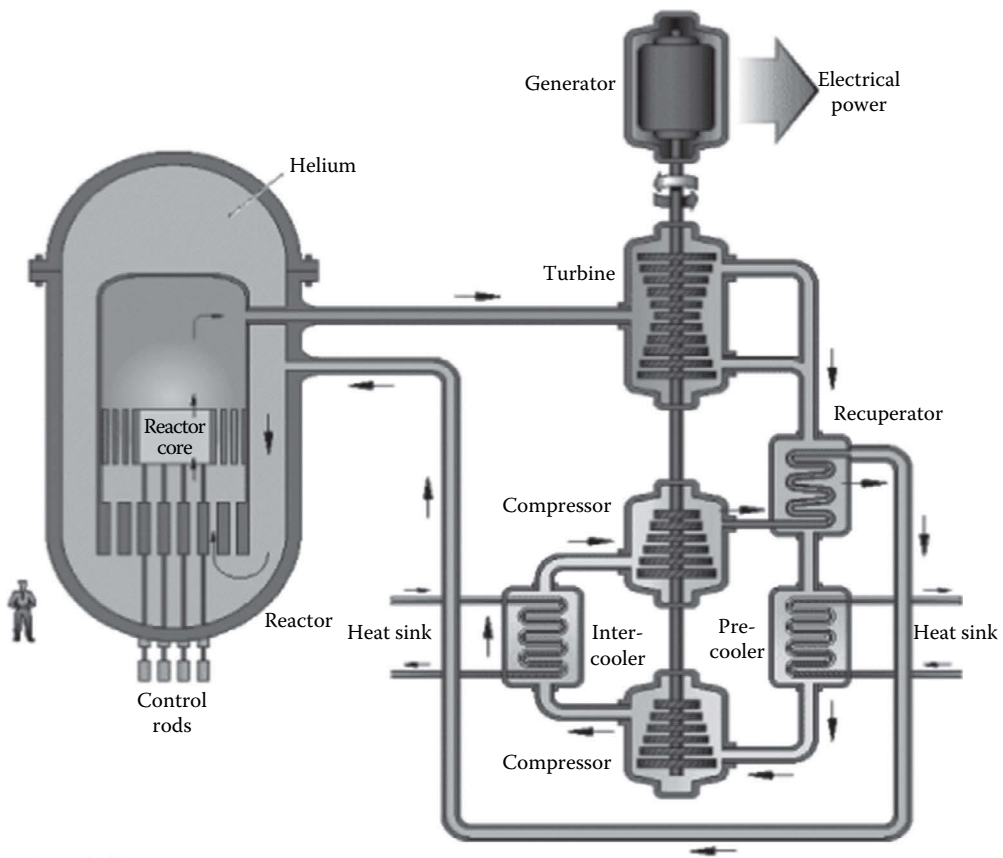


FIGURE 15.5

Gas-cooled fast reactor. (Courtesy of *A Technology Roadmap for Generation IV Nuclear Systems*, U.S. DOE, Washington, DC, 2002.)

fluid, or an indirect Rankine cycle using a secondary working fluid can be used. The high-temperature characteristics of this reactor concept also make it an ideal candidate for cogeneration applications to meet both electricity and hydrogen production, or other high-temperature process heat needs.

15.5.3 Supercritical-Water-Cooled Reactor (SWR)

Supercritical-water-cooled reactor (SWR) is a relatively high-temperature, high-pressure reactor designed to operate above the thermodynamic critical point of water, which is 374°C and 22.1 MPa. Since there is no phase change in the supercritical coolant water, the balance of plant design, shown in Figure 15.7, utilizes a relatively simple, direct cycle power conversion system. The reference design for this concept is a 1700 MWe reactor operating at a pressure of 25 MPa with a reactor outlet temperature ranging between 510°C and 550°C. This reactor can be designed as either a fast neutron spectrum or thermal neutron spectrum reactor. The relatively simple design also allows for the incorporation of passive safety features similar to those of the simplified BWR (discussed earlier). However, unlike

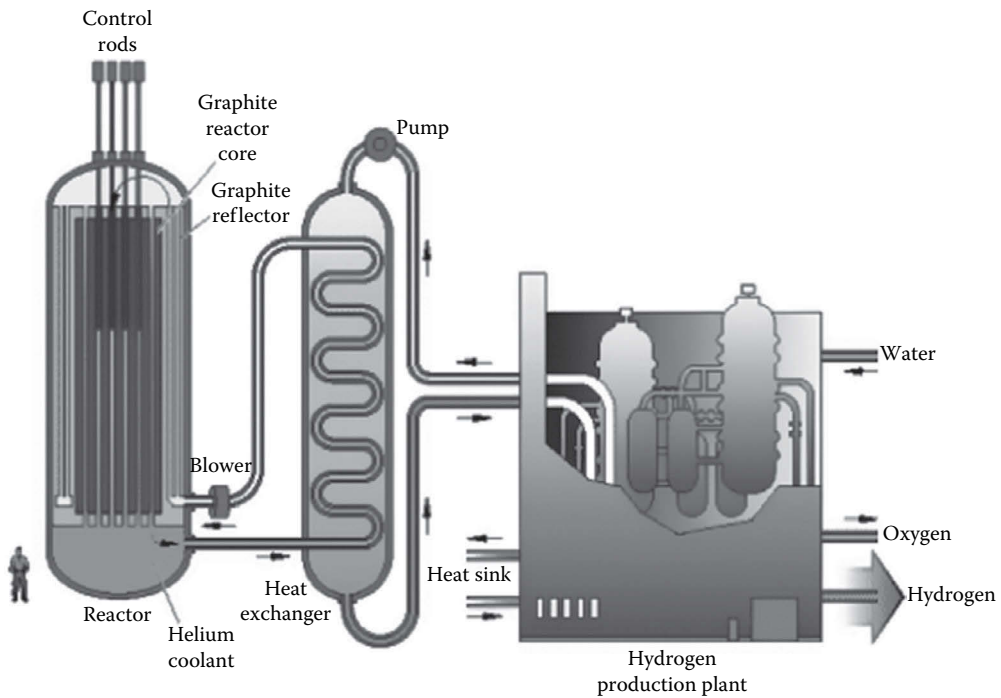


FIGURE 15.6

Very-high-temperature reactor. (Courtesy of *A Technology Roadmap for Generation IV Nuclear Systems*, U.S. DOE, Washington, DC, 2002.)

the previously discussed concepts, lower reactor outlet temperature is not well-suited for the efficient production of hydrogen, which requires minimum temperatures in the range of 850°C–900°C. Therefore, this reactor concept is primarily intended for the efficient, low-cost production of electricity.

15.5.4 Sodium-Cooled Fast Reactor

Sodium-cooled fast reactor (SFR), shown in Figure 15.8, is a sodium-cooled fast-neutron-spectrum reactor designed primarily for the efficient management of actinides and conversion of fertile uranium in a closed fuel cycle. Two reference designs to support different fuel reprocessing options have been defined for this concept. First is a medium-sized, sodium-cooled reactor with a power level between 150 and 500 MW(e) that utilizes uranium-plutonium-minor-actinide-zirconium metal alloy fuel. This reactor concept is supported by a fuel cycle based on pyrometallurgical processing in which the processing facilities are an integral part of the reactor plant design.

The second reactor reference design is a large sodium-cooled reactor with a power output capability between 500 and 1500 MWe that utilizes uranium-plutonium oxide fuel. This reactor design is supported by a fuel cycle based on an advanced aqueous process that would include a centrally located processing facility supporting a number of reactors.

Both versions of this reactor concept would operate at coolant outlet temperatures in the range of 550°C, and are intended primarily for the management of high-level waste

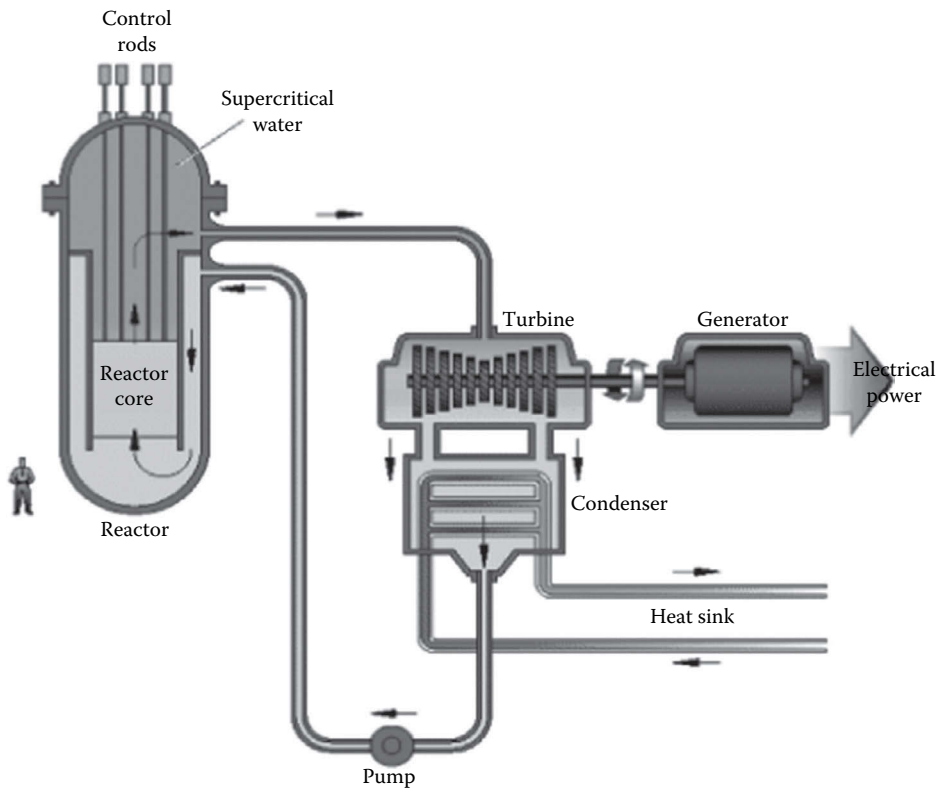


FIGURE 15.7

Supercritical water-cooled reactor. (Courtesy of *A Technology Roadmap for Generation IV Nuclear Systems*, U.S. DOE, Washington, DC, 2002.)

(HLW) and the production of electricity. In addition to design innovations to reduce capital costs, these reactors incorporate a number of enhanced safety features that include long thermal response time, a large margin to coolant boiling, a primary system that operates near atmospheric pressure, and an intermediate sodium system between the radioactive sodium in the primary system and the water and steam in the power plant.

15.5.5 Lead-Cooled Fast Reactor

Lead-cooled fast reactor (LFR) is a fast-neutron spectrum reactor cooled by either molten liquid or a lead-bismuth eutectic liquid metal. It is designed for the efficient conversion of fertile uranium and management of actinides in a closed fuel cycle. The reactor core for this design, shown in Figure 15.9, utilizes a metal- or nitride-based fuel containing fertile uranium and transuranics. As shown in Figure 15.9, LFR relies on natural convection to cool the reactor core. Outlet temperature for the current reactor concept is about 550°C, but with advanced materials, reactor outlet temperatures of 800°C may be possible. An indirect gas Brayton cycle is used to produce electrical power.

There are currently three versions of reference designs for this concept. The smallest design, rated at 50–150 MW(e), is intended for distributed power applications or electricity production on small grids. This reactor design, referred to as a “battery,” features modular

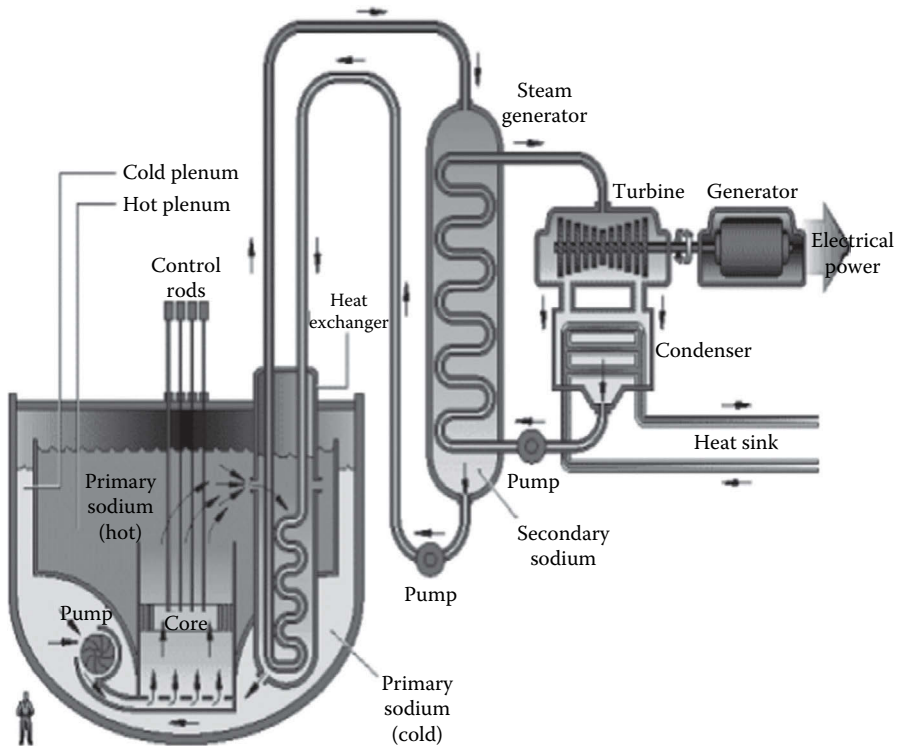


FIGURE 15.8 Sodium-cooled fast reactor. (Courtesy of *A Technology Roadmap for Generation IV Nuclear Systems*, U.S. DOE, Washington, DC, 2002.)

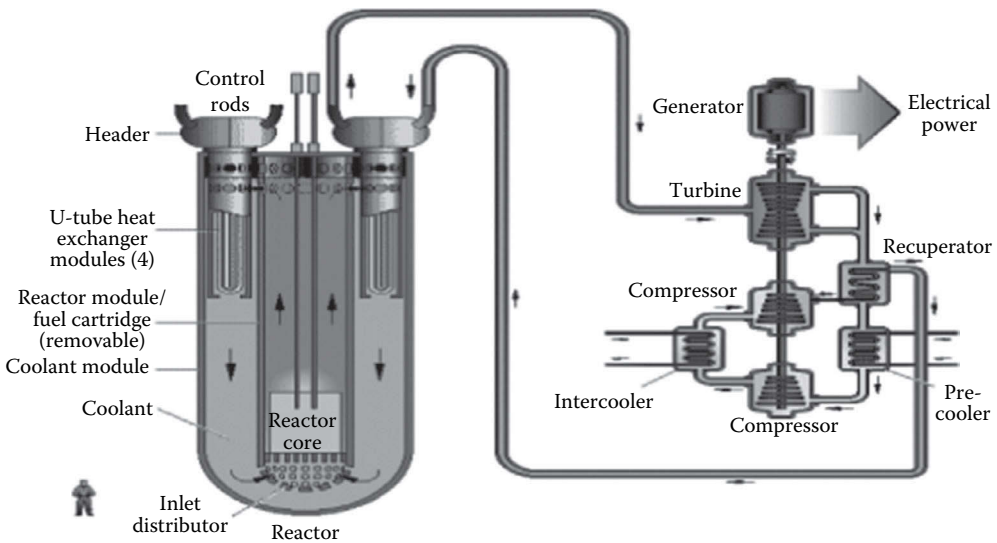


FIGURE 15.9 Lead-cooled fast reactor. (Courtesy of *A Technology Roadmap for Generation IV Nuclear Systems*, U.S. DOE, Washington, DC, 2002.)

design with a factory fabrication “cassette” core. The reactor is designed for very long refueling interval (15–20 years), with refueling accomplished by replacement of the cassette core or reactor module.

The other two versions of this design are a modular system rated at 300–400 MWe and a large plant rated at 1200 MWe. The different power options for this design are intended to fulfill different needs or opportunities in the power market, and be economically competitive with comparable alternative power sources.

15.5.6 Molten Salt Reactor

The molten salt reactor (MSR), shown in Figure 15.10, produces power by circulating a molten salt and fuel mixture through graphite core flow channels. The slowing down of neutrons by the graphite moderator in the core region provides the epithermal neutrons necessary to produce the fission power for sustained operation of the reactor. The heat from the reactor core is then transferred to a secondary system through an intermediate heat exchanger and then through a tertiary heat exchanger to the power conversion system that produces the electric power. The circulating coolant flow for this design is a mixture of sodium, uranium, and zirconium fluorides. In a closed fuel cycle, actinides such as plutonium can be efficiently burned by adding these constituents to the liquid fuel without the need for special fuel fabrication. The reference design for this concept is a 1000 MWe power plant with a coolant outlet of 700°C. To achieve higher thermal efficiencies for this concept, coolant outlet temperatures as high as 800°C may also be possible.

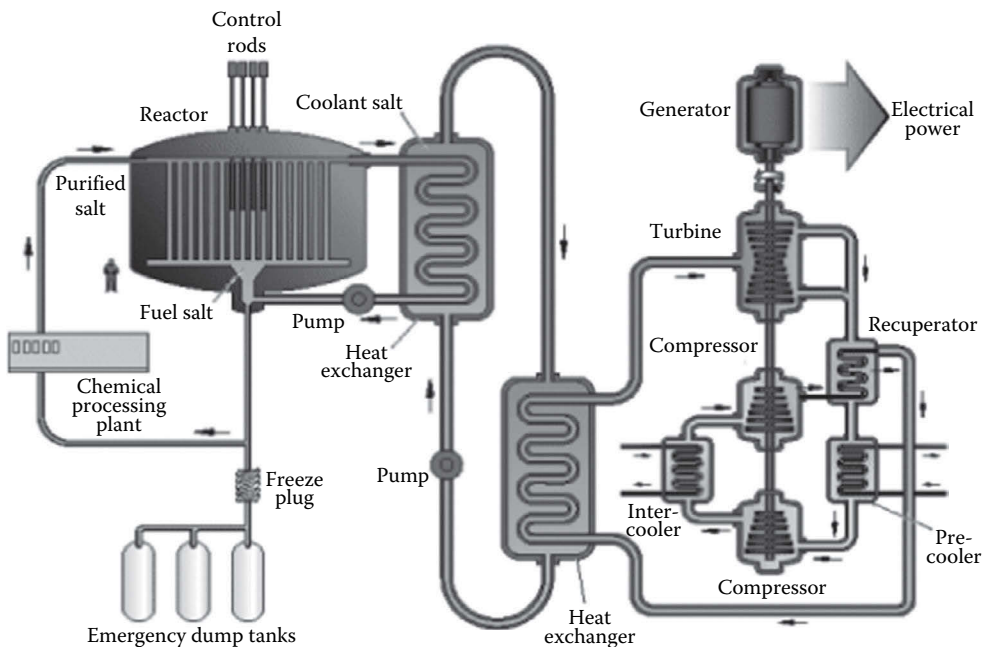


FIGURE 15.10

Molten salt reactor. (Courtesy of *A Technology Roadmap for Generation IV Nuclear Systems*, U.S. DOE, Washington, DC, 2002.)

15.6 Fuel Cycle

The process of following the fuel material from uranium or thorium mine through processing and reactor operation until it becomes waste is called the fuel cycle for nuclear systems. After a discussion of fuel cycle in general, it will be examined by looking at uranium and thorium resources, mining and milling, enrichment, reactor fuel use, spent fuel storage, nuclear materials transportation, and reprocessing. Nuclear waste will be addressed in a separate section.

General discussion of the fuel cycle often includes the terms “open” or “closed.” The open fuel cycle is also called the once-through cycle. In the once-through fuel cycle, the uranium fuel is fabricated and run through the reactor once and then disposed-off as waste. There is no reprocessing of the fuel. In the closed cycle, the fuel is reprocessed after leaving the reactor so that it can be reused to improve overall fuel utilization.

In the open cycle, the fuel is introduced into the reactor for 1–2 years. It is then removed and put into long-term storage for eventual disposal. The impact of this cycle is wastage of about 99% of energy contained in the fuel. The United States adopted the open cycle in 1977 when President Jimmy Carter issued an executive order to stop reprocessing as a part of the fuel cycle. Canada has also adopted the open cycle.

The closed cycle was envisioned when the development of nuclear power began. Uranium and plutonium removed from reactors would be reprocessed and returned to reactors as fuel. Breeder reactors would be used to breed additional plutonium for use in thermal reactors. Thorium could also be used as a breeding material to generate U233 as a reactor fuel. The intent of the closed fuel cycle was to maximize the use of available reactor fuel resources while minimizing the waste generated by operating reactors.

Currently, reprocessing is used in Europe and Japan but the benefits of closed cycle have not been fully realized since there has only been limited use of the separated plutonium. As discussed earlier, the United States and Canada, for reasons described later, have not pursued closed cycle reprocessing of spent fuel. As a result, only a small fraction of the available fuel resources are utilized, and disposal of large quantities of potentially usable spent fuels has become a major issue for the U.S. nuclear industry.

15.6.1 Uranium and Thorium Resources

Uranium is a common material in the earth’s crust. It is also present in sea water. Thorium is about three times more plentiful than uranium. Typical concentrations of uranium measured in parts per million (ppm) are shown in Table 15.4.

TABLE 15.4

Typical Concentrations of Uranium

High-grade ore—2% U	20,000 ppm U
Low-grade ore—0.1% U	1,000 ppm U
Granite	4 ppm U
Sedimentary rock	2 ppm
Earth’s continental crust (avg)	2.8 ppm U
Seawater	0.003 ppm U

Source: World Nuclear Association, Supply of uranium. Information paper, www.world-nuclear.org, August, 2012.

The amount of recoverable uranium is dependent on the price. As the price increases, more material is economically recoverable. Also, more exploration will occur and it is likely that additional orebodies will be discovered. An orebody is defined as an occurrence of mineralization from which the metal, in this case uranium, can be recovered economically. Because of the uncertainties of price and its impact on exploration, any statement of recoverable amounts of uranium is simply a picture at an instant in time and is likely to change many times in the future. There is also a store of highly enriched uranium that is being recovered as nuclear weapons are dismantled. In addition, there are millions of tons of U238 which are the results of previous enrichment activities around the world. U238 can be blended with highly enriched uranium or plutonium to make fuel for nuclear power plants. It can also be used to breed plutonium in FBR fuel cycles.

Table 15.5 presents a list of recoverable resources of uranium. The table is taken from information gathered by the World Nuclear Association from other sources and was generated in 2004.

The 3.5 Mt is enough to fuel the world's current reactors for 50 years assuming the same fuel cycles currently in use. IAEA estimates the world supply at over 14 Mt which provides a supply exceeding 200 years at the current rate of use. This estimate does not include the uranium in phosphate deposits estimated at 22 Mt or the uranium available in sea water estimated at 1400 Mt. In addition, the ability of nuclear reactors to achieve higher burnups (utilize more of the uranium in the fuel) has also increased. This increases the efficiency of uranium use. Since thorium is not included in these fuel supply numbers, and as noted earlier is about three times as plentiful as uranium, there does not appear to be a fuel supply limitation for nuclear power in the foreseeable future.

TABLE 15.5

Known Recoverable Resources of Uranium

	Uranium (Tons)	Total (%)
Australia	1,661,000	31
Kazakhstan	629,000	12
Russia	487,200	9
Canada	468,700	9
Niger	421,000	8
South Africa	279,100	5
Brazil	276,700	5
Namibia	261,000	5
United States	207,400	4
China	166,100	3
Ukraine	119,600	2
Uzbekistan	96,200	2
Mongolia	55,700	1
Jordan	33,800	1
Other	164,000	3
World total	5,327,200	

Source: World Nuclear Association, Supply of uranium. Information paper, www.world-nuclear.org, August 2012.

15.6.2 Mining and Milling

Uranium is being mined using traditional underground and open-pit excavation technologies, and also using in situ leaching or solution mining techniques.

Underground mining is used when the orebody is deep underground, usually greater than 120 m deep. In underground mines, only the orebody material is extracted. Underground mining is hazardous and made more so by high concentrations of radon from the radioactive decay of uranium. Once mined, the extracted ore is sent to a mill where uranium in the ore is concentrated.

Open-pit technology is used when the orebody is near the surface. This leads to the excavation of large amounts of material that does not contain the ore itself. The ore that is recovered is also sent to a mill for further processing.

Solution mining involves the introduction of an aqueous solution into the ore body. The solution, oxygenated ground water, is pumped into the porous orebody and the uranium is dissolved. The uranium-rich solution is then extracted and sent to the mill for further processing.

The milling process for the solid ore material involves crushing the ore and then subjecting it to a highly acidic or alkaline solution to dissolve the uranium. Mills are normally located close to the mining activity and a single mill will often support several mines. The solution containing uranium goes through a precipitation process which yields a material called yellow-cake. The yellow-cake contains about 80% uranium oxide. The yellow-cake is packaged and sent to a conversion and enrichment facility for further processing.

15.6.3 Conversion and Enrichment

Prior to entering the enrichment process, the impure U_3O_8 is converted through a series of chemical processing steps to UF_6 . During these processes, the uranium is purified. Conversion facilities are operating commercially in the United States, Canada, France, the United Kingdom, and Russia. UF_6 is solid at room temperature but converts to its gaseous form at moderate temperature levels making the compound suitable for use in the enrichment process. UF_6 is very corrosive and reacts readily with water. It is transported in large cylinders in its solid state.

Conversion of U_3O_8 to UO_2 is also done at conversion facilities. Natural UO_2 is used in reactors such as CANDU which do not require enriched uranium as fuel.

The first enrichment facilities were operated during the 1940s. Electromagnetic isotope separation process was used to separate the U235 used in the first atomic bomb. The process used a magnetic field to separate U235 from U238 as the ions were accelerated and turned, and they moved differently because of the mass difference. Multiple stages were required and the process was very difficult to run efficiently so it was soon abandoned.

Today, only two processes, gaseous diffusion and gas centrifuge are used commercially. The capacity of enrichment plants is measured in separative work units (SWU). SWU is a complex term that is dependent on the amount of uranium processed, and the concentration of U235 in the product and tails. It is a measure of the amount of energy used in the process.

The first commercial enrichment was carried out in large gaseous diffusions plants in the United States. It has also been used in Russia, the United Kingdom, France, China, and Argentina. Today operating plants exist in the United States, France, and China with a total nominal capacity of 30 million SWU.

In the gaseous diffusion process UF_6 is pumped through a series of porous walls or membranes that allow more of the light U235 to pass through. Because the lighter U235 particles travel faster than heavier U238 particles, more of them penetrate the membrane. This process continues through a series of membranes with the concentration of U235 increasing each time. For commercial reactor fuel, the process continues until U235 concentration is 3%–5%. The slower U238 particles are left behind and collect as a product referred to as “tails.” The tails have a reduced concentration of U235 and are commonly referred to as depleted uranium. This process uses a very large amount of energy and thus is very expensive to operate.

In the centrifuge enrichment process, the gaseous UF_6 is placed in a high speed centrifuge. The spinning action forces out the heavier U238 particles while the lighter U235 particles remain closer to the center. To obtain the enrichment required for power reactor fuel many stages of separation are required. The arrangement is known as a cascade. Again, the process is continued until U235 concentration is 3%–5%. The centrifuge process uses only about 2% of the energy required by gaseous diffusion.

Table 15.6 shows the location and size of enrichment facilities around the world.

15.6.4 Fuel Fabrication and Use

Following enrichment, UF_6 is shipped to a fuel fabrication facility where it is converted to UO_2 and pressed into cylindrical ceramic pellets. The pellets are sintered, heated to high temperature, and inserted in the fuel-cladding tubes. The tubular material is zircaloy, an alloy of zirconium. The tubes are sealed forming fuel rods which are assembled into fuel assemblies and shipped to a reactor for use. All the dimensions of pellets and fuel rods are very carefully controlled to assure uniformity throughout the fuel assemblies.

The primary hazard in the fabrication facility is the potential for an accidental criticality because they are working with enriched uranium. Therefore, all of the processing quantities and the dimensions of the processing vessels must be controlled. This must be done even with the low-enriched uranium.

A typical 1000 MWe reactor will use about 27 tons of UO_2 each year. Typical burnup in current reactors is 33 GWd/t of uranium fed to the reactor. The energy available from the fission of uranium is 1 MW/g of uranium or 1000 GW/t. Using these numbers the actual amount of uranium burned is only 3%–5%. This means that the unused energy available from the spent fuel, if it could be completely burned, is over 95%. During the operation of the reactor some of the U238 is converted to plutonium and that also contributes to the thermal energy of the reactor.

Advanced fuel use in reactors is estimated to be up to 200 GWd/t. In this case, about 80% of the energy available from the uranium remains in the spent fuel. These facts are the driving force behind the questions regarding reprocessing. In the once-through fuel cycle the spent fuel will be disposed of as waste. In the closed cycle, the spent fuel is reprocessed and the remaining uranium and plutonium are recovered.

15.6.5 Reprocessing

In 1940s reactors were operated solely for the production of plutonium to be used in weapons. The fuels from the production reactors were reprocessed in order to recover plutonium. Chemical processes were developed to separate the fission products and uranium from plutonium. The most common process was the PUREX process. This is the process that is used today by countries that reprocess power reactor fuels.

TABLE 15.6

Location, Size, and Type of Enrichment Facilities around the World

Country	Owner/Controller	Plant Name/Location	Capacity (1,000 SWU)
<i>Gaseous diffusion plants</i>			
Argentina	CNEA ☞	Pilcaniyeu [ISSUES]	20
China	CNNC ☞	Lanzhou	900?
France	EURODIF	Tricastin (closed since June 7, 2012)	(10,800)
United States	U.S.-Enrichment Corp. ☞	Paducah, Kentucky ☞ (closed since May 31, 2013)	(11,300)
		Portsmouth, Ohio ☞ (closed since May 11, 2001)	(7,400)
Subtotal			920
<i>Centrifuge plants</i>			
Brazil	INB ☞	Resende	?
China	CNNC	Hanzhong	500
		Lanzhou	500
France	Eurodif	Georges Besse II, Tricastin (under constr.)	2,800
Germany	UrencoDeutschlandGmbH	Gronau	4,200
India	DAE Nuclear Fuel Complex ☞	Ratnahalli, Karnataka	4.5
Iran	AEOI ☞	Natanz [ISSUES]	?
		Qom [ISSUES]	?
Japan	JNC	Ningyo Toge	200
	Japan Nuclear Fuel Limited (JNFL)	Rokkasho-mura	1,050
Korea, DPR		Yongbyon [ISSUES]	8
		Tongchang [ISSUES]	?
Netherlands	Urenco Netherland BV	Almelo	5,550
Pakistan	Pakistan Atomic Energy Commission (PAEC)	Kahuta	5
Russia	Rosatom ☞	Urals Electrochemical Integrated Enterprise (UEIE), ☞ Novouralsk (formerly Sverdlovsk-44, near Ekaterinburg) [ISSUES]	7,000
		Siberian Chemical Combine (SKhK), ☞ Seversk (formerly Tomsk-7) [ISSUES]	4,000
		Electrochemical Plant (ECP), ☞ Zelenogorsk (formerly Krasnoyarsk-45) [ISSUES]	3,000
		Angarsk Electrolytic Chemical Combine (AEKhK), ☞ Angarsk [ISSUES]	2,600
United Kingdom	Urenco UK Ltd.	Capenhurst	5,000
United States	Urenco USA	Lea County, NM (under constr.) [ISSUES]	2,200
Subtotal			38,567.5
Total			39,487.5

Source: WISE Uranium Project, World nuclear fuel facilities, www.wise-uranium.org, November 2013.

The purpose of reprocessing is to recover the uranium and plutonium in the spent fuel. As discussed earlier these materials contain a large amount of potential energy if they are reused as reactor fuel. Plutonium separated in the PUREX process can be mixed with uranium to form a mixed oxide (MOX) fuel. Plutonium from the dismantlement of weapons can be used in the same way.

The potential availability of separated plutonium is seen by some as a potential mechanism for the proliferation of nuclear weapons. This was the basis of the U.S. decision to halt reprocessing. In the 1970s, research on ways to modify the chemical process began, so that plutonium and uranium would remain together at the end of the process. In this method, called co-processing, the short-lived fission products would be separated and the remaining uranium, plutonium, and other actinide elements would remain together. This remaining mixture would be highly radioactive but could be remotely processed into new reactor fuel. A blend of fast neutron and thermal reactors could be used to maximize the use of this material.

The current world wide reprocessing capability is shown in Table 15.7. All of these facilities use the PUREX technology. More than 80,000 tons of commercial fuel have been reprocessed in these facilities.

Three processes are considered to be the mature options for reprocessing fuel. They are PUREX, UREX+, and Pyroprocessing. Each of them has certain advantages and disadvantages.

15.6.5.1 PUREX

The PUREX process is the oldest and most common reprocessing option. It uses liquid-liquid extraction to process light-water reactor spent fuel. The spent fuel is dissolved in nitric acid, and then the acid solution is mixed with an organic solvent consisting of tributyl phosphate in kerosene. Uranium and plutonium are extracted in the organic phase and the fission products remain in the aqueous phase. Further processing allows the separation of uranium and plutonium. The advantage of this process is the long-term experience with the process. The disadvantage is that it cannot separate fission products such as technetium, cesium, and strontium nor can it separate actinides such as neptunium, americium, and curium.

TABLE 15.7

World Commercial Reprocessing Capacity

	Location	Tons/Year
LWR fuel	France, La Hague	1700
	United Kingdom, Sellafield (THORP)	900
	Russia, Ozersk (Mayak)	400
	Japan (Rokkasho)	800
	Subtotal	3800
Other nuclear fuels	United Kingdom, Sellafield	1500
	India	330
	Subtotal	1830
Civilian capacity	Total	5630

Source: Uranium Information Centre, Processing of used nuclear fuel, UIC Nuclear Issues Briefing Paper 72, www.uic.com.au, March 2005.

15.6.5.2 UREX+

The UREX+ process is a liquid–liquid extraction process like PUREX. It can be used for light-water reactor fuels and it includes additional extraction steps that allow separation of neptunium/plutonium, technetium, uranium, cesium/strontium, americium, and curium. The advantage of this process is that it meets the requirements for continuous recycle in light-water reactors and it builds on current technology. The disadvantage is that it cannot be used to process short-cooled fuels and it cannot be used for some specialty fuels being developed for advanced reactors.

15.6.5.3 Pyroprocessing

This process was developed and tested at Experimental Breeder Reactor-2 (EBR-2) by Argonne National Laboratory in the United States. It is an electrochemical process rather than a liquid–liquid extraction process. Oxide fuels are first converted to metals in order to be processed. The metallic fuel is then treated to separate uranium and the transuranic elements from the fission products. The advantage of this process is the ability to process short-cooled and specialty fuels designed for advanced reactors. The disadvantage is that it does not meet the requirements for continuous recycle from thermal reactors but it is ideal for fuel for fast neutron reactors.

15.6.6 Spent Fuel Storage

Spent fuel is routinely discharged from operating reactors. As it is discharged it is moved to the spent fuel storage pool that is an integral part of the reactor facility. Reactors are built with storage pools that will hold fuel from many years of operation. The pools are actively cooled by circulating cooling water. The fuel stored at many older reactors is reaching the capacity of the on-site storage pools. At this point, the fuel is being transferred to dry storage. Dry storage takes place in large metal or concrete storage facilities. These dry facilities are passively cooled by the air circulating around them.

15.6.7 Spent Fuel Transportation

Spent fuel is transported in large engineered containers designated as Type B containers (casks). Casks provide shielding for the highly radioactive fuel so that they can be safely handled. They are made of cast iron or steel. Many of them use lead as the shielding material. They are also designed to protect the environment by maintaining their integrity in case of accident. They are designed to withstand severe accidents including fires, impacts, immersion, pressure, heat, and cold, and are tested as part of the design certification process.

Casks have been used to transport radioactive materials for over 50 years. The IAEA has published advisory regulations for safe transportation of radioactive materials since 1961. Casks are built to standards, designed to meet the IAEA advisory regulations, specified by licensing authorities such as NRC in the United States.

Spent fuel is shipped from reactor sites by road, rail, or water. Larger casks can weigh up to 110 tons and hold about 6 tons of spent fuel. Since 1971, about 7000 shipments of spent fuel (over 35,000 tons) have been transported over 30 million km with no property damage or personal injury, no breach of containment, and a very low-dose rate to the personnel involved.

15.7 Nuclear Waste

Radioactive wastes are produced throughout the reactor fuel cycle. The costs of managing these wastes are included in the costs of the nuclear fuel cycle and thus are part of the electricity cost.

Since these materials are radioactive, they decay with time. Each radioactive isotope has a half-life, which is the time it takes for half of the material to decay away. Eventually, these materials decay to a stable nonradioactive form.

The process of managing radioactive waste involves the protection of people from the effects of radiation. The longer-lived materials tend to emit alpha and beta particles. It is relatively easy to shield people from this radiation but if these materials are ingested the alpha and beta radiation can be harmful. The shorter-lived materials usually emit gamma rays. These materials require greater amounts of shielding.

15.7.1 Types of Radioactive Wastes

The strict definitions of types of radioactive waste may vary from country to country. In the following discussion, more generally accepted terminology will be used.

15.7.1.1 Mine Tailings

Mining and milling of uranium produces a sandy type of waste which contains naturally occurring radioactive elements that are present in uranium ore. The decay of these materials produces radon gas which must be contained. This is often done by covering the tailings piles with clay to contain the radon gas. Technically, tailings are not classified as radioactive waste.

15.7.1.2 Low-Level Wastes

Low-level wastes (LLW) is generated from medical and industrial uses of radioactive materials as well as from the nuclear fuel cycle. In general, these wastes include materials such as paper, clothing, rags, tools filters, soils, etc., which contain small amounts of radioactivity. This radioactivity tends to be short-lived. These materials generally do not have to be shielded during transport and they are suitable for shallow land burial. The volume of these materials may be reduced by compacting or incineration prior to disposal. They make up about 90% of the volume of radioactive waste but contain only about 1% of the radioactivity of all the radioactive waste.

15.7.1.3 Intermediate-Level Wastes

Intermediate-level wastes (ILW) are generated during the operation of nuclear reactors, in the reprocessing of spent fuel, and from the decommissioning of nuclear facilities. These materials contain higher amounts of radioactivity and generally require some shielding during storage and transportation. ILW is generally made up of resins, chemical sludge, fuel cladding, and contaminated materials from decommissioning nuclear facilities. Some of these materials are processed before disposal by solidifying them in concrete or bitumen. They make up about 7% of the volume and have about 4% of the radioactivity of all the radioactive waste.

15.7.1.4 High-Level Wastes

High level waste is generated during the operation of a nuclear reactor. This waste consists of fission products and transuranic elements generated during the fission process. This material is highly radioactive and is also thermally hot so that it must be both shielded and cooled. It accounts for 95% of the radioactivity produced by nuclear power reactors.

15.7.2 Managing HLW from Spent Fuel

The form of HLW from spent fuel is either the spent fuel itself or the waste products from reprocessing. The level of radioactivity from spent fuel falls to about one thousandth of the level it was when removed from the reactor in 40–50 years. This means the heat generated is also greatly reduced.

Currently, there are about 270,000 tons of spent fuel in storage at reactor sites around the world. An additional 12,000 tons are generated each year and about 3,000 tons of this are sent for reprocessing.

When spent fuel reprocessing is used, uranium and plutonium are first removed during reprocessing, and then the much smaller volume of remaining HLW is solidified using a vitrification process. In this process, the fission products are mixed in a glass material, vitrified in stainless steel canisters, and stored in shielded facilities for later disposal.

High-level waste will eventually be disposed-off in deep geologic facilities. Several countries have selected sites for these facilities and they are expected to be commissioned for use after 2015.

15.7.3 Managing Other Radioactive Wastes

Generally, ILW and LLW are disposed by burial. ILW generated from fuel reprocessing will be disposed in deep geological facilities. Some low-level liquid wastes from reprocessing plants are discharged to the sea. These liquids include some distinctive materials such as technetium-99 that can be discerned hundreds of kilometers away. Such discharges are tightly controlled and regulated so that the maximum dose any individual receives is a small fraction of natural background radiation.

Nuclear power stations and reprocessing facilities release small quantities of radioactive gases to the atmosphere. Gases such as krypton-85 and xenon-133 are chemically inert and gases such as iodine-131 have short half-lives. The net effect of these gases is too small to warrant further consideration.

Table 15.8 provides a summary of waste management adopted by countries throughout the world.

15.8 Nuclear Power Economics

Any discussion of the economics of nuclear power involves a comparison with other competitive electric generation technologies. The competing technologies are usually coal and natural gas.

Nuclear power costs include capital costs, fuel cycle costs, waste management costs and the cost of decommissioning after operation. The costs vary widely depending on the

TABLE 15.8

Waste Management for Used Fuel and HLW from Nuclear Power Reactors

Country	Policy	Facilities and Progress Toward Final Repositories
Belgium	Reprocessing	Central waste storage at Dessel Underground laboratory established in 1984 at Mol Construction of repository to begin about 2035
Canada	Direct disposal	Nuclear Waste Management Organisation set up in 2002 Deep geological repository confirmed as policy, retrievable Repository site search from 2009, planned for use in 2025
China	Reprocessing	Central used fuel storage at LanZhou Repository site selection to be completed by 2020 Underground research laboratory from 2020, disposal from 2050
Finland	Direct disposal	Program started in 1983, two used fuel storages in operation Posiva Oy set up in 1995 to implement deep geological disposal Underground research laboratory Onkalo under construction Repository planned from this, near Olkiluoto, to open in 2020
France	Reprocessing	Underground rock laboratories in clay and granite Parliamentary confirmation in 2006 of deep geological disposal, containers to be retrievable and policy “reversible” Bure clay deposit is likely repository site to be licensed in 2015, operating from 2025
Germany	Reprocessing but moving to direct disposal	Repository planning started in 1973 Used fuel storage at Ahaus and Gorleben salt dome Geological repository may be operational at Gorleben after 2025
India	Reprocessing	Research on deep geological disposal for HLW
Japan	Reprocessing	Underground laboratory at Mizunami in granite since 1996 Used fuel and HLW storage facility at Rokkasho since 1995 Used fuel storage under construction at Mutsu, start-up in 2013 NUMO set up in 2000, site selection for deep geological repository underway to 2025, operation from 2035, retrievable
Russia	Reprocessing	Underground laboratory in granite or gneiss in Krasnoyarsk region from 2015, may evolve into repository Sites for final repository under investigation on Kola peninsula Pool storage for used VVER-1000 fuel at Zheleznogorsk since 1985 Dry storage for used RBMK and other fuel at Zheleznogorsk from 2012 Various interim storage facilities in operation
South Korea	Direct disposal, maybe change	Waste program confirmed in 1998, KRWM set up in 2009 Central interim storage planned from 2016
Spain	Direct disposal	ENRESA established in 1984, its plan was accepted in 1999 Central interim storage at Villar de Canas from 2016 (volunteered location) Research on deep geological disposal, decision after 2010
Sweden	Direct disposal	Central used fuel storage facility—CLAB—in operation since 1985 Underground research laboratory at Aspo for HLW repository Osthammar site selected for repository (volunteered location)
Switzerland	Reprocessing	Central interim storage for HLW and used fuel at ZZL Wurenlingen since 2001 Smaller used fuel storage at Beznau Underground research laboratory for high-level waste repository at Grimsel since 1983 Deep repository by 2020, containers to be retrievable

(Continued)

TABLE 15.8 (Continued)

Waste Management for Used Fuel and HLW from Nuclear Power Reactors

Country	Policy	Facilities and Progress Toward Final Repositories
United Kingdom	Reprocessing	Low-level waste repository in operation since 1959 HLW from reprocessing is vitrified and stored at Sellafield Repository location to be on basis of community agreement New NDA subsidiary to progress geological disposal
United States	Direct disposal	DoE responsible for used fuel from 1998, accumulated \$32 billion waste fund Considerable research and development on repository in welded tuffs at Yucca Mountain, Nevada The 2002 Congress decision that geological repository be at Yucca Mountain was countered politically in 2009 Central interim storage for used fuel now likely

Source: World Nuclear Association, Waste management in the nuclear fuel cycle. Information paper, www.world-nuclear.org, December 2012.

location of the generating plant. In countries such as China, Australia, and the United States, coal remains economically attractive because of large accessible coal resources. This advantage could be changed if a charge is made on carbon emissions. In other areas nuclear energy is competitive with fossil fuels even though nuclear costs include the cost of all waste disposal and decommissioning.

15.8.1 Comparison of Generation Technologies

As previously stated, nuclear power costs include spent fuel management, plant decommissioning, and final waste disposal. These costs are not generally included in the costs of other power generation technologies.

Decommissioning costs are estimated to be 9%–15% of the initial cost of a nuclear plant. Since these costs are discounted over the life of the plant, they contribute only a few percent to the investment cost of the plant and have an even lower impact on the electricity generation cost. This impact in the United States is about 0.1–0.2 cent/kWh or about 5% of the cost of electricity produced.

Spent fuel interim storage and ultimate disposal in a waste repository contribute another 10% to the cost of electricity produced. This cost is reduced if the spent fuel is disposed-off directly. This does not account for the energy that could be extracted from the fuel if it was reprocessed.

Costs for nuclear-based electricity generation have been dropping over the last decade. This reduction in the cost of nuclear generated electricity is a result of reductions in nuclear plant fuel, operating, and maintenance costs. However, the capital construction costs for nuclear plants are significantly higher than coal and gas-fired plants. Because the capital cost of nuclear plants contribute more to the cost of electricity than for coal- or gas-fired generation the impact of changes in fuel, operation, and maintenance costs on the cost of electricity generation is less than for coal- or gas-fired generation.

One of the primary contributors to the capital cost of nuclear plants has been the cost of money used to finance nuclear plant construction. The financing costs increase when the time required to license and construct a plant increases. Two factors are leading to the reduction in this portion of the cost. First, especially in the United States, the licensing process is changing so that a plant receives both the construction permit and the operating

license prior to the start of construction. Under this process, there is no large investment in plant hardware prior to completion of a significant portion of the licensing process, leading to a reduction in time required for the plant to begin producing revenue. Second, the new generation of nuclear plants will be highly standardized and modularized. This will allow a significant reduction in the time required to construct a new plant. It is estimated that the time from the start of construction to the start of operation will be reduced from nearly 10 years to 4–5 years. This will have a significant impact on capital costs.

The reduced capital costs associated with the licensing and construction of new nuclear power plants, and the fact that nuclear power is inherently less susceptible to large fluctuations in fuel costs, have made nuclear power an attractive energy option for many countries seeking to diversify their energy mix in the face of rising fossil fuel costs.

15.9 Conclusions

The development of nuclear power began after World War II and continues today. The first power-generating plants were constructed in the late 1950s. During the 1960s and 1970s, there was a large commitment to nuclear power until the accidents occurred at Three Mile Island in 1979 and then at Chernobyl in 1986. The new safety requirements and delays caused by these accidents drove up the costs and at the same time caused a loss of public acceptance. In the United States, many plant orders were canceled and in other countries the entire nuclear programs were canceled.

The ability of nuclear reactors to produce electricity economically and safely without the generation of greenhouse gases has revitalized the interest in nuclear power as an alternative energy source. Many lessons have been learned from the operation of current power plants that have allowed the safety of newly designed plants to be improved. This coupled with the desire of many nations to develop secure energy sources and a diversity of energy options has resulted in the continuing development of a whole new generation of nuclear plants to meet future energy needs.

Nuclear power is also not as susceptible to fluctuation in fuel costs as petroleum and natural gas. As discussed, the supply of uranium is very large, and if it is supplemented with thorium, the fuel supply will seemingly be unlimited. This drives many other aspects of the fuel cycle, such as the choice between closed and open fuel cycles discussed earlier. For example, because of the large uranium resource and the fears of nuclear proliferation, the once-through (open) fuel cycle is favored by many. This will require large, deep, geologic waste repositories for the disposal of large quantities of spent fuel. However, when reprocessing is included in the closed fuel cycle, the amount of needed repository space is greatly reduced but the expense of operation is increased. Finally, it may be possible to essentially eliminate the need for repositories by utilizing advanced fuel cycles that utilize almost all of the energy available in uranium and the other transuranic products of reactor operation.

The need for energy and the use of electricity as the primary energy source for the end-user will drive the increase in electricity generation around the world. The drive to reduce the production of greenhouse gases will contribute to a wider use of nuclear power for electricity generation. The recognition that nuclear power can safely provide large base-load generating capacity at a reasonable cost using known technologies will also be a major factor in its future development.

References

1. World Nuclear Association. Plans for new reactors worldwide. Information paper, www.world-nuclear.org, March 2013.
2. World Nuclear Association. Advanced nuclear power reactors. Information paper, www.world-nuclear.org, September 2013.
3. WISE Uranium Project. World nuclear fuel facilities. www.wise-uranium.org, November 2013.
4. World Nuclear Association. Waste management in the nuclear fuel cycle. Information paper, www.world-nuclear.org, December 2012.
5. UIC Nuclear Issues Briefing Paper #72. Processing of used nuclear fuel. www.uic.com.au, March 2005.
6. World Nuclear Association. Supply of uranium. Information paper, www.world-nuclear.org, August 2012.
7. U.S. DOE Nuclear Energy Research Advisory Committee and the Generation IV International Forum. A technology roadmap for the Generation IV nuclear energy systems, GIF-002-00, December 2002.
8. World Nuclear Association. Small nuclear power reactors. Information paper, www.world-nuclear.org, February 2014.

16

Nuclear Fusion

François Waelbroeck

CONTENTS

16.1 Introduction.....	491
16.2 Fusion Reactions.....	491
16.3 Confinement Concepts.....	492
16.4 Tokamak Reactor Development.....	492
16.5 Fusion Energy Conversion and Transport.....	493
Defining Terms.....	494
References.....	494
For Further Information.....	495

16.1 Introduction

Nuclear fusion holds the promise of providing almost unlimited power for future generations. If the process can be commercialized as envisioned by reactor design studies (Najmabadi et al. 1994), many of the problems associated with central electric power stations could be eliminated. Fusion power plants would not produce the pollution caused by the burning of fossil fuels and would eliminate the concern for meltdown associated with nuclear fission. The amount of radioactive waste material produced by a fusion reactor will be much less than that of a fission reactor since there is essentially no radioactive ash from the fusion reaction. If low activation advanced materials such as silicon carbide composites can be developed for the reactor structural material, the problem of disposal of activated components can also be eliminated.

16.2 Fusion Reactions

Although a number of different atomic nuclei can combine to release net energy from fusion, the reaction of deuterium and tritium (D-T) is the basis of planning for the first generation of fusion reactors. This choice is based on considerations of reactor economy. The D-T reaction occurs at the lowest temperature, has the highest probability for reaction, and provides the greatest output of power per unit of cost (Shannon 1989). The disadvantages of D-T as a fusion fuel are twofold. Tritium does not occur naturally in

nature and must be bred in the fusion reactor or elsewhere. Second, tritium is a radioactive isotope of hydrogen with a relatively long half-life of 12.3 years. Since tritium can readily combine with air and water, special safety procedures will be required to handle the inventory necessary for a fusion reactor. There is hope that a less reactive fuel, such as deuterium alone (D-D), will eventually prove to be an economically acceptable alternative (Shannon 1989). A tantalizing alternative is the reaction between a proton and boron-11 to form three helium nuclei. This offers the prospect of aneutronic fusion, but the conditions necessary to produce energy through this reaction are very difficult to achieve (Rostoker et al. 1997).

16.3 Confinement Concepts

The two main approaches to fusion confinement are magnetic and inertial fusion confinement. Magnetic fusion relies on electric currents running in coils and in the plasma to create a magnetic “bottle” that confines tenuous plasma for long pulses, if not in steady state. The leading concept, the tokamak, has received the majority of research funding for fusion energy development. Other magnetic fusion concepts, such as the stellarator, the spherical torus, reversed-field pinch, and field-reversed configurations, are being developed as possible alternatives to the tokamak (Sheffield 1994). Inertial confinement, by contrast, relies on lasers to compress the fuel to very high densities, leading to an inherently pulsed approach (Moses 2009). Inertial confinement is of interest for research pertaining to weapons stockpile stewardship in addition to fusion energy. Experiments on the National Ignition Facility demonstrated heating of the plasma by fusion products and the generation of more fusion power than deposited into the fuel during the implosion process (Hurricane et al. 2014). Unfortunately, instabilities have so far prevented the ignition of the fuel that is a necessary step in the development of fusion energy. The remainder of this discussion will consider only the tokamak magnetic fusion concept.

16.4 Tokamak Reactor Development

The tokamak device has proved to be the most effective means of producing the conditions necessary for magnetic fusion energy production. Researchers have achieved in excess of 10 MW of D-T fusion power in two tokamaks, the Tokamak Fusion Test Reactor (TFTR) at the Princeton Plasma Physics Laboratory and the Joint European Torus (JET) in the United Kingdom. In another experiment on the JET, researchers sustained 4 MW of fusion power for several seconds (Jacquinot and the Jet Team 1999). The next major experiment, the International Thermonuclear Experimental Reactor (ITER), is being constructed under an international agreement among Europe, Japan, Russia, India, China, Korea, and the United States (Holtkamp 2009). A drawing of the ITER tokamak is shown in Figure 16.1. The ITER is designed to produce a fusion power of 500 MW. It will enable the study of plasma heated primarily by fusion reactions. This will be a significant step on the path to commercial fusion power. Looking beyond ITER, the European Fusion Development

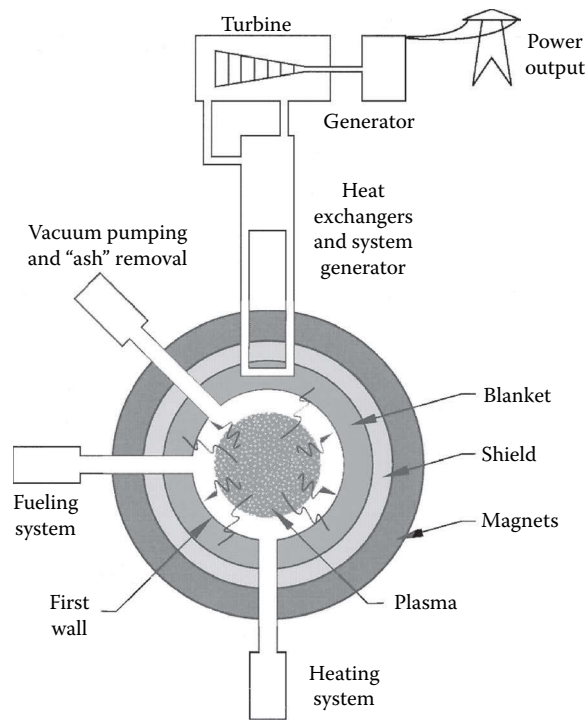


FIGURE 16.2
Schematic diagram of a magnetic fusion reactor power plant.

Defining Terms

Deuterium and tritium: Isotopes of hydrogen as the fuel for fusion reactors.

Half-life: The time required for half of the radioactive material to disintegrate.

Low-activation advanced materials: Structural materials that significantly reduce the radioactivity induced by exposure to fusion neutrons.

Plasma: A gas such as a mixture of deuterium and tritium raised to a very high temperature at which the electrons and the nuclei of the atoms separate. The plasma, consisting of electrons and ions, can conduct electricity and react to magnetic fields.

References

- Holtkamp, N. 2009. The status of the ITER design. *Fusion Engineering and Design* 84, 98.
- Hurricane, O. E. et al. 2014. Fuel gain exceeding unity in an inertially confined fusion implosion. *Nature* 506, 343–348.
- Jacquinot and the JET Team. 1999. Deuterium-tritium operation in magnetic confinement experiments: Results and underlying physics. *Plasma Physics and Controlled Fusion* 41, A13.

- Najmabadi, F. et al. 1994. The ARIES-II and -IV second stability tokamak reactors, Report UCLA-PPG-1461, University of California, Los Angeles, CA.
- Romanelli, F., Federici, G., Horton, L., Neu, R., Stork, D., and Zohm, H. 2013. A roadmap to the realization of fusion energy, *Proceedings of the IEEE 25th Symposium on Fusion Engineering*, p. 1. <https://www.euro-fusion.org/wpcms/wp-content/uploads/2013/01/JG12.356-web.pdf>.
- Rostoker, N., Binderbauer, M. W., and Monkhorst, H. J. 1997. Colliding beam fusion reactor, *Science* 278, 1419–1422.
- Shannon, T. E. 1989. Design and cost evaluation of a generic magnetic fusion reactor using the D-D fuel cycle. *Fusion Technology*, 15(2), 1245–1253 (Part 2B).
- Sheffield, J. 1994. The physics of magnetic fusion reactors. *Reviews of Modern Physics* 66(3), 1015–1103.
- Moses, E. I. 2009. Ignition on the National Ignition Facility: A path towards inertial fusion energy. *Nuclear Fusion* 49, 104022.

For Further Information

The U.S. Department of Energy, Office of Fusion Energy maintains a home page on the World Wide Web. The website <http://www.fofe.er.doe.gov> serves as an excellent source of up-to-date information and provides access to information from most institutions involved in fusion research.



Taylor & Francis

Taylor & Francis Group

<http://taylorandfrancis.com>

17

*Energy Storage Technologies**

Jeffrey P. Chamberlain, Roel Hammerschlag, and Christopher P. Schaber

CONTENTS

17.1 Overview of Storage Technologies	498
17.2 Principal Forms of Stored Energy	499
17.3 Applications of Energy Storage	500
17.4 Specifying Energy Storage Devices.....	501
17.5 Specifying Fuels.....	504
17.6 Electrochemical Energy Storage	505
17.6.1 Secondary Batteries	505
17.6.1.1 Lead-Acid	506
17.6.1.2 Lithium Ion	506
17.6.1.3 Nickel–Cadmium.....	507
17.6.1.4 Nickel Metal Hydride.....	507
17.6.1.5 Sodium–Sulfur	508
17.6.1.6 Zebra	509
17.6.2 Flow Batteries	509
17.6.2.1 Vanadium Redox.....	509
17.6.2.2 Polysulfide Bromide.....	510
17.6.2.3 Zinc Bromide	510
17.6.2.4 Nonaqueous Redox Flow	511
17.6.3 Electrolytic Hydrogen	511
17.7 Direct Electric Storage	511
17.7.1 Ultracapacitors.....	511
17.7.2 SMES.....	512
17.8 Mechanical Energy Storage.....	512
17.8.1 Pumped Hydro.....	512
17.8.2 Compressed Air	513
17.8.3 Flywheels	514
17.9 Direct Thermal Storage.....	515
17.9.1 Sensible Heat	515
17.9.1.1 Liquids.....	515
17.9.1.2 Solids.....	517
17.9.2 Latent Heat.....	517
17.9.2.1 Phase Change	518

* Updated by Jeffrey P. Chamberlain from Chapter 18.1 of *Handbook of Energy Efficiency and Renewable Energy* (F. Kreith and D.Y. Goswami, eds.), Boca Raton, FL: CRC Press, 2007.

17.9.2.2 Hydration–Dehydration Reactions	519
17.9.2.3 Chemical Reaction.....	519
17.10 Thermochemical Energy Storage	519
17.10.1 Biomass Solids	519
17.10.2 Ethanol.....	520
17.10.3 Biodiesel.....	521
17.10.4 Syngas	521
References.....	522

17.1 Overview of Storage Technologies

The availability of affordable and reliable electrical energy storage technologies is crucial to the worldwide effort to transform our electricity and transportation systems and break society's century-long dependence on fossil fuels.

Concerns about energy security and climate change are driving demand for renewable energy generation and storage systems as an alternative to current technologies. While grid energy generation using wind and solar technologies is becoming more common, the lack of cost-effective, high-capacity storage systems has severely limited the use of these technologies. Similarly, shortcomings in storage systems have limited the shift in transportation fuel from petroleum to electricity.¹ Because the current state of knowledge does not allow us to overcome these limitations, revolutionary advances in science and engineering are needed.²

The electric grid is undergoing a transformation that requires electricity storage in order to realize its objectives of low-carbon, reliable operation. Tomorrow's grid uses a highly diverse generation mix with inflexible (i.e., unpredictable) renewable energy sources in both centralized and distributed deployments. While battery-based storage would avoid reliability issues, the cost of batteries (~\$500/kWh for a Na–S battery) is five times that of other storage technologies.³

In parallel, widespread market penetration of electric vehicles (EVs) will require a five-fold cost reduction, from \$500–\$600/kWh to \$100–\$125/kWh. To achieve a 350-mile driving range, EV batteries also must operate at pack-level energy densities of 400 Wh/kg or more, rather than today's 80–100 Wh/kg.

Energy storage will play a more and more critical role in an efficient and renewable energy future, much more so than it does in today's fossil-based energy economy. There are two principal reasons that energy storage will grow in importance with increased development of renewable energy:

1. Many important renewable energy sources are intermittent, and generate when weather dictates, rather than when energy demand dictates.
2. Many transportation systems require energy to be carried with the vehicle.*

* This is almost always true for private transportation systems, and usually untrue for public transportation systems, which can rely on rails or overhead wires to transmit electric energy. However, some public transportation systems such as buses do not have fixed routes and also require portable energy storage.

Energy can be stored in many forms: as mechanical energy in rotating, compressed, or elevated substances, as thermal or electrical energy waiting to be released from chemical bonds, or as electrical charge ready to travel from positive to negative poles on demand.

Storage media that can take and release energy in the form of electricity have the most universal value, because electricity can efficiently be converted either to mechanical or heat energy, while other energy conversion processes are less efficient. Electricity is also the output of three of the most promising renewable energy technologies: wind turbines, solar thermal, and photovoltaics. Storing this electricity in a medium that naturally accepts electricity is favored, because converting the energy to another type usually has a substantial efficiency penalty.

Still, some applications can benefit from mechanical or thermal technologies. Examples are when the application already includes mechanical devices or heat engines that can take advantage of the compatible energy form, lower environmental impacts that are associated with mechanical and thermal technologies, or low cost resulting from simpler technologies or efficiencies of scale.

In this chapter, we group the technologies into five categories: direct electric, electrochemical, mechanical, direct thermal, and thermochemical. Table 17.1 is a summary of all of the technologies covered. Each is listed with indicators of appropriate applications, which are further explained in Section 17.3.

17.2 Principal Forms of Stored Energy

The storage media discussed in this chapter can accept and deliver energy in three fundamental forms: electrical, mechanical, and thermal. Electrical and mechanical energies are both considered high-quality energy, because they can be converted to either of the other two forms with fairly little energy loss (e.g., electricity can drive a motor with only about 5% energy loss, or a resistive heater with no energy loss).

The quality of thermal energy storage depends on its temperature. Usually, thermal energy is considered low quality, because it cannot be easily converted to the other two forms. The theoretical maximum quantity of useful work W_{\max} (mechanical energy) extractable from a given quantity of heat Q is

$$W_{\max} = \frac{(T_1 - T_2)}{T_1} Q,$$

where

T_1 is the absolute temperature of the heat

T_2 is the surrounding, ambient absolute temperature

Any energy storage facility must be carefully chosen to accept and produce a form of energy consistent with either the energy source or the final application. Storage technologies that accept and/or produce heat should as a rule only be used with heat energy sources or with heat applications. Mechanical and electric technologies are more versatile, but in most cases, electric technologies are favored over mechanical, because electricity is more easily transmitted, because there is a larger array of useful applications, and because the construction cost is typically lower.

TABLE 17.1

Overview of Energy Storage Technologies and Their Applications

	Utility Shaping	Power Quality	Distributed Grid	Automotive
<i>Direct electric</i>				
Ultracapacitors		✓		✓
SMES		✓		
<i>Electrochemical</i>				
Batteries				
Lead–acid	✓	✓	✓	
Lithium-ion	✓	✓	✓	✓
Nickel–cadmium	✓	✓		
Nickel metal hydride				✓
Zebra				✓
Sodium–sulfur	✓	✓		
Flow batteries				
Vanadium redox	✓			
Polysulfide bromide	✓			
Zinc bromide	✓			
Electrolytic hydrogen				✓
<i>Mechanical</i>				
Pumped hydro	✓			
Compressed air	✓			
Flywheels		✓		✓
<i>Direct thermal</i>				
Sensible heat				
Liquids			✓	
Solids			✓	
Latent heat				
Phase change	✓		✓	
Hydration–dehydration	✓			
Chemical reaction	✓		✓	
<i>Thermochemical</i>				
Biomass solids	✓		✓	
Ethanol	✓			✓
Biodiesel				✓
Syngas	✓			✓

17.3 Applications of Energy Storage

In Table 17.1, each technology is classified by its relevance in one to four different, principal applications.

Utility shaping is the use of very large capacity storage devices in order to answer electric demand, when a renewable resource is not producing sufficient generation. An example would be nighttime delivery of energy generated by a solar thermal plant during the prior day.

Power quality is the use of very responsive storage devices (capable of large changes in output over very short timescales) to smooth power delivery during switching events, short outages, or plant run-up. Power quality applications can be implemented at central generators, at switchgear locations, and at commercial and industrial customers' facilities. Uninterruptible power supplies (UPS) are an example of this category.

Distributed grid technologies enable energy generation and storage at customer locations, rather than at a central (utility) facility. The distributed grid is an important, enabling concept for photovoltaic technologies, which are effective at a small scale and can be installed on private homes and commercial buildings. When considered in the context of photovoltaics, the energy storage for the distributed grid is similar to the utility shaping application insofar that both are solutions to an intermittent, renewable resource, but distributed photovoltaic generation requires small capacities in the neighborhood of a few tens of MJ, while utility shaping requires capacities in the TJ range.* Renewable thermal resources (solar and geothermal) can also be implemented on a distributed scale, and require household-scale thermal storage tanks. For the purposes of this chapter, district heating systems are also considered a distributed technology.

Automotive applications include battery-electric vehicles (EVs), hybrid gasoline-electric vehicles (HEVs), plug-in hybrid electric vehicles (PHEVs), and other applications that require mobile batteries larger than those used in today's internal combustion engine cars. A deep penetration of automotive batteries also could become important in a distributed grid. Large fleets of EVs or PHEVs that are grid-connected when parked would help enable renewable technologies, fulfilling utility shaping and distributed grid functions as well as their basic automotive function.

Additional energy storage applications exist, most notably portable electronics and industrial applications. However, the four applications described here make up the principal components that will interact in a significant way with the global energy grid.

17.4 Specifying Energy Storage Devices

Every energy storage technology, regardless of category, can be roughly characterized by a fairly small number of parameters. Self-discharge time, unit size, and efficiency serve to differentiate the various categories. Within a category, finer selections of storage technology can be made by paying attention to cycle life, specific energy, specific power, energy density, and power density.

Self-discharge time is the time required for a fully charged, noninterconnected storage device to reach a certain depth of discharge (DOD). DOD is typically described as a percentage of the storage device's useful capacity, so that, for instance, 90% DOD means 10% of the device's energy capacity remains. The relationship between self-discharge time and DOD is rarely linear, so self-discharge times must be measured and compared at a uniform DOD. Acceptable self-discharge times vary greatly: from a few minutes for some power quality applications to years for devices designed to shape annual power production.

Unit size describes the intrinsic scale of the technology, and is the least well defined of the parameters listed here. If the unit size is small compared to the total required capacity

* Storage capacities in this chapter are given in units of MJ, GJ and TJ. 1 MJ = 0.28 kWh, 1 GJ = 280 kWh, and 1 TJ = 280 MWh.

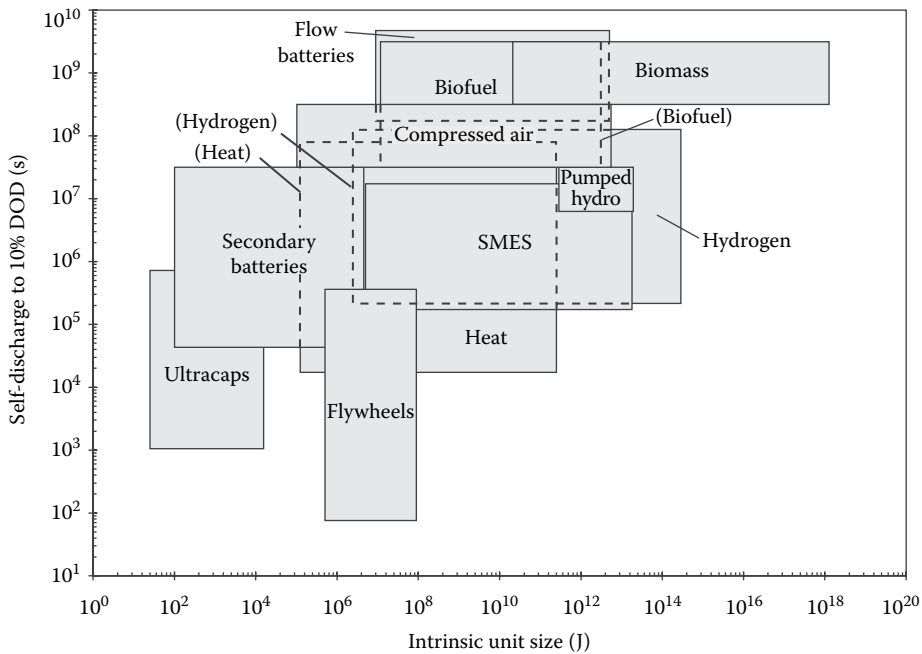


FIGURE 17.1

All storage technologies, mapped by self-discharge time and unit size. Not all hidden lines are shown. Larger self-discharge times are always more desirable, but more or less important depending on the application. Intrinsic unit size does not have a desirability proportional to its value, but rather must be matched to the application.

of a project, complexity and supply shortages can increase the cost relative to technologies with a larger unit size. Some technologies have a fairly large unit size that prohibits small-scale energy storage.

Figure 17.1 maps all of the technologies discussed in this chapter, according to their unit size and 10% self-discharge time. The gamut of technologies available covers many orders of magnitude on each axis, illustrating the broad choice available. Utility shaping applications require a moderate self-discharge time and a large unit size; power quality applications are much less sensitive to self-discharge time but require a moderate unit size. Distributed grid and automotive applications both require a moderate self-discharge time and a moderate unit size.

Efficiency is the ratio of energy output from the device to the energy input. Like energy density and specific energy, the system boundary must be carefully considered when measuring efficiency. It is particularly important to pay attention to the form of energy required at the input and output interconnections, and to include the entire system necessary to attach to those interconnections. For instance, if the system is to be used for shaping a constant-velocity, utility wind farm, then presumably, both the input and output will be AC electricity. When comparing a battery with a fuel cell in this scenario, it is necessary to include the efficiencies of an AC-to-DC rectifier for the battery, an AC-powered hydrogen generation system for the fuel cell system, and DC-to-AC converters associated with both systems.

Efficiency is related to self-discharge time. Technologies with a short self-discharge time will require constant charging in order to maintain a full charge; if discharge occurs much

later than charge in a certain application, the apparent efficiency will be lower, because a significant amount of energy is lost in maintaining the initial, full charge.

Cycle life is the number of consecutive charge–discharge cycles a storage installation can undergo while maintaining the installation’s other specifications within certain, limited ranges. Cycle life specifications are made against a chosen DOD depending on the application of the storage device. In some cases, for example, pressurized hydrogen storage in automobiles, each cycle will significantly discharge the hydrogen canister and the appropriate DOD reference might be 80% or 90%. In other cases, for example, a battery used in a HEV, most discharge cycles may consume only 10% or 20% of the energy stored in the battery. For most storage technologies, cycle life is significantly larger for shallow discharges than deep discharges, and it is critical that cycle life data be compared across a uniform DOD assumption.

Specific energy is a measure of how heavy the technology is. It is measured in units of energy per mass, and in this chapter, we will always report this quantity in MJ/kg. The higher the specific energy, the lighter the device. Automotive applications require high specific energies; for utility applications, specific energy is relatively unimportant, except where it impacts construction costs.

Energy density is a measure of how much space the technology occupies. It is measured in units of energy per volume, and in this chapter, we will always report this quantity in megajoule per liter (MJ/L). The higher the energy density, the smaller is the device. Again, this is most important for automotive applications, and rarely important in utility applications. Typical values for energy density associated with a few automotive-scale energy technologies are listed in Table 17.2, together with cycle life and efficiency data.

Energy density and specific energy estimates are dependent on the system definition. For example, it might be tempting to calculate the specific energy of a flow battery technology by dividing its capacity by the mass of the two electrolytes. But it is important to also include the mass of the electrolyte storage containers, and of the battery cell for a fair and comparable estimate of its specific energy. Thus, the energy density and specific energy are dependent on the size of the specific device; large devices benefit from efficiency of scale with a higher energy density and specific energy.

Specific power and *power density* are the power correlates to specific energy and energy density.

TABLE 17.2

Nominal Energy Density, Cycle Life, and Efficiency of Automotive Storage Technologies

	Energy Density (MJ/L)	Cycle Life at 80% DOD ^a	Electric Efficiency (%)
Ultracapacitors	0.2	50,000	95
Li-ion batteries	1.8	2,000	85
NiMH batteries	0.6	1,000	80
H ₂ at 350 bar	3.0	n/a ^b	47
H ₂ at 700 bar	5.0	n/a	45
Air at 300 bar	<0.1	n/a	37
Flywheels	<0.1	20,000	80
Ethanol	23.4	n/a	n/a

Note: Electric efficiencies are calculated for electric-to-electric conversion and momentary storage.

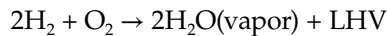
^a Depth of discharge.

^b Not applicable.

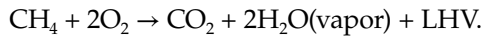
17.5 Specifying Fuels

A *fuel* is any (relatively) homogenous substance that can be combusted to produce heat. Though the energy contained in a fuel can always be extracted through combustion, other processes may be used to extract the energy (e.g., reaction in a fuel cell). A fuel may be gaseous, liquid, or solid. All energy storage technologies in the thermochemical category store energy in a fuel. In the electrochemical category, electrolytic hydrogen is a fuel.

A fuel's *lower heating value (LHV)* is the total quantity of sensible heat released during combustion of a designated quantity of fuel. For example, in the simplest combustion process, that of hydrogen,

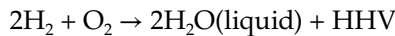


or for the slightly more complex combustion of methane,

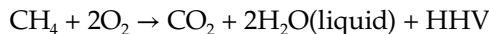


In this chapter, the quantity of fuel is always expressed as a mass, so that LHV is a special case of specific energy. Like specific energy, LHV is expressed in units of MJ/kg in this chapter.

Higher heating value (HHV) is the LHV, plus the latent heat contained in the water vapor resulting from combustion.* For the examples of hydrogen and methane, this means



and



The latent heat in the water vapor can be substantial, especially for the hydrogen-rich fuels typical in renewable energy applications. Table 17.3 lists LHVs and HHVs of fuels

TABLE 17.3

Properties of Fuels

	Chemical Formula	Density (g/L)	LHV (MJ/kg)	HHV (MJ/kg)
Methanol	CH ₃ OH	794	19.9	22.7
Ethanol	C ₂ H ₅ OH	792	26.7	29.7
Methane	CH ₄	0.68	49.5	54.8
Hydrogen	H ₂	0.085	120	142
Dry syngas, airless process ^a	40H ₂ + 21CO + 10CH ₄ + 29CO ₂	0.89	11.2	12.6
Dry syngas, air process ^a	25H ₂ + 16CO + 5CH ₄ + 15CO ₂ + 39N ₂	0.99	6.23	7.01

Source: All except syngas from U.S. Department of Energy, Properties of fuels, Alternative Fuels Data Center 2004.

^a Chemical formulae and associated properties of syngas are representative; actual composition of syngas will vary widely according to manufacturing process.

* The concepts of sensible and latent heat are explained further in Section 17.9.

discussed in this chapter; in the most extreme case of molecular hydrogen, the HHV is some 18% higher than the LHV. Recovery of the latent heat requires controlled condensation of the water vapor; technologies for doing so are described in Chapter 13.

In this chapter, all heating values are reported as HHV rather than LHV. HHV is favored for two reasons. One, its values allow easier checking of energy calculations with the principle of energy conservation. Two, when examining technologies for future implementation, it is wise to keep an intention of developing methods for extracting as much of each energy source's value as possible.

17.6 Electrochemical Energy Storage

17.6.1 Secondary Batteries

A secondary battery allows electrical energy to be converted into chemical energy, stored, and converted back to electrical energy. Batteries are made up of three basic parts: a negative electrode, positive electrode, and an electrolyte (Figure 17.2). The negative electrode gives up electrons to an external load, and the positive electrode accepts electrons from the load. The electrolyte provides the pathway for charge to transfer between the two electrodes. Chemical reactions between each electrode and the electrolyte remove electrons from the positive electrode and deposit them on the negative electrode. This can be written as an overall chemical reaction that represents the states of charging and discharging of a battery. The speed at which this chemical reaction takes place is related to the *internal resistance* that dictates the maximum power at which the batteries can be charged and discharged.

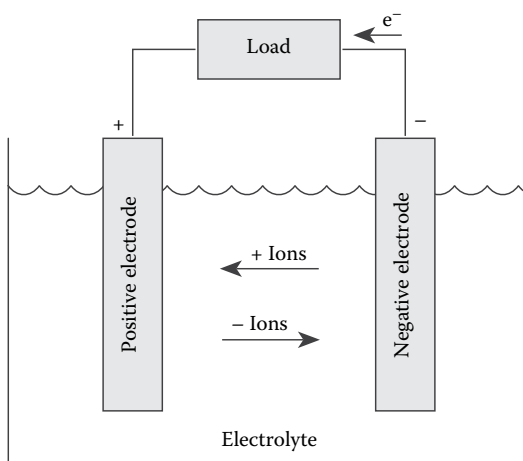


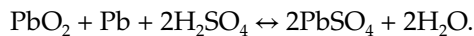
FIGURE 17.2

Schematic of a generalized secondary battery. Directions of electron and ion migration shown are for discharge, so that the positive electrode is the cathode and the negative electrode is the anode. During charge, electrons and ions move in the opposite directions and the positive electrode becomes the anode, while the negative electrode becomes the cathode.

Some batteries suffer from the *memory effect* in which a battery exhibits a lower discharge voltage under a given load than is expected. This gives the appearance of lowered capacity but is actually a voltage depression. Such a voltage depression occurs when a battery is repeatedly discharged to a partial depth and recharged again. This builds an increased internal resistance at this partial DOD, and the battery appears as a result to only be dischargeable to the partial depth. The problem, if and when it occurs, can be remedied by deep discharging the cell a few times. Most batteries considered for modern renewable applications are free from this effect, however.

17.6.1.1 Lead-Acid

Lead-acid is one of the oldest and most mature battery technologies. In its basic form, the lead-acid battery consists of a lead (Pb) negative electrode, a lead dioxide (PbO₂) positive electrode, and a separator to electrically isolate them. The electrolyte is dilute sulfuric acid (H₂SO₄), which provides the sulfate ions for the discharge reactions. The chemistry is represented by



(In all battery chemistries listed in this chapter, left-to-right indicates battery discharge and right-to-left indicates charging.)

There are three main types of lead-acid batteries: the flooded cell, the sealed gel cell, and the sealed absorbed glass mat (AGM) lead-acid battery. The wet cell has a liquid electrolyte, which must be replaced occasionally to replenish the hydrogen and oxygen that escape during the charge cycle. The sealed gel cell has a silica component added to the electrolyte to stiffen it. The AGM design uses a fiberglass-like separator to hold electrolyte in close proximity to the electrodes, thereby increasing efficiency. For both the gel and AGM configurations, there is a greatly reduced risk of hydrogen explosion and corrosion from disuse. These two types do require a lower charging rate, however. Both the gel cells and the AGM batteries are sealed and pressurized so that oxygen and hydrogen, produced during the charge cycle, are recombined into water.

The lead-acid battery is a low-cost and popular storage choice for power quality applications. Its application for utility shaping, however, has been very limited due to its short cycle life. A typical installation survives 1500 deep cycles at a maximum.⁴ Yet, lead-acid batteries have been used in a few commercial and large-scale energy management applications. The largest one is a 140 GJ system in Chino, California, built in 1988. Lead-acid batteries have a specific energy of only 0.18 MJ/kg, so they would not be a viable automobile option apart from providing the small amount of energy needed to start an engine. It also has a poor energy density at around 0.25 MJ/L. The advantages of the lead-acid battery technology are low cost and high power density.

17.6.1.2 Lithium Ion

Lithium ion and lithium polymer batteries, while primarily used in the portable electronics market, are likely to have future use in many other applications. The cathode in these batteries is a lithiated metal oxide (LiCoO₂, LiMO₂, etc.), and the anode is made of graphitic carbon with a layer structure. The electrolyte consists of lithium salts (such as LiPF₆) dissolved in organic carbonates; an example of Li-ion battery chemistry is



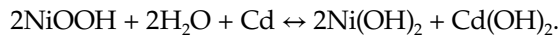
When the battery is charged, lithium atoms in the cathode become ions and migrate through the electrolyte toward the carbon anode where they combine with external electrons and are deposited between carbon layers as lithium atoms. This process is reversed during discharge.

The lithium polymer variation replaces the electrolyte with a plastic film that does not conduct electricity but allows ions to pass through it. The 60°C operating temperature requires a heater, reducing overall efficiency slightly.

Lithium ion batteries have a high energy density of about 0.72 MJ/L and have low internal resistance; so, they will achieve efficiencies in the 90% range and above. They have an energy density of around 0.72 MJ/kg. Their high energy efficiency and energy density make lithium-ion batteries excellent candidates for storage in all four applications we consider here: utility shaping, power quality, distributed generation, and automotive.

17.6.1.3 Nickel–Cadmium

Nickel–cadmium (NiCd) batteries operate according to the chemistry

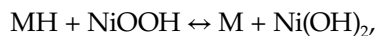


NiCd batteries are not common for large stationary applications. They have a specific energy of about 0.27 MJ/kg, an energy density of 0.41 MJ/L, and an efficiency of about 75%. Alaska's Golden Valley Electric Association commissioned a 40 MW/290 GJ nickel–cadmium battery in 2003 to improve reliability and to supply power for essentials during outages.⁵ Resistance to cold and relatively low cost were among the deciding factors for choosing the NiCd chemistry.

Cadmium is a toxic heavy metal and there are concerns relating to the possible environmental hazards associated with the disposal of NiCd batteries. In November 2003, the European Commission adopted a proposal for a new battery directive that includes recycling targets of 75% for NiCd batteries. However, the possibility of a ban on rechargeable batteries made from nickel–cadmium still remains, and hence, the long-term viability and availability of NiCd batteries continues to be uncertain. NiCd batteries can also suffer from *memory effect*, where the batteries will only take full charge after a series of full discharges. Proper battery management procedures can help to mitigate this effect.

17.6.1.4 Nickel Metal Hydride

The nickel metal hydride (NiMH) battery operates according to the chemistry



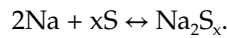
where M represents one of a large variety of metal alloys that serve to take up and release hydrogen. NiMH batteries were introduced as a higher energy density and more environmentally friendly version of the nickel–cadmium cell. Modern NiMH batteries offer up to 40% higher energy density than nickel–cadmium. There is potential for yet higher energy density, but other battery technologies (lithium ion in particular) may fill the same market sooner.

NiMH is less durable than nickel–cadmium. Cycling under heavy load and storage at high temperature reduces the service life. NiMH suffers from a higher self-discharge

rate than the nickel–cadmium chemistry. NiMH batteries have a specific energy of 0.29 MJ/kg, an energy density of about 0.54 MJ/L, and an energy efficiency about 70%. These batteries have been an important bridging technology in the portable electronics and hybrid automobile markets. Their future is uncertain, because other battery chemistries promise higher energy storage potential and cycle life.

17.6.1.5 Sodium–Sulfur

A sodium–sulfur (NaS) battery consists of a liquid (molten) sulfur positive electrode and liquid (molten) sodium negative electrode, separated by a solid beta-alumina ceramic electrolyte (Figure 17.3). The chemistry is as follows:



When discharging, positive sodium ions pass through the electrolyte and combine with the sulfur to form sodium polysulfides. x in the equation is 5 during early discharging, but once free sulfur has been exhausted, a more sodium-rich mixture of polysulfides with lower average values of x develops. This process is reversible as charging causes sodium polysulfides in the positive electrode to release sodium ions that migrate back through the electrolyte and recombine as elemental sodium. The battery operates at about 300°C. NaS batteries have a high energy density of around 0.65 MJ/L and a specific energy of up to 0.86 MJ/kg. These numbers would indicate an application in the automotive sector, but warm-up time and heat-related accident risk make its use there unlikely. The efficiency of this battery chemistry can be as high as 90% and would be suitable for bulk storage applications while simultaneously allowing effective power smoothing operations.⁶

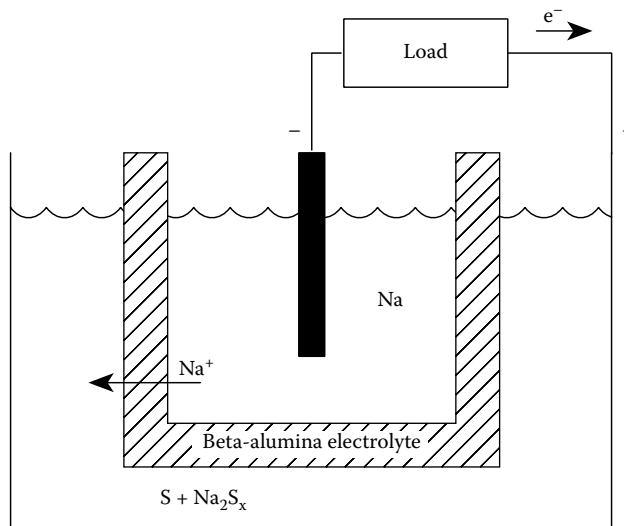
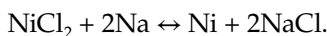


FIGURE 17.3

Sodium–sulfur battery showing discharge chemistry. The sodium (Na) and sulfur (S) electrodes are both in a liquid state and are separated by a solid, beta-alumina ceramic electrolyte that allows only sodium ions to pass. Charge is extracted from the electrolytes with metal contacts; the positive contact is the battery wall.

17.6.1.6 Zebra

Zebra is the popular name for the sodium nickel chloride battery chemistry:



Zebra batteries are configured similarly to sodium–sulfur batteries (see Figure 17.3), and also operate at about 300°C. Zebra batteries boast a greater than 90% energy efficiency, a specific energy of up to 0.32 MJ/kg, and an energy density of 0.49 MJ/L.⁷ Its tolerance for a wide range of operating temperature and high efficiency, coupled with a good energy density and specific energy, make its most probable application the automobile sector, and as of 2003, Switzerland's MES-DEA is pursuing this application aggressively.⁸ Its high energy efficiency also makes it a good candidate for the utility sector.

17.6.2 Flow Batteries

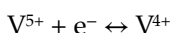
Most secondary batteries use electrodes both as an interface for gathering or depositing electrons, and as a storage site for the products or reactants associated with the battery's chemistry. Consequently, both energy and power density are tied to the size and shape of the electrodes. Flow batteries store and release electrical energy by means of reversible electrochemical reactions in two liquid electrolytes. An electrochemical cell has two compartments, one for each electrolyte, physically separated by an ion-exchange membrane. Electrolytes flow into and out of the cell through separate manifolds and undergo chemical reaction inside the cell, with ion or proton exchange through the membrane and electron exchange through the external electric circuit. The chemical energy in the electrolytes is turned into electrical energy and vice versa for charging. They all work in the same general way but vary in chemistry of electrolytes.⁹

There are some advantages to using the flow battery over a conventional secondary battery. The capacity of the system is scaleable by simply increasing the amount of solution. This leads to cheaper installation costs, as the systems get larger. The battery can be fully discharged with no ill effects and has little loss of electrolyte over time. Because the electrolytes are stored separately and in large containers (with a low surface area to volume ratio), flow batteries show promise to have some of the lowest self-discharge rates of any energy storage technology available.

Poor energy densities and specific energies remand these battery types to utility-scale power shaping and smoothing, though they might be adaptable for distributed generation use. There are three types of flow batteries that are closing in on commercialization: vanadium redox, polysulfide bromide, and zinc bromide. There is a fourth type of flow battery in early stages of R&D that may enable a significant increase in energy density over aqueous systems by enabling operation in a wider voltage window than allowed by water: nonaqueous flow batteries.

17.6.2.1 Vanadium Redox

The vanadium redox flow battery (VRB) was pioneered at the University of New South Wales, Australia, and has shown potentials for long cycle life and energy efficiencies of over 80% in large installations.¹⁰ The VRB uses compounds of the element vanadium in both electrolyte tanks. The reaction chemistry at the positive electrode is



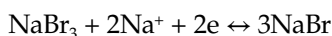
and at the negative electrode is



Using vanadium compounds on both sides of the ion-exchange membrane eliminates the possible problem of cross-contamination of the electrolytes and makes recycling easier.¹¹ As of 2005, two small, utility-scale VRB installations are operating: one 2.9 GJ unit on King Island, Australia, and one 7.2 GJ unit in Castle Valley, Utah.

17.6.2.2 Polysulfide Bromide

The polysulfide bromide battery (PSB) utilizes two salt solution electrolytes, sodium bromide (NaBr) and sodium polysulfide (Na_2S_x). PSB electrolytes are separated in the battery cell by a polymer membrane that only passes positive sodium ions. Chemistry at the positive electrode is



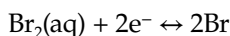
and at the negative electrode is



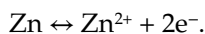
The PSB battery is being developed by Canada's VRB Power Systems, Inc.¹² This technology is expected to attain energy efficiencies of approximately 75%.¹³ Though the salt solutions themselves are only mildly toxic, a catastrophic failure by one of the tanks could release highly toxic bromine gas. Nevertheless, the Tennessee Valley Authority released a finding of no significant impact for a proposed, 430 GJ facility and deemed it safe.¹⁴

17.6.2.3 Zinc Bromide

In each cell of a zinc bromide (ZnBr) battery, two different electrolytes flow past carbon-plastic composite electrodes in two compartments separated by a microporous membrane. Chemistry at the positive electrode follows the equation:



and at the negative electrode:



During discharge, Zn and Br combine into zinc bromide. During charge, metallic zinc is deposited as a thin film on the negative electrode. Meanwhile, bromine evolves as a dilute solution on the other side of the membrane, reacting with other agents to make thick bromine oil that sinks down to the bottom of the electrolytic tank. During discharge, a pump mixes the bromine oil with the rest of the electrolyte. The zinc bromide battery has an energy efficiency of nearly 80%.¹⁵

Exxon developed the ZnBr battery in the early 1970s. Over the years, many GJ-scale ZnBr batteries have been built and tested. Meidisha demonstrated a 1 MW/14 GJ ZnBr battery in 1991 at Kyushu Electric Power Company. Some GJ-scale units are now available preassembled, complete with plumbing and power electronics.

17.6.2.4 Nonaqueous Redox Flow

Current flow battery technologies depend on aqueous electrodes, a choice that limits energy densities to <40 Wh/L as a consequence of low solubilities of redox species and operating voltages that are bounded by water electrolysis.¹⁶ Employing nonaqueous solvents offers a wider window of electrochemical stability that enables cell operation at dramatically higher potentials. Higher cell voltage (>3 V) leads to higher energy density, and typically to higher roundtrip efficiency as well, which together reduce the total cost of energy. Compared to aqueous flow systems, fewer stack layers, lower flow velocities, smaller tanks, and fewer ancillaries are required, which significantly reduces hardware costs and enhances system reliability. In order to capitalize on the inherent benefits of nonaqueous redox flow, several fundamental science challenges must be overcome.

Nonaqueous flow batteries fall into two broad classes of early investigation: solution phase systems, in which electroactive materials are dissolved in the electrolyte,^{17,18} and suspensions of active intercalant hosts, which are essentially fluidized versions of standard solid-state electrodes found in current lithium ion batteries.^{19,20}

17.6.3 Electrolytic Hydrogen

Diatomic, gaseous hydrogen (H_2) can be manufactured with the process of electrolysis; an electric current applied to water separates it into components O_2 and H_2 . The oxygen has no inherent energy value, but the HHV of the resulting hydrogen can contain up to 90% of the applied electric energy, depending on the technology.²¹ This hydrogen can then be stored, and later combusted to provide heat or work, or power a fuel cell (see Chapter 27).

The gaseous hydrogen is low density and must be compressed to provide useful storage. Compression to a storage pressure of 350 bar, the value usually assumed for automotive technologies, consumes up to 12% of the hydrogen's HHV if performed adiabatically, though the loss approaches a lower limit of 5% as the compression approaches an isothermal ideal.²² Alternatively, the hydrogen can be stored in liquid form, a process that costs about 40% of HHV using current technology, and that at best would consume about 25%. Liquid storage is not possible for automotive applications, because mandatory boil-off from the storage container cannot be safely released in closed spaces (i.e., garages).

Hydrogen can also be bonded into metal hydrides using an absorption process. The energy penalty of storage may be lower for this process, which requires pressurization to only 30 bar. However, the density of the metal hydride can be between 20 and 100 times the density of the hydrogen stored. Carbon nanotubes have also received attention as a potential hydrogen storage medium.²³ Hydrogen storage technologies are covered in more detail in Chapter 53.

17.7 Direct Electric Storage

17.7.1 Ultracapacitors

A capacitor stores energy in the electric field between two oppositely charged conductors. Typically, thin conducting plates are rolled or stacked into a compact configuration with a dielectric between them. The dielectric prevents arcing between the plates and allows the plates to hold more charge, increasing the maximum energy storage.

The ultracapacitor—also known as supercapacitor, electrochemical capacitor, or electric double layer capacitor (EDLC)—differs from a traditional capacitor in that it employs a thin electrolyte, in the order of only a few angstroms, instead of a dielectric. This increases the energy density of the device. The electrolyte can be made of either an organic or an aqueous material. The aqueous design operates over a larger temperature range, but has a smaller energy density than the organic design. The electrodes are made of a porous carbon that increases the surface area of the electrodes and further increases energy density over a traditional capacitor.

Ultracapacitors' ability to effectively equalize voltage variations with quick discharges makes them useful for power quality management and for regulating voltage in automotive systems during regular driving conditions. Ultracapacitors can also work in tandem with batteries and fuel cells to relieve peak power needs (e.g., hard acceleration) for which batteries and fuel cells are not ideal. This could help extend the overall life and reduce lifetime cost of the batteries and fuel cells used in HEV and EV. This storage technology also has the advantage of very high cycle life of greater than 500,000 cycles and a 10–12 year lifespan.²⁴ The limitations lie in the inability of ultracapacitors to maintain charge voltage over any significant time, losing up to 10% of their charge per day.

17.7.2 SMES

A superconducting magnetic energy storage (SMES) system is well suited in storing and discharging energy at high rates (high power.) It stores energy in the magnetic field created by direct current in a coil of cryogenically cooled, superconducting material. If the coil were wound using a conventional wire such as copper, the magnetic energy would be dissipated as heat due to the wire's resistance to the flow of current. The advantage of a cryogenically cooled, superconducting material is that it reduces electrical resistance to almost zero. The SMES recharges quickly and can repeat the charge–discharge sequence thousands of times without any degradation of the magnet. A SMES system can achieve full power within 100 ms.²⁵ Theoretically, a coil of around 150–500 m radius would be able to support a load of 18,000 GJ at 1000 MW, depending on the peak field and ratio of the coil's height and diameter.²⁶ Recharge time can be accelerated to meet specific requirements, depending on system capacity.

Because no conversion of energy to other forms is involved (e.g., mechanical or chemical), the energy is stored directly and round-trip efficiency can be very high.⁵ SMES systems can store energy with a loss of only 0.1%; this loss is due principally to energy required by the cooling system.⁶ Mature, commercialized SMES is likely to operate at 97%–98% round-trip efficiency and is an excellent technology for providing reactive power on demand.

17.8 Mechanical Energy Storage

17.8.1 Pumped Hydro

Pumped hydro is the oldest and largest of all of the commercially available energy storage technologies, with existing facilities up to 1000 MW in size. Conventional pumped hydro uses two water reservoirs, separated vertically. Energy is stored by moving water from the

lower to the higher reservoir, and extracted by allowing the water to flow back to the lower reservoir. Energy is stored according to the fundamental physical principle of potential energy. To calculate the stored energy in joules, use the formula:

$$E_s = Vdgh,$$

where

V is the volume of water raised (m^3)

d is the density of water ($1000 \text{ kg}/m^3$)

g is the acceleration of gravity ($9.8 \text{ m}/s^2$)

h is the elevation difference between the reservoirs (m) and is often referred to as the *head*

Though pumped hydro is by nature a mechanical energy storage technology, it is most commonly used for electric utility shaping. During off-peak hours, electric pumps move water from the lower reservoir to the upper reservoir. When required, the water flow is reversed to generate electricity. Some high dam hydro plants have a storage capability and can be dispatched as pumped hydro storage. Underground pumped storage, using flooded mine shafts or other cavities, is also technically possible but probably prohibitively expensive. The open sea can also be used as the lower reservoir if a suitable upper reservoir can be built at close proximity. A 30 MW seawater pumped hydro plant was first built in Yanbaru, Japan, in 1999.

Pumped hydro is most practical at a large scale with discharge times ranging from several hours to a few days. There is over 90 GW of pumped storage in operation worldwide, which is about 3% of global electric generation capacity.²⁷ Pumped storage plants are characterized by long construction times and high capital expenditure. Its main application is for utility shaping. Pumped hydro storage has the limitation of needing to be a very large capacity to be cost effective, but can also be used as storage for a number of different generation sites.

Efficiency of these plants has greatly increased in the last 40 years. Pumped storage in the 1960s had efficiencies of 60% compared with 80% for new facilities. Innovations in variable speed motors have helped these plants to operate at partial capacity, and greatly reduced equipment vibrations, increasing plant life.

17.8.2 Compressed Air

A relatively new energy storage concept that is implemented with otherwise mature technologies is compressed air energy storage (CAES). CAES facilities must be coupled with a combustion turbine, so they are actually a hybrid storage/generation technology.

A conventional gas turbine consists of three basic components: a compressor, combustion chamber, and an expander. Power is generated when compressed air and fuel burned in the combustion chamber drive turbine blades in the expander. Approximately 60% of the mechanical power generated by the expander is consumed by the compressor supplying air to the combustion chamber.

A CAES facility performs the work of the compressor separately, stores the compressed air, and, at a later time, injects it into a simplified combustion turbine. The simplified turbine includes only the combustion chamber and the expansion turbine. Such a simplified turbine produces far more energy than a conventional turbine from the same fuel, because there is potential energy stored in the compressed air. The fraction of output energy

beyond what would have been produced in a conventional turbine is attributable to the energy stored in compression.

The net efficiency of storage for a CAES plant is limited by the heat energy loss occurring at compression. The overall efficiency of energy storage is about 75%.²⁸

CAES compressors operate on grid electricity during off-peak times, and use the expansion turbine to supply peak electricity when needed. CAES facilities cannot operate without combustion, because the exhaust air would exit at extremely low temperatures, causing trouble with brittle materials and icing. If 100% renewable energy generation is sought, biofuel could be used to fuel the gas turbines. There might still be other emissions issues, but the system could be fully carbon neutral.

The compressed air is stored in appropriate underground mines, caverns created inside salt rocks or possibly in aquifers. The first commercial CAES facility was a 290 MW unit built in Hundorf, Germany, in 1978. The second commercial installation was a 110 MW unit built in McIntosh, Alabama, in 1991. The third commercial CAES is a 2700 MW plant under construction in Norton, Ohio. This nine-unit plant will compress air to about 100 bar in an existing limestone mine 2200 ft (766 m) underground.²⁹ The natural synergy with geological caverns and turbine prime movers dictates that these be on the utility scale.

17.8.3 Flywheels

Most modern flywheel energy storage systems consist of a massive rotating cylinder (comprised of a rim attached to a shaft) that is supported on a stator by magnetically levitated bearings that eliminate bearing wear and increase system life. To maintain efficiency, the flywheel system is operated in a low vacuum environment to reduce drag. The flywheel is connected to a motor/generator mounted onto the stator that, through some power electronics, interacts with the utility grid.

The energy stored in a rotating flywheel, in joules, is given by

$$E = \frac{1}{2}I\omega^2,$$

where

I is the flywheel's moment of inertia ($\text{kg}\cdot\text{m}^2$)

ω is its angular velocity ($1/\text{s}^2$)

I is proportional to the flywheel's mass, so energy is proportional to mass and the square of speed. In order to maximize energy capacity, flywheel designers gravitate toward increasing the flywheel's maximum speed rather than increasing its moment of inertia. This approach also produces flywheels with the higher specific energy.

Some of the key features of flywheels are low maintenance, a cycle life of better than 10,000 cycles, a 20-year lifetime, and environmentally friendly materials. Low speed, high mass flywheels (relying on I for energy storage) are typically made from steel, aluminum, or titanium; high speed, low mass flywheels (relying on ω for energy storage) are constructed from composites such as carbon fiber.

Flywheels can serve as a short-term ride-through before long-term storage comes online. Their low energy density and specific energy limit them to voltage regulation and UPS capabilities. Flywheels can have energy efficiencies in the upper 90% range, depending on frictional losses.

17.9 Direct Thermal Storage

Direct thermal technologies, though they are storing a lower grade of energy (heat, rather than electrical or mechanical energy), can be useful for storing energy from systems that provide heat as a native output (e.g., solar thermal, geothermal), or for applications where the energy's commodity value is heat (e.g., space heating, drying).

While thermal storage technologies can be characterized by specific energy and energy density like any other storage technology, they can also be characterized by an important, additional parameter, the delivery temperature range. Different end uses have more or less allowance for wide swings of the delivery temperature. Also, some applications require a high operating temperature that only some thermal storage media are capable of storing.

Thermal storage can be classified into two fundamental categories: sensible heat storage and latent heat storage. Applications that have less tolerance for temperature swings should utilize a latent heat technology.

Input to and output from heat energy storage is accomplished with heat exchangers. The following discussion focuses on the choice of heat storage materials; the methods of heat exchange will vary widely depending on properties of the storage material, especially its thermal conductivity. Materials with higher thermal conductivity will require a smaller surface area for heat exchange. For liquids, convection or pumping can reduce the need for a large heat exchanger. In some applications, the heat exchanger is simply the physical interface of the storage material with the application space (e.g., phase change drywall, see the following).

17.9.1 Sensible Heat

Sensible heat is the heat that is customarily and intuitively associated with a change in temperature of a massive substance. The heat energy E_s stored in such a substance is given by

$$E_s = (T_2 - T_1)cM,$$

where

c is the specific heat of the substance (J/kg-°C)

M is the mass of the substance (kg)

T_1 and T_2 are the initial and final temperatures, respectively (°C)

The specific heat c is a physical parameter measured in units of heat per temperature per mass: substances with the ability to absorb heat energy with a relatively small increase in temperature (e.g., water) have a high specific heat, while those that get hot with only a little heat input (e.g., lead) have a low specific heat. Sensible heat storage is best accomplished with materials having a high specific heat.

17.9.1.1 Liquids

Sensible heat storage in a liquid is with very few exceptions accomplished with water. Water is unique among chemicals in having an abnormally high specific heat of 4186 J/kg-K, and furthermore has a reasonably high density. Water is also cheap and safe. It is the preferred choice for most nonconcentrating solar thermal collectors.

Liquids other than water may need to be chosen if the delivery temperature must be higher than 100°C , or if the system temperature can fall below 0°C . Water can be raised to temperatures higher than 100°C , but the costs of storage systems capable of containing the associated high pressures are usually prohibitive. Water can be mixed with ethylene glycol or propylene glycol to increase the useful temperature range and prevent freezing.

When a larger temperature range than that afforded by water is required, mineral, synthetic, or silicone oils can be used instead. The trade-offs for the increased temperature range are higher cost, lower specific heat, higher viscosity (making pumping more difficult), flammability, and, in some cases, toxicity.

For very high temperature ranges, salts are usually preferred, which balance a low specific heat with a high density and relatively low cost. Sodium nitrate has received the most prominent testing for this purpose, in the U.S. Department of Energy's *Solar Two* project located in Barstow, California.

Liquid sensible heat storage systems are strongly characterized not just by the choice of heat transfer fluid, but also by the system architecture. Two-tank systems store the cold and hot liquids in separate tanks (Figure 17.4). Thermocline systems use a single tank with cold fluid entering or leaving the bottom of the tank and hot fluid entering or leaving the top (Figure 17.5). Thermocline systems can be particularly low cost, because they minimize the required tank volume, but require careful design to prevent mixing of the hot and cold fluid.

One particularly interesting application of the thermocline concept is nonconvecting, salinity-gradient solar ponds, which employ the concept in reverse. Solar ponds are both an energy collection and energy storage technology. Salts are dissolved in the water to introduce a density gradient, with the densest (saltiest) water on the bottom and lightest (freshest) on top. Solar radiation striking the dark bottom of the pond heats the densest water, but convection of the heated water to the top cannot occur, because the density gradient prevents it. Salinity-gradient ponds can generate and store hot water at temperatures approaching 95°C .³⁰

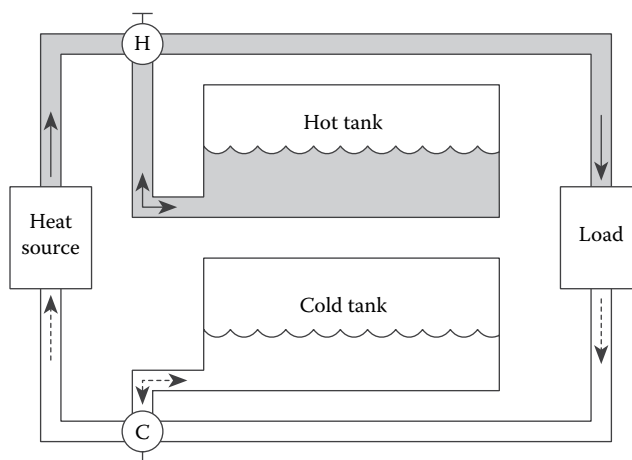
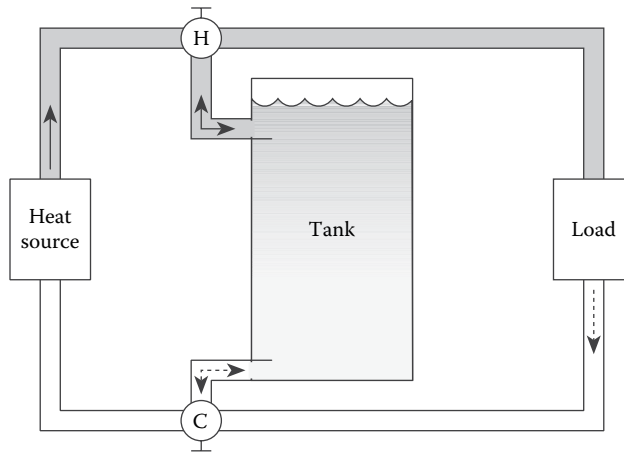


FIGURE 17.4

Two-tank thermal storage system; hot water is shown in gray and cold water is shown in white. When the heat source is producing more output than required for the load, valve H is turned to deposit hot liquid in the tank. When it is producing less than required for the load, the valve is turned to provide supplemental heat from the storage tank. Note that each tank must be large enough to hold the entire fluid capacity of the system.

**FIGURE 17.5**

Thermocline storage tank. Thermocline storage tanks are tall and narrow to encourage the gravity-assisted separation of hot and cold fluid, and include design features (especially at the input/output connectors) to prevent mixing in the stored fluid.

17.9.1.2 Solids

Storage of sensible heat in solids is usually most effective when the solid is in the form of a bed of small units, rather than a single mass. The reason is that the surface-to-volume ratio increases with the number of units, so that heat transfer to and from the storage device is faster for a greater number of units. Energy can be stored or extracted from a thermal storage bed by passing a gas (such as air) through the bed. Thermal storage beds can be used to extract and store the latent heat of vaporization from water contained in flue gases.

Though less effective for heat transfer, monolithic solid storage has been successfully used in architectural applications and solar cookers.

17.9.2 Latent Heat

Latent heat is absorbed or liberated by a phase change or a chemical reaction, and occurs at a constant temperature. A phase change means the conversion of a homogenous substance among its various solid, liquid, or gaseous phases. One very common example is boiling water on the stovetop: though a substantial amount of heat is absorbed by the water in the pot, the boiling water maintains a constant temperature of 100°C. The latent heat E_s stored through a phase change is

$$E_s = lM,$$

where

M is the mass of material undergoing a phase change (kg)

l is the latent heat of vaporization (for liquid–gas phase changes) or the latent heat of fusion (for solid–liquid phase changes), in units of energy per mass (J/kg)

Conservation of energy dictates that the amount of heat absorbed in a given phase change is equal to the amount of heat liberated in the reverse phase change.

Though we use the term *phase change* to refer only to straightforward freezing and melting (Section 179.2.1), many sources use the term *phase change materials (PCMs)* to refer to any substance storing latent heat (including those described in Sections 179.2.2 and 179.2.3 as well).

17.9.2.1 Phase Change

Practical energy storage systems based on a material phase change are limited to solid–solid and solid–liquid phase changes. Changes involving gaseous phases are of little interest due to the expense associated with containing a pressurized gas, and difficulty of transferring heat to and from a gas.

Solid–solid phase changes occur when a solid material reorganizes into a different molecular structure in response to temperature. One particularly interesting example is lithium sulfate (Li_2SO_4) that undergoes a change from a monoclinic structure to a face-centered cubic structure at 578°C , absorbing 214 J/g in the process, more than most solid–liquid phase changes.³¹

Some common chemicals, their melting points, and heats of fusion are listed in Table 17.4. Fatty acids and paraffins received particular attention in the 1990s as candidate materials for the heat storage component of phase change drywall, a building material designed to absorb and release heat energy near room temperature for the purpose of indoor temperature stabilization.³² In this application, solids in the drywall maintain the material's structural integrity even though the PCMs are transitioning between solid and liquid states.

TABLE 17.4
Melting Points and Heats of Fusion for Solid–Liquid Phase Changes

	Melting Point ($^\circ\text{C}$)	Heat of Fusion (J/g)
Aluminum bromide	97	42
Aluminum iodide	191	81
Ammonium bisulfate	144	125
Ammonium nitrate	169	77
Ammonium thiocyanate	146	260
Anthracene	96	105
Arsenic tribromide	32	37
Beeswax	62	177
Boron hydride	99	267
Metaphosphoric acid	43	107
Naphthalene	80	149
Naphthol	95	163
Paraffin	74	230
Phosphoric acid	70	156
Potassium	63	63
Potassium thiocyanate	179	98
Sodium	98	114
Sodium hydroxide	318	167
Sulfur	110	56
Tallow	76	198
Water	0	335

Source: From Kreith, F. and Kreider J.F., *Principles of Solar Engineering*, Taylor & Francis, 1978. With permission.

17.9.2.2 Hydration–Dehydration Reactions

In this process, a salt or similar compound forms a crystalline lattice with water below a *melting point* temperature, and at the melting point, the crystal dissolves in its own water of hydration. Sodium sulfate (Na_2SO_4) is a good example, forming a lattice with ten molecules of water per molecule of sulfate ($\text{Na}_2\text{SO}_4 \cdot 10\text{H}_2\text{O}$) and absorbing 241 J/g at 32°C.³³

Hydration–dehydration reactions have not found significant application in renewable energy systems, though they too have been a candidate for phase change drywall.

17.9.2.3 Chemical Reaction

A wide variety of reversible chemical reactions are available that release and absorb heat (e.g., Ref. [34]). The principal feature of this category of latent heat storage technologies is the ability to operate at extremely high temperatures, in some cases over 900°C. Extremely high temperature applications have focused primarily on fossil and advanced nuclear applications; to date, none of these chemical methods of heat storage have been deployed in commercial renewable energy applications.

17.10 Thermochemical Energy Storage

This section provides an overview of biomass storage technologies from an energetic perspective only. Additional details on biomass fuels are presented in Chapters 39, 49, and 50.

17.10.1 Biomass Solids

Plant matter is a storage medium for solar energy. The input mechanism is photosynthesis conversion of solar radiation into biomass. The output mechanism is combustion of the biomass to generate heat energy.

Biologists measure the efficiency of photosynthetic energy capture with the metric *net primary productivity* (NPP, which is usually reported as a yield in units similar to dry Mg/ha-yr (dry metric tons per hectare per year.) However, to enable comparisons of biomass with other solar energy storage technologies, it is instructive to estimate a *solar efficiency* by multiplying the NPP by the biomass heating value (e.g., MJ/dry Mg) and then dividing the result by the average insolation at the crop's location (e.g., MJ/ha-yr). The solar efficiency is a unitless value describing the fraction of incident solar energy ultimately available as biomass heating value. Most energy crops capture between 0.2% and 2% of the incident solar energy in heating value of the biomass; Table 17.5 shows examples of solar efficiencies estimated for a number of test crops.

The principal method for extracting useful work or electricity from biomass solids is combustion. Hence, the solar efficiencies listed in Table 17.5 need to be multiplied by the efficiency of any associated combustion process to yield a net solar efficiency. For example, if a boiler-based electric generator extracts 35% of the feedstock energy as electricity, and the generator is sited at a switchgrass plantation achieving 0.30% solar capture efficiency on a mass basis, the electric plant has a net solar efficiency of $0.30\% \times 35\% = 0.11\%$. Because biomass is a very low efficiency collector of solar energy, it is very land-intensive compared to photovoltaic or solar thermal collectors, which deliver energy at solar efficiencies

TABLE 17.5

Primary Productivity and Solar Efficiency of Biomass Crops

Location	Crop	Yield (Dry Mg/ha-Year)	Average Insolation (W/m ²)	Solar Efficiency (%)
Alabama	Johnsongrass	5.9	186	0.19
Alabama	Switchgrass	8.2	186	0.26
Minnesota	Willow and hybrid poplar	8–11	159	0.30–0.41
Denmark	Phytoplankton	8.6	133	0.36
Sweden	Enthropic lake angiosperm	7.2	106	0.38
Texas	Switchgrass	8–20	212	0.22–0.56
California	<i>Euphorbia lathyris</i>	16.3–19.3	212	0.45–0.54
Mississippi	Water hyacinth	11.0–33.0	194	0.31–0.94
Texas	Sweet sorghum	22.2–40.0	239	0.55–0.99
Minnesota	Maize	24.0	169	0.79
West Indies	Tropical marine angiosperm	30.3	212	0.79
Israel	Maize	34.1	239	0.79
Georgia	Subtropical saltmarsh	32.1	194	0.92
Congo	Tree plantation	36.1	212	0.95
New Zealand	Temperate grassland	29.1	159	1.02
Marshall Islands	Green algae	39.0	212	1.02
New South Wales	Rice	35.0	186	1.04
Puerto Rico	<i>Panicum maximum</i>	48.9	212	1.28
Nova Scotia	Sublittoral seaweed	32.1	133	1.34
Colombia	Pangola grass	50.2	186	1.50
West Indies	Tropical forest, mixed ages	59.0	212	1.55
California	Algae, sewage pond	49.3–74.2	218	1.26–1.89
England	Coniferous forest, 0–21 years	34.1	106	1.79
Germany	Temperate reedswamp	46.0	133	1.92
Holland	Maize, rye, two harvests	37.0	106	1.94
Puerto Rico	<i>Pennisetum purpurcum</i>	84.5	212	2.21
Hawaii	Sugarcane	74.9	186	2.24
Java	Sugarcane	86.8	186	2.59
Puerto Rico	Napier grass	106	212	2.78
Thailand	Green algae	164	186	4.90

Source: From Klass, D.L., *Biomass for Renewable Energy, Fuels, and Chemicals*, Academic Press, San Diego, CA, 1998. With permission.

over 20% (see Chapters 43 and 47 for a full discussion). However, the capacity of land to store standing biomass over time is extremely high, with densities up to several hundred Mg/ha (and therefore several thousand GJ/ha), depending on the forest type. Standing biomass can serve as very long-term storage, though multiple stores need to be used in order to accommodate fire risk. For short-term storage, woody biomass may be dried, and is frequently chipped or otherwise mechanically treated to create a fine and homogenous fuel suitable for burning in a wider variety of combustors.

17.10.2 Ethanol

Biomass is a more practical solar energy storage medium if it can be converted to liquid form. Liquids allow for more convenient transportation and combustion, and enable

extraction on demand (through reciprocating engines) rather than through a less dispatchable, boiler- or turbine-based process. This latter property also enables its use in automobiles.

Biomass grown in crops or collected as residue from agricultural processes consists principally of cellulose, hemicellulose, and lignin. The sugary or starchy by-products of some crops such as sugarcane, sugar beet, sorghum, molasses, corn, and potatoes can be converted to ethanol through fermentation processes, and these processes are the principal source of ethanol today. Starch-based ethanol production is low efficiency, but does succeed in transferring about 16% of the biomass heating value to the ethanol fuel.³⁵

When viewed as a developing energy storage technology, ethanol derived from cellulose shows much more promise than the currently prevalent starch-based ethanol.³⁶ Cellulosic ethanol can be manufactured with two fundamentally different methods: either the biomass is broken down to sugars using a hydrolysis process, and then the sugars are subjected to fermentation, or the biomass is gasified (see the following), and the ethanol is subsequently synthesized from this gas with a thermochemical process. Both processes show promise to be far cheaper than traditional ethanol manufacture via fermentation of starch crops, and will also improve energy balances. For example, it is estimated that dry sawdust can yield up to 224 L/Mg of ethanol, thus recovering about 26% of the HHV of the sawdust.³⁷ Since the ethanol will still need to be combusted in a heat engine, the gross, biomass-to-useful-work efficiency will be well below this. In comparison, direct combustion of the biomass to generate electricity (per the discussion in Section 17.10.1) makes much more effective use of the biomass as an energy storage medium. Hence, the value of ethanol as an energy storage medium lies mostly in the convenience of its liquid (rather than solid) state.

17.10.3 Biodiesel

As starch-based ethanol is made from starchy by-products, most biodiesel is generated from oily by-products. Some of the most common sources are rapeseed oil, sunflower oil, and soybean oil. Biodiesel yields from crops like these range from about 300 to 1000 kg/ha-year, but the crop as a whole produces about 20 Mg/ha-year, meaning that the gross solar capture efficiency for biodiesel from crops ranges between 1/20 and 1/60 the solar capture efficiency of the crop itself. Because of this low solar capture efficiency, biomass cannot be the principal energy storage medium for transportation needs.³⁸

Biodiesel can also be manufactured from waste vegetable or animal oils; however, in this case, the biodiesel is not functioning *per se* as a solar energy storage medium, so it is not further treated in this work.

17.10.4 Syngas

Biomass can be converted to a gaseous state for storage, transportation, and combustion (or other chemical conversion).³⁹ Gasification processes are grouped into three different classes: *pyrolysis* is the application of heat in anoxic conditions; *partial oxidation* is combustion occurring in an oxygen-starved environment; *reforming* is the application of heat in the presence of a catalyst. All three processes form *syngas*, a combination of methane, carbon monoxide, carbon dioxide, and hydrogen. The relative abundances of the gaseous products can be controlled by adjusting heat, pressure, and feed rates. The HHV of the resulting gas can contain up to 78% of the original HHV of the feedstock, if the feedstock is dry.⁴⁰ Compositions and heating values of two example syngases are listed in Table 17.3.

The equivalent of up to 10% of the gas HHV will be lost when the gas is pressurized for transportation and storage. Even with this loss, gasification is a considerably more efficient method than ethanol manufacture for transferring stored solar energy to a nonsolid medium.

References

1. Srinivasan, V., Batteries for vehicular applications, *Physics of Sustainable Energy, AIP Conference Proceedings*, 1044, 283–296, 2008.
2. Goodenough, J.B., Abruna, H.D., Buchanan, M.V., *Basic Research Needs in Electrical Energy Storage*, Bethesda, MD, 2007. Basic energy sciences workshop report. web.anl.gov/energy-storage-science/publications/ees.rpt.pdf.
3. Grid-scale rampable intermittent dispatchable storage, U.S. Department of Energy—Advanced Research Projects Agency—Energy (ARPA-E), Funding Opportunity Number: DE-FOA-0000290, 2010.
4. EA Technology, Review of electrical energy storage technologies and systems and of their potential for the UK, United Kingdom Department of Trade and Industry, London, U.K., 2004 (URN 04/1876).
5. DeVries, T., World’s biggest battery helps stabilize Alaska, *Modern Power Systems*, 22, 40, 2002.
6. Nourai, A., NaS battery demonstration in the USA, *Electricity Storage Association Spring Meeting*, Electricity Storage Association, Morgan Hill, CA, 2003.
7. Sudworth, J.L., Sodium/nickel chloride (Zebra) battery, *Journal of Power Sources*, 100, 149, 2001.
8. The Zebra, *Fleets & Fuels*, February 17, 2003, p. 8.
9. Price, A., Technologies for energy storage—Present and future: Flow batteries, *2000 Power Engineering Society Meeting*, Seattle, WA, July 16–20, 2000.
10. Skyllas-Kazacos, M., *Recent Progress with the Vanadium Redox Battery*, University of New South Wales, Sydney, Australia, 2000.
11. Menictas, C. et al., Status of the vanadium battery development program, *Proceedings of the Electrical Engineering Congress*, Sydney, Australia, 1994.
12. VRB Power Systems, Inc., <http://www.vrbpower.com>.
13. Wilks, N., Solving current problems, *Professional Engineering*, 13, 27, 2000.
14. Scheffler, P., *Environmental Assessment for the Regenesys Energy Storage System*, Tennessee Valley Authority, 2001.
15. Lex, P. and Jonshagen, B., The zinc/bromide battery system for utility and remote applications, *Power Engineering Journal*, 13, 142, 1999.
16. Weber, A.Z., Mench, M.M., Meyers, J.P., Ross, P.N., Gostick, J.T., and Liu, Q., Redox flow batteries: A review, *Journal of Applied Electrochemistry*, 41(10), 1137–1164, 2011.
17. Brushett, F.R., Jansen, A.N., Vaughey, J.T., and Zhang, Z., Exploratory research of non-aqueous flow batteries for renewable energy storage, *220th Electrochemical Society Meeting*, Boston, MA, October 9–14, 2011.
18. Huskinson, B., Marshak, M.P., Suh, C., Er, S., Gerhardt, M.R., Galvin, C.J., Chen, X., Aspuru-Guzik, A., Gordon, R.G., and Aziz, M.J., A metal-free organic–inorganic aqueous flow battery, *Nature*, 505, 195–198, 2014.
19. Duduta, M., Ho, B.Y., Wood, V.C., Limthongkul, P., Brunini, V.E., Carter, W.C., and Chiang, Y.M., Semi-solid lithium rechargeable flow battery, *Advanced Energy Materials*, 1, 511–516, 2011.
20. Ho, B.Y., An experimental study on the structure-property relationship of composite fluid electrodes for use in high energy density semi-solid flow cells, PhD thesis, MIT, Cambridge, MA, February 2012.

21. Kruger, P., Electric power requirement for large-scale production of hydrogen fuel for the world vehicle fleet, *International Journal of Hydrogen Energy*, 26, 1137, 2001.
22. Bossel, U., Eliasson, B., and Taylor, G., The future of the hydrogen economy: Bright or bleak?, *European Fuel Cell Forum*, Oberrohrdorf, Switzerland, 2003.
23. Dillon, A. et al., Storage of hydrogen in single-walled carbon nanotubes, *Nature*, 386, 377, 1997.
24. Linden, D. and Reddy, T.B., *Handbook of Batteries*, 3rd edn., McGraw-Hill, New York, 2002.
25. Luango, C.A., Superconducting storage systems: An overview, *IEEE Transactions on Magnetics*, 32, 1996.
26. Cheung, K.Y.C. et al., *Large Scale Energy Storage Systems*, Imperial College London, London, U.K., 2003 (ISE2 2002/2003).
27. Donalek, P., Advances in pumped storage, *Electricity Association Spring Meeting*, Chicago, IL, 2003.
28. Kondoh, J. et al., Electrical energy storage systems for energy networks, *Energy Conservation and Management*, 41, 1863, 2000.
29. van der Linden, S., The case for compressed air energy system, *Modern Power Systems*, 22, 19, 2002.
30. Hull, J. et al., *Salinity Gradient Solar Ponds*, CRC Press, 1988.
31. Sørensen, B., *Renewable Energy: Its Physics, Engineering, Environmental Impacts, Economics & Planning*, 3rd edn., Elsevier Academic Press, Burlington, MA, 2004.
32. Neep, D.A., Thermal dynamics of wallboard with latent heat storage, *Solar Energy*, 68, 393, 2000.
33. Goswami, D.Y., Kreith, F., and Kreider, J.F., *Principles of Solar Engineering*, 2nd edn., Taylor & Francis, Philadelphia, PA, 2000.
34. Hanneman, R., Vakil, H., and Wentorf Jr., R., Closed loop chemical systems for energy transmission, conversion and storage, *Proceedings of the Ninth Intersociety Energy Conversion Engineering Conference*, American Society of Mechanical Engineers, New York, 1974.
35. Shapouri, H., Duffield, J.A., and Wang, M., The energy balance of corn ethanol: An update, USDA, Office of Energy Policy and New Uses, Agricultural Economics, 2002 (Rept. No. 813).
36. Hammerschlag, R., Ethanol's energy return on investment: A survey of the literature 1990–present, *Environmental Science & Technology* (submitted).
37. Klass, D.L., *Biomass for Renewable Energy, Fuels, and Chemicals*, Academic Press, San Diego, CA, 1998.
38. Bockey, D. and Körbitz, W., *Situation and Development Potential for the Production of Biodiesel—An International Study*, Union zur Förderung von Oel- und Proteinpflanzen, e.V., Berlin, Germany, 2003.
39. Bridgwater, A.V., The technical and economic feasibility of biomass gasification for power generation, *Fuel*, 74, 631, 1995.
40. Klass, *Biomass for Renewable Energy, Fuels, and Chemicals*, 302.
41. U.S. Department of Energy, Properties of fuels, Alternative Fuels Data Center, 2004.
42. Kreith, F. and Kreider J.F., *Principles of Solar Engineering*, Taylor & Francis, 1978.



Taylor & Francis

Taylor & Francis Group

<http://taylorandfrancis.com>

18

Solar Thermal Energy Conversion

T. Agami Reddy and Jeffrey H. Morehouse

CONTENTS

18.1	Active Solar Heating Systems	526
18.1.1	Introduction	526
18.1.1.1	Motivation and Scope.....	526
18.1.2	Solar Collectors	527
18.1.2.1	Collector Types.....	527
18.1.2.2	Flat-Plate Collectors	529
18.1.2.3	Improvements to Flat-Plate Collector Performance	536
18.1.2.4	Other Collector Types	538
18.1.3	Long-Term Performance of Solar Collectors	540
18.1.3.1	Effect of Day-to-Day Changes in Solar Insolation	540
18.1.3.2	Individual Hourly Utilizability	541
18.1.3.3	Daily Utilizability	545
18.1.4	Solar Systems.....	550
18.1.4.1	Classification.....	550
18.1.4.2	Closed-Loop and Open-Loop Systems	552
18.1.5	Controls	557
18.1.5.1	Corrections to Collector Performance Parameters.....	559
18.1.6	Thermal Storage Systems.....	562
18.1.7	Solar System Simulation	563
18.1.8	Solar System Sizing Methodology.....	566
18.1.8.1	Solar-Supplemented Systems	566
18.1.9	Solar System Design Methods	568
18.1.9.1	Classification.....	568
18.1.9.2	Active Space Heating.....	570
18.1.9.3	Domestic Water Heating.....	573
18.1.9.4	Industrial Process Heat.....	573
18.1.10	Design Recommendations and Costs	578
18.1.10.1	Design Recommendations.....	578
18.1.10.2	Solar System Costs.....	578
References	579
18.2	Passive Solar Heating, Cooling, and Daylighting.....	581
18.2.1	Introduction	581
18.2.1.1	Distinction between a Passive System and Energy Conservation.....	581
18.2.1.2	Key Elements of Economic Consideration	581

18.2.2	Solar Thermosyphon Water Heating	582
18.2.2.1	Thermosyphon Concept	582
18.2.2.2	Thermo-Fluid System Design Considerations.....	584
18.2.3	Passive Solar Heating Design Fundamentals	586
18.2.3.1	Types of Passive Heating Systems.....	586
18.2.3.2	Fundamental Concepts for Passive Heating Design	588
18.2.3.3	Passive Design Approaches.....	588
18.2.3.4	First Level: Generalized Methods	589
18.2.3.5	Load	590
18.2.3.6	Solar Savings Fraction.....	590
18.2.3.7	Load Collector Ratio	590
18.2.3.8	Storage	591
18.2.3.9	Second Level: LCR Method	592
18.2.3.10	Third Level: SLR Method.....	620
18.2.4	Passive Space Cooling Design Fundamentals	624
18.2.4.1	Solar Control.....	624
18.2.4.2	Natural Convection/Ventilation.....	624
18.2.4.3	Evaporative Cooling	627
18.2.4.4	Nocturnal and Radiative Cooling Systems.....	627
18.2.4.5	Earth Contact Cooling (or Heating)	629
18.2.5	Daylighting Design Fundamentals	633
18.2.5.1	Lighting Terms and Units.....	633
18.2.5.2	Approach to Daylighting Design	633
18.2.5.3	Sun-Window Geometry	634
18.2.5.4	Daylighting Design Methods.....	635
18.2.5.5	Daylighting Controls and Economics	648
	Glossary	651
	References.....	651
	For Further Information.....	653

18.1 Active Solar Heating Systems

T. Agami Reddy

18.1.1 Introduction

This section defines the scope of the entire chapter and presents a brief overview of the types of applications that solar thermal energy can potentially satisfy.

18.1.1.1 Motivation and Scope

Successful solar system design is an iterative process involving consideration of many technical, practical, reliability, cost, code, and environmental considerations (Mueller Associates 1985). The success of a project involves identification of and intelligent selection among trade-offs, for which a proper understanding of goals, objectives, and constraints is essential. Given the limited experience available in the solar field, it is advisable to keep solar systems as simple as possible and not be lured by the promise of higher efficiency offered by more complex systems.

Because of the location-specific variability of the solar resource, solar systems offer certain design complexities and concerns not encountered in traditional energy systems.

The objective of this chapter is to provide energy professionals which a fundamental working knowledge of the scientific and engineering principles of solar collectors and solar systems relevant to both the prefeasibility study and the feasibility study of a solar project. Conventional equipment such as heat exchangers, pumps, and piping layout are but briefly described. Because of space limitations, certain equations/correlations had to be omitted, and proper justice could not be given to several concepts and design approaches. Effort has been made to provide the reader with pertinent references to textbooks, manuals, and research papers.

A detailed design of solar systems requires in-depth knowledge and experience in (1) the use of specially developed computer programs for detailed simulation of solar system performance, (2) designing conventional equipment, controls, and hydronic systems, (3) practical aspects of equipment installation, and (4) economic analysis. These aspects are not addressed here, given the limited scope of this chapter. Readers interested in acquiring such details can consult manuals such as Mueller Associates (1985) or SERI (1989).

The lengthy process outlined above pertains to large solar installations. The process is much less involved when a small domestic hot-water system, or unitary solar equipment or single solar appliances such as solar stills, solar cookers, or solar dryers are to be installed. Not only do such appliances differ in engineering construction from region to region, there are also standardized commercially available units whose designs are already more or less optimized by the manufacturers, normally as a result of previous experimentation, both technical or otherwise. Such equipment is not described in this chapter for want of space.

The design concepts described in this chapter are applicable to domestic water heating, swimming pool heating, active space heating, industrial process heat, convective drying systems, and solar cooling systems.

18.1.2 Solar Collectors

18.1.2.1 Collector Types

A solar thermal collector is a heat exchanger that converts radiant solar energy into heat. In essence this consists of a receiver that absorbs the solar radiation and then transfers the thermal energy to a working fluid. Because of the nature of the radiant energy (its spectral characteristics, its diurnal and seasonal variability, changes in diffuse to global fraction, etc.), as well as the different types of applications for which solar thermal energy can be used, the analysis and design of solar collectors present unique and unconventional problems in heat transfer, optics, and material science. The classification of solar collectors can be made according to the type of working fluid (water, air, or oils) or the type of solar receiver used (nontracking or tracking).

Most commonly used working fluids are water (glycol being added for freeze protection) and air. Table 18.1 identifies the relative advantages and potential disadvantages of air and liquid collectors and associated systems. Because of the poorer heat transfer characteristics of air with the solar absorber, the air collector may operate at a higher temperature than a liquid-filled collector, resulting in greater thermal losses and, consequently, a lower efficiency. The choice of the working fluid is usually dictated by the application. For example, air collectors are suitable for space heating and convective drying applications, while liquid collectors are the obvious choice for domestic and industrial hot-water applications. In certain high-temperature applications, special types of oils are used that provide better heat transfer characteristics.

TABLE 18.1

Advantages and Disadvantages of Liquid and Air Systems

Characteristics	Liquid	Air
Efficiency	Collectors generally more efficient for a given temperature difference	Collectors generally operate at slightly lower efficiency
System configuration	Can be readily combined with service hot-water and cooling systems	Space heat can be supplied directly but does not adapt easily to cooling. Can preheat hot-water
Freeze protection	May require antifreeze and heat exchangers that add cost and reduce efficiency	None needed
Maintenance	Precautions must be taken against leakage, corrosion and boiling	Low maintenance requirements. Leaks repaired readily with duct tape, but leaks may be difficult to find
Space requirements	Insulated pipes take up nominal space and are more convenient to install in existing buildings	Duct work and rock storage units are bulky, but ducting is a standard HVAC installation technique
Operation	Less energy required to pump liquids	More energy required by blowers to move air; noisier operation
Cost	Collectors cost more	Storage costs more
State of the art	Has received considerable attention from solar industry	Has received less attention from solar industry

Source: SERI, *Engineering Principles and Concepts for Active Solar Systems*, Hemisphere Publishing Company, New York, 1989.

TABLE 18.2

Types of Solar Thermal Collectors

Nontracking Collectors	Tracking Collectors
Basic flat-plate	Parabolic troughs
Flat-plate enhanced with side reflectors or V-troughs	Fresnel reflectors
Tubular collectors	Paraboloids
Compound parabolic concentrators (CPCs)	Heliostats with central receivers

The second criterion of collector classification is according to the presence of a mechanism to track the sun throughout the day and year in either a continuous or discreet fashion (see Table 18.2). The stationary flat-plate collectors are rigidly mounted, facing toward the equator with a tilt angle from the horizontal roughly equal to the latitude of the location for optimal year-round operation. The compound parabolic concentrators (CPCs) can be designed either as completely stationary devices or as devices that need seasonal adjustments only. On the other hand, Fresnel reflectors, paraboloids, and heliostats need two-axis tracking. Parabolic troughs have one axis tracking either along the east-west direction or the north-south direction. These collector types are described by Kreider (1979) and Rabl (1985).

A third classification criterion is to distinguish between nonconcentrating and concentrating collectors. The main reason for using concentrating collectors is not that *more energy* can be collected but that the thermal energy is obtained at higher temperatures. This is done by decreasing the area from which heat losses occur (called the

receiver area) with respect to the aperture area (i.e., the area that intercepts the solar radiation). The ratio of the aperture to receiver area is called the *concentration ratio*.

18.1.2.2 Flat-Plate Collectors

18.1.2.2.1 Description

The flat-plate collector is the most common conversion device in operation today, since it is most economical and appropriate for delivering energy at temperatures up to about 100°C. The construction of flat-plate collectors is relatively simple, and many commercial models are available.

Figure 18.1 shows the physical arrangements of the major components of a conventional flat-plate collector with a liquid working fluid. The blackened absorber is heated by radiation admitted via the transparent cover. Thermal losses to the surroundings from the absorber are contained by the cover, which acts as a black body to the infrared radiation (this effect is called the *greenhouse effect*), and by insulation provided under the absorber plate. Passages attached to the absorber are filled with a circulating fluid, which

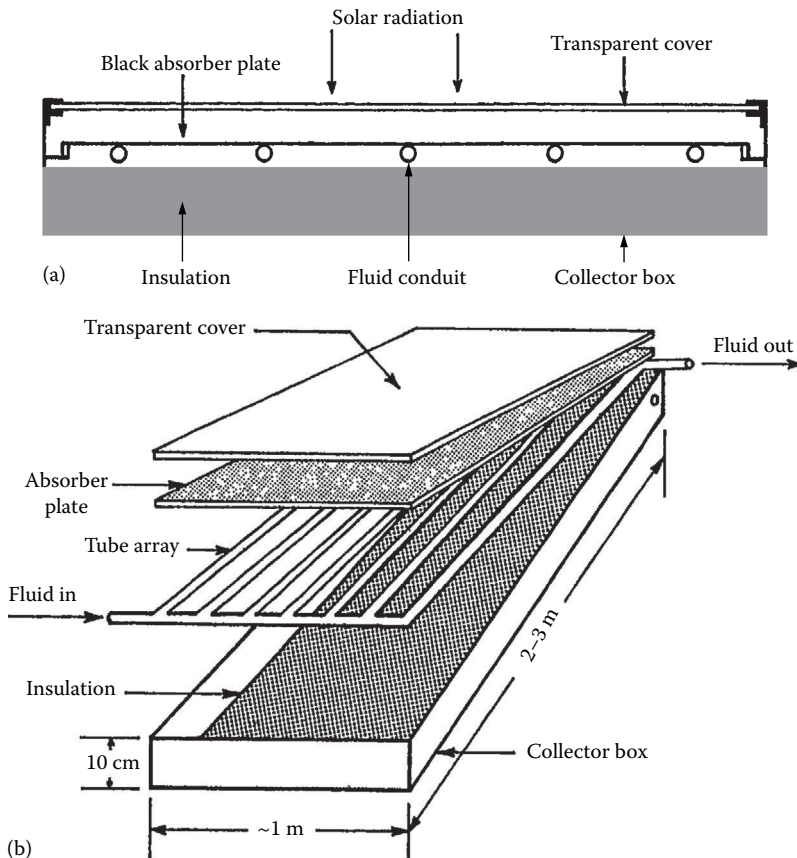


FIGURE 18.1 Cross-section (a) and isometric (b) view of a flat-plate collector.

extracts energy from the hot absorber. The simplicity of the overall device makes for long service life.

The absorber is the most complex portion of the flat-plate collector, and a great variety of configurations are currently available for liquid and air collectors. Figure 18.2 illustrates some of these concepts in absorber design for both liquid and air absorbers. Conventional materials are copper, aluminum, and steel. The absorber is either painted with a dull black paint or can be coated with a *selective surface* to improve performance (see Section 18.1.2.3 for more details). Bonded plates having internal passageways perform well as absorber plates because the hydraulic passageways can be designed for optimal fluid and thermal performance. Such collectors are called *roll-bond* collectors. Another common absorber consists of tubes soldered or brazed to a single metal sheet, and mechanical attachments of the tubes to the plate have also been employed. This type of collector is called a *tube-and-sheet* collector. Heat pipe collectors have also been

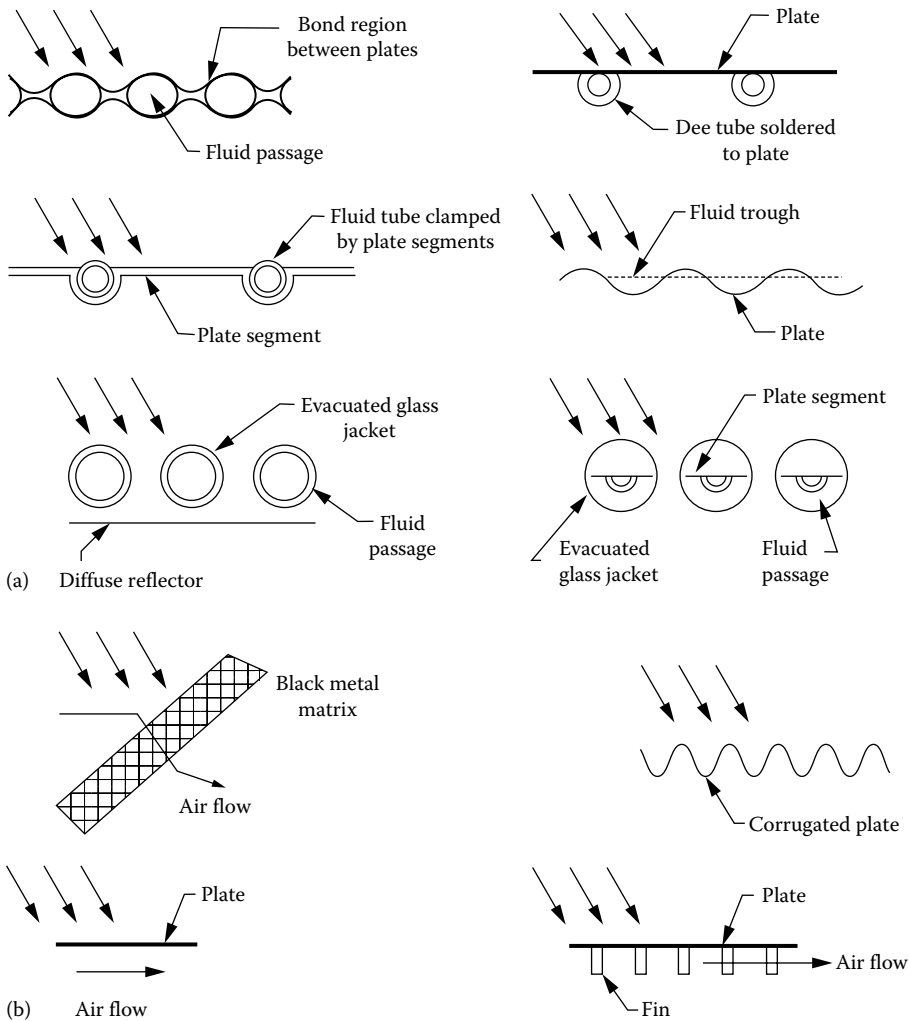


FIGURE 18.2 Typical flat-plate absorber configurations. (a) Air and (b) liquid collectors.

developed, though these are not as widespread as the previous two types. The so-called *trickle type* of flat-plate collector, with the fluid flowing directly over the corrugated absorber plate, dispenses entirely with fluid passageways. Tubular collectors have also been used because of the relative ease by which air can be evacuated from such collectors, thereby reducing convective heat losses from the absorber to the ambient air.

The absorber in an air collector normally requires a larger surface than in a liquid collector because of the poorer heat transfer coefficients of the flowing air stream. Roughness elements and producing turbulence by way of devices such as expanded metal foil, wool, and overlapping plates have been used as a means for increasing the heat transfer from the absorber to the working fluid. Another approach to enhance heat transfer is to use packed beds of expanded metal foils or matrices between the glazing and the bottom plate.

18.1.2.2.2 Modeling

A particular modeling approach and the corresponding degree of complexity in the model are dictated by the objective as well as by experience gained from past simulation work. For example, it has been found that transient collector behavior has insignificant influence when one is interested in determining the long-term performance of a solar thermal system. For complex systems or systems meant for nonstandard applications, detailed modeling and careful simulation of system operation are a must initially, and simplifications in component models and system operation can subsequently be made. However, in the case of solar thermal systems, many of the possible applications have been studied to date and a backlog of experience is available not only concerning system configurations but also with reference to the degree of component model complexity.

Because of low collector time constants (about 5–10 min), heat capacity effects are usually small. Then the instantaneous (or hourly, because radiation data are normally available in hourly time increments only) steady-state useful energy q_C in watts delivered by a solar flat-plate collector of surface area A_C is given by

$$q_C = A_C F' [I_T \eta_0 - U_L (T_{Cm} - T_a)]^+ \quad (18.1)$$

where

F' is the plate efficiency factor, which is a measure of how good the heat transfer is between the fluid and the absorber plate

η_0 is the optical efficiency, or the product of the transmittance and absorptance of the cover and absorber of the collector

U_L is the overall heat loss coefficient of the collector, which is dependent on collector design only and is normally expressed in $W/(m^2 \text{ } ^\circ\text{C})$

T_{Cm} is the *mean* fluid temperature in the collector (in $^\circ\text{C}$)

I_T is the radiation intensity on the plane of the collector (in W/m^2)

The + sign denotes that negative values are to be set to zero, which physically implies that the collector should not be operated when q_C is negative (i.e., when the collector loses more heat than it can collect).

However, because T_{Cm} is not a convenient quantity to use, it is more appropriate to express collector performance in terms of the fluid *inlet* temperature to the collector (T_{Ci}). This equation is known as the classical Hottel–Whillier–Bliss (HWB) equation and is most widely used to predict instantaneous collector performance:

$$q_C = A_C F_R [I_T \eta_0 - U_L (T_{Ci} - T_a)]^+ \quad (18.2)$$

where F_R is called the heat removal factor and is a measure of the solar collector performance as a heat exchanger, since it can be interpreted as the ratio of actual heat transfer to the maximum possible heat transfer. It is related to F' by

$$\frac{F_R}{F'} = \frac{(mc_p)_C}{A_C F' U_L} \left\{ 1 - \exp \left[- \frac{A_C F' U_L}{(mc_p)_C} \right] \right\} \quad (18.3)$$

where $(mc_p)_C$ is the heat capacity of the total fluid flow rate times the specific heat of fluid flowing through the collector.

The variation of (F_R/F') with $[(mc_p)_C/A_C F' U_L]$ is shown graphically in Figure 18.3. Note the asymptotic behavior of the plot, which suggests that increasing the fluid flow rate more than a certain amount results in little improvement in F_R (and hence in q_C) while causing a quadratic increase in the pressure drop.

Factors influencing solar collector performance are of three types: (1) constructional, that is, related to collector design and materials used, (2) climatic, and (3) operational, that is, fluid temperature, flow rate, and so on. The plate efficiency factor F' is a factor that depends on the physical constructional features and is essentially a constant for a given liquid collector. (This is not true for air collectors, which require more careful analysis.) Operational features involve changes in m_C and T_{Ci} . While changes in m_C affect F_R as per Equation 18.3, we note from Equation 18.2 that to enhance q_C , T_{Ci} needs to be kept as low as possible. For solar collectors that are operated under more or less constant flow rates, specifying $F_R \eta_0$ and $F_R U_L$ is adequate to predict collector performance under varying climatic conditions.

There are a number of procedures by which collectors have been tested. The most common is a *steady-state procedure*, where transient effects due to collector heat capacity

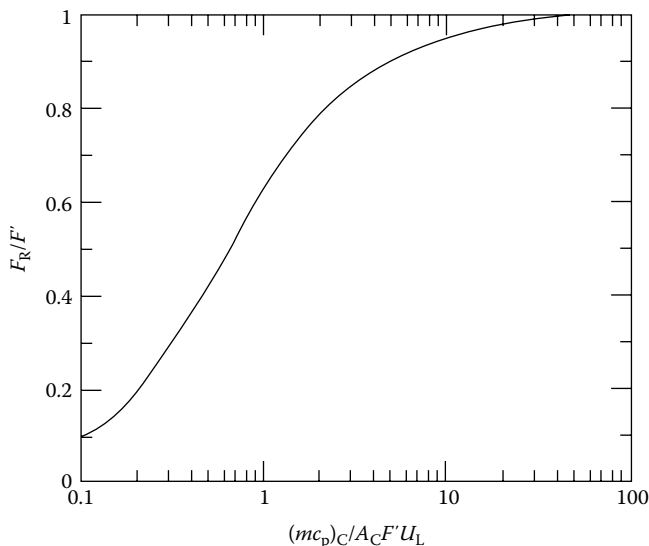


FIGURE 18.3

Variation of F_R/F' as a function of $[(mc_p)_C/(A_C F' U_L)]$. (From Duffie, J. A. and Beckman, W. A., *Solar Engineering of Thermal Processes*, Wiley Interscience, New York, 1980.)

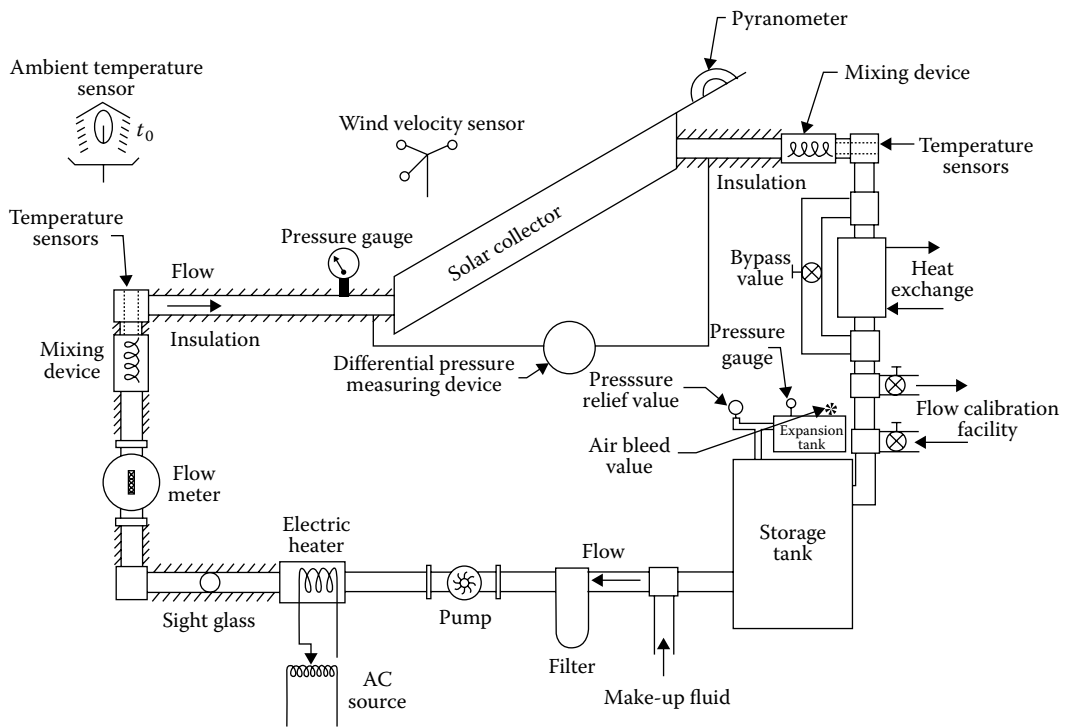


FIGURE 18.4
Set up for testing liquid collectors according to ASHRAE Standard 93-72.

are minimized by performing tests only during periods when radiation and ambient temperature are steady. The procedure involves simultaneous and accurate measurements of the mass flow rate, the inlet and outlet temperatures of the collector fluid, and the ambient conditions (incident solar radiation, air temperature, and wind speed). The most widely used test procedure is the ASHRAE Standard 93-77 (1978), whose test setup is shown in Figure 18.4. Though a solar simulator can be used to perform indoor testing, outdoor testing is always more realistic and less expensive. The procedure can be used for nonconcentrating collectors using air or liquid as the working fluid (but not two phase mixtures) that have a single inlet and a single outlet and contain no integral thermal storage.

Steady-state procedures have been in use for a relatively long period and though the basis is very simple the engineering setup is relatively expensive (see Figure 18.4). From an overall heat balance on the collector fluid and from Equation 18.2, the expressions for the instantaneous collector efficiency under normal solar incidence are

$$\eta_c \equiv \frac{q_c}{A_c I_T} = \frac{(m c_p)_{ci} (T_{co} - T_{ci})}{A_c I_T} \tag{18.4}$$

$$= \left[F_R \eta_n - F_R U_L \left(\frac{T_{ci} - T_a}{I_T} \right) \right] \tag{18.5}$$

where η_n is the optical efficiency at normal solar incidence.

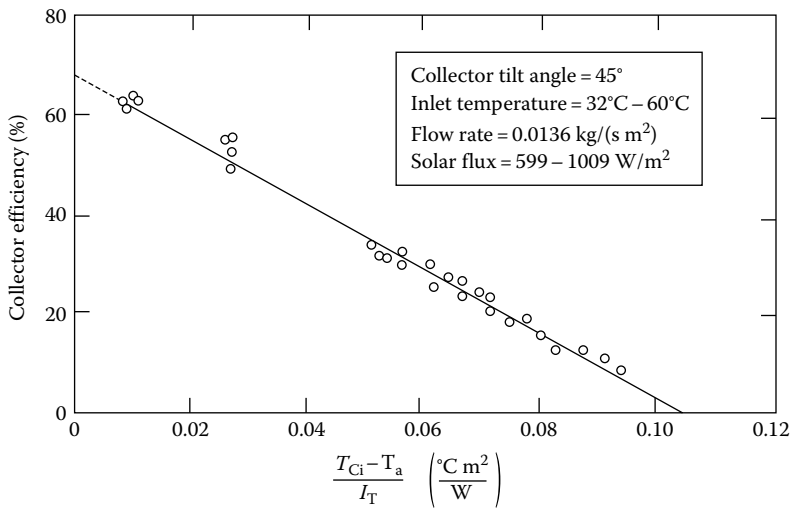


FIGURE 18.5

Thermal efficiency curve for a double glazed flat-plate liquid collector. Test conducted outdoors on a 1.2 m by 1.25 m panel with 10.2 cm of glass fiber back insulation and a flat copper absorber with black coating of emissivity of 0.97. (From ASHRAE Standard 93-77, *Methods of Testing to Determine the Thermal Performance of Solar Collectors*, American Society of Heating, Refrigeration and Air Conditioning Engineers, New York, 1978.)

From the test data, points of η_c against reduced temperature $[(T_{Ci} - T_a)/I_T]$ are plotted as shown in Figure 18.5. Then a linear fit is made to these data points by regression, from which the values of $F_R\eta_n$ and F_RU_L are easily deduced. It will be noted that if the reduced term were to be taken as $[(T_{Cm} - T_a)/I_T]$, estimates of $F'\eta_n$ and $F'U_L$ would be correspondingly obtained.

18.1.2.2.3 Incidence Angle Modifier

The optical efficiency η_0 depends on the collector configuration and varies with the angle of incidence as well as with the relative values of diffuse and beam radiation. The incidence angle modifier is defined as $K_\eta = (\eta_0/\eta_n)$. For flat-plate collectors with 1 or 2 glass covers, K_η is almost unchanged up to incidence angles of 60° , after which it abruptly drops to zero.

A simple way to model the variation of K_η with incidence angle for flat-plate collectors is to specify η_n , the optical efficiency of the collector at normal beam incidence, to assume the entire radiation to be beam, and to use the following expression for the angular dependence (ASHRAE 1978)

$$K_\eta = 1 + b_0 \left(\frac{1}{\cos \theta} - 1 \right) \quad (18.6)$$

where

θ is the solar angle of incidence on the collector plate (in degrees)

b_0 is a constant called the incidence angle modifier coefficient

Plotting K_η against $[(1/\cos \theta) - 1]$ results in linear plots (see Figure 18.6), thus justifying the use of Equation 18.6.

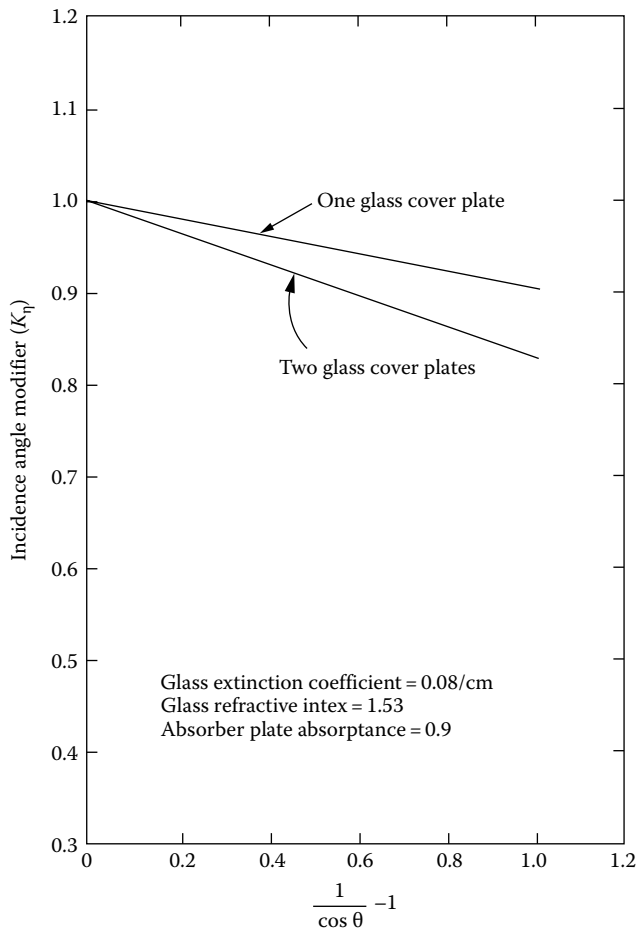


FIGURE 18.6

Incidence angle modifiers for two flat-plate collectors with nonselective coating on the absorber. (Adapted from ASHRAE, Methods of testing to determine the thermal performance of solar collectors, Standard 93-77, American Society of Heating, Refrigeration and Air Conditioning Engineers, New York, 1978.)

We note that for one-glass and two-glass covers, approximate values of b_0 are -0.10 and -0.17 , respectively.

In case the diffuse solar fraction is high, one needs to distinguish between beam, diffuse, and ground-reflected components. Diffuse radiation, by its very nature, has no single incidence angle. One simple way is to assume an equivalent incidence angle of 60° for diffuse and ground-reflected components. One would then use Equation 18.6 for the beam component along with its corresponding value of θ and account for the contribution of diffuse and ground reflected components by assuming a value of $\theta = 60^\circ$ in Equation 18.6. For more accurate estimation, one can use the relationship between the effective diffuse solar incidence angle versus collector tilt given in Duffie and Beckman (1980). It should be noted that the preceding equation gives misleading results with incidence angles close to 90° . An alternative functional form for the incidence angle modifier for both flat-plate and concentrating collectors has been proposed by Rabl (1981).

Example 18.1

From the thermal efficiency curve given in Figure 18.5 determine the performance parameters of the corresponding solar collector.

Extrapolating the curve yields y -intercept = 0.69, x -intercept = 0.105 ($\text{m}^2 \text{ }^\circ\text{C}/\text{W}$). Since the reduced temperature in Figure 18.5 is in terms of the inlet fluid temperature to the collector, Equation 18.5 yields $F_R\eta_n = 0.69$ and $F_RU_L = 0.69/0.105 = 6.57 \text{ W}/(\text{m}^2 \text{ }^\circ\text{C})$. Alternatively, the collector parameters in terms of the plate efficiency factor can be deduced. From Figure 18.5, the collector area = $1.22 \times 1.25 = 1.525 \text{ m}^2$, while the flow rate (m/A_C) = $0.0136 \text{ kg}/(\text{s m}^2)$. From Equation 18.3,

$$F'/F_R = -(0.0136 \times 4190/6.57)\ln[-6.57/(0.0136 \times 4190)] = 1.0625$$

Thus $F'U_L = 6.57 \times 1.0625 = 6.98 \text{ W}/(\text{m}^2 \text{ }^\circ\text{C})$ and $F'\eta_n = 0.69 \times 1.0625 = 0.733$.

Example 18.2

How would the optical efficiency be effected at a solar incidence angle of 60° for a flat-plate collector with two glass covers?

Assume a value of $b_0 = -0.17$. From Equation 18.6, $K_\eta = 0.83$. Thus

$$F_R\eta_0 = F_R\eta_n K_\eta = 0.69 \times 0.83 = 0.57$$

18.1.2.2.4 Other Collector Characteristics

There are three collector characteristics that a comprehensive collector testing process should also address. The collector *time constant* is a measure that determines how intermittent sunshine affects collector performance and is useful in defining an operating control strategy for the collector array that avoids instability. Collector performance is usually enhanced if collector time constants are kept low. ASHRAE 93-77 also includes a method for determining this value. Commercial collectors usually have time constants of about 5 min or less, and this justifies the use of the HWB model (see Equation 18.2).

Another quantity to be determined from collector tests is the collector *stagnation temperature*. This is the equilibrium temperature reached by the absorber plate when no heat is being extracted from the collector. Determining the maximum stagnation temperature, which occurs under high I_T and T_a values, is useful in order to safeguard against reduced collector life due to thermal damage to collectors (namely irreversible thermal expansion, sagging of covers, physical deterioration, optical changes, etc.) in the field when not in use. Though the stagnation temperature could be estimated from Equation 18.2 by setting $q_C = 0$ and solving for T_{Civ} , it is better to perform actual tests on collectors before field installation.

The third collector characteristic of interest is the *pressure drop* across the collector for different fluid flow rates. This is an important consideration for liquid collectors, and more so for air collectors, in order to keep parasitic energy consumption (namely electricity to drive pumps and blowers) to a minimum in large collector arrays.

18.1.2.3 Improvements to Flat-Plate Collector Performance

There are a number of ways by which the performance of the basic flat-plate collectors can be improved. One way is to enhance optical efficiency by treatment of the glass cover thereby reducing reflection and enhancing performance. As much as a 4% increase has been reported (Anderson 1977). Low-iron glass can also reduce solar absorption losses by a few percent.

These improvements are modest compared to possible improvements from reducing losses from the absorber plate. Essentially, the infrared upward reradiation losses from the heated absorber plate have to be decreased. One could use a second glass cover to reduce the losses, albeit at the expense of higher cost and lower optical efficiency. Usually for water heating applications, radiation accounts for about two-thirds of the losses from the absorber to the cover with convective losses making up the rest (conduction is less than about 5%). The most widely used manner of reducing these radiation losses is to use selective surfaces whose emissivity varies with wavelength (as against matte-black painted absorbers, which are essentially gray bodies). Note that 98% of the solar spectrum is at wavelengths less than $3.0\ \mu\text{m}$, whereas less than 1% of the black body radiation from a 200°C surface is at wavelengths less than $3.0\ \mu\text{m}$. Thus selective surfaces for solar collectors should have high-solar absorptance (i.e., low reflectance in the solar spectrum) and low long-wave emittance (i.e., high reflectance in the long-wave spectrum). The spectral reflectance of some commonly used selective surfaces is shown in Figure 18.7. Several commercial collectors for water heating or low-pressure steam (for absorption cooling or process heat applications) are available that use selective surfaces.

Another technique to simultaneously reduce both convective and radiative losses between the absorber and the transparent cover is to use honeycomb material (Hollands 1965). The honeycomb material can be reflective or transparent (the latter is more common) and should be sized properly. Glass honeycombs have had some success in reducing losses in high-temperature concentrating receivers, but plastics are usually recommended for use in flat-plate collectors. Because of the poor thermal aging properties, honeycomb flat-plate collectors have had little commercial success. Currently the most promising kind seems to be the simplest (both in terms of analysis and construction), namely collectors using horizontal rectangular slats (Meyer 1978). Convection can be entirely suppressed provided the slats with the proper aspect ratio are used.

Finally, collector output can be enhanced by using side reflectors, for instance a sheet of anodized aluminum. The justification in using these is their low cost and simplicity. For instance, a reflector placed in front of a tilted collector cannot but increase collector

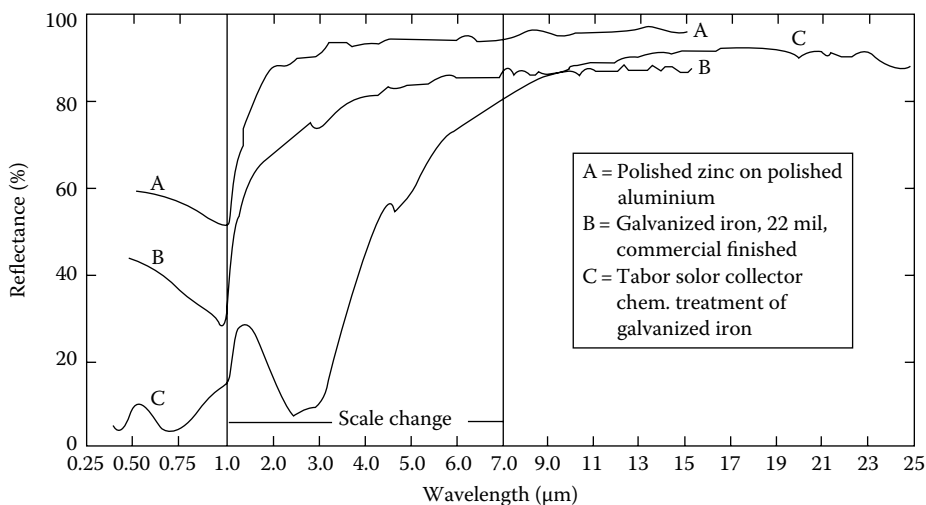


FIGURE 18.7

Spectral reflectance of several surfaces. (From Edwards, D. K. et al., Basic studies on the use of solar energy, Report No. 60-93, Department of Engineering, University of California at Los Angeles, Los Angeles, CA, 1960.)

performance because losses are unchanged and more solar radiation is intercepted by the collector. Reflectors in other geometries may cast a shadow on the collector and reduce performance. Note also that reflectors would produce rather nonuniform illumination over the day and during the year, which, though not a problem in thermal collectors, may drastically penalize the electric output of photovoltaic modules. Whether reflectors are cost-effective depends on the particular circumstances and practical questions such as aesthetics and space availability. The complexity involved in the analysis of collectors with planar reflectors can be reduced by assuming the reflector to be long compared to its width and treating the problem in two dimensions only. How optical performance of solar collectors are affected by side planar reflectors is discussed in several papers, for example Larson (1980) and Chiam (1981).

18.1.2.4 Other Collector Types

18.1.2.4.1 Evacuated Tubular Collectors

One method of obtaining temperatures between 100°C and 200°C is to use evacuated tubular collectors. The advantage in creating and being able to maintain a vacuum is that convection losses between glazing and absorber can be eliminated. There are different possible arrangements of configuring evacuated tubular collectors. Two designs are shown in Figure 18.8. The first is like a small flat-plate collector with the liquid to be heated making

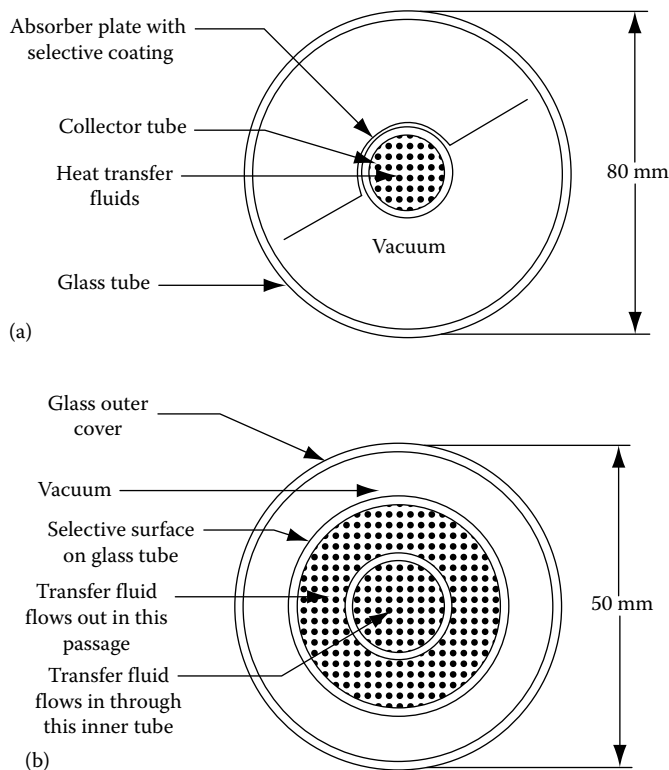


FIGURE 18.8

Two common configurations of tubular vacuum collectors: (a) with absorber plate and fluid single-pass, (b) with concentric tubes and fluid two-pass. (From Charters, W.W.S. and Pryor, T.L., *An Introduction to the Installation of Solar Energy Systems*, Victoria Solar Energy Council, Melbourne, Australia, 1982.)

one pass through the collector tube. The second uses an all-glass construction with the glass absorber tube being coated selectively. The fluid being heated passes up the middle of the absorber tube and then back through the annulus. Evacuated tubes can collect both direct and diffuse radiation and do not require tracking. Glass breakage and leaking joints due to thermal expansion are some of the problems which have been experienced with such collector types. Various reflector shapes (like flat-plate, V-groove, circular, cylindrical, involute, etc.) placed behind the tubes are often used to usefully collect some of the solar energy, which may otherwise be lost, thus providing a small amount of concentration.

18.1.2.4.2 Compound Parabolic Concentrators

The CPC collector, discovered in 1966, consists of parabolic reflectors that funnel radiation from aperture to absorber rather than focusing it. The right and left halves belong to different parabolas (hence the name *compound*) with the edges of the receiver being the foci of the opposite parabola (see Figure 18.9). It has been proven that such collectors are *ideal* in that any solar ray, be it beam or diffuse, incident on the aperture within the acceptance angle will reach the absorber while all others will bounce back to and fro and reemerge through the aperture. CPCs are also called *nonimaging* concentrators because they do not form clearly defined images of the solar disk on the absorber surface as achieved in classical concentrators. CPCs can be designed both as low-concentration devices with large acceptance angles or as high-concentration devices with small acceptance angles.

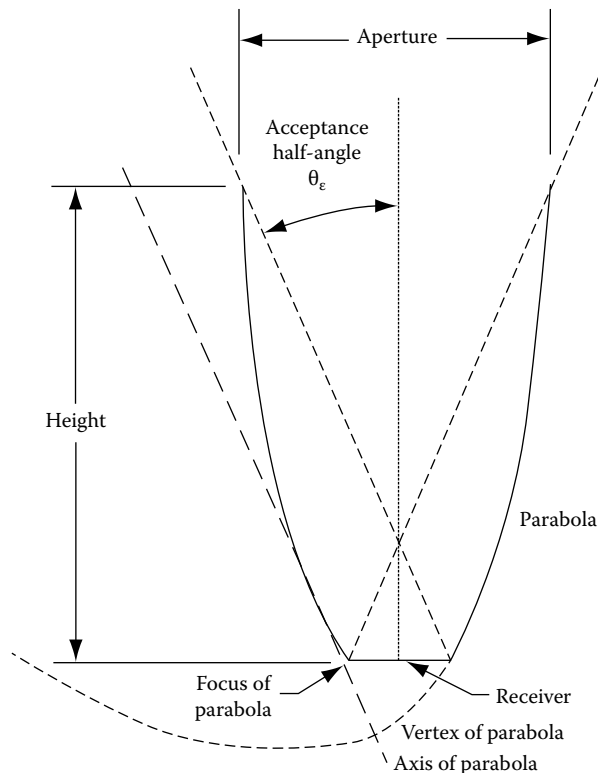
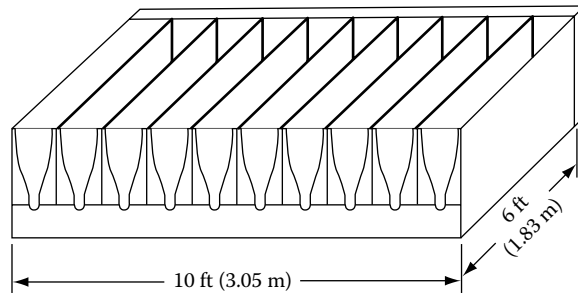


FIGURE 18.9

Cross-section of a symmetrical nontruncated CPC. (From Duffie, J.A. and Beckman, W.A., *Solar Engineering of Thermal Processes*, Wiley Interscience, New York, 1980.)

**FIGURE 18.10**

A CPC collector module. (From SERI, *Engineering Principles and Concepts for Active Solar Systems*, Hemisphere Publishing Company, New York, 1989.)

CPCs with low-concentration ratios (of about 2) and with east-west axes can be operated as stationary devices throughout the year or at most with seasonal adjustments only. CPCs, unlike other concentrators, are able to collect all the beam and a large portion of the diffuse radiation. Also they do not require highly specular surfaces and can thus better tolerate dust and degradation. A typical module made up of several CPCs is shown in Figure 18.10. The absorber surface is located at the bottom of the trough, and a glass cover may also be used to encase the entire module. CPCs show considerable promise for water heating close to the boiling point and for low-pressure steam applications. Further details about the different types of absorber and receiver shapes used, the effect of truncation of the receiver and the optics, can be found in Rabl (1985).

18.1.3 Long-Term Performance of Solar Collectors

18.1.3.1 Effect of Day-to-Day Changes in Solar Insolation

Instantaneous or hourly performance of solar collectors has been discussed in “Flat-Plate Collectors.” For example, one would be tempted to use the HWB Equation 18.2 to predict long-term collector performance at a prespecified and constant fluid inlet temperature T_{Ci} merely by assuming average hourly values of I_T and T_a . Such a procedure would be erroneous and lead to underestimation of collector output because of the presence of the control function, which implies that collectors are turned on only when $q_C > 0$, that is, when radiation I_T exceeds a certain critical value I_C . This critical radiation value is found by setting q_C in Equation 18.2 to zero:

$$I_C = U_L (T_{Ci} - T_a) / \eta_0 \quad (18.7a)$$

To be more rigorous, a small increment δ to account for pumping power and stability of controls can also be included if needed by modifying the equation to

$$I_C = U_L (T_{Ci} + \delta - T_a) / \eta_0 \quad (18.7b)$$

Then, Equation 18.2 can be rewritten in terms of I_C as

$$q_C = A_C F_R \eta_0 [I_T - I_C]^+ \quad (18.8)$$

Why one cannot simply assume a mean value of I_T in order to predict the mean value of q_C will be illustrated by the following simple concept (Klein 1978). Consider the three

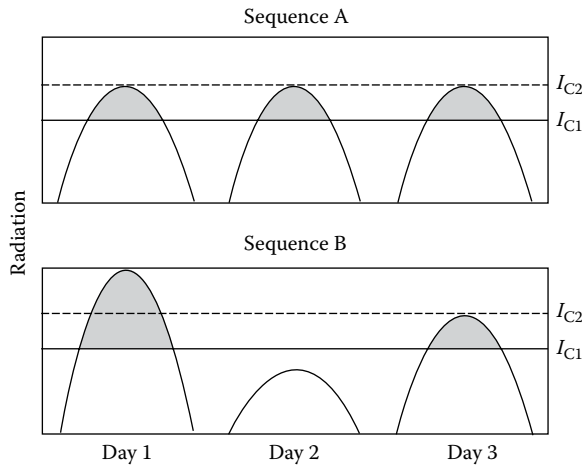


FIGURE 18.11

Effect of radiation distribution on collector long-term performance. (From Klein, S.A., Calculation of flat-plate collector utilizability, *Solar Energy*, 21, 393, 1978.)

identical day sequences shown in sequence A of Figure 18.11. If I_{C1} is the critical radiation intensity and if it is constant over the whole day, the useful energy collected by the collector is represented by the sum of the shaded areas. If a higher critical radiation value shown as I_{C2} in Figure 18.11 is selected, we note that no useful energy is collected at all. Actual weather sequences would not look like that in sequence A but rather like that in sequence B, which is comprised of an excellent, a poor, and an average day. Even if both sequences have the same average radiation over 3 days, a collector subjected to sequence B will collect useful energy when the critical radiation is I_{C2} . Thus, neglecting the variation of radiation intensity from day-to-day over the long term and dealing with mean values would result in an underestimation of collector performance.

Loads are to a certain extent repetitive from day-to-day over a season or even the year. Consequently, one can also expect collectors to be subjected to a known diurnal repetitive pattern or mode of operation, that is, the collector inlet temperature T_{Ci} has a known repetitive pattern.

18.1.3.2 Individual Hourly Utilizability

In this mode, T_{Ci} is assumed to vary over the day but has the same variation for all the days over a period of N days (where $N = 30$ days for monthly and $N = 365$ for yearly periods). Then from Equation 18.8, total useful energy collected over N days during individual hour i of the day is

$$q_{CN}(i) = A_C F_R \bar{\eta}_0 \bar{I}_{Ti} \sum_{i=1}^N \frac{[I_{Ti} - I_c]^+}{\bar{I}_{Ti}} \tag{18.9}$$

Let us define the radiation ratio

$$X_i = \frac{I_{Ti}}{\bar{I}_{Ti}} \tag{18.10}$$

and the critical radiation ratio

$$X_C = \frac{I_C}{I_{Ti}}$$

The modified HWB Equation 18.8 can be rewritten as

$$q_{CN}(i) = A_C F_R \bar{\eta}_0 \bar{I}_{Ti} N \phi_i(x_c) \tag{18.11}$$

where the individual hourly utilizability factor ϕ_i is identified as

$$\phi_i(X_C) = \frac{1}{N} \sum (X_i - X_C)^+ \tag{18.12}$$

Thus ϕ_i can be considered to be the fraction of the incident solar radiation that can be converted to useful heat by an ideal collector (i.e., whose $F_R \eta_0 = 1$). The utilizability factor is thus a *radiation statistic* in the sense that it depends solely on the radiation values at the specific location. As such, it is in no way dependent on the solar collector itself. Only after the radiation statistics have been applied is a collector dependent significance attached to X_C .

Hourly utilizability curves on a *monthly* basis that are independent of location were generated by Liu and Jordan (1963) over 30 years ago for flat-plate collectors (see Figure 18.12). The key climatic parameter which permits generalization is the *monthly clearness index* \bar{K} of the location defined as

$$\bar{K} = \frac{\bar{H}}{\bar{H}_0} \tag{18.13}$$

where

\bar{H} is the monthly mean daily global radiation on the horizontal surface

\bar{H}_0 is the monthly mean daily extraterrestrial radiation on a horizontal surface

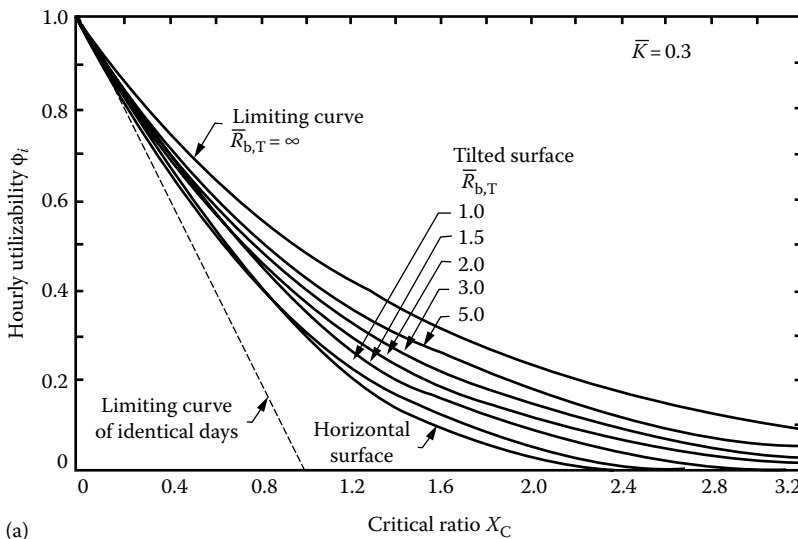


FIGURE 18.12

Generalized hourly utilizability curves of Liu and Jordan (1963) for three different monthly mean clearness indices K . (a) $\bar{K} = 0.3$.

(Continued)

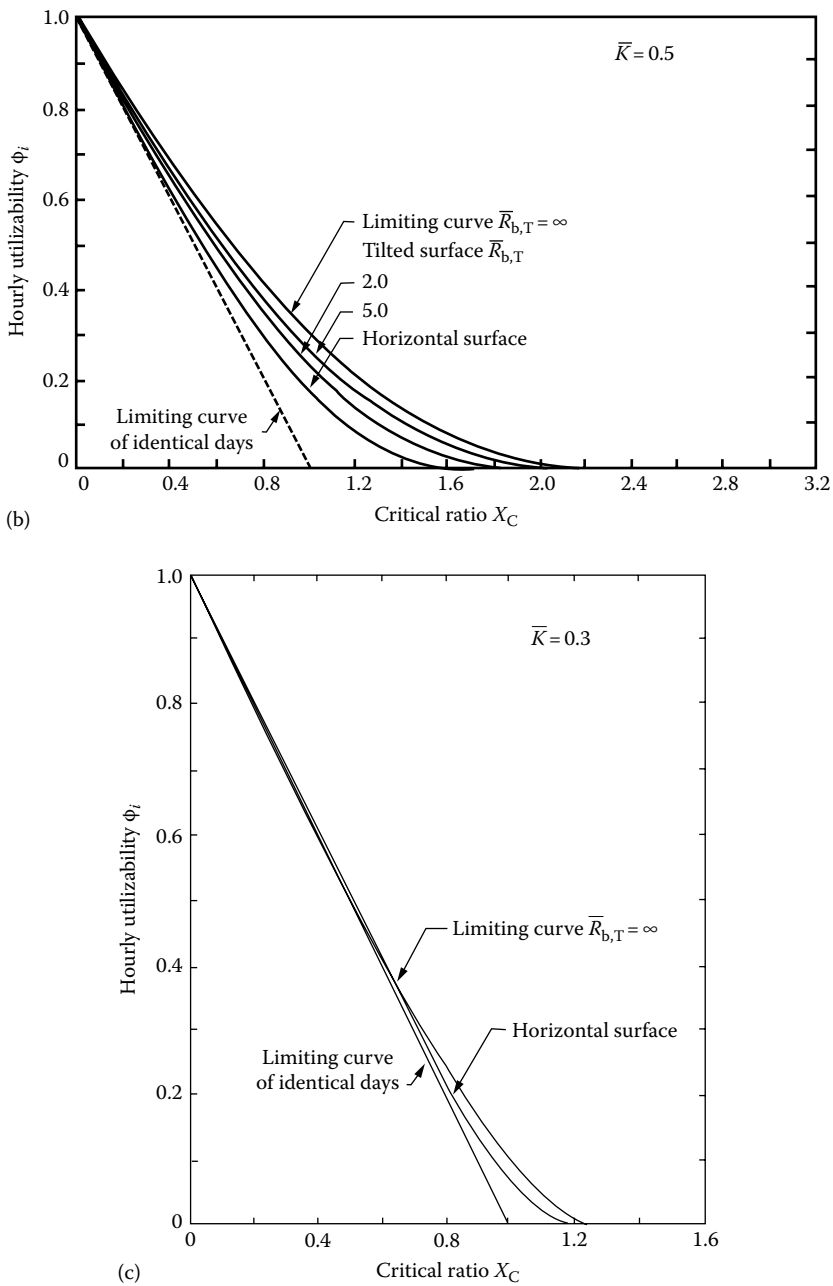


FIGURE 18.12 (Continued)
 Generalized hourly utilizability curves of Liu and Jordan (1963) for three different monthly mean clearness indices K . (b) $\bar{K} = 0.5$, (c) $\bar{K} = 0.7$. (From Liu, B. Y. H. and Jordan, R. C., A rational procedure for predicting the long-term average performance of flat-plate solar energy collectors, *Solar Energy*, 7, 53, 1963.)

Extensive tables giving monthly values of \bar{K} for several different locations worldwide can be found in several books, for example, Duffie and Beckman (1980) or Reddy (1987). The curves apply to equator-facing tilted collectors with the effect of collector tilt accounted for by the factor $\bar{R}_{b,T}$ which is the ratio of the monthly mean daily extraterrestrial radiation on the tilted collector to that on a horizontal surface. Monthly mean daily calculations can be made using the 15th of the month, though better accuracy is achieved using slightly different dates (Reddy 1987). Clark et al. (1983), working from measured data from several U.S. cities, have proposed the following correlation for individual hourly utilizability over monthly time scales applicable to flat-plate collectors only:

$$\begin{aligned}\phi_i &= 0 \quad \text{for } X_C \geq X_{\max} \\ &= (1 - X_C/X_{\max})^2 \quad \text{for } X_{\max} = 2 \\ &= \left| a \left| -[a^2 + (1 + 2a)(1 - X_C/X_{\max})^2]^{1/2} \right| \right| \quad \text{otherwise}\end{aligned}\quad (18.14)$$

where

$$a = (X_{\max} - 1)(2 - X_{\max}) \quad (18.15)$$

and

$$X_{\max} = 1.85 + 0.169(\bar{r}_T/\bar{k}^2) - 0.0696 \cos \beta / \bar{k}^2 - 0.981 \bar{k} / (\cos \delta)^2 \quad (18.16)$$

where

\bar{k} is the monthly mean *hourly* clearness index for the particular hour

δ is the solar declination

β is the tilt angle of the collector plane with respect to the horizontal

\bar{r}_T is the ratio of monthly average hourly global radiation on a tilted surface to that on a horizontal surface for that particular hour

For an isotropic sky assumption, \bar{r}_T is given by

$$\bar{r}_T = (1 - \bar{I}_d \bar{I}) r_{b,T} + \left(\frac{1 + \cos \beta}{2} \right) \bar{I}_d \bar{I} + \left(\frac{1 - \cos \beta}{2} \right) \rho \quad (18.17)$$

where

\bar{I}_d and \bar{I} are the hourly diffuse and global radiation on the horizontal surface

$r_{b,T}$ is the ratio of hourly beam radiation on the tilted surface to that on a horizontal surface (this is a purely astronomical quantity and can be calculated accurately from geometric considerations)

ρ is the ground albedo

Example 18.3

Compute the total energy collected during 11:30–12:30 for the month of September in New York, NY (latitude: 40.75°N, $T_a = 20^\circ\text{C}$) by a flat-plate solar collector of 5 m² area having zero tilt. The collector performance parameters are $F_R \eta_0 = 0.54$ and $F_R U_L = 3.21 \text{ W}/(\text{m}^2 \text{ }^\circ\text{C})$ and the collector inlet temperature is 80°C. The corresponding hourly mean clearness index \bar{k} is 0.44, and the monthly mean hourly radiation on a horizontal surface I_{T1} (11:30–12:30) is 6.0 MJ/(m² h).

From Equation 18.7a, critical radiation $I_C = 3.21 \times (80 - 20)/0.54 = 356.7 \text{ W/m}^2 = 1.28 \text{ MJ}/(\text{m}^2 \text{ h})$. For the average day of September, solar declination $\delta = 2.2^\circ$. Also, because the collector is horizontal $\bar{r}_T = 1$ and $\beta = 0$. Thus from Equation 18.16

$$X_{\max} = 1.85 + 0.169/0.44^2 - 0.0696/0.44^2 - 0.981 \times 0.44/(\cos 2.2)^\circ = 1.93.$$

Also from Equation 18.15, $a = (1.93 - 1)/(2 - 1.93) = 13.29$.

The critical radiation ratio $X_C = 1.28/1.93 = 0.663$.

Because $X_C < X_{\max}$, from Equation 18.14 we have

$$\phi_i(X_C) = |13.29 - [13.29^2 + (1 + 2 \times 13.29)(1 - 0.663/1.93)^2]^{1/2}| = |13.29 - 13.73| = 0.444.$$

Finally, the total energy collected is given by Equation 18.11

$$q_{\text{CN}}(11:30-12:30) = 5 \times 0.54 \times 60 \times 30 \times 0.44 = 214 \text{ MJ/h}$$

18.1.3.3 Daily Utilizability

18.1.3.3.1 Basis

In this mode, T_{Ci} , and hence the critical radiation level, is assumed constant during all hours of the day. The *total* useful energy over N days that can be collected by solar collectors operated all day over n hours is given by

$$Q_{\text{CN}} = A_C F_R \bar{\eta}_0 \bar{H}_T N \bar{\phi} \quad (18.18)$$

where

\bar{H}_T is the average daily global radiation on the collector surface
 $\bar{\phi}$ (called Phibar) is the daily utilizability factor, defined as

$$\bar{\phi} = \frac{N n \sum (I_T - I_C)^+}{\sum \sum I_T} = \frac{1}{Nn} \sum \sum (X_i - X_C)^+ \quad (18.19)$$

Generalized correlations have been developed both at monthly time scales and for annual time scales based on the parameter \bar{K} . Generalized (i.e., location and month independent) correlations for $\bar{\phi}$ on a *monthly* time scale have been proposed by Theilacker and Klein (1980). These are strictly applicable for flat-plate collectors only. Collares-Pereira and Rabl (1979) have also proposed generalized correlations for $\bar{\phi}$ on a monthly time scale which, though a little more tedious to use are applicable to concentrating collectors as well. The reader may refer to Rabl (1985) or Reddy (1987) for complete expressions.

18.1.3.3.2 Monthly Time Scales

The Phibar method of determining the daily utilizability fraction proposed by Theilacker and Klein (1980) correlates $\bar{\phi}$ to the following factors:

1. A geometry factor $\bar{R}_T / \bar{r}_{T,\text{noon}}$ which incorporates the effects of collector orientation, location, and time of year. \bar{R}_T is the ratio of monthly average global radiation on the tilted surface to that on a horizontal surface. $\bar{r}_{T,\text{noon}}$ is the ratio of radiation at noon on the tilted surface to that on a horizontal surface for the average day of the month.

Geometrically, $\bar{r}_{T,\text{noon}}$ is a measure of the maximum height of the radiation curve over the day, whereas \bar{R}_T is a measure of the enclosed area. Generally the value ($\bar{R}_T/\bar{r}_{T,\text{noon}}$) is between 0.9 and 1.5.

2. A dimensionless critical radiation level $\bar{X}_{C,K}$ where

$$\bar{X}_{C,K} = \frac{I_C}{\bar{I}_{T,\text{noon}}} \quad (18.20)$$

with $\bar{I}_{T,\text{noon}}$ the radiation intensity on the tilted surface at noon, given by

$$\bar{I}_{T,\text{noon}} = \bar{r}_{\text{noon}} \bar{r}_{T,\text{noon}} \bar{H} \quad (18.21)$$

where \bar{r}_{noon} is the ratio of radiation at noon to the daily global radiation on a horizontal surface during the mean day of the month which can be calculated from the following correlation proposed by Liu and Jordan (1960):

$$r(W) = \frac{I(W)}{H} = \frac{\pi}{24} (a + b \cos W) \frac{(\cos W - \cos W_s)}{\left(\sin W_s - \frac{\pi}{180} W_s \cos W_s \right)} \quad (18.22)$$

with

$$a = 0.409 + 0.5016 \sin(W_s - 60)$$

$$b = 0.6609 - 0.4767 \sin(W_s - 60)$$

where

W is the hour angle corresponding to the midpoint of the hour (in degrees)

W_s is the sunset hour angle given by

$$\cos W_s = -\tan L \tan \delta \quad (18.23)$$

where L is the latitude of the location. The fraction r is the ratio of hourly to daily global radiation on a horizontal surface. The factors $\bar{r}_{T,\text{noon}}$ and \bar{r}_{noon} can be determined from Equations 18.17 and 18.22, respectively, with $W = 0^\circ$.

The Theilacker and Klein correlation for the daily utilizability for equator-facing flat-plate collectors is

$$\bar{\phi}(X_{C,K}) = \exp\{[a' + b'(\bar{r}_{T,\text{noon}}/\bar{R}_T)][X_{C,K} + c'X_{C,K}^2]\} \quad (18.24)$$

where

$$\begin{aligned} a' &= 7.476 - 20.00\bar{K} + 11.188\bar{K}^2 \\ b' &= -8.562 + 18.679\bar{K} - 9.948\bar{K}^2 \\ c' &= -0.722 + 2.426\bar{K} + 0.439\bar{K}^2 \end{aligned} \quad (18.25)$$

How $\bar{\phi}$ varies with the critical radiation ratio $\bar{X}_{C,K}$ for three different values of \bar{K} is shown in Figure 18.13.

Example 18.4

A flat-plate collector operated horizontally at Fort Worth, Texas ($L = 32.75^\circ\text{N}$), has a surface area of 20 m^2 . It is used to heat 10 kg/min of water entering the collector at a constant temperature of 80°C each day from 6 a.m. to 6 p.m. The collector performance parameters are $F_R \eta_0 = 0.70$ and $F_R U_L = 5.0 \text{ W}/(\text{m}^2 \text{ } ^\circ\text{C})$. Use Klein's correlation to compute the energy collected by the solar collectors during September. Assume $\bar{H} = 18.28 \text{ MJ}/(\text{m}^2\text{-d})$, $\bar{K} = 0.57$ and $\bar{T}_a = 25^\circ\text{C}$. Assume the mean sunset hour angle for September to be 90° .

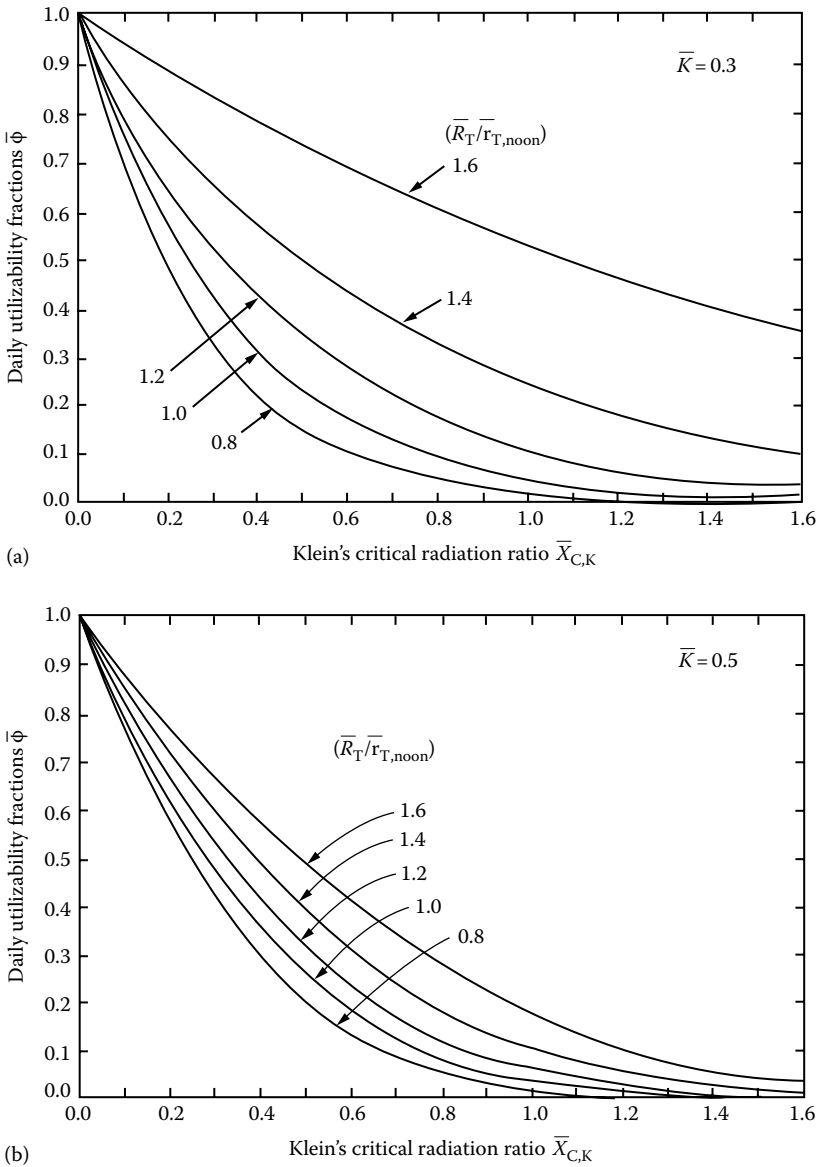


FIGURE 18.13

Generalized daily utilizability curves of Theilacker and Klein (1980) for three different K values. (a) $\bar{K} = 0.3$, (b) $\bar{K} = 0.5$. (Continued)

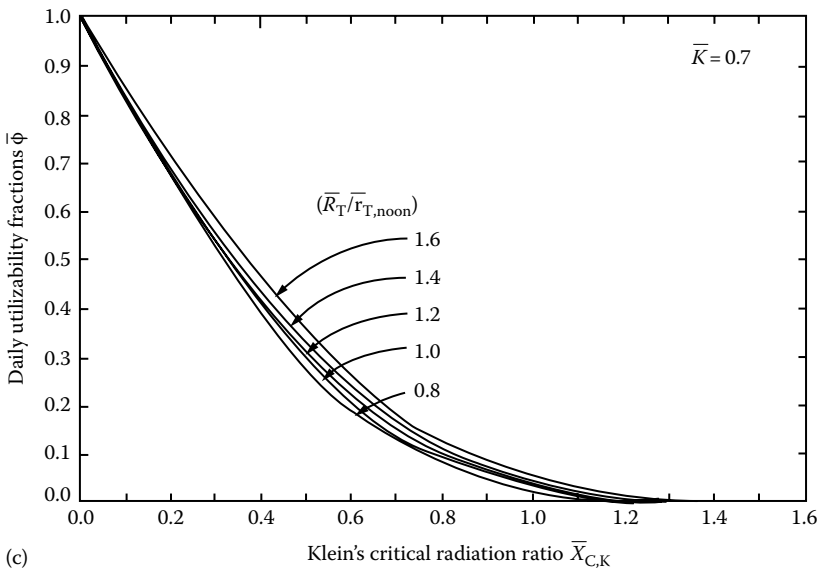


FIGURE 18.13 (Continued)

Generalized daily utilizability curves of Theilacker and Klein (1980) for three different K values. (c) $\bar{K} = 0.7$. (From Theilacker, J.C. and Klein, S.A., Improvements in the utilizability relationships, in *American Section of the International Solar Energy Society Meeting Proceedings*, Phoenix, AZ, 1980, 271pp.)

The critical radiation is calculated first:

$$I_C = (5/0.7)(80 - 25) = 393 \text{ W/m}^2 = 1.414 \text{ MJ}/(\text{m}^2\text{h})$$

For a horizontal surface, $\bar{R}_T = \bar{r}_{T,\text{noon}} = 1$. From Equation 18.22, $r(W = 0) = \pi/24(a + b) = 0.140$. Klein's critical radiation ratio (Section 18.1.10) $\bar{X}_{C,K} = 1.414/(18.28 \times 0.140) = 0.553$. From Equation 18.24, $\bar{\phi} = 0.318$. Finally, from Equation 18.18, the total monthly energy collected by the solar collectors is $Q_{CM} = 20 \times 0.7 \times 30 \times 0.318 \times 18.28 = 2.44 \text{ GJ}/\text{month}$.

18.1.3.3.3 Annual Time Scales

Generalized expressions for the *yearly* average energy delivered by the principal collector types with constant radiation threshold (i.e., when the fluid inlet temperature is constant for all hours during the day over the entire year) have been developed by Rabl (1981) based on data from several U.S. locations. The correlations are basically quadratic of the form

$$\frac{Q_{CY}}{A_C F_R \eta_n} = \tilde{a} + \tilde{b} I_C + \tilde{c} I_C^2 \tag{18.26}$$

where the coefficients \tilde{a} , \tilde{b} , and \tilde{c} are functions of collector type and/or tracking mode, climate, and in some cases, latitude. The complete expressions as revised by Gordon and Rabl (1982) are given in Reddy (1987). Note that the yearly *daytime* average value of T_a should be used to determine I_C . If this is not available, the yearly mean *daily* average value can be used. Plots of Q_{CY} versus I_C for flat-plate collectors that face the equator with tilt equal to the latitude are shown in Figure 18.14. The solar radiation enters these expressions as \tilde{I}_{bn} ,

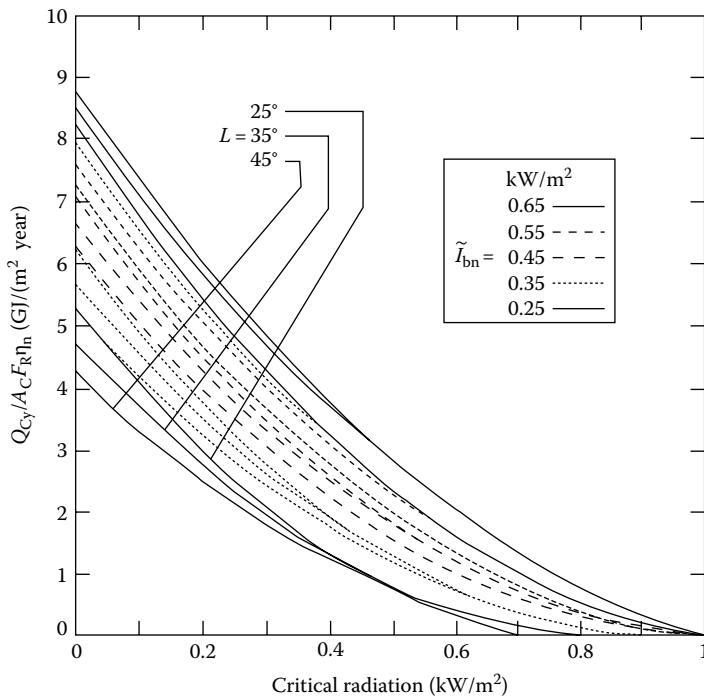


FIGURE 18.14

Yearly total energy delivered by flat-plate collectors with tilt equal to latitude. (From Gordon, J.M. and Rabl, A., *Solar Energy*, 28, 519, 1982.)

the annual average beam radiation at normal incidence. This can be estimated from the following correlation

$$\tilde{I}_{bn} = 1.37\tilde{K} - 0.34 \tag{18.27}$$

where

\tilde{I}_{bn} is in kW/m²

\tilde{K} is the annual average clearness index of the location

Values of \tilde{K} for several locations worldwide are given in Reddy (1987).

This correlation is strictly valid for latitudes ranging from 25° to 48°. If used for lower latitudes, the correlation is said to lead to overprediction. Hence, it is recommended that for such lower latitudes a value of 25° be used to compute Q_{Cy} .

A direct comparison of the yearly performance of different collector types is given in Figure 18.15. A latitude of 35°N is assumed and plots of Q_{Cy} U.S. $(T_{Ci} - T_a)$ have been generated in a sunny climate with $I_{bn} = 0.6$ kW/m². Relevant collector performance data are given in Figure 18.15. The crossover point between flat-plate and concentrating collectors is approximately 25°C above ambient temperature whether the climate is sunny or cloudy.

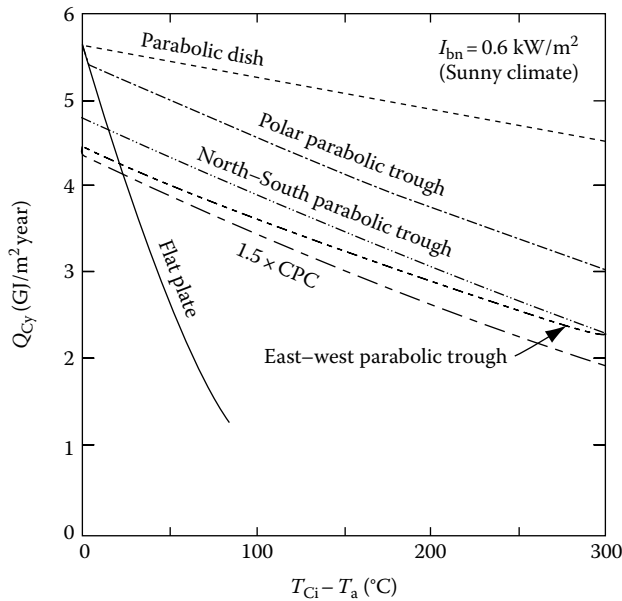


FIGURE 18.15

Figure illustrating the comparative performance (yearly collectible energy) of different collector types as a function of the difference between collector inlet temperature and ambient collector performance parameters $F'\eta_0$ and $F'U_L$ in $W/(m^2 \text{ } ^\circ\text{C})$ are: flat plate (0.70 and 5.0), CPC (0.60 and 0.75), parabolic trough (0.65 and 0.67), and parabolic dish (0.61 and 0.27). (From Rabl, A., Yearly average performance of the principal solar collector types, *Solar Energy*, 27, 215, 1981.)

18.1.4 Solar Systems

18.1.4.1 Classification

Solar thermal systems can be divided into two categories: standalone or solar supplemented. They can be further classified by means of energy collection as active or passive, by their use as residential or industrial. Further, they can be divided by collector type into liquid or air systems, and by the type of storage they use into seasonal or daily systems.

18.1.4.1.1 Standalone and Solar Supplemented Systems

Standalone systems are systems in which solar energy is the only source of energy input used to meet the required load. Such systems are normally designed for applications where a certain amount of tolerance is permissible concerning the load requirement; in other words, where it is not absolutely imperative that the specified load be met each and every instant. This leniency is generally admissible in the case of certain residential and agricultural applications. The primary reasons for using such systems are their low cost and simplicity of operation.

Solar-supplemented systems, widely used for both industrial and residential purposes, are those in which solar energy supplies part of the required heat load, the rest being met by an auxiliary source of heat input. Due to the daily variations in incident solar radiation, the portion of the required heat load supplied by the solar energy system may

vary from day-to-day. However, the auxiliary source is so designed that at any instant it is capable of meeting the remainder of the required heat load. It is normal practice to incorporate an auxiliary heat source large enough to supply the entire heat load required. Thus, the benefit in the solar subsystem is not in its capacity credit (i.e., not that a smaller capacity conventional system can be used), but rather that a part of the conventional fuel consumption is displaced. The solar subsystem thus acts as a fuel economizer.

Solar-supplemented energy systems will be the primary focus of this chapter. Designing such systems has acquired a certain firm scientific rationale, and the underlying methodologies have reached a certain maturity and diversity, which may satisfy professionals from allied fields. On the other hand, unitary solar apparatus are not discussed here, since these are designed and sized based on local requirements, material availability, construction practices, and practical experience. Simple rules of thumb based on prior experimentation are usually resorted to for designing such systems.

18.1.4.1.2 Active and Passive Systems

Active systems are those systems that need electric pumps or blowers to collect solar energy. It is evident that the amount of solar energy collected should be more than the electrical energy used. Active systems are invariably used for industrial applications and for most domestic and commercial applications as well. *Passive systems* are those systems that collect or use solar energy without direct recourse to any source of conventional power, such as electricity, to aid in the collection. Thus, either such systems operate by natural thermosyphon (for example, domestic water heating systems) between collector, storage, and load or, in the case of space heating, the architecture of the building is such as to favor optimal use of solar energy. Use of a passive system for space heating applications, however, in no way precludes the use of a backup auxiliary system. This chapter deals with active solar systems only.

18.1.4.1.3 Residential and Industrial Systems

Basically, the principles and the components used in these two types of systems are alike, the difference being in the load distribution, control strategies, and relative importance of the components with respect to each other. Whereas *residential* loads have sharp peaks in the early morning or in the evening and have significant seasonal variations, industrial loads tend to be fairly uniform over the year. Constant loads favor the use of solar energy because good equipment utilization can be achieved. Because of differences in load distribution, the role played by the storage differs for both applications. Residential loads often occur at times when solar radiation is no longer available. Thus the collector and the storage subsystems interact in a mode without heat withdrawal from the storage. Finally, for economic reasons, many residential systems are designed to operate by natural thermosyphon, in which case no pumps or controls are needed.

On the other hand, for *industrial and commercial* applications, there is no a priori relationship between the time dependence of the load and the period of sunshine. Moreover, a high reliability has to be assured, so the solar system will have to be combined with a conventional system. Very often, a significant portion of the load can be directly supplied by the solar system even without storage. Another option is to use buffer storage for short periods, on the order of a few hours, in case of discontinuous batch process loads. Thus, the proper design of the storage component has to be given adequate consideration.

At present, due to economic constraints as well as the fact that proper awareness of the various installations and operational difficulties associated with larger solar thermal systems is still lacking, solar thermal systems are normally designed either (1) with the no-storage option, or (2) with buffer storage where a small fraction of the total heat demand is only supplied by the solar system.

18.1.4.1.4 *Liquid and Air Collectors*

Although air has been the primary fluid for space heating and drying applications, solar air heating systems have until recently been relegated to second place, mainly as a result of the engineering difficulties associated with such systems. Also, applications involving hot air are probably less common than those needing hot water. Air systems for space heating are well described by Löff (1981).

Even with liquid solar collectors, various configurations are possible, and these can be classified basically as *nontracking* (which include flat-plate collectors and CPCs) or *tracking* collectors (which include various types of concentrating collectors). For low-grade thermal heat, for which solar energy is most suited, flat-plate collectors are far more appropriate than concentrating collectors, not only because of their lower cost but also because of their higher thermal efficiencies at low temperature levels. Moreover, their operation and maintenance costs are lower. Finally, for locations having a high fraction of diffuse radiation, as in the tropics, flat-plate collectors are considered to be thermally superior because they can make use of diffuse radiation as well as beam radiation. Although the system design methodologies presented in this chapter explicitly assume flat-plate collector systems, these design approaches can be equally used with concentrating collectors.

18.1.4.1.5 *Daily and Seasonal Storage*

By *daily storage* is meant systems having capacities equivalent to at most a few days of demand (i.e., just enough to tide over day-to-day climatic fluctuations). In *seasonal storage*, solar energy is stored during the summer for use in winter. Industrial demand loads, which are more or less uniform over the year, are badly suited for seasonal-storage systems. This is also true of air-conditioning for domestic and commercial applications because the load is maximum when solar radiation is also maximum, and vice versa. The present-day economics of seasonal storage units do not usually make such systems an economical proposition except for community heating in cold climates.

18.1.4.2 *Closed-Loop and Open-Loop Systems*

The two possible configurations of solar thermal systems with daily storage are classified as closed-loop or open-loop systems. Though different authors define these differently, we shall define these as follows. A *closed-loop system* has been defined as a circuit in which the performance of the solar collector is directly dependent on the storage temperature. Figure 18.16 gives a schematic of a closed-loop system in which the fluid circulating in the collectors does not mix with the fluid supplying thermal energy to the load. Thus, these two subsystems are distinct in the sense that any combination of fluids (water or air) is theoretically feasible (a heat exchanger, as shown in the figure, is of course imperative when the fluids are different). However, in practice, only water–water, water–air, or air–air combinations are used. From the point of system performance, the storage temperature normally varies over the day and, consequently, so does collector performance. Closed-loop system configurations have been widely used

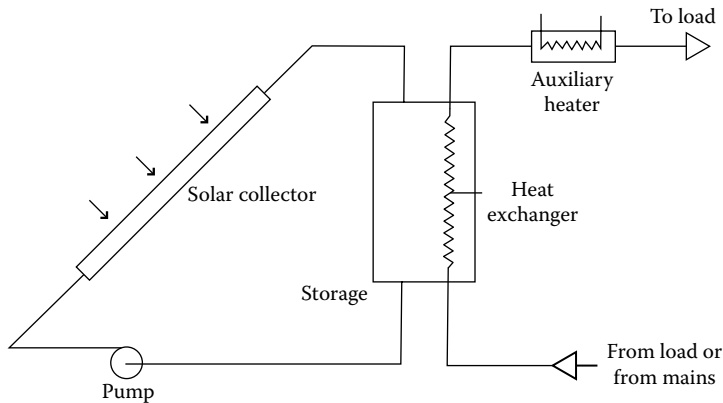


FIGURE 18.16
Schematic of a closed-loop solar system.

to date for domestic hot water and space heating applications. The flow rate per unit collector area is generally around $50 \text{ kg}/(\text{h m}^2)$ for liquid collectors. The storage volume makes about 5–10 passes through the collector during a typical sunny day, and this is why such systems are called *multipass* systems. The temperature rise for each pass is small, of the order of 2°C – 5°C for systems with circulating pumps and about 10°C for thermosyphon systems. An expansion tank and a check valve to prevent reverse thermosyphoning at nights, although not shown in the figure, are essential for such system configurations.

Figure 18.17 illustrates one of the possible configurations of *open-loop systems*. Open-loop systems are defined as systems in which the collector performance is independent of the storage temperature. The working fluid may be rejected (or a heat recuperator can be used) if contaminants are picked up during its passage through the load. Alternatively, the working fluid could be directly recalcitrated back to the entrance of the solar collector field. In all these open-loop configurations, the collector is subject to a given or known inlet temperature specified by the load requirements.

If the working fluid is water, instead of having a continuous flow rate (in which case the outlet temperature of the water will vary with isolation), a solenoid valve can be placed

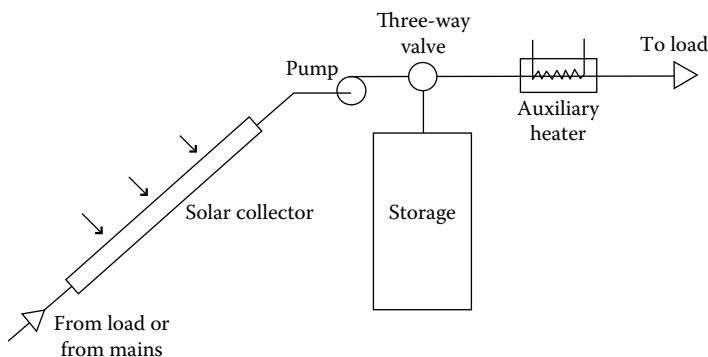


FIGURE 18.17
Schematic of an open-loop solar system.

just at the exit of the collector, set so as to open when the desired temperature level of the fluid in the collector is reached. The water is then discharged into storage, and fresh water is taken into the collector. The solar collector will thus operate in a discontinuous manner, but this will ensure that the temperature in the storage is always at the desired level. An alternative way of ensuring uniform collector outlet temperature is to vary the flow rate according to the incident radiation. One can collect a couple of percent more energy than with constant rate single-pass designs (Gordon and Zarmi 1985). However, this entails changing the flow rate of the pump more or less continuously, which is injurious to the pump and results in reduced life. Of all the three variants of the open-loop configuration, the first one, namely the single-pass open-loop solar thermal system configuration with constant flow rate and without a solenoid valve, is the most common.

As stated earlier, closed-loop systems are appropriate for domestic applications. Until recently, industrial process heat systems were also designed as large solar domestic hot-water systems with high collector flow rates and with the storage tank volume making several passes per day through the collectors. Consequently, the storage tank tends to be fairly well mixed. Also the tank must be strong enough to withstand the high pressure from the water mains. The open-loop single-pass configuration, wherein the required average daily fluid flow is circulated just once through the collectors with the collector inlet temperature at its lowest value, has been found to be able to deliver as much as 40% more yearly energy for industrial process heat applications than the multipass designs (Collares-Pereira et al. 1984). Finally, in a closed-loop system where an equal amount of fresh water is introduced into storage whenever a certain amount of hot water is drawn off by the load, it is not possible to extract the entire amount of thermal energy contained in storage since the storage temperature is continuously reduced due to mixing. This *partial depletion effect* in the storage tank is not experienced in open-loop systems. The penalty in yearly energy delivery ranges typically from about 10% for daytime-only loads to around 30% for nighttime-only loads compared to a closed-loop multipass system where the storage is depleted every day. Other advantages of open-loop systems are (1) the storage tank need not be pressurized (and hence is less costly), and (2) the pump size and parasitic power can be lowered.

A final note of caution is required. The single-pass design is not recommended for *variable* loads. The tank size is based on yearly daily load volumes, and efficient use of storage requires near-total depletion of the daily collected energy each day. If the load draw is markedly lower than its average value, the storage would get full relatively early the next day and solar collection would cease. It is because industrial loads tend to be more uniform, both during the day and over the year, than domestic applications that the single-pass open-loop configuration is recommended for such applications.

18.1.4.2.1 Description of a Typical Closed-Loop System

Figure 18.18 illustrates a typical closed-loop solar-supplemented liquid heating system. The useful energy is often (but not always) delivered to the storage tank via a collector-heat exchanger, which separates the collector fluid stream and the storage fluid. Such an arrangement is necessary either for antifreeze protection or to avoid corrosion of the collectors by untreated water containing gases and salts. A safety relief valve is provided because the system piping is normally nonpressurized, and any steam produced in the solar collectors will be let off from this valve. When this happens, energy dumping is said to take place. Fluid from storage is withdrawn and made to flow through the load-heat exchanger when the load calls for heat. Whenever possible, one should withdraw fluid directly from the storage and pass it through the load, and avoid incorporating the

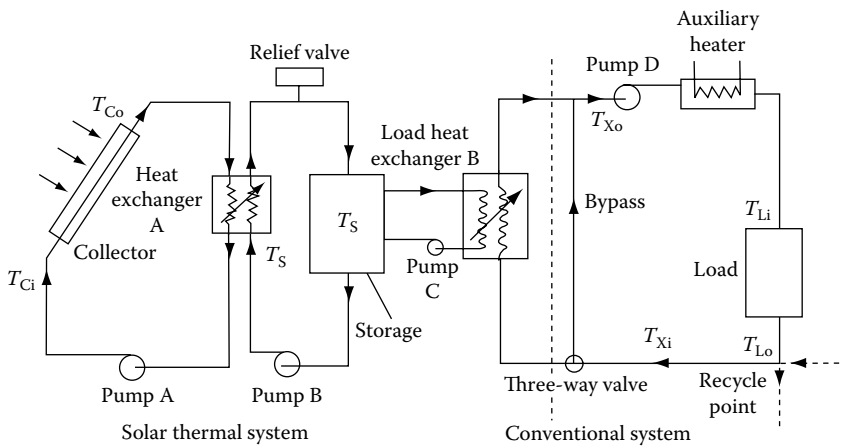


FIGURE 18.18

Schematic of a typical closed-loop system with auxiliary heater placed in series (also referred to as a topping-up type).

load-heat exchanger, since it introduces additional thermal penalties and involves extra equipment and additional parasitic power use. Heat is withdrawn from the storage tank at the top and reinserted at the bottom in order to derive maximum benefit from the thermal stratification that occurs in the storage tank. A bypass circuit is incorporated prior to the load heat exchanger and comes into play

1. When there is no heat in the storage tank (i.e., storage temperature T_S is less than the fluid temperature entering the load heat exchanger T_{Xi})
2. When T_S is such that the temperature of the fluid leaving the load heat exchanger is greater than that required by the load (i.e., $T_{Xo} > T_{Li}$, in which case the three-way valve bypasses part of the flow so that $T_{Xo} = T_{Li}$). The bypass arrangement is thus a differential control device which is said to modulate the flow such that the above condition is met. Another operational strategy for maintaining $T_{Xo} = T_{Li}$ is to operate the pump in a "bang-bang" fashion (i.e., by short cycling the pump). Such an operation is not advisable, however, since it would lead to premature pump failure.

An auxiliary heater of the *topping-up type* supplies just enough heat to raise T_{Xo} to T_{Li} . After passing through the load, the fluid (which can be either water or air) can be recirculated or, in case of liquid contamination through the load, fresh liquid can be introduced. The auxiliary heater can also be placed in parallel with the load (see Figure 18.19), in which case it is called an *all-or-nothing type*. Although such an arrangement is thermally less efficient than the topping-up type, this type is widely used during the solar retrofit of heating systems because it involves little mechanical modifications or alterations to the auxiliary heater itself.

It is obvious that there could also be solar-supplemented energy systems that do not include a storage element in the system. Figure 18.20 shows such a system configuration with the auxiliary heater installed in series. The operation of such systems is not very different from that of systems with storage, the primary difference being that whenever instantaneous solar energy collection exceeds load requirements (i.e., $T_{Co} > T_{Li}$), energy dumping takes place. It is obvious that by definition there cannot be a closed-loop,

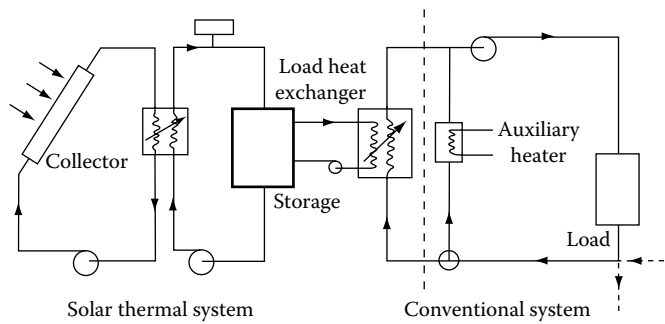


FIGURE 18.19

Schematic of a typical closed-loop system with auxiliary heater placed in parallel (also referred to as an all-or-nothing type).

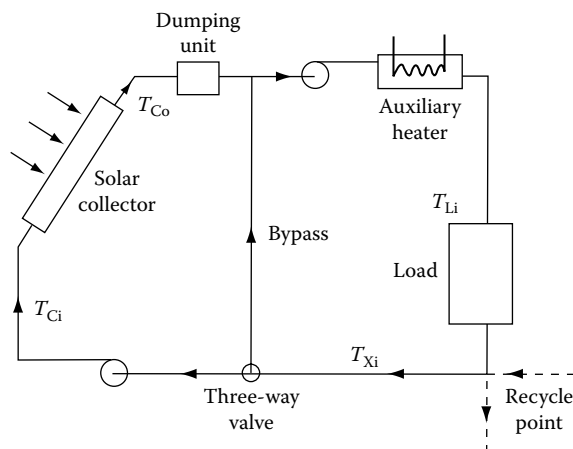
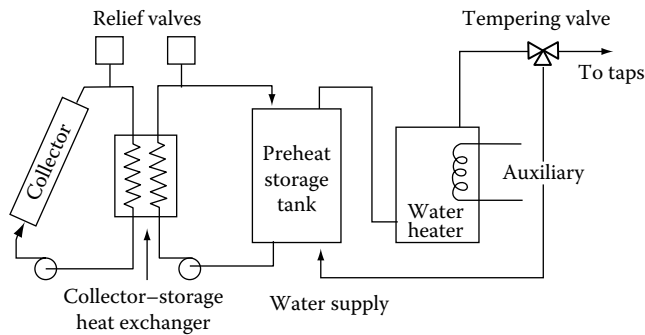


FIGURE 18.20

Simple solar thermal system without storage.

no-storage solar thermal system. Solar thermal systems without storage are easier to construct and operate, and even though they may be effective for 8–10 h a day, they are appropriate for applications such as process heat in industry.

Active closed-loop solar systems as described earlier are widely used for service hot-water systems, that is, for domestic hot water and process heat applications as well as for space heat. There are different variants to this generic configuration. A system without the collector-heat exchanger is referred to having collectors *directly coupled* to the storage tank (as against *indirect coupling* as in Figure 18.16). For domestic hot-water systems, the system can be simplified by placing the auxiliary heater (which is simply an electric heater) directly inside the storage tank. One would like to maintain stratification in the tank so that the coolest fluid is at the bottom of the storage tank, thereby enhancing collection efficiency. Consequently, the electric heater is placed at about the upper third portion of the tank so as to assure good collection efficiency while assuring adequate hot water supply to the load. A more efficient but expensive option is widely used in the United States: the *double tank system*, shown in Figure 18.21. Here the functions of solar storage and auxiliary heating are separated, with the solar tank acting as a preheater for the conventional gas or electric unit. Note that a further system simplification can be achieved for domestic

**FIGURE 18.21**

Schematic of a standard domestic hot-water system with double tank arrangement. (From Duffie, J.A. and Beckman, W.A., *Solar Engineering of Thermal Processes*, Wiley Interscience, New York, 1980.)

applications by placing the load heat exchanger directly inside the storage tank. In certain cases, one can even eliminate the heat exchanger completely.

Another system configuration is the *drain-back* (also called drain-out) system, where the collectors are emptied each time the solar system shuts off. Thus the system invariably loses collector fluid at least once, and often several times, each day. No collector-heat exchanger is needed, and freeze protection is inherent in such a configuration. However, careful piping design and installation, as well as a two-speed pump, are needed for the system to work properly (Newton and Gilman 1981). The drain-back configuration may be either open (vented to atmosphere) or closed (for better corrosion protection). Long-term experience in the United States with the drain-back system has shown it to be very reliable if engineered properly. A third type of system configuration is the *drain-down* system, where the fluid from the collector array is removed only when adverse conditions, such as freezing or boiling, occur. This design is used when freezing ambient temperatures are only infrequently encountered.

Active solar systems of the type described above are mostly used in countries such as the United States and Canada. Countries such as Australia, India, and Israel (where freezing is rare) usually prefer thermosyphon systems. No circulating pump is needed, the fluid circulation being driven by density difference between the cooler water in the inlet pipe and the storage tank and the hotter water in the outlet pipe of the collector and the storage tank. The low fluid flow in thermosyphon systems enhances thermal stratification in the storage tank. The system is usually fail-proof, and a study by Liu and Fanney (1980) reported that a thermosyphon system performed better than several pumped service hot-water systems. If operated properly, thermosyphon and active solar systems are comparable in their thermal performance. A major constraint in installing thermosyphon systems in already existing residences is the requirement that the bottom of the storage tank be at least 20 cm or more higher than the top of the solar collector in order to avoid reverse thermosyphoning at night. To overcome this, spring-loaded one-way valves have been used, but with mixed success.

18.1.5 Controls

There are basically five categories to be considered when designing automatic controls (Mueller Associates 1985): (1) collection to storage, (2) storage to load, (3) auxiliary energy

to load, (4) miscellaneous (i.e., heat dumping, freeze protection, overheating, etc.), and (5) alarms. The three major control system components are sensors, controllers, and actuating devices. Sensors are used to detect conditions (such as temperatures, pressures, etc.). Controllers receive output from the sensors, select a course of action, and signal a system component to adjust the condition. Actuated devices are components such as pumps, valves, and alarms that execute controller commands and regulate the system.

The sensors for the controls must be set, operated, and located correctly if the solar system is to collect solar energy effectively, reduce operating time, wear and tear of active components, and minimize auxiliary and parasitic energy use. Moreover, sensors also need to be calibrated frequently. For diagnostic purposes, it may be advisable to add extra sensors and data acquisition equipment in order to verify system operation and keep track of long-term system operation. Potential problems can be then rectified in time. The reader may refer to manuals by Mueller Associates (1985) or by SERI (1989) for more details on controls pertaining to solar energy systems.

Though single-point temperature controllers or solar-cell-activated controls have been used for activated solar collectors, the best way to do so is by differential temperature controllers. Temperature sensors are used to measure the fluid temperature at collector outlet and at the bottom of the storage tank. When the difference is greater than a set amount, say 5°C , then the controller turns the pump on. If the pump is running and the temperature difference falls below another preset value, say 1°C , the controller stops the pump. The temperature deadband between switching-off and reactivating levels should be set with care, since too high a deadband would adversely affect collection efficiency and too low a value would result in short cycling of the collector pump. Figure 18.22 taken from CSU (1980), shows typical diurnal temperature variations of the liquids at collector exit T_1 and in the storage bottom T_3 as a result of heat withdrawal and/or heat losses from the storage. At about 8:30 a.m., $T_1 > T_3$ and, since there is no flow in the collector, T_1 increases rapidly until the difference ($T_1 - T_3$) reaches the preset activation level (shown as point 1). The collector pump A comes on, and liquid circulation through the collector begins. Because of this cold water surge, T_1 decreases, resulting in a drop of ($T_1 - T_3$) to the preset deactivating level (shown as point 2). The pump switches off, and

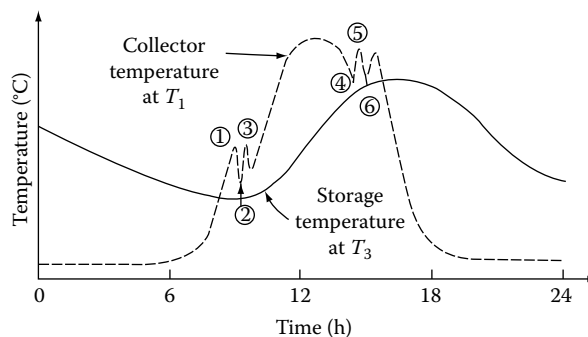


FIGURE 18.22

Typical diurnal variation of collector and storage temperatures. Points 1–3 represent the start-up, shut-down, and re-start cycling operation of the circulating pump at the beginning of the day; points 4–6 represent the shut-down cycling behavior at the end of the day. (From CSU, *Solar heating and cooling of residential buildings—Design of systems*, Manual prepared by the Solar Energy Applications Laboratory, Colorado State University, Fort Collins, CO, 1980.)

liquid flow through the collectors stops. Gradually T_1 increases again, and so on. The number of on-off cycles at system start-up depends on solar intensity, fluid flow rate, volume of water in the collector loop, and the differential controller setting. A similar phenomenon of cycling also occurs in the afternoon. However, the error introduced in solar collector long-term performance predictions by neglecting this cycling effect in the modeling equations is usually small.

18.1.5.1 Corrections to Collector Performance Parameters

18.1.5.1.1 Combined Collector-Heat Exchanger Performance

The use of the heat exchanger A in Figure 18.18 imposes a penalty on the performance of the solar system because T_{Ci} is always higher than T_s , thereby decreasing q_c (see Figure 18.23). The collector-heat exchanger can be implicitly accounted for by suitably modifying the collector performance parameters. Recall from basic heat transfer the concept of heat exchanger effectiveness E defined as the ratio of the actual heat transfer rate to the maximum possible heat transfer rate, that is,

$$E = \frac{(mc_p)_a(T_{ai} - T_{ao})}{(mc_p)_{\min}(T_{ai} - T_{bi})} \quad (18.28a)$$

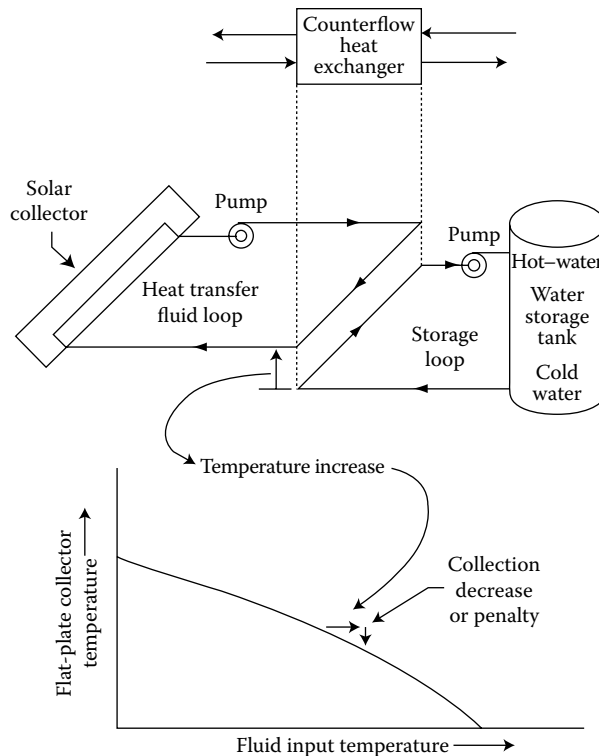


FIGURE 18.23

Heat collection decrease caused by double-loop heat exchangers. (From Cole, R.L. et al. (eds.), Design and installation manual for thermal energy storage, ANL-79-15, Argonne National Laboratory, Argonne, IL, 1979.)

$$= \frac{(mc_p)_b(T_{bo} - T_{bi})}{(mc_p)_{\min}(T_{ai} - T_{bi})} \quad (18.28b)$$

where

$(mc_p)_x$ is the capacitance rate of fluid X (with $X = a$ for the warmer fluid, or $X = b$ for the cooler fluid)

$(mc_p)_{\min}$ is the lower heat capacitance value of either stream

The advantage of this modeling approach is that, to a good approximation, E can be considered constant in spite of variations in temperature levels provided the mass flow rates of both fluids remain constant. Thus, knowing the two flow rates, E , T_{ai} , and T_{bi} , both the exit fluid temperatures can be conveniently deduced. De Winter (1975) has shown that the combined performance of the solar collector and the heat exchanger can be conveniently modeled by replacing the collector heat removal factor F_R by a combined collector-exchanger heat removal factor F'_R such that

$$\frac{F'_R}{F_R} = \left[1 + \frac{F_R U_L A_C}{(mc_p)_C} \left\{ \frac{(mc_p)_C}{E_A (mc_p)_{\min}} - 1 \right\} \right]^{-1} \quad (18.29)$$

where

$(mc_p)_C$ is the capacitance rate of the fluid through the collector

E_A is the effectiveness of heat exchanger A

The variation of F'_R/F_R is shown in Figure 18.24. The plots exhibit the same type of asymptotic behavior with mass flow rate as in Figure 18.3.

The design of the collector-heat exchanger also requires care if the penalty imposed by it on the solar collection is to be minimized. Using a large heat exchanger increases the effectiveness and lowers this penalty; that is, the ratio (F'_R/F_R) is high, but the associated initial and operating costs may be higher. Both these considerations need to be balanced

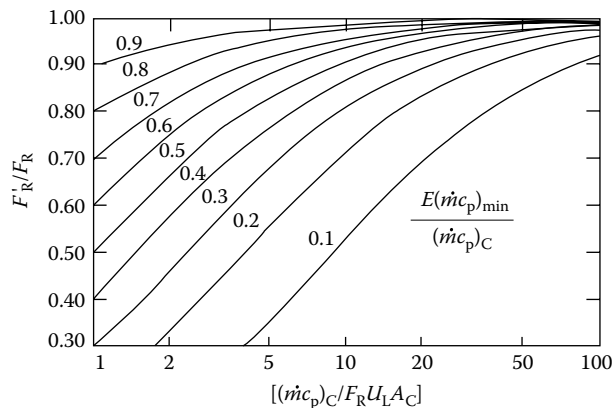


FIGURE 18.24

Variation of collector-heat exchanger correction factor. (From Duffie, J.A. and Beckman, W.A., *Solar Engineering of Thermal Processes*, Wiley Interscience, New York, 1980.)

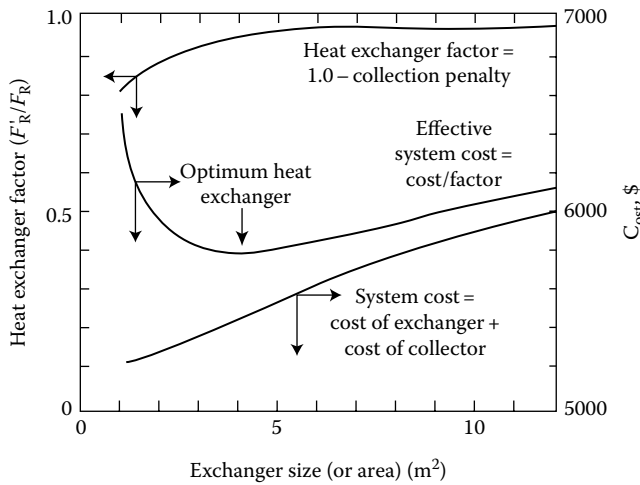


FIGURE 18.25

Typical heat-exchanger optimization plot. (From Cole, R.L. et al. (eds.), Design and installation manual for thermal energy storage, ANL-79-15, Argonne National Laboratory, Argonne, IL, 1979.)

for optimum design (see Figure 18.25). Optimum heat exchanger area A_x can be found from the following equation proposed by Cole et al. (1979):

$$A_x = A_c \left[\frac{F_R U_L C_c}{U_x C_x} \right]^{1/2} \tag{18.30}$$

where

- A_c is the collector area
- C_c is the cost per unit collector area
- C_x is the cost per unit heat exchanger area
- U_x is the heat loss per unit area of the heat exchanger

18.1.5.1.2 Collector Piping and Shading Losses

Other corrections that can be applied to collector performance parameters include those for thermal losses from the piping (or from ducts) between the collection subsystem and the storage unit. Beckman (1978) has shown that these losses can be conveniently taken into consideration by suitably modifying the η_n and U_L terms of the solar collectors as follows:

$$\frac{\eta'_n}{\eta_n} = \left[1 + \frac{u_d A_0}{(mc_p)_C} \right]^{-1} \quad \text{and} \quad \frac{U'_L}{U_L} = \frac{1 - \frac{U_d A_i}{(mc_p)_C} + \frac{U_d (A_i + A_0)}{A_c F_R U_L}}{1 + \frac{U_d A_0}{(mc_p)_C}} \tag{18.31}$$

where

- U_d is the heat coefficient from the pipe or duct
- A_0 is the heat loss area of the outlet pipe or duct
- A_i is the heat loss area of the inlet pipe or duct

When large collector arrays are mounted on flat roofs or level ground, multiple rows of collectors are usually arranged in a sawtooth fashion. These multiple rows must be spaced so that they do not shade each other at low sun angles. Unlimited space is rarely available, and it is desirable to space the rows as close as possible to minimize piping and to keep land costs low. Some amount of shading, especially during early mornings and late evenings during the winter months is generally acceptable. Detailed analysis of shading losses is cumbersome though not difficult and equations presented in standard text books such as Duffie and Beckman (1980) can be used directly.

18.1.6 Thermal Storage Systems

Low-temperature solar thermal energy can be stored in liquids, solids, or phase change materials (PCMs). Water is the most frequently used liquid storage medium because of its low cost and high specific heat. The most widely used solid storage medium is rocks (usually of uniform circular size 25–40 mm in diameter). PCM storage is much less bulky because of the high-latent heat of the PCM material, but this technology has yet to become economical and safe for widespread use.

Water storage would be the obvious choice when liquid collectors are used to supply hot water to a load. When hot air is required (for space heat or for convective drying), one has two options: an air collector with a pebble-bed storage or a system with liquid collectors, water storage, and a load heat exchanger to transfer heat from the hot water to the working air stream. Though a number of solar air systems have been designed and operated successfully (mainly for space heating), water storage is very often the medium selected. Water has twice the heat capacity of rock, so water storage tanks will be smaller than rock-bed containers. Moreover, rock storage systems require higher parasitic energy to operate, have higher installation costs, and require more sophisticated controls. Water storage permits simultaneous charging and discharging while such an operation is not possible for rock storage systems. The various types of materials used as containers for water and rock-bed storage and the types of design, installation, and operation details one needs to take care of in such storage systems are described by Mueller Associates (1985) and SERI (1989).

Sensible storage systems, whether water or rock-bed, exhibit a certain amount of thermal stratification. Standard textbooks present relevant equations to model such effects. In the case of active closed-loop multipass hot-water systems, storage stratification effects can be neglected for long-term system performance with little loss of accuracy. Moreover, this leads to conservative system design (i.e., solar contribution is underpredicted if stratification is neglected). A designer who wishes to account for the effect of stratification in the water storage can resort to a formulation by Phillips and Dave (1982), who showed that this effect can be fairly well modeled by introducing a *stratification coefficient* (which is a system constant that needs to be determined only once) and treating the storage subsystem as fully mixed. However, this approach is limited to the specific case of no (or very little) heat withdrawal from storage during the collection period. Even when water storage systems are highly stratified, simulation studies seem to indicate that modeling storage as a one-dimensional plug-flow three-node heat transfer problem yields satisfactory results of long-term solar system performance.

The thermal losses q_w from the storage tank can be modeled as

$$q_w = (UA_S)(T_S - T_{\text{env}}) \quad (18.32)$$

where

(UA_S) is the storage overall heat loss per unit temperature difference

T_{env} is the temperature of the air surrounding the storage tank

Note that (UA_S) depends (1) on the storage size, which is a parameter to be sized during system design, and (2) on the configuration of the storage tank (i.e., on the length by diameter ratio in case of a cylindrical tank). For storage tanks, this ratio is normally in the range of 1.0–2.0.

18.1.7 Solar System Simulation

A system model is nothing but an assembly of appropriate component modeling equations that are to be solved over time subject to certain forcing functions (i.e., the meteorological data and load data). The resulting set of simultaneous equations can be solved either analytically or numerically.

The analytical method of resolution is appropriate, or possible, only for simplified system configurations and operating conditions. This approach has had some success in the analysis and design of open-loop systems (refer to Reddy 1987, Gordon and Rabl 1986, for more details). On the other hand, numerical simulation can be performed for any system configuration and operating strategy, however, complex. However, this is time-consuming and expensive in computer time and requires a high level of operator expertise.

We shall illustrate the approach of numerical simulation by considering the simple solar system shown in Figure 18.18. Assuming a fully mixed storage tank, the instantaneous energy balance equation is

$$(mc_p)_S(dT_S/dt) = q_C - q_u - q_w \quad (18.33)$$

where

q_C is the useful energy delivered by the solar collector (given by Equation 18.2)

q_w is the thermal loss from the storage tank (given by Equation 18.32)

q_u is the useful heat transferred through the load heat exchanger, which can be determined as shown in the following text

The maximum hourly rate of energy transfer through the load heat exchanger is

$$q_{max} = E_B(mc_p)_{min}(T_S - T_{Xi})\delta_L \quad (18.34)$$

where δ_L is a control function whose value is either 1 or 0 depending upon whether there is a heat demand or not. Since q_{max} can be greater than the amount of thermal energy q_L actually required by the load, the bypass arrangement can be conveniently modeled as

$$q_u = \min(q_{max}, q_L) \quad (18.35)$$

where

$$q_L = (mc_p)_L(T_{Li} - T_{Xi}) \quad (18.36)$$

for water heating and industrial process heat loads. Space heating and cooling loads can be conveniently determined by one of the several variants of the bin-type methods (ASHRAE 1985).

The amount of energy q_{\max} supplied by a topping-up type of auxiliary heater is

$$q_{\max} = q_L - q_u \quad (18.37)$$

Assuming $T_{\text{env}} = T_a$, Equation 18.33 can be expanded into

$$(Mc_p)_s \frac{dT_s}{dt} - A_c F_R [I_T \eta_0 - U_L (T_s - T_a)]^+ - (mc_p)_s (T_s - T_{Xi}) \delta_L - (UA)_s (T_s - T_a) \quad (18.38)$$

The presence of control functions and time dependence of I_T and T_a prevent a general analytical treatment, though, as mentioned earlier, specific cases can be handled. The numerical approach involves expressing this differential equation in finite difference form. After rearranging, one gets

$$T_{s,b} + \frac{\Delta t}{(Mc_p)_s} \{A_c F_R [I_T \eta_0 - U_L (T_{s,b} - T_a)]^+ - (mc_p)_s (T_{s,b} - T_{Xi}) \delta_L - (UA)_s (T_{s,b} - T_a)\} T_{s,f} \quad (18.39)$$

where $T_{s,b}$ and $T_{s,f}$ are the storage temperatures at the beginning and the end of the time step Δt . The time step is sufficiently small (say 1 h) that I_T and T_a can be assumed constant. This equation is repeatedly used over the time period in question (day, month, or year), and the total energy supplied by the collector or to the load can be estimated.

Such methods of simulation, referred as stepwise steady-state simulations, implicitly assume that the solar thermal system operates in a steady-state manner during one time step, at the end of which it undergoes an abrupt change in operating conditions as a result of changes in the forcing functions, and thereby attains a new steady-state operating level. Although in reality, the system performance varies smoothly over time and is consequently different from that outlined earlier, it has been found that, in most cases, taking time steps of the order of 1 h yields acceptable results of long-term performance.

The objective of solar-supplemented energy systems is to displace part of the conventional fuel consumption of the auxiliary heater. The index used to represent the contribution of the solar thermal system is the *solar fraction*, which is the fraction of the total energy required by the load that is supplied by the solar system. The solar fraction could be expressed over any time scale, with month and year being the most common. Two commonly used definitions of the monthly solar fraction are

1. Thermal solar fraction:

$$f_Y = \frac{Q_{UM}}{Q_{LM}} = 1 - \frac{Q_{aux,M}}{Q_{LM}} \quad (18.40)$$

where

Q_{UM} is the monthly total thermal energy supplied by the solar system

Q_{LM} is the monthly total thermal requirements of the load

$Q_{aux,M}$ is the monthly total auxiliary energy consumed

2. Energy solar fraction (i.e., thermal plus parasitic energy):

$$f'_M = \frac{Q'_{UM}}{Q'_{LM}} \quad (18.41)$$

where

Q'_{UM} is Q_{UM} minus the parasitic energy consumed by the solar system

Q'_{LM} is Q_{LM} plus the parasitic energy consumed by the load

Example 18.5

Simulate the closed-loop solar thermal system shown in Figure 18.18 for each hour of a day assuming both collector and load heat exchangers to be absent (i.e., $E_A = E_B = 1$). Assume the following data as input for the simulation: $A_C = 10 \text{ m}^2$, $F_R U_L = 5.0 \text{ W/m}^2 \text{ }^\circ\text{C}$, $F_R \eta_0 = 0.7$, $(mc_p) = 2.0 \text{ MJ/}^\circ\text{C}$ and $(UA)_S = 3 \text{ W/}^\circ\text{C}$. Water is withdrawn to meet a load from 9 a.m. to 7 p.m. (solar time) at a constant rate of 60 kg/h and is replenished from the mains at a temperature of 25°C. The storage temperature at the start (i.e., at 6 a.m.) is 40°C, and the environment temperature is equal to the ambient temperature. The temperature of the water entering the load should not exceed 55°C. The hourly values of the solar radiation on the plane of the collector are given in column 2 of Table 18.3 and the ambient temperature is assumed constant over the day and equal to 25°C. The variation of the optical efficiency with angle of incidence can be neglected.

The results of the simulation are given in Table 18.3. The following equations should permit the reader to verify for himself the results obtained. Simulating the system entails solving the following equations in the sequence given here:

Column 4. Useful energy delivered by the collector (Equation 20.2)

$$q_c = 10[0.7 I_T - 5(3600/10^6)T_{s,b} - 25]^+ \text{ (MJ/h)}$$

The term $(3600/10^6)$ is introduced to convert W/m^2 (the units in which I_T is expressed) into $\text{MJ}/(\text{h m}^2)$. Note that $T_{s,b}$ is taken to be equal to $T_{s,f}$ of the final hour.

Column 5. Thermal losses from the storage tank (Equation 18.32)

$$q_w = 3(3600/10^6)(T_{s,b} - 25) \text{ (MJ/h)}$$

TABLE 18.3

Simulation Results of Example 18.5

(1) Solar Time (h)	(2) I_T (MJ/m ² h)	(3) $T_{s,f}$ (°C)	(4) q_c (MJ/h)	(5) q_w (MJ/h)	(6) q_{max} (MJ/h)	(7) q_L (MJ/h)	(8) q_U (MJ/h)	(9) q_{aux} (MJ/h)
Start		40.00						
6-7	0.37	39.92	0.00	0.16	0.00	0.00	0.00	0.00
7-8	0.95	41.82	3.96	0.16	0.00	0.00	0.00	0.00
8-9	1.54	45.61	7.75	0.18	0.00	0.00	0.00	0.00
9-10	2.00	48.05	10.29	0.22	5.18	754	5.18	2.36
10-11	2.27	50.90	11.74	0.25	5.79	7.54	5.79	1.75
11-12	2.46	53.78	12.56	0.28	6.51	7.54	6.51	1.03
12-13	2.50	56.17	12.32	0.31	7.24	7.54	7.24	0.31
13-14	2.24	57.26	10.07	0.34	7.84	7.54	7.54	0.00
14-15	2.12	57.84	9.03	0.35	8.11	7.54	7.54	0.00
15-16	1.37	55.73	3.68	0.35	8.25	7.54	7.54	0.00
16-17	0.76	51.79	0.00	0.33	7.72	7.54	7.54	0.00
17-18	0.23	48.28	0.00	0.29	6.73	7.54	6.73	0.81
18-19	0.00	45.23	0.00	0.25	5.85	7.54	5.85	1.69
Total	18.81	—	81.41	3.48	69.24	75.40	67.48	7.94

Column 6. The maximum rate of energy that can be transferred from the load can be calculated from Equation 18.34

$$q_{\max} = 60(4190/10^6)(T_{s,b} - 25) \text{ (MJ/h)}$$

Column 7. The thermal energy required by the load (from Equation 18.36)

$$q_L = 60(4190/10^6)(55 - 25) = 7.54 \text{ MJ/h}$$

Column 8. The actual amount of heat withdrawn from storage (Equation 18.35)

$$q_w = \min[\text{column 6, column 7}]$$

Column 9. The amount of energy supplied by the auxiliary heater (Equation 18.2.37)

$$q_{\text{aux}} = \text{column 7} - \text{column 8}$$

The final storage temperature $T_{s,f}$ is now calculated from Equation 18.39

$$T_{s,f} = T_{s,b} + [\text{column 4} - \text{column 8} - \text{column 5}]/2.0$$

From Table 18.3, we note that the solar collector efficiency over the entire day is $[81.41/(18.81 \times 10)] = 0.43$. The corresponding daily solar fraction = $(67.48/75.40) = 0.895$.

18.1.8 Solar System Sizing Methodology

Sizing of solar systems primarily involves determining the collector area and storage size that are most cost effective. Standalone and solar-supplemented systems have to be treated separately since the basic design problem is somewhat different. The interested reader can refer to Gordon (1987) for sizing standalone systems.

18.1.8.1 Solar-Supplemented Systems

18.1.8.1.1 Production Functions

Because of the annual variation of incident solar radiation, it is not normally economical to size a solar subsystem such that it provides 100% of the heat demand. Most solar energy systems follow the *law of diminishing returns*. This implies that increasing the size of the solar collector subsystem results in a less than proportional increase in the annual fuel savings (or alternatively, in the annual solar fraction).

Any model has two types of variables: exogenous and endogenous. The *exogenous parameters* are also called the input variables, and these in turn may be of two kinds. *Variable exogenous parameters* are the collector area A_C , the collector performance parameters $F_R \eta_n$ and $F_R U_L$, the collector tilt, the thermal storage capacity $(mc_p)_s$, the heat exchanger size, and the control strategies of the solar thermal system. On the other hand, the climatic data specified by radiation and the ambient temperature, as well as the end use thermal demand characteristics, are called *constrained exogenous parameters* because they are imposed externally and cannot be changed. The *endogenous parameters* are the output parameters whose values are to be determined, the annual solar fraction being one of the parameters most often sought.

Figure 18.26 illustrates the law of diminishing results. The annual solar fraction f_Y is seen to increase with collector area but at a decreasing rate and at a certain point will reach saturation. Variation of any of the other exogenous parameters also exhibits a similar trend. The technical relationship between f_Y and one or several variable exogenous parameters for a given location is called the *yearly production function*.

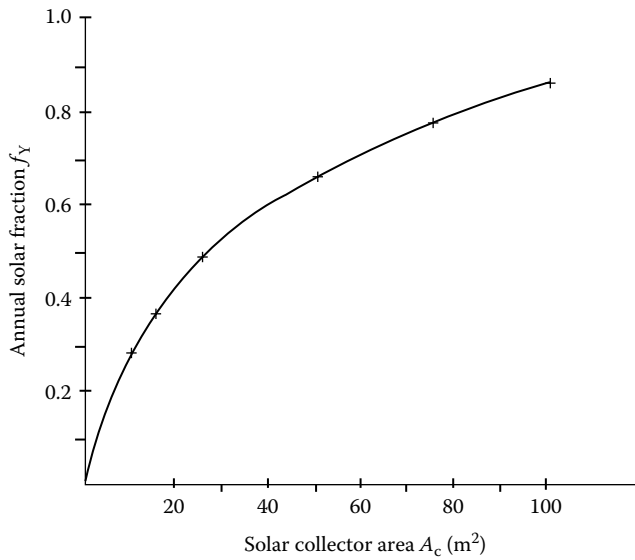


FIGURE 18.26
A typical solar system production function (see Example 18.14).

It is only for certain simple types of solar thermal systems that an analytical expression for the production can be deduced directly from theoretical considerations. The most common approach is to carry out computer simulations of the particular system (solar plus auxiliary) over the complete year for several combinations of values of the exogenous parameters. The production function can subsequently be determined by an empirical curve fit to these discrete sets of points.

Example 18.6

Kreider (1979) gives the following expression for the production function of an industrial solar water heater for a certain location:

$$f_Y = \frac{Q_{UY}}{Q_{LY}} = \left(0.35 - \frac{F_R U_L}{100 F_R \eta_n} \right) \ln \left(1 + \frac{20 F_R \eta_n A_c}{Q_{LY}} \right) \tag{18.42}$$

where

Q_{UY} is the thermal energy delivered by the solar thermal system over the year in GJ/y

Q_{LY} is the yearly thermal load demand, also in GJ/y

$F_R U_L$ is in W/(m² °C)

Note that only certain solar system exogenous parameters figure explicitly in this expression, thereby implying that other exogenous parameters (for example, storage volume) have not been varied during the study. As an illustration, let us assume the following nominal values: $Q_{LY} = 100$ GJ/year, $F_R U_L = 2.0$ W/(m² °C), and $F_R \eta_n = 0.7$. For a 1% increase in collector area A_c , the corresponding percentage increase in Q_{UY} (called elasticity) can be determined:

$$\frac{dQ_{UY}}{Q_{UY}} = \frac{dA_c}{A_c} \left[\left(\frac{Q_{LY}}{20 F_R \eta_n A_c} + 1 \right) \ln \left(1 + \frac{20 F_R \eta_n A_c}{Q_{LY}} \right) \right]^{-1} \tag{18.43}$$

From this, we obtain the expression for *marginal productivity*

$$\frac{dQ_{UY}}{dA_C} = \frac{Q_{UY}}{A_C} \left[\left(\frac{Q_{LY}}{20F_R \eta_n A_C} + 1 \right) \ln \left(1 + \frac{20F_R \eta_n A_C}{Q_{LY}} \right) \right]^{-1} \quad (18.44)$$

Numerical values can be obtained from the preceding expression. Though Q_{UY} increases with A_C , the marginal productivity of Q_{UY} goes on decreasing with increasing A_C , thus illustrating the law of diminishing returns. A qualitative explanation of this phenomenon is that as A_C increases, the mean operating temperature level of the collector increases, thus leading to decreasing solar collection rates. Figure 18.26 illustrates the variation of f_Y with A_C as given by Equation 18.42 when the preceding numerical values are used.

The objective of the sizing study in its widest perspective is to determine, for a given specific thermal end use, the size and configuration of the solar subsystem that results in the most economical operation of the entire system. This economical optimum can be determined using the production function along with an appropriate economic analysis. Several authors—for example, Duffie and Beckman (1980) or Rabl (1985)—have presented fairly rigorous methodologies of economic analysis, but a simple approach is adequate to illustrate the concepts and for preliminary system sizing.

18.1.8.1.2 Simplified Economic Analysis

It is widely recognized that *discounted cash flow analysis* is most appropriate for applications such as sizing an energy system. This analysis takes into account both the initial cost incurred during the installation of the system and the annual running costs over its entire life span.

The economic objective function for optimal system selection can be expressed in terms of either the energy cost incurred or the energy savings. These two approaches are basically similar and differ in the sense that the objective function of the former has to be minimized while that of the latter has to be maximized. In our analysis, we shall consider the latter approach, which can further be subdivided into the following two methods:

1. Present worth or life cycle savings, wherein all running costs are discounted to the beginning of the first year of operation of the system.
2. Annualized life cycle savings, wherein the initial expenditure incurred at the start as well as the running costs over the life of the installation are expressed as a yearly mean value.

18.1.9 Solar System Design Methods

18.1.9.1 Classification

Design methods may be separated into three generic classes. The *simple* category, usually associated with the prefeasibility study phase involves quick manual calculations of solar collector/system performance and rule-of-thumb engineering estimates. For example, the generalized yearly correlations proposed by Rabl (1981) and described in Section 18.1.2 could be conveniently used for year-round, more or less constant loads. The approach is directly valid for open-loop solar systems, while it could also be used for closed-loop systems if an *average* collector inlet temperature could be determined. A simple manner of

selecting this temperature \bar{T}_m for domestic closed-loop multipass systems is to assume the following empirical relation:

$$\bar{T}_m - T_{\text{mains}}/3 + (2/3)T_{\text{set}} \quad (18.45)$$

where

T_{mains} is the average annual supply temperature

T_{set} is the required hot-water temperature (about 60°C–80°C in most cases)

These manual methods often use general guidelines, graphs, and/or tables for sizing and performance evaluation. The designer should have a certain amount of knowledge and experience in solar system design in order to make pertinent assumptions and simplifications regarding the operation of the particular system.

Mid-level design methods are resorted to during the feasibility phase of a project. The main focus of this chapter has been toward this level, and a few of these design methods will be presented in this section. A personal computer is best suited to these design methods because they could be conveniently programmed to suit the designer's tastes and purpose (spreadsheet programs, or better still one of the numerous equation-solver software packages, are most convenient). Alternatively, commercially available software packages such as *f-chart* (Beckman et al. 1977) could also be used for certain specific system configurations.

Detailed design methods involve performing hourly simulations of the solar system over the entire year from which accurate optimization of solar collector and other equipment can be performed. Several simulation programs for active solar energy systems are available, TRNSYS (Klein et al. 1975, 1979) developed at the University of Wisconsin-Madison being perhaps the best known. This public-domain software has technical support and is being constantly upgraded. TRNSYS contains simulation models of numerous subsystem components (solar radiation, solar equipment, loads, mechanical equipment, controls, etc.) that comprise a solar energy system. A user can conveniently hook up components representative of a particular solar system to be analyzed and then simulate that system's performance at a level of detail that the user selects. Thus TRNSYS provides the design with large flexibility, diversity, and convenience of usage.

As pointed out by Rabl (1985), the detailed computer simulations approach, though a valuable tool, has several problems. Judgment is needed both in the selection of the input and in the evaluation of the output. The very flexibility of big simulation programs has drawbacks. So many variables must be specified by the user that errors in interpretation or specification are common. Also, learning how to use the program is a time-consuming task. Because of the numerous system variables to be optimized, the program may have to be run for numerous sets of combinations, which adds to expense and time. The inexperienced user can be easily misled by the second-order details while missing first-order effects. For example, uncertainties in load, solar radiation, and economic variables are usually very large, and long-term performance simulation results are only accurate to within a certain degree. Nevertheless, detailed simulation programs, if properly used by experienced designers, can provide valuable information on system design and optimization aspects at the final stages of a project design.

There are basically three types of mid-level design approaches: the empirical correlation approach, the analytical approach, and the one-day repetitive methods (described fully in Reddy 1987). We shall illustrate their use by means of specific applications.

18.1.9.2 Active Space Heating

The solar system configuration for this particular application has become more or less standardized. For example, for a liquid system, one would use the system shown in Figure 18.27. One of the most widely used design methods is the f -chart method (Beckman et al. 1977; Duffie and Beckman 1980), which is applicable for standardized liquid and air heating systems as well as for standardized domestic hot-water systems. The f -chart method basically involves using a simple algebraic correlation that has been deduced from numerous TRNSYS simulation runs of these standard solar systems subject to a wide range of climates and solar system parameters (see Figure 18.28). Correlations were developed between monthly solar fractions and two easily calculated dimensionless variables X and Y , where

$$X = \frac{(A_C F'_R U_L (T_{\text{Ref}} - \bar{T}_a) \Delta t)}{Q_{\text{LM}}} \quad (18.46)$$

$$Y = A_C F'_R \bar{\eta}_0 \bar{H}_T N / Q_{\text{LM}} \quad (18.47)$$

where

A_C collector area (m^2)

F'_R collector-heat exchanger heat removal factor (given by Equation 18.29)

U_L collector overall loss coefficient ($\text{W}/(\text{m}^2 \text{ } ^\circ\text{C})$)

Δt total number of seconds in the month = $3600 \times 24 \times N = 86,400 \times N$

\bar{T}_a monthly average ambient temperature ($^\circ\text{C}$)

T_{Ref} an empirically derived reference temperature, taken as 100°C

Q_{LM} monthly total heating load for space heating and/or hot water (J)

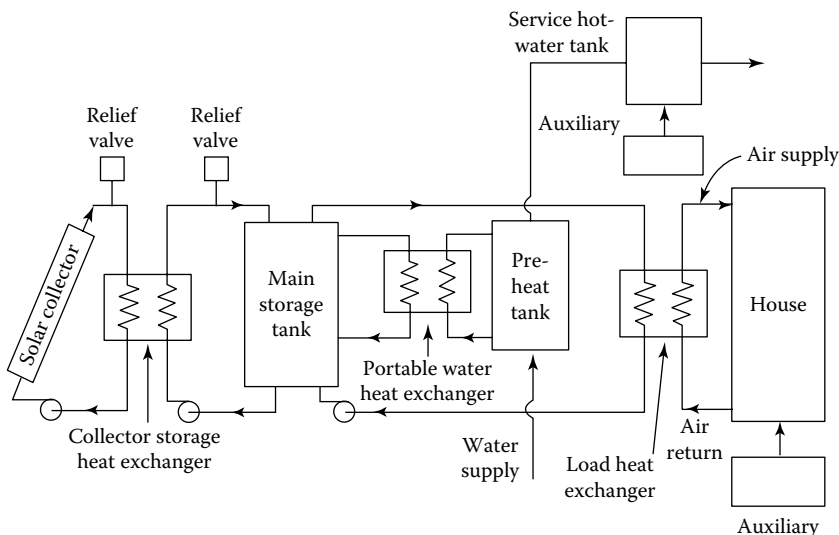


FIGURE 18.27

Schematic of the standard space heating liquid system configuration for the f -chart method. (From Duffie, J.A. and Beckman, W.A., *Solar Engineering of Thermal Processes*, Wiley Interscience, New York, 1980.)

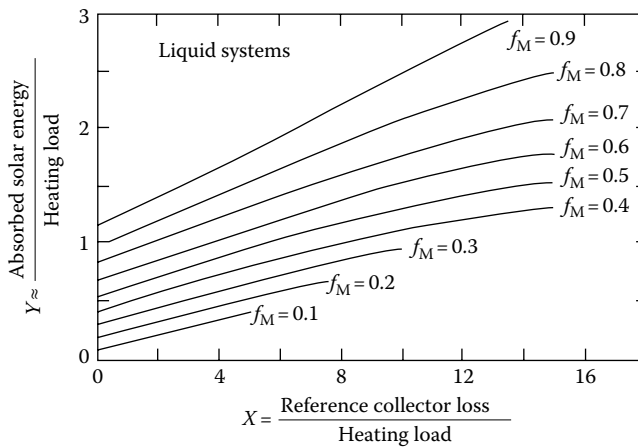


FIGURE 18.28

The f -chart correlation for liquid system configuration. (From Duffie, J.A. and Beckman, W.A., *Solar Engineering of Thermal Processes*, Wiley Interscience, New York, 1980.)

- \bar{H}_T monthly average daily radiation incident on the collector surface per unit area (J/m^2)
- N number of days in the month
- $\bar{\eta}_0$ monthly average collector optical efficiency

The dimensionless variable X is the ratio of reference collector losses over the entire month to the monthly total heat load; the variable Y is the ratio of the monthly total solar energy absorbed by the collectors to the monthly total heat load. It will be noted that the collector area and its performance parameters are the predominant exogenous variables that appear in these expressions. For changes in secondary exogenous parameters, the following corrective terms X_C and Y_C should be applied for liquid systems:

1. For changes in storage capacity:

$$\frac{X_C}{X} = \left(\frac{\text{actual storage capacity}}{\text{standard storage capacity}} \right)^{-0.25} \tag{18.48}$$

where the standard storage volume is 75 L/m^2 of collector area.

2. For changes in heat exchanger size:

$$\frac{Y_C}{Y} = \frac{0.39 + 0.65 \exp[-(0.139(UA)_B]}{(E_L(mc_p)_{\min})} \tag{18.49}$$

The monthly solar fraction for liquid space heating can then be determined from the following empirical correlation:

$$f_M = 1.029Y - 0.065X - 0.245Y^2 + 0.0018X^2 + 0.0215Y^3 \tag{18.50}$$

subject to the conditions that $0 \leq X \leq 15$ and $0 \leq Y \leq 3$. This empirical correlation is shown graphically in Figure 18.28.

A similar correlation has also been proposed for space heating systems using air collectors and pebble-bed storage. The procedure for exploiting the preceding empirical correlations is as follows. For a predetermined location, specified by its 12 monthly radiation and ambient temperature values, Equation 18.50 is repeatedly used for each month of the year for a particular set of variable exogenous parameters. The monthly solar fraction f_M and thence the annual thermal energy delivered by the solar thermal system are easily deduced. Subsequently, the entire procedure is repeated for different values and combinations of variable exogenous parameters. Finally, an economic analysis is performed to determine optimal sizes of various solar system components. Care must be exercised that the exogenous parameters considered are not outside the range of validity of the f -chart empirical correlations.

Example 18.7

(Adapted from Duffie and Beckman 1980). A solar heating system is to be designed for Madison, Wisconsin (latitude 43°N) using one-cover collectors with $F_R\eta_n = 0.74$ and $F_RU_L = 4\text{W}/(\text{m}^2\text{ }^\circ\text{C})$. The collector faces south with a slope of 60° from the horizontal. The average daily radiation on the tilted surface in January is $12.9\text{ MJ}/\text{m}^2$, and the average ambient temperature is -7°C . The heat load is 36 GJ for space heating and hot water. The collector-heat exchanger correction factor is 0.97 and the ratio of monthly average to normal incidence optical efficiency is 0.96 . Calculate the energy delivered by the solar system in January if 50 m^2 of collector area is to be used.

From Equations 18.46 and 18.47, with $A_C = 50\text{ m}^2$,

$$X = 4.0 \times 0.97[100 - (-7)]31 \times 86,400 \times 50/(36 \times 10^9) = 1.54$$

$$Y = 0.74 \times 0.97 \times 0.96 \times 12.9 \times 10^6 \times 31 \times 50/(36 \times 10^9) = 0.38$$

From Equation 18.50, the solar fraction for January is $f_M = 0.26$. Thus the useful energy delivered by the solar system = $0.26 \times 36 = 9.4\text{ GJ}$.

In an effort to reduce the tediousness involved in having to perform 12 monthly calculations, two analogous approaches that enable the annual solar fraction to be determined directly have been developed by Barley and Winn (1978) and Lameiro and Bendt (1978). These involve the computation of a few site-specific empirical coefficients, thereby rendering the approach less general. For example, the *relative-area* method suggested by Barley and Winn enable the designer to directly calculate the annual solar fraction of the corresponding system using four site-specific empirical coefficients. The approach involves curve fits to simulation results of the f -chart method for specific locations in order to deduce a correlation such as:

$$f = c_1 + c_2 \ln(A/A_{0.5}) \quad (18.51)$$

where

c_1 and c_2 are location-specific parameters that are tabulated for several United States locations

$A_{0.5}$ is the collector area corresponding to an annual solar fraction of 0.5 given by

$$A_{0.5} = \frac{A_s(UA)}{(F'_R\eta_0 - F'_R U_L Z)} \quad (18.52)$$

where

A_s and Z are two more location specific parameters

UA is the overall heat loss coefficient of the building

$F'_R\eta_0$ and $F'_R U_L$ are the corresponding solar collector performance parameters corrected for the effect of the collector-heat exchanger

Barley and Winn also proposed a simplified economic life-cycle analysis whereby the optimal collector area could be determined directly. Another well-known approach is the *Solar Load Ratio* (SLR) method for sizing residential space heating systems (Hunn 1980).

18.1.9.3 Domestic Water Heating

The f -chart correlation (Equation 18.50) can also be used to predict the monthly solar fraction for domestic hot-water systems represented by Figure 18.21 provided the water mains temperature T_{mains} is between 5°C and 20°C and the minimum acceptable hot-water temperature drawn from the storage for end use (called the set water temperature T_w) is between 50°C and 70°C. Further, the dimensionless parameter X must be corrected by the following ratio

$$\frac{X_w}{X} = \frac{(11.6 + 1.8T_w + 3.86T_{\text{mains}} - 2.32\bar{T}_a)}{(100 - \bar{T}_a)} \quad (18.53)$$

In case the domestic hot-water load is much smaller than the space heat load, it is recommended that Equation 18.50 be used without the above correction.

18.1.9.4 Industrial Process Heat

As discussed in Section 18.1.4.2.1, two types of solar systems for industrial process heat are currently used: the closed-loop multipass systems (with an added distinction that the auxiliary heater may be placed either in series or in parallel (see Figures 18.18 and 18.19) and the open-loop singlepass system. How such systems can be designed will be described next.

18.1.9.4.1 Closed-Loop Multipass Systems

18.1.9.4.1.1 Auxiliary Heater in Parallel The Phibar- f chart method (Klein and Beckman 1979; Duffie and Beckman 1980; Reddy 1987) is a generalization of the f -chart method in the sense that no restrictions need be imposed on the temperature limits of the heated fluid in the solar thermal system. However, three basic criteria for the thermal load have to be satisfied for the Phibar- f chart method to be applicable: (1) the thermal load must be constant and uniform over each day and for at least a month, (2) the thermal energy supplied to the load must be above a minimum temperature that completely specifies the temperature level of operation of the load, and (3) either there is no conversion efficiency in the load (as in the case of hot water usage) or the efficiency of conversion is constant (either because the load temperature level is constant or because the conversion efficiency is independent of the load temperature level). The approach is strictly applicable to solar systems with the auxiliary heater in parallel (Figure 18.19).

A typical application for the Phibar- f chart method is absorption air-conditioning. The hot water inlet temperature from the collectors to the generator must be above a minimum temperature level (say, 80°C) for the system to use solar heat. If the solar fluid temperature is less (even by a small amount), the entire energy to heat up the water to 80°C is supplied by the auxiliary system.

As a result of continuous interaction between storage and collector in a closed-loop system, the variation of the storage temperature and hence the fluid inlet temperature to the collectors) over the day and over the month is undetermined. The Phibar- f chart method implicitly takes this into account and reduces these temperature fluctuations down to a

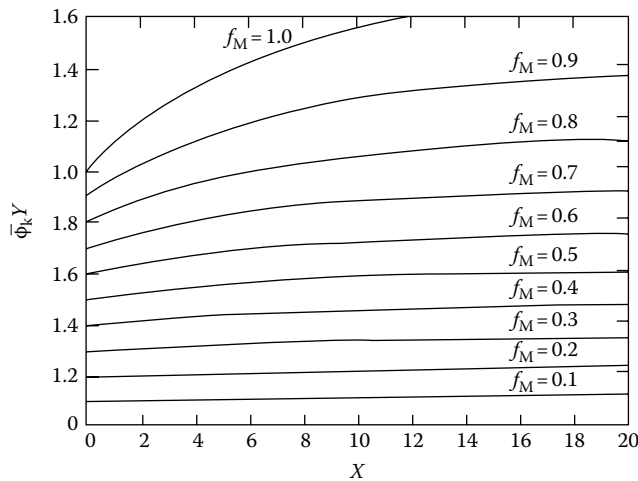


FIGURE 18.29

The Phibar- f chart correlation for a storage capacity of 350 kJ/m² and for a 12 h/day thermal load. (From Duffie, J.A. and Beckman, W.A., *Solar Engineering of Thermal Processes*, Wiley Interscience, New York, 1980.)

monthly mean equivalent storage temperature \bar{T}_S . The determination of this temperature in conjunction with the daily utilizability approach is the basis of the design approach.

The basic empirical correlation of the Phibar- f chart method, shown graphically in Figure 18.29, is as follows:

$$f_M = Y\bar{\phi} - a[\exp(bf_M) - 1][1 - \exp(cX)] \quad (18.54)$$

with $0 < X < 20$ and $0 < Y < 1.6$, and $\bar{\phi}$ is the Klein daily utilizability fraction described in Section 18.1.3.3 and given by Equation 18.24. Y is given by Equation 18.47, and X is now slightly different from Equation 18.46 and is defined as:

$$X = \frac{A_c F_R U_L \Delta t (100^\circ \text{C})}{QLM} \quad (18.55)$$

The values of the constants a , b , and c are given by the following:

1. For an end use load operating between 6 a.m. and 6 p.m. every day of the month,

$$a = 0.015[(mc_p)_s/350 \text{ kJ}/(\text{m}^2 \text{ }^\circ\text{C})]^{-0.76} \text{ for } 175 \leq [(mc_p)_s/A_c] \leq 1400 \text{ kJ}/(\text{m}^2 \text{ }^\circ\text{C}),$$

$$b = 3.85 \quad \text{and} \quad c = -0.15 \quad (18.56)$$

2. For an end use load operating 24 h/day over the entire month,

$$a = 0.043 \text{ only for } [(mc_p)_s/A_c] = 350 \text{ kJ}/(\text{m}^2 \text{ }^\circ\text{C}), \quad b = 2.81, \quad \text{and} \quad c = -0.18 \quad (18.57)$$

It will be noted that $(Y\bar{\phi})$ denotes the maximum solar fraction that would have resulted had T_{Ci} , the inlet temperature to the collector, been equal to T_{Li} throughout the month. The term in Equation 18.54 that is subtracted from $(Y\bar{\phi})$ represents the decrease in the solar fraction as a result of $T_{Ci} > T_{Li}$. The solar fraction computed from Equation 18.54 has to be

corrected for the effect of thermal losses from the storage as well as the presence of the load-heat exchanger, both of which will decrease the solar fraction. For complete details, refer to Duffie and Beckman (1980) or Reddy (1987). Note that Equation 18.54 needs to be solved for f_m in an iterative manner.

18.1.9.4.1.2 Auxiliary Heater in Series The Phibar- f chart method has also been modified to include solar systems with the auxiliary heater in series as shown in Figure 18.18. This configuration leads to higher solar fractions but retrofit to existing systems may be more costly.

In this case, the empirical correlation given by Equation 18.54 has been modified by Braun et al. (1983) as follows:

$$f_M = Y\bar{\phi} - a[\exp(bf_M) - 1][1 - \exp(cX)]\exp(-1.959Z) \quad (18.58)$$

with $Z = Q_{lm}/(C_1 \times 100^\circ\text{C})$ and (1) when there is no load-heat exchanger, C_L is the monthly total load heat capacitance, which is the product of the monthly total mass of water used and the specific heat capacity of water, and (2) when there is a load-heat exchanger present $C_L = E_L \times C_{\min}$, where E_L is the effectiveness of the load-heat exchanger and C_{\min} is the monthly total heat capacitance, which is the lesser of the two fluids rates across the load heat exchanger.

The modified Phibar- f chart is similar to the original method in respect to load uniformity on a day-to-day basis over the month and in assuming no conversion efficiency. The interested may refer to Braun et al. (1983) or Reddy (1987) for complete details.

18.1.9.4.2 Open-Loop Single-Pass Systems

The advantages offered by open-loop single-pass systems over closed-loop multipass systems for meeting constant loads has been described in Section 18.1.4.2. Because industrial loads operate during the entire sun-up hours or even for 24 h daily, the simplest solar thermal system is one with no heat storage (Figure 18.20). A sizable portion (between 25% and 70%) of the daytime thermal load can be supplied by such systems and consequently, the sizing of such systems will be described below (Gordon and Rabl 1982). We shall assume that T_{Li} and T_{Xi} are constant for all hours during system operation. Because no storage is provided, excess solar energy collection (whenever $T_{Ci} > T_{Li}$) will have to be dumped out.

The maximum collector area \hat{A}_C for which energy dumping does not occur at any time of the year can be found from the following instantaneous heat balance equation:

$$P_L = \hat{A}_C \hat{F}_R [I_{\max} \eta_n - U_L (T_{Ci} - T_a)] \quad (18.59)$$

where P_L , the instantaneous thermal heat demand of the load (say, in kW) is given by

$$P_L = m_L c_p (T_{Li} - T_{Xi}) \quad (18.60)$$

and F_R is the heat removal factor of the collector field when its surface area is \hat{A}_C . Since \hat{A}_C is as yet unknown, the value of \hat{F}_R is also undetermined. (Note that though the *total* fluid flow rate is known, the flow rate per unit collector area is not known.) Recall that the plate efficiency factor F' for liquid collectors can be assumed constant and independent of fluid flow rate per unit collector area. Equation 18.59 can be expressed in terms of critical radiation level I_C :

$$P_L = \hat{A}_C \hat{F}_R \eta_n (I_{\max} - I_C) \quad (18.61a)$$

or

$$\hat{A}_C \hat{F}_R \eta_n = \frac{P_L}{(I_{\max} - I_C)} \quad (18.61b)$$

Substituting Equation 18.3 in lieu of F_R and rearranging yields

$$\hat{A}_C = -(m_L c_p / F' U_L) \ln[1 - P_L U_L / (\eta_n (I_{\max} - I_C) m_L c_p)] \quad (18.62)$$

If the actual collector area A_C exceeds this value, dumping will occur as soon as the radiation intensity reaches a value I_D , whose value is determined from the following heat balance:

$$P_L = A_C F_R \eta_n (I_D - I_C) \quad (18.63a)$$

Hence

$$I_D = \frac{I_C + P_L}{(A_C F_R \eta_n)} \quad (18.63b)$$

Note that the value of I_D decreases with increasing collector area A_C , thereby indicating that increasing amounts of solar energy will have to be dumped out.

Since the solar thermal system is operational during the entire sunshine hours of the year, the yearly total energy collected can be directly determined by the Rabl correlation given by Equation 18.26. Similarly, the yearly total solar energy collected by the solar system which has got to be dumped out is

$$Q_{DY} = A_C F_R \eta_n (\tilde{a} + \tilde{b} I_D + \tilde{c} I_D^2) \quad (18.64)$$

The yearly total solar energy delivered to the load is

$$\begin{aligned} Q_{UY} &= Q_{CY} - Q_{DY} \\ &= A_C F_R \eta_n [\tilde{b}(I_C - I_D) + \tilde{c}(I_C^2 - I_D^2)] \end{aligned} \quad (18.65)$$

$$\begin{aligned} &= -(\tilde{b} + 2\tilde{c}I_C)P_L - \tilde{c}P_L^2 / (A_C F_R \eta_n) \\ &= -(\tilde{b} + 2\tilde{c}I_C)P_L - \tilde{c}P_L^2 / (A_C F_R \eta_n) \end{aligned} \quad (18.66)$$

Replacing the value of F_R given by Equation 18.3, the annual production function in terms of A_C is

$$Q_{UY} = -(\tilde{b} + 2\tilde{c}I_C)P_L - \frac{\tilde{c}P_L^2}{\left(\frac{F' \eta_n}{F' U_L}\right)(m_L c_p) \left[1 - \exp\left(-\frac{F' U_L A_C}{m_L c_p}\right)\right]} \quad (18.67)$$

subject to the condition that $A_C > \hat{A}_C$. If the thermal load is not needed during all days of the year due to holidays or maintenance shutdown, the production function can be reduced proportionally. This is illustrated in the following example.

Example 18.8

Obtain the annual production function of an open-loop solar thermal system without storage that is to be set up in Boston, Massachusetts according to the following load specifications: industrial hot water load for 12 h a day (6 a.m. to 6 p.m.) and during 290 days a year, mass flow rate $m_L = 0.25$ kg/s, required inlet temperature $T_{Li} = 60^\circ\text{C}$. Contaminants are picked up in the load, so that all used water is to be rejected and fresh water at ambient temperature is taken in. Flat-plate collectors with tilt equal to latitude with the following parameters are used $F'\eta_n = 0.75$ and $F'U_L = 5.5$ W/(m² °C). The latitude of Boston is $42.36^\circ\text{N} = 0.739$ rad. The yearly $\bar{K} = 0.45$ and $\bar{T}_a = 10.9^\circ\text{C}$. Use the following Gordon and Rabl (1982) correlation:

$$\begin{aligned} Q_{CY}/A_C F_R \eta_n = & [(5.215 + 6.973 I_{bn}) + (-5.412 + 4.293 I_{bn})L + (1.403 - 0.899 I_{bn})L^2] \\ & + [(-18.596 - 5.931 I_{bn}) + (15.468 + 18.845 I_{bn})L + (-0.164 - 35.510 I_{bn})L^2] I_C \\ & + [(-14.601 - 3.570 I_{bn}) + (13.675 - 15.549 I_{bn})L + (-1.620 + 30.564 I_{bn})L^2] I_C^2 \end{aligned}$$

From Equation 18.27, $\tilde{I}_{bn} = 1.37 \times 0.45 - 0.34 = 0.276$ kW/m². The critical radiation level $I_C = 0$, since $T_{Ci} = T_a$. Consequently, Equation 18.26, using the above expression reduces to

$$\begin{aligned} Q_{CY}/(A_C F_R \eta_n) &= 5.215 + 6.973 \times 0.276 + (-5.412 + 4.293 \times 0.276)0.739 \\ &+ (1.403 - 0.899 \times 0.276)0.739^2 \\ &= 4.646 \text{ GJ}/(\text{m}^2\text{y}). \end{aligned}$$

The expression for the dumped out energy is found from Equation 18.64 and the previous expression by replacing I_C by I_D :

$$\begin{aligned} Q_{CY,dump}/(A_C F_R \eta_n) &= 4.646 + [(-18.596 - 5.931 \times 0.276) + (15.468 + 18.845 \times 0.276)0.739 \\ &+ (-0.164 - 35.510 \times 0.276)0.739^2] I_D + [(14.601 - 3.57 \times 0.276) \\ &+ (-13.675 - 15.549 \times 0.276)0.739 + (1.620 + 30.564 \times 0.276)0.739^2] I_D^2 \\ &= 4.646 - 10.40 I_D + 5.83 I_D^2 \text{ (GJ}/\text{m}^2\text{y)} \end{aligned}$$

The thermal energy demand $P_L = 0.25 \times 4.19(60 - 10.9) = 51.43$ kW.

The annual production function is

$$\begin{aligned} Q_{UY}(365/290) &= -(-10.40 + 2\bar{c} \times 0)51.43 - (5.83 \times 51.43^2) / \{(0.75/5.5)(0.25 \times 4.19) \\ &\times [1 - \exp\{-(5.5 \times A_C)/(0.25 \times 4190)\}]\} \end{aligned}$$

or

$$Q_{UY} = 424.96 - 85.78/[1 - \exp(-A_C/190.45)] \text{ (GJ}/\text{y)}$$

Complete details as well as how this approach can be extended to solar systems with storage (see Figure 18.30) can be found in Rabl (1985) or Reddy (1987).

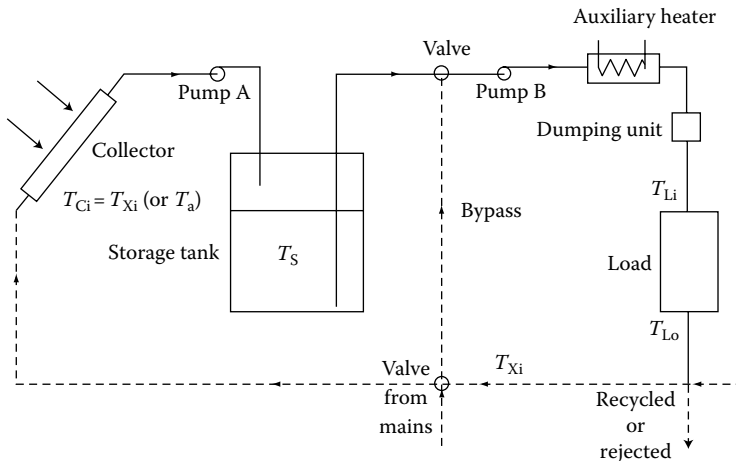


FIGURE 18.30
Open-loop solar industrial hot-water system with storage.

18.1.10 Design Recommendations and Costs

18.1.10.1 Design Recommendations

As mentioned earlier, design methods reduce computational effort compared to detailed computer simulations. Even with this decrease, the problem of optimal system design and sizing remains formidable because of

- The presence of several solar thermal system configuration alternatives.
- The determination of optimal component sizes for a given system.
- The presence of certain technical and economic constraints.
- The choice of proper climatic, technical, and economic input parameters.
- The need to perform sensitivity analysis of both technical and economic parameters.

For most practical design work, a judicious mix of theoretical expertise and practical acumen is essential. Proper focus right from the start on the important input variables as well as the restriction of the normal range of variation would lead to a great decrease in design time and effort. Several examples of successful case studies and system design recommendations are described in the published literature (see, for example, Kutcher et al. 1982).

18.1.10.2 Solar System Costs

How the individual components of the solar system contribute to the total cost can be gauged from Table 18.4. We note that collectors constitute the major fraction (from 15% to 30%), thus suggesting that collectors should be selected and sized with great care. Piping costs are next with other collector-related costs like installation and support structure being also important.

TABLE 18.4
Percentage of Total System Cost by Component

Cost Component	Percentage Range
Collectors	15–30
Collector installation	5–10
Collector support structure	5–20 ^a
Storage tanks	5–7
Piping and specialties	10–30
Pumps	1–3
Heat exchangers	0–5 ^b
Chiller	5–10
Miscellaneous	2–10
Instrumentation	1–3
Insulation	2–8
Control subsystem	4–9
Electrical	2–6

Source: Mueller Associates, *Active Solar Thermal Design Manual*, Funded by U.S. DOE (no. EG-77-C-01-4042), SERI (XY-2-02046-1) and ASHRAE (project no. 40). Baltimore, MD, 1985.

^a For collectors mounted directly on a tilted roof.

^b For systems without heat exchangers.

References

- Anderson, B. 1977. *Solar Energy: Fundamentals in Building Design*. McGraw-Hill, New York.
- ASHRAE. 1985. *Fundamentals*. American Society of Heating, Refrigeration and Air Conditioning Engineers, New York.
- ASHRAE. 1978. Methods of testing to determine the thermal performance of solar collectors, Standard 93-77. American Society of Heating, Refrigeration and Air Conditioning Engineers, New York.
- Barley, C. D. and Winn, C. B. 1978. Optimal sizing of solar collectors by the method of relative areas. *Solar Energy*, 21, 279.
- Beckman, W. A. 1978. Technical note: Duct and pipe losses in solar energy systems. *Solar Energy*, 21, 531.
- Beckman, W. A., Klein, S. A., and Duffie, J. A. 1977. *Solar Heating Design: By the F-Chart Method*. Wiley Interscience, New York.
- Braun, J. E., Klein, S. A., and Pearson, K. A. 1983. An improved design method for solar water heating systems. *Solar Energy*, 31, 597.
- Charters, W. W. S. and Pryor, T. L. 1982. *An Introduction to the Installation of Solar Energy Systems*, pp. 503–127. Victoria Solar Energy Council, Melbourne, Australia.
- Chiam, H. F. 1981. Planar concentrators for flat-plate solar collectors. *Solar Energy*, 26, 503.
- Clark, D. R., Klein, S. A., and Beckman, W. A. 1983. Algorithm for evaluating the hourly radiation utilizability function. *ASME Journal of Solar Energy Engineering*, 105, 281.
- Cole, R. L., Nield, K. J., Rohde, R. R., and Wolosewicz, R. M. (eds.) 1979. Design and installation manual for thermal energy storage, ANL-79-15, pp. 223–397. Argonne National Laboratory, Argonne, IL.
- Collares-Pereira, M., Gordon, J. M., Rabl, A., and Zarmi, Y. 1984. Design and optimization of solar industrial hot water systems with storage. *Solar Energy*, 32, 121.
- Collares-Pereira, M. and Rabl, A. 1979. Derivation of method for predicting the long-term average energy delivery of solar collectors. *Solar Energy*, 23, 223.

- CSU. 1980. Solar heating and cooling of residential buildings—Design of systems. Manual prepared by the Solar Energy Applications Laboratory, Colorado State University. Colorado State University, Fort Collins, CO.
- de Winter, F. 1975. Heat exchanger penalties in double loop solar water heating systems. *Solar Energy*, 17, 335.
- Duffie, J. A. and Beckman, W. A. 1980. *Solar Engineering of Thermal Processes*. Wiley Interscience, New York.
- Edwards, D. K., Nelson, K. E., Roddick, R. D., and Gier, J. T. 1960. Basic studies on the use of solar energy, Report No. 60-93. Department of Engineering, University of California, Los Angeles, CA.
- Gordon, J. M. 1987. Optimal sizing of stand-alone photovoltaic systems. *Solar Cells*, 20, 295.
- Gordon, J. M. and Rabl, A. 1982. Design, analysis and optimization of solar industrial process heat plants without storage. *Solar Energy*, 28, 519.
- Gordon, J. M. and Rabl, A. 1986. Design of solar industrial process heat systems. In *Reviews of Renewable Energy Sources*, Sodha, M. S. Mathur, S. S. Malik, M. A. S., and Kandpal, T. C. (eds.), Chapter 6, pp. 55–177. Wiley Eastern, New Delhi, India.
- Gordon, J. M. and Zarmi, Y. 1985. An analytic model for the long-term performance of solar thermal systems with well-mixed storage. *Solar Energy*, 35, 55.
- Hollands, K. G. T. 1965. Honeycomb devices in flat-plate solar collectors. *Solar Energy*, 9, 159.
- Hunn, B. D. 1980. A simplified method for sizing active solar space heating systems. In *Solar Energy Technology Handbook, Part B: Applications, System Design and Economics*, Dickinson, W. C. and Cheremisinoff, P. N. (eds.), pp. 639–255. Marcel Dekker, New York.
- Klein, S. A. 1978. Calculation of flat-plate collector utilizability. *Solar Energy*, 21, 393.
- Klein, S. A. and Beckman, W. A. 1979. A general design method for closed-loop solar energy systems. *Solar Energy*, 22, 269.
- Klein, S. A., Cooper, P. I., Freeman, T. L., Beekman, D. M., Beckman, W. A., and Doffie, J. A. 1975. A method of simulation of solar processes and its applications. *Solar Energy*, 17, 29.
- Klein, S. A. et al. 1979. TRNSYS—A transient system simulation. User's manual. University of Wisconsin-Madison Engineering Experiment Station Report 38-10. University of Wisconsin, Madison, WI.
- Kreider, J. F. 1979. *Medium and High Temperature Solar Energy Processes*. Academic Press, New York.
- Kutcher, C. F., Davenport, R. L., Dougherty, D. A., Gee, R. C., Masterson, P. M., and May, E. K. 1982. Design approaches for solar industrial process heat systems, SERI/TR-253-1356. Solar Energy Research Institute, Golden, CO.
- Lameiro, G. F. and Bendt, P., 1978. The GFL method for designing solar energy space heating and domestic hot water systems. In: *Proceedings of American Solar Energy Society Conference*, Boulder, CO, Vol. 2, p. 113.
- Larson, D. C. 1980. Optimization of flat-plate collector flat mirror system. *Solar Energy*, 24, 203.
- Liu, B. Y. H. and Jordan, R. C. 1960. The inter-relationship and characteristic distribution of direct, diffuse and total solar radiation. *Solar Energy*, 4, 1.
- Liu, B. Y. H. and Jordan, R. C. 1963. A rational procedure for predicting the long-term average performance of flat-plate solar energy collectors. *Solar Energy*, 7, 53.
- Liu, S. T. and Fanne, A. H. 1980. Comparing experimental and computer-predicted performance for solar hot water systems. *ASHRAE Journal*, 22(5), 34.
- Löf, G. O. G. 1981. Air based solar systems for space heating. In: *Solar Energy Handbook*, Kreider, J. F. and Kreith F. (eds.), pp. 39–44. McGraw-Hill, New York.
- Meyer, B. A. 1978. Natural convection heat transfer in small and moderate aspect ratio enclosures—An application to flat-plate collectors. In: *Thermal Storage and Heat Transfer in Solar Energy Systems*, Kreith, F. Boehm, R. Mitchell, J., and Bannerot, R. (eds.), pp. 555–558. American Society of Mechanical Engineers, New York.
- Mueller Associates. 1985. *Active Solar Thermal Design Manual*. Funded by U.S. DOE (no. EG-77-C-01-4042), SERI(XY-2-02046-1) and ASHRAE (project no. 40). Baltimore, MD.
- Newton, A. B. and Gilman, S. H. 1981. *Solar Collector Performance Manual*. Funded by U. S. DOE (no. EG-77-C-01-4042), SERI(XH-9-8265-1) and ASHRAE (project no. 32, Task 3).

- Phillips, W. F. and Dave, R. N. 1982. Effect of stratification on the performance of liquid-based solar heating systems. *Solar Energy*, 29, 111.
- Rabl, A. 1981. Yearly average performance of the principal solar collector types. *Solar Energy*, 27, 215.
- Rabl, A. 1985. *Active Solar Collectors and Their Applications*. Oxford University Press, New York.
- Reddy, T. A. 1987. *The Design and Sizing of Active Solar Thermal Systems*. Oxford University Press, Oxford, U.K.
- SERL. 1989. *Engineering Principles and Concepts for Active Solar Systems*. Hemisphere Publishing Company, New York.
- Theilacker, J. C. and Klein, S. A. 1980. Improvements in the utilizability relationships. In: *American Section of the International Solar Energy Society Meeting Proceedings*, Phoenix, AZ, 271pp.

18.2 Passive Solar Heating, Cooling, and Daylighting

Jeffrey H. Morehouse

18.2.1 Introduction

Passive systems are defined, quite generally, as systems in which the thermal energy flow is by natural means: by conduction, radiation, and natural convection. A *passive heating system* is one in which the sun's radiant energy is converted to heat upon absorption by the building. The absorbed heat can be transferred to thermal storage by natural means or used to directly heat the building. *Passive cooling systems* use natural energy flows to transfer heat to the environmental sinks: the ground, air, and sky.

If one of the major heat transfer paths employs a pump or fan to force the flow of a heat transfer fluid, then the system is referred to as having an active component or subsystem. Hybrid systems—either for heating or for cooling—are ones in which there are both passive and active energy flows. The use of the sun's radiant energy for the natural illumination of a building's interior spaces is called *daylighting*. Daylighting design approaches use both solar beam radiation (referred to as *sunlight*) and the diffuse radiation scattered by the atmosphere (referred to as *skylight*) as sources for interior lighting, with historical design emphasis on utilizing skylight.

18.2.1.1 Distinction between a Passive System and Energy Conservation

A distinction is made between the energy conservation techniques and passive solar measures. Energy conservation features are designed to reduce the heating and cooling energy required to thermally condition a building: the use of insulation to reduce either heating or cooling loads, and the use of window shading or window placement to reduce solar gains, reducing summer cooling loads. Passive features are designed to increase the use of solar energy to meet heating and lighting loads, plus the use of ambient *coolth* for cooling. For example, window placement to enhance solar gains to meet winter heating loads and/or to provide daylighting is passive solar use, and the use of a thermal chimney to draw air through the building to provide cooling is also a passive cooling feature.

18.2.1.2 Key Elements of Economic Consideration

The distinction between passive systems, active systems, or energy conservation is not critical for economic calculations, as they are the same in all cases: a trade-off between the

life cycle cost of the energy saved (performance) and the life cycle cost of the initial investment, operating, and maintenance costs (cost).

18.2.1.2.1 Performance: Net Energy Savings

The key performance parameter to be determined is the net annual energy saved by the installation of the passive system. The basis for calculating the economics of any solar energy system is to compare it against a *normal* building; thus, the actual difference in the annual cost of fuel is the difference in auxiliary energy that would be used with and without solar. Therefore, the energy saved rather than energy delivered, energy collected, useful energy, or some other energy measure, must be determined.

18.2.1.2.2 Cost: Over and above "Normal" Construction

The other significant part of the economic trade-off involves determining the difference between the cost of construction of the passive building and of the *normal* building against which it is to be compared. The convention, adopted from the economics used for active solar systems, is to define a *solar add-on cost*. Again, this may be a difficult definition in the case of passive designs because the building can be significantly altered compared to typical construction since, in many cases, it is not just a one-to-one replacement of a wall with a different wall, but it is more complex and involves assumptions and simulations concerning the *normal* building.

18.2.1.2.3 General System Application Status and Costs

Almost 500,000 buildings in the United States were constructed or retrofitted with passive features in the 20 years after 1980. Passive heating applications are primarily in single-family dwellings and secondarily in small commercial buildings. Daylighting features that reduce lighting loads and the associated cooling loads are usually more appropriate for large office buildings.

A typical passive heating design in a favorable climate might supply up to one-third of a home's original load at a cost of \$5–\$10 per million Btu net energy saved. An appropriately designed daylighting system can supply lighting at a cost of 2.5¢–5¢ per kWh (Larson et al. 1992a–c).

18.2.2 Solar Thermosyphon Water Heating

Solar hot water heating systems are composed of a collector and a storage tank. When the flow between the collector and tank is by natural circulation, these passive solar hot water systems are referred to as *thermosyphon systems*. This ability of thermosyphon systems to heat water without an externally powered pump has spurred its use in regions where both power is unavailable and power is very expensive.

18.2.2.1 Thermosyphon Concept

The natural tendency of a less dense fluid to rise above a more dense fluid can be used in a simple solar water heater to cause fluid motion through a collector. The density difference is created within the solar collector where heat is added to increase the temperature and decrease the density of the liquid. This collection concept is called a *thermosyphon*, and Figure 18.31 schematically illustrates the major components of such a system.

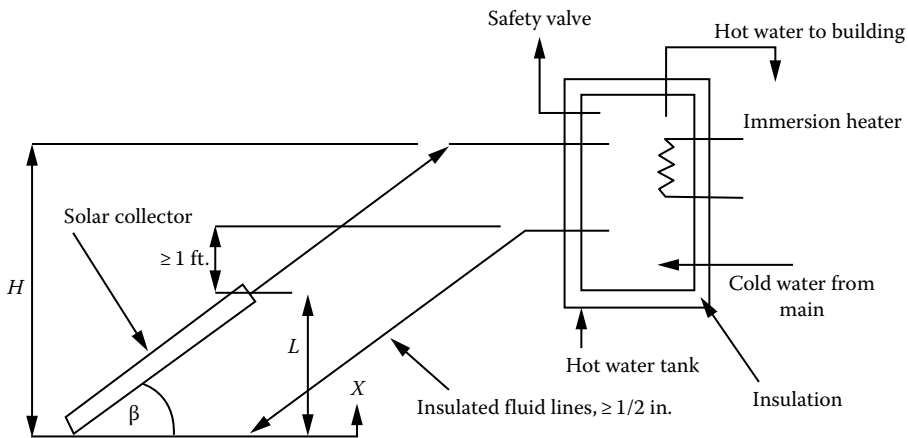


FIGURE 18.31

Schematic diagram of thermosyphon loop used in a natural circulation, service water heating system. The flow pressure drop in the fluid loop must equal the buoyant force pressure $\left[\int_0^L g\rho(x)dx - \rho_{stor}gL \right]$, where $\rho(x)$ is the local collector fluid density and ρ_{stor} is the tank fluid density, assumed uniform.

The flow pressure drop in the fluid loop (ΔP_{FLOW}) must equal the buoyant force pressure difference ($\Delta P_{BUOYANT}$) caused by the differing densities in the hot and cold legs of the fluid loop:

$$\begin{aligned} \Delta P_{FLOW} &= \Delta P_{BUOYANT} \\ &= \rho_{stor}gH - \left[\int_0^L \rho(x)gdx + \rho_{out}g(H-L) \right], \end{aligned} \tag{18.68}$$

where

- H is the height of the legs
- L is the height of the collector (see Figure 18.74)
- $\rho(x)$ is the local collector fluid density
- ρ_{stor} is the tank fluid density (assumed to be uniform)
- ρ_{out} is the collector outlet fluid density (assumed to be uniform)

The flow pressure term, ΔP_{FLOW} , is related to the flow loop system headloss that is in turn directly connected to friction and fitting losses and the loop flow rate:

$$\Delta P_{FLOW} = \oint_{LOOP} \rho d(h_L), \tag{18.69}$$

where

- $h_L = KV^2$, with K being the sum of the component loss velocity factors (see any fluid mechanics text)
- V is the flow velocity

18.2.2.2 Thermo-Fluid System Design Considerations

Because the driving force in a thermosyphon system is only a small density difference and not a pump, larger than normal plumbing fixtures must be used to reduce pipe friction losses. In general, one pipe size larger than that would be used with a pump system is satisfactory. Under no conditions should piping smaller than 1/2 in. (12 mm) national pipe thread (NPT) be used. Most commercial thermosyphons use 1 in. (25 mm) NPT pipe. The flow rate through a thermosyphon system is about 1 gal/ft.² h (40 L/m² h) in bright sun, based on collector area.

Because the hot water system loads vary little during a year, the best angle to tilt the collector is that equal to the local latitude. The temperature difference between the collector inlet water and the collector outlet water is usually 15°F–20°F (8°C–11°C) during the middle of a sunny day (Close 1962). After sunset, a thermosyphon system can reverse its flow direction and lose heat to the environment during the night. To avoid reverse flow, the top header of the absorber should be at least 1 ft. (30 cm) below the cold leg fitting on the storage tank, as shown.

To provide heat during long cloudy periods, an electrical immersion heater can be used as a backup for the solar system. The immersion heater is located near the top of the tank to enhance stratification so that the heated fluid is at the required delivery temperature at the delivery point. Tank stratification is desirable in a thermosyphon to maintain flow rates as high as possible. Insulation must be applied over the entire tank surface to control heat loss. Figure 18.32 illustrates two common thermosyphon system designs.

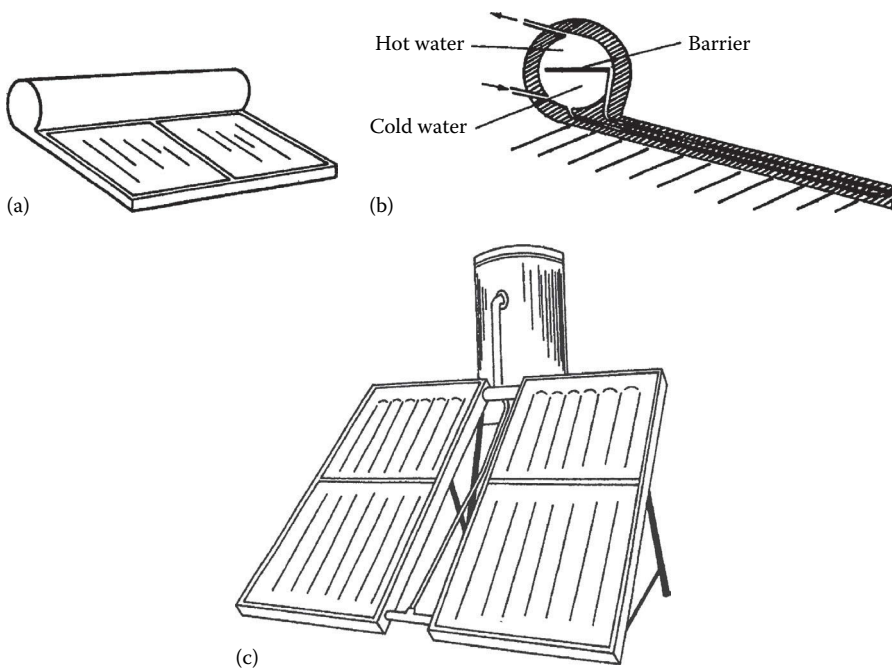


FIGURE 18.32

Passive solar water heaters: (a) compact model using combined collector and storage, (b) section view of the compact model, and (c) tank and collector assembly.

Several features inherent in the thermosyphon design limit its utility. If it is to be operated in a freezing climate, a nonfreezing fluid must be used, which in turn requires a heat exchanger between the collector and potable water storage. (If potable water is not required, the collector can be drained during cold periods instead.) Heat exchangers of either the shell-and-tube type or the immersion-coil type require higher flow rates for efficient operation than that a thermosyphon can provide. Therefore, the thermosyphon is generally limited to nonfreezing climates. A further restriction on thermosyphon use is the requirement for an elevated tank. In many cases, structural or architectural constraints prohibit raised-tank locations. In residences, collectors are normally mounted on the roof, and tanks mounted above the high point of the collector can easily become the highest point in a building. Practical considerations often do not permit this application.

Example 18.9

Determine the *pressure difference* available for a thermosyphon system with 1 m high collector and 2 m high *legs*. The water temperature input to the collector is 25°C, and the collector output temperature is 35°C. If the overall system loss velocity factor (*K*) is 15.6, estimate the system flow velocity.

Solution

Equation 18.68 is used to calculate the pressure difference, with the water densities being found from the temperatures (in steam tables)

$$\rho_{\text{stor}}(25^\circ\text{C}) = 997.009 \text{ kg/m}^3,$$

$$\rho_{\text{out}}(35^\circ\text{C}) = 994.036 \text{ kg/m}^3, \text{ and}$$

$$\rho_{\text{coll.ave.}}(30^\circ\text{C}) = 996.016 \text{ kg/m}^3,$$

(*note*: average collector temperature used in *temperature*) and with $H = 2 \text{ m}$ and $L = 1 \text{ m}$:

$$\begin{aligned} \Delta P_{\text{BUOYANT}} &= (997.009)9.81(2) - [(996.016)9.81(1) + (994.036)9.81(1)], \\ &= 38.9 \text{ N/m}^2 \text{ (Pa)}. \end{aligned}$$

The system flow velocity is estimated from the *system K* given, the pressure difference calculated earlier, taking the average density of the water around the loop (at 30°C), and substituting into Equation 18.69:

$$\Delta P_{\text{BUOYANT}} = (\rho_{\text{loop.ave}})(h_L)_{\text{loop}} = (\rho_{\text{loop.ave}})KV^2,$$

$$V^2 = 38.9/(996.016)(15.6),$$

$$V = 0.05 \text{ m/s}.$$

18.2.3 Passive Solar Heating Design Fundamentals

Passive heating systems contain the five basic components of all solar systems, as described in Chapter 40. Typical passive realizations of these components are

1. Collector: windows, walls, and floors
2. Storage: walls and floors, large interior masses (often, these are integrated with the collector absorption function)
3. Distribution system: radiation, free convection, simple circulation fans
4. Controls: movable window insulation, vents both to other inside spaces or to ambient
5. Backup system: any nonsolar heating system

The design of passive systems requires the strategic placement of windows, storage masses, and the occupied spaces themselves. The fundamental principles of solar radiation geometry and availability are instrumental in the proper location and sizing of the system's *collectors* (windows). Storage devices are usually more massive than those used in active systems and are frequently an integral part of the collection and distribution system.

18.2.3.1 Types of Passive Heating Systems

A commonly used method of cataloging the various passive system concepts is to distinguish three general categories: direct, indirect, and isolated gain. Most of the physical configurations of passive heating systems are seen to fit within one of these three categories.

For direct gain (Figure 18.33), sunlight enters the heated space and is converted to heat at absorbing surfaces. This heat is then distributed throughout the space and to the various enclosing surfaces and room contents.

For indirect gain category systems, sunlight is absorbed and stored by a mass interposed between the glazing and the conditioned space. The conditioned space is partially enclosed and bounded by this thermal storage mass, so a natural thermal coupling is achieved. Examples of the indirect approach are the thermal storage wall, the thermal storage roof, and the northerly room of an attached sunspace.

In the thermal storage wall (Figure 18.34), sunlight penetrates the glazing and is absorbed and converted to heat at a wall surface interposed between the glazing and the heated space. The wall is usually masonry (Trombe wall) or containers filled with water (waterwall), although it might contain phase-change material. The attached sunspace (Figure 18.35) is actually a two-zone combination of direct gain and thermal storage wall. Sunlight enters and heats a direct gain southerly *sunspace* and also heats a mass wall separating the northerly buffered space, which is indirectly heated. The *sunspace* is frequently used as a greenhouse, in which case, the system is called an *attached greenhouse*. The thermal storage roof (Figure 18.36) is similar to the thermal storage wall except that the interposed thermal storage mass is located on the building roof.

The isolated gain category concept is an indirect system, except that there is a distinct thermal separation (by means of either insulation or physical separation) between the thermal storage and the heated space. The convective (thermosyphon) loop, as depicted in Figure 18.31, is in this category and, while often used to heat domestic water, is also used for building heating. It is most akin to conventional active systems in that there is a separate collector and separate thermal storage. The thermal storage wall, thermal storage roof,

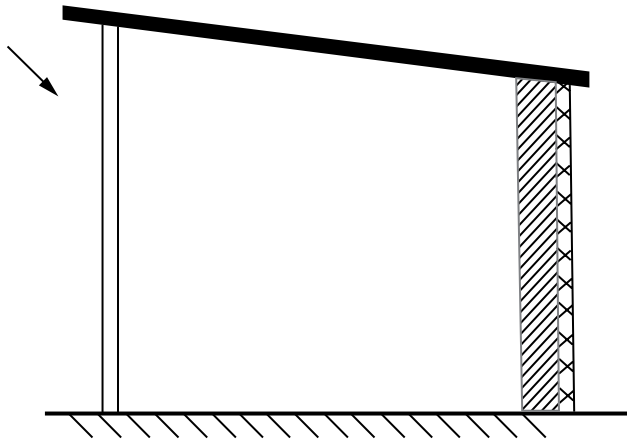


FIGURE 18.33
Direct gain.

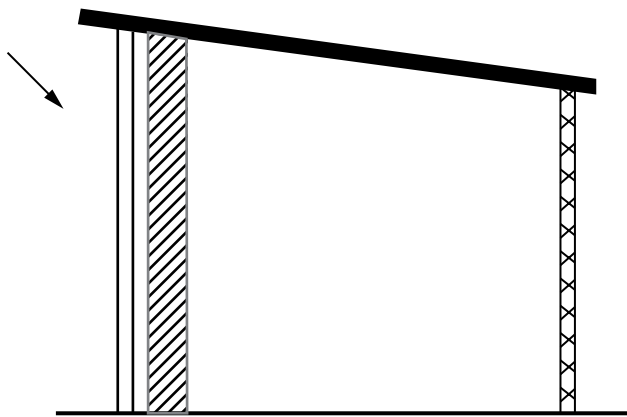


FIGURE 18.34
Thermal storage wall.

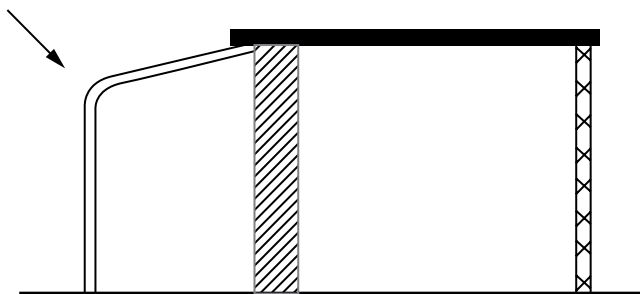


FIGURE 18.35
Attached sunspace.

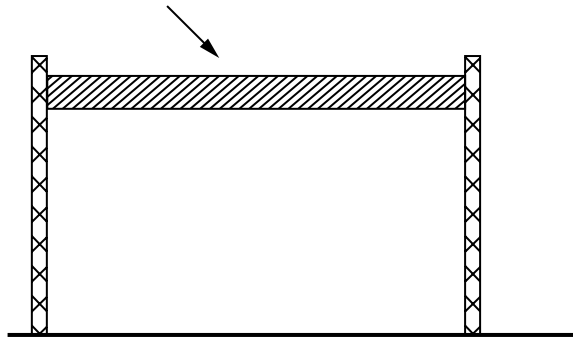


FIGURE 18.36
Thermal storage roof.

and attached sunspace approaches can also be made into isolated systems by insulating between the thermal storage and the heated space.

18.2.3.2 Fundamental Concepts for Passive Heating Design

Figure 18.37 is an equivalent thermal circuit for the building illustrated in Figure 18.34, the Trombe wall-type system. For the heat transfer analysis of the building, three temperature nodes can be identified: room temperature, storage wall temperature, and the ambient temperature. The circuit responds to climatic variables represented by a current injection I_s (solar radiation) and by the ambient temperature T_a . The storage temperature, T_s , and room temperature, T_r , are determined by current flows in the equivalent circuit. By using seasonal and annual climatic data, the performance of a passive structure can be simulated, and the results of many such simulations are correlated to give the design approaches described later in text.

18.2.3.3 Passive Design Approaches

Design of a passive heating system involves selection and sizing of the passive feature type(s), determination of thermal performance, and cost estimation. Ideally, a cost/performance optimization would be performed by the designer. Owner and architect ideas usually establish the passive feature type, with general size and cost estimation available. However, the thermal performance of a passive heating system has to be calculated.

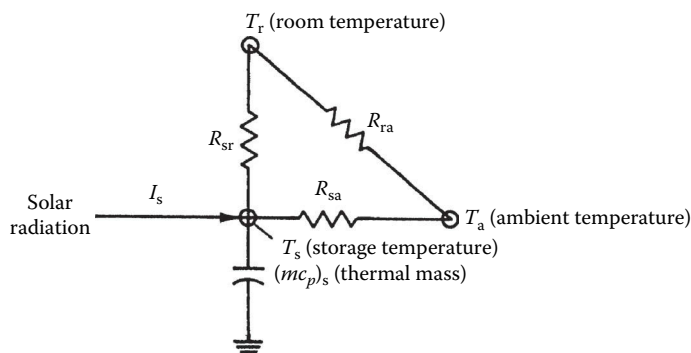


FIGURE 18.37
Equivalent thermal circuit for passively heated solar building in Figure 18.34.

There are several *levels* of methods that can be used to estimate the thermal performance of passive designs. First-level methods involve a rule of thumb and/or generalized calculation to get a starting estimate for size and/or annual performance. A second-level method involves climate, building, and passive system details, which allow annual performance determination, plus some sensitivity to passive system design changes. Third-level methods involve periodic calculations (hourly, monthly) of performance and permit more detailed variations of climatic, building, and passive solar system design parameters.

These three levels of design methods have a common basis in that they all are derived from correlations of a multitude of computer simulations of passive systems (PSDH 1980, 1984). As a result, a similar set of defined terms is used in many passive design approaches:

- A_p , solar projected area, m^2 ($ft.^2$): the net south-facing passive solar glazing area projected onto a vertical plane
- NLC, net building load coefficient, kJ/CDD (Btu/FDD): net load of the nonsolar portion of the building per degree-day of indoor–outdoor temperature difference. The CDD and FDD terms refer to Celsius and Fahrenheit degree-days, respectively
- Q_{net} , net reference load, Wh (Btu): heat loss from nonsolar portion of building as calculated by

$$Q_{net} = NLC \times (\text{number of degree-days}). \quad (18.70)$$

- LCR, load collector ratio, $kJ/m^2 CDD$ ($Btu/ft.^2 FDD$): ratio of NLC to A_p ,

$$LCR = \frac{NLC}{A_p} \quad (18.71)$$

- SSF, solar savings fraction, %: percentage reduction in required auxiliary heating relative to net reference load,

$$SSF = 1 - \frac{\text{Auxiliary heat required } (Q_{aux})}{\text{Net reference load } (Q_{net})}. \quad (18.72)$$

Therefore, using Equation 18.70, the auxiliary heat required, Q_{aux} , is given by

$$Q_{aux} = (1 - SSF) \times NLC \times (\text{number of degree-days}). \quad (18.73)$$

The amount of auxiliary heat required is often a basis of comparison between possible solar designs as well as being the basis for determining building energy operating costs. Thus, many of the passive design methods are based on determining SSF, NLC, and the number of degree-days in order to calculate the auxiliary heat required for a particular passive system by using Equation 18.73.

18.2.3.4 First Level: Generalized Methods

A first estimate or starting value is needed to begin the overall passive system design process. Generalized methods and rules of thumb have been developed to generate initial values for solar aperture size, storage size, solar savings fraction, auxiliary heat required, and other size and performance characteristics. The following rules of thumb are meant to be used with the defined terms presented earlier.

18.2.3.5 Load

A rule of thumb used in conventional building design is that a design heating load of 120–160 kJ/CDD per m² of floor area (6–8 Btu/FDD ft.²) is considered an energy conservative design. Reducing these nonsolar values by 20% to solarize the proposed south-facing solar wall gives rule-of-thumb NLC values per unit of floor area:

$$\text{NLC/floor area} = 100\text{--}130 \text{ kJ/CDD m}^2 \text{ (4.8--6.4 Btu/FDD ft.}^2\text{)}. \quad (18.74)$$

18.2.3.6 Solar Savings Fraction

A method of getting starting-point values for the solar savings fraction is presented in Figure 18.38 (PSDH 1984). The map values represent optimum SSF (in percent) for a particular set of conservation and passive-solar costs for different climates across the United States. With the Q_{net} generated from the NLC rule of thumb (see earlier) and the SSF read from the map, the Q_{aux} can be determined.

18.2.3.7 Load Collector Ratio

The A_p can be determined using the NLC given earlier if the LCR is known. The rule of thumb associated with *good* values of LCR (PSDH 1984) differs depending on whether the design is for a *cold* or *warm* climate:

$$\text{"Good" LCR} = \begin{cases} \text{For cold climate: } 410 \text{ kJ/m}^2 \text{ CDD (20 Btu/ft.}^2 \text{ FDD)} \\ \text{For warm climate: } 610 \text{ kJ/m}^2 \text{ CDD (30 Btu/ft.}^2 \text{ FDD)} \end{cases} \quad (18.75)$$

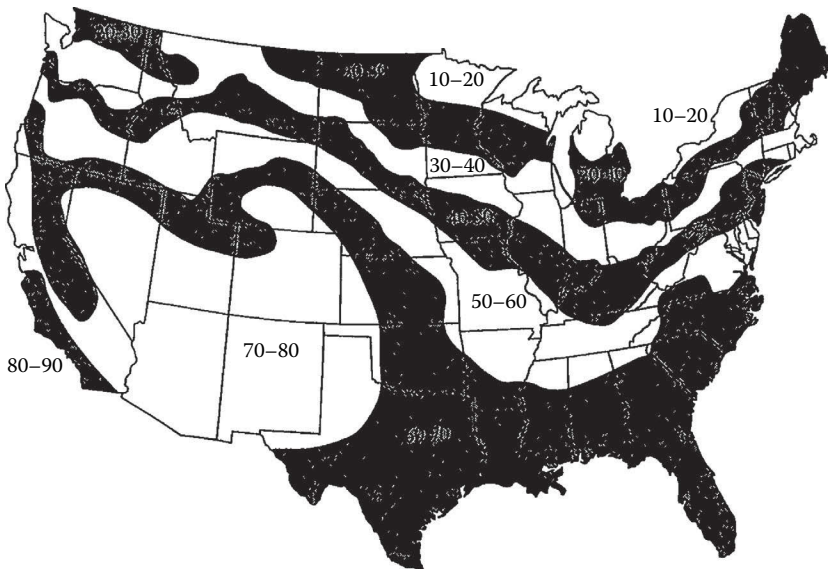


FIGURE 18.38

Starting-point values of solar savings fraction (SSF) in percent. (From PSDH, *Passive Solar Design Handbook*, Part One: Total Environmental Action, Inc., Part Two: Los Alamos Scientific Laboratory, Part Three: Los Alamos National Laboratory. Van Nostrand Reinhold, New York, 1984.)

18.2.3.8 Storage

Rules of thumb for thermal mass storage relate storage material total heat capacity to the solar projected area (PSDH 1984). The use of the storage mass is to provide for heating on cloudy days and to regulate sunny day room air temperature swing. When the thermal mass directly absorbs the solar radiation, each square meter of the projected glazing area requires enough mass to store 613 kJ/°C. If the storage material is not in direct sunlight, but heated from room air only, then four times as much mass is needed. In a room with a directly sunlight-heated storage mass, the room air temperature swing will be approximately one-half the storage mass temperature swing. For room air heated storage, the air temperature swing is twice that of the storage mass.

Example 18.10

A Denver, Colorado, building is to have a floor area of 195 m² (2100 ft.²). Determine rule-of-thumb size and performance characteristics.

Solution

From Equation 18.72, the NLC is estimated as

$$\begin{aligned} \text{NLC} &= (115 \text{ kJ/CDDm}^2) \times (195 \text{ m}^2) \\ &= 22,400 \text{ kJ/CDD} (11,800 \text{ Btu/FDD}). \end{aligned}$$

Using the *cold* LCR value and Equation 18.71, the passive solar projected area is

$$\begin{aligned} A_p &= \frac{\text{NLC}}{\text{LCR}} = \frac{22,400 \text{ kJ/CDD}}{410 \text{ kJ/m}^2 \text{CDD}} \\ &= 54.7 \text{ m}^2 (588 \text{ ft.}^2). \end{aligned}$$

Locating Denver on the map of Figure 18.38 gives an SSF value in the 70%–80% range (use 75%). An annual °C-degree-day value can be found in city climate tables (PSDH 1984; NCDC 1992) and is 3491 CDD (6283 FDD) for Denver. Thus, the auxiliary heat required, Q_{aux} , is found using Equation 18.73:

$$\begin{aligned} Q_{\text{aux}} &= (1 - 0.75)(22,400 \text{ kJ/CDD})(3491 \text{ CDD}) \\ &= 19,600 \text{ MJ} (18.5 \times 10^6 \text{ Btu}) \text{ annually.} \end{aligned}$$

The thermal storage can be sized using directly solar-heated and/or room air heated mass by using the projected area. Assuming brick with a specific heat capacity of 840 J/kg °C, the storage mass is found by

$$\begin{aligned} A_p \times (613 \text{ kJ/C}) &= m \times (840 \text{ J/kg } ^\circ\text{C}), \\ m_d &= 40,000 \text{ kg} (88,000 \text{ lbm}) \text{ [direct sun]}, \\ \text{or } m_a &= 160,000 \text{ kg} (351,000 \text{ lbm}) \text{ [air heated]}. \end{aligned}$$

A more location-dependent set of rules of thumb is presented in PSDH (1980). The first rule of thumb relates solar projected area as a percentage of floor area to solar savings fraction, with and without night insulation of the solar glazing:

A solar projected area of (B1)% to (B2)% of the floor area can be expected to produce a SSF in (location) of (S1)% to (S2)%, or, if R9 night insulation is used, of (S3)% to (S4)%

The values of B1, B2, S1, S2, S3, and S4 are found using Table 18.5 for the location. The thermal storage mass rule of thumb is again related to the solar projected area:

A thermal storage wall should have $14 \text{ kg} \times \text{SSF} (\%)$ of water or $71 \text{ kg} \times \text{SSF} (\%)$ of masonry for each square meter of solar projected area. For a direct gain space, the mass above should be used with a surface area of at least three times the solar projected area, and masonry no thicker than 10–15 cm. If the mass is located in back rooms, then four times the above mass is needed.

Example 18.11

Determine size and performance passive solar characteristics with the location-dependent set of rules of thumb for the house of the previous example.

Solution

Using Table 18.5 with the 195 m² house in Denver yields

Solar projected area = 12%–23% of floor area

= 23.4–44.9 m².

SSF (no night insulation) = 27%–43%.

SSF (R9 night insulation) = 47%–74%.

Using the rule of thumb for the thermal storage mass,

$$m = 17 \text{ kg} \times 43\% \times 44.9 \text{ m}^2$$

$$= 33,000 \text{ kg (72,000 lbm) [Thermal wall or direct gain].}$$

Comparing the results of this example to those of the previous example, the two rules of thumb are seen to produce *roughly* similar answers. General system cost and performance information can be generated with results from rule-of-thumb calculations, but a more detailed level of information is needed to determine design-ready passive system type (direct gain, thermal wall, sunspace), size, performance, and costs.

18.2.3.9 Second Level: LCR Method

The LCR method is useful for making estimates of the annual performance of specific types of passive system(s) combinations. The LCR method was developed by calculating the annual SSF for 94 reference passive solar systems for 219 U.S. and Canadian locations over a range of LCR values. Table 18.6 includes the description of these 94 reference systems for use both with the LCR method and with the solar load ratio (SLR) method described later. Tables were constructed for each city with LCR versus SSF listed for each of the 94 reference passive systems. (Note that the SLR method was used to make the LCR calculations, and this SLR method is described in the next section as the third-level method.) Although the complete LCR tables (PSDH 1984) include 219 locations, Table 18.7 includes only 6 *representative* cities

TABLE 18.5

Values to Be Used in the Glazing Area and SSF Relations Rules of Thumb

City	B1	B2	S1	S2	S3	S4
Birmingham, Alabama	0.09	0.18	22	37	34	58
Mobile, Alabama	0.06	0.12	26	44	34	60
Montgomery, Alabama	0.07	0.15	24	41	34	59
Phoenix, Arizona	0.06	0.12	37	60	48	75
Prescott, Arizona	0.10	0.20	29	48	44	72
Tucson, Arizona	0.06	0.12	35	57	45	73
Winslow, Arizona	0.12	0.24	30	47	48	74
Yuma, Arizona	0.04	0.09	43	66	51	78
Fort Smith, Arkansas	0.10	0.20	24	39	38	64
Little Rock, Arkansas	0.10	0.19	23	38	37	62
Bakersfield, California	0.08	0.15	31	50	42	67
Baggett, California	0.07	0.15	35	56	46	73
Fresno, California	0.09	0.17	29	46	41	65
Long Beach, California	0.05	0.10	35	58	44	72
Los Angeles, California	0.05	0.09	36	58	44	72
Mount Shasta, California	0.11	0.21	24	38	42	67
Needles, California	0.06	0.12	39	61	49	76
Oakland, California	0.07	0.15	35	55	46	72
Red Bluff, California	0.09	0.18	29	46	41	65
Sacramento, California	0.09	0.18	29	47	41	66
San Diego, California	0.04	0.09	37	61	46	74
San Francisco, California	0.06	0.13	34	54	45	71
Santa Maria, California	0.05	0.11	31	53	42	69
Colorado Springs, Colorado	0.12	0.24	27	42	47	74
Denver, Colorado	0.12	0.23	27	43	47	74
Eagle, Colorado	0.14	0.29	25	35	53	77
Grand Junction, Colorado	0.13	0.27	29	43	50	76
Pueblo, Colorado	0.11	0.23	29	45	48	75
Hartford, Connecticut	0.17	0.35	14	19	40	64
Wilmington, Delaware	0.15	0.29	19	30	39	63
Washington, District of Columbia	0.12	0.23	18	28	37	61
Apalachicola, Florida	0.05	0.10	28	47	36	61
Daytona Beach, Florida	0.04	0.08	30	51	36	63
Jacksonville, Florida	0.05	0.09	27	47	35	62
Miami, Florida	0.01	0.02	27	48	31	54
Orlando, Florida	0.03	0.06	30	52	37	63
Tallahassee, Florida	0.05	0.11	26	45	35	60
Tampa, Florida	0.03	0.06	30	52	36	63
West Palm Beach, Florida	0.01	0.03	30	51	34	59
Atlanta, Georgia	0.06	0.17	22	36	34	58
Augusta, Georgia	0.06	0.16	24	40	35	60
Macon, Georgia	0.07	0.15	25	41	35	59
Savannah, Georgia	0.06	0.13	25	43	35	60
Boise, Idaho	0.14	0.28	27	38	48	71

(Continued)

TABLE 18.5 (Continued)

Values to Be Used in the Glazing Area and SSF Relations Rules of Thumb

City	B1	B2	S1	S2	S3	S4
Lewiston, Idaho	0.15	0.29	22	29	44	65
Pocatello, Idaho	0.13	0.26	25	35	51	74
Chicago, Illinois	0.17	0.35	17	23	43	67
Moline, Illinois	0.20	0.39	17	22	46	70
Springfield, Illinois	0.15	0.30	19	26	42	67
Evansville, Indiana	0.14	0.27	19	29	37	61
Fort Wayne, Indiana	0.16	0.33	13	17	37	60
Indianapolis, Indiana	0.14	0.28	15	21	37	60
South Bend, Indiana	0.18	0.35	12	15	39	61
Burlington, Iowa	0.18	0.36	20	27	47	71
Des Moines, Iowa	0.21	0.43	19	25	58	75
Mason City, Iowa	0.22	0.44	18	19	56	79
Sioux City, Iowa	0.23	0.46	20	24	53	76
Dodge City, Kansas	0.12	0.23	27	42	46	73
Goodland, Kansas	0.13	0.27	26	39	47	74
Topeka, Kansas	0.14	0.26	24	35	45	71
Wichita, Kansas	0.14	0.26	26	41	45	72
Lexington, Kentucky	0.13	0.27	17	26	35	58
Louisville, Kentucky	0.13	0.27	18	27	35	59
Baton Rouge, Louisiana	0.06	0.12	26	43	34	59
Lake Charles, Louisiana	0.06	0.11	24	41	32	57
New Orleans, Louisiana	0.05	0.11	27	46	35	61
Shreveport, Louisiana	0.08	0.15	26	43	36	61
Caribou, Maine	0.25	0.30	NR	NR	53	74
Portland, Maine	0.17	0.34	14	17	45	69
Baltimore, Maryland	0.14	0.27	19	30	38	62
Boston, Massachusetts	0.15	0.29	17	25	40	64
Alpena, Michigan	0.21	0.42	NR	NR	47	69
Detroit, Michigan	0.17	0.34	13	17	39	61
Flint, Michigan	0.15	0.31	11	12	40	62
Grand Rapids, Michigan	0.19	0.38	12	13	39	61
Sault Ste. Marie, Michigan	0.25	0.50	NR	NR	50	70
Traverse City, Michigan	0.18	0.36	NR	NR	42	62
Duluth, Minnesota	0.25	0.50	NR	NR	50	70
International Falls, Minnesota	0.25	0.50	NR	NR	47	66
Minneapolis–St. Paul, Minnesota	0.25	0.50	NR	NR	55	76
Rochester, Minnesota	0.24	0.49	NR	NR	54	76
Jackson, Mississippi	0.06	0.15	24	48	34	59
Meridian, Mississippi	0.08	0.15	23	39	34	58
Columbia, Missouri	0.13	0.26	20	30	41	66
Kansas City, Missouri	0.14	0.29	22	32	44	70
Saint Louis, Missouri	0.15	0.29	21	33	41	65
Springfield, Missouri	0.13	0.26	22	34	40	65
Billings, Montana	0.16	0.32	24	31	53	76

(Continued)

TABLE 18.5 (Continued)

Values to Be Used in the Glazing Area and SSF Relations Rules of Thumb

City	B1	B2	S1	S2	S3	S4
Cut Bank, Montana	0.24	0.49	22	23	62	81
Dillon, Montana	0.16	0.32	24	32	54	77
Glasgow, Montana	0.25	0.50	NR	NR	55	75
Great Falls, Montana	0.18	0.37	23	26	56	77
Helena, Montana	0.20	0.39	21	25	55	77
Lewistown, Montana	0.19	0.38	21	25	54	76
Miles City, Montana	0.23	0.47	21	23	60	80
Missoula, Montana	0.18	0.36	15	16	47	68
Grand Island, Nebraska	0.18	0.36	24	33	51	76
North Omaha, Nebraska	0.20	0.48	21	29	51	76
North Platte, Nebraska	0.17	0.34	25	36	50	76
Scottsbluff, Nebraska	0.16	0.31	24	36	49	74
Elko, Nevada	0.12	0.25	27	39	52	76
Ely, Nevada	0.12	0.23	27	41	50	77
Las Vegas, Nevada	0.09	0.18	35	56	48	75
Lovelock, Nevada	0.13	0.25	32	48	53	78
Reno, Nevada	0.11	0.22	31	48	49	76
Tonopah, Nevada	0.11	0.23	31	48	51	77
Winnemucca, Nevada	0.13	0.26	28	42	49	75
Concord, New Hampshire	0.17	0.34	13	15	45	68
Newark, New Jersey	0.13	0.25	19	29	39	64
Albuquerque, New Mexico	0.11	0.22	29	47	46	73
Clayton, New Mexico	0.10	0.20	28	45	45	73
Farmington, New Mexico	0.12	0.24	29	45	49	76
Los Alamos, New Mexico	0.11	0.22	25	40	44	72
Roswell, New Mexico	0.10	0.19	30	49	45	73
Truth or Consequences, New Mexico	0.09	0.17	32	51	46	73
Tucumcari, New Mexico	0.10	0.20	30	48	45	73
Zuni, New Mexico	0.11	0.21	27	43	45	73
Albany, New York	0.21	0.41	13	15	43	66
Binghamton, New York	0.15	0.30	NR	NR	35	56
Buffalo, New York	0.19	0.37	NR	NR	36	57
Massena, New York	0.25	0.50	NR	NR	50	71
New York (Central Park), New York	0.15	0.30	16	25	36	59
Rochester, New York	0.18	0.37	NR	NR	37	58
Syracuse, New York	0.19	0.38	NR	NR	37	59
Asheville, North Carolina	0.10	0.20	21	35	36	61
Cape Hatteras, North Carolina	0.09	0.17	24	40	36	60
Charlotte, North Carolina	0.08	0.17	23	38	36	60
Greensboro, North Carolina	0.10	0.20	23	37	37	63
Raleigh–Durham, North Carolina	0.09	0.19	22	37	36	61
Bismarck, North Dakota	0.25	0.50	NR	NR	56	77
Fargo, North Dakota	0.25	0.50	NR	NR	51	72
Minot, North Dakota	0.25	0.50	NR	NR	52	72

(Continued)

TABLE 18.5 (Continued)

Values to Be Used in the Glazing Area and SSF Relations Rules of Thumb

City	B1	B2	S1	S2	S3	S4
Akron–Canton, Ohio	0.15	0.31	12	16	35	57
Cincinnati, Ohio	0.12	0.24	15	23	35	57
Cleveland, Ohio	0.15	0.31	11	14	34	55
Columbus, Ohio	0.14	0.28	13	18	35	57
Dayton, Ohio	0.14	0.28	14	20	36	59
Toledo, Ohio	0.17	0.34	13	17	38	61
Youngstown, Ohio	0.16	0.32	NR	NR	34	54
Oklahoma City, Oklahoma	0.11	0.22	25	41	41	67
Tulsa, Oklahoma	0.11	0.22	24	38	40	65
Astoria, Oregon	0.09	0.19	21	34	37	60
Burns, Oregon	0.13	0.25	23	32	47	71
Medford, Oregon	0.12	0.24	21	32	38	60
North Bend, Oregon	0.09	0.17	25	42	38	64
Pendleton, Oregon	0.14	0.27	22	30	43	64
Portland, Oregon	0.13	0.26	21	31	38	60
Redmond, Oregon	0.13	0.27	26	38	47	71
Salem, Oregon	0.12	0.24	21	32	37	59
Allentown, Pennsylvania	0.15	0.29	16	24	39	63
Erie, Pennsylvania	0.17	0.34	NR	NR	35	55
Harrisburg, Pennsylvania	0.13	0.26	17	26	38	62
Philadelphia, Pennsylvania	0.15	0.29	19	29	38	62
Pittsburgh, Pennsylvania	0.14	0.28	12	16	33	55
Wilkes-Barre–Scranton, Pennsylvania	0.16	0.32	13	18	37	60
Providence, Rhode Island	0.15	0.30	17	24	40	64
Charleston, South Carolina	0.07	0.14	25	41	34	59
Columbia, South Carolina	0.08	0.17	25	41	36	61
Greenville–Spartanburg, South Carolina	0.08	0.17	23	38	36	60
Huron, South Dakota	0.25	0.50	NR	NR	58	79
Pierre, South Dakota	0.22	0.43	21	23	58	80
Rapid City, South Dakota	0.15	0.30	23	32	51	76
Sioux Falls, South Dakota	0.22	0.45	18	19	57	79
Chattanooga, Tennessee	0.09	0.19	19	32	33	56
Knoxville, Tennessee	0.09	0.18	20	33	33	56
Memphis, Tennessee	0.09	0.19	22	36	36	60
Nashville, Tennessee	0.10	0.21	19	30	33	55
Abilene, Texas	0.09	0.18	29	47	41	68
Amarillo, Texas	0.11	0.22	29	46	45	72
Austin, Texas	0.06	0.13	27	46	37	63
Brownsville, Texas	0.03	0.06	27	46	32	57
Corpus Christi, Texas	0.05	0.09	29	49	36	63
Dallas, Texas	0.08	0.17	27	44	38	64
Del Rio, Texas	0.06	0.12	30	50	39	66
El Paso, Texas	0.09	0.17	32	53	45	72
Forth Worth, Texas	0.09	0.17	26	44	38	64

(Continued)

TABLE 18.5 (Continued)

Values to Be Used in the Glazing Area and SSF Relations Rules of Thumb

City	B1	B2	S1	S2	S3	S4
Houston, Texas	0.06	0.11	25	43	34	59
Laredo, Texas	0.05	0.09	31	52	39	64
Lubbock, Texas	0.09	0.19	30	49	44	72
Lufkin, Texas	0.07	0.14	26	43	35	61
Midland–Odessa, Texas	0.09	0.18	32	52	44	72
Port Arthur, Texas	0.06	0.11	26	44	34	60
San Angelo, Texas	0.08	0.15	29	48	40	67
San Antonio, Texas	0.06	0.12	28	48	38	64
Sherman, Texas	0.10	0.20	25	41	38	64
Waco, Texas	0.06	0.15	27	45	38	64
Wichita Falls, Texas	0.10	0.20	27	45	41	67
Bryce Canyon, Utah	0.13	0.25	26	39	52	78
Cedar City, Utah	0.12	0.24	28	43	48	75
Salt Lake City, Utah	0.13	0.26	27	39	48	72
Burlington, Vermont	0.22	0.43	NR	NR	46	68
Norfolk, Virginia	0.09	0.19	23	38	37	62
Richmond, Virginia	0.11	0.22	21	34	37	61
Roanoke, Virginia	0.11	0.23	21	34	37	61
Olympia, Washington	0.12	0.23	20	29	38	59
Seattle–Tacoma, Washington	0.11	0.22	21	30	39	59
Spokane, Washington	0.20	0.39	20	24	48	68
Yakima, Washington	0.18	0.36	24	31	49	70
Charleston, West Virginia	0.13	0.25	16	24	32	54
Huntington, West Virginia	0.13	0.25	17	27	34	57
Eau Claire, Wisconsin	0.25	0.50	NR	NR	53	75
Green Bay, Wisconsin	0.23	0.46	NR	NR	53	75
La Crosse, Wisconsin	0.21	0.43	NR	NR	52	75
Madison, Wisconsin	0.20	0.40	15	17	51	74
Milwaukee, Wisconsin	0.18	0.35	15	18	48	71
Casper, Wyoming	0.13	0.26	27	39	53	78
Cheyenne, Wyoming	0.11	0.21	25	39	47	74
Rock Springs, Wyoming	0.14	0.28	26	38	54	79
Sheridan, Wyoming	0.16	0.31	22	30	52	75
<i>Canada</i>						
Edmonton, Alberta	0.25	0.50	NR	NR	54	72
Suffield, Alberta	0.25	0.50	28	30	67	85
Nanaimo, British Columbia	0.13	0.26	26	35	45	66
Vancouver, British Columbia	0.13	0.26	20	28	48	60
Winnipeg, Manitoba	0.25	0.50	NR	NR	54	74
Dartmouth, Nova Scotia	0.14	0.28	17	24	45	70
Moosonee, Ontario	0.25	0.50	NR	NR	48	67
Ottawa, Ontario	0.25	0.50	NR	NR	59	80
Toronto, Ontario	0.18	0.36	17	23	44	68
Normandie, Quebec	0.25	0.50	NR	NR	54	74

Source: PSDH, *Passive Solar Design Handbook*, U.S. Department of Energy, Washington, DC, 1980.

Note: NR, not recommended.

TABLE 18.6

Designations and Characteristics for 94 Reference Systems

(a) Overall System Characteristics

<i>Masonry Properties</i>	
Thermal conductivity (<i>k</i>)	
Sunspace floor	0.5 Btu/h/ft./°F
All other masonry	1.0 Btu/h/ft./°F
Density (<i>Q</i>)	150 lb/ft. ³
Specific heat (<i>c</i>)	0.2 Btu/lb/°F
Infrared emittance of normal surface	0.9
Infrared emittance of selective surface	0.1
<i>Solar Absorptances</i>	
Waterwall	1.0
Masonry, Trombe wall	1.0
Direct gain and sunspace	0.8
Sunspace: water containers	0.9
Lightweight common wall	0.7
Other lightweight surfaces	0.3
<i>Glazing Properties</i>	
Transmission characteristics	Diffuse
Orientation	Due south
Index of refraction	1.526
Extinction coefficient	0.5 in. ⁻¹
Thickness of each pane	½ in.
Gap between panes	½ in.
Ared emittance	0.9
<i>Control Range</i>	
Room temperature	65°F–75°F
Sunspace temperature	45°F–95°F
Internal heat generation	0
<i>Thermocirculation Vents (when Used)</i>	
Vent area/projected area (sum of both upper and lower vents)	0.06
Height between vents	8 ft.
Reverse flow	None
<i>Nighttime Insulation (when used)</i>	
Thermal resistance	R9
In place, solar time	5:30 p.m. to 7:30 a.m.
<i>Solar Radiation Assumptions</i>	
Shading	None
Ground diffuse reflectance	0.3

(Continued)

TABLE 18.6 (Continued)

Designations and Characteristics for 94 Reference Systems

(b) Direct-Gain (DG) System Types

Designation	Thermal Storage Capacity ^a (Btu/ft. ² /°F)	Mass Thickness ^a (in.)	Mass-Area-to-Glazing-Area Ratio	No. of Glazings	Nighttime Insulation
A1	30	2	6	2	No
A2	30	2	6	3	No
A3	30	2	6	2	Yes
B1	45	6	3	2	No
B2	45	6	3	3	No
B3	45	6	3	2	Yes
C1	60	4	6	2	No
C2	60	4	6	3	No
C3	60	4	6	2	Yes

(c) Vented Trombe Wall (TW) System Types

Designation	Thermal Storage Capacity ^a (Btu/ft. ² /°F)	Wall Thickness ^a (in.)	ρck (Btu ² /h/ft. ⁴ /°F ²)	No. of Glazings	Wall Surface	Nighttime Insulation
A1	15	6	30	2	Normal	No
A2	22.5	9	30	2	Normal	No
A3	30	12	30	2	Normal	No
A4	45	18	30	2	Normal	No
B1	15	6	15	2	Normal	No
B2	22.5	9	15	2	Normal	No
B3	30	12	15	2	Normal	No
B4	45	18	15	2	Normal	No
C1	15	6	7.5	2	Normal	No
C2	22.5	9	7.5	2	Normal	No
C3	30	12	7.5	2	Normal	No
C4	45	18	7.5	2	Normal	No
D1	30	12	30	1	Normal	No
D2	30	12	30	3	Normal	No
D3	30	12	30	1	Normal	Yes
D4	30	12	30	2	Normal	Yes
D5	30	12	30	3	Normal	Yes
E1	30	12	30	1	Selective	No
E2	30	12	30	2	Selective	No
E3	30	12	30	1	Selective	Yes
E4	30	12	30	2	Selective	Yes

(d) Unvented Trombe Wall (TW) System Types

Designation	Thermal Storage Capacity ^a (Btu/ft. ² /°F)	Wall Thickness ^a (in.)	ρck (Btu ² /h/ft. ⁴ /°F ²)	No. of Glazings	Wall Surface	Nighttime Insulation
F1	15	6	30	2	Normal	No
F2	22.5	9	30	2	Normal	No
F3	30	12	30	2	Normal	No

(Continued)

TABLE 18.6 (Continued)

Designations and Characteristics for 94 Reference Systems

(d) Unvented Trombe Wall (TW) System Types

Designation	Thermal Storage Capacity ^a (Btu/ft. ² /°F)	Wall Thickness ^a (in.)	ρck (Btu ² /h/ft. ⁴ /°F ²)	No. of Glazings	Wall Surface	Nighttime Insulation
F4	45	18	30	2	Normal	No
G1	15	6	15	2	Normal	No
G2	22.5	9	15	2	Normal	No
G3	30	12	15	2	Normal	No
G4	45	18	15	2	Normal	No
H1	15	6	7.5	2	Normal	No
H2	22.5	9	7.5	2	Normal	No
H3	30	12	7.5	2	Normal	No
H4	45	18	7.5	2	Normal	No
I1	30	12	30	1	Normal	No
I2	30	12	30	3	Normal	No
I3	30	12	30	1	Normal	Yes
I4	30	12	30	2	Normal	Yes
I5	30	12	30	3	Normal	Yes
J1	30	12	30	1	Selective	No
J2	30	12	30	2	Selective	No
J3	30	12	30	1	Selective	Yes
J4	30	12	30	2	Selective	Yes

(e) Waterwall (WW) System Types

Designation	Thermal Storage Capacity ^a (Btu/ft. ² /°F)	Wall Thickness (in.)	No. of Glazings	Wall Surface	Nighttime Insulation
A1	15.6	3	2	Normal	No
A2	31.2	6	2	Normal	No
A3	46.8	9	2	Normal	No
A4	62.4	12	2	Normal	No
A5	93.6	18	2	Normal	No
A6	124.8	24	2	Normal	No
B1	46.8	9	1	Normal	No
B2	46.8	9	3	Normal	No
B3	46.8	9	1	Normal	Yes
B4	46.8	9	2	Normal	Yes
B5	46.8	9	3	Normal	Yes
C1	46.8	9	1	Selective	No
C2	46.8	9	2	Selective	No
C3	46.8	9	1	Selective	Yes
C4	46.8	9	2	Selective	Yes

(Continued)

TABLE 18.6 (Continued)

Designations and Characteristics for 94 Reference Systems

(f) Sunspace (SS) System Types

Designation	Type	Tilt (°)	Common Wall	End Walls	Nighttime Insulation
A1	Attached	50	Masonry	Opaque	No
A2	Attached	50	Masonry	Opaque	Yes
A3	Attached	50	Masonry	Glazed	No
A4	Attached	50	Masonry	Glazed	Yes
A5	Attached	50	Insulated	Opaque	No
A6	Attached	50	Insulated	Opaque	Yes
A7	Attached	50	Insulated	Glazed	No
A8	Attached	50	Insulated	Glazed	Yes
B1	Attached	90/30	Masonry	Opaque	No
B2	Attached	90/30	Masonry	Opaque	Yes
B3	Attached	90/30	Masonry	Glazed	No
B4	Attached	90/30	Masonry	Glazed	Yes
B5	Attached	90/30	Insulated	Opaque	No
B6	Attached	90/30	Insulated	Opaque	Yes
B7	Attached	90/30	Insulated	Glazed	No
B8	Attached	90/30	Insulated	Glazed	Yes
C1	Semienclosed	90	Masonry	Common	No
C2	Semienclosed	90	Masonry	Common	Yes
C3	Semienclosed	90	Insulated	Common	No
C4	Semienclosed	90	Insulated	Common	Yes
D1	Semienclosed	50	Masonry	Common	No
D2	Semienclosed	50	Masonry	Common	Yes
D3	Semienclosed	50	Insulated	Common	No
D4	Semienclosed	50	Insulated	Common	Yes
E1	Semienclosed	90/30	Masonry	Common	No
E2	Semienclosed	90/30	Masonry	Common	Yes
E3	Semienclosed	90/30	Insulated	Common	No
E4	Semienclosed	90/30	Insulated	Common	Yes

Source: PSDH, *Passive Solar Design Handbook*, Part One: Total Environmental Action, Inc., Part Two: Los Alamos Scientific Laboratory, Part Three: Los Alamos National Laboratory, Van Nostrand Laboratory, Reinhold, New York, 1984.

^a The thermal storage capacity is per unit of projected area, or, equivalently, the quantity ρck . The wall thickness is listed only as an appropriate guide by assuming $\rho c = 30 \text{ Btu/ft}^3/\text{°F}$.

(Albuquerque, Boston, Madison, Medford, Nashville, and Santa Maria), purely due to space restrictions. The LCR method consists of the following steps (PSDH 1984):

1. Determine the following building parameters:
 - a. Building load coefficient, NLC
 - b. Solar projected area, A_p
 - c. Load collector ratio, $\text{LCR} = \text{NLC}/A_p$
2. Find the short designation of the reference system closest to the passive system design (Table 18.6).

TABLE 18.7

LCR Tables for Six Representative Cities (Albuquerque, Boston, Madison, Medford, Nashville, and Santa Maria)

SSF	0.10	0.20	0.30	0.40	0.50	0.60	0.70	0.80	0.90
Santa Maria, California									3053 DD
WW A1	1776	240	119	73	50	35	25	18	12
WW A2	617	259	159	103	74	54	39	28	19
WW A3	523	261	164	114	82	61	45	33	22
WW A4	482	260	169	119	87	65	48	35	24
WW A5	461	263	175	125	92	69	52	38	26
WW A6	447	263	177	128	95	72	54	40	27
WW B1	556	220	128	85	60	43	32	23	15
WW B2	462	256	168	119	88	66	49	36	25
WW B3	542	315	211	151	112	85	64	47	32
WW B4	455	283	197	144	109	83	63	47	32
WW B5	414	263	184	136	103	79	60	45	31
WW C1	569	330	221	159	118	89	67	49	33
WW C2	478	288	197	143	107	81	61	45	31
WW C3	483	318	228	170	130	100	77	57	40
WW C4	426	280	200	149	114	88	68	51	35
TW A1	1515	227	113	70	48	34	24	17	11
TW A2	625	234	134	89	63	46	33	24	16
TW A3	508	231	140	95	68	50	37	27	18
TW A4	431	217	137	95	69	51	38	28	19
TW B1	859	212	112	71	49	35	25	18	12
TW B2	502	209	124	83	59	43	32	23	15
TW B3	438	201	123	84	60	44	33	24	16
TW B4	400	184	112	76	55	40	30	22	14
TW C1	568	188	105	69	48	35	25	18	12
TW C2	435	178	105	70	50	36	27	19	13
TW C3	413	165	97	64	46	33	25	18	12
TW C4	426	146	82	54	38	27	20	14	10
TW D1	403	170	101	67	48	35	25	18	12
TW D2	488	242	152	105	76	57	42	31	21
TW D3	509	271	175	123	90	67	50	36	25
TW D4	464	266	177	127	94	71	53	39	27
TW D5	425	250	169	122	91	69	52	38	26
TW E1	581	309	199	140	102	76	57	42	28
TW E2	512	283	186	132	97	73	55	40	27
TW E3	537	328	225	164	123	94	71	53	36
TW E4	466	287	199	145	109	83	63	47	32
TW F1	713	198	107	68	47	34	25	18	12
TW F2	455	199	120	81	58	42	31	22	15
TW F3	378	190	120	83	60	45	33	24	16
TW F4	311	169	110	77	57	42	32	23	16
TW G1	450	170	98	65	46	33	24	17	12

(Continued)

TABLE 18.7 (Continued)

LCR Tables for Six Representative Cities (Albuquerque, Boston, Madison, Medford, Nashville, and Santa Maria)

SSF	0.10	0.20	0.30	0.40	0.50	0.60	0.70	0.80	0.90
TW G2	331	163	102	70	51	38	28	20	14
TW G3	278	147	94	66	48	36	27	20	13
TW G4	222	120	78	55	40	30	22	16	11
TW H1	295	137	84	57	41	30	22	16	11
TW H2	226	118	75	52	38	28	21	15	10
TW H3	187	99	64	44	33	24	18	13	9
TW H4	143	75	48	33	24	18	14	10	7
TW I1	318	144	88	59	42	31	23	16	11
TW I2	377	203	132	93	68	51	38	28	19
TW I3	404	226	149	106	78	58	44	32	22
TW I4	387	230	156	113	84	64	48	36	24
TW I5	370	226	155	113	85	65	49	36	25
TW J1	483	271	179	127	94	71	53	39	26
TW J2	422	246	165	119	88	67	50	37	25
TW J3	446	283	199	146	111	85	65	48	33
TW J4	400	254	178	132	100	77	58	43	30
DG A1	392	188	117	79	55	38	26	16	7
DG A2	389	190	121	85	61	45	32	22	14
DG A3	443	220	142	102	77	58	44	31	19
DG B1	384	191	122	86	64	48	35	24	13
DG B2	394	196	127	91	69	53	40	29	19
DG B3	445	222	145	105	80	62	49	37	25
DG C1	451	225	146	104	78	61	47	34	21
DG C2	453	226	148	106	80	63	49	37	25
DG C3	509	254	167	121	92	73	58	45	31
SS A1	1171	396	220	142	98	69	49	34	22
SS A2	1028	468	283	190	135	98	71	50	33
SS A3	1174	380	209	133	91	64	45	31	20
SS A4	1077	481	289	193	136	98	71	50	32
SS A5	1896	400	204	127	86	60	42	29	18
SS A6	1030	468	283	190	135	97	71	50	32
SS A7	2199	359	178	109	72	50	35	24	15
SS A8	1089	478	285	190	133	96	69	48	31
SS B1	802	298	170	111	77	55	40	28	18
SS B2	785	366	224	152	108	79	57	41	27
SS B3	770	287	163	106	74	52	37	26	17
SS B4	790	368	224	152	108	78	57	40	26
SS B5	1022	271	144	91	62	44	31	22	14
SS B6	750	356	219	149	106	77	56	40	26
SS B7	937	242	127	80	54	38	27	19	12
SS B8	750	352	215	146	103	75	55	39	25
SS C1	481	232	144	99	71	52	39	28	19
SS C2	482	262	170	120	88	66	49	36	24

(Continued)

TABLE 18.7 (Continued)

LCR Tables for Six Representative Cities (Albuquerque, Boston, Madison, Medford, Nashville, and Santa Maria)

SSF	0.10	0.20	0.30	0.40	0.50	0.60	0.70	0.80	0.90
SS C3	487	185	107	71	50	36	27	19	13
SS C4	473	235	147	102	74	55	41	30	20
SS D1	1107	477	282	188	132	95	68	48	31
SS D2	928	511	332	232	169	125	92	66	43
SS D3	1353	449	248	160	110	78	56	39	25
SS D4	946	500	319	222	160	117	86	61	40
SS E1	838	378	227	153	108	78	56	40	26
SS E2	766	419	272	190	138	102	75	54	36
SS E3	973	322	178	115	79	56	40	28	18
SS E4	780	393	247	170	122	89	65	47	31
Albuquerque, New Mexico									4292 DD
WW A1	1052	130	62	38	25	18	13	9	6
WW A2	354	144	84	56	39	29	21	15	10
WW A3	300	146	90	62	45	33	24	18	12
WW A4	276	146	93	65	47	35	26	19	13
WW A5	264	148	97	69	50	38	28	21	14
WW A6	256	148	99	70	52	39	30	22	15
WW B1	293	111	63	41	28	20	15	11	7
WW B2	270	147	96	67	49	37	28	20	14
WW B3	314	179	119	84	62	47	35	26	18
WW B4	275	169	116	85	64	49	37	28	19
WW B5	252	159	110	81	61	47	36	27	19
WW C1	333	190	126	89	66	50	38	28	19
WW C2	287	171	115	83	62	47	36	27	18
WW C3	293	191	136	101	77	59	46	34	24
WW C4	264	172	122	91	69	54	41	31	22
TW A1	900	124	60	37	25	17	12	9	6
TW A2	361	130	73	48	33	24	18	13	8
TW A3	293	129	77	52	37	27	20	15	10
TW A4	249	123	76	52	38	28	21	15	10
TW B1	502	117	60	38	26	18	13	9	6
TW B2	291	118	68	45	32	23	17	12	8
TW B3	254	114	68	46	33	24	18	13	9
TW B4	233	104	63	42	30	22	16	12	8
TW C1	332	106	58	37	26	19	14	10	6
TW C2	255	101	58	39	27	20	15	11	7
TW C3	243	94	54	36	25	18	13	10	7
TW C4	254	84	46	30	21	15	11	8	5
TW D1	213	86	50	33	23	17	12	9	6
TW D2	287	139	86	59	43	32	24	17	12
TW D3	294	153	97	68	49	37	27	20	14
TW D4	281	158	104	74	55	41	31	23	16
TW D5	260	151	101	73	54	41	31	23	16

(Continued)

TABLE 18.7 (Continued)

LCR Tables for Six Representative Cities (Albuquerque, Boston, Madison, Medford, Nashville, and Santa Maria)

SSF	0.10	0.20	0.30	0.40	0.50	0.60	0.70	0.80	0.90
TW E1	339	177	113	78	57	43	32	23	16
TW E2	308	168	109	77	56	42	32	23	16
TW E3	323	195	133	96	72	55	42	31	21
TW E4	287	175	120	88	66	50	38	28	20
TW F1	409	108	57	36	24	17	13	9	6
TW F2	260	110	65	43	31	22	17	12	8
TW F3	216	106	66	45	33	24	10	13	9
TW F4	178	95	61	42	31	23	17	13	9
TW G1	256	93	53	34	24	17	13	9	6
TW G2	189	91	56	38	27	20	15	11	7
TW G3	159	82	52	36	26	20	15	11	7
TW G4	128	68	43	30	22	16	12	9	6
TW H1	168	76	45	31	22	16	12	9	6
TW H2	130	66	41	29	21	15	11	8	6
TW H3	108	56	35	25	8	13	10	7	5
TW H4	83	42	27	19	13	10	7	5	4
TW I1	166	73	43	29	20	15	11	8	5
TW I2	221	117	75	52	30	28	21	16	11
TW I3	234	128	83	59	43	32	24	10	12
TW I4	234	137	92	66	49	37	28	21	14
TW I5	226	136	93	67	50	38	29	22	15
TW J1	282	156	102	72	53	40	30	22	15
TW J2	254	146	97	69	51	39	29	22	15
TW J3	269	169	118	86	65	50	38	29	20
TW J4	247	155	106	80	60	46	35	26	18
DG A1	211	97	57	36	22	13	5	—	—
DG A2	227	107	67	46	32	23	16	10	5
DG A3	274	131	83	59	44	34	25	18	10
DG B1	210	97	60	42	30	21	13	6	—
DG B2	232	110	69	49	37	28	21	14	8
DG B3	277	134	85	61	47	37	28	21	14
DG C1	253	120	74	53	39	30	22	14	—
DG C2	271	130	82	59	45	35	26	19	12
DG C3	318	155	96	71	54	43	34	26	18
SS A1	591	187	101	64	44	31	22	16	10
SS A2	531	232	137	92	65	47	34	25	16
SS A3	566	170	90	56	38	27	19	13	8
SS A4	537	230	135	89	63	45	33	23	15
SS A5	980	187	92	56	37	26	18	13	8
SS A6	529	231	136	91	64	47	34	24	16
SS A7	1103	158	74	44	29	20	14	10	6
SS A8	540	226	131	87	61	44	32	23	15
SS B1	403	141	78	50	35	25	18	13	8
SS B2	412	186	111	75	53	39	28	20	14

(Continued)

TABLE 18.7 (Continued)

LCR Tables for Six Representative Cities (Albuquerque, Boston, Madison, Medford, Nashville, and Santa Maria)

SSF	0.10	0.20	0.30	0.40	0.50	0.60	0.70	0.80	0.90
SS B3	372	130	71	46	31	22	16	11	7
SS B4	403	181	106	72	51	37	27	20	13
SS B5	518	127	65	40	27	19	13	9	6
SS B6	390	179	106	73	52	38	28	20	13
SS B7	457	108	54	33	22	16	11	8	5
SS B8	379	171	102	69	49	35	26	19	12
SS C1	270	126	77	52	37	27	20	15	10
SS C2	282	150	97	68	49	37	28	20	14
SS C3	276	101	57	37	26	19	14	10	7
SS C4	277	135	83	57	41	31	23	17	11
SS D1	548	225	130	85	59	43	31	22	14
SS D2	474	253	162	113	82	61	45	33	22
SS D3	683	212	113	72	49	35	25	17	11
SS D4	484	248	156	107	77	57	42	30	20
SS E1	410	176	103	68	48	35	25	18	12
SS E2	390	208	133	92	67	50	37	27	18
SS E3	487	151	80	51	35	25	18	12	8
SS E4	400	195	120	82	59	43	32	23	15
Nashville, Tennessee									3696 DD
WW A1	588	60	24	13	8	5	3	2	1
WW A2	192	70	38	23	15	11	7	5	3
WW A3	161	72	42	27	18	13	9	6	4
WW A4	148	72	43	29	20	14	10	7	5
WW A5	141	74	46	31	22	16	11	8	5
WW A6	137	74	47	32	22	16	12	8	5
WW B1	135	41	19	10	6	3	2	—	—
WW B2	152	78	48	33	23	17	12	9	6
WW B3	179	97	61	42	30	22	16	12	8
WW B4	164	97	65	46	34	25	19	14	9
WW B5	153	93	63	45	33	25	19	14	9
WW C1	193	105	67	46	33	24	18	13	8
WW C2	169	97	63	44	32	24	18	13	8
WW C3	181	115	79	58	43	33	25	18	12
WW C4	164	104	72	53	39	30	23	17	11
TW A1	509	59	25	13	8	5	3	2	1
TW A2	199	64	33	20	13	9	6	4	3
TW A3	160	65	36	23	15	11	8	5	3
TW A4	136	62	36	23	16	11	8	6	4
TW B1	282	57	26	15	9	6	4	3	2
TW B2	161	59	32	20	13	9	6	4	3
TW B3	141	58	32	21	14	10	7	5	3
TW B4	131	54	30	19	13	9	7	5	3
TW C1	188	53	27	16	10	7	5	3	2
TW C2	144	52	28	18	12	8	6	4	2

(Continued)

TABLE 18.7 (Continued)

LCR Tables for Six Representative Cities (Albuquerque, Boston, Madison, Medford, Nashville, and Santa Maria)

SSF	0.10	0.20	0.30	0.40	0.50	0.60	0.70	0.80	0.90
TW C3	139	49	27	17	11	8	5	4	2
TW C4	149	45	23	14	9	7	5	3	2
TW D1	99	33	16	9	5	3	2	1	—
TW D2	164	75	44	29	20	14	10	7	5
TW D3	167	82	49	33	23	17	12	8	5
TW D4	168	91	58	40	29	21	15	11	7
TW D5	160	89	58	40	29	22	16	12	8
TW E1	198	98	59	40	28	20	15	10	7
TW E2	182	95	59	40	29	21	15	11	7
TW E3	197	115	76	54	39	29	22	16	11
TW E4	178	105	70	50	37	27	20	15	10
TW F1	221	50	23	13	8	5	4	2	1
TW F2	139	53	29	18	12	8	6	4	2
TW F3	116	52	30	19	13	9	7	5	3
TW F4	96	47	28	19	13	9	7	5	3
TW G1	137	44	22	13	9	6	4	3	2
TW G2	101	44	25	16	11	8	5	4	2
TW G3	86	41	24	16	11	8	6	4	2
TW G4	69	34	21	14	10	7	5	3	2
TW H1	89	36	20	13	8	6	4	3	2
TW H2	69	33	19	12	9	6	4	3	2
TW H3	59	28	17	11	8	5	4	3	2
TW H4	46	22	13	9	6	4	3	2	1
TW I1	74	26	13	7	4	2	1	—	—
TW I2	125	62	38	25	18	13	9	7	4
TW I3	133	69	43	29	20	15	11	8	5
TW I4	139	78	51	35	26	19	14	10	7
TW I5	137	80	53	37	27	20	15	11	7
TW J1	164	86	54	36	26	19	14	10	6
TW J2	150	82	53	36	26	19	14	10	7
TW J3	165	101	68	49	36	27	20	15	10
TW J4	153	93	63	46	34	25	19	14	10
DG A1	98	34	—	—	—	—	—	—	—
DG A2	130	55	31	19	11	6	—	—	—
DG A3	173	78	47	32	23	16	11	7	2
DG B1	100	36	17	—	—	—	—	—	—
DG B2	134	58	33	22	15	10	6	—	—
DG B3	177	81	49	33	24	18	14	10	6
DG C1	131	52	28	17	9	—	—	—	—
DG C2	161	71	42	28	20	14	10	6	—
DG C3	205	94	57	39	29	22	17	12	8
SS A1	351	100	50	29	19	13	9	6	4
SS A2	328	135	76	49	33	24	17	12	8

(Continued)

TABLE 18.7 (Continued)

LCR Tables for Six Representative Cities (Albuquerque, Boston, Madison, Medford, Nashville, and Santa Maria)

SSF	0.10	0.20	0.30	0.40	0.50	0.60	0.70	0.80	0.90
SS A3	330	87	41	24	15	10	6	4	2
SS A4	331	133	74	47	32	22	16	11	7
SS A5	595	98	43	24	15	10	7	4	2
SS A6	324	132	75	48	32	23	16	11	7
SS A7	668	79	32	17	10	6	4	2	1
SS A8	330	129	71	45	30	21	15	10	6
SS B1	236	74	38	23	15	10	7	5	3
SS B2	258	110	63	41	28	20	14	10	6
SS B3	212	65	32	19	12	8	5	3	2
SS B4	251	105	60	39	27	19	13	9	6
SS B5	307	65	30	17	10	7	4	3	2
SS B6	241	104	60	39	27	19	14	10	6
SS B7	264	52	23	12	7	5	3	2	—
SS B8	233	98	56	36	25	17	12	9	5
SS C1	141	60	33	21	14	10	7	5	3
SS C2	161	81	50	33	23	17	12	9	6
SS C3	149	48	25	15	10	7	4	3	2
SS C4	160	73	43	28	19	14	10	7	5
SS D1	317	119	64	39	26	18	13	8	5
SS D2	287	147	90	61	43	31	23	16	10
SS D3	405	113	55	33	21	14	10	6	4
SS D4	295	144	87	58	40	29	21	15	10
SS E1	229	89	48	29	19	13	9	6	4
SS E2	233	118	72	48	34	24	18	12	8
SS E3	283	77	37	22	14	9	6	4	2
SS E4	242	111	65	43	29	21	15	11	7
Medford, Oregon									4930 DD
WW A1	708	64	24	11	—	—	—	—	—
WW A2	212	73	38	22	13	7	3		
WW A3	174	75	41	25	16	9	5	2	—
WW A4	158	74	43	27	17	11	6	3	1
WW A5	149	75	45	29	19	12	7	4	2
WW A6	144	75	46	30	20	13	8	4	2
WW B1	154	43	16	—	—	—	—	—	—
WW B2	162	80	48	31	21	14	9	6	3
WW B3	190	100	62	41	28	19	13	8	5
WW B4	171	99	65	45	32	23	16	11	7
WW B5	160	95	63	45	32	23	17	12	7
WW C1	205	108	67	45	31	21	15	10	6
WW C2	178	99	63	43	30	22	15	10	6
WW C3	189	117	80	57	42	31	23	16	10
WW C4	170	106	72	52	38	28	21	15	9
TW A1	607	63	25	12	5	—	—	—	—

(Continued)

TABLE 18.7 (Continued)

LCR Tables for Six Representative Cities (Albuquerque, Boston, Madison, Medford, Nashville, and Santa Maria)

SSF	0.10	0.20	0.30	0.40	0.50	0.60	0.70	0.80	0.90
TW A2	222	68	33	19	11	6	2	—	—
TW A3	175	67	36	21	13	8	4	2	—
TW A4	147	64	36	22	14	9	5	3	1
TW B1	327	61	27	14	7	3	—	—	—
TW B2	178	62	32	19	12	7	4	2	—
TW B3	154	60	33	20	12	8	4	2	1
TW B4	143	56	31	19	12	8	5	2	1
TW C1	212	56	27	15	9	5	2	—	—
TW C2	159	55	28	17	11	7	4	2	—
TW C3	154	52	27	16	10	6	4	2	1
TW C4	167	48	24	14	9	5	3	2	—
TW D1	112	34	14	—	—	—	—	—	—
TW D2	177	77	44	28	18	12	8	5	3
TW D3	180	85	50	32	21	14	9	6	3
TW D4	177	93	58	39	27	19	13	9	5
TW D5	168	92	58	40	28	20	14	10	6
TW E1	213	101	60	39	26	18	12	8	4
TW E2	194	98	59	39	27	19	13	9	5
TW E3	208	118	77	53	38	27	20	13	8
TW E4	186	108	71	49	36	26	19	13	8
TW F1	256	53	23	12	5	—	—	—	—
TW F2	153	56	29	17	10	5	2	—	—
TW F3	125	54	30	18	11	7	3	1	—
TW F4	102	48	28	18	11	7	4	2	1
TW G1	153	46	22	12	7	—	—	—	—
TW G2	109	46	25	15	9	5	3	1	—
TW G3	92	42	24	15	9	6	3	2	—
TW G4	74	35	20	13	8	5	3	2	—
TW H1	97	38	20	12	7	4	1	—	—
TW H2	75	34	19	12	7	5	3	1	—
TW H3	63	29	17	10	7	4	3	1	—
TW H4	49	23	13	8	5	3	2	1	—
TW I1	83	27	10	—	—	—	—	—	—
TW I2	133	64	38	24	16	11	7	4	2
TW I3	142	71	43	28	19	13	9	5	3
TW I4	146	80	51	35	25	17	12	8	5
TW I5	144	82	53	37	26	19	13	9	6
TW J1	175	89	54	36	24	17	11	7	4
TW J2	158	85	53	36	25	18	12	8	5
TW J3	173	103	69	48	35	26	18	13	8
TW J4	160	96	64	45	33	24	17	12	8
DG A1	110	35	—	—	—	—	—	—	—
DG A2	142	58	32	18	9	—	—	—	—

(Continued)

TABLE 18.7 (Continued)

LCR Tables for Six Representative Cities (Albuquerque, Boston, Madison, Medford, Nashville, and Santa Maria)

SSF	0.10	0.20	0.30	0.40	0.50	0.60	0.70	0.80	0.90
DG A3	187	82	48	32	22	15	9	5	—
DG B1	110	40	15	—	—	—	—	—	—
DG B2	146	61	35	21	13	7	—	—	—
DG B3	193	84	51	34	24	17	12	7	3
DG C1	144	57	29	13	—	—	—	—	—
DG C2	177	75	44	28	19	12	6	—	—
DG C3	224	98	60	41	29	21	14	10	5
SS A1	415	110	51	28	16	9	4	2	—
SS A2	372	146	79	48	31	21	14	8	5
SS A3	397	96	42	21	10	—	—	—	—
SS A4	379	144	76	46	29	19	12	7	4
SS A5	732	111	45	23	12	5	—	—	—
SS A6	368	143	77	47	30	20	13	8	4
SS A7	846	90	33	14	—	—	—	—	—
SS A8	379	140	73	44	27	17	11	6	3
SS B1	274	81	38	21	12	6	3	—	—
SS B2	288	117	65	40	26	18	12	7	4
SS B3	249	71	33	17	8	—	—	—	—
SS B4	282	113	62	38	25	16	11	7	4
SS B5	368	72	30	15	7	—	—	—	—
SS B6	269	111	62	30	25	17	11	7	4
SS B7	323	58	23	10	—	—	—	—	—
SS B8	262	106	57	35	23	15	9	6	3
SS C1	153	62	33	19	11	5	—	—	—
SS C2	172	83	50	32	22	15	10	6	3
SS C3	166	51	24	13	7	3	—	—	—
SS C4	173	76	43	27	18	12	8	5	3
SS D1	367	129	65	37	22	13	7	3	1
SS D2	318	156	92	60	40	27	18	12	7
SS D3	480	124	57	31	18	10	5	2	—
SS D4	328	153	89	57	38	26	17	11	6
SS E1	262	95	48	27	15	7	—	—	—
SS E2	257	124	73	47	31	21	14	9	5
SS E3	334	84	38	20	10	4	—	—	—
SS E4	269	118	67	42	27	18	12	7	4
Boston, Massachusetts									5621 DD
WW A1	368	28	9	—	—	—	—	—	—
WW A2	119	41	20	12	7	5	3	2	—
WW A3	101	43	24	15	10	6	4	3	1
WW A4	93	44	26	16	11	7	5	3	2
WW A5	89	45	27	18	12	8	6	4	2
WWA6	87	46	28	19	13	9	6	4	3
WW B1	59	—	—	—	—	—	—	—	—

(Continued)

TABLE 18.7 (Continued)

LCR Tables for Six Representative Cities (Albuquerque, Boston, Madison, Medford, Nashville, and Santa Maria)

SSF	0.10	0.20	0.30	0.40	0.50	0.60	0.70	0.80	0.90
WW B2	103	52	31	21	15	10	7	5	3
WW B3	123	66	41	28	20	14	10	7	5
WW B4	118	70	46	33	24	18	13	9	6
WW B5	113	69	46	33	25	18	14	10	7
WW C1	135	72	46	31	22	16	12	8	5
WW C2	121	68	44	31	22	16	12	9	6
WW C3	136	86	60	44	33	25	19	14	9
WW C4	124	78	54	40	30	23	17	12	8
TW A1	324	30	11	4	—	—	—	—	—
TW A2	126	37	18	10	6	4	2	1	—
TW A3	102	39	21	13	8	5	3	2	1
TW A4	88	38	22	14	9	6	4	3	2
TW B1	180	32	13	7	4	2	—	—	—
TW B2	104	36	19	11	7	5	3	2	1
TW B3	92	36	19	12	8	5	3	2	1
TW B4	86	34	19	12	8	5	4	2	1
TW C1	122	32	15	9	5	3	2	1	—
TW C2	95	33	17	10	7	4	3	2	1
TW C3	93	31	16	10	6	4	3	2	1
TW C4	102	29	15	9	6	4	3	2	1
TW D1	45	—	—	—	—	—	—	—	—
TW D2	112	49	28	18	12	9	6	4	3
TW D3	113	54	32	21	15	10	7	5	3
TW D4	121	64	41	28	20	15	11	8	5
TW D5	118	66	42	30	21	16	12	8	6
TW E1	138	67	40	27	18	13	9	7	4
TW E2	130	66	41	28	20	14	10	7	5
TW E3	146	84	56	39	29	21	16	11	8
TW E4	133	78	52	37	27	20	15	11	7
TW F1	134	25	10	4	—	—	—	—	—
TW F2	86	30	16	9	5	3	2	1	—
TW F3	72	31	17	11	7	4	3	2	1
TW F4	61	29	17	11	7	5	3	2	1
TW G1	83	24	11	6	3	2	—	—	—
TW G2	63	26	14	9	5	4	2	1	—
TW G3	54	25	14	9	6	4	3	2	1
TW G4	45	21	12	8	5	4	3	2	1
TW H1	54	21	11	6	4	2	1	—	—
TW H2	44	20	11	7	5	3	2	1	—
TW H3	38	17	10	6	4	3	2	1	—
TW H4	30	14	8	5	3	2	2	1	—
TW I1	30	—	—	—	—	—	—	—	—
TW I2	84	41	24	16	11	8	6	4	2

(Continued)

TABLE 18.7 (Continued)

LCR Tables for Six Representative Cities (Albuquerque, Boston, Madison, Medford, Nashville, and Santa Maria)

SSF	0.10	0.20	0.30	0.40	0.50	0.60	0.70	0.80	0.90
TW I3	91	46	28	19	13	9	7	5	3
TW I4	100	56	36	25	18	13	10	7	5
TW I5	101	58	38	27	20	15	11	8	5
TW J1	114	59	37	25	17	12	9	6	4
TW J2	107	58	37	25	18	13	10	7	4
TW J3	123	75	51	36	27	20	15	11	7
TW J4	115	70	47	34	25	19	14	10	7
DG A1	43	—	—	—	—	—	—	—	—
DG A2	85	34	18	9	—	—	—	—	—
DG A3	125	56	33	22	16	11	7	4	—
DG B1	44	—	—	—	—	—	—	—	—
DG B2	87	36	20	12	7	—	—	—	—
DG B3	129	58	35	24	17	13	9	6	3
DG C1	71	23	—	—	—	—	—	—	—
DG C2	109	47	27	17	12	8	4	—	—
DG C3	151	68	41	28	21	16	12	8	5
SS A1	230	61	29	16	10	6	4	2	1
SS A2	231	93	52	33	22	15	11	7	5
SS A3	205	48	20	10	4	—	—	—	—
SS A4	229	90	49	31	20	14	9	6	4
SS A5	389	58	23	11	6	3	—	—	—
SS A6	226	91	50	32	21	15	10	7	4
SS A7	420	40	12	—	—	—	—	—	—
SS A8	226	86	46	28	19	12	8	6	3
SS B1	151	44	21	12	7	4	2	1	—
SS B2	183	77	43	28	19	13	9	6	4
SS B3	129	36	16	8	3	—	—	—	—
SS B4	176	73	41	26	17	12	8	6	4
SS B5	193	36	15	7	3	—	—	—	—
SS B6	169	72	41	26	18	12	9	6	4
SS B7	157	25	7	—	—	—	—	—	—
SS B8	160	66	37	23	16	11	7	5	3
SS C1	84	33	17	10	6	4	2	1	—
SS C2	110	54	33	22	15	11	8	5	3
SS C3	91	26	12	7	4	2	—	—	—
SS C4	109	48	28	18	12	9	6	4	3
SS D1	206	73	38	22	14	9	5	3	2
SS D2	203	103	63	42	29	21	15	10	6
SS D3	264	69	32	18	10	6	4	2	1
SS D4	208	100	60	39	27	19	14	9	6
SS E1	140	51	25	14	8	4	2	—	—
SS E2	161	80	48	32	22	15	11	7	5
SS E3	177	44	19	10	5	2	—	—	—
SS E4	166	75	43	28	19	13	9	6	4

(Continued)

TABLE 18.7 (Continued)

LCR Tables for Six Representative Cities (Albuquerque, Boston, Madison, Medford, Nashville, and Santa Maria)

SSF	0.10	0.20	0.30	0.40	0.50	0.60	0.70	0.80	0.90
Madison, Wisconsin									7730 DD
WW A1	278	—	—	—	—	—	—	—	—
WW A2	91	27	12	—	—	—	—	—	—
WW A3	77	30	15	8	3	—	—	—	—
WW A4	72	32	17	10	5	—	—	—	—
WW A5	69	33	19	11	7	4	—	—	—
WW A6	67	34	19	12	7	4	2	—	—
WW B1	—	—	—	—	—	—	—	—	—
WW B2	84	41	24	15	10	7	5	3	2
WW B3	102	53	32	21	15	10	7	5	3
WW B4	101	59	39	27	19	14	10	7	5
WW B5	98	59	39	28	20	15	11	8	5
WW C1	113	59	37	25	17	12	8	6	3
WW C2	103	57	37	25	18	13	9	6	4
WW C3	119	75	51	37	28	21	15	11	7
WW C4	109	68	47	34	25	19	14	10	7
TW A1	249	16	—	—	—	—	—	—	—
TW A2	97	26	11	4	—	—	—	—	—
TW A3	79	28	13	7	3	—	—	—	—
TW A4	69	28	15	9	5	3	—	—	—
TW B1	139	20	5	—	—	—	—	—	—
TW B2	81	26	12	6	3	—	—	—	—
TW B3	72	27	13	7	4	2	—	—	—
TW B4	69	26	13	8	5	3	1	—	—
TW C1	96	23	10	4	—	—	—	—	—
TW C2	76	25	12	7	4	2	—	—	—
TW C3	75	24	12	7	4	2	1	—	—
TW C4	84	23	11	6	4	2	1	—	—
TW D1	—	—	—	—	—	—	—	—	—
TW D2	91	39	22	13	9	6	4	2	1
TW D3	93	43	25	16	10	7	5	3	1
TW D4	103	54	34	23	16	12	8	6	4
TW D5	102	56	36	25	18	13	10	7	4
TW E1	115	54	32	21	14	10	7	4	3
TW E2	110	55	34	22	16	11	8	5	3
TW E3	126	72	47	33	24	18	13	9	6
TW E4	116	68	45	32	23	17	13	9	6
TW F1	99	13	—	—	—	—	—	—	—
TW F2	65	20	8	—	—	—	—	—	—
TW F3	55	22	11	5	—	—	—	—	—
TW F4	47	21	11	7	4	2	—	—	—
TW G1	61	14	—	—	—	—	—	—	—

(Continued)

TABLE 18.7 (Continued)

LCR Tables for Six Representative Cities (Albuquerque, Boston, Madison, Medford, Nashville, and Santa Maria)

SSF	0.10	0.20	0.30	0.40	0.50	0.60	0.70	0.80	0.90
TW G2	47	18	8	4	—	—	—	—	—
TW G3	42	18	9	5	3	—	—	—	—
TW G4	35	16	9	5	3	2	—	—	—
TW H1	41	13	6	—	—	—	—	—	—
TW H2	34	14	7	4	2	—	—	—	—
TW H3	29	13	7	4	2	1	—	—	—
TW H4	24	10	6	3	2	1	—	—	—
TW I1	—	—	—	—	—	—	—	—	—
TW I2	68	32	18	12	8	5	3	2	1
TW I3	75	37	22	14	10	7	4	3	2
TW I4	85	47	30	21	15	11	8	5	3
TW I5	87	50	33	23	16	12	9	6	4
TW J1	95	48	29	19	13	9	6	4	3
TW J2	91	48	30	21	14	10	7	5	3
TW J3	106	65	43	31	23	17	12	9	6
TW J4	100	61	41	29	21	16	12	9	6
DG A1	—	—	—	—	—	—	—	—	—
DG A2	68	25	11	—	—	—	—	—	—
DG A3	109	47	28	18	12	8	5	—	—
DG B1	—	—	—	—	—	—	—	—	—
DG B2	70	27	14	6	—	—	—	—	—
DG B3	114	50	30	20	14	10	7	4	—
DG C1	47	—	—	—	—	—	—	—	—
DG C2	91	37	21	13	7	—	—	—	—
DG C3	133	59	35	24	17	13	9	6	3
SS A1	192	47	20	9	3	—	—	—	—
SS A2	200	78	42	26	17	12	8	5	3
SS A3	166	32	—	—	—	—	—	—	—
SS A4	197	74	39	23	15	10	6	4	2
SS A5	329	42	13	—	—	—	—	—	—
SS A6	195	75	40	25	16	11	7	5	3
SS A7	349	22	—	—	—	—	—	—	—
SS A8	192	69	36	21	13	8	5	3	2
SS B1	122	32	13	5	—	—	—	—	—
SS B2	158	64	36	22	15	10	7	5	3
SS B3	100	22	—	—	—	—	—	—	—
SS B4	150	60	33	29	13	9	6	4	2
SS B5	156	24	—	—	—	—	—	—	—
SS B6	145	59	33	20	13	9	6	4	2
SS B7	122	—	—	—	—	—	1—	—	—
SS B8	136	54	29	18	11	7	5	3	2
SS C1	61	20	7	—	—	—	—	—	—
SS C2	90	43	25	16	11	7	5	3	2

(Continued)

TABLE 18.7 (Continued)

LCR Tables for Six Representative Cities (Albuquerque, Boston, Madison, Medford, Nashville, and Santa Maria)

SSF	0.10	0.20	0.30	0.40	0.50	0.60	0.70	0.80	0.90
SS C3	67	16	—	—	—	—	—	—	—
SS C4	90	38	22	13	9	6	4	2	1
SS D1	169	56	26	13	6	—	—	—	—
SS D2	175	86	51	34	23	16	11	7	5
SS D3	221	52	21	10	—	—	—	—	—
SS D4	179	84	49	32	21	15	10	7	4
SS E1	108	34	12	—	—	—	—	—	—
SS E2	135	65	38	24	16	11	7	5	3
SS E3	141	29	8	—	—	—	—	—	—
SS E4	140	61	34	21	14	9	6	4	2

Source: PSDH, *Passive Solar Design Handbook*, Los Alamos National Laboratory, Van Nostrand Reinhold, New York, 1984.

3. Enter the LCR tables (Table 18.7).
 - a. Find the city
 - b. Find the reference system listing
 - c. Determine annual SSF by interpolation using the LCR value from above
 - d. Note the annual heating degree-days (number of degree-days)
4. Calculate the annual auxiliary heat required:

$$\text{Auxiliary heat required} = (1 - \text{SSF}) \times \text{NLC} \times (\text{number of degree-days}).$$

If more than one reference solar system is being used, then find the *aperture-area-weighted* SSF for the combination. Determine each individual reference system SSF using the total aperture area LCR, then take the *area-weighted* average of the individual SSFs.

The LCR method allows no variation from the 94 reference passive designs. To treat off-reference designs, sensitivity curves have been produced that illustrate the effect on SSF of varying one or two design variables. These curves were produced for the six *representative* cities, chosen for their wide geographical and climatological ranges. Several of these SSF *sensitivity curves* are presented in Figure 18.39 for storage wall (Figure 18.39a through c) and sunspace (Figure 18.39d) design variations.

Example 18.12

The previously used 2100 ft.² building with NLC = 11,800 Btu/FDD is preliminarily designed to be located in Medford, Oregon, with 180 ft.² of 12 in. thick vented Trombe wall and 130 ft.² of direct gain, both systems with double glazing, nighttime insulation, and 30 Btu/ft.² thermal storage capacity. Determine the annual auxiliary energy needed by this design.

Solution

Step 1 yields:

$$\text{NLC} = 11,800 \text{ Btu/FDD.}$$

$$A_p = 180 + 130 = 320 \text{ ft.}^2$$

$$\text{LCR} = 11,800/320 = 36.8 \text{ Btu/FDD ft.}^2$$

Step 2 yields: From Table 18.6, the short designations for the appropriate systems are

TWD4 (Trombe wall)

DGA3 (Direct gain)

Step 3 yields: From Table 18.7 for Medford, Oregon, with LCR = 36.8,

TWD4: SSF(TW) = 0.42.

DGA3: SSF(DG) = 0.37.

Determine the *weighted area average* SSF:

$$\text{SSF} = \frac{180(0.42) + 130(0.37)}{320} = 0.39.$$

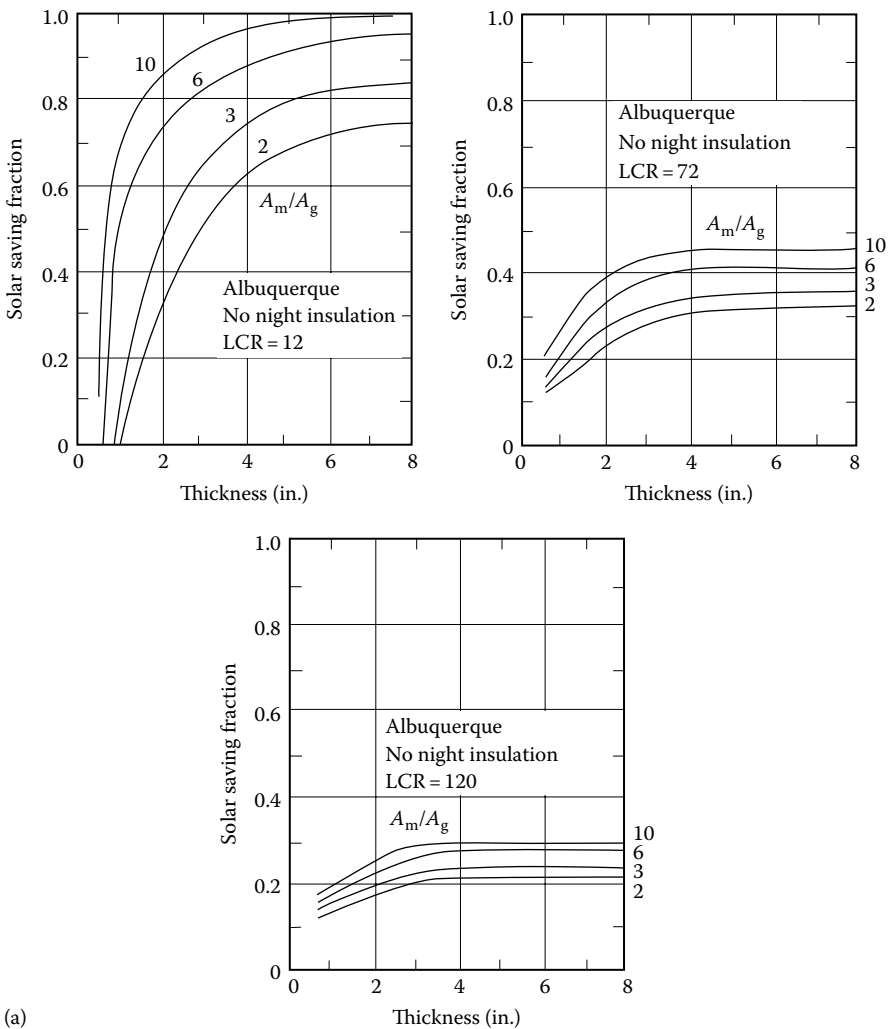


FIGURE 18.39

(a) Storage wall: mass thickness. Sensitivity of SSF to off-reference conditions.

(Continued)

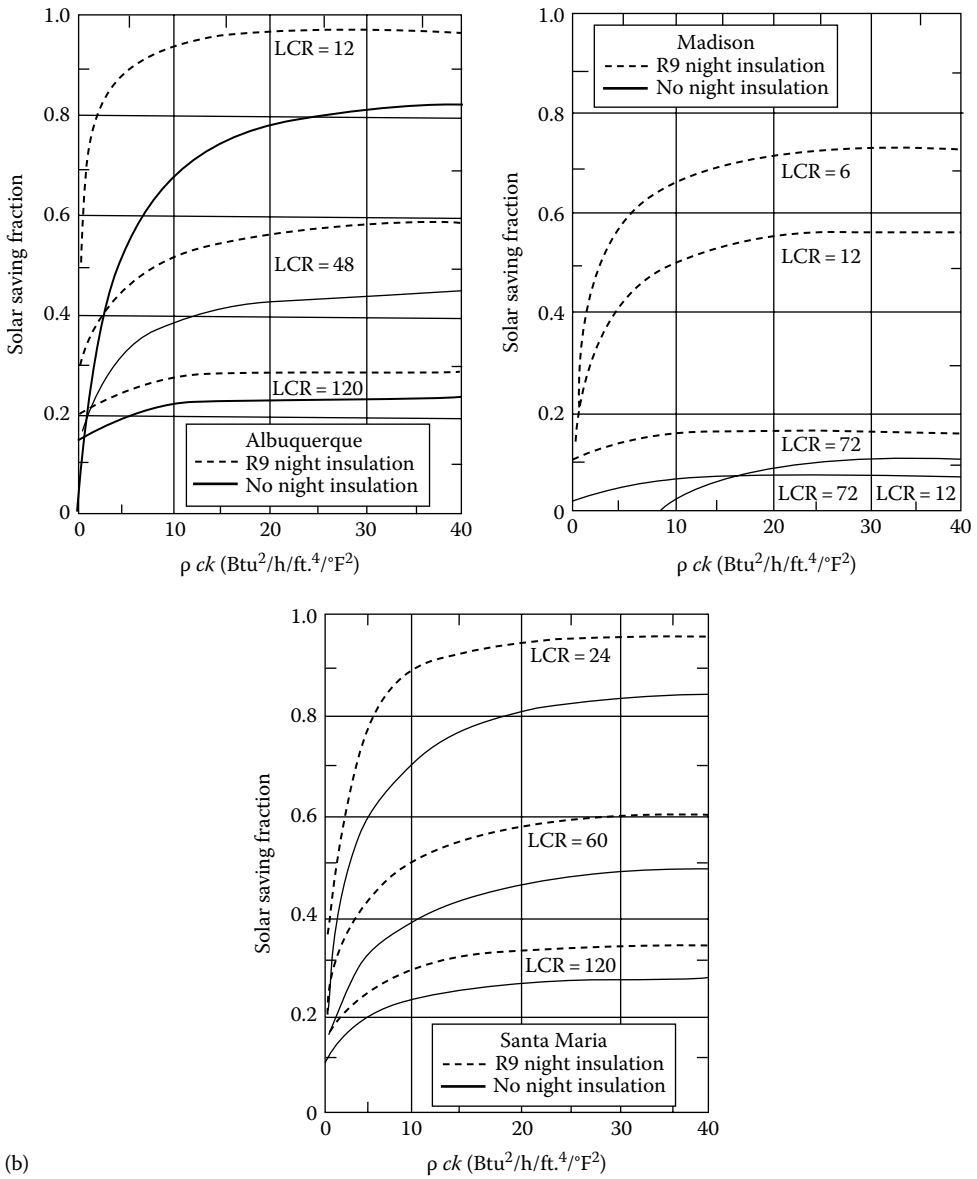


FIGURE 18.39 (Continued)
 (b) Storage wall: pck product.

(Continued)

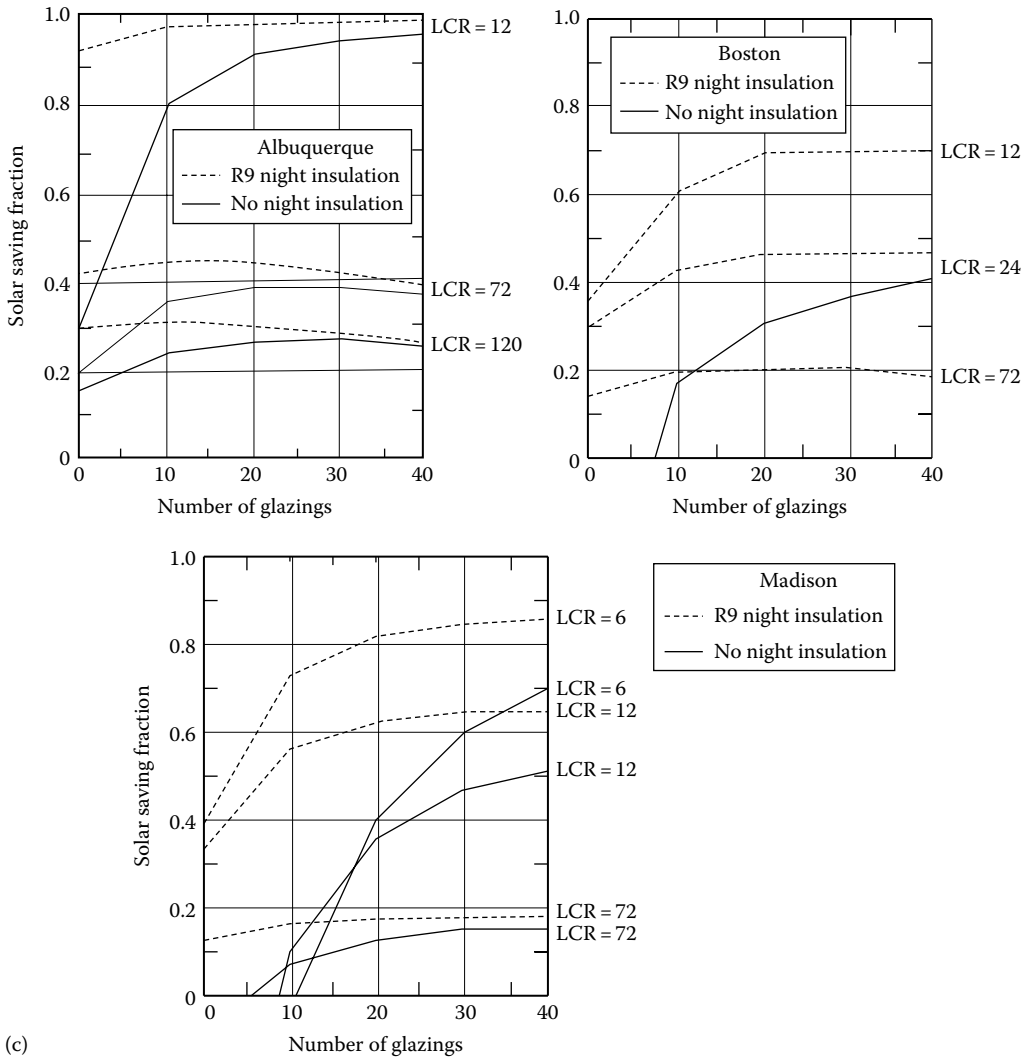


FIGURE 18.39 (Continued)

(c) Storage wall: number of glazings.

(Continued)

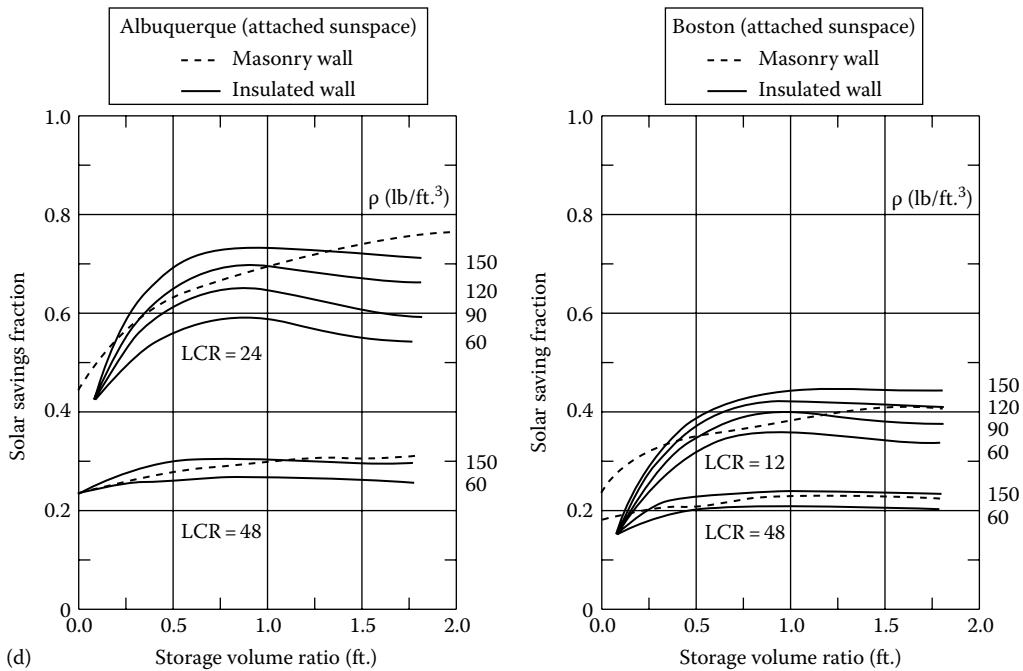


FIGURE 18.39 (Continued)

(d) Sunspace: storage-volume-to-projected-area ratio. (From PSDH, *Passive Solar Design Handbook*, Volume One: Passive Solar Design Concepts, DOE/CS-O127/1, March 1980. Prepared by Total Environmental Action, Inc. (B. Anderson, C. Michal, P. Temple, and D. Lewis); Volume Two: *Passive Solar Design Analysis*, DOE/CS-O127/2, January 1980, Prepared by Los Alamos Scientific Laboratory (J. D. Balcomb, D. Barley, R McFarland, J. Perry, W. Wray and S. Noll), U.S. Department of Energy, Washington, DC, 1980.)

Step 4 yields: Using Equation 18.73 and reading 4930 FDD from Table 18.7,

$$Q_{aux} = (1 - 0.39) \times 11,800 \text{ Btu} \times 4,930 \text{ FDD} = 35.5 \times 10^6 \text{ Btu annually.}$$

Using the reference system characteristics yields, the thermal storage size: Trombe wall (ρck = 30, concrete properties from Table 18.6c):

$$\begin{aligned} m(\text{TW}) &= \text{density} \times \text{area} \times \text{thickness} \\ &= 150 \text{ lbm/ft.}^3 \times 180 \text{ ft.}^2 \times 1 \text{ ft.} \\ &= 27,000 \text{ lbm.} \end{aligned}$$

Direct gain (ρck = 30, concrete properties), using mass-area-to-glazing-area ratio of 6:

$$\text{Mass area} = 6 \times 130 = 780 \text{ ft.}^2 \text{ of 2 in. thick concrete}$$

$$\begin{aligned} m(\text{DG}) &= 150 \text{ lbm/ft.}^3 \times 780 \text{ ft.}^2 \times 1/6 \text{ ft.} \\ &= 19,500 \text{ lbm.} \end{aligned}$$

Using the LCR method allows a basic design of passive system types for the 94 reference systems and the resulting annual performance. A bit more design variation can be obtained by using the sensitivity curves of Figure 18.39 to modify the SSF of a particular reference system. For instance, a direct gain system SSF of 0.37 would increase by approximately 0.03 if the mass–glazing-area ratio (assumed 6) were increased to 10 and would decrease by about 0.04 if the mass–glazing-area ratio were decreased to 3. This information provides a designer with quantitative information for making trade-offs.

18.2.3.10 Third Level: SLR Method

The SLR method calculates monthly performance, and the terms and values used are monthly based. The method allows the use of specific location weather data and the 94 reference design passive systems (Table 18.6). In addition, the sensitivity curves (Figure 18.39) can again be used to define performance outside the reference design systems. The result of the SLR method is the determination of the monthly heating auxiliary energy required that is then summed to give the annual requirement for auxiliary heating energy. Generally, the SLR method gives annual values within $\pm 3\%$ of detailed simulation results, but the monthly values may vary more (PSDH 1984; Duffie and Beckman 1991). Thus, the monthly SLR method is more *accurate* than the rule-of-thumb methods, plus providing the designer with system performance on a month-by-month basis.

The SLR method uses equations and correlation parameters for each of the 94 reference systems combined with the insolation absorbed by the system, the monthly degree-days, and the system's LCR to determine the monthly SSF. These correlation parameters are listed in Table 18.8 as A , B , C , D , R , G , H , and LCRs for each reference system (PSDH 1984). The correlation equations are

$$\text{SSF} = 1 - K(1 - F), \quad (18.76)$$

where

$$K = 1 + G/\text{LCR}, \quad (18.77)$$

$$F = \begin{cases} AX, & \text{when } X < R \\ B - C \exp(-DX), & \text{when } X > R \end{cases} \quad (18.78)$$

$$X = \frac{S/\text{DD} - (\text{LCRs})H}{(\text{LCR})K}, \quad (18.79)$$

and X is called the *generalized solar load ratio*. The term S is the monthly insolation absorbed by the system per unit of solar projected area. Monthly average daily insolation data on a vertical south-facing surface can be found and/or calculated using various sources (PSDH 1984; McQuiston and Parker 1994), and the S term can be determined by multiplying by a transmission and an absorption factor and the number of days in the month. Absorption factors for all systems are close to 0.96 (PSDH 1984), whereas the transmission is approximately 0.9 for single glazing, 0.8 for double glazing, and 0.7 for triple glazing.

TABLE 18.8

SLR Correlation Parameters for the 94 Reference Systems

Type	A	B	C	D	R	G	H	LCRs	STDV
WW A1	0.0000	1.0000	0.9172	0.4841	-9.0000	0.00	1.17	13.0	0.053
WW A2	0.0000	1.0000	0.9833	0.7603	-9.0000	0.00	0.92	13.0	0.046
WW A3	0.0000	1.0000	1.0171	0.8852	-9.0000	0.00	0.85	13.0	0.040
WW A4	0.0000	1.0000	1.0395	0.9569	-9.0000	0.00	0.81	13.0	0.037
WW A5	0.0000	1.0000	1.0604	1.0387	-9.0000	0.00	0.78	13.0	0.034
WW A6	0.0000	1.0000	1.0735	1.0827	-9.0000	0.00	0.76	13.0	0.033
WW B1	0.0000	1.0000	0.9754	0.5518	-9.0000	0.00	0.92	22.0	0.051
WW B2	0.0000	1.0000	1.0487	1.0851	-9.0000	0.00	0.78	9.2	0.036
WW B3	0.0000	1.0000	1.0673	1.0087	-9.0000	0.00	0.95	8.9	0.038
WW B4	0.0000	1.0000	1.1028	1.1811	-9.0000	0.00	0.74	5.8	0.034
WW B5	0.0000	1.0000	1.1146	1.2771	-9.0000	0.00	0.56	4.5	0.032
WW C1	0.0000	1.0000	1.0667	1.0437	-9.0000	0.00	0.62	12.0	0.038
WW C2	0.0000	1.0000	1.0846	1.1482	-9.0000	0.00	0.59	8.7	0.035
WW C3	0.0000	1.0000	1.1419	1.1756	-9.0000	0.00	0.28	5.5	0.033
WW C4	0.0000	1.0000	1.1401	1.2378	-9.0000	0.00	0.23	4.3	0.032
TW A1	0.0000	1.0000	0.9194	0.4601	-9.0000	0.00	1.11	13.0	0.048
TW A2	0.0000	1.0000	0.9680	0.6318	-9.0000	0.00	0.92	13.0	0.043
TW A3	0.0000	1.0000	0.9964	0.7123	-9.0000	0.00	0.85	13.0	0.038
TW A4	0.0000	1.0000	1.0190	0.7332	-9.0000	0.00	0.79	13.0	0.032
TW B1	0.0000	1.0000	0.9364	0.4777	-9.0000	0.00	1.01	13.0	0.045
TW B2	0.0000	1.0000	0.9821	0.6020	-9.0000	0.00	0.85	13.0	0.038
TW B3	0.0000	1.0000	0.9980	0.6191	-9.0000	0.00	0.80	13.0	0.033
TW B4	0.0000	1.0000	0.9981	0.5615	-9.0000	0.00	0.76	13.0	0.028
TW C1	0.0000	1.0000	0.9558	0.4709	-9.0000	0.00	0.89	13.0	0.039
TW C2	0.0000	1.0000	0.9788	0.4964	-9.0000	0.00	0.79	13.0	0.033
TW C3	0.0000	1.0000	0.9760	0.4519	-9.0000	0.00	0.76	13.0	0.029
TW C4	0.0000	1.0000	0.9588	0.3612	-9.0000	0.00	0.73	13.0	0.026
TW D1	0.0000	1.0000	0.9842	0.4418	-9.0000	0.00	0.89	22.0	0.040
TW D2	0.0000	1.0000	1.0150	0.8994	-9.0000	0.00	0.80	9.2	0.036
TW D3	0.0000	1.0000	1.0346	0.7810	-9.0000	0.00	1.08	8.9	0.036
TW D4	0.0000	1.0000	1.0606	0.9770	-9.0000	0.00	0.85	5.8	0.035
TW D5	0.0000	1.0000	1.0721	1.0718	-9.0000	0.00	0.61	4.5	0.033
TW E1	0.0000	1.0000	1.0345	0.8753	-9.0000	0.00	0.68	12.0	0.037
TW E2	0.0000	1.0000	1.0476	1.0050	-9.0000	0.00	0.66	8.7	0.035
TW E3	0.0000	1.0000	1.0919	1.0739	-9.0000	0.00	0.61	5.5	0.034
TW E4	0.0000	1.0000	1.0971	1.1429	-9.0000	0.00	0.47	4.3	0.033
TW F1	0.0000	1.0000	0.9430	0.4744	-9.0000	0.00	1.09	13.0	0.047
TW F2	0.0000	1.0000	0.9900	0.6053	-9.0000	0.00	0.93	13.0	0.041
TW F3	0.0000	1.0000	1.0189	0.6502	-9.0000	0.00	0.86	13.0	0.036
TW F4	0.0000	1.0000	1.0419	0.6258	-9.0000	0.00	0.80	13.0	0.032
TW G1	0.0000	1.0000	0.9693	0.4714	-9.0000	0.00	1.01	13.0	0.042
TW G2	0.0000	1.0000	1.0133	0.5462	-9.0000	0.00	0.88	13.0	0.035
TW G3	0.0000	1.0000	1.0325	0.5269	-9.0000	0.00	0.82	13.0	0.031
TW G4	0.0000	1.0000	1.0401	0.4400	-9.0000	0.00	0.77	13.0	0.030

(Continued)

TABLE 18.8 (Continued)

SLR Correlation Parameters for the 94 Reference Systems

Type	A	B	C	D	R	G	H	LCRs	STDV
TW H1	0.0000	1.0000	1.0002	0.4356	-9.0000	0.00	0.93	13.0	0.034
TW H2	0.0000	1.0000	1.0280	0.4151	-9.0000	0.00	0.83	13.0	0.030
TW H3	0.0000	1.0000	1.0327	0.3522	-9.0000	0.00	0.78	13.0	0.029
TW H4	0.0000	1.0000	1.0287	0.2600	-9.0000	0.00	0.74	13.0	0.024
TW I1	0.0000	1.0000	0.9974	0.4036	-9.0000	0.00	0.91	22.0	0.038
TW I2	0.0000	1.0000	1.0386	0.8313	-9.0000	0.00	0.80	9.2	0.034
TW I3	0.0000	1.0000	1.0514	0.6886	-9.0000	0.00	1.01	8.9	0.034
TW I4	0.0000	1.0000	1.0781	0.8952	-9.0000	0.00	0.82	5.8	0.032
TW I5	0.0000	1.0000	1.0902	1.0284	-9.0000	0.00	0.65	4.5	0.032
TW J1	0.0000	1.0000	1.0537	0.8227	-9.0000	0.00	0.65	12.0	0.037
TW J2	0.0000	1.0000	1.0677	0.9312	-9.0000	0.00	0.62	8.7	0.035
TW J3	0.0000	1.0000	1.1153	0.9831	-9.0000	0.00	0.44	5.5	0.034
TW J4	0.0000	1.0000	1.1154	1.0607	-9.0000	0.00	0.38	4.3	0.033
DG A1	0.5650	1.0090	1.0440	0.7175	0.3931	9.36	0.00	0.0	0.046
DG A2	0.5906	1.0060	1.0650	0.8099	0.4681	5.28	0.00	0.0	0.039
DG A3	0.5442	0.9715	1.1300	0.9273	0.7068	2.64	0.00	0.0	0.036
DG B1	0.5739	0.9948	1.2510	1.0610	0.7905	9.60	0.00	0.0	0.042
DG B2	0.6180	1.0000	1.2760	1.1560	0.7528	5.52	0.00	0.0	0.035
DG B3	0.5601	0.9839	1.3520	1.1510	0.8879	2.38	0.00	0.0	0.032
DG C1	0.6344	0.9887	1.5270	1.4380	0.8632	9.60	0.00	0.0	0.039
DG C2	0.6763	0.9994	1.4000	1.3940	0.7604	5.28	0.00	0.0	0.033
DG C3	0.6182	0.9859	1.5660	1.4370	0.8990	2.40	0.00	0.0	0.031
SS A1	0.0000	1.0000	0.9587	0.4770	-9.0000	0.00	0.83	18.6	0.027
SS A2	0.0000	1.0000	0.9982	0.6614	-9.0000	0.00	0.77	10.4	0.026
SS A3	0.0000	1.0000	0.9552	0.4230	-9.0000	0.00	0.83	23.6	0.030
SS A4	0.0000	1.0000	0.9956	0.6277	-9.0000	0.00	0.80	12.4	0.026
SS A5	0.0000	1.0000	0.9300	0.4041	-9.0000	0.00	0.96	18.6	0.031
SS A6	0.0000	1.0000	0.9981	0.6660	-9.0000	0.00	0.86	10.4	0.028
SS A7	0.0000	1.0000	0.9219	0.3225	-9.0000	0.00	0.96	23.6	0.035
SS A8	0.0000	1.0000	0.9922	0.6173	-9.0000	0.00	0.90	12.4	0.028
SS B1	0.0000	1.0000	0.9683	0.4954	-9.0000	0.00	0.84	16.3	0.028
SS B2	0.0000	1.0000	1.0029	0.6802	-9.0000	0.00	0.74	8.5	0.026
SS B3	0.0000	1.0000	0.9689	0.4685	-9.0000	0.00	0.82	19.3	0.029
SS B4	0.0000	1.0000	1.0029	0.6641	-9.0000	0.00	0.76	9.7	0.026
SS B5	0.0000	1.0000	0.9408	0.3866	-9.0000	0.00	0.97	16.3	0.030
SS B6	0.0000	1.0000	1.0068	0.6778	-9.0000	0.00	0.84	8.5	0.028
SS B7	0.0000	1.0000	0.9395	0.3363	-9.0000	0.00	0.95	19.3	0.032
SS B8	0.0000	1.0000	1.0047	0.6469	-9.0000	0.00	0.87	9.7	0.027
SS C1	0.0000	1.0000	1.0087	0.7683	-9.0000	0.00	0.76	16.3	0.025
SS C2	0.0000	1.0000	1.0412	0.9281	-9.0000	0.00	0.78	10.0	0.027
SS C3	0.0000	1.0000	0.9699	0.5106	-9.0000	0.00	0.79	16.3	0.024
SS C4	0.0000	1.0000	1.0152	0.7523	-9.0000	0.00	0.81	10.0	0.025
SS D1	0.0000	1.0000	0.9889	0.6643	-9.0000	0.00	0.84	17.8	0.028
SS D2	0.0000	1.0000	1.0493	0.8753	-9.0000	0.00	0.70	9.9	0.028

(Continued)

TABLE 18.8 (Continued)

SLR Correlation Parameters for the 94 Reference Systems

Type	A	B	C	D	R	G	H	LCRs	STDV
SS D3	0.0000	1.0000	0.9570	0.5285	-9.0000	0.00	0.90	17.8	0.029
SS D4	0.0000	1.0000	1.0356	0.8142	-9.0000	0.00	0.73	9.9	0.028
SS E1	0.0000	1.0000	0.9968	0.7004	-9.0000	0.00	0.77	19.6	0.027
SS E2	0.0000	1.0000	1.0468	0.9054	-9.0000	0.00	0.76	10.8	0.027
SS E3	0.0000	1.0000	0.9565	0.4827	-9.0000	0.00	0.81	19.6	0.028
SS E4	0.0000	1.0000	1.0214	0.7694	-9.0000	0.00	0.79	10.8	0.027

Source: PSDH, *Passive Solar Design Handbook*, Los Alamos National Laboratory, Van Nostrand Reinhold, New York, 1984.

Example 18.13

For a vented, 180 ft.², double-glazed with night insulation, 12 in. thick Trombe wall system (TWD4) in an NLC = 11,800 Btu/FDD house in Medford, Oregon, determine the auxiliary energy required in January.

Solution

Weather data for Medford, Oregon (PSDH 1984), yields for January ($N = 31$, days): daily vertical surface insolation = 565 Btu/ft.² and 880 FDD, so $S = (31)(565)(0.8)(0.96) = 13,452$ Btu/ft.² month.

$$\text{LCR} = \frac{\text{NLC}}{A_p} = \frac{11,800}{180} = 65.6 \text{ Btu/FDD ft.}^2$$

From Table 18.8 at TWD4: $A = 0$, $B = 1$, $C = 1.0606$, $D = 0.977$, $R = -9$, $G = 0$, $H = 0.85$, LCRs = 5.8 Btu/FDD ft.²

Substituting into Equation 18.77 gives

$$K = 1 + 0/65.6 = 1.$$

Equation 18.79 gives

$$X = \frac{(13,452/880) - (5.8 \times 0.85)}{65.6 \times 1} = 0.16.$$

Equation 18.78 gives

$$F = 1 - 1.0606e^{-0.977 \times 0.16} = 0.09,$$

and Equation 18.76 gives

$$\text{SSF} = 1 - 1(1 - 0.09) = 0.09.$$

The January auxiliary energy required can be calculated using Equation 18.73:

$$\begin{aligned} Q_{\text{aux}}(\text{Jan}) &= (1 - \text{SSF}) \times \text{NLC} \times (\text{number of degree-days}) \\ &= (1 - 0.09) \times 11,800 \times 880 \\ &= 9,450,000 \text{ Btu.} \end{aligned}$$

As mentioned, the use of sensitivity curves (PSDH 1984) as in Figure 18.39 will allow SSF to be determined for many off-reference system design conditions involving storage mass, number of glazings, and other more esoteric parameters. Also, the use of multiple

passive system types within one building would be approached by calculating the SSF for each type system individually using a *combined area* LCR, and then a weighted-area (aperture) average SSF would be determined for the building.

18.2.4 Passive Space Cooling Design Fundamentals

Passive cooling systems are designed to use natural means to transfer heat from buildings, including convection/ventilation, evaporation, radiation, and conduction. However, the most important element in both passive and conventional cooling design is to prevent heat from entering the building in the first place. Cooling conservation techniques involve building surface colors, insulation, special window glazings, overhangs and orientation, and numerous other architectural/engineering features.

18.2.4.1 Solar Control

Controlling the solar energy input to reduce the cooling load is usually considered a passive (versus conservation) design concern because solar input may be needed for other purposes, such as daylighting throughout the year and/or heating during the winter. Basic architectural solar control is normally *designed in* via the shading of the solar windows, where direct radiation is desired for winter heating and needs to be excluded during the cooling season.

The shading control of the windows can be of various types and *controllability*, ranging from drapes and blinds, use of deciduous trees, to the commonly used overhangs and vertical louvers. A rule-of-thumb design for determining proper south-facing window overhang for both winter heating and summer shading is presented in Table 18.9. Technical details on calculating shading from various devices and orientations are found in Olgyay and Olgyay (1977) and ASHRAE (1993).

18.2.4.2 Natural Convection/Ventilation

Air movement provides cooling comfort through convection and evaporation from human skin. ASHRAE (1993) places the comfort limit at 79°F for an air velocity of 50 ft./min (fpm), 82°F for 160 fpm, and 85°F for 200 fpm. To determine whether or not comfort conditions can be obtained, a designer must calculate the volumetric flow rate, Q , which is passing through the occupied space. Using the cross-sectional area, A_x , of the space and the room air velocity, V_a , required, the flow is determined by

$$Q = A_x V_a. \quad (18.80)$$

The proper placement of windows, *narrow* building shape, and open landscaping can enhance natural wind flow to provide ventilation. The air flow rate through open windows for wind-driven ventilation is given by ASHRAE (1993):

$$Q = C_v V_w A_w \quad (18.81)$$

where

Q is the air flow rate (m^3/s)

A_w is the free area of inlet opening (m^2)

V_w is the wind velocity (m/s)

C_v is the effectiveness of opening that is equal to 0.5–0.6 for wind perpendicular to opening and 0.25–0.35 for wind diagonal to opening

TABLE 18.9
South-Facing Window Overhang Rule of Thumb

Length of the overhang = $\frac{\text{window height}}{F}$	
(a) Overhang Factors	(b) Roof Overhang Geometry
North Latitude	F^a
28	5.5–11.1
32	4.0–6.3
36	3.0–4.5
40	2.5–3.4
44	2.0–2.7
48	1.7–2.2
52	1.5–1.8
56	1.3–1.5

Properly sized overhangs shade out hot summer sun but allow winter sun (which is lower in the sky) to penetrate windows

Source: Halacy, 1984.

^a Select a factor according to your latitude. Higher values provide complete shading at noon on June 21; lower values, until August 1.

The stack effect can induce ventilation when warm air rises to the top of a structure and exhausts outside, while cooler outside air enters the structure to replace it. Figure 18.40 illustrates the solar chimney concept, which can easily be adapted to a thermal storage wall system. The greatest stack effect flow rate is produced by maximizing the stack height and the air temperature in the stack, as given by

$$Q = 0.116A_j\sqrt{h(T_s - T_o)} \tag{18.82}$$

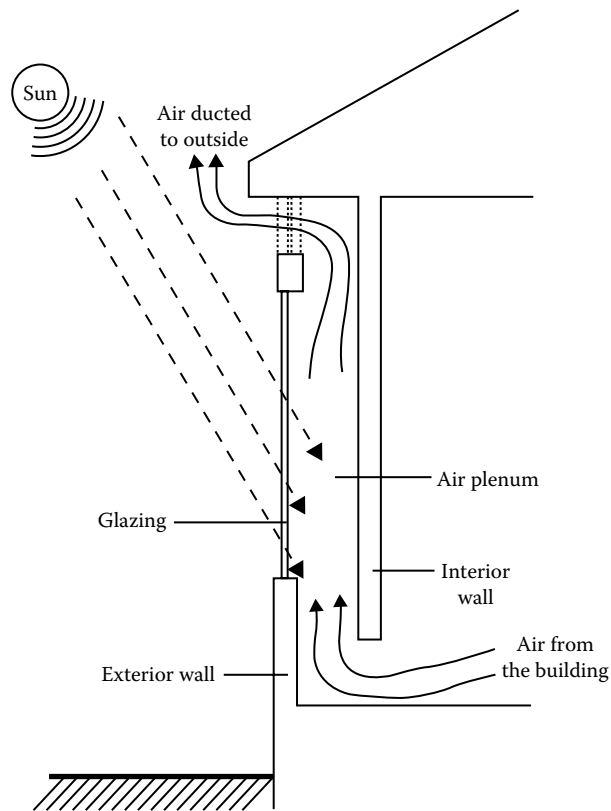
where

- Q is the stack flow rate (m^3/s)
- A_j is the area of inlets or outlets, whichever is smaller (m^2)
- h is the inlet-to-outlet height (m)
- T_s is the average temperature in stack ($^\circ\text{C}$)
- T_o is the outdoor air temperature ($^\circ\text{C}$)

If inlet or outlet area is twice the other, the flow rate will increase by 25%, and by 35% if the areas' ratio is 3:1 or larger (Table 18.10).

Example 18.14

A two-story (5 m) solar chimney is being designed to produce a flow of $0.25 \text{ m}^3/\text{s}$ through a space. The preliminary design features include a $25 \text{ cm} \times 1.5 \text{ m}$ inlet, a $50 \text{ cm} \times 1.5 \text{ m}$ outlet, and an estimated 35°C average stack temperature on a sunny 30°C day. Can this design produce the desired flow?

**FIGURE 18.40**

The stack-effect/solar chimney concept to induce convection/ventilation. (From PSDH, *Passive Solar Design Handbook*, Volume One: Passive Solar Design Concepts, DOE/CS-0127/1, March 1980, Prepared by Total Environmental Action, Inc. (B. Anderson, C. Michal, P. Temple, and Lewis); Volume Two: *Passive Solar Design Analysis*, DOE/CS-0127/2, January 1980, Prepared by Los Alamos Scientific Laboratory (J. D. Balcomb, D. Barley, R McFarland, J. Perry, W. Wray and S. Noll), U.S. Department of Energy, Washington, DC, 1980.)

TABLE 18.10

Ground Reflectivities

Material	ρ (%)
Cement	27
Concrete	20–40
Asphalt	7–14
Earth	10
Grass	6–20
Vegetation	25
Snow	70
Red brick	30
Gravel	15
White paint	55–75

Source: Murdoch, J.B., *Illumination Engineering—From Edison's Lamp to the Laser*, Macmillan, New York, 1985.

Solution

Substituting the design data into Equation 18.82,

$$\begin{aligned} Q &= 0.116(0.25 \times 1.5)[5(5)]^{1/2} \\ &= 0.2 \text{ m}^3/\text{s}. \end{aligned}$$

Because the outlet area is twice the inlet area, the 25% flow increase can be used:

$$Q = 0.2(1.25) = 0.25 \text{ m}^3/\text{s}.$$

(Answer: Yes, the proper flow rate is obtained.)

18.2.4.3 Evaporative Cooling

When air with less than 100% relative humidity moves over a water surface, the evaporation of water causes both the air and the water itself to cool. The lowest temperature that can be reached by this direct evaporative cooling effect is the wet-bulb temperature of the air, which is directly related to the relative humidity, with lower wet-bulb temperature associated with lower relative humidity. Thus, dry air (low relative humidity) has a low wet-bulb temperature and will undergo a large temperature drop with evaporative cooling, while humid air (high relative humidity) can be only slightly cooled evaporatively. The wet-bulb temperature for various relative humidity and air temperature conditions can be found via the *psychrometric chart* available in most thermodynamic texts. Normally, an evaporative cooling process cools the air only part of the way down to the wet-bulb temperature. To get the maximum temperature decrease, it is necessary to have a large water surface area in contact with the air for a long time, and interior ponds and fountain sprays are often used to provide this air–water contact area.

The use of water sprays and open ponds on roofs provides cooling primarily via evaporation. The hybrid system involving a fan and wetted mat, the *swamp cooler*, is by far the most widely used evaporative cooling technology. Direct, indirect, and combined evaporative cooling system design features are described in ASHRAE (1993, 1995).

18.2.4.4 Nocturnal and Radiative Cooling Systems

Another approach to passive convective/ventilative cooling involves using cooler night air to reduce the temperature of the building and/or a storage mass. Thus, the building/storage mass is prepared to accept part of the heat load during the hotter daytime. This type of convective system can also be combined with evaporative and radiative modes of heat transfer, utilizing air and/or water as the convective fluid. Work in Australia (Close et al. 1968) investigated rock storage beds that were chilled using evaporatively cooled night air. Room air was then circulated through the bed during the day to provide space cooling. The use of encapsulated roof ponds as a thermal cooling mass has been tried by several investigators (Hay and Yellott 1969; Marlatt et al. 1984; Givoni 1994) and is often linked with nighttime radiative cooling.

All warm objects emit thermal infrared radiation; the hotter the body, the more energy it emits. A passive cooling scheme is to use the cooler night sky as a sink for thermal radiation emitted by a warm storage mass, thus chilling the mass for cooling

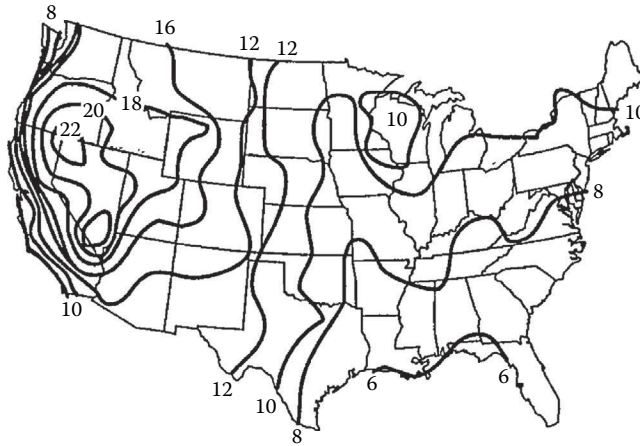


FIGURE 18.41

Average monthly sky temperature depression ($I_{AIR} - I_{SKY}$) for July in °F. (Adapted from Martin, M. and Berdahl, P., *Solar Energy*, 33(314), 321–336, 1984.)

use the next day. The net radiative cooling rate, Q_r , for a horizontal unit surface (ASHRAE 1993) is

$$Q_r = \epsilon\sigma(T_{body}^4 - T_{sky}^4), \tag{18.83}$$

where

- Q_r is the net radiative cooling rate, W/m^2 (Btu/h ft.²)
- ϵ is the surface emissivity fraction (usually 0.9 for water)
- σ is $5.67 \times 10^{-8} W/m^2 K^4$ ($1.714 \times 10^{-9} Btu/h ft.^2 R^4$)
- T_{body} is the warm body temperature, Kelvin (Rankine)
- T_{sky} is the effective sky temperature, Kelvin (Rankine)

The monthly average air–sky temperature difference has been determined (Martin and Berdahl 1984), and Figure 18.41 presents these values for July (in °F) for the United States.

Example 18.15

Estimate the overnight cooling possible for a 10 m², 85°F water thermal storage roof during July in Los Angeles.

Solution

Assume the roof storage unit is black with $\epsilon = 0.9$. From Figure 18.84, $T_{air} - T_{sky}$ is approximately 10°F for Los Angeles. From weather data for LA airport (PSDH 1984; ASHRAE 1993), the July average temperature is 69°F with a range of 15°F. Assuming night temperatures vary from the average (69°F) down to half the daily range (15/2), then the average nighttime temperature is chosen as $69 - (1/2)(15/2) = 65$ °F. Therefore, $T_{sky} = 65 - 10 = 55$ °F. From Equation 18.83,

$$Q_r = 0.9(1.714 \times 10^{-9})[(460 + 85)^4 - (460 + 55)^4]$$

$$= 27.6 Btu/h ft.^2$$

For a 10 h night and 10 m² (107.6 ft.²) roof area,

$$\begin{aligned} \text{Total radiative cooling} &= 27.6(10)(107.6) \\ &= 29,700 \text{ Btu.} \end{aligned}$$

Note that this does not include the convective cooling possible, which can be approximated (at its maximum rate) for still air (ASHRAE 1993) by

$$\begin{aligned} \text{Maximum total } Q_{\text{conv}} &= hA(T_{\text{roof}} - T_{\text{air}})(\text{Time}) \\ &= 5(129)(85 - 55)(10) \\ &= 161,000 \text{ Btu.} \end{aligned}$$

This is a maximum since the 85°F storage temperature will drop as it cools; this is also the case for the radiative cooling calculation. However, convection is seen to usually be the more dominant mode of nighttime cooling.

18.2.4.5 Earth Contact Cooling (or Heating)

Earth contact cooling or heating is a passive summer cooling and winter heating technique that utilizes underground soil as the heat sink or source. By installing a pipe underground and passing air through the pipe, the air will be cooled or warmed depending on the season. A schematic of an open-loop system and a closed-loop air-conditioning system are presented in Figures 18.42 and 18.43, respectively (Goswami and Biseli 1994).

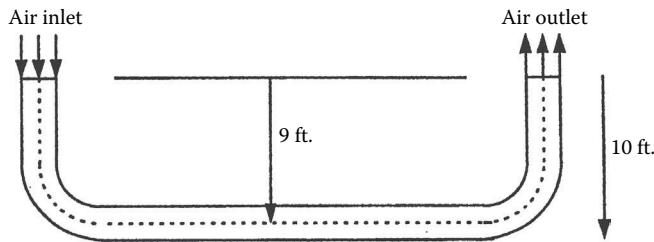


FIGURE 18.42
Open-loop underground air tunnel system.

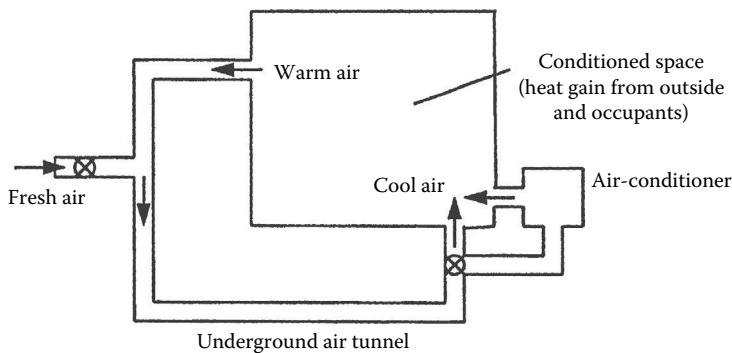


FIGURE 18.43
Schematic of closed-loop air-conditioning system using air tunnel.

The use of this technique can be traced back to 3000 BC when Iranian architects designed some buildings to be cooled by natural resources only. In the nineteenth century, Wilkinson (USDA 1960) designed a barn for 148 cows where a 500 ft. long underground passage was used for cooling during the summertime. Since that time, a number of experimental and analytical studies of this technique have continued to appear in the literature (Krarti and Kreider 1996; Hollmuller and Lachal 2001; De Paepe and Janssens 2003). Goswami and Dhaliwal (1985) have given a brief review of the literature as well as presented an analytical solution to the problem of transient heat transfer between the air and the surrounding soil as the air is made to pass through a pipe buried underground.

18.2.4.5.1 Heat Transfer Analysis

The transient thermal analysis of the air and soil temperature fields (Goswami and Dhaliwal 1985) is conducted using finite elements with the convective heat transfer between the air and the pipe and using semi-infinite cylindrical conductive heat transfer to the soil from the pipe. It should be noted that the thermal resistance of the pipe (whether of metal, plastic, or ceramic) is negligible relative to the surrounding soil.

18.2.4.5.1.1 Air and Pipe Heat Transfer The pipe is divided into a large number of elements and a psychrometric energy balance written for each, depending on whether the air leaves the element (1) unsaturated or (2) saturated.

1. If the air leaves an element as unsaturated, the energy balance on the element is

$$mC_p(T_1 - T_2) = hA_p(T_{\text{air}} - T_{\text{pipe}}). \quad (18.84)$$

T_{air} can be taken as $(T_1 + T_2)/2$. Substituting and simplifying,

$$T_2 = \frac{(1 - (U/2))T_1 + UT_{\text{pipe}}}{1 + (U/2)}, \quad (18.85)$$

where U is defined as

$$U = \frac{A_p h}{mC_p}$$

2. If the air leaving the element is saturated, the energy balance is

$$mC_p T_1 + m(W_1 - W_2)H_{fg} = mC_p T_2 + hA_p(T_{\text{air}} - T_{\text{pipe}}). \quad (18.86)$$

Simplifying gives

$$T_2 = \frac{(1 - (U/2))T_1 + ((W_1 - W_2)/C_p)H_{fg} + UT_{\text{pipe}}}{1 + (U/2)}. \quad (18.87)$$

The convective heat transfer coefficient h in the preceding equations depends on Reynolds number, the shape, and roughness of the pipe.

Using the exit temperature from the first element as the inlet temperature for the next element, the exit temperature for the element can be calculated in a similar way. Continuing this way from one element to the next, the temperature of air at the exit from the pipe can be calculated.

18.2.4.5.1.2 Soil Heat Transfer The heat transfer from the pipe to the soil is analyzed by considering the heat flux at the internal radius of a semi-infinite cylinder formed by the soil around the pipe. For a small element, the problem can be formulated as

$$\frac{\partial^2 T(r,t)}{\partial r^2} + \frac{1}{r} \frac{\partial T(r,t)}{\partial r} = \frac{1}{\alpha} \frac{\partial T(r,t)}{\partial t}, \quad (18.88)$$

with initial and boundary conditions as

$$\begin{aligned} T(r,0) &= T_e, \\ T(\infty,t) &= T_e, \\ -K \frac{\partial T}{\partial r}(r,t) &= q'', \end{aligned}$$

where

T_e is the bulk earth temperature

q'' is also given by the amount of heat transferred to the pipe from the air by convection, that is, $q'' = h(T_{\text{air}} - T_{\text{pipe}})$

18.2.4.5.2 Soil Temperatures and Properties

Kusuda and Achenbach (1965) and Labs (1981) studied the earth temperatures in the United States. According to both of these studies, temperature swings in the soil during the year are dampened with depth below the ground. There is also a phase lag between the soil temperature and the ambient air temperature, and this phase lag increases with depth below the surface. For example, the soil temperature for light dry soil at a depth of about 10 ft. (3.05 m) varies by approximately $\pm 5^\circ\text{F}$ (2.8°C) from the mean temperature (approximately equal to mean annual air temperature) and has a phase lag of approximately 75 days behind ambient air temperature (Labs 1981).

The thermal properties of the soil are difficult to determine. The thermal conductivity and diffusivity both change with the moisture content of the soil itself, which is directly affected by the temperature of and heat flux from and to the buried pipe. Most researchers have found that using constant property values for soil taken from standard references gives reasonable predictive results (Goswami and Ileslamlou 1990).

18.2.4.5.3 Generalized Results from Experiments

Figure 18.44 presents data from Goswami and Biseli (1994) for an open system, 100 ft. long, 12 in. diameter pipe, buried 9 ft. deep. The figure shows the relationship between the pipe inlet-to-outlet temperature reduction ($T_{\text{in}} - T_{\text{out}}$) and the initial soil temperature with ambient air inlet conditions of 90°F , 55% relative humidity for various pipe flow rates.

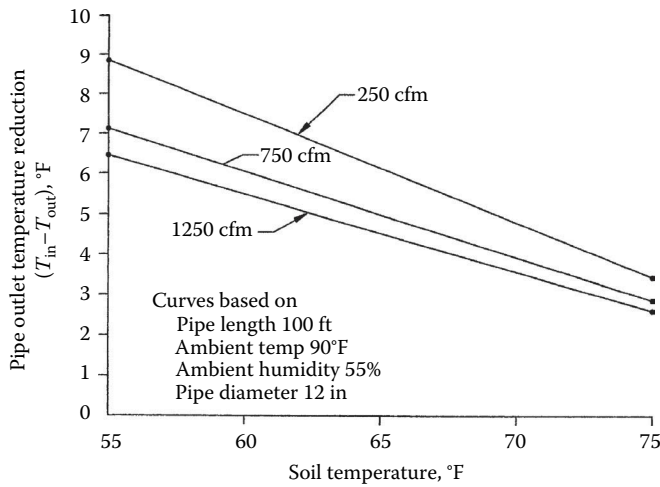


FIGURE 18.44

Air temperature drop through a 100 ft. long, 12 in. diameter pipe buried 9 ft. underground.

Other relations from this same report that can be used with Figure 18.44 data include the following: (1) the effect of increasing pipe/tunnel length on increasing the inlet-to-outlet air temperature difference is fairly linear up to 250 ft.; and (2) the effect of decreasing pipe diameter on lowering the outlet air temperature is slight, and only marginally effective for pipes less than 12 in. in diameter.

Example 18.16

Provide the necessary 12 in. diameter pipe length(s) that will deliver 1500 cfm of 75°F air if the ambient temperature is 85°F and the soil at 9 ft. is 65°F.

Solution

From Figure 18.44, for 100 ft. of pipe at 65°F soil temperature, the pipe temperature reduction is

$$\begin{aligned}
 T_{\text{in}} - T_{\text{out}} &= 6^\circ\text{F} \text{ (at 250 cfm)} \\
 &= 5^\circ\text{F} \text{ (at 750 cfm)} \\
 &= 4.5^\circ\text{F} \text{ (at 1250 cfm)}.
 \end{aligned}$$

Because the *length versus temperature reduction* is linear (see earlier text), the 10°F reduction required (85°F down to 75°F) would be met by the 750 cfm case (5°F for 100 ft.) if 200 ft. of pipe is used. Then, two 12 in. diameter pipes would be required to meet the 1500 cfm requirement.

Answer

Two 12 in. diameter pipes, each 200 ft. long. (*Note:* see what would be needed if the 250 cfm or the 1250 cfm cases had been chosen. Which of the three flow rate cases leads to the *cheapest* installation?)

18.2.5 Daylighting Design Fundamentals

Daylighting is the use of the sun's radiant energy to illuminate the interior spaces in a building. In the nineteenth century, electric lighting was considered an alternative technology to daylighting. Today, the situation is reversed, primarily due to the economics of energy use and conservation. However, there are good physiological reasons for using daylight as an illuminant. The quality of daylight matches the human eye's response, thus permitting lower light levels for task comfort, better color rendering, and clearer object discrimination (Robbins 1986; McCluney 1998; Clay 2001).

18.2.5.1 Lighting Terms and Units

Measurement of lighting level is based on the *standard candle*, where the lumen (lm), the unit of luminous flux (ϕ), is defined as the rate of luminous energy passing through a 1 m² area located 1 m from the candle. Thus, a standard candle generates 4π lumens, which radiate away in all directions. The illuminance (E) on a surface is defined as the luminous flux on the surface divided by the surface area, $E = \phi/A$. Illuminance is measured in either lux (lx), as lm/m², or footcandles (fc), as lm/ft.².

Determination of the daylighting available at a given location in a building space at a given time is important to evaluate the reduction possible in electric lighting and the associated impact on heating and cooling loads. Daylight provides about 110 lm/W of solar radiation, fluorescent lamps about 75 lm/W of electrical input, and incandescent lamps about 20 lm/W; thus, daylighting generates only half to one-fifth the heating that equivalent electric lighting does, significantly reducing the building cooling load.

18.2.5.2 Approach to Daylighting Design

Aperture controls such as blinds and drapes are used to moderate the amount of daylight entering the space, as are the architectural features of the building itself (glazing type, area, and orientation; overhangs and wingwalls; lightshelves; etc.). Many passive and *active* reflective, concentrating, and diffusing devices are available to specifically gather and direct both the direct and diffuse components of daylight to areas within the space (Kinney et al. 2005). Electric-lighting dimming controls are used to adjust the electric light level based on the quantity of daylighting. With these two types of controls (aperture and lighting), the electric lighting and cooling energy use and demand, as well as cooling system sizing, can be reduced. However, the determination of the daylighting position and time illuminance value within the space is required before energy usage, and demand reduction calculations can be made.

Daylighting design approaches use both solar beam radiation (referred to as sunlight) and the diffuse radiation scattered by the atmosphere (referred to as skylight) as sources for interior lighting, with historical design emphasis being on utilizing skylight. Daylighting is provided through a variety of glazing features, which can be grouped as sidelighting (light enters via the side of the space) and toplighting (light enters from the ceiling area). Figure 18.45 illustrates several architectural forms producing sidelighting and toplighting, with the dashed lines representing the illuminance distribution within the space. The calculation of work-plane illuminance depends on whether sidelighting and/or toplighting features are used and the combined illuminance values are additive.

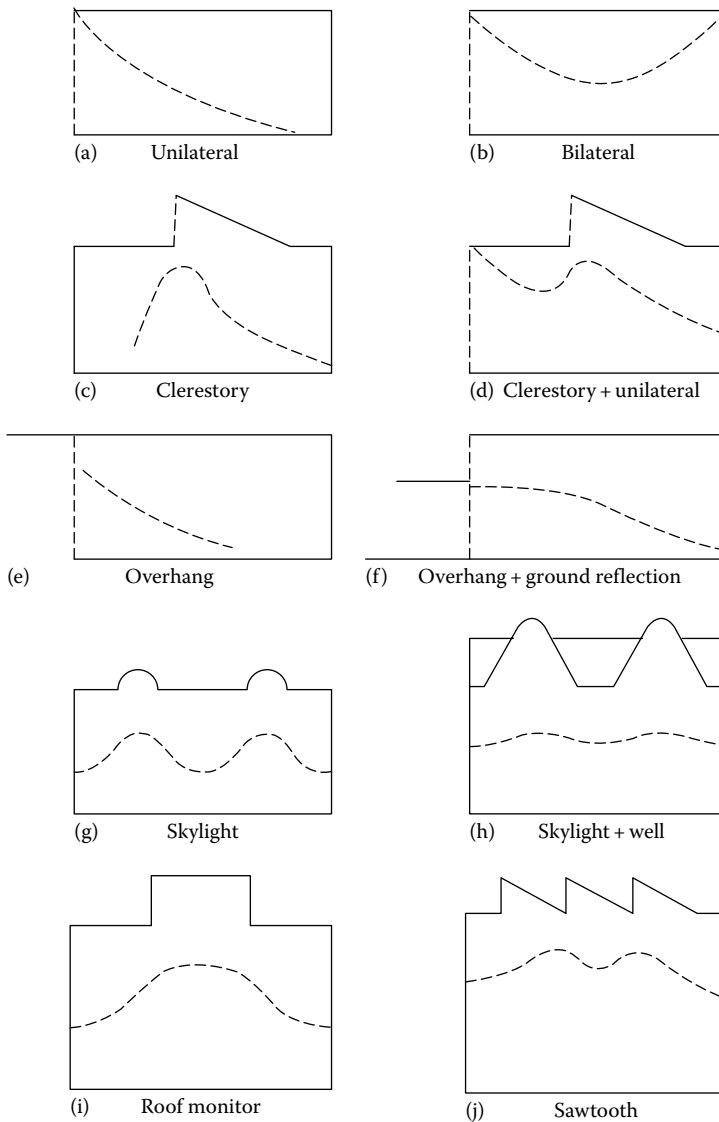


FIGURE 18.45

(a–j) Examples of sidelighting and toplighting architectural features (dashed lines represent illuminance distributions). (From Murdoch, J.B., *Illumination Engineering—From Edison's Lamp to the Laser*, Macmillan, New York, 1985.)

18.2.5.3 Sun-Window Geometry

The solar illuminance on a vertical or horizontal window depends on the position of the sun relative to that window. In the method described here, the sun and sky illuminance values are determined using the sun's altitude angle (α) and the sun-window azimuth angle difference (Φ). These angles need to be determined for the particular time of day, day of year, and window placement under investigation.

18.2.5.3.1 Solar Altitude Angle

The solar altitude angle, α , is the angle swept out by a person's arm when pointing to the horizon directly below the sun and then raising the arm to point at the sun. The equation to calculate solar altitude, α , is

$$\sin \alpha = \cos L \delta \cos H + \sin L \sin \delta, \quad (18.89)$$

where

L is the local latitude (degrees)

δ is the earth-sun declination (degrees) given by $\delta = 23.45 \sin[360(n - 81)/365]$

n is the day number of the year

H is the hour angle (degrees) given by

$$H = \frac{(12 \text{ noon} - \text{time}) \text{ min}}{4}; \quad (+, \text{morning}, -, \text{afternoon}). \quad (18.90)$$

18.2.5.3.2 Sun-Window Azimuth Angle Difference

The difference between the sun's azimuth and the window's azimuth, Φ , needs to be calculated for vertical window illuminance. The window's azimuth angle, γ_w , is determined by which way it faces, as measured from south (east of south is positive, westward is negative). The solar azimuth angle, γ_s , is calculated by

$$\sin \gamma_s = \frac{\cos \delta \sin H}{\cos \alpha}. \quad (18.91)$$

The sun-window azimuth angle difference, Φ , is given by the absolute value of the difference between γ_s and γ_w :

$$\Phi = |\gamma_s - \gamma_w|. \quad (18.92)$$

18.2.5.4 Daylighting Design Methods

To determine the annual lighting energy saved (ES_L), calculations using the lumen method described later should be performed on a monthly basis for both clear and overcast days for the space under investigation. Monthly weather data for the site would then be used to prorate clear and overcast lighting energy demands monthly. Subtracting the calculated daylighting illuminance from the design illuminance leaves the supplementary lighting needed, which determines the lighting energy required.

The approach in the following method is to calculate the *sidelighting* and the *skylighting* of the space separately and then combine the results. This procedure has been computerized (Lumen II/Lumen Micro) and includes many details of controls, daylighting technologies, and weather. ASHRAE (1993) lists many of the methods and simulation techniques currently used with daylighting and its associated energy effects.

18.2.5.4.1 Lumen Method of Sidelighting (Vertical Windows)

The lumen method of sidelighting calculates interior horizontal illuminance at three points, as shown in Figure 18.46, at the 30 in. (0.76 m) work-plane on the room-and-window

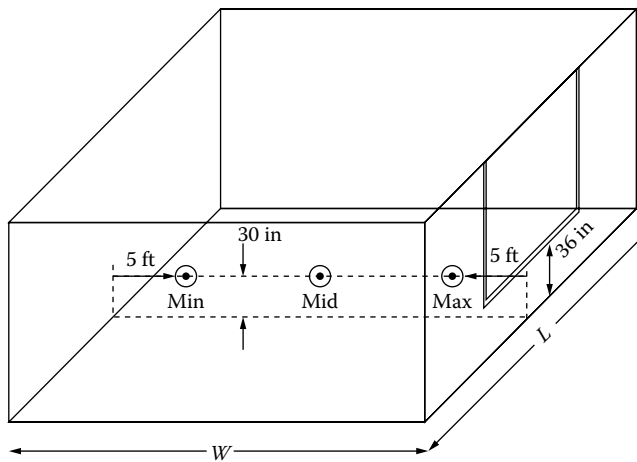


FIGURE 18.46

Location of illumination points within the room (along centerline of window) determined by lumen method of sidelighting.

centerline. A vertical window is assumed to extend from 36 in. (0.91 m) above the floor to the ceiling. The method accounts for both direct and ground-reflected sunlight and skylight, so both horizontal and vertical illuminances from sun and sky are needed. The steps in the lumen method of sidelighting are presented next.

As mentioned, the incident direct and ground-reflected window illuminances are normally calculated for both a cloudy and a clear day for representative days during the year (various months), as well as for clear or cloudy times during a given day. Thus, the interior illumination due to sidelighting and skylighting can then be examined for effectiveness throughout the year.

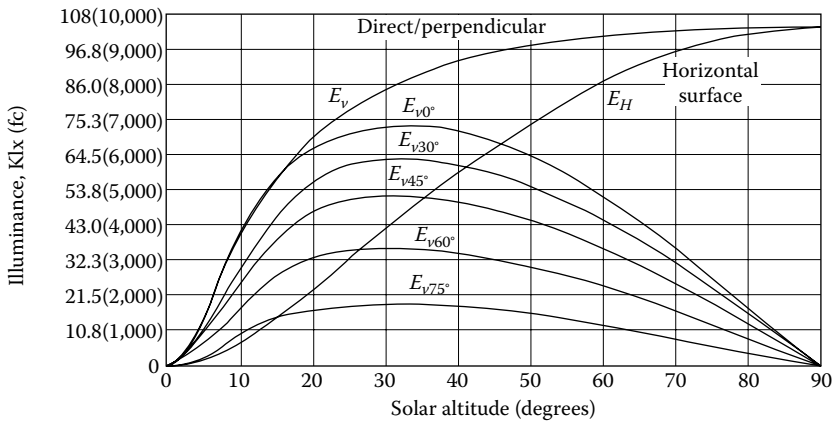
Step 1: Incident direct sky and sun illuminances—The solar altitude and sun-window azimuth angle difference are calculated for the desired latitude, date, and time using Equations 18.89 and 18.92, respectively. Using these two angles, the total illuminance on the window (E_{sw}) can be determined by summing the direct sun illuminance (E_{uw}) and the direct sky illuminance (E_{kw}), each determined from the appropriate graph in Figure 18.47.

Step 2: Incident ground-reflected illuminance—The sun illuminance on the ground (E_{ug}), plus the overcast or clear sky illuminance (E_{kg}) on the ground, makes up the total horizontal illuminance on the ground surface (E_{sg}). A fraction of the ground surface illuminance is then considered diffusely reflected onto the vertical window surface (E_{gw}), where gw indicates from the ground to the window.

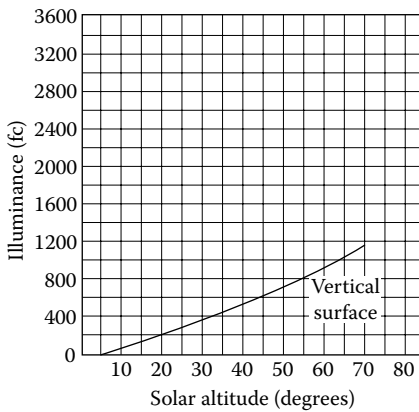
The horizontal ground illuminances can be determined using Figure 18.48, where the clear sky plus sun case and the overcast sky case are functions of solar altitude. The fractions of the ground illuminance diffusely reflected onto the window depend on the reflectivity (ρ) of the ground surface (see Table 18.10) and the window-to-ground surface geometry.

If the ground surface is considered uniformly reflective from the window outward to the horizon, then the illuminance on the window from ground reflection is

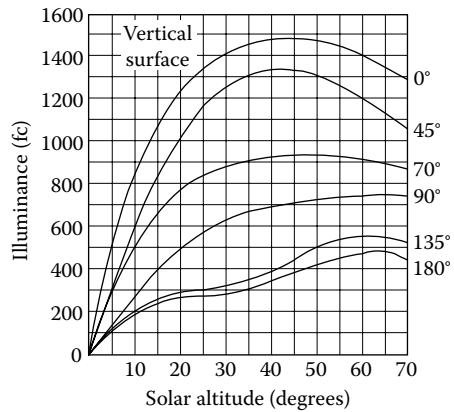
$$E_{gw} = \frac{\rho E_{sg}}{2}. \quad (18.93)$$



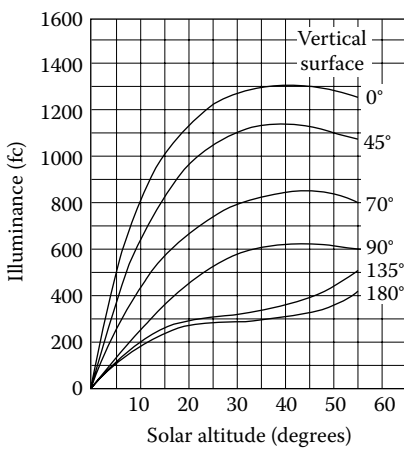
(a) Direct sunlight



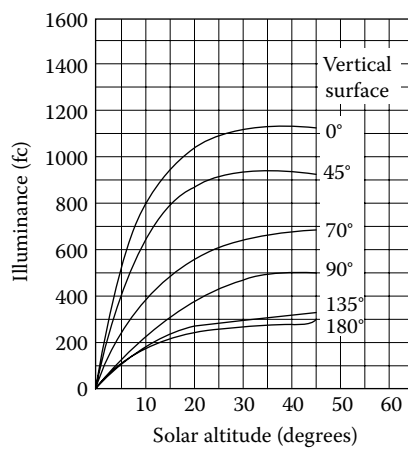
(b) Overcast skylight



(c) Clear summer skylight



(d) Clear autumn/spring skylight



(e) Clear winter skylight

FIGURE 18.47

Illuminance on a vertical surface from (a) direct sunlight and from (b–e) skylight for various sun-window azimuth angle differences. (From IES, *Lighting Handbook, Applications Volume*, Illumination Engineering Society, New York, 1987.)

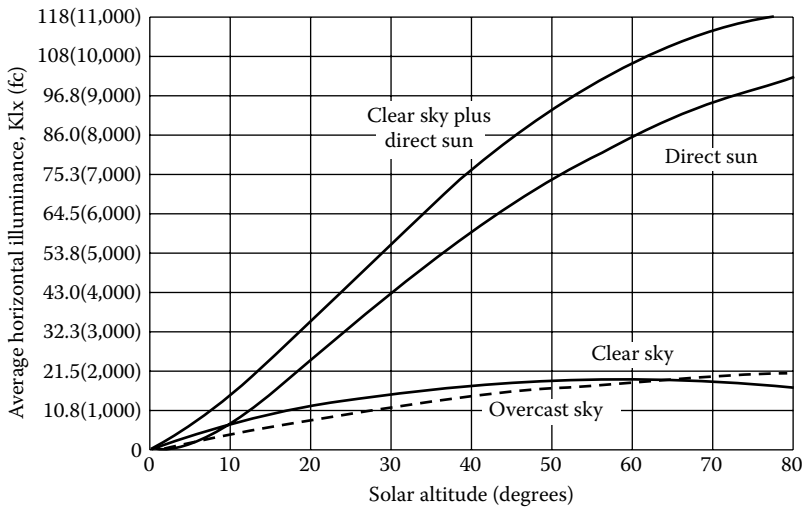


FIGURE 18.48

Horizontal illuminance for overcast sky, clear sky, direct sun, and clear sky plus direct sun. (From Murdoch, J.B., *Illumination Engineering—From Edison’s Lamp to the Laser*, Macmillan, New York, 1985.)

A more complicated ground-reflection case is illustrated in Figure 18.49, where multiple *strips* of differently reflecting ground are handled using the angles to the window where a strip’s illuminance on a window is calculated by

$$E_{gw(\text{strip})} = \frac{\rho_{\text{strip}} E_{sg}}{2} (\cos \theta_1 - \cos \theta_2). \tag{18.94}$$

And the total reflected onto the window is the sum of the strip illuminances:

$$E_{gw} = \frac{E_{sg}}{2} [\rho_1(\cos 0 - \cos \theta_1) + \rho_2(\cos \theta_1 - \cos \theta_2) + \dots + \rho_n(\cos \theta_{n-1} - \cos 90)]. \tag{18.95}$$

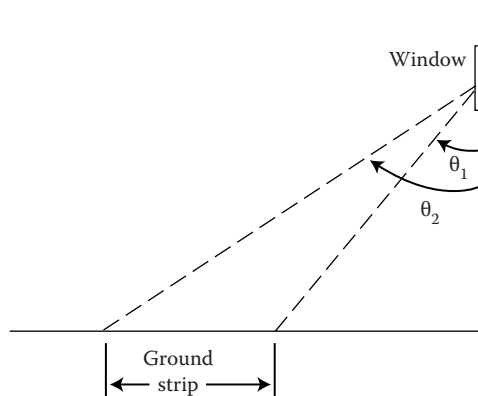


FIGURE 18.49

Geometry for ground *strips*. (From Murdoch, J.B., *Illumination Engineering—From Edison’s Lamp to the Laser*, Macmillan, New York, 1985.)

Step 3: Luminous flux entering space—The direct sky–sun and ground-reflected luminous fluxes entering the building are attenuated by the transmissivity of the window. Table 18.11 presents the transmittance fraction (τ) of several window glasses. The fluxes entering the space are calculated from the total sun–sky and the ground-reflected illuminances by using the area of the glass, A_w :

$$\begin{aligned} \phi_{sw} &= E_{sw} \tau A_w \\ \phi_{gw} &= E_{gw} \tau A_w \end{aligned} \tag{18.96}$$

Step 4: Light loss factor—The light loss factor (K_m) accounts for the attenuation of luminous flux due to dirt on the window (WDD, window dirt depreciation) and on the room surfaces (RSDD, room surface dirt depreciation). WDD depends on how often the window is cleaned, but a 6-month average for offices is 0.83 and for factories is 0.71 (Murdoch 1985).

The RSDD is a more complex calculation involving time between cleanings, the direct–indirect flux distribution, and room proportions. However, for rooms cleaned regularly, RSDD is around 0.94, and for once-a-year-cleaned dirty rooms, the RSDD would be around 0.84.

The light loss factor is the product of the preceding two fractions:

$$K_m = (WDD)(RSDD). \tag{18.97}$$

Step 5: Work-plane illuminances—As discussed earlier, Figure 18.46 illustrates the location of the work-plane illuminances determined with this lumen method of sidelighting.

TABLE 18.11

Glass Transmittances

Glass	Thickness (in.)	τ (%)
Clear	1/3	89
Clear	3/16	88
Clear	1/4	87
Clear	5/16	86
Gray	1/8	61
Gray	3/16	51
Gray	1/4	44
Gray	5/16	35
Bronze	1/8	68
Bronze	3/16	59
Bronze	1/4	52
Bronze	5/16	44
Thermopane	1/8	80
Thermopane	3/16	79
Thermopane	1/4	77

Source: Murdoch, J.B., *Illumination Engineering—From Edison’s Lamp to the Laser*, Macmillan, New York, 1985.

The three illuminances (max, mid, min) are determined using two coefficients of utilization, the C factor, and the K factor. The C factor depends on room length and width and wall reflectance. The K factor depends on ceiling–floor height, room width, and wall reflectance. Tables 18.12 through 18.14 presents C and K values for the three cases of incoming fluxes: sun plus clear sky, overcast sky, and ground reflected. Assumed ceiling and floor reflectances are given for this case with no window controls (shades, blinds, overhangs, etc.). These further window control complexities can be found in Libbey-Owens-Ford Company (1976), IES (1987), and others. A reflectance of 70% represents light-colored walls, with 30% representing darker walls.

The work-plane max, mid, and min illuminances are each calculated by adding the sun- and ground-reflected illuminances, which are given by

$$\begin{aligned} E_{sp} &= \phi_{sw} C_s K_s K_m, \\ E_{gp} &= \phi_{gw} C_g K_g K_m \end{aligned} \quad (18.98)$$

where the “sp” and “gp” subscripts refer to the sky-to-work-plane and ground-to-work-plane illuminances.

Example 18.17

Determine the clear-sky illuminances for a 30 ft. long, 30 ft. wide, 10 ft. high room with a 20 ft. long window with a 3 ft. sill. The window faces 10° E of south, the building is at 32° N latitude, and it is January 15 at 2 p.m. The ground cover outside is grass, the glass is $1/4$ in. clear, and the walls are light colored.

Solution

Following the steps in the *sidelighting* method

Step 1: With $L = 32$, $n = 15$, $H = (12 - 14)60/4 = -30$,

$$\delta = 23.45 \sin[360(15 - 81)/365] = -21.3^\circ.$$

Then, Equation 18.89 yields $\alpha = 41.7^\circ$, Equation 18.91 yields $\gamma_s = -38.7^\circ$, and Equation 18.92 yields

$$\Phi = |-38.7 - (+10)| = 48.7^\circ.$$

From Figure 18.47 with $\alpha = 41.7^\circ$ and $\Phi = 48.7^\circ$

- (a) For clear sky (winter, no sun): $E_{kw} = 875$ fc.
- (b) For direct sun: $E_{uw} = 4,100$ fc.
- (c) Total clear sky plus direct: $E_{sw} = 4,975$ fc.

(Note: A high E_{uw} value probably indicates a glare situation!)

Step 2: Horizontal illuminances from Figure 18.48: $E_{sg} = 4007$ fc.

Then, Equation 18.93 yields, with $\rho_{grass} = 0.06$, $E_{gw} = 222$ fc.

Step 3: From Equation 18.96, with $\tau = 0.87$ and $A_w = 140$ ft.²,

$$\Phi_{sw} = 4975(0.87)(140) = 605,955 \text{ lm.}$$

$$\Phi_{gw} = 222(0.87)(140) = 27,040 \text{ lm.}$$

TABLE 18.12
C and K Factors for No Window Controls for Overcast Sky

Illumination by Overcast Sky																	
C: Coefficient of Utilization								K: Coefficient of Utilization									
Room Length (ft.)		20		30		40		Ceiling Height (ft.)		8		10		12		14	
Wall Reflectance (%)		70	30	70	30	70	30	Wall Reflectance (%)		70	30	70	30	70	30	70	30
Room Width (ft.)		Room Width (ft.)															
Max	20	0.0276	0.0251	0.0191	0.0173	0.0143	0.0137	Max	20	0.125	0.129	0.121	0.123	0.111	0.111	0.0991	0.0973
	30	0.0272	0.0248	0.0188	0.0172	0.0137	0.0131		30	0.122	0.131	0.122	0.121	0.111	0.111	0.0945	0.0973
	40	0.0269	0.0246	0.0182	0.0171	0.0133	0.0130		40	0.145	0.133	0.131	0.126	0.111	0.111	0.0973	0.0982
Mid	20	0.0159	0.0177	0.0101	0.0087	0.0081	0.0071	Mid	20	0.0908	0.0982	0.107	0.115	0.111	0.111	0.105	0.122
	30	0.0058	0.0050	0.0054	0.0040	0.0034	0.0033		30	0.156	0.102	0.0939	0.113	0.111	0.111	0.121	0.134
	40	0.0039	0.0027	0.0030	0.0023	0.0022	0.0019		40	0.106	0.0948	0.123	0.107	0.111	0.111	0.135	0.127
Min	20	0.0087	0.0053	0.0063	0.0043	0.0050	0.0037	Min	20	0.0908	0.102	0.0951	0.114	0.111	0.111	0.118	0.134
	30	0.0032	0.0019	0.0029	0.0017	0.0020	0.0014		30	0.0924	0.119	0.101	0.114	0.111	0.111	0.125	0.126
	40	0.0019	0.0009	0.0016	0.0009	0.0012	0.0008		40	0.111	0.0926	0.125	0.109	0.111	0.111	0.133	0.130

Source: IES, 1979.

TABLE 18.13

C and K Factors for No Window Controls for Clear Sky

Illumination by Clear Sky																	
C: Coefficient of Utilization								K: Coefficient of Utilization									
Room Length (ft.)		20		30		40		Ceiling Height (ft.)		8		10		12		14	
Wall Reflectance (%)		70	30	70	30	70	30	Wall Reflectance (%)		70	30	70	30	70	30	70	30
Room Width (ft.)								Room Width (ft.)									
Max	20	0.0206	0.0173	0.0143	0.0123	0.0110	0.0098	Max	20	0.145	0.155	0.129	0.132	0.111	0.111	0.101	0.0982
	30	0.0203	0.0173	0.0137	0.0120	0.0098	0.0092		30	0.141	0.149	0.125	0.130	0.111	0.111	0.0954	0.101
	40	0.0200	0.0168	0.0131	0.0119	0.0096	0.0091		40	0.157	0.157	0.135	0.134	0.111	0.111	0.0964	0.0991
Mid	20	0.0153	0.0104	0.0100	0.0079	0.0083	0.0067	Mid	20	0.110	0.128	0.116	0.126	0.111	0.111	0.103	0.108
	30	0.0082	0.0054	0.0062	0.0043	0.0046	0.0037		30	0.106	0.125	0.110	0.129	0.111	0.111	0.112	0.120
	40	0.0052	0.0032	0.0040	0.0028	0.0029	0.0023		40	0.117	0.118	0.122	0.118	0.111	0.111	0.123	0.122
Min	20	0.0106	0.0060	0.0079	0.0049	0.0067	0.0043	Min	20	0.105	0.129	0.112	0.130	0.111	0.111	0.111	0.116
	30	0.0054	0.0028	0.0047	0.0023	0.0032	0.0021		30	0.0994	0.144	0.107	0.126	0.111	0.111	0.107	0.124
	40	0.0031	0.0014	0.0027	0.0013	0.0021	0.0012		40	0.119	0.116	0.130	0.118	0.111	0.111	0.120	0.118

Source: IES, 1979.

TABLE 18.14C and K Factors for No Window Controls for Ground Illumination^a

Ground Illumination																	
C: Coefficient of Utilization								K: Coefficient of Utilization									
Room Length (ft.)		20		30		40		Ceiling Height (ft.)		8		10		12		14	
Wall Reflectance (%)		70	30	70	30	70	30	Wall Reflectance (%)		70	30	70	30	70	30	70	30
Room Width (ft.)		Room Width (ft.)															
Max	20	0.0147	0.0112	0.0102	0.0088	0.0081	0.0071	Max	20	0.124	0.206	0.140	0.135	0.111	0.111	0.0909	0.0859
	30	0.0141	0.0012	0.0098	0.0088	0.0077	0.0070		30	0.182	0.188	0.140	0.143	0.111	0.111	0.0918	0.0878
	40	0.0137	0.0112	0.0093	0.0086	0.0072	0.0069		40	0.124	0.182	0.140	0.142	0.111	0.111	0.0936	0.0879
Mid	20	0.0128	0.0090	0.0094	0.0071	0.0073	0.0060	Mid	20	0.123	0.145	0.122	0.129	0.111	0.111	0.100	0.0945
	30	0.0083	0.0057	0.0062	0.0048	0.0050	0.0041		30	0.0966	0.104	0.107	0.112	0.111	0.111	0.110	0.105
	40	0.0055	0.0037	0.0044	0.0033	0.0042	0.0026		40	0.0790	0.0786	0.0999	0.106	0.111	0.111	0.118	0.118
Min	20	0.0106	0.0071	0.0082	0.0054	0.0067	0.0044	Min	20	0.0994	0.108	0.110	0.114	0.111	0.111	0.107	0.104
	30	0.0051	0.0026	0.0041	0.0023	0.0033	0.0021		30	0.0816	0.0822	0.0984	0.105	0.111	0.111	0.121	0.116
	40	0.0029	0.0018	0.0026	0.0012	0.0022	0.0011		40	0.0700	0.0656	0.0946	0.0986	0.111	0.111	0.125	0.132

Source: IES, 1979.

^a Ceiling reflectance, 80%; floor reflectance, 30%.

Step 4: For a clean office room,

$$K_m = (0.83)(0.94) = 0.78.$$

Step 5: From Tables 18.12 through 18.14, for 30 ft. width, 30 ft. length, 10 ft. ceiling, and wall reflectivity 70%,

a. Clear sky

$$C_{s, \max} = 0.0137; K_{s, \max} = 0.125,$$

$$C_{s, \text{mid}} = 0.0062; K_{s, \text{mid}} = 0.110,$$

$$C_{s, \min} = 0.0047; K_{s, \min} = 0.107.$$

b. Ground reflected

$$C_{g, \max} = 0.0098; K_{g, \max} = 0.140.$$

$$C_{g, \text{mid}} = 0.0062; K_{g, \text{mid}} = 0.107.$$

$$C_{g, \min} = 0.0041; K_{g, \min} = 0.0984.$$

Then, using Equation 18.98,

$$E_{\text{sp}, \max} = 605,955(0.0137)(0.125)(0.78) = 809 \text{ fc.}$$

$$E_{\text{sp}, \text{mid}} = 605,955(0.0062)(0.110)(0.78) = 322 \text{ fc.}$$

$$E_{\text{sp}, \min} = 605,955(0.0047)(0.107)(0.78) = 238 \text{ fc.}$$

$$E_{\text{gp}, \max} = 27,040(0.0098)(0.140)(0.78) = 29 \text{ fc.}$$

$$E_{\text{gp}, \text{mid}} = 27,040(0.0062)(0.107)(0.78) = 14 \text{ fc.}$$

$$E_{\text{gp}, \min} = 27,040(0.0041)(0.0984)(0.78) = 9 \text{ fc.}$$

Thus,

$$E_{\max} = 838 \text{ fc.}$$

$$E_{\text{mid}} = 336 \text{ fc.}$$

$$E_{\min} = 247 \text{ fc.}$$

18.2.5.4.2 Lumen Method of Skylighting

The lumen method of skylighting calculates the average illuminance at the interior work-plane provided by horizontal skylights mounted on the roof. The procedure for skylighting is generally the same as that described earlier for sidelighting. As with windows, the illuminance from both overcast sky and clear sky plus sun cases is determined for specific days in different seasons and for different times of the day, and a judgment is then made as to the number and size of skylights and any controls needed.

The procedure is presented in four steps: (1) finding the horizontal illuminance on the outside of the skylight, (2) calculating the effective transmittance through the skylight and

its well, (3) figuring the interior space light loss factor and the utilization coefficient, and finally, (4) calculating illuminance on the work-plane.

Step 1: Horizontal sky and sun illuminances—The horizontal illuminance value for an overcast sky or a clear sky plus sun situation can be determined from Figure 18.48 knowing only the solar altitude.

Step 2: Net skylight transmittance—The transmittance of the skylight is determined by the transmittance of the skylight cover(s), the reflective efficiency of the skylight well, the net-to-gross skylight area, and the transmittance of any light-control devices (lenses, louvers, etc.).

The transmittance for several flat-sheet plastic materials used in skylight domes is presented in Table 18.15. To get the effective dome transmittance (T_D) from the flat-plate transmittance (T_F) value (AAMA 1977), use

$$T_D = 1.25T_F(1.18 - 0.416T_F). \quad (18.99)$$

If a double-domed skylight is used, then the single-dome transmittances are combined as follows (Pierson 1962):

$$T_D = \frac{T_{D1}T_{D2}}{T_{D1}T_{D2} - T_{D1}T_{D2}}. \quad (18.100)$$

If the diffuse and direct transmittances for solar radiation are available for the skylight glazing material, it is possible to follow this procedure and determine diffuse and direct dome transmittances separately. However, this difference is usually not a significant factor in the overall calculations.

The efficiency of the skylight well (N_w) is the fraction of the luminous flux from the dome that enters the room from the well. The well index (WI) is a geometric index (height, h ; length, l ; width, w) given by

$$WI = \frac{h(w+l)}{2wl}, \quad (18.101)$$

and WI is used with the well-wall reflectance value in Figure 18.50 to determine the well efficiency, N_w .

TABLE 18.15

Flat-Plate Plastic Material Transmittance for Skylights

Type	Thickness (in.)	Transmittance (%)
Transparent	1/8–3/16	92
Dense translucent	1/3	32
Dense translucent	3/16	24
Medium translucent	1/8	56
Medium translucent	3/16	52
Light translucent	1/8	72
Light translucent	3/16	68

Source: Murdoch, J.B., *Illumination Engineering—From Edison's Lamp to the Laser*, Macmillan, New York, 1985.

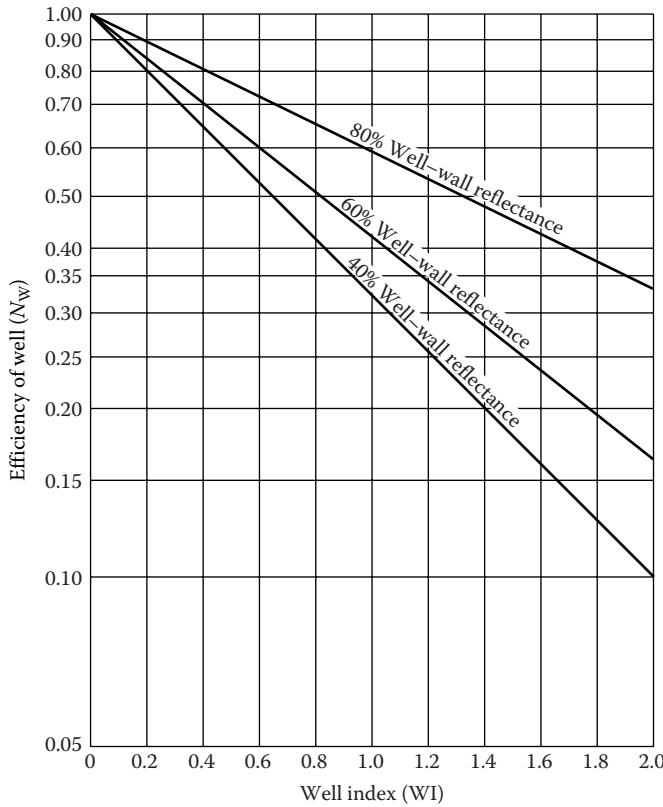


FIGURE 18.50 Efficiency of well versus well index. (From IES (Illumination Engineering Society), *Lighting Handbook, Applications Volume*, Illumination Engineering Society, New York, 1987)

With T_D and N_w determined, the net skylight transmittance for the skylight and well is given by

$$T_n = T_D N_w R_A T_C \tag{18.102}$$

where

- R_A is the ratio of net-to-gross skylight areas
- T_C is the transmittance of any light-controlling devices

Step 3: Light loss factor and utilization coefficient—The light loss factor (K_m) is again defined as the product of the RSDD and the skylight direct depreciation (SDD) fractions, similar to Equation 18.97. Following the reasoning for the sidelighting case, the RSDD value for clean rooms is around 0.94 and 0.84 for dirty rooms. Without specific data indicating otherwise, the SDD fraction is often taken as 0.75 for office buildings and 0.65 for industrial areas.

The fraction of the luminous flux on the skylight that reaches the work-plane (K_w) is the product of the net transmittance (T_n) and the room coefficient of utilization (RCU).

Dietz et al. (1981) developed RCU equations for office and warehouse interiors with ceiling, wall, and floor reflectances of 75%, 50%, and 30%, and 50%, 30%, and 20%, respectively.

$$\text{RCU} = \frac{1}{1 + A(\text{RCR})^B} \quad \text{if } \text{RCR} < 8, \quad (18.103)$$

where

A is 0.0288 and B is 1.560 for offices

A is 0.0995 and B is 1.087 for warehouses

Room cavity ratio (RCR) is given by

$$\text{RCR} = \frac{5h_c(l+w)}{lw}, \quad (18.104)$$

where

h_c is the ceiling height above the work-plane

l and w are the room length and width, respectively

The RCU is then multiplied by the previously determined T_n to give the fraction of the external luminous flux passing through the skylight and incident on the workplace:

$$K_u = T_n(\text{RCU}). \quad (18.105)$$

Step 4: Work-plane illuminance—The illuminance at the work-plane (E_{TWP}) is given by

$$E_{\text{TWP}} = E_H \left(\frac{A_T}{A_{\text{WP}}} \right) K_u K_m, \quad (18.106)$$

where

E_H is the horizontal overcast or clear sky plus sun illuminance from step 1

A_T is the total gross area of the skylights (number of skylight times skylight gross area)

A_{WP} is the work-plane area (generally room length times width)

Note that in Equation 18.106, it is also possible to fix the E_{TWP} at some desired value and determine the required skylight area.

Rules of thumb for skylight placement for uniform illumination include 4%–8% of roof area and spacing less than 1.5 times ceiling-to-work-plane distance between skylights (Murdoch 1984).

Example 18.18

Determine the work-plane *clear sky plus sun* illuminance for a $30 \times 30 \times 10$ ft.³ office with 75% ceiling, 50% wall, and 30% floor reflectance with four 4×4 ft.² double-domed skylights at 2:00 p.m. on January 15 at 32° latitude. The skylight well is 1 ft. deep at with 60% reflectance walls, and the outer- and inner-dome flat-plastic transmittances are 0.85 and 0.45, respectively. The net skylight area is 90%.

Solution

Follow the four steps in the lumen method for skylighting.

Step 1: Use Figure 18.48 with the solar altitude of 41.7° (calculated from Equation 18.93) for the clear sky plus sun curve to get horizontal illuminance:

$$E_H = 7400 \text{ fc.}$$

Step 2: Use Equation 18.99 to determine domed transmittances from the flat-plate plastic transmittances given

$$T_{D_1} = 1.25(0.85)[1.18 - 0.416(0.85)] = 0.89,$$

$$T_{D_2}(T_F = 0.45) = 0.56,$$

and use Equation 18.100 to get total dome transmittance from the individual dome transmittances:

$$T_D = \frac{(0.89)(0.56)}{(0.89) + (0.56) - (0.89)(0.56)} = 0.52.$$

To determine well efficiency, use $WI = 0.25$ from Equation 18.101 with 60% wall reflectance in Figure 18.50 to give $N_w = 0.80$. With $R_A = 0.90$, use Equation 18.102 to calculate net transmittance:

$$T_n = (0.52)(0.80)(0.90)(1.0) = 0.37.$$

Step 3: The light loss factor is assumed to be from *typical* values in Equation 18.97: $K_m = (0.75)(0.94) = 0.70$. The room utilization coefficient is determined using Equations 18.103 and 18.104:

$$RCR = \frac{5(7.5)(30 + 30)}{(30)(30)} = 2.5,$$

$$RCU = [1 + 0.0288(2.5)^{1.560}]^{-1} = 0.89.$$

Equation 18.104 yields $K_u = (0.37)(0.89) = 0.33$.

Step 4: The work-plane illuminance is calculated by substituting these values into Equation 18.106:

$$E_{TWP} = 7400 \left[\frac{4(16)}{30(30)} \right] 0.33(0.70),$$

$$E_{TWP} = 122 \text{ fc.}$$

18.2.5.5 Daylighting Controls and Economics

The economic benefit of daylighting is directly tied to the reduction in lighting electrical energy operating costs. Also, lower cooling-system operating costs are possible due to the reduction in heating caused by the reduced electrical lighting load. The reduction in lighting and cooling system electrical power during peak demand periods could also beneficially affect demand charges.

The reduction of the design cooling load through the use of daylighting can also lead to the reduction of installed or first-cost cooling system dollars. Normally, economics dictate that an automatic lighting control system must take advantage of the reduced lighting/cooling effect, and the control system cost minus any cooling system cost savings should be expressed as a *net* first cost. A payback time for the lighting control system (*net* or not) can

be calculated from the ratio of first costs to yearly operating savings. In some cases, these paybacks for daylighting controls have been found to be in the range of 1–5 years for office building spaces (Rundquist 1991).

Controls, both aperture and lighting, directly affect the efficacy of the daylighting system. As shown in Figure 18.51, aperture controls can be architectural (overhangs, light shelves, etc.) and/or window shading devices (blinds, automated louvers, etc.). The aperture controls generally moderate the sunlight entering the space to maximize/minimize solar thermal gain, permit the proper amount of light for visibility, and prevent glare and beam radiation onto the workplace. Photosensor control of electric lighting allows the dimming (or shutting off) of the lights in proportion to the amount of available daylighting illuminance.

In most cases, increasing the solar gain for daylighting purposes, with daylighting controls, saves more in electrical lighting energy, and the cooling energy associated with the lighting then is incurred with the added solar gain (Rundquist 1991). In determining the annual energy savings total from daylighting, ES_T , the annual lighting energy saved from daylighting, ES_L , is added with the reduction in cooling system energy, ΔES_C , and with the negative of the heating system energy increase ΔES_H :

$$ES_T = ES_L + \Delta ES_C - \Delta ES_H. \quad (18.107)$$

A simple approach to estimating the heating and cooling energy changes associated with the lighting energy reduction is by using the fraction of the year associated with the cooling or heating season (f_C, f_H) and the seasonal coefficient of performance (COP_C, COP_H) of the cooling or heating equipment. Thus, Equation 18.107 can be expressed as

$$ES_T = ES_L + \frac{f_C ES_L}{COP_C} - \frac{f_H ES_L}{COP_H},$$

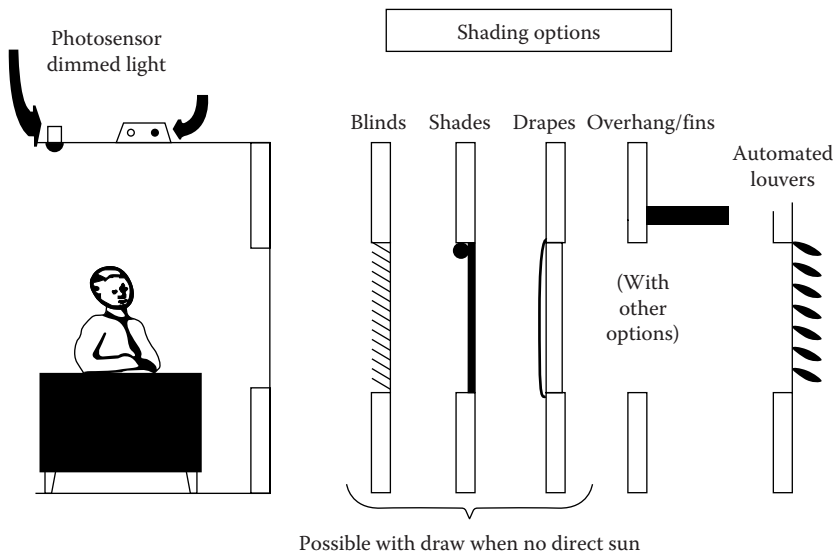


FIGURE 18.51

Daylighting system controls. (From Rundquist, R.A., *ASHRAE J.*, 11, 30–34, November 1991.)

$$ES_T = ES_L + \left(\frac{f_C}{COP_c} - \frac{f_H}{COP_H} \right). \quad (18.108)$$

It should be noted that the increased solar gain due to daylighting has not been included here but would reduce summer savings and increase winter savings. If it is assumed that the increased wintertime daylighting solar gain approximately offsets the reduced lighting heat gain, then the last term in Equation 18.108 becomes negligible.

To determine the annual lighting energy saved (ES_L), calculations using the lumen method described earlier should be performed on a monthly basis for both clear and overcast days for the space under investigation. Monthly weather data for the site would then be used to prorate clear and overcast lighting energy demands monthly. Subtracting the calculated (controlled) daylighting illuminance from the design illuminance leaves the supplementary lighting needed, which determines the lighting energy required.

This procedure has been computerized and includes many details of controls, daylighting methods, weather, and heating and cooling load calculations. ASHRAE (1989) lists many of the methods and simulation techniques currently used with daylighting and its associated energy effects.

Example 18.19

A 30×20 ft² space has a photosensor dimmer control with installed lighting density of 2.0 W/ft². The required workplace illuminance is 60 fc, and the available daylighting illuminance is calculated as 40 fc on the summer peak afternoon. Determine the effect on the cooling system (adapted from Rundquist 1991).

Solution

The lighting power reduction is $(2.0 \text{ W/ft}^2) (30 \times 20) \text{ ft}^2 \times (40 \text{ fc}/60 \text{ fc}) = 800 \text{ W}$. The space cooling load would also be reduced by this amount (assuming CLF = 1.0):

$$\frac{800 \text{ W} \times 3.413 \text{ Btu h/W}}{12,000 \text{ Btu h/ton}} = 0.23 \text{ ton.}$$

Assuming 1.5 ton nominally installed for 600 ft² of space at \$2200/ton, the 0.23 ton reduction is *worth* $0.23 \times \$2200/\text{ton} = \506 . The lighting controls cost about \$1/ft² of controlled area, so the net installed first cost is

$$\text{Net first cost} = \$600 \text{ controls} - \$500 \text{ A/C savings} = \$100.$$

Assuming the day-to-monthly-to-annual illuminance calculations gave a 30% reduction in annual lighting, the associated operating savings can be determined. Lighting energy savings are

$$ES_L = 0.30 \times 2.0 \text{ W/ft}^2 \times 600 \text{ ft}^2 \times 2500 \text{ h/year} = 900 \text{ kWh.}$$

Using Equation 18.108 to also include cooling energy saved due to lighting reduction (with $COP_c = 2.5$, $f_c = 0.5$, and neglecting heating) gives

$$ES_T = 900(1 + 0.5/2.5 - 0) = 1080 \text{ kWh.}$$

At \$0.10 per kWh, the operating costs savings are $\$0.10/\text{kWh} \times 1080 \text{ kWh} = \$108/\text{year}$.

Thus, the simple payback is approximately 1 year (100/108) for the *net* situation and a little over 5.5 years (600/108) against the *controls* cost alone. It should also be noted that the 800 W lighting electrical reduction at peak hours, with an associated cooling energy reduction of $800 \text{ W}/2.5 \text{ COP} = 320 \text{ W}$, provides a peak demand reduction for the space of 1.1 kW, which can be used as the *first-cost savings* to offset control system costs.

Glossary

- Active system:** A system employing a forced (pump or fan) convection heat transfer fluid flow.
- Daylighting:** The use of the sun's radiant energy for illumination of a building's interior space.
- Hybrid system:** A system with parallel passive and active flow systems or one using forced convection flow to distribute from thermal storage.
- Illuminance:** The density of luminous flux incident on a unit surface. Illuminance is calculated by dividing the luminous flux (in lumens) by the surface area (m^2 , ft^2). Units are lux (lx) (lumens/m^2) in SI and footcandles (fc) ($\text{lumens}/\text{ft}^2$) in English systems.
- Luminous flux:** The time rate of flow of luminous energy (lumens). A lumen (lm) is the rate that luminous energy from a 1 candela (cd) intensity source is incident on a 1 m^2 surface 1 m from the source.
- Passive cooling system:** A system using natural energy flows to transfer heat to the environmental sinks (ground, air, and sky).
- Passive heating system:** A system in which the sun's radiant energy is converted to heat by absorption in the system, and the heat is distributed by naturally occurring processes.
- Sidelighting:** Daylighting by light entering through the wall/side of a space.
- Skylight:** The diffuse solar radiation from a clear or overcast sky, excluding the direct radiation from the sun.
- Sunlight:** The direct solar radiation from the sun.
- Toplighting:** Daylighting by light entering through the ceiling area of a space.

References

- AAMA (Architectural Aluminum Manufacturers Association). 1977. Publication 1602.1.1977, *Voluntary Standard Procedure for Calculating Skylight Annual Energy Balance*. AAMA, Chicago, IL.
- ASHRAE (American Society of Heating, Refrigerating and Air-Conditioning Engineers). 1993. Fundamentals. In *ASHRAE Handbook*. ASHRAE, Atlanta, GA.
- ASHRAE (American Society of Heating, Refrigerating and Air-Conditioning Engineers). 1995. Heating, ventilating, and air-conditioning applications. In *ASHRAE Handbook*, pp. 279–127. ASHRAE, Atlanta, GA.
- Clay, R. A. 2001. Green is good for you. *Monitor on Psychology*, 32(4), 40–42.
- Close, D. J., Dunkle, R. V., and Robeson, K. A. 1968. Design and performance of a thermal storage air conditioning system. *Mechanical and Chemical Engineering Transactions*, MC4, 45.
- De Paepe, M. and Janssens, A. 2003. Thermo-hydraulic design of earth-air heat exchanger. *Energy and Buildings*, 35, 389–397.

- Dietz, P., Murdoch, J., Pokoski, J., and Boyle, J. October 1981. A skylight energy balance analysis procedure. *Journal of the Illuminating Engineering Society*, 11, 27–34.
- Duffie, J. A. and Beckman, W. A. 1991. *Solar Engineering of Thermal Processes*, 2nd edn., Wiley, New York.
- Goswami, D. Y. and Biseli, K. M. August 1994. Use of underground air tunnels for heating and cooling agricultural residential buildings. Report EES-78, Florida Energy Extension Service, University of Florida, Gainesville, FL.
- Goswami, D. Y. and Dhaliwal, A. S. May 1985. Heat transfer analysis in environmental control using an underground air tunnel. *Journal of Solar Energy Engineering*, 107, 141–145.
- Goswami, D. Y. and Ileslamlou, S. May 1990. Performance analysis of a closed-loop climate control system using underground air tunnel. *Journal of Solar Energy Engineering*, 112, 76–81.
- Givoni, B. 1994. *Passive and Low Energy Cooling of Buildings*. Van Nostrand Reinhold, New York.
- Halacy, D.S. 1984. *Home Energy*. Rodale Press, Inc., Emmaus, PA.
- Hay, H. and Yellott, J. 1969. Natural air conditioning with roof ponds and movable insulation. *ASHRAE Transactions*, 75(1), 165–177.
- Hollmuller, P. and Lachal, B. 2001. Cooling and preheating with buried pipe systems: Monitoring, simulation and economic aspects. *Energy and Buildings*, 33, 509–518.
- IES. 1979. *Lighting Handbook, Applications Volume*. Illumination Engineering Society, New York.
- IES. 1987. *Lighting Handbook, Applications Volume*. Illumination Engineering Society, New York.
- Kinney, L., McCluney, R., Cler, G., and Hutson, J. 2005. New designs in active daylighting: Good ideas whose time has (finally) come. In *Proceedings of the 2005 Solar World Congress*. August 6–12, 2005, ISES, Orlando, FL.
- Krarti, M. and Kreider, J. F. 1996. Analytical model for heat transfer in an underground air tunnel. *Energy Conversion Management*, 37(10), 1561–1574.
- Kusuda, T. and Achenbach, P. R. 1965. Earth temperature and thermal diffusivity at selected stations in the United States. *ASHRAE Transactions*, 71(1), 965.
- Labs, K. 1981. Regional analysis of ground and above ground climate. Report ORNL/Sub-81/40451/1. Oak Ridge National Laboratory, Oak Ridge, TN.
- Larson, R., Vignola, F., and West, R., eds. 1992. *Economics of Solar Energy Technologies*. American Solar Energy Society, Orlando, FL.
- Libbey-Owens-Ford Company. 1976. *How to Predict Interior Daylight Illumination*. Libbey-Owens-Ford Company, Toledo, OH.
- Marlatt, W., Murray, C., and Squire, S. 1984. Roof Pond Systems Energy Technology Engineering Center. Report No. ETEC 6, April. Rockwell International, New York.
- Martin, M. and Berdahl, P. 1984. Characteristics of infrared sky radiation in the United States. *Solar Energy*, 33(314), 321–336.
- McCluney, R. 1998. Advanced fenestration daylighting systems. In *International Daylighting Conference '98*. Natural Resources Canada/CETC, Ottawa, Ontario, Canada.
- McQuiston, P. C. and Parker, J. D. 1994. *Heating, Ventilating, and Air Conditioning*, 4th edn. Wiley, New York.
- Murdoch, J. B. 1985. *Illumination Engineering—From Edison's Lamp to the Laser*. Macmillan, New York.
- NCDC (National Climactic Data Center). 1992. *Climatology of the U.S. #81*. NCDC, Asheville, NC.
- Olgay, A. and Olgay, V. 1977. *Solar Control and Shading Devices*, Princeton University Press, Princeton, NJ.
- Pierson, O. 1962. *Acrylics for the Architectural Control of Solar Energy*. Rohm and Haas, Philadelphia, PA.
- PSDH. 1980. *Passive Solar Design Handbook*. Volume I: *Passive Solar Design Concepts*, DOE/CS-0127/1, March 1980. Prepared by Total Environmental Action, Inc. (B. Anderson, C. Michal, P. Temple, and D. Lewis); Volume II: *Passive Solar Design Analysis*, DOE/CS-0127/2, January 1980. Prepared by Los Alamos Scientific Laboratory (J. D. Balcomb, D. Barley, R. McFarland, J. Perry, W. Wray and S. Noll). U.S. Department of Energy, Washington, DC.
- PSDH. 1984. *Passive Solar Design Handbook*. Part One: Total Environmental Action, Inc., Part Two: Los Alamos Scientific Laboratory, Part Three: Los Alamos National Laboratory, Van Nostrand Reinhold, New York.

- Robbins, C. L. 1986. *Daylighting—Design and Analysis*. Van Nostrand, New York.
- Rundquist, R. A. November 1991. Daylighting controls: Orphan of HVAC design. *ASHRAE Journal*, 11, 30–34.
- USDA. 1960. *Power to Produce. 1960 Yearbook of Agriculture*. US Department of Agriculture.

For Further Information

General Background Information

The most complete basic reference for passive system heating design is still the 1980 Los Alamos Lab's *Passive Solar Design Handbook*, all three parts. The *ASHRAE Handbook of Fundamentals* is a good general introduction to passive cooling techniques and calculations, with an emphasis on evaporative cooling. *Passive Solar Buildings* and *Passive Cooling*, both published by MIT Press, contain a large variety of techniques and details concerning passive system designs and economics. All the major building energy simulation codes (DOE-2, EnergyPlus, TRNSYS, TSB13, etc) now include passive heating and cooling technologies.

The Illumination Engineering Society's *Lighting Handbook* presents the basis for and details of daylighting and artificial lighting design techniques. However, most texts on illumination present simplified format daylighting procedures. Currently used daylighting computer programs include various versions of Lumen Micro, Lightscape, and Radiance.

Solar Today magazine, published by the American Solar Energy Society, is a readily available source for current practice designs and economics, as well as a source for passive system equipment suppliers.

Technical Publication Information

Many of the current and archival passive solar technical papers are found from the conference proceedings and journals associated with the International Solar Energy Society (ISES), its affiliated American Solar Energy Society (ASES), the American Society of Mechanical Engineering (ASME), and ASHRAE. Also, many of the early passive solar practitioners were architects and builders who published in their specific industry trade journals, as is still the case today. As an Internet search for passive solar articles today will reveal, there are several *new* energy/solar/sustainable technical journals that publish passive solar-related articles.



Taylor & Francis

Taylor & Francis Group

<http://taylorandfrancis.com>

19

Concentrating Solar Thermal Power

Manuel Romero, Jose Gonzalez-Aguilar, and Eduardo Zarza

CONTENTS

19.1	Introduction and Context	656
19.2	Solar Concentration and STP Systems	661
19.2.1	Why Use Concentrating Solar Energy Systems?: Dependence of Efficiency with T	661
19.2.2	Solar Concentrator Beam Quality	665
19.2.3	Solar Concentration Ratio: Principles and Limitations of STP Systems	670
19.3	Solar Thermal Power Plant Technologies.....	671
19.4	Parabolic-Trough Solar Thermal Power Plants.....	675
19.4.1	Operational Principle and Components of the Parabolic-Trough Collector	675
19.4.2	Performance Parameters and Losses in a Parabolic-Trough Collector	681
19.4.3	Efficiencies and Energy Balance in a Parabolic-Trough Collector	686
19.4.4	Industrial Applications for Parabolic-Trough Collectors	688
19.4.4.1	Unfired Boiler System.....	689
19.4.4.2	Flash-Steam Systems	689
19.4.4.3	Direct Steam Generation.....	690
19.4.5	Sizing and Layout of Solar Fields with Parabolic-Trough Collectors	691
19.4.6	Electricity Generation with Parabolic-Trough Collectors	693
19.4.7	Thermal Storage Systems for Parabolic-Trough Collectors.....	695
19.4.7.1	Single-Medium Storage Systems.....	696
19.4.7.2	Dual-Medium Storage Systems.....	698
19.4.8	Direct Steam Generation.....	699
19.4.9	SEGS Plants and State-of-the-Art of Solar Power Plants with Parabolic-Trough Collectors.....	707
19.5	Linear Fresnel Reflectors.....	714
19.5.1	Historical Evolution of Linear Fresnel Reflector Systems	714
19.5.2	Future Technology Development and Performance Trends	716
19.6	Central-Receiver Solar Thermal Power Plants.....	716
19.6.1	Technology Description.....	718
19.6.1.1	Heliostat and Collector Field Technology	719
19.6.2	Solar Receiver	727
19.6.2.1	Tubular Receivers.....	732
19.6.2.2	Volumetric Receivers	734
19.6.3	Experience in Central Receiver Systems.....	739
19.6.3.1	Water–Steam Plants: The PS10 Project	740
19.6.3.2	Molten-Salt Systems: Solar Two and Gemasolar	744

19.7 Dish–Stirling Systems	747
19.7.1 System Description	747
19.7.1.1 Concentrator	748
19.7.1.2 Receiver.....	749
19.7.1.3 Stirling Engine.....	749
19.7.2 Dish–Stirling Developments	750
19.8 Conclusions and Outlook	752
References.....	755

19.1 Introduction and Context

Solar energy has a high exergetic value since it originates from processes occurring at the sun's surface at a blackbody equivalent temperature of approximately 5777 K. Because of this, more than 93% of the energy may be theoretically converted to mechanical work by thermodynamic cycles (Winter et al., 1991) or to Gibbs free energy of chemicals by solarized chemical reactions (Kodama, 2003), including promising hydrogen production processes (Romero and Steinfeld, 2012). According to thermodynamics and Planck's equation, the conversion of solar heat to mechanical work or Gibbs free energy is limited by the Carnot efficiency, and therefore to achieve maximum conversion rates, the energy should be transferred to a thermal fluid, or reactants, at temperatures close to that of the sun.

Even though solar radiation is a source of high temperature and exergy at origin, with a high radiosity of 63 MW/m², sun–earth geometrical constraints lead to a dramatic dilution of flux and to irradiance available for terrestrial use only slightly higher than 1 kW/m² and, consequently, supply of low temperatures to the thermal fluid. It is therefore an essential requisite for solar thermal power (STP) plants and high-temperature solar chemistry applications to make use of optical concentration devices that enable the thermal conversion to be carried out at high solar flux and with relatively little heat loss. A simplified model of an STP plant, also known as concentrating solar power (CSP) plant, is depicted in Figure 19.1.

The optimum STP system design combines a relatively large, efficient optical surface (e.g., a field of high-reflectivity mirrors), harvesting the incoming solar radiation and concentrating it onto a solar receiver with a small aperture area. The solar receiver is a high-absorptance and high-transmittance, low-reflectance, radiative/convective heat exchanger that emulates as closely as possible the performance of a radiative blackbody. An ideal solar receiver would thus have negligible convection and conduction losses. In the case of an STP plant, the solar energy is transferred to a thermal fluid at an outlet temperature high enough to feed a heat engine or a turbine that produces electricity. The solar thermal element can be a parabolic-trough field, a linear Fresnel (LF) reflector field, a central receiver system (CRS), or a field of parabolic dishes, normally designed for a normal incident radiation of 800–900 W/m². Annual normal incident radiation varies from 1600 to more than 3000 kWh/m², allowing from 2000 to more than 3500 annual full-load operating hours with the solar element, depending on the available radiation at the particular site.

Solar transients and fluctuation in irradiance can be mitigated by using an oversized mirror field (solar multiple higher than 1) and then making use of the excess energy to load a thermal or chemical storage system. Hybrid plants with fossil backup burners connected in series or in parallel are also possible. The use of heat storage systems and fossil backup makes STP systems highly flexible for integration with conventional power plant design and

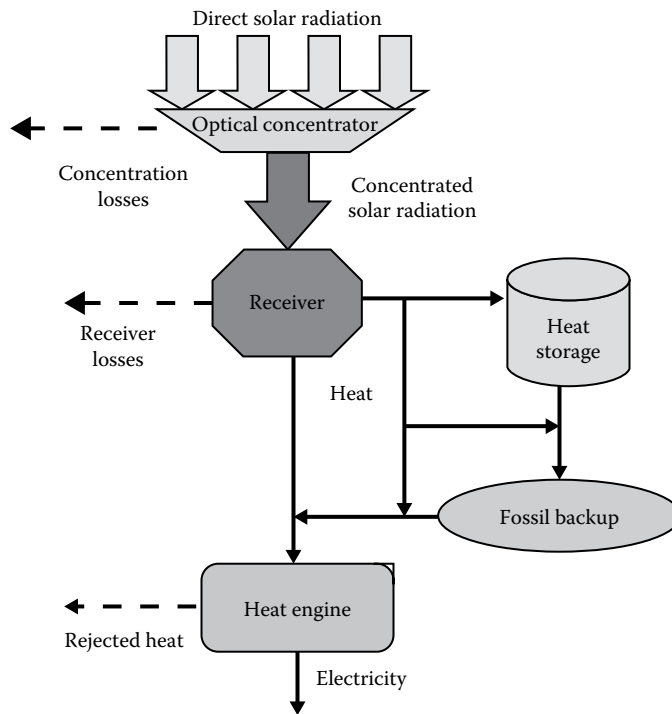


FIGURE 19.1
Flow diagram for a typical solar thermal power plant.

operation and for blending the thermal output with fossil fuel, biomass, and geothermal resources (Mancini et al., 1997). The use of large solar multiples with low-cost heat storage systems of up to 12 h (equivalent at nominal power) facilitates the design of secure-capacity plants supplying between 2000 and 6000 h of operation (equivalent at full load). In addition, hybridization is possible in conventional power plants by using a solar field as a booster or fuel saver in natural gas combined cycles and coal-fired Rankine plants, and may accelerate near-term deployment of projects due to improved economics and reduced overall project risk (Kolb, 1998). Hybridization of a natural gas combined-cycle plant with a solar field acting as a booster is called *integrated solar combined-cycle system (ISCCS)* plant. Three ISCCS plants were implemented in Kuraymat (Egypt), Hassi R'mel (Algeria), and Ain Beni Matar (Morocco) from 2009 to 2012. It is therefore evident that STP can currently supply dispatchable power and meet peaking and intermediate loads at an affordable electricity cost.

Additional advantages of STP are (Morse, 2000) the following:

- Proven capabilities, for example, 354 MW of trough plants in operation in California since 1985 have selectively demonstrated excellent performance, availability, a reduction in investment cost of almost 50%, and significant reductions in O&M cost.
- Modular and thus suitable for large central facilities in the hundreds of MW down to distributed generation in the tens of kW.
- Can be rapidly deployed using entirely domestic resources and existing infrastructure.

- Scale can be significant enough to impact climate-change targets.
- Suitable for both independent power producer and turnkey projects.
- Proven potential for further cost reduction, including those resulting from economies of scale, that is, from mass production of glass, steel, etc.

Electricity production with concentrating solar thermal technologies is not an innovation of the last few years. The French mathematician Augustin Mouchot built a machine able to convert CSP into mechanical work to run a printing press by generating steam (Pifre, 1882). A showcase with a parabolic dish connected to an engine and producing electricity was presented in Paris in 1878. Other remarkable pioneers that deserve recognition are Ericsson (1888), Eneas (1901), Shuman (1913), and Francia (1968). However, solar thermal concentrating technologies were not sufficiently developed for industrial use till the 1970s. The oil crisis triggered R&D on concentrating STP, and several pilot plants were built and tested around the world during the 1980s (Winter et al., 1991). Nevertheless, most of these experiences ended without having reached the final goal of making the concentrating solar thermal technologies commercial. The only exception is the experience accumulated by the LUZ International company in the nine 354 MW total capacity Solar Electricity Generating System (SEGS) plants, which were built between 1984 and 1991, and which have injected more than 16,000 GWh into the Southern California grid since then. All SEGS plants were developed, financed, built, and are still operated on a purely private basis.

However, after the inauguration of the last SEGS plant built by LUZ in 1990 (the plant SEGS IX), no new commercial STP plant was built until 2007, when the plant PS10 was built in Spain and Nevada Solar One was built in the United States. The favorable feed-in tariff implemented in Spain in 2007 led to the construction of more than 40 STP plants in the period 2007–2013, with a total installed power higher than 2.2 GW_e. Public support in the United States led to the construction of more STP plants during the second decade of this century (e.g., SOLANA and Ivanpah plants). Important initiatives are launched in different countries like Chile, South Africa, Morocco, Algeria, India, and others. The main reasons why no commercial plant was built in the period 1991–2007 were (Becker et al., 2002) as follows:

- Financial uncertainties caused by delayed renewal of favorable tax provisions for solar systems in California
- Financial problems and subsequent bankruptcy of the U.S./Israeli LUZ group in 1991, the first commercial developer of private solar power projects
- Rapid drop in fossil energy prices followed by years of worldwide stability at those low levels
- The large STP station unit capacities required to meet competitive conditions for the generation of bulk electricity, resulting in financial constraints due to their inherently large share of capital costs
- Rapidly decreasing depreciation times of capital investments in power plants due to the deregulation of the electricity market and the worldwide shift to private investor ownership of new plant projects
- Drops in cost and enhanced efficiencies of installed conventional power plants, particularly in combined-cycle power plants
- Lack of a favorable financial and political environment for the development of STP plant project initiatives in sunbelt countries

In spite of that, the Cost Reduction Study for Solar Thermal Power Plants prepared for the World Bank in early 1999 (Enermodal, 1999) already concluded that the potential STP market could reach an annual installation rate of 2000 MW of electricity. In the foregoing scenario, this rate would be reached by 2020. Assuming that advanced low-cost STP systems were likely to offer energy output at an annual capacity factor of 0.22 or more, the contribution of STP would be about 24–36 TWh of electricity by 2020 and 1600–2400 TWh by 2050. However, the same study estimated that the current STP capital cost is 2.5–3.5 times higher than the capital cost of a conventional fossil-fueled thermal power plant and showed that the price of electricity generation is between two and four times the conventional generation price. But the potential learning curve is enormous, and technology roadmaps predict that over a 60% cost reduction is possible by 2020, when production costs for solar-only plants could descend below €0.12 per kWh, by combining innovation, mass production, and scaling-up factors (Sargent & Lundy, 2003; Pitz-Paal et al., 2005; Kearney and ESTELA, 2010; IRENA, 2012).

Given the huge solar resource on Earth and the earlier-mentioned cost scenarios, STP is foreseen to impact enormously on the world's bulk power supply by the middle of the century. In Southern Europe alone, the technical potential of STP is estimated at 2000 TWh and in Northern Africa beyond any quantifiable guess (Nitsch et al., 2004). Worldwide, the exploitation of less than 1% of the total STP plant potential would be enough to meet the recommendations of the United Nations "Intergovernmental Panel on Climate Change for Long-Term Climate Stabilization" (Aringhoff et al., 2003; Philibert, 2004). In contrast to conventional fossil plants, concentrating STP plants do not produce CO₂ during operation and are therefore suitable to meet the challenge of keeping standards of living without compromising environmental issues. One MW installed of concentrating STP avoids 688 tons of CO₂ compared to a combined-cycle conventional plant and 1360 tons of CO₂ compared to a conventional coal/steam plant. A 1 m² mirror in the primary solar field produces 400 kWh of electricity/year, avoids 12 tons of CO₂, and contributes to a 2.5 tons savings of fossil fuels during its 25 year operation lifetime. The energy payback time of CSP systems is less than 1 year, and most solar-field materials and structures can be recycled and used again for further plants.

But in terms of electricity grid and quality of bulk power supply, it is the ability to provide dispatchability on demand that makes STP stand out from other renewable energy technologies like PV or wind. Even though the sun is an intermittent source of energy, STP systems offer the advantage of being able to run the plant continuously at a predefined load. Thermal energy storage systems store excess thermal heat collected by the solar field. A typical storage concept consists of two storage tanks filled with a liquid storage medium at different temperatures (Falcone, 1986). When storage is charged, the medium is pumped from the *cold* to the *hot* tank being heated up (directly or indirectly) by the solar heat collected. When storage is discharged, the medium is pumped from the *hot* to the *cold* tank extracting the heat in a steam generator that drives the power cycle. Storage systems, alone or in combination with some fossil fuel backup, keep the plant running under full-load conditions. When solar thermal energy is stored, it is already clear hours in advance when the plant will stop supplying energy. Figure 19.2 shows how stable operation can be extended for several hours after sunset. With an appropriate weather forecast, a 24–48 h prediction of solar capacity appears to be feasible. It should be kept in mind that thermal energy storage systems are designed only to shift the energy a few hours (e.g., from daytime to evening) or days. It cannot compensate the seasonal difference in the solar input, which comes from the changing

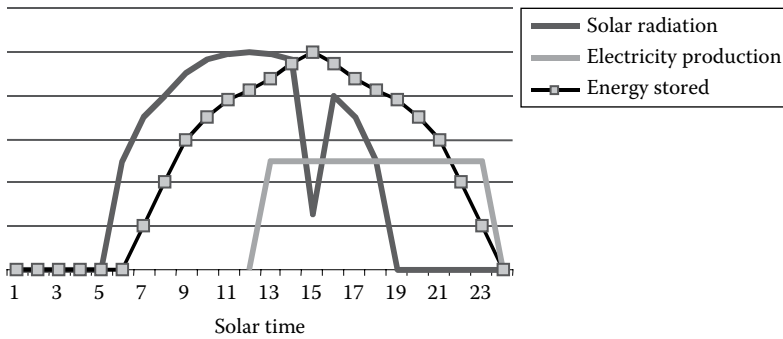


FIGURE 19.2 Extended operation with an only-solar STP plant by using some hours of thermal energy storage.

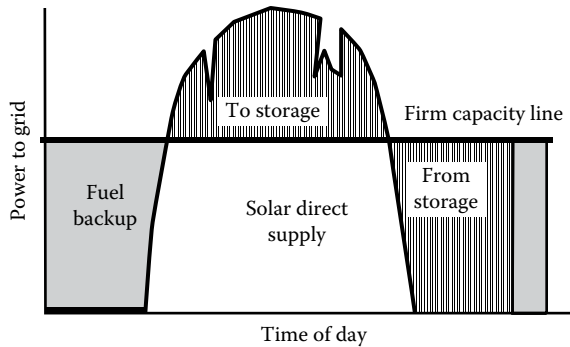


FIGURE 19.3 Example of operational strategy for an STP plant with thermal storage and fuel backup to maintain a constant firm capacity supply round the clock.

duration of sunlight from summer to winter, but with an appropriately small percentage of fossil fuel hybridization, secure capacity can be ensured and investment can be reduced by 30% (Kolb, 1998). Figure 19.3 shows an STP plant providing secure capacity. The thermal storage system supplies most of the energy required by the turbine after sunset. Overnight and early in the morning, operation is ensured by fossil fuel backup. The example shown is a *fuel saver* scheme in which solar energy is used to save fossil fuel during the daytime. There are also other options, like the *power booster* scheme, in which the fossil burner is kept constant all the time, and solar energy is fed into the turbine for peaks during solar hours, in which case the power block can absorb power increments to some extent.

This specific capability of storing high-temperature thermal energy leads to early economically competitive design options, since only the solar portion has to be oversized. This means that there is an incremental cost for the storage system and additional solar field, while the size of the conventional part of the plant (power block) remains the same. Furthermore, storage system efficiencies are high, over 95%. Specific investment costs of less than \$10–\$30 per kWh_{th}, resulting in \$25–\$75 per kWh_e, are

possible today. This STP plant feature is tremendously relevant, since penetration of solar energy into the bulk electricity market is possible only when substitution of intermediate-load power plants of about 4000–5000 h/year is achieved (Pitz-Paal et al., 2005b).

New opportunities are opening up for STP as a result of the global search for clean energy solutions, and new plants are being constructed after more than two decades of interruption (IEA, 2010). Feed-in tariffs, green portfolios, and other environmentally related incentives have been pushing since 2006 for new projects to become a reality in Spain, the United States, Australia, Algeria, and elsewhere (IRENA, 2012).

19.2 Solar Concentration and STP Systems

19.2.1 Why Use Concentrating Solar Energy Systems?: Dependence of Efficiency with T

Explained simply, solar concentration allows *higher-quality* energy to be collected, since higher temperatures, and thereby greater capacity for generating mechanical work, can be achieved. According to the second law of thermodynamics, the higher the operating temperature, T_{op} , is, the better is the efficiency of a heat engine (e.g., the one in an STP plant). The heat engine operating temperature T is directly dependent on the solar receiver, or absorber, outlet temperature.

Moreover, with solar concentration, the receiver–absorber aperture area can be reduced, minimizing infrared losses, which are directly proportional to the emission surface for a given operating temperature. Finally, concentration of solar radiation leads to greater technological development of the absorber and, consequently, to a greater cost reduction potential.

Maximum attainable temperatures in typical fossil fuel burners are on the order of 2100°C. For nuclear fission, the expected maximum useful temperature in Generation-IV gas-cooled reactors is below 1000°C. If higher temperatures are required, a classical solution is to make use of electricity as the heating source, for example, in electric furnaces. The use of electricity for this purpose represents about a 50%–75% conversion loss. In contrast, solar radiation has the potential to reach temperatures close to the apparent temperature of the sun (5777 K).

Solar concentrating systems are characterized by the use of devices, like mirrors or lenses, able to redirect the incident solar radiation received onto a particular surface, collector surface A_c , and concentrate it onto a smaller surface, absorber surface A_{abs} , or absorber. The quotient of these two areas is called the geometric concentration ratio, $\text{Conc} = A_{abs}/A_c$.

Let us assume a simplified model of an STP plant, like the one represented in Figure 19.1, made up of an ideal optical concentrator, a solar receiver performing as a blackbody and therefore having only emission losses (cavity receivers and volumetric receivers theoretically approach this condition), and a turbine or heat engine with Carnot ideal efficiency. System efficiency will depend on the balance of radiative and convective losses in the solar receiver, as shown in Equation 19.1. When the concentrated solar flux impinges on the absorber, its temperature augments and, simultaneously, radiation losses from the absorber surface to the ambient increase. With a thermal fluid cooling the absorber,

when equilibrium, or steady state, is reached, the solar radiation gain equals the sum of infrared emission losses plus the useful energy rejected.

$$\frac{Q_{gain}^*}{A} = \alpha * \text{Conc} * \phi - \sigma * \varepsilon * (T_{abs}^4 - T_{amb}^4) \quad (19.1)$$

where

Q_{gain}^* is the power gain or useful power outlet from solar receiver (W)

A is the absorber aperture area (m²)

α is the hemispherical absorptivity of absorber

Conc is the geometrical concentration ratio

σ is the Stefan–Boltzmann constant (=5.67E–08 W/m² K⁴)

ε is the hemispherical emissivity of absorber

ϕ is the direct normal irradiance (W/m²)

T_{abs} is the temperature (homogeneous) of the absorber (K)

T_{amb} is the effective temperature of ambient or atmosphere *viewed* by the absorber (K)

Solar receiver efficiency, defined as the quotient of power gain flux and concentrated solar radiation flux incident on the receiver (absorber), can be formulated as

$$\eta_{rec} = \frac{(Q_{gain}^*/A)}{\text{Conc} * \phi} \quad (19.2)$$

By substituting Equation 19.1 in 19.2, the dependence of thermal efficiency versus parameters and variables of the receiver is observed.

$$\eta_{rec} = \alpha - \sigma * \varepsilon * \frac{(T_{abs}^4 - T_{amb}^4)}{\text{Conc} * \phi} \quad (19.3)$$

Equation 19.3 is plotted for different concentration ratios in Figure 19.4. This graphic representation, valid for flat absorbers, leads to the following conclusions:

- The maximum theoretical optical efficiency (when $T_{abs} \geq T_{amb}$) is the effective absorptivity of the receiver, α .
- The higher the incident solar flux (Conc * ϕ), the better the optical efficiency.
- The higher the absorber temperature is, the higher the radiative loss is and, therefore, the lower the optical efficiency.
- The higher the effective emissivity, ε , the lower the optical efficiency.

Figure 19.4 shows the evolution of optical efficiency versus temperature and concentration ratio. It also includes the Carnot cycle efficiency, defined as

$$\eta_{Carnot} = \frac{T_{abs} - T_{amb}}{T_{abs}} \quad (19.4)$$

The Carnot cycle efficiency is the ideal efficiency (for reversible processes) that, as observed, increases with temperature and sets the thermodynamic limit of the conversion efficiency of the outlet heat delivered to mechanical work by the receiver.

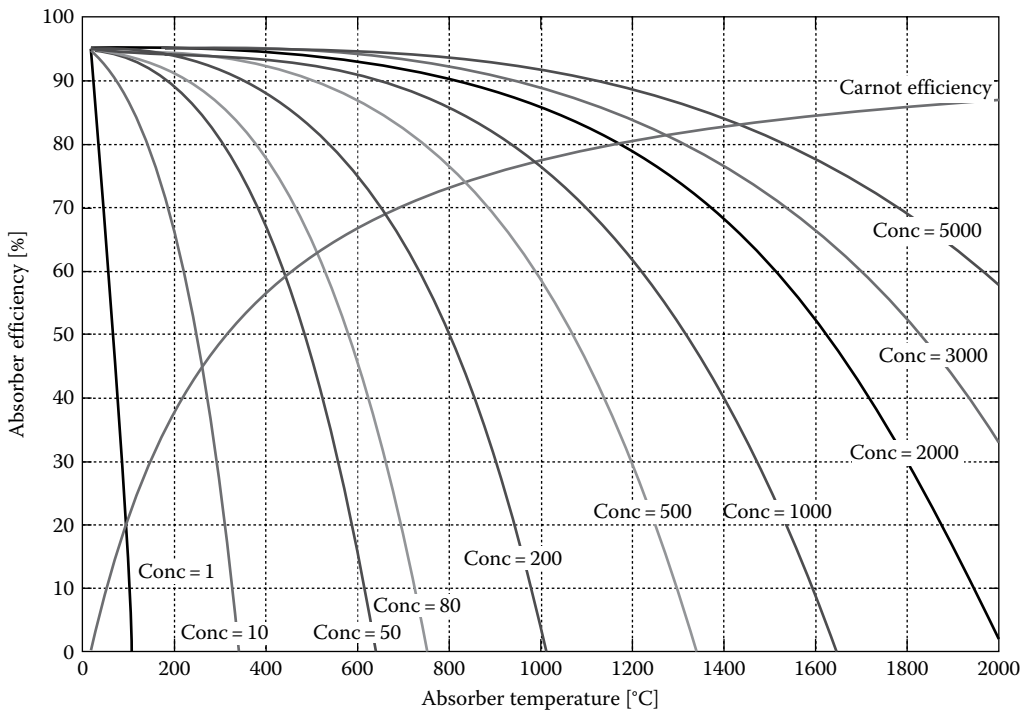


FIGURE 19.4 Efficiency of the solar receiver versus T_{abs} and versus solar concentration ratio, assuming $T_{amb} = 20^\circ\text{C}$, $\phi = 770 \text{ W/m}^2$, and $\alpha = \varepsilon = 0.95$.

As ideal absorber temperature increases, thermal radiation losses increase as well. When losses and gains are equal, the net useful heat is zero, and the receiver should have achieved the maximum temperature or stagnation temperature. The stagnation temperature is described in the following equation and Figure 19.5:

$$T_{abs_max} = \left[\frac{\alpha * \text{Conc} * \phi}{\varepsilon * \sigma} + T_{amb}^4 \right]^{1/4} \tag{19.5}$$

It should be noted that

- A nonselective absorber ($\alpha = \varepsilon = 1$) reaches 95°C in stagnation conditions, without concentration and for the given solar irradiance.
- A selective coating can enable much higher stagnation temperatures to be reached. For instance, at $\text{Conc} = 1000$, the maximum temperature is higher than 1600°C , for $\alpha/\varepsilon = 1$, and about 3200°C , for $\alpha/\varepsilon = 10$ ($\alpha = 1$; $\varepsilon = 0.1$).

From these correlations, it may clearly be concluded that, in terms of solar receiver efficiency, high solar concentrations and low temperatures are the best compromise. For a given concentration ratio, there is an absorber threshold temperature at which radiation losses increase dramatically. However, when analyzing a theoretical STP system, the

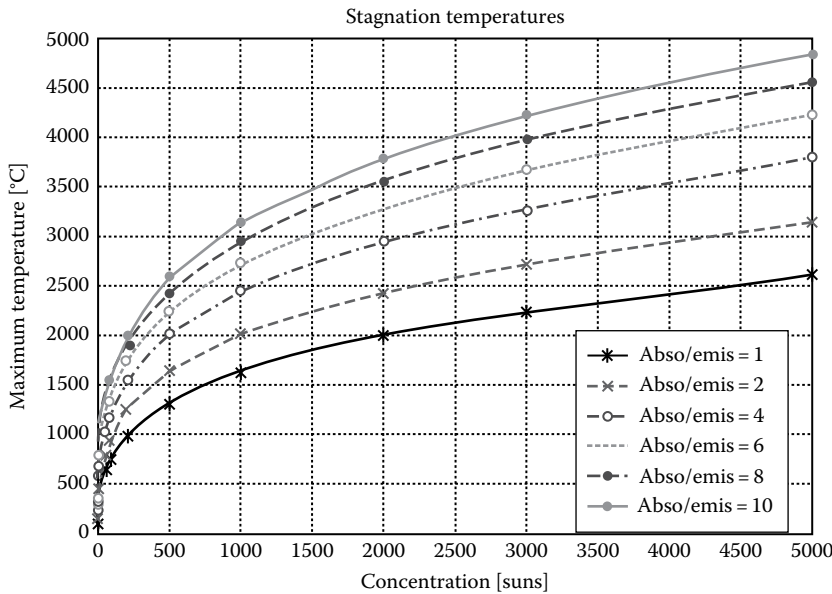


FIGURE 19.5 Stagnation temperatures for a given solar absorber as a function of concentration ratio, for a direct normal irradiance of 770 W/m², ambient temperature of 20°C, α = 1, and different values of emissivity, ε.

convolution of the solar receiver and the heat engine should also be taken into consideration. What is the optimum temperature for a complete system including receiver and Carnot cycle? The combined efficiency of both systems can easily be visualized by multiplying the optical efficiency of the absorber (Equation 19.2) and the Carnot cycle efficiency (Equation 19.4). The result would represent the ideal conversion efficiency of our system from solar radiation to work.

$$\eta_{tot_rec} = \eta_{rec} * \eta_{Carnot} \tag{19.6}$$

Figure 19.6 depicts the combined efficiency of the receiver/heat engine system versus concentration and temperature. It may be observed that for each concentration, the efficiency increases with temperature up to a maximum (Carnot term prevails). Once this peak is achieved, a temperature increment represents a decrement in efficiency (infrared losses at receiver prevail).

As a result, it may be concluded that for any ideal receiver working at a given concentration, there is an optimum temperature, and this temperature can be obtained by

$$\frac{d\eta_{tot_rec}}{dT} = 0 \tag{19.7}$$

Substituting Equations 19.1 through 19.5 into Equation 19.6 and obtaining the derivative, we find a polynomial expression in T_{abs} , and its real (positive) roots give the optimum temperature.

$$4 * \sigma * T_{abs}^5 - 3 * \sigma * \epsilon * T_{amb} * T_{abs}^4 - (\sigma * T_{amb}^5 + \alpha * Conc * \phi * T_{amb}) = 0 \tag{19.8}$$

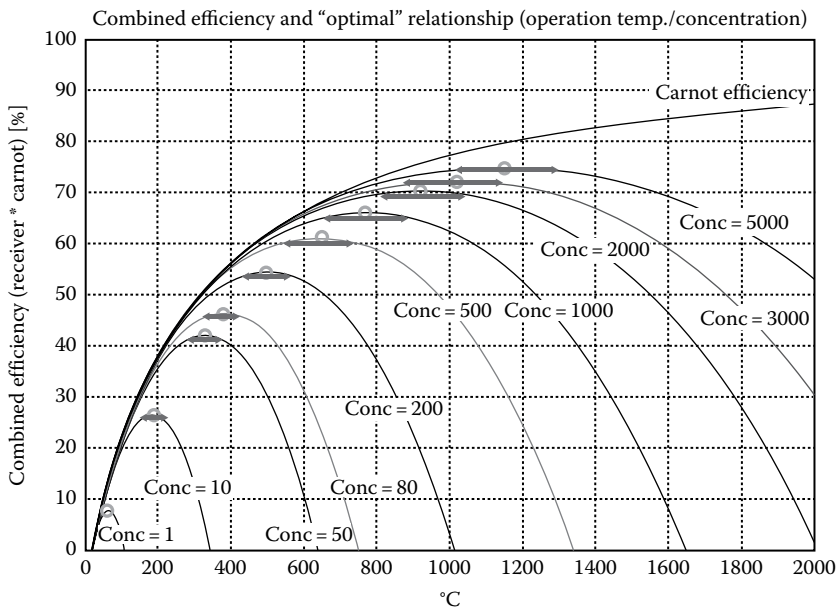


FIGURE 19.6 Combined efficiency of the solar receiver/heat engine system for different solar concentration factors and operation temperatures of the absorber. Direct normal irradiance of 770 W/m^2 , ambient temperature of 20°C , $\alpha = \epsilon = 1$.

Figure 19.6 includes the optimum temperature for the different solar concentrations as calculated from Equation 19.8.

In conclusion, solar concentration is necessary to convert solar energy into mechanical work, and for each geometrical concentration, there is a theoretical optimum absorber operating temperature.

19.2.2 Solar Concentrator Beam Quality

Optical concentration leads to two significant limitations on the practical use of solar radiation that are intrinsic to the characteristics of the radiation source. First, the nonnegligible diffuse solar rays reaching the surface of Earth that do not have a preferential direction are not reflected by the concentrating surface onto the target absorber (energy spillage); therefore, only direct solar radiation from the solar disk can be used. Second, and because of this first restriction, costly mechanical devices are required to track the sun. Consequently, there are practical physical limitations to the concentration level depending on the application (Sizmann, 1991). Sun tracking and use of beam radiation are not the only restrictions. It should also be taken into account that the sun is not a point source of energy at an infinite distance. This means that when solar rays directly from the solar disk reach our observation point at Earth, they are not completely collimated, but at a certain solid angle. The subtended solid angle is $32'$; this means an angular radius of 4.653 mrad or $16'$ of arc; therefore, even an ideal parabolic concentrator would reflect the image of the sun on a spot having the same target-to-mirror solid angle. This means that for an ideal heliostat located 500 m from the optical target or focal point, the theoretical diameter of the spot would be 4.7 m only because of the size

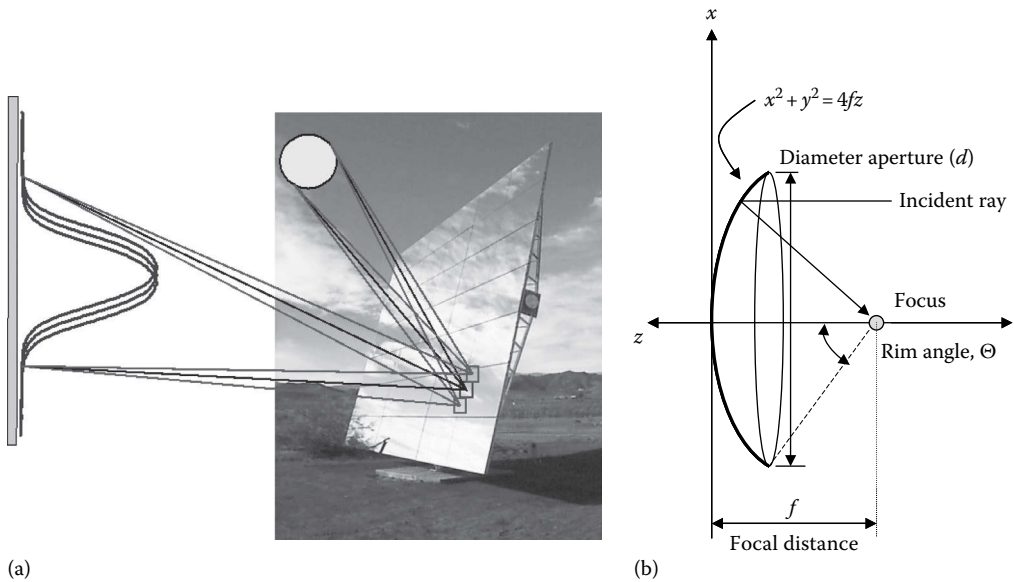


FIGURE 19.7 Configuration of an ideal parabolic concentrator (b) and effect of the size of the sun on the reflected image with a real reflectant surface, heliostat (a).

of the sun. The effect of the size of the sun on the reflected cone for a heliostat and the size of the spot on the target can be observed in Figure 19.7.

Therefore, when designing a real solar concentrator and the aperture of a solar receiver, it is necessary to take into account the minimum size of the spot at a given distance. One additional characteristic of the sun must be considered, the sunshape. Dispersion and absorption effects on the solar photosphere modify the uniform distribution of the expected radiance of an ideal blackbody. Because of that it is more realistic to substitute a *limb-darkened* distribution for the ideal uniform distribution, since the sun is darker near the rim than at the center (Vant-Hull, 1991). Assuming that the sun is an ideal Lambertian emitter, a uniform distribution of radiance (pill-box) with a constant value of $L_0 = 13.23$ MW/m² would be required over the entire solar disk, providing the integrated value of the solar irradiance $E = \int L d\Omega = \pi\theta^2 L_0$, where $\theta = R/D_{ES} = 4.653$ mrad is the ratio between the radius of the solar disk and the Earth–sun distance and Ω the solid angle. For the *limb-darkened* distribution, the following expression of radiance is obtained:

$$\frac{L}{L_0} = 0.36 + 0.84\sqrt{1 - \frac{\xi^2}{\theta_s^2}} - 0.20\left(1 - \frac{\xi^2}{\theta_s^2}\right) \tag{19.9}$$

where

L is the radiance (MW/(m² sr))

L_0 is the radiance at the center of the disk (13.23 MW/m²), for $\xi = 0$

$\xi = r/D_{ES} \leq \theta$ is the radial coordinate normalized to D_{ES}

$\theta_s = R/D_{ES} = 4.653$ mrad

The extraterrestrial irradiance is modified as it enters the atmosphere because of absorption and multiple dispersions, producing the well-known aureole. That is why

better sunshape fit is obtained if the previous radiance distribution is separated into two regions, the central solar disk and the circumsolar region (Rabl, 1985). The ratio between the circumsolar irradiance and direct irradiance varies depending on atmospheric conditions, but in typical sites with good solar radiation, the monthly average does not exceed 5%, provided the operating threshold for system start-up is above 300 W/m². A detailed *ray tracing* analysis reproducing reflection on our solar concentrating surface should take into account the sunshape. To this effect, other factors, like curvature and waviness errors of the reflecting surface, as well as the possible tracking errors in the drive mechanism, must be added. It is relatively simple to approximate all these nonsystematic errors of the concentrator to a standard deviation, $\sigma^2 = \sum \sigma_i^2$, to quantify the beam quality of the reflector. The consequence of the convolution of all the mentioned errors from sun, tracking system, and reflecting surface leads to the real fact that instead of an ideal point-focus parabolic concentrator, Figure 19.7b, the spot and energy profile obtained on a flat absorber can be approximated to a Gaussian shape, Figure 19.7a. The real image obtained is also known as *degraded sunshape*. Subsequently, the designer of a solar receiver should take into account the beam quality of the solar concentrator and the concentrated flux distribution to optimize the heat transfer process.

However, the main interest of a solar concentrator is the energy flux and not the quality of the image. Because of that, 4.65 mrad is a good reference for comparing the extent of optical imperfections. Those errors deflecting the reflected ray significantly less than 4.65 mrad are of minor importance, while deviations over 6 mrad contribute drastically to the reduction of concentration and energy spillage at the receiver aperture.

Solar concentrators follow the basic principles of Snell's law of reflection (Rabl, 1985), as depicted in Figure 19.8. On a specular surface like the mirrors used in STP plants, the reflected solar ray forms an angle with the mirror normal equal to the angle formed by the incoming ray with the normal. On a real mirror with intrinsic and constructional errors, the reflected ray distribution can be described with *cone optics*. The reflected ray direction has an associated error that can be described with a normal distribution function. The errors of a typical reflecting solar concentrator may be either microscopic (specularity) or macroscopic (waviness of the mirror and error of curvature). All the errors together end up modifying the direction of the normal compared to the reference reflecting element. However, it is necessary to discriminate between microscopic and macroscopic errors. Microscopic errors are intrinsic to the material itself and depend on the fabrication process, and can be measured at the lab with mirror samples.

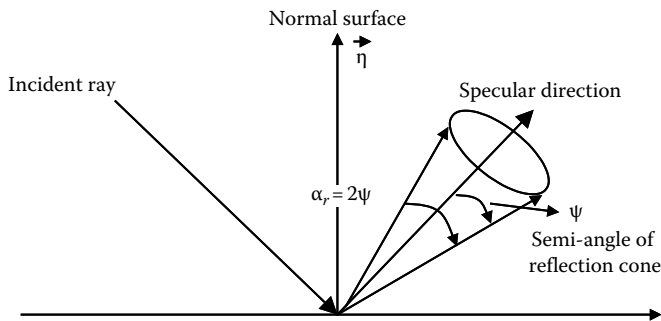


FIGURE 19.8
Geometry of reflection according to the principles of Snell.

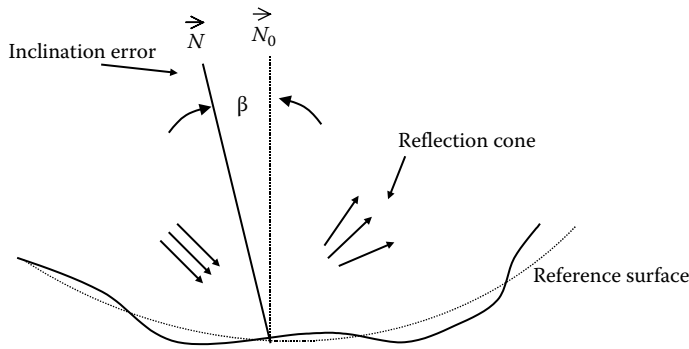


FIGURE 19.9
Normal error produced by grainy texture of the material and deficient curvature of the concentrator.

Macroscopic errors are characteristic of the concentrator itself and the erection process; therefore, they should be measured and quantified with the final system in operation (Biggs and Vittitoe, 1979).

The parameter best defining the *macroscopic* quality of a reflective concentrator is the slope error (β) as shown in Figure 19.9. The slope error is the angle between the normal to the reference surface (\vec{N}_0) and the normal to the real reflecting surface (\vec{N}). The root mean square or RMS, a statistical mean distribution of slope errors, is used to specify the distribution of β on a real surface. For a given differential element of surface (dA), the RMS is obtained as

$$\text{RMS} = \langle \beta^2 \rangle^{1/2} = \left[\frac{\int \beta^2 dA}{\int dA} \right]^{1/2} \tag{19.10}$$

RMS is a deterministic value of the surface errors, but it can be expressed with a probabilistic value as the standard deviation. Since it is more practical to determine the probabilistic error in the reflected image, it is a good idea to translate the RMS of the normals on the reflector to the standard deviation of the reflected rays. For convenience, the value of σ is expressed on a line that intersects and is orthogonal to the normal of the reflector. Assuming a new reference plane r - s placed at a unitary distance, the probability of \vec{N} intersecting the element of surface $dr \cdot ds$ is $F(r, s) \cdot dr \cdot ds$ where $F(r, s)$ is a probability density function normalized to 1 when integrated over the entire plane r - s (Figure 19.10).

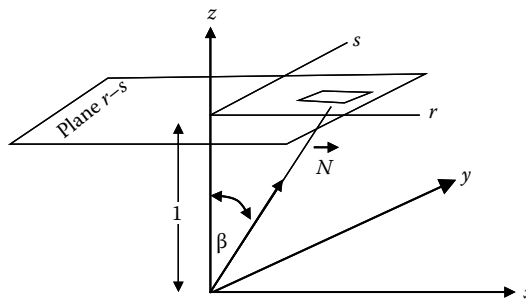


FIGURE 19.10
Translation of the normal error to a new reference plane at a distance 1.

In this case, the probability function can be approximated to a normal distribution function, since further convolution with other errors like specularity, solar tracking, or sunshape leads to a damping effect according to the central limit theorem. In addition, since the total error is the convolution of a series of random surface errors, the distribution is circular normal.

If we use the new coordinates defined for the plane as depicted in Figure 19.10,

$$\rho = \tan \beta = (r^2 + s^2)^{1/2} \tag{19.11}$$

and for those values of ρ close to β , which is the case for actual solar concentrators used in STP plants, the function F may be expressed as

$$F(\rho) = \frac{1}{2\pi\sigma^2} \exp\left[-\frac{\rho^2}{2\sigma^2}\right] \tag{19.12}$$

where the parameter σ is the standard deviation of the reflected ray, and for circular symmetry, $\sigma_r = \sigma_s = \sigma$.

By integrating the previous expression to obtain the RMS of ρ , σ is correlated with β and with the RMS, by the following equation (Biggs and Vittitoe, 1979; Vant-Hull, 1991):

$$\text{RMS} = \langle \rho^2 \rangle^{1/2} = \sigma\sqrt{2} = \langle \beta^2 \rangle^{1/2} \tag{19.13}$$

Summarizing, the beam quality of the concentrating reflector may be expressed by means of three parameters related to the inclination error of the surface elements, the RMS of β , the dispersion σ of the normal, or the dispersion σ of the reflected beam. The total standard deviation of a solar concentrator or beam quality would be the sum of several sources of error:

$$\sigma_C^2 = \sigma_{sp+wav}^2 + \sigma_{curvature}^2 + \sigma_{tracking}^2 \tag{19.14}$$

The total error of the image, also known as degraded sun, would be the convolution of the beam quality of the concentrator with the sunshape:

$$\sigma_D^2 = \sigma_{sunshape}^2 + \sigma_C^2 \tag{19.15}$$

where

- $\sigma_{sunshape}$ is the beam standard deviation due to the sunshape effect (approximately 2.19 mrad)
- σ_{sp+wav} is the beam standard deviation due to specularity and waviness (measured with reflected rays from material samples using a reflectometer)
- $\sigma_{curvature}$ is the beam standard deviation due to curving (should be measured on the concentrator itself)
- $\sigma_{tracking}$ is the beam standard deviation due to aiming point and other drive-mechanism-related sources of error

The association of the flux profile on the target with a Gaussian shape and the determination of the beam quality of the concentrator are useful in identifying the optimum

aperture area of the receiver for a specific fraction of intercepted power. For a given receiver aperture radius length (ρ_A), the probability of $\rho < \rho_A$ may be obtained by integrating (19.12)

$$P(\rho < \rho_A) = 2\pi \int_0^{\rho_A} \rho F(\rho) d\rho = 1 - \exp\left[-\frac{\rho_A^2}{2\sigma^2}\right] \quad (19.16)$$

With this simple correlation, the beam standard deviation (σ) and cone radius (ρ_A) can be correlated by intercepting a certain percentage of reflected power or the probability of $\rho < \rho_A$ (P).

19.2.3 Solar Concentration Ratio: Principles and Limitations of STP Systems

The most practical and simplest primary geometrical concentrator typically used in STP systems is the parabola. Even though there are other concentrating devices like lenses or compound parabolic concentrators (Welford and Winston, 1989), the reflective parabolic concentrators and their analogues are the systems with the greatest potential for scaling up at a reasonable cost. Parabolas are imaging concentrators able to focus all incident paraxial rays onto a focal point located on the optical axis (see Figure 19.7). The paraboloid is a surface generated by rotating a parabola around its axis. The parabolic dish is a truncated portion of a paraboloid. For optimum sizing of the parabolic dish and absorber geometries, the geometrical ratio between the focal distance, f , the aperture diameter of the concentrator, d , and the rim angle, Θ , must be taken into account. The ratio can be deduced from the equation describing the geometry of a truncated paraboloid, $x^2 + y^2 = 4fz$, where x and y are the coordinates on the aperture plane, and z is the distance from the plane to the vertex. For small rim angles, the paraboloid tends to be a sphere, and in many cases, spherical facets are used; therefore, in most solar concentrators, the following correlation is valid:

$$\frac{f}{d} = \frac{1}{4 \tan(\Theta/2)} \quad (19.17)$$

For example, a paraboloid with a rim angle of 45° has an f/d of 0.6 (see Figure 19.11). The ratio f/d increases as the rim angle decreases. A parabolic concentrator with a very small rim angle has very little curvature and the focal point far from the reflecting surface. Because of that, STP systems making use of cavity receivers with small apertures should use small rim angles. Conversely, those STP systems using external or tubular receivers will make use of large rim angles and short focal lengths.

The maximum solar concentration ratio for an ideal perfectly specular 3D paraboloid of rim angle Θ aligned to the sun is (Goswami et al., 2000)

$$C_{\max} = \frac{\sin^2 \Theta}{(4 \sin^2 \theta_s)} \quad (19.18)$$

where θ_s is the semi-angle subtended by the sun, 4.653 mrad ($16'$). For $\Theta = 90^\circ$, $C_{\max} \sim 11,547$.

The thermodynamic limit or maximum concentration ratio for an ideal solar concentrator would be set by the size of the sun and not by the beam quality. By applying the

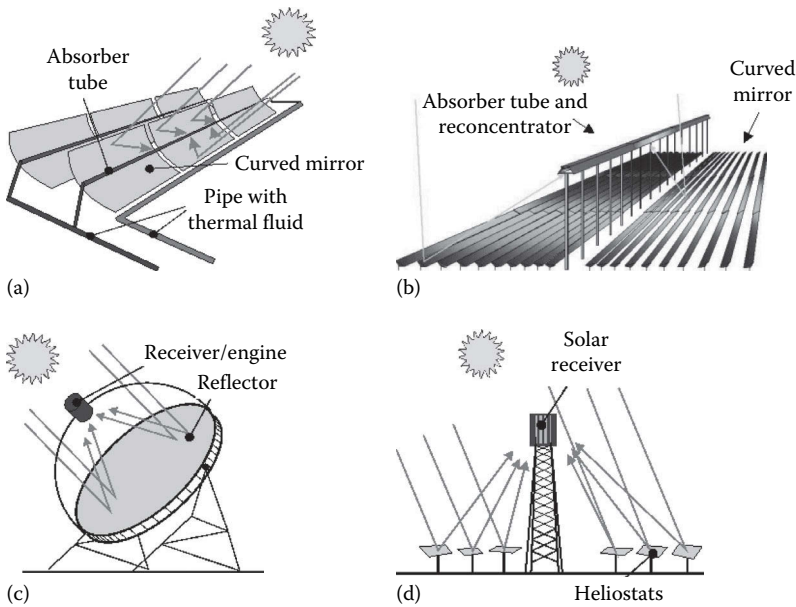


FIGURE 19.11 Schematic diagrams of the four CSP systems scaled up to pilot and demonstration sizes: (a) parabolic trough, (b) linear Fresnel, (c) dish/engine, and (d) central receiver.

geometrical conservation of energy in a solar concentrator, the following expressions are obtained for 3D and 2D systems (for a refraction index, $n = 1$):

$$C_{\max,3D} = \frac{1}{\sin^2 \theta_s} \leq 46,200 \tag{19.19}$$

$$C_{\max,2D} = \frac{1}{\sin \theta_s} \leq 215 \tag{19.20}$$

For real concentrators, the maximum ratios of concentration are much lower, because of microscopic and macroscopic, tracking and mechanical, sunshape, and other errors. Engineers designing a specific STP plant should give special attention to the expected real beam quality and rim angle of the reflecting system to obtain an appropriate sizing of the solar receiver.

19.3 Solar Thermal Power Plant Technologies

STP plants with optical concentration technologies are important candidates for providing the bulk solar electricity needed within the next few decades, even though they still suffer from a lack of public awareness and confidence, especially among scientists and decision makers. Four CSP technologies are today represented at pilot and demonstration scale

(Mills, 2004; Romero and Gonzalez-Aguilar, 2014): parabolic-trough collectors (PTCs), LF concentrator systems, power towers or CRSs, and dish/engine (DE) systems. All the existing pilot plants mimic parabolic geometries with large mirror areas and work under real operating conditions. Reflective concentrators are usually selected since they have better perspectives for scale-up (Figure 19.11).

PTC and LF are 2D concentrating systems in which the incoming solar radiation is concentrated onto a focal line by one-axis tracking mirrors. They are able to concentrate the solar radiation flux 30–80 times, heating the thermal fluid in the receiver. Although commercial PTC and LF plants built until 2013 had a maximum thermal fluid temperature of 395°C, these technologies can achieve higher temperatures if the thermal oil traditionally used is replaced by another working fluid (direct steam generation [DSG] and molten salts), and commercial plants with temperatures up to 500°C are therefore likely to be implemented in a medium term. Although the scale-up effect leads to a significant cost reduction in these plants, thus making implementation of unit powers higher than 50 MW_e advisable, there are also small commercial plants in operation (i.e., the 1 MW_e PTC Saguaro plant in the United States and the 1.4 MW_e LF Puerto Errado plant in Spain). These two STP technologies are well suited for centralized power generation with a Rankine steam turbine/generator cycle in dispatchable markets.

CRS optics is more complex, since the solar receiver is mounted on top of a tower and sunlight is concentrated by means of a large paraboloid that is discretized into a field of heliostats. This 3D concentrator is therefore off-axis, and heliostats require two-axis tracking. Concentration factors are between 200 and 1000, and unit sizes are between 10 and 200 MW, and they are therefore well suited for dispatchable markets and integration into advanced thermodynamic cycles. A wide variety of thermal fluids, like saturated steam, superheated steam, molten salts, atmospheric air, or pressurized air, can be used, and temperatures vary between 300°C and above 1000°C.

Finally, DE systems are small modular units with autonomous generation of electricity by Stirling engines or Brayton mini-turbines located at the focal point. Dishes are parabolic 3D concentrators with high concentration ratios (1000–4000) and unit sizes of 5–25 kW. Their current market niche is in both distributed on-grid and remote/off-grid power applications (Becker et al., 2002).

Typical solar-to-electric conversion efficiencies and annual capacity factors are listed in Table 19.1 (Romero and Steinfeld, 2012). These values have been demonstrated commercially. With current investment costs, all current STP technologies generally thought to require a public financial support strategy for market deployment. Although an independent study promoted by the World Bank at the end of last century (Enermodal, 1999) stated that STP was the most economical technology for solar production of bulk electricity at that time, the significant cost reduction experienced by the photovoltaic panels during the first decade of current century has changed the situation, and STP plants are cheaper only in those places with a high level of direct normal irradiance. However, the added value of dispatchability is still a valuable asset for STP plants when compared with PV plants. Cost data delivered by commercial STP plants show a direct capital costs of 2.5–3.5 times those of a fossil-fueled power plant, and therefore, generation costs of the electricity produced are 2–4 times higher (IRENA, 2012).

Every square meter of STP field can produce up to 1200 kWh thermal energy/year or up to 500 kWh of electricity/year. That means, a cumulative savings of up to 12 tons of carbon dioxide and 2.5 tons of fossil fuel per square meter of STP system over its 25-year lifetime (Geyer, 2002). Although most of the commercial plants installed up

TABLE 19.1

Characteristics of Concentrating Solar Power Systems

	Parabolic Troughs	Central Receiver	Dish/Engine
Power unit	30–140 MW ^a	10–100 MW ^a	5–25 kW
Temperature operation	390°C	565°C	750°C
Annual capacity factor	23%–50% ^a	20%–77% ^a	25%
Peak efficiency	20%	23%	29.4%
Net annual efficiency	11%–16% ^a	7%–20% ^a	12%–25%
Commercial status	Mature	Early projects	Prototypes-demos
Technology risk	Low	Medium	High
Thermal storage	Limited	Yes	Batteries
Hybrid schemes	Yes	Yes	Yes

^a Data interval for the period 2010–2025.

to 2012 used parabolic troughs (11 plants in the United States totaling 415 MW_e, 38 plants in Spain totaling 1975 MW_e, and 3 plants in Morocco, Algeria, and Egypt respectively), this tendency could change because the number of projects promoted with CRS and LF plants is increasing nowadays. The high initial investment required by early commercial plants (\$3000–\$6000 per kW) and the restricted modularity generally motivated by their expensive thermodynamic cycle, combined with the lack of appropriate power purchase agreements and fair taxation policies, led to a vicious circle in which the first generation of commercial grid-connected plants became difficult to implement without market incentives. After two decades of frozen or failed projects, approval in the first decade of this century of specific financial incentives in Europe, the United States, Australia, Algeria, and South Africa paved the way for the launching of the first commercial ventures, and more than 40 STP plants were implemented from 2007 to 2012.

The *parabolic trough* is today considered a fully mature technology (Price et al., 2002). Costs are in the range of \$0.16–\$0.21 per kWh, depending on the boundary conditions for each project (direct normal irradiance available, loan interest rate, etc.), and even up to 30% less in hybrid systems, and technological and financial risks are low. The five plants at the Kramer Junction site (SEGS III–VII) achieved a 30% reduction in operating and maintenance costs, a record annual plant efficiency of 14%, and a daily solar-to-electric efficiency near 20%, as well as peak efficiencies up to 21.5%. Annual plant availability exceeded 98%, and collector field availability was over 99% (Cohen et al., 1999). In view of this advanced state of development, investors were keener to support projects with parabolic troughs, and many companies promoted projects with this technology as soon as public subsidies became available. This was the main reason why most of the commercial STP plants built during the period 2007–2012 used parabolic-trough technology, with either a similar configuration of the SEGS plants or with various hybridization options, including ISCCs.

LF reflector systems are conceptually simple, using inexpensive, compact optics that can produce saturated steam at 150°C–360°C (higher temperatures of about 500°C are pursued for the next generation of LF plants) with land use of less than 10 m²/kW. Therefore the STP technology is best suited for integration with combined-cycle recovery boilers, to replace the steam bled in regenerative Rankine power cycles or for saturated steam turbines. The first commercial experience with LF was the prototype-scale plant developed at the University of Sydney in Australia (Mills and Morrison, 2000). The biggest LF

STP plant in operation in 2012 was Puerto Errado-2 (Spain), with a unit power of 30 MW_e. Taking into account the scale-up effect, LF plants with the unit power of about 100 MW_e were soon promoted after the first small commercial experiences. LF technology is being used in Australian coal-fired power plants as a fuel-saver option to supply 270°C preheat thermal energy to either replace the steam bled in the regenerative Rankine power cycle or for water preheating in the boiler.

Power tower technology, after a proof-of-concept stage, has already started its commercial deployment, although less mature than the parabolic-trough technology. To date, a few CRS commercial plants have been implemented and are in daily operation. At an earlier stage, more than 10 different experimental plants were tested worldwide, generally small demonstration systems of between 0.5 and 10 MW, and most of them operated in the 1980s (Romero et al., 2002). That experience demonstrated the technical feasibility of the CRS power plants and their capability of operating with large heat storage systems. The most extensive operating experience was in the European pilot projects located in Spain on the premises of the Plataforma Solar de Almería (PSA) and in the United States at the 10 MW Solar One and Solar Two facilities located in California. Commercial deployment of CRS plants started in 2007 with the start-up of the Spanish PS10 plant, promoted by the company Abengoa. PS10 plant, with a net unit power of 10 MW_e and a 40 bar/240°C saturated steam Rankine cycle (Osuna et al., 2004), was the first commercial CRS plant in the world. PS10 was followed by the PS20, with a unit power of 20 MW_e. The third CRS commercial plant in the world was the Gemasolar plant, promoted by Torresol Energy in the Spanish province of Seville. Gemasolar, with its molten-salt central receiver and 17 h thermal storage system, has been a significant step forward in the CRS technology. With a unit power of 19 MW_e, this plant can operate round the clock in summertime. The company BrightSource has promoted a challenging CRS plant with 550°C superheated steam receiver, the so-called Ivanpah plant. The 392 MW Ivanpah Plant was connected to the grid in February 2014. Other projects based upon superheated steam and molten salts are under construction in Chile, South Africa, and the United States. In addition to the CRS technologies already implemented in commercial STP plants before 2013 (i.e., saturated steam, superheated steam, and molten salts), the use of open- or closed-loop volumetric air receivers is at R&D stage (Romero et al., 2002).

DE systems are absolutely modular and ideal for unit powers between 5 and 25 kW. Two decades ago, dish–Stirling systems had already demonstrated their high conversion efficiency, concentration of more than 3000 suns, and operating temperatures of 750°C at annual efficiencies of 23% and 29% peak (Stine and Diver, 1994). Unfortunately, DE systems have not yet surpassed the proof-of-reliability operation phase. Only a limited number of prototypes have been tested worldwide, and annual availability above 90% still remains a challenge. Given the fact that autonomous operation and off-grid markets are the first priorities of this technology, more long-endurance test references must be accumulated. DE technology investment costs, which are twice as high as those of parabolic troughs, would have to be dramatically reduced by mass production of specific components, like the engine and the concentrator, although these systems, because of their modular nature, are targeted toward much higher-value markets. DE system industries and initiatives are basically confined to the United States and Europe (Mancini et al., 2003). To date, there has been only one DE commercial plant (the Maricopa plant in the United States), built with 25 kW_e DE systems and a total unit power of 1.5 MW_e. This plant did not achieve the expected performance, and the plant was dismantled in 2012 after 1 year of operation.

19.4 Parabolic-Trough Solar Thermal Power Plants

19.4.1 Operational Principle and Components of the Parabolic-Trough Collector

PTCs are linear-focus concentrating solar devices that convert direct solar radiation into thermal energy and are suitable for working in the 150°C–400°C temperature range (Price et al., 2002).

A PTC is basically made up of a parabolic-trough-shaped mirror that reflects direct solar radiation, concentrating it onto a receiver tube located in the focal line of the parabola. Concentration of the direct solar radiation reduces the absorber surface area with respect to the collector aperture area and thus significantly reduces the overall thermal losses. The concentrated radiation heats the fluid that circulates through the receiver tube, thus transforming the solar radiation into thermal energy in the form of the sensible heat of the fluid. Since a PTC is an optical solar concentrator, it can use only direct solar radiation, and the diffuse solar radiation is lost. Figure 19.12 shows a typical PTC and its components.

PTCs are dynamic devices because they have to rotate around an axis, the so-called tracking axis, to follow the apparent daily movement of the sun. Otherwise, the solar radiation reflected by the parabolic mirrors would not reach the receiver tube. Collector rotation around its axis requires a drive unit. One drive unit is usually sufficient for several parabolic-trough modules connected in series and driven together as a single collector. The type of drive unit assembly depends on the size and dimensions of the collector. Drive units composed of an electric motor and a gearbox combination are used for small collectors (aperture area < 100 m²), while powerful hydraulic drive units are required to rotate large collectors. A drive unit placed on the central pylon is commanded by a local control unit that tells it when and in which direction to rotate the collector to track the sun.

Local control units currently available on the market can be grouped into two categories, depending on the device used to track the sun. These two categories are as follows:

1. Control units based on sun sensors
2. Control units based on astronomical algorithms

Control units in Group (a) use photo cells to detect the sun position, while those in Group (b) calculate the sun vector using very accurate mathematical algorithms that find

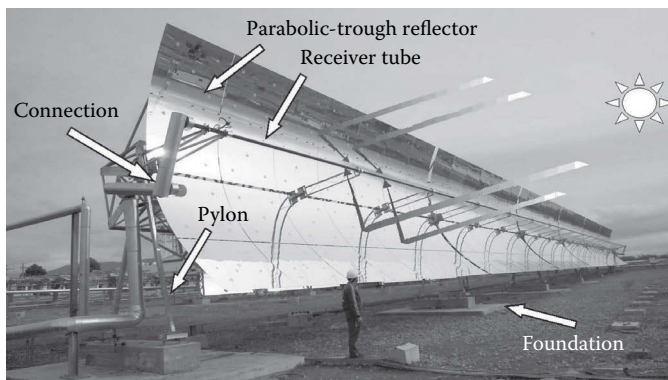


FIGURE 19.12

A typical parabolic-trough collector.

the sun elevation and azimuth every second and measure the angular position of the rotation axis by means of electronic devices (angular encoders or magnetic coded tapes attached to the rotation axis).

Shadow-band and flux-line trackers are in Group (a). Shadow-band trackers are mounted on the parabolic concentrator and face the sun when the collector is in perfect tracking (i.e., the sun vector is within a plane that includes the receiver tube and is perpendicular to the concentrator aperture plane). Two photo sensors, one on each side of a separating shadow wall, detect the sun's position. When the collector is correctly pointed, the shadow wall shades both sensors equally, and their electric output signals are identical.

Flux-line trackers are mounted on the receiver tube. Two sensors are also placed on both sides of the absorber tube to detect the concentrated flux reaching the tube. The collector is correctly pointed when both sensors are equally illuminated and their electrical signals are of the same magnitude.

At present, all commercial PTC designs use a single-axis sun-tracking system. Though PTC designs with two-axis sun-tracking systems have been designed, manufactured, and tested in the past, evaluation results show that they are less cost-effective. Though the existence of a two-axis tracking system allows the PTC to permanently track the sun with an incidence angle equal to 0° (thus reducing optical losses while increasing the amount of solar radiation available at the PTC aperture plane), the length of passive piping (i.e., connecting pipes between receiver pipes of adjacent parabolic troughs on the same collector) and the associated thermal losses are significantly higher than in single-axis collectors. Furthermore, their maintenance costs are higher and their availability lower because they require a more complex mechanical design.

Thermal oils are commonly used as the working fluid in these collectors for temperatures above 200°C , because at these operating temperatures, normal water would produce high pressures inside the receiver tubes and piping. This high pressure would require stronger joints and piping, and thus raise the price of the collectors and the entire solar field. However, the main technical challenges of using water as working fluid in the receiver tubes is not related to the higher pressure, but to process instabilities that could arise in the solar field due to the two-phase flow (i.e., steam and liquid water) circulating inside the receiver tubes (Zarza et al., 1999, 2002).

After a fruitful R&D stage at the PSA, the use of demineralized water for high temperatures/pressures has been already implemented in a 5 MW commercial STP plant built in Thailand by the German company Solarlite, and the feasibility of DSG at 100 bar/ 400°C in the receiver tubes of PTCs has already been proven in the DISS project. For temperatures below 200°C , either a mixture of water/ethylene glycol or pressurized liquid water can be used as the working fluids because only a moderate pressure is required in the liquid phase.

There are many options when choosing the thermal oil to act as working fluid in PTCs. The main limiting factor to be taken into consideration is the maximum oil bulk temperature defined by the manufacturer. Good oil stability is guaranteed by the manufacturer if the maximum bulk temperature is not exceeded. Above this temperature, oil cracking and rapid degradation occur.

The oil most widely used in PTCs for temperatures up to 395°C is VP-1 or Dowtherm-A, which is a eutectic mixture of 73.5% diphenyl oxide/26.5% diphenyl. The main problem with this oil is its high solidification temperature (12°C), which requires an auxiliary heating system when oil lines run the risk of cooling below this temperature. Since the boiling temperature at 1013 mbar is 257°C , the oil circuit must be pressurized with nitrogen, argon, or any other inert gas when oil is heated above this temperature. Blanketing of the entire oil circuit with an oxygen-free gas is a must when working at high temperatures because

high-pressure mists can form an explosive mixture with air. Though there are other suitable thermal oils for slightly higher working temperatures with lower solidification temperatures, they are unaffordable for large solar plants due to their much higher price.

The typical PTC receiver tube is composed of an inner steel pipe surrounded by a glass tube to reduce convective heat losses from the hot steel pipe. The steel pipe has a selective high-absorptivity ($>90\%$), low-emissivity ($<30\%$ in the infrared) coating, which reduces radiative thermal losses. Receiver tubes with glass vacuum tubes and glass pipes with an antireflective coating achieve higher PTC thermal efficiency and better annual performance, especially at higher operating temperatures. Receiver tubes with no vacuum are usually for working temperatures below 250°C , because thermal losses are not so critical at these temperatures. Due to manufacturing constraints, the maximum length of single receiver pipes is less than 6 m, so that the complete receiver tube of a PTC is composed of a number of single receiver pipes welded in series up to the total length of the PTC. The total length of a PTC is usually within 25–150 m.

Figure 19.13 shows a typical PTC vacuum receiver pipe. The outer glass tube is attached to the steel pipe by means of flexible metal differential expansion joints that compensate for the different thermal expansion of glass and steel when the receiver tube is working at nominal temperature. The number of manufacturers of PTC vacuum absorber tubes was small in 2013: the German companies Schott and Siemens, the Italian company Archimede Solar, and the Chinese company HUIYIN. The glass cover is connected to the inner steel tube by means of stainless steel expansion bellows, which compensates the different thermal expansion of the glass cover and steel tubes. The glass-to-metal welding used to connect the glass tube and the expansion bellows is a weak point in the receiver tube and has to be protected from the concentrated solar radiation to avoid high thermal and mechanical stress that could damage the welding. An aluminum shield is usually placed over the bellows to protect the welding.

As seen in Figure 19.13, several chemical getters are placed in the gap between the steel receiver pipe and the glass cover to absorb gas molecules from the fluid that get through the steel pipe wall to the annulus.

PTC reflectors have a high specular reflectance ($>88\%$) to reflect as much solar radiation as possible. Solar reflectors commonly used in PTC are made of back-silvered glass mirrors,

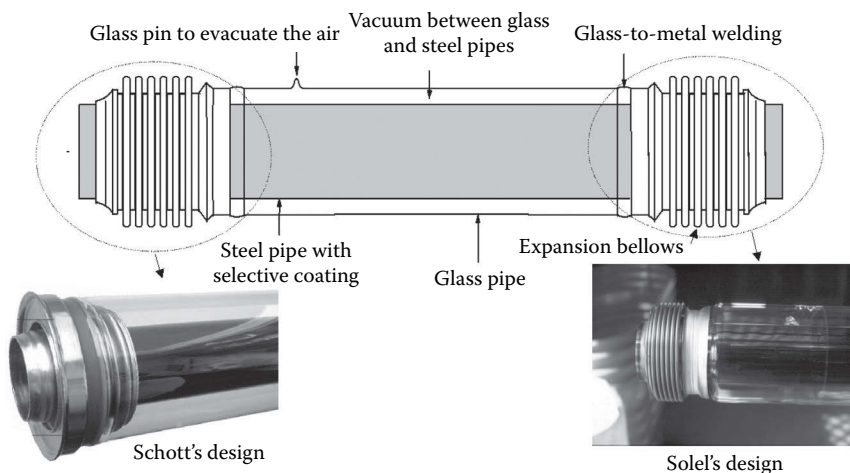


FIGURE 19.13

A typical receiver tube of a PTC.

since their durability and solar spectral reflectance are better than the polished aluminum and metallized acrylic mirrors also available on the market. Solar spectral reflectance is typically 0.93 for silvered glass mirrors and 0.87 for polished aluminum.

Low-iron glass is used for the silvered glass reflectors and the glass receiver envelopes since iron has an absorption peak in the solar spectrum, and therefore glass transmissivity to solar radiation is higher when the iron content is low.

The parabolic-trough reflector is held by a steel support structure on pylons in the foundation. At present, there are several commercial PTC designs. Large STP plant designs are much larger than those developed for industrial process heat (IPH) applications in the range of 125°C–300°C. Examples of PTC designs for IPH applications are the designs developed by the American company IST (Industrial Solar Technology, www.industrialsolartech.com) and the European company Solitem (www.solitem.de). IST and Solitem designs are very similar in size (approx. 50 m total length and 2 m wide) and have aluminum reflectors. SOPOGY (www.sopogy.com), with head offices in Honolulu (Hawaii), developed a 3.7 m long, 1.35 m wide PTC module marketed as Soponova 4.0, which was suitable for both process heat applications and electricity generation with small STP plants.

Two PTC designs conceived for large STP plants are the URSSATrough and EuroTrough, both of which have a total length of 150 m and a parabola width of 5.76 m, with back-silvered thick-glass mirrors and vacuum absorber pipes (Table 19.2). The initial EuroTrough design (Luepfert et al., 2003) was then improved, leading to its successor, the SKAL-ET, the collector installed at the ANDASOL plants in Spain in 2007–2011. The main difference between the URSSATrough and EuroTrough designs is their steel structure: EuroTrough mechanical rigidity to torsion is assured by a steel *torque box* of trusses and beams, while the URSSATrough (www.urssa.es) steel structure is based on the replacement of the torque box by a central steel tube (called the *Torque Tube*) (Figure 19.14). However, assembly of the steel mirror support frames on this central tube must also be highly accurate. The collector design SenerTrough, developed by the Spanish company SENER (www.sener.es), also has a torque tube instead of a torque box. Figure 19.14 shows the steel structures of these two PTC designs: with *torque box* and *torque tube*. The main constraint when developing the mechanical design of a PTC is the maximum torsion at the collector ends, because high torsion would lead to a smaller intercept factor and lower optical efficiency.

PTCs are usually installed with the rotation axis oriented either north–south or east–west; however, any other orientation would be feasible too. The orientation of this type of

TABLE 19.2

Parameters of the ET-150 Parabolic-Trough Collector

Overall length of a single collector (m)	147.5
Number of parabolic-trough modules per collector	12
Gross length of every concentrator module (m)	12.27
Parabola width (m)	5.76
Outer diameter of steel absorber pipe (m)	0.07
Inner diameter of steel absorber pipe (m)	0.055
Number of ball joints between adjacent collectors	4
Net collector aperture per collector (m ²)	822.5
Peak optical efficiency	0.765
Cross section of the steel absorber pipes (m ²)	2.40 × E–03
Inner roughness factor of the steel absorber pipes (m)	4.0 × E–05
Relative roughness of the steel absorber pipes (m)	7.23 × E–04

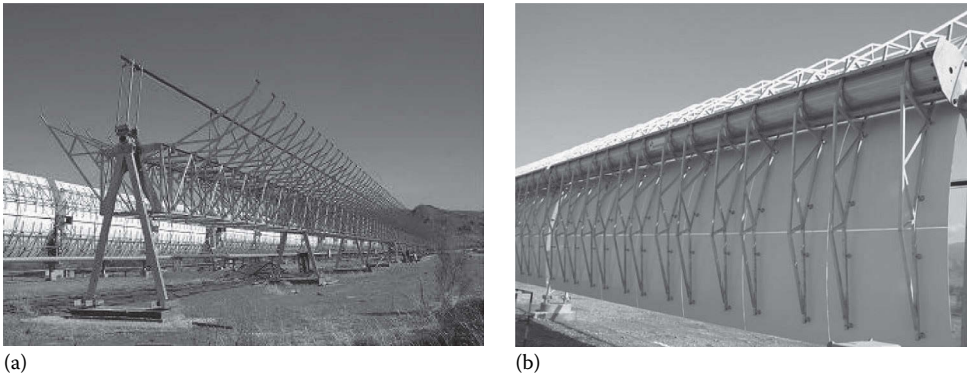


FIGURE 19.14
Steel structures with *torque box* (a) and *torque tube* (b).

solar collector is sometimes imposed by the shape and orientation of the site where they are installed. When the solar field designer can choose solar collector orientation, he must take into consideration that the orientation has a significant influence on the sun incidence angle on the aperture plane of the collectors, which, in turn, affects collector performance. The incidence angle is the angle between the normal to the aperture plane of the collector and the sun's vector, both contained on a plane perpendicular to the collector axis.

Seasonal variations in north–south-oriented trough collector output can be quite wide, depending on the site weather conditions and the geographical latitude. Three to four times more energy is delivered daily during summer months than in the winter at latitudes of about 35°N . Seasonal variations in energy delivery are much smaller for an east–west orientation, usually less than 50%. Nevertheless, a north–south sun-tracking axis orientation usually provides more energy on a yearly basis. This difference in energy output is caused by the different incidence angle of the direct solar radiation onto the aperture plane of the concentrators. Daily variation in the incidence angle is always greater for the east–west orientation, with maximum values at sunrise and sunset and a minimum of 0° every day at solar noon (Rabl, 1985).

So the orientation of the rotation axis of PTCs is a very important design specification, because it strongly affects their performance, and selection of the best orientation depends on the answers to the following questions:

1. Which season of the year should the solar field produce the most energy? If more energy is needed in summer than in winter, the most suitable orientation is north–south.
2. Is it better for energy to be evenly distributed during the year, although in winter, the production is significantly less than in summer? If the answer is “yes,” the best orientation is north–south.
3. Is the solar field expected to supply similar thermal power in summer and winter? If the answer is “yes,” the proper orientation is east–west.

In a typical PTC field, several collectors connected in series make a row, and a number of rows are connected in parallel to achieve the required nominal thermal power output at design point. The number of collectors connected in series in every row depends on the

temperature increase to be achieved between the row inlet and outlet. In every row of collectors, the receiver tubes in adjacent PTCs have to be connected by flexible joints to allow independent rotation of both collectors as they track the sun during the day. These flexible connections are also necessary to allow the linear thermal expansion of the receiver tubes when their temperature increases from ambient to nominal temperature during system start-up. Two main types of flexible connections are available: flexible hoses and ball joints.

Flexible hoses for temperatures below 300°C are composed of an inner hose that can withstand this maximum temperature and an outer metal-braid shield protecting the inner hose. The outer braid is thermally insulated to reduce thermal loss. For higher temperatures, stainless steel bellows are commonly used. This type of hose is not as flexible and causes a significant pressure drop in the circuit because of its high friction coefficient. The minimum bending radius defined by the manufacturer must be taken into consideration to prevent overstressing of the bellows.

Ball joints are another option for flexible connection between the receiver tubes of adjacent collectors. The main benefit of this option is a significantly lower pressure drop because pressure drop for one ball joint is equivalent to a 90° elbow. Another advantage of ball joints is that the connected pipes have two degrees of freedom of movement, because the connected pipes can rotate freely (360°) simultaneously and with a maximum pivot angle of about $\pm 15^\circ$. Ball joints are also provided with an inner graphite sealing to reduce friction and avoid leaks.

Today's PTCs working at temperatures above 300°C are connected by ball joints instead of flexible hoses. Furthermore, the flexible hoses initially installed in the solar power plants in California between 1985 and 1990 are being replaced by ball joints because they are more reliable and have lower maintenance costs. Flexible hoses are likely to suffer from fatigue failures resulting in a leak, while ball joints require only the graphite sealing to be refilled after many thousands of hours of operation. Figure 19.15 shows typical pipe connections: with a flexible hose and with ball joints.

An advanced hybrid element composed of a flex hose and a cylindrical joint has been developed by the German company Senior Flexionics, with a special design to prevent

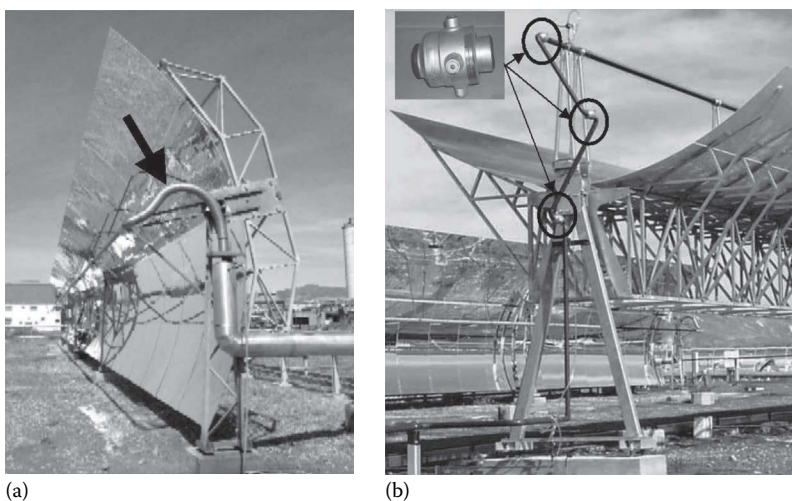


FIGURE 19.15

Flexible hose and ball joint connections to allow collector rotation and linear thermal expansion of receiver tubes: (a) flexible hose and (b) ball joints.

overstressing of the bellows and provide a better reliability. This design (<http://www.seniorflexonics.de>) combines the best features of flex hoses and mechanical seals, while avoiding their disadvantages.

19.4.2 Performance Parameters and Losses in a Parabolic-Trough Collector

Three of the design parameters required for a PTC are the geometric concentration ratio, the acceptance angle, and the rim angle (see Figure 19.16). The concentration ratio is the ratio between the collector aperture area and the total area of the absorber tube, while the acceptance angle is the maximum angle that can be formed by two rays in a plane transversal to the collector aperture so that they intercept the absorber pipe after being reflected by the parabolic mirrors. The concentration ratio, C , is given by the following equation:

$$C = \frac{l_a \cdot l}{\pi \cdot d_o \cdot l} = \frac{l_a}{\pi \cdot d_o} \tag{19.21}$$

where

- d_o is the outer diameter of receiver steel pipe
- l is the collector length
- l_a is the parabola width

The wider the collector acceptance angle is, the less accurate the tracking system has to be, as the collector will not need to update its position as frequently. Usual values of the concentration ratio of PTCs are about 20, although the maximum theoretical value is on the order of 70. High concentration ratios are associated with very small acceptance angles, which require very accurate sun-tracking systems and, consequently, higher costs.

The minimum practical acceptance angle is 32' (0.53°), which is the average solid angle at which the sun sphere is seen from Earth. This means that any PTC with an acceptance angle smaller than 32' would always lose a fraction of the direct solar radiation. In fact, recommended acceptance angles for commercial PTCs are between 1° and 2°. Smaller angles would demand very accurate sun-tracking system and frequent updating of the

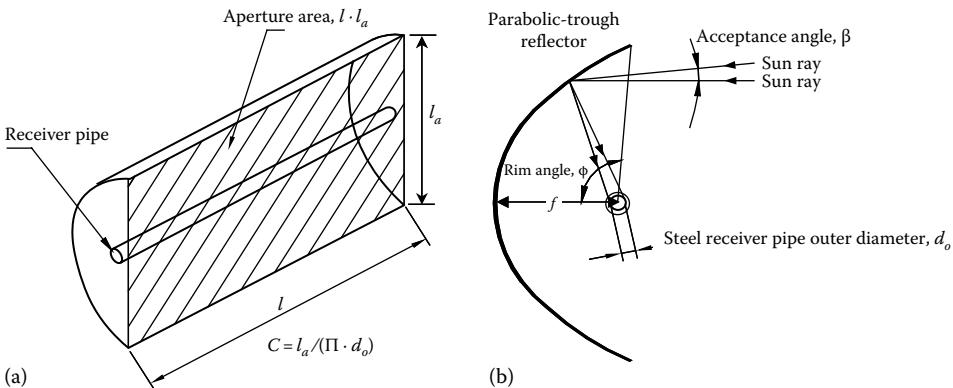


FIGURE 19.16

Concentration ratio and acceptance angle of a parabolic-trough collector: (a) concentration ratio and (b) acceptance angle, β .

collector position, while higher values would lead to small concentration ratios and, therefore, lower working temperatures. So acceptance angle values between 1° and 2° are the most cost-effective.

The rim angle, ϕ , is directly related to the concentrator arc length, and its value can be calculated from Equation 19.22 as a function of the parabola focal distance, f , and aperture width, l_a :

$$\frac{l_a}{4 \cdot f} = \tan \frac{\phi}{2} \quad (19.22)$$

Usual values for rim angles in a PTC are between 70° and 110° . Smaller rim angles are not advisable because they reduce the aperture surface. Rim angles over 110° are not cost-effective because they increase the total reflecting surface without effectively increasing the aperture width.

When direct solar radiation reaches the surface of a PTC, a significant amount of it is lost due to several different factors. The total loss can be divided into three types, which in the descending order of importance are

1. Optical losses
2. Thermal losses from the absorber pipe to the ambient
3. Geometrical losses

The optical losses are associated with four parameters (see Figure 19.17), which are as follows:

1. *Reflectivity, ρ , of the collector reflecting surface:* Since the reflectivity of the parabolic-trough concentrator is less than 1, only a fraction of the incident radiation is reflected toward the receiver tube. Typical reflectivity values of clean silvered-glass mirrors are around 0.93. After washing the mirrors, their reflectivity continuously decreases as dirt accumulates until the next washing. Commercial parabolic-trough mirrors are washed when their reflectivity is of about 0.88–0.9.
2. *Intercept factor, γ :* A fraction of the direct solar radiation reflected by the mirrors does not reach the steel absorber tube due to either microscopic imperfections of

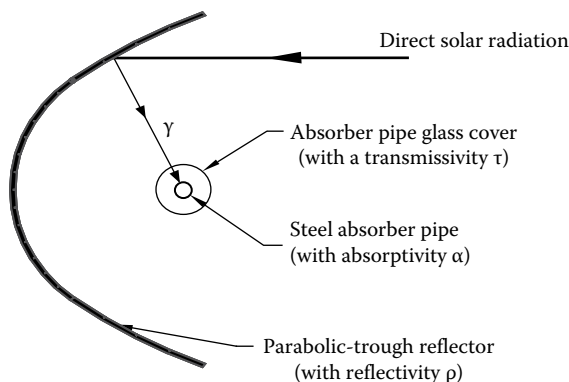


FIGURE 19.17

Optical parameters of a parabolic-trough collector.

the reflectors or macroscopic shape errors in the parabolic-trough concentrators (e.g., imprecision during assembly). These errors cause reflection of some rays at the wrong angle, and therefore they do not intercept the absorber tube. These losses are quantified by an optical parameter called the geometrical intercept factor, Υ_g , which is typically 0.95. Also the flexible bellows connecting the end of the glass cover and the steel tube (see Figure 19.13) reduce the amount of reflected solar radiation that reaches the steel receiver tube, because a fraction of the concentrated solar radiation reflected by the parabolic mirrors is blocked in its way toward the steel receiver tube. This percentage of reflected solar radiation that is blocked by the bellows is quantified by means of the so-called active length factor of the receiver tube, Υ_L , which usually has a value of 0.96–0.97. The overall intercept factor, Υ , is the product of the geometrical intercept factor, Υ_g , and the *active length factor*, Υ_L .

3. *Transmissivity of the glass tube*, τ : The metal absorber tube is placed inside an outer glass tube in order to increase the amount of absorbed energy and reduce thermal losses. A fraction of the direct solar radiation reflected by the mirrors and reaching the glass cover of the absorber pipe is not able to pass through it. The ratio between the radiation passing through the glass tube and the total incident radiation on it gives transmissivity, τ , which is typically $\tau = 0.93$.
4. *Absorptivity of the absorber selective coating*, α : This parameter quantifies the amount of energy absorbed by the steel absorber pipe, compared with the total radiation reaching the outer wall of the steel pipe. This parameter is typically 0.95 for receiver pipes with a cermet coating, while it is slightly lower for pipes coated with black nickel or chrome.

Multiplication of these four parameters (reflectivity, intercept factor, glass transmissivity, and absorptivity of the steel pipe) when the incidence angle on the aperture plane of the PTC is 0° gives what is called the peak optical efficiency of the PTC, $\eta_{opt,0^\circ}$:

$$\eta_{opt,0^\circ} = \rho \times \gamma \times \tau \times \alpha \Big|_{\varphi=0^\circ} \tag{19.23}$$

$\eta_{opt,0^\circ}$ is usually in the range of 0.70–0.76 for clean, good-quality PTCs.

Concerning the second type of losses (i.e., the thermal losses), the total thermal loss in a PTC, $P_{Q,collector \rightarrow ambient}$ is due to radiative heat loss from the steel absorber pipe to ambient, $P_{Q,absorber \rightarrow ambient}$ and convective and conductive heat losses from steel absorber pipe to its outer glass tube, $P_{Q,absorber \rightarrow glass}$. Though this heat loss is governed by the well-known mechanisms of radiation, conduction, and convection, it is a good practice to calculate them all together using the *thermal loss coefficient*, $U_{L,abs}$ according to the following equation, where T_{abs} is the mean steel absorber pipe temperature, T_{amb} is the ambient air temperature, d_o is the outer diameter of the steel absorber pipe, and l is the absorber pipe length (PTC length):

$$P_{Q,collector \rightarrow ambient} = U_{L,abs} \cdot \pi \cdot d_o \cdot l \cdot (T_{abs} - T_{amb}) \tag{19.24}$$

In Equation 19.23, the thermal loss coefficient is given in $(W/m_{abs}^2 K)$ units per square meter of the steel absorber pipe surface. The following equation can be used to find the value of the thermal loss coefficient per square meter of aperture surface of the PTC, $U_{L,col}$:

$$U_{L,col} = \frac{U_{L,abs}}{C} \left(W/m_{col}^2 K \right) \tag{19.25}$$

The heat loss coefficient depends on absorber pipe temperature, which is found experimentally by performing specific thermal loss tests with the PTC working at several temperatures within its typical working-temperature range. Variation in the thermal loss coefficient versus the receiver pipe temperature can usually be expressed with a second-order polynomial equation like Equation 19.26, with coefficients a , b , and c experimentally calculated:

$$U_{L,abs} = a + b \cdot (T_{abs} - T_{amb}) + c \cdot (T_{abs} - T_{amb})^2 \quad (\text{W/m}_{abs}^2 \text{ K}) \quad (19.26)$$

It is sometimes difficult to find values for coefficients a , b , and c valid for a wide temperature range. When this happens, different sets of values are given for smaller temperature ranges. Table 19.3 gives the values of coefficients a , b , and c experimentally calculated by Ajona (1999) for receiver tubes initially installed at SEGS VIII and IX.

A typical value of $U_{L,abs}$ for absorber tubes with vacuum in the space between the inner steel pipe and the outer glass tube is lower than $5 \text{ (W/m}_{abs}^2 \text{ K)}$. High-vacuum conditions are not needed to significantly reduce the convective heat losses. However, the low thermal stability in hot air of the cermet coatings currently used in these receiver tubes requires a high vacuum to assure good coating durability.

The optical properties (i.e., absorptivity and emissivity) of selective coatings used in vacuum receiver tubes for PTCs have been improved in the last years, and new correlations have been developed to calculate the overall thermal loss without using a heat loss coefficient. Nowadays, each receiver tube manufacturer gives the proper correlations to calculate the thermal loss of their tubes, so that the customers have to apply only such correlations.

The optimum space between the steel absorber pipe and the outer glass tube for receivers without vacuum to minimize the convective heat loss is calculated as a function of the Rayleigh number (Ratzel and Simpson, 1979). The possible bowing of the steel pipe has to be considered also in determining the minimum gap, because the possibility of contact with the glass cover has to be avoided.

The third type of losses in a PTC are the geometrical losses, which are due to the incidence angle, ϕ , of direct solar radiation on the aperture plane of the collector. The incidence angle is the angle between the normal to the aperture plane of the collector and the sun's vector, both contained on a plane perpendicular to the collector axis. This angle depends on the day of the year and the time of day. The incidence angle of direct solar radiation is a very important factor, because the fraction of direct radiation that is useful to the collector is directly proportional to the cosine of this angle, which also reduces the useful aperture area of the PTC (see Figure 19.18). The incidence angle reduces the aperture area of a PTC

TABLE 19.3

Values of Coefficients "a," "b," and "c" for a Receiver Tube Installed at SEGS VIII and IX

T_{abs} (°C)	a	b	c
<200	0.687257	0.001941	0.000026
>200; <300	1.433242	-0.00566	0.000046
>300	2.895474	-0.0164	0.000065

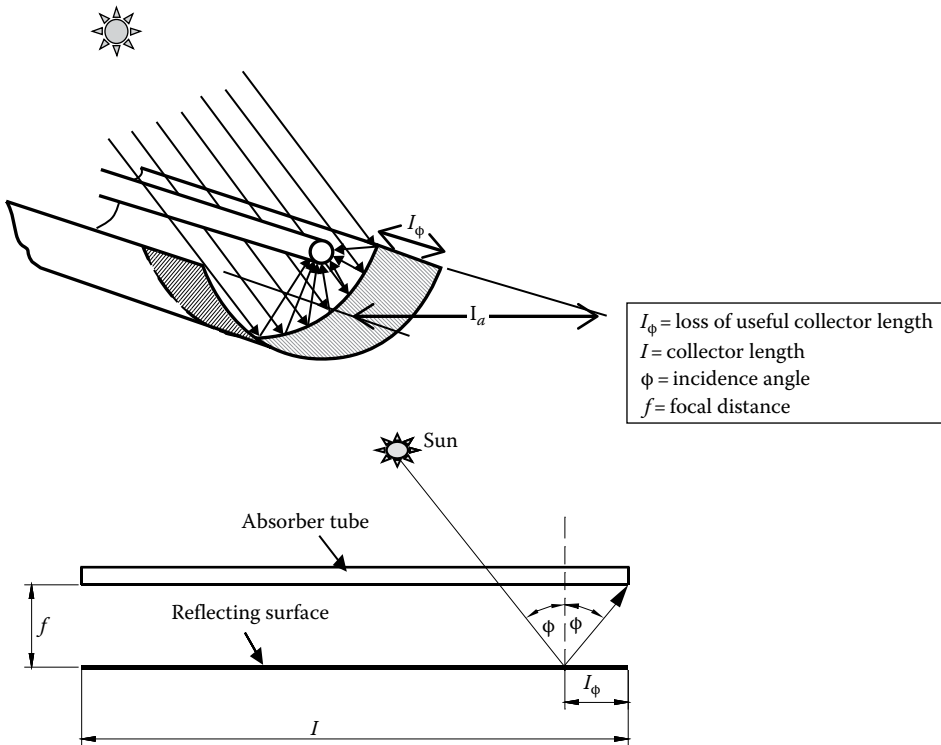


FIGURE 19.18
Geometrical losses at the end of a parabolic-trough collector.

in an amount A_e called the *collector geometrical end losses* and is calculated with Equations 19.27 and 19.28 with the following parameters:

- l_a is the parabola width
- l is the collector length
- f is the focal distance of the parabolic-trough concentrator
- f_m is the mean focal distance in a cross section of the parabolic-trough concentrator
- ϕ is the incidence angle of the direct solar radiation

$$A_e = l_a \cdot l_\phi = l_a \cdot f_m \cdot \tan \phi \tag{19.27}$$

$$f_m = f + \left[\frac{(f \cdot l_a^2)}{(48 \cdot f^2)} \right] \tag{19.28}$$

The incidence angle also affects PTC optical parameters (i.e., mirror reflectivity, selective coating absorptivity, intercept factor, and glass transmissivity) because these parameters are not isotropic. The effect of the incidence angle on the optical efficiency and useful aperture area of a PTC is quantified by the incidence angle modifier, $K(\phi)$, because this parameter includes all optical and geometric losses due to an incidence angle greater than 0° .

The incidence angle modifier, which directly depends on the incidence angle, is usually given by a polynomial equation so that it is equal to 0 for $\phi = 90^\circ$ and 1 for $\phi = 0^\circ$. So, for instance, the incidence angle modifier for an LS-3 collector is given by

$$\begin{aligned}
 K(\phi) &= 1 - 2.23073E - 4x\phi - 1.1E - 4x\phi^2 \\
 &\quad + 3.18596E - 6x\phi^3 - 4.85509E - 8x\phi^4 \quad (0^\circ < \phi < 80^\circ) \\
 K(\phi) &= 0 \quad (85^\circ < \phi < 90^\circ)
 \end{aligned} \tag{19.29}$$

Coefficients of Equation 19.29 are calculated experimentally by means of tests performed with different incidence angles (Gonzalez et al., 2001). The incidence angle of direct solar radiation depends on PTC orientation and sun position, which can be easily calculated by means of the azimuth, AZ , and elevation, EL , angles. For horizontal north–south and east–west PTC orientations, the incidence angle is given by Equations 19.30 and 19.31, respectively. The sun elevation angle is measured with respect to the horizon (positive upward), while azimuth is 0° to the south and positive clockwise.

$$\phi = \arccos \left[1 - \cos^2(EL) \cdot \sin^2(AZ) \right]^{1/2} \tag{19.30}$$

$$\phi = \arccos \left[1 - \cos^2(EL) \cdot \cos^2(AZ) \right]^{1/2} \tag{19.31}$$

19.4.3 Efficiencies and Energy Balance in a Parabolic-Trough Collector

The combination of three different efficiencies

η_{global} is the global efficiency

$\eta_{opt,0^\circ}$ is the peak optical efficiency (optical efficiency with an incidence angle of 0°)

η_{th} is the thermal efficiency

and one parameter

$K(\phi)$ is the incidence angle modifier

describe the performance of a PTC. Their definition is graphically represented in the diagram shown in Figure 19.19, which clearly shows that a fraction of the energy flux incident on the collector aperture plane is lost due to the optical losses accounted for by the peak optical efficiency, while another fraction is lost because of an incidence angle $\phi > 0^\circ$, which is taken into account by the incidence angle modifier, $K(\phi)$. The remaining PTC losses are thermal losses at the absorber tube.

As explained earlier, the peak optical efficiency, $\eta_{opt,0^\circ}$, considers all optical losses that occur with an incidence angle of $\phi = 0^\circ$ (reflectivity of the mirrors, transmissibility of the glass tube, absorptivity of the steel absorber pipe, and the intercept factor). The incidence angle modifier, $K(\phi)$, considers all optical and geometrical losses that occur in the PTC because the incidence angle is $>0^\circ$ (collector end losses, collector center losses, blocking losses due to absorber tube supports, angle dependence of the intercept factor, angle dependence of reflectivity, transmissivity, and absorptivity). Thermal efficiency, η_{th} , includes all absorber tube heat losses from conduction, radiation, and convection.

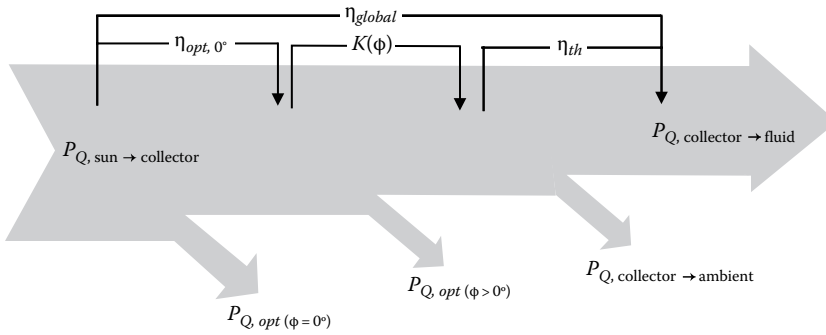


FIGURE 19.19
Diagram of efficiencies and losses in a parabolic-trough collector.

Global efficiency, η_{global} , includes the three kinds of losses that occur in the PTC (optical, geometrical, and heat) and can be calculated as a function of the peak optical efficiency, incidence angle modifier, and thermal efficiency using

$$\eta_{global} = \eta_{opt,0''} \cdot K(\phi) \cdot \eta_{th} \tag{19.32}$$

The global efficiency can also be calculated as the ratio between the net thermal output power delivered by the collector, $P_{Q,collector \to fluid}$, and the solar energy flux incident on the collector aperture plane, $P_{Q,sun \to collector}$, by Equations 19.33 through 19.35:

$$\eta_{global} = \frac{P_{Q,collector \to fluid}}{P_{Q,sun \to collector}} \tag{19.33}$$

$$P_{Q,sun \to collector} = A_c \cdot E_d \cdot \cos(\phi) \tag{19.34}$$

$$P_{Q,collector \to fluid} = q_m \cdot (h_{out} - h_{in}) \tag{19.35}$$

where

- A_c is the collector aperture surface
- E_d is the direct solar irradiance
- ϕ is the incidence angle
- q_m is the fluid mass flow through the absorber tube of the collector
- h_{in} is the fluid specific mass enthalpy at the collector inlet
- h_{out} is the fluid specific mass enthalpy at the collector outlet

The net output thermal power delivered by a PTC can be calculated by means of Equation 19.35 if the fluid mass flow and the inlet and outlet temperatures are known when the collector is in operation. However, these data are not known during the solar field design phase, and the expected net thermal output has to be calculated starting from the values of the direct solar irradiance, ambient air temperature, incidence angle, and PTC optical, thermal, and geometrical parameters. Equation 19.36 can be used for this purpose.

$$P_{Q,collector \to fluid} = P_{Q,sun \to collector} \cdot \eta_{global} = A_c \cdot E_d \cdot \cos(\phi) \cdot \eta_{opt,0''} \cdot K(\phi) \cdot \eta_{th} \cdot F_e \tag{19.36}$$

From a practical standpoint, calculation of the net thermal output power during the design phase is easier if thermal losses in the PTC, $P_{Q,\text{collector} \rightarrow \text{ambient}}$, are used instead of the thermal efficiency, η_{th} . In this case, the net thermal output power is given by the following equation, which must be used in combination with Equation 19.23:

$$P_{Q,\text{collector} \rightarrow \text{fluid}} = A_c \cdot E_d \cdot \cos(\varphi) \cdot \eta_{opt,0'} \cdot K(\varphi) \cdot F_e - P_{Q,\text{collector} \rightarrow \text{ambient}} \quad (19.37)$$

All the parameters used in Equation 19.37 have been explained in the earlier paragraphs, with the exception of the *soiling factor*, F_e , which is $0 < F_e < 1$, and takes into account the progressive soiling of mirrors and absorber tube glass after washing. This means that the reflectivity and transmissivity are usually lower than nominal, and the peak optical efficiency is also lowered. Usual values of F_e are around 0.97, which is equivalent to a mirror reflectivity of 0.90 for mirrors with a nominal reflectivity of 0.93.

19.4.4 Industrial Applications for Parabolic-Trough Collectors

The large potential market existing for solar systems with PTCs can be clearly seen in the statistical data. The U.S. industry consumes about 40% of the total energy demand in that country. Of this, approximately half (about 20% of the total energy consumption) involves IPH suitable for solar applications with PTCs, which are internationally known as IPH applications. As an example of the situation in other countries with a good level of direct solar radiation, industry is also the biggest energy consumer in Spain (more than 50% of the total energy demand), and 35% of the industry demand is in the mid-temperature range (80°C–300°C) for which PTCs are very suitable.

Besides this large potential market for parabolic-trough systems, there is also an environmental benefit that is taken more and more into consideration: contrary to fossil fuels, solar energy does not contaminate, and it is independent of political or economic interruptions of supply (due to war, trade boycott, etc).

Since industrial process energy requirements in the mid-temperature range are primarily met by steam systems, representative configurations of solar steam generation systems are presented in this section with simple diagrams to facilitate their understanding.

Steam is the most common heat transport medium in industry for temperatures below 250°C where there is a great deal of experience with it. Compact steam generators have proven to be extremely reliable. Integration of a solar steam generation system for a given industrial process involves a simple plant interface to feed steam directly into the existing process, with no major facility changes. Medium-temperature steam can be supplied with PTCs in three different ways:

1. Using a high-temperature, low-vapor-pressure working fluid in the solar collectors and transferring the heat to an unfired boiler where steam is produced. Oil is widely used for this purpose.
2. Circulating pressurized hot water in the solar collectors and flashing it to steam in a flash tank. This method is suitable for temperatures that are not too high (below 200°C), because of the high pressure required in the absorber pipes and flash tank for higher temperatures.
3. Boiling water directly in the collectors (the so-called direct steam generation process).

A brief description of each of these methods follows.

19.4.4.1 Unfired Boiler System

Figure 19.20 shows the schematic diagram for an unfired steam boiler system with PTCs. A heat transfer fluid (HTF) is circulated through the collector field, and steam is generated in an unfired boiler. A variation of the system shown in Figure 19.20 incorporates a preheater in the water makeup line, which not only increases the system cost, but also reduces the inlet temperature to the solar field. Water could be circulated in the collector loop, but the fluid generally selected is a low-vapor-pressure, nonfreezing hydrocarbon, or silicon oil. The use of oil overcomes the disadvantages associated with water (high vapor pressure and risk of freezing) and accommodates energy storage, but certain characteristics of these oils cause other problems. Generally, precautions must be taken to prevent the oil from leaking out of the system, which could cause fire. Oil is also expensive and has poorer heat transport properties than water. They are extremely viscous when cold, and a positive displacement pump is sometimes needed to start the system after it has cooled down. The use of a fluid to transfer thermal energy from the solar field to an unfired boiler where steam is produced is internationally known as HTF technology.

The unfired boiler itself is an expensive item requiring alloy tubes for corrosion protection, and it is an additional resistance to heat flow. As in the flash-steam system, the collectors must operate at a temperature some degrees (20°C approx.) above the steam delivery temperature. Because the process steam must be maintained at a certain temperature, the solar-generated steam is delivered at a variable flow rate depending on the solar radiation available at the aperture of the solar collectors. The collector outlet temperature can be held constant by varying the oil flow rate through the collectors as the collected solar energy varies due to cloud passage or any other reason.

19.4.4.2 Flash-Steam Systems

A diagram of a flash-steam system is shown in Figure 19.21. Water at a high enough pressure to prevent boiling is circulated through the collector field and flashed to steam across a throttling valve into a separator. This constant-enthalpy process converts the sensible heat of the water into the latent heat of a two-phase mixture at the conditions prevailing in the separator. The maximum steam quality (i.e., the fraction of total flow that is converted

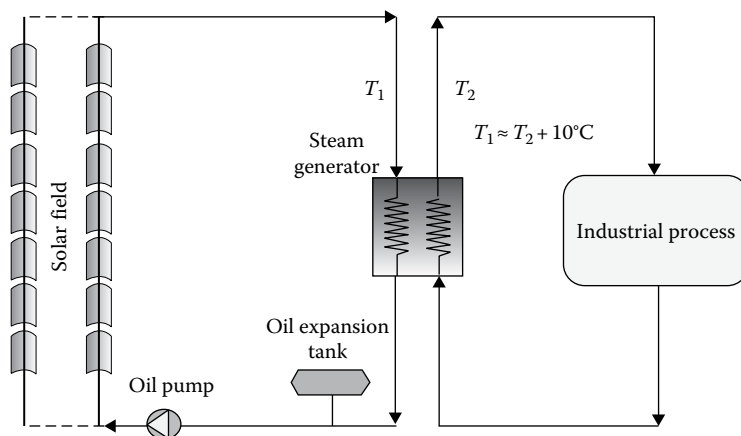


FIGURE 19.20
Unfired-boiler steam-generating system.

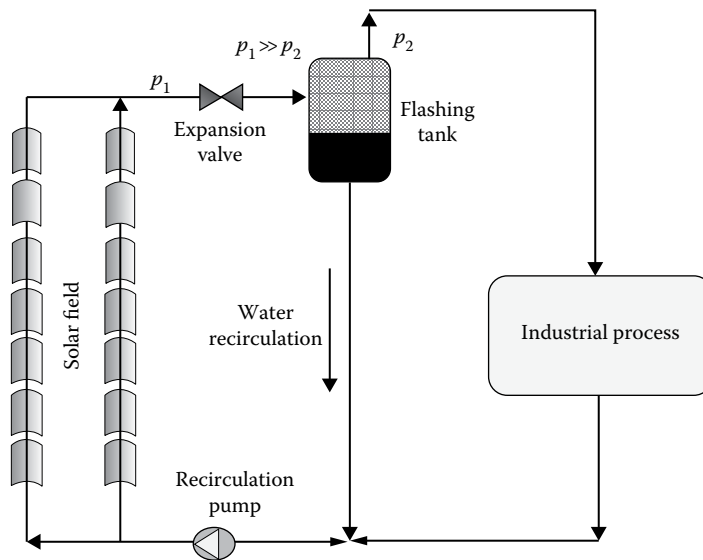


FIGURE 19.21
Flash-steam solar system.

into steam) is less than 10% due to thermodynamic constraints. The steam thus produced is fed into the industrial process, while the water remaining in the flash tank is recirculated to the solar field inlet. Feed-water makeup is injected from the flash tank into the pump suction to maintain the liquid level in the tank.

Using water as an HTF simplifies the construction of a flash-steam system. However, although water is an excellent heat transport medium, freezing problems can occur. Therefore, the freeze protection mechanism must be carefully designed and controlled to ensure that a minimum amount of heat is supplied to the water to prevent freezing due to low ambient temperature.

The disadvantages of the flash-steam system are associated with the steam generation mechanism. Collector temperatures must be significantly higher than the steam delivery temperature to obtain reasonable steam qualities downstream of the throttling valve and to limit the water recirculation rate. But higher temperatures reduce the collector's efficiency. In addition, the circulating pump must overcome the pressure drop across the flash valve, which can be important.

Moreover, the rapid rise in the water vapor pressure at temperatures above 175°C limits the steam pressure that can be achieved by this method to approximately 2 MPa (305 psig) at acceptable levels of electrical power required for pumping. For higher pressures, the electricity consumption of the feed-water pump would be excessive and would jeopardize the efficiency of the whole system.

19.4.4.3 Direct Steam Generation

DSG in the absorber tubes of PTCs is an attractive concept because the average collector operating temperature would be near the steam delivery temperature and because the phase change reduces the required water flow through the circulating pump. The system diagram would be similar to that of the flash-steam system but without a flash valve. The disadvantages of this concept are associated with the thermo-hydraulic problems associated with the two-phase flow existing in the evaporating section of the

solar field. Nevertheless, experiments performed at the PSA in Spain have proven the technical feasibility of DSG with horizontal PTCs at 100 bar/400°C (Zarza et al., 2002).

19.4.5 Sizing and Layout of Solar Fields with Parabolic-Trough Collectors

A typical parabolic-trough solar collector field (Figure 19.22) is composed of a number of parallel rows of several collectors connected in series so that the working fluid circulating through the absorber pipe is heated as it passes from the inlet to the outlet of each row.

The first step in the design of a parabolic-trough solar field is the definition of the so-called design point, which is composed of a set of parameters that determine solar field performance. Parameters to be defined for the *design point* are

- Collector orientation
- Date (month and day) and time of design point
- Direct solar irradiance and ambient air temperature for the selected date and time
- Geographical location of the plant site (latitude and longitude)
- Total thermal output power to be delivered by the solar field
- Solar collector soiling factor
- Solar field inlet/outlet temperatures
- Working fluid for the solar collectors
- Nominal fluid flow rate

If oil is used in the solar field to transfer the energy to an unfired boiler (HTF technology), the selected temperature of the fluid at the solar field outlet must be at least 10°C higher than the steam temperature demanded by the process to be fed. So, for example, if the industrial process to be fed by the solar system requires 300°C steam, the oil temperature at the solar field outlet must be about 315°C. This difference is necessary to compensate for thermal losses between the solar field outlet and the steam generator inlet and the boiler pinch point, which is on the order of (approx.) 5°C–7°C.

Once the design point has been defined, the number of collectors to be connected in series in each row can be calculated using the parameters of the selected PTC (peak optical efficiency, incidence angle modifier, heat loss coefficient, and aperture area) and fluid

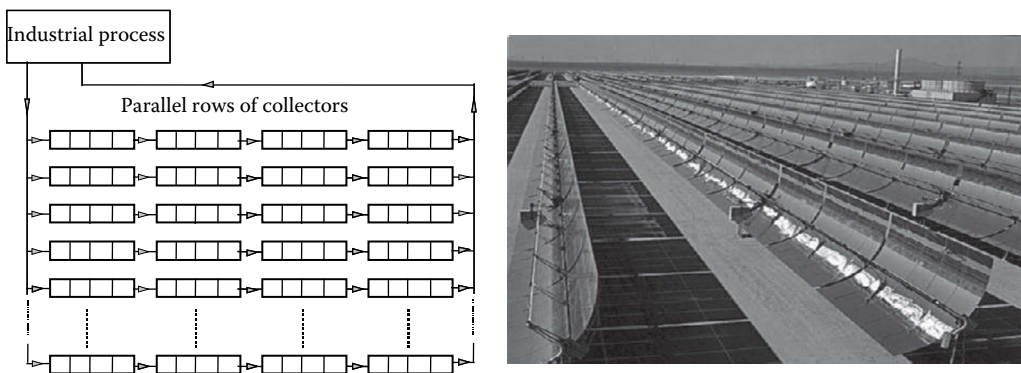


FIGURE 19.22

A typical solar field with parabolic-trough collectors.

(density, heat capacity, and dynamic viscosity). The number of collectors in each row depends on the nominal temperature difference between solar field inlet and outlet, ΔT , and the single collector temperature step, ΔT_c . Thus, if a collector field is intended to supply thermal energy to an unfired boiler that requires a temperature step of 70°C between inlet and outlet, with a nominal inlet temperature of 220°C, the inlet and outlet temperatures in each row will be 220°C and 290°C, respectively, with a $\Delta T = 70^\circ\text{C}$. Once this ΔT has been determined, the number of collectors required in each row, N , is given by the ratio

$$N = \frac{\Delta T}{\Delta T_c}$$

where

N is the number of collectors to be connected in series in a row

ΔT is the required ΔT by the industrial process

ΔT_c is the difference between the single collector nominal inlet and outlet working temperatures

Once the number of collectors to be connected in series in each row has been calculated, the next step is to determine the number of rows to be connected in parallel. This number depends on the thermal power demanded by the industrial process. The procedure for determining the number of rows is very simple when there is no thermal storage system: the ratio between the thermal power demanded by the industrial process and the thermal power delivered by a single row of collectors at design point.

When thermal storage is available, the number of parallel rows is determined in a different way. In this case, the useful thermal energy delivered by a single row of collectors from sunrise to sunset during the design day must be calculated, as well as the thermal energy demanded during the complete day (i.e., 24 h period) by the process to be fed by the solar field. The number of parallel rows required is given by the ratio between the thermal energy demanded by the process and the thermal energy delivered by a single row of collectors.

After sizing the solar field, the designer has to lay out the piping. Three basic layouts are used in solar fields with PTCs. These layouts (direct return, reverse return, and center feed) are shown schematically in Figure 19.23. In all three options, the hot outlet piping is shorter than the cold inlet piping to minimize thermal losses. The advantages and disadvantages in each of these three configurations are explained in following paragraphs.

The *direct-return* piping configuration is the simplest and probably the most extensively used in small solar fields. Its main disadvantage is that there is a much greater pressure difference between the inlets in parallel rows, so that balancing valves must be used to keep flow rates the same in each row. These valves cause a significant pressure drop at the beginning of the array, and thus their contribution to the total system pressure loss is also significant. The result is higher parasitic energy consumption than for the reverse-return layout, where the fluid enters the collector array at the opposite end. Pipe headers with different diameters are used in this configuration to balance array flow. The use of larger pipe headers also results in lower parasitic power requirements, but these could be offset by increases in initial investment costs and thermal energy losses.

The *reverse-return* layout has an inherently more balanced flow. While balancing valves may still be required, the additional system pressure loss is much lower than in a direct-return configuration. (Alternatively, header pipes can be stepped down in size on the inlet side and stepped up on the outlet side to keep flow rate in the headers constant, thereby

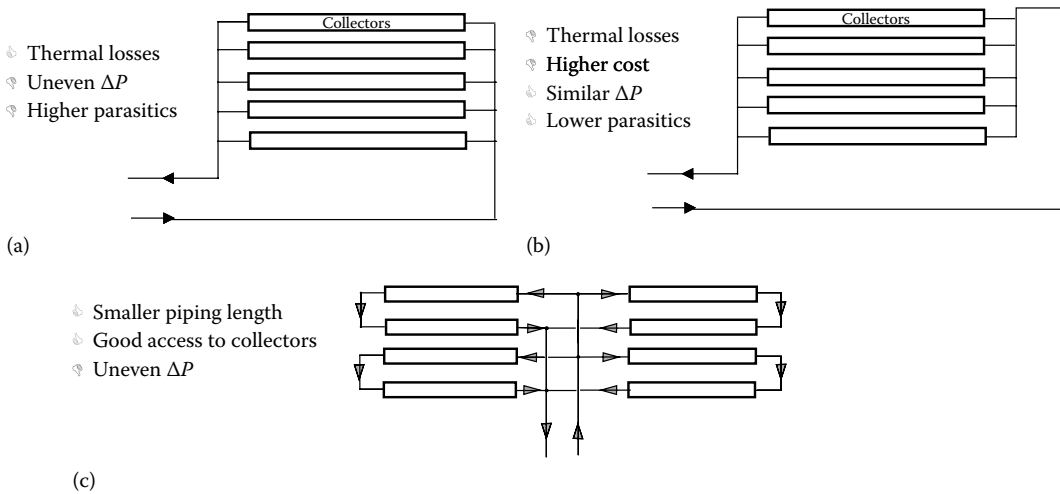


FIGURE 19.23 Solar field layouts for parabolic-trough collectors: (a) direct return, (b) inverse return, and (c) central feed.

providing uniform flow.) The extra length of piping at the solar field inlet is a disadvantage in the reverse-return configuration because of the additional heat loss, although this greatly depends on the solar field inlet temperature. If this temperature is low, additional heat loss is negligible. Adding to pipe length, however, results in higher piping, insulation, and fluid inventory costs.

The *center-feed* configuration is the most widely used layout for large solar fields. Like the direct-return design, pressure balancing valves may be required at the row inlets in very large solar fields, and pressure loss would be thus increased in the solar field. However, this configuration has two important advantages: (1) it minimizes the total amount of piping because there is no pipe running the length of the collector row, and (2) there is direct access to each collector row without buried pipes. This direct access is very important for repair works and solar field washing, which must be performed often in commercial plants to keep a high level of reflectivity, because vehicles have an easy access to each solar collector.

19.4.6 Electricity Generation with Parabolic-Trough Collectors

The current PTC temperature range and their good solar-to-thermal efficiency up to 400°C make it possible to integrate a parabolic-trough solar field in a Rankine water–steam power cycle to produce electricity. The simplified scheme of a typical STP plant using parabolic troughs integrated in a Rankine cycle is shown in Figure 19.24. So far, all the STP plants with parabolic-trough collectors use the HTF technology because steam production by flashing is not suitable for 100-bar superheated-steam pressure, and commercial DSG has not yet been commercially proven for superheated steam at 100 bar.

A parabolic-trough power plant is basically composed of three elements: the solar system, the steam generator, and the power conversion system (PCS; see Figure 19.24). The solar system is composed of a parabolic-trough solar collector field and the oil circuit. The solar field collects the solar energy available in the form of direct solar radiation and converts it into thermal energy as the temperature of the oil circulating through the receiver tubes of the collectors increases.

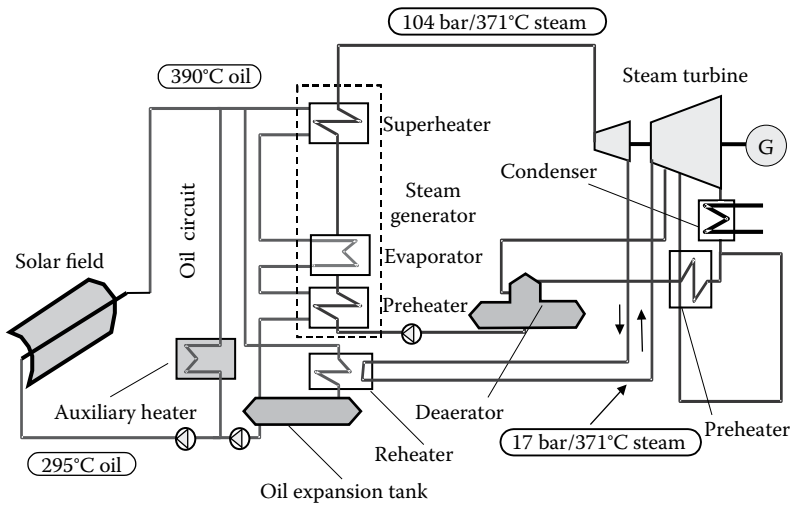


FIGURE 19.24

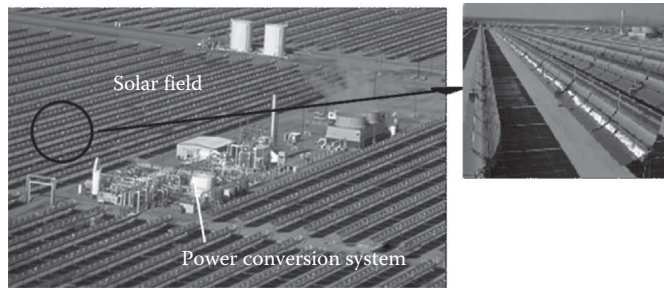
Simplified scheme of a solar thermal power plant with parabolic-trough collectors.

Once heated in the solar field, the oil goes to the steam generator, which is an oil–water heat exchanger where the oil transfers its thermal energy to the water that is used to generate the superheated steam required by the turbine. The steam generator is, therefore, the interface between the solar system (solar field + oil circuit) and the PCS itself. Normally, the steam generator used in these solar power plants consists of three stages:

1. *Preheater*: Where water is preheated to a temperature close to evaporation.
2. *Evaporator*: Where the preheated water is evaporated and converted into saturated steam.
3. *Superheater*: The saturated steam produced in the evaporator is heated in the superheater to the temperature required by the steam turbine.

The PCS transforms the thermal energy delivered by the solar field into electricity, using the superheated steam delivered by the steam generator. This PCS is similar to that of a conventional Rankine power plant, except for the main difference that heat supplied to the conventional Rankine cycle is from fossil fuels, while in the solar plant, the PTCs deliver the required thermal energy.

The superheated steam delivered by the steam generator is then expanded in a steam turbine that drives an electricity generator, which produces the electricity that is delivered to the distribution grid. The steam turbine is usually composed of two consecutive stages, for high- and low-pressure steam. Steam leaving the turbine high-pressure stage goes to a reheater where its temperature rises before entering the low-pressure turbine stage. After this stage, the steam is condensed, and the condensate goes to a water deaerator to remove oxygen and gases dissolved in the water. The steam leaving the turbine low-pressure stage can be condensed either in a wet cooling system (with cooling towers refrigerated by water) or in a dry cooling system (condenser refrigerated by air). The selection of the best cooling system is strongly influenced by the onsite availability of water resources. The main pump takes feed water for the steam generator from the deaerator, thus starting the Rankine thermodynamic cycle again.

**FIGURE 19.25**

Overall view of a solar power plant with parabolic-trough collectors.

Though parabolic-trough power plants usually have an auxiliary gas-fired heater to produce electricity when direct solar radiation is not available, the amount of electricity produced with natural gas is always limited to a reasonable level. This limit changes from one country to another: 25% in California (United States), 15% in Spain (until 2012, because this percentage was reduced to 0% in 2012), and no limit in Algeria. Figure 19.25 shows what an STP plant with PTCs looks like. The PCS is located at the center of the plant, surrounded by the solar field. The plant shown in Figure 19.25 is provided with a wet cooling system, and the steam leaving the cooling towers is clearly shown.

Parabolic-trough power plants can play an important role in achieving sustainable growth because they save about 2000 tons of CO₂ emissions per MW of installed power yearly. Typical solar-to-electric efficiencies of a large STP plant (>30 MW_e) with PTCs are between 15% and 22%, with an average value of about 17%. The yearly average efficiency of the solar field is about 50%.

Though not included in Figure 19.24, a thermal energy storage system can be implemented in parabolic-trough power plants to allow operation of the PCS when direct solar radiation is not available. In this case, the solar field has to be oversized so that it can simultaneously feed the PCS and charge the storage system during sunlight hours. Thermal energy from the storage system is then used to keep the steam turbine running and producing electricity after sunset or during cloudy periods. Yearly hours of operation can be significantly increased, and plant amortization is thus enhanced when a storage system is implemented. However, the required total investment cost is also higher.

19.4.7 Thermal Storage Systems for Parabolic-Trough Collectors

The main problem with using solar radiation is its discontinuity, because it is possible to collect only during sunlight hours. There is an additional limitation when dealing with concentrating solar systems as these systems can collect only the direct solar radiation, so they need clear sky conditions, because clouds block direct solar radiation. Thermal storage systems are implemented to solve these limitations.

When a solar system does not have to supply thermal energy during the night or during cloudy periods, a storage system is not necessary. On the other hand, if the industrial process has to be supplied during periods without direct solar radiation, a storage system has to be implemented to store part of the thermal energy supplied by the solar collectors during the sunlight hours to deliver it when the sun is not available.

Thermal storage systems have three main advantages:

1. Thermal energy can be supplied during hours when direct solar radiation is not available, so that solar energy collection and thermal energy supply do not have to be simultaneous.
2. The solar field inlet can be isolated from possible disturbances at the outlet, because the storage system behaves as a good thermal cushion and avoids feedback of the disturbances affecting the solar field outlet temperature.
3. A constant thermal power level can be supplied to the process if energy is taken from both solar field and thermal storage system, so that the energy taken from the thermal storage complements the energy delivered by the solar field. The variability of the beam solar radiation is thus compensated with thermal energy delivered by the thermal storage system.

The second advantage is very important because it enhances solar field operation on days with frequent cloud transients. No matter how effective solar field control is, the fluid temperature at the outlet is affected by cloud transients, and temperature fluctuations are likely. These fluctuations would immediately affect the working fluid temperature at the inlet if there were not a thermal storage system in between.

The hot water storage system used in low-temperature solar conversion systems (i.e., flat-plate collectors) is not suitable for parabolic-trough systems because the high pressure in the storage tank would make the system too expensive. For this reason, PTCs require the use of a different storage medium. Depending on the medium where the thermal energy is stored, there are two types of systems:

1. Single-medium storage systems
2. Dual-medium storage systems

19.4.7.1 Single-Medium Storage Systems

Single-medium storage systems are those in which the storage medium is the same fluid circulating through the collectors. The most common is thermal oil as both the working fluid and the storage medium. The efficiency of these systems is over 90%. Oil storage systems can be configured in two different ways:

19.4.7.1.1 Systems with a Single Oil Tank

For low-capacity storage systems, thermal energy can be stored in a single tank, in which the oil is stratified by temperature. Energy is stored as latent heat by increasing the temperature of the oil in the tank. Figure 19.26a shows this type of system configuration, in which the solar field can supply hot oil to the tank by means of three-way valves installed at the solar field inlet and outlet, so that all of it or only part of it enters. The density of the thermal oils commonly used as working fluids in these systems strongly varies with temperature. So, for instance, the density of Santotherm 55 oil at 90°C is 842.5 kg/m³, while at 300°C it is 701.4 kg/m³. Due to its lower density, the hot oil entering the storage tank through the top inlet manifold remains in the upper layers inside the tank, while the cold oil always remains at the bottom of the tank. As seen in Figure 19.26a, the boiler supplying the thermal energy demanded by the industrial process can be fed from either the storage tank or the solar field, depending on the position of the three-way valve. When discharging the storage system, the hot oil leaves the tank through the top outlet manifold and returns to the bottom after leaving the boiler. Pump “B2” is used

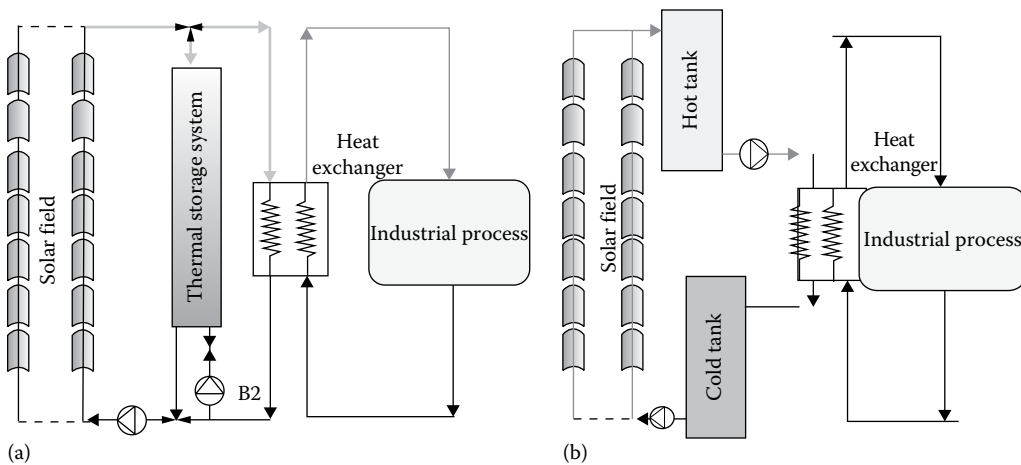


FIGURE 19.26 Thermal storage systems with (a) one and (b) two oil tanks.

exclusively to feed the boiler from the storage tank, when the solar field is not in operation. Cold oil leaves from the bottom of the storage tank and goes to the solar field during daylight hours to be heated and then returned to the top of the storage tank. The storage system is fully charged when all the oil stored in the tank is hot. As already mentioned, the use of a single oil storage tank is feasible only for small storage systems. For high-capacity systems, two oil tanks (i.e., one tank for cold oil and another for hot oil) are needed.

19.4.7.1.2 Systems with Two Oil Tanks

There are two oil tanks in these systems (see Figure 19.26b), one hot tank and one cold tank. The boiler is always fed from the hot tank, and once the oil has transferred heat to the water in the unfired boiler, it goes to the cold tank. This tank supplies the solar field, which at the same time feeds the hot tank with the oil heated by the collectors.

One of the drawbacks of using oil as the storage medium is the need to keep the oil in the storage tank(s) pressurized and inert. Thermal oil has to be kept pressurized above the vapor pressure corresponding to the maximum temperature in the oil circuit to prevent the oil from changing into gas. Fortunately, the vapor pressure of the thermal oils used in these systems is usually low for the 100°C–400°C temperature range, and pressurization is easily maintained by injecting argon or nitrogen. This inert atmosphere also avoids the risk of explosion in the tank from pressurized mists, which are explosive in air.

Another disadvantage of oil systems is the need for appropriate fire-fighting systems, as well as a concrete oil sump to collect any leaks and avoid contamination. All this equipment increases the cost of the storage system. Thermal oil storage systems usually have two safety systems to avoid excessive overpressure inside the tank when temperature increases (the oil expands considerably with temperature):

1. A relief valve to discharge the inert gas into the atmosphere when the pressure inside the tank is over a predefined value. This valve usually works when the pressure inside the tank increases slowly (for instance, during charging).
2. Due to the small section of the relief valve, it cannot dissipate sudden overpressures. There is an additional security device for this purpose: a pressure-rated ceramic rupture disk. This system allows gases to be rapidly evacuated into the

atmosphere. The rupture disk is destructive, because it consists of a ceramic membrane that breaks if the pressure in the tank is higher than calibrated. The rupture disk works only in case of an emergency when overpressure occurs so quickly that the relief valve cannot keep the pressure inside the tank below the limit value.

An additional auxiliary system required in thermal oil storage tanks is a small vessel where gas and volatile compounds produced by oil cracking are condensed and evacuated.

19.4.7.2 Dual-Medium Storage Systems

Dual-medium storage systems are those in which the heat is stored in a medium other than the working fluid heated in the solar collectors. Iron plates, ceramic materials, molten salts, or concrete (Laing et al., 2008) can be used as the storage medium. In these systems, the oil is commonly used as the heat transfer medium between the solar field and the material where the thermal energy is stored in the form of sensible heat. In the case of thermal storage in iron plates, the oil circulates through channels between cast iron slabs placed inside a thermally insulated vessel, transferring thermal energy to them (charging process) or taking it from them (discharging process). When concrete is used as storage medium, the oil circulates through steel tubes installed inside big blocks of concrete.

Molten salts (a eutectic mixture of sodium and potassium nitrates) are nowadays used for dual-medium thermal storage systems in parabolic-trough solar plants. In this case, two tanks are needed: one for cold molten salt and another to store the hot molten salt. Obviously, the lowest temperature is always above the melting point of the salt (250°C, approx.). In this case, a heat exchanger is needed to transfer energy from the oil used in the solar field (heat transfer medium) to the molten salt used for energy storage (storage medium). Figure 19.27 shows the simplified scheme of a parabolic-trough power plant with a molten-salt thermal energy storage system. This type of thermal storage system is currently installed in many Spanish commercial plants, with a storage capacity of 1 GWh in each plant, and it is claimed to be the current most cost-effective option for large commercial solar power plants with large solar shares.

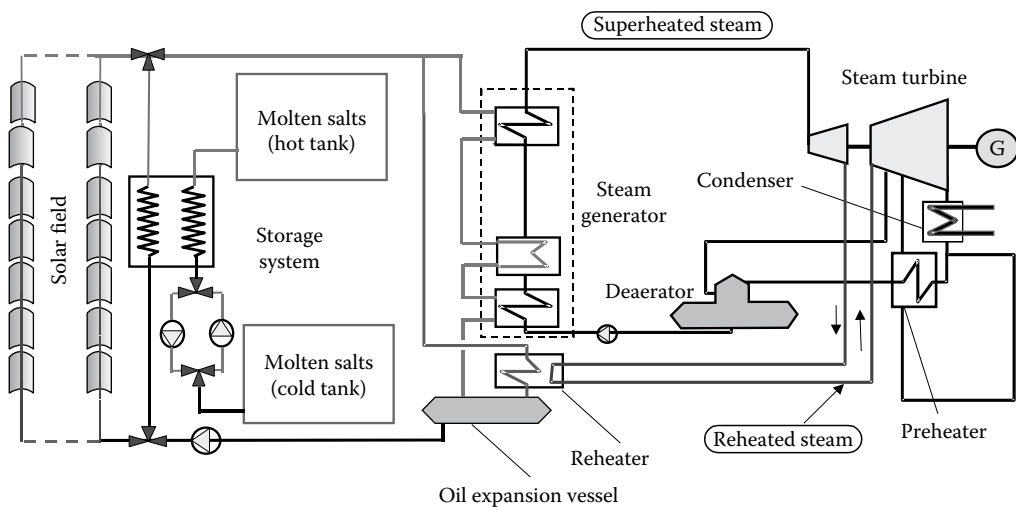


FIGURE 19.27

Scheme of a parabolic-trough power plant with molten-salt storage system.

Thermal storage systems using latent heat, also called phase change material (PCM) storage systems because they use a medium that changes phase during charging and discharging, are under development, and several prototypes have been experimentally tested (Bayón et al., 2010). The storage medium used in the first prototypes was a mixture of NaNO_3 and KNO_3 . The melting temperature of the mixture can be varied from 220°C to 300°C (approx.) changing the percentage of these two components, thus covering a wide range of steam pressures (i.e., 22–100 bar approx.). The main technical constraint of this type of storage systems is the low thermal conductivity of the salt mixture. Although the use of graphite foils to enhance heat transfer has been successfully evaluated, other options are under study and are ready for testing in the short term. However, latent-heat thermal storage systems are not expected to reach the market before 2020. PCM storage systems are required by STP plants with DSG, because the sensible heat storage systems used in HTF plants are not suitable to store the thermal energy released by the steam during its condensation.

19.4.8 Direct Steam Generation

All solar power plants with PTCs implemented to date use thermal oil as the working fluid in the solar field, and they usually follow the general scheme in Figure 19.24, with only slight differences from one plant to another. The technology of these plants has been improved since the implementation of the first commercial plant in 1984 (Lotker, 1991; Price et al., 2002). However, though the collector design and connection between the solar system and the PCS have been improved, some further improvements could still be implemented to reduce costs and increase efficiency. The main limitation to improving their competitiveness is the technology itself: the use of oil as a heat carrier medium between the solar field and the PCS, which entails a high-pressure drop in the oil circuit, limitation of the maximum temperature of the Rankine cycle, and O&M costs of the oil-related equipment. If the superheated steam required to feed the steam turbine in the power block were produced directly in the receiver tubes of the PTCs (i.e., DSG), the oil would be no longer necessary, and temperature limitation and environmental risks associated with the oil would be avoided (Ajona and Zarza, 1994). Figure 19.28 shows the overall scheme of a parabolic-trough power plant with DSG in the solar field. Simplification of overall plant configuration is evident when comparing Figures 19.24 and 19.28.

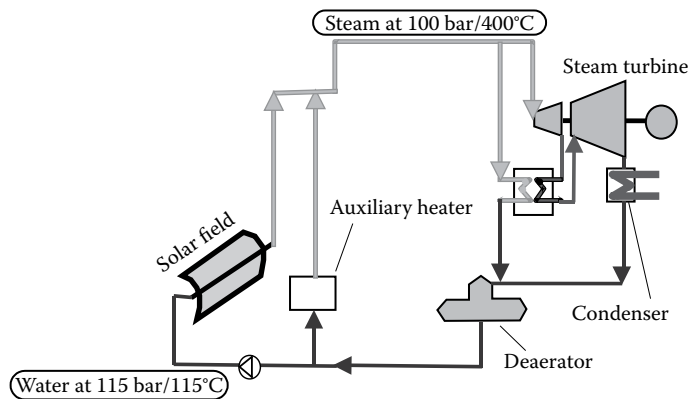


FIGURE 19.28

Simplified scheme of a parabolic-trough power plant with direct steam generation.

DSG has technical advantages that must be considered (Zarza et al., 1999):

- No danger of pollution or fire due to the use of thermal oil at temperatures of about 400°C
- Possibility of raising the maximum temperature of the Rankine cycle above 400°C, the limit imposed by the thermal oil currently used
- Reduction in the size of the solar field, thus reducing the investment cost
- Reduction in operation and maintenance-related costs, as thermal-oil-based systems require a certain amount of the oil inventory to be changed every year, as well as antifreeze protection when the air temperature is below 14°C

However, DSG presents certain challenges as a way to improve the current technology of parabolic-trough solar power plants, due to the two-phase flow (liquid water + steam) existing in the absorber tubes of the solar field evaporating section. The existence of this two-phase flow involves some uncertainties that must be clarified before a commercial plant making use of this technology can be built. Some of these uncertainties are

- Solar field control
- Process stability
- Stress in the receiver pipes
- Higher steam loss (leaks) than oil-based systems

Figure 19.29 shows the typical two-phase flow pattern in a horizontal pipe. As observed in Figure 19.29, four main flow patterns are possible, depending on the surface flow rates in the liquid and steam phases: bubbly, intermittent, stratified, and annular. The borders between adjacent flow patterns are not as well defined as they appear in Figure 19.29, but are rather separated by transition zones.

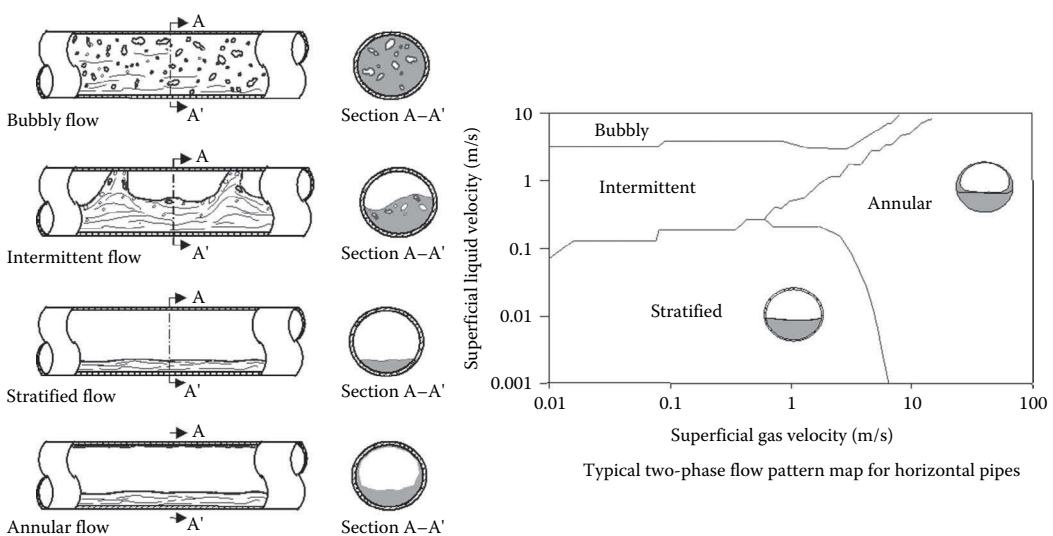


FIGURE 19.29

Two-phase flow configurations and typical flow pattern map for a horizontal receiver pipe.

In bubbly and intermittent flows, the steel absorber pipe inner wall is well wetted, thus avoiding dangerous temperature gradients between the bottom and the top of the pipe when it is heated from one side. The result is a good heat transfer coefficient all the way around the pipe because the liquid phase is not stratified.

In the stratified region (Goebel, 1997), the water is in the bottom of the absorber pipe, while the steam remains above the surface of the water. The result of this stratification is an uneven heat transfer coefficient around the pipe. Wetting of the bottom of the pipe is still very good and so is the heat transfer coefficient. But the cooling effect of the steam is poorer, and the heat transfer coefficient in the top section of the absorber pipe can be very low, resulting in a wide temperature difference of more than 100°C between the bottom and the top of the pipe in a given cross section when it is heated from one side. The thermal stress and bending from this steep temperature gradient can destroy the pipe. Figure 19.30 shows what happens in a cross section of the steel absorber pipe when it is heated underneath (Figure 19.30b, parabolic-trough concentrator looking upward) and from one side (Figure 19.30a, parabolic-trough concentrator looking at the horizon). The figure clearly shows how stratified flow can cause steep temperature gradients only when the vector normal to the aperture plane of the concentrator is almost horizontal (Figure 19.30a).

In the annular region, though there is partial stratification of water at the bottom of the pipe, there is a thin film of water wetting the upper part of the pipe. This film is enough to ensure a good heat transfer coefficient all the way around the pipe, thus avoiding dangerous thermal gradients that could destroy it. Typical absorber pipe cross sections in the stratified and annular regions are also shown in Figure 19.29.

Nevertheless, the technical problems due to water stratification inside the absorber pipes can be avoided if the feed-water mass flow is kept above a threshold level. There are three basic DSG processes, called once-through, injection, and recirculation. These three options require a solar field composed of long rows of PTCs connected in series to perform the

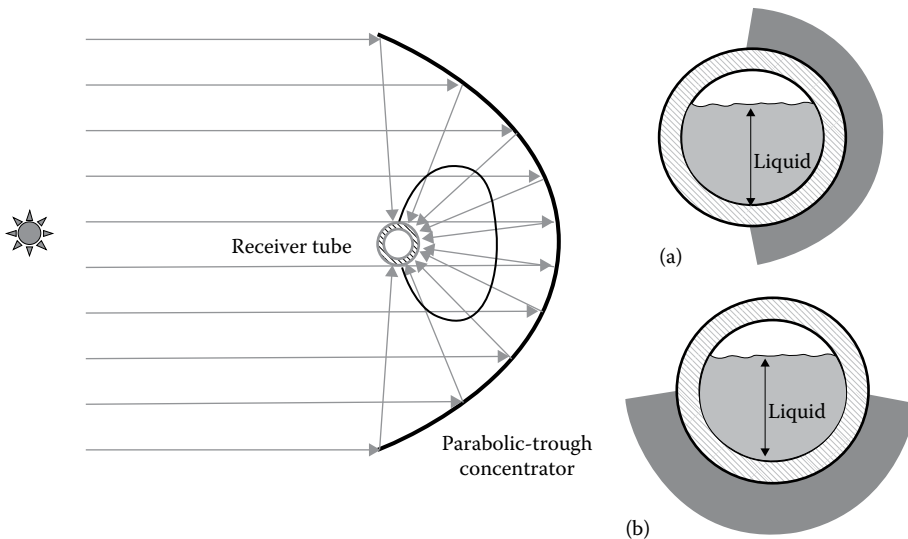


FIGURE 19.30

Liquid-phase stratification and concentrated incident solar flux onto the receiver pipe: (a) solar collector in vertical position; (b) solar collector in horizontal position (looking upward).

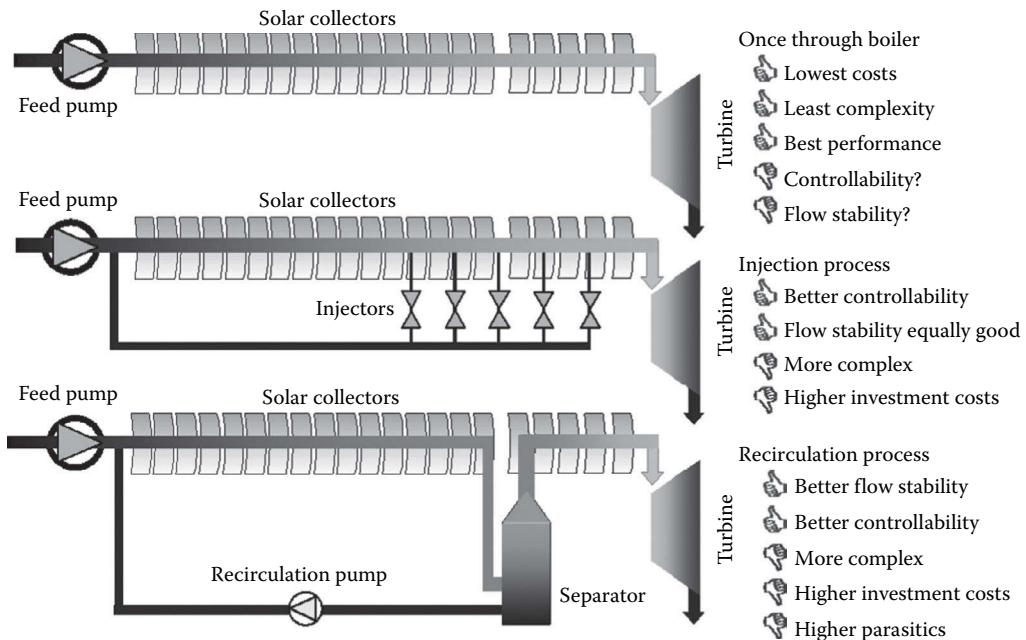


FIGURE 19.31
The three basic DSG processes.

complete DSG process: water preheating, evaporation, and steam superheating. Figure 19.31 summarizes the advantages and disadvantages of the three basic DSG options.

First, in the once-through process, all the feed water is introduced at the collector row inlets and converted into superheated steam as it circulates through the collector rows.

Second, in the injection process, small fractions of feed water are injected along the collector row. The main advantage of this process is the good controllability of the superheated steam parameters at the field outlet. On the downside, this makes the system more complex and increases its cost.

The third option, the so-called recirculation process, is the most conservative one. In this case, a water–steam separator is placed at the end of the evaporating section of the collector row. Feed water enters the solar field inlet at a higher flow rate than the steam to be produced by the system. Only a fraction of this water is converted into steam as it circulates through the collectors of the preheating and evaporating sections. At the end of the evaporating section, the saturated steam is separated from the water by the separator, and the remaining water is recirculated to the solar field inlet by a recirculation pump. The excess water in the evaporating section guarantees good wetting of the receiver pipes and makes stratification of liquid water impossible. Good controllability is the main advantage of this DSG option, but the need for a recirculation pump and the excess water that has to be recirculated from the water–steam separator to the solar field inlet increase system parasitic loads, penalizing overall efficiency.

Figure 19.31 shows that, compared to each other, each of the three basic DSG options has advantages and disadvantages (Zarza et al., 1999), and only their evaluation under real solar conditions can show which option is the best. This is why in 1996 a European consortium launched an R&D project to investigate all the technical questions concerning the DSG process. The name of that project was DIrect Solar Steam (DISS), and it was

developed by partners belonging to all the sectors involved in this technology (i.e., electric utilities, industry, engineering companies, and research centers) in efficient collaboration with other European projects related to PTCs and STP plants (e.g., STEM, ARDISS, GUDE, EuroTrough, PRODISS).

The only DSG life-size test facility available in the world at the end of last century was designed and implemented at the PSA during the first phase of the DISS project to investigate the feasibility of DSG in PTCs under real solar conditions. DISS-phase I started in January 1996 and ended in November 1998, with the financial support of the European Commission. The second phase of the project, also partly funded by the European Commission, started in December 1998 and lasted 37 months.

Though the DISS solar field can be operated over a wide temperature/pressure range, the three main operating modes are as follows:

Solar Field Conditions	Inlet	Outlet
Mode 1	40 bar/210°C	30 bar/300°C
Mode 2	68 bar/270°C	60 bar/350°C
Mode 3	108 bar/300°C	100 bar/375°C

The DISS test facility accumulated more than 8000 h of operation until 2012. The experimental data gathered in the project and the simulation tools that were developed on the basis of test data provided enough information to evaluate and compare the three DSG basic operation modes (i.e., recirculation, injection, or once-through) or any combination of them. Water injectors at the inlet of the solar collectors and water pumps are provided with frequency converters for smooth, efficient speed control from 10% to 100%. This facility is still in operation and delivers very useful information for the short-term commercial deployment of DSG.

The PSA DISS test facility field was initially composed of a single row of 11 PTCs connected in series, with a total length of 550 m and 2700 m² of aperture surface. The collector row is connected to the balance of plant where the superheated steam delivered by the solar field is condensed and used as feed water for the solar field (closed-loop operation).

The DISS test facility implemented at the PSA in DISS-phase I was improved during the subsequent years, and it became a very flexible and powerful life-size test facility, suitable not only for investigating thermo-hydraulic aspects of DSG under real solar conditions, but also for evaluating optimized components and O&M procedures for commercial DSG solar plants. Figure 19.32 shows the present schematic diagram of the PSA DISS facility. A water–steam separator (marked TK-4 in Figure 19.32) connects the end of the evaporating section to the inlet of the steam superheating section when the facility is operated in recirculation mode. Two additional collectors were added to the first row in 2003, so it is currently 750 m long with an aperture area of 3822 m², with a nominal thermal power of 1.8 MW_{th} and a maximum 400°C/100 bar superheated steam production of 1 kg/s.

The DISS project results proved the feasibility of the DSG process in horizontal PTCs, and important know-how was acquired by the project partners regarding the thermo-hydraulic parameters of the liquid water–steam flow in DSG solar fields within a wide range of pressures (30–100 bar). Experimental results were evaluated and complemented with results from lab-scale experiments and simulation tools. So several models developed in the past to calculate the pressure drop in pipes with two-phase flow were compared with the project's experimental results, and the models with the most accurate simulation results were identified. The proposed Chisholms (1980) and Friedel models proved to be the best match (Zarza, 2004).

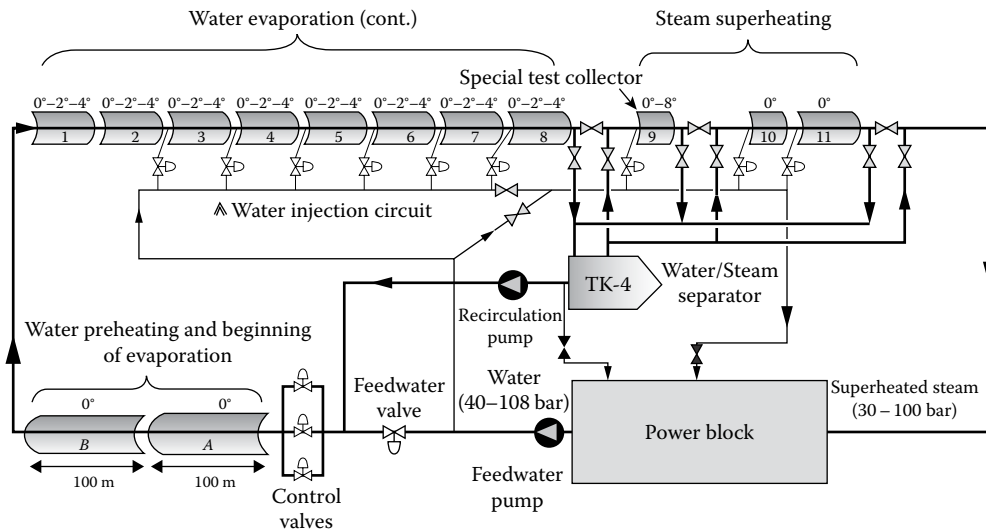


FIGURE 19.32
Schematic diagram of the PSA DISS test facility.

The good match between experimental data and simulation results obtained with finite-element models for the temperature profile in the DSG absorber pipes was another conclusion achieved in the DISS project. It was proven that the temperature gradients in the steel absorber pipes are within safe limits for a wide range of mass fluxes. Results concerning pressure drop and temperature gradients in the absorber pipes of the DISS collector row enabled accurate simulation and design tools for large DSG commercial solar fields to be developed (Eck et al., 2003) and was one of the major contributions of DISS to the development of the DSG technology.

Different possibilities (i.e., inner capillary structures and displacers) for enhancing heat transfer in the DSG absorber pipes were also investigated; however, experimental results showed that the absorber pipes do not need these devices to keep the temperature gradients within safe limits.

Several control schemes for once-through and recirculation operation modes were developed and evaluated with good results in the project. As initially expected, it was found that the temperature and pressure of the superheated steam produced by the solar field can be controlled more easily in recirculation mode, though an efficient control was achieved also for the once-through mode.

The influence of the inclination of the absorber pipes on the thermo-hydraulic parameters of the two-phase flow was investigated also. Tests at 30, 60, and 100 bar were performed in two positions, horizontal and tilted 4° . Though inclination of the absorber pipe reduced the stratified region, the test results obtained without inclination clearly showed that inclination of the absorber pipes is not required to guarantee sufficient cooling for the wide range of operating conditions investigated in the project.

Of the three DSG basic processes (i.e., injection, recirculation, and once-through), experimental results showed that recirculation is the most feasible option for financial, technical, and O&M-related parameters of commercial application. Test results showed good stability of the recirculation process even with a low recirculation ratio, thus making possible the use of small, cheap water–steam separators in the solar field.

The experience and know-how acquired in DISS was applied to the INDITEP project (2002–2005) in designing the first pre-commercial DSG solar power plant, in which the thermal energy delivered by a DSG solar field is used to feed a superheated-steam Rankine cycle (Zarza et al., 2004). The INDITEP project (Rueda et al., 2003) was the logical continuation of the DISS project, because the design and simulation tools developed in it for DSG solar fields were used in INDITEP, and most of the partners had also been involved in the previous project. INDITEP was promoted by a Spanish-German consortium of engineering companies, power equipment manufacturers, research centers, and businesses involved in the energy market: Iberdrola Ingeniería Consultoría (project Coordinator), CIEMAT, DLR, FLAGSOL GmbH, FRAMATONE, GAMESA Energía Servicios S.A., INITEC Tecnología S.A., Instalaciones Inabensa S.A., and ZSW. The European Commission also provided financial assistance.

Three basic requirements were defined for the design of this first pre-commercial DSG solar power plant:

1. The power block had to be robust and operable under flexible conditions in order to assure durability and reliability. Higher priority was therefore given to power block robustness and flexibility, while efficiency was considered less critical for this first DSG plant.
2. The plant must be small in order to limit the financial risk. Operating stability of a multi-row DSG solar field under uneven distribution of solar radiation and solar radiation transients must be proven.
3. The solar field must operate in recirculation mode because the DISS project demonstrated that the recirculation mode is the best option for commercial DSG solar fields (Eck and Zarza, 2002).

A 5.47 MW_e power block was selected for this plant to meet the first two requirements. Though, due to its small size, this power block is not very highly efficient, its robustness was guaranteed by the manufacturer with references from facilities already in operation. Figure 19.33 shows a schematic diagram of the power block design and its main parameters (Table 19.4).

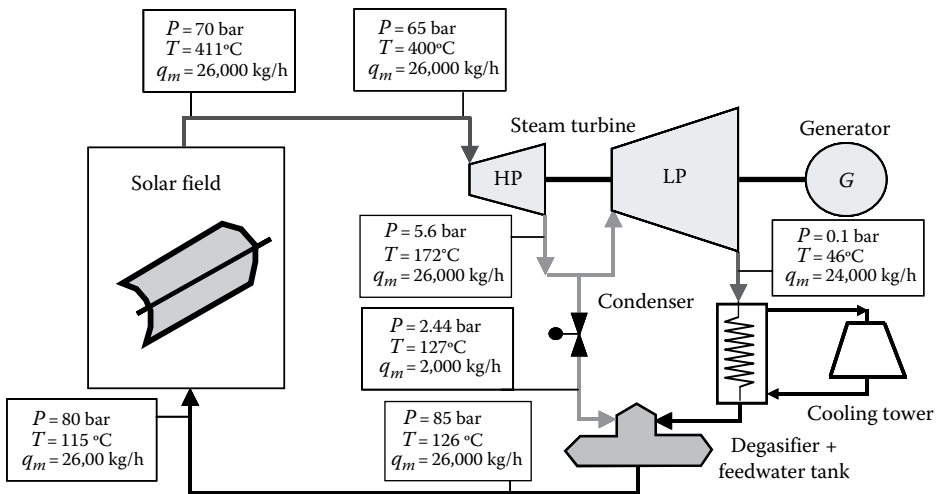


FIGURE 19.33
Schematic diagram of the power block designed for the DSG plant INDITEP.

TABLE 19.4

INDITEP Project 5 MW_e DSG Solar Power Plant Power Block Parameters

Manufacturer	KKK
Gross power (kW _e)	5,472
Net power (kW _e)	5,175
Net heat rate (kJ/kWh)	14,460
Gross efficiency (%)	26.34
Net efficiency (%)	24.9

The DSG solar field design consists of 70 ET-100 PTCs developed by the European EuroTrough consortium with financial support from the European Commission. This collector was chosen over the LUZ company’s LS-3 collector, which is in use at the most recent SEGS plants erected in California (United States), because of its improved optical efficiency and lighter steel structure (Luepfert et al., 2003).

The seven parallel rows of ET-100 PTC axes are oriented north–south to collect the largest amount of solar radiation per year, even though the differences in solar field thermal energy output in winter and summer are more significant than with east–west orientation. Figure 19.34 shows the schematic diagram of a typical solar field collector row at design point. Every row is made up of 10 collectors: 3 collectors for preheating water + 5 collectors for evaporating water + 2 collectors for superheating steam. The end of the boiling section and the inlet of the superheating steam section in every row are connected by a compact water–steam separator, which in turn drains into a larger shared vessel. Water from the separator in every row goes to the final vessel from which it is then recirculated to the solar field inlet by the recirculation pump.

The temperature of the superheated steam produced in each row of collectors would be controlled by means of a water injector placed at the inlet of the last collector. The amount of water injected at the inlet of the last collector in every row is increased or decreased by the control system to keep the superheated steam temperature at the outlet of the row as close as possible to the set point defined by the operator.

Due to the lack of public financial support, the DSG plant designed in INDITEP could not be implemented. However, the experience and know-how gained in the projects DISS and INDITEP were used to implement a first 5 MW_e DSG STP plant in Kanchanaburi Province,

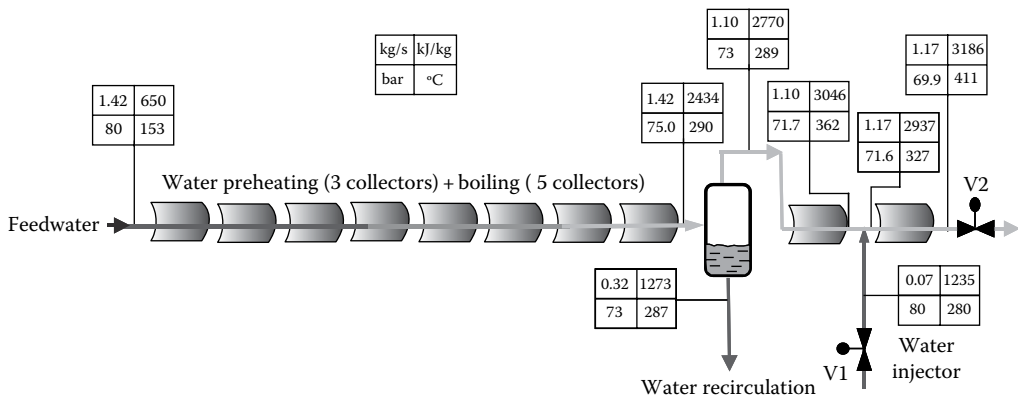


FIGURE 19.34

Scheme of a typical row of collectors in the DSG plant designed in INDITEP.

Thailand (http://www.solarlite.de/en/project_kanchanaburi.cfm) by the German company Solarlite with the collaboration and scientific support of DLR. The name of this plant is TSE-1, and it has a collector area of 45,000 m². The nominal solar field output steam temperature/pressure is 330°C/30 bar. This plant proved the commercial feasibility of the recirculation process for DSG in PTCs.

Keeping in mind the benefits of the once-through process when compared to the recirculation process, a German consortium composed of DLR and the company Solarlite launched in 2011 the project DUKE (Durchlaufkonzept – Entwicklung und Erprobung) with the financial support of the German government, the collaboration of PSA, and a duration of 3 years to study the commercial feasibility of the once-through process. The DISS test facility was improved in 2012–2013 within the framework of the project DUKE with the installation of three additional PTCs and new instrumentation. Experimental results delivered by DUKE will be essential for the commercial future of the DSG once-through process.

19.4.9 SEGS Plants and State-of-the-Art of Solar Power Plants with Parabolic-Trough Collectors

From a commercial standpoint, PTCs are the most successful technology for generating electricity with solar thermal energy. More than 50 commercial STP plants with PTCs were in operation in 2012, with a total output power of more than 2.5 GW_e. The first nine plants, called the SEGS (Solar Electricity Generating Systems) I–IX, which use thermal oil as the working fluid (HTF technology), were designed and implemented by the LUZ International Limited company from 1985 to 1990. All the SEGS plants are located in the Mojave Desert, northwest of Los Angeles, California. With their daily operation and over 2.2 million square meters of PTCs, SEGS plants are this technology's best example of commercial maturity and reliability. Their plant availability is over 98%, and their solar-to-electric annual efficiency is in the range of 14%–18%, with a peak efficiency of 22% (DeMeo and Galdo, 1997; Price et al., 2002). All SEGS plant configurations are similar to that shown in Figure 19.24, with only slight differences between one plant and another (Table 19.5).

The success of the SEGS plants was very important to get the support of bankers and investors for the commercial projects implemented in Spain and other countries later on. In fact, the configuration of the commercial STP plants implemented 20 years later than the SEGS plants was almost the same. The main difference between SEGS and more recent STP plants with parabolic troughs is the installation of a big thermal storage system using

TABLE 19.5

SEGS Plants Installed by LUZ International Limited

Plant	Net Capacity (MW _e)	Location	Inauguration
SEGS I	14	Dagget, CA	1984
SEGS II	30	Dagget, CA	1985
SEGS III	30	Kramer Jn, CA	1986
SEGS IV	30	Kramer Jn, CA	1986
SEGS V	30	Kramer Jn, CA	1987
SEGS VI	30	Kramer Jn, CA	1988
SEGS VII	30	Kramer Jn, CA	1988
SEGS VIII	80	Harper Lake, CA	1989
SEGS IX	80	Harper Lake, CA	1990

a mixture of molten salts, thus improving the plant dispatchability. The SEGS plant configuration was modified by LUZ from one plant to another in order to achieve higher efficiencies and lower O&M costs, so the only plant with a thermal energy storage system was SEGS I, which had a two-tank oil storage system. LUZ came to the conclusion that the auxiliary gas heater had to be implemented in the oil circuit because plant operating procedures were more difficult with the auxiliary heater installed in the water–steam circuit. LUZ research and development in the design and improvement of the solar collector field components and integration of the power block achieved higher plant efficiencies and provided a technology for large solar power plants, leading to a reduction in the cost of the solar field per m^2 to about 75% of the first SEGS plant, and solar system thermal efficiency was increased 8% (Harats and Kearney, 1989).

Figure 19.35 shows an aerial view of the SEGS III and IV plants. The layout chosen by LUZ for the solar fields is the so-called Central Feed, because it allows easy washing and maintenance access to all the collector rows. The power block (steam generator, steam turbine, electricity generator, condenser, etc.) building is located in the center of the collector field.

The SEGS IX plant, put into operation in 1990, was the last one installed by LUZ before its bankruptcy in 1991. Although LUZ had projects for another four plants to be erected in Harper Lake in a very advanced stage, they were cancelled due to the company's bankruptcy. LUZ had increased the net nominal power of the SEGS plants from 14 MW_e (SEGS I) to 80 MW_e (SEGS VIII and IX).

In SEGS plants VIII and IX (see Figure 19.24), there is no gas-fired steam reheater and the steam turbine has two stages working with steam at $371^\circ\text{C}/104$ bar and $371^\circ\text{C}/17$ bar, respectively. The thermal oil is heated in the solar collectors up to a temperature of approximately 390°C , and split into two parallel circuits, the steam generator and reheater. In the steam-generating circuit, the oil passes through a steam superheater, boiler, and preheater, generating steam at 371°C and 104 bar. This steam expands in the first stage of the turbine, passing to a reheater thermally fed by the other oil circuit, reheating steam to 371°C and 17 bar. During June, July, August, and September, the auxiliary gas boiler is put into operation to keep the turbine working at full load during peak-demand hours. For the rest of the time, the steam turbine is mainly driven by the solar system only (Table 19.6).



FIGURE 19.35
Aerial view of the SEGS III and IV plants.

TABLE 19.6

Basic Characteristics of the SEGS I-IX Plants

	SEGS I	SEGS II	SEGS III	SEGS IV	SEGS V	SEGS VI	SEGS VII	SEGS VIII	SEGS IX
Starting up	December 1984	December 1985	December 1986	December 1986	October 1987	December 1988	December 1988	December 1989	September 1990
Investment (M\$)	62	96	101	104	122	116	117	231	
Electricity yearly production (MWh)	30,100	80,500	92,780	92,780	91,820	90,850	92,646	252,750	256,125
Estimated life (years)	20	25	30	30	30	30	30	30	30
No. of stages of the turbine	1	2	2	2	2	2	2	2	2
Solar steam (P, T) (bar, °C)	248/38	300/27	327/43.4	327/43.4	327/43.4	371/100	371/100	371/104	371/104
Steam with gas (P, T) (bar, °C)	417/37	510/104	510/104	510/104	510/100	510/100	510/100	371/104	371/104
Efficiency in solar mode (%)	31.50	29.40	30.60	30.60	37.70	37.50	37.50	37.60	37.60
Efficiency with gas (%)	—	37.30	37.40	37.40	37.40	39.50	39.50	37.60	37.60
<i>Solar field</i>									
Collector type	LS-1/LS-2	LS-1/LS-2	LS-2	LS-2	LS-2	LS-2	LS-3	LS-3	LS-3
Aperture area (m ²)	82,960	188,990	230,300	230,300	233,120	188,000	194,280	464,340	483,960
Working temperature	279	321	349	349	349	390	390	390	390
Inlet/outlet collector field temperature, (°C)	241/307	248/320	248/349	248/349	248/349	293/393	293/390	293/390	293/390
Type of oil	ESSO 500	M-VP1	M-VP1	M-VP1	M-VP1	M-VP1	M-VP1	M-VP1	M-VP1
Oil volume (m ³)	3,217	379	403	404	461	372	350		

LUZ Industries developed three generations of PTCs, called LS-1, LS-2, and LS-3. The LS-1 and LS-2 designs are conceptually very similar. The main differences are the overall dimensions. The parabolic reflectors are glass panels simply screwed to helicoidal steel tube frames that provide the assembly with the required integrity and structural stiffness.

The LS-3 collector is twice as long as the LS-2, with a parabola 14% wider, which reduces the number of flexible connections, local control units, temperature sensors, hydraulic drives, and similar equipment by more than half. However, the LS-3 design represents a change in collector philosophy, more than a change in scale. While the LS-2 model used a torque tube to provide the required stiffness, the LS-3 is made of a central steel space frame that is assembled on-site with precision jigs. The result of this innovation is a lighter and more resistant structure, with highly accurate operation in heavy winds (Table 19.7).

The electricity produced by the SEGS plants is sold to the local utility under individual 30-year contracts for every plant. To optimize the profitability of these plants, it is essential to produce the maximum possible energy during peak-demand hours, when the electricity price is the highest. The gas boilers can be operated for this, either to supplement the solar field or alone. Nevertheless, the total yearly electricity production using natural gas was limited at that time by the Federal Commission for Energy Regulation in the United States to 25% of the overall yearly production.

Peak-demand hours are when there is the most electricity consumption, and therefore, the tariff is the highest. Off-peak and super off-peak hours are when electricity consumption is low, and the electricity price is therefore also lower. At present, 16% of the SEGS plants' annual net production is generated during summer peak-demand hours, and the revenues from this are on the order of 55% of the annual total. These figures show how important electricity generated during peak-demand hours is for the profitability of these plants.

TABLE 19.7

Characteristics of the LS-1, LS-2, and LS-3 Collectors

	LS-1	LS-2	LS-3
Solar tracking accuracy (°)	0.10	0.10	0.10
Maximum wind velocity to operate (km/h)	56	56	56
Steel structure based on	Steel tube	Steel tube	Space frame
Selective coating of absorber tubes	Black Cr	Black Cr	Cermet
Absorptivity/transmissivity (%)	94/94	94/95	96/95
Emissivity (%)	39 (300°C)	24 (300°C)	18 (350°C)
Focal distance of the solar concentrator	0.68	1.49	1.71
Aperture angle	85	80	80
Reflectivity (%)	94	94	94
Trough aperture (m)	2.5	5	5.76
Absorber steel pipe outer diameter (mm)	42	70	70
Geometric concentration	19	23	26
Overall length (m)	50.2	47.1	99.0
Distance between supports (m)	6.3	8.0	12.0
Mirrors surface per collector (m ²)	128	235	545
Maximum working temperature (°C)	307	350	390
Distance between parallel rows (m)	7	12.5/15	17
Intercept factor (%)	87	89	93

Thanks to the continuous improvements in the SEGS plants, the total SEGS I cost of \$0.22 per kWh_e for electricity produced was reduced to \$0.16 per kWh_e in the SEGS II and down to \$0.09 per kWh_e in SEGS IX (Kearney and Cohen, 1997).

The other important contribution to the profitability of the SEGS plants was the favorable tax laws it took advantage of. The large tax rebate was a crucial factor in the economic feasibility of the SEGS plants. The eventual reduction in these tax exemptions was overcome by the considerable cost reduction from one plant to another achieved by LUZ. The significant reduction in both fossil fuel prices and tax exemptions made it impossible for the SEGS plants to maintain the profit margin they had had at the beginning, resulting in the bankruptcy of the company and the cancellation of the planned erection of more SEGS plants.

Another factor that led to the bankruptcy of LUZ was the short time in which one SEGS plant had to be fully implemented to obtain tax benefits. A plant had to be installed in less than 12 months. For the last 80 MW_e plant (SEGS X), this short leeway required around-the-clock construction work, which rocketed the investment cost and made it impossible for a SEGS X to be financially successful, and its construction was therefore cancelled in the middle of 1991 as a consequence of LUZ's bankruptcy (Lotker, 1991).

Though LUZ achieved a significant cost reduction in the SEGS plants, the current cost of electricity produced by modern parabolic-trough solar power plants is higher, and it must still be further reduced before it can become competitive with conventional power plants and PV plants (Pitz-Paal et al., 2005). Without tax incentives or an adequate premium for electricity generated by this type of plants, they are not profitable, because current investment and O&M costs demand a public support strategy for commercial development. At present, the direct capital cost is about three times that of a fossil-fueled power plant, and the generating cost is about three times higher. Annual thermal efficiency (solar-to-useful thermal energy delivered) of commercial parabolic-trough solar fields is about 50%. This means a yearly savings of about 0.45 ton of CO₂ emissions and 0.1 ton of fossil fuel per square meter of PTC (Geyer, 2002).

In spite of their environmental benefits, there are some barriers to the commercial use of this technology. The main barriers at present are the high investment cost (\$3500–\$6000 per kW, depending on plant size and thermal storage capacity) and the minimum size of the power block required for high thermodynamic efficiency. However, these barriers are shared by all the STP technologies currently available (i.e., CRSs, Dish Stirling systems, and LF concentrator systems) (Romero et al., 2004). The high investment cost can be compensated with public incentives in the form of tax credits or favorable feed-in tariffs. The favorable feed-in tariff implemented in Spain in 2007 and the tax credits and loan guarantees in the United States for STP plants opened the door to many commercial projects, thus achieving a total installed power of more than 2.5 GW_e with PTCs at the end of 2012.

Since the size limit imposed in Spain for STP plants (i.e., 50 MW_e) had no technical reasoning behind, several commercial projects with unit powers higher than 100 MW_e were promoted in other countries at the beginning of the second decade in this century. The SOLANA plant promoted by Abengoa, Arizona, with a unit power of 280 MW_e and a 6 h thermal storage system with molten salts, is a good example of these large STP plants.

At the time of writing the technology commercially available for parabolic-trough power plants is the HTF technology, which uses oil as the heat carrier between the solar field and the power block, while thermal storage systems with molten salts in two tanks is the preferred option. The promotion of many commercial projects since 2007 has led to the development of many new collector designs (URSSATrough, SenerTrough, SkyTrough, etc.) with good mechanical and geometrical quality and lower and lower manufacture and assembly costs.



FIGURE 19.36

The UltimateTrough prototype installed in a commercial solar power plant in Southern California. (Courtesy of Flabeg.)

These new collector designs have been specially developed for large solar fields. Although most of the new collector designs developed in the period 2007–2013 had similar dimensions and features (150 m length, 5.76 m parabola width, 1.7 m focal distance), very innovative designs with much bigger aperture area have been developed keeping in mind the future installation of very large solar fields. The UltimateTrough design is the best example of new collectors with very large aperture area. With an aperture of 1689 m², a parabola width of 7.5 m, and a length of 240 m, UltimateTrough was specially designed for STP plants with a unit power of 100 MW_e or more, although it can be used for smaller plants also. Figure 19.36 shows the UltimateTrough collector prototype installed in an STP plant in Southern California for evaluation.

More than 2 GW_e were installed in the period 2007–2013 with PTCs in Spain, the United States, and Mediterranean and North Africa region, and several countries (Morocco, South Africa, and others) had launched national programs to install STP plants and promote solar thermal electricity production.

Most of the commercial STP plants installed in the period 2007–2013 with PTCs have the configuration showed either in Figure 19.24 (plants without thermal storage) or Figure 19.27 (plants with molten-salt thermal storage systems), and only 3 plants had a parabolic-trough solar field integrated in the bottoming cycle of a combined-cycle gas-fired power plant. This configuration is called the integrated solar combined-cycle system (ISCCS) configuration. Though the contribution of the solar system to the overall plant power output is small (10%–15% approx.) in the ISCCS configuration, it seems to be a good approach to market penetration in some countries, which is why the World Bank is promoting ISCCS plants in developing countries (Geyer et al., 2003). Figure 19.37 shows the schematic diagram of a typical ISCCS plant.

The first commercial plant with PTCs in Europe was the ANDASOL-I plant (Aringhoff et al., 2002a,b), a SEGS-like plant with a 6 h molten-salt thermal storage system. Figure 19.38 is an aerial view of ANDASOL-I.

The financial crisis in 2011 made some countries change their mind concerning the promotion of STP plants. This was the case of Spain, where the legal framework implemented in 2007 was significantly modified in 2012 and 2013 to reduce the incomes of the STP plants owners, and the feed-in tariff was cancelled for new plants. Studies performed

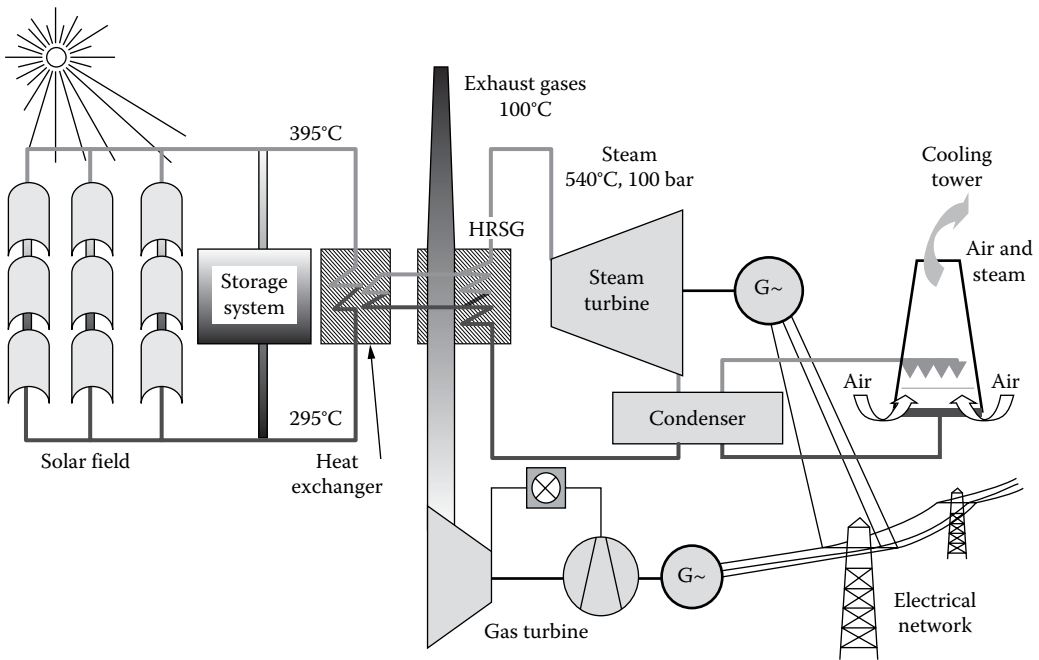


FIGURE 19.37
Schematic diagram of a typical ISCCS (integrated solar combined-cycle system) plant.

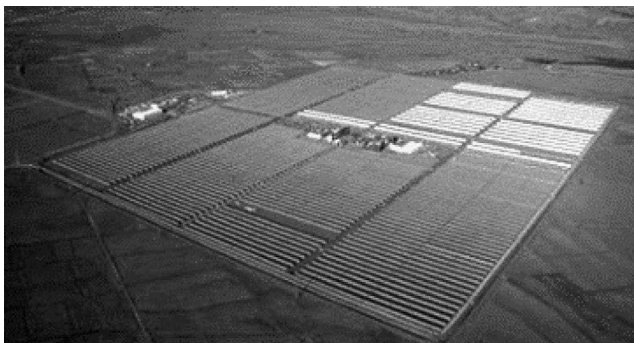


FIGURE 19.38
Aerial view of the Spanish ANDASOL-I plant.

in the second decade of this century have pointed out the possibility of achieving a significant midterm cost reduction in parabolic-trough technology (Enermodal, 1999; Sargent & Lundy, 2003; Kearney and ESTELA, 2010). Mass production and component improvement through R&D would lead to an electricity cost fully competitive with conventional power plants in 2025. It is therefore clear that parabolic-trough technology must seek ways to become more competitive with conventional power plants. The European Solar Thermal Electricity Association (ESTELA) issued a strategic research agenda in 2013 with the recommended R&D topics to speed up the cost reduction of electricity produced by STP plants. This document is available at www.estelasolar.eu. Within the potential improvements for cost reduction, DSG of high-pressure/high-temperature superheated steam in

the receiver pipes seems to be one of the promising ways to achieve this goal, because the thermal oil currently used in the HTF technology as the working fluid and the associated equipment (oil/water heat exchanger required to produce the superheated steam, oil circuit, expansion vessel, etc.) would be no longer needed. Improvement of thermal storage systems and development of receiver tubes for higher temperatures are two other important R&D topics.

Also in the United States, a national R&D program called *The SunShot Initiative* was launched in February 2011 to achieve a significant cost reduction in CSTP technologies. The SunShot Initiative is a collaborative national effort to make the United States a leader in the global clean energy race by fueling solar energy technology development. The vision of SunShot is to make the total cost of solar energy economically viable for everyday use. This initiative is aimed at reducing the total installed cost of solar energy systems by 75%.

The future of STP plants with PTCs strongly depends on the cost reduction achieved for future plants, because photovoltaic panels have significantly reduced their cost, and a similar cost reduction must be achieved by STP plants to compete with that technology, even taking into account the benefit of the STP plants' dispatchability.

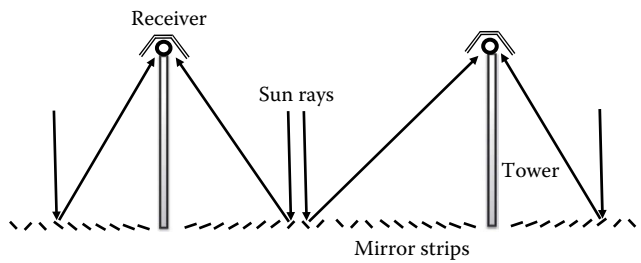
19.5 Linear Fresnel Reflectors

LF reflectors are composed by an array of linear (or slightly bent) mirror strips that independently move and collectively focus on absorber lines suspended from elevated towers. Reflective segments are close to the ground and can be assembled in a compact way up to 1 ha/MW. This technology aims at achieving the performance of parabolic troughs with lower costs. They are characterized by a fixed linear focus where the absorber is static (Mills, 2004). However, optical efficiency is lower than that of parabolic troughs due to a higher impact of the incidence angle and the cosine factor. Consequently, operating temperature at the working fluid is usually lower, typically between 150°C and 350°C. By this reason, LF technology has been historically applied to generate saturated steam via direct in-tube steam generation and use into ISCCS or in regenerative Rankine cycles, though current R&D is aiming at higher temperatures above 400°C (Platzer, 2009).

LF reflectors typically make use of lower cost non-vacuum thermal absorbers where the stagnant air cavity provides significant thermal insulation, light reflector support structures close to the ground, low-cost flat float glass reflector, and low-cost manual cleaning, because the reflectors are at human height (Kalogirou, 2004). The LFs also have much better ground utilization, typically using 60%–70% of the ground area compared to about 33% for a trough system and lower O&M costs due to more accessible reflectors.

19.5.1 Historical Evolution of Linear Fresnel Reflector Systems

After some pioneering experiences (Francia, 1968; Di Canio et al., 1979), the first serious development undertaken on the compact LF reflector system was proposed at the University of Sydney in 1993. The concept is composed by a single field of reflectors together with multiple linear receivers (see Figure 19.39). Each reflector is able to change

**FIGURE 19.39**

Scheme of compact LF system with a multi-tower array and dynamic aiming strategy of mirror strips.

their focal point from one receiver to another during the day in order to minimize shading and shadow losses in the dense reflector field. This system covers about 71% of the ground compared with 33% for parabolic-trough systems (Mills and Morrison, 1999). In 2000, the company Solarmundo built a 2400 m² LF prototype collector field with such a technology at Liege, Belgium, but test results were not reported. Later the company moved to Germany and was renamed Solar Power Group (SPG). SPG signed an exclusivity cooperation agreement with DSD Industrieanlagen GmbH (renamed to MAN Ferrostaal Power Industry in 2005). A 800 kW LF pilot operating at 450°C has already been tested in the PSA, Spain (Bernhard et al., 2008; Hautmann et al., 2009).

Back in Australia, in early 2002, a new company, Solar Heat and Power Pty Ltd. (SHP), made extensive changes to the engineering design of the reflectors to lower cost and has become the first to commercialize LF technology. SHP initiated in 2003 for Macquarie Generation, Australia's largest electricity generator, a demonstration project of 103 MW_{th} (approximately 39 MW_e) plant with the aim of supplying preheat to the coal-fired Liddell power station. Phase 1 of the project, completed in 2004, resulted in a 1350 m² segment not connected to the coal-fired plant and was used to trial initial performance, and it first produced steam at 290°C in July 2004. The expansion to 9 MW_{th} was completed by 2008. Activities of the company moved to the United States and were continued by Ausra, Palo Alto. Ausra established a factory of components, tubular absorbers, and mirrors in Las Vegas and built the Kimberlina 5 MW demonstration plant in Bakersfield at the end of 2008. In 2010, Ausra was purchased by AREVA, which is presently committed to the commercial deployment of this technology.

The third technology player after SPG/MAN and AREVA is the German company NOVATEC Solar, formerly NOVATEC Biosol. The technology of NOVATEC is based upon its collector Nova-1 aimed to produce saturated steam at 270°C. They have developed a serial production factory for prefabricated components, a 1.4 MW small commercial plant, PE-1, in Puerto Errado, Murcia, Spain, which has been grid connected since March 2009, and a second 30 MW commercial plant, PE-2 (with a mirror surface of 302,000 m²), also built in Murcia, Spain. NOVATEC is promoting 50 MW plants mixing PTC and LF fields, where LF provides preheating and evaporation and PTC field takes over superheating. The company claims that this hybridization results in 22% less land use and higher profitability. In March 2011, ABB acquired a 35% shareholding in Novatec Solar. In September 2011, Novatec Solar claimed that its technology has successfully generated superheated steam at temperatures above 500°C at its 1.4 MW demonstration plant in Murcia, Spain, by implementing a receiver containing vacuum absorber (Selig, 2011).

In last few years, new companies have explored the application of Fresnel technologies for electricity generation. SkyFuel Inc., Albuquerque, New Mexico, is developing the Linear Power Tower™, a Fresnel based on concept designed to use a high-temperature molten-salt HTE, and it incorporates thermal energy storage. In Europe, the French company CNIM is developing its own technology for the boiler part of the plant focusing on direct superheated steam generation and LF principle. A first prototype (800 m²) has been built, commissioned, and pretested in 2010 (Lehaut, 2010).

19.5.2 Future Technology Development and Performance Trends

Even though some solid commercial programs are underway on LF, still it is early to have consolidated performance data with respect to electricity production. The final optimization would integrate components development to increment temperature of operation and possible hybridization with other STP systems like parabolic troughs.

There are many possible types of receivers, including evacuated tube and PV modules, but the most cost-effective system seems to be an inverted cavity receiver. In the case of SHP technology, the absorber is a simple parallel array of steam pipes at the top of a linear cavity, with no additional redirection of the incoming light from the heliostats to minimize optical losses and the use of hot reflectors. In the case of SPG technology, the absorber is a single tube surmounted by a hot nonimaging reflector made of glass, which must be carefully manufactured to avoid thermal stress under heating and exhibit some optical loss. Both systems can produce saturated steam or pressurized water. At present, AREVA and NOVATEC are looking for new absorbers able to work at temperatures above 450°C. By 2015, according to developers, LF can be expected to be operating with superheated steam at 500°C yielding an efficiency improvement of up to 18.1% relative to current saturated steam operation at 270°C (Kearney and ESTELA, 2010).

For reflectors, automation is a key issue that has been demonstrated by NOVATEC. Additional effort should be given to the optimized demonstration of multitower arrays to maximize ground coverage ratios. However, it is the lack of reliable information regarding annual performance and daily evolution of steam production that should be targeted as a first priority. Still some concerns remain regarding the ability to control steam production, because of the pronounced effect of cosine factor in this kind of plants. This dynamic performance would also affect the potential integration with other STE systems such as PTC or CRS. Until now, most comparative assessments vis-à-vis parabolic troughs are not economically conclusive, revealing the need to use much larger fields to compensate lower efficiencies. In order to achieve break-even costs for electricity with current LF technology, the cost target for the Fresnel solar power plants needs to be about 55% of the specific costs of parabolic-trough systems (Dersch et al., 2009).

19.6 Central-Receiver Solar Thermal Power Plants

CRSs with large heliostat fields and solar receivers located on top of a tower are deploying the first generation of grid-connected commercial plants from 2007. The CRS power plant technology can be considered as sufficiently mature after the pioneering experience of several 0.5–10 MW pilot plants in the early 1980s and the subsequent improvement of such key components as heliostats and solar receivers in many later projects merging

international collaboration during the past 20 years. Solar-only plants like Gemasolar and PS10 and hybrid configurations like SOLGAS, CONSOLAR, or SOLGATE have provided a portfolio of alternatives that have led to the first scaled-up plants for the period 2007–2014. The first small 10–20 MW projects, still non-optimized, already reveal a dramatic cost reduction over previous estimates and provide a path for a realistic LEC milestone of \$0.08 per kWh by 2030.

In power towers, incident sunrays are tracked by large mirrored collectors (heliostats), which concentrate the energy flux onto radiative/convective heat exchangers called solar receivers, where energy is transferred to a thermal fluid. After energy collection by the solar subsystem, the thermal energy conversion to electricity is quite similar to fossil-fueled thermal power plants and the earlier-described parabolic-trough system power block.

Reflective solar concentrators are employed to reach the temperatures required for thermodynamic cycles (Mancini et al., 1997). In power towers or CRSs, the solar receiver is mounted on top of a tower, and sunlight is concentrated by means of a large paraboloid that is discretized into a field of heliostats (Figure 19.40). CRSs have a high potential for midterm cost reduction of electricity produced since there are many intermediate steps between their integration in a conventional Rankine cycle up to the higher exergy cycles using gas turbines at temperatures above 1300°C, leading to higher efficiencies and throughputs.

The typical optical concentration factor ranges from 200 to 1000. Because of economy of scale, 10–100 MW plant sizes are chosen, even though advanced integration schemes are claiming the economics of smaller units as well (Romero et al., 2000a,b). The high solar flux incident on the receiver (averaging between 300 and 1000 kW/m²) enables operation at relatively high temperatures of up to 1000°C and integration of thermal energy into more efficient cycles in a step-by-step approach. CRS can be easily integrated in fossil plants for hybrid operation in a wide variety of options and has the potential for generating electricity with high annual capacity factors through the use of thermal storage. With storage, CRS plants are able to operate over 4500 h/year at nominal power (Kolb, 1998).

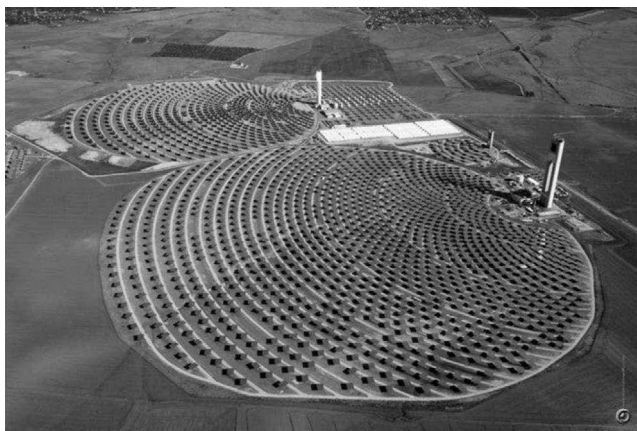


FIGURE 19.40

Aerial view of the first commercial solar towers in the world. PS20 with 20 MW at the front and the PS10 with 11 MW at upper left. Heliostat field layout is formed by hundreds of tracking mirrors focusing concentrated light onto the receiver aperture. PS20 and PS10 have been developed by Abengoa Solar and are located in Sanlúcar la Mayor, Spain. (Courtesy of Abengoa Solar, Sanlúcar la Mayor, Spain.)

19.6.1 Technology Description

A solar power tower, or CRS, plant may be described in terms of the following subsystems:

- Collector system, or heliostat field, created with a large number of two-axis tracking units distributed in rows.
- Solar receiver, where the concentrated flux is absorbed. It is the key element of the plant and serves as the interface between the solar portion of the plant and the more conventional power block.
- Heat exchanger system, where an HTF may be used to carry the thermal energy from the receiver to the turbine.
- Heat storage system, with which system dispatchability is ensured during events like cloud passages and can adapt to demand curves.
- Fossil fuel backup for hybrid systems with a more stable output.
- Power block, including steam generator and turbine alternator.
- Master control, UPS, and heat rejection systems.

A detailed description and historical perspective of all the subsystems would be excessive, given the large number of configurations and components tested to date. Because of their higher temperatures, CRSs have been able to make use of a diversity of thermal fluids, such as air, water–steam, molten nitrate salt, and liquid sodium. In general, the components that impact the most on investment cost are the heliostat field, the tower receiver system, and the power block. The heliostat field and solar receiver systems distinguish solar thermal tower power plants from other CSP plants and are therefore given more attention in the following. In particular, the heliostat field is the single factor with the most impact on plant investment, as seen in Figure 19.41. Collector field and power block together represent about 72% of the typical solar-only plant (without fossil backup) investment, of which heliostats represent 60% of the solar share. Even though the solar receiver impacts the capital investment much less (about 14%), it can be considered the most critical subsystem

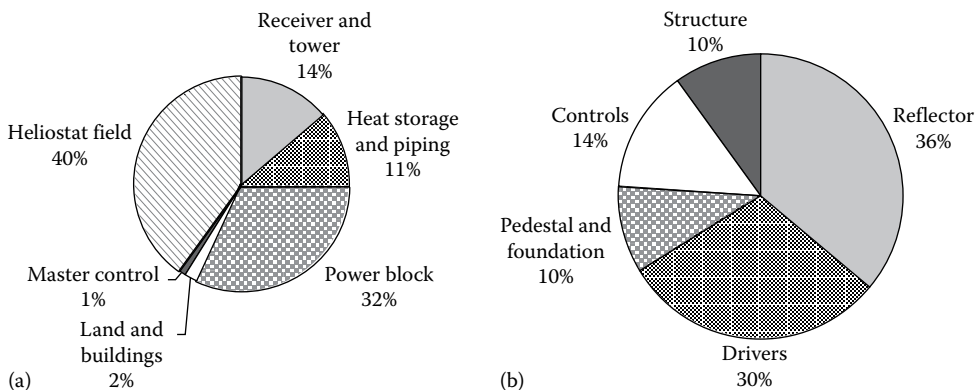


FIGURE 19.41

(a) Investment costs breakdown for a CRS plant, only solar. As it can be observed, the heliostat field and the power block are the most impacting subsystems on plant investment. (b) Breakdown of production cost for a single heliostat distributed among its main components. Reflector and tracking mechanism are in this case the most capital intensive components.

in terms of performance, since it centralizes the entire energy flux exchange. The largest heliostat investment is the drive mechanism and reflecting surface, which alone are almost 70% of the total.

19.6.1.1 Heliostat and Collector Field Technology

The collector field consists of a large number of tracking mirrors, called heliostats, and a tracking control system to continuously focus direct solar radiation onto the receiver aperture area. During cloud passages and transients, the control system must defocus the field and react to prevent damage to the receiver and tower structure.

Heliostats fields are characterized by their off-axis optics. Since the solar receiver is located in a fixed position, the entire collector field must track the sun in such a way that each and every heliostat individually places its surface normal to the bisection of the angle subtended by sun and the solar receiver. Figure 19.42 shows the variability of elevation angles in a heliostat field and identifies the elevation angle. The geometrical definition of the inclination angle n of a single heliostat is a function of the tower height, its distance from the tower, and the incidence angle of the sun. Assuming z_s is the heliostat vertical dimension and z_T is the geometrical tower height above ground, the so-called optical tower height may be defined as the elevation of the center of the receiver aperture area above the pivot point of the heliostat ($z_T - z_s/2$).

$$\psi = h + n - 90^\circ \text{ (}^\circ\text{)} \tag{19.38}$$

$$90^\circ - n = \arctan \left[\frac{(z_T - (z_s/2))}{x} \right] + \psi \text{ (}^\circ\text{)} \tag{19.39}$$

$$n = \frac{180^\circ - h - \arctan [(z_T - (z_s/2))/x]}{2} \text{ (}^\circ\text{)} \tag{19.40}$$

Heliostat field performance is defined in terms of the optical efficiency, which is equal to the ratio of the net power intercepted by the receiver to the product of the direct insolation and the total mirror area. The optical efficiency includes the cosine effect, shadowing, blocking, mirror reflectivity, atmospheric attenuation, and receiver spillage (Falcone, 1986).

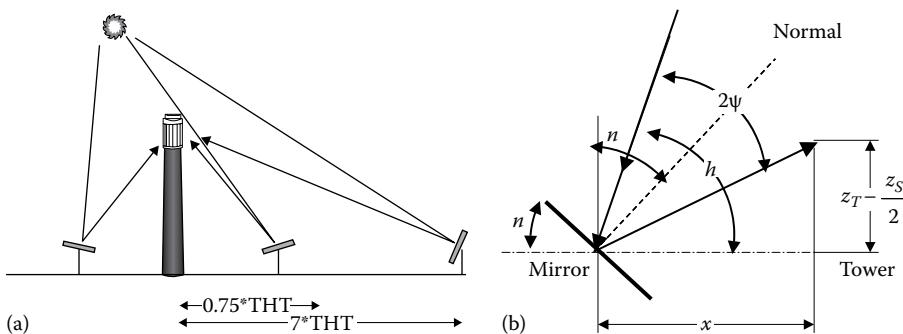


FIGURE 19.42

(a) Visualization of the off-axis optics of heliostats representing different inclination angles of mirrors located in a heliostat field. (b) Geometrical definition of elevation angle n .

Because of the large area of land required, complex optimization algorithms are used to optimize the annual energy produced by unit of land, and heliostats must be packed as close as possible so the receiver can be small and concentration high. However, the heliostats are individual tracking reflective Fresnel segments subject to complex performance factors, which must be optimized over the hours of daylight in the year, by minimizing the cosine effect, shadowing and blocking, and receiver spillage. Since the reflective surface of the heliostat is not normal to the incident rays, its effective area is reduced by the cosine of the angle of incidence ψ ; the annual average $\cos \psi$ varies from about 0.9 at two tower heights north of the tower to about 0.7 at two tower heights south of the tower. Of course, annual average cosine is highly dependent on site latitude. Consequently, in places close to the equator, a surround field would be the best option to make best use of the land and reduce the tower height. North fields improve performance as latitude increases (south fields in the Southern Hemisphere), in which case, all the heliostats are arranged on the north side of the tower. Representative surround and north collector field configurations are depicted in Figure 19.43.

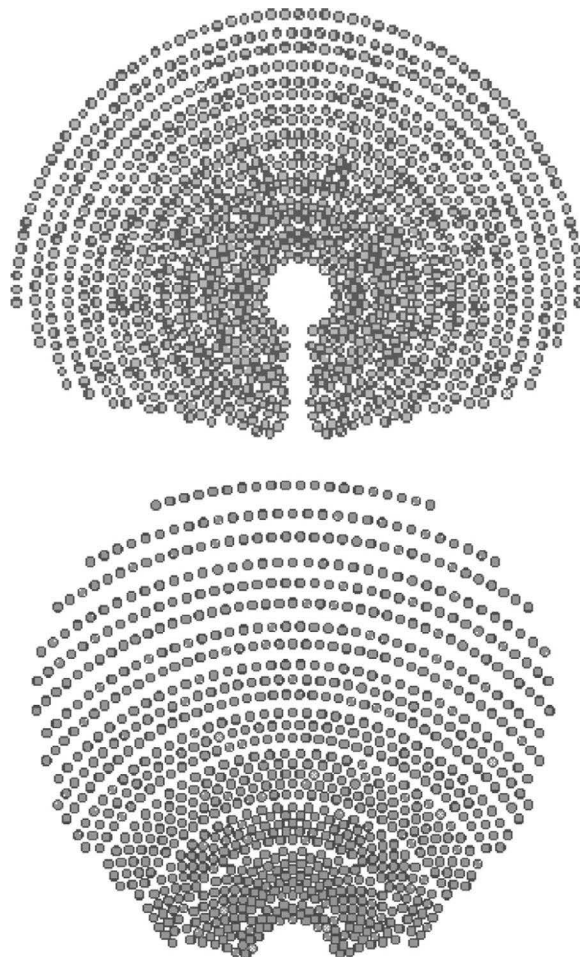


FIGURE 19.43

Representation of optimized fields for a latitude of 36° with surround field (top) and north field (bottom) configurations.

Another point to be considered in the layout is the heliostat dimensions. If the heliostats are spaced too close together, their corners could collide, so mechanical limits preclude pedestal spacing closer than the maximum dimension of the heliostat (i.e., the diagonal or diameter of the heliostat, D_m). This causes a significant disadvantage when the aspect ratio (height/width) differs greatly from 1.

Blocking of reflected rays is also an important limitation on spacing heliostats. Blocking is produced by neighboring heliostats. To avoid blocking losses, the distance Δx between the heliostat rows must be calculated according to the following equation:

$$\Delta x = x \frac{z_s}{z_r} \tag{19.41}$$

Shading produced by neighboring heliostats also has to be taken into account. This occurs mostly at low sun angles and in the middle of the field where blocking conditions would allow close spacing. The shadows move during the day and year, as does the heliostat orientation, so there is no simple rule. In addition, the tower or other objects may also cast a shadow over part of the heliostat field. Usually shadowing in the field is calculated by projecting the outlines of the heliostats aligned, the tower, and anything else that casts a shadow onto a plane perpendicular to the center sunray. Shadowed portions of any heliostat appear in the overlapping areas in this projection. Classical computer codes like HELIOS provide this calculation (Biggs and Vittitoe, 1979).

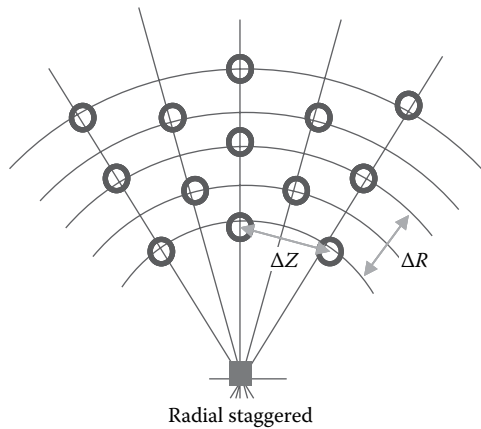
Not all the sunlight that clears the heliostats reaches the vicinity of the receiver. Some of the energy is scattered and absorbed by the atmosphere. This effect is referred to as the attenuation loss (Falcone, 1986). This factor increases when water vapor or aerosol content in the atmosphere is high and is typically anywhere between 5% and 15% in a solar field. Atmospheric attenuation is usually expressed as a function or experimental correlation depending on the range of heliostat inclination.

The size of the image formed by each heliostat depends on mirror focusing and canting and on the size of the heliostat and errors, as expressed by its beam quality. Because of that, there is an intercept factor for a given receiver aperture area. Some of the energy spills over around the receiver. While spillage can be eliminated by increasing the size of the receiver, at some point, increased size becomes counterproductive because of the resulting increased receiver losses and receiver costs.

The combination of all these factors influencing the performance of the heliostat field should be optimized to determine an efficient layout. There are many optimization approaches to establish the radial and azimuthal spacing of heliostats and rows. One of the most classic, effective, and widespread procedures is the *radial staggered* pattern, as shown in Figure 19.44, originally proposed by the University of Houston in the 1970s (Lips and Vant-Hull, 1978). Typical radially staggered field spacing at 35° latitude using square low-cost heliostats can be expressed by

$$\frac{\Delta R}{\Delta D_m} = \frac{1.009}{\Theta} - 0.063 + 0.4803\Theta \tag{19.42}$$

$$\frac{\Delta Z}{\Delta D_m} = 2.170 - 0.6589\Theta + 1.247\Theta^2 \tag{19.43}$$

**FIGURE 19.44**

Radial staggered field layout, where ΔZ represents the azimuthal spacing and ΔR represents the radial spacing.

where Θ represents the receiver elevation angle in radians:

$$\Theta = \arctan \left[\frac{(z_T - (z_S/2))}{x} \right]$$

Integral optimization of the heliostat field is decided by a trade-off between cost and performance parameters. Heliostats, land, and cabling network must be correlated with costs. Cost and performance also often have reverse trends, so that when heliostats are packed closer together, blocking and shadowing penalties increase, but related costs for land and wiring decrease. A classical code in use since the 1980s for optimization of central receiver subsystems is DELSOL3 (Kistler, 1986). In DELSOL3, heliostat field layout is optimized for tower height and solar receiver geometry. Figure 19.45 shows a breakdown of efficiency maps for the different performance factors in a typical one-sided north heliostat field. It may be deduced that the heliostat density is greatest at the inner boundary and decreases with increasing radial distance from the tower. The average land coverage ratio is typically 0.20–0.25.

The radially staggered distribution clearly creates *prearranged* grids based on the tower height versus row-to-radius ratio. This geometrical procedure provides a smart solution to the problem with good optimization of computing resources. However, with today's computers, it is possible to calculate the yearly energy available at any point in a site for a given tower height, the *yearly normalized energy surface* (YNES). Yearly efficiency maps can be generated based on the cosine factor, the spillage factor, and the site atmospheric attenuation coefficient using real direct normal irradiance (DNI) data, within a reasonable computing time. It is therefore easy to find the place where the yearly energy available is the highest for location of the first heliostat. It is also possible to calculate the effect of shadowing and blocking by this heliostat on the YNES, so YNES can be recalculated, and the best position for the next heliostat can be found. Although this iterative method is time consuming, it is worthwhile if either the efficiency of the solar plant can be increased or the capital cost can be reduced. This YNES-based layout method enables better flexibility than predetermined gridding strategies (Sánchez and Romero, 2006).

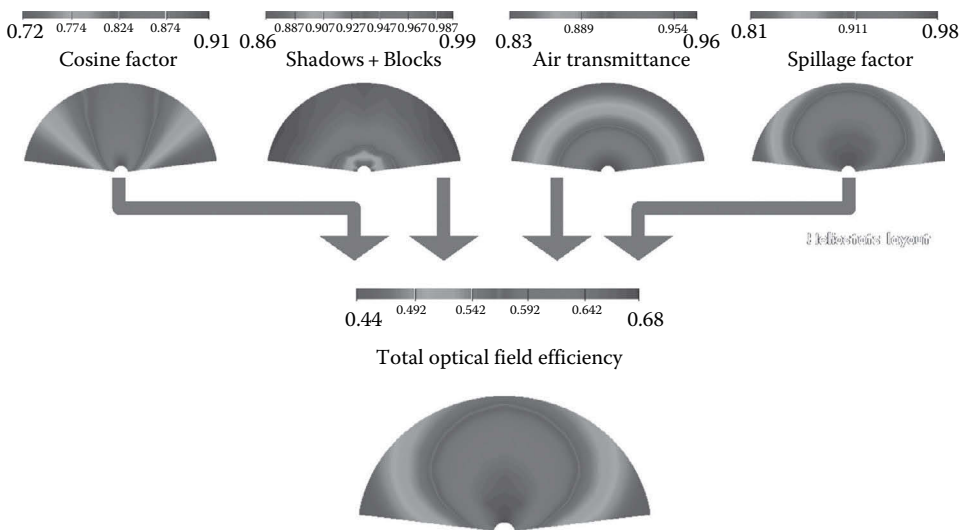


FIGURE 19.45 Mapping of total optical efficiency of a north-field area of heliostats and its breakdown into cosine factor, shadowing and blocking, air transmittance, and receiver spillage.

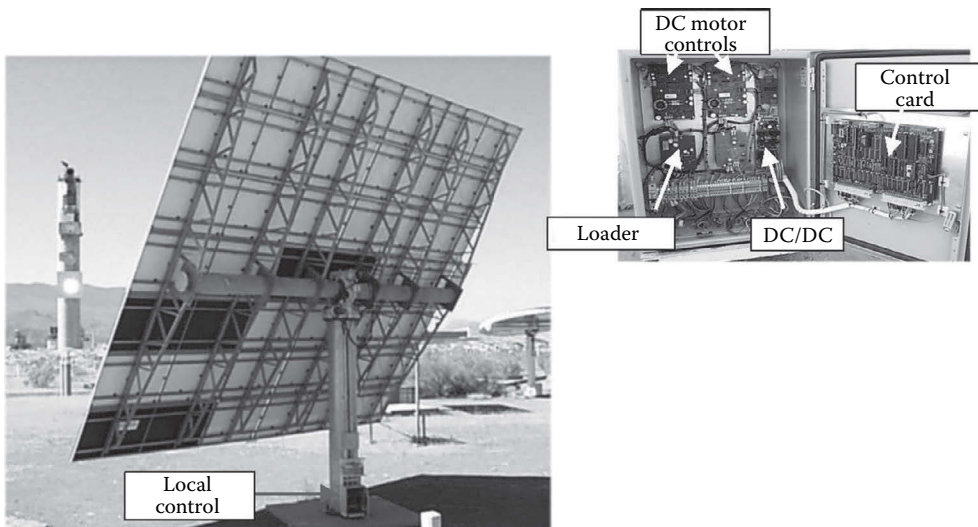


FIGURE 19.46 Rear view of the heliostat COLON SOLAR of 70 m² with typical T-shape structure and torque tube. The control box is located at the bottom of the pedestal. The reflected image is shown at the Lambertian target located on the tower.

Mature low-cost heliostats consist of a reflecting surface, a support structure, a two-axis tracking mechanism, pedestal, foundation, and control system (Figure 19.46). The development of heliostats shows a clear trend from the early first-generation prototypes, with a heavy, rigid structure, second-surface mirrors, and reflecting surfaces of around 40 m² (Mavis, 1989), to the current commercial designs with large 100–120 m² reflecting surfaces, lighter structures, and lower-cost materials (Romero et al., 1991).

Since the first-generation units, heliostats have demonstrated beam qualities below 2.5 mrad that are good enough for practical applications in solar towers, so the main focus of development is directed at cost reduction. Two basic approaches are being pursued to reduce per m² installed cost.

The first approach is devoted to increasing the reflective area by employing curved surfaces made up of several mirror facets. Each facet surface typically goes from 3 to 6 m². This increment in optical surface results in a cost reduction, since some components, like the drive mechanism, pedestal, and control, do not increase linearly. However, there is a limit to this advantage, since the larger the area, the higher the optical errors and washing problems are also.

The second line of development is the use of new light-reflective materials like polymer reflectors and composites in the supporting structure, such as in the stretched-membrane heliostats. The stretched-membrane drum consists of a metal ring to which prestressed 0.4 mm stainless-steel membranes are welded. One of the membranes is glued to a polymer reflector or thin mirrors. A vacuum is created inside the plenum with a controlled blower to ensure curvature.

In Spain, some developments worthy of mention are the 70 m² COLON SOLAR prototype (Osuna et al., 1999), the 105 m² GM-100 (Monterreal et al., 1997), and more recently, the 90 and 120 m² Sanlúcar heliostats (Osuna et al., 2004). In the United States, a similar development in glass/metal technology was the 150 m² ATS heliostat (Alpert and Houser, 1990). The stretched-membrane milestone is the 150 m² Steinmuller heliostat ASM-150 with an excellent beam quality of 2 mrad (Weinrebe et al., 1997). In spite of the good quality achieved by stretched membranes, projected costs are higher than the more mature glass/metal units.

Eventually, 120 m² heliostats were adopted for the first commercial tower power plants PS10 and PS20 promoted by the company Abengoa Solar (Osuna et al., 2004). The company SENER has developed a similar 115 m² heliostat for its Gemasolar plant. Estimated production costs of large-area glass/metal heliostats for sustainable market scenarios are around \$130–\$200 per m². Large-area glass/metal units make use of glass mirrors supported by metallic frame facets.

Recently, some developers are introducing substantial changes in the conception of heliostat design. A number of projects based upon the paradigm of maximum modularity and mass production of components are claiming small-size heliostats as a competitive low-cost option. Companies like BrightSource, eSolar, Aora, or Cloncurry are introducing heliostat units of only a few m². The small heliostats have better optical efficiency, and even they can be flat mirrors compared to curved and canted facets in the large heliostats. This advantage and the easier transportation to the site with minimal installation works can lead to a further decrease in the heliostats costs. BrightSource with an ambitious program of large projects is making use of single-facet 7.3 m² heliostats (Silberstein et al., 2009), and the company eSolar with a multitower plant configuration presents a highly innovative field with ganged heliostats of extremely small size (1.14 m² each) that implies the large number of 12,180 units for a single 2.5 MW tower (Schell, 2009). If such small heliostats may reach installed costs below \$200 per m², it can be understood only under aggressive mass production plans and preassembly during manufacturing process by reducing on-site mounting works. Annual performance and availability of those highly populated fields are still under testing.

The drive mechanism is in charge of independent azimuthal and elevation movement, in such a way that the specular surface follows the sun position and reflects the beam onto the focal point. The ratio between the angle of incidence and the reflected ray leads

to angular errors doubling at the target. It is therefore crucial for a tracking system to be highly accurate. Heliostat drives should have the following characteristics:

- Sufficiently robust to support their own weight, the movable structure, and wind loads, and be rigid enough to avoid low-frequency vibrations.
- Able to generate extremely slow movement, with high reduction ratios (up to 40,000:1).
- Highly accurate positioning (use of encoders) and no free movement.
- Able to ensure relatively fast return to stow position in case of high winds or other dangerous weather conditions, and other events.
- Resistance to outdoor exposure.
- Easy maintenance.
- Low-cost manufacture and operation.

The most common drive mechanism configuration makes use of worm-gear systems for both elevation and azimuth axes (Figure 19.47). Both gears are essentially analogous in terms of tooth shape and reduction ratio. In many cases, there is a first planetary reduction step and then a second worm-gear reduction step at the outlet. The advantage of the

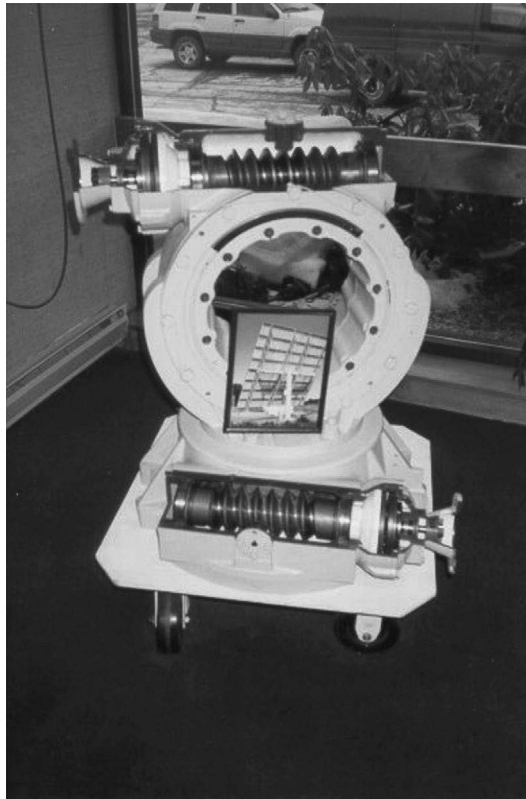


FIGURE 19.47

Detail of a typical worm-gear drive mechanism. At the bottom, the azimuthal actuator located on top of the pedestal is shown. The upper worm actuates against the gear connected to the torque tube.

planetary system is the high ratio of reduction in a limited space. The worm gear provides high reduction ratios at high momentums. However, worm gears are less efficient because of the stress of high friction. This stress has a positive reaction, since the self-locking worm comes to a halt whenever the angle of friction between the worm thread and the gear teeth is higher than the nominal design angle.

Mature glass/metal faceted heliostats report availabilities over 95% and beam qualities of 2.4–2.8 mrad. Yearly average reflectivity of a heliostat field reaches 85%–92%. Faceted heliostats with curved mirrors require canting of the facets to form a large paraboloid. In Figure 19.48, the effect of canting facets can be seen.

Control of CRSs is more complicated than other types of STP plants since optics are off-axis, and each and every heliostat individually tracks the sun. The control system in a CRS is naturally separated into the heliostat field control system (HFCS) and the receiver and power system control system (RPSCS) (Yebra et al., 2004). The main purpose of the HFCS is to keep each heliostat positioned at the desired coordinates at all times, depending on power system

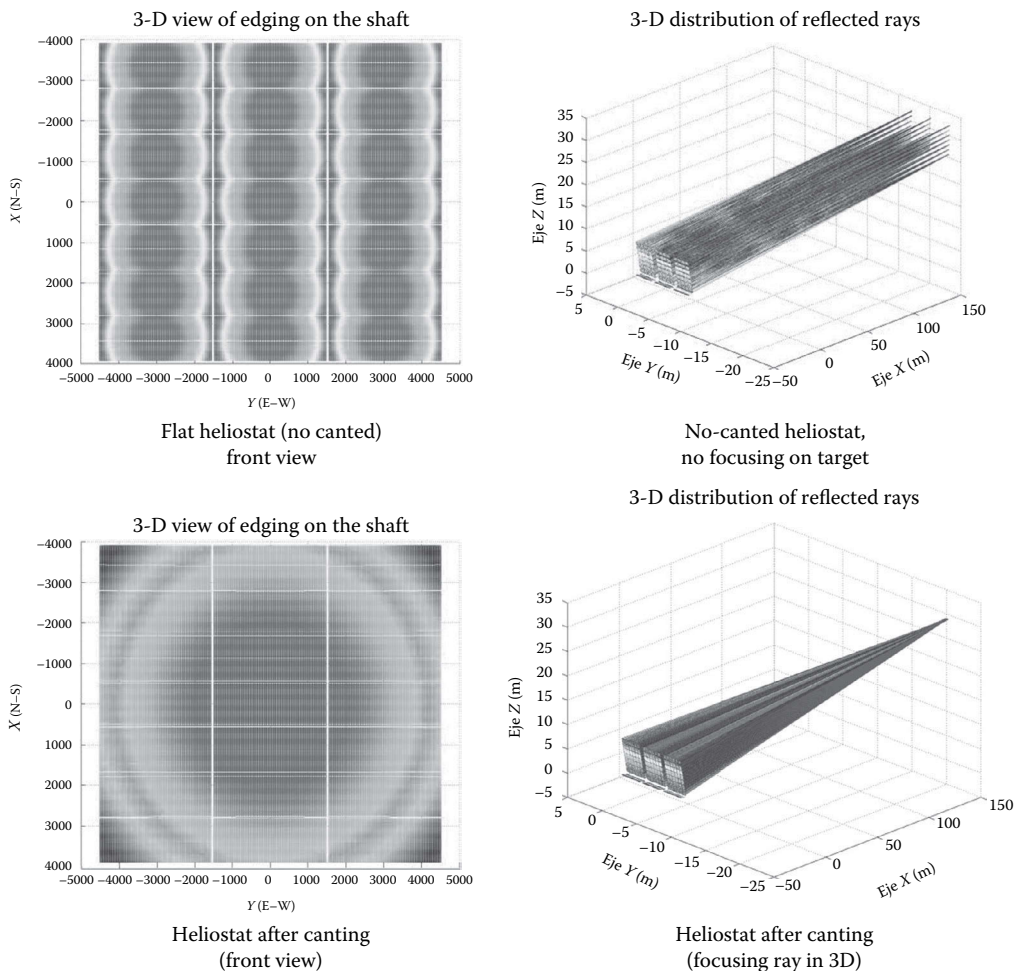


FIGURE 19.48

Effect of canting facets in a glass metal heliostat. In the upper part, it can be observed that a flat heliostat with curved facets is not focusing in a single image. In the lower part, a canted heliostat is depicted.

demand. The general purpose of the HFCS is to generate a uniform time–spatial distribution of the temperature on the volumetric receiver by controlling the timed insertion of an associated group of heliostats at predefined aiming points on the receiver by modifying the aiming-point coordinates and changing from one heliostat group to another during operation. This is accomplished by an HFCS aiming-point strategy (Garcia-Martín et al., 1999). The current trend in control systems is a distributed control, with a hard real-time operating system, integrating heterogeneous hardware and software platforms in real time, that guarantees a deterministic response to external (physical environment) and internal (operator interface) events. The RPSCS regulates the pressure and temperature of the HTF, and steam generator.

The heliostat local control is responsible for all the emergency and security maneuvers and sun-tracking calculations, as well as communication with the control room. The current trend is to increase the heliostat intelligence and autonomy. In addition, some drive mechanism options consider the use of wireless communications and PV-power supply, eliminating the need for cabling and trenching. This is the case of the stand-alone heliostat developed at the PSA in Spain, where a field of 92 such heliostats is in operation (García et al., 2004).

19.6.2 Solar Receiver

In a solar power tower plant, the receiver is the heat exchanger where the concentrated sunlight is intercepted and transformed into thermal energy useful in thermodynamic cycles. Radiant flux and temperature are substantially higher than in parabolic troughs, and therefore, high technology is involved in the design, and high-performance materials should be chosen. The solar receiver should mimic a blackbody by minimizing radiation losses. To do so cavities, black-painted tube panels or porous absorbers able to trap incident photons are used. In most designs, the solar receiver is a single unit that centralizes all the energy collected by the large mirror field, and therefore high availabilities and durability are a must. Just as cost reduction is the priority for further development in the collector field, in solar receivers, the priorities are thermal efficiency and durability. Typical receiver absorber operating temperatures are between 500°C and 1200°C, and incident flux covers a wide range between 300 and over 1000 kW/m². The picture in Figure 19.49 clearly shows the high flux to be withstood by the receiver.

Thermal and optical losses are the key parameters for quantifying the efficiency of a solar receiver.

$$\eta_{rec} = (\alpha\tau_w) + (\alpha\varepsilon_w) \frac{\sigma T_w^4}{C \cdot \phi} - (\varepsilon\bar{\rho}) \frac{\sigma T^4}{C \cdot \phi} - U \frac{(T - T_a)}{C \cdot \phi} \quad (19.44)$$

This equation is the result of the energy balance of gains and losses in the receiver, with an absorber surface at temperature T . In some cases, the receiver has a transparent window that absorbs part of the incident radiation at a temperature, T_w , higher than the ambient, T_a . The concentrated solar irradiance ($C \cdot \phi$) is absorbed with an efficiency of $(\alpha\tau_w)$. The radiation must often go through a transparent window, where it is partially absorbed, before reaching the absorber surface, reflected and transmitted onto the absorber. These not-so-simple effects are represented by the apparent window transmittance, τ_w . Likewise, the second term in Equation 19.44 expresses the energy emitted of temperature T_w from the hot window toward the absorber. Therefore, this second term adds gains to the first. The loss terms are of two different types. The most important in a central receiver represents energy thermally radiated by the absorber through the receiver aperture. These radiation



FIGURE 19.49

Lateral view of the 80 m concrete tower of the CESA-1 facility located at the Plataforma Solar de Almería in Spain. The concentrated flux is aiming a standby position previous to start operation.

losses depend on the emissivity of the absorber and on thermal radiation reflectivity ρ_w of the window. In the product $(\varepsilon\bar{\rho})$, $\bar{\rho}$ indicates $(1 - \rho_w)$ or $(\alpha_w + \tau_w)$.

The absorber convective, or conductive, loss to the ambient is determined by the heat loss coefficient U , which depends on the temperature and the forced convection due to wind. In good central receiver designs, U can be sufficiently reduced by thermal insulation and decreased aperture area; therefore, U is basically expressed as a convective loss heat transfer coefficient. Generally, this coefficient is obtained from the dimensionless Nusselt number and subsequently as a function of numbers like Reynolds (Re), Prandtl (Pr), and Grashof (Gr). Forced convection is determined by combinations of the Re and Pr numbers, while natural convection is characterized by Pr and Gr numbers.

In the solar tower, the convective heat loss is calculated differently depending on whether the receiver is a cavity or a cylindrical external receiver. A typical simple mixed convection coefficient for an external receiver can be obtained calculated (Siebers and Kraabel, 1984) as

$$U_{mix} = \left(h_{forced}^{3.2} + h_{nat}^{3.2} \right)^{1/3.2} \quad (19.45)$$

where

$h_{nat} = 9.09 \text{ (W/m}^2 \text{ }^\circ\text{C)}$ for an average absorber temperature of 480°C

h_{forced} is separated into three cases depending on the receiver diameter (Kistler, 1986)

In all cases, the Reynolds number is $Re = (1.751 \times 10^5)D$.

Case 1: $D \leq 4.0$ m	$h_{forced} = \left(\frac{1}{D}\right) \cdot \left(0.3 + 0.488 \cdot Re^{0.5} \cdot \left(1.0 + \left(\frac{Re}{282000}\right)^{0.625}\right)^{0.8}\right) \cdot 0.04199$
Case 2: $4.0 < D \leq 125.0$	$h_{forced} = 14.0$
Case 3: $D > 125.0$ m	$h_{forced} = 33.75 \cdot D^{-0.19}$

For a cavity receiver, the convective heat loss can be directly calculated as (Kistler, 1986) follows:

$$Q_{conv} = Q_{forced} + Q_{nat} \text{ (W)} \tag{19.46}$$

$$Q_{forced} = 7631 \frac{A}{W_{ap}^{0.2}} \tag{19.47}$$

$$Q_{nat} = 5077 \cdot A_{cav} \tag{19.48}$$

where

A is the aperture area (m^2)

W_{ap} is the aperture width (m)

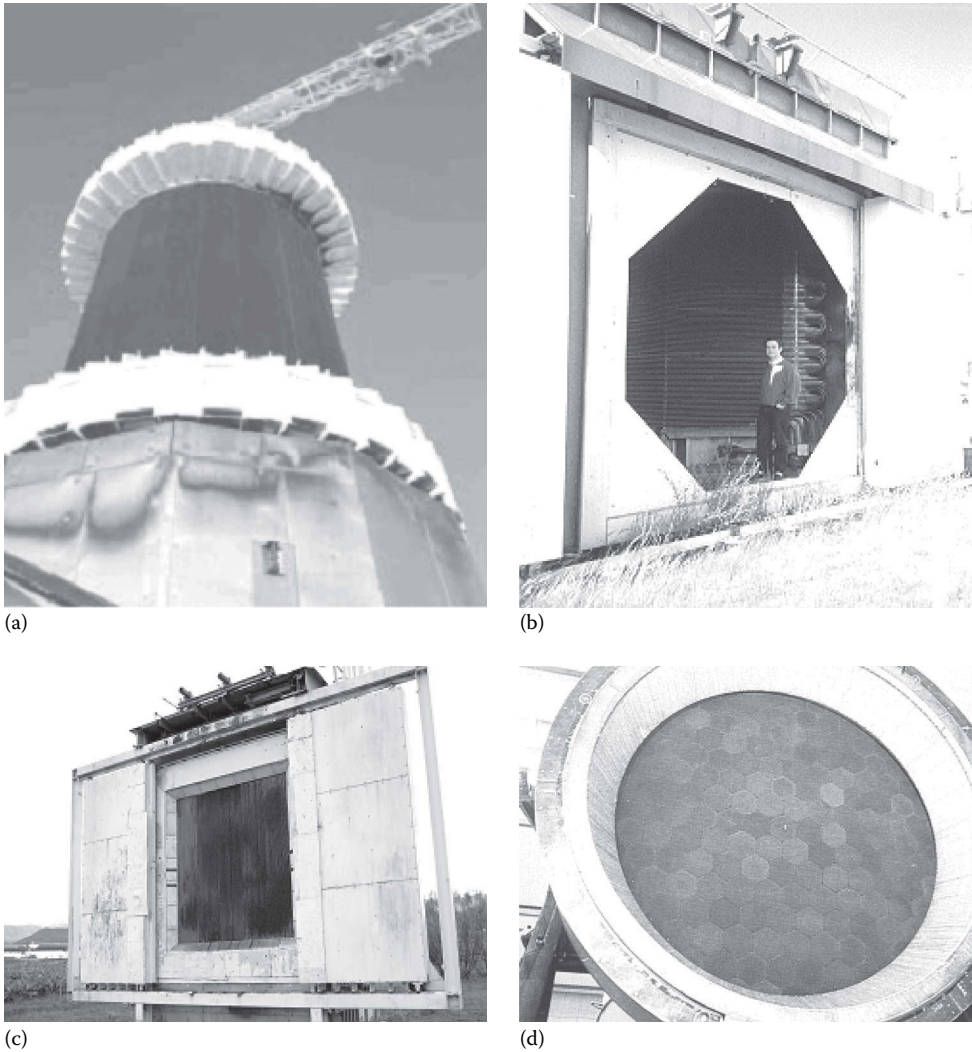
A_{cav} is the approximation to total area inside cavity (m^2)

For more detailed correlations applicable to convection losses in different kinds of solar receivers, Becker and Vant-Hull (1991) is recommended.

There are different solar receiver classification criteria depending on the construction solution, the use of intermediate absorber materials, the kind of thermal fluid used, or heat transfer mechanisms. According to the geometrical configuration, there are basically two design options, external and cavity-type receivers. In a cavity receiver, the radiation reflected from the heliostats passes through an aperture into a box-like structure before impinging on the heat transfer surface. Cavities are constrained angularly and subsequently used in north-field (or south-field) layouts. External receivers can be designed with a flat plate tubular panel or in a cylindrical shape. Cylindrical external receivers are the typical solution adopted for surround heliostat fields. Figure 19.50 shows examples of cylindrical external, billboard external, and cavity receivers.

Receivers can be directly or indirectly irradiated depending on the absorber materials used to transfer the energy to the working fluid (Becker and Vant-Hull, 1991). Directly irradiated receivers make use of fluids or particle streams able to efficiently absorb the concentrated flux. Particle receiver designs make use of falling curtains or fluidized beds. Darkened liquid fluids can use falling films. In many applications, and to avoid leaks to the atmosphere, direct receivers should have a transparent window. Windowed receivers are excellent solutions for chemical applications as well, but they are strongly limited by the size of a single window, and therefore clusters of receivers are necessary.

The key design element in indirectly heated receivers is the radiative/convective heat exchange surface or mechanism. Basically, two heat transfer options are used, tubular panels and volumetric surfaces. In tubular panels, the cooling thermal fluid flows inside the tube and removes the heat collected by the external black panel surface by convection. It is therefore operating as a recuperative heat exchanger. Depending on the HTF

**FIGURE 19.50**

Different configurations of solar receivers. From left to right and top to bottom: (a) external tubular cylindrical, (b) cavity tubular, (c) billboard tubular, and (d) volumetric.

properties and incident solar flux, the tube might undergo thermo-mechanical stress. Since heat transfer is through the tube surface, it is difficult to operate at an incident flux above 600 kW/m^2 (peak). Table 19.8 shows how only with high thermal conductivity liquids like sodium, it is possible to reach operating fluxes above 1 MW/m^2 . Air-cooled receivers have difficulties working with tubular receivers because of the lower heat transfer coefficients, as already found in the German-Spanish GAST project where two tubular receivers, one metal and one ceramic, were tested at the PSA in Spain (Becker and Boehmer, 1989). To improve the contact surface, a different approach based on wire, foam, or appropriately shaped materials within a volume is used. In volumetric receivers, highly porous structures operating as convective heat exchangers absorb the concentrated solar radiation. The solar radiation is not absorbed on an outer surface, but

TABLE 19.8

Operating Temperature and Flux Ranges of Solar Tower Receivers

Fluid	Water–Steam	Liquid Sodium	Molten Salt (Nitrates)	Volumetric Air
Flux (MW/m^2)				
Average	0.1–0.3	0.4–0.5	0.4–0.5	0.5–0.6
Peak	0.4–0.6	1.4–2.5	0.7–0.8	0.8–1.0
Fluid outlet temperature ($^{\circ}C$)	490–525	540	540–565	700–800 (>800)

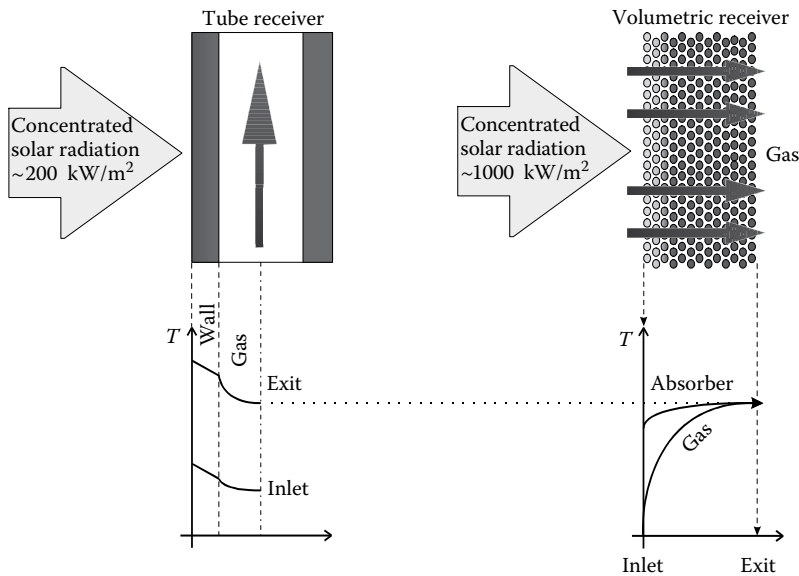


FIGURE 19.51
Heat transfer principles in tubular and volumetric receivers.

inside the structure *volume*. The heat transfer medium (mostly air) is forced through the porous structure and is heated by convective heat transfer. Figure 19.51 shows a comparison of the two absorber principles. Volumetric absorbers are usually made of thin heat-resistant wires (in knitted or layered grids) or either metal or ceramic (reticulated foams, etc.) open-cell matrix structures. Good volumetric absorbers are very porous, allowing the radiation to penetrate deeply into the structure. Thin substructures (wires, walls, or struts) ensure good convective heat transfer. A good volumetric absorber produces the so-called volumetric effect, which means that the irradiated side of the absorber is at a lower temperature than the medium leaving the absorber. Under specific operating conditions, volumetric absorbers tend to have an unstable mass flow distribution. Receiver arrangements with mass flow adaptation elements (e.g., perforated plates) located behind the absorber can reduce this tendency, as well as appropriate selection of the operating conditions and the absorber material.

Selection of a particular receiver technology is a complex task, since operating temperature, heat storage system, and thermodynamic cycle influence the design. In general, tubular technologies allow either high temperatures (up to 1000°C) or high pressures (up to 120 bar), but not both (Kribus, 1999). Directly irradiated or volumetric receivers allow even higher temperatures but limit pressures to below 15 bar.

19.6.2.1 Tubular Receivers

The most common systems used in the past have been tubular receivers where concentrated radiation is transferred to the cooling fluid through a metal or ceramic wall. Conventional panels with darkened metal tubes have been used with steam, sodium, and molten salts for temperatures up to 500°C–600°C. Much less experience is available on tubular receivers with gas, though temperatures in the range of 800°C–900°C are possible. Cavity receivers have been tested in France (Themis) and Spain (IEA-SSPS-CRS project and CESA-1 plant). External tubular receivers were used in Solar One (United States), IEA-SSPS-CRS (Spain), and Solar Two (United States) (Grasse et al., 1991; Pacheco and Gilbert, 1999). Other experimental systems using water–steam and tubular receivers were Nio in Japan, Eurelios in Italy, and SES-5 in the former Soviet Union.

Solar One in Barstow, California, used a once-through superheated water–steam receiver. It operated from 1984 to 1988 and was the largest central receiver in the world for two decades. It was an external cylindrical receiver made up of twenty-four 1 m wide by 14 m long rectangular panels (Figure 19.52). The six panels on the south side were feed-water preheat units. Preheated water was then transferred to once-through boilers and superheaters on the north side. The tubes in each panel were welded throughout their length and painted black with Pyromark® paint. The design specifications were for steam at 516°C and a pressure of 100 bar. Up to 42 MW_{th} could be absorbed by the receiver. The initial thermal efficiency was 77% for an absorbed power of 34 MW_{th}. After painting it black and curing the surface, it increased to 82% with $\alpha = 0.97$. Almost constant thermal losses have been verified (4.5–5 MW_{th}) for this kind of receiver, due basically to radiation losses and

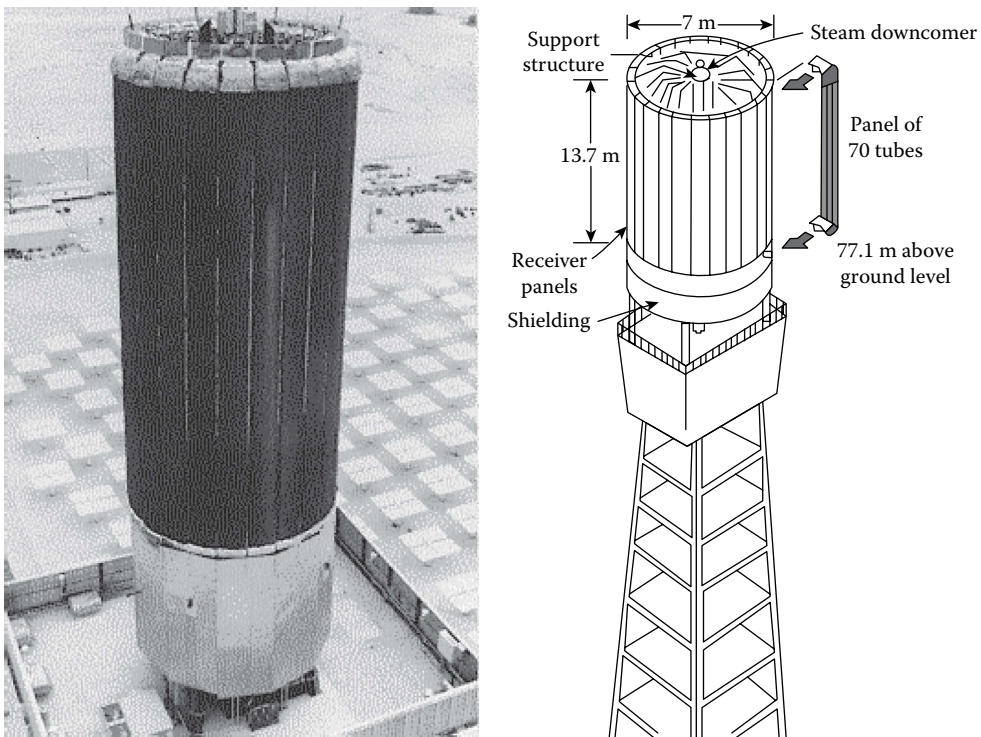


FIGURE 19.52

External cylindrical tubular receiver used in Solar One power plant, Barstow, California.

operating the receiver at constant temperature by regulating the mass flow rate. One of the main problems found during testing was overheating and deformation in the superheating section because of solar transients and poor heat transfer (Radosevich and Skinrood, 1989). Cracking and leaking were observed at the top of the boiler tubes after 18 months of operation. The temperature gradient between the edges and the center of the tubes can go up to 111°C during start-ups and shutdowns.

CESA-1, which operated 1631 h between 1983 and 1986 in Almería, Spain, was a north-facing water–steam cavity receiver. The 3.4 m square aperture was tilted 20° to the heliostat field. The receiver panel configuration and position of the steam drum are shown in Figure 19.53. The boiler consisted of three panels of A-106 Gr B carbon steel tubes, with an effective surface of 48.6 m^2 , and a superheater made of X-20 Cr Mo V 121 steel. The 6.7 MW maximum incident power on the receiver produced superheated steam at 110 kg/cm^2 and 525°C . As in Solar One, operating problems and noticeable deformations were found in the superheating zone, requiring it to be operated with lower flux. Also because of that, operation had to proceed slowly during start-up and transients, penalizing efficiency. More than 45 min were required to reach nominal conditions (Sánchez, 1986).

Molten-salt tubular receivers are represented by the Themis system (cavity) and Solar Two (cylindrical external), and subsequently applied to the commercial project Gemasolar. In a molten-salt system, cold salt at about 290°C is pumped from a tank at ground level to the receiver mounted atop a tower where it is heated by concentrated sunlight to 565°C . Using molten salts as receiver coolant provides a number

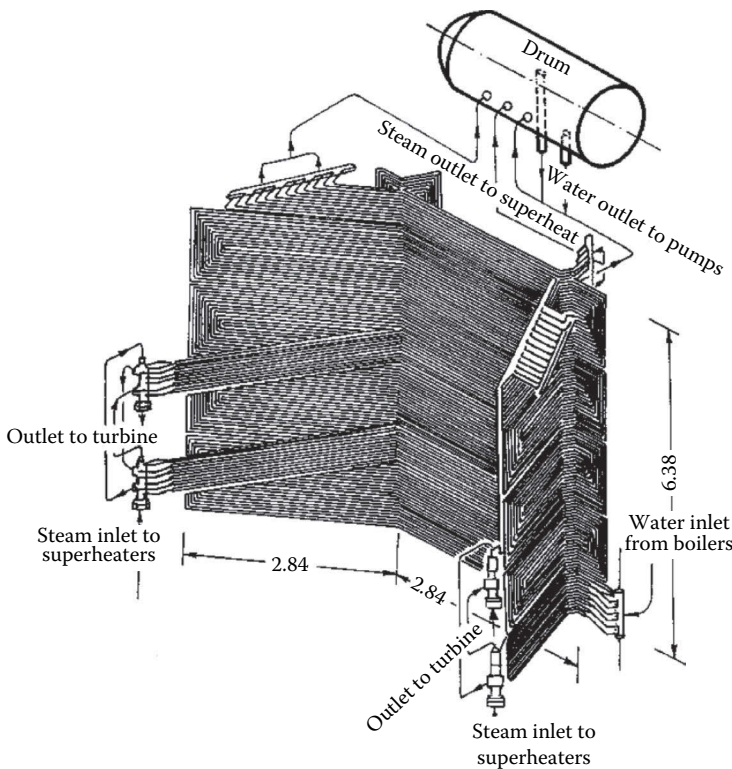


FIGURE 19.53

Inner view of tubular panels and drum of the water–steam cavity receiver used in the CESA-1 project in Spain.

of benefits because there is no phase change, and it is possible to heat up to 565°C without the problems associated in tubes with superheating sections. Mixtures of 60% sodium nitrate and 40% potassium nitrate have been extensively tested with satisfactory results in France and the United States. Molten nitrates provide good thermal conductivity (0.52 W/m K) and heat capacity (1.6 kJ/kg K) at relatively low prices. Molten nitrate salt, though an excellent thermal storage medium, can be a troublesome fluid to deal with because of its relatively high freezing point (220°C). To keep the salt molten, a fairly complex heat trace system must be employed. (Heat tracing is composed of electric wires attached to the outside surface of pipes. Pipes are kept warm by way of resistance heating.) Problems were experienced during the start-up of Solar Two due to the improper installation of the heat trace. Though this problem has been addressed and corrected, research is needed to reduce the reliance on heat tracing in these plants. Also, valves can be troublesome in molten-salt service. Special packings must be used, oftentimes with extended bonnets, and leaks are not uncommon. Furthermore, freezing in the valve or packing can prevent it from operating correctly. While today's valve technology is adequate for molten-salt power towers, design improvements and standardization would reduce risk and ultimately reduce O&M costs (De Meo and Galdo, 1997).

Solar Two, tested between 1996 and 1999 (Pacheco et al., 2000), is still the technical reference for molten-salt tubular receivers. The 42 MW absorber consisted of a 6.2 m–high and 5.1 m–diameter cylinder, with 768 2 cm–diameter tubes. Reported efficiency with no wind was 88% for 34 MW absorbed (86% with wind under 8 km/h). Peak concentrated solar flux was 800 kW/m² and average 400 kW/m². Though reported efficiency was close to nominal, during the 3 years of operation, there were many incidents, and modifications and repairs to avoid freezing and obstructions in tubes, downcomers, manifolds, valves, and pipelines. The consequence was a very limited experience in long-term testing. Some attempts were made in the early 1990s to simplify molten-salt receivers by removing the salt-in-tube heat exchanger and introducing open-air falling-film flat plates (Romero et al., 1995). Table 19.9 summarizes typical operating temperatures, incident flux, pressures, and efficiencies in tubular water–steam and molten-salt receivers.

19.6.2.2 Volumetric Receivers

As already mentioned, volumetric receivers use highly porous structures for the absorption of the concentrated solar radiation deep inside (in the *volume*) the structure. Volumetric receivers can work open to the ambient or enclosed by a transparent window. With metal absorbers, it is possible to achieve air outlet temperatures up to 850°C, and with ceramic fibers, foams, or monoliths (SiC), the temperature can surpass 1000°C (Avila-Marin, 2011).

TABLE 19.9

Summary of Operational Range for Tubular Water–Steam and Molten-Salt Receivers

Receivers Water–Steam	Molten-Salt Receivers
Temperature fluid outlet 250°C/525°C	Temperature outlet 566°C
Incident flux 350 kW/m ²	Incident flux 550 kW/m ²
Peak flux 700 kW/m ²	Peak flux 800 kW/m ²
Pressure 100–135 bar	
Efficiency 80%–93%	Efficiency 85%–90%

The main advantages of an air-cooled volumetric receiver are as follows:

- The air is free and fully available at the site.
- No risk of freezing.
- Higher temperatures are possible, and therefore the integration of solar thermal energy into more efficient thermodynamic cycle looks achievable.
- No phase change.
- Simple system.
- Fast response to transients or changes in incident flux.
- No special safety requisites.
- No environmental impact.

Open volumetric receivers have made dramatic progress since the pioneering experiences of the late 1970s (Sanders, 1979) and early 1980s (Fricker et al., 1988). More than 20 absorbers and prototypes in the 200–300 kW_{th} range have been tested in the Sulzer test bed at the PSA (Becker et al., 1989, 1992; Hoffschmidt et al., 2001). Wire mesh, knitted-wire, foam, metal, and ceramic monolith volumetric absorbers have been developed worldwide. The relatively large number of volumetric prototypes tested has demonstrated the feasibility of producing hot air at temperatures of 1000°C and upward and with aperture areas similar to those used in molten-salt or water–steam receivers. Average flux of 400 kW/m² and peaks of 1000 kW/m² have been proven, and their low-inertia and quick sun-following dispatchability are excellent. Comparative assessments have demonstrated that wire mesh has the lowest thermal losses (Table 19.10). This can mainly be explained by the very high porosity of the absorber, which permits a large portion of the irradiation to penetrate deep into its volume. The choice of ceramics as the absorber material makes higher gas outlet temperatures possible. In particular, siliconized SiC has been revealed as a good option because of its high thermal conductivity. Even though ceramic absorbers have lower efficiencies at 680°C (this is the reference temperature for applications where hot air is used as the HTF to produce superheated

TABLE 19.10

Properties and Efficiencies Reported for Several Absorber Materials Tested at the Plataforma Solar de Almería ($D_{m,p}$ = Mean Pore Diameter)

Type of Receiver	Designed by	Absorber Structure	Porosity (V_p/V_{tot})	$D_{m,p}$ (mm)	Absorber Thickness (mm)	Material	Thermal Conductivity (500°C) (W/m K)	Efficiency (680°C) (%)
Metallic wire	Sulzer	Wire mesh	0.95	2.5	35	Stainless steel	20	75
Ceramic foam	Sandia	Amorphous foam	0.8	1.0	30	Al ₂ O ₃	25	54
Metallic foils	Interatom/ Emitec	Prismatic channels	0.9	1.0	90	X ₅ CrAl ₂ O ₅	20	57
Ceramic foils	DLR/ Ceramtec	Prismatic channels	0.4	3.0	92	SiSiC	80	60
Ceramic cups	DLR/ Stobbe	Prismatic channels	0.5 + 0.12 apert.	2.1	80	SiSiC	80	60

steam in a heat exchanger), they have demonstrated efficiencies about 80% at temperatures of 800°C. With higher solar flux and temperatures, more compact designs and smaller receivers can be developed.

A milestone in the experimental scale-up of open volumetric receivers was the Technology Program Solar Air Receiver (TSA) project, under the leadership of the German Steinmüller company. A 2.5 MW_{th} air-cooled receiver was tested on top of the PSA CESA-1 tower late in 1991. The TSA experimental setup was a small-scale PHOEBUS-type receiver (Schmitz-Goeb and Keintzel, 1997), in which atmospheric air is heated up through a wire mesh receiver to temperatures on the order of 700°C to produce steam at 480°C–540°C and 35–140 bar, in a heat recovery steam generator with a separate superheater, reheater, evaporator, and economizer feeding a Rankine turbine-generator system. All the hardware, including receiver, steam generator, and heat storage, was located atop the CESA-1 tower. Average solar flux at the receiver aperture was 0.3 MW/m². The HFCS was implemented with heuristic algorithms to obtain an automatic aiming strategy able to maintain stationary flux and air outlet temperature (Garcia-Martin et al., 1999). One of two blowers controlled the air mass flow rate through the receiver and the other the air through the steam generator. The 1000 kWh capacity thermocline storage system (alumina pellets) was enough to allow 30 min of nominal off-sun operation. Depending on the load, it could be charged, bypassed, or discharged. The 3 m-diameter absorber was made of hexagonal wire mesh modules (Figure 19.54). The TSA receiver was successfully operated by DLR and CIEMAT for a total of nearly 400 h between April and December 1993 (Haeger, 1994), and for shorter periods in 1994 and 1999, demonstrating that a receiver outlet temperature of 700°C could easily be achieved within 20 min of plant start-up and receiver thermal efficiencies up to 75% were obtained as shown in Figure 19.55.

A significant number of volumetric prototypes have been reported unable to reach nominal design conditions because of local cracks and structural damages. Those failures were, in many cases, caused by thermal shock, material defects, or improper operation. In the middle 1980s, some projects promoted by the German Aerospace Center (DLR) studied the fluid dynamics and thermal mechanisms inherent in volumetric absorbers (Hoffschmidt et al., 2001). One of the conclusions of these studies was that in highly porous absorber materials, the air flow through the absorber structure is unstable under high solar flux, which leads to the destruction (cracks or melting) of the absorber structure by local overheating (Pitz-Paal et al., 1996). As a consequence of this analysis, a new approach

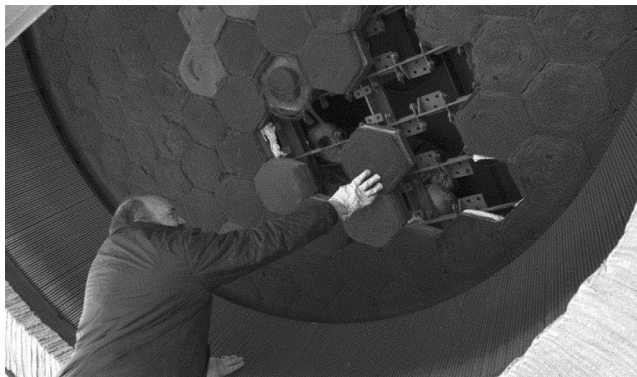


FIGURE 19.54

Front view of the TSA volumetric receivers. The absorber was composed of hexagonal pieces of wire mesh. The outer ring includes the air return system.

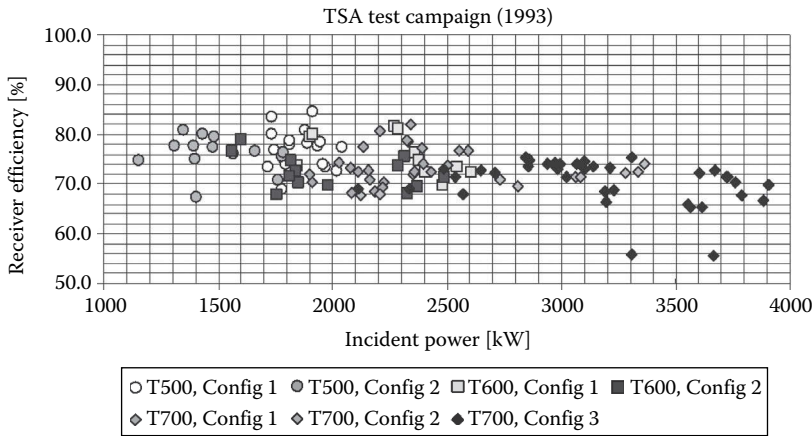


FIGURE 19.55

TSA receiver efficiency at different temperatures and incident powers during test campaign carried out in 1993.

developed monolithic ceramic absorbers able to work at high temperatures and fluxes due to their high thermal conductivity and geometric modularity, which were put to use first in the German-Spanish HiTRec project (Hoffschmidt et al., 1999) and afterward in the European SOLAIR project (Hoffschmidt et al., 2002).

The HiTRec–SOLAIR receiver principle is shown in Figure 19.56. A stainless steel support structure on the back of a set of ceramic absorber modules forms the base of the receiver. Similar to ceramic burner tubes, the absorber modules are separated from the back and allowed to expand both axially and radially with thermal expansion of the modules or movement of the stainless steel construction behind them during start-up or shut-down. The absorber modules are spaced to avoid touching adjacent modules. The support structure is a double-sheet membrane, which may be cooled by either ambient or returned air. Tubes attached to the absorber cups pass through holes in the front sheet and are

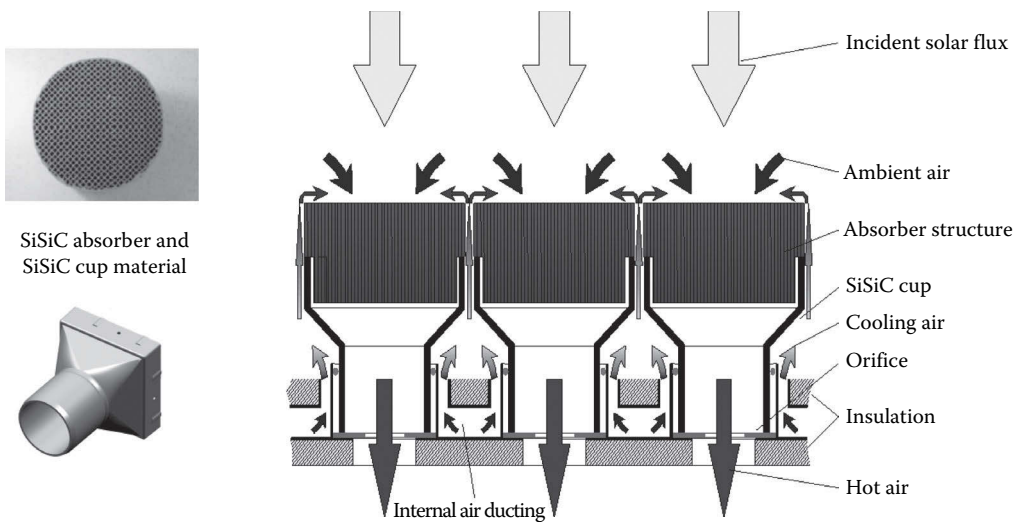


FIGURE 19.56

Principle of volumetric receivers used in HiTRec and SOLAIR projects.

welded to the rear sheet. The cooling air circulates between the two sheets and, as it leaves through the sides of the segments, also cools the support structure. The air reaches the absorber aperture through the spaces between the segments. Outgoing air and ambient air are mixed and sucked back into the segments. As they penetrate the absorber structure, the air is heated up by convection. On leaving the absorber structure, the hot air is ducted to the bottom of the cup. There an orifice, previously sized according to solar flux simulations, adjusts the air mass flow rate to compensate the expected solar flux profile over the aperture and to provide homogeneous outlet air temperatures from the cups. Then, the air passes through the tubes hosting the cups and across the holes in the rear sheet of the membrane.

A first milestone in the development of this type of receiver was the qualification of the 200 kW HiTRec-II receiver (Hoffschmidt et al., 2003). Testing lasted from November 2000 through May 2001. During the course of the test program, the HiTRec-II receiver was operated over a period of 38 days, accumulating a total of 155 operating hours with a thermal efficiency of up to $76\% \pm 7\%$ at 700°C . Eventually, a SOLAIR 3 MW prototype was developed, installed, and tested in the TSA test bed in the PSA and therefore connected to the heat storage thermocline, the steam generator, and the air circuit. The receiver was designed as a real modular absorber, which was assembled from 270 ceramic modules measuring 140 mm^2 . Each module consisted of a square absorber structure glued to a SiSiC cup. The cups were square at the aperture, but round at the back. The honeycomb absorber structure was made of recrystallized SiC with a normal open porosity of 49.5%. The SOLAIR-3000 receiver had a total aperture surface of 5.67 m^2 . During testing, the incident solar radiation is reflected by the heliostat field and concentrated on the ceramic volumetric absorber with an average flux density of 0.5 MW/m^2 . The air leaves the absorber outlet at 700°C – 750°C . The system was evaluated during 2003 and 2004 presenting an air return ratio (ARR) of 0.5, efficiency of $(72 \pm 9)\%$ at a temperature of 750°C , and efficiency of $(74 \pm 9)\%$ at 700°C . Efficiencies were estimated at over 85% (and up to 89%) for outlet air temperatures in the range of 590°C – 630°C and mean incident solar fluxes of 310 – 370 kW/m^2 (Agrafiotis et al., 2007).

Though simplicity and operating results are satisfactory, it is obvious that open volumetric receiver thermal efficiencies must be improved to achieve cost-effective plant designs able to replace tubular receivers (Palero et al., 2008). In addition, there have not yet been any long-term endurance tests, radiation losses must be further reduced, and the ARR should be improved in open receiver designs. Plant performance analysis leads to the conclusion that ARR in a PHOEBUS-type receiver should be close to 70% to keep air-cooled solar plants in the same efficiency range as other power tower plants cooled with molten-salt or water-steam (Marcos et al., 2004).

The future use of open volumetric receivers in more efficient thermodynamic cycles, with air return temperatures up to 500°C , and more, may lead to even more stringent requirements for the ARR. Assuming a target air-mixing efficiency of at least 0.93 or higher, it means that for air return temperatures of 200°C , ARR should be over 0.8 and for temperatures above 400°C , the ARR should be raised to 0.9.

Another option for working with closed-loop air circuits is the use of windowed volumetric receivers. One attractive application is based upon solar receivers as the preheating chamber of a gas turbine (Romero et al., 2002). In 1996, the German Aerospace Center (DLR) initiated a specific development program called REFOS for the purpose of producing an optimum 350 kW windowed-module design able to work at temperatures up to 1000°C and with pressures up to 15 bar. The aim of the REFOS project was to develop, build, and test modular pressurized volumetric receivers under representative operating conditions

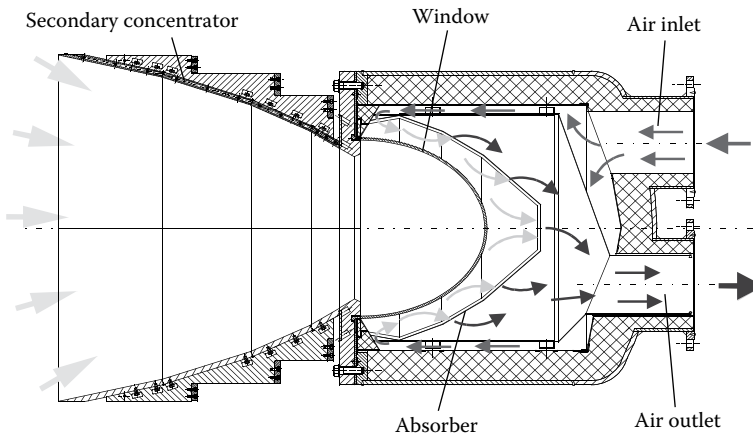


FIGURE 19.57
Example of 350 kW REFOS module.

for coupling to gas turbines. Emphasis was on testing solar preheating of air, accompanied by basic materials research. The REFOS receiver consists of a cylindrical vessel containing a curved knitted absorber. A quartz dome is used to pressurize the air cycle. A hexagonal secondary concentrator with a 1.2 m inner diameter is used to increment the flux density and protect the window flange. The hexagonal shape was selected to optimize the layout of cluster packing in such a way that the REFOS modules can be used in either small or large power plants (Figure 19.57). Typical REFOS module specifications are as follows:

- Absorbed thermal power (design point): 350 kW per unit
- Absolute pressure (operation): 15 bar
- Air outlet temperature: 800°C for metal absorber and up to 1000°C for ceramics
- Temperature increment per module: 150°C
- Receiver efficiency (including secondary): 80% at design point

Several modules have been tested at the PSA under cooperation agreements between DLR and CIEMAT. In the most extensive tests performed in 1999, the design conditions were demonstrated with a single module operating at air outlet temperatures of 800°C at 15 bar, at power levels up to 400 kW_{th}. More than 247 h of testing proved the feasibility of the receiver, which reached a maximum temperature of 1050°C without incurring damage (Buck et al., 2002). Thermal efficiencies were between 63% and 75%.

19.6.3 Experience in Central Receiver Systems

Although there have been a large number of STP tower projects, only a few have culminated in the construction of an entire experimental system. Table 19.11 lists the experimental systems that have been tested all over the world before commercial projects started in 2006. In general terms, as observed, they are characterized as being small demonstration systems between 0.5 and 10 MW, and most of them were operated in the 1980s (Entropie, 1982; Falcone, 1986; Grasse et al., 1991). The thermal fluids used in the receiver have been liquid sodium, saturated or superheated steam, nitrate-based molten salts, and air. All of

TABLE 19.11

Experimental CRS Facilities in the World

Project	Country	Power (MW _e)	Heat Transfer Fluid	Storage Media	Beginning Operation
SSPS	Spain	0.5	Liquid sodium	Sodium	1981
Eurelios	Italy	1	Steam	Nitrate salt/water	1981
Sunshine	Japan	1	Steam	Nitrate salt/water	1981
Solar One	United States	10	Steam	Oil/rock	1982
CESA-1	Spain	1	Steam	Nitrate salt	1982
MSEE/Cat B	United States	1	Nitrate salt	Nitrate salt	1983
Themis	France	2.5	Hitech salt	Hitech salt	1984
SPP-5	Russia	5	Steam	Water-steam	1986
TSA	Spain	1	Air	Ceramic	1993
Solar Two	United States	10	Nitrate salt	Nitrate salt	1996
CONSOLAR	Israel	0.5 ^a	Pressurized air	Fossil hybrid	2001
SOLGATE	Spain	0.3	Pressurized air	Fossil hybrid	2002

^a Thermal.

them can easily be represented by flow charts, where the main variables are determined by working fluids, with the interface between power block and the solar share.

The set of experiences referred to has served to demonstrate the technical feasibility of the CRS power plants, whose technology is sufficiently mature. The most extensive experience has been collected by several European projects located in Spain at the premises of the PSA (Grasse et al., 1991), and the 10 MW Solar One (Radosevich and Skinrod, 1989) and Solar Two plants (Pacheco and Gilbert, 1999) in the United States. Since the early 1990s, most proposals for the first generation of commercial plants have focused on nitrate salt and air as the receiver HTFs, since a joint U.S./German study identified their potential and economics in power tower plants (Chavez et al., 1993), though in Spain, parallel initiatives have developed saturated steam designs (Silva et al., 1999). Several penetration strategies have been proposed since then, and many more may be developed in the future, since solar towers have the great advantage of admitting very open integration designs depending on the dispatching scenarios, annual capacity factors, and hybridization schemes. At present, water-steam and molten salts are the HTFs being selected for the first generation of commercial plants.

19.6.3.1 Water-Steam Plants: The PS10 Project

Production of superheated steam in the solar receiver has been demonstrated in several plants, such as Solar One, Eurelios, and CESA-1, but operating experience showed critical problems related to the control of zones with dissimilar heat transfer coefficients like boilers and superheaters (Grasse et al., 1991). Better results regarding absorber panel lifetime and controllability have been reported for saturated steam receivers. In particular, the Solar Thermal Enhanced Oil Recovery pilot plant, which proved to be highly reliable for oil extraction using direct injection of steam, was successfully operated in Kern County, California, for 345 days in 1983 (Blake et al., 1985). The good performance of saturated steam receivers was also qualified at the 2 MW Weizmann receiver that produced steam at 15 bar for 500 h in 1989 (Epstein et al., 1991). Even though technical risks are reduced by saturated steam receivers, the outlet temperatures are significantly lower than those of superheated steam, making applications where heat storage is replaced by fossil fuel backup necessary.

At present, estimated costs of electricity production from the solar share of hybrid systems are \$0.08–\$0.15 per kWh, whereas expected costs for solar-only plants are in the range of \$0.15–\$0.20 per kWh. The implementation of hybridized systems is one of the paths leading to a breakthrough in the financial barriers to the deployment of solar electricity technologies as it reduces the initial investment (Kolb, 1998). The use of hybrid plants with the low technological risk of a CRS with saturated steam as the working fluid is the starting point. Two projects subsidized by the European Commission, the SOLGAS project promoted by SODEAN and the COLON SOLAR project promoted by the Spanish utility, SEVILLANA (Ruiz et al., 1999), established the strategy of market penetration on the basis of the integration of saturated steam receivers in cogeneration systems and repowering of combined cycles. The size of the cavity receiver was optimized to supply 21.8 MW_{th} to the fluid at 135 bar and 332.8°C outlet temperature. The collector subsystem consisted of 489 heliostats (each with a 70 m² reflective surface) and a 109 m tower. As observed in Table 19.12, the use of low-temperature receivers and phase-change saturated steam yields a much higher thermal efficiency of up to 92% at nominal load. The table shows a theoretical comparison between a typical volumetric air-cooled receiver working at 700°C air outlet temperature and saturated steam receiver at 250°C thermal outlet. Both are cavity receivers with an incident power of 45 MW (Osuna et al., 2004).

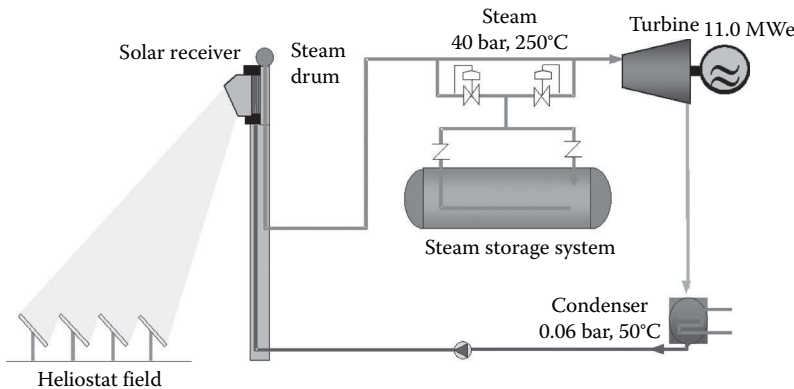
Integrating power towers into existing combined-cycle plants can create issues with respect to heliostat field layout, since the solar field is forced to make use of sites near gas pipelines and industrial areas. Land becomes a nonnegligible share of plant cost, and site constraints lead to layout optimization and subsequent optical performance problems. This was the case of the COLON heliostat field, which represented a real design challenge, because of the significant restrictions imposed by the available site (Romero et al., 1999). The hybrid solar-gas scheme predicts solar production costs below \$0.11 per kWh and annual solar shares in the range of 8%–15%. The lack of public support schemes for hybrid STP plants in Spain at that time led to project abortion, and the plant was never built.

The follow-up of the COLON SOLAR project was finally a solar-only saturated steam plant called PS10 (Planta Solar 10 MW). PS10 came about as a consequence of the Spanish legal framework for a special regime of feed-in tariffs for renewable electricity, issued in March 2004. PS10 is located on the Casa Quemada estate (37.2° latitude), 15 km west of the city of Seville (Spain). The 11 MW plant was designed to achieve an annual electricity production of 23 GWh at an investment cost of less than \$4000 per kW. The project made use of available, well-proven technologies like the glass-metal heliostats developed by the Spanish Inabensa company and the saturated steam cavity receiver developed by the TECNICAL company to produce steam at 40 bar and 250°C (Osuna et al., 2004). The plant is a solar-only system with saturated steam heat

TABLE 19.12

Comparison of Thermal Losses and Efficiency in Air Volumetric and Saturated Steam Receivers for the PS10 Project

Losses	Air (%)	Steam (%)
Reflection	7.9	2.0
Radiation	8.6	0.8
Convection	0.0	2.6
Spillage	5.0	2.1
Air return	3.7	0.0
Total efficiency	74.8	92.4

**FIGURE 19.58**

Basic scheme of PS10 solar thermal power plant with saturated steam as thermal fluid.

storage able to supply 50 min of plant operation at 50% load. The system makes use of 624,121 m² heliostats, distributed in a north-field configuration, a 90 m-high tower, a 15 MWh heat storage system, and a cavity receiver with four 4.8 × 12 m tubular panels. The basic flow diagram selected for PS10 is shown in Figure 19.58. Though the system makes use of a saturated steam turbine working at extremely low temperature, the nominal efficiency of 30.7% is relatively good. This efficiency is the result of optimized management of waste heat in the thermodynamic cycle. At the turbo-generator exit, the steam is sent to a water-cooled condenser, working at 0.06 bar. The condenser outlet is preheated with 0.8 and 16-bar steam bled from the turbine. The output of the first preheater is sent to the deaerator, which is fed with steam again bled from the turbine. A humidity separator is installed between the high- and low-pressure sections of the turbine to increase steam quality in the last stages of expansion. A third and last preheater fed with steam from the receiver increases water temperature to 245°C. When mixed with water returned from the drum, 247°C receiver feed water is obtained. As summarized in Table 19.13, the combination of optical, receiver, and power block

TABLE 19.13

Annual Energy Balance for the PS10 Plant at Nominal Conditions and Annual Basis

Nominal Rate Operation

Optical efficiency	77.0%	67.5 → 51.9 MW
Receiver and heat handling efficiency	92.0%	51.9 → 47.7 MW
Thermal power to storage		11.9 MW
Thermal power to turbine		35.8 MW
Thermal power/electric power efficiency	30.7%	35.8 → 11.0 MW
<i>Total efficiency at nominal rate</i>	21.7%	

Energetic Balance in Annual Basis

Mean annual optical efficiency	64.0%	148.63 → 95.12 GWh
Mean annual receiver and heat-handling efficiency	90.2%	95.12 → 85.80 GWh
Operational efficiency (start-up/stop)	92.0%	85.80 → 78.94 GWh
Operational efficiency (breakages, O&M)	95.0%	78.94 → 75.00 GWh
Mean annual thermal energy/electricity efficiency	30.6%	75.00 → 23.0 GWh
<i>Total annual efficiency</i>	15.4%	

efficiencies leads to a total nominal efficiency at design point of 21.7%. Total annual efficiency decreases to 15.4%, including operational losses and outages. PS10 is a milestone in the CRS deployment process, since it is the first solar power tower plant developed for commercial exploitation. Commercial operation started on June 21, 2007. Since then, the plant is performing as specified. The construction of PS20, a 20 MW_e plant with the same technology as PS10, followed. PS20 started operation in May 2009. With 1255 heliostats (120 m² each) spread over 90 ha and with a tower of 165 m high, the plant is designed to produce 48.9 GWh/year (Figure 19.40).

Saturated steam plants are considered a temporary step to the more efficient superheated steam systems. Considering the problems found in the 1980s with superheated steam receivers, the current trend is to develop dual receivers with independent absorbers, one of them for the preheating and evaporation, and another one for the superheating step. The experience accumulated with heuristic algorithms in central control systems applied to aiming point strategies at heliostat fields allows achieving a flexible operation with multi-aperture receivers. The company Abengoa Solar, developer of PS10 and PS20, has already designed a superheated steam receiver for a new generation of water–steam plants to be implemented in the first CRS project in South Africa (Fernandez-Quero et al., 2005). The most advanced strategy is the program initiated by the BrightSource PLT. BrightSource has already built a demonstration plant of 6 MW_{th} located at the Negev desert in June 2008 (Silberstein et al., 2009). The final objective of BrightSource is to promote plants producing superheated steam at 160 bar and temperature of 565°C (named DPT550). With those characteristics, they expect up to 40% conversion efficiency at the power block for unit sizes between 100 and 200 MW. The receiver is cylindrical, dual, and with a drum. The first commercial project producing superheated steam is Ivanpah Solar in California of 380 MW, with three towers. The plant is expected to connect to the grid in 2014.

The combination of recent initiatives on small heliostats, compact modular multitower fields, and production of superheated steam may be clearly visualized in the development program of the company eSolar. This company proposes a high degree of modularity with power units of 46 MW covering 64 ha, consisting of 16 towers and their corresponding heliostat fields sharing a single central power block. With replication, modularity sizes up to 500 MW and upward may be obtained (Tyner and Pacheco, 2009). Two modules of 2.5 MW each were installed in 2009 by eSolar in Lancaster, California. Each receiver had two independent cavities, and the heliostat layout consisted of identical arrays to maximize replication and modularity. Each tower is associated with 12,180 flat heliostats of 1.14 m² each (Schell, 2009). The receivers are dual-cavity, natural-circulation boilers. Inside the cavity, the feed water is preheated with economizer panels before entering the steam drum. A downcomer supplies water to evaporator panels where it is boiled. The saturated water/vapor mixture returns to the drum where the steam is separated, enters superheater panels, and reaches 440°C at 6.0 MPa. Each receiver absorbs a full-load power of 8.8 MW_{th}.

A comparative analysis of system integration schemes for megawatt-range DSG central receiver STP plants reveals that the differences between superheated steam and saturated steam schemes may be minimized in some extent given the fact that dual receivers involve two apertures and worse thermal efficiencies (Sanz-Bermejo et al., 2014). Superheated steam systems at 550°C and pressure between 60 and 80 bar obtain the best results. However, the increment of efficiency versus saturated solar plant at 69 bar is just 2.3% in the best case, and if the 69-bar saturated system integrates an intermediate reheat process, it can even achieve the same performance level of superheated

systems. It is also relevant to mention that saturated conditions at 40 bar provide similar performance than superheated system operating at 500°C.

19.6.3.2 Molten-Salt Systems: Solar Two and Gemasolar

The Solar One Pilot Plant successfully demonstrated operation of a utility-scale power tower plant. The Solar One receiver heated subcooled water to superheated steam, which drove a turbine. The superheated steam was also used to charge an oil-rock thermocline storage system. Solar One operated for 6 years from 1982 to 1988, the last three of which were devoted to power production (Radosevich and Skinrod, 1989). Although Solar One successfully demonstrated the feasibility of the power tower concept, the thermal storage system was inadequate for operating the turbine at peak efficiency, because the storage system operated only between 220°C and 305°C, whereas the receiver outlet (and design turbine inlet) temperature was 510°C. The primary mode of operation was directly from receiver outlet to turbine input, bypassing the thermal storage system, and storage provided auxiliary steam during offline periods.

For high annual capacity factors, solar-only power plants must have an integrated cost-effective thermal storage system. One such thermal storage system employs molten nitrate salt as the receiver HTF and thermal storage media. To be usable, the operating range of the molten nitrate salt, a mixture of 60% sodium nitrate and 40% potassium nitrate, must match the operating temperatures of modern Rankine cycle turbines. In a molten-salt power tower plant, cold salt at 290°C is pumped from a tank at ground level to the receiver mounted atop a tower where it is heated by concentrated sunlight to 565°C. The salt flows back to ground level into another tank. To generate electricity, hot salt is pumped from the hot tank through a steam generator to make superheated steam. The superheated steam powers a Rankine cycle turbine. A diagram of a molten-salt power tower is shown in Figure 19.59. The collector field can be sized

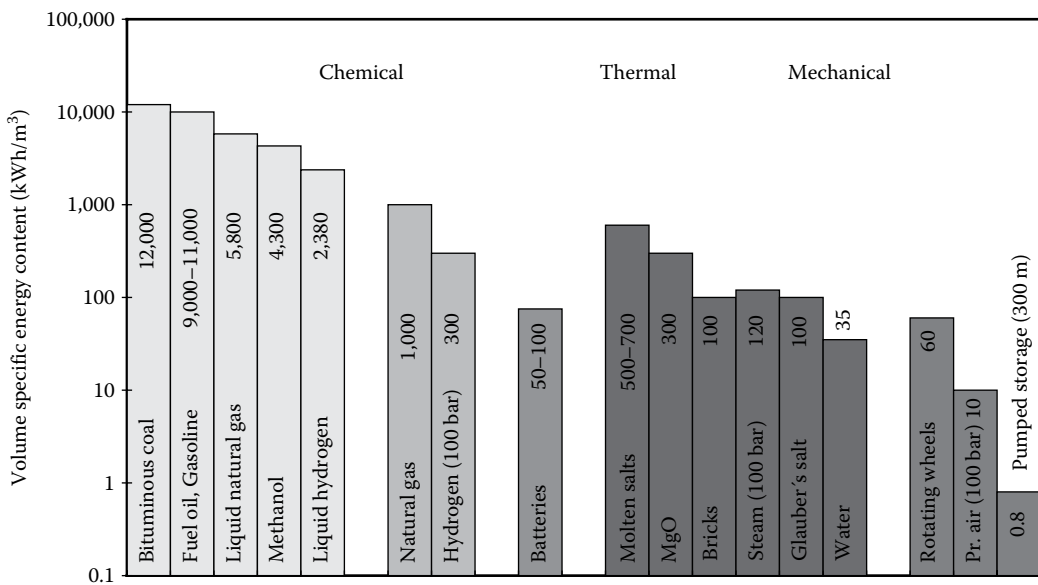
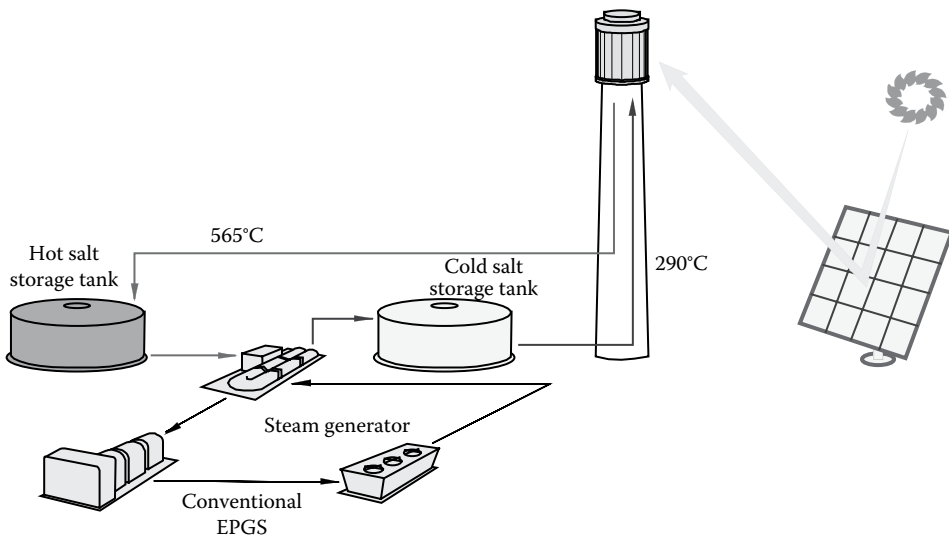


FIGURE 19.59 Schematic of a molten-salt central receiver system with cylindrical tubular receiver.

**FIGURE 19.60**

Comparison of volume energy storage capacity for several chemical, thermal, and mechanical media.

to collect more power than is demanded by the steam generator system, and the excess salt is accumulated in the hot storage tank. With this type of storage system, solar power tower plants can be built with annual capacity factors up to 70%. As molten salt has a high energy storage capacity per volume (500–700 kWh/m³), as shown in Figure 19.60, they are excellent candidates for STP plants with large capacity factors. Even though nitrate salt has a lower specific heat capacity per volume than carbonates, they still store 250 kWh/m³. The average heat conductivity of nitrates is 0.52 W/m K, and their heat capacity is about 1.6 kJ/kg K. Nitrates are a cheap solution for large storage systems. The cost of the material is \$0.70 per kg or \$5.20 per kWh_{th}. Estimates for large systems including vessels are in the range of \$13 per kWh_{th}.

Several molten-salt development and demonstration experiments have been conducted over the past two and half decades in the United States and Europe to test entire systems and develop components. The largest demonstration of a molten-salt power tower was the Solar Two project, a 10 MW power tower located near Barstow, California.

The purpose of the Solar Two project was to validate the technical characteristics of the molten-salt receiver, thermal storage, and steam generator technologies; improve the accuracy of economic projections for commercial projects by increasing the capital, operating, and maintenance cost database; and distribute information to utilities and the solar industry to foster a wider interest in the first commercial plants. The Solar Two plant was built at the same site as the Solar One pilot plant and reused much of the hardware including the heliostat collector field, tower structure, 10 MW turbine, and balance of plant. A new, 110 MWh_{th} two-tank molten-salt thermal storage system was installed, as well as a new 42 MWh_{th} receiver, a 35 MWh_{th} steam generator system (535°C, 100 bar), and master control system (Kelly and Singh, 1995).

The plant began operating in June 1996. The project successfully demonstrated the potential of nitrate-salt technology. Some of the key results were the following: receiver efficiency was measured at 88%, the thermal storage system had a measured round-trip efficiency of over 97%, and the gross Rankine-turbine cycle efficiency was 34%, all of

which matched performance projections. The collector field performance was less than predicted, primarily due to the low availability of the heliostats (85%–95% versus 98% expected), the degradation of the mirrored surfaces, and poor heliostat canting. Most of the heliostat problems were attributed to the fact that the heliostat field had sat idle and unmaintained for 6 years between Solar One shutdown and Solar Two start-up. The overall peak-conversion efficiency of the plant was measured at 13.5%. The plant successfully demonstrated its ability to dispatch electricity independently from solar collection. On one occasion, the plant operated around the clock for 154 h straight (Pacheco et al., 2000). The plant met daily performance projections when the actual heliostat availability was accounted for. Although there were some plant start-up issues, and it did not run long enough to establish annual performance or refine operating and maintenance procedures, the project identified several areas where the technology could be simplified and its reliability improved. On April 8, 1999, testing and evaluation of this demonstration project was completed, and it was shut down.

To reduce the risks associated with scaling-up hardware, the first commercial molten-salt power tower should be approximately three times the size of Solar Two (Zavoico et al., 2001). One attempt to prove scaled-up molten-salt technology is the Gemasolar project (Figure 19.61) promoted, built, and operated by Torresol Energy, a joint venture between the Spanish SENER and MASDAR initiative from Abu Dhabi (Ortega et al., 2006). Table 19.14 summarizes the main technical specifications of Gemasolar project. With only 17 MW_e, the plant that connected to the grid in summer 2011 is designed to produce 112 GWh_e/year. A large heliostat field of 304,750 m² (115 m² each heliostat) is oversized to supply 15 h equivalent heat storage capacity. The plant is designed to operate around the clock in summertime, leading to an annual capacity factor of 74%. Fossil backup corresponding to 15% of annual production is added. The levelized energy costs are estimated to be approximately \$0.16 per kWh. Gemasolar represents a breakthrough for solar technology in terms of time-dispatch management (Burgaleta et al., 2009; García and Calvo, 2012).

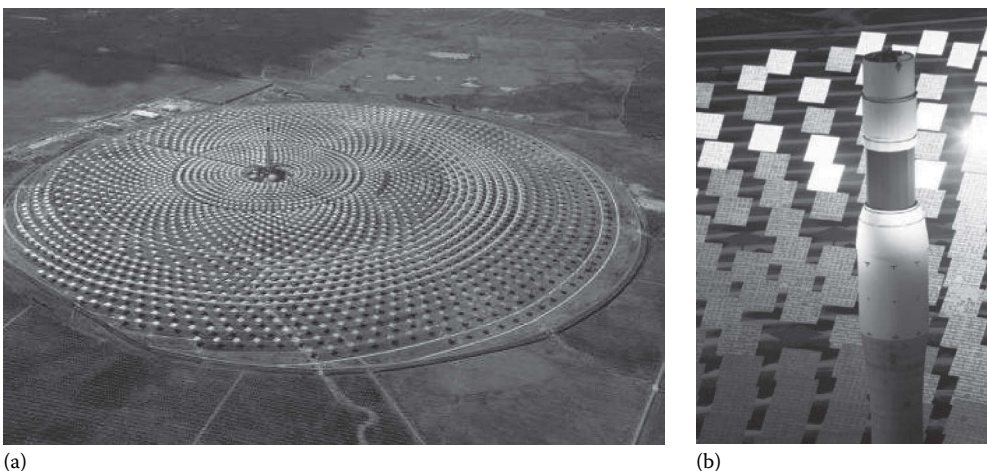


FIGURE 19.61

Aerial view of Gemasolar plant located in South Spain, the largest commercial solar central receiver system in operation by end 2013 with a circular-shape heliostat field (a). Lateral view of cylindrical solar receiver (b). (Courtesy of Torresol Energy, Spain.)

TABLE 19.14

Technical Specifications and Design Performance of the Gemasolar Project

Technical Specifications	
Heliostat field reflectant surface	304,750 m ²
Number heliostats	2,650
Land area of solar field	142 ha
Receiver thermal power	120 MW _{th}
Tower height	145 m
Heat storage capacity	15 h
Power at turbine	17 MW _e
Power NG burner	16 MW _{th}
Operation	
Annual electricity production	112 MWh _e
Production from natural gas (annual)	15%
Capacity factor	74%

19.7 Dish–Stirling Systems

STP plants can also be applied to distributed generation through parabolic dishes in which a power conversion unit (PCU) is attached by an arm directly to the concentrator. Although there have been other modular PCU system initiatives in the past, like the dish/Brayton tested by Cummins and DLR (Buck et al., 1996) or the use of dish farms to produce superheated steam designed to feed a centralized Rankine cycle in Georgia (Alvis, 1984), it is the dish–Stirling system that has demonstrated from the earliest prototypes high peak conversion efficiencies of above 30% solar-to-electric and a daily average of up to 25%. Dish–Stirling systems are considered as efficient technology to convert solar energy into electricity. This high conversion efficiency is due to their high concentration ratios (up to 3000×) and high working temperatures of above 750°C (Stine and Diver, 1994).

19.7.1 System Description

Dish–Stirling systems track the sun and focus solar energy onto a cavity receiver, where it is absorbed and transferred to a heat engine/generator. An electrical generator, directly connected to the crankshaft of the engine, converts the mechanical energy into electricity (AC). To constantly keep the reflected radiation at the focal point during the day, a sun-tracking system continuously rotates the solar concentrator on two axes following the daily path of the sun. With current technologies, a 5 kW_e dish–Stirling system would require 5.5 m diameter concentrator, and for 25 kW_e, the diameter would have to increase up to 10 m. Stirling engines are preferred for these systems because of their high efficiencies (40% thermal to mechanical), high power density (40–70 kW/L), and potential for long-term, low-maintenance operation. Dish–Stirling systems are modular, that is, each system is a self-contained power generator, allowing their assembly in plants ranging in size from a few kilowatts to tens of megawatts (Mancini et al., 2003).

Global efficiency of the system can be defined as

$$\eta = \eta_C * \eta_R * \eta_{Stir} * \eta_{Gen} = \frac{P}{A_C * I} \quad (19.49)$$

where

- η_C is the concentrator efficiency
- η_R is the receiver efficiency
- η_{Stir} is the Stirling engine efficiency
- η_{Gen} is the generator efficiency
- P is the gross power generated
- A_C is the projected concentrator area
- I is the direct normal irradiance

19.7.1.1 Concentrator

The concentrator is a key element of any dish–Stirling system. The curved reflective surface can be manufactured by attached segments, by individual facets, or by a stretched membrane shaped by a continuous plenum. In all cases, the curved surface should be coated or covered by aluminum or silver reflectors. Second-surface glass mirrors, front surface thin-glass mirrors, or polymer films have been used in various different prototypes.

First-generation parabolic dishes developed in the 1980s were shaped with multiple, spherical mirrors supported by a trussed structure (Lopez and Stone, 1992). Though extremely efficient, this structure concept was costly and heavy. The introduction of automotive industry concepts and manufacturing processes has led to optimized commercial versions like the 25 kW SunCatcher system developed by the company Stirling Energy Systems (SES), which has peak efficiency rating of 31.25%, for converting solar energy-to-grid quality electricity. Large monolithic reflective surfaces can be obtained by using stretched membranes in which a thin reflective membrane is stretched across a rim or hoop. A second membrane is used to close off the space behind forming a partially evacuated plenum between them, giving the reflective membrane an approximately spherical shape. This concept was developed by the German SBP company in the 1990s, and several prototypes have been tested at the PSA in Spain (Schiel et al., 1994). An alternative to the single stretched membrane in large units is a composition of a number of small circular rings, each with their corresponding membrane (Beninga et al., 1997).

Another example of concentrator developments in dish–Stirling systems is the Eurodish prototype (Figure 19.62). The concentrator consists of 12 single segments made of fiber glass resin. When mounted, the segments form an 8.5 m–diameter parabolic shell. The shell rim is stiffened by a ring truss to which bearings and the Stirling support structure are later attached. Thin 0.8 mm–thick glass mirrors are glued onto the front of the segments for durable, high reflectivity of around 94% (Keck et al., 2003).

Solar tracking is usually done by two different methods (Adkins, 1987):

1. Azimuth-elevation tracking by an orientation sensor or by calculated coordinates of the sun performed by the local control.
2. Polar tracking, where the concentrator rotates about an axis parallel to the earth's axis rotation. The rate of rotation is constant and equal to 15° per h. Declination angle movement is only $\pm 23.5^\circ$ per year (0.016° per h) and therefore adjusted from time to time.



FIGURE 19.62

Example of segmented parabolic concentrators. Rear and front views of two Eurodish prototype tested at the Plataforma Solar de Almería, Spain.

19.7.1.2 Receiver

As in central receivers and parabolic-trough absorbers, the receiver absorbs the light and transfers the energy as heat to the engine's working gas, usually helium or hydrogen. Thermal fluid working temperatures are between 650°C and 750°C. This temperature strongly influences the efficiency of the engine. Because of the high operating temperatures, radiation losses strongly penalize the efficiency of the receiver; therefore, a cavity design is the optimum solution for this kind of system.

Two different heat transfer methods are commonly used in parabolic dish receivers (Diver, 1987). In directly illuminated receivers, the same fluid used inside the engine is externally heated in the receiver through a pipe bundle. Although this is the most conventional method, a good high-pressure, high-velocity, heat-transfer gas like helium or hydrogen must be used. In indirect receivers, an intermediate fluid is used to decouple solar flux and working temperature from the engine fluid. One such method is heat pipes, which employ a metal capillary wick impregnated with a liquid metal heated up through the receiver plate and vaporized. The vapor then moves across the receiver and condenses in a cooler section, transferring the heat to the engine. The phase change guarantees good temperature control, providing uniform heating of the Stirling engine (Moreno et al., 2001).

19.7.1.3 Stirling Engine

Stirling engines solarized for parabolic dishes are externally heated gas-phase engines in which the working gas is alternately heated and cooled in constant-temperature, constant-volume processes (Figure 19.63b). This possibility of integrating additional external heat in the engine is what makes it an ideal candidate for solar applications. Since the Stirling cycle is very similar to the Carnot cycle, the theoretical efficiency is high. High reversibility is achieved since work is supplied to and extracted from the engine at isothermal conditions. The clever use of a regenerator that collects the heat during constant-volume cooling and heating substantially enhances the final system efficiency. For most engine designs, power is extracted kinematically by rotating a crankshaft connected to the pistons by a connecting rod. An example of a kinematic Stirling engine is shown in Figure 19.63a. Though, theoretically, Stirling engines may have a high life-cycle projection, the actual

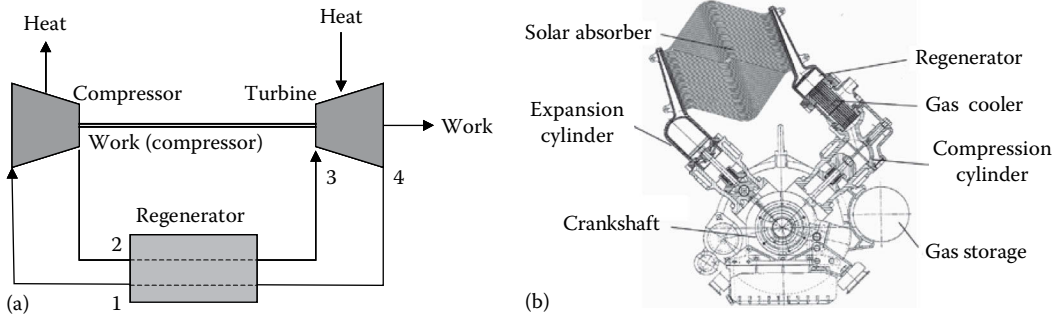


FIGURE 19.63

(a) Representation of the ideal Stirling cycle. (b) Kinematic Stirling engine V-160 of 10 kW_e manufactured by Solo Kleinmotoren with pistons situated in V and connected to a tubular array heat exchanger.

fact is that today their availability is still not satisfactory, as an important percentage of operating failures and outages are caused by pistons and moving mechanical components. Availability is therefore one of the key issues, since it must operate for more than 40,000 h in 20-year lifetime, or 10 times more than an automobile engine. One option to improve availability is the use of free-piston designs. Free-piston engines make use of gas or a mechanical spring so that mechanical connections are not required to move reciprocating pistons. Apparently, they are better than kinematic engines in terms of availability and reliability. The most relevant program in developing dishes with free-piston technology was promoted by Cummins in the United States in 1991. Unfortunately, there were technical problems with the PCU and the project was cancelled (Bean and Diver, 1995). The last 10 years, the company Infinia Solar has developed several prototypes and test fields for 3 kW free piston systems derived from satellite applications, though still extended operation is needed. Due to the flexibility of the heat source, a Stirling engine can also be operated with a solar/fossil or solar/biomass hybrid receiver (Laing and Trabling, 1997), making the system available during cloudy periods and at night.

19.7.2 Dish–Stirling Developments

Like the other CSP technologies, practical dish–Stirling development started in the early 1980s. Most development has concentrated in the United States and Germany, and though developed for commercial markets, they have been tested in a small number of units (Stine and Diver, 1994).

The first generation of dishes was a facet-type concentrator with second-surface mirrors that already established concentration records ($C = 3000$) and had excellent performances, though their estimated costs for mass production were above \$300 per m². Their robust structures were extremely heavy, weighing in at 100 kg/m² (Grasse et al., 1991). The 25 kW Vanguard-1 prototype built by Advanco was operated at Rancho Mirage, California, in the Mojave Desert in production mode for 18 months (February 1984 to June 1985), and results were published by EPRI (Droher and Squier, 1986).

This system was 10.7 m in diameter with a reflecting surface of 86.7 m² and a 25 kW PCU made by United Stirling AB model 4-95 Mark II. This engine had four cylinders with a 95 cm³ cylinder displacement. Cylinders were distributed in parallel and assembled in a square. They were connected to the regenerator and cooler and had double-acting pistons. The working gas was hydrogen at a maximum pressure of 20 MPa and temperature of 720°C.

Engine power was controlled by varying the working-gas pressure (Schiel, 1999). The Advanco/Vanguard system, with a net conversion efficiency (including ancillary systems) of more than 30%, still holds the world's conversion record.

McDonnell Douglas later developed another somewhat improved dish system making use of the same technology and the same engine. The dish was 10.5 m and 25 kW. The 88 m² parabolic dish consisted of 82 spherically curved glass facets. Six of these units were produced and installed at sites around the United States for testing in operation. Southern California Edison continued to evaluate the system later. Reported performances and efficiencies were similar to those of Advanco/Vanguard (Lopez and Stone, 1992). The project was frozen for several years until in 1996, SES acquired the intellectual and technology rights to the concentrator and the U.S. manufacturing rights to what is now called the Kockums, 4-95 Stirling engine-based PCU (Mancini et al., 2003). Under a DOE-industry cost-sharing project to commercialize the dish–Stirling system for emerging markets, SES started testing and improvement of several units in different locations in the United States and South Africa. More than 100,000 h of operation accumulated for all the systems have been reported (Stone et al., 2001; Mancini et al., 2003). Daily efficiency has been found to be 24%–27% and the annual average 24%, and what is even more important, they have claimed availabilities of 94% at irradiances of just over 300 W/m². The redesigned 25 kW_e system named SunCatcher has been qualified in a commercial basis at the Maricopa Solar Plant in Arizona. The plant totaled 1.5 MW with 60 dishes and started operation in January 2010. This plant did not achieve the expected performance obtained at previous prototypes testing, and it was dismantled in 2012 after 1 year of operation.

Since the pioneering Vanguard dish records, with the exception of SES, most of the design options have been directed at the development of lowering costs by such strategies as less demanding temperatures, thereby penalizing efficiency, and introducing lighter and less expensive reflectors made of polymers or thin glass glued onto resin-based structures. These dishes, which have a lower optical performance, were first used in non-Stirling applications, with lower operating temperatures, such as the Shenandoah (Solar Kinetics) and Solar Plant 1 in Warner Springs (LaJet) (Grasse et al., 1991). Typical concentrations were in the range of 600–1000, and working temperatures were in the range of 650°C. Several prototypes were developed by Acurex, LaJet, GE, SKI, and SBP. These developments were followed up in the United States by SAIC (Mayette et al., 2001) and WGA (Diver et al., 2001) under the DOE-industry R&D program, Dish Engine Critical Components (Mancini et al., 2003).

The most extensive testing of this light material concept has been done with the stretched-membrane concentrator developed in Germany by Schlaich, Bergermann und Partner (SBP). More than 50,000 h of testing have been accumulated in the six-prototype field, promoted by SBP and Steinmüller, and evaluated at the PSA in Spain (Schiel et al., 1994). The concentrator is a single 7.5 m–diameter facet made of a single 0.23 mm thick preformed stainless-steel stretched membrane. Thin-glass mirrors are bonded to the stainless-steel membrane. The membrane is pre-stretched beyond its elastic limit using a combination of the weight of water on the front and vacuum on the back, to form a nearly ideal paraboloid. Then, a slight active vacuum within the membrane drum preserves the optical shape. The V-160 engine, originally produced by Stirling Power Systems, is at present manufactured by the German company Solo Kleinmotoren (Figure 19.63). The engine sweeps 160 cm³ of helium with two pistons. The engine has an efficiency of 30% and reported overall conversion efficiency of 20.3% (Figure 19.64). The figure demonstrates the high dispatchability of dish–Stirling systems at part loads.

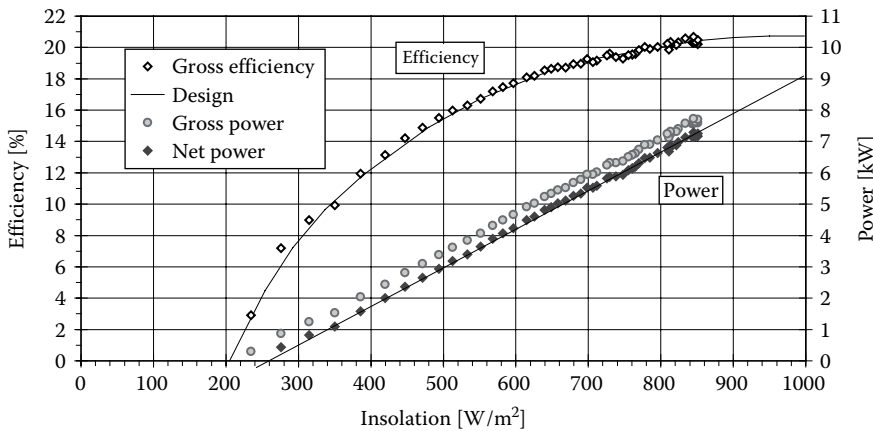


FIGURE 19.64

Input/output parameters and performance measured for a 9 kW SBP stretched membrane dish–Stirling system tested in Almería, Spain.

Though stretched membranes had excellent optical results, the economics revealed production costs higher than expected. The successor of the SBP membrane dishes is the EuroDish system. The EuroDish project is a joint venture undertaken by the European Community, German/Spanish Industry (SBP, MERO, Klein + Stekl, Inabensa), and research institutions DLR and CIEMAT. The new design replaces the stretched-membrane concentrator with a glass-fiber composite shell onto which glass mirrors are bonded with an adhesive. The engine used in the EuroDish is the next-generation SOLO Kleinmotoren 161. Two new 10 kW EuroDish units, shown in Figure 19.62, were installed at the Plataforma Solar de Almeria, Spain, early in 2001 for testing and demonstration. In a follow-up project called EnviroDish, additional units were deployed in France, India, Italy, and Spain to accumulate operating experience at different sites. The peak solar-to-net-electric energy conversion efficiency of the system is expected to be 21%–22%, based on the experience of former projects with the same engine. The peak system efficiency was first measured at 20%. The estimated annual production of a EuroDish system operating in Albuquerque, New Mexico, is 20,252 kWh of electricity with 90% availability and an annual efficiency of 15.7% (Mancini et al., 2003). SBP and the associated EuroDish industry have performed cost estimates for a yearly production rate of 500 units/year (5 MW/year) and 5000 units/year, which corresponds to 50 MW/year. The actual cost of the 10 kW unit without transportation and installation cost and excluding foundations is approximately U.S. \$10,000 per kW. The cost projections at production rates of 500 and 5000 units/year are U.S. \$2500 per kW and U.S. \$1500 per kW, respectively.

19.8 Conclusions and Outlook

From the 1970s to the 1990s, the development of solar thermal electricity technologies remained restricted to a few countries, and only a few, though important, research institutions and industries were involved. The situation has dramatically changed since 2006 with the approval of specific feed-in-tariffs or power purchase agreements in Spain and

the United States. Both countries, with more than 3 GW of projects by the end 2013, are leading the commercialization of STP. Other countries such as India, China, South Africa, Chile, Australia, Morocco, Algeria, and Saudi Arabia adopted the STP technology in their portfolios. Subsequently, a number and variety of engineering and construction companies, consultants, technologists, and developers committed to STP are rapidly growing and moving to global markets. A clear indicator of the globalization of STE commercial deployment for the future energy scenario has been elaborated by the International Energy Agency (IEA). This considers STP to play a significant role among the necessary mix of energy technologies for halving global energy-related CO₂ emissions by 2050 (IEA, 2010b). This scenario would require capacity addition of about 14 GW/year (55 new STP plants of 250 MW each). However, this new opportunity is introducing an important stress to the developers of STP. In a period of less than 5 years, in different parts of the world, these developers of STP are forced to move from strategies oriented to early commercialization markets based upon special tariffs, to strategies oriented to a massive production of components and the development of large amounts of projects with less profitable tariffs. This situation is speeding up the implementation of second-generation technologies, like DSG or molten-salt systems, even though in some cases, still some innovations are under assessment in early commercialization plants or demonstration projects.

Parabolic trough is the technology widely used nowadays in commercial projects, though other technologies like LF reflectors and CRSs are developing the first grid-connected projects and reveal promising impacts on cost reduction (Romero and Gonzalez-Aguilar, 2011). The projected evolution of levelized electricity costs (LECs) of different CSP technologies is depicted in Figure 19.65. LEC reduction is expected from mass production, scaling-up, and R&D. A technology roadmap promoted by the European Industry Association ESTELA (Kearney and ESTELA, 2010) states that by 2015, when most of the improvements currently under development are expected to be implemented in new plants, energy production boosts greater than 10% and cost decreases up to 20% are expected to be achieved. Furthermore, economies of scale resulting from plant size increase will also contribute

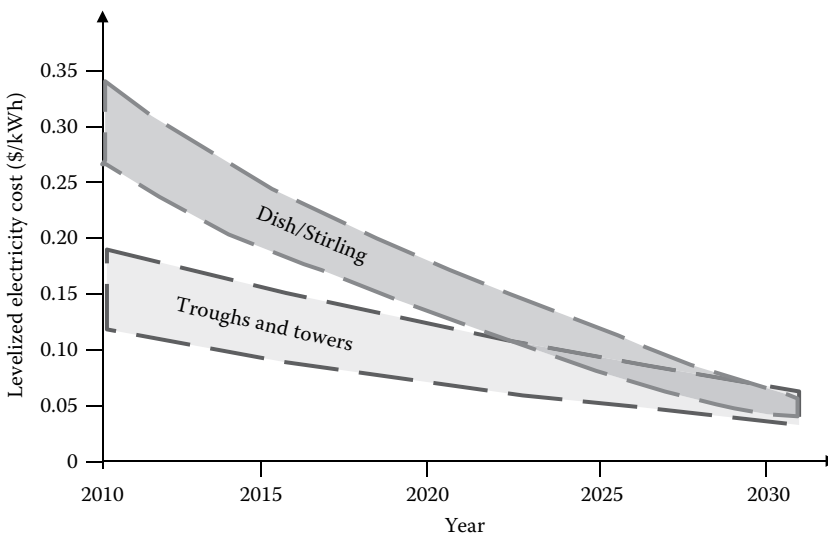


FIGURE 19.65

Evolution of levelized electricity cost for STP technologies based upon technology roadmaps and industry.

to reduce plants' CAPEX per MW installed up to 30%. STP deployment in locations with very high solar radiation further contributes to the achievement of cost competitiveness of this technology by reducing costs of electricity up to 25%. All these factors can lead to electricity generation cost savings up to 30% by 2015 and up to 50% by 2025, reaching competitive levels with conventional sources (e.g., coal/gas with stabilized electricity costs <€10 cents/kWh). Similar projections are published in another recent roadmap issued by the IEA (2010) and IRENA (2012).

The first generation of commercial SPT projects adopted technologies and concepts that have matured in the last 30 years. They were based on conservative designs and schemes that do not necessarily exploit the enormous potential of concentrated solar energy. Figure 19.66 illustrates the situation. Current technologies are based on solar receivers

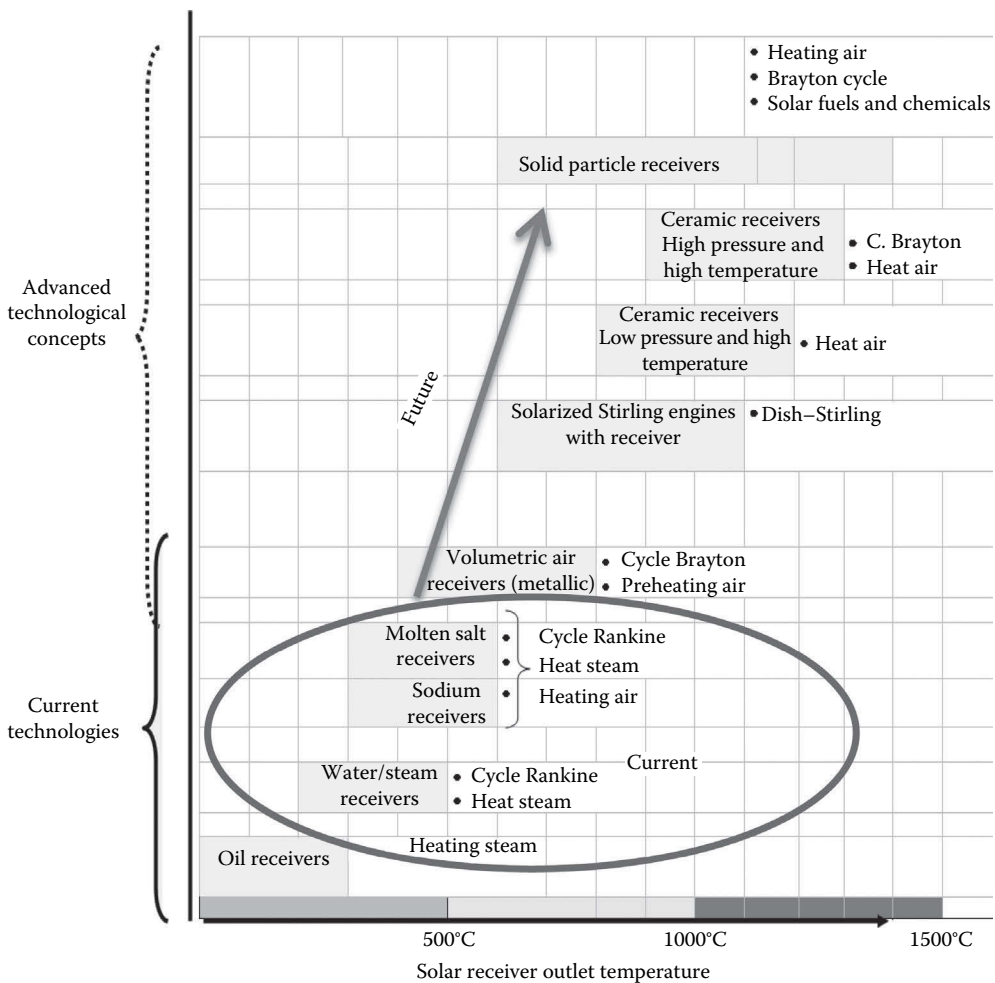


FIGURE 19.66

Evolution of STP. Current technologies are based on solar receivers that operate with thermal oil or water–steam at working temperatures usually below 500°C, coupled to steam-based Rankine cycles. Next generation of technologies allows surpassing 1000°C and enable higher efficiencies via Brayton and combined cycles, as well as the thermochemical production of solar fuels.

operating at moderate solar concentration ratios with thermal oil or water–steam at working temperatures usually below 500°C, which are coupled to steam-based Rankine cycles. As a consequence, solar-to-electricity conversion efficiencies are below 20%, the application of energy storage is limited, the water consumption and land use are relatively high, the power block integration is rather inefficient, and the thermochemical routes to produce solar fuels are beyond reach. Next generations of STP plants should allow surpassing 1000°C and enable higher efficiencies via Brayton and combined cycles as well as better integration of thermal storage (Romero and Steinfeld, 2012). Novel receiver concepts based on volumetric absorption of directly irradiated porous structures and particles, with alternative thermal fluids (e.g., air), operate at higher solar concentration ratios and promise more efficient solar energy capture and conversions. Moreover, these advance concepts open the door to the thermochemical production of solar fuels. The solar concentrating technologies better adapted for these high-temperature applications are solar towers (CRS), whose current development mainly for power generation is paving the ground for future high-flux/high-temperature thermochemical applications.

Challenges and key general topics for the medium- to long-term R&D are improved designs of materials and components, increased system efficiency through higher operating temperatures, high reliability during unattended operation, hybrid solar/fossil fuel plants with small solar share, and solar share increase through integration of storage. R&D is multidisciplinary, involving optics, materials science, thermal engineering, and control and measurement techniques. Specifically, for PTC and LF systems, R&D is aimed at lighter and lower-cost structural designs including front surface mirrors with high solar-weighted reflectivity of about 95%; high-absorptance (>96%) coatings for tube receivers able to operate at above 500°C; medium-temperature thermal energy storage systems based on PCMs, molten salts, concrete, and packed bed of rocks suitable for solar-only systems; improvement in overall system O&M, including mirror cleaning, integral automation, and unattended control; system cost reductions and efficiency improvements by DSG; and alternative HTFs such as air. For CRS systems, R&D is aimed at improvements in the heliostat field as a result of superior optical properties, lower cost structures, and better control; development of water/superheated steam and advanced air-cooled volumetric receivers using wire mesh absorbers or ceramic monoliths and foams; advanced thermocline storage systems based on packed bed of ceramic materials (especially suitable for solar air receivers) and high-temperature thermochemical storage; and distributed control architectures, system integration, and hybridization in high-efficiency electricity production schemes. For DE, R&D is aimed at volumetric receivers coupled to Stirling and Brayton engines; improvements in mirrors and support structures; and improvements in system integration and control for fully automation, parasitic loads reduction, start-up optimization, and hybrid Stirling–Brayton operation.

References

- Adkins, D.R. (November 1987). Control strategies and hardware used in solar thermal applications. SAND86-1943, Sandia National Laboratories, Albuquerque, NM.
- Agrafiotis, C.C., Mavroidis, I., Konstandopoulos, A.G., Hoffschmidt, B., Stobbe, P., Romero, M., Fernández-Quero, V. (2007). Evaluation of porous silicon carbide monolithic honeycombs as volumetric receivers/collectors of concentrated solar radiation. *Solar Energy Materials & Solar Cells* 91, 474–488.

- Ajona, J.I. (1999). Electricity generation with distributed collector systems. In: *Solar Thermal Electricity Generation*. Edited by CIEMAT, Madrid, Spain, pp. 5–77.
- Ajona, J.I., Zarza, E. (1994). Benefits potential of electricity production with direct steam generation in parabolic troughs. In: Popel, O., Fris, S., and Shchedrova, E., eds. *Proceedings of the Seventh International Symposium on Solar Thermal Concentrating Technologies*. Institute for High Temperature of Russian Academy of Science, Moscow, Russia, pp. 300–314.
- Alpert, D.J., Houser, R.M. (1990). Performance evaluation of large-area glass-mirror heliostats. In: Gupta, B.P., Traugott, W.H., eds. In: *Research, Development and Applications of Solar Thermal Technology*. Editorial: Hemisphere, NY, pp. 91–100.
- Alvis, R.L. (1984). Some solar dish/heat engine design consideration. Technical Report SAND84-1698, Sandia National Laboratories, Albuquerque, NM.
- Aringhoff, R., Aubrey, C., Brakmann, G., Teske, S. (2003). *Solar Thermal Power 2020*. Greenpeace International/European Solar Thermal Power Industry Association, Amsterdam, the Netherlands.
- Aringhoff, R., Geyer, M., Herrmann, U., Kistner, R., Nava, P., Osuna, R. (2002a). AndaSol-50 MW solar plants with 9 hour storage for Southern Spain. In: Steinfeld, A., ed. *Proceedings of the 11th SolarPACES International Symposium on Concentrated Solar Power and Chemical Energy Technologies*, September 4–6, 2002, Zurich, Switzerland, pp. 37–42.
- Aringhoff, R. et al. (2002b). 50 MW solar plants with 9 hour storage for Southern Spain. In: *Proceedings of the 11th International Symposium on Concentrating Solar Power and Chemical Energy Technologies*, Zurich, Switzerland.
- Avila-Marin, A.L. (2011). Volumetric receivers in solar thermal power plants with central receiver system technology: A review. *Solar Energy* 85, 891–910.
- Bayón, R., Rojas, E., Valenzuela, L., Zarza, E., León, J. (2010). Analysis of the experimental behaviour of a 100 kWth latent heat storage system for direct steam generation in solar thermal power plants. *Applied Thermal Engineering* 30, 2673–2651.
- Bean, J.R., Diver, R.B. (1995). Technical status of the dish/stirling joint venture program. In: *Proceedings of the 30th IECEC*, Orlando, FL, pp. 2.497–2.504. Report SAND95-1082C, Sandia National Laboratories, Albuquerque, NM.
- Becker, M., Boehmer, M. (1989). GAST: The gas cooled solar tower technology program. In: *Proceedings of the Final Presentation*, Springer-Verlag, Berlin, Germany.
- Becker, M., Böhmer, M., Meinecke, W., Unger, E. (1989). Volumetric receiver evaluation. SSPS Technical Report No. 3/89, Cologne, Germany.
- Becker, M., Cordes, S., Böhmer, M. (1992). The development of open volumetric receivers. In: *Proceedings of the Sixth International Symposium on Solar Thermal Concentrating Technologies*, September 28–October 2, 1992, Vol. II. CIEMAT, Madrid, Spain, pp. 945–952.
- Becker, M., Meinecke, W., Geyer, M., Trieb, F., Blanco, M., Romero, M., Ferriere, A. (2002). Solar thermal power plants. In: EUREC Agency, ed. *The Future for Renewable Energy 2: Prospects and Directions*. James & James Science Publishers Ltd., London, U.K., pp. 115–137.
- Becker, M., Vant-Hull, L.L. (1991). Thermal receivers. In: Winter, C.J., Sizmann, R.L., Vant-Hull, L.L., eds. *Solar Power Plants*. Springer-Verlag, Berlin, Germany, pp. 163–197.
- Beninga, K., Davenport, R., Sellars, J., Smith, D., Johansson, S. (1997). Performance results for the SAIC/STM prototype dish/stirling system. In: *ASME International Solar Energy Conference*, Washington, DC, pp. 77–80.
- Bernhard, R., Hein, S., de Lalaing, J., Eck, M., Eickhoff, M., Pfänder, M., Morin, G., Häberle, A. (2008). Linear Fresnel collector demonstration on the PSA, part II—Commissioning and first performance tests. In: *Proceedings of the 14th Solar Paces Symposium*, Las Vegas, NV. <http://www.nrel.gov/docs/gen/fy08/42709CD.zip>. Last accessed date March 30, 2015.
- Biggs, F., Vittitoe, C.N. (1979) The Helios model for the optical behavior of reflecting solar concentrators. Report SAND76-0347, Sandia National Laboratories, Albuquerque, NM.
- Blake, F.A., Gorman, D.N., McDowell, J.H. (1985). *ARCO Central Receiver Solar Thermal Enhanced Oil Recovery Project*. ARCO Power Systems, Littleton, CO.

- Buck, R., Bräuning, T., Denk, T., Pfänder, M., Schwarzbözl, P., Tellez, F. (2002). Solar-hybrid gas turbine-based power tower systems (REFOS). *Journal of Solar Energy Engineering* 124, 2–9.
- Buck, R., Heller, P., Koch, H. (1996). Receiver development for a Dish-Brayton system. In: *Solar Engineering 1996*, ASME, San Antonio, TX, pp. 91–96.
- Burgaleta, J.I., Arias, S., Salbidegoitia, I.B. (2009). Operative advantages of a central tower solar plant with thermal storage system. In: *Proceedings of the SolarPACES 2009* (CD). Ref. Manuscript: 11720, September 15–18, 2009, Berlin, Germany. DLR, Stuttgart, Germany.
- Chavez, J.M., Kolb, G.J., Meinecke, W. (1993). In: Becker, M., Klimas, P.C., eds. *Second Generation Central Receiver Technologies—A Status Report*. Verlag C.F. Müller GmbH, Karlsruhe, Germany.
- Chisholms, D. (1980). Two-phase flow in bends. *International Journal of Multiphase Flow* 6, 363–367.
- Cohen, G.E., Kearney, D.W., Kolb, G.J. (1999). Final report on the operation and maintenance improvement program for concentrating solar power plants. SAND99-1290, Sandia National Laboratories, Albuquerque, NM, Printed June 1999.
- DeMeo, E.A., Galdo, J.F. (December 1997). Renewable energy technology characterizations. TR-109496 Topical Report, U.S. DOE, Washington, DC and EPRI, Palo Alto, CA.
- Dersch, J., Morin, G., Eck, M., Häberle, A. (2009). Comparison of linear Fresnel and parabolic trough collector systems—System analysis to determine break even costs of linear Fresnel collectors. In: *Proceedings of the SolarPACES 2009* (CD). Ref. Manuscript: 15162, September 15–18, 2009, Berlin, Germany. DLR, Stuttgart, Germany.
- Di Canio, D.G., Treytl, W.J., Jur, F.A., Watson, C.D. (April 1979). Line focus solar thermal central receiver research study—Final report. Prepared for U.S. Department of Energy, DOE/ET/20426-1. FMC Corporation, Santa Clara, CA.
- Diver, R., Andraka, C., Rawlinson, K., Thomas, G., Goldberg, V. (2001). The Advanced Dish Development system project. In: Kleis, S.J., Bingham, C.E., eds. *Proceedings of Solar Forum 2001 Solar Energy: The Power to Choose* (CD-ROM), April 21–25, 2001, Washington, DC. ASME, New York.
- Diver, R.B. (1987). Receiver/reactor concepts for thermochemical transport of solar energy. *Journal of Solar Energy Engineering* 109(3), 199–204.
- Droher, J.J., Squier, S.E. (1986). Performance of the Vanguard solar dish-stirling engine module. Technical Report EPRI AP-4608, Electric Power Research Institute, Palo Alto, CA.
- Eck, M., Zarza, E. (2002). Assessment of operation modes for direct solar steam generation in parabolic troughs. In: Steinfel, A., eds. *Proceedings of the 11th SolarPACES International Symposium on Concentrated Solar Power and Chemical Energy Technologies*, Zurich, Switzerland, pp. 591–598.
- Eck, M., Zarza, E., Eickhoff, M., Rheinländer, J., Valenzuela, L. (2003). Applied research concerning the direct steam generation in parabolic troughs. *Solar Energy* 74, 341–351.
- Eneas, A. (1901). US Patent 670,917.
- Enermodal Engineering Ltd. (May 5, 1999). Cost reduction study for solar thermal power plants. Final Report. Prepared by Enermodal Engineering Ltd. in Association with Marbek Resource Consultants Ltd., by Contract of World Bank/GEF, Washington, DC.
- Entropie (1982). Centrales à Tour: Conversion Thermodynamique de l'Énergie Solaire, Entropie No. 103, Special Journal Issue.
- Epstein, M., Liebermann, D., Rosh, M., Shor, A.J. (1991). Solar testing of 2 MW(th) water/steam receiver at the Weizmann Institute solar tower. *Solar Energy Materials* 24, 265–278.
- Ericsson, J. (1888). The sun motor. *Nature* 38, 321.
- Falcone, P.K. (1986). A handbook for solar central receiver design. SAND86-8009, Sandia National Laboratories, Livermore, CA.
- Fernandez-Quero, V., Osuna, R., Romero, M., Sanchez, M., Ruiz, V., Silva, M. (2005). EURECA: Advanced receiver for direct superheated steam generation in solar towers, as an option for increasing efficiency in large low cost direct steam generation plants. In: Goswami, D.Y., Vijayaraghaveng, S., Campbell-Howe, R., eds. *Proceedings of the 2005 Solar World Congress ISES-2005*, August 6–12, Orlando, FL. American Solar Energy Society, Boulder, CO.

- Francia, G. (1968). Pilot plants of solar steam generation systems. *Solar Energy* 12, 51–64.
- Fricker, H.W., Silva, M., García, C., Winkler, C., Chavez, J. (1988). Design and test results of the wire receiver experiment Almeria. In: Gupta, B.K., ed. *Proceedings of the Fourth International Workshop on Solar Thermal Technology*, Santa Fe, NM. Hemisphere Publishing, New York, pp. 265–277.
- García, E., Calvo, R. (2012). One year operation experience of Gemasolar plant. In: *Proceedings of the SolarPACES 2012*, September 11–14, 2012, Marrakech, Morocco.
- García, G., Egea, A., Romero, M. (2004). Performance evaluation of the first solar tower operating with autonomous heliostats: PCHA project. In: Ramos, C., Huacuz, J., eds. *Proceedings of the 12th SolarPACES International Symposium*, S3-231 (CD-ROM), October 6–8, 2004, Oaxaca, Mexico.
- García-Martín, F.J., Berenguel, M., Valverde, A., Camacho, E.F. (1999). Heuristic knowledge-based heliostat field control for the optimization of the temperature distribution in a volumetric receiver. *Solar Energy* 66(5), 355–369.
- Geyer, M. (2002). Panel 1 briefing material on status of major project opportunities. The current situation, issues, barriers and planned solutions. In: *International Executive Conference on Expanding the Market for Concentrating Solar Power (CSP)—Moving Opportunities into Projects*, June 19–20, 2002, Berlin, Germany.
- Geyer, M., Romero, M., Steinfeld, A., Quaschnig, V. (2003). International Energy Agency—Solar power and chemical energy systems. Annual Report 2002, DLR, Printed March 2003. May be downloaded at www.solarpaces.org. Last accessed date March 30, 2015.
- González, L., Zarza, E., Yebra, L. (2001). Determinación del Modificador por Angulo de Incidencia de un colector solar LS-3, incluyendo las pérdidas geométricas por final de colector. Technical Report DISS-SC-SF-30, Almería, Spain, Plataforma Solar de Almería.
- Goswami, Y., Kreith, F., Kreider, J.F. (2000). *Principles of Solar Engineering*, 2nd edn. Taylor & Francis Group, New York.
- Grasse, W., Hertlein, H.P., Winter, C.J. (1991). Thermal solar power plants experience. In: Winter, C.J., Sizmann, R.L., Vant-Hull, L.L., eds. *Solar Power Plants*. Springer-Verlag, Berlin, Germany, pp. 215–282.
- Haeger, M. (July 1994). Phoebus technology program: Solar Air Receiver (TSA). PSA Tech. Report: PSA-TR02/94.
- Harats, Y., Kearney, D. (1989). Advances in parabolic trough technology in the SEGS plants. In: Fanne, A.H., Lund, K.O., eds. *Proceedings of the 11th Annual American Society of Mechanical Engineers Solar Energy Conference*, San Diego, CA. American Society of Mechanical Engineers, New York, pp. 471–476.
- Hautmann, G., Selig, M., Mertins, M. (2009). First European Linear Fresnel power plant in operation—Operational experience & outlook. In: *Proceedings of the SolarPACES 2009* (CD). Ref. Manuscript: 16541, September 15–18, 2009, Berlin, Germany. DLR, Stuttgart, Germany.
- Hoffschmidt, B., Fernández, V., Konstandopoulos, A.G., Mavroidis, I., Romero, M., Stobbe, P., Téllez, F. (2001). Development of ceramic volumetric receiver technology. In: Funken, K.-H., Bucher, W., eds. *Proceedings of the Fifth Cologne Solar Symposium*, June 21, 2001, Forschungsbericht 2001–2010. DLR, Cologne, Germany, pp. 51–61.
- Hoffschmidt, B., Fernandez, V., Pitz-Paal, R., Romero, M., Stobbe, P., Téllez, F. (2002). The development strategy of the HitRec volumetric receiver technology—Up-scaling from 200kWth via 3MWth up to 10MWel. In: *Proceedings of the 11th SolarPACES International Symposium on Concentrated Solar Power and Chemical Energy Technologies*, September 4–6, 2002, Zurich, Switzerland, pp. 117–126.
- Hoffschmidt, B., Pitz-Paal, R., Böhmer, M., Fend, T., Rietbrock, P. (1999). 200 kWth open volumetric air receiver (HiTRec) of DLR reached 1000°C average outlet temperature at PSA. *Journal de Physique IV, France* 9, Pr3-551–Pr3-556.
- Hoffschmidt, B., Téllez, F.M., Valverde, A., Fernández-Reche, J., Fernández, V. (February 2003). Performance evaluation of the 200-kWth HiTRec-II open volumetric air receiver. *Journal of Solar Energy Engineering* 25, 87–94.

- IEA (2010). Technology Roadmap—Concentrating Solar Power. Available at: <http://www.iea.org>. Last accessed date March 30, 2015.
- IEA (2010b). Energy Technology Perspectives 2010—Scenarios and Strategies to 2050.
- IRENA (2012). Concentrating solar power. Renewable energy technologies: Cost analysis series. Volume 1: Power Sector, Issue 2/5. International Renewable Energy Agency. Available at: www.irena.org/Publications. Last accessed date March 30, 2015.
- Kalogirou, S.A. (2004). Solar thermal collectors and applications. *Progress in Energy and Combustion Science* 30(3), 231–295.
- Kearney, A.T., ESTELA (2010). *Solar Thermal Electricity 2025*. ESTELA, Brussels, Belgium. <http://www.estelasolar.eu/index.php?id=22>. Last accessed date March 30, 2015.
- Kearney, D.W., Cohen, G.E. (1997). Current experiences with the SEGS parabolic trough plants. In: Becker, M., Böhmer, M., eds. *Proceedings of the Eighth International Symposium on Solar Thermal Concentrating Technologies*, Vol. 1, Colonia, Germany, 1996. C.F. Müller, Heidelberg, Germany, 1997, pp. 217–224.
- Keck, T., Heller, P., Weinrebe, G. (June 2003). Envirodish and Eurodish—System and status. In: *Proceedings of the ISES Solar World Congress*, Göteborg, Sweden.
- Kelly, B., Singh, M. (1995). Summary of the final design for the 10 MWe solar two central receiver project. *Solar Engineering, ASME* 1, 575.
- Kistler, B.L. (1986). A user's manual for DELSOL3: A computer code for calculating the optical performance and optimal system design for solar thermal central receiver plants. Sandia Report, SAND86-8018, Sandia National Laboratories, Albuquerque, NM.
- Kodama, T. (2003). High-temperature solar chemistry for converting solar heat to chemical fuels. *Progress in Energy and Combustion Science* 29, 567–597.
- Kolb, G.J. (1998). Economic evaluation of solar-only and hybrid power towers using molten-salt technology. *Solar Energy* 62, 51–61.
- Kribus, A. (1999). Future directions in solar thermal electricity generation. In: *Solar Thermal Electricity Generation*. Colección documentos CIEMAT. CIEMAT, Madrid, Spain, pp. 251–285.
- Laing, D., Lehmann, D., Bahl, C. (2008). Concrete storage for solar thermal power plants and industrial process heat. In: *Proceedings of the Third International Renewable Energy Storage Conference (IRES III)*, November 24–25, 2008, Berlin, Germany.
- Laing, D., Trabling, C. (1997). Second generation sodium heat pipe receivers for USAB V-160 stirling engine: Evaluation of on-sun test results using the proposed IEA guidelines and analysis of heat pipe damage. *ASME Journal of Solar Energy Engineering* 119(4), 279–285.
- Lehaut, C. (2010). Construction, start-up and performance tests of a direct steam generation CSP Fresnel module. In: *Proceedings of the SolarPACES 2010*, Perpignan, France.
- Lipps, F.W., Vant-Hull, L.L. (1978). A cellwise method for the optimization of large central receiver systems. *Solar Energy* 20, 505–516.
- Lopez, C., Stone, K., (1992). Design and performance of the Southern California Edison stirling dish. In: *Proceedings of the ASME International Solar Energy Conference*, Maui, HI, pp. 945–952.
- Lotker, M. (1991). Barriers to commercialization of large-scale solar electricity: Lessons learned from LUZ experience. Informe técnico SAND91-7014, Sandia National Laboratories, Albuquerque, NM.
- Luepfert, E., Zarza, E., Schiel, W., Osuna, R., Esteban, A., Geyer, M., Nava, P., Langenkamp, J., Mandelberg, E. (2003). Eurotrough collector qualification complete—Performance test results from PSA. In: *Proceedings of the ISES 2003 Solar World Congress (CD)*, Göteborg, Sweden.
- Mancini, T., Heller, P., Butler, B., Osborn, B., Schiel, W., Goldberg, V., Buck, R., Diver, R., Andraka, C., Moreno, J. (2003). Dish-Stirling systems: An overview of development and status. *International Journal of Solar Energy Engineering* 125, 135–151.
- Mancini, T., Kolb, G.J., Prairie, M. (1997). Solar thermal power. In: Boer, K.W. ed., *Advances in Solar Energy: An Annual Review of Research and Development*, Vol. 11. American Solar Energy Society, Boulder, CO.
- Marcos, M.J., Romero, M., Palero, S. (2004). Analysis of air return alternatives for CRS-type open volumetric receiver. *Energy* 29, 677–686.

- Mavis, C.L. (1989). A description and assessment of heliostat technology. SAND87-8025, Sandia National Laboratories, Enero.
- Mayette, J., Davenport, R, Forristall, R. (2001). The Salt River Project SunDish dish-stirling system. In: Kleis, S.J., Bingham, C.E., eds. *Proceedings of the Solar Forum 2001 Solar Energy: The Power to Choose* (CD-ROM), April 21–25, 2001, Washington, DC. ASME, New York.
- Mills, D. (2004). Advances in solar thermal electricity technology. *Solar Energy* 76, 19–31.
- Mills, D.R., Morrison, G.L. (1999). Compact linear Fresnel reflector solar thermal powerplants. *Solar Energy* 68, 263–283.
- Mills, D.R., Morrison, G.L. (2000). Compact linear Fresnel reflector solar thermal power plants. *Solar Energy* 68, 263–283.
- Monterreal, R., Romero, M., García, G., Barrera, G. (1997). Development and testing of a 100 m² glass-metal heliostat with a new local control system. In: Claridge, D.E., Pacheco, J.E., eds. *Solar Engineering*. ASME, New York, pp. 251–259.
- Moreno, J.B., Modesto-Beato, M., Rawlinson, K.S., Andracka, C.E., Showalter, S.K., Moss, T.A., Mehos, M., Baturkin, V. (2001). Recent progress in heat-pipe solar receivers. SAND2001-1079, 36th Intersociety Energy Conversion Engineering Conference, Savannah, GA, pp. 565–572.
- Morse, F.H. (2000). *The Commercial Path Forward for Concentrating Solar Power Technologies: A Review of Existing Treatments of Current and Future Markets*. Morse Associates, Inc., By Contract of Sandia National Laboratories and U.S. DOE, Washington, DC.
- Nitsch, J., Krewitt, W., Langniss, O. (2004). Renewable energies in Europe, *Encyclopedia of Energy* 5, 313–331 (Elsevier Inc., San Diego, USA).
- Ortega, J.I., Burgaleta, J.I., Tellez, F. (2006). Central receiver system (CRS) solar power plant using molten salt as heat transfer fluid. In: Romero, M., Martínez, D., Ruiz, V., Silva, M., Brown, M., eds. *Proceedings of the 13th International Symposium on Concentrated Solar Power and Chemical Energy Technologies*, June 20, 2006, Seville, Spain. CIEMAT, Madrid, Spain.
- Osuna, R., Cerón, F., Romero, M., García, G. (1999). Desarrollo de un prototipo de heliostato para la planta Colón Solar. *Energía XXV*(6), 71–79.
- Osuna, R., Fernández, V., Romero, S., Romero, M., Sanchez, M. (2004). PS10: A 11-MW solar tower power plant with saturated steam receiver. In: Ramos, C., Huacuz, J., eds. *Proceedings of the 12th SolarPACES International Symposium*, S3-102 (CD-ROM), October 6–8, 2004, Oaxaca, Mexico.
- Pacheco, J.E., Gilbert, R. (1999). Overview of recent results of the Solar Two test and evaluations program. In: Hogan, R., Kim, Y., Kleis, S., O'Neal, D., Tanaka, T., eds. *Renewable and Advanced Energy Systems for the 21st Century RAES'99*, RAES99-7731, April 11–15, 1999, Maui, Hawaii. ASME, New York.
- Pacheco, J.E., Reilly, H.E., Kolb, G.J., Tyner, C.E. (2000). Summary of the solar two test and evaluation program. In: *Proceedings of the Renewable Energy for the New Millennium*, March 8–10, 2000, Sydney, New South Wales, Australia, pp. 1–11.
- Palero, S., Romero, M., Castillo, J.L. (2008). Comparison of experimental and numerical air temperature distributions behind a cylindrical volumetric solar absorber module. *Journal of Solar Energy Engineering* 130, 011011-1–011011-8.
- Philibert, C. (2004). International energy technology collaboration and climate change mitigation, case study 1: Concentrating solar power technologies. OECD/IEA Information Paper, Paris, France. COM/ENV/EPOC/IEA/SLT(2004)8.
- Pifre, A. (1882). A solar printing press. *Nature* 21, 503–504.
- Pitz-Paal, R. et al. (February 2005b). In: Pitz-Paal, R., Dersch, J., Milow, B., eds. *ECOSTAR Roadmap Document for the European Commission, SES-CT-2003-502578*. Deutsches Zentrum für Luft- und Raumfahrt e.V., Cologne, Germany.
- Pitz-Paal, R., Dersch, J., Milow, B., Téllez, F., Zarza, E., Ferriere, A., Langnickel, U., Steinfeld, A., Karni, J., Popel, O. (2005). A European roadmap for concentrating solar power technologies (ECOSTAR). In: *Proceedings Submitted to ISEC2005, 2005 International Solar Energy Conference*, August 6–12, 2005, Orlando, FL.

- Pitz-Paal, R., Hoffschmidt, B., Böhmer, M., Becker, M. (1996). Experimental and numerical evaluation of the performance and flow stability of different types of open volumetric absorbers under non-homogeneous irradiation. *Solar Energy*, Köln, Germany 60(3/4), 135–159.
- Platzer, W.J. (2009). Linear Fresnel collector as an emerging option for concentrating solar thermal power. In: *Proceedings of the ISES Solar World Congress 2009*, Johannesburg, South Africa.
- Price, H., Luepfert, E., Kearney, D., Zarza, E., Cohen, G., Gee, R., Mahoney, R. (2002). Advances in parabolic trough solar power technology. *International Journal of Solar Energy Engineering* 124, 109–125.
- Rabl, A. (1985). *Active Solar Collectors and Their Applications*. Oxford University Press, New York, pp. 59–66.
- Radosevich, L.G., Skinrood, A.C. (1989). The power production operation of Solar One, the 10 MWe solar thermal central receiver pilot plant. *Journal of Solar Energy Engineering* 111, 144–151.
- Ratzel, C.A., Simpson, C.E. (1979). Heat loss reduction techniques for annular receiver design. Informe técnico SAND78-1769, Sandia National Laboratories, Albuquerque, NM.
- Romero, M., Buck, R., Pacheco, J.E. (2002). An update on solar central receiver systems, projects, and technologies. *International Journal of Solar Energy Engineering* 124, 98–108.
- Romero, M., Conejero, E., Sánchez, M. (1991). Recent experiences on reflectant module components for innovative heliostats. *Solar Energy Materials* 24, 320–332.
- Romero, M., Fernández, V., Sánchez, M. (1999). Optimization and performance of an optically asymmetrical heliostat field. *Journal de Physique IV, France* 9, Pr3-71–Pr3-76.
- Romero, M., González Aguilar, J. (2011). Chapter 3: Solar thermal power plants: From endangered species to bulk power production in sun-belt regions. In: Rao, K.R., ed. *Energy & Power Generation Handbook*. ASME Three Park Avenue, New York.
- Romero, M., González Aguilar, J. (2014). Solar thermal CSP technology. *WIREs Energy and Environment* 3, 42–59. doi: 10.1002/wene.79.
- Romero, M., Marcos, M.J., Osuna, R., Fernández, V. (2000a). Design and implementation plan of a 10 MW solar tower power plant based on volumetric-air technology in Seville (Spain). In: Pacheco, J.D., Thornbloom, M.D., eds. *Solar Engineering 2000—Proceedings of the ASME International Solar Energy Conference*, June 16–21, 2000, Madison, WI. ASME, New York.
- Romero, M., Marcos, M.J., Téllez, F.M., Blanco, M., Fernández, V., Baonza, F., Berger, S. (2000b). Distributed power from solar tower systems: A MIUS approach. *Solar Energy* 67(4–6), 249–264.
- Romero, M., Martínez, D., Zarza, E. (2004). Terrestrial solar thermal power plants: On the verge of commercialization. In: European Space Agency, ed. *Proceedings of the Fourth International Conference on Solar Power from Space-SPS'04*, June 30–July 2, 2004, Granada, Spain, pp. 81–89. Noordwijk, the Netherlands.
- Romero, M., Sanchez-Gonzalez, M., Barrera, G., Leon, J., Sanchez-Jimenez, M. (1995). Advanced salt receiver for solar power towers. In: *Solar Engineering* 1, 657–664. Stine, W.B., Tanaka, T., Claridge, D.E., eds. ASME, New York.
- Romero, M., Steinfeld, A. (2012). Concentrating solar thermal power and thermochemical fuels. *Energy & Environmental Science* 5, 9234–9245.
- Rueda, F. et al. (October 2003). Project INDITEP. First Yearly Report. IBERDROLA Ingeniería y consultoría, Madrid, Spain.
- Ruiz, V., Silva, M., Blanco, M. (1999). Las centrales energéticas termosolares. *Energía* XXV(6), 47–55.
- Sánchez, F. (1986). Results of Cesa-1 plant. In: Konstanz, B.M., ed. *Proceedings of the Third International Workshop on Solar Thermal Central Receiver Systems*, Berlin, Germany. Springer, New York, pp. 46–64.
- Sánchez, M., Romero, M. (2006). Methodology for generation of heliostat field layout in central receiver systems based on yearly normalized energy surfaces. *Solar Energy* 80, 861–874.
- Sanders Associates Inc. (October 1979). 1/4-Megawatt solar receiver. Final Report, DOE/SF/90506-1.
- Sanz-Bermejo, J., Gallardo-Natividad, V., Gonzalez-Aguilar, J., Romero, M. (2014). Comparative system performance analysis of direct steam generation central receiver solar thermal power plants in megawatt range. *Journal of Solar Energy Engineering* 136, 010908-1.

- Sargent & Lundy (October 2003). Assessment of parabolic trough and power tower solar technology cost and performance forecasts. Report: NREL/SR-550-34440, National Renewable Energy Laboratory, Golden, CO.
- Schell, S. (2009). Design and evaluation of eSolar's heliostat fields. In: *Proceedings of the SolarPACES 2009* (CD), Berlin, Germany, September 15–18, 2009. DLR, Stuttgart, Germany.
- Schiel, W. (1999). Dish/Stirling systems. In: *Solar Thermal Electricity Generation*. Colección documentos CIEMAT. CIEMAT, Madrid, Spain, pp. 209–250.
- Schiel, W., Keck, T., Kern, J., Schweitzer, A. (1994). Long term testing of three 9 kW dish/Stirling systems. In: *Solar Engineering, ASME 1994 Solar Engineering Conference*, pp. 541–550.
- Schiel, W., Schweizer, A., Stine, W. (1994). Evaluation of the 9-kW Dish/Stirling system of Schlaich Bergermann und Partner using the proposed IEA Dish/Stirling performance analysis guidelines. In: *Proceedings of the 29th IECEC*, Monterey, CA, pp. 1725–1729.
- Schmitz-Goeb, M., Keintzel, G. (1997). The Phoebus solar power tower. In: Claridge, D.E., Pacheco, J.E., eds. *Proceedings of the 1997 ASME International Solar Energy Conference*, April 27–30, 1997, Washington, DC, pp. 47–53.
- Selig, M. (2011). Commercial CSP plants based on Fresnel collector technology. In: *Proceedings of the SolarPACES 2011*, Granada, Spain.
- Shuman, F. (1913). The most rational source of energy: Tapping the sun's radiant energy directly. *Scientific American* 109, 350.
- Siebers, D.L., Kraabel, J.S. (April 1984). Estimating convective energy losses from solar central receivers. SAND84-8717, Sandia National Laboratories, Livermore, CA.
- Silberstein, E., Magen, Y., Kroyzer, G., Hayut, R., Huss, H. (2009). Brightsource solar tower pilot in Israel's Negev operation at 130 bar @ 530°C superheated steam. In: *Proceedings of the SolarPACES 2009* (CD), September 15–18, 2009, Berlin, Germany. DLR, Stuttgart, Germany.
- Silva, M., Blanco, M., Ruiz, V. (1999). Integration of solar thermal energy in a conventional power plant: The COLON SOLAR project. *Journal de Physique IV, Symposium Series 9*, Pr3-189–Pr3-194.
- Sizmann, R.L. (1991). Solar radiation conversion. In: Winter, C.J., Sizmann, R.L., Vant-Hull, L.L., eds. *Solar Power Plants*. Springer-Verlag, Berlin, Germany, pp. 17–83.
- Stine, W., Diver, R.B. (1994). A compendium of solar dish/Stirling technology. Report SAND93-7026, Sandia National Laboratories, Albuquerque, NM.
- Stone, K., Leingang, E., Rodriguez, G., Paisley, J., Nguyen, J., Mancini, T., Nelving, H. (2001). Performance of the SES/Boeing dish Stirling system. In: Kleis, S.J., Bingham, C.E., eds. *Proceedings of the Solar Forum 2001 Solar Energy: The Power to Choose* (CD-ROM), April 21–25, 2001, Washington, DC. ASME, New York.
- Tyner, C.E., Pacheco, J.E. (2009). eSolar's power plant architecture. In: *Proceedings of the SolarPACES 2009* (CD), September 15–18, 2009, Berlin, Germany. DLR, Stuttgart, Germany.
- Vant-Hull, L.L. (1991). Solar radiation conversion. In: Winter, C.J., Sizmann, R.L., Vant-Hull, L.L., eds. *Solar Power Plants*. Springer-Verlag, Berlin, Germany, pp. 84–133.
- Weinrebe, G., Schmitz-Goeb, M., Schiel, W. (1997). On the performance of the ASM150 stressed membrane heliostat. In: *Solar Engineering: 1997 ASME/JSME/JSSES International Solar Energy Conference*, April 27–30, Washington, DC.
- Welford, W.T., Winston, R. (1989). *High Collection Non-Imaging Optics*. Academic Press, New York.
- Winter, C.J., Sizmann, R.L., Vant-Hull, L.L., eds. (1991). *Solar Power Plants*. Springer-Verlag, Berlin, Germany.
- Yebra, L., Berenguel, M., Romero, M., Martínez, D., Valverde, A. (2004). Automation of solar plants. In: *Proceedings of EuroSun2004*, Vol. I. DGS, Munich, Germany and PSE, Freiburg, Germany, pp. 978–984.
- Zarza, E. (2004). *Generación Directa de Vapor con Colectores Solares Cilindro Parabólicos. Proyecto Direct Solar Steam (DISS)*. CIEMAT, Madrid, Spain.
- Zarza, E. et al. (1999). DISS-phase I project. Final Project Report. CIEMAT, Madrid, Spain.
- Zarza, E., Rojas, M.E., González, L., Caballero, J.M., Rueda, F. (2004). INDITEP: The first DSG pre-commercial solar power plant. In: *Proceedings to the 12th Solar PACES International Symposium*, October 6–8, 2004, Oaxaca, Mexico.

- Zarza, E., Valenzuela, L., Leon, J., Hennecke, K., Eck, M., Weyers, D.-H., Eickhoff, M. (2002). Direct steam generation in parabolic troughs. Final results and conclusions of the DISS project. In: Steinfeld, A., ed. *Book of Proceedings of the 11th SolarPACES International Symposium on Concentrated Solar Power and Chemical Energy Technologies*, September 4–6, 2002, Zurich, Switzerland. Paul Scherrer Institute, Villigen, Switzerland, pp. 21–27.
- Zavoico, A.B., Gould, W.R., Kelly, B.D., Grimaldi, I., Delegado, C. (2001). Solar power tower (SPT) design innovations to improve reliability and performance—Reducing technical risk and cost. In: *Proceedings of Forum 2001 Conference*, April 21–25, 2001, Washington, DC.



Taylor & Francis

Taylor & Francis Group

<http://taylorandfrancis.com>

20

Photovoltaics Fundamentals, Technology and Application

Roger Messenger, D. Yogi Goswami, Hari M. Upadhyaya, Senthilarasu Sundaram, Aruna Ivaturi, Stephan Buecheler, and Ayodhya N. Tiwari

CONTENTS

20.1 Photovoltaics.....	766
20.1.1 Introduction	766
20.1.2 PV Cell.....	768
20.1.2.1 $p-n$ Junction	768
20.1.2.2 Illuminated $p-n$ Junction	770
20.1.2.3 Properties of the PV Cell.....	772
20.1.3 Manufacture of Solar Cells.....	774
20.1.3.1 Manufacture of Crystalline and Multicrystalline Silicon PV Cells.....	774
20.1.3.2 Amorphous Silicon and Multijunction Thin-Film Fabrication	777
20.1.4 PV Modules and PV Arrays	778
20.1.5 Sun and PV Array Orientation	779
20.1.6 PV System Configurations.....	780
20.1.7 PV System Components.....	782
20.1.7.1 Maximum Power Trackers and Linear Current Boosters	782
20.1.7.2 Inverters.....	783
20.1.7.3 Balance of System Components	784
20.1.8 PV System Examples	787
20.1.8.1 Stand-Alone PV Well Pump System.....	787
20.1.8.2 Stand-Alone System for a Remote Schoolhouse	788
20.1.8.3 Straightforward Utility-Interactive PV System.....	791
20.1.9 Present Status of Technology and Future Challenges for PV Systems	792
Nomenclature	794
References.....	795
20.2 Thin-Film PV Technology	796
20.2.1 Introduction	796
20.2.1.1 Historical and Current Developments	796
20.2.1.2 Cost Potentials and Material Availability Issues.....	801
20.2.2 Thin-Film Silicon Solar Cells	806
20.2.2.1 Material and Properties	806
20.2.2.2 Deposition Techniques	808
20.2.2.3 Amorphous Silicon Solar Cells and Configurations.....	808
20.2.2.4 Flexible a -Si Solar Cells and Modules	813
20.2.3 Cadmium Telluride Solar Cells	816
20.2.3.1 Material and Properties	816
20.2.3.2 CdTe Solar Cell Device Structure	817

20.2.3.3	Deposition Techniques.....	820
20.2.3.4	Flexible CdTe Solar Cells.....	821
20.2.4	Cu(In,Ga)Se ₂ Solar Cells.....	821
20.2.4.1	Material and Properties	821
20.2.4.2	CIGS Solar-Cell Configuration.....	823
20.2.4.3	Deposition and Growth of CIGS Absorber	825
20.2.4.4	Flexible CIGS Solar Cells.....	827
20.2.5	Cu ₂ ZnSn(S, Se) ₄ or CZTS Solar Cells	829
20.2.5.1	Material and Properties	829
20.2.5.2	CZTS Solar Cell Configuration	830
20.2.5.3	Deposition and Growth of CZTS (CZTSSe) Absorber	830
20.2.6	New-Generation Solar Cells.....	833
20.2.6.1	Perovskite Solar Cells	834
20.2.7	Environmental Concerns and Cd Issue.....	835
20.2.8	Conclusions.....	836
References.....		838
20.3	Concentrating PV Technologies.....	845
20.3.1	Introduction	845
20.3.2	CPV Technology.....	847
20.3.2	CPV Market	848
20.3.4	Energy Payback.....	848
20.3.5	Qualification Standards	849
References.....		849

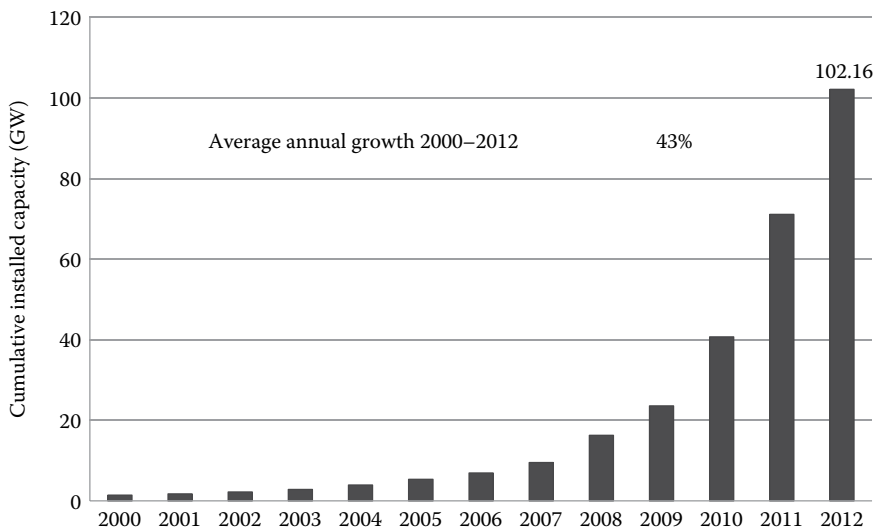
20.1 Photovoltaics

Roger Messenger and D. Yogi Goswami

20.1.1 Introduction

Photovoltaic (PV) conversion is the direct conversion of sunlight into electricity with no intervening heat engine. PV devices are solid state; therefore, they are rugged and simple in design and require very little maintenance. Perhaps the biggest advantage of solar PV devices is that they can be constructed as stand-alone systems to give outputs from micro-watts to megawatts. That is why they have been used as the power sources for calculators, watches, water pumping, remote buildings, communications, satellites and space vehicles, and even megawatt-scale power plants. PV panels can be made to form components of building skin, such as roof shingles and wall panels. With such a vast array of applications, the demand for PVs is increasing every year. With net metering and governmental incentives, such as feed-in laws and other policies, grid-connected applications such as building-integrated PV have become cost-effective even where grid electricity is cheaper. As a result, the worldwide growth in PV production has averaged over 43% per year from 2000 to 2012 and 61% from 2007 to 2012 (see Figure 20.1). The cumulative installed global PV capacity grew to over 100 GW by the end of 2012.

In the early days of solar cells in the 1960s and 1970s, more energy was required to produce a cell than it could ever deliver during its lifetime. Since then, dramatic improvements

**FIGURE 20.1**

Worldwide production of PV panels. (From EPIA, Global market outlook for photovoltaics, European Photovoltaic Industries Association, Brussels, Belgium, <http://www.epia.org>.)

have taken place in the efficiencies and manufacturing methods. The present energy pay-back periods have been reduced to 0.68 for thin-film CdTe cells to less than 2 years for crystalline silicon cells [1]. The costs of PV panels have come down from about \$30 to less than \$1 per peak watt over the last three decades.

With panel costs as low as \$0.55/W (large quantities) to \$2/W (retail), the system costs are in the range of about \$1.50/W for megawatt-range systems to about \$3–\$4/W for small systems, and the PV systems have finally become cost-effective for on-grid applications. The PV panel costs are reaching the limits of cost reduction; however, the costs of the balance of the system (BOS) have room for further reduction. The U.S. Department of Energy has a goal to reduce the BOS costs, which would bring the total costs of a PV system down to \$1/W and the cost of power to \$0.06/kWh [1b]. At present, module efficiencies are as high as 21%. The main constraint on the efficiency of a solar cell is related to the bandgap of the semiconductor material of a PV cell. As explained later in this chapter, a photon of light with energy equal to or greater than the bandgap of the material is able to free up one electron, when absorbed in the material. However, the photons that have energy less than the bandgap are not useful for this process. When absorbed on the cell, they just produce heat. And for the photons with more energy than the bandgap, the excess energy above the bandgap is not useful in generating electricity. The excess energy simply heats up the cell. These reasons account for a theoretical maximum limit on the efficiency of a conventional single junction PV cell to less than 30%. The actual efficiency is even lower because of the reflection of light from the cell surface, shading of the cell due to current collecting contacts, internal resistance of the cell, and recombination of electrons and holes before they are able to contribute to the current.

The limits imposed on solar cells due to bandgap can be partially overcome by using multiple layers of solar cells stacked on top of each other, each layer with a bandgap higher than the layer below it. For example (Figure 20.2), if the top layer is made from a cell of material A (bandgap corresponding to λ_A), solar radiation with wavelengths less than λ_A would be absorbed to give an output equal to the hatched area A.

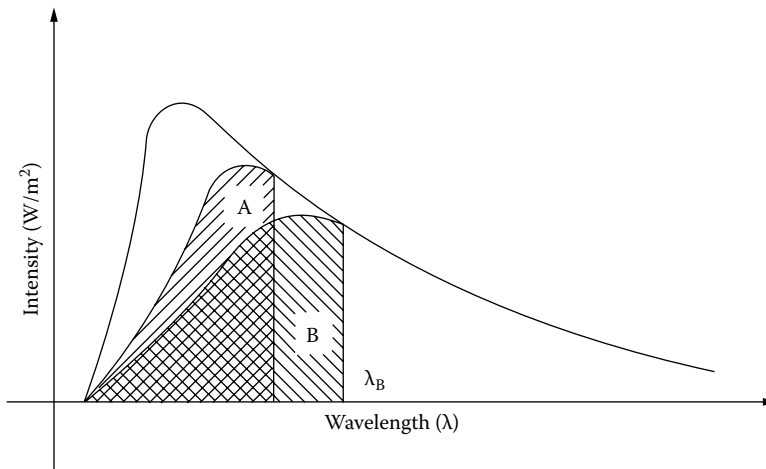


FIGURE 20.2

Energy conversion from a two-layered stacked PV cell. (From Goswami, D.Y. et al., *Principles of Solar Engineering*, 2nd edn., Taylor & Francis, Philadelphia, PA, 2000.)

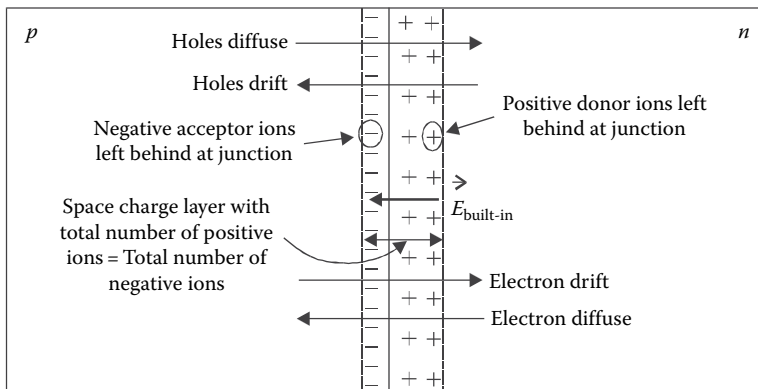
The solar radiation with wavelength greater than λ_A would pass through A and be converted to give an output equal to the hatched area B. The total output and therefore the efficiency of this tandem cell would be higher than the output and the efficiency of each single cell individually. The efficiency of a multijunction cell can be about 50% higher than a corresponding single cell. The efficiency would increase with the number of layers. For this concept to work, each layer must be as thin as possible, which puts a very difficult if not an insurmountable constraint on crystalline and polycrystalline cells to be made multijunction. As a result, this concept is being investigated mainly for thin-film amorphous or microcrystalline solar cells. Efficiencies as high as 37.7% have been reported for multijunction cells in the literature [2]. For concentrated PV, efficiencies as high as 44% have been reported [2].

In this chapter, the physics of PV electrical generation will be briefly reviewed, followed by a discussion of the PV system design process. Several PV system examples will be presented, then a few of the latest developments in crystalline silicon PV will be summarized, and finally, some of the present challenges (2004–2005) facing the large-scale deployment of PV energy sources will be explored. Emphasis will be on nonconcentrating, crystalline or multicrystalline silicon, terrestrial PV systems, since such systems represent nearly 95% of systems currently being designed and built. However, the design procedures outlined at the end of the chapter also can be applied to other PV technologies, such as thin films. While multijunction III–V semiconductor concentrating PV cells have been fabricated with efficiencies that are double the efficiencies of silicon cells, the cost of these cells is so high that their use is only justified in extraterrestrial applications. As a result, the typical reader of this material will not become involved in the use of these technologies.

20.1.2 PV Cell

20.1.2.1 p–n Junction

PV cells have been made with silicon (Si), gallium arsenide (GaAs), copper indium diselenide (CIS), cadmium telluride (CdTe), and a few other materials. The common denominator of PV cells is that a *p–n* junction, or the equivalent, such as a Schottky junction, is


FIGURE 20.3

The p - n junction showing electron and hole drift and diffusion. (From Messenger, R. and Ventre, G., *Photovoltaic Systems Engineering*, 2nd edn., CRC Press LLC, Boca Raton, FL, 2004.)

needed to enable the PV effect. Understanding the p - n junction is thus at the heart of understanding how a PV cell converts sunlight into electricity.

Figure 20.3 shows a Si p - n junction.

The junction consists of a layer of n -type Si joined to a layer of p -type Si, with an uninterrupted Si crystal structure across the junction. The n -layer has an abundance of free electrons and the p -layer has an abundance of free holes. Under thermal equilibrium conditions, meaning that temperature is the only external variable influencing the populations of free holes and electrons, the relationship between hole density, p , and electron density, n , at any given point in the material, is given by

$$np = n_i^2, \quad (20.1)$$

where n_i is approximately the density of electrons or holes in intrinsic (impurity-free) material. When impurities are present, then $n \cong N_d$ and $p \cong N_a$, where N_d and N_a are the densities of donor and acceptor impurities. For Si, $n_i \cong 1.5 \times 10^{10} \text{ cm}^{-3}$ at $T = 300 \text{ K}$, while N_d and N_a can be as large as 10^{21} cm^{-3} . Hence, for example, if $N_d = 10^{18}$ on the n -side of the junction, then $p = 2.25 \times 10^2 \text{ cm}^{-3}$.

Both electrons and holes are subject to random diffusion within the Si crystalline structure, so each tends to diffuse from regions of high concentration to regions of low concentration. The enormous concentration differences of hole and electron concentrations between the n -side and the p -side of the junction cause large concentration gradients across the junction. The net result is that the electrons diffuse across the junction into the p -region and the holes diffuse across the junction into the n -region, as shown in Figure 20.3.

Before formation of the junction, both sides of the junction are electrically neutral. Each free electron on the n -side of the junction comes from a neutral electron donor impurity atom, such as arsenic (As), while each free hole on the p -side of the junction comes from a neutral hole donor (acceptor) impurity atom, such as boron (B). When the negatively charged electron leaves the As atom, the As atom becomes a positively charged As ion. Similarly, when the positively charged hole leaves the B atom, the B atom becomes a negatively charged B ion. Thus, as electrons diffuse to the p -side of the junction, they leave behind positively charged electron donor ions that are covalently bound to the Si lattice. As holes diffuse to the n -side of the junction, they leave behind negatively charged hole

donor ions that are covalently bound to the Si lattice on the p -side of the junction. The diffusion of charge carriers across the junction thus creates an electric field across the junction, directed from the positive ions on the n -side to the negative ions on the p -side, as shown in Figure 20.3. Gauss’s law requires that electric field lines originate on positive charges and terminate on negative charges, so the number of positive charges on the n -side must be equal to the number of negative charges on the p -side.

Electric fields exert forces on charged particles according to the familiar $f = qE$ relationship. This force causes the charge carriers to drift. In the case of the positively charged holes, they drift in the direction of the electric field, that is, from the n -side to the p -side of the junction. The negatively charged electrons drift in the direction opposite the field, that is, from the p -side to the n -side of the junction. If no external forces are present other than temperature, then the flows of holes are equal in both directions and the flows of electrons are equal in both directions, resulting in zero net flow of either holes or electrons across the junction. This is called the law of detailed balance, which is consistent with Kirchhoff’s current law.

Carrying out an analysis of electron and hole flow across the junction ultimately leads to the development of the familiar diode equation:

$$I = I_0 \left(e^{\frac{qV}{kT}} - 1 \right), \tag{20.2}$$

where

q is the electronic charge

k is Boltzmann’s constant

T is the junction temperature in K

V is the externally applied voltage across the junction from the p -side to the n -side of the junction

20.1.2.2 Illuminated p - n Junction

Figure 20.4 illustrates the effect of photons impinging upon the junction area.

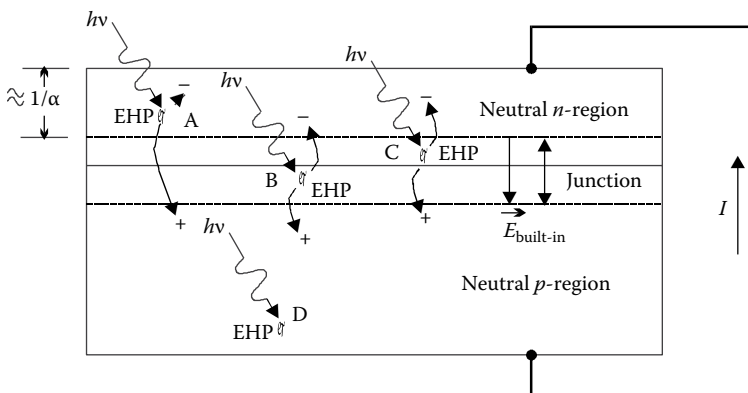


FIGURE 20.4

The illuminated p - n junction showing desirable geometry and the creation of electron–hole pairs. (From Messenger, R. and Ventre, G., *Photovoltaic Systems Engineering*, 2nd edn., CRC Press LLC, Boca Raton, FL, 2004.)

The energy of a photon is given in the following equation, where λ is the wavelength of the photon, h is Planck's constant (6.625×10^{-34} J s), and c is the speed of light (3×10^8 m/s):

$$e = h\nu = \frac{hc}{\lambda}, \quad (20.3)$$

The energy of a photon in electron volts (eV) becomes $1.24/\lambda$, if λ is in μm ($1 \text{ eV} = 1.6 \times 10^{-19}$ J). If a photon has an energy that equals or exceeds the semiconductor bandgap energy of the p - n junction material, then it is capable of creating an electron-hole pair (EHP). For Si, the bandgap is 1.1 eV, so if the photon wavelength is less than 1.13 μm , which is in the near-infrared region, then the photon will have sufficient energy to generate an EHP.

Although photons with energies higher than the bandgap energy can be absorbed, one photon can create only one EHP. The excess energy of the photon is wasted as heat. As photons enter a material, the intensity of the beam depends upon a wavelength-dependent absorption constant, α . The intensity of the photon beam as a function of penetration depth into the material is given by $F(x) = F_0 e^{-\alpha x}$, where x is the depth of penetration into the material. Optimization of photon capture, thus, suggests that the junction should be within $1/\alpha$ of the surface to ensure transmission of photons to within a diffusion length of the p - n junction, as shown in Figure 20.4.

If an EHP is created within one minority carrier diffusion length, D_x , of the junction, then, on the average, the EHP will contribute to current flow in an external circuit. The diffusion length is defined to be $L_x = \sqrt{D_x \tau_x}$, where D_x and τ_x are the minority carrier diffusion length and lifetime for electrons, respectively, in the p -region if $x = n$, and D_x and τ_x are the minority carrier diffusion length and lifetime for holes, respectively, in the n -region if $x = p$. So the idea is to quickly move the electron and hole of the EHP to the junction before either has a chance to recombine with a majority charge carrier. In Figure 20.4, points A, B, and C represent EHP generation within a minority carrier diffusion length of the junction. But if an EHP is generated at point D, it is highly unlikely that the electron will diffuse to the junction before it recombines.

The amount of photon-induced current flowing across the junction and into an external circuit is directly proportional to the intensity of the photon source. Note that the EHPs are swept across the junction by the built-in E-field, so the holes move to the p -side and continue to diffuse toward the p -side external contact. Similarly, the electrons move to the n -side and continue to diffuse to the n -side external contact. Upon reaching their respective contacts, each contributes to external current flow if an external path exists. In the case of holes, they must recombine at the contact with an electron that enters the material at the contact. Electrons, on the other hand, are perfectly happy to continue flowing through an external copper wire.

At this point, an important observation can be made. The external voltage across the diode that results in significant current flow when no photons are present is positive from p to n . The diode current and voltage are defined in this direction, and the diode thus is defined according to the passive sign convention. In other words, when no photons impinge on the junction, the diode dissipates power. But when photons are present, the photon-induced current flows OPPOSITE to the passive direction. So current LEAVES the positive terminal, which means that the device is *generating* power. This is the PV effect. The challenge to the manufacturers of PV cells is to maximize the capture of photons and, in turn, maximize the flow of current in the cell for a given incident photon intensity. Optimization of the process

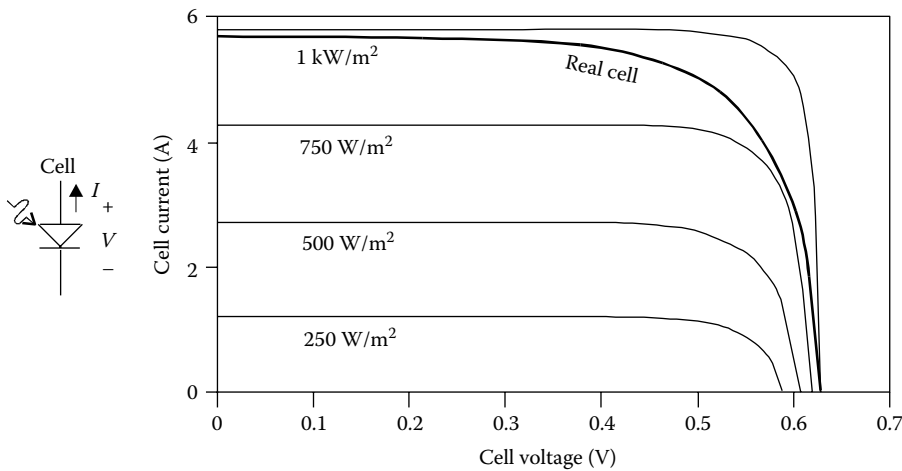


FIGURE 20.5

*I-V characteristics of real and ideal PV cells under different illumination levels. (From Messenger, R. and Ventre, G., *Photovoltaic Systems Engineering*, 2nd edn., CRC Press LLC, Boca Raton, FL, 2004.)*

is discussed in detail in [4]. When the photocurrent is incorporated into the diode equation, the result is

$$I = I_{\ell} - I_0 \left(e^{\frac{qV}{kT}} - 1 \right) \cong I_1 - I_0 e^{\frac{qV}{kT}}. \quad (20.4)$$

Note that in (20.4), the direction of the current has been reversed with respect to the cell voltage. With the active sign convention implied by (20.4), the junction device is now being defined as a cell, or PV cell. Figure 20.5 shows the *I-V* curves for an ideal PV cell and a typical PV cell, assuming the cell has an area of approximately 195 cm².

It is evident that the ideal curve closely represents that of an ideal current source for cell voltages below 0.5 V, and it closely represents that of an ideal voltage source for voltages near 0.6 V. The intersection of the curve with the *V* = 0 axis represents the short-circuit current of the cell. The intersection of the curve with the *I* = 0 axis represents the open-circuit voltage of the cell. To determine the open-circuit voltage of the cell, simply set *I* = 0 and solve (20.4) for *V*_{OC}. The result is

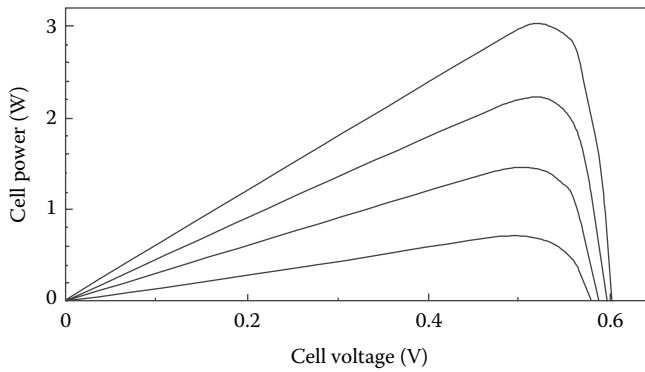
$$V_{OC} = \frac{kT}{q} \ln \frac{I_1}{I_0}. \quad (20.5)$$

The direct dependence of *I* on *I*₁ and the logarithmic dependence of *V*_{OC} on *I*₁ is evident from (20.4) and (20.5) as well as from Figure 20.5.

The departure of the real curve from the ideal prediction is primarily due to unavoidable series resistance between the cell contacts and the junction.

20.1.2.3 Properties of the PV Cell

Another property of the *I-V* curves of Figure 20.5 is the presence of a single point on each curve at which the power delivered by the cell is a maximum. This point is called the

**FIGURE 20.6**

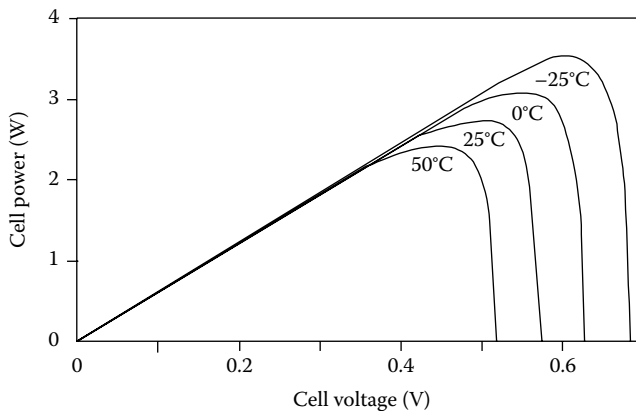
Power vs. voltage for a PV cell for four illumination levels. (From Messenger, R. and Ventre, G., *Photovoltaic Systems Engineering*, 2nd edn., CRC Press LLC, Boca Raton, FL, 2004.)

maximum power point of the cell and is more evident when cell power is plotted vs. cell voltage, as shown in Figure 20.6.

Note that the maximum power point of the cell remains at a nearly constant voltage as the illumination level of the cell changes.

Not shown in Figure 20.5 or 20.6 is the temperature dependence of the photocurrent. It turns out that I_0 increases rapidly with temperature. Thus, despite the KT/q multiplying factor, the maximum available power from a Si PV cell decreases at approximately $0.47\%/^{\circ}\text{C}$, as shown in Figure 20.7.

Furthermore, the maximum power voltage also decreases by approximately this same factor. An increase of 25°C is not unusual for an array of PV cells, which corresponds to a decrease of approximately 12% in maximum power and in maximum power voltage. Because of this temperature degradation of the performance of a PV cell, it is important during the system design phase to endeavor to keep the PV cells as cool as possible.

**FIGURE 20.7**

Temperature dependence of the power vs. voltage curve for a PV cell. (From Messenger, R. and Ventre, G., *Photovoltaic Systems Engineering*, 2nd edn., CRC Press LLC, Boca Raton, FL, 2004.)

20.1.3 Manufacture of Solar Cells

20.1.3.1 Manufacture of Crystalline and Multicrystalline Silicon PV Cells

While crystalline and multicrystalline silicon PV cells require highly purified, electronic-grade silicon, the material can be about an order of magnitude less pure than semiconductor-grade silicon and still yield relatively high-performance PV cells. Recycled or rejected semiconductor-grade silicon is often used as the feedstock for PV-grade silicon. Once adequately refined silicon is available, a number of methods have been devised for the production of single-crystal and multicrystalline PV cells. Single-crystal Si PV cells have been fabricated with conversion efficiencies just over 20%, while conversion efficiencies of champion multicrystalline Si PV cells are about 16% [5,6].

Single-crystal Si cells are almost exclusively fabricated from large single-crystal ingots of Si that are pulled from molten, PV-grade Si. These ingots, normally *p*-type, are typically on the order of 200 mm in diameter and up to 2 m in length. The Czochralski method (Figure 20.8a) is the most common method of growing single-crystal ingots.

A seed crystal is dipped in molten silicon doped with a *p*-material (Boron) and drawn upward under tightly controlled conditions of linear and rotational speed and temperature. This process produces cylindrical ingots of typically 10 cm diameter, although ingots of 20 cm diameter and more than 1 m long can be produced for other applications. An alternative method is called the float zone method (Figure 20.8b). In this method, a polycrystalline ingot is placed on top of a seed crystal and the interface is melted by a heating coil around it. The ingot is moved linearly and rotationally, under controlled conditions. This process has the potential to reduce the cell cost. Figure 20.9 illustrates the process of manufacturing a cell from an ingot.

The ingots are sliced into wafers that are approximately 0.25 mm thick. The wafers are further trimmed to a nearly square shape, with only a small amount of rounding at the corners. Surface degradation from the slicing process is reduced by chemically etching the wafers. In order to enhance photon absorption, it is common practice to use a preferential etching process to produce a textured surface finish. An *n*-layer is then diffused into the wafer to produce a *p-n* junction, contacts are attached, and the cell is then encapsulated into a module (Figure 20.10).

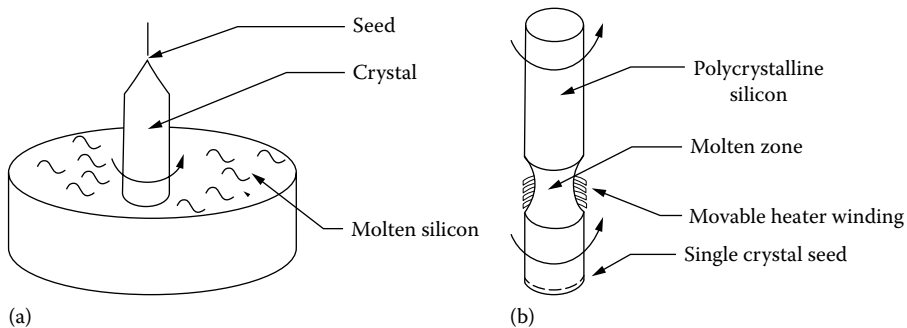
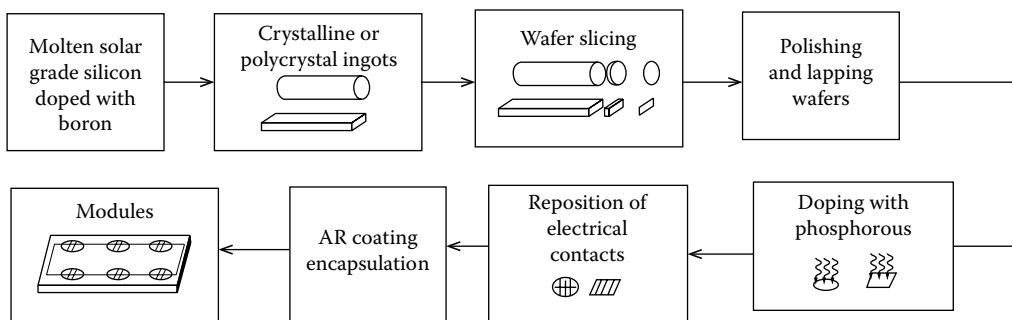
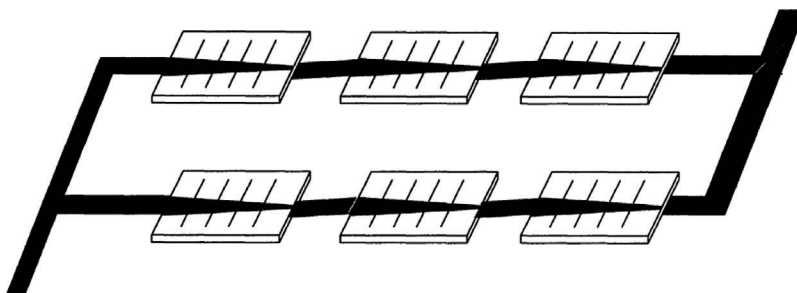


FIGURE 20.8

Crystalline silicon ingot production methods: (a) Czochralski method and (b) float zone method. (From Goswami, D.Y. et al., *Principles of Solar Engineering*, 2nd edn., Taylor & Francis, Philadelphia, PA, 2000.)

**FIGURE 20.9**

Series of processes for the manufacture of crystalline and polycrystalline cells. (From Goswami, D.Y. et al., *Principles of Solar Engineering*, 2nd edn., Taylor & Francis, Philadelphia, PA, 2000.)

**FIGURE 20.10**

Assembly of solar cells to form a module. (From Goswami, D.Y. et al., *Principles of Solar Engineering*, 2nd edn., Taylor & Francis, Philadelphia, PA, 2000.)

Detailed accounts of cell and module fabrication processes can be found in [2,4,6,7].

Growing and slicing single-crystal Si ingots are highly energy intensive and, as a result, impose a relatively high energy cost on this method of cell fabrication. This high energy cost imposes a lower limit on the cost of production of a cell, and although the cell will ultimately generate as much energy as was used to produce it, the energy payback time (EPBT) is longer than desirable. Reducing the energy cost of cell and module fabrication has been the subject of a great deal of research over the past 40 years. The high energy cost of crystalline Si led to the work on thin films of amorphous Si, CdTe, and other materials, which is described later in this handbook. A great deal of work has also gone into developing methods of growing Si in a manner that will result in lower energy fabrication costs.

Three methods that are less energy intensive are now commonly in use—crucible growth, the EFG process, and string ribbon technology. These methods, however, result in the growth of multicrystalline Si, which, upon inspection, depending upon the fabrication process, has a speckled surface appearance, as opposed to the uniform color of single-crystal Si. Multicrystalline Si has electrical and thermodynamic characteristics that match single-crystal Si relatively closely, as previously noted.

The crucible growth method involves pouring molten Si into a quartz crucible and carefully controlling the cooling rate (Figure 20.11).

A seed crystal is not used, so the resulting material consists of a collection of zones of single crystals with an overall square cross section. It is still necessary to saw the ingots

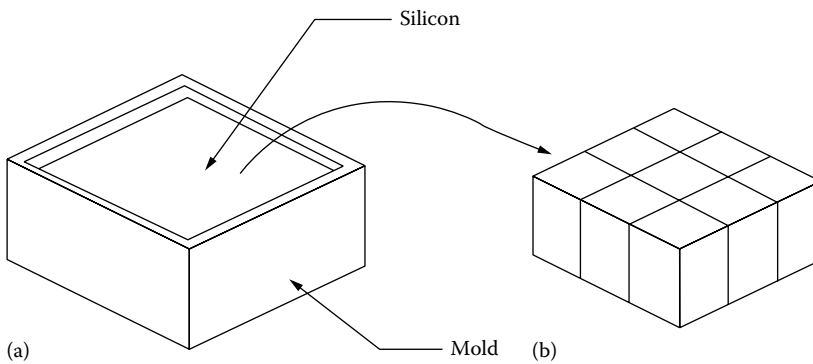


FIGURE 20.11

Polycrystalline ingot production. (a) Mold, (b) polycrystalline ingot. (From Goswami, D.Y. et al., *Principles of Solar Engineering*, 2nd edn., Taylor & Francis, Philadelphia, PA, 2000.)

into wafers, but the result is square wafers rather than round wafers that would require additional sawing and corresponding loss of material. Wafers produced by this method can achieve conversion efficiencies of 15% or more [2].

The edge-defined film-fed growth (EFG) process is another method currently being used to produce commercial cells [8]. The process involves pulling an octagon tube, 6 m long, with a wall thickness of 330 μm , directly from the Si melt. The octagon is then cut by a laser along the octagonal edges into individual cells. Cell efficiencies of 14% have been reported for this fabrication method [5]. Figure 20.12 illustrates the process.

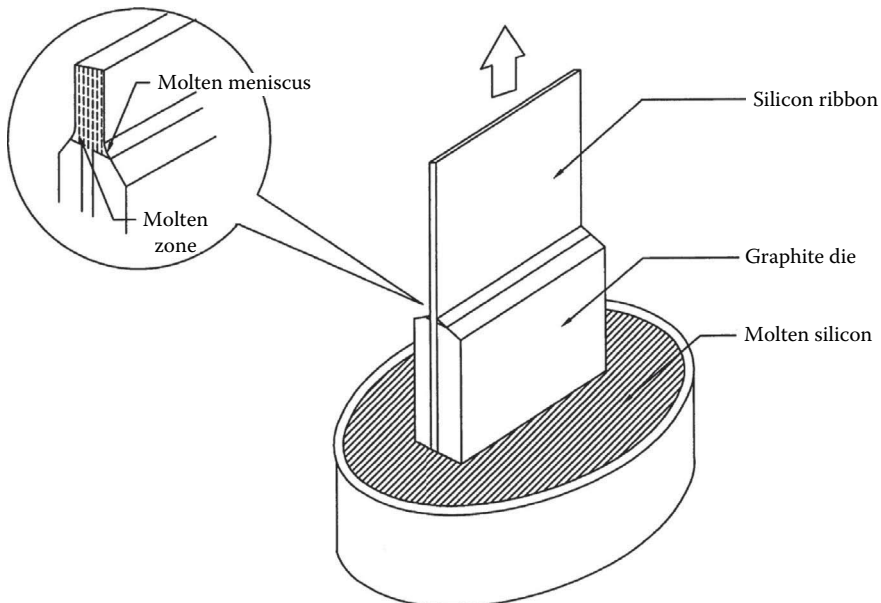
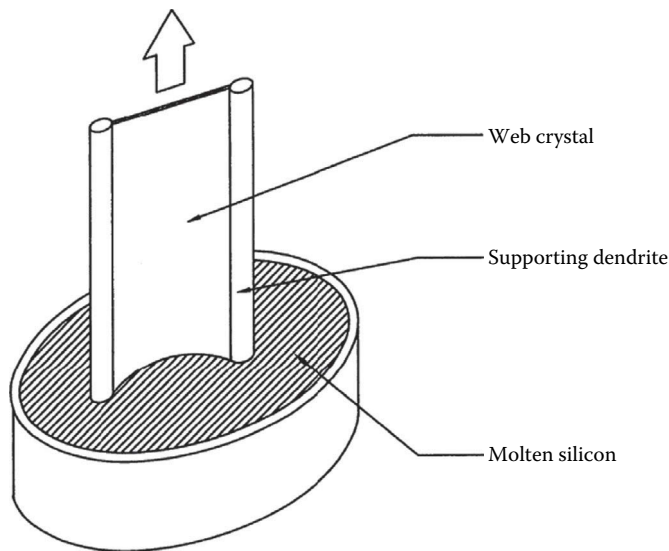


FIGURE 20.12

Thin-film production by EFG. (From Goswami, D.Y. et al., *Principles of Solar Engineering*, 2nd edn., Taylor & Francis, Philadelphia, PA, 2000.)

**FIGURE 20.13**

Thin-film production by dendritic web growth. (From Goswami, D.Y. et al., *Principles of Solar Engineering*, 2nd edn., Taylor & Francis, Philadelphia, PA, 2000.)

A third method of fabrication of multicrystalline Si cells involves pulling a ribbon of Si, or dendritic web, from the melt (Figure 20.13).

Controlling the width of the ribbon is the difficult part of this process. High-temperature string materials are used to define the edges of the ribbon. The string materials are pulled through a crucible of molten Si in an Ar atmosphere after the attachment of a seed crystal to define the crystal structure of the ribbon. The nonconducting string material has a coefficient of thermal expansion close to that of Si, so during the cooling process, the string material will not affect the Si crystallization process [6]. The ribbons of Si are then cut into cells, typically rectangular in shape, as opposed to the more common square configuration of other multicrystalline technologies. Once the multicrystalline wafers have been fabricated, further processing is the same as that used for single-crystal cells.

20.1.3.2 Amorphous Silicon and Multijunction Thin-Film Fabrication

Amorphous silicon (*a*-Si) cells are made as thin films of *a*-Si:H alloy doped with phosphorous and boron to make *n* and *p* layers, respectively. The atomic structure of an *a*-Si cell does not have any preferred orientation. The cells are manufactured by depositing a thin layer of *a*-Si on a substrate (glass, metal, or plastic) from glow discharge, sputtering, or chemical vapor deposition (CVD) methods. The most common method is by an RF glow discharge decomposition of silane (SiH_4) on a substrate heated to a temperature of 200°C–300°C. To produce *p*-silicon, diborane (B_2H_6) vapor is introduced with the silane vapor. Similarly, phosphene (PH_3) is used to produce *n*-silicon. The cell consists of an *n*-layer, and intermediate undoped *a*-Si layer, and a *p*-layer on a substrate. The cell thickness is about 1 μm . The manufacturing process can be automated to produce rolls of solar cells from rolls of substrate. Figure 20.14 shows an example of roll-to-roll *a*-Si cell manufacturing equipment using a plasma CVD method.

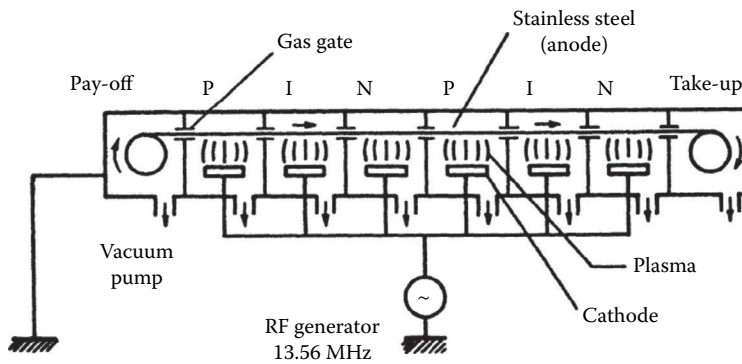


FIGURE 20.14

A schematic diagram of a roll-to-roll plasma CVD machine. (Adapted from www.ase-international.com.)

This machine can be used to make multijunction or tandem cells by introducing the appropriate materials at different points in the machine.

The four previously mentioned cell fabrication techniques require contacts on the front surface and on the back surface of the cells. Front surface contacts need to cover enough area to minimize series resistance between cell and contact, but if too much area is covered, then photons are blocked from entering the crystal. Thus, it is desirable, if possible, to design cells such that both contacts are on the back of the cell. Green and his PV team at the University of South Wales have devised a buried contact cell [9] that has both contacts on the back and also is much thinner, thus much less material intensive, than conventional Si cells. In conventional cells, charge carrier flow is perpendicular to the cell surface, while in the buried contact cell, even though the multiple $p-n$ junctions are parallel to the cell surfaces, charge carrier flow is parallel to the cell surfaces. The fabrication process involves depositing alternate p -type and n -type Si layers, each about $1\ \mu\text{m}$ thick, on an insulating substrate or superstrate. Grooves are laser cut in the layers and contacts are deposited in the grooves. Elimination of the ingot and wafer steps in processing, along with the reduced amount of material used, reduces correspondingly the energy overhead of cell production. Conversion efficiencies in excess of 20% and high cell fill factors have been achieved with this technology.

20.1.4 PV Modules and PV Arrays

Since individual cells have output voltages limited to approximately 0.5 V and output currents limited to approximately 7 A, it is necessary to combine cells in series and parallel to obtain higher voltages and currents. A typical PV module consists of 36 cells connected in series in order to produce a maximum power voltage of approximately 17 V, with a maximum power current of approximately 7 A at a temperature of 25°C . Such a module will typically have a surface area of about $10\ \text{ft}^2$. Modules also exist with 48 or more series cells so that three modules in series will produce the same output voltage and current as four 36-cell modules in series. Other larger modules combine cells in series and in parallel to produce powers up to 300 W per module.

Modules must be fabricated so the PV cells and interconnects are protected from moisture and are resistant to degradation from the ultraviolet component of sunlight. Since the modules can be expected to be exposed to a wide range of temperatures, they

must be designed so that thermal stresses will not cause delamination. Modules must also be resistant to blowing sand, salt, hailstones, acid rain, and other unfriendly environmental conditions. And, of course, the module must be electrically safe over the long term. A typical module can withstand a pressure of 50 psf and large hailstones and is warranted for 25 years. Details on module fabrication can be found in [4,7,10].

It is important to realize that when PV cells with a given efficiency are incorporated into a PV module, the module efficiency will be less than the cell efficiency, unless the cells are exactly identical electrically. When cells are operated at their maximum power point, this point is located on the cell I - V curve at the point where the cell undergoes a transition from a nearly ideal current source to a nearly ideal voltage source. If the cell I - V curves are not identical, since the current in a series combination of cells is the same in each cell, each cell of the combination will not necessarily operate at its maximum power point. Instead, the cells operate at a current consistent with the rest of the cells in the module, which may not be the maximum power current of each cell.

When modules are combined to further increase system voltage and/or current, the collection of modules is called an array. For the same reason that the efficiency of a module is less than the efficiencies of the cells in the module, the efficiency of an array is less than the efficiency of the modules in the array. But since a large array can be built with subarrays that can operate essentially independently of each other, in spite of the decrease in efficiency at the array level, PV arrays that produce in excess of 1 MW are in operation at acceptable efficiency levels. The bottom line is that most efficient operation is achieved if modules are made of identical cells and if arrays consist of identical modules.

20.1.5 Sun and PV Array Orientation

As explained in detail in Chapter 6, total solar radiation is composed of components, direct or beam, diffuse, and reflected. In regions with strong direct components of sunlight, it may be advantageous to have a PV array mount that will track the sun. Such tracking mounts can improve the daily performance of a PV array by more than 20% in certain regions. In cloudy regions, tracking is less advantageous.

The position of the sun in the sky can be uniquely described by two angles—the azimuth, γ , and the altitude, α . The azimuth is the deviation from true south. The altitude is the angle of the sun above the horizon. When the altitude of the sun is 90° , the sun is directly overhead.

Another convenient, but redundant, angle, is the hour angle, ω . Since the earth rotates 360° in 24 h, it rotates 15° each hour. The sun thus appears to move along its arc 15° toward the west each hour. The hour angle is 0° at solar noon, when the sun is at its highest point in the sky during a given day. In this handbook, we have a sign convention such that the hour angle and the solar azimuth angle are negative before noon and positive after noon. For example, at 10 a.m. solar time, the hour angle will be -30° .

A further important angle that is used to predict the sun's position is the declination, δ . The declination is the apparent position of the sun at solar noon with respect to the equator. When $\delta = 0$, the sun appears overhead at solar noon at the equator. This occurs on the first day of fall and on the first day of spring. On the first day of Northern Hemisphere summer (June 21), the sun appears directly overhead at a latitude, L , of 23.45°N of the equator. On the first day of winter (December 21), the sun appears directly overhead at a latitude of 23.45° south of the equator. At any other latitude, the altitude $\alpha = 90^\circ - |L - \delta|$ when the sun is directly south (or north), that is, at solar noon. At solar noon, the sun is directly south for $L > \delta$ and directly north for $L < \delta$. Note that if L is negative, it refers to the Southern Hemisphere.

Several important formulas for determining the position of the sun [4,11] include the following, where n is the day of the year with January 1 being day 1:

$$\delta = 23.45^\circ \sin \frac{360[n - 80]}{365}, \quad (20.6)$$

$$\omega = \pm 15^\circ (\text{hours from local solar noon}), \quad (20.7)$$

$$\sin \alpha = \sin \delta \sin L + \cos \delta \cos L \cos \omega, \quad (20.8)$$

and

$$\cos \gamma = \frac{\cos \delta \sin \omega}{\cos \alpha}. \quad (20.9)$$

Solution of (20.6 through 20.9) shows that for optimal annual performance of a PV array, it should face directly south and should be tilted at an angle approximately equal to the latitude, L . For best summer performance, the tilt should be at $L - 15^\circ$, and for best winter performance, the array should be tilted at an angle of $L + 15^\circ$.

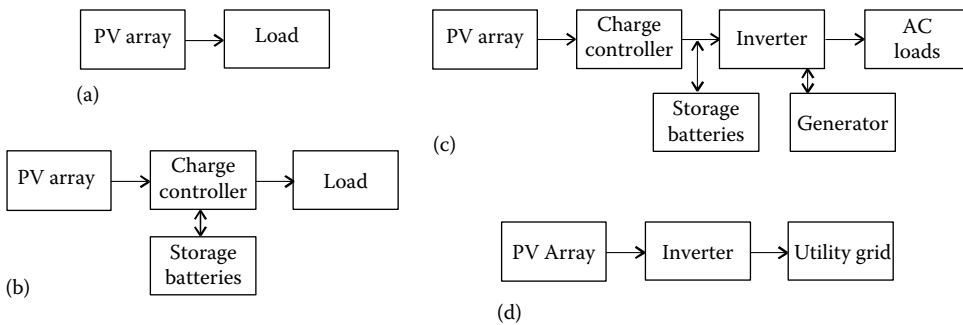
While (20.6 through 20.9) can be used to predict the location of the sun in the sky at any time on any day at any location, they cannot be used to predict the degree of cloud cover. Cloud cover can only be predicted on a statistical basis for any region, and thus the amount of sunlight available to a collector will also depend upon cloud cover. The measure of available sunlight is the peak sun hour (psh). If the sunlight intensity is measured in kW/m^2 , then if the sunlight intensity is integrated from sunrise to sunset over 1 m^2 of surface, the result will be measured in kWh. If the daily kWh/m^2 is divided by the peak sun intensity, which is defined as $1 \text{ kW}/\text{m}^2$, the resulting units are hours. Note that this hour figure multiplied by $1 \text{ kW}/\text{m}^2$ results in the daily kWh/m^2 . Hence the term peak sun hours, since the psh is the number of hours the sun would need to shine at peak intensity to produce the daily sunrise to sunset kWh. Obviously the psh is also equivalent to $\text{kWh}/\text{m}^2/\text{day}$. For locations in the United States, the National Renewable Energy Laboratory [12] publishes psh for fixed and single-axis tracking PV arrays at tilts of horizontal, latitude -15° , latitude, latitude $+15^\circ$, and vertical. NREL also tabulates data for double-axis trackers. These tables are extremely useful for determining annual performance of a PV array.

20.1.6 PV System Configurations

Figure 20.15 illustrates four possible configurations for PV systems.

Perhaps the simplest system is that of Figure 20.15a in which the output of the PV module or array is directly connected to a DC load. This configuration is most commonly used with a fan or a water pump, although it is likely that the water pump will also use a linear current booster (LCB) between the array and the pump motor. Operation of the LCB will be explained later.

The configuration of Figure 20.15b includes a charge controller and storage batteries so the PV array can produce energy during the day that can be used day or night by the load. The charge controller serves a dual function. If the load does not use all the energy produced by the PV array, the charge controller prevents the batteries from overcharge.

**FIGURE 20.15**

Several examples of PV systems: (a) direct-coupled DC system, (b) DC system with battery backup, (c) AC system with battery backup and fossil generator, and (d) grid-connected system.

While flooded lead–acid batteries require overcharging about once per month, frequent overcharging shortens the lives of the batteries. As the batteries become discharged, the charge controller disconnects the load to prevent the batteries from overdischarge. Normally PV systems incorporate deep discharge lead–acid batteries, but the life of these batteries is reduced significantly if they are discharged more than 80%. Modern charge controllers typically begin charging as constant current sources. In the case of a PV system, this simply means that all array current is directed to the batteries. This is called the *bulk* segment of the charge cycle. Once the battery voltage reaches the bulk voltage, which is an owner programmable value, as determined by the battery type and the battery temperature, the charging cycle switches to a constant voltage mode, commonly called the *absorption* mode. During the absorption charge mode, the charge controller maintains the bulk charge voltage for a preprogrammed time, again depending upon manufacturers' recommendations. During the absorption charge, battery current decreases as the batteries approach full charge. At the end of the bulk charge period, the charging voltage is automatically reduced to the *float* voltage level, where the charging current is reduced to a *trickle* charge.

Since quality charge controllers are microprocessor controlled, they have clock circuitry so that they can be programmed to automatically subject the batteries to an *equalization* charge approximately once a month. The equalization mode applies a voltage higher than the bulk voltage for a preset time to purposely overcharge the batteries. This process causes the electrolyte to bubble, which helps to mix the electrolyte as well as to clean the battery plates. Equalization is recommended *only* for flooded lead–acid batteries. Sealed varieties can be seriously damaged if they are overcharged.

Figure 20.16 shows the currents and voltages during the bulk, absorption, and float parts of the charging cycle. Note that all settings are programmable by the user in accordance with manufacturers' recommendations. Some charge controllers incorporate maximum power tracking as a part of their charge control algorithm. Since the maximum power voltage of a module or an array is generally higher than needed to charge the batteries, the array will not normally operate at its maximum power point when it is charging batteries, especially if the array temperature is low. For example, if it takes 14.4 V to charge a 12.6 V battery, and if a module maximum power voltage is 17, then the charging current can be increased by a factor of $17/14.4$, or approximately 18%, assuming close to 100% efficiency of the maximum power tracker (MPT).

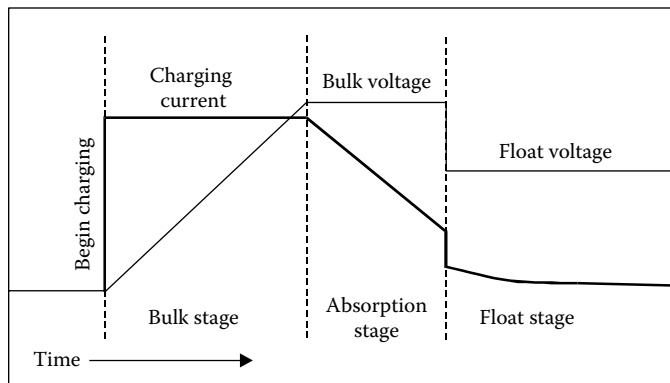


FIGURE 20.16
Charging cycle for typical PV charge controller.

The configuration of Figure 20.15c incorporates an inverter to convert the DC PV array output to AC and a backup generator to supply energy to the system when the supply from the sun is too low to meet the needs of the load. Normally, the backup generator will be a fossil-fueled generator, but it is also possible to incorporate wind or other renewable generation into the system. In this case, the charge controller prevents overcharge of the batteries. The inverter is equipped with voltage sensing circuitry so that if it detects the battery voltage going too low, it will automatically start the generator so the generator will provide power for the load as well as provide charging current for the batteries. This system is called a hybrid system, since it incorporates the use of more than one energy source.

The first three configurations are stand-alone systems. The fourth system, shown in Figure 20.15d, is a grid-connected, or utility-interactive, system. The inverter of a utility-interactive system must meet more stringent operational requirements than the stand-alone inverter. The inverter output voltage and current must be of *utility-grade* quality. This means that it must have minimal harmonic content. Furthermore, the inverter must sense the utility, and if utility voltage is lost, the inverter must shut down until utility voltage is restored to within normal limits.

20.1.7 PV System Components

20.1.7.1 Maximum Power Trackers and Linear Current Boosters

The LCB was mentioned in conjunction with the water pumping example. The function of the LCB is to match the motor I - V characteristic to the maximum power point of the PV array, so that at all times the array delivers maximum power to the load. Note that the LCB acts as a DC-to-DC transformer, converting a higher voltage and lower current to a lower voltage and higher current, with minimal power loss in the conversion process. A more general term that includes the possibility of converting voltage upward defines the maximum power tracker (MPT). Figure 20.17 shows the operating principle of the LCB and MPT.

Note that normally the I - V characteristic of the load will not intersect the I - V characteristic of the PV array at the maximum power point of the array, as shown by points A,

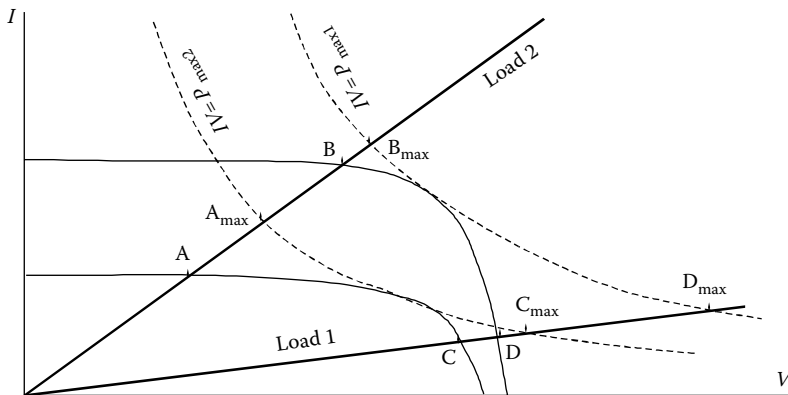


FIGURE 20.17

Operation of the LCB or MPT. (From Messenger, R. and Ventre, G., *Photovoltaic Systems Engineering*, 2nd edn., CRC Press LLC, Boca Raton, FL, 2004.)

B, C, and D for the two loads and the two sunlight intensity levels. For the lower-intensity situation, the characteristic of load 1 intersects the array characteristic at point C and the characteristic of load 2 intersects the array characteristic at point A. The two hyperbolas are the loci of points where the I - V product is equal to the maximum available power from the array at the particular sunlight intensity. Hence, the intersection of these hyperbolas with the load characteristics represents the transfer of all available power from the array to the load. While the increase in power for points B and C is not particularly impressive, as shown by points B_{\max} and C_{\max} , the increase in power for points A and D is considerably greater, as shown by points A_{\max} and D_{\max} . The assumption here, of course, is 100% efficiency in the transformation. In fact, efficiencies in excess of 95% are not unusual for quality MPT and LCB devices.

The final observation for Figure 20.17 is that points A_{\max} and B_{\max} occur at voltages below the maximum power voltages of the array, while C_{\max} and D_{\max} occur at voltages above the maximum power voltages of the array. Since the input voltage and current of the MPT or LCB are the maximum power voltage and current of the array, the MPT or LCB output voltage and current points A_{\max} and B_{\max} represent down-conversion of the array voltage and points C_{\max} and D_{\max} represent up-conversion of the array voltage. These forms of conversion are discussed in power electronics books, such as [13]. The difference between the MPT and the LCB is that the LCB only performs a down-conversion, so the operating voltage of the load is always below the maximum power voltage point of the array. The terms LCB and MPT are often used interchangeably for down-conversion, but normally LCB is limited to the description of the black box that optimizes performance of pumps, while MPT is used for more general applications.

20.1.7.2 Inverters

Inverters convert DC to AC. The simplest inverter converts DC to square waves. While square waves will operate many AC loads, their harmonic content is very high, and as a result, there are many situations where square waves are not satisfactory. Other more suitable inverter output waveforms include the quasi-sine wave and the utility-grade sine

wave. Both are most commonly created by the use of multilevel H-bridges controlled by microprocessors. There are three basic configurations for inverters: stand-alone, grid-tied, and UPS. The stand-alone inverter must act as a voltage source that delivers a prescribed amplitude and frequency rms sine wave without any external synchronization. The grid-tied inverter is essentially a current source that delivers a sinusoidal current waveform to the grid that is synchronized by the grid voltage. Synchronization is typically sufficiently close to maintain a power factor in excess of 0.9. The UPS inverter combines the features of both the stand-alone and the grid-tied inverter, so that if grid power is lost, the unit will act as a stand-alone inverter while supplying power to emergency loads. IEEE Standard 929 [14] requires that any inverter that is connected to the grid must monitor the utility grid voltage, and if the grid voltage falls outside prescribed limits, the inverter must stop delivering current to the grid. Underwriters Laboratory (UL) Standard 1741 [15] provides the testing needed to ensure compliance with IEEE 929.

While it may seem to be a simple matter to shut down if the utility shuts down, the matter is complicated by the possibility that additional utility-interactive PV systems may also be online. Hence, it may be possible for one PV system to *fool* another system into thinking that it is really the utility. To prevent this *islanding* condition, sophisticated inverter control algorithms have been developed to ensure that an inverter will not appear as the utility to another inverter. Some PV system owners do not want their PV system to shut down when the utility shuts down. Such a system requires a special inverter that has two sets of AC terminals. The first set, usually labeled AC IN, is designed for connection to the utility. If the utility shuts down, this set of terminals disconnects the inverter output from the utility, but continues to monitor utility voltage until it is restored. When the utility connection is restored, the inverter will first meet the needs of the emergency loads and then will feed any excess output back to the main distribution panel.

The second set of terminals is the emergency output. If the utility shuts down, the inverter almost instantaneously transfers into the emergency mode, in which it draws power from the batteries and/or the PV array to power the emergency loads. In this system, the emergency loads must be connected to a separate emergency distribution panel. Under emergency operation, the loads in the main distribution panel are without power, but the emergency panel remains energized. Such a system is shown in Figure 20.18.

The reader is referred to [4,13] for detailed explanations of the operation of inverters, including the methods used to ensure that utility-interactive inverters meet UL 1741 testing requirements.

20.1.7.3 Balance of System Components

Aside from the array, the charge controller, and the inverter, a number of other components are needed in a code-compliant PV system. For example, if a PV array consists of multiple series-parallel connections, as shown in Figure 20.19, then it is necessary to incorporate fuses or circuit breakers in series with each series string of modules, defined as a source circuit.

This fusing is generally accomplished by using a source circuit combiner box as the housing for the fuses or circuit breakers, as shown in Figure 20.19. The combiner box should be installed in a readily accessible location. The PV output circuit of Figure 20.19 becomes the input to the charge controller, if a charge controller is used. If multiple

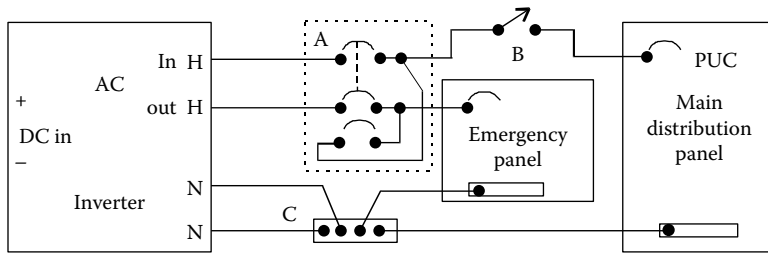


FIGURE 20.18
Example of PV source and output circuits.

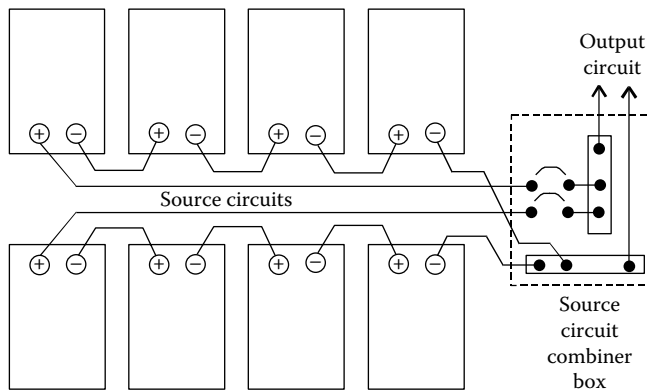
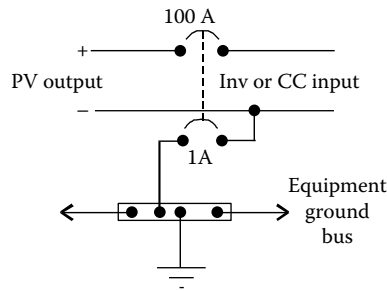


FIGURE 20.19
Use of GFDI.

parallel source circuits are used, it may be necessary to use more than one charge controller, depending upon the rating of the charge controller. When more than one charge controller is used, source circuits should be combined into separate output circuits for each charge controller input. In a utility-interactive circuit with no battery backup, a charge controller is not necessary. The PV output circuit connects directly to the inverter through either a DC disconnect or a DC ground fault detection and interruption (GFDI) device.

A GFDI device is required by the *National Electrical Code* (NEC) [16] whenever a PV array is installed on a residential rooftop. The purpose of the device is to detect current flow on the grounding conductor. The grounding conductor is used to ground all metal parts of the system. In a properly installed and operating system, no current will flow on the grounding conductor. Normally the negative conductor of the PV array is grounded, but this ground, if properly installed, will be attached to the grounding conductor at only one point, as shown in Figure 20.20, where the negative PV output conductor is connected to the equipment grounding bus through the 1 A circuit breaker. The 1 A circuit breaker is ganged to the 100 A circuit breaker so that if the current through the 1 A circuit breaker exceeds 1 A, both breakers will trip. When the two circuit breakers open, current flow on both the PV output circuit conductors and the grounding conductor is interrupted. If the

**FIGURE 20.20**

Utility-interactive PV system connections to emergency loads and to utility.

fault current on the grounding conductor was the result of an arcing condition between one of the PV circuit conductors and ground, the arc will be extinguished, thus preventing a fire from starting.

The NEC also requires properly rated disconnects at the inputs and outputs of all power conditioning equipment. An additional disconnect will be needed at the output of a charge controller as well as between any battery bank and inverter input or DC load center. If the disconnect is to disconnect DC, then the NEC requires that it be rated for DC. Additional disconnects are needed at the output of any inverter. If the inverter is utility interactive with battery backup for emergency loads, it is desirable to include an inverter bypass switch at the inverter output in case inverter maintenance is required without interruption of power to emergency loads. In addition to the inverter bypass switch, many utilities require a visible, lockable, accessible, load break, disconnect between the inverter output and the point of utility connection. This switch is for use by the utility if they deem it necessary to disconnect the inverter from the line for any reason.

The point of utility connection for a utility-interactive system will normally be a back-fed circuit breaker in a distribution panel. This circuit breaker is to be labeled so maintenance workers will recognize it as a source of power to the distribution panel. Figure 20.18 shows the connections for an inverter bypass switch (A), the utility disconnect switch (B), and the point of utility connection circuit breaker (PUC). The figure also shows a neutral bus (C) for the connection of neutrals for the main distribution panel, the emergency panel, and the inverter. Operation of the inverter bypass switch is as follows: The two-pole unit and the one-pole unit are ganged together so that either both are off or only one is on. Under normal operation, the two-pole unit is on and the one-pole unit is off. This connects the utility to the inverter and the inverter emergency output to the emergency panel. When the two-pole is off and the one-pole is on, the utility is connected to the emergency panel and the inverter is bypassed. When both are off, the utility is disconnected from both the inverter and the emergency panel. It is interesting to note that if the PUC circuit breaker in the main distribution panel is turned off, the inverter will interpret this as an interruption in utility power and will shut down the feed from inverter to main distribution panel. Thus, the energized portions of the circuit breaker will be the same as the energized portions of the other circuit breakers in the panel. When it is on, both sides of the circuit breaker will be energized. When it is off, only the line side will be energized.

Article 690 of the NEC governs the sizing of conductors in the PV system. The serious designer should carefully review the requirements of this article, especially since many PV systems use low-voltage DC where voltage drop in the connecting wiring can be a problem. Sizing of conductors must be done carefully.

Chapter 6 provides information about storage batteries.

20.1.8 PV System Examples

20.1.8.1 Stand-Alone PV Well Pump System

As long as the depth of the well, the well replenishment rate, and the necessary flow rate are known, a PV pumping system can be designed. PV pumping systems are so common, in fact, that they often come in kits that include PV modules, a pump controller (LCB), and a pump. Pump manufacturers generally provide specifications that indicate, for a given pumping height, the amount of water pumped and the current drawn by the pump for specified pump voltages.

As an example, consider a system designed to pump 2000 gal/day from a well that is 200 ft deep and has a replenishment rate that exceeds the desired pumping rate. Assume the location for the pumping system has a minimum of 5 psh/day. This means that the 2000 gal must be pumped in 5 h, which corresponds to a pumping rate of $2000 \text{ gal}/300 \text{ min} = 6.67 \text{ gpm}$. One pump that meets this requirement is a 1.0 HP pump that will pump 7.6 gpm to a height of 200 ft. Under these pumping conditions, the pump will draw 6.64 A at a DC voltage of 105 V. An 875 W PV array is recommended for the operation of this system by the distributor. Note that $(6.64 \text{ A}) \times (105 \text{ V}) = 697 \text{ W}$, indicating that the recommended PV array is rated at 125% of the system requirements.

Before committing to this system, however, it should be compared with a system that uses battery storage and a smaller pump. The cost of the 1.0 HP pump is close to \$1800, while a 0.25 HP pump that will pump 2.15 GPM while consuming 186 W can be purchased for about \$500. This pump will need to pump for 15.5 h to deliver the 2000 gal, so the energy consumption of the pump will be $(186 \text{ W}) \times (15.5 \text{ h}) = 2884 \text{ Wh}$. If the pump runs at 24 V DC, this corresponds to $2884 \div 24 = 120 \text{ Ah/day}$. For PV storage, deep discharge lead–acid batteries are normally used, and it is thus necessary to ensure that the batteries will provide adequate storage for the pump without discharging to less than 20% of full charge. Thus, the battery rating must be at least $120 \div 0.8 = 150 \text{ Ah}$ for each day of storage. If the water is pumped into a tank, then the water itself is a form of energy storage, and if the tank will hold several days' supply of water, then the batteries will only need to store enough energy to operate the pump for a day. If it is less expensive to use more batteries than to use a larger water tank, then additional batteries can be used.

So, finally, a sensible system will probably consist of a $\frac{1}{4}$ HP pump, an MPT charge controller for the batteries, and a minimum of 150 Ah at 24 V of battery storage. With the MPT controller, the array size, assuming 5 psh minimum per day, becomes $(2884 \text{ Wh}) \times 1.25 \div (5 \text{ h}) = 721 \text{ W}$, where the 1.25 factor compensates for losses in the array due to operation at elevated temperatures, battery charging and discharging losses, MPT losses, and wiring losses. This array can be conveniently achieved with 120 W modules configured in an array with two in series and three in parallel, as shown in Figure 20.21.

As a final note on the pumping system design, it is interesting to check the wire sizes. The NEC gives wire resistance in terms of Ω/kft . It is good design practice, but not an

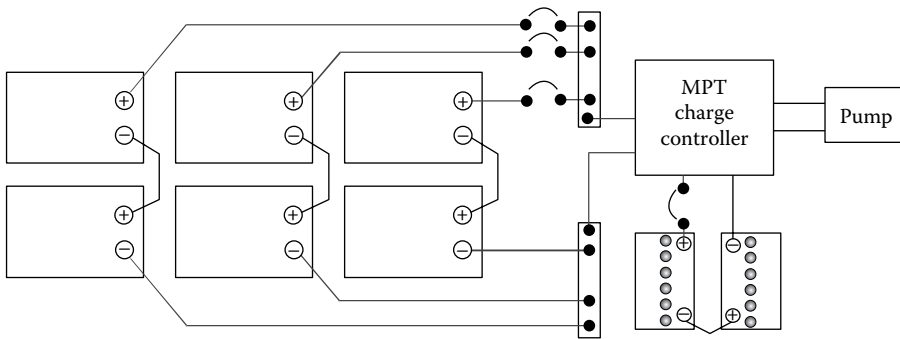


FIGURE 20.21
Water pumping system with battery storage and MPT charge controller.

absolute requirement, to keep the voltage drop in any wiring at <2%. The overall system voltage drop must be <5%. The wire size for any run of wire can thus be determined from

$$\Omega/\text{kft} \leq \frac{(\%VD)V_S}{0.2 \cdot I \cdot d}, \quad (20.10)$$

where

%VD is the allowed voltage drop in the wiring expressed as a percentage

V_S is the circuit voltage

I is the circuit current

d is the one-way length of the wiring

For the PV source circuit wiring, V_S will be about 34 V and I will be about 7 A. If the one-way source circuit length is 40 ft, then, for 2% voltage drop, (20.10) evaluates to $\Omega/\text{kft} = 1.2143$. NEC (Chapter 9 Table 8 in Reference [16]) shows that #10 solid Cu wire has 1.21 Ω/kft , while #10 stranded Cu has 1.24 Ω/kft . So either type of #10 will keep the %VD very close to 2%. Since #10 THWN-2 is rated to carry 40 A at 30°C, it is adequate for the job even under most derating conditions. Since the pump will be submersed, it will need 200 ft of wire just to get out of the well. If the controller is close to the well, then d will be approximately 210 ft. Thus, for $I = (186 \text{ W}) \div (24 \text{ V}) = 7.75 \text{ A}$, and $V_S = 24 \text{ V}$, (20.10) yields $\Omega/\text{kft} = 0.1475$, which requires #1/0 Cu according to NEC (Chapter 9 Table 8 in Reference [16]). A 3% voltage drop would allow the use of #2 Cu. In either case, this is a good example of how wire size may need to be increased to keep voltage drop at acceptable levels when relatively low-voltage DC is used. The 30°C ampacity of #2 Cu, for example, is 130 A. So even the small, low-voltage DC pump may not be the best choice. With inverter price decreasing and reliability increasing, and with AC motors generally requiring less maintenance than DC motors, at the time this article is being read, it may be more cost-effective to consider a 120 or 240 V AC pump for this application.

20.1.8.2 Stand-Alone System for a Remote Schoolhouse

Stand-alone system design requires a tabulation of the system loads, generally expressed in ampere hours (Ah) at the battery voltage. Suppose, for example, it is desired to provide power for 400 W of lighting, 400 W of computers, and 200 W of refrigeration, all at 120 V AC. Suppose that all of the loads operate for 8 h/day. This means the load to be met is 8 kWh/day

at 120 V AC. If this load is supplied by an inverter that operates with 92% efficiency, then the batteries must supply the inverter with $8 \div 0.92 = 8.7$ kWh/day. If the inverter input is 48 V DC, then the daily load in Ah is $(8700 \text{ Wh}) \div (48 \text{ V}) = 181$ Ah. To meet the needs for 1 day of operation, the batteries should thus be rated at 125% of 181 Ah = 226 Ah. But for a stand-alone system, it is usually desirable to provide more than 1 day of storage. For this system, 3 days would be more common, so a total of 678 Ah at 48 V should be used.

If an MPT charge controller is used, then the array can be sized based upon the daily system Wh and the available daily psh, taking losses into account. First of all, battery charging and discharging are only about 90% efficient. So to get 181 Ah *out* of the batteries, it is necessary to design for $181 \div 0.9 = 201$ Ah *in* to the batteries. At 48 V, this is 9648 Wh. Next, it is necessary to include a 10% degradation factor for array maintenance, mismatch, and wiring losses and another 15% factor for elevated array operating temperature. So the array should be designed to produce $9,648 \div 0.9 \div 0.85 = 12,612$ Wh/day. Assuming a worst-case psh = 5 h/day, this means an array size of $12,612 \div 5 = 2,522$ W will be needed.

This can be achieved with twenty 125 W modules in a 4-series-by-5-parallel array, or with 15 167 W modules in a 3-series-by-5-parallel array, or by any number of other module combinations that do not exceed the charge controller maximum input voltage limit when running open circuit. It must be remembered that to achieve the nominal 48 V source circuit output, it may take two, three, or four modules in series. Thus, each additional parallel module will require additional series modules to achieve the system voltage.

Figure 20.22 shows the block diagram of the schoolhouse system.

To this point, wind loading of the array has not been mentioned. In areas of high wind loads, the size of the module and the mounting method may or may not be adequate to meet high wind loading conditions. The final check on any PV system design must be a determination of whether the system will blow away in a high wind. This is especially undesirable considering the cost of a system as well as the fact that many systems are installed to provide power during emergencies, one of which might be a hurricane.

As a final note on system design, if an MPT charge controller is not used, then the array should be sized to provide 110% of the daily battery input Ah, using the maximum power current of the array. In this case, the daily battery input Ah is 201, so the array should be designed for 221 Ah. For 5 psh, this converts to an array current of 20.2 A. The 125 W modules have a 7 A maximum power current, so this means six in parallel will produce 42 A, which is close to the required amount. So the MPT controller saves four modules, or 500 W. At \$4/W, this is a savings of \$2000, which more than pays for the additional cost of the MPT charge controller.

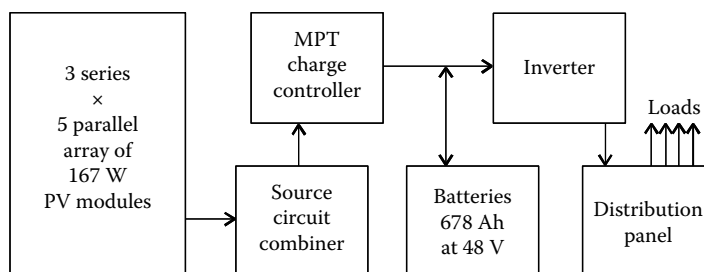


FIGURE 20.22
Block diagram of schoolhouse PV system.

It is interesting to look at a life cycle cost of the schoolhouse system. Using a discount rate of 5% and an inflation rate of 3%, an LCC cost estimate can be tabulated. In Table 20.1, it is assumed that the batteries are 12 V, 110 Ah, sealed, AGM lead–acid, deep-cycle batteries with a rated lifetime of 8 years and a cost of \$150 each.

To compare this system with a gasoline generator, note that the generator would need to generate 8 kWh/day for 20 years by operating 8 h/day over this period. A typical small gasoline generator will generate 4 kWh/gal [4], so will require 2 gal of gasoline per day. The generator will require an oil change every 25 h, a tune-up every 300 h, and a rebuild every 3000 h. The LCC analysis for the generator is shown in Table 20.2. Clearly, the PV system is the preferred choice. And this does not even account for the noise-free, pollution-free performance of the PV system.

TABLE 20.1

Life Cycle Costs of a Stand-Alone Photovoltaic System for a Schoolhouse

Item	Cost (\$)	Present Worth (\$)	LCC (%)
<i>Capital costs</i>			
Array	10,000	10,000	38.1
Batteries	3,600	3,600	13.7
Array mount	1,250	1,250	4.8
Controller	500	500	1.9
Inverter	500	500	1.9
BOS	1,000	1,000	3.8
Installation	2,000	2,000	7.6
<i>Recurring costs</i>			
Annual inspection	50	839	3.2
<i>Replacement costs</i>			
Batteries—8 years	3,600	3,087	11.8
Batteries—16 years	3,600	2,646	10.1
Controller—10 years	500	413	1.6
Inverter—10 years	500	413	1.6
Totals		26,247	100

TABLE 20.2

Life Cycle Costs of a Gasoline Generator for a Schoolhouse

Item	Cost (\$)	Present Worth (\$)	LCC (%)
<i>Capital costs</i>			
Generator	750	750	2
<i>Recurring costs</i>			
Annual fuel	1825	30,593	73
Annual oil changes	235	3,939	9
Annual tune-ups	345	4,107	10
Annual rebuilds	146	2,447	6
		41,836	100

20.1.8.3 Straightforward Utility-Interactive PV System

Since utility-interactive PV systems are backed up by the utility, they do not need to be sized to meet any particular load. Sometimes they are sized to meet emergency loads, but if the system does not have emergency backup capabilities, then they may be sized to fit on a particular roof, to meet a particular budget, or to incorporate a particular inverter. Suppose the sizing criterion is the inverter, which has the following specifications:

DC input	Input voltage range	250–550 V
	Maximum input current	11.2 A
AC output	Voltage	240 V, 1 ϕ
	Nominal output power	2200 W
	Peak power	2500 W
	Total harmonic distortion	<4%
	Maximum efficiency	94%

Note that if the input voltage is 550 V and the input current is 11.2 A, the input power would be 6160 W. Since the peak output power of this inverter is 2500 W, it would not make sense to use a 6160 W array, since most of the output would be wasted, and it might be easier to damage the inverter. So an array size of about 2500 W would make better sense.

Since cloud focusing can increase the short-circuit output current of a module by 25%, the array rated short-circuit current should be kept below $11.2 \div 1.25 = 8.96$ A. The number of modules in series will depend upon the maximum voltage of the array at low temperatures remaining <550 V and the minimum array voltage at high array operating temperatures remaining >250 V.

NEC (Table 690.7 in Reference [16]) specifies multipliers for open-circuit voltages for different low-temperature ranges. For design purposes, suppose the coldest array temperature will be -25°C and the hottest array temperature will be 60°C . NEC (Table 690.7 in Reference [16]) requires a multiplier of 1.25 for the array open-circuit voltage, so the maximum rated array open-circuit voltage must be less than $550 \div 1.25 = 440$ V. If the open-circuit voltage of a module decreases by $0.47\%/^{\circ}\text{C}$, then it will decrease by $35 \times 0.47 = 16.45\%$ when the module is operated at 60°C . Thus, the 25°C rated array open-circuit voltage needs to be greater than $250 \div 0.8355 = 299$ V.

The next step is to look at PV module specifications. One module has $P_{\text{max}} = 125$ W, $V_{\text{OC}} = 21.0$ V, and $I_{\text{SC}} = 7.2$ A. Thus, the maximum number of these modules in series will be $440 \div 21.0 = 20.95$, which must be rounded down to 20. The minimum number in series will be $299 \div 21.0 = 14.24$, which must be rounded up to 15. Checking power ratings gives 2500 W for 20 modules and 1875 W for 15 modules. Since 2500 W does not exceed the inverter rated maximum output power, and since the array will normally operate below 2500 W, it makes sense to choose 20 modules, as long as the budget can afford it and as long as there is room for 20 modules wherever they are to be mounted. Figure 20.15d shows the block diagram for this system.

The life cycle cost of this type of system is usually looked at somewhat differently than that of the schoolhouse system. In this case, the cost of electricity generated is usually compared with the cost of electricity from the utility, neglecting pollution and other externalities. In regions with an abundance of trained installers, it is currently possible to complete a grid-connected installation for less than \$7/W. The installed cost of the 2,500 W system would thus be approximately \$17,500. It is reasonable to expect an average daily output of

10 kWh for this system in an area with an average of 5 psh. The value of the annual system output will thus be approximately \$365 at \$0.10/kWh. This amounts to a simple payback period of 48 years—almost double the expected lifetime of the system.

Of course, what is not included in the analysis is the significant amount of CO₂ production that is avoided, as well as all the other pollutants associated with nonrenewable generation. Also not included are the many subsidies granted to producers of nonrenewable energy that keep the price artificially low. For that matter, it assumes that an abundance of fossil fuels will be available at low cost over the lifetime of the PV system. Finally, it should be remembered that the energy produced by the PV system over the lifetime of the system will be at least four times as much as the energy that went into the manufacture and installation of the system.

If the cost of the system could be borrowed at 3% over a period of 25 years, the annual payments would be \$1005. Thus, if a grid-connected system is considered, unless there is a subsidy program, it could not be justified with simple economics. It would be purchased simply because it is the right thing to do for the environment. Of course, if the installation cost were less, the value of grid electricity were more, and the average sunlight were higher, then the numbers become more and more favorable. If the values of externalities, such as pollution, are taken into account, then the PV system looks even better.

Because of the cost issue, as well as local PUC regulations or lack of them, ill-defined utility interface requirements, etc., few grid-connected PV systems are installed in areas that do not provide some sort of incentive payments. In some cases, PV system owners are paid rebates based on dollars per watt. The problem with this algorithm is that there is no guarantee that the system will operate properly. In other cases, PV system owners are guaranteed a higher amount per kWh for a prescribed time, which guarantees that the system must work to qualify for incentive payments. In fact, at present, more kW of PV is installed annually in grid-connected systems than are installed in stand-alone systems [17].

20.1.9 Present Status of Technology and Future Challenges for PV Systems

The PV technology has made tremendous progress in the last decade, where the PV system deployment around the world has been increasing at an average annual rate of more than 50%. The costs of PV panels have come down by an order of magnitude over the last decade. The present panel costs for both polycrystalline silicon and thin-film panels are less than \$0.75/W, which has resulted in the system costs of \$2–\$2.50/W for small-scale systems and around \$1.50–\$2.00/W for large-scale systems. Large-scale PV systems are being constructed in the range 1 MW to as large as hundreds of MW. The challenge is to reduce the panel costs further to less than \$0.50/W and the BOS costs also to less than \$0.50/W, which will make PV competitive without government incentives. For PV panels, this will be achieved by further improvements in panel efficiencies. As of 2013, the efficiencies achieved in the laboratory for the various PV technologies are given in Table 20.3. Efficiency table for concentrating PV is given in Section 20.3.

The PV industry is currently engaged in an effort to ensure quality control at all levels of system deployment, including manufacturing, distribution, design, installation, inspection, and maintenance. At this point in time (2013), most of the technical challenges for PV system components have been overcome. PV modules are very reliable, and most are warranted for 25 years. Reliability of other system components continues to improve, and at this point, PV system power conditioning equipment has proven to operate very reliably.

TABLE 20.3Confirmed Terrestrial Cell and Submodule Efficiencies Measured under the Global AM1.5 Spectrum (1000 W/m²) at 25°C

Classification	Effic. (%)	Area (cm ²)	V _{oc} (V)	J _{sc} (mA/cm ²)	FF (%)
<i>Silicon</i>					
Si (crystalline)	25.0 ± 0.5	4.00 (da)	0.706	42.7	82.8
Si (multicrystalline)	20.4 ± 0.5	1.002 (ap)	0.664	38.0	80.9
Si (thin-film transfer)	20.1 ± 0.4	242.6 (ap)	0.682	38.14	77.4
Si (thin-film submodule)	10.5 ± 0.3	94.0 (ap)	0.492	29.7	72.1
<i>III-V cells</i>					
GaAs (thin film)	28.8 ± 0.9	0.9927 (ap)	1.122	29.68	86.5
GaAs (multicrystalline)	18.4 ± 0.5	4.011 (t)	0.994	23.2	79.7
InP (crystalline)	22.1 ± 0.7	4.02 (t)	0.878	29.5	85.4
<i>Thin-film chalcogenide</i>					
CIGS (cell)	19.6 ± 0.6	0.996 (ap)	0.713	34.8	79.2
CIGS (submodule)	17.4 ± 0.5	15.993 (da)	0.6815	33.84	75.5
CdTe (cell)	18.3 ± 0.5	1.005 (ap)	0.857	26.95	77.0
<i>Amorphous/nanocrystalline Si</i>					
Si (amorphous)	10.1 ± 0.3	1.036 (ap)	0.886	16.75	67.8
Si (nanocrystalline)	10.1 ± 0.2	1.199 (ap)	0.539	24.4	76.6
<i>Photochemical</i>					
Dye sensitized	11.9 ± 0.4	1.005 (da)	0.744	22.47	71.2
Dye sensitized (submodule)	9.9 ± 0.4	17.11 (ap)	0.719	19.4	71.4
<i>Organic</i>					
Organic thin film	10.7 ± 0.3	1.013 (da)	0.872	17.75	68.9
Organic (submodule)	6.8 ± 0.2	395.9 (da)	0.798	13.50	62.8
<i>Multijunction devices</i>					
InGaP/GaAs/InGaAs	37.7 ± 1.2	1.047 (ap)	3.014	14.57	86.0
a-Si/nc-Si/nc-Si (thin film)	13.4 ± 0.4	1.006 (ap)	1.963	9.52	71.9
a-Si/nc-Si (thin-film cell)	12.3 ± 0.3	0.962 (ap)	1.365	12.93	69.4
a-Si/nc-Si (thin-film submodule)	11.7 ± 0.4	14.23 (ap)	5.462	2.99	71.3

Source: Adapted from Green, M.A. et al., *Prog. Photovolt. Res. Appl.*, 21, 11, 2013.

Notes: ap, aperture area; t, total area; da, designated illumination area; nc-Si, nanocrystalline or microcrystalline Silicon; a-Si, amorphous silicon.

So, once installed properly, modern PV systems require very little maintenance. In fact, systems without batteries require almost no maintenance.

The biggest challenge for PV systems is storage. As the contribution of PV in the grid continues to increase, the electrical utilities are becoming more concerned with the transients in the grid due to solar radiation transients. Battery storage, however, is very expensive. With the cost of battery storage of over \$500/kWh_e, batteries are not cost-effective in large-scale systems. Although a great deal of battery and supercapacitor research is being conducted around the world, the costs are not expected to get below \$100/kWh_e in this decade.

If the cost of a PV system were to be measured in energy units, then perhaps the importance of PV systems would become more obvious. By the early 1980s, Odum and Odum [17] and Henderson [18] had proposed using the Btu as the international monetary standard.

However, at that time, they reported that the EPBT of PV panels was more than their entire lifetime. In the last decade, Battisti and Corrado [19] reported EPBTs of approximately 3 years and $\text{CO}_{2\text{eq}}$ payback times of about 4 years for PV systems. Since that time, the EPBTs have come down further. By 2011, the EPBTs of commercial rooftop PV systems had reduced to as little as 0.68 year for CdTe technology and 1.96 years for monocrystalline silicon [1]. Since the life expectancy of a PV system exceeds 20–25 years, this equates to as much as 30:1 return on the energy invested.

Nomenclature

C	Speed of light (3×10^8 m/s)
D_x	Minority carrier diffusion length
E	Energy of photon (eV)
$F(x)$	Intensity of the photon beam as a function of penetration depth into the material
F_0	Initial intensity of the photon beam at the material surface
h	Planck's constant (6.625×10^{-34} J s)
I	Current (A)
I_1	Short-circuit current (A)
k	Boltzmann's constant (1.381×10^{-23} J/K)
L	Latitude angle
L_x	Diffusion length
n	Electron concentration
n	Day of year
N_a	Density of acceptor impurities
N_d	Density of donor impurities
n_i	Intrinsic carrier concentration
p	Hole concentration
P_{max}	Maximum power (W)
Q	Charge of an electron (1.602×10^{-19} C)
T	Junction temperature (K)
V	Voltage (V)
V_{OC}	Open-circuit voltage (V)
X	Depth of penetration into material

Symbols

Λ	Wavelength (μm)
A	Absorption constant
A	Altitude angle of the sun
Δ	Declination angle
Γ	Azimuth angle of the sun
Ω	Hour angle
Ω	Resistance (ohm)
τ_x	Minority carrier lifetime

Acronyms

$a\text{-Si}$	Amorphous silicon
CVD	Chemical vapor deposition

EHP	Electron–hole pair
GFDI	Ground fault detection and interruption
HIT	Heterojunction with intrinsic thin layer
LCB	Linear current booster
MPT	Maximum power tracker
psh	Peak sun hour

References

1. Wild-Scholten, M.J., Energy payback time and carbon footprint of commercial photovoltaic systems. *Solar Energy Materials and Solar Cells*. 2013, 119: 296–305.
- 1b. USDOE, http://www1.eere.energy.gov/solar/sunshot/reducing_technology_costs.html (accessed May 2014).
2. Green, M.A. et al., Solar cell efficiency tables. *Progress in Photovoltaics: Research and Applications*. 2013, 21: 1–11.
3. Goswami, D.Y. et al., *Principles of Solar Engineering*, 2nd edn. Taylor & Francis, Philadelphia, PA, 2000.
4. Messenger, R. and Ventre, G., *Photovoltaic Systems Engineering*, 2nd edn. CRC Press LLC, Boca Raton, FL, 2004.
5. Rosenblum, A.E. et al., *Proceedings of the 29th IEEE Photovoltaic Specialists Conference*, 2002, pp. 58–61.
6. Hanoka, J.I., *Proceedings of the 29th IEEE Photovoltaic Specialists Conference*, 2002, pp. 66–69.
7. Saitoh, T., Progress of highly reliable crystalline si solar devices and materials. In: Goswami, D.Y. and Boer, Karl W. (Eds.), *Advances in Solar Energy*, Vol. 16, Chapter 5. American Solar Energy Society, Boulder, CO, 2005, pp. 129–154.
8. www.ase-international.com (For information on EFG process).
9. Green, M.A. and Wenham, S.R., Novel parallel multijunction solar cell. *Applied Physics Letters*. 1994, 65: 2907.
10. Bohland, J., Accelerated aging of PV encapsulants by high intensity UV exposure. In: *Proceedings of the 1998 Photovoltaic Performance and Reliability Workshop*, Cocoa Beach, FL, November 3–5, 1998.
11. Markvart, T. (Ed.). *Solar Electricity*. John Wiley & Sons, Chichester, U.K., 1994.
12. National Renewable Energy Laboratory, 30-year average of monthly solar radiation, 1961–1990, Spreadsheet Portable Data Files. http://rredc.nrel.gov/solar/old_data/nsrdb/redbook/sum2/ (accessed May 2014).
13. Krein, P.T., *Elements of Power Electronics*. Oxford University Press, New York, 1998.
14. IEEE 929-2000, IEEE recommended practice for utility interface of residential and intermediate photovoltaic (PV) systems. IEEE Standards Coordinating Committee 21, Photovoltaics, IEEE, 2000.
15. UL 1741, Standard for static inverters and charge controllers for use in photovoltaic power systems. Underwriters Laboratories, Inc., Northbrook, IL, May, 1999.
16. NFPA 70, National electrical code, 2002 Ed. National Fire Protection Association, Quincy, MA, 2002.
17. Odum, H.T. and Odum, E.C., *Energy Basis for Man and Nature*, 2nd edn. McGraw-Hill, New York, 1981.
18. Henderson, H., *The Politics of the Solar Age: Alternatives to Economics*. Anchor Press/Doubleday, Garden City, NY, 1981.
19. Battisti, R. and Corrado, A., Evaluation of technical improvements of photovoltaic systems through life cycle assessment methodology. *Energy*, 2005, 30: 952–967.

20.2 Thin-Film PV Technology

Hari M. Upadhyaya, Senthilarasu Sundaram, Aruna Ivaturi, Stephan Buecheler, and Ayodhya N. Tiwari

20.2.1 Introduction

20.2.1.1 Historical and Current Developments

Crystalline silicon (*c*-Si) technology has a lion's share in the present photovoltaic (PV) industry, contributing more than 85% through the cells and modules based on poly-, mono-, and multicrystalline wafer technology (Mints and Donnelly 2011). The recent growth rate of PV industry and market is phenomenal, with a substantial surge on average over 40% recorded globally during the last decade and expected to sustain the trend from short to medium time frame. During the early developmental phase of *c*-Si PV technology, the continuous feedstock support offered by Si-based electronics industry played a key role in its growth. The high purity and even second-grade wafer materials obtained at a relatively cheaper price proved favorable for PV industry as they led to a reasonable efficiency (η) figures for standard size modules (average $\eta > 16\%$ – 18%) and extremely good performance stability (more than 25 years) that are two essential requirements for any technology to successfully demonstrate its potential for market (Chopra et al. 2004; Jäger-Waldau 2004). However, continuously increasing demand for PV modules and the need for low-cost PV options in the last decade had stretched these advantages to the limit and had exposed some inherent disadvantages of *c*-Si technology, such as the scarcity of feedstock material, costly processing of materials and device fabrication steps, as well as the inability for monolithic interconnections. These, in turn, had restricted the potential of Si wafer technology and made it difficult to achieve PV module production cost below €1/W (1€ is about U.S. \$1.35), which was considered essential for cost-competitive generation of solar electricity (Hegedus and Luque 2003; von Roedern et al. 2005; Zweibel 2000). However, recently, there has been a dramatic upsurge in the production of *c*-Si modules in China for the last 2 years, which were made available at and below \$0.6/W and as low as \$0.50/W in some cases. While there is speculation that the low module cost from China perhaps did not reflect the real costs, the fact remains that the PV module prices have seen significant reduction in the recent years. The PV module cost depends on the total manufacturing cost of the module per square area, conversion efficiency, and long-term performance stability. Figure 20.23 gives an estimate of achievable cost with *c*-Si technology and comparison with projected achievable costs with other PV technologies. It was generally agreed that *c*-Si wafer technology would be unable to meet the low-cost targets, while thin-film technologies will have the potential to provide a viable alternative in the near future. However, the cost of modules from China available for as low as \$0.50/Wp recently has made these speculations look very weak as the gap between thin film and *c*-Si modules has shrunk considerably. Although the thin-film PV still has better potential to lower the cost of modules further, this will require appreciable increase in the energy conversion efficiencies of the technologies, in order to stay in competition with *c*-Si. Recently, the cost projection by First Solar for CdTe modules has shown a competitive cost of \$0.49/W for the module efficiencies over 14%. It is thus clear that thin-film technologies have to significantly improve their efficiencies in order to stay in competition with *c*-Si (Osborne 2013). The world record efficiency of 20.4% for small area and 17% efficient CdTe champion modules announced recently by First Solar and 20.9% small area efficiency

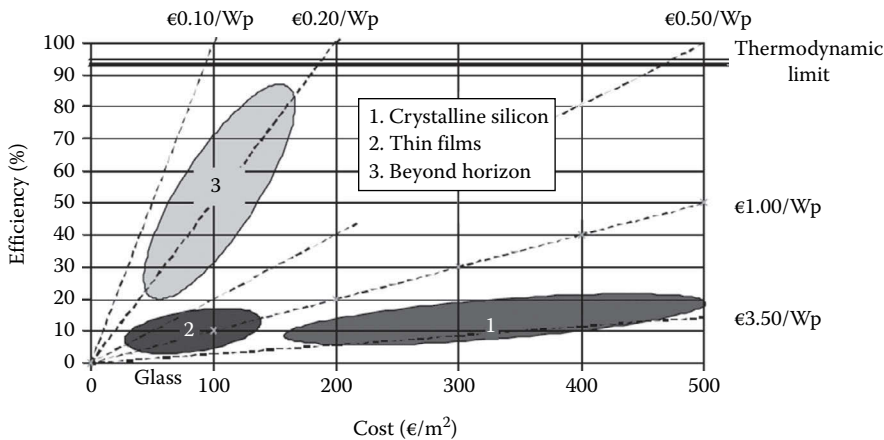


FIGURE 20.23

Comparison of estimated costs achievable with different PV technologies as a function of manufacturing cost (€/m²) and conversion efficiency. (Courtesy M. Green, UNSW, Sydney, New South Wales, Australia.)

achieved on CIGS technology by Solar Frontier and 16.4% CIGS modules by Avancis definitely show a great promise in a short span of time.

The PV market although appears to be promising, the share of the technologies remains very difficult to predict. An optimistic and ambitious forecast by Hanergy Solar with their multigigawatt production in a few years' time on *a*-Si, along with production on CIGS technology as well, provides a projection of about 50% market share by 2018 (Hanergy Annual Report 2013). However, a more conservative approach adopted by NPD Solarbuzz provides a forecast of around 10% share of thin-film technologies by 2020 (Colville 2014).

Figure 20.24 (NREL 2013) summarizes the best laboratory scale (cell area less than 1 cm²) efficiencies of some prominent thin-film technologies. Out of these, an efficiency of 20.8% achieved at ZSW (has been improved further by Solar Frontier to 20.9% on CIS recently), with CIGS, makes it the most efficient thin-film PV device that has narrowed the gap further between existing *c*-Si and thin-film technologies.

Silicon wafers are fragile, solar cell area is limited by the wafer size, and the modules are bulky, heavy, and nonflexible. To overcome some of the problems of *c*-Si wafer technology, efforts were made to develop monocrystalline and polycrystalline thin-film silicon solar cells on glass substrates, as reviewed by Bergmann (1999). However, these efforts to develop efficient crystalline silicon thin films on glass (CSG) have not gained much success over these years and efficiencies have been limited around or just over 10% mark with much more processing costs involved. One of the techniques used to form poly-Si films on glass has been based on solid phase crystallization (SPC) and had resulted in 10.5% efficient cells (Keevers et al. 2007). The open circuit voltage (V_{oc}) up to 500 mV was one of the stumbling blocks for its progress. The TU-Hamburg-Harburg and Helmholtz-Zentrum Berlin, Germany, presented a new type of poly-Si thin-film solar cell on glass using electron-beam crystallization (EBC) through liquid phase and have achieved an improved V_{oc} of 545 mV (Amkreutz et al. 2011). The EBC process is based on a line-shaped electron beam, which is scanned across the silicon layer on glass with a typical rate of 1 cm/s. Recently, an analogue laser crystallization (LC) process has been investigated as an alternative to EBC, using which the University of New South Wales in Australia and Suntech R&D, Australia, have

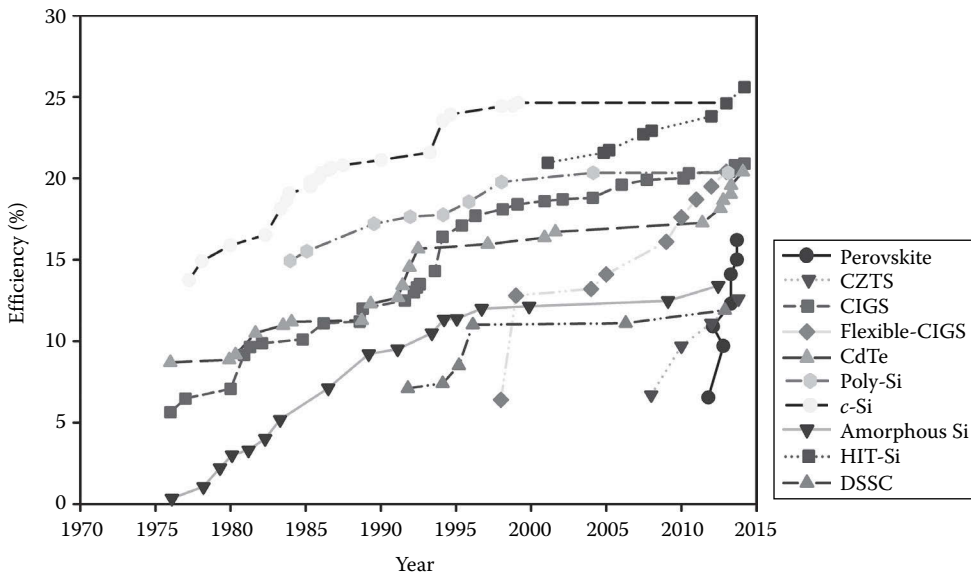


FIGURE 20.24

Development of *champion* thin-film solar cell efficiencies with emerging PV. (Based on Efficiency chart, National Renewable Energy Laboratory (NREL), 2014, <http://www.nrel.gov/ncpv/>.)

recently reached a new record single-junction efficiency of 11.7% for poly-Si thin-film solar cells on glass (Dore et al. 2014). A current status and some latest developments on CSG have been covered in a report (Becker et al. 2013) recently. It is expected that by using the aforementioned techniques, 15% efficient single junction CSG can be achieved in near future (Rech 2013).

It has been realized that application of thin-film technologies to grow solar cells and modules based on other materials can prove to be an alternative to the silicon-wafer technologies. However, the efficiency of the thin-film PV technologies has to match or exceed the current *c*-Si technology. Thin-film deposition of materials of required quality and suitable properties depends on the processes used and the control of several parameters. However, once optimized, these methods provide over an order of magnitude cheaper processing cost and low energy payback time, which is certainly a big advantage. For example, even at lower module efficiencies as compared to *c*-Si, the cost of CdTe modules have lower payback time owing to less energy intensive and easier processing steps involved.

Research on alternative to *c*-Si already started over four decades back, considering that it has low absorption coefficient ($\sim 10^3 \text{ cm}^{-1}$) and its narrow bandgap ($E_g \sim 1.1 \text{ eV}$). Some of the most interesting semiconducting materials that have received considerable attention are cadmium telluride (CdTe), gallium arsenide (GaAs), indium phosphide (InP), zinc phosphide (Zn_3P_2), copper sulfide (Cu_2S), copper indium diselenide (CIS), copper indium gallium diselenide (CIGS), and copper zinc tin diselenide (CZTS). These all have the electronic and optical properties suitable for the efficient utilization of the sun's spectrum (see Table 20.4 for bandgaps). Multijunction solar cells based on III-V materials (GaAs, InP, GaSb, GaInAs, GaInP, etc.) show high efficiency, exceeding 35%, but due to the high production cost and low abundance of their constituent applications materials, these solar cells are not considered suitable for cost-effective terrestrial applications though they are still very important for space PV applications.

TABLE 20.4

Bandgap of Different Semiconductor Materials Suitable as Light Absorber in Solar Cells

Compound/Alloys	Bandgap (eV)	Compound/Alloys	Bandgap (eV)
<i>c</i> -Si	1.12	Zn ₃ P ₂	1.50
<i>a</i> -Si	1.70	CuInSe ₂	1.04
GaAs	1.43	CuGaSe ₂	1.68
InP	1.34	Cu(In,Ga)Se ₂	1.20
Cu ₂ S	1.20	CuInS ₂	1.57
CdTe	1.45	Cu(In,Ga)(S,Se) ₂	1.36
Cu ₂ ZnSnS ₄	1.5	Cu ₂ ZnSnSe ₄	1.0

Thin-film technology has answers and potential to eliminate many existing bottlenecks of *c*-Si PV programs experienced at different levels from module production to its applications viz. space programs and BIPV. Thin-film PV modules are manufactured on either rigid glass substrates or flexible substrates (thin metallic or plastic foils). Some of the advantages of the thin-film technologies are the following:

- The high absorption coefficient ($\sim 10^5 \text{ cm}^{-1}$) of the absorber materials is about 100 times higher than *c*-Si (Figure 20.25); thus, about 1–2 μm of material thickness is sufficient to harness more than 90% of the incident solar light. This helps in reducing the material mass significantly to make modules cost effective.
- The estimated energy payback time of the thin-film PV is considerably lower than that of *c*-Si PV. Estimation suggests that CdTe has the lowest payback time among all PV technologies. With recent improved cell and modules efficiencies of 17%, the payback time could be as low as 6 months.

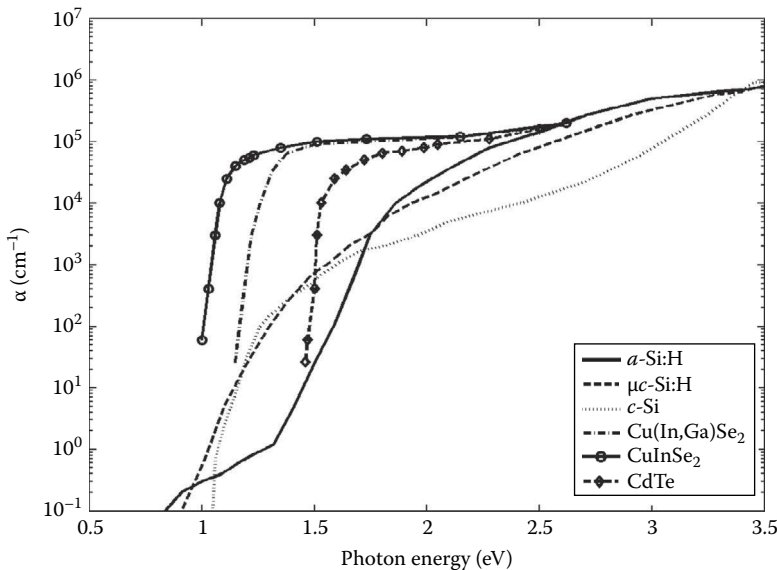


FIGURE 20.25

The optical absorption (α) versus photon energy of the *c*-Si and some of the prominent light-absorbing materials that are used in thin-film solar cells.

- The formation of heterojunction and better device engineering for reduction of photon absorption losses and enhanced collection of photogenerated carriers are possible.
- Large-area deposition (in the order of m^2) along with the monolithic integration (interconnection of cells during processing of rigid and flexible devices) is possible that minimizes area losses, handling, and packaging efforts.
- Roll-to-roll manufacturing of flexible solar modules is possible that gives high throughput and thus can further reduce the energy payback time significantly.
- Tandem or multijunction devices could be realized to utilize full solar spectrum to achieve higher efficiency devices. A theoretical limit of 66.7% had been estimated for large number of multiple junction, which can cover the entire spectrum of the sun (Honsberg et al. 2001; Shockley and Queisser 1961).
- Flexible and lightweight PV facilitates several attractive applications.

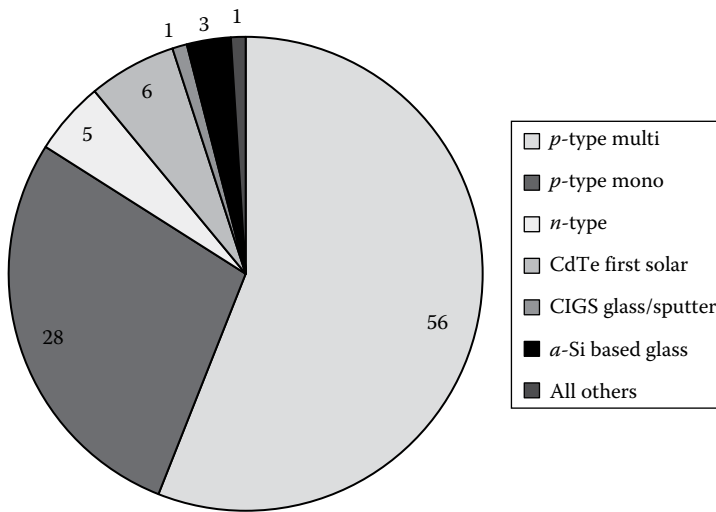
Historically, cadmium sulfide and copper sulfide (CdS/Cu_2S) heterojunctions were one of the early technologies almost contemporary to *c*-Si but could not survive due to the astounding success of *c*-Si technology that was efficient, stable, backed by electronic industries and widely supported by space programs. Despite Cu_xS having stability issues, the technology went to pilot production in the late 1970s or early 1980s. But with the advent of *a*-Si and CdTe thin-film solar cells, it was abandoned before mid-1980s.

Currently, *a*-Si, CdTe, and CIGS are considered the mainstream thin-film technologies. Out of these, *a*-Si has suffered some setbacks due to difficulties in improving the stabilized efficiency numbers and bankruptcy issues of the leading company United Solar recently; however, there is a good promise on reemergence of this technology with newer ways of achieving high efficiency in the future. Besides, CdTe and CIGS have not only proven potential to become leading technologies, but they have already achieved significant production capacities around multi-GW per year recently through the efforts of First Solar and Solar Frontier. Currently, the world record efficiencies in both CdTe and CIGS technologies are led by the aforementioned companies.

Figure 20.26 gives the market share of all the leading PV technologies including *c*-Si based on the cumulative deployment by 2013. Their thin-film market share is about 10%, with CdTe being leader, with 6% share on absolute scale.

Recently, several companies have started production-related activities and production volume is expected to increase during next few years. Recent developments on a new technology on organic and dye-sensitized solar cells (DSSCs), especially solid-state perovskite-based solar cells (a kind of solid state analogue of DSSCs), appear to be quite interesting. The efficiency figures for this technology has taken an unprecedented leap from near 4% in 2009 (Kojima et al. 2009) to 17% in 2014 (Snaith and coworkers 2014; Bennett 2014) (described in a separate section later). These technologies with their low-temperature and cheaper processing cost on flexible substrates (Docampo et al. 2013; Kumar et al. 2013) make them potentially very attractive for various niche applications. However, there are important issues of instability and degradation, which need to be addressed. Perovskite solar cells are at infancy of their development at the moment and would require considerable efforts and time to come out as a commercially viable option.

Table 20.5 summarizes the current status of thin-film solar cell and module development at laboratory and industrial level on rigid and flexible substrates (with one exception). These contain some latest developments and global efforts to make thin-film PV technology a viable option for cost-effective and competitive electrical energy production.

**FIGURE 20.26**

Worldwide market share of the dominant PV technologies by cumulative deployment end 2013. (Adapted from The worldwide market share of the dominant PV technologies by cumulative deployment end 2013, Solar Buzz, Report on PV equipment quarterly, 2013, <http://www.solarbuzz.com/reports/pv-equipment-quarterly>.)

20.2.1.2 Cost Potentials and Material Availability Issues

Estimates in the past decade had suggested that solar cell production costs as low as €0.30/W are possible depending on the volume of production (Bruton et al. 1997; Keshner and Arya 2004; Woodcock et al. 1997). At present, there is a significantly large gap between the efficiencies of the solar cells at the R&D level and those at the industrial modules level because of the process scalability–related issues during the early phase of industrial development. The current production cost of the thin-film PV modules is rather high because of low volume of production through pilot-production lines or small capacity (less than 30 MW) plants. However, with larger production volumes and higher module efficiencies, the cost is expected to decrease significantly in near future. It is estimated on the basis of the trend derived from the past experiences of cumulative production versus price variations (learning curve) that the module prices decrease by 20% for every doubling of the cumulative production (Surek 2003). These trends had predicted that with a growth rate of 25%, the cumulative production would reach ~75 GW by year 2020 and the target cost below \$1/Wp was achievable with existing thin-film technologies. It is striking to note that the cumulative production in 2013 was alone close to 140 GW and set to achieve annual production of about 50 GW in 2014 (Burger 2013). More surprisingly, what was not believed at that time, the *c*-Si technology has tremendously brought down the module cost to as low as \$0.5/Wp (Metha 2013). An excellent cost estimation and projection of the PV technologies has been made by U.S. Department of Energy (Sunshot Vision Study February 2012), with a mission to achieve future affordable electricity price below grid parity. This in-depth analysis was conducted by the National Renewable Energy Laboratory (NREL) with contributions from the Solar Energy Industries Association, Solar Electric Power Association, and many other related organizations.

Currently, the conventional module assembly procedures used by the *c*-Si industries and adopted by thin-film industries restrict the overall cost of the thin-film modules.

TABLE 20.5

Efficiencies of Solar Cells and Modules Based on Rigid and Flexible Substrates for Various Technologies

	Types of Solar Cells	Companies/ Institutions	Efficiency (%)	Area (cm ²)(Designed Area Illumination [da]; Aperture Area [ap]; Total Area [t])	Test Center (and Date)	Description/Comments	References
Silicon single cell	Si (crystalline)	University of New South Wales	25.0 ± 0.5	4.00 (da)	Sandia (3/1999)	Structure is similar to passivated emitter and rear locally diffused (PERL) structure. Adopted hexagonally symmetric honeycomb surface structure.	Zhao et al. (1998)
	Si (multicrystalline)	Fraunhofer institute for solar energy (FhG-ISE).	20.4 ± 0.5	1.002 (ap)	NREL (5/2004)	Wet oxidation for rear surface passivation.	Schultz et al. (2004)
	Si (large crystalline)	Panasonic	24.7 ± 0.5	101.8 (t)	AIST (12/2012)	Heterojunction with intrinsic thin layer.	Kinoshita et al. (2011)
	Si (large multicrystalline)	Q-Cells	19.5 ± 0.4	242.7 (t)	FhG ISE(03/2011)	Laser-fired contacts.	Engelhart et al. (2010)
	Si (thin-film transfer)	Solexel	20.1 ± 0.4	242.6 (ap)	NREL (10/2012)	A large area (15.6 cm × 15.6 cm) but thin (43 μm) silicon cell transferred from a reusable template.	Moslehi et al. (2012)
Silicon Modules	Si (crystalline)	University of New South Wales/ Goehermann	22.9 ± 0.6	778 (da)	Sandia (9/1996)	A flat-plate module made from 50 single cells.	Zhao et al. (1997)
	Si (large crystalline)	SunPower	22.4 ± 0.6	15775 (da)	NREL (8/2012)		Swanson (2012)
	Si (multicrystalline)	Q-Cells	18.5 ± 0.4	14661 (ap)	FhG-ISE (1/2012)	60 serial cells connected.	Pvtech.org
	Si (thin-film poly crystalline)	Pacific Solar	8.2 ± 0.2	661 (ap)	Sandia (7/2002)	Thin film coated on glass with <2 μm thickness.	Basore (2002)

(Continued)

TABLE 20.5 (Continued)

Efficiencies of Solar Cells and Modules Based on Rigid and Flexible Substrates for Various Technologies

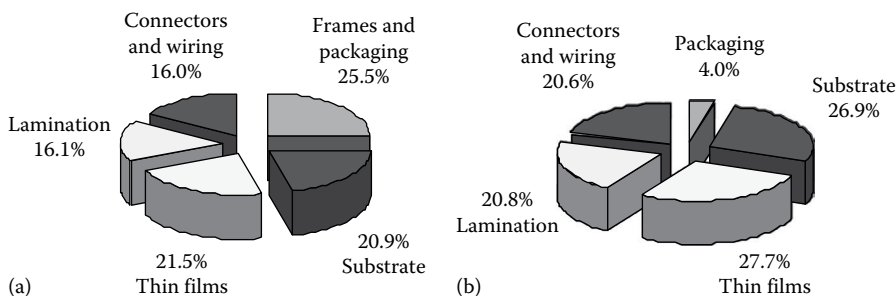
	Types of Solar Cells	Companies/ Institutions	Efficiency (%)	Area (cm ²)(Designed Area Illumination [da]; Aperture Area [ap]; Total Area [t])	Test Center (and Date)	Description/Comments	References
Thin-film solar cells	GaAs thin film	Alta devices	28.8 ± 0.9	0.9927 (ap)	NREL (5/2012)	Single-junction devices under nonconcentrated sunlight.	Kayes et al. (2011)
	GaAs (multicrystalline)	Research Triangle Institute, NC, United States	18.4 ± 0.5	4.011 (t)	NREL (11/1995)	Thin film grown on Ge substrates.	Venkatasubramanian et al. (1997)
	InP (crystalline)	Spire	22.1 ± 0.7	4.02 (t)	NREL (4/1990)	MOCVD grown with graded bandgap.	Keavney et al. (1990)
	Cu(In,Ga)Se ₂	ZSW	20.8 ± 0.6	0.9974 (ap)	FhG-ISE (10/2013)	CIGS on glass substrate.	Jackson et al. (2011)
	Cu(In,Ga)Se ₂	Empa	20.4 ± 0.4		FhG-ISE(9/2012)	CIGS thin film on polyamide flexible solar cells.	Chirilă et al. (2013)
	GaInP	NREL	20.8 ± 0.6	0.2491 (ap)	NREL (5/2013)	Made from high bandgap.	Geisz et al. (2013)
	CdTe	First Solar & GE Tech	20.4 ± 0.4	1.0055 (ap)	Newport (6/2013)		Firstsolar.com
	CuInGaSse (CIGSS)	Showa Shell/ Tokyo University of Science	19.7 ± 0.5	0.496 (da)	AIST (11/2012)	Efficiency extracted from 30 × 30 cm ² sized submodule.	Nakamura et al. (2013)
	Cu ₂ ZnSnS ₄ (CZTS)	Solar Frontier & IBM labs	12.6 ± 0.5	0.42 (da)	AIST (7/2013)		Cleantechnia.com
	Perovskite thin film	EPFL	14.1 ± 0.3	0.2090 (ap)	Newport (5/2013)	Sensitization approach. Perovskite replaced dye molecules.	Burschka et al. (2013)

(Continued)

TABLE 20.5 (Continued)

Efficiencies of Solar Cells and Modules Based on Rigid and Flexible Substrates for Various Technologies

	Types of Solar Cells	Companies/ Institutions	Efficiency (%)	Area (cm ²)(Designed Area Illumination [da]; Aperture Area [ap]; Total Area [t])	Test Center (and Date)	Description/Comments	References
Excitonic solar cells	Organic thin film	Mitsubishi Chemicals	11.1 ± 0.3	0.159 (ap)	AIST (10/2012)		Service (2011)
	DSSCs	Sharp	11.9 ± 0.4	1.005 (da)	AIST (9/2012)	Monolithic dye sensitized solar cells .	Komiya et al. (2011)
	DSSCs) minimodule	Sony	9.9 ± 0.4	17.11 (ap)	AIST (8/2010)	Eight parallel cells .	Morooka et al. (2009)
	DSSCs submodule	Sharp	8.8 ± 0.3	398.9 (da)	AIST (9/2012)	26 series cells connected .	Komiya et al. (2011) and Kawai (2013)
	Organic (minimodule)	Toshiba	8.5 ± 0.3	25.02 (da)	AIST (8/2013)	Four series cells connected.	Hosoya et al. (2013)
	Organic (submodule)	Toshiba	6.8 ± 0.2	395.9 (da)	AIST (10/2012)	15 series cells connected.	Hosoya et al. (2012)
Multijunction Solar cells	5J GaAs/InP bonded	Spectrolab	38.8 ± 1.9	1.021 (ap)	NREL (7/2013)	5 junctions.	Chiu et al. (2014)
	InGaP/GaAs/InGaAs	Sharp	37.9 ± 1.2	1.047(ap)	AIST (2/2013)		Sasaki et al. (2013)
	<i>a</i> -Si/nc-Si/nc-Si (thin film)	LG electronics	13.4 ± 0.4	1.006 (ap)	NREL (7/2012)		Ahn et al. (2012)
	<i>a</i> -Si/nc-Si (thin-film cells)	Kaneka	12.3 ± 0.4	0.962 (ap)	AIST (7/2011)		Kaneka-solar.com
	<i>a</i> -Si/nc-Si (thin-film minimodule)	Kaneka	9.9 ± 0.4	14.23 (ap)	AIST (9/2004)		Yoshimi et al. (2003)
Concentrator cell	Si (single cell)	Amonix	27.6 ± 1.0	1.00 (da)	FhG-ISE (11/2004)	92 suns illumination using backcontact method.	Slade and Garboushian (2005)
	GaAs (single cell)	FhG-ISE	29.1 ± 1.3	0.0505 (da)	FhG-ISE (3/2010)	Concentrated at 117 suns.	FhG-ISE
	CIGS (thin film)	NREL	22.8 ± 0.9	0.100 (ap)	NREL (8/2013)	15 suns illumination.	NREL
	InGaP/GaAs/InGaAs	Sharp	44.4 ± 2.6	0.1652 (da)	FhG-ISE (4/2013)	302 suns illumination on inverted metamorphic cells.	Sharp Press Release (2012)

**FIGURE 20.27**

Distributions and breakup of the materials cost in (a) framed and (b) unframed *a*-Si based modules.

Thus, the advantage of using *less material* in thin-film technology under *back end* schemes of assembling is drastically reduced. Some frameless mounting schemes (PV laminates on membranes) have also been developed and pursued for *a*-Si technology, which were shown to have potential to bring significant reduction in cost (Arya 2004). Figure 20.27 shows distribution of materials costs in framed (a) and unframed (b) Si-based modules. As may be compared, the cost of packaging and framing components has been drastically lowered from 25.5% to only 4%, which is significant; consequently, the cost reduction in materials and its processing will have more meaning with further advancements in technologies of all the components.

Tuttle et al. (2000, 2005) had given cost estimates of CIGS solar modules from 2 to 2000 MW/year capacity production plants including cost of equipment and materials. Similarly, there are several reviews and reports available that summarize the cost potential of thin-film modules in terms of different component costs and address some future concerns related with the cost and availability of materials: In, Ga, Se, and Te used in the leading thin-film technologies and future electricity generation cost estimation (Gross et al. 2013). An estimate in the subcontractor's report at NREL (Keshner and Arya 2004) suggested a decade ago that the production of these elements had to be accelerated in order to fulfill the demand of 2–3 GW/year generation of electricity.

An important report (out of DoE Solar Energy Technologies Programme and PV FAQ, www.nrel.gov) also exists (U.S. Department of Energy 2005) that brings the judgment in favor of In, Ga, and Se and speculates that Ga and Se will not be constrained by supply, and a steady production growth rate of 0.16% per year for Se would be sufficient to meet the demand of annual PV production of 20 GW/year by 2050. Furthermore, it is also estimated that In will also keep a steady supply as it is a by-product of Zn, which is relatively higher in abundance and more in demand by various industries. There could be some concern about the availability of Te for multi-GW plants, but with the advancement in thin-film technology, the thickness of the material may be reduced by implementation of light-trapping schemes, thus relieving the burden on production of materials also through clever and efficient recycling methods. A good account of material scarcity issues (such as the sustainability of Te and In materials) that might arise when the production will reach several tens of GW capacity for the CdTe and CIGS technologies has been addressed by Candelise et al. 2011. The estimations made by the authors after reviewing the literature on claims of In and Te scarcity suggest that there is a high uncertainty in the estimates of the resource-constrained thin-film PV potential as well as in data and methodologies used to assess future availability of the targeted materials. The reviewed evidence does not support the contention that the availability of tellurium and

indium will necessarily constrain CdTe and CIGS technologies respectively in their ability to supply expected future PV market growth.

In the following sections, the frontline thin-film technologies such as *a*-Si, CdTe, and CIGS, along with some of the emerging technologies such as CZTS and recently explored perovskite solar cells, are discussed in detail relating to their material and device aspects, current status, and issues related with environmental concerns.

20.2.2 Thin-Film Silicon Solar Cells

20.2.2.1 Material and Properties

The oil crisis of early 1970s gave an impetus to the PV R&D activities and several concepts for thin-film PV started to emerge. The first report on thin-film *a*-Si based solar cells appeared in 1976 (Carlson and Wronski 1976). It took only 5 years to see the indoor consumer products appearing in the market with this technology in the 1980s, although it took a significant amount of time to understand the basics of the material and device properties and their inherent bottlenecks. Amorphous-Si is now the most studied and applied material for thin-film solar cells as compared to its other counterparts. Silicon has the advantage of the material being in abundance in the earth's crust; therefore, following the trends of *c*-Si technology, *a*-Si has developed over the years into an industrially mature technology (Rech and Wagner 1999). Besides, *a*-Si has several other non-PV applications that provided it an additional standing.

Crystalline Si has long-range atomic ordering extending up to a few centimeters size in the single crystals, whereas *a*-Si has got short-range atomic ordering of less than 1 nm, and thus, the material is not a crystal. Amorphous silicon has a disordered lattice showing localized tetrahedral bonding schemes but with broken Si-Si bonds of random orientation, as shown in Figure 20.28. These broken (or unsaturated) bonds are called *dangling bonds* and contribute to the defect density in the material. Because of disorder, the momentum conservation rules are relaxed and a higher absorption coefficient (α) is observed in *a*-Si material. The absorption coefficient of *a*-Si is about two orders of magnitude higher than the *c*-Si; thus, it only requires a couple of micron thickness for effective absorption and utilization of solar spectrum. However, due to predominant disordered structure, high

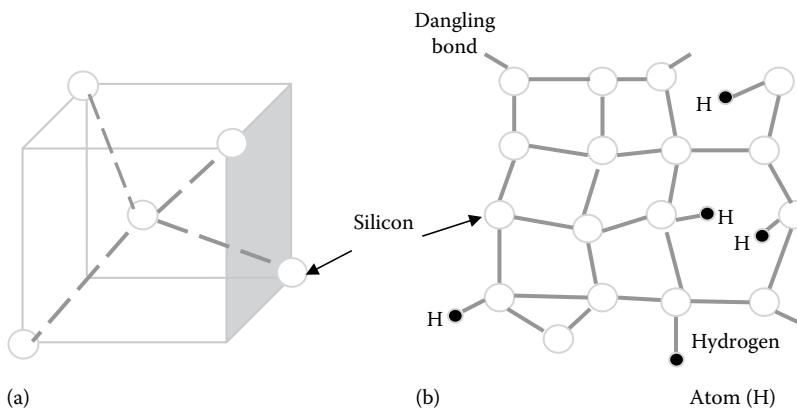


FIGURE 20.28

A schematic presentation of tetrahedral bonding scheme in crystalline Si (a) and network of *a*-Si:H exhibiting broken silicon atom dangling bonds, which are passivated by hydrogen atoms (b).

density ($\sim 10^{19} \text{ cm}^{-3}$) of localized defect states is created within the energy gap that causes the Fermi level pinning, and hence the material cannot be doped because the defect states act as trap for all free carrier generated in the material.

One effective way to overcome this problem is to passivate the unsaturated bonds of *a*-Si with the help of small size atoms that could get into the crystal and attach themselves with the available bonds. This is precisely done by adding 5%–10% atomic hydrogen into *a*-Si, which attaches itself to the uncoordinated bonds due to its high activity; this reduces the dangling bonds density from $\sim 10^{19}$ to $\sim 10^{15} \text{ cm}^{-3}$. At this order of defect density, the required doping of material is possible, and hence, the material can be made as *p*- or *n*-type using boron and phosphorous as dopants. However, the defect density still remains so high that even with high doping, the Fermi level is not significantly shifted; it remains mostly within the donor and defect levels at the center of the gap in the case of *n*-doping.

Amorphous silicon may be considered as an alloy of silicon with hydrogen. The distortion of the bond length and bond angle after passivation with hydrogen modifies the defect distribution and consequently changes the optical and electronic properties. By changing the deposition conditions (Guha et al. 1981, 1986; Vetterl et al. 2000), hydrogen-diluted microcrystalline silicon (μc -Si) can be obtained, which has rather different properties. Figure 20.25 compares the absorption coefficient of the *a*-Si:H, *c*-Si, and μc -Si:H along with some of the other PV materials. The absorption bands (plateau) appearing at low energy values for *a*-Si:H and μc -Si are ascribed to the presence of large density of midgap defects and band tail states. The absorption coefficient (α) of *c*-Si (mono-crystalline silicon wafers) and microcrystalline thin-film Si has more or less same onset of transition, but μc -Si has higher α in low wavelength (λ) region. However, α for μc -Si is lower than of *a*-Si; therefore, thicker μc -Si layers are required compared to *a*-Si for the absorption of solar spectrum. A stacked combination of the two—microcrystalline and amorphous Si layers—is attractive for absorption of the most useful part of the spectrum in thin layers. This has been successfully employed first by IMT Neuchatel, Switzerland, and later by several other groups to develop *a*-Si/ μc -Si tandem (also often called *micromorph*) solar cells.

The bandgap of *a*-Si can also be tailored by addition of O, C, and Ge to produce amorphous materials of wider or narrower bandgaps, for example, with the addition of C and Ge in *a*-Si:H, bandgaps of 2.2–1.1 eV are achievable but with inferior electronic properties. Table 20.6 provides the list of these alloys with their respective bandgaps. Suitable *a*-SiC:H and *a*-SiGe:H for solar cell devices have bandgaps ~ 2.0 and 1.3 eV, respectively.

TABLE 20.6

Energy Bandgaps (E_g) of Certain Alloys of *a*-Si:H with Germanium and Carbon Used in Multiple Junction Solar Cell Structures

Material (Semiconductor/Alloy)	E_g min (eV)	E_g max (eV)
<i>c</i> -Si	1.1	1.1
μc -Si:H	1.0	1.2
<i>a</i> -Si:H	1.7	1.8
<i>a</i> -SiC:H	2.0 (in 20% C)	2.2
<i>a</i> -SiGe:H	1.3 (in 60% Ge)	1.7
<i>a</i> -Ge:H	1.1	

20.2.2.2 Deposition Techniques

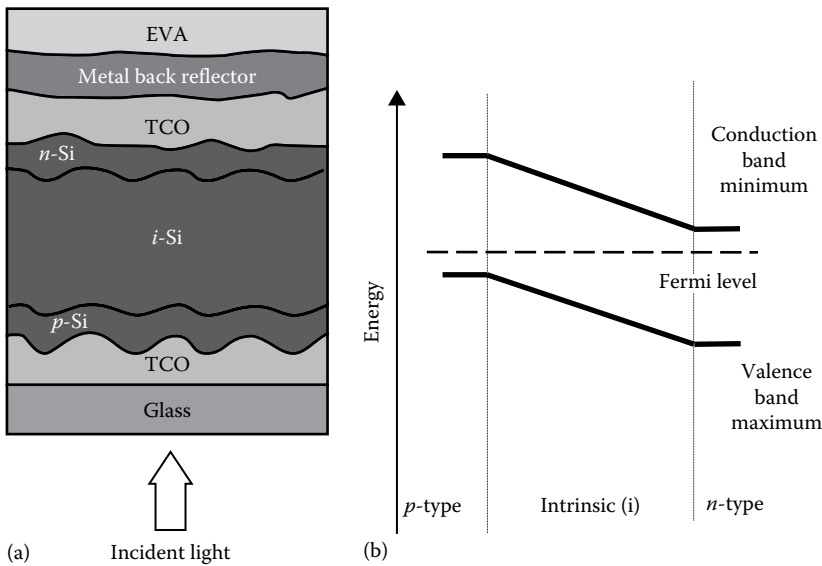
Perhaps the most important feature of *a*-Si material is that a wide range of temperatures, from room temperature to 400°C, can be used for its deposition. Room temperature deposition allows the use of a variety of substrates, viz., glass, metal, and plastic, and in particular the possibility to use low-cost plastic polyethylene terephthalate (PET) could be of significant advantage in reducing the cost of the modules. There are various processes used for the deposition of the *a*-Si:H material. Silane (SiH₄), which is the basic precursor gas, is used in nearly all processes using chemical vapor deposition (CVD) method but excluding sputtering that is not preferred for active semiconductor layers in *a*-Si:H. Typical deposition temperature for *a*-Si:H has to be below 500°C; otherwise, the incorporation of hydrogen in the film is not possible. At low substrate temperatures, the predissociation of SiH₄ does not take place easily. Hence, room temperature deposited layers give rise to inferior quality and efficiency. Therefore, plasma is used for dissociation of silane gas. Two most commonly used methods are plasma-enhanced chemical vapor deposition (PECVD) and glow discharge CVD. Typically, 13.56 MHz plasma excitation frequencies with optimal plasma excitation power at 0.1–1 mbar pressure are used. SiH₄ always diluted with hydrogen (~10%) is used in the deposition of *a*-Si:H, while increasing hydrogen dilution results in μ c-Si:H layers, but with lower growth rates. The typical deposition rates for *a*-Si cells (in R&D) is ~1 Å/s and results in fairly long deposition times (50 min for 0.3 μ m thick *a*-Si:H cell and 5 h for a 1.8 μ m thick μ c-Si:H cell), while 3 Å/s or higher deposition rates are generally preferred in production plants. For high deposition rates, the deposition technologies based on very high frequency (VHF) microwave, and high-pressure plasma are currently being pursued at R&D level. Rates as high as 10 Å/s have been achieved at laboratory scale.

Alternative deposition methods using hot wire CVD (HWCVD) technique, electron cyclotron resonance reactor (ECR), and also the combination of HWCVD and PECVD are also being carried out to increase the deposition rate. A detailed account of some of these techniques can be found in the following references: Carabe and Gandia (2004), Deng and Schiff (2003), Klein et al. (2004), Lechner and Schade (2002), Shah et al. (2004), Shah et al. (2013), and Sopori (2003).

20.2.2.3 Amorphous Silicon Solar Cells and Configurations

The conventional *p*-*n* junction configuration for *a*-Si:H-based solar cells suffers from inherent limitations due to the presence of large number of defect states even after H-passivation. The doping of *a*-Si:H further increases this concentration, which reduces the average lifetime of the free carriers as a result of very high recombination probabilities and low diffusion lengths ~0.1 μ m; thus, solar cells in the *p*-*n* configuration do not work and are not considered suitable. The basic structure of *a*-Si solar cell configuration is a *p*-*i*-*n* junction shown in Figure 20.29a, which illustrates qualitatively the thickness of different layers grown in the device in the *superstrate* configuration along with applied texturing (roughness) of the transparent conducting electrodes for enhanced light trapping in *a*-Si layer, as will be described later.

The *p*-*i*-*n* type configuration for *a*-Si solar cell was introduced by Carlson et al. at RCA laboratories, United States (Carlson and Wronski 1976), where an intrinsic (i) layer of *a*-Si:H is sandwiched between the *n*- and *p*-type doped layers of *a*-Si:H or its alloys. Because of very short lifetime (or high recombination) of the carriers, the doped layers do not contribute to the photocurrent generation, that is, the photons absorbed in these

**FIGURE 20.29**

The schematic representation of single junction *a*-Si solar cell in superstructure configuration (a) and the energy band diagram of the *p-i-n* solar cell structure (b). Ethylene vinyl acetate (EVM) is the polymer coating used for encapsulation of solar cell.

layers contribute to optical losses, but these *p*- and *n*-layers build up the electrical field across the *i*-layer. This electrical field drives the electrons and holes in opposite direction that are photogenerated in *i*-layer, which essentially acts as the absorber layer in *a*-Si:H solar cells. The electrical field depends on the doping concentration of *p*- and *n*-layers as well as the thickness of the *i*-layer. Because the *p*- and *n*-doped layers do not contribute to the photocurrents and can cause further recombination of the generated carriers before sweeping across the layer, it is essential to minimize their thickness that is typically ~10–30 nm. There is an upper limit to the thickness of the *i*-layer (~0.5 μm), because charge defects reduce the effective field, and thus, if the width of the *i*-layer exceeds the space charge width, then the extra width would act as *dead* layer without actually contributing to photocurrent.

20.2.2.3.1 Stability and Recombination Issues in *a*-Si Solar Cell

The initial results of *a*-Si cells in the 1970s indicated very promising potential for attaining efficiencies well above 10%. However, it was soon observed and realized that *a*-Si solar cells suffer from an inherent problem of light-dependent degradation on their performance under continuous light exposure, later attributed to Staebler–Wronski effect (SWE) (Staebler and Wronski 1977). It was observed that in a timescale of a few months, the performance of the cells dropped about 30%–40%, then stabilized at efficiency lower than the initial values. This initial drop in performance is significant and takes the edge off the promise shown by this cheaper alternative to *c*-Si technology, keeping it much below the efficiency threshold limit (generally accepted ~12% module efficiency for thin-film vacuum-based technologies). An explanation for the light-induced degradation (SWE) is that with light exposure, the Si–H bonds break and further increase the density of the dangling bonds. Thus, the system is driven into an excited or higher energy

state, with active defect centers leading to higher recombination of the free carriers and hence reduction in efficiency. The efficiency drop depends on the illumination level and operating temperature of the solar cell. It has been observed that efficiencies may be partially recovered on heating the cells. The heating recovery depends on the temperature of the cells, that is, annealing at 70°C helps in stabilizing the system better than at room temperature.

The control of defect (trap) states and dangling bonds passivation for effective doping of the *a*-Si:H layers are significant in the *a*-Si cell's overall design. The first inherent problem of the technology is that the SWE cannot be eliminated but can be reduced by engineering of device structure, for example, by employing a thinner *i*-layer at the expense of absorption loss. It has been verified by several groups that efficiency degradation in *a*-Si solar cells and modules with thinner *i*-layer is lower. The second problem is that the doping of the *a*-Si leads to an increase of the trap density, leading to a pronounced recombination effects in the device; therefore, limiting the thickness of the doped layers to 10–30 nm is needed for minimized recombination effects. The limits on *i*-layer and *n*- and *p*-doped layer thicknesses together have a direct bearing on the overall device structure and performance stability.

20.2.2.3.2 *a*-Si Solar Cell Configurations

An advantage of *a*-Si is that the solar cells can be grown in both *superstrate* and *substrate* configurations as shown in Figure 20.30. In the *superstrate* configuration, the cell is grown in the *p-i-n* sequence (starting with *p*-layer followed by *i* and *n* layers) onto a substrate that must be transparent (such as glass), and hence, this configuration is not suitable for metal or highly opaque polymeric substrates. On the other hand, the *substrate* configuration can be grown on any type of substrates that could be rigid glass or flexible metal or polymer foil. It bears *n-i-p* configuration (cell growth starting with *n*-layer followed by *i* and *p* layers), and the light enters through the last grown *p*-layer.

Generally, *a*-Si solar cells on glass are available in the *superstrate* configuration starting with the transparent conducting oxides (TCOs) window having *p-i-n* layers grown on it followed by another TCO layer and a metallic back reflector layer, as shown in Figure 20.30.

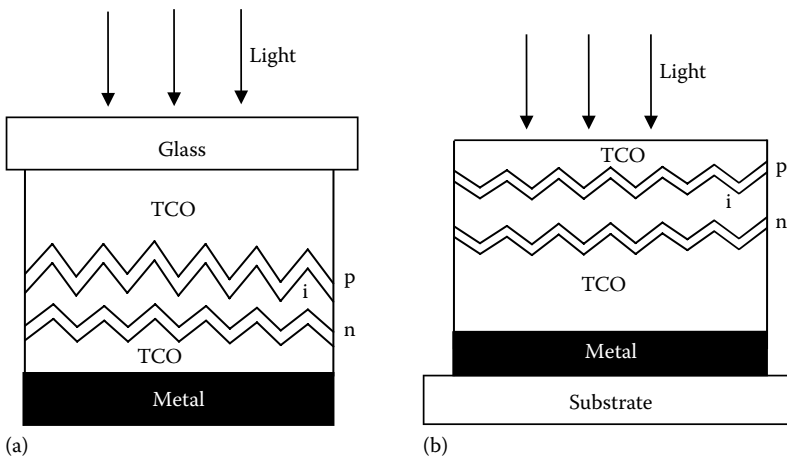


FIGURE 20.30

Schematic presentation of *a*-Si solar cell in *superstrate* (*p-i-n*) configuration (a) and *substrate* (*n-i-p*) configuration (b).

One of the leading United States-based companies in *a*-Si (unfortunately out of business now due to bankruptcy in 2013), United Solar (USOC, formerly USSC), had been using *substrate* configuration for roll-to-roll production of cells on stainless steel (SS) and polymer foils. The layers can be grown in *n-i-p* or *p-i-n* sequence but irrespective of the *substrate* or *superstrate* configuration, incident light is allowed through the *p*-side, as it has higher bandgap than *i*- or *n*-parts. Also, because the mobility of holes is smaller as compared to electrons, a thin front *p*-layer supports hole collection in the device (Rech and Wagner 1999).

The choice of TCO material as well as its electrical and optical properties is not only important for electrical contacts but also for efficient light trapping through the device. Light trapping is essential for efficient performance of *a*-Si solar cells where device thickness is limited by several inimical factors: for example, thinner *i*-layer is desired for minimizing light-induced performance degradation. Consequently, the thickness of intrinsic layer that acts as an absorber is generally limited to only ~300 nm, which is not sufficient for absorption of a large part of solar spectrum. In order to effectively utilize the incident photons, the applied strategies are to reduce the reflection through refractive index grading structures for the entire spectral wavelength range cell response and allow multiple scattering of light for enhanced absorption of photons in the *i*-layer. These are achieved by an antireflection coating used on the glass, where the light enters into the PV module, and also through suitable surface texture of TCO with the feature sizes comparable to the wavelength and application of metal reflectors. For detailed description of TCOs and light scattering, refer to the publications by Goetzberger et al. (2003), Granqvist (2003), Muller et al. (2004), and Shah et al. (2004). TCOs such as $\text{SnO}_x\text{:F}$, ITO, and ZnO:Al have been extensively used in *a*-Si solar cells. Some of the requirements for a good *a*-Si:H solar cells are the following:

- Glass and front TCO should have a high (>80%) transparency over the whole spectral range.
- TCO with a sheet resistance of at the most 10–15 Ω /square (high conductivity) to be obtained by enhancing carrier mobility rather than the carrier concentration to minimize free carrier absorption over the near-infrared region.
- TCO layers and doped silicon layers, which do not contribute to photogeneration and collection, should be kept as thin as possible and have very low absorption coefficients.
- TCO layer should not degrade by chemical reduction during *a*-Si:H deposition.
- Use of back reflectors with as little absorption as possible.

The properties of doped and intrinsic layers have been widely studied, and layers are employed in optimized conditions. However, light trapping through various structure and patterns are relatively recent advancements and thus open up much more scope in the improvement of the device performance (Granqvist 2003; Muller et al. 2004). There are other innovations related with device architecture by making use of tandem or multiple junction and heterojunction cells for efficiency and stability improvements, which are discussed in the following sections.

20.2.2.3.3 Multiple Junction or Tandem Solar Cells

The light-induced degradation (SWE) has become the biggest bottleneck of the *a*-Si technology and it has serious implications. Besides, the general effects of high density of trap and recombination centers have put restrictions on the thickness of the device

layers, which consequently limits the absorption of the incoming light. The clever $p-i-n$ configuration once thought with great promise of good efficiency at cheaper cost was also masked by this instability component. To work within the limits of intrinsic layer thickness of ~ 300 nm and making use of different light-trapping arrangements, the concept of tandem cells using double and triple junctions has been thoroughly pursued worldwide. Single junction a -Si solar cells are hardly used these days because of low efficiency and stability problems. Multijunction solar cells are used for better utilization of solar spectrum and to improve the stability of the solar cells. The state-of-the-art efficiency for single junction solar cells of small area is 9.3%, while for double junction it is 12.4%, and for triple junction with a -Si:H and its alloys 13.0% efficiency has been achieved (Guha 2004). Figure 20.31 schematically presents different multijunction structures. The developments of multijunction solar cells are based on following strategies:

1. The first strategy for tandem design is based on the use of only a -Si:H intrinsic layers shown in Figure 20.31a. Such double junction devices have been developed by Fuji Electric & Co., Japan, and Phototronics (part of RWE Schott), Germany, and others. A stabilized laboratory efficiency of $\sim 8.5\%$ and module efficiency at about 5.5% are commercially available (Diefenbach 2005; Ichikawa et al. 1993).
2. The second strategy includes the use of a -Si and Ge alloys with different bandgap (lower than 1.7 eV) combinations to form tandem junctions, where the top cell is 1.7 eV a -Si:H based and bottom cells have a -SiGe:H alloy layers of lower (1.5–1.3 eV) bandgaps, as shown in Figure 20.31b. United Solar (USSC) has developed 13% stabilized efficiency triple junction solar cell (small area) in *substrate* configuration and is selling their triple junction modules on SS at stabilized efficiency of about 6.5%.
3. The third strategy introduced in 1994 by IMT Neuchatel, Switzerland, is based on a novel concept of combining μc -Si:H (with a bandgap of 1.1 eV)- and a -Si:H (with a bandgap of 1.7 eV)-based solar cells. This has a promising potential because of significantly reduced light-dependent degradation effect in tandem solar cell (Meier et al. 1994; Shah et al. 2004). The only degradation observed comes from a -Si part, which is optimized at 0.2–0.3 μm , while the μc -Si:H layer is kept around 1–2 μm . Figure 20.31c shows the schematic of the design in $p-i-n/p-i-n$ configuration on a rigid glass substrate. Kaneka Corporation, Japan, had achieved large-area modules ($910 \times 455 \text{ mm}^2$) of initial efficiency $\sim 13.2\%$ and with stabilized efficiency approaching toward 10%. Using the concept of intermediate TCO reflector layer for novel light trapping, Yamamoto et al. (2004) have shown an initial efficiency of 14.7% for a test cell. The reason for a good efficiency of the cells lies in the spectral response of the combination of 1.7 eV a -Si:H-based cells and 1.1 eV μc -Si:H-based second part. The superposition of the two results in a quantum efficiency spreading around 80% between 500 and 800 nm, covering a large part of the solar spectrum.

20.2.2.3.4 Hybrid Solar Cells

Amorphous silicon cells have been combined with nanocrystalline silicon junction and the cells of other materials, for example, junction with CIGS (Mitchell et al. 1988a; Yamamoto et al. 1998). Another significant development in the design is the formation

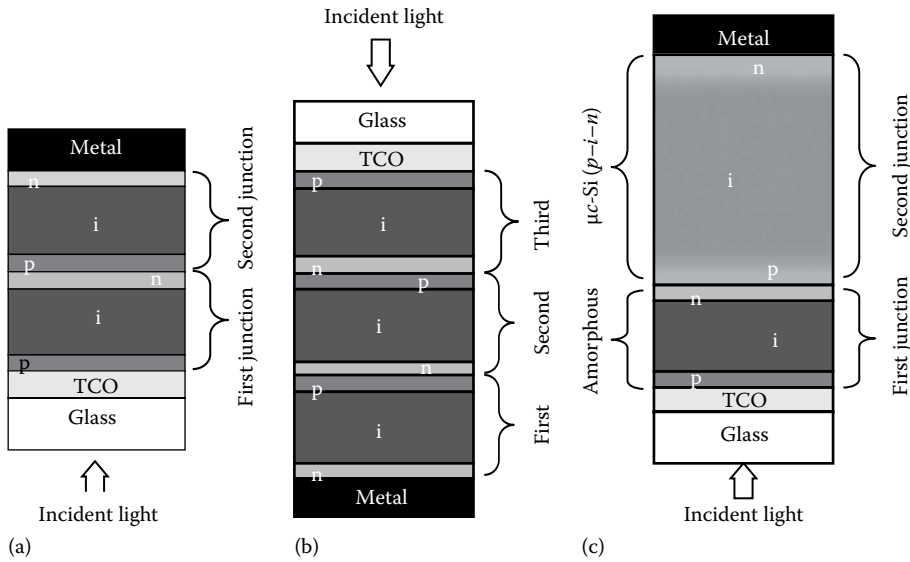


FIGURE 20.31

The schematics of multijunction cell architecture showing double junction *superstrate* configuration (a), triple junction in *substrate* configuration (b), and *micromorph* junction in *superstrate* configuration (c), that is, glass/TCO/*p-i-n* (*a-Si:H*)/*p-i-n* ($\mu\text{c-Si:H}$).

of a thick/thin type of interface structure (heterostructure) between *a-Si:H* layer and *c-Si* wafer referred to as heterojunction with intrinsic thin-film layer (HIT) cells that were developed by Sanyo, Japan. Efficiency close to 21% over a cell area 101 cm² was reported (Sakata et al. 2000) initially with a good promise. This technology uses *n*-type of Cz-silicon wafer as the base (light absorber) and low-temperature processes with the device structure being *a-Si(p⁺)/a-Si(i)/c-Si(n)/a-Si(i)/a-Si(n⁺)*. The intrinsic *a-Si* layer is important as it contacts *c-Si* at both ends, and provides passivation as well as extra stability to the system. As per reports of Sanyo, the cells had exhibited excellent stability. Subsequently, further improvement in efficiencies was reported by Sanyo crossing 23% mark and recently record efficiency has been claimed by Panasonic corporation for crystalline silicon-based PV cell of a *practical size* (101 cm²) with an efficiency of 24.7%. Japan's Institute of Advanced Industrial Science and Technology has evaluated the efficiency (Gifford 2013).

20.2.2.4 Flexible *a-Si* Solar Cells and Modules

20.2.2.4.1 Monolithic Modules

All solar modules require a number of solar cells to be electrically connected in series to provide power, depending on size and cell efficiency. Additional processing steps such as attachment of leads and encapsulation for protection against external influences are done to finalize the module structure. The *superstrate* configuration has advantages for monolithic electrical interconnection of solar cells to form solar modules since substrate (glass, polymer) is insulating. While in *substrate* configuration individual large-area solar cells are mechanically connected, cell to cell, as done in *c-Si* technology, USSC, United States, follows this electrical contacting approach for triple junction *a-Si* solar cells on steel foils.

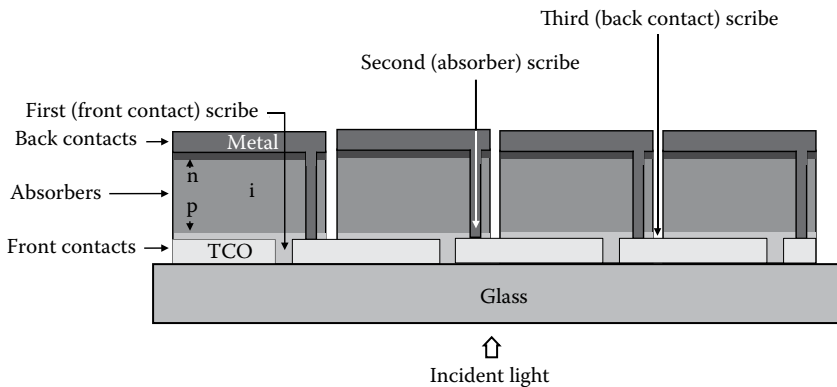


FIGURE 20.32

Schematic presentation of a monolithic module design with a single junction *a*-Si cell in *superstrate* configuration. Similar strategy can also be used for modules on polymer foils or multijunction solar cells, which may have different sequence of layers.

Figure 20.32 illustrates the monolithic interconnection scheme to develop solar modules in *superstrate* configuration. For interconnection of solar cells, layers are laser-scribed in three stages: first separating front TCO contact, then scribing *a*-Si layers to connect individual cells, and finally isolating the conducting backelectrode to obtain series interconnection. This approach removes the need for separating and connecting of cells, which is time consuming, costly, and complex in conventional *c*-Si technology.

20.2.2.4.2 Flexible *a*-Si Solar Cells

Another important perspective of thin-film PV technology is the flexible modules that are lucrative owing to their applications related with strategic space and military use, integration in roofs and facades of buildings, portable power source, automobiles, consumer electronics, value-added products, etc. Therefore, the technology has attracted recently major players of thin-film PV to venture in this area. Because they can be available in different shades (even semitransparent), shapes, and sizes, these flexible *a*-Si solar cells once were potential candidates for low-to-medium range of power applications.

Some of the prominent companies that were involved in the production (as on year 2007) and development of flexible *a*-Si based modules are listed in Table 20.7 (some significant record efficiencies may also be found in Table 20.5). Out of these, United States-based United Solar, Iowa thin films, and Japanese companies like Sanyo and Fuji had entered into relatively large-scale production, while European companies such as Flexcell (Switzerland) and Akzo Nobel (the Netherlands) were also involved in production plants for consumer electronics-oriented market. *a*-Si offers cheaper processing and materials cost; however, for it to remain as frontline thin-film technology would mainly depend on its efficiency for larger module with high throughput, which is the biggest bottleneck for the technology. Module efficiency above ~12% and a long-term (more than 30 years) stable performance of the large-area modules would make it compete effectively with *c*-Si and remain the leader among other thin-film counterparts if low-cost modules could be developed with production processes that give high throughput and yield. Oerlikon solar had created a world record of stabilized efficiency of over 10% modules for single junction *a*-Si solar cells (Benagli et al. 2009). Despite these successes, the lack of dynamism in this technology area had been due to stagnant efficiency of *a*-Si by most of the manufacturers, while other thin-film technologies are growing faster.

TABLE 20.7

Summary of the Companies Active in Flexible *a*-Si Thin-Film Si PV. Generally, the Module Efficiencies Are in 3%–8% Range (as in Year 2007)

Companies	Technology	Production	Remarks
United solar ^a	Triple junction SiGe alloys On SS RF-PECVD	30 MW line, RF-PECVD, modules, and consumer products	Modules between 6.5% and 6.8%. Cutting-assembling process modules with 8% for military and space application
VHF-Technology	<i>a</i> -Si on PEN, polyimide VHF-PECVD	Pilot production and consumer products	Product efficiency ~4%
Iowa thin-film technology (ITFT)	<i>a</i> -Si on polyamide, RF-PECVD	Pilot production and consumer products	Product efficiency ~4%
Fuji Electric	<i>a</i> -Si/ <i>a</i> -Si on polyamide RF-PECVD	Pilot production and consumer products	Feed-through contacts through the substrates, 7% module, 8% active area stable efficiency
Sanyo	<i>a</i> -Si on plastic RF-PECVD	Consumer products	
Canon	μ -Si:H/ <i>a</i> -Si:H on SS (VHF-PECVD)	Development	
Akzo Nobel	Amorphous <i>p-i-n</i> on Al RF-PECVD	Development, pilot line	Al sacrificial substrate dissolved after cell deposition

^a The company United Solar; the largest *a*-Si manufacturer went bankrupt in 2013.

The future of larger-scale amorphous silicon solar panels does not look very bright: Sharp retired 160 out of their 320 MW production capacity in Japan earlier in 2014. Optisolar, Signet Solar, Unisolar, and many other companies that were touting the amorphous technology are acquired, bankrupt, or closed (energyinformative.org). The *a*-Si technology could return back to gain the thin film market leadership only when the SWE effect of the degradation of cells could be tackled (Fehr et al. 2014; Yu et al. 2014).

Efforts are ongoing in countries around the world to overcome this barrier, especially in Japan where this technology is widely accepted. A good account on the future of *a*-Si technology was presented at Asian PVSEC meeting in Taiwan (Konagai 2013). Under Japan's NEDO mission PV2030+, the target module conversion efficiencies of *a*-Si thin-film solar cells are 14% for 2017 and 18% for 2025. To attain these goals, conventional *a*-Si/ μ -Si double-junction tandem solar cells must be superseded by triple-junction solar cells. The development targets of triple-junction solar cells include those for *a*-Si/ μ -Si/ μ -Si and *a*-Si/*a*-SiGe/ μ -SiGe structures as well as for the *a*-Si/*a*-SiGe/ μ -Si structure. Under this strategy, two collaborative university–industry research consortia that focus on innovative Si thin-film solar cells have been initiated. One is the *thin-film full-spectrum solar cells* project of METI/NEDO and the other is the *Si nanowire solar cells* project of MEXT/JST. In each project, which involves a study period of 5–7 years, domestic research organizations as well as foreign countries have been included, with a budget that exceeds four billion yen over the entire period.

With a success in the efficiency figures in *a*-Si technology, Hanergy Solar in China (who are currently producing thin film PV up to 3 GW) along with a few other Chinese companies (who have ambitious plan to use this technology for BIPV and BAPV [Building Attached PV]) have also set their eyes on this technology for enhanced production in coming years. A European roadmap for *a*-Si technology was built around these factors some time ago with a short-term goal of 15% stabilized cell efficiency from 2008 to 2013,

through fundamental understanding of electronic properties of the layers and the interfaces followed by an increase up to 17% by 2020 (Sinke 2007).

20.2.3 Cadmium Telluride Solar Cells

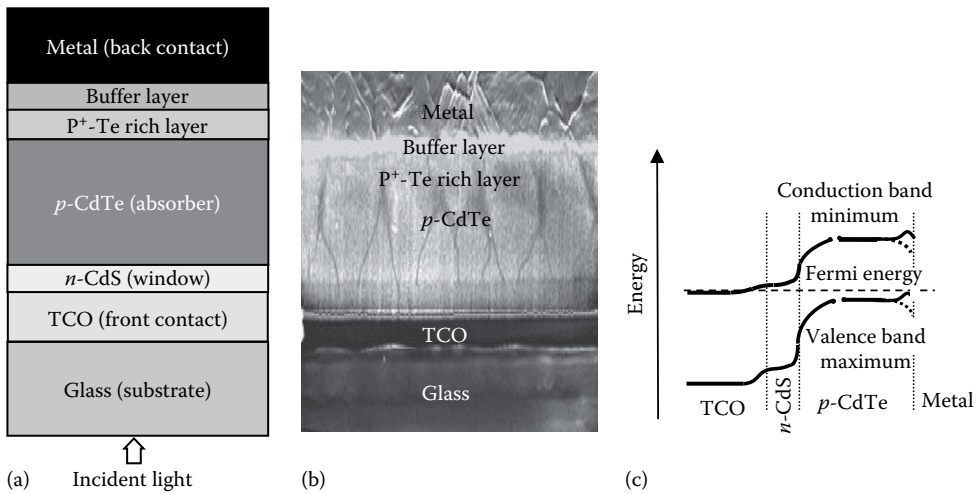
20.2.3.1 Material and Properties

Cadmium telluride (CdTe) is a direct band-gap material and comes under the family of II–VI materials referred to as metal chalcogenides. Its band-gap energy of ~ 1.45 eV is quite favorable for the requirement of highest conversion of solar spectrum into electricity with a single junction solar cell. Besides, very high optical absorption (10^5 cm $^{-1}$, see Figure 20.25) and *p*-type conductivity make it an ideal material for PV application. It has a *zincblende* crystal structure and a simple phase diagram as the constituents have high vapor pressure. The layers of CdTe can be deposited using a number of processes and the compound can easily be grown in stoichiometric form at temperatures over 400°C. Like other II–VI materials, the electronic doping is controlled by substitution of atoms at vacancy sites. While *n*-type doping control is relatively easier, it is difficult to vary the doping concentration in *p*-type CdTe because of compensation effects. The most common CdTe thin-film solar cell structure comprises of a *p*-type CdTe absorber layer and *n*-type CdS-based window layer forming a heterojunction, which has an intermixed interface region.

First development of CdTe heterojunction solar cell started around 1962 using *n*-CdTe in combination with Cu $_x$ Te (Bonnet 2004; Cusano 1963; Lebrun 1966). Though 5%–6% efficiencies were achieved, the cells suffered from degradation due to Cu diffusion from Cu $_x$ Te (similar to CdS/Cu $_x$ S solar cells). A breakthrough in 1972 was achieved when a new heterojunction structure between CdTe and CdS was developed by Bonnet and Rabenhorst (1972) and 6% efficiency was reported. Current solar cell structures are based on the device structure shown in Figure 20.33. By 2001, significant progress had raised the efficiency to 16.5% (Wu et al. 2002). Historical developments of CdTe PV technology have been reviewed by McCandless and Sites (2003).

The most attractive features of CdTe compound are its chemical simplicity and the robust stability. Because of its highly ionic nature, the surfaces and grain boundaries (GBs) tend to passivate and are not detrimental (that is a reason that polycrystalline CdTe solar cells are more efficient than single crystal counterpart). CdTe material is inherently stable under solar spectrum since its bonding strength of ~ 5.7 eV is much higher than the incident photon energy of the solar spectrum. This accounts for the excellent material stability and device performance. CdTe is not only stable for terrestrial applications, but it has also been demonstrated that CdTe has excellent stability under high-energy photon and electron irradiation for space applications, superior to Si, GaAs, CIGS, etc. (Bätzner et al. 2004).

Table 20.5 lists the efficiency of the CdTe solar cells reported by laboratories and prominent manufacturers. The theoretical efficiency of CdTe solar cell is estimated by detailed balance calculations to be $\sim 32\%$ ($J_{sc} \sim 31$ mA/cm 2 and $V_{oc} \sim 1.1$ V), which is higher than *c*-Si; therefore, there is plenty of scope for improvement in the conversion efficiency in the future. Important issues in R&D are shallow acceptor doping of the CdTe absorber, formation of good ohmic contact on *p*-CdTe, and reduction of optical absorption losses from the CdS and TCO front contact layers. These are some inherent critical issues requiring further investigation to achieve cell efficiency well above 20% with single junction device. Progress of CdTe technology has also been hampered because of perception involving environmental concerns due to cadmium and shall be discussed later in Section 20.2.7.

**FIGURE 20.33**

Schematic presentation of CdTe/CdS solar cell in *superstrate* configuration showing different layers and their nomenclature (a), a corresponding SEM picture illustrating different layers (b), and the energy band diagram of the solar cell (c).

20.2.3.2 CdTe Solar Cell Device Structure

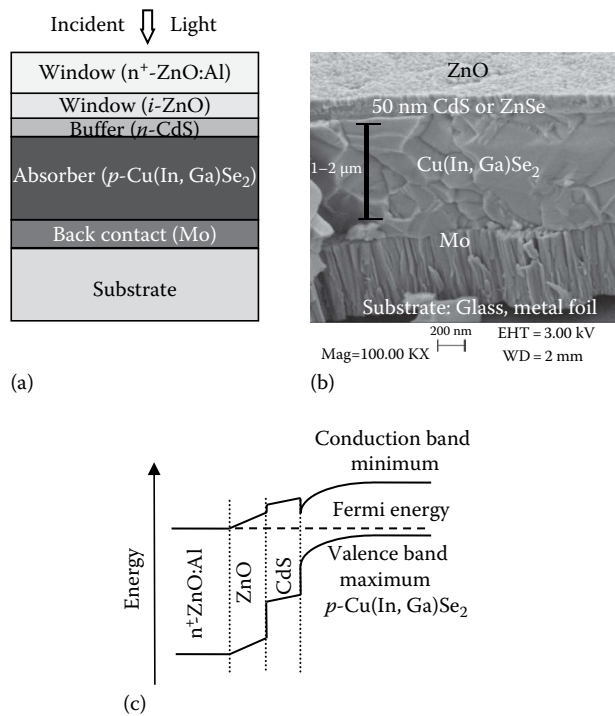
The CdTe solar cells can be grown in both *substrate* and *superstrate* configurations. Until today the highest efficiencies have been achieved in *superstrate* configuration. Figure 20.33a gives the schematics of CdTe solar cell grown on TCO-coated glass substrate in a *superstrate* configuration. The glass substrate can be a low-cost soda lime glass for processing temperature below 600°C or alkali-free glass (generally borosilicate) for high-temperature processing above 600°C.

Substrate configuration would allow CdTe to be deposited on opaque substrates such as metal or polyimide foils. Stability of the backcontact especially was believed to be the main limiting factor in this configuration, as CdTe/CdS layers need to be grown at so high temperatures where interdiffusion degrades the CdTe backcontact interface and cells are shunted. Only recently, the *substrate* configuration was reconsidered and the development of a novel doping method allowed solar cell efficiencies close to 14% (Kranz et al. 2013a) (Figure 20.34).

In the *superstrate* configuration layers of TCO, CdS, CdTe and the metal backcontact are sequentially grown on glass substrates. There are some intermediate processing steps that will be described later. An antireflecting coating on the glass rear surface is often applied to reduce the reflection at the air–glass interface. The incident light passes through the glass, TCO, and CdS and gets absorbed in CdTe layer where it creates electron–hole pairs that contribute to the PV power.

20.2.3.2.1 TCO Front Electrical Contact

A highly transparent and *n*-type conducting TCO layer with an electron affinity below 4.5 eV is required to form an ohmic contact and to have good band alignment with *n*-CdS. Most of the TCOs such as SnO_x:F, ITO, ZnO:Al, and Cd₂SnO₄ (cadmium stannate) have been used in combination with a highly resistive and transparent (HRT) layer such as resistive ZnO, SnO_x, or Zn₂SnO₄ to grow high-efficiency solar cells (Wu et al. 2002).

**FIGURE 20.34**

Schematic presentation of CIGS solar cell in *substrate* configuration (a), SEM cross-section image of CIGS device showing microstructure of layers (b), and the qualitative energy band diagram of CIGS solar cell (c).

The bilayer (combination of high and low resistive TCO stack) is often used to protect against shunts caused by pinholes in thin CdS layers. Most commonly used TCO in industrial production is SnO_x:F and often with a thin ITO layer. ITO front contacts are often sensitive to annealing treatment. An increase in electron affinity from around 4 to 5 eV can be caused by oxidation or PDT.

20.2.3.2.2 *n*-Type Window Layer

CdS is commonly used as *n*-type window layer material. The energy bandgap of CdS is 2.4 eV with intrinsic *n*-type electrical conductivity and it forms a heterojunction with CdTe layer. A typical thickness of as-deposited CdS layer used in solar cells is in the range of 10–500 nm. During high-temperature steps of cell processing, this thickness can be effectively reduced because of interdiffusion with CdTe. A thin CdS layer (10–50 nm) is desired to minimize the photon absorption losses so that maximum number of photons can reach the CdTe layer. However, there has to be a compromise because very thin CdS may lead to a lower open circuit voltage and fill factor through shunting in the device. CdS layers can be grown by different methods such as chemical bath deposition (CBD), evaporation, sublimation, vapor transport (VT), metal organic chemical vapor deposition (MOCVD), and sputtering (Ferekides et al. 1993; McCandless and Sites 2003; Romeo et al. 1999, 2004a).

The relatively low energy bandgap of CdS leads to significant parasitic absorption losses of high-energy photons. Alternative materials with increased energy band-gap values such as oxygenated CdS or Zn(O,S) are under investigation in order to increase the current density toward the theoretical maximum.

20.2.3.2.3 CdTe Absorber Layer

The CdTe thin film is the most important component as it absorbs the incident solar light and contributes to the photogenerated current. Because of its direct band-gap properties, only about 2 μm thick material is sufficient to absorb the most useful part of the solar spectrum. CdTe layers may be grown by a variety of vacuum and nonvacuum methods classified into high-temperature and low-temperature processes. Some of the commonly used high-temperature methods are closed space sublimation (CSS), VT, or vapor transport deposition (VTD) with deposition temperature above 500°C, while methods such as electrodeposition (ED), screen printing (SP), chemical spraying (CS), high vacuum evaporation (HVE), and sputtering with deposition temperature below 450°C are classified under low-temperature processes (McCandless and Sites 2003; Romeo et al. 2004a). Depending on deposition methods, the typical thickness of CdTe layer in solar cells is in the range of 2–6 μm .

20.2.3.2.4 Junction Activation Treatment

The as-deposited CdTe/CdS solar cells always exhibit poor PV properties and thus require a special annealing treatment that improves the cell efficiency considerably (by a factor of 3–5). This is done by subjecting the CdTe/CdS stacks to a heat treatment under Cl–O ambient between 350 and 600°C. This is known as *CdCl₂ treatment* or *junction activation treatment*. After this annealing treatment, a significant enlargement of grain size, by a factor of 5–20, is observed in CdTe grown by low-temperature deposition methods, as can be seen in the Figure 20.33b. The grain size of HVE CdS is in the range of 0.1–0.3 μm and the layers are rough. If the CdS is grown by a CBD, then it consists of small grains of about 0.1 μm widths. A treatment with CdCl₂ recrystallizes the CdS layers so that some of the small grains coalesce together and form bigger grains of 0.5 μm width (Romeo et al. 2004a). In case of high-temperature grown CdTe, this annealing treatment recrystallization is observed, but the grain size near the top surface does not increase since the grains are already few microns large even in as-deposited condition.

For high-temperature growth processes, there is a tendency of CdS_xTe_{1-x} formation by the conversion of small CdS grains into CdTe due to interdiffusion at the interface and little or low grain growth is noticed after the activation treatment. A stable CdS/CdTe interface can be obtained for 6% diffusion of sulfur atoms. However, under nonequilibrium conditions, the diffusion of S decreases the thickness of the CdS films causing pinholes and eventually leads to shorting paths across the junction. This is a critical problem in CdTe solar cells, restricting the application of thinner CdS as desired to minimize the optical absorption losses. Nevertheless, a thermal treatment of CdS layer prior to CdTe deposition is frequently applied to restrict the interdiffusion of S. The formation of CdS_xTe_{1-x} after activation actually helps in reducing the lattice mismatch between CdS and CdTe but only marginally as compared to improvement in electrical changes induced by Cl, O, and S. Apart from reduction in density of stacking faults and misfit dislocation, there is an overall increase in the shallow-acceptor concentration in CdTe, leading to enhanced *p*-doping in CdTe after annealing. In particular, the GB regions become more *p*-doped, owing to preferred GB diffusion and segregation of Cl and O. As a result, increased charge carrier collection efficiency is measured and efficiency increases by a factor of 3–5.

20.2.3.2.5 Problems of Electrical Backcontact and Stability

An important issue in CdTe solar cell technology is the formation of efficient and stable ohmic contact on *p*-CdTe layer. For an ohmic contact to form on a *p*-type semiconductor, the work function of the metal should be higher than the sum of the bandgap and the

electron affinity of the semiconductor; otherwise, Schottky contact is formed. For *p*-CdTe layer, a metal with a work function higher than 5.7 eV is needed since CdTe has a bandgap of 1.45 eV and electron affinity is 4.3 eV. Metals with such high work functions are not available. To overcome this problem, a heavily doped *p*-CdTe surface is created with the help of chemical etching and a buffer layer of high carrier concentration is often applied. Subsequent postdeposition annealing diffuses some buffer material into CdTe where it changes the band edges as a result of change in the interface state density. Thereby a lowering in interface barrier height and width results, which enables a quasi-ohmic or tunneling contact between the metal and CdTe, as shown in Figure 20.33c. Commonly used buffer layer/metallization combinations are Cu/Au, Cu/graphite, or graphite pastes doped with Hg and Cu. But backcontacts containing Cu in any form are often not stable with time as Cu migration from the backcontact leads to efficiency degradation with time. However, alternate processes were being developed, among them Sb₂Te₃/Mo and Sb/Mo contacts that have provided high-efficiency and long-term stable solar cells (Abken and Bartelt 2002; Bätzner et al. 2001, 2004; Romeo et al. 2004b).

20.2.3.3 Deposition Techniques

HVE is a simple deposition method where CdTe and CdS are congruently evaporated from crucible/boats on substrates at 150°C for CdS and ~300°C for CdTe. In this process, the layers are grown in a high vacuum (~10⁻⁵ Torr), but the distance between the source material and substrate is kept in the range of 10–30 cm. This allows the use of substrates at relatively lower temperature. Typical deposition rates vary between 2 and 10 μm/h. Solar cells of ~12%–16% efficiency have been achieved by Stanford University, United States; ETH Zurich, Switzerland; and IEC, Delaware, United States (Fahrenbruch et al. 1992; McCandless et al. 1999; Perrenoud et al. 2011a).

Sputtering is another process that involves a vacuum system with ionized gases forming plasma discharge, where a CdTe target (a few mm thick plate) attached to one electrode is used as the source material. The energetic ionized atoms from plasma strike the target and remove the material atoms, and consequently, a CdTe layer gets deposited on the substrate, which is placed on the counterelectrode facing the target. Sputtering methods are suitable for large-area deposition in an industrial environment, but because of difficulty in maintaining stoichiometry, they are considered not very suitable for compound semiconductors. However, 14% efficiency has been achieved with this process at University of Toledo, United States (Compaan et al. 2004).

CSS and VT are the prominent and industrially used processes for CdTe deposition owing to its very high rate (2–5 μm/min) of deposition. The CSS process consists of an arrangement involving the placement of a graphite crucible with the source material (CdTe compound) in a high vacuum chamber (~10⁻⁵ Torr). The CdTe compound sublimates at around 600°C and is deposited onto the substrate, which is kept with a separation of 1–5 mm above the crucible and heated typically above 550°C. Antec Solar GmbH in Germany uses this method for industrial production of 60 × 120 cm² modules on a 10 MW capacity plant. Parma University, Italy; University of South Florida, United States; and NREL, United States, have also used this method and cells of 15.5%–16.5% efficiency have been achieved. First Solar, United States, uses a variant of CSVT where instead of compound, elemental vapors are used (First Solar 2005; McCandless and Dobson 2004; Romeo et al. 2004c). First Solar is the most successful CdTe company to date with an annual production capacity of approximately 2 GWp for modules on 60 × 120 cm² glass substrates. First Solar and GE global research have contributed to improve the CdTe-based solar cell efficiency

significantly. GE global research has achieved a ground-breaking efficiency of 19.6% on glass substrates. Early 2014, First Solar communicated 20.4% solar cell efficiency and a very remarkable full scale module efficiency of 17% (First Solar 2014).

Details of other alternative methods such as SP, spray pyrolysis, MOCVD, CVD, atomic layer deposition (ALD), and ED may be found in articles (Bonnet and Rabenhorst 1972; Romeo et al. 2004c). For flexible substrates such as polymers low-temperature methods like sputtering, HVE and ED are suitable.

20.2.3.4 Flexible CdTe Solar Cells

Even though the technology of CdTe solar cells on glass substrates has matured and efficiencies exceeding 17% on module level have been achieved, not much effort has gone in developing these devices on flexible substrates. The R&D on flexible CdTe has been supported by NASA and defense agencies in the United States. Because of high radiation tolerance, superior to conventional Si and GaAs solar cells, against high-energy electron and proton irradiation, these solar cells are also attractive for space applications in addition to terrestrial applications.

Though the CdTe solar cells can be grown in *substrate* configuration, one of the hurdles in the development of high-efficiency CdTe solar cells on metallic substrates is that most of the metal foils do not form efficient ohmic contact with CdTe and it is difficult to incorporate an additional buffer layer as ohmic contact to increase the cell efficiency. The criteria of matching thermal expansion coefficients and work function limit the choice of available substrate materials. Another reason is that during CdCl₂ annealing treatment, diffusion of impurities changes the ohmic contact properties. Recently, by optimization of the interfaces and doping methods, flexible CdTe solar cells on metal foil have been realized with an efficiency of 11.5%. On glass substrate, an efficiency of 13.6% has been obtained with similar substrate configuration, which with little bit of more optimization over 16% can provide production avenues of CdTe on a range of both rigid and flexible substrates (Kranz et al. 2013b). Further, latest status and details on the CdTe solar cells development have been reported by Professor Ayodhya Tiwari's group at EMPA, Switzerland (Kranz et al. 2013c).

The choice of an appropriate substrate is a crucial factor for flexible solar cells in the *superstrate* configuration because the substrate should be optically transparent and should withstand the high processing temperature. Most of the CdTe/CdS cell fabrication techniques require temperatures in the range 450°C–500°C. Therefore, low-temperature (less than 450°C) deposition processes are required. However, NREL (United States) and EMPA (Switzerland) have reported 14.0% and 13.6% efficiency flexible cells on flexible glass and polymer foil, respectively (Kranz et al. 2013d). On polyimide foil first monolithically interconnected minimodules were demonstrated, yielding efficiencies of 8% (Perrenoud et al. 2011b). These devices were grown with HVE method, which is suitable for roll-to-roll deposition, but the concept for industrial production is yet to be demonstrated (Mathew et al 2004; Romeo et al. 2004c).

20.2.4 Cu(In,Ga)Se₂ Solar Cells

20.2.4.1 Material and Properties

Compound semiconductors from the I–III–VI₂ series of periodic table, such as CIS, copper gallium diselenide (CGS), and their mixed alloys CIGS, are often simply referred to as *chalcopyrites* because of their tetragonal crystal structure. These materials are easily prepared

in a wide range of compositions, and their corresponding phase diagrams have been intensively investigated. Changing the stoichiometry and extrinsic doping can vary their electrical conductivity. However, for the preparation of solar cells, only slightly Cu-deficient compositions of *p*-type conductivity are suitable. Depending on the $[\text{Ga}]/[\text{In} + \text{Ga}]$ ratio, the bandgap of CIGS can be varied continuously between 1.04 and 1.68 eV. The current high-efficiency devices are prepared with bandgap in the range 1.15–1.25 eV; this corresponds to a $[\text{Ga}]/[\text{In} + \text{Ga}]$ ratio between 20% and 30%. Layers with higher Ga content, as needed to increase the bandgap toward ~1.5 eV, are of inferior electronic quality and yield lower efficiency cells.

Other chalcopyrites such as CuInS_2 and CuInTe_2 were also investigated earlier but cell efficiencies were rather low and the R&D focus was made on CIS. Interest in CuInS_2 resurfaced with the development of ~11.4% efficient cells at HMI Berlin. A spin-off company, Sulfurcell, based in Berlin, started setting up a pilot production line in 2003. The device structure of the CuInS_2 solar cell is quite similar to CIGS solar cells in terms of other constituent layers.

The first CIS solar cell was developed with single-crystal material and ~12% efficiency was reported in 1974 (Wagner et al. 1974) and the first thin-film solar cell was reported by Kazmerski in 1976 by developing ~4% cells obtained with the evaporation of CuInSe_2 material (Kazmerski et al. 1976). The real breakthrough in CIS thin-film technology came with the pioneering work of Boeing Corp., United States, where they used three-source evaporation of Cu, In, and Se elements and raised the efficiency from 5.7% in 1980 to above 10% in 1982 (Mickelsen and Chen 1981, 1982). Despite the apparent complexity of material system, this efficiency jump clearly showed promising potential of the material. Later in 1987, Arco Solar, United States, raised the cell efficiency to ~14% by using a different CIS deposition process where stacked metal layer was selenized under H_2Se ambient (Mitchell et al. 1988b). Subsequent improvements in efficiency were attained by the EUROCIS consortium in Europe and later at NREL, United States, who reported efficiency of ~19.5% (Ramanathan et al. 2003). Efficiency improvements over the Boeing process occurred due to addition of Ga and S for band-gap engineering, addition of Na in absorber layer, optimization of the *n*-CdS (hetero-junction part of the cell), and transparent front electrical contact layers.

The first industrial production of CIS modules was started by Siemens (later Shell solar) based on the Arco Solar technology, whereas other companies such as Wurth Solar and Global Solar started development of CIS solar modules using coevaporation methods. Several other companies have been investigating various other methods of deposition such as paste printing, ED, etc. but up to now, these technologies have been less successful as compared to vacuum-based technologies.

The phase diagram of the ternary compound is described by pseudobinary phase diagram of the binary analogue, for example, Cu_2Se and In_2Se_3 phase for CuInSe_2 ternary. Single-phase chalcopyrite CuInSe_2 exists at small copper deficiency, whereas for Cu-rich compositions, a mixed phase of Cu_xSe with CuInSe_2 forms that is not suitable for PV devices. For In-rich compositions, defect-chalcopyrite phase (CuIn_3Se_5) forms, that is generally *n*-type. Despite an apparent complicated crystal structure and multicomponent system, the material properties of the PV relevant compounds are fault tolerant and not particularly affected by minor deviations from stoichiometry in Cu-deficient range. Further, surfaces and GBs in CIGS compounds are easy to passivate, resulting in high-efficiency cells even with submicron grain-size materials.

The PV grade Cu-deficient CIGS material has a tetragonal crystal structure having vacancies and interstitials, which act favorably, especially because the material is self-healing,

owing to the defect relaxation caused by highly mobile Cu-ions and its interaction with vacancies. Defects created in CIGS by external influence (e.g., radiation) are immediately healed up. This is an inherent advantage of the CIGS material, leading to highly stable CIGS solar cells. However, care must be taken for proper encapsulation of devices against highly damped conditions; otherwise, the degradation of electrical contacts (TCO or Mo) in moisture can lead to minor degradations in performance. Therefore, stability of encapsulated CIGS solar cells is not a problem as proven by field tests conducted by ZSW, Shell, and NREL. CIGS is also tolerant against space radiation being superior to Si, and GaAs single crystal cells, but somewhat inferior to CdTe.

20.2.4.2 CIGS Solar-Cell Configuration

The CIGS solar cells can be grown in both *substrate* and *superstrate* configurations, but the *substrate* configuration gives the highest efficiency owing to favorable process conditions (Figure 20.34). *Superstrate* structures were investigated in the early 1980s, but efficiency was below 5%. However, recent efforts have improved the efficiency to ~13%. This has been possible with the introduction of undoped ZnO instead of CdS buffer layer and coevaporation of Na_xSe during the CIGS deposition. Further, bifacial CIGS solar cells with both front and rear transparent conducting contacts were also investigated (Nakada and Mizutani, 2002; Nakada et al. 2004).

20.2.4.2.1 Electrical Backcontact

CIGS solar cells in substrate configuration can be grown on glass as well as metal and polymer foils. Molybdenum (Mo), grown by sputtering or e-beam evaporation, is the most commonly used electrical backcontact material for CIGS solar cells. The growth of the solar cell starts with the deposition of Mo on the substrate, which forms an electrically conducting backelectrode with CIGS. When CIGS is grown on Mo, an interface layer of MoSe₂ is automatically formed, which helps in ohmic transport between CIGS and Mo. Recently, alternative backcontact materials have been explored, but industrial production is still based on Mo layers.

20.2.4.2.2 CIGS Absorber Layer

Because of a high absorption coefficient, a 2 μm thick layer is sufficient for absorption of maximum incident radiation. CIGS layers can be grown with a variety of deposition methods (as described later). Although the grain size and morphology (surface roughness) depends on deposition methods, high efficiencies >13% have been achieved with most of the methods, which indicate that GBs in CIGS are benign and can be easily passivated. High-efficiency cells have *p*-type Cu(In,Ga)Se₂ bulk, while a defect-chalcopyrite Cu(In,Ga)₃Se₅ phase in the form of thin layer segregates at the top surface that is *n*-type especially when doped by cation atoms diffusing from the buffer layer. It is believed that this inverted surface, leading to *p-n* homojunction in CIGS absorber, is crucial for high-efficiency cells.

20.2.4.2.3 Buffer Layer

Several semiconductor compounds with *n*-type conductivity and bandgaps between 2.0 and 3.4 eV have been applied as a buffer to form a heterojunction in CIGS solar cells. However, CdS remains the most widely investigated buffer layer, as it has continuously yielded high-efficiency cells on different type of absorber layers. CdS for highest-efficiency CIGS cells is commonly grown by CBD, which is a low-cost, large-area process. However, its incompatibility with in-line vacuum-based production methods is a matter of concern.

Although CBD-grown CdS serves as a reference for highest efficiency, physical vapor deposition (PVD)-grown CdS layers yield lower efficiency cells. Thin layers grown by PVD often do not show uniform coverage of CIGS and are less effective in chemically engineering the interface properties between the buffer and the absorber. The trend in buffer layers has been to substitute CdS with *Cd-free* wide-bandgap semiconductors and to replace the CBD technique with in-line-compatible processes. Alternative materials such as In_2S_3 , ZnO, ZnS, ZnSe, etc. using different methods viz. PVD, RF sputtering, metal organic chemical vapor deposition (MOCVD), ALD, or a novel technique called ion layer gas reaction (ILGAR) have been explored (Bhattacharya and Ramanathan 2004; Chaisitsak et al. 2001; Ohtake et al. 1995; Olsen et al. 2002; Spiering et al. 2003). A record efficiency of 20.9% has been achieved for CBD-Zn(O,S) buffer layer by Solar Frontier (2014). Most industries are currently using CBD-CdS, but Solar Frontier has shown 17.8% efficiency on 819 cm^2 sub-module developed with CBD-grown ZnS(O,OH) buffer layers (Nakamura et al. 2012).

20.2.4.2.4 Front Electrical Contact

TCOs with bandgaps of above 3 eV are the most appropriate and have become the ultimate choice for front electrical contact due to their excellent optical transparency (greater than 85%) and reasonably good electrical conductivity. Today, CIGS solar cells employ either ITO or, more frequently, RF-sputtered Al-doped ZnO. A combination of an intrinsic and a doped ZnO layer is commonly used. Although this double layer yields consistently higher efficiencies, the beneficial effect of intrinsic ZnO is still under discussion. Doping of the conducting ZnO layer is achieved by group III elements, particularly with aluminum. However, investigations show boron to be a feasible alternative because it yields a high mobility of charge carriers and a higher transmission in the long-wavelength spectral region, giving rise to higher currents. For high-efficiency cells, the TCO deposition temperature should be lower than 150°C in order to avoid the detrimental interdiffusion across CdS/CIGS interface. RF sputtering is not considered suitable for industrial production; therefore, alternative sputtering and CVD methods are investigated and used.

20.2.4.2.5 Sodium Incorporation in CIGS

One of the breakthrough in CIGS PV technology happened when the alumina or borosilicate glass substrate was replaced by soda-lime glass to match the thermal expansion coefficients, which resulted in substantial efficiency improvement (Hedström et al. 1993). It was subsequently realized that sodium (Na) plays an important role in high-efficiency CIGS solar cells because it affects the microstructure (grain size), and passivates the GBs, leading to changes in electronic conductivity by up to two orders of magnitude. The overall effect is efficiency improvement primarily because of an increase in the open circuit voltage (V_{oc}) and fill-factor (FF) of the solar cells. Most commonly, Na is introduced into CIGS by diffusion from the soda-lime glass substrate during the absorber deposition. However, sodium incorporation from such an approach is neither controllable nor reliable; therefore, alternative methods to add Na from external sources are used either during or after the deposition of CIGS layers. These methods include the coevaporation or the deposition of a thin precursor of a Na compound such as NaF, Na_2Se , or Na_2S for CIGS on Na-free substrates, which include soda-lime glass covered with barrier layers Al_2O_3 , Si_3N_4 , etc. as used by Shell Solar (Kessler and Rudmann 2004). These barrier layers inhibit sodium diffusion from the glass substrate. CIGS on flexible substrates (metal and polyimide foils) also need controlled incorporation of sodium, which is provided from a precursor layer applied prior or after the CIGS growth as PDT.

20.2.4.2.6 Potassium Incorporation in CIGS

Another breakthrough in CIGS PV technology happened when potassium was introduced in a controlled manner. Results on enameled steel substrates, which contain a high amount of potassium, indicated a beneficial effect of potassium on the device performance (Wuerz et al. 2012). These observations inspired the development of a PDT where KF is evaporated onto the finished CIGS absorber layer in the presence of selenium, which led to a new record efficiency of 20.4% (Chirilă et al. 2013). Remarkably, this has been achieved with a low-temperature process on flexible polyimide substrate. The KF PDT induces a surface modification of the CIGS, resulting in a copper depletion and Cd enrichment. Introduced in the high-temperature process, the KF PDT enabled further efficiency improvement to 20.5% (Stolt 2014) and 20.8% (Jackson et al. 2014).

20.2.4.3 Deposition and Growth of CIGS Absorber

There are number of processes used for the deposition of the CIGS thin films, some of them are briefly described:

20.2.4.3.1 Coevaporation Processes

As described earlier, vacuum evaporation is the most successful technique for deposition of CIGS absorber layers for highest-efficiency cells. Vacuum evaporation method involves simultaneous evaporation of the constituent elements from multiple sources in single or sequential processes during the whole absorber deposition process. While a variation of the In to Ga ratio during the deposition process leads to only minor changes in the growth kinetics, the variation of the Cu content strongly affects the film growth. Thus, different coevaporation growth procedures are classified by their Cu evaporation profile (Figure 20.35).

One variant of coevaporation is a bilayer process (also called the *Boeing process*), which originates from the work of Mickelsen and Chen (1982) and yields larger grain sizes compared to the constant rate (single stage) process. This is attributed to the formation of a Cu_xSe phase during the Cu-rich first stage that improves the mobility of group III atoms during growth.

The highest efficiencies in laboratories are achieved with the so-called *three-stage* process, introduced by NREL, United States (Gabor et al. 1994). With this process CIGS layer is obtained by starting the deposition of an $(\text{In,Ga})_x\text{Se}_y$ precursor, followed by the codeposition of Cu and Se until Cu-rich overall composition is reached, and finally, the overall Cu concentration is readjusted by subsequent deposition of In, Ga, and Se. CIGS films prepared by the three-stage process exhibit a large-grained smooth surface, that reduces the junction area and is thereby expected to reduce the number of defects at the junction and yield high efficiency. Several groups worldwide have developed 16%–20.8% efficiency cells using CIGS grown with three-stage process.

20.2.4.3.2 Selenization of Precursor Materials

This is another approach of obtaining CIGS thin films. This sequential process is favorable due to its suitability for large-area film deposition with good control of the composition and film thickness following the initial success of Arco Solar in 1987. Such processes consist of the deposition of a precursor material obtained by sputtering, evaporation, ED, paste printing, spray pyrolysis, etc. followed by thermal annealing in controlled reactive or inert

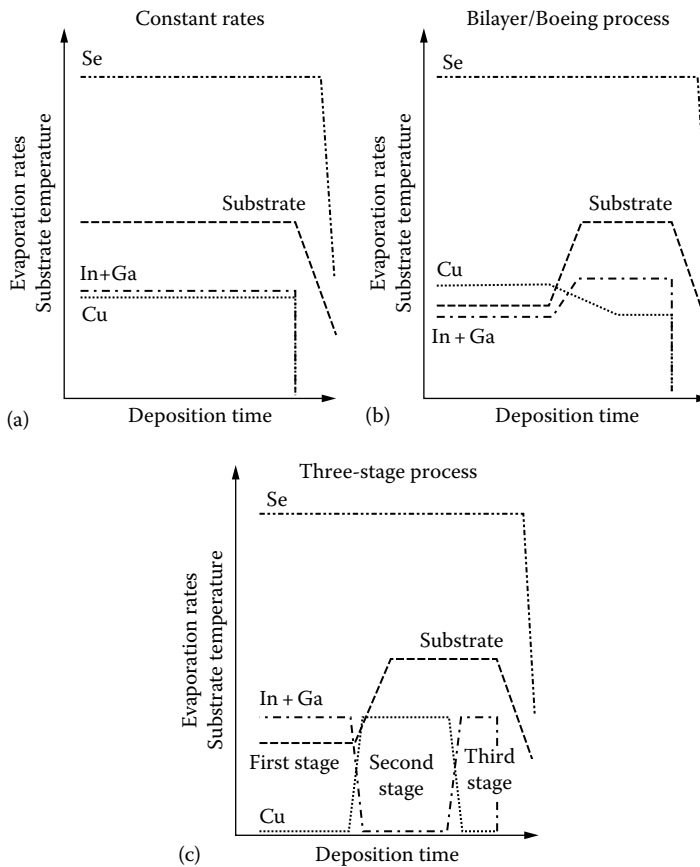
**FIGURE 20.35**

Diagram representing the recipes in the coevaporation processing steps in the deposition of $\text{Cu}(\text{In,Ga})\text{Se}_2$ used for (a) constant rate, (b) bilayer or Boeing, and (c) three-stage process.

atmosphere for optimum compound formation via the chalcogenization reaction as illustrated in Figure 20.36. The precursor materials are either stacked metal layers or a stack of their compound and alloys. Shell Solar, United States, and Solar Frontier (Showa Shell), Japan, use sputtering technique for precursor deposition and production of large-area solar modules up to $60 \times 120 \text{ cm}^2$, yielding maximum efficiencies of 13% on $30 \times 30 \text{ cm}^2$ modules (Karg 2001; Kushiya et al. 2003; Palm et al. 2004).

20.2.4.3.3 Alternative CIGS Growth Processes

There is a substantial interest to use nonvacuum methods for CIGS deposition. An innovative approach utilizes the stability of the oxides to produce nanosized precursor particles (Eberspacher et al. 2001; Kaelin et al. 2004; Kapur et al. 2001). Nanosized metal oxides are mixed in an ink suspension that allows low-cost, large-area deposition by doctor blading, SP, or spraying of the precursor. Such nonvacuum deposition of precursors allows a very efficient material utilization of almost 100% of the nonabundant metals indium and gallium. A selenization treatment converts precursor into CIGS layer, and solar cell efficiencies of over 13% have been achieved by ISET, United States. One of the drawbacks of

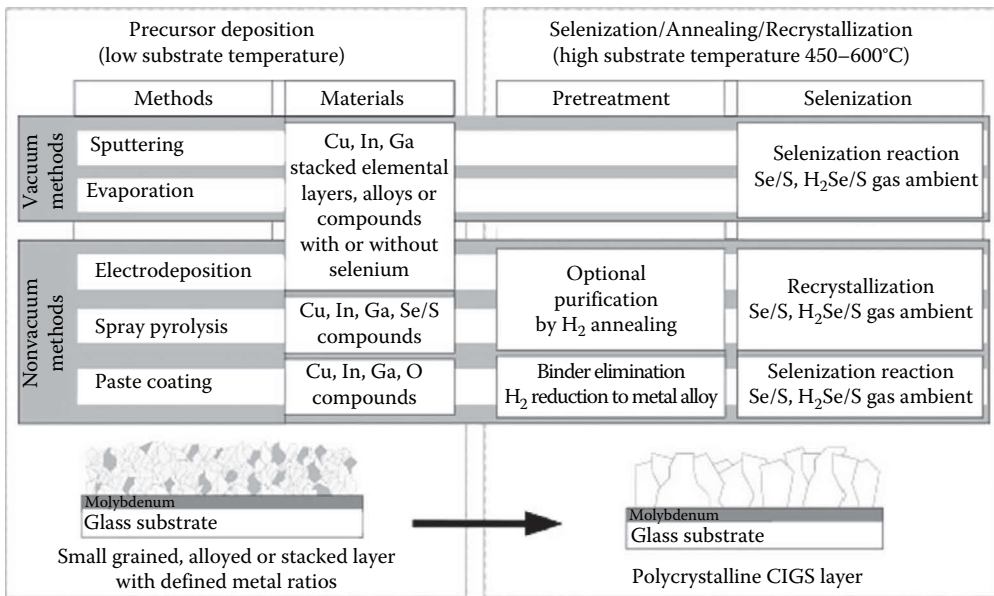


FIGURE 20.36

Schematic of the various processes for selenization of precursor materials.

the process is the toxicity of the H₂Se gas used for selenization. However, recent efforts are being made to selenize printed precursors with Se vapors (Kaelin et al. 2004).

The CIGS compound can also be formed directly by ED from a chemical bath (Hodes et al. 1986). Several groups including EDF-CNRS, France; CIS solar technologies, Germany; CISCuT, Germany, etc. have been using such approaches and obtained cells with efficiencies around or greater than 10% viz. 9.4% from single pot ED (Duchatelet et al. 2012) and 13.4% aperture efficiency on flexible foil achieved by Solo Power (Osborne 2012). Nexcis, France, reported an efficiency of 15.9% with ED followed by an RTP selenization treatment (Bermudez 2013).

The European consortium SCALENANO, which has received around EUR 7.5 million in EU funding, is scheduled to complete its work in July 2015. The consortium applies innovative process based on the ED of nanostructured precursors, as well as alternative processes with very high potential throughput and process rates. The researchers have demonstrated the scalability of ED-based processes for the synthesis of very homogeneous large areas of thin-film chalcogenide absorbers with medium-area solar modules with cell efficiency of 15.4% (http://cordis.europa.eu/news/rcn/36210_en.html). With a hybrid approach that uses additional vacuum deposition on electrodeposited precursor layer, efficiencies as high as 15.4% have been achieved at NREL, United States.

20.2.4.4 Flexible CIGS Solar Cells

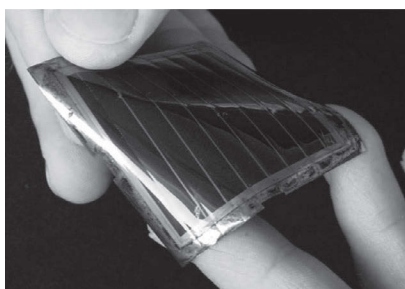
Probably the ultimate advantage of thin-film technology is the application of roll-to-roll manufacturing for production of monolithically interconnected solar modules leading to low energy payback time because of high-throughput processing and low cost of overall system. A large number of activities on highly efficient, stable, and flexible thin-film modules based on CIGS have recently drawn much interest for flexible solar cells on

metal and plastic foils. Apart from the expected high-efficiency and long-term stability for terrestrial applications, flexible CIGS has excellent potential for space application because of their space-radiation-tolerant properties, which are two to four times superior to the conventional Si and GaAs cells. Lightweight and rollable solar array structures will not only reduce the overall cost of space-deployable solar modules but also can substantially save on the launching cost of satellites.

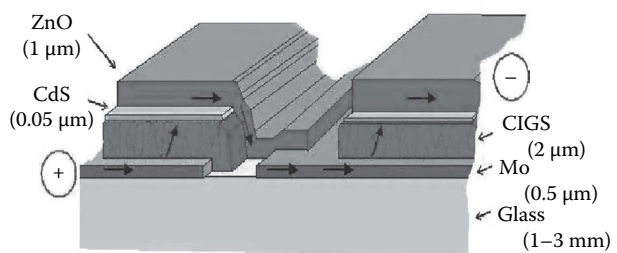
Development and current status of flexible CIGS solar cells have been reviewed by Kessler and Rudmann (2004). Flexible CIGS cells can be grown on polyimide and on a variety of metals, for example, SS, Mo, Ti, etc. Therefore, the choice of substrate is important as there are some advantages and disadvantages: (1) The density of usable metals is four to eight times higher than polymer; therefore, cells on metals are heavier. (2) Metals are conducting and have rough surfaces; therefore, monolithic module development is difficult, which in contrast is easier on polymer foils. (3) SS foils need an extra barrier layer against detrimental impurity (e.g., Fe) diffusion of the metal into the CIGS during deposition. (4) Metal foils can withstand high deposition temperatures (550–600°C), which leads to higher efficiency than on polymer foils, which are not suitable for processing temperature greater than 450°C.

High record efficiencies of flexible CIGS solar cells are 17.7% (Pianezzi et al. 2012) on SS, 18.6% on enameled steel (Powalla et al. 2014), and 20.4% on polymer foil (Chirilă et al. 2013). Several research groups and industries are involved in the development of flexible solar cells; a recent review of the technological status of CIGS-based PVs including activities on flexible substrate is given by (Reinhard et al. 2013) EMPA, Switzerland. The solar modules on SS foils are not monolithically connected; they are made by connecting individual cells into large-area cell with an overlap method. The basic schematic cross-section of a monolithic module on glass is shown in Figure 20.37 along with a flexible prototype mini-module developed on polymer foil by ZSW and ETH, Zurich (research group relocated to EMPA, Switzerland), within a European collaborative project.

Table 20.8 gives an overview of different flexible solar cell technologies, including the organic and TiO₂-based dye-sensitized PV technologies. Because of the late start in R&D, flexible CIGS and CdTe solar cells are industrially less mature compared to *a*-Si cells. However, high cell efficiency and inherent stability advantages indicate promising potential for these technologies.



(a)



(b)

FIGURE 20.37

Flexible monolithic CIGS modules showing a prototype minimodule on a polymer foil (a) and schematic cross-section of the module (image taken from the website of ZSW) exhibiting the material component layers and their interconnect patterns (b).

TABLE 20.8

Overview of Different Flexible Solar Cell Technologies

	CIGS	CdTe	Amorphous Silicon	Organic and Titanium Oxide
Lab efficiency on plastic foil	20.4% (Single junction cell)	14% (Single junction cell)	9.8% (Single junction cells) ^a 8% ^a –12% ^a (multijunction cell)	5%–8%
Lab efficiency on metal foil	18.7% ^b (single junction cell)	11.5% (single junction cell)	14.6 ^a /13% (multijunction cell)	
Industrial efficiency (typical values)	10%–14%	Not yet demonstrated	4%–8% ^a (available on plastic and metal foils)	Not yet demonstrated
Stability under light	Material stable	Material stable	Degrades	Stability not proven

^a Initial values measured before light-induced degradation of solar cells.^b Value not certified.

20.2.5 $\text{Cu}_2\text{ZnSn(S, Se)}_4$ or CZTS Solar Cells

Currently, CdTe and CIGS technologies dominate the thin-film PV market with 1 GW/year production capacity barrier surpassed first time for CdTe devices in 2009 by First Solar (Wolden et al. 2011) and for CIGS in 2011 by Solar Frontier (Hering 2011). Despite the impressive growth rates in these technologies, two issues—absorber layer component abundance (scarcity of indium and tellurium) and toxicity (heavy metal cadmium)—represent potential road blocks for pervasive deployment of these thin-film chalcogenide-based PV technologies. For the aforementioned reasons, there has been strong motivation to find alternatives to the two leading thin-film chalcogenide absorbers that use low-cost, abundant elements. In this context, various absorbers that use earth-abundant metals such as SnS (Ramakrishna Reddy et al. 2006), FeS₂ (pyrite) (Smestad et al. 1990), Cu₂S (Martinuzzi 1982), and Cu₂ZnSn(S,Se)₄ (CZTSSe) (Barkhouse et al. 2012) have been explored. The current status of CZTSSe technology and its development has been summarized by EMPA group in Switzerland (Fella et al. 2013). Among these, only Cu₂S and CZTSSe have exceeded the lower performance efficiency limit for commercial interest of 10% (Barkhouse et al. 2012; Hall et al. 1981) when compared with CIGS and CdTe, which have achieved 20.9% (Solar Frontier 2014) and 20.4% (First Solar 2014) efficiency values, respectively, for individual devices. However, Cu₂S technology was dropped from serious consideration in the 1980s owing to device instability arising from facile Cu diffusion into the semiconductor layers, leading to degradation of the device junction. Despite being in its infancy, CZTSSe technology can be considered a current favorite in terms of prospective Earth-abundant metal systems to supplement the existing CIGS and CdTe technologies, in the quest for more ubiquitous solar energy deployment.

20.2.5.1 Material and Properties

CZTSSe has a number of useful properties that could lead to its massive use as an abundant, nontoxic, and low-cost absorber for thin-film PV solar cells. It is a compound semiconductor whose intrinsic point defects lead to its *p*-type conductivity. It has a direct bandgap and has an absorption coefficient greater than $\sim 10^4 \text{ cm}^{-1}$, suitable for thin-film PV applications (Chan et al. 2010; Ito and Nakazawa 1988; Xinkun et al. 2012). Its bandgap can be tuned to lay in the range 1.0 eV for Cu₂ZnSnSe₄ and 1.5 eV for Cu₂ZnSnS₄ (Chen et al.

2009; Timmo et al. 2010). The bandgap of CZTSSe can also be tuned by incorporation of Ge and Ge-containing materials having smaller bandgap than their Ge-free counterparts (Ford et al. 2011). This tunability is of particular interest for the manufacturing of absorbers with a bandgap between 1.1 and 1.5 eV, which allow theoretical efficiencies higher than 30% (Shockley and Queisser 1961). The knowledge gathered from CIGS solar cells fabrication could be tuned and adapted directly for CZTS solar cells. The GBs seem to have the same beneficial properties for CZTS as for CIGS, such as enhanced minority carrier collection taking place at the GB (Li et al. 2012).

20.2.5.2 CZTS Solar Cell Configuration

Since the CZTS solar cell configuration is similar to that of the CIGS (or CIGSSe) (already described in the previous sections), the present section would avoid going into the details about the same.

Although CZTS single crystals had been grown and analyzed in 1967 (Nische et al. 1967), however, the PV effect of the CZTS films was reported only in 1988 (Ito and Nakazawa 1988). The fabricated heterodiode consisted of a transparent cadmium-tin-oxide thin film and a CZTS thin film on an SS substrate. An open-circuit voltage of 165 mV was obtained with the device. In 1997, Friedlmeier et al. fabricated thin-film solar cells using a CZTS layer as the light absorber in contact with an *n*-CdS/ZnO window layer. The best energy conversion efficiency produced by the cells was 2.3%. This record was later broken by Katagiri's group in 1999 that produced a CZTS solar cell with 2.63% power conversion efficiency. In this cell, the CZTS film was deposited on a Mo-coated soda lime glass (SLG) substrate. By optimization of the sulfurization process, the efficiency of the solar cells was increased to 5.45% in 2003, and then to 6.7% in 2008. Two review papers regarding the efficiency milestones achieved in CZTS-based thin-film solar cells were reported by Katagiri (2005) and Katagiri et al. (2009a), respectively. Todorov et al. (2010) reported 9.6% efficient CZTS-based thin-film solar cells. In this cell, the CZTS thin film was partly selenized to have a broader spectral photoresponse. The current record value of 11.1% is reported by Barkhouse et al. (2012). Figure 20.38 gives the power conversion efficiency in the record CZTSSe thin-film devices versus year, showing constant progress in the technology.

CdS has been observed to have suitable band offset with CZTS, and until now, the most efficient solar cells were obtained with a CdS buffer layer (Nagoya et al. 2011). At the absorber/buffer interface, CZTS is Cu poor, similar to CIGS (Bär et al. 2011). Moreover, sodium incorporation seems to have the same effects on CZTS as in CIGS. It promotes the growth of larger grains, enhances conductivity, and has a significant effect on film morphology, as was demonstrated by SLG/borosilicate substrate comparison and dipping in Na₂S (Hlaingo Oo et al. 2011; Prabhakar and Jampana 2011). However, Na diffusion in CIGS is observed to be larger than in CZTS. It is interesting to note that oxidation of the CZTS absorber by dipping in deionized water (Katagiri et al. 2009a) or O₂ annealing (Repins et al. 2012) before deposition of CdS seems to improve efficiencies. As for CIGS, reducing the time between absorber synthesis and CdS deposition to the minimum is of utmost importance (Grenet et al. 2012).

20.2.5.3 Deposition and Growth of CZTS (CZTSSe) Absorber

The investigations on the phase equilibrium in the Cu₂S-ZnS-SnS₂ system showed that single phase CZTS crystals is a challenge as it can only be grown in a very narrow region (Oleksyuk et al. 2004). Secondary phases such as ternary and quaternary compounds are

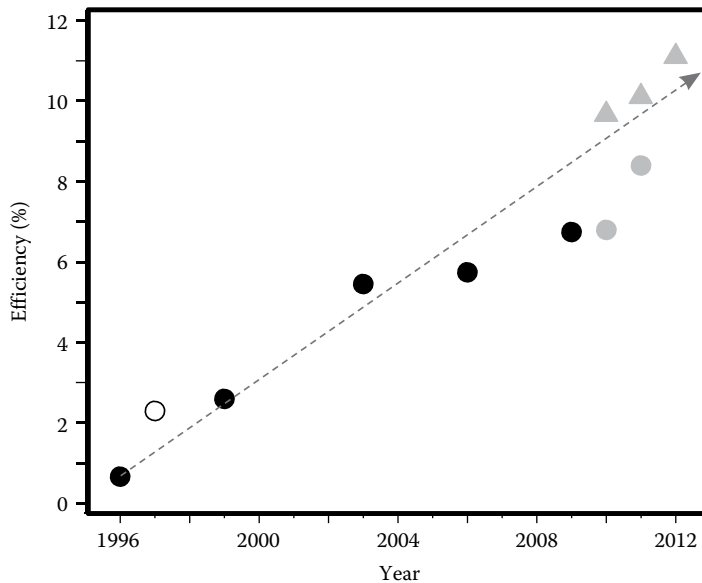


FIGURE 20.38

Power conversion efficiency in the record CZTSSe thin-film devices versus year, showing consistent progress. Data for pure sulfur-containing materials (CZTS) are represented by circles, whereas data for kesterites in which Se has been introduced are represented by triangles. The laboratories responsible for each record are Nagaoka Nat. College of Technology (black), University of Stuttgart (white), and IBM Corp. (gray). The dotted arrow is a guide to the eye. (From Mitzi et al. 2013.)

much easier to form than CZTS. Therefore, it is quite challenging to deposit CZTS thin film without the significant presence of secondary phases. Moreover, in contrast to CIGS, the elements in CZTS synthesis are prone to evaporation and sublimation. Zn sublimates at 430°C (Teeter et al. 2011), SnSe at 350°C (Redinger et al. 2011a), and SnS at 370°C and Sn evaporates at 400°C (Weber et al. 2010; Yoo et al. 2012). Moreover, high temperatures promote CZTS decomposition that can be avoided by atmosphere control (Redinger et al. 2011b).

The possibility of replacing the rare In with readily available Zn and Sn while retaining key semiconductor properties, such as nearly identical bandgap to the highly successful chalcopyrite absorbers, makes CZTSSe particularly attractive for large-scale PV production. This potential has given significant research impetus not only toward the fabrication of higher performance CZTSSe devices with traditional vacuum deposition techniques such as sputtering and coevaporation but also to explore a variety of alternative lower-cost and high-throughput fabrication approaches. Some of these alternative methods include spray pyrolysis, ED, photochemical deposition, *monograin* deposition, and direct liquid-coating techniques, including pure-solution, particle-based, and hybrid slurry ink deposition. The details of these techniques have been covered in an extensive review article by Mitzi et al. (2013).

20.2.5.3.1 Sputtering

Sputtering has been the first and one of the most extensively explored vacuum-based routes to CZTSSe film deposition (Ito and Nakazawa 1988). Katagiri et al. have investigated a series of sequential sputtering approaches comprising different stacked and cosputtered precursor configurations followed by high-temperature sulfurization anneals. The results from these studies laid the foundation for CZTSSe technology, establishing key process

parameters such as optimal elemental ratios (generally, Cu-poor and Zn-rich relative to the ideal CZTSSe stoichiometry) (Katagiri et al. 2009b). After a series of improvements, including soaking in deionized water after film deposition to remove surface oxide impurities, a power conversion efficiency of 6.77% was achieved for a pure sulfide CZTS device (Katagiri et al. 2008). Recently, CZTSSe devices were prepared by cosputtering from compound targets of $\text{Cu}_x(\text{S,Se})_y$, $\text{Zn}_x(\text{S,Se})_y$, and $\text{Sn}_x(\text{S,Se})_y$ in an argon atmosphere, followed by annealing in an SnS and S_2 gas atmosphere, and devices with efficiencies of as high as 8% have been reported (Chawla and Clemens 2012).

20.2.5.3.2 Coevaporation

In contrast to the CIGSSe technology, CZTSSe deposition using coevaporation has encountered significant challenges during especially in the classical configuration where the substrate is maintained at high temperature while delivering precisely controlled elemental fluxes. In addition to the typically volatile Se and S in chalcopyrite absorbers, Sn re-evaporation also occurs during CZTSSe deposition (Friedlmeier et al. 1997). This issue was addressed by introducing a faster coevaporation process in which Sn loss could be mitigated. One way to go around this issue is by adding continuous Sn overpressure throughout the whole high-temperature process, including part of the cooling stage as indicated in a recent NREL report (Repins et al. 2011). Using this approach, device efficiencies of as high as 9.2% for pure selenide CZTSSe devices have been achieved (Repins et al. 2012). Currently, the best performing coevaporated CZTS (pure sulfide) devices have reached efficiencies of 8.4%, using a process developed at IBM that consists of coevaporation onto a low-temperature substrate followed by a short anneal at atmospheric pressure (Shin et al. 2011).

20.2.5.3.3 Nonvacuum Deposition Approaches

From the early years of CZTSSe development, it was well understood that a combination of cheap readily available materials combined with a reliable low-cost fabrication approach could revolutionize the PV industry. Three approaches based on pure solutions, nanoparticles, or hybrid particle–solutions, respectively, have been particularly pursued. Of these, the third category of inks, comprising a combination of dissolved and solid active components, has so far been the most successful CZTSSe fabrication approach. It advantageously uses the binding action of dissolved metal chalcogenide species to produce dense, compact layers and additionally bypasses the solubility limitation of pure solution approaches by introducing particle components that further provide densification and crack-deflection benefits. Recently, Yang and coworkers (Hsu et al. 2012) studied the chemical pathways involved in the hydrazine-based deposition and heat treatment process. The precursor ink was dried at room temperature resulting in the integration of copper and tin chalcogenide complexes to form a bimetallic framework, with hydrazine and hydrazinium molecules as spacers. After mild thermal annealing, the spacers are removed and the $\text{Cu}_2\text{Sn}(\text{Se,S})_3 + \text{Zn}(\text{Se,S}) \rightarrow \text{Cu}_2\text{ZnSn}(\text{Se,S})_4$ reaction is triggered. The described reaction pathway contains fewer steps than most deposition processes, which typically start with elemental or binary chalcogenides (Hsu et al. 2012). By use of this hybrid solution–nanoparticle approach, a record efficiency of 9.7% was reported in 2010 by the IBM group (Todorov et al. 2010). The method was further refined to yield 10.1% power conversion efficiency in 2011 (Barkhouse et al. 2012) and most recently to the 11.1% level (Todorov et al. 2011), which represents the current world record for the kesterite-based system.

The efficiency improvement in the CZTS technology has been significant in a short span of time, and this gives a hope that this technology can provide alternatives to the material

sustainable issues for In and Ga in CIGS. It may be noted that the In and Ga materials are the by-products of the Zn smelting factories, and so ramping up the production of CZTS technology will also enable the sustained supply of In and Ga, leading to sustained and regenerative production along with CZTS technology growth.

20.2.6 New-Generation Solar Cells

The beginning of 1990s has seen the emergence of new and disruptive technologies viz. dye-sensitized and later organic solar cells (Grätzel 2000), which followed completely different device approach of bulk-heterojunction formation in the nanometer length regime, which can be referred to as new generation solar cells. DSSCs are nanocomposites of mesoporous TiO₂ and inorganic dyes (typically ruthenium complexes); they created a breakthrough by achieving relatively high conversion efficiency ~10% through the use of rather inexpensive and abundant materials (O'Regan and Grätzel 1991).

The solar cell action in the aforementioned device on the illumination of light is initiated by excitonic electron–hole pair generation and dissociation leading to a charge separation at the nanointerface. These devices are therefore termed as *excitonic* or organic–inorganic or hybrid solar cells. Unlike conventional *p–n* homojunction (*c–Si*) solar cells, the absorption of photons and electron transport is mediated via two dissimilar constituents, viz., dyes and *n*-type nanocrystalline TiO₂, respectively, while the holes are transported through a hole-transporting material (HTM), which could be a redox liquid electrolyte or ion-conducting polymeric electrolyte (quasisolid state) or quantum dot sensitized or hole-conducting conjugated polymer material or small molecules or perovskites (solid state).

Although the initial results had been remarkable, the liquid junction DSSC technology appears to have now reached a state of stagnation in the efficiency values, with an increase from about 10% to 12.3% only in the span of over 20 years. This technology had also suffered from the lack of sensitizer dyes with wider spectral coverage, atmospheric degradation, and engineering issues such as encapsulation and sealing of the liquid junction device, which had prevented this technology from making a mark in commercialization. Incidentally, there has been a breakthrough in an attempt to solve these issues with the development of solid-state DSSC, in the form of the mesoscopic perovskite solar cells developed in parallel by Michael Grätzel and coworkers at EPFL, Switzerland (Burschka et al. 2013), and Henry Snaith and coworkers at Oxford University (Lee et al. 2012) with efficiencies ~10% and 11%, respectively, initially which had moved up to over 17% (Bennett 2014; Snaith 2014) toward the end of 2013. A comprehensive detail on these developments including liquid-, quasi-, and solid-state DSSCs (or perovskite cells) has been reported (Upadhyaya et al. 2013) and has been described briefly in the following section.

A significant achievement was made toward the development of DSSC/CIGS tandem (Liska et al. 2006) solar cell, which resulted then with over 15% efficient cells with 1.42 V open circuit voltage (using a physical stack of DSSC and CIGS cells with 4 wired configuration with DSSC cell efficiency about 8% and CIGS efficiency about 13%), bringing a step jump in efficiencies. The monolithic two-wire DSSC/CIGS tandem was not successful because of issues of corrosion caused by liquid electrolyte component (Wenger et al. 2009). However, with solid-state analogues of DSSC or perovskite solar cells available with higher efficiencies, it is anticipated that the tandem cells up to 27% efficiencies could be developed (Kim et al. 2013; Kranz et al. 2013).

20.2.6.1 Perovskite Solar Cells

Apart from the aforementioned listed thin-film solar cells, there are a new generation of thin-film solar cells along with DSSCs and organic solar cells that have emerged recently. Attempts have been going on over many years to find an alternative to the liquid electrolytes and to obtain, thus, an improved DSSC, which will have ease of fabrication, less complication in the sealing and encapsulation of the device, possibility for monolithic interconnection of the cells within the module, and therefore also increased performance and lower cost. However, a class of solar cells based on perovskite structured semiconductors has emerged and rapidly reached conversion efficiencies of more than 15% (Figure 20.39), as listed in Table 20.5.

Most commonly, $\text{CH}_3\text{NH}_3\text{PbI}_3$ -based organic-inorganic perovskite materials have been used in these types of solar cells, which are having high charge carrier mobility. High mobility is important because, together with high charge carrier lifetimes, it means that the light-generated electrons and holes can move large enough distances to be extracted as current, instead of losing their energy as heat within the cell (Hodes 2013). Moreover, the perovskite solar cells can be deposited by low-temperature methods such as solution process (spin coating) and thermal evaporation methods. The advantages of the solid-state DSSCs over the liquid DSSCs are obvious: less complications involved in the manufacturing equipment, easy possibility for producing monolithically interconnected modules, easier sealing, and encapsulation of the modules (similar to the processes employed for other thin-film solar cells). Although the efficiency values reached for small-size individual solar cells can be considered to be satisfactory, and should basically provide a great commercialization potential for this technology in the future, especially thanks to the fact that we have here a true solid-state device, the stability and longevity of the device is yet to be ascertained. Although the perovskites are cheaper than the conventional dyes and have wider spectral coverage, they are susceptible to temperature and humidity. Temperature around 95°C can bring structural

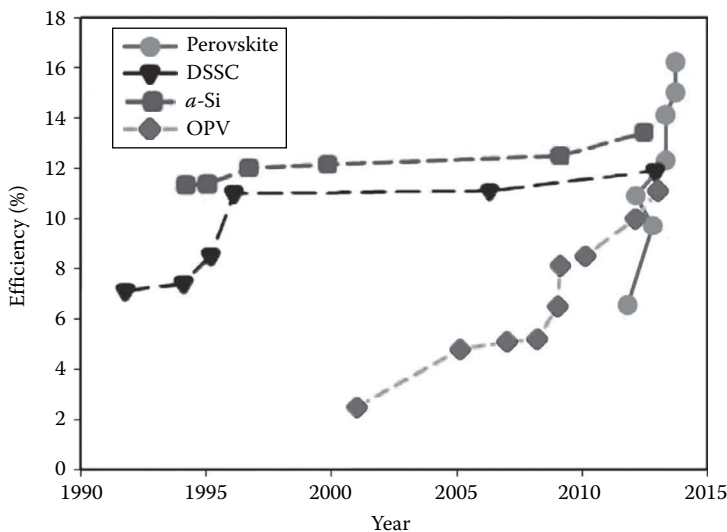


FIGURE 20.39

Comparing the rate of increase in perovskite solar cell efficiencies with the other thin-film PV technologies. (From Hodes, G., *Science*, 342, 317, 2013.)

transformation in the materials and also atmospheric moisture can lead to degradation as well. Thus, a strong barrier layer would be required for desired stability toward moisture ingress. In addition other variants of perovskites will have to be found out with intrinsic temperature stability issues. Besides, other critical issues of long-term stability of the devices are the stability of the organic spiro-OMeTAD layer, and the need for the perovskites with Pb-free compounds, to cover the environmental concerns.

20.2.7 Environmental Concerns and Cd Issue

The CdTe and CIGS thin-film technologies have demonstrated excellent potential for cost-effective production of solar electricity. However, these technologies, especially the CdTe, suffer from the perception of toxicity of constituent element Cd, which is used in the form of a stable compound in thin-film modules. Often raised issues such as the risks or hazards in handling CdTe technology are associated with the materials used during the processing and fabrication of CdTe/CdS and CdS/CIGS solar cells along with the risks associated during the cradle to grave operating lifetime of these modules. The environmental and health hazard (E&H) issues of CdTe solar modules have been extensively investigated by several independent agencies including the national laboratories in Europe and United States (Fthenakis and Zweibel 2003; Fthenakis et al. 1999, 2004). There are a number of reports now available, which support CdTe technology against any serious threat arising even under worst-case scenarios. Under extreme conditions like fire under basement and leaching from broken modules, the theoretical models show that even if all the Cd compounds were to be released, Cd concentrations within the near vicinity to the CdTe PV system are below human health screening levels (Beckmann and Mennenga 2011; Dutta et al. 2012; Sinha et al. 2011). An interesting report also provides a supporting argument in favor of CdTe technology analyzed during earthquakes or tsunami in Japan (Matsuno 2013). While First Solar program of module recycling is already available and supports their confidence (<http://www.firstsolar.com/en/technologies-and-capabilities/recycling-services>), the chance of Cd compounds and other potentially harmful materials getting into the ambient environment from the PV plant during its lifetime is also negligible. The current power generation technologies using coal have a large amount of Cd emitted in the environment in an uncontrolled manner, with the amount far exceeding the expected emission from CdTe modules even under exceptional conditions (e.g., fire). Even the dominant PV technologies based on Si solar cells have larger life cycle Cd emissions due to the embodied energy being larger for these devices (Fthenakis et al. 2008).

While CdTe technology has no chance to do away with Cd, there is some maneuverability in CIGS technology in the elimination of very thin (typically ~50 nm) CdS buffer layer, and so the quest for alternative buffer layer is being successfully pursued. Initial success has already been achieved as CIGS solar cells of 16%–18.8% and modules of 13.4% have been developed with alternative *Cd-free* buffers (Hedström et al. 1993; Kushiya 2004). Recently, coevaporation of CIGS in an inline single-stage process is used to fabricate solar cell devices with up to 18.6% conversion efficiency using a CdS buffer layer and 18.2% using a $Zn_{1-x}Sn_xO_y$ (Cd-free) buffer layer. Furthermore, a 15.6 cm² minimodule, with 16.8% conversion efficiency, has been made with the same layer structure as the CdS baseline cells, showing the excellent uniformity. These cell results were externally verified (Lindahl et al. 2013).

Referring to the perception and concerns on Cd issues, V. Fthenakis (Sr. Chemical Engineer, Brookhaven national Laboratory) and K. Zweibel (Manager, Thin film

partnership program, NREL, United States) had presented a detailed account of their studies during their presentations at the 2003 NCPV program review meeting in the United States (Fthenakis et al. 2004) that confirmed that CdTe panels would be almost benign with almost zero emission (0.01 g/GW h) as compared to its counterparts oil (44.3 g/GW h) and coal (3.7 g/GW h), with no associated health hazards, and gave a clean chit to CdTe technology. The following points emerged out of the studies:

Cadmium is a by-product of zinc, lead, and copper mining. It constitutes only 0.25% of its main feedstock ZnS (sphalerite). Cadmium is released into the environment from phosphate fertilizers, burning fuels, mining and metal processing operations, cement production, and disposing of metal products. Releases from disposed Cd products, including Ni–Cd batteries, are minimum contributors to human exposure because Cd is encapsulated in the sealed structures. Most human cadmium exposure comes from ingestion and most of that stems from the uptake of cadmium by plants, through fertilizers, sewage sludge, manure, and atmospheric deposition. Although long-term exposure to elemental cadmium, a carcinogen, has detrimental effect on kidneys and bones, limited data exist in toxicology. However, CdTe compound is more stable and less soluble than Cd element and therefore likely to be much less toxic.

Considering the electrolytic refinery production of CdTe powders (from Cd wastes from Zn, iron, and steel industries), there would be an emission of 0.001% Cd gaseous emission. This would correspond to 0.01 g/GW h, which is significantly less as compared to the perceptions and hypes created by some who estimate it at 0.5 g/GW h based on other crude processes or unsubstantiated data. The only potential hazard that could come to any ones' mind would be the building fire. It has also been estimated quantitatively that the maximum temperature of a basement on fire is ~900°C, which is still less than the melting point of CdTe (1041°C). Besides, the vapor pressure at 800°C for CdTe is ~2.5 Torr (0.003 atmosphere), so this minimizes the risks further, and once sealed between glass plates, any Cd vapor emission is unlikely. The main conclusion of the studies was that the environmental risks associated with CdTe-based technology are minimal. Every energy source or product may present some direct or indirect environmental health and safety hazards and those of CdTe should by no means be considered a problem; the following conclusions were drawn:

- Cd is produced as a by-product of Zn and can either be put to beneficial uses or discharged to the environment posing another risk.
- CdTe in PV is much safer than other current Cd uses.
- CdTe PV uses Cd about 2500 times more efficient than Ni–Cd batteries.
- Occupational health risks are well managed.
- Absolutely no emission during PV operation.
- A risk from fire emission is minimal.
- CdTe technology and modules are safe and do not pose significant risks.

20.2.8 Conclusions

1. PV market is booming with a phenomenal surging growth rate of over 40% for more than a decade despite a downturn observed in the worldwide economy recently. The cumulative PV production capacity was ~140 GW by 2013, while 50 GW production is anticipated in 2014 alone. This is in contrary to the belief in the last decade

that high demand for cost-effective PV installations with more consumer-oriented choices can neither be met by the *c*-Si wafer technology nor is expected to achieve low production cost targets of below €1/W, which is a myth now.

2. An upsurge in the PV production and an artificial module price crisis created by Chinese manufacturers has brought a radical drop in the module prices well below \$0.6/W_p since 2011. This strategy has wiped away the PV industries in Europe and has caused a PV manufacturing base shift toward the Asia, with China, Taiwan, and Korea taking this opportunity and leading the show through their natural advantage of cheaper material supply and cheaper human resources available.
3. Thin-film PV has clearly demonstrated an excellent potential for cost-effective generation of solar electricity using CdTe technology by First Solar in the United States and CIGS technology by Solar Frontier in Japan currently aiming to produce 2 GW capacities annually. While the world record cell efficiencies of 20.4% for CdTe and 20.9% for CIGS have already matched/surpassed polycrystalline Si efficiency of 20.4%, the module efficiencies have also shown significant figures of 17% and 16.4% for CdTe and CIGS, respectively. In fact, thin-film PV market has gained stability from *c*-Si production and market leadership with almost 90% share. It is anticipated that a mix of *c*-Si and thin-film PV technologies will cater the market needs in near to midterm future, followed by the dominance of thin-film and other PV technologies in long term.
4. The *a*-Si technology has suffered a setback mainly because of the stagnancy and the low efficiency figures arising from the intrinsic light-dependent degradation issues. This has resulted in the bankruptcy of the United Solar company in 2013, which was the largest manufacturer of triple junction *a*-Si technology on steel foils. Efforts are underway in Japan through NEDO programs to overcome these barriers for a successful relaunching of this technology, which will have wider application in BIPV and BAPV sectors in the future.
5. Thin-film PV industries are growing fast; however, there are several issues:
 - a. Reducing the gap between lab efficiency and larger area industrial production efficiency. This is achievable with the design of better equipment with in situ diagnostics. Nonavailability of standard deposition system for thin-film PV has been a problem, so effort is needed to develop large-area equipment suitable for thin-film PV.
 - b. Unlike *c*-Si technology, which allows the process and equipment availability off the shelf, there is no availability of processing equipment and the optimized processes for thin-film PV technologies, which are only under the proprietary control of the companies involved. Although companies like Manz Solar (<http://www.manz.com/>) have taken initiatives in this direction, this is not enough to cover the entire promise.
 - c. To lower the cost, increase the throughput and the yield, efforts are needed for further simplification and increased robustness of the process and device structures.
 - d. If multi-giga and terawatt PV facilities are to be successful for a safer and prosperous world, further improvements in the device structures along with optimized material utilisation (low wastage) have to be achieved for attaining efficiencies greater than 25%.

References

- Abken, A. E. and Bartelt, O. J. 2002. *Thin Solid Films*, 403–404, 216–222.
- Ahn, S. W., Lee, S. E., and Lee, H. M. D. 2012. Presented at *27th European Photovoltaic Solar Energy Conference*, Frankfurt, Germany, 24–28 September 2012, p. 3AO5.1.
- Amkreutz, D., Müller, J., Schmidt, M., Hänel, T., and Schulze, T. F. 2011 *Progress in Photovoltaics*, 19, 937–945.
- Arya, R. R. 2004. In *Proceedings of the 19th European Photovoltaic Conference*, Paris, June 7–11, 2004, <http://apache.solararch.ch/pdf/KonferenzParisInternet.pdf>.
- Barkhouse, D. A. R., Gunawan, O., Gokmen, T., Todorov, T. K., and Mitzi, D. B. 2012. *Progress in Photovoltaics: Research and Applications*, 20, 6–11.
- Basore, P. A. 2002. In *Proceedings of 29th IEEE Photovoltaic Specialists Conference*, May 19–24, 2002, pp. 49–52, <http://ieeexplore.ieee.org/xpl/mostRecentIssue.jsp?punumber=8468>.
- Bär, M., Schubert, B. A., Marsen, B., Krause, S., Pookpanratana, S., Unold, T., Weinhardt, L., Heske, C., and Schock, H.-W. 2011. *Applied Physics Letters*, 99, 112103.
- Bätzner, D. L., Romeo, A., Terheggen, M., Döbeli, M., Zogg, H., and Tiwari, A. N. 2004. *Thin Solid Films*, 451, 536–543.
- Bätzner, D. L., Romeo, A., Zogg, H., Wendt, R., and Tiwari, A. N. 2001. *Thin Solid Films*, 387, 151–154.
- Becker, C., Amkreutz, D., Sontheimer, T., Preidel, V., Lockau, D., Haschke, J., Jogschies, L. et al. 2013. *Solar Energy Materials and Solar Cells*, 119, 112–123.
- Beckmann, J. and Mennenga, A. 2011. Calculation of emissions when there is a fire in a photovoltaic system made of cadmium telluride modules. Bavarian Environmental Agency, Augsburg, Germany.
- Benagli, S., Borrello, D., Vallat, E., Meier, J., Kroll, U., Hötzel, J., Bailat, J. et al. 2009. In *Proceedings of 24th European Photovoltaic Solar Energy Conference*, Hamburg, Germany, September 21–25, 2009, pp. 2293–2298, <http://www.solarplaza.com/event/24th-european-photovoltaic-solar-energy-conference>.
- Bennett, P. 2014. http://www.solarpowerportal.co.uk/news/oxford_professor_recognised_by_materials_research_society_for_solar_3309.
- Bergmann, R. B. 1999. *Applied Physics A* 69, 187–194.
- Bermudez, V. 2013. Nexcis, CIGS technology from R&D to industry. Presented at *the Fifth Photovoltaic Thin-Film Week*, Berlin, Germany, April 2013, https://www.helmholtz-berlin.de/projects/pvcomb/events/tfw13/index_en.html.
- Bhattacharya, R. N. and Ramanathan, K. 2004. *Solar Energy*, 77, 679–683.
- Bonnet, D. 2004. In *Proceedings of the 19th European Photovoltaic Solar Energy Conference*, Paris, June 7–11, 2004, pp. 1657–1664, <http://apache.solararch.ch/pdf/KonferenzParisInternet.pdf>.
- Bonnet, D. and Rabenhorst, H. 1972. In *Proceedings of the Ninth PV Specialists Conference*, pp. 129–132.
- Bruton, T. M., Woodcock, J. M., Roy, K., Garrard, B., Alonso, J., Nijs, J., Räuber, A. et al. 1997. Final report European Commission Project RENA-CT94-0008 “MUSICFM”.
- Burger, B. 2013. Photovoltaics report, Fraunhofer, ISE, BMU, EEG 2013 and BMWi Energiedaten, Freiburg, October 24, 2014. <http://www.ise.fraunhofer.de/de/downloads/pdf-files/aktuelles/photovoltaics-report-in-englischer-sprache.pdf>.
- Burschka, J., Pellet, N., Moon, S. J., Humphry-Baker, R., Gao, P., Nazeeruddin, M. K., and Grätzel, M. 2013. *Nature*, 499, 316–319.
- Candelise, C., Spiers, J., and Gross, R. 2011. Materials availability for thin film (TF) PV technologies development: A real concern? ICEPT/WP/2011/001, Imperial College Centre for Energy Policy and Technology, London, U.K., <https://workspace.imperial.ac.uk/icept/Public/Materials%20for%20PV%20ICEPT%20format.pdf>.
- Carabe, J. and Gandia, J. J. 2004. *Opto-Electronics Reviews* 12, 1–6.
- Carlson, D. and Wronski, C. 1976. *Applied Physics Letters*, 28, 671–673.
- Chaisitsak, S., Yamada, A., and Konagai, M. 2001. In *Proceedings of the Materials Research Society Spring Meeting*, p. 668.

- Chan, C. P., Lam, H., and Surya, C. 2010. *Solar Energy Materials Solar Cells*, 94, 207–211.
- Chawla, V. and Clemens, B. 2012. In *Proceedings of 38th IEEE Photovoltaics Specialists Conference*, Austin, TX, June 3–8, 2012, pp. 002990–002992. <http://www.ieee-pvsc.org/PVSC38/>.
- Chen, S., Gong, X. G., Walsh, A., and Wei, S. H. 2009. *Applied Physics Letters*, 94, 041903(1–3).
- Chirilă, A., Reinhard, P., Pianezzi, F., Bloesch, P., Uhl, A. R., Fella, C., Kranz, L. et al. 2013. *Nature Materials*, 12, 1107–1111.
- Chiu, P. T., Law, D. C., Woo, R. L., Singer, S. B., Bhusari, D., Hong, W. D., Zakaria, A. et al. 2014. *IEEE Journal of Photovoltaics*, 4, 493–497.
- Chopra, K. L., Paulson, P. D., and Dutta, V. 2004. *Progress in Photovoltaics: Research Application*, 12, 69–92.
- Colville, F. 2014. http://www.pv-tech.org/guest_blog/npd_solarbuzz_upgrades_uk_pv_market_to_2.5gw_in_2014.
- Compaan, A. D., Gupta, A. K., Lee, S., Wang, S., and Drayton, J. 2004. *Solar Energy*, 77, 815–822.
- Cusano, D. A. 1963. *Solid State Electronics*, 6, 217–232.
- Deng, X. and Schiff, E. A. 2003. Amorphous silicon based solar cells. In *Handbook of Photovoltaic Science and Engineering*, A. Luque and S. Hegedus (Eds.), pp. 505–565. Wiley, New York.
- Duchatelet, A., Chassaing, E., Savidand, G., Vannier, R. N., and Lincot, D. 2012. One-step electrochemical deposition of Cu–In–Ga mixed oxide thin films for low-cost CIGS solar cells. In presented at the *27th European Photovoltaic Solar Energy Conference and Exhibition*, pp. 2805–2807, September 2012. doi: 10.4229/27thEUPVSEC2012-3DV.3.34.
- Diefenbach, K. H. 2005. *Photon International*, 48–67.
- Docampo, P., Ball, J. M., Darwich, M., Eperon, G. E., and Saith, H. J. 2013. *Nature Communications*, 4, 2761–2767.
- Dore, J., Ong, D., Varlamov, S., Egan, R., and Green, M. A. 2014. *IEEE Journal of Photovoltaics*, 4, 33–39.
- Durr, M., Schmid, A., Obermaier, M., Rosselli, S., Yasuda, A., and Nelles, G. 2005. *Nature Materials*, 4, 607–611.
- Dutta, V., Vamsi Krishna, K., Sreekrishnan, T. R., and Singh, U. P. 2012. http://www.fitt-iitd.org/downloads/First%20Solar_Final%20Report_24-08-2012.pdf.
- Eberspacher, C., Fredric, C., Pauls, K., and Serra, J. 2001. *Thin Solid Films* 387, 18–22.
- Engelhart, P., Wendt, J., Schulze, A., Klenke, C., Mohr, A., Petter, K., Stenzel, F. et al. 2010. In *Energy Procedia, First International Conference on Silicon Photovoltaics, Energy Procedia*, 8 (2011) 313–317, www.Elsevier.com/locate/procedia.
- Fahrenbruch, A., Bube, R., Kim, D., and Lopez-Otero, A. 1992. *International Journal of Solar Energy* 12, 197–222.
- Fehr, M., Schnegg, A., Rech, B., Astakhov, O., Finger, F., Bittl, R., Teutloff, C., and Lips, K. 2014. *Physical Review Letters*, 112, 066403(1–5).
- Fella, C. M., Romanyuk, Y. E., and Tiwari, A. N. 2013. *Solar Energy Materials and Solar Cells*, 119, 276–277.
- Ferekides, C., Britt, J., Ma, Y., and Killian, L. 1993. In *Proceedings of 23rd IEEE, PV Specialists Conference*, pp. 389–393, <http://iee-ee.eng.usf.edu/ferekides/plist.html>.
- First Solar. 2005. <http://www.firstsolar.com/index.html>.
- First Solar. 2014. <http://investor.firstsolar.com/releasedetail.cfm?ReleaseID=828273>.
- Ford, G. M., Guo, Q., Agrawal, R., and Hillhouse, H. W. 2011. *Chemistry of Materials*, 23, 2626–2629.
- Friedlmeier, T. M., Wieser, N., Walter, T., Dittrich, H., and Schock, H. W. 1997. In *Proceeding of the 14th European Conference of Photovoltaic Science and Engineering and Exhibition*, p. 1242.
- Fthenakis, V., Morris, S., Moskowitz, P., and Morgan, D. 1999. *Progress in Photovoltaics*, 7, 489–497.
- Fthenakis, V. and Zweibel, K. 2003. CdTe PV: Real and perceived EHS risks. In Prepared for the *NCPV and Solar Program Review Meeting*, Denver, CO, March 24–26, 2003, <http://www.nrel.gov/docs/fy03osti/33561.pdf>.
- Fthenakis, V. M., Fuhrmann, M., Heiser, J., and Wang, W. 2004. Presented at the *19th European PV Solar Energy Conference*, Paris, France, June 7–11, 2004, p. 5BV.1.32, https://www.bnl.gov/pv/files/pdf/abs_176.pdf.
- Fthenakis, V. M., Kim, H. C., and Alsema, E. 2008. *Environmental Science and Technology*, 42, 2168–2174.

- Gabor, A. M., Tuttle, J. R., Albin, D. S., Contreras, M. A., Noufi, R., and Hermann, A. M. 1994. *Applied Physics Letters*, 65, 198–200.
- Geisz, J. F., Steiner, M. A., Garcia, I., Kurtz, S. R., and Friedman, D. J. 2013. *Applied Physics Letters*, 103, 041118 (1–5).
- Gifford, J. 2013. http://www.pv-magazine.com/news/details/beitrag/panasonic-hits-247-cell-efficiency_100010185/#ixzz2yFQcp1fv.
- Goetzberger, A., Hebling, C., and Schock, H. W. 2003. *Materials Science and Engineering*, R40, 1–46.
- Granqvist, C. G. 2003. *Advance Materials*, 15, 1789–1803.
- Grätzel, M. 2000. *Progress in Photovoltaics: Research and Applications*, 8, 171–186.
- Grenet, L., Bernardi, S., Kohen, D., Lepoittevin, C., Noël, S., Karst, N., Brioude, A., Perraud, S., and Mariette, H. 2012. *Solar Energy Materials and Solar Cells*, 101, 11–14.
- Gross, R.D., Heptonstall, P., Greenacre, P., Candelise, C., Jones, F., and Castillo, A. November 2013. Presenting the future: An assessment of future costs estimation methodologies in the electricity generation sector. A report by the UKERC Technology & Policy Assessment Function, REF UKERC/RR/TPA/2013/001, UKERC.
- Guha, S. 2004. *Solar Energy*, 77, 887–892.
- Guha, S., Narsimhan, K. L., and Pietruszko, S. M. 1981. *Journal of Applied Physics*, 52, 859–860.
- Guha, S., Yang, J., Nath, P., and Hack, M. 1986. *Applied Physics Letters*, 49, 218–219.
- Hall, R. B., Birkmire, R. W., Phillips, J. E., and Meakin, J. D. 1981. *Applied Physics Letters*, 38, 925–926.
- Hanergy Annual Report. 2013. http://www.hanergysolargroup.com/pdf/ew_0566frp-20140407q4.pdf.
- Hedström, J., Ohlsen, H., Bodegard, M., Kylner, A., Stolt, L., Hariskos, D., Ruckh, M., and Schock, H. W. 1993. In *Proceedings of the 23rd IEEE Photovoltaic Specialists Conference*, pp. 364–371, http://www.appropedia.org/Photovoltaic_materials_abundance_limitations_literature_review.
- Hegedus, S. S. and Luque, A. 2003. Status, trends, challenges and the bright future of solar electricity from photovoltaics. In *Handbook of Photovoltaic Science and Engineering*, A. Luque and S. Hegedus (Eds.), pp. C113–C678. Wiley, New York.
- Hering, G. 2011. *Photon International*, 4, 186–218.
- Hlaingo Oo, W., Johnson, J., Bhatia, A., Lund, E., Nowell, M., and Scarpulla, M. 2011. *Journal of Electronic Materials*, 40, 2214–2221.
- Hodes, G. 2013. *Science*, 342, 317–318.
- Hodes, G., Lokhande, C. D., and Cahen, D. 1986. *Journal of Electrochemistry Society*, 133, C113.
- Honsberg, C. B., Corkish, R., and Bremner, S. P. 2001. In *Proceedings of 17th European Photovoltaic Solar Energy Conference*, Munich, Germany, October 22–26, 2001, pp. 22–26. http://web2.etaflorence.it/cms/index.php?page=17ma-conferenza-ed-esposizione-europea-sull-energia-solare-fotovoltaica&hl=en_US.
- Hosoya, M., Oooka, H., Nakao, H., Gotanda, T., Hayase, R., Nakano, Y., and Saito, M. 2012. In *Proceedings of 73rd Fall Meeting of Japan Society of Applied Physics*, September 11–14, 2012, pp. 12–380. <http://www.osa.org/en-us/publications/>.
- Hosoya, M., Oooka, H., Nakao, H., Gotanda, T., Mori, S., Shida, N., Hayase, R., Nakano, Y., and Saito, M. 2013. In *Proceedings of 93rd Annual Meeting of the Chemical Society of Japan*, March 22–25, 2013, pp. 21–37. http://www.chemistryviews.org/details/event/2766931/Chemical_Society_of_Japan_93rd_Spring_Annual_Meeting.html.
- Hsu, W. C., Bob, B., Yang, W., Chung, C. H., and Yang, Y. 2012. *Energy and Environmental Sciences*, 5, 8564–8571. <http://cleantechnica.com/2013/12/18/new-czts-solar-cell-efficiency-record/>.
- http://cordis.europa.eu/news/rcn/36210_en.html.
- <http://www.firstsolar.com/en/technologies-and-capabilities/recycling-services> <http://www.kaneka-solar.com>.
- <http://www.manz.com/>.
- Ichikawa, Y., Fujikake, S., Takayama, R., Saito, S., Ota, H., Yoshida, T., Ihara, T., and Sakai, H. 1993. In *Proceedings of 23rd IEEE Photovoltaic Specialists Conference*, p. 27.
- Ito, K. and Nakazawa, T. 1988. *Japanese Journal of Applied Physics*, 27, 2094–2097.

- Jackson, P., Hariskos, D., Lotter, E., Paetel, S., Wuerz, R., Menner, R., Wischmann, W., and Powalla, M. 2011. *Progress in Photovoltaics: Research and Applications*, 19, 894–897.
- Jackson, P., Hariskos, D., Wuerz, R., Wischmann, W., and Powalla, M. 2014. *Physica Status Solidi (RRL)*, 8, 219–222.
- Jäger-Waldau, A. 2004. *Solar Energy*, 77, 667–678.
- Kaelin, M., Rudmann, D., and Tiwari, A. N. 2004. *Solar Energy*, 77, 749–756.
- Karg, F. H. 2001. *Solar Energy Materials and Solar Cells*, 66, 645.
- Kapur, V. K., Fisher, M., and Roe, R. 2001. In *Proceedings of the 2001 MRS Spring Meeting*, San Francisco, CA, April 16–20, 2001, p. 668, H2.6.1-7, <http://www.mrs.org/spring2001/>.
- Katagiri, H. 2005. *Thin Solid Films*, 480, 426–432.
- Katagiri, H., Jimbo, K., Maw, W. S., Oishi, K., Yamazaki, M., Araki, H., and Takeuchi, A. 2009a. *Thin Solid Films*, 517, 2455–2460.
- Katagiri, H., Jimbo, K., Tahara, M., Araki, H., and Oishi, K. 2009b. *Material Research Society Symposium Proceedings*, 1165, M01–M04.
- Katagiri, H., Jimbo, K., Yamada, S., Kamimura, T., Maw, W. S., Fukano, T., Ito, T., and Motohiro, T. 2008. *Applied Physics Express*, 1, 041201(1–2).
- Kawai, M. 2013. Nikkei Electronics. http://techon.nikkeibp.co.jp/english/NEWS_EN/20130131/263532/.
- Kayes, B. M., Nie, H., Twist, R., Spruytte, S. G., Reinhardt, F., Kizilyalli, I. C., and Higashi, G. S. 2011. In *Proceedings of the 37th IEEE Photovoltaic Specialists Conference*, June 19–24, 2011, pp. 000004–000008.
- Kazmerski, L., White, F., and Morgan, G. 1976. *Applied Physics Letters*, 29, 268–269.
- Keavney, C. J., Haven, V. E., and Vernon, S. M. 1990. In *Proceedings of 21st IEEE Photovoltaic Specialists Conference*, pp. 141–144.
- Keevers, M. J., Young, T. L., Schubert, U., and Green, M. A. 2007. In *Proceedings of 22nd European Photovoltaic Solar Energy Conference*, Milan, Italy, September 3–7, pp. 1783–1790.
- Keshner, M. S. and Arya, R. 2004. NREL/SR-520-36846. <http://www.nrel.gov/docs/fy05osti/36846.pdf>.
- Kessler, F. and Rudmann, D. 2004. *Solar Energy*, 77, 685–695.
- Kim, S., Kasashima, S., Sicanugrist, P., Kobayashi, T., Nakada, T., Konagai, M. 2013. *Solar Energy Materials and Solar Cells*, 119, 214–218.
- Kinoshita, T., Fujishima, D., Yano, A., Ogane, A., Tohoda, S., Matsuyama, K., Nakamura, Y. et al. 2011. In *Proceedings of 26th European Photovoltaic Solar Energy Conference*, September 5–9, 2011 pp. 871–874, <http://www.eea.europa.eu/events/26th-european-photovoltaic-solar-energy-6>.
- Klein, S., Repmann, T., and Brammer, T. 2004. *Solar Energy*, 77, 893–908.
- Kojima, A., Teshima, K., Shirai, Y., and Miyasaka, T. 2009. *Journal of American Chemical Society*, 131, 6050–6051.
- Komiya, R., Fukui, A., Murofushi, N., Koide, N., Yamanaka, R., Katayama, H. 2011. Technical digest. In *21st International Photovoltaic Science and Engineering Conference*, Fukuoka, Japan, 2C-50-08, http://www.researchsea.com/html/calendar.php/aid/6371/cid/1/research/_pvsec-21_21st-international-photovoltaic-science-and-engineering-conference.html?PHPSESSID=k0o28evdgdjkjp845701b5vm20.
- Konagai, M. 2013. Presented at *Asian Photovoltaic Science and Engineering Conference*.
- Kranz, L., Buecheler, S., and Tiwari, A. N. 2013a. *Solar Energy Materials and Solar Cells*, 119, 278–280.
- Kranz, L., Gretener, C., Perrenoud, J., Schmitt, R., Pianezzi, F., Mattina, F. L., Blösch, P. et al. 2013b. *Nature Communications*, 4, 2306–2313.
- Kranz, L., Gretener, C., Perrenoud, J., Jaeger, D., Gerstl, S. S. A., Schmitt, R., Buecheler, S., and Tiwari, A. N. 2013c. *Advanced Energy Materials*, 2014, 4, 1301400.
- Kranz, L., Jäger, T., Reinhard, P., Hagendorfer, H., Romanyuk, Y. E., Buecheler, S., and Tiwari, A. N. 2013d. In presented at the *Materials Research Society Fall Meeting*, Boston, MA, December 1–6, 2013.
- Kumar, M. H., Yantara, N., Dharani, S., Grätzel, M., Mhaisalkar, S., Boix, P. P., and Mathews, N. 2013. *Chemical Communications*, 49, 11089–11091.

- Kushiya, K. 2004. *Solar Energy*, 77, 717–724.
- Kushiya, K., Ohshita, M., Hara, I., Tanaka, Y., Sang, B., Nagoya, Y., Tachiyuki, M., and Yamase, O. 2003. *Solar Energy Materials and Solar Cells*, 75, 171–178.
- Lebrun, J. 1966. *Revue de Physique Appliquee* 1, 204–210.
- Lechner, P. and Schade, H. 2002. *Progress in Photovoltaics: Research Applications*, 10, 85–97.
- Lee, M. M., Teuscher, J., Miyasaka, T., Murakami, T. N., and Snaith, H. J. 2012. *Science*, 338, 643–647.
- Li, J. B., Chawla, V., and Clemens, B. M. 2012. *Advanced Materials* 24, 720–723.
- Lindahl, J., Zimmermann, U., Szaniawski, P., Törndahl, T., Hultqvist, A., Salomé, P., Platzer-Björkman, C., and Edoff, M. 2013. *IEEE Journal of Photovoltaics*, 3, 1100–1105.
- Liska, P., Thampi, K. R., Grätzel, M., Brémaud, D., Rudmann, D., Upadhyaya, H. M., and Tiwari, A. N. 2006. *Applied Physics Letters*, 88, 203103.
- Mathew, X., Enriquez, J. P., Romeo, A., and Tiwari, A. N. 2004. *Solar Energy*, 77, 831–838.
- Martinuzzi, S. 1982. *Thin Solid Films*, 517, 2455–2460.
- Matsuno, Y. 2013. <http://park.itc.u-tokyo.ac.jp/matsuno/files/FS%20Tsunami%20Risk%20Review%20English.pdf>.
- McCandless, B., Youm, I., and Birkmire, R. 1999. *Progress in Photovoltaics*, 7, 21–30.
- McCandless, B. E. and Dobson, K. D. 2004. *Solar Energy*, 77, 839–856.
- McCandless, B. E. and Sites, J. R. 2003. Cadmium telluride solar cells. In *Handbook of Photovoltaic Science and Engineering*, A. Luque and S. Hegedus (Eds.), pp. 617–657. Wiley, Chichester, U.K.
- Meier, J., Dubail, S., Fluckinger, R., Fischer, D., Keppner, H., and Shah, A. 1994. In *Proceedings of the First World Conference on Photovoltaic Energy*, pp. 409–412.
- Metha, S. 2013. PV technology and cost outlook, 2013–2017. <http://www.greentechmedia.com/research/report/pv-technology-and-cost-outlook-2013-2017>.
- Mickelsen, R. and Chen, W. 1981. In *Proceedings of the 15th IEEE Photovoltaic Specialist Conference*, Orlando, FL, pp. 800–804.
- Mickelsen, R., and Chen, W. 1982. In *Proceedings of the 16th IEEE Photovoltaic Specialist Conference*, pp. 781–785.
- Mints, P. and Donnelly, J. 2011. Navigant Consulting Photovoltaic Service Program. Report NPS-Supply6. <http://www.navigantresearch.com/research/photovoltaic-manufacturer-shipments-capacity-competitive-analysis-20112012>.
- Mitchell, K., Eberspacher, C., Ermer, J., and Pier, D. 1988a. In *Proceedings of the 20th IEEE Photovoltaic Specialists Conference*, September 26–30, 1988, pp. 1384–1389.
- Mitchell, K. C., Ermer, E. J., and Pier, D. 1988b. In *Proceedings of 20th IEEE Photovoltaic Specialists Conference*, September 26–30, 1988, p. 1384.
- Mitzi, D. B., Gunawan, O., Todorov, T. K., and Barkhouse, D. A. R. 2013. *Philosophical Transactions of Royal Society A*, 371:20110432.
- Morooka, M., Ogura, R., Orihashi, M., and Takenaka, M. 2009. *Electrochemistry*, 77, 960–965.
- Moslehi, M. M., Kapur, P., Kramer, J., Rana, V., Seutter, S., Deshpande, A., Stalcup, T. et al. 2012. Presented at *PV Asia Pacific Conference (APVIA/PVAP)*, October 22–24, 2012.
- Muller, J., Rech, B., Springer, J., and Vanecek, M. 2004. *Solar Energy*, 77, 917–930.
- Nagoya, A., Asahi, R., and Kresse, G. 2011. *Journal of Physics of Condensed Matter*, 23, 404203.
- Nakada, T., Hirabayashi, Y., Tokado, T., Ohmori, D., and Mise, T. 2004. *Solar Energy*, 77, 739–747.
- Nakada, T. and Mizutani, M. 2002. *Japanese Journal of Applied Physics*, 41, 165–167.
- Nakamura, M., Chiba, Y., Kijima, S., Horiguchi, K., Yanagisawa, Y., Sawai, Y., Ishikawa, K., and Hakuma, H. 2012. In *Proceedings of the 38th IEEE Photovoltaics Specialists Conference*, Austin, TX, June 3–8, 2012, pp. 1807–1810.
- Nakamura, M., Yamaguchi, K., Chiba, Y., Hakuma, H., Kobayashi, T., and Nakada, T. 2013. Presented at *39th IEEE Photovoltaic Specialist Conference*, Tampa, FL, June 16–21, 2013, pp. 0849–0852.
- Nische, R., Sargent, D. F., and Wild, P. 1967. *Journal of Crystal Growth*, 1, 52.
- NREL. <http://www.nrel.gov/cdte>.
- Ohtake, Y., Kushiya, K., Ichikawa, M., Yamada, A., and Konagai, M. 1995. *Japanese Journal of Applied Physics*, 34, 5949–5955.

- Oleksyuk, I. D., Dudchar, I. V., and Piskach, L. V. 2004. *Journal of Alloys and Compounds*, 368, 135–143.
- Olsen, L., Eschbach, P., and Kundu, S. 2002. In *Proceedings of the 29th IEEE Photovoltaic Specialists Conference*, New Orleans, LO, pp. 652–655.
- O'Regan, B. and Grätzel, M. 1991. *Nature*, 353, 737–740.
- Osborne, M. March 2012. *PV Tech News*. http://www.pv-tech.org/news/solopower_sets_13.4_flex_cigs_aperture_efficiency_record_backed_by_nrel.
- Osborne, M. 2013. http://www.pvtech.org/news/has_first_solar_retaken_the_lowest_cost_pv_manufacturer_mantle.
- Palm, J., Probst, V., and Karg, F. H. 2004. *Solar Energy*, 77, 757–765.
- Perrenoud, J., Kranz, L., Buecheler, S., Pianezzi, F., and Tiwari, A. N. 2011a. *Thin Solid Films*, 519, 7444–7448.
- Perrenoud, J., Schaffner, B., Buecheler, S., and Tiwari, A. N. 2011b. *Solar Energy Materials and Solar Cells*, 95, S8–S12.
- Pianezzi, F., Chirilă, A., Blösch, P., Seyrling, S., Buecheler, S., Kranz, L., Fella, C., and Tiwari, A. N. 2012. *Progress in Photovoltaics: Research and Applications*, 20, 253–259.
- Powalla, M., Witte, W., Jackson, P., Paetel, S., Lotter, E., Wuerz, R., Kessler, F. et al. 2014. *IEEE Journal of Photovoltaics*, 4, 440–446.
- Prabhakar, T. and Jampana, N. 2011. *Solar Energy Materials Solar Cells*, 95, 1001–1004.
- Ramakrishna Reddy, K. T., Kotewara Reddy, N., and Miles, R. W. 2006. *Solar Energy Materials Solar Cells*, 90, 3041–3046.
- Ramanathan, K., Contreras, M. A., Perkins, C. L., Asher, S., Hasoon, F. S., Keane, J., Young, D. et al. 2003. *Progress in Photovoltaics: Research and Applications*, 11, 225–230.
- Rech, B. 2013. https://www.helmholtz-berlin.de/forschung/oe/enma/si-pv/arbeitsgebiete/duenschichtszellen/index_en.html.
- Rech, B. and Wagner, H. 1999. *Applied Physics A*, 69, 155–167.
- Redinger, A., Berg, D. M., Dale, P. J., Djemour, R., Gutay, L., Eisenbarth, T., Valle, N., and Siebentritt, S. 2011a. *IEEE Journal of Photovoltaics*, 1, 200–206.
- Redinger, A., Berg, D. M., Dale, P. J., and Siebentritt, S. 2011b. *Journal of American Chemical Society*, 133, 3320–3323.
- Reinhard, P., Buecheler, S., and Tiwari, A. N. 2013. *Solar Energy Materials Solar Cells*, 119, 287–290.
- Repins, I., Beall, C., Vora, N., DeHart, C., Kuciauskas, D., Dippo, P., To, B., Mann, J., Hsu, W.-C., Goodrich, A., and Noufi, R. 2012. *Solar Energy Materials and Solar Cells*, 101, 154–159.
- Repins, I., Vora, N., Beall, C., Wei, S.-H., Yan, Y., Romero, M., Teeter, G., Du, H., To, B., Young, M., and Noufi, R. 2011. <http://www.nrel.gov/docs/fy11osti/51286.pdf>.
- Romeo, A., Bätzner, D. L., Zogg, H., Tiwari, A. N., and Vignali, C. 1999a. *Solar Energy Materials and Solar Cells*, 58, 209–218.
- Romeo, A., Khrypunov, G., Kurdesau, F., Bätzner, D. L., Zogg, H., and Tiwari, A. N. 2004a. In *Technical Digest of the International PVSEC-14*, Bangkok, Thailand, pp. 715–716.
- Romeo, A., Terheggen, M., Abou-Ras, D., Bätzner, D. L., Haug, F.-J., Kälin, M., Rudmann, D., and Tiwari, A. N. 2004b. *Progress in Photovoltaics: Research and Applications*, 12, 93–111.
- Romeo, N., Bosio, A., Canevari, V., and Podesta, A. 2004c. *Solar Energy*, 77, 795–801.
- Romeo, N., Bosio, A., Tedeschi, R., Romeo, A., and Canevari, V. 1999b. *Solar Energy Materials and Solar Cells*, 58, 209–218.
- Sakata, H., Kawamoto, K., Taguchi, M., Baba, T., Tsuge, S., Uchihashi, K., Nakamura, N., and Kiyam, S. 2000. In *Proceedings of the 28th IEEE Photovoltaic Specialists Conference*, September 15–22, 2000, pp. 7–12, <http://ieeexplore.ieee.org/xpl/mostRecentIssue.jsp?punumber=7320>.
- Sasaki, K., Agui, T., Nakaido, K., Takahashi, N., Onitsuka, R., and Takamoto, T. 2013. *Proceedings of Ninth International Conference on Concentrating Photovoltaics Systems*, Miyazaki, Japan.
- Schultz, O., Glunz, S. W., and Willeke, G. P. 2004. *Progress in Photovoltaics: Research and Applications*, 12, 553–558.
- Service, R. 2011. *Science*, 332, 293.
- Shah, A., Meier, J., Buechel, A., Kroll, U., Steinhäuser, J., Meillaud, F., and Schade, H. 2004. Presented at the *ICCG5 Conference in Saarbrücken (D)*, July 4–8, 2004.

- Shah, A., Moulin, E., and Ballif, C. 2013. *Solar Energy Materials and Solar Cells*, 119, 311–316.
- Sharp Corporation. Press Release. 2012. <http://sharp-world.com/corporate/news/120531.html>.
- Shin, B., Gunawan, O., Zhu, Y., Bojarczuk, N. A., Chey, S. J., and Guha, S. 2011. *Progress in Photovoltaics: Research and Applications*, 21, 72–76.
- Shockley, W. and Queisser, H. J. 1961. *Journal of Applied Physics*, 32, 510–519.
- Sinha, P., Balas, R., and Krueger, L. 2011. In *Proceedings of 37th IEEE Photovoltaics Specialists Conference*, Washington, June 19–24, 2011, pp. 2025–2030.
- Sinke, W. C. 2007. A strategic research agenda for photovoltaic solar energy technology. Hamburg, Germany, September 14–18, 2015, www.eupvplatform.org.
- Slade, A. and Garboushian, V. 2005. In *Technical Digest of 15th International Photovoltaic Science and Engineering Conference*, Shanghai, China, October 10–15, 2005, p. 701.
- Smestad, G. P., Ennaoui, A., Fiechter, S., Hofmann, W., Tributsch, H., and Kautek, W. 1990. *Proceedings of SPIE, Optical Materials Technology for Energy Efficiency and Solar Energy Conversion IX*, Vol. 1272, p. 67.
- Snaith, H. J. 2014. Presented at the APEX (Advancing the Efficiency and Production Potential of Excitonic Solar Cells), RCUK-DST India Project Meeting in New Delhi, India.
- Solar Frontier. 2014. <http://www.solar-frontier.com/eng/news/2014/C031367.html>.
- Sopori, B. 2003. In *Handbook of Photovoltaic Science and Engineering*, A. Luque and S. Hegedus (Eds.), pp. 359–363. Wiley, New York.
- Spiering, S., Hariskos, D., Powalla, M., Naghavi, N., and Lincot, D. 2003. *Thin Solid Films*, 431–432, 359–363.
- Staebler, D. L. and Wronski, C. R. 1977. *Applied Physics Letters*, 31, 292.
- Stolt, L. 2014. Henergy/Solibro. Presented at the Fifth International Workshop on CIGS Solar Cell Technology (IW-CIGSTech 5), Berlin, Germany, April 2–3, 2014.
- Sunshot Vision Study. Department of Energy, USA assessment report, <http://energy.gov/downloads/sunshot-vision-study>.
- Surek, T. 2003. In *Proceeding of Third World Conference on PV Energy Conversion*, May 11–18, 2003, p. 2507.
- Swanson, R. 2012. Presented at the *Challenges in PV Science, Technology, and Manufacturing: A Workshop on the Role of Theory, Modeling and Simulation*, Purdue University, August 2–3, 2012.
- Teeter, G., Du, H., Leisch, J. E., Young, M., Yan, F., Johnston, S., Dippo, P. et al. 2011. In *Proceedings of 35th IEEE Photovoltaic Specialists Conference*, June 20–25, 2010, pp. 650–655.
- Timmo, K., Altosaar, M., Raudoja, J., Muska, K., Pilvet, M., Kauk, M., Varema, T., Danilson, M., Volobujeva, O., and Mellikov, E. 2010. *Solar Energy Materials and Solar Cells*, 94, 1889–1892.
- Todorov, K., Reuter, K. B., and Mitzi, D. B. 2010. *Advanced Materials*, 22, E156–E159.
- Todorov, T., Gunawan, O., Chey, S. J., Goislard de Monsabert, T., Prabhakar, A., and Mitzi, D. B. 2011. *Thin Solid Films*, 519, 7378–7381.
- Tuttle, J. R., Schuyler, T., Choi, E., and Freer, J. 2005. In *Proceedings of 20th European Photovoltaic Solar Energy Conference and Exhibition*, Barcelona, Spain, June 6–10, 2005.
- Tuttle, J. R., Szalaj, A., and Keane, J. 2000. In *Proceedings of the 28th IEEE Photovoltaic Specialists Conference*, September 15–22, 2000, pp. 1042–1045.
- Upadhyaya, H. M., Senthilarasu, S., Hsu, M. H., and Kishore Kumar, D. 2013. *Solar Energy Materials and Solar Cells*, 119, 291–295.
- Venkatasubramanian, R., O’Quinn, B. C., Hills, J. S., Sharps, P. R., Timmons, M. L., Hutchby, J. A., Field, H., Ahrenkiel, A., and Keyes, B. 1997. In *Conference Record of 25th IEEE Photovoltaic Specialists Conference*, May 13–17, 1996, pp. 31–36.
- Vetterl, O., Finger, F., Carius, R., Hapke, P., Houben, L., Kluth, O., Lambertz, A., Mück, A., Rech, B., and Wagner, H. 2000. *Solar Energy Materials and Solar Cells*, 62, 97–108.
- von Roedern, B., Zweibel, K., and Ullal, H. S. 2005. In *Proceedings of 31st IEEE Photovoltaic Specialists Conference*, January 3–7, 2005, pp. 183–188.
- Wagner, S., Shay, J., Migliorato, P., and Kasper, H. 1974. *Applied Physics Letters*, 25, 434.
- Weber, A., Mainz, R., and Schock, H. W. 2010. *Journal of Applied Physics*, 107, 013516.
- Wenger, S., Seyrling, S., Tiwari, A. N., and Grätzel, M. 2009. *Applied Physics Letters*, 94, 173508.

- Wolden, C. A., Kurtin, J., Baxter, J. B., Repins, I., Shaheen, S. E., Torvik, J. T., Rockett, A. A., Fthenakis, V. M., and Aydil, E. S. 2011. *Journal of Vacuum Science and Technology A*, 29, 030801.
- Woodcock, J. M., Schade, H., Maurus, H., Dimmler, B., Springer, J., and Ricaud, A. 1997. In *Proceedings of the 14th European Photovoltaic Solar Energy Conference*, Barcelona, Spain, pp. 857–860.
- Wu, X., Keane, J. C., Dhere, R. G., DeHart, C., Duda, A., Gessert, T. A., Asher, S., Levi, D. H., and Sheldon, P. 2002. In *Proceedings of the 17th European Photovoltaic Solar Energy Conference*, Munich, Germany, pp. 995–1000.
- Wuerz, R., Eicke, A., Kessler, F., Paetel, S., Efimenko, S., and Schlegel, C. 2012. *Solar Energy Materials and Solar Cells*, 100, 132–137.
- www.energyinformative.org/best-thin-film-solar-panels-amorphous-cadmium-telluride-cigs/.
- www.pvtech.org/news/q_cells_sets_two_new_world_records_for_multi_crystalline_and_quasi_mono_sol.
- Xinkun, W., Wei, L., Shuying, C., Yunfeng, L., and Hongjie, J. 2012. *Journal of Semiconductors*, 33, 022002.
- Yamamoto, K., Nakajima, A., Yoshimi, M., Sawada, T., Fukuda, S., Suezaki, T., Ichikawa, M. et al. 2004. *Solar Energy*, 77, 939–949.
- Yamamoto, K., Toshimi, M., Suzuki, T., Tawada, Y., Okamoto, T., and Nakajima, A. 1998. Presented at *the Materials Research Society Spring Meeting*, San Francisco, CA, April 13–17, 1998.
- Yoo, H., Kim, J., and Zhang, L. 2012. *Current Applied Physics*, 1052–1057.
- Yoshimi, M., Sasaki, T., Sawada, T., Suezaki, T., Meguro, T., Matsuda, T., Santo, K. et al. 2003. In presented at *Third World Conference on Photovoltaic Energy Conversion*, May 11–18, 2003, pp. 1566–1569.
- Yu, L., Misra, S., Wang, J., Qian, S., Foldyna, M., Xu, J., Shi, Y., Johnson, E., and Cabarrocas, P. R. 2014. *Scientific Reports*, 4, 4357–4364.
- Zhao, J., Wang, A., Green, M. A., and Ferrazza, F. 1998. *Applied Physics Letters*, 73, 1991–1993.
- Zhao, J., Wang, A., Yun, F., Zhang, G., Roche, D. M., Wenham, S. R., and Green, M. A. 1997. *Progress in Photovoltaics*, 5, 269–276.
- Zweibel, K. 2000. *Solar Energy Materials & Solar Cells*, 63, 375–386.

20.3 Concentrating PV Technologies

D. Yogi Goswami

20.3.1 Introduction

The current state of solar cell development is illustrated in Figure 20.40. While single-junction silicon solar cells dominate today's solar industry, the rapid rise in efficiency versus time (experience curve) of the multijunction cells makes this a particularly attractive technology path. The high efficiency, in comparison with single junction cells, such as silicon, is obtained by stacking several junctions in series, electrically isolated by tunnel diodes, as explained in Section 20.1. These can be qualitatively viewed by adding the voltages of three junctions in series, while maintaining the current of a single junction (Figure 20.40).

Under concentrated sunlight, multijunction (GaInP/GaAs/GaInNAs) solar cells have demonstrated an efficiency of 44.4% within the lab, as compared to silicon cells' best efficiency of 25%. This means that, in sunny areas, a multijunction concentrator system can generate almost twice as much electricity as a silicon panel with the same area.

Table 20.9 gives the efficiencies of CPV submodules achieved as of 2012.

The concentrating optics focus the light onto a small area of cells, reducing the area of the solar cells by a factor of, typically, 500–1000 times. The reduced cell area overcomes the

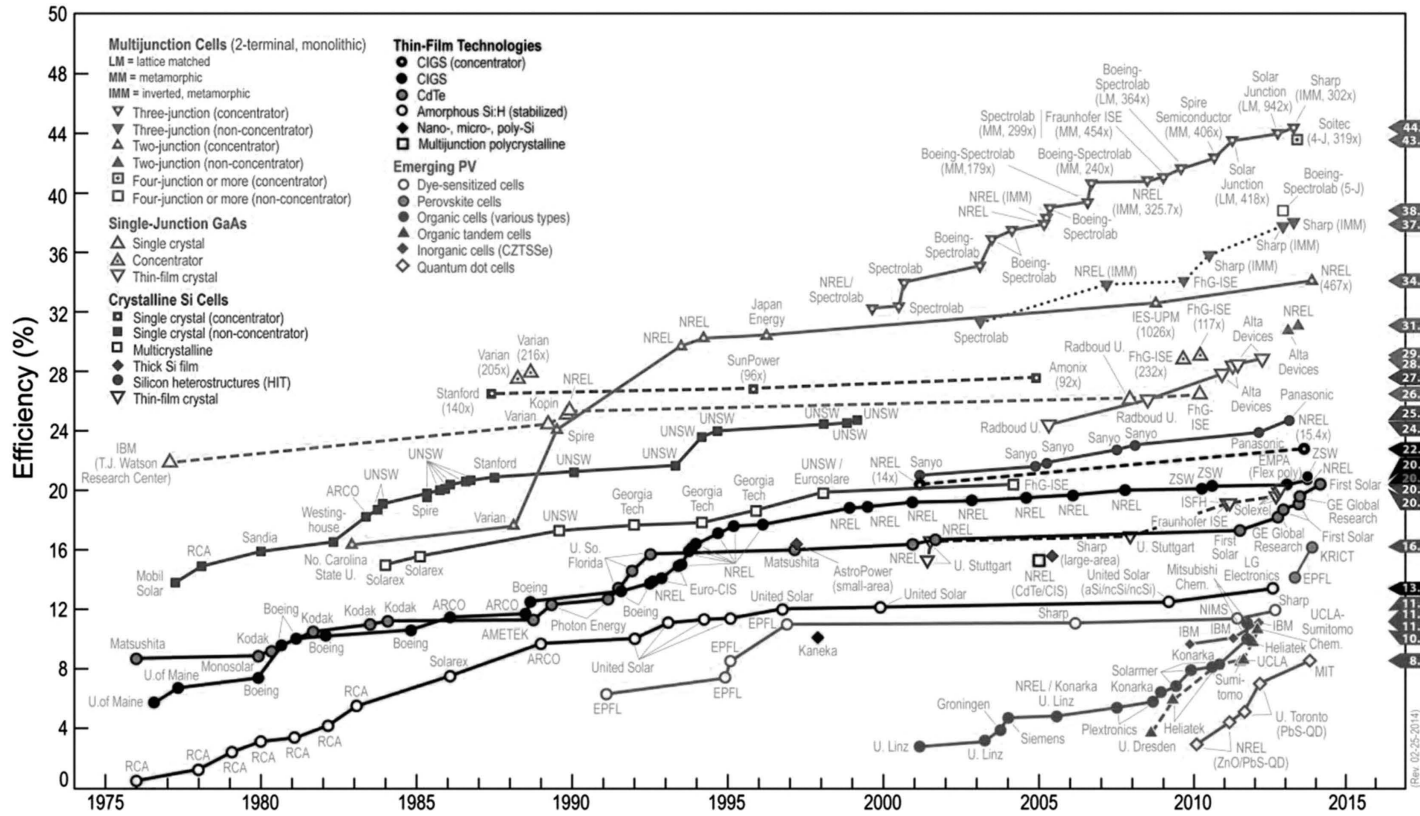


FIGURE 20.40 World record conversion efficiencies for various PV technologies. (From NREL, Best research cell efficiencies, National Renewable Energy Laboratory, Golden, CO, 2014, <http://www.nrel.gov>.)

TABLE 20.9

Terrestrial Concentrator Cell Efficiencies (Measured under ASTM G-173-03 Direct Beam AM1.5 Spectrum at a Cell Temperature of 25°C)

Classification	Efficiency (%)	Area (cm ²) ^a	Intensity (Suns)
<i>Single cells</i>			
GaAs	29.1 ± 1.3	0.505 (da)	117
Si	27.6 ± 1.0	1.00 (da)	92
<i>Multijunction cells (monolithic)</i>			
GaInP/GaAs/GaInNAs	44.0 ± 3	0.3104 (ap)	942
InGaP/GaAs/InGaAs	43.5 ± 2.6	0.167 (da)	306
GaInP/GaInAs/Ge	41.6 ± 2.5	0.3174 (da)	364
<i>Submodule</i>			
GaInP/GaAs; GaInAsP/GaInAs	38.5 ± 1.9	0.202 (ap)	20
<i>Modules</i>			
Si	20.5 ± 0.8	1,875 (ap)	79
Triple junction	33.5 ± 0.5	10,674.8 (ap)	N/A
<i>Notable exceptions</i>			
Si (large area)	21.7 ± 0.7	20.0 (da)	11

Source: Adapted from Green, M.A. et al., *Progress in Photovoltaics: Research and Applications*, 21, 1, 2013.

^a ap, aperture area; da, designated illumination area.

increased cell cost. The cell cost is diminished in importance and is replaced by the cost of optics. Thus, in high direct insolation locations, the multijunction concentrator technology has the potential to reduce the cost of solar electricity. As a side benefit, the cells are more efficient under concentration, provided a reasonable cell temperature can be maintained. The technology has been extended to four junctions and could be extended to even five junctions if efficiency benefits justify added cost. The efficiency is a moving target; today's triple junction cell efficiency is nearly 45%. Thus, one may reasonably extrapolate that multijunction cells may reach 50% efficiency in the future. Using less cell material for a given power output has attraction to cell manufacturers that are having trouble producing sufficient material to keep up with demand. It is worth mentioning that this technology was first developed and proven in the space program, where specific power (power/mass) is a more important consideration than cost.

20.3.2 CPV Technology

CPV technologies may use any concentrators developed for concentrating thermal technologies, including parabolic trough or parabolic dishes, compound parabolic concentrators (CPCs), or Fresnel concentrators. The concentrations achieved depend on the type of concentrators used. The CPV systems are classified as low, medium, or high concentrations, depending on the concentration ratio as shown in Table 20.10.

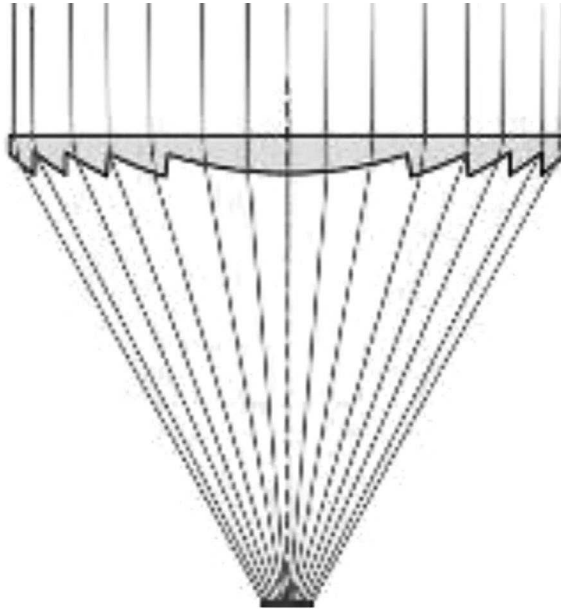
The most common type of concentrator is based on Fresnel concentrator as shown in Figure 20.41.

For low concentration CPV, silicon or even CdTe or CIGS panels may be used. However, for very high concentrations, triple junction cells of III–V compounds are used.

TABLE 20.10

CPV Concentration Classes

Class of CPV	Typical Concentration Ratio	Type of Converter
High concentration	>400×	Multijunction
Medium concentration	~3×–100×	Silicon or other cells
Low concentration	<3×	Silicon modules

**FIGURE 20.41**

Fresnel concentrator optics used in the most common CPV panels.

20.3.2 CPV Market

In 2004, less than 1 MW of concentrator PV systems was installed, out of a total world PV market of 1200 MW, and for some time, the market share of CPV remained extremely small. However, a dramatic reduction in cost of a CPV system from \$3.54/W in 2012 to \$2.62/W in 2013 increased the CPV installation to 160 MW in 2013 (Melkonyn 2013).

Amonix, Inc., of Torrance, California, spent more than 15 years developing five generations of CPV prototypes that led to a 35 kW CPV system installed in Arizona by Arizona Public Service (Amonix 2005). Since then, they have completed the largest CPV system of 30 MW in Alamosa, Colorado, in 2012. As of 2014, there are 54 companies developing or marketing CPV systems around the world. With reduction in the prices and increase in the efficiency, the global market for CPV is expected to grow at a very high rate (Mendelsohn et al. 2012).

20.3.4 Energy Payback

CPV system costs are much more sensitive to the price of steel than to the price of silicon. In this regard, CPV systems share similar concerns with the wind industry (McConnell 2002). Other technological similarities with wind systems include the low cost of production

plants, suitability for distributed and large-scale utility generation, modularity, moving parts, and the need for a good resource, be it wind or solar.

Such observations suggest that CPV systems could follow in the footsteps of wind systems. It seems plausible that CPV system costs can approach wind system costs (typically U.S. 80¢/W today—or about the same as projected CPV costs) if only because common materials (e.g., steel, glass, plastic) are dominant and because production plant costs are relatively low. Also consistent with these observations are recent estimates of energy payback for CPV technologies that are very close to values published for wind turbines at good wind sites. Specifically, the energy payback has been estimated at 8 months for a CPV system in a site having a good solar resource (Bett et al. 2005). More recently, the Fraunhofer Institute for Solar Energy in Freiburg, Germany, estimated the energy payback period for a CPV system in Italy as about 9 months (Fraunhofer ISE 2013).

20.3.5 Qualification Standards

Qualification standards help developers design their new products by identifying weaknesses before production and project installation. They give customers the confidence that their project investments will pay off. In short, they can contribute immensely to a technology's successful market entry.

Fortunately, the CPV industry thought about this situation in the 1990s. Standards take years to develop because the process is based on consensus. Companies do not want standards that are unnecessarily strict or require expensive test procedures. Customers want standards that ensure good product performance. So input from both groups—companies and customers—as well as from relatively objective research organizations leads to an accepted set of test procedures vital for successful CPV market. The first CPV standard (IEEE 2001) was published in 2001. This standard, however, was most suitable for US concentrator PV technologies using Fresnel lenses. The International Electrotechnical Commission (IEC) with input from engineers from more than 10 countries has been developing a standard suitable for concentrators using mirrors or lenses with solar concentration ratios ranging from a couple of suns to thousands of suns. The IEC issued their standard IEC 62108 in 2007 as a comprehensive CPV standard (IEC 2007). They are also working on new standards for solar trackers and safety.

References

- Amonix, Inc. 2014. <http://www.amonix.com>.
- Bett, A.W., Siefer, G., Baur, C.B., Riesen, S.V., Peharz, G., Lerchenmuller, H., and Dimroth, F. 2005. G. SFLATCON concentrator PV: Technology ready for the market. Presentation at *the 20th European PV Solar Energy Conference and Exhibition*.
- Fraunhofer ISE. 2013. Photovoltaics report, November 2013. <http://www.ise.fraunhofer.de>.
- Green, M.A., Emery, K., Hishikawa, Y., Warta, W., and Dunlop, E.D., 2013. Solar cell efficiency tables. *Progress in Photovoltaics: Research and Applications*, 21: 1–11.
- IEC. 2007. IEC Standard 62108: Concentrator photovoltaic (CPV) modules and assemblies—Design qualification and type approval. International Electrochemical Commission, Geneva, Switzerland. <http://www.iec.ch>.
- IEEE. 2001. IEEE recommended practice for qualification of concentrator photovoltaic receiver sections and modules. IEEE Standard, pp. 1523–2001.

- McConnell, R. 2002. Large scale deployment of concentrating PV: Important manufacturing and reliability issues. Proceedings of the First International Conference on Solar Electric Concentrators, NREL/EL-590-32461.
- Melkonyn, M. 2013. *The World Market for Concentrated Photovoltaics (CPV) 2013 Edition*, IHS, Inc, Englewood, CO.
- Mendelsohn, M., Lowden, T., and Canavan, B. 2012. Utility-scale concentrating solar power and photovoltaics projects: A technology and market overview, NREL/TP-6A20-51137, April 2012. <http://www.nrel.gov>.
- NREL. 2014. Best research cell efficiencies. National Renewable Energy Laboratory, Golden, CO. <http://www.nrel.gov>.

21

Wind Energy Conversion

Dale E. Berg

CONTENTS

21.1	Introduction.....	852
21.2	Wind Turbine Aerodynamics.....	855
21.2.1	Aerodynamic Models.....	860
21.2.1.1	Momentum Models.....	860
21.2.1.2	Vortex Models.....	864
21.2.1.3	Limitations Common to the Momentum and Vortex Models.....	866
21.2.1.4	Computational Fluid Dynamics Models.....	866
21.2.1.5	Hybrid Models.....	867
21.2.1.6	Model Results.....	867
21.3	Offshore Wind.....	868
21.3.1	Offshore Platform Hydrodynamics.....	869
21.4	Wind Turbine Loading.....	869
21.5	Wind Turbine Structural Dynamic Considerations.....	870
21.5.1	Horizontal-Axis Wind Turbine Structural Dynamics.....	870
21.5.2	Vertical-Axis Wind Turbine Structural Dynamics.....	872
21.6	Peak Power Limitation.....	873
21.7	Turbine Subsystems.....	875
21.7.1	Electrical Power Generation Subsystem.....	875
21.7.2	Yaw Subsystem.....	878
21.7.3	Control Subsystem.....	878
21.7.3.1	Safety Controller.....	878
21.7.3.2	Operational Controller.....	879
21.7.3.3	Turbine Power/Load Control Programming.....	879
21.8	Other Wind Energy Conversion Considerations.....	882
21.8.1	Wind Turbine Materials.....	882
21.8.2	Wind Turbine Installations.....	883
21.8.3	Wind Power Integration into Grid Operations and the Need for Forecasting.....	884
21.8.3.1	Grid Integration.....	884
21.8.3.2	Wind Forecasting.....	885
21.8.4	Energy Payback Period.....	886
21.8.5	Wind Turbine Costs.....	886
21.8.6	Environmental Concerns.....	890
	References.....	891
	For Further Information.....	894

21.1 Introduction

Wind power supplied about 2.6% of the world electricity demand in 2013 (up from 0.6% in 2005), and the size of that contribution is growing rapidly. Wind energy is the most rapidly expanding source of energy in the world today; over the past 10 years, the worldwide installed capacity of wind energy has grown at an average rate of nearly 25% per year, leading to an installed nameplate capacity at the end of 2012 of about 286,000 MW [1]. As of January 2013, China was the world leader in cumulative installed wind power capacity, with about 75,400 MW installed, followed by the United States with 60,200, Germany with 31,500, Spain with 22,500, India with 18,600, the United Kingdom with 9,100, Italy with 8,000, France with 7,600, Canada with 6,200, and Portugal with 4,400. This 60,000 MW of wind power capacity in the United States reflects a 5-year average annual growth rate of over 29%; it is sufficient to power approximately 15.2 million American households, providing 3.5% of the U.S. electricity consumption in 2012. Over 21% of U.S. electricity providers had wind in their generation mix in 2012, and 42% of new U.S. generating capacity added in 2012 was wind. On April 15, 2012, wind provided a peak of 56.7% of Xcel Energy's generated electricity in Colorado [2].

The cost to generate wind energy decreased dramatically from more than 30 cents (U.S.) per kilowatt-hour (¢/kW h) in the early 1980s to under 4¢/kW h (at the best sites) in 2004. The cost has since increased somewhat, in spite of continuing technology improvements, as a result of worldwide increases in steel, concrete, and transportation costs that have led to increases in the prices of wind turbines. The large increases in the cost of natural gas and other fossil fuels prior to 2010 made wind-generated electricity a lower-cost option than natural gas for many utilities adding generating capacity, but recent drilling technology advances have led to significant increases in the U.S. natural gas supply and decreases in its cost. The long-term impacts of these technology advances on the price of natural gas and on how well wind can compete for new generating capacity remain to be seen.

There is considerable anecdotal evidence that the first wind machines may have been built over 2000 years ago, perhaps in China, but there is no firm evidence to support this conjecture. However, there is considerable written evidence that the windmill was in use in Persia by AD 900, perhaps as early as AD 640. Figure 21.1 illustrates the main features of this type of mill. The center vertical shaft was attached to a millstone, and horizontal beams or arms were attached to the shaft above the millstone. Bundles of reeds attached vertically to the outer end of the arms acted as sails, turning the shaft when the wind blew. The surrounding structure was oriented so that the prevailing wind entered the open portion of the structure and pushed the sails downwind. The closed portion of the structure sheltered the sails from the wind on the upwind pass. The primary applications of these machines were to grind or mill grain and to pump water; they became generally known as *windmills*. The wind machines of today may look much different from those first machines, but the basic idea remains the same—use the power in the wind to generate useful energy. Modern wind machines, called *wind turbines*, tend to have a small number of airfoil-shaped blades, in contrast to the older windmills that usually had several flat or slightly curved blades (such as the American multiblade water pumper shown in Figure 21.2). The reasons for this difference in blade number will be examined a little later.

Although there are many different configurations of wind turbines, most of them can be classified as either horizontal-axis wind turbines (HAWTs), which have blades that rotate about a horizontal axis parallel to the wind, or vertical-axis wind turbines (VAWTs), which have blades that rotate about a vertical axis perpendicular to the wind.

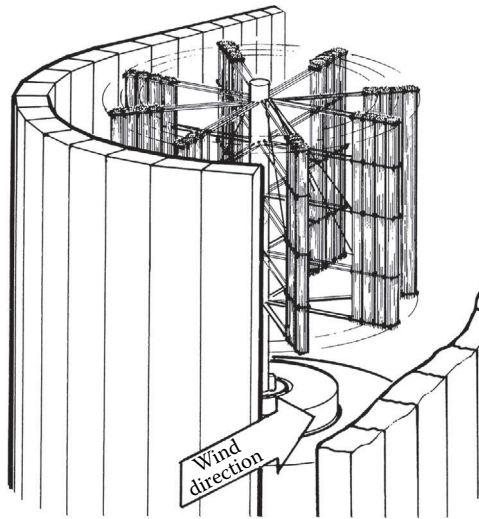


FIGURE 21.1
Illustration of ancient Persian windmill.



FIGURE 21.2
Typical American multiblade windmill. (Courtesy of Nolan Clark, U.S. Department of Agriculture.)

Figure 21.3 illustrates the main features of these configurations; they both contain the same major components, but the details of those components differ significantly.

According to Shepherd [3], the terms *horizontal* and *vertical* associated with these classifications are a potential source of confusion. Although they now refer to the driving shaft on which the rotor is mounted, in the past, the terms referred to the plane in which the rotor turned. Thus, the ubiquitous multibladed water-pumper type of windmill shown in Figure 21.2, now referred to as a *horizontal-axis machine*, had a rotor that turned in a vertical

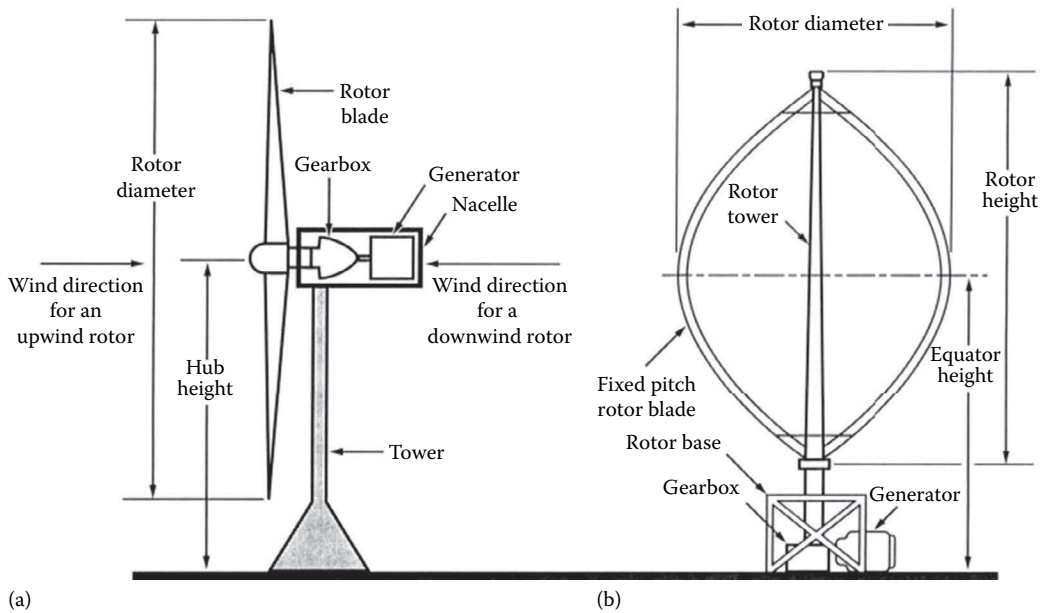


FIGURE 21.3 Schematic of basic wind turbine configurations: (a) horizontal-axis wind turbine (HAWT) and (b) vertical-axis wind turbine (VAWT).

plane, so it was, at one point, known as a *vertical* mill. Likewise, the earliest windmills, such as the one illustrated in Figure 21.1, had rotors that turned in a horizontal plane and were known as *horizontal* windmills.

As shown in Figure 21.3, HAWTs and VAWTs have very different configurations. Each configuration has its own set of strengths and weaknesses. HAWTs usually have all of their drive train (the transmission, generator, and any shaft brake) equipment located in a nacelle or enclosure mounted on a tower as shown; their blades are subjected to cyclic stresses due to gravity as they rotate, and their rotors must be oriented (yawed) so the blades are properly aligned with respect to the wind. HAWTs may readily be placed on tall towers to access the stronger winds typically found at greater heights. The most common type of modern HAWT is the propeller-type machine, and these machines are generally classified according to the rotor orientation (upwind or downwind of the tower), blade attachment to the main shaft (rigid or hinged), maximum power control method in high winds (full or partial-span collective or individual blade pitch or blade stall), and the number of blades (generally two or three blades).

VAWTs, on the other hand, usually have most of their drive train on the ground, their blades do not experience cyclic gravitational stresses, and their rotors do not require orientation with respect to the wind. However, VAWT blades are subject to severe alternating aerodynamic loading due to rotation of the blades upwind and downwind during each revolution of the rotor, and VAWTs cannot readily be placed on tall towers to exploit the stronger winds at greater heights. The most common types of modern VAWTs are the Darrieus turbines, with curved, fixed-pitch blades, and the “H” or “box” turbines with straight fixed-pitch blades. Virtually all of these turbines rely on blade stall (loss of lift and increase in drag as the blade angle of attack increases at high wind speeds) for maximum power control in high winds. Although there are still a few manufacturers of VAWTs today, the overwhelming majority of wind turbine manufacturers devote their efforts to developing better (and usually larger) HAWTs.

While the fuel for wind turbines is free, the initial cost of a wind turbine is a very large contributor to the cost of energy (COE) for that turbine. In order to minimize that COE, wind turbine designs must be optimized for the particular site or wind environment in which they will operate. Trial and error methods were very commonly used to develop early, small turbines, but these methods become very expensive and time-consuming when used to design and/or optimize larger turbines. A large optimized wind turbine can be developed at a reasonable cost only if the designers can accurately predict the performance of conceptual machines and use modeling to investigate the effects of design alternatives. The following discussion describes the basic phenomena that enable a machine to convert wind to mechanical energy and then presents several of the models that have been developed to predict the aerodynamic, hydrodynamic, and structural dynamic performance of wind turbines.

21.2 Wind Turbine Aerodynamics

Items exposed to the wind are subjected to forces in both the drag direction (parallel to the air flow) and the lift direction (perpendicular to the air flow). The earliest wind machines, known as *windmills*, used the drag on the blades to produce power, but many windmill designs over the last few centuries did make limited use of lift to increase their performance. For predominantly drag machines, such as those illustrated in Figures 21.1 and 21.2, larger numbers of blades result in higher drag and, thus, produce more power; therefore, these machines tend to have many blades. The old Dutch windmills, such as the one shown in Figure 21.4, utilized lift as well as drag, and since lift devices must be widely separated to generate the maximum possible amount of power, those machines evolved with a relatively small number of blades. The high-lift, low-drag shapes that were developed for airplane wings and propellers in the early part of the twentieth century (commonly referred to as *airfoils*) were quickly incorporated into wind machines to produce the first modern wind machines, usually known as *wind turbines*. An example of a typical modern wind turbine is shown in Figure 21.5. Modern wind turbines use the lift generated by the blades to produce power, and since the blades must be widely separated to generate the maximum amount of lift, wind turbines have a small number of blades. The following paragraphs contrast the characteristics of the drag- and lift-type machines.

Figure 21.6 illustrates the flow field about a moving drag device. The drag results from the relative velocity between the wind and the device, and the power that is generated by the device (the product of the drag force and the translation or blade velocity) may be expressed as

$$P = Dlv = \left[0.5\rho(U - v)^2 \right] C_D clv \quad (21.1)$$

where

P is the power extracted from the wind

D is the drag force per unit length in the span direction (perpendicular to the page)

l is the length of device in the span direction (perpendicular to the page)

v is the translation (or blade) velocity

ρ is the air density

U is the steady free-stream wind velocity

C_D is the drag coefficient (= Drag / ((1/2) ρclU^2), a function of device geometry)

c is the device width (perpendicular to the wind, in the plane of the page)



FIGURE 21.4
Example of Dutch windmill. (Courtesy of Richard A. Neiser, Jr.)



FIGURE 21.5
G.E. 1.5 MW wind turbines near Lamar, Colorado.

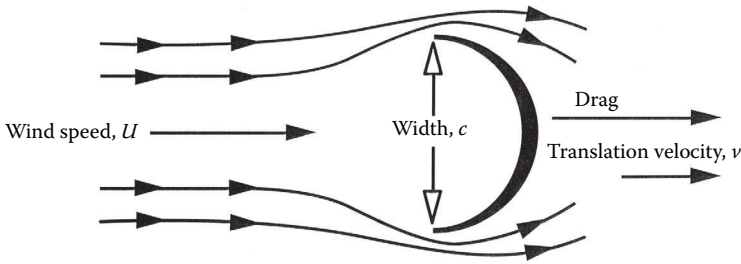


FIGURE 21.6
Schematic of translating drag device.

The translation (or blade) velocity of the device must always be less than the wind velocity, or no drag is generated and no power is produced. The power extraction efficiency of the device may be expressed as the ratio of the power extracted by the device to the power available in the wind passing through the area occupied by the device (the projected area of the device), a ratio known as the *power coefficient*, C_p . From Equation 7.1, the available power is

$$P_A = \frac{1}{2} \rho U^3 A = \frac{1}{2} \rho U^3 cl \tag{21.2}$$

where $A (=cl)$ is the area of the device projected perpendicular to the wind.

For a drag machine, C_p , using Equations 21.1 and 21.2, is

$$C_p = \frac{P}{(1/2)\rho U^3 cl} = \frac{v}{U} \left[1 - \frac{v}{U} \right]^2 C_D \tag{21.3}$$

Now consider a device that utilizes lift to extract power from the wind, that is, an airfoil. Figure 21.7 depicts an airfoil that is moving at some angle relative to the wind and is

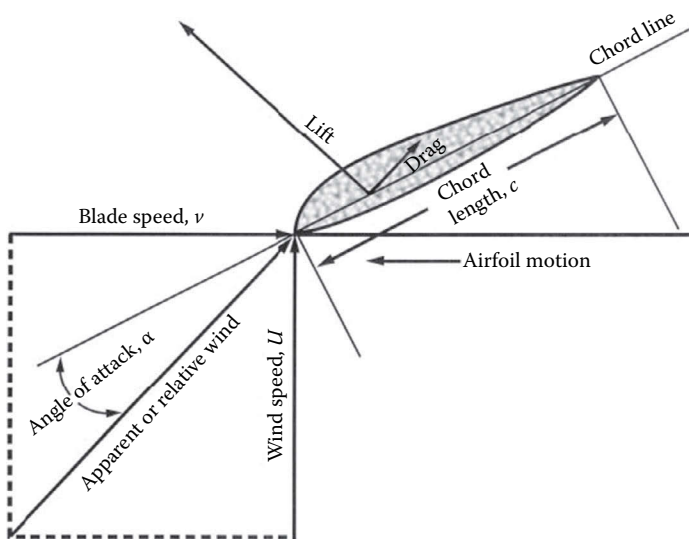


FIGURE 21.7
Schematic of translating lift device.

subject to both lift and drag forces. The relative wind across the airfoil is the vector sum of the wind velocity, U , and the blade velocity, v . The angle between the direction of the relative wind and the airfoil chord (the straight line from the leading edge to the trailing edge of the airfoil) is termed the angle of attack, α . The power extracted by this device may be expressed as

$$P = \frac{1}{2} \rho U^3 c l \left[C_L - C_D \frac{v}{U} \right] \sqrt{1 + \left(\frac{v}{U} \right)^2} \quad (21.4)$$

where

c is the chord length

C_L is the lift coefficient ($= \text{Lift} / ((1/2) \rho c l U^2)$, a function of airfoil shape and α)

The other quantities are as defined for Equation 21.1, but C_D is now a function of airfoil shape and α . Lift and drag coefficients for some common airfoils may be found in Refs. [4–9]. In this case, the projected area of the device is cl , and the power coefficient, using Equations 21.3 and 21.4, is

$$C_P = \frac{v}{U} \left[C_L - C_D \frac{v}{U} \right] \sqrt{1 + \left(\frac{v}{U} \right)^2} \quad (21.5)$$

Keep in mind that Equations 21.3 and 21.5 express the performance coefficients of these devices in terms of the *projected area* of the individual device. Figure 21.8 presents experimental lift and drag coefficient values for the S-809 airfoil, an airfoil designed by the National Renewable Energy Laboratory (NREL) for use on small HAWTs [10]. As the angle of attack increases beyond approximately 9° , the lift levels off and then drops slightly, and the drag begins to rise fairly rapidly. This is due to separation of the flow from the upper surface of the airfoil, a flow condition referred to as *stall*. Figure 21.9 compares Equations 21.3 and 21.5 using $C_L = 1.0$ and $C_D = 0.10$ for the airfoil (conservative values for modern airfoils, as seen from Figure 21.8), and a drag coefficient of 2.0 (the maximum possible) for the drag device. The airfoil has a maximum power coefficient of about 15, compared with 0.3 for the drag device; that is, it extracts 50 times more power per unit of device surface area. Of course, the airfoil must be translated across the wind to produce power, but this is easily achieved with rotating machines such as wind turbines.

As mentioned earlier, lift-type machines tend to have only a few blades, while drag-type machines tend to have many blades. Thus, the difference in the turbine performance coefficient (now based on the rotor frontal area rather than the blade or bucket frontal area) of actual wind machines is much less than that might be expected from the analysis presented earlier—a well-designed lift-type machine may achieve a peak power coefficient (based on the area covered by the rotating turbine blades) of 0.5–0.59, while a pure drag-type machine will achieve a peak power coefficient of no more than 0.2. Some of the multibladed drag-type windmills actually utilize a blade shape that creates some lift, and they may achieve power coefficients of 0.3 or a little higher. The drag machines rotate slowly (the blade translation velocity cannot exceed the effective wind speed) and produce high torque, while the lift machines rotate quickly (to achieve a high translation velocity) and produce low torque. The slow rotating, high-torque drag machines are very well suited for

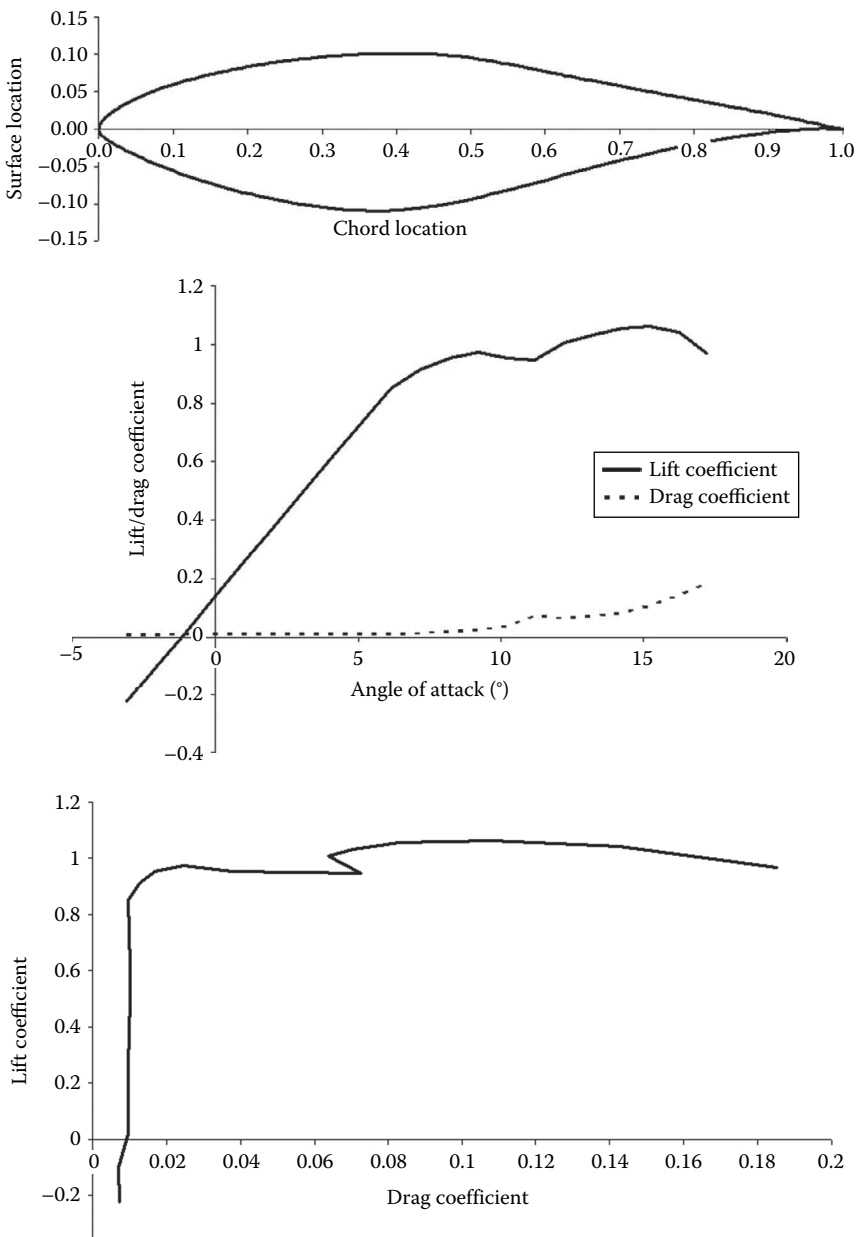


FIGURE 21.8 Profile and performance characteristics of the S-809 airfoil.

mechanical power applications such as milling grain and pumping water. On the other hand, extensive experience has shown that fast-rotating, lift-type machines are much easier to adapt to electrical generators and can produce electricity at a significantly lower COE than can the drag-type machines.

Because of their superior performance in electrical generation applications, only lift-type machines will be considered in the remainder of this discussion.

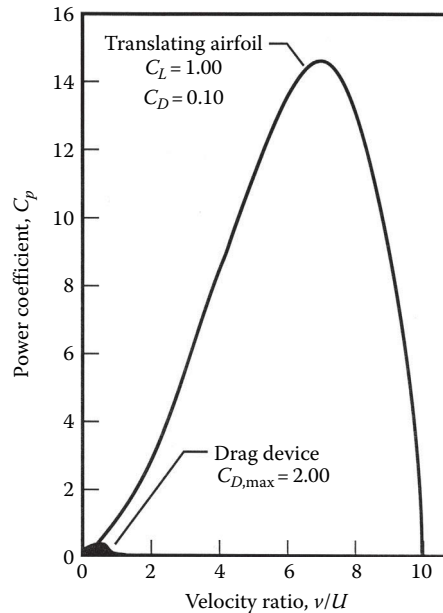


FIGURE 21.9
Comparison of power coefficients for drag-type and lift-type devices.

21.2.1 Aerodynamic Models

The aerodynamic analysis of a wind turbine has two primary objectives: (1) to predict the aerodynamic performance or power production of the turbine, and (2) to predict the detailed time-varying distribution of aerodynamic loads acting on the turbine rotor blades. In general, the same models are used to accomplish both objectives. Accurate prediction of turbine aerodynamic performance does not guarantee accurate prediction of the loading distribution—the performance predictions result from the integration of time-averaged aerodynamic lift and drag over the entire turbine, and significant errors may be present in the detailed lift and drag predictions but balance out in the performance predictions. While there is a considerable body of data showing good agreement of predicted performance with measured performance, especially for codes that have been tailored to give good results for the particular configuration of interest, there are very few data available against which to compare detailed load-distribution predictions.

The aerodynamics of wind turbines are far too complex to model with simple formulas that can be solved with handheld calculators; computer-based models ranging from very simplistic to very complex are required. Several commonly used aerodynamic models are described in the following paragraphs.

21.2.1.1 Momentum Models

The simplest aerodynamic model of an HAWT is the actuator disk or momentum model in which the turbine rotor is modeled as a single porous disk. This analysis was originally adapted for wind turbine use by Betz [11] from the propeller theory developed by Froude [12] and Lanchester [13]. To develop the equations for this model, the axial force acting on the rotor is equated to the time rate of change of the momentum of the air stream passing through the rotor. The mass of air that passes through the rotor disk is assumed to remain

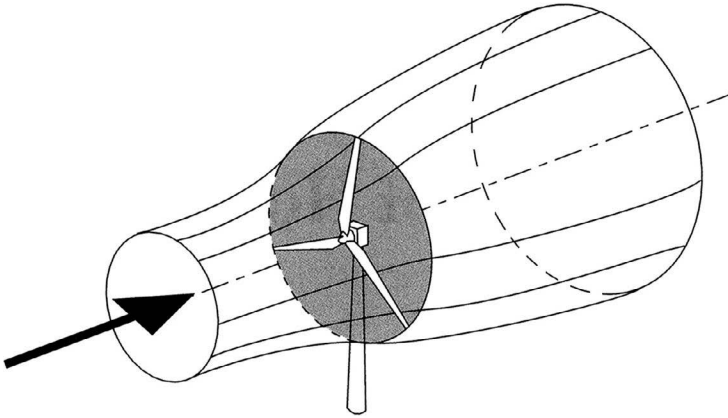


FIGURE 21.10
Schematic of stream-tube for horizontal-axis wind turbines.

separate from the surrounding air and only the air passing through the disk slows down. That mass of air with a boundary surface of circular cross section, extended upstream and downstream of the rotor disk, is shown in Figure 21.10. No air flows across the lateral boundary of this *stream-tube*, so the mass flow rate of air at any position along the stream-tube will be the same. Because the air is incompressible, the decrease in the velocity of the air passing through the disk must be accompanied by an increase in the cross-sectional area of the stream-tube to maintain the same mass flow. The presence of the turbine causes the air approaching from the upstream to gradually slow down; thus, the velocity of the air arriving at the rotor disk is already lower than the free-stream wind speed. As mentioned earlier, this causes the stream-tube to expand. In addition, the static pressure of the air rises to compensate for the decrease in kinetic energy.

As the air passes through the rotor disk, there is a drop in static pressure; the air immediately downstream of the disk is below the atmospheric pressure level, but there is no instantaneous change in velocity. As the air continues downstream, the static pressure gradually increases until it again comes into equilibrium with the surrounding atmosphere, and the velocity drops accordingly. This region of the flow is referred to as the *wake*. Thus, the difference in flow conditions between the far upstream and the far wake is a decrease in kinetic energy, but no change in static pressure.

Utilizing conservation of mass, conservation of axial momentum, the Bernoulli equation, and the first law of thermodynamics, and assuming isothermal flow, the power produced by the turbine (the product of the axial force and the air velocity at the rotor) may be readily derived. From the conservation of axial momentum, the thrust on the rotor, T , may be expressed as

$$T = \dot{m}(U - v_w) = \rho A v (U - v_w) \quad (21.6)$$

where

\dot{m} is the mass flow rate of air ($=\rho A v$)

v is the wind velocity at the rotor disk

v_w is the wind velocity far downstream of the rotor disk (in the wake)

U is the wind velocity far upstream of the disk

A is the area of the rotor disk

The thrust may also be expressed in terms of the pressure drop caused by the rotor

$$T = A(p_u - p_d) \quad (21.7)$$

where

p_u is the pressure just upwind of the rotor disk

p_d is the pressure just downwind of the rotor disk

The Bernoulli equation, applied just upwind of the rotor and just downwind of the rotor, yields

$$p_\infty + \frac{1}{2}\rho U^2 = p_u + \frac{1}{2}\rho v_u^2 \quad (21.8)$$

$$p_d + \frac{1}{2}\rho v_d^2 = p_w + \frac{1}{2}\rho v_w^2 \quad (21.9)$$

where the subscripts ∞ , u , d , and w denote far upwind of the rotor, immediately upwind of the rotor, immediately downwind of the rotor, and far downwind of the rotor, respectively.

The pressures are equal far upwind of the rotor and far downwind of the rotor ($p_\infty = p_w$), and the velocity is the same just upwind and just downwind of the rotor ($v_u = v_d$). Substituting Equations 21.8 and 21.9 into Equation 21.7 yields

$$T = A \left[\left(\frac{1}{2}\rho U^2 - \frac{1}{2}\rho v_u^2 \right) - \left(\frac{1}{2}\rho v_d^2 - \frac{1}{2}\rho v_w^2 \right) \right] = \frac{1}{2}\rho A (U^2 - v_w^2) \quad (21.10)$$

Equating 21.6 and 21.10 then yields

$$v = \frac{1}{2}(U + v_w) \quad (21.11)$$

That is, the velocity at the rotor disk is equal to the mean of the free-stream and wake velocities; thus, the velocity change between the free-stream and the wake is twice the change between the free-stream and the disk.

The power produced at the rotor, assuming isothermal flow and ambient pressure in the wake, is the product of the thrust and the velocity at the rotor:

$$\begin{aligned} P &= Tv = \frac{1}{2}\rho A (U^2 - v_w^2)v = \frac{1}{2}\rho A (U - v_w)(U + v_w)v \\ &= \frac{1}{2}\rho A [2(U - v)]2vv = 2\rho A (U - v)v^2 \end{aligned} \quad (21.12)$$

Now, define

$$a = \frac{(U - v)}{U} \quad (21.13)$$

which is commonly known as the *axial interference factor*. Using this in Equation 21.12 and rearranging yields

$$P = 2\rho A(aU)(1 - a)^2U^2 = 2\rho AU^3a(1 - a)^2 \tag{21.14}$$

The power coefficient for the turbine, then, is (utilizing Equations 21.2 and 21.14)

$$C_p = \frac{P}{P_A} = \frac{2\rho AU^3a(1 - a)^2}{(1/2)\rho AU^3} = 4a(1 - a)^2 \tag{21.15}$$

This is maximized for $a = 1/3$, yielding $C_{p,max} = 16/27 = 0.593$ as the maximum possible performance coefficient for a lift-type machine, a maximum often referred to as the *Betz limit*. Expressed in slightly different terms, this equation shows that a lift-type HAWT turbine can extract no more than 59.3% of the energy available in the wind passing through the rotor!

The typical performance of various types of wind machines is compared to the Betz limit in Figure 21.11, where the variations of the turbine power coefficients with the *tip-speed ratio* (the ratio of the speed of the blade tip to the free-stream wind speed) are presented. Even though the maximum performance of modern HAWTs and VAWTs is well above that of the older, drag-type machines such as the Dutch windmill and the American multiblade windmill, it is still somewhat below the Betz limit. Some HAWTs have demonstrated peak performance coefficients approaching 52%.

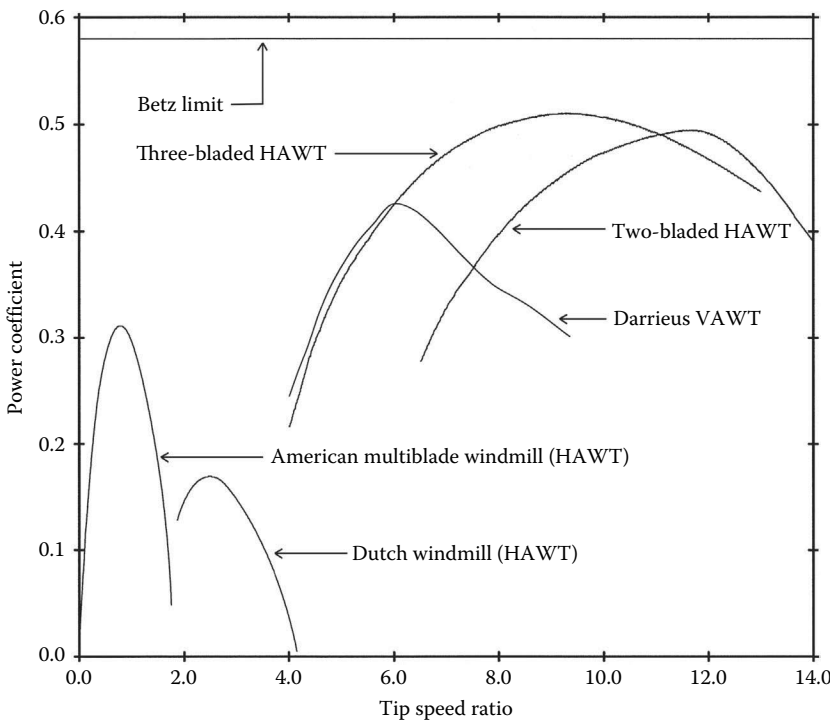


FIGURE 21.11
Typical performance of various types of wind turbines.

For HAWTs, the momentum model can be expanded to the widely used blade element momentum (BEM or BEMT) model in which the blades are divided into small radial elements, and local flow conditions at each element are used to determine blade forces and loads on those elements. To obtain accurate predictions, these models typically incorporate numerous modifications to account for blade and turbine wake effects, the three-dimensional flow near blade tips, the thick blade sections near the root, blade stall at high wind speeds, and unsteady effects associated with blade stall. Additional information on these models may be found in Hansen and Butterfield [14], Wilson [15], and Snel [16].

A very similar derivation yields a momentum model for the VAWT. This model may be expanded into the multiple stream-tube (the turbine rotor is modeled as multiple actuator disks, rather than just one) and the double-multiple stream-tube models (multiple actuator disks, with separate ones modeling the upwind and downwind passes of the rotor blades) that are the VAWT equivalent of the HAWT blade element model. Additional information on these models may be found in Touryan et al. [17], Wilson [15], and Paraschivoiu [18]. A recent paper by Simão Ferreira and Scheurich [19] shows that, although these models may predict turbine power production fairly accurately, they are not accurate when it comes to prediction of blade loads; more physically realistic models such as vortex codes or CFD codes must be used to accurately predict VAWT blade loads.

Momentum-based models are extremely popular with wind turbine designers because they are simple, fast, and fairly accurate for performance prediction, especially after they are tuned for a particular configuration. However, they are approximate because they are based upon the assumptions of flow conditions that are fixed in time and space, while the flow conditions around a wind turbine are constantly changing. These models cannot predict the effects of yawed flow, unsteady aerodynamics, and other complex flows that are present on wind turbines, all of which can have large impacts on turbine performance and loads. In some cases, specialized codes based on experimental results are used to approximate some of these effects, but these codes are limited to specific turbine sizes and geometries. In other cases, more realistic models such as vortex-based models, full computational fluid dynamics (CFD) models, and hybrid models are used to estimate these effects.

21.2.1.2 Vortex Models

Vortex models are usually more properly referred to as lifting line or lifting surface models, depending on whether a lifting line or a lifting surface formulation is used to model the blades. In the lifting line method, each rotor blade is modeled as a series of segmented *bound line vortices* located at the blade 1/4-chord line, as illustrated in Figure 21.12a. Line vortex strengths, defined by the blade lift at each radial location, are associated with the vortex line segments. The lifting surface method represents the blade in more detail, as a distribution of vortex line segments over the blade surface, as illustrated in Figure 21.12b. Either of these models will generate both trailing vorticity (perpendicular to the span of the blade) due to the differences in vortex strength along the blade span and shed vorticity (parallel to the span of the blade) due to time-dependent changes in vortex strength that are shed into the wake as the turbine rotates. These vortex methods lend themselves to the modeling of unsteady problems, as the shed vorticity models the time-dependent changes in the blade bound vortex strength. Solutions are achieved by impulsively starting the turbine in a uniform flow field and allowing the computational flow field to develop until it reaches a steady-state or periodic condition.

The manner in which the transport of the vorticity in the turbine wake is modeled depends on whether a free-wake or a fixed (or prescribed) wake model is used. In the

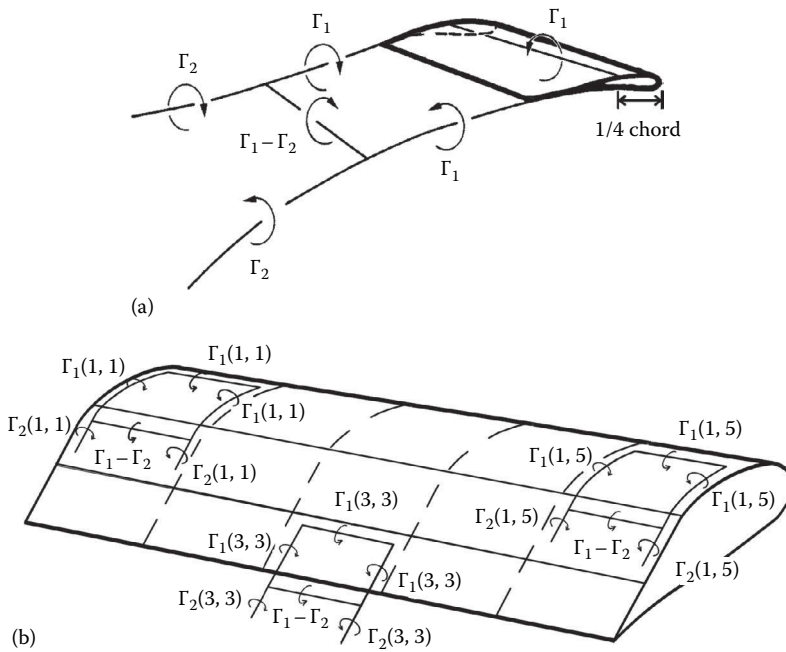


FIGURE 21.12

Schematic of lifting line and lifting surface models of turbine blades: (a) lifting line model and (b) lifting surface model (Note: Each of the surface panels [15 shown here] is represented by a vortex system such as the three sketched here).

free-wake model, the vorticity is allowed to convect, stretch, and rotate as it is transported through the wake. However, the movement of each line vortex is influenced by the presence of all of the other line vortices, including those on the blade. As the computation progresses in time, the number of vortices that must be followed and the time required to calculate the vortex interactions both grow very quickly. In order to minimize the need for large computer resources, the fixed or prescribed wake models have been developed. In these models, the geometry of the wake is modeled as either fixed or described by only a few parameters, and the vortex interactions in the wake are no longer directly calculated. The result is a much faster execution time, but the accuracy of the predicted power generation and blade loads depends very heavily upon the fidelity with which the specified wake approximates the actual physical wake. The three-dimensional, lifting-surface, free-wake formulation is the most physically realistic of the vortex models, but a computer program implementing such a model will require a large amount of computer resources and time. Experience has shown that the dramatic increase in computer resources required by such a model does not yield significantly more accurate predictions than what can be obtained with a three-dimensional, lifting-line, fixed-wake model. A major problem with vortex codes is finding a good balance between model simplification (and the associated limitations on fidelity), computation time, and desired accuracy. The improved physical fidelity of the vortex models relative to the momentum models results in more accurate solutions, assuming the turbine is represented in adequate detail and the solution time increment is sufficiently short. While vortex models have not been widely used in the wind industry in the past, they are seen to be gaining popularity today, as the continuing increases in

computer speed make their use in optimizing simulation studies quite feasible. While they model the turbine and flow field with less accuracy than CFD models and thus, can be expected to yield less accurate results, they require far, far less computer resources while incorporating much greater fidelity than is present in momentum models. Additional information on vortex models for both HAWTs and VAWTs may be found in Kocurek [20], Snel [16], and Strickland et al. [21]. Murray and Barone [22] describe the development of a current-generation vortex model program that is capable of analyzing both HAWTs and VAWTs, including those with unconventional geometries.

21.2.1.3 Limitations Common to the Momentum and Vortex Models

Both the momentum-based and the vortex models normally utilize airfoil performance characteristic tables (lift and drag coefficients as functions of angle of attack, such as are shown in Figure 21.8) and air velocity to determine the blade lift and drag. These performance tables are generated from static two-dimensional wind tunnel test results or from static two-dimensional airfoil design code predictions. The table contents are modified with empirical, semiempirical, or analytic methods and used to estimate blade loads under the three-dimensional, dynamic conditions actually experienced by the turbine blades. The greatest difficulty in obtaining accurate load distribution predictions with either the momentum models or the vortex models is the challenge of accurately determining the appropriate airfoil performance characteristics.

21.2.1.4 Computational Fluid Dynamics Models

CFD, in a broad sense, is the solution of the partial differential equations describing the flow field by approximating these equations with algebraic expressions (discretizing them) and then solving those expressions numerically with the aid of a computer. Within the wind energy community, the term CFD normally refers to the numerical solution of the unsteady Reynolds-averaged Navier–Stokes (RaNS) equations [23,24], often restricted to four partial differential equations (one conservation of mass equation and conservation of momentum equations in three orthogonal directions) that describe general ideal-gas, incompressible, nonreacting, fluid flow.

One might argue that the most detailed and physically realistic method of predicting the performance of and loads on a wind turbine is to utilize CFD to model the airflow around the turbine and through the rotor, calculating the airfoil lift and drag directly. The flow field in the vicinity of the wind turbine is approximated as a computational grid of variable density, and the discretized Navier–Stokes equations are applied to each element of that grid. The computational grid close to the turbine blades must be very, very dense in order to capture the details of the airflow around the blades; it becomes less dense as the distance from the blades becomes greater, and the effect of the blades on the airflow decreases. The resulting set of simultaneous equations must be solved, frequently in a time-marching manner, to determine the time-dependent nature of the entire flow field.

Duque et al. [25] describe a 2002 CFD investigation of a wind turbine in which they utilized a complex grid with 11.5 million points to model the flow around a 10 m diameter HAWT rotor and tower combination. A steady-flow solution (rotor facing directly into the wind) for that model at a single wind speed, utilizing eight PC processors, each operating at 1.4 GHz in a parallel processor computer configuration, required approximately 26 h. An unsteady-flow solution (rotor yawed at an angle to the wind) with the same computing resources required over 48 h for each rotor revolution. Obviously, these

computations can be performed much more quickly with the computing resources available today. Sørensen et al. [26], Johansen et al. [27], and Chow and van Dam [28,29] report other CFD modeling efforts.

At this point, CFD is suitable for research use or final design verification only—it is still too slow and requires far too many computer resources to be considered for use as a routine design tool. CFD also suffers from some shortcomings that limit its accuracy in performance and loads calculations. First, it does not consistently yield highly accurate results for airfoil lift and drag, because it cannot adequately model the transition of flow over the airfoil surface from laminar, well-ordered, basically two-dimensional flow to inherently three-dimensional and unsteady turbulent flow that is accompanied by rapid fluctuations in both velocity and pressure (most wind turbines today utilize airfoils that will experience such a transition in the flow). Second, most CFD models today cannot adequately predict the effects of separated flow, especially three-dimensional separated flow, such as will occur near the hub of the wind turbine rotor under most operating conditions. In spite of these limitations, CFD models, when run by an expert who devotes a lot of effort to validate the results, can yield very useful information, as illustrated by the work reported in Chow and van Dam [28,29]. Efforts to improve the accuracy of CFD codes continue.

21.2.1.5 Hybrid Models

The hybrid model approach is an attempt to get the increased accuracy that CFD models are capable of without the heavy computing resources. It typically models the airflow in the immediate vicinity of the airfoil and close to the turbine with the discretized Navier–Stokes equations, similar to the procedure used by the CFD models. However, to model the mostly undisturbed flow away from the turbine, the model uses nonviscous or potential flow equations that are much less complex and that can be solved much faster than the Navier–Stokes equations. The two solutions must be merged at the boundary between the two regions. The result is a code with the accuracy of the CFD model, but one that requires an order of magnitude less computing resources to solve. Xu and Sankar [30] and Schmitz and Chattot [31] describe two such codes. Even these hybrid models require a large amount of computer resources and are too slow and expensive to be utilized for parametric optimization studies; they are apt to be reserved for research work or detailed analysis of a proposed turbine design.

21.2.1.6 Model Results

None of these aerodynamic models is capable of accurately predicting the performance of and detailed loads on an arbitrary wind turbine operating at a variety of wind speeds. In order to have high confidence in the code predictions for a turbine design, the code must be calibrated against the measured performance and loads obtained from turbines of similar size and shape. Simms et al. [32] report on the ability of 19 codes based on the earlier models to predict the distributed loads on and performance of an upwind HAWT with a 32.8 ft (10 m) diameter rotor that was tested in the NASA/Ames 80 ft by 120 ft (24.4 m by 36.6 m) wind tunnel in 2000. Although the rotor was small compared to the 262 ft (80 m) diameter and larger commercial turbines that are being built today, a panel of experts from around the world concluded that it was large enough to yield results representative of what would be observed on the larger turbines. The comparisons of the code predictions and the experimental results were, in general, poor—turbine power predictions ranged from 30% to 275% of measured, and blade-bending moment predictions ranged

from 85% to 150% of measured for what is considered to be the most easy-to-predict conditions of no yaw, steady state, and low wind speed. Many aerodynamic code developers have spent considerable effort over the years since that comparison attempting to identify the sources of the discrepancies and improving the accuracy of their various codes.

In 2006, the Energy Research Center of the Netherlands led a second wind tunnel test of a heavily instrumented 15 ft (4.5 m) diameter wind turbine in the Germany/Dutch Wind tunnel organization 31 ft × 31 ft (9.5 m × 9.5 m) open-jet wind tunnel. This effort, known as the Model Experiments in Controlled Conditions or MEXICO experimental campaign, was funded by the European Union Framework Programme 5. An extensive literature list dealing with the experiment and related analyses is available on the MEXICO experiment website at www.mexnext.org/resultsstatus. Calculations from several models have been compared to the MEXICO results, with generally good qualitative agreement between calculations and measurements down to the flow detail level, even in yawed conditions. However, none of the calculations have been able to accurately predict both the velocities and the loads; they all overpredict the velocities and/or overpredict the loads. While one explanation for the anomalies could be tunnel effects rather than model inaccuracies, that has not been supported by CFD calculations such as that performed by Réthoré et al. [33].

Additional information and references on wind turbine aerodynamics models may be found in Manwell et al. [34] and Burton et al. [35] for HAWTs and in Touryan et al. [17], Wilson [15], and Murray and Barone [22] for VAWTs.

Most wind turbine companies today continue to use the very fast momentum-based models for design optimization purposes, in spite of the approximations and inaccuracies that are inherent in these models. The analysts doing the studies tweak these models to get good comparison with measurements from an existing turbine and then use them to predict performance and loads for new turbines that are fairly close in size and geometry to the existing turbine. If the new turbine is significantly different in size and shape from the reference turbine, the performance predictions are considered to be subject to considerable error. Performance tests on a prototype of the new turbine are required to further refine the actual performance and loads. There does appear to be a trend toward adapting a vortex-based code to replace the momentum-based codes in these applications, and that should reduce the amount of error inherent in the predictions. Performance tests on prototypes of new turbines will still be required with these codes, however, to refine the actual performance and loads.

21.3 Offshore Wind

All of the wind power development in the United States to date is land-based, most of it in the West and Midwest, where the wind offers a good resource and there are large areas of land available on which to place wind farms. However, this resource is far from the major metropolitan centers near the coastline, and building the transmission line capacity that is necessary to carry the power to those centers is very, very expensive. The offshore wind resource, on the other hand, is very large, and much of it is relatively close to major coastal metropolitan areas (see Figure 7.8), making the possibility of offshore wind attractive, in spite of the additional costs involved. In Europe, where very little land is available for siting turbines, large amounts (over 6 GW) of offshore wind have been installed at shallow-water sites (water depth of less than 30 m), fixed to the seafloor (the turbines are mounted on piles driven into the seafloor or on concrete gravity bases) in the past decade.

21.3.1 Offshore Platform Hydrodynamics

When turbines are located offshore, regardless of the depth of the water, the turbine supporting platform is subjected not only to the wind-generated loads transmitted through the turbine to its base, as is the case for the land-based turbine, but also to water-generated (or hydrodynamic) loads. In addition, the mounting platform now experiences a much larger range of motion than would the gravity foundation of a typical land-based turbine. Thus, the analysis of the wind turbine becomes much more complex—the platform must be modeled as a moving body, subjected to the hydrodynamic loads, that is coupled to the flexible wind turbine structure at the base. At shallow water sites of less than about 30 m water depth, the turbine can economically be mounted on a monopile driven into the seabed or on a conventional concrete gravity foundation (both referred to as fixed-bottom support platforms). For these turbines, the analysis of the hydrodynamic loads acting on the platform can be approximated by applying a number of simplifying assumptions. However, at greater water depth, fixed-bottom support platforms are no longer economically feasible. For water depths between 30 and 60 m, space-frame substructures, including tripods, quadpods, or lattice frames, will be required to maintain the strength and stiffness requirements at the lowest possible cost. At depths of 60 m and greater, economics drive the selection of a floating support platform moored to the sea bottom [36]. The offshore oil and gas industry has demonstrated the long-term survivability of offshore floating structures, so the technical feasibility is not in question, but high-fidelity modeling and accurate analysis are required to enable the development of economical floating platforms.

These more complex structures and hydrodynamic loading in the deeper waters can no longer be adequately modeled with the simplifying assumptions that are typically used for the shallow-water fixed-bottom platforms. Many frequency- and time-domain analyses have investigated wind turbines mounted in water depths in excess of 30 m, but they all contain approximations and limitations. Jonkman provides a very comprehensive review of the analyses that have been done and the approximations and limitations inherent in them [36]. Rather than attempting to summarize the development of the very complex hydrodynamics modeling here, I refer you to Jonkman [36] for a detailed explanation of his development of models that accurately represent the hydrodynamic and mooring forces acting on the floating platform. He has incorporated these models into the NREL-supported HydroDyn code; that code, used in conjunction with the publically available and NREL-supported FAST code for wind turbine modeling and analysis, is capable of analyzing the transient response of a wide variety of offshore wind turbine/support platform/mooring system configurations in waters of moderate to great depth.

21.4 Wind Turbine Loading

Wind turbines are typically fatigue-driven structures; they normally fail not as the result of a single application of a large-amplitude load, but as a result of the repeated application and removal (or cycling) of small-amplitude loads. Each load cycle causes microscopic damage to the structure, and the accumulated effect of many, many cycles of varying amplitude eventually leads to failure of the structure, a process referred to as fatigue failure. In general, the smaller the amplitude of the load, the larger the number of load cycles

the structure can withstand before failing. Therefore, it is very important that the loads acting on a wind turbine be well understood; if the loads are larger than expected, fatigue failure may occur much earlier than anticipated. If the loads are smaller than expected, the turbine will more expensive than necessary for the desired lifetime.

The wind is random or stochastic in nature, with significant short-term variations or turbulence in both direction and velocity. Wind turbine aerodynamic loads may be regarded as falling into one of two broad categories—the deterministic loads occurring in narrow frequency bands resulting from the mean steady atmospheric wind, wind shear, rotor rotation, and other deterministic effects, and the random loads occurring over all frequencies resulting from the wind turbulence. Prior to about 1995, the deterministic loads were frequently predicted with an aerodynamics code, such as those described earlier, utilizing a uniform wind input, while the random loads were estimated with empirical relations. However, turbine designers now recognize that this approach may lead to serious underprediction of both the maximum and random blade loads, resulting in costly short-term component failures. Most analysts today utilize an aerodynamics performance code with a wind model that includes a good representation of the turbulence of the wind in all three dimensions to predict long-term wind turbine loads. The appropriate method of determining the wind-induced extreme events and random loads that limit the lifetime of a turbine remains the subject of ongoing research.

In contrast, designers of offshore turbines can look to the offshore oil and gas industry for guidance on hydrodynamic loading analysis, and Jonkman [36] and others have developed quite comprehensive hydrodynamic load simulation capabilities.

Any lack of knowledge about loads that the turbine/mounting platform will encounter is typically compensated for in the design process by incorporation of large safety margins, leading to excess material and cost.

Civil engineers have spent decades developing statistical methods for predicting wind and wave loads on offshore drilling platforms, to help reduce the cost and increase the reliability of those platforms. The wind turbine industry is now starting to apply that technology to predict the wind and wave loads on wind turbines.

21.5 Wind Turbine Structural Dynamic Considerations

Input loads resulting from wind and, in the case of offshore turbines, waves, together with dynamic interactions of the turbine components with each other, result in forces, moments, and motions in wind turbines, phenomena referred to as structural dynamics. By applying various analysis methods, the impact of changes in turbine configurations, controls, and subsystems on the behavior of the turbine can be predicted. General wind turbine structural dynamic concerns and methods of analysis are discussed in the following paragraphs.

21.5.1 Horizontal-Axis Wind Turbine Structural Dynamics

Small horizontal-axis turbine designs usually use fairly rigid, high-aspect-ratio (the blade length is much greater than the blade chord) blades, cantilevered from a rigid hub and main shaft. As turbine size increases, the flexibility of the components tends to increase, even if the relative scales remain the same, so the blades on larger turbines tend to be

quite flexible, and the hub and main shaft tend to be far less rigid than corresponding components on the small turbines. The entire drive train assembly is mounted on and yaws about a tower that may also be flexible. These structures have many natural vibration modes, and some of them may be excited by the wind or the blade rotation frequency to cause a *resonance* condition, amplifying vibrations and causing large stresses in one or more components. Operating at a resonance condition can quickly lead to component failure and result in the destruction of the turbine. Careful structural analysis during the turbine design may not guarantee that the turbine will not experience a resonance condition, as analysis techniques are not infallible, but ignoring the analysis altogether or failing to properly conduct parts of it may dramatically increase the probability that the turbine will experience one or more resonance conditions, leading to early failure. While the relatively rigid small turbines are not likely to experience these resonance problems, the very flexible, highly dynamic larger turbines may well experience resonance problems unless they are very carefully designed and controlled. Turbines that operate over a range of rotational speeds (variable-speed turbines) are especially challenging to design. The designer will usually try to minimize the number of resonances that occur within the operational speed range and then implement a controller that will avoid operating at those resonance conditions. The actual resonances typically depend on the rotor speed, and the severity of the resonance depends on the wind speed, so the controller logic can become quite complicated.

It is possible to develop techniques in the frequency domain to analyze many aspects of the turbine dynamics. The frequency-domain calculations are fast, but they can be applied only to linear, time-invariant systems and therefore cannot deal with some important aspects of wind turbine operations such as aerodynamic stall, start-up and shut-down operations, variable-speed operation, and nonlinear control system dynamics. In spite of these limitations, frequency-domain solutions of modal formulations are frequently used in the preliminary design of a wind turbine, when quick analyses of many configurations are required.

The large relative motion between the rotor and the tower frequently precludes the use of standard commercial finite-element analysis codes and requires the use of a model constructed specifically for the analysis of wind turbines. Development of such a model can be a rather daunting task, as it requires the formulation and the solution of the full nonlinear governing equations of motion. The model must incorporate the yaw motion of the nacelle, the pitch control of the blades, any motion and control associated with hinged blades, the time-dependent interaction between the rotor and the supporting tower, etc. If the full equations of motion are developed with either finite-element or multibody dynamics formulations, the resultant models contain moderate numbers of elements and potential motions (degrees of freedom or DOF), and significant computer resources are required to solve the problem. On the other hand, a modal formulation utilizing limited DOF may be able to yield an accurate representation of the wind turbine, resulting in models that do not require large computing resources. The development of the modal equations of motion may require somewhat more effort than does the development of the finite-element or multibody equations, and the equations are apt to be more complex. The modal degrees of freedom must include, at a minimum, blade bending in two directions, blade motion relative to the main shaft, drive train torsion, tower bending in two directions, and nacelle yaw. Blade torsion (twisting about the long axis) is not normally included in current modal models, but it may become more important as the turbine sizes continue to increase and the blades become more flexible. The accuracy of some modal formulations is limited by their inability to model the direction-specific nonlinear variation of airfoil lift with an

angle of attack that occurs as a result of aerodynamic stall. However, this is not an inherent limitation of the technique, and some modal formulations are free of this limitation. These modal formulations (NREL's wind-turbine-specific FAST [36] is an example of such a code) are extremely fast running and are arguably the most widely used HAWT structural analysis tools today.

The most accurate structural dynamics models utilize general, commercially available finite-element codes such as ABAQUS [37] or multibody dynamics codes such as ADAMS [38] or wind-turbine-specific multibody dynamics codes such as HAWC2 [39] and BLADED [40]. These require significantly more computer resources than do modal formulation codes, but they can still be run fairly quickly on a PC. FAST, the NREL wind-turbine-specific version of ADAMS, HAWC2, and BLADED have been verified through measurements and comparisons with other codes, and they include all of the modules required to simulate both land-based and offshore wind turbines, including both aerodynamic and hydrodynamic loading.

All of these structural dynamics codes use separate aerodynamics codes, most based on BEM models, to furnish the aerodynamic loads that act on the turbine blades.

Regardless of the methods used in preliminary design, the state of the art in wind turbine structural analysis today is to use highly detailed multibody or finite-element-based, time-accurate structural codes, coupled with blade loadings derived from BEM-based aerodynamics models and support platform loadings derived from hydrodynamic models (for offshore configurations) to analyze the turbine behavior for the detailed final design calculations.

Malcolm and Wright [41] and Molenaar and Dijkstra [42] provide reviews of some of the available land-based HAWT dynamics codes that have been developed, together with their limitations. Buhl et al. [43] compare some of the land-based HAWT dynamics codes that have been extensively verified and that are widely used today, and Quarton [44] provides a good history of the development of land-based HAWT wind turbine analysis codes. More general finite-element dynamics codes are described in [45,46], and additional information on both land-based and offshore HAWT dynamics models can be found in Manwell et al. [34] and Burton et al. [35].

21.5.2 Vertical-Axis Wind Turbine Structural Dynamics

Darrieus turbine designs normally use relatively slender, high-aspect-ratio structural elements for the blades and supporting tower. As with large HAWTs, the result is a very flexible, highly dynamic structure, with many natural modes of vibration that again must be carefully analyzed to ensure that the turbine will avoid structural resonance conditions under all operating environments. The guy cables and turbine support structure can typically be analyzed with commercial or conventional finite-element codes, but the tower and blades require a more refined analysis, usually requiring the use of a finite-element code possessing options for analyzing rotating systems. With such a code, the blades and tower of a VAWT are modeled in a rotating coordinate frame, resulting in time-independent interaction coefficients. The equations of motion must incorporate the effects of the steady centrifugal and gravitational forces, the aerodynamic loading due to the turbulent wind, the hydrodynamic loading due to the water waves and current for offshore configurations), and the forces arising from rotating coordinate system effects. Detailed information on finite-element modeling of land-based VAWTs may be found in Lobitz and Sullivan [47], and information on more general finite-element modeling that includes offshore VAWTs may be found in Owens et al. [48].

21.6 Peak Power Limitation

All turbines incorporate some method of regulating or limiting the peak power produced. The entire turbine, including the rotor, the transmission, and the generator, must be sized to handle the loads associated with peak power production. While high winds (above, say, 25 m/s) contain large amounts of available power, they do not occur very often, and the energy that can be captured is very small. This is illustrated in Figure 21.13 for the Amarillo, TX, airport. In this figure, the power density is the power per unit of rotor area (normalized to yield a value under the curve of unity) that is available for capture by a wind turbine. This takes into account the amount of time that the wind actually blows at each wind speed (the probability density that is also shown on the figure). Amarillo does occasionally experience very high winds, but as seen from this probability density, that does not happen very often, and the energy that could be captured from winds above 24 m/s is negligible.

Generators and transmissions operate most efficiently at their design conditions, typically close to their maximum capacity. These efficiencies drop off quickly at conditions below design. Cost trade-off studies reveal that it is far more cost effective to limit the maximum power level to that achieved at wind speeds of, say, 13–14 m/s and to shut the turbine down completely at a cutout wind speed of, say, 26 m/s, as illustrated in Figure 21.14, than to try to capture the maximum amount of power at the higher wind speeds. Limiting the peak power limits the peak loads that the entire drive train, the tower structure, and the blades must withstand, so the turbine can be built with far less material (and at lower cost) than that required for a turbine that generates peak power at a wind speed of 25 m/s. Under these conditions, the transmission and generator are operating near design conditions a good part of the time, so they are operating at close to their maximum efficiency. The additional energy captured due to the increase in generator and transmission efficiencies at the lower wind speeds is usually many times greater than that lost due to limiting

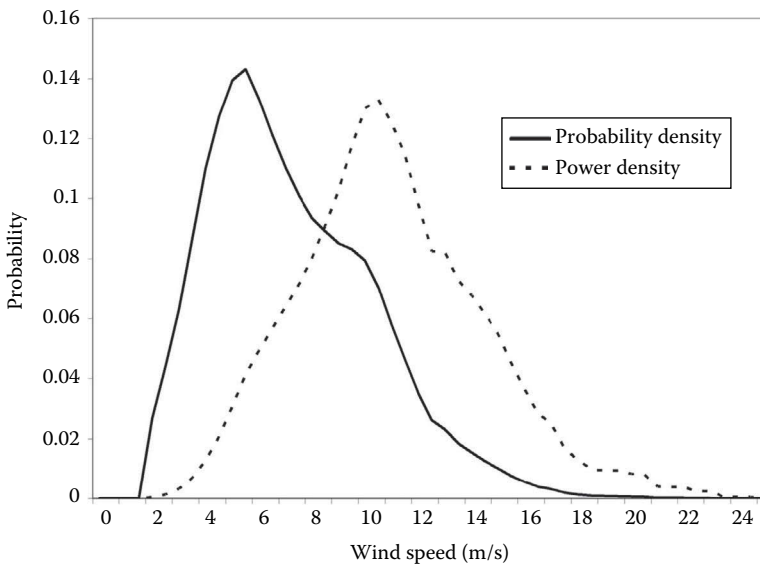


FIGURE 21.13 Wind speed and wind power probability densities for Amarillo, TX, airport.

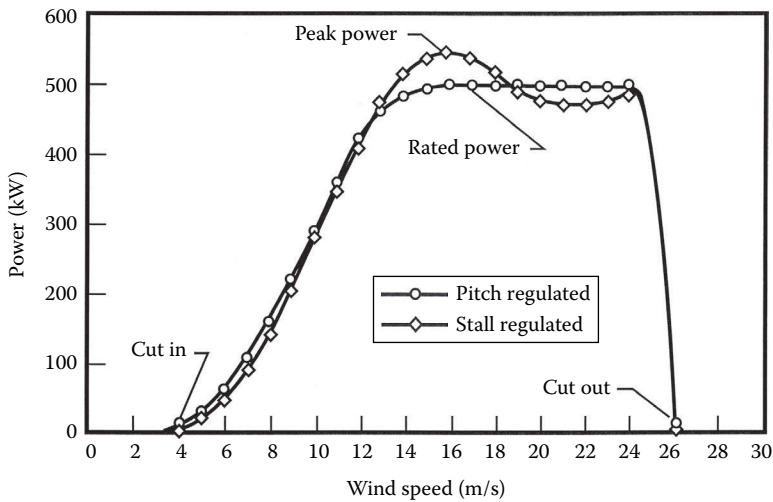


FIGURE 21.14

Sample power curves for stall-regulated and pitch-regulated wind turbines.

the peak power at the rather infrequent winds above 14 m/s (refer to the wind speed distribution in Figure 21.13).

Most small horizontal-axis turbines incorporate passive features, such as tail vanes and furling, that turn the rotor so the rotor axis is no longer aligned with the wind in order to limit peak power production in high winds. Older turbines and some small turbines are designed with fixed-pitch blades and rely on airfoil stall at high winds to limit the maximum power output of the machine. However, nearly all modern large horizontal-axis turbines now use blade pitch control, where either the entire blade or a portion of it is rotated about the blade longitudinal axis to change the effective angle of attack, and thus the power output, of the blade to limit peak power. The blade may be rotated so as to decrease the effective angle of attack as the wind speed increases (commonly referred to as *pitch to feather*), causing decreased blade lift and limiting the peak power to the desired level, or it may be rotated to increase the effective angle of attack (commonly referred to as *pitch to stall*), causing blade stall and limiting peak power. Either pitch to feather or pitch to stall results in better average peak power control than can be achieved with fixed-pitch stall control.

Although pitch-to-feather control results in decreased drag loads at high winds, a major disadvantage is poor peak-power control during high-wind stochastic conditions—sudden increases in wind speed will result in corresponding increases in angle of attack, loads, and power generation. Power excursions can exceed twice the rated power levels before the high-inertia blade pitch system can compensate for gust-induced wind speed increases. Blade stall control (either fixed pitch or pitch to stall), on the other hand, results in better peak power control at high winds. Major disadvantages of stall control include increased blade drag loads as the wind speed increases (even after stall) and possible large dynamic loads due to wind turbulence.

Most VAWTs utilize stall regulation with fixed-pitch blades to control peak power, but some straight-bladed VAWTs are equipped with full-span passive or active pitch controls.

Pitch control can be either passive or active. The pitch control may be included in each blade mounted on a very simple hub, it may be incorporated into a sophisticated hub with

blades that are nothing special, or it may be distributed between the hub and the blades. Therefore, discussions about turbine pitch control normally refer to the combination of hub and blades—the rotor.

- Passive pitch-control techniques automatically adjust the blade pitch angle by using hub-mounted cams activated by centrifugal loads or by using tailored blade materials that permit the blade to twist toward feather or stall under high loads. These devices are very carefully tailored to maintain peak performance at lower wind speeds but limit the peak power and blade loads at high wind speed. A major disadvantage of these techniques is that they cannot readily be adapted to site-specific conditions—a hardware change is required to make any changes to the control.
- Active-pitch control rotors are equipped with one or more motors (typically mounted on the hub) to change the blade pitch angle on command from the turbine controller. These rotors are much more expensive than fixed-pitch stall control blades, but they open the possibility for much refined control of the turbine, potentially leading to reductions in loads for the entire drive train. Changes to the control can usually be implemented by simply changing the controller software program.

Sample power curves for fixed-pitch stall regulated and active pitch (pitch to feather) 500 kW turbines are shown in Figure 21.14.

21.7 Turbine Subsystems

The wind turbine incorporates many subsystems, in addition to the actual turbine, in order to generate power. The electrical power generation, yaw, and control systems are the only ones that will be discussed here.

21.7.1 Electrical Power Generation Subsystem

Once a wind turbine has converted the kinetic energy in the wind into rotational mechanical energy, that rotational energy is usually converted by a generator into electricity that can be readily transported to where it is needed. In many configurations, the generator input shaft speed is much higher than the turbine shaft speed, requiring the use of a speed-up transmission (or *gearbox*) that increases the turbine shaft speed to that required by the generator. Other configurations utilize *direct-drive* (DD) generators to eliminate this need for a gearbox with the generator input shaft directly connected to the turbine drive shaft.

In the past, most grid-connected turbines have utilized either synchronous or induction generators. Synchronous generators are more complex and tend to be more expensive than induction generators, but they provide excellent voltage and frequency control of the generated power and can deliver reactive power to the grid. However, these generators are not intrinsically self-starting (the turbine blades are usually pitched to start the turbine, which drives the generator), do not provide power-train damping, and require sophisticated controls for connecting to the grid, as the output frequency

(and thus, the speed of the generator) must be precisely matched to the grid frequency before the connection is made.

Induction generators, in contrast, have a simple, rugged construction; they may readily be used as motors to spin a turbine up to speed; they are cheaper than synchronous generators; they may be connected to and disconnected from the grid relatively easily, and they provide some power-train damping to smooth out the cyclic torque variations inherent in the wind turbine output. However, they require reactive power from either power electronics or the grid, and they can contribute to frequency and voltage instabilities in the grid to which they are connected. These adverse effects can usually be solved fairly quickly and at low cost with modern power electronics. Induction generators are, therefore, the most common type found on wind turbines.

Synchronous *permanent magnet* (PM) generators replace the separate excitation, slip rings, and rotor windings (with associated losses) of a typical synchronous machine with powerful PMs, leading to a simple, rugged construction. Virtually all PM generators utilize *rare-earth* (RE) materials for the PMs due to the very high flux density that can be achieved with these materials. The power produced by PM generators is usually variable-voltage and variable-frequency AC that must be converted to DC or to fixed-voltage and fixed-frequency AC with power electronics before it can be fed into the grid. Even with this requirement for additional power electronics, these machines tend to achieve higher efficiency at low power ratings (92.9% at 25% load versus 94.4% at full load) than either induction or synchronous generators, leading to increased energy capture. The cost of these generators has historically been somewhat higher than that of induction or synchronous generators, due primarily to the high cost of the RE material, but technology advances have resulted in price decreases, making the technology quite competitive with the older technologies. As a result, PM generators are becoming very common. Fuchs et al. [49] describe the development of a PM generator for wind turbine use.

While the earlier discussion covers the generator technologies most commonly used on wind turbines in the past, many other types of technologies are used today. Discussion of those generator technologies may be found in Manwell et al. [34] and Burton et al. [35].

Direct-drive generators are normally synchronous machines (with either conventional or permanent magnet excitation) of special design, built with a sufficient number of poles to permit the generator rotor to rotate at the same speed as the wind turbine rotor. This eliminates the need for a gearbox or transmission. Benefits of a direct-drive generator include a drive train with far fewer parts, leading to potentially higher reliability and lower maintenance, and a lower system tower-top weight. The primary drawback to a direct-drive generator is the very high torque that it must handle; the power produced by the rotor is proportional to torque multiplied by rpm, so the torque that is applied to the generator goes up as the generator operating rpm decreases. A typical 1.5 MW turbine rotor rpm might be 15 rpm, with a conventional generator rpm of 1800 rpm. Replacing this generator with a direct-drive generator would drop the generator rpm to 15 rpm, requiring a direct-drive generator torque rating of $1800/15 = 120$ times that of the conventional generator. Direct-drive generators are usually used in conjunction with power electronic converters to decouple the generator from the network and provide flexibility in the voltage and frequency requirements of the generator.

Direct-drive PM generators require very strong magnetic fields (and corresponding large amounts of RE materials), due to the very high torque levels at which the generators must operate. In large amounts, RE components are still quite expensive, as China is currently the primary source, and they are severely limiting export. Thus, direct-drive

PM generators tend to be more expensive than more conventional direct-drive generators. Moderate-speed PM generators (lower rotational speed than traditional synchronous or induction generators, but higher rotational speed than direct-drive generators) operate at much reduced torque levels and thus require much less RE. This configuration still requires the use of a gearbox, but it can be a fairly simple single-stage design due to the moderate speed step-up requirements.

The direct-drive generator technology advantage in reduced drive train weight increases with size, but as the power rating approaches the 8–10 MW range, current technology results in generators that rapidly grow larger and heavier, due to the high torque requirements. This, in turn, requires a heavier tower structure to carry the extra weight and torque. These large generators also present design challenges. As with PM generators, an alternative then becomes a relatively light, single-stage gearbox with a much smaller, lighter generator that still offers many of the direct-drive advantages.

Most older turbines (built prior to about 2000) operated at a single fixed rotational speed, but many newer turbines, and especially the large ones, are variable speed, operating within a fixed range of rotational speeds. Variable-speed turbine operation offers several major advantages over fixed-speed operation:

1. The aerodynamic efficiency of the rotor at low to moderate wind speeds may be improved by lowering the rotational speed to keep the turbine operating close to the optimum tip-speed ratio, maximizing the power coefficient. At higher wind speeds, the turbine rotates at maximum rotational speed, and the blades are either in stall or are pitched to limit peak power. The rotor speed may also be adjusted to fine-tune peak power regulation.
2. System dynamic loads may be attenuated by the inertia of the rotor as it speeds up and slows down in response to wind gusts.
3. The turbine may be operated in a variety of modes, including operation at maximum efficiency to maximize energy capture at lower wind speeds and operation to minimize fatigue damage.

As mentioned earlier, for variable-speed operation, certain rotational speeds within the operating-speed range will likely excite turbine vibration modes, causing structural resonance and increased rates of fatigue damage. These rotational speeds must be avoided during operation, leading to complex control schemes.

Variable-speed operation is possible with any type of generator, including direct-drive and PM generators. As is the case for fixed-speed, direct-drive and PM generators, variable-speed operation results in variable-frequency/variable-voltage AC power. Interfacing the turbine to the power grid requires the use of power electronics to convert this power to high-quality, constant-frequency/constant-voltage AC power. Several methods have been developed for accomplishing this with sophisticated power electronics (see, e.g., Smith [50]), but research to develop improved methods with higher efficiencies continues. Manwell et al. [34] and Burton et al. [35] give brief overviews of some common types of power converters and provide references for more extensive discussions of these devices.

For a conventional, non-PM generator, electrical efficiency tends to drop off rapidly as the generated power falls below the rated generator capacity, so single-generator wind turbines tend to be very inefficient at low wind speeds. Some turbine designs address this deficiency by incorporating multiple smaller generators; at low wind speed, only

one generator is attached to the drive train, with more being added as the wind speed increases. The net result is that each generator operates close to its rated power much of the time, increasing the overall generator efficiency. Similar increases in generator efficiency at low power levels can be obtained with a single generator utilizing pole switching or multiple windings. Other generator designs that overcome this loss in efficiency at lower power levels have been developed in recent years.

21.7.2 Yaw Subsystem

The rotor of an HAWT must be oriented so that the rotor axis is parallel to the wind direction for peak power production. While small turbines usually rely on passive systems, such as tail vanes, to accomplish this, most large upwind HAWTs and a few downwind HAWTs incorporate active yaw control systems, using a wind direction sensor and a drive motor/gear system to orient the rotor with respect to the wind direction. Most downwind HAWTs are designed to utilize the wind itself to automatically orient the rotor. Active yaw systems tended to be extremely problematic in early turbines, basically because the loads acting on them were not well understood. Yaw loads are much better understood today, and these systems are no longer a major problem area.

As mentioned earlier, VAWTs do not require orientation with respect to the wind and thus do not require yaw systems.

21.7.3 Control Subsystem

One or more control systems are needed to integrate the operation of the many components of a wind turbine and to safely generate power. In a very general sense, a wind turbine control system consists of a number of sensors, a number of actuators, and a system of hardware and software that processes the signals from the sensors to generate signals to control the actuators. A turbine usually contains a minimum of two distinct controllers—a safety controller that will override all other controllers to bring the turbine to a safe state (usually stopped, with the brakes applied) in case of an abnormal event, and an operational controller that handles the normal operation of the turbine. Any particular turbine may incorporate many additional secondary or slave controllers, each of which handles only a limited number of tasks. An example of a secondary/slave controller might be a blade pitch controller that pitches the blades to follow a predetermined schedule during start-up and shutdown of the turbine and that pitches the blades as necessary to regulate the power output of the turbine at the rated level in above-rated wind speeds.

21.7.3.1 Safety Controller

The safety controller acts as a backup to the operational controller and any secondary or slave controllers; it takes over if the other controllers fail to maintain the turbine in a safe operating mode. It is normally triggered by the activation of certain safety sensors (such as excessive vibration, excessive rotor speed, or excessive generator power) that are independent of the sensors connected to the operational and/or slave controllers, but it may also be activated by an operator-controlled emergency stop button. This system must be as independent from the normal operations control system as possible and must be designed to be fail-safe and highly reliable, since it may be the last line of defense to save a

turbine from self-destruction. The safety controller will normally consist of a hard-wired fail-safe circuit monitoring a number of sensors. If any of the sensors indicates a problem, the safety controller assumes full turbine control and ensures that the turbine is brought to a safe condition. This might include, for example, de-energizing all electrical systems, pitching the blades to the feather position, and engaging the spring-applied emergency brakes (that are held off in normal operation).

21.7.3.2 Operational Controller

The regular operational controller is usually computer or microprocessor based; a basic turbine operational controller will normally start and stop the machine; connect the generator to or disconnect the generator from the power grid, as needed; control the operation of the yaw and pitch systems (if present); perform diagnostics to monitor the operation of the machine; and perform normal or emergency shutdown of the turbine as required.

For older turbines, the operational controller was frequently a fairly generic device that was simply added to the turbine and then programmed with either hardware or software modifications to implement the control functions specific to that particular turbine. The operational controllers on newer turbines, especially the large, variable-speed/variable-pitch machines, incorporate much more intelligence than the old, generic type, and they are custom tailored (with software) to reflect the capabilities and characteristics of each specific turbine. Modern controllers (or, more accurately, the turbine control software programs) are usually designed from scratch as an integral component of the wind turbine and must be included in the models of system aerodynamics and structural dynamics to obtain accurate estimates of loads and motions. The controller dictates how the pitch, rotor speed, and generator torque systems are used to limit peak power and/or torque, control rotor speed, maximize energy capture, trade-off energy capture and load mitigation, reduce power fluctuations, control power quality, actively control some turbine dynamics, or perform many other functions. These controllers may consist of a single physical unit performing all of the assigned tasks, or they may consist of multiple physical units, each performing a small number of tasks, all coordinated by a supervisory controller.

21.7.3.3 Turbine Power/Load Control Programming

The operational control hardware mentioned in the last section must be programmed to perform the appropriate functions for the turbine. This section discusses some of the specific scenarios that may be implemented in the control system.

Figure 21.15 illustrates the three distinct operational regions of wind turbine operation, which are as follows:

1. Region 1 is where the wind speed is too low to overcome the drive train resistance of the turbine.
2. Region 2 is that region between the cut-in wind speed (where the turbine starts to generate power) and the rated wind speed (where the turbine reaches rated or maximum power).
3. Region 3 is between the rated wind speed and the shut-down wind speed (where the turbine is shut down to protect it).

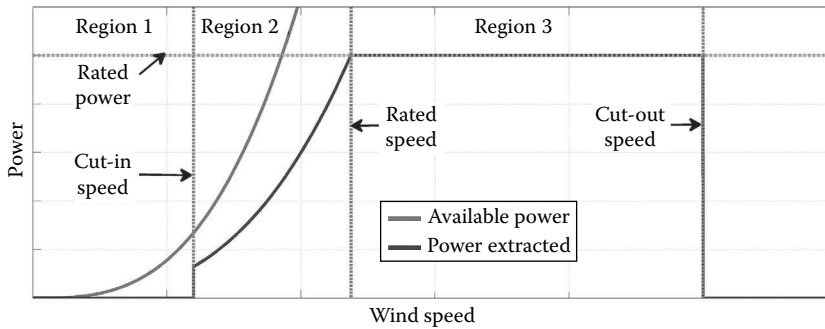


FIGURE 21.15
Wind turbine operating regions and ideal turbine power curve.

The pitch and rotor rotational speed capabilities of a turbine determine how the turbine controller can increase energy capture and limit blade and generator loads in these regions. The ideal path of turbine power as a function wind speed, as shown on Figure 21.15, requires that the turbine be operated at maximum efficiency in region 2 and then limit the power production in region 3. This requires that the rotor rotational speed (commonly referred to as the rotor speed) be correlated to the wind speed throughout region 2 so that the turbine is always operating at its maximum efficiency (the turbine $C_{p,max}$ curve), and the turbine must be able to dump excess power in order to limit the turbine power and wind-induced loads in region 3.

The early turbines were restricted to constant rotor speed and fixed blade pitch (referred to as constant speed/fixed pitch). These turbines are constrained to follow some suboptimal energy capture path through region 2 (the precise path depends on the preset blade pitch and the fixed rotor speed). They rely on blade stall to limit peak power and loads in region 3, but stall can lead to some very high power peaks and loads in this region in response to positive wind gusts. Large turbine design has evolved through the years to include variable rotor speed and variable blade pitch (referred to as variable-speed/variable-pitch) capabilities that enable modern turbine controllers to better approximate the ideal power path of Figure 21.15 and capture more energy. These capabilities enable the turbine (as directed by the control program) to very closely follow the optimal turbine performance path; within region 2, the turbine sets the optimum blade pitch angle and then operates at the rotor speed that optimizes turbine performance at each wind speed; within region 3, the turbine operates at maximum rotor speed and utilizes blade pitch to control peak power and wind-induced loads. The turbines may also utilize the variable rotor speed capability to smooth out power and load fluctuations due to wind gusts throughout regions 2 and 3.

The turbine controller determines the precise manner in which these capabilities are utilized. It is typically designed with two distinct operating algorithms for the two regions, with some kind of transition between the two that mitigates the very large drive train loads that can result from an abrupt switch between the variable-speed/fixed-pitch operation in region 2 and the fixed-speed/variable pitch operation in region 3. This transition usually results in a lowering of the actual power curve in the vicinity of change between the operating regions—some energy capture is sacrificed to mitigate drive train loading. A turbine is normally designed to spend a lot of time in this transition region in order to maximize energy capture, so even a small lowering of the power curve here can result in considerable energy capture loss over time. Given the reality that a 1% loss in energy capture for every turbine results in income loss of over \$2 million annually for 1 GW of

installed capacity, there is a tremendous amount of interest in optimizing control in this region to maximize power while minimizing loads.

Many other areas of control offer the opportunity to increase energy capture and/or mitigate loads. A few of those areas are mentioned in the following paragraphs.

Early variable-pitch turbines utilized collective blade pitch, where all the blades pitch the same amount at the same time, often driven by a single motor. As turbines became larger, this design changed to use an electric motor for each blade, enabling each blade to be pitched independently of the others. Research has shown that utilizing this capability has the potential to significantly decrease blade fatigue loads [51]. However, this control strategy leads to increased use of blade pitch motors; retrofitting it on existing turbines could lead to early pitch motor burnout. In addition, implementation of this capability without an update to the existing turbine controller software has sometimes been found to lead to a small loss in turbine energy capture. This technology remains the subject of active research.

The blades on large turbines are very large; some exceed 80 m in length. Pitching a blade of this size is slow, and this limits the amount of load mitigation that can be achieved with full-span pitch. One variation on active blade pitch is the use of only a portion of the airfoil surface (typically including the blade tip) as a control surface. Adjusting the pitch (and, thus, the lift and drag) of this portion of the blade independently of the remainder of the blade (so-called partial-span control) can be used to control the peak power output of the turbine. This control surface is usually much smaller than the full blade, so it can respond to wind changes and mitigate loads much faster than can the full-span blade. However, partial-span devices have proven to be very difficult to integrate into a blade, and the gaps between the devices and the surrounding blade tend to generate noise.

Some recent research work has investigated the use of very small load control devices that can generate large changes in lift and drag while experiencing small loads. The chord-wise dimensions of these devices are typically on the order of 1% of the blade chord; their small size means they can be activated very quickly to alleviate excess loads, and they are less likely to create large amounts of noise. Mayda et al. [52] discuss the use of CFD to investigate the effects of some of these devices. An excellent summary of work on this concept prior to 2009 may be found in a survey article written by Barlas and van Kuik [53], while Barlas et al. [54] and Berg et al. [55] provide information on two recent demonstration efforts.

Other areas of controls research include the following:

- Maximizing turbine and/or wind-farm-generated power while mitigating structural loads.
- Maximizing turbine and/or wind farm power quality.
- Preview control, where the wind is measured upwind of the turbine and load mitigation and/or enhanced energy capture actions can be initiated before the wind actually strikes the turbine.
- Maximum power point control, where the controller *learns* the exact method of operation that will yield the maximum possible power output (especially in region 2), rather than relying on a nominal maximum efficiency curve.

While traditional turbine controls seem to work fairly well for the fixed-bottom offshore turbines, the field of offshore floating wind turbine control is so new that very little is known about what will be needed.

21.8 Other Wind Energy Conversion Considerations

The actual turbine system is the single most important and most costly item of a wind energy conversion system, but there are many other aspects of the system that must be considered and carefully optimized before wind energy can be produced at a cost-competitive price. These aspects include things like turbine siting, installation and foundations; operating and maintenance costs; manufacturing processes; transport of components to the site; turbine payback period; wind energy COE and environmental concerns. Turbine siting has already been discussed in Chapter 7. This section will discuss only materials, installations, grid integration, wind forecasting, energy payback period, wind turbine costs and COE, and some environmental concerns. Additional information, including extensive reference lists, on all of these aspects can be found in Manwell et al. [34], Burton et al. [35], and Spera [56].

21.8.1 Wind Turbine Materials

As mentioned earlier, wind turbines are fatigue critical structures (their design is driven by consideration of the cyclic fatigue loads they must endure), and the number of fatigue cycles they experience in a 20–30-year design life is three orders of magnitude beyond the 10^6 cycles that has been the common limit of fatigue data for most materials. Most of the materials used in the construction of wind turbines are typical of those materials that are used in other rotating machinery and towers—relatively common structural materials such as metal, wood, concrete, and glass-fiber-reinforced plastic (GFRP) composites. Towers are typically made of steel; a few have been built of concrete. Drive trains, generators, transmissions, and yaw drives are made of steel. These components can readily be designed so they experience very low stresses and will have a fatigue life of 20–30 years. HAWT blades, however, must be built with a minimum of lightweight material to minimize the gravity-induced cyclic loads on the blades, drive train, and tower. Over the past 20 years or so, high-cycle fatigue databases for many potential blade materials have been developed specifically for wind turbine applications. Mandell and Samborsky [57] and Mandell et al. [58] describe the main U.S. high-cycle fatigue database; the latest database, together with new reports and recent publications and presentations regarding the database, may be found at www.coe.montana.edu/composites/. De Smet and Bach [59] and Kensche [60] describe the European counterpart, which has now been included in the OPTIMAT materials database maintained by the WMC Knowledge Centre of the Netherlands. The latest version of this database is available at www.wmc.eu/optimatblades_optidat.php, and a reference document describing the contents of the database is provided by Nijssen [61].

The material with the best all-around structural properties for wind turbine blades appears to be carbon-fiber/epoxy composite, but it is significantly more expensive than other potential materials. In light of that, the blade material of choice today (as it has been for the past couple of decades) is GFRP, due to the high strength and stiffness that can be obtained, the ease of tailoring blades made of GFRP to handle the loads, and the relatively low cost of GFRP [62]. However, the trend to larger and larger turbines, with the resultant increase in blade weight and flexibility, has created intense interest in utilizing some carbon fiber in the blades to decrease weight and add stiffness. The expense of carbon fiber, even in the cheapest form available today, means that turbine designers must incorporate it into blades in a cost-effective manner. According to Griffin [63] and Jackson et al. [64], one very efficient method of utilizing carbon fiber is to place it in the longitudinal spar

caps, near the maximum thickness area of the blade, where its lightweight and extra stiffness yield maximum benefits.

Obviously, the materials must be protected from the environment in some fashion. While paints and gel coats have been deemed adequate for most land-based installations in the past, long-term exposure to sunlight and high winds (and the dust and debris carried by those high winds) has resulted in considerable degradation of the GFRP blades, especially the leading edges, leading to considerable loss of turbine performance. Quantifying the performance loss due to this surface degradation is an active research area at the current time [65].

The offshore environment is much different and much more demanding than the onshore environment. Testing techniques must be developed to determine the suitability of materials proposed for use in offshore turbines. Miller et al. [66] describe the challenges they have encountered in developing techniques to evaluate the performance of composite materials in a seawater environment and present some initial results.

21.8.2 Wind Turbine Installations

Chapter 7 of this handbook discusses wind turbine siting considerations in some depth. Although individual turbines or small clusters of turbines may be used to provide power to small loads such as individual residences or businesses, the most common arrangement for producing large amounts of energy from the wind is to locate many wind turbines in close proximity to each other in a wind farm or wind park. Figure 21.16 is a photograph of several of the General Electric 1.5 MW turbines comprising the 204 MW New Mexico Wind Energy Center in eastern New Mexico (mentioned earlier in the case study in Chapter 7), while Figure 21.17 shows a few of the turbines in the huge offshore



FIGURE 21.16

Typical land-based wind farm installation—New Mexico Wind Energy Center in eastern New Mexico.



FIGURE 21.17

Offshore wind farm installation—London Array Wind Farm in Thames River Estuary, United Kingdom. (Courtesy of London Array Limited.)

London Array. Operating turbines in this manner leads to lower COE, as fixed construction costs, such as electrical grid interconnections and project development and management costs, and fixed maintenance costs, such as cranes, replacement parts, and repair facilities, can be spread over a larger investment. As of the date this is written (November 2013), the offshore London Array wind power project in the United Kingdom is the world's largest wind farm. The fleet of 175 wind turbines stationed in the salty waters of the outer Thames estuary, where the river Thames empties into the North Sea, boasts a nameplate capacity of 630 MW, enough to power nearly half a million U.K. homes.

21.8.3 Wind Power Integration into Grid Operations and the Need for Forecasting

The following discussion borrows heavily from two papers that have been recently published in the *IEEE Power & Energy Magazine* [67,68].

21.8.3.1 Grid Integration

One common argument that wind energy critics raise is that grid systems are capable of accepting power only from *dispatchable* (capable of providing the operator-specified amount of power at any time) power systems; wind's inherent variability precludes its efficient integration into a grid system. Most conventional generators are, in reality, quite constrained in their ability to quickly change their output to a desired amount of power and must be operated with careful consideration of their start-up times, minimum run times, and ramp-rate limitations, and all conventional generators are subject to occasional failure—thus, even they cannot be considered to be truly dispatchable. Wind can usually adjust output very quickly within the range between zero and the power available from the wind, while many conventional units ramp slowly and within a more limited range. In fact, the components of the electric power system have always been uncertain and variable to some degree, but the addition of wind energy (or other variable sources of energy)

increases the need to directly manage these attributes in more sophisticated ways; the growth of wind energy is forcing the development of the next generation of tools and practices for continued efficient and reliable electric system operations.

At the current time, larger markets are, in general, more adept at handling higher wind penetration rates for several reasons:

- Larger markets are typically more geographically diverse, and this diversity of wind resources reduces the short-term fluctuations and forecast errors in the wind power.
- Larger markets typically use centralized wind power forecasts and sophisticated tools for scheduling power resources.
- Larger markets typically have made a larger effort to better understand the issues specific to a high penetration of variable resources and to find methods of alleviating those issues.

In general, analysis by system operators has shown the need for increased generation fleet flexibility (for all types of generation units), including flexibility from the wind plants.

Several grids in the United States, including New York Independent System Operator, Alberta Electric System Operator, Energy Reliability Council of Texas (ERCOT), Midcontinent Independent System Operator, California Independent System Operator, and the PJM regional transmission organization have successfully integrated extensive amounts of wind into their systems, and they are all preparing for significantly more in the near future [67]. Most of these grids have integrated wind into their security-constrained economic dispatch systems to allow the grid operator to treat wind the same as they treat other power plants, requiring them to furnish precise levels of output for the next few minutes and penalizing them if they fail to deliver. The keys to these successful integrations are the use of 5-minute (the de facto North American standard interval) rolling dispatch—rebalancing the calls for power from all resources every 5 minutes—and the demonstrated reliable persistence of wind over that time frame.

ERCOT, which efficiently dispatches wind and uses energy dispatch and non-spinning reserves (no spinning reserves) to compensate for wind uncertainty, has carried out detailed analysis of the costs of wind variability and uncertainty for the 9% of their energy supplied by wind in 2011. They have concluded that the costs of wind power variability and day-ahead forecast uncertainty together amount to only 1%–2% of the value of that wind-generated energy, with about one-third of that amount due to variability and two-thirds due to the day-ahead uncertainty attributable to imperfect wind power forecasts.

While this discussion has focused on integration of wind into North American grid systems, European grids have experienced similar success in integrating wind, utilizing a different approach for aggregating wind plant output and an hourly dispatch schedule.

21.8.3.2 Wind Forecasting

The success of these operators in integrating wind energy into their systems is not to say that there is no need to continue to advance the state of the art in wind power forecasting; additional improvements will help reduce those wind-related additional costs and will be of great value to system operators, wind plant owners, financial traders, and even traditional generators. However, better forecasts will likely be more valuable for smaller grid systems with less generating options and a lower frequency of dispatch than for the huge grid systems with very frequent dispatching discussed earlier.

Wind power predictions or forecasts utilize a combination of weather forecasting models and wind farm-specific models (to model the complexity and interactions of wind turbines with each other and with the localized terrain). Weather forecasts and wind power forecasts are far from perfect, but, as seen earlier, experience has shown that forecasts do not need to be perfect to be very useful and valuable; currently available forecasting models perform reasonably well for several days in the future and may be marginally adequate for large grid operators.

While a cheap and simple wind power forecast can be produced with no real-time data using a publicly available numeric weather prediction model to provide the wind speed and combining that with geographic location, wind power plant size, and a turbine power curve, having more data means getting better forecasts, up to a point. Basic data such as the geographic center of the wind power plant, turbine hub height, measures of the metered power output of the power plant, and historic output data will greatly improve the simple forecast mentioned earlier. On the other hand, forecasting systems that make use of great volumes of data are frequently cumbersome and complex; the cost-effectiveness of such approaches may well be lower than that of simpler methods. The continuing goal must be to improve both the accuracy of numerical weather prediction models (by improving our fundamental knowledge of the physics involved) and the quality, quantity, and timeliness of the environmental data required to define the initial state of the atmosphere, ocean, and land surface for those models.

Not all interested parties will derive the same benefits from these improved wind forecasts. For some grid operators (especially smaller ones, with limited generator options available), the ability to more precisely forecast rapid increases or decreases in available wind power (ramp forecasting) may be of great value as that will directly affect the ability of these operators to match energy demand and supply. On the other hand, increasing the precision of ramp forecasting might not be a major issue if the grid system has gas combustion turbines online that can readily adapt to rapid changes in wind contribution, but increasing the certainty associated with 1–5 day-ahead forecasts may enable that operator to confidently plan maintenance on conventional generators.

Significant advances in forecasting are being made, with high-quality wind power forecasts now available from a number of forecast providers and new research promising continued incremental improvements in the future. Cooperation between the public and private sectors is needed to maximize that rate of improvement. When these advances are combined with the appropriate operating practices and market rules that are now evolving, increasing amounts of wind energy will be economically and reliably integrated into our power system.

21.8.4 Energy Payback Period

A certain amount of energy is used in the manufacture, installation, and eventual scrapping of any energy-producing machine. The time required for the machine to generate as much energy as was used in its manufacture, installation, and end-of-life scrapping is referred to as the *energy payback period*. Studies by Krohn [69] and Milborrow [70] have found that the energy payback period for modern wind turbines ranges between 3 and 10 months, depending on the wind speed at the site and the details of turbine manufacturing and installation. This payback period is among the shortest for any type of electricity producing technology.

21.8.5 Wind Turbine Costs

By the mid- to late-1990s, the configuration for utility-scale wind turbines had evolved to the three-bladed upwind design. About this time, the University of Sunderland in the

United Kingdom developed a set of scaling tools for wind turbines, together with several models to predict the impact of machine size on turbine components. That work was further advanced by DOE-funded efforts starting in about 2000. In 2005, researchers at NREL's National Wind Technology Center began developing a spreadsheet model of these scaling relationships. The result is a set of models that can be used to project the total COE for a wind turbine over a range of sizes and configurations; they are not intended to predict turbine *pricing* [71]. These models allow projections of costs for both land-based and offshore technologies, though the offshore technologies are very early in their development, and forecast costs are very rough.

The model cost estimates are based on turbine rating, rotor diameter, hub height, and other key turbine descriptors. Cost scaling functions have been developed for major components and subsystems. Annual energy production is estimated based on the Weibull probability of wind speeds. The cost metric used is the levelized cost of energy (LCOE), given by

$$\text{LCOE} = \frac{(\text{ICC} \times \text{FCR}) + \text{AOE}}{(\text{AEP}_{\text{net}}/1000)}$$

where

ICC (initial capital cost) in \$/kW is the sum of the turbine system cost and the balance of station cost

FCR (fixed charge rate) in % is the annual amount per dollar of initial capital cost needed to cover the capital cost, a return on debt and equity, and various other fixed charges

AOE (annual operating expense) in \$/kW/year includes land lease cost, levelized operations and maintenance cost, and levelized replacement/overhaul cost

AEP_{net} in MW h/MW/year is the net annual energy production

LCOE values are expected to be greater than actual wind energy prices because these calculations do not include the value of the production tax credit or any other renewable energy credit or subsidy.

NREL recently issued a report documenting their use of this model to develop their estimate for the cost of both land-based and offshore wind energy in the United States for 2011 [72]. In this report, their land-based turbine is a 1.5 MW machine with a hub height of 80 m at 50 m wind speed of 7.25 m/s (7.75 m/s at hub height). The turbine is assumed to be included in a 200 MW wind farm of 133 turbines. Their offshore or fixed-bottom turbine is a 3.6 MW machine with a hub height of 90 m at 50 m wind speed of 8.4 m/s (8.0 at hub height). This turbine is assumed to be included in a 500 MW wind farm of 139 turbines, mounted on monopile foundations in an average water depth of 15 m and situated 20 km from shore. Additional details on terminology, study assumptions, and calculations may be found in the NREL reports [71,72].

Results of the study for the land-based turbine are presented in Table 21.1, while the results for the offshore turbine are presented in Table 21.2; the LCOE for the land-based turbine is \$72/MW h, while for the offshore turbine, it is \$225/MW h. Again, keep in mind that these figures are not intended to reflect actual energy prices, but rather to reflect relative costs of these electricity-generating projects at this point in time.

The installed capital costs for the two configurations as given in Tables 21.1 and 21.2 are summarized in Figures 21.18 and 21.19. From these results, it is obvious that reductions in any single component of capital cost will not lead to dramatic changes in turbine COE.

TABLE 21.1

Initial Capital Cost Breakdown for Land-Based Turbine

	1.5 MW (\$/kW)	1.5 MW (\$/MW h)
Rotor	292	9
Blades	178	5
Hub	53	2
Pitch mechanism and bearings	57	2
Drive train, nacelle	667	19
Low-speed shaft	36	1
Bearings	20	1
Gearbox	144	4
Mechanical brake, high-speed coupling	2	*
Generator	91	3
Variable-speed electronics	108	3
Yaw drive and bearing	32	1
Mainframe	126	4
Electrical connections	76	2
Hydraulic, cooling system	17	*
Nacelle cover	16	*
Control, safety system, and condition monitoring	30	1
Tower	296	9
Turbine capital cost	1286	37
Turbine transportation	63	2
Permitting	1	*
Engineering	7	*
Meteorological mast and power performance engineering	5	*
Access road and site improvement	42	1
Site compound and security	5	*
Control and operation and maintenance building	4	*
Turbine foundation	68	2
Turbine erection	59	2
Medium-voltage electrical material	76	2
Medium-voltage electrical installation	25	1
Collector substation	26	1
Project management	17	*
Development	25	1
Balance of station	446	13
Market price adjustment	196	6
Contingency fund	112	3
Soft costs	307	9
Construction financing cost	60	2
Total capital cost	2098	61
Levelized replacement cost	11	3
Labor, equipment, facilities (O&M)	17	5
Land lease cost	7	2
Annual operating expenses	35	11
Net annual energy production (MW h/MW/year)	3263	
Levelized cost of energy (\$/MW h)	72	

Source: Tegen, S. et al., 2011 Cost of wind energy review, NREL/TP-500-56266, National Renewable Energy Laboratory, Golden, CO, 2013.

TABLE 21.2
Initial Capital Cost Breakdown for Offshore Turbine

	3.6 MW (\$/kW)	3.6 MW (\$/MW h)
Turbine capital cost	1789	62
Development (i.e., permits, engineering, and site assessment)	58	2
Project management	117	4
Support structure	1021	35
Port and staging	73	3
Electrical infrastructure	540	19
Transportation and installation	1109	38
Balance of station	2918	101
Insurance	94	3
Surety bond (decommissioning)	165	6
Contingency fund	471	16
Soft costs	730	25
Construction financing cost	163	6
Total capital cost	5600	194
Levelized replacement cost	40	12
Labor, equipment, facilities (O&M)	46	22
Outer continental shelf lease cost	21	6
Annual operating expenses	107	40
Net annual energy production (MW h/MW/year)	3406	
Levelized cost of energy (\$/MW h)	225	

Source: Tegen, S. et al., 2011 Cost of wind energy review, NREL/TP-500-56266, National Renewable Energy Laboratory, Golden, CO, 2013.

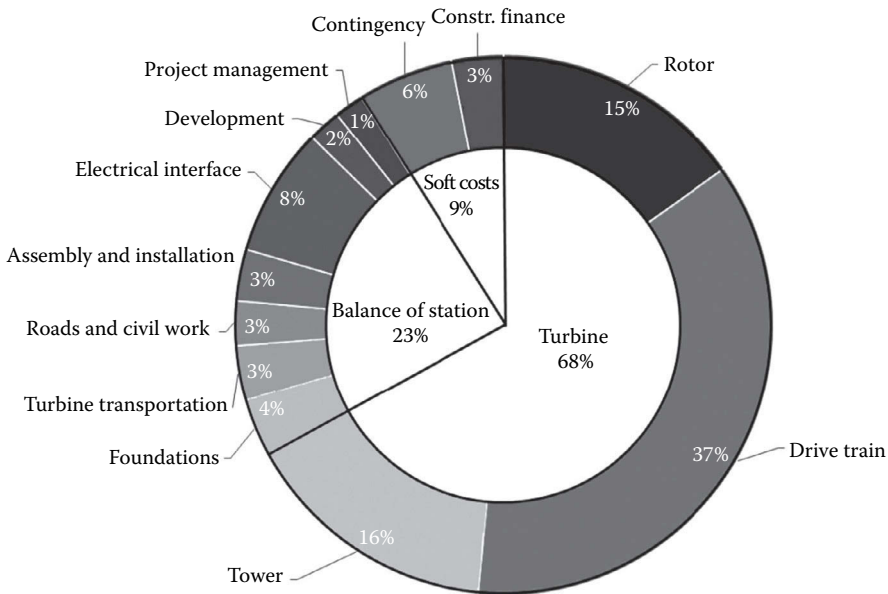


FIGURE 21.18
Initial capital cost breakdown for land-based wind turbine. (From Tegen, S. et al., 2011 Cost of wind energy review, NREL/TP-500-56266, National Renewable Energy Laboratory, Golden, CO, 2013.)

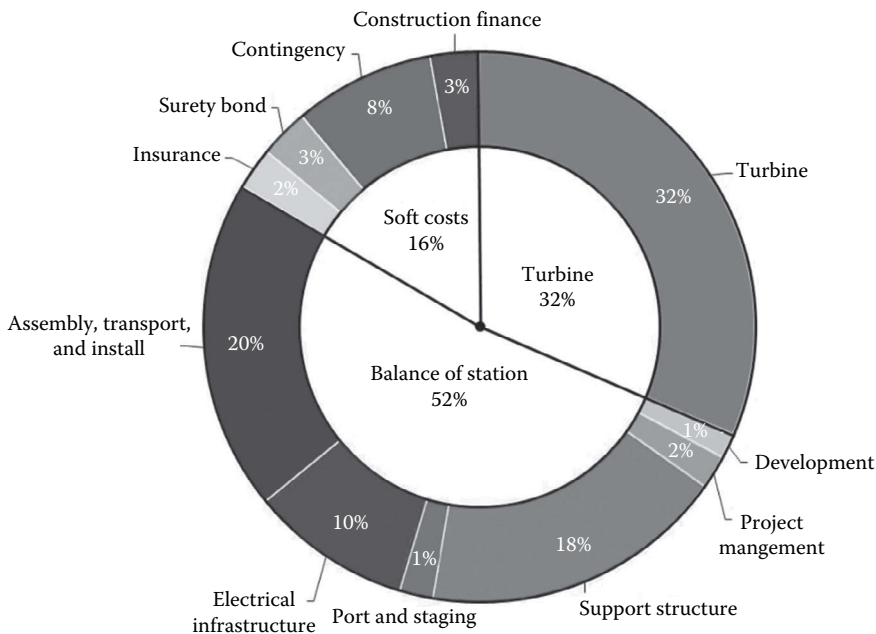


FIGURE 21.19

Initial capital cost breakdown for offshore wind turbine. (From Tegen, S. et al., 2011 Cost of wind energy review, NREL/TP-500-56266, National Renewable Energy Laboratory, Golden, CO, 2013.)

For example, the rotor contribution to the capital costs (and the total COE) of the land-based turbine is only 13%, so a 20% decrease in the rotor contribution only yields a 3% decrease in total COE; the drive train contribution to the total capital costs is 37%, so a 20% decrease there yields only a 7% decrease in total COE. On the other hand, any improvement in a component that leads to increased turbine energy production may lead to a significant decrease in COE. A 20% increase in rotor energy capture at no additional capital or O&M cost, for example, would lead directly to a 20% decrease in COE.

21.8.6 Environmental Concerns

Although wind turbines generate electricity without causing any air pollution or creating any radioactive wastes, like all human-built structures, they do cause an impact on the environment. Wind turbines require a lot of land, but only about 5% of that land is used for turbine foundations, roads, electrical substations, and other wind farm application. The remaining 95% of the land is available for other uses such as farming or livestock grazing.

Wind turbines do generate noise as well as electricity, but with proper siting restrictions, noise should not be a problem with newer wind turbines. Current industry standards call for characterization of turbine noise production and rate of decay of that noise with distance as part of the turbine testing process, so noise information is readily available. Since noise decreases quickly with distance from the source, the noise level due to a typical large modern wind turbine 300 m distant is usually roughly comparable to the typical noise level in the reading room of a library. Placing wind turbines at appropriate distances from local homes has proven to be an effective means of suppressing perceived noise, in most cases. However, certain weather conditions in some locations can cause focusing of

turbine-generated noise, leading to propagation of that noise to much greater distances and resulting in great irritation for nearby residents.

The visual impact of wind turbines is extremely subjective. What one person considers highly objectionable, another might consider as attractive or at least not objectionable. The relatively slow rotation of today's large wind turbines is viewed by most people as far less intrusive than the fast rotation of the early small turbines. Visual impact can be minimized through careful design of a wind farm. The use of a single model of wind turbine in a wind farm and uniform spacing of the turbines help alleviate concerns in this area. Computer simulation can be very helpful in evaluating potential visual impacts before construction begins.

References

1. BTM Consult, Navigant Research. 2013. International Wind Energy Development: World market update 2012.
2. American Wind Energy Association. 2013. AWEA U.S. Wind Industry Annual Market Report Year Ending 2012.
3. Shepherd, D. 1994. Historical development of the windmill. In: Spera, D., ed., *Wind Turbine Technology, Fundamental Concepts of Wind Turbine Engineering*. ASME Press, New York, pp. 1–46.
4. Miley, S.J. 1982. A catalog of low Reynolds number airfoil data for wind turbine applications. RFP-3387, Department of Aerospace Engineering, Texas A&M University, College Station, TX.
5. Abbott, I.H. and von Doenhoff, A.E. 1959. *Theory of Wind Sections Including a Summary of Airfoil Data*. Dover Publications, New York.
6. Selig, M.S., Guglielmo, J.J., Broeren, A.P., and Giguere, P. 1995. *Summary of Low-Speed Airfoil Data*, Vol. 1. SoarTech Publications, Virginia Beach, VA.
7. Selig, M.S., Lyon, C.A., Giguere, P., Ninham, C.P., and Guglielmo, J.J. 1996. *Summary of Low-Speed Airfoil Data*, Vol. 2. SoarTech Publications, Virginia Beach, VA.
8. Lyon, C.A., Broeren, A.P., Giguere, P., Gopalathnam, A., and Selig, M.S. 1997. *Summary of Low-Speed Airfoil Data*, Vol. 3. SoarTech Publications, Virginia Beach, VA.
9. Selig, M.S. and McGranahan, B.D. 2004. Wind tunnel aerodynamic tests of six airfoils for use on small wind turbines; period of performance: October 31, 2002–January 31, 2003. NREL Report SR-500-34515, National Renewable Energy Laboratory, Golden, CO.
10. Somers, D.M. 1997. Design and experimental results for the S809 airfoil. NREL Report SR-440-6918, National Renewable Energy Laboratory, Golden, CO.
11. Betz, A. 1920. Das maximum der theoretisch möglichen ausnützung des windes durch windmotoren. *Zeitschrift für das gesamte Turbinenwesen*, 26, 307–309.
12. Froude, R.E. 1889. On the part played in propulsion by differences of fluid pressure. *Transactions of the Institute of Naval Architects*, 30, 390–405.
13. Lanchester, F.W. 1915. A contribution to the theory of propulsion and the screw propeller. *Transactions of the Institute of Naval Architects*, 57, 98–116.
14. Hansen, A.C. and Butterfield, C.P. 1993. Aerodynamics of horizontal-axis wind turbines. *Annual Review of Fluid Mechanics*, 25, 115–149.
15. Wilson, R.E. 1994. Aerodynamic behavior of wind turbines. In: Spera, D., ed., *Wind Turbine Technology, Fundamental Concepts of Wind Turbine Engineering*. ASME Press, New York, pp. 215–282.
16. Snel, H. 2003. Review of aerodynamics for wind turbines. *Wind Energy*, 6, 203–211.
17. Touryan, K.J., Strickland, J.H., and Berg, D.E. 1987. Electric power from vertical-axis wind turbines. *Journal of Propulsion and Power*, 3(6), 481–493.
18. Paraschivoiu, I. 2002. *Wind Turbine Design with Emphasis on Darrieus Concept*. Polytechnic International Press, Montreal, Quebec, Canada.

19. Simão Ferreira, C. and Scheurich, F. 2013. Demonstrating that power and instantaneous loads are decoupled in a vertical-axis wind turbine. *Wind Energy*, 17, 385–396.
20. Kocurek, D. 1987. Lifting surface performance analysis for horizontal-axis wind turbines. SERI/STR-2 17 3163, Solar Energy Research Institute, Golden, CO.
21. Strickland, J.H., Smith, T., and Sun, K. 1981. A vortex model of the Darrieus turbine: An analytical and experimental study. SAND81-7017, Sandia National Laboratories, Albuquerque, NM.
22. Murray, J.C. and Barone, M. 2011. The development of CACTUS, a wind and marine turbine performance simulation code. In: *Proceedings of the 49th AIAA Aerospace Sciences Meeting*, Orlando, FL, AIAA-2011-147.
23. Xu, G. and Sankar, L.N. 1999. Computational study of horizontal-axis wind turbines. In: *A Collection of the 1999 ASME Wind Energy Symposium Technical Papers*, ASME, pp. 192–199.
24. Sørensen, N.N. and Hansen, M.O.L. 1998. Rotor performance predictions using a Navier–Stokes method. In: *A Collection of the 1998 ASME Wind Energy Symposium Technical Papers*, ASME, pp. 52–59.
25. Duque, E.P.N., Burkland, M.D., and Johnson, W. 2003. Navier–Stokes and comprehensive analysis performance predictions of the NREL phase VI experiment. In: *A Collection of the 2003 ASME Wind Energy Symposium Technical Papers*, ASME, pp. 43–61.
26. Sørensen, N., Michelsen, J., and Schreck, S. 2002. Navier–Stokes predictions of the NREL phase VI rotor in the NASA Ames 80 ft. × 120 ft. wind tunnel. *Wind Energy*, 5(2/3), 151–169.
27. Johansen, J., Sørensen, N., Michelsen, J., and Schreck, S. 2003. Detached-eddy simulation of flow around the NREL phase-VI rotor. In: *Proceedings of the 2003 European Wind Energy Conference and Exhibition*, Madrid, Spain.
28. Chow, R. and van Dam, C.P. 2012. Verification of computational simulations of the NREL 5 MW rotor with a focus on inboard flow separation. *Wind Energy*, 15, 967–981.
29. Chow, R., and van Dam, C.P. 2013. Computation investigations of blunt trailing-edge and twist modifications to the inboard region of the NREL 5 MW rotor. *Wind Energy*, 16, 445–458.
30. Xu, G. and Sankar, L.N. 2002. Application of a viscous flow methodology to the NREL phase VI rotor. In: *A Collection of the 2002 ASME Wind Energy Symposium Technical Papers*, ASME, pp. 83–93.
31. Schmitz, S. and Chattot, J.-J. 2005. Influence of the vertical wake behind wind turbines using a coupled Navier–Stokes/vortex-panel methodology. In: *Proceedings of the Third MIT Conference on Computational Fluid and Solid Mechanics*, Cambridge, MA, pp. 832–836.
32. Simms, D., Schreck, S., Hand, M., and Fingersh, L. 2001. NREL unsteady aerodynamics experiment in the NASA–Ames wind tunnel: A comparison of predictions to measurements. NREL Report TP-500-29494, National Renewable Energy Laboratory, Golden, CO.
33. Réthoré, P.-E., Sørensen, N., Zahle, A., Bechmann, A., and Madsen, H.A. 2011. MEXICO wind tunnel and wind turbine modelled in CFD, *29th AIAA Applied Aerodynamics Conference*, June 27–30, 2011, Honolulu, Hawaii, AIAA-2011-3373.
34. Manwell, J.F., McGowan, J.G., and Rogers, A.L. 2010. *Wind Energy Explained: Theory, Design and Application*, 2nd edn. Wiley, Chichester, U.K.
35. Burton, T., Sharpe, D., Jenkins, N., and Bossanyi, E. 2011. *Wind Energy Handbook*, 2nd edn. Wiley, Chichester, U.K.
36. FAST. NWTC Computer-Aided Engineering Tools (FAST by Jason Jonkman, Ph.D.). <http://wind.nrel.gov/designcodes/simulators/fast/>, last modified October 28, 2013; accessed November 22, 2013.
37. 2005. *ABAQUS Analysis User's Manual, Version 6.5*. ABAQUS, Inc., Providence, RI. <http://www.abaqus.com>.
38. MSC ADAMS. 2006. <http://www.mscsoftware.com>.
39. HAWC2, Danish Technical University, Wind Energy Section, <http://www.hawc2.dk/> (accessed November, 2013).
40. BLADED, Garrad Hassan, <http://www.gl-garradhassan.com/en/GHBladed.php>.
41. Malcolm, D.J. and Wright, A.D. 1994. The use of ADAMS to model the AWT-26 prototype. In: *Proceedings of the 1994 ASME Wind Energy Symposium*, New Orleans, LA, pp. 125–132.

42. Molenaar, D.P. and Dijkstra, S. 1999. State-of-the-art of wind turbine design codes: Main features overview for cost-effective generation. *Wind Engineering*, 23(5), 295–311.
43. Buhl, M.L., Jr., Wright, A.D., and Pierce, K.G. 2000. Wind turbine design codes: A comparison of the structural response. In: *A Collection of the 2000 ASME Wind Energy Symposium Technical Papers*, ASME, pp. 12–22.
44. Quarton, D.C. 1998. The evolution of wind turbine design analyses—A twenty year progress review. *Wind Energy*, 1, 5–24.
45. RCAS Theory Manual, Version 2.0. 2002. United States (US) Army Aviation and Missile COMmand/AeroFlightDynamics Directorate (USAAMCOM/AFDD) Technical Report (TR), USAAMCOM/AFDD TR 02-A-005. US Army Aviation and Missile Command, Moffett Field, CA.
46. Bir, G.S., and Chopra, I. 1994. University of Maryland Advanced Rotorcraft Code (UMARC) theory manual. Technical Report UM-AERO 94-18, Center for Rotorcraft Education and Research, University of Maryland, College Park, MD.
47. Lobitz, D.W. and Sullivan, W.N. 1983. A comparison of finite-element prediction and experimental data for forced response of DOE 100 kW VAWT. In: *Proceedings of the Sixth Biennial Wind Energy Conference and Workshop*, Minneapolis/St. Paul, MN, pp. 843–853.
48. Owens, B.C., Hurtado, J.E., Paquette, J., Griffith, D.T., and Barone, M. 2013. Aeroelastic modeling of large offshore vertical-axis wind turbines: Development of the offshore wind energy simulation toolkit. In: *Proceedings of the 54th AIAA/ASME/ASCE/AHS/ASC Structures, Structural Dynamics, and Materials Conference*, Boston, MA, AIAA-2013-1552.
49. Fuchs, E.F., Erickson, R.W., Carlin, P.W., and Fardou, A.A. 1992. Permanent magnet machines for operation with large speed variations. In: *Proceedings of the 1992 American Wind Energy Association Annual Conference*, American Wind Energy Association, Washington, DC, pp. 291–297.
50. Smith, G.A. 1989. Electrical control methods for wind turbines. *Wind Engineering*, 13(2), 88–98.
51. Bossanyi, E.A. 2003. Individual blade pitch control for load reduction. *Wind Energy*, 6, 119–128.
52. Mayda, E.A., van Dam, C.P., and Yen-Nakafuji, D. 2005. Computational investigation of finite width microtabs for aerodynamic load control. In: *A Collection of the 2005 ASME Wind Energy Symposium Technical Papers*, ASME, pp. 424–436.
53. Barlas, T.K. and van Kuik, G.A.M. 2010. Review of state of the art in smart rotor control research for wind turbines. *Progress in Aerospace Sciences*, 46(1), 1–27.
54. van Wingerden, J.W., Hulskamp, A., Barlas, T., Houtzager, I., Bersee, H., van Kuik, G.A.M., and Verhaegen, M. 2010. Two-degree-of-freedom active vibration control of a prototyped “smart” rotor. *IEEE Transactions on Control Systems Technology*, 19(2), 284–296.
55. Berg, J.C., Barone, M.F., and Resor, B.R. 2013. Field test results from the Sandia SMART rotor. In: *Proceedings of the 51st AIAA Aerospace Sciences Meeting*, Grapevine (Dallas/Ft. Worth Region), TX, AIAA-2013-1060.
56. Spera, D., ed. 1994. *Wind Turbine Technology, Fundamental Concepts of Wind Turbine Engineering*. ASME Press, New York.
57. Mandell, J.F. and Samborsky, D.D. 1997. DOE/MSU composite material fatigue database: Test methods, materials, and analysis. SAND97-3002, Sandia National Laboratories, Albuquerque, NM.
58. Mandell, J.F., Samborsky, D.D., and Cairns, D.S., 2002. Fatigue of composite material and substructures for turbine blades. SAND2002-077, Sandia National Laboratories, Albuquerque, NM.
59. De Smet, B.J., and Bach, P.W. 1994. Database FACT: Fatigue of composites for wind turbines. ECN-C-94-045, ECN, Petten, the Netherlands.
60. Kensch, C.W., ed. 1996. Fatigue of materials and components for wind turbine rotor blades. EUR 16684, European Commission, Luxembourg, Belgium.
61. Nijssen, R. 2006. OptiDAT—Database reference document. OB_TC_R018, Rev. 005, Document Number 10224. www.wmc.eu/optidat_files/Optidat%20reference%20document.pdf (accessed November, 2013).

62. Sutherland, H.J. 2000. A summary of the fatigue properties of wind turbine materials. *Wind Energy*, 3(1), 1–34.
63. Griffin, D.A. 2004. Blade system design studies volume II: Preliminary blade designs and recommended test matrix. SAND2004-0073, Sandia National Laboratories, Albuquerque, NM.
64. Jackson, K.J., Zuteck, M.D., van Dam, C.P., Standish, K.J., and Berry, D. 2005. Innovative design approaches for large wind turbine blades. *Wind Energy*, 8(2), 141–171.
65. Ehrmann, R.S., White, E.B., Maniaci, D.C., Chow, R., Langel, C.M., and van Dam, C.P. 2013. Realistic leading-edge roughness effects on airfoil performance. In: *Proceedings of the 31st AIAA Applied Aerodynamics Conference*, San Diego, CA, AIAA-2013-2800.
66. Miller, D., Mandell, J., Samborsky, D., Hernandez-Sanchez, B., and Griffith, D. 2012. Performance of composite materials subjected to salt water environments. In: *Proceedings of the 53rd AIAA/AMSE/ASCE/AHS/ASC Structure, Structural Dynamics and Materials Conference*, Honolulu, HI, AIAA-2012-1575.
67. Ahlstrom, M., Blatchford, J., Davis, M., Duchesne, J., Edelson, D., Focken, U., Lew, D. et al. November/December 2011. Atmospheric pressure—Weather, wind forecasting and energy market operations. *IEEE Power & Energy Magazine*, 9(6), 97–107.
68. Ahlstrom, M., Bartlett, D., Collier, C., Duchesne, J., Edelson, D., Gesino, A., Keyser, M. et al. November/December 2013. Knowledge is power—Efficiently integrating wind energy and wind forecasts. *IEEE Power & Energy Magazine*, 11(6), 45–52.
69. Krohn, S. 1997. *The Energy Balance of Modern Wind Turbines*, WindPower Note No. 16. Danish Wind Turbine Manufacturers Association, Copenhagen, Denmark.
70. Milborrow, D. Dispelling the myths of energy payback time. *Wind Stats Newsletter*, 11(2), 1–3.
71. Fingersh, L., Hand, M., and Laxson, A. 2006. Wind turbine design cost and scaling model. NREL/TP-500-40566, National Renewable Energy Laboratory, Golden, CO.
72. Tegen, S., Lantz, E., Hand, M., Maples, B., Smith, A., and Schwabe, P. 2013. 2011 Cost of wind energy review. NREL/TP-500-56266, National Renewable Energy Laboratory, Golden, CO.

For Further Information

Excellent summaries of HAWT and VAWT aerodynamic principles together with extensive reference lists, are presented by Hansen and Butterfield [14], and by Touryan et al. [17], respectively. Vol. 1(1) of *Wind Energy*, Wiley, 1998 contains a comprehensive set of review papers covering wind turbine rotor aerodynamics, design analysis, and overall system design, and excellent updates on the status of wind turbine aeroelasticity and aerodynamics and be found in articles in Vol. 6(3), 2003 of that journal.

The latest developments in the field of wind energy in the United States and Europe may be found in the following annual conference proceedings:

Proceedings of WINDPOWER American Wind Energy Association (AWEA), Washington, DC, www.awea.org.

Proceedings of the European Wind Energy Association, European Wind Energy Association, Brussels, Belgium, www.ewea.org.

The books by Manwell et al. [34], Spera [56] and Burton et al. [35] contain a wealth of fairly current information on wind energy conversion, history, and technology, together with extensive reference lists.

Extensive information on wind energy conversion technology may also be found on the World-Wide Web. Excellent sites to start with include those of the U.S. National Renewable Energy Laboratory, Wind Energy Technology Center at www.nrel.gov/nwtc/, the Sandia National Laboratories, Wind Energy Technology Department at http://energy.sandia.gov/?page_id=344, the Danish Technical University, Department of Wind Energy at www.vindenergi.dtu.dk, the American Wind Energy Association at www.awea.org, the European Wind Energy Association at www.ewea.org, and the Danish Wind Energy Association at www.windpower.org/en.



Taylor & Francis

Taylor & Francis Group

<http://taylorandfrancis.com>

22

Biomass Conversion Process for Energy Recovery

Mark M. Wright and Robert C. Brown

CONTENTS

22.1 Biomass Conversion to Heat and Power	897
22.1.1 Biomass Energy Systems.....	898
22.1.2 Biomass to Heat and Power	898
22.1.2.1 Direct Combustion.....	898
22.1.2.2 Combustion Equipment.....	901
22.1.2.3 Co-Firing	902
22.1.2.4 Gasification	902
22.1.2.5 Gasification Equipment.....	904
22.1.2.6 Heat and Power Cycles.....	907
References.....	912
22.2 Biomass Conversion to Fuels.....	913
22.2.1 Biomass to Solid Fuels.....	913
22.2.2 Biomass to Gaseous Fuels.....	914
22.2.2.1 Biogas.....	914
22.2.2.2 Light Gases.....	915
22.2.2.3 Synthetic Gas	916
22.2.3 Biomass to Liquid Fuels.....	917
22.2.3.1 Alcohols.....	918
22.2.3.2 Biodiesel	922
22.2.3.3 Mixed Alcohols.....	924
22.2.3.4 Gasoline and Diesel	924
22.2.3.5 Hydrothermal Processing.....	926
22.2.4 Biofuel Properties.....	926
References.....	927

22.1 Biomass Conversion to Heat and Power

Biomass can be converted into a combination of heat, power, and a variety of fuels via thermal conversion processes. Heat and power are the primary products from direct biomass combustion, but they are often coproducts in other thermal processes. Thermal processes can convert biomass into solid (charcoal, torrefied biomass), gas (biogas, synthetic gas), and liquid (ethanol, biodiesel, gasoline) products. Modern biorefineries convert biomass into a combination of these energy products and chemicals. The contents of

this section can be grouped into two main topics: (1) an overview of the energy efficiency of biomass conversion systems and (2) descriptions of common industrial biomass conversion technologies.

22.1.1 Biomass Energy Systems

Biomass conversion processes involve a large number of complex thermodynamic phenomena occurring through multiple system units or steps. Each step may involve mass or heat transfer and chemical reactions. The overall system's efficiency will depend on its ability to recover heat and/or maximize the output of desired products.

The first law of thermodynamics provides a framework for evaluating changes in energy within a system in relation to heat and work transfer across the system's boundary. It requires that the net heat transfer into a system be equal to the work done by the system plus the change in energy within the system. A thermodynamic system is a region in space delineated for analysis. The first law of thermodynamics requires that the energy change of macroscopically identifiable forms of energy be accounted for as heat and/or work transfer, and changes in internal, kinetic, or gravitational energy.

Biomass energy systems range from portions of a single equipment to multiple units or facilities in which biomass is transformed to heat, power, or other energy forms. A majority of biomass facilities focus on the production of one or two products (typically heat and power). However, some facilities produce a wide range of products, including heat, power, chemicals, and fuels. These systems can be compared based on their efficiency once an energy balance is established. The energy efficiency (η) for a system is defined as

$$\eta = \frac{E_{out}}{E_{in}} = \frac{(\text{Fuel} + \text{Steam} + \text{Power})}{(\text{Biomass} + \text{Fuel})} \quad (22.1)$$

where

the energy inputs consist typically of biomass and heat or electricity from fossil fuels, nuclear, solar, wind, geothermal energy, and others

the energy output includes any combination of recovered heat, electricity, and fuels

Table 22.1 shows representative efficiency values for different biomass conversion systems.

22.1.2 Biomass to Heat and Power

There are numerous routes to convert the chemical energy in biomass into heat or electric power. Direct combustion releases heat that can be used in Stirling engines or Rankine steam power cycles. Alternatively, thermal treatment with low-oxygen concentrations yields intermediate materials with varying energy properties. Carbonization and slow pyrolysis produce a charcoal material with high-carbon concentration. Biomass gasification results in a combustible gas. Fast pyrolysis generates mostly a liquid fuel. Each of these processes will be discussed in further detail later. This section will discuss direct combustion and co-firing for heat and power production.

22.1.2.1 Direct Combustion

Combustion converts chemical energy directly into heat via rapid oxidation of the fuel. Primary products from combustion of carbonaceous products include carbon dioxide

TABLE 22.1

Facility Efficiency and Capacity Comparison of Biomass Conversion Systems

Technologies	Efficiency (%)	Typical Size
Combined heat and power (CHP) [1]	LHV	MWe Output
Co-firing	35–40	10–50
Dedicated steam cycles	30–35	5–25
IGCC	30–40	10–30
Gasific + engine CHP	25–30	0.2–1
Stirling engine CHP	11–20	<0.1
Solid fuels	LHV	MW _{th} Input
Torrefaction [2]	96	<25
Slow pyrolysis [3]	72	<25
Carbonization [3]	65	<50
Liquid fuels		
Corn ethanol [4]	50	400
Cellulosic ethanol [5]	45	400
Fast pyrolysis gasoline [5]	54	<400
Gasification Fischer–Tropsch [5]	53	>400

(CO₂) and water. Secondary products result from incomplete combustion or reactions with fuel-bound nitrogen (N₂), sulfur, and other impurities. Combustion conditions vary depending on the heating value and moisture content of the fuel, the amount of air used to burn the fuel, and heat losses from the furnace. Flame temperatures can exceed 1600°C.

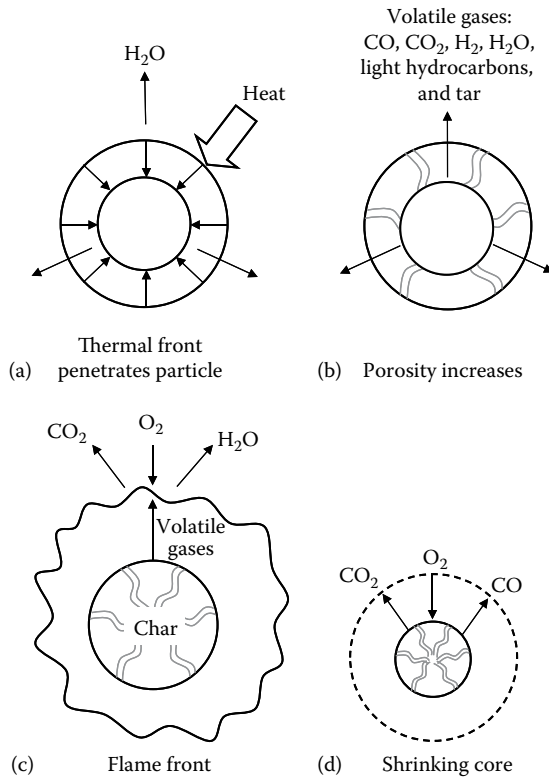
Solid fuel combustion takes place in four steps (see Figure 22.1): heating and drying, pyrolysis, flaming combustion, and char combustion [6]. Chemical reactions do not occur during heating and drying. During heating and drying, a thermal front drives advances into the interior of the particle while driving water away. The particle temperature will not rise high enough for pyrolysis until most of the water has been released.

Pyrolysis, the second step during combustion, is a complex series of thermally driven chemical reactions. Pyrolysis decomposes organic compounds in the fuel [7]. It proceeds at low temperatures depending on the plant material. Hemicellulose pyrolyzes at temperatures between 150°C and 300°C, cellulose at 275°C–350°C, and lignin pyrolysis initiates at 250°C–500°C.

Pyrolysis produces a wide range of volatile compounds with types and quantities dependent on the fuel and heating rate. The products include carbon monoxide (CO), CO₂, methane (CH₄), and high-molecular-weight compounds that condense to a tarry liquid if cooled before they are able to burn. These condensable compounds may form fine droplets, which constitute much of the smoke associated with smoldering fires. The pyrolysis thermal front leaves behind pores that penetrate from the surface to the core of the particle.

Both volatile gases and the resulting pyrolysis char can be oxidized if sufficient oxygen is available. Volatile gas oxidation above the solid fuel results in flaming combustion. The ultimate products of volatile combustion are CO₂ and H₂O, although a variety of intermediate chemical compounds can exist in the flame including CO, condensable organic materials, and long chains of carbon known as soot. In fact, hot, glowing soot is responsible for the familiar orange color of wood fires.

The combustion flame will consume all intermediate compounds given sufficient temperature, turbulence, and time. High combustion temperatures assure that chemical

**FIGURE 22.1**

Processes of solid fuel combustion: (a) heating and drying, (b) pyrolysis, (c) flaming combustion, and (d) char combustion.

reactions proceed at high rates. Turbulent or vigorous mixing of air with fuel allows all fuel molecules to come into contact with oxygen molecules. Long residence times are needed for the fuel to be completely consumed. Lack of good combustion conditions results in a variety of noxious organic compounds, including CO, soot, polycyclic aromatic hydrocarbons (PAH), and the particularly toxic families of chlorinated hydrocarbons known as furans and dioxins. Both CO and CO₂ may form on or near the surface of burning char (see Equation 22.2 [6]):



CO will completely oxidize if there is sufficient oxygen and residence in the immediate vicinity of the char particle; otherwise, it will appear in the flue gas as a pollutant.

The third step in solid fuel combustion involves char solid–gas reactions also known as glowing combustion, and they are responsible for the familiar red-hot embers in a fire. Char consists mostly of carbon with small quantities of mineral matter. Char oxidation occurs when there is mass transfer of oxygen to the char surface rather than by chemical

kinetics. Oxygen mass transfer is very fast at the elevated combustion temperatures. Oxygen may react with char at the surface or penetrate through pores depending on the particle porosity, reactivity, and combustion temperature. Surface oxidation results in a shrinking core, whereas pore oxidation yields a constant diameter particle with increasing porosity.

22.1.2.2 Combustion Equipment

Combustors convert fuel chemical energy into heat embedded in high-temperature exhaust gases. This heat can be utilized in a variety of applications, including space heating, drying, and power generation. However, with the exception of kilns used by the cement industry, most solid-fuel combustors today are designed to produce either low-pressure steam for process heat or high-pressure steam for power generation. Combustors designed to raise steam are known as boilers. Some boiler designs include distinct sections for combustion, and high- and low-temperature heat transfer; these sections are called furnace, radiative, and convective segments, respectively. Other designs may not include clear, distinct separations between the processes of combustion and heat transfer.

Solid-fuel combustors can be categorized as grate-fired systems, suspension burners, or fluidized beds [8], as shown in Figure 22.2. The first burner systems developed were grate-fired, which evolved during the late nineteenth and early twentieth century into a variety of automated systems. The spreader-stoker is the most common system, and it consists of a fuel feeder that mechanically or pneumatically flings fuel onto a moving grate where the fuel burns. Most of the ash falls off the end of the moving grate, but some fly ash can appear in the flue gas. Combustion efficiencies for grate systems rarely exceed 90%.

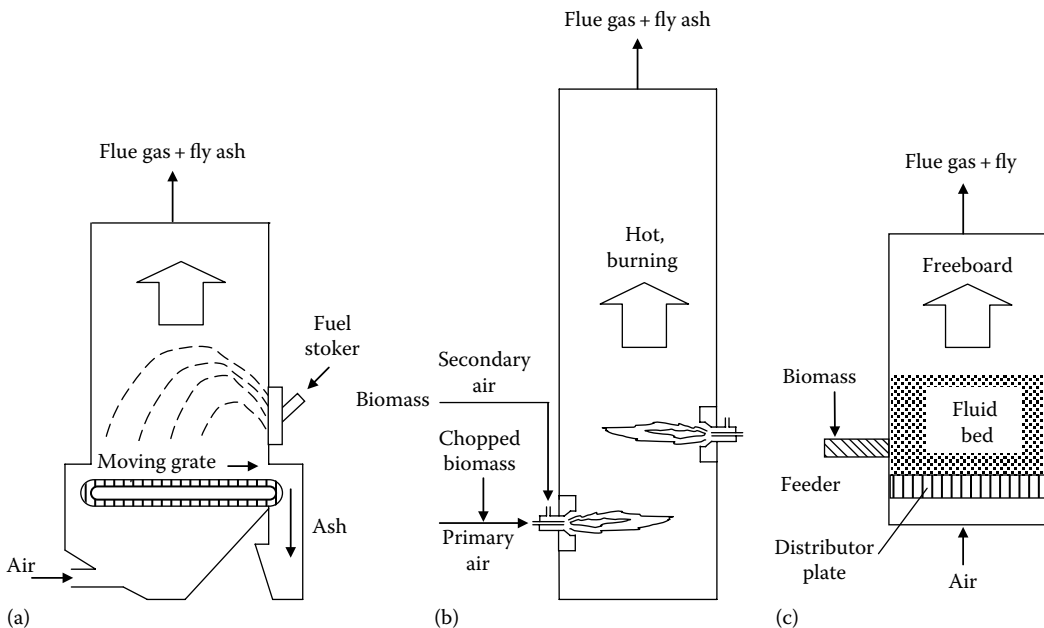


FIGURE 22.2
Common types of combustors: (a) grate-fired, (b) suspension, and (c) fluidized.

Suspension burners employ a stream of rising air to suspend the fuel as fine powder. The fuel burns in a fireball and radiates heat to tubes that contain water to be converted into steam. Suspension burners are also known as pulverized coal (PC) boilers, and they have dominated the U.S. power industry since World War II. They achieve high volumetric heat release rates and combustion efficiencies of more than 99%. However, they are not designed to burn coarse particles and are notorious generators of nitrogen oxides. Feeding employs pulverizers designed to reduce the particle size enough to burn in suspension. The fuel particles remain suspended in the primary airflow prior to feeding to the burner section through ports where it burns as a rising fireball. A secondary air stream helps complete the combustion process. Steam tubes arrayed in banks of heat exchanges (waterwall, superheaters, and economizer) absorb the combustion gas heat before the gas exits through a bag house. Bag houses are designed to capture suspended ash.

Fluidized bed combustors are a relatively recent innovation in boiler design. They operate by injecting air into the bottom of the boiler to suspend a bed of sand or other granular, refractory material. The suspension produces a turbulent mixture of air and sand. This environment achieves high heat and mass transfer rates and is suitable for burning a wide range of fuel types. The unit can be operated as low as 850°C due to the large thermal mass of the sand bed. The low temperature helps reduce the formation of N₂ compounds. A commercial market for fluidized bed boilers developed during the 1980s.

22.1.2.3 Co-Firing

Biomass co-firing is the notion of supplementing a primary fuel, often coal, with biomass [9]. Coal burners are often designed to operate with specifications that can only tolerate small quantities (less than 20%) of biomass because of its combustion behavior. Co-firing is commonly employed to take advantage of economic or environmental benefits. For example, lumber mills or pulp and paper companies can use co-firing as an alternative to landfilling waste. Governmental environmental constraints can also drive the use of co-firing in existing boilers.

Wood-fired power plants have capacities of 20–100 MW and heat rates of about 12,500 Btu/kW h. Coal-fired power plants by comparison are much larger and have improved heating rates of 10,250 Btu/kW h or lower. The lower heating rate and limited capacity of wood-fired power plants could ultimately limit the use of direct combustion to convert biomass into power.

22.1.2.4 Gasification

Gasification is a thermal process characterized by an oxygen-deficient environment and temperatures above 750°C. In this environment, most carbonaceous material converts into a flammable gas consisting of CO, hydrogen (H₂), CH₄, CO₂, and smaller quantities of heavier hydrocarbons. Gasification may take place with either air or pure oxygen input. Air gasification yields gas with high N₂ content commonly known as producer gas; gas from oxygen gasification is known as synthetic gas or syngas. Steam may also be introduced into the gasification environment as an oxygen carrier. Gasification requires heat input that is delivered either internally from partial combustion of the feed input or via external heaters. Gasification performance depends on the ability to introduce oxygen and heat into its environment. Residual material from biomass gasification includes unconverted carbon (char) and ash.

The gasification process involves four primary steps [10]: heating and drying, pyrolysis, gas–solid reactions, and gas–phase reactions. These steps are illustrated in Figure 22.3. As in combustion, heating and drying evaporates all feed moisture before the particle temperature increases to gasification temperatures. Pyrolysis occurs once the thermal front penetrates the particle, resulting in the release of volatile gases via pores of increasing number and size. The volatile gases include all gasification final products as well as tar. Tar consists of heavy and extremely viscous hydrocarbon compounds. After the pyrolysis step, these gases react with the particle surface, which is now primarily char, in a series of gas–solid endothermic and exothermic reactions that increase the yield of light gases. Finally, released gases continue to react in the gas–phase until they reach equilibrium conditions.

The heating and drying, and pyrolysis steps during gasification are similar to those of combustion. However, in the case of gasification, pyrolysis yields a larger quantity of tarry material because of insufficient oxygen and/or temperature to decompose the heavier compounds. Much of this tar elutriates from the particle and accumulates upon condensation. Where gasification differs from combustion is in the gas–solid and gas–phase reactions.

Gas–solid reactions include carbon–oxygen, Boudouard, carbon–water, and hydrogenation reactions shown in Equations 22.3. The carbon–oxygen reaction is highly exothermic and key to driving the Boudouard and carbon–water reactions, which are endothermic.

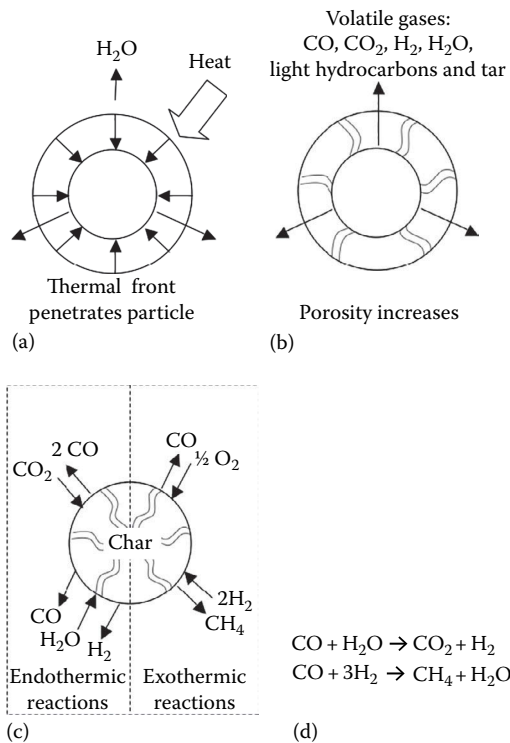
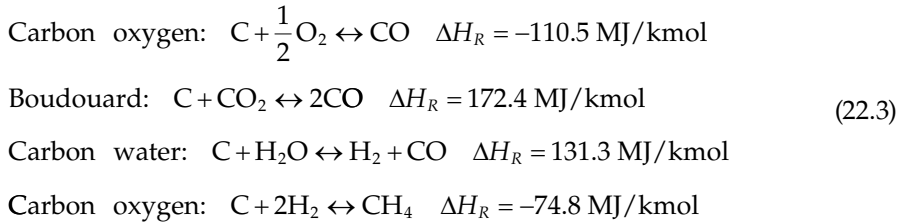


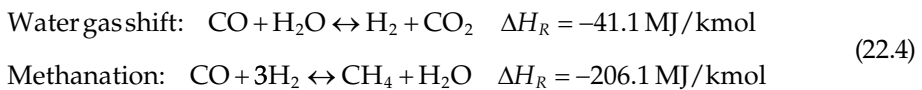
FIGURE 22.3 Thermal gasification process steps: (a) heating and drying, (b) pyrolysis, (c) gas–solid reactions, and (d) gas–phase reactions.

The carbon–oxygen and Boudouard reactions yield CO, whereas the carbon–water reaction yields H₂ and CO. This H₂ goes on to react exothermically with C to yield CH₄. The amount of H₂ involved in gas–solid reactions is relatively small:



Chemical equilibrium calculations predict that almost all carbon should react and form gas compounds. Practical systems typically achieve greater than 90% carbon conversion. Industrial engineers devote significant efforts to increase the carbon conversion by optimizing material treatment, equipment design, and operation parameters. In general, smaller particle sizes, longer residence times, and higher temperatures will increase carbon conversion. However, there are practical limitations that prevent the attainment of near-equilibrium conversions.

Gas–phase reactions consist of the exothermic water gas shift (WGS) and methanation reactions (see Equations 22.4). These reactions are significant because they determine the ultimate H₂:CO ratio in the gas. The H₂:CO ratio is an important parameter in synthetic fuel applications. WGS tends to increase the H₂ gas concentration, which is desirable for fuel synthesis, and the methanation reaction increases CH₄, which is important for combustion applications. Both reactions are favored by low temperatures despite slower reaction rates at lower temperatures. Thus, the common strategy to shift yields toward the products is to introduce steam or increase the partial pressure of H₂ depending on whether more H₂ or CH₄ is desired, respectively.



22.1.2.5 Gasification Equipment

Gasification equipment can be classified based on the choice of oxygen input and heat delivery method. Gasifiers can be air-blown, or oxygen-blown with and without steam. They can be heated directly or indirectly. Direct heating air-blown gasifiers dilute syngas with N₂, resulting in a low calorific value of 5–6 MJ per standard cubic meter. Avoiding N₂-dilution with pure oxygen feed increases the calorific value to between 13 and 14 MJ/m³. Direct heating increases CO₂ concentration, which has a similar energy dilution effect as N₂. Indirect heating gasifiers achieve the highest syngas calorific energy value with as much as 20 MJ/m³ [11].

Direct heating air-blown gasifiers present the simplest and lowest cost option. These characteristics have made them attractive for commercial applications. However, the excess N₂ concentration increases the size of downstream equipment and results in energy penalties for heating applications. Despite these challenges, producer gas from air-blown gasifiers have been employed in furnaces, boilers, and engines. N₂ can also be problematic

for synthetic fuel applications because in the best of cases it simply increases vessel sizes, and in some applications participates negatively in chemical reactions.

Oxygen-blown gasifiers have a smaller footprint but at the significant cost of requiring an oxygen separation unit. They generate a high-quality syngas for heat or fuel synthesis applications. Downstream equipment are also much smaller due to the N_2 avoided. Another advantage is that oxygen-blown gasifiers can be very efficient with carbon conversion rates of 95% and higher. They can achieve temperatures of up to 1800°C . At these temperatures, syngas composition approaches equilibrium and contains limited quantities of tar, char, and light hydrocarbons [12]. These temperatures are above the ash melting temperature, resulting in a layer of hot, liquid ash called slag that collects on the reactor surface. Slag properties are critical for proper operation of high-temperature gasifiers. They can substitute for refractory material by regulating heat transfer between the reaction chamber and external walls. For this reason, the slag layer has to be maintained within a tight thickness tolerance. Excess slag flows to the bottom of the reactor where it is collected.

Indirect heating gasifiers provide reaction heat from external sources and can avoid the use of air or oxygen. Without oxygen addition, gasification products include higher concentrations of primary volatile compounds, char, and tar. These products can continue to react in the gas phase depending on the residence time and operating conditions. In principle, indirect heating gasifiers can operate at temperatures of up to 1500°C . However, most of these systems operate between 600°C and 850°C due to heat transfer limitations. These gasifiers produce syngas with low N_2 and CO_2 concentrations than air- or oxygen-blown gasifiers but yield moderate quantities of tar and dust.

An alternative classification for gasifier designs is based on the contact method between the oxidizing agent and the feedstock input. By this classification, there are four main types of gasifiers: updraft (countercurrent), downdraft (concurrent), fluidized bed, and entrained flow [13]. Figure 22.4 illustrates these different designs.

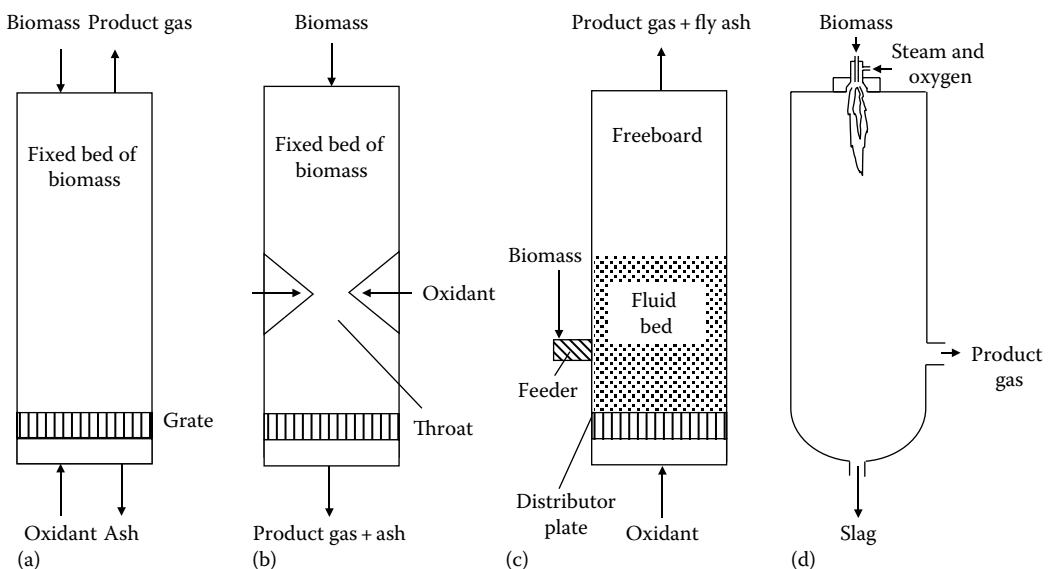


FIGURE 22.4

Common types of biomass gasifiers: (a) updraft, (b) downdraft, (c) fluidized bed, and (d) entrained flow.

The simplest and earliest design is the updraft gasifier, which evolved from charcoal kilns and blast furnaces. Updraft gasifiers resemble grate furnaces with chipped fuel admitted from above and below stoichiometric air input from below. Reaction temperatures close to the grate are very high and combustion processes dominate. At this location, oxygen gets depleted rapidly but hot H_2O and CO_2 reduce char to H_2 and CO . The fuel cools down as it moves toward the grate, but temperatures remain high enough to heat, dry, and pyrolyze the fuel. Updraft gasifiers yield high quantities of tar (50 g/m^3), making them unsuitable for many biomass energy applications.

Downdraft gasifiers were introduced in the nineteenth century following the introduction of induced draft fans capable of drawing air downward along with fuel. Contemporary designs introduced an arrangement of tuyeres to admit air or oxygen directly into a region known as the throat where combustion forms a bed of hot char. With this design, pyrolysis volatiles are forced through the bed of hot char, thereby increasing gas–solid reactions. These reactions increase tar cracking making a producer gas have with low tar concentrations less than 1 g/m^3 . These low tar concentrations make producer gas suitable for engine fuel. Strict requirements of particle size, ash, and moisture content make operation difficult. Slagging and ash sintering in the concentrated oxidation zone present another disadvantage. Mechanical and design measures can alleviate these problems such as the use of rotating ash grates. Downdraft gasifier capacities are limited to a maximum size of about 400 kg/h .

Fluidized bed gasifiers operate by introducing a gas stream flowing upward through a bed of inert particulate material to form a turbulent mixture of gas and solid. The bed material constitutes a well-mixed environment that approaches a theoretical continuously stirred tank reactor (CSTR). Thus, the temperature is uniformly kept at 700°C – 850°C throughout the bed, although hot spots may form if improper mixing occurs. This design does not provide distinct regions for the various gasification steps. Feedstock is introduced into this environment at rates that maintain a low fuel to inert weight ratio. Since fuel is injected in the base of the bed, much of the tar can be cracked within the fluidized bed. However, a key portion of fluidized bed gasifiers is the freeboard. The freeboard is a large insulated space above the bed where further tar cracking, gas–phase, and some gas–solid reactions can take place. Fluidized bed gasifiers achieve intermediate tar levels of about 10 g/m^3 . Fluidized bed gasifiers can convert a wide range of feedstock with few material property requirements. They can scale to large size, making them suitable for both fuel synthesis and electric power applications. Disadvantages include high power consumption to move gas through the bed; high exit gas temperatures; and relatively high particulate burdens in the gas due to the abrasive forces acting within the bed.

The entrained flow reactor is the fourth gasifier design. This reactor was developed for steam-oxygen gasification of PC at temperatures above 1200°C . They can achieve carbon conversion rates that approach 100%, produce trace tar quantities, and convert ash to molten slag. These properties make it attractive for both fuel synthesis and power generation applications. They can operate over a wide range of pressures, which allows them to be built at relatively smaller sizes. The key challenges for entrained flow gasifiers, particularly related to biomass applications, are requirements for small particle sizes, high operating temperatures, and low alkali levels. It is expensive to pulverize biomass, and biomass moisture and alkali content are comparably high for most feedstock. Pretreatment methods including torrefaction and pyrolysis can overcome many of these challenges [2].

There are many potential permutations of gasifier design and operation parameters. Furthermore, each gasifier design can be operated with various combinations of air/

TABLE 22.2

Producer Gas Composition from Various Kinds of Gasifiers

Gasifier Type	Gaseous Constituents (vol.% Dry)						Gas Quality	
	H ₂	CO	CO ₂	CH ₄	N ₂	HHV (MJ/m ³)	Tars	Dust
Air-blown updraft	11	24	9	3	53	5.5	High (≈10 g/m ³)	Low
Air-blown downdraft	17	21	13	1	48	5.7	Low (≈1 g/m ³)	Medium
Air-blown fluidized bed	9	14	20	7	50	5.4	Medium (≈10 g/m ³)	High
Oxygen-blown downdraft	32	48	15	2	3	10.4	Low (≈1 g/m ³)	Low
Indirectly-heated fluidized bed	31	48	0	21	0	17.4	Medium (≈10 g/m ³)	High

Sources: Higman, C. and Van Der Burgt, M., *Gasification*, Gulf Professional Publishing, Burlington, MA, 2008; Milne, T.A. et al., Biomass gasifier “tars”: Their nature, formation, and conversion, Technical report, NREL//TP-570-25357, National Renewable Energy Laboratory, Golden, CO, 1998.

oxygen and steam input, resulting in different product compositions. Keeping this in mind, Table 22.2 shows typical composition, energy content, and quality of gas from the various gasifiers discussed previously.

22.1.2.6 Heat and Power Cycles

Biomass combustion processes can be combined with a variety of steam and power cycles to generate electricity. These include the classical Stirling, Rankine, and Brayton cycles, as well as fuel cells and combined cycles. A majority of U.S. power generation comes from conventional steam turbines with growing contributions from gas turbines (see Figure 22.5).

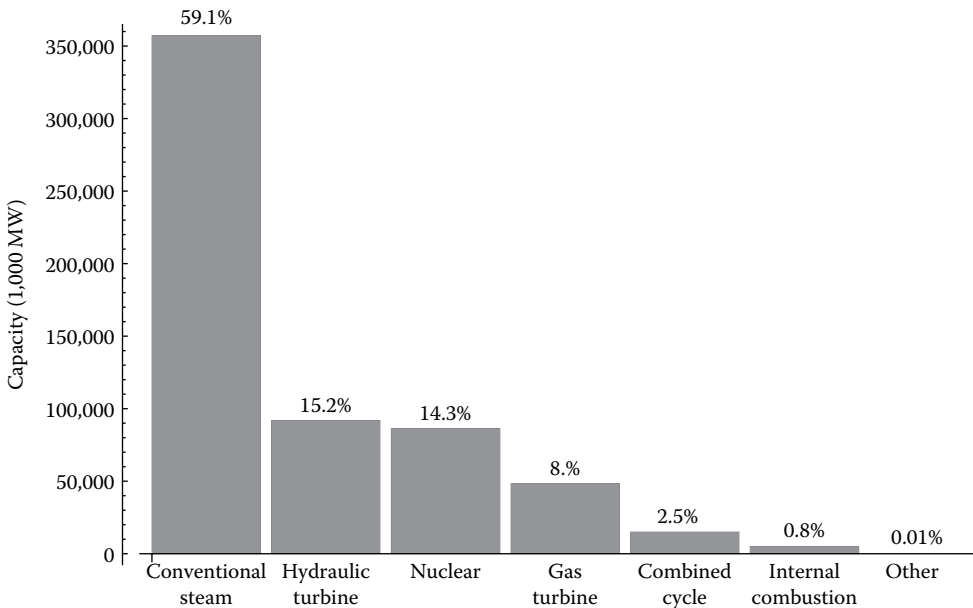


FIGURE 22.5

U.S. electric power generation capacity by generator/cycle type. (From Anon., Biomass for power generation and CHP, 2007)

Many of these systems could utilize biomass by simply co-firing or combining with the cycles described in this section.

22.1.2.6.1 Stirling Cycle

The Stirling cycle employs heat from an external combustion engine to raise the temperature of an internal fluid undergoing a thermodynamic cycle [14]. The internal fluid never comes in contact with the combustion fuel, which lowers maintenance costs and pollution emissions. This arrangement also increases the tolerance to contaminants, which makes this cycle attractive for use with “dirty” fuels.

The Stirling cycle is similar to the Rankine cycle in its use of an external combustion process. In theory, Stirling cycles offer a higher thermodynamic efficiency than Rankine cycles. In practice, Stirling engines achieve relatively modest efficiencies and net power output of a few kilowatts. Their major obstacle might be high costs, which have so far prevented significant market entry.

22.1.2.6.2 Rankine Cycle

The Rankine cycle resembles the Stirling cycle in its use of an external combustion engine [15]. Figure 22.6 illustrates the major units found in a Rankine cycle. Fuel is fed from a bunker and pulverized before combustion in the furnace. Superheaters raise steam from the hot gas exiting the furnace. Low-temperature heat is recovered in the economizer before gas cleaning through baghouses and rejection through the stack. The Rankine cycle depicted uses steam to operate a steam turbine, which drives a generator to produce electric power.

The Rankine steam power cycle has been the foundation of stationary power generation for over a century. Although Brayton cycles employing gas turbines and electrochemical cycles based on fuel cells will constitute much of the growth in power generation in

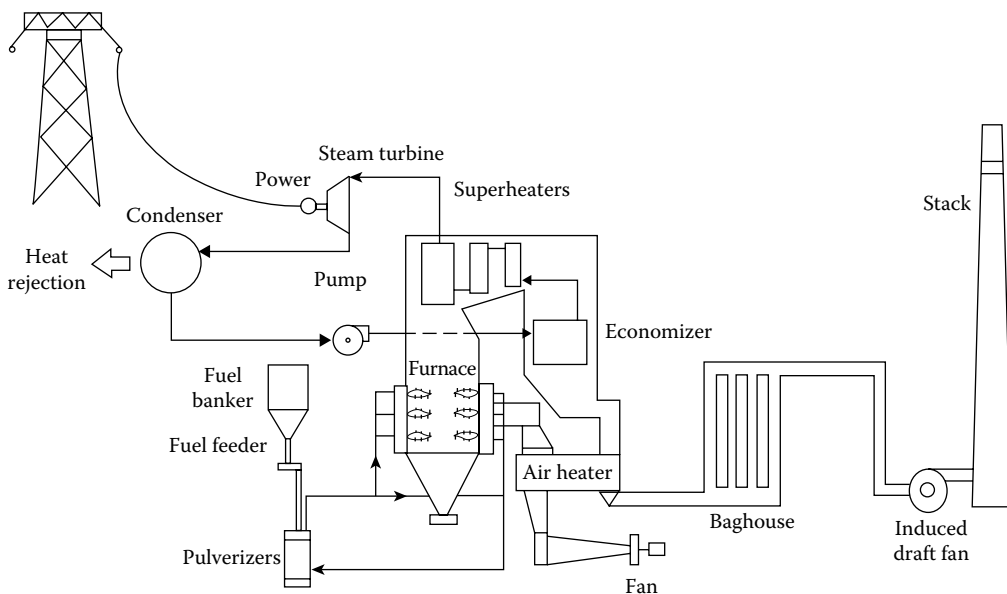


FIGURE 22.6
Rankine steam power plant.

the future, steam power plants will continue to supply the majority of electric power for decades to come. Steam power plants will find new applications in combination with advanced generation technologies. The reason for the Rankine cycle's preeminence has been its ability to directly fire coal and other inexpensive solid fuels. Constructed at scales of several hundred megawatts, the modern steam power plant can convert as much as 45% of chemical energy in fuel to electricity at a cost of \$0.02–\$0.05/kilowatt.

Utility-scale steam power plants are not expected to dominate future growth in electric power infrastructure in the United States. These giant plants take several years to plan and construct, which decreases their financial attractiveness in increasingly deregulated power markets. Coal and other fossil fuels burned in these plants are the major sources of air pollution, including sulfur and nitrogen oxides, both of which are precursors to acid rain and the latter an important factor in smog formation; fine particulate matter, which is implicated in respiratory disease in urban areas; and heavy metals, the most prominent being mercury, which accumulates in the biosphere to toxic levels. Substitution of biorenewable resources such as wood and agricultural residues for coal in existing power plants could substantially reduce pollution emissions, although these plants are so large that the locally available biomass resources could supplant only a small fraction of the total energy requirement. Small-scale steam power plants sized for use of local biomass resources have low thermodynamic efficiencies, on the order of 25%, making them wasteful of energy resources.

22.1.2.6.3 *Brayton Cycle*

The Brayton cycle produces electric power by expanding hot gas through a turbine [16]. These gas turbines operate at temperatures approaching 1300°C compared to inlet temperatures of less than 650°C for steam turbines used in Rankine cycles. Although this difference in inlet temperature would suggest that Brayton cycles have much higher thermodynamic efficiencies than Rankine cycles, the Brayton cycle also has a much higher exhaust temperature than does the Rankine cycle. Gas turbine exhaust temperatures are in the range of 400°C–600°C, whereas steam turbine exhaust temperatures are on the order of 20°C. Furthermore, Brayton cycles, which contain both gas compressor and gas turbine, have more sources of mechanical irreversibilities, further degrading thermodynamic efficiencies, which may only be marginally higher than the best Rankine steam cycles. However, improvements in gas turbine technology that allow operation at higher temperatures and pressures are expected to increase Rankine cycle efficiency for large power plants to greater than 50%, although 30% is more realistic for gas turbines sized appropriately for biomass power plants.

The two general classes of gas turbines for power generation are heavy-duty industrial turbines and lightweight aeroderivative gas turbines. The aeroderivatives are gas turbines originally developed for commercial aviation but adapted for stationary electric power generation. They are attractive for bioenergy applications because of their high efficiency and low unit capital costs at the modest scales required for biomass fuels.

Gas turbines are well suited to gaseous and liquid fuels that are relatively free of contaminants that rapidly erode or corrode turbine blades. In this respect, gas turbine engines are not suitable for directly firing most biomass fuels. Solid biomass releases significant quantities of alkali metals, chlorine, mineral matter, and lesser amounts of sulfur upon burning. These would be entrained in the gas flow entering the expansion turbine where they would quickly contribute to blade failure. Cleaning large quantities of hot flue gas is not generally considered an economical proposition. Even the gas released from anaerobic digestion contains too much hydrogen sulfide (H₂S) to be directly burned in a gas turbine without first chemically scrubbing the gas to remove this corrosive agent.

Nevertheless, gas turbine engines are considered one of the most promising technologies for bioenergy because of the relative ease of plant construction, cost-effectiveness in a wide range of sizes (from tens of kilowatts to hundreds of megawatts), and the potential for very high thermodynamic efficiencies when employed in advanced cycles. The key to their success in bioenergy applications is converting the biomass to clean-burning gas or liquid before burning it in the gas turbine combustor.

22.1.2.6.4 Fuel Cells

Among the most exciting new energy technologies are fuel cells, which directly convert chemical energy into work, thus bypassing the restriction on efficiency imposed by the Carnot relationship [17]. This does not imply that fuel cells can convert 100% of chemical enthalpy of a fuel into work, as the process still must conform to the laws of thermodynamics. In practice, irreversibilities limit their conversion efficiencies to 35%–60%, depending upon the fuel cell design. Thus, fuel cells can produce significantly more work from a given amount of fuel than can heat engines. However, carbonaceous fuels must first be reformed to H_2 before they are suitable for use in fuel cells. The energy losses associated with fuel reforming must be included when determining the overall fuel-to-electricity conversion efficiency of a fuel cell.

The gas mixture produced by a biomass gasifier contains dust and tar that must be removed or greatly reduced for most applications, including power generation in fuel cells. Removal of tar would ideally be performed at elevated temperatures. If the gas is to be used in fuel cells, further cleaning is required to remove ammonia (NH_3), hydrogen chloride (HCl), and H_2S [18]. To obtain high-energy efficiency, trace contaminant removal must be performed at elevated temperatures for fuel cells that operate at relatively high temperatures. Low-temperature fuel cells cannot tolerate CO, which can be removed by the WGS reaction. The catalysts that facilitate the shift reaction, however, are poisoned by trace contaminants, which must be removed prior to the shift reactors. One method for removing H_2S and HCl is the use of a fixed bed of calcined dolomite or limestone and zinc titanate at temperatures around 630°C. This is followed by steam reforming at high temperature (750°C–850°C) to destroy tar and NH_3 [19].

22.1.2.6.5 Combined Cycles

In an effort to enhance energy conversion efficiency, combined cycle power systems have been developed, which recognize that waste heat from one power cycle can be used to drive a second power cycle [20]. Combined cycles would be unnecessary if a single heat engine could be built to operate between the temperature extremes of burning fuel and the ambient environment. However, temperature and pressure limitations on materials of construction have prevented this realization. Combined cycles employ a topping cycle operating at high temperatures and a bottoming cycle operating on the rejected heat from the topping cycle. Most commonly, combined cycle power plants employ a gas turbine engine for the topping cycle and a steam turbine plant for the bottoming cycle, achieving overall efficiencies of 60% or higher.

Clean-burning fuel from biomass for use in a combined cycle can be obtained by thermal gasification. Integrated gasification/combined cycle (IGCC) power is illustrated in Figure 22.7. Compressed air enters an oxygen plant, which separates oxygen from the air. The oxygen is used to gasify biomass in a pressurized gasifier to produce medium heating-value producer gas. The producer gas passes through cyclones and a gas clean-up system to remove particulate matter, tar, and other contaminants that may adversely affect gas turbine performance

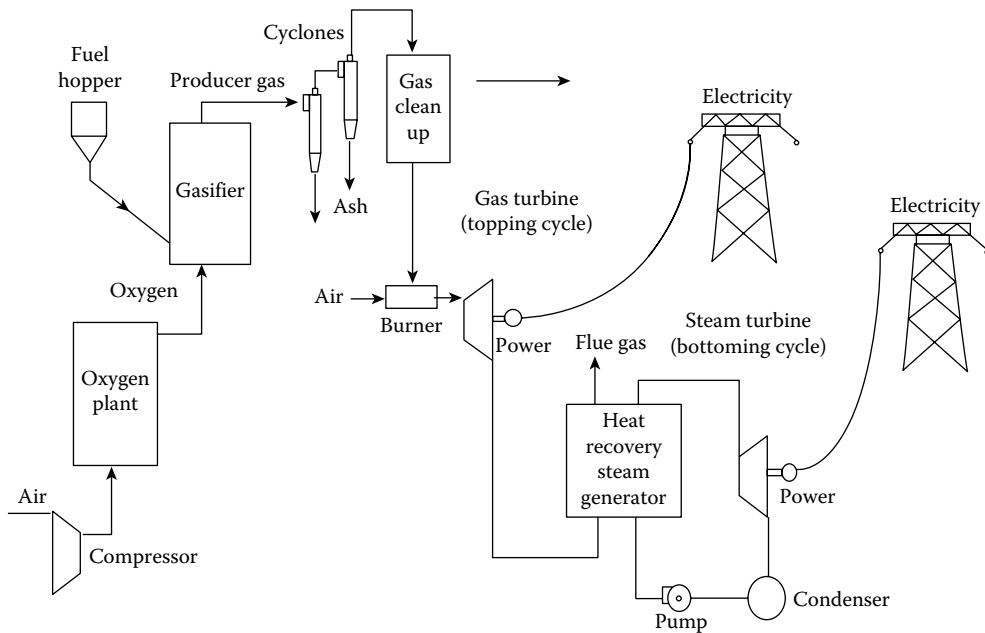


FIGURE 22.7

Integrated gasification/combined cycle power plant (IGCC) based on a gas turbine topping cycle.

(alkali and chloride being the most prominent among these). These clean-up operations are best performed at high temperature and pressure to achieve high cycle efficiency. The clean gas is then burned in air and expanded through a gas turbine operating as a “topping” cycle. The gas exits the turbine at temperatures ranging between 400°C and 600°C. A heat recovery steam generator produces steam for a “bottoming” cycle that employs a steam turbine. Electric power is produced at two locations in this plant, yielding thermodynamic efficiencies exceeding 47%.

Integrated gasifier/combined cycle systems based on gas turbines are attractive for several reasons. These reasons include their relative commercial readiness and the expectation that they can generate electricity at the lowest cost of all possible biomass power options.

An alternative to IGCC is to generate steam for injection into the gas turbine combustor, which increases mass flow and power output from the turbine. This variation, called a steam-injected gas-turbine (STIG) cycle [20,21] is less capital intensive than IGCC since it does not employ a steam turbine. The STIG cycle is commercially developed for natural gas; lower flammability limits for producer gas make steam injection more problematic for biomass-derived producer gas. The intercooled steam-injected gas turbine (ISTIG) is an advanced version of the STIG. This cycle further improves thermodynamic efficiency by cooling gas flow between several stages of compression (intercooling).

Figure 22.8 illustrates an IGCC power plant based on a molten carbonate fuel cell [18]. Biomass is gasified in oxygen to yield producer gas. Gasification occurs at elevated pressure to improve the yield of CH_4 , which is important for proper thermal balance of this fuel cell. Hot-gas clean up to remove particulate matter, tar, and other contaminants is followed by expansion through a gas turbine as part of a topping power cycle. The pressure

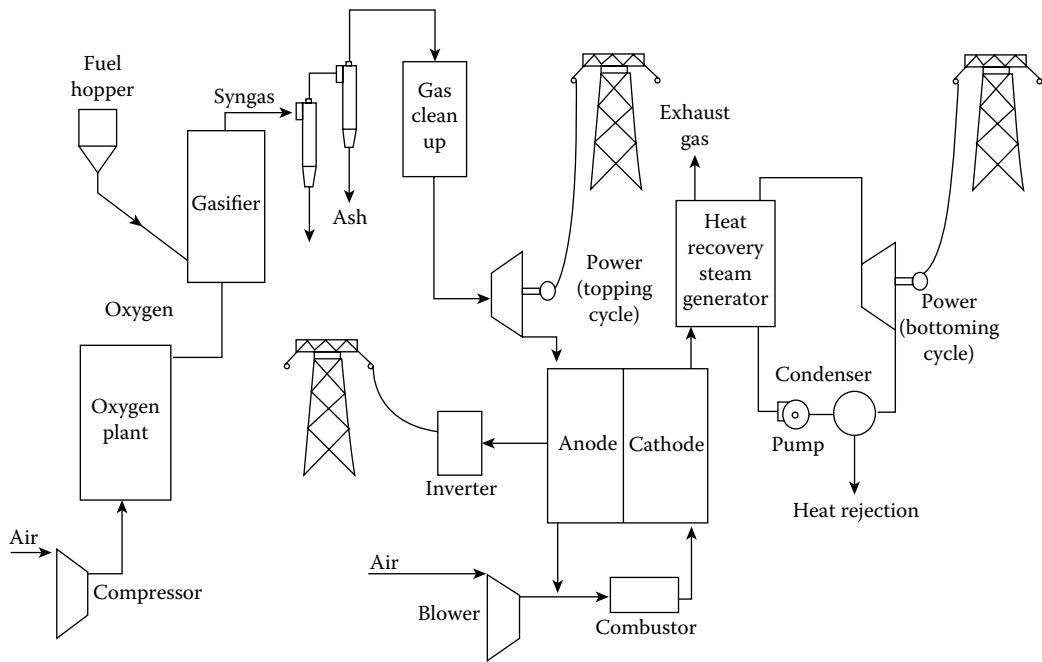


FIGURE 22.8
Combined cycle power plant based on high-temperature fuel cells.

and temperature of the producer gas is sufficiently reduced after this to admit it into the fuel cell. High-temperature exhaust gas exiting the cathode of the fuel cell enters a heat recovery steam generator, which is part of a bottoming cycle in the integrated plant. Thus, electricity is generated at three locations in the plant for an overall thermodynamic efficiency reaching 60% or more.

References

1. Anon. Biomass for power generation and CHP, International Energy Agency, France, Paris, 2007 <http://www.iea.org/publications/freepublications/publication/essentials3.pdf>.
2. PCA Bergman and JHA Kiel. Torrefaction for biomass upgrading. Technical Report ECN-RX-05-180, Petten, the Netherlands, November 2005.
3. L Nan and G Best. Integrated energy systems in China—The cold northeastern region experience. Food and Agriculture Organization of the United Nations, Rome, Italy, 1994.
4. MQ Wang. The GREET Spreadsheet Model: Greenhouse gases and regulated emissions and energy use in transportation, GREET 1 2011 Version. Center for Transportation Research, Energy Systems Division, Argonne National Laboratory, Lemont, IL, 2009.
5. RP Anex et al. Techno-economic comparison of biomass-to-transportation fuels via pyrolysis, gasification, and biochemical pathways. *Fuel*, 89(S1):S29–S35, November 2010.
6. DA Tillman. *The Combustion of Solid Fuels and Wastes*. Academic Press, San Diego, CA, 1991.
7. JV Kumar and BC Pratt. Compositional analysis of some renewable biofuels. *American Laboratory*, 28(8):15–20, 1996.

8. RL Bain and RP Overend. Biomass-fired power generation. *Fuel Processing Technology*, 54.1:1–16, 1998.
9. M Sami, K Annamalai, and M Wooldridge. Co-firing of coal and biomass fuel blends. *Progress in Energy and Combustion Science*, 27(2):171–214, 2001.
10. RC Brown. *Biorenewable Resources: Engineering New Products from Agriculture*. Iowa State Press, A Blackwell Publishing Company, Ames, IA, pp. 59–75, 2003.
11. RL Bain and K Broer. Gasification. In *Thermochemical Processing of Biomass: Conversion into Fuels, Chemicals and Power*, R Brown and C Stevens (eds.), 1st edn., Vol. 3. John Wiley & Sons, pp. 47–76, 2011.
12. Anon. Siemens fuel gasification technology. Siemens AG, Erlangen, Germany, 2012. <http://www.energy.siemens.com/us/pool/hq/power-generation/fuel-gasifier/fuel-gasification-technology-for-integrated-gasificationbrochure.pdf> (accessed March 2015).
13. AV Bridgwater. The technical and economic feasibility of biomass gasification for power generation. *Fuel*, 74(5):631–653, 1995.
14. AJ Organ. *Thermodynamics and Gas Dynamics of the Stirling Cycle Machine*. Cambridge University Press, Cambridge, U.K., 1992.
15. JG Singer. *Combustion, Fossil Power Systems: A Reference Book on Fuel Burning and Steam Generation*. Combustion Engineering Windsor, Babylon, NY, 1981.
16. A Poullikkas. An overview of current and future sustainable gas turbine technologies. *Renewable and Sustainable Energy Reviews*, 9(5):409–443, 2005.
17. J Larminie, A Dicks, and MS McDonald. *Fuel Cell Systems Explained*, Vol. 2. Wiley, Chichester, U.K., 2003.
18. Anon. *Fuel Cell Handbook*, 5th edn. U.S. Department of Energy, Morgantown, WV, 2000. www.netl.doe.gov.
19. DJ Stevens. Hot gas conditioning: recent progress with larger-scale biomass gasification systems. National Renewable Energy Laboratory, NREL Subcontractor Report (NREL/SR-510-29952), Golden, CO, 2001.
20. RH Williams et al. Advanced gasification-based biomass power generation. In *Renewable Energy: Sources for Fuels and Electricity*, TB Johansson, H Kelly, AK N Reddy, R Williams, and L Burnham (eds.), pp. 729–785, 1993.
21. M Jonsson and J Yan. Humidified gas turbines—A review of proposed and implemented cycles. *Energy*, 30(7):1013–1078, 2005.

22.2 Biomass Conversion to Fuels

22.2.1 Biomass to Solid Fuels

Low energy density and high moisture content are two key disadvantages of using biomass as a solid fuel. Both can be overcome with thermal pretreatment methods. Torrefaction and (slow) pyrolysis are two main approaches to converting a significant portion of biomass into a high-energy-density solid fuel.

Biomass torrefaction is similar to the coffee roasting process. Both take place at moderate temperatures of about 250°C without oxygen addition and residence times of 30 min or more. The process is mostly endothermic, but torrefaction gases can be consumed to provide necessary heat. Torrefaction evolves over three main steps. Initially, the feedstock will simply absorb heat until the feed moisture evaporates. The next step involves the release of some volatile gases. Finally, the biomass undergoes minor chemical restructuring becoming dark, brittle, and hydrophobic. Material yields can be as low as 70 wt.% with corresponding energy yields of more than 90 wt.% [1].

Torrefied biomass resembles charcoal in appearance and physical properties. It is easier to pulverize, has a higher energy content (>20 MJ/kg), and can be stored for longer periods without absorbing moisture and with minimal microbial degradation [2]. These properties make it attractive for direct combustion, co-firing, and entrained flow gasification applications.

Slow pyrolysis is a higher-intensity form of torrefaction [3]. Slow pyrolysis conditions consist of an inert environment with temperatures above 400°C and residence times of more than 30 min. This process releases a greater amount of pyrolysis volatiles resulting in solid yields of <30 wt.%. The solid product shares many similarities with torrefied biomass including a higher heating value (HHV) of about 30 MJ/kg. However, its products are not well suited to synthetic fuel applications.

Finally, carbonization, which takes place at temperatures of 450°C – 600°C , yields about 35 wt.% solids with a similar HHV as slow pyrolysis charcoal. Carbonization can convert large feed sizes without prior grinding. It is also the simplest of technologies to operate in part because the product requirements are less strict than other thermal processes.

22.2.2 Biomass to Gaseous Fuels

Anaerobic digestion and gasification are two of the main ways to convert biomass into gaseous fuels. Both pathways generate a combustible gas: biogas and synthetic gas (syngas), respectively. Biogas is relatively inexpensive to produce, but has a smaller range of applications than syngas. This section will discuss the technologies that enable biomass fuel gas production.

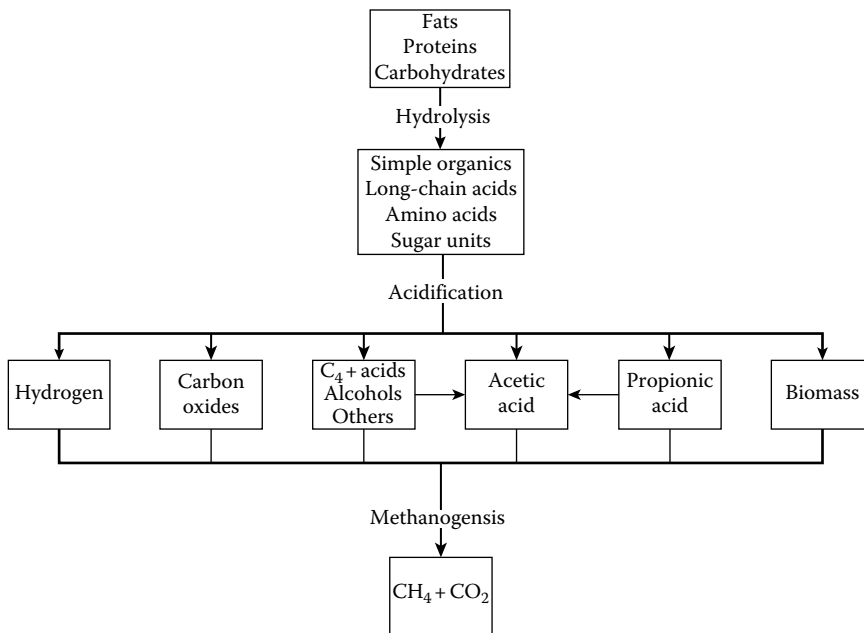
22.2.2.1 Biogas

In the absence of oxygen, bacteria decompose organic wastes into a mixture of CH_4 , CO_2 , and trace gases. The decomposition productivity is sensitive to feedstock properties including moisture and ash content. Anaerobic digestion yields vary from 23 to over 250 m^3/Mg (wet basis) with a methane content of 55%–75% by volume with an energy efficiency of about 60%.

Methane is the primary component in biogas, which makes it a candidate for substituting natural gas in many applications. Clean biogas is suitable for engine generator sets, small gas turbines, and some kinds of fuel cells. However, biogas often contains contaminants like sulfur that must be removed before use in some equipment.

Anaerobic digestion involves several complicated steps illustrated in Figure 22.9 [4]. During this process, several bacteria species break down proteins, carbohydrates, and fats into simple acids, alcohols, and gaseous compounds via hydrolysis and acidification. The final step is methanogenesis, where most of the intermediate organics decompose to CH_4 and CO_2 .

On the other hand, the anaerobic digester systems where these processes take place are simple (see Figure 22.9). Anaerobic digesters operate as batch, semi-batch, or continuous units (Figure 22.10). Reactor designs include batch, plug-flow, continuously stirred tank, upflow, and two-tank reactors. The most common reactor design is the batch system in which most of the digestion steps take place within a single vessel. Improvements to this design aim to increase contact time between bacteria and the organic wastes and/or to separate and control the environments for acid-forming and methane-forming bacteria. There are numerous parameters to optimize the performance of anaerobic digestion: pretreatments, heating, mixing, nutrient addition, bacteria selection, and pH to name a few.

**FIGURE 22.9**

Microbial phases in anaerobic digestion. (Adapted from Klass, D., *Biomass for Renewable Energy, Fuels, and Chemicals*, Academic Press, San Diego, CA, 1998c, p. 462.)

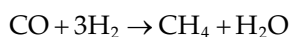
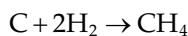
The effluent from these systems is a mixture of biogas and sludge. Biogas often requires scrubbing to remove hydrogen sulfide in order to minimize emissions of sulfur dioxide (SO_2). Digested sludge contains materials that bacteria are unable to digest within the timescales of most systems: lignin, mineral matter, and water. Digested sludge is amenable to use as a fertilizer.

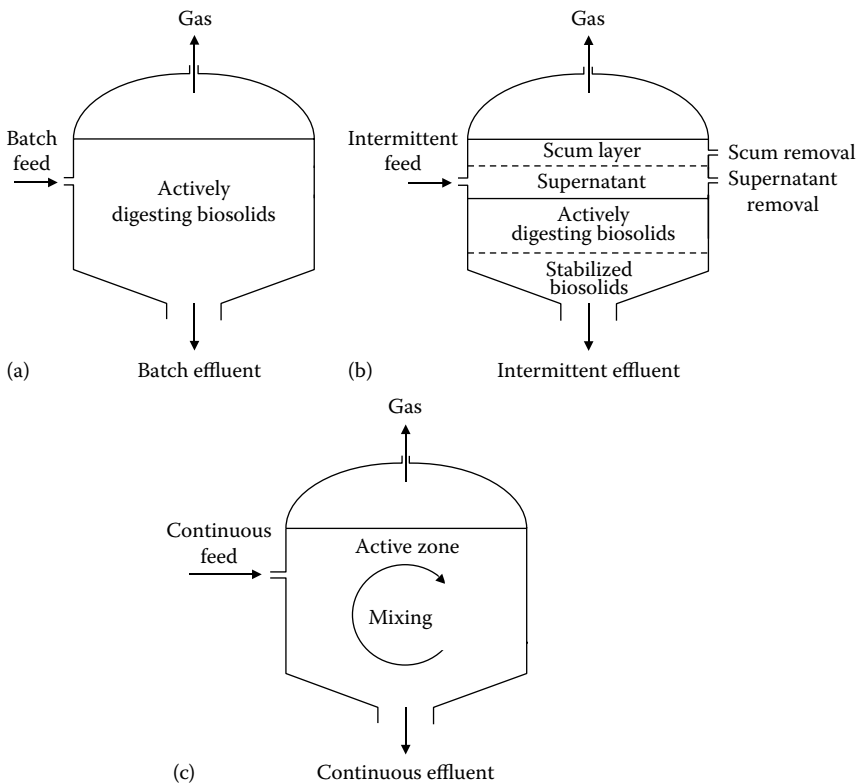
22.2.2.2 Light Gases

The ideal transportation fuel is a stable liquid at ambient temperature and pressure that can be readily vaporized and burned within an engine. However, some gaseous compounds are potential transportation fuels by increasing their density through compression. Among these gaseous transportation fuels are hydrogen, methane, ammonia, and dimethyl ether (DME).

Hydrogen can be manufactured from syngas via the water–gas shift reaction. This moderately exothermic reaction is best performed at relatively low temperatures in one or more stages with the aid of catalysts. Biomass to hydrogen processes face the same fuel delivery challenges as hydrogen from fossil sources in addition to the increased costs associated with using biomass.

Methane can be the main product of gasification under conditions known as hydrogasification (see Equation 22.5) [5]:



**FIGURE 22.10**

Types of anaerobic digesters: (a) batch fed, (b) intermittently fed, and (c) continuously stirred and fed.

Although methane is more easily pressurized or liquefied than hydrogen, its density is still too low to be an attractive transportation fuel except in some urban mass transit applications [6].

Ammonia is produced by the Haber process (see Equation 22.5) at 200 bar and 500°C [7]:



As a widely employed agricultural fertilizer, the United States already has in place production, storage, and distribution infrastructure for its use.

DME, like liquefied petroleum gas, is a nontoxic, flammable gas at ambient conditions, which is easily stored as a liquid under modest pressures [8]. It can be produced from syngas and can substitute for diesel after minor engine modifications.

22.2.2.3 Synthetic Gas

Biomass gasification generates syngas, which is attractive for energy applications because of its H_2 , CO , and CH_4 contents. As discussed previously, syngas composition varies by reactor operating conditions and can be tailored to specific applications. The two main syngas applications are power generation and fuel synthesis.

Clean syngas can replace natural gas use in gas turbines without major equipment modifications. It is often employed in coal-based integrated gasification/combined cycle,

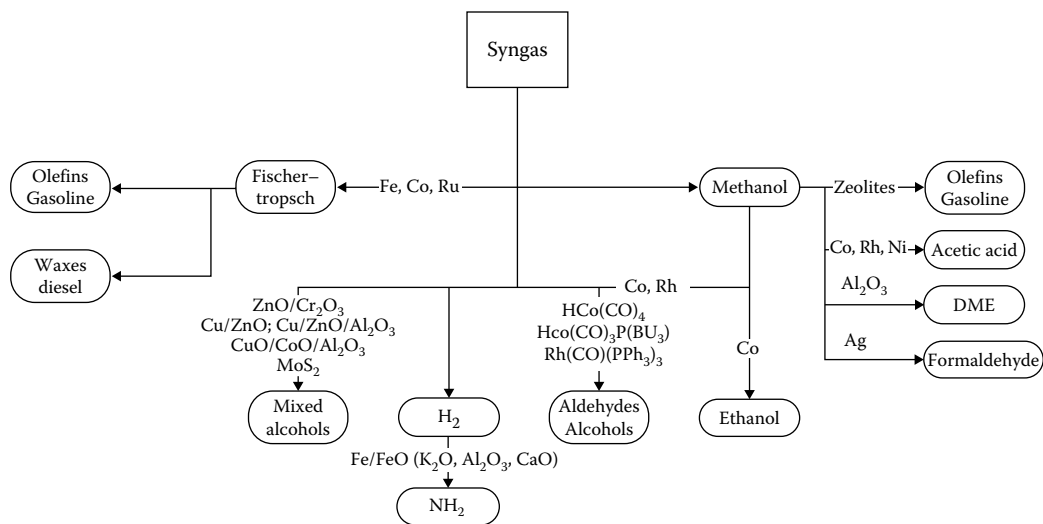


FIGURE 22.11

Catalytic pathways for converting synthetic gas to fuels. (Adapted from Spath, P.L. and Dayton, D.C., Preliminary screening-technical and economic assessment of synthesis gas to fuels and chemicals with emphasis on the potential for biomass-derived syngas, Technical Report, DTIC Document, National Renewable Energy Laboratory NREL/TP-510-34929, pp. 1–160, 2003.)

but efforts to reduce greenhouse gas emissions could encourage co-firing of biomass in these systems. However, the low cost of natural gas coupled with the lower construction costs of gas-based systems makes it unlikely that new facilities will be built to convert solid fuels to syngas for power applications.

Fuel synthesis converts solid carbonaceous materials into higher-value liquid fuels. While solid fuels such as coal and biomass are valued below \$100 per Mg, liquid fuels including gasoline and diesel often have prices of over \$1000 per Mg. These higher prices reflect the value of high energy density, portability, and fuel consistency. Solid fuels can be pretreated to improve these characteristics, and they have been historically used in portable applications including onboard passenger vehicle fuels. However, the mass production of liquid fuel engines has led to the development of numerous pathways to produce synthetic fuels [9].

Figure 22.11 shows several catalytic pathways for converting syngas into liquid fuels [10]. A large number of catalysts can convert syngas into Fischer–Tropsch liquids (FTLs), alcohols, short-chained hydrocarbons, and ammonia via H₂ synthesis. DME, ethanol, methanol, formaldehyde, acetic acid, olefins, and gasoline can be synthesized following syngas conversion to methanol. Details for these pathways will be discussed in the following section.

This wide range of fuels highlights the versatility of syngas. Thus, syngas from inexpensive, renewable, environmentally friendly sources could replace fossil fuels in a variety of applications. However, the development of any of these pathways depends heavily on a variety of technical, economic, and policy constraints.

22.2.3 Biomass to Liquid Fuels

Almost 25% of energy consumption in the United States goes to transportation. Approximately half of this amount comes from imported petroleum. Thus, the development of

transportation fuels from biorenewable resources is a priority if decreased dependence on foreign sources of energy is to be achieved. Table 22.3 lists properties of both traditional and bio-based transportation fuels.

Traditional transportation fuels are classified as gasoline, diesel fuel, or jet fuel. Gasoline is intended for spark-ignition (Otto cycle) engines; thus, it is relatively volatile but resistant to autoignition during compression. Diesel fuel is intended for use in compression-ignition (Diesel cycle) engines; thus, it is less volatile compared to gasoline and more susceptible to autoignition during compression. Jet fuel is designed for use in gas turbine (Brayton cycle) engines, which are not limited by autoignition characteristics but otherwise have very strict fuel specifications for reasons of safety and engine durability.

Gasoline is a mixture of hundreds of different hydrocarbons obtained from a large number of refinery process streams that contain between 4 and 12 carbon atoms with boiling points in the range of 25°C–225°C. Most of the mixture consists of alkanes with butanes and pentanes added to meet vapor pressure specifications. A few percent of aromatic compounds are added to increase octane number, the figure of merit used to indicate the tendency of a fuel to undergo premature detonation within the combustion cylinder of an internal combustion engine. The higher the octane number, the less likely a fuel will detonate until exposed to an ignition source (electrical spark). Premature detonation is responsible for the phenomenon known as engine knock, which reduces fuel economy and can damage an engine. Various systems of octane rating have been developed, including research octane and motor octane numbers. Federal regulation in the United States requires gasoline sold commercially to be rated using an average of the research and motor octane numbers. Gasoline rated as “regular” has a commercial octane number of about 87 while premium grade is 93.

Diesel fuel, like gasoline, is also a mixture of light distillate hydrocarbons but with lower volatility and higher viscosity. Because diesel fuel is intended to be ignited by compression rather than by a spark, its autoignition temperature is lower than for gasoline. The combustion behavior of diesel fuels are conveniently rated according to cetane number, an indication of how long it takes a fuel to ignite (ignition delay) after it has been injected under pressure into a diesel engine. A high cetane number indicates short ignition delay, for example, no. 2 diesel fuel has a cetane number of 37–56, while gasoline has a cetane number <15.

Jet fuel is designated as either Jet A fuel or Jet B fuel. Jet A fuel is a kerosene type of fuel with relatively high flash point, whereas Jet B fuel is a wide-boiling-range fuel, which more readily evaporates.

Bio-based transportation fuels, also known as biofuels, are currently dominated by ethanol and biodiesel. Ethanol, by virtue of its high octane number, is suitable for use in spark-ignition engines, while the high cetane numbers of biodiesel, which are methyl or ethyl esters formulated from vegetable or animal fats, make them suitable for use in compression-ignition engines. However, there are other candidate liquid biofuels including methanol, mixed alcohols, and FTLs, as well as gaseous biofuels including hydrogen, methane, ammonia, and DME, which will also be discussed.

22.2.3.1 Alcohols

22.2.3.1.1 Corn Ethanol

Ethanol is the dominant biofuel with global production exceeding 50 billion L. The majority of this ethanol comes from Brazilian sugarcane and the U.S. corn grain. Microbes convert these sugar-rich crops into alcohols with relative ease and at low cost. Two major corn-to-ethanol facilities have been operated in the United States: dry grind and wet-milling.

TABLE 22.3

Comparison of Ignition and Combustion Properties of Transportation Fuels

Fuel Type	Fossil Fuel-Derived			Biomass-Derived					
	Gasoline	No. 2 Diesel Fuel	Methanol	Ethanol	Biodiesel	Fischer-Tropsch A	Hydrogen	Methane	Dimethyl Ether
Specific gravity ^a	0.72–0.78	0.85	0.796	0.794	0.886	0.770	0.071 (liq)	0.422 (liq)	0.660
Kinematic viscosity at 20°C–25°C (mm ² /s)	0.8	2.5	0.75	1.51	3.9	2.08	105 ^b	16.5 ^b	0.227
Boiling point range (°C)	30–225	210–235	65	78	339	164–352	–253	–162	–24.9
Flash point (°C)	–43	52	11	13	188	58.5		–184	—
Autoignition temperature (°C)	370	254	464	423	—	—	566–582	540	235
Octane no. (research)	91–100	—	109	109	—	—	>130	>120	—
Octane no. (motor)	82–92	—	89	90	—	—	—	—	—
Cetane no.	<15	37–56	<15	<15	55	74.6	—	—	>55
Heat of vaporization (kJ/kg)	380	375	1185	920	—	—	447	509	402 ^d
Lower heating value (MJ/kg)	43.5	45	20.1	27	37	43.9	120	49.5	28.88

^a Measured at 16°C except for liquefied gases, which are saturated liquids at their respective boiling points.

^b Munson et al. [11].

^c Perry and Green [12].

^d Kajitani et al. [13].

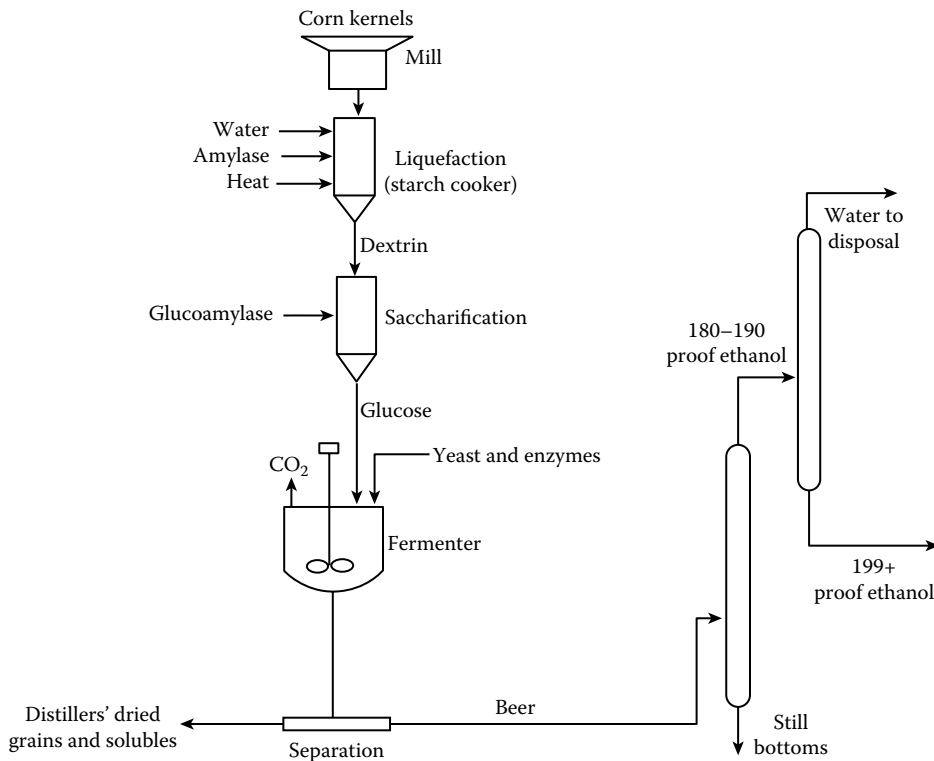


FIGURE 22.12
Dry grind corn to ethanol.

Dry grind ethanol plants, shown in Figure 22.12, grind the whole kernel while wet-milling plants soak the grain with water and acid to separate the corn germ, fiber, gluten, and starch components before mechanical grinding [14]. The capital investment for dry grind is less than that for a comparably sized wet-milling plant. However, the higher value of its by-products, greater product flexibility, and simpler ethanol production can make a wet-milling plant a more profitable investment.

Dry grind ethanol takes place in four major steps: pretreatment, cooking, fermentation, and distillation. Pretreatment consists of grinding the corn kernel into flour “meal,” which is mixed with water, enzymes, and ammonia. This mixture (“mash”) is then “cooked” to reduce bacteria levels. After cooling, the mash is sent to the fermenter where it remains for 40 h or more. The beer resulting from fermentation consists of a mixture of ethanol and stillage. Energy-intensive distillation of the beer is necessary to separate the stillage and water content from the ethanol and achieve maximum concentrations of 95%. This is followed by further purification to 100% ethanol using molecular sieves.

A modern dry grind plant will produce over 2.7 gal of ethanol per bushel of corn processed. Yields of coproducts per bushel of corn are 7.7–8.2 kg (17–18 lb) of dry distiller’s grain with solubles and 7.3–7.7 kg (16–17 lb) of carbon dioxide evolved from fermentation, the latter of which can be sold to the carbonated beverage industry. As a rule of thumb, the three products are produced in approximately equal weight per bushel. Table 22.4 shows ethanol yields for various feedstock.

TABLE 22.4

Ethanol Yields from Various Biorenewable Resources

Feedstock	Yield (L/Mg)
Apples	64
Barley	330
Cellulose	259
Corn	355–370
Grapes	63
Jerusalem artichoke	83
Molasses	280–288
Oats	265
Potatoes	96
Rice (rough)	332
Rye	329
Sorghum (sweet)	44–86
Sugar beets	88
Sugarcane	160–187
Sweet potatoes	125–143
Wheat	355

Sources: Klass, D., *Biomass for Renewable Energy, Fuels, and Chemicals*, Academic Press, San Diego, CA, 1998a, p. 356; Klass, D., *Biomass for Renewable Energy, Fuels, and Chemicals*, Academic Press, San Diego, CA, 1998b, pp. 341–344; Klass, D., *Biomass for Renewable Energy, Fuels, and Chemicals*, Academic Press, San Diego, CA, 1998c, p. 462.

Costs for ethanol from corn grain have been developed by the USDA [15] for the dry mill process. Capital costs for a 40 million gal/year ethanol plant were estimated at \$46.7 million with fuel production costs of \$1.03 per gal (2006).

22.2.3.1.2 Cellulosic Ethanol

Much of the carbohydrate in plant materials is structural polysaccharides, providing shape and strength to the plant. This structural material, known as lignocellulose, is a composite of cellulose fibers embedded in a cross-linked lignin–hemicellulose matrix [16]. Depolymerization to basic plant components is difficult because lignocellulose is resistant to both chemical and biological attack [17]. However, depolymerization is necessary for microbes to efficiently convert cellulosic biomass into alcohols.

Cellulose to ethanol consists of four steps: pretreatment, enzymatic hydrolysis, fermentation, and distillation [14]. Of these, pretreatment is the most costly step, accounting for about 33% of the total processing costs [18]. An important goal of all pretreatments is to increase the surface area of lignocellulosic material, making the polysaccharides more susceptible to hydrolysis. Thus, comminution, or size reduction, is an integral part of all pretreatments.

Enzymatic hydrolysis was developed to better utilize both cellulose and hemicellulose from lignocellulosic materials. Three basic methods for hydrolyzing structural polysaccharides in plant cell walls to fermentable sugars are available: concentrated acid hydrolysis, dilute acid hydrolysis, and enzymatic hydrolysis [17,19]. The two acid processes hydrolyze both hemicellulose and cellulose with very little pretreatment beyond comminution of the lignocellulosic material to particles of about 1 mm size. The enzymatic process must be preceded by extensive pretreatment to separate the cellulose, hemicellulose, and lignin fractions.

Although thermodynamic efficiencies for the conversion of carbohydrates to ethanol can be calculated, it is more typical to report the volumetric yield of ethanol per unit mass of feedstock. The yield of ethanol from energy crops varies considerably. Among sugar crops, sweet sorghum yields 80 L/ton, sugar beets yield 90–100 L/ton, and sugarcane yields 75 L/ton. Among starch and inulin crops, the ethanol yield is 350–400 L/ton of corn, 400 L/ton of wheat, and 90 L/ton of Jerusalem artichoke. Among lignocellulosic crops, the potential ethanol yield is 400 L/ton of hybrid poplar, 450 L/ton for corn stover, 510 L/ton for corn cobs, and 490 L/ton for wheat straw.

Researchers at the National Renewable Energy Laboratory [20] developed a design report showing capital costs of \$114 million and operating costs of \$1.07 per gal (2000) of ethanol for a 69 million gal/year ethanol plant.

22.2.3.1.3 *Butanol*

Ethanol has several limitations as a transportation fuel, including its affinity for water, which prevents it from being fully compatible with the existing fuel infrastructure, and its low volumetric heating value, which is only two-thirds that of gasoline. For this reason, fermentations that produce metabolites other than ethanol have been proposed. Alternative fermentations could produce hydrophobic molecules that are less oxidized than ethanol including higher alcohols (most prominently butanol), fatty acids, fatty alcohols, esters, alkanes, alkenes, and isoprenes.

Butanol is of particular industrial interest because of its high compatibility with the existing vehicle technologies. In addition to a higher heating value than ethanol, butanol can power existing gasoline engines without major modifications. In fact, gasoline engines can operate on up to 100% butanol blends. This would overcome the 10% volumetric blend limit of ethanol to gasoline in modern vehicles. The challenges for butanol are mostly associated with its production. Butanol production proceeds through either the intermediate hydrocarbon propylene or acetaldehyde. The propylene route employs a rhodium catalyst. The acetaldehyde pathway is a fermentation process commonly known as the acetone–butanol–ethanol (ABE) process. The ABE process shares many similarities with corn fermentation. However, it suffers from low product specificity and yield due in part to high butanol toxicity to the fermenting microorganisms [21]. Low product yields and butanol concentrations in the bioreactors are key reasons for higher butanol production capital and fuel costs relative to ethanol fermentation [22]. There are recent industry indications that some of these challenges have been overcome to allow rapid conversion of existing corn ethanol facilities to butanol.

22.2.3.2 *Biodiesel*

There is growing global interest to produce biodiesel from lipid-rich biomass. There are abundant sources of inexpensive lipid-rich biomass including dedicated, fast-growing crops like jatropha, oils from food waste, and algae-based oils. Lipids are a large group of hydrophobic, fat-soluble compounds produced by plants and animals for high-density energy storage. Triglycerides of fatty acids, commonly known as fats and oils depending upon their melting points, are among the most familiar form of lipids and have been widely used in recent years for the production of diesel fuel substitutes. The solution to this problem is to convert the triglycerides into methyl esters or ethyl esters of the fatty acids, known as biodiesel, and the by-product 1,2,3-propanetriol (glycerol).

A wide variety of plant species produce triglycerides in commercially significant quantities, most of it occurring in seeds [15]. Average oil yields range from 15,000 L/km² for cottonseed to 81,400 L/km² for peanut oil although intensive cultivation might double these numbers.

Soybeans are responsible for more than 50% of world production of oilseed, representing 4882 million bbl/year. The average oil yield for soybeans is 38,300 L/km² [15]. A higher-yielding crop is oil palm, already grown in plantations for vegetable oil production [23].

Although oil palm yields are 10 times higher than soybeans, some environmentalists are concerned that its cultivation for fuel production will encourage rainforest destruction. However, several oil seed crops have been identified that could be grown on wasteland or even saline soils, which reduces concerns about competition for food crops and rainforest destruction. These alternative oil seed crops include jatropha, Chinese tallow tree, and salicornia [24,25].

Triglycerides can be converted into transportation fuels via transesterification [26]. The process, described in Figure 22.13, has been commercialized for the production of biodiesel. Although biodiesel can substitute for diesel fuel, it has some shortcomings. Fatty acid methyl esters found in biodiesel are subject to microbial or oxidative attack, making them unsuitable in applications requiring long-term fuel storage. Low-temperature performance of biodiesel is sometimes problematic.

For these reasons, hydrogenation is being evaluated as a replacement for transesterification in the production of lipid-based biofuels [26]. Hydrogenation includes a number of reactions: large molecules are broken into smaller molecules; carbon-carbon double bonds are converted into more stable single bonds; molecular structures are rearranged; and undesirable atoms such as sulfur, nitrogen, and oxygen are removed from the hydrogenated compounds. In the case of lipids, hydrogenation yields alkanes, which are highly desirable fuel molecules.

Finally, lipid-rich microalgae might be grown in brackish water or even in seawater [27]. Algae can produce as much as 60% of their body weight as lipids when deprived of key nutrients such as silicon for diatoms or nitrogen for green algae. They employ relatively low substrate concentrations, on the order of 10–40 g/L. However, algae require the proper combination of brackish water, CO₂, and sunlight, which could limit the number of sites

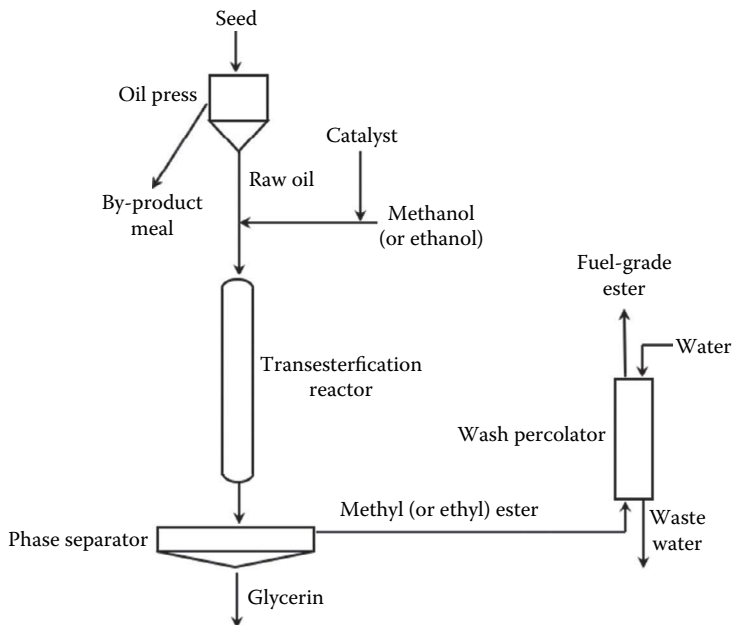


FIGURE 22.13

Conversion of triglycerides to methyl (or ethyl) esters and glycerol (biodiesel synthesis).

where this process would be profitable. Berkeley researchers have estimated that biofuels from algae would require break-even oil prices of \$332 per bbl [28].

22.2.3.3 Mixed Alcohols

Thermochemical technologies can also produce alcohols as an alternative to biochemical conversion. Mixed alcohol synthesis dates back to before the development of Fischer–Tropsch synthesis. Both processes employ similar catalytic materials and operating conditions. Mixed alcohol synthesis involves the conversion of syngas over copper, zinc, and/or cobalt catalysts at temperatures of 300°C and 6.8 MPa pressure. The syngas H₂:CO ratio should be between 1.0 and 1.2. One of the main challenges for mixed alcohol biorefineries is the need to market their coproducts. Mixed alcohols contain mostly ethanol (>70 wt%), but the longer-chained alcohols (propanol, butanol, and pentanol) need to be marketed separately. Market availability for these coproducts would help improve the economics of mixed alcohol synthesis (see work by NREL [29]).

22.2.3.4 Gasoline and Diesel

22.2.3.4.1 Fischer–Tropsch Synthesis

FTLs from biomass have antecedents in the coal-to-liquids industry. Germany extensively developed the Fischer–Tropsch process during World War II when it was denied access to petroleum-rich regions of the world. Likewise, when South Africa faced a world oil embargo during their era of apartheid, they employed Fischer–Tropsch technology to sustain its national economy. A comprehensive bibliography of Fischer–Tropsch literature can be found on the web [30].

Fischer–Tropsch catalysis produces a large variety of hydrocarbons including light hydrocarbon gases, paraffinic waxes, and alcohols according to the generalized reaction (22.6):



FTL composition depends on the process selectivity. Process selectivity is affected by various factors including catalyst and feed gas properties. The Anderson–Schulz–Flory distribution describes the probability of hydrocarbon chain growth where the molar yield for a carbon chain can be calculated using the following equation [31]:

$$C_n = \alpha^{n-1}(1 - \alpha) \quad (22.7)$$

where α is the chain growth probability of a hydrocarbon of length n . Light hydrocarbons (mostly methane) can be fed into a gas turbine to provide power. FTLs can be separated into various products in a process similar to petroleum distillation.

Product distribution is a function of temperature, pressure, feed gas composition (H₂/CO), catalyst type, and composition [32]. Depending on the types and quantities of Fischer–Tropsch products desired, either low- (200°C–240°C) or high-temperature (300°C–350°C) synthesis at pressures ranging between 10 and 40 bar is used. For example, high gasoline yield can be achieved using high process temperatures and an iron catalyst. Fischer–Tropsch synthesis requires careful control of the H₂/CO ratio to satisfy the stoichiometry of the synthesis reactions as well as avoid deposition of carbon on the

catalysts (coking). The optimal H_2/CO ratio for the production of naphtha and diesel range fuels sold in Western markets is 2:1.

Swanson et al. developed an analysis of FTL fuels from biomass [33]. Their estimates of a 2000 Mg/day corn stover facility found capital costs of \$498–\$606 million with minimum fuel selling prices of \$4.27 and \$4.83 per gal of gasoline equivalent depending on whether the process was based on a fluid bed or entrained flow gasifier.

22.2.3.4.2 Bio-Oil Upgrading

Pyrolysis is the thermal decomposition of organic compounds in the absence of oxygen. The resulting product streams depend on the rate and the duration of heating. Liquid yields exceeding 70% are possible under conditions of fast pyrolysis, which is characterized by rapid heating rates (up to $1000^\circ\text{C}/\text{s}$), moderate reactor temperatures (450°C – 600°C), short vapor residence times (<0.5 s), and rapid cooling at the end of the process. Rapid cooling is essential if high-molecular-weight liquids are to be condensed rather than further decomposed to low-molecular-weight gases.

Pyrolysis liquid, also known as bio-oil, is a low-viscosity, dark-brown fluid with up to 15%–20% water, which contrasts with the black, tarry liquid resulting from slow pyrolysis [34]. Fast pyrolysis liquid is a complicated mixture of organic compounds arising from thermal degradation of carbohydrate and lignin polymers in biomass [35]. The liquid is highly oxygenated, approximating the elemental composition of the feedstock, which makes it highly unstable. The HHV of pyrolysis liquids ranges between 17 and 20 MJ/kg with liquid densities of about $1280\text{ kg}/\text{m}^3$. Assuming conversion of 72% of the biomass feedstock to liquid on a weight basis, yields of pyrolysis oil are about 135 gal/ton.

Production of pyrolysis oils and its coproducts involves several steps [36], which are illustrated in Figure 22.14. Lignocellulosic feedstock, such as wood or agricultural residues, is milled to a fine powder to promote rapid reaction. The particles are augured into the pyrolysis reactor where they are rapidly heated and converted into condensable vapors, liquid aerosols, noncondensable gases, and charcoal. These products are

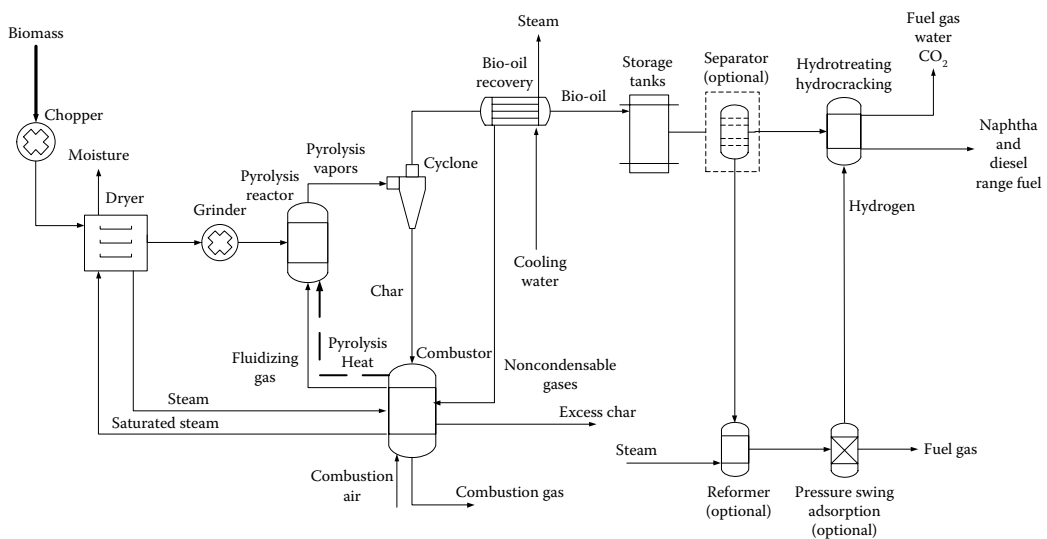


FIGURE 22.14

Biomass fast pyrolysis and bio-oil hydrotreating/hydrocracking to gasoline and diesel.

transported out of the reactor into a cyclone operating above the condensation point of pyrolysis vapors where the charcoal is removed. Vapors and gases are transported to a quench vessel where a spray of pyrolysis liquid cools vapors sufficiently for them to condense. The noncondensable gases, which include flammable carbon monoxide, hydrogen, and methane, are burned in air to provide heat for the pyrolysis reactor. The condensable liquids consist of a mixture of hundreds of organic compounds commonly known as bio-oil.

Bio-oil can be upgraded using conventional oil refinery processes. The most common of these processes are hydrotreating and hydrocracking. Hydrotreating can remove most of the bio-oil impurities such as nitrogen, alkali metals, and oxygen carried over from the original biomass. The purpose of hydrocracking is to break down heavy hydrocarbons with long carbon chain lengths into compounds within the naphtha and diesel range (7–20 carbon atoms). Bio-oil contains organic compounds with molecular weights of several hundred grams per mole. These compounds can be cracked into lighter hydrocarbons increasing the yield of naphtha and diesel range fuels. Hydrocracking consumes significant quantities of hydrogen, which can be obtained by reforming bio-oil or natural gas within the facility [37].

Gasoline and diesel from corn stover fast pyrolysis followed by bio-oil upgrading could cost between \$2.00 and \$3.10 per gal for a 2000 Mg/day biorefinery [36,38]. This facility would generate 35.4 million gal/year.

22.2.3.5 Hydrothermal Processing

Hydrothermal processing (HTP) is the use of water at near-critical-state conditions (374°C, 22.1 MPa) for thermochemical conversion. At temperatures below (subcritical) and above (supercritical) the critical point, water exhibits unique properties attractive for biomass depolymerization and product extraction [39]. HTP encompasses a wide range of operating temperatures (200°C–600°C) and pressures (5–40 MPa). At lower temperatures, the process is often called liquefaction, and its primary products are a mixture of organic liquids commonly known as bio-crude. At higher temperatures, the primary products are methane and hydrogen [40].

HTP presents several benefits compared to other thermochemical processes: feedstock flexibility, heat integration, and tunable chemical reactions. HTP reactors can convert a wide range of materials including high-moisture-content feedstock. However, alkali metals can affect the equipment lifetime. High water temperatures allow for heat integration opportunities. As long as the water retains its latent heat, it can be reheated with small energy input. Excess heat can be recovered upon cooling spent reaction media. Finally, fine-tuning of process temperature, pressure, and catalytic media can significantly improve product selectivity and yield.

Researchers at the Pacific Northwest National Laboratory have developed preliminary techno-economic analyses for HTP of various types of biomass [41]. However, there are limited industrial data to support detailed cost estimates of this technology.

22.2.4 Biofuel Properties

Biomass can be converted to a wide range of biofuels with significantly different combustion properties as shown in Table 22.3. Combustion properties determine the suitability of the biofuel to different engines and combustion equipment. In general, a combination of these properties determines the ultimate fuel performance, but a single factor may make the fuel unsuitable for a specific equipment.

Most of the global biofuel production has focused on ethanol and biodiesel. These fuels can be blended in small quantities with traditional fossil fuels. Conventional engines can operate with low levels of ethanol and biodiesel blends. In the United States, both E10 and E85 (ethanol:gasoline blends of 10% and 85% ethanol, respectively) have been marketed to consumers. The most common biodiesel blend in the United States is B20 with other blends ranging from 5% to 100% biodiesel. Both E85 and B20 typically require modern engines with modifications to adjust for the biofuel properties.

There is growing interest in the production of drop-in biofuels. Drop-in fuels refer to gasoline and diesel-type biofuels that can operate in existing gasoline engines without modifications. Companies have been able to produce drop-in biofuels that meet most of the specifications required by modern vehicles via several of the pathways discussed previously. The use of existing engines and infrastructure is one of the advantages of producing drop-in biofuels. On the other hand, hydrocarbons in first-generation drop-in biofuels have some minor differences compared to fossil fuels that are still being addressed. Researchers continue to study innovative ways of synthesizing fuels with improved combustion properties that could not only replace but also improve upon conventional gasoline and diesel.

References

1. Bergman, P. C. A. and J. H. A. Kiel (November 2005). Torrefaction for biomass upgrading. Technical Report ECN-RX-05-180, Petten, the Netherlands.
2. Medic, D., M. Darr, A. Shah, B. Potter, and J. Zimmerman (2012). Effects of torrefaction process parameters on biomass feedstock upgrading. *Fuel* 91(1), 147–154.
3. Nachenius, R., F. Ronsse, R. Venderbosch, and W. Prins (2012). Biomass pyrolysis. *Chemical Engineering for Renewables Conversion* 42, 75.
4. Klass, D. (1998). *Biomass for Renewable Energy, Fuels, and Chemicals*. Academic Press, San Diego, CA, p. 356.
5. Reed, T. (1981). *Biomass Gasification: Principles and Technology*. Noyes Data Corp., Park Ridge, NJ.
6. Vieira de Carvalho, A. J. (1982). Natural gas and other alternative fuels for transportation purposes. *Energy* 10(2), 187–215.
7. Satterfield, C. (1991). *Heterogeneous Catalysis in Industrial Practice*. McGraw-Hill Book Co., New York.
8. Sorenson, S. (2001). Dimethyl ether in diesel engines: Progress and perspectives. *Journal of Engineering for Gas Turbines and Power* 123, 652.
9. Probst, R. F. and E. R. Hicks (May 2006). *Synthetic Fuels*. Dover Publications, Dover, NY.
10. Spath, P. L. (2003). Preliminary screening-technical and economic assessment of synthesis gas to fuels and chemicals with emphasis on the potential for biomass-derived syngas. Technical Report, National Renewable Energy Laboratory NREL/TP-510-34929, 1–160.
11. Munson, B. et al. (1994). *Fundamentals of Fluid Mechanics*, 2nd edn. John Wiley & Sons, New York, Table 1.6.
12. Perry, R. and W. Green (1984). *Perry's Chemical Engineers' Handbook*, 6th edn. McGraw-Hill, New York, Chapter 3.
13. Kajitani, S. et al. (1997). Engine performance and exhaust characteristics of direct-injection diesel engine operated with DME. Society of Automotive Engineers Inc., Warrendale, PA, p. 35.
14. Bailey, B. (1996). Performance of ethanol as a transportation fuel. In C. Wyman (ed.), *Handbook on Bioethanol*, Vol. 1. Taylor & Francis Group, London, U.K., pp. 37–58.
15. Kwiatkowski, J., A. McAloon, F. Taylor, and D. Johnston (2006). Modeling the process and costs of fuel ethanol production by the corn dry-grind process. *Industrial Crops & Products* 23(3), 288–296.

16. Rowell, R., R. Young, and J. Rowell (1997). *Paper and Composites from Agro-Based Resources*. CRC Press, Boca Raton, FL.
17. Schell, D., J. McMillian, and G. Philippidis (1992). Ethanol from lignocellulosic biomass. *Advances in Solar Energy* 7, 373–448.
18. Lynd, L. R. (1996). Overview and evaluation of fuel ethanol from cellulosic biomass: Technology, economics, the environment and policy. *Annual Reviews in Energy and the Environment* 21(1), 403–465.
19. Wayman, M. and S. Parekh (1990). *Biotechnology of Biomass Conversion: Fuels and Chemicals from Renewable Resources*. Open University Press, Philadelphia, PA.
20. Aden, A., M. Ruth, K. Ibsen, J. Jechura, K. Neeves, J. Sheehan, B. Wallace, L. Montague, and A. Slayton (2002). Lignocellulosic biomass to ethanol process design and economics utilizing co-current dilute acid prehydrolysis and enzymatic hydrolysis for corn stover. Technical Report NREL//TP-510-32438, National Renewable Energy Laboratory, Golden, CO.
21. Ezeji, T. C., N. Qureshi, and H. P. Blaschek (2007). Bioproduction of butanol from biomass: From genes to bioreactors. *Current Opinion in Biotechnology* 18(3), 220–227.
22. Pfromm, P. H., V. Amanor-Boadu, R. Nelson, P. Vadlani, and R. Madl (2010). Bio-butanol vs. bio-ethanol: A technical and economic assessment for corn and switchgrass fermented by yeast or clostridium acetobutylicum. *Biomass and Bioenergy* 34(4), 515–524.
23. Openshaw, K. (2000). A review of *Jatropha curcas*: An oil plant of unfulfilled promise. *Biomass and Bioenergy* 19(1), 1–15.
24. Glenn, E., J. O'Leary, M. Watson, T. Thompson, and R. Kuehl (1991). *Salicornia bigelovii* torr.: An oilseed halophyte for seawater irrigation. *Science* 251(4997), 1065–1067.
25. Kumar, A. and S. Sharma (2008). An evaluation of multipurpose oil seed crop for industrial uses (*Jatropha curcas* L.): A review. *Industrial Crops & Products* 28.1, 1–10.
26. Kram, J. W. (January 2009). Aviation alternatives. *Biodiesel Magazine*, available online at <http://www.biodieselmagazine.com/articles/3071/aviation-alternatives>.
27. Klass, D. (1998). *Biomass for Renewable Energy, Fuels, and Chemicals*. Academic Press, San Diego, CA, pp. 341–344, 462.
28. Lundquist, T., I. Woertz, N. Quinn, and J. Benemann (2010). *A Realistic Technology and Engineering Assessment of Algae Biofuel Production*. Energy Biosciences Institute, Berkeley, CA, p. 1.
29. Dutta, A., R. L. Bain, and M. J. Bidy (May 2010). Techno-economics of the production of mixed alcohols from lignocellulosic biomass via high-temperature gasification. *Environmental Progress & Sustainable Energy* 29(2), 163–174.
30. Anon. (2005). Fischer–Tropsch archive, www.fischer-tropsch.org (accessed March 2015).
31. Schulz, H. (1999). Short history and present trends of Fischer–Tropsch synthesis. *Applied Catalysis A, General* 186(1–2), 3–12.
32. Tijmensen, M., A. Faaij, C. Hamelinck, and M. van Hardeveld (2002). Exploration of the possibilities for production of Fischer–Tropsch liquids and power via biomass gasification. *Biomass and Bioenergy* 23(2), 129–152.
33. Swanson, R., A. Platon, J. Satrio, and R. Brown (2010). Techno-economic analysis of biomass-to-liquids production based on gasification. *Fuel* 89, S11–S19.
34. Czernik, S. and A. Bridgwater (2004). Overview of applications of biomass fast pyrolysis oil. *Energy and Fuels* 18(2), 590–598.
35. Piskorz, J. and D. Scott (1987). The composition of oils obtained by the fast pyrolysis of different woods. Preprint Paper, *American Chemical Society, Division of Fuel Chemistry* 32(2).
36. Wright, M. M., D. E. Daugaard, J. A. Satrio, and R. C. Brown (2010). Techno-economic analysis of biomass fast pyrolysis to transportation fuels. *Fuel* 89(Suppl. 1), S2–S10 (Techno-economic comparison of biomass-to-biofuels pathways).
37. Wright, M. M., Y. Roman-Leshkov, and G. H. William. (2012). Investigating the techno-economic tradeoffs of hydrogen source using a response surface model of drop-in biofuel production via biooil upgrading. *Biofuels, Bioproducts and Biorefining* 6(5), 503–520.
38. Brown, T. R., R. Thilakarathne, R. C. Brown, and G. Hu (2013). Techno-economic analysis of biomass to transportation fuels and electricity via fast pyrolysis and hydroprocessing. *Fuel* 106, 463–469.

39. Ye, P., L. Cheng, H. Ma, B. Bujanovic, M. Goundalkar, T. Amidon, H. Xie, and N. Gathergood (2011). *Biorefinery with Water*. John Wiley & Sons, Hoboken, NJ.
40. Peterson, A., F. Vogel, R. Lachance, M. Froling, M. Antal Jr., and J. Tester (2008). Thermochemical biofuel production in hydrothermal media: A review of sub- and supercritical water technologies. *Energy & Environmental Science* 1(1), 32–65.
41. Elliott, D. C., G. G. Neuenschwander, T. R. Hart, L. Rotness, A. H. Zacher, D. Santosa, C. Valkenburg, S. Jones, and S. Tjokro Rahardjo (2009). *Catalytic Hydrothermal Gasification of Lignin-Rich Biorefinery Residues and Algae*, pp. 1–25. Pacific Northwest National Laboratory, Richland, WA.



Taylor & Francis

Taylor & Francis Group

<http://taylorandfrancis.com>

23

Geothermal Power Generation

Kevin Kitz

CONTENTS

23.1	Introduction.....	932
23.2	Definition and Use of Geothermal Energy	933
23.3	Requirements for Commercial Geothermal Power Production.....	934
23.3.1	Definition of a Geothermal Resource (Heat, Permeability, Water).....	934
23.3.2	Improving a Geothermal Resource through Human Intervention.....	936
23.3.3	Geothermal Energy as a “Renewable” Resource	937
23.3.4	Economic Access	938
23.3.4.1	Economic Access: Wellhead Energy Cost.....	938
23.3.4.2	Economic Access: Electricity Transmission	939
23.3.4.3	Economic Access: Viable Market	941
23.3.5	Economic Access: Power Plant Cost.....	946
23.3.5.1	Capital Costs	946
23.3.5.2	Operating Costs.....	947
23.4	Exploration and Assessment of Geothermal Resources	948
23.4.1	Overview.....	948
23.4.2	Exploration and Discovery	949
23.4.3	Risk of Exploration	950
23.5	Management of the Geothermal Resource for Power Production.....	951
23.5.1	Goals of Resource Management	952
23.5.1.1	Minimizing Development Capital Cost.....	952
23.5.1.2	Residual Brine Management	954
23.5.1.3	Clean-Water Injection Placement to Enhance Steam Production.....	955
23.5.2	Resource Chemistry	956
23.5.3	Barriers to Resource Management	957
23.5.3.1	Incomplete Information	957
23.5.3.2	Capital Limitations and Sunk Costs.....	958
23.5.3.3	Economic Impetus	958
23.5.4	Resource Characterization	959
23.6	Geothermal Steam Supply (from Wellhead to Turbine).....	963
23.6.1	Overview of Steam/Brine Separation for Steam Turbine Supply.....	963
23.6.2	Multipressure Steam Flash and Separation	964
23.6.3	Steam Pipeline Operation.....	965
23.6.4	Steam Washing Prior to Steam Turbine Admission	965
23.6.5	Turbine Washing to Remove Scale Buildup.....	966

23.7	Geothermal Power Production—Steam Turbine Technologies	967
23.7.1	Overview of Geothermal Power Generation Technologies	967
23.7.2	Steam Turbine Conversion.....	967
23.7.3	Condensing Steam Turbine Process	968
23.7.4	Design of Geothermal Turbines.....	971
23.7.5	Design of Heat-Rejection Systems	971
23.7.6	Geothermal Condenser Gas-Removal Systems.....	972
23.8	Geothermal Power Production—Binary Power Plant Technologies	973
23.8.1	Binary Power Plant Advantages	973
23.8.1.1	Silica Solubility	974
23.8.1.2	Lower Parasitics vs. Cycle Inefficiency	974
23.8.1.3	Compactness	974
23.8.2	Types of Binary Systems	975
23.8.2.1	Subcritical Pentane Binary Power Plants.....	975
23.8.2.2	Supercritical Hydrocarbon Binary Power Plants	975
23.8.2.3	Ammonia–Water Binary Power Plants	976
23.8.3	Binary Power Plants for Pressurized Geothermal Brine	976
23.8.4	Integrated Steam Turbine and Binary Power Plants.....	977
23.8.4.1	The Geothermal Combined Cycle Process.....	978
23.8.4.2	Silica Solubility Limits.....	978
23.8.4.3	Compare and Contrast	979
23.9	Environmental Impact	980
23.9.1	Geothermal Power Plant Emissions.....	980
23.9.1.1	CO ₂ Emissions	980
23.9.1.2	H ₂ S and SO _x Emissions	981
23.9.1.3	NO _x Emissions.....	981
23.9.1.4	Particulate Emissions	982
23.9.2	Land Use	982
23.10	Additional Information on Geothermal Energy	982
	References.....	983

23.1 Introduction

Roman mythology holds that humans obtained fire from the gods on Mount Olympus to meet their needs for light and heat. In much of today's industrialized world, the use of electricity has edged out fire for these age-old needs. However, the convenient use of electricity is now faced with increasing cost and concerns about the availability and environmental consequences of the fuels that are needed to produce it. Can those Roman gods again come to mankind's aid?

Deep below Mount Olympus, Vulcan toils over his forge. The forge glows red as Vulcan hammers out weapons for the gods, including Jupiter's own thunderbolts. Vulcan's forge is stoked by geothermal energy that humans, too, have used for the production of electricity since 1904, starting in the very homeland of the Romans.

Geothermal power production in the United States approached 18,000 GW h in 2005,¹ or an average of more than 2000 MW over the year. It does so on an around-the-clock basis, providing baseload power to several western utilities in California, Nevada, Hawaii,

Utah and starting in 2006, Alaska. The power generated has very low emissions and is immune to price fluctuations in the fossil fuel markets. Similar benefits are derived around the world from plants operating in 24 countries worldwide, including Italy, the Philippines, Indonesia, Kenya, New Zealand, and Iceland. In Iceland, geothermal power not only provides 16.6% of the electric power generated every year, but 54% of the total primary energy use in the country, including the 87% of households that are heated by geothermal water.² Worldwide direct use of geothermal energy is documented in 76 countries.³

This chapter examines geothermal power technologies and the issues involved in further utilization of geothermal energy for the production of electric power.

23.2 Definition and Use of Geothermal Energy

Geothermal energy is present on Earth from two sources:

1. As heat that flows upward and outward across the entire surface of the world from the very deep (mantle and core) radioactive decay of uranium, thorium, and potassium. In most regions of the world, this energy flux is too small to be commercially useful for any purpose.
2. As localized heat resulting from the movement of magma into the earth's crust. In some areas of the world, most frequently along the so-called "Ring of Fire," this localized heat, with high heat flux and high temperatures, can be found between the surface and 10,000 ft below ground. Where such heat flux meets the requisite conditions, geothermal energy can be developed for multiple and varied purposes. Where temperatures are sufficiently high, geothermal energy may be used for electric power generation. This form of geothermal energy is the subject of this chapter.

Geothermal energy was first used for experimental power generation in Larderello, Italy, on July 4, 1904, by Prince Piero Ginori Conti. However, commercial development followed slowly thereafter. The Larderello site also saw the first commercial geothermal power plant (250 kW) in 1913, as well as the first large-power installation in 1938 (69 MW). It would be 20 years before the next large geothermal power installation would be built: halfway around the world in Wairakei, New Zealand, with the first unit—commissioned in 1958—that, under a steady development program, grew to 193 MW of installed capacity by 1963. In the United States, the installation of the first unit (11 MW) of what was to become the largest geothermal power complex in the world, The Geysers, in Sonoma County, California, occurred in 1960. Over the next quarter-century, a total of 31 turbine generator sets were installed at The Geysers, with a nameplate capacity of 1890 MW. Plant retirements and declining steam supply have since reduced generation at The Geysers to an annual average generation of 1020 MW from 1421 MW of installed capacity—still the largest geothermal field in the world.¹

Since those early efforts, Lund et al. report that a total of 2564 MW of geothermal power generation capacity is currently installed in the United States, generating approximately 2000 MW of annual average generation. In 2005, worldwide annual geothermal power

was estimated at 56,875 GW h from 8,932 MW of installed capacity.³ These values put the United States and worldwide geothermal power plant capacity factors* at 78% and 73%, respectively.

Geothermal energy is also utilized in direct-heat uses for space heating, recreation and bathing, and industrial and agricultural uses. Geothermal energy in direct-use application is estimated to have an installed capacity of 12,100 MW thermal, with an annual average energy use of 48,511 GW h/year energy equivalent.³ This excludes ground-coupled heat pumps (GCHPs, see below). In the United States, the first geothermal heating district was installed in Boise, Idaho, in 1892, and is still in operation today.

GCHPs are also often referred to as *geothermal*. GCHP units are reported by Lund to have 15,721 MW of installed capacity and 24,111 GW h of annual energy, representing 56.5% and 33.2% of worldwide direct use, respectively.³ It should be noted that although these numbers are reported as “geothermal,” in many instances the ground temperature is primarily controlled not by the flow of heat from below the surface, but by the annual average ambient temperature of the location, which is a solar phenomenon. From the numbers above, it can be seen that GCHPs provide an additional worldwide energy production of almost 50% more than that provided by geothermal electric power generation. For more information on GCHP usage, see Chapter 27.

This chapter will cover the technologies and issues in the utilization of geothermal energy for electric power generation, with a particular focus on the issues facing the development of new capacity, both technical and economic. Although the technologies of geothermal energy for power and for direct use are quite different, the issues covered in this chapter related to reservoir issues, and the economic factors affecting or controlling the development and maintenance of the reservoirs are often the same or similar.

23.3 Requirements for Commercial Geothermal Power Production

For new geothermal power to be installed, or an existing geothermal power plant to continue operating, commercial geothermal power production requires two major elements: a geothermal resource and economic access.

23.3.1 Definition of a Geothermal Resource (Heat, Permeability, Water)

A geothermal resource for power production comprises three major elements: heat, sufficient reservoir permeability, and water.

1. Heat is clearly the first element for commercial power generation. Most commercial geothermal resources produce fluids from reservoirs with a resource temperature of at least 320°F. However, there are examples of geothermal fields with lower temperature fluids. Nonetheless, resource temperature is a good first indicator of economic viability, see Table 23.1. As can be calculated from the table, the flow requirements for a 60 MW plant are 18 million lb/h of 300°F geothermal liquid, but only 4 million lb/h of geothermal liquid if the reservoir temperature is 450°F.

* Capacity factor is defined as the actual generation produced compared to the theoretical generation that would be produced in 1 year with the power plant running at full rated capacity.

TABLE 23.1

Power Generation Potential from a Range of Resource Temperatures

1000 lbm Geothermal Fluid of	Electrical Generation (kW h)	Power Plant Type ^a (see Later Sections)
Liquid at 300°F	3.3	Binary
Liquid at 350°F	5.6	Single-flash steam
Liquid at 400°F	10.4	Double-flash steam
Liquid at 450°F	14.5	Double-flash steam
Steam at 350°F	53.5	Dry steam

Source: From DiPippo, R., *Geothermal Power Plants: Principles, Applications and Case Studies*, Elsevier Advanced Technology, Oxford, U.K., 2005, p. 424.

^a The column labeled “power plant type” is the technology used as a basis for the power generation calculation. All plant types are used over a larger range of temperatures than that indicated in the table.

2. *Permeability* describes the ability of the reservoir fluid (water or steam) to flow through the rock formation. Permeability allows deep-seated geothermal heat sources to create a geothermal resource through the convection (flow under the influence of heating and cooling) of hot water or steam. The convection of the geothermal fluids through the reservoir heats a large volume of rock, thereby storing a large quantity of energy over a period of tens of thousands of years. Geothermal reservoir permeability is dynamic, with the hotter fluids dissolving minerals and increasing permeability, and the cooling fluids depositing minerals and restricting permeability. Reservoir permeability is what allows the extraction of that stored heat through a relatively few number of wells in commercial geothermal developments.

Matrix permeability is the ability of the fluid to flow through the bulk rock itself. Fresh water wells, natural gas wells, and oil wells are frequently observed to obtain a significant portion of their total flow from matrix permeability. In other words, the fluids enter the wellbore as uniform flow along an area of unfractured rock. Sufficient matrix permeability is rare in geothermal wells that will support commercially significant flow rates.

Fracture permeability is low most geothermal wells which obtain the majority of total wellbore inflow through naturally occurring fractures in the rock. Pervasive fracturing allows a single well to obtain flow contributions from a large area at high flow rates, even where the matrix permeability is low. In most cases, the fractures extend over large areas and volumes as a result of tectonically active areas, but some fields have been discovered and developed that essentially comprise a single fault system (which may be comprised of multiple fractures in the rock). In such fields, only wellbores that cross the fault produce geothermal fluid at commercial rates.

3. Water is the motive fluid for geothermal power production. It may be brought to the surface as steam from one of the few (but typically large) geothermal steam fields, such as Larderello (Italy), The Geysers (California), and Kamojang (Indonesia). A water–steam combination may also be produced to the surface from high-temperature liquid-dominated or liquid-and-steam reservoirs. In low- or moderate-temperature resources, pressurized water may be pumped to the surface using downhole pumps.

The development of new geothermal power plants and the expansion and maintenance of existing geothermal fields depends on the three elements of heat, permeability, and water.

The three occur simultaneously in relatively few places around the world, but there remain many thousands of megawatts of undeveloped worldwide and U.S. resources. Over the long term, the natural resource base for geothermal power could be supplemented with human intervention to create new systems or enhance existing systems.

23.3.2 Improving a Geothermal Resource through Human Intervention

The terms *hot dry rock* (HDR) or *hot fractured rock* (HFR) refer to a family of experimental technologies that are not yet commercially proven. The objective is to establish one or more of the missing elements of a commercial geothermal resource (specifically, permeability or water) where a heat source already exists. HDR experiments have been undertaken as research projects by the U.S. Department of Energy and similar agencies in Europe and Japan. The problems are daunting and the costs are high; U.S. DOE funding, for example, has diminished substantially from its maximum in the 1980s.

The concept behind HDR and HFR is to drill a well into the hot rock and then pump water into the well at very high pressure, causing the rock to fracture. The fractures provide a heat transfer surface and flow path allowing water to be pumped from the surface into an injection well, circulated through the man-made fractures, and ultimately recovered in a production well some distance away from the injection well. The theory is straightforward; unfortunately, the implementation to date has not been.

As of 2005, the first privately-funded HFR development had commenced at the Cooper Basin in southern Australia, and it will be watched closely for its success. The developer's plans call for an initial installation of a 3 MW power plant if the fracturing process is successful.⁵

If HDR and HFR technology is developed and implemented in significant quantities over the next 20 years, the geothermal reservoir management strategies and the energy-to-power conversion technologies will be much the same as that described in the rest of this chapter.

Between the naturally-occurring resource base and the potential man-made resource base of HDR/HFR is the enhanced geothermal system (EGS). EGS technologies seek to supplement a naturally occurring geothermal resource primarily by the addition of more liquid, or by stimulation of wells to tie into a larger, naturally occurring fracture network. The goal of EGS is to extend the life or capacity of existing fields, rather than the creation of an entirely new resource, as is being attempted at the Cooper Basin described above. There have been many studies, evaluations, and proposals to date, and the use of EGS at The Geysers project—including those plants owned and operated by Calpine* and NCPA†—has been a proven success.

At The Geysers, two pipelines bring 77,000 m³/day (20 million gal/day) of treated wastewater from adjoining cities to the mountains where The Geysers facilities are located. The water serves to replace that which has been depleted from The Geysers over its approximately 50 year operating history. Stark et al. report that tracer tests show that 40% of the injected water is recovered as steam within a year. The injection of the water from just one of the two pipelines (delivering about 55% of the total wastewater) is forecast to result in an annual average generation increase of 84 MW. With a parasitic pump load of 9 MW, the annual average benefit is roughly 75 MW.⁶

* Calpine Corporation, <http://www.calpine.com>.

† Northern California Power Agency, <http://www.ncpa.com>.

23.3.3 Geothermal Energy as a “Renewable” Resource

Throughout this chapter, declines in flow rates from geothermal wells and output from geothermal power plants are discussed. What does this mean in terms of whether geothermal energy is renewable?

In recent years many thoughtful papers have been published on the renewability and sustainability of geothermal energy... However, no universally accepted definitions of the words “renewability” and “sustainability” seem to exist and definitions used often have ambiguities...⁷

From a thermodynamic point of view, it may seem that the only true renewable geothermal development would be one in which the extraction rate is the same as the natural heat influx rate into the system. However, reservoir simulations and field observations frequently reveal that the natural heat influx rate increases as production occurs, due to pressure changes that allow more hot liquid to flow into the system. Therefore, operating at a “nonrenewable” level increases the ultimate energy extraction from the resource. More importantly, a true “renewable” level of energy extraction would very often be sub-economic, and is therefore of little interest in the development of geothermal resources for society’s benefit.

Another definition argues that, as long as the power or heat usage from the resource continues at a constant level for hundreds of years, it approximates a true renewable resource, although it may be termed a “sustainable resource.” Again, this is an interesting theoretical discussion, but not one that actually is put into practice in the development of most geothermal resources, for both the reasons of economics and an inability to know what this actual level would be.

Sanyal (2004) argues that sustainable geothermal development occurs if the project maintains its output, including make-up well drilling, over the amortization period of the power plant.⁷ This definition recognized the critical role that economics plays in actual natural resource development decisions. In short, projects are developed to meet economic requirements. This is true of any new power project, whether geothermal, another renewable source, or a fossil-fired resource. Section 23.3.4, will illustrate why the question of sustainable development for a 50-year period, let alone a 300-year period, will not play a role in the development decisions for a particular geothermal resource. The reason, in summary, is that even at a mere 50 years in the future, there are no meaningful economic consequences to development decisions made today when using a discounted cash flow analysis.

More valuable than the theoretical discussion of whether geothermal energy is renewable, sustainable, both, or neither, is to look at the history of geothermal development. Geothermal use at Larderello, Italy, is over 200 years old, starting with mineral extraction in the early 1800s and including almost 100 years of commercial power generation. During the last 100 years of power generation, turbines have been renewed or replaced, power output has grown and shrunk and grown again, and new methods of extracting more energy have been developed. In fact, geothermal power generation in 2003 was higher than any other year, with 5.3 billion kW h produced.⁸

Many further decades of geothermal power generation are expected from the Larderello region, as well as Wairakei, The Geysers, and other fields that are approaching 50 years of power generation. Geothermal power-generating facilities only very rarely cease operation, although few will reach their 50th anniversary at their maximum generation level.

23.3.4 Economic Access

Given that a geothermal resource exists—whether naturally occurring or developed with EGS or HDR technologies—the resource will be economically viable for power generation only if the four elements of economic access are met: wellhead energy cost, electricity transmission, a market for the electric power, and the power plant cost.

23.3.4.1 Economic Access: Wellhead Energy Cost

Wellhead energy cost is the total cost to bring useable geothermal energy to the surface and to return the cooled geothermal fluids to the reservoir. The thermodynamic condition (pressure, temperature, and flow rate) of the geothermal energy at the surface will influence the capital cost of the power plant. The wellhead energy cost is the result of the combined effects of the productivity of the well, the cost to drill the well, and the enthalpy (or available energy) of the fluid that is produced from the well, among other aspects. These factors vary widely from field to field, and even within a single field.

- Well productivity is the ability of the well to bring fluid to the surface at a temperature and pressure useful for power generation. Clearly, the more fluid that is produced by each well, the fewer wells are needed for a given power plant size, and therefore the lower the total cost of the geothermal well-field development. Less obvious is the fact that highly-productive wells can also have a major impact on the cost and design of the power plant itself.
- Highly-productive wells allow the power plant inlet pressure to be increased (and thereby increase the available energy) on plants that directly use the geothermal steam in a turbine. An increase in the power plant inlet pressure can allow the size of the plant to be increased, because last-stage turbine blades can only be built to a limited maximum size in geothermal service and in binary power plant turbines as well (see Sections 23.5 and 23.6). Alternatively, for plants contractually limited to a particular megawatt capacity, e.g., 60 MW, higher inlet pressures reduce the amount of fluid that must be extracted from the reservoir and delivered to the power plant, thereby reducing the size of the heat rejection system and the injection capacity (two major components of geothermal power costs, as will be discussed in later sections).
- In binary power plants (see Section 23.6) with pumped wells, highly productive wells not only reduce the direct drilling costs, but also reduce the number of pumps that must be installed (at an installed 2005 cost of roughly \$500,000 each). Even more importantly, the pumps can be set at a shallower depth, thereby reducing the pump parasitic loads. The energy for the production pump parasitic loads (400–1000 hp per pump) is supplied by the power plant itself. Again, the productivity of the wells will either reduce the size of the plant that must be built to meet contractual and pump parasitic obligations, or can increase the amount of power available for sale from a particular power plant. The combined effect of fewer wells and more power sales dramatically increase the economic viability of a new or expansion geothermal binary power plant development. Well injectivity is a similar issue for the disposal of the residual geothermal liquids for both binary and steam power plants.
- The energy production rate (a combination of mass flow, temperature, and steam content) of production wells vary from field to field, often varying substantially

within a given field itself, and almost always changes over time for a particular well. In steam power plants, high-enthalpy wells can result either from a high-temperature portion of the field, or as a result of what is termed “excess steam” production. Excess steam occurs when the enthalpy of the produced fluid is higher than the enthalpy of the reservoir fluid as a whole due to the greater mobility of the steam through the reservoir rock than liquid water. In pumped brine binary power plants, high-enthalpy wells are simply wells with higher flowing temperatures. For both steam and binary power plants, higher enthalpy wells result in lower power plant cost, as the benefits of the higher enthalpy are found in lower drilling costs (fewer wells), lower heat-rejection system costs (higher available energy per unit mass into the plant), and lower brine-injection costs (less produced fluid).

- The depth of geothermal resources is highly variable, with most geothermal resources produced between depths of 1500–7000 ft below surface, although resources commonly exist outside of this range. One example of a shallow resource is the Salt Wells field in Nevada, in which the production and injection wells are between 450 and 750 ft deep. One particular well at that field is reported to be only 470 ft deep and to be capable of between 4 and 5 MW of power from 140°C (284°F) fluid. The drilling time for this well was only 12 days.⁹ The cost of the well is on the order of hundreds of thousands of dollars. By contrast, make-up wells drilled at one field in the Philippines almost 25 years after the start of production had a true vertical depth of over 10,000 ft, and an even greater measured depth due to the lateral reach of the well. The cost of these wells between 2001 and 2003 was on the order of \$3 million to \$5 million each. At the Puna geothermal project in Hawaii, drilling is difficult and the location remote, so the daily drilling cost is high. Wells drilled in 2005 cost approximately \$6 million, and were drilled to a depth of about 6000 ft.

There is no threshold value for the wellhead energy cost below which geothermal development is viable and above which it is not. Rather, there is a continuum in which the effects of transmission, market, and the power plant cost affect to varying degrees the ability to construct a new geothermal plant.

For existing power plants, the wellhead energy cost determines whether or not a make-up well will be economical, and ultimately the end of make-up well drilling. After make-up well drilling ends, geothermal power plants enter a period of slow decline in the output of the power plant over the coming years and decades. Although the plant is no longer able to achieve its initial rated capacity, it will continue to operate economically, literally for decades. There are very few examples of geothermal resources that, once in operation, shut down completely.

23.3.4.2 Economic Access: Electricity Transmission

With a suitable geothermal resource and a viable market for geothermal power, the link between the two is transmission. As with other renewable and nonrenewable energy sources, transmission can be a significant issue in the viability of development of a new geothermal resource, or in the expansion of an existing geothermal power facility.

Occasionally, geothermal resources are found in close proximity to existing transmission access. Examples include Steamboat Springs, Nevada and Raft River, Idaho. For these developments, the cost of transmission access is low, and transmission line construction and interconnection does not play a major role in the development of the resource.

However, geothermal resources often occur at substantial distances from existing transmission, and entail the need for considerable capital expenditures on the transmission system to deliver the power to the customer. If the field is large enough, the long transmission lines and expenses can be justified. Two separate subsea cables were built in the Philippines to transport hundreds of megawatts of electricity generated from geothermal resources from islands with small native loads to the main load center on the island of Luzon.

The cost of the transmission line has most often been the responsibility of the utility that was receiving the power (e.g., Pacific Gas and Electric for the power generated at The Geysers), whereas in more recent years, the development of the power line has been the responsibility of the geothermal developer in the United States. The power price offered to geothermal and other renewable developers may fail to recognize this cost (e.g., the Idaho PURPA posted rate), yet the cost must still be borne by the developer, and as such, the cost of transmission construction can become a substantial burden to the project economics. A 107-mile-long dedicated transmission line was built and paid for by a consortium of geothermal power developers in the Imperial Valley, California, to deliver some 500 MW of power to a common customer, Southern California Edison. After the line was built, it was turned over to the local utility, the Imperial Irrigation District, for ongoing operation and maintenance.

When a transmission system is used to deliver power and the transmission lines are owned by an entity other than the ultimate purchaser of the power, the use of that transmission system incurs wheeling costs. Wheeling costs comprise a monthly reservation/use fee and a power loss that can be paid either with funds or with power delivered to the transmission entity. Typically, wheeling charges are not charged by the utility that actually is receiving the power under contract. "Pancaked charges" refers to the circumstances in which power crosses multiple transmission segments owned by different entities, incurring separate transmission charges through each segment. The losses assessed by each utility usually are not based on actual losses for the power being transmitted, but represent a system-wide average apportioned out to the users of the system on a pro-rata basis. In the United States, wheeling protocols are established by the FERC (Federal Energy Regulatory Commission).

Common wheeling charges are 1%–5% for losses, plus \$1000–\$3000 per MW-month for the reservation costs for firm capacity. Therefore, wheeling through more than one, and often even only one, utility becomes prohibitive. As a result, the viability of development is strongly influenced by the willingness of the utility in whose control area the power plant is located to accept the power. Delivery to the closest utility generally eliminates wheeling fees and losses and improves the economic viability of the plant. On the other hand, having only a single party with whom to negotiate a contract puts the developer in a difficult position.

In deregulated markets, such as the United States, transmission reservations are the mechanism by which a power plant ensures access to the market for the life of the contract. The ability to obtain that reservation is critical to development, or else the geothermal development may face greatly increased transmission costs for transmission upgrades or longer transmission lines. One of the advantages of geothermal power as opposed to wind power is the efficiency of transmission usage. Both resources must reserve transmission capacity for their peak delivery, e.g., 100 MW. Wind will typically deliver between 25 and 40 MW on an annual average basis, while geothermal will typically deliver about 90–95 MW. On the transmission system peak hours, the difference in utilization will be even greater, due to the intermittency of the wind resource and the typical incentives in

a geothermal contract to be on-line during peak hours. A geothermal power plant can be expected to be on-line and at near-full capacity for over 95% of the peak hours.

Where transmission system capacity is limited, geothermal and other baseload resources will make much greater use of that capacity. Comparisons of new generation costs seldom account for the efficiency and hidden costs of transmission usage, which is unfortunate in the evaluation of the economics of geothermal power generation, because it is so efficient in its use of transmission capacity.

23.3.4.3 Economic Access: Viable Market

Power generation, regardless of the technology, is a highly specialized form of manufacturing. As with all manufactured products, there must be a place to sell the manufactured product. Therefore, for new geothermal power to come online, regardless of how low the wellhead energy cost and even if transmission is readily available and affordable, without a market, there is no development. Market consists of three elements: willing buyer, price vs. characteristics, and contract provisions. The first two are much the same for all power developments, whether renewable or otherwise. For geothermal power, there are unique contract provisions that must be present for realistic expansion of the role of geothermal power in the electrical demand of the United States.

23.3.4.3.1 Willing Buyer

The willing buyer must be just that: “willing” and a “buyer.” In the United States, this rare beast has been found in a number of geothermal development habitats over the last 40 years. More recently, the captive breeding program seems to be showing success. A much larger number of willing buyers have been observed, as many U.S. electric utilities have been stung first by wild swings in natural gas prices, second by 2004–2005 gas prices climbing from \$4 or less to over \$10 per million Btu, with long-term price forecasts for gas remaining high, and lastly by state-mandated renewable energy targets.

From 1960 through roughly the mid-1980s, geothermal development in the United States (and in many places around the world) was most commonly undertaken by two parties: the resource developer and the local utility. The resource developer drilled wells and built cross-country pipelines to deliver a flow of steam or mixed brine and steam to the power plant boundary. The resource developer also was responsible for injection of the residual liquids, both brine and condensed steam. The local electric utility—i.e., the willing buyer—used the steam to generate power. Under this U.S. development model, the utility met the mandate of its monopoly franchise to supply power. The utility also met its investor’s objective of investing in new facilities, the power plant and transmission lines, for which it was able, under its monopoly, to earn a regulated rate of return on the invested capital dollars. However, an inherent inefficiency was created in this development model by having two owners who each had different economic drivers, separate operating groups that worked side by side, double administration costs, and other factors. One common and unfortunate outcome of the two-owner model occurred because the steam was sold on a \$/MW h basis instead of on the energy content of the steam. The consequence was that the power plant owner built inefficient power plants because inefficiency is cheaper than efficiency, if one only looks at the power plant cost. Of course, the consequence was that the steam developer had to drill additional risky and expensive wells to supply additional steam for the inefficient power plant. Those few contracts that had steam sales based on energy content saw exactly the opposite effect in power plant design. The power plants tended to be very efficient to minimize steam use

(fuel cost). The net result of two-owner operation was that the price of geothermal power was comparatively high and resource utilization was inefficient.

With the widespread occurrence of independent power producers (IPP) in the United States in the mid-1980s, a regulated utility could theoretically obtain a lower price through the integrated operation of geothermal field and power plant and could meet its mandate for power supply, but by buying power from the IPP, the utility could not meet the objectives of its shareholders for new investment. The IPP developer's objective of building a power plant put it in direct competition with the utility for the return on investment in new power plant capacity. Under the IPP model, each megawatt of capacity installed by an IPP directly equates to less investment by the utility in baseload power (potentially \$700,000–\$1,700,000 per MW). Consequently, because the utility faces a reduced rate base (the capital on which the utility is allowed to earn a return), the IPP faces an intrinsic unwillingness in the utility to procure the output of a new geothermal (or any other type of fuel) plant. Although geothermal development should, in theory, thrive under the IPP model, the reality is that utilities in the United States have shown little interest in bringing on new geothermal development unless forced to do so in the interest of the ratepayer by governmental authority.

From the mid-1980s through the mid-2000s, many geothermal power plants were built exclusively because of the Federal PURPA* regulations and the consequent requirement of state public utility commissions for the utility to buy the power at a published avoided cost. For example, California's Standard Offer Number Four resulted in the construction of several of the Salton Sea and Heber Units, among others, in the late 1980s and early 1990s. Idaho's Posted Rate 10 MW PURPA contracts resulted in the development of the Raft River Geothermal Power Plants in southern Idaho, with anticipated operation dates of 2007 through 2009. In California and Nevada, the passage of Renewable Portfolio Standards has also spurred utilities to contract for geothermal power to comply with state law. Both PURPA and the RPS have created utility buyers, but they have not necessarily been "willing." The state RPSs and the prospect of a federal RPS is now emerging as a major factor in the decision of utilities to sign contracts for IPP-developed geothermal (and other renewable) power plants, in spite of the fact that it is against the interests of their shareholders, though not their ratepayers.

23.3.4.3.2 *Price of Delivered Power*

The price vs. the characteristics for the electrical energy is the most obvious component of a viable market. The characteristics of geothermal power are very attractive and rare in the renewable power industry. It is price-stable, has low to negligible environmental impact, and has a steady, predictable, and reliable output.

The unit price paid for geothermal-generated electrical power must cover the expense of the power plant and the wellfield development, as well as the often long and expensive exploration phase. In addition, the price paid per MW h must satisfy annual cash flow requirements and the return on investment sought by the geothermal developer. As most contracts from the late 1990s onward are not in the public domain, it is hard to know what constitutes an adequate price for electricity generated from geothermal energy. A few that have emerged are described below.

In 2003, the power purchase prices awarded to three geothermal power plants after a round of renewables bidding in Nevada were inadvertently released. The contracts were for both the power output and environmental attributes ("green tags," carbon credits, etc.).

* PURPA is the Public Utility Regulatory Policies Act.

Two were for expansions to existing power plants. One price was less than \$45 per MW h, and the other was more than \$52 per MW h. The third contract was for a greenfield power plant at under \$50 per MW h. All were for resources with temperatures greater than 320°F. Only the power plant that bid the highest price was ever built. The other plants proposed power purchase prices too low to actually accomplish development drilling, build the power plant, and close financing. The prices bid for these plants were offered before the 2004–2005 worldwide run-up in steel prices that had a tremendous negative impact on the cost of building a geothermal power plant with its miles of steel well casing, miles of steel surface piping, and enormous steel heat exchangers.

In January 2005, the Idaho Public Utility Commission approved a 20-year PURPA contract to supply power from the U.S. Geothermal, Inc.* Raft River Geothermal Power Plant for an initial price of \$52.70, escalating at 2.3% per year.¹⁰ This gives an equivalent leveled price of \$60.99. Although Raft River is a greenfield development, the production and injection wells were drilled in the late 1970s, with those costs written off by previous owners.

In May 2005, two 10 MW contracts were announced at a fixed price of \$57.50 per MW h with an annual escalation of 1.5%. These contracts were for expansions to existing power plants at two different fields in southern California (Heber and East Mesa). The price includes the value for the energy, as well as the environmental attributes. The contract also allowed for the sharing of U.S. federal production tax credits (PTCs) with the power purchasers.¹¹ The leveled price, excluding the PTCs, would be about \$63. Speaking at the groundbreaking of an additional 8 MW expansion of the Heber facility, Robert Foster, the President of Southern California Edison, said, "I like... the geothermal plant... because we know that these plants produce reliable power 24 × 7. Unlike other forms of renewable energy, I know that this energy will always be there and we don't need to have shadow generation to support geothermal power. Even though we like to have dispatchable[†] power, we can forego dispatchability for the reliability of geothermal power."¹¹

An international benchmark is the Sarulla, Indonesia, development, in which the state oil company drilled the wells for the power plant and the power plant developer was responsible for the power plant and pipeline system (excluding the cost of transmission and drilling.) The power price was bid at approximately \$45 per MW h in 2005 by two companies. Price escalations and adjustment factors are not available at the time of this writing.

An adequate selling price for the generated electrical power in a geothermal development is determined in part by resource temperature (higher temperature means lower power plant price), wellhead energy costs, power plant size (smaller requires higher price) and whether the new power plant is greenfield or an expansion (expansion can take advantage of existing infrastructure and personnel costs). Within the geothermal community, the general rule of thumb is that for geothermal resources above 300°F, a true grassroots geothermal power plant must sell power for \$60–\$65 per MW h for at least 20 years, for an all-in project (wells, pipelines, power plant, and transmission). Expansions to existing facilities can reduce the cost by 10%–15%,¹² or roughly a \$5–\$15 per MW h reduction, with most of the savings being in a lower drilling failure rate, use of the existing transmission line, and sharing of operating personnel and spare well capacity. Figure 23.1 provides representative cost elements in a geothermal power development.

* U.S. Geothermal, Inc., <http://www.usgeothermal.com>.

† A dispatchable plant can be ordered to vary its load from zero to full load to meet the needs of the electric power grid.

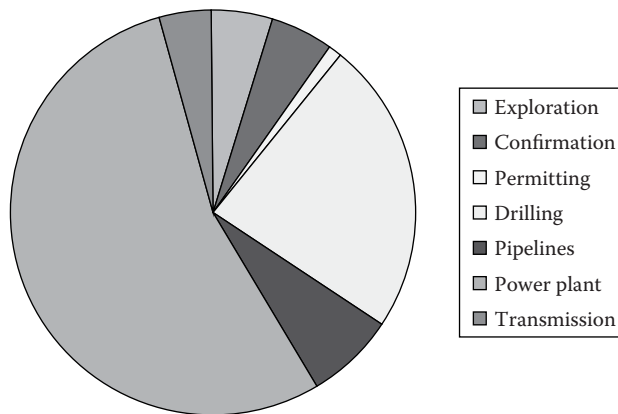


FIGURE 23.1

Typical cost breakdown of geothermal power projects. (From Hance, C.N., Factors affecting the costs of geothermal power development, Geothermal Energy Association and the U.S. Department of Energy, Washington, DC, 2005.)

23.3.4.3.3 Contract Provisions for Operation

Contract provisions for a viable geothermal power market are twofold: those governing once the plant is up and operating, and those that govern prior to the operation date.

Baseload: The nature of geothermal power plants lead to the general requirement that geothermal plant contracts allow them to operate *baseloaded** at full available capacity. Three factors lead to this requirement: low variable costs (see Table 23.2), high plant availability, and high fuel/plant capacity factor.

Geothermal plants have low variable costs, which are those costs resulting from changes in plant output. Therefore, any dispatch order that reduces the output of the geothermal plant simply raises the cost of power during noncurtailed periods to recover the fixed costs. The geothermal power plant operates most effectively and at greatest economic efficiency at full baseload.

Geothermal power generation typically operates at a 95%–99% plant availability (hours capable of operation per year divided by hours per year). What this means is that as long as the plant has permission to operate, it will generate power, because it also has a high fuel availability. By contrast, wind generation also has high mechanical availability, but because the wind is not blowing all the time (no or low “fuel” availability), the plants do not generate, even though they are “available.” Although there is little difference in wind and geothermal generation plant mechanical availability, the capacity factors are very different because of the nature of the fuel supply.

Geothermal power plants typically operate at high capacity factor (MW h generated per year divided by the product of hours per year and plant capacity).† The high mechanical availability and the steady flow of energy from the production wells means that geother-

* The term baseload refers to the minimum amount of power continuously required by a utility’s customers over a 24 h or annual basis. A baseloaded plant is one that remains on-line at all hours of the day at maximum or near maximum output to serve that demand.

† The fuel-capacity factor is useful in addition to the plant-capacity factor, because after make-up drilling is completed, the power plant mechanical capacity remains essentially constant, but the resource capacity declines. Consequently, the power plant capacity factor drops each year, even though the power plant maybe converting essentially 90%–99% of the available fuel supply. The output and performance of the plant remains highly predictable, however, on both an hourly and annual basis.

TABLE 23.2

Comparison of Fixed and Variable Costs for Geothermal and Fossil-Fired Plants

Cost Category	Geothermal Power Plant with Wells and Piping		Fossil-Fuel Power Plant	
	Variable Cost	Fixed Cost	Variable Cost	Fixed Cost
Fuel costs to increase plant output from 50% to 100%	Geothermal royalties (1%–5% of gross power sales)	Drill wells and build pipelines, mostly before start-up of plant	Essentially entire additional fuel cost	Not applicable
Cost/savings to stop plant and restart later	Low cost savings other than royalties. Low additional costs other than ongoing fixed costs	May have to vent steam to air rather than shut-in wells, and expose wells to thermal cycling damage	Fuel savings when stopped. Fuel costs to keep warm or cold start plus start/stop related maintenance costs	Not applicable
Fixed operating personnel costs (number of MW that carry cost of each staff person)	Not applicable	10–13 people for 0–15 MW = 1–1.5 MW/person 13–18 people for 40–120 MW = 2–8 MW/person	Not applicable	15–20 people for 250–550 MW = 13–36 MW/person
Fixed capital costs	Not applicable	\$1400–\$3000 per kW of capacity	Not applicable	\$700–\$1300 per kW of capacity

mal power plants as a class are unsurpassed by any other generation technology, whether renewable, fossil-fueled, nuclear, or hydro.

Seasonal Pricing: Another contractual provision in many geothermal power supply contracts is for the utility to have seasonal pricing. For example many California and Nevada geothermal contracts have prices that are higher in the summer and lower in the spring and fall. This provides the geothermal plant operator incentive for the power plant to be online in the peak summer hours, when replacement power is the most expensive for the utility. The reliable and predictable summer peak output is one of the advantages for a utility (and its ratepayers) to have available energy sources using biomass, geothermal power, and solar generation. Because summer peak power spot market costs and the cost for simple-cycle gas turbine generation can commonly rise to over \$150 per MW h in the summer, the reliable fixed-cost prices of nonintermittent resources reduce the cost of meeting summer peak loads.

23.3.4.3.4 Contract Provisions for New Geothermal Development

Unique contract provisions are advantageous for *development* of new grassroots geothermal power plants as opposed to the expansion of an existing geothermal power plant. The expansion of an existing geothermal power plant is based on the historical performance of the geothermal resource. Therefore, operators of existing plants can commit to definitive start-up schedules and subsequent liquidated damages (LD) for missing those schedules. This is not so with new geothermal plants. Unique contract provisions can assist in the development of a grassroots geothermal power plant by recognizing and mitigating the risks, uncertainties, and costs of such development.

One unique challenge to the development of a grassroots geothermal power plant can be a contractual “chicken and egg” situation in which two events must occur, neither of which can occur before the other has been satisfied. The first of these is that it is very difficult and expensive, if not almost impossible, to secure funding for exploration drilling without a power sales contract. Geothermal energy, in comparison to natural gas or oil, is neither transportable nor does it have an automatic market after its discovery. Therefore, before risking the large capital for an exploration program, investors (whether as shareholders or venture capital) want a utility commitment to buy the geothermal power if a commercial resource is discovered. On the other hand, it is often not possible to sign a power sales contract without a proven resource, because the power sales contract may contain a large LD clause for failure to deliver the contracted power by a contracted date, and may include the requirement to post a large bond.

One solution for those utilities that would like to add geothermal power to their mix of resources to consider contracts with geothermal developers that recognize the risk, uncertainty, and cost in the discovery of a new geothermal field. Such contracts would not contain penalties for failure to discover a resource, but will assure the developer a market should their exploration efforts be fruitful. Provisions of the contract to protect the utility can include the following:

1. A price acceptable to the utility.
2. An expiration date 2–5 years beyond the date on which the contract is signed, by which time the developer must produce a resource discovery report or forfeit the contract.
3. A requirement for a notice of intent from the developer to deliver first power to the utility after 2–3 years.
4. The requirement for bonds or LDs for failure to deliver after the submission of the notice of intent.

The delay between the notice of intent and first power is of minor consequence for the developer, as the cycle time from resource confirmation to commercial operation will generally be 2 years or more, and the delay gives the utility the necessary time to time to plan for the delivery of the power. There are no statistics on success rates for grassroots exploration to power plant commercial operation under such a contract scenario, but it is likely that a utility that wants 50 MW of geothermal power should plan on signing resource discovery and power purchase contracts for between 75 and 100 MW from two or more exploration prospects.

23.3.5 Economic Access: Power Plant Cost

Power plant costs comprise two elements: the capital cost and the operating cost.

23.3.5.1 Capital Costs

Capital costs vary according to four major variables:

1. *Resource temperature*: Higher temperature resources have lower \$/MW capital cost. Table 23.1 indicates the first benefit of higher temperature, namely lower flows, and hence, fewer wells and smaller components are needed. However,

the reduction of the size of the heat rejection system (condenser and cooling system) required per megawatt of capacity is also of great value. Higher-temperature fuel sources require much less cooling than lower-temperature sources. This is illustrated by a comparison of fossil-fuel power plants and geothermal plants in which geothermal power plants may have a heat rejection system eight times as large per megawatt as that in a combustion-turbine combined cycle plant.

2. *Power technology*: Power plants using a binary process generally have a cost several hundred dollars per kilowatt higher than power plants using only steam turbine technology. However, this is not universally true, and binary power technology plants have won numerous open bids around the world over suppliers of steam turbine technology.
3. *Wet or dry cooling*: Steam flash power plants generally use wet cooling with the water supplied by the condensed geothermal steam. Binary power plants can use wet or dry cooling. In most climates, wet cooling gives an advantage in net plant output over dry cooling, and also causes less capacity degradation than dry cooling in the peak summer hours. Because these peak hours are generally the utility's most expensive hours, wet cooling offers utilities a benefit. However, there is often not water available (neither condensed geothermal steam nor meteoric waters) for a binary power plant cooling system, and therefore, dry cooling is used.
4. *Plant size*: Larger plants and larger machines are less expensive per kilowatt of installed capacity than smaller plants and smaller machines. This occurs both because of the general economy of scale of machine size, as well as a distribution of fixed costs (e.g., civil engineering, roads, site preparation, instrumentation, insulation, and paint) over a greater plant size.

23.3.5.2 Operating Costs

Geothermal plants have low variable costs, which are direct costs resulting from changes in plant output. Fixed operating costs are those costs that exist even if the power plant is not operating, e.g., personnel and interest on loans. If output is reduced, the staff costs are the same, the fuel costs are the same (i.e., the amortization of the well costs), and chemical use changes negligibly. Thus, there are no cost savings with a reduction in geothermal plant output other than the royalty paid to the holder of the geothermal rights. For all intents and purposes, a geothermal power plant has only fixed operating costs. Table 23.2 illustrates the difference in variable costs between a geothermal plant and a combined cycle plant using a combustion turbine. The table illustrates why baseloaded operation is optimal for geothermal power plant cost structure whereas a dispatchable operation fits the cost structure of fossil-fired power plants.

Not only does reducing the output from a geothermal plant not reduce operating costs, but throttling a geothermal turbine to reduce its power output actually has a negative effect on long-term operations, because it increases scale formation at the turbine inlet. Reducing the flow from geothermal wells on a regular basis, as would be required if the plant is not operated at baseload, can also induce damage in both the wellbore and the steel well casing in certain geothermal fields due to thermal or pressure cycling.

23.4 Exploration and Assessment of Geothermal Resources

Geothermal resources capable of sustaining commercial electrical production require specialized methods of exploration and assessment. To finance the high initial capital cost of a geothermal power plant and wellfield, the equity and debt providers must be assured that a geothermal reservoir is capable of sustaining the expected amount of energy production for a period of 20–30 years. Likewise, the purchaser of power, typically a local electrical utility, must have adequate assurances to justify entering into a long-term power purchase agreement (PPA). The geothermal industry has developed a suite of exploration and reservoir assessment techniques which provide the assurances required by all parties involved in a particular project.

Even when an active geothermal system is found, many geothermal discoveries do not lead to commercial development for a host of reasons, as discussed previously. This does not necessarily mean that a particular geothermal resource is forever noncommercial. Raft River (Idaho), Salt Wells (Nevada), and other resources under development in 2005 were discovered, drilled, and assessed in the 1970s and 1980s and were deemed noncommercial. Today, these resources are under commercial development, through a combination of improvements in exploration techniques, changing electrical power and natural gas markets, and advances in geothermal power technology.

Although this section is written from the perspective of geothermal development for power production, the same considerations and approaches are used for geothermal resources developed for direct-use applications.

23.4.1 Overview

The discovery of a geothermal resource and the assessment that it will be capable of sustaining 20–30 years of commercial production is a complex and costly undertaking, and has been the subject of entire books and many journal articles. This section is meant to provide a brief overview of the subject, much like learning geography while looking out the window of the space shuttle at the earth passing by below. In that brief glance, the shape of some of the continents would be largely visible, and one might be able to discern some forest, desert, and cities.

The process of geothermal exploration generally begins with the observation of surface manifestation of geothermal heat; for example, hot springs, fumaroles, or surface deposits of silica (sinters). However, some geothermal resources have no surface manifestations, and are discovered by accident when drilling takes place for purposes unrelated to geothermal development. Several commercial geothermal fields in the western United States have been discovered through the drilling of irrigation wells or mineral exploration holes.

From this initial surface exploration, detailed geoscientific work is undertaken to characterize and assess the size of the geothermal resource underlying the visible manifestations. After a promising resource is identified by the geoscientific study, wells must be drilled to prove the existence of the essential elements of a commercially viable geothermal resource, as described in Section 23.3.1, i.e., heat, permeability, and fluid. The critical first step in the drilling campaign is to drill a discovery well that is capable of producing commercial quantities of hot fluid. With the successful completion and testing of one or more additional wells, the process of exploration ends and the resource is considered “proven.”

Finally, the remaining wells for the development must be drilled. Once the geothermal resource is under production, pressure, temperature and chemistry of the

reservoir are monitored to evaluate and optimize resource production, and to make plans for further development (Section 23.5).

23.4.2 Exploration and Discovery

Surface geoscientific investigations are the first step in the process of discovery. These investigations include geochemical analysis of hydrothermal manifestations (hot springs, fumaroles, mudpots, etc.) and surface geologic mapping, including the type and extent of rock units, hydrothermal mineralization and surface expression of faulting, fracturing, and other structural features. Surface mapping techniques have been greatly enhanced by the use of remote sensing (satellite imagery). Together, these methods may indicate the ultimate resource temperature, provide clues as to the resource structure, and provide evidence of the vigor and extent of the resource. If a water sample can be obtained from a hot spring, the geochemistry, via various chemical “geothermometers,” can provide an indication of the maximum temperature to which the water was heated on its journey to the surface. However, the surface geoscience does not provide a good definition of the depth to the commercial geothermal reservoir, nor can it define its lateral extent or ultimate productivity. Not all hot springs are indications of commercial geothermal power resources, even if the geothermometers indicate a high-temperature origin of the fluid; the geothermometers can be erroneous, or, even if high-temperature water is available, it may not be producible at commercially viable flow rates.

The second step is geophysical investigation to map the lateral extent, depth, and distribution of permeability of the active geothermal system. These investigations and their objective may include those listed in Table 23.3.

The cost of conducting and interpreting a typical suite of geophysical surveys can vary greatly, depending on the individual characteristics of a particular exploration project. The total cost is dependent on the methods chosen, overall size of the area to be explored, the maximum depth to be explored, surface topography and the remoteness of the site. For example, an effective geophysical program to explore and define a small geothermal reservoir in Nevada may cost as little as \$150,000, whereas a program in the remote jungles of Indonesia may cost in excess of \$1,500,000.

TABLE 23.3
Geophysical Investigations for Geothermal Exploration

Exploration Tool	Objective	Indicative of
Resistivity	Detection of a clay cap, transition depth to high temperature mineralization	Convecting geothermal system that has deposited minerals to seal-off the top of the system
Seismic reflection	Faulting, structure	Flow paths (good drilling targets), structural block volume
Microearthquake monitoring	Identify active faulting and fracturing	Fracture permeability, fracture density, injection and production drilling targets
Magnetics	Loss of iron minerals	Convecting geothermal system
Geodesy	Active surface deformation	Rapid natural subsidence overlying active rift zones
Self potential	Map natural ground voltage	Shallow active hydrothermal systems
Microgravity	Faulting, mineral deposits	Flow paths, convecting geothermal system
Shallow wells	Temperature gradient	High heat flux, possible max T at depth, lateral reservoir extents

The third, and final, step is the riskiest and most expensive portion of the exploration program: the exploration drilling to determine if the resource is commercially viable. The exploration drilling program can involve both full-size development wells (commonly final casing size of 9–13 in. with reservoir hole diameter of 8–12 in.) and slim holes (final casing size of 6 in. or less and reservoir hole diameter of 5.5 in. or less). Slim hole wells have the advantage of costing only about two-thirds to three-fourths that of a full-size well, but have little commercial value, even if drilled into the heart of the resource. Depending on terrain, remoteness, road requirements, possible maximum resource temperature, depth, and other factors, the cost of the first exploration well will often exceed \$2,000,000, and may reach \$5,000,000 for deep or remote locations. Unexpected drilling problems can result in enormous cost overruns or the total loss of a wellbore and all the investment in it. Rare shallow resources may see exploration wells at less than \$1 million. Follow-up wells, if drilled at the same time, will save on the order of several hundred thousand dollars as a result of shared mobilization and construction costs.

Typically, three to eight wells will be required to prove and delineate an undeveloped geothermal resource, depending on the efficacy of the exploration program used to target the wells, the size of the first power plant, and other factors that cannot be predicted prior to drilling. Sometimes a nonproductive well will eventually be used for injection, so the investment may not be altogether wasted if a particular well fails to encounter commercial production. There are instances when, even after a multiwell exploration program, the resource that is discovered cannot be economically developed at all.

After the first (or, preferably, two or more) well(s) have been drilled and found to flow with commercial temperatures and flow rates, a long-term flow test and an interference test will be conducted. The budget for the flow test, with cross-country pipelines, staff, instrumentation, chemical sampling, interpretation, logistics, travel, and so on, can cost \$200,000–\$500,000, although long multiwell tests can incur greater costs.

The final stage of the geothermal reservoir assessment process is the analysis of the well and reservoir flow testing data. This analysis is done using established reservoir engineering techniques in which the behavior of the geothermal reservoir is numerically simulated at the proposed production rates for the expected duration of the power plant life, typically 20–30 years. The numerical model is used to investigate different production and injection strategies to optimize the resource development strategy. Positive results of this analysis are an essential factor for obtaining the debt and equity financing required for completing the wellfield and initiating power plant construction.

23.4.3 Risk of Exploration

A modest exploration budget of \$2–\$10 million, staged over the phases above, may suffice for many geothermal resources, but much greater budgets are well documented. Western GeoPower Corp. is a company seeking to commercialize the South Meager Creek Geothermal Project in British Columbia. Because they are a public company, various aspects of their development work are available in the public domain and can be used as a case study.¹³

The company raised over U.S. \$24 million for corporate expenses and a three-well exploration program in the remote area where the resource was located; the program was executed in 2004–2005. As of the time of this writing, the three wells had been drilled, but not flow-tested. These exploration wells were targeted on the basis of previously-drilled wells and surface exploration over the previous 20 years since the resource was first

identified. Temperatures in the three wells were announced to have ranged from 240°C to 260°C (460°F to 500°F), which demonstrates that the thermal basis for the targeting was sound. Western GeoPower has not yet announced whether the other elements of a commercial geothermal resource (permeability and water), per Section 23.3.1, have been discovered.

Regardless of whether or not a geothermal power plant is eventually developed at South Meager Creek, the exploration program demonstrates the potentially high risks and high costs of grassroots geothermal resource exploration. Not only was there substantial cost, but it has taken two decades for the exploration project to get to its current state.

Both geothermal and wind resources are renewable energy sources that must be converted at the location at which they are found, but it is much more difficult to demonstrate a viable commercial geothermal resource than a commercial wind resource. The cost of an array of wind exploration towers, the data collection, and analysis is miniscule by comparison with the cost of geothermal resource exploration. Additionally, the time to prove a commercial wind resource is much shorter. These cash and time costs not only affect the ease and extent of exploration, but the power price that must be obtained to pay for the exploration. The resource discovery process is by far the greatest disadvantage and barrier to expanding geothermal power generation. The costs and risks are why geothermal exploration is most often undertaken outside of the United States with strong government support or with government funding. In the United States, continued DOE support of exploration and discovery through cost-share programs will be necessary to bring significant quantities of new geothermal resources under development.

In spite of the barriers to exploration and discovery of commercial geothermal resources, they are discovered, developed, and electric power is delivered to the transmission grid. The remainder of this chapter is dedicated to these processes, from the resource (fuel) management issues to the power cycles.

23.5 Management of the Geothermal Resource for Power Production

Geothermal resource management initially seeks to ascertain the initial and long-term behavior of the geothermal reservoir so as to select the optimal power process for the particular geothermal resource, including the changing conditions that might be encountered over the first 20 years. Second, geothermal resource management seeks to design the geothermal resource development to meet short- and long-term economic goals that may include some or all of the following: minimizing invested capital cost in the wells and the power plant, maximizing the power plant installed capacity that the resource can support, and minimizing operating costs.

The complexities and issues of geothermal resource management have no equivalent in any other electric power generation technology, whether conventional or renewable.

- The fuel supply is located 2,000–10,000 ft below the surface, and may be more than 10 cubic miles in volume.
- The response of the resource to development plays a huge role in the overall economic and generation performance of the resource, but the details of the response are largely unknowable until after the resource is under full production for a number of years.

- The “fuel supply” almost invariably changes with time, and as a result, the power plant either must be operated off-design or modified to meet the new conditions.
- Through much of the resource life, make-up wells will need to be sited and drilled to maintain adequate geothermal energy supply to the power plant, which is a combination of flow rate and pressure or temperature.

Although the management of natural gas and oil fields face many of the same issues, fossil-fuel power plants are seldom tied to a single and solitary gas or oil resource.

In this section, the issues involved in managing the geothermal resource, and how the characteristics of the fuel supply interact with the design and operation of the power plant, will be examined. Case studies illustrate successes, changes, and occasional failures in geothermal resource management.

Section 23.5 begins with the large goals, examines some of the subgoals, and ends with the beginning—the characterization of the geothermal resource for the selection of the power process.

23.5.1 Goals of Resource Management

Geothermal energy production is the science and technology of heat recovery. At commercially-significant extraction and power generation rates, the heat extraction rate from the production wells is almost always far greater than the natural heat addition rate that created the geothermal resource. The energy balance is closed by extraction of the heat-in-place in the volume of the reservoir, i.e., cooling of the geothermal resource.

$$\text{Heat produced out of the geothermal system per year} - \text{Natural heat inflow to geothermal system per year} = \text{Cooling of geothermal system per year.}$$

The geothermal resource volume is large, however, so the cooling is a long, slow process that allows the geothermal resource to be productive for many decades. (Some of the issues of renewability and sustainability in geothermal power are addressed in Section 23.3.4.) Therefore, the overall strategic goal of resource management is efficient heat mining (cooling) of the geothermal resource. Four of the most important resource management subgoals include (1) minimizing the capital cost of the development, (2) residual brine management (if applicable), (3) injection placement to enhance production, and (4) geothermal fluid monitoring and control, including chemistry, rate, pressure, and temperature.

23.5.1.1 Minimizing Development Capital Cost

To achieve heat recovery from the resource, geothermal fluids (steam or brine) must move through and be heated by the rock. Boiling is the most efficient mechanism, because of the high heat transfer rates of vaporization and the high heat capacity of steam. The native, in-place water is the primary mechanism for many years of the production. Geothermal reservoir rock porosities are most commonly in the range of 3%–10%, but may be as high as 20% in sedimentary systems.

As discussed in Section 23.3, matrix flow of fluid through the bulk rock occurs at only very low rates, so much of the heat of the reservoir volume must transfer by the much slower process of conduction through the rock to the fracture surfaces, where liquid is mobile and heating or vaporization can more readily occur. (This also explains part of the difficulty of creating the HDR/HFR geothermal resources of Section 23.3.2.) The native-state fluid

mass is not sufficient to achieve the goal of heat mining the reservoir. This can only be achieved by flowing supplemental water through the resource. Therefore, the placement of the residual geothermal fluids through the injection wells can have a large effect on the overall capability of the field over the long term. From an ideal heat transfer perspective, the optimal development would be to have many production wells drilled into the hottest areas of the field, with many injection wells ringing the production area to sweep heat and provide pressure support to the production wells. Unfortunately, the need to manage and limit the capital cost of the development intrudes on this Utopian development, and forces geothermal resource developers to seek compromises to the ideal.

Figure 23.2 illustrates a deliverability curve for a hypothetical well producing a mixture of steam and brine. The curve segments are as follows:

- Segment A to B is an unstable flow regime (not all wells have this segment).
- Segment B to C is increasing flow due to greater differential pressure between wellbore and reservoir.
- Segment C to D is the same as B to C, except for an increasingly dominant frictional pressure loss in the wellbore or fractures feeding the wellbore that reduces flow rate at a faster rate than in the segment from B to C.

In the Utopian geothermal development, the well would be operated somewhere just to the right of point B, because point B has the highest available energy per unit mass, and will therefore allow the greatest cumulative power generation over time from the resource. However, there is not much flow at point B, and thus a large number of wells and long lengths of connecting pipelines would be required. This is an unacceptable barrier to economic commercial development, in part because of the high capital, and in part because the additional generation occurs so far in the future that its present worth value is minimal, as discussed in Section 23.5.3. Therefore, a much more common optimization of the wells is to maximize the energy production from the wells (shown as point E on the dashed line in Figure 23.2); doing so minimizes the amount of money invested in production wells because of the high energy production per well. The disadvantages to

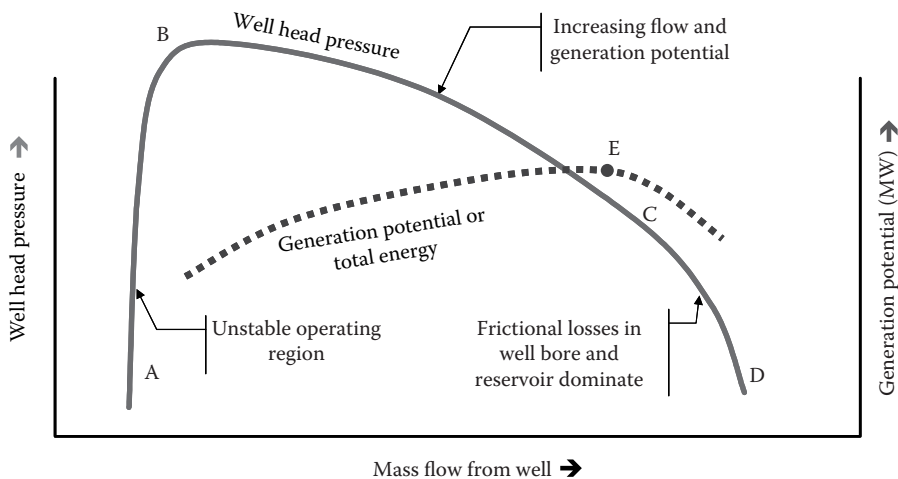


FIGURE 23.2
A hypothetical free-flowing geothermal production well deliverability curve.

this strategy stem from larger flows per megawatt-hour of generation that result in higher injection well costs (more spent fluid because of lower available energy per pound), higher power plant heat rejection costs (lower useful energy per unit mass), lower ultimate field capacity, and more make-up drilling sooner. The choice of the exact operating point on this curve is much more complex than a single number, but these two extremes (point B and point C) illustrate two of the important issues. A third issue is the provisions of the power sales contract. Power sales contracts that do not limit the output capacity of the field, and in which the field capacity can be fully developed in a short period of time, will tend to push the optimal operating point closer to point B because point B maximizes the ultimate field capacity. Those in which the power sales limit is much smaller than the capacity limit of the field will tend to push the operating point toward point C.

The knowledge of how a resource will respond to development can often be used to minimize the capital cost of the development. For example, at the Salak geothermal field in Indonesia, the reservoir modeling prior to production indicated that there was a region of the reservoir that would quickly evolve from producing a mixture of steam and brine to almost entirely steam production. Wells and a power plant were located in this area to minimize piping costs and to capture the benefit of lower brine handling and injection costs that resulted from the production of nearly dry steam.

23.5.1.2 Residual Brine Management

A large variety of operating practices has developed around the world over the use and disposal of brine, from primarily the two-phase (steam and brine) reservoirs. This is because in two-phase reservoirs, the reservoir pressure is primarily controlled by the steam pressure in the reservoir, whereas in primarily liquid reservoirs, the reservoir pressure is strongly influenced by the injection of the liquids back into the reservoir. A table of options and applications for use of the residual brine is presented in Table 23.4.

TABLE 23.4

Uses of Separated Brine in Worldwide Geothermal Power Operations

Option	Use of Separated Brine	Fields in Which it is Used ^a
1	Surface disposal	Wairakei, New Zealand (river disposal). Cerro Prieto, Mexico (evaporation ponds). Tiwi, Philippines (ocean disposal in early years of operation). Svartsengi, Iceland (The Blue Lagoon swimming, bathing, and health spa)
2	District or sensible heating	Nesjavellir, Iceland (indirect heat exchange with fresh water to supply district heating in Reykjavik)
3	Separated hot brine injected back in geothermal reservoir after a single flash due to silica saturation	Bacon–Manito, Philippines. Tiwi, Philippines (current operation). Salak, Indonesia
4	Separated hot brine used as source for binary power plant, and then reinjected	Mak-Ban, Philippines. Rotokawa, Kawerau, and Mokai, New Zealand. Brady Hot Spring, Nevada
5	Hot brine flashed multiple times for steam to power plant, and then brine reinjected	Salton Sea, California. Mt. Apo, Philippines. Hatchobaru, Japan
6	Minerals extraction, followed by reinjection	Salton Sea, California. (After a four-stage flash process, silica is precipitated to stabilize the brine for injection. The silica is disposed in landfill. A multiyear, multimillion dollar effort to recover zinc was abandoned in 2004.)

^a Examples, not a complete list.

In geothermal reservoirs, both heat mining and pressure support are managed by injection well placement. When this is accomplished according to objective, the results can be seen and monitored in the production well characteristics. Injection well placement is best accomplished in a manner similar to Goldilocks and the three bears: not too close (rapid cooling of produced fluids), not too far (no benefit), but just right (reservoir management).

When separated brine is disposed of through injection, the brine is generally injected into either the bottom of the reservoir or outside the reservoir. The location of the brine disposal is a difficult task, and in the history of many geothermal fields, brine injection locations have had to be adjusted at least once during the life of the field, usually because the injection wells are too close and cold-water breakthrough is observed. If the injection is ideally placed, it provides both pressure support for the production wells, as well as "mining" of the stored heat of the reservoir rocks as the injectate flows from the high-pressure zone of the injection to the low-pressure zone of the production well. However, if the injection well is too close or if the injection well encounters a highly permeable crack linking the production and injection areas, cold injectate can enter a production area, and quickly reduce the enthalpy (temperature or steam content) of the fluid produced by that zone. Therefore, in many instances, the preferred option is to inject some portion of the total injectate volume in steam/brine systems effectively outside of the geothermal reservoir, sacrificing the benefits of in-field injection, but also avoiding the potentially severe consequences of enthalpy loss at the production wells. As a result of the need to move injection distant from production, it is common in geothermal fields to have injection pipelines several miles long that carry the brine to distant injection wells.

As with almost every situation in geothermal resource development not tied to conservation of energy or mass, there are exceptions to the long injection pipeline option. The particular characteristics of the deep vertical fracturing of the Steamboat Hills (Nevada) geothermal resource have allowed a large-capacity injection well to operate without negative consequences to nearby production wells. In most geothermal fields, such geographic proximity would have resulted in cold water breakthrough to the production well within a very short time, perhaps on the order of days or months.

23.5.1.3 Clean-Water Injection Placement to Enhance Steam Production

The dryout of a region of a reservoir can occur when the water present in the region is no longer sufficient to remove the heat that is stored in the rock. At that point, the adoption of a new clean-water injection strategy can improve a number of the negative consequences of that dryout: specifically, loss of production, superheat, and acid gas production.

As dryout occurs, the temperature of the rock and the heat stored therein remain high, but there is no water to capture or transfer the heat. Production declines, and as it does, the pressure drops. Steam passing through rock that has a temperature higher than the saturation temperature of the steam's pressure becomes superheated. Superheated steam, upon mixing at the surface with wells that are not superheated, can evaporate the water from the brine flowing from other wells. If the brine rates are low enough and the evaporation is high enough, minerals will precipitate in the pipelines or separation vessels.

Superheated steam is also capable of carrying hydrochloric acid gases produced from certain rock formations out of the reservoir. Because the gases are extremely hydrophilic, they can only pass through the reservoir and into the steel-lined wellbore if no water is present. The hydrochloric gases are harmless to the steel as long as the steam is superheated. They can be removed at the surface by one of several methods: mixing with large quantities of water, mixing with smaller quantities of brine (which is naturally buffered

against changes in pH), or, in some instances, by caustic injection into the pipeline. However, if scrubbing of the hydrochloric acid is not accomplished before the onset of condensation, the rate of corrosion at the condensation point can be so high that the steel pipe wall can be thinned to failure in less than a year.

Injection into the reservoir can be used to solve all three problems. Adding water to the dried-out region through injection not only provides the means to increase production and heat-mining, it eliminates the superheat, and with the elimination of the superheat, also eliminates the acid gas production and pipeline scaling.

23.5.2 Resource Chemistry

The geothermal water and steam that are produced contain the chemical signatures of the rocks and processes (e.g., boiling) through which they have passed. Measuring the steam and brine chemistry is an important tool in the exploration process for new geothermal resources, in determining the brine processing requirements of the power cycle, and as an ongoing activity in developed geothermal resources for analyzing the response of the resource to production and for resource management planning. Examples include:

- In the exploration phase, geothermal water is collected from surface springs or fumaroles for clues as to the nature of the geothermal resource. For example, the relative concentrations of sodium, calcium, magnesium, and potassium in the water tell geochemists whether the fluid started out hot and then cooled (indicating a high-temperature resource elsewhere and indicating commercial geothermal resource potential) or whether the observed temperature of the fluid is close to the maximum temperature of the resource (not hot enough for power production).
- The extreme example of geothermal fluid chemistry is the Salton Sea (California) geothermal brine that contains more than 200,000 ppm total dissolved solids (TDS), or 20%, in its native state in the reservoir. The high TDS is a result of the high temperatures and the marine sediments that comprise the geothermal reservoir. The brine is produced and is flashed to steam at four pressures (~250, 125, 20, and 0 psig). In so doing, the brine becomes supersaturated with respect to silica and other minerals and salts, resulting in large chemical processing facilities necessary to prepare the brine for injection back into the geothermal reservoir. The silica treatment processes can either reduce the pH to prevent precipitation in the equipment or, alternatively, the silica can be removed from the brine by the controlled precipitation of the silica in tanks and vessels.
- Silica concentration is primarily a function of the reservoir temperature, but the concentration of silica determines how far the brine temperature can be lowered (how much energy can be extracted) before the onset of silica scaling. The power process is frequently designed to prevent silica from reaching saturation. In such cases, the operating point of the well is pushed to the left of point C in Figure 23.2, regardless of other considerations. The injection of acid or chemicals to inhibit the precipitation of silica can be used to lower the minimum allowable brine temperature and extract more energy from the brine. Another strategy to extract more energy from the brine is to use a binary power plant after the first steam flash. This strategy is discussed in more detail in Section 23.7.
- Tritium (an artifact of atmospheric nuclear weapons testing) detected in the geothermal steam or water indicates that young groundwater is entering the

geothermal reservoir as a result of geothermal exploitation. Native-state geothermal water, which has typically been underground for tens of thousands of years, contains no detectable tritium. Tritium from groundwater may occur in the geothermal reservoir as a result of intentional injection programs to replenish water, such as at The Geysers, or the result of unwanted cold water influx from the surface. At Tiwi (Philippines), the cold water in question has quenched several square miles of productive resource. The advancing surface water could be detected in the tritium concentrations long before the temperature indicated a cooling process was occurring at the well.

- Increasing salt concentrations and other mineral concentrations indicate the return of injected brine from flash steam plants. Again, this can occur long before a change in production temperature is measured. If the rate of cooling is negligible or small, these chemical signatures indicate successful heat mining through the injection program.

23.5.3 Barriers to Resource Management

In most human endeavors, the best results come by starting with the end in mind. This is true of geothermal resource development and resource management as well. By understanding the particular resource the wells can be placed to ideally collect and convert the geothermal energy stored in the reservoir. Unfortunately, in practice, the ideal placement of the production and injection wells may be either impractical or even impossible for three reasons: incomplete information, capital limitations and sunk costs, and economic impetus.

23.5.3.1 Incomplete Information

First, many aspects of the geothermal resource are simply not known in the early stages of development of a new resource. Such incomplete information includes whether cold water from injection will short-circuit to the production wells, how strong the natural influx to the system will be, or where that influx will actually occur. In fact, the exact area and volume of the resource is commonly not even known until 10 years or more after the onset of production.

The Geysers facility illustrates this point. The unit 1 power plant went into operation in 1960, and the final power plant—the J.W. Aidlin Plant that began operation in 1989—brought the total installed capacity to 1890 MW, although deratings and retirements commenced soon thereafter. However, reservoir information and analysis was not complete, even in the mid-1980s. Two additional power plants were ordered and never completed because there was insufficient steam for their operation. Therefore, the geothermal resource management strategy is dynamic and evolving from the beginning. As more information becomes available about the resource over time, the knowledge of the resource improves, and the decisions about its management more informed.

A surprising and interesting example of this evolving knowledge has occurred in recent years at Larderello, Italy. Almost 100 years after the start of power generation, it now appears that the historical development in the Larderello area is at the top of a much larger and deeper regional system, perhaps 400 km² in size and between 3,000 and 4,000 m deep (10,000–13,000 ft). Plans have been announced to begin drilling and developing this deep hot resource in 2007 with 11 deep-production wells.⁸

23.5.3.2 Capital Limitations and Sunk Costs

There may be capital limitations and sunk costs that must be taken into account in well placement decisions. For example, suppose that it would be ideal to inject the cooled brine to the north of the power plant, but an unsuccessful exploration well will serve as an injection well to the east, saving over a million dollars. In one development in Indonesia, a well that was targeted as an injection well was found, after being drilled, to have a very large production capacity. However, pipelines were already under construction, the well was distant from the power plant, and production well capacity had already been essentially completed. What was needed for plant operation was injection capacity, so the well was used for injection. Time and capital constraints forced the decision, even though it was against the ideal resource management strategy. This example also illustrates the first point about incomplete information at the onset of the project.

23.5.3.3 Economic Impetus

The third driver for well placement decisions is the economic impetus. The economic test criterion used for investment decisions is discounted cash flow, in which decisions are based largely on achieving the highest net present value or the lowest net present cost in which all costs and earnings are brought back to the present at an assumed discount or interest rate. For public (government) development, that discount rate may vary from 5% to 15%; for development by private corporations, the rate for normal equipment and operational investments is typically 9%–12%, but for resource development issues is not uncommonly as high as 20%, due to the greater risk and uncertainty. The lower the discount rate, the more important future performance is to the total value of the project, as viewed by “today’s” decision makers. The converse is also true, and in fact dominates spending decisions for resource management at the start of the development. Suppose that the publishers of this text elected to develop a new geothermal power plant named “CRC #1.” They are sharp businesspeople, and are told by their resource development experts that there are several resource development options that can be pursued. Both strategies produce the same income with the same expenses for the first 15–20 years. However, the second strategy will produce significantly more value in the outer years because of better resource management. They perform a discounted cash flow calculation and develop in Table 23.5. The conclusion that is reached

TABLE 23.5

Amount of Spending that can be Justified “Today” for a Savings or Earnings of \$10 Million in the Future

Discount Rate Scenario	Economically Justified Spending “Today” at a Discount Rate of				
	0%	4%	11%	15%	20%
\$10 Million value in 15 years	\$10,000,000	\$5,552,645	\$2,090,043	\$1,228,945	\$ 649,055
\$10 Million value in 20 years	\$10,000,000	\$4,563,869	\$1,240,339	\$611,003	\$ 260,841
\$10 Million value in 30 years	\$10,000,000	\$3,083,187	\$436,828	\$151,031	\$42,127
\$10 Million value in 50 years	\$10,000,000	\$1,407,126	\$54,182	\$9,228	\$1,099

is that, for an investment as risky as resource performance in 15–20 years, the corporation will use a discount rate of 15%–20%. The table shows that the resource managers have a budget to optimize the resource development of between \$0.25 and \$1.2 million (the highlighted area in Table 23.5) to create \$10 million of value. In most cases, this will not be sufficient to implement an enhanced resource management plan. At the extreme, in looking at resource development strategies that would create the \$10 million value in 50 years, the table shows that less than \$10,000 of additional spending today can be justified at a 15% discount rate and only \$1,000 at a 20% discount rate. In short, there is virtually no economic impetus for resource development decisions that yield a benefit after 50 years.

Even if not implemented at the onset of the resource development, some resource management strategies will be able to be implemented at a later date. However, other decisions are irreversible, such as inefficiency in the conversion of the resource to electrical power. Conversion inefficiency directly reduces the total generation from the resource (megawatt-hours), but may also ultimately lead to a reduction in the installed capacity of the field (megawatts). While this is clear from the beginning, if such additional generation does not occur for 30 years, Table 23.5 demonstrates that the generation is of inconsequential value at the time of initial development. A scenario under which this occurs is where the generation contract for the geothermal field is limited to a given output.

Suppose that a PPA is for 100 MW average over the year. With the high-efficiency power plant, the resource is forecast to provide 100 MW for 40 years before beginning its decline. With the lower-efficiency (and less expensive) power plant, the plant is forecast to be able to maintain 100 MW for 25 years. In terms of today's decision making, the value of the additional 15 years of full-capacity generation are of marginal value, and the economic calculations will almost certainly show that the power plant and resource strategy with the lower capital cost is the preferred investment strategy "today."

The same calculations also apply to the efficiency of nonrenewable natural resources, such as natural gas and petroleum. Straight discounted cash flow calculations provide little incentive for the conservation of depletable natural resources for a time frame greater than 20 years. However, at the end of the 20 years, the impact of the inefficiency can be very large on the future value.

23.5.4 Resource Characterization

An early task of the geothermal resource management team is to characterize the resource based on the exploration and initial development wells. The characteristic of the fluids that will be produced from the well must be determined: steam only, brine and steam, or brine only. Subsequent tasks must address the design issues within each resource type.

Table 23.6 provides a list of some of the design issues and options that derive from this first basic resource characterization. The characteristics of the wells will determine the options for the power cycle, and from that the configuration of the surface facilities. As illustrated in Table 23.6, there are three types of resources that are used in the two dominant power plant types: steam power plants and binary power plants, as discussed in detail in subsequent sections.

TABLE 23.6

Geothermal Facilities Design Parameters Resulting from the Geothermal Resource Type

Wells Flow: Design Issue	Steam Only	Steam and Brine Two-Phase Flow	Brine Only
<i>Representative fields</i>	Geysers, California Lardarello, Italy Kamojang, Indonesia	Cerro Prieto, Mexico Coso, California Wairakei, New Zealand Mak-Ban, Philippines Miravalles, Costa Rica	East Mesa, California Steamboat Springs, Nevada Raft River, Idaho
<i>Production well design</i>			
Production of fluid to surface by	Free flow	Free flow	Pumped
Well design—flow	Minimize pressure drop (velocity) to maximize flow	Maximize flow, but must maintain high velocity to lift liquid out of the well	12-in. inside diameter (min) to deepest expected pump installation depth
Well design—pressure	Maximum reservoir pressure (generally less than 600 psi, and falls with time)	Saturation pressure at maximum temperature. (generally less than 400 psi, but can be 2000 psi.)	Often less than 200 psi at surface and less than 600 psi for pumps at the zero flow condition
Production pump parasitic load	Not applicable	Not applicable	Usually between 5% and 8% of gross generator output, but can be as high as 15%
<i>Surface facility design</i>			
Production pipeline network	Steam only to power plant. Build with large cross-section for low pressure drop. Condensate knockout pots must be provided	Two-phase flow to separators requires high velocities and pressure drop to prevent slugging. After separator, two pipelines of single phase steam and separated brine	Single-phase liquid flow to binary power plant or separator. Size pipe for low pressure drop. Water hammer at start-up is an issue
Brine steam separator	Not applicable	Required. installed vessel cost greater than \$600,000 per 10–20 MW	Only required if steam turbine to be used
Steam washing system to remove impurities and condensate	Usually required on a continuous basis. Installed cost greater than \$500,000 per 10–90 MW	Same	Not required
<i>Power plant design</i>			
Power plant location	Center of initial and long-term production. Usually accomplished	Same goal. Not uncommonly, the center of production (make-up well drilling) moves away from the power plant site as new resource is discovered, resulting in large pipeline costs and available energy loss	Same goal. Usually accomplished, as these tend to be smaller and better-defined geothermal resources

(Continued)

TABLE 23.6 (Continued)

Geothermal Facilities Design Parameters Resulting from the Geothermal Resource Type

Wells Flow: Design Issue	Steam Only	Steam and Brine Two-Phase Flow	Brine Only
Steam turbine	Single pressure entry Size from 5 to 125 MW. Most commonly 25–75 MW	Size as per other geothermal steam turbines 1. Single inlet pressure, as for steam only resource 2. Multiple inlet pressures on same or multiple turbines (needs multiflash design of brine system)	Not commonly used Size is less than 40 MW
Binary power plant Size has historically been 1–8 MW per turbine/ generator set. Since 2004, size has increased to 20 MW/T/G	Not applicable	1. Can be used for recovery of energy from brine instead of multiple flashes 2. Can be used instead of steam turbine on small plants	Most commonly used instead of steam turbine
Geothermal combined cycle power plant	Has not been used in practice, but could be	1. Steam turbine with binary plant used as steam turbine condenser 2. Brine energy recovered in separate binary plant	Not applicable
Effect of brine chemistry on total available energy	Not applicable	Determines lowest temperature to which brine can be flashed without scaling Temperature can be lowered by adding acid	Determines the lowest brine temperature at discharge of binary plant heat exchangers to avoid scaling. Acid addition lowers temperature
Condenser	Generally sub-atmospheric. Direct contact of cooling water and steam, unless H ₂ S abatement is required, then shell and tube often used	Same, unless a geothermal combined cycle unit is used	Same for steam-only plants Generally supra-atmospheric for binary plants
Condenser gas removal equipment	Large to handle 0.5%–8% NCG in steam. Sized for NCGs and air infiltration Creates large parasitic steam or power load	Same Not applicable for geothermal-combined cycle units	Small. Sized only for minimal breakdown of hydrocarbon and air infiltration
Cooling System	Water-cooled, usually uses condensed steam as make-up water for cooling tower	Same for steam turbine plants Most often air-cooled for binary and geothermal combined cycle plants	Usually air-cooled condenser, unless surface water or steam condensate is available. Air cooling creates a large parasitic load and summer capacity loss

(Continued)

TABLE 23.6 (Continued)

Geothermal Facilities Design Parameters Resulting from the Geothermal Resource Type

Wells Flow: Design Issue	Steam Only	Steam and Brine Two-Phase Flow	Brine Only
Abatement of H ₂ S gas contained in geothermal steam	If required by regulators	Same	Not required for an all-binary system, as H ₂ S never leaves brine
<i>Surplus fluid design</i>			
Brine injection pipeline	Not applicable	Often long and expensive. Lengths of 0.5–1 mile from production area, or longer	Same as steam/brine system
Brine injection wells	Not applicable	Required, generally 1 well/10–40 MW (Often negative wellhead pressure)	Required, generally 1 well/3–10 MW (usually positive wellhead pressure)
Cooling water blowdown well	Usually required. One per power plant	Same. Should not mix with brine because of corrosion/precipitation if condensate is used in cooling tower Not required for geothermal combined cycle, as steam condensate is not oxygenated and can be mixed into brine	Not required for binary-only power plant
Fluid injection or disposal strategy	Inject cooling tower blowdown to regenerate steam (80% is evaporated in cooling tower). Supplement with fresh water injection. Water injection can minimize the production of hydrochloric acid gas with the steam	1. Generally, all brine and condensate must be injected into or outside of the active reservoir for reservoir management (heat mining, steam flow and pressure support) and environmental compliance 2. Rarely, some may be surface disposed to evaporation pond, river, or ocean to reduce capital and operating costs, but may be against best reservoir management practice	Always reinjected to maintain a high reservoir liquid level because of the production well pumps
Parasitic load of injection	Cooling tower blowdown pump load is very small, approaching zero	Generally pump load is small because of two-phase reservoir	Pump loads can consume 3%–7% of total gross generator output

23.6 Geothermal Steam Supply (from Wellhead to Turbine)

The first two columns of Table 23.6 discuss resources in which steam is produced from the wells, as opposed to the third column, in which only pressurized brine is produced. In almost every case, the steam that is produced from these wells is used in a steam turbine. In this section, the technology of handling geothermal steam from the wellhead to the geothermal steam turbine is discussed.

23.6.1 Overview of Steam/Brine Separation for Steam Turbine Supply

In the vast majority of geothermal fields in the world, a two-phase mixture of steam and brine is brought to the surface through the production wells. The brine must be separated from the steam before delivering the steam to the turbine. Separators of many different configurations are in use throughout the world, but the most common is a vertical vessel with a tangential entry to centrifugally separate the steam and brine. The level of purity of the steam varies between that which meets the geothermal standard of 0.1–0.5 ppm of chloride to over 10 ppm chloride.

Steam purity is typically measured by the chloride content of the steam condensate. However, the chloride itself is seldom intrinsically a problem to the alloys employed in a geothermal steam turbine. Rather, chloride is a convenient measure of the co-contaminants that are much harder to measure: mostly silica, but other minerals as well. Where these minerals are carried in the steam to the turbine, they may precipitate primarily on the first-stage stationary blades, reducing efficiency and eventually restricting plant capacity as well. The consequences and treatment of these mineral deposits are further discussed in Section 23.6.5.

With typical geothermal brine chloride levels, the separators need to achieve over 99.5% dryness to achieve the lower steam chloride concentration objective. The greatest challenge in doing so is to minimize the pressure drop through the vessel. The pressure drop has two negative consequences. The first is that the pressure drop results in an unrecoverable loss of available energy (reduced efficiency). Second, it results in a higher pressure at the wellhead, which reduces flow from the well (moving the operating point toward “B” in Figure 23.2), thereby requiring more wells (greater capital cost) to supply a given steam demand.

Where high-chloride (high-silica) steam is produced from the separators, steam washing must be employed to clean the steam before admission to the turbine, with a consequent parasitic steam loss as described below. While the commitment to, and investment in, steam purity at the discharge of the flash separation vessel varies from field to field, it is, in fact, better in practice to “put a fence at the top of the cliff, than an ambulance at the bottom.”¹⁴ In other words, the best practice in geothermal design is to first ensure high-efficiency separation (the fence) and not rely on the steam-washing system (the ambulance) at the power plant to prevent scaling of the turbine. Steam washing is defined and described below in Section 23.6.5.

Figure 23.3 illustrates a modern high-efficiency, low-pressure-drop geothermal steam separator designed by Sinclair Knight Mertz Consultants.* The two-phase mixture of steam and brine from the wells on the right enters the vessel through a special lemniscate entry (providing lower entrance turbulence than a tangential entry). The brine is separated

* Sinclair Knight Mertz Consulting, <http://www.skmconsulting.com>.

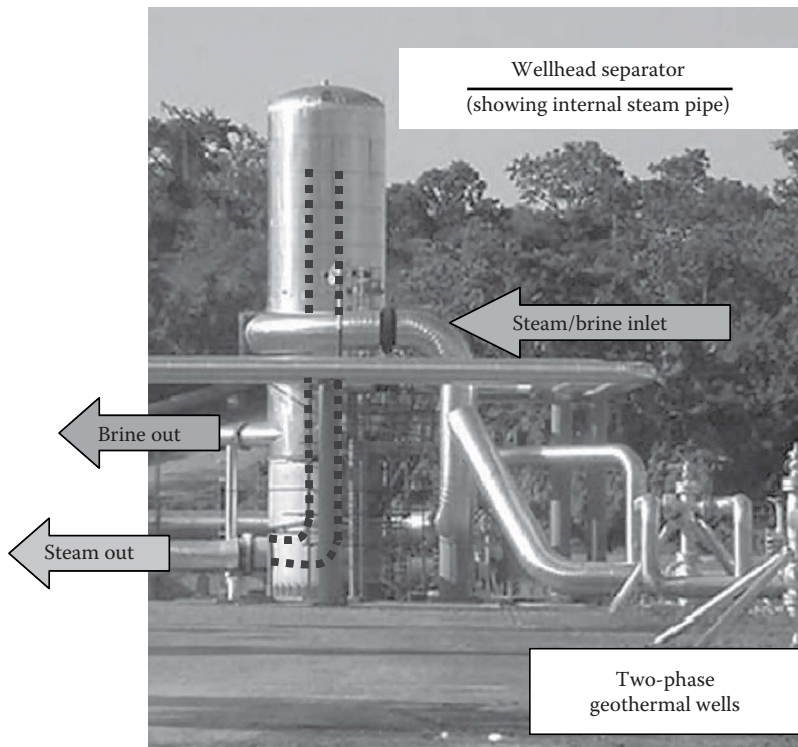


FIGURE 23.3
Annotated photo of a high-efficiency steam separator.

by the centrifugal motion of the steam flowing upward. The steam enters an exit pipe at the top, flowing downward to exit through the bottom of the vessel. The brine exits tangentially through the vessel side-wall below the inlet.

23.6.2 Multipressure Steam Flash and Separation

The number of steam pressures (flashes) that are taken from the brine varies from field to field. Each time the brine is flashed, additional energy is extracted from the brine by delivering a supply of steam to the power plant at a lower pressure, but the concentration of minerals in the residual brine is increased. Many fields use only one flash to avoid silica saturation of the brine. Multiple flashes can quickly drive the brine past the silica saturation point by the combined effect of cooling and concentration due to the extraction of steam. Where multiple-flash separation is used, it is usually limited to two flash pressures. At the CalEnergy* Salton Sea facilities, turbines are driven off of as many as three separate flashes, producing turbine inlet pressures of roughly 250, 100, and 10 psig (actual pressures vary among the various plants) with a final flash at atmospheric pressure that is vented, but a large silica precipitation facility is employed to desupersaturate the silica from the brine to prevent pipeline and injection well fouling.

Figure 23.4 illustrates a multistage steam separation and cleaning process from the well to the turbine inlets. Brine from the first separator is flashed to the lower pressure across

* CalEnergy Generation, <http://www.calenergy.com>.

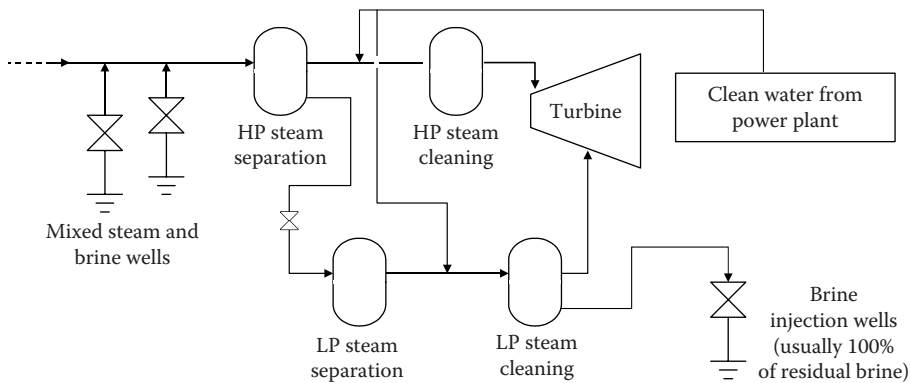


FIGURE 23.4
Geothermal double-flash process with steam cleaning.

the level control valve of the higher pressure separator. Commonly, each flow of steam is washed with geothermal steam condensate from the power plant before entering the turbine. Residual brine is injected.

23.6.3 Steam Pipeline Operation

Steam pressures used in geothermal power generation are often less than 120 psig at the turbine inlet, and the steam pipelines are sized to keep steam velocities low. Thus, on large-steam turbine installations, there may be many miles of 30–42 in. pipeline snaking along roads and hillsides to bring the steam to the power plant.

These long pipelines introduce various operational problems. The pressure drop that occurs over such long distances represents an unrecoverable loss of available energy.* The long distances and the transport of saturated steam can also lead to considerable condensation in the pipelines, especially during windy, rainy, or snowy weather. Condensed steam must be removed from the pipeline either in knockout pots with steam traps, or in the steam scrubbing vessel near the turbine inlet to prevent water damage to the turbine.

23.6.4 Steam Washing Prior to Steam Turbine Admission

After the steam is brought to the edge of the power plant from the dry steam wells or the separators, the steam at many facilities is washed by injecting steam condensate from the power plant condenser into the steam line. Typical flow rates look to achieve a total moisture of 1%–2.5%, or about 10,000–25,000 lb/h (up to 50 gal/min) for a common 55 MW power plant using about 1 million lb/h of steam. For each 100 lb of condensate injected into the steam flow, approximately 22 lb of steam is condensed. This condensed steam also helps to scrub the vapor, but the condensation is essentially a parasitic load. In a large facility, with poor steam quality, the wash water can represent as much as one megawatt of steam flow. The condensation and any injected water are removed in the power plant moisture removal vessel that immediately precedes the turbine.

* A wellhead separator pressure of 160 psia and a turbine inlet pressure of 110 psia are commonly seen. Assuming a constant condenser pressure of 101 mm Hg_a (4 in.), this pressure drop between wellhead and turbine represents up to a 7% loss of available energy.

The moisture removal vessel can be either a centrifugal separator or a vane-type demister. Pad-type demisters are not used because they are prone to scaling. The Porta-Test Whirlscrub® V Gas Scrubber* is used upstream of many United States and worldwide geothermal steam turbines to ensure low-moisture steam is delivered to the turbine.

When high-efficiency steam separation is successfully implemented for wells producing a two-phase mixture of steam and brine, steam washing is unnecessary on a continuous basis. Even if a high-efficiency separator is used, a moisture removal vessel is still required to protect the turbine from entrained water and/or solids that may originate in the pipeline between the separator and the moisture removal vessel.

23.6.5 Turbine Washing to Remove Scale Buildup

The consequence of insufficient steam purity and contaminant cleanup is that the turbine first-stage nozzle diaphragms will develop a layer of scale that restricts the steam passage. A schematic illustration of the turbine pressure and generation response to inlet nozzle scale build-up and removal through turbine washing is shown in Figure 23.5. As scaling occurs, the operator will allow the turbine inlet pressure to increase to maintain plant contracted output. As the scaling and pressure build up, the pressure limit of the turbine casing is eventually reached, and at that point, further scaling of the turbine results in reduction of the of turbine output due to decreased steam flow.

Turbine scaling occurs as the steam passes across the first-stage stationary blades. Entrained microdroplets of liquid with dissolved impurities evaporate as they cross the blades. The impurities are left behind, and scale buildup is the result.

Over the years, various experiments have been undertaken to remove the built-up scale with online turbine washing. Early efforts took the unit off-line and injected water at reduced rotating speeds. Later, low load injection of water into the turbine inlet was tried. Eventually, however, it became the widely accepted practice to inject water into the turbine at almost full-load to clean off scaling and restore design operating conditions. This practice has evolved in part by consideration of the actual operation of a low-pressure geothermal turbine. In normal operation, the saturated steam enters the turbine with condensation forming as the steam passes through the turbine to produce work. A typical

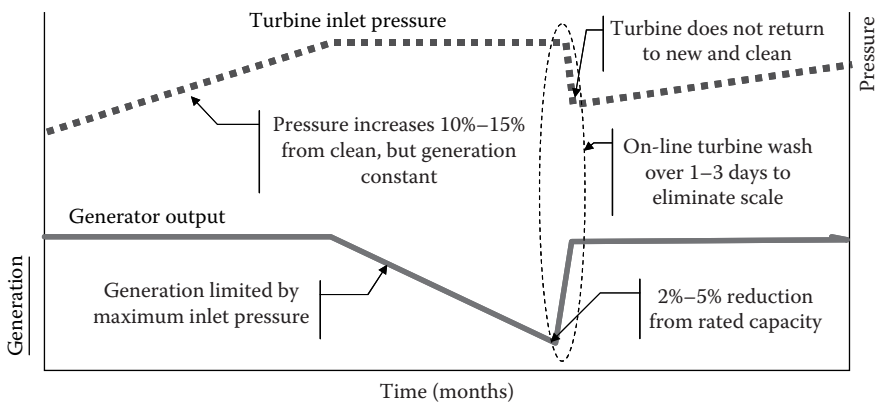


FIGURE 23.5

Response of turbine to scaling of the first stage nozzles and to an on-line turbine wash (schematic-not to scale).

* <http://www.natcogroup.com/>.

geothermal steam turbine operating around 120 psia inlet pressure and 2 psia condenser pressure (4 in. Hg, absolute) has an exhaust moisture of 14%–16% less interstage moisture drains. Therefore, adding 1%–2% moisture to the steam entering the turbine for short periods of time does not represent a large deviation from normal operating conditions.

23.7 Geothermal Power Production—Steam Turbine Technologies

23.7.1 Overview of Geothermal Power Generation Technologies

Two conversion technologies dominate the geothermal power industry: Direct steam turbines in an open-loop Rankine cycle configuration, and binary power plants using a hydrocarbon (pentane or butane) in the boilers and turbines in a closed-loop organic Rankine cycle (ORC). Geothermal combined cycle (GCC) units marry the two technologies. Ammonia/water binary power plant technologies have been proposed as a potential third power cycle option, with one such plant having been built as of 2006, and additional plants planned for operation in the coming years. Table 23.7 lists the 2004 breakdown of worldwide installed capacity.

Steam turbines represent 95% of the installed capacity of geothermal power plants worldwide, including the steam turbines of the integrated steam turbine and binary power plants. Binary power plant technologies, discussed in Section 23.8, represent the remaining 5% of installed worldwide capacity.

23.7.2 Steam Turbine Conversion

Geothermal power plants using steam as the motive fluid are open-cycle systems in which geothermal energy in the form of steam is admitted to the power plant, the energy is extracted, and the residual brine and condensed steam are then discharged from the plant to surface disposal, or injection, as described above. Gases contained in the steam are vented to the atmosphere. Because there are no fuel handling systems, boilers, superheaters, ash systems, or other systems related to the burning of fuel, geothermal steam power plants

TABLE 23.7

Breakdown of Geothermal Power Technologies Worldwide

Resource Type	Power Plant Type	Installed Capacity (MW)	Number of Units
Dry steam	Steam turbine	2460	63
Flash steam	Steam turbine	5831	210
Pressurized brine, including residual brine from a flash steam plant	Organic Rankine cycle (ORC)	274	154
Steam/brine	Integrated steam turbine and ORC, or ORC only	306	39
Pressurized brine	Binary-Kalina cycle (ammonia)	2	1
	Total	8873	467

Source: DiPippo, R., *Geothermal Power Plants: Principles, Applications and Case Studies*, Elsevier Advanced Technology, Oxford, U.K., 2005, pp. 404–405.

are very simple. It is referred to as an “open” cycle because the condensed steam is not returned to a boiler in a closed-loop circuit. The steam from the geothermal resource is delivered to the turbine inlet and may originate from either dry steam wells or from the separated steam of wells producing a brine/steam mixture.

There are three main steam power processes in use around the world: steam turbines without condensers (atmospheric discharge), steam turbines with subatmospheric condensers, and steam turbines integrated with binary power plants.

In a few installations worldwide, the steam turbine may exhaust directly to atmosphere. It is an inefficient mode of operation since 50% of the available energy is lost when discharged at atmospheric pressure. From an economic perspective, the loss of 50% of the available energy does not justify long-term operation of atmospheric discharge turbines, because with only the addition of a condenser and cooling tower, the output of the facility can be roughly doubled with no additional resource development. However, atmospheric discharge turbines are sometimes used to prove reservoir capability because of rapid installation and low cost. In other places, they have been used when CO₂ content in the steam was over 5%. The use of atmospheric discharge turbines provides another example of the trade-offs that occur between long-term efficiency benefits and economic constraints as discussed in Section 23.5.3.

Geothermal combined-cycle steam/binary power plants also use a steam turbine that discharges at slightly above atmospheric pressure. However, instead of the steam venting to the atmosphere, the steam is condensed and energy recovered in the vaporizers and preheaters of the binary power plant. In this way, the energy of the exhaust steam is captured in the power conversion cycle of the binary power plant. More details on this process and advantages of this “combined cycle” technology are discussed in Section 23.8.4.

Most of the total installed worldwide geothermal generating capacity is from steam turbines in which the geothermal steam is admitted to the turbine at between 15 and 250 psia and exits the turbine at subatmospheric pressures of between 1.0 and 2.5 psia. The condenser is cooled by water from a cooling tower. The steam rate (pounds/kilowatt-hour) of the turbines is determined by the turbine efficiency (usually slightly better than 80%, including entrance and leaving losses), inlet pressure, and the condenser pressure. Figure 23.6 is a photo of the world’s largest-capacity (110 MW net rated output) single shaft geothermal steam turbine, in the Fuji Electric* shop before its installation at the Wayang Windu (Indonesia) geothermal power project. The design inlet and condenser pressures are 150 and 1.7 psia, respectively, using a 27 in. long last stage blade.¹⁵

23.7.3 Condensing Steam Turbine Process

Figure 23.7 is a general illustration of a dry steam power process. Steam is produced from the geothermal reservoir through multiple wells and delivered to the power plant through cross-country pipelines. The steam is always passed through a moisture removal vessel before entering the turbine to ensure that no particles or slugs of water reach the turbine. In many installations around the world, the steam is washed before entering this vessel to remove any impurities (see Section 23.6.4).

The basic process for a single-flash steam process is much the same, as shown in Figure 23.8. The key difference is that a two-phase mixture of brine and steam are produced from the geothermal reservoir to the surface. A centrifugal separator removes the steam for delivery to the power plant (Section 23.6.1), and the brine is injected back into the reservoir.

* Fuji Electric Systems Co., Ltd., <http://www.fesys.co.jp>.

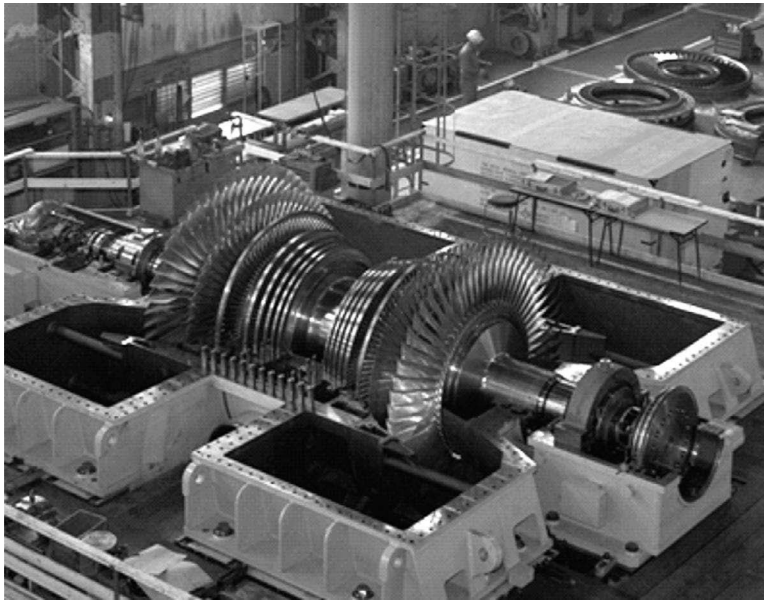


FIGURE 23.6
The Wayang Windu 110 MW geothermal turbine. (Photo courtesy of Fuji Electric Systems Co., Ltd., Tokyo, Japan.)

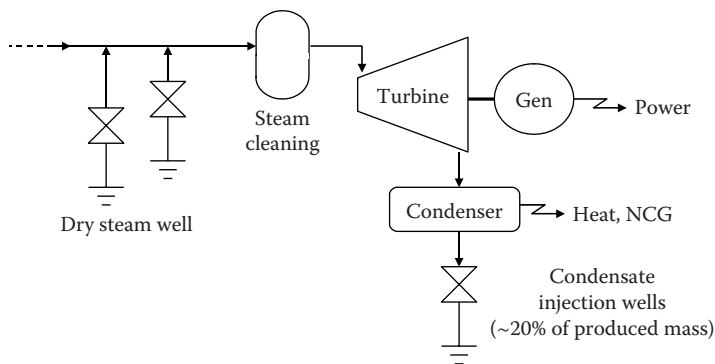


FIGURE 23.7
Geothermal dry steam power process (water cooled).

Figure 23.9 is a typical process-flow diagram for a geothermal power plant using a steam turbine and a condenser. In this illustration, steam is supplied from dry steam wells or a flash separation process at only one pressure (i.e., there is no low pressure turbine inlet). The steam is also used directly in the gas removal ejectors. Steam exiting the turbine is condensed in a direct contact condenser that is supplied with cold water from a cooling tower. The condensed steam and the cooling water are returned to the cooling tower. Approximately 80% of the steam to the power plant is evaporated in the cooling tower, and the remaining 20% forms the cooling tower blowdown. In hot arid climates, the amount of water evaporated can be greater than 100% during the hottest hours of the day and greater than 90% over a 24 h period. The steam contains noncondensable

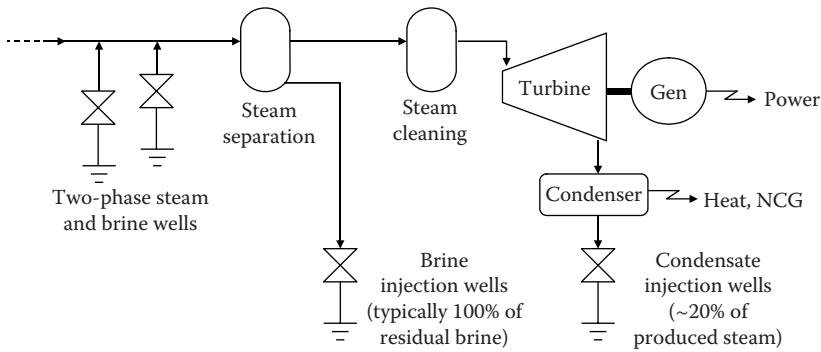


FIGURE 23.8 Geothermal single-flash steam power process (water cooled).

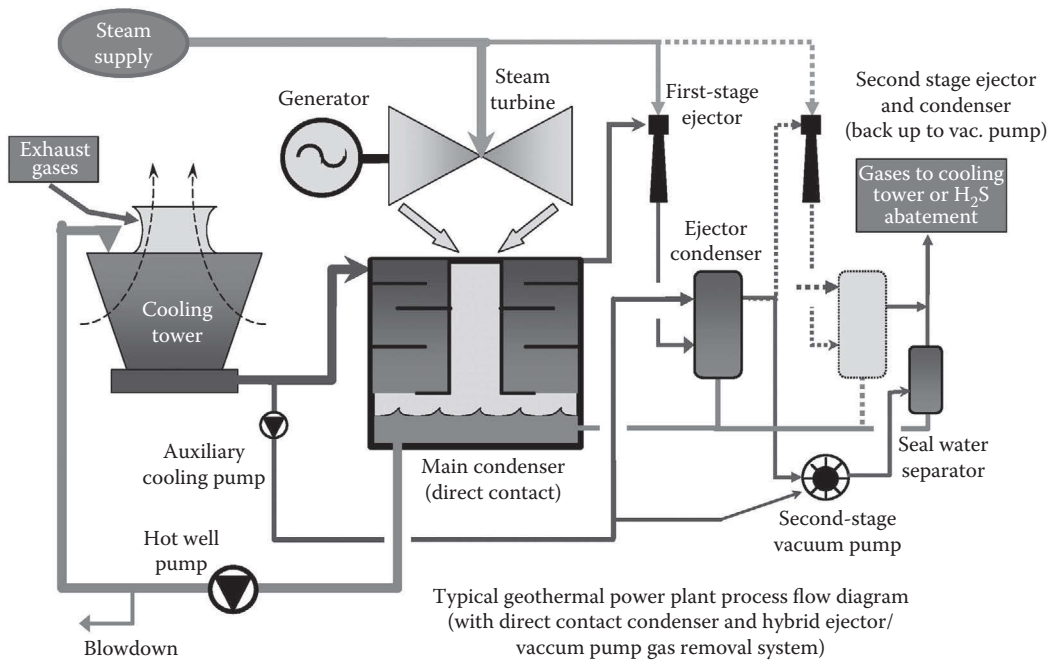


FIGURE 23.9 Geothermal steam power plant with direct contact condenser. (From Williamson, K.H. et al., *Proc. IEEE*, 89(12), 1783, 2001.)

gases (NCG), primarily CO₂, but also H₂S and other trace gases. These gases must be removed from the condenser to keep a low turbine exhaust pressure.

In Figure 23.9, geothermal steam is used as the motive force for the first-stage ejector to compress the NCG. The ejector steam is condensed in the direct-contact ejector condenser (the intercondenser), with the condensed steam and cooling water being returned to the main condenser. The NCG from the intercondenser is compressed in a second stage to atmospheric pressure either by the vacuum pump or by a second-stage ejector with an aftercondenser. The amount of steam used by the ejector and the size of the vacuum pump motor is related to the size of the power plant and the NCG content of the steam.

The vacuum pump is the primary system because it is more efficient than an ejector. The second-stage ejector is shown as a backup system because it has lower capital costs than a standby stainless steel compressor. Stainless steel is required throughout the NCG system because of the corrosiveness of moist CO₂ gases. The NCGs are dispersed using the cooling tower fans. If H₂S abatement is required, it is installed between the discharge of the second stage of compression and the cooling tower. The gas removal system is discussed in greater detail in Section 23.7.6.

23.7.4 Design of Geothermal Turbines

Geothermal steam can be a virtual chemical soup that varies from field to field. In most cases, the steam is saturated as it enters the turbine, and has a moisture content approaching or even exceeding 15% as it leaves the turbine for subatmospheric discharge turbines. The combination of scaling tendency, potential corrosivity, and high moisture content heavily influences the design of geothermal turbines.

Geothermal turbines generally use the same alloys as low pressure turbines in fossil fuel power plants, but with small variations in the alloy composition of the blades and rotors to enhance the alloy's ability to withstand the corrosive environment of geothermal steam. Detailed design can be just as important as alloy selection. For example, by using long-radius transitions and avoiding notches in the design of geothermal turbine parts, especially in the blade attachment areas, the stresses are more evenly applied and the blades and rotors are much less susceptible to cracking and failure.

The last-stage turbine blades are exposed to high moisture content, which requires methods to minimize blade leading edge erosion. Both erosion-resistant alloy shields and blade-surface hardening are used to resist the impingement of water on the last-stage blades. In addition to moisture, the specter of corrosion once again strongly influences the design of geothermal turbines at the last stage.

Last-stage blade size is a key element in the maximum size geothermal turbine that can be built. Geothermal turbine last-stage blades are designed for lower combined stresses than equivalent blades in conventional power plants. Because a large portion of last-stage blades stresses is proportional to the steam flow, this results in lower steam flows (per square foot of exhaust area) than in conventional power plants. High moisture content—the result of using saturated steam at the turbine inlet—tends to limit blade size to about 660 mm (26 in.) for turbines operating at 3600 rpm (60 Hz power), and its equivalent of about 765 mm (30 in.) for turbines operating at 3000 rpm (50 Hz power). The combined effect of the limited blade length and the reduced flow rate per unit area limit the maximum size that can be achieved in a geothermal turbine/generator. Thus, it is common to see two to three 55–70 MW turbines installed in a single powerhouse, rather than a single 200 MW unit. As discussed above, the largest two-flow geothermal turbine/generator (two rows of last-stage blades with steam inlet in the middle) ever built was Wayang Windu in Indonesia, with a rated net output of 110 MW.

23.7.5 Design of Heat-Rejection Systems

A second area affecting geothermal competitiveness is the heat-rejection system comprising the condenser, cooling tower, and cooling water pumps. The heat-rejection system of geothermal power plants can be up to eight times as large as a combustion-turbine combined-cycle power plant per kilowatt of output because of the low available energy per mass of steam at the inlet to the geothermal turbine. The heat-rejection system of any

geothermal power plant, whether for a steam turbine or binary plant, represents a very large capital cost burden for the project.

Where H_2S abatement is required, modern plants are most often built with shell-and-tube condensers. Thus, shell-and-tube is found in most steam condensers in United States geothermal power plants. Outside of the United States, the majority of geothermal steam condensers are direct-contact. In this system, steam exiting the turbine encounters either water sprayed from nozzles or droplets from trays. Heat transfer is much more efficient. The higher the gas content of the steam, the larger the advantage that direct-contact condensers bring. The disadvantages are that the cooling water is exposed to the CO_2 , H_2S , and ammonia, thereby providing substantial biological growth potential in the circulating water. Counteracting this is the high blowdown rate in a direct-contact geothermal cooling system.

Cooling tower make-up water comes from the condensed geothermal steam. In most circumstances, between 70% and 80% of the steam that enters the turbine is eventually evaporated in the cooling tower. The remaining 30%–20% steam is condensed and not evaporated, and is the source of the cooling system blowdown. Although the low cycles of concentration in the cooling water help control biological growth in the system, at the same time, the high blowdown rates result in it being relatively expensive to dose the water with biocides, since the biocides are quickly washed out of the system. Additionally, the presence of H_2S and NH_3 in the cooling water substantially reduces the efficacy of conventional biocide treatments. Cooling tower blowdown is most commonly injected back into the geothermal reservoir.

23.7.6 Geothermal Condenser Gas-Removal Systems

In addition to the challenges of mechanical design of the steam turbine and the size of the cooling and condenser system, the steam also contains large quantities of noncondensable gases (NCG). Average NCG compositions for two fields in the Philippines are shown in Table 23.8.

As a consequence of high NCG content in the geothermal steam, the gas-removal systems of geothermal power plants dwarf the gas-removal systems of conventional power plants. For example, the power plants at Tiwi, with a gas content of about 3%, can use either a two-stage steam jet gas ejector that consumes 110,000 lb of steam/h, or a hybrid system of first-stage ejector and second-stage liquid ring vacuum pump (consuming 33,000 lb of steam/h and 0.6 MW of electrical load). This is summarized in tabular form in Table 23.9. The two systems were designed for different gas loads, but both systems place a tremendous parasitic load on the plant. The two-stage ejector consumes an additional 11% steam over that used by the turbine, while the ejector hybrid consumes only 3.4% of the turbine steam, but also consumes 1.2% of the net electric output of the facility.

TABLE 23.8

NCG Amount and Composition in Steam at Tiwi and Mak-Ban, Philippines

Field	Percent Gas in Steam (wt%)	Gas Composition (mol%)								
		CO_2	H_2S	NH_3	CH_4	H_2	N_2	O_2	He	As, Hg
Tiwi	2.8	97.9	1.24	0.04	0.05	0.31	0.45	0.04	0.001	Trace
Mak-Ban	0.5	88.7	6.9	0.08	0.22	1.24	2.61	0.10	0.006	Trace

TABLE 23.9

Parasitic Steam and Power for Condenser Gas Removal at Tiwi, Philippines, for One 55 MW Unit

Option	Design Gas Load % Steam	Parasitic Steam		Parasitic Power	
		Ejector Flow (lb/h)	% of Turbine Flow	kW	% of Rated Capacity
Two-stage ejector	2.8	110,000	11.1	Not applicable	
Ejector hybrid	2.8	33,000	3.4	635	1.2

The higher the NCG content is above 1% in the steam, the greater the incentive to cut the parasitic steam usage with mechanical gas compression. This may take the form of ejector hybrids, as discussed above, or to eliminate the ejector altogether using an all-mechanical compressor. As in most aspects of geothermal design, a variety of solutions is employed.

Whatever the particular compressor system used, the additional cost of compressor systems is usually justified by the reduction of production wells required to supply the ejectors with steam, by an increase in the turbine steam supply at a geothermal field that is short of steam, or looking to maximize installed capacity. However, the electric parasitic load can have considerable negative implications on plant revenue, and for this reason, it is sometimes avoided on newer installations. The reason that the electric loads of mechanically driven compressors can have large impacts on revenue is found in the size limitation of the geothermal turbine, as discussed above. If the turbine size is limited (e.g., by last-stage blade size), then adding parasitic electric load reduces the power that can be sold, and hence reduces revenue. This is, once again, an example of the need to sacrifice efficiency in the short term to obtain higher net present value in a discounted cash flow calculation.

23.8 Geothermal Power Production—Binary Power Plant Technologies

Section 23.7 presented the technologies and strategies of the geothermal power plant that directly uses geothermal steam in the turbine. In Section 23.8, the use of geothermal steam and brine as an energy source but not as the power plant working fluid (that which drives the turbine) is discussed. The power plants that use these two fluids are known as *binary power plants*. All of the closed-loop working fluid cycles used in geothermal energy production, with a few exceptions, are Rankine cycles with a hydrocarbon as the working fluid.

23.8.1 Binary Power Plant Advantages

If one were to consider an idealized geothermal system in which the thermodynamics of pure water and steam played the dominant role in decision-making, there may not be a large role for the binary geothermal power plant. However, one does not have to delve too far into the reality of geothermal development before the advantages of the binary geothermal power plant in some applications become apparent. Some of these reasons have already been discussed in the preceding pages. Two of the most important answers to the question “Why binary?” are provided below.

23.8.1.1 Silica Solubility

As noted in several earlier sections, avoiding the precipitation of silica is a requirement for successful long-term geothermal well and pipeline operations. The precipitation of silica is a function of three factors: time, concentration, and temperature. Time is easily extended by the addition of acid to the geothermal brine, but for inexplicable reasons, this straightforward and easy solution is widely ignored. That leaves concentration and temperature as the factors within the control of the power process designer.

A brine that starts out at 450°F in the reservoir, when introduced into a steam separator at a pressure of 135 psia, will flash off approximately 12% of the initial water mass as steam. If there is a second flash at 35 psia, the total water mass flashed to steam is 21%. In such a flash process, two factors are at work increasing the potential of forming silica scale: mineral concentration in the brine and lower brine temperature. The physical properties that inhibit scale precipitation are that amorphous silica solubility is greater than the quartz silica solubility, and the often-slow kinetics of amorphous silica precipitation.

In contrast, the geothermal heat is transferred to the working fluid in a binary power plant without concentrating the silica by flashing off steam from the brine. Therefore, the temperature of the brine can be lowered further before the amorphous silica precipitation temperature is reached. Because of the silica solubility limit, the binary power plant can extract more energy from the produced brine (lower temperature) than a flash plant is capable of, especially where pH modification of the brine (acid addition) is not used. This can be true either on wells that are pumped and in which pressurized brine is delivered to the power plant, or after the brine has been flashed once and the binary plant is then installed to make use of the heat in the residual brine.

23.8.1.2 Lower Parasitics vs. Cycle Inefficiency

In a binary plant, a heat exchanger must be used to transfer the heat from the geothermal fluid to the power plant working fluid. As such, there is an inherent loss of efficiency from the process, as well as the capital cost of the heat exchanger itself. There is also a cycle feed pump, a significant power consumer that has no counterpart at all in a geothermal steam turbine power plant. On the other hand, in a plant directly using geothermal steam, the process of removing NCGs from the condenser is also an inherent loss of efficiency and a significant capital cost that does not exist in a binary power plant. How the two options balance out is dependent on site-specific factors, but conceptually, there are offsetting advantages and disadvantages, making the thermodynamic and economic balance closer than it might appear at first glance.

The exception to the offsetting advantages of binary plants versus direct steam plants occurs when the use of binary also forces the use of air-cooled condensers instead of water-cooled condensers and evaporative cooling towers. The water-cooled direct contact condenser has lower capital cost, higher efficiency, and lower parasitic loads than an air-cooled condenser system in all but the coldest climates.

23.8.1.3 Compactness

Binary power plants operate with working pressures much higher than those used for low-temperature flash power plants. This translates to smaller pipes and eliminates flash separators and scrubbers on pressurized brine systems; additionally, the condensers have smaller volumes because of the much higher condenser pressures of the working fluids.

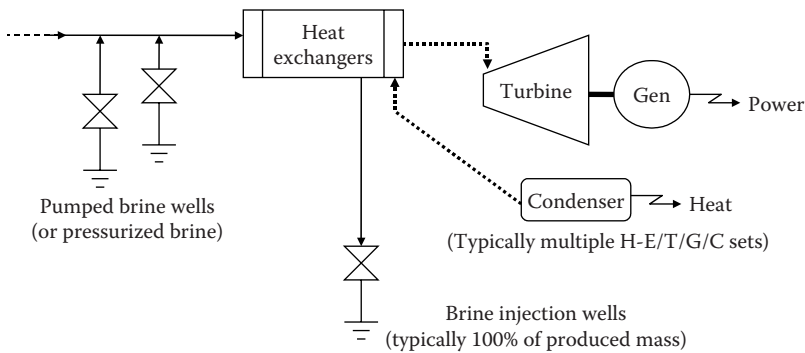


FIGURE 23.10
Pressurized brine binary power process (air or water cooled).

23.8.2 Types of Binary Systems

There are two types of binary power systems currently in use, both of which are based on hydrocarbons, and a third currently under development that is based on using an ammonia–water mixture as the working fluid. A fourth binary power system based on commercial refrigeration equipment is also under development, with a 200 kW demonstration project starting operation in Alaska at Chena Hot Springs in 2006. All of these power cycles are similar to that shown in Figure 23.10.

23.8.2.1 Subcritical Pentane Binary Power Plants

The geothermal fluids (brine or steam) are used to boil pentane as the power cycle working fluid in an ORC. The pentane passes through a turbine coupled to a generator and is then condensed. The cooled geothermal fluid is injected back into the geothermal reservoir.

The use of pressurized geothermal water from pumped wells in a subcritical pentane-based power plant is the most prevalent method to utilize geothermal resources from 280°F to 320°F. This system is also used to extract additional energy and power from the residual brine from single-flash flash plants all around the world.

Where two-phase geothermal fluid is available instead of pressurized brine, the two-phase fluids can be used in one of two ways. In some instances, both the steam and the brine are used in the vaporizers and preheaters. On larger facilities, it is more common to see a mixture of steam turbines and ORC plants. This type of integrated facility is made up of a pressurized brine facility of the type described above and a geothermal combined-cycle facility. In the geothermal combined-cycle facility, geothermal steam is first passed through a steam turbine and then condensed in a binary power plant.

23.8.2.2 Supercritical Hydrocarbon Binary Power Plants

Several hydrocarbon-based binary power plants have been built that use supercritical isobutane as the working fluid in an ORC. The pinch point is eliminated in the vaporizer in the supercritical regime. Although there is a theoretical thermodynamic benefit to a supercritical power cycle, the market has not embraced these plants because they tend to be much more expensive than the subcritical plants.

23.8.2.3 Ammonia–Water Binary Power Plants

Several different power cycles have been proposed based on ammonia-water systems. The potential advantages and disadvantages that all ammonia systems share over hydrocarbon-based binary systems include:

- Higher heat-capacity fluid means smaller heat exchangers and less parasitic load from the working fluid cycle feed pumps.
- Higher pressures result in smaller vapor equipment components.
- The boiling point changes with water/ammonia concentration, providing a boiling point glide instead of a single pinch point temperature, increasing thermodynamic efficiency.
- Condensation temperature changes with concentration, again providing a glide instead of a pinch point and a higher thermodynamic efficiency.
- The design of the heat exchangers is more complex to achieve the glides.
- There is a tradeoff of ammonia toxicity for hydrocarbon flammability.
- Ammonia has been used in refrigeration cycles for a century, providing a wealth of practical operating knowledge, even though few ammonia-based power plants exist.
- Ammonia vapor and steam have similar molecular weights (17 and 18 g/mol, respectively), which theoretically means that conventional steam turbines could be used, with little modification; if true, it would allow a rapid step up in turbine size to 30 MW or more and for the competitive bidding for supply of the turbine.
- Ammonia cycles are more complex, with more exchangers and cycle pumps.

In spite of the net benefit of the potential advantages, only one 2 MW geothermal plant has been installed to date, in Husavik, Iceland, using one of many Kalina cycle ammonia–water technologies. Plans to install additional Kalina cycle plants at Salt Wells, Nevada, and a 42 MW plant at Cove Fort, Utah, have been announced.

23.8.3 Binary Power Plants for Pressurized Geothermal Brine

Ormat Technologies* has developed a binary power plant approach, using subcritical pentane-based Rankine cycle technology, that commercially dominates the pressurized brine market. Because of that dominance, their technology will be used to illustrate the principles of the binary power plant design in this section. The technology has also been used in some instances in which the wells produce a mixture of steam and brine. These same basic power plants are now also being used to generate power from natural gas pipeline compressors exhaust gas waste heat.

Ormat started out designing and building small binary plants. One of their first installations was at the East Mesa field in California near the Mexican border. The ORMESA I plant began operation in 1987 and was comprised of 26 individual boiler/turbine/condenser units, with a total output of 24 MW. Since the East Mesa installation, Ormat has steadily increased the size of their units in the pursuit of both economy of scale and efficiency, and hence, lower installed cost (\$/kW). Initially, Ormat technology was based on a modular design, in which the economy of scale of a single large plant was traded off in

* Ormat Technologies, <http://www.ormat.com>.

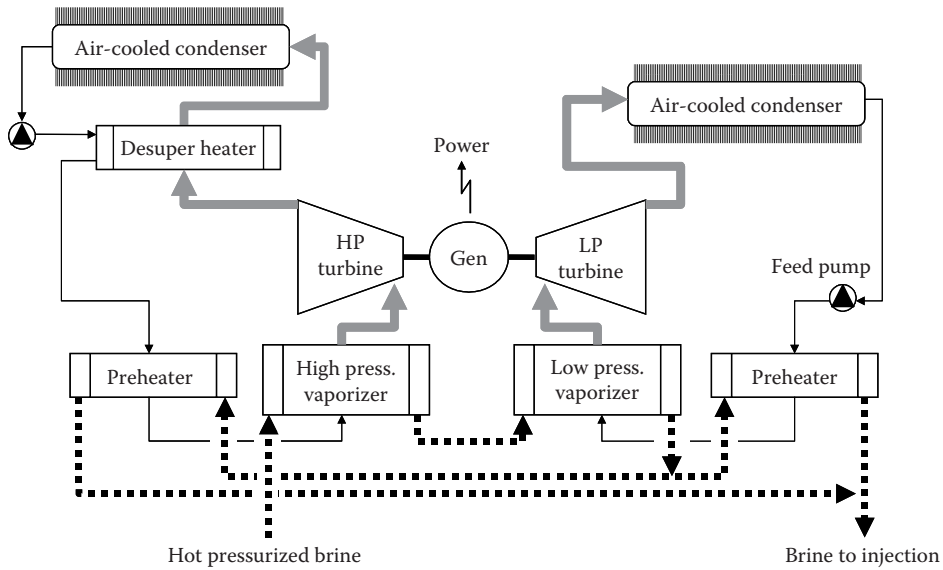


FIGURE 23.11
Ormat two-level subcritical pentane power cycle.

favor of the economy of scale of many smaller standardized, modular, factory-assembled skid-mounted units that required minimal field construction. Ormat now also offers a larger T/G unit comprised of a high- and low-pressure turbine coupled to opposite ends of a single generator, with the capability to deliver 20 MW to the grid.

The basic ORC process design used by Ormat is illustrated in Figure 23.11. The hot pressurized geothermal brine, whether from a pumped well or as residual brine from a flash plant, enters the high-pressure (HP) vaporizer to generate HP pentane vapor for the HP turbine. The geothermal fluid exits the HP turbine and enters the low-pressure (LP) vaporizer, which generates vapor for the LP turbine. From the LP vaporizer, the geothermal fluid splits between the preheaters of the LP and HP vaporizers. The pentane for the LP turbine is pumped out of the condenser to the preheaters and into the vaporizers. Pentane vapor passes through the turbine and into the condenser. The HP pentane cycle is similar, except that the pentane from the condenser is first pumped to a desuperheater located between the turbine discharge and the condenser.

Examples of where pressurized brine from the wells is used directly in the binary power plant include Soda Lake and Steamboat Springs in Nevada, as well as Heber and East Mesa in California.

Binary power plants have been installed to capture the waste energy of several geothermal power plant hot brine discharges. Examples include Brady Hot Springs (Nevada), Mak-Ban (Philippines), Los Azufres (Mexico), Miravalles (Costa Rica), and Wairakei (New Zealand). There also remain many locations where binary power plants could be installed on existing steam flash plants.

23.8.4 Integrated Steam Turbine and Binary Power Plants

In other locations, steam turbine(s) and binary power units have been combined into a single facility. Integrated facilities are installed at fields where the geothermal fluid is produced to the surface as a mix of steam and brine, rather than pumped and pressurized brine.

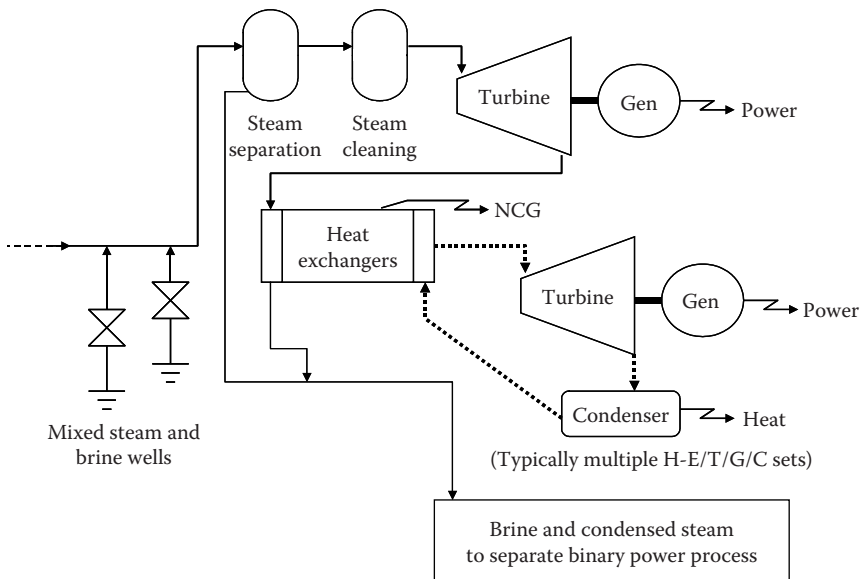


FIGURE 23.12
Integrated brine steam combined cycle binary power process (air cooled).

The largest integrated facilities are those of Ormat Technologies, and are based on the integration of the pressurized brine ORC and what is referred to as GCC plants. See Figure 23.12.

23.8.4.1 The Geothermal Combined Cycle Process

The brine/steam mix flows from the production well to a separator. Brine from the separator is directed to a pressurized brine binary power plant, as described above.

Steam from the separator is cleaned and delivered to a steam turbine. The steam turbine faces the same inlet steam quality issues as were discussed in Section 23.8. However, because the turbine discharges at near-atmospheric pressures, the previously discussed concerns about last-stage blade length and moisture-induced erosion are eliminated. With the elimination of these two issues, cycle optimization of the geothermal resource can be undertaken without a cap on the maximum turbine inlet pressure. The available mass and the optimized pressure of the steam result in varying steam turbine sizes and outputs at different geothermal fields.

At the larger GCC units (see Table 23.10), the steam that discharges from the steam turbine is divided among multiple binary units. Each binary unit condenses the steam in a process of heating and vaporizing the binary unit working fluid. The condensed steam is mixed back into the brine to reduce silica scaling potential. In some instances, small steam turbines are coupled to one end of a generator, with the steam discharged used in a binary plant with the pentane turbine coupled to the other end of the generator. In most cases, the condensers for the binary power plant are air-cooled.

23.8.4.2 Silica Solubility Limits

In fields with a steam/brine mix, the GCC competes directly with multflash steam technology. The GCC can produce greater output where flash plants have elected to use a

TABLE 23.10

Examples of Ormat Geothermal Combined Cycle Projects

Year	Project Name and Location	Project Net Output (MW)	Description of the Air-Cooled Power Plant
1996	Upper Mahiao, Leyte, Philippines	125	Four geothermal steam turbines that feed multiple binary units for 120 MW of net output. An additional 5 MW of power are generated by other binary units using the geothermal brine
2000	Mokai, New Zealand	60	One geothermal steam turbine that feeds multiple binary units for 50 MW of net output. Ten megawatts of power are generated by binary units using the geothermal brine

single flash to control silica (SiO_2) scaling, resulting in a brine discharge temperature of 300°F or greater. The same temperature limitation of the single-flash technology does not apply to the GCC, so the GCC is able to capture more energy from a given brine flow and therefore generate more power. Although it may at first seem counter-intuitive, the hotter the resource and thus the more steam that is produced in the flash process, the more advantage the GCC will have.

In a flash process, hotter brine results in a greater silica concentration in the reservoir fluid. Hotter brine also results in more flash, and therefore more concentration of the silica. The silica solubility limit controls the separated brine temperature, and therefore the minimum allowable flash pressure and temperature. Thus, because of the silica concentration, higher geothermal resource temperatures also result in a higher brine temperature that must be discharged from the flash plant.

Although the integrated binary plant also uses the initial flash in the steam turbine of the GCC, the condensed steam is mixed back into the brine flow. As a result, the final brine temperature can be lower without risking silica scaling. Consequently, more energy is available to the integrated binary power plant than is available to the flash-only plant. The binary plant advantage would be reduced if more geothermal operators were willing to use acid to slightly lower the pH of the brine and retard the kinetics of the silica precipitation.

23.8.4.3 Compare and Contrast

The GCC technology has some additional advantages and disadvantages over a single- or multiple-flash plant when compared side-by-side for a particular geothermal resource. The large advantage that the GCC obtains in greater energy availability due to the silica solubility limits is discussed in the paragraph above. The larger units that Ormat has developed in recent years will also help to make them more competitive through an economy of scale. Another advantage is obtained by discharging the steam turbine at slightly above atmospheric pressure. In this way, the NCGs are vented without the cost or parasitic load of the gas removal equipment that is needed when the steam turbine exhaust is at sub-atmospheric pressure, as occurs with the steam flash process. Since the steam condensate is mixed back into the brine with the GCC, the cost of an oxygenated fluid disposal well may be eliminated.

The advantages that the steam-turbine process holds over the GCC are: (1) the ability to use large equipment (up to a single 110 MW turbine); (2) no need for large heat exchangers (vaporizers and preheaters) and the intrinsic thermodynamic and capital cost penalty they entail; and (3) the steam flash process uses wet cooling from the condensed steam, whereas the GCC uses dry cooling, resulting in a higher final condenser temperature.

Thus, the steam process regains some of the thermodynamic disadvantage incurred by the silica solubility limit and the gas removal system parasitic steam load by having a lower power plant heat-rejection temperature and, thereby, greater available energy.

23.9 Environmental Impact

The generation of electric power will have an environmental impact, regardless of the energy source used. A large unregulated strip mine and unabated emissions from an old coal plant would probably represent the extreme negative end of the spectrum in its environmental impact to land, water, and air, but would not be particularly relevant to discussions of environmental impacts of power generation in the United States. Understanding the other end of the spectrum is much more complex. Solar and wind generation would seem to have zero emissions, but both of these require fossil-fired generation to back them up during periods when these generation technologies are unavailable or erratic. These “firming” requirements increase emissions from fossil-fired plants, and result in them not being the zero-emission technology that they might otherwise seem to be. What this shows is that even renewable technologies have negative environmental consequences. Society’s need for new sources of electric power generation, which cannot be served by conservation and efficiency, will result in negative environmental impacts.

Like other renewable technologies, geothermal power generation must be evaluated on a site-specific basis to accurately determine its environmental impacts. Two areas of environmental impact relevant to the use of geothermal energy, emissions and land use, are discussed below.

23.9.1 Geothermal Power Plant Emissions

Air emissions and clean air are the most-discussed environmental benefits of renewable-energy electric power generation, especially with the concern of the effect of greenhouse gases on global warming. Like other renewable energy sources, the emissions from geothermal power are generally low compared to fossil-fired generation. However, certain geothermal resources with high gas content may approach that of a natural gas fired power plant with regards to CO₂ emissions, but this is a rare exception. The concentrated CO₂ discharged from such units does make CO₂ capture feasible. The actual emissions from geothermal power plants are dependent on the highly variable gas content of the geothermal fluids that are being produced and the nature of the geothermal power process. Table 23.11 gives representative emissions of geothermal power plants compared to fossil-fired generation sources.

Pumped binary power plants have no emissions, except for fugitive leaks of the working fluid. As discussed above, the gases are still present in the brine, but because the pressure is never lowered below the bubble pressure of the gases, they remain in solution and are injected back into the geothermal resource.

23.9.1.1 CO₂ Emissions

Flash-steam power plants have emissions on the order of magnitude described, but vary according to the particular resource characteristics and whether the power process is

TABLE 23.11

Emissions from Generation Sources

Plant/Fuel	Emissions Rate (lb/MW h)				Notes
	NO _x	SO ₂	CO ₂	Particulates	
<i>Conventional power plants</i>					
Coal	4.3	10.4	2190	2.2	
Coal—life cycle	7.4	14.8	—	20.3	— ^a
Natural gas	3.0	0.2	1210	0.1	— ^b
Avg. of all U.S. plants	3.0	6.0	1390	—	[18]
<i>Geothermal power plants</i>					
Pumped geothermal brine	0	0	0	Negligible	— ^c
Geothermal flash steam plants	0	Negligible with abatement to 0.35	60 (avg.) some plants <120 to >900	Negligible	— ^d
Dry steam resources	Trace	Negligible with abatement	90 (Geysers) some plants <120 to >900	Negligible	

Source: Kagel, A. et al., *A Guide to Geothermal Energy and the Environment*, Geothermal Energy Association, Washington, DC, 2005, p. 39.

^a Kagel reports that this includes the emissions from the mining and transportation of coal to the power plant.

^b Kagel reports as an average of direct fired, combined cycle, and simple cycle plants.

^c Cooling tower drift only, if water cooling is used. Air-cooled plants have zero particulate emissions.

^d 150–900 lb/MW h of CO₂ is added to Kagel’s reported numbers for both flash and steam plants. It is based on 0.7%–5% CO₂ in the geothermal steam and 18–20 klb/MW h steam usage in the power plant. These are realistic, though nonproject-specific, values for some high-gas geothermal resources worldwide.

single-flash, double-flash, or coupled to a binary system. Most geothermal flash steam resources have NCG content of between 0.5% and 2% in the steam, which, when coupled with either double flash or a binary system, results in the reported values. However, for those systems that operate with only a single flash and have NCG content of up to 5% in the steam, the CO₂ emissions can reach the 900 lb/MW h reported in the above table.

Like the flash steam plants, the emissions from a dry steam power plant are dependent on the particular resource being considered.

23.9.1.2 H₂S and SO_x Emissions

For geothermal power plants with some form of H₂S abatement, sulfur emissions are negligible to very low, as shown in the table. For those plants without H₂S abatement, the released H₂S eventually converts to SO₂, and can be on the same order of magnitude as U.S. coal plant emissions for geothermal resources with high-H₂S content in the NCGs.

Except for California and the western United States, few geothermal plants worldwide operate H₂S abatement systems. StretfordTM and Lo-CatTM are the most common H₂S abatement technologies for gas-phase H₂S emissions. The use of bioreactors is an emerging technology for abatement, one in which sulfur-loving bacteria are used to convert the H₂S to sulfate. Bioreactors have been independently developed and put into operation at the Salton Sea, California, and in Wairakei, New Zealand.

23.9.1.3 NO_x Emissions

The reason NO_x emissions are reported as “negligible” instead of zero for the dry steam plants is a consequence of the early H₂S abatement technology installed at The Geysers

TABLE 23.12

30-Year Land Use

Energy Source	Land Use (m ² /GW h)
Coal, including mining	3642
Solar thermal	3561
Central station photovoltaic	3237
Wind, including roads	1335
Geothermal, including roads and pipelines	404

Source: Brophy, P., *Renewab. Energy*, 10, 374, 1997.

that incinerates the H₂S and then scrubs it out of the gas stream using the cooling water. The incineration also produces small amounts of nitrogen oxides. Since those early efforts at H₂S abatement, the geothermal industry has primarily used a cold catalytic conversion of H₂S to elemental sulfur, which has no NO_x emissions.

23.9.1.4 Particulate Emissions

Air-cooled plants have no particulate emissions, whereas water-cooled plants have only the evaporated minerals remaining from cooling tower drift, the quantity of which will be a function of the TDS in the cooling water. This quantity of particulate is negligible.

23.9.2 Land Use

Compared to other renewable energy sources, geothermal power developments have low land use and visual impact. The total geothermal development of wells and power plant may occur over many square miles, but the actual land occupied by the facilities is small. Some negative impacts may be attributed when a geothermal development occurs in a roadless area. There is a visual impact from the pipelines running from wells to power plant, and from the cooling tower steam plume on a cold day. When an air-cooled power cycle is used, geothermal power generation achieves its minimum visual impact. The fenced area of the power plant itself may be no larger than a couple of acres for up to 20 MW of net generation. The height of the air-cooled condenser, the highest point in the plant, is less than 25 ft above ground level. Overall, the land-use impact of geothermal development is small. Table 23.12 provides the total land use of various renewable and coal power technologies.

23.10 Additional Information on Geothermal Energy

This chapter has touched on only some of the many topics in the field of geothermal energy—a subject to which entire books have been devoted. Some additional geothermal energy information sources are provided in this section.

For a broad view on the subject of geothermal energy, including many direct-use applications such as aquaculture, district heating, industrial heat use, environmental issues and financing, a recent book, *Geothermal Energy—Utilization and Technology*, edited by Mary Dickson and Mario Fanelli, is an excellent resource. Each chapter has been written by an

expert of geothermal subject matter. At the end of each chapter are questions, answers, and references regarding the particular subject matter of that chapter.

Another recent book, *Geothermal Power Plants: Principles, Applications and Case Studies*, authored by Ronald DiPippo, provides some coverage of geothermal exploration, drilling, and reservoir engineering, with a primary focus on geothermal power generation. The book covers the conversion technologies, thermodynamics, equipment, and operation, and includes several detailed case studies of particular geothermal power plant developments.

In addition, there are a number of excellent geothermal resources on the World Wide Web.

Geo-Heat Center, http://geoheat.oit.edu/	Focus is direct use. Excellent online library. Software and databases
Geothermal Resources Council, www.geothermal.org/	GRC bulletin and transaction articles. Must be a member of the GRC to download articles
Geothermal Energy Association, www.geo-energy.org	The U.S. geothermal industry trade association several excellent broad research articles available for download including three papers on Geothermal Energy Costs, Environmental Impact, and Employment
International Geothermal Association, http://iga.igg.cnr.it/index.php	Downloadable papers from the last two world geothermal conferences

References

1. Lund, J. W., Bloomquist, R., Gordon, B., Tonya, L., and Renner, J. 2005. The United States of America country update—2005. *Geothermal Resources Council Transactions*, 29, 817–830.
2. Ragnarsson, Á. 2005. Geothermal development in Iceland (2000–2004). In: *Proceedings of the World Geothermal Congress*, Antalya, Turkey, 11pp.
3. Lund, J. W. 2005. Worldwide utilization of geothermal energy—2005. *Geothermal Resources Council Transactions*, 29, 831–836.
4. DiPippo, R. 2005. *Geothermal Power Plants: Principles, Applications and Case Studies*. Elsevier Advanced Technology, Oxford, U.K.
5. Wyborn, D., de Graaf, L., and Hann, S. 2005. Enhanced geothermal development in the Cooper Basin, South Australia. *Geothermal Resources Council Transactions*, 29, 151–155.
6. Stark, M. A., Box, W. T. Jr., Beall, J. J., Goyal, K. P., and Pingol, A. S. 2005. The Santa Rosa-Geysers recharge project, Geysers geothermal field, California. *Geothermal Resources Council Transactions*, 29, 144–150.
7. Sanyal, S. 2004. Defining the sustainability and renewability of geothermal power. *Geothermal Resource Council Bulletin*, July/August, 149–151.
8. Capetti, G. and Ceppatelli, L. 2005. Geothermal power generation in Italy, 2000–2004 update report. In *Proceedings of the World Geothermal Congress*, Antalya, Turkey, 7pp.
9. State of Nevada, Division of Minerals. 2005. Nevada geothermal update. <http://minerals.state.nv.us/>.
10. Idaho Public Utilities Commission Order # 29692, Case No. IPC-E-05-1, January 24, 2005. <http://www.puc.idaho.gov>.
11. Ormat Technologies News Release, May 6, 2005. http://www.ormat.com/index_news.htm (accessed December 2005).
12. Hance, C. N. 2005. Factors affecting the costs of geothermal power development. Geothermal Energy Association and the U.S. Department of Energy, Washington, DC.

13. Western GeoPower. 2005. Corporation website. <http://www.geopower.ca/newsreleases.htm> (accessed December 2005).
14. Phil Lory of Sinclair Knight Mertz Consulting, Personal communication.
15. Fuji Electric Systems. 2005. *Wayang Windu Project Information Bulletin*, GEC82-12. Fuji Electric Systems, Tokyo, Japan.
16. Williamson, K. H., Gunderson, R. P., Hamblin, G. M., Gallup, D. L., and Kitz, K. 2001. Geothermal power technology. *Proceedings of the IEEE*, 89(12), 1783–1792.
17. Kagel, A., Bates, D., and Gawell, K. 2005. *A Guide to Geothermal Energy and the Environment*. Geothermal Energy Association, Washington, DC.
18. Kagel's source reported as US EPA. Average power plant emissions from EPA 2000 emissions data. <http://www.epa.gov/cleanenergy/egrid/highlights>.
19. Kagel, A. Citing data from Brophy, P. 1997. Environmental advantages to utilization of geothermal energy. *Renewable Energy*, 10, 374.

24

Waste-to-Energy Combustion

Charles O. Velzy and Leonard M. Grillo

CONTENTS

24.1	Introduction	986
24.2	Waste Quantities and Characteristics	986
24.2.1	Waste Quantities	987
24.2.2	Waste Characteristics	988
24.3	Design of WTE Facilities	990
24.3.1	General Features	990
24.3.1.1	Types of Facilities	990
24.3.1.2	Operation and Capacity	992
24.3.1.3	Siting	993
24.3.2	Fuel Handling	994
24.3.2.1	Refuse Receipt, Processing, and Storage	994
24.3.2.2	Refuse Feeding	995
24.3.3	Combustion Principles	995
24.3.4	Furnaces	1003
24.3.5	Boilers	1008
24.3.5.1	Refractory Furnace with Waste Heat Boiler	1008
24.3.5.2	Mass-Fired Water Wall Units	1008
24.3.5.3	RDF-Fired Water Wall Units	1009
24.3.6	Residue Handling and Disposal	1009
24.3.7	Other Plant Facilities	1011
24.4	Air Pollution Control Facilities	1011
24.4.1	Particulate Control	1012
24.4.2	Gaseous Emission Control	1014
24.4.3	Organic Compound Control	1016
24.4.4	Trace Metals	1019
24.5	Performance	1022
24.6	Costs	1023
24.7	Status of Other Technologies	1025
24.7.1	Modular Systems	1025
24.7.2	Fluidized Beds	1026
24.7.3	Pyrolysis and Gasification	1026
24.8	Future Issues and Trends	1027
References	1028

24.1 Introduction

One of the most serious issues facing urbanized areas today is development of cost-effective environmentally acceptable disposal of the community's solid waste. The solid waste generated in a community may be collected by private companies or governmental entities, or portions by both, but the assurance that the waste is ultimately disposed of in an environmentally safe manner is a governmental responsibility.

Solid waste management is a major issue in the United States, because of increasing concerns with environmental problems. One potential solution is to use municipal solid waste, which, for all practical purposes is a renewable commodity, for the generation of electricity. An analysis by Penner and Richards⁵³ showed that incineration of municipal waste, even after 30% of the waste was recycled, could provide as much electric power as eight large nuclear or coal generating stations. Their analysis further concluded that this could provide 1%–2% of the total electric energy needs in the United States at prices competitive with coal-fired base load power plants.

The basic technology for modern waste-to-energy combustion was developed in Europe during the 1960s and 1970s. This technology, which has been modified and improved since its development, has been widely implemented in the United States. However, despite the fact that incineration of solid waste can decrease its volume ninefold and ameliorate the final waste disposal into landfills, the full potential of utilizing solid waste for energy production is not being realized because of widespread fears regarding environmental pollution. In preparing this chapter, the realities of the situation have been taken into account and the discussion emphasizes the prevention of pollution as much or more than the production of power from waste. Waste-to-energy combustion in modern facilities with adequate environmental safeguards and careful monitoring has been shown to be a safe and cost-effective technology that is likely to increase in importance during the next decade.

Two conditions usually point to the use of combustion processes in treating municipal solid waste prior to ultimate disposal: the waste is collected in an urbanized area with little or no conveniently located land for siting of sanitary landfills (need for volume reduction); and markets exist for energy recovered from the combustion process, and possibly for reclaimed materials, with the energy attractively priced. Even some rural areas are currently considering waste to energy facilities.

Modern waste-to-energy (WTE) plants reflect significant advances that have been made in addressing the technical and practical difficulties of material handling, combustion control, and flue gas cleanup. In the early days of waste incineration, when air pollution regulations were undemanding or nonexistent, relatively simple, fixed-grate plants operating on a single- or two-shift basis were common. However, with increasingly stringent air pollution control regulations, more complex plants requiring continuous operation are now being built.

24.2 Waste Quantities and Characteristics

Municipal solid waste (MSW) as used herein refers to solid waste collected from residences and commercial, light industrial and institutional waste. It does not include heavy industrial waste, which is another problem and varies widely in quantity and

characteristics, depending on the industry and specific industrial plant. Changes in packaging practices and improvements in the general standard of living have resulted in significant increases in the quantities of solid waste generated over the past 50 years. Additionally, increasing emphasis on and participation in the recycling of wastes by local communities has resulted in significant variations in quantity and characteristics of MSW at the local community level. All of these factors must be considered when planning a WTE facility. Chapter 48 gives more information on waste availability.

24.2.1 Waste Quantities

In the United States approximately 120 million tons of MSW were generated in 1970, increasing to 220 million tons in 1998.²³ MSW generation is projected to increase to almost 260 million tons by the year 2015.²⁵ At the local level the quantity of solid waste generated varies geographically, daily, and seasonally, according to the effectiveness of the local recycling initiatives, and differences in socioeconomic conditions.⁶⁰

Over the past 40 years, numerous studies by EPA,²¹ APWA,⁵⁴ and others⁶⁷ have indicated that urbanized areas in this country generate approximately 2.0 lb/capita/day of MSW from residences and another 2.0 lb/capita/day from commercial and institutional facilities, on a national average basis. Thus, a typical community of 100,000 inhabitants would generate about 200 tons/day of gross MSW discards averaged over a 1-year time period.

These projections are subject to adjustments related to specific community characteristics. Thus, communities in the south, with longer active growing seasons than those in the north, tend to produce and collect more yard waste. Recent requirements for on-site disposal and/or composting of yard waste is changing this variable. Rural communities tend to produce less waste per capita than highly urbanized areas because of their greater potential for on-site waste disposal. In the past, the communities in the north tended to produce more waste in the winter due to the prevalence of heating of homes with solid fuels, which produced large quantities of ashes for disposal. Variations in yard wastes and ashes produced from home heating with solid fuels are also examples of variations in MSW quantities related to seasonal effects. Seasonal variations in MSW generation have been noted to range $\pm 15\%$ from the average, while daily variations in waste collections may range up to $\pm 50\%$ from the average, depending largely on number of collections per week. Daily variations in waste quantities are more important in designing certain plant components, while geographic and seasonal effects are more important in establishing plant size.

Waste quantities are also affected by the effectiveness of local recycling initiatives and by socioeconomic conditions. EPA studies have indicated an increase, nationally, in waste recycling from 6.6% in 1960–1970, to 16.2% in 1990,²² and 28.2% in 1998.²⁴ The national recycling rate had increased to 34% and 87.2 million tons by 2013,²⁵ at which time it is expected to level off.* A community in New England⁷ projected a 14.0% drop in MSW generation between 1989 and 1991 due to recycling activities in the community, and a 6.0% drop due to the recession during this period in this region of the country. A 15% drop in MSW collections was noted in a Long Island community during a recessionary period in 1972. The impact of recycling on MSW generation should be considered in plant sizing, while the impact of recessionary periods on plant economics may require specific consideration during project planning.

* The EPA updates figures annually. The most up-to-date information is available at www.epa.gov/solidwaste/nonhaz/municipal.

24.2.2 Waste Characteristics

It is important in approaching the design of a WTE facility that one consider the potential variations in both physical and chemical composition of MSW. Historically, one of the most troublesome areas in WTE plants has been materials handling systems. To successfully select materials handling system components and design an integrated process, one must have adequate information on the variability and extremes of the physical size and shape the solid waste facility must handle, the bulk density and angle of repose of the material, and the variation in noncombustible content. This information generally is not available from published surveys and reports, and can only be secured through inspection of the MSW in the field. Materials handling equipment for refuse feeding and residue handling must be large enough and oriented properly to pass the largest bulky items in the MSW, and large enough and rugged enough to handle the quantities of materials required to meet plant design capacity, or the plant will experience expensive periods of down time and might have to be derated.

In the design of the furnace/boiler portion of WTE facilities, the refuse characteristics of interest are the calorific value, moisture content, proportion of noncombustibles, and other components (such as heavy metals, chlorine, and sulfur) whose presence during combustion will result in the need for flue gas cleanup. The capacity of a WTE furnace boiler is roughly inversely proportional to the calorific or heating value of the waste. Table 24.1 illustrates the variation in waste characteristics that has been observed in studies defining the average solid waste composition in the United States since 1960.

As indicated in Table 24.1, approximately 35%–40% of the combustible fraction of MSW is composed of cellulosic material such as paper and wood. This percentage has remained relatively constant over the past 20 years, even after taking into account the

TABLE 24.1

Generation, Materials Recovery, Composting, Combustion with Energy Recovery and Discards of MSW, 1960–2013 (in Millions of Tons)

Activity	1960	1970	1980	1990	2000	2005	2009	2011	2012	2013
Generation	88.1	121.1	151.6	208.3	243.5	253.7	244.6	250.5	251.0	254.1
Recovery for recycling	5.6	8.0	14.5	29.0	53.0	59.2	61.9	66.4	65.3	64.7
Recovery for composting ^a	neg.	neg.	neg.	4.2	16.5	20.6	20.7	20.6	21.3	22.4
Total materials recovery	5.6	8.0	14.5	33.2	69.5	79.8	82.6	87.0	86.6	87.2
Discards after recovery	82.5	113.0	137.1	175.0	174.0	173.9	162.0	163.5	164.4	167.0
Combustion with energy recovery ^b	0.0	0.4	2.7	29.7	33.7	31.6	29.0	31.8	32.2	32.7
Discards to landfill, other disposal ^c	82.5	112.6	134.4	145.3	140.3	142.3	133.0	131.7	132.2	134.3

Note: neg., negligible = less than 5000 tons or 0.05%.

^a Composting of yard trimmings, food and other MSW organic material. Does not include backyard composting.

^b Includes combustion of MSW in mass burn or refuse-derived fuel form, and combustion with energy recovery of source separated materials in MSW (e.g., wood pallets, tire-derived fuel).

^c Discards after recovery minus combustion with energy recovery. Discards include combustion without energy recovery. Details might not add to totals due to rounding.

greater than fourfold increase in recycling percentage achieved over this period. The remainder of the combustible content is composed of various types of plastics, rubber, and leather. The heat released by burning cellulose is approximately 8000 Btu/lb (on a dry basis), while that released by plastics, rubber, and leather is significantly higher on a per pound, dry basis. Heat released by burning garbage (on a dry basis) is only slightly less than cellulose. However, the moisture content of garbage has been observed to range from 50% to 75%, by weight, while that of the cellulosic fraction of MSW usually ranges from 15% to 30%.

In recent years, it has been observed that the higher heating value (HHV) of the combustible portion of MSW (moisture and ash free) averages about 9400 Btu/lb. Considering the recent changes in MSW composition following recycling (increase in plastics while cellulosic material has remained relatively constant), this moisture and ash free HHV has probably increased to 9500 Btu/lb. Taking 9500 Btu/lb as the moisture and ash free heat content of MSW, Table 24.2 illustrates the variation in as-received heat content that one could expect in MSW with moisture content ranging from 20% to 50% by weight and non-combustible content ranging from 25% by weight (earliest period) to approximately 15% by weight (currently).

Moisture content is a highly important and also a highly variable characteristic of waste materials. The moisture content of MSW is generally around 25%, but has been observed to vary from 15% to 70%. This variation may be due, for example, to seasonal variations in precipitation, the nature of the waste (e.g., grass clippings vs. paper) and the method of storage and collection (e.g., open vs. closed containers/trucks). Thus, after a heavy rain, the moisture content of the solid waste may be so high that it may be difficult to sustain combustion. The combustion of solid waste usually can proceed without supplementary fuel when the heat value is greater than 3500–4000 Btu/lb (8140–9300 kJ/kg). This type of variation in MSW composition must be considered in the design of WTE facilities.

The ultimate or elemental analysis of the combustible portion of the MSW refers to the chemical analysis of the waste for carbon, hydrogen, oxygen, sulfur, chlorine, and nitrogen. This information is used to estimate the heat content of waste, moisture, and ash free; to predict the composition of the flue gases; and, from the last three elements (sulfur, chlorine, and nitrogen), to assess the possible impact of waste combustion on air pollution. A typical analysis of solid waste is presented in Table 24.3.

TABLE 24.2

Variation in Heat Content of MSW

Noncombustible (%)	15		25	
	Comb. (%)	Heat Cont. (Btu/lb)	Comb. (%)	Heat Cont. (Btu/lb)
<i>Moisture%</i>				
20	65	6125	55	5225
30	55	5225	45	4275
40	45	4275	35	3325
50	35	3225	25	2375

TABLE 24.3

Analysis of Solid Waste

	Percent by Weight	
	West Europe	United States
<i>Proximate analysis</i>		
Combustible	42.1	50.3
Water	31.0	25.2
Ash and inert material	26.9	24.5
Total	100	100
<i>Ultimate (elemental) analysis of combustibles</i>		
Carbon	51.1	50.9
Hydrogen	7.1	6.8
Oxygen	40.1	40.3
Nitrogen	1.2	1.0
Sulfur	0.5	0.4
Chlorine	—	0.6
Total	100	100

Sources: From Domalski, E.S. et al., The chlorine content of municipal solid waste from Baltimore County, Maryland, and Brooklyn, NY, in: *Proceedings 1986 National Waste Processing Conference*, Denver, CO, June 1–4, 1986, ASME, New York, pp. 435–448; Seeker, W.R. et al., *Municipal Waste Combustion Study: Combustion Control of Organic Emissions*, EPA, Research Triangle Park, NC, 1987; Suess, M.J. et al., *Solid Waste Management Selected Topics*, WHO Regional Office for Europe, Copenhagen, Denmark, 1985.

Note: Gross heat value, as fired = 3870 Btu/lb (9000 kJ/kg).

24.3 Design of WTE Facilities

The primary function of a WTE facility is to reduce solid waste to an inert residue with minimum adverse impact on the environment. Thermal efficiency, in terms of maximizing the capture of energy liberated in the combustion process, is of secondary importance. WTE facilities are usually classified as mass-burn systems, or refuse-derived fuel (RDF) systems.

24.3.1 General Features

24.3.1.1 Types of Facilities

Mass-burn systems are large facilities (usually over 200 tons/day) that burn, as-received, unprocessed MSW which is extremely heterogeneous. Most mass-burn systems burn the waste in a single combustion chamber under conditions of excess air (i.e., more than is needed to complete combustion) (see Figure 24.1). The waste is burned on a sloping, moving grate, which helps agitate the MSW and mixes it with combustion air. Many different proprietary grate systems exist.

In refuse-derived fuel (RDF) systems, usually large facilities, the MSW is first processed (see Figure 24.2) by mechanical means to produce a more homogeneous material prior to introduction into a furnace/boiler. Several types of RDF can be made—coarse, fluff, powder, and densified. These differ in complexity and horsepower requirements of the waste processing facilities, size of particle produced, and whether or not the

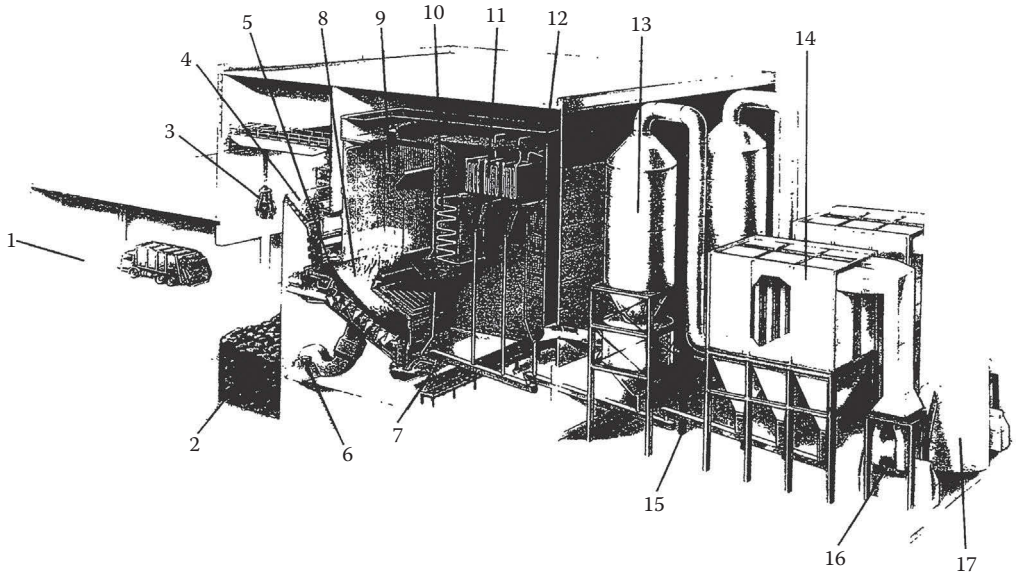


FIGURE 24.1
 A typical Covanta facility. (1) Tipping floor, (2) refuse holding pit, (3) feed crane, (4) feed chute, (5) Martin stoker grate, (6) combustion air fan, (7) Martin residue discharger and handling system, (8) combustion chamber, (9) radiant zone (furnace), (10) convection zone, (11) superheater, (12) economizer, (13) dry gas scrubber, (14) bag-house or electrostatic precipitator, (15) fly ash handling system, (16) induced draft fan, and (17) stack.

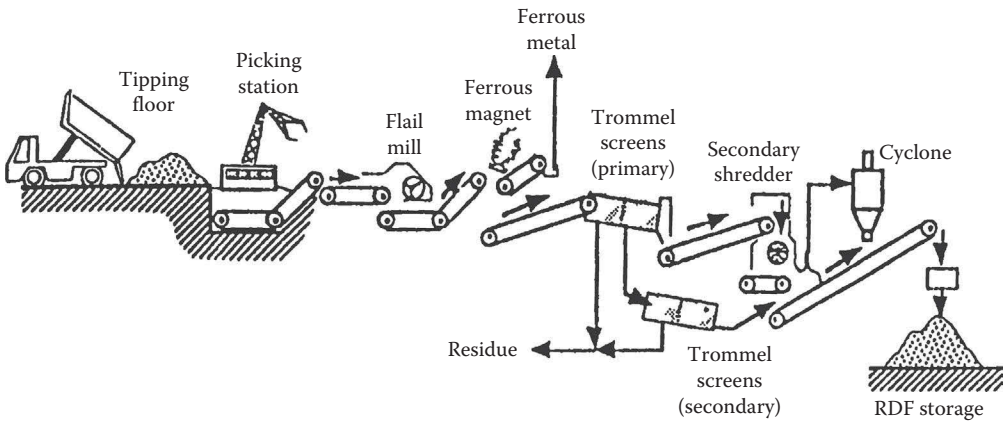


FIGURE 24.2
 RDF processing system.

material is compacted under pressure into pellets, briquettes, or similar forms. The coarse type of RDF is the most common form produced at this time.

RDF can be burned in one of the two types of boilers. It can be used as the sole or primary fuel in dedicated boilers (see Figure 24.3) or it can be co-fired with conventional fossil fuels in existing industrial or utility boilers. One advantage of these systems is that RDF can be produced at one location for use at a nearby off-site boiler, allowing for flexibility in locating processing facilities. Also, some materials, such as steel and glass, can be recovered for recycling during the initial processing step.

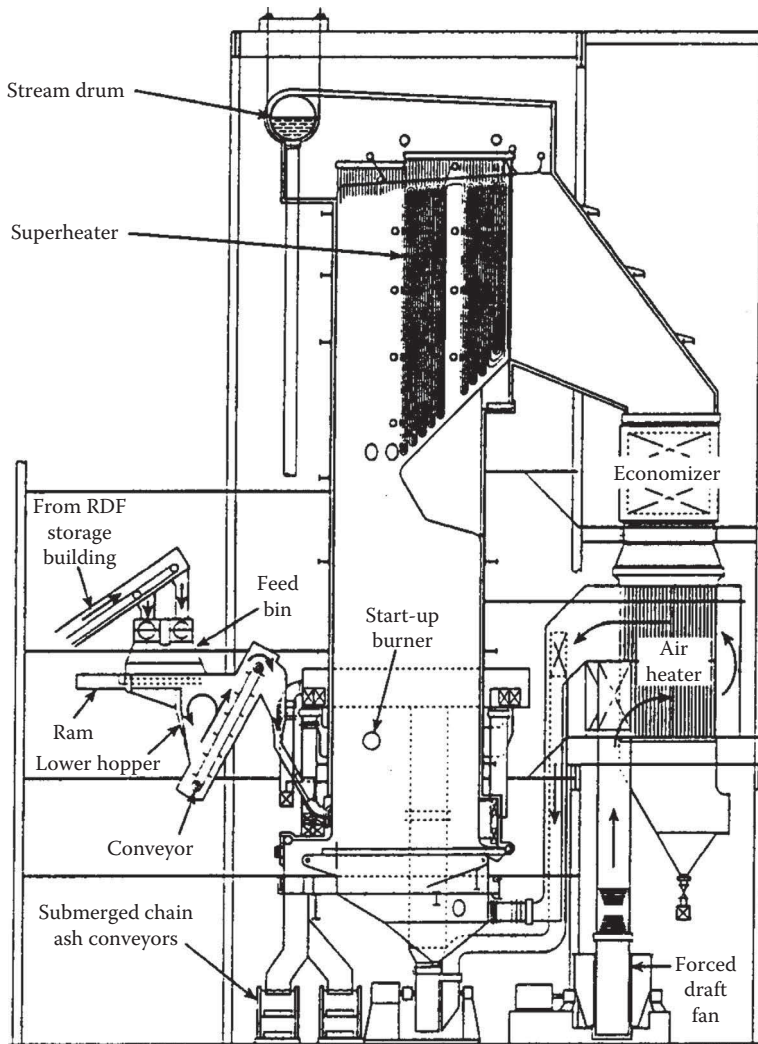


FIGURE 24.3
West Palm Beach, FL, RDF-fired boiler by the Babcock and Wilcox Company.

Mass-burn and RDF systems together account for 86 of the 98 currently operating waste-to-energy facilities and 98% of the waste combustion capacity. Modular units, described briefly later, account for the other 12 units and 2% of the waste combustion capacity.³⁹

24.3.1.2 Operation and Capacity

The capacity to be provided in a facility is a function of the area and population to be served; and the rate of refuse production for the population served. A small plant (100 tons/day) without energy recovery might not be operated on weekends. For capacities above 400 tons/day, or any plant with energy recovery, economic and/or equipment operating considerations usually dictate three-shift operation, 7 days/week.

If collection records, preferably by weight, are available for the community, forecasts for determining required plant capacity can be made with reasonable accuracy. If records are not available, refuse quantities for establishing plant size may be approximated by assuming a refuse generation rate of 4.0 lb/capita/day when there is little or no waste from industry. Of course, in planning for plant capacity, the impact of local recycling activities on both quantity and characteristics of MSW must be considered as discussed earlier.

Other factors must be taken into account in establishing the size or capacity of a facility. Should the facility serve only one community, or should it be regional and serve several communities? What are the possible benefits of economies of scale? What is the impact of the cost of hauling refuse to a central point on overall project economics? There is substantial evidence available at present to show that implementation becomes much more difficult as the number of separate political jurisdictions is increased. Imposition of regional plans on local jurisdictions to achieve economies of scale, where it cannot be conclusively demonstrated that such regional plans make sound economic sense based on the total cost of the solid waste management plan, including the cost of transporting the solid waste to the regional facility, is, at best, unwise. Economies of scale in these projects have tended to be illusory, while haul costs to gather sufficient waste together to achieve the economies of scale have tended to be ignored in developing total project economics.

24.3.1.3 Siting

One of the key issues to face in implementing a WTE project is locating a site for the facility. Since MSW is usually delivered to these plants by truck, inevitably there will be substantial truck traffic in the vicinity of the plants. The equipment and processes used in these plants are industrial in nature. They are generally noisy at the source and tend to produce dust and odors. These facts indicate that it is desirable to site such plants in industrial or commercial areas.⁴⁵ It has been contended, as cited in a 1989 OTA report⁶⁸ "that sites are sometimes selected to avoid middle- and higher-income neighborhoods that have sufficient resources to fight such development."

Plants should be located near major highways to minimize the impact from increased truck traffic. As shown by operating WTE plants in Europe and the United States, it is possible to control all nuisance conditions by proper attention to the details of plant design. The local impact of truck deliveries to the plant can be minimized by providing sufficient length of access road so that refuse truck queuing does not take place on public highways. Odors and noise can be confined to the plant building. Odors and fugitive dust can be destroyed by collecting plant air and using it for combustion air supply. Noise should be attenuated at the source to maintain healthful working conditions. In all cases, there is no need to adversely impact the surrounding neighborhood. Proper attention to architectural treatment can result in a structure that blends into its surroundings; if sited in industrial or commercially zoned areas.

Since considerable vertical distance is frequently required in the passage of MSW through a mass-burn WTE plant, there is an advantage in a sloping or hillside site. Collection trucks can deliver MSW at the higher elevation, while residue trucks operate at the lower elevation, requiring minimum site regrading. This consideration does not generally apply to RDF plants.

24.3.2 Fuel Handling

24.3.2.1 Refuse Receipt, Processing, and Storage

Scales, preferably integrated into an automated record keeping system, should be provided to record the weight of MSW delivered to the WTE plant. Either the entire tipping area or individual tipping positions should be enclosed so as to control potential nuisance conditions in the vicinity of the plant, such as blowing papers, dust, and/or odors. The number of tipping positions provided should take into consideration the peak number of trucks expected per hour at the facility and should be located so the trucks have adequate time and room to maneuver to and from the dumping positions while minimizing queue time.

Collections usually are limited to one 8 h daily shift 5 days/week (sometimes with partial weekend collection) while burning will usually be continuous, so ample storage must be provided. This usually requires 2–3 days of refuse storage at most WTE plants. Seasonal and cyclic variations should also be a consideration in establishing plant storage requirements.

Refuse storage in large mass-burn plants is normally in long, relatively narrow, and deep pits extending along the front of the furnaces. It will generally be necessary to rehandle the refuse dumped from the trucks. In some mass-burn plants and in RDF plants, floor dumping and storage of the MSW either on the dump floor or in shallow, relatively wide pits is common practice.

When computing the dimensions required for storage of as-received MSW, the required volume may be determined based on an MSW bulk density of from 400 to 600 lb/yd³ (240–360 kg/m³).^{54,61} Other factors to consider in sizing and laying out refuse storage facilities in WTE plants is that refuse flows very poorly and can maintain an angle of repose greater than 90°. Thus, MSW is commonly stacked in storage facilities to maximize storage capacity.

Sizing a refuse storage pit requires the use of empirical data, judgment, site constraints, and knowledge of plant layout and operations. The pit should be at least long enough to provide sufficient truck tipping positions so that the trucks are not unduly delayed in discharging their waste (tipping) into the pit. It has been found in practice that it takes an average of 10 min for the truck to perform the tipping operation. This time may be shorter for packer trucks and longer for transfer vehicles. Each tipping position must provide at least 14 ft of unobstructed width for this operation. Ideally, 20 ft should be allowed for each tipping position to allow for convenient truck access and space for armored building support columns.

The pit should be capable of holding a minimum of 3 days' storage at the facility's maximum continuous rating. The desired volume should be based on a bulk density of about 500 lb/cycle of waste. The dimensions of the pit will be dependent on site constraints and the facility design. The pit is usually at least as long as the width of all the boilers it feeds. The depth will be dependent on groundwater conditions, but should be 30–45 ft deep if possible. The total volume of storage should equal the volume in the pit up to the tipping floor level plus the volume above the tipping floor assuming the waste is stacked at a 45° from the charging floor wall to the tipping floor. The remainder of the pit will be used for the grapple to move waste away from the tipping positions. After the waste has been stacked, the grapple can remove the material against the tipping floor wall and form a trench, since the waste will maintain a vertical face when stacked.

At most newer and more successful RDF plants, after receiving the MSW in a floor dump type of operation, the MSW is loaded onto conveyors that carry the material

to flail mills or trommels with bag-breaking blades. These facilities break apart the bags containing the waste, allowing glass and some metals to be separated from the remaining MSW. The separated MSW, primarily the light combustible fraction, is then reduced in size. Removal of the glass prior to the size reduction process alleviates the problem, experienced in earlier plants, of contamination of combustible material with glass shards.

Processes to produce powdered fuel or RDF fuel pellets, although interesting, have not been developed to a state of commercial availability. A process to produce RDF by "hydro-pulping" after being attempted in two full-scale plants, was not commercially successful.

24.3.2.2 Refuse Feeding

Batch feeding of MSW, practiced in the past in mass-burn plants, is undesirable and is not practiced in modern plants. In the larger mass-burn plants, the solid waste is usually moved from the storage pit to a charging hopper by a traveling bridge crane and an orange-peel type of grapple. The grapple size is established by a duty cycle analysis, taking into account the quantity of material that must be moved from the pit to the furnaces, the distances over which the material must be moved, allowable crane speeds, and the need to rehandle (mixing and/or stacking) material in the pit. Grapples can range in size from 1.5 to 8 yd³ (1–6 m³) capacity and larger.

The crane used in this service should be capable of meeting the severest of duty requirements.⁵² The load lifting capability is established by adding to the grapple weight, 1.5 times the volumetric capacity of the grapple times a density of MSW of 600–800 lb/yd³ (360–480 kg/m³).³⁷ In the past, the crane has been operated from an air-conditioned cab mounted on the bridge. However, crane operation is now centralized in a fixed control room, usually located at the charging floor elevation and either over the tipping positions opposite the charging hoppers or in the vicinity of the charging hoppers.

In modern mass-burn plants, the MSW is deposited from the crane grapple into a charging hopper. The charging hopper, which is built large enough to prevent spillage on the charging floor and with slopes steep enough to prevent bridging, is placed on top of a vertical feed chute that discharges the MSW into the furnace. The feed chute may be constructed of water cooled steel plates or steel plates lined with smooth refractory material. The chute is normally at least 4 ft (1.2 m) wide, to pass large objects with a minimum of bridging, and the width of the furnace. It is kept full of refuse to prevent uncontrolled admission of air into the furnace. The refuse is fed from the bottom of the feed chute into the furnace by a portion of the mechanical grate, or by a ram. The ram generally provides better control of the rate of feed into the furnace than the older technique of using a portion of the mechanical grate for refuse feed.

In RDF plants, conveyors, live bottom bins, and pneumatic handling of the size-reduced MSW combustible material have been utilized. The fuel material is usually blown into these furnaces, where it is partially burned while in suspension, with combustion being completed on grates at the bottom of the furnace. These fuel feeding systems are generally more complex than the mass-burn systems.

24.3.3 Combustion Principles

Combustion is the rapid oxidation of combustible substances with release of heat. Oxygen is the sole supporter of combustion. Carbon and hydrogen are by far the most important of the combustible substances. These two elements occur either in a free or combined state

TABLE 24.4

Elements and Compounds Encountered in Combustion

Substance	Molecular Symbol	Molecular Weight	Form	Density (lb/ft ³)
Carbon	C	12.0	Solid	—
Hydrogen	H ₂	2.0	Gas	0.0053
Sulfur	S	32.1	Solid	—
Carbon monoxide	CO	28.0	Gas	0.0780
Oxygen	O ₂	32.0	Gas	0.0846
Nitrogen	N ₂	28.0	Gas	0.0744
Nitrogen atmos.	N _{2atm}	28.2	Gas	0.0748
Dry air		29.0	Gas	0.0766
Carbon dioxide	CO ₂	44.0	Gas	0.1170
Water	H ₂ O	18.0	Gas/liquid	0.0476
Sulfur dioxide	SO ₂	64.1	Gas	0.1733
Oxides of nitrogen	NO _x	—	Gas	—
Hydrogen chloride	HCl	36.5	Gas	0.1016

Source: From Hecklinger, R.S., *Combustion*, in: *The Engineering Handbook*, Dorf, R.C. (ed.), CRC Press, Inc., Boca Raton, FL, 1996.

in all fuels—solid, liquid, and gaseous. Sulfur is the only other element considered to be combustible. In combustion of MSW, sulfur is a minor constituent with regard to heating value. However, it is a concern in design of the air pollution control equipment. The only source of oxygen considered here will be the oxygen in the air around us.

Table 24.4 displays the elements and compounds that play a part in the combustion process. The elemental and molecular weights displayed are approximate values which are sufficient for combustion calculations. Nitrogen is listed as chemical nitrogen N₂, with a molecular weight of 28.0 and as atmospheric nitrogen, N_{2atm}, which is a calculated figure to account for trace constituents of dry air. Water occurs as a vapor in air and in the products of combustion and as a liquid or vapor constituent of MSW fuel.

A U.S. standard atmosphere of dry air has been defined as a mechanical mixture of 20.947% O₂, 78.086% N₂, 0.934% Ar (argon), and 0.033% CO₂ by volume.⁴³ The percentages of argon and carbon dioxide in air can be combined with chemical nitrogen to develop the following compositions of dry air by volume and by weight that can be used for combustion calculations:

Constituent	% by Volume	% by Weight
Oxygen, O ₂	20.95	23.14
Atmospheric nitrogen, N _{2atm}	79.05	76.86

Atmospheric air also contains some water vapor. The level of water vapor in air, or its humidity, is a function of atmospheric conditions. It is measured by wet and dry bulb thermometer readings and a psychrometric chart. If specific data are not known, the American Boiler Manufacturers Association recommends a standard of 0.013 lb of water per pound of dry air, which corresponds to 60% relative humidity and a dry bulb temperature of 80°F.

Table 24.5 displays the chemical reactions of combustion. These reactions result in complete combustion; that is, the elements and compounds unite with all the oxygen with which they are capable of entering into combination. In actuality, combustion is a more complex process in which heat in the combustion chamber causes intermediate

TABLE 24.5
Chemical Reactions of Combustion

Combustible	Reaction
Carbon	$C + O_2 = CO_2$
Hydrogen	$2H_2 + O_2 = 2H_2O$
Sulfur	$S + O_2 = SO_2$
Carbon monoxide	$2CO + O_2 = 2CO_2$
Nitrogen	$N_2 + O_2 = 2NO$
Nitrogen	$N_2 + 2O_2 = 2NO_2$
Nitrogen	$N_2 + 3O_2 = 2NO_3$
Chlorine	$4Cl + 2H_2O = 4HCl + O_2$

Source: From Hecklinger, R.S., Combustion, in: *The Engineering Handbook*, Dorf, R.C. (ed.), CRC Press, Inc., Boca Raton, FL, 1996.

reactions leading up to complete combustion. An example of intermediate steps to complete combustion would be when carbon reacts with oxygen to form carbon monoxide and, later in the combustion process, the carbon monoxide reacts with more oxygen to form carbon dioxide. The combined reaction produces precisely the same result as if an atom of carbon combined with a molecule of oxygen to form a molecule of carbon dioxide in the initial reaction. An effectively controlled combustion process results in well less than 0.01% of the carbon in the fuel leaving the combustion chamber as carbon monoxide; and the remaining 99.99% of the carbon in the fuel leaves the combustion process as carbon dioxide. It should also be noted with regard to Table 24.5 that some of the sulfur in a fuel may combust to SO_3 rather than SO_2 with a markedly higher release of heat. However, it is known that only a small portion of the sulfur will combust to SO_3 and some of the sulfur in fuel may be in the form of pyrites (FeS_2), which do not combust at all. Therefore, only the SO_2 reaction is given. Also, some nitrogen is converted to oxides of nitrogen (NO_x), and some chlorine is converted to hydrogen chloride in the presence of moisture in the flue gas. While these components do not factor into the combustion calculations, they are important for the purpose of establishing air pollution control requirements.

Factors directly affecting furnace design are the moisture and the combustible content of the solid waste to be burnt and the volatility of the material to be burnt. The means for temperature control and sizing of flues and other plant elements should be based on design parameters that result in large sizes. Combustion controls should provide satisfactory operation for loads below the maximum rated capacity of the units.

The combustible portion of MSW is composed largely of cellulose and similar materials originating from wood, mixed with appreciable amounts of plastics and rubber, as well as some fats, oils, and waxes. The heat released by burning dry cellulose is approximately 8,000 Btu/lb, while that released by certain plastics, rubber, fats, oils, and so on, may be as high as 17,000 Btu/lb. If MSW consists of five parts cellulose and one part plastics, rubber, oil, and fat, the heat content of the dry combustible matter only is approximately 9500 Btu/lb.

The heat released in combustion of basic combustible substances is displayed in Table 24.6. The heating value of a substance can be expressed either as higher (or gross) heating value or as lower (or net) heating value. The higher heating value takes into account the fact that water vapor formed or evaporated in the process of combustion includes the latent heat of vaporization, which could be recovered if the products of combustion are reduced in temperature sufficiently to condense the water vapor to

TABLE 24.6

Heat of Combustion

Combustible	Molecular Symbol	Heating Value (Btu/lb)	
		Gross	Net
Carbon	C	14,100	14,100
Hydrogen	H ₂	61,100	51,600
Sulfur	S	3,980	3,980
Carbon monoxide	CO	4,350	4,350

Source: From Hecklinger, R.S., *Combustion*, in: *The Engineering Handbook*, Dorf, R.C. (ed.), CRC Press, Inc., Boca Raton, FL, 1996.

liquid water. The lower heating value is predicated on the assumption that the latent heat of vaporization will not be recovered from the products of combustion.

The heat released during combustion may be determined in a bomb calorimeter, a device with a metal container (bomb) immersed in a water jacket. A 1 g MSW sample is burned with a known quantity of oxygen, and the heat released is determined by measuring the increase in temperature of the water in the water jacket. Since the bomb calorimeter is cooled to near ambient conditions, the heat recovery measured includes the latent heat of vaporization as the products of combustion are cooled and condensed in the bomb. That is, the bomb calorimeter inherently measures higher heating value (HHV). It has been customary in the United States to express heating value as HHV. In Europe and elsewhere, heating value is frequently expressed as the lower heating value (LHV).

Heating value can be converted from HHV to LHV if weight decimal percentages of moisture and hydrogen (other than the hydrogen in moisture) in the fuel are known, using the following formula:

$$\text{LHV}_{\text{Btu/lb}} = \text{HHV}_{\text{Btu/lb}} - [\% \text{H}_2\text{O} + (9 \times \% \text{H}_2)] \times (1050 \text{ Btu/lb}) \quad (24.1)$$

$$\text{LHV}_{\text{J/kg}} = \text{HHV}_{\text{J/kg}} - [(9 \times \% \text{H}_2) + \% \text{H}_2\text{O}] \times (2240 \text{ kJ/kg}) \quad (24.2)$$

For example (using data from Table 24.9),

$$\text{LHV}_{\text{Btu/lb}} = \text{HHV}_{\text{Btu/lb}} - [\% \text{H}_2\text{O} + (9 \times \% \text{H}_2)] \times 1050 \text{ Btu/lb}$$

$$\text{LHV}_{\text{Btu/lb}} = 4940 - [0.30 + (9 \times 0.047)] \times 1050$$

$$\text{LHV}_{\text{Btu/lb}} = 4940 - [0.30 + 0.42] \times 1050$$

$$\text{LHV}_{\text{Btu/lb}} = 4940 - 756 = \text{Btu/lb}$$

Another method for determining the approximate higher heating value for MSW is to perform an ultimate analysis and then apply Dulong's formula:

$$\text{HHV}_{(\text{Btu/lb})} = 14,544 \text{ C} + 62,028 \left(\text{H}_2 - \frac{\text{O}_2}{8} \right) + 4,050 \text{ S} \quad (24.3)$$

where C, H₂, O₂, and S represent the decimal proportionate parts by weight of carbon, hydrogen, oxygen, and sulfur in the fuel. The term O₂/8 is a correction used to account for hydrogen which is already combined with oxygen in the form of water. For example (using data from Table 24.9)

$$\text{HHV}_{(\text{Btu/lb})} = 14,544 C + 62,028 \left(\text{H}_2 - \frac{\text{O}_2}{8} \right) + 4,050 S$$

$$\text{HHV} = 14,544 \times 0.257 + 62,028 \left(0.048 - \frac{0.21}{8} \right) + 4,050 \times 0.001$$

$$\text{HHV} = 3,738 + 62,028(0.047 - 0.026) + 4.0$$

$$\text{HHV} = 3,738 + 62,028 \times 0.021 + 4.0$$

$$\text{HHV} = 3738 + 1303 + 4 = 5045 \text{ Btu/lb}$$

An alternate method of estimating the HHV is to multiply the approximate dry combustible HHV of 9500 Btu/lb by the weight fraction of combustibles:

$$\text{HHV} = 9500 \times (1 - \text{moisture} - \text{ash})$$

$$\text{HHV} = 9500 \times (1 - 0.30 - 0.18)$$

$$\text{HHV} = 9500 \times 0.52 = 4940 \text{ Btu/lb}$$

The American Society for Testing and Materials (ASTM) publishes methods for determining the ultimate analysis of solid fuels such as MSW. The ultimate analysis of a fuel is developed through measures of carbon, hydrogen, sulfur, nitrogen, ash, and moisture content. Oxygen is normally determined "by difference"; that is, once the percentages of the other components are measured, the remaining material is assumed to be oxygen. For solid fuels, such as MSW, it is frequently desirable to determine the proximate analysis of the fuel. The procedure for determining the proximate analysis is also prescribed by ASTM. The qualities of the fuel measured in percentage by weight are moisture, volatile matter, fixed carbon, and ash. This provides an indication of combustion characteristics of a solid fuel. As a solid fuel is heated to combustion, first the moisture in the fuel evaporates, then some of the combustible constituents volatilize (gasify) and combust as a gas with oxygen, and the remaining combustible constituents remain as fixed carbon in a solid state and combust with oxygen to form carbon dioxide. The material remaining after combustion is complete is the ash. MSW, with a high percentage of volatiles and a low percentage of fixed carbon, burns with much flame.

Table 24.7 displays ignition temperatures for combustible substances in MSW. The ignition temperature is the temperature to which the combustible substance must be raised before it will unite in chemical combination with oxygen. Thus, the temperature must be reached and oxygen must be present for combustion to take place. Ignition temperatures are not fixed temperatures for a given substance. The actual ignition temperature is influenced by combustion chamber configuration, oxygen fuel ratio, and synergistic effect of

TABLE 24.7

Ignition Temperatures

Combustible	Molecular Symbol	Ignition Temperature (°F)
Carbon (fixed)	C	650
Hydrogen	H ₂	1080
Sulfur	S	470
Carbon monoxide	CO	1170

Source: From Stultz, S.C. and Kitto, J.B. (Eds.), *Steam: Its Generation and Use*, 40th edn., The Babcock and Wilcox Co., Barberton, OH, 1992.

TABLE 24.8

Theoretical Combustion Air

Combustible	Pounds per Pound of Combustible					
	Required for Combustion			Products of Combustion		
	O ₂	N _{atm}	Air	CO ₂	H ₂ O	N _{atm}
Carbon	2.67	8.87	11.54	3.67		8.87
Hydrogen	8.00	26.57	34.57		9.00	26.57
Sulfur	1.00	3.32	4.32	2.00		3.32
Carbon monoxide	0.57	1.89	2.46	1.57		1.89

Source: From Hecklinger, R.S., *Combustion, The Engineering Handbook*, Dorf, R.C. (ed.), CRC Press, Inc., Boca Raton, FL, 1996.

multiple combustible substances. The ignition temperature of MSW is the ignition temperature of its fixed carbon component. The volatile components of MSW are gasified but not ignited before the ignition temperature is attained.

The oxygen, nitrogen, and air data displayed in Table 24.8 represent the weight of air theoretically required to completely combust one pound of a combustible substance. The weight of oxygen required is the ratio of molecular weight of oxygen to molecular weight of the combustion constituent as displayed in Table 24.5. The weights of nitrogen and air required are calculated from the percentage by weight constituents of dry air. In actuality, to achieve complete combustion, air in excess of the theoretical requirement is required for complete combustion to increase the likelihood that all of the combustible substances are joined with sufficient oxygen to complete combustion. The level of excess air required in the combustion of MSW depends on the configuration of the combustion chamber, the nature of the fuel firing equipment, and the effectiveness of mixing combustion air with the MSW. An excess air level of 80% is commonly associated with combustion of MSW in modern WTE facilities. Excess air is generally monitored using an oxygen analyzer at the economizer outlet. The type of analyzer used at waste-to-energy facilities generally reports percent wet oxygen. The dry oxygen can be estimated by assuming 15% moisture in the flue gas using the following equation:

$$\text{Dry oxygen} = (\text{wet oxygen}) / (1 - \text{percent moisture}/100), \text{ or } \text{dry oxygen} = (1.176)(\text{wet oxygen})$$

Excess air can be approximated by the following equation:

$$\text{Excess air} = 55.2 - 10.46 \times (\text{dry O}_2) + 1.4 \times (\text{dry O}_2)^2$$

where dry O₂ is the percentage dry oxygen in the flue gas.

Excess air serves to dilute and thereby reduce the temperature of the products of combustion. The reduction of temperature tends to reduce the heat energy available for useful work. Therefore, the actual excess air used in the combustion process is a balance between the desire to achieve complete combustion and the objective of maximizing the heat energy available for useful work.

It is frequently useful to know the temperature attained by combustion. The heat released during combustion heats the products of combustion to a calculable temperature. It must be understood that the calculation procedure presented here assumes complete combustion and that no heat is lost to the surrounding environment. Thus, it is a temperature that is useful to compare one combustion process with another. The heat available for heating the products of combustion is the lower heating value of the fuel. The increase in temperature is the lower heating value divided by the mean specific heat of the products of combustion. The mean specific heat is a function of the constituent products of combustion ($W_{P.C.}$) and the temperature. To approximate the theoretical temperature attainable, one can use a specific heat of 0.55 Btu/lb/°F for water vapor (W_{H_2O}) and 0.28 Btu/lb/°F for the other gaseous products of combustion ($W_{P.C.} - W_{H_2O}$). Thus, the formula approximating the temperature attained during combustion is

$$T_{\text{comb}} = T + \frac{\text{LHV}_{\text{Btu/lb}}}{0.55W_{\text{H}_2\text{O}} + 0.28(W_{\text{P.C.}} - W_{\text{H}_2\text{O}})} \quad (24.4)$$

For example (using data from Table 24.9)

$$T_{\text{comb}} = T_{\text{ambient}} + \frac{\text{LHV}_{\text{Btu/lb}}}{0.55W_{\text{H}_2\text{O}} + 0.28(W_{\text{P.C.}} + W_{\text{H}_2\text{O}})}$$

If the ambient temperature is assumed to be 60°F, then

$$T_{\text{comb}} = 60 + \frac{4184}{0.55 \times 0.81 + 0.28(7.55 - 0.81)}$$

$$T_{\text{comb}} = 60 + \frac{4184}{0.45 + 1.89} = 60 + \frac{4184}{2.34}$$

$$T_{\text{comb}} = 1848 \cong 1850^\circ\text{F}$$

Typical combustion calculations are provided in Table 24.9 for MSW to determine the products of the combustion process. Each of the combustible substances combines and completely combusts with oxygen as displayed in Table 24.5. The weight ratio of oxygen to the combustible substance is the ratio of molecular weights. Table 24.8 displays the weight or volume of oxygen theoretically required for complete combustion of one pound of the combustible substance. Sulfur dioxide from combustion of sulfur in fuel is combined with CO_2 in the sample calculation as a matter of convenience. If desired, a separate column can be prepared for sulfur dioxide in the products of combustion. Oxygen in the fuel combines with the combustible substances in the fuel, thereby reducing the quantity of air required to achieve complete combustion. The sample calculation uses the weight percentages of oxygen

TABLE 24.9

Sample Calculation for Municipal Solid Waste (MSW)

Air Calculations (80% Excess Air)				
Ultimate Analysis				
Substance	Fraction% by Weight	Oxygen Required for Combustion, lb/lb of Element	Theoretical Oxygen, lb/lb of Element	Theoretical Dry Air, lb/lb of Element
Carbon	0.279	2.67	0.745 ^a	3.218 ^b
Hydrogen	0.037	8.00	0.296 ^a	1.279 ^b
Oxygen	0.209	—	—	—
Nitrogen	0.005	—	—	—
Sulfur	0.002	1.00	0.002 ^a	0.009 ^b
Ash	0.187			
Fuel moisture	0.281			
Total	1.000		1.043	4.505
Less oxygen in fuel			(0.209)	(0.903) ^c
Air				
Required at 100% theoretical air			0.834	3.603
180% of theoretical air (80% excess air)			1.501	6.485
Excess			0.667	2.882
HHV = 5100 Btu/lb				
Products of Combustion			lb/lb of Element	lb of Product
Carbon dioxide			3.67	1.024 ^d
Moisture from hydrogen			9.00	0.333 ^d
Oxygen			0.667 ^e	
Nitrogen			4.989 ^f	
Sulfur dioxide			2.00	0.004 ^d
Moisture from fuel			1.00	0.281 ^d
Moisture from air			0.084 ^g	
Total moisture			0.698 ^h	
Total			7.382	
LHV = 5100 - [0.281 + (9 × 0.037)] × 1050 = 4455 Btu/lb				
Temperature developed in combustion = 60 + 4455 / [(0.698 × 0.55) + (7.382 - 0.698) × 0.28] = 2035°F				
Check:				
Total products of combustion = 180% of theoretical air + moisture from air + fraction percent by weight of C, H, O, N, S, and moisture				
7.382 = 6.485 + 0.084 + 0.279 + 0.037 + 0.209 + 0.005 + 0.002 + 0.281 = 7.382				

^a Weight percent of element times oxygen required for combustion.
^b Theoretical oxygen times 4.32.
^c Amount of theoretical air due to oxygen in fuel.
^d Weight percent of element times lb/lb of element.
^e Excess oxygen.
^f 180% of theoretical dry air times 0.7686 plus weight percent of nitrogen in fuel.
^g Moisture in combustion air = 0.013 times 180% of theoretical air (0.013 lb moisture per lb of dry air at 80°F and 60% relative humidity).
^h Total of moisture from combustion of hydrogen, moisture in fuel, and moisture from air.
ⁱ Heat capacity of water vapor.
^j Heat capacity of dry flue gas.

to reduce the theoretical air requirements and the nitrogen in the products of combustion. The decimal percentage of excess air is multiplied by the total theoretical air requirement to establish the weight of excess air and the total air requirement including excess air.

24.3.4 Furnaces

While the general principles of a modern waste combustor burning as-received MSW are common to all types, the specific solid waste combustion process is rather complex. The waste is heated by contact with hot combustion gases or preheated air, and by radiation from the furnace walls. Drying occurs in a temperature range of 122°F–302°F (50°C–150°C). At higher temperatures, volatile matter is formed by complicated thermal decomposition reactions. This volatile matter is generally combustible and, after ignition, produces flames. The remaining material is further degased and burns much more slowly. In an RDF furnace (see Figure 24.3), most of the volatile matter and some of the fixed carbon is burned in suspension while the remaining fixed carbon is combusted on a grate at the bottom of the furnace.

The complexity of the combustion of solid waste streams results from the nature of the decomposition and burning reactions and their association with heat transfer, air flow, and diffusion. In most waste combustors, combustion takes place while the solids are supported on and conveyed by a grate. Since the early 1960s, most MSW incinerators have incorporated one of a number of available proprietary grate systems that allow continuous feed of unscreened waste into and movement through furnaces with integral boiler facilities. The grate performs several functions: provides support for the refuse, admits underfire air through openings in the grate surface, transports the solid waste from feed mechanism to ash quench, agitates the bed, and serves to agitate and redistribute the burning mass.

The basic design factors which determine furnace capacity are grate area and furnace volume. Also, the available capacity and method of introducing both underfire and overfire air will influence, to a lesser extent, furnace capacity. Required grate area, in a conservative design, is normally determined by limiting the burning rate to between 60 and 70 lb/ft² h (290–340 kg/m² h) of grate area.⁵⁴ This is based on limiting the heat release rate loading on the grate to 250,000–300,000 Btu/ft² of grate per h (2.8–3.4 GJ/m²/h).

Furnace volume required is established by the rate of heat release from the fuel. Thus, furnace volume is generally established by using heat release rates ranging from 12,500 to 20,000 Btu/ft³/h (450–750 MJ/m³/h), with the lower heat release rate being more desirable from the standpoint of developing a conservative design. A conservative approach to design in this area is desirable because of probable periodic operation above design capacity to meet short-term higher than normal refuse collections and possible receipt of high heat-content waste.

Water wall units burning as-received MSW have been built as small as 75–100 tons/day (68–91 tons/day) capacity. However, the cost per ton of rated capacity of such units is relatively high. A more common unit size for both mass-burn and RDF furnaces is 250–1000 tons/day (225–900 tons/day), while water wall mass-fired units have been built as large as 750–1200 tons/day (675–1090 tons/day) capacity.⁵

The primary objective of a mechanical grate in a mass-burn furnace is to convey the refuse from the point of feed through the burning zone to the point of residue discharge with a proper depth of fuel and sufficient retention time to achieve complete combustion. The refuse bed should be agitated so as to enhance combustion. However, the agitation

should not be so pronounced that particulate emissions are unreasonably increased. The rate of movement of the grate or its parts should be adjustable to meet varying conditions or needs in the furnace.

In the United States over the past 20 years, several types of mechanical grates have been used in continuous feed furnaces burning as-received MSW. These include reciprocating grates (see Figure 24.4), rocking grates (see Figure 24.5), roller grates (see Figure 24.6),

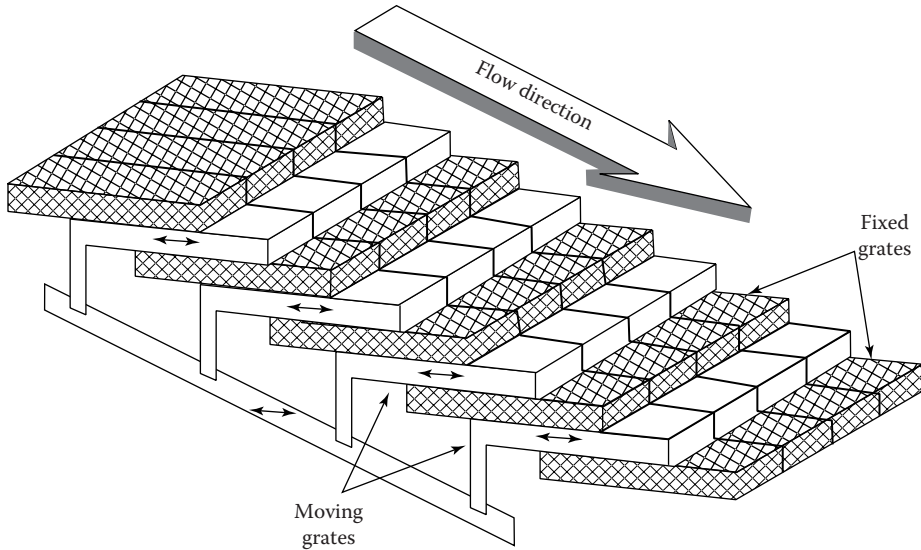


FIGURE 24.4
Reciprocating grates.

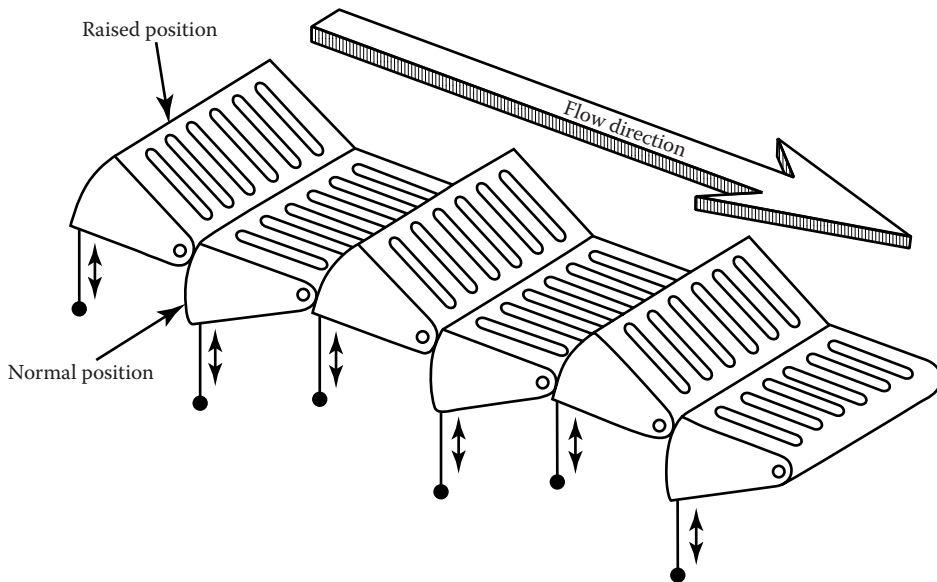


FIGURE 24.5
Rocking grates.

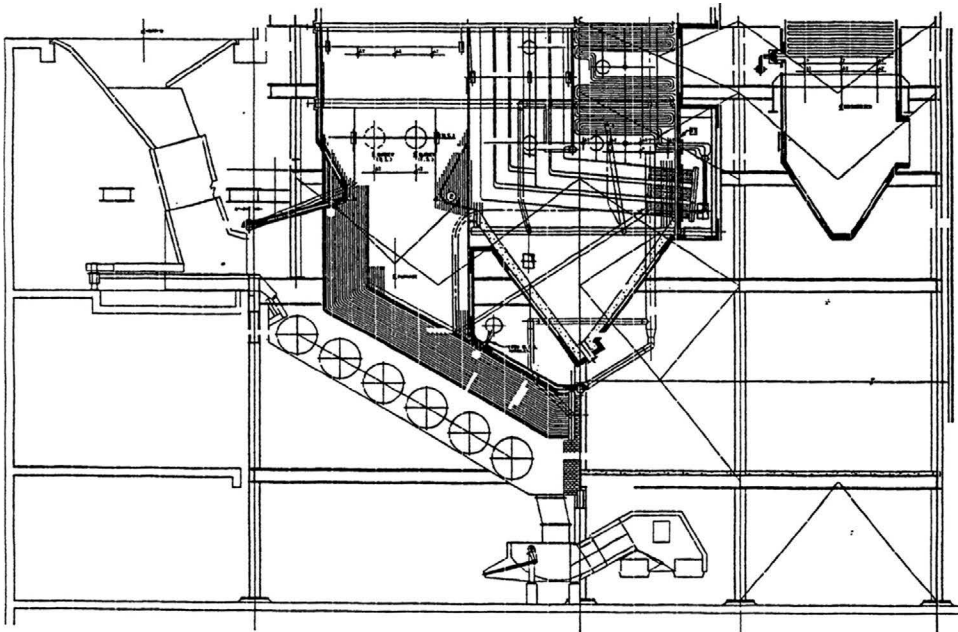


FIGURE 24.6
Roller grate system by Covanta Energy Group.

and water wall rotary combustors for mass-burn units, and traveling grates for RDF units (see Figure 24.3). The reciprocating grates, rocking grates, and roller grates agitate and move the refuse material through the furnace by the movement of the grate elements and the incline of the grate bed. Additional agitation is obtained, particularly in the reciprocating grate, by drops in elevation between grate sections. The rotary combustor slowly rotates to tumble the refuse material, which is conveyed through the inside of the cylinder. The combustor is inclined from the horizontal so that gravity assists in moving the material through the unit. The traveling grate conveys the refuse through the furnace on the grate surface. Stirring is accomplished by building the grate in two or more sections, with a drop between sections to agitate the material.

Other grate systems have been developed in Europe for burning as-received MSW, some of which are currently being utilized in plants being constructed or in operation in the United States. The roller grate, or so-called Dusseldorf System (see Figure 24.6), uses a series of 5 or more rotating cylindrical grates, or drums, placed at a slope of about 30° .⁵⁷ The refuse is conveyed by the surface of the drums, which rotate in the direction of refuse flow, and is agitated as it tumbles from drum to drum. Underfire air is introduced through the surface of the drums. Both the Von Roll and the Martin grates use a reciprocating motion to push the refuse material through the furnace. However, in the Martin grate (see Figure 24.7), the grate surface slopes steeply down from the feed end of the furnace to the ash discharge end and the grate sections push the refuse uphill against the flow of waste, causing a gentle tumbling and agitation of the fuel bed.

Another variable feature in the various grate designs is the percentage of open area to allow for passage of underfire air.⁷³ These air openings vary from approximately 2% to 30%

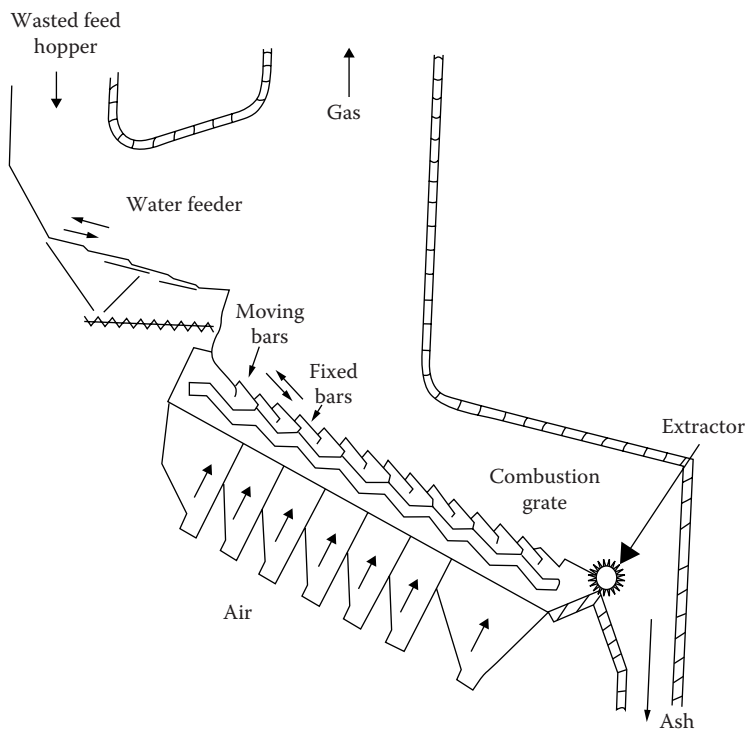


FIGURE 24.7

Martin system. (From Braun, H., Metzger, M., and Vogg, H., *Zur Problematik der Quecksilber-Abscheidung aus Rauchgasen von Mullverbrennungsanlagen*, Vol. 1, Teil 2, 1985.)

of the grate surface area. The smaller air openings tend to limit the quantity of siftings dropping through the grates and create a pressure drop that assists in controlling the point of introduction of underfire air. RDF grates generally have a smaller percentage of air openings. Larger air openings make control of underfire air more difficult but allow for continuous removal of fine material, which could interfere with the combustion process, from the fuel bed.

Furnace configuration is largely dictated by the type of grate used. In the continuous feed mechanical grate system, the furnace is rectangular in plan and the height is dependent upon the volume required by the limiting rate of heat release cited earlier. An optimum furnace configuration would provide sufficient volume for retention of gases in the high-temperature zone of maximum fuel volatilization long enough to ensure complete combustion, and would be arranged so that the entire volume is effectively utilized. Temperatures are usually high enough with present-day refuse for proper combustion. Turbulence should be provided by a properly designed overfire air system.

With present-day mass-fired water wall furnaces, the use of refractories in furnace construction has been minimized but not eliminated. Refractory materials may be used to line charging chutes, provide a transition enclosure between the top of the grates and the bottom of the water walls, a protective coating on the water wall tubes, and an insulating layer between the hot gases and the metal walls of flues downstream of the primary combustion chamber. Refractory brick used in a charging chute must be able to withstand high temperatures, flame impingement, thermal shock, slagging, spalling, and abrasion. The protective coating on the water wall tubes must be

relatively dense castable material with a relatively high heat conductivity.⁷⁴ Insulating refractories used in flues downstream from the boilers, on the other hand, should have a low heat conductivity.

Refractories are generally classified according to their physical and chemical properties, such as resistance to chemical attack, hardness, strength, heat conductivity, porosity, and thermal expansion.⁴⁹ The material may be cast in brick in a variety of shapes and laid up with air-setting or thermal-setting mortar, or may be used in a moldable or plastic form. Material used in waste combustor construction includes "high duty" and "superduty" fireclay brick, phosphate-bonded alumina material, and silicon carbide, among others. In selecting the proper materials for application in this type of service, because the variety of materials is so great and the conditions of service so varied and severe,¹⁶ advice of a recognized manufacturer should be sought.

As indicated in the section on combustion calculations, the combustion process requires oxygen to complete the reactions involved in the burning process. The air that must be delivered in the furnace to supply the exact amount of oxygen required for completion of combustion is called the stoichiometric air requirement. Additional air supplied to the furnace is called excess air and is usually expressed as a percentage of the stoichiometric requirements.

The total air supply capacity in a waste combustor must be greater than the stoichiometric requirement for combustion because of imperfect mixing and to assist in controlling temperatures, particularly with dry, high heat-content refuse. The total combustion air requirements can range from 6 to 8 lb of air/lb of refuse for mass-fired water wall furnaces, and slightly less for RDF facilities.

In the modern mass-burn mechanical grate furnace chamber, at least two blower systems should be provided to supply combustion air to the furnace—one for underfire or undergrate air and the other for overfire air. Underfire air, admitted to the furnace from under the grates and through the fuel bed, is used to supply primary air to the combustion process and to cool the grates.

Overfire air may be introduced in two levels. Air introduced at the first level, called secondary air, immediately above the fuel bed, is used to promote turbulence and mixing, and to complete the combustion of volatile gases driven off the bed of burning solid waste. The second row of nozzles, which are generally located higher in the furnace wall, allow the introduction of air, called tertiary air, into the furnace to promote additional mixing of gases and for temperature control.

Blower capacities should be divided so that the underfire air blower is capable of furnishing half to two-thirds of the total calculated combustion air requirements, while the overfire blower should have a capacity of about half of the total calculated air requirements. Setting these capacities requires some judgment related to assessing how great a variation is anticipated in refuse heat contents during plant operation. Variable frequency drivers on the fan motors or dampers on fan inlets and air distribution ducts should be provided for control purposes.

Pressures on underfire air systems in mass-burn units for most U.S. types of grates will normally range from 2 to 5 in. of water. European grates frequently require a higher pressure. The pressure on the overfire air should be high enough that the air, when introduced into the furnace, produces adequate turbulence without impinging on the opposite wall. This is normally accomplished by the use of numerous relatively small (1½–3 in. in diameter) nozzles at pressures of 20 in. of water or higher.

Recirculated flue gas is sometimes used in part for underfire air and tempering air. Using recirculated flue gas as combustion air reduces the quantity of fresh air needed,

thereby increasing thermal efficiency and minimizing thermal NO_x formation. It can also be used as tempering air to control the temperature of the flue gas entering the boiler.¹³ The duct work for recirculated flue gas is highly susceptible to corrosion due to the presence of acid gases. For this reason, it is critical that the recirculated gas be taken from the system after the pollution control devices.

In an RDF-fired, spreader-stoker type of unit, the combustible material is generally introduced through several air-swept spouts in the front water wall, is partially burned in suspension, and then falls onto a grate on which combustion is completed as the partially burned material is conveyed to the residue discharge under the front water wall face of the furnace. Densified RDF can also be burned in such units. The RDF can furnish all the combustible input to the system, or it may be co-fired with a fossil fuel, generally coal.

Some combustion air in RDF-fired units is introduced with the fuel through the air-swept feed spouts to distribute the fuel on the grate. Additional air is introduced into the furnace higher in the water wall area to enhance turbulence and mixing in the unit and/or to control temperatures. This additional combustion air supply is similar to the tertiary air utilized in the mass-burn units.

24.3.5 Boilers

Substantial quantities of heat energy may be recovered during the thermal destruction of the combustible portions of MSW. Systems that have been successfully used to recover this energy include mass-fired refractory combustion chambers followed by a convection boiler section; a mass-fired water wall unit where the water wall furnace enclosure forms an integral part of the boiler system and an RDF semisuspension-fired spreader-stoker/boiler unit. Each system has apparent advantages and disadvantages.

24.3.5.1 Refractory Furnace with Waste Heat Boiler

In a refractory furnace waste heat boiler unit, energy extraction efficiencies are generally lower, assuming the same boiler outlet temperatures, than with the other systems. Approximately 50%–65% of the heat generated in the combustion process may be recovered with such systems. These units can produce approximately 2–3 lb steam/lb of normal MSW (heat content = 4500 Btu/lb), versus 3 or more lb/lb MSW in mass-fired water wall units. This lower efficiency of steam generation is caused by larger heat losses due to higher excess air quantities needed with such units to control furnace temperatures so that furnace refractories are not damaged. However, the boilers in such units, if properly designed and operated, generally are less susceptible to boiler tube metal wastage problems than the other systems listed earlier.

24.3.5.2 Mass-Fired Water Wall Units

Mass-fired water wall units are the most widely utilized type of heat recovery unit in this field today. In this type of unit, the primary combustion chamber is fabricated from closely spaced steel tubes through which water circulates. This water wall lined, primary combustion chamber incorporated into the overall boiler system is followed by a convection type of boiler surface. It has been found desirable in these plants to coat a substantial height of the primary combustion chamber, subject to higher temperatures and flame impingement, with a thin coating of a silicon carbide type of refractory material

or inconel and to limit average gas velocities to under 15 ft/s (4.5 m/s) in this portion of the furnace. Gas velocities entering the boiler convection bank should be less than 30 ft/s (9.0 m/s).⁷⁴ Efficiency of heat recovery in such units has been found to range generally from 65% to 75%, with steam production usually above 3 lb of steam/lb of normal as-received MSW. Water table studies have been used occasionally in some larger units to check on combinations of furnace configuration and location of overfire combustion of air nozzles.²⁷

24.3.5.3 RDF-Fired Water Wall Units

As pointed out earlier, RDF may be burned in a semisuspension-fired spreader-stoker/boiler unit where the RDF is introduced through several air-swept spouts in the front water wall, partially burns in suspension, and then falls on a grate on which combustion is completed. In this type of unit, the water wall lined primary combustion enclosure (furnace) may be followed by a superheater (usually), a convection boiler heat transfer surface, and (sometimes) an economizer surface.

Efficiencies of RDF-fired boilers generally range from 65% to 80% of the heat input from the RDF. Steam production from RDF would normally be expected to be somewhat greater than 3 lb of steam/lb of RDF. However, when one takes into account the combustible material lost in the processing of as-received MSW to produce the RDF, steam production normally will fall to about 3 lb of steam/lb of as-received MSW.³⁵

If the energy recovered from the combustion of as-received MSW or RDF is to be used to produce electricity, some superheating is desirable, if not necessary. Since boiler tube metal wastage in these plants is, at least partially, a function of tube metal temperature¹⁰ and steam is a less efficient cooling medium than water, superheater surface is more prone to metal wastage problems than other areas of boiler tubing. Tube metal temperatures, above which metal wastage can be a significant operational problem, are generally thought to range from 650°F to 850°F (345°C–455°C). These temperatures are lower than those for maximum efficiency of electrical generation by steam driven turbines. It is desirable to consider this in facility design to reduce plant downtime and minimize maintenance costs.

In the 1980s and early 1990s a so-called full-suspension combustion concept was attempted in which finely shredded combustible material from MSW was blown into the furnace through nozzles located one-half to two-thirds up the height of the water wall furnace enclosure. In this type of unit most of the RDF, usually composed of smaller sized particles than in the semisuspension-fired unit was supposed to burn in suspension. This concept was not successful due to problems related to the additional handling of the RDF and greater power required to achieve a finer shred. Also, some boilers seemed to experience a greater tendency for slag formation in the boiler. While the concept initially anticipated that the RDF would completely burn in suspension, experience indicated that this does not occur. Accordingly, dump grates became a necessity in such furnace boiler units to allow for completion of combustion prior to water quenching of the residue. This concept has been abandoned.

24.3.6 Residue Handling and Disposal

The residue from a well-designed, well-operated mass-fired incinerator burning as-received refuse will include the noncombustible material in the MSW and usually somewhat less than 3% of the combustibles. The nature of this material will vary from relatively

fine, light ash, burned tin cans, and partly melted glass to large, bulky items such as lawn mowers and bicycles.

In most modern WTE plants bottom ash residue is discharged from the end of the furnace grate through a chute into a trough filled with water. Removal from the trough may be either by a ram discharger onto a conveyor or by a flight conveyor to an elevated storage hopper from which it is discharged to a truck. If a water-filled trough with a flight conveyor is used, normally two troughs are provided, arranged so that the residue can be discharged through either trough. The second trough serves as a standby. Fly ash, residue collected in the air pollution control equipment downstream of the furnace/boiler, is usually returned back to and mixed with the bottom ash.

A key feature in the design of ash discharge facilities is provision for sealing the discharge end of the furnace to prevent uncontrollable admission of air. This seal is usually provided by carrying the ash discharge chute at least 6 in. (15 cm) below the water surface in the receiving trough. In the design of the conveyor mechanism, the proportions should be large because the material frequently contains bulky metal items and wire, potential causes of jamming. Also, the residue material tends to be extremely abrasive. A grizzly screen is often used to remove oversized bulky materials from the residue prior to its being loaded onto trucks for delivery to the landfill.

Residue is usually taken to a landfill for final disposal. Many modern facilities dispose of their residue at monofills (landfills that accept WTE plant residue only). The volume of material remaining for ultimate disposal will range from 5% to 15% of that received at the plant. Many plants currently operating in the United States that weigh MSW received at the plant and residue discharged from the furnaces, indicate that the weight of MSW is only reduced by from 40% to 50%. However, as much as one-third of the residue weight in these plants may be attributed to incomplete drainage of the material prior to its discharge into the final transportation container. The ram-type ash discharger used in European and most large U.S. plants generally achieves much better dewatering of residues than older water-filled trough, ash drag residue handling systems. These systems can achieve 65%–75% weight reduction.

The main components of ash are inert materials of low solubility, such as silicates, clay, and sand. Aluminum, calcium, chlorine, iron, selenium, sodium, and zinc are major elements in all particles and, along with carbon, can comprise over 10% by weight of the ash.²⁰

A broad range of trace metals and organic compounds may be found in fly and bottom ash. Data on ash composition are difficult to compare, however, because they reflect different types and sizes of facilities, unknown sample collection methodology and sample size at each facility, interlab variation in testing procedures (even using the same test), and the heterogeneous nature of MSW itself. In addition, the presence of a substance in ash does not mean that it will enter the environment. Its fate depends on its solubility, how the ash is managed, and whether the ash is subject to conditions that cause leaching.⁴⁷

Metals tend to be distributed differently in fly and bottom ash. Most volatile and semi-volatile metals, such as arsenic, mercury, lead, cadmium, and zinc, tend to be more concentrated or “enriched” in fly ash.^{59,70} Less volatile metals, such as aluminum, chromium, iron, nickel, and tin, typically are concentrated in bottom ash.^{58,59}

Organic chemicals also exhibit differing distributions. Dioxin/furan and polychlorinated biphenyls (PCBs) tend to be enriched in fly ash, while other chemicals such as polycyclic-aromatic hydrocarbons (PAHs) and phthalates tend to be concentrated in bottom ash.⁷⁰ Concentrations of dioxins/furans in fly ash exhibit a wide range, but they are significantly lower in ash from modern facilities than in ash from older incinerators.^{32,71,79}

From a regulatory standpoint, a number of different testing procedures have been developed and utilized by regulatory agencies over the past several years in an attempt to predict the behavior of MSW residues deposited in landfills. Most of these methods were developed to predict leaching characteristics of residues deposited in landfills with raw or as-received MSW. Test results using these methods have been quite variable. However, as pointed out earlier, most modern WTE facilities dispose of their residue in monofills.⁶⁸ Tests of leachate from such monofills indicate metals concentrations below extraction procedure (EP) toxicity limits, and in most cases below U.S. drinking water standards.⁶⁸ Most test data show little or no leaching of organic chemicals.^{33,68}

Following a court decision in the mid-1990s that ash residue from combustion of MSW is not exempt from the rules and regulations for hazardous waste, regulators have required testing of ash residues as they are discharged from the plant, i.e., separately if bottom ash and fly ash are discharged separately, and combined if they are combined prior to discharge from the plant. Bottom ash is alkaline and usually tests as nonhazardous, while fly ash is acidic and frequently tests as hazardous. When the fly ash is mixed with bottom ash prior to discharge from the plant, the alkaline bottom ash neutralizes the smaller quantities of acidic fly ash. The mixture tests as nonhazardous and can be disposed of in the normal monofill.

24.3.7 Other Plant Facilities

The balance of the plant equipment is similar to that used in fossil-fuel-fired boiler facilities. However, there are differences. Thus, the combustion of MSW produces a highly corrosive environment for boiler tube materials. Metal chlorides are believed to be primarily responsible for boiler tube corrosion problems.⁴⁰ The most important factors in high temperature corrosion are metal temperature, gas temperature, temperature gradient between gas temperature and metal temperature, deposit characteristics, and temperature fluctuations.¹ For this reason, boiler tubes are generally fabricated using corrosion-resistant alloys. Boiler tube shields or weld overlay cladding of boiler tubes with inconel are also used in highly corrosive/erosive areas.⁴⁰

Some waste-to-energy facilities incorporate an air heater to preheat combustion air. Finned tubes plug quickly due to the large quantity of flyash in the flue gas. These air heaters are always of the bare tube design.

Since thermal efficiency is not an overriding concern in waste-to-energy facilities, many plants have one, or at most two, feedwater heaters. Some have only a deaerator for feedwater heating, unlike conventional power plants which have several stages of feedwater heaters.

24.4 Air Pollution Control Facilities

Potential emissions from the combustion of MSW may be broadly classified into particulates, gaseous emissions, organic compounds, and trace metals. The concern is to reduce emissions so as to adequately protect public health. This is achieved using good combustion practice and equipment specially designed to remove the targeted pollutants.

During the 1980s and 1990s, the emission requirements for air pollution control equipment became more stringent as the USEPA promulgated new standards. The most recent standards were published in the December 19, 1995 Federal Register as 40 CFR Part 60 Subpart Cb.^{4,72} These standards established emission limits for large (over 248 tons/day

TABLE 24.10

Emission Limits for Large Combustor Units

Parameter	Limit	Conditions
Particulates	27 mg/DSCM	Corrected to 7% oxygen
Opacity	10%	6 min average
Cadmium	0.04 mg/DSCM	Corrected to 7% oxygen
Lead	0.49 mg/DSCM	Corrected to 7% oxygen
Mercury	Lesser of 0.08 mg/DSCM or 85% removal	Corrected to 7% oxygen
SO ₂	Lesser of 31 ppmv or 75% removal	Corrected to 7% oxygen 24 h geometric mean
HCl	Lesser of 31 ppmv or 95% removal	Corrected to 7% oxygen
Dioxin/furans	60 ng/DSCM-ESP 30 ng/DSCM—all others	Corrected to 7% oxygen
NO _x	220 ppmv—water wall	Corrected to 7% oxygen
	250 ppmv—rotary water wall	Corrected to 7% oxygen
	250 ppmv—RDF	Corrected to 7% oxygen
	240-fluidized bed	Corrected to 7% oxygen

TABLE 24.11

Emission Limits for Small Combustor Units

Parameter	Limit	Conditions
Particulates	70 mg/DSCM	Corrected to 7% oxygen
Opacity	10%	6-min average
Cadmium	0.10 mg/DSCM	Corrected to 7% oxygen
Lead	1.6 mg/DSCM	Corrected to 7% oxygen
Mercury	Lesser of 0.08 mg/DSCM or 85% removal	Corrected to 7% oxygen
SO ₂	Lesser of 80 ppmv or 50% removal	Corrected to 7% oxygen 24 h geometric mean
HCl	Lesser of 250 ppmv or 50% removal	Corrected to 7% oxygen
Dioxin/furans	125 ng/DSCM	Corrected to 7% oxygen
NO _x	No limit	Corrected to 7% oxygen

[225 Mg/day]) and small (under 248 tons/day [225 Mg/day]) combustor units. Tables 24.10 and 24.11 contain a summary of those standards.

24.4.1 Particulate Control

Particulates have been a matter of concern and regulatory agency attention for some time. The initial concern was from the standpoint of reducing gross particulate emissions that were both an aesthetic and a potential public health problem. Current interest and concern is directed toward better control of submicron-size particles⁷⁵ and other pollutants.

Electrostatic precipitators were the most commonly used gas cleaning device for particulate emission control in municipal waste combustors in the 1970s and early 1980s. They were designed to achieve high collection efficiencies (99% or higher) and meet the air emissions standards at the time. As emission standards became more stringent for particulates, fabric filters became more prevalent. Many electrostatic precipitators were replaced with fabric filters due to the 1995 regulations.

Fabric filters can operate at high efficiency, even in the submicron particle size range. They became widely used in the late 1980s because of the increasing emphasis of regulatory agencies on acid gas control and lower particulate emission levels. Baghouses are more effective than electrostatic precipitators for acid gas scrubbing when preceded by a spray dryer. The original bags used in these facilities had a limited life at high temperatures. Experiments using different materials of construction have led to longer bag life.

The scrubber/fabric filter control systems have been shown to be capable of operating at a particulate emission level of 20 mg/Nm³ (0.009 gr/dscf) and lower (see Table 24.12). The material selected for the filter bags can have an important effect on filtering efficiency and the emission level thus achieved. In general, test results to date for the scrubber/fabric indicate lower particulate emissions than those for electrostatic precipitators on WTE plants. However, in general, electrostatic precipitators have not been designed to meet emission levels as low as those specified for fabric filter installations. Electrostatic precipitators following spray drying absorbers in Europe have been tested at particulate emission levels of 1–8 mg/Nm³ (0.00045–0.0036 gr/dscf). The reliability and overall economics of the various control processes must be considered when making a selection of equipment to meet these very low emission control requirements. Data are available⁶⁸ on emission levels for approximately 30 different specific elements, many of them heavy metals. Elements found to occur in stack emission from municipal waste combustors are lead, chromium, cadmium, arsenic, zinc, antimony, mercury, molybdenum, calcium, vanadium, aluminum, magnesium, barium, potassium, strontium, sodium, manganese, cobalt, copper, silver, iron, titanium, boron, phosphorus, tin, and others.

Since the condensation point for metals such as lead, cadmium, chromium, and zinc is above 570°F (300°C), the removal efficiency for such metals is highly dependent on the particulate removal efficiency. Some metal compounds, particularly chlorides such as AsCl₃ at 252°F (122°C) and SnCl₄ at 212°F (100°C), have condensation points below 300°C. For such compounds, particulate collection temperatures will be a factor in collection efficiency. High removal (over 99%) has been observed for most metals for highly efficient (over 99%) particulate removal systems operating at appropriate temperatures.

TABLE 24.12

Particulate Emissions from Municipal Waste Combustors

	Particulates (gr/dscf) ^a at 12% CO ₂
Plant G (1983); EP	0.0321
Plant T (1984); DS, BH	0.012
Plant M (1984); DS, EP	0.0104
Plant W (1985); DS, BH	0.004
Plant P (1985); EP	0.0163
Plant T (1986); EP	0.007
Plant M (1986); DS, BH	0.007

Source: From Velzy, C.O., U.S. Experience in combustion of municipal solid waste, presented at the *APCA Specialty Conference on Regulatory Approaches for Control of Air Pollutants*, Atlanta, GA, February 20, 1987.

Notes: EP, electrostatic precipitator; DS, dry scrubber; BH, bag house.

^a Grains per dry standard cubic foot.

24.4.2 Gaseous Emission Control

Gaseous emissions such as SO_2 , HCl, CO, NO_x and hydrocarbons have recently become a concern in municipal waste combustors and their emissions are now regulated. Acid gas emissions are controlled by scrubbing devices. Carbon monoxide, NO_x , and hydrocarbons are controlled by good combustion practice. Oxides of nitrogen in some cases also require control equipment in the form of selective noncatalytic reduction (SNCR) to reduce NO_x to acceptable levels.

Common gaseous emission factors, based on tests at a number of waste-to-energy plants, are shown in Table 24.13. High carbon monoxide and hydrocarbon emissions are caused by incomplete combustion and/or upsets in combustion conditions. High nitrogen oxide emissions are generally caused by high combustion temperatures. Hydrogen chloride (and hydrogen fluoride) and sulfur oxides, on the other hand, are directly a function of the chlorine (fluorine) and sulfur content in the fuel. The highest emissions, cited in Table 24.13, are from older, poorly controlled plants without significant pollution control equipment. Hydrogen chloride (and hydrogen fluoride) and sulfur oxides are best removed by acid gas scrubbing devices using chemical treatment. Initial efforts at acid gas control used wet collectors. However, this type of flue gas cleaning equipment is subject to problems such as corrosion, erosion, generation of acidic waste water, wet plumes, and, not least, high operating cost. Because of these problems, various semiwet and dry methods of cleaning flue gases have been developed and installed. These methods of gas treatment are based on the injection of slurried or powdered lime, limestone, or dolomite; adsorption; and absorption; followed by chemical conversion.⁶⁸ Since the reactivity of these lime materials is rather low, a multiple of the stoichiometric quantity is normally required to obtain a satisfactory cleaning effect. High removal efficiencies can be achieved for HCl, but reduction of SO_2 and SO_3 is more difficult to achieve and maintain. Slaked lime is highly reactive and stoichiometric ratios of 1.2–1.7 have been used for 97%–99% HCl removals and 60%–90%

TABLE 24.13

Gaseous Emission Factors for Municipal Waste Combustors (lb/ton)

	New York Incinerators	Test Results U.S. Plants	Martin Plants	EPA Data Base Tests through 1988	
	1968–1969	1971–1978	1984–1986	Mass-Burn	RDF
Carbon monoxide	—	3.7–9.3	0.2	0.06–16.2	1.0–5.2
Nitrogen oxides	—	0.5–2.2	5.0–6.0	0.5–4.5	2.5–3.2
Hydrocarbons	0.1–22.1	1.1	0.015–0.006	0.01–0.1	0.005–0.01
Hydrochloric acid	1.4–8.6	4.6–14.5	5.0–0.2	0.05–5.7	0.02–9.3
Sulfur oxides	1.3–8.0	0.8–2.2	1.0–2.0	0.05–4.8	0.05–2.3

Sources: From Carrotti, A.A. and Smith, R.A., *Gaseous Emissions from Municipal Incinerators*, USEPA Publication No. SW-18C, 1974; Cooper Engineers, Inc., *Air Emissions Tests of a Deutsche Babcock Anlagen, Dry Scrubber System at the Munich North Refuse-Fired Power Plant*, 1985; Cooper Engineers, Inc., *Air Emissions and Performance Testing of a Dry Scrubber (Quench Reactor)*, Dry Venturi and Fabric Filter System Operating on Flue Gas from Combustion of Municipal Solid Waste in Japan, West County Agency of Contra Costa County Waste Co-Disposal/Energy Recovery Project, May, 1995; Hahn, J.L. et al. (Ogden Martin Systems, Inc.), and Weiland, H. et al. (Martin GmbH), in: *Proceedings of the 1986 National Waste Processing Conference*, Denver, CO, June 1–4, 1986, ASME, New York; Murdoch, J.D. and Gay, J.L., Material recovery with incineration, Monmouth County, NJ, in: *Proceedings of 27th Annual International Solid Waste Exposition*, Tulsa, OK, SWANA, Silver Springs, MD (Pub. #GR-0028), August 14–17, 1989, p. 329; Velzy, C.O., Standards and control of trace emissions from refuse-fired facilities, in: *Municipal Solid Waste as a Utility Fuel*, EPRI Conference Proceedings, Madison, WI, November 20–22, 1985.

SO₂ reductions, depending on operating conditions and particulate collector (fabric filters having demonstrated higher removal efficiencies than electrostatic precipitators).

Lime injection into a scrubber/fabric filter system has resulted in removal efficiencies of 90%–99% for HCl and 70%–90% SO₂, provided that the flue gas temperature and the stoichiometric ratio for lime addition are suitable. This combination of processes has reduced HCl levels below 20 ppm and SO₂ to levels below 30 ppm for MSW waste-to-energy plants. This technology has also been extensively used in other applications for acid gas removal. The scrubber/electrostatic precipitator combination has been shown to provide about 90% HCl removal, but typically less SO₂ removal (about 50%). Since this removal efficiency does not meet the most recent regulations, many electrostatic precipitators have been replaced with baghouses. Lime injection into the furnace has also been tested with some success (about 50%–70% efficiency), but fails to meet the most recent regulations.

Some sampling to determine HF removal has been reported. In general, HF removal normally follows HCl removal (i.e., is usually over 90%–95%).

Carbon monoxide and hydrocarbon emissions are best controlled by maintaining proper combustion conditions. Nitrogen oxide emissions are controlled by ammonia injection or by use of combustion control techniques such as limitation of combustion temperatures or recirculation of flue gases. Note in the last column of Table 24.13 that attempts to limit hydrocarbon emissions by improving combustion conditions and raising furnace operating temperatures seem to have resulted in increasing the level of NO_x emissions.

Selective noncatalytic reduction (SNCR) appears to be the most practical method of reducing NO_x emissions for most municipal waste combustors. SNCR involves the use of ammonia to reduce NO_x to nitrogen and water. The SNCR reaction occurs at a temperature of 1600°F–2100°F. At lower temperatures, a catalyst is required to promote the reaction (selective catalytic reduction, or SCR). SCR is not used on municipal waste combustors. Tests conducted at a municipal waste combustor demonstrated that NO_x emission levels of 150 ppmv (45%–55% reduction) can be achieved with SNCR.⁴

Thermodynamic equilibrium considerations indicate that under excess air conditions and with temperatures of 1472°F (800°C) and higher, maintained in a completely mixed reactor for a suitable period of time, emissions of organic or hydrocarbon compounds should be at nondetectable levels. However, measurements at operating plants, particularly those constructed prior to the early to mid-1980s, indicated significant emissions of trace organic or hydrocarbon compounds, some of which are toxic. These tests indicated that the basic objective of combustion control, thorough mixing of combustion products with oxygen at a temperature that is sufficiently high to provide for the rapid destruction of all organic or hydrocarbon compounds, had not been achieved in these early WTE plants.

If the fuel, or the gas driven off of the fuel bed, is not adequately mixed with air, fuel-rich pockets will exist containing relatively high levels of hydrocarbons, which then can be carried out of the combustion system. Kinetic considerations indicate that such hydrocarbons can be destroyed rapidly in the presence of oxygen at elevated temperatures. Also, if too much combustion air is introduced into the combustion chamber, either in total or in a particular area of the chamber, temperatures will be reduced, combustion reactions can be quenched, and hydrocarbons carried out of the combustion system. Achieving the goal of proper combustion control, destruction of all hydrocarbon compounds to form carbon dioxide and water, will minimize emission of potentially toxic substances as well as other compounds that may be precursors and capable of forming toxic compounds downstream in cooler regions of the boiler.

Table 24.13 shows that the hydrocarbons can vary significantly, frequently over relatively short periods of time, based on measurements at older municipal waste combustors.

The highest levels shown in this table occurred in one of the older plants and no doubt indicate very poor combustion conditions. Tests at modern WTE plants indicate consistently low levels of hydrocarbons, which are indicative of good combustion control. In modern, well-designed and -operated plants, photochemical oxidants and PAH are in concentrations too low to cause any known adverse health effects. Tests^{55,66} for other substances that might be of concern, such as polychlorinated biphenyls (PCBs), generally have found levels discharged to the atmosphere to be so low as to have a negligible impact on the environment.

24.4.3 Organic Compound Control

Organic compounds for which emission data are available include polychlorinated dibenzodioxins (PCDDs), polychlorinated dibenzofurans (PCDFs), chlorobenzenes (CBs), chlorophenols (CPs), polycyclic aromatic hydrocarbons (PAHs), and PCBs. A number of other organic compounds, including aldehydes, chlorinated alkanes, and phthalic acid esters, have also been identified in specific testing programs. Since dioxin/furan emissions have generated the most interest over the past several years, there are more data for these compounds, in particular for the tetrahomologues, and especially the 2,3,7,8-substituted isomers. The other compounds have been less frequently reported in the literature. The reason for this emphasis is the toxicity of dioxin/furan to laboratory animals and the perceived risk to humans.

Upset conditions in energy-from-waste plants can lead to local air-deficient conditions resulting in the emission of organic compounds. PAHs are formed during fuel-rich combustion as a consequence of free radical reactions in the high temperature flame zone. In addition, it is found that in the presence of water cooled surfaces, such as found in oil-fired home-heating furnaces, a high fraction of the polycyclic compounds are oxygenated. Similar free radical reactions probably take place in fuel-rich zones of incinerator flames yielding PAH, oxygenated compounds such as phenols, and, in the presence of chlorine, some dioxin/furan. The argument for the synthesis of dioxin/furan at temperatures of 400°F–800°F is supported by the increase in the concentration of these pollutants across a heat recovery boiler downstream of the refractory lined combustion chamber of a waste combustor.

This free radical mechanism appears to be the dominant source of dioxin/furan in municipal waste combustors. These compounds may also be present as contaminants in a number of chemicals, most notably chlorinated phenols and polychlorinated biphenyls (PCBs). Their presence in MSW results from the use of these chemicals, discontinued in some cases, as fungicides and bactericides for the phenol derivatives, or the use of PCBs as heat exchanger and capacitor fluids. These compounds are expected to survive in a furnace combustion chamber only if large excesses in the local air flow cool the gases to below the decomposition or reaction temperature. Dioxin/furan can also be produced by condensation reactions involving the chlorinated phenols and biphenyls. The observed formation of dioxin/furan when fly ash from MSW incinerators is heated to temperatures of 480°F (250°C) suggest such catalyzed condensation reactions of chlorinated phenols. PCBs are precursors to furan, and pyrolysis of PCBs in laboratory reactors at elevated temperatures for a few seconds has yielded furan.

The available test data clearly show that dioxin/furan exit the boilers and, depending on the emission control devices employed, some fraction enters the atmosphere either as gases or adsorbed onto particulates. In addition, the solids remaining behind in the form of fly ash and bottom ash contain most of the same compounds, and these become another potential source of discharge to the environment.

Emission data for total dioxin/furan generally fall into three main categories:

1. Low emissions, in the range of 20–130 ng/Nm³
2. Medium emissions, from 130 to 1000 ng/Nm³
3. High emissions, over 1000 ng/Nm³

Average dioxin/furan emission from older plants ranges from about 500 to 1000 ng/Nm³. The lower emission levels tend to be associated with newer, well-operated mass-fired facilities such as water wall plants, and with modular, starved or controlled air types of incinerators (see Table 24.14). In most test programs, adequate operating data were not collected to correlate emissions with operations. Researchers in the field theorize that combustion conditions can play a role in minimizing emissions, and several studies^{63,68,69} were conducted in Canada and the United States to define that role more exactly.

Emissions from MSW combustion contain small amounts of many different dioxin/furan isomers. While individual dioxin/furan isomers have widely differing toxicities, the 2,3,7,7-TCDD isomer, present as a small proportion of the total dioxin/furan, is of greatest known toxicological concern. Based on animal studies it has been generally concluded that other 2,3,7,8-substituted dioxin/furan isomers, in addition to the 2,3,7,8-TCDD, are also likely to be of toxicological concern. A method for expressing the relative overall toxicological impact of all dioxin/furan isomers, as so-called “2,3,7,8-TCDD toxic equivalents,” was developed in the mid-1980s² and has been used by the EPA intermittently in its regulatory efforts since this time.

In this method, emissions are sampled, extracted, and analyzed for all constituent isomers of dioxin/furan. A system of toxicity weighting factors from the existing toxicological data (based almost entirely on animal studies) is applied to each constituent dioxin/furan isomer and the results are summed to arrive at the 2,3,7,8-TCDD toxic equivalent. An example of dioxin/furan test results expressed as 2,3,7,8-TCDD toxic equivalents, using three different systems of weighting factors, is shown in Table 24.15.

Emission control systems consisting of a scrubber/fabric filter have been evaluated for dioxin emissions.³⁴ Recently dioxin removal efficiencies exceeding 99% were obtained, which resulted in dioxin concentrations at the stack that approach the detection limit of the sampling and analytical equipment currently available. Emissions of furan followed a similar range of values as dioxin with the scrubber/high efficiency particulate removal

TABLE 24.14

Summary of Average Total PCDD/PCDF Concentrations from MSW Combustion in Modern Plants (ng/Nm³, dry, at 12% CO₂)

	Total PCDD PCDF
Peekskill, NY, electrostatic precipitator only (1985)	100.25
Wurzburg, FRG, dry scrubber-baghouse (1985)	49.95
Tulsa, OK, electrostatic precipitator only (1986)	34.45
Marion Co., OR, dry scrubber-baghouse (1986)	1.55

Sources: From Hahn, J.L. et al. (Ogden Martin Systems, Inc.), and Weiand, H. et al. (Martin GmbH), in: *Proceedings of the 1986 National Waste Processing Conference*, Denver, CO, June 1–4, 1986, ASME, New York; NYS Department of Environmental Conservation Bureau of Toxic Air Sampling, Division of Air Resources, Preliminary Report on Westchester RESCO RRF, January 8, 1986; Ogden Projects, Inc., Environmental test report, Walter B. Hall Resource Recovery Facility, October 20, 1986; Ogden Projects, Inc., Environmental test report, Marion County Solid Waste-to-Energy Facility, December 5, 1986.

TABLE 24.15

Toxic Equivalent Emissions by U.S. EPA, Swedish, and California Methods

Facility	Toxic Equivalents ng/Nm ³ at 12% CO ₂		
	U.S. EPA	Swedish	California
Peekskill, NY	1.62	3.83	9.73
Tulsa, OK	0.7	1.74	4.75
Wurzburg, FRG	0.37	0.81	2.11
Marion Co., OR	0.11	0.16	0.29
From WHO Workshop; Naples, Italy			
Max. from avg. oper.	25.0	52.78	134.5
Achievable with no acid gas cleaning	0.9	2.2	5.94

Sources: From Hahn, J.L. and Sussman, D.B., Dioxin emissions from modern, mass-fired, stoker/boilers with advanced air pollution control equipment, presented at *Dioxin '86*, Fukuoka, Japan, September 1986; NYS Department of Environmental Conservation Bureau of Toxic Air Sampling, Division of Air Resources, Preliminary Report on Westchester RESCO RRF, January 8, 1986; Ogden Projects, Inc., Environmental test report, Walter B. Hall Resource Recovery Facility, October 20, 1986; Ogden Projects, Inc., Environmental test report, Marion County Solid Waste-to-Energy Facility, December 5, 1986; Vogg, H. et al., Recent findings on the formation and decomposition of PCDD/PCDF in solid municipal waste incineration, ISWA/WHO, Specialized Seminar, Copenhagen, Denmark, January, 1987; World Health Organization, Report on PCDD and PCDF Emissions from Incinerators for Municipal Sewage, Sludge and Solid Waste—Evaluation of Human Exposure, from WHO Workshop, Naples, Italy, March, 1986.

combination reducing furan to very low or nondetectable levels. Additional reductions of over 50% can be achieved by activated carbon injection.⁴

Some limited data on emissions of CB, CP, PCB, and PAH are available. Most sampling programs for dioxin/furan have unfortunately neglected to analyze for these compounds. Maximum levels from Canadian studies³⁴ are as included in Table 24.16 along with some data from tests on U.S. plants.³³ The scrubber/fabric filter technology generally demonstrated removal rates of 80%–99% for these compounds in these studies.

Very few studies report on other organic products in the flue gas. Some data from tests on older plants have been reported for aldehydes and certain other volatile hydrocarbons.³ Such data are not available for newer plants.

The conventional combustion gas measurements include CO, total hydrocarbons (THCs), CO₂, and H₂O. Both CO and THC have been of interest as potential surrogates for dioxin/furan emissions; however, no strong correlations have been found in previous studies. In fact, very few studies have attempted to determine CO and dioxin/furan

TABLE 24.16Organic Emissions (ng/Nm³)

Chemical Emitted	U.S. Plants	Canadian Pilot Plant	
	Before Particulate Removal	Before Particulate Removal	After Scrubber/Fabric Filter
CB	10,000–500,000	17,000	3000
CP	22,000–80,000	30,000	8000
PCB	—	700	Nondetectable (ND)
PAH	ND to 5,600,000	30,000	130

Sources: From Battelle Columbus Labs, Characterization of stack emissions from municipal refuse-to-energy systems, National Technical Information Service, PB87-110482, October 1982; Hay, D.J. et al. (Environment Canada), and Marenlette, L. (Flakt Canada, Ltd.), The national incinerator testing and evaluation program: An Assessment of (A) two-stage incineration (B) pilot scale emission control, Report EPS 3/UP/2, September 1986.

TABLE 24.17

Lime Addition with Baghouse, Percent Removal of Organics

	Dry System				Wet/Dry System	
	110°C	125°C	140°C	200°C	140°C	140°C Recycle
CB	95	98	98	62	>99	>99
PCB	72	>99	>99	54	>99	>99
PAH	84	82	84	98	>99	79
CP	97	99	99	56	99	96

Sources: From Hay, D.J. et al. (Environment Canada), and Marenlette, L. (Flakt Canada, Ltd.), The national incinerator testing and evaluation program: An assessment of (A) two-stage incineration (B) pilot scale emission control, Report EPS 3/UP/2, September 1986.

emission data for several operating conditions on the same combustor to develop a correlation. On the other hand, several authors have attempted to correlate CO and dioxin/furan data obtained from several different facilities. From such comparisons, it appears that low CO levels (below 100 ppm) are associated with low dioxin/furan emissions.³⁸ High CO levels of several 100 ppm and even over 1000 ppm have been associated with high dioxin/furan emissions. During poor or upset combustion conditions, CO levels of several thousand ppm have been observed and THC levels have risen from a typical 1–5 ppm to 100 ppm and more. Since one of the measures available to combustor operators to optimize combustion control is to minimize CO production, one would assume from these general correlations that this would also tend to minimize dioxin/furan emissions, along with emissions of other trace chlorinated hydrocarbons. THC is not as useful as CO as an indicator of proper combustion because of problems in sampling to consistently obtain a representative sample for analysis at the analytical instrument.

Table 24.17 shows operating results achieved using dry and semidry lime injection followed by a baghouse for removal of trace organic pollutants from waste combustor emissions.

24.4.4 Trace Metals

Trace metals are not destroyed during combustion, and the composition of wastes therefore provides, on a statistical basis, the measure of the total inorganic residue. The distribution of trace metals between bottom ash and ash carried over to the air pollution control device is dependent upon the design and operation of the combustor and the composition of the feed. The amount of ash carried up and with the flue gases discharged from a burning refuse bed increases with increasing underfire air rate and with bed agitation. Modular incinerators (described later in Section 24.7) with low underfire air flow rates tend to have lower particulate emissions than conventional mass-burn units and RDF units for this reason. In addition, the amount of ash carried from the combustion chamber will be influenced by the particle size of the inorganic content of the MSW.

The distribution of trace metals between the different components of refuse has a strong influence on the fate of the trace metals. For example, TiO₂ used as a pigment in paper products, has a particle size of about 0.2 μm and will tend to be carried off by the flue gases passing through the refuse bed, whereas TiO₂ present in glass will remain with the glass in the bottom ash. Up to 20% of the inorganic content of the waste will be entrained from burning refuse beds to form fly ash particles. The remainder will end up in the residue.

Volatile metals and their compounds, usually present in trace amounts in the feed, will vaporize from the refuse and condense in the cooler portions of a furnace either as an ultra fine aerosol (size less than 1 μm) or on the surface of the fly ash, preferentially on the surface of the finer ash particles. A large fraction of certain elements in the feed, such as mercury, will be volatilized.

Since mercury is a very volatile metal, it exists in vapor phase at temperatures as low as 68°F–122°F (20°C–50°C). Several studies have indicated that sufficient cooling of the flue gas (typically below 140°C, based on test results conducted to date) and a highly efficient particulate removal system to remove the particles on which the mercury has been adsorbed^{6,8,80} are both required to achieve high mercury removal. High mercury removal has been obtained for the scrubber/fabric filter system, provided that the flue gas is adequately cooled (see Table 24.18).

Test results with carbon injection at two municipal waste combustors demonstrated that the EPA emission guidelines of 80 mg/dscm or 85% reduction in mercury emissions can be achieved with a spray dryer, fabric filter and carbon injection.⁴

Elements such as sodium (Na), lead (Pb), zinc (Zn), and cadmium (Cd), will be distributed between the volatiles and the residue in amounts that depend on the chemical and physical form in which the elements are present. For example, sodium in glass will be retained in the residue but that in common salt will partially disassociate and be discharged with the emission gases.

Some of the data on metal emissions that are available from tests on resource recovery plants is shown in Table 24.19. Note that the emission of trace metals can be dramatically limited at WTE plants by the use of high-efficiency particulate control devices that are installed on modern facilities.

While sampling for metal emissions is fairly well established, in order to obtain enough sample to analyze at highly controlled sources, samples times are extremely long, sometimes over 8 h using the U.S. EPA Method 5 sample train (relatively low sample rate). Several studies^{28,29,41} of waste combustor emissions in the United States in the 1970s concluded that “municipal incinerators can be major sources of Cd, Zn, Sb and possibly Sn....” This conclusion is based on the relative concentration of these materials in the total suspended particulate catch. However, two of the three plants tested in these studies utilized inefficient air pollution control facilities. Thus, particulate emissions in these plants were relatively high when compared to the German and Japanese plant

TABLE 24.18

Lime Addition with Baghouse Mercury Concentrations ($\mu\text{g}/\text{km}^3$ at 8% O_2)

Operation Dry System	Inlet	Outlet	%Removal
230°F (110°C)	440	40	90.9
260°F (125°C)	480	23	97.9
285°F (140°C)	320	20	93.8
390°F (>200°C)	450	610	0
Wet-dry system			
140°C	290	10	94.7
140°C ← recycle	350	19	94.7

Source: From Hay, D.J. et al. (Environment Canada), and Marenlette, L. (Flakt Canada, Ltd.), The national incinerator testing and evaluation program: An assessment of (A) two-stage incineration (B) pilot scale emission control, Report EPS 3/UP/2, September 1986.

TABLE 24.19

Trace Metal Emissions Test Results

	Japanese Plant Uncontrolled	Braintree Mass. Part. Rem. Eff. 74%	German Plants	Japanese Plants	Tulsa, OK	Dry Scrubber, Fab. Filter	
						Marion, Co., OR	Pilot Plant Canada
Arsenic (As) (lb/ton × 10 ⁻³)	<0.4	0.125	0.09	<0.0016	—	—	0.00033– 0.00064
Beryllium (Be) (lb/ton × 10 ⁻³)	<0.3	0.00027	0.002	<0.0016 ^a	0.000025	0.000021	—
Cadmium (Cd) (lb/ton × 10 ⁻³)	0.7	1.30	0.25	0.11	—	—	ND–0.006
Chromium (Cr) (lb/ton × 10 ⁻³)	16.0	0.34	0.185	0.026	—	—	ND–0.016
Lead (Pb) (lb/ton × 10 ⁻³)	17.0	42.4	10.0	0.1	3.5	0.29	ND–0.08
Mercury (Hg) (lb/ton × 10 ⁻³)							
on particulates	0.5	0.11	0.067	0.03	—	—	—
Vapor phase	0.8	4.38 ^a	—	0.90	3.5	2.9	0.16–9.83
Selenium (Se) (lb/ton × 10 ⁻³)	<0.3	—	—	<0.0016	—	—	—
Particulates (lb/ton)	25.7	1.3	0.5	0.19	0.13	0.16	<0.01

Sources: From Clark, L., Case history of a 240 ton day resource recovery project: Part II, in: *Proceedings of the 1996 National Waste Processing Conference*, ASME, New York, 1996, pp. 235–248; Hahn, J.L. and Sofaer, D.S. 1988. Variability of NO_x emissions from modern mass-fired resource recovery facilities, Paper No. 88-21.7, presented at the *81st Annual Meeting of Air Pollution Control Association*, Dallas, TX, June 1988; Ogden Projects, Inc., Environmental test report, Walter B. Hall Resource Recovery Facility, October 20, 1986; Ogden Projects, Inc., Environmental test report, Marion County Solid Waste-to-Energy Facility, December 5, 1986; Velzy, C.O., Standards and Control of Trace Emissions from Refuse-Fired Facilities, in: *Municipal Solid Waste as a Utility Fuel*, EPRI Conference Proceedings, Madison, WI, November 20–22, 1985.

^a Total on particulate and vapor phase.

data in Table 24.19, which is similar to emission data from most modern mass-burn and RDF waste-to-energy plants in the United States.⁶⁸ Note also in Table 24.19 that, as the efficiency of particulate control improves, trace metal emissions generally decrease, and in most cases decrease significantly. Even though there is ample evidence from test data¹⁷ to indicate that heavy metals tend to concentrate on the finer particulates, there is also evidence from test results to show that at high particulate removal efficiency (99% ±), high trace metal removal (99% ±) is achieved. Thus, the conclusion in these studies of waste combustors quoted earlier is not valid for WTE plants utilizing efficient air pollution control devices.

The important operating parameters for such equipment are flue gas temperature and composition, contact time, relative velocity of particles and gas stream, and possible activation of particles. See Tables 24.18 and 24.20 for operating results achieved using dry and semidry lime injection followed by a baghouse for removal of heavy metal pollutants from waste combustor emissions.

TABLE 24.20

Lime Addition with Baghouse, Metal Concentrations ($\mu\text{g}/\text{km}^3$ at 8% O_2)

Metal	Inlet	Outlet	Removal
Zinc	77,000–108,000	5–10	96 → 99.99
Cadmium	1,000–3,500	1.0–0.6	96 → 99.96
Lead	34,000–44,000	1–6	95 → 99.98
Chromium	1,400–3,100	0.2–1	>99.92
Nickel	700–2,500	0.4–2	>99.81
Arsenic	80–150	0.02–0.07	>99.95
Antimony	800–2,200	0.2–0.6	>99.92
Mercury	190–480	10–610	0 → 90

Sources: From Carlsson, K., *Waste Manage. Res.*, 4, 15, 1986; Hay, D. et al. (Environment Canada), and Marenlette, L. (Flakt Canada, Ltd.), The national incinerator testing and evaluation program: An assessment of (A) two-stage incineration (B) pilot scale emission control, Report EPS 3/UP/2, September, 1986.

24.5 Performance

Mass burning of MSW is the most highly developed and commercially proven combustion process presently available for reducing the volume of MSW prior to ultimate disposal of residuals on the land, and for extracting energy from the waste.⁷⁰ Hundreds of such plants, incorporating various grate systems and boiler concepts, which differ in details of design, construction, and quality of operation, have been built throughout the world since the mid-1960s. Mass-burn systems are generally furnished with a guaranteed availability of 85%, while in practice availabilities of 90%–95% have been achieved.⁶⁸ Availability cannot approach 100% because standard maintenance practice requires periodic shutdowns. The newest mass-burn facilities seem capable of achieving high reliability, based on their performance in Europe, Japan, and the United States.

Refuse-derived fuel (RDF) facilities became popular during the 1970s. The early plants were generally designed with the intent to remove and recycle metals, glass, and other marketable materials, with the remaining fraction, RDF, to be burned in an existing boiler as a replacement fuel. Those types of facilities all failed and are no longer in operation. The main reasons for failure were that the recycled materials were highly contaminated with waste and were not marketable, and the boilers were not designed to handle the inconsistent RDF that was being fed to them.

The RDF approach quickly evolved to produce a fuel with a known specification to be burned in a dedicated boiler designed specifically to burn that fuel. The materials which were removed were sold, if possible, or landfilled. The primary difference in philosophy between the two types of RDF plants was that the early ones treated the RDF as the "waste" that contaminated the recovered materials, and the newer generation treated the recovered materials as the "waste" that contaminated the RDF. The newer generation RDF facilities which were designed in this manner have been successful.

Fluidized bed technology has been used outside the United States to combust solid waste for several years. One advantage of fluidized bed combustion is that the boiler is more efficient than those in mass-burn or spreader-stoker facilities. Also, fluidized bed combustion produces lower NO_x emissions than other incineration methods. Although lower, these NO_x emissions must still be controlled with additional air pollution control equipment, as with other combustion facilities. Fluidized bed combustion also has the advantage of

being able to add limestone with the sand in the bed to assist in acid gas removal. However, a scrubber is still needed to reduce emissions to permitted levels.⁴⁶

The major disadvantage to a fluidized bed facility is that it does not have a long-term proven track record in the United States. Also, the size of the units are small when compared to the size needed for typical U.S. waste-to-energy facilities.⁴⁶

24.6 Costs

It is extremely difficult to obtain accurate, consistent, and comparable WTE plant construction cost data from which to develop information which might be useful in predicting a planned new plant's construction cost during the study stage of a project. However, a 1988 study⁵⁶ has developed such data (appropriate for the time frame of mid-1987), which is confirmed in general by this author's personal experience. This study indicates that for the upper 90% confidence limit for the smallest facility, and the largest facility, the construction costs would range as indicated below:

1. A small modular combustion unit with a waste heat boiler and a capacity of less than 250 TPD—\$68,000 and \$40,000 per ton of daily MSW processing capability. (In most instances, such plants don't incorporate the same degree of equipment redundancy, and/or the same quality of equipment as the larger plants.)
2. A small refractory wall furnace with waste heat boiler and dry scrubbers of between 200 and 500 TPD capacity—\$90,000 and \$70,000 per ton of daily MSW processing capability.
3. A small, field erected, water wall congeneration or electric generation facility with dry scrubbers of between 500 and 1,500 TPD capacity—\$112,000 and \$85,000 per ton of daily MSW processing capability.
4. A large, field erected, water wall congeneration or electric generation facility with a dry scrubber between 2,000 and 3,000 TPD capacity—\$129,000 and \$112,000 per ton of daily MSW processing capability.

In this study,⁵⁶ the construction costs were said to include the vendor quote for construction plus contingency, utility interconnection expenses, and any identified allowances clearly associated with the construction price. All other costs, such as land acquisition, interest during construction, development costs, and management fees were not considered or included, where known, due to their highly project specific nature.

The following specific observations were made by the authors at the conclusion of this study.⁵⁶

1. Capital construction price decreases with increasing size within size ranges and increases with a higher-value energy product.
2. Price is also affected by the construction, procurement, and air pollution control methods employed.
3. Refuse-derived fuel and mass burning water wall facilities are competitively priced with each other.

The effect of plant capacity on capital costs or mass-burn plants is shown in Figure 24.8. Capital costs for other types of plants are similar.

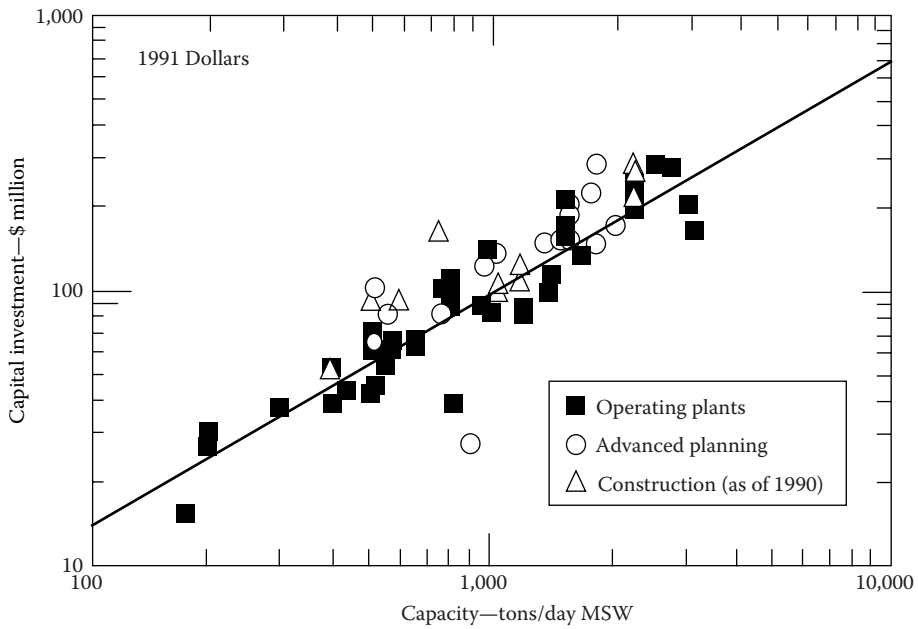


FIGURE 24.8 Effect of plant capacity on capital costs for mass-burn facilities (electricity only), excluding costs associated with collection (e.g., trucks).

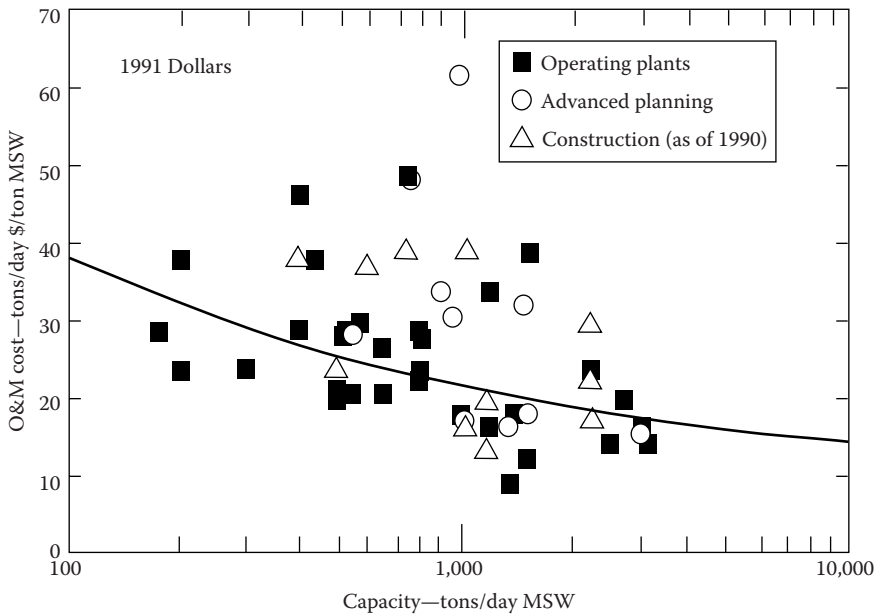


FIGURE 24.9 Effect of plant capacity on O&M costs for mass-burn facilities (electricity producing only), excluding costs associated with collection (e.g., trucks).

With respect to operating costs and/or tipping fees, information is even more difficult to obtain from which to develop costs for planning purposes. Costs cited in the literature from 1989 through 1994 range from \$40 to \$80 per ton of daily rated MSW processing capability.^{18,42,41,77,78} Tipping fees on Long Island, which has generally high labor rates, high power costs, and very long hauls for residue disposal, have been noted to range up to \$110 per ton of daily rated MSW processing capability.²⁶ Plants in other parts of the country where plant operating cost elements are significantly lower have been found to have tipping fees closer to \$40 per ton.⁷ Thus, tipping fees for a specific facility would have to be developed based on cost factors for that specific plant.

The effect of plant capacity on O&M costs for mass-burn plants is shown in Figure 24.9. Information is so limited on other types of plants, and the costs are so dependent on local conditions that we do not feel that curves developed for other types of plants would be useful.

24.7 Status of Other Technologies

Several other technologies have been used to a small extent to burn MSW and beneficially use the energy produced in the combustion process. Their use in the future depends on numerous factors, perhaps the most important of which is full-scale demonstration of successful, reliable operation, after which total operational costs are shown to be competitive with mass-burn and/or RDF combustion costs.

24.7.1 Modular Systems

Modular systems, generally utilized in smaller plants, are assemblies of factory-prefabricated major components joined together in the field to form a total operational system. They have been built in individual unit sizes up to just over 100 tons/day capacity, combined into plants of just over 400 tons/day capacity. Modular systems are similar to mass-burn systems in that they combust unprocessed MSW, but they feature two combustion chambers, and the MSW is charged into the system with a hydraulic ram and combustion takes place on a series of stationary hearths. MSW is pushed from one hearth to the next by hydraulic rams. Two types of modular systems have been built and operated: starved air and excess air.

The primary chamber of a starved air modular system is usually operated in a slightly oxygen-deficient ("starved air") environment. The volatile portion of the MSW is vaporized in this chamber and the resulting gases flow into the secondary chamber. The secondary chamber operates in an excess air condition, and combustion of the gases driven off the MSW is essentially completed in this chamber. An excess air modular system operates in a manner similar to a field erected boiler system, with excess air injected into the primary chamber.

One advantage of these units, as indicated in the section on costs, is low cost. Another advantage is that factory prefabrication of major system components can result in shortening of the field construction time. One disadvantage of the two-chamber modular system is that waste burn out in the residue is not always complete, which increases ash quantities and reduces the efficiency of energy recovery.⁶⁹ Energy recovery efficiency is also reduced

due to generally higher “excess air” levels carried in these units. Also, combustion control is generally less effective in this type of unit, increasing the possibility of discharge of trace organic emissions. As pointed out earlier, these types of units generally utilize a lower quality of equipment and include less redundancy than larger mass-fired water wall and RDF WTE plants. Modular plants are responsible for about 2% of the total MSW burned at this time in the United States.

24.7.2 Fluidized Beds

Fluidized bed combustion (FBC) differs from mass-burn and RDF combustion in that the fuel is burned in “fluid suspension”—entrained along with particles of sand in an upward flow of turbulent air at a temperature controlled to 1500°F–1600°F (816°C–971°C). To date, it has been used primarily to burn sewage sludge, industrial waste, and coal and has been used to combust RDF in one facility in the U.S. Fluidized bed combustion of MSW is more commonly used in some European countries.

“Bubbling” FBC designs retain the material near the bottom of the furnace, while “circulating” designs allow bed material to move upward and then be returned near the bottom of the bed for further combustion. The reason for the interest in this combustion technique to burn RDF is the potential for these designs to provide more consistent combustion because of the extreme turbulence and the proximity of the RDF waste particles to the hot sand particles.⁴⁶ Such systems also require lower combustion temperatures than mass-burn and current RDF systems.

24.7.3 Pyrolysis and Gasification

Pyrolysis is the chemical decomposition of a substance by heat in the absence of oxygen. It generally occurs at relatively low temperatures (900°F–1100°F, compared with 1800°F for mass-burn). The heterogeneous nature of MSW makes pyrolysis reactions complex and difficult to control. Besides producing larger quantities of solid residues that must be managed for ultimate disposal, pyrolysis produces liquid tar and/or gases that are potentially marketable energy forms. The quality of the fuel products depends on the material fed into the reactor (e.g., moisture, ash, cellulose, trace constituent content) and operating conditions (e.g., temperature and particle size).⁶⁸

Gasification is similar to pyrolysis in that it is the chemical decomposition of the substance by heat in the absence of oxygen. However, gasification occurs at temperatures of approximately 2200°F (1200°C). The reaction produces a synthetic gas with a heat content of approximately 250 Btu/cf. The approximate composition by volume on a dry basis is 25%–42% carbon monoxide, 25%–42% hydrogen, 10%–25% carbon dioxide, and 3%–4% nitrogen and other constituents. The synthetic gas is then cooled rapidly to reduce formation of dioxins and cleaned.⁶²

Several prototype pyrolysis facilities were built in the 1970s with grants from EPA. These facilities were unable to produce quality fuels in substantial quantities. No one in the United States has yet successfully developed and applied the pyrolysis or gasification technology to MSW combustion. However, the use of pyrolysis and gasification for MSW management still attracts attention in other countries. Additional reading for pyrolysis and gasification technologies is available.⁹⁴⁴

24.8 Future Issues and Trends

It has been demonstrated by actual experience that modern mass-burn and RDF-fired MSW WTE plants can be designed and operated with reasonable assurance of continuous service and without adversely affecting nearby neighborhood property values. Allegations that WTE plant sites are situated adjacent to neighborhoods of low-income, disadvantaged, or minority populations ignore the specific technical siting criteria outlined earlier (i.e., adjacent to major highways, low land cost, industrial type area, etc.) which are generally followed in siting such facilities. Such areas frequently are closer to low-income neighborhoods than to middle- and higher-income neighborhoods.⁶⁸

In 1994 the Supreme Court found that a local community could not force the MSW from that community to be taken to a specific facility such as a WTE plant.²⁴ This court decision was a major blow to the WTE industry bringing most planning and construction of new facilities to a halt in the mid-1990s. Many communities, when considering solid waste disposal options, have opted for low cost landfill disposal because of concern over impacts of higher cost WTE alternatives on taxes. At some point in the not too distant future, as the current landfills are rapidly filled, WTE technology will have to be utilized to solve the solid waste disposal problem. Some signs of this new interest in WTE technology are already occurring.

Another issue facing WTE plants is the uncertain future of regulatory requirements, both from the standpoint of legislation and from that of the regulatory agencies. In the past, legislation has been passed by Congress calling for Best Available Control Technology (BACT), then Lowest Achievable Emission Requirements (LAER), and then, most recently, Maximum Achievable Control Technology (MACT). The impact of this legislation, each calling for significant reductions in allowable emissions (absent any indication of the existence of a significant public health problem or benefit), has been to require extensive retrofits of existing plants and addition of equipment to proposed new plants, all at substantial expense without proven benefit and, in many cases, without prior proof of operational viability. Most facilities have opted to upgrade the air pollution control equipment and continue to operate.

Several positive actions are occurring in the field. Thus, most project developers have recognized the desirability of implementing a proactive program early in the project planning process to involve the public, particularly those in the vicinity of the proposed facility.⁶⁰ Also, the potential for materials recycling, which had been overenthusiastically embraced a number of years ago (state recycling goals as high as 70%, with some local communities projecting that their entire quantity of MSW could be managed through recycling), is gradually being recognized.⁴⁵ Franklin Associates²³ projects an increase in the recycling rate of from 22% in 1993 to 30% by the year 2000. Much of this increase in recycling is to come from increases in recovery of paper materials and diversion of yard wastes to composting. The impact of these changes in waste composition on energy available at WTE plants will be minimal, with the reduction in moisture content due to diversion of yard wastes being a positive factor.

The need to generate electric energy and safely manage the MSW generated by modern civilization, particularly in the vicinity of major metropolitan areas, together with the proven performance of modern WTE plants, indicate that this technology will be utilized to dispose of a portion of this country's solid waste and provide electricity.

References

1. Albina, D., Millrath, K., and Themelis, N., Effects of feed composition on boiler corrosion in waste-to-energy plants, in: *Proceedings of the 12th Annual North American Waste to Energy Conference*. ASME, New York, pp. 99–109, 2004.
2. Barnes, D., Rump session, *Chemosphere*, 14 (6–7), 987–989, 1985.
3. Battelle Columbus Labs, Characterization of stack emissions from municipal refuse-to-energy systems, National Technical Information Service, PB87-110482, October, 1981.
4. Bauer, J. P. and Wofford, J., Compliance with the new emissions guidelines for existing municipal waste combustion facilities, in: *Proceedings 1996 National Waste Processing Conference*. ASME, New York, 1996, pp. 9–18.
5. Beltz, P. R., Engdahl, R. B., and Dartoy, J., Evaluation of European refuse-fired energy systems design practices, summary, conclusions and inventory, prepared for U.S. EPA by Battelle Laboratories, Columbus, OH, 1979.
6. Bergstrom, J. G. T., Mercury behavior in flue gases, *Waste Management and Research*, 4(1), 57–64, 1986.
7. Bilmes, J. S., Impact of the recession and recycling on solid waste processing facilities in New England, in: *Proceedings 1992 National Waste Processing Conference*. ASME, New York, May 1992, pp. 351–360.
8. Braun, H., Metzger, M., and Vogt, H., *Zur Problematik der Quecksilber-Abscheidung aus Rauchgasen von Mullverbrennungsanlagen*, Vol. 1, Teil 2, 1985.
9. Bridgewater, A. (Ed.), *Pyrolysis and Gasification of Biomass and Waste*. CPL Press, Newbury, U.K., 2003.
10. Bryers, R. W. (Ed.), *Ash Deposits and Corrosion due to Impurities in Combustion Gases*. Hemisphere Publishing Corp., New York, 1978.
11. Carlsson, K., Heavy metals from energy-from-waste plants—Comparison of gas cleaning systems, *Waste Management & Research*, 4(1), 15–20, 1986.
12. Carrotti, A. A. and Smith, R. A., Gaseous emissions from municipal incinerators, USEPA Publication No. SW-18C, 1974.
13. Clark, L., Case history of a 240 ton day resource recovery project: Part II, in: *Proceedings of the 1996 National Waste Processing Conference*. ASME, New York, pp. 235–248, 1996.
14. Cooper Engineers, Inc., *Air Emissions Tests of a Deutsche Babcock Anlagen, Dry Scrubber System at the Munich North Refuse-Fired Power Plant*, February 1985. Report by Cooper Engineers.
15. Cooper Engineers, Inc., *Air Emissions and Performance Testing of a Dry Scrubber (Quench Reactor), Dry Venturi and Fabric Filter System Operating on Flue Gas From Combustion of Municipal Solid Waste in Japan*, West County Agency of Contra Costa County Waste Co-Disposal/Energy Recovery Project, May 1995. Report by Cooper Engineers.
16. Criss, G. H. and Olsen, R. A., The chemistry of incinerator slags and their compatibility with fireclay and high alumina refractories, in: *Proceedings 1968 National Incinerator Conference*. ASME, New York, 1968, pp. 75–88.
17. Dannecker, W., Schadstoffmessungen bei mullverbrennungsanlagen, *VGB Kraftwerkstechnik*, 63(3), 237–243, 1983.
18. Davis, C. F., Annual snapshot of six large scale RDF projects, in: *Proceedings 1992 National Waste Processing Conference*. ASME, New York, May 1992, pp. 75–88.
19. Domalski, E. S., Ledford A. E., Jr., Bruce, S. S., and Churney, K. L., The chlorine content of municipal solid waste from Baltimore County, Maryland, and Brooklyn, NY, in: *Proceedings 1986 National Waste Processing Conference*, Denver, CO. ASME, New York, June 1986, pp. 435–448.
20. Eighmy, T. T., Collins, M. R., DiPietro, J. V., and Guay, M. A., Factors affecting inorganic leaching phenomena from incineration residues. Paper presented at *the Conference on Municipal Solid Waste Technology*, San Diego, CA, 1989.

21. Franklin Associates, Ltd., Characterization of municipal solid waste in the United States, 1960–2000, Report prepared for U.S. EPA, NTIS No. PB87-17323, Prairie Village, KS, July 25, 1986.
22. Franklin Associates, Ltd., Characterization of municipal solid waste in the United States, 1960 to 2000 (Update 1988), Report prepared for U.S. EPA, Office of Solid Waste and Emergency Response, Prairie Village, KS, March 30, 1988.
23. Franklin Associates, Ltd., Characterization of municipal solid waste in the United States (1994 Update), Report prepared for U.S. EPA Office of Solid Waste and Emergency Response, Prairie Village, KS, November, 1994.
24. Franklin, M. A., Solid waste stream characteristics, in: *Handbook of Solid Waste Management*, Tchobanoglous, G. and Kreith, F. (eds.), 2nd edn., Chapter 5. McGraw Hill, 2002.
25. EPA, www.epa.gov/solidwaste/nonhaz/municipal, accessed January 15, 2015.
26. Freeman, D., Waste-to-energy fights the fires of opposition, *World Wastes*, 37(1), 24, 1994.
27. Fryling, G. R. (Ed.), *Combustion Engineering*. Combustion Engineering, Inc., New York, 1966.
28. Greenberg, P. R., Zoller, W. H., and Gordon, G. E., Composition and size distributions of particles released in refuse incineration, *Environmental Science and Technology*, ACS, 12(5), 566–573, 1978.
29. Greenberg, R. R., Gordon, G. E., Zoller, W. H., Jacko, R. B., Neuendorf, D. W., and Yost, K. J., Composition of particles from the Nicosia Municipal Incinerator, *Environmental Science and Technology*, ACS, 12(11), 1329–1332, 1978.
30. Hahn, J. L., VonDemfange, H. P., Zurlinden, R. A., Stianche, K. F., and Seelinger, R. W. (Ogden Martin Systems, Inc.), and Weiland, H., Schetter, G., Spichal, P., and Martin, J. E. (Martin GmbH), Innovative technology for the control of air pollution at waste-to-energy plants, in: *Proceedings of the 1986 National Waste Processing Conference*, Denver, CO. ASME, New York, June 1986.
31. Hahn, J. L. and Sussman, D. B., Dioxin emissions from modern, mass-fired, stoker/boilers with advanced air pollution control equipment. Presented at the *Dioxin'86*, Fukuoka, Japan, September 1986.
32. Hahn, J. L. and Sofaer, D. S., Variability of NO_x emissions from modern mass-fired resource recovery facilities, Paper No. 88-21.7. Presented at the *81st Annual Meeting of Air Pollution Control Association*, Dallas, TX, June 1988.
33. Hasselriis, F., The environmental and health impact of waste combustion—The rush to judgment versus getting the facts first, in: *Proceedings 1992 National Waste Processing Conference*. ASME, New York, May 1992, pp. 361–369.
34. Hay, D. J., Finkelstein, A., Klicius, R. (Environment Canada), and Marenlette, L. (Flakt Canada, Ltd.), The national incinerator testing and evaluation program: An assessment of (A) two-stage incineration (B) pilot scale emission control, Environment Canada, Report EPS 3/UP/2, September 1986.
35. Hecklinger, R. S., The relative value of energy derived from municipal refuse, *Journal of Energy Resources Technology*, 101, 251–259, 1979.
36. Hecklinger, R. S., Combustion, in: *The Engineering Handbook*, Dorf, R.C. (ed.). CRC Press, Inc., Boca Raton, FL, 1996.
37. Kaiser, E. R., Zeit, C. D., and McCaffery, J. B., Municipal incinerator refuse and residue, in: *Proceedings 1968 National Incinerator Conference*. ASME, New York, 1968, pp. 142–153.
38. Kilgroe, J. D., Lanier, W. S., and Von Alten, T. R., Development of good combustion practice for municipal waste combustors, in: *Proceedings 1992 National Waste Processing Conference*. ASME, New York, May 1992, pp. 145–156.
39. Kiser, J. V. L. and Zannes, M., The 2000 L.W.S.A. directory of waste-to-energy plants. Integrated Waste Services Association, Washington, DC, 2002.
40. Lai, G., Corrosion mechanisms and alloy performance in waste-to-energy boiler combustion environments, in: *Proceedings of the 12th Annual North American Waste to Energy Conference*. ASME, New York, 2004, pp. 91–98.
41. Law, S. L. and Gordon, G. E., Sources of metals in municipal incinerator emissions, *Environmental Science and Technology*, ACS, 13(4), 432–438, 1979.
42. Leavitt, C., Calculating the costs of waste management, *World Wastes*, 37(4), 42, 1994.

43. Lide, D. R., *CRC Handbook of Chemistry and Physics*, 71st edn. CRC Press, Boca Raton, FL, 1990.
44. Malkow, T., Novel and innovative pyrolysis and gasification technologies for energy efficient and environmentally sound MSW disposal, *Waste Management*, 24, 53–79, 2004.
45. Michaels, A., Solid waste forum, *Public Works*, March 1995, p. 72.
46. Minott, D. H., Operating principles and environmental performance of fluid-bed energy recovery facilities, Paper No. 88-21.9. Presented at the *81st Annual Meeting of Air Pollution Control Association*, June 1989.
47. Murdoch, J. D. and Gay, J. L., Material recovery with incineration. Monmouth County, NJ, in: *Proceedings of 27th Annual International Solid Waste Exposition*, Tulsa, OK. SWANA, Silver Springs, MD (Pub. #GR-0028), August 1989, p. 329.
48. NYS Department of Environmental Conservation, Bureau of Toxic Air Sampling, Division of Air Resources, Preliminary Report on Westchester RESCO RRF, January 8, 1986.
49. Norton, F. H., Refractories, *Marks Standard Handbook for Mechanical Engineers*, 8th edn. McGraw-Hill, New York, 1978, pp. 6.172–6.173.
50. Ogden Projects, Inc., Environmental test report, Walter B. Hall Resource Recovery Facility, October 20, 1986.
51. Ogden Projects, Inc., Environmental test report, Marion County Solid Waste-to-Energy Facility, December 5, 1986.
52. O'Malley, W. R., Special factors involved in specifying incinerator cranes, in: *Proceedings 1968 National Incinerator Conference*. ASME, New York, 1968, pp. 114–123.
53. Penner, S. S. and Richards, M. B., Estimates of growth rates for municipal-waste incineration and environmental controls costs for coal utilization in the U.S., *Energy: The International Journal*, 14, 961, 1989.
54. Public Administration Service, *Municipal Refuse Disposal*, 3rd edn. American Public Works Association, Chicago, IL, 1970.
55. Richard, J. J. and Junk, G. A., Polychlorinated biphenyls in effluents from combustion of coal/refuse, *Environmental Science and Technology*, ACS, 15(9), 1095–1100, 1981.
56. Rigo, H. G. and Conley, A. D., Waste-to-energy facility capital costs, in: *Proceedings 1988 National Waste Processing Conference*. ASME, New York, May 1988, pp. 23–28.
57. Rogus, C. A., An appraisal of refuse incineration in Western Europe, in: *Proceedings 1966 National Incinerator Conference*. ASME, New York, 1966, pp. 114–123.
58. Sawell, S. E., Bridle, T. R., and Constable, T. W., Leachability of organic and inorganic contaminants in ashes from lime-based air pollution control devices on a municipal waste incinerator, Paper No. 87-94A. Presented at the *80th Annual Meeting of Air Pollution Control Association*, New York, June 1987.
59. Sawell, S. E. and Constable, T. W., NITEP Phase IIB: Assessment of contaminant leachability from the residues of a mass burning incinerator, Vol. VI of National Incinerator Testing and Evaluation Program, The Combustion Characterization of Mass Burning Incinerator Technology, Environment Canada, Toronto, Ontario, Canada, August 1988.
60. Scarlett, T., WTE report focuses on socioeconomics, *World Wastes*, 37(5), 14, 1994.
61. Scherrer, R. and Oberlaender, B., Refuse pit storage requirements, in: *Proceedings 1990 National Waste Processing Conference*. ASME, New York, June 1990, pp. 135–142.
62. Schilli, J., The fourth dimension for waste management in the United States: Thermoselect gasification technology and the hydrogen energy economy, in: *Proceedings of the 12th Annual North American Waste to Energy Conference*. ASME, New York, 2004, pp. 251–258.
63. Seeker, W. R., Lanier, W. S., and Heap, M. P., *Municipal Waste Combustion Study: Combustion Control of Organic Emissions*, EPA, Research Triangle Park, NC, January 1987.
64. Stultz, S. C. and Kitto, J. B. (Eds.), *Steam: Its Generation and Use*, 40th edn. The Babcock and Wilcox Co., Barberton, OH, 1992.
65. Suess, M. J. et al., *Solid Waste Management Selected Topics*. WHO Regional Office for Europe, Copenhagen, Denmark, 1985.

66. Timm, C. M., Sampling survey related to possible emission of polychlorinated biphenyls from the incineration of domestic refuse, NTIS Publication No. PB-251-285, National Technical Information Service, U.S. Department of Commerce, Springfield, VA, 1975.
67. U.S. Congress, Office of Technology Assessment, Generation and composition of MSW, *Facing America's Trash, What Next for Municipal Solid Waste*, OTA-A-424, Chapter 3. U.S. Government Printing Office, Washington, DC, October 1989.
68. U.S. Congress, Office of Technology Assessment, Incineration, *Facing America's Trash, What Next for Municipal Solid Waste*, OTA-A-424, Chapter 6. U.S. Government Printing Office, Washington, DC, October 1989.
69. U.S. Environmental Protection Agency, Municipal waste combustion study, Report to congress, EPA/530-SW-87-021a, Washington, DC, 1987.
70. U.S. Environmental Protection Agency, Characterization of municipal waste combustor ashes and leachates from municipal solid waste landfills, monofills and codisposal sites, Prepared by NUS Corporation for Office of Solid Waste and Emergency Response, EPA/530-SW-87-028A, Washington, DC, 1987.
71. U.S. Environmental Protection Agency, Municipal waste combustion multipollutant study, characterization emission test report, office of air quality planning and standards, EMB Report No. 87-MIN-04, Research Triangle Park, NC, September 1988.
72. U. S. Environmental Protection Agency, Standards for performance for stationary sources and emission guidelines for existing sources—Municipal waste combustors, 40 CFR, Part 60, Subpart Cb, December 19, 1995.
73. Velzy, C. O., The enigma of incinerator design, in: *Incinerator and Solid Waste Technology*. ASME, New York, 1975, pp. 65–74.
74. Velzy, C. O., 30 Years of refuse fired boiler experience, Presented at *the Engineering Foundation Conference*. Franklin Pierce College, Rindge, NH, July 17, 1978.
75. Velzy, C. O., Trace emissions in resource recovery—Problems, issues and possible control techniques, in: *Proceedings of the DOE-ANL Workshop; Energy from Municipal Waste: State-of-the-Art and Emerging Technologies*, Argonne National Laboratory Report ANL/CNSV-TM-137, Lemont, IL, February, 1984.
76. Velzy, C. O., Standards and control of trace emissions from refuse-fired facilities, in: *Municipal Solid Waste as a Utility Fuel*, EPRI Conference Proceedings, Madison, WI, November 20–22, 1985.
77. Velzy, C. O., U.S. Experience in combustion of municipal solid waste. Presented at *the APCA Specialty Conference on Regulatory Approaches for Control of Air Pollutants*, Atlanta, GA, February 20, 1987.
78. Velzy, C. O., Considerations in planning for an energy-from-waste incinerator. Presented at *the New Techniques and Practical Advice for Problems in Municipal Waste Management*, Toronto, Ontario, Canada, April 1–2, 1987.
79. Visalli, J. R., A comparison of dioxin, furan and combustion gas data from test programs at three MSW incinerators, *Journal of the Air Pollution Control Association*, 37(12), 1451–1463, 1987.
80. Vogg, H., Braun, H., Metzger, M., and Schneider, J., The specific role of cadmium and mercury in municipal solid waste incineration, *Waste Management and Research*, 4(1), 65–73, 1986.
81. Vogg, H., Metzger, M. and Stieglitz, L., Recent findings on the formation and decomposition of PCDD/PCDF in solid municipal waste incineration, ISWA/WHO, Specialized Seminar, Copenhagen, Denmark, January 1987.
82. World Health Organization, Report on PCDD and PCDF emissions from incinerators for municipal sewage, sludge and solid waste—Evaluation of human exposure, from WHO Workshop, Naples, Italy, March 1986.



Taylor & Francis

Taylor & Francis Group

<http://taylorandfrancis.com>

25

Fuel Cells

Xianguo Li

CONTENTS

25.1	Introduction	1034
25.2	Principle of Operation for Fuel Cells	1035
25.3	Typical Fuel Cell Systems	1036
25.4	Performance of Fuel Cells	1037
25.4.1	Reversible Cell Potential	1038
25.4.2	Effect of Operating Conditions on Reversible Cell Potential	1042
25.4.3	Energy Conversion Efficiency	1046
25.4.3.1	Definition of Energy Conversion Efficiency	1046
25.4.3.2	Reversible Energy Conversion Efficiency for Fuel Cells	1047
25.4.3.3	Carnot Efficiency: The Reversible Energy Conversion Efficiency for Heat Engines	1048
25.4.3.4	Equivalency of Carnot and Fuel Cell Reversible Efficiency	1049
25.4.3.5	Possibility of Over 100% Fuel Cell Efficiency: Is It Real or Hype?	1050
25.4.4	Practical Fuel Cell Efficiency and Energy Loss Mechanisms	1052
25.4.4.1	Reversible Energy Loss and Reversible Energy Efficiency	1052
25.4.4.2	Mechanism of Irreversible Energy Losses	1054
25.4.4.3	Amount and Rate of Waste Heat Generation	1056
25.4.4.4	Various Forms of Irreversible Energy Conversion Efficiency	1057
25.4.5	Efficiency Loss in Operating Fuel Cells: Stoichiometry, Utilization, and Nernst Loss	1059
25.5	Fuel Cell Electrode Processes	1062
25.6	Cell Connection and Stack Design Considerations	1063
25.7	Six Major Types of Fuel Cells	1066
25.7.1	Alkaline Fuel Cells	1067
25.7.2	Polymer Electrolyte Membrane Fuel Cells	1069
25.7.2.1	Introduction	1069
25.7.2.2	Basic Operating Principle	1070
25.7.2.3	Acceptable Contamination Levels	1071
25.7.2.4	Major Technological Problems	1071
25.7.2.5	Technological Status	1072
25.7.2.6	Applications	1072
25.7.3	Direct Methanol Fuel Cells	1073
25.7.3.1	Introduction	1073
25.7.3.2	Basic Operating Principle	1074
25.7.3.3	Acceptable Contamination Levels	1074

25.7.3.4	Major Technological Problems	1074
25.7.3.5	Technological Status	1075
25.7.3.6	Applications	1075
25.7.4	Phosphoric Acid Fuel Cells	1075
25.7.5	Molten Carbonate Fuel Cells	1076
25.7.5.1	Introduction	1076
25.7.5.2	Basic Operating Principle	1077
25.7.5.3	Acceptable Contamination Levels	1078
25.7.5.4	Major Technological Problems	1078
25.7.5.5	Technological Status	1079
25.7.5.6	Applications	1079
25.7.6	Solid Oxide Fuel Cells	1079
25.7.6.1	Introduction	1079
25.7.6.2	Basic Operating Principle	1080
25.7.6.3	Acceptable Contamination Levels	1081
25.7.6.4	Major Technological Problems	1081
25.7.6.5	Technological Status	1082
25.7.6.6	Applications	1082
25.8	Summary	1082
	References	1083

25.1 Introduction

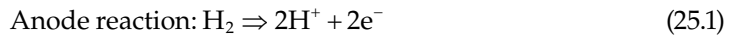
A fuel cell is an electrochemical device that directly converts the chemical energy of a fuel and oxidant into electric energy. Such a direct one-step conversion avoids the inefficient multistep processes involved in heat engines via combustion, thus eliminating the emission of chemical pollutants. Besides being efficient and clean, fuel cell is also compatible with renewable energy sources and carriers for sustainable development and energy security. Fuel cell offers additional advantages for both mobile and stationary applications, including quiet operation without vibration and noise, thus capable of on-site applications. Its inherent modularity allows for simple construction and operation with possible applications for dispersed, distributed, and portable power generation. Its fast response to the changing load condition while maintaining high efficiency makes it ideally suited to load following applications. Its potential high efficiency also represents less chemical, thermal, and carbon dioxide emissions for the same amount of energy conversion and power generation. Hence, fuel cell is often regarded as one of the advanced energy technologies of the future.

At present, fuel cells are being used routinely in space applications and have been under intensive development for terrestrial use, such as for utilities and zero-emission vehicles. There exist a variety of fuel cells, which are classified based on their operating temperature such as low- and high-temperature fuel cells, and the type of ion migrating through the electrolyte, etc. However, the choice of electrolyte defines the properties of a fuel cell. Hence, fuel cells are often named by the nature of the electrolyte used. There are presently six major fuel cell technologies at varying stages of development and commercialization. They are alkaline, phosphoric acid, polymer electrolyte membrane (PEM), molten carbonate, solid oxide, and direct methanol fuel cells (DMFCs). This chapter provides a

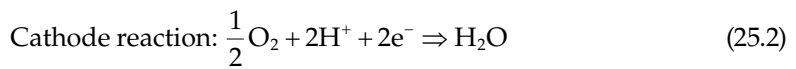
summary of fundamentals and the state-of-the-art technology for these types of fuel cell, while detailed information regarding their electrochemical reactions, operation principles, construction and design, and specific areas of applications can be found elsewhere [1–7].

25.2 Principle of Operation for Fuel Cells

A fuel cell is composed of three active components: a fuel electrode (anode), an oxidant electrode (cathode), and an electrolyte sandwiched in-between. Figure 25.1 illustrates the basic operational principle of fuel cells with a typical acid electrolyte fuel cell, where it is seen that molecular hydrogen is delivered from a gas flow stream to one of the electrodes, often named anode (or fuel electrode), and it reacts electrochemically in the anode as follows:



The hydrogen (fuel) is oxidized at the anode/electrolyte interface into hydrogen ion or proton H^+ and an electron e^- . The protons migrate through the (acid) electrolyte, while the electrons are forced to transfer through an external circuit, both arriving at another electrode that is often referred to as cathode (or oxidant electrode). At the cathode, the protons and electrons react with the oxygen supplied from an external gas flow stream, forming water:



Thus, oxygen is reduced into water at the cathode by combining with H^+ and e^- . Now both the electric current and the mass transfer form a complete circuit. The electrons go

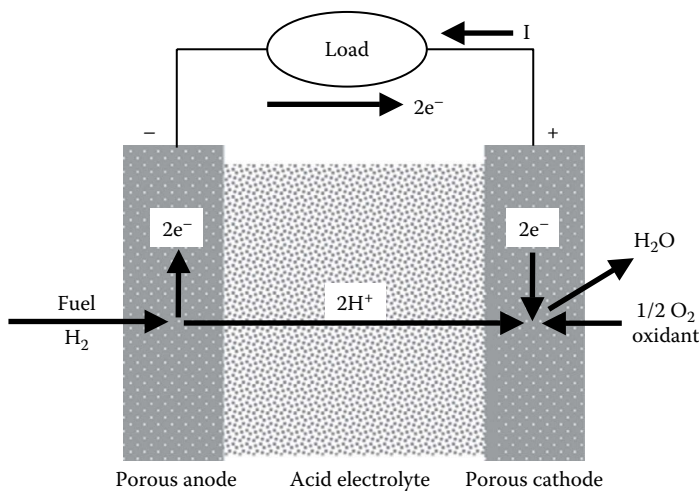
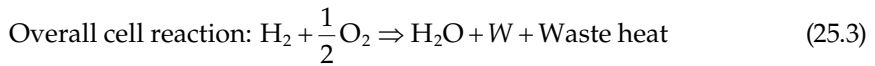


FIGURE 25.1
Schematic of a typical acid electrolyte fuel cell.

through the external electric circuit and do work on the electric load, constituting the useful electric energy output from the fuel cell. At the same time, waste heat is also generated due to the electrochemical reactions occurring at the anode and the cathode, as well as due to protons migrating through the electrolyte and electrons transporting in the solid portion of the electrodes and the external circuit. As a result, the overall cell reaction can be obtained by summing these two half-cell reactions to yield



where W stands for the useful electric energy output from the fuel cell. Although the half-cell reactions may be quite different in different types of fuel cells, to be described later, the overall cell reaction remains exactly the same as the equation shown earlier.

Therefore, the by-products of the electrochemical reactions described earlier are water and waste heat. They should be continuously removed from the cell in order to maintain its continuous isothermal operation for electric power generation. This need for the continuous removal of water and heat results in the so-called water and heat (thermal) management, which may become the two critical issues for the design and operation of some types of fuel cells. In general, they are not easy tasks to accomplish.

25.3 Typical Fuel Cell Systems

In general, a fuel cell power system involves more than just fuel cell itself because fuel cell needs a steady supply of qualifying fuel and oxidant as reactants for continuous generation of electric power. The oxidant is usually pure oxygen for specialized applications like in space and some military applications, and is almost invariably air for terrestrial and commercial applications. Depending on the specific types of fuel cells, both fuel and oxidant streams need to meet certain impurity requirements before being qualified as adequate for fuel cell operations. Therefore, a fuel cell power system is usually composed of a number of subsystems for fuel processing, oxidant conditioning, electrolyte management, cooling or thermal management, and reaction product removal, etc. A schematic of a typical rudimentary fuel cell system is illustrated in Figure 25.2. Normally, a power-conditioning unit is required to convert the DC electric power into AC power because fuel cell generates DC power while most of electric equipment operates on AC. The waste heat produced in the fuel cell power section is often integrated through a series of heat exchangers into the fuel cell system for better energy efficiency, and it is also possible for some types of fuel cells to use the waste heat as the heat source for either cogeneration or bottoming cycles for additional electric energy generation. The cogeneration of heat and hot water (and sometimes steam) along with electricity increases the overall energy efficiency of the fuel cell system to as much as 85% or more. Heat is critical to human survival, for example, for space heating and household use. Both heat and steam are significantly important commodity in industrial processes, in addition to many other practical applications.

The DC-to-AC inverter is a fairly mature technology, due to the incorporation of semiconductor and integrated circuit technology, and its conversion efficiency is very high, as much as 96% for megawatt-size power plants. The fuel processor converts the primary and/or portable fuel (such as natural gas, low-sulfur distillate, naphtha, methyl fuel—mostly

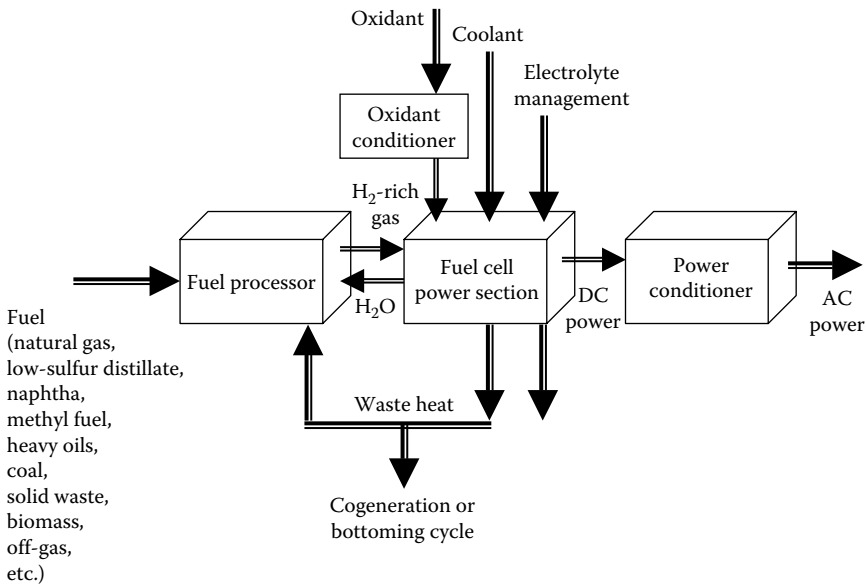


FIGURE 25.2
Schematic of a typical rudimentary fuel cell system.

methanol, heavy oils, coal, solid waste, biomass, etc.) into H₂ and CO. These secondary fuels (H₂ and CO) are considerably more electrochemically active in the electrochemical cell stack than the primary fuels. Even though fuel processing technology is highly advanced and efficient, it typically accounts for a third of the power plant size, weight, and cost for the hydrocarbon-fuelled fuel cell power plants; roughly, the electrochemical fuel cell stack accounts another third of the size, weight, and cost, while the ancillary components and subsystems associated with air supply, thermal management, water recovery and treatment, cabinet ventilation, and system control and diagnostics (or often referred to as the balance of the plant) accounts for the remaining third. In fuel cell systems, the most important subsystem is the electrochemical fuel cell stack, and fuel processor is the second major subsystem if hydrocarbon fuels are used as the primary fuel.

25.4 Performance of Fuel Cells

Although numerous studies have been conducted, aiming at developing fuel cell as a practical source of power, some confusion and misconception exist about the thermodynamic performance of fuel cell and its comparison with heat engines [2,8–10]. In this section, the fundamental principles, the first and second laws of thermodynamics, will be used to derive the idealized best possible performance, namely, the reversible cell potential and the reversible energy conversion efficiency of fuel cell. The effect of the operating conditions on the cell performance will be given, such as temperature, pressure, and reactant concentrations. The maximum possible efficiency for fuel cell will be compared with the Carnot efficiency, the maximum possible efficiency for heat engines against which fuel cell is competing for commercial success. Then, the possibility of over 100% efficiency for fuel cell will

be analyzed and ruled out based on the fundamental principles. Finally, various energy loss mechanisms in a fuel cell will be described, including both reversible and irreversible losses; the amount and rate of heat generation in an operating fuel cell will be derived; various forms of efficiency for fuel cell will be defined; and further energy losses in operating fuel cells will be considered as the Nernst loss due to limited utilization (or stoichiometry) of the reactants supplied to the cell.

25.4.1 Reversible Cell Potential

In a fuel cell, the chemical energy of a fuel and an oxidant is directly converted into electrical energy, which is exhibited in terms of cell potential and electrical current output. The maximum possible electrical energy output and the corresponding electrical potential difference between the cathode and the anode are achieved when the fuel cell is operated under thermodynamically reversible conditions. This maximum possible cell potential is called reversible cell potential, one of the important parameters for fuel cells, and it is derived in this section.

A thermodynamic system* model is shown in Figure 25.3 for the analysis of fuel cell performance. It is a control volume system for the fuel cell to which fuel and oxidant streams enter and product or exhaust stream exits. The fuel cell is located inside a thermal bath in order to maintain the desired system temperature T . The reactant streams (fuel and oxidant) and the exhaust stream are considered to have the same temperature T and

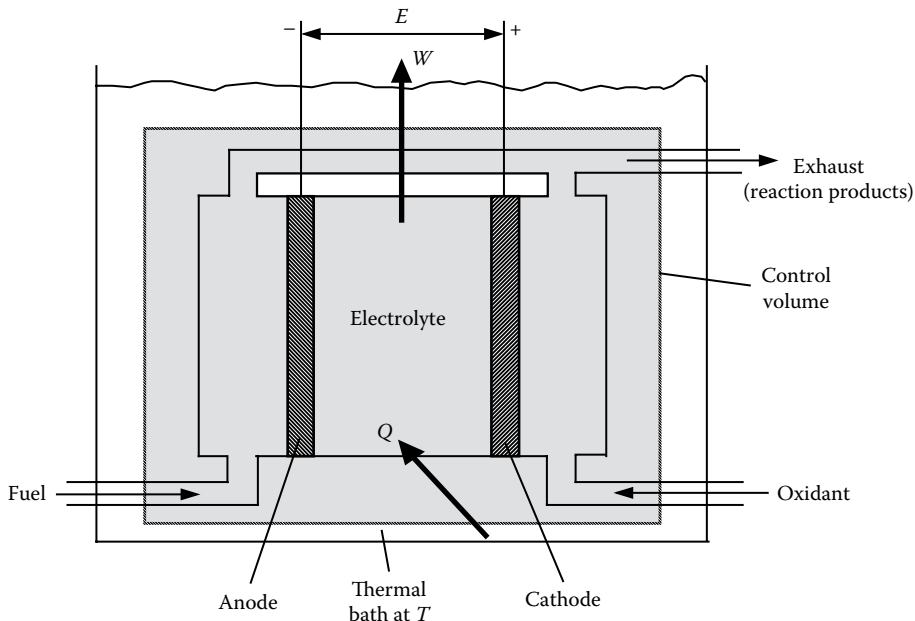
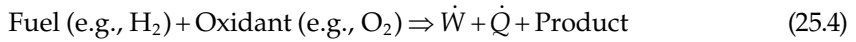


FIGURE 25.3
A thermodynamic model of fuel cell system.

* A thermodynamic system, or simply system, is a collection of matter under study (or analysis) in thermodynamics, whereas the jargon "fuel cell system" in fuel cell literature usually denotes the fuel cell power plant that consists of fuel cell stack(s) and auxiliary equipment (also called balance of the plant)—see Section 25.3, for example. In this chapter, a fuel cell system may imply both meanings. However, the context will tell which it is meant to be.

pressure P . It is assumed that the fuel and oxidant inflow and the exhaust outflow are steady; the kinetic and gravitational potential energy changes are negligible. Further, the overall electrochemical reactions occurring inside the fuel cell system boundary is described as follows:



where

\dot{W} is the rate of work done by the system

\dot{Q} is the rate of heat transferred into the system from the surrounding constant temperature thermal bath, which may, or may not, be in thermal equilibrium with the fuel cell system at the temperature T and pressure P

For hydrogen/oxygen fuel cells, the reaction product is water. Then, the first and second laws of thermodynamics can be written, respectively, for the present fuel cell system, as

$$\frac{dE_{C.V.}}{dt} = [(\dot{N}h)_F + (\dot{N}h)_{Ox}]_{in} - [(\dot{N}h)_{Ex}]_{out} + \dot{Q} - \dot{W} \quad (25.5)$$

$$\frac{dS_{C.V.}}{dt} = [(\dot{N}s)_F + (\dot{N}s)_{Ox}]_{in} - [(\dot{N}s)_{Ex}]_{out} + \frac{\dot{Q}}{T} + \dot{\phi}_s \quad (25.6)$$

where

\dot{N} is the molar flow rate

h is the (absolute) enthalpy per unit mole

s is the specific entropy on a mole basis

$\dot{\phi}_s$ is the rate of entropy generation due to irreversibilities

The subscripts “F,” “Ox,” and “Ex” stand for fuel, oxidant, and exhaust stream, respectively. “KE” and “PE” denote kinetic and gravitational potential energies that are being carried in and out of the system by the mass flow.

For a steady process, there are no temporal changes in the amount of energy $E_{C.V.}$ and entropy $S_{C.V.}$ within the control volume system, hence, $dE_{C.V.}/dt = 0$ and $dS_{C.V.}/dt = 0$. Therefore, Equations 25.5 and 25.6 can be simplified as follows:

$$\dot{N}_F(h_{in} - h_{out}) + \dot{Q} - \dot{W} = 0 \quad (25.7)$$

$$\dot{Q} = -T\dot{\phi}_s - \dot{N}_F T(s_{in} - s_{out}) \quad (25.8)$$

where

$$h_{in} = \left(h_F + \frac{\dot{N}_{Ox}}{\dot{N}_F} h_{Ox} \right)_{in} \quad \text{and} \quad h_{out} = \frac{\dot{N}_{Ex}}{\dot{N}_F} h_{Ex} \quad (25.9)$$

where

h_{in} is the amount of enthalpy per mole of fuel carried into the system by the reactant inflow

h_{out} is the amount of enthalpy per mole of fuel taken out of the system by the exhaust stream

Similarly,

$$s_{\text{in}} = \left(s_{\text{F}} + \frac{\dot{N}_{\text{Ox}}}{\dot{N}_{\text{F}}} s_{\text{Ox}} \right)_{\text{in}} \quad \text{and} \quad s_{\text{out}} = \frac{\dot{N}_{\text{Ex}}}{\dot{N}_{\text{F}}} s_{\text{Ex}} \quad (25.10)$$

are the amount of entropy per mole of fuel brought into, and carried out of, the system by the reactant inflow, and the outgoing exhaust stream containing the reaction products, respectively.

Substitution of Equation 25.8 into Equation 25.7 yields

$$\dot{W} = \dot{N}_{\text{F}}(h_{\text{in}} - h_{\text{out}}) - \dot{N}_{\text{F}}T(s_{\text{in}} - s_{\text{out}}) - T\dot{\varphi}_s \quad (25.11)$$

Let

$$w = \frac{\dot{W}}{\dot{N}_{\text{F}}}, \quad q = \frac{\dot{Q}}{\dot{N}_{\text{F}}}, \quad \text{and} \quad \varphi_s = \frac{\dot{\varphi}_s}{\dot{N}_{\text{F}}} \quad (25.12)$$

represent, respectively, the amount of work done, heat transferred, and entropy generated per unit mole of fuel. Equations 25.8 and 25.11 then become

$$q = -T\varphi_s - T(s_{\text{in}} - s_{\text{out}}) = T\Delta s - T\varphi_s \quad (25.13)$$

$$w = (h_{\text{in}} - h_{\text{out}}) - T(s_{\text{in}} - s_{\text{out}}) - T\varphi_s \quad (25.14)$$

Because the enthalpy and entropy changes for the fuel cell reaction are defined as

$$\Delta h = h_{\text{out}} - h_{\text{in}} \quad \text{and} \quad \Delta s = s_{\text{out}} - s_{\text{in}} \quad (25.15)$$

Equation 25.14 can also be expressed as

$$w = -\Delta h + T\Delta s - T\varphi_s = -[(h - Ts)_{\text{out}} - (h - Ts)_{\text{in}}] - T\varphi_s \quad (25.16)$$

From the definition of the Gibbs function (per mole of fuel) $g = h - Ts$, Equation 25.14 or 25.16 can also be written as

$$w = -(g_{\text{out}} - g_{\text{in}}) - T\varphi_s = -\Delta g - T\varphi_s \quad (25.17)$$

Because by the second law of thermodynamics, entropy can be generated but can never be destroyed, we know $\varphi_s \geq 0$, and also the absolute temperature (in Kelvin scale) $T > 0$ by the third law of thermodynamics, the maximum possible work (i.e., useful energy) output from the present system occurs when $\varphi_s = 0$, or under the thermodynamically reversible condition, since the change in the Gibbs function is usually negative for useful fuel cell reaction. Therefore, from Equation 25.17, it is clear that the maximum possible work output from the present fuel cell system is equal to the decrease in Gibbs function, or

$$w_{\text{max}} = -\Delta g \quad (25.18)$$

for all reversible processes, regardless of the specific type of fuel cells involved. In fact, it might be pointed out that in the derivation of Equations 25.17 and 25.18, no specifics about the control volume system have been stipulated; hence, they are valid for any energy conversion systems.

For a fuel cell system, the electrical energy output is conventionally expressed in terms of the cell potential difference between the cathode and the anode. Since the (electrical) potential is the (electrical) potential energy per unit (electrical) charge, its SI unit is J/C, which is more often called volt or simply V. Potential energy is defined as the work done when a charge is moved from one location to another in the electrical field, normally external circuits. For the internal circuit of fuel cells, such as the one shown in Figure 25.3, electromotive force is the terminology often used, which is also defined as the work done by transferring 1 C (coulomb) positive charge from a low to a high potential. Hence, electromotive force also has the SI unit of J/C, or V. We shall adopt the terminology of cell potential, instead of electromotive force, from now on, and we shall use the notation E to represent the cell potential. Because normally electrons are the particles transferred that carry electrical charge, we may express the work done by a fuel cell as follows:

$$w \text{ (J/mol fuel)} = E \times (\text{Coulombs of electron charge transferred/mol fuel})$$

or

$$w = E \times (nN_0e) = E \times (nF) \tag{25.19}$$

where

- n is the number of moles of electrons transferred per mole of fuel consumed
- N_0 is the Avogadro's number ($=6.023 \times 10^{23}$ number of electrons/mol electron)
- e is the electric charge per electron ($=1.6021 \times 10^{-19}$ C/electron)

Since $N_0e = 96,487$ C/mol electron $= F$ is known as the Faraday constant, the cell potential becomes, from Equation 25.17,

$$E = \frac{w}{nF} = \frac{-\Delta g - T \wp_s}{nF} \tag{25.20}$$

Hence, the maximum possible cell potential, or the reversible cell potential E_r , becomes

$$E_r = -\frac{\Delta g}{nF} \tag{25.21}$$

From the reversible cell potential given earlier, Equation 25.20 can also be rewritten as

$$E = E_r - \frac{T \wp_s}{nF} = E_r - \eta \tag{25.22}$$

where

$$\eta = \frac{T \wp_s}{nF} \tag{25.23}$$

is the cell voltage loss due to irreversibilities (or entropy generation). Clearly, the actual cell potential can be calculated by subtracting the cell voltage loss from the reversible cell potential. Alternatively, the amount of entropy generation per mole of fuel consumed can be determined as

$$\wp_s = \frac{nF\eta}{T} = \frac{nF(E_r - E)}{T} \tag{25.24}$$

Thus, the amount of entropy generation, representing the degree of irreversibilities (the degree of deviation from the idealized reversible condition), for the fuel cell reaction process can be measured once the cell potential E and the cell operating temperature T are known.

Note that the Gibbs function is a thermodynamic property, determined by state variables such as temperature and pressure. Hence, the change in the Gibbs function for the fuel cell reaction discussed here

$$\Delta g = \Delta h - T\Delta s \quad (25.25)$$

is also a function of the system temperature T and pressure P , as is the reversible cell potential. The specific effect of the operating conditions, such as temperature, pressure, and reactant concentrations, on the reversible cell potential will be presented in the next section. If the reaction occurs at the standard reference temperature and pressure (25°C and 1 atm), the resulting cell potential is usually called the standard reversible cell potential E_r° ,* or

$$E_r^\circ(T_{\text{ref}}) = -\frac{\Delta g(T_{\text{ref}}, P_{\text{ref}})}{nF} \quad (25.26)$$

If pure hydrogen and oxygen are used as reactants to form product water, then $E_r^\circ(25^\circ\text{C}) = 1.229\text{ V}$ for the product water in liquid form, and $E_r^\circ(25^\circ\text{C}) = 1.185\text{ V}$ for the product water in vapor form. The difference in E_r° corresponds to the energy required for the vaporization of water. It might be pointed out that any fuel containing hydrogen (including hydrogen itself, hydrocarbons, alcohols, and to a lesser extent coal) has two values for Δg and Δh , one higher and one lower, depending on whether the product water is in the form of liquid or vapor. Hence, care should be taken when referring to reversible cell potential and energy efficiency to be discussed later in Section 25.4.3.

The standard reversible cell potential, E_r° , can be determined for any other electrochemical reactions. Some of the potential fuel cell reactions and the resulting E_r° are shown in Table 25.1 along with other relevant parameters. From this table, it might be noted that E_r° should be approximately above 1 V in order for the reaction to be realistic for fuel cell application. This is because if E_r° is $\ll 1\text{ V}$, and considering the cell voltage loss that inevitably occurs in practical fuel cells due to irreversibilities, the actual cell potential might become too small to be useful for practical applications. Therefore, the rule of thumb is, for any proposed fuel and oxidant, to calculate E_r° and to see if E_r° is on the order of 1 V or larger before proceeding to any further work on it.

25.4.2 Effect of Operating Conditions on Reversible Cell Potential

The most important operating conditions that influence fuel cell performance are the operating temperature, pressure, and reactant concentrations. For many useful electrochemical reactions, the entropy change is negative and is almost constant with the change of temperature to a good approximation, provided the temperature change

* In the literature, the superscript “°” sometimes denotes the value at the standard “reference condition” of 25°C and 1 atm, and sometimes it also refers to parameters evaluated at 1 atm. The latter meaning has been adopted in this chapter.

TABLE 25.1

Standard Enthalpy and Gibbs Function of Reaction for Candidate Fuels and Oxidants, and Corresponding Standard Reversible Cell Potential as well as Other Relevant Parameters (at 25°C and 1 atm)

Fuel	Reaction	n	$-\Delta h$ (kJ/mol)	$-\Delta g$ (kJ/mol)	E_r° (V)	η^a (%)
Hydrogen	$H_2 + 0.5O_2 \rightarrow H_2O(l)$	2	286.0	237.3	1.229	82.97
	$H_2 + Cl_2 \rightarrow 2HCl(aq)$	2	335.5	262.5	1.359	78.33
	$H_2 + Br_2 \rightarrow 2HBr(aq)$	2	242.0	205.7	1.066	85.01
Methane	$CH_4 + 2O_2 \rightarrow CO_2 + 2H_2O(l)$	8	890.8	818.4	1.060	91.87
Propane	$C_3H_8 + 5O_2 \rightarrow 3CO_2 + 4H_2O(l)$	20	2221.1	2109.3	1.093	94.96
Decane	$C_{10}H_{22} + 15.5O_2 \rightarrow 10CO_2 + 11H_2O(l)$	66	6832.9	6590.5	1.102	96.45
Carbon monoxide	$CO + 0.5O_2 \rightarrow CO_2$	2	283.1	257.2	1.333	90.86
Carbon	$C(s) + 0.5O_2 \rightarrow CO$	2	110.6	137.3	0.712	124.18 ^b
	$C(s) + O_2 \rightarrow CO_2$	4	393.7	394.6	1.020	100.22 ^b
Methanol	$CH_3OH(l) + 1.5O_2 \rightarrow CO_2 + 2H_2O(l)$	6	726.6	702.5	1.214	96.68
Formaldehyde	$CH_2O(g) + O_2 \rightarrow CO_2 + H_2O(l)$	4	561.3	522.0	1.350	93.00
Formic acid	$HCOOH + 0.5O_2 \rightarrow CO_2 + H_2O(l)$	2	270.3	285.5	1.480	105.62 ^b
Ammonia	$NH_3 + 0.75O_2 \rightarrow 1.5H_2O(l) + 0.5N_2$	3	382.8	338.2	1.170	88.36
Hydrazine	$N_2H_4 + O_2 \rightarrow 2H_2O(l) + N_2$	4	622.4	602.4	1.560	96.77
Zinc	$Zn + 0.5O_2 \rightarrow ZnO$	2	348.1	318.3	1.650	91.43
Sodium	$Na + 0.25H_2O + 0.25O_2 \rightarrow NaOH(aq)$	1	326.8	300.7	3.120	92.00

Source: Appleby, A.J., Characteristics of fuel cell systems, in: Blomen, L.J.M.J. and Mugerwa, M.N., eds., *Fuel Cell Systems*, Chapter 5, Plenum Press, New York, 1993.

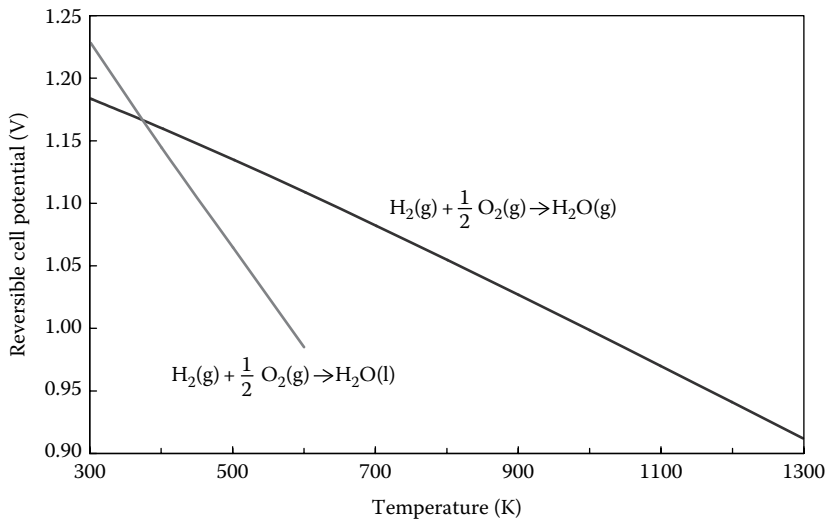
^a Energy conversion efficiency.

^b There is a conceptual problem with these efficiency data; see Section 25.4.3.5 for explanation.

$T - T_{ref}$ is not too large. Then, the effect of temperature on the reversible cell potential may be written as [1]

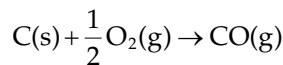
$$E_r(T, P) = E_r(T_{ref}, P) + \left(\frac{\Delta s(T_{ref}, P)}{nF} \right) (T - T_{ref}) \quad (25.27)$$

It must be emphasized that the expression given in Equation 25.27 is an approximation. Strictly speaking, the reversible cell potential at any temperature and pressure should be determined from Equation 25.21 by calculating first the property changes for the particular fuel cell reaction involved. Such a procedure has been followed for the hydrogen and oxygen reaction to form gaseous water, and the results are presented in Figure 25.4. Clearly, the reversible cell potential indeed decreases almost linearly as temperature is increased over a large temperature range. However, it is noticed that the reversible cell potential is larger for product water as liquid at low temperatures, but it decreases much faster than the gaseous water as product when temperature is increased. So that at temperatures slightly above about 373 K, the reversible cell potential for liquid water product actually becomes smaller. This may seem odd, but it is because at such high-temperature pressurization is necessary to keep the product water in liquid form as the reactants, hydrogen and oxygen, are fed at 1 atm. Also notice that the critical temperature for water is about 647 K, beyond which distinct liquid state does not exist for water, hence the shorter curve shown for the liquid water case in Figure 25.4.

**FIGURE 25.4**

Effect of temperature on the reversible cell potential of a hydrogen–oxygen fuel cell for the reaction of $\text{H}_2 + 1/2\text{O}_2 \rightarrow \text{H}_2\text{O}$ at the pressure of 1 atm.

As pointed out earlier, the entropy change for most of fuel cell reactions is negative; consequently, the reversible cell potential decreases as temperature is increased as shown in Figure 25.4. However, for some reactions such as



the entropy change is positive, for example, $\Delta s = 89 \text{ J}/(\text{mol fuel K})$ at the standard reference temperature and pressure. As a result, the reversible cell potential for this type of reactions will increase with temperature, which is clearly seen in Figure 25.5 for the reversible cell potential as a function of temperature for a number of important fuel cell reactions.

The effect of pressure on reversible cell potential can be expressed as [1]

$$E_r(T, P) = E_r(T, P_{\text{ref}}) - \frac{\Delta N \mathfrak{R} T}{nF} \ln \left(\frac{P}{P_{\text{ref}}} \right) \quad (25.28)$$

where ΔN represents the total number of mole changes for all the gaseous species involved in the fuel cell reaction. This equation indicates that the pressure dependence of the reversible cell potential is a logarithmic function, and hence the dependence becomes weaker as pressure P is increased. Figure 25.6 shows the effect of pressure on the reversible cell potential for hydrogen/oxygen fuel cell for both liquid and vapor water as the reaction product. It is seen that the reversible cell potential increases with pressure, very fast for low-pressure values, gradually slowing down for higher-pressure values. Also, the pressure effect is larger for liquid water as the product, because of the larger coefficient arising from the larger change in the number of moles between the product and the reactant, ΔN .

It might be also emphasized that the pressure effect is small on the reversible cell potential at low temperatures, as shown in the earlier example. However, this effect increases

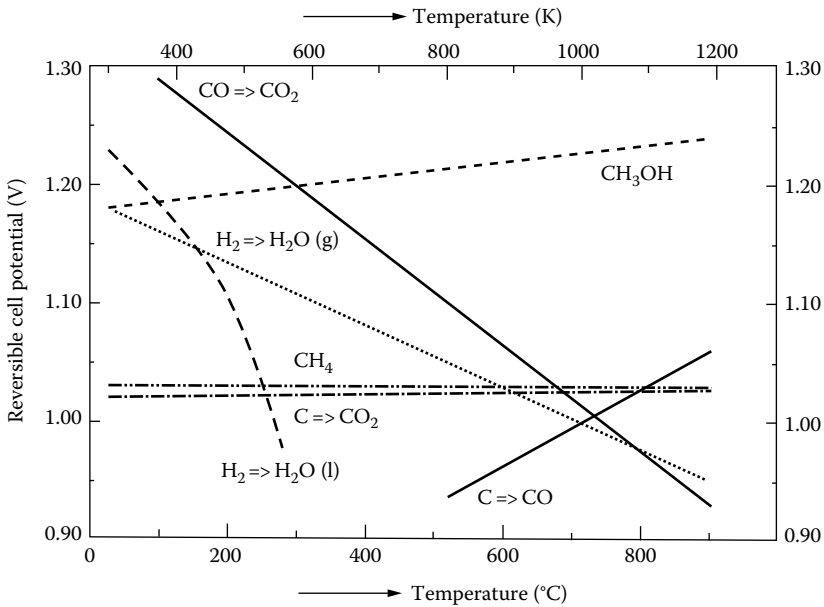


FIGURE 25.5 Standard reversible cell potential, E_r , as a function of temperature for the most important fuel cell reactions at the pressure of 1 atm. (From Barendrecht, E., *Electrochemistry of fuel cells*, in: Blomen, L.J. M.J. and Mugerwa, M.N., eds., *Fuel Cell Systems*, Plenum Press, New York, 1993.)

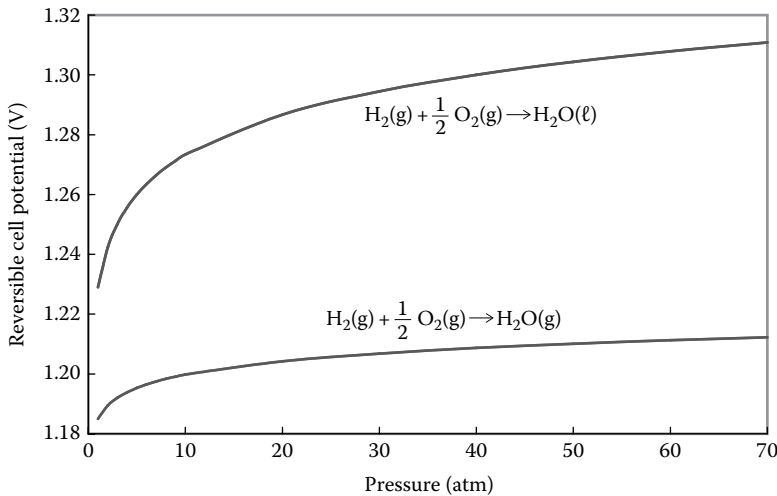


FIGURE 25.6 Standard reversible cell potential, E_r , as a function of pressure for the fuel cell reaction of $\text{H}_2(\text{g}) + 1/2\text{O}_2 \rightarrow \text{H}_2\text{O}$ at the temperature of 25°C .

significantly at high temperatures because the pressure effect coefficient, $-\Delta N \mathcal{R} T / (nF)$, is directly proportional to temperature.

It might be pointed out that for high-temperature fuel cells, the dependence of the actual cell potential E on the pressure follows closely the results given in Equation 25.28, whereas a significant deviation occurs for the low-temperature fuel cells. The difference arises from

the fact that at high temperatures, the reaction kinetics are very fast and pressurization primarily increases the reactant concentration, hence better performance directly. At low temperatures, the reaction kinetics are slow, and higher reactant concentration does not yield a proportional increase in the cell potential due to the significant cell potential loss associated with the slow kinetics.

When the fuel, oxidant, and exhaust streams contain chemically inert gas species, the reversible cell potential will be lowered due to the dilution effect of the inert species and can be derived as [1]

$$E_r(T, P_i) = E_r(T, P) - \frac{\mathcal{R}T}{nF} \ln K \quad (25.29)$$

where P_i is the partial pressure of the reactant in the fuel and oxidant streams, and

$$K = \prod_{i=1}^{N_g} \left(\frac{P_i}{P} \right)^{(v_i' - v_i'')/v_F} \quad (25.30)$$

is defined similar to the equilibrium constant for partial pressure (but they are not the same); N_g is the total number of gas species in the reacting system, excluding the solid and liquid species; v_i' and v_i'' are the number of moles of species i in the reactant and product mixtures, respectively. Equation 25.29 is the general form of the Nernst equation, representing the effect of the reactant and product concentrations on the reversible cell potential. When the reactant streams contain inert diluents for a given operating temperature and pressure, the diluents will cause a voltage loss for the reversible cell potential, and the amount of loss is generally called the Nernst loss, and its magnitude is equal to the second term on the right-hand side of Equation 25.29.

25.4.3 Energy Conversion Efficiency

25.4.3.1 Definition of Energy Conversion Efficiency

The efficiency for any energy conversion process or system is often defined as*

$$\eta = \frac{\text{Useful energy obtained}}{\text{Energy available for conversion that's an expense}} \quad (25.31)$$

Based on this definition, it is well known that 100% energy conversion efficiency is possible by the first law of thermodynamics, but is not possible by the second law of thermodynamics for many energy conversion systems that produce power output, such as steam and gas turbines, internal combustion engines, which involve irreversible losses of energy. These thermal energy conversion systems are often referred to as heat engines.

* Note that in literature η is commonly used as efficiency in thermodynamics, whereas it is also conventionally used as overpotential, or voltage loss, for fuel cell analysis, as in electrochemistry. In this chapter, η is used for both efficiency and overpotential in order to be consistent with the respective convention, and its meaning would become clear from the context.

25.4.3.2 Reversible Energy Conversion Efficiency for Fuel Cells

For the present fuel cell system described in Figure 25.3, the energy balance equation, Equation 25.5, can be written, on a per unit mole of fuel basis, as

$$h_{\text{in}} - h_{\text{out}} + q - w = 0 \quad \text{or} \quad h_{\text{in}} - h_{\text{out}} = -q + w \quad (25.32)$$

which indicates that the enthalpy change, $-\Delta h = h_{\text{in}} - h_{\text{out}}$, provides the energy available for conversion into the useful energy exhibited as work here, and it is the expense to be paid for the useful work output. At the same time, waste heat, q , is also generated, which would represent a degradation of energy. The amount of waste heat generated can be determined from the second law expression, Equation 25.6 or 25.13, as

$$q = T\Delta s - T\phi_s \quad (25.33)$$

and the useful energy output as work is, from Equation 25.17 or combining Equations 25.32 and 25.33

$$w = -\Delta g - T\phi_s \quad (25.34)$$

Therefore, the energy conversion efficiency for the fuel cell system described in Figure 25.3 becomes, according to Equation 25.31,

$$\eta = \frac{w}{-\Delta h} = \frac{\Delta g + T\phi_s}{\Delta h} \quad (25.35)$$

Note that both Δh and Δg are negative for power generation systems, including fuel cells as it is clearly shown in Table 25.1. By the second law, the entropy generation per unit mole of fuel is

$$\phi_s \geq 0 \quad (25.36)$$

and the equality holds for all reversible processes, whereas entropy is always generated for irreversible processes. Therefore, the maximum possible efficiency allowed by the second law is, when the process is reversible (i.e., $\phi_s = 0$),

$$\eta_r = \frac{w_{\text{max}}}{-\Delta h} = \frac{\Delta g(T, P)}{\Delta h(T, P)} \quad (25.37)$$

Since both the enthalpy and Gibbs function changes depend on the system temperature and pressure, the same holds for the energy conversion efficiency. It should be pointed out that in the earlier derivation, no assumption specifically related to fuel cell has been made; the only assumption made is that the energy conversion system for power production is reversible for all processes involved. Thus, Equation 25.37 is valid for any power production system, be it electrochemical converter like fuel cells or conventional thermal energy converter like heat engines, as long as the process is reversible. Hence, it may be called the *second law or reversible efficiency*, since it is the maximum possible efficiency that is allowed by the second law of thermodynamics. In what follows, we will demonstrate that the maximum possible efficiency for conventional heat engines, the well-known Carnot efficiency, is really the second law efficiency applied specifically to the conventional thermal power cycles, thus is equivalent to Equation 25.37.

25.4.3.3 Carnot Efficiency: The Reversible Energy Conversion Efficiency for Heat Engines

Consider a heat engine operating between two temperature thermal energy reservoirs (TER), one at a high temperature T_H and the other at a low temperature T_L , as shown in Figure 25.7. The heat engine obtains energy from the high-temperature TER in the form of heat with the quantity q_H ; a portion of this heat is converted to work output w , and the remainder is rejected to the low-temperature TER in the amount of q_L as waste heat. Applying the first and second laws to the heat engine, we have

$$\text{First law:} \quad w = q_H - q_L \quad (25.38)$$

$$\text{Second law:} \quad \wp_{s,\text{HE}} = \frac{q_L}{T_L} - \frac{q_H}{T_H} \quad (25.39)$$

where $\wp_{s,\text{HE}}$ represents the amount of entropy production during the energy conversion process by means of the heat engine. From Equation 25.39, the amount of heat rejection can be determined as

$$q_L = \frac{T_L}{T_H} q_H + T_L \wp_{s,\text{HE}} \quad (25.40)$$

The efficiency for the heat engine is, by the definition of Equation 25.31,

$$\eta = \frac{w}{q_H} \quad (25.41)$$

Substituting Equations 25.38 and 25.40 into 25.41 yields

$$\eta = 1 - \frac{T_L}{T_H} - \frac{T_L}{q_H} \wp_{s,\text{HE}} \quad (25.42)$$

As pointed out earlier, the second law of thermodynamics dictates that the entropy generation within the heat engine can never be negative; at most, it can vanish under the

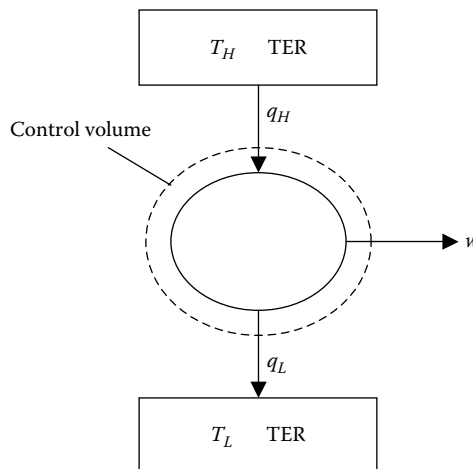


FIGURE 25.7
Thermodynamic system model of heat engines operating between two temperature thermal energy reservoirs.

thermodynamically reversible condition. Therefore, the maximum possible efficiency for the heat engine is achieved if the process is reversible ($\phi_{s,HE} = 0$):

$$\eta_{r,HE} = 1 - \frac{T_L}{T_H} \tag{25.43}$$

This is the familiar Carnot efficiency, giving the upper bound for the efficiency of all heat engines. Because $T_L < T_H$, the low-temperature $T_L \neq 0$ by the third law of thermodynamics, and the high-temperature T_H is finite, 100% efficiency is not possible by the second law for any energy conversion system that produces power output using heat engines, such as steam and gas turbines and internal combustion engines, because of the second law requirement that the entropy generation term must never be negative. In contrast, 100% efficiency is possible by the first law, which merely states the principle of energy conservation.

25.4.3.4 Equivalency of Carnot and Fuel Cell Reversible Efficiency

As shown earlier, both the Carnot efficiency and the reversible energy conversion efficiency for fuel cell, Equation 25.37, are the maximum possible efficiency allowed by the second law; the former is applied specifically to heat engines, while the latter is derived for fuel cells. Therefore, they must be related somehow as they both are the maximum possible efficiency dictated by the second law. In this section, we demonstrate that they are actually equivalent, just expressed in a different form, under a suitable condition for the comparison.

Suppose, for a heat engine, the high-temperature TER is maintained at T_H by the combustion of a fuel with an oxidant, both reactants are originally at the temperature of T_L , as shown schematically in Figure 25.8. It is assumed that both the fuel and the oxidant are the same as used in Figure 25.3 for the derivation of fuel cell performance; the combustion process is carried out at the same system pressure P in a controlled manner such that the combustion products leave the TER at the pressure P and temperature T_L . Neglecting

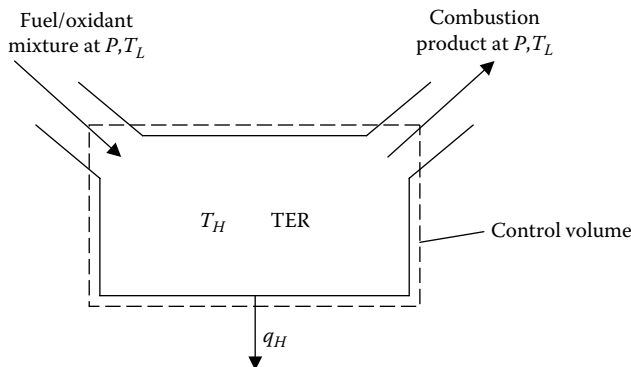


FIGURE 25.8 Thermodynamic system model of high-temperature thermal energy reservoir (TER) maintained by combustion process of a fuel/oxidant mixture.

the changes in the kinetic and gravitational potential energy, the first and second laws become, for the high-temperature TER,

$$\text{First law:} \quad q_H = h_R - h_P = -\Delta h(T_L, P) \quad (25.44)$$

$$\text{Second law:} \quad \wp_{s, \text{TER}} = (s_P - s_R) + \frac{q_H}{T_H} = \Delta s(T_L, P) + \frac{q_H}{T_H} \quad (25.45)$$

After rearranging, Equation 25.45 gives the temperature T_H resulting from the combustion process

$$T_H = \frac{q_H}{\wp_{s, \text{TER}} - \Delta s(T_L, P)} \quad (25.46)$$

Substitution of Equations 25.44 and 25.46 into 25.42 leads to

$$\eta = \frac{\Delta g(T_L, P)}{\Delta h(T_L, P)} + \frac{T_L}{\Delta h(T_L, P)} (\wp_{s, \text{HE}} + \wp_{s, \text{TER}}) \quad (25.47)$$

where $\Delta g(T_L, P) = \Delta h(T_L, P) - T_L \Delta s(T_L, P)$ is the change in the Gibbs function between the reaction product and the reactant. If all the processes within the heat engine and high-temperature TER are reversible ($\wp_{s, \text{HE}} = 0$ and $\wp_{s, \text{TER}} = 0$), then Equation 25.47 reduces to

$$\eta_r = \frac{\Delta g(T_L, P)}{\Delta h(T_L, P)} \quad (25.48)$$

which is exactly the same as Equation 25.37—the efficiency expression derived for fuel cells. Note that in order for the combustion process to be reversible (i.e., $\wp_{s, \text{HE}} = 0$) theoretically, there should be no product dissociations and no incomplete combustion products or by-products (such as pollutants) formed, and the perfect combustion products should consist of stable chemical species only, as would be obtained from an ideal and complete stoichiometric reaction. Therefore, it may be stated that any reversible heat engine operating under the maximum temperature limit allowed by a *perfect* combustion of a fuel/oxidant mixture has the same efficiency as that of a reversible isothermal fuel cell using the same fuel and oxidant and operating at the same temperature as that of the low-temperature TER. Or simply stated, the maximum possible efficiency is the same for both fuel cells and heat engines.

It should be emphasized that combustion process is inherently irreversible, and other irreversibilities occur in the heat engine as well so that the actual efficiency for heat engine is much lower than the maximum allowed by the second law. Similarly, fuel cells can never achieve, although it is quite possible to achieve very closely the maximum possible efficiency allowed by the second law. Therefore, the actual energy efficiency for fuel cells is typically much higher than the heat engine. The various mechanisms of irreversible losses in fuel cells will be described later in this chapter.

25.4.3.5 Possibility of Over 100% Fuel Cell Efficiency: Is It Real or Hype?

It is well known that no heat engine could have efficiency of 100% or more, including the ideal Carnot efficiency, as discussed earlier. However, it has been reported that the ideal

fuel cell efficiency, η_r , according to Equation 25.37, could be over 100% in principle for some special fuel cell reactions (e.g., [2,8]), even though it is unachievable in practice. This has also sometimes been used as evidence that fuel cells could have higher energy efficiency than the competing heat engines. Is this realistic even under the thermodynamically reversible condition? The answer is negative! With the following analysis, we can show that this is really due to a conceptual error in stretching the application of Equation 25.37 beyond its validity range.

Consider the thermodynamic model system used for fuel cell analysis, as shown in Figure 25.3. The amount of heat transfer from the surrounding thermal bath to the fuel cell system is given in Equation 25.33 for practical fuel cells. Under the thermodynamically reversible condition, the amount of heat transfer becomes

$$q = T\Delta s = \Delta h - \Delta g \quad (25.49)$$

For most of fuel cell systems, Δs is negative (i.e., $\Delta s < 0$ just like Δh and Δg), indicating that heat is actually transferred from the fuel cell to the ambient environment, or heat is lost from the fuel cell system, rather than the other way around. Hence, the second law efficiency, according to Equation 25.37,

$$\eta_r = \frac{\Delta g}{\Delta h} = \frac{\Delta h - T\Delta s}{\Delta h} = 1 - \frac{T\Delta s}{\Delta h} < 1 \quad (25.50)$$

is $< 100\%$, as it should be by the common perception of the parameter called efficiency.

However, for some special reactions, such as



the entropy change Δs is positive. Physically, it indicates that the fuel cell absorbs heat from the ambient and converts it completely into electrical energy along with the chemical energy of the reactants. This is equivalent to stating that the less useful form of energy, heat, is converted completely into the more useful form of energy, electric energy, without the generation of entropy (i.e., reversible condition) during the conversion process when Equation 25.37 is used for the efficiency calculation—such a process is clearly a violation of the second law. Therefore, the second law efficiency for this particular fuel cell reaction becomes larger than 100%, that is, a physically impossible result, when Equation 25.37 is utilized for the efficiency calculation for this type of fuel cell reactions. According to Equation 25.37, the reversible fuel cell efficiency for the reaction shown in Equation 25.51 would be equal to $\eta_r = 124\%$ at the standard temperature and pressure, 163% at 500°C and 1 atm, and 197% at 1000°C and 1 atm.

The root of the problem from the straightforward application of Equation 25.37 leading to the physically impossible result of over 100% energy efficiency is as follows. At atmospheric temperature for fuel cell operations, the energy from the thermal bath (or the atmosphere) as heat may be free. But at elevated temperatures, external means must be employed to keep the thermal bath at temperatures above the ambient atmospheric temperature, which constitutes an expense. Therefore, the heat from the thermal bath to the fuel cell system is no longer a free energy input; rather, it is part of the energy input that has to be paid for. By definition, Equation 25.31, the efficiency definition for fuel cells, has to be modified accordingly, such that the ideal reversible efficiency will be no longer over 100% for fuel cells. Thus, we conclude that the reversible fuel cell

efficiency shown in Equation 25.37 is valid only for fuel cell reactions where the entropy change between the product and reactant is negative (hence, heat is lost from the fuel cell), and it cannot be applied for reactions with positive entropy change, such as the one given in Equation 25.51.

25.4.4 Practical Fuel Cell Efficiency and Energy Loss Mechanisms

From the preceding analysis, it is clear that energy loss in fuel cells occurs under both reversible and irreversible conditions. We will describe each type of energy loss mechanisms and associated expression for energy conversion efficiency in fuel cells.

25.4.4.1 Reversible Energy Loss and Reversible Energy Efficiency

The energy loss in fuel cells under reversible conditions is equal to the heat transferred (or lost) to the environment, as given:

$$q = T\Delta s = \Delta h - \Delta g \quad (25.49)$$

because of the negative entropy change for the fuel cell reaction. The associated energy conversion efficiency, which has been called the reversible energy conversion efficiency, has been derived and given in Equation 25.37 or 25.50. Combining Equation 25.49 with 25.50 yields

$$\eta_r = \frac{\Delta g}{\Delta h} = \frac{\Delta g}{\Delta g + T\Delta s} \quad (25.52)$$

Dividing the numerator and the denominator by the factor (nF), and utilizing Equations 25.21 and 25.52 becomes [1]

$$\eta_r = \frac{E_r}{E_r - T(\partial E_r / \partial T)_p} \quad (25.53)$$

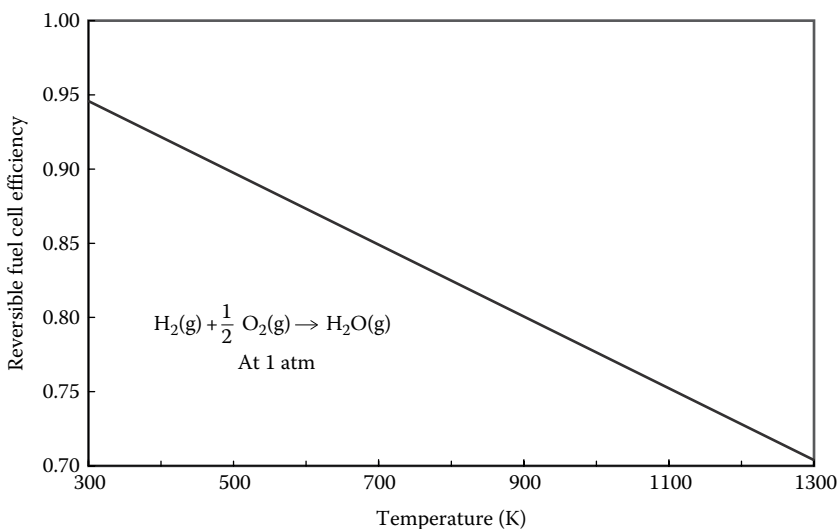
Therefore, when the entropy change is negative, as described earlier, the reversible efficiency, η_r is <100%, and the reversible cell potential decreases with temperature; and according to Equation 25.53, the reversible efficiency, η_r also decreases with temperature. For example, for H_2 and O_2 reaction forming gaseous water at 1 atm pressure,

$$\left(\frac{\partial E_r}{\partial T} \right)_p = -0.2302 \times 10^{-3} \text{ V/K}$$

at 25°C, and the reversible efficiency is about 95% at 25°C, and it becomes 88% at 600 K and 78% at 1000 K. Figure 25.9 illustrates the reversible efficiency as a function of temperature for the hydrogen and oxygen reaction with gaseous water as the reaction product. It is seen that the reversible efficiency decreases almost linearly. For most fuel cell reactions,

$$\left(\frac{\partial E_r}{\partial T} \right)_p = -(0.1-1.0) \times 10^{-3} \text{ V/K}$$

at 25°C and 1 atm; hence, the reversible efficiency is typically around 90%.

**FIGURE 25.9**

The reversible fuel cell efficiency (based on LHV) as a function of temperature for the reaction of $\text{H}_2 + 1/2\text{O}_2 \rightarrow \text{H}_2\text{O}(\text{g})$ occurring at 1 atm pressure.

However, for the reaction of carbon and oxygen to form carbon monoxide, as shown in Equation 25.51, the entropy change is positive, and the reversible cell potential increases with temperature, as presented previously; hence, the reversible efficiency will also increase with temperature, according to Equation 25.53. But as discussed previously, the efficiency expression, Equation 25.52 or 25.53, is not valid for such reactions.

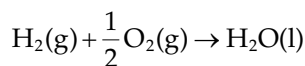
From the reversible energy efficiency, Equation 25.37, and dividing the numerator and the denominator by the factor (nF), we have, after utilizing the reversible cell potential, Equation 25.21

$$\eta_r = \frac{E_r}{(-\Delta h/nF)} = \frac{E_r}{E_{tn}} \quad (25.54)$$

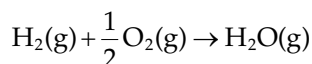
where

$$E_{tn} = -\frac{\Delta h}{nF} \quad (25.55)$$

is called thermoneutral voltage (or potential), a voltage a fuel cell would have if all the chemical energy of the fuel and oxidant is converted to electric energy (i.e., 100% energy conversion into electricity). For example, for the reaction



$E_{tn} = 1.48 \text{ V}$, and the corresponding reversible efficiency is $\eta_r = 83\%$ at 25°C and 1 atm, whereas at the same temperature and pressure, for the reaction



$E_{tn} = 1.25 \text{ V}$, and the corresponding reversible efficiency is $\eta_r = 95\%$.

From this discussion, it is noted that for hydrogen and oxygen reaction, the reversible cell efficiency can differ by as much as 14%, depending on whether the product water is liquid or vapor, or whether the higher (HHV) or lower heating value (LHV) is used for the efficiency calculation under identical operating conditions. For most of the hydrocarbon fuels that contain hydrogen (including hydrogen itself, hydrocarbons, alcohols, and to a lesser extent coal), there exist two values for the change in the enthalpy and Gibbs function, for example,

$$\text{For natural gas (methane, CH}_4\text{): } \frac{\text{LHV}}{\text{HHV}} = 0.90$$

$$\text{For coals of typical hydrogen and water content: } \frac{\text{LHV}}{\text{HHV}} \sim 0.95 \text{ on a dry basis}$$

Therefore, different efficiency values result, depending on which heating value ($-\Delta h$) is used for the efficiency calculation. Typically, in fuel cell analysis, the HHV is used unless stated otherwise, and this convention will be used throughout this chapter unless explicitly stated otherwise.

It should be emphasized that from the preceding analysis, it is known that for most fuel cell reactions, the reversible efficiency, η_r , decreases as the fuel cell operating temperature is increased. This effect is important in considering high-temperature fuel cells, namely, the molten carbonate fuel cells (MCFCs) and the solid oxide fuel cells (SOFCs). For example, Figure 25.9 indicates that the reversible cell efficiency is reduced to lower 70% (based on LHV) for hydrogen and oxygen reaction at the typical operating temperature of 1000°C for SOFCs, as opposed to around 95% at 25°C as discussed earlier. This significant reduction in the reversible cell efficiency seems to work against high-temperature fuel cells. However, the irreversible losses, to be described later, decrease drastically as temperature is increased, so that the practical fuel cell performance (such as efficiency and power output under practical operating condition) increases. Therefore, further analysis should be done for efficiency under practical operating condition rather than the idealized reversible condition, which is the focus of the following discussion.

25.4.4.2 Mechanism of Irreversible Energy Losses

For fuel cells, the reversible cell potential and the corresponding reversible efficiency are obtained under the thermodynamically reversible condition, implying that there is no rigorous occurrence of continuous reaction or electrical current output. For practical applications, a useful amount of work (electrical energy) is obtained only when a reasonably large current I is drawn from the cells because the electrical energy output is through the electrical power output, which is defined as

$$\text{Power} = EI \quad \text{or} \quad \text{Power Density} = EJ \quad (25.56)$$

However, both the cell potential and efficiency decrease from its corresponding (equilibrium) reversible values because of irreversible losses when current is increased. These irreversible losses are often called polarization, overpotential, or overvoltage* in

* The terms "polarization," "overpotential," and "overvoltage" have been loosely used in the literature to denote cell potential (or voltage) loss. However, they do have some subtle differences [1] that are neglected here so that these words can be used interchangeably.

literature, and they originate primarily from three sources: activation, ohmic, and concentration polarization. The actual cell potential as a function of current is the result of these polarizations; therefore, a plot of the cell potential vs. current output is conventionally called a polarization curve. It should be noticed that the magnitude of electrical current output depends largely on the active cell area; therefore, a better measure is the current density, J (A/cm²) instead of current, I , itself, and the unit A/cm² is often used rather than A/m² as the unit for the current density because square meter is too large to be used for fuel cell analysis.

A typical polarization curve is illustrated in Figure 25.10 for the cell potential as a function of current density. The ideal cell potential–current relation is independent of the current drawn from the cell, and the cell potential remains equal to the reversible cell potential. The difference between the thermoneutral voltage and the reversible cell potential represents the energy loss under the reversible condition (the reversible loss). However, the actual cell potential is smaller than the reversible cell potential and decreases as the current drawn is increased due to the three mechanisms of irreversible losses: activation, ohmic, and concentration polarization. The activation polarization, η_{act} , arises from the slow rate of electrochemical reactions, and a portion of the energy is lost (or spent) on driving up the rate of electrochemical reactions in order to meet the rate required by the current demand. The ohmic polarization, η_{ohm} , arises due to electrical resistance in the cell, including ionic resistance to the flow of ions in the electrolyte and electronic resistance to the flow of electrons in the rest of the cell components. Normally, the ohmic polarization is linearly dependent on the cell current. Concentration polarization, η_{conc} , is caused by the slow rate of mass transfer resulting in the depletion of reactants in the vicinity of active reaction sites and the overaccumulation of reaction products

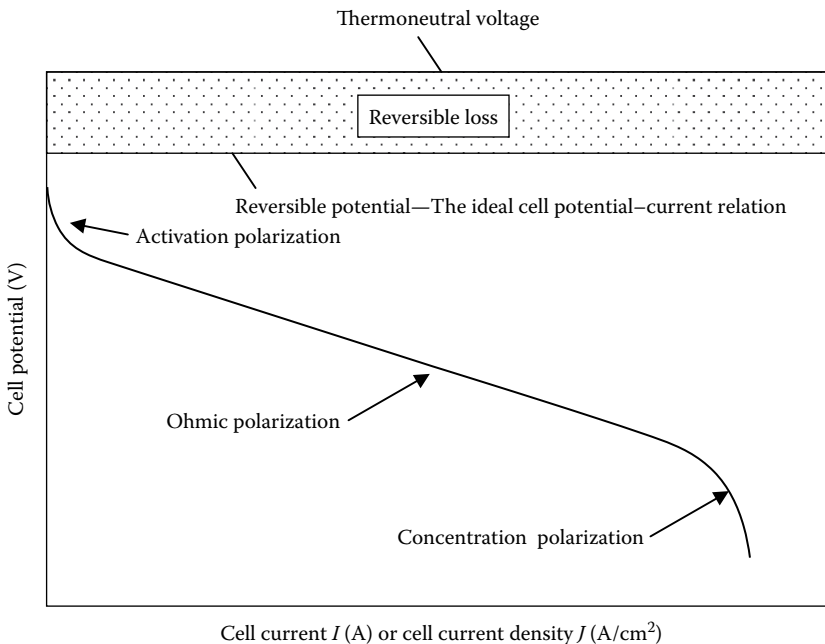


FIGURE 25.10

Schematic of a typical polarization curve. The cell potential for a fuel cell decreases as the current drawn from the cell is increased due to activation, ohmic, and concentration polarizations.

that block the reactants from reaching the reaction sites. It usually becomes significant, or even prohibitive, at high current density when the slow rate of mass transfer is unable to meet the high demand required by the high current output. As shown in Figure 25.10, concentration polarization is often the cause of rapid cell potential decrease to zero. The current (density) corresponding to the zero cell potential is often called the limiting current (density), and evidently, it is controlled by the concentration activation. From Figure 25.10, it is also clear that activation polarization is dominant at small current densities, while concentration polarization is predominant at high current densities. The linear drop in the cell potential due to resistance loss occurs at intermediate current densities, and practical fuel cell operation is almost always located within the ohmic polarization region. It should be emphasized that these three loss mechanisms actually occur simultaneously in an operating cell, despite their different influences at the different current density conditions.

Figure 25.10 also indicates that even at zero current output from the fuel cell, the actual cell potential is smaller than the idealized reversible cell potential. This small difference in cell potential is directly related to the chemical potential difference between the cathode and the anode. So that even at zero external load current, there are electrons delivered to the cathode, where oxygen ions are formed, and migrate through the electrolyte to the anode where they deionize to release electrons. The electron released migrates back to the cathode to continue the process or *exchange*. The ionization/deionization reactions proceeding at a slow rate yield an extremely small current, often called exchange current I_0 or exchange current density J_0 , and the cell potential is reduced below the reversible cell potential. Therefore, exchange current arises from the electrons migrating through the electrolyte rather than through the external load, and about 0.1–0.2 V of cell potential loss results from the exchange process. Consequently, the efficiency of a real fuel cell is about 8%–16% lower than the reversible cell efficiency, η_r , even at close to zero current output.

The exchange current density J_0 is very small; it is at least about 10^{-2} A/cm² for H₂ oxidation at the anode, and about 10^{-5} times slower for O₂ reduction at the cathode. In comparison, the O₂ reduction process at the cathode is so slow that competing anodic reactions play a significant role, such as oxidation of electrocatalyst, corrosion of electrode materials, and oxidation of organic impurities in the anode structure. All these anodic reactions result in the corrosion of electrodes, thereby limiting the cell life unless appropriate countermeasures are taken.

It should be pointed out that the cell potential loss resulting from the exchange current diminishes when the current drawn through the external load is increased beyond a certain critical value. As the external current is increased, the cell potential decreases as shown in Figure 25.10; thus, the driving force for the exchange current is reduced, leading to a smaller exchange current—this is the only form of energy loss that decreases when the external current is increased.

25.4.4.3 Amount and Rate of Waste Heat Generation

From the earlier discussion, it becomes clear that the actual cell potential E is lower than the reversible cell potential E_r , and the difference is due to the potential losses arising from the earlier irreversible loss mechanisms. Therefore,

$$E = E_r - (\eta_{\text{act}} + \eta_{\text{ohm}} + \eta_{\text{conc}}) \quad (25.57)$$

The irreversible energy loss as heat (or waste heat generation) per mole fuel consumed can be easily obtained, because the entropy generation is, according to Equations 25.24 and 25.57,

$$\phi_s = \frac{nF(E_r - E)}{T} = \frac{nF(\eta_{act} + \eta_{ohm} + \eta_{conc})}{T} \quad (25.58)$$

Then, Equation 25.13 becomes for the total heat loss from the fuel cell

$$q = T\Delta s - T\phi_s = \underbrace{T\Delta s}_{\text{Reversible loss}} - \underbrace{nF(\eta_{act} + \eta_{ohm} + \eta_{conc})}_{\text{Irreversible losses}} \quad (25.59)$$

Since the entropy change is negative ($\Delta s < 0$) for most fuel cell reactions, the heat transfer is negative as well, implying that energy as heat is lost from the fuel cell shown in Figure 25.3 for both reversible and irreversible losses.

Because $T\Delta s = \Delta h - \Delta g$ by the definition of the Gibbs function change for fuel cell reactions, Equation 25.59 can be written as

$$\frac{q}{nF} = \frac{T\Delta s}{nF} - (\eta_{act} + \eta_{ohm} + \eta_{conc}) = \frac{\Delta h - \Delta g}{nF} - (\eta_{act} + \eta_{ohm} + \eta_{conc}) \quad (25.60)$$

Considering the definition for the thermoneutral voltage and the reversible cell potential, the earlier expression becomes

$$\frac{q}{nF} = -E_{tm} + E_r - (\eta_{act} + \eta_{ohm} + \eta_{conc}) \quad (25.61)$$

Combining with Equation 25.57, Equation 25.61 reduces to

$$\frac{q}{nF} = -(E_{tm} - E) \quad (25.62)$$

Hence, the equivalent cell potential loss due to the energy loss in the fuel cell as heat is equal to the difference between the thermoneutral voltage and the actual cell potential.

The rate of heat loss per mole fuel consumed in the fuel cell, Equation 25.59, can be expressed as an equivalent power loss:

$$P_{\text{HeatLoss}} = I \left(\frac{q}{nF} \right) = -I(E_{tm} - E) = I \left[\frac{T\Delta s}{nF} - (\eta_{act} + \eta_{ohm} + \eta_{conc}) \right] \quad (25.63)$$

This expression is important in determining the cooling requirements of fuel cell stacks.

25.4.4.4 Various Forms of Irreversible Energy Conversion Efficiency

After the earlier description of the irreversible energy losses, we can now introduce several forms of energy efficiency that would be useful in the analysis of fuel cell performance.

25.4.4.4.1 Voltage Efficiency, η_E

The voltage efficiency is defined as

$$\eta_E = \frac{E}{E_r} \quad (25.64)$$

Because the actual cell potential E is compared with the maximum possible cell potential E_r , allowed by the second law, the voltage efficiency is really a specific form of the exergy efficiency, representing the degree of departure of the cell operation from the idealized thermodynamically reversible condition. As shown in Equation 25.57, $E < E_r$, hence $\eta_E < 1$.

25.4.4.4.2 Current Efficiency, η_I

The current efficiency is a measure of how much current is produced from a given amount of fuel consumed in the fuel cell reaction, and it is defined as

$$\eta_I = \frac{I}{nF(dN_F/dt)} \quad (25.65)$$

where dN_F/dt represents the rate of fuel consumption in the fuel cell (mol/s). The current efficiency would be <100% if part of the reactants participate in non-current-productive side reactions, called parasitic reactions, such as reactant crossover through the electrolyte region, incomplete conversion of reactants to the desired products, reaction with the cell components, or even reactant leakage from the cell compartment due to sealing problem. For example, in DMFCs, about 20% of the liquid methanol can cross over to the cathode side through the proton-conducting polymer membrane, implying the current efficiency is only about 80% for such cells. However, for most practical fuel cells, especially at operating conditions where the current output is sufficiently larger than zero (without the effect of exchange current discussed previously), the current efficiency is about 100%. This is because for practical fuel cells, all the parasitic reactions are undesirable and would have been removed by appropriate design.

25.4.4.4.3 Overall Free Energy Conversion Efficiency, η_{FC}

The overall free energy conversion efficiency is defined as the product of the reversible efficiency, voltage, and current efficiency:

$$\eta_{FC} = \eta_r \times \eta_E \times \eta_I \quad (25.66)$$

If the current efficiency is 100% as is often the case for well-designed practical fuel cells, substituting the definitions for the various efficiencies into the earlier equation lead to

$$\eta_{FC} = \frac{E}{E_{th}} \quad (25.67)$$

Therefore, the overall free energy conversion efficiency is really the overall efficiency for energy conversion process occurring within the fuel cell. Because the thermoneutral voltage is a fixed value for a given fuel and oxidant under a given operating condition of temperature and pressure, the overall energy conversion efficiency for fuel cells is proportional to the actual cell potential,

$$\eta_{FC} \sim E \quad (25.68)$$

This is a significantly important result. Once the actual cell potential is determined, the energy conversion efficiency of the fuel cell is known as well. This is the primary reason that in fuel cell literature, it is almost always that the cell polarization curve is given without specifically showing the cell energy efficiency as a function of the current. Further, Equation 25.68 implies that the fuel cell efficiency will depend on the current output in the same way as the cell potential, that is, decrease as the current output is increased.

25.4.4.4 Fuel Cell System Efficiency, η_s

Since a fuel cell system is composed of one or multiple fuel cell stacks and auxiliary equipment, which would also have its own energy efficiency of η_{aux} , the total fuel cell system efficiency is

$$\eta_s = \eta_{FC} \times \eta_{aux} \quad (25.69)$$

25.4.5 Efficiency Loss in Operating Fuel Cells: Stoichiometry, Utilization, and Nernst Loss

In an operating fuel cell, reactant composition changes between the inlet and outlet of the fuel cell along the flow path over the electrode surface because reactants are consumed to yield current output and reaction products are formed along the way as well. The change in reactant composition results in additional loss of cell potential beyond those losses described in the preceding section. This potential loss arises from the fact that the cell potential E adjusts to the lowest electrode potential given by the Nernst equation, Equation 25.29, for the various reactant compositions at the exit of the anode and cathode chambers. This is because electrodes are usually made of good electronic conductors, and consequently, they are isopotential surfaces. The cell potential E may not exceed the minimum local value set by the Nernst equation. This additional cell potential loss is often also called the Nernst loss, which is equal to the difference between the inlet and exit Nernst potentials determined based on the inlet and exit reactant compositions. According to Equation 25.29, this additional cell potential loss due to the consumption of reactants in the cell is when the reactant streams are arranged in a concurrent flow:

$$\eta_N = \frac{\mathcal{R}T}{nF} \ln K_{out} - \frac{\mathcal{R}T}{nF} \ln K_{in} = \frac{\mathcal{R}T}{nF} \ln \frac{K_{out}}{K_{in}} \quad (25.70)$$

In the case of a fuel cell where both fuel and oxidant flows are in the same direction (concurrent), the minimum Nernst potential occurs at the flow outlet. When the reactant flows are in counterflow, cross-flow, or more complex arrangements, it becomes difficult to determine the location of the minimum potential due to the reactant consumption. Appropriate flow channel design for the anode and cathode sides can minimize the Nernst loss.

Equation 25.70 also implies that the Nernst loss will be extremely large and approach infinity if all the reactants are consumed in the in-cell electrochemical reaction leading to zero reactant concentration at the cell outlet. To reduce the Nernst loss to an acceptable level for practical fuel cell operations, reactants are almost always supplied more than the stoichiometric amount required for the desired current production. The actual amount of reactants supplied to a fuel cell is often expressed in terms of a parameter called stoichiometry, S_i :

$$S_i = \frac{\text{Molar flow rate of reactants supplied to a fuel cell}}{\text{Molar flow rate of reactants consumed in the fuel cell}} = \frac{\dot{N}_{in}}{\dot{N}_{consumed}} \quad (25.71)$$

For example, for proton exchange membrane (PEM) fuel cells, typical operation uses $S_t \approx (1.1\text{--}1.2)$ for H_2 and $S_t \approx 2$ for O_2 (pure or in air). Therefore, stoichiometry really represents the actual flow rate for the reactant delivered to the fuel cell. Because there are normally at least two types of reactants for fuel cell, one as fuel and another as oxidant, stoichiometry can be defined for either reactant.

Alternatively, reactant flow rate can be expressed in terms of a parameter called utilization, U_t :

$$U_t = \frac{\text{Molar flow rate of reactants consumed in the fuel cell}}{\text{Molar flow rate of reactants supplied to the fuel cell}} = \frac{\dot{N}_{\text{consumed}}}{\dot{N}_{\text{in}}} \quad (25.72)$$

Clearly, stoichiometry and utilization are inversely proportional to each other.

For properly designed practical fuel cells, no reactant crossover or leakage out of the cell may occur in general; therefore, the rate of reactant consumed within the cell is equal to the difference between the rate of molar flow into and out of the cell. For example, the stoichiometry for the fuel may be expressed as

$$S_{t,F} = \frac{\dot{N}_{F,\text{in}}}{\dot{N}_{F,\text{consumed}}} = \frac{\dot{N}_{F,\text{in}}}{\dot{N}_{F,\text{in}} - \dot{N}_{F,\text{out}}} = \frac{1}{U_{t,F}} \quad (25.73)$$

Effect of reactant utilization on the reversible cell potential is illustrated in Figure 25.11. It is seen that the reactant composition at the cell outlet decreases; hence, the reversible cell potential decreases as well when the utilization factor is increased. The decrease is rapid when utilization goes beyond about 90%. In practical fuel cell operation, 100% utilization

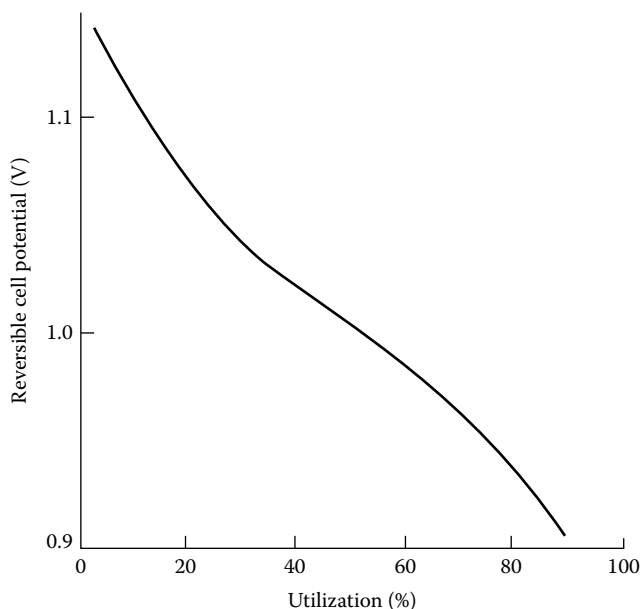


FIGURE 25.11

Reversible cell potential as a function of reactant utilization (both fuel and oxidant utilizations are set equal) for a molten carbonate fuel cell operating at 650°C and 1 atm. Reactant compositions at the cell inlet: 80% H_2 /20% CO_2 mixture saturated with $\text{H}_2\text{O}(\text{g})$ at 25°C for the fuel gas, and 60% CO_2 /30% O_2 /10% inert gas mixture for the oxidant gas. (From Hirschenhofer, J.H. et al., *Fuel Cells: A Handbook* (Rev. 3), U.S. Department of Energy, Washington, DC, 1994.)

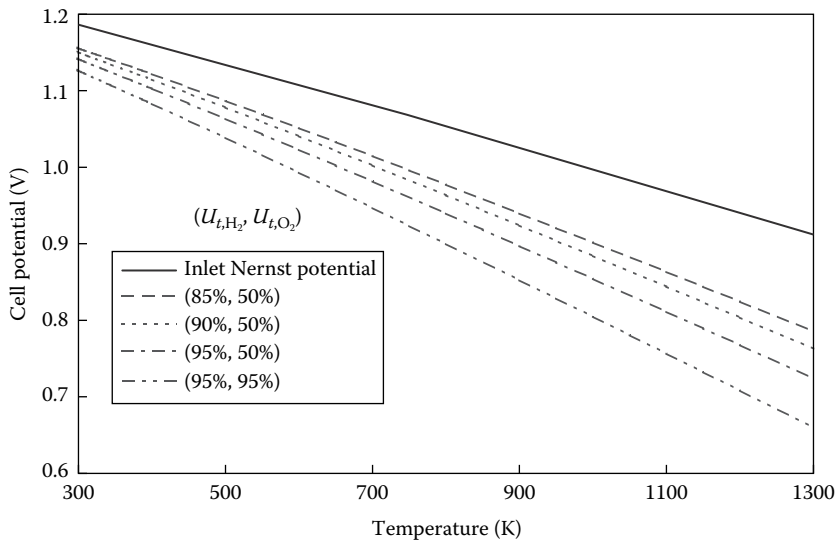


FIGURE 25.12

Inlet and outlet Nernst potential as a function of temperature and utilization for the reaction of $\text{H}_2(\text{g}) + \text{O}_2(\text{g}) \rightarrow \text{H}_2\text{O}(\text{g})$ at 1 atm.

(or unity stoichiometry) will result in reactant concentrations vanishing at the cell exit; then, the Nernst loss becomes dominant and the cell potential is reduced to zero—this is certainly an undesirable situation that needs to be avoided. Therefore, typical operation requires that the utilization be about 80%–90% for fuel and 50% for oxidant in order to balance the Nernst loss with the parasitic losses associated with the reactant supply.

As shown in Equation 25.70, the additional Nernst loss due to the reactant depletion in the cell is directly proportional to the cell operating temperature. Figure 25.12 shows the reversible cell potential at the cell inlet and outlet for hydrogen and oxygen reaction forming gaseous water product at 1 atm as a function of temperature. The outlet Nernst potentials (i.e., the reversible cell potential at the cell outlet) are determined for oxygen utilization of 50%, and hydrogen utilizations of 85%, 90%, and 95%, respectively, as well as for the utilization of 95% for both hydrogen and oxygen. It is clearly seen that the outlet Nernst potential decreases when either utilization or temperature is increased.

If pure hydrogen is used as fuel, the anode compartment can be designed as a dead-end chamber for hydrogen supply. Similarly, if pure oxygen is used as oxidant, a dead-end cathode compartment can be employed. However, inert impurities in the reactant gas will accumulate at the anode and cathode compartments, and they must be removed either periodically or continuously in order to maintain a good fuel cell performance. Periodic purging or continuous bleeding can be implemented for this purpose, but this results in a small loss of fuel, and hence <100% utilization.

From the earlier discussion, it is evident that 100% utilization for reactants is practically an unwise design. Since in-cell fuel utilization will never be 100% in practice, the determination of in-cell energy conversion efficiency and the cell potential must take utilization factor into consideration. If the fuel exiting the fuel cell is discarded (not recirculated back to the cell or not utilized for other useful purpose such as providing heat for fuel preprocessing), then the overall energy conversion efficiency must be equal to the overall fuel cell efficiency given in Equation 25.66 multiplied by the utilization to take into account the fact that not all the fuel is being used for electric energy production.

25.5 Fuel Cell Electrode Processes

The thermodynamic process described in the previous section for a fuel cell is a gross underestimate of what happens in reality. It has been identified that there are many physical (i.e., transport of mass, momentum, and energy) and chemical processes involved in the overall electrochemical reactions in the porous fuel cell electrodes that influence the performance of fuel cells. The transport processes involving the mass transfer of reactants and products play a prominent role in the performance of porous electrodes in fuel cells, and those involving heat transfer and thermal management are important in fuel cell systems. Some of the important physical and chemical processes occurring in porous fuel cell electrodes during electrochemical reactions for liquid electrolyte fuel cells are the following [4]:

1. Initially, the reactant stream consists of multicomponent gas mixture, for example, the fuel stream typically contains hydrogen and water vapor, as well as carbon dioxide and even some carbon monoxide, whereas the oxidant stream usually has oxygen, nitrogen, water vapor, carbon dioxide, etc. The molecular reactant (such as H_2 or O_2) is transferred to the porous electrode surface from the reactant stream through the mechanism of convection and then transported through the porous electrode, primarily by diffusion, to reach the gas/electrolyte interface.
2. The reactant dissolves into the liquid electrolyte at the two-phase interface.
3. The dissolved reactant then diffuses through the liquid electrolyte to arrive at the electrode surface.
4. Some pre-electrochemical homogeneous or heterogeneous chemical reactions may occur, such as electrode corrosion reaction, or impurities in the reactant stream may react with the electrolyte.
5. Electroactive species (which could be reactant itself as well as impurities in the reactant stream) are adsorbed onto the solid electrode surface.
6. The adsorbed species may migrate on the solid electrode surface, principally by the mechanism of diffusion.
7. Electrochemical reactions then occur on the electrode surface wetted by the electrolyte—the so-called three-phase boundary, giving rise to electrically charged species (or ions and electrons).
8. The electrically charged species and other neutral reaction product such as water, still adsorbed on the electrode surface, may migrate along the surface due to diffusion in what has been referred to as post-electrochemical surface migration.
9. The adsorbed reaction products become desorbed.
10. Some post-electrochemical homogeneous or heterogeneous chemical reactions may occur.
11. The electrochemical reaction products (neutral species, ions, and electrons) are not only transported away from the electrode surface, mainly by diffusion, but also influenced, for the ions, by the electric field setup between the anode and the cathode. The electron motion is dominated by the electric field effect.
12. The neutral reaction products diffuse through the electrolyte to reach the reactant gas/electrolyte interface.
13. Finally, the products will be transported out of the electrode and the cell in the gas form.

Normally, any of the 13 processes can influence the performance of a fuel cell, exhibiting the complex nature of a fuel cell operation. For well-designed practical fuel cells, the earlier electrode processes might be grouped into the following three major steps:

1. *Delivery of molecular reactant to the electrode surface:* This step involves a number of physical and chemical processes preceding the electrochemical reaction, and it generally includes the transport of molecular reactant from the gas phase supply outside the electrode structure to the liquid electrolyte surface, typically through the porous electrode structure, then the dissolution of molecular reactant into the liquid electrolyte, followed by the diffusion of the dissolved reactant through the electrolyte to the electrode surface, and finally the adsorption of the reactant on the electrode surface.
It might be pointed out that the delivery of the electrons and ions to the electrode surface is as important as the delivery of molecular reactant since they are all needed for the electrochemical reactions to occur at the electrode surface.
2. *Reduction or oxidation of the adsorbed molecular reactant at the electrode surface in the presence of electrolyte:* This is the step for electrochemical reactions that produce electric current. The reactions occur only at the electrode surface that is covered by the electrolyte, hence, often referred to as the three-phase boundary or active reaction sites. Significant increase in the reactive sites is essential for good fuel cell performance.
3. *Removal of the reaction products from the electrode surface for the regeneration of the reaction sites and for the continuous production of electric current:* This step is especially important for low-temperature acid electrolyte fuel cells, because product water is formed at the cathode and is in the liquid form. Liquid water accumulation in the porous electrode structure may block the transport of molecular oxygen to the reaction sites, severely hindering the process described in step (1), thereby degrading the cell performance due to oxygen starvation at the reaction sites. Such a phenomenon is often referred to as the *water flooding* of electrodes, a critical issue for PEM fuel cells (PEMFCs).

25.6 Cell Connection and Stack Design Considerations

The potential of a working cell is typically around 0.7–0.8 V, and it is normally too small for practical applications, also because of the limited power available from a single cell. Therefore, many individual cells are connected (or stacked) together to form a fuel cell stack. Although many stacking configurations are possible, the overpotential associated with the transport processes discussed in this chapter imposes limitations and technical difficulties, making cell stacking one of the significant technical challenges in the drive for the fuel cell commercialization. We will briefly discuss the stacking options later and the associated transport-related issues.

The electrical connection among the individual cells may be arranged in parallel or in series, as shown in Figure 25.13. The parallel connection still provides a low voltage output from the stack, but a very high current output since the stack current is the sum of the current produced in each cell. Such an extremely large current flow will cause an

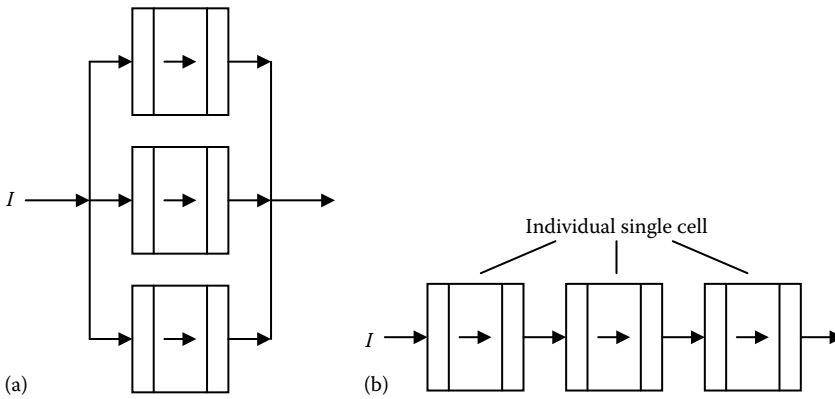


FIGURE 25.13 Cell connection (stacking) configurations: (a) parallel connection and (b) series connection. The arrow in the diagram represents the direction of the current flow.

excessively large ohmic voltage loss in the stack components and at the surface contacts among the components. Thus, parallel connection is typically avoided unless for small current or power applications.

Series connection can have two typical arrangements: unipolar and bipolar, as shown in Figure 25.14. Unipolar design has one fuel stream supplying fuel to two anodes for the two adjacent cells, and one oxidant stream delivering oxidant to two cathodes for the two adjacent cells. This arrangement of one reactant stream serving for two adjacent electrodes simplifies the reactant flow channel design. However, it forces the electrical current generated

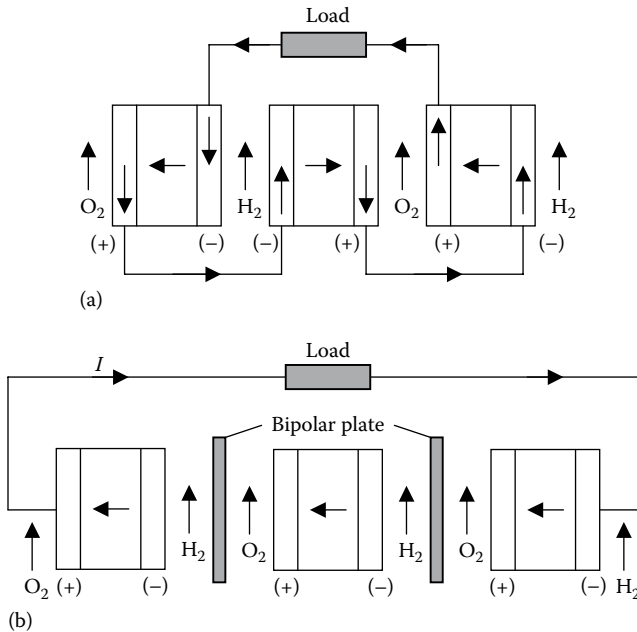


FIGURE 25.14 Series cell connection (stacking) configurations: (a) unipolar arrangement with the edge collection of the current generated in each cell and (b) bipolar arrangement with the end-plate collection of the current.

in each cell to be collected at the edge of the electrodes. Since electrode is very thin (<1 mm), while the other electrode dimensions (in the direction of the current flow) are at least on the order of centimeters or larger, the ohmic resistance tends to be very large. Thus, edge collection of current, although used in early fuel cell stack designs, is generally avoided in recent fuel cell stack development, primarily due to the excessively large ohmic voltage losses.

The bipolar arrangement has the current flow normal to the electrode surface, instead of along the electrode surface as in the unipolar arrangement; thus, the current flow path is very short while the cross-sectional area available for the current flow is very large. The ohmic voltage loss for this case is very small in comparison, and bipolar design is favored in recent fuel cell stack technology. However, this end-plate collection of current results in the complex design for the reactant flow channels and complex organization for the reactant stream, and the bipolar plate has to fulfill several functions simultaneously in order to obtain a good overall stack performance. Bipolar plates serve as current collectors, for reactant delivery to the electrode surface, for cell reaction product removal (such as water), and for the integrity of the cell/stack. These functions for the bipolar plates may be contradictory to each other, and the optimal design for the bipolar plates represents one of the significant technical challenges for practical fuel cells.

A typical configuration of a bipolar plate is shown in Figure 25.15. The reactant flow follows the flow channels made on the bipolar plate, thus distributing the reactant over the

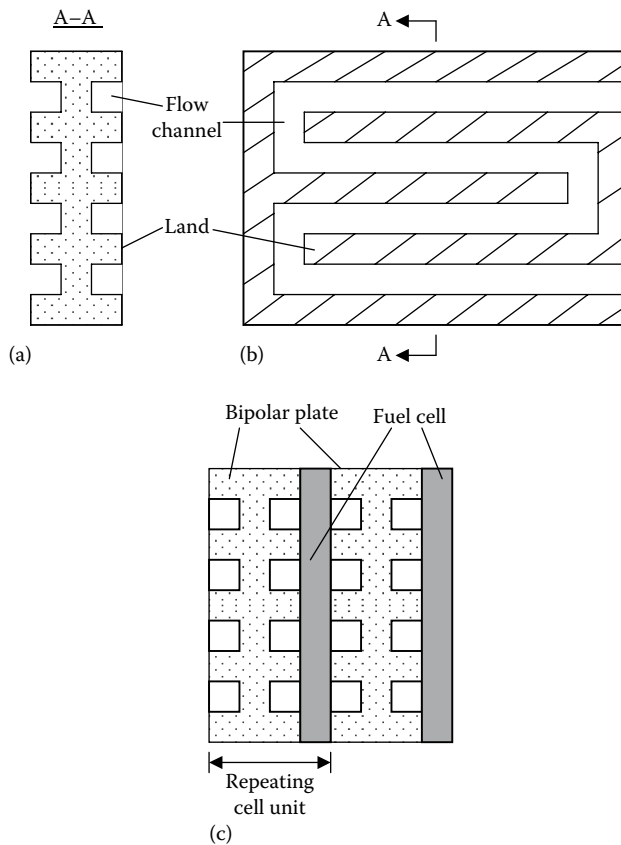


FIGURE 25.15

Typical configuration of a bipolar plate: (a) cross-sectional view, (b) face view, and (c) repeating cell unit in a stack.

electrode surface. On the other hand, the land between the adjacent flow channels serves as the passage for the current flow from one cell to the next. Therefore, a wide flow channel is beneficial for the reactant distribution over the electrode surface and for the reaction product removal, while a wide land is beneficial for the electron flow and for the mechanical integrity of the cells and the entire stack. Normally, the same cell unit as shown in Figure 25.15c is repeated to form a stack. The plate at the end of the stack has flow channels only on one side of its surfaces.

From the cell repeating unit in a stack, it is clear that the reactant concentration decreases along the flow direction following the flow channel design and into the electrode due to convective and diffusional mass transfer. Thus, the concentration field is three dimensional, so is the electrical field due to the flow channels made on the bipolar plate surfaces, the nonuniform rate of electrochemical reactions in the catalyst layers, and the three-dimensional distribution of the reactant concentrations and the temperature. Therefore, an accurate prediction of the cell performance requires a three-dimensional analysis based on solving the conservation equations governing the transport phenomena of the reactant flow, species concentration, temperature, and electric fields, incorporating the in-cell electrochemical reaction processes, thus posing significant challenges to fuel cell designers.

25.7 Six Major Types of Fuel Cells

Fuel cell technology has been developed and improved dramatically in the past few years, and this has captured once again public as well as industry's attention concerning the prospect of fuel cells as practical power sources for terrestrial applications. At present, fuel cell technology is being routinely used in many specific areas, notably in space explorations, where fuel cell operates on pure hydrogen and oxygen with over 70% efficiency and drinkable water as the only by-product. There are now approximately over 200 fuel cell units for terrestrial applications operating in 15 countries; impressive technical progress has been achieved in terms of higher power density and better performance as well as reduced capital and maintenance and operation cost, and is driving the development of competitively priced fuel cell-based power generation systems with advanced features for terrestrial use, such as utility power plants and zero-emission vehicles. In light of decreasing fossil fuel reserves and increasing energy demands worldwide, fuel cell will probably become one of the major energy technologies with fiercest international competition in the twenty-first century.

The major terrestrial commercial applications of fuel cells are electric power generation in the utility industry and as a zero-emission powertrain in the transportation sector. For these practical applications, the efficiencies of fuel cells range somewhere between 40% and 65% based on the LHV of hydrogen. Typically, the cell electric potential is only about 1 V across a single cell, and it decreases due to various loss mechanisms under operational conditions. Thus, multiple cells are required to be connected together in electrical series in order to achieve a useful voltage for practical purposes, and these connected cells are often referred to as a fuel cell stack. A fuel cell system consists of one or multiple fuel cell stacks connected in series and/or parallel, and the necessary auxiliaries whose composition depends on the type of fuel cells and the kind of primary fuels used. The major accessories include thermal management (or cooling) subsystem, fuel supply, storage and processing subsystem, and oxidant (typically air) supply and conditioning subsystem.

TABLE 25.2

Operational Characteristics and Technological Status of Various Fuel Cells

Type of Fuel Cells	Operating Temperature (°C)	Power Density (mW/cm ²) (Present) Projected	Projected Rated Power Level (kW)	Fuel Efficiency (Chemical to Electrical)	Lifetime Projected (h)	Capital Cost Projected (U.S. \$ per kW)	Areas of Application
AFC	60–90	(100–200) >300	10–100	40–60	>10,000	>200	Space, mobile
PAFC	160–220	(200) 250	100–5,000	55	>40,000	3000	Dispersed and distributed power
PEMFC	50–80	(350) >600	0.01–1,000	45–60	>40,000	>200	Portable, mobile, space, stationary
MCFC	600–700	(100) >200	1,000–100,000	60–65	>40,000	1000	Distributed power generation
SOFC	800–1000	(240) 300	100–100,000	55–65	>40,000	1500	Baseload power generation
DMFC	90	(230) ?	0.001–100	34	>10,000	>200	Portable, mobile

Note: ? indicates that the projected value achievable in the near future is not available.

In this section, a summary of the state-of-the-art technology for the six major types of fuel cells is presented, including

1. Alkaline fuel cells (AFCs)
2. Polymer electrolyte membrane fuel cells (PEMFCs)
3. DMFCs
4. Phosphoric acid fuel cells (PAFCs)
5. MCFCs
6. SOFCs

Five of them are classified based on their electrolytes used, including the alkaline, phosphoric acid, PEM, molten carbonate, and solid oxide. DMFC is classified based on the fuel used for electricity generation. Table 25.2 provides a summary of the operational characteristics and application of the six major types of fuel cell.

25.7.1 Alkaline Fuel Cells

AFCs give the best performance among all the fuel cell types under the same or similar operating conditions when running on pure hydrogen and oxygen. Hence, they are among the first fuel cells to have been studied and taken into development for practical applications, and they are the first type of fuel cells to have reached successful routine applications, mainly in space programs such as space shuttle missions in the United States and similar space exploration endeavors in China and Europe, where pure hydrogen and

oxygen are used as reactants. Because of their success in space programs, AFCs are also the type of fuel cells on which probably the largest number of fuel cell development programs has begun in the world in an effort to bring them down to terrestrial applications, particularly in Europe. However, almost all the AFC development programs have come to an end. At present, the only few activities related to the AFC RD&D are in Europe.

The AFCs have the highest energy conversion efficiency among all types of fuel cells under the same operating conditions if pure hydrogen and pure oxygen are used as the reactants. That was one of the important reasons that AFCs were selected for the U.S. space shuttle missions. The AFCs used in the shuttle missions are operated at about 200°C for better performance (i.e., high energy conversion efficiency of over 70% and high power density that is critical for space applications), and the alkaline electrolyte is potassium hydroxide (KOH) solution immobilized in an asbestos matrix. As a result, the AFCs operate at high pressure in order to prevent the boiling and depletion of the liquid electrolyte. Consequently, these severe operating conditions of high temperature and high pressure dictate extremely strict requirement for cell component materials that must withstand the extreme corrosive oxidizing and reducing environment of the cathode and the anode. To meet these requirements, precious metals such as platinum, gold, and silver are used for the construction of the electrodes, although these precious metals are not necessary for the electrochemical reactions leading to electric power generation. Each shuttle flight contains 36 kW AFC power system. Its purchase price is about U.S. \$28.5 million, and it costs NASA additional \$12–\$19 million annually for operation and maintenance. Although the manufacturer claims about 2400 h of lifetime, NASA's experience indicates that the real lifetime is only about 1200 h. With sufficient technology development, 10,000 h are expected as the life potential (or upper limit) for the AFC system. This belief is based on the nature of the AFC systems and the data accumulated on both stacks and single cells.

The typical working temperature of AFC power systems aimed at commercial and terrestrial applications ranges from 20°C to 90°C, and the electrolyte is a KOH solution (30%–35%). There are four different cell types investigated:

1. Cell with a free liquid electrolyte between two porous electrodes
2. ELOFLUX cell with liquid KOH in the pore systems
3. Matrix cell where the electrolyte is fixed in the electrode matrix
4. The falling film cell

Many technical challenges have been encountered in the development of AFCs. The most important ones are as follows:

- *Preparation method of the electrodes:* The electrodes consist of porous material that is covered with a layer of catalyst. In general, it is very difficult to distribute the catalyst at the surface and to produce a defined pore system for the transport of the reactants.
- *Costs of the electrodes, stacks, and fuel cell systems:* The preparation of electrodes with noble metal catalysts is very expensive. In general, the electrodes are manufactured in small-scale production with high overhead costs.
- *Lifetime of the electrode/degradation:* The electrolyte is very corrosive, and the catalyst materials are sensitive to high polarization. Using nickel and silver as catalysts, in order to reduce the costs of the fuel cell, leads to a high degradation of these catalysts.

- *Diaphragm made of asbestos*: The diaphragm of low-temperature AFCs is made of asbestos. But this material is hazardous for health, and in some countries, its use is even banned. Therefore, new diaphragms should be developed, but it is difficult to find a material with a similar performance in alkaline electrolyte.
- *Carbon dioxide-contaminated fuel and oxidant streams (carbonation of electrolyte and electrodes)*: The electrolyte intolerance of carbon dioxide is the most important disadvantage of air-breathing AFCs with reformat gases from primary fossil fuels.

Other problems associated with the AFC power systems are the concerns for the safety and reliability of AFC power systems. For example, the liquid KOH electrolyte contained in an asbestos matrix can withstand only a 5 psi limit of pressure differential between the anode and cathode reactant gases. This dictates the need for sophisticated pinpoint pressure control during the operation including transient, start-up, and shutdown processes. It is also a safety issue because of its greater likelihood of the reactants mixing in the AFC system with the possibility of a serious fire breaking out. In terms of general safety considerations, the use of the corrosive potassium hydroxide electrolyte in the AFCs represents the need for hazardous material handling, and the handling of asbestos matrix poses potential hazard to one's health. With flowing reactant gases, the potential for the gradual loss of the liquid electrolyte, drying of the electrolyte matrix, reactant crossover of the matrix, and ensuing life-limiting reactant mixing (or actual AFC stack failure due to fire) is very real in the AFC system.

The major technical challenge is that alkaline electrolytes, like potassium or sodium hydroxide, do not reject carbon dioxide, even the 300–350 ppm of carbon dioxide in the atmospheric air is not tolerated (carbon dioxide concentration in both cathode and anode gases must be <10–100 ppm by volume), while terrestrial applications almost invariably require the use of atmospheric air as oxidant due to technical and economic considerations. For municipal electric applications, hydrocarbon fuels, especially natural gas, are expected to be the primary fuel, and their reformation into hydrogen-rich gases invariably contain a significant amount of carbon dioxide, for example, steam-reforming of the natural gas results in the reformat gas consisting approximately of 80% hydrogen, 20% carbon dioxide, and a trace amount of other components such as carbon monoxide. Carbonaceous products of aging and corrosion shorten AFC life; they degrade the alkaline electrolyte. Whether originating as impurities in the gaseous reactants or from some fuel cell materials, oxides of carbon will chemically react with the alkaline electrolyte and produce irreversible decay that will decrease performance and shorten life. Consequently, AFCs are currently restricted to specialized applications where pure hydrogen and oxygen are utilized. The revival of this technology will depend almost completely on the successful curing of *CO₂ syndrome*—the efficient and economic scrubbing of carbon dioxide, even though claims have been made of successful resolution of carbon dioxide poisoning in the AFCs. This is especially true for utility applications, although some optimistic estimate indicates that the AFC stack costs are similar to all other low-temperature fuel cell systems, and the production costs for the AFC systems seem to be the lowest. A price of about U.S. \$400–\$500 per kW has been quoted by using today's technologies and today's knowledge in large-scale production. However, small-scale commercial production cost is estimated to be 5–10 times higher.

25.7.2 Polymer Electrolyte Membrane Fuel Cells

25.7.2.1 Introduction

The PEMFC is also called solid polymer (electrolyte) fuel cell. It is perhaps the most elegant of all fuel cell systems in terms of design and mode of operation. It was the first type of fuel

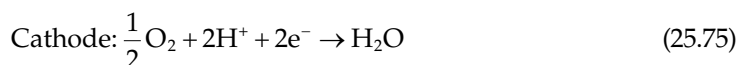
cell that was put into practical application (in Gemini space missions from 1962 to 1966). It consists of a solid polymeric membrane acting as the electrolyte. The solid membrane is an excellent proton conductor, sandwiched between two platinum-catalyzed porous carbon electrodes. It has fast start capability and yields the highest output power density among all types of the fuel cells. Because of the solid membrane as the electrolyte, there is no corrosive fluid spillage hazard, and there is lower sensitivity to orientation. It has no volatile electrolyte and has minimal corrosion concerns. It has truly zero pollutant emissions with potable liquid product water when hydrogen is used as fuel. As a result, the PEMFC is particularly suited for vehicular power application, although it is also being considered for stationary power application, albeit to a lesser degree.

The proton-conducting polymer membrane belongs to a class of materials called ionomers or polyelectrolytes, which contain functional groups that will dissociate in the presence of water. The dissociation produces ions fixed to the polymer and simple counterions that can freely exchange with ions of the same sign from the solution. The current available polyelectrolytes have cation as the counterion. In the case of hydrogen, the cation is proton. Therefore, the membrane must be fully hydrated in order to have adequate ion conductivity. As a result, the fuel cell must be operated under conditions where the product water does not evaporate faster than it is produced, and the reactant gases, both hydrogen and oxygen, need to be humidified. Therefore, water and thermal management in the membrane become critical for efficient cell performance, are fairly complex, and require dynamic control to match the varying operating conditions of the fuel cell. Because of the limitation imposed by the membrane and problems with water balance, the operating temperature of PEMFCs is usually $<120^{\circ}\text{C}$, typically at 80°C . This rather low operating temperature requires the use of noble metals as catalysts in both the anode and cathode side with generally higher catalyst loadings than those used in PAFCs.

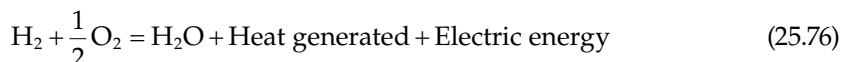
Currently, the polymer electrolyte used is made of perfluorinated sulfonic acid membrane, or it is essentially acid, though in solid polymeric form. Hence, PEMFCs are essentially acid electrolyte fuel cells, with its operational principle essentially the same as PAFCs. As a result, most of PEMFC design, material selection, component fabrication, etc., are similar to those of PAFCs. The only difference is the humidification of reactant gases dictated by the membrane performance. Reactant humidification is often achieved by a number of techniques, for example, by passing gas stream through a water column, by using in-stack humidification section of cell and membrane arrangement, and by spraying water into the reactant streams. In the early stage of the PEMFC development, the membranes were based on polystyrene, but since 1968, a Teflon-based product, named Nafion by DuPont, is used. This offers high stability, high oxygen solubility, and high mechanical strength.

25.7.2.2 Basic Operating Principle

The PEM is essentially acid electrolyte; PEMFC requires hydrogen gas as the fuel and oxygen (typically air) as the oxidant. The half-cell reactions are



and the overall cell reaction is



The current PEMFCs use perfluorinated sulfonic acid membrane (almost exclusively Nafion from DuPont) as the proton-conducting electrolyte; carbon paper or cloth as the anode and cathode backing layers; and platinum or its alloys, either pure or supported on carbon black, as the catalyst. The bipolar plate with the reactant gas flow fields is often made of graphite plate. The stoichiometry is around 1.1–1.2 for the fuel and 2 for the oxidant (oxygen). The PEMFCs usually operate at about 80°C and 1–8 atm pressure. The pressures, in general, are maintained equal on either side of the membrane. Operation at high pressure is necessary to attain high power densities, particularly when air is chosen as the cathodic reactant.

To prevent the membrane dryout leading to local hot spot (and crack) formation, performance degradation, and lifetime reduction, both fuel and oxidant streams are fully humidified, and the operating temperature is limited by the saturation temperature of water corresponding to the operating pressure. The product liquid water formed at the cathode does not dissolve in the electrolyte membrane and is usually removed from the cell by the excessive oxidant gas stream. The accumulation of liquid water in the cathode backing layer blocks the oxygen transfer to the catalytic sites, thus resulting in the phenomenon called *water-flooding* causing performance reduction. Local hot and cold spots will cause the evaporation and condensation of water. Thus, an integrated approach to thermal and water management is critical to PEMFCs' operation and performance, and a proper design must be implemented.

25.7.2.3 Acceptable Contamination Levels

As an acid electrolyte fuel cell operating at low temperature, the PEMFC is primarily vulnerable to carbon monoxide poisoning. Even a trace amount of CO drastically reduces the performance levels, although CO poisoning effect is reversible and does not cause permanent damages to the PEMFC system. Further, the performance reduction due to CO poisoning takes a long time (on the order of 2 h) to reach steady state. This transient effect may have profound implication for transportation applications. Therefore, the PEMFC requires the use of a fuel virtually free of CO (must be less than a few ppm). Also high-quality water free of metal ions should be used for the cell cooling and reactant humidification to avoid the contamination of the membrane electrolyte. This requirement has a severe implication on the materials that can be used for cell components. On the other hand, carbon dioxide does not affect PEMFC operation and performance except through the effect of reactant dilution (the Nernst loss).

25.7.2.4 Major Technological Problems

For practical applications, PEMFC performance in terms of energy efficiency, power density (both size and weight), and capital cost must be further improved. This can be accomplished by systematic research in the following:

1. *New oxygen reduction electrocatalysts*: This includes the reduction of precious metal platinum and its alloys loading from 4 to 0.4 mg/cm² or lower without affecting the long-term performance and the lifetime, and the development of CO-tolerant catalysts.
2. New types of polymer electrolyte with higher oxygen solubility, thermal stability, long life, and low cost. A self-humidified membrane or a polymer without the need of humidification will be ideal for PEMFC operation and performance enhancement with significant simplification of system complexities and reduction of the cost.

3. Profound changes in oxygen (air) diffusion electrode structure to minimize all transport-related losses. The minimization of all transport losses is the most promising direction for PEMFC performance improvement.
4. Optimal thermal and water management throughout the individual cells and the whole stack to avoid local hot and dry spot formation and to avoid *water-flooding* of the electrode.

In addition to the earlier issues, the development of low-cost lightweight materials for the construction of reactant gas flow fields and bipolar plates is one of the major barriers to PEMFCs' large-scale commercialization. The successful solution of this problem will further increase the output power density. Additional issues include optimal design of flow fields with the operating conditions, and an appropriate selection of materials and fabrication techniques. It has been reported that over 20% improvement in the performance of PEMFC stacks can be obtained just by appropriate design of flow channels alone. The current leading technologies for bipolar plate design include injection-molded carbon-polymer composites, injection-molded and carbonized amorphous carbon, assembled three-piece metallic, and stamped unitized metallic.

25.7.2.5 Technological Status

PEMFCs have achieved a high power density of over 1 kW/kg and 0.7 kW/L, perhaps the highest among all types of the fuel cells currently under development. It is also projected that the power density may be further improved, up to 2–3 kW/L, with unitized metallic (stainless steel) bipolar plates. The capital cost has been estimated to vary from the most optimistic of \$1,500 per kW to the most pessimistic of \$50,000 per kW at the current technology and is projected to reach approximately \$200–\$300 per kW, assuming a 10–20-fold reduction in the membrane and catalyst cost and also considering mass production. It is expected that PEMFC technology is about 5–10 years from commercialization, and pre-commercial demonstration for buses and passenger vehicles are under way with increasing intensity, and the first demonstration for residential combined heat and power application just began at the end of 1999. However, application of PEMFCs in powering portable and mobile electronics such as laptops has already been started.

25.7.2.6 Applications

PEMFCs have a high power density, a variable power output, and a short start-up time due to low operating temperature; the solid polymer electrolyte is virtually corrosion free and can withstand a large pressure differential (as high as 750 psi reported by NASA) between the anode and cathode reactant gas streams. Hence, PEMFCs are suitable for use in the transportation sector. Currently, they are considered the best choice for zero-emission vehicles as far as present-day available fuel cell technologies are concerned. Their high power density and small size make them primary candidates for light-duty vehicles, though they are also used for heavy-duty vehicles. For high-profile automobile application, pure hydrogen and air are used as reactants at the present. However, conventional gasoline and diesel engines are extremely cheap, estimated to cost about \$30–\$50 per kW. Therefore, the cost of PEMFC systems must be lowered at least by two to three orders of magnitude in order to be competitive with the conventional heat engines in the transportation arena.

For electricity generation from the hydrocarbon fuels, a reformer with carbon monoxide and sulfur cleaning is necessary. It is estimated that the cost of the reforming system is about the same as the fuel cell stack itself, which is also the same as the cost of other ancillary systems. Apart from the high cost, the optimal chemical to electric conversion efficiency is around 40%–45%, and the low operating temperature makes the utilization of the waste heat difficult, if at all possible, for the reforming of hydrocarbon fuels, cogeneration of heat, and combined cycles. On the other hand, conventional thermal power plants with combined gas and steam turbines have energy efficiency approaching 60% with a very low capital cost of U.S. \$1000 per kW. Therefore, the best possible application of the PEMFC systems interesting to utility industry is the use of PEMFCs in the size of tens to hundreds of kW range for remote region and also a possibility for residential combined heat and power application.

In addition, NASA is conducting a feasibility study of using the PEMFC power systems for its space programs (mainly space shuttle missions) in place of its current three 12 kW AFC power modules. As discussed in Section 25.7.1, NASA is motivated by the extremely high cost, low lifetime, and maintenance difficulty associated with its current AFC systems. Currently, NASA's feasibility study is in its second phase by using parabolic flight tests in airplanes to simulate low-gravity environment. If all goes well, NASA will conduct real-time tests in shuttles in a couple of years.

25.7.3 Direct Methanol Fuel Cells

25.7.3.1 Introduction

All the fuel cells reviewed earlier for commercial applications require the use of gaseous hydrogen directly or liquid/solid hydrocarbon fuels, for example, methanol, reformed to hydrogen as the fuel. Pure oxygen or oxygen in air is used as the oxidant. Hence, these fuel cells are often referred to as hydrogen–oxygen or hydrogen–air types of fuel cells. The use of gaseous hydrogen as a fuel presents a number of practical problems, such as storage system weight and volume as well as handling and safety issues especially for consumer and transportation applications. Although liquid hydrogen has the highest energy density, the liquefaction of hydrogen needs roughly one-third of the specific energy, and the thermal insulation required increases the volume of the reservoir significantly. The use of metal hydrides decreases the specific energy density, and the weight of the reservoir becomes excessive. The size and the weight of a power system are extremely important for transportation applications, as they directly affect the fuel economy and vehicle capacity, although they are less critical for stationary applications. The low volumetric energy density of hydrogen also limits the distance between vehicle refueling.

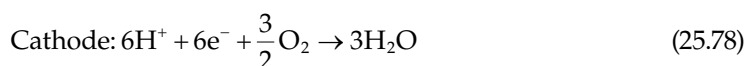
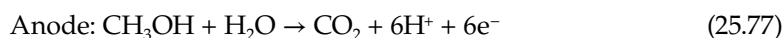
Methanol as a fuel offers ease of handling and storage, and potential infrastructure capability for distribution. Methanol also has a higher theoretical energy density than hydrogen (5 kW h/L compared with 2.6 kW h/L for liquid hydrogen). Easy refueling is another advantage for methanol. However, in the conventional hydrogen–air or hydrogen–oxygen fuel cells, a reformer is needed that adds complexity and cost as well as production of undesirable pollutants such as carbon monoxide. The addition of a reformer also increases response time.

Therefore, direct oxidation of methanol is an attractive alternative in view of its simplicity from a system point of view. The DMFCs utilizing PEM have the capability of efficient heat removal and thermal control through the circulating liquid, and elimination of humidification required to avoid membrane dryout. These two characteristics have to be accounted

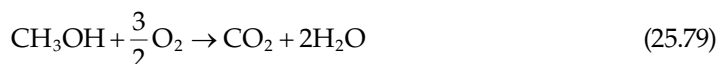
for in the direct and indirect hydrogen systems, which impact their volume and weight, consequently the output power density.

25.7.3.2 Basic Operating Principle

The DMFC allows the direct use of an aqueous, low concentration (3%) liquid methanol solution as the fuel. Air is the oxidant. The methanol and water react directly in the anode chamber of the fuel cell to produce carbon dioxide and protons that permeate the PEM and react with the oxygen at the cathode. The half-cell reactions are as follows:



and the net cell reaction is



Because the PEM (typically Nafion 117) is used as the electrolyte, the cell operating temperature must be less than the water boiling temperature to prevent the dryout of the membrane. Typically, the operating temperature is around 90°C, and the operating pressure ranges from one to several atmospheres.

25.7.3.3 Acceptable Contamination Levels

The system is extremely sensitive to carbon monoxide (CO) and hydrogen sulfide (H₂S). Carbon monoxide may exist as one of the reaction intermediaries and can poison the catalyst used. There are arguments whether CO is present in the anode during the reaction. Sulfur may be present if methanol is made of petroleum oils and needs to be removed.

25.7.3.4 Major Technological Problems

The PEM used in the DMFCs is Nafion 117, which is the same as employed in the PEMFCs. Although it works well in both types of cells, it is expensive with only one supplier. Since the electrolyte in DMFCs is essentially acid, expensive precious metals (typically platinum or its alloys) are used as the catalyst. However, the most serious problem is the so-called methanol crossover. This phenomenon is caused by the electro-osmotic effect. When the protons migrate through the electrolyte membrane, a number of water molecules are dragged along with each proton, and because methanol is dissolved in liquid water on the anode side, methanol is dragged through the membrane electrolyte to reach the cathode side together with the protons and water. Fortunately, the methanol at the cathode is oxidized into carbon dioxide and water at the cathode catalyst sites, producing no safety hazards. But the methanol oxidation in cathode does not produce useful electric energy. The development of a new membrane with low methanol crossover is a key to the success of DMFCs.

Such a low methanol crossover membrane has a number of advantages. First, it reduces the methanol crossover, enhancing fuel utilization, hence energy efficiency. Second, it reduces the amount of water produced at the cathode, leading to a lower activation and concentration

polarization, thus allowing higher cell voltage at the same operating current. Third, it allows higher methanol concentration in the fuel stream, resulting in better performance.

25.7.3.5 Technological Status

DMFCs are the least developed among all the fuel cell technologies. Though methanol itself has simpler storage requirements than hydrogen and is simpler to make and transport, its electrochemical activity is much slower than that of hydrogen, that is, its oxidation rate is about four orders of magnitude smaller than that of hydrogen. Also, the conversion takes place at low temperature (about 80°C–90°C), and the contaminant problem is a serious issue.

The state-of-the-art performance is an energy conversion efficiency of 34% (from methanol to electricity) at 90°C using 20 psig air, at a cell voltage of 0.5 V (corresponding to a voltage efficiency of 42%) together with the methanol crossover accounting for 20% of the current produced (equivalent to a fuel efficiency of 80%). This 20% methanol crossover occurs when the fuel stream used is an aqueous solution containing only 3% methanol. It has been projected that with the better membrane under development and improvement of membrane electrode assembly, a cell voltage of 0.6 V can be achieved with only 5% methanol crossover. This is equivalent to 50% voltage efficiency and 95% fuel efficiency, resulting in an overall stack efficiency of 47% (from methanol to electricity). The DMFC system efficiency will be lower due to running the necessary auxiliary systems.

The DMFC power system is underdeveloped, and until now, nobody could demonstrate any feasibility for commercialization. It remains at a scale of small demonstration in the sub-kW range. As such, no system cost estimate is available or has ever been carried out. However, the current DMFCs basically use the same cell components, materials, construction, and fabrication techniques as the PEMFCs; therefore, it is expected that the system and component costs will be similar to that of the PEMFCs. It is said that one company in the world has recently been formed to explore the potential of the DMFC systems and to develop DMFC for transportation practical applications. However, the DMFC system is at least 10 years away from any realistic practical applications, judging from the progress of other types of fuel cells in the past.

25.7.3.6 Applications

DMFCs offer a potential for high power density and cold-start capabilities, a convenience for onboard fuel storage and compatibility with existing refueling infrastructure. Therefore, DMFCs are the most attractive for applications where storage or generation of hydrogen causes significant effort and has a negative impact on the volume and weight of the system. As a result, DMFCs have a great potential for transportation applications ranging from automobiles, trains and ships, etc. For utility applications, small DMFC units have potential for use in residential and office buildings, hotels and hospitals, etc., for the combined electricity and heat supply (cogeneration). Since methanol can be made from agricultural products, the use of methanol is also compatible with renewable energy sources to allow for sustainable development.

25.7.4 Phosphoric Acid Fuel Cells

The PAFC is the most advanced type of fuel cells and is considered to be *technically mature* and ready for commercialization after nearly 30 years of RD&D and over half-a-billion-dollar expenditure. Therefore, the PAFC has been referred to as the first-generation fuel cell

technology. Unlike the AFC systems that were primarily developed for space applications, the PAFC was targeted initially for terrestrial applications with the carbon dioxide-containing air as the oxidant gas and hydrocarbon-reformed gas as the fuel for electrochemical reactions and electric power generation.

The basic components of a PAFC are the electrodes consisting of finely dispersed platinum catalyst or carbon paper, SiC matrix holding the phosphoric acid, and a bipolar graphite plate with flow channels for fuel and oxidant. The operating temperature ranges between 160°C and 220°C, and it can use either hydrogen or hydrogen produced from hydrocarbons (typically natural gas) or alcohols as the anodic reactant. In the case of hydrogen produced from a reformer with air as the anodic reactant, a temperature of 200°C and a pressure as high as 8 atm are required for better performance. PAFCs are advantageous from a thermal management point of view. The rejection of waste heat and product water is very efficient in this system, and the waste heat at about 200°C can be used efficiently for the endothermic steam-reforming reaction. The waste heat can also be used for space heating and hot water supply.

However, the PAFC cannot tolerate the presence of carbon monoxide and H₂S, which are commonly present in the reformed fuels. These contaminants poison the catalyst and decrease its electrochemical catalytic activity. A major challenge for using natural gas reformed fuel, therefore, lies in the removal of carbon monoxide to a level of <200–300 ppm. Carbon monoxide tolerance is better at the operating temperature of above 180°C. However, removal of sulfur is still essential. Further, the PAFC has a lower performance, primarily due to the slow oxygen reaction rate at the cathode. Therefore, PAFC is typically operated at higher temperature (near 200°C) for better electrochemical reactivity and for smaller internal resistance, which is mainly due to the phosphoric acid electrolyte. As a result, PAFC exhibits the problems of both high- and low-temperature fuel cells, but possibly none of the advantages of either option.

The PAFC system is the most advanced fuel cell system for terrestrial applications. Its major use is in on-site integrated energy systems to provide electrical power in apartments, shopping centers, office buildings, hotels and hospitals, etc. These fuel cells are commercially available in the range from 24 V, 250 W portable units to 200 kW on-site generators. PAFC systems of 0.5–1.0 MW are being developed for use in stationary power plants of 1–11 MW capacity. The power density of PAFC system is about 200 mW/cm², and the power density for 36 kW brassboard PAFC fuel cell stack has been reported to be 0.12 kW/kg and 0.16 kW/L. The most advanced PAFC system is the PC-25 from the International Fuel Cells in Connecticut, United States. It costs about U.S. \$3000 per kW (the best technology possible for the PAFCs), while the conventional thermal power generation system costs only about U.S. \$1000 per kW. Thus, it is believed that the PAFC is not commercially viable at present, even though U.S. DOE and DOD have been subsidizing half of the cost (\$1500 per kW) in order to gain operational and maintenance experience for practical fuel cell systems. Although Japan seems determined to push ahead for the fuel cell technology, interest in the PAFC systems is waning in the United States and Europe.

25.7.5 Molten Carbonate Fuel Cells

25.7.5.1 Introduction

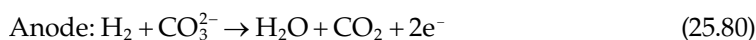
The MCFC is often referred to as the second-generation fuel cell because its commercialization is normally expected after the PAFC. It is believed that the development and technical maturity of the MCFC is about 5–7 years behind the PAFC. At present, the

MCFC has reached the early demonstration stage of pre-commercial stacks, marking the transition from fundamental and applied R&D toward product development. MCFCs are being targeted to operate on coal-derived fuel gases or natural gas. This contrasts with the PAFCs, as discussed earlier, which prefer natural gas as primary fuel.

The MCFC operates at higher temperature than all the fuel cells described so far. The operating temperature of the MCFC is generally around 600°C–700°C, typically 650°C. Such high temperature produces high-grade waste heat, which is suitable for fuel processing, cogeneration, or combined cycle operation, leading to higher electric efficiency. It also yields the possibility of utilizing carbonaceous fuels (especially natural gas) directly, through internal reforming to produce the fuel (hydrogen) ultimately used by the fuel cell electrochemical reactions. This results in simpler MCFC systems (i.e., without external reforming or fuel processing subsystem), less parasitic load, and less cooling power requirements, hence higher overall system efficiency as well. The high operating temperature reduces voltage losses due to reduced activation, ohmic, and mass transfer polarization. The activation polarization is reduced to such an extent that it does not require expensive catalysts as low-temperature fuel cells do, such as PAFCs and PEMFCs. It also offers great flexibility in the use of available fuels, say, through in situ reforming of fuels. It has been estimated that the MCFC can achieve an energy conversion efficiency of 52%–60% (from chemical energy to electrical energy) with internal reforming and natural gas as the primary fuel. Some studies have indicated that the MCFC efficiency of methane to electricity conversion is the highest attainable by any fuel cell or other single-pass/simple cycle generation scheme.

25.7.5.2 Basic Operating Principle

An MCFC consists of two porous gas-diffusion electrodes (anode and cathode) and a carbonate electrolyte in liquid form. The electrochemical reaction occurring at the anode and the cathode is



and the net cell reaction is



Besides the hydrogen oxidation reaction at the anode, other fuel gases such as carbon monoxide, methane, and higher hydrocarbons are also oxidized by conversion to hydrogen. Although direct electrochemical oxidation of carbon monoxide is possible, it occurs very slowly compared to that of hydrogen. Therefore, the oxidation of carbon monoxide is mainly via the water–gas shift reaction



which, at the operation temperature of the MCFC, equilibrates very rapidly at using catalysts such as nickel. Therefore, carbon monoxide becomes a fuel, instead of a contaminant

as in the previously described low-temperature fuel cells. Direct electrochemical reaction of methane appears to be negligible. Hence, methane and other hydrocarbons must be steam-reformed, which can be done either in a separate reformer (external reforming) or in the MCFC itself (the so-called internal reforming).

As a result, water and carbon dioxide are important components of the feed gases to the MCFCs. Water, produced by the main anode reaction, helps to shift the equilibrium reactions to produce more hydrogen for the anodic electrochemical reaction. Water must also be present in the feed gas, especially in low-Btu (i.e., high CO content) fuel mixtures, to avoid carbon deposition in the fuel gas flow channels supplying the cell, or even inside the cell itself. Carbon dioxide, from the fuel exhaust gas, is usually recycled to the cathode as it is required for the reduction of oxygen.

The MCFCs use a molten alkali carbonate mixture as the electrolyte, which is immobilized in a porous lithium aluminate matrix. The conducting species is carbonate ions. Lithiated nickel oxide is the material of the current choice for the cathode, and nickel, cobalt, and copper are currently used as anode materials, often in the form of powdered alloys and composites with oxides. As a porous metal structure, it is subject to sintering and creeping under the compressive force necessary for stack operation. Additives such as chromium or aluminum form dispersed oxides and thereby increase the long-term stability of the anode with respect to sintering and creeping. MCFCs normally have about 75%–80% fuel (hydrogen) utilization.

25.7.5.3 Acceptable Contamination Levels

MCFCs do not suffer from carbon monoxide poisoning, and in fact, they can utilize carbon monoxide in the anode gas as the fuel. However, they are extremely sensitive to the presence of sulfur (<1 ppm) in the reformed fuel (as hydrogen sulfide, H₂S) and oxidant gas stream (SO₂ in the recycled anode exhaust). The presence of HCl, HF, HBr, etc., causes corrosion, while trace metals can spoil the electrodes. The presence of particulates of coal/fine ash in the reformed fuel can clog the gas passages.

25.7.5.4 Major Technological Problems

The main research efforts for the MCFCs are focused on increasing the lifetime and endurance, and reducing the long-term performance decay. The main determining factors for the MCFC are electrolyte loss, cathode dissolution, electrode creepage and sintering, separator plate corrosion, and catalyst poisoning for internal reforming.

Electrolyte loss results in increased ohmic resistance and activation polarization, and it is the most important and continuously active factor in causing the long-term performance degradation. It is primarily a result of electrolyte consumption by the corrosion/dissolution processes of cell components, electric potential-driven electrolyte migration, and electrolyte vaporization. Electrolyte evaporation (usually Li₂CO₃ and/or K₂CO₃) occurs either directly as carbonate or indirectly as hydroxide.

The cathode consists of NiO, which slowly dissolves in the electrolyte during operation. It is then transported toward the anode and precipitates in the electrolyte matrix as Ni. These processes lead to a gradual degradation of cathode performance and the shorting of the electrolyte matrix. The time at which shorting occurs depends not only, via NiO solubility, on the CO₂ partial pressure and the cell temperature, but also on the matrix structure, that is, on the porosity, pore size, and in particular, thickness of the matrix. Experience indicates that this cell-shortening mechanism tends

to limit stack life to about 25,000 h under the atmospheric reference gas conditions and much shorter for real operating conditions.

Electrode, especially anode, creepage and sintering (i.e., a coarsening and compression of electrode particles) result in increased ohmic resistance and electrode polarization. NiO cathodes have quite satisfactory sinter and creepage resistance. Creep resistance of electrodes has important effect on maintaining low contact resistance of the cells and stacks. The corrosion of the separator plate depends on many factors, such as the substrate, possible protective layers, composition of the electrolyte, local potential and gas composition, and the oxidizing and reducing atmospheres at the cathode and anode, respectively. Poisoning of the reforming catalyst occurs for direct internal reforming MCFCs. It is caused by the evaporation of electrolyte from the cell components and condensation on the catalyst, which is the coldest spot in the cell, and by liquid creep within the cell.

25.7.5.5 Technological Status

MCFC technology is in the first demonstration phase and under the product development with full-scale systems at the 250 kW to 2 MW range. The short-term goal is to reach a lifetime of 25,000 h, and the ultimate target is 40,000 h. It is estimated that the capital cost is about U.S. \$1000–\$1600 per kW for the MCFC power systems. The cost breakdown is, at full-scale production levels, about one-third for the stack and two-thirds for the balance of the plant. It is also generally accepted that the cost of raw materials will constitute about 80% of total stack costs. Although substantial development efforts supported by fundamental research are still needed, the available knowledge and number of alternatives will probably make it possible to produce pre-commercial units in the earlier part of the coming decade at a capital cost of U.S. \$2000–\$4000 per kW. Pre-competitive commercial units may be expected some years later by which time further cost reduction to full competitiveness will be guided by extensive operating experience and increased volume production.

25.7.5.6 Applications

The MCFC is being developed for their potential as baseload utility generators. However, their best application is in distributed power generation and cogeneration (i.e., for capacities <20 MW in size), and in this size range, MCFCs are 50%–100% more efficient than turbines—the conventional power generator. Other applications have been foreseen, such as pipeline compressor stations, commercial buildings, and industrial sites in the near term and repowering applications in the longer term. Due to its high operation temperature, it has only very limited potential for transportation applications. This is because of its relatively low power density and long start-up times. However, it may be suitable as a powertrain for large surface ships and trains.

25.7.6 Solid Oxide Fuel Cells

25.7.6.1 Introduction

SOFCS have emerged as a serious alternative high-temperature fuel cell, and they have been often referred to as the third-generation fuel cell technology because their commercialization is expected after the PAFCs (the first generation) and MCFCs (the second generation).

SOFC is an all-solid-state power system, including the electrolyte, and it is operated at high temperature of around 1000°C for adequate ionic and electronic conductivity of

various cell components. The all solid-state cell composition makes the SOFC system simpler in concept, design, and construction; two-phase (gas–solid) contact for the reaction zone reduces corrosion and eliminates all the problems associated with the liquid electrolyte management. The high-temperature operation results in fast electrochemical kinetics (i.e., low activation polarization) and no need for noble metal catalysts. The fuel may be gaseous hydrogen, H₂/CO mixture, or hydrocarbons because the high-temperature operation makes the internal in situ reforming of hydrocarbons with water vapor possible. It is specially noticed that CO is no longer a contaminant; rather, it becomes a fuel in SOFCs. Even with external reforming, the SOFC fuel feedstock stream does not require the extensive steam reforming with shift conversion as it does for the low-temperature fuel cell systems. More important, the SOFC provides high-quality waste heat that can be utilized for cogeneration applications or combined cycle operation for additional electric power generation. The SOFC operating condition is also compatible with the coal gasification process, which makes the SOFC systems highly efficient when using coal as the primary fuel. It has been estimated that the chemical to electrical energy conversion efficiency is 50%–60%, even though some estimates go as high as 70%–80%. Also, nitrogen oxides are not produced, and the amount of carbon dioxide released per kW h is around 50% less than for power sources based on combustion because of the high efficiency.

25.7.6.2 Basic Operating Principle

As mentioned earlier, both hydrogen and carbon monoxide can be directly oxidized in the SOFCs. Hence, if hydrogen or hydrogen-rich gas mixture is used as fuel, and oxygen (or air) is used as oxidant, the half-cell reaction becomes



and the overall cell reaction becomes



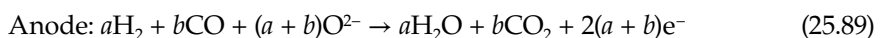
However, if carbon monoxide is provided to the anode instead of hydrogen, the anode reaction becomes



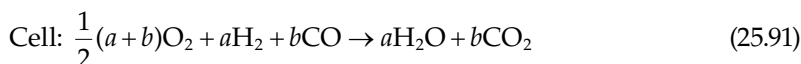
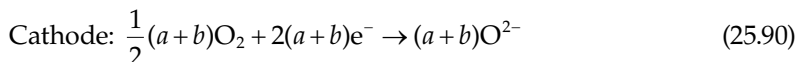
With the cathode reaction remaining the same, the cell reaction becomes



If the fuel stream contains both hydrogen and carbon monoxide as is the case for hydrocarbon reformed gas mixture, especially from the gasification of coal, the oxidation of hydrogen and carbon monoxide occurs simultaneously at the anode, and the combined anode reaction becomes



Consequently, the corresponding cathode and overall cell reactions become



The solid electrolyte in SOFCs is usually yttria-stabilized zirconia (YSZ); thus, a high-operating temperature of around 1000°C is required to ensure adequate ionic conductivity and low ohmic resistance. This is especially important because the cell open-circuit voltage is low, compared with low-temperature fuel cells, typically around 0.9–1 V under the typical working conditions of the SOFCs. The high-temperature operation of the SOFCs makes the activation polarization very small, resulting in the design operation in the range dominated by the ohmic polarization. The conventional material for the anode is nickel–YSZ–cermet, and cathode is usually made of lanthanum–strontium–manganite. Metallic current collector plates of a high-temperature corrosion-resistant chromium-based alloy are typically used.

25.7.6.3 Acceptable Contamination Levels

Because of high temperature, the SOFCs can better tolerate impurities in the incoming fuel stream. They can operate equally well on dry or humidified hydrogen or carbon monoxide fuel or on mixtures of them. But hydrogen sulfide (H_2S), hydrogen chloride (HCl), and ammonia (NH_3) are impurities typically found in coal-gasified products, and each of these substances is potentially harmful to the performance of SOFCs. The main poisoning factor for SOFCs is H_2S . Though the sulfur tolerance level is approximately two orders of magnitude greater than other fuel cells, the level is below 80 ppm. However, studies have shown that the effect of hydrogen sulfide (H_2S) is reversible, meaning that the cell performance will recover if hydrogen sulfide is removed from the fuel stream or clean fuel is provided after the contaminant poison has occurred.

25.7.6.4 Major Technological Problems

The high-temperature operation of the SOFCs places stringent requirements on materials used for cell construction, and appropriate materials for cell components are very scarce. Therefore, the key technical challenges are the development of suitable materials and the fabrication techniques. Of the material requirements, the most important consideration is the matching of the thermal expansion coefficients of electrode materials with that of the electrolyte to prevent cracking or delamination of SOFC components either during high-temperature operation or heating/cooling cycles. One of the remedies for the thermal expansion mismatch is to increase the mechanical toughness of the cell materials by developing either new materials or doping the existing materials with SrO and CaO .

The electrode voltage losses are reduced when the electrode material possesses both ionic and electronic conductivities (the so-called mixed conduction), for which the electrochemical reactions occur throughout the entire surface of the electrode rather than only at the three-phase interface of, for example, the cathode, the air (gas phase), and the electrolyte. Therefore, it is important for performance enhancement to develop mixed-conduction materials for both the cathode and the anode that have good thermal expansion match with the electrolyte used and good electrical conductivity to reduce the ohmic polarization, which dominates the SOFC voltage losses.

Another focus of the current development is the intermediate-temperature SOFCs operating at around 800°C for better matching with the bottoming turbine cycles and lessening requirements for the cell component materials. Again, appropriate materials with adequate electrical conductivity are the key areas of the development effort, and thermal expansion matching among the cell components is still necessary.

25.7.6.5 Technological Status

There are three major configurations for SOFCs: the tubular, flat plate, and monolithic. Even though the SOFC technology is in the developmental stage, the tubular design has gone through development at Westinghouse Electric Corporation since the late 1950s and is now being demonstrated at user sites in a complete operating fuel cell power unit of nominal 25 kW (40 kW maximum) capacity. The flat plate and the monolithic designs are at a much earlier development status typified by subscale, single cell, and short stack development (up to 40 cells). The present estimated capital cost is U.S. \$1500 per kW, but is expected to be reduced with improvements in technology. Therefore, the SOFCs may become very competitive with the existing technology for electric power generation. However, it is believed that the SOFC technology is at least 5–10 years away from the commercialization.

25.7.6.6 Applications

SOFCs are very attractive in electrical utility and industrial applications. The high operating temperature allows them to use hydrogen and carbon monoxide from natural gas steam reformers and coal gasification plants, a major advantage as far as fuel selection is concerned. SOFCs are being developed for large (>10 MW, especially 100–300 MW) baseload stationary power plants with coal as the primary fuel. This is one of the most lucrative markets for this type of fuel cells.

A promising field for SOFCs is the decentralized power supply in the MW range, where the SOFC gains interest due to its capability to convert natural gas without external reforming. In the range of one to some tenths of a MW, the predicted benefits in electrical efficiency of SOFC-based power plants over conventional methods of electricity generation from natural gas can be achieved only by an internal-reforming SOFC. So internal reforming is a major target of present worldwide SOFC development.

25.8 Summary

This chapter is focused on fuel cell, including the basic principle of operation, system composition, and balance of plants, the performance and the design considerations, as well as the state-of-the-art technology. The performance of fuel cell is analyzed in terms of the cell potential and energy conversion efficiency under the idealized reversible and practical irreversible conditions, and misconception regarding fuel cell energy efficiency is clarified. The effect of operating conditions, namely, temperature, pressure, and reactant concentration, on the reversible cell potential is also given. It is shown that both fuel cells and heat engines have the same maximum theoretical efficiency, which is equivalent to the Carnot efficiency, when operating on the same fuel and oxidant. However, fuel cells have less irreversibilities in practice, resulting in higher practical efficiencies. Further, possibilities of over 100% fuel

cell efficiency are ruled out from the fundamental principles. Both reversible and irreversible energy loss mechanisms are described for fuel cells, expression for waste heat generation in a fuel cell is derived, and various forms of fuel cell efficiency are defined. Finally, the Nernst potential loss arising from the reactant consumption in practical cells is considered, and issues related to reactant utilization are outlined. Then, important physical and chemical processes occurring in fuel cell electrodes are provided, which relate to the transport phenomena and electrochemical reactions for current generation. These processes affect how the cells are connected together to form fuel cell stack of different sizes for desired power output.

Finally, the characteristics, technological status, and preferred area of applications are summarized for each of the six major types of fuel cells. AFCs have the best performance when operating on pure hydrogen and oxygen; its intolerance of carbon dioxide hinders its role for terrestrial applications. Significant progress is being made for PEMFC, although it is still too expensive to be competitive in the marketplace today. However, PEMFC is believed to be the most promising candidate for transportation application because of its high power density, fast start-up, high efficiency, and easy and safe handling. But until its cost is lowered by at least orders of magnitude, it will not be economically acceptable. Due to the difficulty of onboard fuel (hydrogen) storage and the lack of infrastructure for fuel (hydrogen) distribution, DMFCs are believed by some to be the most appropriate technology for vehicular application. PEMFCs are expected to be 5–10 years away from commercialization, while the DMFCs are at the early stage in their technological development. DMFCs also have considerable potential for portable applications. PAFC is the most commercially developed fuel cell, operating at intermediate temperatures. PAFCs are being used for combined heat and power applications with high energy efficiency. The high-temperature fuel cells like MCFCs and SOFCs may be most appropriate for cogeneration and combined cycle systems (with gas or steam turbine as the bottoming cycle). The MCFCs have the highest energy efficiency attainable from methane to electricity conversion in the size range of 250 kW to 20 MW; whereas the SOFCs are best suited for baseload utility applications operating on coal-derived gases. It is estimated that the MCFC technology is about 5–10 years away from commercialization, and the SOFCs are probably years afterward.

References

1. X. Li, *Principles of Fuel Cells*. Taylor & Francis, New York, 2006.
2. A. J. Appleby and F. R. Foulkes, *Fuel Cell Handbook*. Van Nostrand Reinhold, New York, 1989.
3. L. J. M. J. Blomen and M. N. Mugerwa, eds., *Fuel Cell Systems*. Plenum Press, New York, 1993.
4. J. H. Hirschenhofer, D. B. Stauffer, and R. R. Engleman, *Fuel Cells: A Handbook* (Rev. 3). U.S. Department of Energy, Washington, DC, 1994.
5. K. Kordesch and G. Simader, *Fuel Cells and Their Applications*. VCH, New York, 1996.
6. A. J. Appleby, Fuel cell technology: Status and future prospects. *Energy* 21, 521–653, 1996.
7. W. Vielstich, H. Gasteiger, and A. Lamm, eds., *Handbook of Fuel Cells—Fundamentals, Technology, Applications*. Wiley, New York, 2003.
8. A. J. Appleby, Characteristics of fuel cell systems. In: L. J. M. J. Blomen and M. N. Mugerwa, eds., *Fuel Cell Systems*, Chapter 5. Plenum Press, New York, 1993.
9. X. Li, Fuel cells and their thermodynamic performance. In: *Proceedings of the Energy Week Conference & Exhibition, ASME and API*, Book V, Vol. IV, Houston, TX, January 1997, pp. 346–356.
10. X. Li, *Int. J. Fuel cells—The environmentally friendly energy converter and power generator. International Journal of Global Energy Issues* 17(1/2), 68–91, 2002.
11. E. Barendrecht, Electrochemistry of fuel cells. In: L. J. M. J. Blomen and M. N. Mugerwa, eds., *Fuel Cell Systems*. Plenum Press, New York, 1993, pp. 73–119.



Taylor & Francis

Taylor & Francis Group

<http://taylorandfrancis.com>

26

Direct Energy Conversion

Mysore L. Ramalingam, Jean-Pierre Fleurial, and George Nolas

CONTENTS

26.1 Thermionic Energy Conversion.....	1085
26.1.1 Introduction.....	1085
26.1.2 Principles of Thermionic Energy Conversion.....	1086
26.1.2.1 Surface Work Function.....	1087
26.1.2.2 Interelectrode Motive Distribution.....	1087
26.1.2.3 Electron Saturation Current.....	1088
26.1.3 Types of Thermionic Converters.....	1089
26.1.4 Converter Output Characteristics.....	1089
26.1.5 Thermodynamic Analysis.....	1090
26.1.6 Design Transition to Space Reactors—Concluding Remarks.....	1091
26.2 Thermoelectric Power Conversion.....	1092
26.2.1 Introduction.....	1092
26.2.2 Thermoelectric Effects.....	1092
26.2.3 Thermoelectric Applications.....	1093
26.2.3.1 Power Generation.....	1094
26.2.3.2 Refrigeration.....	1095
26.2.4 Additional Considerations.....	1098
Nomenclature.....	1099
Defining Terms.....	1099
References.....	1100
For Further Information.....	1101

26.1 Thermionic Energy Conversion

Mysore L. Ramalingam

26.1.1 Introduction

Thermionic energy conversion (TEC) is the process of converting heat directly to useful electrical work by the phenomenon of thermionic electron emission. This fundamental concept can be applied to a cylindrical version of the planar converter, considered the building block for space nuclear power systems (SNPS) at any power level. Space nuclear reactors based on TEC can produce power in the range of 5 kWe–5 MWe, a spectrum that

serves the needs of current users such as National Aeronautics and Space Administration (NASA), United States Air Force (USAF), United States Department of Energy (USDOE), and Ballistic Missile Defense Organization (BMDO). Electrical power in this range is currently being considered for commercial telecommunication satellites, navigation, propulsion, and planetary exploration missions.

The history of thermionic emission dates back to the mid-1700s when Charles Dufay observed that electricity is conducted in the space near a red-hot body. Although Thomas Edison requested a patent in the late 1800s, indicating that he had observed thermionic electron emission while perfecting his electric light system, it was not until the 1960s that the phenomenon of TEC was adequately described theoretically and experimentally (Hatsopoulos and Gryftopoulos 1973). These pioneering activities have led to the development of thermionic SNPS that could potentially be augmented by Brayton and Stirling cycle generators to produce additional power from waste heat in NASA manned lunar and martian exploration missions (Ramalingam and Young 1993).

26.1.2 Principles of Thermionic Energy Conversion

Figure 26.1 represents a schematic of the essential components and processes in an elementary thermionic converter (TC). Electrons “boil-off” from the emitter material surface, a refractory metal such as tungsten, when heated to high temperatures (2000 K) by a heat source. The electrons then traverse the small interelectrode gap, to a colder (1000 K) collector surface where they condense, producing an output voltage that drives the current through the electrical load and back to the emitter. The flow of electrons through the electrical load is sustained by the temperature difference and the difference in **surface work functions** of the electrodes.

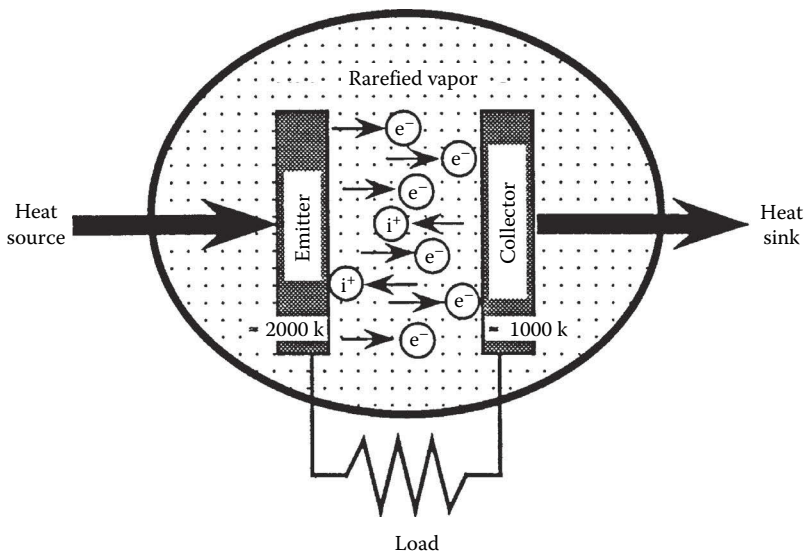


FIGURE 26.1
Schematic of an elementary TEC.

26.1.2.1 Surface Work Function

In a simple form, the energy required to separate an electron from a metal surface atom and take it to infinity outside the surface is termed the electron work function or the work function of the metal surface. The force experienced by an electron as it crosses an interface between a metal and a rarefied vapor can be represented by the **electron motive**, Ψ , which is defined as a scalar quantity whose negative gradient at any point is a measure of the force exerted on the electron at that point (Langmuir and Kingdon 1925). At absolute zero the kinetic energy of the free electrons would occupy quantum energy levels from zero to some maximum value called the Fermi level. Each energy level contains a limited number of free electrons, similar to the electrons contained in each electron orbit surrounding the nucleus of an atom. Fermi energy, m , corresponds to the highest energy of all free electrons at absolute zero. At temperatures other than absolute zero some of the free electrons begin to experience energies greater than that at the Fermi level. Thus, the electron work function Φ , would be defined as

$$\Phi = \Psi_T - \mu \tag{26.1}$$

where Ψ_T represents the electron motive or energy at some temperature, T , above absolute zero.

26.1.2.2 Interelectrode Motive Distribution

Figure 26.2 provides a schematic representation of the electron motive distribution in the interelectrode space of a thermionic converter. Under ideal conditions of particle transport, the motive varies linearly from Ψ_{EM} , the motive just outside the emitter, to Ψ_{CO} , the

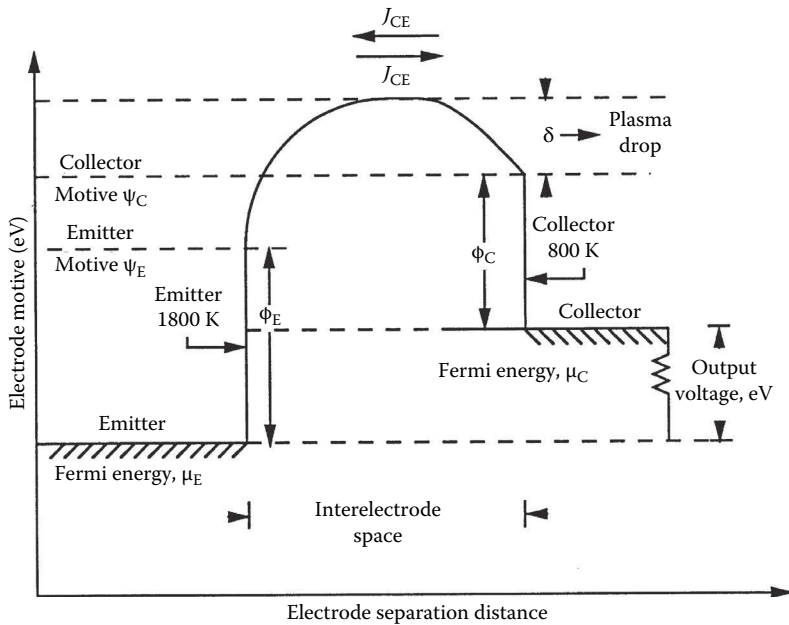


FIGURE 26.2
Electron motive distribution in the interelectrode gap.

motive outside the collector surface. The magnitudes of the Fermi energies of the emitter and collector relative to Ψ_{EM} and Ψ_{CO} are clearly indicated. The internal voltage drop of the converter is defined as;

$$\Delta V = \frac{\Psi_{EM} - \Psi_{CO}}{e} \quad (26.2)$$

In a conventional thermionic converter, the emitter and collector are not at the same temperature, but to a good approximation, the output voltage, neglecting **lead losses** and **particle interaction losses**, can be represented by the relationship.

$$V = \frac{\mu_{CO} - \mu_{EM}}{e} \quad (26.3)$$

Since a real thermionic converter has an ionizing medium to improve its performance, a similar motive distribution can be defined for the ions. It is sufficient to state that the ion interelectrode motive has a slope equal and opposite to the corresponding electron interelectrode motive. The ions are, therefore, decelerated when the electrons are accelerated and vice versa.

26.1.2.3 Electron Saturation Current

In the absence of a strong influence from an external electrical source, the electron current ejected from a hot metal at the emitter surface into the vacuum ionizing medium is termed the *electron saturation current*. As this quantity depends on the number of free electrons $N(\epsilon_x)$, Fermi-Dirac statistics provide the means to compute the number of free electrons, $N(\epsilon_x) d\epsilon_x$, incident on a unit area within the metal in unit time with energies corresponding to the motion normal to the area, between ϵ_x and $\epsilon_x + d\epsilon_x$. For energies greater than the Fermi energy, the functional dependence of $N(\epsilon_x)$ on ϵ_x is given by (Fowler 1955)

$$N(\epsilon_x) \approx \left[\frac{4\pi m_e kT}{h^3} \right] \left[\exp \left\{ \frac{-\epsilon_x - \mu}{kT} \right\} \right] \quad (26.4)$$

where

m_e is the mass of the electron = 9.108×10^{-28} g

h is Planck's constant = 4.140×10^{-15} eV s.

The electron saturation current density, J_{sat} , for a uniform surface, is found by integrating $N(\epsilon_x)$ in the range of ϵ_x from Ψ_T to infinity for all $\Psi_T - \mu > kT$, which is the case for almost all materials and practical temperatures. The result of the integration yields

$$J_{sat} = AT^2 \exp \left[-\frac{\Psi_T - \mu}{kT} \right] \quad (26.5)$$

or

$$J_{sat} = AT^2 \exp \left[-\frac{\Phi}{kT} \right] \quad (26.6)$$

where A is the Richardson constant ≈ 120 A/cm² K².

Equation 26.6, which is the most fundamental and important relationship for the design of a thermionic converter, is called the Richardson-Dushman Equation (Richardson 1912). On similar lines, the ion saturation current density for a converter with an ionizing medium is given by the relationship (Taylor and Langmuir 1933):

$$\tilde{J}_{\text{isat}} = \frac{ep_g}{(2\pi m_g k T_g)^{0.5} (1 + 2 \exp\{[V_i - \Phi/kT]\})} \quad (26.7)$$

where p_g , T_g , m_g , and V_i are the pressure, temperature, mass, and first ionization energy, respectively, of the ionizing medium.

26.1.3 Types of Thermionic Converters

Thermionic converters can be broadly classified as vacuum thermionic converters and vapor thermionic converters, depending on the presence of an ionizing medium in the interelectrode gap. In vacuum thermionic converters the interelectrode space is evacuated so that the space is free of particles other than electrons and the two electrodes are placed very close together, thereby neutralizing the negative space charge buildup on the electrode surface and reducing the total number of electrons in transit. Due to machining limitations, vacuum converters have been all but completely replaced by vapor-filled thermionic converters. In vapor-filled thermionic converters, the interelectrode space is filled with a rarefied ionizing medium at a vapor pressure generally on the order of 1–10 Torr. The vapor generally used is cesium as it is the most easily ionized of all stable gases and this can be provided through an external two-phase reservoir or an internal graphite reservoir (Young et al. 1993). The vapor neutralizes the negative space charge effect by producing positive ions at the electrode surfaces and gets adsorbed on the surfaces, thereby altering the work function characteristics.

26.1.4 Converter Output Characteristics

Figure 26.3 represents the output current-voltage characteristics for various modes of operation of the vacuum and vapor-filled thermionic converters. Characteristics obtained by not considering particle interactions in the interelectrode gap are generally considered ideal output characteristics. The figure essentially displays three types of converter output current-voltage characteristics, an ideal characteristic, an ignited mode characteristic, and an unignited mode characteristic. For an ideal converter in the interelectrode space the net output current density consists of the electron current density, J_{EMCO} flowing from emitter to collector diminished by the electron current density J_{COEM} flowing from collector to emitter and the ion-current density \tilde{J}_{iEMCO} flowing from emitter to collector. Thus,

$$J_{\text{net}} = J_{\text{EMCO}} - J_{\text{COEM}} - \tilde{J}_{\text{iEMCO}} \quad (26.8)$$

By expressing the individual terms as functions of ϕ , T , and V

$$J_{\text{net}} = AT_{\text{EM}}^2 \exp\left[-\frac{\Phi_{\text{EM}}}{kT_{\text{EM}}}\right] - AT_{\text{CO}}^2 \exp\left[-\frac{\Phi_{\text{EM}} - eV}{kT_{\text{CO}}}\right] - \tilde{J}_{\text{EMS}} \exp[-(\Psi_{\text{EM}} - \Psi_{\text{CO}})kT_{\text{EM}}] \quad \text{for } eV < \Phi_{\text{EM}} - \Phi_{\text{CO}} \quad (26.9)$$

Similar relationships can be generated for various types of thermionic converters.

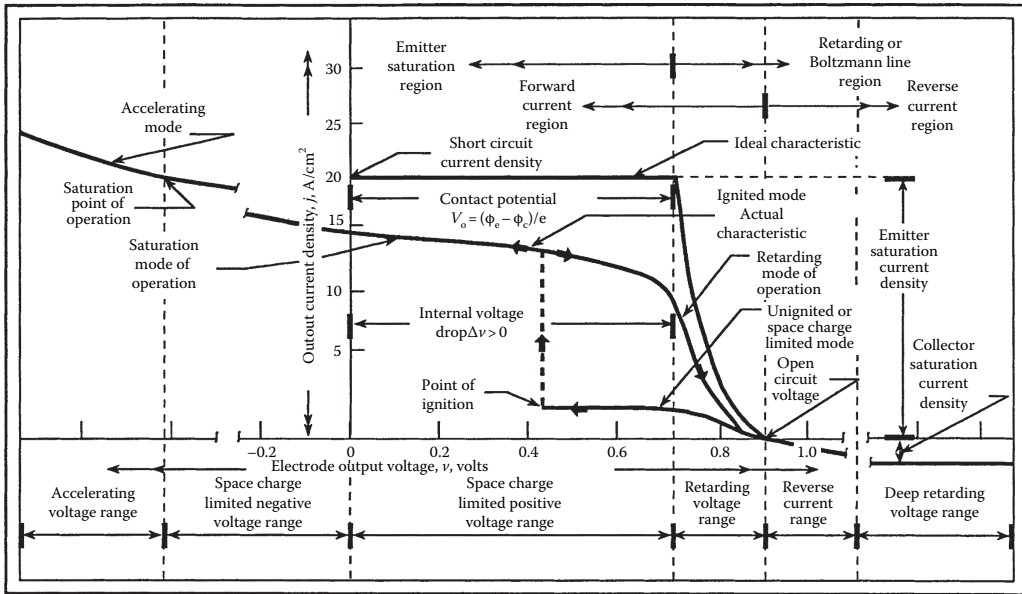


FIGURE 26.3 Thermionic diode output current density characteristics and nomenclature.

26.1.5 Thermodynamic Analysis

In thermodynamic terms a thermionic converter is a heat engine that receives heat at high temperature, rejects heat at a lower temperature, and produces useful electrical work while operating in a cycle analogous to a simple vapor cycle engine. Based on the application of the first law of thermodynamics to the control volumes around the emitter (Houston 1959; Angrist 1976),

$$\text{Energy in} = \text{Energy out} \tag{26.10}$$

i.e.,

$$q_{CB} + q_{JH} + q_{HS} = q_{EC} + q_{WB} + q_{CD} + q_{RA} \tag{26.11}$$

where, by using the terminology in Figure 26.2, each of the terms in Equation 26.11 can be elaborated as follows:

1. Energy supplied by back emission of the collector:

$$q_{CB} = J_{COEM} \left[\Phi_{CO} + \delta + V + \frac{2kT_{CO}}{e} \right] \tag{26.12}$$

2. Energy supplied by joule heating of lead wires and plasma:

$$q_{JH} = 0.5 [J_{EMCO} - J_{COEM}]^2 (R_{LW} + R_{PL}) \tag{26.13}$$

3. Energy dissipated by electron cooling:

$$q_{EC} = J_{EMCO} \left[\Phi_{CO} + \delta + V - \Phi_{EM} + \left(\frac{2kT_{EM}}{e} \right) \right] \quad (26.14)$$

4. Energy dissipated due to phase change by electron evaporation:

$$q_{WB} = J_{EM} \Phi_{EM} \quad (26.15)$$

5. Energy dissipated by conduction through the lead wires and plasma:

$$q_{CD} = \Delta T \left[\frac{K_{LW} A_{LW}}{A_e L_{LW}} + \frac{K_{PL} A_{PL}}{A_e L_{IG}} \right] \quad (26.16)$$

where

K represents thermal conductivity

LW is the lead wires

PL is the plasma

IG is the interelectrode gap

6. Energy dissipated by radiation from emitter to collector:

$$q_{RA} = 5.67 \times 10^{-12} (T_{EM}^2 - T_{CO}^4) (\epsilon_{EM}^{-1} + \epsilon_{CO}^{-1} - 1)^{-1} \quad (26.17)$$

Substitution for the various terms in Equation 26.10 yields q_{HS} , the energy supplied to the emitter from the heat source.

The thermal efficiency of the thermionic converter is now expressed as

$$\eta_{TH} = \left[V \frac{(J_{EMCO} - J_{COEM})}{q_{HS}} \right] \quad (26.18)$$

26.1.6 Design Transition to Space Reactors—Concluding Remarks

All the fundamentals discussed so far for a planar thermionic converter can be applied to a cylindrical version which then becomes the building block for space power systems at any power level. In a thermionic reactor, heat from the nuclear fission process produces the temperatures needed for thermionic emission to occur. The design of a thermionic SNPS is a user-defined compromise between the required output power and the need to operate reliably for a specified lifetime. Based on the type of contact the emitter has with the nuclear fuel, the power systems can be categorized as “in-core” or “out-of-core” power systems. At this stage it suffices to state that the emitter design for in-core systems is extremely complex because of its direct contact with the hot nuclear fuel.

26.2 Thermoelectric Power Conversion

Jean-Pierre Fleurial and George Nolas

26.2.1 Introduction

The advances in materials science and solid-state physics during the 1940s and 1950s resulted in intensive studies of thermoelectric effects and related applications in the late 1950s and through the mid-1960s (Rowe and Bhandari 1983). The development of semiconductors with good thermoelectric properties made possible the fabrication of thermoelectric generators and refrigerators. Being solid-state devices, thermoelectric systems offer unique advantages such as being highly reliable with long operational lifespans, small sizes, and for refrigeration applications, vibration-free operation. They can also be used in a wide range of temperatures (200–1300 K). Their limited conversion efficiencies, however, relegate these devices to only specialized applications. As the following sections will emphasize, the performance of those devices is closely associated with the magnitude of the dimensionless figure of merit, ZT , of the thermoelectric semiconductor materials (Nolas et al. 2001).

Thermoelectric materials known since the early 1960s have been extensively developed. Although significant improvements of the thermoelectric properties of these materials have been achieved, the average ZT over the temperature range of operation is currently no more than 1 over the entire 100–1500 K temperature range (Figure 26.4a and b). To expand the use of thermoelectric devices to a wide range of applications will require improving ZT by at least a factor of 2. There is no theoretical limitation on the value of ZT , and new research and approaches are now focusing on the investigation of new materials and nanoscale thermoelectric enhancements (Rowe 2012; Koumoto and Mori 2013).

26.2.2 Thermoelectric Effects

Thermoelectric devices are based on two transport phenomena: the Seebeck effect for power generation and the Peltier effect for electronic refrigeration. If a steady temperature gradient is applied along a conducting sample, the initially uniform charge carrier distribution is disturbed as the free carriers located at the high-temperature end diffuse to the low-temperature end. This results in the generation of a back emf which opposes any further diffusion current. The open-circuit voltage when no current flows is the Seebeck voltage. When the junctions of a circuit formed from two dissimilar conductors (n- and p-type semiconductors) connected electrically in series but thermally in parallel are maintained at different temperatures T_1 and T_2 , the open-circuit voltage V developed is given by $V = S_{pn}(T_1 - T_2)$, where S_{pn} is the Seebeck coefficient expressed in $\mu\text{V K}^{-1}$.

The complementary Peltier effect arises when an electrical current I passes through the junction. A temperature gradient is then established across the junctions and the corresponding rate of reversible heat absorption \dot{Q} is given by $\dot{Q} = \Pi_{pn}I$, where Π_{pn} is the Peltier coefficient expressed in W A^{-1} or V . There is actually a third, less-important phenomenon, the Thomson effect, which is produced when an electrical current passes along a single conducting sample over which a temperature gradient is maintained. The rate of reversible heat absorption is given by $\dot{Q} = \beta I(T_1 - T_2)$, where β is the Thomson coefficient expressed in V K^{-1} . The three coefficients are related by the Kelvin relationships:

$$S_{pn} = \frac{\Pi_{pn}}{T} \quad \text{and} \quad \frac{dS_{pn}}{dT} = \frac{\beta_p - \beta_n}{T} \quad (26.19)$$

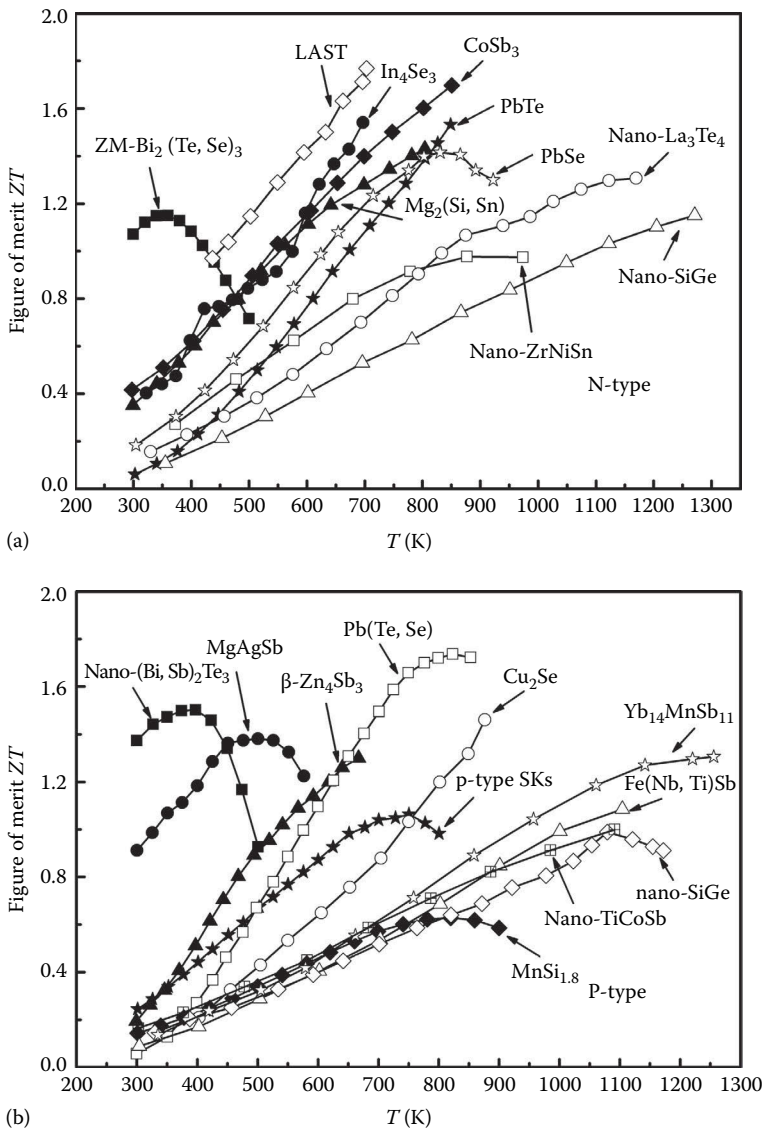


FIGURE 26.4

(a) ZT versus temperature of state-of-the-art n-type thermoelectric materials. (b) ZT versus temperature of state-of-the-art p-type thermoelectric materials.

26.2.3 Thermoelectric Applications

The schematic of a thermoelectric device, or module, on Figure 26.5, illustrates the three different modes of operation: power generation, cooling, and heating. The *thermoelectric module* is a standardized device consisting of several p- and n-type legs connected electrically in series and thermally in parallel, and bonded to a ceramic plate on each side (typically alumina). The modules are fabricated in a great variety of sizes, shapes, and number of thermoelectric couples and can operate in a wide range of currents, voltages, powers, and efficiencies. Complex, large-scale thermoelectric systems can be easily designed and

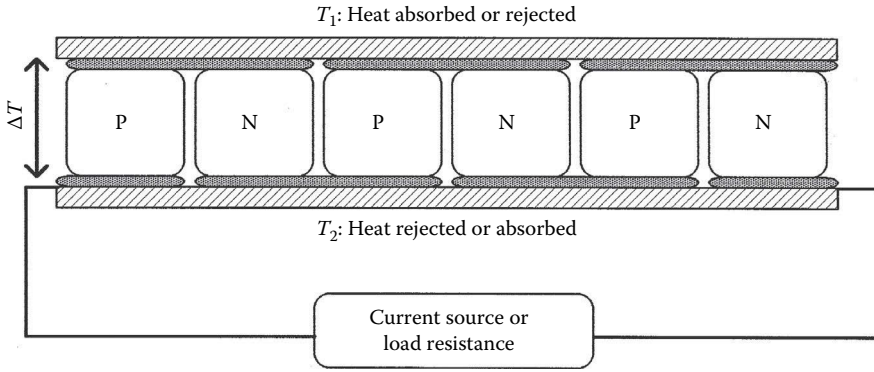


FIGURE 26.5
Schematic of a thermoelectric module.

built by assembling various numbers of these modules connected in series or in parallel depending on the type of applications.

26.2.3.1 Power Generation

When a temperature gradient is applied across the thermoelectric device, the heat absorbed at the hot junction (Figure 26.5, hot side $T_h - T_1$ and cold side, $T_c - T_2$) will generate a current through the circuit and deliver electrical power to the load resistance R_L (Harman and Honig 1967). The conversion efficiency η of a thermoelectric generator is determined by the ratio of the electrical energy, supplied to the load resistance, to the thermal energy, absorbed at the hot junction, and is given by

$$\eta = \frac{R_L I^2}{S_{pn} I T_h + K(T_h - T_c) - (1/2) R I^2} \tag{26.20}$$

where

K is the thermal conductance in parallel

R is the electrical series resistance of one $p-n$ thermoelectric couple

The electrical power P_L generated can be written as

$$P_L = \frac{S_{pn} (T_h - T_c)^2 R_L}{(R_L + R)^2} \tag{26.21}$$

The thermoelectric generator can be designed to operate at maximum power output, by matching the load and couple resistances, $R_L = R$. The corresponding conversion efficiency is

$$\eta = \frac{T_h - T_c}{(3/2)T_h + (1/2)T_c + (1/4)Z_{pn}^{-1}} \tag{26.22}$$

where Z_{pn} is the figure of merit of the $p-n$ couple given by

$$Z_{pn} = \frac{S_{pn}^2}{RK} \tag{26.23}$$

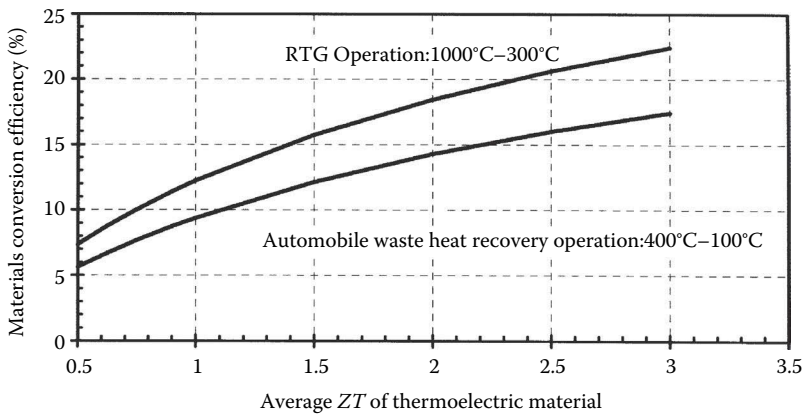


FIGURE 26.6

Maximum conversion efficiency η_{max} as a function of the average material figure of merit ZT , calculated using Equation 26.25 for two systems operating in different temperature ranges: the radioisotope generator (RTG) used for deep space missions and an automobile waste heat recovery generator.

The figure of merit can be optimized by adjusting the device geometry and minimizing the RK product. This results in Z_{pn} becoming independent of the dimensions of the thermoelectric legs. Moreover, if the p - and n -type legs have similar transport properties, the figure of merit, $Z_{pn} = Z$, can be directly related to the Seebeck coefficient S , electrical conductivity σ or resistivity ρ , and thermal conductivity λ of the thermoelectric material:

$$Z = \frac{S^2}{\rho\lambda} = \frac{S^2\sigma}{\lambda} \tag{26.24}$$

The maximum performance η_{max} of the generator is obtained by optimizing the load-to-couple-resistance ratio, leading to the maximum energy conversion efficiency expressed as

$$\eta_{max} = \frac{T_h - T_c}{T_h} \frac{\sqrt{1 + Z_{pn}T_{av}} - 1}{\sqrt{1 + Z_{pn}T_{av}} + (T_c / T_h)} \tag{26.25}$$

It must be noted that the maximum efficiency is thus the product of the Carnot efficiency, less than unity, and of a material-related efficiency, increasing with increasing Z_{pn} values as illustrated in Figure 26.6.

26.2.3.2 Refrigeration

When a current source is used to deliver electrical power to a thermoelectric device, heat can be pumped from T_1 to T_2 and the device thus operates as a refrigerator (Figure 26.5, hot side $T_h = T_2$ and cold side, $T_c = T_1$). As in the case of a thermoelectric generator the operation of a thermoelectric cooler depends solely upon the properties of the p - n thermocouple materials expressed in terms of the figure of merit Z_{pn} and the two temperatures T_c and T_h (Goldsmid 1986). The conversion efficiency or coefficient of performance, COP, of a thermoelectric refrigerator is determined by the ratio of the cooling power pumped at the cold junction to the electrical power input from the current source and is given by

$$COP = \frac{S_{pn}T_cI - (1/2)RI^2 - K(T_h - T_c)}{S_{pn}(T_h - T_c)I + RI^2} \tag{26.26}$$

There are three different modes of operation which are of interest to thermoelectric coolers. A thermoelectric cooler be designed to operate at maximum cooling power, Q_{cmax} , by optimizing the value of the current:

$$I_{Q_{cmax}} = \frac{S_{pn}T_c}{R} \quad \text{and} \quad Q_{cmax} = \frac{1}{2} \frac{(ST_c)^2}{R} - K(T_h - T_c) \tag{26.27}$$

Similarly, the conditions required for operating at maximum efficiency, COP_{max} , across a constant temperature gradient, are determined by differentiating Equation 26.26 with respect to I , with the solution:

$$I_{COP_{max}} = \frac{K(T_h - T_c)c}{S_{pn}T_{av}} (1 + \sqrt{1 + Z_{pn}T_{av}}) \tag{26.28}$$

$$COP_{max} = \frac{T_c}{T_h - T_c} - \frac{\sqrt{1 + Z_{pn}T_{av}} - (T_h/T_c)}{\sqrt{1 + Z_{pn}T_{av}} + 1} \tag{26.29}$$

By reversing the input current to the device, the thermoelectric refrigerator can become a heat pump, with T_1 being the hot junction temperature. The expression of the maximum conversion efficiency of the heat pump is very similar to Equation 26.29 because of the following relationship:

$$(COP_{max})^{heat\ pump} = 1 + (COP_{max})^{refrigerator} \tag{26.30}$$

The maximum COP expression in Equation 26.29 is similar to the one derived for the conversion efficiency η of a thermoelectric generator in Equation 26.25. However, there is a major difference between the COP_{max} and η_{max} parameters. Clearly, η_{max} increases with increasing ΔT values but is limited by the Carnot efficiency (Equation 26.22) which is less than 1, while COP_{max} in Equation 26.20 increases with decreasing ΔT values and can reach values much larger than 1. Figure 26.7 represents the variations

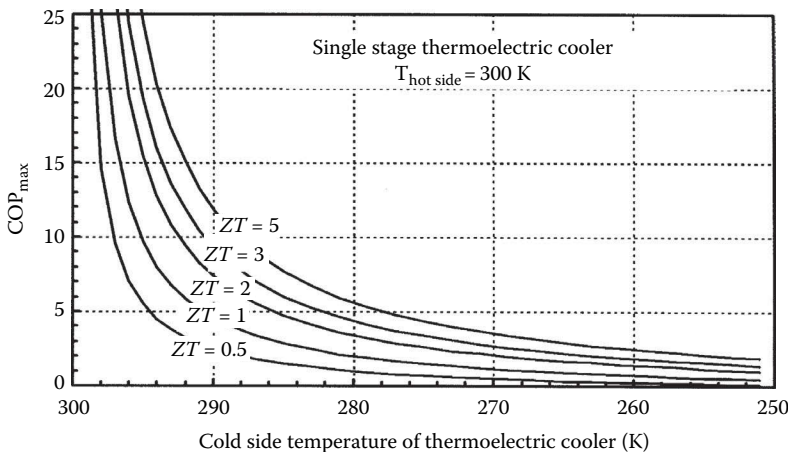


FIGURE 26.7 Maximum material coefficient of performance COP_{max} of a single-stage thermoelectric cooler calculated using Equation 26.29 as a function of the cold-side temperature (hot-side temperature of 300 K). Curves corresponding to various values of the average material figure of merit are displayed.

of the COP_{max} of a thermoelectric cooling device optimized for working voltage and geometry as a function of average ZT values and temperature differences (hot junction temperature at 300 K). The average ZT value for current state-of-the-art commercially available materials (Bi_2Te_3 -based alloys) is about 0.8. For example, it can be seen that a COP_{max} of 4 is obtained for a $(T_h - T_c)$ difference of 10 K, meaning that to pump 8 W of thermal power only 2 W of electrical power needs to be provided to the thermoelectric cooling device. This also means that 10 W of thermal power will be rejected at the hot side of the cooler.

The operation of a thermoelectric refrigerator at maximum cooling power necessitates a substantially higher input current than the operation at maximum efficiency. This is illustrated by calculating the variations of the maximum COP and cooling power with the input current and temperature difference which have been plotted in Figures 26.8 and 26.9. The calculation was based on the properties of a thermoelectric cooler using state-of-the-art Bi_2Te_3 -based alloys, and the arbitrary units are the same for both graphs. It can be seen that $I_{COP_{max}}$ increases while $I_{Q_{c,max}}$ decreases with increasing ΔT . Also, it is possible to operate at the same cooling power with two different current values.

Finally, the third problem of interest for thermoelectric coolers is to determine the maximum temperature difference, ΔT_{max} , that can be achieved across the device. As shown on Figure 26.9, by operating at maximum cooling power and extrapolating Equation 26.27 to $Q_{c,max} = 0$, ΔT_{max} is given by

$$\Delta T_{max} = \frac{1}{2} Z_{pn} T_c^2 \quad \text{and} \quad T_{cmin} = \frac{\sqrt{1 + 2Z_{pn} T_h} - 1}{Z_{pn}} \tag{26.31}$$

where T_{cmin} corresponds to the lowest cold-side temperature achievable. If the cooler operates at a ΔT close to ΔT_{max} or higher, it becomes necessary to consider a cascade arrangement with several stages. The COP of an n-stage thermoelectric cooler is optimized if the

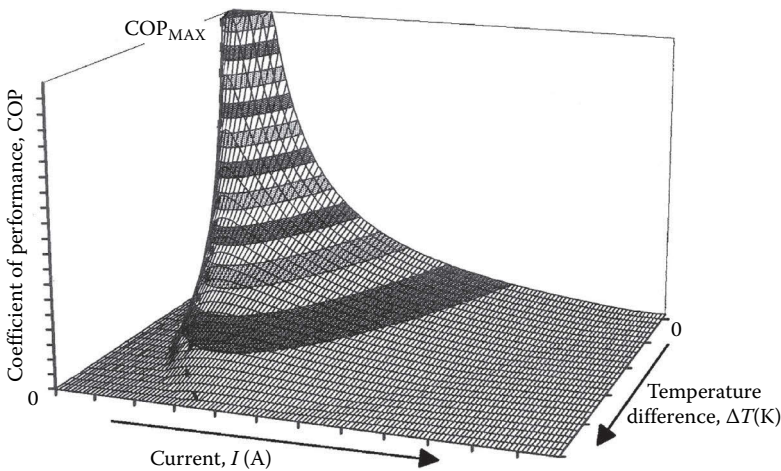


FIGURE 26.8 Three-dimensional plot of the variations of the COP of a thermoelectric cooler as a function of the operating current and the temperature difference.

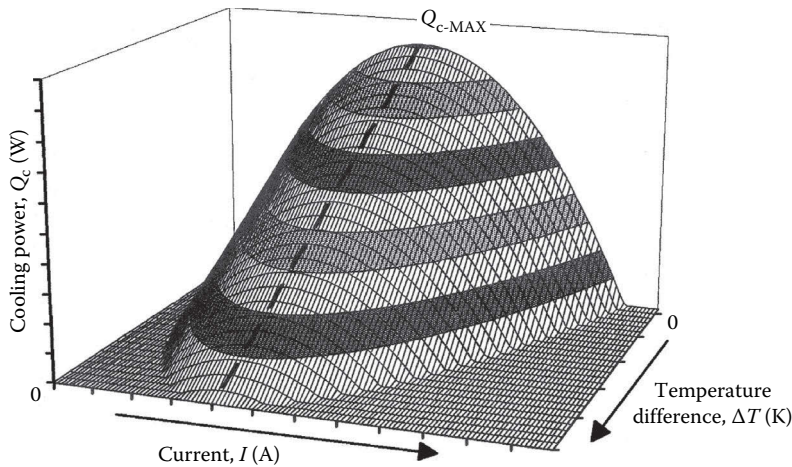


FIGURE 26.9

Three-dimensional plot of the variations of the cooling power of a thermoelectric cooler as a function of the operating current and the temperature difference.

COP of each stage, COP_i is the same, which requires $\Delta T_i/T_{i-1}$ to be the same for each stage. The overall maximum COP is then expressed as

$$\text{COP}_{\max} = \frac{1}{(\prod_{i=1}^n (1 + (1/\text{COP}_i)) - 1)} \quad (26.32)$$

Finally, a comparison of thermoelectric and thermionic refrigeration may be in order. If one assumes $ZT = 4$ is possible in thermoelectric materials and $\Phi = 0.3$ eV is possible for a thermionic emitter, it is clear that thermionic refrigeration is more than viable (Nolas and Goldsmid 1999). In both cases, practical device-related consideration will tend to lower performance; however, this simple comparison quickly reveals the need for new material developments for both technologies.

26.2.4 Additional Considerations

When considering the operation of an actual thermoelectric device, several other important parameters must be considered. The thermal and electrical contact resistances can substantially degrade the device performance, in particular for short lengths of the thermoelectric legs. For example, the conversion efficiency of a radioisotope generator system is about 20% lower than the value calculated in Figure 26.6 for the thermoelectric materials only. The electrical contact resistance arises from the connection (see Figure 26.5) of all the legs in series. Typical values obtained for actual generators and coolers are $10\text{--}25 \mu\Omega \text{ cm}^2$. The thermal contact resistance is generated by the heat-transfer characteristics of the ceramic plates and contact layers used to build the thermoelectric module. The heat exchangers and corresponding heat losses should also be taken into account. The thermoelectric material's mechanical properties also need to be taken into consideration as well as its thermal expansion in comparison with the ceramics and other materials that are in thermal contact with it. In addition, the transport properties of the thermoelectric materials vary with temperature, as illustrated in Figure 26.4a and b. When a thermoelectric device is operating across a wide temperature range, these variations should be factored into any calculation of its performance.

Nomenclature

COP	Coefficient of performance
COP_{\max}	Maximum coefficient of performance
COP_i	Coefficient of performance of the i th stage of a multistage thermoelectric cooler
I	Current intensity
$I_{COP_{\max}}$	Current intensity required to operate a thermoelectric cooler at maximum conversion efficiency
$I_{Q_{\max}}$	Current intensity required to operate a thermoelectric cooler at maximum cooling power
K	Thermal conductance
Q	Rate of reversible heat absorption
R	Electrical resistance
R_L	Load resistance
P_L	Electrical power delivered to the load resistance
S	Seebeck coefficient
S_{pn}	Seebeck coefficient of a p - n couple of thermoelements
T_1	Temperature
T_2	Temperature
T_{av}	Average temperature across the thermoelectric device
T_c	Cold-side temperature of a thermoelectric device
T_{\min}	Minimum cold-side temperature which can be achieved by a thermoelectric cooler
T_h	Hot-side temperature of a thermoelectric device
V	Voltage; open-circuit voltage
Z	Thermoelectric figure of merit
Z_{pn}	Thermoelectric figure of merit of a p - n couple of thermoelements
ZT	Dimensionless thermoelectric figure of merit
β	Thomson coefficient
β_p	Thomson coefficient for the p -type thermoelement
β_n	Thomson coefficient for the n -type thermoelement
ΔT	Temperature difference across a thermoelectric device
ΔT_{\max}	Maximum temperature difference which can be achieved across a thermoelectric cooler
η	Thermoelectric conversion efficiency
η_{\max}	Maximum thermoelectric conversion efficiency
λ	Thermal conductivity
Π_{pn}	Peltier coefficient
ρ	Electrical resistivity

Defining Terms

Coefficient of performance: Electrical to thermal energy conversion efficiency of a thermoelectric refrigerator, determined by the ratio of the cooling power pumped at the cold junction to the electrical power input from the current source.

Dimensionless figure of merit: The performance of a thermoelectric device depends solely upon the properties of the thermoelectric material, expressed in terms of the dimensionless figure of merit ZT , and the hot-side and cold-side temperatures. ZT is calculated as the square of the Seebeck coefficient times the absolute temperature divided by the product of the electrical resistivity to the thermal conductivity. The best ZT values are obtained in heavily doped semiconductors, such as Bi_2Te_3 alloys, PbTe alloys, and Si-Ge alloys.

Electron motive: A scalar quantity whose negative gradient at any point is a measure of the force exerted on an electron at that point.

Free electrons: Electrons available to be extracted from the emitter for thermionic emission.

Heat source: Electron bombardment heating of the emitter.

Lead losses: Voltage drop as a result of the built-in resistance of the leads and joints.

Particle interaction losses: Voltage drop in the interelectrode gap as a result of particle collisions and other interactions.

Stage: Multistage thermoelectric coolers are used to achieve larger temperature differences than possible with a single-stage cooler composed of only one module.

Surface work function: A measure of the electron-emitting capacity of the surface.

Thermionic energy conversion: Energy conversion from heat energy to useful electrical energy by thermionic electron emission.

Thermoelectric module: Standardized device consisting of several p- and n-type legs connected electrically in series and thermally in parallel, and bonded to a ceramic plate on each. The modules are fabricated in a great variety of sizes, shapes, and number of thermoelectric couples.

Thermoelectric leg: Single thermoelectric element made of n-type or p-type thermoelectric material used in fabricating a thermoelectric couple, the building block of thermoelectric modules. The geometry of the leg (cross-section-to-length ratio) must be optimized to maximize the performance of the device.

References

- Angrist, S. W. 1976. *Direct Energy Conversion*. 3rd edn. Allyn and Bacon, Boston, MA.
- Fowler, R. H. 1955. *Statistical Mechanics*. 2nd edn. Cambridge University Press, New York.
- Hatsopoulos, G. N. and Gyftopoulos, E. P. 1973. *Thermionic Energy Conversion*, Vol. 1, MIT Press, Cambridge, MA.
- Goldsmid, H. J. 1986. *Electronic Refrigeration*. Pion Ltd., London, U.K.
- Hannan, T. C. and Honig, J. M. 1967. *Thermoelectric and Thermomagnetic Effects and Applications*. McGraw-Hill, New York.
- Houston, J. M. 1959. Theoretical efficiency of the thermionic energy converter. *J. Appl. Phys.*, 30, 481–487.
- Koumoto, K. and Mori, T. (Eds.) 2013. *Thermoelectric Nanomaterials*. Springer, Heidelberg, Germany.
- Langmuir, I. and Kingdon, K. H. 1925. Thermionic effects caused by vapors of alkali metals. *Proc. R. Soc. Lond. A*, 107, 61–79.

- Nolas, G. S. and Goldsmid, H. J. 1999. A comparison of projected thermoelectric and thermionic refrigerators. *J. Appl. Phys.*, 85/8, 4066.
- Nolas, G. S., Sharp, J. W., and Goldsmid, H. J. 2001. *Thermoelectrics: Basics Principles and New Materials Developments*. Springer, Heidelberg, Germany.
- Ramalingam, M. L. and Young, T. J. 1993. The power of thermionic energy conversion. *Mech. Eng.*, 115 (9), 78–83.
- Richardson, O. W. 1912. Some applications of the electron theory of matter. *Philos. Mag.*, 23, 594–626.
- Rowe, D. M. (Ed.) 2012. *CRC Handbook on Thermoelectrics and Its Energy Harvesting on Materials, Preparation and Characterization*. Taylor & Francis, Boca Raton, FL.
- Rowe, D. M. and Bhandari, C. M. 1983. *Modern Thermoelectrics*. Reston Publishing, Reston, VA.
- Taylor, J. B. and Langmuir, I. 1933. The evaporation of atoms, ions and electrons from cesium films on tungsten. *Phys. Rev.*, 44, 423–458.
- Young, T. J., Thayer, K. L., and Ramalingam, M. L. 1993. Performance simulation of an advanced cylindrical thermionic fuel element with a graphite reservoir. Presented at *28th AIAA Thermophysics Conference*, Orlando, FL.

For Further Information

- Cayless, M. A. 1961. Thermionic generation of electricity. *Br. J. Appl. Phys.*, 12, 433–442.
- Hatsopoulos, G. N. and Gryftopoulos, E. P. 1979. *Thermionic Energy Conversion*. Vol. 2. MIT Press, Cambridge, MA.
- Hernquist, K. G., Kanefsky, M., and Norman, F. H. 1959. Thermionic energy converter. *RCA Rev.*, 19, 244–258.
- Ramalingam, M. L. 1993. The advanced single cell thermionic converter program, WL-TR-93-2112, USAF Technical Report, Dayton, OH.
- Rasor, N. S. 1960. Figure of merit for thermionic energy conversion. *J. Appl. Phys.*, 31, 163–167.
- The *Proceedings of the Annual International Conference on Thermoelectrics* are published annually by the International Thermoelectric Society (ITS). These proceedings provide the latest information on thermoelectric materials research and development as well as thermoelectric devices and systems. The ITS also publishes a semiannual newsletter. For ITS membership or questions related to thermoelectrics, you may contact the current ITS secretary: Dr. Jean-Pierre Fleurial, Jet Propulsion Laboratory, MS 277–212, Pasadena, CA 91109. Phone (818)-354–4144. Fax (818) 393–6951. E-mail jean-pierre.fleurial@jpl.nasa.gov
- Rowe, D. M. 1996. *CRC Handbook of Thermoelectrics*. CRC Press Inc., Boca Raton, FL, became available in 1996. This handbook covers all current activities in thermoelectrics.



Taylor & Francis

Taylor & Francis Group

<http://taylorandfrancis.com>

Appendix A: The International System of Units, Fundamental Constants, and Conversion Factors

Nitin Goel

The International system of units (SI) is based on seven base units. Other derived units can be related to these base units through governing equations. The base units with the recommended symbols are listed in Table A.1. Derived units of interest in solar engineering are given in Table A.2.

Standard prefixes can be used in the SI system to designate multiples of the basic units and thereby conserve space. The standard prefixes are listed in Table A.3.

Table A.4 lists some physical constants that are frequently used in solar engineering, together with their values in the SI system of units.

Conversion factors between the SI and English systems for commonly used quantities are given in Table A.5.

TABLE A.1

The Seven SI Base Units

Quantity	Name of Unit	Symbol
Length	Meter	m
Mass	Kilogram	kg
Time	Second	s
Electric current	Ampere	A
Thermodynamic temperature	Kelvin	K
Luminous intensity	Candela	cd
Amount of a substance	Mole	mol

TABLE A.2

SI Derived Units

Quantity	Name of Unit	Symbol
Acceleration	Meters per second squared	m/s^2
Area	Square meters	m^2
Density	Kilogram per cubic meter	kg/m^3
Dynamic viscosity	Newton-second per square meter	N s/m^2
Force	Newton (= 1 kg m/s ²)	N
Frequency	Hertz	Hz
Kinematic viscosity	Square meter per second	m^2/s
Plane angle	Radian	rad
Potential difference	Volt	V
Power	Watt (= 1 J/s)	W
Pressure	Pascal (= 1 N/m ²)	Pa
Radiant intensity	Watts per steradian	W/sr
Solid angle	Steradian	sr
Specific heat	Joules per kilogram–Kelvin	J/kg K
Thermal conductivity	Watts per meter–Kelvin	W/m K
Velocity	Meters per second	m/s
Volume	Cubic meter	m^3
Work, energy, heat	Joule (= 1 N/m)	J

TABLE A.3

English Prefixes

Multiplier	Symbol	Prefix	Multiplier	Multiplier Symbol
10^{12}	T	Tera	10^3	M (thousand)
10^9	G	Giga	10^6	MM (million)
10^6	m	Mega		
10^3	k	Kilo		
10^2	h	Hecto		
10^1	da	Deka		
10^{-1}	d	Deci		
10^{-2}	c	Centi		
10^{-3}	m	Milli		
10^{-6}	μ	Micro		
10^{-9}	n	Nano		
10^{-12}	p	Pico		
10^{-15}	f	Femto		
10^{-18}	a	Atto		

TABLE A.4

Physical Constants in SI Units

Quantity	Symbol	Value
Avogadro constant	N	$6.022169 \times 10^{26} \text{ kmol}^{-1}$
Boltzmann constant	k	$1.380622 \times 10^{-23} \text{ J/K}$
First radiation constant	$C_1 = 2\pi^5 h^6 C^2$	$3.741844 \times 10^{-16} \text{ Wm}^2$
Gas constant	R	$8.31434 \times 10^3 \text{ J/kmol K}$
Planck constant	h	$6.626196 \times 10^{-34} \text{ Js}$
Second radiation constant	$C_2 = hc/k$	$1.438833 \times 10^{-2} \text{ m K}$
Speed of light in a vacuum	C	$2.997925 \times 10^8 \text{ m/s}$
Stefan–Boltzmann constant	σ	$5.66961 \times 10^{-8} \text{ W/m}^2 \text{ K}^4$

TABLE A.5
Conversion Factors

Physical Quantity	Symbol	Conversion Factor
Area	A	1 ft ² = 0.0929 m ²
		1 acre = 43,560 ft ² = 4047 m ²
		1 hectare = 10,000 m ²
		1 square mile = 640 acres
Density	ρ	1 lb _m /ft ³ = 16.018 kg/m ³
Heat, energy, or work	Q or W	1 Btu = 1055.1 J
		1 kWh = 3.6 MJ
		1 Therm = 105.506 MJ
		1 cal = 4.186 J
Force	F	1 ft lb _f = 1.3558 J
		1 lb _f = 4.448 N
Heat flow rate, refrigeration	q	1 Btu/h = 0.2931 W
		1 ton (refrigeration) = 3.517 kW
		1 Btu/s = 1055.1 W
Heat flux	q/A	1 Btu/h ft ² = 3.1525 W/m ²
Heat-transfer coefficient	h	1 Btu/h ft ² F = 5.678 W/m ² K
Length	L	1 ft = 0.3048 m
		1 in. = 2.54 cm
		1 mi = 1.6093 km
		1 lb _m = 0.4536 kg
Mass	m	1 ton = 2240 lb _m
		1 tonne (metric) = 1000 kg
Mass flow rate		1 lb _m /h = 0.000126 kg/s
Power		1 hp = 745.7 W
		1 kW = 3415 Btu/h
		1 ft lb _f /s = 1.3558 W
		1 Btu/h = 0.293 W
Pressure	p	1 lb _f /in. ² (psi) = 6894.8 Pa (N/m ²)
		1 in. Hg = 3,386 Pa
		1 atm = 101,325 Pa (N/m ²) = 14.696 psi
Radiation	l	1 langley = 41,860 J/m ²
		1 langley/min = 697.4 W/m ²
Specific heat capacity	c	1 Btu/lb _m °F = 4187 J/kgK
Internal energy or enthalpy	e or h	1 Btu/lb _m = 2326.0 J/kg
		1 cal/g = 4184 J/kg
Temperature	T	T (°R) = (9/5)T (K)
		T (°F) = [T (°C)](9/5) + 32
		T (°F) = [T (K) - 273.15](9/5) + 32
Thermal conductivity	k	1 Btu/h ft °F = 1.731 W/m K
Thermal resistance	R _{th}	1 h °F/Btu = 1.8958 K/W
Velocity	V	1 ft/s = 0.3048 m/s
		1 mi/h = 0.44703 m/s

(Continued)

TABLE A.5 (Continued)

Conversion Factors

Physical Quantity	Symbol	Conversion Factor
Viscosity, dynamic		1 lb _m /ft s = 1.488 Ns/m ²
		1 cP = 0.00100 Ns/m ²
Viscosity, kinematic	ν	1 ft ² /s = 0.09029 m ² /s
		1 ft ² /h = 2.581 × 10 ⁻⁵ m ² /s
Volume	V	1 ft ³ = 0.02832 m ³ = 28.32 L
		1 barrel = 42 gal (U.S.)
		1 gal (U.S. liq.) = 3.785 L
		1 gal (U.K.) = 4.546 L
Volumetric flow rate	\dot{Q}	1 ft ³ /min (cfia) = 0.000472 m ³ /s
		1 gal/min (GPM) = 0.0631 L/s



Taylor & Francis

Taylor & Francis Group

<http://taylorandfrancis.com>

Appendix B: Solar Radiation Data

Nitin Goel

The altitude and azimuth of the sun are given by

$$\sin \alpha = \sin L \sin \delta_s + \cos \phi \cos \delta_s \cos h_s \quad (\text{A2.1})$$

and

$$\sin a_s = -\frac{\cos \delta_s \sin h_s}{\cos \alpha} \quad (\text{A2.2})$$

where

α is the altitude of the sun (angular elevation above the horizon)

L is the latitude of the observer

δ_s is the declination of the sun

h_s is the hour angle of sun (angular distance from the meridian of the observer)

a_s is the azimuth of the sun (measured eastward from north)

From Equations A2.1 and A2.2 it can be seen that the altitude and azimuth of the sun are functions of the latitude of the observer, the time of day (hour angle), and the date (declination).

Figure A2.1b through g provides a series of charts, one for each 5° of latitude (except 5°, 15°, 75°, and 85°) giving the altitude and azimuth of the sun as a function of the true solar time and the declination of the sun in a form originally suggested by Hand. Linear interpolation for intermediate latitudes will give results within the accuracy to which the charts can be read.

On these charts, a point corresponding to the projected position of the sun is determined from the heavy lines corresponding to declination and solar time.

To find the solar altitude and azimuth:

1. Select the chart or charts appropriate to the latitude.
2. Find the solar declination δ corresponding to the date.
3. Determine the true solar time as follows:
 - a. To the *local standard time* (zone time) add 4' for each degree of longitude the station is east of the standard meridian or subtract 4' for each degree west of the standard meridian to get the *local mean solar time*.
 - b. To the *local mean solar time* add algebraically the equation of time; the sum is the required *true solar time*.
4. Read the required altitude and azimuth at the point determined by the declination and the true solar time. Interpolate linearly between two charts for intermediate latitudes.

It should be emphasized that the solar altitude determined from these charts is the true geometric position of the center of the sun. At low solar elevations terrestrial refraction may considerably alter the apparent position of sun. Under average atmospheric refraction the sun will appear on the horizon when it actually is about 34' below the horizon; the effect of refraction decreases rapidly with increasing solar elevation. Since sunset or sunrise is defined as the time when the upper limb of the sun appears on the horizon, and the semi-diameter of the sun is 16', sunset or sunrise occurs under average atmospheric refraction when the sun is 50' below the horizon. In polar regions especially, unusual atmospheric refraction can make considerable variation in the time of sunset or sunrise.

The 90°N chart is included for interpolation purposes; the azimuths lose their directional significance at the pole.

Altitude and azimuth in southern latitudes: To compute solar altitude and azimuth for southern latitudes, change the sign of the solar declination and proceed as above. The resulting azimuths will indicate angular distance from *south* (measured eastward) rather than from north.

(a)

FIGURE A2.1

Description of method for calculating true solar time, together with accompanying meteorological charts, for computing solar-altitude and azimuth angles, (a) Description of method. (Continued)

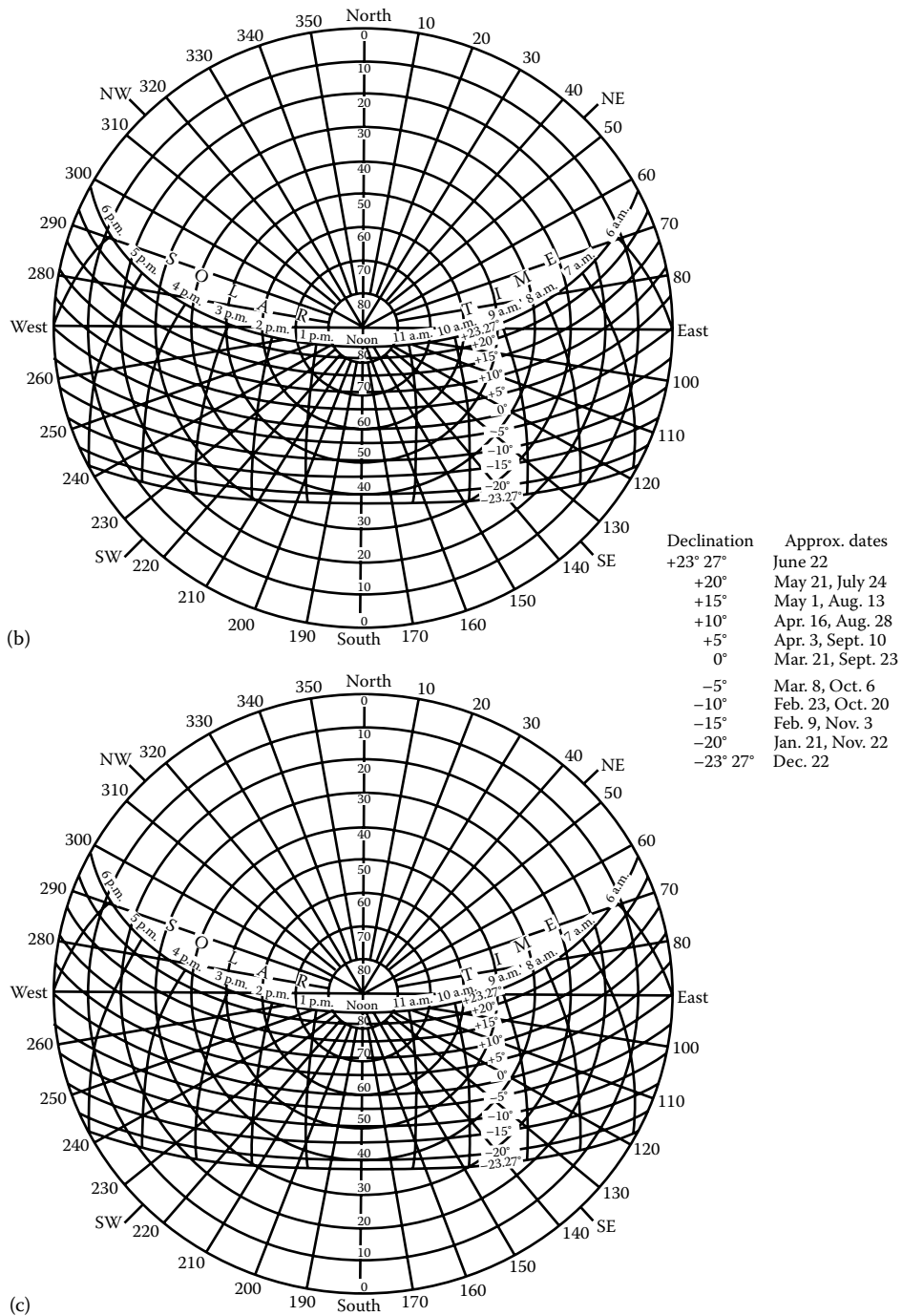


FIGURE A2.1 (Continued)
 Description of method for calculating true solar time, together with accompanying meteorological charts, for computing solar-altitude and azimuth angles, (b) chart, 25°N latitude; (c) chart, 30°N latitude. (Continued)

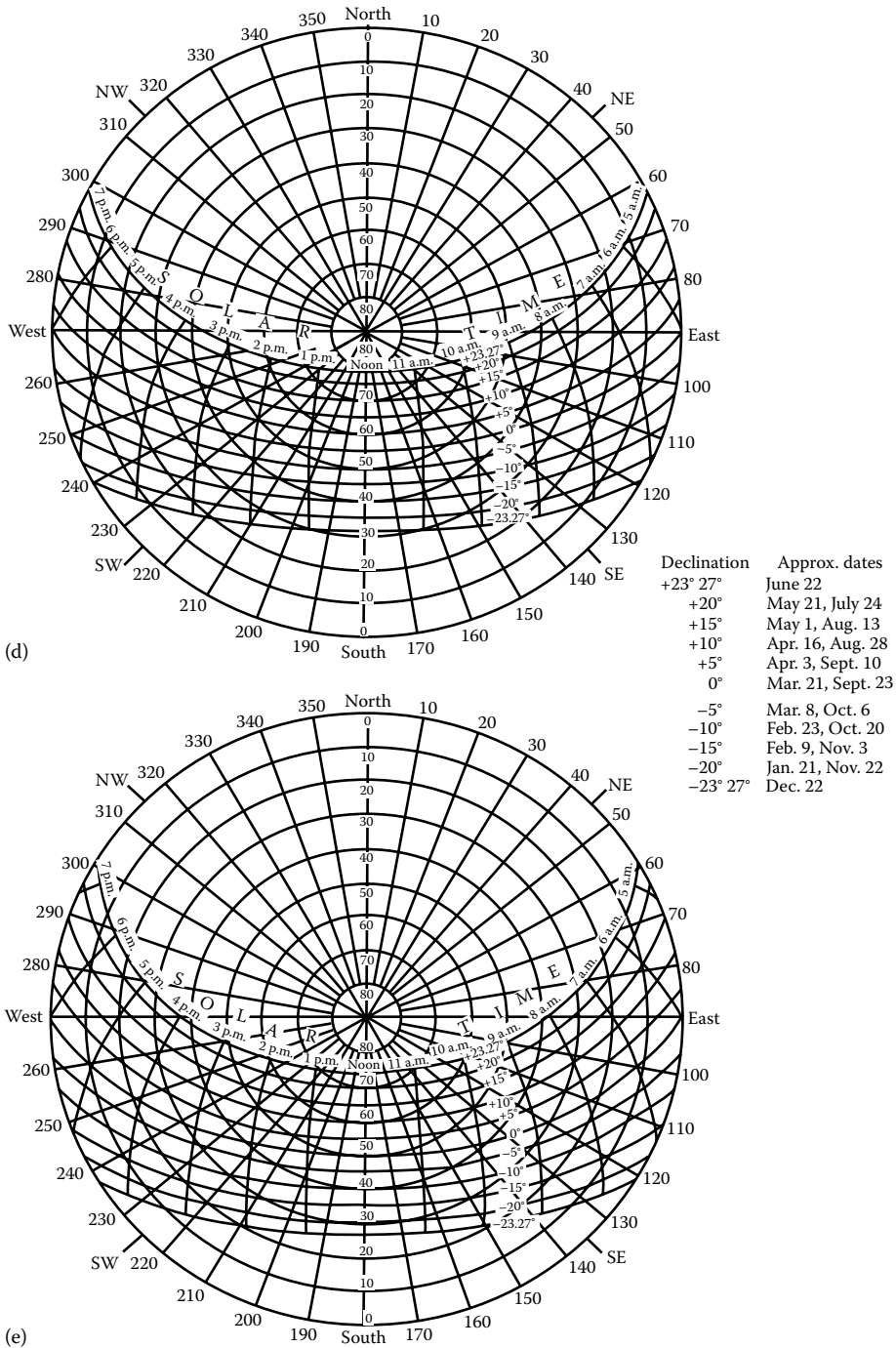


FIGURE A2.1 (Continued)

Description of method for calculating true solar time, together with accompanying meteorological charts, for computing solar-altitude and azimuth angles, (d) chart, 35°N latitude; (e) chart, 40°N latitude; (f) chart, 45°N latitude; (g) chart, 50°N latitude. (Continued)

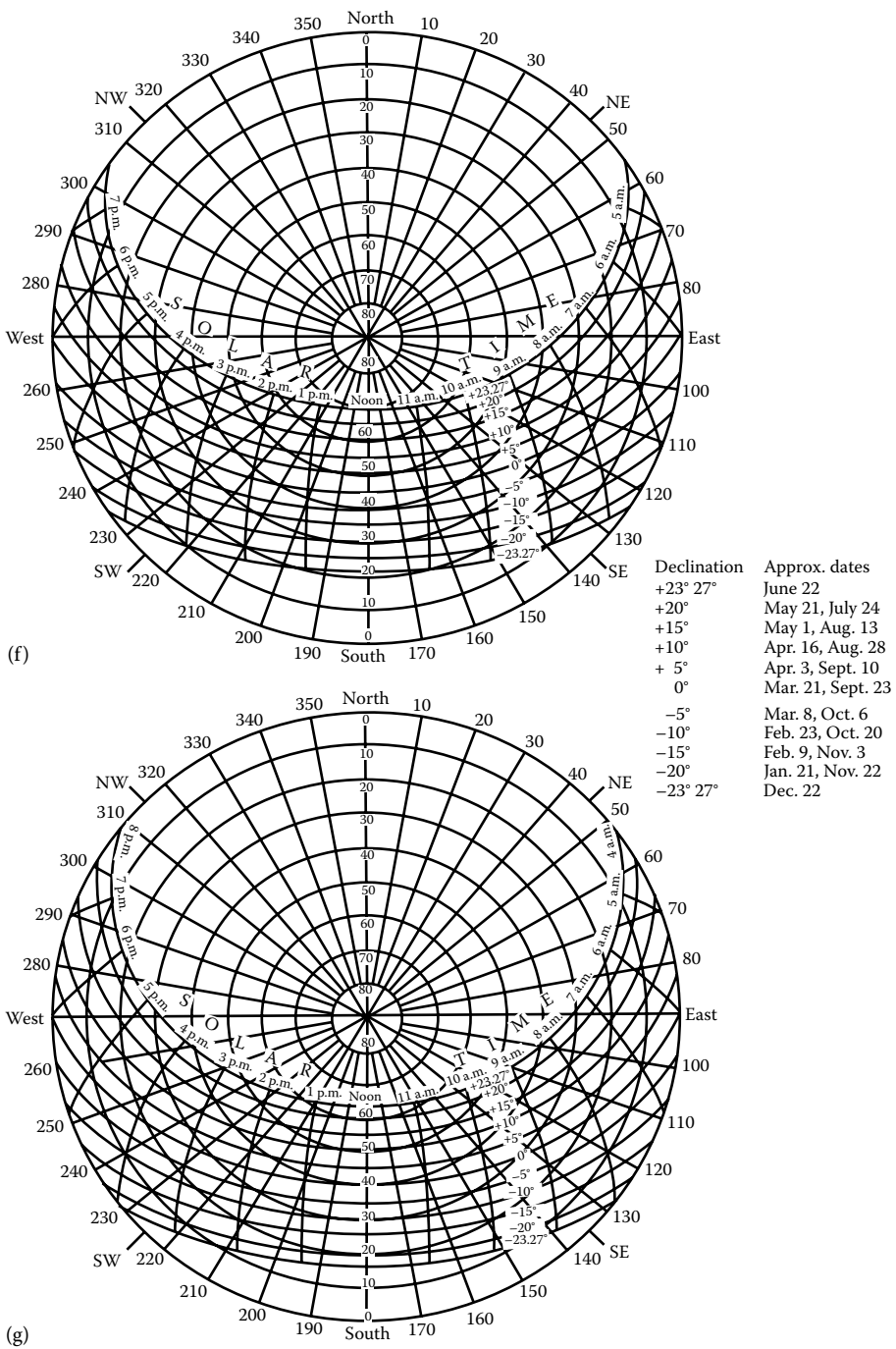


FIGURE A2.1 (Continued)

Description of method for calculating true solar time, together with accompanying meteorological charts, for computing solar-altitude and azimuth angles, (f) chart, 45°N latitude; (g) chart, 50°N latitude. (Description and charts reproduced from the "Smithsonian Meteorological Tables" with permission from the Smithsonian Institute, Washington, DC.)

(Continued)

TABLE A2.1

Solar Irradiance for Different Air Masses

Wavelength	Air Mass; $\alpha = 0.66$; $\beta = 0.085^a$				
	0	1	4	7	10
0.290	482.0	0.0	0.0	0.0	0.0
0.295	584.0	0.0	0.0	0.0	0.0
0.300	514.0	4.1	0.0	0.0	0.0
0.305	603.0	11.4	0.0	0.0	0.0
0.310	689.0	30.5	0.0	0.0	0.0
0.315	764.0	79.4	0.1	0.0	0.0
0.320	830.0	202.6	2.9	0.0	0.0
0.325	975.0	269.5	5.7	0.1	0.0
0.330	1059.0	331.6	10.2	0.3	0.0
0.335	1081.0	383.4	17.1	0.8	0.0
0.340	1074.0	431.3	24.9	1.8	0.1
0.345	1069.0	449.2	33.3	2.5	0.2
0.350	1093.0	480.5	40.8	3.5	0.3
0.355	1083.0	498.0	48.4	4.7	0.5
0.360	1068.0	513.7	57.2	6.4	0.7
0.365	1132.0	561.3	68.4	8.3	1.0
0.370	1181.0	603.5	80.5	10.7	1.4
0.375	1157.0	609.4	89.0	13.0	1.9
0.380	1120.0	608.0	97.2	15.6	2.5
0.385	1098.0	609.8	104.5	17.9	3.1
0.390	1098.0	623.9	114.5	21.0	3.9
0.395	1189.0	691.2	135.8	26.7	5.2
0.400	1429.0	849.9	178.8	37.6	7.9
0.405	1644.0	992.8	218.7	48.2	10.6
0.410	1751.0	1073.7	247.5	57.1	13.2
0.415	1774.0	1104.5	266.5	64.3	15.5
0.420	1747.0	1104.3	278.9	70.4	17.8
0.425	1693.0	1086.5	287.2	78.9	20.1
0.430	1639.0	1067.9	295.4	81.7	22.6
0.435	1663.0	1100.1	318.4	92.2	26.7
0.440	1810.0	1215.5	368.2	111.5	33.8
0.445	1922.0	1310.4	415.3	131.6	41.7
0.450	2006.0	1388.4	460.3	152.6	50.6
0.455	2057.0	1434.8	486.9	165.2	56.1
0.460	2066.0	1452.2	504.4	175.2	60.8
0.465	2048.0	1450.7	515.7	183.3	65.1
0.470	2033.0	1451.2	527.9	192.0	69.8
0.475	2044.0	1470.3	547.3	203.7	75.8
0.480	2074.0	1503.4	572.6	218.1	83.1
0.485	1976.0	1443.3	562.4	219.2	85.4
0.490	1950.0	1435.2	572.2	228.2	91.0
0.495	1960.0	1453.6	592.9	241.9	98.7
0.500	1942.0	1451.2	605.6	252.7	105.5

(Continued)

TABLE A2.1 (Continued)

Solar Irradiance for Different Air Masses

Wavelength	Air Mass; $\alpha = 0.66$; $\beta = 0.085^a$				
	0	1	4	7	10
0.505	1920.0	1440.1	607.6	256.4	108.2
0.510	1882.0	1416.8	604.4	257.8	110.0
0.515	1833.0	1384.9	597.3	257.6	111.1
0.520	1833.0	1390.0	606.1	264.3	115.2
0.525	1852.0	1409.5	621.3	273.9	120.7
0.530	1842.0	1406.9	626.9	279.4	124.5
0.535	1818.0	1393.6	627.7	282.8	127.4
0.540	1783.0	1371.7	624.5	284.4	129.5
0.545	1754.0	1354.2	623.2	286.8	132.0
0.550	1725.0	1336.6	621.7	289.2	134.5
0.555	1720.0	1335.7	625.5	293.0	137.3
0.560	1695.0	1319.2	622.0	293.3	138.3
0.565	1705.0	1330.0	631.3	299.6	142.2
0.570	1712.0	1338.4	639.5	305.6	146.0
0.575	1719.0	1346.9	647.8	311.6	149.6
0.580	1715.0	1346.7	652.0	315.7	152.8
0.585	1712.0	1347.3	656.6	320.0	156.0
0.590	1700.0	1340.7	657.7	322.6	158.3
0.595	1682.0	1329.4	656.4	324.1	160.0
0.600	1660.0	1319.6	655.8	325.9	162.0
0.605	1647.0	1311.0	661.3	333.6	168.2
0.610	1635.0	1307.9	669.6	342.8	175.5
0.620	1602.0	1294.2	682.4	359.9	189.7
0.630	1570.0	1280.9	695.6	377.8	205.2
0.640	1544.0	1272.1	711.4	397.9	222.5
0.650	1511.0	1257.1	723.9	416.9	240.1
0.660	1486.0	1244.2	730.2	428.6	251.6
0.670	1456.0	1226.8	733.8	438.9	262.5
0.680	1427.0	1209.9	737.4	449.5	273.9
0.690	1402.0	1196.2	742.9	461.3	286.5
0.698	1374.6	1010.3	546.1	311.8	181.6
0.700	1369.0	1175.3	743.7	470.6	297.7
0.710	1344.0	1157.4	739.2	472.1	301.5
0.720	1314.0	1135.1	731.7	471.6	304.0
0.728	1295.5	1003.1	582.3	351.7	212.5
0.730	1290.0	1117.8	727.1	479.0	307.7
0.740	1260.0	1095.1	718.9	471.9	309.8
0.750	1235.0	1076.6	713.2	472.4	313.0
0.762	1205.5	794.0	357.1	163.6	69.1
0.770	1185.0	1039.2	700.8	472.7	318.8
0.780	1159.0	1019.4	693.6	472.0	321.1
0.790	1134.0	1000.3	686.7	471.4	323.6
0.800	1109.0	981.2	679.4	470.5	325.8

(Continued)

TABLE A2.1 (Continued)

Solar Irradiance for Different Air Masses

Wavelength	Air Mass; $\alpha = 0.66$; $\beta = 0.085^a$				
	0	1	4	7	10
0.806	1095.1	874.4	547.7	355.9	234.4
0.825	1048.0	931.6	654.3	459.6	322.8
0.830	1036.0	921.8	649.3	457.3	322.1
0.835	1024.5	912.4	644.4	455.2	321.5
0.846	998.1	476.2	181.0	85.9	44.2
0.860	968.0	506.4	212.0	107.4	58.3
0.870	947.0	453.8	174.7	84.0	43.8
0.875	436.5	449.2	173.4	83.6	43.7
0.887	912.5	448.6	178.3	87.7	46.7
0.900	891.0	448.9	183.7	92.3	50.0
0.907	882.8	455.2	190.9	97.6	53.7
0.915	874.5	461.5	198.5	103.2	57.5
0.925	863.5	279.0	73.6	28.0	12.1
0.930	858.0	221.8	46.9	15.4	6.0
0.940	847.0	313.4	95.0	39.6	18.5
0.950	837.0	296.5	86.3	35.0	16.0
0.955	828.5	321.1	102.3	44.1	21.2
0.965	811.5	344.4	120.4	55.1	27.8
0.975	794.0	576.9	346.0	224.6	150.1
0.985	776.0	544.6	316.1	201.2	132.4
1.018	719.2	617.5	391.0	247.5	156.7
1.082	620.0	512.9	290.4	164.4	93.1
1.094	602.0	464.1	303.1	210.8	149.9
1.098	596.0	503.7	304.1	183.6	110.9
1.101	591.8	504.8	362.7	267.3	198.8
1.128	560.5	135.1	27.7	9.1	3.6
1.131	557.0	152.2	35.3	12.6	5.3
1.137	550.1	143.1	31.7	11.0	4.5
1.144	542.0	191.2	57.4	24.2	11.6
1.147	538.5	174.5	48.2	19.3	8.8
1.178	507.0	399.3	195.1	95.4	46.6
1.189	496.0	402.2	214.5	114.4	61.0
1.193	492.0	424.0	310.8	233.3	176.6
1.222	464.3	391.8	235.3	141.3	84.9
1.236	451.2	390.8	254.1	165.2	107.4
1.264	426.5	329.2	209.7	140.0	94.3
1.276	416.7	342.6	238.6	172.6	126.3
1.288	406.8	347.3	216.1	134.4	83.7
1.314	386.1	298.3	137.6	63.5	29.3
1.335	369.7	190.6	85.0	46.7	27.7
1.384	343.7	5.7	0.1	0.0	0.0
1.432	321.0	44.6	5.4	1.3	0.4
1.457	308.6	85.4	20.6	7.7	3.3

(Continued)

TABLE A2.1 (Continued)

Solar Irradiance for Different Air Masses

Wavelength	Air Mass; $\alpha = 0.66$; $\beta = 0.085^a$				
	0	1	4	7	10
1.472	301.4	77.4	17.4	6.2	2.6
1.542	270.4	239.3	165.9	115.0	79.7
1.572	257.3	222.6	168.1	130.4	102.1
1.599	245.4	216.0	166.7	131.5	104.5
1.608	241.5	208.5	157.4	122.1	95.7
1.626	233.6	206.7	160.7	127.5	101.9
1.644	225.6	197.9	152.4	120.1	95.5
1.650	223.0	195.7	150.9	119.1	94.7
1.676	212.1	181.9	114.8	72.4	45.7
1.732	187.9	161.5	102.5	65.1	41.3
1.782	166.6	136.7	75.6	41.8	23.1
1.862	138.2	4.0	0.1	0.0	0.0
1.955	112.9	42.7	14.5	6.8	3.6
2.008	102.0	69.4	35.8	17.7	6.4
2.014	101.2	74.7	45.5	28.8	17.8
2.057	95.6	69.5	41.3	25.3	14.8
2.124	87.4	70.0	35.9	18.4	9.5
2.156	83.8	66.0	32.3	15.8	7.7
2.201	78.9	66.1	49.1	38.0	29.7
2.266	72.4	61.6	46.8	36.8	29.3
2.320	67.6	57.2	43.2	33.8	26.8
2.338	66.3	54.7	39.9	30.4	23.4
2.356	65.1	52.0	36.3	26.5	19.6
2.388	62.8	36.0	18.7	11.7	7.8
2.415	61.0	32.5	15.8	9.4	6.0
2.453	58.3	29.6	13.7	7.9	5.0
2.494	55.4	20.3	6.8	3.2	1.7
2.537	52.4	4.6	0.4	0.1	0.0
2.900	35.0	2.9	0.2	0.0	0.0
2.941	33.4	6.0	1.0	0.3	0.1
2.954	32.8	5.7	0.9	0.3	0.1
2.973	32.1	8.7	2.2	0.9	0.4
3.005	30.8	7.8	1.8	0.7	0.3
3.045	28.8	4.7	0.7	0.2	0.1
3.056	28.2	4.9	0.8	0.2	0.1
3.097	26.2	3.2	0.4	0.1	0.0
3.132	24.9	6.8	1.7	0.7	0.3
3.156	24.1	18.7	12.6	8.9	6.3
3.204	22.5	2.1	0.2	0.0	0.0
3.214	22.1	3.4	0.5	0.1	0.0
3.245	21.1	3.9	0.7	0.2	0.1
3.260	20.6	3.7	0.6	0.2	0.1
3.285	19.7	14.2	8.5	5.1	2.8

(Continued)

TABLE A2.1 (Continued)

Solar Irradiance for Different Air Masses

Wavelength	Air Mass; $\alpha = 0.66$; $\beta = 0.085^a$				
	0	1	4	7	10
3.317	18.8	12.9	6.9	3.5	1.3
3.344	18.1	4.2	0.9	0.3	0.1
3.403	16.5	12.3	7.8	5.1	3.2
3.450	15.6	12.5	8.9	6.7	5.0
3.507	14.5	12.5	9.9	8.1	6.7
3.538	14.2	11.8	8.8	6.9	5.5
3.573	13.8	10.9	5.4	2.6	1.3
3.633	13.1	10.8	8.3	6.7	5.5
3.673	12.6	9.1	6.1	4.6	3.5
3.696	12.3	10.4	8.2	6.7	5.6
3.712	12.2	10.9	9.0	7.6	6.5
3.765	11.5	9.5	7.2	5.9	4.8
3.812	11.0	8.9	6.7	5.4	4.4
3.888	10.4	8.1	5.6	4.0	2.9
3.923	10.1	8.0	5.6	4.2	3.1
3.948	9.9	7.8	5.5	4.0	3.0
4.045	9.1	6.7	4.1	2.6	1.5
Total Wm^3	1353	889.2	448.7	255.2	153.8

Source: From Thekaekara, M. P. 1974. *The Energy Crisis and Energy from the Sun*, Institute for Environmental Sciences.

W/m^2 μm ; H_2O 20 mm; O_3 3.4 mm.

^a The parameters α and β are measures of turbidity of the atmosphere. They are used in the atmospheric transmittance equation C1 includes Rayleigh and ozone attenuation.

TABLE A2.2Monthly Averaged, Daily Extraterrestrial Insolation on a Horizontal Surface (Units: Wh/m²)

Latitude (deg)	January	February	March	April	May	June	July	August	September	October	November	December
20	7415	8397	9552	10,422	10,801	10,868	10,794	10,499	9791	8686	7598	7076
25	6656	7769	9153	10,312	10,936	11,119	10,988	10,484	9494	8129	6871	6284
30	5861	7087	8686	10,127	11,001	11,303	11,114	10,395	9125	7513	6103	5463
35	5039	6359	8153	9869	10,995	11,422	11,172	10,233	8687	6845	5304	4621
40	4200	5591	7559	9540	10,922	11,478	11,165	10,002	8184	6129	4483	3771
45	3355	4791	6909	9145	10,786	11,477	11,099	9705	7620	5373	3648	2925
50	2519	3967	6207	8686	10,594	11,430	10,981	9347	6998	4583	2815	2100
55	1711	3132	5460	8171	10,358	11,352	10,825	8935	6325	3770	1999	1320
60	963	2299	4673	7608	10,097	11,276	10,657	8480	5605	2942	1227	623
65	334	1491	3855	7008	9852	11,279	10,531	8001	4846	2116	544	97

TABLE A2.3

Worldwide Global Horizontal Average Solar Radiation (Units: MJ/sq. m-day)

Position	Lat	Long	January	February	March	April	May	June	July	August	September	October	November	December
<i>Argentina</i>														
Buenos Aires	34.58 S	58.48 W	24.86	21.75	18.56	11.75	8.71	7.15	7.82	8.75	14.49	16.66	24.90	21.93
<i>Australia</i>														
Adelaide	34.93 S	138.52 E	20.99	17.50	20.15	18.27	17.98	—	18.81	19.64	20.11	20.88	20.57	20.72
Brisbane	27.43 S	153.08 E	25.36	22.22	13.25	16.61	12.23	11.52	9.70	15.10	17.61	19.89	—	—
Canberra	35.30 S	148.18 E	28.20	24.68	20.56	14.89	10.29	6.62	—	12.33	16.88	24.06	26.00	25.77
Darwin	12.47 S	130.83 E	26.92	23.40	18.13	13.62	9.30	7.89	9.41	11.15	14.85	18.87	23.43	22.34
Hobart	42.88 S	147.32 E	—	—	—	10.09	7.26	6.04	5.72	9.21	13.54	18.12	—	—
Laverton	37.85 S	114.08 E	22.96	20.42	15.59	13.40	7.48	6.10	6.54	10.43	13.24	18.76	—	—
Sydney	33.87 S	151.20 E	21.09	21.75	17.63	13.63	9.78	8.79	7.62	12.84	16.93	22.10	—	—
<i>Austria</i>														
Wien	48.20 N	16.57 E	3.54	7.10	8.05	14.72	16.79	20.87	19.89	17.27	12.55	8.45	3.51	2.82
Innsbruck	47.27 N	11.38 E	5.57	9.28	10.15	15.96	14.57	17.65	18.35	17.26	12.98	9.08	4.28	3.50
<i>Barbados</i>														
Husbands	13.15 N	59.62 W	19.11	20.23	—	21.80	19.84	20.86	21.55	22.14	—	—	18.30	16.56
<i>Belgium</i>														
Ostende	51.23 N	2.92 E	2.82	5.75	9.93	15.18	16.74	16.93	18.21	18.29	11.71	6.15	2.69	1.97
Melle	50.98 N	3.83 E	2.40	4.66	8.41	13.55	14.23	13.28	15.71	15.61	10.63	5.82	2.40	1.59
<i>Brunei</i>														
Brunei	4.98 N	114.93 E	19.46	20.12	22.71	20.54	19.74	18.31	19.38	20.08	20.83	17.51	17.39	18.12
<i>Bulgaria</i>														
Chirpan	42.20 N	25.33 E	6.72	6.79	8.54	13.27	17.25	17.39	19.85	14.61	12.53	8.52	5.08	5.09
Sofia	42.65 N	23.38 E	4.05	6.23	7.93	9.36	12.98	19.73	19.40	17.70	14.71	6.44	—	3.14
<i>Canada^a</i>														
Montreal	45.47 N	73.75 E	4.74	8.33	11.84	10.55	15.05	22.44	21.08	18.67	14.83	9.18	4.04	4.01
Ottawa	45.32 N	75.67 E	5.34	9.59	13.33	13.98	20.18	20.34	19.46	17.88	13.84	7.38	4.64	5.04

(Continued)

TABLE A2.3 (Continued)

Worldwide Global Horizontal Average Solar Radiation (Units: MJ/sq. m-day)

Position	Lat	Long	January	February	March	April	May	June	July	August	September	October	November	December
Toronto	43.67 N	79.38 E	4.79	8.15	11.96	14.00	18.16	24.35	23.38	—	15.89	9.40	4.72	3.79
Vancouver	49.18 N	123.17 E	3.73	4.81	12.14	16.41	20.65	24.04	22.87	19.08	12.77	7.39	4.29	1.53
<i>Chile</i>														
Pascua	27.17 S	109.43 W	19.64	16.65	—	11.12	9.52	8.81	10.90	12.29	17.19	20.51	21.20	22.44
Santiago	33.45 S	70.70 W	18.61	16.33	13.44	8.32	5.07	3.66	3.35	5.65	8.15	13.62	20.14	23.88
<i>China</i>														
Beijing	39.93 N	116.28 W	7.73	10.59	13.87	17.93	20.18	18.65	15.64	16.61	15.52	11.29	7.25	6.89
Guangzhou	23.13 N	113.32 E	11.01	6.32	4.04	7.89	10.53	12.48	16.14	16.02	15.03	15.79	11.55	9.10
Harbin	45.75 N	126.77 E	5.15	9.54	17.55	20.51	20.33	17.85	19.18	16.09	13.38	14.50	10.50	6.98
Kunming	25.02 N	102.68 E	9.92	11.26	14.38	18.00	18.53	17.37	11.95	18.47	15.94	12.45	11.96	13.62
Lanzhou	36.05 N	103.88 E	7.30	12.47	10.62	18.91	17.40	20.40	20.23	17.37	13.23	10.21	8.22	6.43
Shanghai	31.17 N	121.43 E	7.44	10.31	11.78	14.36	14.23	16.79	14.63	11.85	15.96	12.03	7.73	8.70
<i>Columbia</i>														
Bogota	4.70 N	74.13 W	17.89	—	19.37	16.58	14.86	—	15.42	18.20	17.05	14.58	14.20	16.66
<i>Cuba</i>														
Havana	23.17 N	82.35 W	—	14.70	18.94	20.95	22.63	18.83	21.40	20.19	16.84	16.98	13.19	13.81
<i>Czech</i>														
Kucharovice	48.88 N	16.08 E	3.03	5.85	9.88	14.06	20.84	19.24	21.18	19.41	13.61	6.11	3.47	2.12
Churanov	49.07 N	13.62 E	2.89	5.82	9.24	13.18	21.32	15.68	20.51	19.49	12.84	5.68	3.36	2.99
Hradec Kralov	50.25 N	15.85 E	3.51	5.94	10.58	15.95	20.42	18.43	17.17	17.92	11.86	6.27	2.45	1.89
<i>Denmark</i>														
Copenhagen	55.67 N	12.30 E	1.83	3.32	7.09	11.12	21.39	24.93	—	13.92	10.10	5.20	2.81	1.23
<i>Egypt</i>														
Cairo	30.08 N	31.28 E	10.06	12.96	18.49	23.04	21.91	26.07	25.16	23.09	21.01	—	11.74	9.85
Mersa Matruh	31.33 N	27.22 E	8.38	11.92	18.47	24.27	24.17	—	26.67	26.27	21.92	18.28	11.71	8.76

(Continued)

TABLE A2.3 (Continued)

Worldwide Global Horizontal Average Solar Radiation (Units: MJ/sq. m-day)

Position	Lat	Long	January	February	March	April	May	June	July	August	September	October	November	December
<i>Ethiopia</i>														
Addis Ababa	8.98 N	38.80 E	—	11.39	—	12.01	—	—	—	6.33	9.35	11.71	11.69	11.50
<i>Fiji</i>														
Nandi	17.75 S	177.45 E	20.82	20.65	20.25	18.81	15.68	14.18	15.08	16.71	19.37	20.11	21.78	25.09
Suva	48.05 S	178.57 E	20.37	17.74	16.22	13.82	10.81	12.48	11.40	—	—	18.49	19.96	20.99
<i>Finland</i>														
Helsinki	60.32 N	24.97 E	1.13	2.94	5.59	11.52	17.60	16.81	20.66	15.44	8.44	3.31	0.97	0.63
<i>France</i>														
Agen	44.18 N	0.60 E	4.83	7.40	10.69	17.12	19.25	20.42	21.63	20.64	15.56	8.41	5.09	5.01
Nice	43.65 N	7.20 E	6.83		11.37	17.79	20.74	24.10	24.85	24.86	15.04	10.99	7.08	6.73
Paris	48.97 N	2.45 E	2.62	5.08	7.21	12.90	14.84	13.04	15.54	16.30	10.17	5.61	3.14	2.20
<i>Germany</i>														
Bonn	50.70 N	7.15 E	2.94	5.82	8.01	14.27	15.67	14.41	18.57	17.80	11.70	6.15	3.42	1.90
Nuremberg	53.33 N	13.20 E	3.23	6.92	9.08	15.69	15.71	18.21	21.14	17.98	12.43	8.15	2.79	2.51
Bremen	53.05 N	8.80 E	2.36	4.93	8.53	14.52	14.94	14.52	19.40	15.02	10.48	6.27	2.80	1.66
Hamburg	53.63 N	10.00 E	1.97	3.96	7.59	12.32	14.11	12.69	19.00	14.11	10.29	6.45	2.33	1.43
Stuttgart	48.83 N	9.20 E	3.59	7.18	9.22	15.81	17.72	17.44	22.21	19.87	12.36	7.81	3.19	2.54
<i>Ghana</i>														
Bole	9.03 N	2.48 W	18.29	19.76	19.71	19.15	16.61	—	—	13.68	16.29	17.27	17.33	15.93
Accra	5.60 N	0.17 W	14.82	16.26	18.27	16.73	18.15	13.96	13.86	13.49	15.32	19.14	18.16	14.23
<i>Great Britain</i>														
Belfast	54.65 N	6.22 W	2.00	3.60	6.85	12.00	15.41	15.09	15.46	13.56	11.49	4.63	2.34	1.24
Jersey	49.22 N	2.20 W	2.76	5.65	9.51	14.98	18.51	17.83	18.14	18.62	12.98	6.16	3.26	2.83
London	51.52 N	0.12 W	2.24	3.87	7.40	12.01	12.38	13.24	16.59	16.23	12.59	5.67	2.87	1.97
<i>Greece</i>														
Athens	37.97 N	23.72 E	9.11	10.94	15.70	20.91	23.85	25.48	24.21	23.08	19.03	13.29	5.98	6.64
Sikiwna	37.98 N	22.73 E	7.60	8.16	11.99	21.06	22.62	24.32	23.56	21.73	17.30	11.75	9.45	6.35

(Continued)

TABLE A2.3 (Continued)

Worldwide Global Horizontal Average Solar Radiation (Units: MJ/sq. m-day)

Position	Lat	Long	January	February	March	April	May	June	July	August	September	October	November	December
<i>Guadeloupe</i>														
Le Raizet	16.27 N	61.52 W	14.88	18.10	20.55	19.69	20.26	20.65	20.65	20.24	18.47	17.79	13.49	14.38
<i>Guyana</i>														
Cayenne	4.83 N	52.37 W	14.46	14.67	16.28	17.57	—	14.92	17.42	18.24	20.52	—	22.69	17.04
<i>Hong Kong</i>														
King's Park	22.32 N	114.17 W	12.34	7.39	6.94	9.50	11.38	13.60	16.70	17.06	15.91	16.52	14.19	10.00
<i>Hungary</i>														
Budapest	47.43 N	19.18 E	2.61	7.46	11.14	14.46	20.69	19.47	21.46	19.72	12.88	7.96	2.95	2.47
<i>Iceland</i>														
Reykjavik	64.13 N	21.90 W	0.52	2.02	6.25	11.77	13.07	14.58	16.83	11.35	9.70	3.18	1.00	0.65
<i>India</i>														
Bombay	19.12 N	72.85 E	18.44	21.00	22.72	24.52	24.86	19.75	15.84	16.00	18.19	20.38	19.18	17.81
Calcutta	22.53 N	88.33 E	15.69	18.34	20.09	22.34	22.37	17.55	17.07	16.55	16.52	16.90	16.35	15.00
Madras	13.00 N	80.18 E	19.09	22.71	25.14	24.88	23.89	—	18.22	19.68	19.51	16.41	14.76	15.79
Nagpur	21.10 N	79.05 E	18.08	21.01	22.25	24.08	24.79	19.84	15.58	15.47	17.66	20.10	18.98	17.33
New Delhi	28.58 N	77.20 E	14.62	18.25	20.15	23.40	23.80	19.16	20.20	19.89	20.08	19.74	16.95	14.22
<i>Ireland</i>														
Dublin	53.43 N	6.25 W	2.51	4.75	7.48	11.06	17.46	19.11	15.64	13.89	9.65	5.77	2.93	—
<i>Israel</i>														
Jerusalem	31.78 N	35.22 E	10.79	13.01	18.08	23.79	29.10	31.54	31.83	28.79	25.19	20.26	12.61	10.71
<i>Italy</i>														
Milan	45.43 N	9.28 E	—	6.48	10.09	13.17	17.55	16.32	18.60	16.86	11.64	5.40	3.52	2.41
Rome	41.80 N	12.55 E	—	9.75	13.38	15.82	15.82	18.89	22.27	21.53	16.08	8.27	6.41	4.49
<i>Japan</i>														
Fukuoka	33.58 N	130.38 E	8.11	8.72	10.95	13.97	14.36	12.81	13.84	16.75	13.92	11.86	10.05	7.30

(Continued)

TABLE A2.3 (Continued)

Worldwide Global Horizontal Average Solar Radiation (Units: MJ/sq. m-day)

Position	Lat	Long	January	February	March	April	May	June	July	August	September	October	November	December
Tateno	36.05 N	140.13 E	9.06	12.17	11.00	15.78	16.52	15.26	—	—	—	9.60	8.55	8.26
Yonago	35.43 N	133.35 E	6.25	7.16	10.87	17.30	16.72	15.44	17.06	19.93	12.41	10.82	7.50	5.51
<i>Kenya</i>														
Mombasa	4.03 S	39.62 E	22.30	22.17	22.74	18.49	18.31	17.41	—	18.12	21.03	22.97	21.87	21.25
Nairobi	1.32 S	36.92 E	—	24.10	21.20	18.65	14.83	15.00	13.44	14.12	19.14	19.38	16.90	18.27
<i>Lithuania</i>														
Kaunas	54.88 N	23.88 E	1.89	4.43	7.40	12.97	18.88	18.74	21.41	15.79	10.40	5.64	1.80	1.10
<i>Madagascar</i>														
Antananarivo	18.80 S	47.48 E	15.94	13.18	13.07	11.53	9.25	8.21	9.32	—	—	16.43	15.19	15.62
<i>Malaysia</i>														
Kualalumpur	3.12 N	101.55 E	15.36	17.67	18.48	16.87	15.67	16.24	15.32	15.89	14.62	14.13	13.54	11.53
Piang	5.30 N	100.27 E	19.47	21.35	23.24	20.52	18.63	19.32	17.17	16.96	15.93	16.01	18.35	17.37
<i>Martinique</i>														
Le Lamentin	14.60 N	61.00 W	17.76	20.07	22.53	21.95	22.42	21.23	20.86	21.84	20.23	19.87	14.08	16.25
<i>Mexico</i>														
Chihuahua	28.63 N	106.08 W	14.80	—	—	—	26.94	26.28	24.01	24.22	20.25	19.55	10.57	15.79
Orizabita	20.58 N	99.20 E	19.49	23.07	27.44	27.35	26.04	25.05	—	27.53	21.06	17.85	15.48	12.93
<i>Mongolia</i>														
Ulan Bator	47.93 N	106.98 E	6.28	9.22	14.34	18.18	20.50	19.34	16.34	16.65	14.08	11.36	7.19	5.35
Uliasutai	47.75 N	96.85 E	6.43	10.71	14.83	20.32	23.86	20.46	21.66	17.81	15.97	10.92	7.32	5.08
<i>Morocco</i>														
Casablanca	33.57 N	7.67 E	11.46	12.70	15.93	21.25	24.45	25.27	25.53	23.60	19.97	14.68	11.61	9.03
<i>Mozambique</i>														
Maputo	25.97 S	32.60 E	26.35	23.16	19.33	20.54	16.33	14.17	—	—	—	22.55	25.48	26.19

(Continued)

TABLE A2.3 (Continued)

Worldwide Global Horizontal Average Solar Radiation (Units: MJ/sq. m-day)

Position	Lat	Long	January	February	March	April	May	June	July	August	September	October	November	December
<i>Netherlands</i>														
Maastricht	50.92 N	5.78 E	3.20	5.43	8.48	14.82	14.97	14.32	18.40	17.51	11.65	6.51	3.01	1.72
<i>New Caledonia</i>														
Koumac	20.57 S	164.28 E	24.89	21.15	16.96	18.98	15.67	14.55	15.75	17.62	22.48	15.83	27.53	26.91
<i>New Zealand</i>														
Wilmington	41.28 S	174.77 E	22.59	19.67	14.91	9.52	6.97	4.37	5.74	7.14	12.50	16.34	19.07	24.07
Christchurch	43.48 S	172.55 E	23.46	19.68	13.98	8.96	6.47	4.74	5.38	6.94	13.18	17.45	18.91	24.35
<i>Nigeria</i>														
Benin City	6.32 N	5.60 E	14.89	17.29	19.15	17.21	16.97	15.04	10.24	12.54	14.37	15.99	17.43	15.75
<i>Norway</i>														
Bergen	60.40 N	5.32 E	0.46	1.33	3.18	8.36	19.24	16.70	16.28	10.19	6.53	3.19	1.36	0.35
<i>Oman</i>														
Seeb	23.58 N	58.28 E	12.90	14.86	21.22	22.22	25.30	24.02	23.46	21.66	20.07	18.45	15.49	13.12
Salalah	17.03 N	54.08 E	16.52	16.92	18.49	20.65	21.46	16.92	8.52	11.41	17.14	18.62	16.42	—
<i>Pakistan</i>														
Karachi	24.90 N	67.13 E	13.84	—	—	19.69	20.31	16.62	—	—	—	—	12.94	11.07
Multan	30.20 N	71.43 E	12.29	15.86	18.33	22.35	22.57	21.65	20.31	20.44	20.57	15.91	12.68	10.00
Islamabad	33.62 N	73.10 E	10.38	12.42	16.98	22.65	—	25.49	20.64	18.91	14.20	15.30	10.64	8.30
<i>Peru</i>														
Puno	15.83 S	70.02 W	14.98	12.92	16.08	20.03	17.45	17.42	15.74	15.32	16.11	16.18	14.24	13.90
<i>Poland</i>														
Warszawa	52.28 N	20.97 E	1.73	3.83	7.81	10.53	19.22	17.11	20.18	15.00	10.65	4.95	2.39	1.68

(Continued)

TABLE A2.3 (Continued)

Worldwide Global Horizontal Average Solar Radiation (Units: MJ/sq. m-day)

Position	Lat	Long	January	February	March	April	May	June	July	August	September	October	November	December
Kolobrzeg	54.18 N	15.58 E	2.50	3.25	8.86	15.21	20.79	20.50	17.19	16.46	7.95	5.75	1.78	1.18
<i>Portugal</i>														
Evora	38.57 N	7.90 W	9.92	12.43	17.81	18.69	23.57	29.23	28.75	23.77	20.17	—	6.81	4.57
Lisbon	38.72 N	9.15 W	9.24	11.60	17.52	18.49	24.64	29.02	28.14	22.20	19.76	13.56	7.18	4.83
<i>Romania</i>														
Bucuresti	44.50 N	26.13 E	7.05	10.22	12.04	16.53	18.97	22.16	23.19	—	17.17	9.55	4.82	—
Constania	44.22 N	28.63 E	5.62	9.28	14.31	20.59	23.23	25.80	27.98	24.22	16.91	11.89	6.19	5.10
Galati	45.50 N	28.02 E	6.09	9.33	14.31	17.75	21.77	22.74	25.55	19.70	14.05	11.26	6.32	5.38
<i>Russia</i>														
Alexandovsko	60.38 N	77.87 E	1.34	4.17	9.16	17.05	21.83	21.34	20.26	13.05	10.16	4.68	1.71	0.68
Moscow	55.75 N	37.57 E	1.45	3.96	8.09	11.69	18.86	18.12	17.51	14.17	10.92	4.03	2.28	1.29
St. Petersburg	59.97 N	30.30 E	1.03	3.11	4.88	12.24	20.59	21.55	20.43	13.27	7.83	2.93	1.16	0.59
Verkhoyansk	67.55 N	133.38 E	0.21	2.25	7.61	15.96	19.64	—	—	14.12	7.59	3.51	0.54	—
<i>St. Pierre & Miquelon</i>														
St. Pierre	46.77 N	56.17 W	4.43	6.61	12.50	17.57	18.55	17.84	19.95	16.46	12.76	8.15	3.69	3.33
<i>Singapore</i>														
Singapore	1.37 N	103.98 E	19.08	20.94	20.75	18.20	14.89	15.22	13.92	16.66	16.51	15.82	13.81	12.67
<i>South Korea</i>														
Seoul	37.57 N	126.97 E	6.24	9.40	10.34	13.98	16.35	17.49	10.65	12.94	11.87	10.35	6.47	5.14
<i>South Africa</i>														
Cape Town	33.98 S	18.60 E	27.47	25.57	—	15.81	11.44	9.08	8.35	13.76	17.30	22.16	26.37	27.68
Port Elizabeth	33.98 S	25.60 E	27.22	22.06	19.01	15.29	11.79	11.13	10.73	13.97	18.52	23.09	23.15	27.26
Pretoria	25.73 S	28.18 E	26.06	22.43	20.52	16.09	15.67	13.67	15.19	18.65	21.62	21.75	24.82	23.43
<i>Spain</i>														
Madrid	40.45 N	3.72 W	7.73	10.53	15.35	21.74	22.81	22.05	26.27	22.90	18.89	10.21	8.69	5.56

(Continued)

TABLE A2.3 (Continued)

Worldwide Global Horizontal Average Solar Radiation (Units: MJ/sq. m-day)

Position	Lat	Long	January	February	March	April	May	June	July	August	September	October	November	December
<i>Sudan</i>														
Wad Madani	14.40 N	33.48 E	21.92	24.01	23.43	25.17	23.92	23.51	22.40	22.85	21.75	20.47	20.19	19.21
Elfasher	13.62 N	25.33 E	21.56	21.84	24.54	25.29	24.31	24.15	22.87	21.19	22.58	23.85	—	—
Shambat	15.67 N	32.53 E	23.90	27.38	—	27.45	23.21	26.15	23.55	25.46	24.05	23.51	23.82	22.53
<i>Sweden</i>														
Karlstad	59.37 N	13.47 E	1.26	3.13	5.02	14.01	19.90	16.70	20.92	14.14	10.52	3.98	1.47	0.94
Lund	55.72 N	13.22 E	1.97	3.47	6.66	12.48	17.83	13.38	18.74	14.99	10.39	5.45	1.82	1.21
Stockholm	59.35 N	18.07 E	1.32	2.69	4.75	13.21	15.58	14.79	20.52	14.48	10.50	4.04	1.19	0.83
<i>Switzerland</i>														
Geneva	46.25 N	6.13 E	2.56	7.21	9.46	17.07	20.98	19.78	22.38	20.50	13.62	8.44	3.31	2.87
Zurich	47.48 N	8.53 E	2.31	7.02	7.54	15.04	16.33	16.73	20.28	18.32	12.52	7.18	2.64	2.29
<i>Thailand</i>														
Bangkok	13.73 N	100.57 E	16.67	19.34	23.00	22.48	20.59	17.71	18.02	16.04	16.23	16.81	18.60	16.43
<i>Trinidad & Tobago</i>														
Crown Point	11.15 N	60.83 W	13.05	15.61	15.17	16.96	17.61	15.37	13.16	13.08	12.24	8.76	—	—
<i>Tunisia</i>														
Sidi Bouzid	36.87 N	10.35 E	7.88	10.38	13.20	17.98	25.12	26.68	27.43	24.33	18.87	12.11	9.37	6.72
Tunis	36.83 N	10.23 E	7.64	9.88	14.79	31.61	25.31	26.03	26.60	20.37	19.58	12.91	9.35	7.16
<i>Ukraine</i>														
Kiev	50.40 N	30.45 E	2.17	4.87	11.15	12.30	20.49	—	18.99	18.55	9.72	9.84	3.72	2.52
<i>Uzbekistan</i>														
Tashkent	41.27 N	69.27 E	7.27	10.81	15.93	23.60	25.21	29.53	28.50	26.68	20.76	13.25	8.61	4.59
<i>Venezuela</i>														
Caracas	10.50 N	66.88 W	14.25	13.56	16.30	15.56	15.69	15.56	16.28	17.11	17.04	15.14	14.74	13.50
St. Antonio	7.85 N	72.45 W	11.78	10.54	10.65	12.07	12.65	21.20	14.68	15.86	16.62	15.32	12.28	11.28
St. Fernando	7.90 N	67.42 W	14.92	16.82	16.89	—	—	14.09	13.78	14.42	14.86	15.27	14.25	13.11

(Continued)

TABLE A2.3 (Continued)

Worldwide Global Horizontal Average Solar Radiation (Units: MJ/sq. m-day)

Position	Lat	Long	January	February	March	April	May	June	July	August	September	October	November	December
<i>Vietnam</i>														
Hanoi	21.03 N	105.85 E	5.99	7.48	8.73	13.58	19.10	21.26	19.85	19.78	20.67	14.78	12.44	13.21
<i>Yugoslavia</i>														
Beograd	44.78 N	20.53 E	4.92	6.27	10.64	14.74	20.95	22.80	22.09	20.27	15.57	11.24	6.77	4.99
Kopaonik	43.28 N	20.80 E	7.03	10.93	14.75	12.78	13.54	20.43	22.48	—	20.14	11.61	6.26	4.64
Portoroz	45.52 N	13.57 E	5.11	7.84	13.75	17.30	23.66	22.31	25.14	21.34	13.40	8.98	6.04	3.92
<i>Zambia</i>														
Lusaka	15.42 S	28.32 W	16.10	18.02	20.24	19.84	17.11	16.37	19.45	20.72	21.68	23.83	23.85	20.52
<i>Zimbabwe</i>														
Bulawayo	20.15 S	28.62 N	20.03	22.11	21.03	18.09	17.15	15.36	16.46	19.49	21.55	23.44	25.08	23.46
Harare	17.83 S	31.02 N	19.38	19.00	19.22	17.67	18.35	16.10	14.55	17.87	21.47	23.98	19.92	21.88

Source: Voeikov Main Geophysical Observatory, Russia: Internet address: http://wrdc-mgo.nrel.gov/html/get_data-ap.html.

Note: Data for 872 locations is available from these sources in 68 countries.

^a Source for Canadian Data: Environment Canada: Internet address: <http://www.ec.gc.ca/envhome.html>.

TABLE A2.4

Average Daily Solar Radiation on a Horizontal Surface in U.S.A. (Units: MJ/sq. m-day)

Position	January	February	March	April	May	June	July	August	September	October	November	December	Average
<i>Alabama</i>													
Birmingham	9.20	11.92	15.67	19.65	21.58	22.37	21.24	20.21	17.15	14.42	10.22	8.40	16.01
Montgomery	9.54	12.49	16.24	20.33	22.37	23.17	21.80	20.56	17.72	14.99	10.90	8.97	16.58
<i>Alaska</i>													
Fairbanks	0.62	2.77	8.31	14.66	17.98	19.65	16.92	12.36	7.02	3.20	1.01	0.23	8.74
Anchorage	1.02	3.41	8.18	13.06	15.90	17.72	16.69	12.72	8.06	3.97	1.48	0.56	8.63
Nome	0.51	2.95	8.29	15.22	18.97	19.65	16.69	11.81	7.72	3.63	0.99	0.09	8.86
St. Paul Island	1.82	4.32	8.52	12.72	14.08	14.42	12.83	10.33	7.84	4.54	2.16	1.25	7.95
Yakutat	1.36	3.63	7.72	12.61	14.76	15.79	14.99	12.15	7.95	3.97	1.82	0.86	8.18
<i>Arizona</i>													
Phoenix	11.58	15.33	19.87	25.44	28.85	30.09	27.37	25.44	21.92	17.60	12.95	10.56	20.56
Tucson	12.38	15.90	20.21	25.44	28.39	29.30	25.44	24.08	21.58	17.94	13.63	11.24	20.44
<i>Arkansas</i>													
Little Rock	9.09	11.81	15.56	19.19	21.80	23.51	23.17	21.35	17.26	14.08	9.77	8.06	16.24
Fort Smith	9.31	12.15	15.67	19.31	21.69	23.39	23.85	24.46	17.26	13.97	9.88	8.29	16.35
<i>California</i>													
Bakersfield	8.29	11.92	16.69	22.15	26.57	28.96	28.73	26.01	21.35	15.90	10.33	7.61	18.74
Fresno	7.61	11.58	16.81	22.49	27.14	29.07	28.96	25.89	21.12	15.56	9.65	6.70	18.62
Long Beach	9.99	12.95	17.03	21.60	23.17	24.19	26.12	24.08	19.31	14.99	11.24	9.31	17.83
Sacramento	6.93	10.68	15.56	21.24	25.89	28.28	28.62	25.32	20.56	14.54	8.63	6.25	17.72
San Diego	11.02	13.97	17.72	21.92	22.49	23.28	24.98	23.51	19.53	15.79	12.26	10.22	18.06
San Francisco	7.72	10.68	15.22	20.44	24.08	25.78	26.46	23.39	19.31	13.97	8.97	7.04	16.92
Los Angeles	10.11	13.06	17.26	21.80	23.05	23.74	25.67	23.51	18.97	14.99	11.36	9.31	17.72
Santa Maria	10.22	13.29	17.49	22.26	25.10	26.57	26.91	24.42	20.10	15.67	11.47	9.54	18.62
<i>Colorado</i>													
Boulder	7.84	10.45	15.64	17.94	17.94	20.47	20.28	17.12	16.07	12.09	8.66	7.10	14.31

(Continued)

TABLE A2.4 (Continued)

Average Daily Solar Radiation on a Horizontal Surface in U.S.A. (Units: MJ/sq. m-day)

Position	January	February	March	April	May	June	July	August	September	October	November	December	Average
Colorado Springs	9.09	12.15	16.13	20.33	22.26	24.98	23.96	21.69	18.51	14.42	9.99	8.18	16.81
<i>Connecticut</i>													
Hartford	6.70	9.65	13.17	16.69	19.53	21.24	21.12	18.51	14.76	10.68	6.59	5.45	13.74
<i>Delaware</i>													
Wilmington	7.27	10.22	13.97	17.60	20.33	22.49	21.80	19.65	15.79	11.81	7.84	6.25	14.65
<i>Florida</i>													
Daytona Beach	11.24	13.85	17.94	22.15	23.17	22.03	21.69	20.44	17.72	14.99	12.15	10.33	17.38
Jacksonville	10.45	13.17	17.03	21.12	22.03	21.58	21.01	19.42	16.69	14.20	11.47	9.65	16.47
Tallahassee	10.33	13.29	16.92	21.24	22.49	22.03	20.90	19.65	17.72	15.56	11.92	9.77	16.81
Miami	12.72	15.22	18.51	21.58	21.46	20.10	21.10	20.10	17.60	15.67	13.17	11.81	17.38
Key West	13.17	16.01	19.65	22.71	22.83	22.03	22.03	21.01	18.74	16.47	13.85	15.79	18.40
Tampa	11.58	14.42	18.17	22.26	23.05	21.92	20.90	19.65	17.60	16.01	12.83	11.02	17.49
<i>Georgia</i>													
Athens	9.43	12.38	16.01	20.21	22.03	22.83	21.80	20.21	17.26	14.42	10.45	8.40	16.29
Atlanta	9.31	12.26	16.13	20.33	22.37	23.17	22.15	20.56	17.49	14.54	10.56	8.52	16.43
Columbus	9.77	12.72	16.47	20.67	22.37	22.83	21.58	20.33	17.60	14.99	11.02	9.09	16.62
Macon	9.54	12.61	16.35	20.56	22.37	22.83	21.58	20.21	17.26	14.88	10.90	8.86	16.50
Savanna	9.99	12.72	16.81	21.01	22.37	22.60	21.80	19.76	16.92	14.65	11.13	9.20	16.58
<i>Hawaii</i>													
Honolulu	14.08	16.92	19.42	21.24	22.83	23.51	23.74	23.28	21.35	18.06	14.88	13.40	19.42
<i>Idaho</i>													
Boise	5.79	8.97	13.63	18.97	23.51	26.01	27.37	23.62	18.40	12.26	6.70	5.11	15.90
<i>Illinois</i>													
Chicago	6.47	9.31	12.49	16.47	20.44	22.60	22.03	19.31	15.10	10.79	6.47	5.22	13.85
Rockford	6.70	9.77	12.72	16.58	20.33	22.49	22.15	19.42	15.22	10.79	6.59	5.34	14.08
Springfield	7.50	10.33	13.40	17.83	21.46	23.51	23.05	20.56	16.58	12.26	7.72	6.13	15.10

(Continued)

TABLE A2.4 (Continued)

Average Daily Solar Radiation on a Horizontal Surface in U.S.A. (Units: MJ/sq. m-day)

Position	January	February	March	April	May	June	July	August	September	October	November	December	Average
<i>Indiana</i>													
Indianapolis	7.04	9.99	13.17	17.49	21.24	23.28	22.60	20.33	16.35	11.92	7.38	5.79	14.76
<i>Iowa</i>													
Mason City	6.70	9.77	13.29	16.92	20.78	22.83	22.71	19.76	15.33	10.90	6.59	5.45	14.31
Waterloo	6.81	9.77	13.06	16.92	20.56	22.83	22.60	19.76	15.33	10.90	6.70	5.45	14.20
<i>Kansas</i>													
Dodge City	9.65	12.83	16.69	21.01	23.28	25.78	25.67	22.60	18.40	14.42	10.11	8.40	17.49
Goodland	8.97	11.92	16.13	20.44	22.71	25.78	25.55	22.60	18.28	14.08	9.65	7.84	17.03
<i>Kentucky</i>													
Lexington	7.27	9.88	13.51	17.60	20.56	22.26	21.46	19.65	16.01	12.38	7.95	6.25	14.54
Louisville	7.27	10.22	13.63	17.83	20.90	22.71	22.03	20.10	16.35	12.38	7.95	6.25	14.76
<i>Louisiana</i>													
New Orleans	9.77	12.83	16.01	19.87	21.80	22.03	20.67	19.65	17.60	15.56	11.24	9.31	16.35
Lake Charles	9.77	12.83	16.13	19.31	21.58	22.71	21.58	20.33	18.06	15.56	11.47	9.31	16.58
<i>Maine</i>													
Portland	6.70	9.99	13.78	16.92	19.99	21.92	21.69	19.31	15.22	10.56	6.47	5.45	13.97
<i>Maryland</i>													
Baltimore	7.38	10.33	13.97	17.60	20.21	22.15	21.69	19.19	15.79	11.92	8.06	6.36	14.54
<i>Massachusetts</i>													
Boston	6.70	9.65	13.40	16.92	20.21	22.03	21.80	19.31	15.33	10.79	6.81	5.45	14.08
<i>Michigan</i>													
Detroit	5.91	8.86	12.38	16.47	20.33	22.37	21.92	18.97	14.76	10.11	6.13	4.66	13.63
Lansing	5.91	8.86	12.49	16.58	20.21	22.26	21.92	18.85	14.54	9.77	5.91	4.66	13.51
<i>Minnesota</i>													
Duluth	5.68	9.31	13.74	17.38	20.10	21.46	21.80	18.28	13.29	8.86	5.34	4.43	13.29
Minneapolis	6.36	9.77	13.51	16.92	20.56	22.49	22.83	19.42	14.65	9.99	6.13	4.88	13.97

(Continued)

TABLE A2.4 (Continued)

Average Daily Solar Radiation on a Horizontal Surface in U.S.A. (Units: MJ/sq. m-day)

Position	January	February	March	April	May	June	July	August	September	October	November	December	Average
Rochester	6.36	9.65	13.17	16.58	20.10	22.15	22.15	19.08	14.54	10.11	6.25	5.11	13.74
<i>Mississippi</i>													
Jackson	9.43	12.38	16.13	19.87	22.15	23.05	22.15	19.08	14.54	10.11	6.25	5.11	13.74
<i>Missouri</i>													
Columbia	8.06	10.90	14.31	18.62	21.58	23.62	23.85	21.12	16.69	12.72	8.29	6.70	15.56
Kansas City	7.95	10.68	14.08	18.28	21.24	23.28	23.62	20.78	16.58	12.72	8.40	6.70	15.44
Springfield	8.52	11.02	14.65	18.62	21.24	23.05	23.62	21.24	16.81	13.17	8.86	7.27	15.67
St. Louis	7.84	10.56	13.97	18.06	21.12	23.05	22.94	20.44	16.58	12.49	8.18	6.59	15.22
<i>Montana</i>													
Helena	5.22	8.29	12.61	17.15	20.67	23.28	25.21	21.24	15.79	10.45	6.02	4.43	14.20
Lewistown	5.22	8.40	12.72	17.15	20.33	23.05	24.53	20.78	15.10	10.22	5.91	4.32	13.97
<i>Nebraska</i>													
Omaha	7.50	10.33	13.97	18.06	21.24	2.40	23.51	20.56	16.01	11.81	7.61	6.13	15.10
Lincoln	7.33	10.10	13.65	16.22	19.26	21.21	22.15	18.87	15.44	11.54	7.76	6.20	14.16
<i>Nevada</i>													
Elko	7.61	10.56	14.42	18.85	22.71	25.67	26.69	23.62	19.31	13.63	8.29	6.70	16.58
Las Vegas	10.79	14.42	19.42	24.87	28.16	30.09	28.28	25.89	22.15	17.03	12.15	9.88	20.33
Reno	8.29	11.58	16.24	21.24	25.10	27.48	28.16	24.98	20.56	14.88	9.31	7.38	17.94
<i>New Hampshire</i>													
Concord	6.81	10.11	13.97	16.92	20.21	21.80	21.80	19.08	14.99	10.45	6.47	5.45	14.08
<i>New Jersey</i>													
Atlantic City	7.38	10.22	13.97	17.49	20.21	21.92	21.24	19.19	15.79	11.92	8.06	6.36	14.54
Newark	6.93	9.77	13.51	17.26	19.76	21.35	21.01	18.85	15.33	11.36	7.27	5.68	13.97

(Continued)

TABLE A2.4 (Continued)

Average Daily Solar Radiation on a Horizontal Surface in U.S.A. (Units: MJ/sq. m-day)

Position	January	February	March	April	May	June	July	August	September	October	November	December	Average
<i>New Mexico</i>													
Albuquerque	11.47	14.99	19.31	24.53	27.60	29.07	27.03	24.76	21.12	17.03	12.49	10.33	19.99
<i>New York</i>													
Albany	6.36	9.43	12.95	16.69	19.53	21.46	21.58	18.51	14.65	10.11	6.13	5.00	13.51
Buffalo	5.68	8.40	12.15	16.35	19.76	22.03	21.69	18.62	14.08	9.54	5.68	4.54	13.29
New York City	6.93	9.88	13.85	17.72	20.44	22.03	21.69	19.42	15.56	11.47	7.27	5.79	14.31
Rochester	5.68	8.52	12.26	16.58	19.87	21.92	21.69	18.51	14.20	9.54	5.68	4.54	13.29
<i>North Carolina</i>													
Charlotte	8.97	11.81	15.67	19.76	21.58	22.60	21.92	19.99	16.92	13.97	9.99	8.06	16.01
Wilmington	9.31	12.15	16.24	20.44	21.92	22.60	21.58	19.53	16.69	14.08	10.56	8.52	16.13
<i>North Dakota</i>													
Fargo	5.79	9.09	13.17	16.92	20.56	22.37	23.17	19.87	14.31	9.54	5.68	4.54	13.74
Bismarck	6.12	9.75	13.88	17.43	21.45	23.01	24.06	20.12	15.21	10.61	6.28	4.84	14.39
<i>Ohio</i>													
Cleveland	5.79	8.63	12.04	16.58	20.10	22.15	21.92	18.97	14.76	10.22	6.02	4.66	13.51
Columbus	6.47	9.09	12.49	16.58	19.76	21.58	21.12	18.97	15.44	11.24	6.81	5.34	13.74
Dayton	6.81	9.43	12.83	17.03	20.33	22.37	22.37	19.65	15.90	11.47	7.04	5.45	14.20
Youngstown	5.79	8.40	11.92	15.90	19.19	21.24	20.78	18.06	14.31	10.11	6.02	4.77	13.06
<i>Oklahoma</i>													
Oklahoma City	9.88	1.25	16.47	20.33	22.26	24.42	24.98	22.49	18.17	14.54	10.45	8.74	17.15
<i>Oregon</i>													
Eugene	4.54	7.04	11.24	15.79	19.99	22.37	24.19	21.01	15.90	9.65	5.11	3.75	13.40
Medford	5.34	8.52	13.17	18.62	23.39	26.23	27.82	23.96	18.62	11.92	6.02	4.43	15.67
Portland	4.20	6.70	10.68	15.10	18.97	21.24	22.60	19.53	14.88	9.20	4.88	3.52	12.61

(Continued)

TABLE A2.4 (Continued)

Average Daily Solar Radiation on a Horizontal Surface in U.S.A. (Units: MJ/sq. m-day)

Position	January	February	March	April	May	June	July	August	September	October	November	December	Average
<i>Pacific Islands</i>													
Guam	16.35	17.38	19.65	20.78	20.56	19.76	18.28	17.49	17.49	16.58	15.79	15.10	17.94
<i>Pennsylvania</i>													
Philadelphia	7.04	9.88	13.63	17.26	19.99	22.03	21.46	19.42	15.67	11.58	7.72	6.02	14.31
Pittsburgh	6.25	8.97	12.61	16.47	19.65	21.80	21.35	18.85	15.10	10.90	6.59	5.00	13.63
<i>Rhode Island</i>													
Providence	6.70	9.65	13.40	16.92	19.99	21.58	21.24	18.85	15.22	11.02	6.93	5.56	13.97
<i>South Carolina</i>													
Charleston	9.77	12.72	16.81	21.12	22.37	22.37	21.92	19.65	16.92	14.54	11.02	9.09	16.58
Greenville	9.20	12.04	15.90	19.99	21.58	22.60	21.58	19.87	16.81	14.08	10.22	8.18	16.01
<i>South Dakota</i>													
Pierre	6.47	9.54	13.85	17.94	21.46	24.08	24.42	21.46	16.35	11.24	7.04	5.45	14.99
Rapid City	6.70	9.88	14.20	18.28	21.46	24.19	24.42	21.80	16.92	11.81	7.50	5.79	15.33
<i>Tennessee</i>													
Memphis	8.86	11.58	15.22	19.42	22.03	23.85	23.39	21.46	17.38	14.20	9.65	7.84	16.24
Nashville	8.29	11.13	14.65	19.31	21.69	23.51	22.49	20.56	16.81	13.51	8.97	7.15	15.67
<i>Texas</i>													
Austin	10.68	13.63	17.03	19.53	21.24	23.74	24.42	22.83	18.85	15.67	11.92	9.99	17.49
Brownsville	10.33	13.17	16.47	19.08	20.78	22.83	23.28	21.58	18.62	16.13	12.38	9.88	17.03
El Paso	12.38	16.24	20.90	25.44	28.05	28.85	26.46	24.30	21.12	17.72	13.63	11.47	20.56
Houston	9.54	12.26	15.22	18.06	20.21	21.69	21.35	20.21	17.49	15.10	11.02	8.97	15.90
San Antonio	10.88	13.53	16.26	17.35	21.10	23.87	24.92	22.81	19.22	15.52	11.50	9.98	17.24
<i>Utah</i>													
Salt Lake City	6.93	10.45	14.76	19.42	23.39	26.46	26.35	23.39	18.85	13.29	8.06	6.02	16.47
<i>Vermont</i>													
Burlington	5.79	9.20	13.06	16.47	19.87	21.69	21.80	18.74	14.42	9.43	5.56	4.43	13.40

(Continued)

TABLE A2.4 (Continued)

Average Daily Solar Radiation on a Horizontal Surface in U.S.A. (Units: MJ/sq. m-day)

Position	January	February	March	April	May	June	July	August	September	October	November	December	Average
<i>Virginia</i>													
Norfolk	8.06	10.90	14.65	18.51	20.78	22.15	21.12	19.42	16.13	12.49	9.09	7.27	15.10
Richmond	8.06	10.90	14.76	18.62	20.90	22.49	21.58	19.53	16.24	12.61	8.97	7.15	15.22
<i>Washington</i>													
Olympia	3.63	6.02	9.99	14.20	18.06	20.10	21.12	18.17	13.63	7.95	4.32	3.07	11.70
Seattle	3.52	5.91	10.11	14.65	19.08	20.78	21.80	18.51	13.51	7.95	4.20	2.84	11.92
Yakima	4.88	7.95	12.83	17.83	22.49	24.87	25.89	22.26	16.92	10.68	5.56	4.09	17.76
<i>West Virginia</i>													
Charleston	7.04	9.65	13.40	17.15	20.21	21.69	20.90	18.97	15.56	11.81	7.72	6.02	14.20
Elkins	6.93	9.43	12.83	16.35	19.08	20.56	19.99	18.06	14.88	11.13	7.27	5.79	13.51
<i>Wisconsin</i>													
Green Bay	6.25	9.31	13.17	16.81	20.56	22.49	22.03	18.85	14.20	9.65	5.79	4.88	13.74
Madison	6.59	9.88	13.29	16.92	20.67	22.83	22.37	19.42	14.76	3.41	6.25	5.22	14.08
Milwaukee	6.47	9.31	12.72	16.69	20.78	22.94	22.60	19.42	14.88	10.22	6.25	5.11	13.97
<i>Wyoming</i>													
Rock Springs	7.61	10.90	15.10	19.42	23.17	26.01	25.78	22.94	18.62	13.40	8.40	6.70	16.58
Sendan	6.47	9.77	13.97	17.94	20.90	23.85	24.64	21.69	16.47	11.24	7.15	5.56	14.99

Source: National Renewable Energy Laboratory, USA., Internet address: <http://rredc.nrel.gov/solar>.

TABLE A2.5

Reflectivity Values for Characteristic Surfaces

Surface	Average Reflectivity
Snow (freshly fallen or with ice film)	0.75
Water surfaces (relatively large incidence angles)	0.07
Soils (clay, loam, etc.)	0.14
Earth roads	0.04
Coniferous forest (winter)	0.07
Forests in autumn, ripe field crops, plants	0.26
Weathered blacktop	0.10
Weathered concrete	0.22
Dead leaves	0.30
Dry grass	0.20
Green grass	0.26
Bituminous and gravel roof	0.13
Crushed rock surface	0.20
Building surfaces, dark (red brick, dark paints, etc.)	0.27
Building surfaces, light (light brick, light paints, etc.)	0.60

Source: Hunn, B.D. and Calafell, D.O., *Solar Energy*, Vol. 19, 1977, p. 87; see also List, R.J., *Smithsonian Meteorological Tables*, 6th edn., Smithsonian Institution Press, 1949, pp. 442–443.

Note: Integrated over solar spectrum and angle of incidence.

Appendix C: Properties of Gases, Vapors, Liquids, and Solids

Nitin Goel

TABLE A3.1

Properties of Dry Air at Atmospheric Pressures between 250 and 1000 K

$T, ^\circ\text{K}$	$\rho, \text{kg/m}^3$	$c_p, \text{kJ/kg K}$	$\mu, \text{kg/m s} \times 10^5$	$\nu, \text{m}^2/\text{s} \times 10^6$	$k, \text{W/m K}$	$\alpha, \text{m}^2/\text{s} \times 10^4$	dPr
250	1.4128	1.0053	1.488	9.49	0.02227	0.13161	0.722
300	1.1774	1.0057	1.983	15.68	0.02624	0.22160	0.708
350	0.9980	1.0090	2.075	20.76	0.03003	0.2983	0.697
400	0.8826	1.0140	2.286	25.90	0.03365	0.3760	0.689
450	0.7833	1.0207	2.484	28.86	0.03707	0.4222	0.683
500	0.7048	1.0295	2.671	37.90	0.04038	0.5564	0.680
550	0.6423	1.0392	2.848	44.34	0.04360	0.6532	0.680
600	0.5879	1.0551	3.018	51.34	0.04659	0.7512	0.680
650	0.5430	1.0635	3.177	58.51	0.04953	0.8578	0.682
700	0.5030	1.0752	3.332	66.25	0.05230	0.9672	0.684
750	0.4709	1.0856	3.481	73.91	0.05509	1.0774	0.686
800	0.4405	1.0978	3.625	82.29	0.05779	1.1951	0.689
850	0.4149	1.1095	3.765	90.75	0.06028	1.3097	0.692
900	0.3925	1.1212	3.899	99.3	0.06279	1.4271	0.696
950	0.3716	1.1321	4.023	108.2	0.06525	1.5510	0.699
1000	0.3524	1.1417	4.152	117.8	0.06752	1.6779	0.702

TABLE A3.2

Properties of Water (Saturated Liquid) between 273 and 533 K

<i>T</i>			<i>c_p</i> , kJ/kg °C	ρ , kg/m ³	μ , kg/m s	<i>k</i> , W/m °C	<i>Pr</i>	
K	°F	°C						
273	32	0	4.225	999.8	1.79×10^{-3}	0.566	13.25	
277.4	40	4.44	4.208	999.8	1.55	0.575	11.35	1.91×10^9
283	50	10	4.195	999.2	1.31	0.585	9.40	6.34×10^9
288.6	60	15.56	4.186	998.6	1.12	0.595	7.88	1.08×10^{10}
294.1	70	21.11	4.179	997.4	9.8×10^{-4}	0.604	6.78	1.46×10^{10}
299.7	80	26.67	4.179	995.8	8.6	0.614	5.85	1.91×10^{10}
302.2	90	32.22	4.174	994.9	7.65	0.623	5.12	2.48×10^{10}
310.8	100	37.78	4.174	993.0	6.82	0.630	4.53	3.3×10^{10}
316.3	110	43.33	4.174	990.6	6.16	0.637	4.04	4.19×10^{10}
322.9	120	48.89	4.174	988.8	5.62	0.644	3.64	4.89×10^{10}
327.4	130	54.44	4.179	985.7	5.13	0.649	3.30	5.66×10^{10}
333.0	140	60	4.179	983.3	4.71	0.654	3.01	6.48×10^{10}
338.6	150	65.55	4.183	980.3	4.3	0.659	2.73	7.62×10^{10}
342.1	160	71.11	4.186	977.3	4.01	0.665	2.53	8.84×10^{10}
349.7	170	76.67	4.191	973.7	3.72	0.668	2.33	9.85×10^{10}
355.2	180	82.22	4.195	970.2	3.47	0.673	2.16	1.09×10^{11}
360.8	190	87.78	4.199	966.7	3.27	0.675	2.03	
366.3	200	93.33	4.204	963.2	3.06	0.678	1.90	
377.4	220	104.4	4.216	955.1	2.67	0.684	1.66	
388.6	240	115.6	4.229	946.7	2.44	0.685	1.51	
399.7	260	126.7	4.250	937.2	2.19	0.685	1.36	
410.8	280	137.8	4.271	928.1	1.98	0.685	1.24	
421.9	300	148.9	4.296	918.0	1.86	0.684	1.17	
449.7	350	176.7	4.371	890.4	1.57	0.677	1.02	
477.4	400	204.4	4.467	859.4	1.36	0.665	1.00	
505.2	450	232.2	4.585	825.7	1.20	0.646	0.85	
533.0	500	260	4.731	785.2	1.07	0.616	0.83	

Source: Adapted from Brown, A.I. and Marco, S.M., Introduction to Heat Transfer, 3rd edn., McGraw-Hill Book Company, New York, 1958.

TABLE A3.3

Emittances and Absorptances of Materials

Substance	Short-Wave Absorptance	Long-Wave Emittance	$a \epsilon$
Class I substances: Absorptance to emittance ratios less than 0.5			
Magnesium carbonate, $MgCO_3$	0.025–0.04	0.79	0.03–0.05
White plaster	0.07	0.91	0.08
Snow, fine particles, fresh	0.13	0.82	0.16
White paint, 0.017 in. on aluminum	0.20	0.91	0.22
Whitewash on galvanized iron	0.22	0.90	0.24
White paper	0.25–0.28	0.95	0.26–0.29
White enamel on iron	0.25–0.45	0.9	0.28–0.5
Ice, with sparse snow cover	0.31	0.96–0.97	0.32
Snow, ice granules	0.33	0.89	0.37
Aluminum oil base paint	0.45	0.90	0.50
White powdered sand	0.45	0.84	0.54
Class II substances: Absorptance to emittance ratios between 0.5 and 0.9			
Asbestos felt	0.25	0.50	0.50
Green oil base paint	0.5	0.9	0.56
Bricks, red	0.55	0.92	0.60
Asbestos cement board, white	0.59	0.96	0.61
Marble, polished	0.5–0.6	0.9	0.61
Wood, planed oak	—	0.9	—
Rough concrete	0.60	0.97	0.62
Concrete	0.60	0.88	0.68
Grass, green, after rain	0.67	0.98	0.68
Grass, high and dry	0.67–0.69	0.9	0.76
Vegetable fields and shrubs, wilted	0.70	0.9	0.78
Oak leaves	0.71–0.78	0.91–0.95	0.78–0.82
Frozen soil	—	0.93–0.94	—
Desert surface	0.75	0.9	0.83
Common vegetable fields and shrubs	0.72–0.76	0.9	0.82
Ground, dry plowed	0.75–0.80	0.9	0.83–0.89
Oak woodland	0.82	0.9	0.91
Pine forest	0.86	0.9	0.96
Earth surface as a whole (land and sea, no clouds)	0.83		10^{10}
Class III substances: Absorptance to emittance ratios between 0.8 and 1.0			
Grey paint	0.75	0.95	0.79
Red oil base paint	0.74	0.90	0.82
Asbestos, slate	0.81	0.96	0.84
Asbestos, paper			0.93–0.96
Linoleum, red–brown	0.84	0.92	0.91
Dry sand	0.82	0.90	0.91
Green roll roofing	0.88	0.91–0.97	0.93

(Continued)

TABLE A3.3 (Continued)

Emittances and Absorptances of Materials

Substance	Short-Wave Absorptance	Long-Wave Emittance	$a \epsilon$
Slate, dark grey	0.89	—	
Old grey rubber			0.86
Hard black rubber	—	0.90–0.95	
Asphalt pavement	0.93	—	—
Black cupric oxide on copper	0.91	0.96	0.95
Bare moist ground	0.9	0.95	0.95
Wet sand	0.91	0.95	0.96
Water	0.94	0.95–0.96	0.98
Black tar paper	0.93	0.93	1.0
Black gloss paint	0.90	0.90	1.0
Small hole in large box, furnace, or enclosure	0.99	0.99	1.0
“Hohlraum,” theoretically perfect black body	1.0	1.0	1.0
Class IV substances: Absorptance to emittance ratios greater than 1.0			
Black silk velvet	0.99	0.97	1.02
Alfalfa, dark green	0.97	0.95	1.02
Lampblack	0.98	0.95	1.03
Black paint, 0.017 in. on aluminum	0.94–0.98	0.88	1.07–1.11
Granite	0.55	0.44	1.25
Graphite	0.78	0.41	1.90
High ratios, but absorptances less than 0.80			
Dull brass, copper, lead	0.2–0.4	0.4–0.65	1.63–2.0
Galvanized sheet iron, oxidized	0.8	0.28	2.86
Galvanized iron, clean, new	0.65	0.13	5.0
Aluminum foil	0.15	0.05	3.00
Magnesium	0.3	0.07	4.3
Chromium	0.49	0.08	6.13
Polished zinc	0.46	0.02	23.0
Deposited silver (optical reflector) untarnished	0.07	0.01	
Class V substances: Selective surfaces ^a			
Plated metals: ^b			
Black sulfide on metal	0.92	0.10	9.2
Black cupric oxide on sheet aluminum	0.08–0.93	0.09–0.21	
Copper (5×10^{-5} cm thick) on nickel or silver-plated metal			
Cobalt oxide on platinum			
Cobalt oxide on polished nickel	0.93–0.94	0.24–0.40	3.9
Black nickel oxide on aluminum	0.85–0.93	0.06–0.1	14.5–15.5
Black chrome	0.87	0.09	9.8
Particulate coatings:			
Lampblack on metal			
Black iron oxide, 47 μm grain size, on aluminum			

(Continued)

TABLE A3.3 (Continued)

Emittances and Absorptances of Materials

Substance	Short-Wave Absorptance	Long-Wave Emittance	$a \epsilon$
Geometrically enhanced surfaces: ^c			
Optimally corrugated greys	0.89	0.77	1.2
Optimally corrugated selectives	0.95	0.16	5.9
Stainless-steel wire mesh	0.63–0.86	0.23–0.28	2.7–3.0
Copper, treated with NaClO, and NaOH	0.87	0.13	6.69

Source: From Anderson, B., *Solar Energy*, McGraw-Hill Book Company, 1977. With permission.

^a Selective surfaces absorb most of the solar radiation between 0.3 and 1.9 μm , and emit very little in the 5–15 μm range—the infrared.

^b For a discussion of plated selective surfaces, see Daniels, *Direct Use of the Sun's Energy*, especially Chapter 12.

^c For a discussion of how surface selectivity can be enhanced through surface geometry, see Hollands, K.G.T., Directional selectivity emittance and absorptance properties of vee corrugated specular surfaces, *J. Sol. Energy Sci. Eng.*, 3, July 1963.

TABLE A3.4

Thermal Properties of Metals and Alloys

Material	k , Btu/(h)(ft) (°F)				c , Btu/(lb _m)(°F)	ρ , lb _m /ft ³	α , ft ² /h
	32°F	212°F	572°F	932°F	32°F	32°F	32°F
Metals							
Aluminum	117	119	133	155	0.208	169	3.33
Bismuth	4.9	3.9	—	—	0.029	612	0.28
Copper, pure	224	218	212	207	0.091	558	4.42
Gold	169	170	—	—	0.030	1203	4.68
Iron, pure	35.8	36.6	—	—	0.104	491	0.70
Lead	20.1	19	18	—	0.030	705	0.95
Magnesium	91	92	—	—	0.232	109	3.60
Mercury	4.8	—	—	—	0.033	849	0.17
Nickel	34.5	34	32	—	0.103	555	0.60
Silver	242	238	—	—	0.056	655	6.6
Tin	36	34	—	—	0.054	456	1.46
Zinc	65	64	59	—	0.091	446	1.60
Alloys							
Admiralty metal	65	64	—	—	—	—	—
Brass, 70% Cu, 30% Zn	56	60	66	—	0.092	532	1.14
Bronze, 75% Cu, 25% Sn	15	—	—	—	0.082	540	0.34
Cast iron							
Plain	33	31.8	27.7	24.8	0.11	474	0.63
Alloy	30	28.3	27	—	0.10	455	0.66
Constantan, 60% Cu, 40% Ni	12.4	12.8	—	—	0.10	557	0.22
18-8 Stainless steel,							
Type 304	8.0	9.4	10.9	12.4	0.11	488	0.15
Type 347	8.0	9.3	11.0	12.8	0.11	488	0.15
Steel, mild, 1% C	26.5	26	25	22	0.11	490	0.49

Source: Kreith, F., *Principles of Heat Transfer*, PWS Publishing Co., Boston, MA, 1997.

TABLE A3.5

Thermal Properties of Some Insulating and Building Materials

Material	Average, Temperature, °F	k , Btu/(h)(ft) (°F)	c , Btu/(lb _m) (°F)	ρ , lb _m /ft ³	a , ft ² /h
Insulating materials					
Asbestos	32	0.087	0.25	36	-0.01
	392	0.12	—	36	-0.01
Cork	86	0.025	0.04	10	-0.006
Cotton, fabric	200	0.046	—	—	—
Diatomaceous earth, powdered	100	0.030	0.21	14	-0.01
	300	0.036	—	—	—
	600	0.046	—	—	—
Molded pipe covering	400	0.051	—	26	26
	1600	0.088	—	—	—
Glass Wool					
Fine	20	0.022	—	—	—
	100	0.031	—	1.5	—
	200	0.043	—	—	—
Packed	20	0.016	—	—	—
	100	0.022	—	6.0	—
	200	0.029	—	—	—
Hair felt	100	0.027	—	8.2	—
Kaolin insulating brick	932	0.15	—	27	—
	2102	0.26	—	—	—
Kaolin insulating firebrick	392	0.05	—	19	—
	1400	0.11	—	—	—
85% magnesia	32	0.032	—	17	—
	200	0.037	—	17	—
Rock wool	20	0.017	—	8	—
	200	0.030	—	—	—
Rubber	32	0.087	0.48	75	0.0024
Building materials					
Brick					
Fire-clay	392	0.58	0.20	144	0.02
	1832	0.95	—	—	—
Masonry	70	0.38	0.20	106	0.018
Zirconia	392	0.84	—	304	—
	1832	1.13	—	—	—
Chrome brick	392	0.82	—	246	—
	1832	0.96	—	—	—
Concrete					
Stone	-70	0.54	0.20	144	0.019
10% Moisture	-70	0.70	—	140	-0.025

(Continued)

TABLE A3.5 (Continued)

Thermal Properties of Some Insulating and Building Materials

Material	Average, Temperature, °F	k , Btu/(h)(ft) (°F)	c , Btu/(lb _m) (°F)	ρ , lb _m /ft ³	a , ft ² /h
Glass, window	-70	-0.45	0.2	170	0.013
Limestone, dry	70	0.40	0.22	105	0.017
		Sand			
Dry	68	0.20	—	—	95
10% H ₂ O	68	0.60	—	—	100
Soil					
Dry	70	-0.20	0.44	—	-0.01
Wet	70	-1.5	—	—	-0.03
		Wood			
Oak \perp to grain	70	0.12	0.57	51	0.0041
to grain	70	0.20	0.57	51	0.0069
Pine \perp to grain	70	0.06	0.67	31	0.0029
to grain	70	0.14	0.67	31	0.0067
Ice	32	1.28	0.46	57	0.048

Source: Kreith, R., *Principles of Heat Transfer*, PWS Publishing Co., Boston, MA, 1997.

TABLE A3.6
Saturated Steam and Water—SI Units

Temperature, K	Pressure, MN/m ²	Specific Volume, m ³ /kg		Specific Energy Internal, kJ/kg		Specific Enthalpy, kJ/kg			Specific Entropy, kJ/kg K	
		v_f	v_g	u_f	u_g	h_f	h_{fg}	h_g	s_f	s_g
273.15	0.0006109	0.0010002	206.278	-0.03	2375.3	-0.02	2501.4	2501.3	-0.0001	9.1565
273.16	0.0006113	0.0010002	206.136	0	2375.3	+0.01	2501.3	2501.4	0	9.1562
278.15	0.0008721	0.0010001	147.120	+20.97	2382.3	20.98	2489.6	2510.6	+0.0761	9.0257
280.13	0.0010000	0.0010002	129.208	29.30	2385.0	29.30	2484.9	2514.2	0.1059	8.975
283.15	0.0012276	0.0010004	106.379	42.00	2389.2	42.01	2477.7	2519.8	0.1510	8.9008
286.18	0.0015000	0.0010007	87.980	54.71	2393.3	54.71	2470.6	2525.3	0.1957	8.8279
288.15	0.0017051	0.0010009	77.926	62.99	2396.1	62.99	2465.9	2528.9	0.2245	8.7814
290.65	0.0020000	0.0010013	67.004	73.48	2399.5	73.48	2460.0	2533.5	0.2607	8.7237
293.15	0.002339	0.0010018	57.791	83.95	2402.9	83.96	2454.1	2538.1	0.2966	8.6672
297.23	0.0030000	0.0010027	45.665	101.04	2408.5	101.05	2444.5	2545.5	0.3545	8.5776
298.15	0.003169	0.0010029	43.360	104.88	2409.8	104.89	2442.3	2547.2	0.3674	8.5580
302.11	0.004000	0.0010040	34.800	121.45	2415.2	121.46	2432.9	2554.4	0.4226	8.4746
303.15	0.004246	0.0010043	32.894	125.78	2416.6	125.79	2430.5	2556.3	0.4369	8.4533
306.03	0.005000	0.0010053	28.192	137.81	2420.5	137.82	2423.7	2561.5	0.4764	8.3951
308.15	0.005628	0.0010060	25.216	146.67	2423.4	146.68	2418.6	2565.3	0.5053	8.3531
309.31	0.006000	0.0010064	23.739	151.53	2425.0	151.53	2415.9	2567.4	0.5210	8.3304
312.15	0.007000	0.0010074	20.530	163.39	2428.8	163.40	2409.1	2572.5	0.5592	8.2758
313.15	0.007384	0.0010078	19.523	167.56	2430.1	167.57	2406.7	2574.3	0.5725	8.2570
314.66	0.008000	0.0010084	18.103	173.87	2432.2	173.88	2403.1	2577.0	0.5926	8.2287
316.91	0.009000	0.0010094	16.203	183.27	2435.2	183.29	2397.7	2581.0	0.6224	8.1872
318.15	0.009593	0.0010099	15.258	188.44	2436.8	188.45	2394.8	2583.2	0.6387	8.1648
318.96	0.010000	0.0010102	14.674	191.82	2437.9	191.83	2392.8	2584.7	0.6493	8.1502
323.15	0.012349	0.0010121	12.032	209.32	2443.5	209.33	2382.7	2592.1	0.7038	8.0763
327.12	0.015000	0.0010141	10.022	225.92	2448.7	225.94	2373.1	2599.1	0.7549	8.0085

(Continued)

TABLE A3.6
Saturated Steam and Water—SI Units

Temperature, K	Pressure, MN/m ²	Specific Volume, m ³ /kg		Specific Energy Internal, kJ/kg		Specific Enthalpy, kJ/kg			Specific Entropy, kJ/kg K	
		v_f	v_g	u_f	u_g	h_f	h_{fg}	h_g	s_f	s_g
328.15	0.015758	0.0010146	9.568	230.21	2450.1	230.23	2370.7	2600.9	0.7679	7.9913
333.15	0.019940	0.0010172	7.671	251.11	2456.6	251.13	2358.5	2609.6	0.8312	7.9096
333.21	0.020000	0.0010172	7.649	251.38	2456.7	251.40	2358.3	2609.7	0.8320	7.9085
338.15	0.025030	0.0010199	6.197	272.02	2463.1	272.06	2346.2	2618.3	0.8935	7.8310
342.25	0.030000	0.0010223	5.229	289.20	2468.4	289.23	2336.1	2625.3	0.9439	7.7686
343.15	0.031190	0.0010228	5.042	292.95	2469.6	292.98	2333.8	2626.8	0.9549	7.7553
348.15	0.038580	0.0010259	4.131	313.90	2475.9	313.93	2221.4	2635.3	1.0155	7.6824
349.02	0.040000	0.0010265	3.993	317.53	2477.0	317.58	2319.2	2636.8	1.0259	7.6700
353.15	0.047390	0.0010291	3.407	334.86	2482.2	334.91	2308.8	2643.7	1.0753	7.6122
354.48	0.050000	0.0010300	3.240	340.44	2483.9	340.49	2305.4	2645.9	1.0910	7.5939
358.15	0.057830	0.0010325	2.828	355.84	2488.4	355.90	2296.0	2651.9	1.1343	7.5445
359.09	0.060000	0.0010331	2.732	359.79	2489.6	359.86	2293.6	2653.5	1.1453	7.5320
363.10	0.070000	0.0010360	2.365	376.63	2494.5	376.70	2283.3	2660.0	1.1919	7.4797
363.15	0.070140	0.0010360	2.361	376.85	2494.5	376.92	2283.2	2660.1	1.1925	7.4791
366.65	0.080000	0.0010386	2.087	391.58	2498.8	391.66	2274.1	2665.8	1.2329	7.4346
368.15	0.084550	0.0010397	1.9819	397.88	2500.6	397.96	2270.2	2668.1	1.2500	7.4159

Source: Bolz, R.E. and Tuve, G.L. (Eds.), *CRC Handbook of Tables for Applied Engineering Science*, 2nd edn., Chemical Rubber Co., Cleveland, OH, 1973.

Subscripts: f refers to a property of liquid in equilibrium with vapor; g refers to a property of vapor in equilibrium with liquid; fg refers to a change by evaporation.

TABLE A3.7

Superheated Steam—SI Units

Pressure (MN/m ²) (Saturation Temperature) ^a		Temperature									
		50°C	100°C	150°C	200°C	300°C	400°C	500°C	700°C	1000°C	1300°C
		323.15 K	373.15 K	423.15 K	473.15 K	573.15 K	673.15 K	773.15 K	973.15 K	1273.15 K	1573.15 K
0.001 (6.98°C) (280.13K)	<i>v</i>	149.093	172.187	195.272	218.352	264.508	310.661	356.814	449.117	587.571	726.025
	<i>u</i>	2445.4	2516.4	2588.4	2661.6	2812.2	2969.0	3132.4	3479.6	4053.0	4683.7
	<i>h</i>	2594.5	2688.6	2783.6	2880.0	3076.8	3279.7	3489.2	3928.7	4640.6	5409.7
	<i>s</i>	9.2423	9.5129	9.7520	9.9671	10.3443	10.6705	10.9605	11.4655	12.1019	12.6438
0.002 (17.50°C) (290.65 K)	<i>v</i>	74.524	86.081	97.628	109.170	132.251	155.329	178.405	224.558	293.785	363.012
	<i>u</i>	2445.2	2516.3	2588.3	2661.6	2812.2	2969.0	3132.4	3479.6	4053.0	4683.7
	<i>h</i>	2594.3	2688.4	2793.6	2879.9	3076.7	3279.7	3489.2	3928.7	4640.6	5409.7
	<i>s</i>	8.9219	9.1928	9.4320	9.6471	10.0243	10.3506	10.6406	11.1456	11.7820	12.3239
0.004 (28.9°C) (302.11 K)	<i>v</i>	37.240	43.028	48.806	54.580	66.122	77.662	89.201	112.278	146.892	181.506
	<i>u</i>	2444.9	2516.1	2588.2	2661.5	2812.2	2969.0	3132.3	3479.6	4053.0	4683.7
	<i>h</i>	2593.9	2688.2	2783.4	2879.8	3076.7	3279.6	3489.2	3928.7	4640.6	5409.7
	<i>s</i>	8.6009	8.8724	9.1118	9.3271	9.7044	10.0307	10.3207	10.8257	11.4621	12.0040
0.006 (36.16°C) (309.31 K)	<i>v</i>	24.812	28.676	32.532	36.383	44.079	51.774	59.467	74.852	97.928	121.004
	<i>u</i>	2444.6	2515.9	2588.1	2661.4	2812.2	2969.0	31323	3479.6	4053.0	4683.7
	<i>h</i>	2593.4	2688.0	2783.3	2879.7	3076.6	3279.6	3489.1	3928.7	4640.6	5409.7
	<i>s</i>	8.4128	8.6847	8.9244	9.1398	9.5172	9.8435	10.1336	10.6386	11.2750	11.8168
0.008 (41.51°C) (314.66 K)	<i>v</i>	18.598	21.501	24.395	27.284	33.058	38.829	44.599	56.138	73.446	90.753
	<i>u</i>	2444.2	2515.7	2588.0	2661.4	2812.1	2969.0	3132.3	3479.6	4053.0	4683.7
	<i>h</i>	2593.0	2687.7	2783.1	2879.6	3076.6	3279.6	3489.1	3928.7	4640.6	5409.7
	<i>s</i>	8.2790	8.5514	8.7914	9.0069	9.3844	9.7107	10.0008	10.5058	11.1422	11.6841
0.010 (45.81°C) (318.96 K)	<i>v</i>	14.869	17.196	19.512	21.825	26.445	31.063	35.679	44.911	58.757	72.602
	<i>u</i>	2443.9	2515.5	2587.9	2661.3	2812.1	2968.9	3132.3	3479.6	4053.0	4683.7
	<i>h</i>	2592.6	2687.5	2783.0	2879.5	3076.5	3279.6	3489.1	3928.7	4640.6	5409.7
	<i>s</i>	8.1749	8.4479	8.6882	8.9038	9.2813	9.6077	9.8978	10.4028	11.0393	11.5811

(Continued)

TABLE A3.7 (Continued)
 Superheated Steam—SI Units

Pressure (MN/m ²) (Saturation Temperature) ^a		Temperature									
		50°C	100°C	150°C	200°C	300°C	400°C	500°C	700°C	1000°C	1300°C
		323.15 K	373.15 K	423.15 K	473.15 K	573.15 K	673.15 K	773.15 K	973.15 K	1273.15 K	1573.15 K
0.020 (60.06°C) (333.21 K)	<i>v</i>	7.412	8.585	9.748	10.907	13.219	15.529	17.838	22.455	29.378	36.301
	<i>u</i>	2442.2	2514.6	2587.3	2660.9	2811.9	2968.8	3132.2	3479.5	4053.0	4683.7
	<i>h</i>	2590.4	2686.2	2782.3	2879.1	3076.3	3279.4	3489.0	3928.6	4640.6	5409.7
0.040 (75.87°C) (349.02 K)	<i>s</i>	7.8498	8.1255	8.3669	8.5831	8.9611	9.2876	9.5778	10.0829	10.7193	11.2612
	<i>v</i>	3.683	4.279	4.866	5.448	6.606	7.763	8.918	11.227	14.689	18.151
	<i>u</i>	2438.8	2512.6	2586.2	2660.2	2811.5	2968.6	3132.1	3479.4	4052.9	4683.6
0.060 (85.94°C) (359.09 K)	<i>h</i>	2586.1	2683.8	2780.8	2878.1	3075.8	3279.1	3488.8	3928.5	4640.5	5409.6
	<i>s</i>	7.5192	7.8003	8.0444	8.2617	8.6406	8.9674	9.2577	9.7629	10.3994	10.9412
	<i>v</i>	2.440	2.844	3.238	3.628	4.402	5.174	5.944	7.484	9.792	12.100
0.080 (93.50°C) (366.65 K)	<i>u</i>	2435.3	2510.6	2585.1	2659.5	2811.2	2968.4	3131.9	3479.4	4052.9	4683.6
	<i>h</i>	2581.7	2681.3	2779.4	2877.2	3075.3	3278.8	3488.6	3928.4	4640.4	5409.6
	<i>s</i>	7.3212	7.6079	7.8546	8.0731	8.4528	8.7799	9.0704	9.5757	10.2122	10.7541
0.100 (99.63°C) (372.78 K)	<i>v</i>	1.8183	2.127	2.425	2.718	3.300	3.879	4.458	5.613	7.344	9.075
	<i>u</i>	2431.7	2508.7	2583.9	2658.8	2810.8	2968.1	3131.7	3479.3	4052.8	4683.5
	<i>h</i>	2577.2	2678.8	2777.9	2876.2	3074.8	3278.5	3488.3	3928.3	4640.4	5409.5
0.200 (120.23°C) (393.38 K)	<i>s</i>	7.1775	7.4698	7.7191	7.9388	8.3194	8.6468	8.9374	9.4428	10.0794	10.6213
	<i>v</i>	1.4450	1.6958	1.9364	2.172	2.639	3.103	3.565	4.490	5.875	7.260
	<i>u</i>	2428.2	2506.7	2582.8	2658.1	2810.4	2967.9	3131.6	3479.2	4052.8	4683.5
	<i>h</i>	2572.7	2676.2	2776.4	2875.3	3074.3	3278.2	3488.1	3928.2	4640.3	5409.5
	<i>s</i>	7.0633	7.3614	7.6134	7.8343	8.2158	8.5435	8.8342	9.3398	9.9764	10.5183
	<i>v</i>	0.6969	0.8340	0.9596	1.0803	1.3162	1.5493	1.7814	2.244	2.937	3.630
	<i>u</i>	2409.5	2496.3	2576.9	2654.4	2808.6	2966.7	3130.8	3478.8	4052.5	4683.2
	<i>h</i>	2548.9	2663.1	2768.8	2870.5	3071.8	3276.6	3487.1	3927.6	4640.0	5409.3

(Continued)

TABLE A3.7 (Continued)

Superheated Steam—SI Units

Pressure (MN/m ²) (Saturation Temperature) ^a	Temperature										
	50°C	100°C	150°C	200°C	300°C	400°C	500°C	700°C	1000°C	1300°C	
	323.15 K	373.15 K	423.15 K	473.15 K	573.15 K	673.15 K	773.15 K	973.15 K	1273.15 K	1573.15 K	
0.300 (133.55°C) (406.70 K)	<i>s</i>	6.6844	7.0135	7.2795	7.5066	7.8926	8.2218	8.5133	9.0194	9.6563	10.1982
	<i>v</i>	0.4455	0.5461	0.6339	0.7163	0.8753	1.0315	1.1867	1.4957	1.9581	2.4201
	<i>u</i>	2389.1	2485.4	2570.8	2650.7	2806.7	2965.6	3130.0	3478.4	4052.3	4683.0
0.400 (143.63°C) (416.78 K)	<i>h</i>	2522.7	2649.2	2761.0	2865.6	3069.3	3275.0	3486.0	3927.1	4639.7	5409.0
	<i>s</i>	6.4319	6.7965	7.0778	7.3115	7.7022	8.0330	8.3251	8.8319	9.4690	10.0110
	<i>v</i>	0.3177	0.4017	0.4708	0.5342	0.6548	0.7726	0.8893	1.1215	1.4685	1.8151
0.500 (151.86°C) (425.01 K)	<i>u</i>	2366.3	2473.8	2564.5	2646.8	2804.8	2964.4	3129.2	3477.9	4052.0	4682.8
	<i>h</i>	2493.4	2634.5	2752.8	2860.5	3066.8	3273.4	3484.9	3926.5	4639.4	5408.8
	<i>s</i>	6.2248	6.6319	6.9299	7.1706	7.5662	7.8985	8.1913	8.6987	9.3360	9.8780
	<i>v</i>		0.3146	0.3729	0.4249	0.5226	0.6173	0.7109	0.8969	1.1747	1.4521
	<i>u</i>		2461.5	2557.9	2642.9	2802.9	2963.2	328.4	3477.5	4051.8	4682.5
	<i>h</i>		2618.7	2744.4	2855.4	3064.2	3271.9	3483.9	3925.9	4639.1	5408.6
	<i>s</i>		6.4945	6.8111	7.0592	7.4599	7.7938	8.0873	8.5952	9.2328	9.7749

Source: Bolz, R.E. and Tuve, G.L. (Eds.) *CRC Handbook of Tables for Applied Engineering Science*, 2nd edn., Chemical Rubber Co., Cleveland, OH, 1973.

^a Symbols: *v*, specific volume, m³/kg; *u*, specific internal energy, U/kg; *h*, specific enthalpy, kJ/kg; *s*, specific entropy, kJ/K kg.



Taylor & Francis

Taylor & Francis Group

<http://taylorandfrancis.com>

Appendix D: Ultimate Analysis of Biomass Fuels

Nitin Goel

Material	Ca (%)	H ₂ ^a (%)	O ₂ ^a (%)	N ₂ ^a (%)	S ^a (%)	A ^a (%)	HHV (kJ/kg) ^b
Agricultural wastes							
Bagasse (sugarcane refuse)	47.3	6.1	35.3	0.0	0.0	11.3	21,255
Feedlot manure	42.7	5.5	31.3	2.4	0.3	17.8	17,160
Rice hulls	38.5	5.7	39.8	0.5	0.0	15.5	15,370
Rice straw	39.2	5.1	35.8	0.6	0.1	19.2	15,210
Municipal solid waste							
General	33.9	4.6	22.4	0.7	0.4	38.0	13,130
Brown paper	44.9	6.1	47.8	0.0	0.1	1.1	17,920
Cardboard	45.5	6.1	44.5	0.2	0.1	3.6	18,235
Corrugated boxes	43.8	5.7	45.1	0.1	0.2	5.1	16,430
Food fats	76.7	12.1	11.2	0.0	0.0	0.0	38,835
Garbage	45.0	6.4	28.8	3.3	0.5	16.0	19,730
Glass bottles (labels)	0.5	0.1	0.4	0.0	0.0	99.0	195
Magazine paper	33.2	5.0	38.9	0.1	0.1	22.7	12,650
Metal cans (labels, etc.)	4.5	0.6	4.3	0.1	0.0	90.5	1,725
Newspapers	49.1	6.1	43.0	0.1	0.2	1.5	19,720
Oils, paints	66.9	9.6	5.2	2.0	0.0	16.3	31,165
Paper food cartons	44.7	6.1	41.9	0.2	0.2	6.9	17,975
Plastics							
General	60.0	7.2	22.6	0.0	0.0	10.2	33,415
Polyethylene	85.6	14.4	0.0	0.0	0.0	0.0	46,395
Vinyl chloride	47.1	5.9	18.6	(Chlorine = 28.4%)	20,535		
Rags	55.0	6.6	31.2	4.6	0.1	2.5	13,955
Rubber	77.7	10.3	0.0	0.0	2.0	10.0	26,350
Sewage							
Raw sewage	45.5	6.8	25.8	3.3	2.5	16.1	16,465
Sewage sludge	14.2	2.1	10.5	1.1	0.7	71.4	4,745
Wood and wood products							
Hardwoods							
Beech	51.6	6.3	41.5	0.0	0.0	0.6	20,370
Hickory	49.7	6.5	43.1	0.0	0.0	0.7	20,165

(Continued)

Material	Ca (%)	H ₂ ^a (%)	O ₂ ^a (%)	N ₂ ^a (%)	S ^a (%)	A ^a (%)	HHV (kJ/kg) ^b
Maple	50.6	6.0	41.7	0.3	0.0	1.4	19,955
Poplar	51.6	6.3	41.5	0.0	0.0	0.6	20,745
Oak	49.5	6.6	43.4	0.3	0.0	0.2	20,185
Softwoods							
Douglas fir	52.3	6.3	40.5	0.1	0.0	0.8	21,045
Pine	52.6	6.1	40.9	0.2	0.0	0.2	21,280
Redwood	53.5	5.9	40.3	0.1	0.0	0.2	21,025
Western hemlock	50.4	5.8	41.4	0.1	0.1	2.2	20,045
Wood products							
Charcoal (made at 400°C)	76.5	3.9	15.4	0.8	0.0	3.4	28,560
Charcoal (made at 500°C)	81.7	3.2	11.5	0.2	0.0	3.4	31,630
Douglas fir bark	56.2	5.9	36.7	0.0	0.0	1.2	22,095
Pine bark	52.3	5.8	38.8	0.2	0.0	2.9	20,420
Dry sawdust pellets	47.2	5.5	46.3	0.0	0.0	1.0	20,500
Ripe leaves	40.5	6.0	45.1	0.2	0.1	8.1	16,400
Plant wastes							
Brush	42.5	5.9	41.2	2.0	0.1	8.3	18,370
Evergreen trimmings	49.5	6.6	41.2	1.7	0.2	0.8	6,425
Garden plants	48.0	6.8	41.3	1.2	0.3	2.4	8,835
Grass	48.4	6.8	41.6	1.2	0.3	1.7	18,520

^a All percentages on moisture-free basis.

^b 1 kJ/kg = 0.43 Btu/lbm.

Index

- “Atoms for Peace” speech, 457
1990 Clean Air Act Amendments, effect of on
 transportation of coal, 46–47
2,3,7,8-TCDD, 1017
3PRH bottoming cycles, 315, 319, 359
40 CFR Part 60, 1011–1012
450 scenario, 14–15, 28
- A**
- a*-Si cells, 800, 806–807
 configurations, 810–811
 deposition techniques for, 808
 fabrication of, 777–778
 flexible, 814–816
 stability and recombination issues in,
 809–810
- a*-Si:H cells
 configurations for, 808–809
 deposition techniques for, 808
- ABAQUS, 872
- Abengoa, 674, 724
- Absolute efficiency, 276
- Absorber pipes
 enhancing heat transfer in, 704
 flow in, 700–701
- Absorbers
 compound parabolic concentrators, 539–540
 design of, 731
 design of for flat-plate collectors, 530
 flat-plate solar collectors, 662–664, 667
 ideal temperatures of, 663–664
 reducing losses from, 537–538
 use of in tubular receivers, 732–734
 use of in volumetric receivers, 734–739
- Absorption carbon capture, 295
- Absorption charge mode, 781
- Absorption effects, 666
- Absorptivity, 683
- AC solar array systems, 782
- Acceptance angle, 681–682
- Acid electrolyte fuel cell, 1035, 1071. *See also*
 PEMFCs
- Acid rain, combustion of coal and, 48
- Acoustic flow meters, 277
- ACPR nuclear reactors, 467
- Active length factor, 683
- Active pitch control rotors, 875
- Active solar systems, 551
 closed-loop, 554–557
 controls for, 557–562
 design recommendations and costs, 578–579
- Active space heating, design approach for,
 570–573
- AD process, microbial phases in, 915
- ADAMS, 872
- Additive manufacturing, use of to reduce inlet
 temperature gaps, 352
- Adiabatic saturators
 definition of, 221
 use of with gas turbines, 218
- Adsorption carbon capture, 295
- Advanced boiling water reactors (AWBRs), 465
- Advanced fossil fuel power systems.
 See AFFPS
- Advanced gas-cooled reactor (AGR), 460
- Advanced heavy-water reactor (AHWR), 468
- Advanced power systems, categories of, 283
- Advanced pressurized water reactor (APWR),
 466–467
- Advanced thermal reactors, 465–466. *See also*
 Generation III nuclear reactors
- Aeroderivative gas turbines, air standard cycle
 calculations for, 317–318
- Aerodynamic loading, 869–870
- Aerodynamic models of wind turbines,
 860–868
- AES nuclear reactors, 467
- AFFPS, 435
 cogeneration, 364–367
 combustion technologies, 335–345
 determinants for, 296–301
 fuel cell hybrid system, 305–306
 fuel flexibility, 369–372
 GTCC high performance cycles, 355–360
 GTCC technology, 351–355
 indirectly fired gas turbines, 361–362
 operational flexibility, 367–369
 repowering, 362–364
 thermodynamics of, 308–319
 USC power plants, 345–351
 use of GTCC system for benchmark, 319
- Agricultural residues, 66
- Air
 use of as a working fluid, 527–528
 use of to cool gas turbines, 220

- Air gasification, 902
- Air heat transfer, 630–631
- Air mass ratio, 102–103
- Air pollution
 - control of from MSW combustion, 996–997
 - emission requirements, 1011–1012
 - gaseous emission control, 1014–1016
 - organic compound control, 1016–1019
 - particulate control, 1012–1013
 - trace metals from MSW residue, 1019–1022
- Air quality control, 286, 417–423
- Air quality control systems. *See* AQCS
- Air separation unit (ASU), 290, 392–393, 434
- Air solar collectors, 552
- Air staging, 339
- Air standard power cycles, 230
 - calculations for heavy duty GTs, 317–318
 - idea Diesel cycle, 232–233
 - ideal Otto cycle, 230–232
- Air temperature, transient thermal analysis of, 630–631
- Air throttling, 234
- Air-blown gasifiers, 904–905
- Air-cooled volumetric receivers, 735
- Air–fuel mixture
 - SI engine emissions levels and, 242–243
 - SI engines, 236–238
- Airfoils, 855. *See also* Wind turbines
 - performance characteristics, 866
- Alcohols
 - butanol, 922
 - cellulosic ethanol, 921–922
 - corn ethanol, 918–921
 - mixed, 924
- Algae, 69
- Alkaline fuel cells (AFCs), 1067–1069
- All-or-nothing auxiliary heaters, 555–556
- Allam cycle, 299
- Alloy steels, 381–382
- Alloying elements, 383
- Alpha iron, 383
- Altitude angle, 91, 635, 779
- American Petroleum Institute (API) gravity
 - scale. *See* API gravity
- American Society of Heating, Refrigerating, and Air-Conditioning Engineers. *See* ASHRAE
- American Society of Testing and Materials. *See* ASTM
- Amine-based absorption/stripper process, 296
- Ammonia
 - leakage of from SCR converters, 243
 - production of from biomass, 916
- Ammonia–water binary power plants, 976
- Amorphous silicon PV cells. *See* a-Si cells
- Anaerobic digestion. *See also* AD process
 - conversion of biomass to biogas using, 914–915
- Anaerobic digestors, 916
- ANDASOL, 678
- ANDASOL-I plant, 712
- Anemometers, 159–160
 - selection of, 160
- Aneutronic fusion, 492
- Angle of incidence, 106
- Ångström–Page regression equation, 113–114
- Angular dependence, 534
- Anisotropic of diffuse solar radiation, 118–119
- Annual lighting energy saved, 635
- Annual normal incident radiation, 656
- Anodes in fuel cells, 1035
- Anthracite, 34–36
 - reserves of, 39–40
- Antiknock index, 245
- Aora, 724
- Aperture-area-weighted SSF, 615
- API gravity, 59
 - definition of, 60
- AQCS, 286
 - use of in FFPS, 295
- Archimede Solar, 677
- ARDISS, 703
- Area–velocity measurements, 276
- AREVA, 715
- Areva-EdF-CGNPC nuclear reactor, 467
- Ash content of coal, 36–39
- Ash discharge facilities, 1010
- Ash fusibility, 39
- ASHRAE
 - clear sky model, 103–105
 - Standard 93-77, 533
- Asphalt, 55
- ASTM
 - alloy steel specifications, 382
 - coal property analysis, 36–39
 - coal rank classification scheme of, 34–36
 - Standard D975, 246
 - Standard D976, 246
 - Standards Part 47, 244–245
- Atmea1 nuclear reactor, 467
- Atmospheric IGFC, 307–308
- ATS heliostat, 724
- Attached sunspace, 586–587
- Ausra, 715
- Austenite, 383

- Australia
 - evolution of LF reflector systems in, 714–715
 - hot fractured rock development in, 936
 - use of linear Fresnel systems in, 673–674
- Autoignition, 228
- Autoignition temperature, 370
- Automatic generation control (AGC), 368
- Automotive storage technologies, 501
 - energy density, cycle life, and efficiency of, 503
- Auxiliary heaters, 555–556
 - designs for closed-loop multipass systems, 573–575
- Auxiliary power, 287
- Auxiliary technologies, 284
- Azimuth angle, 91, 635, 779

- B**
- Baghouses
 - use of in gaseous emission control, 1015
 - use of in organic compound control, 1019
- Balance of plant (BOP), 293
- Balance of the system (BOS) costs, 767
- Ball joints, use of in connecting PTCs, 679–681
- Bandgap
 - effect of on solar cell efficiency, 767
 - semiconductor materials used in solar cells, 799
 - tailoring for *a*-Si, 807
- Bang-bang control, 555
- Barometric pressure, determination of air density using, 161
- Barrel swirl, 236
- Base load, 320
- Baseloaded, 944
- Bat fatalities, impact of wind facilities, 150
- Batch feeding of MSW, 995
- Batteries
 - capacity of in PHEVs, 8
 - flow, 509–511
 - lead-acid, 506
 - lithium ion, 506–507
 - nickel metal hydride, 507–508
 - nickel-cadmium, 507
 - secondary, 505–506
 - sodium-sulfur, 508
 - zebra, 509
- Beam radiation, 101
- Beam solar radiation, measurement of, 126–127
- Belgium, nuclear power capacity in, 461
- Berzelius, 82
- Best Available Control Technology (BACT), 1027
- Betz limit, 863
- Binary power plants, 938, 947
 - advantages of, 973–974
 - integration of steam turbines in, 977–980
 - pressurized geothermal brine, 976–977
 - types of, 975–976
- Bio-oil upgrading, 925–926
- Biodiesel, 918
 - production of from biomass, 922–924
- Biofuels, 8, 918
 - drop-in, 927
 - ethanol, 918–922
 - production of, 19–21
 - properties of, 926–927
 - world production of, 20–21
- Biogas, 914–915
- Biomass
 - analysis of, 64–65
 - co-firing, 902
 - conversion of to heat and power, 897–898 (*See also* Biomass conversion)
 - definition of, 61
 - demand for, 4
 - land use for production of, 69–71
 - physical and thermochemical properties of, 63
 - potential of, 19–21
 - productivity data, 63
 - role of in future energy mix, 27–28
 - solar energy conversion to, 61–63
 - torrefied, 913–914
 - total energy potential of, 14
- Biomass conversion, 898
 - biofuel properties, 926–927
 - combustion equipment, 901–902
 - direct combustion, 898–901
 - facility efficiency and capacity comparison, 899
 - gaseous fuels, 914–917
 - gasification, 902–904
 - gasification equipment, 904–907
 - gasification equipment types, 905
 - heat and power cycles, 907–912
 - liquid fuels, 917–926
 - processes of solid fuel combustion, 900
 - solid fuels, 913–914
- Biomass crops
 - nominal annual yields of, 69
 - primary productivity and solar efficiency of, 520
- Biomass energy systems, 898
- Biomass fuels, thermal performance of, 64
- Biomass gasification, 898

- Biomass properties, plant composition, 63–64
- Biomass resources, 66
- algae, 69
 - energy crops, 67–68
 - waste materials, 66–67
- Biomass solids, thermochemical energy storage by, 519–520
- Biomass storage technologies
- biodiesel, 521
 - ethanol, 520–521
 - syngas, 521–522
- Biorenewable resources, 66–67
- Bipolar fuel cell connections, 1064–1066
- Bird fatalities, impact of wind facilities, 149–150
- Bituminous coal, 35–36
- analysis of, 38–39
 - reserves of, 39–40
- Blade cooling, 219–220
- Blade element momentum (BEM), 864
- Blade stall control, 874
- BLADED, 872
- Blades for steam turbines, 199–200
- Blast furnace gas (BFG), 289–290
- Blocking losses, 721
- Blowdown, wastewater from, 296
- Blowers, capacity of in MSW furnaces, 1007
- BN-series of fast neutron reactors, 469–470
- Boiler feed pump (BFP), 204
- Boilers, 901
- design of in WTE facilities, 988
 - mass-fired water wall units, 1008–1009
 - RDF-fired water wall systems, 1009
 - refractory furnace with waste heat, 1008
 - steam, 196–198
 - suitable alloys for construction of, 383–384
 - tube corrosion in, 1011
- Boiling water reactors (BWRs), 457, 459
- Boost pressure, 247–250
- Bottom ash, 1010
- Bottom dead center (BDC)
- four-stroke SI engines, 225
 - two-stroke SI engines, 227
- Bottoming cycles, 196
- use of in waste energy recovery, 250–252
- Boudouard reaction, 903–904
- Boundary Dam Power Station CCS project, 407
- Box turbines, 854
- Brake mean effective pressure (bmep),
- calculation of, 235
- Brake work, 234–235
- Brake-specific fuel consumption (bsfc),
- calculation of, 235
- Brayton cycle, 209, 213–215, 292, 297, 909–910
- impact of constant-volume heat addition on, 341–342
 - supercritical CO₂, 376–379
- Brayton gas turbine cycles, state-of-the-art, 297
- Brayton–Rankine combined cycle. *See also* GTCC
- calculating thermal efficiency of, 311–314
- Breeder reactors, 478
- BREST nuclear reactor, 469
- BrightSource, 674, 724, 743
- Bubbly flow, 701
- Building integrated PV (BIPV), 17, 799
- use of *a*-SI thin film technology for, 815
- Building-attached photovoltaics (BAPV), 815
- Buildings, effect of on wind speed, 154–155
- Bulb turbines, 260
- Bulk segment, 781
- Buoyant force pressure difference, 583
- Buried contact cells, 778
- Burning velocity, 371
- Butane (C₄H₁₀). *See* Hydrocarbons
- Butanol, 922
- C**
- C-P&R correlation, 115–118
- model of, 119–122
- c-Si technology, 796–797, 806–807
- C4 plants, conversion of solar energy by, 62
- Cadmium, environmental concerns, 835–836
- Cadmium telluride solar cells. *See* CdTe solar cells
- California
- geothermal power transmission in, 940
 - use of geothermal energy in, 933
- Calorific values, use of in coal property analysis, 37–38
- Campbell–Stokes sunshine recorder, 128–129
- Canada
- installed wind power capacity in, 852
 - nuclear power reactors in, 459–460
 - use of heavy-water reactors in, 468
- CANDU reactor, 459–460, 480
- EC6, 468
- CAP1000 nuclear reactor (China), 465
- Capital charge factor, 320
- Capital costs
- CRS plants, 718
 - estimating for FFPS, 319–323
 - geothermal power plants, 946–947
 - learning curve for FOAK technologies, 322

- minimization of for geothermal development, 952–954
 - nuclear power, 488–489
 - PTC systems, 711
 - STP plants, 659, 672
 - wind turbines, 886–890
 - WTE facilities, 1023–1025
- Carbon, combustible portion of in MSW, 995–996
- Carbon capture and sequestration. *See* CCS
- Carbon capture systems, types of, 295–296
- Carbon fiber, use of for wind turbines, 882
- Carbon fixation pathways, 62
- Carbon monoxide
- combustion conditions and production of, 900
 - emissions from IC engines, 240–241
 - emissions of from MSW incineration, 1014–1016
 - emissions of in flue gas, 295
 - production of from MSW combustion, 997
 - reduction of in coal combustion, 339–340
- Carbon sequestration, 10
- Carbon–oxygen reactions, 903–904
- Carbon–water reactions, 903–904
- Carbonization, 898, 914
- Carburetors, 236
- Carnot cycle, 308
- comparison of with Rankine cycle, 193–194
 - efficiency of, 662
- Carnot efficiency
- equivalency of with reversible efficiency, 1049–1050
 - fuel cells, 1048–1049
- Carnot factor
- characterization of bottoming cycles using, 310–311
 - contemporary heat engines, 316–317
- Carnot limit, 305
- Carnot target, 309
- Cascaded HAT (CHAT), 359–360
- Case studies, initial wind farm development in New Mexico, 171–173
- Catalytic combustor, reduction of emissions using, 339
- Catalytic converters, emission control using, 243
- Catalytic gasifiers, 308
- Catalytic hydromethanation, 399
- Cathodes in fuel cells, 1035
- Cavitation of hydraulic turbines, 270
- Cavity receivers, 729, 731
- CCS, 284. *See also* Post-combustion carbon capture system
- proposed technologies for, 298–300
 - use of with IGCC power plants, 391–392
- CdTe PV modules, 796–797, 800
- environmental concerns, 835–836
- CdTe solar cells
- absorber layer, 819
 - deposition techniques for, 820–821
 - device structure, 817
 - electrical backcontact and stability issues, 819–820
 - flexible, 821
 - junction activation treatment, 819
 - material and properties of, 816
 - n*-type window layer, 818
 - schematic of, 817
 - TCO front electrical contact configuration, 817–818
- Cellulose, 64
- Cellulosic ethanol, 921–922
- Cellulosic material, characteristics of in MSW, 989
- Center-feed configuration of solar fields, 693
- Central receiver systems. *See* CRSs
- Centrifugal blower, 248
- Centrifuge uranium enrichment, 480–481
- Ceramic materials
- use of for gas turbine coatings, 220
 - use of for thermal energy storage, 698
- Ceramic matrix composites, 389–390
- potential use of with reheat combustion, 357
 - use of to reduce inlet temperature gaps, 352
- CESA-1, 733
- Cetane index, 246
- Cetane number, 240, 246, 918
- CFD models, 866–867
- Chalcopyrites, 821–823. *See also* CIGS solar cells
- Chalder Hall nuclear power plant, 462
- Champion thin-film solar cell efficiencies, 798
- Chaplecross nuclear power plant, 462
- Char, 899–900
- oxidation of, 900–901
 - production of in gasification process, 903
- Charge cooling, 250
- Chemical looping combustion (CLC), 299, 416–417
- Chemical spraying (CS), 819
- Chemical vapor deposition (CVD), 777–778, 808
- China
- CAP1000 nuclear reactor, 465
 - coal use in, 10–11
 - energy use in, 2–4

- HTR-PM nuclear reactor, 468
- increase in electricity-generating capacity, 6
- power capacity of, 4
- power production in, 4
- production of c-Si modules in, 796
- solar collectors in, 17–18
- use of nuclear power in, 12
- Chinooks, 138
- Chisholm's model, 703
- Chlorinated hydrocarbons, combustion
 - conditions and production of, 900
- Chromium, 383
- CI engines, 224
 - basic operation of, 228–229
 - combustion in, 239–240
 - compression ratio, 231–232
 - emission reduction, 243
 - fuels for, 245–246
 - knock in, 240
 - particulate emissions from, 241–242
 - power output control in, 234
 - supercharging, 247–248
 - turbocharging, 248–250
- CIGS solar cells, 797, 800, 812
 - absorber layer, 823
 - alternative growth processes for, 826–827
 - buffer layer, 823–824
 - coevaporation process, 825–826
 - configurations, 817–818, 823–825
 - cost estimates for, 805
 - electrical backcontact, 823
 - environmental concerns, 835–836
 - flexible, 827–829
 - front electrical contact, 824
 - material and properties, 821–823
 - potassium incorporation in, 825
 - selenization of precursor materials, 825–827
 - sodium incorporation in, 824
- Circulating fluidized bed (CFB) combustion, 339–341
- Circumsolar radiation, 118–119
- Clean Air Act Amendments (1990), effect of on transportation of coal, 46–47
- Clean coal technology, 10
- Clear sky illuminance, 642
- Clear sky radiation model, 103–105
- Climate change, 7, 27–28
- Cloncurry, 724
- Closed heaters, 203–204
- Closed-cycle gas turbines, 217
 - use of in FFPS, 292
- Closed-cycle reprocessing, 478
- Closed-loop multipass systems
 - design of with auxiliary heater in parallel, 573–574
 - design of with auxiliary heater in series, 574–575
- Closed-loop solar systems, 552–553
 - description of, 554–557
- Closed-loop steam cooling. *See also* H-System
 - use of to reduce TIT–RIT temperature loss, 355–357
- Closed-space sublimation. *See* CSS
- Cloud cover, 780
- Cloud point, 246
- Co-firing, 902
- CO₂ emission factor, 333–334
- CO₂ emissions, 295, 333. *See also* Hydrocarbons
 - coal combustion and, 48
 - combustion conditions and production of, 900
 - flash-steam power plants, 980–981
 - increasing electricity-generating capacity and, 6
 - transportation sources of, 6
 - use of renewable energy sources to decrease, 5
- CO₂ sequestration, 27
- Coal, 289
 - analysis and properties of, 36–39
 - average properties of, 333
 - combustion of, 332–334
 - composition and classification, 33–36
 - conversion processes, 39
 - demand for, 4
 - effect of quality of on plant performance, 349
 - emissions from, 5
 - environmental aspects of, 47–48
 - global reserves of, 10–11
 - maceral groups, 34
 - oxy-fuel combustion of, 408–410
 - rank classification scheme, 34–36
 - reserve to production ratio (R/P), 10–11
 - reserves of, 39–40
 - resources, 40
 - role of in future energy mix, 27–28
 - spot prices for, 324
 - terminology, 40–41, 49–50
 - transportation of, 41, 46–47
 - type of, 33–34
 - world recoverable reserves of, 44–46
- Coal combustion, technology to limit emissions from, 339–340
- Coal gasification, 391–397

- Coal-fired steam power plants, 191–192
 - potential conversion efficiency improvements, 345–348
- Coalification, 34
 - definition of, 49
- Coatings, use of in gas turbines, 220
- Code predictions for turbine design, 867–868
- COE
 - standard formulation of, 319
 - wind turbines, 855, 886–890
- Coefficient of performance (COP)
 - definition, 1099
 - thermoelectric refrigeration, 1095–1098
- Coevaporation processes, 825–826
 - use of for CZTS deposition, 832
- Cogeneration, 291, 364–367. *See also* Combined heat and power
 - measuring effectiveness of, 365–367
- Coke oven gas (COG), 289
- Coking properties, 38
- Collares-Pereira and Rabl correlation. *See* C-P&R correlation
- Collector fields, 719–727
- Collector time constant, 536
- COLON SOLAR, 723–724, 741
- Combined collector-heat exchanger
 - performance, 559–561
- Combined cycle system, 217
 - definition of, 221
 - fuels used in, 289
 - power generation by, 910–912
- Combined heat and power (CHP), 291, 364–367. *See also* Cogeneration
 - measuring effectiveness of, 365–367
- Combined-cycle gas turbine power plant. *See* GTCC power plants
- Combined-cycle power plants, integration of power towers into, 741
- Combined-cycle steam power plants, 192
- Combustible portion of MSW, ultimate analysis of, 989
- Combustion
 - calculations for biomass fuels, 65
 - chemical looping, 299, 416–417
 - chemical reactions of, 997
 - coal, 332–334
 - elements and compounds encountered in, 996
 - emission limits for, 1012
 - equipment, 901–902
 - heat of, 998
 - methane, 332
 - principles of in WTE facilities, 995–1003
 - properties of transportation fuels, 919
- Combustion cycles, four-stroke SI engine, 224
- Combustion dynamic instability, 371
- Combustion efficiency, 211
 - definition of, 222
- Combustion flame, 899–900
- Combustion of MSW, 76–78
- Combustion process
 - abnormal, 238–239
 - CI engines, 228–229
 - four-stroke SI engines, 225
 - normal, 237–238
 - two-stroke Si engines, 225, 227–228
- Combustion reaction, 330–334
- Combustors, gas turbines, 221
- Commercial geothermal power production, 934–947. *See also* Geothermal power
- Commercial solar systems, 551–552
- Compact steam generators, 688
- Composting, recovery of materials from MSW, 76–78
- Compound parabolic concentrators. *See* CPCs
- Compressed air energy storage (CAES), 513–514
- Compressed natural gas (CNG), 58. *See also* Natural gas
- Compression ignition engines. *See* CI engines
- Compression ratio, 230
 - CI engines, 231–232
 - SI engines, 231–232
- Computational fluid dynamics models. *See* CFD models
- Concentrating collectors, 528–529
- Concentrating photovoltaic technologies. *See* CPV technologies
- Concentrating reflectors, beam quality of, 668–670
- Concentrating solar collectors, 17
- Concentrating solar power. *See* CSP
- Concentrating solar power plants. *See* CSP systems
- Concentrating solar thermal power
 - outlook for, 752–755
 - research and development, 714
- Concentrating solar thermal power plants (CSP), 17
- Concentration ratio, 529
- Concrete, use of for thermal energy storage, 698
- Concurrent gasifiers, 905–906
- Condensate heaters, 203–204
- Condensate pumps, 205
- Condenser gas-removal systems, 972–973
- Condensing steam turbines, 968–971
- Condensors for steam turbines, 204–205
- Cone optics, 667

- CONSOLAR, 717
 Constant-pressure heat addition, 340–341
 ideal Diesel cycle, 232–233
 Constant-pressure turbocharging, 248–249
 Constant-volume heat addition, 341
 ideal Otto cycle, 230–232
 Constrained exogenous parameters, 566
 Containers and packaging, recovery of from
 MSW, 74–76
 Control systems
 design of for solar thermal applications,
 557–562
 parabolic trough collectors, 675–676
 Controlled circulation boilers, 197
 Controlled retractable injection point. *See* CRIP
 underground coal gasification
 Convective heat loss, 728–729
 Convective losses, reduction of in solar
 collectors, 537
 Conversion of uranium, 83
 Cooling systems, load reduction using
 daylighting controls, 648–651
 Cooling tower makeup water, 296
 Copper-indium gallium diselenide thin films.
 See CIGS solar cells
 Coriolis forces, 138
 Corn, conversion of solar energy by, 62
 Corn ethanol, 918–921. *See also* Ethanol
 Corrosion, 381
 Cost, solar add-on, 582
 Cost of energy. *See* COE
 Costs
 geothermal power plants, 946–947
 solar thermal systems, 578–579
 WTE facilities, 1023–1025
 Countercurrent gasifiers, 905–906
 CPCs, 528, 539–540
 CPRG model, 120–122
 CPV technologies, 845–848
 energy payback, 848–849
 market for, 848
 qualification standards, 849
 Creep, 380–381
 CRIP underground coal gasification, 397–398
 Criteria pollutants, 295
 Crop yields, 69
 Cross-flow turbines, 259
 CRSs, 670–672, 674, 727–742
 control of, 726–727
 experience with, 739–740
 heliostat and collector field technology,
 719–727
 investment cost breakdown for, 718
 molten-salt systems, 744–747
 solar thermal power plants, 716–717
 technology description, 718–719
 tubular receivers, 732–734
 volumetric receivers, 734–739
 water–steam plants, 740–744
 Crucible growth method, 775
 Crude oil, 244
 classification of, 51
 world refining capacity, 55
 Cryogenic separation, 406
 Crystalline silicon PV cells, manufacture of,
 774–777
 Crystalline silicon thin films. *See* c-Si
 technology
 Crystalline silicon thin films on glass. *See* CSG
 thin films
 CSG thin films, 797–798
 CSP
 collectors, 670–672 (*See also* specific
 collectors)
 electricity production with, 658
 reasons for using, 661–665
 technologies, 671–672
 CSP systems, 656
 characteristics of, 673
 environmental advantages of, 659
 CSS, 819
 use of for CdTe deposition, 820
 Cu(In,Ga)Se₂ solar cells. *See* CIGS solar cells
 Cu₂ZnSn(S,Se)₄ solar cells. *See* CZTS solar cells
 Cup anemometers, 159
 Curtis, Charles, 210
 Cut-off ratio, 233
 Cycle efficiency, Diesel, 233
 Cycle life, 503
 Cycle variants, gas turbine efficiency and,
 355–360
 Cyclic fatigue, 882
 Cyclone furnaces, 339
 Cylinder volume, 231
 Cylindrical external receivers, 729
 Czochralski method, 774
 CZTS solar cells, 829
 configuration, 830
 deposition and growth of absorber, 830–833
 material and properties, 829–830
- D**
 D-T reaction, 491–492
 energy conversion and transport, 493–494
 Daily solar energy storage, 552

- Daily utilizability fraction, 546–548
- Dangling bonds, 806–807, 810
- Darrieus turbines, 854
 - structural dynamics of, 872
- Data
 - collection and handling of, 166
 - processing and reporting, 169–171
 - protection and storage of, 167
 - retrieval frequency, 167
 - screening of, 168–169
 - solar radiation, 129–131
 - validation of, 167–168
 - verification of, 169
- Data loggers, 162–164
- Data sensors
 - sampling rates and statistical quantities, 164–165
 - towers and mounting, 165–166
- Daylighting
 - controls and economics, 648–651
 - definition of, 581
 - design approach, 633–634
 - design fundamentals, 633
 - design methods, 635–648
 - sun-window geometry, 634–635
- DC solar array systems, 780–781
- DC-to-AC inverters, 1036
- Deadbands, 558
- Deaerators (DA), 204
- Declination, 91, 779
- Decommissioning costs, nuclear power plants, 488
- Dedicated energy crops, 61
- Degraded sunshape, 667
- Degree of recuperation, 379
- Delivered power, price of from geothermal resources, 942–943
- Demonstrated reserve base (DRB), 41
 - U.S., 42–43
- Demonstrated resources, 41
- Dendritic web growth, thin-film production by, 777
- Densified RDF, 1008
- Department of Energy (US). *See* DOE
- Depleted uranium, 481
- Deposition techniques
 - a*-Si solar cells, 808
 - CdTe absorber layer, 819
 - CdTe solar cells, 820–821
 - CIGS absorber, 825–827
 - CZTS absorber, 831–833
 - thermal barrier coatings, 390–391
- Depressions, effect of on wind speed, 155–156
- Depth of discharge (DOD), 501
- Deriaz hydraulic turbines, 267
- Design cooling load, reduction of using daylighting, 648–651
- Design methods
 - active solar space heating, 570–573
 - classification of for solar systems, 568–569
 - domestic solar hot water heating, 573
 - IPH applications of active solar heating, 573–578
 - recommendations for active solar applications, 578
- Design point parameters, 691
- Design specific speed, 263
- Desuperheating, 203–204
- Detailed design methods, 569
- Detonation combustion, 344
- Deuterium-deuterium reaction (D-D reaction), 492
- Deuterium-tritium reaction. *See* D-T reaction
- Diesel cycle, 232–233, 292, 297
- Diesel engines. *See also* CI engines
 - combustion chamber design for, 228–229
 - combustion in, 239–240
- Diesel fuel, 245–246, 918
- Diesel knock, 240
- Differential temperature controllers, 558
- Diffuse radiation, 633
 - anisotropic of, 118–119
- Diffusion coatings, 390
- Diffusion combustors, 335
- Diffusion flame design of gas turbines, 221
 - fuels for, 289
- Diffusion flame lift-off length (FLoL), 239–240
- Dimensionless figure of merit (*ZT*)
 - definition, 1099
 - magnitude of in thermoelectric materials, 1092–1098
- Dimethyl ether (DME), production of from biomass, 916
- DIN EN 10020, alloy steel specifications, 381–382
- Dioxins
 - combustion conditions and production of, 900
 - control of from MSW combustion, 1016–1019
- Direct combustion, 898–901
- Direct electric storage
 - SMES, 512
 - ultracapacitors, 511–512

- Direct gain systems, 586
 - Direct heat, use of geothermal energy for, 934
 - Direct heating air-blown gasifiers, 904–905
 - Direct injection (DI) engines, 225, 228
 - Direct methanol fuel cells. *See* DMFCs
 - Direct radiation, 101
 - Direct solar radiation, measurement of, 126–127
 - Direct Solar Steam project. *See* DISS project
 - Direct steam generation. *See* DSG
 - Direct thermal storage, 515
 - latent heat, 517–519
 - sensible heat, 515–517
 - Direct-coupled DC PV array system, 780–781
 - Direct-drive generators, 876–877
 - Direct-return piping configuration, 692
 - Directional solidification (DS) superalloys, 388–389
 - Directly coupled systems, 557
 - Directly irradiated receivers, 729
 - Discovered oil resources, 51
 - definition of, 60
 - Discovery of geothermal resources, 949–950
 - Dish-Stirling systems, 674, 747
 - concentrators, 748–749
 - description of, 747–748
 - developments in, 750–752
 - receiver, 749
 - use of Stirling engines, 749–750
 - Dish/engine collectors, 670–672, 674
 - DISORT, 122
 - Dispersion effects, 666
 - DISS project, 676, 702–704
 - Distillate fuel oil, 54
 - Distributed grid technologies, 501
 - Distributed photovoltaic systems. *See* Photovoltaics
 - DLN combustion, 295
 - estimation of CO and NO_x from, 334–339
 - DLN combustors, reducing pollutants from, 335–339
 - DMFCs, 1073–1074
 - acceptable contamination levels, 1074
 - applications of, 1075
 - basic operating principle, 1074
 - major technological problems, 1074–1075
 - technological status, 1075
 - DOE
 - Biomass Feedstock and Property Database, 65
 - Energy Information Administration (EIA) (*See* EIA)
 - Domestic solar hot water heating
 - design method for, 573
 - use of closed-loop systems for, 554–557
 - Double-reheat cycle, 297
 - Double-tank solar systems, 556–557
 - Downdraft gasifiers, 905–906
 - Dowtherm-A, 676
 - DPT550, 743
 - Draft tubes
 - importance of for flow stability, 266
 - numerical modeling of, 273–274
 - Drag devices, 855
 - power coefficients for, 860
 - translating, 857
 - Drain cooler approach (DCA), 203
 - Drain-back systems, 557
 - Drain-down systems, 557
 - Dresden Nuclear Power Plant, 457
 - Drop-in fuels, 927
 - Drum-type boilers, 197
 - Dry grind ethanol, 920–921
 - Dry low NO_x combustion. *See* DLN combustion
 - Dry natural gas, world production of, 55–56, 58
 - DSG, 676, 690–691
 - advantages of, 700
 - research and development for, 713–714
 - use of in PTC plants, 699–707
 - DSSCs, 800, 833
 - Dual catalytic converters, 243
 - Dual-axis tracking, 528
 - Dual-medium storage systems, 698–699
 - Dufay, Charles, 1086
 - DUKE, 707
 - Durable goods, recovery of from MSW, 74–76
 - Dusseldorf System, 1005
 - Dye dilution test method, 276
 - Dye-sensitized solar cells. *See* DSSCs
- ## E
- E class gas turbines, air standard cycle
 - calculations for, 317–318
 - Earth, thermal energy within, 177–178
 - Earth contact cooling, 629–632
 - Earth-sun geometric relationship, 86–87, 90–92
 - shadow-angle protractor, 95–98
 - solar time and angles, 92–93
 - sun-path diagram, 93–94
 - East-west sun-tracking axis orientation, 679
 - Easterlies, 138–139
 - ECN Phyllis database, 65
 - Economic access for geothermal resources
 - electricity transmission, 939–941
 - power plant costs, 946–947
 - viable market, 941–946
 - wellhead energy cost, 938–941

- Economic and Simplified boiling water reactor (ESBWR), 466
- Economic considerations, elements of for
 - passive solar systems, 581–582
- Economics, daylighting controls and, 648–651
- Economizer, 197
- Eddystone 1 (AEP), 303
- Edge-defined film-fed growth (EFG) process, 776
- Edison, Thomas, 1086
- Efficiency
 - energy storage, 502
 - engine fuel conversion, 235
 - gas turbines, 211–212
 - hydraulic turbines, 262
 - measures of, 276
 - Otto cycle, 230–232
 - parabolic trough collectors, 686–688
 - volumetric, 235–236
- Effusion cooling, 352
- EGR
 - use of in CI engines, 240
 - use of in two-stroke engines, 227
- EGR system, development of for use with DLN combustors, 337–338
- EIA, crude oil classification and estimated world reserves, 51–54
- Eisenhower, President Dwight D., 457
- Electric generators for FFPS, 292
- Electric power generation
 - economic analysis of, 319–330 (*See also* LCOE)
 - U.S. capacity by generator/cycle type, 907
- Electric storage, direct, 511–512
- Electric vehicles, 8
 - energy storage with, 501
- Electrical backcontact, 819–820
 - CIGs solar cells, 823
- Electrical energy, price of delivered geothermal power, 942–943
- Electrical energy storage technologies, 498–499
- Electrical power generation subsystem, 875–878
- Electricity, 6
 - demand for, 5–6
 - production, 6
 - transmission of geothermal power, 939–941
- Electricity generation, use of PTCs for, 693–695
- Electricity-generating capacity, addition to 2040, 6
- Electro-hydraulic governors, 269
- Electrochemical energy storage
 - batteries, 505–509
 - electrolytic hydrogen, 511
 - flow batteries, 509–511
- Electrodeposition (ED), 819, 827
- Electrodes, processes of in fuel cells, 1062–1063
- Electron cyclotron resonance reactor (ECR) deposition, 808
- Electron motive, 1087
 - definition, 1100
- Electron saturation current, 1088–1089
- Electron–hole pair (EHP), creation of, 771
- Electrostatic precipitators, 1012–1013
- Elemental analysis, 63–64
 - combustible portion of MSW, 989, 999
- Elling, Jens William Aegidius, 210
- Emissions. *See also* specific pollutants
 - air pollution control requirements, 1011–1012
 - carbon monoxide, 240–241
 - control of from IC engines, 242–243
 - NO_x, 241
 - unburned hydrocarbons, 241
- Endogenous parameters, 566
- Energy
 - availability of from wind, 141–151
 - forecast of future mix, 27–28
 - global needs and resources, 2–4
 - per capita consumption, 22–24
 - production of from geothermal wells, 938–939
- Energy balance, parabolic trough collectors, 686–688
- Energy conservation
 - distinction of from passive solar systems, 581
 - role of, 22–26
- Energy consumption, global, 2–3, 51–53
- Energy conversion efficiency
 - definition, 1046
 - fuel cell, 1047
 - heat engines, 1048–1049
 - irreversible, 1057–1058
- Energy crops, 67–68
- Energy density, 503
- Energy losses
 - irreversible, 1054–1056
 - reversible, 1052–1054
- Energy payback period
 - CPV technologies, 848–849
 - PV cells, 775
 - thin-film PV cells, 798–799
 - wind power, 886
- Energy policies, potential for renewable energy, 14–15
- Energy Reliability Council of Texas (ERCOT), 885
- Energy saving potential, 25–26

- Energy storage
 - devices for, 501–503
 - electrochemical, 505–509
 - electrolytic hydrogen, 511
 - flow batteries, 509–511
 - mechanical, 512–515
 - specifications for fuels, 504–505
 - thermochemical, 519–522
 - Energy storage technologies
 - applications of, 500–501
 - electrical, 498–499
 - Engine efficiency, 211
 - Engine fuel conversion efficiency, 235
 - Enhanced coal bed methane (ECBM)
 - technology, 408
 - Enhanced geothermal systems (EGS), 936
 - Enhanced oil recovery (EOR) application, 298, 407–408
 - Enrichment facilities for uranium, 83–84, 480–481
 - Enthalpy, reversible cell potentials, 1043
 - Entrained flow gasifiers, 905–906
 - Environmental barrier coatings (EBCs), 390
 - Environmental concerns, wind facilities, 149–151
 - Enzymatic hydrolysis, 921
 - Equatorial doldrums, 138–139
 - Equivalence ratio, 237, 331
 - ERSATZ, 130
 - eSolar, 724, 743
 - ESTELA, 713
 - ET-100 PTC, 706
 - ET-150 parabolic trough collector, parameters of, 678
 - Ethane (C₂H₆). *See* Hydrocarbons
 - Ethanol, 918
 - cellulosic, 921–922
 - corn, 918–921
 - world production of, 20–21
 - yields of from biorenewable resources, 921
 - EuroDish project, 749, 752
 - Europe
 - energy use in, 2–3
 - MEXICO wind project of, 868
 - nuclear fuel reprocessing in, 478
 - nuclear power plant licensing in, 465
 - per capita energy consumption, 22–23
 - use of volumetric receivers in, 737–738
 - European pressurized water reactor (EPR), 465
 - European Solar Thermal Electricity Association. *See* ESTELA
 - EuroTrough, 678, 703
 - Evacuated tubular collector, 538–539
 - Evaporative cooling, 627
 - use of for GT inlet conditioning, 354
 - Evolutionary pressurized water reactor (EPR), 465
 - Excess air ratio, 331
 - Excitation systems, 208
 - Excitonic solar cells, 833
 - Exergy, 310
 - Exhaust emissions
 - control of from IC engines, 242–243
 - harmful constituents, 240–242
 - Exhaust gas clean-up systems, 198
 - Exhaust gas recirculation. *See* EGR
 - Exhaust heat, recovery of from gas turbines, 216
 - Exhaust waste energy recovery, 250–252
 - Exinite, 34
 - Exit velocity head, 262
 - Exogenous parameters, 522
 - Expanders, 209. *See also* Gas turbines
 - Expansion process
 - definition of, 222
 - turbine efficiency in, 211
 - Exploration of geothermal resources, 949–950
 - risk of, 950–951
 - Extended Zel'dovich mechanism, 334
 - External combustion engines (XCE)
 - gas turbines, 210
 - use of in FFPS, 292
 - External cylindrical tubular receiver, 732
 - External receivers, 729
 - External tubular receivers, 732
 - Extraterrestrial solar radiation, 99–100
 - spectral distribution, 98
 - Extratropical cyclones, 138
- F**
- F*-chart design method, 570–573
 - Fabric filters, 1013
 - Failure mechanisms, 380–381
 - Fast breeder reactors (FBR), 469
 - FAST code, 872
 - Fast neutron reactors, 469–470
 - Fast pyrolysis, 898
 - Feed-in tariffs (FIT)
 - construction of STPs in Spain due to, 658
 - solar thermal power plants, 711
 - Feedstocks
 - organic composition of, 64
 - waste materials as, 67
 - Feedwater booster pump, 205
 - Feedwater heaters, 203–204
 - Fermi level, 1087

- Ferrite, 383
- FFPS
 - air quality control systems, 417–423
 - auxiliary equipment, 294–296
 - combustion in, 330–345
 - design objectives, 316
 - expected advances in, 298
 - future technologies, 305–308 (*See also* AFFPS)
 - impact of CCS on performance of, 402–404
 - impact of renewable technologies on duty cycle of, 367–369
 - main equipment, 292–294
 - materials used for components in, 380–387
 - past technologies, 302–303
 - present technologies, 304–305
 - schema for, 290–291
 - suitable alloys for boiler construction, 383–384
 - system components, 291–292
 - wastewater treatment, 429–430
 - water treatment systems, 424–429
 - zero liquid discharge wastewater treatment, 430–433
- Field tests of hydraulic turbines, 276277
- Finished petroleum products, 54
- Finite-element modeling, VAWTs, 872
- Finland
 - European pressurized water reactor, 465
 - nuclear power capacity in, 461
- Firing temperature, 352. *See also* RIT
- First-of-a-kind technologies. *See* FOAK technologies
- Fiscal incentives
 - necessity of for solar power plants, 711
 - new STP plant construction, 673
- Fischer–Tropsch liquids (FTLs), 289, 917
 - synthesis of from biomass, 924–925
- Fission products, 84
- Fixed carbon content, 34–36
 - definition of, 49
- Fixed O&M costs, rule-of-thumb for GTCC, 323–324
- Fixed wake models, 865
- Fixed-speed turbine orientation, 877
- Flame lift-off length (FLoL), 239–240
- Flame speed, 371
- Flame temperature, 331–332
 - reduction of in combustors, 335
- Flammability ratio, 370
- Flash-steam systems, 689–690
- Flat absorbers, 662–664, 667
- Flat-plate collectors, 529
 - daily utilizability, 546–548
 - description of, 529–531
 - incidence angle modifier, 534–535
 - individual hourly utilizability, 541–545
 - modeling, 531–534
 - performance improvements, 537–538
 - pressure drop across, 536
 - stagnation temperature of, 536
 - stationary, 528
 - time constant of, 536
- Flexible *a*-Si solar cells, 814–816
- Flexible CdTe solar cells, 821
- Flexible CIGS solar cells, 827–829
- Flexible joints, use of in connecting PTCs, 679–681
- Float voltage, 781
- Float zone method, 774
- Flooded lead–acid batteries, 781
- Flow batteries, 509–511
- Flow control, use of for speed regulation of hydraulic turbines, 268
- Flow rate, field tests to measure, 276277
- Flue gas
 - methods of treatment, 1014–1016
 - pollutant emissions in, 295
 - recirculation of in MSW combustion, 1007–1008
- Fluid inlet temperature, 531
- Fluidized bed combustion (FBC), 339–341, 902, 1022, 1026
- Fluidized bed gasifiers, 905–906
- Flux-line trackers, 676
- Fly ash, 1010
- Flywheel energy-storage systems, 514
- FOAK technologies, estimating project costs for, 322–323
- Foehn winds, 138
- Food waste, percentage of in municipal solid waste, 73
- Forest residues, 66
- Fossil fuel power systems. *See* FFPS
- Fossil fuel reserves, 11. *See also* specific sources
- Fossil fuel steam power plants. *See also* Steam power plants
 - efficiencies of, 192
- Fossil fuels, demand for, 4
- Four-stroke IC engines
 - indicator diagram for, 234
 - volumetric efficiency, 235–236
- Four-stroke SI engines, 224
 - basic operation of, 224–226
- Fracking, 288

- Fracture permeability, 935
- Frame machines, 351. *See also* J class gas turbines
- France
 installed wind power capacity in, 852
 nuclear power reactors in, 461
- Francis hydraulic turbines, 260
 efficiency of, 267
 performance characteristics, 266–267
- Free electrons
 definition of, 1100
 electron saturation current and, 1088
- Free energy conversion efficiency, 1058
- Free swelling index, 38
- Free-wake model, 865
- Frequency-domain calculations, 871
- Fresnel concentrators, 847–848
- Fresnel reflectors. *See* Linear Fresnel reflectors
- Friedel model, 703
- Fuel cell hybrid system, 305–306
- Fuel cell systems, 1036–1037
 power generation by, 910
 thermodynamic model of, 1038
- Fuel cell utilization factor (UF), 306
- Fuel cells, 1034–1035
 alkaline, 1067–1069
 Carnot efficiency, 1048–1049
 connection and stack design considerations, 1063–1066
 direct methanol, 1073–1075
 efficiency loss in, 1059–1061
 efficiency of, 1050–1052
 efficiency of and energy loss mechanisms, 1052–1056
 electrode processes, 1062–1063
 energy conversion efficiency of, 1046
 equivalency of Carnot and reversible efficiency, 1049–1050
 irreversible energy losses, 1054–1056
 molten carbonate, 1076–1079
 operational characteristics and technological status of, 1067
 performance of, 1037–1038
 phosphoric acid, 1076–1077
 polymer electrolyte membrane, 1069–1073
 principle of operation for, 1035–1036
 reversible cell potential, 1038–1042
 reversible energy conversion efficiency for, 1047
 solid oxide, 1079–1082
 types of, 1066–1067
 use of as power generation systems, 305–306
 waste heat generation by, 1056–1057
- Fuel chargeable to power (FCP), 367
- Fuel conversion efficiency (FCE), use of waste energy recovery to increase, 250–252
- Fuel cycle for nuclear power systems, 478–484
 fuel fabrication and use, 481
 mining and milling of uranium, 480
 reprocessing, 481, 483–484
 spent fuel storage, 484
 spent fuel transportation, 484
 uranium and thorium resources, 478–479
 uranium conversion and enrichment, 480–481
- Fuel electrodes, 1035
- Fuel flexibility, 369–372
- Fuel injection systems, 236
- Fuel moisturization, 338–339
- Fuel saver scheme, 660
- Fuel staging, 339
- Fuel synthesis, 917
- Fuel systems for FFPS, 294–295
- Fuel utilization factor, 365
- Fuel-capacity factor, 944
- Fuel-rich catalytic combustion, 339
- Fuel–air ratio, 237
 SI engine emissions levels and, 242–243
- Fuels
 energy storage specifications, 504–505
 properties of, 370, 504
- Fukushima nuclear accident, effect of on growth of nuclear power, 461
- Furans
 combustion conditions and production of, 900
 control of from MSW combustion, 1016–1019
- Furnaces
 design of in WTE facilities, 988
 factors affecting design of, 997
 solid waste combustion in, 1003–1008
- Fusion
 confinement, 492
 energy conversion and transport, 493–494
- Fusion power plants, potential of, 491
- Fusion reactions, 491–492
- Future energy mix, forecast of, 27–28
- G**
- Gadolinium zirconate (GdZ) coatings, 391
- Gamma iron, 383
- Garbage, moisture content of, 989
- Gas. *See also* Oil; Petroleum
 classification of, 54–55
 resource base, 53

- Gas centrifuges, uranium enrichment using, 480–481
- Gas engines, 372. *See also* IC engines; Reciprocating engines; Reciprocating engine emissions from, 374
 - low-quality waste heat recovery from, 375–377
- Gas turbine Brayton cycles
 - calculating efficiencies of, 311–313
 - cycle pressure ratios of, 297
- Gas turbine combined cycle power systems. *See* GTCC power plants
- Gas turbine combustors, use of in FFPS, 293
- Gas turbine-based repowering options, 364
- Gas turbine–modular helium reactor (GT-MHR), 469
- Gas turbines, 209
 - combustors, 221
 - comparison of with reciprocating engines, 372–375
 - cycle analysis, 211
 - cycle configurations, 213–215
 - cycles, 212–213
 - efficiency of, 211–212, 222
 - evolution of, 304–305
 - fuel and firing, 210–211
 - fuel flexibility of, 369–372
 - fuels used in, 288
 - history of, 210
 - materials, 220
 - mechanical product features, 221
 - NO_x production in combustors of, 334–339
 - state-of-the-art, 283, 352–353
 - steam-cooled, 297
 - thermal barrier coatings for, 390–391
 - three-pressure reheat bottoming cycles (*See* 3PRH bottoming cycles)
 - upper temperature limit, 219–220
 - use of exhaust from to power steam turbines, 217
 - use of for power generation, 909–910
 - use of in FFPS, 291–293
 - use of superalloys for, 388
- Gas-cooled fast reactor (GFR) system, 472–473
- Gas-cooled reactors, 460
 - high-temperature, 468–469
- Gas-phase reactions, 904
- Gas-turbine combined-cycle plants, efficiencies of, 209
- Gas–solid reactions, 903–904
- Gaseous diffusion, uranium enrichment using, 481
- Gaseous emission control, 1014–1016
- Gaseous fuels, 288
 - biomass conversion to, 914–917
- Gasification, 289, 294–295, 391–397, 902–904
 - equipment, 904–907
 - equipment types, 905
 - MSW, 1026
 - production of light gases from biomass, 915–916
- Gasoline, 244–245, 918
 - additives, 245
 - Fischer–Tropsch liquids (FTLs), 924–925
- GAST project, 730
- Gemasolar plant, 674, 717, 724, 733–734, 746–747
- Generalized solar load ratio, 620
- Generation III nuclear reactors, 462, 464–465
 - fast neutron reactors, 469–470
 - heavy-water reactors, 468
 - high-temperature gas-cooled reactors, 468–469
 - light-water reactors, 465–468
- Generation IV International Forum (GIF), 471
- Generation IV nuclear reactors, 471–472
 - gas-cooled fast reactor system, 472–473
 - lead-cooled fast reactor, 475–477
 - molten salt reactor, 477
 - sodium-cooled fast reactor, 474–476
 - supercritical-water-cooled reactor, 473–475
 - very-high-temperature reactor, 472–474
- Generators
 - auxiliaries, 207–208
 - excitation, 208
 - turbine, 875–878
 - use of in steam power plants, 206–208
 - ventilation, 207
- Geometric concentration ratio, 681
- Geometric correction factors (GCFs), 125–126
- Geometrical losses, 684–685
- Geostrophic winds, 138
- Geothermal combined-cycle steam power plants, 968, 978–979
- Geothermal condenser gas-removal systems, 972–973
- Geothermal energy, 177
 - definition and use of, 933–934
 - renewability of, 937
- Geothermal energy systems, types of, 178
- Geothermal power
 - binary power plant technologies, 973–977
 - contract provisions for new development, 945–946
 - contract provisions for operation, 944–945
 - environmental impact of, 980–982
 - market for, 941–946
 - price of delivered power, 942–943

- requirements for commercial production of, 934–947
- steam turbine technologies for production of, 967–973
- Geothermal resources
 - barriers to management of, 957–959
 - characterization of, 959–962
 - chemistry of, 956–958
 - definition of, 934–936
 - economic access, 938–947
 - exploration and assessment of, 948–951
 - improving through human intervention, 936
 - management of for power production, 951–957
 - temperature of, 946–947
- Geothermal steam supply, 963–967
- Geothermal systems
 - costs of, 946–947
 - design parameters for, 960–962
 - emissions from, 980–982
 - enhancing steam production in, 955–957
 - operating costs of, 947
 - residual brine management in, 954–955
- Geothermal turbines, design of, 971
- Geothermal wells, capital limitations on placement of, 958–959
- Germany
 - installed wind power capacity in, 852
 - phase out of nuclear power in, 462
- Geysers The, 933
 - use of EGS at, 936
- GFDI devices, use of in solar arrays, 785
- Gibbs free energy, conversion of solar heat to, 656
- Gibbs function, reversible cell potentials, 1043
- Gieseler plastometer test, 38
- Glass
 - percentage of in municipal solid waste, 73
 - transmittances of, 639
- Glass-fiber-reinforced plastic (GFRP)
 - composites, use of for wind turbines, 882
- Glazing area, values for, 593–597
- Global climate change, 7, 27–28
- Global commercial reprocessing capacity, 483
- Global crude oil refining capacity, 55
- Global efficiency, 687
- Global energy figures
 - electricity-generating capacity, 6
 - energy consumption, 2–3, 51–53
 - energy demand, 5–6
 - land use for biomass production, 70–71
 - natural gas reserves, 57
 - new construction of nuclear power plants, 462–464
 - nuclear power plants, 457–458
 - uranium enrichment facilities, 482
 - wind power potential, 149
- Global wind patterns, 139
- Glow discharge CVD, 808
- Glow plugs, 229
- GOES, 131–132
- Governors, use of for speed regulation of hydraulic turbines, 268–270
- Grate systems, use of in MSW furnaces, 1003–1007
- Grate-fired systems, 901
- Gray–King assay test, 38
- Greenhouse effect, 529
- Grid integration, wind power, 884–885
- Grid-connected solar systems, 782
- Grid-tied inverters, 784
- Griggs–Putnam index of deformation, 154
- Gross calorific value, 34–36
 - definition of, 49
 - measurement of, 38
- Gross output, 287
- Ground fault detection and interruption devices. *See* GFDI devices
- Ground illuminance, 643
- Ground reflectivities, 626
- Ground-coupled geothermal heat pump systems, 934
- GTCC, 351–355
 - calculating thermal efficiency of, 311–316
 - comparison of high performance cycles, 360
 - comparison of with reciprocating engines, 372–375
 - efficiency improvement parameters, 355
 - net cycle efficiency map, 354
 - outage factors, 325
 - power augmentation options, 353
 - rule-of-thumb O&M costs estimates, 323–324
 - startup curves, 369
- GTCC power plants, 294–295
 - auxiliary power for, 287
 - bottoming cycle steam conditions in, 297
 - comparison of with USC power plants, 350–351
 - efficiency wall of, 304
 - exhaust temperatures, 390
 - fuels used in, 288–289
 - operational flexibility of, 367–369
 - use of fuel moisturization technology in, 338–339
 - use of intercooling in, 357
- GUDE, 703

H

- H class gas turbines, 283
 - estimating O&M costs for, 323–324
- H turbines, 854
- H-System, 297
 - use of to reduce TIT–RIT temperature loss, 355–357
- H₂S emissions from geothermal power plants, 981
- Haber process, 916
- Hahn, Otto, 81
- HAWC2, 872
- HAWTs, 852–854
 - CFD models for, 866–867
 - classification of, 854
 - momentum models of, 860–864
 - peak performance coefficients for, 863
 - structural dynamics, 870–872
 - vortex models for, 864–866
 - yaw control systems, 878
- Haynes 263, 387
- Head, 258
 - availability of to impulse turbines, 265–266
- Heat
 - biomass conversion to, 897–898, 907–912
 - geothermal, 934
- Heat addition
 - constant-pressure, 232–233, 340–341
 - constant-volume, 230–232
 - irreversibility of, 310, 318
 - natural gas combustion, 330–332
- Heat engines
 - Carnot factor of, 316–317
 - crucial nature of for FFPS, 305
 - reversible energy conversion efficiency for, 1048–1049
 - thermodynamic cycles, 296–297
 - use of Kelvin–Planck statement to analyze, 308
- Heat exchangers, use of in steam power plants, 203–204
- Heat flow, 177–178
- Heat loss coefficient, 684
- Heat pipe collectors, 530–531
- Heat rate (HR), 286
 - cost analyses and, 327–329
- Heat recovery repowering, 364
- Heat recovery steam generators. *See* HRSGs
- Heat removal factor, 532
- Heat sinks for FFPS, 292
- Heat source, definition of for thermoelectric applications, 1100
- Heat sources for FFPS, 292
- Heat transfer
 - air and pipe, 630
 - analysis of, 630–631
 - soil, 630–631
- Heat transfer fluid technology. *See* HTF technology
- Heat-rejection systems, 971–972
- Heaters for steam power plants, 203–204
- Heating load, 590
- Heavy-duty industrial gas turbines, 351. *See also* J class gas turbines
 - use of reheat combustion with, 357
- Heavy-water reactors, 468
- Height layers, 159
- HELIOS, 721
- Heliostat drives, 724–725
 - characteristics of, 725
- Heliostat field control system (HFCs), 726
- Heliostat fields, 716–717, 719–727
- Hemicellulose, 64
- Herbaceous energy crops (HECs), 67
- Heterojunction with intrinsic thin-film layer cells. *See* HIT cells
- Heterojunctions, 800
- HHV, 287, 504
 - biomass, 64–65
 - combustible portion of MSW, 989
 - combustion of MSW, 997–999
 - efficiency measures of gas turbines using, 211
- High fogging, 354
- High vacuum evaporation. *See* HVE
- High-cycle fatigue, 882
- High-enthalpy wells, 939
- High-level wastes (HLW), 486
 - managing from spent fuel, 486
 - waste management of, 487–488
- High-performance power systems. *See* HIPPS
- High-pressure steam conditions, 297
- High-temperature gas-cooled reactors, 468–469
- Higher heating value. *See* HHV
- Hill diagram, 263–264
- HIPPS, 361–362
- HIT cells, 813
- HiTRec project, 737–738
- Holocellulose, 67
- Holzwarth turbine, 343
- Homogeneous combustion process, four-stroke SI engines, 225
- Honeycomb material, use of to reduce losses from collectors, 537
- Horizontal sky and sun illuminances, 645

- Horizontal skylights, 644–648
- Horizontal solar radiation, models based on
long-term measures of, 113–123
- Horizontal-axis machines, 853
- Horizontal-axis wind turbines. *See* HAWTs
- Hot dry rock (HDR), 936
- Hot fractured rock (HFR), 936
- Hot gas cleanup, 391
- Hot gas path (HGP)
parts, 297
temperatures, 352
use of superalloys for component
manufacturing, 388–389
- Hot reheat (HRH) steam, 297
- Hot wire CVD (HWCVD), 808
- Hottel–Whillier–Bliss (HWB) equation, 531
- Hour angle, 91
- HRSGs, 218
controlled warming of, 368–369
effectiveness of, 315
exergy destruction in, 358–359
increasing effectiveness of, 376
use of in FFPS, 294
- HTF technology, 689
use of in SEGS plants, 707
- Human Development Index (HDI), relationship
to per capita energy use, 23–24
- Humid air turbine (HAT) cycle, 218, 283,
359–360
definition of, 222
- Humming, 371
- Hurricanes, 138
- HUTYIN, 677
- HVE, 819
use of for CdTe deposition, 820
- Hybrid electric vehicles (HEVs), energy storage
with, 501
- Hybrid gas turbine fuel cell, 305–306
- Hybrid models for wind turbines, 867
- Hybrid power plants, 656–657, 740–741
integration of CRS technologies in, 717
- Hybrid solar cells, 812–813, 833
- Hybrid vehicles, 8
- Hydraulic fracturing, 288. *See also* Fracking
- Hydraulic turbines
cavitation and setting of, 270
classification of, 258
description of, 258–261
efficiency of, 262
field tests of, 276277
model testing of, 271
numerical simulations of, 271–275
performance characteristics, 265–267
performance comparisons, 267
performance of, 262–264
power available, 261–262
scaling formulae for, 263–264
speed regulation, 268–270
- Hydrocarbons
combustion conditions and production of,
900
emissions of from MSW incineration,
1014–1016
physical properties of, 58–59
unburned, 241
- Hydrodynamic loading, modeling of, 869
- Hydrogasification, 915–916. *See also* Gasification
- Hydrogen, 288
combustible portion of in MSW, 995–996
use of as a fuel, 295, 399–401
use of as a transportation fuel, 8
- Hydrogenation reaction, 903–904
production of biodiesel using, 923
- Hydrokinetic turbines, 277–278
- Hydropower
numerical simulations of facility
components, 271–275
total energy potential of, 14
typical installation, 258
- Hydrothermal processing, 926
- I**
- I*–*V* curves for ideal PV cells, 772
- IC engines
air standard power cycles, 230–233
carbon monoxide emissions from, 240–241
combustion in, 236–240
control of emissions from, 242–243
exhaust waste energy recovery, 250–252
fuels for, 244–246
gas turbines, 210
intake pressurization, 247
open mechanical energy cycles in, 233–236
supercharging, 247–248
turbocharging, 248–250
types and basic operation of, 224–229
use of in FFPS, 291
- Ideal Carnot cycle, 309
- Ideal Diesel cycle, 232–233
- Ideal Otto cycle, 230–232
- IGCC power plants, 10, 283, 295, 391–397,
910–912
blocks, 392
capital cost estimates for, 322
emissions from, 396–397

- IGFCs, 307
 - atmospheric, 307–308
 - pressurized, 308
- Ignition delay period, 228
- Ignition properties of transportation fuels, 919
- Ignition quality, 245–246. *See also* Cetane number
- Illuminance, 633
- Illuminances
 - clear sky, 642
 - ground, 643
 - horizontal sky and sun, 645
 - incident direct sky and sun, 636
 - incident ground reflected, 636–638
 - overcast sky, 641
 - work-plane, 633, 639–640, 644
- Illuminated p - n junction, 770–772
- Impulse turbines, 258–259
 - control of flow in, 262
 - performance characteristics, 265–266
 - performance comparison with reaction turbines, 267
- Incidence angle, 679, 685–686
 - modifiers for flat-plate collector, 534–535
- Incident radiation, 656
- Inconel 617, 387
- Independent power producers (IPPs), 942
- Index tests of flow, 277
- India
 - coal use in, 10–11
 - electricity-generating capacity of, 6
 - energy use in, 2–3
 - fast breeder test reactor in, 469
 - installed wind power capacity in, 852
 - use of heavy-water reactors in, 468
- Indicated mean effective pressure (imep),
 - calculation of, 234
- Indicated resources, 41
- Indicated work, 234
- Indicator diagram, 234
- Indirect gain systems, 586
- Indirect heating gasifiers, 905
- Indirect injection (IDI) engines, 228
- Indirectly coupled systems, 553
- Indirectly fired gas turbines, 361–362
- Indirectly heated receivers, 729–730
- INDITEP project, 705–706
- Individual hourly utilizability, 541–545
- Indonesia, electricity-generating capacity of, 6
- Induction generators, 876
- Industrial process compressors, use of
 - intercoolers with, 216
- Industrial process heat applications. *See* IPH applications
- Industrial sector
 - applications for PTCs in, 688
 - use of direct steam generation in, 690–691
 - use of flash steam systems in, 699–690
 - use of unified boiler systems in, 689
- Industrial solar systems, 551–552
- Industrial Solar Technology (IST), 678
- Inertial CO₂ extraction system (ICES), 405
- Inertial fusion confinement, 492
- Inferred resources, 41
- Injection process, 702
- Inlet air fogging, 218
- Inlet foggers, 354
- Insolation, 99
 - effect of day-to-day changes in, 540–541
- Installed nameplate capacity, 852
- Intake pressurization, IC engines, 247–250
- Integral optimization of heliostat fields, 722
- Integrated gasification combined-cycle (IGCC) plants. *See* IGCC power plants
- Integrated gasification fuel cells. *See* IGFCs
- Integrated solar combined-cycle system plants. *See* ISCCS plants
- Intercept factor, 682–683
- Intercooled recuperated (ICR) machines, 216, 357
- Intercoolers, 216
 - definition of, 222
 - use of in turbochargers, 249–250
- Intercooling, use of in gas turbine power plants, 357
- Interelectrode motive distribution, 1087–1088
- Intermediate-level wastes (ILW), 485
- Intermittent flow, 701
- Internal combustion engines. *See* IC engines
- Internal reformation, use of in NGFC system, 308
- Internal resistance, 505
- International Organization of Standardizations. *See* ISO
- International Solar Radiation Data Base, 131
- International Thermonuclear Experimental Reactor (ITER), 492–493
- Intertinite, 34
- Inverted cavity receivers, 716
- Inverters, DC-to-AC, 783–784, 1036
- IPH applications
 - closed-loop multipass system design, 573–575
 - design methods for, 573–578

- open-loop single pass system design, 575–578
 - use of closed-loop systems for, 556
 - use of parabolic trough collectors for, 678
- IRIS pressurized water reactor, 467
- Iron, 383
- Iron plates, use of for thermal energy storage, 698
- Irradiance, mitigation of fluctuation in, 656
- Irreversible energy conversion efficiency, forms of, 1057–1058
- Irreversible energy losses, 1054–1056
- ISCCS plants, 657, 673, 712–713
- Islanding condition, 784
- ISO
 - coal classification, 36
 - COE calculations, 320
- Iso-octane, 245
- Isolated gain systems, 586, 588
- Italy
 - installed wind power capacity in, 852
 - use of geothermal energy in, 933
 - use of tubular receivers in, 732
- Ivanpah, 658, 674
- J**
- J class gas turbines, 283, 351–355
 - air standard cycle calculations for, 317–318
 - estimating O&M costs for, 323–324
- Japan
 - advanced boiling water reactor in, 465
 - advanced pressurized water reactor in, 466
 - development of Generation III nuclear reactors in, 465
 - nuclear fuel reprocessing in, 478
 - nuclear power reactors in, 461
 - use of tubular receivers in, 732
- Jet fuel, 54, 918
- Jevons, W.S., 302
- Joint European Torus (JET), 492
- Junction activation treatment, 819
- K**
- K class gas turbines, air standard cycle calculations for, 317–318
- Kalina cycle, 283, 358–359
- Kaplan hydraulic turbines, 260
 - efficiency of, 267
 - use of index testing for, 277
- Kazakhstan
 - BN-350 nuclear reactor in, 469
 - VBER-300 nuclear reactor in, 468
- Kelvin–Planck statement of 2nd law of thermodynamics, 308
- Kerena nuclear reactor, 467
- Kerosene, 54
- Kewaunee nuclear power plant, 462
- Kinematic engines, 453
- Kinematic Stirling engine, 750
- Klaproth, Martin Heinrich, 81
- Knock
 - CI engines, 240
 - SI engines, 238
- Kockums 4-95 Stirling-engined based PCU, 751
- Korea Advanced Liquid Metal Reactor (KALIMER), 470
- Korean Next-Generation Reactor, 467
- L**
- Land breezes, 138
- Land disposal of MSW, 76–78
- Land use
 - biomass production, 70–71
 - geothermal power plants, 982
- Lardello geothermal energy site, 933, 937
- Large-eddy simulation (LES), numerical modeling using, 272–275
- Latent heat, 504
 - hydration-dehydration reactions, 519
 - storage of in phase change materials, 518
 - storage of with chemical reactions, 519
 - use of for direct thermal storage, 517–519
- Latent heat storage systems, 699
- Latitude, 91
- Law of diminishing returns, 566
- LCOE, 319–323
 - similar technology requirements of, 324–325
 - wind turbines, 887
- LCR, 589–590
 - passive solar heating system design using, 592–620
 - tables for representative cities, 602–615
- Lead losses, 1088
 - definition of, 1100
- Lead time, 320–321
- Lead-acid batteries, 506
- Lead-cooled fast reactor (LFR), 475–477
- Lead-acid batteries, use of in solar systems, 781
- Lean catalytic lean burn (LCL), 339
- Lean premix (LPM) combustion, 336–339. *See also* DLN combustion
- Lean-premixed process, 221
- Levelized cost of energy. *See* LCOE

- LHV, 287, 504
 biomass, 64–65
 combustion of MSW, 997–999
 efficiency measures of gas turbines using, 211
- LHV basis, efficiencies of gas-turbine combined-cycle plants, 209
- Life cycle cost, 363
- Lift devices, 857–859
 power coefficients for, 860
- Lifting line model, 864–865
- Lifting surface model, 864–865
- Light gases, production of by biomass conversion, 915–916
- Light loss factor, 639, 646–648
- Light-induced degradation, 809–810
 use of multijunction cells to combat, 811–812
- Light-water graphite-moderated reactors, 461
- Light-water nuclear reactors, 465–468
- Lighting, terms and units, 633
- Lightning protection devices, 165
- Lignin, 63–64
- Lignite, U.S. reserves of, 39–40
- Lignocellulose, 63–64
 energy crops, 67–68
- Limb-darkened distribution, 666
- Lime injection
 control of trace metal emissions with, 1021
 use of in gaseous emission control, 1015
 use of in organic compound control, 1019
- Linear current booster (LCB), 782–783
 use of in PV arrays, 780
- Linear Fresnel collectors, 670–672
 integration of in combined-cycle plants, 673–674
- Linear Fresnel reflectors, 714
 future development and performance trends, 716
 historical evolution of, 714–716
- Linear Power Tower, 716
- Linked vertical well. *See* LVW underground coal gasification
- Liptinite, 34
- Liquefied natural gas (LNG), 56. *See also* Natural gas
 production of, 58
- Liquefied refinery gases, 54
- Liquid electrolyte fuel cells, 1062
- Liquid fuels, 288
- Liquid sensible heat storage, 515–517
- Liquid solar collectors, 552
- Liquid-metal-cooled fast-breeder reactors (LMFBRs), 461
- Lithium ion batteries, 506–507
- Liu and Jordan (LJ) method, 115
- LNB, estimation of CO and NO_x from, 334–335
- Load, 589–590
 predictions for wind turbines, 867–868
 time dependence of, 551
- Load reduction, use of daylighting controls for, 648–651
- London Array, 883–884
- Long-term measured horizontal radiation
 circumsolar, 118–119
 models of, 113
 monthly solar radiation on tilted surfaces, 115–118
 spectral models, 122–123
- Longwall mining, 48
- Low cycle fatigue (LCF), 368
- Low specific speed hydraulic turbines, 259
- Low-level wastes (LLW), 485
- Low-pressure-ratio recuperated cycle, 216–217
- Low-quality waste heat recovery, 375–377
- Lower heating value. *See* LHV
- Lowest Achievable Emission Requirements (LAER), 1027
- Lubricants, 55
- Lumen method of skylighting, 644–648
- Luminous flux, 639
- LUZ International, 707. *See also* SEGS plants
 bankruptcy of, 711
 parabolic trough collectors of, 710
- LVW underground coal gasification, 397–398
- M**
- MACC, 327
- Macerals, 34
 definition of, 49
- Macroscopic errors, 667
- Magnetic fusion confinement, 492
 tokamak reactor development, 492–493
- Magnox reactors, 460
- Main step-up transformers, 293
- Makeup water treatment, 296
- MAN Ferrostaal Power Industry, 715
- Manganese, 383
- Manure, 66
- Maricopa Solar Plant, 674, 751
- Martin grates, 1005–1006
- MASDAR, 746
- Mass-burn systems, 990–992
 furnaces, 1003–1007
 particulate emissions from, 1019–1022
 performance of, 1022–1023

- Mass-fired incinerators, residue handling and disposal, 1009–1011
- Mass-fired water wall units, 1008–1009
- Material flows methodology, 73
- Matrix permeability, 935
- Maximum acceptable increase in capital cost.
See MACC
- Maximum Achievable Control Technology (MACT), 1027
- Maximum power trackers (MPT), 782–783
- Maximum useful temperatures, energy sources and, 661
- MCFCs, 305, 1076–1077
 - acceptable contamination levels, 1078
 - air utilization factor, 306
 - applications of, 1079
 - basic operating principle, 1077–1078
 - major technological problems, 1078–1079
 - technological status, 1079
- Measured resources, 40
- Mechanical energy storage, 499
 - compressed air, 513–514
 - flywheels, 514
 - pumped hydro, 512–513
- Mechanical grates, use of in MSW furnaces, 1003–1007
- Mechanical work, conversion of solar heat to, 656
- Membrane carbon capture, 295
- Mercury, emissions of from MSW, 1020
- Mercury and Air Toxics Standards (MATS), 345
- Metal chlorides, boiler tube corrosion due to, 1011
- Metallurgical coals, 38
- Metals
 - condensation point for, 1013
 - degradation of in FFPS, 380–381
 - emissions from MSW incineration, 1019–1022
 - percentage of in municipal solid waste, 73
- Meteorological towers, sensor mounting on, 165–166
- Methanation, 295, 398–399, 904, 914–915
- Methanation unit, 290
- Methane, 289. *See also* Hydrocarbons
 - production of from biomass, 914–916
 - stoichiometric combustion of, 332
- Methanol, direct oxidation of, 1073
- METOSAT, 131
- MEXICO (Model Experiments in Controlled Conditions), 868
- Microrystalline silicon ($\mu\text{-Si}$), 807
- Microalgae, conversion of to biodiesel, 923–924
- Micromorph solar cells, 807
- Microscopic errors, 667
- Mid-level design methods, 569
- Miller cycle engine, 224
- Minable coal, 41
- Mine tailings, 485
- Mineral matter, 36
- Minimum emissions compliance load (MECL), 336, 368
- Mixed alcohols, 924
- Mixed oxide (MOX) fuel, 483
 - reprocessing of, 483
- Mixed-flow runners, 260. *See also* Runner configurations
- Model testing of hydraulic turbines, 271
- Modeling
 - flat-plate collectors, 531–534
 - solar system simulation, 563–566
 - use of TRNSYS for, 570–573
- Modified Wobbe index (MWI), 371–372
- MODTRAN, 122
- Modular incinerators, 1019–1022, 1025–1026
- Moisture content
 - coal, 36–37
 - MSW, 989
- Molten carbonate fuel cells. *See* MCFCs
- Molten salt reactor (MSR), 477
- Molten salts
 - use of for thermal energy storage, 698–699
 - use of in SEGS PTCs, 708
- Molten-salt central receivers, 674
- Molten-salt tubular receivers, 733–734
- Molybdenum, 383
- Momentum models, 860–864
 - limitations of, 866
- Monolithic modules, 813–814
- Monsoons, 138
- Monte Carlo simulation, use of for project cost estimation, 329–330
- Monthly clearness index, 115, 542
- Motor gasoline, 54
- Motor method for octane rating, 244–245
- Motor octane number (MON), 245
- Mountain winds, 138
 - effect of terrain on speed of, 155–156
- MSW
 - air pollution control facilities for, 1011–1022
 - batch feeding of, 995
 - biorenewable resources in, 66–67
 - characteristics of, 988–990
 - definition of, 73
 - distribution of trace metals in, 1019–1022
 - electricity generating capacity of, 19
 - fluidized bed combustion, 1026

- generation and recovery of, 74–76
 - generation of in US, 77
 - incinerators, 1003–1008
 - management of, 76–78
 - materials and products in, 73–74
 - particulate emissions from combustors, 1013
 - processing of, 994–995
 - pyrolysis and gasification of, 1026
 - quantities of, 988
 - residue handling and disposal, 1009–1011
 - ultimate analysis of, 999
 - MSW combustion, 76–78, 995–1003, 1022–1023
 - modular systems for, 1025–1026
 - Multicrystalline silicon PV cells, manufacture of, 774–777
 - Multijunction solar cells, 798, 811–812
 - configurations, 813
 - use of in concentrating PV systems, 845
 - Multipass solar collector systems, 543
 - Multipressure steam flash, 964–965
 - Municipal solid waste. *See* MSW
- N**
- n*-doping, 807
 - n*-type window layer, 818
 - n-i-p* configuration, 810–811
 - Nafion 117, 1074
 - Nanowire solar cells, 815
 - Naphthas, 55, 244–245
 - NASA
 - PEMFC studies by, 1072–1073
 - use of thermionic energy conversion by, 1086
 - National Climatic Data Center. *See* NCDC
 - National Electrical Code (NEC)
 - Article 690 of, 787
 - requirements of for PV arrays, 786
 - National Ignition Facility, 492
 - National Oceanic and Atmospheric Administration. *See* NOAA
 - National Renewable Energy Laboratory. *See* NREL
 - National Solar Radiation Database (NSRDB), 130
 - Natural circulation boilers, 197
 - Natural convection/ventilation, 624–627
 - Natural gas
 - combustion reaction, 330–332
 - consumption of, 56
 - demand for, 4
 - efficiency of gas turbines using, 211
 - global reserves of, 10
 - liquids, 54
 - oxy-fuel combustion of, 410–413
 - production measurement, 58
 - reserves and resources, 56–57
 - role of in future energy mix, 27–28
 - spot prices for, 324
 - terminology, 60
 - use of in auxiliary heaters, 695
 - world production of, 55–56
 - world reserves of, 57
 - Natural gas fuel cells. *See* NGFCs
 - NCDC, solar radiation data of, 130
 - Nernst loss, 1059–1061
 - Net building load coefficient (NLC), 589–590
 - Net energy savings, 582
 - Net head, 262
 - Net output, 287
 - Net primary production (NPP), 519
 - Net skylight transmittance, 645
 - Net thermal output, 687–688
 - New Mexico Wind Energy Center, 883–884
 - New-generation solar cells, 833–834
 - Next-generation nuclear reactor technologies, 462, 464–465
 - fast neutron reactors, 469–470
 - gas-cooled fast reactor system, 472–473
 - Generation IV, 471–472
 - heavy-water reactors, 468
 - high-temperature gas-cooled reactors, 468–469
 - lead-cooled fast reactor, 475–477
 - light-water reactors, 465–468
 - molten salt reactor, 477
 - sodium-cooled fast reactor, 474–476
 - supercritical-water-cooled reactor, 473–475
 - very-high-temperature reactor, 472–474
 - NGFCs, 307–308
 - Nickel, 383
 - Nickel metal hydride (NiMH) batteries, 507–508
 - Nickel-based superalloys, 388
 - Nickel-cadmium batteries, 507
 - Nitrogen oxides. *See* NO_x emissions
 - No-load speed, 268
 - NOAA, solar radiation data of, 130
 - Nocturnal cooling systems, 627–629
 - Non-heat engines, 305
 - Non-OECD Asian countries, electricity-generating capacity of, 6
 - Non-spinning reserve, 368
 - Nonaqueous redox flow batteries, 511
 - Nonconcentrating collectors, 528
 - sensible heat storage in water, 515
 - Noncondensable gas (NCG), 969–970
 - compositions of in geothermal systems, 972–973

- Nondurable goods, recovery of from MSW, 74–76
- Nontracking solar collectors, 552
- Nonvacuum deposition techniques, use of for CZTS deposition, 832–833
- North America, energy use in, 2–3
- North-south sun-tracking axis orientation, 679
- Nova-1, 715
- NOVATEC Solar, 715–716
- NO_x emissions, 295. *See also* Hydrocarbons
 coal combustion, 48, 339–340
 combustion in gas turbines and, 334–339
 geothermal power plants, 981–982
 IC engines, 241
 MSW combustion, 1022–1023
 reduction of using SNCR, 1014–1015
- NREL
 FAST code, 872
 National Solar Radiation Database (NSRDB), 130
 peak sun hour figures, 780
 S-809 airfoil, 858
 wind resource maps of, 146–148
 wind turbine cost modeling, 887–890
- NSAT, 131
- Nuclear fission, 81–82, 456
- Nuclear fuel cycle, 82–84
- Nuclear fuels
 processing of, 82–84
 sources of, 81–82
- Nuclear fusion, 12
 confinement, 492
 energy conversion and transport, 493–494
 potential of, 491
 tokamak reactor development, 492–493
- Nuclear power
 comparison of generation technologies, 488–489
 economics of, 486, 488
 growth of, 461–462
 role of in future energy mix, 27
- Nuclear power plants
 global, 457–458
 life extension, 461–462
 new construction of worldwide, 462–464
 tokamak reactor development, 492–493
 worldwide distribution by reactor type, 447–461
- Nuclear power reactors, 461
 boiling water reactors (BWRs), 459
 development of current technologies, 457
 gas-cooled reactors, 460
 Generation III, 462, 464–470
 Generation IV technologies, 471–477
 pressurized heavy-water reactor, 459–460
 pressurized water reactors, 457–459
 small modular reactors, 470
 waste management for used fuel from, 487–488
- Nuclear power systems
 fuel cycle, 478–484
 goals for Generation IV technologies, 471–472
- Nuclear power technology, 456
- Nuclear resources, 11–13
 fuel regeneration, 12
- Nuclear waste, 485–486
 types of, 485–486
- O**
- Octane number, 918
- Octane rating, 244–245
- OECD countries, per capita energy use in, 23–24
- Offshore gross wind resource, 149
- Offshore wind installations, 868
 platform hydrodynamics, 869
- Ohmic contact, stability of in CdTe solar cells, 819–820
- Oil. *See also* Petroleum
 classification of crude, 51
 demand for, 4
 global reserves of, 9–10
 resource base, 53
 role of in future energy mix, 27
 transitioning away from, 8
 use of for transportation, 7–8
 world refining capacity, 55
 world reserves of, 51–54
- Oil crops, 67
- Once-through boilers, 197
- Once-through cycle, 478, 702, 704, 707
- Once-through superheated water–steam receiver, 732
- Open cycle, 478
- Open heaters, 203
- Open volumetric receivers, 735
- Open-cycle gas turbines, use of in FFPS, 291
- Open-loop single pass systems, design methods for, 575–578
- Open-loop solar thermal systems, 553–554
- Open-pit mining, uranium, 480
- Operating costs, geothermal power plants, 947
- Operating fuel cells, efficiency loss in, 1059–1061

- Operational flexibility, 367–369
- Optical concentration, 665
CRSs, 717
STP plants with, 671–674
- Optical efficiency, 662
enhancing, 536
flat-plate collectors, 534
heliostat fields, 719–727
- Optical losses
in power towers, 727
in PTCs, 682
- OPTIMAT materials database, 882
- Optimum pressure ratio, 213–214
- Orbital combustion process (OCP), 227–228
- Orebody, 479
- Organic chemicals, presence of in MSW ash residue, 1010
- Organic composition of plants, 63–64
- Organic compound emission control, 1016–1019
- Organic Rankine cycle (ORC), 250–252, 287
low-quality waste recovery using, 376
- Organisation for Economic Cooperation and Development. *See* OECD countries
- Ormat Technologies, 976–977
- Otto cycle, 230–232, 292, 297
- Output characteristics of thermionic converters, 1089–1090
- Over-fire air (OFA), 339
- Overall free energy conversion efficiency, 1058
- Overcast sky illuminance, 641
- Overfire air, 1007
- Overlay coatings, 390
- Overpotential, 1054–1055
- Overvoltage, 1054–1055
- Oxidation catalytic converters, 243, 381
- Oxy-fuel combustion, 283, 290, 295, 299
coal, 408–410
natural gas, 410–413
supercritical CO₂, 413–416
- Oxygen
mass transfer of in biomass conversion, 900–901
role of in MSW combustion, 995–1003
- Oxygen-blown gasifiers, 905
- P**
- p-i-n* junctions, 808–809
- p-n* junction, 768–770
illuminated, 770–772
- PAHs, 1016
combustion conditions and production of, 900
- Pancaked charges, 940
- Paper and paperboard products, percentage of
in municipal solid waste, 73
- Parabolic concentrators, 670–671, 748–749
configuration of, 666
errors of, 667–668
sun tracking by, 665
- Parabolic trough collector systems. *See* PTC systems
- Parabolic trough collectors. *See* PTCs
- Parabolic trough STPs, 675–681
- Parasitic power consumption, 287
- Part-flow cycle, 378–379
- Partial depletion effect, 554
- Partial oxidation, 521
- Particle interaction losses, 1088
definition of, 1100
- Particle receiver designs, 729
- Particulate control, 1012–1013
Diesel engines, 243
- Particulate emissions, geothermal power plants, 982
- Particulate matter, emissions of in flue gas, 295
- Particulates, emissions of from Diesel engines, 241–242
- Passive cooling systems, design fundamentals, 624–632
- Passive pitch control, 875
- Passive solar cooling systems, definition of, 581
- Passive solar heating systems
definition of, 581
design approaches, 588–589
design fundamentals, 588
designations and characteristics of, 598–601
fundamental design concepts, 588
general application status and costs, 582
generalized design methods, 589
performance estimation using LCR method, 592–620
SLR correlation parameters, 621–623
SLR method for calculating performance of, 620–624
types of, 586–588
- Passive solar systems, 551
distinction of from energy conservation, 581
economic considerations, 581–582
- Passive solar thermosyphon systems, 582–585.
See also Thermosyphon systems
- Payback period, wind energy, 886
- PCBs, 1016
- PE-1, 715
- Peak optical efficiency, 686

- Peak power, limitation of for wind turbines, 873–875
- Peak sun hour (psh), 780
- Pebble-bed modular reactor, 468–469
- Peltier effect, 1092
- Pelton-type hydraulic turbines, 259
 - efficiency of, 267
 - head values for, 266
- PEMFCs, 1069–1070
 - acceptable contamination levels, 1071
 - applications of, 1072–1073
 - basic operating principle, 1070–1071
 - major technological problems, 1071–1072
- Permanent-magnet generators, 876
 - direct-drive, 876–877
- Permeability, 935
- Perovskite solar cells, 834–835
 - solid-state, 800
- Pescara turbine, 343
- Petra Nova project, 407
- Petrochemical feedstock, 55
- Petroleum. *See also* Oil
 - product classification, 54–55
 - use of for transportation, 7–8
- PFB combustion system, 210–211, 340, 362–363
- Phase change materials (PCM), 699
 - solar thermal storage in, 562
 - storage of thermal energy in, 517
- PHEVs, 8
 - energy storage with, 501
- Phibar method, 545–548
 - use of in IPH design methods, 573–578
- Philippines, geothermal power transmission in, 940
- Philo 6 (AEP), 303
- PHOEBUS-type receivers, 736
- Phosphoric acid fuel cells (PAFCs), 1075–1076
- Photobioreactors, 69
- Photosynthesis, steps and efficiencies of, 62
- Photovoltaic arrays. *See* PV arrays
- Photovoltaic cells. *See* PV cells
- Photovoltaic conversion, 766–767
- Photovoltaic detectors, 127
- Photovoltaic modules. *See* PV modules
- Photovoltaic panels. *See* PV panels
- Photovoltaic systems. *See* PV systems
- Photovoltaic technologies. *See* PV technologies
- Photovoltaics (PV). *See also* PV cells
 - increasing use of, 17
 - role of in future energy mix, 27–28
 - worldwide installed capacity, 766–767
- Pipe heat transfer, 630–631
- Piping losses, 561–562
- Pitch control, 874–875
- Pitch speed capability, 880–881
- Pitch to feather control, 874
- Pitch to stall control, 874
- Pitting corrosion, 381
- Plant composition, impact of on biomass energy, 63–64
- Plant deformation, 153
- Plasma-enhanced CVD (PECVD), 808
- Plastics, percentage of in municipal solid waste, 73
- Plataforma Solar de Almeria. *See* PSA
- Plug-in hybrid electric vehicles. *See* PHEVs
- Plutonium
 - reprocessing of, 481, 483–484
 - use of in breeder reactors, 478
- Polar jets, 138–139
- Polarization, 1054–1055
- Policies for renewable energy, potential of, 14–15
- Policy change, potential for renewable energy, 14–15
- Pollutants, emissions of in flue gas, 295
- Polychlorinated biphenyls. *See* PCBs
- Polycrystalline PV cells, manufacture of, 774–777
- Polycyclic aromatic hydrocarbons. *See* PAHs
- Polymer electrolyte membrane fuel cells. *See* PEMFCs
- Polymer electrolyte membranes, use of in DMFCs, 1073–1074
- Polysulfide bromide batteries (PSB), 510
- Porta-Test Whirllyscrub V Gas Scrubber, 966
- Portugal, installed wind power capacity in, 852
- Post-combustion carbon capture system, 401–408
 - use of in FFPS, 295–296
- Potassium, incorporation of in CIGS solar cells, 825
- Power
 - availability of in hydraulic turbines, 261–262
 - biomass conversion to, 897–898, 907–912
- Power block design, 705
- Power booster scheme, 660
- Power coefficient, 857–858
- Power cycles, air standard, 230–233
- Power density, 503, 873
 - two-stroke SI engines, 227
- Power generating capacity, 907
 - growth of nuclear power, 461
- Power generation, use of thermoelectric devices for, 1094–1095

- Power production. *See also* Electric power generation
gas turbines, 212–213
management of geothermal resource for, 951–959
- Power quality (PQ), 501
- Power sector, primary energy use by, 5
- Power supply, contribution of STP to, 659
- Power towers, 672, 674, 717, 727–742. *See also* CRSs
experience with, 739–740
heliostat and collector field technology, 719–727
molten-salt systems, 744–747
technology description, 718–719
tubular receivers, 732–734
volumetric receivers, 734–739
water–steam plants, 740–744
- Power/load control programming, 879–881
- Pre-combustion carbon capture, 295
- Pre-combustion chamber, 229
- Premixed flame, 336
- Prescribed wake models, 865
- Pressure, effect of on reversible cell potential, 1044–1045
- Pressure drop, flat-plate collectors, 536
- Pressure swing adsorption, 399–400
- Pressure-gain combustion, 283, 340–345
- Pressure–time technique, 276
- Pressurized fluidized bed combustion. *See* PFB combustion system
- Pressurized geothermal brine, 976–977
- Pressurized heavy-water reactor, 459–460
- Pressurized IGFCs, 308
- Pressurized water reactors (PWRs), 457–459
- Pressurizing intake air, 247–250
- Primary energy consumption, 3
- Primary energy use, major sectors of, 5–6
- Prime movers, types of in FFPS, 291–292
- PRISM nuclear reactor, 469
- Probabilistic methods for cost estimation, 329–330
- Probability density, 873
- Process contingencies, 321
- PRODISS, 703
- Producer gas, 902
composition of from various gasifiers, 907
- Project contingencies, 321
- Project cost estimates, 320–321. *See also* TPI
- Propane (C₃H₈). *See* Hydrocarbons
- Propeller anemometers, 159
- Propeller turbines. *See also* Reaction turbines
efficiency of, 267
performance characteristics, 266–267
- Prospecting for wind energy sites, 152–153
biological indicators, 153
effects of topography, 153–157
- Proved oil resources, definition of, 60
- Proven oil reserves, 9
- Proximate analysis, 63–64, 332
coal, 36–38
definition of, 49
- Proximate ash content, 36
- PS10, 658, 674, 717, 724, 740–744
- PS20, 724, 743
- PSA, 674
- PTC systems, use of direct steam generation in, 699–707
- PTCs, 528, 670–672
barriers to commercial use of, 711
connection of in series, 679–681
costs of, 673
efficiencies and energy balances in, 686–688
electricity generation with, 693–695
industrial applications for, 688–691
LS collectors, 710
new designs for, 711–713
operational principles and components of, 675–691
orientation of the rotation axis, 679
performance parameters and losses in, 681–686
sizing and layout of solar fields with, 691–693
solar power plants with, 711–714
thermal storage systems for, 695–699
- Puerto Errado-2, 674
- Pulsating combustor engines, 343
- Pulse converter turbocharging, 249
- Pulse turbocharger, 249–250
- Pulse(d) detonation combustion (PDC), 344
- Pulverized coal (PC)
boiler construction, 383–384
use of in FFPS, 294
- Pumped hydro, 512–513
numerical modeling of, 273
- PUREX process, 483
- PV arrays, 778–779
balance of system components in, 784–787
sunlight and orientation of, 779–780
- PV cells. *See also* solar cells
CdTe, 816–821
CIGS, 821–829
combination of into modules and arrays, 778–779
CZTS, 829–833
efficiency of, 767–768, 793

- hybrid, 812–813
 - illuminated p - n junction, 770–772
 - new generation, 833–835
 - p - n junction, 768–770
 - properties of, 772–773
 - PV charge controller, 781–782
 - PV modules, 778–779
 - a -Si solar cells and configurations, 808–813
 - cost potentials, 801, 805
 - deposition techniques for a -Si solar cells, 808
 - efficiencies of, 802–804
 - materials availability issues, 805–806
 - PV panels, costs of, 766–767
 - PV systems
 - components of, 782–787
 - configurations of, 780–782
 - present status of technology and future challenges, 792–794
 - stand-alone PV well pump system, 787–788
 - stand-alone system for remote schoolhouse, 788–790
 - utility-interactive example, 791–792 (*See also* Utility-interactive PV systems)
 - PV technologies
 - concentrating, 845–849
 - worldwide market share of, 801
 - Pyranometer, 124–126
 - measurement of solar radiation with, 126–127
 - Pyrheliometer, 124
 - Pyrolysis, 521–522
 - bio-oil upgrading, 925–926
 - MSW, 1026
 - role of in biomass conversion to solid fuels, 913–914
 - solid fuel combustion, 899–900
 - thermal gasification and, 903
 - Pyroprocessing, 484
- Q**
- Quiescent chamber engine, 228
- R**
- Raceway ponds, 69
 - Radar, impact of wind facilities on, 151
 - Radial runners, 260. *See also* Runner configurations
 - Radial staggered heliostat field layout, 721–722
 - Radiation distribution, effect of on solar collector performance, 541
 - Radiation statistic, 542
 - Radiative cooling systems, 627–629
 - Radiative losses, reduction of in solar collectors, 537
 - Radiative transfer numerical models, 122–123
 - Radioactive waste materials, 82, 84, 456, 485–486
 - management of radioactive gases, 487–488
 - types of, 485–486
 - Raft River Geothermal Power Plant, 943
 - RAM, 324–327
 - Range tests, 168
 - Rank, definition of for coal classification, 49
 - Rankine bottoming cycle. *See* RBC
 - Rankine cycle, 192, 250–251, 292, 908
 - analysis of, 192–195
 - combination of with topping cycles, 196
 - increasing efficiency of, 194
 - integration of CRSs in, 717
 - integration of PTCs in, 693–694
 - Ranking SCO_2 cycle, 379
 - RANS equations, use of for simulation of hydraulic turbines, 271–272
 - Raptors, impact of wind facilities on, 150
 - Ray tracing analysis, 667
 - RBC, 297
 - thermodynamic calculations of efficiency, 309–311
 - RDF systems, 990–992, 1022
 - furnace grates in, 1005–1007
 - particulate emissions from, 1019–1022
 - production of fuel pellets in, 995
 - RDF-fired water wall systems, 1009
 - Reaction turbines, 258, 260
 - cavitation issues with, 270
 - control of flow in, 262
 - performance characteristics, 266–267
 - performance comparison with impulse turbines, 267
 - Reactor fuel, 456
 - Reactor technologies, 461
 - boiling water reactors (BWRs), 459
 - development of, 457
 - gas-cooled reactors, 460
 - Generation III, 462, 464–470
 - plant life extension, 461–462
 - pressurized heavy-water reactor, 459–460
 - pressurized water reactors, 457–459
 - small modular reactors, 470
 - Real options theory, 329–330
 - Reburning, 339
 - Receiver and power system control system (RPSCS), 726–727
 - Receiver tubes, 677

- Reciprocating engines. *See* Recips
- Reciprocating grates, 1004
- Reciprocating IC engines, 224
- Recips
 - Carnot factor for bottoming cycle of, 376
 - comparison of with gas turbines, 372–375
 - stationary power generation examples, 374
 - use of in FFPS, 291
- Recirculation process, 702, 704
- Recoverable oil resources, definition of, 60
- Recoverable reserves
 - coal, 41
 - oil, 9–10, 51
- Recovery rates, 78
 - products in MSW, 74–76
- Recuperated gas turbines, 209, 215
 - definition of, 222
- Recuperated SCO₂ cycle, 377–379
- Recycling, 987
 - recovery of materials from MSW, 76–78
- Reduced boiling water reactor (PBWR), 468
- Reduced moderation water reactor (RMWR), 468
- Reduction catalytic converters, 243
- Reed valves, 227
- Reflective parabolic concentrators, 670–671
- Reflective solar concentrators, 717
- Reflectivity, 682
- Reflectors
 - concentrating, 668–670
 - performance improvement of solar collectors using, 537–538
 - use of in parabolic trough collectors, 677–678
- Reforming, 521
- REFOS, 738–739
- Refractories, 1006–1007
- Refractory furnace with waste heat boilers, 1008
- Refrigeration, use of thermoelectric devices for, 1095–1098
- Refuse
 - feeding, 995
 - receipt, processing, and storage of, 994–995
- Refuse-derived fuel (RDF) systems. *See* RDF systems
- Regenerable solid solvent carbon capture, 295
- Regenerative cycle, 194
 - gas turbines, 215–216
- Reheat combustion, 313, 357–358
 - Carnot factor and, 318
- Reheat combustion gas turbine, air standard cycle calculations for, 317–318
- Reheaters, 198, 216
- Relational tests, 169
- Relative efficiency, 276
- Reliability, availability, and maintenance. *See* RAM
- Renewable energy (RE). *See also* specific sources
 - biomass potential, 19–21
 - biomass resources, 66–69
 - elements of economic consideration, 581–582
 - energy storage for, 498–499
 - present status and potential of, 13–15
 - resource summary, 21–22
 - role of in future energy mix, 27–28
 - solar energy conversion to biomass, 61–63
 - solar energy potential, 16–18
 - wind energy resource, 143–149
 - wind power potential, 15–16
 - wind resource assessment, 152–157
 - wind resource evaluation, 157–171
- Renewable energy resources, geothermal energy, 937
- Renewable energy sources, electricity production from, 5–6
- Repowering, 362–364
- Reprocessing, 478, 481, 483–484
 - PUREX process, 483
 - pyroprocessing, 484
 - UREX+ process, 484
- Research and development, solar thermal power plants, 713
- Research method for octane rating, 244–245
- Research octane number (RON), 245
- Reserve base, 41
 - global recoverable coal resources, 44–46
- Reserve to production ratio (R/P), 10–11
- Reserve-return layout of solar fields, 692–693
- Residential solar systems, 551
- Resonance condition, 871
- Reversible cell potential, 1038–1042
 - effect of operating conditions on, 1042–1046
- Reversible energy conversion efficiency, 1047, 1052–1054
 - equivalency of with Carnot efficiency, 1049–1050
 - heat engines, 1048–1049
- Reversible energy loss, 1052–1054
- Reynolds-averaged Navier–Stokes (RANS) equations. *See* RANS equations
- RF glow discharge decomposition, 777
- Rich catalytic lean burn (RCL), 339
- Ridges, effect of on wind speed, 155–156
- Rim angle, 681–682
- RIT, 352
- Rock storage systems, 562
- Rocking grates, 1004

- Roll-bond collectors, 530
- Roller grates, 1004–1005
- Room surface dirt depreciation, 639
- Room-and-pillar mining, 47–48
- Root mean square (RMS), use of to quantify slope errors, 668–669
- Roots blower, 248
- Rotor inlet temperature. *See* RIT
- Rotor speed capability, 880
- Rotors for steam turbines, 200–201
- Runaway speed, 268
- Runner configurations
 - hydraulic turbine efficiency and, 262
 - impulse turbines, 259
 - numerical modeling of, 273
 - performance comparisons, 267
 - reaction turbines, 260
- Russia
 - fast nuclear reactors in, 469
 - nuclear power reactors in, 461

- S**
- S-809 airfoil, 858
- Sac volume, 241
- Safety controller, 878–879
- Salinity-gradient ponds, sensible heat storage in, 516–517
- Salt velocity testing method, 276
- San Onofre nuclear power plant, 462
- Sanlúcar heliostats, 724
- Satellite data
 - estimation of solar resource from, 132–134
 - use of to map solar radiation, 131–132
- Saturated steam plants, 741–744
- SBDART, 122
- Scaling factor, 688
- Scaling formulae for hydraulic turbines, 263–264
- Schott, 677
- Screen printing (SP), 819
- Scrubber/fabric filter control systems, 1013
- Sea breezes, 138
- Seasonal pricing, geothermal power, 945
- Seasonal solar energy storage, 552
- Secondary batteries, 505–506
 - lead-acid, 506
 - lithium ion, 506–507
 - nickel metal hydride, 507–508
 - nickel-cadmium, 507
 - sodium-sulfur, 508
 - zebra, 509
- Seebeck effect, 1092
- Seed crystals, use of to fabricate silicon PV cells, 774–776
- SEGS plants, 658, 673, 707–721
 - basic characteristics of, 709
- Selective catalytic reduction (SCR), 198, 243, 295, 335
- Selective noncatalytic reduction. *See* SNCR
- Selective surfaces, use of to reduce losses from collectors, 537
- Selective surfaces on flat-plate collectors, 530
- Selenization, 825–827
- Self-discharge time, 501–503
- Semiconductor materials, use of on PV cells, 796–801. *See also* PV cells
- Semipermanent global wind patterns, 139
- SENER, 678, 724, 746
- SenerTrough, 678
- Sensible heat, 504, 515
 - storage in liquids, 515–517
 - storage in solids, 517
- Sensible storage systems, 562–563
- Sensitivity curves, 615–619
- Sensor coatings, 391
- Sensor technology
 - control of solar systems using, 558
 - data collection and handling, 166–171
 - sampling rates and statistical quantities, 164–165
 - specifications for wind data instruments, 162
 - towers and mounting, 165–166
 - use of for wind resource evaluation, 159–165
- Separated brine, uses of in geothermal power operations, 954–955
- Separative work units (SWU), 480
- Sequential combustion, 357–358. *See also* Reheat combustion
- SEVILLANA, 741
- Shading, heliostat placement and, 721
- Shading losses, 561–562
- Shadow map, 97
- Shadow-angle protractor, 95–98
- Shadow-band trackers, 676
- Shaft power producers for FFPS, 292
- Shassroen, Fritz, 81
- Shell-and-tube heat exchangers, use of in steam turbines, 204–205
- Shippingport Atomic Power Station, 457
- Short rotation woody crops (SRWCs), 67
- SI engines, 224
 - abnormal combustion, 238–239
 - air throttling in, 234
 - combustion in, 236–237

- compression ratio, 231–232
- control of emissions from, 242–243
- fuels for, 244–245
- normal combustion process, 237–238
- supercharging, 247–248
- turbocharging, 248–250
- Si *p-n* junction, 769–770
- Si PV cells, manufacture of, 774–777
- Sibbutiminous coal, 34
 - reserves of, 39–40
- Sidelighting, 633–634
 - lumen method of, 635–644
- Siemens, 677
- Silica
 - concentrations of in geothermal reservoirs, 956
 - solubility limits of, 978–979
 - solubility of, 974
- Silicon, 383
- Silicon nitride, use of for gas turbine coating, 220
- Silicon thin-film solar cells. *See* Si PV cells
- Silicon wafers, 797
- Similitude of hydraulic turbines, 262–264
- Simple design methods, 568–569
- Single-axis sun-tracking systems, 528, 676
- Single-crystal (SC) superalloys, 388–389
- Single-crystal Si PV cells, manufacture of, 774–777
- Single-medium storage systems, 696–698
- Single-pass open-loop solar thermal systems, 554
- Single-point temperature controllers, 558
- SKAL-ET, 678
- Sky diffuse radiation, 101
- SkyFuel Inc., 716
- Skylight, 633
 - definition of, 581
- Skylighting, lumen method of, 644–648
- Slag, 39
- Slagging combustion technology, 339
- Slope error, use of root mean square to quantify, 668–669
- SLR, 592
 - calculation of passive solar heating performance using, 620–624
- Small modular reactors (SMRs), 470
- SMES, direct electric storage with, 512
- Smith–Kaplan hydraulic turbines, 260–261
- SNCR, use of to reduce NO_x emissions from MSW incineration, 1014–1015
- Snell's law of reflection, 667
- SO₂ emissions. *See also* Hydrocarbons
 - geothermal power plants, 981
 - MSW incineration, 1014–1016
- Societal concerns, wind facilities, 149–151
- SODEAN, 741
- Sodium, incorporation of in CIGS solar cells, 824
- Sodium nickel chloride batteries, 509
- Sodium-cooled fast reactor (SFR), 474–476
- Sodium–sulfur batteries, 508
- SOFCs, 305, 1079–1080
 - acceptable contamination levels, 1081
 - applications of, 1082
 - basic operating principles, 1080–1081
 - major technological problems, 1081–1082
 - programs currently researching, 306–307
 - technological status, 1082
 - use of syngas by, 307–308
 - utilization factor, 306
- Softwoods, 67
- Soil
 - heat transfer, 630–631
 - temperatures and properties, 631
 - transient thermal analysis of temperature, 630–631
- SOLAIR project, 737–738
- SOLANA, 658, 711
- Solar absorbers, stagnation temperatures for, 663–664
- Solar add-on cost, 582
- Solar altitude angle, 91, 635, 779
- Solar angles. *See also* specific angles
 - definitions for on a tilted surface, 105–112
- Solar azimuth angle, 91, 635, 779
- Solar beam radiation, 633
- Solar cells. *See also* PV cells
 - assembly of, 775
 - bandgap of semiconductor materials used in, 799
 - CdTe, 816–821
 - CIGS, 821–829
 - CZTS, 829–833
 - efficiencies of, 16, 802–804
 - future of, 815
 - hybrid, 812–813
 - manufacture of Si PV cells, 774–777
 - multijunction and tandem, 811–812
 - new generation, 833–835
- Solar chimney concept, 625–626
- Solar concentration ratio, 670–671
- Solar concentration, STP systems and, 661–671
- Solar concentrators
 - beam quality, 665–671
 - errors of, 667–668

- Solar constant, 99
- Solar control, 624
- Solar declination, 87, 90
- Solar Electricity Generating System plants. *See* SEGS plants
- Solar energy
 - conversion of to biomass, 61–63
 - economic considerations, 581–582
 - exergetic value of, 656
 - growth potential of, 16–18
 - role of in future energy mix, 27–28
 - storage of by STP plants, 659–661
- Solar energy storage, use of biomass for, 519–522
- Solar ephemeris, 88–89
- Solar fields
 - new PTC designs for, 712–714
 - sizing and layout of, 691–693
- Solar fraction, 564
- Solar gain, increasing for daylighting purposes, 649
- Solar Heat and Power Pty Ltd., 715
- Solar hot water heating
 - absorber losses during, 537
 - design method for, 573
 - thermosyphon systems, 582–585
 - use of closed-loop systems for, 554–557
- Solar insolation, 99
 - effect of day-to-day changes in, 540–541
- Solar load ratio. *See* SLR
- Solar noon, 779
- Solar One, 658, 732–733, 744
- Solar ponds, sensible heat storage in, 516–517
- Solar Power Group (SPG), 715
- Solar power systems (SPS), Stirling, 450–453
- Solar power towers. *See* CRSs
- Solar radiation, 85–86, 98–99
 - anisotropic of, 118–119
 - atmospheric extinction of, 101–103
 - attenuation of, 102
 - data, 129–131
 - detectors for instrumentation, 127–128
 - estimation of terrestrial, 100–101
 - extraterrestrial, 99–100
 - hourly and daily on tilted surfaces, 119–122
 - instruments for measuring, 124–127
 - mapping using satellite data, 131–134
 - measurement of, 123
 - measurement of sunshine duration, 128
 - models based on long-term measures of, 113–123
 - monthly estimation models, 112
 - spectral measurements, 128–129
 - thermal storage of, 695–699
 - on a tilted surface, 105–112
 - use of in wind-flow modeling, 161
 - wideband spectral measurements of, 129
- Solar receivers, 656, 717, 727–742
 - convection losses in, 728–729
 - direct configuration of, 730
 - efficiency of, 662–664, 727
 - tubular, 732–734
 - volumetric, 734–739
- Solar reflectors, use of in parabolic trough collectors, 677–678
- Solar savings fraction. *See* SSF
- Solar steam generation systems, 688
- Solar Stirling power systems, 450–453
- Solar system design, 527
- Solar thermal collectors
 - compound parabolic concentrators, 539–540 (*See also* CPCs)
 - corrections to performance parameters, 559–562
 - evacuated tubular, 538–539
 - factors influencing performance of, 532
 - flat-plate, 529–538 (*See also* Flat-plate collectors)
 - long-term performance of, 540–550
 - pipng and shading losses, 561–562
 - pressure drop across, 536
 - stagnation temperature, 536
 - time constant of, 536
 - types of, 527–529
- Solar thermal energy, storage of, 562–563
- Solar Thermal Enhanced Oil Recovery pilot plant, 740
- Solar thermal power systems. *See* STP systems
- Solar thermal systems
 - active, 551
 - classification of, 550–552
 - closed- and open-loop systems, 552–557
 - costs, 578–579
 - daily and seasonal storage, 552
 - design methods, 568–578
 - design of active space heating, 570–573
 - design recommendations, 578
 - liquid and air collectors, 552
 - passive, 551
 - simplified economic analysis for, 568
 - simulation of, 562–566
 - sizing methodology, 566–568
 - solar-supplemented, 550–551
 - stand-alone, 550
- Solar time, 92–93, 779
- Solar Two, 733–734, 745–746

- Solar zenith angle, 91
- Solar-cell-activated controls, 558
- Solar-supplemented energy systems, 550–551, 555–557
 - production functions of, 566–568
 - simplified economic analysis of, 568
- Solar-supplemented systems, simplified
 - economic analysis for, 568
- Solar-to-electric conversion efficiencies, 672–673
- Solarlite, 676, 707
- Solarmundo, 715
- SOLGAS, 717
- SOLGATE, 717
- Solid fuels
 - biomass conversion to, 913–914
 - processes of combustion of, 899–900
 - ultimate analysis of, 999
- Solid oxide fuel cells. *See* SOFCs
- Solid polymer (electrolyte) fuel cells. *See* PEMFCs
- Solid waste, quantities and characteristics of, 988–990
- Solid waste management. *See* MSW
- Solid-fuel combustors, 901–902
- Solid-liquid phase changes, 518
 - melting points and heats of fusion for, 518
- Solid-solid phase changes, 518
- Solid-state perovskite-based solar cells, 800
- Solids, storage of sensible heat in, 517
- Solitem, 678
- SOLMET, 130
- Solution mining, uranium, 480
- SOPOGY, 678
- Soponova 4.0, 678
- Sorghum, conversion of solar energy by, 62
- Source circuit, 784–785
- South Africa, development of the pebble-bed modular reactor in, 468–469
- South-facing windows, 624–625
- Soybeans, conversion of to biodiesel, 923
- Space heating
 - design of active solar systems for, 570–573
 - use of active closed-loop solar systems for, 557
- Space nuclear power systems (SNPS), 1085
 - use of thermionic converters in, 1091
- Spain
 - construction of new STP plants in, 711–713
 - heliostat technology in, 723–724
 - history of linear Fresnel reflector systems in, 715
 - installed wind power capacity in, 852
 - nuclear power capacity in, 461
 - PS10 project in, 741–744 (*See also* PS10)
 - STP plant in, 674
- Spark gap, 236
 - normal combustion process, 237–238
- Spark ignition engines. *See* SI engines
- Spark plugs, 224
- Specific energy, 503
- Specific power, 503
- Specific speed, 259
 - definition of, 263
 - practical range of for reaction turbines, 266
 - values of for impulse turbines, 266
- Spectral distribution, extraterrestrial solar radiation, 98
- Spectral models of solar radiation, 122–123
- Spectral solar radiation, measurement of, 128–129
- Speed regulation for hydraulic turbines, 268–270
- Spent fuel, 456
 - interim storage costs, 488
 - managing high-level wastes from, 486
 - storage of, 484
 - transportation of, 484
 - waste management of, 487–488
- Spinning reserve, 368
- Split-compression cycle, 378–379
- Spray attemperators, 198
- Spreader-stoker facilities, 1022
- Sputtering
 - use of for CZTS deposition, 831–832
 - use of for deposition on CdTe solar cells, 820
- SSF, 589–590
 - aperture-area-weighted, 615
 - sensitivity curves, 615–619
 - values for, 593–597
- Stack design considerations, 1063–1066
- Stack effect, 625–626
- Staebler-Wronski effect (SWE), 809–810
 - use of multijunction cells to combat, 811–812
- Stagnation temperature, 536, 663
- Stainless steel, 381–382
- Stall control, 874
- Stand-alone inverters, 784
- Stand-alone solar systems, 550
- Standard candle, 633
- Standard fuels, classification of, 54–55
- Starch crops, 67
- Steady-state procedures, use of to test flat-plate collectors, 532–534
- Steady-state simulations, 564
- Steam
 - enhancing production of, 955–957

- heat transport in, 688
- pipeline operation in geothermal systems, 965
- Steam boilers, 196–197
 - drum-type, 197
 - major components of, 197–198
 - use of in FFPS, 293
- Steam coals, 38
- Steam cooling of gas turbines, 220
 - definition, 222
- Steam drum, 197
- Steam flash power plants, 947
- Steam generators, 196–198
 - stages of, 694
- Steam methane reformer, 290
- Steam methane reforming (SMR), 295, 399–400
 - use of in natural gas fuel cells, 307
- Steam power plants, 191–192, 939
 - auxiliary power for, 287
 - efficiencies of, 192
 - exhaust gas clean-up systems for, 198
 - generators, 206–208
 - heat exchangers in, 203–205
 - pumps, 205
 - Rankine, 908–909
 - Ranking cycle analysis, 192–195
 - use of boilers in, 196–198
 - use of topping and bottoming cycles in, 196
 - use of turbines in, 198–203
- Steam RBCs, state-of-the-art, 297
- Steam turbines, 198–199, 965–967
 - blading, 199–200
 - choosing arrangements for, 201–202
 - conversion, 967–968
 - cylinders and bolting, 202
 - geothermal, 938
 - integration of in binary power plants, 977–980
 - materials for, 202, 385–386
 - rotors, 200–201
 - steam/brine separation for, 963–964
 - use of exhaust from gas turbines to power, 217
 - use of in FFPS, 293
 - valves, 203
- Steam-injected gas-turbine (STIG) cycle, 218, 911
 - definition of, 222
- Steam-tubes, 861
- Steel, 381
- Steinmuller heliostat ASM-150, 724
- STEM, 703
- Sterling cycle, thermodynamics of, 447–450
- Sterling, Reverend Robert, 447
- Still gas, 55
- Sterling cycle, 292, 908
- Sterling engines, 450–453
 - use of dish-Sterling systems, 749–750
- Stirred reactor model, 331
- Stodola, Aurel, 302
- Stoichiometric combustion, 330–334
- Stoichiometry, 1059–1061
- Storage
 - applications, 500–501
 - closed-loop solar systems, 554–557
 - devices for, 501–503
 - direct electric, 511–512
 - direct thermal, 515–519
 - electrochemical energy, 505–509
 - electrolytic hydrogen, 511
 - flow batteries, 509–511
 - mechanical energy, 512–515
 - passive solar heating systems design, 591–592
 - refuse, 994–995
 - solar thermal, 551–552
 - solar thermal energy, 562–563
 - temperatures in active solar systems, 558
 - thermochemical energy, 519–522
- Storage capacities, 501
- Storage media, 499
- Storage systems, 498–499
- Stored energy, principal forms of, 499
- STP systems, 656. *See also* CSP systems
 - advantages of, 656–658
 - capital costs of, 659, 672
 - central receiver, 716–717
 - dish-Sterling, 747–752
 - outlook for, 752–755
 - plant technologies, 671–674
 - potential market for, 659
 - principles and limitations of, 670–671
 - reasons for lack of new facilities, 658
 - solar concentration and, 661–671
 - system efficiency, 661–665
 - use of in IPH applications, 678
 - use of PTCs in, 711–714
- Straflo turbines, 260
- Straight-run gasoline, 245. *See also* Naphthas
- Stress, 380
- Stress corrosion cracking (SCC), 381
- Stretched-membrane concentrator, 751
- Structural dynamics
 - HAWTs, 870–872
 - VAWTs, 872
- Subcritical pentane binary power plants, 975
- Substitute natural gas (SNG), 289, 295, 398–399

- Substrate solar cell configuration, 810–811
- Subtropical jets, 138–139
- Sugarcane, conversion of solar energy by, 62
- Sulfur
 - combustion of coal and emissions of, 48
 - combustion of in MSW, 996–997
- Sulfur dioxide. *See* SO₂ emissions
- Sun angles, 92–93
 - definitions for on a tilted surface, 105–112
- Sun tracking, 528, 665, 675–676
 - axis orientations for, 679
 - parabolic concentrators, 748
- Sun–earth geometric relationship, 86–87, 90–92
 - shadow-angle protractor, 95–98
 - solar time and angles, 92–93
 - sun-path diagram, 93–94
- Sun-path diagram, 93–94
- Sun-window azimuth angle difference, 635
- Sun-window geometry, 634–635
- SunCatcher system, 748
- Sunk costs, 958
- Sunlight, 633
 - definition of, 581
- Sunshape, 666–667
 - degraded, 667
- Sunshine
 - instruments for measuring, 124–127
 - measurement of duration, 128
- Sunshine switch, 128
- Sunshot Initiative, 714
- Sunspace, 586–587
- Superalloys, 387–390
 - example chemical composition of, 387
 - use of in gas turbines, 220
 - use of in USC power plant boiler
 - construction, 385
- Supercharging, 224, 247–248
- Superconducting magnetic energy storage system. *See* SMES
- Supercritical CO₂ cycle (SCO₂ cycle), 283, 299, 376–379
 - oxy-fuel combustion with, 413–416
- Supercritical coal power plants. *See also* Steam power plants
 - efficiencies of, 192
- Supercritical double-reheat power plants, 303
- Supercritical hydrocarbon binary power plants, 975–976
- Supercritical pulverized coal (SCPC) plants, 396
- Supercritical-water-cooled reactor (SWR), 473–475
- Superheated steam systems, 743
- Superheaters, 197–198
- Superstrate solar cell configuration, 810–811
- Surface ignition, 238–239
- Surface mining, 48
- Surface work function, 1087
 - definition of, 1100
- Suspension burners, 902
- Swamp coolers, 627
- Swirl ratio, 228
- Switchyard, 293
- Switzerland, nuclear power capacity in, 461
- Synchronous AC generators, use of in FFPS, 293
- Synchronous generators, 875–876
- Syngas, 288, 391–397, 521–522, 902, 915–916
 - catalytic pathways for conversion of to fuels, 917
 - generation of by biomass gasification, 916–917
 - generation of in indirect heating gasifiers, 904
 - generation of in oxygen-blown gasifiers, 905
 - use of in fuel cells, 307–308
- Synthetic fuels, production of, 391
- System checks, 169
- System reliability, 164
- T**
- T*–*s* plots
 - heat transfer from recuperator/regenerator, 215
 - use of for gas turbine cycles, 212–213
- T&D systems, geothermal power, 939–941
- Tailwater elevations, turbine cavitation and, 270
- Tandem solar cells, 811–812
- Tankless storage technologies, biomass solids, 519–520
- Tax incentives, necessity of for solar power plants, 711
- TCOs, 810–811
 - front electrical contact configuration for CdTe solar cells, 817–818
- TCR, 321
- Technology Program Solar Air Receiver project, 736
- Technology readiness level. *See* TRL
- Temperature
 - effect of on reversible cell potential, 1042–1044
 - geothermal resources, 946–947
 - stagnation, 536
- Temperature sensors, use of in active solar systems, 558
- Temperature–entropy plots. *See* *T*–*s* plots

- Terminal temperature difference (TTD), 203–204
- Terrestrial solar radiation, 86, 138
 - clear sky radiation model, 103–105
 - estimation of, 100–103
 - on a tilted surface, 105–112
- Thailand
 - DSG solar thermal power plant in, 707
 - electricity-generating capacity of, 6
- Theilacker and Klein correlation, 545–548
- Themis system, 733
- Thermal barrier coatings (TBC), 388
 - application of on components, 390–391
 - use of to reduce inlet temperature gaps, 352
- Thermal efficiency, 286, 686
 - definition of for power cycles, 230–231
 - flat-plate collectors, 534
 - improving in coal-fired power plants, 345–348
- Thermal energy, 177–178
- Thermal energy storage (TES), 499, 659–661
- Thermal fluids, use of in CRSs, 718
- Thermal gasification, 902–904
 - equipment for, 904–907
 - process steps, 903
- Thermal loss coefficient, 683
- Thermal losses, 683, 727
 - flat-plate collectors, 529
 - pipng and shading, 561–562
- Thermal memory coatings, 391
- Thermal NO_x mechanism, 334
- Thermal oils, 676–677, 689
 - use of as working fluids, 527–528
 - use of for energy storage, 696–698
 - use of in SEGS plants, 707
- Thermal storage, 562–563, 591–592
 - direct, 515–519
 - dual-medium systems, 698–699
 - single-medium systems, 696–698
 - sizing and layout of solar fields, 692
 - systems for parabolic trough collectors, 695–699
- Thermal storage beds, 517
- Thermal storage roof, 588
- Thermal storage wall, 586–587
- Thermionic converters
 - electron saturation current, 1088–1089
 - interelectrode motive distribution, 1087–1088
 - output characteristics, 1089–1090
 - schematic of, 1086
 - surface work function, 1087
 - thermodynamic analysis of, 1090–1091
 - types of, 1089
 - use of in space power systems, 1091
- Thermionic energy conversion (TEC), 1085–1086
 - definition of, 1100
 - principles of, 1086–1089
- Thermochemical energy storage, 519
 - biodiesel, 521
 - biomass solids, 519–520
 - ethanol, 520–521
 - syngas, 521–522
- Thermochemical technologies, use of for biomass conversion, 924
- Thermocline systems, sensible heat storage in, 516–517
- Thermodynamic analysis of thermionic converters, 1090–1091
- Thermodynamic model of fuel cell system, 1038
- Thermodynamic test method, 276–277
- Thermodynamics
 - AFFPS, 308–319
 - Stirling cycle, 447–450
- Thermoelectric applications, 1093–1094
 - power generation, 1094–1095
 - refrigeration, 1095–1098
- Thermoelectric detectors, 127–128
- Thermoelectric effects, 1092–1093
- Thermoelectric legs, 1093–1095
 - definition of, 1100
- Thermoelectric modules, 1093–1094
 - definition of, 1100
- Thermoelectric power conversion, 1092
- Thermopiles, 127
- Thermosyphon systems, 557
 - concept, 582–583
 - solar hot water heating using, 582–585
 - thermo-fluid system design considerations, 584–585
- Thin-film full-spectrum solar cells, 815
- Thin-film PV technology
 - advantages of, 799–800
 - cost potentials, 801, 805
 - efficiencies, 797
 - historical and current developments, 796–801
 - material availability issues, 805–806
- Thin-film silicon solar cells. *See also a-Si cells; Si PV cells*
 - fabrication of, 776–778
 - material and properties, 806–807
- Thoma's sigma, 270
- Thompson effect, 1092

- Thorium, 82
 - resources of, 478–479
 - use of in breeder reactors, 478
- Thorium reserves, 12
- Three-dimensional, lifting-surface, free-wake model, 865
- Throttle steam conditions, 297
- Tilted surfaces
 - hourly and daily solar radiation on, 119–122
 - terrestrial radiation on, 105–112
- Time to rupture, 381
- Tip-speed ratio, 863
- TIT, 312
 - definition of, 352
 - E class, 342–344
 - improving cycle performance by increasing, 318
 - NO_x emission as a function of, 335
 - use of fuel moisturization to increase, 338
- TIT-RIT temperature loss, 352
 - use of closed-loop steam cooling to reduce, 355–357
- TMV data sets, 130
- Tokamak Fusion Test Reactor (TFTR), 492
- Tokamak magnetic fusion, 492
- Tokamak reactor development, 492–493
- Top dead center (TDC)
 - CI engines, 228
 - four-stroke SI engines, 224–225
 - two-stroke SI engines, 225
- Toplighting, 633–634
- Topography, effects of on wind speed, 153–157
- Topping cycles, 196
- Topping-up auxiliary heaters, 555–556
- Toroidal bowl combustion chamber, 228–229
- Torque boxes, 678
- Torque tubes, 678
- Torrefied biomass, 913–914
- Torresol Energy, 674
- Total capital requirement. *See* TCR
- Total plant investment. *See* TPI
- Total primary energy supply, fuel shares in, 13
- TPI, 321
- Trace metals
 - distribution of in MSW, 1019–1022
 - presence of in MSW ash residue, 1010
- Tracking axis, 675
- Tracking solar collectors, 552, 675–676
- Trade winds, 138–139
- Transesterification, production of biodiesel using, 922–923
- Transition to alternative fuels, 10
- Translating drag device, 857
- Transmission and distribution systems. *See* T&D systems
- Transmission reservations, 940
- Transmissivity, 683
- Transparent conducting oxides. *See* TCOs
- Transportation
 - use of for distribution of coal, 41, 46–47
 - use of primary energy by, 6–8
- Transportation fuels
 - ignition and combustion properties of, 919
 - traditional, 918
 - use of light gases for, 915–916
- Trend tests, 169
- Trickle charge, 781
- Trickle type flat-plate collectors, 531
- Triglycerides, conversion of, 922–924
- Tritium, 491–492
- TRL, 299–300
 - DOE Office of Fossil Energy definitions for, 301
- TRNSYS, 569
 - modeling active space heating design using, 570–573
- Trombe wall, 586
- Tube turbines, 260
- Tube-and-sheet collectors, 530
- Tubular collectors, 531
 - evacuated, 538–539
- Tubular receivers, 732–734
 - heat transfer principles in, 731
- Tumble swirl, 236
- Turbine control
 - operational controller, 879
 - power/load control programming, 879–881
 - safety controller, 878–879
- Turbine efficiency, 211–212
 - definition of, 222
- Turbine generators, 875–878
- Turbine inlet temperature. *See* TIT
- Turbine reheat, 216
- Turbine runners, 258. *See also* Runner
 - configurations
- Turbine vane cooling, 219–220
- Turbines
 - hydraulic (*See* Hydraulic turbines)
 - hydrokinetic, 277–278
 - impact of wind facilities on environment, 149–151
 - orientation of, 877
 - steam, 198–203
- Turbocharging, 224, 248–250
- Turbulence
 - intensity, 170

- SI engine combustion, 236
 - use of large-eddy simulation for modeling of, 272–275
 - wind farm siting and measurements of, 161
 - Turgo turbines, 259
 - Two-axis sun-tracking systems, 528, 676
 - Two-phase flow, 700
 - Two-stroke SI engines, 224
 - basic operation of, 225–228
 - Two-tank thermal storage system, 516
 - Type, definition of for coal classification, 49
- U**
- Ultimate analysis, 332
 - biomass, 64
 - coal, 37–39
 - combustible portion of MSW, 989, 999
 - definition of, 49
 - Ultimate recoverable oil reserves, 9
 - UltimateTrough, 712
 - Ultra-supercritical (USC) coal plants. *See* USC power plants
 - Ultracapacitors, 511–512
 - Unburned hydrocarbons (UHCs)
 - emissions of from IC engines, 241
 - emissions of gas engines *vs.* GTCC, 374
 - reduction of in coal combustion, 339–340
 - Underfire air, 1007
 - Underground coal gasification (UGC), 397–398
 - Underground mining, uranium, 480
 - Unified boiler systems, 689
 - Unipolar fuel cell connections, 1064–1065
 - Unit size, 501–502
 - United Kingdom
 - installed wind power capacity in, 852
 - London Array wind power project, 883–884
 - nuclear power reactors in, 460
 - United States
 - advanced pressurized water reactor in, 466–467
 - coal reserves in, 39–40
 - development of Generation III nuclear reactors in, 465
 - electric power generation capacity by generator/cycle type, 907
 - energy use in, 2–4
 - geothermal power production in, 932–933
 - heliostat technology in, 724
 - history of linear Fresnel reflector systems in, 715
 - installed wind power capacity in, 852
 - nuclear power capacity in, 461
 - nuclear power plants in, 457
 - per capita energy consumption, 22–23
 - STP plants in, 673–674
 - Sunshot Initiative, 714
 - United States Department of Energy. *See* DOE
 - Unity stoichiometry, 1060
 - Updraft gasifiers, 905–906
 - Upper temperature limit, gas turbines, 219–220
 - UPS inverters, 784
 - Uranium, 81–82
 - conversion and enrichment of, 480–481
 - fuel fabrication and use, 481
 - known recoverable resources of, 479
 - milling of, 480
 - mine tailings, 485
 - mining of, 480
 - processing of, 82–84
 - reprocessing of, 483–484
 - use of in breeder reactors, 478
 - world commercial reprocessing capacity, 483
 - Uranium reserves, 12
 - Uranium-235, fission of, 456
 - Urea-selective catalytic reduction (SCR), 243
 - URSSATrough, 678
 - USC power plants, 283, 345–351
 - comparison of with GTCC power plants, 350–351
 - potential alloys for boiler construction in, 384–385
 - use of superalloys in, 388
 - Utility shaping, 500
 - Utility-interactive PV systems, 786
 - example of, 791–792
 - Utilizability
 - daily, 546–548
 - hourly and daily solar radiation on tilted surfaces, 119
 - individual hourly, 541–545
 - Utilizability factor, 542
 - Utilization coefficient, 646–648
 - Utilization in fuel cells, 1059–1061
- V**
- Vacuum receiver pipes, 677
 - Vacuum thermionic converters, 1089
 - Validation tests
 - range tests, 168
 - relational tests, 169
 - trend tests, 169
 - Valley winds, 138
 - Valves for steam turbines, 203
 - Vanadium, 383

- Vanadium redox flow batteries (VRB), 509–510
 - Vane cooling, 219–220
 - Vanguard-1 prototype, 750
 - Vapor thermionic converters, 1089
 - Vapor transport (VT), use of for CdTe deposition, 820
 - Vapor transport deposition. *See* VTD
 - Variable exogenous parameters, 566
 - Variable O&M costs, rule-of-thumb for GTCC, 323–324
 - Variable-pitch turbines, 881
 - Variable-speed turbine orientation, 877
 - Variations in wind speed, 138–140
 - VAWTs, 852–854
 - classification of, 854
 - momentum model for, 864
 - structural dynamics, 872
 - vortex models for, 864–866
 - VBER nuclear reactors, 467–468
 - Velocity head, 261–262
 - Velocity predictions for wind turbines, 867–868
 - Ventilation for steam generators, 207
 - Vertical wind profile, 142–143
 - effects of terrain on, 154–155
 - Vertical wind shear, 142–143
 - determination of, 159–165
 - exponent, 170
 - Vertical windows, lumen method of sidelighting, 635–644
 - Vertical-axis wind turbines. *See* VAWTs
 - Very-high frequency deposition techniques, 808
 - Very-high-temperature reactor (VHTR), 472–474
 - Viscosity, Diesel fuels, 246
 - Vitrinite, 34
 - Volatile gas oxidation, 899
 - Volatile matter, 34–36
 - definition, 50
 - production of by pyrolysis, 899
 - release of from coal, 36
 - Volatile metals, emissions of from MSW, 1020
 - Volatile organic compounds (VOC), emissions of in flue gas, 295
 - Volatility of gasoline fuels, 244
 - Voltage efficiency, 1058
 - Volume energy storage capacity, 744–745
 - Volumetric efficiency, 235
 - Volumetric receivers, 734–739
 - heat transfer principles in, 731
 - von Ohain, Hans, 210
 - Von Roll grates, 1005
 - Vortex models, 864–866
 - limitations of, 866
 - VP-1, 676
 - VTD, 819
 - VVER-TOI nuclear reactors, 467
- W**
- Wankel rotary engine, 224
 - Waste biomass, definition of, 61
 - Waste combustors, air supply capacity in, 1007
 - Waste energy recovery (WER), 250–252
 - Waste heat, 1036
 - generation of by fuel cells, 1056–1057
 - optimized management of, 742
 - Waste heat recovery (WHR), low-quality, 375–377
 - Waste heat recovery (WHR) heat exchangers, use of in FFPS, 292
 - Waste management, radioactive wastes, 487–488
 - Waste materials, biorenewable resources in, 66–67
 - Waste recycling, 987
 - Waste stream, estimation of using material flows methodology, 73
 - Waste-to-energy combustion, 986
 - Waste-to-energy facilities. *See* WTE facilities
 - Wastewater
 - treatment of from FFPS, 296, 429–430
 - use of in EGS, 936
 - Water
 - use of as a thermal fluid, 676, 690
 - use of as a working fluid, 527–528, 553
 - use of for geothermal power production, 935
 - use of for sensible heat storage, 515–517
 - use of for solar thermal storage, 562–563
 - use of to cool gas turbines, 220
 - Water gas shift (WGS), 904
 - use of in fuel cell systems, 910
 - Water heating, solar thermosyphon, 582–585
 - Water treatment systems, 424–427
 - usage minimization, 427–429
 - use of in FFPS, 296
 - Water wall units
 - mass-fired, 1008–1009
 - RDF-fired, 1009
 - use of in MSW furnaces, 1003–1007
 - Water–gas shift reaction, 915
 - Water–steam cavity receiver, 733
 - Waterwall, 586
 - Waxes, 55
 - Wayang Windu geothermal power project, 968–969

- Weather Year for Energy Calculations data sets.
See WYEC data sets
- Websites
- agricultural statistics, 69
 - biomass, 63
 - DOE Office of Fusion Energy, 495
 - geothermal energy, 983
 - IPH application designs, 678
 - solar radiation data, 122, 131
 - spectral models of solar radiation, 122
 - wind turbine material characteristics, 882
- Weibull distribution, 144
- Weizmann receiver, 740
- Wellhead energy cost, 938–941
- Westinghouse AP1000 nuclear reactor, 465
- Wet compression, 354
- Wheeling charges, 940
- Whittle, Frank, 210
- Wicket gates, 259
 - numerical modeling of, 272–273
 - use of for flow control, 269
- Wideband spectral solar radiation measurements, 129
- Wind direction vanes, 160–161
- Wind energy
 - conversion considerations, 882–891
 - worldwide installed capacity of, 852
- Wind energy development sites, prospecting for, 152–157
- Wind energy potential (WEP), 145
- Wind energy resource (WER), 143–149
 - assessment of, 152–157
 - evaluation of, 157–171
 - maps of for the United States, 146–148
- Wind facilities
 - impact of on radar, 151
 - impacts of on birds and bats, 149–151
- Wind farms
 - initial development example, 171–173
 - site assessment, 157–171
- Wind forecasting, 885–886
- Wind origins, 137–140
- Wind patterns, 139
- Wind power, 141–142, 852
 - environmental/societal restrictions, 149–151
 - grid integration of, 884–885
 - growth potential of, 15–16
 - offshore, 868–869
 - role of in future energy mix, 27–28
- Wind power density, 119, 171
- Wind shear, 142–143
 - vertical exponent, 170
- Wind speed
 - distribution of, 144–145
 - effects of topography on, 153–157
 - site assessment and, 155–156
 - variations in, 138–140
- Wind turbines
 - aerodynamic loading of, 869–870
 - aerodynamics of, 855–860
 - classification of, 852–854
 - components used in complex cycles, 215–219
 - computational fluid dynamics models of, 866–867
 - control subsystem for, 878–881
 - cost of energy for, 855
 - costs of, 886–890
 - electrical power generation subsystem, 875–878
 - environmental concerns, 890–891
 - hybrid models for, 867
 - impacts of on birds and bats, 149–151
 - installations of, 883–884
 - limitations of momentum and vortex models, 866
 - load prediction, 161
 - materials used for, 882–883
 - momentum models of, 860–864
 - offshore platform hydrodynamics, 869
 - operational regions of, 879
 - orientation of, 877
 - peak power limitation, 873–875
 - power extraction efficiency of, 857–858
 - structural dynamic considerations, 870–872
 - terrain classification and siting of, 153–157
 - velocity and load predictions, 867–868
 - vortex models for, 864–866
 - yaw system, 878
- Windmills, 852–854
- Window dirt depreciation (WDD), 639
- Windowed receivers, 729
- Windows
 - solar illuminance, 634
 - south-facing, 624–625
 - vertical, 635–644
- Winter–Kennedy taps, 277
- Wobbe index (WI), 371–372
- Woody crops, 67
- Work-plane illuminance, 633, 639–640, 644
- Working fluids, 527–528, 553
- World Bank, promotion of ISCCS construction by, 712
- World commercial reprocessing capacity, 483
- World crude oil refining capacity, 55
- World electricity production, 6

- World energy consumption, 2–3, 51–53
 - World energy demand, 5
 - per capita consumption, 22–23
 - World energy resources, 8
 - biomass potential, 19–21
 - coal, 10–11, 44–46
 - conventional oil, 9–10
 - distribution of solar thermal collector markets, 18
 - fossil fuel reserves, 11
 - natural gas, 10, 57
 - nuclear, 11–13
 - oil, 54
 - renewable energy, 13–15
 - solar energy potential, 16–18
 - thorium, 82
 - total primary energy supply, 13
 - uranium, 82
 - wind energy potential, 15–16
 - World Meteorological Organization (WMO),
 - solar radiation data of, 130
 - World primary energy demand, 2
 - World Radiation Data Center (WRDC), solar radiation data of, 130
 - World uranium enrichment facilities, 482
 - Worldwide energy figures
 - annual geothermal power, 933–934
 - conversion efficiencies for PV technologies, 846
 - fossil-fuel-fired electricity generation, 282
 - installed capacity of wind energy, 852
 - market share of PV technologies, 801
 - new nuclear plant construction, 462–464
 - nuclear power plants, 457–458
 - PV panel production, 766–767
 - Worm-gear drive mechanism, 725–726
 - WTE facilities
 - air pollution control, 1011–1022
 - boilers in, 1008–1009
 - combustion principles, 995–1003
 - costs, 1023–1025
 - furnaces in, 1003–1008
 - materials handling systems in, 988
 - operation and capacity of, 992–993
 - performance of, 1022–1023
 - regulatory requirements, 1027
 - residue handling and disposal, 1009–1011
 - siting of, 993
 - types of, 990–992
 - WYEC data sets, 130
- Y**
- Yard trimmings, percentage of in municipal solid waste, 73
 - Yearly average energy, 548–550
 - Yearly normalized energy surface (YNES), 722
 - Yield strength, 381
- Z**
- Zebra batteries, 509
 - Zenith angle, 91
 - Zero Emission Power and Steam (ZEPS) power plant, 415–416
 - Zero liquid discharge (ZLD) plants, 296, 430–433
 - Zinc bromide batteries, 510
 - ZT, magnitude of in thermoelectric materials, 1092–1098